

FAA CENTER OF EXCELLENCE FOR ALTERNATIVE JET FUELS & ENVIRONMENT

Annual Technical Report

2025

For the period

October 1, 2024 – September 30, 2025

Boston University
Georgia Institute of Technology
Massachusetts Institute of Technology
Missouri University of Science and Technology
Oregon State University
Pennsylvania State University
Purdue University
Stanford University
University of Dayton
University of Hawaii
University of Illinois
University of North Carolina
University of Pennsylvania
University of Tennessee
University of Washington
Washington State University





This work was funded by the US Federal Aviation Administration (FAA) Office of Environment and Energy as a part of ASCENT Project AJFE under FAA Award Number 13-C. Any opinions, findings, and conclusions or recommendations expressed in this material are those of the authors and do not necessarily reflect the views of the FAA or other ASCENT Sponsors.



Table of Contents

Overview Michael P. Wolcott and R. John Hansman, Center Directors	1
Project 001(A) | Alternative Jet Fuel Supply Chain Analysis Lead Investigator: Michael P. Wolcott	7
Project 001(B) | Alternative Jet Fuel Supply Chain Analysis Lead Investigator: Scott Q. Turn	28
Project 001(C) | Alternative Jet Fuel Supply Chain Analysis Lead Investigator: Farzad Taheripour	51
Project 001(D) | Alternative Jet Fuel Supply Chain Analysis Lead Investigator: Lara Fowler	56
Project 001(E) | Alternative Jet Fuel Supply Chain Analysis Lead Investigator: Timothy Rials	66
Project 001(F) | Alternative Jet Fuel Supply Chain Analysis Lead Investigators: Florian Allroggen, Raymond L. Speth	80
Project 002 | Understanding Changes in Aviation Emissions Due to SAF with New Combustor Technology Lead Investigator: Philip D. Whitefield	90
Project 003 | Cardiovascular Disease and Aircraft Noise Exposure Lead Investigator: Junenette L. Peters	94
Project 018 | Community Measurements of Aviation Emission Contributions to Ambient Air Quality Lead Investigator: Kevin J. Lane	110
Project 019 | Development of Aviation Air Quality Tools for Airshed-Specific Impact Assessment: Air Quality Modeling Lead Investigator: Saravanan Arunachalam	128
Project 022 | Evaluation of FAA Climate Tools: Aviation Portfolio Management Tool (APMT) Lead Investigator: Donald Wuebbles	176
Project 023 | Analytical Approach for Quantifying Noise from Advanced Operational Procedures Lead Investigator: R. John Hansman	179
Project 025 | Shock Tube Studies of the Kinetics of Jet Fuels Lead Investigator: Ronald K. Hanson	184
Project 031 | Alternative Jet Fuel Test and Evaluation Lead Investigator: Zachary West	191



Project 033 | Alternative Fuels Test Database Library Lead Investigator: Tonghun Lee	203
Project 037 | CLEEN II System-level Assessment Lead Investigator: Dimitri N. Mavris	217
Project 038 | Rotorcraft Noise Abatement Procedure Development Lead Investigator: Kenneth S. Brentner	232
Project 044 | Aircraft Noise Abatement Procedure Modeling and Validation Lead Investigator: R. John Hansman	245
Project 049 | Urban Air Mobility Noise Reduction Modeling Lead Investigator: Kenneth S. Brentner	253
Project 051 | Combustion Concepts for Next-Generation Aircraft Engines Lead Investigator: Raymond L. Speth	269
Project 052 | Comparative Assessment of Electrification Strategies for Aviation Lead Investigators: Florian Allroggen, Raymond L. Speth	275
Project 053 | Validation of Low Exposure Noise Modeling by Open-Source Data Management and Visualization Systems Integrated with AEDT Lead Investigator: Juan J. Alonso	288
Project 054 | AEDT Evaluation and Development Support Lead Investigators: Dimitri N. Mavris, Michelle Kirby	292
Project 055 | Noise Generation and Propagation from Advanced Combustors Lead Investigator: Timothy Lieuwen	347
Project 056 | Turbine Cooling Through Additive Manufacturing Lead Investigator: Reid A. Berdanier	386
Project 057 | Support for Supersonic Aircraft En-Route Noise Efforts in ICAO CAEP Lead Investigator: Victor W. Sparrow	406
Project 058 | Improving Policy Analysis Tools to Evaluate Higher-Altitude Aircraft Operations Lead Investigator: Raymond L. Speth	424
Project 059(B) | Jet Noise Modeling and Measurements to Support Reduced LTO Noise of Supersonic Aircraft Technology Development Lead Investigators: Krishan K. Ahuja	433
Project 059(C) | Modeling Supersonic Jet Noise Reduction with Global Resolvent Modes Lead Investigators: Daniel J. Bodony	506
Project 059(D) | Physics-Based Analyses and Modeling for Supersonic Aircraft Exhaust Noise Lead Investigator: Sanjiva K. Lele	517



Project 059(E) | Moderate-Fidelity Simulations for Efficient Modeling of Supersonic Aircraft Noise Lead Investigator: Philip Morris	537
Project 060 | Analytical Methods for Expanding the AEDT Aircraft Fleet Database Lead Investigator: Dimitri N. Mavris	549
Project 061 | Noise Certification Streamlining Lead Investigators: Dimitri N. Mavris, Michael Balchanos	552
Project 062 | Noise Model Validation for AEDT Lead Investigators: Dimitri N. Mavris, Victor W. Sparrow	617
Project 064 | Alternative Design Configurations to Meet Future Demand Lead Investigators: Dimitri N. Mavris, Michelle Kirby	637
Project 065(A) | Fuel Testing Approaches for Rapid Jet Fuel Prescreening Lead Investigator: Joshua Heyne	674
Project 065(B) | Fuel Testing Approaches for Rapid Jet Fuel Prescreening Lead Investigator: Tonghun Lee	699
Project 066 | Evaluation of High Thermal Stability Fuels Lead Investigator: Joshua Heyne	714
Project 067 | Impact of Fuel Heating on Combustion Performance and Lean Combustion Characterization Lead Investigators: Robert P. Lucht, Carson D. Slabaugh	735
Project 068 | Combustor Wall Cooling with Dirt Mitigation Lead Investigator: Reid A. Berdanier	748
Project 069 | Transitioning a Research nvPM Mass Calibration Procedure to Operations Lead Investigator: Philip D. Whitefield	772
Project 070 | Reduction of nvPM Emissions from Aero-Engine Fuel Injectors Lead Investigator: Wenting Sun	777
Project 071 | Predictive Simulation of nvPM Emissions in Aircraft Combustors Lead Investigator: Suresh Menon	791
Project 072 | Aircraft Noise Exposure and Market Outcomes in the United States Lead Investigators: R. John Hansman, Christopher R. Knittel, Florian Allroggen	841
Project 073 | Fuel Composition Impact on Combustor Durability Lead Investigator: Scott Stouffer	849
Project 075 | Improved Engine Fan Broadband Noise Prediction Capabilities Lead Investigator: Sheryl Grace	861



Project 077 | Measurements to Support Noise Certification for UAS and UAM Vehicles and Identify Noise Reduction Opportunities Lead Investigator: Eric Greenwood	879
Project 078 | Contrail Avoidance Decision Support and Evaluation Lead Investigator: Ian A. Waitz	905
Project 079 | Novel Noise Liner Development Enabled by Advanced Manufacturing Lead Investigator: Nicholas Meisel	916
Project 080(A) | Hydrogen and Power-to-Liquid Concepts for Sustainable Aviation Fuel Production Lead Investigators: Manuel Garcia-Perez, Michael P. Wolcott	933
Project 080(B) | Hydrogen and Power-to-Liquid Concepts for Sustainable Aviation Fuel Production Lead Investigator: Florian Allroggen	945
Project 082(A) | CAEP Stringency Analysis Modeling Lead Investigators: Dimitri N. Mavris, Michelle Kirby	953
Project 082(B) | Integrated Noise and CO_2 Standard Setting Analysis Lead Investigator: Raymond L. Speth	960
Project 083 | NO_x Cruise/Climb Metric System Development Lead Investigator: Raymond L. Speth	964
Project 084 | Noise Modeling of Advanced Air Mobility Flight Vehicles Lead Investigators: R. John Hansman, Jacqueline Huynh	971
Project 085 | Strategies for Improving En-Route Fuel Efficiency Lead Investigator: Dimitri N. Mavris	984
Project 086 | Study on the Use of Broadband Sounds to Mitigate Sleep Disruption Due to Aircraft Noise Lead Investigator: Mathias Basner	1015
Project 088 | A Method for Rapidly Assessing Jet Fuel Compatibility with Non-Metallic Materials Lead Investigators: John Graham, Gina Roesch	1022
Project 089 | Characterization of Compositional Effects on Dielectric Constant Lead Investigator: Zachary West	1045
Project 090 | World Fuel Survey Lead Investigator: Zachary West	1052
Project 091(B) | Environmental Impacts of High-Altitude and Space Vehicle Emissions Lead Investigator: Donald Wuebbles	1060
Project 092 | Advanced Two-Stage Turbine Rig Development Lead Investigator: Reid A. Berdanier	1064



Project 093(A) | Collaborative Research Network for Global SAF Supply Chain Development Lead Investigators: Florian Allroggen, Raymond L. Speth	1077
Project 093(B) | Collaborative Research Network for Global SAF Supply Chain Development Lead Investigator: Scott Q. Turn	1085
Project 093(C) | Collaborative Research Network for Global SAF Supply Chain Development: Latin America and Caribbean Case Lead Investigators: Manuel Garcia-Perez, Michael P. Wolcott	1096
Project 094 | Probabilistic Unmanned Aircraft Systems (UAS) Trajectory and Noise Estimation Tool Lead Investigators: Dimitri N. Mavris, Holger Pfaender	1104
Project 095 | Assessment of Fuel Cells for Powering Modern Business Jets Lead Investigator: Dimitri N. Mavris	1126
Project 096 | Future Transportation System Opportunities and Constraints Lead Investigators: Dimitri N. Mavris, Holger Pfaender	1149
Project 097 | FAST-Tech System Level Assessment Lead Investigators: Dimitri N. Mavris	1182
Project 098 | Low Emissions Lean Pre-Mixed Pre-Vaporized Combustion Technology for Subsonic Civil Transport Lead Investigator: Adam Steinberg	1187
Project 099 | Conceptual Analysis of Cryogenic Hydrogen Distribution to Airports Lead Investigator: Jacob Leachman	1199
Project 100 | U.S.-Canada SAF Supply Chain Analysis Lead Investigator: Michael P. Wolcott	1211
Project 101 | Sustainable Aviation Fuel Repository Lead Investigator: Joshua Heyne	1225
Project 102 | Assessment on Contrail Formation via Combustion of SAF Lead Investigator: Tonghun Lee	1239
Project 103 | Pareto Efficient SAF Yield and Blending Lead Investigator: Joshua Heyne	1252
Project 104 (A) | Methodology for Assessing Changes in Soil Organic Carbon Lead Investigator: Lara Fowler	1277
Project 104 (B) | Methodology for Assessing Changes in Soil Organic Carbon Lead Investigator: Farzad Taheripour	1281
Project 104 (C) | Methodology for Assessing Changes in Soil Organic Carbon Lead Investigator: Timothy Rials	1285



Project 105 | Quantification of Trace Levels of Sulfur Using ICP-MS Lead Investigator: Zachary West	1293
Project 106 (A) | Integration of Turbine Operational Parameters into Aerothermal System Analyses Lead Investigator: Dimitri N. Mavris	1299
Project 106 (B) | Integration of Turbine Operational Parameters into Aerothermal System Analyses Lead Investigator: Reid A. Berdanier	1313
Publications Index	1319
Funding Tables	1335



Overview

This report covers the period October 1, 2024, through September 30, 2025. The Center was established by the authority of FAA solicitation 13-C-AJFE-Solicitation. The ASCENT website can be viewed at ascent.aero. The next meetings will be held during the months of April, May, and June 2026.

Over the last year, the ASCENT team has made great strides in research, outreach, and education. The team's success includes the following:

- **65 active research projects*.**

The projects are divided into seven main categories: alternative fuels, combustion products, noise, operations, tools, aircraft technology innovation, and supersonics. See the project category descriptions for more detail on each category and a summary of the projects. Funding for these projects comes from the FAA in partnership with Transport Canada.

*Note that projects 001, 059, 065, 082, 093, 104 and 106 include several separately funded projects within a single project number. Individual report sections are provided for each of these funded "sub-projects" and are titled Projects 001A-E, 059A-E, 065A-B, 082A-B, 093A-C, 104A-C and 106A-B.

- **152 publications, reports, and presentations by the ASCENT team.**

Each project report includes a list of publications, reports, and presentations. A comprehensive list of the publications, reports, and presentations for all projects is available in the publications index.

- **235 students participated in aviation research with the ASCENT team.**

ASCENT research projects were supported by 199 graduate students and 36 undergraduate students. Each project report includes the names and roles of the graduate and undergraduate students in the investigator's research. Students are selected by the investigators to participate in this research.

- **75 active industry partners involved in ASCENT.**

ASCENT's industry partners play an important role in the Center. Industry partners may contribute matching funds, participate on the Advisory Board, or both. Advisory Board members provide insight into the views of stakeholders, advice on activities and priorities of the Center's co-directors and ensure research will have practical application. The board does not influence FAA policy. Industry partners also play a role in some of the research projects, providing matching funds, resources, and expertise to the project investigators.

Leadership

Dr. Michael P. Wolcott
Center Director and Technical Lead for Alternative Jet Fuels Research
Washington State University
(509) 335-6392, wolcott@wsu.edu

Dr. R. John Hansman
Center Co-Director and Technical Lead for Environmental Research
Massachusetts Institute of Technology
(617) 253-2271, rjhans@mit.edu

Dr. Jonathan Male
Director of Energy Systems and Research Support
Washington State University
jonathan.male@wsu.edu

Dr. Anna Oldani
Chief Scientific and Technical Advisor for Environment and Energy, Office of Environment and Energy
Federal Aviation Administration
anna.oldani@faa.gov



Research Topics

Research projects within ASCENT are divided into seven categories: alternative fuels, combustion products, noise, operations, tools, aircraft technology innovation, and supersonics. The list below includes all ASCENT funded research projects. This report includes research on active projects only. Reports for projects marked as COMPLETE are available on the ASCENT website at: https://ascent.aero/topic/complete/.

Alternative Fuels

The development of alternative jet fuels (AJFs) is of great interest to an array of aviation stakeholders, including aircraft and engine manufacturers and airlines. Alternative fuels that are produced from non-fossil feedstocks provide alternatives that create jobs in rural areas and lessen our reliance on foreign petroleum supplies.

Effective research and development, co-funded by the federal government and industry, enables AJF development by reducing the costs of producing renewable fuel. ASCENT research provides the scientific expertise and data to evaluate the benefits associated with these alternative fuels. ASCENT's collaborative R&D activities focus on evaluating promising aviation fuel pathways to ensure social benefits, reduce technical uncertainties, inform aviation combustion products policies, and promote private sector investment in production.

Projects include:

- 001A-F – Alternative Jet Fuel Supply Chain Analysis
- 025 – National Jet Fuels Combustion Program – Area #1: Chemical Kinetics Combustion Experiments
- 026 – (COMPLETE) National Jet Fuels Combustion Program – Area #2: Chemical Kinetics Model Development and Evaluation
- 027 – (COMPLETE) National Jet Fuels Combustion Program – Area #3: Advanced Combustion Tests
- 028 – (COMPLETE) National Jet Fuels Combustion Program – Area #4: Combustion Model Development and Evaluation
- 029A – (COMPLETE) National Jet Fuels Combustion Program – Area #5: Atomization Tests and Models
- 030 – (COMPLETE) National Jet Fuels Combustion Program – Area #6: Referee Swirl-Stabilized Combustor Evaluation/Support
- 031 – Alternative Jet Fuels Test and Evaluation
- 032 – (COMPLETE) Worldwide LCA of GHG Emissions from Petroleum Jet
- 033 – Alternative Fuels Test Database Library
- 034 – (COMPLETE) National Jet Fuels Combustion Program – Area #7: Overall Program Integration and Analysis
- 052 – Comparative Assessment of Electrification Strategies for Aviation
- 065A-B – Fuel Testing Approaches for Rapid Jet Fuel Prescreening
- 066 – Evaluation of High Thermal Stability Fuels
- 067 – Impact of Fuel Heating on Combustion and Emissions
- 073 – Combustor Durability with Alternative Fuel Use
- 080A-B – Hydrogen and Power-to-Liquid (PtL) Concepts for SAF Production
- 088 – A Method for Rapidly Assessing Jet Fuel Compatibility with non-Metallic Materials
- 089 – Characterization of Compositional Effects on Dielectric Constant
- 090 – World Fuel Survey
- 093A-C – Collaborative Research Network for Global SAF Supply Chain Development
- 099 – Conceptual Analysis of Cryogenic Hydrogen Distribution to Airports
- 100 – U.S.-Canada Cross-Border SAF Supply Chain Analysis
- 101 – Sustainable Aviation Fuel Repository
- 102 – Assessment of Contrail Formation via Combustion of Sustainable Aviation Fuel
- 103 – Pareto Efficient SAF Yield and Blending
- 104 – Methodology for Assessing Changes in Soil Organic Carbon
- 105 – Quantification of Trace Levels of Sulfur Using ICP-MS

Combustion Products

The demand for passenger and cargo air transportation has and continues to grow rapidly. According to the U.S. Bureau of Transportation Statistics (BTS), in 2023 there were 946 million domestic air travelers. The 2024 FAA Aerospace Forecast calls for U.S. carrier domestic passenger growth over the next 20 years to average 2.5 percent per year. This staggering



growth is accompanied by airport expansions and increases in combustion products from aircraft, ground services equipment, and vehicle traffic on and near airports.

ASCENT researchers are analyzing data and improving predictive models to understand the effects of combustion products from aircraft and ground vehicles, create and refine analytical techniques at both airport-specific and global scales, and assess how policy changes affect combustion products and related impacts.

Projects include:

- 002 – (COMPLETE) Ambient Conditions Corrections for Non-Volatile PM Emissions Measurements
- 013 – (COMPLETE) Micro-Physical Modeling & Analysis of ACCESS 2 Aviation Exhaust Observations
- 014 – (COMPLETE) Analysis to Support the Development of an Aircraft CO2 Standard
- 018 – Community Measurement of Aviation Emission Contribution of Ambient Air Quality
- 019 – Development of Improved Aviation Emissions Dispersion Capabilities for AEDT
- 020 – (COMPLETE) Development of NAS wide and Global Rapid Aviation Air Quality
- 021 – (COMPLETE) Improving Climate Policy Analysis Tools
- 022 – Evaluation of FAA Climate Tools
- 024 – (COMPLETE) Emissions Data Analysis for CLEEN, ACCESS, and Other Recent Tests
- 032 – (COMPLETE) Worldwide LCA of GHG Emissions from Petroleum Jet Fuel
- 039 – (COMPLETE) Naphthalene Removal Assessment
- 047 – (COMPLETE) Clean Sheet Supersonic Aircraft Engine Design and Performance
- 048 – (COMPLETE) Analysis to Support the Development of an Engine nvPM Emissions Standard
- 051 – Combustion Concepts for Next-Generation Aircraft Engines
- 052 – Comparative Assessment of Electrification Strategies for Aviation
- 058 – Improving Policy Analysis Tools to Evaluate Higher-Altitude Aircraft Operations
- 064 – Alternative Design Configurations to Meet Future Demand
- 069 – Transitioning a Research nvPM Mass Calibration Procedure to Operations
- 070 – Reduction of nvPM emissions via innovation in aero-engine fuel injector design
- 071 – (COMPLETE) Predictive Simulation of nvPM Emissions in Aircraft Combustors
- 074 – (COMPLETE) Low Emissions Pre-Mixed Combustion Technology for Supersonic Civil Transport
- 078 – Contrail Avoidance Decision Support and Evaluation
- 082A-B – Integrated Noise and Emissions CO_2 Standard Setting Analysis
- 083 – NOx Cruise/Climb Metric System Development
- 085 – Strategies for Improving En-Route Fuel Efficiency
- 091A-B – Environmental Impacts of High Altitude and Space Vehicle Emissions

Noise

ASCENT researchers are working to fully understand community noise impacts of aviation including how aircraft noise affects human health and wellbeing and how elements such as motion and atmospheric parameters affect noise. They are also creating tools for analyzing aircraft noise, informing policies related to noise, and conducting outreach and education about aircraft noise reduction efforts.

Projects include:

- 003 – Cardiovascular Disease and Aircraft Noise Exposure
- 004 – (COMPLETE) Estimate of Noise Level Reduction
- 005 – (COMPLETE) Noise Emission and Propagation Modeling
- 007 – (COMPLETE) Civil, Supersonic Over Flight, Sonic Boom (Noise) Standards Development
- 008 – (COMPLETE) Noise Outreach
- 009 – (COMPLETE) Geospatially Driven Noise Estimation Module
- 017 – (COMPLETE) Pilot Study on Aircraft Noise and Sleep Disturbance
- 038 – Rotorcraft Noise Abatement Procedures Development
- 040 – (COMPLETE) Quantifying Uncertainties in Predicting Aircraft Noise in Real-world Situations
- 041 – (COMPLETE) Identification of Noise Acceptance Onset for Noise Certification Standards of Supersonic Airplane
- 042 – (COMPLETE) Acoustical Model of Mach Cut-off
- 043 – (COMPLETE) Noise Power Distance Re-Evaluation
- 044 – Aircraft Noise Abatement Procedure Modeling and Validation



- 049 – Urban Air Mobility Noise Reduction Modeling
- 053 – Validation of Low Exposure Noise Modeling by Open Source Data Management and Visualization Systems Integrated with AEDT
- 055 – Noise Generation and Propagation from Advanced Combustors
- 057 – Support for Supersonic Aircraft En-route Noise Efforts in ICAO CAEP
- 059A-E – Modeling and Measurements of Supersonic Civil Transport Jet Noise
- 061 – (COMPLETE) Noise Certification Streamlining
- 062 – Noise Model Validation for AEDT
- 063 – Parametric Noise Modeling for Boundary Layer Ingesting Propulsors
- 072 – Aircraft Noise Exposure and Market Outcomes in the US
- 075 – Improved Engine Fan Broadband Noise Prediction Capabilities
- 076 – Improved Open Rotor Noise Prediction Capabilities
- 077 – Measurements to Support Noise Certification for UAS/UAM Vehicles and Identify Noise Reduction Opportunities
- 079 – Novel Noise Liner Development Enabled by Advanced Manufacturing
- 082A-B – Integrated Noise and Emissions CO_2 Standard Setting Analysis
- 084 – Noise Modeling of Advanced Air Mobility Flight Vehicles
- 086 – Study on the Use of Broadband Sounds to Mitigate Sleep Disruption Due to Aircraft Noise
- 094 – Probabilistic Unmanned Aircraft Systems (UAS) Trajectory and Noise Estimation Tool

Operations

Aviation operations result in fuel burn, combustion products, and noise impacts. The nature and scale of these effects depend on a number of related factors, including:

- Aircraft flight paths and profiles,
- Schedule and frequency of operations, and
- Aircraft fleet mix.

ASCENT research focuses on identifying and accelerating the implementation of operational concepts that will improve and maintain the efficiency of the National Airspace System.

Projects include:

- 006 – (COMPLETE) Rotorcraft Noise Abatement Operating Conditions Modeling
- 015 – (COMPLETE) Cruise Altitude and Speed Optimization
- 016 – (COMPLETE) Airport Surface Movement Optimization
- 023 – Analytical Approach for Quantifying Noise from Advanced Operational Procedures
- 038 – Rotorcraft Noise Abatement Procedures Development
- 044 – Aircraft Noise Abatement Procedure Modeling and Validation
- 053 – Validation of Low Exposure Noise Modeling by Open-Source Data Management and Visualization Systems Integrated with AEDT
- 085 – Strategies for Improving En-Route Fuel Efficiency

Tools

The aviation system operation involves complex interactions between many different components when aircraft are on the ground, taking off, in the air, and when landing. Aviation system operations also require the understanding of how to optimize aviation activities, which is best done by implementing advanced modeling tools.

The Federal Aviation Administration's suite of modeling tools have been developed to characterize and quantify the interdependences of aviation-related noise and combustion products, impacts on human health and welfare, and the costs and market impacts to industry and consumers under varying policies, technologies, operations, and market scenarios.

The ASCENT researchers are further developing and expanding the capabilities of these modeling tools in a variety of ways, from improving the way basic physical properties are represented and effectively modeled to how new technologies will enter the aircraft fleet and identifying the benefits of such technologies.



Projects include:

- 009 – (COMPLETE) Geospatially Driven Noise Estimation Module
- 011 – (COMPLETE) Rapid Fleet-wide Environmental Assessment Capability
- 012 – (COMPLETE) Aircraft Design and Performance Assessment Tool Enhancement
- 035 – (COMPLETE) Airline Flight Data Examination to Improve flight Performance Modeling
- 036 – (COMPLETE) Parametric Uncertainty Assessment for AEDT2b
- 037 – CLEEN II Technology Modeling and Assessment
- 040 – (COMPLETE) Quantifying Uncertainties in Predicting Aircraft Noise in Real-world Situations
- 043 – (COMPLETE) Noise Power Distance Re-Evaluation (NPD+C) to Include Airframe Noise in AEDT
- 045 – (COMPLETE) Takeoff/Climb Analysis to Support AEDT APM Development
- 046 – (COMPLETE) Surface Analysis to Support AEDT APM Development
- 049 – Urban Air Mobility Noise Reduction Modeling
- 053 – Validation of Low Exposure Noise Modeling by Open-Source Data Management and Visualization Systems Integrated with AEDT
- 054 – AEDT Evaluation and Development Support
- 058 – Improving Policy Analysis Tools to Evaluate Higher-Altitude Aircraft Operations
- 060 – (COMPLETE) Analytical Methods for Expanding the AEDT Aircraft Fleet Database
- 062 – Noise Model Validation for AEDT

Aircraft Technology Innovation

The evolution of airframes and engines has resulted in modern designs that significantly reduce aviation fuel use, combustion products and noise on a per-flight basis. ASCENT researchers conduct the analyses, modeling and testing required to demonstrate the viability of innovative airframe, engine and flight management technologies that reduce noise, combustion products, and fuel burn. Future innovations will drive further improvements, and the ASCENT research helps accelerate technology development.

Projects include:

- 010 – Aircraft Technology Modeling and Assessment
- 037 – CLEEN II System Level Assessment
- 047 – (COMPLETE) Clean Sheet Supersonic Aircraft Engine Design and Performance
- 050 – (COMPLETE) Over-Wing Engine Placement Evaluation
- 051 – Combustion Concepts for Next-Generation Aircraft Engines
- 052 – Comparative Assessment of Electrification Strategies for Aviation
- 055 – Noise Generation and Propagation from Advanced Combustors
- 056 – Turbine Cooling through Additive Manufacturing
- 059A-E – Modeling and Measurements of Supersonic Civil Transport Jet Noise
- 063 – Parametric Noise Modeling for Boundary Layer Ingesting Propulsors
- 064 – Alternative Design Configurations to Meet Future Demand
- 066 – Evaluation of High Thermal Stability Fuels
- 067 – Impact of Fuel Heating on Combustion and Emissions
- 068 – Combustor Wall Cooling with Dirt Mitigation
- 070 – Reduction of nvPM Emissions Via Innovation in Aero-Engine Fuel Injector Design
- 074 – (COMPLETE) Low Emissions Pre-Mixed Combustion Technology for Supersonic Civil Transport
- 075 – Improved Engine Fan Broadband Noise Prediction Capabilities
- 076 – Improved Open Rotor Noise Prediction Capabilities
- 077 – Measurements to Support Noise Certification for UAS/UAM Vehicles and Identify Noise Reduction Opportunities
- 092 – Advanced Two-State Turbine Rig Development
- 095 – Assessment of Fuel Cells for Powering Modern Business Jets
- 096 – Future Transportation System Opportunities and Constraints
- 097 – FAST-Tech System Level Assessment
- 098 – Low Emissions Lean Pre-Mixed, Pre-Vaporized Combustion Technology for Subsonic Civil Transport
- 106 – Integration of Turbine Operational Parameters into Aerothermal System Analysis



Supersonics

ASCENT supersonics research supports implementation of new technologies by advancing the understanding of the perception of sonic boom noise over a range of sonic boom levels, assessing Mach cut-off levels that will allow supersonic flight over land and furthering development of supersonic aircraft noise certification standards.

Projects include:

- 007 – (COMPLETE) Civil, Supersonic Over Flight, Sonic Boom (Noise) Standards Development
- 010 – Aircraft Technology Modeling and Assessment
- 022 – Evaluation of FAA Climate Tools
- 041 – (COMPLETE) Identification of Noise Acceptance Onset for Noise Certification Standards of Supersonic Airplanes
- 042 – (COMPLETE) Acoustical Model of Mach Cut-off
- 047 – (COMPLETE) Clean Sheet Supersonic Aircraft Engine Design and Performance
- 057 – Support for Supersonic Aircraft Noise Efforts in ICAO CAEP
- 058 – Improving Policy Analysis Tools to Evaluate Aircraft Operations in the Stratosphere
- 059A-E – Jet Noise Modeling to Support Low Noise Supersonic Aircraft Technology Development
- 074 – (COMPLETE) Low Emissions Pre-Mixed Combustion Technology for Supersonic Civil Transport



Project 001(A) Alternative Jet Fuel Supply Chain Analysis

Washington State University

Project Lead Investigator

Michael P. Wolcott
Regents Professor
Department of Civil & Environmental Engineering
Washington State University
PO Box 642910
Pullman, WA 99164-2910
509-335-6392
wolcott@wsu.edu

University Participants

Washington State University (WSU)

- P.I.s: Michael P. Wolcott, Regents Professor; Christina Sanders, Acting Director, Division of Governmental Studies and Services; Manuel Garcia-Perez, Professor; Xiao Zhang, Professor; and Ji Yun Lee, Associate Professor
- FAA Award Number: 13-C-AJFE-WaSU-023, 026
- Period of Performance: October 1, 2024, to September 30, 2025
- Tasks:
  1. Prepare and assess design cases
  2. Evaluate the most promising biorefinery concepts for alternative jet fuel (AJF) production
  3. Supplement and maintain the current inventory of biorefinery infrastructures that are useful for AJF production, as identified in the conversion design cases
  4. Update Community Asset and Attribute Model (CAAM) Measures and perform a community social asset assessments
  5. Refine and deploy facility siting tools to determine regional demand and potential conversion sites to be used in regional analyses
  6. Perform a refinery-to-wing stakeholder assessment.
  7. Conduct a supply chain analysis
  8. Provide analytical support for regional Commercial Aviation Alternative Fuels Initiative (CAAFI) and U.S. Department of Agriculture (USDA) jet fuel projects
  9. CAAFI collaboratively supports research, development, demonstration and deployment efforts on sustainable aviation fuel (SAF)/AJF

Project Funding Level

The ASCENT Project 001A has received $5,155,056 in Federal Aviation Administration (FAA) funding over its lifetime, $3,886490 in matching funds, and state-committed graduate school contributions for four doctoral students. Faculty time for Michael Wolcott, Manuel Garcia-Perez, and Xiao Zhang contributed to the cost share.

Investigation Team

Washington State University

Prof. Michael P. Wolcott (P.I.), Tasks 3, 5, 7, and 8
Christina Sanders (co-P.I.)
Season Hoard (co-P.I.)
Prof. Manuel Garcia-Perez (co-P.I.), Tasks 1, 2, and 7
Xiao Zhang (co-P.I.), Tasks 1 and 2
Associate Prof. Ji Yun Lee (co-P.I.)
Daniel Mueller (faculty), Tasks 4,6
Michael Gaffney (faculty), Tasks 4, 6



Kristin Brandt (adjoint faculty)
Dane Camenzind (staff engineer)
Lina Pilar Martinez Valencia (postdoctoral research associate)
Chenxi Wang (postdoctoral research associate)
Santheeb Balaji Velmurugan (graduate student)
Claudia Marcela Valderrama (graduate student)
Nasimeh Rashidi (graduate student)

Commercial Aviation Alternative Fuels Initiative
Steve Csonka, Office of the Executive Director

Collaborating Researchers

University of Tennessee (UT)
Burton English
Edward Yu

University of Hawaii (UH)
Scott Turn

Massachusetts Institute of Technology (MIT)
Florian Allroggen

Volpe National Transportation Systems Center (Volpe)
Kristin C. Lewis

Project Overview

As part of an effort to realize an "aviation system in which air traffic will move safely, swiftly, efficiently, and seamlessly around the globe," the FAA set a series of goals and supporting outcomes, strategies, and performance metrics (Hileman et al., 2013). The goal entitled "Sustaining our Future" outlines several strategies collectively aimed at reducing the environmental and energy impacts of the aviation system. To achieve this goal, the FAA set an aspirational goal for the aviation industry to utilize one billion gallons of AJF by the year 2018. This goal was created according to economic, emission, and overall feasibility perspectives (Richard, 2010; Staples et al., 2014). Over the past several years, the goals for United States (U.S.) AJF use have been updated with the SAF Grand Challenge that the U.S. will produce three billion gallons of SAF by 2030, with an increase to 35 billion gallons in 2050 with a minimum reduction of 50% in lifecycle greenhouse gases.

Most approaches to supply chain analyses for AJF optimize feedstock-to-refinery and refinery-to-wing transportation logistics (Bond et al., 2014). One of the greatest barriers to large-scale AJF production is the high capital of greenfield facilities, which translates to risk in the investment community (Huber & Corma, 2007). The cost of cellulosic ethanol plants ranges from $10 to $13 per gallon capacity (Hileman & Stratton, 2014); moreover, the additional processing steps required to convert the intermediate to a drop-in AJF could increase this cost to more than $25 per gallon capacity (Hileman, 2013).

Motivated by the realities of converting these initial commercialization efforts into second-generation AJF, researchers have considered alternative conversion scenarios, including the transitioning of existing facilities (Brown, 2013). The conversion of existing refineries to produce renewable diesel and AJF has been completed on first phase conversions at the following refineries: World Energy®'s Paramount, California, refinery; Montana Renewables™, Great Falls, Montana, refinery; Marathon®'s Dickinson, North Dakota, refinery; Marathon's Martinez Renewables, Matinez, California, refinery; and Phillips 66®'s Rodeo Renewed, Rodeo, California, refinery. Research on approaches for achieving the SAF Grand Challenge goals

® World Energy is a registered trademark of World Management Group, LLC, Boston, Massachusetts.
™ Montana Renewables is a trademark of Montana Renewables, LLC, Great Falls, Montana, a subsidiary of Calumet, Inc.
® Marathon is a registered trademark of Marathon Petroleum Company LP, Findlay, Ohio.
® Phillips 66 is a registered trademark of Phillips 66 Company, Houston, Texas.



for AJF consumption has relied on "switching" scenarios, in which existing and planned capacities are used to produce drop-in fuel (Malina, 2012). These approaches require the identification of existing industrial assets, similar to refinery conversions, which can be targeted for future AJF production. Thus, siting becomes not only an exercise for optimizing feedstock transportation but also a necessary task for aligning this critical factor with the existing infrastructure, markets within regions, and the appropriate social capital for developing this new industry (Henrich, 2007; Seber et al., 2014).

To date, all published AJF supply chain analyses have been limited to stand-alone jet fuel production technologies that do not generate bioproducts. Hence, future studies must consider the potential techno-economic and environmental benefits of using the existing industrial infrastructure and the production of co-products with respect to the development of jet fuel production scenarios.

Design cases of stand-alone AJF production facilities will be used in supply chain evaluations. Social asset modeling is not well developed, and efforts are likely to be hampered by difficulties in quantifying social assets when compared with improved environmental performance or reductions in AJF costs. However, the community characteristics of a potential site must be considered when determining preferred locations for a new biorefinery. Community resistance or enthusiasm for the AJF industry can strongly influence the success or failure of a facility (Martinkus et al., 2014; Rijkhoff et al., 2017). Thus, community social asset modeling efforts conducted within this project, such as those based on the CAAM, will inform disciplinary applications and advances. Social factors can have substantial effects, either positive or negative, on project adoption and implementation, particularly in high-technology or energy-related projects (Lewis et al., 2012; Martinkus et al., 2012; Mueller et al., 2020). The consideration of social factors in site selection and implementation decisions can maximize positive social support and minimize opposition and social negatives, thereby substantially promoting the success of a project. In this regard, the CAAM originally piloted in the Northwest Advanced Renewables Alliance (NARA) project was designed to provide a quantitative rating of select social factors at the county level (Martinkus et al., 2014).

Focusing on regional supply chains, this research aims to identify the key barriers that must be overcome to meet AJF targets. Our team will address this overall goal by developing tools to support the AJF supply chain assessment performed at Volpe. Our efforts will provide facility siting analyses that assess conversion design cases combined with regional supply chain assets and social capacity assessments for communities to act collectively toward development goals. Finally, a refinery-to-wing stakeholder assessment will support modeling and accounting of AJF distribution for downstream fuel logistics.

References

Bond, J. Q., Upadhye, A. A., Olcay, H., Tompsett, G. A., Jae, J., Xing, R., Alonso, D. M., Wang, D., Zhang, T., Kumar, R., Foster, A., Sen, S. M., Maravelias, C. T., Malina, R., Barrett, S. R. H., Lobo, R., Wyman, C. E., Dumesic, J. A., & Huber, G. W. (2014). Production of renewable jet fuel range alkanes and commodity chemicals from integrated catalytic processing of biomass. *Energy & Environmental Science*, *7*(4), 1500–1523. https://doi.org/10.1039/C3EE43846E

Brown, N. (2013, November 20). *FAA alternative jet fuel activities* [Conference presentation]. Continuous Lower Energy, Emissions & Noise (CLEEN) Consortium, Atlanta, Georgia.,

Henrich, E. (2007, August 29-31). *The status of FZK concept of biomass gasification* [Conference presentation]. 2nd European Summer School on Renewable Motor Fuels, Warsaw, Poland.

Hileman, J. I., De la Rosa Blanco, E., Bonnefoy, P. A., & Carter, N. A. (2013). The carbon dioxide challenge facing aviation. *Progress in Aerospace Sciences*, *63*, 84–95. https://doi.org/10.1016/j.paerosci.2013.07.003

Hileman, J. I., & Stratton, R. W. (2014). Alternative jet fuel feasibility. *Transport Policy*, *34*, 52–62. https://doi.org/10.1016/j.tranpol.2014.02.018

Hileman, J. (2013). *Overview of FAA alternative jet fuel activities* [Meeting presentation]. Biomass R&D Technical Advisory Committee, Washington DC.

Huber, G. W., & Corma, A. (2007). Synergies between bio- and oil refineries for the production of fuels from biomass. *Angewandte Chemie International Edition*, *46*(38), 7184–7201. https://doi.org/10.1002/anie.200604504

Lewis, K., Mitra, S., Xu, S., Tripp, L., Lau, M., Epstein, A., Fleming, G., & Roof, C. (2012). *Alternative jet fuel scenario analysis report* (Publication No. DOT/FAA/AEE/2011-05). U.S. Department of Transportation, Bureau of Transportation Statistics. http://ntl.bts.gov/lib/46000/46500/46597/DOT-VNTSC-FAA-12-01.pdf

Malina, R. (2012, November 27). *HEFA and F-T jet fuel cost analyses* [Presentation]. Massachusetts Institute of Technology, Laboratory for Aviation and the Environment.

Martinkus, N., Kulkarni, A., Lovrich, N., Smith, P., Shi, W., Pierce, J., & Brown, S. (2012, August 27-31). *An innovative approach to identify regional bioenergy infrastructure sites* [Conference presentation]. 55th International



Convention of Society of Wood Science and Technology, Beijing, China. https://www.swst.org/wp/meetings/AM12/ppts/smith_paul.pdf

Martinkus, N., Shi, W., Lovrich, N., Pierce, J., Smith, P., & Wolcott, M. (2014). Integrating biogeophysical and social assets into biomass-to-alternative jet fuel supply chain siting decisions. *Biomass and Bioenergy*, *66*, 410-418. https://doi.org/10.1016/j.biombioe.2014.04.014

Mueller, D., Hoard, S., Roemer, K., Sanders, C., & Rijkhoff, S. (2020). *Quantifying the Community Capitals Framework: strategic application of the Community Assets and Attributes Model. Community Development*, *51*(5), 535–555. https://doi.org/10.1080/15575330.2020.1801785

Richard, T. L. (2010). Challenges in scaling up alternative jet fuels infrastructure. *Science, 329*(5993):793-796. http://dx.doi.org/10.1126/science.1189139

Rijkhoff, S. A. M., Hoard, S. A., Gaffney, M. J., & Smith, P. M. (2017). Communities ready for takeoff Integrating social assets for biofuel site-selection modeling. *Politics and the Life Sciences: The Journal of the Association for Politics and the Life Sciences*, *36*(1), 14–26.

Seber, G., Malina, R., Pearlson, M. N., Olcay, H., Hileman, J. I., & Barrett, S. R. H. (2014). Environmental and economic assessment of producing hydroprocessed jet and diesel fuel from waste oils and tallow. *Biomass and Bioenergy*, *67*, 108–118. https://doi.org/10.1016/j.biombioe.2014.04.024

Staples, M. D., Malina, R., Olcay, H., Pearlson, M. N., Hileman, J. I., Boies, A., & Barrett, S. R. H. (2014). Lifecycle greenhouse gas footprint and minimum selling price of renewable diesel and jet fuel from fermentation and advanced fermentation production technologies. *Energy & Environmental Science*, *7*(5), 1545–1554. https://doi.org/10.1039/C3EE43655A

Task 1 – Prepare and Assess Design Cases

Washington State University

Objectives

In previous years, our team has worked toward completing reviews and final reports of design cases for six stand-alone AJF technologies (Table 1) and four relevant industries (i.e., sugarcane, pulp and paper, corn ethanol, and petroleum refineries). The status of each stand-alone AJF techno-economic analysis (TEA) and report is shown in Table 1. Results on pyrolysis and alcohol-to-jet (ATJ) pathways have been published in the referenced peer-reviewed journals. The work conducted from October 1, 2024, to September 30, 2025, focused on the following objectives:

1. Conduct a detailed analysis of a new AJF pathway for hydrothermal liquefaction (HTL) processing.
2. Conduct TEA on the integration of lignin co-product technologies in the ATJ pathway to determine the potential for reducing fuel costs.
3. Develop a new case report focusing on a technology review, an evaluation of lipid conversion processes (hydroprocessed esters and fatty acids [HEFA], catalytic hydrothermolysis [CH], SBI BioEnergy,® FORGE Hydrocarbons,™ Tyton Bioenergy Solutions,™ and decarboxylation), and new technologies for the production of alternative lipids (HTL and sugar-to-lipid).
4. Prepare manuscripts for publication.

® SBI Bioenergy is a registered trademark of SBI Bioenergy, Inc., Edmonton, Alberta, Canada.
™ FORGE is a trademark of FORGE Hydrocarbons Corporation, Oakville, Ontario, Canada.
™ Tyton Bioenergy Solutions is a trademark of Tyton Bioenergy Solutions, Danville, Virginia.



Table 1. Evaluated stand-alone alternative jet fuel technologies. TEA: techno-economic analysis.

Fuel Type	Literature Review/Design Report Date	Publications	Techno-Economic Analysis (TEA) Model
Pyrolysis	Literature review based on a design report, 138 pages (2017)	*Energy Fuel, 33*(6), 4683–4720, 2019. https://doi.org/10.1021/acs.energyfuels.9b00039; *Fuel Process Technology, 195*:106140, 2019. https://doi.org/10.1016/j.fuproc.2019.106140	A standardized TEA is complete and has been posted on the Washington State University repository.
Alcohol-to-jet (ATJ)	Literature review based on a design report, 28 pages (2015)	*ChemSusChem, 11*(21), 3728-3741, 2018. https://doi.org/10.1002/cssc.201801690	A standardized TEA is complete and has been posted on the Washington State University repository.
Synthetic kerosene and synthetic aromatic kerosene (SK-SAK)	Literature review based on a design report, 36 pages (2015)	Manuscript based on the case design report in preparation	This work was based on a Sasol® process, for which we have not found any significant development since 2016. Because of a lack of adequate process information/data on SK-SKA production from renewable feedstock, we are not able to build a reliable TEA.
Direct sugar-to-hydrocarbon	Literature review based on a design report, 88 pages (2017)	*Biomass and Bioenergy, 145:105942,* 2021. https://doi.org/10.1016/j.biombioe.2020.105942	A standardized TEA is complete and available for use by partners.
Virent® BioForming process	Literature review based on a design report, 46 pages (2015)	*Biomass and Bioenergy, 145:105942,* 202. https://doi.org/10.1016/j.biombioe.2020.1059421	A standardized TEA is complete and available for use by partners.
Catalytic hydrothermolysis (CH)	Literature review based on a design report, 35 pages (2018)	*Renewable and Sustainable Energy Reviews, 115:111516,* 2021. https://doi.org/10.1016/j.rser.2021.111516; *Data in Brief, 39:107514,* 2021. https://doi.org/10.1016/j.rser.2021.111516	A standardized TEA is complete and has been posted on the Washington State University repository.
Gasification Fischer Tropsch (GFT)	No literature review conducted	*Biomass and Bioenergy, 145:105942,* 2021. https://doi.org/10.1016/j.biombioe.2020.105942	A standardized TEA is complete and has been posted on the Washington State University repository.

® Sasol is a registered trademark of Sasol Limited, Gauteng, South Africa.
® Virent is a registered trademark of Virent, Inc., Madison, Wisconsin.



Fuel Type	Literature Review/Design Report Date	Publications	Techno-Economic Analysis (TEA) Model
Microchannel GFT (microGFT)	No exhaustive literature review written, capital costs found in the open literature for microchannel FT deemed unreliable	Capital cost results deemed unreliable	A standardized microGFT TEA was completed; however, the cost information is considered unreliable.
Hydroprocessed esters and fatty acids (HEFA)	No literature review conducted	*Biomass and Bioenergy, 145:105942,* 2021. https://doi.org/10.1016/j.biombioe.2020.105942	A standardized TEA is complete and has been posted on the Washington State University repository.

Research Approach

Background

A detailed literature review was conducted and prepared design case reports on six AJF pathways were prepared, including pyrolysis, ATJ, synthetic kerosene, direct sugar-to-hydrocarbon, Virent BioForming (now owned by Marathon Petroleum Corporation), and CH. Our team has also collected data from the literature to conduct TEAs for these pathways. The results from these design cases were applied in the development of supply chains and the identification of synergies that may eventually lead to the construction of integrated AJF production systems that take advantage of the infrastructure in a given region. An analysis of the locations of existing infrastructure demonstrated that the U.S. can be divided into regions according to the dominant biomass. Thus, we believe that the generation of advanced biorefinery concepts focused on petroleum refineries, pulp and paper mills, sugarcane mills, and corn ethanol mills is a viable approach for evaluating the synergy among AJF pathways, existing infrastructure, and co-products. Thus, our team can then compare the biorefinery concepts developed for each technology to identify the most promising approach, which can subsequently be used in supply chain analyses.

Stand-alone design case reports were generated by reviewing relevant research in the academic literature and public information provided by commercial entities developing the corresponding technology. The published manuscripts were subjected to an industrial expert review. The reports provide details regarding the processes involved in each conversion pathway and outline the technology readiness and particular barriers to implementation. Publicly available information regarding the commercial processes and research literature will provide a foundation of information to be used in modeling efforts. In cases lacking detailed process engineering information, as possible new models were built to estimate the parameters needed to complete assessments such as techno-economic modeling and supply chain modeling. Aspen Plus primarily generates process models and details, including mass balances, energy balances, energy requirements, and equipment size and cost. These results will also provide the basis for a comparative analysis of design cases, which identify the key advantages and markets for each technology.

Each design case has the following components:

- Feedstock requirements
- Companies developing/commercializing the technology
- Current locations of units in the U.S. and worldwide
- Block and flow diagram of the technology
- Unit operations and process conditions (e.g., reactor type, separation unit type, catalysts, product yield, and jet fuel yield)
- Properties of the produced jet fuel
- Identification of potential intermediates
- Current and potential uses of wastes and effluents
- Developed co-products



- Potential methods for coprocessing intermediates, wastes, and co-products by using existing infrastructure (e.g., petroleum refineries or pulp and paper mills)
- Preliminary TEA
- Technological challenges and gaps

The ASCENT Project 001A team has submitted technical reports and supplementary Microsoft® Excel® files with mass and energy balances and TEAs for the pathways listed. Furthermore, we have conducted a strategic analysis to identify the overall weaknesses of the technologies under study. All files are available for Project 001 team members.

- Pyrolysis-bio-oil hydro-treatment concept (hydro-treated depolymerized cellulosic jet): The TEA is complete.
- ATJ: A manuscript with information on the mass and energy balances and the TEA has been published.
- Fischer Tropsch (FT): Two design cases have been prepared for biomass gasification. The first case focuses on microreactors, and the second design case is applicable to technology based on larger standard reactors (reviews on the TEAs for gasification FT (GFT) and microchannel GFT have been completed. However, the limited reliability of the microreactor capital costs hinders the value of the practical impact of our microreactor TEA study. The TEAs are available for use by partners. In addition to gasification, the harmonized TEA was updated to include power-to-liquids with assistance from collaborators at MIT.
- HEFA: A stochastic TEA was created in MATLAB® and was confirmed to match the completed, deterministic TEA when the assumptions and costs match (the deterministic TEA review is complete). The TEA is now available for use.
- CH: The TEA is complete.
- A stochastic Excel-based spreadsheet version of the HEFA, ATJ, and FT TEAs were developed and shared for internal review.
- All TEAs were updated to include (1) 2021 cost year, (2) updated operating expense (OPEX) costs, (3) up-to-date feedstock costs, and (4) the addition of a second economic analysis perspective.

Milestones

- Updated all open-source TEAs to 2021 cost year.
- Updated the five SAF technology TEAs to include policies defined in the 2022 Inflation Reduction Act and revised in the 2025 One Big Beautiful Bill Act. Users can now model a variety of policy time horizons, values, and company structure scenarios. Specifically, the clean fuel production credit termed 45Z.

Major Accomplishments

A manuscript entitled “Comparison of techno-economic and environmental performance of alternative jet fuel production technologies” has been prepared, reviewed, and updated in preparation for FAA review. The ASCENT Project 001A team intends to submit these manuscripts to the FAA for review within the next four months. The team is working on the construction of a TEA for lignin extraction and utilization in a biorefinery process.

Our team has assisted the International Civil Aviation Organization (ICAO), and the Committee on Aviation Environmental Protection (CAEP) through participation in the previous Fuels Task Group (FTG), now Working Group 5 (WG5) and the Long-Term Aspirational Goal Task Group. An Excel spreadsheet of publicly announced global AJF producers has been updated, and the work with ICAO WG5 for integrating the historical portion of these data with their database is ongoing. Revised fuel projections were requested by and provided to the Modelling and Databases Group (MDG)-and Forecast and Economic Analysis Support Ground (FESG) at the FTG8 meeting on September 23-27, 2024, in Montreal, Canada. The methodology of projecting potential AJF production is under review, and a new methodology is under development. In addition, a separate U.S. database that does not include ICAO-specific assumptions and data is being maintained to assist in tracking progress toward meeting the SAF Grand Challenge goals.

Six Excel spreadsheet-based TEAs have been published on the WSU repository site to make these tools publicly available for analysis. These TEAs include HEFA, ATJ, FT with both solid and gaseous feedstocks, FT feedstock preparation, pyrolysis, and CH. The TEAs are being used by other ASCENT member universities and interested industry and government parties. These spreadsheet TEAs were updated and reposted in the 2025.

® Microsoft and Excel are registered trademarks of Microsoft Corporation in the United States and other countries.
® MATLAB is a registered trademark of The MathWorks Inc., Natick, Massachusetts.



We continued to generate data from the design cases and make these data available to ASCENT Project 001A partners to assist with supply chain analysis and techno-economic modeling by improving the conversion and cost figure database values.

Publications

Brandt, K., Martinez-Valencia, L., Camenzind, D., Martulli, A., Malina, R., Allroggen, F., & Wolcott, M. (2025). Pragmatic assessment of meeting the 2030 U.S. sustainable aviation fuel goal. *Biomass and Bioenergy, 206*. https://10.1016/j.biombioe.2025.108516

Outreach Efforts

Our results have been presented to the FAA, USDA Office of the Chief Economist (OCE), U.S. Department of Energy, ICAO, and CAAFI. Six harmonized TEAs have been posted on the WSU Research Repository for public use. The team has also made several presentations for graduate and undergraduate students.

Awards

None.

Student Involvement

Santheeb Velmurugan participated in the creation, editing, and updating of design cases for methanol-to-jet (MTJ).

Plans for Next Period

- Submit MTJ review paper for journal publication.
- Submit "Lipid and bio-processing technologies: process intensification and continuous flow-through reaction (PICFTR), lipid-to-hydrocarbon (LTH), Tyton, decarboxylation, and coprocessing" for journal publication (or as a report).
- Complete MTJ Aspen process model and subsequent harmonized TEA.
- Updated harmonized TEAs to 2024 cost year for use in ICAO WG5 "Rules of Thumb" update.
- Continue to support ICAO work through participation in the WG5. This includes the regularly scheduled SAF database updates and volume projections, additional work on chain of custody documents and potentially guidance, and the requested to update the SAF "Rules of Thumb" including evaluation of adding co-processing.

References

National Renewable Energy Laboratory. (2018). *Process design and economics for the conversion of lignocellulosic biomass to hydrocarbon fuels and coproducts: 2018 biochemical design case update* (Publication No. NREL/TP-5100-71949). https://www.nrel.gov/docs/fy19osti/71949.pdf

Task 2 – Evaluate the Most Promising Biorefinery Concepts for AJF Production

Washington State University

Objective

In continuation of work completed from previous years, the ASCENT Project 001A team completed our evaluation of biorefinery scenarios for AJF production using corn ethanol, sugarcane, and pulp and paper mills and petroleum refineries. The objective of this task is to conduct detailed TEAs on the integration of lignin co-product technologies and the ATJ pathway to determine the potential for reducing fuel costs.

Research Approach

Background

In this task, our team used design cases for existing infrastructure, AJF production technology, and identified co-products to generate new biorefinery concepts for petroleum refineries, pulp and paper mills, sugarcane mills, and corn ethanol mills. The results from this effort will allow us to identify and select the most commercially feasible biorefinery concepts.



Major technical gaps or barriers to the commercialization of each biorefinery concept will also be determined from the results of this study.

The integration of process technologies was assessed via an approach similar to that for the stand-alone design cases. The integration concepts were developed by pairing stand-alone cases with these concepts to evaluate the economic and environmental advantages of the integration approaches. Over this period, our team has conducted detailed analyses of ATJ conversion and integration with pulp mill operations. Our team has also investigated the potential contribution of lignin co-products to the overall process economy.

A dry-grind corn ethanol mill with a capacity of 80 million gallons of ethanol per year was studied to evaluate potential biorefinery scenarios for AJF production. Similarly, a sugarcane mill with a sugarcane processing capacity of 12,444 tons per day that produces raw sugar, molasses, surplus bagasse, and surplus electricity, was studied. The petroleum refinery used as the base case processes 120,000 barrels of crude oil per day. Five AJF technologies were studied: (1) Virent BioForming, (2) ATJ, (3) direct sugar-to-hydrocarbon, (4) fast pyrolysis, and (5) GFT. A standardized methodology was adopted to compare the biorefinery concepts for a dry-grind corn ethanol mill, sugarcane mill, and petroleum refinery in several integration scenarios with six jet fuel production scenarios. For all cases, our team estimated the fuel minimum selling price (MSP) and greenhouse gas emissions.

A manuscript on the integration of ATJ technologies with pulp mill infrastructure was published. Three additional manuscripts were published with results for corn ethanol mills (2021), sugarcane mills (2022), and petroleum refineries (2021).

P-graph is a tool to identify combinatorially feasible technological structures from basic unit operations. Biochemical technologies - Virent's BioForming, Alcohol to Jet, and gasification were the focus of p-graph analysis. These studies suggested that acetic acid co-production could increase the economic viability of these technologies. The p-graph work has been completed. We are currently working on the final report of this task.

In this year, the ASCENT Project 001A team has begun the process of refining the Aspen process model (Figure 1) to analyze MTJ production. There are three units in the MTJ process: (1) olefination of methanol (MTO), (2) hydrogenation of oligomers, and (3) fractionation of aviation fuel base stock. The Honeywell® UOP Renewable Jet Fuel Process™/hydro MTO process was referenced to generate C2 and C3 olefins as input feedstocks for oligomerization reaction, and the oligomerized products are hydrotreated to be used as the precursors for SAF. In addition to the Aspen model development, we drafting a paper titled "Methanol to sustainable aviation fuel" in collaboration with Pacific Northwest National Laboratory based on comments from an internal review.

® Honeywell and the UOP Renewable Jet Fuel Process are trademarks of Honeywell International, Inc., in the United States and other countries.

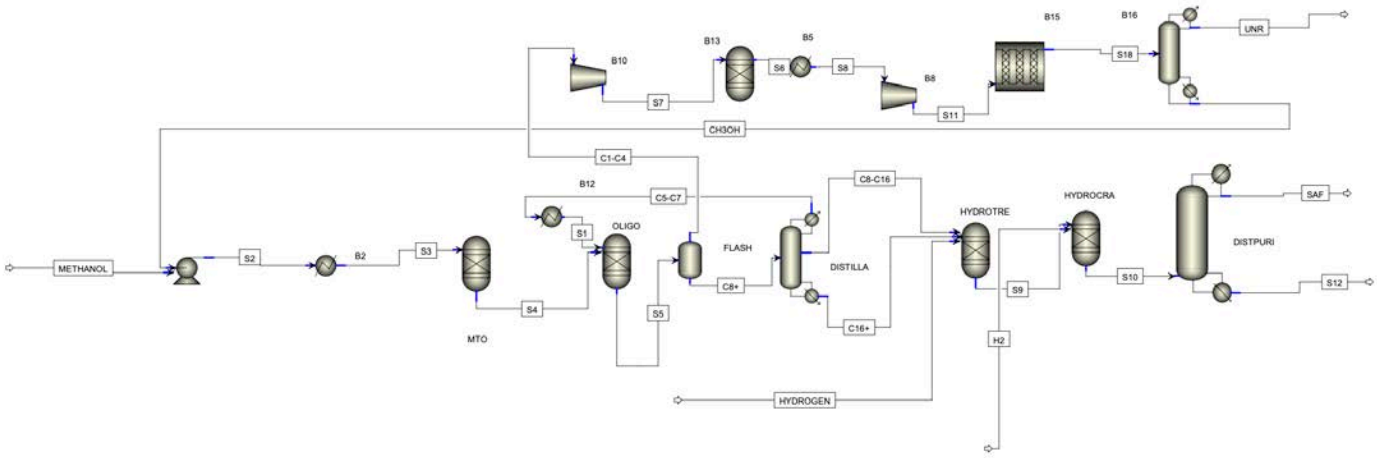


Figure 1. Aspen Plus flow sheet for methanol to aviation fuel base stocks.

Major Accomplishments
None.

Publications
None.

Outreach Efforts
None.

Awards
None.

Student Involvement
Graduate students, Claudia Marcela Valderrama and Santheeb Velmurugan, have received training in this project.

Plans for Next Period
- Complete a preliminary TEA analysis of MTJ conversion and the internal review of the review paper and submit it to the FAA internal review and then submit it for peer-reviewed journal publication.
- Pending completion of the initial Aspen model, begin work on a TEA to model the economics of MTJ and the impacts of technical and policy options.
- Complete a report or peer-reviewed manuscript titled “Lipid and bio-processing technologies: an insight into bioconversion potential of process intensification and continuous flow-through reaction (PICFTR), lipid to hydrocarbon (LTH) and TYTON bioenergy.”



Task 3 – Supplement and Maintain the Current Inventory of Biorefinery Infrastructures that are Useful for AJF Production, as Identified in the Conversion Design Cases

Washington State University

Objective

The objective of this task is to provide the required periodic evaluation of the databases to add new facilities or update the status of closed facilities in each category to ensure that the geospatially specific assets are current.

Research Approach

The use of existing infrastructure assets is a key component of retrofit approaches for advances in this industry. To differentiate between the relative values of various options, the specific assets must be valued with respect to their potential use within a conversion pathway. Regional databases of industrial assets that might be utilized by a developing AJF industry have been assessed on the national level. These baseline databases have been compiled from a variety of sources, including industry associations, universities, and news outlets. These databases will be expanded, refined, and validated as the conversion design cases indicate additional needs for regional analyses.

Milestones

- Evaluated the databases as necessary to add new facilities or to change the status of closed facilities in each category, to ensure that the geospatially specific assets are current.
- Converted the geospatial infrastructure data for use in supply chain resiliency models.

Major Accomplishments

- Compiled, validated, and shared National databases with the ASCENT Project 001A teams upon request. All metadata are available for use in regional analyses.
- Updated the count, scale and location of wood pellet mills.
- Geolocated the soybean and canola crushers in the U.S. with facility scale information.
- Geolocated large-capacity animal slaughter facilities in the U.S. For facilities in the Western U.S., capacities of facilities were found using public sources.

Publications

None.

Outreach Efforts

None.

Awards

None.

Student Involvement

None.

Plans for Next Period

This task will be closed out with a final infrastructure write-up and the most recent version of each database posted on the WSU repository next year.

Task 4 – Update CAAM Measures

Washington State University

Objective

The objective of this task is to update the CAAM with the latest available data.



Research Approach
Based on a community capitals framework, the ASCENT Project 001A team created the CAAM, which provides quantitative indicators of four social assets: social, cultural, human, and political capital. The CAAM provides quantitative proxy measures of qualitative concepts for initial site-selection assessments. Variations of the model have been applied to the Pacific Northwest, Idaho, Montana, Colorado, and Wyoming. Manuscripts on applications of the CAAM have been published in *Community Development*, *Politics and Life Sciences*, *Biomass & Bioenergy*, and *Frontiers in Energy Research*. The CAAM is currently being updated with the latest available data, with plans to make the CAAM more publicly accessible for use. As the social capital data have not been updated for several years, the research team is updating the data or creating our own measures to be validated in future use.

Milestones
- Conducted an investigation of alternative social capital data sources and measures.
- Met with another research team regarding additional data for potential cultural capital use, the Cultural Vitality Index (CVI) data from Creative West (formerly WESTAF).
- Validated the CAAM by using a private company.

Major Accomplishments
None.

Publications
None.

Outreach Efforts
None.

Awards
None.

Student Involvement
None.

Plans for Next Period
None. This task is complete.

Task 5 – Refine and Deploy Facility Siting Tools to Determine Regional Demand and Potential Conversion Sites to be Used in Regional Analyses
Washington State University

Objective
The objective of this task is to develop tools to site potential conversion facilities. Two primary tools are needed for this task: (1) a generalized tool to site initial locations that meet the needs of a specific conversion facility type and (2) a tool to select optimal conversion facility sites from the initial set of locations.

Research Approach
The ASCENT Project 001A team began developing a geospatial siting pre-selection (GSP) tool in early 2019. This tool is a Python®-based script that automates ArcGIS® to produce points representing locations that suit the needs of a conversion facility. The GSP tool uses a combination of buffer and cost datasets. Buffer datasets ensure that a candidate is sited in proximity to the necessary infrastructure, such as roads, rails, and natural gas pipelines. Because the candidate set generated by using only buffers will be very large, cost datasets have been added to distinguish candidates from each

® Python is a registered trademark of Python Software Foundation, Beaverton, Oregon.
® ARCGIS is a registered trademark of Environmental Systems Research Institute, Inc., Redlands, California.



other. Cost datasets represent geospatially variable costs, including electricity, natural gas, and transportation. In early 2020, a graphic user interface was added to the GSP tool to make it more user-friendly. An additional script was developed in 2022 to model the transportation cost inputs for the GSP tool based on the local density of feedstock, the maximum feasible travel distance from the facility for feedstock collection, and regional road characteristics. This script also includes a rudimentary user interface. In 2023, our team performed a retrospective analysis of corn ethanol plants using the GSP, with the objective of performing a pseudo-validation. This study showed that the facility locations of the mature ethanol supply chain were in areas that the GSP would have prioritized for siting, indicating that the tool is likely a good fit for other similar supply chains, such as SAF supply chains. The team also performed an extensive study in 2023 to show how the number of candidates and locations of candidates affect the optimization model solution time. The results of this study showed that a small number of candidates generated by the GSP performed significantly better than the same number of points laid out in a square grid.

The Many-Step Transshipment Solver (MASTRS) is a Python-based script that models large supply chains across multiple levels by building and solving mixed-integer linear programming problems. The model starts with feedstock spread across many locations and then models the distribution and conversion of feedstock into biofuels and other co-products through multiple levels of intermediate facilities that may include temporary storage, pre-treatment, and fuel production, before new products are sent to their destinations. Intermediate facilities may include existing facilities or new candidate facilities that are generated by the GSP tool. The MASTRS output shows the flow of materials throughout the supply chain and the most cost-efficient capacities and locations for new facilities.

The modeling combination of GSP and MASTRS scripts has been implemented for several regional supply chains. MASTRS was first implemented for the Pacific Northwest oilseed-to-jet-fuel supply chain in 2018. Since 2019, the GSP and MASTRS scripts have been used together for two supply chain models for both the production of jet fuel from forest residuals and lumber production byproducts in the Pacific Northwest. The first supply chain model uses single-stage conversion at integrated biorefineries, and the second supply chain model is a multi-stage model with distributed preprocessing facilities.

Milestones

- Updated the GSP tool to Python 3 so that it can function with ArcGIS Pro.
- Made substantial improvements have been made regarding tool accessibility for new potential users along with the expansion of tool capabilities.

Major Accomplishments

None.

Publications

None.

Outreach Efforts

None.

Awards

None.

Student Involvement

None.

Plans for Next Period

- Continue the process for publishing manuscripts that define the GSP and MASTRS tools.
- Continue implementing the GSP and MASTRS tools in regional supply chain analyses upon request.



Task 6 – Perform a Refinery-to-Wing Stakeholder Assessment

Washington State University

Objective

The objective of this task is to extend the stakeholder assessment to a limited sample of informed stakeholders in the remaining sections of the country to provide insight into market and industry dynamics, with the aim of optimizing successful outcomes.

Research Approach

Conduct online surveys of key stakeholders to inform market and industry dynamics.

Milestones

None.

Major Accomplishments

None.

Publications

None.

Outreach Efforts

None.

Awards

None.

Student Involvement

None.

Plans for Next Period

None. This task is complete.

Task 7 – Conduct a Supply Chain Analysis

Washington State University
U.S. Department of Transportation Volpe Center

Objective

The objective of this task is to design and implement a dynamic fuel mapping tool, which significantly advances our methodology for wildfire risk assessment across a supply chain network. WSU and Volpe have each developed modeling tools that apply transshipment optimization to model the geospatial layout of developing supply chains. A comparison of these tools would be useful to identify the strengths and weaknesses of each tool.

Research Approach

Focusing on the use of woody-biomass-to-jet-fuel conversion via fast pyrolysis and the upgrading of a supply chain centered in the northern Rocky Mountains, a series of comparison studies was conducted by using optimization tools from Volpe and WSU. Each modeling approach was required to determine sites for new pyrolysis depots and upgrades to refineries. Forest production data were provided by the land use and resource allocation (LURA) model from the University of Idaho. Pyrolysis depot locations were selected by candidate generation tools included in each approach, and existing petroleum refineries were used as candidates for upgrading refineries. Cities, ports, and airport hubs throughout the U.S. West Coast and Rocky Mountain regions were used as markets for road transportation fuel, bunker fuel, and jet fuel.



In this task, we propose a novel hybrid dynamic fuel mapping methodology that combines a deep learning architecture and traditional classification algorithms. More specifically, the approach integrates a binary U-Net-based semantic segmentation model with a pixel-wise K-Nearest Neighbors (KNN) classifier to leverage the complementary strengths of both methods. The U-Net model first generates a binary mask distinguishing non-burnable and vegetated areas, effectively capturing large-scale spatial patterns and linear features critical for fire behavior modeling. The KNN classifier then performs detailed pixel-level classification of vegetation areas into fuel categories based on the Scott and Burgan fuel models. The methodology is implemented using free and publicly available Harmonized Landsat Sentinel-2 (HLS) imagery with a 30-m resolution, enabling near-real-time monitoring with a revisit interval of 2 to 3 days. The results demonstrate that the hybrid approach significantly improves spatial coherence of the fuel maps generated compared to using KNN or U-Net alone. Moreover, the model effectively captures dynamic vegetation changes. The resulting tool can be used to dynamically monitor the availability and distribution of burnable biomass feedstock while simultaneously leveraging live environmental data to conduct a comprehensive, near real-time assessment of immediate and projected wildfire risk to key supply chain network assets.

Milestones
None.

Major Accomplishments
- Studied five feedstock types for producing AJF: (1) agricultural residues and grasses, (2) forest residues, (3) urban wood waste, (4) oilseeds, and (5) fats, oils, and greases (FOG).
- Submitted a journal manuscript titled “Satellite imagery-based dynamic fuel mapping for wildfire risk assessment” for FAA review.

Publications
None.

Outreach Efforts
None.

Awards
None.

Student Involvement
Nasimeh Rashidi, a PhD student in Civil & Environmental Engineering at WSU, has worked on this task.

Plans for Next Period
- Utilize regional supply chain tools to assess forest residuals for SAF using pyrolysis methods.
- Submit a journal paper, “Satellite imagery-based dynamic fuel mapping for wildfire risk assessment.”

Task 8 – Provide Analytical Support for Regional CAAFI and USDA Jet Fuel Projects
Washington State University

Objectives
The objectives of this task are to (1) develop a readiness-level tools to assess the status of regional SAF production projects and to use supply chain and stand-alone design cases to support TEA and supply chain analysis, (2) assess the regional feedstock, conversion pathways, and MSP for SAF manufactured in U.S. regions, (3) support CAAFI requested analyses, and (4) deploy and enhance ASCENT tools for use in ICAO/CAEP/WG5.

Research Approach
The ASCENT Project 001A team assisted the regional USDA Bioenergy Alliance Network of the Rockies (BANR) team by deploying TEA and supply chain analysis for their project. This effort focused on the use of softwood forest salvage



feedstock in a thermochemical conversion process to produce fuels and co-products. The facility siting tools discussed in Task 5 (i.e., GSP and MASTRS) were implemented for the BANR supply chain and Port of Seattle project. For BANR, optimal locations for facility siting, supply chain configurations, and fuel production at different price points were calculated.

The Port of Seattle project required a detailed feedstock survey for forest residuals, municipal solid waste, and lipids. Each feedstock was quantified and then paired with a compatible SAF conversion pathway to determine the SAF MSP by using ASCENT-developed TEAs.

Federal (Renewable Fuel Standard, Inflation Reduction Act) and state (California, Oregon, Washington, Illinois) policies in the U.S. that incentivize the production of AJF, its co-products, or feedstock (i.e., green dihydrogen [H_2], carbon dioxide [CO_2] capture and utilization) were mapped in a series of flow charts. An initial decision support tool was programmed using Python and converted to an Excel spreadsheet to facilitate its sharing among stakeholders. This tool enables a user to identify applicable policies for specific scenarios and returns generalized values per volume of fuel or mass of feedstock. Values can be selected for different time ranges, confidence interval values, and multiple summary statistics. Graphics were added to the tool in addition to options to export the data. The decision tool underwent ASCENT and external stakeholder review. The output from this tool is a direct input into the harmonized TEAs to more accurately determine the economic viability of an AJF production pathway in the U.S. This was published in 2025 with a peer-reviewed paper.

Information about facilities and infrastructure has been supplemented with information about the current consumption of feedstocks. Using information from the U.S. Census Bureau, U.S. Energy Information Administration, California Air Resources Board, and annual company reports, our team has compiled data that show how lipid feedstocks have been consumed for fuels in the U.S. since HEFA fuels were first produced in the U.S. in 2014.

A financial model that uses a system dynamics approach was conceptualized and developed. This model analyzes the effects of federal and state policies on the financial performance of projects to produce SAF. This model can perform both deterministic and stochastic analyses. Three conversion technologies (i.e., HEFA, ATJ, FT) and nine feedstocks (including FOGs; vegetable oil; municipal solid waste; forest and agricultural residues; first- and second-generation ethanol; direct air capture; and flue gas) have been analyzed. The team assessed the influence of green hydrogen, renewable electricity and gas, and carbon capture utilization and storage on the financial metrics, based on calculations performed by MIT colleagues. A draft manuscript of this work is under internal review.

As continuation of the technical support to the ICAO/CAEP/WG5 on fuel accounting and reporting systems, a review paper titled “A dual sustainable aviation strategy: voluntary markets and regulatory frameworks” is being drafted and submitted to Renewable and Sustainable Energy Reviews. The paper aims to be a critical review on the impacts of regulatory and voluntary frameworks on the industry, examining their correlation to the development of sustainable supply chains, and the scaling up of the renewable energy. The collaboration with the Fuel Accounting Systems ad hoc group of the Technology Production and Policy subgroup continues on a Study of Fuel Accounting Systems for International Aviation as part of the CAEP/14 Cycle Tasks S.12.01 and S.12.02. An initial report outline was presented at the CAEP/14 WG5 Second meeting, and a preliminary report has been prepared and is under discussion. The report presents a review of fundamental concepts, updated information on regulatory and voluntary frameworks, and a survey of existing fuel accounting systems.

Technical support to the ICAO/CAEP/WG5 was provided. This support included (1) maintenance of the global database of SAF fuel production announcements, (2) revision of the potential AJF fuel production projections, and (3) preparation for the requested third version to the ICAO SAF “Rules of Thumb.”

An assessment of the practical pathway to meet the U.S. AJF goals was completed and a journal article was written, reviewed and was in the final stages of the publication process at the end of the period of performance. This paper used harmonized assumptions as a companion paper from the National Renewable Energy Laboratory that is in process. Our team also completed a maximum feedstock price analysis for the USDA OCE for SAF manufactured using the HEFA pathway. The maximum price of each analyzed feedstock was determined for a variety of policy scenarios. This work has been extended and revised following the One Big Beautiful Bill Act to be written into a paper with University of Tennessee, Knoxville (UTK) as the lead authors using policy to determine volumes of soybean oil and second crop oils for different price and policy support scenarios.



An inventory of domestic and imported lipid feedstocks was created to support potential AJF production. The inventory includes production quantities, prices and locations of various lipids used in fuels including canola oil, soybean oil, corn oil, beef tallow, hog fats, and used cooking oil. Additionally, information about supply elasticity, competition from other markets and recent trends in international trade are also included.

Milestones

- Submitted manuscript "A Dual Sustainable Aviation Strategy: Voluntary Markets and Regulatory Frameworks" to *Renewable and Sustainable Energy Reviews*.
- Supported ICAO/CAEP/WG5 AJF global database and fuel production projections.

Major Accomplishments

None.

Publications

None.

Outreach Efforts

- Participated (Wolcott, M.) in the MassPort New England Regional SAF Workshop at Volpe National Transportation Laboratory held June 5, 2025, in Cambridge, Massachusetts.
- Participated (Wolcott, M.) on the review team for the new University of Maine project, "USDA Sustainable Wood to Fuel and Fish Feed," on September 30, 2025.

Presentations

Brandt, K.; Wolcott, M. (2025, August 21). *Sustainable Aviation Fuels: Supply Chains and Policy*. Eastern Washington Sustainable Aviation Fuel Tour. Pullman, Washington. Group included county legislators, regional port personnel, Alaska Airlines, Boeing and regional non-governmental organizations.

Brandt, K.; Echeverria Paredes, P.; Camenzind, D.; Wolcott, M. (2025, October 15). *ICAO WG5 Work Update* [Meeting presentation]. Fall 2025 ASCENT Meeting, Alexandria, Virginia.

Awards

None.

Student Involvement

None.

Plans for Next Period

- Complete publication of "A dual sustainable aviation strategy: voluntary markets and regulatory frameworks" (review paper) that was submitted.
- Submit "Spurring Technological Innovation, Industry Development and Decarbonization Through Sustainable Aviation Fuel Policy in Canada and the U.S.," a paper that is under internal review.
- Publish joint paper with UTK that covers the volume of oilseed lipids that match the maximum price biorefineries can pay given different policy scenarios.

Task 9 – CAAFI Collaborative Support of Research, Development, Demonstration and Deployment Efforts on SAF/AJF

CAAFI's Office of the Executive Director

Objectives

The objective of this task includes the responsibilities for the CAAFI's Office of the Executive Director to:

- Maintain familiarity with U.S. government, academic and industry SAF activities, and provide expertise in fostering the development and commercialization of SAF as enabled by the various pursuits or interests of these parties.



- Provide technical support to the FAA Office of Environment and Energy (AEE) and other agencies associated with the SAF Grand Challenge, as well as to other academic and commercial contributors.
- Lead or assist in facilitating public and private stakeholder engagement with SAF development, ASTM International fuel qualification, and related activities.
- Be responsible for executing an annually updated set of goals and priorities via a work plan approved by FAA AEE as well as the CAAFI Steering Group.

Research Approach

The CAAFI reinforces the value proposition of synthetic aviation turbine fuels (SATF), including SAF, through use of communications, outreach, and direct stakeholder engagement. CAAFI enhances the SATF Fuel Qualification approach through participation, advisement, and facilitation of producer and original equipment manufacturer (OEM) engagement in the ASTM qualification process, as well as internal coordination discussions with CAAFI research and development (R&D) and certification teams. CAAFI works to seek alignment of efforts to enable commercial SAF deployment, via leveraging research, partnering across U.S. government agencies, facilitating partnerships among supply chain stakeholders (typically both directly with individual companies and through various trade associations), and supporting innovative fuel acquisition processes. CAAFI implements and shares best practices across the SAF enterprise, including by providing tools and integrating information to support communication and understanding among diverse stakeholders. Finally, CAAFI will support the implementation of the SAF Grand Challenge roadmap by leveraging the above activities to facilitate the execution of the work streams and activities in the roadmap (https://www.energy.gov/sites/default/files/2022-09/beto-saf-gc-roadmap-report-sept-2022.pdf).

All of the above activities are supported through broad exchange of information among SAF stakeholders at our regularly occurring discussions, CAAFI webinars, and via pertinent conferences, workshops, and ad hoc meetings. Pertinent observations from more formal public activities are published on the CAAFI website: http://www.caafi.org.

CAAFI provides information resources and credible expert technical support to the SAF community through:

- An updated and cohesive communications strategy to leverage a range of outlets for technical information and information exchange.
- A continuously updated CAAFI website with greater functionality, usability across devices, and expanded content.
- Continued and expanded direct interaction with supply chain participants who seek out CAAFI leadership for information, advice, and coordination with other entities.
- Continued and expanded dissemination of information through events, conferences, interviews, written articles, and journal publications.

CAAFI coordinates and aligns with U.S. government agencies' activities in support of the SAF Grand Challenge (biweekly meetings throughout the execution period):

- Regularly coordinating with the Federal SAF Interagency Working Group on needs, goals, and priorities. Providing input on SAF Grand Challenge execution and performance tracking and supporting SAF Grand Challenge work team efforts and tasks.
- Communicating federal funding and program developments to the broader SAF community.
- Communicating the need for long-term, sustained policy support to meet the SAF Grand Challenge goals.
- Collaborating with stakeholders to develop key SAF communications and informational materials (e.g., infographics) that (1) reference the best available data and (2) highlight the potential economic benefits (employment, etc.), environmental, and social benefits of SAF.
- Promote consistency for coherent and clear messaging.

CAAFI facilitates ongoing efforts by jet fuel industry practitioners in committees such as ASTM D02, hosted by ASTM International:

- Development of a specification for SATF that can be used at higher blend levels up to 100% (complete) synthesized fuels.
- Assessment of options for a more generalized specification for SATF based on composition and other characteristics.
- Evaluation and approval of new SATF pathways.
- Establishment of additional specifications leveraging existing refining infrastructure to produce SAF.



- Support for clearinghouse, prescreening, and other SATF testing for fuel analysis and qualification in collaboration with the FAA-funded ASCENT Center of Excellence.

CAAFI promotes harmonization of sustainability evaluation approaches and tools by:

- Facilitating broader acceptance of methodologies to assess the environmental, social, and economic performance of SAF.
- Facilitating research, demonstration, and commercial scale projects relating to regenerative agriculture/soil organic carbon sequestration.
- Fostering integration with developments in carbon capture and sequestration.
- Identifying concerns about carbon management and permanence with supply chain partners.

CAAFI enables continuing and expanding international engagement through:

- Input to the ICAO through events and direct engagement with working group participants.
- Coordination with other CAAFI-like organizations around the globe to align and complement work efforts.
    - Specific engagement with aireg in this period, including participation in their SAF Conference 2025 in June in Berlin.
- Collaboration with global SAF stakeholders on messaging.

Leveraging the above efforts to advance the use and commercial production of SAF by fostering strategic partnerships, identifying opportunities and aligning deployment efforts:

- Facilitating team development to respond to funding opportunities to develop novel feedstocks, SAF commercialization projects, and supply chains.
- Supporting the development of commercial agreements across the SAF supply chain to enable SAF production and use.
- Fostering other supply chain development and deployment partnerships.
- Developing an approach to collaboration with the established biofuel and energy industry and the agricultural sector.

Milestones

- Continued progress on CAAFI via each of the above listed support approaches.
- Released a new CAAFI Website.
- Progressed the concept of a Commercial Engagement Readiness Level Framework (release dependent of resource allocation for the coming year).
- Released a revised Feedstock Readiness Level Framework (along with an informational webinar).
- Executed the next North American SAF Conference & Expo in Minneapolis, Minnesota, on September 22-24, 2025.

Major Accomplishments

- Worked collaboratively with BBI International and SAF Magazine, CAAFI co-produced and executed the North American SAF Conference and Expo in Minneapolis, Minnesota on September 22-24, 2025.
    - The event showcased many updates for SAF value chain development, as well as providing a forum for major messaging from industry and government.
    - The event also addressed challenging issues currently facing the SAF industry, as well as highlighting opportunities across the value chain.
    - Approximately 300 attendees were able to connect with exhibitors showcasing the latest technologies and services in the industry, as well as with their peers in discussing how to move the SAF community forward.

Outreach Efforts

Outreach effort for this task included workshop participation, presentations, general discussions, panel moderation, interviews, and student seminars. The following is a list of outreach efforts participated in during this reporting period:

Tim Hughes

- Canola meeting, Bardwell, Kentucky, December 18, 2024
- Kentucky Commodity Conference, Bowling Green, Kentucky, January 15-16, 2025
- KY Ag Expo, Owensboro, Kentucky, January 29, 2025
- West KY Ag Conference, Water Valley, Kentucky, January 31, 2025
- Iowa Renewable Fuels Summit, Altoona, Iowa, February 03-04, 2025



- National Farm Machinery Show, Louisville, Kentucky, February 12-13, 2025
- Renewable Fuels Association Conference, Nashville, Tennessee, February 18, 2025
- Covercress Engagement, Livermore, Kentucky, February 19, 2025
- USDA Outlook Forum, Crystal City, Virginia, February 26-28, 2025
- Commodity Classic, Denver, Colorado, March 02-05, 2025
- Illinois Sustainable Fuels Conference, Chicago, Illinois, March 12-13, 2025
- BBI International Biomass Conference, Atlanta, Georgia, March 18-20, 2025
- IL focus collaboration: University of Illinois, National Corn Ethanol Research Center, Crysalis, Illinois, April 14-18, 2025
- Fastmarkets Biofuels & Feedstocks Americas 2025, Chicago, Illinois, May 05-07, 2025
- Pennycres Field Day, Macomb, Illinois, May 21-22, 2025
- Sustainable Fuels Summit, Omaha, Nebraska, June 08-11, 2025
- CA SAF Research Assets, San Francisco, California, September 01-03, 2025
- BBI/CAAFI NA SAF Conference & Expo, Minneapolis, Minnesota, September 21-24, 2025

Steve Csonka

- SEATAC SAF Workshop, Seattle, Washington, October 07-09, 2024
- SE Regional SAF Workshop, Atlanta, Georgia, October 14-15, 2024
- DOE Co-processing Workshop, Long Beach, California, October 16-18, 2024
- NBAA BACE Aviation Sustainability workshops, Las Vega, Nevada, October 22-24, 2024
- ASCENT Fall Meeting Advisory Committee, Washington DC, October 29-31, 2024
- SAE-SMC-CRC Annual, Columbus, Ohio, November 12, 2024
- Airbus Sustainability Forum, Washington DC, November 13-14, 2024
- AFCC Conference, Washington DC, November 19-22, 2024
- DOE Deploy, Washington DC, December 04-05, 2024
- ASTM D02 Biennial, Anaheim, California, December 09-12, 2024
- IL IMA Conference, Chicago, Illinois, March 12-13, 2025
- Marquis Collaboration, Hennepin, Illinois, March 14, 2025
- ABLC, Washington DC, March 17-21, 2025
- ASTM Meeting, Brussels, Belgium, April 07-11, 2025
- IL focus collaboration: University of Illinois, National Corn Ethanol Research Center, Crysalis, Illinois, April 14-18, 2025
- ASCENT Spring Meeting SAF, Knoxville, Tennessee, April 21-23, 2025
- CRC Meeting, UDRI, Dayton, Ohio, April 29-May 01, 2025
- IN HPLC Summit, Indianapolis, Indiana, May 06-07, 2025
- SPARC Conclusion Meeting, Tampa, Florida, May 11-14, 2025
- GLBRC Annual & SAIB Meeting, Milwaukee, Wisconsin, Mary 19-22, 2025
- MASSPORT Workshop, Cambridge, Massachusetts, June 04-06, 2025
- HYCO1 Visit, and EPC Conference, Houston, Texas, June 10-12, 2025
- CBI Annual & SAIB Meeting, Asheville, North Carolina, June 16-19, 2025
- AIREG Annual, Berlin, Germany, June 23-24, 2025
- SAF Summit Brussels, Belgium, June 25-26, 2025
- MN SAF Hub Session, Minneapolis, Minnesota, July 22, 2025
- AAIC & IOCC, Fairbanks, Alaska, August 31-September 04, 2025
- Cascadia Meeting, Seattle, Washington, September 05-06, 2025
- ARGUS NAm RFS LCFS, Monterey, California, September 15-18, 2025
- BBI NAm SAF C&E, Minneapolis, Minnesota, September 21-24, 2025

Awards

None.

Student Involvement

Student involvement activities occur on a continuing basis via engagement with the universities associated with the Bioenergy Research Centers (i.e., Great Lakes Bioenergy Research Center, Center for Bioenergy Innovation, and their



partner institutions), ASCENT Advisory Board Meetings, and USDA National Institute of Food and Agriculture/Agriculture and Food Research Initiative Coordinated Agricultural Projects Sustainable Agricultural Systems efforts (i.e., the Sustainability Programming for Ag Retailers & Certified Crop Consultants [SPARC] and IPREFER). Members of the CAAFI Office of the Executive Director also participate annually in various University forums that promote student engagement in SAF activities (e.g., Fairbanks, Alaska activities highlighted above).

Plans for Next Period

None. CAAFI is no longer funded through ASCENT.



Project 001(B) Alternative Jet Fuel Supply Chain Analysis

University of Hawai‘i

Project Lead Investigator

Scott Q. Turn
Researcher
Hawai‘i Natural Energy Institute
University of Hawai‘i
1680 East-West Rd., POST 109
Honolulu, HI 96822
808-956-2346
sturn@hawaii.edu

University Participants

University of Hawai‘i (UH)

- P.I.: Scott Q. Turn, Researcher
- FAA Award Number: 13-C-AJFE-UH, Amendment 005
- Period of Performance: October 1, 2015, to August 4, 2021
- Tasks:
  1.
     1.1 Inform regional supply chains.
     1.2 Identify supply chain barriers in the Hawaiian Islands.

- FAA Award Number: 13-C-AJFE-UH, Amendment 007
- Period of Performance: October 1, 2016, to August 4, 2021
- Tasks:
  2.
     2.1 Inform regional supply chains.
     2.2 Support Indonesian alternative jet fuel (AJF) supply initiatives.

- FAA Award Number: 13-C-AJFE-UH, Amendment 008
- Period of Performance: August 1, 2017, to August 4, 2021
- Tasks:
  3.
     3.1 National lipid supply availability analysis
     3.2 Hawai‘i Regional Project

- FAA Award Number: 13-C-AJFE-UH, Amendment 011
- Period of Performance: May 31, 2019, to August 4, 2021
- Task:
  4. Hawai‘i Regional Project

- FAA Award Number: 13-C-AJFE-UH, Amendment 013
- Period of Performance: June 5, 2020, to August 4, 2021
- Task:
  5. Hawai‘i Regional Project

- FAA Award Number: 13-C-AJFE-UH, Amendment 017
- Period of Performance: October 1, 2021, to September 30, 2022
- Task:



6. Hawai‘i Regional Project

- FAA Award Number: 13-C-AJFE-UH, Amendment 019
- Period of Performance: December 22, 2022, to December 31, 2023
- Task:
  7. Hawai‘i Regional Project

- FAA Award Number: 13-C-AJFE-UH, Amendment 025
- Period of Performance: August 12, 2024, to September 30, 2026
- Task:
  8. Hawai‘i Regional Project

Project Funding Level

Under **FAA Award Number 13-C-AJFE-UH, Amendment 005**, the Alternative Jet Fuel Supply Chain Analysis–Tropical Region Analysis project received $75,000 in funding from the Federal Aviation Administration (FAA) and cost-share funding of $75,000 from the State of Hawai‘i.

Under **FAA Award Number 13-C-AJFE-UH, Amendment 007**, the Alternative Jet Fuel Supply Chain Analysis–Tropical Region Analysis project received $100,000 in funding from the FAA, cost-share funding of $75,000 from the State of Hawai‘i, and $25,000 of in-kind cost match in the form of salary support for Scott Turn from UH.

Under **FAA Award Number 13-C-AJFE-UH, Amendment 008**, the Alternative Jet Fuel Supply Chain Analysis–Tropical Region Analysis project received $125,000 in funding from the FAA and cost-share funding of $125,000 from the State of Hawai‘i.

Under **FAA Award Number 13-C-AJFE-UH, Amendment 011**, the Alternative Jet Fuel Supply Chain Analysis–Tropical Region Analysis project received $200,000 in funding from the FAA and cost-share funding of $200,000 from the State of Hawai‘i.

Under **FAA Award Number 13-C-AJFE-UH, Amendment 013**, the Alternative Jet Fuel Supply Chain Analysis–Tropical Region Analysis project received $200,000 in funding from the FAA and cost-share funding of $200,000 from the State of Hawai‘i.

Under **FAA Award Number 13-C-AJFE-UH, Amendment 019**, the Alternative Jet Fuel Supply Chain Analysis–Tropical Region Analysis project received $150,000 in funding from the FAA and cost-share funding of $150,000 from the State of Hawai‘i.

Under **FAA Award Number 13-C-AJFE-UH, Amendment 025**, the Alternative Jet Fuel Supply Chain Analysis–Tropical Region Analysis project received $150,000 in funding from the FAA and cost-share funding of $150,000 from the State of Hawai‘i.

Investigation Team

University of Hawai‘i

Dr. Scott Turn (P.I.; Hawai‘i Natural Energy Institute), All Tasks
Dr. Trevor Morgan (assistant researcher; Hawai‘i Natural Energy Institute), Tasks 1–3
Dr. Richard Ogoshi (assistant researcher; Department of Tropical Plant and Soil Sciences), Tasks 1 and 2
Dr. Adel H. Youkhana (junior researcher; Department of Tropical Plant and Soil Sciences), Tasks 1 and 2
Dr. Curtis Daehler (professor; Department of Botany), Task 1
Ms. Sharon Chan (junior researcher; Hawai‘i Natural Energy Institute), Tasks 2, 5, and 7
Mr. Gabriel Allen (undergraduate student; Department of Biochemistry, Task 2
Dr. Jinxia Fu (assistant researcher; Hawai‘i Natural Energy Institute), Task 3
Dr. Quang Vu Bach (assistant researcher; Hawai‘i Natural Energy Institute), Tasks 3,4, 6, and 8
Ms. Sabrina Summers (undergraduate student; Department of Bioengineering), Task 3
Ms. Sarah Weber (undergraduate student; Department of Molecular Biosciences and Biotechnology), Task 3
Mr. Taha Elwir (undergraduate student; Department of Chemistry), Task 3



Dr. Donna Lee (energy crop analyst, Hawai'i Natural Energy Institute), Task 5 and 7
Dr. Elmar Villota (postdoctoral researcher, Hawai'i Natural Energy Institute), Task 5 and 7

Other Lead Personnel

University of Tennessee
Prof. Tim Rials (co-P.I.)
Prof. Edward Yu (co-P.I.)

Washington State University (WSU)
Prof. Michael Wolcott (P.I.)
Prof. Manuel Garcia-Perez (co-P.I.)

Volpe National Transportation Systems Center (Volpe)
Kristin Lewis (principal technical advisor and P.I.)

The Pennsylvania State University
Prof. Lara Fowler (P.I.)

Project Overview

The research effort under **Task 1** has two objectives. The first objective is to develop information on regional supply chains for use in creating scenarios of future alternate jet fuel (AJF) production in tropical regions. Outputs from this project may be used as inputs to regional supply chain analyses being developed by the FAA and Volpe. The second objective is to identify key barriers in regional supply chains that must be overcome to produce substantial quantities of sustainable aviation fuel (SAF) in the Hawaiian Islands and similar tropical regions.

The project goals of Task 1 are as follows:

- Review and summarize the following:
  - The available literature on biomass feedstocks for the tropics.
  - The available literature on pretreatment and conversion technologies for tropical biomass feedstocks.
  - The available literature on geographic information system (GIS) datasets available for assessing AJF production systems in the tropics.
- Identify AJF supply chain barriers in the Hawaiian Islands.

The research effort under Task 2 has two objectives. The first objective is to develop information on regional supply chains for use in creating scenarios for future SAF production in tropical regions. Outputs from this project may be used as inputs to regional supply chain analyses being developed by the FAA and Volpe. This objective includes the development of fundamental property data for tropical biomass resources to support supply chain analysis. The second objective is to support the memorandum of understanding between the FAA and the Indonesian Directorate General of Civil Aviation to promote the development and use of sustainable alternative aviation fuels.

The project goals of Task 2 are as follows:

- Support the Volpe and Commercial Aviation Alternative Fuels Initiative (CAAFI) Farm to Fly 2.0 supply chain analysis.
- Use GIS-based estimates of fiber crop production potential to develop preliminary technical production estimates of jet fuel in Hawai'i.
- Develop fundamental property data for tropical biomass resources.
- Transmit data and analysis results to other ASCENT Project 001 researchers to support the improvement of existing tools and best practices.
- Support Indonesian SAF supply initiatives.

The research effort under Task 3 has two objectives. The first objective is to support a national lipid supply availability analysis that will inform industry development and guide policy. The second objective is to conduct a targeted supply chain analysis for a SAF production facility based on the Hawai'i regional project.

The project goals of Task 3 are as follows:



- Support ASCENT partners conducting the national lipid supply availability analysis by contributing information on tropical oilseed availability.
- Evaluate supply chains for targeted waste streams and purpose-grown crops in Hawai‘i to a location in the principal industrial park on the island of O‘ahu.

For the research effort under Task 4, the main objective is to conduct bench-scale testing of tropical feedstocks for use in targeted supply chain analysis for a SAF production facility based on the Hawai‘i Regional Project initiated under Amendment 008.

The project goals of Task 4 are as follows:
- Survey bench-scale systems available for relevant SAF conversion technology options.
- Down-select from the available bench-scale systems to no more than two systems capable of conducting feedstock testing and quantifying product yields and contaminant concentrations.
- Conduct bench-scale feedstock tests and quantify product yields, quality, and contaminant concentrations.

The project goals of Task 5 are as follows:
- Conduct tropical oil-to-SAF supply chain analyses.
- Develop management strategies for elements present in construction and demolition (C&D) waste that affect use in thermochemical-conversion-based SAF production pathways.

The project goals of Task 6 are as follows:
- Explore the impacts of HB2386 on waste management in Hawai‘i and potential for waste-based SAF production systems.

The project goals of Task 7 are as follows:
- Evaluate greenhouse gas (GHG) implications of tropical oil-to-SAF supply chains in Hawai‘i based on life cycle methods.

The project goals of Task 8 are as follows:
- Evaluate GHG implications of waste management use for SAF production in Hawai‘i based on life cycle methods.

Task 1.1 – Inform Regional Supply Chains

University of Hawai‘i

Objectives

The objective of this task includes (1) reviewing the archival literature on existing tropical crops and potential new crops that could provide feedstocks for SAF production, and (2) reviewing relevant pretreatment and conversion technology options and experiences with the feedstocks identified in the first objective.

Research Approach

Task 1.1

The archival literature was reviewed to construct an updated database of relevant citations for tropical crops; new potential energy crops were identified and added to the database. Available information on agronomic practices, crop rotation, and harvesting techniques was included. The database was shared to serve as a resource for the ASCENT Project 001 team and Volpe analyses of regional supply chains.

Task 1.2

A database of relevant pretreatment and conversion technology options, and experiences with potential tropical feedstock materials, was assembled from the archival literature and from existing ASCENT Project 001 team shared resources. Of particular interest were inventories of material and energy flows associated with the pretreatment and conversion unit operations fundamental to the design of sustainable systems and underlying analyses. Pairings of pretreatment and conversion technology options provided a starting point for the evaluation of tropical biorefineries that can be integrated into the ASCENT Project 001 team and Volpe activities.



Milestones

Task 1.1

- Identified a target list of databases to search for relevant literature.
- Provided an interim report summarizing progress in the literature search.

Task 1.2

- Identified a target list of databases to search for relevant literature.
- Provided an interim report summarizing progress in the literature search.

Major Accomplishments

This work has been completed. A report was produced for each of the two activities, and the two reports were combined into a manuscript published in the journal *Energy & Fuels* (Morgan et al., 2019).

Publications

Peer-reviewed Journal Publication

Morgan, T. J., Youkhana, A., Ogoshi, R., Turn, S. Q., & Garcia-Perez, M. (2019). Review of biomass resources and conversion technologies for alternative jet fuel production in Hawai'i and tropical regions. *Energy & Fuels, 33*(4), 2699–2762. https://doi.org/10.1021/acs.energyfuels.8b03001

Outreach Efforts

On February 21, 2018, the P.I. participated in a ThinkTech Hawai'i broadcast focused on SAFs, with collaborators from WSU and CAAFI (https://www.youtube.com/watch?v=Ci4oWITPRKQ&feature=youtu.be).

Awards

None.

Student Involvement

None.

Plans for Next Period

None.

Task 1.2 – Identify Supply Chain Barriers in the Hawaiian Islands

University of Hawai'i

Objective

The objective of this task was to identify key barriers in regional supply chains that must be overcome to produce substantial quantities of SAF in the Hawaiian Islands and similar tropical regions.

Research Approach

The UH developed the Hawai'i Bioenergy Master Plan for the State of Hawai'i (http://www.hnei.hawaii.edu/wp-content/uploads/Hawaii-Bioenergy-Master-Plan.pdf), which was completed in 2009. In that plan, UH was tasked with determining whether Hawai'i had the capability to produce 20% of land transportation fuels and 20% of electricity from bio-based resources. To this end, the plan included assessments of (a) land and water resources that can support biomass feedstock production, (b) potential biomass resources and their availability, (c) technology requirements, (d) infrastructure requirements to support logistics, (e) economic impacts, (f) environmental impacts, (g) availability of human capital, (h) permitting requirements, and (i) limitations to developing complete value chains for biomass-based energy systems. In keeping with the stakeholder-driven development of the Hawai'i Bioenergy Master Plan, barriers to the development of regional supply chains for ASCENT were identified through interactions with key stakeholder groups. Green Initiative for Fuels Transition Pacific (GIFTPAC) meetings are held quarterly and attended by biofuel development interests in Hawai'i, including representatives of large landowners, producers of first-generation biofuels, petroleum refineries, electric utilities, the Hawai'i State Energy Office, U.S. Pacific Command, biofuel entrepreneurs, county government officials, and UH. Additional stakeholders are invited as necessary to fill gaps in information and the value chain. These meetings serve as



excellent opportunities to receive stakeholder input, identify barriers to supply chain development, and organize data collection efforts that span supply chain participants.

Milestones

- Introduced activities at the next regularly scheduled GIFTPAC meeting after contract execution.
- Prepared an interim report outlining two tropical supply chain scenarios developed in consultation with the ASCENT Project 001 team, with input from GIFTPAC participants.

Major Accomplishments

This task has been completed. A stakeholder meeting was held and documented in a report submitted to the FAA. The stakeholders identified barriers to SAF production in Hawai'i and ranked the barriers in order of importance as follows:

1. Economic constraints (e.g., high costs of entry for production factors such as land) throughout the entire production chain.
2. Issues associated with access to capital, including high initial risks and uncertain returns on investment.
3. Insufficient government support in the form of incentives and favorable policies to encourage long-term private investment.
4. Cost, availability, and competition for water.
5. SAF production technologies (emerging but not yet demonstrated to have full commercial viability); and
6. Insufficient or inadequate infrastructure (e.g., harbors, roads, fuel distribution infrastructure, irrigation systems) to support the entire production chain.

Several of these barriers also arise at locations in the continental United States; however, those related to water and infrastructure are unique characteristics of an island state.

Publications

None.

Outreach Efforts

This activity engaged stakeholders to identify barriers to SAF production in Hawai'i. Preparation included reviewing stakeholder lists from previous activities. Facilitators appropriate to the stakeholder group were retained. The stakeholder meeting included a presentation of the scope and goals of the larger ASCENT program and other aspects of the UH ASCENT project.

Awards

None.

Student Involvement

None.

Plans for Next Period

None. This task is complete, but stakeholder outreach activities will continue under other tasks, as outlined below.

References

Hawai'i Natural Energy Institute. (n.d.). *Hawai'i Natural Energy Institute*. hnei.hawaii.edu

Task 2.1 – Inform Regional Supply Chains

University of Hawai'i

Objectives

To build on activities from fiscal year 2016, additional supporting analyses will be conducted for proposed supply chains in Hawai'i, including the following:



Task 2.1.1.
Support the Volpe and CAAFI Farm to Fly 2.0 supply chain analysis.

Task 2.1.2.
Use GIS-based estimates of fiber crop production potential to develop preliminary technical production estimates of jet fuel in Hawai‘i.

Task 2.1.3.
Develop fundamental property data for tropical biomass resources.

Task 2.1.4.
Transmit data and analysis results to support the improvement of existing tools (e.g., Policy Analysis System Model [POLYSYS]; https://bioenergykdf.net/content/polysys).

Research Approach

Task 2.1.2 has been conducted by using GIS data to identify areas suitable for purpose-grown crop production of feedstocks for SAF production in Hawai‘i. The approach has used GIS layers for land capability class (LCC), slope, and zoning as preliminary screens for suitability. Lands are classified by the Natural Resources Conservation Service with ratings from 1 to 6. LCCs 1–3 are generally suitable for agricultural production, LCC 4 can be productive with proper management, and LCCs 5 or 6 can support less intensive production and may be suitable for forestry. The slopes of terrains affect aspects of production, including mechanization and erodibility. An elevation GIS layer was used to derive a slope layer. Zoning layers were acquired from Hawai‘i state and county GIS offices. Only agricultural zoning was deemed suitable for this analysis.

The EcoCrop model was used to develop yield models for the crops selected in Task 1 according to annual rainfall and mean minimum monthly temperature data. EcoCrop includes model parameters on sugarcane, bana grass, five species of eucalyptus, *Gliricidia*, *Leucaena*, *Pongamia*, *Jatropha*, and sorghum. The parameters for sugarcane have been used to provide a base case assessment for comparison with historical sugarcane acreage and yield. Through sensitivity analysis, the model can be tuned to account for differences between parameters developed from global sugar production and a century of production experience in Hawai‘i that has been refined through plant breeding to adapt sugarcane varieties to a wide variety of agro-ecosystems. The analysis has purposely avoided land-use conflict with food production by limiting suitability to areas capable of sustaining AJF feedstocks under rain-fed conditions. Areas suitable for SAF production that do not conflict with current agricultural land use (i.e., fallow land) have also been identified.

Pongamia (*Millettia pinnata*) was the initial focus of Task 2.1.3. *Pongamia* is an oilseed-bearing leguminous tree with production potential in Hawai‘i and Florida. The tree produces pods containing oil-bearing seeds. Pods, oilseed cake, and oil were evaluated from trees growing on the island of O‘ahu. Fundamental measurements of chemical composition were conducted and reported. Torrefaction of pods as a coproduct in oil production has been conducted. An investigation of pretreatment methods to improve pod feedstock properties for thermochemical conversion applications has been completed.

Milestones

- Identified target opportunities to augment POLYSYS, the Alternative Fuel Transportation Optimization Tool (https://trid.trb.org/view/1376122), and conversion modules.
- Reviewed previously developed GIS information layers for tropical fiber crops and identified updating requirements.
- Conducted preliminary estimates of SAF technical potential in Hawai‘i, according to previously developed GIS information layers.

Major Accomplishments

The GIS-based analysis of SAF production potential is ongoing. The assessment of potential lands meeting the requirements for LCC, slope, and land-use zoning has been completed. The EcoCrop model was implemented to predict yield as a function of the minimum mean monthly temperature and annual rainfall. This process identified potential SAF feedstock crops for land areas capable of supporting their production under both rain-fed and irrigated conditions. This analysis provided information necessary for determining cropping patterns and assessing costs for transport to processing



facility locations. The EcoCrop model's prediction of sugarcane potential was determined, and the results were compared with historical sugarcane acreage, both rain-fed and irrigated. The EcoCrop's upper and lower values for temperature and rainfall that support optimal sugarcane production were varied to calibrate the prediction against historical acreage. The difference between the EcoCrop values and those representative of conditions in Hawai'i is attributable to improvements due to plant breeding and unique combinations of environmental conditions (e.g., the relatively young volcanic soils present in high-rainfall areas on the island of Hawai'i that enable high drainage rates and accommodate sugar production).

Calibration of the EcoCrop model using historical sugarcane planted acreages was completed in 2018. This effort used a confusion matrix approach for validation (resulting in a kappa value >0.4) and demonstrated that the mean annual temperature was a better indicator of environmental capability than the minimum mean monthly temperature recommended by the EcoCrop developers. This effort highlights the need to adapt models to local conditions. Model predictions for suitable cropping are being compared with current land uses to provide another indicator of agreement.

The GIS analysis of SAF feedstock production potential has been completed. Statewide working maps for each of the species have been summarized in a draft report currently undergoing internal review (Chan et al., draft). This report will serve as the basis for a journal article publication.

Dr. Curtis Daehler (UH, Department of Botany) has completed a report assessing the invasiveness of *Pongamia*. Retrospective analyses have shown that predictive weed risk assessment systems correctly identify many major pest plants, but their predictions are not 100% accurate. The purpose of this study was to collect field observations of *Pongamia* planted around O'ahu to identify direct evidence of *Pongamia* escaping from plantings and becoming an invasive weed. Seven field sites were visited in various environments across O'ahu. Although some *Pongamia* seedlings were found in the vicinity of some *Pongamia* plantings, particularly in wetter, partly shaded environments, almost all observed seedlings were restricted to areas directly beneath the canopies of mother trees. This finding suggests a lack of effective seed dispersal away from *Pongamia* plantings. According to its current behavior in the field, *Pongamia* is not invasive or established outside of cultivation on O'ahu. Because of its limited seed dispersal and low rates of seedling establishment beyond the canopy, the risk of *Pongamia* becoming invasive can be mitigated through monitoring and targeted control of any rare escapes in the vicinity of plantings. Because seeds and seed pods are dispersed by water, future risks of *Pongamia* escape and unwanted spread can be minimized by avoiding planting at sites near flowing water, near areas exposed to tides, or on or near steep slopes. Although vegetative spread by root suckers was not observed around plantings on O'ahu, monitoring for vegetative spread around plantations is recommended; unwanted vegetative spread might become a concern in the future that could be addressed with localized mechanical or chemical control.

Pods, oilseed cake, and oil have been evaluated from a number of trees growing on the island of O'ahu. TerViva,® a company pursuing *Pongamia* commercialization, provided material from orchards on O'ahu. Fundamental measurements of chemical composition were made for seeds, pods, extracted oil, and post-extraction seed material. The measured values included carbon, hydrogen, nitrogen, and sulfur elemental composition; energy content; volatile matter, fixed carbon, and ash content; and trace element composition. Oils were characterized by peroxide value, iodine value, fatty acid profile, free fatty acid content, flash point, density, viscosity, and phase transition temperatures. The chemical composition and fuel properties of the oilseed cake and the pod material were characterized. A manuscript summarizing the results of this effort has been published in the journal *ACS Omega* (Fu et al., 2021a).

Coproduct evaluation of *Pongamia* pod feedstock for thermochemical conversion has been conducted. Evaluation included both untreated pods and pods pretreated by a torrefaction process to improve their properties. Torrefaction produces a material with improved grindability, storage stability, diminished oxygen content, and microbial availability. The effects of process conditions on feedstock properties relevant to thermochemical conversion technologies, proximate and ultimate composition, heating value, and Hardgrove grindability index were measured. The chemical structure, reactivity, and changes in elemental composition of the torrefied materials were also investigated. A manuscript summarizing the results of this effort has been published in the journal *Fuel* (Fu et al., 2021b).

Pongamia seedpods are recognized as a potential feedstock for SAF production because of the relatively high oil content of the seeds. *Pongamia* pods are byproduct residues available after seed separation. Pods have high chlorine and potassium content that may be problematic in thermochemical energy conversion systems. Leaching experiments were performed to

® TerViva is a registered trademark of TerViva, Inc., Alameda, California.



remove inorganic constituents of the pods and thereby decrease the potential for fouling, slagging, and agglomeration. A manuscript summarizing the results of this effort has been published in the journal *Fuel* (Fu et al., 2021c).

The state tree of Hawai'i, *Aleurites moluccanus* (commonly known as kukui and candlenut), is an oil-nut-bearing tree frequently found in the tropics. Nuts from a number of these trees growing on the island of O'ahu were collected, and the nutshell, oilseed cake, and oil components were fractionated and analyzed for common properties necessary for designing SAF production systems. Results were published in the journal *ACS Omega* (Fu et al., 2023).

Publications

Peer-reviewed Journal Publications

Fu, J., Summers, S., Morgan, T. J., Turn, S. Q., & Kusch, W. (2021a). Fuel properties of pongamia (*Milletia pinnata*) seeds and pods grown in Hawaii. *ACS Omega*, *6*, 9222–9233. https://doi.org/10.1021/acsomega.1c00635

Fu, J., Summers, S., Turn, S. Q., & Kusch, W. (2021b). Upgraded pongamia pod via torrefaction for the production of bioenergy. *Fuel, 291,* 120260. https://doi.org/10.1016/j.fuel.2021.120260

Fu, J., Allen, G., Weber, S., Turn, S. Q., & Kusch, W. (2021c). Water leaching for improving fuel properties of pongamia pod: Informing process design. *Fuel, 305,* 121480. https://doi.org/10.1016/j.fuel.2021.121480

Fu, J., Weber, S., & Turn. S. Q. (2023). Comprehensive characterization of kukui nuts as feedstock for energy production in Hawai'i. *ACS Omega, 8*(25), 22567-22574. https://doi.org/10.1021/acsomega.3c00860

Written Report

Chan, S., Ogoshi, R. & Turn, S. (2024, draft*). Feedstocks for sustainable jet fuel production: An assessment of land suitability in Hawaii*. A draft report has been prepared, and a draft manuscript is under preparation for publication.

Outreach Efforts

Outreach in this task has focused on interactions with TerViva, a startup company, which has identified *Pongamia* germplasm production and marketing as the central focus of its business plan.

Chan, S., Ogoshi, R. & Turn, S. (2020, July 6-9). *Feedstocks for Sustainable Jet Fuel Production: An Assessment of Land Suitability in Hawaii* [Poster presentation]. 28th European Biomass Conference & Exhibition, Virtual.

Fu, J., Summers, S. & Turn, S. (2020, October 5-7). *Upgraded Millettia Pinnata Pod via Torrefaction for the Production of Bioenergy in Hawai'i* [Oral presentation]. 2020 Thermal & Catalytic Sciences Virtual Symposium, Virtual.

Turn, S. (2019, December 3). *Regional Supply Chain Analysis for Alternative Jet Fuel Production in the Tropics* [Poster presentation]. Hawai'i Aviation and Climate Action Summit, Honolulu, Hawai'i.

Fu, J., Allen, G., Weber, S., Turn, S. Q., & Kusch, W. (2021, August 22-26). *Water Leaching for Improving Fuel Properties of Pongamia Pods* [Oral and Virtual presentation]. American Chemical Society Fall 2021 National Meeting, Atlanta, Georgia.

Fu, J., Summers, S. & Turn, S. (2021, April 5-16). *Upgraded Millettia Pinnata Pod via Torrefaction for the Production of Bioenergy in Hawai'i* [virtual and oral presentation]. American Chemical Society Spring 2021 National Meeting, Virtual.

Fu, J., Weber, S. & Turn, S. (2022, August 21-25). *Comprehensive Characterization of Kukui Nuts for Bioenergy Production in Hawaii* [Oral presentation]. American Chemical Society Fall 2022 National Meeting & Exposition, Chicago, Illinois.

Awards

A poster entitled "Feedstocks for Sustainable Jet Fuel Production: An Assessment of Land Suitability in Hawai'i" (Chan et al., 2020) was presented at the European Biomass Conference & Exhibition held virtually on July 6–9, 2020, and received the Best Visual Presentation Award.

Student Involvement

Three undergraduate students are involved in the project. Their primary responsibility is processing and analyzing samples of biomass materials selected for evaluation as potential SAF feedstocks. The *Pongamia* torrefaction work was the focus of an Undergraduate Research Opportunity Program project for Sabrina Summers, a bioengineering and chemistry double major. The results of her work were presented at the American Chemical Society Fall 2019 National Meeting in San Diego,



California. The *Pongamia* pod leaching work was the focus of an Undergraduate Research Opportunity Program project for Gabriel Allen, a biochemistry major.

Plans for Next Period
None. This task is complete.

Task 2.2 – Support Indonesian AJF Supply Initiatives
University of Hawai'i

Objective
This task supports the memorandum of understanding between the FAA and Indonesian Directorate of General Civil Aviation to promote the development and use of sustainable alternative aviation fuels. Under the coordination of the FAA, efforts to establish points of contact and coordinate with Indonesian counterparts are ongoing.

Research Approach
To begin this process, the team will work with FAA to establish points of contact to coordinate efforts with Indonesian counterparts. Members of the Indonesian Aviation Biofuels and Renewable Energy Task Force include Universitas Indonesia, Institut Teknologi Bandung, and Universitas Padjadjaran. A prioritized list of tasks will be developed in consultation with Indonesian counterparts, and data required to inform sustainability and supply analyses, and potential sources of information will be identified. The information collected may include Indonesian jet fuel use and resources for SAF production, airport locations, and annual and monthly jet fuel consumption patterns. Characterization of sustainable biomass resources with potential for use in producing SAF supplies may include developing preliminary GIS mapping information of their locations and distributions, and preliminary estimates of their technical potential.

Milestones
- Identify points of contact at Indonesian universities participating in the Aviation Biofuels and Renewable Energy Task Force.
- Identify research needs and develop a project plan.
- Develop data for potential projects.

Major Accomplishments
The P.I. traveled to Jakarta, Indonesia, in the first week of August 2017 and met with the following individuals:
- Cesar Velarde Catolfi-Salvoni (International Civil Aviation Organization [ICAO])
- Dr. Wendy Aritenang (ICAO)
- Dr. Ridwan Rachmat (Head of Research Collaboration, Indonesian Agency for Agricultural Research and Development)
- Sylvia Ayu Bethari (Head of Aviation Fuel Physical and Chemical Laboratory, Research and Development Centre for Oil and Gas Technology)
- Dr. Ina Winarni (Forest Product Research and Development Center, Ministry of Environment and Forestry)
- Dr. SD Sumbogo Murti (Center of Technology Energy Resources and Chemical Industry, Agency for the Assessment and Application of Technology)

The activities of the tropical supply chain analysis effort were presented to the group, and a general discussion followed. From this introductory meeting, it was concluded that the Indonesian counterparts would seek agreement on how to move forward with future cooperation.

In November 2018, the P.I. traveled to Jakarta, Indonesia, and met with Dr. Wendy Aritenang of the ICAO Jakarta office. The same trip included meetings with renewable energy researchers at Universitas Indonesia. After the meeting, Dr. Aritenang suggested several points of contact for future engagement: Frisda Panjaitan from the Palm Oil Research Institute and Tatang Soerawidjaja, Tirto Prakoso Brodjonegoro, and Imam Reksowardojo from the Bandung Institute of Technology.

In October 2022, the P.I. traveled to Jakarta, Indonesia, and met with Dr. Wendy Aritenang. The following day, the P.I. and Dr. Aritenang traveled to Bandung, West Java, Indonesia, to visit the Bandung Institute of Technology and met with faculty



members Professor Adiwan Aritenang (Department Head of Regional Planning) and Professors Tatang Soerawidjaja, Tirto Prakoso Brodjonegoro, and Iman Reksowardojo, from the Faculty of Industrial Technology, Bandung Institute of Technology. Ongoing UH ASCENT activities were presented, and the Bandung Institute of Technology researchers discussed their SAF-related research efforts.

Publications
None.

Outreach Efforts
Outreach efforts by the P.I. are described in the Major Accomplishments section above. In addition, the P.I. participated in the Asia Pacific Economic Cooperation event, "Energy Transition toward Carbon Neutrality, APEC BCG Economy Thailand 2022: Tech to Biz," in Bangkok, Thailand, and gave an oral presentation entitled "US Initiatives on Sustainable Aviation Fuel."

Awards
None.

Student Involvement
None.

Plans for Next Period
None. This task is complete.

Task 3.1 – National Lipid Supply Availability Analysis
University of Hawai'i

Objective
The objective of this task is for the ASCENT Project 001 team to provide support to ASCENT partners working on a national lipid supply availability analysis by sharing data on tropical oilseed availability developed under previous years' activities.

Research Approach
This support will include estimates of *Pongamia* production capability in the state of Hawai'i, in addition to assessments of waste cooking oil and tallow.

Milestones
Milestones will coincide with the schedule of the lead institution (WSU) for the national lipid supply analysis.

Major Accomplishments
Additional seeds and pods were collected from the *Pongamia* trees on the UH campus, Foster Botanical Garden, and Ke'ehi Lagoon Beach Park. Large quantities (tens of kilograms) of material were acquired from TerViva's plantings on the O'ahu North Shore for use in oil evaluation. Two oilseed presses were acquired, and safety documents were developed. Pods, oilseed cake, and oil were evaluated from a number of trees growing on the island of O'ahu. Fundamental measurements of chemical composition were made for seeds, pods, extracted oil, and post-extraction seed material. The measured values included carbon, hydrogen, nitrogen, and sulfur elemental composition; energy content; volatile matter, fixed carbon, and ash content; and trace element composition. Oils were characterized by peroxide value, iodine value, fatty acid profile, free fatty acid content, flash point, density, viscosity, and phase transition temperatures. The development of coproducts from pods and oilseed cake was explored.

Areas in Hawai'i with agricultural zoning suitable for rain-fed production of *Pongamia* have been identified. Conflicts with the current agricultural land use have been identified.

The waste oil resources in Hawai'i are estimated to be on the order of 2 to 3 million gallons per year, according to the de facto population, and are directed to biodiesel production.



Publications

Peer-reviewed Journal Publication

Fu, J., Summers, S., Morgan, T. J., Turn, S. Q., & Kusch, W. (2021). Fuel properties of pongamia (*Milletia pinnata*) seeds and pods grown in Hawaii. *ACS Omega, 6*(13), 9222–9233. https://doi.org/10.1021/acsomega.1c00635

Outreach Efforts

Data were presented at the April 2019 ASCENT review meeting in Atlanta, Georgia.

Awards

None.

Student Involvement

Three undergraduate students (Sabrina Summers, Sarah Weber, and Taha Elwir) are involved in the project. Their primary responsibility is processing and analyzing samples of biomass materials selected for evaluation as potential SAF feedstocks.

Plans for Next Period

None. This task is complete. Results will underpin future tasks.

Task 3.2 – Hawai‘i Regional Project

University of Hawai‘i

Objectives

A supply chain based on fiber feedstocks transported to a conversion facility located at the Campbell Industrial Park (CIP) on O‘ahu will be evaluated (Figure 1). The CIP is the current site of two oil refineries. C&D wood waste from the PVT Land Company™’s landfill could provide a primary source of feedstock. Other sources will be evaluated from elsewhere on O‘ahu and outer islands, including municipal solid waste streams from outer islands and mining of current waste-in-place stocks. Waste streams and purpose-grown crops form the basis of a hub-and-spoke supply system, with the hub located on O‘ahu. Pipelines for jet fuel transport are in place from CIP to Daniel K. Inouye International Airport and the adjacent Joint Base Pearl Harbor-Hickam. Other coproduct offtakers for alternative diesel fuel include the Hawaiian Electric Company and several military bases, including Schofield Barracks (~50-megawatt alternative fuel-capable power plant under development) and Marine Corps Base Hawai‘i located in Kaneohe Bay. Hawai‘i Gas,® a local gas utility, is also seeking alternative sources of methane if methane or feedstock suitable for methane production is available as a coproduct. Hawai‘i Gas currently offtakes feedstock (naphtha) from the refinery.

™ PVT Land Company is a trademark of PVT Land Company LTD., Nanakuli, Hawai‘i.
® Hawai‘i Gas is a registered trademark of The Gas Company, LLC, Honolulu, Hawai‘i.



Figure 1. Possible Locations of Value Chain Participants for a Fiber-Based Alternative Jet Fuel Production Facility at the Campbell Industrial Park, O'ahu.

Research Approach

Task 3.2.G1. Analyze Feedstock-conversion-pathway Efficiency, Product Slate (including coproducts), and Maturation
To build on activities from previous years, additional supporting analyses will be conducted for proposed supply chains in Hawai'i, as follows:

- Subtask 3.2.G1.1. Assess feedstock suitability for conversion processes (e.g., characterization, conversion efficiencies, and contaminants) (UH and WSU [Manuel Garcia-Perez])
- Subtask 3.2.G1.2. Acquire data on feedstock size reduction, particle size of materials, and bulk densities (UH, WSU [Manuel Garcia-Perez])
- Subtask 3.2.G1.3. Evaluate coproducts at every step of the supply chain (ASCENT Project 001 team)

Task 3.2.G2. Assess the Scope of Techno-Economic Analysis (TEA) Issues
This task will determine the current TEA status of targeted SAF production technologies that use fiber feedstocks as production inputs (UH, WSU [Manuel Garcia-Perez], Purdue University [Wally Tyner]).



Task 3.2.G3. Conduct a Screening-level GHG Life-Cycle Assessment (LCA)
This task will conduct screening-level GHG LCA on the proposed target supply chains and SAF conversion technologies.
Subtasks:

- Subtask 3.2.G3.1. Assess Massachusetts Institute of Technology (MIT) waste-based GHG LCA tools in the context of application to Hawai'i (MIT [Mark Staples])
- Subtask 3.2.G3.2. Assess requirements to link previously completed eucalyptus energy and GHG analysis to the edge of the plantation with available GHG LCA information for conversion technology options (MIT [Mark Staples], UH)
- Subtask 3.2.G3.3. Identify and fill information/data gaps

Task 3.2.G4. Identify Supply Chain Participants/Partners
Subtasks:

- Subtask 3.2.G4.1. Define C&D landfill case
- Subtask 3.2.G4.2. Identify eucalyptus in existing plantations, landowners, leaseholders/feedstock producers, harvesting contractors, truckers, etc. (UH)
- Subtask 3.2.G4.3. Define other feedstock systems as identified (ASCENT Project 001 team)

Task 3.2.G5. Develop an Appropriate Stakeholder Engagement Plan
Subtasks:

- Subtask 3.2.G5.1. Review stakeholder engagement methods and plans from past work to establish baseline methods (UH, WSU [Season Hoard])
- Subtask 3.2.G5.2. Identify and update engagement strategies according to the updated Community Social Asset Modeling/Outreach support tool (UH, WSU [Season Hoard])

Task 3.2.G6. Identify and Engage Stakeholders
Subtasks:

- Subtask 3.2.G6.1. Identify stakeholders along the value chain and create a database based on value chain location (UH)
- Subtask 3.2.G6.2. Conduct a stakeholder meeting by using the instruments developed in Task 3.2.G5 (UH, WSU [Season Hoard])
- Subtask 3.2.G6.3. Analyze stakeholder response and feedback to the process (UH, WSU [Season Hoard])

Task 3.2.G7. Acquire Transportation-network and Other Regional Data Needed for the Freight and Fuel Transportation Optimization Tool and Other Modeling Efforts
Subtasks:

- Subtask 3.2.G7.1. Acquire necessary data to evaluate harbor capacities and current usage (UH, Volpe [Kristin Lewis], WSU [Michael Wolcott])
- Subtask 3.2.G7.2. Acquire data on inter-island transport practices (UH, Volpe [Kristin Lewis], WSU [Michael Wolcott])

Task 3.2.G8. Evaluate Infrastructure Availability
Subtasks:

- Subtask 3.2.G8.1. Evaluate inter-island shipping options and applicable regulation (UH, Volpe [Kristin Lewis], WSU [Michael Wolcott])
- Subtask 3.2.G8.2. Evaluate transport or conveyance options from conversion location to end users and applicable regulation (UH, Volpe [Kristin Lewis], WSU [Michael Wolcott])

Task 3.2.G9. Evaluate Feedstock Availability
Subtasks:

- Subtask 3.2.G9.1. Refine ground-truth prior evaluations of options for purpose-grown feedstock supply (UH)
- Subtask 3.2.G9.2. Conduct projections of future C&D waste supply and mining of waste-in-place on O'ahu, municipal solid waste, and mining of waste-in-place on other islands (UH)

Task 3.2.G10. Develop a Regional Proposal
This task will use the information collected in Tasks 3.2.G1–3.2.G9 to develop a regional project proposal.



Milestone
A single milestone is associated with each of the subtask activities identified in the Research Approach section above.

Major Accomplishments
The characteristics of the feedstock generated at the landfill have been determined and summarized in a publication (Bach et al., 2021).

The elemental compositions of feedstock materials have been used as the basis for equilibrium analysis of gasification systems using oxygen, steam, and steam–oxygen mixtures to inform process design.

The material flows relevant to the screening-level GHG analysis of C&D waste as SAF feedstock have been assembled. Preliminary discussions of GHG analysis of C&D-based SAF systems with landfill operators have been initiated.

The plans for solid waste management from all counties in Hawai‘i have been used to provide a broader picture of the waste stream composition, diversion, recycling practices, and planned uses.

Publications
Peer-reviewed Journal Publications

Bach, Q. V., Fu, J., & Turn, S. (2021). Construction and demolition waste-derived feedstock: fuel characterization of a potential resource for sustainable aviation fuels production. *Frontiers in Energy Research, 9,* 711808. https://doi.org/10.3389/fenrg.2021.711808

Bach, Q. V. & Turn, S. (2024, draft). *Fate of arsenic and other inorganic elements during gasification of construction and demolition wastes – thermochemical equilibrium calculations.* Draft manuscript in process.

Outreach Efforts
Results of the fuel sampling, fuel analyses, and gasification equilibrium analyses were presented at the October ThermoChemical Biomass 2019 Conference in Chicago, Illinois.

Information from this task was included in the talk “Regional Supply Chain Analysis for Alternative Jet Fuel Production in the Tropics” presented at the Hawai‘i Aviation and Climate Action Summit, December 3, 2019, at the Hawai‘i State Capitol, Honolulu, Hawai‘i.

Data acquired under this task were presented to the management of PVT Land Company and their consultants from Simonpietri Enterprises and T. R. Miles Technical Consultants, Inc.

A poster entitled “Construction and Demolition Waste as an Alternative Energy Source: Fuel Characterization and Ash Fusion Properties” was presented at the 2020 Thermal & Catalytic Sciences Virtual Symposium.

Discussion with Dr. Kristin Lewis and Volpe staff on the addition of Hawai‘i transportation infrastructure to the Freight and Fuel Transportation Optimization Tool was initiated and deferred until a clearer definition of the system emerges.

As suggested by FAA management, UH worked with the Servicios y Estudios para la Navegación Aérea y la Seguridad Aeronáutica (SENASA) to identify a counterpart university in the Canary Islands, Spain. Universidad de la Laguna (ULL) was selected, and a memorandum of understanding was signed between UH and ULL. A nondisclosure agreement was subsequently signed among SENASA, ULL, UH, and the Spanish company Abengoa Energía, S.A. Regularly scheduled meetings have been held biannually with Professor Dr. Ricardo Guerrero Lemus from ULL to discuss common research themes and were continued in 2023.

Awards
None.

Student Involvement
Three undergraduate students (Sabrina Summers, Sarah Weber, and Taha Elwir) have been involved in sample preparation and in operating the laboratory analytical equipment used for sample analysis.



Plans for Next Period

Manuscripts covering the prediction of gasification product streams including contaminant concentrations will be completed and submitted. Comparative data from bench-scale gasification tests (see Task 4) at ThermoChem Recovery International facilities were received in October 2023. These data will be supplemented with the results of C&D waste sample analyses using a differential thermal analyzer paired with an inductively coupled plasma mass spectrometer (DTA-ICPMS) to provide information on the release of inorganic elements as a function of temperature. Contracting for DTA-ICPMS analytical services at the University of California, Davis, Interdisciplinary Center for Plasma Mass Spectrometry was completed in 2025. With these experimental data, the manuscripts will be completed. Note: Although this was anticipated to be completed in 2025, computer/software issues with the DTA-ICPMS have delayed the analysis and thus the manuscript preparation and the completion of this task. When these data become available, the results from Tasks 3, 4, and 5.2 will be summarized in a combined manuscript. Otherwise, this task is complete.

References

Bach, Q. V., Fu, J., & Turn, S. (2021). Construction and demolition waste-derived feedstock: fuel characterization of a potential resource for sustainable aviation fuels production. *Frontiers in Energy Research, 9,* 711808. https://doi.org/10.3389/fenrg.2021.711808

Task 4 – Hawai‘i Regional Project

University of Hawai‘i

Objective

This task builds upon results from the previous years' work under the Hawai‘i Regional Project, with a focus on the data and analysis necessary to plan a project that uses C&D waste as feedstock for SAF production. The Task 4 objective is to use C&D feedstock characterization data and thermochemical equilibrium analysis from the previous years to conduct bench-scale gasification tests and to quantify the product gas yield, composition, and contaminant concentrations. These results will be compared with equilibrium prediction used to identify contaminants that must be addressed before end use and will provide the basis for designing contaminant control systems.

Research Approach

Bench-scale gasification tests will be conducted on samples of C&D wastes characterized in the earlier tasks, to measure product yields, identify contaminants, and investigate element partitioning between product phases.

The information gained from the tests will be used to identify opportunities to improve TEA, identify co-products, inform supply chain participants and stakeholders, and identify necessary infrastructure improvements.

Milestones

- Identify and evaluate capabilities of experimental bench-scale facilities for gasifier tests.
- Specify system performance parameters to be measured.
- Specify techniques to sample and analyze contaminants.
- Select and engage an experimental bench-scale facility for testing.
- Prepare and ship feedstock from Hawai‘i to the experimental test facility.
- Conduct tests, reduce data, and prepare a summary report of the results.

Major Accomplishments

Operational measurements to be conducted as part of the bench-scale tests were summarized, and a test plan was developed; these were used as the basis for entertaining proposals for test services.

Through a competitively structured proposal process, ThermoChem Recovery International, Inc., was engaged to provide bench-scale test services for C&D waste feedstock and other opportunity fuels of relevance to Hawai‘i and the tropics.

A synthetic C&D waste recipe was developed according to the results published in the journal *Frontiers in Energy Research* (Bach et al., 2021). Component fractions in the recipe were determined by a least-squares approach to matching critical fuel characteristics, including volatile matter, fixed carbon, and ash content; higher heating value; and concentrations of



the elements Na, Mg, Al, Si, P, S, Cl, K, Ca, Ti, Cr, Mn, Fe, Cu, Zn, As, Ru, and Pb. This recipe will enable a reproducible C&D waste fuel lot to be assembled and will aid in decreasing test-to-test variability.

In November and December 2021, tests were conducted in the bench-scale facility at the ThermoChem Recovery International facility in Durham, North Carolina. After shakedown testing was completed, two subsequent tests were conducted: (1) a test using *Leucaena leucocephela* stemwood, and (2) a test using synthetic C&D waste. Test reports for the two bench-scale gasification tests at ThermoChem Recovery International facilities were finalized in October 2023.

Publications

Peer-reviewed Journal Publication

Bach, Q. V., Fu, J., & Turn, S. (2021). Construction and demolition waste-derived feedstock: fuel characterization of a potential resource for sustainable aviation fuels production. *Frontiers in Energy Research, 9,* 711808. https://doi.org/10.3389/fenrg.2021.711808

Outreach Efforts

A presentation entitled "Hawai'i Energy Crop and Urban Waste Feedstock Updates" was presented at the ASCENT Spring Meeting in Honolulu, Hawai'i.

Awards

None.

Student Involvement

None.

Plans for Next Period

Results from Tasks 3, 4, and 5.2 will be summarized in a combined manuscript. Otherwise, this task is complete.

Task 5 – Hawai'i Regional Project

University of Hawai'i

Objective

Task 5.1: Tropical Oil-to-SAF Supply Chain Analysis

The objective of this task is to develop a model for tropical oil supply chains for SAF and associated coproducts. Hawai'i will be the initial focus, but the modeling tools will be developed for wider use in island settings.

Task 5.2: Contaminants in the Gasification of C&D waste

The objective of this task is to develop management strategies for elements present in C&D waste that affect its use as a feedstock for thermochemical conversion.

Research Approach

Task 5.1

Prior ASCENT EcoCrop GIS modeling activities identified the growing locations for *Pongamia*, kamani, croton, and *Jatropha*, according to suitable environmental conditions, geography, and zoning. If unavailable, the primary data on the chemical and physical characteristics of these tropical oils and their coproducts (e.g., pods/shell and oilseed cake) were acquired. The project will use these earlier results as the basis for developing supply chain models for AJF production. The model results will identify feedstock production areas as well as locations and scales of primary processing sites for shell and pod separation, oil extraction from seeds, and oil conversion to SAF. Potential sources of hydrogen from oilseed coproducts, other renewable resources, and fossil sources will be analyzed and included in the model. Options for points of production, SAF production technologies (e.g., Applied Research Associates® [ARA], SBI BioEnergy, Inc.® [SBI], or FORGE

® Applied Research Associates is a registered trademark of Applied Research Associates, Inc., Albuquerque, New Mexico.
® SBI BioEnergy, Inc. is a registered trademark of SBI BioEnergy, Inc., Edmonton, Alberta, Canada.



Hydrocarbons™ [Forge]), transportation strategies, and blend ratios at airports (or for specific end users, e.g., the military) across Hawai'i will affect model outcomes and will be evaluated. Options for co-products such as animal feeds and high-value materials will be evaluated and incorporated into the model decision-making process. Criteria used to drive the model solution might include minimizing SAF production costs while meeting a minimum total production benchmark or a minimum blending rate for annual state jet fuel consumption. Other criteria, such as system resiliency to extreme weather events and climate change, provision of environmental services, and stakeholder acceptability, will also be of importance and will be used to evaluate model solutions.

Task 5.2
Thermochemical gasification of biorenewable resources is the initial conversion process for two entry points to AJF production: (1) synthesis gas used in the direct production of Fischer–Tropsch (FT) liquids, and/or (2) green/renewable hydrogen used in biorefineries for hydrotreating lipids or in existing petroleum-refining activities for the production of hybrid jet fuel. Urban wood waste from C&D activities provides a reliable source of biorenewable material and requires a tipping fee for disposal, characteristics that enhance its attractiveness as feedstock. The negative aspects of C&D feedstock are its physical and chemical inhomogeneity. In the latter case, the inorganic elements present in the feedstock can negatively influence the gasification process (e.g., corrosion of, or accumulation on, reactor working surfaces, bed material agglomeration, catalyst deactivation, or pollutant emissions). Using data generated from previous ASCENT Project 001 tasks, this project will assess methods for managing contaminants in C&D feedstocks. This project will be based on gasification systems proposed for the production of synthesis gas/FT liquids and green hydrogen. The technology options for contaminant removal or conversion to benign forms will be assessed at each step in the conversion process, including presorting at the waste generation site, sorting/diversion at the C&D waste intake facility, removal by physical/chemical/other methods before gasification, in-situ reactor control methods, and gas cleanup. The technology options based on existing process industries and the scientific literature will be considered. Laboratory-scale testing of removal techniques will be conducted to provide a preliminary assessment of selected promising technology options. The integrated gasification process options and contaminant control options will be evaluated as complete systems to guide system design and to enable system comparisons. The risks associated with technology options will also be assessed to guide implementation and risk mitigation of the system as a whole. The impacts of processing scale (e.g., Mg waste/day) on the selection of technology options will also be assessed.

Milestones

Task 5.1.
A model framework was established for an oilseed-based SAF supply chain in an island setting, using the scenario of Hawai'i.

Task 5.2.
A review of options for managing contaminants along the supply chain was completed, and bench-scale tests to confirm the efficacy of options were conducted.

Major Accomplishments

On the basis of the *Pongamia* production areas identified by GIS analysis in Task 3 (described above), sites for processing *Pongamia* (pod and seed separation, oil extraction from seed) have been evaluated on each island. Candidate processing sites in the analysis included (a) brownfield sites with industrial zoning and (b) greenfield sites identified as lands with a slope of less than 5%, a contiguous area of 50 hectares, and agricultural zoning. The ArcGIS® "minimized impedance" and "origin-destination" analysis tools were used to determine transportation cost index values for all potential processing facility locations, using the *Pongamia* production estimates and the road network distances from production sites to candidate processing sites. Analyses were performed for each island and included four *Pongamia* production scenarios.

A cost of production analysis for *Pongamia* based on a 25-year orchard lifetime was completed. As *Pongamia* has not been grown commercially in Hawai'i, the analysis included assumptions about the cultural practices and input application rates. The analysis was summarized and shared with stakeholders and subject matter experts for review and comment. Feedback has been incorporated. Analysis has been extended to project a pathway for industry development, assuming values for the number of trees planted per year and their cumulative productivity. The production scenarios are being used to

™ FORGE Hydrocarbons is a trademark of FORGE Hydrocarbons Corporation, Oakville, Ontario, Canada.
® ArcGIS is a registered trademark of ERSI, Redlands, California.



explore processing facility scales and technology options that include the unit operations of drying, decortication, oil extraction, and distribution of oil and meal components to the refinery on O'ahu and animal feeding locations across Hawai'i, respectively. Discussions with equipment vendors for drying, decortication, and oil extraction equipment have provided the basis for cost estimates for each of the processing steps. The Hawai'i Public Utilities Commission (PUC) regulates property motor carriers, and this includes the transport of agricultural products. Property carriers are classified by the types of commodities transported and the nature of services performed. Motor carrier tariffs published by the PUC were surveyed on each island and hourly, distance, zone-to-zone, and commodity-based rates were compiled to estimate transport costs of harvested seed pods and extracted oil. Costs for interisland shipping of extracted oil in bulk isotainers were compiled. Costs for pongamia production and processing on Hawai'i island with resulting oil transported and landed on O'ahu totaled $2,083 per Mg of pongamia oil.

In an earlier review, camelina (*Camelina sativa*) was not previously identified as a candidate oil seed crop for production in Hawai'i but is nonetheless being pursued as a cover crop in rotation with food crops such as onions, lettuce, etc. In response to interest in producing camelina, UH developed new GIS analysis approaches to evaluate potential production areas. Unlike annual and perennial crops, camelina matures in approximately 90 days requiring that the growing season be matched to shorter time windows of temperature and rainfall availability. Hawai'i's varied climates, both geographically and seasonally, would require intensive management if grown under rainfed conditions and could require shifting production locations throughout the year. Use of camelina as a cover crop with irrigated food production could alleviate the need to match the plant growth requirements with monthly rainfall. Results of the UH analysis have been used by Pono Pacific to target production areas, engage growers for planting camelina trials, and discuss policy with state executive and legislative branches. The analysis also underpinned a proposal to the U.S. Department of Energy program, Regional Resource Hubs for Purpose-Grown Energy Crops with Pono Pacific and Hawai'i Agriculture Research Center.

Kukui (*Aleurites moluccanus*) is the Hawai'i State tree and bears a nut whose kernel contains 60% extractable oils. Previous work has characterized the fuel properties of the oil, meal, and nut fractions. Kukui is extensively distributed across the Hawai'i landscape zoned for conservation, but little has been done to explore agricultural zoning areas suitable for production. A GIS-based assessment of kukui production using the Eco-Crop model has been initiated.

Elemental analyses of C&D waste from earlier tasks were used as inputs for the thermochemical equilibrium calculation in FACTSage™ 8.0 under different gasification conditions (e.g., bed material, oxidizer, etc.). The results show that the predictions of hydrogen gas (H_2), carbon monoxide (CO), and carbon dioxide (CO_2) in product gas are in good agreement with literature data. In addition, gasification in steam yields the highest H_2 content while that in oxygen yields the lowest. The elements As, Br, Cl, K, Mn, Mo, Na, Pb, S, and Zn were found in the gas phase at different concentrations depending on the feedstock composition and gasification conditions. Some elements (Br, Cl, K, Pb, and Zn) appear to be more volatile than others (As, Na, and S). The elements Ca, Si, P, Ti, Cr, Fe, Ni, Cu, Sr, Ru, and Ba were primarily presented in solid and/or slag phases. Olivine bed material captured a portion of arsenic during the gasification process due to the presence of nickel in its chemical composition. Arsenic species in the product gas stream are predicted to deactivate Fe- and Co-based FT catalysts in downstream processes. It is possible to remove arsenic compounds by cooling hot product gas; however, cooling may also result in the condensation of high molecular weight organic compounds (tar). Copper and nickel can be employed as arsenic sorbents with sorptive capacity directly linked to the metals' mass.

Publications

None.

Outreach Efforts

The results of feedstock analyses have been regularly shared with personnel from Par Hawai'i, the refinery located on the island of O'ahu, and with Pono Pacific, a land management company engaged in sustainable agricultural development. Par Hawai'i has announced plans to produce SAF in partnership with Hawaiian Airlines. Pono Pacific is pursuing oilseed production to supply Par Hawai'i with lipids for SAF production via the production pathway for hydroprocessed esters and fatty acids. Mitsubishi Corporation (Americas) personnel interested in SAF-related investment opportunities in Hawai'i have

™ FactSage is a trademark of Thermfact/CRCT, Montreal, Canada, and GTT-Technologies, Aachen, Germany. FactSage is a thermochemical software and database package developed jointly between Thermfact/CRCT (Montreal, Canada; www.crct.polymtl.ca) and GTT-Technologies (Aachen, Germany; www.gtt-technologies.de) and is the result of over 30 years of collaborative efforts. The FactSage web site is www.factsage.com.



requested briefings on oil seed opportunities. Outreach has also included staff from the Hawai'i State Energy Office's Energy Efficiency and Renewable Energy (EERE) branch and Decarbonization Program.

A presentation entitled "Hawai'i Energy Crop and Urban Waste Feedstock Updates" was presented at the ASCENT Spring 2024 Meeting in Honolulu, Hawai'i.

A poster entitled "Thermochemical Equilibrium Prediction of Ash Behavior during Gasification of Construction and Demolition Waste" was presented at the conference TC Biomass: The International Conference on Thermochemical Conversion Science: Biomass & Municipal Solid Waste to RNG, Biofuels & Chemicals on September 10–12, 2024, in Itasca, Illinois.

A poster entitled "Alternative Jet Fuel Supply Chain Tropical Region Analysis, Pongamia Supply Chain Optimization" was presented at the ASCENT Fall 2024 Meeting in Alexandria, Virginia.

A presentation entitled "Hawai'i Energy Crop Updates" was presented at the ASCENT Spring 2025 Meeting in Knoxville, Tennessee.

The project principal investigator participated in the Hawai'i State Energy Office's Biofuels Working Group and the Hawai'i Energy Policy Forum. Both groups engage Hawaii energy stakeholders and SAF is an active topic.

Awards
None.

Student Involvement
None.

Plans for Next Period
Task 5.1
Results from this task will be summarized in a manuscript, otherwise this task is complete.

Task 5.2
Results from Tasks 3, 4, and 5.2 will be summarized in a combined manuscript, otherwise this task is complete.

Task 6 – Hawai'i Regional Project
University of Hawai'i

Objective
The task activities in Year 6 will explore the impacts of Hawai'i State Legislative Bill HB2386 on waste management and the potential for waste-based SAF production systems. HB2386 requires 0.5-mile buffer zones around waste and disposal facilities (including landfills) and restricts facilities from land with conservation-district zoning.

Research Approach
The goal of this task is to assess and evaluate the impacts of HB2386 on waste management strategies in Hawai'i. HB2386 was disruptive to disposal practices for C&D waste on the island of O'ahu, and its impacts are currently not fully understood. The aims of Task 6 are to collect updated waste generation data, elucidate how HB2386 will affect current management strategies, and develop scenarios for waste-based SAF production under the new regulatory environment. The impacts of HB2386 on the capacity to perform landfill mining will also be considered. A preliminary assessment of restricted and unrestricted sites for waste and disposal facilities will be reviewed and refined, as necessary.

Milestone
Evaluated the impacts of removing or diminishing the role of an active C&D landfill as a supply chain participant.



Major Accomplishments

An assessment of available data on urban waste flows across the state has been completed. Sources have included county solid waste management plans, annual reports by county solid waste management offices, and annual legislative reports prepared by the state solid and hazardous waste management branch. Based on these data, estimates of solid waste production across the state have been assembled. Waste composition data available at the county level have been used to generate production estimates of combustible and noncombustible fractions as well as biogenic and nonbiogenic fractions. The enactment of HB2386 has restricted expansion of the existing C&D landfill on Oʻahu and delayed the siting of new landfills on the islands of Oʻahu and Kauaʻi. Six scenarios for managing waste across the state as an integrated system have been developed. Three of the scenarios split the waste resource between the existing Covanta Honolulu Resource Recovery Venture (H-POWER) waste to an energy plant on Oʻahu and a waste-to-SAF production plant using gasification and FT technology. The other three scenarios assume that the H-POWER waste-to-energy plant is decommissioned and all of the state's waste is delivered to a larger SAF production facility. Diverting food waste and plastics from the waste streams were also included as scenario options; food waste has alternative use as animal feed or for anaerobic digestion feedstock and plastics are nonbiogenic. Estimates of production potential from the six waste utilization scenarios were completed. Scenarios where H-POWER was decommissioned yielded the highest SAF production values ranging from 38 to 45 million gallons annually. Diverting food waste and plastics from the material fueling the SAF process accounts for the difference of 7 million gallons per year. The scenario with the lowest SAF production potential, 18 million gallons per year, was the result of diverting waste to H-POWER and excluding both food waste and plastics.

Publications

None.

Outreach Efforts

A poster entitled "Municipal Solid Waste (MSW)-based SAF (Alternative Jet Fuel Supply Chain Tropical Region Analysis)" was presented at the ASCENT Fall review meetings (2024 and 2025) in Alexandria, Virginia.

Awards

None.

Student Involvement

None.

Plans for Next Period

Results from Tasks 6 and 8 will be summarized in a manuscript, otherwise this task is complete.

Task 7 – Hawaiʻi Regional Project

University of Hawaiʻi

Objective

The objective of this task is to assess and evaluate the GHG implications of a *Pongamia*-based feedstock supply chain for SAF production. Activities proposed for Task 7 will continue to develop the information needed for the Hawaiʻi Regional Projects begun in previous years. These activities will support efforts by the State of Hawaiʻi and Hawaiʻi energy service providers to reduce GHG emissions. Task activities will explore the GHG intensity of *Pongamia* as a feedstock producer in Hawaiʻi regional pathways.

Research Approach

Based on analyses from previous years, life cycle inventories (LCIs) for *Pongamia* production, oil extraction, and oil conversion to SAF will be completed. The LCIs will be used to conduct GHG assessments of *Pongamia*-based SAF production systems. Different *Pongamia* land use scenarios, extraction options, and conversion technologies can be considered and compared.

Milestone

Produce a complete set of LCIs for the *Pongamia* production system.



Major Accomplishments
Production scenarios developed in Task 5 have been used to identify inputs for orchard production of *Pongamia*. This includes material and energy requirements for nursery production of saplings, site preparation, planting and stand establishment, cultural practice (fertilization, weed control, and pruning), harvesting, and orchard removal at the end of productive life. The basis for transport of harvested material between the orchard and processing sites has been established.

Publications
None.

Outreach Efforts
The project principal investigator participated in the Hawaii State Energy Office's Biofuels Working Group and the Hawai‘i Energy Policy Forum. Both groups engage Hawai‘i energy stakeholders and SAF and GHG reduction are active topics.

Awards
None.

Student Involvement
None.

Plans for Next Period
Drying, decortication, and oil extraction scenarios currently under development in Task 5 will provide the basis for material and energy flows for *Pongamia* processing. Data for oil and byproduct transport from processing sites to refining assets on O‘ahu and animal production facilities will be finalized.

Task 8 – Hawai‘i Regional Project
University of Hawai‘i

Objective
The objective of this task is to assess and evaluate the GHG implications of waste based SAF production in Hawai‘i. Activities proposed for Task 8 will continue to develop the information needed for the Hawai‘i Regional Projects begun in previous years. These activities will support efforts by the State of Hawai‘i and Hawai‘i energy service providers to reduce GHG emissions. Task activities in Year 8 will focus on waste-based feedstocks that address MSW and construction and demolition waste currently generated and disposed of in landfills across the state.

Research Approach
Based on analyses from Task 6, waste production across the state will be considered as a single resource to be managed for SAF production. Available data on waste generation by island, waste composition by island, transportation requirements, and conversion technologies will be used as the basis for developing scenarios for SAF production given existing waste management practices. These scenarios will be used to evaluate GHG intensity of SAF production scenarios.

Milestone
Developed scenarios for waste-to-SAF production options based on available county and state data reporting.

Major Accomplishments
An assessment of available data on urban waste flows across the state has been completed. Nine scenarios for managing waste across the state as an integrated system have been developed and were used as the basis for comparing greenhouse gases impacts. Two scenarios continued using local landfills with landfill gas recovery and either flaring or electricity production. The City & County of Honolulu has considered shipping MSW to west coast landfills as a disposal option as recently as 2024. Four out-of-state shipping scenarios were considered that included landfill gas recovery with flaring and electricity production as well as enhanced sorting and recycling prior to shipment. These six landfill scenarios were evaluated using the U.S. Environmental Protection Agency Waste Reduction Model (WARM) v16 and openLCA v2.0.4 software.



The three remaining scenarios assumed a waste-to-SAF production plant using gasification and FT technology. The first SAF scenario used the entire state waste stream, the second diverted food waste, and the third case diverted food waste and mixed plastics. Based on these three scenarios of waste management for SAF production, preliminary estimates of GHG intensity were developed based on the contributions from feedstock transportation, fuel production, ash disposal, SAF production, and combustion of nonbiogenic components. The scenario that diverted food waste and mixed plastics from the feedstock stream yielded the lowest GHG intensity, 32 g CO_2e/MJ. The highest value, 48 g CO_2e/MJ of SAF, corresponded to the scenario where food waste was diverted and mixed plastics were included in the feedstock steam. SAF production across all scenarios ranged from 25 to 30 million gallons annually, roughly 4 to 5% of the state's annual jet fuel consumption.

Publications
None.

Outreach Efforts
A poster entitled "MSW-based SAF (Alternative Jet Fuel Supply Chain Tropical Region Analysis)" was presented at the ASCENT Fall 2024 review meeting in Alexandria, Virginia.

Awards
None.

Student Involvement
None.

Plans for Next Period
Results from Tasks 6 and 8 will be summarized in a manuscript, otherwise this task is complete.



Project 001(C) Alternative Jet Fuel Supply Chain Analysis

Purdue University

Project Lead Investigator

Farzad Taheripour
Research Professor
Department of Agricultural Economics
Purdue University
403 Mitch Daniels Blvd.
West Lafayette, IN 47906-2056
765-494-4612
tfarzad@purdue.edu

University Participants

Purdue University

- P.I.: Farzad Taheripour, Research Professor
- FAA Award Number: 13-C-AJFE-PU, Amendments 25, 29, 34, 36, 41, 46, 48, 51, 55
- Period of Performance: October 1, 2024, to September 30, 2025
- Tasks:
  1. Provide analyses on induced land use change (ILUC) and direct land use change (DLUC) emissions and other analyses related to land use changes (LUC) at global, regional, and country levels for national and international biofuel programs that tend to promote supplies of clean fuels. This task provides the required support to calculate a portion of the carbon intensity (CI) of sustainable aviation fuel (SAF) pathways and other biofuels that are related to LUCs.
  2. Collect data, conduct data analyses, and develop economic models to support the United States (U.S.) government agencies and the International Civil Aviation Organization (ICAO)/Committee on Aviation Environmental Protection (CAEP)/Working Group 5 (WG5) – Aviation Fuels, to develop techno-economic analysis (TEA) in degerming profitability and feasibility of SAF pathways under alternative economic conditions and policy environments.
  3. Improve agro-ecological zone-emission factor (AEZ-EF) model and its emission factors to follow the 2019 International Panel of Climate Change (IPCC) guidelines in assessing land use emission factors and better measure the vegetation and soil organic carbon (SOC) contents of land cover items at a global scale. [This task has been moved to the ASCENT Project 104B (award number 13-C-AJFE-PU-058)].

Project Funding Level

This project received funding from the Federal Aviation Administration (FAA) as follows:

- Award received prior to this period of performance
  - Amendment 3: $250,000
  - Amendment 6: $110,000
  - Amendment 10: $230,000
  - Amendment 15: $373,750
  - Amendment 19: $400,000
  - Amendment 29: $400,000
  - Amendment 36, 41: $523,000
  - Amendment 46, $350,000
  - Amendment 48, $350,000
  - Amendment 51, $394,844
- Award received for the current period of performance
  - Amendment 55, $399,865



Current cost sharing for this project year was provided by Neste US, Inc.

Investigation Team

Prof. Farzad Taheripour (P.I.), All Tasks
Prof. Dominique van der Mensbrugghe (co-P.I.), Task 3
Prof. Qianlai Zhuang (co-P.I.), Task 3
Maksym Chepeliev, (co-P.I.; research economist), Task 1
Erwin Corong (co-P.I.; research economist), Task 1
Angel Aguiar (research economist), Task 1
EhsanReza Sajedinia (PhD student), All Tasks
Shuo Chen (PhD student), Task 3
Xiangyu Liu (PhD student), Task 3
Ye Yuan (PhD student), Task 3
Lauren Benavidez (PhD student), All Tasks

Project Overview

The research team of ASCENT Project 001C has worked on the three main tasks listed above and made major progress on each task in this performance time period. The first task is focused on providing analyses on ILUC and DLUC assessments for the national and international policies that tend to promote production and consumption of SAF and non-SAF biofuels including corn ethanol, sugarcane ethanol, and biodiesel produced from several types of vegetable oils. This task also considers advancing methodologies for ILUC and DLUC calculations.

The second task aims at supporting the U.S. government agencies and ICAO/CAEP/WG5 subgroups, including the Core Life Cycle Assessment (LCA), Technology, Production, and Policy (TPP), and Sustainability subgroups, to accomplish their tasks and achieve their goals. This task considers developing TEA for determining the profitability and feasibility of SAF pathways under alternative economic conditions and policy environments.

The third task focused on various activities including updating the AEZ-EF model to adopt the 2019 IPCC guidelines in assessing lands use emission factors, assessing the existing data and approaches that provide land use emission factors used in the AEZ-EF model; and studying and proposing a methodology to measure, check, and verify changes in the soil carbon content of cropland including SOC at the farm level due to production of SAF or other biofuels.

Task 1 – Provide Required Analyses on ILUC at Global, Regional, and Country Levels

Purdue University

Objectives

The objectives of this task focus on calculating ILUC values and their updates for new SAF pathways, improving ILUC modeling approaches, collecting required data to more accurately estimate ILUC, updating the global trade analysis project for biofuel (GTAP-BIO) database to represent the global economy in recent years, and providing analyses that help to better elucidate LUCs across the world.

Research Approach

Our team collected the required data and developed required analyses for both TEA and LCA to determine the cost structure of each new SAF pathway to be included in the GTAP-BIO model to support ILUC calculations. We then used the modified model to assess the LUCs associated with new SAF pathways.

Milestones

- Calculated new ILUC values upon request by the ICAO/CAEP/WG5.
- Developed a new GTAP-BIO database, which represents the global economy in 2014.
- Added several SAF pathways to the new GTAP-BIO database. This new database has been used to develop the required analyses for the 40B provision of the Inflation Reduction Act of 2022.



Major Accomplishments

Accomplishments in Task 1 include providing various assessments for SAF that could be produced in Brazil using corn alcohol-to-jet (ATJ) technology and developing ILUC values for palm oil Hydroprocessed Esters and Fatty Acids (HEFA) that can be produced in South America and Sub-Saharan Africa. Several pathways were also examined for the 45Z provision of the Inflation Reduction Act of 2022. The pathways included for the 45Z provision of the Inflation Reduction Act of 2022 were two U.S. corn ethanol cases, U.S. soybean biodiesel, U.S. soybean renewable diesel, U.S./Canadian canola biodiesel, U.S./Canadian canola renewable diesel U.S. sorghum ethanol, two Brazilian sugarcane ethanol cases, and five cellulosic fuel pathways using miscanthus, switchgrass, poplar, willow, and energy sorghum.

Publications

Written Report

ANL. (2024). *Expansion of Carbon Calculator for Land Use and Land Management Change from Biofuels Production (CCLUB) to Address Induced Land Use Changes and Other Indirect Effects of Clean Fuel Production for R&D GREET2024*. Argonne National Laboratory (ANL).

Taheripour, Sajedinia, Chepeliev, and Aguiar have contributed to developing this report and its Appendix A.

Presentations/Working Papers

- CAEP/14-WG5_1-WP05 – ILUC value estimation, May 12-16, 2025, Virtual.
- CAEP/14-WG5_1-WP06 – Model Improvement and modelling time, May 12-16, 2025, Virtual.
- CAEP/14-WG5_2_IP05 – Standard GTAP, GTAP-BIO, and CORSIA GTAP-BIO models and their databases, October 27-37, 2025, São Paulo, Brazil.
- CAEP/14-WG5_2-WP015 – Progress ILUC values determination, October 27-37, 2025, São Paulo, Brazil.

Outreach Efforts

- Participated (Dr. Taheripour) in ASCENT Advisory Group meetings in Fall 2024 and Spring 2025 and shared the findings of this research with the ASCENT community.
- Participated and presented (Dr. Taheripour) the results of this project at the following conferences, seminars, and meetings related to biofuels and their land use effects:
  - 2025 Sustainability Workshop, Clean fuel conference, April 7-9, 2025, Kansas City, Missouri.
  - 2025 American and Applied Economic Association (AAEA) Annual Meeting, July 27-29, 2025, Denver, Colorado.
- Reviewed (Dr. Taheripour) many academic papers for various journals that provide publications in research areas associated with Task 1.

Awards

None.

Student Involvement

- EhsanReza Sajedinia, current PhD student, Purdue University, for data collection and running simulations
- Lauren Benavidez, current PhD student, Purdue University, for data collection and working with land use emission data and models

Plans for Next Period

The new Cycle of ICAO CAEP began in 2025. Following the request by WG5, our team plans to use a new version of GTAP-BIO model that represents the world economy in 2017 and represents corn-soy double cropping system in Brazil to update the ILUC values for all Carbon Offsetting and Reduction Scheme for International Aviation (CORSIA) SAF pathways. In addition, we will develop required ILUC assessments to support the U.S. policies regarding biofuels production and use.



Task 2 – Collect Data, Conduct Analyses, and Develop Economic Models to Support Policy Decision at National and International Levels for SAF and Other Biofuels

Purdue University

Objectives

The objective of this task is to (1) develop required analyses to support policy decision at national and international levels to promote supplies of cleaner fuels such as SAF and non-SAF pathways for aviation and road transportation, (2) coordinate with the WG5 subgroups to avoid conflicts between the ILUC subgroup activities and activities performed by other subgroups, and (3) collaborate with the U.S. government agencies to coordinate policy decision on SAF and non-SAF pathways.

Research Approach

This task considers various assignments and components. Our team uses standard methods to support WG5 subgroups, including the Core LCA, TPP, and Sustainability subgroups. We collected data and used economic models including GTAP-BIO and provided appropriate analyses to accomplish this task. Dr. Taheripour collaborates with the ILUC, Core LCA, TPP, and Sustainability subgroups of the ICAO/CAEP/WG5.

Milestones

- Developed analyses and models to support WG5 subgroups,
- Calculated LUCs for SAF pathways.
- Provided required economic analysis.

Major Accomplishments

Supporting International Activities

In addition to participating in meetings with WG5 subgroups and reviewing their working and information papers, Dr. Taheripour collaborated with the WG5 secretary and co-rapporteurs to develop reports for ICAO Steering Group meetings. One major accomplishment was developing the required analyses for the 45Z provision of the Inflation Recovery Act of 2022. Dr. Taheripour participated in the CAEP14/WG5-1 and CAEP14/WG5-2 meetings and many sub-group meetings and was involved in several tasks and document preparation activities for these meetings. He also responded to other subgroup requests for help and collaboration. He has led efforts in ILUC modeling and ILUC-related tasks associated with other subgroups. He also joined various meeting with the U.S. government agencies and provided various presentations to discuss and explain ILUC modeling.

Supporting Domestic U.S. Policy Decision

Dr. Taheripour also collaborated with U.S. government agencies such as the FAA, U.S. Department of Agriculture (USDA), U.S. Environmental Protection Agency (EPA), U.S. Department of Energy (DOE), and Argonne Research Library to develop modeling practices for the use in the U.S. domestic policy analysis regarding the provision of 40B and 45Z of the Inflation Reduction Act of 2022.

Publications

The ILUC related reports are noted under Task 1.

Outreach Efforts

- See outreach efforts under Task 1.
- Reviewed (Dr. Taheripour) many academic papers for various journals that provide publications in research areas associated with Task 2.
- Attended (Dr. Taheripour, Dr. Chepeliev, Dr. Aguiar, Sajedinia, Chen, and Yuan) the ASCENT Advisory Group meetings in Fall 2024 and Spring 2025 and discussed the findings of this task with members of this community.

Awards

None.



Student Involvement

- EhsanReza Sajedinia, current PhD student, Purdue University, for data collection and running simulations
- Shuo Chen, current PhD student, Purdue University, for data collection and running simulations
- Xiangyu Liu, current PhD student, Purdue University, for data collection and running simulations
- Ye Yuan, current PhD student, Purdue University, for data collection and running simulations
- Lauren Benavidez, current PhD student, Purdue University, for data collection and running simulations

Plans for Next Period

- Collaborate with the Core LCA subgroup to refine the mythology of assessing changes in soil carbon content at the farm level.
- Continue to support WG5 subgroups, including the Core LCA, TPP, and Sustainability subgroups, in accomplishing the required LCAs for new SAF pathways.
- Continue to develop the required TEAs to include the cost structure of new SAF pathways in the GTAP-BIO database.
- Continue to collaborate with the U.S. government agencies to establish the U.S. domestic policy towards the SAF and non-SAF biofuel pathways.

Task 3 – Improvements in AEZ-EF Model

Purdue University

This task has been moved to ASCENT Project 104B (Award Number: 13-C-AJFE-PU-058).



Project 001(D) Alternative Jet Fuel Supply Chain Analysis

The Pennsylvania State University

Project Lead Investigator

Lara Fowler
Professor of Teaching, Penn State Dickinson Law
Affiliate Faculty, Penn State School of International Affairs
The Pennsylvania State University
231 Katz Building
University Park, PA 16802
814-865-4806
Lbf10@psu.edu

University Participants

The Pennsylvania State University

- P.I.s: Lara Fowler, Professor of Teaching, Penn State Dickinson Law; Anne Menefee, Assistant Professor of Energy and Mineral Engineering (starting with funding period beginning June 14, 2022); Armen Kemanian, Professor of Production Systems and Modeling (starting with funding period beginning June 14, 2022; soil related activities transitioning to Project 104); and Seth Blumsack, Professor of Energy Policy and Economics and International Affairs
  - Researchers: Michael Helbing, Executive Director, Penn State Center for Energy Law and Policy; Ekrem Korkut, Legal Research Postdoctoral Associate (position ended June 30, 2024); Yuning Shi, Post Doc, Penn State College of Ag Sciences; Saurabh Bansal, Professor of Supply Chain Management (involvement ended in 2022); Thomas Chase Lam, Graduate Student, John and Willie Leone Family Department of Energy and Mineral Engineering; Emmy Wang, MS Candidate, Agricultural and Environmental Plant Science; Alicia Costello, MS Candidate, Ecology.
- FAA Award Number: 13-C-AJFE-PSU, RISK-INFORMED ALTERNATIVE JET FUEL (AJF)
- Periods of Performance: **Period A:** August 1, 2017, to January 31, 2022; **Period B:** June 14, 2022, to November 13, 2023; **Period C:** October 1, 2022, to September 30, 2023; and **Period D:** July 1, 2023, to September 30, 2026 (time period extended to 2026 through no-cost extension).
- Tasks:

  Period A (August 1, 2017, to January 31, 2022)

  1.
     1.3.1 Risk–reward profit-sharing modeling for first facilities
     1.3.2 Additional quantification of risk and uncertainties in supply chains (foundational part of Task 1.3.1)
     1.3.3 Supply chain risk analysis tools for farmer adoption
     1.4.1 National survey of current and proposed state and federal programs that monetize ecosystem services
     1.4.3 Support of stakeholder engagement efforts

  Period B (June 14, 2022, to November 13, 2023)

  1. Law and Policy Research
     1.1 Research existing federal law and policy drivers
     1.2 Research existing state and regional law and policy drivers
     1.3 Research proposed legislation (federal and state)
     1.4 Research other law/policy issues, as identified by the ASCENT Project 001 team
  2. Support Stakeholder Engagement Efforts
     2.1 Work with ASCENT Project 001 team to identify stakeholder engagement opportunities
     2.2 Develop a list of potential stakeholders critical to discussion
     2.3 Develop agenda/materials for critical discussions; meeting facilitation as needed
  3. Carbon Capture and Sequestration (CCS)
     3.1 Work with ASCENT Project 001 team members to identify critical questions, and refine the scope of work related to CCS



3.2 Conduct literature review regarding CCS and its potential use in conjunction with AJFs
3.3 Draft a review manuscript examining opportunities to integrate CCS and AJF

4. Organic Soil Carbon
   4.1 Work with ASCENT Project 001 team members to identify critical questions, and refine the scope of work related to soil organic carbon (SOC)
   4.2 Conduct literature review regarding SOC and its potential relation to AJF
   4.3 Draft review manuscript examining opportunities for SOC and AJF

Period C (October 1, 2022, to September 30, 2023)

1. Law and Policy Research
   1.1 Research existing and proposed federal law and policy drivers
   1.2 Research existing and proposed state and regional law and policy drivers
   1.3 Research other law/policy issues, as identified by the ASCENT Project 001 team
2. Support Stakeholder Engagement Efforts
   2.1 Work with ASCENT Project 001 team to identify stakeholder engagement opportunities
3. Carbon Capture and Sequestration
   3.1 Research integration of CCS
   3.2 Work with ASCENT Project 001 team to refine the scope of work and current needs
   3.3 Research and review paper on geologic carbon storage potential, with emphasis on permanence and risks (both technical and legal)
4. Organic Soil Carbon
   4.1 Refine global modeling systems using Level 3 Global Administrative Areas (GADM), soils from the International Soil Reference and Information Centre (ISRIC), and weather data from the North American Land Data Assimilation System (NLDAS)
   4.2 Use machine learning to generate SOC profiles for business as usual (BAU) conditions, or machine learning and combination of Cycles for automated SOC stock calculations; the initial geographic target is the continental United States (CONUS)
   4.3 Apply Cycles-A to the task of fitting sustainable aviation fuel (SAF) crops in the current agricultural matrix of the United States (U.S.), with focus on oil crops as an example
   4.4 Complete a SOC modeling manuscript with the goal of standardizing methods for SOC (and nitrous oxide) calculations in relation to the carbon intensity (CI) of BAU and SAF production scenarios

Period D. (July 1, 2023, to September 30, 2026)

1. Law and Policy Research
   1.1 Research existing and proposed federal law and policy drivers
   1.2 Research existing and proposed state and regional law and policy drivers
   1.3 Research other law/policy issues, as identified by the ASCENT Project 001 team.
2. Support Stakeholder Engagement Efforts
   2.1 Work with ASCENT Project 001 team to identify stakeholder engagement opportunities
3. Carbon Capture and Sequestration
   3.1 Research integration of CCS
   3.2 Work with ASCENT Project 001 team to refine the scope of work and current needs
   3.3 Research and review paper on geologic carbon storage potential, with emphasis on permanence and risks (both technical and legal)
4. Organic Soil Carbon
   4.1 Refine global modeling systems using Level 3 GADM, soils from the ISRIC, and weather data from the NLDAS
   4.2 Use machine learning to generate SOC profiles for BAU, or machine learning and combination of Cycles for automated SOC stock calculations; the initial geographic target is CONUS
   4.3 Apply Cycles-A to the task of fitting SAF crops in the current agricultural matrix of the U.S., with focus on oil crops as an example
   4.4 Complete a SOC modeling manuscript with the goal of standardizing methods for SOC (and nitrous oxide) calculations in relation to the CI of BAU and SAF production scenarios

Washington State University (WSU)

- Michael Wolcott, Regents Professor (for funding period from June 14, 2022, to November 13, 2023)
- Kristin Brandt, Staff Engineer (through funding period ending January 31, 2022)



University of Kentucky (UK)
- Burt English, Institute Professor (for work through April 2022); now retired.

Project Funding Level

FAA funding: $150,000 (for Period D, July 1, 2023, to September 30, 2026)
Matching from Penn State: $150,000
Total funding: $300,000

Investigation Team

Period A (August 1, 2017, to January 31, 2022)
- Task 1.3.1 (Bansal; supported by Brandt and English): Risk–reward profit-sharing modeling for first facilities
- Task 1.3.2 (Bansal; supported by Brandt and English): Additional quantification of risk and uncertainties in supply chains (foundational part of Task 1.3.1)
- Task 1.3.3 (Bansal; supported by Brandt and English): Supply chain risk analysis tools for farmer adoption
- Task 1.4.1 (Fowler; supported by Korkut): National survey of current and proposed state and federal programs that monetize ecosystem services
- Task 1.4.3 (Fowler; supported by Korkut): Support of stakeholder engagement efforts

Period B (June 14, 2022, to November 13, 2023)
- Task 1.1 (Fowler, supported by Korkut): Research on existing federal law and policy drivers
- Task 1.2 (Fowler, supported by Korkut): Research on existing state and regional law and policy drivers
- Task 1.3 (Fowler, supported by Korkut): Research on proposed legislation (federal and state)
- Task 1.4 (Fowler, supported by Korkut): Research on other law/policy issues, as identified by the ASCENT Project 001 team
- Task 2.1 (Fowler, supported by Korkut): Work with the ASCENT Project 001 team to identify stakeholder engagement opportunities
- Task 2.2 (Fowler, supported by Korkut): Development of a list of potential stakeholders critical to discussion
- Task 2.3 (Fowler, supported by Korkut): Development of agenda/materials for critical discussions; meeting facilitation as needed
- Task 3.1 (Menefee): Work with ASCENT Project 001 team members to identify critical questions and refine the scope of work related to CCS
- Task 3.2 (Menefee): Conduct literature review regarding CCS and its potential use in conjunction with AJFs
- Task 3.3 (Menefee): Draft a review manuscript examining opportunities to integrate CCS and AJF
- Task 4.1 (Kemanian, supported by Wolcott): Work with ASCENT Project 001 team members to identify critical questions, and refine the scope of work related to SOC
- Task 4.2 (Kemanian, supported by Wolcott): Conduct literature review regarding SOC and its potential relation to AJF
- Task 4.3 (Kemanian, supported by Wolcott): Draft review manuscript examining opportunities for SOC and AJF.

Period C (October 1, 2022, to September 30, 2023)
- Task 1.1 (Fowler, supported by Helbing and Korkut): Research on existing and proposed federal law and policy drivers
- Task 1.2 (Fowler, supported by Helbing and Korkut): Research on existing and proposed state and regional law and policy drivers
- Task 1.3 (Fowler, supported by Helbing and Korkut): Research on other law/policy issues, as identified by the ASCENT Project 001 team
- Task 2.1: (Fowler, supported by Helbing and Korkut) Work with ASCENT Project 001team to identify stakeholder engagement opportunities
- Task 3.1 (Menefee & Helbing): Research on integration of CCS
- Task 4.1 (Kemanian & Shi): Accounting for SOC and nitrous oxide emissions using agroecosystem models

Period D (July 1, 2023, to September 30, 2026):
- Task 1.1 (Fowler, supported by Helbing and Korkut [through June 30, 2024]): Research on existing and proposed federal law and policy drivers
- Task 1.2 (Fowler, supported by Helbing and Korkut [through June 30, 2024]): Research on existing and proposed state and regional law and policy drivers



- Task 1.3 (Fowler, supported by Helbing and Korkut [through June 30, 2024]): Research on other law/policy issues, as identified by the ASCENT Project 001 team
- Task 2.1: Work with ASCENT Project 001 team to identify stakeholder engagement opportunities
- Task 3.1 (Menefee, Helbing, & Lam): Research on integration of CCS
- Task 4.1 (Kemanian, Shi, Wang, & Costello; with Wang & Costello funded through Project 104): Accounting for SOC and nitrous oxide emissions using agroecosystem models

Project Overview

For the first period of performance (Period A), this project focused on developing a qualitative and quantitative understanding of factors to help establish biofuel supply chains for AJFs. Although efforts are being made to establish these supply chains, many face challenges because of a lack of clarity regarding the incentives that stakeholders would require to engage in these supply chains and devote their resources to investing in the facilities required for these supply chains. To this end, this project has two goals:

1. Develop pro forma cash flows that represent the financial status of various participants in biofuel supply chains for AJFs, to inform a transparent risk-sharing tool; and
2. Understand the policy landscape in various parts of the U.S. to encourage AJF supply chains and identify additional policy initiatives that may be needed.

During the second period of performance (Period B), this project continued to focus on understanding the law and policy drivers associated with AJF and expanded its focus to include two new areas—CCS and SOC—and their potential linkages to AJF.

During the third and fourth periods of performance (Periods C and D), this project continues to stay up to date on the law and policy changes associated with AJF and has also started to focus on important opportunities and knowledge gaps surrounding CCS and SOC. Two new PIs, Dr. Anne Menefee and Dr. Armen Kemanian, were on-boarded to focus on these emerging areas and provide relevant expertise across the ASCENT Project 001 team.

Periods A-B, Summary of All Tasks

The Pennsylvania State University

In this section, we briefly summarize the work done under all tasks in Periods A and B. Complete reports of activity during these periods can be found in annual reports for years 2024 and earlier.

During Periods A and B, research team members performed a number of research tasks designed to develop a qualitative and quantitative understanding of factors driving the establishment of biofuel supply chains for AJFs.

- The research team developed four Microsoft Excel® models using data from techno-economic analysis models developed by WSU to serve as a risk-sharing tool for better understanding of risks faced by supply chain members.
- Researchers developed a new econometric approach to quantify the probability distributions of uncertain quantities, such as yield or demand; that method was described in two manuscripts, which are listed among the publications below.
- The team performed a survey to better understand farmers' risk tolerance in certain situations. The results of this survey were presented in a manuscript that was submitted to the sponsor.
- An extensive effort was undertaken to survey and summarize current and proposed state and federal programs to monetize ecosystem services. That effort resulted in one peer-reviewed publication and four white papers, all of which are listed below.
- Throughout the project, we have worked to engage stakeholders and facilitate effective dialogue to help bridge gaps among producers, industry, government, and other affected stakeholders.
- In Period B, we initiated our work to study the integration of CCS into supply chains for AJF. We also begam our research into critical questions regarding the effects of SOC on sustainability efforts related to AJF.

® Microsoft and Excel are registered trademarks of Microsoft Corporation in the United States and other countries.



Publications

Peer-reviewed journal publications

Bansal, S., & Gutierrez, G. J. (2020). Estimating uncertainties using judgmental forecasts with expert heterogeneity. *Operations Research*, *68*(2), 363-380. doi: 10.1287/opre.2019.1938

Korkut, E. & Fowler, L. B. (2021). Regulatory and policy analysis of production, development and use of sustainable aviation fuels in the United States." *Frontiers in Energy Research*, *9,* 750514. doi:10.3389/fenrg.2021.750514.

Written reports

Bansal, S., & Wang, T. (2019). Using subjective probability distributions to support supply chain decisions for innovative agribusiness products. Report for the *Federal Aviation Administration*. https://s3.wp.wsu.edu/uploads/sites/2479/2021/05/ASCENT-Project-001D-attachment-1.pdf

Bansal, S., & Gutierrez, G. J. (2021). Optimal aggregation of individual judgmental forecasts to support decision making in an R&D program. Submitted to *Operations Research*. https://s3.wp.wsu.edu/uploads/sites/2479/2021/05/ASCENT-Project-001D-attachment-2.pdf

Korkut, E., & Fowler, L. (2021). *Regulatory and Policy Analysis of Productions, Development and Use of Sustainable Aviation Fuels in the United States* [White paper, draft]. Pennsylvania State University. 2021_01_08_SAF paper draft_ circulated for review_KCL_NB (1).docx

Western U.S. policy manuscript (with a focus on Washington State, last updated in 2019): Southeast Bioenergy Law & PolicyDraft3.docx

Southeast policy manuscript (with a focus on Tennessee): Southeast Bioenergy Law & PolicyDraft3.docx

Hawaii policy manuscript: Hawaiian Biofuel Law & Policy_v5.docx

Periods C-D, Task 1- Law and Policy Research

The Pennsylvania State University

Objectives

Stay up to date with existing and proposed federal law and policy drivers affecting SAF, including participation by the U.S. in international discussions and agreements (Task 1.1).

- Research existing and proposed state law and policy drivers (Task 1.2).
- Explore other issues identified by the ASCENT Project 001 team as needed (Task 1.3).

Research Approach

Following up on our previous law and policy research, the ASCENT Project 001 team stayed abreast of developments related to the One Big Beautiful Bill Act provisions related to SAF as well as broader legal developments that could have an impact on SAF. In addition, a 50-state survey of laws and policies impacting SAF development was completed and developed into presentations and a draft paper.

Milestone

At biweekly team meetings and semi-annual conferences, updates were provided on legal research topics. Email updates were sent as appropriate regarding significant legal developments.

Major Accomplishments

A presentation on the “50-State Survey” was presented in April 2025 at the SAF Spring Meeting in Knoxville, TN. Fifty-state survey research was also presented in poster form at the Penn State Climate Solutions Symposium in May 2025 and the ASCENT Fall Meeting in October 2025. In addition, Helbing led a team of ASCENT researchers exploring avenues of future research.

Publications

Peer-reviewed journal publications

Korkut, E. & Fowler, L. B. (2021). ”Regulatory and policy analysis of production, development and use of sustainable aviation fuels in the United States." *Frontiers in Energy Research*, *9,* 750514. doi:10.3389/fenrg.2021.750514.



A manuscript presenting the 50-state survey research has been drafted and will be presented for FAA review early in the next cycle.

Outreach Efforts

Presentations

Helbing, M. (2024, October). *Flying into the Future: Sustainable Aviation Fuel and the Policies Impacting its Development* [Oral presentation]. Penn State Earth and Environmental Systems Institute EarthTalks Series.

Helbing, M. (2024, November). *Session 5: Discussion of other policy options that might merit review under the SAFGCR Action Area 4 - Policy Valuation and Analysis, Workstream PA.3 – Inform SAF Policy* [Panelist in oral presentation] Alternative Fuels & Chemicals Coalition's SAF Workshop, Oxon Hill, MD.

Johnson, M., & Helbing, M., (2025, April). *50-state Survey* [Oral presentation]. Spring 2025 ASCENT Sustainable Aviation Fuel Meeting, Knoxville, TN.

Poster

Johnson, M., Helbing, M., & Fowler, L. (2025, May). *A 50-state Survey of Sustainable Aviation Fuel Policy.* [Poster]. Penn State Climate Solutions Symposium.

Awards

None.

Student Involvement

Third-year law student, Mary Johnson, researched policies affecting SAF development in all 50 states and presented her research at the ASCENT SAF Spring Meeting in Knoxville, TN, in April 2025.

Plans for Next Period

Our team will continue to work with the ASCENT Project 001 team to identify potential law and policy concerns and opportunities. Our team will also continue to explore how SAF and renewable natural gas might be developed in synergistic ways. We will complete the manuscript documenting the data from our 50-state survey and hope to publish it once it is approved by the FAA. We also plan to explore the possibility of creating and maintaining a website to make this information available to the public. Depending on available funding, we also hope to extend our research to include economic and logistical research into government programs such as low-carbon fuel standards and the One Big Beautiful Bill Act. Our team will continue to engage with other ASCENT Project 001 team members on evaluating areas for future research.

Periods C-D, Task 2 - Support Stakeholder Engagement Efforts

The Pennsylvania State University

Objective

Facilitate dialogue among producers, industry, government, and other affected stakeholders.

Research Approach

Our work under this objective has focused on stakeholder engagement and facilitation of effective dialogue to help bridge gaps among producers, industry, government, and other affected stakeholders. This role supports the needs of other team members.

Milestone

These efforts have supported stakeholder engagement efforts led by other teams, including but not limited to the regional partners identified in ASCENT Project 001.

Major Accomplishments

Our team has continued to participate in discussions and calls related to potential stakeholder engagement needs. Those discussions this year included conversations with Steve Csonka from the Commercial Aviation Alternative Fuels Initiative (CAAFI) and other members of the ASCENT research team. We have also held calls with officials from both the Pittsburgh



International Airport and the Philadelphia International Airport to discuss their SAF initiatives. Through networking at various events, we have also established relationships with representatives from Lanza Jet and Third Way, among others.

Publications
None.

Outreach Efforts
Michael Helbing attended the North American SAF Conference and Expo in Minneapolis, MN, in September 2025.

In June 2025, Fowler and Kemanian were part of a Pennsylvania delegation that traveled to Denmark to explore and understand the Danish biogas industry, which is significantly more advanced and integrated to the energy matrix and agricultural nutrient management than American biogas. This experience provided Fowler and Kemanian with an understanding of how the biogas industry in Denmark came to be so advanced as well as enhanced relationships with biogas stakeholders, including several Pennsylvania officials. This tour also highlighted opportunities for turning biogas co-products into sustainable aviation fuel.

Helbing has also had informal conversations about SAF at meetings not specifically dedicated to SAF, including the Penn State Climate Solutions Symposium and a project meeting of CO2-SMART: A National Science Foundation Industry/University Cooperative Research Center.

Awards
None.

Student Involvement
None.

Plans for Next Period
Work will continue with other ASCENT partners to facilitate work to support the U.S. delegation to the International Civil Aviation Organization (ICAO) Committee on Aviation Environmental Protection (CAEP) Working Group 5. Specifically, the aim is to deepen relationships with the Fueling Aviation's Sustainable Transition SAF grant recipients affiliated with the Philadelphia and Pittsburgh airports in Pennsylvania. We will also work with stakeholders to perform research into the impacts of government programs like low-carbon fuel standards and the One Big Beautiful Bill Act. As needed, support will be provided to working groups.

Periods C-D, Task 3 - Carbon Capture and Sequestration
The Pennsylvania State University

Objectives
- Work with ASCENT Project 001 team to identify critical questions and needs surrounding the potential for CCS in SAF/AJF supply chains and support other tasks looking to integrate aspects of CCS (e.g., carbon footprint, techno-economic, and feasibility analyses).
- Conduct literature review to understand the potential opportunities, challenges, research needs, etc.

Research Approach
The initial stages of the CCS task involved in-depth literature review to understand knowledge gaps and existing pathways to integrate CCS into SAF/AJF supply chains. Our approach and objectives were refined through discussions with the ASCENT Project 001 team to focus more on policy and risk related to CCS and to identify hurdles that need to be addressed to (1) enable integration into SAF/AJF supply chains and (2) achieve real and quantifiable emission reductions. As a result of those efforts, Dr. Anne Menefee and Michael Helbing finalized a white paper that has been distributed among ASCENT Project 001 team members and is now currently available on the Penn State Center for Energy Law and Policy website.



This project year, the work has expanded to developing regional U.S. case studies incorporating life cycle assessment to identify opportunities and challenges for CCS both on the side of fuel production and carbon dioxide (CO_2) transport/end use. We are developing the life-cycle assessment (LCA) framework in alignment with Carbon Offsetting and Reduction Scheme for International Aviation (CORSIA) guidance. This work is intended for a paper that will provide realistic assessments of SAF-CCS feasibility, based on realistic examples of AJF production facilities and the practical and logistical considerations of geologic CO_2 storage.

Milestone
PI Menefee along with researcher Helbing finalized a white paper discussing technical and policy research about CCS in SAF development. PI Menefee has also been involved in the CCS ad hoc group and sustainability working group.

Major Accomplishments
A white paper was drafted and circulated discussing the technical and policy research about CCS in SAF development. Menefee and Helbing also presented this paper at ASCENT Project 001 team meetings.

Publications
Menefee, A., Helbing, M. (2025). *Carbon Capture and Storage in Sustainable Aviation Fuel Supply Chains* [White paper]. PennState Center for Energy Law and Policy. https://celp.psu.edu/wp-content/uploads/2025/01/SAF-CCS-white-paper-final-January-2025.pdf

Outreach Efforts
None.

Awards
None.

Student Involvement
In this project year, Menefee has brought on a graduate student, Thomas Lam (M.S. in Chemical Engineering, University of Virginia). Lam is working with Menefee and Helbing on current research initiatives, developing case studies for incorporation of CCS into AJF supply chains with quantitative LCA analysis focused on how CCS impacts carbon intensity.

Plans for Next Period
Menefee and Helbing will continue to work with student Lam to develop an LCA model and accompanying paper discussing the feasibility of CCS in SAF production using realistic scenarios, alongside tradeoffs with respect to emission reductions and economic/logistical considerations.

Periods C-D, Task 4 - Organic Soil Carbon
The Pennsylvania State University

Objectives
Incorporate Penn State expertise on soil carbon and nitrogen cycling in the context of the calculation of the carbon intensity of SAF. This includes incorporating carbon cycling modeling and the inclusion of uncertainty bounds, methods for standardizing calculations that encompass baseline (or reference) scenarios and SAF production scenarios. These methods need to be applicable worldwide, but the initial focus is CONUS. In addition, it is expected that similar work accounting for the nitrogen cycle including the carbon footprint associated with the use of fertilizers and an accounting for the emissions of nitrous oxide, whose equivalent carbon footprint can surpass that of SOC both as a positive or negative climate forcing. These objectives will transition to ASCENT Project 104, now established.

Research Approach
The research approach for this task includes developing a standard method to account for land use and SAF production using Earth Stats and level three GADM to report calculations on a field basis but also on political units of relevance that are standardized around the world. This task also includes overlaying the NLDAS climate databases (reanalysis), and ISRIC soils, so that the model Cycles (developed in Dr. Kemanian's lab) can be operated through the cropland domain. Finally,



this task includes using machine learning combined with a standard initialization procedure to estimate steady state soil carbon stocks under BAU and alternative SAF production scenarios.

Milestone

The team established a stable database of land use, weather data, and soils, along with automated methods to run simulations with Cycles, and downloaded and curated the USDA-Natural Resources Conservation Service (NRCS) pedon database for machine learning analysis. This database has been augmented for soils, which enables adding the source of the soil data used in simulations to the uncertainty analysis. The proper allocation of biomass to rainfed and irrigated land, as well as carbon inputs from animal manure, has been resolved at the county level. We now aim at completing estimations of carbon inputs from crop residues. Only corn has been completed so far, with excellent results.

Major Accomplishments

Dr. Yuning Shi updated the global weather data from the Global Land Data Assimilation System (GLDAS) reanalysis database, to allow simulation of any crop rotation worldwide.

Dr. Yuning Shi and Dr. Armen Kemanian started developing a two-dimensional (2D) version of the model Cycles that will allow simulation of nitrous oxide fluxes in systems with banding of nitrogen fertilizer or manure. Banding is a common practice in crop production. Ignoring nitrogen banding can lead to gross underestimations of nitrogen uptake by crops and alter nitrous oxide emission estimates. The 2D version relies on the use of C-language Variable-coefficients ODE solver (CVODE), a solver for a system of ordinary differential equations maintained by the Lawrence Livermore National Laboratory. So far, water transport in 2D is still being tested, including infiltration that is resolved using a modification of the Green and Ampt method, and water redistribution using Richards equation.

Publications

Dr. Armen Kemanian co-authored a manuscript positing that the return to the soil of high-lignin fermentation byproducts, (i.e., the leftovers of fermenting cellulosic materials for ethanol or other products) can balance or overcome the otherwise expected SOC losses from the removal of corn residues. The manuscript was published in *Environmental Research Letters* on August 2, 2024 (Lynd et al., 2024).

Peer-Reviewed Journal Publication

Lynd, L., Kemanian, A., Smith, J., Richard, T. L., Arifi, A., Bozzetto, S., Fabbri, C., Field, J., Pries, C. H., Kubis, M. (2024). Soil application of high-lignin fermentation byproduct to increase the sustainability of liquid biofuel production from crop residues*, Environmental Research Letters, 19*(8). doi: 10.1088/1748-9326/ad601a

Outreach Efforts

Presentations

Kemanian, A. (2024, October). *Risk-Informed Alternative Jet Fuel (AJF) Supply Chain Analysis: Top-Down Modeling of Soil Organic Carbon in Cropland* [Oral presentation]. Fall 2024 ASCENT Advisory Committee Meeting.

Posters

Posters from students have been added to the corresponding section of the report for ASCENT Project 104.

Awards

None.

Student Involvement

P.I. Armen Kemanian hired Emmy Wang, MS Candidate, Agricultural and Environmental Plant Science, and Alicia Costello, MS Candidate, Ecology, to contribute to this research. Both presented posters at the ASCENT 2025 Fall Meeting in Alexandria, VA.

Plans for Next Period

As a joint-effort by the Penn State team working on ASCENT Projects 001 and 104, the top-down modeling of the SOC balance at the county level presented in the ASCENT meeting in Alexandria, VA, in October 2024 is being refined. The



results will be summarized in a draft article for publication. Specifically, the analysis to date used SOC from the STATSGO (U.S. General Soil Map) database; it will be replaced (or duplicated) with the global Soil Grids database from the ISRIC. Carbon input, which was estimated using only grain yield and forage yield, will be updated with a longer statistical time series from the National Agricultural Statistical Service and parsed for rainfed and irrigated land, although the analysis will only focus on rainfed soils. As reported before, the analysis has been completed for corn, and we are proceeding with estimates of carbon inputs from other crops. The target journals are *Global Change Biology – Bioenergy* (Oxford) and *Energy Advances* (Royal Society of Chemistry). This manuscript will complete the transition of SOC and nitrogen work from ASECENT Project 001 to ASCENT Project 104.



Project 001(E) Alternative Jet Fuel Supply Chain Analysis

University of Tennessee

Project Lead Investigator

Timothy Rials
Professor and Associate Dean
AgResearch, University of Tennessee
2506 Jacob Dr., Knoxville, TN 37996
865-946-1130
trials@utk.edu

University Participants

University of Tennessee (UT)

- P.I.: T. Edward Yu, Professor
- FAA Award Number: 13-C-AJFE-UTenn, Amendments 22
- Period of Performance: October 1, 2024, to September 30, 2025
- Tasks:
  1. Estimate regional feedstock supply for sustainable aviation fuel (SAF)
  2. Analyze the risk factors reported by publicly traded biofuel companies
  3. Assess the stakeholder perceptions of the SAF supply chain for its deployment
  4. Collaborate with other ASCENT team members on feedstock supply and facility location analysis

Project Funding Level

Total estimated project funding: $200,000
Total federal and non-federal funds: $200,000
The UT Institute of Agriculture, in support of the project, provided faculty and staff salaries and graduate student tuition.

Investigation Team

Timothy Rials (Project Director – PD), Task 4
T. Edward Yu (P.I.), Tasks 1–4
Carlos Trejo-Pech (faculty), Task 2
Ricky Chen (faculty), Tasks 3
David Hughes (faculty), Task 3
Hannah Williams (Research Associate), Tasks 1 and 3
Bijay Regmi (MS student), Tasks 1 and 4
Bishal Bista (MS student), Task 2

Project Overview

UT leads the project's feedstock production analysis for the Southeast region of the United States (U.S.). This component targets the need to assess regional forest and agricultural biomass feedstock resources and delineate the sustainability impacts associated with feedstock choices. UT also leads the national lipid supply availability analysis to develop information on the potential effects and feasibility of using lipids to supply SAF. The UT team facilitates regional deployment and production of SAF by understanding stakeholders' perspectives throughout the SAF supply chain to expedite the development and scaling. Additionally, UT collaborates with other ASCENT team members on feedstock supply and facility location analysis.

Task 1 - Estimate Regional Feedstock Supply for Sustainable Aviation Fuel

University of Tennessee

Objectives

- Assess the impacts of feedstock quality on the supply chains and economics of SAF produced from logging residues via fast pyrolysis/hydrotreatment in the Southeast U.S.
- Develop a SAF supply chain from winter canola for the two major U.S. air cargo hubs: Memphis International Airport (MEM) and Louisville Muhammad Ali International Airport (SDF).

Research Approach

Using forestry biomass (e.g., logging residues) for SAF production to replace fossil-based jet fuel has been suggested as a potential means to mitigate carbon emissions from the aviation sector. However, the quality of the feedstock, particularly the ash content, can adversely affect bio-oil yield and SAF production using the fast pyrolysis/hydrotreatment process, and potentially its supply chain optimization. Previous research often assumes fixed biofuel yields and neglects the variability in feedstock quality when optimizing the supply chain. Thus, this study seeks to address this gap in the literature by employing a two-stage mixed-integer linear programming (MILP) model to investigate the influence of varying ash content in logging residues on the potential maximum supply quantity (MSQ) and net revenue (NR) of SAF production. Figure 1 presents the supply chain network and the modeling structure. Two scenarios were conducted in the Southeastern U.S.: (1) assuming constant ash content, and (2) accounting for the heterogeneous ash content in logging residues.

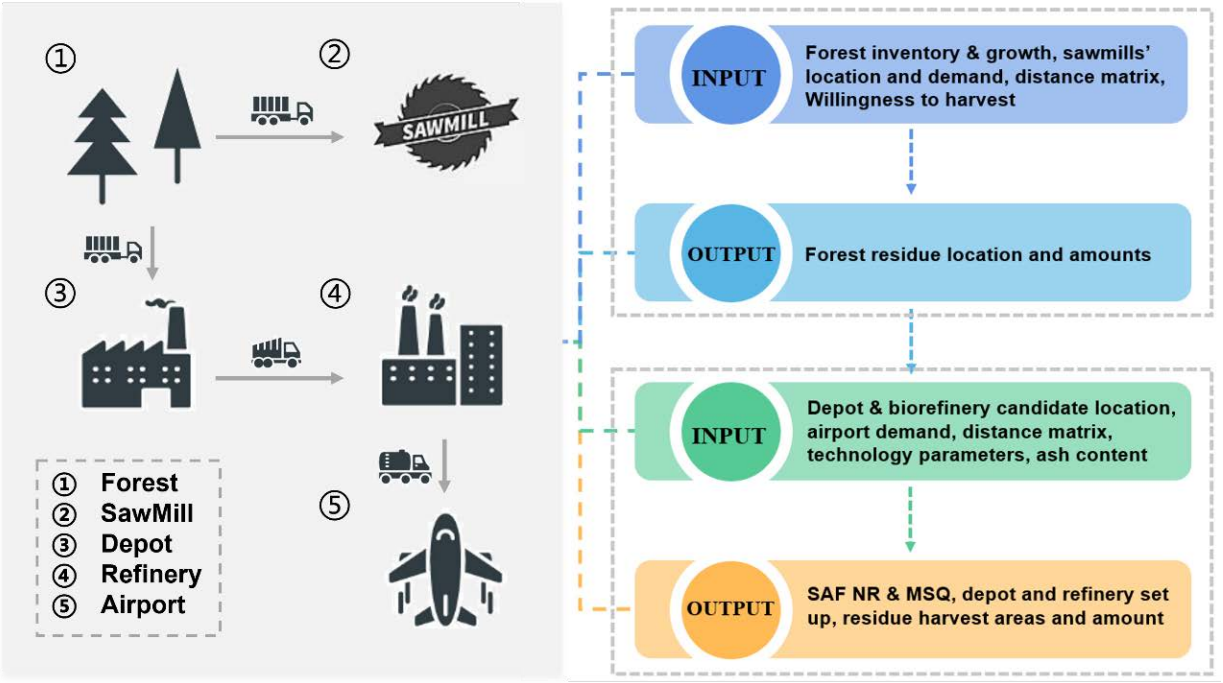


Figure 1. Diagram of logging residue-based SAF supply chain network and model structure.
Note: NR: net revenue; MSQ: maximum supply quantity.

In addition to biomass feedstock, intermediate crops cultivated during winter have gained recent attention as SAF feedstocks via the hydro-processed ester fatty acid (HEFA) pathway. We applied our previously established winter canola supply chain optimization model to evaluate the economic and potential volume of SAF to two major U.S. air cargo hubs, i.e., MEM and SDF airports. We have been expanding the cultivation area beyond Tennessee and Kentucky when locating winter canola production areas around those two major air cargo hubs.



Milestones

- Completed and presented the results of the forestry biomass for SAF production and developed a manuscript that has been revised and resubmitted.
- Updated the winter canola data files and incorporated them with the winter canola supply chain model.

Major Accomplishments

The impact of incorporating feedstock ash content variability on the economic and supply chains of the optimization model is considerable. Table 1 summarizes the differences in the optimal logging residue supply chain outputs between the fixed ash content case and heterogeneous ash case. The lower SAF production and higher production cost when considering ash content variations in logging residues are due to lower conversion throughput (i.e., lower bio-oil yield from the same amount of logging residues) in areas with high ash content. Neglecting ash variations in feedstock and using a constant ash content and fixed bio-oil yield likely overestimates feedstock availability and the corresponding SAF production, as shown in the constant ash content scenario.

Table 1. Optimization outputs of the assuming fixed and heterogeneous ash contents in logging residues.

	No Ash Variation	Spatially Heterogeneous Ash Variation	Difference
Annual SAF Production (million gal)	629.	540	↓89 (-14.10%)
Other Biofuels (million gal)	446	384	↓62 (-13.90%)
Number of Biorefineries	18	16	↓2
Avg. Biorefinery Capacity (million gal/year)	80	77	↓3 (-3.75%)
Number of Depots	85	80	↓5
Total Production Cost ($/gallon)	5.76	5.92	↑0.16 (2.78%)
- Harvest Cost	0.38	0.41	↑0.03 (7.89%)
- Stumpage Coste	0.11	0.11	--
- Preprocessing Cost	1.44	1.55	↑0.11 (7.64%)
- Conversion Cost	3.25	3.25	--
- Transport: Site > Depot	0.37	0.38	↑0.01 (2.70%)
- Transport: Deport > Refinery	0.2	0.22	↑0.02 (10.00%
- Transport: Refinery > Airport	0.02	0.02	--
SAF Selling Price ($/gallon)	9.09	9.09	Fixed
Net Revenue ($/gallon)	3.33	3.17	↓0.16 (-4.80%)

SAF: sustainable aviation fuel

As illustrated in Figure 2, the model selects 18 refineries under the constant-ash scenario (top panel). In contrast, the heterogeneous-ash scenario results in the selection of only 16 refineries (bottom panel), leading to the exclusion of two sites: Meriwether, GA (60 million gal) and Cleveland, NC (60 million gal). Additionally, one site is relocated from Wilson, TN, to Davidson, TN, approximately 51 miles away. Among the remaining operational sites, the model adjusts facility capacity with notable disparities: one site reduces capacity by 30 million gal, two sites each downsize capacity by 20 million gal, two sites each lower capacity by 10 million gal, and only one site increases capacity by 10 million gal. Consequently, accounting for feedstock ash variability results in an overall reduction of 200 million gal in capacity compared to the constant-ash scenario.

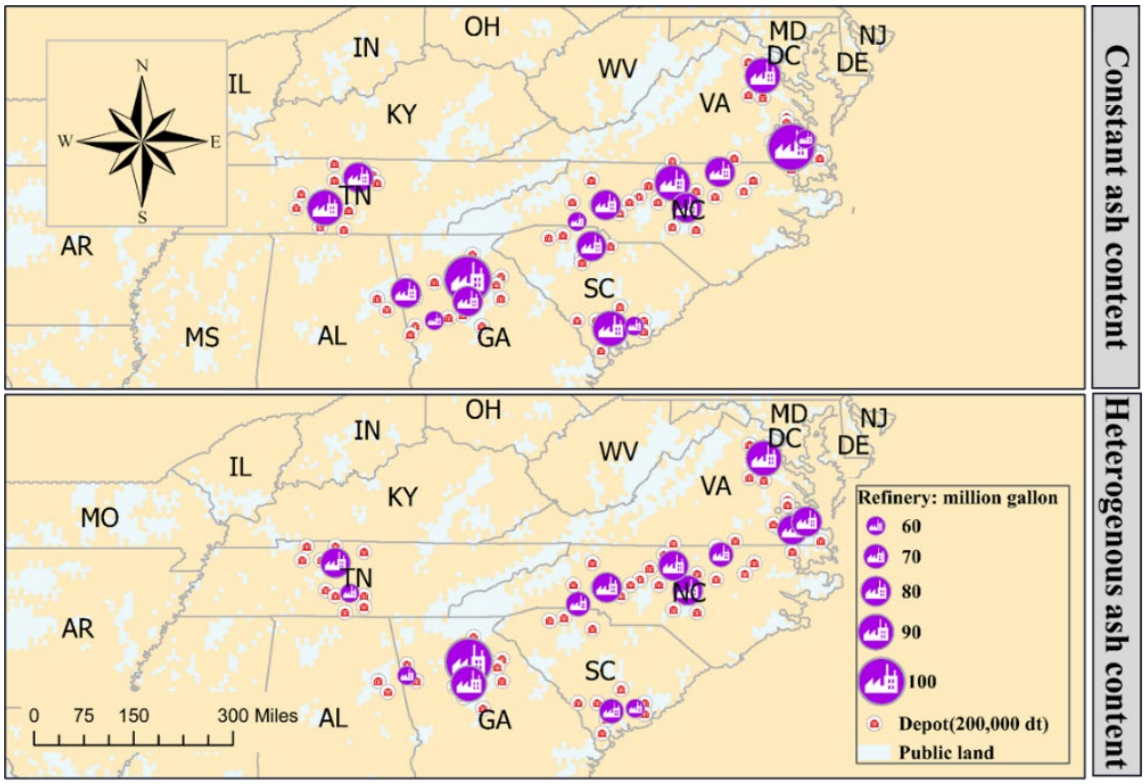


Figure 2. Graphic of placement comparison of preprocessing and conversion facilities.

Publications

Bolakhe, K., Yu, T. E., Sykes, V., Smith, A., & Boyer, C. N. (Manuscript revised and resubmitted for publication). *Assessing a Sustainable Aviation Fuel Supply Chain from Winter Canola and Its Carbon Intensity Considering Feedstock Yield Variations*.

Li, P., Yu, T.E., Labbé, N., Abdoulmoumine, N., Garcia-Perez, M., Hoyt, K.P., & English, B.C. (2026). Spatial Optimization of the Sustainable Aviation Fuel Supply Chains from Forest Residues via Fast Pyrolysis/Hydrotreatment Considering Feedstock Ash Content Variability. *Biomass and Bioenergy*, 208:108793. https://doi.org/10.1016/j.biombioe.2025.108793

Outreach Efforts

The study results have been disseminated at various professional meetings. Our team also shared the work with the Tennessee Department of Agriculture.

Conference Presentations

Yu, T. E. (2024, September 30 – October 3). *Biomass Feedstock Supply Chain Modeling and Decision Tools for Sustainable Aviation Fuels* [Conference presentation]. 2024 Frontiers in Biorefining 7th International Conference, St. Simons Island, Georgia.

Yu, T. E., Li, P., Labbé, N., Abdoulmoumine, N., Garcia-Perez, M., & Hoyt, K. (2024, November 20-22) *Sustainable Aviation Fuel Supply Chains Optimization from Forest Residues Considering Feedstock Ash Content Variability* [Conference presentation]. 2024 AFCC Global Biobased Economy Conference, Washington DC.

Awards

2025 Outstanding Master's Thesis Award for Kumar Bolakhe's master's thesis, titled "Stochastic Optimization of Canola-Based Sustainable Aviation Fuel in the Southeastern US," awarded by the Southern Agricultural Economics Association.



2025 Outstanding Master's Thesis Award Honorable Mention for Kumar Bolakhe's master's thesis, titled "Stochastic Optimization of Canola-Based Sustainable Aviation Fuel in the Southeastern US," awarded by the Agricultural and Applied Economics Association.

Student Involvement

Kumar Bolakhe, a previous MS student, developed the winter canola supply chain optimization model. Bijay Regmi, a current MS student, is updating the data files for the winter canola supply chain for the major air cargo hubs.

Plans for Next Period

- Continue to work on regional SAF analysis using winter canola as feedstock.
- Incorporate life-cycle analysis to supply chain analysis.

Task 2 - Analyze the Risk Factors Reported by Publicly Traded Biofuel Companies

University of Tennessee

Objectives

One of the biggest challenges in an emerging industry is the significant uncertainty investors face. Given the high level of uncertainty in the immature biofuel industry, such as SAF, the primary objective of this study was to identify and assess the risks biofuel firms face. The study evaluated the risk factors, or specific risks, reported by biofuel firms to the U.S. Securities and Exchange Commission (SEC).

Research Approach

This study analyzed the risks disclosed by a sample of biofuel firms that listed their securities on U.S. exchange markets. The study primarily evaluated two risk metrics, prevalence and relevance, across 25 specific risks (or risk factors) listed in Table 2 and Table 3 from 2017 to 2021. Risk prevalence measures the extent to which a risk affects the biofuel industry. It represents the number of firms in the sample that report a particular risk each year, or equivalently, the proportion of firms that report it. Risk relevance measures the severity of a risk by considering the frequency with which a risk is reported/discussed by firms in their annual reports, as well as the importance or priority assigned by firms to that particular risk. The risk relevance metric was validated by comparing it with other widely used risk metrics, including the Z-score and the debt-to-equity ratio, which typically measure overall firm risk. The analysis was conducted for all firms in the sample, as well as for subsets of focused and diversified biofuel firms. Identification of risk metrics by quadrants, combined with quantile regression analysis, allowed us to identify the critical risks.

Table 2. External risk factors analyzed in the study.

Political	Economic	Social	Technological
Biofuel regulation	Feedstock markets	Public opposition	Conversion technology
Environmental	Biofuel markets	Public perception	Fuel compatibility
Infrastructure	Competing fuel markets		Intellectual property
International	Energy markets		Cybersecurity
General regulations	Competition		
	General economic conditions		
	Stock price risk		



Table 3. Primary activities and support activities risk factors analyzed in the study.

Primary Activities	Support Activities
Facilities development	General management
Profitable operations	Risk management
	Financing
	Contracting
	Mergers and acquisitions

Milestones

- Performed risk analysis of the publicly traded biofuel firms.
- Published a peer-reviewed journal article for this study.

Major Accomplishments

Figure 3 plots the medians of prevalence (panel A) and relevance (panel B) by risk category. Primary activities, support activities, economic, and political sources of risk were ranked above or around the median values of the biofuel industry. In contrast, the social and technological risk categories were below the overall medians. Figure 3 suggests that firm managers consider internal factors, classified into primary and support activities, more relevant than external factors, likely because managers are more exposed to daily internal activities than to external factors, which are considered in less frequent strategic management assessments.

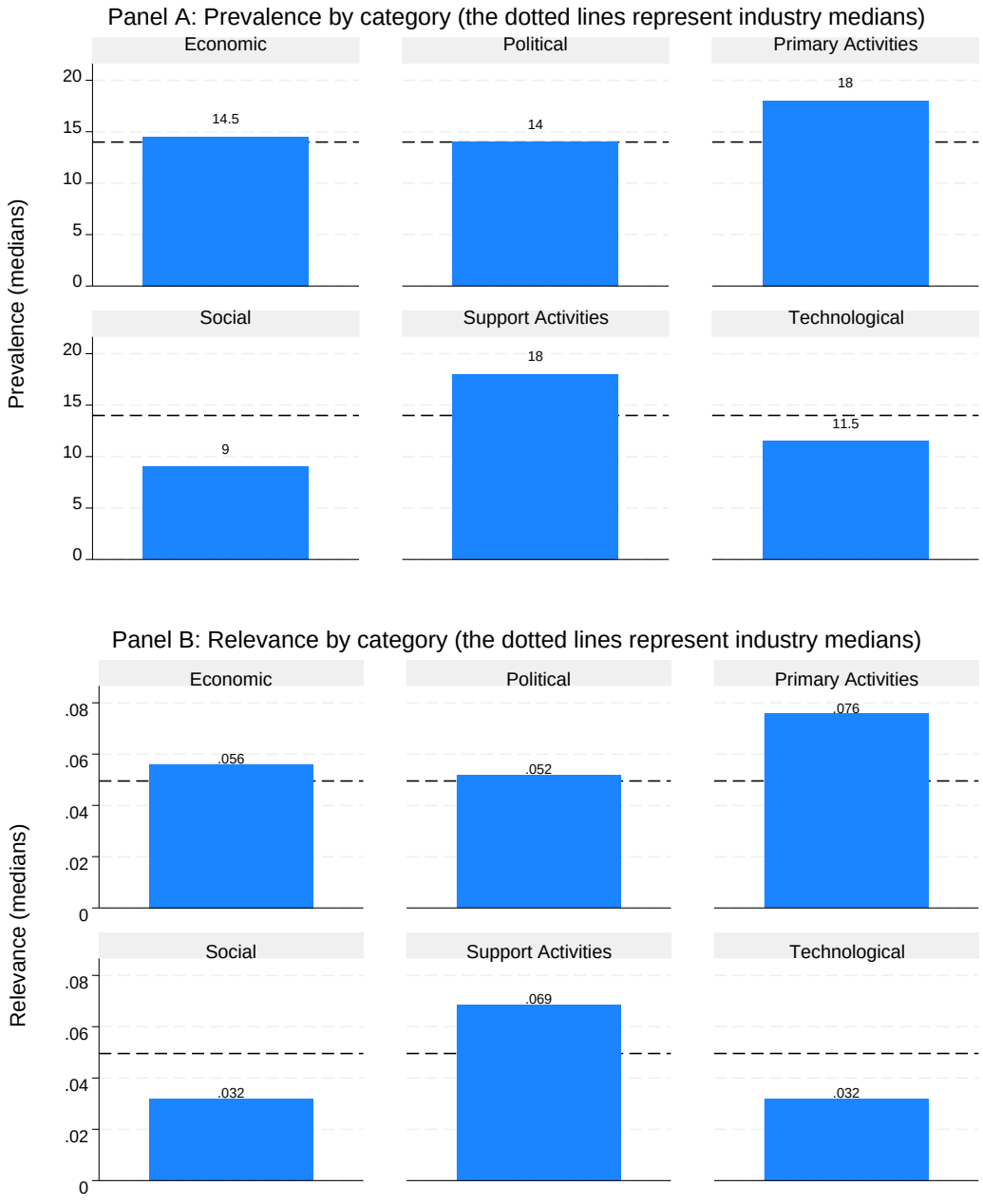


Figure 3. Prevalence and relevance by risk category for biofuel firms over 2017-2021.

The quantile regression results, presented in Table 4, help us identify critical risks. The dependent variable for the regression was the risk metric relevance, and the explanatory variable was the binary variable created for each risk. A risk was identified as critical if the risk's relevance median was statistically equal to or higher than the median of all other risks in the quantile regression. The critical risks included biofuel regulation, biofuel markets, feedstock markets, conversion technologies, profitable operations, financing, and risk management. Environmental and contracting risks were also critical.



Table 4. Regressions for risk relevance of biofuel firms from 2017 to 2021.

	Risk relevance (medians)		
	In the group	Not in the group	Regression coefficient
Political:			
Biofuel regulation	0.0777	0.0474	0.0303***
Environmental	0.0474	0.0493	-0.002
Infrastructure	0.0381	0.0503	-0.0122***
International	0.0517	0.0490	0.003
General regulations	0.0669	0.0474	0.0195**
Economic:			
Feedstock markets	0.0694	0.0474	0.022***
Biofuel markets	0.1117	0.0474	0.0644***
Competing fuel markets	0.0514	0.0490	0.002
Energy markets	0.0496	0.0475	0.002
Competition	0.0475	0.0493	-0.002
General economic conditions	0.0753	0.0474	0.028***
Stock price	0.0291	0.0503	-0.0212***
Social:			
Public opposition	0.0250	0.0503	-0.0253***
Public perception	0.0375	0.0503	-0.0128***
Technological:			
Conversion technology	0.0442	0.0503	-0.006
Fuel compatibility	0.0315	0.0503	-0.0188*
Intellectual property	0.0246	0.0503	-0.0257***
Cybersecurity	0.0369	0.0503	-0.0134***
Primary Activities:			
Facilities development	0.0519	0.0475	0.004
Profitable operations	0.1010	0.0474	0.0536***
Support Activities:			
General management	0.0421	0.0503	-0.0082**
Risk management	0.1438	0.0474	0.0964***
Financing	0.0957	0.0474	0.0483***
Contracting	0.0759	0.0474	0.0286**
Mergers and acquisitions	0.0345	0.0503	-0.0158***

Publications

Peer-Reviewed Journal Publication

Trejo-Pech, C. O., Bista, B., Yu, T. E., & Larson, J. A. (2025). An Analysis of the Risk Narrative Disclosed by Publicly Traded Biofuel Firms. *Energy Strategy Reviews, 62*, 101927. https://doi.org/10.1016/j.esr.2025.101927

Outreach Efforts

The preliminary findings were shared with some biofuel companies for feedback.

Awards

None.

Student Involvement

An MS student, Bishal Bista, calculated the risk metrics in the study.

Plans for Next Period

The analysis could be updated with more recent data if additional funding is available.

Task 3 - Assess the Stakeholder Perceptions of the SAF Supply Chain for its Deployment

University of Tennessee

Objectives

The UT team facilitates regional deployment and production of SAF by understanding stakeholders' perspectives throughout the SAF supply chain to expedite its development and scaling.

Research Approach

For airlines to commit to using SAF, there must be reliable consumer demand. This study evaluated whether airline campaign videos could change consumers' perceptions and understanding of SAF and their willingness to pay a premium. We surveyed American air travelers who were adults and had flown at least once in the past year, using an international market research company (Qualtrics) in February 2025. The study involved two airline campaign videos: Delta Air Lines and United Airlines, which served as the treatment groups. A total of 1,327 valid responses were collected, with 444 participants viewing Delta Air Lines' campaign video, 445 participants watching United Airlines' video, and 438 participants in a control group. We also used the best-worst scaling (BWS) analysis to identify what features of SAF are most and least important to U.S. air travelers.

Major Accomplishments

Figure 4 indicates that the campaign videos increased respondents' acceptance of SAF. The blue bar represents the control group that did not watch either of the campaign videos. The yellow bar refers to the treatment group before watching the video, while the green bar represents the treatment group after watching the video. For both statements in the figure, the share of choosing “strongly agree” significantly increased, while the share of “neither agree nor disagree” group decreased.

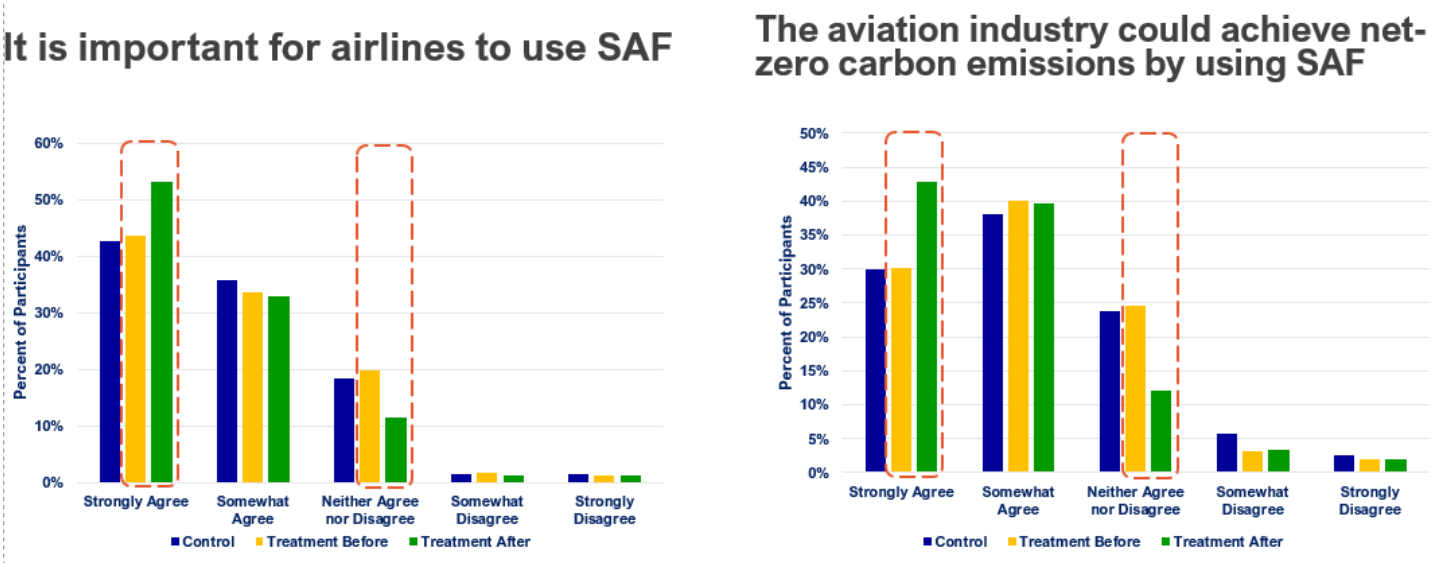


Figure 4. Charts of air travelers' perceptions about the importance of using sustainable aviation fuel (SAF) for flights.

Figure 5 presents the impact of the campaign video on air travelers' knowledge of SAF. The distribution of respondents' knowledge clearly shifted right. Most respondents received four points before watching the video. However, after watching the video, more than 70% of respondents received scores greater than five points. Table 4 shows more details about the composition of the changes. The videos improved the overall knowledge scores by nearly 41%, with more than 68% of the respondents knowing more about SAF after treatment. Interestingly, the video impact varied slightly by airline. Knowledge of both SAF benefits and feedstocks improved, with more progress on feedstocks.

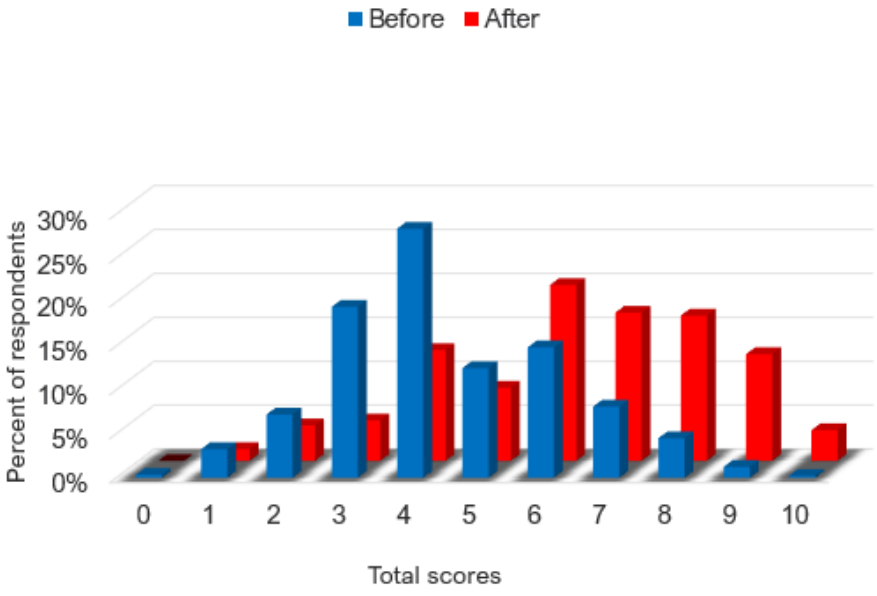


Figure 5. Graph of U.S. air travelers' knowledge scores about SAF before and after the campaign video.



Table 5. Summary of U.S. air travelers' knowledge before and after the campaign video.

Group Name	Total Scores before Treatment	Total Score after Treatment	Percent of Improved Total Scores	Number of People with Improved Scores	Number of People in Group	Percent of People with Improved Score
Overall	3974	5601	40.94%	612	889	68.84%
Airline Campaign Subgroups:						
Delta	2017	2846	41.10	316	444	71.17%
United	1957	2755	40.78%	296	445	66.52%
SAF Question Subgroups:						
Benefits	2654	2814	6.03%	287	889	32.28%
Feedstocks	1320	2787	111.14%	580	889	65.24%

Figure 6 shows most of the participants were willing to pay a premium for their last flight if fueled by SAF. Also, participants who purchased higher-class tickets were willing to pay a larger premium. For instance, most air travelers who paid their last air ticket prices less than $1,000 were willing to pay the SAF premium up to 10% of the ticket price. However, travelers who paid more than $1,500 for the last ticket were willing to pay a much higher premium.



Figure 6. WTP for SAF premium vs. price paid for the last ticket.

Regression analysis in Table 6 revealed that respondents who better understood SAF's benefits from the campaign videos were more inclined to pay the premium. Furthermore, age, gender, education, the number of flights taken per year, air ticket prices, and awareness of changing weather patterns influenced the willingness to pay the premium. Our findings suggest that improving public perception and knowledge of SAF is essential for its further development.



Table 6. Regression results of the willingness to pay (WTP) for sustainable aviation fuel (SAF) premium.

Variables	Model 1	Model 2	Model 3
Air ticket price paid last flight	0.33 (0.033)***	0.32 (0.032)***	0.32 (0.033)***
Number of flights last year	0.17 (0.048)***	0.16 (0.049)***	0.16 (0.048)***
Age	-0.13 (0.016)***	-0.12 (0.16)***	-0.12 (0.016)***
Gender	-0.29 (0.100)**	-0.26 (0.102)*	-0.26 (0.102)*
Education	-0.05 (0.034)	-0.05 (0.034)	-0.05 (0.034)
Weather pattern change	0.048 (0.073)***	0.47 (0.073)***	0.048 (0.074)***
Delta	0.14 (0.122)	--	--
United	-0.05 (0.124)	--	--
Δ in benefit scores	--	0.08 (0.031)**	0.08 (0.031)**
Δ in feedstock scores	--	-0.09 (0.028)***	-0.09 (0.028)***
Perception Δ of importance of SAF	--	--	0.18 (0.084)*
Perception Δ of NetZero from SAF	--	--	0.08 (0.031)
LR chi2(8)	297.89	308.63	311.39
Prob>chi2	0.000	0.000	0.000

Note: N=1326; standard errors in parenthesis;
*** p<0.05, ** p<0.01, *** p<0.001**

The BWS analysis results, presented in Figure 7, show that carbon emission reduction and local air quality improvement are the top two features of SAF considered by U.S. households. Findings suggest that consumers prioritize the environmental benefits of SAF over other features. This perspective remains largely consistent across various demographics, including both those who watched and did not watch the SAF videos, as well as across genders and age groups.

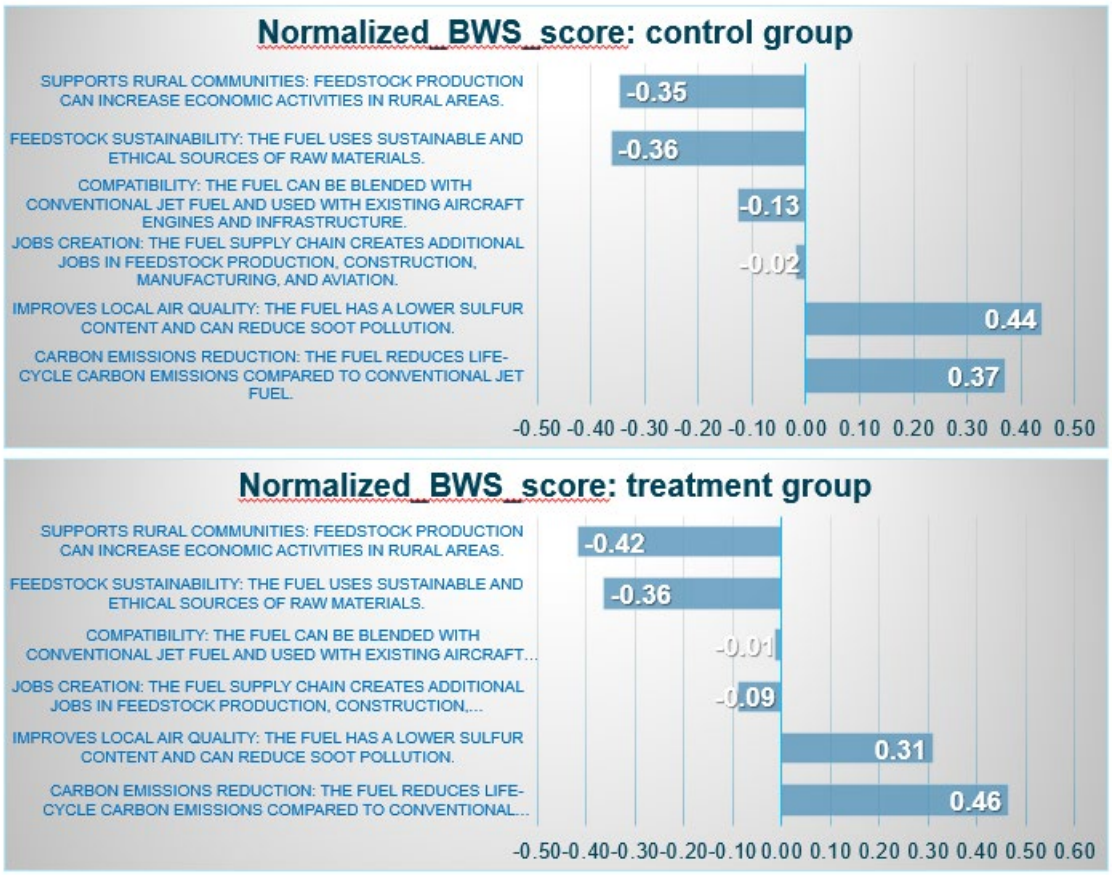


Figure 7. Chart of the best-worst scaling analysis results of the SAF features.

Publications

None.

Outreach Efforts

We shared our findings with an industry group (Airlines for America) and government agencies for their feedback and input.

Conference Presentation

Yu, T. E., Meyer, E., & Chen, X. (2025, July 9-11). *Consumers' Perception and Knowledge of Sustainable Aviation Fuel and Their Willingness to Pay a Premium* [Conference presentation]. The 1st International Conference on Sustainable Aviation Research, Dublin, Ireland.

Awards

Best Paper Award, International Conference of Sustainable Aviation Research, 2025 (Yu et al., 2025).

Student Involvement

An undergraduate student, Emma Meyer, participated in the survey design and analysis, and composed an undergraduate thesis titled "The Impact of Airline Campaign Video on Consumers' Perception and Knowledge of Sustainable Aviation Fuel and Their Willingness to Pay."



Plans for Next Period

- Develop manuscripts from the survey results to examine the impacts of airlines' SAF campaign videos on air travelers' perception and knowledge about SAF and their willingness to pay for SAF premium.

Task 4 - Collaborate with other ASCENT Team Members on Feedstock Supply and Facility Location Analysis

University of Tennessee

Objective

Collaborate with other ASCENT Project 001 teams, e.g., U.S. Department of Transportation Volpe Center (Volpe) or Washington State University (WSU), to conduct feedstock supply and facilitate location analysis.

Research Approach

This task involves exchanging necessary input with other teams through research efforts. The approach varies based on the topic and scope of research.

Milestones

- Worked with WSU in Techno-economic Analysis (TEA) assessment and the impact of government programs on oilseed markets
- Worked with Volpe to examine the Freight and Fuel Transportation Optimization Tool (FTOT) model for winter canola supply chains.

Major Accomplishments

We obtained some preliminary output but will need to further examine the analyses.

Publications

None.

Outreach Efforts

None.

Awards

None.

Student Involvement

Bijay Regmi, an MS student, has worked closely with Volpe to validate the winter canola supply chains from FTOT.

Plans for Next Period

Finalize the analysis with WSU and develop a manuscript of the oilseed analysis.



Project 001(F) Alternative Jet Fuel Supply Chain Analysis

Massachusetts Institute of Technology
Hasselt University

Project Lead Investigators

Dr. Florian Allroggen
Principal Research Scientist
Laboratory for Aviation and the Environment
Massachusetts Institute of Technology
77 Massachusetts Ave, Building 33-328, Cambridge, MA 02139
617-715-4472
fallrogg@mit.edu

Dr. Raymond L. Speth
Senior Research Scientist
Laboratory for Aviation and the Environment
Massachusetts Institute of Technology
77 Massachusetts Ave, Building 33-322, Cambridge, MA 02139
617-253-1516
speth@mit.edu

University Participants

Massachusetts Institute of Technology (MIT)

- P.I.: Dr. Florian Allroggen
- FAA Award Number: 13-C-AJFE-MIT, Amendment Nos. 003, 012, 016, 028, 033, 040, 048, 055, 058, 067, 082, 088, 096, 115, 132, 135, 142, and 143
- Period of Performance: August 1, 2014, to August 31, 2027
- Tasks (for reporting period October 1, 2024, to September 30, 2025):
  1. Support and provide leadership for United States (U.S.) participation in the International Civil Aviation Organization (ICAO) Committee on Aviation Environmental Protection (CAEP) to enable appropriate crediting of the use of sustainable aviation fuels (SAF) under the Carbon Offsetting and Reduction Scheme for International Aviation (CORSIA)
  2. Support U.S. participation in the ICAO CAEP by establishing default values and other lifecycle assessments for use under CORSIA
  3. *(omitted, led by Hasselt University)*
  4. Support knowledge sharing and coordination across all ASCENT Project 001 universities working on SAF supply chain analyses.

Hasselt University (UHasselt or UH, through subaward from MIT)

- P.I.: Prof. Robert Malina
- FAA Award Number: MIT Subaward Purchase Order No. 753374
- Period of Performance: September 1, 2016, to September 30, 2026
- Tasks (for reporting period October 1, 2024, to September 30, 2025):
  1. Support and provide leadership for U.S. participation in ICAO CAEP to enable appropriate crediting of the use of SAFs under CORSIA
  2. Support U.S. participation in the ICAO CAEP by establishing default values and other lifecycle assessments for use under CORSIA
  3. Contribute to the development of fuel production assessment for CORSIA-eligible fuels (CEF)
  4. *(omitted, led by MIT)*



Project Funding Level

$4,560,000 FAA funding and $4,560,000 matching funds. Sources of match are approximately $723,200 from MIT, plus 3rd party in-kind contributions of $809,000 from Byogy Renewables, Inc., and $1,038,000 from Oliver Wyman Group, and $1,155,000 from NuFuels LLC, and $401,000 from Savion Aerospace Corp., and $433,800 from Earth Force Technologies.

Investigation Team

Massachusetts Institute of Technology

Dr. Florian Allroggen (P.I.), All MIT tasks
Dr. Raymond L. Speth (co-P.I.), MIT Task 1
Dr. Niamh Keogh (research scientist), MIT Task 1 & 2
Tae Joong Park (graduate research assistant), MIT Tasks 1 & 2

Hasselt University

Prof. Robert Malina (P.I.), All UHasselt Tasks
Dr. Alessandro Martulli (postdoctoral associate), All UHasselt Tasks

Project Overview

The overall objectives of ASCENT Project 001 are to (a) derive information on regional supply chains to explore scenarios for future SAF production and (b) identify supply-chain-related obstacles to commercial-scale production in the near term and to larger-scale adoption in the longer term. For the reporting period, the MIT/UHasselt team contributed to these goals by (a) providing leadership in the ICAO CAEP Core LCA (CLCA) subgroup of the Fuels Task Group (FTG), now ICAO CAEP Working Group 5 (WG5), which has been tasked with calculating life-cycle greenhouse gas (GHG) emissions associated with the use of SAF, (b) performing core life-cycle GHG emission analyses to enable the inclusion of additional SAF pathways under CORSIA or to verify CLCA values calculated by other institutions, (c) contributing to SAF availability assessments, and (d) contributing to knowledge transfer among the A01 team.

Task 1 – Support and Provide Leadership for U.S. Participation in ICAO CAEP to Enable Appropriate Crediting of the Use of SAFs under CORSIA

Massachusetts Institute of Technology
Hasselt University

Objectives

The overall objective of this task is to provide leadership and support to the FAA in its engagement with the ICAO CAEP FTG (now WG5) to maintain and further develop CORSIA. The specific focus of the work during this reporting period was to (a) finalize amendments to the CORSIA actual value method for including fuels produced from with high electricity inputs and/or with atmospheric or waste gas carbon sources, (b) support finalizing documents for the CAEP 13 meeting, and (c) support development of the work program for WG5 for the CAEP 14 cycle.

Research Approach

To achieve the goals outlined above, the team continued to co-lead the CLCA subgroup of the FTG, now WG5. Prof. Malina acted as a co-lead of the CLCA subgroup and Dr. Allroggen leads the ad-hoc group (AHG) to develop methods for fuels with significant electricity input, which also covered carbon sourcing methods. Prof. Malina's role ensures that Prof. Malina remains a focal point of CLCA research and that specific research tasks can be guided efficiently and effectively; Dr. Allroggen's role ensures leadership on developing novel methods for fuels that were previously not captured in CORSIA. Research conducted in support of the leadership roles is discussed below.

Actual Value Method for Including Fuels Produced with High Electricity Inputs and from Atmospheric or Waste Gas Carbon Sources

Based on research reported during previous reporting periods, the MIT team helped finalize the methods proposal for fuels produced with high electricity inputs and from atmospheric or waste gas carbon sources. Specific text proposals were revised and discussed within FTG:



- For electricity sourcing, key amendments include the addition of a novel electricity sourcing method, which is now included in Section 10 of the Actual Value document. This section discusses the required sourcing documentation, as well as additionality, deliverability, temporal matching, and sustainability certification requirements for electricity sourced for CEF production. Taken together, these elements are meant to replicate chain of custody considerations. They were considered necessary to (a) provide a technology-neutral assessment methodology and (b) avoid concerns at the grid level, especially for impacts and grid stability. A detailed discussion of the underlying rationale can be found in the report for the previous reporting period.
- For carbon sourcing, the MIT team helped finalize new provisions that allow the use of atmospheric and waste gas carbon sources under the actual value document. Key edits include required revisions of the system boundary (now included in Section 2.2.1) and detailed provisions on how waste and residue gases of fossil and biogenic origin can be utilized (now in Section 2.4). Furthermore, a definition and criteria to identify waste and residue gases were included in Section 4 of the document. A detailed discussion of the underlying rationale can be found in reports for the previous reporting periods.

During the CAEP 14 cycle, the MIT team has begun supporting the work of the electricity AHG by researching the sensitivity of default LCA values to electricity carbon intensities. This included understanding when contributions of electricity could vary significantly from default assumptions. Initial analyses show substantial variability in this sensitivity across the default pathways. While electricity contributions to the default value for most pathways do not vary by more than 4g carbon dioxide equivalent (CO_2e) per MJ of fuel within reasonable ranges of electricity carbon intensity (CI) (see Figure 1), some pathways, including mostly ethanol-to-Jet (ETJ) pathways, can produce significant deviations.

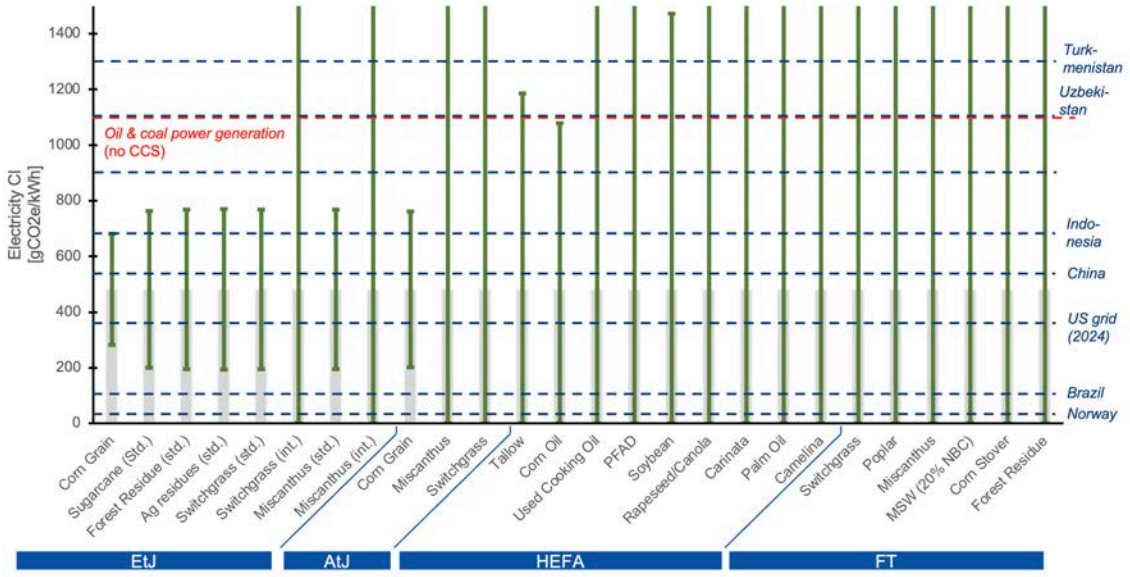


Figure 1. Ranges of electricity carbon intensity, which maintains electricity contribution within 4 gCO_2e per MJ of fuel of the default assumption. Default assumption grid assumption for the analysis is shown in the gray bar.

Support Finalizing Documents for the CAEP 13 Meeting

In wrapping up the CAEP 13 cycle, the MIT team supported finalization of documents for presentation to the CAEP 13 meeting. This included reviewing overview and status papers on FTG's work during the CAEP 13 cycle, as well as reviewing and finalizing concrete amendment proposals brought forward by FTG (see above as an example for the electricity and carbon sourcing method) and talking points for the U.S. team at the CAEP 13 meeting. Furthermore, the MIT team discussed inputs with FAA to help formulate the U.S. positions and leadership role of the U.S.



Support Development of the Work Program for WG5 for the CAEP 14 Cycle
During the CAEP 13 meeting, WG5 was established to take over the tasks of the FTG during the CAEP 14 cycle. WG5 was tasked with further advancing the methods to assess CEFs for consideration under CORSIA. During this reporting period, the MIT team supported development of a work program for the CAEP 14 cycle for WG5. In particular, the team co-led development of the work program for the CLCA group. This included identification of pathways for developing default LCA values (see below) and discussion and prioritization of areas to enhance methods (including further refinements on how electricity is considered in LCA values). The MIT team supported WG5 leadership to develop specific proposals for workplans; it further supported the US delegation in ensuring that U.S. priorities are reflected in the work plans.

Milestones

- UHasselt and MIT have brought forward analyses to support progress in the areas outlined above. The results have been presented to the FTG and WG5 during FTG and WG5 meetings and numerous CLCA subgroup and expert meetings.
- UHasselt and MIT experts participated in and contributed to FTG and WG5 meetings, including CAEP13/FTG9 as well as CAEP14_WG5_1 (May 2025), and CAEP13_WG5_2 (October 2025).

Major Accomplishments

- The CORSIA Actual Value document has been amended with proposed methods on electricity sourcing and use of additional carbon sources.
- Detailed work plans for the CAEP 14 cycle have been developed and presented to WG5.

Publications

- CAEP14_WP5_1_WP03: Update of the work of the CLCA subgroup
- CAEP14_WP5_2_WP09: Update of the work of the CLCA subgroup
- CAEP14_WP5_2_WP13: Proposal to the WG5 Board on feedstock classification
- CAEP14_WP5_2_WP20: Work Program of the Electricity Sourcing AHG in the CAEP 14 cycle.

Outreach Efforts

- Communicated progress on this task during weekly briefing calls with the FAA and other U.S. delegation members to the FTG and WG5, as well as during numerous FTG and WG5 teleconferences between meetings.
- Participated in and contributed to FTG meetings (UHasselt and MIT experts), including CAEP13/FTG9 as well as CAEP14_WG5_1 (May 2025) and CAEP13_WG5_2 (October 2025).
- Led an AHG to prepare concrete proposals for revision of the actual value document to enable the use of additional carbon sources and significant electricity use.

Student Involvement

Tae Joong Park (graduate student, MIT) was involved in this task.

Plans for Next Period

Subject to additional funding of the project, continue work in WG5, including:

- Calculate and propose default CLCA values for additional pathways.
- Continue to lead the CLCA Subgroup (Prof. Malina) and the Electricity Sourcing AHG (Dr. Allroggen).

Task 2 – Support U.S. Participation in ICAO CAEP by Performing CLCA to Establish Default Values for Use Under CORSIA

Massachusetts Institute of Technology
Hasselt University

Objectives

During the CAEP/11, CAEP/12, and CAEP/13 cycle, the MIT ASCENT Project 001 team took leadership in applying the agreed-upon CLCA method to establish default CLCA values for CEFs. However, the list of pathways is not exhaustive, and further CLCA analysis is required to enable the inclusion of SAF technologies nearing commercialization. During the



current reporting period, the team supported the calculation of palm oil mill effluent (POME) hydroprocessed ester and fatty acid (HEFA) fuel default LCA value using the U.S.-developed Greenhouse gases, Regulated Emissions, and Energy use in Technologies (GREET) model.

Research Approach

CLCA of HEFA fuel from POME

The team estimated the life cycle GHG emissions of HEFA from POME. The feedstock is a palm oil mill effluent which is included in the positive list of wastes, residues and by products of the palm oil industry. The system boundaries of calculations as well as the specific data sources used for the calculation are summarized in Table 1. The results are shown in Table 2.

Table 1. General assumptions for estimating the core life-cycle analysis emissions of hydroprocessed ester and fatty acid (HEFA) fuels from palm oil mill effluent (POME). CORSIA: Carbon Offsetting and Reduction Scheme for International Aviation; GREET: greenhouse gases, regulated emissions, and energy use in transportation, ICAO: International Civil Aviation Organization, SAF: sustainable aviation fuel.

Stage	Modeling assumptions
Feedstock collection and pre-treatment	Feedstock is assumed to be collected from the POME pond by pump (electricity use). Steam, electricity and various chemicals are used as inputs in the pre-treatment stage. As this step is assumed to take place in Malaysia, the electricity grid mix and the natural gas emission factors of Malaysia are used. Data on the electricity grid mix for Malaysia are sourced from Ember-energy (2023). Electricity use is taken from Sharvini et al. (2020). The natural gas emission factors are computed assuming a 99% offshore gas production in Malaysia.
Feedstock transportation	The POME oil is assumed to be transported first by truck (315 km) to Port Klang from where it is transported to the Port of Rotterdam by ocean tanker (14985 km). Electricity input for the pumping is included.
Fuel production	Hydrogen requirements for POME oil were adjusted from those for soybean hydrogen consumption using the molar stoichiometry of the hydroprocessing reactions. The fatty acid composition of POME oil is taken from data submitted to ICAO. Other energy and utility inputs taken from other HEFA fuels considered under CORSIA. As the SAF production step is assumed to take place in Europe, electricity grid mix and adjusted natural gas emission factors of Europe are used. The natural gas emission factor for Europe is computed in GREET assuming a 33% imported liquified natural gas (LNG).
Fuel transportation and distribution	According to default data from the GREET model, 63%, 8% and 29% of the fuel were assumed to be transported 80 km by truck, 837 km by barge, and 1288 km by rail, respectively. Back-haul is assumed to be empty.

Table 2. Estimated greenhouse gas (GHG) emissions from palm oil mill effluent (POME) sustainable aviation fuel (SAF) production. Data in g CO_2e/MJ_{SAF}.

Stage	POME
Feedstock collection and pre-treatment	3.23
Feedstock transportation	3.71
SAF production	9.83
SAF transportation	0.38

A sensitivity analysis was conducted around key parameters in order to understand the need for clarification in the pathway specification column of the default value table in the ICAO Document “CORSIA Default Life Cycle Emissions Values For CORSIA Eligible Fuels.” (ICAO, 2025) The results are detailed in Table 3 and Table 4.



Table 3. Sensitivity analysis results for power, coal, and natural gas (NG) requirements.

Variation in g-CO_2e/MJ	-20%	-10%	Baseline	+10%	+20%
Power requirements	-0.17	-0.09	17.15	+0.09	+0.17
NG requirements	-1.44	-0.72	17.15	+0.72	+1.44

Table 4. Sensitivity analysis results for power, coal, and natural gas requirements. GHG: greenhouse gas.

g-CO_2e/MJ	Natural Gas (baseline)	Coal	Solar	Nuclear
GHG emission	17.15	21.80 (+4.65)	12.89 (-4.27)	12.93 (-4.22)

Milestones

- Documented research performed in working papers and information papers submitted to the FTG and WG5.
- Discussed the work outlined above with various technical experts.

Major Accomplishments

Inclusion of POME HEFA pathway in CORSIA

Publications

Written report

CAEP14/WG05_02/WP14: Proposal to the FTG Board on a default LCA value for POME HEFA.

Student Involvement

None.

Outreach Efforts

- Communicated progress on this task during weekly briefing calls with the FAA and other U.S. delegation members to the FTG and WG5, as well as during numerous FTG and WG5 teleconferences between meetings.
- Participated in and contributed to FTG meetings (UHasselt and MIT experts), including CAEP13/FTG9 as well as CAEP14_WG5_1 (May 2025) and CAEP13_WG5_2 (October 2025).

Plans for Next Period

Continue to perform attributional CLCA to establish default values for use under CORSIA, subject to additional funding of the project.

References

Ember-energy. (2023). *Electricity Data Explorer*. https://ember-energy.org/data/electricity-data-explorer/?data=co2_intensity&fuel=total&entity=Malaysia

ICAO. (2025). *CORSIA supporting document: CORSIA eligible fuels – Life cycle assessment methodology* (Version 7). International Civil Aviation Organization. https://www.icao.int/sites/default/files/environmental-protection/CORSIA/Documents/CORSIA%20Eligible%20Fuels/CORSIA_Supporting_Document_CORSIA-Eligible-Fuels_LCA_Methodology_V7.pdf

Sharvini, S. R., Noor, Z. Z., Chong, C. S., Stringer, L. C., & Glew, D. (2020). Energy generation from palm oil mill effluent: A life cycle assessment of two biogas technologies. *Energy, 191*, 116513. https://doi.org/10.1016/j.energy.2019.116513

Task 3 – Contribute to the Development of the Fuel Production Assessment for CEFs

Hasselt University

Objective

The objective of this task is to contribute to the development of the fuel production assessment for CEFs to the year 2030 and beyond, based on detailed information gathered in a fuel production database. During the reporting period, the team worked jointly with researchers from Washington State University to maintain and update the SAF production analysis database used for the WG5 fuel projections. Three work streams were developed: (1) update of the SAF short-term production projections, (2) revision of the methodology for developing the short-term production projections, and (3) publish SAF production development trajectories in the peer reviewed literature.

Research Approach

Update of the SAF Short-term Production Projections

In line with previous projections, the projection analysis considers a set of four production scenarios (Low, Moderate, High, and High+). The different scenarios are representative of more pessimistic or optimistic expectations on the development of the SAF market in the short-term. Table 5 details the scenario definitions. While not explicitly modeled, the gradient of parameters chosen in the scenarios with regard to success rates and product slate assumptions is reflective of different levels of policy support for SAF deployment through 2030 (Table 6).

Table 5. Definition of short-term scenarios. *Note*: Code 1: Company has SAF production plans, Code 2: SAF production mentioned but no specific plans & process relevant to SAF, Code 3: process relevant to SAF, but no SAF production plans mentioned; Maturity levels A (very high), B (high), C (moderate) and D (low) are considered. SAF: sustainable aviation fuel.

Scenario	Code	Maturity	Facility Jet Fuel Ratio	A	B	C
Low	1	A,B	Actual or low %	25%	10%	0%
Moderate	1-2	A,B,C	Actual or low %	50%	25%	10%
High	1-3	A,B,C	Actual or high % for 1-2 Actual or low % for 3	75%	50%	25%
High +	1-3	A,B,C	High %	75%	50%	25%

Table 6. Policy-mapping of scenarios. SAF: sustainable aviation fuel.

Scenario	Implicit SAF Policy landscape
Low	No policy support for SAF
Moderate	Some level of policy support for SAF, but lower than for road transportation biofuels
High	Level-playing field between SAF and road transportation biofuels
High+	SAF-emphasis in policies

The updated projections employ the International Air Transport Association SAF production estimate as starting point. For 2024, this value amounted to 1 million tonnes (Mt). Notably, the difference between the actual 2024 SAF production value and the estimates from the database and scenario definition is significantly larger in the High and High+ scenarios. This difference is primarily due to the inclusion of production volumes from facilities that use a technology that can be used for SAF production, but whose operators have not announced that they will actually produce SAF. In 2024, such facilities account for 40% and 79% of the projected production for the year 2024 in the High and High+ scenarios, respectively.

The use of actual production data for the baseline year (2024) results in a sharp increase between actual SAF production in 2024 and projected production in 2025 for the High and High+ scenarios (825% and 1,721% production growth between 2024 and 2025 for the High and High+ scenarios, respectively). This rapid increase is unlikely to occur. While keeping the



projected 2030 values from the two scenarios as-is, we smoothen the ramp-up to the 2030 values using a market diffusion approach previously used for the FTG fuel projections. The diffusion model scales the curve to align with actual production in 2024 and scenario-based estimates for 2030, providing a modified projection of SAF production from 1 Mt/year in 2024 to the maximum production level for 2030 using data derived from scenario definition and database data for the High and High+ scenarios.

Table 7 shows the updated annual results for the four scenarios through 2030 using the short-term production database without adjustments to the High and High+ scenarios. For the four scenarios (Low, Moderate, High, and High+), SAF volumes in the year 2030 range from 2.29 Mt in the Low scenario, to 32.13 Mt in the High+ scenario.

Table 7. Annual global (domestic and international) sustainable aviation fuel (SAF) production by scenario (2024 - 2030), without adjustments for the High and High+ scenarios. Data in million tonnes per year (Mt/year).

Year	Low	Moderate	High	High+
2024	1	1	1	1
2025	1.21	3.17	9.25	18.21
2026	1.56	4.17	12.27	21.25
2027	2.05	5.46	16.60	25.63
2028	2.05	5.91	19.83	28.87
2029	2.13	6.17	20.40	29.43
2030	2.29	6.85	23.09	32.13

Revision of the Methodology for SAF Short-term Production Projections

In April 2025, following the release of the latest production projections, the need to revise the projection methodology was highlighted. In July 2025, a review and potential revision of the short-term production projection methodology was proposed. Three main limitations in the current short-term production projections methodology were identified: (1) definition of short-term production projections scenarios, (2) maturity level definition, and 3) discrepancy between two data types, production and capacity volumes.

The definition of the current short-term production projections scenarios results in significant volume disparities between the High/High+ and the Low/Moderate scenarios. This is primarily due to the inclusion of facilities which use a technology that can be used for SAF production, but whose operators have no announced intentions to produce SAF (code 3 facilities). Moreover, the disparity is amplified by the assumed jet fuel production in the overall output. The High and High+ scenarios apply a high jet fuel ratio (for code 1 and 2 facilities), while the Low and Moderate scenarios assume a low jet fuel ratio when actual SAF production data are unavailable. The suggested revision of the short-term production projections scenarios definition includes two changes: (1) excluding all facilities that use a technology that can be used for SAF production, but whose operators have not announced that they will produce SAF, and (2) adjusting the assumed jet fuel ratio.

Concerns associated with the maturity level definition focus on the imbalanced distribution of entries across the different maturity levels. The suggested revision is to revise the categorization criteria by focusing on the individual facility rather than the production company. For example, instead of “Company has a plant under construction” the criteria could be reframed as “Facility under construction.”

The third limitation concerns the discrepancy between actual production and announced capacity data used in the short-term production projections. Current projections rely on announced capacity volumes. However, actual production data reveal that realized production levels are often considerably lower than the projected volumes from capacity announcements. This results in a discontinuity between historical production and forward projections. The suggested adjustment to address this limitation is to use actual production data for the first year of the short-term production projections, while adopting the 2030 capacity-based forecast as the final value across all scenarios. The interpolation between these points would follow the smoothing method already applied in the High and High+ scenarios in the last short-term production projections.



SAF Production Development Trajectories
The team published two papers in the peer reviewed literature that provide insights into the short- and medium-term projections for SAF production. One paper focuses on global and European trajectories, while another paper discusses the U.S. trajectories.

Milestone
Updated SAF short-term production projections and methods.

Major Accomplishments
- Developed the SAF production relational database in SQL (structured query language).
- Published overviews of SAF development trajectories in the peer reviewed literature.

Publications
ICAO papers
- CAEP14_WG5_PlenaryMeeting 1_WP01: SAF Short-term Production Projections Update, April 2025
- CAEP14_WG5_1_IP09: SAF Short-term Projections Update, May 2025
- CAEP14_WG5_1_IP08: SAF Short-term Production Projections Methodology Updates, October 2025

Peer-Reviewed Journal Publications
Martulli, A., Brandt, K., Allroggen, F., & Malina, R. (2025). The potential scale-up of sustainable aviation fuels production capacity to meet global and EU policy targets. *Nature Communications, 16*, 11619. https://www.nature.com/articles/s41467-025-66686-9

Brandt, K., Martinez-Valencia, L., Camenzind, D., Martulli, A., Malina, R., Allroggen, F., & Wolcott, M. (2025). Pragmatic assessment of meeting the 2030 U.S. sustainable aviation fuel goals. *Biomass and Bioenergy, 206*, 108516. https://doi.org/10.1016/j.biombioe.2025.108516

Outreach Efforts
Communicated progress on this task during weekly briefing calls with the FAA and other U.S. delegation members to the FTG and WG5, as well as during numerous FTG and long-term global aspirational goal (LTAG) teleconferences.

Awards
None.

Student Involvement
None.

Plans for Next Period
- Continue the revision of the SAF short-term production projections methodology and provide a revised methodology during CAEP14/W03 meeting in March 2026.
- Provide a new update of the SAF short-term production projections during a plenary meeting of WG5 scheduled for May 2026.

Task 4 – Support Knowledge Sharing and Coordination Across All A01 Universities Working on SAF Supply Chain Analyses
Massachusetts Institute of Technology

Objective
The objective of this task is to provide support for coordination of work by all ASCENT Project 001 universities on SAF supply chain analysis. The sharing of methods and results decreases the replication of work on similar topics among ASCENT Project 001 universities.



Research Approach
The MIT A01 team performed several functions to accomplish this task. Specifically, the team participated in bi-weekly ASCENT Project 001 coordination teleconferences, which served as a venue to discuss progress in various grant tasks and learn about the activities of other ASCENT universities.

Milestone
Presented current research to other ASCENT universities.

Major Accomplishments
Participated in bi-weekly ASCENT Project 001 coordination teleconferences and presentation of current research to other ASCENT universities.

Publications
None.

Outreach Efforts
Participated in bi-weekly ASCENT Project 001 coordination teleconferences and presentation of current research to other ASCENT universities.

Awards
None.

Student Involvement
None.

Plans for Next Period
Continue to engage in bi-weekly teleconferences and other events to disseminate MIT's ASCENT Project 001 work.



Project 002 Understanding Changes in Aviation Emissions Due to SAF with New Combustor Technology

Missouri University of Science and Technology, Aerodyne Research Inc., and The Boeing Company, and Gulfstream

Project Lead Investigator

Philip D. Whitefield
Professor Emeritus of Chemistry
Department of Chemistry
Missouri University of Science and Technology
400 W 11th Street, Rolla, MO 65409
573-465-7876
pwhite@mst.edu

University Participants

Missouri University of Science and Technology (MS&T)

- P.I.: Prof. Philip D. Whitefield
- FAA Award Number: 13-C-AJFE-MST, Amendments 002, 003, 005, 008, 010, 012, 019, 030 and 033
- Period of Performance: September 18, 2014, to December 31, 2026
- Tasks:
  1- 3. Perform the ground testing associated with an in-flight emissions study on a wide-body airframe and a business jet
    3.1. Plan the test matrices for up to a 3-week deployment to a ground testing venue to be provided by the sponsoring original equipment manufacturer (OEM)
    3.2. Prepare the MS&T and Aerodyne® instrument packages housed in mobile laboratories, including calibration of the individual particulate matter (PM) mass number and compositional systems
    3.3. Transport and set up the MS&T and Aerodyne instrument packages
    3.4. Execute the test matrices defined in Task 1 – 3.1
    3.5. Tear-down and transport the mobile laboratories and test personnel to their home locations
    3.6. Conduct post-test data reduction and analysis including participation in post-test
    3.7. Prepare and deliver interim and final reports
    3.8. Coordinate the procurement, fuel properties analysis, delivery, handling, and loading logistics for various fuels in support of emissions testing

Project Funding Level

Project	Funding	Matching	Source
13-C-AJFE-MST-002	$1,288,836.34	$1,288,836.34	EMPA letter
--	$284,613.66	$284,613.66	Transport Canada
13-C-AJFE-MST-003	$500,000.00	$500,000.00	EMPA letter
13-C-AJFE-MST 005	$500,000.00	$500,000.00	EMPA letter
13-C-AJFE-MST-008	$579,234.00	$579,234.00	EMPA letter
13-C-AJFE-MST-010	$725,500.00	$725,500.00	EMPA letter
13-C-AJFE-MST-012	$1,217,221.00	$1,217,221.00	EMPA letter

® Aerodyne is a registered trademark of Aerodyne Research, Inc., Billerica, Massachusetts.



Project	Funding	Matching	Source
13-C-AJFE-MST-019	$521,246.00	$521,246.00	GE letter
13-C-AJFE-MST-030	$3,050,812.00	$3,050,812.00	Boeing letter
13-C-AJFE-MST-033	$2,513,003.00	$2,513,003.00	Boeing letter

EMPA = Swiss Federal Laboratories for Materials Science and Technology
GE = General Electric

Investigation Team

Missouri University of Science and Technology Prof. Philip Whitefield, (P.I.)
Prof. Klaus Woelk, (co-P.I.)
Steven Achterberg, (research technician)

Aerodyne Research, Inc.
Dr. Richard Miake-Lye, (subcontractor)

The Boeing Company (Boeing)
Dr. Steven Baughum, (subcontractor)
Dr. William Griffin, (subcontractor)

Gulfstream Aerospace Corporation
Dr. Brian Cook, (subcontractor)

Project Overview

Objectives

In the last quarter of 2022, a decision was made to re-target the ASCENT Project 002 to focus on emissions impacts measurements resulting from the adoption of sustainable aviation fuels (SAF) by current and future anticipated global commercial fleets. Funds were de-obligated and re-obligated to underwrite the cost of these new emissions measurements. The ASCENT Project 002 MS&T team, with the guidance of emissions specialists at Boeing,® Pratt and Whitney® (P&W), and Gulfstream,® proposed to make three high-priority ground-based field measurement campaigns of nonvolatile particulate matter (nvPM) and combustion gas emissions from engines on a commercial widebody transport, a business jet aircraft, and a new technology combustor burning both conventional fuels and candidate SAF. These measurements were scheduled to occur in three 21-day test campaigns in the fourth quarter (Q4) of 2023 (Boeing/ecoDemonstrator; see Link 1 below), and in 2024 Q4 (Gulfstream; see Link 2 below). The third field campaign with a novel combustor technology at P&W after being delayed due to test cell access was eventually cancelled and was replaced by a follow-up ground-based and airborne campaign with Gulfstream, scheduled to take place in April 2026. The analysis and reporting of the data arising from the Boeing and first (ground-based) Gulfstream studies are underway. Each campaign has or will be preceded by test design, planning, and preparation, beginning in the second quarter of 2023. The cost to ASCENT Project 002 has been, and will be, to (a) support the MS&T team's participation in and management of the three ground-based emission studies and (b) defray some of the costs incurred for the fuels (i.e., SAFs and conventional jet fuels) that has or will be burned to conduct both ground-based and in-flight emissions testing. During this reporting period, the ecoDemonstrator and the first ground-based Gulfstream subprojects are in the post-test analysis stage. Planning and preparation for the follow-up ground-based and airborne with Gulfstream are underway.

Link 1 - https://aviationweek.com/special-topics/sustainable-aviation-fuel/boeing-737-10-ecodemonstrator-tackles-saf-contrail-study
Link 2 - https://www.gulfstreamnews.com/en/news/?id=c106d3c5-ffa0-4cf1-adc7-292e3a56dfea&utm

® Boeing is a registered trademark of The Boeing Company, Seattle, Washington.
® Pratt & Whitney is a registered trademark of RTX Corporation, Farmington, Connecticut.
® Gulfstream is a registered trademark of Gulfstream Aerospace Corporation, Savannah, Georgia



Work Schedule

- Task 1– 3 describes the work required to successfully perform the ground testing associated with an in-flight emissions study on a wide-body airframe (potentially the Boeing-sponsored ecoDemonstrator study), a business jet (the Gulfstream studies)
- Task 1 – 3.1: Plan the test matrices for up to a 3-week deployment to a ground testing venue to be provided by the sponsoring OEM (Boeing, Seattle, WA; Gulfstream, Savannah, GA). This planning exercise has been undertaken in coordination with the National Aeronautics and Space Administration Mobile Aerosol Laboratory team who are participating in the Boeing and Gulfstream ground tests.
- Task 1 – 3.2: Prepare the MS&T and Aerodyne instrument packages housed in mobile laboratories, including calibration of the individual PM mass number and compositional systems.
- Task 1 – 3.3: Transport and set up the MS&T and Aerodyne instrument packages (mobile laboratories). This task includes deployment of test personnel to the test site and the interconnection of the instrument packages to the communal sampling probe assembly. During this setup activity, sampling system loss analyses will be performed.
- Task 1 – 3.4: Execute the test matrices defined in Task 1 – 3.1
- Task 1 – 3.5: Tear down and transport the mobile laboratories and test personnel to their home locations.
- Task 1 – 3.6: Conduct post-test data reduction and analysis including participation in post-test workshops whose locations and times are yet to be defined.
- Task 1 – 3.7: Prepare and deliver interim and final reports.
- Task 1 – 3.8: The OEMs, with the assistance of the Federal Aviation Administration (FAA), through this effort, have or will coordinate the procurement, fuel properties analysis, delivery, handling, and loading logistics for various fuels in support of the 2023–2025 emissions testing.

  In the case of the ecoDemonstrator subproject, the fuels burned are as follows:
  - Fuel 1: Low-sulfur Jet A, per ASTM D1655 (ASTM, 2023), total percentage by mass maximum objective of 0.0001 (maximum total sulfur target of 1 ppm)
  - Fuel 2: 100% hydroprocessed esters and fatty acids (HEFA)-straight paraffinic jet fuel (SPK), per ASTM D7566 (ASTM, 2022), Tables 1, A2.1, and A2.2
  - Fuel 3: Approved SAF blend (e.g., 30% HEFA-SPK), per ASTM D7566, Table 1

  In the case of the first Gulfstream subproject, the fuels burned are as follows:
  - Fuel 1: 100% HEFA- SPK
  - Fuel 2: 30%/70% HEFA-SPK/Jet A Blend
  - Fuel 3: 100% Conventional Jet A

Milestones

- Task 1 – 3.1: COMPLETED for Boeing, first and second Gulfstream
- Task 1 – 3.2: COMPLETED for Boeing, first and second Gulfstream
- Task 1 – 3.3: COMPLETED for Boeing and first Gulfstream
- Task 1 – 3.4: COMPLETED for Boeing and first Gulfstream
- Task 1 – 3.5: COMPLETED for Boeing and first Gulfstream

Major Accomplishments

- Reconfigured ASCENT Project 002 objectives, with new configuration in action.
- Successfully completed planning and preparation phase for SAF studies with Boeing and Gulfstream,
- Successfully completed ground tests with Boeing and first Gulfstream, with data deposited in appropriate archives.

Publications

Whitefield, P. (2025, October). *Understanding Changes in Aviation Emissions due to SAF with New Combustor Engine Technology* [Oral presentation]. ASCENT Advisory Board Meeting, Alexandria, Virginia.

Achterberg, A, Whitefield, P., & Woelk, K. (2025, October 8). *Gulfstream Ground Test Campaign October 2024* [Oral Presentation]. ICAO CAEP WG3 Meeting.



Outreach Efforts

Currently in negotiation with Aerodyne, Carnegie Mellon University, Gulfstream, P&W, Airbus America,® and Embraer® for future follow-on or new SAF focused studies

Awards

None.

Student Involvement

One graduate student (Lauren Kehoe) was employed in this project and four undergraduate research assistants (Justin Patek, Joshua Carpenter, Zane and Zachary Achterberg) were employed in pre- and post-test activities, including individual component testing and calibration, and data reduction.

Plans for Next Period

- Complete Task 1 – 3.4: For Second Gulfstream Study.
- Complete Task 1 – 3.5: For Second Gulfstream Study.
- Complete Task 1 – 3.6: For Boeing, and both Gulfstream studies.
- Complete Task 1 – 3.7: For Boeing, and both Gulfstream studies.
- Complete Task 1 – 3.8: For Second Gulfstream Study.
- Negotiate, plan, and prepare with Gulfstream, P&W, Airbus America, and Honeywell® for future follow-on or new SAF-focused studies.
- Communicate results and conclusions from the three field campaigns with publications and presentations.

References

ASTM International. (2022). *ASTM D7566-22: Standard Specification for Aviation Turbine Fuel Containing Synthesized Hydrocarbons*. https://doi.org/10.1520/D7566-22

ASTM International. (2023). *ASTM D1655-22a: Standard Specification for Aviation Turbine Fuels*. https://doi.org/10.1520/D1655-22A

® Airbus is a registered trademark of Airbus Operations GmbH, Hamburg, Germany.
® Embraer is a registered trademark of Embraer S.A., San Jose Dos Campos, Brazil.
® Honeywell is a registered trademark of Honeywell International, Inc., Charlotte, New Jersey.



Project 003 Cardiovascular Disease and Aircraft Noise Exposure

Boston University

Project Lead Investigator

Junenette L. Peters
Associate Professor
Department of Environmental Health
Boston University School of Public Health
715 Albany St., T4W, Boston, MA 02118
617-358-2552
petersj@bu.edu

University Participants

Boston University

- P.I.s: Prof. Jonathan Levy (university P.I.), Prof. Junenette Peters (project P.I.)
- FAA Award Number: 13-C-AJFE-BU-032
- Period of Performance: October 1, 2024, to September 30, 2025
- Tasks:
  1. Present on noise and health research in the United States (U.S.).
  2. Perform preliminary analyses of an intermediary risk factor (diabetes) and aircraft noise exposure.
  3. Develop a data analysis plan and perform preliminary analyses of generalized anxiety disorder and aircraft noise exposure.
  4. Develop a data analysis plan and perform preliminary analysis of incident depression and aircraft noise exposure.
  5. Develop analysis plan and submit manuscript proposal on sleep outcomes and aircraft noise exposure.
  6. Review and rerun analyses, and revise manuscript on cardiovascular disease and aircraft noise exposure.
  7. Receive participant addresses, perform data processing for linking with new cohort and develop data use procedures.
  8. Define request for noise data for additional year and airports.

Massachusetts Institute of Technology

- Sub-P.I. and co-P.I.: Prof. R. John Hansman (sub-P.I.), Dr. Florian Allroggen (sub-co-P.I.)
- Task (Boston University and Massachusetts Institute of Technology):
  1. Prepare a final draft of the report on study results related to 2018 Federal Aviation Administration (FAA) Reauthorization, Act Section 189 for policymakers.

Project Funding Level

Total funding (3-year funding): $2,161,609
Matching funds: $2,161,609
Sources of matching funds: Nonfederal donors to the Nurses' Health Study (NHS) and Women's Health Initiative (WHI) cohorts

Investigation Team

Boston University

Prof. Junenette Peters (P.I.)
Prof. Jonathan Levy (P.I.)



Dr. Levy participates in noise exposure assessment and provides expertise in the areas of predictive modeling and air pollution. Dr. Peters is responsible for directing all aspects of the proposed study, including study coordination, design and analysis plans, and co-investigator meetings.

Harvard University/Brigham and Women's Hospital
Prof. Francine Laden
Prof. Jaime Hart
Dr. Tianyi Huang (*now at the National Institutes of Health*)
Dr. Susan Redline

Dr. Laden and Dr. Hart are our NHS sponsors for this ancillary study. Dr. Hart assigns aircraft noise exposures to the geocoded address history coordinates of each cohort member. Dr. Laden and Dr. Hart also assist in documenting data from the NHS, on the basis of their previous experience in research on air pollution and chronic disease outcomes in these cohorts and in performing appropriate analyses of hypertension, cardiovascular, metabolic, and mental health outcomes. Dr. Redline and Dr. Tianyi Huang guide efforts related to noise and sleep disturbance in the NHS and WHI.

University of North Carolina
Dr. Eric Whitsel
James Stewart

Dr. Whitsel is our WHI, National Longitudinal Study of Adolescent to Adult Health (Add Health), and Hispanic Community Health Study/Study of Latinos (HCHS/SOL) sponsor for the ancillary studies. Along with James Stewart, Dr. Whitsel assigns aircraft noise exposure to the geocoded addresses of cohort members. Dr. Whitsel also assists in documenting data from these cohorts based on multiple years of combined leadership and service for the WHI and Add Health morbidity and mortality classification, outcomes adjudication, and ancillary study committees.

Massachusetts Institute of Technology
Prof. R. John Hansman (sub-P.I.)
Dr. Florian Allroggen (sub-co-P.I.)

Dr. Hansman and Dr. Allroggen are responsible for the economic impact analysis and visibility analysis (both analyses reported in previous reports) and participate in drafting the report for policymakers.

Project Overview

Exposure to aircraft noise has been associated with physiological responses and psychological reactions (Bluhm & Eriksson, 2011; Hatfield et al., 2001), including sleep disturbances, sleep-disordered breathing, nervousness, and annoyance (Hatfield et al., 2001; Rosenlund et al., 2001). However, the extent to which aircraft noise exposure increases the risk of adverse health outcomes is still not well understood. The literature, formerly primarily European studies, provided early evidence of a relationship between aircraft noise and self-reported hypertension (Rosenlund et al., 2001), increased blood pressure (Haralabidis et al., 2008; Jarup et al., 2008; Haralabidis et al., 2011; Evrard et al., 2017), antihypertensive medication use (Bluhm & Eriksson, 2011; Greiser et al., 2007; Franssen et al., 2004; Floud et al., 2011), and incidence of hypertension (Eriksson et al., 2010; Dimakopoulou et al., 2017; Kourieh et al., 2022). One study found that aircraft noise exposure was associated with incident diabetes (Eze et al., 2017). Other studies found a stronger but marginal association between aircraft noise and incident diabetes in women and an association with waist circumference (Eriksson et al., 2014; Sakhvidi et al., 2018). Experimental, community, and traffic noise exposures have been related to heart rate variability (El Aarbaoui & Chaix, 2020; El Aarbaoui et al., 2017; Sim et al., 2015; Walker et al., 2016; Kraus et al., 2013), and few studies have reported on heart rate variability relative to aircraft noise (Schmidt et al., 2021). Findings of a cardiovascular relationship were supported by a report by the World Health Organization European Centre for Environmental Health and later studies by researchers, which evaluated the association between residential exposure to environmental noise and cardiovascular disease and found substantial evidence for biological plausibility and positive associations between environmental noise and hypertension, myocardial infarction, and ischemic heart disease (Babisch & Kim, 2011; WHO, 2018, Münzel et al., 2024; Münzel et al., 2025).

The goal of this ongoing project is to continue to examine the potential health impacts attributable to noise exposure resulting from aircraft flights. This project also leverages other ongoing work within ASCENT and is responsive to



Section 189 of the FAA Reauthorization Act of 2018 (Pub. L. 115-254), which called for a study on the potential health and economic impacts attributable to aircraft overflight noise and an assessment of the relationship between a perceived increase in aircraft noise and increases in aircraft visibility. To date, our work has leveraged existing collaborations with well-recognized and respected studies that have followed over 250,000 participants through the course of their lives to understand factors that affect health. These studies include the NHS and Nurses' Health Study II (NHSII) as well as the Health Professionals Follow-Up Study. Furthermore, this work has aligned with a concluded effort funded by the National Institutes of Health to examine these associations in the WHI. The research team continues to leverage aircraft noise data for 90 U.S. airports from 1995 to 2019 and has linked these data to demographic, lifestyle, and health data for the participants of long-term health studies. These studies have provided considerable geographic coverage of the U.S., including all of the geographic areas specified in Section 189. Furthermore, our work to date has also included a first-of-its-kind empirical assessment of the economic impacts on businesses located beneath flight paths at selected U.S. airports responsive to the requirements set forth in Section 189 of the FAA Reauthorization Act of 2018.

Our team recently added to the literature by reporting on U.S. studies evaluating the degree to which aircraft noise affects health. A suggestive positive association was found between aircraft noise exposure and the risk of hypertension (Kim et al., 2022). However, there are fewer studies on the potential effect of noise on mental health (Seidler et al., 2017; Wright et al., 2018). Updated guidelines from the World Health Organization reported a lack of high-quality evidence for aircraft noise and mental health and highlighted the need for additional high-quality studies (WHO, 2018; Clark et al., 2020) with one high-quality study (Eze et al., 2020) and a review of evidence and mechanisms, thereafter (Hahad et al., 2025). Potential biological mechanisms of action of noise on health include induced release of stress hormones (Ising & Kruppa, 2004; Spreng, 2000; Selander et al., 2009; Lefevre et al., 2017) and markers of inflammation and oxidative stress, effects on vascular function (Münzel et al., 2017), and indirect effects on sympathetic activity, which is associated with adverse metabolic outcomes (Selander et al., 2009; Grassi, 2006; Mancia et al., 2006; Mancia et al., 2007). To better understand these potential relationships, our team increased the diversity of participants in our studies with a focus on vulnerable populations by adding the HCHS/SOL and Add Health cohorts. Furthermore, the potential impacts of aircraft noise on additional health outcomes beyond those previously explored are being evaluated, including cardiovascular intermediaries and mental health outcomes in NHS, NHSII, WHI, HCHS/SOL, and Add Health.

The overall aims for this multi-year project as it relates to our continuing efforts are as follows:

Tasks under Amendment No. 38:

1. Assign new aircraft noise exposures to geocoded participant addresses for NHS.
   a. Intersect geocoded addresses with day–night average sound level (DNL) aircraft noise exposure levels newly available for 2019 for the currently included 90 airports and for 2015 and 2019 for additional airports.
2. Increase personnel effort (postdoctoral fellow) on noise and health analyses.

Tasks under Amendment No. 32:

1. Assign aircraft noise exposures over time to geocoded participant addresses for HCHS/SOL and Add Health.
   a. Intersect geocoded addresses with DNL and equivalent sound levels for night (L_{night}) and day (L_{day}) aircraft noise exposure levels currently available from 1995 to 2015.
   b. Estimate the percent of participants across noise exposure categories and assess overall trends in participant noise exposure levels over time, including an evaluation of sociodemographic and other predictors of aircraft noise exposure to facilitate the design and interpretation of epidemiological analyses.
2. Estimate the potential association between cardiovascular intermediaries and aircraft noise exposure.
   a. Develop analysis plans and manuscript proposals to gain approval to investigate potential relationships between aircraft noise exposure and health intermediaries or cardiometabolic markers such as adiposity and heart rate variability in the NHS, WHI, HCHS/SOL, and Add Health cohorts.
   b. Perform statistical analyses, undergo manuscript reviews, and present and publish results.
3. Investigate the potential impact of aircraft noise exposure on mental health.
   a. Conduct an in-depth literature search to identify relevant mental health outcomes.
   b. Determine the applicable assessments of these outcomes (i.e., depression and anxiety) within the various cohort studies.
   c. For each cohort, develop an analysis plan and gain approval of manuscript proposals on the potential relationships between aircraft noise exposure and mental health outcomes.
   d. Perform statistical analyses, undergo manuscript reviews, and present and publish results.
4. Explore the addition of noise-related survey questions to Nurses' Health Study 3 (NHS3).



Tasks under Amendment No. 16 as it relates to Section 189 are as follows:

1. Prepare a final draft of the study report related to Section 189 of the FAA Reauthorization Act of 2018 (Pub. L. 115-254) for policymakers.

Task 1 – Present on Aircraft Noise and Health Research in the United States

Boston University

Objective

The aim of this task is to present on U.S.-based research on aircraft noise exposure and health outcomes.

Research Approach

Presentations highlighting published, current, and planned research on aircraft noise exposure and health outcomes in U.S. cohorts were developed and delivered.

Milestone

- Presented on research efforts and results.

Major Accomplishments

- Presented on aircraft noise and health research to the following organizations (e.g., Figure 1):
  - International Society for Environmental Epidemiology (ISEE) Conference, Atlanta, GA, August 17-20, 2025.
  - International Society of Exposure Science (ISES) Conference (Joint with ISEE), Atlanta, GA, August 17-20, 2025.
  - Aviation Noise and Emissions Symposium, Las Vegas, NV, March 11-12, 2025.

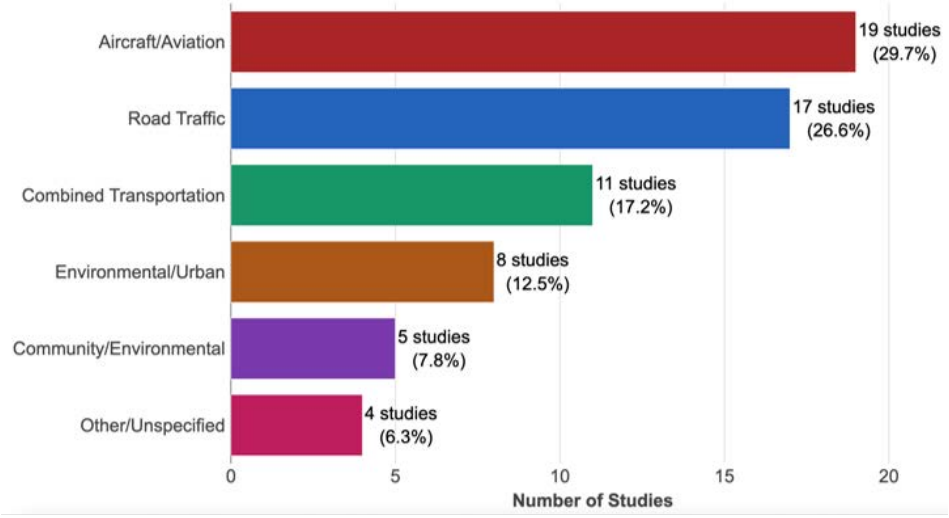


Figure 1. Chart of the number of U.S.-based studies by type of noise exposure

Task 2 – Perform Preliminary Analyses of an Intermediary Risk Factor (Diabetes) and Aircraft Noise Exposure

Boston University, Harvard University

Objective

The aim of this task is to generate preliminary results on aircraft noise and diabetes.

Research Approach

An analysis plan was developed for studying diabetes and aircraft noise and approval obtained from the NHS oversight committee. Statistical analysis was designed, and a large set of a priori variables were selected to be examined as confounders and/or effect modifiers. Appropriate datasets were compiled to perform descriptive statistics analysis. We ran preliminary analysis of the form of the relationship between aircraft noise and diabetes risk.

Milestone

- Produced preliminary results to investigate aircraft noise and the risk of diabetes.

Major Accomplishments

- Performed preliminary analyses on the relationship between aircraft noise and risk of diabetes (Table 1 and Table 2).

Table 1. Number of participants in the Nurses' Health Study (NHS) and Nurses' Health Study 2 (NHSII) at risk for diabetes (did not have diabetes at the time of the first noise measure) and those who developed diabetes during the study period according to day-night average sound level (DNL) categories.

Model	NHS		NHSII	
DNL (dB)	**At Risk**	**Cases**	**At Risk**	**Cases**
<45	90,946	7,076	100,968	6,391
45–49	4,340	313	5,281	276
50–54	2,018	165	2,419	137
55–59	751	60	954	56
60–64	179	17	238	20
≥65	39	3	55	7
Total	98,273	7,634	109,915	6,887



Table 2. Table detailing preliminary results on the relationship between aircraft noise and the risk of diabetes with hazard ratios (95% confidence intervals) across day-night average sound level (DNL) in the Nurses' Health Study (NHS), Nurses' Health Study 2 (NHSII), and meta-analyzed across cohorts. Adjusted for age, race/ethnicity, individual-level and neighborhood-level socioeconomic status, and air pollution.

Cohort	Model	Exposure Category	Hazard Ratio (95% CI)
NHS	Unadjusted	≥45 vs <45 dB	1.04 (0.95 to 1.13)
		≥50 vs <50 dB	1.11 (0.98 to 1.27)
		≥55 vs <55 dB	1.14 (0.91 to 1.42)
	Adjusted	≥45 vs <45 dB	1.01 (0.92 to 1.11)
		≥50 vs <50 dB	1.06 (0.93 to 1.21)
		≥55 vs <55 dB	1.03 (0.82 to 1.29)
NHS**II**	Unadjusted	≥45 vs <45 dB	1.02 (0.92 to 1.11)
		≥50 vs <50 dB	1.12 (0.99 to 1.28)
		≥55 vs <55 dB	1.34 (1.08 to 1.65)
	Adjusted	≥45 vs <45 dB	1.01 (0.92 to 1.11)
		≥50 vs <50 dB	1.08 (0.94 to 1.23)
		≥55 vs <55 dB	1.23 (0.99 to 1.52)
Meta-Analysis	Unadjusted	≥45 vs <45 dB	1.03 (0.94 to 1.09)
		≥50 vs <50 dB	1.12 (1.02 to 1.23)
		≥55 vs <55 dB	1.24 (1.06 to 1.45)
	Adjusted	≥45 vs <45 dB	1.01 (0.94 to 1.08)
		≥50 vs <50 dB	1.07 (0.97 to 1.17)
		≥55 vs <55 dB	1.13 (0.95 to 1.35)

Task 3 – Develop Data Analysis Plan and Perform Preliminary Analyses of Generalized Anxiety Disorder and Aircraft Noise Exposure

Boston University, Harvard University

Objective

The aim of this task is to generate a data analysis plan and conduct preliminary results on aircraft noise and generalized anxiety disorder.

Research Approach

An analysis plan was developed for studying generalized anxiety disorder and aircraft noise. Approval was obtained from the NHS oversight committee. Statistical analysis was designed, and a large set of a priori variables were selected to be examined as confounders and/or effect modifiers. Appropriate datasets were compiled to perform descriptive statistics analysis. We ran preliminary analysis of the form of the relationship between aircraft noise and prevalence of generalized anxiety disorder.

Milestones

- Received approval of study aircraft noise and generalized anxiety disorder.



- Produced preliminary results to investigate these associations.

Major Accomplishments

- Submitted a research analysis plan and received approval from the NHS oversight committee.
- Generated preliminary descriptive characterization of the sample population and determined the number of individuals exposed to DNL (Table 3).
- Generated preliminary results on the relationship between aircraft noise and prevalence of generalized anxiety disorder (Figure 2).

Table 3. Number of participants in Nurses' Health Study 2 (NHSII) with generalized anxiety disorder during the study period according to day-night average sound level (DNL) categories.

DNL (dB)	At Risk
<45	30,928
45–49	2,463
50–54	1,205
≥55	505
Total	35,101

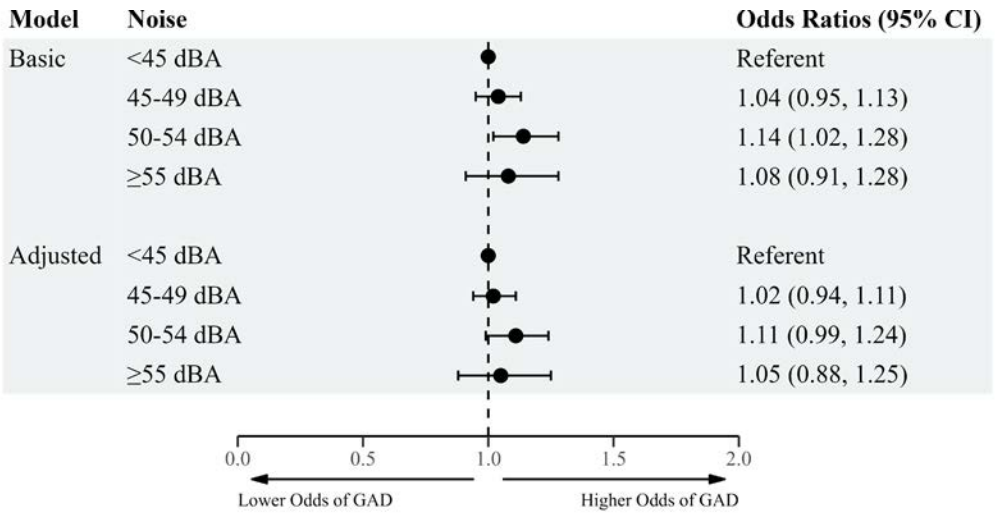


Figure 2. Preliminary results on the relationship between aircraft noise and prevalence of generalized anxiety disorder (GAD) with prevalence odds ratios (95% confidence intervals) across day-night average sound level (DNL) in the Nurses' Health Study 2 (NHSII) cohort. Adjusted models include age, time period, race/ethnicity, individual- and neighborhood-level socioeconomic status, region, air pollution, and population density.

Task 4 – Develop Data Analysis Plan and Perform Preliminary Analysis of Incident Depression and Aircraft Noise Exposure

Boston University, Harvard University

Objective

The aim of this task is to generate a data analysis plan and conduct preliminary results on aircraft noise with incident depression and depressive symptoms.

Research Approach

An analysis plan was developed for studying incident depression and depressive symptoms with aircraft noise and approval obtained from the NHS oversight committee. Statistical analysis was designed, and a large set of a priori variables were selected to be examined as confounders and/or effect modifiers. Appropriate datasets were compiled to perform descriptive statistics analysis. We ran preliminary analysis of the form of the relationship between aircraft noise and incident depression.

Milestones

- Received cohort approval to study aircraft noise and incident depression.
- Produced preliminary results to investigate these associations.

Major Accomplishments

- Submitted a research analysis plan and obtained approval from the NHS oversight committee.
- Generated descriptive characteristics of the sample population and determined the number of individuals exposed to DNL at baseline (Table 4).
- Generated preliminary results on the relationship between aircraft noise and incident depression (Figure 3).

Table 4. Number of participants in Nurses' Health Study 2 (NHSII) at risk of depression (have not been diagnosed with depression at the time of the first noise measure) and those who developed depression during the study period according to day-night average sound level (DNL) categories.

DNL (dB)	At Risk	Cases
<45	15,066	2,702
45–49	2,078	339
50–54	1,034	161
≥55	19	55
Total	18,705	3,257

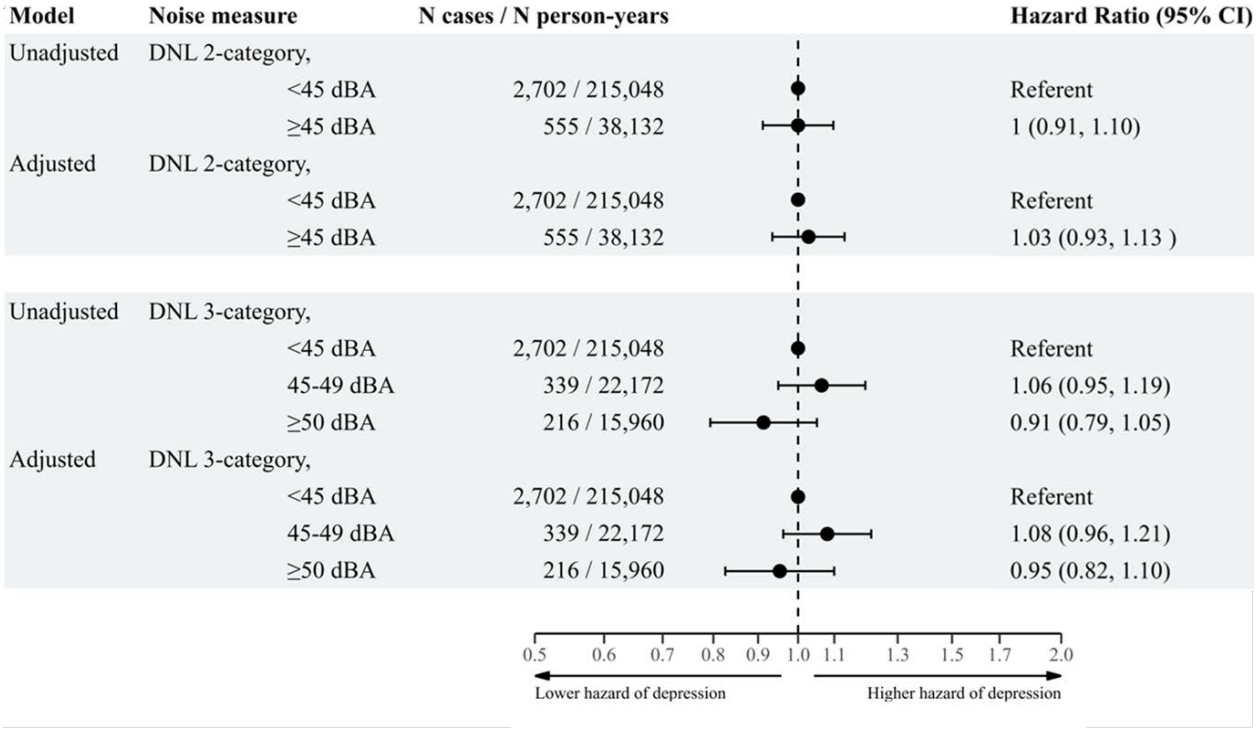


Figure 3. Preliminary results on the relationship between aircraft noise and incident depression with hazard ratios (95% confidence intervals) of associations across day-night average sound level (DNL) in the Nurses' Health Study 2 (NHSII) cohort. Adjusted models include age, time period, race/ethnicity, individual- and neighborhood-level socioeconomic status, region, air pollution, and population density.

Task 5 – Develop Analysis Plan and Submit Manuscript Proposal on Sleep Outcomes and Aircraft Noise Exposure

Boston University, University of North Carolina, Harvard University

Objective

The aim of this task is to study the association between aircraft noise and sleep.

Research Approach

Research will be performed within the WHI, which contains multiple questions on sleep outcomes (Table 5) as well as a validated sleep scale. Noise exposure data were linked to the WHI cohorts' geocoded addresses. A manuscript proposal was developed and submitted and statistical analysis designed for studying aircraft noise and sleep quality. Manuscript proposal was approved by the WHI Proposal and Presentation (P&P) committee. Variables will be selected a priori to be examined as confounders and/or effect modifiers. Appropriate datasets will be compiled to perform descriptive statistics and primary analysis.

Milestones

- Received cohort approval to study aircraft noise and sleep outcomes.
- Produced preliminary characterization of study population.

Major Accomplishments

- Coordinated with a sleep expert to develop analysis plan to study the association between aircraft noise and sleep in the WHI.



- Prepared and submitted a manuscript proposal to WHI's P&P committee and received approval.
- Generated descriptive statistics of the study participants.

Table 5. Preliminary overview of sleep questions and responses in a Women's Health Initiative (WHI) cohort of 116,707 participants.

Question	Response				
	No	<1/week	1-2/week	3-4/week	5+/week
Trouble falling asleep	58%	18%	13%	6%	4%
Waking at night	28%	17%	21%	18%	22%
Waking earlier than planned	41%	21%	19%	11%	7%
Trouble falling back asleep	48%	20%	17%	9%	6%
Napping during day	47%	22%	17%	8%	4%
Falling asleep during day	25%	22%	26%	16%	10%
Using medication for sleep	76%	9%	5%	3%	6%
Question			**Response**		
	Very restless	Restless	Average	Restful	Very restful
Rate the quality of your sleep	2%	14%	42%	29%	13%
Question			**Response**		
	<6 hours	6 hours	7 hours	8 hours	9+ hours
Average hours of sleep per night	8%	28%	37%	22%	4%

Note: Percentages may not sum to 100% due to missing data and rounding

Task 6 – Review and Rerun Analyses, and Revise Manuscript on Cardiovascular Disease and Aircraft Noise Exposure

Boston University, University of North Carolina

Objective

The aim of this task is to finalize the results and manuscript of a study of aircraft noise exposure and cardiovascular disease (CVD).

Research Approach

Analysis that was previously run but not published as part of a dissertation on aircraft noise and CVD in the WHI will be reviewed and rerun with the intent of addressing some differing results in two sub-components of the WHI (the clinical trial and observational study cohorts). Additional analyses will be performed to identify the source of sub-cohort differences via propensity matching the two populations on demographic and health data. The draft manuscript will be revised, reviewed by co-authors, and submitted to a peer-reviewed journal.

Milestones

- Reevaluated assumptions and criteria for analysis of aircraft noise and CVD.
- Reevaluated and reran statistical analysis code.

Major Accomplishments

- Determined updated assumptions and criteria for analyses.
- Rewrote, updated previous statistical code to run successfully on the WHI servers for review and comparison with previous results.



- Generated data to evaluate demographic and health differences between the sub-cohorts (Table 6).

Table 6. Characteristics of participants in two sub-components (clinical trial and observational study cohorts) of the study of noise and cardiovascular disease in the Women's Health Initiative (WHI).

	Population	
	Observational Study	**Clinical Trial**
Total	24,710	17,682
Age (years; mean and sd)	63 (7.2)	63 (6.8)
Employed (%)	9,650 (39%)	7,316 (41%)
Smoking, current (%)	1,640 (6.6%)	1,513 (8.6%)
Smoking, past (%)	10,271 (42%)	7,036 (40%)
Smoking, never (%)	12,799 (52%)	9,133 (52%)
BMI (kg/m^2; mean, sd)	27 (5.8)	29 (6.0)
Family history of CVD	16,252 (66%)	11,608 (66%)

Note: Body Mass Index (ratio of height to weight) as BMI; Standard deviation abbreviated as sd.

Task 7 – Receive Participant Addresses, Perform Data Processing for Linking with New Cohort and Develop Data Use Procedures

Boston University, University of North Carolina

Objective

The aim of this task is to prepare participant addresses for linking airport noise data to participants' geocoded addresses.

Research Approach

The missing addresses for HCHS/SOL participants were requested and received from HCHS/SOL and geocoding processing was performed. Institutional Review Board (IRB) revision and approval was obtained. Our team collaborated in the development and execution of a data use agreement and procedures for use of aircraft noise exposure estimates.

Milestones

- Received IRB approval.
- Received and processing the missing geocoded addresses needed to link noise data.

Major Accomplishments

- Revised IRB protocol to include noise research and received approval.
- Met with HCHS/SOL committee regarding data use agreement for aircraft noise data use.
- Started processing addresses including data cleaning and data de-duplication to prepare for geocoding and data linking (Figure 4).

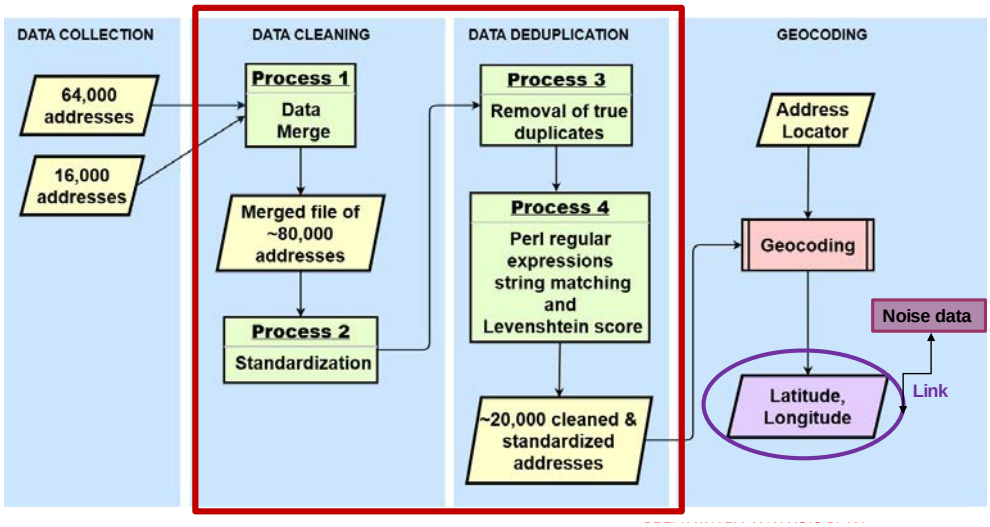


Figure 4. Data processing steps (highlighted) for the Hispanic Community Health Study/Study of Latinos (HCHS/SOL) participant addresses in preparation for linkage with the aircraft noise data.

Task 8 – Define Request for Noise Data for Additional Year and Airports

Boston University, University of North Carolina, Harvard University

Objective

The aim of this task is to define the aircraft noise data request and obtain data for an additional year and additional airports.

Research Approach

More recent data were requested to add to the 5-year incremental data received for 1995 to 2015. The year 2019 was chosen as the additional year to avoid anomalies related to 2020. The locations of participants were reviewed, particularly in new cohorts such as HCHS/SOL, to request 2015 and 2019 data for additional relevant airports not included in the 90 airports previously provided. For the 2019 DNL data, a quality and format review will be performed for the 90 airports before requesting additional metrics and airports. Then data for other metrics (e.g., nighttime noise) will be requested.

Milestone

Requested and obtained data for additional years and airports for additional metric.

Major Accomplishments

- Reviewed aircraft noise DNL format for 2019 aircraft noise data.
- Determined data needs and additional data request and order of delivery.

Task 9 – Prepare the Final Draft of the Report on Study Results Related to 2018 FAA Reauthorization Act, Section 189 for Policymakers

Boston University, Massachusetts Institute of Technology

Objective

The aim of this task is to develop a report of overall study results in response to 2018 FAA Reauthorization Act, Section 189 for policymakers.



Research Approach

Summarized FAA Reauthorization Act of 2018 (Pub. L. 115-254), Section 189, *STUDY ON POTENTIAL HEALTH AND ECONOMIC IMPACTS OF OVERFLIGHT NOISE*, and provided the background of the study, study methods and data, study findings, and conclusions.

Milestone

- Generated a final report on the overall study results in response to Section 189 for policymakers.

Major Accomplishment

- Submitted a final draft of the report summarizing the overall study results in relation to Section 189.

Publications

Peer-Reviewed Journal Publications

Bozigar, M., Laden, F., Hart, J. E., Redline, S., Huang, T., Whitsel, E. A., Nelson, E. J., Grady, S. T., Levy, J. I., & Peters, J. L. (2024). Aircraft noise exposure and body mass index among female participants in two Nurses' Health Study prospective cohorts living around 90 airports in the United States. *Environment International, 187*, 108660. doi: 10.1016/j.envint.2024.108660. PMID: 38677085

Bozigar, M., Huang, T., Redline, S., Hart, J. E., Grady, S. T., Nguyen, D. D., James, P., Nicholas, B., Levy, J. I., Laden, F., & Peters J. L. (2023). Associations between aircraft noise exposure and self-reported sleep duration and quality in the United States-Based prospective Nurses' Health Study cohort. *Environmental Health Perspectives, 131*(4), 47010. doi: 10.1289/EHP10959

Grady, S. T., Hart, J. E., Laden, F., Roscoe, C., Nguyen, D. D., Nelson, E. J., Bozigar, M., VoPham, T., Manson, J. E., Weuve, J., Adar, S. D., Forman, J. P., Rexrode, K., Levy, J. I., & Peters, J. L. (2023). Associations between long-term aircraft noise exposure, cardiovascular disease, and mortality in US cohorts of female nurses. *Environmental Epidemiology, 7*(4), e259. doi: 10.1097/EE9.0000000000000259

Kim, C. S., Grady, S. T., Hart, J. E., Laden, F., VoPham, T., Nguyen, D. D., Manson, J. E., James, P., Forman, J. P., Rexrode, K. M., Levy, J. I. & Peters, J. L. (2022). Long-term aircraft noise exposure and risk of hypertension in the Nurses' Health Studies. *Environmental Research*, *207*, 112195.

Nguyen, D. D., Levy, J. I., Kim, C., Lane, K. J., Simon, M. C., Hart, J. E., Whitsel, E. A., VoPham, T., Malwitz, A., & Peters, J. L. (2023). Characterizing temporal trends in populations exposed to aircraft noise around U.S. airports: 1995–2015. *Journal of Exposure Science and Environmental Epidemiology*. https://doi.org/10.1038/s41370-023-00575-5

Nguyen, D. D., Whitsel, E. A., Wellenius, G. A., Levy, J. I., Leibler, J. H., Grady, S. T., Stewart, J. D., Fox, M. P., Collins, J. M., Eliot, M. N., Malwitz, A., Manson, J. E., & Peters, J. L. (2023). Long-term aircraft noise exposure and risk of hypertension in postmenopausal women. *Environmental Research, 218*, 115037. doi: 10.1016/j.envres.2022.115037

Peters, J. L., Grady, S. T., Laden, F., Nelson, E., Bozigar, M., Hart, J. E., Manson, J. E., Huang, T., Redline, S., Kaufman, J. D., Forman, J. P., Rexrode, K. M., & Levy, J. I. (2024). Long-term nighttime aircraft noise exposure and risk of hypertension in a prospective cohort of female nurses. *International Journal of Hygiene and Environmental Health, 12*(263), 114457. doi: 10.1016/j.ijheh.2024.114457. PMID: 39270405

Outreach Efforts

Presentations

- Presented an oral presentation on current progress during the ASCENT Fall Meeting (October 29–31, 2024) and ASCENT Spring Noise and Operations Meeting (April 14–15, 2025)
- Presented an oral presentation entitled "Characterizing temporal trends in populations exposed to aircraft noise around U.S. airports: 1995–2015" at the Aviation Noise and Emissions Symposium (March 11-12, 2025)
- Presented an oral presentation entitled "Residential exposure to aircraft noise and depression risk in a U.S. prospective cohort" at the Joint Annual Meeting of ISES and ISEE 2025 (August 17-20, 2025).

Awards

None.



Student Involvement

The dissertation of Daniel Nguyen (doctoral graduate, Boston University) included a characterization of the temporal trends in aviation noise surrounding U.S. airports. Daniel Nguyen graduated in the spring of 2022 and is currently working for the Centers for Disease Control and Prevention.

The dissertation of Stephanie Grady (doctoral candidate, Boston University) includes developing and performing statistical analyses on noise and hypertension risk, cardiovascular event risk, and biomarkers of neurodegeneration. Stephanie Grady graduated in the spring of 2024 and is currently working as a postdoctoral fellow at Boston University.

Plans for Next Period

(October 1, 2025, to September 30, 2026)

- Generate results, draft the manuscript, and publish on the relationship between aircraft noise exposure and mental health outcomes (e.g., depression and anxiety).
- Generate results and draft the manuscript on the relationship between aircraft noise exposure and sleep outcomes.
- Review analyses, finalize the manuscript, and publish on aircraft noise exposure and cardiovascular disease.
- Link aircraft noise data to geocoded addresses of participants in the additional cohort.
- Process and link aircraft noise data for additional years and locations.

References

Babisch, W., & Kim, R. (2011). *Environmental noise and cardiovascular disease. WHO European Centre for Environmental Health, ed. Burden of disease from environmental noise: Quantification of healthy life years lost in Europe*. World Health Organization, 15-44.

Bluhm, G., & Eriksson, C. (2011). Cardiovascular effects of environmental noise: research in Sweden. *Noise and Health, 13*(52), 212-216.

Bozigar, M., Laden, F., Hart, J. E., Redline, S., Huang, T., Whitsel, E. A., Nelson, E. J., Grady, S. T., Levy, J. I., & Peters, J. L. (2024). Aircraft noise exposure and body mass index among female participants in two Nurses' Health Study prospective cohorts living around 90 airports in the United States. *Environment International, 187*, 108660. doi: 10.1016/j.envint.2024.108660. PMID: 38677085

Clark, C., Crumpler, C., & Notley, H. (2020). Evidence for environmental noise effects on health for the United Kingdom policy context: a systematic review of the effects of environmental noise on mental health, wellbeing, quality of life, cancer, dementia, birth, reproductive outcomes, and cognition. *International Journal of Environmental Research and Public Health, 17*(2), 393.

Dimakopoulou, K., Koutentakis, K., Papageorgiou, I., Kasdagli, M. I., Haralabidis, A. S., Sourtzi, P., Samoli, E., Houthuijs, D., Swart, W., Hansell, A. L., & Katsouyanni, K. (2017). Is aircraft noise exposure associated with cardiovascular disease and hypertension? Results from a cohort study in Athens, Greece. *Occupational and Environmental Medicine, 74*(11), 830-837.

El Aarbaoui, T., & Chaix, B. (2020). The short-term association between exposure to noise and heart rate variability in daily locations and mobility contexts. Journal of Exposure Science & Environmental Epidemiology, 30(2), 383-393.

El Aarbaoui, T., Méline, J., Brondeel, R., & Chaix, B. (2017). Short-term association between personal exposure to noise and heart rate variability: The RECORD MultiSensor Study. *Environmental Pollution, 231*, 703-711.

Eriksson, C., Bluhm, G., Hilding, A., Östenson, C. G., & Pershagen, G. (2010). Aircraft noise and incidence of hypertension—gender specific effects. *Environmental Research, 110*(8), 764-772.

Eriksson, C., Hilding, A., Pyko, A., Bluhm, G., Pershagen, G., & Östenson, C. G. (2014). Long-term aircraft noise exposure and body mass index, waist circumference, and type 2 diabetes: a prospective study. *Environmental Health Perspectives, 122*(7), 687-694.

Evrard, A. S., Lefèvre, M., Champelovier, P., Lambert, J., & Laumon, B. (2017). Does aircraft noise exposure increase the risk of hypertension in the population living near airports in France?. *Occupational and Environmental Medicine, 74*(2), 123-129.

Eze, I. C., Foraster, M., Schaffner, E., Vienneau, D., Héritier, H., Rudzik, F., Thiesse, L., Pieren, R., Imboden, M., von Eckardstein, A., Schindler, C., Brink, M., Cajochen, C., Wunderli, J. M., Röösli, M., & Probst-Hensch, N. (2017). Long-term exposure to transportation noise and air pollution in relation to incident diabetes in the SAPALDIA study. *International Journal of Epidemiology, 46*(4), 1115-1125.



Eze, I. C., Foraster, M., Schaffner, E., Vienneau, D., Pieren, R., Imboden, M., Wunderli, J. M., Cajochen, C., Brink, M., Röösli, M., & Probst-Hensch, N. (2020). Incidence of depression in relation to transportation noise exposure and noise annoyance in the SAPALDIA study. *Environment international*, *144*, 106014.

Floud, S., Vigna-Taglianti, F., Hansell, A., Blangiardo, M., Houthuijs, D., Breugelmans, O., Cadum, E., Babisch, W., Selander, J., Pershagen, G., Antoniotti, M. C., Pisani, S., Dimakopoulou, K., Haralabidis, A. S., Velonakis, V., Jarup, L., & Hyena Study Team. (2011). Medication use in relation to noise from aircraft and road traffic in six European countries: results of the HYENA study. *Occupational and Environmental Medicine, 68*(7), 518-524.

Franssen, E. A. M., Van Wiechen, C. M. A. G., Nagelkerke, N. J. D., & Lebret, E. (2004). Aircraft noise around a large international airport and its impact on general health and medication use. *Occupational and Environmental Medicine, 61*(5), 405-413.

Grassi, G. (2006). Sympathetic overdrive and cardiovascular risk in the metabolic syndrome. *Hypertension Research, 29*(11), 839-847.

Greiser, E., Janhsen, K., & Greiser, C. (2007). Air traffic noise increases prescriptions of cardiovascular drugs in the vicinity of a major airport. *Epidemiology, 18*(5), S33.

Hahad, O., Kuntic, M., Al-Kindi, S., Kuntic, I., Gilan, D., Petrowski, K., Daiber, A., Munzel, T. (2025). Noise and mental health: evidence, mechanisms, and consequences. *Journal of Exposure Science and Environmental Epidemiology, 35*, 16–23.

Haralabidis, A. S., Dimakopoulou, K., Velonaki, V., Barbaglia, G., Mussin, M., Giampaolo, M., Selander, J., Pershagen, G., Dudley, M. L., Babisch, W., Swart, W., Katsouyanni, K., Jarup, L. & HYENA Consortium. (2011). Can exposure to noise affect the 24 h blood pressure profile? Results from the HYENA study. *Journal of Epidemiology & Community Health, 65*(6), 535-541.

Haralabidis, A. S., Dimakopoulou, K., Vigna-Taglianti, F., Giampaolo, M., Borgini, A., Dudley, M. L., Pershagen, G., Bluhm, G., Houthuijs, D., Babisch, W., Velonakis, M., Katsouyanni, K., Jarup, L., & HYENA Consortium. (2008). Acute effects of night-time noise exposure on blood pressure in populations living near airports. *European Heart Journal, 29*(5), 658-664.

Hatfield, J., Job, R. F. S., Carter, N. L., Peploe, P., Taylor, R., & Morrell, S. (2001). The influence of psychological factors on self-reported physiological effects of noise. *Noise and Health, 3*(10), 1-13.

Ising, H., & Kruppa, B. (2004). Health effects caused by noise: evidence in the literature from the past 25 years. *Noise Health, 6*(22), 5–13.

Jarup, L., Babisch, W., Houthuijs, D., Pershagen, G., Katsouyanni, K., Cadum, E., Dudley, M. L., Savigny, P., Seiffert, I., Swart, W., Breugelmans, O., Bluhm, G., Selander, J., Haralabidis, A., Dimakopoulou, K., Sourtzi, P., Velonakis, M., Vigna-Taglianti, F., HYENA Study Team (2008). Hypertension and exposure to noise near airports: the HYENA study. *Environmental Health Perspectives, 116*(3), 329-333.

Kim, C. S., Grady, S. T., Hart, J. E., Laden, F., VoPham, T., Nguyen, D. D., Manson, J. E., James, P., Forman, J. P., Rexrode, K. M., Levy, J. I. & Peters, J. L. (2022). Long-term aircraft noise exposure and risk of hypertension in the Nurses' Health Studies. *Environmental Research, 207*, 112195.

Kourieh, A., Giorgis-Allemand, L., Bouaoun, L., Lefèvre, M., Champelovier, P., Lambert, J., Laumon, B., & Evrad, A. (2022). Incident hypertension in relation to aircraft noise exposure: results of the DEBATS longitudinal study in France. *Occupational and Environmental Medicine. 79,* 268-276.

Kraus, U., Schneider, A., Breitner, S., Hampel, R., Rückerl, R., Pitz, M., Geruschkat, U., Belcredi, P., Radon, K., & Peters, A. (2013). Individual daytime noise exposure during routine activities and heart rate variability in adults: a repeated measures study. *Environmental Health Perspectives, 121*(5), 607-612.

Lefèvre, M., Carlier, M. C., Champelovier, P., Lambert, J., Laumon, B., & Evrard, A. S. (2017). Effects of aircraft noise exposure on saliva cortisol near airports in France. *Occupational and Environmental Medicine, 74*(8), 612-618.

Mancia, G., Bousquet, P., Elghozi, J. L., Esler, M., Grassi, G., Julius, S., Reid, J., & Van Zwieten, P. A. (2007). The sympathetic nervous system and the metabolic syndrome. *Journal of Hypertension, 25*(5), 909-920.

Mancia, G., Dell'Oro, R., Quarti-Trevano, F., Scopelliti, F., & Grassi, G. (2006). Angiotensin–sympathetic system interactions in cardiovascular and metabolic disease. *Journal of Hypertension, 24*, S51-S56.

Münzel, T., Daiber, A., Engelmann, N., Röösli, M., Kuntic, M., & Banks, J. L. (2025). Noise causes cardiovascular disease: it's time to act. *Journal of Exposure Science and Environmental Epidemiology, **35***, 24–33.

Münzel, T., Molitor, M., Kuntic, M., Hahad, O., Röösli, M., Engelmann, N., Basner, M., Daiber, A., & Sørensen, M. (2024). Transportation noise pollution and cardiovascular health. *Circulation Research, 134*(9), 1113-1135.

Münzel, T., Daiber, A., Steven, S., Tran, L. P., Ullmann, E., Kossmann, S., Schmidt, F. P., Oelze, M., Xia, N., Li, H., Pinto, A., Wild, P., Pies, K., Schmidt, E. R., Rapp, S., & Kröller-Schön, S. (2017). Effects of noise on vascular function, oxidative stress, and inflammation: mechanistic insight from studies in mice. *European Heart Journal, 38*(37), 2838-2849.



Peters, J. L., Grady, S. T., Laden, F., Nelson, E., Bozigar, M., Hart, J. E., Manson, J. E., Huang, T., Redline, S., Kaufman, J. D., Forman, J. P., Rexrode, K. M., & Levy, J. I. (2024). Long-term nighttime aircraft noise exposure and risk of hypertension in a prospective cohort of female nurses. *International Journal of Hygiene and Environmental Health, 12*(263), 114457. doi: 10.1016/j.ijheh.2024.114457. PMID: 39270405

Rosenlund, M., Berglind, N., Pershagen, G., Järup, L., & Bluhm, G. (2001). Increased prevalence of hypertension in a population exposed to aircraft noise. *Occupational and Environmental Medicine, 58*(12), 769-773.

Sakhvidi, M. J. Z., Sakhvidi, F. Z., Mehrparvar, A. H., Foraster, M., & Dadvand, P. (2018). Association between noise exposure and diabetes: a systematic review and meta-analysis. *Environmental Research, 166*, 647-657.

Schmidt, F. P., Herzog, J., Schnorbus, B., Ostad, M. A., Lasetzki, L., Hahad, O., Schäfers, G., Gori, T., Sørensen, M., Daiber, A., & Münzel, T. (2021). The impact of aircraft noise on vascular and cardiac function in relation to noise event number: a randomized trial. *Cardiovascular Research 117*(5):1382-1390.

Seidler, A., Hegewald, J., Seidler, A. L., Schubert, M., Wagner, M., Dröge, P., Haufe, E., Schmitt, J., Swart, E., & Zeeb, H. (2017). Association between aircraft, road and railway traffic noise and depression in a large case-control study based on secondary data. *Environmental Research, 152*, 263-271.

Selander, J., Bluhm, G., Theorell, T., Pershagen, G., Babisch, W., Seiffert, I., Houthuijs, D., Breugelmans, O., Vigna-Taglianti, F., Antoniotti, M. C., Velonakis, E., Davou, E., Dudley, M. L., Järup, L., & HYENA Consortium. (2009). Saliva cortisol and exposure to aircraft noise in six European countries. *Environmental Health Perspectives, 117*(11), 1713-1717.

Sim, C. S., Sung, J. H., Cheon, S. H., Lee, J. M., Lee, J. W., & Lee, J. (2015). The effects of different noise types on heart rate variability in men. *Yonsei Medical Journal, 56(*1), 235-243.

Spreng, M. (2000). Possible health effects of noise induced cortisol increase. *Noise and Health, 2*(7), 59-63.

Walker, E. D., Brammer, A., Cherniack, M. G., Laden, F., & Cavallari, J. M. (2016). Cardiovascular and stress responses to short-term noise exposures—A panel study in healthy males. Environmental Research, 150, 391-397.

World Health Organization. (2018). *Environmental noise guidelines for the European region*. World Health Organization. Regional Office for Europe.

Wright, D. M., Newell, K., Maguire, A., & O'Reilly, D. (2018). Aircraft noise and self-assessed mental health around a regional urban airport: a population based record linkage study. *Environmental Health, 17*(1), 1-10.



Project 018 Measurements of Aviation Emission Contributions to Ambient Air Quality

Boston University School of Public Health

Project Lead Investigator

Kevin J. Lane
Associate Professor
Department of Environmental Health
Boston University School of Public Health
715 Albany St. T4W
Boston, MA 02118
617-414-8457
klane@bu.edu

University Participants

Boston University School of Public Health (BUSPH)

- P.I.s: Kevin J. Lane, Assistant Professor; Jonathan I. Levy, Professor and Chair
- FAA Award Number: 13-C-AJFE-BU, Amendment 7
- Period of Performance: August 30, 2023, to September 30, 2025 ***(BU POP extended through September 30, 2026)***
- Tasks:
  1. Continued targeted mobile and stationary monitoring near the Boston Logan International Airport (BOS) to allow for future analyses of changing aviation source contributions to inform source attribution
  2. Conduct an ambient air pollution monitoring campaign near Dulles International Airport
  3. Provide data to ASCENT Project 019 to conduct calibration and validation of ambient air pollution dispersion models developed by ASCENT Project 019

Project Funding Level

The Federal Aviation Administration (FAA) provided $649,000 in funding. Matching funds were provided by a non-federal donor to the Women's Health Initiative cohort studies as cost-sharing support to Boston University through ASCENT Project 003.

Investigation Team

Boston University School of Public Health

Prof. Jonathan I. Levy, ScD (ASCENT BUSPH Director and ASCENT Project 018 Co-Investigator: Professor of Environmental Health, Chair of the Department of Environmental Health) is the Boston University P.I. for ASCENT. He initiated ASCENT Project 018 and serves as the director of BUSPH ASCENT research.

Prof. Kevin J. Lane, PhD (ASCENT Project 018 P.I.: Associate Professor of Environmental Health, Department of Environmental Health) joined the ASCENT Project 018 team in July 2017. Dr. Lane has expertise in the assessment of ultrafine particle (UFP) exposure, geographic information systems, statistical modeling of large datasets, and cardiovascular health outcomes associated with air pollution exposure. He has contributed to study design and data analysis strategies and, as of October 1, 2017, took over the primary responsibility for project execution. Dr. Lane also contributes to the manuscripts and reports produced.

Dr. Prasad Patil (Assistant Professor) is a machine-learning and regression modeling expert who is assisting Dr. Lane with modeling of the 2017–2019 UFP data.

Sean Mueller (doctoral student) has been analyzing aviation-related particulate number concentration (PNC) results obtained during COVID-19. Daniel Kojis is a doctoral student examining model generalizability and transferability between sites.



Breanna van Loenen and Maria Bermudez (research assistants) are supporting the analysis of mobile monitoring (MM) and stationary monitoring data.

Tufts University

Dr. John Durant, PhD (Associate Professor) oversees the Tufts Air Pollution Monitoring Laboratory (TAPL) team, leads the development of field study design, and contributes to scientific manuscript preparation.

Dr. Neelakshi Hudda, PhD (Research Professor) joined the ASCENT Project 018 team in September 2020 and is managing the TAPL team as well as mobility data analysis, field study design and implementation, and scientific manuscript preparation.

Camille Gimilaro, Olivia Moore, Isabelle Woollacott, and Lily Sandholm (undergraduate students) are working on the MM platform and helping to clean the air pollution data.

Project Overview

The primary goal of ASCENT Project 018 for 2024–2025 was to conduct an air pollution monitoring campaign beneath flight paths to and from BOS, using a protocol specifically designed to determine the magnitude and spatial distribution of UFPs in the vicinity of arrival flight paths. Data were collected to assess whether aircraft emissions, particularly arrival emissions, significantly contribute to UFP concentrations at appreciable distances from BOS. Task 1 aims to further investigate the contributions of variation sources to PNCs at stationary sites using regression and machine-learning models at BOS. Tasks 2 and 3 leverage the infrastructure previously developed for our field campaign and enable measurements that address a broader set of research questions than those evaluated in the previous monitoring year, with additional data collection for nitrogen dioxide (NO_2) and sulfur dioxide (SO_2) to inform dispersion model validation work being conducted by ASCENT Project 019.

Our team continued our monitoring campaign to the summer of 2025 to collect and analyze near-airport air pollution measurements to determine the contributions of in-flight arrival and departure aircraft to ground-based concentrations. State-of-the-art air pollution monitoring technology that can measure different air pollutants every 1–5 s has been used. Stationary sites have been established at varying distances from flight paths for BOS, with measurements collected across multiple seasons. An MM system (electric vehicle) outfitted with the same monitoring equipment has also been employed to drive in airport neighborhoods to better characterize geographic variations in air pollution. Statistical analyses will compare the stationary and mobile measurements with flight activity data from the United States, FAA, and meteorology to determine aircraft contributions to ground measurements. Our team will compare these source attribution estimates with comparable outputs from atmospheric dispersion models.

A summary of all project methods and data collection is included below to describe the continued application of ASCENT Project 018 data and 2024–2025 study tasks.

Task 1 – Continue Targeted Mobile and Stationary Monitoring near the Boston International Airport to Allow for Analyses of Changing Aviation Source Contributions to Inform Source Attribution

Objectives

The mobile and fixed-site monitoring data collected under ASCENT Project 018 were analyzed to investigate the spatiotemporal patterns of aviation-related contributions to UFP, as well as the relative influence of flight arrivals and departures in different locations and underneath flights approaching different runways. Broadly, this effort builds on the methodological foundation developed under ASCENT Project 018 and within earlier PARTNER projects, in which our team developed and applied statistical techniques to model short-term pollution measurements with high variability and high autocorrelation. The fact that these data were collected during the pandemic across time periods in which flight activity changed substantially while traffic followed slightly different patterns provides a “natural experiment” that will enhance our ability to conduct source attribution.

Research Approach

Our team has used two statistical approaches to quantify aviation contributions to ambient air quality. First, multivariable generalized linear models were used to examine the association between air pollutant concentrations and real-time flight



activity, accounting for aircraft locations in space relative to the monitor and including terms for wind speed/direction, temperature, mixing height, and other relevant meteorological covariates. Second, machine-learning regression models, such as random forest modeling and gradient boosts, were applied to improve model performance, while applying Shapley (SHAP) analysis to provide source attribution quantification. Each study site was modeled individually to assess the location-specific impact of aircraft arrivals and departures along with meteorological and other local environmental conditions, and in future work, combined models will be explored. Because of the complexity of interactions among predictors (i.e., flight activity will be influenced by wind speed and direction, which will also affect plume dispersion and resulting concentrations at individual monitors), our team explored advanced statistical techniques for covariate selection and model assembling, including random forest regression and other machine-learning regression techniques. Preliminary findings from the application of machine-learning techniques to our UFP measurements indicate that machine-learning methods are able to explain more variability than generalized linear models or related techniques. These predictions will subsequently be shared with ASCENT Project 019, where investigators are developing comparable estimates of aviation-attributable concentrations near BOS, and we will conduct analyses to compare predictions from dispersion models and regression models.

MM data were used to (a) generate summary statistics characterizing the spatial and spatiotemporal variability of measured pollutants in the study area, (b) aid in source attribution, and (c) build and evaluate spatially explicit predictive models of pollutant concentrations in East Boston, Chelsea, Revere, and Winthrop in Massachusetts. Exploratory spatial data analyses were performed to identify areas of clustering for spatial autocorrelation of PNC within the MM routes, which may warrant further analysis or special treatment in subsequent modeling efforts. Source apportionment of measured pollutants and drivers of variability in the MM data were examined via geographically weighted regression and/or cluster analysis.

With each of the regression models, the amount of measured air pollution attributable to flight is estimated on a short-term and long-term basis. In other words, by zeroing out the flight activity terms and determining the predicted concentrations, the portion of measured concentrations attributable to aircraft arrivals and departures can be ascertained.

Broadly, these analyses make multiple important contributions not available elsewhere. Our team worked with a unique dataset of stationary and mobile measurements collected over the first 2 years of the COVID-19 pandemic in a variety of locations near a major airport. Advanced statistical techniques were applied to better ascertain source contributions. This work builds upon the aviation air pollution exposure literature and yields novel insights.

Milestones

- Completed mobile and stationary monitoring and spatiotemporal data collection and preliminary analysis to elucidate the limitations of stationary monitoring alone in determining accurate UFP exposure across geographic locations around BOS.
- Published two manuscripts, with an additional three manuscripts being prepared for submission.
- Presented at the Aviation Emissions Characterization (AEC) meeting and ASCENT Fall and Spring 2025 meetings (Kevin Lane).

Major Accomplishments

During this year we have successfully published two manuscripts focused on aim 1. A summary of each paper is provided below.

Mueller, S., Patil, P., Levy, J., Hudda, N., Durant, J. L., Gause, E., van Loenen, B. D., Bermudez, M., Geddes, J. A., & Lane, K. J. (2025). Quantifying Aviation-Related Contributions to Ambient Ultrafine Particle Number Concentrations Using Interpretable Machine Learning. *Environmental Science & Technology, 59*(37), 19942-19952. doi: 10.1021/acs.est.5c07989.

Mueller et al. (2025) applies interpretable machine learning (XGBoost with SHAP analysis) to quantify aviation-related contributions to ultrafine PNCs near the airport using an 8-year dataset from BOS. By integrating runway-specific flight activity, on-ground operations, road traffic, and meteorology, the model achieved strong predictive performance (R^2 = 0.66; coefficient of determination) and revealed that aircraft arrivals exert the greatest influence on PNC, particularly under crosswind conditions that enable lateral plume dispersion. Meteorological factors such as wind direction, planetary boundary layer height, and temperature strongly modulate aviation impacts, with shallow mixing layers and cold conditions amplifying concentrations. These findings highlight the complex, nonlinear interactions between aircraft

emissions and atmospheric dynamics, providing a high-resolution framework for exposure assessment and informing strategies to mitigate UFP pollution near airports.

Figure 1 illustrates the spatial context of the study site and its relationship to BOS. Panel (a) shows the airport's runway configuration and the monitoring site located approximately 4 km northwest of the airport, positioned to capture aviation-related UFP emissions under southeasterly winds. Panel (b) presents a wind rose summarizing hourly wind data from 2014–2022, highlighting that impact-sector winds (135°–175°) occur about 7% of the time, placing the site downwind of the airport. This figure establishes the physical basis for interpreting observed UFP patterns and underscores the importance of wind direction in determining aviation influence on local air quality.

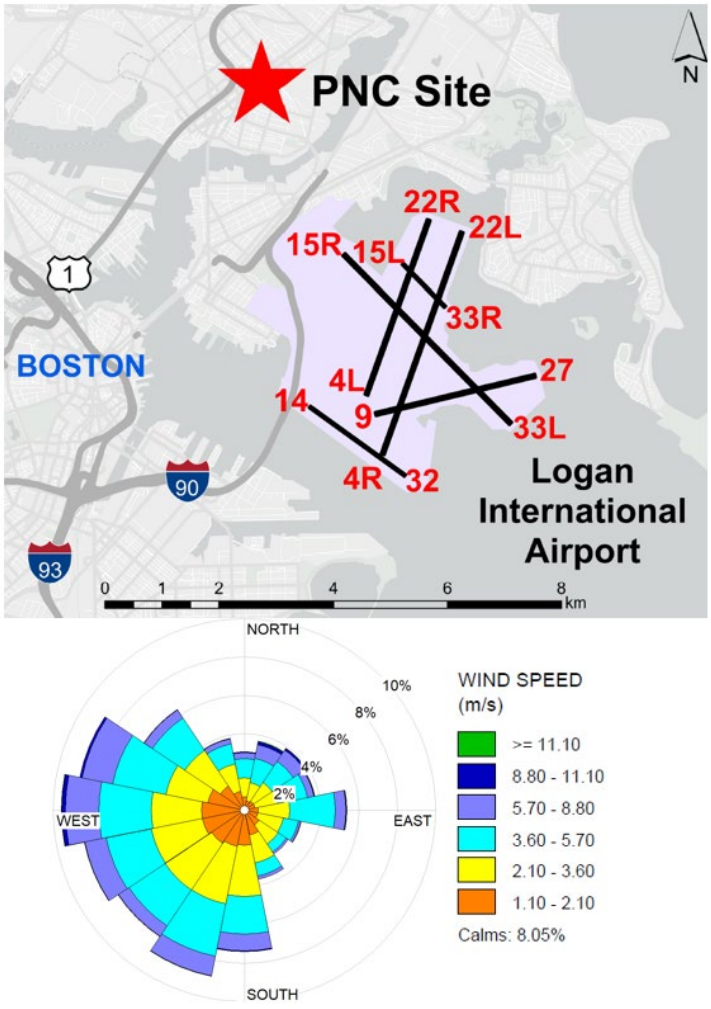


Figure 1. (a) Runway configuration at Logan International Airport and location of the monitoring site. (b) Wind rose 2014-2022 hourly data from the HRRR model.

Figure 2 consists of two panels summarizing feature importance and directional dependencies derived from SHAP analysis. Panel (a) ranks the top 15 predictors of PNC by mean absolute SHAP value (MASV), showing that meteorological variables—particularly surface wind direction, temperature, and wind speed—dominate model influence, followed by road traffic and specific runway operations (notably arrivals on 22L and departures on 22R). Panel (b) displays pollution roses of SHAP values for these aviation and traffic features, revealing that aircraft contributions peak under high-speed southeasterly

winds, while road traffic shows minimal wind dependence. Together, these plots demonstrate the nonlinear and episodic nature of aviation impacts compared to more stable roadway contributions.

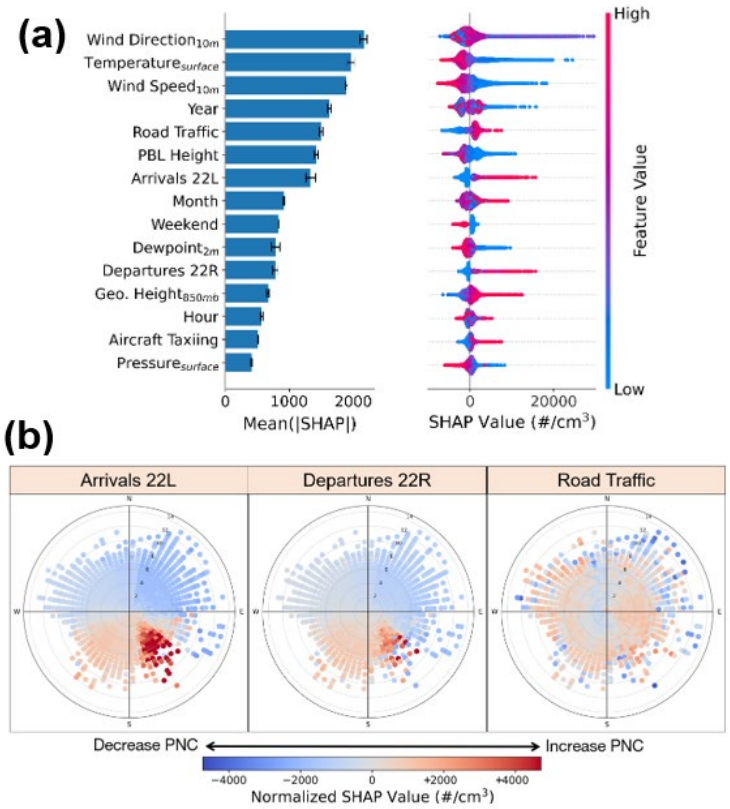


Figure 2. (a) Top 15 features ranked by mean absolute SHAP values (MASV), representing their contributions to predicted PNC (particles/cm³). Left: MASV with error bars (±1 standard deviation) across model runs (n = 10). Right: distribution of SHAP values colored by feature value. (b) Pollution roses showing binned hourly average SHAP values (normalized to 99th percentile) for aircraft arrivals on runway 22L, aircraft departures on runway 22R, and automobile road traffic, plotted against wind direction and speed.

Figure 3 presents bivariate partial dependence plots illustrating the joint marginal effects of wind direction and runway operations on predicted PNC. Results for runways 22L and 22R show minimal marginal effects under their typical southwest wind alignment but substantial increases during southeast crosswinds, with departures exerting stronger per-operation impacts than arrivals. Runway 15R, aligned with the impact sector, shows elevated contributions from arrivals during high activity periods, while departures have negligible influence—likely due to rapid climb-out and plume dispersion. This figure highlights how operational patterns and wind conditions interact to shape aviation-related PNC variability.

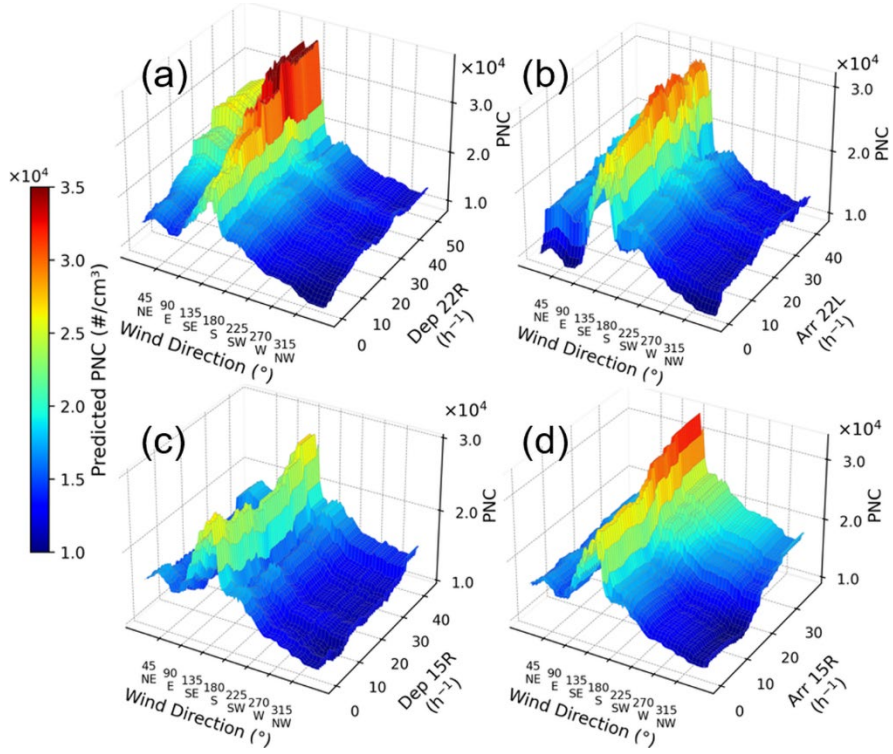


Figure 3. Bivariate partial dependence plots for predicted particle number concentration (particles/cm^3) showing the joint marginal contribution of surface wind direction and operations on runways (a) 22R (b) 22L (c-d) 15R.

Overall, this work shows our team successfully developed a machine-learning model to predict PNCs based on changing meteorology and flight activity variables. PNC data were collected by TSI® water-based condensation particle counters (CPC) at 1-s resolution and then aggregated to 15-min and hourly averages. The model was developed based on 2017 data collected from six stationary air monitoring sites along the 4R/4L runways, which is the most frequently used arrival pathway into BOS. PNC data were collected by CPC devices at 1-s resolution and then merged into hourly averages as a proxy for the total UFP.

van Loenen, B. D., Black-Ingersoll, F., Durant, J. L., Levy, J. I., Patil, P., Mueller, S., Gause, E., Hudda, N., Bermudez, M., & Lane, K. J. (2025). Aircraft Arrival and Departure Contributions to Ultrafine Particle Size Distribution in a Near-Airport Community. *Environmental Science & Technology, 59*(25), 12853-12864. doi:10.1021/acs.est.5c04799.

Van Loenen et al. (2025) examines particle size distribution and source attribution. Aviation activities influenced UFP concentrations and size distributions at monitoring sites near BOS. Using 21 months of continuous monitoring near BOS, the study measured particle size distributions across 32 channels and linked them to flight activity and meteorological conditions. Results show that, overall, PNC were significantly higher when the site was downwind of the airport, with nucleation-mode particles (particularly 8–12 nm) dominating during these conditions. Arrivals contributed disproportionately to UFP exposure, producing smaller modal diameters (9–11 nm) and higher PNC compared to departures, which were associated with larger Aitken-mode particles (39–52 nm).

Our principal component analysis confirmed that nucleation-mode particles strongly correlate with arrival activity, especially under downwind conditions. The findings highlight that exposure to aviation-related UFP is primarily driven by landing aircraft rather than departures, and that particle size distribution can serve as a robust indicator for source attribution. This work underscores the importance of incorporating size-resolved measurements in air quality assessments

® TSI is a registered trademark of TSI Incorporated, Shoreview, Minnesota.

and suggests that mitigation strategies should consider the unique characteristics of aviation emissions to protect public health.

Figure 4 provides a comparison of the PNC size distribution aggregated to hourly level. Figure 4 panel (a) provides map of the monitoring site in Winthrop, MA, showing its spatial relationship with BOS runways and nearby highways. The site is located approximately 1 km from the runway endpoints, directly beneath common landing and departure paths for runways 9 and 27. This figure emphasizes the strategic positioning of the monitoring location to capture aviation-related UFP emissions while minimizing interference from roadway traffic, as the nearest major highway is over 4 km away. The map also illustrates the surrounding geography, including Boston Harbor and Deer Island, which helps contextualize potential secondary sources and prevailing wind directions. Figure 4(B) displays polar plots of hourly averaged UFP concentrations for particles smaller than 30 nm, stratified by wind speed and direction. The plots reveal that nucleation-mode particles (particularly those between 9–11 nm) exhibit sharp concentration spikes during westerly winds, which place the monitoring site downwind of the airport. This pattern strongly supports aviation as the dominant source of these particles under impact-sector conditions. Larger particles do not show similar directional dependence, reinforcing the unique size signature of aircraft emissions. The figure visually demonstrates how meteorology interacts with source activity to influence near-airport particle size distribution.

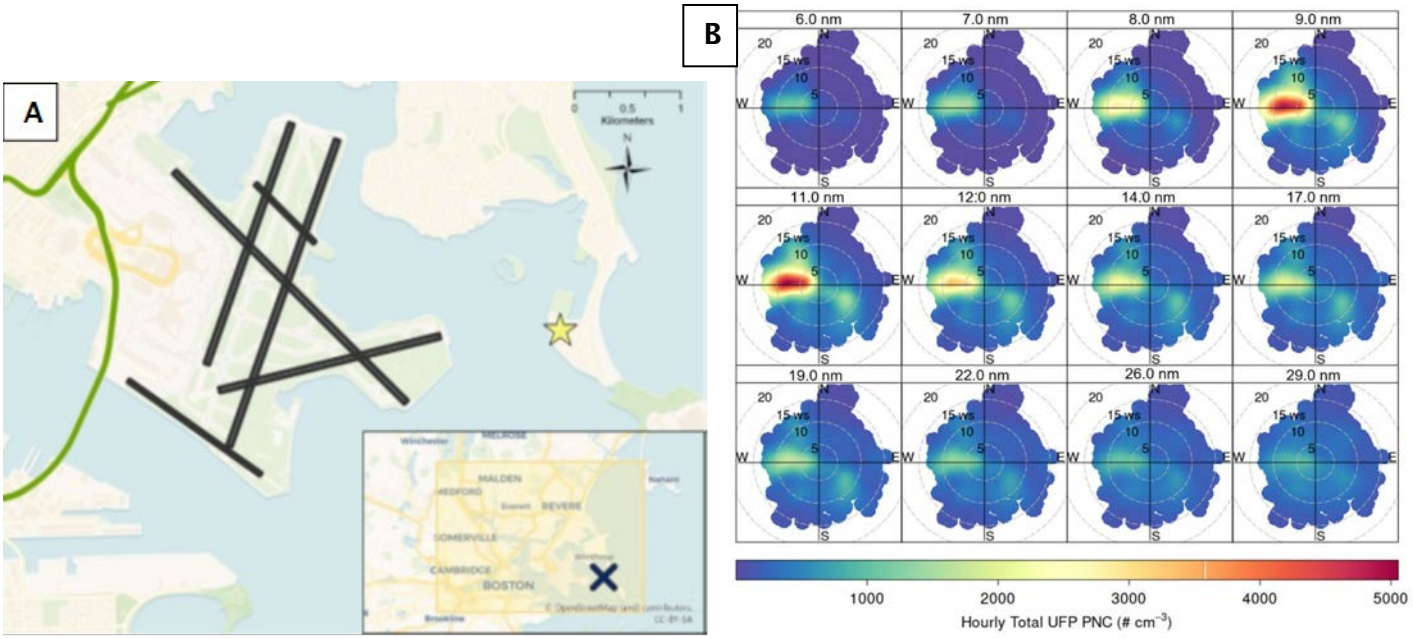


Figure 4. Panel (a) Location of monitoring site in Winthrop, MA; Panel (b) pollution polar plots of hourly average UFP contributions.

Figure 5 compares particle size distributions during two operational scenarios: hours dominated by arrivals on runway 27 versus departures on runway 9. Arrivals produce a narrow peak centered at 9–11 nm, with particles in the 7–17 nm range accounting for more than half of total PNC. In contrast, departures yield a broader distribution dominated by Aitken-mode particles (29–108 nm), peaking around 39–52 nm. Total PNC during arrivals is nearly four times higher than during departures, and peak modal concentrations differ by a factor of nine. This figure underscores the distinct size profiles associated with landing versus takeoff operations and highlights arrivals as the primary contributor to nucleation-mode particles in the study area.

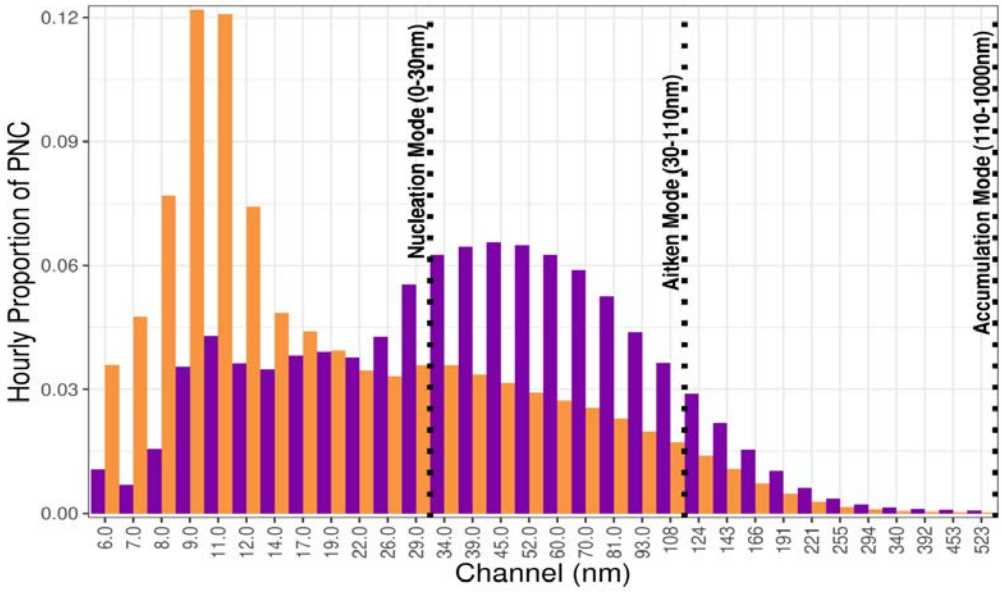


Figure 5. Proportion of total hourly PNC attributed to specific particle sizes during the arrivals scenario (orange, five or more arrivals on runway 27) and the departures scenario (purple, five or more departures on runway 9).

The principal component analysis model (PCA) identified three clusters, with Cluster A—composed of the smallest particle sizes (<30 nm)—closely associated with aviation activity indicators such as arrivals on runway 27 and departures on 33L. Within this cluster, particles between 8–12 nm exhibit the strongest cohesion, confirming their role as markers of aircraft emissions. Larger particles (39–294 nm) form an opposing cluster, indicating an inverse relationship with aviation activity. This visualization provides statistical evidence that nucleation-mode particles are most representative of aviation sources, particularly under downwind conditions. Figure 6 consists of two panels: (a) contributions of particle size bins to PCA variance and (b) overall particle size distribution across the 21-month study period. Panel (a) shows that nucleation-mode particles (<30 nm), especially those around 10–12 nm, dominate variance explained by the first two principal components, aligning with aviation-specific clusters identified earlier. Aitken-mode particles contribute modestly, while accumulation-mode particles (>200 nm) have negligible influence. Panel (b) confirms a persistent size distribution peak at 9–11 nm throughout the monitoring period, reinforcing the strong and consistent impact of aircraft emissions on UFP exposure.

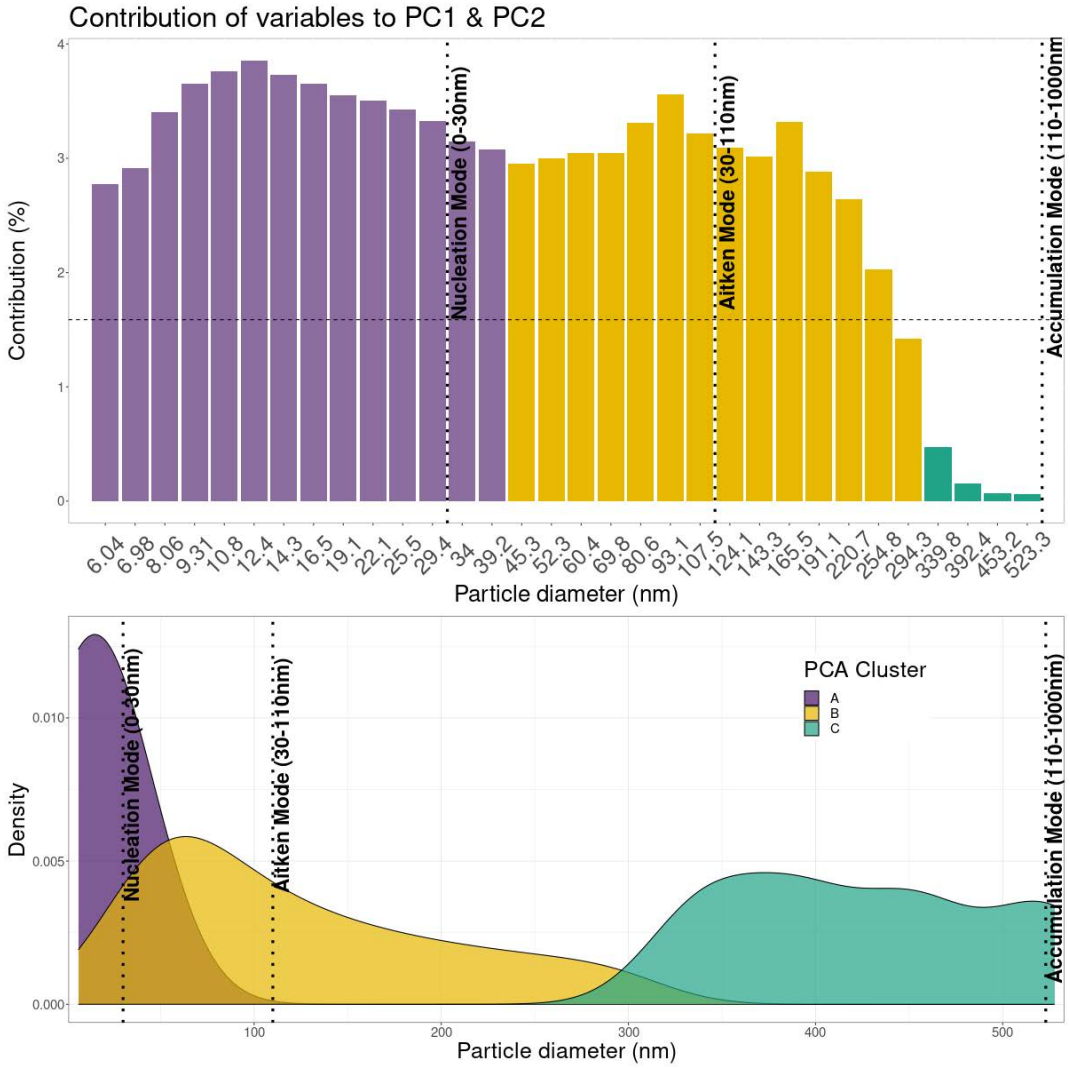


Figure 6. Two charts showing contributions of PC1 and PC2 to variance explained in Model 2 among particle size variables only.

Our team plans to continue to collect PNC data near BOS and we are in the process of expanding models to all study areas by combining the MM data with stationary models.

Publications

Chung, C. S., Lane, K. J., Black-Ingersoll, F., Kolaczyk, E., Schollaert, C., Li, S., Simon, M. C., & Levy, J. I. (2023). Assessing the impact of aircraft arrival on ambient ultrafine particle number concentrations in near-airport communities in Boston, Massachusetts. *Environmental Research, 225* (15 May 2023). https://doi.org/10.1016/j.envres.2023.115584

Mueller, S. C., Hudda, N., Levy, J. I., Durant, J. L., Patil, P., Lee, N. F., Weiss, I., Tatro, T., Duhl, T., Lane, K. (2022). Changes in ultrafine particle concentrations near a major airport following reduced transportation activity during the COVID-19 pandemic. *Environmental Science & Technology Letters, 9*(9), 706-711. https://doi.org/10.1021/acs.estlett.2c00322

Mueller, S., Patil, P., Levy, J., Hudda, N., Durant, J. L., Gause, E., van Loenen, B. D., Bermudez, M., Geddes, J. A., & Lane, K. J. (2025). Quantifying Aviation-Related Contributions to Ambient Ultrafine Particle Number Concentrations Using



Interpretable Machine Learning. *Environmental Science & Technology, 59*(37): 19942-19952. doi: 10.1021/acs.est.5c07989. https://pubs.acs.org/doi/10.1021/acs.est.5c07989

van Loenen, B. D., Black-Ingersoll, F., Durant, J. L., Levy, J. I., Patil, P., Mueller, S., Gause, E., Hudda, N., Bermudez, M., & Lane, K. J. (2025). Aircraft Arrival and Departure Contributions to Ultrafine Particle Size Distribution in a Near-Airport Community. *Environmental Science & Technology, 59*(25):12853-12864. doi:10.1021/acs.est.5c04799. https://pubs.acs.org/doi/full/10.1021/acs.est.5c04799

Outreach Efforts

- Lane, K. J., "Health Effects of Fine Particulate Matter, Ultrafine Particle Exposure and Co-Benefits of SAF." Presented at Commercial Aviation Alternative Fuels Initiative (CAAFI) Webinar Series: Air Quality & Non-CO2 Benefits of Sustainable Aviation Fuel (SAF.) June 4, 2025.
- Lane, K. J., "Measurements of Aviation-Related Air Quality Lessons Learned from Ultrafine Particle Studies In Massachusetts." Presented to the Massachusetts Environmental Policy Act (MEPA) Review Committee. June 16, 2025.
- Durant, J. L. "Mobile monitoring findings from ASCENT Project 018 research." Presented to the MEPA Review Committee. July 21, 2025.
- Presented ASCENT Project 018 air pollution monitoring and modeling at the ASCENT Fall 2024 meeting.

Presentation

Mueller, S., Patil, P., Levy, J. I., Hudda, N., Durant, J. L., Gause, E., Loenen, B. V., & Lane, K. J. (2024, October 20-24). *Examining Impacts of Cross-Validation Approaches on Machine Learning Model Performance for Ultrafine Particle Exposure Assessment* [Oral presentation]. International Society for Exposure Science 2024 Annual Meeting, Montreal, Canada.

Awards

None.

Student Involvement

Sean Mueller, PhD student in the Department of Environmental Health, Boston University
Daniel Kojis, PhD student in the Department of Biostatistics, Boston University

Plans for Next Period

- Publish our remaining three manuscripts.
- Develop a combined stationary and MM machine-learning model using data from 2020–2024.

Task 2 - Conduct an Ambient Air Pollution Monitoring Campaign Near Dulles International Airport

Boston University School of Public Health

Objectives

To expand the generalizability of our work conducted at BOS, our team conducted mobile and stationary monitoring in 2024-2025 at Dulles International Airport (IAD). This offered various levels of complexity of urban sources, operations and meteorology in addition to our Boston data to support future modeling efforts for both ASCENT Projects 018 and 019. To date, the majority of UFP aviation monitoring and modeling has been conducted at only a few United States airports (i.e., BOS, Seattle-Tacoma International Airport [SEA], and Los Angeles International Airport [LAX]). While our team and other researchers have used these measurements to quantify source contributions, the generalizability and transferability of our findings to other airports need to be systematically analyzed. This is planned for the next statement of work (SOW) for ASCENT Project 018 to analyze the data collected in 2024-2025. Specifically, key factors need to be assessed that can impact the ground-level concentrations and thus the relative contribution of airport-related sources. This includes the complexity of urban sources surrounding the airport, airport operations, meteorology, and terrain. By studying these factors systematically, adjustments are made in modeling and the resulting estimates. An additional limitation of previous studies is that they have often either been very time-intensive or unable to fully characterize source contributions. Our

team, therefore, also wants to help determine a more efficient approach for monitoring and characterizing the air quality impacts at other airports.

Research Approach

Our team initiated stationary monitoring and MM at the new site (IAD). Our team aims to investigate the following questions: (1) Can we distinguish an airport's impact on air quality near the airport? If so, what is the impact? 2) How do we develop a generalized understanding of the impact around airports? To initiate the IAD monitoring campaign, the team has collected and analyzed stationary and mobile data in different wind conditions. Preliminary stationary monitoring data were collected at multiple locations near the airport in 2023, with longer-term monitoring at three locations from 2023 to 2024 identified in Figure 6. The initial simultaneous stationary data collected from November 1, 2023, to Summer 2024 was used to create pollution roses that inform the scale and magnitude of impact (Figure 8).

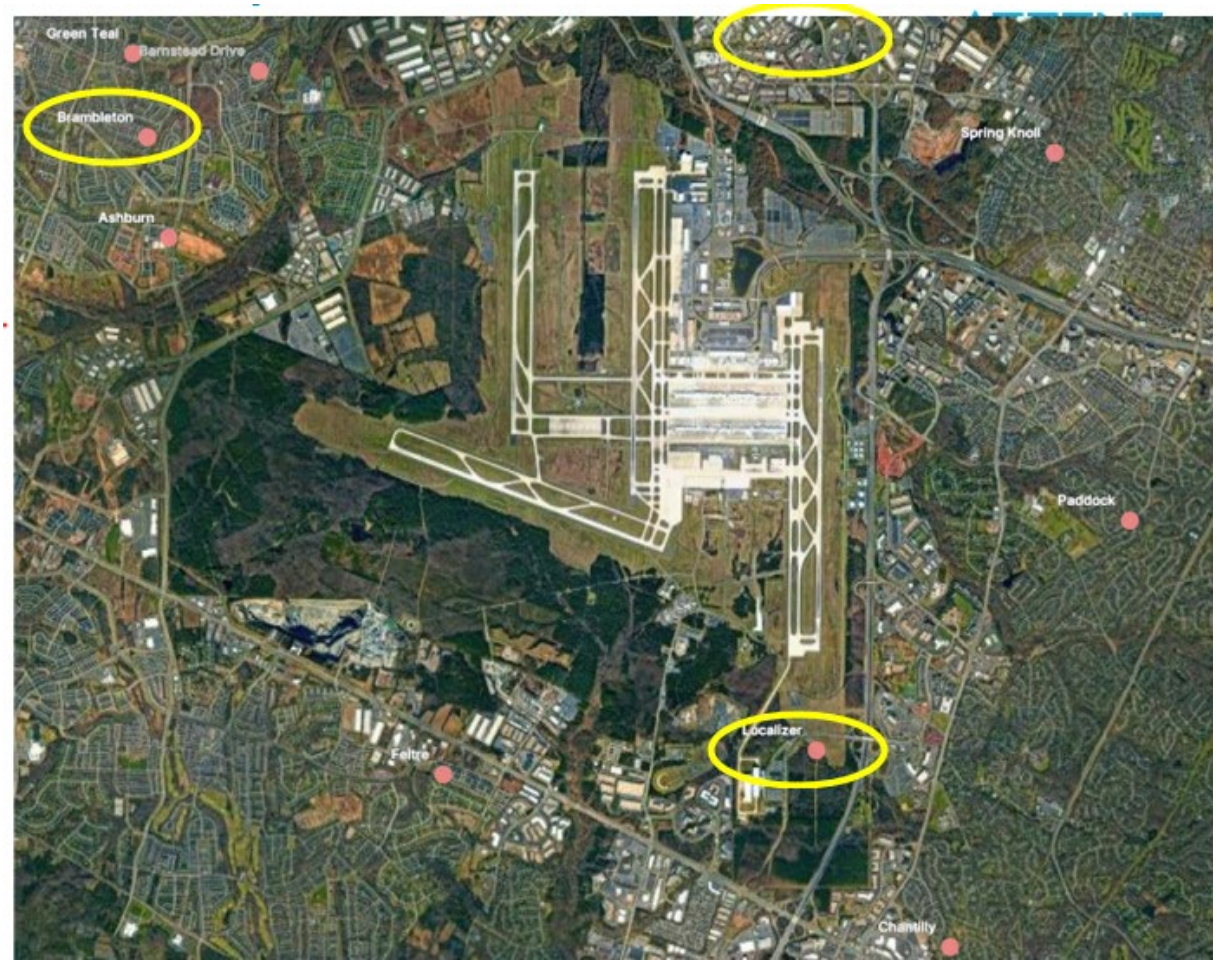


Figure 7. Stationary monitoring locations and data collection for 2024-2025.

Milestones

- Presented our findings at the AEC Roadmap/ASCENT meeting in May 2024 with a showing of the electric vehicle (EV) and instrumentation and monitoring equipment.
- Presented results at the Fall 2024 ASCENT meeting.

Major Accomplishments

Our team has collected over 15 million 1-second measurements of PNC covering three seasons of stationary monitoring near IAD. In Figure 8, each dot represents the hourly average UFP number concentration as a function of wind direction and wind speed. The bearing of each point represents the (hourly average) direction from which the wind is deriving. The distance of each point from the center is proportional to the hourly average wind speed from 0 mph (near the center) to 10 mph (near the outside). The windrose at left indicates the main directions from which the wind derives at IAD. Northwest winds are common in winter; southwest winds are common in summer. The UFP rose for Localizer shows that (for winter months) the highest concentrations occur during northwest winds. The UFP rose for Brambleton shows that (for winter months) the highest concentrations occur during southeast winds. These impacts clearly point to the airport as being a major source of PNC at these two sites. Notice that the black dots are as high as 100,000 particle/cm^3.

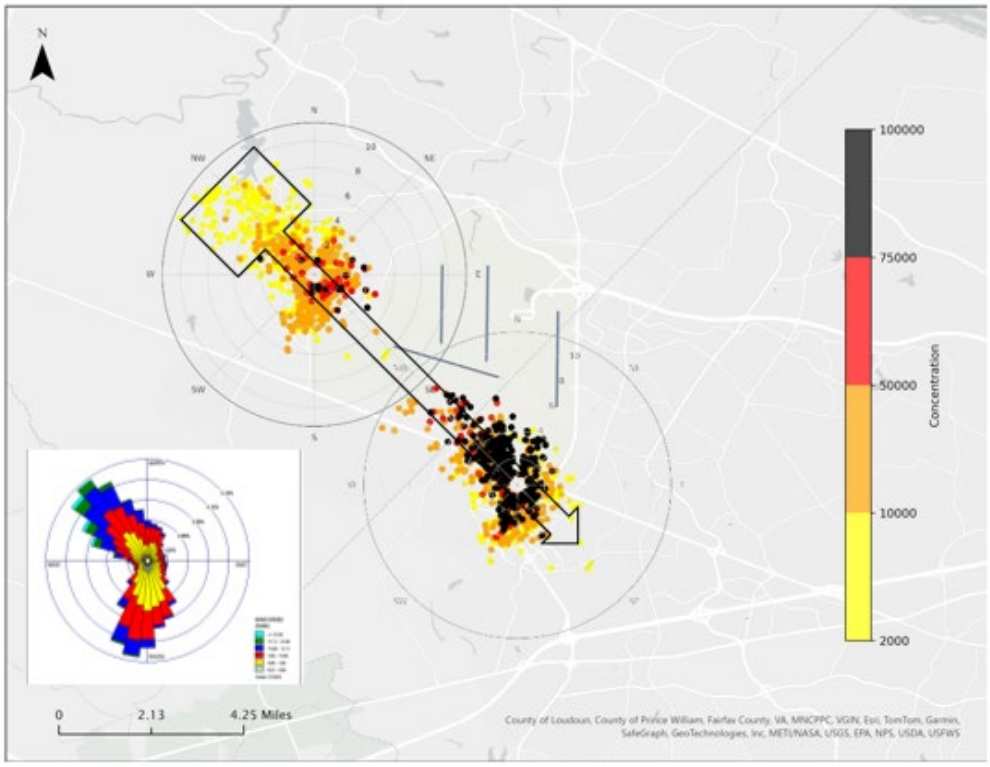


Figure 8. Pollution rose plot for the data at two long-term monitoring sites from fall 2023 through winter 2024 at Dulles International Airport.

Using MM data, we compared exposures to PNC and NO_2 to identify meteorological and aviation conditions that produce simultaneous peaks in both pollutants. Figure 9 illustrates MM results for PNC and NO_2 on a day with steady south-southeast winds, when the monitoring route was downwind of the airport and aircraft were flying over the airport neighborhood. Measurements were collected at 1-second intervals along a 15–20 m route. Spatial patterns for PNC and NO_2 revealed a clear downwind dispersion with a distance-decay gradient, particularly pronounced for UFP. While both pollutants exhibited some similar spatial trends, distinct differences were observed, including far-field NO_2 contributions linked to departures versus landings.

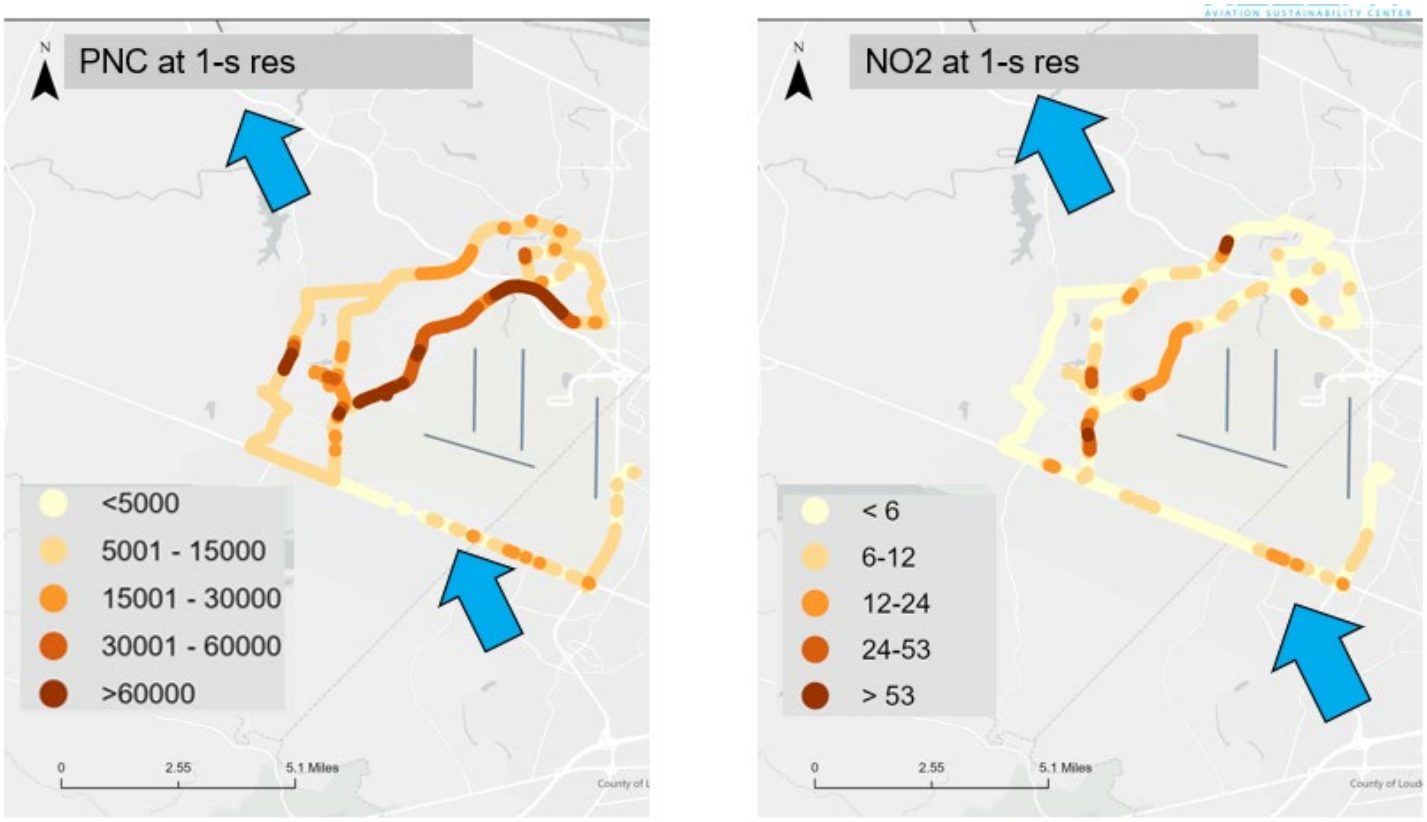


Figure 9. Comparison of particle number concentration (PNC) and nitrogen dioxide (NO_2) mobile monitoring (MM) data.

This MM map in Figure 10 displays the 5th percentile concentrations rolling averages of 30-s data. The wind was blowing from the northeast to the southwest at a speed of 5.6 mph.

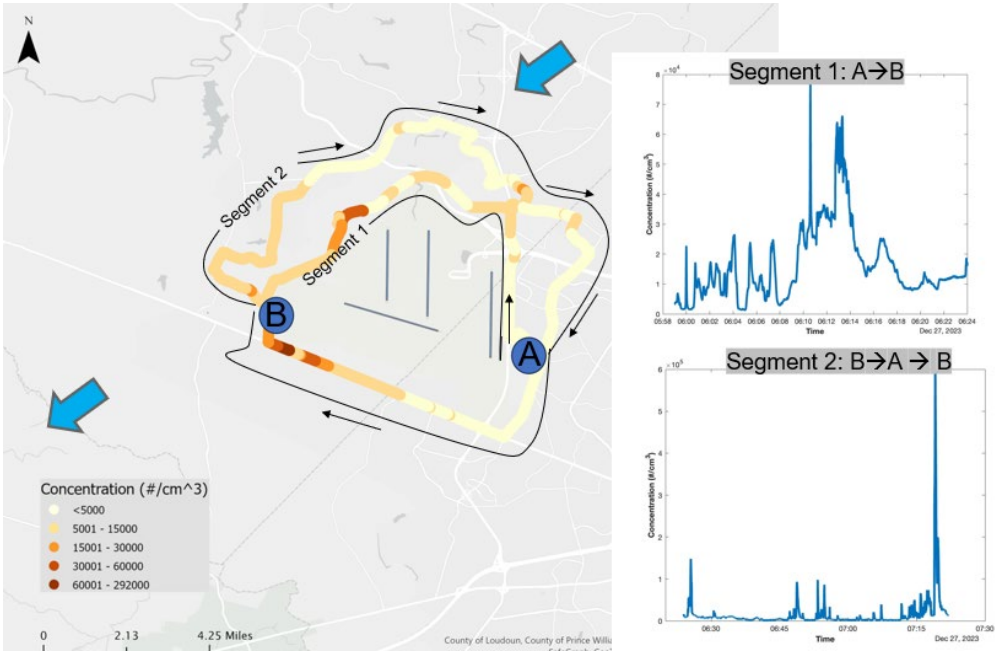


Figure 10. An example of mobile monitoring (MM) results for particle number concentration (PNC) and nitrogen dioxide (NO_2) concentrations for a single day with steady south-southeast winds downwind of BOS.

Publications

A manuscript is being developed on the descriptive analyses of the UFP data near IAD.

Outreach Efforts

- Presented our findings at the Spring AEC/ASCENT meeting in May 2024 with a showing of the EV and instrumentation and monitoring equipment.
- Presented results at the Fall 2025 ASCENT meeting.

Awards

None.

Student Involvement

Camille Gimilaro, doctoral student in Civil and Environmental Engineering, Tufts University.

Plans for Next Period

- Continue collecting air pollution data by moving NO_2 and SO_2 equipment to the stationary monitoring sites in Spring 2026.
- Conduct analysis on the transferability of UFP and NO_2 models developed under ASCENT Projects 018 and 019 to IAD in future years of the project. This will inform source attribution statistical models and the AERMOD Modeling System.[1]

[1] AERMOD is a steady-state plume model that incorporates air dispersion based on planetary boundary layer turbulence structure and scaling concepts.

Task 3 – Provide Data to ASCENT Project 019 to Conduct Calibration and Validation of Ambient Air Pollution Dispersion Models Developed by ASCENT Project 019

Boston University School of Public Health

Objectives

Our team is collecting data on $NO/NO_2/NO_x$ at three different sites in Revere, East Boston and South Boston, MA, and data on SO_2 in East Boston, MA, to inform calibration and validation of dispersion models created by ASCENT Project 019. Development of descriptive analyses of these datasets continued to inform the ASCENT Project 019 data analysis efforts. Our estimates of aviation-attributable $NO/NO_2/NO_x$ concentrations will be directly shared with ASCENT Project 019 for comparison with dispersion model estimates in future study periods. While our team has constructed numerous regression models for source attribution within ASCENT Project 018, the richness of these datasets (including multiple pollutants, both fixed-site and mobile measurements over a lengthy period, and the potential for synthesizing multiple fixed-site and mobile measurements for the same period) will allow for key refinements that will improve estimation and directly inform dispersion model validation.

Research Approach

Our team has continued working directly with ASCENT Project 019, with the long-term objective of improving dispersion modeling and quantifying arrival and takeoff aircraft contributions to NO_2 and SO_2 concentrations near BOS. In collaboration with ASCENT Project 019, data are shared to provide monitored data and to coordinate the collection of flight activity data to be used in both projects. Team members from ASCENT Project 018 and ASCENT Project 019 are coordinating support of each other's continued progress. ASCENT Project 018 staff have prepared analysis-ready datasets that combine all of our stationary air pollution monitoring data from the 2024 and 2025 monitoring campaign merged with relevant and timely meteorology data as well as runway-specific flight activity data at BOS and have shared these datasets with ASCENT Project 019 for use in their dispersion models.



Location	Species measured
Evans	UFP, NO, NO2
Revere	UFP, NO, NO2, NOx
Saratoga St	UFP (via FMPS), NO, NO2, NOx, SO2

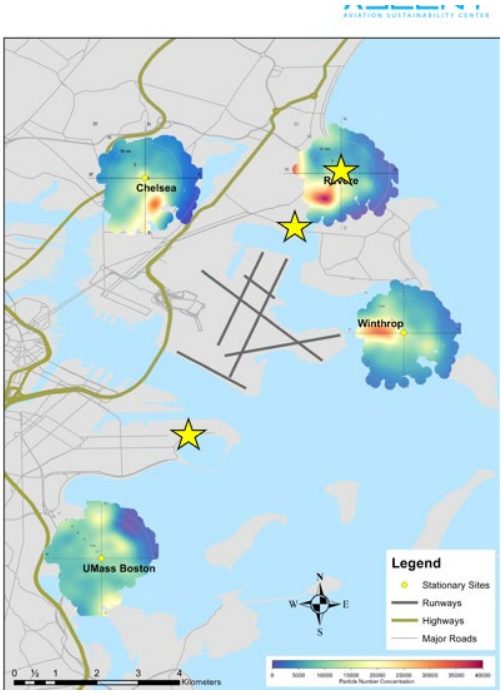
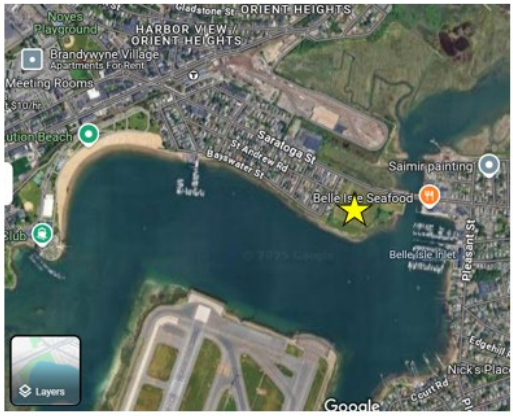


Figure 11. Pollution distribution by wind direction and wind speed for each monitoring site from previous analyses along with starred locations for monitoring sites for 2024-2025 campaign.

Figure 12 illustrates the monitoring site zoomed in along with the equipment location.

Site Name	Monitor Model	Configuration	Distance from Nearest Runway (km)	Pollutants	Measurement Range	Operating Dates
Saratoga St. East Boston	T200 NO2 Analyzer, 6400T SO2 Analyzer, TSI FMPS 3091	Outdoor: in field on Massport property	< 0.48 km	PNC size distribution, NO/NO2/NO x, SO2	NO/NO2/NOX 0-50 ppb / 0-20 ppm; SO2 = 0-50ppb TO 0-20 ppm; PNC = 5.6-560 nm	Spring 2024 – present







T200 - NO, NO2, NOx

Range: 0-50 ppb / 0-20 ppm

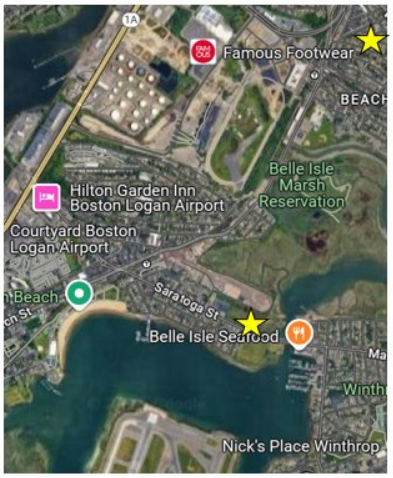
6400T / 6400TH

Sulfur Dioxide Analyzer



Fast Mobility Particle Sizer (FMPS) 3091

Site Name	Monitor Model	Configuration	Distance from Nearest Runway (km)	Pollutants	Measurement Range	Operating Dates
Revere	T500U CAPS NO2 Analyzer; 2Btech NO/NO2/Nox analyzer; TSI CPC 3783	Outdoor: ground floor backyard; Residential	2.3	PNC	NO2 = 0-5 ppb to 0-1 ppm; TO 0-20 ppm; PNC = 7.0 nm	Spring 2024 – present





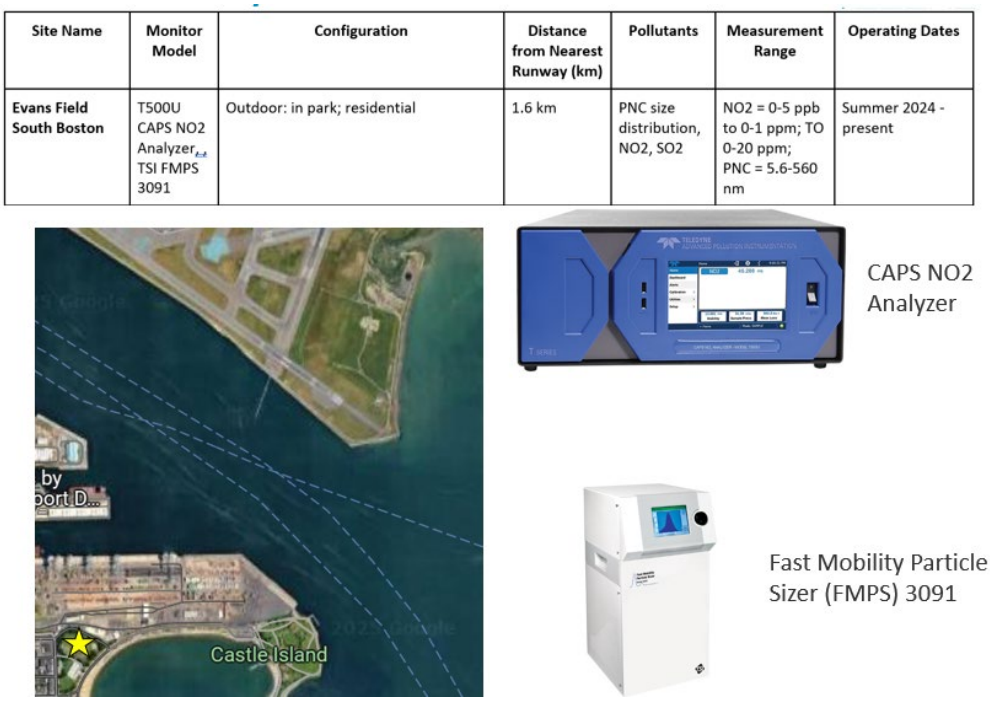
CAPS NO2 Analyzer



2B Tech405 nm NO/NO2/NOx Analyzer



TSI CPC 3783



Site Name	Monitor Model	Configuration	Distance from Nearest Runway (km)	Pollutants	Measurement Range	Operating Dates
Evans Field South Boston	T500U CAPS NO2 Analyzer, TSI FMPS 3091	Outdoor: in park; residential	1.6 km	PNC size distribution, NO2, SO2	NO2 = 0-5 ppb to 0-1 ppm; TO 0-20 ppm; PNC = 5.6-560 nm	Summer 2024 - present

Figure 12. Monitoring site locations, equipment and setup.

This sharing of resources across projects allows both teams to avoid duplicating efforts, thus accelerating research progress. Sharing data also ensures that the results of our individual modeling approaches will be comparable, thus providing helpful context in interpreting the varied approaches. To facilitate data sharing between project groups, ASCENT Project 018 has granted access to their internal data storage and analysis server cluster environment to members of ASCENT Project 019.

Milestones

- Prepared similar analysis-ready data for the current and ongoing stationery and MM campaigns around BOS that are ready to be shared when needed.
- Created a data-processing pipeline to periodically clean and prepare collected datasets during the current monitoring campaign.
- Used ASCENT Project 018 data to prepare multiple publications by the ASCENT Project 019 team.

Major Accomplishments

- Shared all analysis-ready data from the 2024-2025 monitoring period with the ASCENT Project 019 team.
- Held meetings to exchange knowledge and collaborate on model interpretation.

Publications

None.

Outreach Efforts

None.

Awards

None.



Student Involvement

None.

Plans for Next Period

- Continue to provide ASCENT Project 019 with additional raw air pollution data as well as modeled PNC and NO_2 and SO_2 contributions.



Project 019 Development of Aviation Air Quality Tools for Airport-Specific Impact Assessment: Air Quality Modeling

University of North Carolina at Chapel Hill

Project Lead Investigator

Saravanan Arunachalam, PhD
Research Professor
Institute for the Environment
University of North Carolina at Chapel Hill
123 W. Franklin St., Suite 330B
Chapel Hill, NC 27516
919-966-2126
sarav@email.unc.edu

University Participants

University of North Carolina at Chapel Hill (UNC Chapel Hill)

- P.I.: Saravanan Arunachalam, Research Professor and Deputy Director
- FAA Award Number: 13-C-AJFE-UNC Amendments 1–21
- Period of Performance: October 1, 2024, to September 30, 2026
- Tasks:
  1. Develop and evaluate a new dispersion model for aircraft sources
  2. Develop and evaluate a multiscale Weather Research and Forecasting (WRF)-Sparse Matrix Operator Kernel Emissions (SMOKE)-Community Multiscale Air Quality (CMAQ) model application for Boston Logan International Airport (BOS) focused on ultrafine particles (UFP)
  3. Implement volatile particulate matter (PM) plume-scale modeling into a CMAQ application

Project Funding Level

The Federal Aviation Administration (FAA) provided $650,000 in funding. The Barr Foundation provided matching cost-share via the Harvard Center for Climate, Health, and the Global Environment.

Investigation Team

Prof. Saravanan Arunachalam, P.I., UNC Chapel Hill Institute for the Environment
Dr. Gavendra Pandey, Air Quality Dispersion Modeler, UNC Chapel Hill Institute for the Environment
Hyeongseok “Darby” Kim, Graduate Student, UNC Chapel Hill Institute for the Environment
Brian Naess, Geographic Information Systems Specialist, UNC Chapel Hill Institute for the Environment
Dr. Huy Tran, Air Quality Modeler, UNC Chapel Hill Institute for the Environment
Rachel Snead, Aircraft Emissions Modeler, UNC Chapel Hill Institute for the Environment
Dr. Akula Venkatram, Consultant, University of California at Riverside

Project Overview

Aviation is predicted to grow steadily in upcoming years (Boeing, 2010); thus, a variety of aviation environmental policies will be required to meet emission reduction goals in aviation-related air quality and health impacts. Tools are needed to rapidly assess the implications of alternative policies for an evolving population and atmosphere. In the context of the International Civil Aviation Organization’s (ICAO) Committee on Aviation Environmental Protection, additional approaches are required to determine the implications of global aviation emissions.

The overall objective of this project is to develop a new aircraft-specific dispersion model and continue the development and implementation of tools, both domestically and internationally, to allow for an assessment of year-to-year changes in



significant health outcomes. These tools must be acceptable to the FAA (in the context of Destination 2025) and/or other decision makers. More importantly, this new model must have the capability to address the 1-hour form of the nitrogen dioxide (NO_2) National Ambient Air Quality Standard (NAAQS) in the United States (U.S.), as well as to support National Environmental Policy Act (NEPA) and/or NAAQS analyses that may be needed by airports. The developed methods must also rapidly provide output to support a variety of "what if" analyses and other investigations. While the tools for use within and outside the U.S. need not be identical, several goals are desirable for both cases:

- Enable the assessment of premature mortality and morbidity risks due to aviation-attributable PM having a diameter up to 2.5 μm ($PM_{2.5}$), ozone (O_3), and other pollutants known to exert significant health impacts.
- Capture airport-specific health impacts at regional and local scales.
- Account for the impact of landing/take-off (LTO) versus non-LTO emissions, including a separation of effects.
- Allow for an assessment of a wide range of aircraft emission scenarios, including differential growth rates and emission indices.
- Account for changes in non-aviation emissions.
- Allow for assessments of sensitivity to meteorology.
- Provide domestic and global results.
- Include quantified uncertainties and differences with respect to U.S. Environmental Protection Agency (EPA) practices, which are to be minimized when scientifically appropriate.
- Be computationally efficient, such that tools can be used in time-sensitive rapid turnaround contexts and for uncertainty quantification.

During this period of performance, the team at the University of North Carolina at Chapel Hill Institute for the Environment (UNC-IE) performed work on Tasks 1–3.

Task 1 - Develop and Evaluate a New Dispersion Model for Aircraft Sources

University of North Carolina at Chapel Hill

Objectives

The FAA's Aviation Environmental Design Tool (AEDT) is currently coupled with the American Meteorological Society/EPA Regulatory Model (AERMOD[1]) dispersion model for modeling aircraft sources and is the required regulatory model in the U.S. for modeling airport-level aircraft operations during LTO cycles.

Recent studies have shown several limitations in the use of AERMOD for modeling aircraft sources. The Airport Modeling Advisory Committee developed a series of recommendations in 2011 to improve jet exhaust modeling. Since then, the Airport Cooperative Research Program (ACRP) Project 02-08 developed guidance for airport operators on conducting measurements and modeling of air quality at airports, published in ACRP Report 71 (Kim et al., 2012), with a measurement and modeling study conducted at Dulles International Airport (IAD). Subsequently, the ACRP Project 02-58 developed the final ACRP Report 171 (Arunachalam, Valencia, et al., 2017) providing dispersion modeling guidance for airport operators for local air quality and health. This study applied four different models—AERMOD, CALPUFF,[2] Second Order Closure Integrated Puff Model with Chemistry (SCICHEM), and the United Kingdom's Atmospheric Dispersion Modeling System for Airports (ADMS-Airport)—for the Los Angeles International Airport (LAX) and compared model predictions with high-resolution measurements taken during the LAX Air Quality Source Apportionment Study (AQSAS). Each of these reports identified several limitations with AERMOD and developed a series of recommendations for improving dispersion modeling of aircraft emissions for airport-level air quality.

In 2017, UNC-IE developed the C-AIRPORT dispersion model for application to LAX (Arunachalam, Isakov, et al., 2017). Initially, C-AIRPORT was designed to be part of the C-TOOLS series of community-scale, web-based modeling systems. The objective of C-TOOLS was to create a web-based interface for modeling multiple source types for short-term or long-term pollutant concentration averages and for analyzing various "what if" scenarios to assess changes in air quality at local scales due to changes in inputs. C-AIRPORT used a line source-based approach to model aircraft sources, based upon the

[1] AERMOD is a steady-state plume model that incorporates air dispersion based on planetary boundary layer turbulence structure and scaling concepts.
[2] CALPUFF is an advanced non-steady state air quality dispersion model maintained and distributed by Lake Environmental.



C-LINE modeling system (Barzyk et al., 2015), and a preliminary evaluation of the algorithms against LAX AQSAS was conducted. Preliminary results at LAX core sites showed that nitrogen oxide (NO_x) model estimates from all sources were generally comparable to observations except for slight overpredictions, given lack of plume rise. However, overall, aircraft contribution seems low compared to other sources. Further, investigation is needed to continue the evaluation of C-AIRPORT.

Under the previous year's funding, UNC-IE completed development of a modeling framework that addresses known limitations from the above tasks and proposed a viable and suitable approach for modeling pollutants from aircraft sources. The primary objective of this plan was to demonstrate that a robust, improved pollutant dispersion model for aircraft can be developed for U.S. regulatory compliance purposes. The proposed new model will disperse pollutants from aircraft sources in a more technically and scientifically advanced manner (compared with current AERMOD capabilities), with the ultimate goal of becoming a potential U.S. regulatory compliance tool, based on future discussions with FAA and EPA. This plan will include an itemized list of known limitations along with a corresponding proposed developmental approach and recommendations for addressing the limitations.

As part of the proposed ASCENT research under this task, we will continue to implement the plan with a specific focus on four broad areas. This report provides a very high-level summary here, because the specifics of this implementation have been described in previous documents and reports that were independently developed earlier.

Our approach is to ensure that the new model will be "robust" and based on the state of science on physical and chemical processes and associated algorithms.

Source Characterization
Existing approaches in AEDT/AERMOD treat aircraft sources as an area source segment. In the ongoing work, our team is developing two aircraft dispersion models. The first is a simple analytical steady-state plume model, referred to as the aircraft dispersion model (ADM), while the second is a grid-based unsteady-state model, referred to as GADM. In ADM, surface-level aircraft sources are treated as area sources, whereas airborne sources are modeled as pseudo-volume sources. Conversely, in GADM, all aircraft sources are treated as volume sources. To generate input emissions for these models, our team has developed an emission processor called AEDT2ADM. This processor utilizes high-resolution aircraft movement datasets from the AEDT. AEDT2ADM is continuously adapted to enhance its usability for other existing models too, such as AERMOD.

Physical Processes
In previous years, our team already developed an aircraft plume-rise algorithm for the area/volume sources framework (Pandey et al., 2023) by assuming that the different types of aircraft contributing to emissions in any one of the area/volume sources can be represented by a "typical" aircraft whose characteristics computed through a weighted average of the characteristics of aircraft that pass through the area/volume source. Emissions from an aircraft are treated as line thermals that have horizontal momentum and buoyancy. This algorithm is used in ADM and GADM.

In addition to plume rise, our team will go beyond the initial implementation developed during the previous year, with a new focus on the following:

a. Treatment of dispersion under low wind conditions and assessment of effects of atmospheric stability
b. Treatment of dry and wet deposition
c. Incorporation of aircraft downwash effects
d. Treatment of complex terrain and building downwash

Chemical Processes
Our team will go beyond the initial implementation of the previous year, with a new focus on the following:

a. The 1-hr form of the NO_2 NAAQS. The 1-hour form of the NO_2 NAAQS is a critical issue for air quality around U.S. airports, with several modeling studies showing overestimates compared with observations. It is important that the new model performs adequately to capture this short-term form of the NO_2 NAAQS.
b. A new detailed chemical mechanism for NO_2 including the generic reaction set (Valencia et al., 2018; Venkatram et al., 1994) or other components.
c. Version of the aerosol treatment as included in the CMAQ and SCICHEM and described by Chowdhury et al. (2015).



Model Evaluation

a. Ongoing model evaluation has involved evaluating model predictions using only measurements from the LAX AQSAS for winter 2012. Our team will now consider developing and testing the model for other case studies, including the following:
   1. LAX AQSAS for Summer 2012
   2. One of three airports (Copenhagen, Madrid, and Zurich) with measurements being undertaken as part of the European Union (EU) Assessing aviation emission Impact on local Air quality at airports: Towards Regulation (AVIATOR) project, a new measurement-modeling study called AVIATOR undertaken in Europe through funding from the EU.[3]
      i) Our team will rely on the AVIATOR team to provide emission inventories for the chosen airport. If emission inventories are not directly available for use, we will obtain airport operations data for the campaign period and develop an inventory using the AEDT.
   3. New measurements from the ASCENT Project 018 investigators at BOS and IAD
      i) This is a new collaboration that will help focus on both designing the monitoring campaign to assist in obtaining valuable data for characterizing the impact of aircraft emissions on air quality and developing the ADM, as well as in source attribution of the measured fields to the aircraft or other source types.

b. Model evaluation will focus on the model's ability to capture the behavior of the plume related to aircraft sources during LTO cycles at an airport, while comparing with available observations and identifying strengths and weaknesses compared with another existing model.

c. In collaborating with Boston University (BU), we will rely on BU to perform appropriate cleanup and quality assurance/control of observation data before using these data in our model evaluation routines. Our team will also work closely with BU to ensure appropriate and careful interpretation of the data. UNC-IE and BU have collaborated extensively on similar projects in the past, and we expect to obtain a robust model measurement and modeling assessment from the BOS study.

Research Approach

1. Source Characterization

Aircraft LTO emissions contribute to surface air quality in and around an airport. Dispersion modeling helps to quantify the effects of aircraft emissions on surface air quality. We started working on two tasks: (1) understand the effects of airborne aircraft emissions on surface air quality and (2) understand the effects of varying numbers of sources in dispersion modeling. Although there are many studies on the effects of aircraft surface emissions on surface air quality, the effects of airborne emissions on surface air quality in dispersion modeling remain poorly understood. To accomplish both tasks, UNC-IE updated the Python®-based emissions processor AEDT2ADM (developed earlier for ADM) that generates the required input files for the AERMOD dispersion model. We hope to complete these tasks in the next performance period.

2. Physical Processes

2.1 Development and Implementation of an Aircraft Plume Rise Algorithm in AERMOD

Aircraft emissions, especially during the LTO cycle, play a significant role in degrading the air quality in and around airports. Unlike stationary sources, these emissions are characterized by high forward momentum and thermal buoyancy due to jet engine exhaust, which affects how pollutants disperse in the atmosphere. Neglecting these characteristics in a dispersion model frequently results in an overprediction of ground-level pollutant concentrations near airports. Recently, Pandey et al. (2023) implemented this unique but complex characteristic of aircraft plume dynamics in the EPA's regulatory model AERMOD, and further in Pandey et al. (2024), extensively evaluated this algorithm using observations from the LAX AQSAS, conducted at LAX in 2012. They found that AERMOD performs significantly better after the inclusion of aircraft-specific plume rise. This algorithm was subsequently promulgated by EPA as an ALPHA option in AERMOD version 23132. It is publicly available to use as a research option (ALPHA) within the recent version of AERMOD 24142. Here, we presented the updates on this aircraft plume rise algorithm and its evaluation against the LAX AQSAS 2012 and Boston 2024 studies.

2.1.1 Aircraft Plume Rise Methodology within AERMOD

The existing aircraft plume rise algorithm within AERMODv24142 has a simplified assumption of plume dynamics; it takes all the emissions from all different types of aircraft in any one of the fixed area sources and represents them as a "typical" aircraft. The characteristics of this typical aircraft are a weighted average of all actual aircraft that pass through that area source.

[3] https://aviatorproject.eu/

® Python is a registered trademark of Python Software Foundation, Beaverton, Oregon.



According to this existing algorithm, an exhaust plume behaves as follows:

a. It starts as a line of hot air driven by the aircraft's forward momentum. This initial thrust causes the plume to expand horizontally as it travels away from the aircraft.
b. Once the plume slows down to the speed of the surrounding wind, buoyancy takes over.
c. The plume stops rising when it either hits a layer of stable air and loses its lift or when atmospheric turbulence becomes strong enough to break it apart.

The horizontal momentum and the buoyancy of the line thermal associated with jet aircraft emissions are related to aircraft engine characteristics: thrust, fuel burn rate, aircraft velocity, air-fuel ratio, rated power, and engine bypass ratio. Details of the formulation are provided in Pandey et al. (2023).

Overall, this existing algorithm separately calculates the plume rise generated because of horizontal momentum and buoyancy and combines both of them. Due to this, it is unable to accurately capture the characteristics of plume dynamics that are governed by plume velocity causing the algorithm to calculate significantly high plume rise values. To overcome these issues, we modified this into a new, aircraft-specific plume rise algorithm within AERMOD.

2.1.1.1 Reformulated Aircraft Plume Rise Algorithm

From the incompleteness in the existing aircraft plume rise algorithm, we have updated it and describe these updates below. It builds upon our improved understanding of plume rise of emissions from aircraft sources and could be readily incorporated into AERMOD. Here, we have given brief information about the updated aircraft-specific plume rise algorithm.

The calculations of heat rejection, exhaust temperature, and buoyancy flux are identical to the existing algorithm. However, we updated the interaction of the buoyancy-induced plume with the horizontal momentum plume using the following equations:

Plume rise due to buoyancy, z_p, is governed by:

$$\frac{dz_p}{dt} = w_p, \quad \text{(Eq. 1)}$$

where w_p is the buoyancy-induced vertical velocity given by combining the momentum and energy balances on the plume element,

$$\frac{d}{dt}\left(r^2 w_p\right) = F_o. \quad \text{(Eq. 2)}$$

The radius of the plume r grows through the combined effect of shear between the rising plume and the surrounding air and atmospheric turbulence:

$$\frac{dr}{dt} = \beta w_p + \sigma_w, \quad \text{(Eq. 3)}$$

where $\beta = 0.6$ is an entrainment constant, and σ_w is the standard deviation of the vertical velocity fluctuations of the surrounding atmosphere.

Solving the above equations results in the final combined plume rise.

Note that the radius of the plume grows in response to the effects of both horizontal motions caused by exhaust momentum and the vertical motion caused by buoyancy.

2.1.1.2 Computation of Plume Rise Magnitudes

We have compared the plume-rise magnitudes from both algorithms— the publicly available AERMOD version 24142 (Plume Rise_Old) and the updated one presented here (Plume Rise_New)— for all LTO modes. For this, we calculated final plume-rise values up to 1000 m downwind of the source by considering all possible combinations of engine parameters (fuel burn rate, thrust, by-pass ratio, and rated power [for shaft-based engines]) for each LTO mode, over a single stable meteorological hour (wind speed, 3.5 m/s; temperature, 298.15 K; surface roughness length, 0.03 m; Monin-Obukhov length, 100 m; surface friction velocity, 0.5 m/s; and mixing height, 200 m).

New plume rise values are significantly lower than old plume rise values at each LTO mode (Figure 1). These were also consistent with the light detection and ranging (LiDAR) experiment measured values by Wayson et al. (2008).

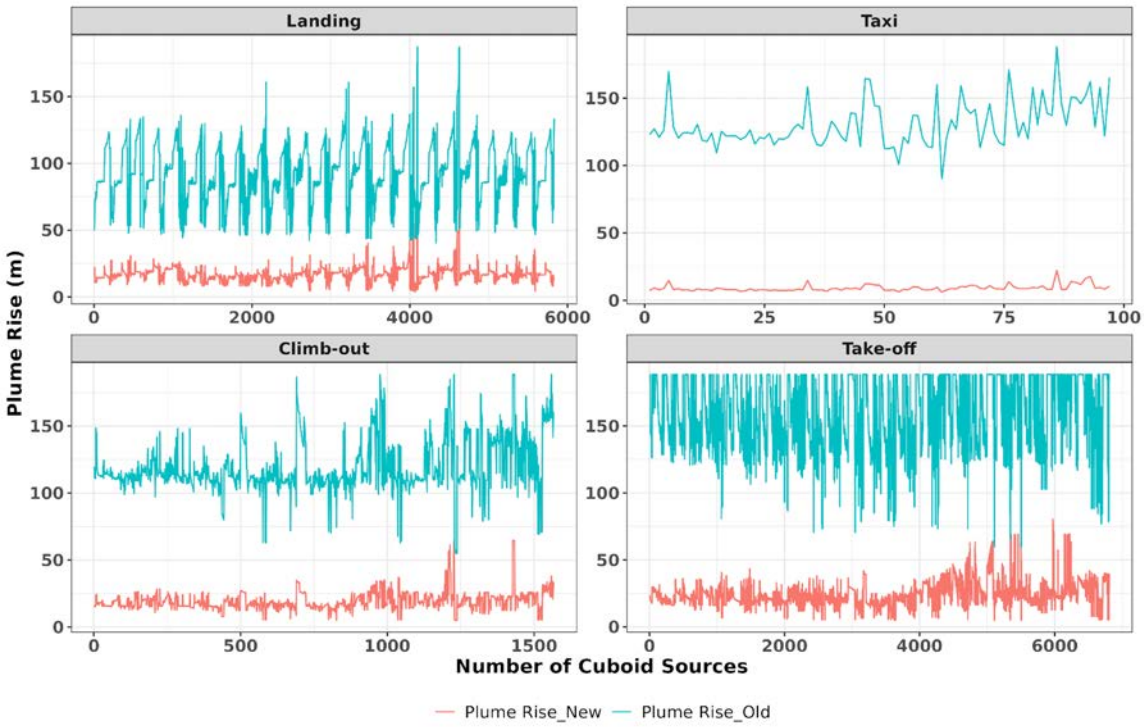


Figure 1. Comparison of old and new plume rise magnitudes for a single stable meteorological hour.

2.1.1.3 Step-Size Sensitivity

We have performed a sensitivity analysis based on the variation in step-size, Δx, by calculating the time taken by AERMOD using the new plume rise algorithm for a one-day LAX Summer 2012 study. In Table 1, from the old to new plume-rise (50 m step size) algorithm in AERMOD for one day, the runtime increases almost three times. All runs were performed on the UNC High Performance Computer (HPC) Longleaf server.

Table 1. AERMOD runtime comparison between old and new plume-rise algorithms. AQSAS: Air Quality Source Apportionment Study, HPC: high performance computer, LAX: Los Angeles International Airport, UNC: University of North Carolina.

Plume Rise Algorithm	Step Size (m)	UNC HPC Longleaf (AMDEPYC7702 x86_64 processor)	Run Time (hh:mm:ss)	Data Period (LAX AQSAS Summer 2012)
Old	NA	C1306ie01	00:14:50	One day
New	1	C1306ie01	23:26:12	One day
New	10	C1306ie01	02:35:41	One day
New	20	C1306ie01	01:25:33	One day
New	40	C1306ie01	00:50:16	One day
New	50	C1306ie01	00:43:18	One day

2.1.2 Case Study Applications

Here, we evaluated AERMOD with and without the aircraft-specific plume rise (old and new) options for the LAX AQSAS for 2012 and BOS Field Study for 2024.

2.1.2.1 Los Angeles International Airport Study

2.1.2.1.1 Site Description

To evaluate the air quality impact of LAX, a major global travel hub, the LAX AQSAS was conducted in 2012 (Figure 2). This study involved two intensive six-week monitoring campaigns during the winter and summer seasons, measuring pollutants like NO_x and sulfur dioxide (SO_2) at several locations in and around the airport. The main focus of this field study was at four "core" sites: AQ, CN, CS, and CE (Tetra Tech, 2013). The details of this study can be found in several studies (Arunachalam, Valencia, et al., 2017; Pandey et al., 2024, 2022).

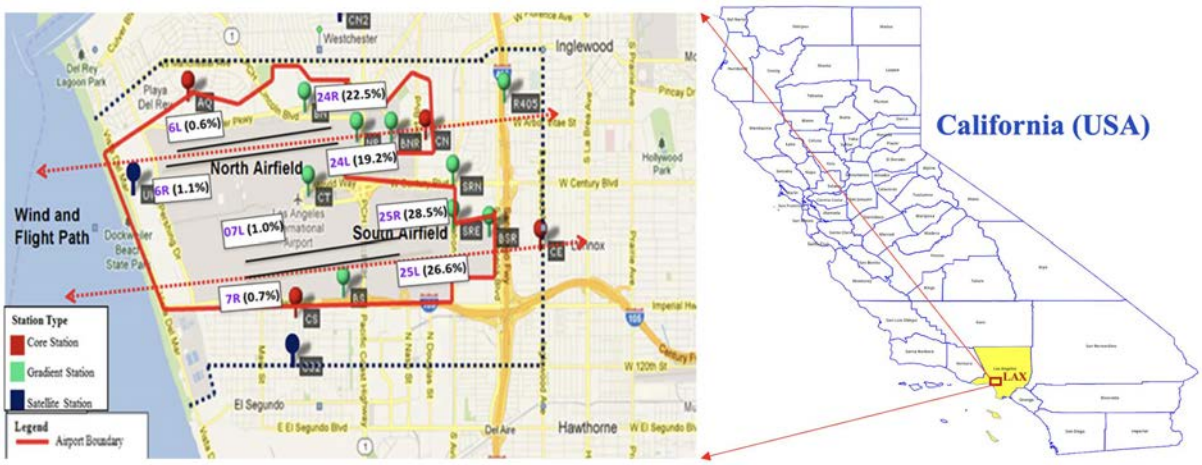


Figure 2. Locations of core, gradient, and satellite monitoring sites at Los Angeles International Airport (LAX). The red rectangle on the right surrounds Los Angeles County, containing the LAX airport, shown in greater detail on the inset map on the left. Adapted from ACRP Report 179 (Arunachalam, Valencia, et al., 2017).

2.1.2.1.2 Meteorological Data Input

The meteorological data for the AERMOD model were created using the AERMET[4] processor. In AERMET, as an input, surface observations from LAX airport, upper air data from a station in San Diego, California, and 1-min weather data from LAX were utilized. Further details on how the meteorological input files were created have been documented in several studies (Arunachalam, Valencia, et al., 2017; Pandey et al., 2024, 2022).

However, Pandey et al. (2022) identified a key limitation with the standard AERMET output: it doesn't fully characterize the heterogeneous/complex behavior of the turbulent internal boundary layer (IBL) that forms, especially on the shoreline at coastal sites. When cool ocean air blows over the warmer land of the airport, it creates an IBL. This layer enhances more mixing and dispersion of pollutants than AERMET would normally predict under stable conditions. To address this, Pandey et al. (2022) modified the meteorological data generated by AERMET.

2.1.2.1.3 Observation Data

A detailed analysis of observed SO_2 and NO_x concentrations and an explanation of potential contributions from aircraft activity during LTO operations are given in Pandey et al. (2024).

[4] AERMET is a meteorological data preprocessor for AERMOD. AERMET processes commercially available or custom on-site met data and creates two files: a surface data file and a profile data file.

2.1.2.1.4 Emission Data

Aircraft emissions of SO_2 and NO_x were calculated using the FAA's AEDT model, which models all the LTO models as distinct area sources of varying sizes. Non-aircraft emissions, which include sources like the nearby Chevron® refinery, road traffic, parking lots, and marine vessels, were taken from the emissions inventory generated during the LAX AQSAS 2012 study. A detailed discussion of the emissions inventory can be found in several studies (Arunachalam, Valencia, et al., 2017; Pandey et al., 2024, 2022).

We utilized both seasons' SO_2 and NO_x concentrations data to evaluate the aircraft-specific plume rise algorithms. However, here we have presented only the summer season results.

2.1.2.2 Boston Logan International Airport Study

To assess the robustness of the plume rise algorithm, we evaluated AERMOD using another dataset from the BOS Field Study. It was conducted by BU ASCENT Project 018 teams in the spring/summer and winter seasons of 2024. We received NO_x and SO_2 observation data from both monitoring periods, and we have extensively analyzed the dataset at UNC-IE. Here, we present the 2024 spring/summer season results, as we currently only have emissions for aircraft and non-aircraft sources for the spring/summer period. Based on the aircraft emissions inventory for the spring/summer of 2024, we have extracted the observation data for March 31 to July 31, 2024, to compare against the model. The results for this period are presented below.

2.1.2.2.1 Site Description

BOS is one of the main airports in the U.S. The BOS 2024 study involved extensive four-month (123 days) monitoring campaigns during the 2024 spring/summer season of 2024 (March 31 to July 31, 2024), measuring pollutants like NO_x and SO_2 at several locations around the airport. In the study, NO_x measurements were recorded at three locations: Revere (approximately 2.3 km from the start of runway 04R/22L and 2.4 km from the start of runway 04L/22R), Saratoga (approximately 0.7 km from the start of runway 04R/22L and 0.8 km from the start of runway 04L/22R), and Evans (approximately 1.8 km from the start of 14/32 runway), whereas SO_2 measurements were captured at only the Saratoga site (Figure 3). Out of the 123-day monitoring period, NO_x measurements were available for 49 days at Revere, 53 days at Saratoga, and 12 days at Evans (Figure 4). For SO_2, 91 days of data were available (Figure 4, Table 2).

Here, model estimates were compared with 1-hr averaged SO_2 and NO_x concentrations measurements made at all sites for the spring/summer season at BOS.

® Chevron is a registered trademark of Chevron Intellectual Property, LLC, Houston, Texas.



Figure 3. Locations of monitoring sites and surface meteorological stations for the Boston Logan International Airport 2024 study.

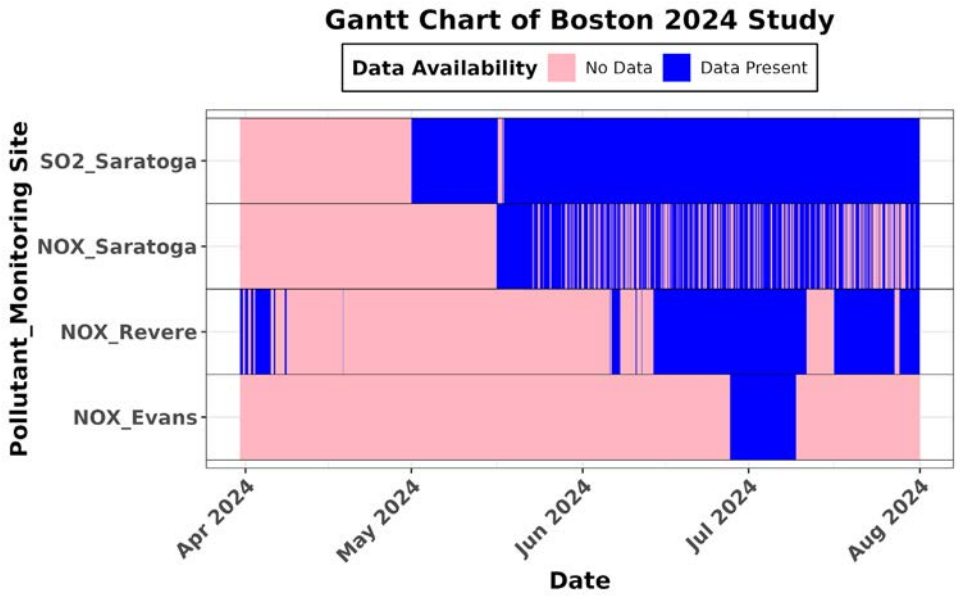


Figure 4. Data availability at all four sites for sulfur dioxide (SO_2) and nitrogen oxides (NO_x) pollutants in the Boston Logan International Airport 2024 study.

Table 2. Data availability at all four sites for sulfur dioxide (SO_2) and nitrogen oxide (NO_x) pollutants in the Boston Logan International Airport 2024 study.

Pollutant	Site	Data Available Day (Hours)	Total Day (Hours)	Data Availability (%)
SO_2	Saratoga	91 (2186)	123 (2952)	74.05
NO_x	Saratoga	53 (1266)	123 (2952)	42.89
	Revere	49 (1186)	123 (2952)	40.18
	Evans	12 (287)	123 (2952)	9.72

2.1.2.2.2 Meteorological Data Input

To create the meteorological input files to run AERMOD for the 2024 spring/summer season, it was necessary to run AERMET, the meteorological preprocessor for AERMOD. For this, hourly surface meteorological data were acquired from the weather station at BOS (WMO 72509 or WBAN 14739) (Figure 3) for the spring/summer of 2024, including 1-min and 5-min wind data. The nearest radiosonde station in Gray, Maine (KGYX) (WMO 74389 and WBAN 54762), was used for upper air data. AERMINUTE (version 15272) uses 1-min and 5-min data to generate a more accurate average wind condition for each hour than the data from the surface weather station. AERMET (version 24142) was run with the ADJ_U* option enabled. The AERSURFACE tool (version 20060) was used to estimate surface roughness length, albedo, and Bowen ratio for the study. Land cover, impervious, and canopy data files from 2016 were used as inputs for the tool to generate the necessary input files for AERMET. Twelve equally distributed sectors were drawn around the airport's weather station with a radius of 1 km. All land-use sectors were assigned as Airport.

Figure 5 represents the wind rose plot for the 2024 spring/summer season, showing the frequency of counts by wind direction as a percentage. During the study period, most of the winds are westerly or southwesterly (Figure 5). This wind rose plot suggests that the Saratoga and Revere sites were downwind during the study, and the Saratoga site was impacted by aircraft emissions through south-westerly winds.

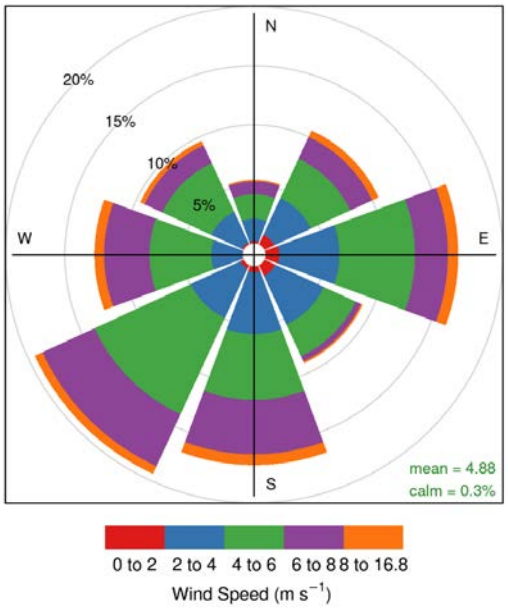


Figure 5. Wind rose plot of the 2024 spring/summer season, showing the frequency of counts by wind direction as a percentage for the Boston Logan International Airport 2024 study.

2.1.2.2.3 Observation Data

The observed SO_2 and NO_x concentration distributions are presented in box-and-whisker plots for each hour of the spring/summer season in Figure 6 and Figure 7 below, with one monitoring site and three monitoring sites, respectively. In Figure 6 and Figure 7, the boxes' top, middle, and bottom edges indicate 75th, 50th, and 25th percentile values, and the top and bottom whiskers show the values corresponding to 1.5 times the interquartile range (IQR). The colors of the dots on each plot represent the wind direction, whereas hollow black dots represent the mean value of overall concentrations for each hour. The higher SO_2 concentrations were measured at the Saratoga site from 7 AM onwards due to the southwesterly wind (180–270 degrees wind sector) contributions (Figure 6). There was a constant 0.1 ppb value at each hour that represents the minimum detection level (LOD) value (Figure 6).

The NO_x concentrations also have the same patterns as SO_2 at each hour for the Revere and Saratoga sites (Figure 7). The higher NO_x concentrations occurred in the early morning and late-night hours when the winds were south-westerly, which suggested that there was a strong signal of aircraft-related activity at these sites. On the other hand, at Evans, when the winds were north easterly or north westerly, we see the higher concentrations and aircraft-related contributions.

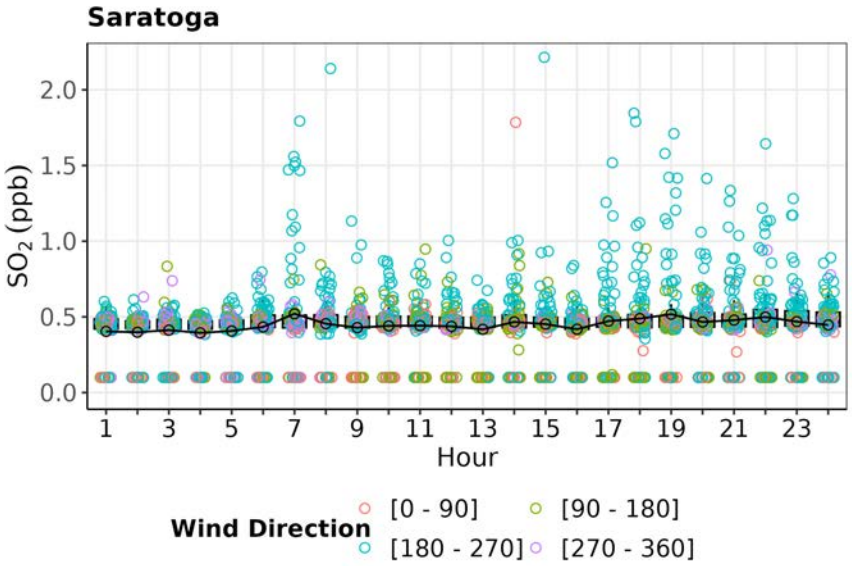


Figure 6. Box-and-whisker plots of measured sulfur dioxide (SO_2) concentrations at the Saratoga site during the 2024 spring/summer season for the Boston Logan International Airport 2024 study. Black hollow dots represent the mean value of overall concentrations at the site for each hour.

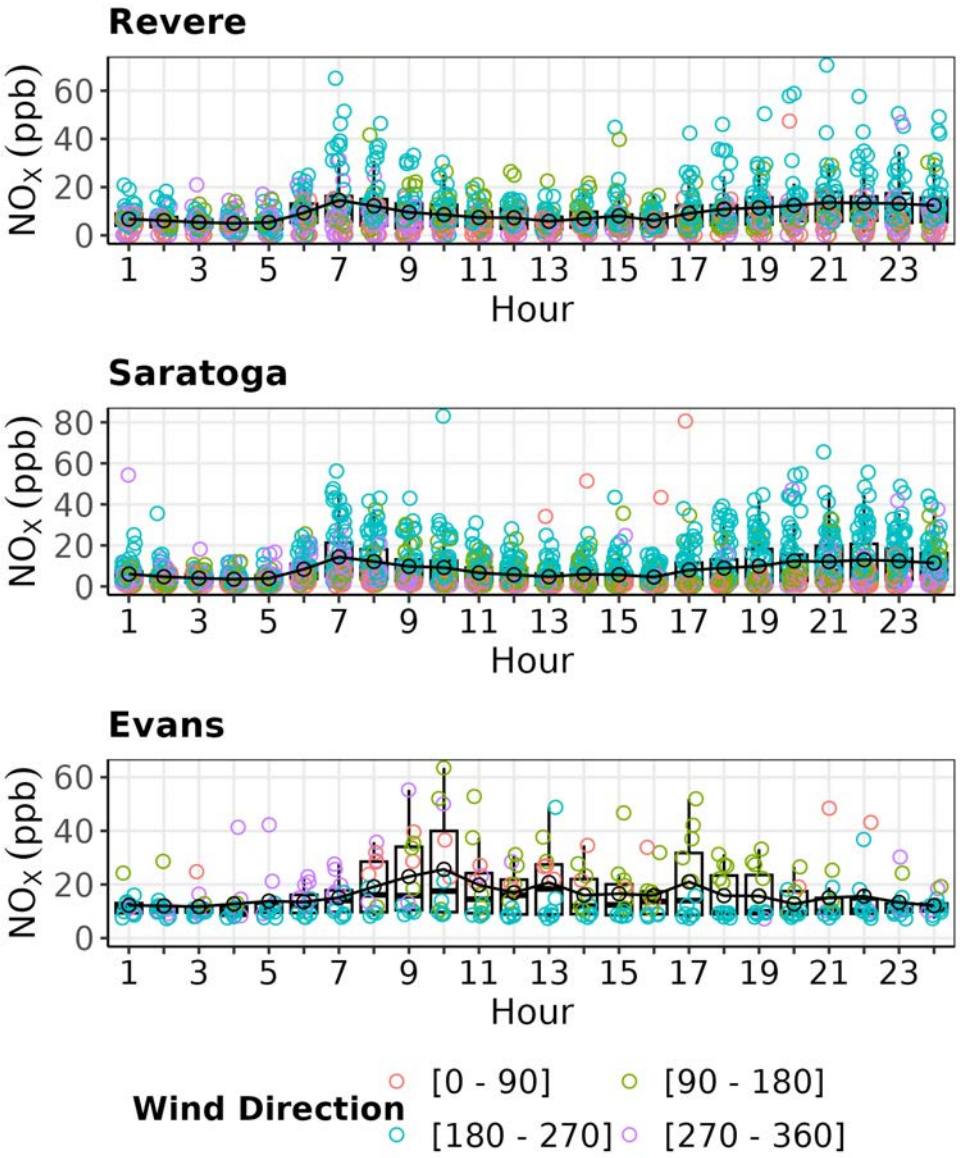


Figure 7. Box-and-whisker plots of measured nitrogen oxide (NO_x) concentrations at the Revere, Saratoga, and Evans sites during the 2024 spring/summer season for the Boston Logan International Airport 2024 study. Black hollow dots represent the mean value of overall concentrations at each site for each hour.

2.1.2.2.3.1 Additional Observation Data Analysis

To compare the pollutant concentration values at BU monitoring sites (Revere, Saratoga, and Evans) with nearby monitoring sites, we collected Air Quality System (AQS) data at other sites located within a 50-km radius of BOS for the 2024 study period. BU had provided UNC-IE with the cleaned hourly observation datasets for nitric oxide (NO), NO_2, and total NO_x at Evans, Revere, and Saratoga, MA, as well as cleaned SO_2 data at Saratoga. The locations of these sites are labeled in Figure 8, and data sources are denoted with "(BU)" for Boston University monitoring sites and "(EPA)" for background AQS monitoring sites.

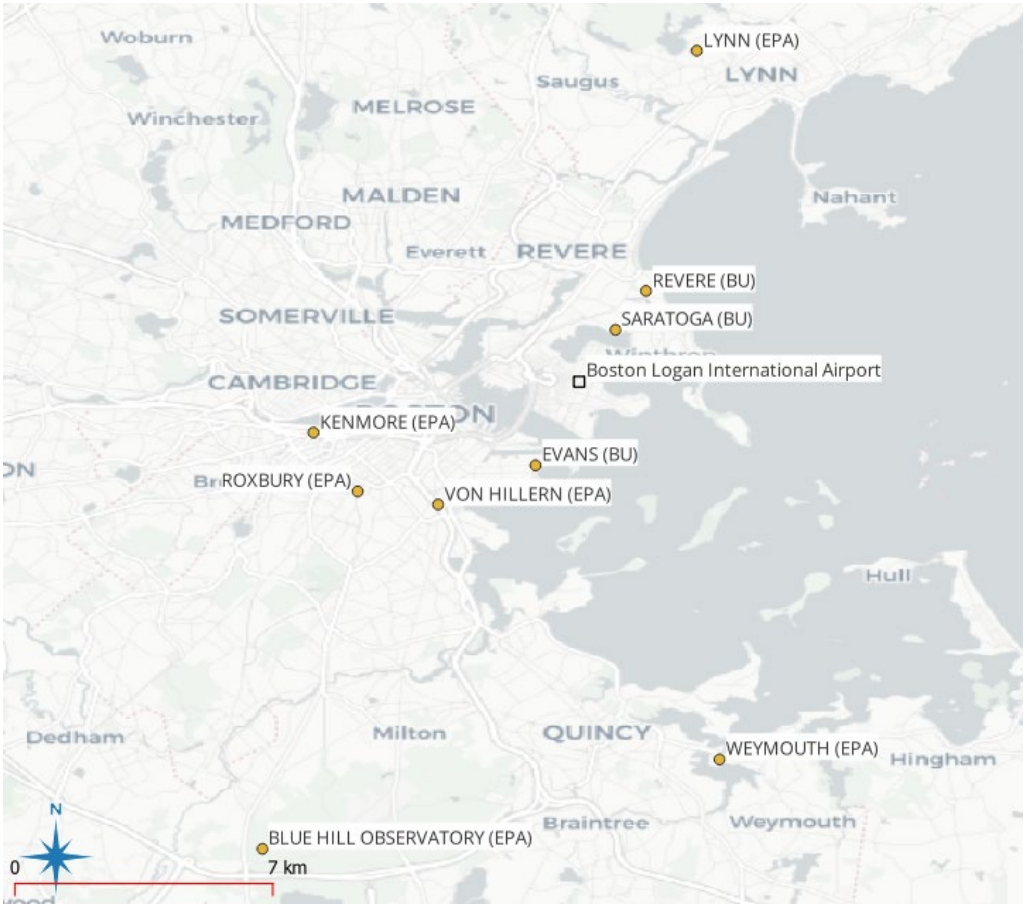


Figure 8. Boston Logan International Airport monitoring sites within 50km, denoted with "(BU)," and EPA AQS background monitoring sites, denoted with "(EPA)," over the Boston region.

We conducted a comparative analysis between the BU monitoring data and the background AQS monitoring site data (Figure 9). Based on the temporal coverage and data completeness, the study period of March 31 to July 31, 2024, was selected. We found that both types of monitoring sites had reasonable concentration values, and sites with relatively lower and higher concentrations were explained based on their farther or closer proximity to center-city Boston, respectively.

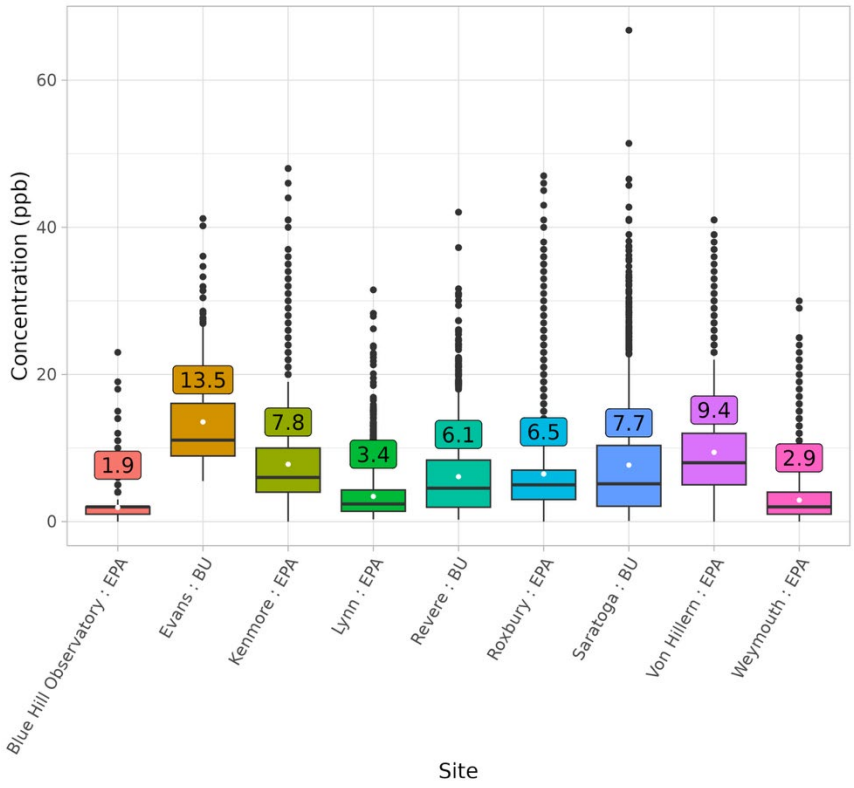


Figure 9. Box and whisker plots of NO_2 hourly concentrations at BU monitoring sites and AQS background sites from 3/31/2024 to 7/31/2024 (Values in each box and whisker indicate the means of the distributions). BU: Boston University, EPA: U.S. Environmental Protection Agency.

2.1.2.2.4 Emissions Data

Aircraft emissions of SO_2 and NO_x were calculated using the FAA's AEDT, which models all the LTO models as distinct area sources of varying sizes. This emissions dataset was provided by the U.S. Department of Transportation Volpe Center (Volpe). Non-aircraft emissions were extracted from EPA's Emission Modeling Platform version 2022v1. Here, we describe the processing of aircraft and non-aircraft emissions for this study.

2.1.2.2.4.1 Aircraft Emissions

AEDT is a publicly available software program used to support the research and regulatory compliance of aircraft and related airport-activity emissions. Using what is known as "threaded-track (TT) data" from the MITRE Corporation (MITRE), aircraft activity parameters are inserted into the AEDT model to estimate emissions at different segments of flights. Parameters such as aircraft engine and airframe specifications, operation type (i.e., arrival, departure, etc.), and operation times are combined with information in the AEDT program's integrated airport and aircraft database. With all these parameters, the AEDT can calculate fuel consumption, emissions, and generate AERMOD inputs for dispersion modeling.

Individual flight operations at BOS were acquired from MITRE for April–July 2024 and injected into the AEDT (version 3g) database using a series of scripts to process raw aircraft movements into the modeling domain and assign fleet data (i.e., unique airframe, engine type, and engine modification) to each operation. Aircraft operations were categorized as either arrivals or departures and assigned to one of the default flight profiles (which assigns the weight of the aircraft) within the AEDT based on the operation's stage length (related to the flight distance) and airframe. Operations were linked to specific runway ends based on the identifier provided in the raw dataset.

Information on aircraft ground movements was unavailable in the MITRE dataset. To estimate emissions from aircraft's taxi movements, operations were assigned to one of four terminal areas at the airport based on the airline operator named in



the flight operation. BOS has four terminals that aircraft use for commercial operations: A, B, C, and E. In general, terminals A, B, and C handle domestic air travel, while terminal E handles international air travel. BOS maintains a list of the terminals used by the different airline operators, by arrival and departure operations (source). The taxi network, which is made up of taxi paths and their associated taxiways, was manually created using satellite imagery of BOS. Taxiways in the AEDT are defined as a set of geographical points along which the aircraft travels, and taxi paths are a series of taxiways that link a runway end to a gate (or, in this case, terminal) and vice versa. Runway ends and terminals were linked via the shortest taxi route possible. AEDT's Delay and Sequencing Module (DSQM) then modeled aircraft ground movements given the defined taxi network and operations schedule. The DSQM ensures aircraft do not occupy the same location at the same time by creating queues as needed, thus determining the time an aircraft spends in taxi. Queues typically occur near the runway ends as aircraft are appropriately spaced for departures. The AEDT assumes arrival aircraft do not queue and taxi directly to their assigned terminal without delay.

For the AEDT to create the hourly emission (HRE) input files to run dispersion via AERMOD, it is necessary to run AERMET, the meteorological preprocessor to AERMOD. Files output from AERMET are used by the AEDT to model aircraft performance and thus calculate the associated emissions. For this evaluation, hourly surface meteorological data and upper air data files were taken, similar to those discussed in Section 2.1.2.2.2.

All emissions are aggregated to each modeling hour, by source, and are converted into AERMOD source-specific emission rates that can vary by hour (via HRE file). Calculated emissions from each flight operation were split across various ground and airborne segments. Within the dispersion workflow of the AEDT, emissions are only calculated for flights up to 914 m above field elevation (AFE). For this study, aircraft were from 914 m AFE up to 15 km from the airport on departure and up to 25 km from the airport upon arrival. The AEDT allocates airport-related emissions into spatially fixed emission sources that can be read by AERMOD. Aircraft sources were defined using default AEDT preferences; the study was run twice – once with aircraft emissions characterized by area sources with plume rise implementation and once without plume rise implementation. When using AREA source characterization, aircraft on the ground were defined with areas of 20 m by 20 m, an initial vertical dispersion dimension of 4.1 m, and a release height of 12 m. Airborne emissions were characterized with 200 m by 200 m areas spaced every 20 m vertically starting at 22 m AFE until 300 m AFE. Emissions between 300 m AFE and 914 m AFE were represented by sources positioned halfway between, or 607 m AFE. Additionally, the initial lateral dispersion dimension was based on an initial lateral dispersion dimension ratio of 4.3 per the EPA-suggested value in the AERMOD User's Guide. Additional details on how AEDT 3g sets up the AERMOD input files can be found in the AEDT 3g Technical Manual (Ross et al., 2024).

2.1.2.2.4.1.1 Reproduction of Aircraft Spring/Summer Emissions

We received the .bak file for the 2024 AEDT BOS study from Volpe in December 2024. In March 2025, UNC-IE received methodological documentation from Volpe describing the setup of the 2024 BOS Study within the AEDT. The study was built using aircraft-movement data from MITRE to provide necessary inputs to the AEDT model. In the methodological documentation, Volpe detailed the steps taken to process the MITRE data into a format usable for AEDT. UNC-IE developed its own series of Structured Query Language (SQL) scripts based on this documentation to process the MITRE data according to the criteria needed for a dispersion study in the AEDT. This also involved matching aircraft information in the MITRE data to the pre-existing set of aircraft data available in the AEDT FLEET database. Since UNC-IE was attempting to recreate the study using their own scripting approach, and the exact nuances in Volpe's approach were not defined, the process of aligning the aircraft the same as the original study became difficult to replicate. After some months on this task, UNC-IE and Volpe agreed that pre-processed MITRE data with AEDT-assigned aircraft information would be provided to support the process of replicating the study. Since aircraft information is linked to AEDT data using the best available information, there is not always a one-to-one match for an aircraft profile. This introduces some randomization and best-guess approaches, which make the aircraft assignments nearly impossible to entirely replicate. Even when Volpe provided the pre-processed MITRE data with FLEET assignments, it did not entirely match their original study setup. The taxi network configurations remained the same as the settings defined by Volpe in the original setup. Tracks were created for each air operation based on runway information provided in the MITRE dataset and airport layout information already included in the AEDT for BOS.

We collaborated with Volpe over several months to replicate the original study as accurately as possible, holding several calls to troubleshoot any issues that had arisen in the process. By the end of June 2025, UNC-IE successfully reproduced the study configuration. However, the results from both the Volpe and UNC-IE simulations were later determined to be preliminary, as subsequent review identified an issue in the taxi configuration setup that inadvertently increased taxi



segment lengths. UNC-IE will resolve these issues and will perform the AERMOD evaluation again using the updated AEDT aircraft emissions during the next period of performance.

2.1.2.2.4.2 Non-Aircraft Emissions

UNC-IE developed a comprehensive non-aircraft emissions inventory for BOS using a 1.33 km by 1.33 km gridded domain covering an 18.2 km by 16.9 km area over BOS (Figure 3, Figure 10). Non-aircraft emissions were filtered out from EPA's Emission Modeling Platform version 2022v1 (EMP2022v1)[5] for relevant sources within the domain and subsequently processed by using the SMOKE model version 5.1.[6] Non-aircraft emissions consider both surface and elevated source types. Surface source types include residential wood combustion (rwc), livestock, open burnings, mobile vehicles (on-road), solvents usages, non-road vehicles and equipment (non-road), railway and terminals, and others. Elevated source types include oil and gas production and processing, energy generation facilities, commercial marine vessels (CMV), and other industrial and commercial point sources. Emissions from surface source types were mapped to the 1.33 km by 1.33 km grid cells, each simulated as area sources in AERMOD. Elevated source types were processed at a facility-specific level and were simulated in AERMOD as point sources with associated coordinates and stack parameters. Temporal profiles provided with the EMP2022v1 were applied to non-aircraft emissions to aggregate annual emissions from short tons per year to hourly emissions in grams per second as required by AERMOD.

Special treatments to CMV emissions improved the accuracy of its spatial distributions. We derived these from geographic information system (GIS) datasets points of actual CMV activities, including shipping channels and seaport locations (Figure 10). Emissions were allocated based on quadrant location and channel depth, with activity fractions calculated for both port and underway points. Nonpoint sources, such as residential wood combustion, nonroad, and rail, were processed using SMOKE at an hourly resolution per grid cell. A tool was developed to convert these outputs into AERMOD-ready files, simulating each grid cell as a squared AREA source. Source grouping strategies were evaluated based on emission strength and proximity to monitoring sites. The approach was revised to use National Emission Inventory (NEI) 2022v1 directly, improving spatial and temporal accuracy over the original plan to scale NEI 2017 data, and daily AERMOD-ready outputs were generated for April through August 2022.

[5] https://www.epa.gov/air-emissions-modeling/2022v1-emissions-modeling-platform
[6] https://www.cmascenter.org/smoke/

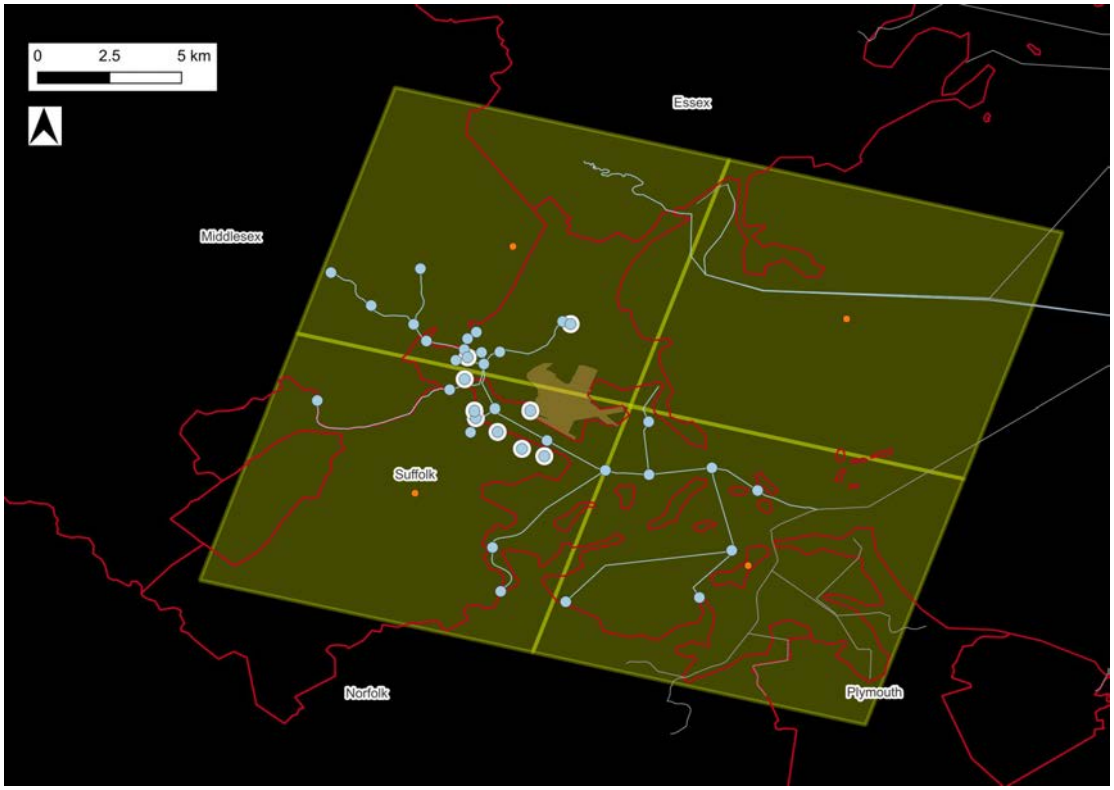


Figure 10. The GIS representation shows the relevant 12 km grid cells (yellow) overlaid on top of our domain with county boundaries in red and the airport footprint in brown. Also shown are the selected lines from the National Waterway Network Lines (NWNL), representing shipping channels (grey) that intersected our domain (light blue), and NWNL start and end points to represent underway activity (blue points). Seaport locations from Massachusetts Department of Environmental Protection's online GIS portal (white/blue dots) were used as port locations for hoteling emissions. Several underway points located in grid 191-388 were removed to simplify processing due to low emissions in that corresponding grid cell, as the vast majority of underway emissions were allocated to grid cells 190-387, 190-388, and 191-387.

Overall, the contribution of aircraft emissions was substantial when compared to non-aircraft sources, representing about 82% of the SO_2 and 26% of the NO_x emissions, respectively (Table 3). This highlights that aircraft were a dominant source of SO_2 emissions and a significant contributor to NO_x emissions within the BOS study area.

Table 3. Total tons per day of sulfur dioxide (SO_2) and nitrogen oxides (NO_x) aircraft and non-aircraft emissions in the 2025 spring/summer season for the Boston Logan International Airport study.

Source Type	Pollutant/Emissions (tons per day)	
	SO_2	NO_x
Aircraft	0.41	4.96
Non-Aircraft	0.50	19.24

2.1.3 Model Results

AERMOD modeled concentrations were compared with the observed SO_2 and NO_x concentrations from the LAX and BOS studies. To better understand how aircraft emissions affect air quality at the core monitoring sites, we analyzed concentrations based on prevailing wind sectors. We grouped the concentrations into 18, 20-degree wind direction sectors: (0 – 20], (20 – 40], (40 – 60], (60 – 80], (80 – 100], (100 – 120], (120 – 140], (140 – 160], (160 – 180], (180 – 200], (200 –



220], (220 – 240], (240 – 260], (260 – 280], (280 – 300], (300 – 320], (320 – 340], and (340 – 360], to assess how emissions from different directions influence each receptor site.

To evaluate the impact of our AERMOD model modifications, we compared results at the four core sites for the summer season of the LAX study and at three sites in spring/summer for the BOS study. This analysis was included: (i) ratio of mean modeled and mean measured concentrations at each site for various wind sectors, and (ii) hourly quantile-quantile (Q-Q) distribution plots at each site for filtered wind directions based on the prevailing wind sectors to assess the impact of aircraft emissions. In addition to this, this study also included model performance using common statistical measures, such as fractional bias based on the top 26 robust highest concentrations (FB) (Cox and Tikvart, 1990) and fraction of model predictions within a factor of two of the corresponding measurements (FAC2) (Chang and Hanna, 2004). These statistical measures are recommended by EPA to measure the performance of any dispersion model, especially for regulatory applications. Overall, these measures helped to determine how accurately the modified AERMOD reproduces observed concentrations.

The different model scenarios in AERMOD, with and without aircraft plume rise options, and with and without shoreline meteorology, were named as:

a. *Default*: The meteorological inputs were baseline AERMET outputs, and the plume rise option within AERMOD (version 24142) is not modeled. This corresponds to the default AERMOD setting that was normally used to predict the air quality impact of aircraft-related emissions.
b. *Old Plume Rise*: Same as 1., except that plume rise was modeled using the ALPHA option "ARCFTOPT" of AERMOD (version 24142); the methodology was described in Pandey et al. (2023).
c. *New Plume Rise*: Same as 1., except that the aircraft plume rise option used the updated plume rise algorithm described in this paper in Section 2.
d. *Shoreline OldPR*: Same as 2. except that the meteorological inputs were modified to account for shoreline and urban effects described in Pandey et al. (2022). This scenario was applicable only for the LAX study.
e. *Shoreline NewPR*: Same as 3., except that the meteorological inputs were modified to account for shoreline and urban effects described in Pandey et al. (2022). This scenario was applicable only for the LAX study.

2.1.3.1 Los Angeles International Airport Study

2.1.3.1.1 Concentrations Averaged over Wind Direction Sectors

Figure 11 and Figure 12 compared the model-predicted mean SO_2 and NO_x concentrations (from the five model scenarios described in Section 2.1.3 above), averaged over 18 wind direction sectors of 20 degrees, with the corresponding observed/measured mean concentrations at the four core sites (AQ, CN, CS, and CE) for the summer season in the LAX study. The dashed line (-----) represents the one-to-one line. The solid lines above and below the one-to-one line on the y-axis correspond to a factor of two intervals.

Here, we see differences across all five model scenarios. However, to understand which specific wind sectors affect each monitoring site, first, we need to focus on the comparison between the *Default*, *Old Plume Rise*, and *New Plume Rise* scenarios. By examining how these three differ, we can identify the specific wind direction sectors that contribute most to the ratio of modeled to measured concentration variations at each site. In contrast, for wind sectors where all three scenarios produce overlapping concentration patterns, we infer that the plume rise treatment had little to no impact, and the results are largely consistent across these three model scenarios.

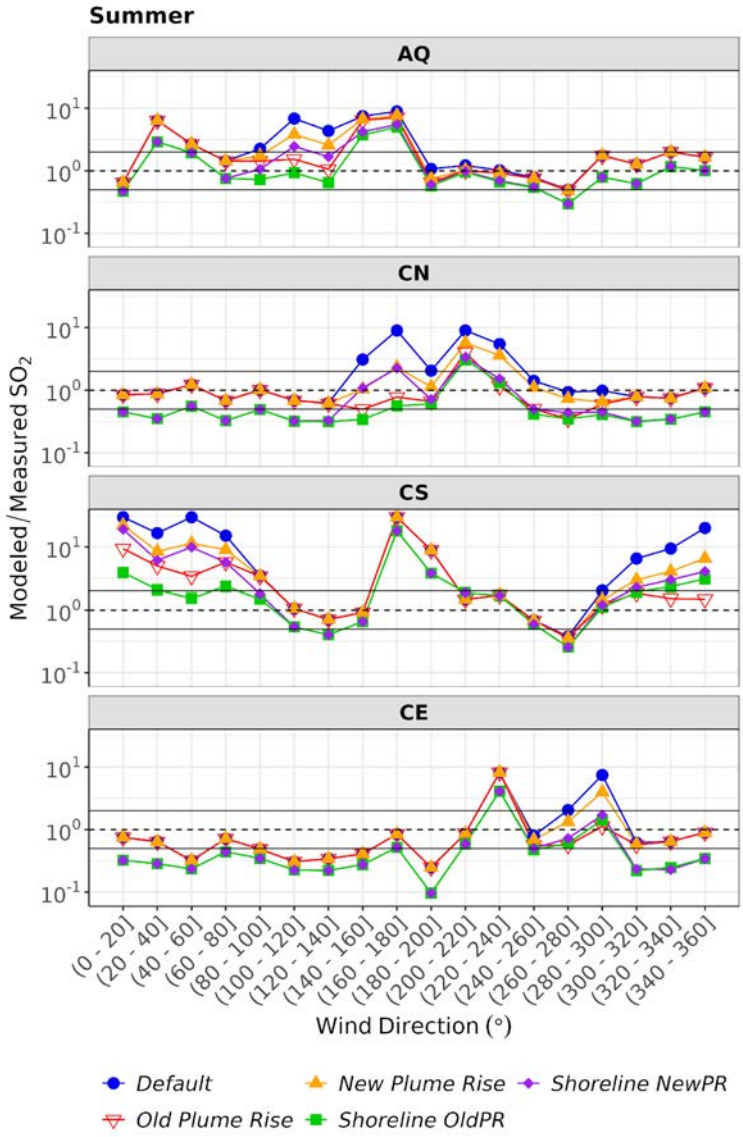


Figure 11. Ratio of modeled to measured SO_2 concentrations at all four core sites (AQ, CN, CS, and CE) during the 2012 summer season at Los Angeles International Airport.

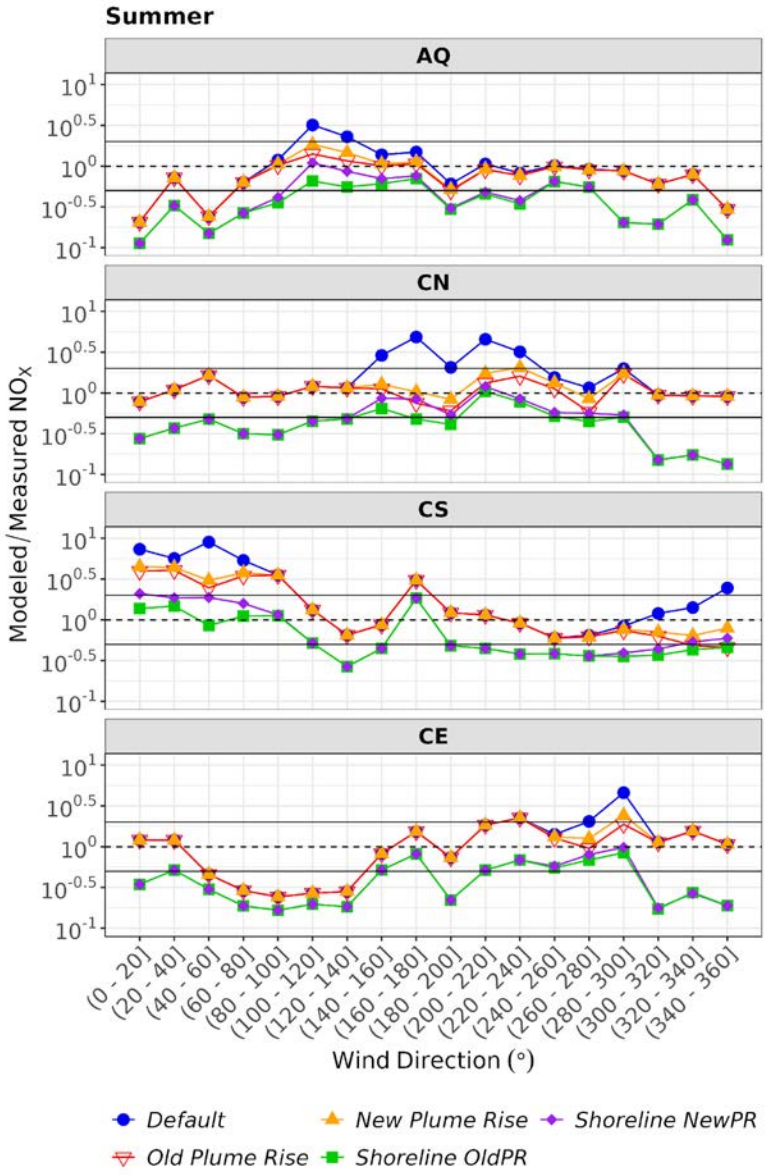


Figure 12. Ratio of modeled to measured NO_x concentrations at all four core sites (AQ, CN, CS, and CE) during the 2012 summer season at Los Angeles International Airport.

2.1.3.1.1.1 Sulfur Dioxide Concentrations

In Figure 11, there are noticeable differences across the *Default*, *Old Plume Rise*, and *New Plume Rise* model scenarios on the wind sectors at: AQ site (80 – 100], (100 – 120], (120 – 140], (140 – 160], (160 – 180], and (180 – 200]; CN site (140 – 160], (160 – 180], (180 – 200], (200 – 220], and (220 – 240]; CS site (0 – 20], (20 – 40], (40 – 60], (60 – 80], (280 – 300], (300 – 320], (320 – 340], (340 – 360]; and CE site (240 – 260], (260 – 280], (280 – 300] in both seasons. Other than these sectors, the differences across these three model scenarios were little to almost negligible at each site for both seasons.

From this, we can evaluate the performance of all five model scenarios at these site-specific wind sectors. Here, we hypothesize that *Shoreline NewPR* should perform better than other scenarios, as it had both new modifications: one based on the updated aircraft plume rise algorithm and the second, as Pandey et al. (2022) discussed, based on meteorology.



In Figure 11, *Shoreline NewPR* predicted the modeled to measured SO_2 values mostly on the one-to-one line, and only a few instances were within a factor of two lines across all the impacted wind sectors at all sites except site CS, where it was reducing the peaked values but not within the FAC2 lines, as the *Default* model predictions were higher compared to the other sites. Overall, the updated aircraft plume rise algorithm is enhancing the concentrations compared to the old plume rise algorithm, as the updated plume rise algorithm predicted the low plume rise values better.

2.1.3.1.1.2 Nitrogen Oxides Concentrations

NO_x concentration results were similar to SO_2 at all four core sites. NO_x ratio results exhibited patterns similar to those observed for SO_2, with *Shoreline NewPR* predictions aligning closely with the one-to-one line, and most values falling within the FAC2 range across the impacted wind sectors at all sites, except for CS, where peak values were reduced but still fall outside the FAC2 range due to the *Default* scenario's higher predictions, especially on (0 – 20], (20 – 40], (40 – 60], (60 – 80] wind sectors (Figure 12).

Based on all the prevailing wind direction findings, in the next section, we have presented hourly quantile-quantile distribution plots at each site for filtered wind sectors to assess the impact of aircraft emissions.

2.1.3.1.2 Overall Concentration Distribution Analysis (Quantile-Quantile Distribution Analysis)

For strong model performance and capability, especially for air quality regulation, it is important to predict high concentrations accurately. To assess this, unpaired concentration distribution plots, commonly referred to as Q-Q plots, were utilized. In these plots, both modeled and observed concentrations were first filtered based on the airport-impacted wind direction, as discussed in Section 2.1.3. At the CN site, we increased the wind direction bin from [140 – 240] to [140 – 250] to include the partial plume rise effect on the next wind direction bin concentrations. Similarly, at the CS site, we filtered the concentrations from 270 degrees instead of 280 degrees, because in the (260 – 280] bin, we could see a slight change from the *Default* to *New Plume Rise* scenario. After that, we ranked from highest to lowest and then plotted against each other. The dashed line (------) represents the one-to-one relationship, indicating a perfect agreement between modeled and observed values. The solid lines with slopes of one-half and two denote underpredictions and overpredictions, respectively. The Q-Q plots were developed using 1-hr averaged SO_2 and NO_x concentrations for both winter and summer seasons, comparing our five model scenarios: *Default*, *Old Plume Rise*, *New Plume Rise*, *Shoreline OldPR*, and *Shoreline NewPR* (see Figure 11 and Figure 12).

2.1.3.1.2.1 Sulfur Dioxide Concentrations

The high- to mid-range concentrations improved substantially from *Default* to *New Plume Rise* and even further with the *Shoreline NewPR* scenario at all sites (Figure 13). At AQ and CS sites, the overpredictions were improved with *Shoreline NewPR,* but there was still a slight overprediction, especially at higher concentrations (Figure 13). On the other hand, at the CN site, most of the concentrations fell a one-to-one line with the *Shoreline NewPR* scenario, and at the CE site, high concentrations came close to a one-to-one line (Figure 13).

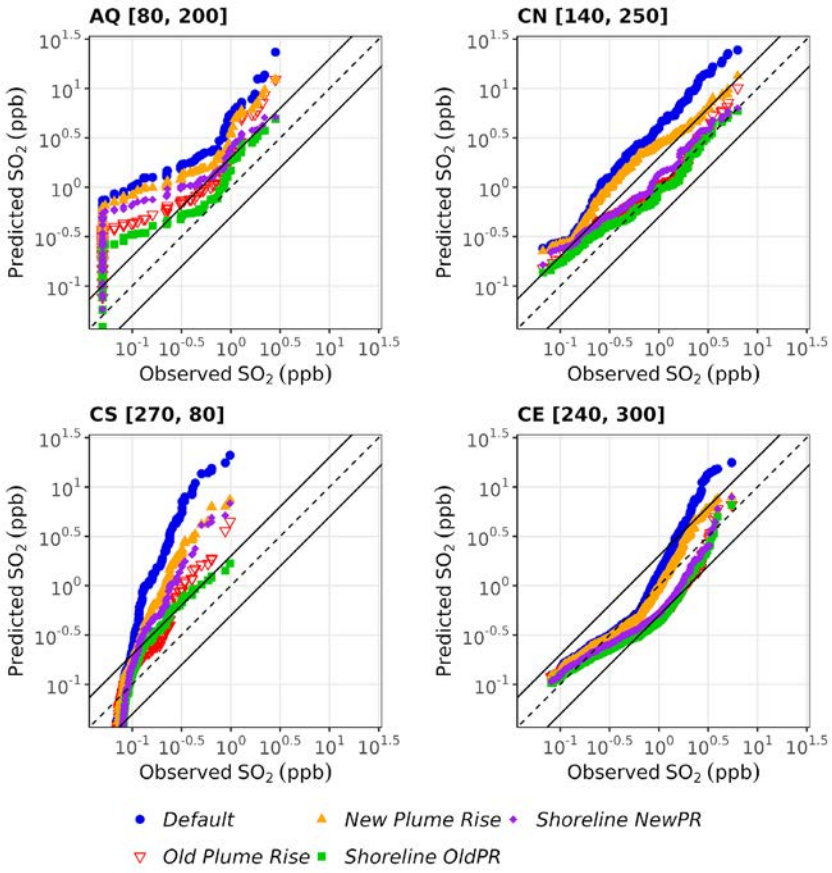


Figure 13. Q-Q plots show the effect of aircraft-specific plume rise and modifying meteorological inputs for the summer season SO_2 concentrations at each site for specific wind directions.

Since regulatory applications of AERMOD emphasize concentrations at the upper end of the modeled distribution, it was important to evaluate the modified model's performance using statistics derived from the top 26 robust highest modeled and observed concentrations, as recommended by EPA (Cox and Tikvart, 1990). These statistics are summarized in Table 4.



Table 4. Fractional Bias (FB) based on the top 26 highest SO_2 concentrations, FAC2 (factor of two), and the ratio of robust highest SO_2 concentrations (Ratio_RHC) for the 2012 summer season.

Site	Model	Statistical Measures		
		FAC2 (%)	FB	Ratio_RHC
AQ [80, 200]	*Default*	1	-1.51	7.17
	Old Plume Rise	25	-1.15	3.72
	New Plume Rise	1	-1.28	4.56
	Shoreline OldPR	51	-0.71	2.10
	Shoreline NewPR	12	-0.82	2.39
CN [140, 250]	*Default*	0	-1.32	4.85
	Old Plume Rise	98	-0.46	1.60
	New Plume Rise	6	-0.65	1.97
	Shoreline OldPR	99	0.16	1.17
	Shoreline NewPR	88	-0.20	1.22
CS [270, 80]	*Default*	36	-1.85	25.84
	Old Plume Rise	81	-1.21	4.09
	New Plume Rise	44	-1.60	9.04
	Shoreline OldPR	63	-0.59	1.84
	Shoreline NewPR	37	-1.49	6.82
CE [240, 300]	*Default*	89	-1.25	4.37
	Old Plume Rise	79	-0.21	1.23
	New Plume Rise	100	-0.69	2.06
	Shoreline OldPR	69	-0.01	1.01
	Shoreline NewPR	100	-0.13	1.14

The fractional bias (FB) was defined by:

$$FB = 2\frac{(Measured - Modeled)}{(Measured + Modeled)} \quad \text{(Eq. 4)}$$

FAC2 referred to the fraction of modeled values within a factor of two of the corresponding measured/observed values. The ratio of the robust highest concentrations (RHC; Ratio_RHC), was the ratio of the modeled RHC to that of the measured, where the RHC of each set was computed using the 26 highest values. The positive FB and the values of the Ratio_RHC relative to unity suggested the underestimation of the highest pollutant concentrations during field study.

Table 4 shows the statistical measures from all five model scenarios at all four core sites. At all sites, the peak ratio (PR) based on top 26 robust highest concentrations improved significantly. At the AQ site, it improved from 7.17 to 2.39 when we used the *Shoreline NewPR* model scenario. At the CN site, it decreased from 4.85 to 1.22. At the CS site, it became closer to its ideal value of one, decreasing from 25.84 to 6.82, and at CE site, from 4.37 to 1.14. The fraction of model predictions to the observations, FAC2, also improved and more closely reached the ideal value of 100, especially at CN and CE sites.

2.1.3.1.2.2 Nitrogen Oxides Concentrations

At all sites, the *Default* scenario overpredicted higher NO_x concentrations, whereas, after the inclusion of plume rise, these higher concentrations better matched the one-to-one line (Figure 14). In addition, with *Shoreline NewPR,* all the high

concentrations at all sites came close to a one-to-one line, especially at the CN site; mid to high range concentrations lay on a one-to-one line (Figure 14). Table 5 shows the statistical measures for all model scenarios. Ratio_RHC was also improved significantly from 6.81 to 0.94, and 98% of concentrations were within a FAC2. At the CE site, *Shoreline NewPR* slightly underestimated the mid-level concentrations, whereas at the AQ and CS sites, the higher concentrations were still overpredicted but within FAC2 lines (Figure 14). Overall, at AQ and CS sites, the Ratio_RHC improved significantly and came closer to its ideal value of 1. FAC2 was also 99% and 49%, respectively, at these two sites (Table 5).

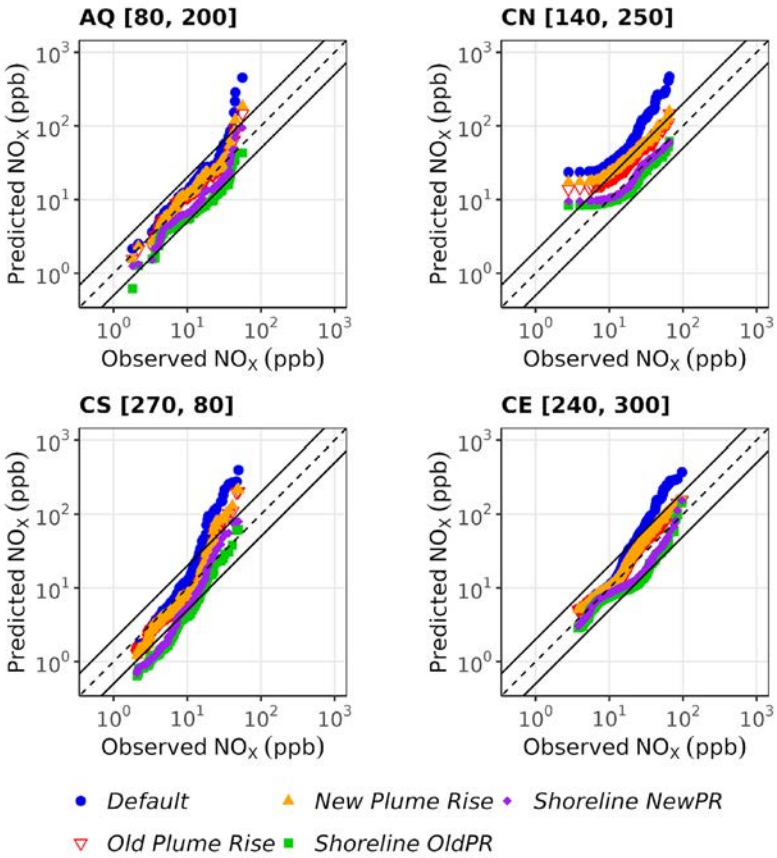


Figure 14. Q-Q plots show the effect of aircraft-specific plume rise and modifying meteorological inputs for the summer season nitrogen oxides (NO_x) concentrations at each site for specific wind directions.



Table 5. Fractional Bias (FB) based on the top 26 highest NO_x concentrations, FAC2 (factor of two), and the ratio of robust highest NO_x concentrations (Ratio_RHC) for the 2012 winter and summer seasons.

Site	Model	Statistical Measures		
		FAC2 (%)	FB	Ratio_RHC
AQ [80, 200]	*Default*	90	-1.27	4.45
	Old Plume Rise	98	-0.47	1.62
	New Plume Rise	97	-0.77	2.24
	Shoreline OldPR	65	0.29	0.74
	Shoreline NewPR	99	-0.22	1.25
CN [140, 250]	*Default*	0	-1.43	6.01
	Old Plume Rise	90	-0.59	1.84
	New Plume Rise	30	-0.70	2.07
	Shoreline OldPR	98	0.17	0.84
	Shoreline NewPR	98	0.06	0.94
CS [270, 80]	*Default*	82	-1.52	7.27
	Old Plume Rise	94	-1.13	3.57
	New Plume Rise	93	-1.18	3.89
	Shoreline OldPR	22	-0.07	1.07
	Shoreline NewPR	49	-0.59	1.84
CE [240, 300]	*Default*	82	-1.24	4.29
	Old Plume Rise	100	-0.38	1.47
	New Plume Rise	100	-0.51	1.69
	Shoreline OldPR	85	0.10	0.90
	Shoreline NewPR	100	-0.06	1.06

2.1.3.2 Boston Logan International Airport Study

2.1.3.2.1 Concentrations Averaged over Wind Direction Sectors

Figure 15 and Figure 16 compared the model-predicted mean SO_2 and NO_x concentrations (from three of the model scenarios described in Section 2.1.3: *Default*, *Old Plume Rise,* and *New Plume Rise*), averaged over 18 wind direction sectors of 20 degrees, with the corresponding observed/measured mean concentrations at Evans, Saratoga, and Revere sites (SO_2 at Saratoga only) for the spring/summer season in the BOS study. The dashed line (-----) represents the one-to-one line. The solid lines above and below the one-to-one line on the y-axis correspond to a factor of two intervals.

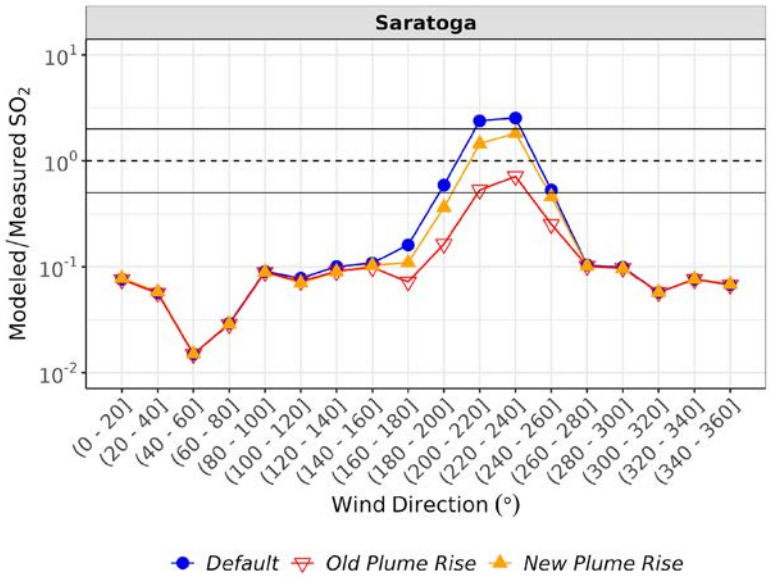


Figure 15. Ratio of modeled to measured sulfur dioxide (SO_2) concentrations at the Saratoga site, during the 2024 spring/summer season at Boston Logan International Airport.

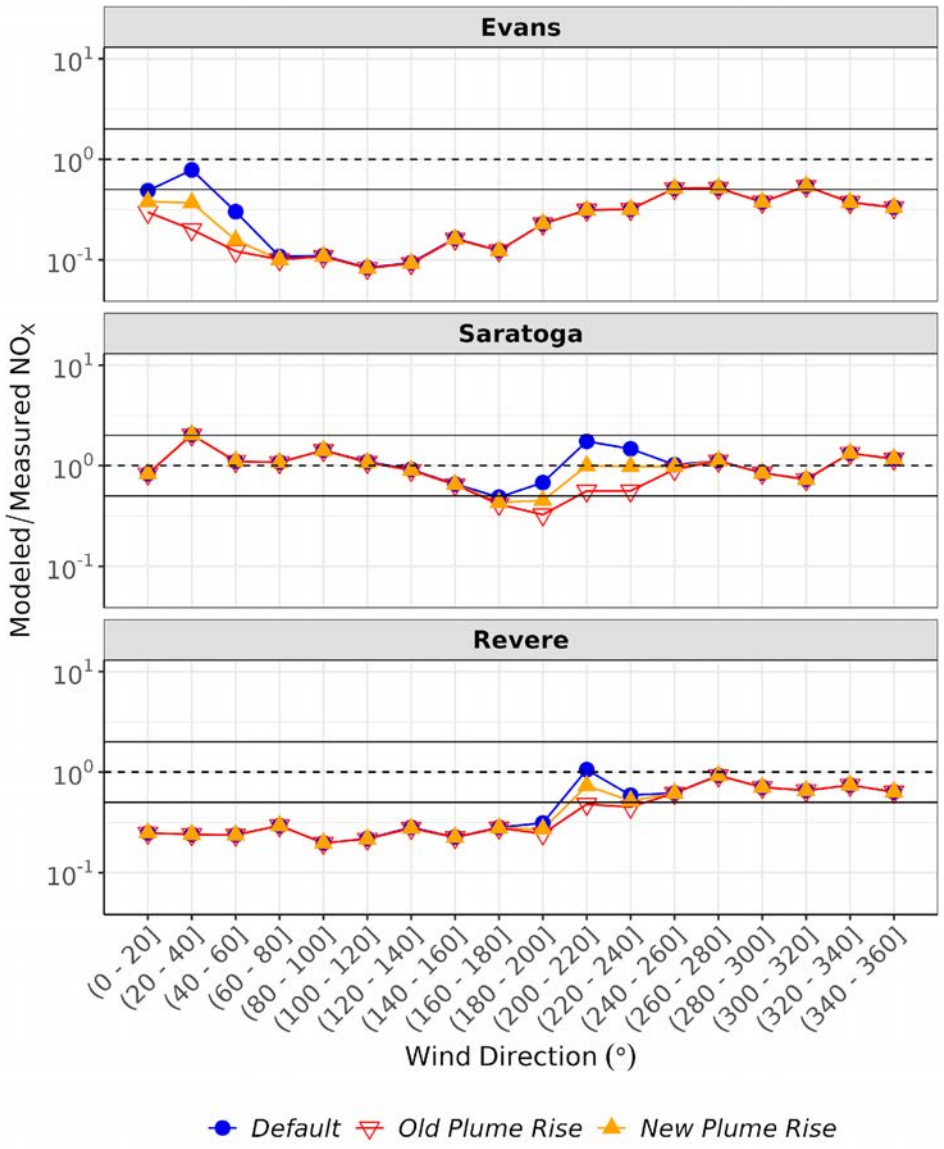


Figure 16. Ratio of modeled to measured nitrogen oxides (NO_x) concentrations at all three sites (Evans, Saratoga, and Revere) during the 2024 spring/summer season at Boston Logan International Airport.

Here, we see differences across all three model scenarios. However, to understand which specific wind sectors affect each monitoring site, first, we needed to focus on the comparison between the *Default*, *Old Plume Rise*, and *New Plume Rise* scenarios. By examining how these three differ, we can identify the specific wind direction sectors that contributed most to the ratio of modeled to measured concentration variations at each site. In contrast, for wind sectors where all three scenarios produced overlapping concentration patterns, we infer that the plume rise treatment had little to no impact, and the results are largely consistent across these three model scenarios.

2.1.3.2.1.1 Sulfur Dioxide Concentrations

In Figure 15, there are noticeable differences across the *Default*, *Old Plume Rise*, and *New Plume Rise* model scenarios on the wind sectors at: Saratoga site (160 – 180], (180 – 200], (200 – 220], and (220 – 240], and (240 – 260]. Other than these sectors, the differences across these three model scenarios were little to almost negligible.

In Figure 15, *New Plume Rise* predicted the modeled to measured SO_2 values slightly above the one-to-one line, and only a few were underpredicted and were not within a factor of two lines on all the impacted wind sectors, whereas with the *Old Plume Rise*, these values were highly underpredicted. Overall, the updated aircraft plume rise algorithm is enhancing the concentrations compared to the old plume rise algorithm, as the updated plume rise algorithm predicted the low plume rise values better.

2.1.3.2.1.2 Nitrogen Oxides Concentrations

For NO_x, the modeled-to-measured mean NO_x ratio results of the *New Plume Rise* model scenario were better compared to the *Old Plume Rise* model scenario, especially at the Saratoga site, where most of the values were on a one-to-one line in the wind direction bin from 200 to 260 degrees (Figure 16). At the Revere site, both *Old Plume Rise* and *New Plume Rise* model scenarios underpredicted the mean-modeled to mean-measured values for the impacted wind direction sectors 180 to 240 degrees, where we have seen a noticeable change from *Default* to any plume rise model scenario (Figure 16).

2.1.3.2.2 Overall Concentration Distribution Analysis (Quantile-Quantile Distribution Analysis)

The Q-Q plots were developed using 1-hour averaged SO_2 and NO_x concentrations for the 2024 spring/summer season, comparing three model scenarios: *Default*, *Old Plume Rise*, and *New Plume Rise*. Here, we filtered the observed/measured and modeled concentrations for specific wind sectors at each site (see Figure 15 and Figure 16).

2.1.3.2.2.1 Sulfur Dioxide Concentrations

At Saratoga, the mid to high SO_2 concentrations were highly overpredicted by the *Default* model scenario, whereas, after the inclusion of aircraft-specific plume rise *Old Plume Rise*, these high concentrations reduce substantially (highly underpredicted) (Figure 17). However, after updating the current plume rise algorithm, the model predications improved significantly and came close to a one-to-one line, but, still, there was a slight overprediction with the *New Plume Rise* model scenario (Figure 17).

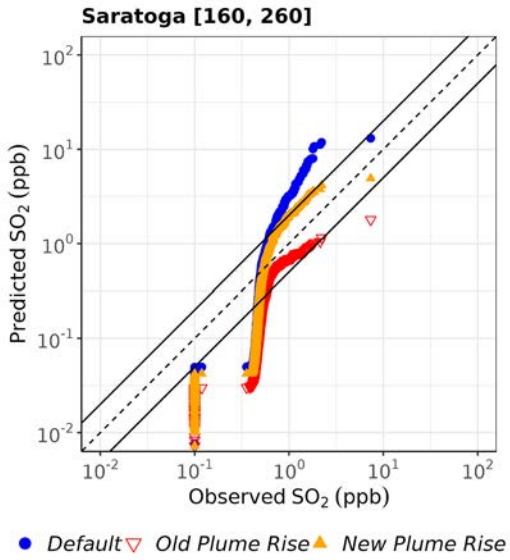


Figure 17. Q-Q plots showing the effect of aircraft-specific plume rise for the spring/summer season SO_2 concentrations at the Saratoga site for specific wind directions.

Table 6 summarizes the EPA-recommended statistics utilized. FAC2 was improved from 40 to 50% with the *New Plume Rise* model scenario. The significant improvement in the ratio of the top 26 robust highest concentrations came down from 4.30 to 1.50.

Table 6. Fractional Bias (FB) based on the top 26 highest SO_2 concentrations, FAC2 (factor of two), and the ratio of robust highest SO_2 concentrations (Ratio_RHC) for 2024 spring/summer seasons at Boston Logan International Airport.

Site	Model	Statistical Measures		
		FAC2 (%)	FB	Ratio_RHC
Saratoga [160, 260]	*Default*	40	-1.25	4.30
	Old Plume Rise	27	0.90	0.38
	New Plume Rise	50	-0.40	1.50

2.1.3.2.2.2 Nitrogen Oxides Concentrations

For NO_x concentrations, Figure 18 shows the Q-Q distributions at all three sites for the specific wind sectors at each site. At Evans, the *Default* model scenario overpredicted all concentrations, whereas with the inclusion of any plume rise, all of them fall within FAC2 lines and close to a one-to-one line. From Table 7, we observe that the ratio of the top 26 robust highest concentrations improved from 3.14 to 1.08, and FAC2 improved from 0 to 100% with the *New Plume Rise* model scenario.

At Saratoga and Revere, higher-end overpredictions from the *Default* model scenarios were significantly improved with the *New Plume Rise* scenario, and most of the mid to high range concentrations lay on a one-to-one line (Figure 18). Ratio_RHC improved from 3.96 to 0.91 and from 1.97 to 0.72 at Saratoga and Revere sites, respectively (Table 7).

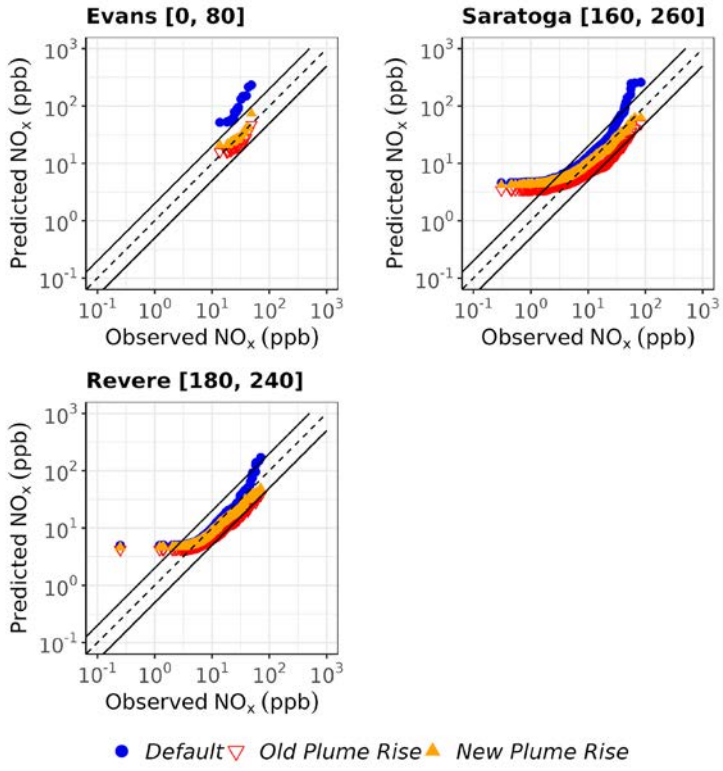


Figure 18. Q-Q plots showing the effect of aircraft-specific plume rise for the spring/summer season NO_x concentrations at each site for specific wind directions.



Table 7. Fractional Bias (FB) based on the top 26 highest NO_x concentrations, FAC2 (factor of two), and the ratio of robust highest NO_x concentrations (Ratio_RHC) for the 2024 spring/summer season.

Site	Model	Statistical Measures		
		FAC2 (%)	FB	Ratio_RHC
Evans [0, 80]	*Default*	0	-1.29	3.14
	Old Plume Rise	100	0.31	0.78
	New Plume Rise	100	-0.02	1.08
Saratoga [160, 260]	*Default*	85	-1.19	3.96
	Old Plume Rise	70	0.45	0.63
	New Plume Rise	92	0.09	0.91
Revere [180, 240]	*Default*	97	-0.65	1.97
	Old Plume Rise	91	0.62	0.63
	New Plume Rise	98	0.33	0.72

2.1.4 Summary

The effectiveness of incorporating the updated aircraft plume-rise option into AERMOD was evaluated by comparing modeled concentrations with field measurements, with a particular focus on wind directions most affected by aircraft emissions for the LAX 2012 and BOS 2024 field studies. For both SO_2 and NO_x, AERMOD's performance improved noticeably across all monitoring sites once the revised plume-rise formulation was applied. The *New Plume Rise* model scenario improved the modeled concentrations significantly, especially for mid to high range concentrations.

The updated algorithm generally produced lower plume-rise estimates for each aircraft LTO mode. These reduced plume-rise values led to higher near-field modeled concentrations, resulting in a better match with observed concentration values. The evaluation also demonstrated that the updated plume-rise approach performs consistently across different airports and study conditions, confirming the robustness and broad applicability of the new algorithm within AERMOD.

2.2 Los Angeles International Airport Summer Study Model Comparison against LASPORT

We received LASPORT (**LAS**AT (**La**grangian **S**imulation of **A**erosol **T**ransport) for Air**port**s) model SO_2 and NO_x results for the summer 2012 LAX AQSAS on September 15, 2025, from Dr. Ulf Janicke (Janicke Consulting, Germany).

LASPORT results only included aircraft, ground support equipment, and auxiliary power unit sources' contributions. For the comparison against AERMOD model results, we added the background source contributions (AERMOD modeled) with LASPORT results. We analyzed the modeled results using the original meteorology for the AERMOD model. For LASPORT, it had only one set of results, so it was assumed that these were generated using the original meteorology. Here, for model comparison, we used the following AERMOD model scenarios: *Default*: AERMOD without plume rise; *Old Plume Rise*: AERMOD with old plume rise (was implemented in AERMODv24142); *New Plume Rise*: AERMOD with new plume rise (updated recently as discussed above).

Figure 19 and Figure 20 show the Q-Q concentration distribution among models in original meteorology for SO_2 and NO_x pollutants, respectively.

Q-Q distribution plots for SO_2 show that LASPORT and AERMOD with the *New Plume Rise* model scenario are very close for mid to high range concentrations, especially at CN and CE (Figure 19). The PR (also referred to as the Ratio of RHC) based on the top 26 robust highest concentrations was slightly higher than its ideal value of one for both models, and the fraction of predictions within FAC2 values was better in *New Plume Rise* than LASPORT, especially at sites CN, CS, and CE (Figure 19).

In Figure 20, all model scenarios were overpredicting the higher concentrations at all sites.

Based on the above, we concluded that our *New Plume Rise* scenario performed as well as, if not better than, LASPORT under most conditions for both pollutants. However, one should note that LASPORT doesn't include a plume rise algorithm due to the potential to underestimate, instead focusing on parameterization of plume dynamics.

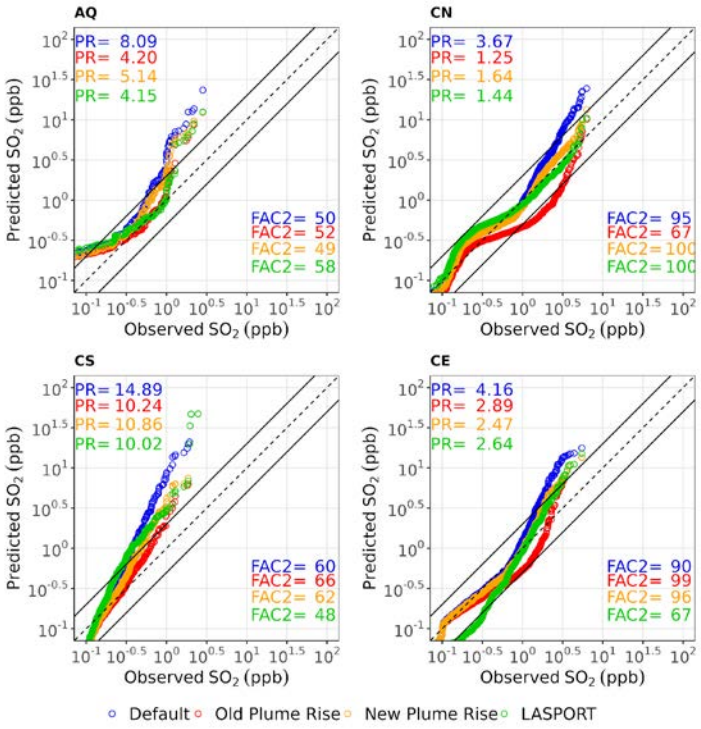


Figure 19. Q-Q distribution of SO_2 concentrations at all four core sites (AQ, CN, CS, and CE) for summer 2012 at Los Angeles International Airport. PR metric in these plots refer to peak ratio of robust highest concentrations. FAC2 refers to % predictions within a factor of two of observations.

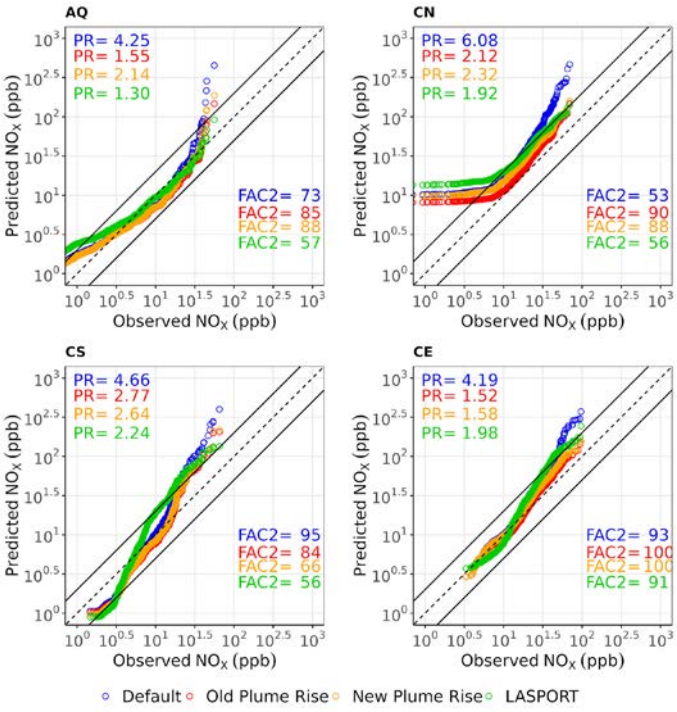


Figure 20. Q-Q distribution of NO_x concentrations at all four core sites (AQ, CN, CS, and CE) for summer 2012 at LAX. PR metric in these plots refer to peak ratio of robust highest concentrations. FAC2 refers to % predictions within a factor of two of observations.

3. Chemical Processes

3.1 Implementation of a New NOX Chemistry Option (GRS7) in AERMOD

As discussed in the previous period of performance, UNC-IE developed a new GRS7 chemistry option to AERMOD (version 23132) and compared its performance against AERMOD's existing chemistry options, including Ozone Limiting Method (OLM), Ambient Ratio Method 2 (ARM2), Travel Time Reaction Method (TTRM), Plume Volume Molar Ratio Method (PVMRM), and Generic Reaction Set Method (GRSM), in simulating NO_2 at four core sites (CN, CS, CE, and AQ) in LAX airport during winter (February 1, 2012, to March 13, 2012) and summer (July 18, 2012, to August 28, 2012) episodes. GRS7 is an improved version of AERMOD's beta GRSM chemistry option: GRSM has only two reactions (photolysis of NO_2 to NO and oxidation of NO to NO_2), whereas GRS7 also considers photolysis and oxidation of reactive organic compounds in the NO_x chemistry cycle.

Overall, all chemistry options underestimated observed NO_2; this behavior was attributed mainly to underestimation of NO_x. At the four core monitoring sites, we found that NO_2 prediction was marginally improved in GRS7 over GRSM (mean bias was lowered by 0.1 ppb [3%] in GRS7 over GRSM). Differences between the two chemistry options are largest in the morning hours when background O_3 is low (< 30 ppb) and mean bias was lowered by 1.2 ppb (14%) on average between 07:00 – 09:00 in GRS7. GRSM and GRS7 have identical NO_2 performance in the remaining hours of the day when background O_3 was sufficient; NO_x is low during nighttime when there is lack of photolysis.

As discussed in Venkatram et al. (1998), chemistry age has important implications in determining species' concentration outcomes from chemical reactions. In case of the LAX study, we found that the greater the chemistry age, the more NO_2 concentration is formed from the GRSM and GRS7 chemistry options. Meanwhile, AERMOD limits chemistry age (also known as travel time) of GRSM and TTRM to one hour. As shown in Table 8, we found that at the four core sites (CE, CS, CN and AQ), the median travel times were within one hour but occasionally exceeded this limit. At the monitoring site CE2 (see Figure 2 for location), located southeast about 5.5 km away from LAX, the travel time well exceeded one hour. Since chemical reactions should be estimated in the same time duration it takes for the air mass to travel from source to receptors, it is unreasonable to limit chemistry age to one hour for receptors far away from LAX center, such as CE2.



Our hypothesis is that differences in simulated NO_2 between GRS7 and GRSM were marginal at the four core sites (CE, CN, CS, and AQ) due to their close proximities to emission sources in LAX, and the differences would become larger at receptors farther downwind. Furthermore, if travel time was not limited to one hour, differences between GRSM and GRS7 become even larger, especially at further downwind distances from emissions sources at LAX.

Table 8. Travel time (seconds) from source to selected monitoring stations in Los Angeles International Airport.

Station	Average	Median	95 pct	Max
CE2	5973	5328	12217	17903
CE	1306	966	3503	6593
CS	2602	1891	7530	13069
CN	1321	899	3898	8297
AQ	2753	1726	8064	16062

3.2 Model Configuration

To verify the hypothesis presented above in Section 3.1, UNC-IE utilized the same AERMOD (version 23132) configurations (e.g., plume rise treatment for aircraft emissions and modified meteorological inputs) that were applied in Pandey et al. (2024) and implementation of the GRS7 chemistry option. Emission input data were processed using the FAA's AEDT3e for LAX-related emissions (i.e., aircraft, taxi, gates) and the EDMS emission inventory for LAX for non-aircraft sources. Emissions from aircrafts, taxi segments, and gates were all simulated as AREA sources.

We extended the receptors to a 10 km by 15 km grid spaced 500 km apart and centered on LAX (Figure 21). We modified the AERMOD source code to un-limit travel time, so that chemical reactions were simulated for the same duration as the source-to-receptors travel time.

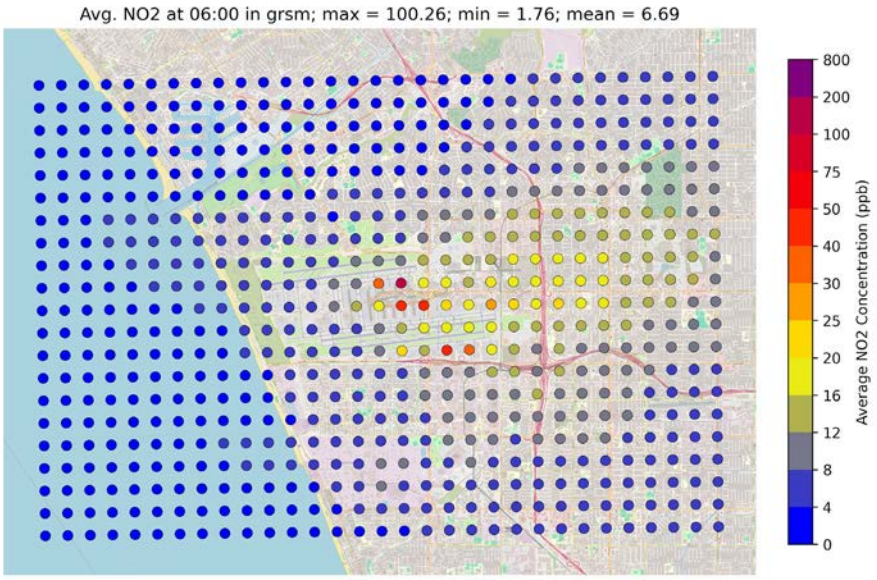


Figure 21. Example of simulated nitrogen dioxide (NO_2) concentrations on the 500 m horizontal resolution receptor grid over Los Angeles International Airport.

3.3 Summary of Findings

Figure 22 shows simulated averaged NO_2 concentrations from GRSM at 6:00 am and 7:00 am local time. Note that this time window is when background O_3 was lowest, thereby increasing the importance of volatile organic compounds (VOC) in GRS7 for the NO-to-NO_2 conversion because O_3 is low. Figure 23 shows differences between the GRS7 and GRSM options,

with the one-hour travel time limitation still in place. We found larger differences between GRS7 and GRSM (up to 5 ppb) at receptors further away from LAX (e.g., receptors on the east side of Interstate I-405). Removing the travel time limitation in GRS7 further enhances the differences between GS7 and GRSM, as shown in Figure 24.

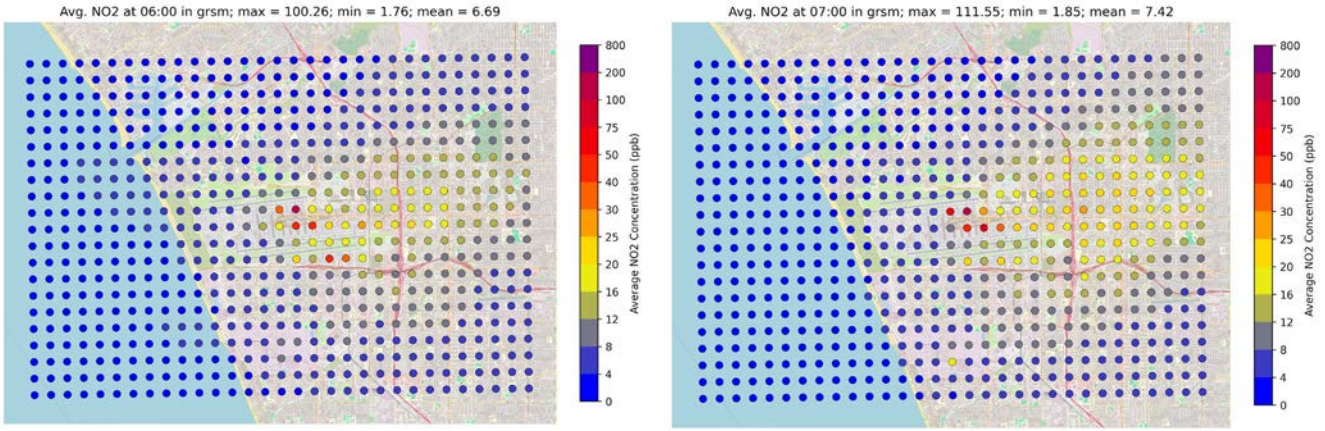


Figure 22. Average nitrogen dioxide (NO_2) concentration as simulated at 6:00 am (left) and 7:00 am (right) local time with the GRSM chemistry option over a 500 m receptor grid. These average concentrations were filtered for hours when wind direction was between 225–315 degrees, which is when AERMOD exhibits the best performance at the four core sites.

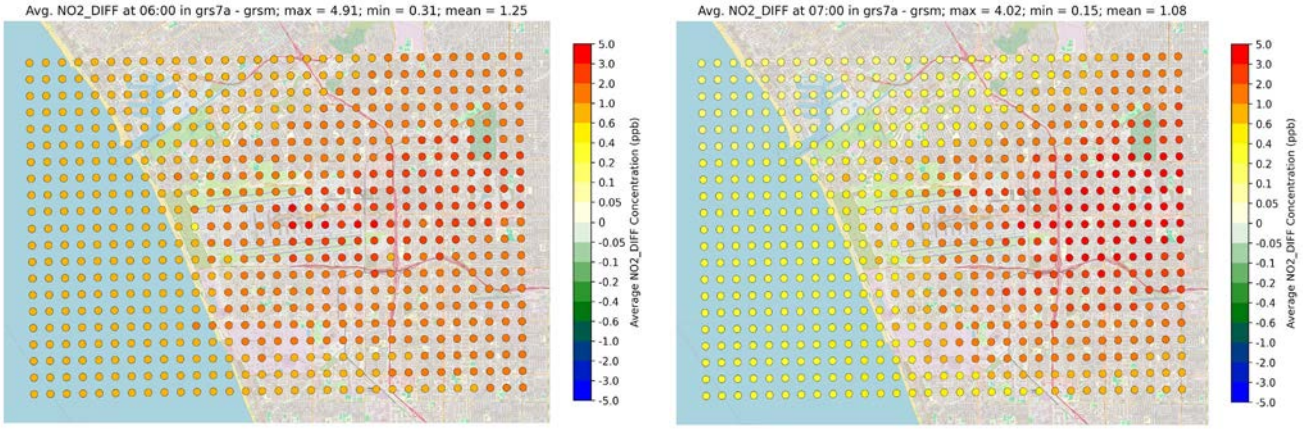


Figure 23. Differences (GRS7 – GRSM) in simulated hourly-average nitrogen dioxide (NO_2) concentrations at 6:00 am (left) and 7:00 am (right) local time over a 500 m receptor grid. Similar to Figure 22, these average concentrations were filtered for hours when wind direction was between 225–315 degrees, which is when AERMOD exhibits the best performance at the four core sites.

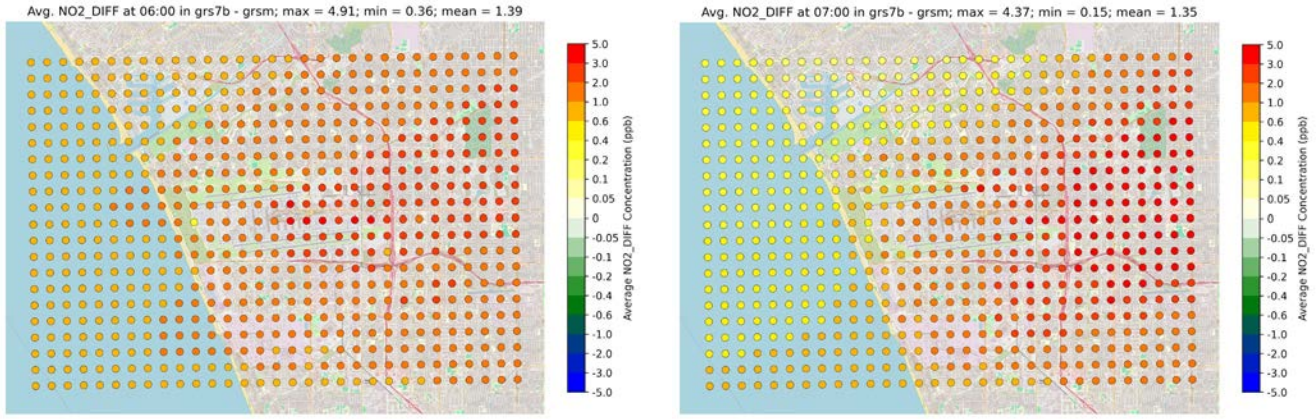


Figure 24. Differences (GRS7 – GRSM) in simulated hourly-average nitrogen dioxide (NO_2) concentrations at 6:00 am (left) and 7:00 am (right) local time over a 500 m receptor grid, with the travel time limitation removed. Similar to Figure 22, these average concentrations were filtered for hours when wind direction was between 225–315 degrees, which is when AERMOD exhibits the best performance at the four core sites.

4. Development of Aircraft Dispersion Model

4.1 Preparing ADM/GADM Emission Inputs

A Python3-based emission processor "AEDT2ADM" was developed to create the emissions input for ADM and GADM. This emission processor's input data files are the AEDT flight segment and performance data. During this period of performance, UNC-IE initiated a substantial update to the AEDT2ADM tool, aiming to significantly expand its capabilities for generating AERMOD-ready input files. Previously limited to polygon-based runway and taxiway ground sources at LAX only, the tool is now being upgraded to support any airport using all gridded sources, including both surface and airborne emissions. The Version 7 update introduces support for VOLUME sources and enables the generation of input files compatible with plume-rise algorithms. To enhance flexibility, the tool is being tested with BOS data to ensure applicability across different airports. Using polygon-based ground source shapes at BOS, UNC-IE successfully created airborne and gridded ground sources. A separate script was developed to summarize segment-level AEDT data, detailing flight counts and emissions by engine type. Comparative analysis of hourly flight activity between BOS (2024) and LAX (2012) revealed discrepancies in BOS data aggregation due to challenges in aggregating segment-level AEDT data to the hourly scale without double counting. This analysis helped UNC-IE refine the process of aggregating and interpreting AEDT segment-level data. Work on Version 7 is ongoing, with a focus not only on evaluating performance at a different airport, but also in evaluating output for VOLUME sources.

4.2 Model Evaluation

This task was on hold during this performance period as our priority was to enhance the aircraft-plume rise algorithm.

Milestones

- Successfully compared AERMOD with plume rise results against the LASPORT dispersion model.
- Extensively analyzed the observation data collected at BOS for the 2024 spring/summer and winter seasons.
- Successfully re-produced the AEDT-generated aircraft emissions for the 2024 spring/summer season for the BOS study.
- Set up the AEDT for the 2024 winter season for the BOS study.

Major Accomplishments

- Successfully updated (using enhanced plume dynamics approach) and implemented the aircraft plume rise algorithm.



Publications

- Published the AREA source meander paper in the *Journal of the Air & Waste Management Association* on October 30, 2024.

Outreach Efforts

- Presented in Alexandria, Virginia, at the ASCENT Fall 2024 meeting on October 29–30, 2024,
- Presented virtually at the ASCENT Spring 2025 meeting on May 14, 2025

Awards

None.

Student Involvement

None.

Plans for Next Period

- Finalize the updated aircraft-plume rise algorithm and optimize the run time.
- Draft a detailed paper on the updated aircraft plume rise algorithm and its evaluation against LAX and BOS data.
- Generate the aircraft emissions inventory using AEDT for the 2024 winter season for the BOS study.
- Perform a detailed AERMOD analysis for the Boston winter study.
- Finalize a detailed paper on GRS7 implementation and evaluation.
- Finalize the ADM and GADM models with all physical and chemical components.

References

Arunachalam, S., Isakov, V., Barzyk, T., Venkatram, A., Weil, J., Naess, B., Valencia, A., Seppanen, C., & Brandmeyer, J. (2017, October 9-12). *C-AIRPORT: a new web-based air quality model for community-scale assessments around airports* [Conference presentation]. 18th International Conference on Harmonization within Atmospheric Dispersion Modelling for Regulatory Purposes, Bologna, Italy.

Arunachalam, S., Valencia, A., Woody, M. C., Snyder, M. G., Huang, J., Weil, J., Soucacos, P., Webb, S., Airport Cooperative Research Program, Transportation Research Board, & National Academies of Sciences, Engineering, and Medicine. (2017). *Dispersion modeling guidance for airports addressing local air quality health concerns*. Transportation Research Board. https://doi.org/10.17226/24881

Barzyk, T. M., Isakov, V., Arunachalam, S., Venkatram, A., Cook, R., & Naess, B. (2015). A near-road modeling system for community-scale assessments of traffic-related air pollution in the United States. *Environmental Modelling & Software, 66*, 46–56. https://doi.org/10.1016/j.envsoft.2014.12.00

Boeing. (2010). *Boeing Projects $700 Billion Commercial Airplanes Market in North America*. Retrieved March 9, 2025, from https://boeing.mediaroom.com/2010-09-02-Boeing-Projects-700-Billion-Commercial-Airplanes-Market-in-North-America

Chowdhury, B., Karamchandani, P. K., Sykes, R. I., Henn, D. S., & Knipping, E. (2015). Reactive puff model SCICHEM: Model enhancements and performance studies. *Atmospheric Environment, 117*, 242–258. https://doi.org/10.1016/j.atmosenv.2015.07.012

Chang, J. C., & Hanna, S. R. (2004). Air quality model performance evaluation. *Meteorology and Atmospheric Physics, 87*(1–3), 167–196. https://doi.org/10.1007/s00703-003-0070-7

Cox, W. M., & Tikvart, J. A. (1990). A statistical procedure for determining the best performing air quality simulation model. *Atmospheric Environment. Part A. General Topics, 24*(9), 2387–2395. https://doi.org/10.1016/0960-1686(90)90331-G

Ross, J., Ahearn, M., Boeker, E., Cumper, J., Downs, R., Goetzinger, S., Gorshkov, S., Malwitz, A., Mittelman, A., Nicholas, B., Reherman, C., Roof, C., Simon, M., Tosa, Y., Wilson, A., DiPardo, J., Majeed, M., Hwang, S., Kuiper, B., & Augustine, S. (2024). *Aviation environmental design tool (AEDT) 3g technical manual*. Federal Aviation Administration. https://www.researchgate.net/publication/386868562_Aviation_Environmental_Design_Tool_AEDT_3g_Technical_Manual

Janicke, U. (2024). Application of Effective Conversion Rates between NO and NO_2 in a Standard Airport Dispersion Model System. *Atmosphere, 15*(5), 574. https://doi.org/10.3390/atmos15050574

Kim, B., Rachami, J., Robinson, D., Robinette, B., Wyle, K. N., Arunachalam, S., Davis, N., Baek, B. H., Shankar, U., Talgo, K.,



Yang, D., Hanna, A. F., Wayson, R. L., Noel, G., Gliff, S. S., Zhao, Y., Hopke, P. K., Kumar, P., Airport Cooperative Research Program, … National Academies of Sciences, Engineering, and Medicine. (2012). *Guidance for quantifying the contribution of airport emissions to local air quality*. Transportation Research Board. https://doi.org/10.17226/22757

Pandey, G., Venkatram, A., & Arunachalam, S. (2022). Evaluating AERMOD with measurements from a major U.S. airport located on a shoreline. *Atmospheric Environment, 294*, 119506. https://doi.org/10.1016/j.atmosenv.2022.119506

Pandey, G., Venkatram, A., & Arunachalam, S. (2023). Accounting for plume rise of aircraft emissions in AERMOD. *Atmospheric Environment, 314*, 120106. https://doi.org/10.1016/j.atmosenv.2023.120106

Pandey, G., Venkatram, A., & Arunachalam, S. (2024). Accounting for plume rise of aircraft emissions and shoreline meteorology enhances AERMOD's description of concentrations measured around Los Angeles airport. *Journal of the Air & Waste Management Association*, 74(10), 726–742. https://doi.org/10.1080/10962247.2024.2394104

Tetra Tech, Inc. (2013). *LAX Air Quality and Source Apportionment Study - Volume 2. Executive Summary*. Los Angeles World Airports.

Valencia, A., Venkatram, A., Heist, D., Carruthers, D., & Arunachalam, S. (2018). Development and Evaluation of the R-LINE Model Algorithms to Account for Chemical Transformation in the Near-road Environment. *Transportation Research. Part D, Transport and Environment, 59*, 464–477. https://doi.org/10.1016/j.trd.2018.01.028

Venkatram, A., Karamchandani, P., Pai, P., & Goldsteins, R. (1994). The development and application of a simplified ozone modeling system (SOMS). *Atmospheric Environment, 28*(22), 3665–3678. https://doi.org/10.1016/1352-2310(94)00190-V

Venkatram, A., Du, S., Hariharan, R., Carter, W., & Goldstein, R. (1998). The concept of species age in photochemical modeling. Atmospheric Environment, 32(20), 3403–3413. https://doi.org/10.1016/S1352-2310(98)00032-6

Wayson, R. L., Fleming, G. G., Noel, G., MacDonald, J., Eberhard, W. L., McCarty, B., Marchbanks, R., et al. (2008). *Lidar Measurement of Exhaust Plume Characteristics from Commercial Jet Turbine Aircraft at The Denver International Airport* (No. FAA-AEE-08-02). U.S. Department of Transportation and NOAA Earth System Research Laboratory. https://rosap.ntl.bts.gov/view/dot/9522/dot_9522_DS1.pdf

Task 2 - Develop and Evaluate a Multiscale WRF-SMOKE-CMAQ Model Application for BOS Focused on UFPs

University of North Carolina at Chapel Hill

Objectives

In this project, our team partnered with ASCENT Project 018 investigators from BU to focus on modeling BOS across various spatial scales. The primary objective was to conduct a thorough intercomparison of measurements and models, with a special emphasis on UFP, mass, and number concentrations resulting from aircraft emissions.

To achieve this goal, we delved into the utilization of two distinct modeling approaches: the CMAQS and Second-order Closure Integrated Puff (SCIPUFF) with SCICHEM models. The SCICHEM model stands out for its integration of comprehensive gas-, aqueous-, and aerosol-phase chemistry within the advanced Gaussian puff model SCIPUFF (Chowdhury, 2015). Noteworthy is its capacity to characterize aircraft impacts with high precision in the immediate vicinity of the source as a series of puffs, thereby offering a significant advancement in the estimation of aircraft-attributable PM compared with previous assessments, notwithstanding its potential large computational times.

It is crucial to highlight that while both CMAQ and SCICHEM share a common aerosol treatment, SCICHEM excels in capturing fine-scale details around the airport. A key outcome of this project is the enhancement of predictions related to aircraft-attributable PM compared with previous estimates. It is worth noting that the use of SCICHEM, which focuses solely on PM mass concentrations, necessitated the development of postprocessing routines. These routines were designed to convert PM mass into a UFP number concentration (UFPNC) using a methodology consistent with CMAQ. Additionally, it is important to mention that, until now, SCICHEM has not been employed to predict UFPNC. This effort introduces a novel avenue of research in our project, showcasing our commitment to develop novel model approaches for source treatment. During this period of performance, our focus has only been on CMAQ, and SCICHEM efforts will be continued later.

In 2017, ASCENT Project 018 investigators made multiple measurements of UFPs at seven locations south and west of BOS. Our team collaborated with BU to obtain these measurements to perform an intercomparison against model outputs.

CMAQ-AEDT Application for Boston Logan International Airport
To complete this task, our team used a nested application of the WRF-SMOKE-CMAQ modeling system, including the AEDT. CMAQ applied to the northern hemisphere at a resolution of 108 km is downscaled to determine the beginning and boundary conditions for the outermost grid, which is set at a resolution of 12 km. The larger-scale conditions are suitably captured for the outermost grid through the nesting down method. From the immediate outer grid, the next 4-km and 1.33-km grids are nested down in accordance with typical modeling procedures. A transition and improvement of atmospheric conditions are made by this nested technique, which permits a more accurate and thorough depiction of the dynamics as spatial resolution increases. We used the following to develop this application:

- Meteorology from Modern-Era Retrospective analysis for Research and Applications (MERRA) (Rienecker et al., 2011) downscaled with WRF v3.8 (Skamarock et al., 2008)
- Background emissions from NEI processed through SMOKE v3.6 (Baek & Seppanen, 2018)
- Aircraft emissions for the 2017 BOS study from the AEDT processed through AEDT Proc (Baek et al., 2012)
- CMAQ v5.33 enhanced with the new aircraft-specific emissions module (Appel et al., 2021)

Development of Aircraft Emission Inventory for Boston Logan International Airport by using AEDT
The TT is derived solely from radar surveillance sources. One of the primary data feeds to the Center for Advanced Aviation System Development (CAASD) is the National Offload Program (NOP) which provides coverage at 158 Terminal Radar Approach Control (TRACON) and 20 Air Route Traffic Control Centers (ARTCC). The ARTCC facilities provide a post-processed set of Common Message Set (CMS) data, whereas the TRACON facilities come directly from Standard Terminal Automation Replacement System (STARS) or Automated Radar Terminal System (ARTS) facilities, each reporting a separate post-processed data format (108 ARTS facilities and 50 STARS facilities). Both ARTCC and STARS facilities compute multi-sensor fused reports, whereas the ARTS facilities provide individual radar sensor reports. ARTCC data have the largest spatial coverage per facility, with a high-quality flight plan and metadata reported at 12 second updates. TRACON facilities have higher fidelity position measurements reported at roughly 4 second updates but are generally limited in this coverage to about 60 nautical miles (NM) of the airport and contain sparser flight metadata.

TT flight operation data have information about each aircraft operation (e.g., aircraft type, airport, runway, and time of arrival and departure, etc.) and has detailed information about each aircraft operation with real-time tracking, including time, latitude, longitude, and altitude. Our main goal is to enhance our modeling simulation to encompass a whole month of January and July 2017, with TT by using the AEDT. Our team utilized AEDT version 3g to create a BOS-specific emission inventory that corresponds with the BU's UFP measurement campaign's duration. Using real-time aircraft operation data to create emissions guarantees more precise calculation of the emissions in the airport vicinity across the designated time frame, compared to other emissions inventories.

Comparison of Boston Logan International Airport Emissions with Different Aircraft Emission Inventories
EPA provides aircraft emissions estimates in the NEI as a point source for all airports in the U.S. Thus, for BOS, our team has aircraft emissions during LTO assigned to a single latitude/longitude. While NEI emission inventory provides us with a starting point for use in CMAQ, two different approaches for emission creation were explored to better understand aircraft impact on air quality.

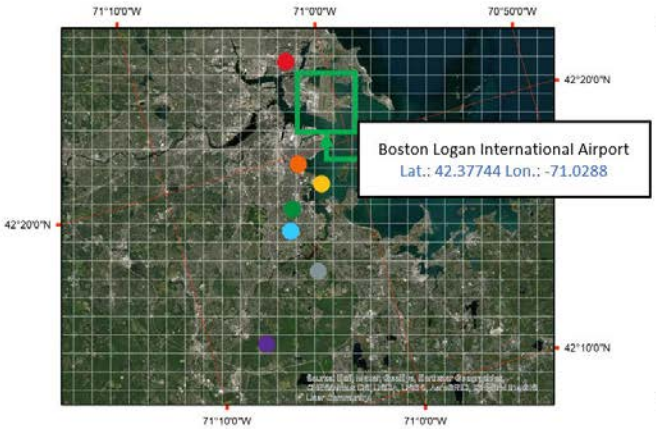
- The emission scenarios considered in this study are:
  - NoBOS: Background emission inventory based on NEI 2017 by excluding BOS
  - AEDT2d-2017-N: 2017 NEI based emissions inventory for BOS, generated using AEDT version 2d
  - AEDT2d-2017-S: 2017 global straight line segment data provided by Volpe for BOS, generated using AEDT version 2d
  - AEDT3g-2017-T: 2017 Thread Track flight operations data by MITRE, generated using AEDT version 3g

Besides improvement in spatial allocation in developing emissions estimates, treatment of particle size distribution was also refined in CMAQ as follows:

- Aircraft Specific Aerosol Size Distribution (ASASD) was applied only for BOS emissions in this study:
  - Geometric Mean Diameter (GMD): 60 nm - 23.2 nm (Moore et al., 2017)
  - Geometric Standard Deviation (GSD): 1.7 nm - 1.56 nm (Moore et al., 2017)
  - Both Geometric Mean Diameter and Standard Deviation (GMDSD) changed as above

Assessment of Ultrafine Particles through Field Observations
The ASCENT Project 018 team at BU made field observations of UFPNC in 2017 at seven fixed sites along the aircraft arrival and departure pathways, near BOS in Figure 25. These monitoring stations were selected because of the varying distances

and UFPNC contributions from BOS. The only one in the northern part of the airport is Chelsea (CHE). Two of the monitoring stations in the southern regions (N1 and N2) are the closest to the airport. Two intermediate sites (I1 and I2) are in the middle, and the last two monitoring stations (far sites F1 and F2) are the furthest distance. UFPNC measurement data were collected from January to September 2017.



Location	Distance (km)	Color
Airport	-	Green Box
CHE	4	Red
N1	3	Orange
N2	4	Yellow
I1	7	Green
I2	9	Light Blue
F1	12	Gray
F2	17	Purple

Figure 25. CMAQ-based modeling at high resolution 1.33 km by 1.33 km with location of seven monitoring sites near Boston Logan International Airport. CHE: Chelsea.

Research Approach

CMAQ-AEDT Application for Boston Logan International Airport

UFP concentrations at BOS were simulated using the WRF-SMOKE-CMAQ modeling framework in Figure 26. The WRF model was used to create meteorological data. The sigma vertical coordinate system, with 35 vertical layers that reach up to 50 hPa (lowest layer of approximately 10 to 20 m above ground level), was used for this work.

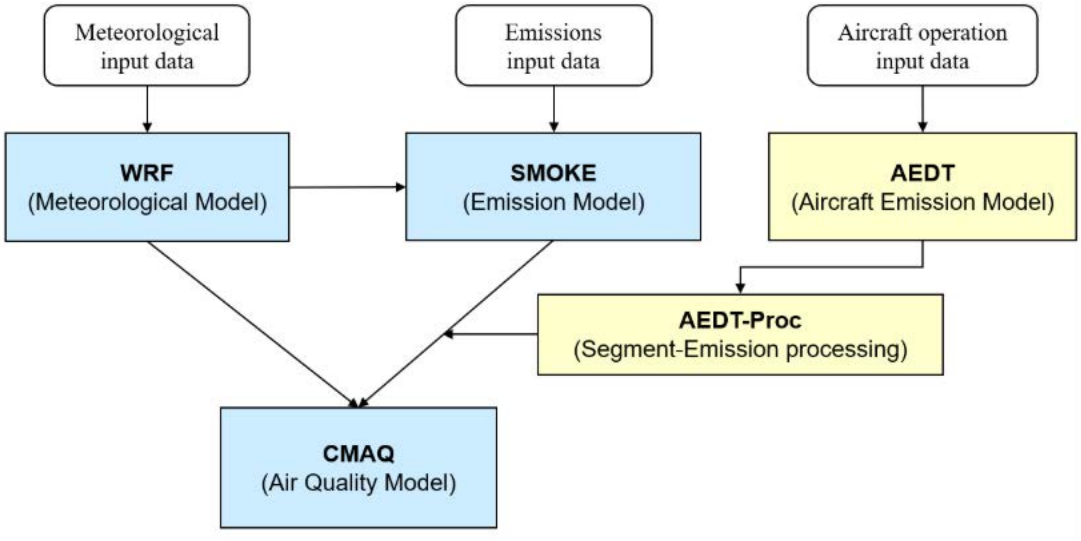


Figure 26. CMAQ application schematic for Boston Logan International Airport with Aviation Environmental Design Tool (AEDT). CMAQ: Community Multiscale Air Quality, SMOKE: Sparse Matrix Operator Kernel Emissions, WRF: Weather Research and Forecasting.



Background emissions were generated based on the 2017 NEI using the SMOKE processing system, except for emissions that came from BOS by using AEDT2d-2017-N. The particle mass concentration was computed using CMAQ configured with the aerosol module version 6 (AERO6) for the aerosol chemistry and the revision 3 of the Carbon Bond 6 mechanism (CB6r3) for the gas-phase chemistry. CMAQ converts particle mass concentration into Particle Number Concentration (PNC) using particle diameter, particle size distribution, and assumed particle density information (Binkowski & Roselle, 2003). PNC is estimated by CMAQ for the entire mass and thus one cannot distinguish between non-volatile particulate matter (nvPM) and volatile particulate matter (vPM) components for the concentrations predicted by CMAQ. Per Equations 5 and 6, our team used a number of parameters for Aitken mode (i) and accumulation mode (j) for total particle number ($N_{i,j}$), particle geometric diameter ($D_{g\,i,j}$), particle geometric standard deviation ($\sigma_{g\,i,j}$), upper diameter cut (UDC), and lower diameter cut (LDC), using the error function (ERF) (Jiang et al., 2006; Meng & Seinfeld, 1994) approach for the concentration of UFPNC. LDC was set at 0.07 µm due to the instrument's low detection limit (LDL) and defined UDC at 0.1 µm, consistent with the UFP definition (Hughes et al., 1998). Our team used a 15-day spin-up period from June 16 to June 30 for the month of July 2017. Initial and boundary conditions were based on the 108-km Northern Hemisphere domain ("108NHEMI").

$$UFP\ number\ for\ Aitken\ mode\ =\ \frac{N_i}{2}\left[1+ERF\left(\frac{lnln\left(\frac{UDC}{D_i}\right)}{\sqrt{2}ln\sigma_i}\right)\right]\ -\ \frac{N_i}{2}\left[1+ERF\left(\frac{lnln\left(\frac{LDC}{D_i}\right)}{\sqrt{2}ln\sigma_i}\right)\right] \quad \text{(Eq. 5)}$$

$$UFP\ number\ for\ accumulation\ mode\ =\ \frac{N_j}{2}\left[1+ERF\left(\frac{lnln\left(\frac{UDC}{D_j}\right)}{\sqrt{2}ln\sigma_j}\right)\right]\ -\ \frac{N_j}{2}\left[1+ERF\left(\frac{lnln\left(\frac{LDC}{D_j}\right)}{\sqrt{2}ln\sigma_j}\right)\right] \quad \text{(Eq. 6)}$$

Our team modeled CMAQ with 35 layers and horizontal resolutions of 12 km, 4 km, and 1.33 km for the study period. Apart from the Aircraft Emission Inventories (AEI) for BOS, all simulations used the same default CMAQ parameters, except aircraft-specific aerosol size distribution.

Development of AEDT Emission Inventory for Boston Logan International Airport by UNC-IE

The key differences among these inventories are in how the segments are spatially and temporally distributed. In AEDT2d-2017-N, aircraft LTO emissions are lumped into the surface layer at a few coordinates based on aircraft type, with a uniform temporal profile for all airports. In contrast, both AEDT2d-2017-S and AEDT3g-2017-T distribute emissions along flight paths with hourly temporal resolution. AEDT2d-2017-S simplifies segments as straight-line paths centered on the airport, illustrating that emissions spread over regions where no runways exist due to the generalized representation of departure and arrival paths. On the other hand, AEDT3g-2017-T confines emissions to the actual corridors of aircraft movement along runways at BOS, yielding emissions in the correct places.

For example, Figure 27 provides the NEI-based spatial mapping and a snapshot (July 3, 2017, at 09:00 EST) of spatial allocation for the straight-segment and TT operations. In the AEDT2d-2017-N (green markers), emissions are assigned to only two grid cells at the airport property and treated as point sources. AEDT2d-2017-S (red) disperses emissions along straight routes radiating from the airport's center, while AEDT3g-2017-T (blue) follows the actual flight trajectories aligned with runways. This underscores that the 3-dimensional (3D) AEI (especially AEDT3g-2017-T) captures the spatial pattern of emissions more realistically than the 2-dimensional (2D) AEI.



Figure 27. Spatial allocation differences among AEDT2d-2017-N (no temporal information) (green), AEDT2d-2017-S (red), and AEDT3g-2017-T (blue) on July 3, 2017, at 9:00 AM (1.33 km × 1.33 km grid).

Comparison of Boston Logan International Airport Emissions with Different Air Emissions Inventories

Our team compared the monthly total mass of major pollutants from the three BOS AEIs to calculate how the choice of emissions model affects the overall emission quantities. In Table 9, we summarize the total emissions for AEDT2d-2017-N (NEI-based), AEDT2d-2017-S (segment-based), and AEDT3g-2017-T (TT-based) for both January and July. The pollutants include the nvPM, volatile fuel organics (PMFO), volatile sulfate PM (PMSO), hydrocarbon (HC), NO_x, SO_2, and carbon monoxide (CO).

For January 2017, nvPM shows the highest (0.66 short tons) with AEDT2d-2017-N; others were between 0.40–0.42 short tons. AEDT3g-2017-T exhibited the highest PMFO among AEIs, while AEDT2d-2017-S was lower than AEDT3g-2017-T and AEDT2d-2017-N. PMSO, which is derived from SO_2 via assumed conversion rates in AEDT, is the highest in AEDT3g-2017-T, even though SO_2 shows the highest in AEDT2d-2017-N, suggesting AEDT2d-2017-N might use a lower conversion rate value in AEDT version 2d. Three AEIs show different magnitudes within PM components.

HC and CO remain the highest with AEDT2d-2017-N. NO_x is the only pollutant which is similar across all three AEIs (102–115 short tons). AEDT3g-2017-T aligns with AEDT2d-2017-N for PMFO, NO_x, SO_2, and CO. AEDT2d-2017-S had the lowest emissions in most categories due to fewer flight numbers than AEDT3g-2017-T.

Table 9. Monthly total aircraft emissions inventories (short tons/year) in January (Jan) and July (Jul) for non-volatile particulate matter (nvPM), volatile fuel organics (PMFO), volatile sulfate PM (PMSO), Hydrocarbon (HC), (Nitrogen oxides (NO_x), sulfur dioxides (SO_2), and carbon monoxide (CO).

Month	AEI	nvPM	PMFO	PMSO	HC	NO_x	SO_2	CO
Jan	AEDT2d-2017-N	0.66	0.36	0.13	28.54	102.19	14.16	231.98
	AEDT2d-2017-S	0.40	0.08	0.31	6.10	115.23	8.37	76.38
	AEDT3g-2017-T	0.42	0.40	0.50	15.67	113.12	13.67	205.39
Jul	AEDT2d-2017-N	0.82	0.45	0.16	35.67	127.74	17.69	289.97
	AEDT2d-2017-S	0.50	0.11	0.41	8.78	150.03	11.34	112.54
	AEDT3g-2017-T	0.53	0.51	0.62	21.01	142.88	16.88	281.13



The pattern of pollutants in July 2017 is broadly similar to January, though absolute amounts are slightly different, reflecting seasonal differences in number of operations, not meteorology. For nvPM, AEDT2d-2017-N is 0.82 short tons, whereas both AEDT3g-2017-T (0.53 short tons) and AEDT2d-2017-S (0.50 short tons) are lower. For PMFO, AEDT3g-2017-T is the highest, and AEDT2d-2017-S is the lowest. PMSO is also the highest in AEDT3g-2017-T, followed by AEDT2d-2017-S and AEDT2d-2017-N. For the gaseous pollutants in July, AEDT2d-2017-N stands out with the highest HC, SO_2, and CO emissions among the three. For NO_x emissions, all AEIs are relatively similar (around 127–150 short tons) for July, as in January. Overall, emissions in July suggest that the AEDT2d-2017-S inventory underestimates emissions for almost all pollutants (except NO_x). The AEDT2d-2017-N and AEDT3g-2017-T can either overestimate or underestimate AEIs for some pollutants. Understanding AEI discrepancies is important because these will influence the modeled UFP.

Assessment of Ultrafine Particles through Field Observations

Figure 28 presents diurnal variation of observed UFPNC and modeled UFPNC with seven modeling scenarios (NoBOS, AEDT2d-2017-N Base/GMDSD, AEDT2d-2017-S Base/GMDSD, and AEDT3g-2017-T Base/GMDSD) at seven measurements near BOS. The top subplots at each site show the UFPNC diurnal variation, and the bottom subplots indicate the diurnal BOS contribution to UFPNC by AEIs compared to NoBOS.

At CHE, the only monitoring station located northwest of BOS (4km), the observations show UFPNC spikes during rush hour at 7:00 AM and 8:00 PM. All modeled scenarios were able to reproduce the diurnal shape, but all overestimated observed UFPNC in the morning (5-10 h) and nighttime (21-5 h) and underestimated observed UFPNC in the evening (18-21 h). The BOS contribution fraction in GMDSD scenarios reaches around 5–20% at 8:00 to 9:00 PM at CHE.

At N1, the observed UFPNC is higher than 8,000 #/cm³ throughout the daytime, but modeled UFPNC underestimated during the daytime, except in the early morning. The AEDT3g-2017-T GMDSD scenario only shows noticeable diurnal contribution to UFPNC at 5:00 AM (10%) and 9:00 PM (10%). N2 shows similar observed UFPNC and modeled UFPNC diurnal variations. At I1 and I2, observed UFPNC reaches 20,000 and 15,000 #/cm³, respectively, around 7:00 to 8:00 PM, which might be a result of the I-93 highway. The modeled BOS contribution to UFPNC in GMDSD scenarios dropped to 3–4% during the morning peak at I1 and I2.

At F1, CMAQ was able to reproduce the UFPNC diurnal shape, even though modeled UFPNC underestimates the observed UFPNC, but the BOS contribution to UFPNC in AEDT3g-2017-T was about 2%. The maximum BOS contribution at F2 was around 0.3%, indicating the dilution of AEs at a farther distance. Figure 28 demonstrates that CMAQ underestimates the magnitude of observed UFPNC, except at CHE. CMAQ with the GMDSD scenario captures the spatial gradient in airport influence (highest at the nearest sites, moderate at the intermediate sites, and negligible at the farthest sites) and calculates the contribution of an aviation source that cannot be distinguished from other sources in observation.

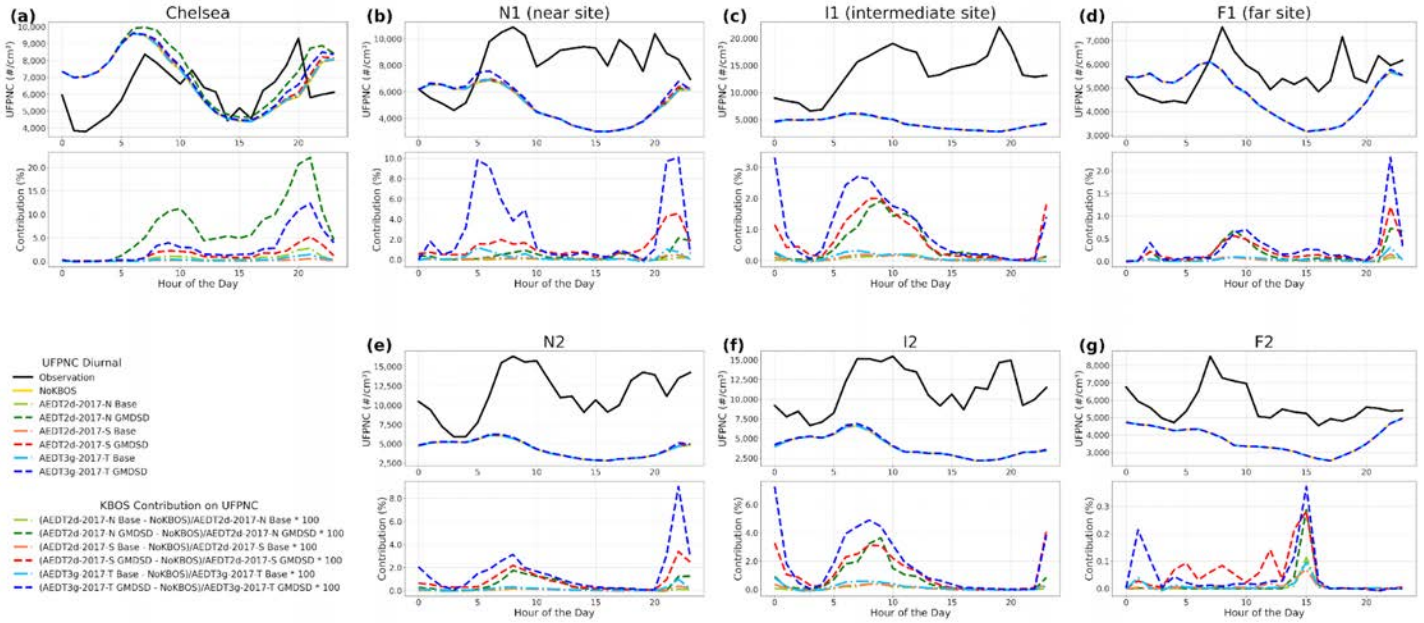


Figure 28. Diurnal variation of ultrafine particles number concentration (UFPNC) (top subplots) and diurnal BOS contribution to UFPNC (bottom subplots) at seven monitoring stations (CHE [Chelsea], near sites [N1 and N2], intermediate sites [I1 and I2], and far sites [F1 and F2]) with observations and seven scenarios.

Milestones

- Completed the development of 3D BOS inventories with TT flight operations using the AEDT for January and July 2017 and repeated CMAQ simulations.
- Completed a comprehensive draft of a paper exploring UFPNC at BOS, and it is currently undergoing thorough review by the co-authors.

Major Accomplishments

- Use TT data for BOS to create our own airport-level inventory, gaining AEDT track creation skills and a further understanding of aircraft operation data in running the AEDT.

Publications

None.

Outreach Efforts

- Hyeongseok (Darby) Kim presented a poster, "Measurement and Modeled Ultrafine Particles from Aircraft Landing and Takeoff Operations at Boston Logan Airport (KBOS)," at the 23rd Annual CMAS Conference, held in Chapel Hill, North Carolina, on October 21–23, 2024.

Awards

None.

Student Involvement

Hyeongseok (Darby) Kim is a PhD student involved in this task performing CMAQ simulations and AEDT modeling.

Plans for Next Period

- Finalize the BOS UFPNC paper and submit it to a peer-reviewed journal.



References

Appel, K. W., Bash, J. O., Fahey, K. M., Foley, K. M., Gilliam, R. C., Hogrefe, C., Hutzell, W. T., Kang, D., Mathur, R., Murphy, B. N., Napelenok, S. L., Nolte, C. G., Pleim, J. E., Pouliot, G. A., Pye, H. O. T., Ran, L., Roselle, S. J., Sarwar, G., Schwede, D. B., . . . Wong, D. C. (2021). The Community Multiscale Air Quality (CMAQ) model versions 5.3 and 5.3.1: System updates and evaluation. *Geoscientific. Model Development, 14*(5), 2867–2897. https://doi.org/10.5194/gmd-14-2867-2021

Baek, B. H., Arunachalam, S., Woody, M., Vennam, P. L., Omary, M., Binkowski, F., & Fleming, G. (2012, October 15-17). *A new interface to model global commercial aircraft emissions from the FAA Aviation Environmental Design Tool (AEDT) in air quality models* [Conference presentation]. 11th Annual CMAS Conference, Chapel Hill, North Carolina.

Baek, B. H., & Seppanen, C. (2018). *Sparse Matrix Operator Kernel Emissions (SMOKE) modeling system*. Zenodo. https://doi.org/10.5281/zenodo.1421403

Binkowski, F. S., & Roselle, S. J. (2003). Models-3 Community Multiscale Air Quality (CMAQ) model aerosol component 1. Model description. *Journal of Geophysical Research: Atmospheres, 108*(D6). https://doi.org/10.1029/2001JD001409

Chowdhury, B. (2015). Reactive puff model SCICHEM: Model enhancements and performance studies. *Atmospheric Environment*, 117, 242-258. https://doi.org/10.1016/j.atmosenv.2015.07.012

Hughes, L. S., Cass, G. R., Gone, J., Ames, M., & Olmez, I. (1998). Physical and chemical characterization of atmospheric ultrafine particles in the Los Angeles area. *Environmental Science & Technology*, 32(9), 1153–61. https://doi.org/10.1021/es970280r

Jiang, W., Smyth, S., Giroux, E., Roth, H., & Yin, D. (2006). Differences between CMAQ fine mode particle and $PM_{2.5}$ concentrations and their impact on model performance evaluation in the Lower Fraser Valley. *Atmospheric Environment*, 40(26), 4973–85. https://doi.org/10.1016/j.atmosenv.2005.10.069

Meng, Z., & Seinfeld, J. H. (1994). On the source of the submicrometer droplet mode of urban and regional aerosols. *Aerosol Science and Technology*, 20(3). 253–65. https://doi.org/10.1080/02786829408959681

Moore, R. H., Shook, M. A., Ziemba, L. D., DiGangi, J. P., Winstead, E. L., Rauch, B., Jurkat, T., Thornhill, K. L., Crosbie, E. C., Robinson, C., Shingler, T. J., Anderson, B. E. (2017). Take-off engine particle emission indices for in-service aircraft at Los Angeles International Airport. *Scientific Data, 4*(1), 170198. https://doi.org/10.1038/sdata.2017.198

Rienecker, M. M., Suarez, M. J., Gelaro, R., Todling, R., Bacmeister, J., Liu, E., Bosilovich, M. G., Schubert, S. D., Takacs, L., Kim, G., Bloom, S., Chen, J., Collins, D., Conaty, A., da Silva, A., Gu, W., Joiner, J., Koster, R. D., Lucchesi, R., . . . Woollen, J. (2011). MERRA: NASA's modern-era retrospective analysis for research and applications. *Journal of Climate*, 24(14), 3624-3648. https://doi.org/10.1175/JCLI-D-11-00015.1

Skamarock, W. C., Klemp, J., Dudhia, J., Gill, D. O., Barker, D., Wang, W., & Powers, J. G. (2008). *A description of the advanced research WRF version 3*. University Corporation for Atmospheric Research. https://doi.org/10.5065/D68S4MVH

Task 3 - Implement Volatile Particulate Matter Plume-Scale Modeling into a Community Multiscale Air Quality Application

University of North Carolina at Chapel Hill

Objectives

In previous work, UNC-IE accounted for the formation of non-traditional secondary organic aerosols (SOA) from the oxidation of semi-volatile organic compounds (SVOC) and intermediate-volatility organic compounds (IVOC) emitted from aircraft, and we utilized alternative emission estimates from the Aerosol Dynamics Simulation Code (ADSC). ADSC is a one-dimensional, plume-scale model that estimates engine-specific PM emissions and the emission of SVOCs and IVOCs under ambient conditions, accounting for relative humidity (RH) and temperature. To extend this work, ADSC for a vPM has been developed by Aerodyne. This model uses the vPM modeling tool developed and enhanced by National Aeronautics and Space Administration (NASA). FAA used ADSC for a parametric analysis of vPM to provide an additional physical perspective on vPM properties and evolution for quantities that are difficult to measure directly or continuously. This is because the engine exit plane is too hot for the condensable species to be in the particle phase, so only the nvPM particles are present at the exit plane.



The parametric set of vPM modeling studies usually spans the range of experimental conditions that have been measured or may be measured in the foreseeable future. These studies also enable an assessment of impacts on vPM properties, such as size and composition due to changes in fuel sulfur contents (FSC) and on fuel HC levels and composition. The interactions between these changes in condensable species and existing soot particles are tracked as a function of FSC, HC concentrations, HC profiles, and concentrations modeled at some distance from downstream (e.g., 0 m to 1000 m) (Wong, 2015). We propose to take advantage of this parameterization and extend previous work by Woody et al. (2016) and Jones and Miake-Lye (2024) to obtain vPM emission indices (EIs) to calculate vPM emissions considering vPM parameters for an airport-level air quality study. We hypothesize that this capability will enable accurate characterization of $PM_{2.5}$ formation at local scales in the immediate vicinity of the airport and enhance air quality health impact studies. With resources permitting, we will develop this application for a single airport next year and apply to airports nationwide with a more recent emission inventory.

Research Approach

Research on Aerosol Dynamics Simulation Code

UNC-IE reviewed previous ADSC modeling work and explored the optimal CMAQ configuration to be used given recent advances in CMAQ version 5.5. We also established contact with Aerodyne to obtain the latest version of the ADSC with vPM treatment to get EIs to calculate aircraft emission for vPM. We obtained the ADSC and ran a series of tests to ensure that we can benchmark the model. After obtaining initial benchmarking results, we ran the model for multiple combinations of engines and atmospheric conditions to create a lookup table for use in CMAQ, and we can also use the EI values from Aerodyne's study. We have worked closely with Aerodyne to document model issues as they come up for future references and updates.

1) **ADSC Modeling Work for vPM**
   - The new parametrization for vPM modeling will be completed, particularly for PMSO and PMFO. The new vPM approach would use EI_{PMFO} and EI_{PMSO}, generated by ADSC. The EI will be multiplied by the fuel burn from AEDT results to calculate aircraft emissions. FSC was also chosen to span a range of values that are representative of those found in aviation fuel.
     - Less than 5-15 ppm FSC to be representative of sustainable aviation fuel (SAF) or the ND-MAX/ECLIF2 campaign's fuels (Schripp et al., 2022)
     - 680 ppm FSC (0.068 weight percent) based on Doc 9889, Airport Air Quality Manual, Second Edition, 2020 from ICAO (ICAO, 2020)

2) **CMAQ Application of vPM for BOS**
   - For this assignment, we adapted the same WRF-SMOKE-CMAQ modeling system methodology from Task 2, but we added ADSC to calculate vPM emissions for aircraft before processing through AEDT-Proc by multiplying fuel burn rate from AEDT output (Figure 29).

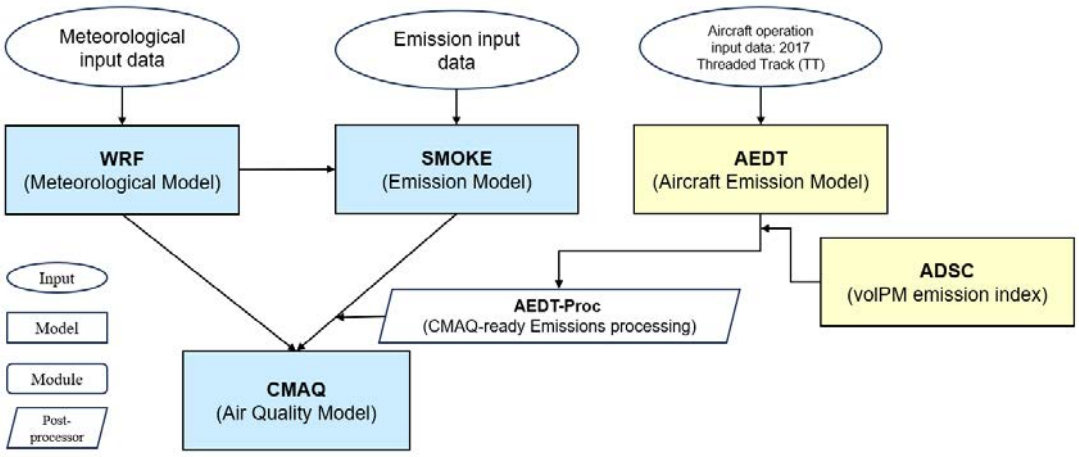


Figure 29. Community Multiscale Air Quality (CMAQ) application schematic for Boston Logan International Airport with Aerosol Dynamics Simulation Code (ADSC) and Aviation Environmental Design Tool (AEDT). SMOKE: Sparse Matrix Operator Kernel Emissions, WRF: Weather Research and Forecasting.

3) **Contribution of vPM on SOA and UFPNC**
   - For this application, the emission inventories pertaining to non-aviation sectors draw upon data provided by the EPA's NEI for 2017, which are projected from NEI 2016. To enhance our vPM emissions for aircraft, we aim to procure BOS-specific airport-level emission inventories for the year 2017 directly from AEDT through TT operations. Also, the AEDT fuel burn results will be extracted and multiplied with the EIs from ADSC for vPM to calculate aircraft emissions. The following emissions scenarios are considered:
     i. BOS emissions in NEI 2017 (based on AEDT) during LTO cycles
     ii. BOS emissions exported by AEDT version 3g during LTO cycles for 2017
     iii. BOS emissions generated by Fuel Burn from AEDT with EI_{PMSO} and EI_{PMFO} from ADSC
   - Seasonal changes in vPM play a central role in understanding aircraft-related air quality impacts, and this work explores how SOA and UFP seasonal patterns shift when vPM emissions are recalculated using specific particle size bins (e.g., Aitken mode [0–20 nm] and accumulation mode [20–100 nm]). Our team also examines how FSC influences particulate mass, number, and the evolving size distribution within CMAQ, providing a more complete view of how PM nucleates and condenses as they mix and dilute in the atmosphere after being emitted from aircraft. We will assess how SAF alters the contribution of vPM, offering insights into the benefits of SAF from an air quality perspective.

Milestones
None.

Major Accomplishments
- Obtained ADSC with vPM treatment from Aerodyne and installed and ran the model to create a new lookup table for use in CMAQ.

Publications
None.

Outreach Efforts
None.

Awards
None.



Student Involvement

Hyeongseok (Darby) Kim is a PhD student involved in this task performing ADSC-CMAQ modeling.

Plans for Next Period

- Create flight operations as an AEDT input data format and run the AEDT for BOS for January and July 2017.
- Run ADSC and create vPM emissions by multiplying AEDT results.
- Conduct CMAQ modeling using the new vPM emissions.

References

ICAO. (2020). *Airport Air Quality Manual* (Doc 9889). International Civil Aviation Organization. https://store.icao.int/en/airport-air-quality-manual-doc-9889

Jones, S. H., & Miake-Lye, R. C. (2024). Parameterization of H_2SO_4 and organic contributions to volatile PM in aircraft plumes at ground idle. *Journal of the Air & Waste Management Association, 74*(7), 490-510. https://doi.org/10.1080/10962247.2024.2354820

Schripp, T., Anderson, B. E., Bauder, U., Rauch, B., Corbin, J. C., Smallwood, G. J., Lobo, P., Crosbie, E. C., Shook, M. A., Miake-Lye, R. C., Yu, Z., Freedman, A., Whitefield, P. D., Robinson, C. E., Achterberg, S. L., Köhler, M., Oßwald, P., Grein, T., Sauer, D., LeClercq, P. (2022). Aircraft engine particulate matter emissions from sustainable aviation fuels: Results from ground-based measurements during the NASA/DLR campaign ECLIF2/ND-MAX. *Fuel, 325*, 124764. https://doi.org/10.1016/j.fuel.2022.124764

Wong, H.-W. (2015). Roles of Organic Emissions in the Formation of Near Field Aircraft-Emitted Volatile Particulate Matter: A Kinetic Microphysical Modeling Study. *Journal of Engineering for Gas Turbines and Power, 137*(7). https://doi.org/10.1115/1.4029366

Woody, M., Wong, H.-W., West, J. J., & Arunachalam, S. (2016). Multiscale predictions of aviation-attributable $PM_{2.5}$ for U.S. airports modeled using CMAQ with plume-in-grid and an aircraft-specific 1-D emission model. *Atmospheric Environment, 147*, 384-394. http://dx.doi.org/10.1016/j.atmosenv.2016.10.016



Project 022 Evaluation of FAA Tools: Aviation Portfolio Management Tool (APMT)

University of Illinois at Urbana-Champaign

Project Lead Investigator

Dr. Donald Wuebbles
Department of Atmospheric Sciences
University of Illinois
105 S. Gregory Street
Urbana, IL 61801
Tel: (217) 244-1568
Fax: (217) 244-4393
Email: wuebbles@illinois.edu

University Participants

University of Illinois at Urbana-Champaign

- P.I.: Dr. Donald Wuebbles
- FAA Award Number: 13-C-AJFE-UI-040
- Period of Performance: October 1, 2024, to September 30, 2025
- Tasks:
  1. Revisiting High-speed Civil Transports and Their Potential Effects on Ozone and Climate
  2. Assisting International Civil Aviation Organization (ICAO) Committee on Aviation Environmental Protection (CAEP) with preparation of various reports concerning emissions from the aviation sector

Project Funding Level

Support from the Federal Aviation administration (FAA) over this time period was about $200,000, with an additional $200,000 in matching in-kind support from the German Aerospace Center (DLR), Germany.

Investigation Team

Dr. Donald Wuebbles (P.I.), All Tasks
Swarnali Sanyal and Dharmendra Singh (postdoctoral students), responsible for conducting studies and performing analyses using the Community Earth System Model (CESM) Whole Atmosphere Community Climate Model (WACCM), a 3-dimensional (3D) atmospheric climate-chemistry model

Task 1 - Revisiting High-Speed Civil Transports
Task 2 – Assisting ICAO

University of Illinois at Urbana-Champaign

Major Goals

This project utilizes state-of-the-art modeling and technical knowledge to analyze the potential global environmental effects of aircraft and to perform analyses that underpin the development of analytical tools that can assess the costs and benefits to inform decision making on technology development. The studies rely on state-of-the-art models of the earth system that can provide useful scientific input for considerations by decision makers. The analyses in the project will aid decision making by translating complex models into simpler tools for use in cost-benefit analyses.



Objectives

To quantify the costs and benefits of using advanced aircraft and engine technologies, the FAA uses tools that are underpinned by state-of-the-art technical knowledge. These tools are used to inform decision making by providing the benefits and costs of various options that could enable technology development. The overall objective of this project is to enhance our understanding of the relationships between subsonic and proposed supersonic aircraft and the atmospheric state, and the development and evaluation of the capabilities, limitations, and uncertainties of metrics and simple models (e.g., Aviation Portfolio Management Tool [APMT]) to assist decision makers. This project will use state-of-the-art geophysical models of the earth system that fully represent tropospheric and stratospheric processes to evaluate the costs and benefits of technologies that could advance subsonic aviation and enable supersonic aviation. Specific project goals include the following: (1) science-based evaluation of analytical tools used by the FAA, (2) development of ideas and concepts for the next-generation treatment of aviation's effects on the earth system, (3) updated evaluation and analyses of the science of aviation effects on atmospheric composition, and (4) evaluation of potential environmental effects from assumed fleets of supersonic commercial and business jet aircraft to compare with their benefits in terms of decreased time for air travel.

Research Approach

The study uses the state-of-the-art WACCM that is part of the range of models within the CESM, developed through community-coordinated efforts by the National Center for Atmospheric Research (NCAR). The version of the WACCM used here has 66 layers from the ground to above the mesosphere and provides a comprehensive treatment of tropospheric and stratospheric (and above) chemical processes. The WACCM is one of the most advanced models worldwide for studying atmospheric processes and one of the few with a complete representation of stratospheric and mesospheric processes and higher; for example, it is one of very few models to represent the quasi-biennial oscillation that is important to stratospheric ozone. It has a comprehensive treatment of gas phase, particle based, and heterogeneous chemistry. This makes the WACCM ideal for the study of the environmental impacts from supersonic and subsonic aircraft.

Results & Discussion

Various companies and academic institutions have been actively considering the designs of supersonic aircraft. As these new designs are developed, the environmental impact on ozone and climate of these realistic fleets needs to be explored. Using emissions for two different supersonic commercial aircraft designs and associated mature fleets from the Massachusetts Institute of Technology (MIT), models for atmospheric physics and chemistry were run at the University of Illinois and at MIT. Analyses of the resulting derived effects on the atmosphere were then completed, and we have now completed a joint journal paper.

New sensitivity studies have been started to examine the effects of different parameters on the ozone and radiative forcing effects from supersonic transport (SST) fleets.

Analyses of the radiative forcing for contrail formation and contrail cirrus for the current commercial aviation fleet and the projected 2035 aviation fleet were analyzed using the global atmospheric model. A journal article has now been completed.

For the ICAO, Dr. Wuebbles coauthored three reports for the ICAO Impacts and Science Group (ISG), one based on the contrail workshop and another on nitrogen oxides (NO_x) emissions from aviation, and he co-led one report that updates understanding of potential environmental impacts of supersonic aircraft. All three reports were published by ICAO in Spring 2025.

Milestones

- Completed new studies of supersonic fleets, and our results are being evaluated for comparison with similar modeling studies made by MIT for the potential impacts on ozone and climate of several fleets of supersonic aircraft based on aircraft designs made by MIT. A journal article is being completed.
- Completed and published a review of contrail science.
- Completed and submitted special reports to ICAO.



Publications

Peer-Reviewed Journal Publications

Singh, D. K., Sanyal, S., & Wuebbles, D. J. (2024). Understanding the role of contrails and contrail cirrus in climate change: A global perspective. *Atmospheric Chemistry and Physics, 24*(16). doi:10.5194/acp-24-9219-2024

Singh, D. K., & Wuebbles, D. J. (2025). Aviation contrail climate forcing through 2035: Implications for sustainable aviation pathways. *Earth's Future,* submitted.

Sanyal, S., Oh, L. J., Kulkarni, R., Eastham, S., and Wuebbles, D.J. (2025) Ozone and Climate Impacts of Future Supersonic Aircraft: A Multimodel Evaluation with WACCM and GEOS-Chem. *Earth's Future*, submitted.

Written Reports

Eastham, S. D., Wuebbles, D. J., Sparrow, V. W., Rhodes, D., Grewe, V., Baughcum, S. L., Delhaye, D., & Penanhoat, O. (2025). *I.03 Update on Understanding of Potential Impacts of Supersonic Aircraft*. Special report for the International Civil Aviation Organization (ICAO), The United Nations, Montreal.

Lee, D. S., Dickson, N., Altuntas, O., Arunachalam, S., Barrett, S., Baughcum, S., Bonne, N., Block, A., Boehm, A., Brons, R., Burkhardt, U., Carter, W., Catalano, F., Claro, G., Delhaye, D., Eastham, S., Gettelman, A., Goobie, S., Johansson, D., Kagaya, R., Kanji, Z., Kärcher, B., Kim, B., de Leon, R. R., Manneville, A., Marizy, C., McDonald, T., Medvedev, Y., Miller, C., Moore, R., Mwangi, F., Ngo, D., Owen, B., Rollins, A., Stettler, M., Stromatas , S., Swann P., van Velthoven, P., Voigt, C., Wells, N., Wuebbles, D., & Yin, F. (2025). *CAEP Impacts and Science Group (ISG) Contrail Science Workshop Report*. Special report for the International Civil Aviation Organization (ICAO), The United Nations, Montreal.

Prashanth, P., Hauglustaine, D., Arunachalam, S., Eastham, S., Grewe, V., Miake-Lye, R., Skowron, A., Speth, R., Turgut, E. T., Van Velthoven, P., & Wuebbles, D. (2025). *I.01 Air Quality and Climate Impacts Interdependencies and Trade-Offs of Aviation Emissions.* Special report for the International Civil Aviation Organization (ICAO), The United Nations, Montreal.

Outreach Efforts

- Presented at ASCENT Meetings in Fall 2024 and May 2025.
- Presented at the FAA Air Emissions Characterization Roadmap meeting in May 2025.
- Presented at U.S. Department of Energy PRE-TRAILS workshop on aviation emissions in October 2024.
- Participated (Dr. Wuebbles) in ICAO ISG meetings (monthly).

Awards

None.

Student Involvement

Three postdoctoral students, Swarnali Sanyal, Rachana Pradhan, and Dharmendra Singh, were responsible for the analyses and modeling studies within the project and leading the initial preparation of the project reports.

Plans for Next Period

- Complete any revisions required by external reviewers to publish the SST and the contrail papers.
- Use the results from this study to inform the development of Aviation Portfolio Management Tool – Impacts Climate (APMT-IC) for supersonic impacts (ASCENT Project 058).
- Update analyses of subsonic aircraft fleets for current and projected future time periods.
- Complete sensitivity analyses of potential supersonic aircraft fleets to enhance understanding of the envelop of potential impacts on ozone and radiative forcing from such aircraft.
- Dr. Wuebbles is co-leading the development of a new report on contrails for ICAO that updates the current scientific understanding of contrails, contrail cirrus and the interactions between aerosols and clouds. This report will be developed throughout 2026, with the aim of completing and submitting the report to ICAO by June 2027.



Project 023 Analytical Approach for Quantifying Noise from Advanced Operational Procedures

Massachusetts Institute of Technology

Project Lead Investigator

R. John Hansman
T. Wilson Professor of Aeronautics & Astronautics
Department of Aeronautics & Astronautics
Massachusetts Institute of Technology
Room 33-303
77 Massachusetts Avenue
Cambridge, MA 02139
617-253-2271
rjhans@mit.edu

University Participants

Massachusetts Institute of Technology (MIT)

- P.I.: R. John Hansman
- FAA Award Number: 13-C-AJFE-MIT, Amendment Nos. 008, 015, 022, 031, 046, and 051
- Period of Performance: October 1, 2024, to September 30, 2025
- Tasks:
  1. Evaluate factors limiting the ability to develop and utilize low-environmental-impact flight procedures.
  2. Review current and proposed air traffic management (ATM) modernization plans for potential environmental impact benefits.
  3. Identify potential opportunities for incorporating operational environmental optimization.
  4. Propose a path forward for high-potential opportunities.

Project Funding Level

The Federal Aviation Administration (FAA) provided $860,000 in funding, and matching funds totaling $860,000 were provided by MIT (approximately $80,000) and the Massachusetts Port Authority (Massport) (approximately $780,000).

Investigation Team

Prof. R. John Hansman (P.I.), All Tasks
Sandro Salgueiro (graduate student), All Tasks
Clement Li (graduate student), All Tasks
Zhishen Wang (graduate student), All Tasks
Mina Cezairli (graduate student), All Tasks

Project Overview

In this project, the team is evaluating the noise reduction potential of advanced operational procedures in the terminal (arrival and departure) phases of flight. The noise impact of these procedures is not well understood or modeled in current environmental analysis tools, presenting an opportunity for further research to facilitate ATM system modernization. This project leverages a noise analysis framework previously developed at MIT under ASCENT Project 023 to evaluate a variety of sample procedures. In conjunction, this project contributes to the memorandum of understanding between the FAA and Massport to identify, analyze, and recommend procedure modifications at Boston Logan International Airport (BOS).



Task 1 - Evaluate Factors Limiting the Ability to Develop and Utilize Low-environmental-impact Flight Procedures

Massachusetts Institute of Technology

Objectives

The objective of this task is to identify factors driving operational stakeholder acceptance constraints, which limit when low-environmental-impact procedures may be utilized and, consequently, also impact the feasibility of their implementation. Interviews with stakeholders may be conducted to better understand the operational requirements that different stakeholders have in the context of procedure acceptance.

Research Approach

- Review relevant literature, including prior human-in-the-loop studies, to identify the effects of novel performance-based navigation (PBN) flight procedure concepts on air traffic control (ATC) and pilot tasks.
- Identify the relationship between operational stakeholder concerns and safety, in the context of the implementation of advanced low-noise flight procedure concepts.

Major Accomplishments

- Identified potential mechanisms to mitigate stakeholder concerns, including new merging and spacing tools and collision mitigation capabilities.
- At BOS, monitored the use of overlay RNAV (Area Navigation) GPS approach procedures throughout the year using flight trajectory data, and identified usage rates for different aircraft and airlines.

Task 2 - Review Current and Proposed ATM Modernization Plans for Potential Environmental Impact Benefits

Massachusetts Institute of Technology

Objectives

This task involves the review of historical, current, and proposed ATM capabilities that influence how operational stakeholders perceive the acceptance of new flight procedure concepts. Examples of capabilities to be analyzed include ATC decision support tools (including merging and spacing tools), trajectory-based operations (TBO), and aircraft navigation capabilities. Both United States and international capabilities are to be reviewed.

Research Approach

- Review relevant literature on both existing and proposed ATM modernization plans, including ATC and pilot decision support tools.
- Analyze noise monitor data from BOS to evaluate noise benefits achieved with the implementation of new low-noise procedures that were developed as part of prior work.

Major Accomplishments

- Identified a legacy set of ATC decision support tools used for merging and spacing of aircraft on final approach.
- Identified current efforts towards deployment of new merging and spacing tools, including the Terminal Sequencing and Spacing (TSAS) tool in the United States and Point Merge in Europe.
- Obtained a large set of noise monitor and aircraft trajectory data for a full year of operations at BOS, enabling new quantitative analyses on the noise effects of procedure changes.
- Analyzed raw noise monitor data for a new overwater required-navigation-performance (RNP AR) approach implemented at BOS (runway 33L).
    - Preliminary results show a significant noise reduction associated with the new procedure as measured at a highly impacted area, matching prior modeling results.
- Analyzed raw noise monitor data and flight trajectory data for new departure procedures serving runways 15R, 22L, and 22R at BOS.



- Preliminary results showed noise reduction associated with the new procedures as measured in a highly impacted area.
- Analyzed raw noise monitor data and flight trajectory data for the new arrival procedure serving runway 22L at BOS, which started to be flown in July 2025.

Task 3 - Identify Potential Opportunities for Incorporating Operational Environmental Optimization

Massachusetts Institute of Technology

Objectives

The objective of this task is to consider the potential of the ATM modernization capabilities identified in Task 2 to address the limitations identified in Task 1 or to enable environmentally desirable trajectories. Potential enhancements or additional capabilities will be identified.

Research Approach

Review potential effects of ATC and pilot support tools identified in Task 2 towards mitigating the operational stakeholder concerns identified in Task 1.

Major Accomplishments

- Leveraged flight trajectory data to compare track miles between the old procedures and the new overwater RNP AR approach implemented at BOS (runway 33L)
  - Preliminary results showed a reduction in track miles flown, leading to fuel burn benefits for the RNP AR procedure.
- Leveraged flight trajectory data to compare track miles between old and new procedures for new departure procedures serving runways 15R, 22L, and 22R at BOS.
  - Preliminary results revealed a reduction in track miles flown in all three of the new departure procedures, leading to fuel burn benefits.

Task 4 - Propose a Path Forward for High-potential Opportunities

Massachusetts Institute of Technology

Objectives

The objective of this task is to synthesize findings from Tasks 1, 2, and 3 to identify key capability development paths that could enable concepts of low-environmental-impact flight procedures. Areas of investigation will include requirements for each capability, functions served by it, and what changes it may drive in the roles and training of operational stakeholders (controllers and pilots).

Research Approach

- Synthesize findings from Tasks 1, 2, and 3 and identify development paths for future low-noise capabilities.

Major Accomplishments

- Not applicable, pending conclusion of Tasks 1, 2, and 3

Publications

Cezairli, M., Salgueiro, S., & Hansman, R. J. (2025). Implementation Analysis of Low-Noise Performance-Based Navigation Flight Procedures at Boston Logan Airport. *Journal of Air Transportation, 33*(3), 274-284. https://doi.org/10.2514/1.D0475

Cezairli, M., Salgueiro, S., & Hansman, R. J. (2024) Analysis of the Implementation of Low-Noise PBN Flight Procedures at Boston Logan Airport. [Conference presentation.] AIAA Aviation 2024 Forum, Las Vegas, Nevada. https://doi.org/10.2514/6.2024-3856

Hansman, R. J., Salgueiro, S., Huynh, J., Li, C., Jansson, M., Mahseredjian, A., & Zimmer, K. (2021). *Block 2 procedure recommendations for Logan Airport community noise reduction*. MIT international Center of Air Transportation. https://hdl.handle.net/1721.1/131242

Hansman, R. J., Jensen, L., Huynh, J., O'Neill, G., & Yu, A. (2017). *Block 1 procedure recommendations for Logan Airport community noise reduction*. MIT international Center of Air Transportation. http://hdl.handle.net/1721.1/114038

Salgueiro, S., & Hansman, R. J. (2023). *Identifying, Visualizing, and Communicating Constraints in PBN Flight Procedure Design* [Conference presentation]. AIAA Aviation 2023 Forum, San Diego, California. https://doi.org/10.2514/6.2023-3968

Salgueiro, S., Thomas, J., Li, C., & Hansman, R. J. (2021, January 11-21). *Operational noise abatement through control of climb profile on departure* [Conference presentation]. AIAA SciTech 2021 Forum, virtual. https://doi.org/10.2514/6.2021-0007

Thomas, J, & Hansman, J. (2019). Framework for analyzing aircraft community noise impacts of advanced operational flight procedures. *Journal of Aircraft*, 6(4). https://doi.org/10.2514/1.C035100

Thomas, J., Yu, A., Li, C., Toscano, P., & Hansman, R. J. (2019, June 17-21). *Advanced operational procedure design concepts for noise abatement* [Seminar presentation.] Thirteenth USA/Europe Air Traffic Management Research and Development Seminar, Vienna, Austria.

Yu, A., & Hansman, R. J. (2019, January 7-11). *Approach for representing the aircraft noise impacts of concentrated flight tracks*. [Conference presentation.] AIAA Aviation Forum, Dallas, Texas.

Outreach Efforts

- September 27, 2017: Poster to the ASCENT Advisory Board
- December 5, 2017: Call with Boeing to discuss procedure noise impact validity
- March 16, 2018: Discussion with Minneapolis-Saint Paul International Airport about metrics
- April 4, 2018: Poster to the ASCENT Advisory Board
- May 7, 2018: Presentation to the FAA 7100.41 PBN Working Group
- June 24, 2018: Discussion with air traffic controllers about dispersion concepts
- July 23, 2018: Briefing at the FAA Joint University Program research update meeting
- October 9, 2018: Poster to the ASCENT Advisory Board
- November 8, 2018: Presentation to the Airline Industry Consortium
- March 3, 2019: Presentation at the Aviation Noise and Emissions Symposium
- October 15, 2019: Presentation to the ASCENT Advisory Board
- November 12, 2019: Presentation to the Airline Industry Consortium
- May 21, 2020: Meeting with operational stakeholders from the FAA 7100.41 process to discuss Block 2 concepts
- September 23, 2021: Public hearing to present Block 2 procedure recommendations for BOS
- Numerous community meetings
- Numerous briefings to politicians representing eastern Massachusetts (local, state, and federal)
- Briefing to the FAA Management Advisory Council
- In-person outreach and collaboration with Massport, an operator at Boston Logan Airport, and an ASCENT Advisory Board member
- April 1, 2022: Presentation of a summary of lessons learned from the Boston project to an audience of FAA, Massport, and HMMH stakeholders
- August 16, 2022: Presentation of work on flight procedure constraints at the FAA Technical Center in Atlantic City, New Jersey, as part of the Joint University Program
- September 20–21, 2022: 7100.41 Working Group meeting at the Boston terminal radar approach control facilities (ASCENT Project 090); presentation to air traffic and airline stakeholders on flight procedures proposed for BOS as part of Block 2; approval received for all presented procedures for further implementation work
- April 9–10, 2024: Presentation to the ASCENT Advisory Board
- October 29–31, 2024: Poster to the ASCENT Advisory Board
- April 14–15, 2025: Presentation to the ASCENT Advisory Board

Awards

- 2018 Department of Transportation/FAA Centers of Excellence Outstanding Student of the Year Award to Jacqueline Thomas
- 2021 Massachusetts Port Authority Logan Stars Award to the MIT International Center for Air Transportation research group



- 2023 American Institute of Aeronautics and Astronautics Orville and Wilbur Wright Graduate Award to Sandro Salgueiro

Student Involvement

Graduate students have been involved in all aspects of this research in terms of analysis, documentation, and presentation.

Plans for Next Period

The next phase of this project will focus on the continuation of all tasks, with a particular focus on the analysis of ATM modernization plans and the identification of potential noise benefits enabled by future capabilities. Current efforts include the analysis of noise monitor data from BOS, which will be used to quantify the change in noise impacts due to the implementation of Block 1 and Block 2 procedures.

Project 025 Shock Tube Studies of the Kinetics of Jet Fuels

Stanford University

Project Lead Investigator

Ronald K. Hanson
Woodard Professor
Mechanical Engineering Department
Stanford University
452 Escondido Mall
650-723-6850
rkhanson@stanford.edu

University Participants

Stanford University

- P.I.: Prof. Ronald K. Hanson
- FAA Award Number: 13-C-AJFE-SU-027
- Period of Performance: October 1, 2024, to September 30, 2025
- Task:
  1. Chemical kinetics combustion experiments.

Project Funding Level

In 2024–2025, the Federal Aviation Administration (FAA) provided $400,000 in funding and Stanford University provided $400,000 in 1:1 matching funds.

Investigation Team

Prof. Ronald K. Hanson, P.I., research direction
Jesse W. Streicher, Research Scientist, research management
Miguel Figueroa Labastida, Postdoctoral fellow, research assistance
Andrew R. Klingberg, Graduate Student, research assistance

Project Overview

This year's efforts focused on advancing Fourier transform infrared (FTIR)-based tools for rapid fuel prescreening by integrating compositional inference, thermochemical property estimation, and comparative modeling analysis. First, we extended our spectral-surrogate framework to predict key thermochemical properties, demonstrating that molecular-species information inferred from vapor-phase mid-infrared (IR) spectra can be used to accurately estimate specific heat, enthalpy, and entropy. Second, we evaluated the generality of an existing molecular-weight prediction model by testing it against a new set of World Jet Fuel Survey (WJFS) samples. Additionally, we developed an improved model tailored to this fuel population. Finally, we systematically compared three representations of the FTIR spectrum, including raw cross-section data, Principal component analysis (PCA)-reduced features, and spectral moments, to quantify their impacts on predictive accuracy, reproducibility, and model development complexity. Together, these studies refine the methodological foundation needed for spectrum-based characterization of aviation fuels and support the development of reliable, data-driven prescreening tools for emerging fuel candidates. In parallel, an instrumentation upgrade to the Thermo Fisher Scientific® Nicolet™ iS50 FTIR system expanded our measurement capabilities and will further enhance future model development.

® Thermo Fisher Scientific and Nicolet are registered trademarks of Thermo Fisher Scientific, Inc., Waltham, Massachusetts.

Task 1 – Chemical Kinetics Combustion Experiments

Stanford University

Objectives

This work is aimed at developing fuel prescreening tools based on the IR absorption cross-section measurements of jet fuels and their constituent molecules. Specific fuel analysis objectives include developing effective strategies for correlating (a) chemical, physical, and combustion properties, and (b) functional group and molecular species composition of jet fuels with their IR spectra.

Research Approach

An important goal of the current research is to characterize jet fuel composition and properties based on the fuel's mid-IR absorption spectrum, measured using a FTIR spectrometer. Over the past five years, a database of spectroscopic measurements and property data for a variety of jet fuels and jet fuel components has been collected. Using this database, we have developed linear and nonlinear correlations between the spectroscopic properties of jet fuels with fuel composition and with important physical/chemical properties such as density, derived cetane number, net heat of combustion, and flash point. Here, we present an overview of this year's research areas: using compositional inference to predict thermochemical properties, refining a property prediction model for WJFS fuels, and evaluating how alternative FTIR spectral representations (raw spectra, PCA-reduced data, and spectral moments) impact model accuracy.

Thermochemical Property Prediction

Traditional approaches for estimating thermochemical properties of real jet fuels rely on constructing a simplified surrogate mixture that approximates the bulk fuel. Because real fuels contain hundreds of molecular species, these surrogates are typically limited to only two to four neat hydrocarbons selected to reproduce a small set of global physical properties (e.g., density, hydrogen-to-carbon ratio, or average carbon number). Once selected, the thermochemical properties of the surrogate are computed as the mole-fraction-weighted sum of the property contributions from each component. While effective for broad characterization, this approach is fundamentally constrained by the limited number of components and by the reliance on global properties, which limits its ability to capture detailed molecular-level features that strongly influence heat capacity, enthalpy, and entropy.

In contrast, an FTIR-based approach (Strategy 4) leverages the rich spectral information contained in vapor-phase mid-IR measurements to inform surrogate formulation. Instead of constraining the surrogate to just a few components, we begin by measuring the vapor-phase FTIR spectrum of the real fuel and then identify the mixture of neat-component spectra that best reconstructs the measured spectrum. Because vapor-phase absorption cross sections are linearly additive, the reconstructed "spectral surrogate" is not restricted in component count and can incorporate contributions from a broad set of reference molecules. This year, we expanded and utilized a reference library containing vapor-phase spectra and thermochemical data for 35 hydrocarbons, spanning paraffins, isoparaffins, cycloalkanes, and aromatics. Both the spectrum and the thermochemical properties of these components are linearly additive, enabling consistent mapping between spectral fit and thermochemical prediction.

Table 1 provides an overview of the neat-component reference library. By leveraging this library and the spectral additivity principle, Strategy 4 allows the surrogate mixture to more accurately reproduce the molecular structure of the target fuel, which in turn yields accurate predictions of specific heat, enthalpy, and entropy.

Table 1. Overview of reference library of neat components. The library includes vapor-phase spectra and thermochemical data for 35 hydrocarbons.

	Molecular class			
	n-paraffins	Isoparaffins	Cycloparaffins	Aromatics
C number range	C_6 to C_{16}	C_6 to C_{16}	C_6 to C_{10}	C_6 to C_9
Count	10	9	5	11

35 reference components

To obtain the spectral surrogate, a constrained linear least-squares optimization is used to determine the mole fractions of the neat components. The optimization enforces non-negativity of all component fractions, ensures that the mixture fractions sum to unity, and matches the average carbon and hydrogen numbers of the target fuel. Using these constraints, the solver identifies the combination of reference spectra that best reproduces the measured vapor-phase FTIR spectrum of Jet-A fuel. The resulting surrogate mixture captures the major spectral features of the fuel, with remaining differences primarily arising from gaps in the reference library; these discrepancies can be further reduced by expanding the set of available neat-component spectra. Figure 1 presents a comparison between the measured Jet-A (A2) spectrum and Strategy-4-derived spectral reconstruction, illustrating the close match achieved by the surrogate.

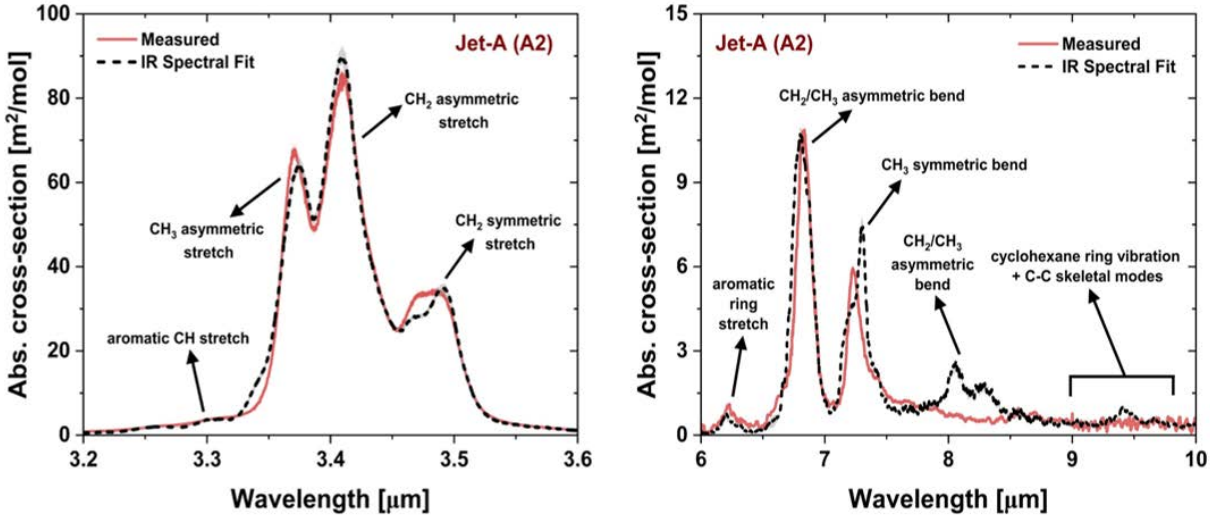


Figure 1. Comparison of measured Jet-A spectrum and the spectrum obtained from Strategy 4.

The thermochemical properties of the surrogate were obtained using National Aeronautics and Space Administration (NASA) polynomial fits for each neat component, which provide temperature-dependent values of specific heat (Cp), enthalpy (H), and entropy (S). Using the mole fractions determined by the spectral fitting procedure, the Cp, H, and S of Jet-A fuel were calculated as linear combinations of the component contributions across a range of temperatures. The resulting estimates agree well with values reported from established Jet-A surrogate models (Figure 2), demonstrating the consistency of the spectral-surrogate approach. Minor differences between models are expected due to variations in component selection and reference data, but these discrepancies are small and are not anticipated to significantly influence global combustion predictions.

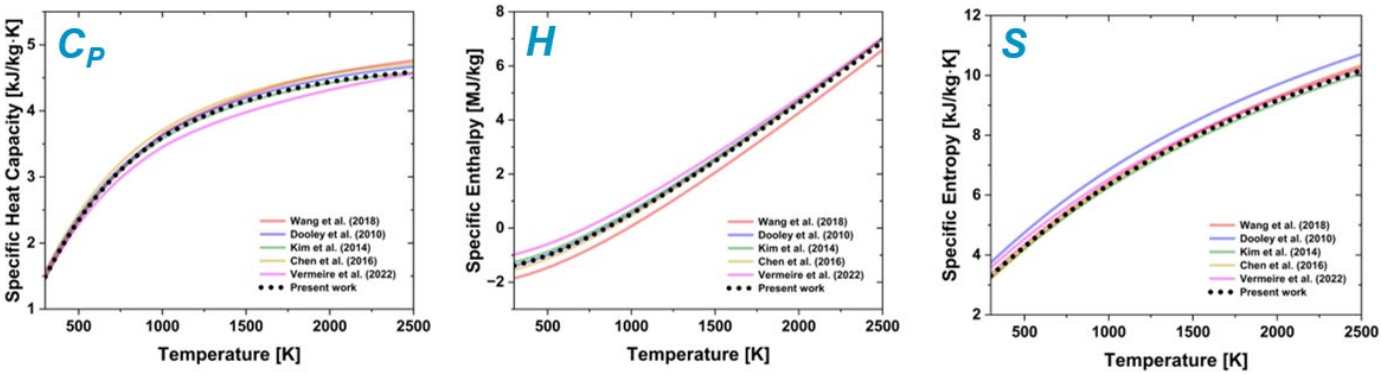


Figure 2. Comparison of specific heat capacity, specific enthalpy, and specific entropy for Jet- predicted from the spectral surrogate (black points) with Jet-A surrogates from the literature.

Adiabatic flame temperature calculations were used as a quantitative metric to assess the performance of the FTIR-based surrogate relative to conventional surrogate formulations. Across a wide range of equivalence ratios, the IR-inferred surrogate (Strategy 4) produces flame temperatures that closely match those obtained from established Jet-A surrogate models (Figure 3), indicating that the spectral surrogate preserves the key thermochemical characteristics governing combustion behavior. Together, these results demonstrate that FTIR measurements, paired with compositional inference, enable accurate prediction of temperature-dependent fuel properties. This approach provides a robust pathway for evaluating the reactivity and combustion performance of novel or emerging fuel candidates during the prescreening process.

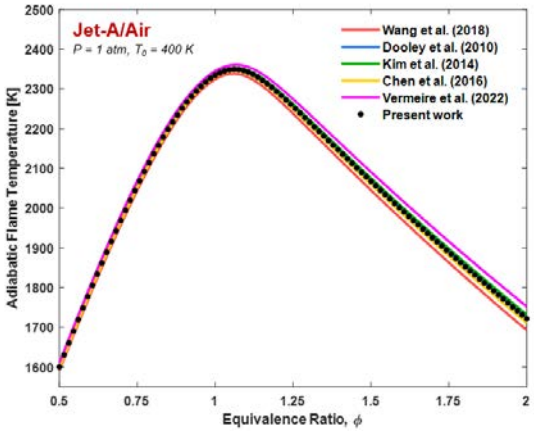


Figure 3. Comparison of simulated adiabatic flame temperature using predicted thermochemical properties from Strategy 4 and Jet-A surrogates from literature.

World Jet Fuel Survey Property Prediction

To evaluate the generality of our existing molecular-weight prediction model, we applied the previously published model of Boddapati et al. (2024) to a new set of WJFS samples. We received 39 WJFS fuels along with property data for 38 of them, and each sample was analyzed using its measured vapor-phase FTIR spectrum. The original model had been trained on a diverse dataset consisting of 47 neat hydrocarbons, 164 simple binary and ternary blends, and 16 jet fuels. When tested on the 38 WJFS samples, however, the model consistently overpredicted molecular weight, indicating that the training set did not fully capture the compositional variability present in the new fuels. This outcome demonstrated the need to further generalize or tailor the existing model for broader fuel classes.

To address this limitation, we developed a new molecular-weight prediction model trained exclusively on the WJFS data. Using 34 samples for training and holding out 4 for testing, the new model produced substantially improved predictive accuracy. This result highlights the importance of selecting a training dataset that closely reflects the fuels of interest, particularly when targeting property prediction for complex real-world mixtures. Figure 4 compares the performance of the original model with the WJFS-trained model and illustrates the improved agreement achieved when the model is calibrated to the specific fuel population. In the improved-model plot (right), blue points mark the samples used for training, and red points denote the held-out test samples that provide an unbiased evaluation of model performance.

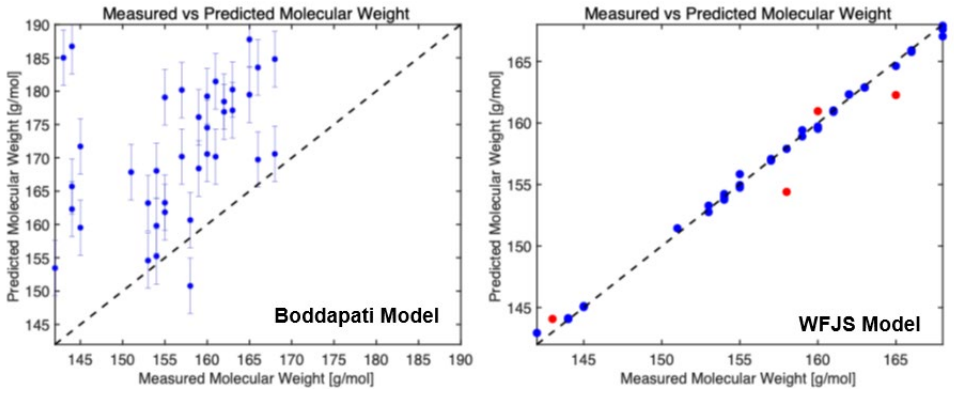


Figure 4. Comparison of molecular-weight prediction performance between the previously developed model and the model trained specifically on WJFS samples.

Model Input Comparison

Our FTIR-based modeling framework was expanded to compare three different spectral input representations: (1) raw vapor-phase FTIR spectra, (2) principal-component–reduced spectra, and (3) spectral-moment descriptors. Using a dataset of 267 fuel spectra, we evaluated how each representation affected both predictive accuracy and model robustness across multiple training subsets. Raw spectra offer the highest physical interpretability (each wavelength corresponds directly to an absorption cross section) but the tens of thousands of input features increase the chance of overfitting and can cause models to select slightly different wavelength regions each time they are retrained. PCA-reduced spectra address this challenge by compressing the data into a small number of orthogonal components that capture the dominant variance in the dataset; however, these components blend many wavelengths and thus are less directly tied to specific functional groups. Spectral moments provide a middle ground: they dramatically reduce the number of features while maintaining physical interpretability. For each predefined functional-group wavelength region, we compute a set of statistical descriptors (including area (zeroth moment), centroid (first moment), width, and skewness) that summarize the shape and strength of the absorption band. Because these features are user-defined rather than model-selected, spectral moments remained consistent across training subsets and offered the highest reproducibility, whereas raw and PCA-based representations provided the strongest predictive accuracy for properties such as molecular weight and density. Table 2 summarizes the three FTIR representations used in model development.

Table 2. Overview of different input representations of the FTIR spectrum used for model development.

Raw Spectrum	Principal Components	Spectral Moments
Physically interpretable: Wavelengths tied to functional groups	**Harder to interpret:** Features are blends of all wavelengths	**Physically interpretable:** Moments tied to functional groups
Large feature set: Tens of thousands → overfitting risk	**Compact feature set:** Captures variance well	**Compact feature set:** Pre-defined and dataset-independent
Stability: Specific wavelengths may change between models	**Stability:** Dependent on dataset composition, but generally consistent	**Stability:** Constant across datasets as the features are determined by user

Figure 5 compares the predictive performance of models trained using the three spectral input representations. For this analysis, all 267 vapor-phase spectra were used to construct the full feature sets for the raw spectrum, PCA-reduced spectrum, and spectral-moment descriptors. A linear regression model was trained for each representation, with hyperparameters optimized through cross-validation. Overall, both the raw-spectrum and PCA-based models achieved the highest accuracy for predicting density, with the raw spectrum slightly outperforming PCA on average. Spectral moments also produced strong predictions but remained the weakest of the three methods in terms of absolute accuracy. These results indicate that when the training dataset adequately represents the fuels of interest, raw or PCA-based inputs are

preferred for maximizing predictive performance. Spectral moments remain valuable, however, when stability, reproducibility, or interpretability are the primary objectives.

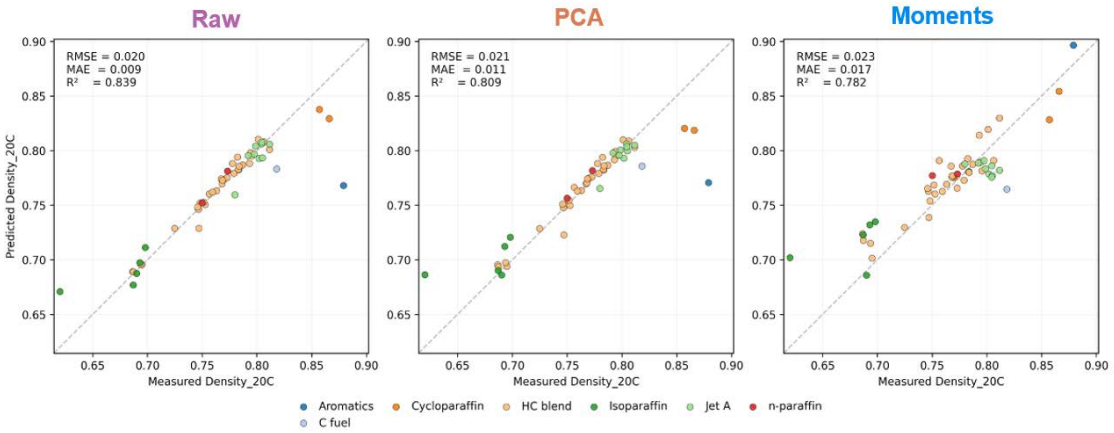


Figure 5. Density property prediction model results using the raw FTIR spectrum, principal components, and spectral moments as the input features for model training.

Instrumentation Update

This year, we acquired a new FTIR spectrometer (Thermo Fisher Scientific Nicolet iS50), which significantly expands our experimental capabilities. The Nicolet iS50 provides an extended spectral range from 1 to 200 micrometers, higher signal-to-noise ratios, improved purge control, and enhanced stability for both vapor-phase and liquid-phase measurements. Compared to our previous instrument (Thermo Fisher Scientific® Nicolet™ 6700), the broader wavelength coverage enables characterization of longer-wavelength absorption features associated with aromatics, fuel additives, and other functional groups. The system is equipped with a heated optical cell capable of vapor-phase measurements up to 300 degrees Celsius and an Attenuated Total Reflectance (ATR) crystal cell for accurate analysis of liquid-phase samples.

Looking forward, these improvements will allow us to build a unified training set containing both vapor-phase and liquid-phase spectra for each fuel, evaluate how spectral phase influences property prediction performance, and ultimately develop a combined liquid–vapor modeling framework that delivers optimal accuracy across all fuel properties.

Milestone

- Presented reporting of experimental results and analysis at the Spring ASCENT meeting (April 2025).

Major Accomplishments

- Extended the FTIR-based compositional inference framework to predict thermochemical properties such as specific heat, enthalpy, and entropy.
- Evaluated and improved molecular-weight prediction performance using a new set of WJFS samples.
- Compared raw spectra, PCA-reduced spectra, and spectral moments to assess how spectral representations influence model accuracy and robustness.
- Set up and began operating the new Nicolet iS50 FTIR spectrometer, enabling expanded spectral measurements and improved data quality.

Publications

Peer-reviewed journal publication

Boddapati, V., Ferris, A. M., & Hanson, R. K. (2024). Predicting the physical and chemical properties of sustainable aviation fuels using elastic-net-regularized linear models based on extended-wavelength FTIR spectra, *Fuel, 356*, 129557. https://doi.org/10.1016/j.fuel.2023.129557



Outreach Efforts
Our thermochemical property prediction work was presented at the Spring ASCENT SAF Meeting (April 23-24, 2025),

Awards
None.

Student Involvement
Graduate students are actively involved in the acquisition and analysis of all experimental data and model development. Andrew Klingberg (current graduate student) and Miguel Figueroa Labastida (current postdoctoral fellow) performed the IR spectral analysis/fuel prescreening. Jesse Streicher (current research scientist) has additionally contributed to the project through research management.

Plans for Next Period
- Continue to expand the training dataset by adding FTIR spectra and property data for additional hydrocarbons across a broad range of molecular classes.
- Acquire and analyze additional SAF samples with varied compositions to further validate and refine the property-prediction strategies.
- Compile paired vapor-phase and liquid-phase FTIR spectra for each fuel to create a unified training set.
- Develop an integrated liquid–vapor modeling framework that achieves optimal predictive accuracy for all targeted fuel properties.



Project 031 Alternative Jet Fuel Test and Evaluation

University of Dayton Research Institute

Project Lead Investigator

Zachary West, PhD
Principal Research Engineer
Group Leader, Fuel Science
University of Dayton
300 College Park
Dayton, OH 45458
937-255-4062
zachary.west@udri.udayton.edu

University Participants

University of Dayton Research Institute (UDRI)

- P.I.: Zachary West, Group Leader
- FAA Award Number: 13-C-AJFE-UD
- Overall Period of Performance: April 8, 2015, to September 30, 2026
- Tasks:
  - Period of Performance: April 8, 2015, to March 14, 2016; Amendment No. 006
    1. Evaluate the performance of candidate alternative fuels via the ASTM D4054 approval process
  - Period of Performance: August 13, 2015, to August 31, 2016; Amendment No. 007
    2. Evaluate the performance of candidate alternative fuels via the ASTM D4054 approval process
  - Period of Performance: August 5, 2016, to August 31, 2017; Amendment No. 012
    3. Manage the evaluation and testing of candidate alternative fuels
  - Period of Performance: July 31, 2017, to August 31, 2019; Amendment No. 016
    4. Manage the evaluation and testing of candidate alternative fuels
  - Period of Performance: August 30, 2018, to August 31, 2019; Amendment No. 021
    5. Manage the evaluation and testing of candidate alternative fuels
  - Period of Performance: Extended period of performance end from September 10, 2019, to September 9, 2020; Amendment No. 023
  - Period of Performance: February 5, 2020, to February 4, 2021; Amendment No. 025
    6. Manage the evaluation and testing of candidate alternative fuels
  - Period of Performance: Extended period of performance end from September 9, 2019, to September 9, 2021; Amendment No. 028
  - Period of Performance: February 4, 2021, to February 5, 2022; Amendment No. 032
    7. Manage the evaluation and testing of candidate alternative fuels
  - Period of Performance: August 10, 2021, to February 10, 2022; Amendment No. 033
    - No-cost extension (Amendment No. 033 is not task-specific)
  - Period of Performance: October 1, 2021, to September 30, 2022; Amendment No. 038
  - Period of Performance: October 1, 2022, to September 30, 2023; Amendment No. 043
  - Period of Performance: October 1, 2023, to September 30, 2024; Amendment No. 049
    - No-cost extension
  - Period of Performance: March 19, 2024, to March 18, 2025; Amendment No. 052
  - Period of Performance: August 26, 2024, to September 30, 2024; Amendment No. 056
    - Redirect funds awarded on Amendment No. 024 to ASCENT Project 031
  - Period of Performance: March 19, 2025, to September 30, 2025; Amendment No. 057
    - No-cost extension
  - Period of Performance: February 3, 2025, to September 30, 2025; Amendment No. 060
    - Redirect funds awarded on Amendment Nos. 027, 030, & 039 to ASCENT Project 031a



- Period of Performance: September 16, 2025, to September 30, 2026; Amendment No. 064
  - No-cost extension

Project Funding Level

Amendment	Funding
Amendment No. 006	$309,885
Amendment No. 007	$99,739
Amendment No. 012	$693,928
Amendment No. 016	$999,512
Amendment No. 021	$199,966
Amendment No. 025	$1,926,434
Amendment No. 032	$1,049,700
Amendment No. 038	$499,784
Amendment No. 043	$1,499,940
Amendment No. 052	$1,999,834
Amendment No. 060	$122,534
Total	**$9,401,256**

In-kind cost sharing has been obtained from the following organizations:

Organization	Funding	**Year of** Commitment
LanzaTech	$ 55,801	2015
UDRI -- internal funds	$ 43,673	2016
LanzaTech	$ 381,451	2016
Neste	$ 372,000	2017
Boeing	$ 2,365,338	2017
Shell	$ 280,000	2019
IHI	$ 1,150,328	2019
Shell	$ 325,000	2020
Global Bioenergies	$ 6,875,900	2021
Global Bioenergies	$ 290,000	2021
Revo	$ 625,873	2024
University of Sheffield	$ 11,975	2024
Topsoe	$268,893	2025
Phillips 66	$101,000	2025
Total	**$13,147,232**	

Investigation Team

Dr. Zachary West (P.I.)
Carlie Anderson (staff scientist)
Dr. Amanda Arts (staff scientist)
Shane Kosir (staff scientist)
Susan Mueller (staff scientist)
Linda Shafer (staff scientist)



Dr. Willie Steinecker (staff scientist)
Maria Baker (other professional)
April Landsaw (other professional)
CJ Nesbit (undergraduate student)
Taylor Nicely (undergraduate student)

Project Overview

Alternative jet fuels, also known as synthetic aviation turbine fuel (SATF) or sometimes sustainable aviation fuel (SAF), offer the potential benefits of reduced global environmental impacts, greater national energy security, and stabilized fuel costs for the aviation industry. The Federal Aviation Administration (FAA) is committed to the advancement of "drop-in" SATF. The successful adoption of alternative fuels requires approval for use by the aviation community (i.e., original equipment manufacturers [OEM] and regulators), followed by large-scale production of fuel that is cost-competitive and meets the safety standards for conventional jet fuel. Alternative jet fuels must undergo rigorous testing to become qualified for use and to be incorporated into ASTM International specifications.

Cost-effective, coordinated performance testing capability (in accordance with ASTM D4054 [ASTM, 2023b]) is needed to support the evaluation of promising alternative jet fuels. The objective of this project is to provide the necessary capability to support fuel testing and evaluation of novel alternative jet fuels.

The proposed program should provide the following capabilities:

- Identify alternative jet fuels, including blends with conventional jet fuel, with the potential to be economically viable and to support FAA's NextGen environmental and SAF Grand Challenge goals for testing.
- Perform engine, component, rig, or laboratory tests, or any combination thereof, to evaluate the performance of alternative jet fuels in accordance with ASTM D4054.
- Identify and conduct unique testing, beyond that defined in ASTM D4054, to support the evaluation of alternative jet fuels for inclusion in ASTM International jet fuel specifications.
- Obtain baseline and alternative jet fuel data to assess the effects of alternative jet fuels on aircraft performance, maintenance requirements, and reliability.
- Coordinate efforts with activities sponsored by the United States (U.S.) Department of Defense and/or other governmental parties that may be supporting relevant work.
- Report relevant performance data for the alternative fuels tested, including quantified effects of the alternative fuel on aircraft and/or engine performance and air-quality relative to conventional jet fuel; share reported data with the FAA National Jet Fuel Combustion Program, the ASCENT Center of Excellence membership, and the broader aviation fuels community, e.g., ASTM International, Coordinating Research Council (CRC), International Air Transport Association (IATA), and International Association for Stability, Handling and Use of Liquid Fuels (IASH).

Tasks 1 and 2 - Evaluate the Performance of Candidate Alternative Fuels via the ASTM D4054 Approval Process and Manage the Evaluation and Testing of Candidate Alternative Fuels

University of Dayton Research Institute

Objective

Cost-effective, coordinated performance testing capability (in accordance with ASTM D4054) is needed to support the evaluation of promising alternative jet fuels. The objective of this project is to provide the capability necessary to support (a) the evaluation of to-be-determined alternative fuels selected in coordination with the FAA and (b) a fuel testing and evaluation project with specific alternative fuels in mind.

Research Approach

The intent of this program is to provide the capability needed to perform specification and fit-for-purpose evaluations of candidate alternative fuels, with the aim of providing a path through the ASTM D4054 approval process. The UDRI team can perform many of these evaluations and is prepared to work with other organizations, such as the Southwest Research Institute (SwRI) and OEMs, with unique test capabilities, as needed. These assessments include additional engine, auxiliary



power unit, component, and rig evaluations. The UDRI testing capabilities include our campus laboratory facilities and limited efforts at the laboratories of the Fuels Branch of the U.S. Air Force Research Laboratory.

Table 1 and Table 2 list examples of the Tier 1 and Tier 2, respectively, measurements that can be provided by UDRI and its partners.

Table 1. Example Tier 1 Properties.

Test Description	Method
Acidity	ASTM D3242
Aromatics	ASTM D6379
Mercaptan Sulfur	ASTM D3227
Sulfur Content	ASTM D5453
Carbon and Hydrogen Mass	ASTM D5291C
FAME	IP 585
Physical Distillation	ASTM D86
Flash Point	ASTM D93
Freezing Point	ASTM D5972
Net Heat of Combustion	ASTM D4809
Smoke Point	ASTM D1322
Copper Strip Corrosion	ASTM D130
Thermal Stability	ASTM D3241
Existent Gum	ASTM D381 or IP 540
MSEP (Microseparometer Index)	ASTM D3948

Table 2. Example Tier 2 Properties.

Test Description	Method
Bulk Detailed Hydrocarbon Type Composition	UDRI FC-M-101 or FED-STD-791, Method 7508
Hydrocarbon Composition	ASTM D2425
Trace Materials – Polar Organics	UDRI FC-M-102
Total Nitrogen Content	ASTM D4629
Total Halogens (Fluorine, Chlorine)	ASTM D7359
Trace Elements (ICP-MS)	UDRI FC-M-107
Simulated Distillation	ASTM D2887
Thermal Stability, Breakpoint	ASTM D3241
Lubricity (BOCLE)	ASTM D5001
Response to Lubricity Improver	ASTM D5001
Viscosity vs Temperature	ASTM D7042
Specific Heat vs Temperature	ASTM E2716



Test Description	Method
Density vs Temperature	ASTM D4052
Surface Tension vs Temperature	ASTM D1331A
Isentropic Bulk Modulus vs Temperature	FED-STD-791, Method 7507
Thermal Conductivity vs Temperature	ASTM D7896
Water Solubility vs Temperature	ASTM D6304
Air Solubility	FC-M-103
True Vapor Pressure vs Temperature	ASTM D6378 or D2879
Dielectric Constant vs Density	IP 638
Electrical Conductivity and Response to Static Dissipator	ASTM D2624
Storage Stability - Peroxides	ASTM D3703
Storage Stability - Potential Gum	ASTM D5304
Flammability Limits	ASTM E681
Autoignition Temperature	ASTM E659
Hot Surface Ignition Temperature	ISO 20823
Preliminary materials compatibility (Nitrile, Fluorosilicone, Fluorocarbon [Viton] Elastomers)	ASTM D4054 Annex 3 (optical dilatometry)
Derived Cetane Number	ASTM D6890

Extended Physical and Chemical Characterization
In addition to the above physical and chemical fuel evaluation capabilities, UDRI has extensive experience in evaluating microbial growth in petroleum-derived and alternative fuels. These evaluations include standard laboratory culturing and colony counting methods, as well as advanced techniques, such as quantitative polymerase chain reaction and metagenomic sequencing. These methods enable quantitative measurements of microbial growth rates in candidate alternative fuels for comparison with petroleum fuels.

UDRI has extensive experience in the evaluation of elastomer degradation upon exposure to candidate alternative fuels. Various methods are used to evaluate seal swell and O-ring fixture leakage, including optical dilatometry, sealing pressure measurements, fuel partitioning into the elastomer, and the use of a pressurized temperature-controlled O-ring test device.

Moreover, UDRI can perform fuel–material compatibility testing by using ASTM D4054 procedures for fuel soak testing, post-exposure nonmetallic and metallic material testing, and surface and microstructural evaluation. The 68 “short-list” materials and 255 materials on the complete list can be tested.

Milestones

The schedule for this project is dependent on the receipt of alternative fuel candidates for testing. As candidate fuels are received, a testing schedule will be established via coordination with the FAA and collaborators. Our existing relationships with these organizations will help expedite this process.



Major Accomplishments

Virent Synthesized Aromatic Kerosene

Virent's synthesized aromatic kerosene (SAK) is an aromatics-only stream produced from a sugar feedstock. The OEM committee has recommended that this candidate be evaluated as a blend with petroleum jet fuel. Some additional testing has been requested (including additional materials and stability tests) in order to proceed through the ASTM qualification process. Virent's parent company, Marathon Petroleum Co. (MPC), has decided to close the Virent research facility; further activities for approval of this SAK will be handled with MPC directly.

Council of Scientific and Industrial Research-Indian Institute of Petroleum

The Council of Scientific and Industrial Research-Indian Institute of Petroleum (CSIR-IIP) has developed a single-step process to convert lipids (i.e., plant-derived oil and animal-derived fats) into hydrocarbons containing aromatic compounds. Multiple fuel samples have been received, and Tier 1 and Tier 2 testing have been completed. The OEM committee has recommended that this fuel proceed along the ASTM full approval pathway (rather than the Fast Track process). OEMs have reviewed the Phase I research report and feedback has been provided to CSIR-IIP. An additional sample has been submitted to UDRI for complete Tier 1 and Tier 2 analysis prior to proceeding.

XOM and UOP's Methanol-to-Jet: Synthetic Paraffinic Kerosene

ExxonMobil® (XOM) and Honeywell®-UOP (UOP) balloted the methanol-to-jet (MTJ) synthetic paraffinic kerosene (SPK) pathway in ASTM International sub-committee D02.0J as a modification to ASTM D7566 (ASTM, 2023c) Annex A5 (i.e., to include methanol as a feedstock). The initial ballot had some negative votes, which is typical; the XOM and UOP teams plan to address the negative votes and incorporate the feedback prior to resubmitting the ballot in 2026.

Topsoe's Methanol-to-Jet: Cycloparaffinic Kerosene with Aromatics

Topsoe received feedback from the OEM panel regarding the MTJ cycloparaffinic kerosene with aromatics (CKA) blending component. The MTJ-CKA fluid is considered to be more 'fully formulated' with respect to hydrocarbon classes—'fully formulated' in this sense meaning the blend component contains most/all of the traditional classes of hydrocarbons to include iso-, n-, cyclo-alkanes, along with aromatics. It is anticipated that the OEM review panel and Topsoe will work out an appropriate path forward in early 2026.

Revo

The Revo fuel is a hydroprocessed ester and fatty acid (HEFA)-type fuel containing a higher level of cycloparaffins. Three fuel samples have been received, and Tier 1 and Tier 2 testing have been completed. Revo decided to perform some process optimization and submitted an additional sample, from a production plant, for testing prior to submitting a research report to the OEM panel.

OMV

The OMV ReOil® candidate is produced from waste plastic pyrolysis oil (WPPO). The OEM committee has approved this fuel for entry to the Fast Track process after reviewing initial fuel property and composition data. Testing is complete on multiple fuel samples. The earlier recommendation to OMV of producing a WPPO feedstock specification faced large technical challenges within ASTM International, and it was decided, with OEM panel support, to abandon the creation of a standalone feedstock specification. OMV will redirect efforts toward using ASTM D7566 for all necessary definitions of feedstock, process, and product.

CleanJoule®

Tier 1 and Tier 2 data were generated for the CleanJoule® isoprene derived synthesized cycloparaffins (SCP) blending component. A research report was submitted for OEM panel review. Feedback and path forward conversations are anticipated in the first half of 2026.

® ExxonMobil is a registered trademark of Exxon Mobil Corporation, Spring, Texas.
® Honeywell is a registered trademark of Honeywell International, Inc., Charlotte, New Jersey.
® ReOil is a registered trademark of OMV Downstream GmbH, Vienna, Austria.
® CleanJoule is a registered trademark of CleanJoule, LLC, Salt Lake City, Utah.



UPM
Tier 1 and Tier 2 data were measured for the UPM candidate synthetic blended component (SBC) derived from crude tall oil (CTO). UPM has submitted additional process samples which have undergone preliminary analysis. UPM has been reporting updates to the OEM review panel and within ASTM International. A path forward is anticipated in 2026.

BioVeritas
BioVeritas submitted the first sample of an SPK, derived solely from ketones, for Tier 1 and Tier 2 testing. Additional samples are anticipated in 2026 that are produced from FOG + ketone streams.

Shell® IH²® Cycloparaffinic Kerosene
The qualification path forward for this product is on indefinite hold from the producer while they work to generate larger volumes of blending component. Tier 3 testing was requested by the OEM panel because of the high cycloparaffin content of the blending component (and uncertainties about how high cycloparaffin content might influence key operability properties).

Publications

Written Reports

Supporting Data for ASTM D7566 revision:

ASTM International. (2018). *Evaluation of LanzaTech-PNNL Ethanol Based Alcohol-to-Jet (LT-PNL ATJ) Synthetic Paraffinic Kerosenes (ATJ-SPKs)* [Research report, D02-1884].

ASTM International. (2019). R*enewable Jet Fuel Produced by Catalytic Hydrothermolysis (CH)* [Research report, D02-1914] (Addendum).

ASTM International. (2020). *Evaluation of Synthesized Paraffinic Kerosene from Algal Oil Extracted from Botryococcus braunii (IHI Bb-SPK)* [Fast Track Research Report, D02-1925].

ASTM International. (2022). *CHJ Pathway: ReadiJet™ Renewable Jet Fuel Produced by Catalytic Hydrothermolysis (CH*) [Research Report, D02-2039].

ASTM International. (2023). *Evaluation of Alcohol-To-Jet Synthetic Kerosene with Aromatics (ATJ-SKA) Fuels and Blends* [Research Report, D02-2056].

ASTM International. (2023). *Evaluation of Global Bioenergies' Isobutene Derived Synthetic Paraffinic Kerosene (IBN-SPK)* [Research Report, D02-2054].

Supporting Data for ASTM D1655 revision

ASTM International. (2020). *Modification of ASTM D1655: Co-Processing of Fischer-Tropsch Feedstocks with Petroleum Hydrocarbons for Jet Production using Hydrotreating & Hydrocracking WK69614* [Research Report, D02-1929].

Outreach Efforts

The ASCENT Project 031 activities were presented at the spring and fall ASCENT semi-annual meetings in 2024 and 2025. Routine meetings are scheduled with the OEM technical review panel—meeting frequency online is about every two weeks and in-person about three times per year—as well as direct meetings with producers (frequency is about every other week). Additionally, the project has been briefed at the following conferences and meetings:

- United Kingdom Ministry of Defence (MoD) Aviation Fuels Committee (AFC) Meeting, Bristol, United Kingdom, March 19-20, 2024
- CRC Aviation Committee Meeting, Alexandria, Virginia, April 29 – May 2, 2024
- United Kingdom MoD AFC Meeting, Manchester, United Kingdom, March 18-19, 2025
- ASTM International D02.0J Sub-committee meeting, Brussels, Belgium, April 9, 2025
- CRC Aviation Committee Meeting, Dayton, Ohio, April 28 – May 1, 2025

Awards

None.

Student Involvement

An undergraduate student, Taylor Nicely, assisted with the analysis of FC-M-102 (polars quantification).

® Shell is a registered trademark of Shell Trademark Management B.V., The Hague, The Netherlands.
® IH² is a registered trademark of Gas Technology Institute, Des Plaines, Illinois.

Plans for Next Period

- Continue discussions/education with new fuel producers
- Prepare for additional ASTM D4054 Clearinghouse candidate submissions for evaluation

Tasks 3 and 4 - Manage the Evaluation and Testing of Candidate Alternative Fuels

University of Dayton Research Institute

Objective

The objective of this work is to manage the evaluation and testing of candidate alternative jet fuels (i.e., SATF, SBC, and SAF) in accordance with ASTM D4054 (see Figure 1).

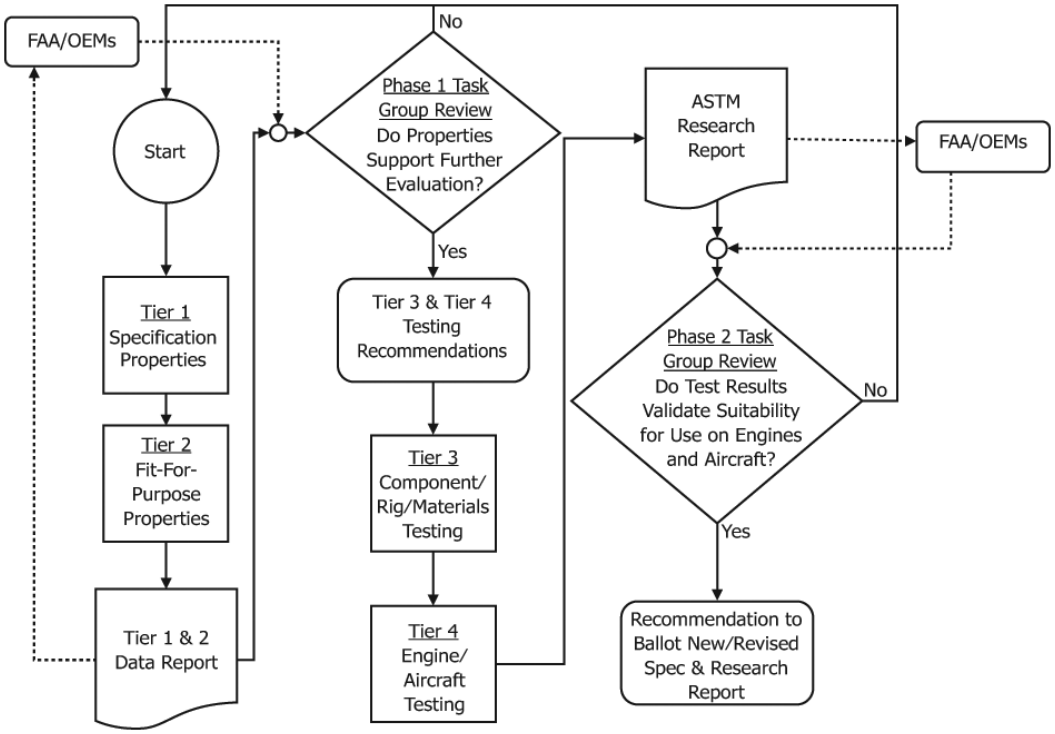


Figure 1. Overview approval process of new aviation fuels from ASTM D4054.

Research Approach

UDRI will subcontract with other research organizations, testing laboratories, and/or OEMs to conduct the following tasks in support of the evaluation and ASTM specification development for alternative jet fuels. The purpose of this project is to manage and coordinate the ASTM D4054 evaluation process to facilitate the transition of alternative fuels to commercial use.

Subtask 1: General Support

- Develop and make available an ASTM D4054 process guide describing logistical procedures for the handling of test fuels, documentation requirements, test report issuance and delivery, and contact information, to provide clear instructions for candidate-fuel producers entering the ASTM D4054 process.

Subtask 2: Phase 1 Support

- Coordinate the handling of Phase 1 candidate test fuel samples for Tier 1 and Tier 2 testing.



- Review process descriptions provided by the fuel producer to determine the acceptability for incorporation into the Phase 1 research report.
- Review test data from Tier 1 and Tier 2 testing to determine acceptability for incorporation into the Phase 1 research report.
- Issue and deliver a Phase 1 research report to OEMs.
- Review and respond to comments regarding the Phase 1 research report, as submitted by the OEMs, in conjunction with the fuel producer.
- Conduct additional Tier 1 or Tier 2 testing in response to OEM comments, as required.
- Review and consolidate OEM requirements for ASTM D4054 Tier 3 and Tier 4 testing, as submitted by the OEMs.
- Deliver consolidated ASTM D4054 Tier 3 and Tier 4 testing requirements to the fuel producer.

Subtask 3: Phase 2 Support

- Coordinate the funding and scheduling of ASTM D4054 Tier 3 and Tier 4 testing with OEMs and other test facilities.
- Coordinate the handling of Phase 2 candidate test fuel samples for Tier 3 and Tier 4 testing.
- Review test data from Tier 3 and 4 testing to determine acceptability for incorporation into the Phase 2 research report.
- Issue and deliver the Phase 2 research report to OEMs.
- Review and respond to comments submitted by OEMs regarding the Phase 2 research report in conjunction with the fuel producer.
- Conduct additional Tier 3 or Tier 4 testing in response to OEM comments, as required.
- Issue and deliver Phase 2 research report addenda reporting the additional Tier 3 or Tier 4 test results, as required.

Subtask 4: OEM Review Meetings

- Schedule periodic OEM meetings to review the testing status and research report evaluations.
- Identify suitable meeting venues and support equipment.
- Develop agendas and coordinate with attendees for participation in these meetings.
- Record meeting minutes, including agreements, commitments, and other action items.
- Issue and distribute meeting minutes to all attendees.

Subtask 5: Single-laboratory Two-dimensional Gas Chromatography Method Documentation

- Document UDRI two-dimensional gas chromatography (GCxGC) methods for hydrocarbon type analysis.
- Develop reference materials for the creation of GCxGC hydrocarbon type templates.
- Measure single-laboratory precision of GCxGC methods.

Subtask 6: Multi-laboratory GCxGC Method Documentation

- Validate the precision of GCxGC methods across multiple laboratories.
- Identify alternative GCxGC methods, including column selection and order and modulation techniques.
- Perform a correlation study to determine the agreement among laboratories, methods, and hardware choices.

Milestones

The schedule for this project is dependent on the receipt of alternative fuel candidates for testing. As candidate fuels are received, a testing schedule will be established via coordination with the FAA and collaborators. Our existing relationships with these organizations will help expedite this process.

Major Accomplishments

Detailed Hydrocarbon Type Analysis (via GCxGC)

The ASCENT Project 031 team has further advanced the accessibility and reporting of detailed hydrocarbon type analysis methods using GCxGC technology. In collaboration with the U.S. Navy and U.S. Air Force partners, a Federal Standard Method (FED-STD-791F, Method 7508) was recently published and successfully balloted for inclusion in ASTM D4054. The method is accessible for download from the website https://quicksearch.dla.mil/qssearch.aspx by searching for "FED-STD-791" under the Document ID category.



Inductively Coupled Plasma Mass Spectrometry
Observations of inconsistent results for dissolved metal/elemental concentrations in fuel evaluated in the ASTM D4054 Clearinghouse have prompted an evaluation of these analyses. In particular, the phosphorus results have presented an issue in ongoing evaluations. UDRI acquired an inductively coupled plasma mass spectrometry (ICP-MS) system and has developed new methods for measuring phosphorous (P) and silicon (Si) via standard addition, as these atoms have interferences that preclude the use of an external calibration curve. In addition to method advancements with P and Si, our team has strived to improve the robustness (i.e., accuracy, precision, and ease of use) of the overall method. The ASCENT Project 031 team have briefed our findings at the Coordinating Research Council Aviation Meeting in Alexandria, Virginia (April 29-May 2, 2024), American Chemical Society (ACS) Fall 2023 national meeting in Denver, Colorado (August 17-21, 2024), and the International Association of Stability, Handling and Use of Liquid Fuels (IASH) 2024 conference in Louisville, Kentucky (September 8-12, 2024). A UDRI test method, FCM-107, has been issued based on this research (UDRI, 2023).

Civil Aviation Administration of China
The Chinese government had approached the FAA/OEM committee with a request to evaluate two jet fuel additives for approval for use. These additives include a static dissipator additive and a corrosion inhibitor/lubricity improver additive. These additives have been received, and testing data were reported to the Chinese delegation. Some technical gaps were mentioned and follow up testing is being finalized at the EU SAF clearing house sponsored by the European Union Aviation Safety Agency (EASA).

OEM Committee Coordination
Ongoing efforts in ASTM OEM committee coordination continued during this period. These efforts involve coordinating in-person engine and airframer OEM meetings, which have typically occurred in concert with the biannual ASTM Committee D02.0J sessions and at the annual United Kingdom MoD AFC meeting. During travel restrictions due to the COVID-19 pandemic, these meetings occurred virtually and more frequently, once or twice per month. SwRI continues to receive funding to aid in coordinating the OEM meetings and in communicating with the OEMs for discussions and research report reviews of new candidate alternative jet fuels.

The ASCENT Project 031 team will continue to look for additional ways to optimize and improve the ASTM D4054 process to streamline approval of alternative jet fuels, while maintaining safe operations. Some areas of future improvement our team has identified include the standardization of laboratory testing results (for bespoke Tier 2 testing), creation of a phase I research report template, development of standardized research report feedback, creation and adoption of an OEM review panel terms of reference, and development of an online OEM technical review panel management tool.

Support for Other Related FAA Projects
Due to UDRI's fuel testing capabilities, the ASCENT Project 031 team has supported jet fuel testing for other related FAA projects including fuel samples received from Gulfstream® and Pratt & Whitney.® Similar to our support for the Boeing® EcoDemonstrator program (ca. 2023), our team provided sample analysis to monitor fuel composition and properties during fuel movements in testing campaigns involving synthetic jet fuels or SBCs. Fuel samples have included two HEFA-SPKs, two Jet A fuels, and blends of HEFA-SPK + Jet A (for a total of 13 fuel samples). Measurements have included, but were not limited to, mono-aromatics, di-aromatics, total aromatics, smoke point, naphthalenes, hydrogen content, gross heat of combustion, net heat of combustion, total sulfur, total nitrogen, flashpoint, density, viscosity, and vapor pressure.

Publications

Written Reports

Testing Method of Lubricants, Liquid Fuels, and Related Products: 7508.0—Method for Detailed Hydrocarbon Analysis of Middle Distillate Fuels by Two-Dimensional Gas Chromatography, Fed.-Std.-791F (2024). https://assist.dla.mil

UDRI. (2018). *Flow modulation GCxGC for Hydrocarbon Type Analysis of Conventional and Alternative Aviation Fuels: UDRI Method FC-M-101.* University of Dayton Research Institute (UDRI), Dayton, Ohio, Report No. UDR-TR-2018-40.

UDRI. (2018). *Identification and Quantification of Polar Species in Conventional and Alternative Aviation Fuel Using SPE-GCxGC: UDRI Method FC-M-102.* University of Dayton Research Institute (UDRI), Dayton, Ohio, Report No. UDR-TR-2018-41.

® Gulfstream is a registered trademark of Gulfstream Aerospace Corporation, Savannah, Georgia
® Pratt & Whitney is a registered trademark of RTX Corporation, Farmington, Connecticut.
® Boeing is a registered trademark of The Boeing Company, Seattle, Washington.

UDRI. (2021). *Reverse Phase Thermal Modulation GCxGC for Hydrocarbon Type Analysis of Conventional and Alternative Aviation Fuels: UDRI Method FC-M-106*. University of Dayton Research Institute (UDRI), Dayton, Ohio,
UDRI. (2023). *UDRI Method FC-M-107: Trace Elemental Determination in Jet Fuel via ICP-MS*. Dayton Research Institute (UDRI), Dayton, Ohio, Report No. UDR-TR-2023-117.

Recent Posters & Presentations

Arts, A. M., Landsaw, A., West, Z. J. (2024, August 20). *Determination of Trace Metals in Aviation Turbine Fuel via ICP-MS* [Poster presentation]. American Chemical Society Fall 2024, Denver, Colorado.
Arts, A. M., Landsaw, A., West, Z. J. (2024, September 8-12). *Determination of Trace Metals in Aviation Turbine Fuel via ICP-MS* [Poster presentation]. 18th International Conference on Stability, Handling and Use of Liquid Fuels, Louisville, Kentucky.
West, Z., Zabarnick, S. (2024, March 19-20). *FAA ASCENT Center of Excellence D4054 Clearinghouse Update* [Conference presentation]. UK MoD Aviation Fuels Committee Meeting, Bristol, United Kingdom.
West, Z. (2024, April 29-May 2). *D4054 Clearinghouse* [Meeting presentation]. 2024 CRC Aviation Committee Meeting, Alexandria, Virginia.

Outreach Efforts

Presentations on ASCENT Project 031 activities were given at the spring and fall ASCENT meetings. Meetings were held with the OEM team, FAA, fuel producers, and other attendees at numerous virtual FAA/OEM meetings (generally two meetings per month). Our team met with multiple candidate-fuel producers including:

- Bioleum®
- BioVeritas
- British Petroleum
- Captis Aire
- Chevron®
- CleanJoule
- CSIR-IIP
- ExxonMobil
- Honeywell UOP
- Marathon Petroleum Corp.
- OMV
- Phillips 66®
- Revo
- Sulzer®
- Universal Fuel Technologies
- UPM
- Vertimass
- Visolis

Awards

None.

Student Involvement

An undergraduate student, Taylor Nicely, assisted with the analysis of FC-M-102 (polars quantification). An undergraduate student, CJ Nesbit, assisted with ASTM D2887 (ASTM, 2023a; SimDis) analysis.

Plans for Next Period

- Continue coordination of the OEM committee reviews.
- Hold both in-person and virtual OEM committee meetings.

® Bioleum is a registered trademark of Comstock IP Holdings, LLC, Milton, Georgia.
® Chevron is a registered trademark of Chevron Intellectual Property, LLC, Houston, Texas.
® Phillips 66 is a registered trademark of Phillips 66 Company, Houston, Texas.
® Sulzer is a registered trademark of Sulzer Ltd., Houston, Texas.



References

ASTM International. (2023a). *ASTM D2887-22e1: Standard Test Method for Boiling Range Distribution of Petroleum Fractions by Gas Chromatography*. https://doi.org/10.1520/D2887-22E01

ASTM International. (2023b). *ASTM D4054-22: Standard Practice for Evaluation of New Aviation Turbine Fuels and Fuel Additives*. https://doi.org/10.1520/D4054-22

ASTM International. (2023c). *ASTM D7566-22: Standard Specification for Aviation Turbine Fuel Containing Synthesized Hydrocarbons*. https://doi.org/10.1520/D7566-22

Testing Method of Lubricants, Liquid Fuels, and Related Products: 7508.0—Method for Detailed Hydrocarbon Analysis of Middle Distillate Fuels by Two-Dimensional Gas Chromatography, Fed.-Std.-791F (2024). https://assist.dla.mil

UDRI. (2023). *UDRI Method FC-M-107: Trace Elemental Determination in Jet Fuel via ICP-MS.* Dayton Research Institute (UDRI), Dayton, Ohio, Report No. UDR-TR-2023-117.



Project 033 Alternative Fuels Test Database Library

University of Illinois at Urbana-Champaign

Project Lead Investigator

Tonghun Lee
Professor
Mechanical Science and Engineering
University of Illinois at Urbana-Champaign (UIUC)
1206 W. Green St.
Urbana, IL 61801
517-290-8005
tonghun@illinois.edu

University Participants

University of Illinois at Urbana-Champaign

- P.I.: Tonghun Lee, Professor
- FAA Award Number: 13-C-AJFE-UI-038
- Period of Performance: October 1, 2024, to September 30, 2025
- Tasks:
  1. Online database development
  2. Chemical kinetic mechanism development

Project Funding Level

Federal Aviation Administration (FAA) funding level: $150,000
Cost-sharing: Software license support from Reaction Design (ANSYS)

Investigation Team

Tonghun Lee (P.I.), All Tasks
Emily Grinage (Graduate Student), All Tasks

Project Overview

This study continues development of a data library (Alternative Jet Fuels Test Database [AJFTD]). The functions of this database are (1) to serve as a comprehensive repository of conventional and sustainable aviation fuel (SAF) test data for the commercial aviation sector and (2) to provide fuel analysis techniques applicable to the rapid assessment and prescreening of novel SAFs. Currently, the repository comprises over 24,000 fuel samples and their respective test data, available for download to approved users of the project website. Figure 1 shows the main database web portal, currently housed at the University of Illinois at Urbana-Champaign (https://altjetfuels.illinois.edu). Database data include results from national laboratories, research efforts, airports, and other sources. In 2020, all compiled database data were converted to a new nonstructured query language (NoSQL) format by using a JavaScript® object notation (JSON) schema. This nonrelational structure allows the data to be analyzed using a variety of computational codes.

The catalog of data currently available in the database is primarily assembled from four separate sources. Fuels with POSF (Air Force Research Laboratory fuel database code) number designations were added from the internal database maintained by the Air Force Research Laboratory at Wright Patterson Air Force Base. The second dataset was obtained from Petroleum Quality Information System reports of the Naval Air Systems Command and corresponds to a compilation of fuel data primarily geared for government use. The third set was provided by Metron Aviation, consisting of fuel properties from samples collected at airports through a previous ASCENT project. The dataset resulting from this study has proven

® JavaScript is a registered trademark of Oracle America, Inc., Redwood Shores, California.

valuable by showing the landscape of fuels currently used in commercial aviation and will guide our future efforts focused on capturing this type of data in real time. The final dataset was obtained from the National Jet Fuel Combustion Program within ASCENT.

Though the database already contains a uniquely large collection of publicly available jet fuel data, data collection efforts are ongoing. Data collection is continuing to be pursued both domestically, focusing on airport and United States (U.S.) refinery data, and internationally, focusing on European sustainable aviation programs. The database documents SAF development and usage trends globally to increase understanding of global fuel infrastructure and variability. Multiple tools for fuel analysis have been implemented on the project website over the years to aid researchers in understanding SAFs. Machine learning techniques for fuel property analysis have been developed. More recently, a graphical interface for assessing fuel two-dimensional gas chromatography (GCxGC) composition information was added to the website. Analysis efforts now encompass the determination of suitable surrogate fuels to model novel SAFs and the rapid development of chemical kinetic models to predict behavior of SAFs in combustion regimes.

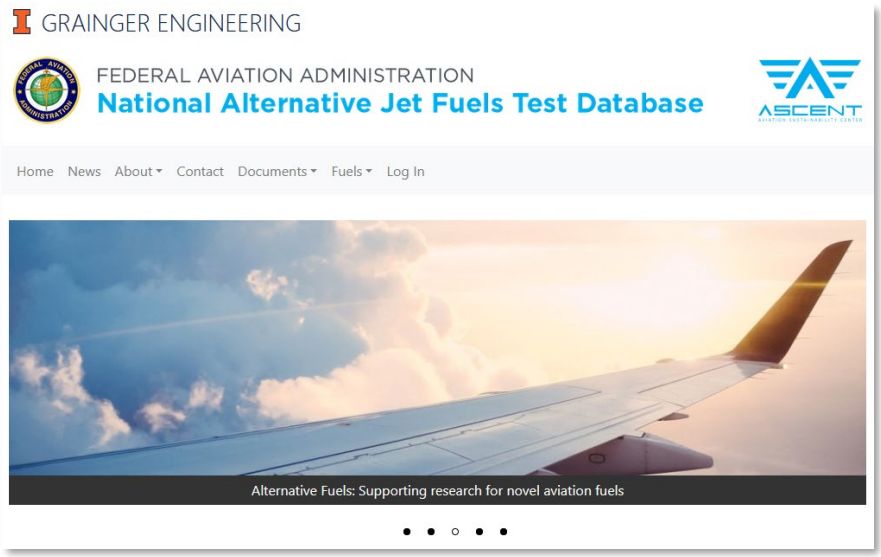


Figure 1. Alternative Jet Fuels Test Database (AJFTD) main webpage (altjetfuels.illinois.edu).

The current goals for the website include:

- Developing a common data schema and storage protocols with the World Fuel Survey.
- Strengthening connections with domestic airports for ongoing real-time data sharing.
- Initiating data sharing with international programs such as ALIGHT and NewJET.
- Developing and refining a methodology for chemical kinetics development based on website data.

Task 1 focuses on data collection and website development efforts, while Task 2 elaborates on the development of an analysis tool for inclusion on the database website.

Task 1 – Online Database Development

University of Illinois at Urbana-Champaign

Objectives

The main objective of this task was to expand and improve the database and its website. Currently, AJFTD is the second generation of the project website, with new capabilities and improvements consistently being added. Bugs are fixed as they are discovered, and improvements to the user interface and ease of data access are constant considerations. Data



acquisition efforts continue to obtain new data for inclusion on the database. The main Task 1 objectives are summarized as follows:

- Upgrade user interface to aid in the access of fuel data.
- Debug interface where needed.
- Establish fuel data sharing with target domestic airports.
- Establish fuel data sharing with U.S. refineries and other fuel sources.
- Forge connections with European programs such as ALIGHT and NewJET.

Research Approach

Website Upkeep

An integral part of website upkeep is building administrative tools to refine the user experience over time. To that end, new administrative capabilities were introduced this year to monitor user activity. These new features track site traffic, search behavior, and filter usage, providing invaluable metrics for maintaining reliability and relevancy site wide.

- **Fuel Search and Download Logs.** Administrators can now monitor which fuels are searched and downloaded. This information gives detailed context of what information is relevant to users and can help steer further database improvements.
- **Unique User Activity.** Administrators can track the number of unique users logged in to the database on a daily or weekly basis. This information is a useful metric to confirm the relevancy of the database.

Figure 2 shows a summary of the weekly activity for the National Alternative Jet Fuels Test Database.

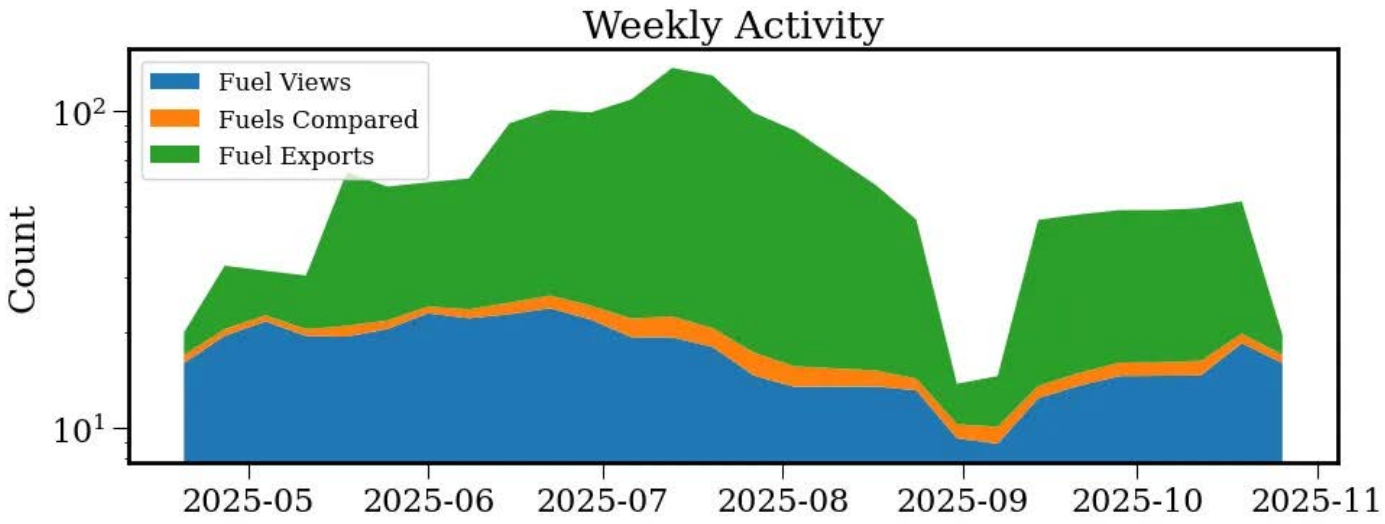


Figure 2. Database Activity Summary.

New administrator functions will continue to be developed, allowing administrators more power to customize website features for the benefit of users.

Website Upgrades

An effective user interface is essential to streamline access to relevant fuel data and support impactful research. Improvements are consistently considered and implemented. Last year, a large effort went into improving the fuels search page. The page now loads quickly, displaying only 10 fuels per page by default. Streamlined search filters appear on the left, featuring dropdown, multi-select, and intuitive buttons to control search updates (see Figure 3). Users can view individual or multiple fuels at a time with the 'Compare Selected' option. While the redesign significantly improved usability, inconsistent formatting in legacy data left some fuels improperly tagged for relevant searches. This year, tags were standardized across all fuel entries to ensure alignment with the search filters.

In the database's second generation, fuel entries were migrated from standard Certificates of Analysis (CoA) tables to structured JSON format to ensure compatibility with JETSCREEN. Storing each entry as structured JSON rather than tabular records improves interoperability and enables more efficient processing, including the search filtering schema. Most search filters mapped cleanly to existing JSON fields, however not all JSONs had an explicit entry for fuel class. The fuel classes in this filter include Alternative, Blend, Conventional, Engineered, and Sustainable Aviation Fuel. For some data sources like airport data, the fuel class "Conventional" is implied, but was not explicitly stated or tagged as such in the respective JSON files. Therefore, if a user were to search under this filter, the search results would not include all relevant fuels. To resolve this, the dataset was audited and backfilled, so all fuel entries are explicitly tagged, and a required "fuel_class" field with a controlled vocabulary is now enforced for all imports.

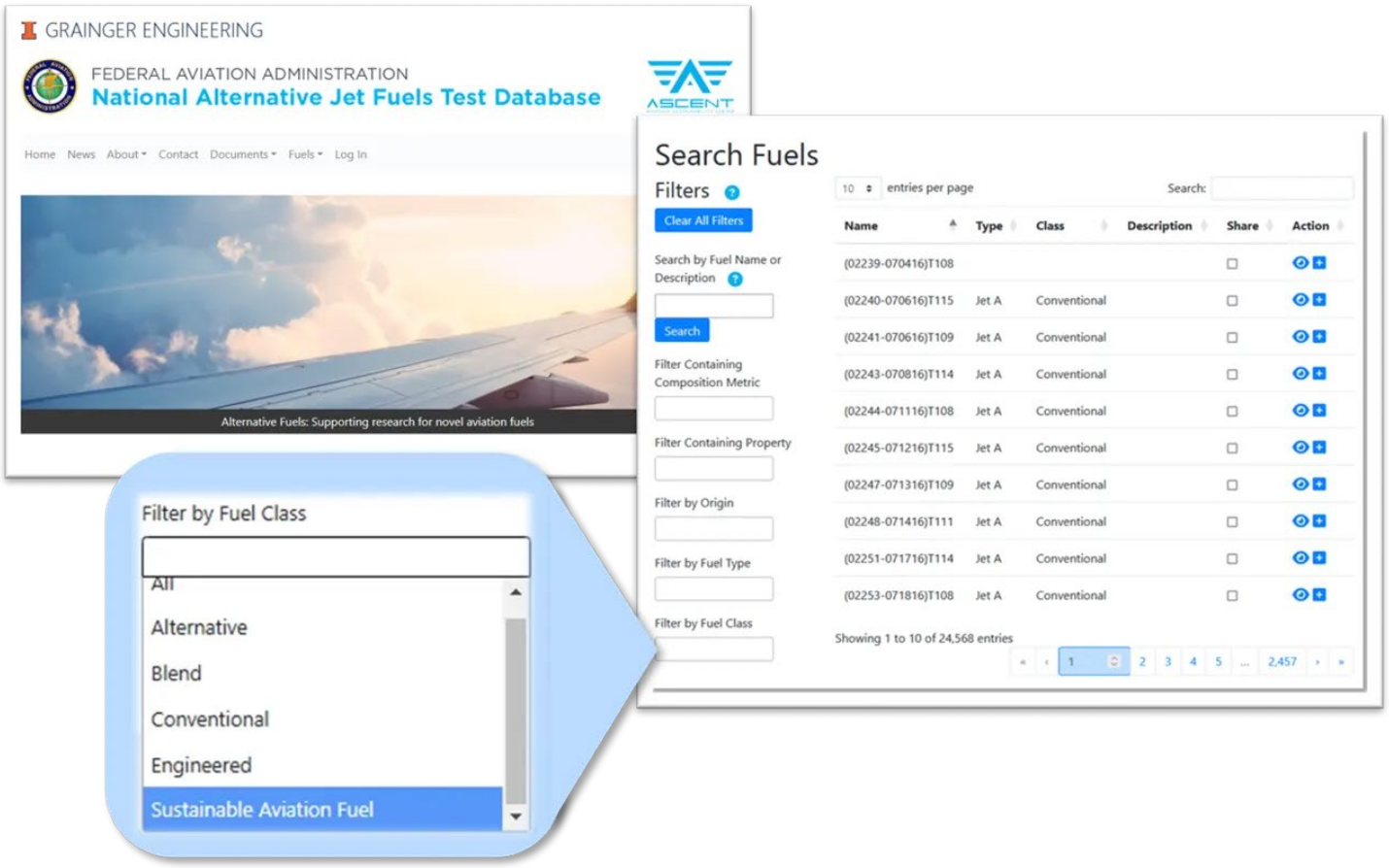


Figure 3. Fuel Class Filter on Search Page.

Airport Data Collection

AJFTD actively sources new data to capture trends in jet-fuel usage over time and region. In the past, 11 different domestic airports have provided fuel data to the database through a connection with Metron Aviation. These airports are indicated by black squares and their airport code in Figure 4. In the years since, our team has sought to establish robust connections with a few key airports in the U.S. to set up a foundation for real-time data sharing. The targeted airports are the Chicago O'Hare International Airport (ORD), Seattle-Tacoma International Airport (SEA), San Francisco International Airport (SFO), Daniel K. Inouye International Airport (HNL), and airports in the New York city region, which are governed by a common port authority. In the prior year, datasets from SFO (2021–2023) and SEA (2023) were received. These datasets are going through the standard pipeline of format conversion and vetting for integration onto the database. Communication has been sent to HNL and the New York Port Authority, and some progress has been made in obtaining data. These efforts are ongoing and will continue in the next year.

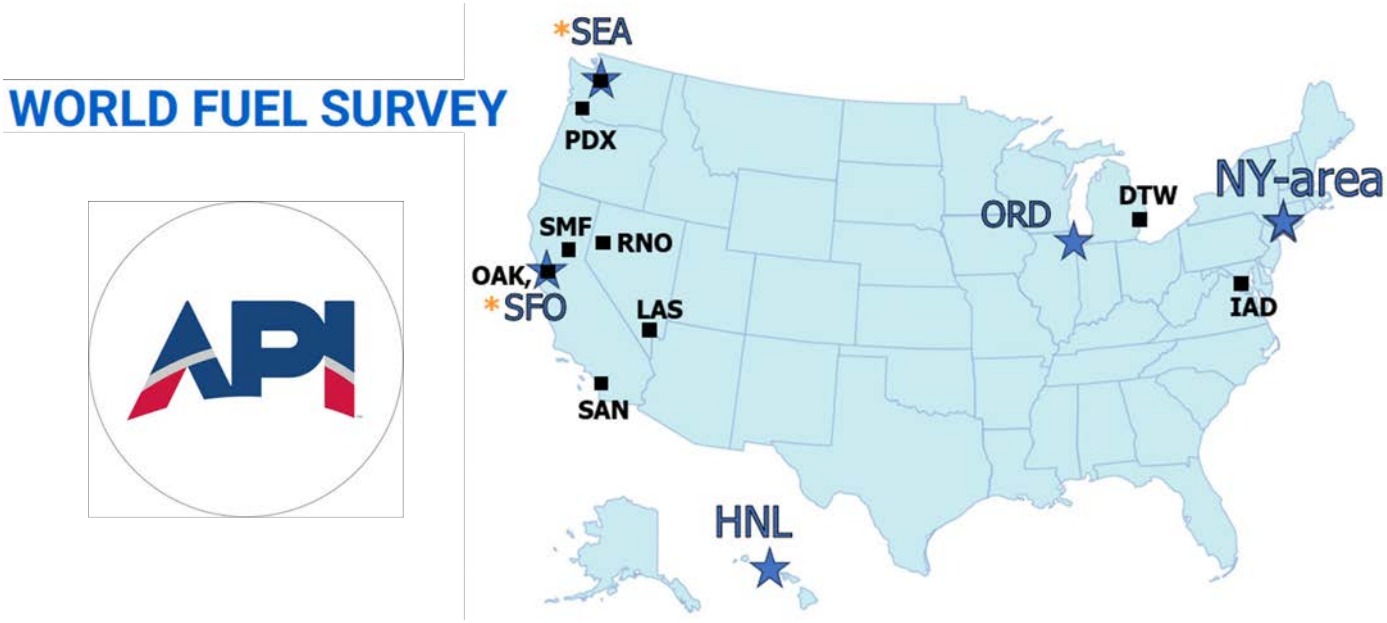


Figure 4. Data Collection Targets for Project Year.

World Fuel Survey
This project year involved connection and collaboration with ASCENT Project 090: World Fuel Survey. Meetings with the Volpe National Transportation Systems Center and University of Dayton Research Institute were held to establish a common data storage method and to begin aligning data formats across projects. The World Fuel Survey data informs international jet fuel production and property trends. While it will be published as a standalone set, it will also be integrated into the database once it is approved for public release. Its addition will expand the scope and diversity of fuels represented. One day, these projects may be integrated into one common database under the FAA, and coordinating data structure among the projects will help streamline that process and reduce the need for extensive reformatting in the future.

API 2022 Jet Fuel Survey
Early this year, connections were established with the Fuel Technologies Team Lead conducting a survey of 2022 CoA/Refinery Certificates of Quality from various American Petroleum Institute (API) refineries nationwide. Phase I of the survey was completed in April 2025 and resulted in the collection of over 25,000 CoAs. The volume of these data has significant impact, nearly doubling the database's existing fuel entries and broadening the range of fuels represented. This survey is ongoing, as API continues to collect data from 2023 onward. The magnitude of this data volume has also highlighted potential improvements to the importer framework of AJFTD to make future data integration as seamless and efficient as possible.

Research Program Data Collection
In addition to U.S. sources, connection with European programs provides valuable breadth to the database. The AJFTD's past connection with JETSCREEN in Europe established a foundation for data sharing with international programs and showed the value of cross-regional collaboration. European programs (ALIGHT and NewJET are our current targets for data collection overseas, as they focus on SAF deployment and aviation emissions). Last year marked the first time a representative from the AJFTD attended the ECATS conference in Europe to share information about the database, present its capabilities to a broader audience, and initiate connections with representatives of ALIGHT and NewJET. This outreach increased international visibility of the database and opened new opportunities for collaboration. Strengthening these connections and converting initial discussions into active data-sharing efforts is an ongoing priority of the project.



Milestones

3 months

- Followed up with representatives at HNL.
- Connected with API Jet Fuel Survey Taskforce.
- Established data storage options with World Fuel Survey.

6 months

- Added new administrator functionality to the AJFTD.
- Standardized fuel tagging across all data entries.
- Presented updates at the Spring SAF ASCENT meeting.
- Received final dataset from API 2022 Jet Fuel Survey.

9 months

- Identified new target airports for data collection.
- Began CoA to JSON conversion for new datasets.

12 months

- Presented updates at the Fall 2025 ASCENT meeting.

Major Accomplishments

Connections with API, the World Fuel Survey, HNL, and the New York Port Authority have been secured and are expected to lead to increased data collection in the coming years. In addition, new administrative tools and data formatting improvements will lead to improved usability of the database. Standardized data formatting and integration lays the groundwork for the implementation of more complex analysis techniques in the future, which will help shape the future of SAF in commercial aviation.

Publications

None.

Outreach Efforts

In both the Spring and Fall of 2025, project updates were shared at the ASCENT semiannual conferences. These presentations led to productive discussions regarding fuel data acquisition, database usage, and avenues for further outreach.

The database has been made accessible at https://altjetfuels.illinois.edu.

Awards

None.

Student Involvement

This project was primarily conducted by a graduate student, Emily Grinage.

Plans for Next Period

In the next period, the focus on data collection from target airports will be emphasized. Obtaining further data samples from HNL will be prioritized. In addition, the team will continue pursuing connection with the New York Port Authority to share our data collection vision. Meetings with ALIGHT and NewJET leaders are anticipated as well.

The improvement of the database website will continue with efforts such as:

- **Search interface refinement.** The new fuels search page will continue to be tested to assure the feature is free of bugs. Minor improvements will continue to be made.
- **Improved analysis tools.** A tool to rapidly generate kinetic mechanisms for further jet fuel performance analysis is underway. Implementation of this analysis feature will begin in the next term.

Task 2 – Chemical Kinetic Mechanism Development

University of Illinois at Urbana-Champaign

Objectives

The objective of this task is to evaluate approaches for rapidly generating chemical kinetic mechanisms for aviation fuels, for eventual integration into AJFTD. Such mechanisms are essential for combustion simulations (e.g., computational fluid dynamics) which significantly decrease time and cost to certify new fuels. As SAFs become more prevalent, timely mechanism development becomes critical. However, building and reducing detailed mechanisms can demand significant computational time and resources, especially for emerging fuels with uncertain properties. Accelerated, reliable methods for constraining and generating mechanisms are essential for broader SAF adoption. This effort examines these methods and opportunities for improvements. The major goals of this task are:

- Outline and implement a robust methodology for the rapid development of mechanisms for any novel SAF with limited experimental data.
- Demonstrate selected approach in mechanism generation for CycloSAF.
- Quantify uncertainties and effectiveness of the constraining approach.

Research Approach

Methodology

New SAFs are initially produced in very small fuel volumes. Fuel producers are reluctant to scale fuel production to commercial quantities until the SAF has been approved and certified for use on an existing aircraft. Prescreening with combustion models is therefore critical for estimating FAA compliance and informing investment decisions. Given the limited volumes of fuel available, such models must be accurate while relying on as little experimental data as possible. Commonly used experimental data include GCxGC and ignition delay time measurements. GC×GC can extract detailed compositional information from small samples, which provides the basis for the mechanism-development approach presented here.

The methodology for mechanism determination outlined for 2025 is summarized in Figure 5. This approach is an expanded version of a general methodology outlined in the year prior. GCxGC data gives details about a fuel's composition, which informs the creation of an appropriate surrogate fuel to model a SAF of interest. Surrogate determination for SAFs with novel compositions can be particularly difficult, especially if there is limited literature on the specific hydrocarbons that make up the fuel. To make use of the abundance of kinetics research in a way that is applicable to hydrocarbon behavior that has not been carefully studied, a generalized approach using a fuel's functional groups was developed.

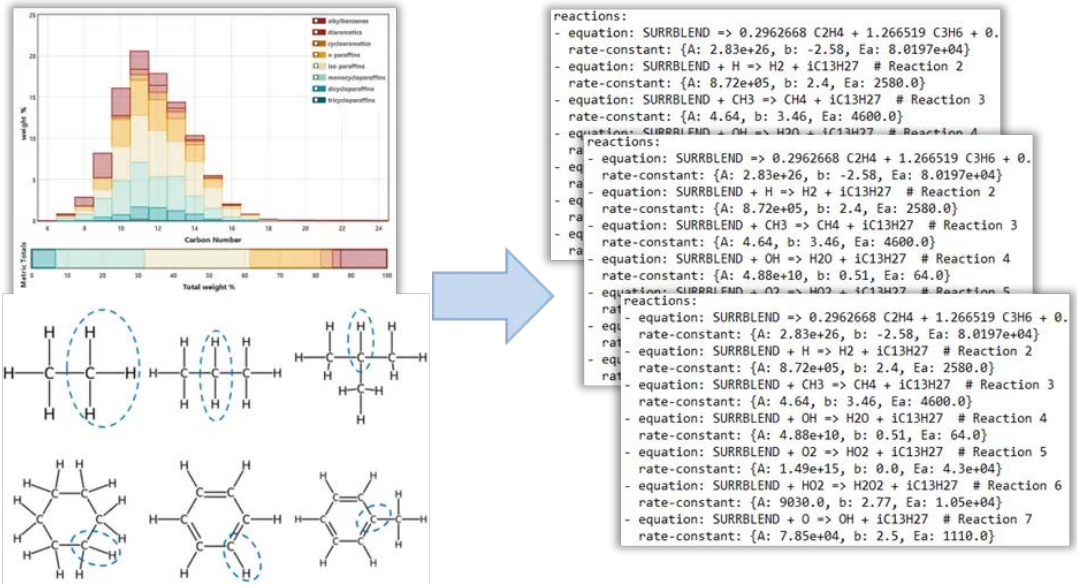


Figure 5. General kinetics approach: transforming Fuel GCxGC data into a mechanism using Chemical Functional Groups.

Figure 6 provides a more detailed overview of the generalized approach for mechanism determination for any SAF. If the fuel's composition is known, a surrogate can be formulated to closely match the properties of the actual fuel. Once a surrogate is created, established kinetic mechanisms are used to simulate the breakdown of the surrogate in various combustion environments, such as shock tubes or plug flow reactors. The results from these simulations inform the stoichiometric coefficients for a set of reactions that govern the initial breakdown of the chosen SAF and its primary decomposition pathways. This set of reactions forms the Hybrid Chemistry (HyChem) mechanism structure. Once the stoichiometric coefficients and rates of these breakdown reactions are determined, the new model is constrained towards experimental data to determine which experiments are most critical in rapidly developing mechanisms for new SAFs.

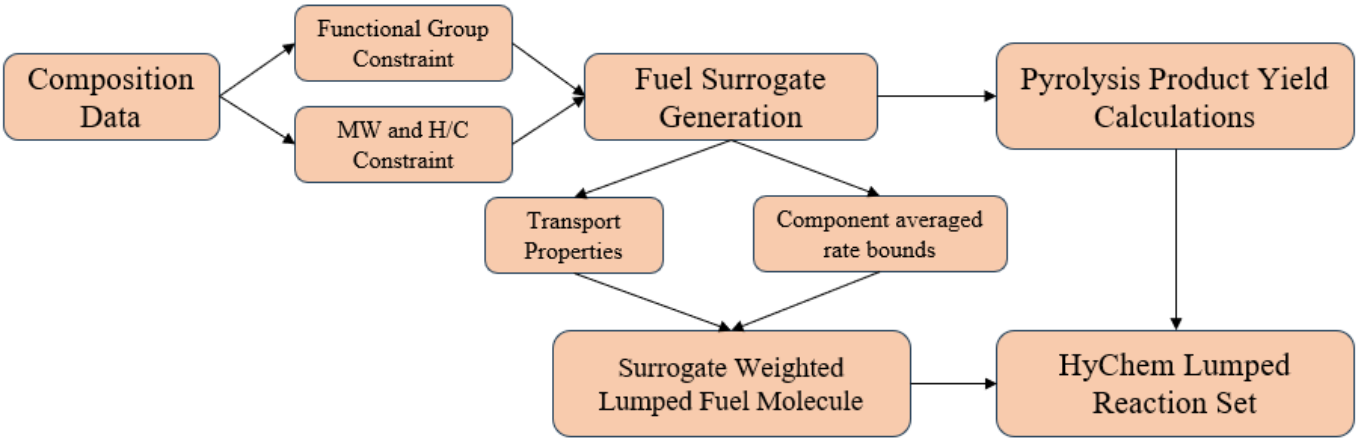


Figure 6. General methodology to generate kinetic mechanism for any fuel

Preliminary Implementation

The feasibility of this method was tested last year by creating a mechanism for an alcohol-to-jet (ATJ) fuel manufactured by



Gevo® (POSF 11498). ATJ was chosen due to the availability of experimental data for this fuel in the literature. The current approach has been modified to broaden its applications to fuels with limited data available, as this is the case for most new SAFs being prescreened for certification. This improved approach will be demonstrated by creating a mechanism for CycloSAF, a fuel manufactured by CleanJoule.™ CycloSAF is unique in that it is made up almost entirely of 10-carbon cyclo-alkanes. The certification of such a fuel would have significant impact on SAF requirements. ASTM 7566 (ASTM, 2023) currently requires SAF's to include 8% aromatics to ensure proper volume swell characteristics needed for O-ring compatibility in the jet engine. Cyclo-alkanes exhibit volume swell properties similar to aromatics while producing substantially less soot. Like many SAFs early in the certification pipeline, there is very limited experimental data and literature available on CycloSAF's behavior. This presents a unique challenge in the previously developed surrogate fuel modeling approach.

To perform simulations on a surrogate fuel, the surrogate must be comprised of species that are already modeled in an existing kinetic mechanism. Many existing detailed mechanisms have been designed for jet fuels made primarily of normal-alkanes and iso-alkanes. Some cyclo-alkanes are represented, but there are no existing mechanisms with large cyclic species like those in CycloSAF. Instead of modeling the surrogate fuel with C10 cyclo-alkanes, it can be modeled to match the functional groups that would be found in the fuel. Functional groups of hydrocarbon species can be determined from nuclear magnetic resonance (NMR) or estimated from GCxGC data. This surrogate modeling approach has been used in several research efforts, namely the creation of FGMech, a mechanism generation method used and validated for 14 surrogate fuel mixtures and 12 real fuels (Zhang & Sarathy, 2020). Functional group matching has been shown to reasonably capture ignition and combustion characteristics. As a result, functional-group-based surrogates can be used as an additional constraint when generating surrogates for novel compositions.

CycloSAF is primarily made up of three cyclo-alkane species that are not in any existing chemical kinetic mechanisms. Both Dimethylcyclo-octane (DMCO) species have an 8-carbon ring and two methyl groups. Para-menthane is a 6-carbon ring with 3 methyl groups and an additional carbon branch. Details on these species structures and functional groups present can be seen in Figure 7. The weight percents of respective functional groups were used as a constraint in generating a surrogate fuel, in addition to matching molecular weight and hydrogen-to-carbon ratio. Functional groups contain key information about how a fuel molecule will break down. Constraining the surrogate to the fuel's functional groups preserves site-specific bond breaking behavior, and conserves hydrogen/carbon (H/C) ratio. Matching molecular weight ensures that transport properties like density, viscosity, and diffusion are modeled properly. While matching the functional groups of a fuel in a surrogate model is a good approximation for the local bond behavior, it does not consider global molecular effects like ring strain. Because of this uncertainty, a distribution of 1,000 fuel surrogates was created to further understand how these effects would propagate through the mechanism generation pipeline. This uncertainty analysis is still in process, but the remaining steps in this methodology use the surrogate fuel composition that most closely matches experimental data for ignition delay time.

® Gevo is a registered trademark of Gevo, Inc., Englewood, Colorado.
™ CleanJoule is a trademark of CleanJoule, Inc., West Valley City, Utah.

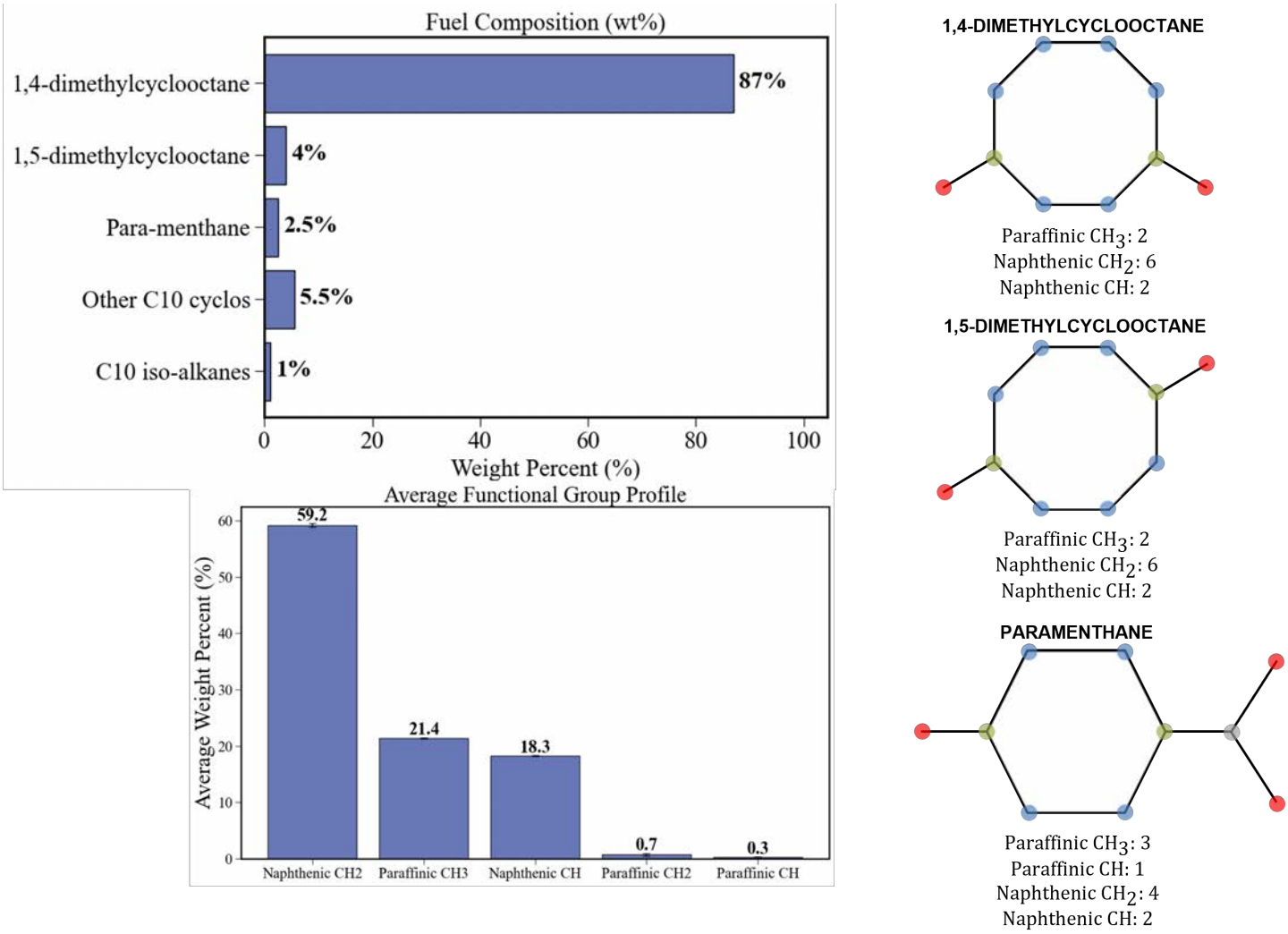


Figure 7. CycloSAF composition and species functional groups.

Once a surrogate fuel model has been constructed, the fuel can be used in various simulated combustion events to further develop our kinetic mechanism. A HyChem structure was adopted for the mechanism determination approach. In this structure, the fuel is treated as one "lumped" fuel molecule with properties representative of the fuel of interest. A set of approximately 20 reactions describe the breakdown of this "lumped" fuel molecule into smaller hydrocarbon products, or pyrolysis products. From here, a large, descriptive model applicable to any jet fuel handles reactions of these smaller hydrocarbons. For HyChem, this large model is the USC-II[1] mechanism.

The creators of HyChem postulated that most jet fuels have the same key pyrolysis products. Complex jet fuels will break down into many different hydrocarbons, but of these, only about eight smaller hydrocarbon species will be strongly present and will govern the behavior of the post-pyrolysis species mixture. Then, for any new SAF of interest, a researcher need only determine which of these key products are produced from the pyrolysis of the SAF, and what the ratios of the products are to one another. The creators of HyChem determined these pyrolysis products by conducting extensive plug flow reactor and shock tube experiments and directly measuring or calculating product concentrations (Wang et. al.,

[1] The USC II mechanism was developed at the University of Southern California by Professor Hai Wang. This mechanism aims at representing a wide variety of combustion scenarios.



2018). For the purposes of this project, the goal is to avoid using the high fuel volumes and long experimentation times necessary to conduct these tests. Instead, the plug flow reactor and shock tube experiments were simulated as closely as possible using Cantera[2] simulations. Cantera simulation inputs were the previously determined surrogate blend for CycloSAF.

The Cantera simulation results for the CycloSAF surrogates were used to determine which of the key pyrolysis products were represented and their ratios to one another. This information fed into the mechanism structure in the form of the stoichiometric coefficients of fuel-specific reactions governing the high- and low-temperature breakdown of the lumped fuel molecule. Two sub-mechanism variants were evaluated: (i) a 16-reaction structure, consistent with the prior ATJ mechanism, and (ii) a 20-reaction set that adds an additional H-abstraction reaction ($Fuel \rightarrow R + H$)and low-temperature pathways ($ROO \leftrightarrow Q + HO_2, QOOH \rightarrow QO + OH,\ QO + OH \rightarrow Pyrolysis\ Products$). The additional reactions in sub-mechanism (ii) were included because comparisons with detailed kinetic mechanisms show that H-abstraction and alkylperoxy/ hydroperoxyalkyl radical (ROO/QOOH) conversion are dominant low-temperature channels for cycloalkane fuels.

At this point, the HyChem CycloSAF mechanism had been modified only in terms of stoichiometric coefficients in the reactions, and not in terms of the reactions' rates. In the previous approach (2024), rates of the lumped fuel breakdown reactions were determined using a Hybrid Response Surface Network followed by a Stochastic Gradient Descent Ensemble (HRSN-SGDE) approach. This approach has been described in more detail in past reports and publications by UIUC (Oh et al., 2023; Wiersema et al., 2024a; Wiersema et al., 2024b). This machine learning approach can rapidly estimate ignition delay measurements instead of calculating them from a set of input conditions. While this model can quickly output sets of reaction rate coefficients that will satisfy ignition delay data, training the model for every novel SAF is not ideal. For this reason, another approach was taken for reaction rate approximation. The HRSN-SGDE approach can still be used for rate refinement if necessary.

To quickly approximate the reaction rates for the HyChem structure reactions, an effective rate constant was calculated from corresponding reaction rates of the surrogate component fuels. For example, take the reaction:

$$\mathrm{CycloSAF} \rightarrow e_d\left(C_2H_4 + \lambda_3 C_3H_6 + \lambda_{\{4,1\}} C_4H_8 + \lambda_{\{4,i\}} iC_4H_8\right) + b_d[\chi C_6H_6 + (1\text{-}\chi)C_7H_8] + \alpha H + (2\text{-}\alpha)CH_3$$

This reaction describes the breakdown of the CycloSAF lumped fuel molecule into pyrolysis products. The variables e_d, λ_i, b_d, χ, α are determined from the prior shock tube and plug flow reactor simulations. To approximate the rate at which the above reaction takes place, a weighted average of corresponding surrogate component rates was conducted.

This effective rate constant for this reaction would then be (Equation 1):

$$\sum_i X_i k(T)_i \qquad \text{(Eq. 1)}$$

where i = all species in the surrogate fuel composition, X_i is the mole fraction of each surrogate component, and $k(T)_i$ is its respective rate function for the reaction of reach respective surrogate component breaking down to pyrolysis products.

The colored lines in Figure 8 show the respective rate functions for the breakdown of each surrogate component into pyrolysis products. The dotted line is the calculated effective rate for the CycloSAF lumped fuel molecule for different temperatures ranging from 500 to 2500 K. Arrhenius parameters A, Ea, and n are fitted to this effective rate curve. This procedure is done for every reaction in the lumped HyChem sub-mechanism to generate a consistent set of rates for the surrogate fuel.

[2] Cantera is an open-source suite of tools for problems involving chemical kinetics, thermodynamics, and transport processes. Cantera is a sponsored project of NumFOCUS®, a 501(c) nonprofit charity in the U.S. NumFOCUS is a registered trademark of NumFOCUS, Inc., Austin, Texas.

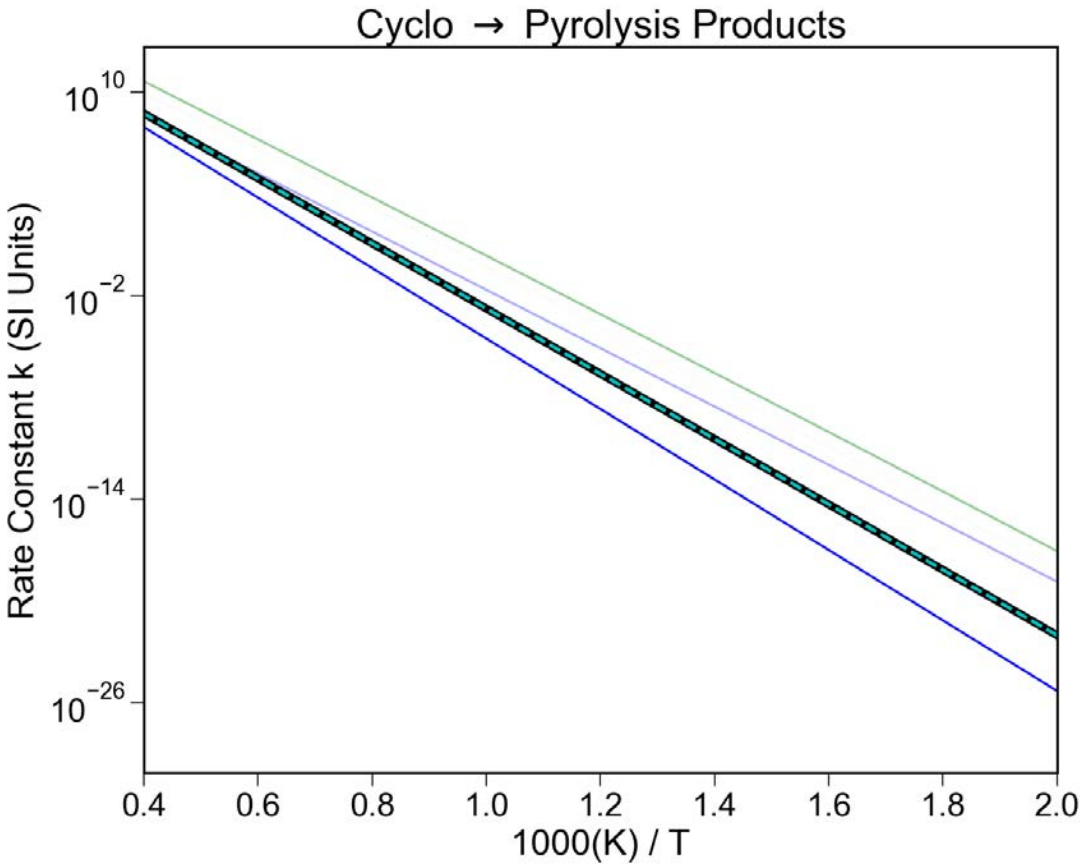
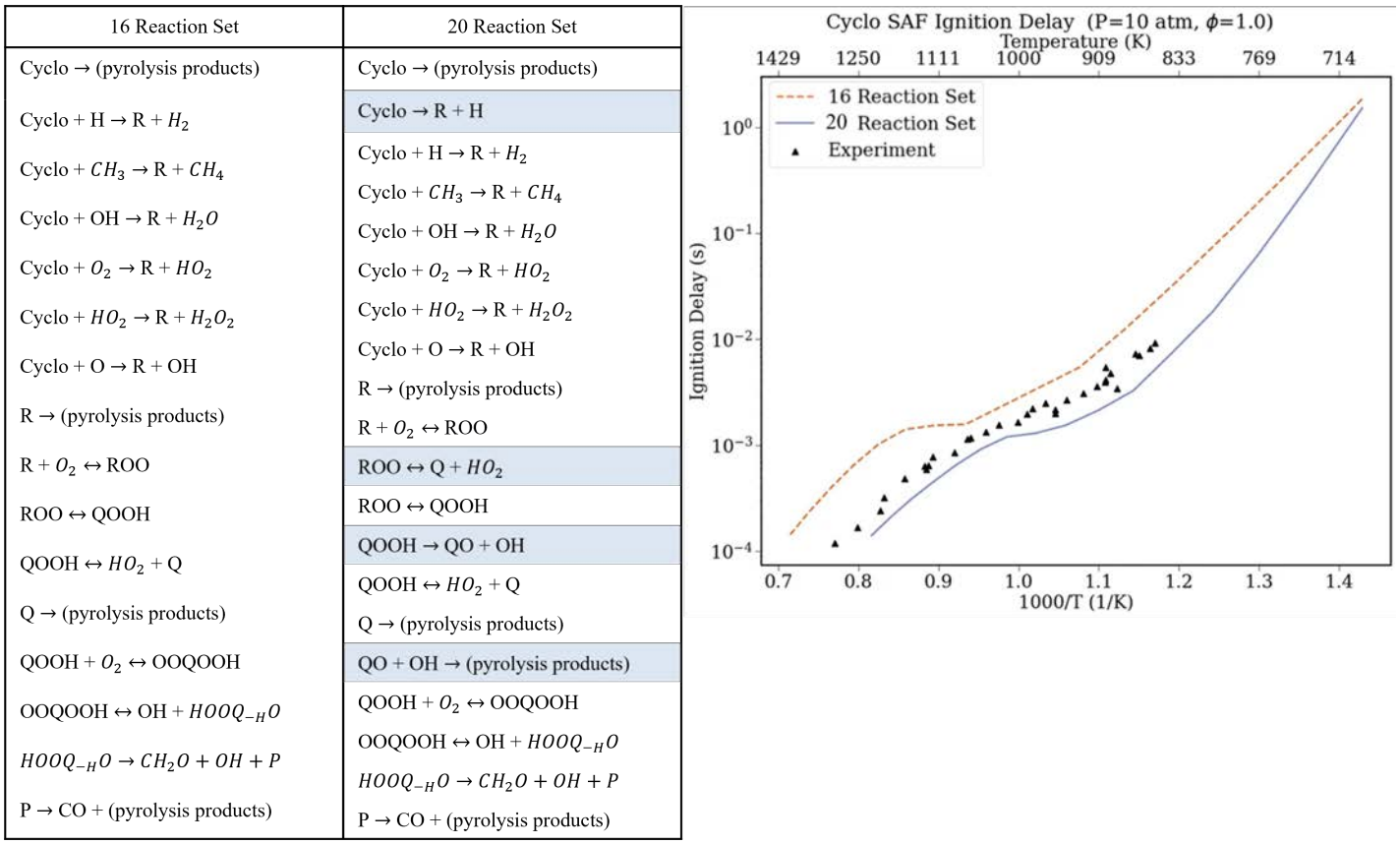


Figure 8. Surrogate Component and Lumped Fuel Molecule Rate Comparison.

Once the reaction rate parameters of our two sub-mechanism variations are complete, the resulting kinetic mechanisms were used to simulate ignition delay time across a wide temperature range, 700 to 1400 K. These results are displayed in Figure 9. The mechanism with 20 lumped pyrolysis reactions seems to underpredict ignition delay time, and the smaller sub-mechanism overpredicts. The Rapid Compression Machine needed to collect low temperature ignition delay data for CycloSAF has been at capacity, but once these data have been collected, further investigation will be performed to refine reaction rate parameters and investigate uncertainties. This methodology shows promise in its ability to approximate combustion parameters like ignition delay time for any fuel with known composition and basic combustion data. Because it does not rely on machine learning or large optimization routines, it can be scaled into a fast-running tool within the database framework.



16 Reaction Set	20 Reaction Set
Cyclo → (pyrolysis products)	Cyclo → (pyrolysis products)
Cyclo + H → R + H_2	Cyclo → R + H
Cyclo + CH_3 → R + CH_4	Cyclo + H → R + H_2
Cyclo + OH → R + H_2O	Cyclo + CH_3 → R + CH_4
Cyclo + O_2 → R + HO_2	Cyclo + OH → R + H_2O
Cyclo + HO_2 → R + H_2O_2	Cyclo + O_2 → R + HO_2
Cyclo + O → R + OH	Cyclo + HO_2 → R + H_2O_2
R → (pyrolysis products)	Cyclo + O → R + OH
R + O_2 ↔ ROO	R → (pyrolysis products)
ROO ↔ QOOH	R + O_2 ↔ ROO
QOOH ↔ HO_2 + Q	ROO ↔ Q + HO_2
Q → (pyrolysis products)	ROO ↔ QOOH
QOOH + O_2 ↔ OOQOOH	QOOH → QO + OH
OOQOOH ↔ OH + $HOOQ_{-H}O$	QOOH ↔ HO_2 + Q
$HOOQ_{-H}O$ → CH_2O + OH + P	Q → (pyrolysis products)
P → CO + (pyrolysis products)	QO + OH → (pyrolysis products)
	QOOH + O_2 ↔ OOQOOH
	OOQOOH ↔ OH + $HOOQ_{-H}O$
	$HOOQ_{-H}O$ → CH_2O + OH + P
	P → CO + (pyrolysis products)

Figure 9. CycloSAF HyChem Mechanism Comparison – Ignition Delay Time.

Milestone

3 months
- Identified areas of improvement to existing methodology.

6 months
- Outlined generalizable surrogate fuel modeling approach with functional groups.
- Identified an appropriate existing model for running surrogate simulations for CycloSAF.

9 months
- Determined surrogate fuel model for CycloSAF.
- Conducted surrogate simulations to emulate original HyChem methodology.
- Set up additional simulation framework from updated HyChem methodology to model low temperature pathways.
- Estimated reaction stoichiometric coefficients for fuel breakdown reactions.

12 months
- Simulation and comparison of initial CycloSAF mechanisms.
- Begin packaging scripts into one adaptable tool.

Major Accomplishments

A repeatable and significant methodology for rapid development of chemical kinetic models based on limited experimental data has been outlined and tested on a SAF with novel composition. A new surrogate modelling approach has been created based on the chemical functional groups of a fuel. Two variations of kinetic mechanisms for CycloSAF have been created and are being further refined as more data becomes available. Methods have been outlined to quantify the uncertainties in mechanism determination in future work.



Publications
None.

Outreach Efforts
In Spring and Fall of 2025, project updates were shared at the ASCENT semiannual meetings. These presentations led to productive discussions regarding fuel data acquisition, database usage, and avenues for further outreach.

Awards
None.

Student Involvement
This project was primarily conducted by one graduate student (Emily Grinage).

Plans for Next Period
In the next period, work will continue with the mechanism determination approach. Attention will be paid to the following areas:

- **CycloSAF model analysis.** Overall, the mechanism determination approach has been demonstrated with CycloSAF with reasonable agreement with experimental data, however there is room to further refine the model to low temperature data once it becomes available. Additional methods for improving rate calculations for the lumped pyrolysis reactions will be explored.
- **Uncertainty Quantification.** The functional group surrogate fuel modelling approach does not account for global molecule behavior, such as ring strain, etc. Uncertainties in model performance due to this approximation need to be further quantified and reduced.
- **AJFTD Implementation.** However, aspects of the approach have yet to be completely designed or implemented. Determining the stoichiometric coefficients of pyrolysis products is the bottleneck in this mechanism generation approach. Multiple simulations must be performed with the fuel surrogate using an existing detailed mechanism. The framework to host an equivalent tool on the website must be further investigated.

References
ASTM International. (2023). *ASTM D7566-22: Standard Specification for Aviation Turbine Fuel Containing Synthesized Hydrocarbons*. https://doi.org/10.1520/D7566-22

Wang, H., Xu, R., Wang, K., Bowman, C., Hanson, R., Davidson, D., Brezinsky, K., & Egolfopoulos, F. N. (2018). A physics-based approach to modeling real-fuel combustion chemistry - I. Evidence from experiments, and thermodynamic, chemical kinetic and statistical considerations. *Combustion and Flame, 193*, 502-519. https://doi.org/10.1016/j.combustflame.2018.03.019

Oh, J.-H., Wiersema, P., Kim, K., Mayhew, E., Temme, J., Kweon, C.-B., & Lee, T. (2023). Fast uncertainty reduction of chemical kinetic models with complex spaces using hybrid response-surface networks. *Combustion and Flame*, 253. https://doi.org/10.1016/j.combustflame.2023.112772

Wiersema, P., Oh, J. H., Kim, K., Godsell, A., & Lee, T. (2024a). Analysis of constraining a chemical kinetic mechanism using hybrid response surface networks. *Proceedings of the Combustion Institute*, 40(1–4). https://doi.org/10.1016/j.proci.2024.105522

Wiersema, P. W., Kim, K., Mayhew, E., Temme, J., Kweon, C.-B. M., & Lee, T. (2024b). Development of a gasoline and jet fuel blend kinetic mechanism using hybrid response surface networks. In *AIAA Scitech 2024 Forum*, AIAA 2024-0176. https://doi.org/10.2514/6.2024-0176

Zhang, X., & Sarathy, S. M. (2020). A functional-group based approach to modeling real-fuel combustion chemistry – II: Kinetic model construction and validation. *Combustion and Flame,* 223, 475-489. https://doi.org/10.1016/j.combustflame.2020.10.039



Project 037 CLEEN II System-level Assessment

Georgia Institute of Technology

Project Lead Investigator

Dimitri Mavris
Regents Professor
School of Aerospace Engineering
Georgia Institute of Technology
Mail Stop 0150
Atlanta, GA 30332-0150
(404) 894-1557
dimitri.mavris@ae.gatech.edu

University Participants

Georgia Institute of Technology (Georgia Tech)

- P.I.s: Prof. Dimitri Mavris, Dr. Jimmy Tai
- FAA Award Number: 13-C-AJFE-GIT-055
- Period of Performance: October 1, 2024, to December 31, 2025
- Tasks:
  1. Finalizing Continuous Lower Energy, Emissions, and Noise (CLEEN) Fleet Benefit Assessment Assumptions
  2. Continuation of CLEEN III Modeling of Aircraft Technologies and Advanced Configurations
  3. Emissions Assessment Options
  4. Host CLEEN Consortium

Project Funding Level

The Federal Aviation Administration (FAA) provided $425,000 in funding to Georgia Tech. Georgia Tech has agreed to a total of $425,000 in matching funds. This total includes salaries for the project director and research engineers, as well as funding for computing, financial, and administrative support, including meeting arrangements. Georgia Tech has also agreed to provide tuition remission for students, paid from state funds.

Investigation Team

Prof. Dimitri Mavris, (P.I.)
Dr. Jimmy Tai, (co-P.I.)
Brennan Stewart, program management/noise modeling
Holger Pfaender, (technical lead), fleet modeling
Supporting Engineers: Zhimin Liu, Carl Johnson, and Barbara Sampaio Felix
Students: Joao De Azevedo, Tabitha D'Amato, Dante Cyrus, James Tsangarides, Kayley Lewis, Ballard Huey, Nathaniel Green, Flavius Penescu, Aniela Zaremski, Akash Shiri, Anna Conroy, Vishwa Malaisamy, Samal Siddharth, Anika Chawla, Adi Arora, Nicholas He, Suhanna Bamzai, Ellen Wang, and Thomas Prosser

Project Overview

The objective of this research project is to support the FAA by independently modeling and assessing the technologies that are being developed under the CLEEN II and CLEEN III programs. This will involve direct coordination and data sharing with CLEEN-funded companies to accurately model the environmental benefits of these technologies at vehicle and fleet levels.

Georgia Tech was previously selected to perform all system-level assessments for the CLEEN program under Partnership for Air Transportation Noise and Emission Reduction (PARTNER) Project 036 and ASCENT Project 010. As a result, Georgia Tech is in a unique position from both the technical and programmatic standpoints to continue the system-level assessments for CLEEN II. From a technical perspective, Georgia Tech has significantly enhanced the Environmental Design



Space (EDS) to incorporate advanced, adaptive, and operational technologies targeting fuel burn, noise, and emissions. EDS has been successfully applied to all CLEEN I contractor technologies including the following: General Electric® (GE) open rotor, twin annular premixing swirler (TAPS) II combustor, Flight Management System (FMS)-Engine, and FMS-Airframe; Pratt & Whitney® geared fan; Boeing® adaptive trailing edge and ceramic matrix composite (CMC) nozzle; Honeywell® hot section cooling and materials; and Rolls-Royce® turbine cooling technologies. In 2024, Georgia Tech stated that all CLEEN II Technology modeling had been completed as well and delivered results to the FAA quantifying the impacts of the CLEEN I and II programs in the areas of fuel burn reduction/cost savings, nitrogen oxides (NO_x) reduction, and noise reduction.

Georgia Tech has also gained extensive experience in communicating system-level modeling requirements to industry engineers and translating the impacts to fleet-level fuel burn, noise, and emissions assessments. This broad technical knowledge base covering detailed aircraft and engine design, as well as high-level benefits assessments, places Georgia Tech in a unique position to assess CLEEN III technologies.

Because the goal of this work is to conduct fleet-level assessments for aircraft representative of future “in-service” systems, Georgia Tech will need to create system-level EDS models using a combination of both CLEEN II/III and other public domain N+1 and N+2 technologies. The outcomes of the technology and fleet assumptions-setting workshops conducted under ASCENT Project 010 are used for this effort. Non-CLEEN technologies for consideration, along with potential future fleet scenarios, will help to bound the impact of CLEEN II/III on future fleet fuel burn, emissions, and noise.

Work conducted during this period of performance examined the impact of updates to some of the CLEEN Fleet assessment assumptions. Phase II of the CLEEN program, made the decisions to use the same assumptions as phase I of the CLEEN program. These assumptions were finalized in approximately 2015. There have been significant changes to the aviation market since the assumptions were originally set. CLEEN III plans to update the fleet assumptions to better align with current trends in the aviation industry. This year of work examined the impact of some of these assumption changes on the CLEEN III Fleet as compared to CLEEN II. Georgia Tech also continued the modeling of CLEEN III technologies while working with CLEEN Contractors. This work is being conducted under a non-disclosure agreement (NDA) due to its proprietary nature, so only minimal updates can be provided publicly.

Georgia Tech also worked on creating alternative emission assessment capabilities inside of EDS. Currently, NO_x is predicted according to the landing and takeoff (LTO) cycle, which utilizes an assumption for how long the engine is at various power levels. Georgia Tech added functionality to EDS to compute NO_x emissions along notional takeoff trajectories predicted by EDS. This will provide an estimate of NO_x tied to the takeoff performance of each aircraft, rather than solely being tied to engine performance. Additionally, Georgia Tech explored methods of implementing non-volatile particulate matter (nvPM) Emissions inside of EDS. These metrics will not be utilized by the current phase of CLEEN program, but there is increased interest in tracking or regulating these metrics in the wider aerospace community, so Georgia Tech explored these metrics should they be required for future analysis under the CLEEN program.

Georgia Tech had been planning to host the Spring 2025 CLEEN consortium, (a series of meetings where CLEEN contractors report progress updates to the FAA twice a year), on campus in Atlanta, Georgia. However, restrictions on non-essential government travel in early 2025, as a part of wider cost savings and governmental efficiency pushes, necessitated that the spring 2025 consortium was ultimately held remotely.

Next year’s work will focus on implementing CLEEN III technologies into EDS as test data become available, finalizing a baseline fleet performance scenario, and conducting a preliminary fleet assessment provided a sufficient number of technology modeling tasks are completed.

Milestones

The major milestones which were planned for this performance period and their planned due dates are listed below, (the major accomplishment section will discuss which were achieved).

® General Electric is a registered trademark of General Electric Company, Schenectady, New York.
® Pratt & Whitney is a registered trademark of RTX Corporation, Farmington, Connecticut.
® Boeing is a registered trademark of The Boeing Company, Seattle, Washington.
® Honeywell is a registered trademark of Honeywell International, Inc., Charlotte, New Jersey.
® Rolls-Royce is a registered trademark of Rolls-Royce PLC, London, England.



Task No.	Milestone	Planned Due Date
1	Finalizing CLEEN Fleet Benefit Assessment Assumptions	December 31, 2025
2	Continuation of CLEEN III Modeling of Aircraft Technologies and Advanced Configurations	December 31, 2025
3	Development of Alternative Emissions Assessment Options within EDS	September 30, 2025
4	Host CLEEN Consortium	May 30, 2025

Major Accomplishments

- Analyzed the impact of fleet assumptions updates on CLEEN III Fleet Assessment.
- Continued modeling progress of CLEEN III Technologies.
- Included alternative NO_x emission assessment options in EDS and accessed nvPM prediction options.

Task 1 - CLEEN Fleet Benefit Assessment Assumptions

Georgia Institute of Technology

Objectives

The objective of this task is to finalize the CLEEN Fleet Benefit Assessment assumptions. During this period of performance, Georgia Tech implemented updated assumptions in the Fleet Assessment Environment and began to analyze their impact.

Research Approach

The reports *Project 037 CLEEN II System-level Assessment* (Mavris et al., 2023 and Mavris et al., 2024) for the previous periods of performance details the initial updates to the Fleet Assessment Assumption from CLEEN II. This period of performance focused on implementing those assumptions and evaluating the impact on the fleet study. This is being done ahead of the CLEEN III fleet study to examine some of the key changes and evaluate if the results are reasonable.

The fleet assessment introduces new vehicles by replacing older retiring aircraft and ordering new aircraft to meet increased demand. The replacement matrix, as shown in Figure 1, informs the fleet study which vehicles would comprise the new introductions for each vehicle class for any year. These new introductions would be from either replacing retiring vehicles or vehicles purchased to meet increased demand. An assumption is made that it takes about four years to transition to delivering solely the next generation of vehicles. An example of how to read the replacement matrix is that in the year 2028, 75% of regional jet replacements will consist of N1 generation of vehicles while the other 25% will consist of N2 generation of vehicles.

The assumptions used in CLEEN I/II was that the baseline best-in-class vehicles (which would be infused with technologies to create notional vehicles) were based on what was available in 2015. Between 2015 and 2020, a new generation of vehicles would come into services comprising the N1 generation of vehicles, which would feature CLEEN I technologies, (some, but not all CLEEN I technologies made it into service comprising this generation of vehicles). These dates were chosen to roughly correspond to introductions of actual aircraft such as the Boeing B737-8, Embraer® E190-E2, and Boeing B787-10. Before these introductions, the 2015 best-in-class is used for new deliveries.

In CLEEN I/II, it was assumed there would be N2 generation of vehicles coming into service in the 2020s which would be used for the introduction of CLEEN II technologies. However, the trend in the aviation industry that occurred is that the 2020s has not seen the introduction of new vehicles (outside of the delayed 777x). Therefore, CLEEN III will be updating the assumption regarding when CLEEN II technologies will be introduced on a new generation of vehicles to the mid-2030s, which will likely correspond with the introduction of CLEEN III technologies. Figure 2 shows the effect difference delaying the introduction of a new generation of vehicles from the mid-2020s to the mid-2030s. Relative to the assumptions in CLEEN I/II, in 2050 under the CLEEN III assumptions, the N1 generation is predicted to have approximately 70% increased annual operations, while the N2 generation is predicted to have approximately 37% less annual operations.

® Embraer is a registered trademark of Embraer S.A., San Jose Dos Campos, Brazil.



These assumptions are reflected by current trends in the aviation industry. As of December 31, 2025, Boeing has 4,869 unfilled orders for the 737 and 1,076 unfilled orders for the 787 (Boeing, 2025). As of December 31, 2025, Airbus® has 1,793 outstanding orders for the A320neo and 5,348 outstanding orders for the A321neo (Airbus, 2025). Embraer Air as of quarter (Q)2 2025 has 190 outstanding firm orders for the E195-E2 in their backlog (Embraer, 2025). These backlog of orders align well with Georgia Tech's fleet analysis assumptions which has delivery of this generation of vehicles continuing for the foreseeable future.

What this means for the CLEEN fleet assessment is that technologies which made it into service on the N1 generation of vehicles will be in operation on a larger percentage of the overall fleet, while CLEEN II technologies, which will be now be introduced in a 2035 generation of vehicles, will be in operation on a smaller percentage of the overall fleet by 2050. The potential fleet benefit of technologies is influenced by how many vehicles are in the fleet in which the technology is present. These statements are meant not to quantify the impact of these changes, as a full fleet assessment with the CLEEN III assumptions has not been performed. Additionally, a later introduction of these technologies might enable these technologies to express further benefits beyond 2050, and these technologies will be introduced on more technologically advanced vehicles. These factors should be considered when analyzing the impact of CLEEN technologies on the CLEEN III fleet assessment when examining the results.

Vehicle	Timeframe	2015	2016	2017	2018	2019	2020	2021	2022	2023	2024	2025	2026	2027	2028	2029	2030	2031	2032	2033	2034	2035
RJ	N+1	0	0	0	25	50	75	100	100	100	100	100	100	100	75	50	25	0	0	0	0	0
RJ	N+2	0	0	0	0	0	0	0	0	0	0	0	0	0	25	50	75	100	100	100	100	100
LSA	N+1	0	25	50	75	100	100	100	100	100	100	75	50	25	0	0	0	0	0	0	0	0
LSA	N+2	0	0	0	0	0	0	0	0	0	0	25	50	75	100	100	100	100	100	100	100	100
STA	N+1	0	0	0	25	50	75	100	100	100	75	50	25	0	0	0	0	0	0	0	0	0
STA	N+2	0	0	0	0	0	0	0	0	0	25	50	75	100	100	100	100	100	100	100	100	100
LTA	N+1	0	0	0	25	50	75	100	100	100	100	100	100	100	100	100	75	50	25	0	0	0
LTA	N+2	0	0	0	0	0	0	0	0	0	0	0	0	0	0	0	25	50	75	100	100	100
VLA	N+1	0	0	0	0	0	25	50	75	100	100	100	100	75	50	25	0	0	0	0	0	0
VLA	N+2	0	0	0	0	0	0	0	0	0	0	0	0	25	50	75	100	100	100	100	100	100

Figure 1. CLEEN I/II fleet replacement matrix assumptions.

® Airbus is a registered trademark of Airbus Operations GmbH, Hamburg, Germany.

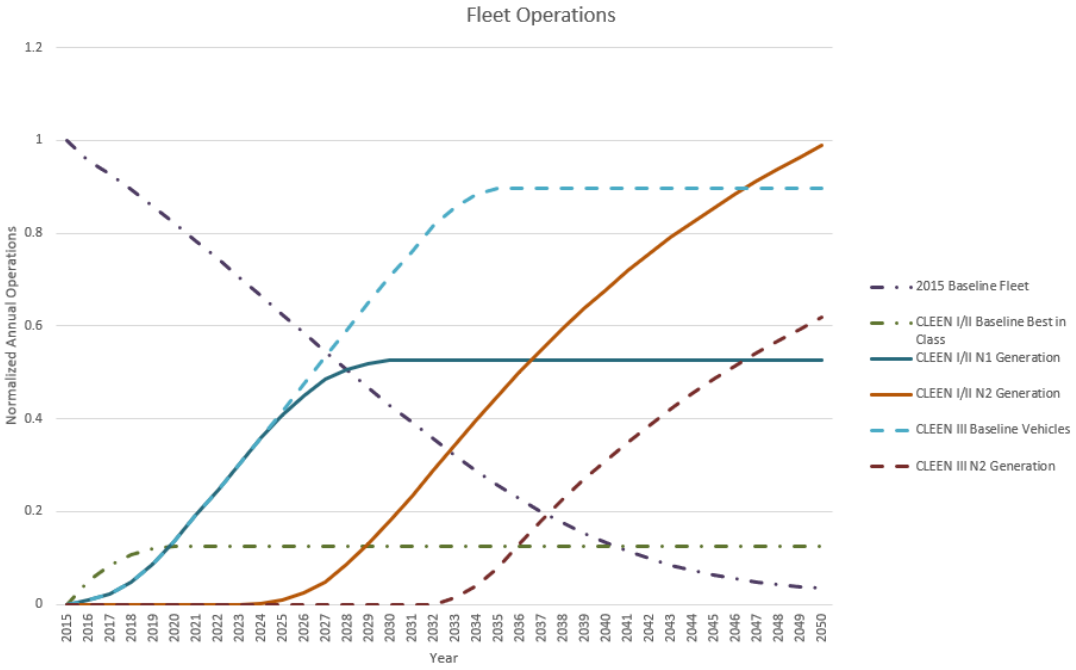


Figure 2. Projected fleet assessment operations of different vehicle generations. CLEEN: Continuous Lower Energy, Emissions, and Noise.

Steps for completion of the fleet study include the steps listed below. These will guide work for the next period of performance.

- Selected updated best-in-class reference vehicles and new fleet analysis assumptions (previously completed).
- Create and calibrate best-in-class reference vehicles (previously completed).
- Implement updated fleet replacement assumptions (completed this period).
- Implement updated base year fleet makeup.
- Implement updated demand growth forecasts.
- Run fleet study for non-CLEEN technology Infused vehicles using public tech Technology Impact Matrix (TIM).
- Run fleet study for CLEEN technology infused vehicles (completion is dependent on Task 2).
- Compare CLEEN and non-CLEEN fleet study results to establish CLEEN III program benefits.

Task 2 - Continuation of CLEEN III Modeling of Aircraft Technologies and Advanced Configurations

Georgia Institute of Technology

Objectives

The objective of this task is to estimate the impacts of CLEEN relevant technologies at the vehicle system-level, each of these technologies must be modeled regarding their impacts to aircraft fuel burn, noise, and emissions using EDS.

Research Approach

Georgia Tech was previously selected to perform all system-level assessments for the CLEEN program under ASCENT Project 010. Because the ultimate goal of this work is to conduct fleet-level assessments for aircraft representative of future “in-service” systems, Georgia Tech will need to create system-level EDS models using a combination of both CLEEN (Phases I, II, and III) and other public domain near-term and midterm Entry into Service (EIS) technologies. Vehicle system-level modeling for all relevant CLEEN technologies will be performed using EDS.



Table 1 presents a list of CLEEN technologies funded under Phase III of the program which as suitable for the Fleet Assessment. The efforts related to sustainable aviation fuel (SAF) funded under CLEEN III are excluded from this list as they are outside the scope of Georgia Tech's fleet assessment. Mavris et al. (2024) noted that the CLEEN II technology modeling process had been completed, as well as noting which areas of the primary fleet analysis metrics each technology affects. Due to the proprietary nature of the modeling work, as Georgia Tech works directly with each CLEEN contractor under an NDA, specific details of the modeling efforts cannot be provided. However, with Phase III of the CLEEN Program publicly slated to concluded in 2026 as noted in Orton (2024), Georgia Tech is engaged with all contractors with the goal of delivering fleet assessment results after all contractor modeling has concluded, and data have been integrated into Georgia Tech's modeling environment.

Table 1. CLEEN III Technologies and Impact Area.

Contractor	Technology/Model Impact Area	Fuel Burn	NO_x	Noise
Boeing	Quiet Landing Gear			X
	Quiet High Lift System			X
	Advanced Inlet	X		X
	Intelligent Operations	X		X
Collins	Large Cell Novel Core Exhaust			X
Delta/MDS/America's Phenix	Fan Leading Edge Protective Coating	X		
GE	MESTANG III	X		
	Open Fan	X		X
	Advanced Thermal Management	X		
	Hybrid Electric Integrated Generation	X		
	Combustor Technology	X	X	
	Advanced Acoustics			X
Honeywell	High Pressure Core	X	X	X
	Highly Efficient Fan	X		X
	Compact low-pressure turbine	X		
Pratt and Whitney	Fan Noise Technologies			X
	Fan Performance Technologies	X		
	Combustor – Swirlers			X
	Combustor – Cooling Technologies	X		
	Combustor- Low Pattern Factor	X		
	Combustor – NO_x Reduction		X	
Rolls-Royce	Centrifugal Compressor	X		
Safran	Short Inlet			X



Task 3 - Emissions Assessment Options

Georgia Institute of Technology

Objective

Georgia Tech has provided the NO_x emissions fleet benefit assessments for both of the first two phases of the CLEEN program. As the CLEEN program continues through Phase III, Georgia Tech will work on expanding the assessment capabilities used in delivering this NO_x emissions benefits in addition to assessing if nvPM emissions can be predicted to ensure that ASCENT Project 037 has the capability to be ready for any future shifts in emission metrics modeling.

Research Approach

NO_x emitted in the LTO cycle has been exclusively considered as LTO emissions for FAA CLEEN program level metric by which to assess fleet benefits. The landing and take-off cycle computes NO_x emissions through a combination of engine performance metrics and an assumed operation cycle (European Environment Agency & EASA, 2016). The LTO cycle uses the times described in Table 2 in the calculation of LTO emissions. The aircraft emission rate per operation conditions is multiplied by the assumed time in each operation mode to get the LTO emissions.

This formulation results in LTO emissions cycle results in NO_x emissions being a function of only the engine performance. By being decoupled from airframe performance, changes to the aerodynamics or weight of the aircraft (which could result in varying thrust levels and time to climb away from the terminal airspace) have no impact on the NO_x as predicted by this cycle. This cycle has benefits in that it allows NO_x to be quantified by entirely public information using the data in the International Civil Aviation Organization (ICAO) Emission Database (ICAO, 2021), as the operational assumptions are fixed and the emissions metrics are all publicly reported by the European Union Aviation Safety Agency (EASA) for engines above 6,000 lbf (26.78 kN). However, this comes at the cost of being decoupled from the aerodynamics and takeoff/landing weight of the aircraft.

Georgia Tech has developed the capability to assess NO_x in a more comprehensive way to ensure Georgia Tech maintains the capability to model any future standards for NO_x metrics. Two additional emissions approaches have been developed for fleet benefit articulation. In the previous period of performance, it was reported that Georgia Tech added the capability to our Flight Optimization System analysis to assess NO_x over the full mission. Full mission NO_x considers NO_x produced by aircraft across the complete mission, not just around the airport. The other metric, terminal mission NO_x, considers NO_x produced by aircraft below an altitude of 3,000 ft. This assessment approach, though a less common standard than LTO NO_x, considers installation effects, aircraft LTO trajectory, and actual engine operations in this window of the mission. A description for the implementation for each functionality is described in Mavris et al. (2024). Georgia Tech has completed development of the terminal area NO_x capability during this performance period.

Below are examples of Georgia Techs analysis of the NO_x emissions using these metrics as assessed in EDS for a Georgia Tech Notional 787-8 with Notional Engine model of a GEnx-1B70. Table 2 shows the LTO cycle NO_x calculations, (please note numbers have been rounded to the nearest tenth of a decimal). Figure 3 shows the cumulative NO_x build up over the course of a notional mission. Figure 4 shows the cumulative NO_x over course of a notional takeoff.

Table 2. Example of landing and takeoff (LTO) nitrogen oxides (NO_x) cycle for a notional 787 as calculated by Environmental Design Space (EDS).

Segment	Time (min)	EI NOx (g NOx/kg Fuel)	Fuel Flow Rate (lbm/s)	NOx per Engine (lbs)
Taxi	26	4.9	0.5	3.8
Approach	4	11.1	1.5	4.0
Takeoff	0.7	35.3	5.4	8.0
Climb	2.2	20.6	4.5	12.2
Total	N/A	N/A	N/A	28.1

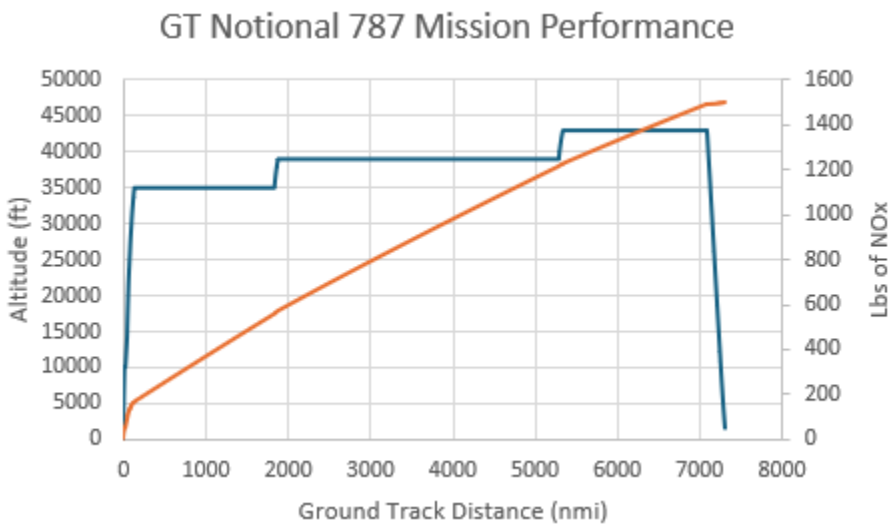


Figure 3. Example of full mission nitrogen oxides (NO_x) build up for notional 787 in Environmental Design Space (EDS).

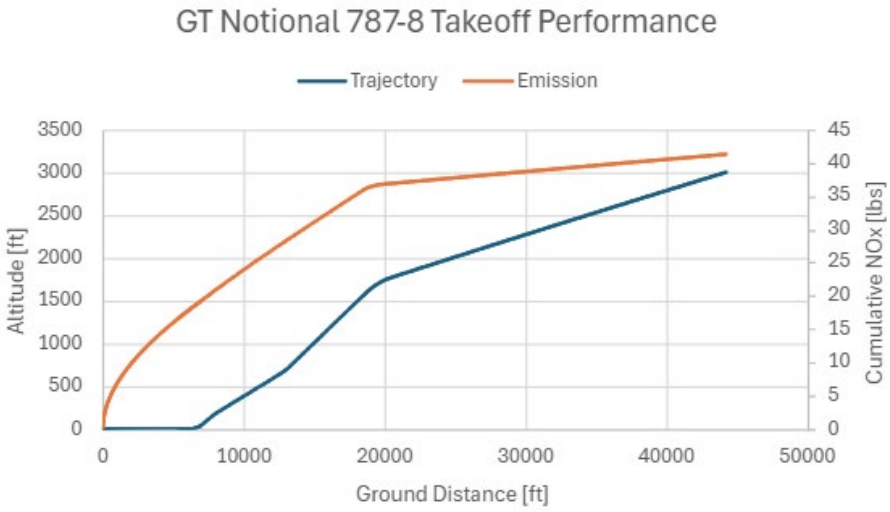


Figure 4. Example of Takeoff nitrogen oxides (NOx) build up for notional 787 in Environmental Design Space (EDS).

Although Georgia Tech now has the capability to model alternative NO_x metrics, both Georgia Tech and the FAA agree that LTO NO_x will remain the standard for the CLEEN III program. However, Georgia Tech will continue to develop EDS emission analysis capabilities which might become metrics of interest in future phases of the CLEEN program.

Another metric of interest of growing interest to the aviation industry is nvPM emissions. Georgia Tech does not currently have the capabilities to predict this metric as a part of our EDS analysis. However, this emission is of interest due to its contribution to contrail creation. Georgia Tech explore nvPM predictions through the application of the Mission Emissions Estimation Methodology (MEEM) method as described in Ahrens et al. (2022) as well as exploring if a P3T3 correlation could be created by regressing data in the ICAO Emissions Database (ICAO, 2021). To explore these methods, Georgia Tech attempted to fit nvPM data for PW1100G, GEnx-1B, and the CF6 engine families. Figure 5 to Figure 7 below show the nvPM levels plotted against thrust. These engines were selected to provide two modern and one older engine examples.

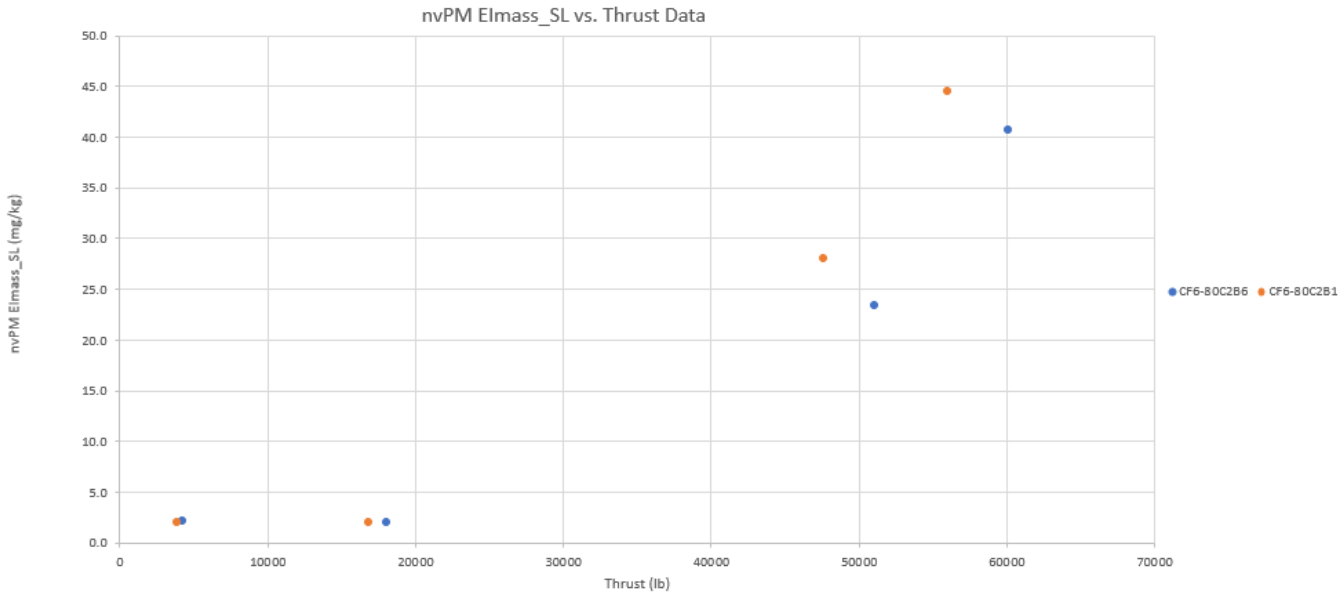


Figure 5. CF6 family non-volatile particulate matter (nvPM) emission mass vs. thrust from ICAO Emission Database.

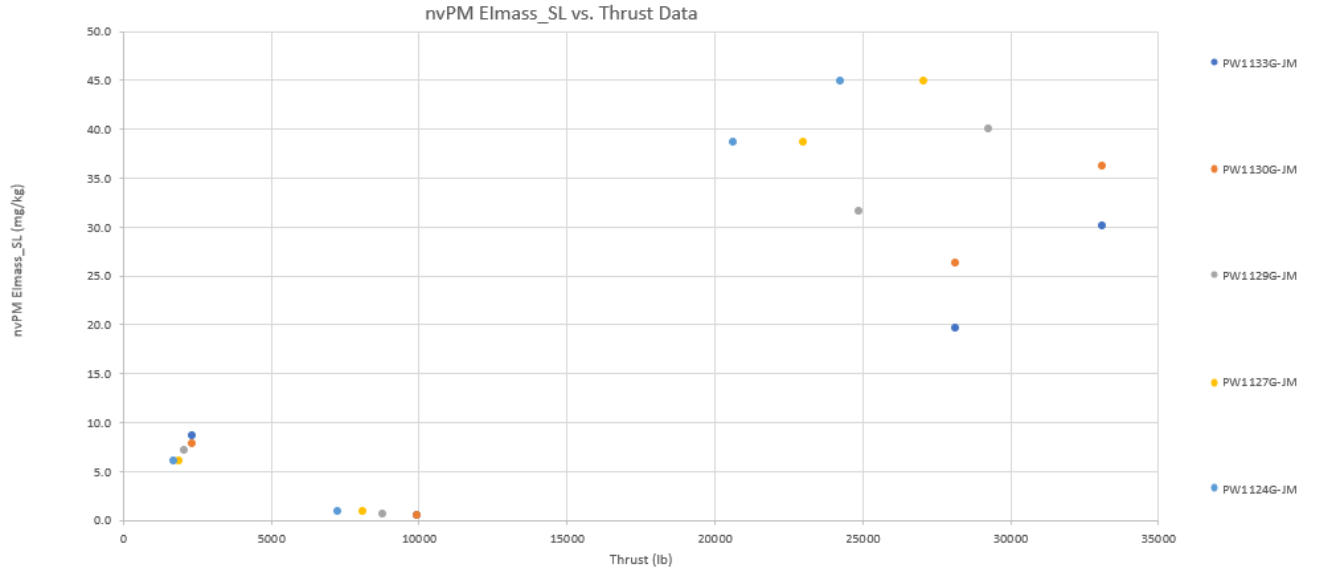


Figure 6. PW1100G family non-volatile particulate matter (nvPM) emission mass vs. thrust from ICAO Emission Database.

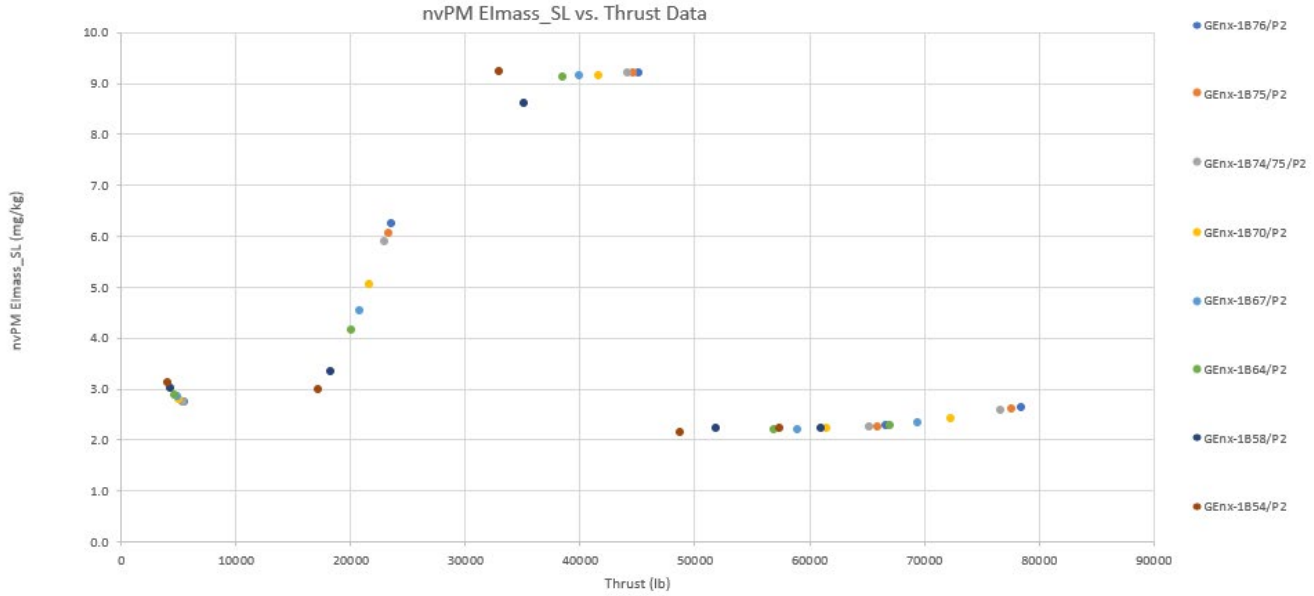


Figure 7. GEnx family non-volatile particulate matter (nvPM) emission mass vs. thrust from ICAO Emission Database.

Georgia Tech explored the MEEM method as outlined by Ahrens et al. (2022). The paper by Ahern outlines a four-step procedure to predict nvPM emissions. Figure 8 to Figure 10 show the process described in step 3 of Ahern which is either a four- or five-point linear interpolation fit over the certification data from the ICAO databank. This linear interpolation fits well as it passes through each of the certification points; however, it is only valid for a specific engine and does not provide a basis for extrapolation. Nevertheless, Georgia Tech was able to apply this method to predict operational nvPM by combining these piecewise linear interpolations with the process described in Step 4 of Ahern to correct for nvPM at altitude. This correction uses the ratio of the pressure at the combustor entrance (P3) at the altitude over the pressure at combustor entrance on the ground as shown in Equation 1 below. Steps 1 and 2 of Ahern describe a process of estimating, thrust, temperature, and pressure on the ground and at altitude are needed to apply this proposed method, but these are unnecessary in Georgia Tech's implementation of this method as these values are predicted in the engine model generated by EDS.

$$EI_{mass,Alt} = EI_{mass,GR}\left(\frac{P3_{ALT}}{P3_{GR}}\right)^{1.35} 1.1^{2.5} \quad \text{(Eq. 1)}$$

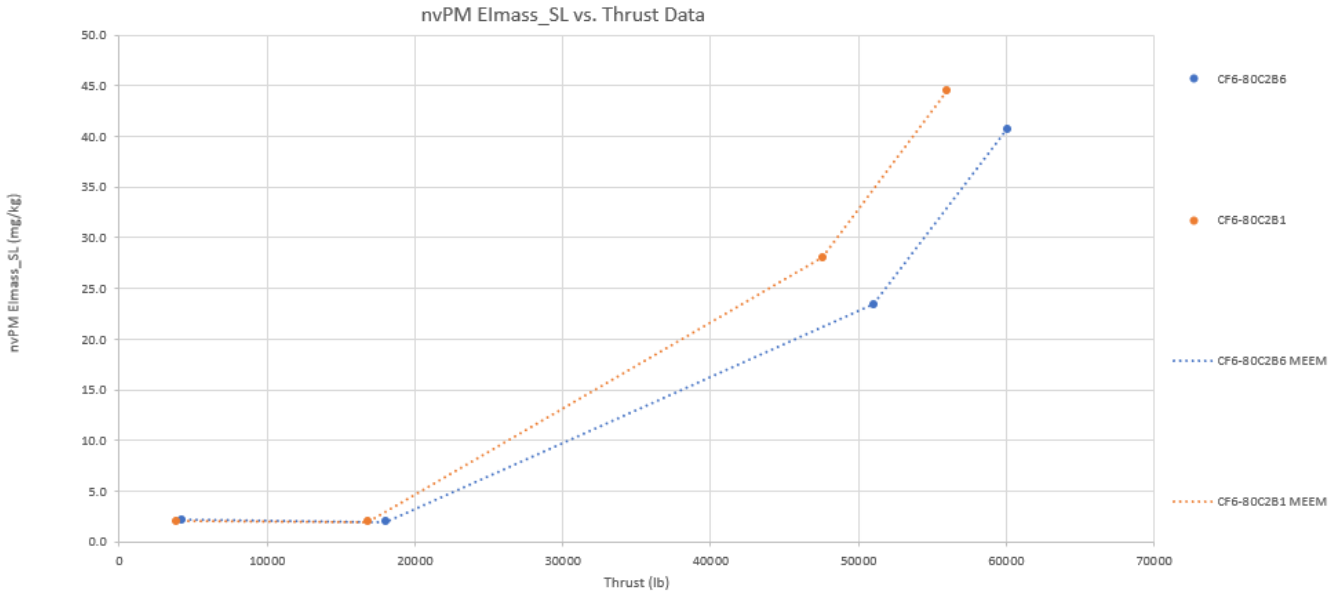


Figure 8. Mission Emissions Estimation Methodology (MEEM) interpolation applied to Cf6 family.

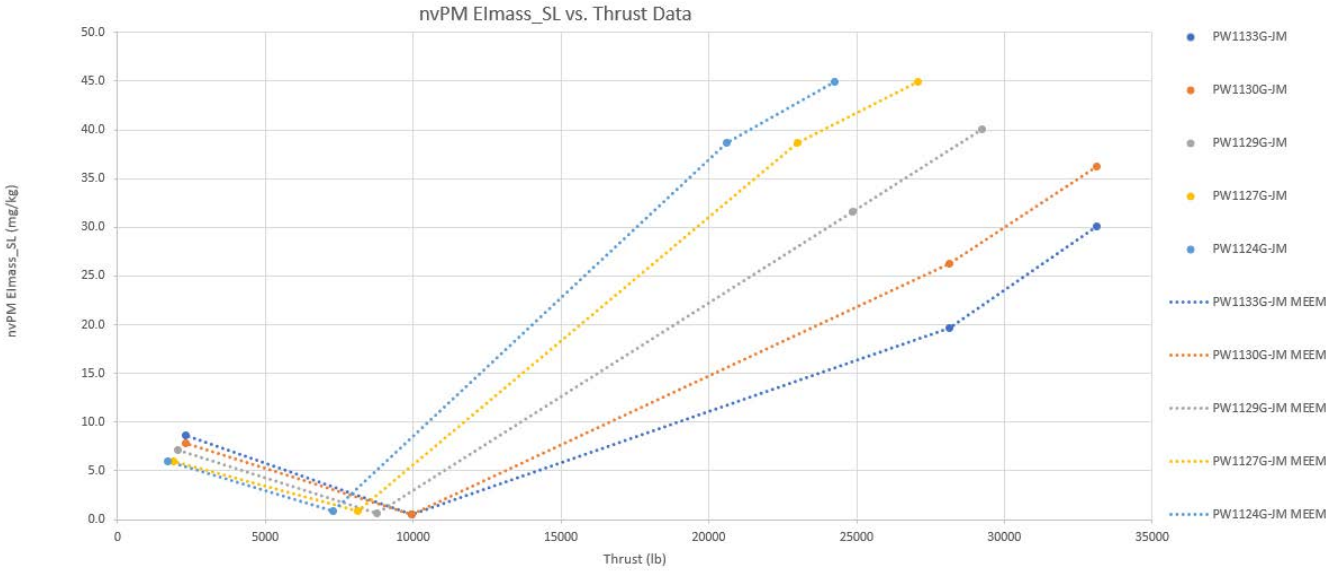


Figure 9. Mission Emissions Estimation Methodology (MEEM) interpolation applied to Pw1100g family.

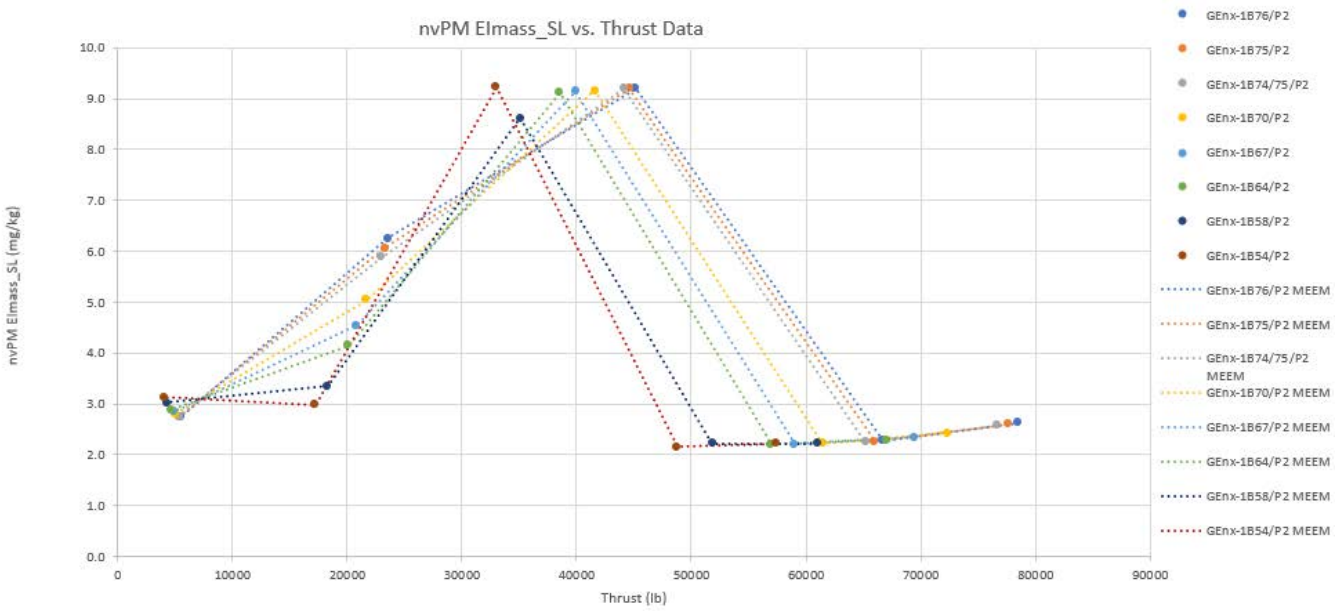


Figure 10. Mission Emissions Estimation Methodology (MEEM) method interpolation applied to GEnx family.

Georgia Tech also explored developing a P3T3 correlation to predict nvPM equations. P3T3 correlations are widely used method in industry for predicting certain emission index based on the pressure and temperature at the combustor inlet, (station 3). However, these methods require often proprietary engine performance data. Georgia Tech has a methodology where the proprietary engine performance data are replaced with engine performance data from Notional Flight Optimization System (NPSS) engine models to approximate a P3T3 correlation. Georgia Tech uses this method in NO_x predictions. Georgia Tech attempted to extend this method to nvPM predictions with mixed results which are shown in Figure 11 to Figure 13. It should be noted that without proprietary engine data, the data points in these charts, which correspond to certification thrust levels show on the previous figures, come from Georgia Tech's notional NPSS engine models.

It quickly became apparent that the three engine families had very different NO_x emissions characteristic which would make fitting a regression challenging. The CF6 family showed monotonically increase in nvPM emissions with thrust. The PW1100G family showed that the engines were most efficient at the approach thrust level, and the GEnx engines have the worst emissions at the climb thrust level and the best at the takeoff thrust level. The PW1100g and CF6 engine families also show a variation in the slope of the nvPM emissions with the thrust level among the different ratings in the engine family with the derated engines showing a greater rise in nvPM emissions with thrust. Georgia Tech was unable to create a correction which could account for the differences in the engine rating. So, while this method was able to provide a somewhat acceptable P3T3 correlation for the GEnx and CF6 family, the PW1100G P3T3 correlation performed particularly poorly.

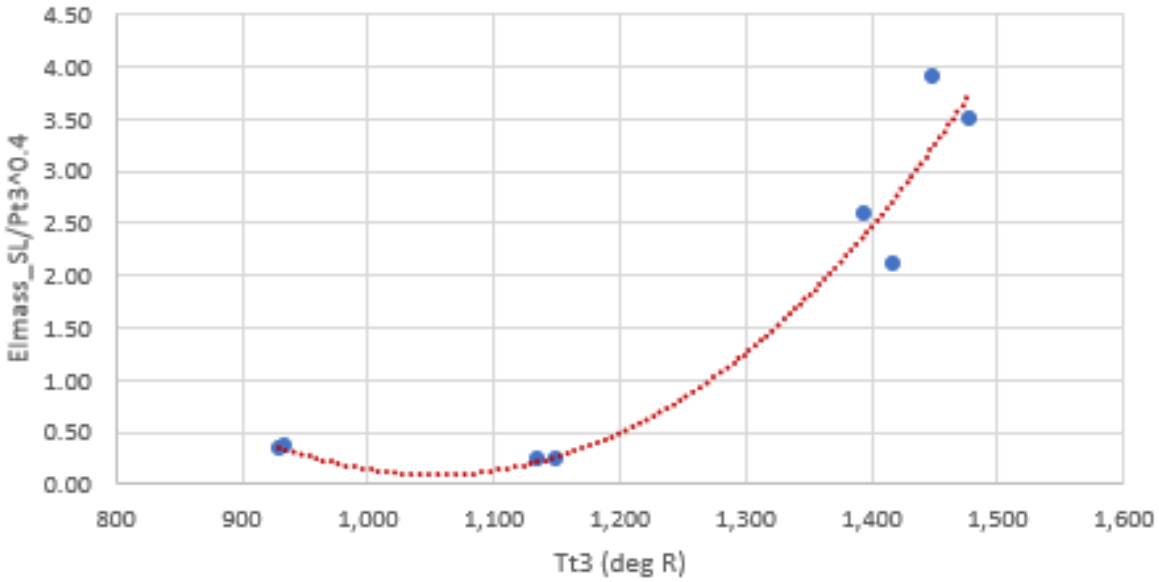


Figure 11. Georgia Tech nvPM P3T3 correlation against certification points for notional CF6 engines.

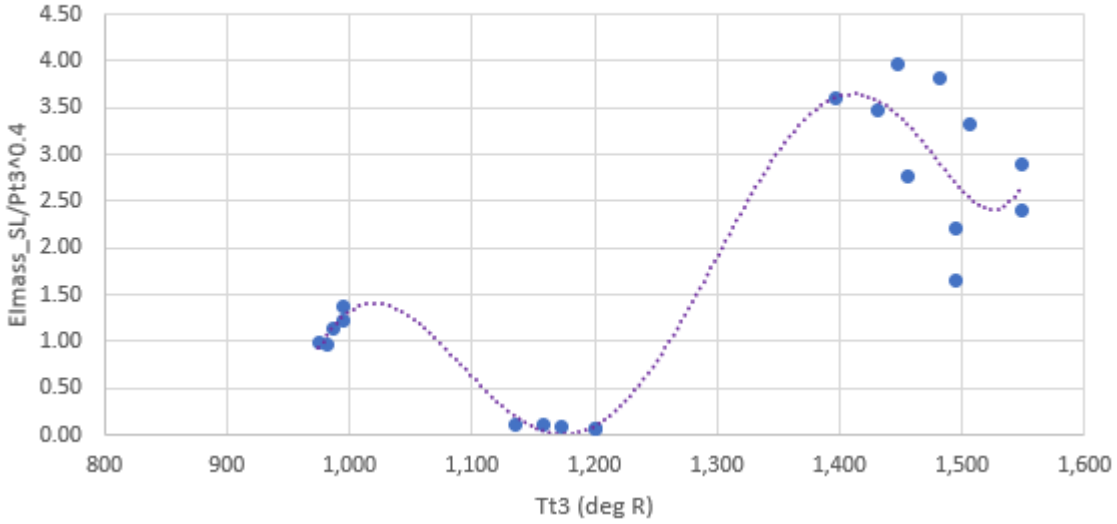


Figure 12. Georgia Tech nvPM P3T3 correlation against certification points for notional pw1100g engines.

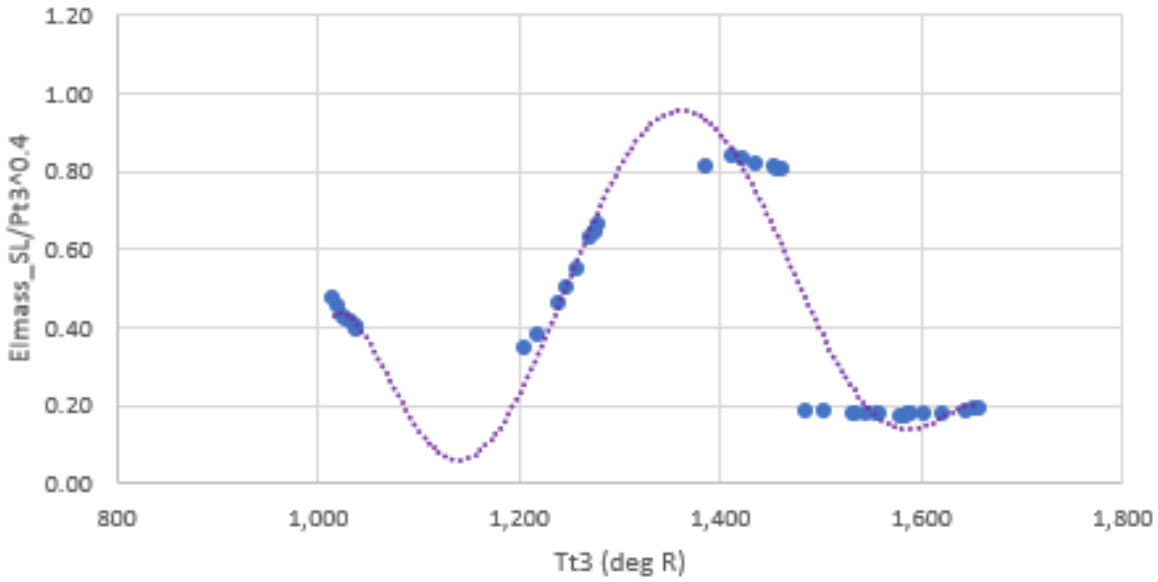


Figure 13. Georgia Tech nvPM P3T3 correlation against certification points for notional GEnx engines.

As a result of this task, Georgia Tech has the capabilities of predicting NO_x emissions over the course of the entire mission and for all operations below 3,000 ft. Georgia Tech can also predict nvPM emissions using the two methods described previously. However, the MEEM method is merely an interpolation and will not be suitable for extrapolation, and Georgia Tech attempt at fitting a P3T3 correlation had mixed success for different engine families.

Task 4 – Host CLEEN Consortium

Georgia Institute of Technology

Objective

Georgia Tech and the FAA had coordinated to host the CLEEN Spring 2025 Consortium on campus at Georgia Tech in Atlanta, Georgia.

Research Approach

The CLEEN Consortium is a bi-annual event where CLEEN contractors report out progress and updates to the FAA on the current state of their CLEEN programs. This gives the government a chance to ensure that the program remains on track, and allows them to invite other government entities, (such as National Aeronautics and Space Administration representatives), and select academia representation, (Georgia Tech), to participate in these reviews and provide feedback to the FAA. Georgia Tech allocated resources to coordinate with FAA resolving the logistics of hosting a CLEEN Consortium and coordinating with contractors. Georgia Tech also was coordinating with Delta to include a facility tour as a part of the CLEEN Consortium Agenda for government attendees. This coordination continued until late February when it became apparent that restrictions on non-essential travel, such as those in Executive Order 14222 (Exec. Order No. 14,222, 2025) which came as a part of wider governmental cost savings and wider efficiency pushes, would require that the CLEEN Consortium be hosted virtually. Plans for Georgia Tech to host the CLEEN Consortium were cancelled with mutual agreement between the FAA and Georgia Tech.

Publications

None.



Outreach Efforts

The Georgia Tech attended the spring and fall CLEEN Consortium in 2025 which included the opportunity for students to observer industry prevent their contributions to the ASCENT program and how professional engineering reviews are conducted.

Awards

None.

Student Involvement

Over the course of 2025, 19 different graduate students received funding from this effort. Note that all 19 students were not funded simultaneously. One of the graduate students (Joao De Azevedo) is on a doctoral track, and the other 18 students (Tabitha D'Amato, Dante Cyrus, James Tsangarides, Kayley Lewis, Ballard Huey, Nathaniel Green, Flavius Penescu, Aniela Zaremski, Akash Shiri, Anna Conroy, Vishwa Malaisamy, Samal Siddharth, Anika Chawla, Adi Arora, Nicholas He, Suhanna Bamzai, Ellen Wang, and Thomas Prosser) are on master's degree track. One additional student, Dante Cyrus, supported this project while receiving funding from the U.S. Air Force.

Plans for Next Period

- Focus on implementing CLEEN III technologies into EDS as data become available.
- Finalize a baseline fleet performance scenario.
- Conduct a preliminary fleet assessment provided that sufficient number of technology modeling tasks are completed.

References

Airbus. (2025). *Orders and deliveries, Commercial Aircraft*. https://www.airbus.com/en/products-services/commercial-aircraft/orders-and-deliveries

Ahrens, D., Méry, Y., Guénard, A., & Miake-Lye, R. (2022) *A New Approach To Estimate Particulate Matter Emissions From Ground Certification Data: The nvPM Mission Emissions Estimation Methodology (MEEM).* The American Society of American Engineers. https://asmedigitalcollection.asme.org/GT/proceedings/GT2022/85994/V03AT04A035/1148716

Boeing. (2025). *Commercial, Orders & Deliveries*. https://www.boeing.com/commercial

Embraer. (2025). *Orders and deliveries*. https://www.embraer.com/eca/orders-deliveries/en/

European Environment Agency, European Union Aviation Safety Agency. (2016). *European aviation environmental report 2016*. https://op.europa.eu/en/publication-detail/-/publication/796e6041-fc83-11e5-b713-01aa75ed71a1/language-en

Exec. Order No. 14,222. 90 FR 11095 (2025). https://www.federalregister.gov/documents/2025/03/03/2025-03527/implementing-the-presidents-department-of-government-efficiency-cost-efficiency-initiative

ICAO. (2021). ICAO Aircraft Emissions Databank. International Civil Aviation Organization. https://www.easa.europa.eu/en/domains/environment/icao-aircraft-engine-emissions-databank

Mavris, D., & Kirby, M. (2024). *Project 082(A) Integrated Noise and CO2 Standard Setting Analysis*. FAA Center of Excellence for Alternative Jet Fuels & Environment. https://ascent.aero/project/integrated-noise-and-co2-standard-setting-analysis/

Mavris, D., Tai, J., & Brooks, J. (2023). *Project 037 CLEEN II System-level Assessment*. FAA Center of Excellence for Alternative Jet Fuels & Environment. https://s3.wp.wsu.edu/uploads/sites/2479/2024/08/2023-ASCENT-Annual-Report.pdf

Mavris, D., Tai, J., & Brooks, J. (2024). *Project 037 CLEEN II System-level Assessment*. FAA Center of Excellence for Alternative Jet Fuels & Environment. https://s3.wp.wsu.edu/uploads/sites/2479/2025/06/ASCENT-2024-Annual-Report.pdf

Orton, A. (2024). *FAA Office of Environment & Administration Energy Overview and Update.* FAA Center of Excellence for Alternative Jet Fuels & Environment. https://www.faa.gov/sites/faa.gov/files/Nov-2024FAA-Environment-and-Energy-RD-Overview.pdf



Project 038 Rotorcraft Noise Abatement Procedure Development

The Pennsylvania State University, Continuum Dynamics, Inc.

Project Lead Investigator

Kenneth S. Brentner
Professor of Aerospace Engineering
Department of Aerospace Engineering
The Pennsylvania State University
308 ECoRE Bldg, 556 White Course Drive
University Park, PA
814-865-6433
ksbrentner@psu.edu

University Participants

The Pennsylvania State University (Penn State or PSU)

- P.I.: Kenneth S. Brentner, Professor of Aerospace Engineering
- FAA Award Number: 13-C_AJFE-PSU-038, Amendment No. 119
- Period of Performance: October 1, 2024, to August 30, 2025
- Tasks:
  1. Shrouded rotor noise modeling
  2. Broadband noise prediction enhancement
  3. PSUDEPSim aircraft model updates
  4. Application of noise prediction enhancements to abatement procedure analysis
  5. Demonstrate PSU Noise Prediction System (PSU-NPS) at Volpe National Transportation Systems Center (Volpe) and Federal Aviation Administration (FAA) Technical Center

Project Funding Level

The project's previous funding ended on December 31, 2023, and was not renewed until August 2024, with FAA funding of $181,000; Continuum Dynamics, Inc. (CDI; point of contact: Dan Wachspress) providing $150,000 of cost sharing in the form of a 1-yr license for the Comprehensive Hierarchical Aeromechanics Rotorcraft Model (CHARM) rotorcraft comprehensive analysis software to Penn State and the FAA or their designee. Supernal will provide $140,000 in-kind support in the form of costs accrued to collect and extract datasets from a flying testbed Bell® 407 as well as engineering hours. Due to the funding gap, task names did not change for this report.

Investigation Team

Kenneth S. Brentner, P.I., Penn State; acoustic prediction lead on all tasks
Joseph F. Horn, co-P.I., Penn State; flight simulation lead, support for all tasks
Daniel A. Wachspress, co-P.I., CDI; rotor loads, wake integration, and CHARM coupling
Mrunali Botre, co-P.I., CDI; support for rotor loads, wake integration, and CHARM coupling
Salma Ibnoukhaiber, Undergraduate Research Assistant, Penn State; broadband noise enhancement, and documentation of PSU-NPS for Volpe and other users.
Bhaskar Mukherjee, Ph.D. student (graduated August 2025), broadband noise, task overview and planning.

® Bell is a registered trademark of Textron Innovations, Inc., Providence, Rhode Island.



Project Overview

Rotorcraft noise consists of several components, including rotor noise, engine noise, and gearbox and transmission noise. Rotor noise is typically the dominant component of rotorcraft noise to which the community is exposed upon takeoff and landing, and along the flight path of the helicopter. Rotor noise arises from multiple noise sources, including thickness noise and loading noise (the combination of these two is known as rotational noise), blade–vortex interaction (BVI) noise, high-speed impulsive (HSI) noise, and broadband noise. Each noise source has its own unique directivity pattern around the helicopter. Furthermore, aerodynamic interactions among rotors, interactions between the airframe wake and a rotor, and unsteady time-dependent loading generated during maneuvers typically increase loading noise. The combination of all potential rotor noise sources makes the prediction of rotorcraft noise highly complex, although not all noise sources are present at any given time in the flight (e.g., BVI noise usually occurs during descent, and HSI noise occurs only during high-speed forward flight).

In ASCENT Project 006, "Rotorcraft Noise Abatement Operating Conditions Modeling," the project team coupled a MATLAB®-based flight simulation code with Comprehensive Hierarchical Aeromechanics Rotorcraft Model (CHARM) aerodynamics code and Penn State's noise prediction code PSU-WOPWOP to form an integrated rotorcraft noise prediction capability for evaluating noise abatement procedures. This system calculates noise generated due to the motion and operating aerodynamic pressures on the main and tail rotor blades. The system did not model engine noise or HSI noise; however, engine noise is generally not a dominant contributor to far-field sound noise levels compared to noise from rotor blade motion and airloads. In addition, HSI occurs primarily during high-speed forward flights and is therefore not typically encountered during routine civil helicopter operations. Comparing predictions against Bell 430 flight test data (Snider et al., 2013) demonstrated reasonable agreement for select flight conditions. This system was then used to draft a plan for a flight test.

Representative helicopters were recommended for development of noise abatement procedures in ASCENT Project 38. These helicopters were selected to enable determination of whether noise abatement procedures could be developed for various categories of helicopters (i.e., two-blade light, four-blade light, two-blade medium, etc.) or whether aircraft-specific design considerations would be required. Aircraft models were established for the following aircraft: Bell 430, Sikorsky® S-76C+ and S-76D, Bell 407 and 206L, Airbus® EC130 and AS350, and Robinson® R66 and R44. Predictions were made before the 2017 FAA/National Aeronautics and Space Administration (NASA) noise abatement flight test to provide guidance for the flight test (see *ASCENT Project 038 Annual Report 2017*). After the flight test, a comparison of *A*-weighted sound pressure level time histories and sound exposure level contour plots revealed a problem in the broadband noise prediction, which was subsequently corrected (see *ASCENT Project 038 Annual Report 2018*). Initial validation comparisons demonstrated that the simulations were within several dBA of the flight test data; however, some discrepancies in the simulations (simplifications) remained, thus requiring a detailed examination. Work was also performed on the PSU-NPS, including modifying PSU-WOPWOP to output plots of the maximum dBA, as plotted in the flight test. Further work was conducted to enhance the postprocessing of noise data to enable a direct comparison with flight test data. Detailed analysis of the noise components and noise sources was performed for several helicopters in the 2017 FAA/NASA flight test (see *ASCENT Project 038 Annual Report 2019*). Further enhancements were added to compute moving averages and devise strategies for window overlapping in the post processing of predicted noise data (see *ASCENT Project 038 Annual Report 2020*). In the cases studied, de-Dopplerization (used in flight test data processing) and moving observers (used in noise predictions to eliminate Doppler effects) were demonstrated to be effectively equivalent (typically within 0.5 dB or less). Next a comparison of the effectiveness of noise abatement procedures by helicopter class was performed by using the 2017 and 2019 flight test data (see *ASCENT Project 038 Annual Report 2021*). In particular, the Bell 205, 206, and 407 aircraft were compared for various flight conditions in the flight tests. In the predictions, the Pegg broadband noise prediction did not work as well for some aircraft, and a simple scaling of the broadband noise was considered as a potential correction. Unfortunately, no clear relationship with the scaling among aircraft was observed. In addition, an analysis of the 2019 FAA/NASA flight test was performed by comparison of prediction and experimental data for 3° and 4.5° descents for both left and right turns at different bank angles (25° and 45°, respectively) for two aircraft (Bell 205 and Sikorsky S-76D). Preliminary coupling between the Penn State noise predictions system and Volpe's Advanced Acoustics Model (AAM) software was implemented (see *ASCENT Project 038 Annual Report 2022*). Expanding on preliminary work on

® MATLAB is a registered trademark of The MathWorks, Inc., Natick, Massachusetts.
® Sikorsky is a registered trademark of Sikorsky Aircraft Corporation, Stratford, Connecticut.
® Airbus is a registered trademark of Airbus Operations GmbH, Hamburg, Germany.
® Robinson is a registered trademark of Robinson Helicopter Company, Incorporated, Torrance, California.



shrouded rotor noise prediction that began in 2021, CHARM's panel method was used to model a duct (see *ASCENT Project 038 Annual Report 2023*). Predictions from this approach showed favorable agreement with experimental data for an isolated ducted rotor (Cuppoletti et al., 2022). This work was further extended to modeling of the EC130 tail rotor (Fenestron®), where the shroud was modeled using a lifting panel in CHARM and noise predictions (see *ASCENT Project 038 Annual Report 2024*). For the EC130 helicopter in out-of-ground-effect hover conditions, predicted sound pressure levels showed good agreement with measured data from the 2017 flight test at several ground microphone locations. The Pegg broadband noise prediction model was also rederived, revealing the foundational equations and a potential pathway for recalibrating the model for different helicopters using flight test data. ASCENT Project 038 also transitioned to using a new version of the noise prediction system developed under ASCENT Project 049. The system was revalidated against flight test data for several helicopters and maneuvers investigated over the years in ASCENT Project 038.

The objective of this continuing project is to reduce the need for flight testing of each rotorcraft of interest for continued development of low-noise operating procedures. Existing guidance in the Fly Neighborly program is based on recommendations from manufacturers, is nonmandatory, and often available for only limited rotorcraft models and design types. Other methods for developing noise abatement procedures at the FAA and NASA are empirical, based on previous flight measurements of specific aircraft. The current project enables analysis of new flight procedures and noise analysis strategies through computations. This year's efforts included further analysis and investigation of the 2017 and 2019 FAA/NASA noise abatement flight tests, development of shrouded rotor noise modeling for rotorcraft models with such features, updating the flight simulator and enhancing couplings, and preparing documentation and training materials to enable the FAA and their partners to use the PSU-NPS.

Task 1 - Shrouded Rotor Noise Modeling

The Pennsylvania State University

Objectives

Prediction of shrouded rotor noise has been a major barrier in predicting noise from helicopters such as the Airbus EC130 (with a Fenestron). The primary objective of this task is to utilize shrouded rotor noise prediction capabilities developed as part of task 38 (ASCENT Annual Report 2022-2023) and test its efficacy against flight test measurements of helicopters equipped with a Fenestron. Modeling techniques and their impact are studied and documented.

Research Approach

The 2017 NASA/FAA flight test (Watts et al., 2019) provided acoustic measurements for the EC130 helicopter in hover and various forward flight maneuvers. The shrouded tail rotor geometry was estimated based on publicly available images, including the uneven blade spacing. CHARM is used to derive airloads for the main and tail rotors along with the shroud. The stators and struts in the Fenestron are not currently modeled in CHARM.

Milestones

- Model EC130 helicopter Fenestron in CHARM and PSU-WOPWOP.
- Evaluate the acoustic impact of unevenly spaced Fenestron blades.
- Predict the noise from Airbus EC-130 aircraft flown in the 2017 FAA/NASA flight test.

Major Accomplishments

A CHARM-based lifting-line and panel representation of the EC130 helicopter rotors was developed (see ASCENT Annual Report 2023 – 2024, Task 1). The model incorporated the estimated uneven blade spacing and an extracted shroud geometry, with the rotor blades represented as flat lifting surfaces using CHARM's vortex lattice method and the shroud represented as a three-dimensional (3D) panel surface (see Figure 1). Comparisons with the 2017 NASA/FAA hover measurements showed agreement within 2 – 4 dB at several microphone locations, demonstrating the model's ability to capture key Fenestron acoustic features.

® Fenestron is a registered trademark of Airbus Helicopters, Marignane Cedex, France.



Figure 1. CHARM panel representation of EC130 Fenestron helicopter shrouded tail rotor.
(as modeled by Sagar Peddanarappagari)

A survey of shrouded-tail-rotor noise studies has provided new guidance for improving the current model. Work from Airbus and ONERA (Office National d'Études et de Recherches Aérospatiales) indicates that rotor–stator aerodynamic interaction is a dominant noise source in hover. You et al. (2016), using Unsteady Reynolds-Averaged Navier-Stokes simulations, demonstrated that rapid, periodic fluctuations in blade loading are driven by stator blockage. This suggests that CHARM's lifting-panel method should be capable of capturing first-order interaction effects once the stator blades and central shaft are included as 3D panel geometry (the present CHARM model includes only the shroud surface).

Fenestron tail rotor noise prediction in forward flight is complicated by flow separation and the increasing importance of acoustic scattering. A significant portion of the thrust needed to counterbalance main rotor torque is provided by lift on the tail rotor fin, requiring lower thrust produced by the Fenestron in forward flight. This has been found to result in significant flow separation around the hub by Gardarein et al. (2006), placing the rotor blades in a highly turbulent inflow. This behavior is also evident in the experimentally measured blade surface pressure data near the tip reported by Gardarein et al. (2010). In addition, Falissard et al. (2011) found that neglecting acoustic scattering by the cylindrical shroud can lead to discrepancies of up to 10 dBA between measured and predicted levels. Accurately modeling these acoustically important phenomena is computationally demanding: capturing separated flow typically requires well-resolved computational fluid dynamics simulations, and acoustic scattering calculations are also prone to issues in numerical convergence (Lee, 2017).

To address such challenges more generally, the Airbus Helicopters MOTUS framework (Guntzer et al., 2025) was developed to leverage flight test data to correct deficiencies in noise prediction. First, a database of de-Dopplerized noise hemispheres from flight tests that span a range of operating conditions is constructed. Filtering the high-frequency broadband noise out, tonal noise from the main and tail rotors are separated at each microphone in the hemisphere. The prediction system is then used to calculate noise at these microphones in the database. The differences between the predicted and measured noise levels for the main and tail rotors are then stored as "masks" Depending on the quality of the experimental data, these masks can be applied as a function of individual frequency bins and microphone locations, a level shift to the integrated sound pressure level that vary with microphone location, or as a uniform shift in levels applied to the entire hemisphere (independent on microphone position).

Publications

Peddanarappagari, S. (2024). *Updates to Penn State Rotor Noise Prediction System for Rotorcraft* [Master's thesis, Pennsylvania State University]. The Pennsylvania State University. https://etda.libraries.psu.edu/catalog/28748ssp5319

Outreach Efforts

None.

Awards

None.



Student Involvement

Bhaskar Mukherjee, a graduate assistant, completed his PhD degree and conducted a literature review identifying key challenges in Fenestron tail rotor noise modeling, recommending approaches to improve predictions using flight test data. Salma Ibnoukhaiber, an undergraduate research assistant, completed her bachelor's degree and performed work to update and extend a user's manual for the PSU-NPS. Salma also helped prepare example cases and a distribution package for the PSU-NPS. Rupak Chaudhary, a Ph.D. student worked on the project to develop and refine PSU-NPS test cases.

Plans for Next Period

- Explore a semi-empirical approach like the Airbus Helicopters MOTUS framework to avoid the impractical computational expenses associated with modeling Fenestron tail rotor noise. Tools for main and tail rotor tonal noise separation have been developed under ASCENT Project 077 (Rachaprolu & Greenwood, 2024), thus allowing the processing of flight test data measured for EC130 (Watts et. al., 2019) and generation of the hemisphere database.
- Obtain and evaluate the "Masks" for different steady flight conditions while predicting noise during maneuvers.

References

Reed, N., & Cuppoletti, D. R. (2022). Implications of Rotor–Rotor Interaction in Noise Generation of UAM Vehicles with Counter-Rotating Configurations. AIAA Scitech 2022 Forum, Paper AIAA 2022-2168. https://doi.org/10.2514/6.2022-2168 [arc.aiaa.org]

Falissard, F., Desmerger, F., Gardarein, P., Binet, L., & Camus, J. (2011, May 3-5). *Aeroacoustic Flight Test and Data Analysis for the Validation of Fenestron Noise Computations.* American Helicopter Society 67th Annual Forum 12, Virginia Beach, Virginia.

Gardarein, P., Falissard, F., Binet, L. & Camus, J.-C. (2010, September 7). Validation of Aerodynamic and Aeroacoustic Computations of a Fenestron in Real Flight Conditions [Conference paper]. 36th European Rotorcraft Forum, Paris, France.

Gardarein, P., Canard, S. & Prieur, J. (2006). Unsteady Aerodynamic and Aeroacoustic Simulations of a Fenestron Tail Rotor. In *Annual Forum Proceedings - AHS International*, 1-12.

Guntzer, F., Caillet, J., Cariou, C., Pinacho, J. Dieumegard, P., & León, E. R. (2025). A comprehensive helicopter acoustic modeling tool based on simulation and experiment. *CEAS Aeronautical Journal, 16*, 1213–1225. https://doi.org/10.4050/F-0080-2024-1409

Lee, S. (2017). Review: The Use of Equivalent Source Method in Computational Acoustics. *Journal of Computational Acoustics, 25*(1), 1630001. https://doi.org/10.1142/S0218396X16300012

Rachaprolu, J. S., & Greenwood, E. (2024). Helicopter Noise Source Separation Using an Order Tracking Filter. *Journal of the American Helicopter Society, 69*, 1–9. https://doi.org/10.4050/F-0078-2022-17433

Snider, R., Samuels, T., Goldman, B., & Brentner, K. S. (2013). Full-scale rotorcraft broadband noise prediction and its relevance to civil noise certification criteria. Proceedings of the 69th American Helicopter Society International Annual Forum, Phoenix, Arizona, May 21–23, 2013, Vol. 2, pp. 1293–1307.Watts, M. E., Greenwood, E., Smith, C. D. & Stephenson, J. H. (2019). *Noise Abatement Flight Test Data Report* (NASA/TM-2019-220264). National Aeronautics and Space Administration.

You, J. H., Breitsamter, C. & Heger, R. (2016). Numerical investigations of Fenestron™ noise characteristics using a hybrid method. *CEAS Aeronautical Journal, 7*(2), 185–207. https://doi.org/10.1007/s13272-015-0180-1

Task 2 - Broadband Noise Prediction Enhancement

The Pennsylvania State University

Objective

Helicopter broadband noise has been shown to be important for flight conditions where BVI is absent. The objective of this task (Task 8.2 in the 2023-2024 proposal) is to enhance the existing helicopter broadband noise modeling capabilities of the PSU noise prediction system. The task aims to investigate improvements in physics-based and empirical modeling methods.

Research Approach

Previous work ASCENT Project 038 by Botre (2020) and Zachos (2022) has revealed deficiencies in broadband noise predictions for several helicopters on the order of 6 decibels. However, the prediction methodology largely relied on the

empirical Pegg (1979) model. The model calibrated originally from flight test data of medium-weight helicopters offers no path for re-calibration using newly measured flight test data (Watts et al., 2019). Zachos (2022) attempted scaling the Pegg model using an offset determined from flight test data (Watts et al., 2019). While this approach had limited success, it did reveal the potential benefits of re-calibrating the Pegg model. Broadband noise modeling for electric vertical take-off and landing (eVTOL) aircraft in ASCENT Project 049 has largely relied on first principle methods and can also be applied to helicopters.

Milestones

- Explore new methods for scaling Pegg model.
- Incorporate broadband noise prediction methods from ASCENT Project 049.

Major Accomplishments

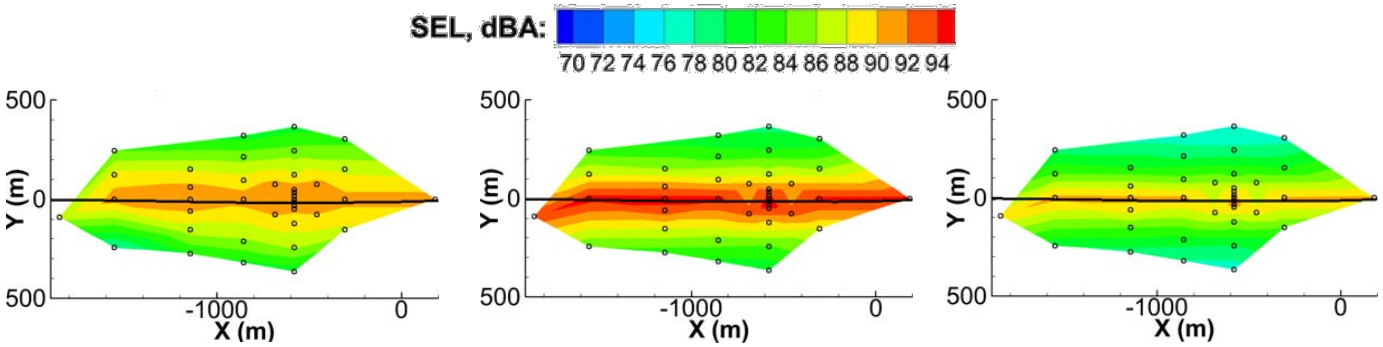
Previous work in ASCENT Project 039 by Botre (2020), Zachos (2022) revealed a trend of broadband noise overprediction by the Pegg model (Pegg, 1979) for several helicopters. During a review of the implementation of the model in PSU-WOPWOP a potentially major source of error was discovered (Mukherjee, 2025). In a discussion on the implementation of the Pegg model in PSU-WOPWOP, Goldman (2012) relates a key input variable, the mean lift coefficient of the rotor ($\bar{C}_L$) with the rotor thrust (T) as follows:

$$\bar{C}_L = \frac{6T}{\rho A_B V_T^2} \quad \text{(Eq. 1)}$$

Here, ρ is the density of air, A_B is the rotor disk area and V_T is the rotor tip speed. However, this expression is not the same as the definition provided by Hubbard (1953) and Schlegel et al. (1966). These reports were found to be the foundation on which Pegg (1979) derived the semiempirical model (complete derivation can be found in pgs. 168 – 171, Mukherjee, 2025). Instead of the tip speed of the rotor V_T, the original expression for $\bar{C}_L$ used the speed at a distance 0.7*tip-radius ($V_{0.7}$) as follows:

$$\bar{C}_L = \frac{T}{\frac{1}{2}\rho A_B (V_{0.7})^2} = \frac{4.081T}{\rho A_B V_T^2} \quad \text{(Eq. 2)}$$

Thus, the current implementation of the Pegg model in PSU-WOPWOP was overestimating $\bar{C}_L$ by a factor of ≈ 1.5. This in turn was shown by Mukherjee (2025, pg. 173) to result in an overprediction of 1.67 dBA to 13.39 dBA depending on the value of $\bar{C}_L$. The impact of this was demonstrated by Mukherjee (2025) when evaluating noise predictions of a Bell 206L helicopter in 80 knots level flight against flight test data (Watts et al., 2019). Figure 2 shows the sound exposure level (SEL) contours on a grid of ground microphones from three different datasets: Figure 2a shows the flight test data, Figure 2b shows PSU-WOPWOP predictions based on Goldman (2012) implementation of the Pegg model, while Figure 2c shows PSU-WOPWOP predictions based on the corrected Pegg model by Mukherjee (2025).



(a) Flight test (b) Pegg implementation (Goldman 2012) (c) Pegg Corrected (Mukherjee 2025)

Figure 2. Bell 206L 80 knots level flight.
(Flight test data and PSU-WOPWOP input files shared by Dr. Mrunali Botre)



Publications

Mukherjee, B. (2025). *Noise of Multirotor Electric Aircraft* [Doctoral dissertation, The Pennsylvania State University]. The Pennsylvania State University. https://etda.libraries.psu.edu/catalog/22433bxm437

Outreach Efforts

None.

Awards

None.

Student Involvement

Bhaskar Mukherjee, a graduate assistant, completed his PhD degree and documented the derivation of the Pegg model, identified and corrected a major source of overprediction by the Pegg model's implementation in PSU-WOPWOP.

Plans for Next Period

- Complete further testing of this correction to the implementation of the Pegg model in PSU-WOPWOP by evaluating noise from additional helicopter maneuvers previously documented to have overpredictions. Once confirmed, the correction will be included in a new release of PSU-WOPWOP to its users in industry, government and academia.

References

Botre, M. (2020). *Rotorcraft noise prediction system validation and analysis for generating noise abatement procedures* [Doctoral dissertation, The Pennsylvania State University]. The Pennsylvania State University. https://etda.libraries.psu.edu/catalog/18150mcb355

Goldman, B.A. (2012). *Modifications to PSU-WOPWOP For Enhanced Noise Prediction Capabilities*. [Master's thesis, The Pennsylvania State University]. The Pennsylvania State University. https://etda.libraries.psu.edu/catalog/16434

Hubbard, H. H. (1953) *Propeller-Noise Charts for Transport Airplanes* (NACA TN 2968). National Advisory Committee for Aeronautics. https://ntrs.nasa.gov/citations/19930084076

Mukherjee, B. (2025). *Noise Of Multirotor Electric Aircraft* [Doctoral dissertation, The Pennsylvania State University]. The Pennsylvania State University. https://etda.libraries.psu.edu/catalog/22433bxm437

Pegg, R. J. (1979). *A Summary and Evaluation of Semi-Empirical Methods for the Prediction of Helicopter Rotor Noise* (NASA-TM-80200). National Aeronautics and Space Administration. https://ntrs.nasa.gov/citations/19800007615

Schlegel, R., King, R. & Mull, H. (1966). *Helicopter Rotor Noise Generation and Propagation* (USAAVLABS TECHNICAL REPORT 66-4). Defense Technical Information Center. https://doi.org/10.21236/AD0645884

Watts, M. E., Greenwood, E., Smith, C. D. & Stephenson, J. H. (2019). *Noise Abatement Flight Test Data Report* (NASA/TM-2019-220264). National Aeronautics and Space Administration.

Zachos, D. R. (2022). *Noise Prediction of Rotorcraft Acoustics for a Conceptual eVTOL Design and Conventional Helicopters* [Doctoral dissertation, The Pennsylvania State University]. The Pennsylvania State University. https://etda.libraries.psu.edu/catalog/19211drz5061

Task 3 - PSUDEPSIM Aircraft Model Updates

The Pennsylvania State University

Objective

Since the transition from the old noise prediction system based on the Helosim flight simulation code (Botre, 2020), helicopter input files need to be adapted for the newly developed PSUDEPSim (Theron et al., 2020). The objective of this task is to transfer input files for helicopters from the old system and validate it with the new noise prediction system (also used in ASCENT Project 049).

Research Approach

Parameters representing the geometry, aerodynamics and dynamics of the helicopter are required for fully coupled flight simulation. Using previously documented values (Botre, 2020), new input files are to be generated based on the format in the DEPSim manual (Theron et al., 2022). Flight test trajectories are simulated using the new system, and noise results validated.

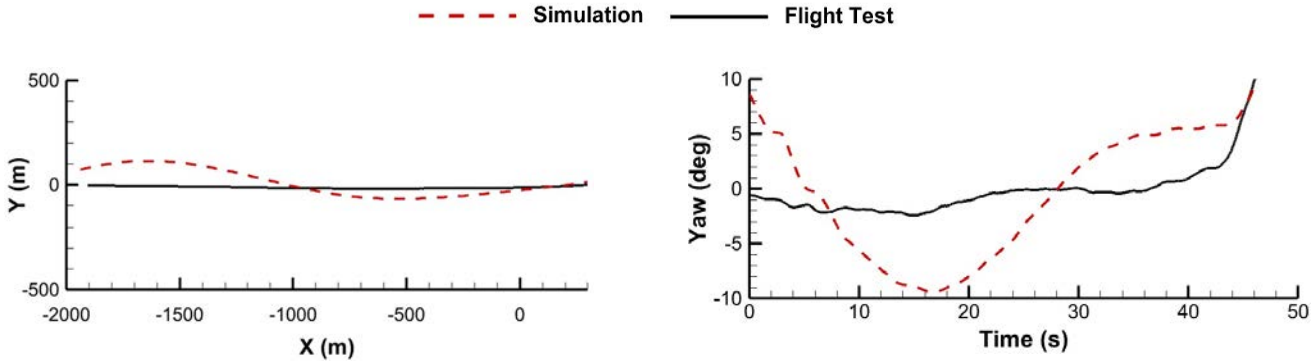
Milestones

- Generate new helicopter input files for PSUDEPSim.
- Validate noise from maneuvers from various helicopter models against measured flight test data.

Major Accomplishments

The Helosim and DEPSim flight simulation codes share very similar helicopter input file formats, both requiring the same set of parameters defining the geometry, mass, and inertia of the blades and aircraft. This allows the following helicopter models to be imported from Helosim into DEPSim with minimal changes: Robinson R44 and R66, Bell 206 and 407, and Airbus AS350. However, unlike Helosim, DEPSim is not limited to helicopters only and therefore uses a different set of input parameters for the flight controller. As a result, default values for several of these parameters are initially used for all helicopter models.

Using these default values, however, appears to result in inaccurate simulations of a given flight condition. For example, Figure 3a shows the X–Y trajectory of a Bell 206L helicopter in 80-knot level flight (+X being the direction of flight). Two datasets are plotted: flight test data (Watts et al., 2019) and DEPSim simulation results. Figure 3a, which uses the default controller input parameters, shows a trajectory deviation of nearly 100 m (≈330 ft) along the Y direction. This indicates that the trajectory-following controller has larger error in tracking the aircraft yaw angle, which is corroborated by Figure 3b.

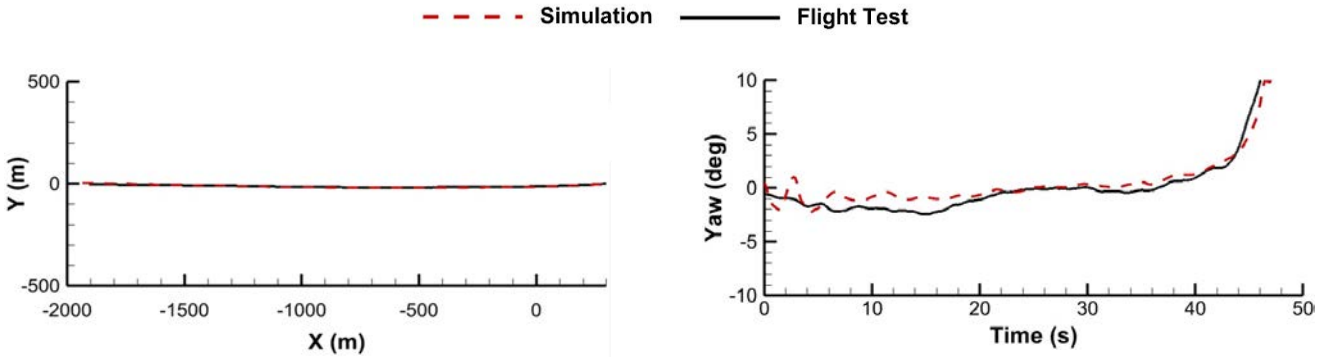


(a) Trajectory (top-view)

(b) Yaw angle

Figure 3. Trajectory tracking error in DEPSim simulation: Bell 206L, 80kts level flight.

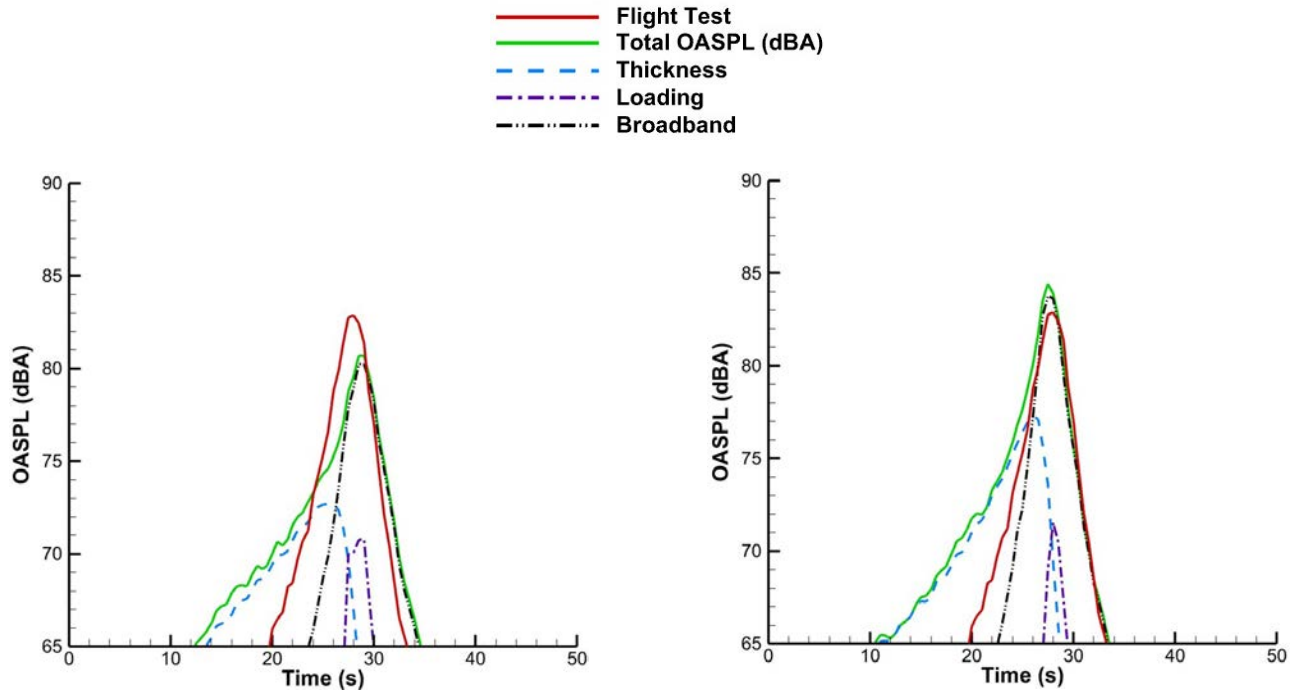
Two issues can be observed in Figure 3b: (1) the values oscillate, and (2) they overshoot. These issues are resolved by adjusting the values of the controller damping ratio and bandwidth, which affect the magnitude of oscillations and the command response time, respectively. Adjusting these parameters leads to a significant improvement in trajectory tracking, as shown in Figure 4, where the yaw angle can now be observed to track the flight test data much more accurately.



(a) Trajectory (top-view) (b) Yaw angle

Figure 4. DEPSim simulation with tuned trajectory following controller: Bell 206L, 80kts level flight.

The impact of accurately tracking flight test data on predicted noise can be seen in Figure 5, where the variation of integrated sound pressure level (A-weighted) with time is plotted for a microphone situated right below the trajectory of the helicopter. The peak level and a 10 dBA drop is captured well once the flight control parameters are tuned (Figure 5b), thus capturing the SEL more accurately. Note that the initial overprediction is currently hypothesized to be a result of acoustic shielding by the fuselage that is not captured in the predictions.



(a) Before tuning (b) After tuning

Figure 5. Bell 206 at 80kts level flight: Comparison of measured and predicted (Before & After tuning) A-weighted overall sound pressure level (dBA) vs. time (mic below helicopter flight trajectory)



Publications
None.

Outreach Efforts
None.

Awards
None.

Student Involvement
Salma Ibnoukhaiber, a first-year master's student in Aerospace Engineering, is working on tuning helicopter models in DEPSim and improving simulation match with flight test data.

Plans for Next Period
- Continue to improve the trajectory tracking for the Robinson R44 and R66, along with documenting the procedures used to achieve these improvements in the noise prediction system manual. The 2023–2024 ASCENT Annual Report demonstrated that the AS350 and Bell 407 helicopters could be simulated in DEPSim with acceptable accuracy. After updating the input parameters for the trajectory-following controller, the Bell 206L is now also being simulated successfully.

References
Botre, M. (2020). Rotorcraft noise prediction system validation and analysis for generating noise abatement procedures. PhD dissertation, The Pennsylvania State University.

Theron, J.-P., Horn, J. F., & Wachspress, D. A. (2020). An integrated simulation tool for e-VTOL aeromechanics and flight control analysis. Presented at the Aeromechanics for Advanced Vertical Flight Technical Meeting, 2020.

Theron, J.-P., Horn, J. F., Wachspress, D. A., Keller, J. D., & Sharma, A. (2022). Investigation of stability and disturbance rejection trade-offs for an e-VTOL controller. Presented at the Aeromechanics for Advanced Vertical Flight Technical Meeting, 2022.

Watts, M. E., Greenwood, E., Smith, C. D. & Stephenson, J. H. (2019). *Noise Abatement Flight Test Data Report* (NASA/TM-2019-220264). National Aeronautics and Space Administration.

Task 4 - Application of Noise Prediction Enhancements to Abatement Procedure Analysis
The Pennsylvania State University

Objective
The objective of this task is to design, test and demonstrate helicopter noise abatement procedures using the new and improved Penn State noise prediction system.

Research Approach
While previous work has demonstrated the ability of the new noise prediction system to predict noise from steady flight conditions such as hover, level flight, the system also needs to be validated against flight test data for maneuvers such as turns. Differences between predicted noise levels and measured need to be understood before using the system to generate new trajectories for noise abatement procedures.

Milestones
- Validate against maneuvers such as turns, accelerating climb etc.
- Demonstrate accuracy of the system in capturing important acoustic events such as blade vortex interactions (BVI), etc.

Major Accomplishments
It is crucial to have a robust and accurate noise prediction system in place before work on designing abatement procedures begins. A long-standing issue of broadband noise overprediction by the Pegg model was corrected as part of Task 2. With



the introduction of a new trajectory-following controller in PSUDEPSim, input parameters are now being updated to improve agreement with flight test data (Task 3). The previous version of the noise prediction system, based on PSUHeloSim, successfully simulated the following aircraft: Airbus AS350 and EC130, Bell 206 and 407, Robinson R44 and R66, and Sikorsky S76D. To date, the AS350 and Bell 206 models have been successfully exported to PSUDEPSim and validated within the new noise prediction system.

In parallel, a literature review was conducted to expand the scope of this task for next year by incorporating considerations of safety and pilot workload in abatement procedure design. Existing guidance for avoiding BVI during arrival maneuvers often involves steep, decelerating descents that can require high pilot workload, particularly under tailwind conditions (Rapoza et al., 2019). PSUDEPSim provides several simulation output parameters that can support preliminary assessment of maneuver safety and workload. For example, rotor torques can be compared against model-specific limits to assess the safety margin. Actuator response can be used to assess the control authority, while rate of stick activity can be used to estimate pilot workload.

Publications
None.

Outreach Efforts
None.

Awards
None.

Student Involvement
Bhaskar Mukherjee, a graduate assistant, completed his PhD degree and coordinated improvements to the noise prediction system and identify flight simulation parameters that can be used to assess maneuver safety and pilot workload to enable development of more acceptable noise abatement procedures.

Plans for Next Period
- Formalize the processing of PSUDEPSim flight simulation output parameters for maneuvers to provide more quantitative insight into flight safety and pilot workload.
- Simulate the arrival and departure procedures from the 2017 FAA/NASA flight test with the new system and analyze the derived safety parameters.

References
Rapoza, A. S., Page, J. A. & Jacobs, E. (2019*). iFlyQuiet Procedures Demonstration: Application of Fly Neighborly Procedures in East Hampton, NY*. U.S. Department of Transportation, John A. Volpe National Transportation Systems Center. https://rosap.ntl.bts.gov

Task 5 - Update PSU-NPS Documentation and Sample Cases
The Pennsylvania State University

Objective
The objective of the current task is to generate updated documentation of the noise prediction system, including user instructions and best practices. A user manual will be distributed to FAA, Volpe, and the FAA Technical Center along with the system for beta testing.



Research Approach

A user manual with instructions on compilation, installation and usage of the system will be documented first. The manual will also contain a brief description of the theoretical background of the components of the noise prediction system. Validation cases will be provided along with a list of best user practices. Based upon the feedback received from beta testers at Penn State and partners at FAA, the manual and the system will be updated accordingly.

Milestones

- Document installation and setup of DEPSim, CHARM, and PSU-WOPWOP including the coupling.
- Describe the file structure of the input files including a list of parameters required to simulate new helicopters.
- Identify validation cases and include necessary input files for users to test the system.

Major Accomplishments

Significant progress was made this year toward finalizing the documentation and sample case materials for the PSU-NPS. The PSU-NPS manual is now nearing completion and will be delivered with the system distribution package. It serves as a comprehensive user guide for operating the modular, physics-based framework developed to simulate rotorcraft flight dynamics and predict acoustic emissions. Across eight chapters, the manual provides structured step-by-step guidance on system configuration, execution, and interpretation of results, enabling users to reliably set up simulations and understand the underlying physical modeling. The table of contents of the PSU-NPS manual is shown in Figure 6.

1 Introduction 3
1.1 Helicopter Noise Background . . . 3
1.2 Introduction to PSU-NPS . . . 4
1.3 Case Example to Operate PSU-NPS: AS350 . . . 5

2 PSU-NPS Description 6
2.1 PSUDEPSim . . . 7
2.2 CHARM . . . 8
2.3 PSU-WOPWOP . . . 8
2.4 Simulation Modes . . . 8
2.4.1 Coupled vs Uncoupled Flight Simulation . . . 8
2.4.2 Aperiodic vs Quasi-periodic Data . . . 9
2.5 System Validation . . . 9

3 Installation and Setup 11
3.1 DEPSim . . . 11
3.2 CHARM . . . 12
3.3 PSU-WOPWOP . . . 12

4 PSU-NPS File Structure 13
4.1 DEPSim Root File Listing . . . 14
4.2 *Include* and *DEPSim.cpp.V2* . . . 14
4.3 *AircraftModels* . . . 14
4.4 *PSUDEPSim* . . . 15
4.5 *Binary2CSV* . . . 15

5 PSU-NPS Input Files 17
5.1 DEPSim . . . 17
5.1.1 *SimFile.inp* . . . 17
5.1.2 *PSUDEPSimInputData.txt* . . . 19
5.1.3 *CHARMInputFiles* . . . 20
5.1.4 *Case File* . . . 20
5.1.5 *Command File* . . . 20
5.2 CHARM . . . 21
5.2.1 Run Characteristics Input File (*.inp) . . . 21
5.2.2 Blade Geometry Input File (*bg.inp) . . . 21
5.2.3 Blade Dynamics Input File (*bd.inp) . . . 23
5.2.4 2-D Airfoil Section Data Input File (*af.inp) . . . 25
5.3 PSU-WOPWOP . . . 25
5.3.1 Case File . . . 25
5.3.2 Namelist Input File . . . 26

6 PSU-NPS Output Files 40
6.1 DEPSim . . . 40
6.1.1 *HeloSimOutXXX.bin* . . . 40
6.1.2 *DEPSimRuns.log* . . . 40
6.1.3 Trim State Vectors . . . 41
6.2 CHARM . . . 41
6.3 PSU-WOPWOP . . . 41
6.3.1 Pressure Files . . . 42
6.3.2 Sound Pressure Levels Files . . . 42
6.3.3 Spectrum Files . . . 42
6.3.4 Sigma Surfaces . . . 43

7 Utility Programs 44
7.1 Plot_results.m . . . 44
7.2 GenFlightTestCaseCmd.m . . . 45
7.3 FlightTestComparisonPlot.m . . . 47
7.4 ProcessForWOPWOP.m . . . 48
7.5 read_nc_files_amedee.m . . . 50

8 Examples to Operate the Noise Prediction System 53
8.1 Predict Noise Using PSU-NPS: AS350 - Level Flight (Run No. 289154) . . . 53
8.1.1 Initial Model Creation . . . 54
8.1.2 DEPSim Simulation: Coupled Example (PSUDEPSim + CHARM Rotor Model) . . . 55
8.1.3 PSU-WOPWOP noise prediction . . . 59
8.1.4 Steady Level Flight Validation . . . 65

Appendix I: Input Reference Tables 68
PSUDEPSimInput.txt . . . 68

Figure 6. PSU-Noise Prediction System Manual: Table of Contents.

The manual covers both introductory and technical elements necessary for effective use of the system. It begins with background information on helicopter noise theory and introduces the AS350 maneuver example, which is used throughout the document to demonstrate the practical use of the system. Later chapters describe the main components of PSU-NPS and explain how simulation setup choices, such as selecting coupled versus uncoupled modes, or using aperiodic versus quasi-periodic data, which can influence prediction accuracy. The manual also provides instructions for installation and setup, outlines the directory structure for DEPSim and CHARM, and presents detailed explanations of all required input files, including parameter definitions and their physical meaning. Guidance on output files, available MATLAB visualization tools, and step-by-step operation examples such as the AS350 80 kts level-flight case and planned additions including the



Bell 206L and R44 examples—are also included. Instructions for using sigma-surface visualizations to support debugging of blade motion, loads, and thickness will be added as well.

In parallel with the manual, the PSU-NPS distribution package (Figure 7) has been assembled and is nearing readiness for distribution, pending final verification of all executables. The package includes the full NPS manual, a readme file describing the directory structure, and six major folders. Three folders—DEPSim, CHARM, and PSUWOPWOP—contain the system executables and example input/output files for the AS350 80-kt level-flight case, serving as baseline reference cases for validation. A documentation folder consolidates all manuals, including those for each individual code. The NPS folder contains the aircraft models (AS350, Bell 206L, Bell 407, R44, R66), case and command files, CHARM and DEPSim input files, simulation files, MATLAB analysis scripts, and an NPS_Run_Results directory where simulation outputs will be stored. The sixth folder, FlightTest_wopwop_processing, includes the executables and MATLAB scripts used to process flight-test data through WOPWOP, with CHARM serving as the tool for generating the corresponding WOPWOP input files.

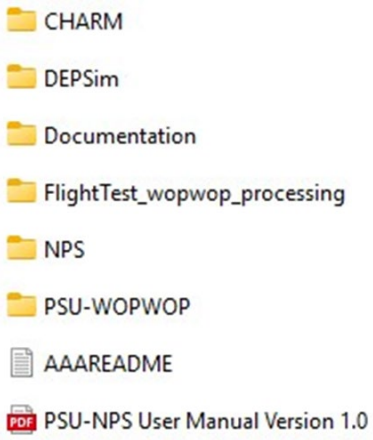


Figure 7. PSU-Noise Prediction System Package.

Publications
None.

Outreach Efforts
None.

Awards
None.

Student Involvement
Salma Ibnoukhaiber, a first-year master's student in Aerospace Engineering, has been working on developing the user manual and packaging the noise prediction system for distribution to users in the government and industry.

Plans for Next Period
- Formalize processing of PSUDEPSim flight simulation output parameters for maneuvers to provide more quantitative insight into flight safety and pilot workload.
- Simulate arrival and departure procedures from the 2017 FAA/NASA flight test with the new system and analyze the derived safety parameters.

References
None.



Project 044 Aircraft Noise Abatement Procedure Modeling and Validation

Massachusetts Institute of Technology

Project Lead Investigator

R. John Hansman
T. Wilson Professor of Aeronautics & Astronautics
Department of Aeronautics & Astronautics
Massachusetts Institute of Technology
Room 33-303
77 Massachusetts Avenue
Cambridge, MA 02139
617-253-2271
rjhans@mit.edu

University Participants

Massachusetts Institute of Technology (MIT)

- P.I.: Prof. R. John Hansman
- FAA Award Number: 13-C-AJFE-MIT, Amendment Nos. 050, 057, 073, 084, 105, 109, 115, 126, 133, and 143
- Period of Performance: September 1, 2018, to August 31, 2027
- Tasks:
  1. Review and identify relevant machine learning and data-mining techniques
  2. Apply data-mining techniques to relevant noise monitor, aircraft, operator, and flight dynamics data
  3. Expand approach to the analysis of additional airports and aircraft types
  4. Identify operational factors which influence the community noise at specific locations
  5. Assess implications of results to the design of noise abatement procedures

University of California - Irvine (via sub-award from MIT)

- P.I.(s): Prof. Jacqueline Huynh
- Award Number: MIT Subaward Purchase Order No. 523807
- Period of Performance: September 1, 2020, to September 30, 2026
- Tasks:
  1. Review and identify relevant machine learning and data-mining techniques
  2. Apply data-mining techniques to relevant noise monitor, aircraft, operator, and flight dynamics data
  3. Expand approach to the analysis of additional airports and aircraft types
  4. Identify operational factors which influence the community noise at specific locations
  5. Assess implications of results to the design of noise abatement procedures

Project Funding Level

$995,000 Federal Aviation Administration (FAA) funding and $995,000 matching funds. Sources of match are approximately $201,300 from MIT and $793,700 from Massachusetts Port Authority.

Investigation Team

Massachusetts Institute of Technology

Prof. R. John Hansman, (P.I.), Tasks 1-5
Brandon Hadfield, (graduate student), Tasks 1-5
Sandro Salgueiro, (graduate student, graduated), Tasks 1-5
Merek Homola, (graduate student), Tasks 1-5
Clement Li, (Postdoc), Tasks 1-5



Phillip Hood, (undergraduate student), Tasks 1-5

University of California, Irvine
Prof. Jacqueline Huynh, (co-P.I.), Tasks 1-5
Trinity Lee, (graduate student), Tasks 1-5
Melissa Lepe, (graduate student), Tasks 1-5

Project Overview

This project uses empirical noise data to develop validation methods from noise and flight surveillance datasets and to improve existing noise models. Field measurements of aircraft noise on approach and departure have historically shown significant variation (on the order of 10 dB), which has traditionally been attributed to factors such as varied power settings, aircraft configuration differences, and propagation effects. Recent analyses of this and other ASCENT projects have attempted to account for these factors but have been constrained by limited detailed flight data. This project explores approaches to combine emerging sources of flight data from flight data recorders (FDR) and other sources such as Automatic Dependent Surveillance-Broadcast (ADS-B) with current and emerging networks of ground noise monitors, to validate or improve aircraft noise models and to validate proposed noise abatement procedures. The rise of data-mining techniques has substantially enabled new insights and modeling capabilities based on the use of large datasets without requiring full a priori knowledge of all relevant physics. The development of advanced data-mining approaches applied to noise modeling is expected to provide insight into aircraft noise prediction for refining or validating noise models and for developing strategies for noise mitigation, through either new aircraft technologies or operational changes. Furthermore, improved noise modeling capabilities are expected to enable more informed decision making for stakeholders considering the options and consequences of operational or technological changes, thus facilitating the minimization of noise impacts on communities. Because noise is becoming an increasingly important factor in operational decisions regarding airports in the National Airspace System, an accurate understanding of noise impacts is necessary to minimize unnecessary disruptions to, or inefficiencies in, National Airspace System operations.

Task 1 – Review and Identify Relevant Machine Learning and Data Mining Techniques

Massachusetts Institute of Technology
University of California, Irvine

Objectives

Machine learning and data-mining techniques appropriate for evaluating relationships between noise monitor, aircraft, operator, and flight dynamics data will be reviewed and identified. These may include, but are not limited to, supervised machine learning on monitor-by-monitor basis, clustering and correlating resulting clusters to noise levels, identification of features/states relevant to observed noise, and intermonitor correlation analysis to investigate trajectory-level effects.

Research Approach

- Identify potential existing data sources for noise validation.
- Develop model of aircraft flight profiles by using existing surveillance (e.g., ADS-B or Airport Surface Detection Equipment, Model-X) data to generate noise estimates (readily available surveillance data are easier and less expensive to acquire than FDR data and data from dedicated flight tests).
- Evaluate flight profiles to understand why some procedures are quieter than others.

Milestones

- Identified Seattle Tacoma International Airport (SEA) noise monitor networks as potential sources of noise data for assessments.
- Identified the OpenSky database as a source of flight procedure data for noise assessments.
- Identified relevant machine learning techniques beyond simple linear regressions to correlate noise levels to operational factors.



Major Accomplishments

- Identified multilinear regression, clustering, airline grouping, XGBOOST and residual analysis as data-based modeling approaches to understand changes in noise as a function of operational and weather factors.

Publications

None.

Outreach Efforts

The ASCENT Project 044 team participated in the following outreach efforts:

- Collaborated with Port of Seattle to obtain noise data for arrivals and departures over 3 years.
- Participated in weekly teleconferences and meetings with FAA Technical Monitors.
- Performed outreach and collaboration with Massport, an operator at Boston Logan International Airport (BOS), and ASCENT Advisory Board members.
- Presented at the biannual ASCENT Advisory Board meetings.

Awards

None.

Student Involvement

Graduate and undergraduate students have been involved in all aspects of this research in terms of analysis, documentation, and presentation.

Plans for Next Period

Techniques to complete residuals analysis to understand factors contributing to noisy versus quiet airframes will be pursued, along with discussions with airlines about related possible sources of noise.

Task 2 – Apply Data Mining Techniques to Relevant Noise Monitor, Aircraft, Operator, and Flight Dynamics Data

Massachusetts Institute of Technology
University of California, Irvine

Objectives

Machine learning and data-mining techniques identified in Task 1 will be applied to relevant noise monitor, aircraft, operator, and flight dynamics data. The process will begin with SEA noise and OpenSky surveillance data for several aircraft types. Additional data inferred data states, such as flight operation type, will also be considered. From this analysis, the trends or features relevant to the observed noise will be assessed, along with the identification of possible correlations between datasets.

Research Approach

- Identify methods to correct variations in modeled noise due to flap setting, aircraft weight, and ambient atmospheric conditions; apply these methods to departures and approaches at SEA.
- Acquire ADS-B data from the OpenSky Network and atmospheric data from the National Oceanic and Atmospheric Administration's High-Resolution Rapid Refresh; use these data to estimate weight from true airspeed and atmospheric attenuation from relative humidity and temperature.

Milestones

- Developed a method to relate OpenSky surveillance operational data to atmospheric data and noise monitor data at particular time stamps.
- Developed a departure and approach weight estimation method based on ADS-B speed profiles, presented at American Institute of Aeronautics and Astronautics (AIAA) AVIATION 2025.
- Developed a method to assign flap deployment based on speed for each aircraft.



Major Accomplishments

- Developed a data-driven approach for assessing departure noise as a function of various operational, weather, and carrier factors, presented at AIAA SciTech 2025.
- Identified contributing noise factors for departure and arrival procedures of Boeing 737-800 aircraft at SEA from 3 years of noise monitor recordings, presented at AIAA SciTech 2025
- Demonstrated the impacts of aircraft operation and weather on modeled and measured noise over noise monitors of interest at SEA for both approaches and departures.
- Multivariate linear regressions and XGBOOST analysis resulted in moderate R^2 values for single monitor events.
- Airline grouping was found to provide more insight into the full procedural impact on multiple noise monitors.

Publications

Published Conference Proceedings

Lepe, M., Homola, M., Li, C., Lee, T., Hood, P., Huynh, J. L., & Hansman, R. J. (2025, January). Multifactor Analysis of Operational Factors Contributing to Aircraft Overflight Noise Variation. AIAA 2025-2004. AIAA SciTech 2025 Forum. https://doi.org/10.2514/6.2025-2004

Homola, M., Lepe, M., Trávník, M., Huynh, J. L., & Hansman, R. J. (2025, July). *Take-Off and Landing Weight Estimation From ADS-B Airspeed Profiles*. AIAA 2025-3309. AIAA AVIATION Forum and ASCEND 2025. https://doi.org/10.2514/6.2025-3309

Outreach Efforts

- Participated in weekly teleconferences and meetings with FAA Technical Monitors.
- Performed outreach and collaboration with Massport, an operator at BOS, and ASCENT Advisory Board members.
- Presented at the biannual ASCENT Advisory Board meetings.
- Presented to the major United States Airlines.

Awards

None.

Student Involvement

Graduate and undergraduate students have been involved in all aspects of this research in terms of analysis, documentation, and presentation.

Plans for Next Period

The additional data-mining techniques, such as residual analysis on loud and quiet airframes will be applied on approach and departure radar, weather, and noise monitor data for multiple aircraft types.

Task 3 – Expand Approach to the Analysis of Additional Airports and Aircraft Types

Massachusetts Institute of Technology
University of California, Irvine

Objectives

The data-mining approaches and analysis process from Task 2 will be expanded to additional airports and aircraft types. The modeling approach will be applied to gather data for the additional aircraft and locations. Potential trends or features relevant to the observed noise will be assessed for the larger dataset.

Research Approach

- Examine relevant noise monitor networks at different airports.
- Outreach to different airports to obtain noise monitor data.
- Expand approach to the analysis of additional airports and aircraft types.



Milestone
- Identified and reached out to obtain noise monitor date for analysis from BOS and John Wayne Airport (SNA).

Major Accomplishments
- Collected 3 years of approach and departure noise data at BOS and SNA for analysis.
- Collected 3 years of flap settings and weight data at SNA.
- Expanded analysis to Boeing 737-700 and Airbus A320 aircraft.

Publications
Student Thesis

Lee, T. (2025). A Data-Driven Approach to Aircraft Noise Variation and Operational Efficiency Analysis. *UC Irvine Masters Thesis*. ProQuest ID: Lee_uci_0030M_19549. Merritt ID: ark:/13030/m5mt5fxm. Retrieved from https://escholarship.org/uc/item/6tf709kc

Outreach Efforts
- Participated in weekly teleconferences and meetings with FAA Technical Monitors.
- Performed outreach and collaboration with Massport, an operator at BOS, and ASCENT Advisory Board members.
- Presented at the biannual ASCENT Advisory Board meetings.

Awards
None.

Student Involvement
Graduate and undergraduate students have been involved in all aspects of this research in terms of analysis, documentation, and presentation.

Plans for Next Period
The data-mining approaches and analysis process from Task 2 will be expanded to procedures flown at BOS.

Task 4 – Identify Operational Factors Which Influence the Community Noise at Specific Locations
Massachusetts Institute of Technology
University of California, Irvine

Objective
Operational factors from the large dataset and applied data-mining techniques in Task 3 will be used to identify any operational factors which influence the community noise. Any observed differences in monitors, airport, and aircraft type will be identified to highlight location- or vehicle-specific trends.

Research Approach
- Use data-mining techniques and big data to assess factors with the highest influences on noise levels.

Milestones
- Observed and identified a variety of departure and approach procedures in surveillance data at SEA and SNA.
- Used different data-mining approaches such as multivariate correlations, clustering, and machine learning applied to the data at SEA to examine trends in variables affecting aircraft noise, including those due to aircraft weight, thrust, distance to the monitor, airspeed, ambient atmospheric conditions, and compounding factors

Major Accomplishments
- Measured noise levels versus weight, thrust, speed, altitude, weather factors, and airline were examined through a multivariate approach for departures and arrivals.

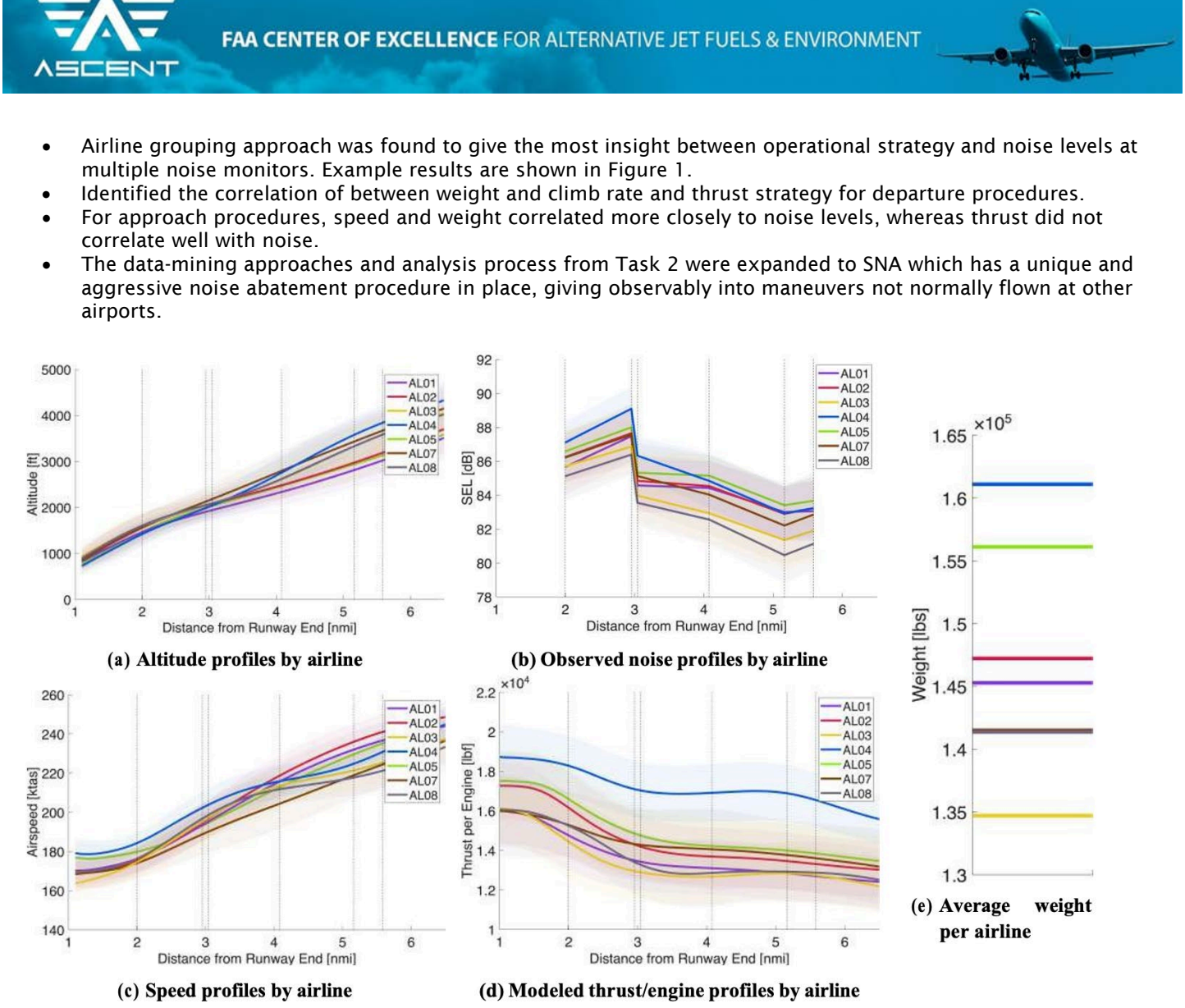


Figure 1. Boeing 737-800 southbound departure profiles for 3 years of operations at SEA for different airlines. Bold lines represent averages, and shaded areas represent region within one standard deviation.

Publications

None.

Outreach Efforts

- Participated in weekly teleconferences and meetings with FAA Technical Monitors.
- Performed outreach and collaboration with Massport, an operator at BOS, and ASCENT Advisory Board members.
- Presented at the biannual ASCENT Advisory Board meetings.

Awards

None.



Student Involvement
Graduate and undergraduate students have been involved in all aspects of this research in terms of analysis, documentation, and presentation.

Plans for Next Period
Any observed differences in monitors, airport, and aircraft type will be identified to highlight location- or vehicle-specific trends. In particular, the differences in analysis for procedures at BOS, SEA, and SNA will be examined to evaluate the effectiveness of these noise abatement procedures by a direct comparison.

Task 5 – Assess Implications of Results to the Design of Noise Abatement Procedures

Massachusetts Institute of Technology
University of California, Irvine

Objectives
Implications from Task 4 will be considered in the design of noise abatement arrival and departure procedures. Different flight operations will be explored and may include cockpit procedures, published procedures, and air traffic control procedures. Results may influence recommended noise abatement techniques and opportunities to improve existing procedures and noise modeling methods.

Research Approach
- Treat noise monitoring data from different airports as experimental data, which could serve as a benchmark for comparing loud versus quiet flights.
- Determine whether learnings can be applied to future departure and approach noise abatement procedure designs.

Milestone
- Performed initial examination of quiet versus loud departure and arrival procedures from 3 years of SEA and SNA data.

Major Accomplishments
- Identified weather factors such as relative humidity, temperature, and wind magnitude and direction to have some correlations, albeit weaker, with the measured noise levels on departure.
- Found aircraft altitude and thrust levels to have the strongest correlations with measured noise for the departure procedures examined, whereas velocity and weight had stronger correlations on arrivals.
- A new, low-noise procedure that was implemented for BOS runway 22L arrivals started to be flown, with preliminary flight trajectory analysis showing utilization of the new procedure.

Publications
Cezairli, M., Salgueiro, S., & Hansman, R. J. (2024). Implementation Analysis of Low-Noise Performance-Based Navigation Flight Procedures at Boston Logan Airport. *Journal of Air Transportation, 33*(3), 274-284. https://doi.org/10.2514/1.D0475

Outreach Efforts
- Participated in weekly teleconferences and meetings with FAA Technical Monitors.
- Performed outreach and collaboration with Massport, an operator at BOS, and ASCENT Advisory Board members.
- Presented at the biannual ASCENT Advisory Board meetings.

Awards
None.



Student Involvement

Graduate and undergraduate students have been involved in all aspects of this research in terms of analysis, documentation, and presentation.

Plans for Next Period

The next phase of this project will evaluate how additional variables identified in the previous tasks influence aircraft noise and will inform the design of future advanced flight procedures intended to reduce aircraft noise.



Project 049 Urban Air Mobility Noise Reduction Modeling

The Pennsylvania State University
Continuum Dynamics, Inc.

Project Lead Investigator

Kenneth S. Brentner
Professor of Aerospace Engineering
Department of Aerospace Engineering
The Pennsylvania State University
308 ECoRE Bldg, 556 White Course Drive
University Park, PA
814-865-6433
ksbrentner@psu.edu

University Participants

The Pennsylvania State University (Penn State or PSU)

- P.I.: Kenneth S. Brentner, Professor of Aerospace Engineering
- FAA Award Number: 13-C-AJFE-PSU-049, Amendment No. 120
- Period of Performance: August 23, 2024, to August 22, 2025
- Tasks:
  1. Predict and investigate turbulence interaction noise
  2. Compare predictions with flight tests
  3. Investigate time-varying broadband noise of multirotor aircraft
  4. Develop and investigate departure and arrival transition maneuvers
  5. Upgrade and document electric vertical take-off and landing (eVTOL) of noise prediction system

Project Funding Level

The project's previous funding ended December 31, 2023, and was not renewed until August 2024, with the FAA providing $305,000 in funding. Blue Ridge Research and Consulting, LLC (BRRC) will provide $8,975 in-kind support to attend research and biannual meetings, and review software and documentation. Sikorsky, A Lockheed Martin Company, will provide $186,000 in-kind support to attend recuring meetings, provide aircraft configuration data, and acoustic flight measurements for verification and validation of the Penn State noise prediction system (PSU-NPS). Supernal will provide $121,000 in-kind support in the form of costs accrued to collect and extract datasets from a flying testbed Bell 407 as well as engineering hours. Continuum Dynamics, Inc. (point of contact: Dan Wachspress) will provide $225,000 of cost sharing in the form of a 1-year license for the CHARM™ rotorcraft comprehensive analysis software to the Federal Aviation Administration (FAA) for its designee and to industrial partners BBRC and Sikorsky. Total cost sharing: $540,975.00.

Investigation Team

The Pennsylvania State University

Kenneth S. Brentner (P.I.; acoustic prediction lead), Tasks 1-5
Eric Greenwood (co-P.I.; acoustics prediction/analysis), Tasks 1-5
Joseph F. Horn (co-P.I.; flight simulation lead), Tasks 2, 4, and 5
Bhaskar Mukherjee, PhD student (graduated August 2025), software coupling, establishing new aircraft models, developing simulations for new aircraft types, performing acoustic predictions, and developing flight abatement procedures), Tasks 1-5
Ze Feng (Ted) Gan, PhD student (graduated May 2025), investigation of broadband noise modulation, Task 3

™ CHARM is a trademark of Continuum Dynamics, Inc., Ewing, New Jersey.



Continuum Dynamics, Inc.
Daniel A. Wachspress and Mrunali Botre (co-P.I.; rotor loads, wake integration, and CHARM coupling),
Tasks 1, 2, 4, and 5

Project Overview

A wide variety of unconventional configurations for urban air mobility (UAM) and eVTOL aircraft, most with many electrically driven propellers and lifting rotors, have been proposed and are currently under development by companies worldwide. These novel configurations comprise a new category of aircraft that will require certification and show acceptable noise levels received by people on the ground during their urban operations. Unlike helicopters, eVTOL aircraft have limited flight test data and lack mature, empirically derived noise models developed from such data (e.g., the Pegg (1979) helicopter broadband noise model). Therefore, first-principles (methods based on universal laws of physics) noise predictions of these aircraft will be important to gain insight into the complex noise generation mechanisms, the acoustics and performance of the vehicle at different flight phases, and to inform developments of noise certification standards and noise modeling standards. In the absence of flight test data for multirotor UAM and eVTOL vehicles, noise measurements of unmanned aircraft systems (UAS) can be leveraged to provide insight into their noise characteristics. For example, ASCENT Project 077 has produced relevant datasets, since UAS measurements are often more practical to obtain because the aircraft are more accessible and can be built and tested locally. In this report, the terms UAM and eVTOL are used synonymously, whereas UASs are eVTOL drones.

Because UAM vehicles will probably have lower tip speeds to achieve acceptable noise levels, broadband noise is expected to become the dominant rotor noise source. Accordingly, rapid physics-based modeling of rotor broadband noise is a prominent goal of this project and motivates building upon prior validated noise-prediction capabilities. In ASCENT Project 038, the helicopter noise prediction system initially developed in ASCENT Project 006 was successful in accurately predicting the noise of helicopters (usually within sound exposure levels of 1 to 3 dBA), when the predictions were compared with results from an FAA/National Aeronautics and Space Administration (NASA) rotorcraft noise abatement flight test performed in August and October 2017. Sound exposure level contours from the flight test were compared with predictions for several flight procedures. The noise prediction system developed in ASCENT Project 038 consisted of the PSU HeloSim flight dynamics simulation code coupled to the CHARM aeromechanics modeling software and the PSU-WOPWOP noise prediction code. This combination with the flight simulation code was demonstrated to be important for noise prediction, which markedly improved when the simulation was modified to track the time-dependent aircraft position, velocity, and attitude flown in an individual run, rather than the nominal flight path.

To build upon the success of ASCENT Project 038 (focused on helicopter noise), ASCENT Project 049 employs an analogous approach of coupling a flight simulation code with CHARM and PSU-WOPWOP. The PSU HeloSim flight simulation component of the noise prediction system used in ASCENT Project 038 was replaced with PSU Distributed Electric Propulsion Simulator (DEPSim), a flight simulation code designed for many electrically driven rotors with unique control strategies to fly such vehicles effectively. Coupling of PSUDEPSim with CHARM was performed in work outside ASCENT, whereas PSUDEPSim–CHARM coupling with PSU-WOPWOP was performed in this project. The resulting noise prediction system has since been adopted in ASCENT Project 038, providing a common framework in which upgrades developed in either can project directly benefit the other.

The goal of this project is to develop a noise prediction system to analyze the noise from UAM and eVTOL vehicles with unique configurations under any flight conditions. Emphasis is placed on modeling the unique features of UAM and eVTOL configurations not commonly seen in conventional rotorcraft, such as rotors with variable rotation speed, and complex unsteady aerodynamic interactions between the many rotors and the airframe. Another goal is to use the noise prediction system developed in this project to provide guidance on how to fly these vehicles in a quiet manner through flight operations. Because the analysis and computations are based on fundamental physics, noise abatement procedures for novel vehicles can be developed.

Task 1 – Prediction and Investigation of Turbulent Interaction Noise

The Pennsylvania State University

Objective

Noise due to turbulent interactions in multirotor electric aircraft is an important contributor to high-frequency broadband noise, which strongly influences perceived annoyance. Key sources of turbulence include atmospheric boundary-layer and

rotor wake/vortex-core interactions, which are especially relevant in hover (in and out of ground effect) and low-speed climb/descent. The objective of this task is to integrate PSU-MulTINoise (developed under ASCENT Project 049) into the noise prediction system. PSU-MulTINoise computes unsteady airloads on blade sections and lifting surfaces (e.g., wings) due to turbulence interactions and exports it to PSU-WOPWOP for noise prediction.

Research Approach

PSU-MulTINoise currently accepts turbulent intensity and length scale to characterize turbulence via the von Kármán spectrum (von Kármán, 1948) and calculates unsteady airloads generated on an airfoil. This spectrum can be used to characterize small-scale isotropic turbulence commonly observed in the atmosphere. A preliminary investigation on the impact of atmospheric turbulence on eVTOL aircraft noise is conducted. A new reference tiltrotor aircraft has also been developed to represent eVTOL aircraft designs such as the Joby Aviation® S4.

Milestones

- Developed a utility code that can generate a profile of atmospheric boundary layer and turbulent parameters dependent on local topography and weather conditions.
- Modeled a new tiltrotor reference aircraft (PSU Reference Aircraft 3 [PSU-RA3]) based on Joby Aviation S4.
- Investigated the Impact of atmospheric turbulence on a nominal transition maneuver.

Major Accomplishments

Task 1 of the ASCENT Project 049 Annual Report 2023–2024 described the integration of PSU-MulTINoise, a time-domain broadband noise prediction method based on Amiet's leading-edge noise theory (1975), into a quasi-steady implementation of PSU-NPS. This coupled framework was then used to conduct a preliminary investigation on noise generated by rotor blades interacting with the turbulence in low-altitude atmospheric boundary-layer (Mukherjee et al., 2025). Flight simulations of notional Airbus® AS350 helicopter and PSU-RA3 tiltrotor eVTOL aircraft indicated that not including the effects of atmospheric boundary-layer turbulence interaction led to an underprediction of noise levels. Surface roughness, an aerodynamic parameter representing the effective drag and turbulence generation caused by the ground, was found to be an important factor. Due to the low rotor tip-Mach number of PSU-RA3, atmospheric boundary-layer turbulence contributed more significantly to noise relative to AS350 helicopter.

A key limitation identified was the assumption of isotropic turbulence, i.e., the statistical properties of turbulent velocity fluctuations are identical in all directions. Prior work by Amiet et al. (1990) demonstrated that this assumption leads to overprediction of rotor broadband noise. In reality, turbulence approaching the rotor disk undergoes mean-flow contraction and streamline curvature, which stretch and tilt turbulent eddies. This process produces anisotropic turbulence, with the strongest stretching typically occurring along the rotor axis. The resulting deformation reduces the axial (upwash) velocity fluctuations, thereby reducing the unsteady lift on the blades and broadband noise levels. When anisotropy is neglected (i.e., turbulence is assumed isotropic at the rotor disk), these reduced upwash fluctuations are not captured, and the predicted noise can be overestimated by as much as 20 dB (Amiet et al., 1990). Consequently, it is essential that anisotropic turbulence effects be incorporated for accurate prediction of turbulence interaction noise.

This is carried out using rapid distortion theory (RDT), which assumes that turbulence does not significantly modify the mean flow and therefore behaves as a passive field that is convected by the mean motion. Under this approximation, eddies are stretched and reoriented by the mean-flow gradients, while viscous damping and nonlinear turbulence interactions are neglected. Amiet et al. (1990) began by assuming isotropic turbulence far upstream. As this turbulence is convected toward the rotor, the mean inflow accelerates and turns around the disk, producing strong contractions and curved streamlines. Amiet computed the resulting distortion using the deformation tensor of the mean flow, which quantifies how an infinitesimal fluid element is stretched, tilted, and reshaped as it moves from the upstream region to the rotor plane.

Here, the deformation tensor is obtained directly from CHARM's free-wake solution. CHARM allows users to extract the velocity field on an arbitrarily defined grid, enabling detailed characterization of the flow around the rotor. In this work, the flowfield is sampled on a structured three-dimensional grid that encloses the rotor and extends several rotor radii upstream, downstream, and laterally (refer to Figure 1). CHARM outputs the three velocity components at every grid point,

® Joby Aviation is a registered trademark of Joby Aero, Inc., Santa Cruz, California.
® Airbus is a registered trademark of Airbus S.A.S., France.

which are then azimuthally averaged to represent the mean flow experienced by a fluid particle as it convects around the rotor.

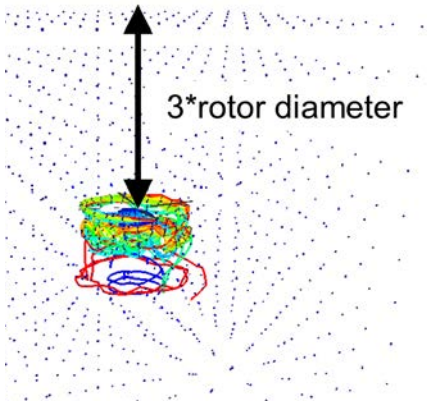
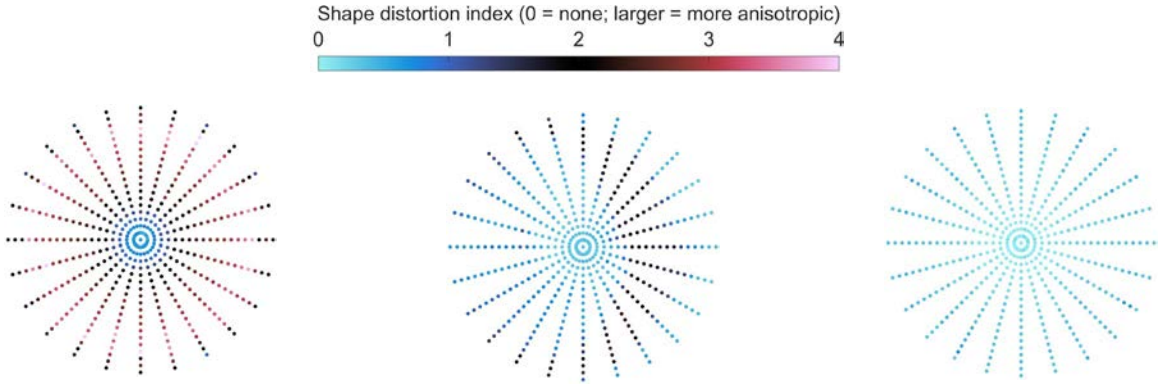


Figure 1. A grid of points measuring flow velocities around a hovering rotor in CHARM.

Following the procedure of Simonich et al. (1990), the deformation tensor is constructed by numerically tracing mean-flow streamlines backward in time from the rotor disk to a far-upstream reference region. Seed points are first placed across the rotor disk. For each seed point, a streamline is integrated backward through the CHARM-predicted mean flow to determine the upstream origin of that fluid element. By comparing the relative displacement of neighboring streamlines, i.e., how an initially orthogonal fluid element is stretched, tilted, and sheared during convection the local deformation tensor is computed.

Figure 2 shows the resulting shape distortion index for an isolated rotor operating in three conditions: hover, axial climb, and edgewise flight. This index measures how unevenly the turbulence is stretched by the mean flow. It is zero when the deformation is isotropic (equal in all directions) and increases as the flow becomes more anisotropic due to shear or directional stretching. Consistent with the findings of Amiet et al. (1990), hover exhibits the strongest deformation, followed by edgewise flight, while axial climb shows the weakest distortion of the incoming turbulence.



(a) Hover (b) Edgewise flight (c) Axial climb

Figure 2. Shape distortion index plotted for seed points on rotor disc.

Publications

None.



Outreach Efforts
None.

Awards
None.

Student Involvement
Bhaskar Mukherjee, a graduate assistant who recently completed his PhD, worked on improving turbulence interaction broadband noise predictions in the PSU-NPS by incorporating turbulence distortion effects estimated using RDT.

References
Amiet, R. K. (1975). Acoustic radiation from an airfoil in a turbulent stream. *Journal of Sound and Vibration, 41*, 407–420.

Amiet, R. K., Simonich, J. C. & Schlinker, R. H. (1990). Rotor noise due to atmospheric turbulence ingestion. II – Aeroacoustic results. *Journal of Aircraft*, 27, 15–22.

Mukherjee, B., Ibnoukhaiber, S. & Brentner, K. (2025, January 5-9). *Impact of AAM Operations on Airport Noise* [Conference paper]. Transportation Research Board (TRB) 104th Annual Meeting, Washington, D.C.

Pegg, R. J. (1979). *A summary and evaluation of semi-empirical methods for the prediction of helicopter rotor noise*. National Aeronautics and Space Administration (NASA), NASA-TM-80200. https://ntrs.nasa.gov/api/citations/19800007615/downloads/19800007615.pdf

Simonich, J. C., Amiet, R. K., Schlinker, R. H. & Greitzer, E. M. (1990). Rotor noise due to atmospheric turbulence ingestion. I - Fluid mechanics. *Journal of Aircraft*, 27, 7–14.

von Kármán, T. (1948). Progress in the statistical theory of turbulence. *Proceedings of the National Academy of Sciences of the United States of America, 34*(11), 530–539.

Task 2 – Comparison Between Predictions and Flight Tests
The Pennsylvania State University

Objectives
This task is focused on comparing noise predictions with acoustic data measured in outdoor flight and anechoic chamber tests. The physics of eVTOL and UAS aircraft operations result in high-frequency broadband noise to be the dominant source. Time-averaged broadband noise predictions from the PSU-NPS are compared with experimental data. Differences between both are analyzed to identify methods for improving the prediction. In parallel, experimental data are analyzed to identify characteristics of time-varying broadband noise, with a focus on the impact of blade azimuth phase offsets between rotors during flight.

Research Approach
Noise from a reconfigurable hexacopter in hover was measured on a ground microphone array as part of ASCENT Project 077. Broadband noise predictions using the BPM self-noise model (Brooks et al., 1989) was compared with experimentally measured spectrum. Differences were analyzed, and improvements to the model were made along with its implementation in PSU-WOPWOP.

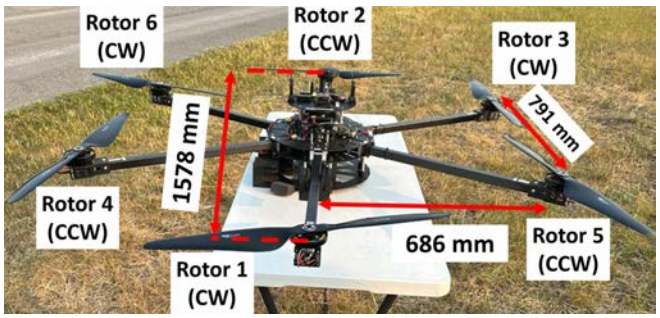
Simple prediction models for time-varying multirotor broadband noise were developed by supplementing analytical models with flight test and anechoic chamber measurements collected for ASCENT Project 077. These include measurements of the rotor azimuth phase and rotor rotation rates. Summation of the modulation of individual rotors represents the first step towards more formal prediction models. Summation of the broadband noise modulation of multiple rotors makes assumptions not previously validated in the literature, which are discussed and validated below.

Milestones
- Modified the BPM model for smaller unmanned aerial vehicle (UAV)-sized blades that helps improve predictions.
- Developed analysis and prediction frameworks for characterizing multirotor broadband noise modulation, including characterizing the variability of noise with time and between repeated flights.

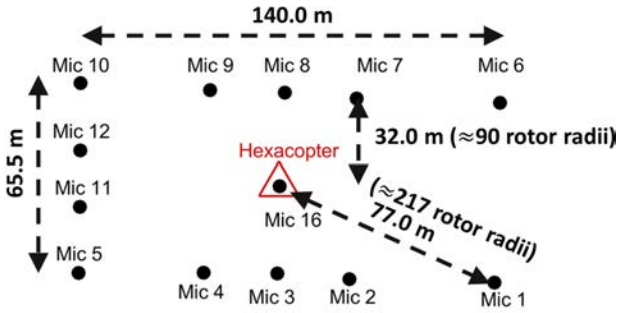
Major Accomplishments

Mukherjee (2025) recently introduced a correction to the semi-empirical Brooks, Pope, and Marcolini (BPM) broadband airfoil self-noise prediction model (Brooks et al., 1989). This addressed an implicit assumption of acoustic compactness in the original formulation. Acoustic compactness is defined using the blade chord-to-wavelength (acoustic) ratio: when the ratio is greater than 1, the blade is considered acoustically compact; when it is less than 1, the blade is considered acoustically noncompact. While helicopter blades are generally acoustically compact, the much smaller rotors used on small Unmanned Aerial Systems (sUAS) are typically acoustically noncompact.

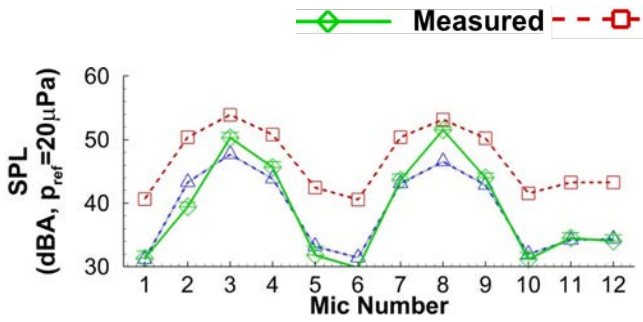
The impact of this correction was demonstrated through comparisons between outdoor noise measurements of the PSU reconfigurable hexacopter (Figure 3a) collected using a ground microphone grid (Figure 3b) and broadband noise predictions generated using the BPM model. Figure 3c and Figure 3d present the A-weighted integrated sound pressure level (SPL) for microphones 1–12, plotted against measured noise for hover conditions at 20 and 40 ft, respectively. Two broadband prediction datasets are shown: the original BPM model assuming acoustic compactness (BPM_C) and the corrected model accounting for acoustic noncompactness (BPM_{NC}). The original BPM model with compact directivity (BPM_C) greatly overestimated the SPLs of the hexacopter hovering at 20 ft, with a median absolute deviation of 8.7 dBA for microphones 1 to 12. Using BPM_{NC} reduced the median absolute deviation to 1 dBA. At 40 ft, the overestimation by BPM_C decreased, yielding a median absolute deviation of approximately 2.8 dBA. Accounting for noncompactness (BPM_{NC}) reduced the deviation to 1.5 dBA.



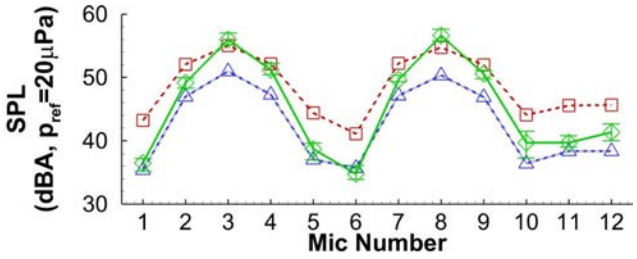
(a) PSU Reconfigurable hexacopter flown for outdoor test



(b) Microphone grid layout



(c) Hexacopter in hover, 20 ft altitude: variation in measured and predicted SPL for microphones 1 – 12



(d) Hexacopter in hover, 40 ft altitude: variation in measured and predicted SPL for microphones 1 – 12

Figure 3. PSU hexacopter in hover, measured vs. noise prediction (Mukherjee, 2025). BPM: Brooks, Pope, and Marcolini, SPL: sound pressure level.

For all sources of self-noise, the BPM model scales the SPLs using two sets of terms: an analytical scaling function and additional functions tuned using measured flow and acoustic data. The analytical scaling equation was derived from an expression by Ffowcs Williams and Hall (1970) estimating the acoustic intensity (I) for an observer in the far-field as $I \approx \frac{M^5 \delta}{r_e^2}$. Here M, δ, r_e are the flow Mach number, boundary layer thickness, and distance from trailing edge to observer,

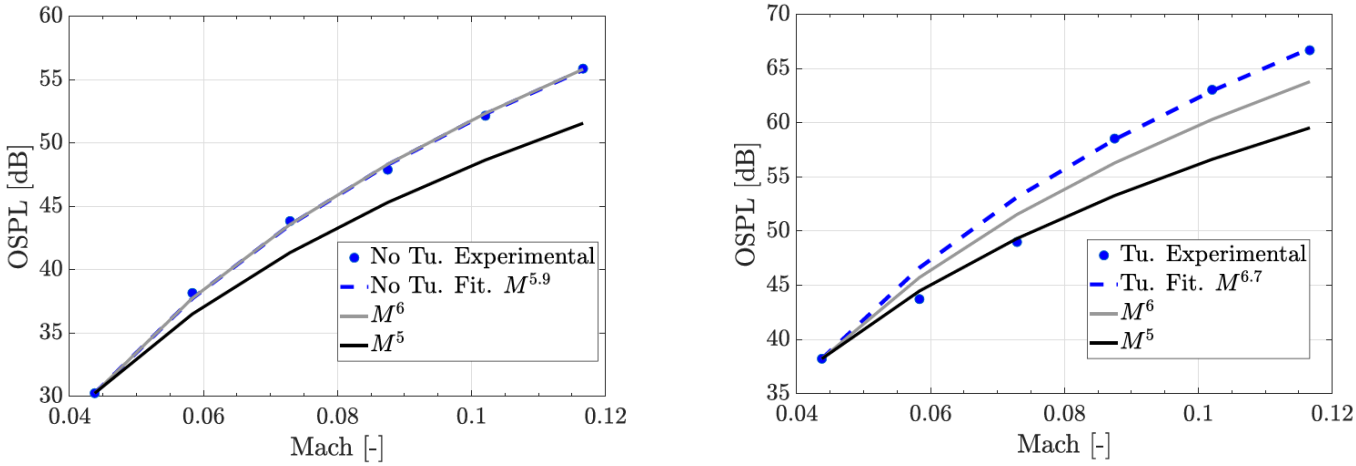


respectively. Brooks et al. (1989) found that the predicted spectra agreed better when δ was replaced by the boundary layer displacement thickness δ^*, giving $I \approx \frac{M^5\,\delta^*}{r_e^2}$. Therefore, Equation 1 for predicting turbulent boundary layer trailing edge (TBL-TE) noise was written as follows:

$$\boldsymbol{SPL_{TBLTE} = 10\,log_{10}\left(\frac{\delta^* M^5 L\,\overline{D}_h}{r_e^2}\right) + A(\delta^*, St)} \qquad \text{(Eq. 1)}$$

Here L is the airfoil span, while $\overline{D}_h$ is the directivity function that was updated to improve sUAS broadband noise predictions. The function A is an empirical correction depending on the boundary layer displacement thickness and flow Strouhal number (St) that is used to match experimentally measured SPL_{TBLTE}.

Recent experimental data from Botero-Bolívar et al. (2024) provided additional insight into the scaling of trailing edge noise with Mach number (M). Noise measurements for a NACA 63018 airfoil have shown that the integrated overall sound pressure level (OASPL) can scale anywhere between M^6 and M^7 depending on the turbulence levels in flow around the airfoil. Figure 4a shows that in a non-turbulent inflow, trailing edge noise scales with M^6, whereas in a turbulent inflow (Figure 4b) the scaling increases to $M^{6.7}$.



(a) Non-turbulent inflow (b) Turbulent inflow

Figure 4. Overall sound pressure level scaling of far-field trailing edge noise with inflow velocity for the NACA 63018, (Botero-Bolívar et al., 2024). OSPL: overall sound pressure level.

Similar trends can also be observed in the experimental acoustic data published by Brooks et al. (1989), which formed the basis for tuning the BPM model originally. In their extensive measurement campaign, noise from a NACA 0012 airfoil was recorded at angles of attack ranging from 0° to 20° and over Reynolds numbers between 1×10^5 and 6.3×10^5. Although Brooks et al. (1989) did not publish OASPL values directly, they reported one-third-octave spectra for nearly 104 flow conditions. These data were digitized from the original report and processed to estimate OASPL.

Figure 5 shows the resulting OASPL trends in the original dataset used for BPM model tuning. The angle of attack (AOA) appears to be the primary factor driving variations in the scaling exponent. At AOA = 0°, noise scales approximately as $M^{4.3}$. As AOA increases, the exponent rises, reaching about $M^{7.6}$ at AOA = 19.8°. This behavior is consistent with the increased turbulence intensity near the trailing edge at higher AOAs. Because these trends deviate significantly from the default M^5 scaling, they highlight the need to update the BPM model accordingly.

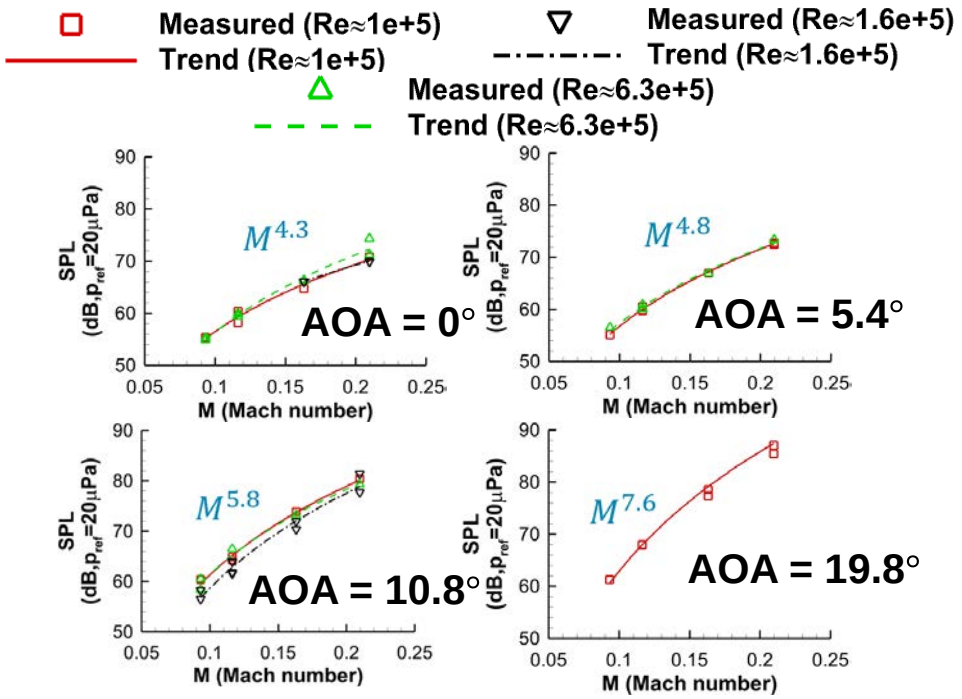


Figure 5. Scaling of far-field trailing-edge noise in data by Brooks et al. (1989). AOA: angle of attack, Re: Reynolds number.

Publications

Mukherjee, B. (2025). *Noise of Multirotor Electric Aircraft* [Doctoral dissertation, The Pennsylvania State University]. Penn State University Libraries, University Park, Pennsylvania.

Outreach Efforts

None.

Awards

None.

Student Involvement

Bhaskar Mukherjee, a graduate assistant who recently completed his PhD, worked on updating the semiempirical BPM broadband noise prediction model for improved prediction of high-frequency noise from small UAS and eVTOL aircraft.

References

Botero-Bolívar, L., dos Santos, F. L., Venner, C. H. & de Santana, L. D. (2024). Trailing-edge far-field noise and noise source characterization in high inflow turbulence conditions. *Journal of the Acoustical Society of America,155*, 803–816.

Brooks, T. F., Pope, D. S., & Marcolini, M. A. (1989). *Airfoil self-noise and prediction* (RP-1218). National Aeronautics and Space Administration. https://ntrs.nasa.gov/api/citations/19890016302/downloads/19890016302.pdf

Ffowcs Williams, J. E., & Hall, L. H. (1970). Aerodynamic sound generation by turbulent flow in the vicinity of a scattering half plane. *Journal of Fluid Mech*anics*, 40*, 657.

Mukherjee, B. (2025). *Noise of Multirotor Electric Aircraft* [Doctoral dissertation, The Pennsylvania State University]. Penn State University Libraries, University Park, Pennsylvania.

Task 3 – Investigate Time-Varying Broadband Noise of Multirotor Aircraft

The Pennsylvania State University

Objectives

One objective of this task is to determine the significance of time-varying multirotor broadband noise (multirotor broadband noise modulation) using flight test measurements. For clarity, time-varying broadband noise refers to the changes over time in noise levels across a wide range of frequencies, whereas broadband noise modulation refers to the cases where those level changes follow a periodic or quasiperiodic pattern at a particular modulation frequency (for example, once per blade passage or once per rotor revolution). With these definitions, this objective is motivated by anechoic chamber measurements taken for ASCENT Project 077 and analyzed in Task 2 of the *2023 Annual Report for ASCENT Project 049*, which found that the importance of time-varying multirotor broadband noise depends significantly on the blade azimuth phase offsets between rotors. This is contrary to predictions in the literature, which predict broadband noise to be fairly constant with time for many rotors, with the modulation depth decreasing as the number of rotors increases (Li & Lee, 2022).

Another objective of this task is to determine the significance and physical sources of broadband noise modulation at modulation frequencies not at the blade-passage frequency (BPF). Broadband noise modulation with the BPF was studied in Task 2 above, but other modulation frequencies were also observed in this work. Psychoacoustics studies of small multirotor UAS report significant noise modulation amplitudes at modulation frequencies much lower than the BPF; and the physical causes responsible for this modulation remain unclear (Gwak et al., 2020; Torija & Nicholls, 2022; Ramos-Romero et al., 2023).

One possible cause of low frequency modulation for multi-rotor aircraft with high BPFs is the presence of beating effects, or simply 'beats' for short. Beats arise when tones have closely spaced frequencies, resulting in modulation at a frequency equal to the difference of the tonal frequencies (Feynman et al., 2011). Although beats are typically studied as tones, one could hypothesize that there exists an analogous phenomenon for broadband noise modulation (i.e., for two amplitude-modulated, broadband noise signals with closely spaced modulation frequencies). However, this has not been studied in the literature.

Closely spaced BPFs are likely to arise in flight for aircraft with electric rotors with variable rotation speeds (for example, the flight controller may command slightly different rotor rotation speeds to trim the aircraft in hover or axial flight, to counteract the presence of atmospheric disturbances).

Research Approach

Flight test measurements of a hexacopter UAS collected for ASCENT Project 077 are analyzed using advanced signal processing methods such as envelope and cyclostationary analysis. Although these methods have not been widely applied to rotorcraft noise analysis, their fine time resolution enables deeper understanding and more precise and accurate quantification of multirotor broadband noise modulation, including the influence of variations in azimuthal phase.

Prediction models were developed by supplementing simple analytical and numerical models with anechoic chamber measurements collected for ASCENT Project 077. These include not only noise measurements, but also measurements of the time histories of rotor rotation rates.

Milestones

- Determined that time-varying multirotor broadband noise is significant in flight.
- Determined the significance of beats of broadband noise modulation.
- Developed analysis and prediction frameworks for characterizing beats of broadband noise modulation.

Major Accomplishments

Gan's work under ASCENT Project 049 is summarized in the doctoral dissertation *Time-Varying Noise of Electric Multirotor Aircraft* (2025). Using data measured in the Penn State anechoic chamber, Gan (2025) showed that the broadband SPL of a single rotor in hover rises and falls within each revolution modulating at the BPF. The primary contributor was found to be kinematic effects associated with rotation, including periodic changes in source–observer distance. This behavior is



quantified using cyclostationary analysis, in which short-time broadband levels are computed over many overlapping windows and then ensemble-averaged while tracking blade azimuth.

Baars and Ragni (2024) investigated the same underlying phenomenon for an isolated benchmark rotor in the Delft[1] A-Tunnel over a range of advance ratios. Their analysis uses time–frequency methods (wavelet transform) to relate the BPF component to the envelope of the high-frequency broadband content. They also confirm that the broadband modulation depth does not impact its time-averaged spectrum. Extending their analysis, it is also reported that the magnitude and phase of time-varying broadband noise depend on operating condition, even at fixed rotor speed.

Publications

Gan, Z. F. (2025). *Time-Varying Noise of Electric Multirotor Aircraft* [Doctoral dissertation, The Pennsylvania State University]. Penn State University Libraries, University Park, Pennsylvania.

Outreach Efforts

None.

Awards

None.

Student Involvement

Ze Feng (Ted) Gan, a graduate assistant who recently completed his PhD, investigated time-varying broadband noise for this task.
Bhaskar Mukherjee, a graduate assistant who recently completed his PhD, worked on interpreting Ze Feng (Ted) Gan's results and connecting the findings to recent literature.

Plans for Next Period

- Study tonal beats and compare their importance to the significance of beats of broadband noise modulation.
- Validate the prediction approach outlined here using flight test measurements taken in ASCENT Project 077, including different maneuvers.

References

Baars, W. J. & Ragni, D. (2024). Low-Frequency Intensity Modulation of High-Frequency Rotor Noise. *AIAA Journal,* 62, 3374–3390. https://doi.org/10.2514/1.J063610

Task 4 – Develop and Investigate Departure and Arrival Transition Maneuvers

The Pennsylvania State University

Objective

The objective of this task is to design departure and arrival maneuvers aiming to balance the requirements of noise and performance for various eVTOL configurations.

Research Approach

Previous work in ASCENT Project 049 (see the 2023 Annual Report for ASCENT Project 049) analyzed a notional lift-plus-cruise aircraft departure transition maneuver using the Penn State noise prediction system. The analysis used multiple flight simulations to evaluate how different control strategies and trajectories affect aircraft performance and noise. However, the conclusions were limited by known deficiencies in the noise modeling, particularly the incomplete prediction of high-frequency broadband noise generated by aerodynamic interactions between rotor wakes and other components. These broadband sources are important during hover and low-speed flight, which define key portions of departure and arrival maneuvers at low altitude. Consequently, the transition-maneuver noise must be re-evaluated by developing and

[1] Delft University of Technology

validating prediction models for these additional broadband noise sources while minimizing the associated increase in computational cost.

Milestones

Improve perpendicular Blade-Vortex Interaction (BVI) noise predictions.

Major Accomplishments

A recent experimental investigation of the generation of broadband noise from small rotors in hover and forward flight by Lößle et al. (2025) revealed several key insights into the dominant mechanisms. The results include acoustic source maps for three octave bands in the 1 kHz - 8 kHz range calculated using beamforming. Figure 6 marks the location of maximum sound emission in frequencies in the 1 kHz - 8 kHz range for the Aero-naut® CAM Carbon Light 16×6 rotor spinning at 3,000 and 4,000 rotations per minute (RPM) in hover. The position is at the trailing edge near the 80% span (x_B/R). This demonstrates the dominance of trailing edge noise in hover. Experimental flow visualizations have also revealed the presence of perpendicular blade vortex interaction from the tip vortex of a rotor in hover (Figure 7).

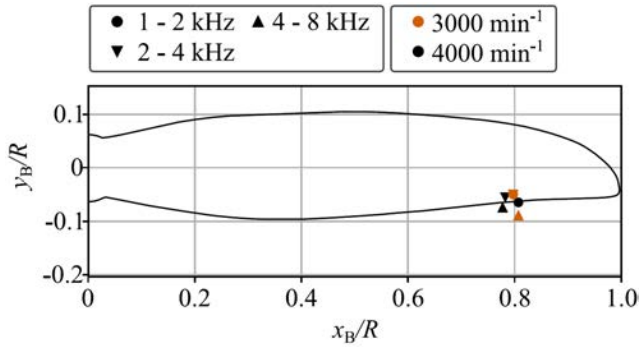


Figure 6. Position of the maximum sound emission on the rotor blade of the CAM Carbon Light 16 × 6 rotor in hover at rotational speeds 3,000 and 4,000 rotations per minute (RPM) (Lößle et al., 2025).

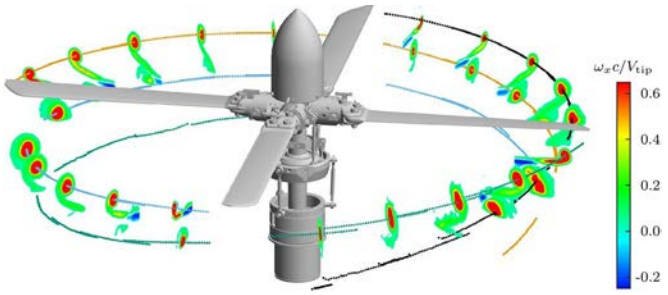


Figure 7. Rotor operating in hover: three-dimensional vortex locations with normalized vorticity contour (Brakumann et al., 2021).

At Penn State University, Zahirudin (2025) measured aerodynamic performance and acoustic data from a single 4-bladed rotor operating in hover at the Flow-Through Anechoic Chamber. The blade has a radius of 9 in. (0.23 m) with a linear distribution of twist and taper (further details can be found in Zahirudin et al. (2021). It is mounted on a shaft where a load cell measures the loads and moments generated, while the rotor speed was measured using a laser tachometer. Figure 8 shows the circular array of microphones installed to allow the measurement of noise at different elevation angles (θ_m) relative to the rotor plane.

® Aero-naut is a registered trademark of Aero-naut Modellbau GmbH + Co. KG, Reutlingen, Germany.

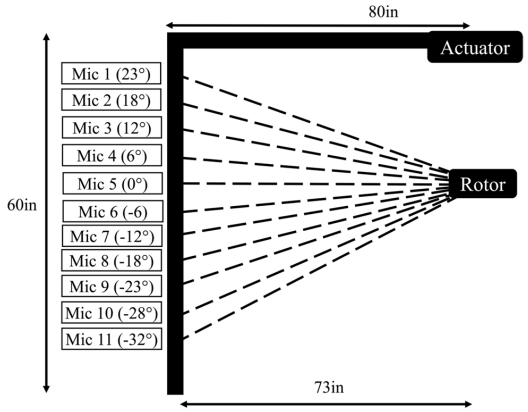
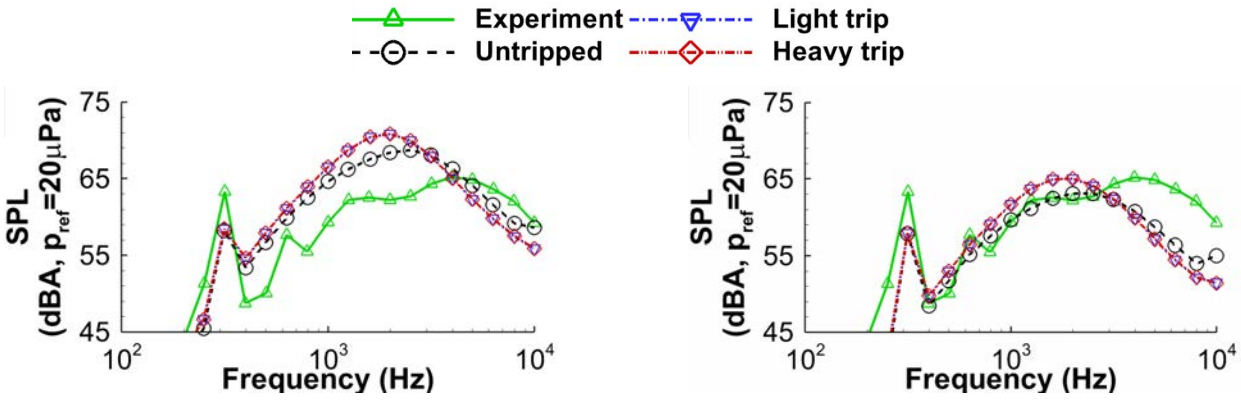


Figure 8. Microphone elevation angles (R. Zahirudin et al., 2021).

Noise during hover was investigated for the 4-bladed rotor operating around a speed of 4,500 RPM (470 rad/s), generating a thrust of 11.15 lbf ($C_T = 0.02126$). Rotor aerodynamics was simulated using the free-wake code CHARM, where the code trimmed the pitch to match the experimentally measured thrust. The resulting airloads were exported to PSU-WOPWOP, and noise predictions were compared with measurement at microphone 8 ($\theta_m = -18°$). Deterministic thickness and loading were calculated using the blade geometry and unsteady airloads calculated in CHARM, while broadband noise was calculated using the semi-empirical BPM self-noise prediction model developed by Brooks et al. (1989).

As discussed in Task 2, PSU-WOPWOP was updated by Mukherjee (2025) to correct the effects of acoustic compactness on noise predicted by the BPM model. This correction was found to be important in improving the prediction of rotors typically used in sUASs. Input parameters for the BPM model include the section angle of attack (obtained from CHARM), flow velocity (estimated kinematically in PSU-WOPWOP). A key modeling choice is the boundary layer state: untripped, light trip, and heavy trip. The BPM model does not internally determine the appropriate condition, so it must be specified based on the local flow physics. The CHARM solution indicates that the maximum Reynolds number across the blade sections is 1.5×10^5, which is consistent with predominantly laminar flow (untripped). Figure 9 plots the one-third-octave spectra measured at microphone 8 along with predictions for all three boundary layer trip conditions.



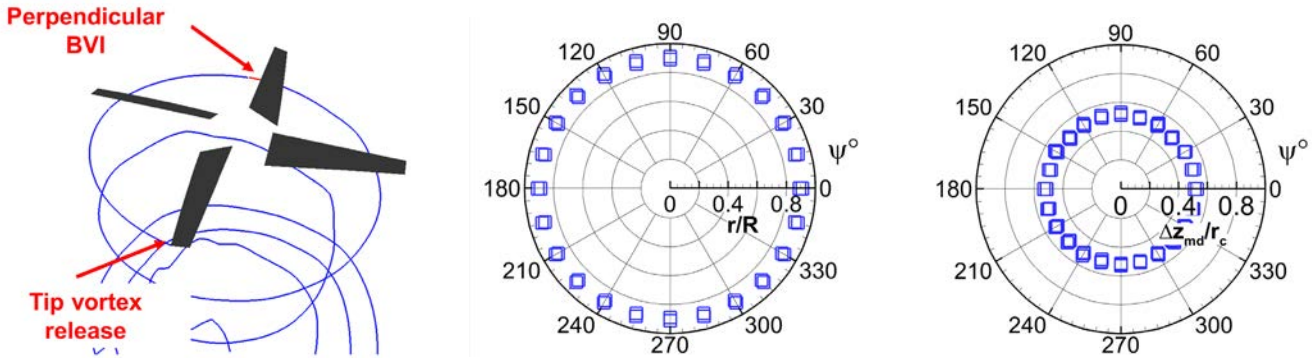
(a) BPM_C (b) BPM_{NC}

Figure 9. Measured noise and prediction at mic 8: single 4-bladed rotor in hover (Ω = 470 rad/s, C_T = 0.02126). BPM: Brooks, Pope, and Marcolini, SPL: sound pressure level. Subscripts: C – compact, NC - noncompact

The predictions seem to underpredict the first tonal peak at ≈ 315 Hz by about 4 dBA, and the cause of this discrepancy is currently unknown. Using the compact (original) directivity function BPM_C, Figure 9a shows that the broadband noise is

overpredicted by 6 – 8 dBA. This is removed in Figure 9b, when the noncompact formulation BPM_{NC} is used. As expected, untripped boundary-layer case performs best overall, matching the measured spectrum between 400 Hz and 2,500 Hz to within 1 dBA. Despite the significantly improved predictions obtained with BPM_{NC}, a pronounced peak near 4,000 Hz remains underpredicted by 5 – 6 dBA. This peak is suspected to be associated with trailing-edge noise generated by perpendicular BVI.

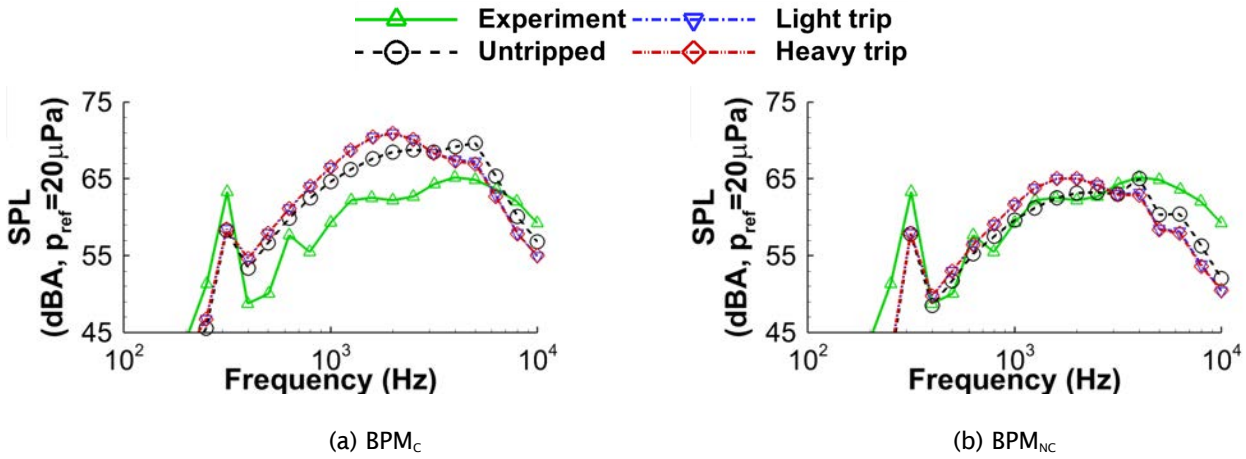
Further insight is obtained by analyzing CHARM's free-wake solution. Wake visualization (Figure 10a) reveals the presence of perpendicular BVI clustered near the non-dimensional radial position $r/R \approx 0.89$ (Figure 10b), with r denoting the radial distance from the center of the hub and R the rotor tip radius. Figure 10c plots the ratio of the vortex miss distance Δz_{md} to the vortex core radius r_c. Values less than 1 indicate that the vortex interacts with the blade. In this case, $\Delta z_{md}/r_c \approx 0.5$, implying that the center of the vortex core passes through the blade plane, i.e., a strong perpendicular BVI event.



(a) CHARM wake visualization (b) Wake interaction locations across one revolution (c) Miss distance ratio ($\Delta z_{md}/r_c$)

Figure 10. Perpendicular blade-vortex interaction (BVI): Single 4-bladed rotor in hover (Ω = 470 rad/s, C_T = 0.02126).

Since the peak in the measured data near 4,000 Hz is hypothesized to be a result of perpendicular BVI, an ad-hoc model was developed that leveraged the BPM airfoil self-noise model to represent the trailing edge noise generated by perpendicular BVI while retaining a low computational cost. Among the model's various self-noise sources, the trailing edge bluntness vortex shedding noise appeared most suitable to represent the vortex shedding resulting from perpendicular BVI. Knowing the location of perpendicular BVI interaction (Figure 10b), bluntness vortex shedding noise from these blade sections were calculated using the maximum thickness of the section as an input to the model. This resulted in the predictions now capturing a second peak around 4,000 Hz as observed in Figure 11. While the compact formulation BPM_C still overpredicts significantly, BPM_{NC} prediction now accurately captures the 4,000 Hz peak.



(a) BPM_C (b) BPM_{NC}

Figure 11. Measured noise and ad hoc prediction at mic 8: single 4-bladed rotor in hover (Ω = 470 rad/s, $C_T = 0.02126$). BPM: Brooks, Pope, and Marcolini, SPL: sound pressure level. Subscripts: C – compact, NC - noncompact

Publications
None.

Outreach Efforts
None.

Awards
None.

Student Involvement
Bhaskar Mukherjee, a graduate assistant who recently completed his PhD, worked on developing new approaches to modeling perpendicular BVI noise using the BPM self-noise model.

Plans for Next Period
- Compare noise measurements at other microphones against predictions to further validate the correction in the BPM model for acoustic noncompactness and ad hoc model proposed to capture trailing edge noise from perpendicular BVI.
- Revisit hover noise measurements for the PSU hexacopter (Task 2, Figure 3a) to validate predictions from the ad-hoc model for perpendicular BVI.

References
Braukmann, J. N., Goerttler, A., Wolf, C. C., Schwarz, C. & Raffel, M. (2021). Combining simultaneous density and velocity measurements of rotor blade tip vortices under cyclic pitch conditions. *Exp Fluids*, 62, 197.

Brooks, T. F., Pope, D. S., & Marcolini, M. A. (1989). *Airfoil self-noise and prediction*. NASA Reference Publication NASA RP-1218, NASA Langley Research Center, 142. https://ntrs.nasa.gov/api/citations/19890016302/downloads/19890016302.pdf

Lößle, F., Schmid, R., Kostek, A. A., Ernst, D., Schwarz, C., Braukmann, J. N., & Wolf, C. C. (2026). Experimental investigation of broadband noise generation of a small rotor in hover and forward flight. *CEAS Aeronautical Journal, 17*, 245-258. https://doi.org/10.1007/s13272-025-00845-y (published May 2025, issue date January 2026)

Mukherjee, B. (2025). *Noise of Multirotor Electric Aircraft* [Doctoral dissertation, The Pennsylvania State University]. Penn State University Libraries, University Park, Pennsylvania.



Raja Zahirudin, R. A. (2025). *Stacked Rotor Design Variations for Acoustics and Performance* [Doctoral dissertation, The Pennsylvania State University]. Penn State University Libraries, University Park, Pennsylvania. https://etda.libraries.psu.edu/catalog/23758ror5201

Zahirudin, R. A., Greenwood, E., Weitsman, D., & Palacios, J. I. (2021). The Development of a Coaxial Acoustics Test System for Rotor Noise. *Proceedings of the Vertical Flight Society 77th Annual Forum*. https://doi.org/10.4050/F-0077-2021-16682

Task 5 – Upgrade and Document eVTOL Noise Prediction System

The Pennsylvania State University

Objective

The objective of this task is to document the eVTOL noise prediction system and its components, including example cases, such that new users can easily learn to use this tool. Work in this task is being coordinated with Task 5 (ASCENT Project 038) as the two projects converge on using the same noise prediction system for helicopters and eVTOL aircraft.

Research Approach

In addition to documentation describing how to use the noise prediction system, example cases are provided to highlight new prediction capabilities and file formats. These example cases also serve as validation cases to ensure that the system is operating as expected. Example cases are automatically validated according to a regression testing procedure (checksuite).

Milestones

- Documented new prediction capabilities for time-varying broadband noise, as summarized in Task 3 above.
- Updated the existing PSU-WOPWOP user manual to include instructions on how to predict time-varying broadband noise.
- Provided example cases and updated the checksuite to automatically validate the file formats of these new time-varying noise results.

Major Accomplishments

The PSU-WOPWOP manual has been updated to document the implementation of corrections to the BPM broadband self-noise prediction model developed under Task 2. Digitization of the experimental data published by Brooks et al. (1989) is expected to allow development of new cases for the checksuite that can be used to automatically validate future development of PSU-WOPWOP code and maintain code correctness.

Publications

None.

Outreach Efforts

None.

Awards

None.

Student Involvement

Bhaskar Mukherjee, a graduate assistant who recently completed his PhD, worked on upgrading the noise prediction system by improving broadband noise prediction methods developed under Task 1 and 2 of this project.

Plans for Next Period

Updates to broadband noise prediction models developed in ASCENT Project 049 need to be merged with the code package of PSU-NPS developed and documented as part of Task 5, ASCENT Project 038. Predictions from the models developed here will also be compared against flight test data measured for helicopters that are being analyzed in ASCENT Project 038. The long-term goal is to have a universal system that can predict helicopter and multirotor electric aircraft noise accurately.



References

Brooks, T. F., Pope, D. S., & Marcolini, M. A. (1989). Airfoil self-noise and prediction (p. 142). National Aeronautics and Space Administration (NASA), NASA Langley Research Center, NASA RP-1218. https://ntrs.nasa.gov/api/citations/19890016302/downloads/19890016302.pdf



Project 051 Combustion Concepts for Next-generation Aircraft Engines

Massachusetts Institute of Technology

Project Lead Investigator

Raymond L. Speth
Principal Research Scientist
Associate Director, Laboratory for Aviation and the Environment
Massachusetts Institute of Technology
77 Massachusetts Ave, Building 33-310, Cambridge, MA 02139
(617) 253-1516
speth@mit.edu

University Participants

Massachusetts Institute of Technology (MIT)

- P.I.: Dr. Raymond L. Speth
- FAA Award Number: 13-C-AJFE-MIT, Amendment Nos. 061, 071, 079, 097, 115, 123, 128, 133, and 143
- Period of Performance: February 5, 2020, to August 31, 2027 (reporting here with the exception of funding level and cost sharing only for the period October 1, 2024, to September 30, 2025)
- Tasks:
  1. Develop a nitrogen oxide (NO_x) emissions model for a reacting jet-in-crossflow environment
  2. Modeling plasma-assisted combustion for NO_x emissions reduction in aircraft gas turbines

Project Funding Level

The Federal Aviation Administration (FAA) provided $1,250,000 in funding and $1,250,000 in matching funds were provided by MIT and third party in-kind contributions. Sources of the matching funds are approximately $317,200 from MIT, plus third party in-kind contributions of $674,000 from NuFuels, LLC, and $258,800 from Earth Force Technologies.

Investigation Team

Dr. Raymond L. Speth, (P.I.), Tasks 1 and 2
Dr. Jayant Sabnis, (co-investigator), Tasks 1 and 2
Yang Chen, (graduate student), Task 1
Matthew Quiram, (graduate student), Task 2

Project Overview

With advances in material technology in the past 50 years, aircraft engines with higher pressure and temperature ratios have been designed to improve the engine's total efficiency and reduce fuel consumption. However, the increase in combustor temperatures tends to produce higher NO_x emissions, which account for a substantial portion of aviation's environmental impact. Therefore, novel low-emissions combustion technologies are needed for the reduction of aircraft engines' emissions, along with the high fuel efficiency of next generation aircraft and engine design.

The objective of the current project is thus to evaluate the performance of various novel combustion concepts in emissions and efficiency. This study would then facilitate the selection of promising high-performance concepts for further development, which would eventually lead to a reduced aviation impact on public health and climate. Throughout the current project, innovative numerical modeling techniques for emissions, combustion chemistry, and combustor internal aerodynamics are developed to enable efficient and accurate evaluation of the performance of different concepts.



The first model currently being developed is a Lagrangian diffusive strip NO_x emissions model for a reacting jet-in-crossflow, where the present focus is on integration of the chemistry and aerodynamics component models. This model will offer the benefits of simulating detailed NO_x formation mechanism, capturing the emissions impacts from aerodynamics, and a low computational cost for wide-range parametric studies. This technique fills the gap between the traditional modeling methods of chemical reactor network and computational fluid dynamics. Chemistry and flame solvers, including Cantera[1] (Goodwin et al., 2024) and Ember (Speth, 2017) are utilized in this development.

The second concept under investigation is plasma-assisted combustion for low-NO_x, gas-turbine relevant Jet-A operation. In this work, non-thermal plasma discharges are integrated into combustor simulations to extend lean blow-off limits with the goal of reducing overall NO_x emissions. This requires the development of a Jet-A reaction mechanism that is tailored to account for NO_x formation and destruction in the presence of plasma. The resulting mechanism will be applied to Cantera-based reactor network and one-dimensional (1D) flame models that can handle the two-way coupling of electron energy distribution and electron impact reactions. By systematically comparing plasma and non-plasma cases, this work aims to identify the operating regimes in which plasma actuation enables leaner combustion with a net reduction in NO_x, as well as regimes where plasma is likely to increase NO_x.

References

Goodwin, D.G., Moffat, H. K., Schoegl, I., Speth, R. L. & Weber, B. W. (2024). *Cantera: an object-oriented software toolkit for chemical kinetics, thermodynamics, and transport processes* (Version 3.1.0). Zenodo, doi: 10.5281/zenodo.14455267. https://www.cantera.org

Speth, R. L. (2017). *Ember: a quasi-one-dimensional, unsteady flame solver* (Version 1.4.0). Zenodo, doi: 10.5281/zenodo.1004752. https://github.com/speth/ember

Task 1 – Develop a NO_x Emissions Model for a Reacting Jet-in-crossflow Environment

Massachusetts Institute of Technology

Objectives

Various emissions modeling techniques are utilized for the development of novel combustion concepts with low NO_x emissions. Among these techniques, chemical reactor network (CRN) methods have high fidelity in capturing detailed chemistry and low computational cost, allowing optimizing of a wide range of model design parameters. However, the simulation of aerodynamics effects on NO_x emissions, such as flame straining effects or multi-stream mixing effects, have been limited in the CRN approach. The aerodynamic effects in the CRN method are typically represented by different combinations of well-stirred reactors (WSR) that assume complete mixing and plug-flow reactors (PFR) that assume no mixing. Then, a weighted average of WSR and PFR components can be employed to approximate a finite-rate mixing process. This type of CRN representation usually requires a large amount of experimental data for model calibration as the representation lacks aerodynamics constraints. This data requirement of CRN models can thus limit their use in studying novel combustion concepts where little experimental information is available.

As a remedy, reacting-flow computational fluid dynamics (CFD) methods are employed to explore cutting-edge combustion concepts. CFD captures detailed aerodynamic constraints in multi-dimensional space such that aerodynamic effects on NO_x emissions can be simulated. However, for a typical Eulerian-grid-based CFD method, this requires a dense computational grid across multiple dimensions, resulting in a high computational cost. This computational cost generally makes only reduced-order chemistry mechanisms affordable for simulating both combustion chemistry and NO_x emissions. The reduced-order mechanisms can then undermine the accuracy of the simulations in capturing certain NO_x formation pathways like the prompt NO_x mechanism. The high computational cost of CFD methods can also limit the number of cases simulated, leading to only a small number of a combustor's design parameters being explorable in a CFD study.

The tradeoff between CFD and CRN methods can be observed in previous studies on NO_x emissions in a reacting-jet-in-crossflow (RJICF) environment. An RJICF is a two-stream mixing flow structure with typically one high-speed jet penetrating

[1] Cantera is an open-source suite of tools for problems involving chemical kinetics, thermodynamics, and transport processes. Cantera is a sponsored project of NumFOCUS®, a 501(c) nonprofit charity in the United States. NumFOCUS is a registered trademark of NumFOCUS, Inc., Austin, Texas.



nearly perpendicularly into a lower speed crossflow. This flow structure is widely utilized in many low-emissions combustion concepts, such as the quench zone in a rich-quench-lean (RQL) combustor and the injection plate for hydrogen (H_2) micro-mixing combustors. The quick mixing in an RJICF, attributable to its complex vortical structures, reduces NO_x emissions by shorting the high-temperature combustion time or quenching the high post-flame temperature. Previous studies thus investigated how different RJICFs' design features, such ask jet momentum ratio and jet diameter, affect the mixing behavior and the subsequent NO_x emissions. The compromise in performance between a CFD and CRN method can be seen in these studies. CRN-based studies simulated the jet-and-crossflow mixing process with approximations ranging from an instantaneous mixing to a two-step piecewise-constant-rate mixing. However, detailed reaction mechanisms, such as the GRI-series with prompt and thermal NO_x formation pathways, were used, along with parametric studies across more than 20 test cases. In contrast, CFD-based studies modeled the detailed jet interactions with the complex vortex groups in RJICF, but the chemistry simulations were limited to only two-step reaction mechanisms or flamelet-based tabulated chemistry methods. Likely due to high computational cost, parametric studies with CFD were also limited to around one to five cases. Therefore, there exists value in developing a NO_x emissions model for RJICF that balances the high-fidelity chemistry available in a CRN with the detailed aerodynamic simulation available in CFD while maintaining moderate computational costs for parametric studies.

A Lagrangian diffusive strip (LDS) method potentially offers a balance between CFD and CRN methods. It is a chemical analogy to the momentum boundary layer method widely used to study the near-wing aerodynamics of an airplane. To capture the mixing process in RJICF, the LDS method models a 1D convection-diffusion-reaction process within chemical boundary layers between the jet and the crossflow. Each chemical boundary layer is then transported by an external flow field, approximated by a potential flow around a simplified representation of the RJICF's vortex groups. Detailed aerodynamic effects on NO_x formation can then be simulated by the potential flow field straining the NO_x-producing chemical boundary layers. With the assumption of an inviscid, incompressible external flow field, the computational cost of the LDS method can be dramatically lower than a traditional Eulerian CFD method that defines a computational grid throughout the whole flow domain. To further reduce the computational cost, the three-dimensional RJICF process is reduced to a two-dimensional simulation by assuming pure convection along the jet direction. The chemical boundary layers on the cross-sectional plane perpendicular to the jet centerline can then be integrated starting from the jet's root in a parabolic CFD fashion. The reduction in computational cost from the aerodynamics simplification is then used to accommodate detailed chemistry and a wide-ranging parametric study.

Milestones

- Develop a finite volume formulation for the Ember transient flame solver to ensure conservation of specific quantities of interest.
- Develop an entrainment-dilation model to simulation the two-way coupling effect between the chemical boundary layer and the jet dynamics.
- Develop a chemical boundary layer re-segmentation function to maintain the stability of the simulation through adaptive grid refinement and small flow structure absorption.

Major Accomplishments

- The finite volume Ember chemical solution reduces species conservation error from the original 10% after 10 ms of simulation down to below 0.2%.
- The jet dilation modeling captures the linear growth trend of the jet width for a free jet problem.
- The muti-segment merging and remeshing process allows stable jet simulation to 1 ms, capturing the major region of interest for NO_x emissions estimation.

Publications

None.

Outreach Efforts

Results were presented to the FAA ASCENT Project Manager during regular bi-weekly teleconferences.

Awards

None.



Student Involvement

This task was conducted by Yang Chen, working under the supervision of Dr. Jayant Sabnis and Dr. Raymond Speth.

Plans for Next Period

- Incorporate the Ember chemical solver into the model to enable NO_x emissions modeling after the non-reacting simulation of the RJICF model.
- Complete further model validation for the determination of correct vortex dynamics in the external flow and the correct heat release physics.

Task 2 – Modeling Plasma-assisted Combustion for NO_x Emissions Reduction in Aircraft Gas Turbines

Massachusetts Institute of Technology

Objective

Plasma-assisted combustion (PAC) has been shown to improve ignition and extend lean blow-off (LBO) limits in a range of fuel and combustor configurations (Pilla et al., 2006; Lacoste et al., 2013). In most practical implementations, plasma actuation is delivered through nanosecond repetitively pulsed discharges that deposit high electric field bursts on nanosecond-timescales driving non-thermal electron-impact chemistry. Several studies suggest that this electron-impact chemistry contributes to additional pathways for the formation of NO_x (Xiong et al., 2019). In certain cases, this may outweigh the NO_x benefits of leaner operation. Other experiments have demonstrated that it is possible to reduce NO_x relative to a non-plasma baseline under specific operating conditions and discharge parameters (Shashsavari et al., 2023). Thus, PAC's impact on NO_x is an open design question, and a predictive modeling approach is needed to navigate this trade space.

Current PAC modeling work has focused on simple fuels (e.g., methane, hydrogen, or ammonia), which have an abundance of experimentally verified reaction data. However, the relevant fuel for practical aircraft turbine applications is a kerosene-like aviation fuel, and the goal of this work is to assess whether PAC can be used in a realistic combustor geometry and mission profile to lower net NO_x emissions when both plasma-generated NO_x and the benefits of leaner operation are taken into account. Addressing this question requires a modeling approach that combines a reduced Jet-A reaction mechanism tailored to NO_x formation and destruction in the presence of non-thermal plasmas, with a two-way coupled representation of the electron energy distribution and plasma chemistry that can be used in reactor network and 1D flame models.

In this task, we build on previous development of plasma reaction capabilities within our primary combustion modeling tool, Cantera, and implement and electron energy distribution function (EEDF) computation using a two-term approximation of the Boltzmann equation. This allows the EEDF to evolve self-consistently with the gas state and provides more reliable electron-impact rate coefficients for reactions which contribute to NO_x formation and destruction under the conditions relevant to aircraft gas turbines.

In parallel, we will develop a plasma-augmented reaction mechanism for a representative Jet-A surrogate that is specifically designed for zero and 1D NO_x and PAC studies. Experimental electron-impact cross-sections and rate coefficients for reactions involving hydrocarbons larger than methane are sparse. Many of these must therefore be derived from scaling laws and, where these models are unavailable, emulate plasma discharge effects by applying calibrated multipliers to surrogate reactions. The mechanism will retain the reduced structure necessary for tractable reactor-network and 1D flame calculations, while incorporating additional excitation, ionization, dissociation, and quenching processes that are known to influence combustion properties and NO_x formation and destruction.

Our team began by evaluating how combustion and plasma discharge parameters (e.g., equivalence ratio, inlet temperature, residence time, pulse frequency, and reduced electric field) affect NO_x/carbon monoxide (CO) emissions in a simple well-stirred reactor for the aforementioned reaction mechanism. Building on the insights gathered from the well-stirred reactor model, we then extend the analysis to reactor network representations of staged combustor architectures to evaluate the effect of PAC on engine conditions representative of realistic operations (i.e., idle, approach, cruise, and takeoff). This would allow for the identification of the most favorable operating conditions and plasma discharge parameters.



Complementary 1D flame simulations can be used to resolve the local structure of PAC-stabilized flames, with and without plasma, to understand where and when NO_x is produced within the flame and post flame region. These calculations will clarify how pulsed discharges modify temperature profiles, radical pools, and residence times in high temperature zones, and how these changes translate into both LBO extension and NO_x trends. The combination of reactor networks and 1D flame models enables us to connect local plasma flame interaction physics to overall combustor emissions in a way that is directly relevant to engine design.

The aim of this work is to create combustion models that can quantify the trade-offs between plasma enhanced lean operability and NO_x emissions across the aircraft operating envelope. As well as the ability to determine the combinations of plasma and combustion parameters where plasma actuation offers a potential NO_x reduction benefit and where it is unlikely to be advantageous.

Milestones

- Successful Implementation of two-term Boltzmann equation approximation in Cantera.
- Creation of a computationally stable reduced Jet-A-NO_x-plasma reaction mechanism, built on the HyChem "A2NOx" skeletal mechanism (Saggese et al., 2020).
- Adaptation of RQL combustor model to implement pulsed discharges in the primary zone.
- Creation of a well-stirred reactor simulation to evaluate NO_x production using various plasma discharge and combustion parameters.

Major Accomplishments

- Validation of Cantera Boltzmann solver functionality against results from Pavan (2023).
- Functionality of Jet-A-NO_x-plasma reaction mechanism within a well-stirred reactor with pulsed plasma discharges.

Publications

None.

Outreach Efforts

None.

Awards

None.

Student Involvement

This task was conducted by graduate student Matthew Quiram working under the supervision of Dr. Raymond Speth.

Plans for Next Period

- Continue using the well-stirred reactor model to evaluate which combinations of plasma and combustion parameters may provide the greatest emissions benefit compared to the non-plasma baseline.
- Create a zero-dimensional reactor network simulation using a combustor architecture representative of an aircraft gas turbine that could use plasma assisted combustion to extend its LBO limit.
- Use the insights gathered from the well-stirred reactor simulations to help determine parameters and engine operating conditions which may provide a net reduction in NO_x emissions.

References

Lacoste, D. A., Moeck, J. P., Durox, D., Laux, C. O., & Schuller, T. (2013). Effect of Nanosecond Repetitively Pulsed Discharges on the Dynamics of a Swirl-Stabilized Lean Premixed Flame. *Journal of Engineering for Gas Turbines and Power*, 135(101501). https://doi.org/10.1115/1.4024961

Pavan, C. A. (2023). Nanosecond Pulsed Plasmas in Dynamic Combustion Environments [Thesis, Massachusetts Institute of Technology]. Massachusetts Institute of Technology. https://dspace.mit.edu/handle/1721.1/151492

Pilla, G., Galley, D., Lacoste, D. A., Lacas, F., Veynante, D., & Laux, C. O. (2006). Stabilization of a Turbulent Premixed Flame Using a Nanosecond Repetitively Pulsed Plasma. *IEEE Transactions on Plasma Science*, 34(6), 2471–2477. https://doi.org/10.1109/TPS.2006.886081

Saggese, C., Wan, K., Xu, R., Tao, Y., Bowman, C. T., Park, J.-W., Lu, T., & Wang, H. (2020). A physics-based approach to modeling real-fuel combustion chemistry – V. NOx formation from a typical Jet A. *Combustion and Flame, 212*, 270–278. https://doi.org/10.1016/j.combustflame.2019.10.038

Shahsavari, M., Konnov, A. A., Bai, X.-S., Valera-Medina, A., Li, T., & Jangi, M. (2023). Synergistic effects of nanosecond plasma discharge and hydrogen on ammonia combustion. *Fuel, 348*, 128475. https://doi.org/10.1016/j.fuel.2023.128475

Xiong, Y., Schulz, O., Bourquard, C., Weilenmann, M., & Noiray, N. (2019). Plasma enhanced auto-ignition in a sequential combustor. *Proceedings of the Combustion Institute, 37*(4), 5587–5594. https://doi.org/10.1016/j.proci.2018.08.031



Project 052 Comparative Assessment of Electrification Strategies for Aviation

Massachusetts Institute of Technology

Project Lead Investigators

Florian Allroggen
Principal Research Scientist
Laboratory for Aviation and the Environment
Department of Aeronautics and Astronautics
Massachusetts Institute of Technology
77 Massachusetts Ave, Building 33-328
Cambridge, MA 02139
617-715-4472
fallrogg@mit.edu

Raymond Speth
Senior Research Scientist
Laboratory for Aviation and the Environment
Department of Aeronautics and Astronautics
Massachusetts Institute of Technology
77 Massachusetts Ave, Building 33-322
Cambridge, MA 02139
617-253-1516
speth@mit.edu

University Participants

Massachusetts Institute of Technology (MIT)

- P.I.: Dr. Florian Allroggen
- FAA Award Number: 13-C-AJFE-MIT, Amendment Nos. 062, 072, 080, 093, 098, 115, 121, 128, 133, 138, and143
- Period of Performance: February 5, 2020, to August 31, 2027
- Tasks (reported for the period October 1, 2024, to September 30, 2025):
  1. Develop a suite of roadmaps for aircraft electrification (covered in previous reporting periods; not reported for this period)
  2. Develop a system-level engineering model of power conversion processes and aircraft energy requirements
  3. Develop a model for analyzing the economics and emissions of electrification strategies (improved modeling capabilities for liquid methane (LCH_4) covered under Task 2 for more coherent presentation).
  4. Analyze the system-level costs and benefits of the electrification strategies
  5. Analyze the benefits of energy storage for power-to-liquid (PtL) fuel production (covered in previous periods; not reported during the current reporting period)

Project Funding Level

$2,185,000 Federal Aviation Administration (FAA) funding and $2,185,000 matching funds. Sources of match are approximately $404,100 from MIT, plus 3rd party in-kind contributions of $460,000 from NuFuels, LLC, and $110,000 from Savion Aerospace Corporation, and $214,000 from Google, LLC, and $996,900 from Earth Force Technologies.

Investigation Team

Dr. Florian Allroggen, (P.I.), All tasks
Dr. Raymond Speth, (co-P.I.), Tasks 1, 2, and 4
Dr. Niamh Keogh, Tasks 2 and 4



Dr. Prashanth Prakash, Task 1, 2, and 4
Dr. Nicolas Gomez-Vega, (postdoctoral associate), Task 2
Dr. Arthur Brown, (postdoctoral associate), Task 4
Bjarni Kristinsson, (graduate researcher), Task 2

Project Overview

The long-term goal of this project is to quantify the costs and impacts of various electrification approaches for commercial aviation. The electrification pathways include battery-electric ("all-electric") aircraft, as well as aircraft using drop-in sustainable aviation fuels (SAF) made with substantial electricity input (PtL) and electricity-intensive non-drop-in fuels, such as liquid hydrogen and methane. The project helps identify the best approach for using one unit of electric energy to power aviation. For this purpose, we develop both system-level engineering and system-level economic models, to assess electricity generation, fuel production, fuel transportation and storage, aircraft energy requirements, and aircraft operations. The models analyze different electrification pathways by using what can be described as a "power station to wake" approach. They quantify differences in costs and impacts associated with each electrification approach and compare them to a set of baseline aircraft powered by petroleum-derived fuels or drop-in SAFs made from biomass or waste streams. The outputs are used in a cost–benefit analysis, which provides insights into the net benefits associated with each technology.

Task 2 – Develop a System-level Engineering Model of Power Conversion Processes and Aircraft Energy Requirements

Massachusetts Institute of Technology

Objective

The goal of this task is to develop and apply system-level models of the value-chain power conversion processes, including energy generation, conversion into an energy carrier, transportation, and use onboard the aircraft. The goal of this effort is to understand which fuel most efficiently uses energy to power aviation. In the reporting period, we have made progress on two research streams within Tasks 2 and 3 (both are discussed here for cohesive presentation):

1. *Evaluation of supply chains for non-drop-in energy carriers for aviation:* Activities during this reporting period cover a detailed study of LCH_4 as an energy carrier for aviation, including challenges and opportunities. Key questions include:
   a. How much methane can be produced annually via biogenic material, including consideration of methanation from waste gas streams?
   b. What is the feasibility of supply chains, including placement of liquefaction facilities, associated utilities and fuel tanks, and costs across different airports?
   c. How much CH_4 will leak from the supply chain, including assessing the first-order impacts of such leakage?

2. *Detailed modeling and sizing of aircraft and their subsystems:* Activities during the reporting period include improving our understanding of the aircraft performance implications of different non-drop-in carriers. Areas of focus include:
   a. Modeling of hydrogen-fueled aircraft including their off-design performance
   b. Design and analysis of methane-fueled aircraft
   c. Advances for modeling fuel-cell powered aircraft design
   d. Development of a modular engine simulation model that could work with alternative propulsion architectures and new fuels

   This work builds on accomplishments in previous periods on (1) how the design of the fuel tank affects hydrogen aircraft energy demand and (2) how heat exchangers can be integrated into the jet engine to reduce energy demand. Higher fidelity models were developed, including capabilities to assess off-design performance, detailed turbomachinery performance maps, and a model for how turbine cooling affects engine performance. Such capabilities extend to unconventional propulsion systems for which new models are needed. While there are existing engine models that could handle a broad set of propulsion architectures, these are slow and not well suited for optimization at the aircraft level.

Milestones

Evaluation of Alternative Non-drop-in Energy Carriers for Aviation

- Selected LCH_4 for detailed analysis. The preliminary results remain promising and the team continues to refine the system-level assessment.
- Completed a preliminary value chain model of producing LCH_4 via anerobic digestion, considering waste and residue feedstocks.

Detailed Aircraft and Subsystem Modeling

- Completed the aircraft design models for cryogenic fuels with turbofan propulsion. Two conference papers have been prepared to disseminate the findings at American Institute of Aeronautics and Astronautics (AIAA) SciTech. A poster was prepared for the FAA ASCENT Fall meeting.
- Developed a preliminary version of a propulsion system model, named PowerCycles.jl, with much higher computational speed than existing open-source alternatives. This model is coupled to the MIT Transport Aircraft System OPTimization (TASOPT) tool to enable a broader set of propulsion architectures.
- Merged models for fuel-cell-powered aircraft using ducted fans and electric motors into TASOPT.jl. The models are ready to be used to design aircraft using fuel cells as an energy conversion system.

Major Accomplishments

Detailed Study of the LCH_4 Supply Chains for Aviation

During the current year, a detailed supply chain model for LCH_4 production was built under this project. It includes (but is not limited to) the following elements:

Methane Production Pathways

Multiple routes are available to produce methane as shown in Figure 1. Anaerobic digestion of biomass is the predominant pathway. It produces, on average, a 1:1 molar ratio of methane and carbon dioxide (CO_2). For the biomethane to be viable for commercial use, the biogenic CO_2 must be removed. The stream of biogenic carbon dioxide can be mixed with hydrogen to produce methane via three routes (see Figure 1). The methanation (Sabatier reaction) is the preferred pathway as the preferred nickel catalyst is low cost for a chemical catalyst, and the reaction has on the order of 95% methane selectivity at approximately 650 K and 5 bar.

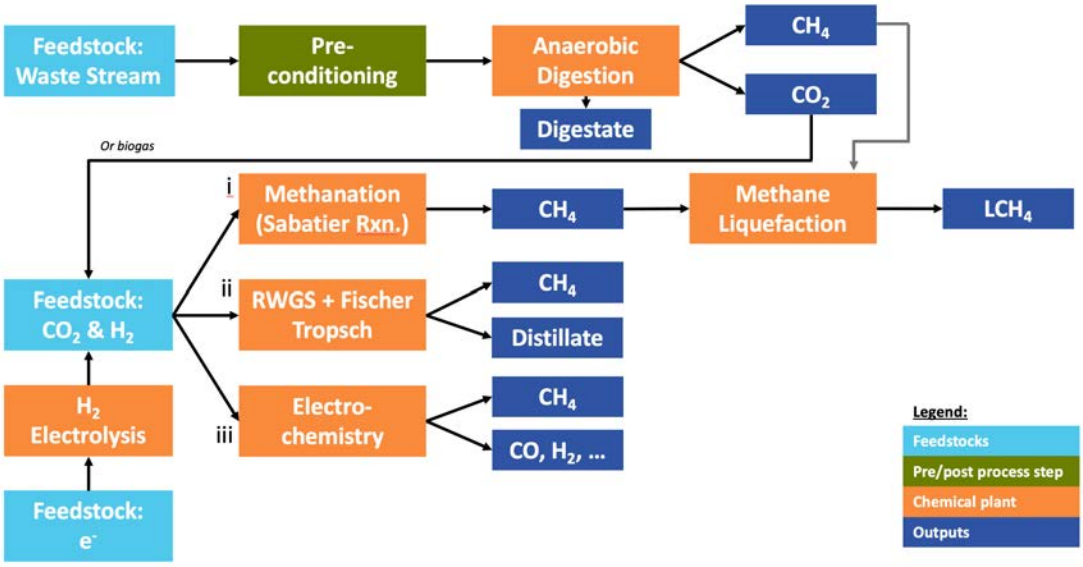


Figure 1. Overview of potential methane synthesis pathways.

Methane Production Potential

In 2019, the aviation industry consumed roughly 12 EJ of primary energy from jet fuel. In the first pass, we assess how 12 EJ of methane could be produced from biomass sources via anaerobic digestion. Sixteen waste and residue feedstocks were identified as potential scalable sources of CH_4, based on the literature's availability of conversion yields via anaerobic digestion. The literature search was focused on significant sources of available waste, and residues found by ASCENT Project 093's work. Figure 2 summarizes the availability of these 16 feedstocks considered, and their methane yields. Anaerobic digestion with pretreatment of all available feedstocks (mean residue scenario) results in 12 EJ of methane (lower heating value) on an annual basis. Note that not all of this potential CH_4 can be economically produced due to local availability and macro-economic factors (cost of debt, cost of equity).

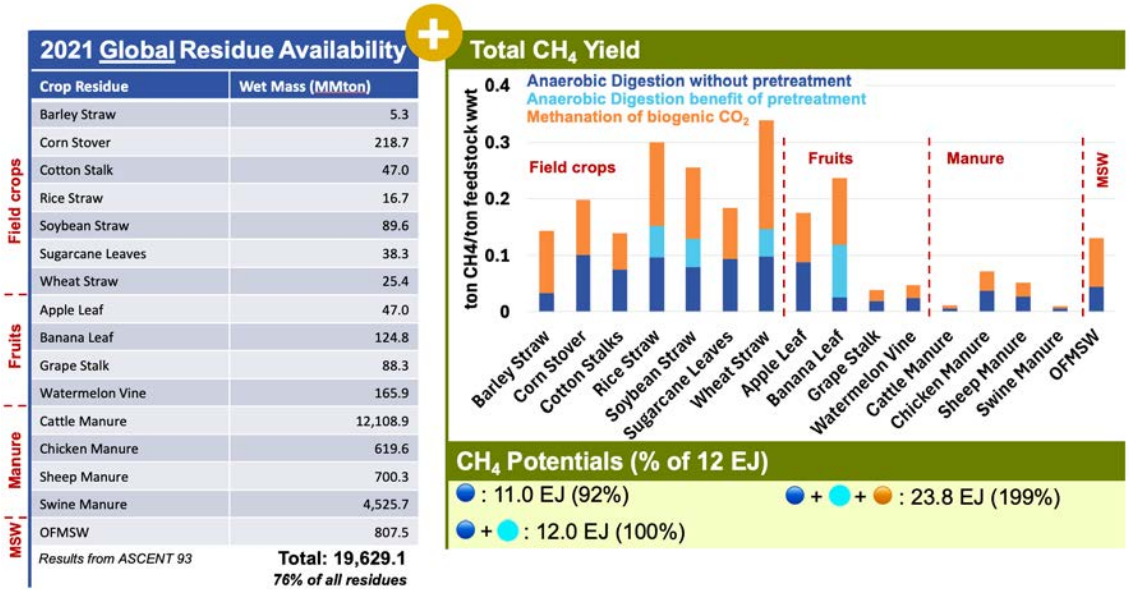


Figure 2. Residual biomass availability (mean residue scenario) and conversion yields to methane. Values are preliminary.

Technoeconomic Analysis of LCH_4 Production

Technoeconomic analysis can provide insight into the competitiveness of methane via anaerobic digestion from an economic angle. A discounted cash flow rate of return model was created to simulate the operational lifetime of an anaerobic digestion facility and determine the minimum selling price for methane in different locations.

An algorithm was then developed to allocate the limited supply of methane to airports globally. The goal was to have a fast algorithm that represents how a global supply chain of methane may develop, without sizing and modeling the whole supply chain network in detail. Figure 3 shows the model results for at-pump LCH_4 mean minimum selling price (MSP) at United States (U.S.) airports. A mean residue scenario is utilized, and the fuel demand from narrowbody aircraft is considered only (40-45% of global aviation fuel demand). The liquefaction premium of methane in the U.S. is modelled to be $0.43/gal Jet-A on an equivalent energy basis.

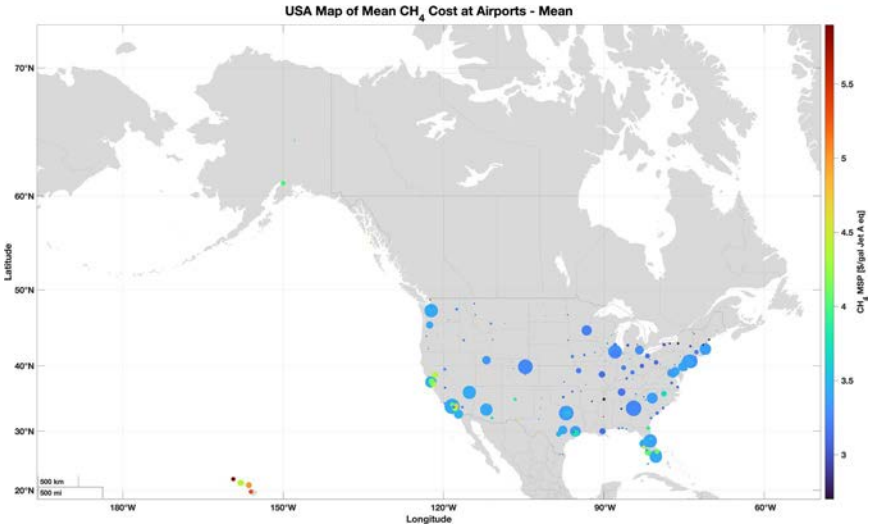


Figure 3. Preliminary liquid methane (LCH_4) pump price at United States airports, assuming only methane (CH_4) produced via anaerobic digestion and the mean residue-waste scenario.

Figure 4 displays the global at-pump price of LCH_4 at airports. The MSP is given in $/L Jet A on an equivalent energy basis to allow for better comparison with jet fuel costs.

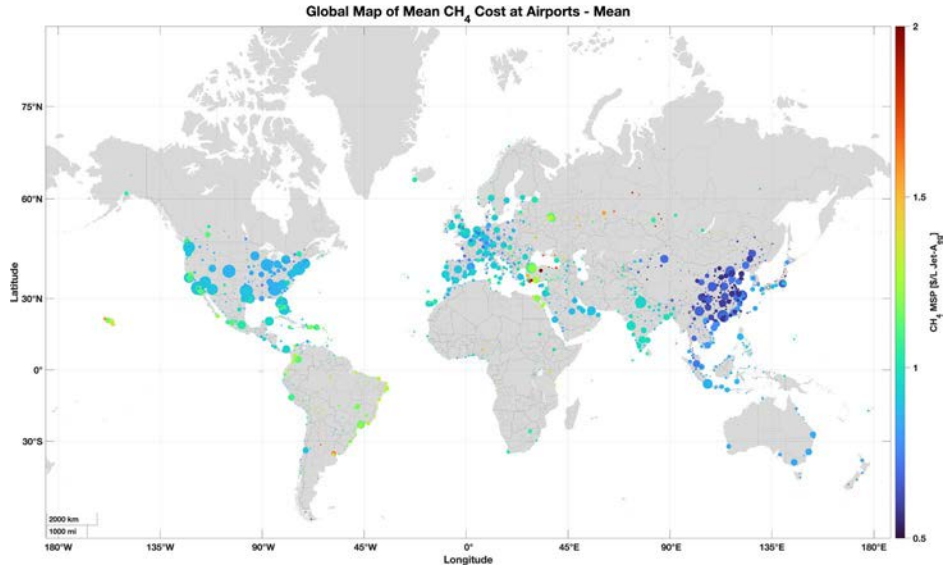


Figure 4. Preliminary liquid methane (LCH_4) pump price at airports globally, assuming only methane (CH_4) produced via anaerobic digestion and the mean residue-waste scenario.

Detailed Aircraft and Subsystem Modeling

Hydrogen-fueled Aircraft

In the studies conducted in the previous reporting period, hydrogen aircraft were optimized to complete one sizing mission. In the updated studies developed during this reporting period, the objective was to minimize the sum of the normalized energy demands across one sizing mission and four off-design missions with different ranges and ground temperatures (see Table 1). This is important as aircraft are regularly used on missions which do not match their design mission. The sensitivity parameters were chosen given their potential impacts on aircraft design, fuel tank, and engine



performance. The range in off-design missions 1 and 2 represents the 75% percentile by passenger-mile of missions flown by representative aircraft according to the 2019 OAG dataset; the range in off-design missions 3 and 4 represents the 50% percentile. The ground temperature in the sizing mission and off-design missions 1 and 3 is the standard sea-level temperature; the (higher) ground temperature in off-design missions 2 and 4 represent takeoff on a summer day.

Table 1. Payloads, ranges, and ground temperatures for the sizing and off-design missions.

	Short haul	Medium haul	Long haul
Payload in sizing mission (t)	11.50	17.55	38.59
Payload in off-design missions (t)	11.89	20.47	46.93
Range in sizing mission	4074 km (2200 nmi)	5556 km (3000 nmi)	14445 km (7800 nmi)
Range in off-design mission 1	1250 km (675 nmi)	2593 km (1400 nmi)	10556 km (5700 nmi)
Range in off-design mission 2	1250 km (675 nmi)	2593 km (1400 nmi)	10556 km (5700 nmi)
Range in off-design mission 3	833 km (450 nmi)	1759 km (950 nmi)	8334 km (4500 nmi)
Range in off-design mission 4	833 km (450 nmi)	1759 km (950 nmi)	8334 km (4500 nmi)
Ground temperature in sizing mission (K)	288.2	288.2	288.2
Ground temperature in off-design mission 1 (K)	288.2	288.2	288.2
Ground temperature in off-design mission 2 (K)	303.2	303.2	303.2
Ground temperature in off-design mission 3 (K)	288.2	288.2	288.2
Ground temperature in off-design mission 4 (K)	303.2	303.2	303.2

Figure 5 shows the payload-fuel energy intensity (PFEI; a non-dimensional measure of energy per passenger mile) for a jet fuel aircraft and hydrogen aircraft with two fuel tank options: a single-walled tank and a double-walled tank.

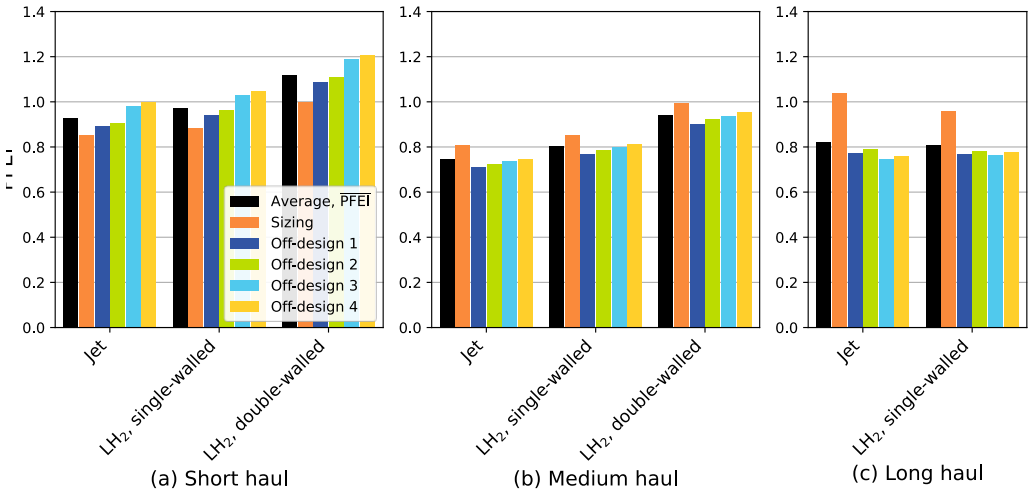


Figure 5. Normalized energy demand (payload-fuel energy intensity [PFEI]) for different aircraft fuels, fuel tank options, and missions.

Our previous study on heat exchangers integrated into the jet engine was revised with higher-fidelity models, including novel performance maps for the turbomachinery and a model for how cooling affects the efficiency of the engine's turbine. The latter model had a significant effect on the results, making one of the heat exchanger placement options more attractive, namely the cooler of turbine cooling air. Figure 6 shows the relative change in aircraft parameters, including the thrust-specific fuel consumption (TSFC) and lift-to-drag ratio (L/D), averaged across the five design missions. The results show that improvements in normalized energy demand on the order of 10% are possible if multiple heat exchangers are used.

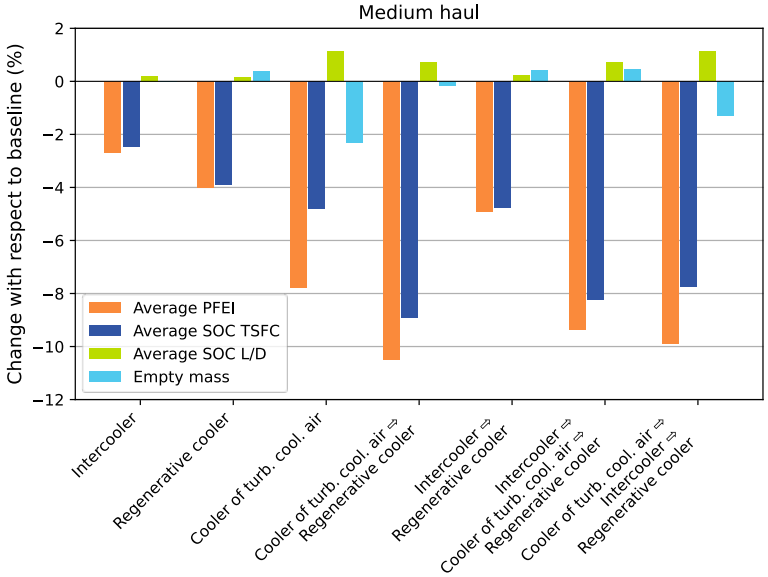


Figure 6. Relative change in hydrogen aircraft parameters with respect to a baseline with no heat exchangers. Thrust-specific fuel consumption (TSFC) and lift-to-drag ratio (L/D) values are at start of cruise (SOC).

Design and Analysis of Methane-fueled Aircraft
The aircraft design models for cryogenic fuels developed under ASCENT Project 052 were applied to design a liquid methane-fueled aircraft with a 250-passenger capacity and a range of 4,500 nautical miles; an equivalent jet-fuel aircraft was also designed for comparison. A preliminary mission-by-mission comparison of energy demand, as measured by a non-dimensional metric (the PFEI) is shown in Figure 7. Averaged across five missions (one sizing mission and four off-design missions), the methane aircraft has a 10.8% higher average PFEI than the jet-fuel analog, indicating a higher energy demand. We attribute this to the methane aircraft having a heavier fuselage as the fuel is carried in insulated fuel tanks in the fuselage, heavier wings due to the absence of bending moment relief from the fuel and increased drag due to the longer fuselage.

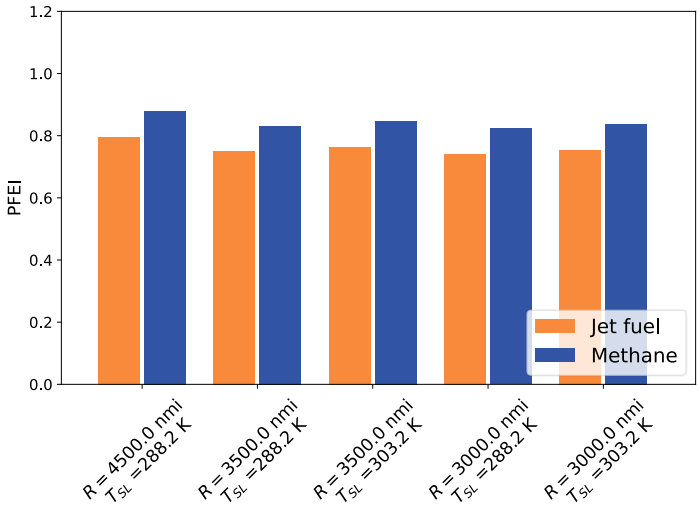


Figure 7. Energy demand (measured with payload-fuel energy intensity [PFEI]) of jet fuel and methane aircraft for one sizing and four off-design missions. Note that the mission ranges are not identical to those in Table 1.

Modular Engine Model
Our modular engine model can simulate the main components found in aircraft engines, such as compressors, turbines, burners or splitters, and combine them to form an independent engine. We have compared the performance of this engine model against the state-of-the-art open-source equivalent, pyCycle (Hendricks & Gray, 2019). In particular, we modeled the same high-bypass-ratio two-spool turbofan that is given as an example in the pyCycle source code. We find that our engine model produces results within 0.3% of the state at all stations in the engine. Comparing the runtimes, pyCycle with a tabular thermodynamic model takes 3.06 s to solve the design point of the turbofan engine and 7.85 s to solve both a design and off-design points; our engine model takes a median of 28.4 ms to solve the design problem and 37.7 ms to solve the off-design problem. This demonstrates that our model can already offer up to two orders of magnitude improvement in speed as compared to the best open-source alternative.

Publications

Presentations

Gomez-Vega, N., Tan, D. Y., Prashanth, P., Barrett, S. R., Speth, R. L., & Allroggen, F. (2025, January). *Influence of Fuel Tank Design on the Energy Demand of Hydrogen Aircraft* [Conference presentation paper]. AIAA SCITECH 2025 Forum, Orlando, Florida, 1243. https://doi.org/10.2514/6.2025-1243

Gomez-Vega, N., Prashanth, P., Speth, R. L., & Allroggen, F. (2025, January). *Hydrogen Aircraft Design With Heat-Exchanger-Enhanced Turbofan Engines* [Conference presentation paper]. AIAA SCITECH 2025 Forum, Orlando, Florida, 0089. https://doi.org/10.2514/6.2025-0089

During the reporting period, a journal paper expanding on these two conference papers was prepared and submitted for publication.



Outreach Efforts

Bjarni Örn Kristinsson shared the latest findings of the alternative non-drop-in energy carrier analysis at the 2025 ASCENT Spring meeting in Knoxville, Tennessee. A derivative of the 2025 ASCENT Spring presentation was given at the Zero Impact Aviation Alliance in May 2025, hosted at MIT. Dr. Gomez-Vega attended the AIAA SciTech 2025 conference in January 2025 in Orlando, Florida.

Student Involvement

During the reporting period, the MIT graduate student involved in this task was Bjarni Örn Kristinsson.

Plans for Next Period

Detailed Study of the LCH_4 Aviation System

- Complete the technoeconomic analysis of methanation via renewable energy sources.
- Develop an LCA model to estimate the gCO_{2eq}/MJ on a per-feedstock and country basis.
- Complete the LCH_4 analysis and submit a paper to a journal.

References

Hendricks, E. S., Gray, J. S. (2019). pyCycle: A tool for efficient optimization of gas turbine engine cycles. *Aerospace, 6*(8), 87. https://doi.org/10.3390/aerospace6080087

Task 4 – Analyze the System-level Costs and Benefits of the Electrification Strategies

Massachusetts Institute of Technology

Objectives

The objective of this task is to develop system-level analyses for comparing various electrification strategies while integrating the engineering and assessment models developed previously. During the current reporting period, the ASCENT Project 052 team focused on assessing the airport infrastructure required to replace current nine-passenger airliners (mostly regional air mobility [RAM]) with fully electric aircraft. Specifically, our team conducted a case study for Bethel Municipal Airport in Alaska. Estimates for number and type of chargers, airport power requirements for charging, and electric generation infrastructure (wind turbines, solar panels, and/or battery energy storage systems) were produced.

Research Approach

RAM is a category of airline service flying aircraft with few (≤9) seats to regional airports. About 550,000 such flights took place in the U.S. in 2019. RAM airliners are candidates for replacement with fully electric aircraft. This is because current batteries have low specific energy (energy per unit mass) relative to hydrocarbon fuels and are therefore too heavy to power single-aisle or long-haul airliners. By contrast, the small number of passengers and short ranges (typically ≤500 miles) of RAM flights means that battery-electric RAM airliners may be possible with current battery technology. Potential benefits of electric RAM include lower costs, particularly fuel and maintenance. In addition, tailpipe emissions from burning hydrocarbon fuels are eliminated.

The goal of this project is to assess the electrical infrastructure required to support battery-electric RAM operations. This is done in three steps. Firstly, a schedule of existing RAM flights is assembled from schedule data for the year 2019. Secondly, all flights are replaced with electric aircraft, and the electricity consumed during each flight is computed with a physics-based aircraft performance model. Finally, the electrical infrastructure required at each airport (i.e., chargers, electricity generation and transmission infrastructure, etc.) is assessed.

Milestones

- Selected Bethel, Alaska, for a case study. A dataset of RAM flights was assembled from OAG data using circular flights (flights that both departed from and arrived in Bethel, with one or more stops elsewhere).
- Estimated the number of chargers, power per charger, and airport electrical loads from charging based on a custom algorithm that used airline turnaround time requirements as an input.

- Sized electrical infrastructure (wind turbines, solar panels, and/or battery energy storage systems) to meet the charging loads using the National Laboratory of the Rockies' (NLR) Renewable Energy Optimization (REopt) tool. Power curtailment and cost estimates were obtained.

Major Accomplishments

Bethel, Alaska, was selected for a case study because it is the busiest airport in the U.S. by number of RAM arrivals, averaging about 65 per day in 2019. Bethel is not connected to the highway transport system, so the only way to reach Anchorage (the nearest large city) in a timely fashion is by air.[1] The RAM flights connect Bethel to dozens of outlying villages, each of which typically has a few hundred residents. Bethel is used as a hub for these flights because Bethel's airport (unlike those of the outlying villages) can handle single-aisle passenger airliners, which connect Bethel to Anchorage. Figure 8 shows a map of Alaska including Anchorage, Bethel, and the outlying connected villages. Figure 9 shows a map of the busiest RAM route in the area: the route from Bethel to the outlying villages of Kipnuk and Chefornak.



Figure 8. Map of Alaska showing Anchorage, Bethel (blue and black square), and the outlying villages connected to Bethel by RAM flights.

[1] 82% of communities in Alaska lack access to the road system and are similarly dependent on air travel.

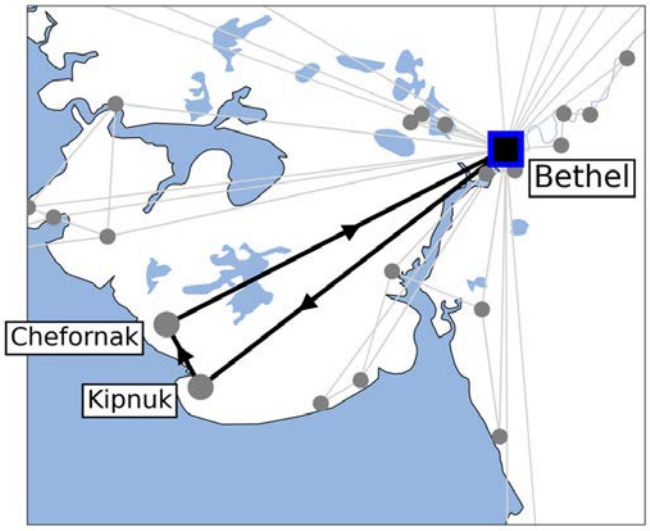


Figure 9. Bethel-Kipnuk-Chefornak-Bethel is the busiest RAM route in the Bethel area, averaging 5-6 flights per day. Connections to some other villages are also shown.

Electric RAM airline operations in the Bethel area can use Bethel as a recharging hub, assuming an aircraft battery capacity of 1,833 kWh. This capacity is sufficient to fly the most demanding mission in the dataset plus a 45-minute loiter, consistent with night visual flight rules (VFR) reserve requirements. The outlying villages served by these flights do not require charging infrastructure. Aircraft recharging must occur simultaneously with passenger loading and unloading to avoid disrupting airline schedules because charging time is comparable to turnaround time.

A summary of our charging analysis results assuming a 30-minute turnaround is provided in Table 2. The maximum output power required to recharge all flights within 30 minutes (3.1 MW) is too high for cable-based fast charging. However, two pantograph-based fast chargers (each of which can typically charge at about 1-2 MW) may together be enough to meet the 3.1-MW requirement. Also, the peak airport power draw required to recharge all flights within 30 minutes (21 MW) exceeds the generating capacity of Bethel's electrical grid (14.4 MW). The peak and average loads on Bethel's grid in 2019 were even lower: 7.3 MW and 5.0 MW, respectively. New electric generation infrastructure is therefore needed to operate electric RAM flights with short turnarounds from Bethel, or changes to flight schedules are needed.

Table 2. Summary of charging results for a 30-minute turnaround.

Number of chargers	13
Max charger output power	3.10 MW
Max charging C-rate	1.69
Average grid power draw	2.08 MW
Peak grid power draw	21.0 MW

Number of chargers, charger power, and grid power (peak and average) as a function of turnaround time are shown in Figure 10 and Figure 11. These two figures show that turnaround time requirements must be carefully considered. Shorter turnarounds induce the following tradeoffs: reduced aircraft battery cycle life because of increased charging C-rates; fewer but more powerful chargers; and higher grid peak power draw, requiring more electrical ground infrastructure.

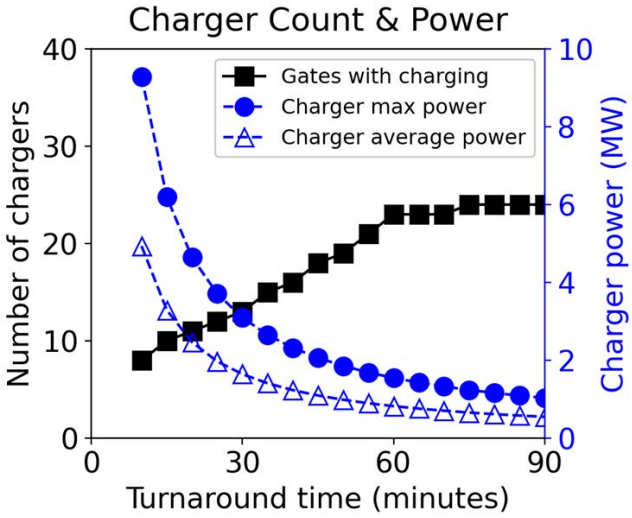


Figure 10. Number of chargers and charger power (average and maximum) as a function of turnaround time.

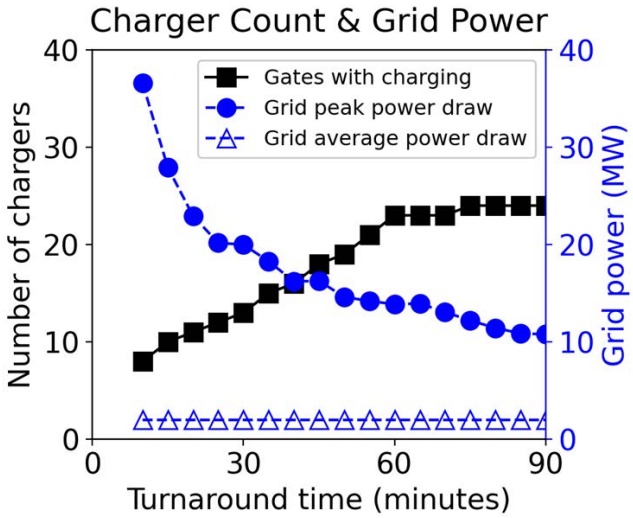


Figure 11. Number of chargers and grid power (average and maximum) as a function of turnaround time.

Electrical infrastructure (wind turbines, solar panels, and/or battery energy storage systems) to meet the charging loads for all flights was sized using NLR's REopt tool. Results including installed distributed energy resources (DER), curtailment fractions (the fraction of electrical energy that is lost due to curtailment) and costs including up-front capital expenses (CapEx) and levelized cost of energy (LCOE) are provided in Table 3.



Table 3. Installed distributed energy resources (DERs), curtailment fractions, and cost estimates for different combinations of electrical infrastructure.

	Wind + battery	Solar + battery	Wind + solar + battery
Installed wind	41.0 MW	-	9.1 MW
Installed solar	-	178.6 MW	13.2 MW
Installed battery	144.4 MWh 21.8 MW	469.3 MWh 22.8 MW	79.9 MWh 21.6 MW
Wind curtailment	88.9%	-	69.3%
Solar curtailment	-	87.2%	32.1%
Upfront CapEx	$458.8m	$1840.4m	$312.6m
LCOE ($/kWh)	$1.443	$5.878	$1.028

Table 3 shows that sizing, curtailment, and costs vary with the type of DERs selected: wind + battery, solar + battery, and wind + solar + battery. Solar + wind + battery is the least expensive option as measured by both upfront CapEx and LCOE. This is because solar and wind power were sized by different times of the year:

- The wind + battery case was sized by a period in late March/early April 2019 in which no wind was available for about 4 days, requiring a large and expensive battery to supply power. The wind turbines are oversized for the rest of the year as indicated by the curtailment fraction of 88.9% (i.e., almost 90% of the available wind energy on an annual basis was not used due to low demand).
- The solar + battery case was sized by a period in late December 2019 in which little light was available due to short day length, also requiring a large and expensive battery to supply power. The solar panels are oversized for the rest of the year as indicated by the curtailment fraction of 87.2%.
- The wind + solar + battery case is cheaper than either energy source alone because wind power is available when little solar power is available and vice versa. This is illustrated by the lower curtailment fractions: 69.3% and 32.1% for wind and solar, respectively.

The LCOE for the wind + solar + battery case was $1.028/kWh. However, a typical commercial electricity price in Bethel in 2025 is only $0.568/kW; the new electrical infrastructure required for electric RAM flights is almost twice as expensive to operate as Bethel's existing grid. Recall that electric RAM charging requires more power than the grid can provide. Therefore, further cost reductions may be necessary.

Publications

None.

Outreach Efforts

Dr. Brown gave a poster presentation at the 2024 ASCENT Fall meeting in Washington, D.C., and a slide-based presentation at the 2025 ASCENT Spring meeting in Knoxville, Tennessee, to disseminate the findings. Dr. Brown also gave a slide-based presentation at the Zero Impact Aviation Alliance meeting in May 2025, hosted at MIT.

Student Involvement

None.

Plans for Next Period

Over the coming reporting period, the team will elaborate on the Bethel, Alaska, case study. Specifically, we will refine our estimates for electrical infrastructure size and cost; we will also estimate the sensitivity to the turnaround time requirement. We will further assess options for reducing infrastructure costs, possibly including diesel generators and/or power curtailment to avoid having to oversize renewable electricity generating infrastructure. Finally, we will investigate ways of generalizing the results across additional airports.



Project 053 Validation of Low Exposure Noise Modeling by Open-Source Data Management and Visualization Systems Integrated with AEDT

Stanford University

Project Lead Investigator

Juan J. Alonso
Vance D. and Arlene C. Coffman Professor
James and Anna Marie Spilker Chair of Aeronautics & Astronautics
Department of Aeronautics & Astronautics
Stanford University
Stanford, CA 94305
(650) 723-9954
jjalonso@stanford.edu

University Participants

Stanford University

- P.I.(s): Prof. Juan J. Alonso
- FAA Award Number: 13-C-AJFE-SU-022
- Period of Performance: October 1, 2024, to September 30, 2025
- Tasks
  1. Complete prototype of Metroplex Overflight Noise Analysis (MONA), including Aviation Environmental Design Tool (AEDT) integration. **Complete.**
  2. Validation and verification of AEDT noise predictions in day-night average sound level (DNL) 55-65 dB areas. Completed study (for arrivals into San Francisco International Airport [SFO] 28L/R only) and submitted journal paper, which was published in March 2024.
  3. Data science formats and scientific computing for large-scale airspace analyses. **Complete.**
  4. Viable alternative approach routes into the San Francisco Bay Area metroplex. **Pending/de-scoped**.

Project Funding Level

The current expected tasks for this reporting period were placed on hold during fiscal year (FY) 2025 due to a delay in funding. As of November 2025 (at the writing of this report), we have not received information regarding when the funds will become available to complete the tasks we had proposed. For this reason, the remainder of this report simply provides a summary of past accomplishments and a description of the plan to (a) complete the assessment of the accuracy of AEDT's noise predictions including departure operations and (b) prepare the release of the software developed in Project 053 for open-source distribution and use. The total expect funding for FY 2025 was $350,000 to cover all activities described below.

Investigation Team

The investigation team is made up of the faculty, graduate and undergraduate students, and collaborators listed below with their respective areas of expertise/areas of contribution and the period of time their involvement was expected:

Juan J. Alonso (P.I., Stanford Aeronautics & Astronautics): overall responsibility for the project and its technical and administrative elements.

Brian Munguía (Graduate Student, Stanford Aeronautics & Astronautics): AEDT, cloud-based AEDT study execution, AEDT debugging; departures study development and initial debugging. During the period of performance (October 1, 2024, to September 30, 2025) Mr. Munguía was expected to perform tasks in support of the development of departure operations, noise model accuracy assessments, and journal paper submission.



Donald Jackson (Collaborator, software developer): overall MONA project infrastructure (servers, databases, hardware/ software monitoring), Geographic Information System (GIS), web-based visualization deployment, technical guidance. During the period of performance, Mr. Jackson was expected to help develop our open-source software and prepare it for release, together with an additional software developer (to be determined). He did continue to maintain our infrastructure database, and to ingest and curate the noise data from our sensors and from those from SFO/EnviroSuite® (October 1, 2024, to September 30, 2025), so as not to lose any data during the hiatus in funding.

Thomas Rindfleisch (Co-P.I., Sr. Research Scientist, Emeritus, Stanford University): noise monitoring and filtering, aircraft trajectory collection/processing, visualization, data analysis. During the period of performance, Mr. Rindfleisch would have worked to analyze results of our calculations and experimental measurements and would have worked to help prepare all the data for our journal submission and to generate the main manuscript in collaboration with Prof. Alonso. (October 1, 2024, to September 30, 2025).

Project Overview

The MONA project was started to provide real-time and objective data, analyses, and reports to key stakeholders and policy makers to mitigate the noise impacts of the deployment of new NextGen procedures. This system (a) collects and archives air traffic data using a network of antennae and automatic dependent surveillance-broadcast (ADS-B) receivers, (b) analyzes noise impacts using a variety of metrics, (c) visualizes resulting large-scale datasets, and (d) uses a network of sound-level monitors (SLM) to validate and enhance the quality of noise predictions. The focus of ASCENT Project 053 is to improve upon the noise predictions of MONA through tighter integration with AEDT. In particular, our work is focused on the following three tasks: (1) integrate and automate AEDT's noise analysis capabilities, (2) validate and verify (V&V) AEDT's noise predictions in DNL 55-65 dB areas, and (3) propose software engineering/architectural choices for future AEDT development to enhance usability in multiple workflows including Application Programming Interface (API) formulation, visualization interfaces, resilient data acquisition and storage, and cloud computing.

The expected benefits of this project mirror the tasks mentioned above, including (a) ability to automate complex noise analyses in metroplexes so they are available in near-real time after the preceding 24-hr period, (b) a better understanding of the accuracy of AEDT's current noise models in high- (DNL >65 dB) and low-noise (DNL 55-65 dB) areas and the reasons for the discrepancies (if any) in existing predictions, and (c) recommendations to software developers on flexible architectures and APIs for AEDT so that the tool is more versatile and generally applicable. AEDT predictions are built around the policy context of an average annual day. The majority of the V&V results produced and shared by the MONA team have focused on a cumulative daily basis for which flight track data are directly collected. The project thus far has managed to automate the cloud-based analysis (using many parallel instances of AEDT) of *every flight into SFO for a period of an entire year (July 1, 2021-June 30, 2022)* and, therefore, some of our results, included in the March 2024 journal publication, now contain DNL levels based on the flight operations collected through MONA system. The focus of the work we have done so far is on arrivals into SFO with main attention paid to arrivals on runways 28L/R. Having created the entire framework and having generated data for a full year of arrivals operations, the effort during this past year focused exclusively on creating, submitting, and providing reviews for a journal publication including all of our results to date. The final journal publication in *The Journal of the Acoustical Society of America* (JASA) was made available online and published in Volume 155, Issue 3 in March 2024. The full citation for this work, which includes all of our results to date is:

Rindfleisch, T. C., Alonso, J. J., Jackson, D. C., Munguia, B. C., & Bowman, N. W. (2024). A Large-Scale Validation Study of AEDT Noise Modeling for Aircraft Arrivals. *The Journal of the Acoustical Society of America, 155*(3), 1928-1949. https://doi.org/10.1121/10.0025276

Background and Previous Accomplishments

The MONA project started approximately 7 years ago with the main objective of providing real-time and objective data, analysis, and reports to key stakeholders and policy makers to help in mitigating the noise impacts of the deployment of new NextGen procedures. Since then, we have put together and deployed a system that (a) collects, archives, and makes available air traffic data using a series of networked antennae and ADS-B receivers 24/7, (b) analyzes noise impacts using a variety of metrics (based on both a MONA-developed noise prediction tool and the noise prediction tools within AEDT), (c) visualizes resulting large-scale datasets in a simple, user-friendly fashion using both a bespoke website and Uber®'s

® EnviroSuite is a registered trademark of Envirosuite Holdings Pty Ltd, North Sydney, Australia.
® Uber is a registered trademark of Uber Technologies, Inc., San Francisco, California.



kepler.gl and deck.gl large-scale data visualization toolboxes, and (d) has deployed a small network of low-cost, Stanford-owned, sound-level monitors scattered across the South Bay part of the Bay Area and has included the data from the noise monitors deployed by SFO to cross-calibrate measurements by MONA and SFO monitors, collect noise measurements more widely geographically, and enhance noise predictions so they describe exactly the actual noise levels experienced.

The longer-term objectives of the MONA project are to (a) ensure the validation and verification of all noise predictions provided (by AEDT or other tools) in both areas near the airport and in other areas further away from the airport, (b) achieve full automation of complex noise analyses in regions around airports in the US, including AEDT-based noise predictions, (c) make all results web-accessible for in-depth interpretations of historical and proposed changes, (d) eventually study potential alternative traffic patterns in complex airspace to mitigate aviation environmental impacts, and (e) export the proven/validated MONA technology to other airport regions via open-source software/hardware.

The MONA system has matured considerably over the past few years to the point that a full-system prototype has now been operational for some time. In fact, for all arrival operations into SFO, we consider the system to be fully operational. To recall the main elements of the system, the MONA team has deployed a small network of ADS-B/multilateration (MLAT) antennae and has completed the software necessary to merge the data streams from all of these antennae including de-duplication of sightings, identification of aircraft equipment and routes flown, physical interpolation of data missing from the joint observations, and archiving (in appropriate database formats) of the information collected for successive analysis. Moreover, for arrival operations, we have spent considerable time and effort understanding the best ways to utilize the AEDT (by understanding the ways to most accurately model aircraft trajectories, aircraft equipment, and aircraft noise) so that any comparisons between experimental data and the results obtained from AEDT may be affected as little as possible by confounding variables. In fact, we have spent time in using AEDT in multiple ways including the standard version of AEDT that is approved for regulatory use in the U.S. and an improved version that leverages higher-fidelity aircraft performance models (BADA 4) and detailed descriptions of individual aircraft trajectories (using the so-called altitude and speed controls that result from the ADS-B data and their post-processing).

The MONA system has achieved a level of integration with FAA's AEDT software that enables fully-automatic processing of noise exposure at arbitrary receptor locations for arrival routes into the San Francisco Bay Area airports. The JASA publication includes our published and most accurate and comprehensive assessment of the comparison between AEDT predictions and noise-monitoring stations created to date, with an entire year of flights observed at multiple locations. In total, more than 200,000 datapoints give statistical significance to the results that we have obtained, that are presented here, and that we submitted for peer-reviewed publication.

Again, direct research efforts were halted during this past year of performance. Because of this, we do not report on any progress but include the description of the tasks that would have been pursued, for reference, in the section titled "Plans for Next Period"

Task 2 - AEDT Noise Prediction Assessment in DNL 55-65 and DNL > 65 dB Areas

Stanford University

Our team has previously reported on the development of the MONA system, the data that it acquires, the information processing (both to prepare and post-process AEDT simulations and to filter and curate experimental noise data) that is necessary to V&V the predictions, and the preliminary observations from all the data collected and produced. Our FY 2024 report, in particular, focused on the statistically-significant characterization of the discrepancies between the measured noise at two different noise-monitoring stations and the predictions using AEDT in various ways with increasing levels of modeling fidelity. The reader is referred to the report for more details. By *statistically significant* we mean that the observations and conclusions are based on large amounts of data that are deemed to have converged probability distributions and statistical moments (e.g., expected value/mean and standard deviations). In other words, we do not attempt to draw conclusions about the predictive qualities of AEDT noise models based on 5 to 10 flights (as has been common in the literature) but that, rather, we focus on large-enough numbers of observations: at least 10,000 flights/datapoints for the main aircraft types and over 200,000 flights, over a 12-month period, for our entire study.



Moreover, the actual data we drew conclusions from were highly curated to eliminate any noise events that are unlikely to be the result of aircraft overflights alone, as well as other situations where multiple aircraft may have passed over a noise-monitoring station nearly simultaneously. This is to say that we feel confident that the data presented in prior publications (both the JASA paper and previous annual reports) are of the highest quality possible. The data presented and the associated conclusions/observations, with the obvious limitations that they apply to SFO and to arrival operations at SFO, were peer reviewed and approved for publication.

Outreach Efforts

No specific outreach efforts were pursued during the period of performance due to the delay in funding.

Awards

None.

Student Involvement

Due to the delay in funding, no student involvement took place this past year. The main PhD Candidate in the project, Mr. Brian Munguía shifted his contributions to other active projects.

Plans for Next Period

Our future efforts in ASCENT Project 053, assuming the availability of funds, will focus on completing the full study, including arrivals (discussed in the FY 2024 report) and departures (to be completed) to develop a complete picture of the areas where AEDT-R and AEDT-AE can and cannot provide the required accuracy in the noise predictions and to more effectively pinpoint areas of potential noise modeling improvements that may be undertaken by AEDT developers to continuously improve the quality of the predictions and, therefore, the quality of proposed new routes accounting for noise impacts on the ground. The outcome of such studies is expected to be more efficient arrivals and departure routes that minimize the noise radiated to the overflown communities. We will also carry out a number of studies to further improve the accuracy of modeling using the AEDT, including terrain and ground effects. Finally, we will continue to improve, modularize, and document key elements of our MONA system software so that it can be used more effectively for our own studies, but so it can also be shared with other researchers to conduct similar studies at different institutions and airports. A second journal paper is expected to be prepared detailing the entire set of results but focusing on the departure routes. We expect the predictions for departure routes, which are dominated by engine noise, to produce better results than those that we have achieved for arrivals.



Project 054 AEDT Evaluation and Development Support

Georgia Institute of Technology

Project Lead Investigator

Prof. Dimitri N. Mavris
Director, Aerospace Systems Design Laboratory
School of Aerospace Engineering
Georgia Institute of Technology
275 Ferst Drive NW, Atlanta, GA 30332
(404) 894-1557
dimitri.mavris@ae.gatech.edu

Dr. Michelle Kirby
Chief, Civil Aviation Division
Aerospace Systems Design Laboratory
School of Aerospace Engineering
Georgia Institute of Technology
275 Ferst Drive NW, Atlanta, GA 30332
(404) 385-2780
michelle.kirby@ae.gatech.edu

University Participants

Georgia Institute of Technology (Georgia Tech)

- P.I.s: Dr. Dimitri N. Mavris, Dr. Michelle Kirby, Dr. Ameya Behere
- FAA Award Numbers: 13-C-AJFE-GIT-098, 114, and 122
- Period of Performance: September 24, 2021, to September 20, 2023
- Tasks:
  1. Improved departure modeling
  2. Arrival profile modeling
  3. Full flight modeling
  4. System testing and evaluation of the Aviation Environmental Design Tool (AEDT)
  5. Supersonic transport (SST) aircraft modeling in the AEDT (formerly ASCENT Project 010)

Project Funding Level

Georgia Tech has received $900,000 in funding for this project. In terms of cost-share details, Georgia Tech has agreed to a total of $900,000 in matching funds. This total includes salaries for the project director, research engineers, and graduate research assistants, as well as computing, financial, and administrative support, including meeting arrangements. Georgia Tech has also agreed to provide tuition remission for the students, paid for by state funds.

Investigation Team

Prof. Dimitri N. Mavris, (P.I.), Tasks 1-5
Dr. Michelle Kirby, (co-Investigator), Tasks 1-5
Dr. Ameya Behere, (co-Investigator), Tasks 1-5
Mr. Jirat Bhanpato, (research faculty), Tasks 1-5
Dr. Raphael Gautier, (research faculty), Tasks 1-5
Ranya Almarzooqi, (graduate student), Task 1
Vishnu Sankar Manivasakan, (graduate student), Task 1
Keletso Mmlane, (graduate student), Task 1
Anushka Moharir, (graduate student), Task 2
Hansen Lian, (graduate student), Task 2



Nitya Maruthuvakudi Venkatram, (graduate student), Tasks 3 and 5
Hyungu Choi, (graduate student), Task 3
Yash Vinod, (graduate student), Task 3
Bogdan Dorca, (graduate student), Task 4
Santusht Sairam, (graduate student), Task 4
Fahraan Badruddin (graduate student), Task 4

Project Overview

This project provides data and methods to continue to improve modeling of aircraft weight, takeoff thrust, and departure and arrival procedures within the Federal Aviation Administration's (FAA) AEDT, as well as the AEDT's full flight modeling capabilities. Some of the modeling assumptions in the AEDT are considered excessively conservative and could be improved through use of industry and airport flight operation data. Funding for this project will continue to support the implementation of these methods and data in the AEDT. To facilitate these efforts, the Georgia Tech team will use real-world flight data and noise monitoring data to improve departure, full flight, and arrival modeling.

Task 1 – Improved Departure Modeling

Georgia Institute of Technology

Objective

This task aims to improve departure profile modeling in the AEDT. Over the past few years, this task provided recommendations for new noise abatement departure procedures (NADP) to be implemented in the AEDT, improving how flight trajectories are modeled and consequently, giving more accurate fuel consumption and emissions metric results.

In the previous reporting period, departure profile modeling efforts focused on identifying why existing AEDT departure procedures did not adequately represent observed operations in the 2021 Threaded Track (TT) and Flight Operations Quality Assurance (FOQA) calendar year (CY)2023 datasets. That work examined the role of aircraft energy share percentage (ES%) and takeoff weight in departures, classified key operational "anchors" for characteristics such as flap transitions, landing gear retraction, thrust cutbacks, level-offs, and constant calibrated airspeed (CAS) segments. Dynamic time warping (DTW) was used to cluster CY2023 FOQA departures using these anchors to determine distinct departure procedures for AEDT implementation.

Building on that foundation, this year's objective is to evaluate whether real-world departure operations can be represented in the AEDT using the existing AEDT procedures and previously developed NADP profiles when assessed on noise. Specifically, the task (1) clusters FOQA departures to existing AEDT/NADP profiles based on noise under flight path (NUFP) similarity, and (2) validates these cluster assignments by checking that key operational anchors for thrust cutback and acceleration segments as well as fuel burn over the corresponding segments, agree between the FOQA derived fixed point profiles (FPP) and their matched procedures within defined tolerances.

To present these findings, this report first describes the methodology used to construct NUFP from AEDT noise outputs for FPPs and existing profiles, to assign FPPs to existing procedures based on NUFP through clustering, and to extract and compare anchors and fuel burn for all flights in these clusters. It then summarizes the clustering and validation results for Airbus® A321-232 departures at several airports, highlights where existing profiles capture noise and operations well and where they do not, and concludes with planned next steps for refining the anchor detection and determining whether additional procedures are necessary to be defined in the AEDT.

Background and Previous Work

Prior work established that, for the TT-2021 dataset, none of the existing AEDT departure profiles provided a consistently accurate representation of observed operations, even when accounting for ES% and takeoff weight variations. The previous reporting period then used CY2023 FOQA data to (1) identify and classify operational anchors for departures (flaps, landing gears, thrust cutback, level-offs, constant CAS), (2) build FPPs in the AEDT to acquire performance and noise results for FOQA departures, and (3) apply DTW and related metrics to cluster flights by trajectory and thrust profiles, and to compare these clusters to existing AEDT and NADP procedures.

® Airbus is a registered trademark of Airbus Operations GmbH, Hamburg, Germany.

Initial clustering highlighted that trajectory-based similarity alone is not always aligned with noise patterns. Some flights with visibly different thrust and altitude profiles produced similar noise footprints, while others with very slight trajectory differences produced significantly different noise. This motivated the shift toward a noise-centric clustering method using NUFP as the basis for determining whether real-world operations can be represented by existing departure procedures.

Research Approach

The following section provides a detailed explanation of the methodology used in this reporting period to evaluate whether real-world departure operations can be represented in the AEDT using existing AEDT and NADP procedures. The overall process is summarized in Figure 1, which shows how FOQA data are used to build FPPs in the AEDT, obtain NUFP, and classify key operational anchors. NUFP for each FPP is then compared with the existing procedure library to determine the closest match, after which the assigned cluster is validated using anchor alignment and cumulative fuel burn. Flights that satisfy these validation checks are considered to be appropriately represented by their assigned procedures, while flights that do not indicate potentially the need for additional or modified departure procedures. The subsections that follow describe each step of this process: NUFP construction and clustering as well as anchor and fuel-based validation.

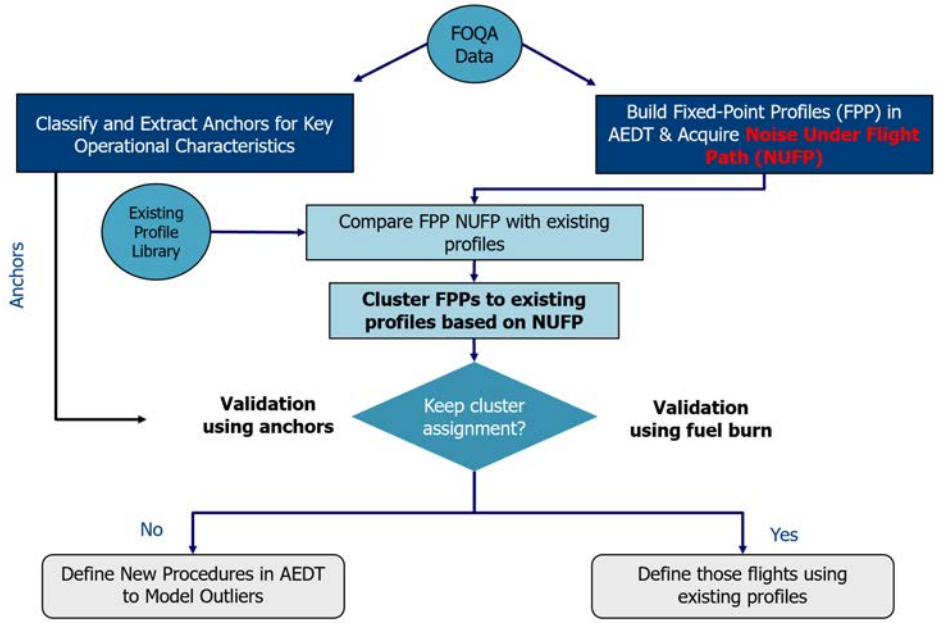


Figure 1. Overall clustering and validation process. AEDT: Aviation Environmental Design Tool, FOQA: Flight Operations Quality Assurance, NUFP: noise under flight path.

Methodology

Data and Scope

This year's analysis uses FOQA CY2023 departures, focusing on A321-232 operations from multiple airports. The NUFP-based clustering and validation were applied to A321-232 departures from Denver International Airport (KDEN), Hartsfield-Jackson Atlanta International Airport (KATL), and Los Angeles International Airport (KLAX). There were 1,987 A321-232 departures considered for KATL, 441 A321-232 departures considered for KDEN, and 532 A321-232 departures considered for KLAX.

Each of these departures is modeled in the AEDT through creating FPP that follow the observed trajectory. The AEDT is then used to compute noise on its standard receptor grid. These FPPs are compared to a library of existing AEDT departure procedures (STANDARD, International Civil Aviation Organization [ICAO]A, ICAOB, etc.) and NADP profiles (NADP 1 and 2 profiles with multiple thrust derate settings) to determine which procedure best matches each FOQA departure in terms of NUFP.



Construction of NUFP

NUFP is a one-dimensional representation of sound exposure level (SEL) directly underneath the aircraft's ground track. For each FPP, the AEDT is first run to obtain full SEL grids on the receptor layout for that airport. The aircraft ground track distance versus time, as well as the latitude and longitude over time, is taken from AEDT performance reports. A KDTree search is then used to find receptors close to the ground track; receptors within roughly 0.08 nmi of the track (about 1.5 times the receptor spacing) are kept ensuring that at least one receptor lies near each point along the trajectory.

To focus on the part of the noise footprint most relevant for NUFP clustering, the receptor set is filtered by SEL threshold. Several thresholds were tested (75, 85, and 95 dB); however, these tests showed that the 95 dB captures only the loudest part of the footprint and misses smaller differences that matter for clustering, while 75 dB retains enough of the footprint shape to separate different procedures without being dominated by far-field noise. As a result, the 75 dB NUFP was used as the primary basis for clustering.

Receptors at or above 75 dB SEL are ordered along cumulative ground track distance from the start of takeoff roll. This produces SEL as a function of cumulative distance from liftoff for each flight. For comparison with existing AEDT/NADP procedures, the NUFP curves for the FPP and the procedures are truncated at the point where either profile reaches 15,000 ft above field elevation (AFE), so that both curves cover a common downrange segment.

NUFP Similarity and Assignment to Existing Procedures

Initial work compared NUFP using distribution-based metrics such as Wasserstein distance and Hausdorff distance applied to the cumulative SEL distributions. These methods capture some differences between procedures but also produced cases where flights with clearly different thrust cutback heights or climb gradients looked “similar” in terms of NUFP because the distributions overlapped. This showed that NUFP needed to be compared as a curve along distance, not just a set of values.

The current approach, therefore, compares the full SEL versus cumulative distance curves. For a given FPP and AEDT/NADP procedure, the two NUFP curves are interpolated to a common set of cumulative distance points over their shared range up to 15,000 ft AFE. The mean absolute error (MAE) and root mean square error (RMSE) between the two curves are then computed. MAE captures average differences in SEL along the path, while RMSE emphasizes larger local mismatches. These two error measures are normalized and combined into a single similarity score. For each FPP, this score is computed against every AEDT/NADP procedure, and the procedure with the lowest score is taken as the best NUFP match for the FOQA departure. All flights whose NUFP best matches a given procedure are grouped into a cluster labeled by that procedure.

This assignment is done separately for each airport and airframe. Comparing results across KDEN, KATL, and KLAX allows for analyzing how local runway layout, elevation, and typical operating practices affect which procedures appear in the cluster library and how many flights each procedure represents.

Anchor Classification

NUFP similarity alone does not guarantee that two departures follow the same procedure in terms of thrust and speed changes, the NUFP-based cluster assignments are checked using operational anchors for the departures. All anchors are defined along cumulative ground track distance but checks also use altitude at the anchor to ensure that events occur at reasonable heights.

Thrust cutback begin (CUT) is defined as the earliest point after an altitude gate where the smoothed thrust profile shows a clear drop and then levels off. Specifically, the algorithm looks for the earliest point between 800 ft and 4,000 ft AFE where thrust drops by at least 8% over a 0.5 nmi window, followed by a flat segment with less than about 2% thrust decrease over 0.3 nmi. This identifies both the cutback and the start of the reduced thrust climb segment.

Initial acceleration begin (AB) and end (AE) are derived from true airspeed after cutback. The method computes the change in speed over a window a roughly 0.5 nmi. The begin point is classified as the first sustained increase in speed of at least 10 kt over 0.4 nmi, and the end point is where the speed gain drops back to about 2 kt over a similar distance. This captures the main acceleration phase where flap settings are changed and the aircraft transitions toward a climb schedule with higher speed. Final acceleration begin (FAB) and end are defined similarly but occurs after AE, with lower speed thresholds (about 5 kt over 0.3 nmi for FAB begin and 2 kt over 0.3 for final acceleration end) to reflect the smaller accelerations at higher altitude.



These anchors are extracted both for each FPP and for each AEDT/NADP procedure to provide a consistent set of reference points for comparison. For anchor validation, altitude checks are used to ensure that anchors occur at comparable heights: CUT is compared using a 1,500 ft altitude tolerance, and AB/FAB and AE use tolerances of about 1,600 ft and 2,200 ft, respectively.

Validation Using Anchors and Fuel Burn

Once flights have been assigned to procedures based on NUFP and the anchors have been classified, each flight-procedure pair is checked against several validation rules. The aim is to determine whether the NUFP similarity corresponds to a genuinely similar procedure in terms of its thrust, speed, and trajectory.

For each anchor (CUT, AB, AE, FAB), the difference in location between the FPP and the matched procedure is computed, along with the altitude difference. An anchor is considered aligned if it occurs within altitude tolerance and within a profile-specific distance or timing tolerance. In addition to individual anchors, an anchor order rule is applied: AE must occur after both CUT and AB, and FAB must occur after or around AE, which allows for both discrete final acceleration classification and continuous final acceleration segments.

Fuel burn is checked using cumulative fuel burn from the performance reports for the FPPs and matched procedure. Cumulative fuel is evaluated at cutback, and the fuel used over the acceleration windows (AB to AE and AE to AB) is summed. The FPP and procedure values are compared using a symmetric relative error method. A flight is considered to pass the fuel check if the combined error across cutback and the acceleration windows is within 25%. Previous work showed that, for the majority of flights, cumulative fuel burn over these windows is within this bound when the operations are consistent.

FAB is treated somewhat differently from the other anchors. As final acceleration can appear as either a discrete event or continuous increase in speed, FAB alignment is a soft check. FAB must respect the anchor order rule, but mismatches in exact FAB location are not counted as hard failures.

When these validation rules were first applied with fixed thresholds, some profiles had high outlier rates even when visual inspection suggested that the operations were reasonably similar. To address this, thresholds for anchor alignment were tuned per profile. For each profile, the distribution of anchor errors among the flights mapped to that profile is computed, and the profile-specific threshold for that anchor is set to the 80th percentile of the empirical error distribution, with an upper cap of 1.6 times the original base threshold. This keeps thresholds tied to observed variability while preventing them from becoming so large that they no longer enforce a meaningful match.

Results and Discussions

NUFP Clustering at KATL

The NUFP clustering analysis for 1,987 A321-232 departures from KATL reveals a structured and highly non-uniform distribution of operational departure profiles. A total of 38 distinct clusters were identified as shown in Figure 2. Although the absolute number of clusters appears large, the cluster size distribution is strongly skewed: only a small subset of clusters contains the majority of the 1,987 flights, while the remainder form a long tail of clusters with very few flights.

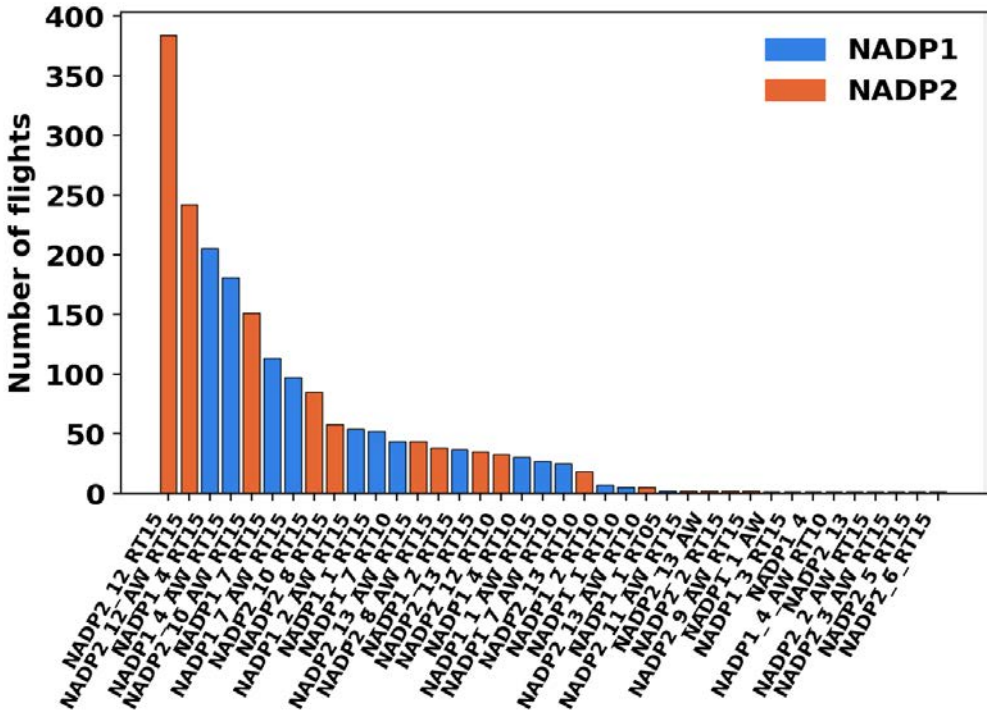


Figure 2. KATL flight distribution among clusters. NADP: noise abatement departure procedures.

All clusters mapped to NADPs, specifically NADP1 and NADP2 variants with RT10 and RT15 thrust-reduction settings. These same procedures repeatedly emerged as the closest NUFP matches because their SEL-distance curves reflect the general shape and noise levels seen in the NUFP of real-world operations.

Despite the relatively large number of total clusters (38), the overall distribution reveals a small number of dominant profiles that account for the majority of departures. These dominant clusters correspond to NADP 1_7 and NADP 2_12. Overall, a small set of NADP1 and NADP2 RT variants effectively capture the dominant NUFP behavior at KATL, while the clusters with very few flights reflect infrequent or non-routine noise patterns,

NUFP Clustering at KLAX

For KLAX, NUFP clustering was applied to 532 A321-232 departures, resulting in 66 clusters as shown in Figure 3. Similar to KATL, the cluster size distribution is dominated by a few high-membership clusters, with the remainder forming a long tail of small clusters.

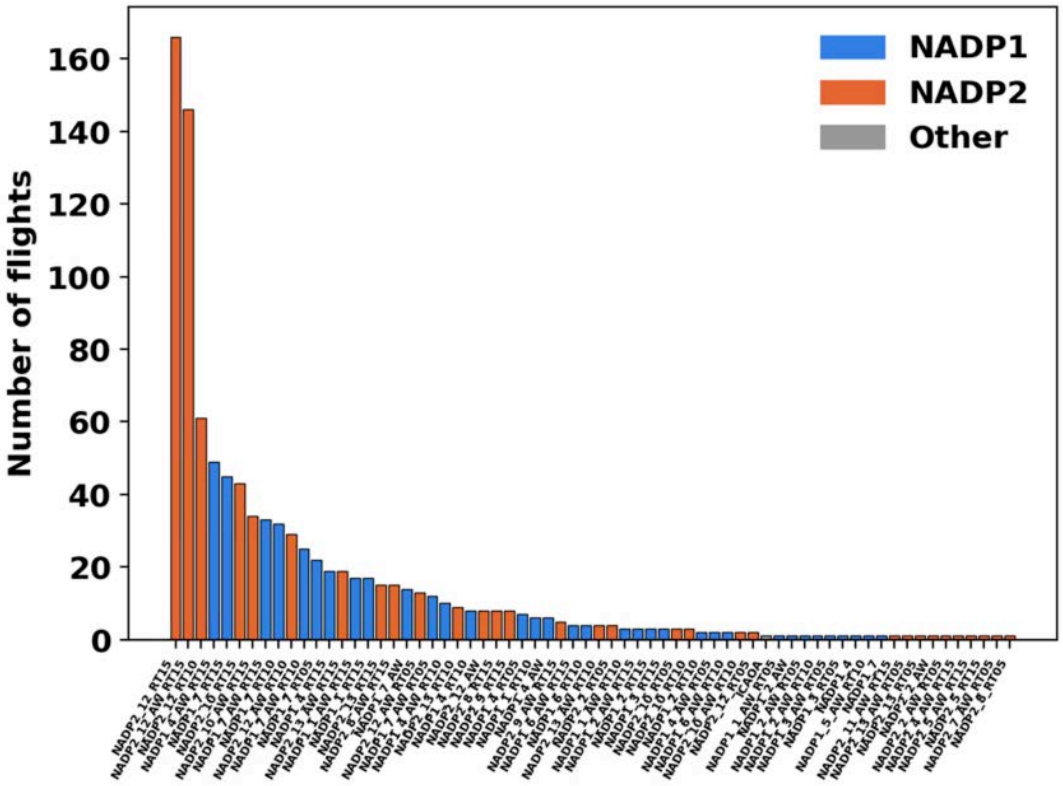


Figure 3. KLAX flight distribution among clusters. NADP: noise abatement departure procedures.

Most flights mapped to NADP2 RT15 and RT10 procedures. NADP 1 variants appear but represent a smaller share of flights compared to KATL. This is likely due to differences in airport elevation and location, impacting noise-abatement constraints and air traffic control procedures. A single flight matched to an ICAOA procedure; however, this does not seem to be a common operation for A321-232s taking off from KLAX.

A321-232s taking off from KLAX produced a larger tail of small clusters than KATL. Non-RT profiles appear within this long tail of clusters, but account for relatively few flights. However, the key observation remains the same: the most common NUFP distributions correspond to a narrow group of NADP procedures.

NUFP Clustering at KDEN

The NUFP clustering for 441 A321-232 departures from KDEN resulted in 43 distinct clusters Figure 4. As at the other airports in this study, the cluster size distribution is highly skewed (i.e., a small number of profiles account for most flights, while most profiles contain only a few flights). When profiles are sorted by membership, the six largest clusters each contain more than 20 flights and together represent about 61% of all departures. An intermediate set of 11 clusters (6–20 flights each) accounts for roughly 26% of the data, while the remaining 26 clusters each contain five or fewer flights, together representing about 12% of departures. This long tail indicates that KDEN A321-232 operations are dominated by a handful of NADP procedures, namely the NADP2_12 and NADP1_7 variants with RT10 and RT15.

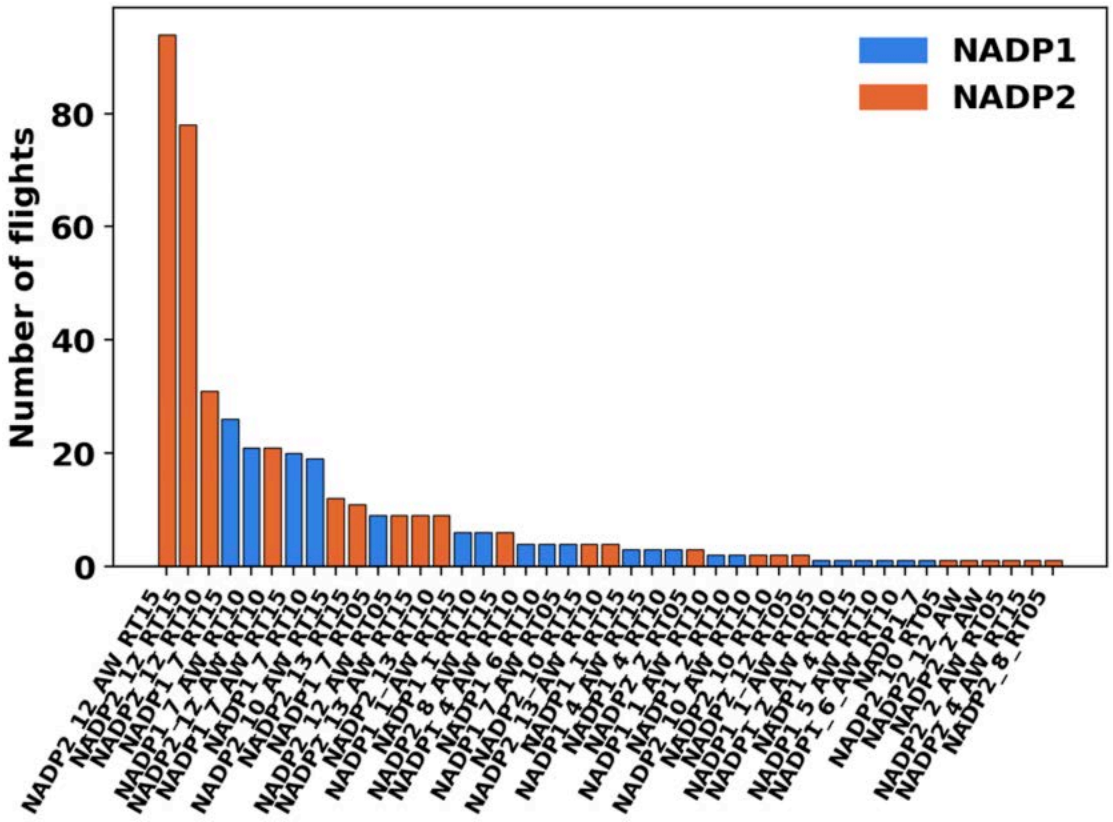


Figure 4. KDEN flight distribution among clusters. NADP: noise abatement departure procedures.

All KDEN profiles were NADP1 or NADP2 variants, aggregating across profiles, approximately 69% of flights are assigned to NADP2 procedures and 31% to NADP1, indicating a clear predominance of NADP2 operations in the NUFP matching results.

The NADP2_12_AW_RT15, NADP2_12_RT15, and NADP2_12_RT10 clusters alone account for just over 45% of all A321-232 departures at KDEN. Smaller but still substantial contributions come from several NADP1_7 variants (e.g., NADP1_7_RT15, NADP1_7_AW_RT10, NADP1_7_AW_RT15, NADP1_7_RT10), each representing 15–30 flights. Overall, the KDEN clustering results indicate that A321-232 departures are strongly organized around NADP2 profiles, with NADP1 profiles providing a secondary set of procedures.

NUFO Clustering Results

Across all three airports, the NUFP clustering results show that A321-232 departures are overwhelmingly organized around a compact set of NADP1 and NADP2 procedures with different RT settings, while many additional clusters contain only a few flights each. At KATL, 1,987 departures form 38 clusters that all match NADP-style profiles; at KLAX, 532 departures form 66 clusters, with almost all clusters mapped to NADP1/NADP2 and a single flight matching an ICAO A procedure; and at KDEN, 441 departures form 43 clusters, with every flight assigned to a NADP variant and about 69% of flights mapped to NADP2. Thus, existing AEDT procedures appear only marginally in the NUFP matching (one KLAX case), whereas NADP profiles systematically capture NUFP for real-world operations more accurately. This indicates that a relatively small library of NADP-based profiles, including key NADP1/NADP2 RT variants, can effectively represent observed A321-232 departure behavior across the three airports and provides a focused basis for enhancing AEDT departure modeling.

Validation Results for A321-232 Departures for KATL

Following NUFP-based clustering, each flight underwent anchor-level validation to assess how closely individual FOQA departures aligned with their cluster's procedural characteristics. Out of 1,987 flights, 378 were flagged as outliers,



corresponding to a validation rate of approximately 81%. This indicates that most flights followed consistent anchor sequencing and climb-profile shapes.

Anchor-Level Validation:

- Cutback (CUT) has the highest pass rate (97.6%), indicating that the thrust-reduction event occurs at consistently similar locations across flights.
- Acceleration anchors show more variability, with AB having the lowest pass rate (79.7%), while AE is somewhat more consistent (84.9%).
- Anchor-order (Order) checks pass for 87.3% of flights, indicating that the expected sequence (CUT → AB → AE) is followed in most cases.
- Fuel-based validation (Fuel) shows that 90% of flights remain within ±25% of the procedure's cumulative fuel burn over the acceleration windows, suggesting good overall agreement between FOQA FPPs and their assigned NADP procedures.

Validation Results for A321-232 Departures for KLAX
524 A321-232 departures were validated, 99 were classified as outliers (≈ 18.9%).

Anchor-Level Validation:

- CUT has a pass rate of 97.9%.
- Followed by AB: 93.5%
- 88.4% have no AE failure
- Final Acceleration Begin (FAB): 100% (i.e., no flight has FAB listed as a failure)
- The order anchor has a pass rate of 98.9%.
- The fuel anchor has a 96.9% pass rate.

Validation Results for A321-232 Departures for KDEN
Following cluster assignment, each of the 441 KDEN departures underwent anchor-level and fuel-based validation against its matched NUFP profile. Of these flights, 79 were flagged as outliers, corresponding to an outlier rate of approximately 17.9%. The remaining 362 flights (82.1%) passed all validation checks and are considered well represented by their assigned NUFP procedures.

Anchor-level pass rates are summarized below, computed over all 441 flights:

- CUT a pass rate of 98.4%.
- AB a pass rate of 92.3%.
- AE a pass rate of 88.9%.
- Order a pass rate of 99.1%.
- Fuel a pass rate of 99.1%.

The validation results suggest the following patterns for KDEN A321-232 departures:

- Cutback and anchor order are highly consistent. Almost all flights satisfy the cutback and order criteria, indicating that the thrust-reduction event and the overall temporal sequence of cutback → acceleration are very stable features across the dataset.
- Acceleration anchors are the primary source of deviation. Most validation failures involve AB and/or AE, which is consistent with those anchors being more sensitive to intra-procedure variability.
- Fuel-based checks show strong agreement. Only four flights fail the fuel check, indicating that cumulative fuel burn over the cutback and acceleration windows generally agrees well with the NUFP-assigned procedures.

In summary, the KDEN validation results show that most A321-232 departures are well captured by their NUFP-assigned NADP1 or NADP2 profiles, with a moderate outlier fraction driven primarily by variability in acceleration-phase anchors rather than by cutback or fuel behavior. These findings complement the clustering results by demonstrating that the dominant NUFP procedures at KDEN are not only frequently used but also flown with generally high internal consistency.

Conclusion
For all three airports, the NUFP validation results indicate that the assigned procedures capture A321-232 departure behavior with a high degree of internal consistency, with roughly 80% of flights passing all checks at each airport (81% at



KATL, 81.1% at KLAX, 82.1% at KDEN). Cutback and anchor-order tests are the most robust, with pass rates above about 97% everywhere, showing that the thrust-reduction event and the overall CUT → AB → AE sequence are implemented very consistently in practice. Acceleration anchors are the main source of deviations: AB and AE have the lowest pass rates at each airport, especially AB at KATL, confirming that the acceleration phase is where most intra-procedure variability appears. Fuel-based validation is strong at all three airports, with at least 90% of flights within the specified fuel-burn bounds and pass rates near 97–99% at KLAX and KDEN. Taken together, these results show that the NUFP-assigned NADP1/NADP2 profiles not only dominate procedurally but are also flown in a repeatable way, with a relatively small outlier fraction driven primarily by variations in the acceleration segment rather than by gross differences in cutback location, event ordering, or fuel usage.

Outlier Behavior and Directional Sensitivity at KATL

This section summarizes the validation outlier behavior observed for A321-232 departures. The goal is to distinguish true procedural deviations from artifacts of the current anchor-detection and validation logic.

Of the 1,987 flights at KATL, 378 grouped into 38 NUFP-based clusters (approximately 19%) failed at least one validation check and were classified as outliers. To understand where validation is most sensitive, the 378 outlier flights were decomposed by the specific anchor checks that failed, shown in Figure 5. The anchor-combination histogram shows that approximately 87% of all outlier flags are tied to the acceleration phase anchors. AE-only failures account for about 42% of the outliers, AB-only failures contribute another 41%, and combined AB+AE failures add roughly 3–4%. This concentration in AB and AE confirms that most outliers arise during the transition between cutback and climb acceleration rather than at thrust reduction itself.

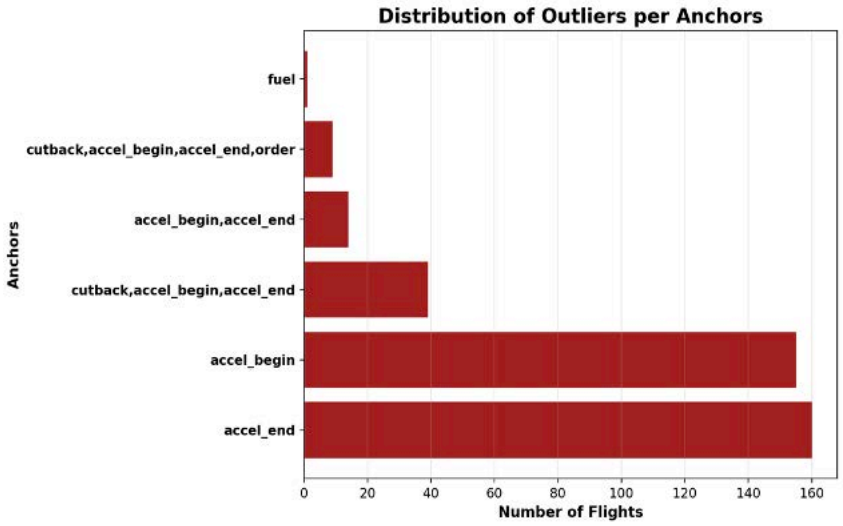


Figure 5. Match failures specific to anchor checks.

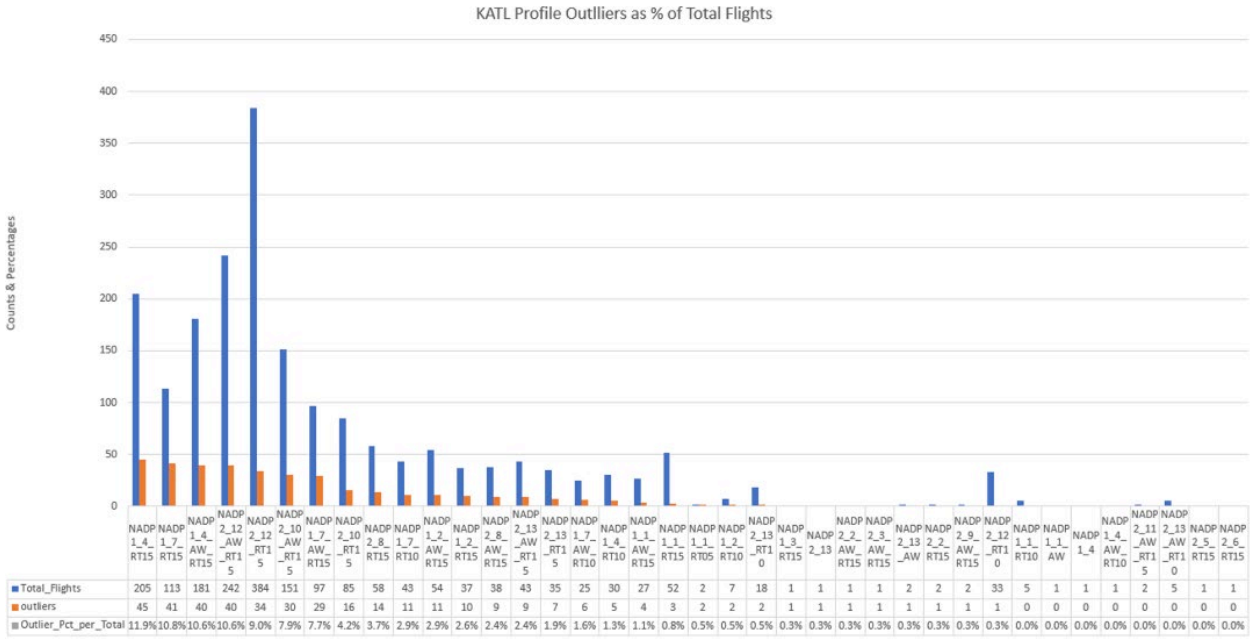
Secondary combinations of anchors account for the remaining outliers. Roughly 10.3% of outliers involve simultaneous mismatches in CUT, AB, and AE, while about 2.4% show additional order-related discrepancies (CUT + AB + AE + Order). These cases typically reflect compound effects where slight misplacement of cutback interacts with acceleration detection and ordering, rather than fundamentally different departure procedures. Fuel-driven mismatches are negligible: only about 0.26% of outliers are caused by the fuel check, consistent with the broader finding that 90% of all flights are within ± 25% of expected fuel burn. This supports the interpretation that the performance-based validation remains robust and that the main tuning need lies in acceleration-phase anchor thresholds.

Aggregating outliers by matched NUFP profile shows in Figure 6 that approximately 70% of all outliers are associated with just seven profiles. All these profiles are flown with RT15 thrust-reduction settings and are largely NADP1 variants, with a smaller but still significant contribution from NADP2 profiles. The key high-outlier profiles are:

- NADP1_4_RT15



- NADP1_7_RT15
- NADP1_4_AW_RT15
- NADP2_12_RT15
- NADP2_12_AW_RT15
- NADP2_10_AW_RT15
- NADP1_10_AW_RT15



	NADP 1_4_ RT15	NADP 1_7_ RT15	NADP 1_4_ AW_ RT15	NADP 2_12 _AW _RT1 5	NADP 2_12 _RT1 5	NADP 2_10 _AW _RT1 5	NADP 1_7_ AW_ RT15	NADP 2_10 _RT1 5	NADP 2_8_ RT15	NADP 1_7_ RT10	NADP 1_2_ AW_ RT15	NADP 1_2_ RT15	NADP 2_8_ AW_ RT15	NADP 2_13 _AW _RT1 5	NADP 2_13 _RT1 5	NADP 1_7_ AW_ RT10	NADP 1_4_ RT10	NADP 1_1_ AW_ RT15	NADP 1_1_ RT15	NADP 1_1_ RT05	NADP 1_2_ RT10	NADP 2_13 _RT1 0	NADP 1_3_ RT15	NADP 2_13	NADP 2_2_ AW_ RT15	NADP 2_3_ AW_ RT15	NADP 2_13 _AW	NADP 2_2_ RT15	NADP 2_9_ AW_ RT15	NADP 2_12 _RT1 0	NADP 1_1_ RT10	NADP 1_1_ AW	NADP 1_4	NADP 1_4_ AW_ RT10	NADP 2_11 _AW _RT1 5	NADP 2_13 _AW _RT1 0	NADP 2_5_ RT15	NADP 2_6_ RT15
Total_Flights	205	113	181	242	384	151	97	85	58	43	54	37	38	43	35	25	30	27	52	2	7	18	1	1	1	1	2	2	2	33	5	1	1	1	2	5	1	1
outliers	45	41	40	40	34	30	29	16	14	11	11	10	9	9	7	6	5	4	3	2	2	2	1	1	1	1	1	1	1	1	0	0	0	0	0	0	0	0
Outlier_Pct_per_Total	11.9%	10.8%	10.6%	10.6%	9.0%	7.9%	7.7%	4.2%	3.7%	2.9%	2.9%	2.6%	2.4%	2.4%	1.9%	1.6%	1.3%	1.1%	0.8%	0.5%	0.5%	0.5%	0.3%	0.3%	0.3%	0.3%	0.3%	0.3%	0.3%	0.3%	0.0%	0.0%	0.0%	0.0%	0.0%	0.0%	0.0%	0.0%

Figure 6. Outlier flights matched to NUFP profiles and shown as a percentage of total flights at Hartsfield-Jackson Atlanta International Airport (KATL). NADP: noise abatement departure procedures.

Taken together, these profiles capture most outlier flights. At this stage, the analysis treats the association between high RT settings, NADP1 procedures, and outliers as a correlation rather than a proven causal link; some of these profiles also carry substantial traffic, which naturally increases their outlier counts. Further normalization and profiling are planned before drawing stronger conclusions about causality.

A second analysis examined the percentage of outliers within each profile Figure 7. Profiles with very small sample sizes (1–2 flights) sometimes show outlier rates above 50% or even 100%, but these represent only nine outliers in total (≈2.4% of all outliers) and are treated as case-by-case anomalies rather than evidence of systemic issues. For statistical robustness, the evaluation was restricted to profiles with at least seven flights. Within this subset, the highest outlier rates are again associated with NADP1 procedures:

- NADP1_7_RT15 (~36%)
- NADP1_7AW_RT15 (~30%)
- NADP1_2_RT10 (~29%)
- NADP1_2_RT15 (~27%)
- NADP1_7_RT10 (~26%)
- NADP1_4_RT15 (~22%)

NADP1 combinations with RT10 or RT15 continue to dominate the high-outlier segment.

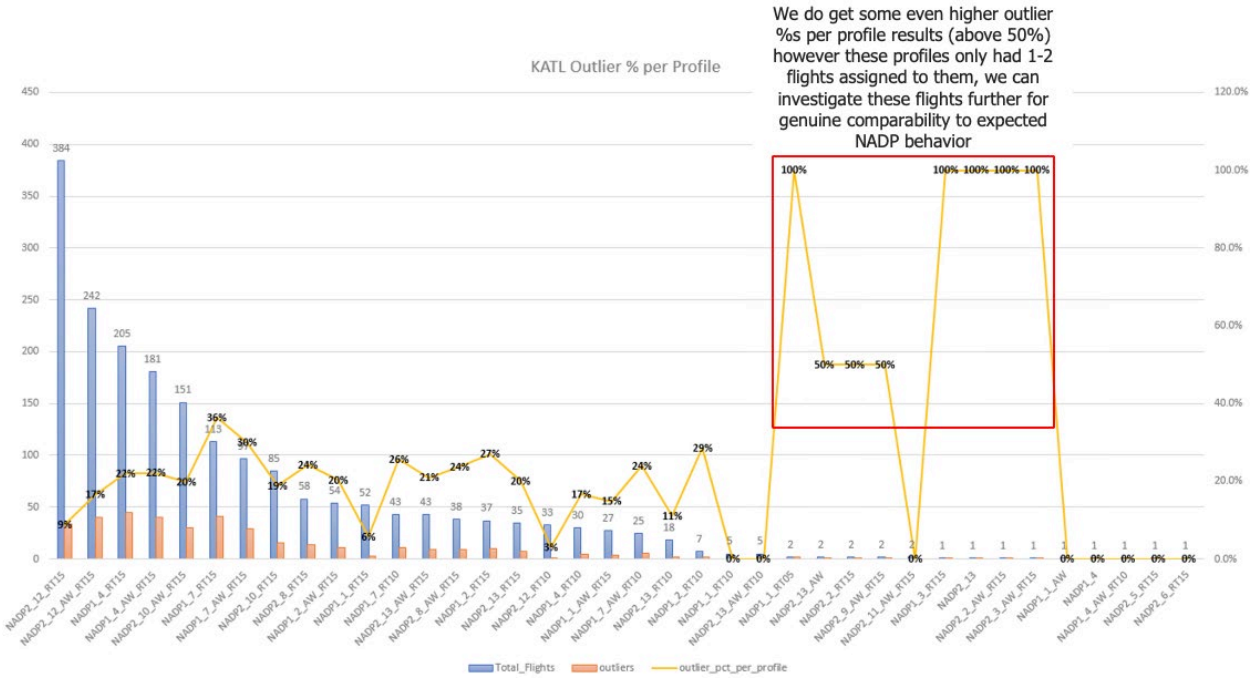


Figure 7. Hartsfield-Jackson Atlanta International Airport (KATL) percentage of outliers matched to each profile. NADP: noise abatement departure procedures.

Detailed cluster plots were generated for representative high-outlier profiles, including NADP1_4_RT15, NADP1_7_AW_RT15 (shown in Figure 8 and Figure 9), NADP1_7_RT10, and NADP1_7_RT15 (shown in Figure 10 and Figure 11). In each case, speed- and altitude-versus-distance traces for outlier flights are overlaid against the corresponding reference NADP profile. Visual inspection shows that the overall climb shapes of the outlier flights remain closely aligned with the nominal procedure: cutback occurs in the expected region, the acceleration segment transitions into clean climb, and the general trajectory family is preserved.

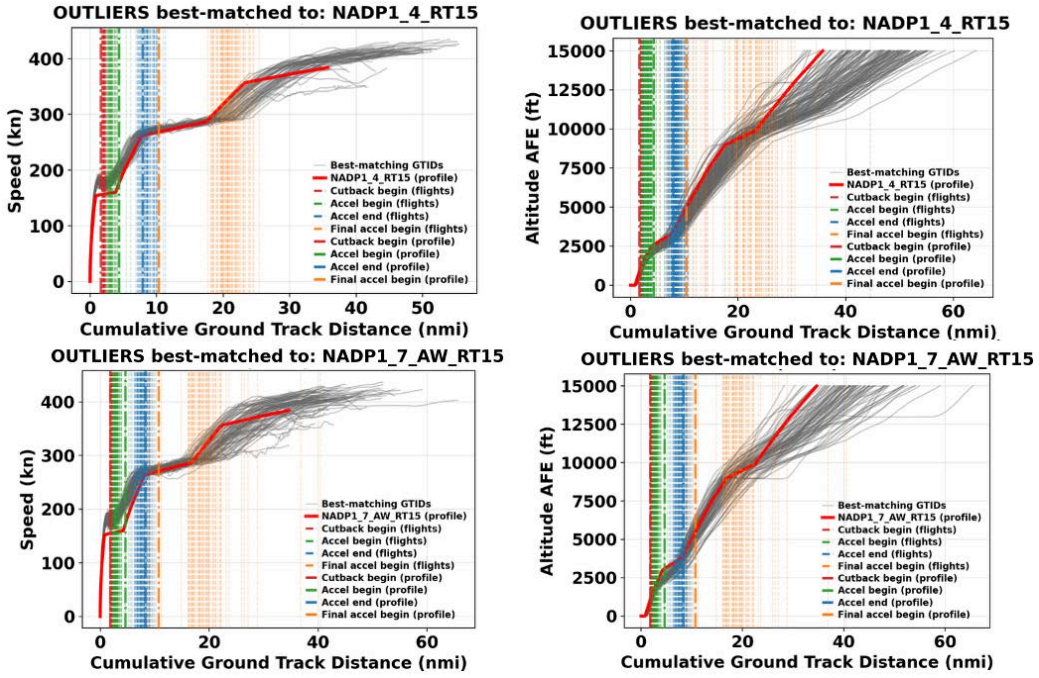


Figure 8. Cluster examples - NADP1_4_RT15 and NADP1_7_AW_RT15 (speed and altitude vs. cumulative ground tract distance [CGTD] plots). NADP: noise abatement departure procedures.

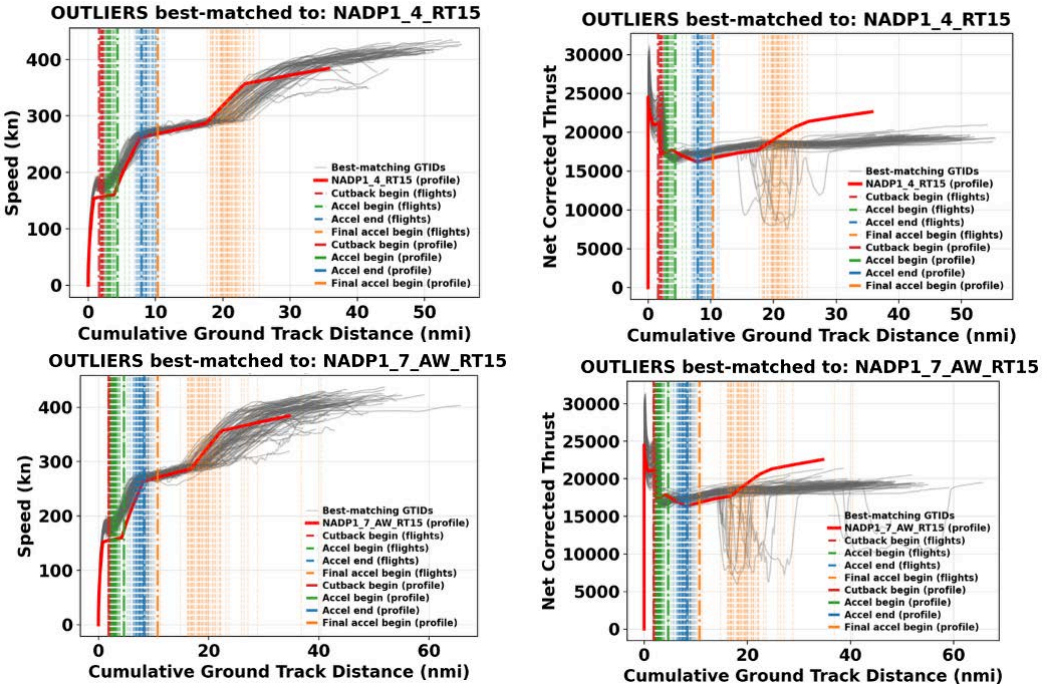


Figure 9. Cluster examples - NADP1_4_RT15 and NADP1_7_AW_RT15 (speed and net corrected thrust vs. cumulative ground tract distance [CGTD] plots). NADP: noise abatement departure procedures.

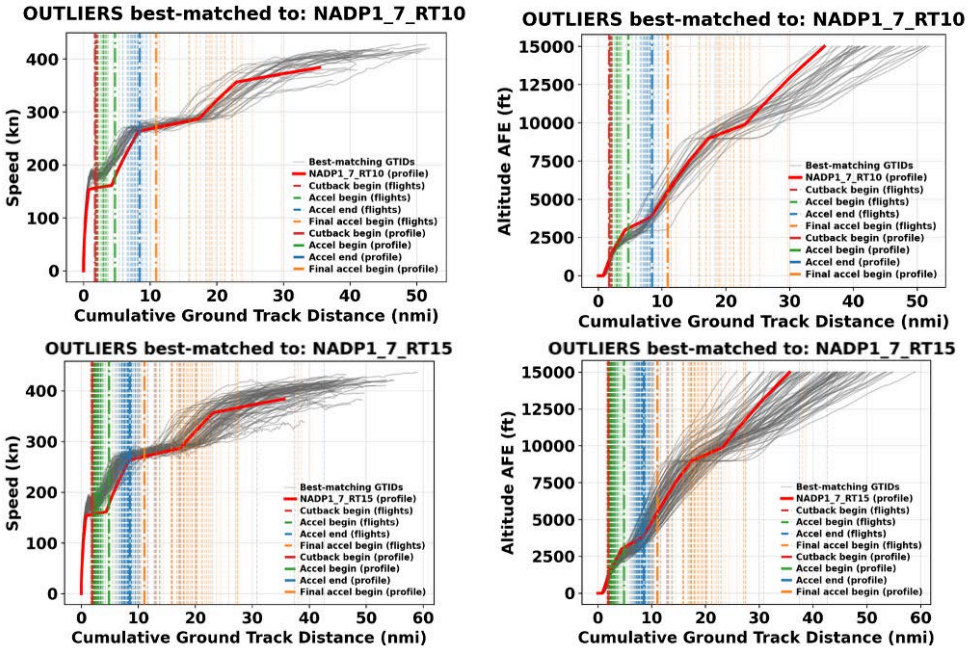


Figure 10. Cluster examples - NADP1_7_RT10 and NADP1_7_RT15 (speed and altitude vs. cumulative ground tract distance [CGTD] plots). NADP: noise abatement departure procedures.

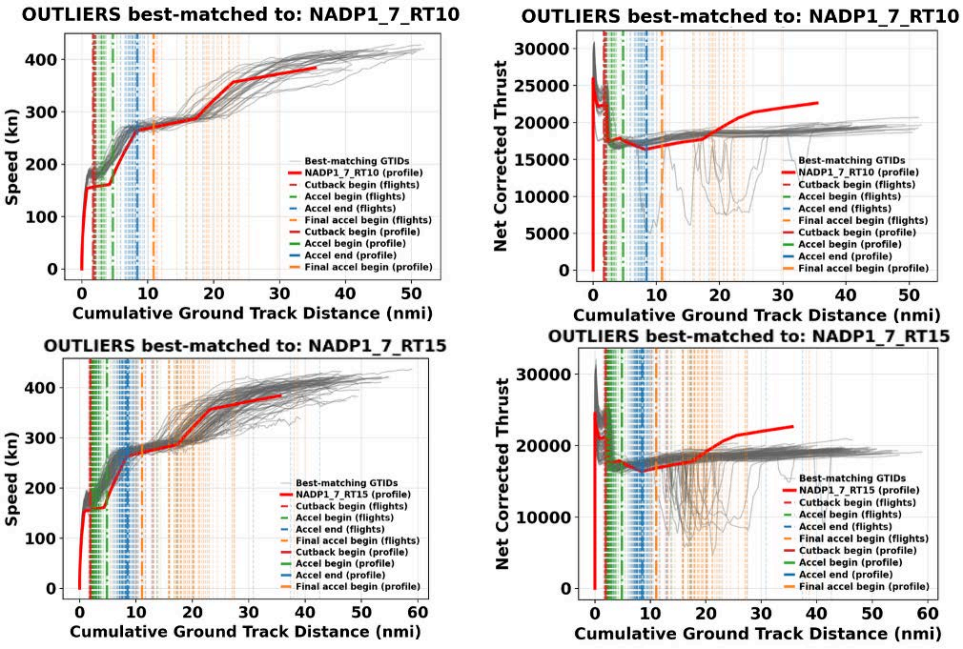


Figure 11. Cluster examples - NADP1_7_RT10 and NADP1_7_RT15 (speed and net corrected thrust vs. cumulative ground tract distance [CGTD] plots). NADP: noise abatement departure procedures.

The primary differences lie in the exact altitude and distance at which AB and AE are detected. Outlier flights tend to show modest shifts in these anchors relative to the reference profile, even though the broader pattern is consistent. FAB markers, included for visualization, further highlight that much of the late-phase variation is driven by FOQA data noise, sampling resolution, and small differences in thrust derate or weight, rather than fundamentally different procedures.

Net corrected thrust plots for the same clusters reinforce this interpretation. The thrust traces follow the same qualitative pattern as the reference NADP curves, but changes in derate level (e.g., RT10 versus RT15) modify climb performance enough to shift the altitude of the acceleration phase. Under the current validation tolerances, these shifts are sufficient to trigger AB and AE failures, even when the operational intent and overall NADP structure are preserved.

For clusters with the very highest outlier rates (100% failures, such as NADP1_1_RT05 and NADP1_3_RT15, as shown in Figure 12 and Figure 13), all primary anchors fail simultaneously: cutback begin, AB, and AE. Yet the speed and altitude traces again closely follow the NADP1 reference shapes. In these cases, the thrust decrease at "cutback" is often smaller than the 8% threshold used in the current logic, so the algorithm never registers a formal cutback event. Combined with derate-driven changes in acceleration timing and the presence of level-offs, this leads to systematic anchor misdetections and multi-anchor failures, even for flights that are procedurally consistent.

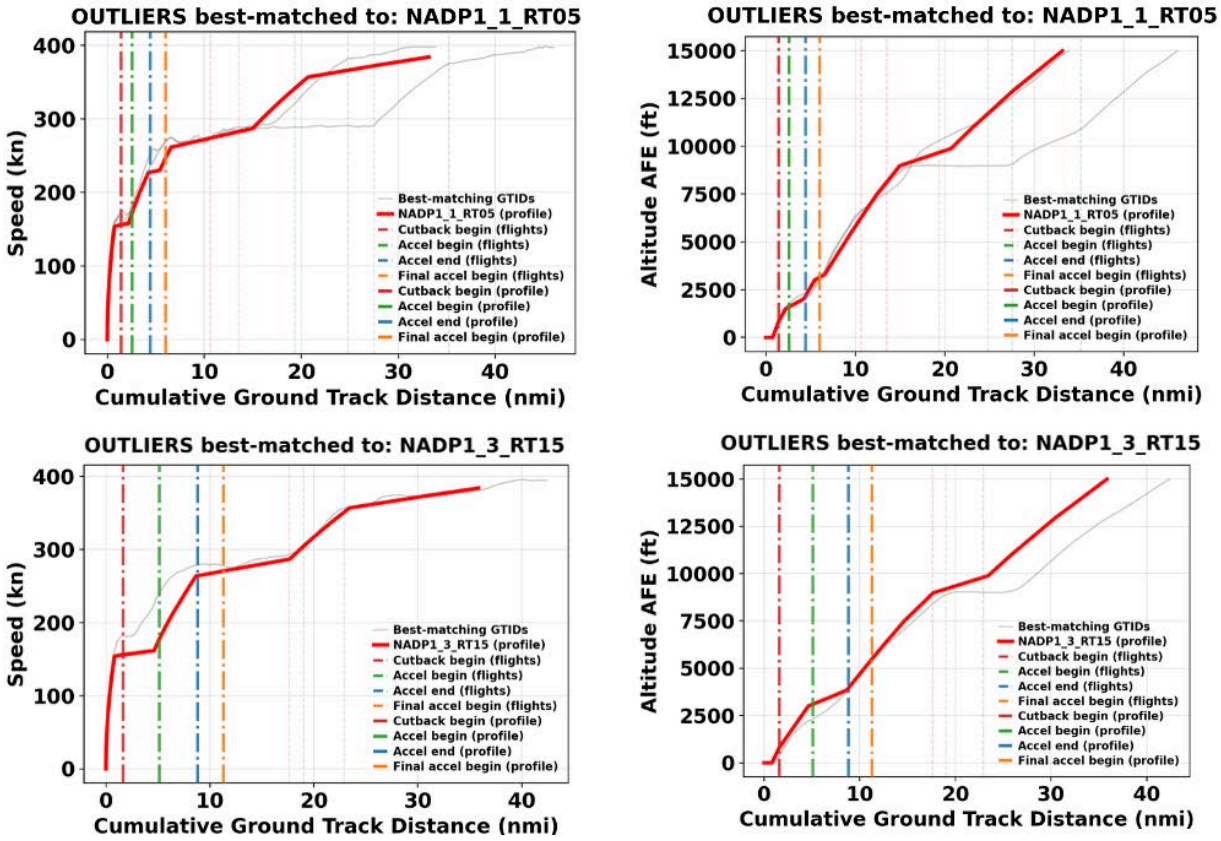


Figure 12. Cluster examples - NADP1_1_RT05 and NADP1_1_RT05 (speed and altitude vs. cumulative ground tract distance [CGTD] plots). NADP: noise abatement departure procedures.

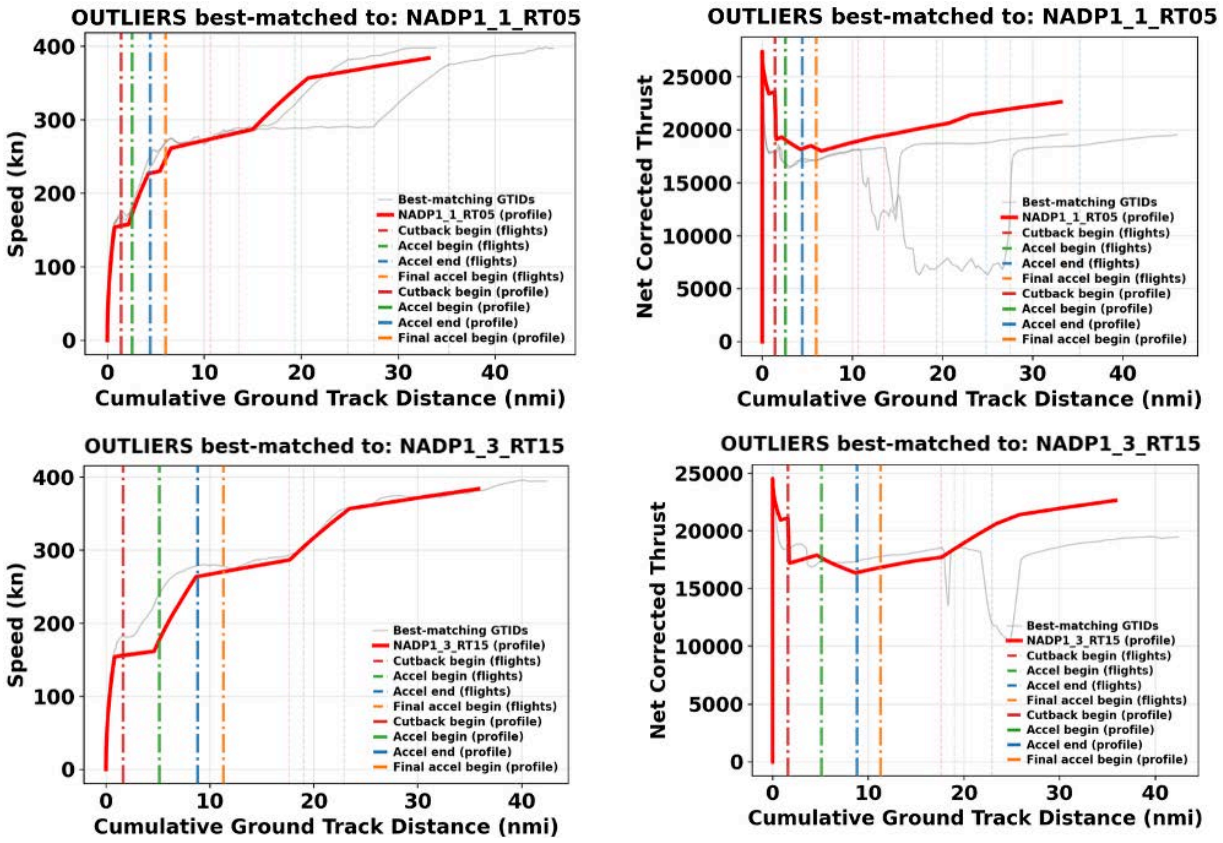


Figure 13. Cluster examples - NADP1_3_RT15 and NADP1_3_RT15 (speed and net corrected thrust vs. cumulative ground tract distance [CGTD] plots). NADP: noise abatement departure procedures.

To place the observed KATL level-off effects in context, a broader analysis was conducted across the full CY 2023 FOQA dataset (approximately 49,647 departures and 596 city pairs). Only about 5% of flights contain at least one level-off segment in the departure phase, indicating that level-offs are relatively rare in the overall population. The top 10 origins account for roughly 74% of these level-offs, driven largely by high-traffic hubs such as KATL, KDTW, and KSEA, with additional contributions from airports like Fort Lauderdale-Hollywood International Airport (KFLL), KDEN, Cancun International Airport (MMUN), KSLC, KLAX, and KJFK. These concentration patterns are interpreted primarily as volume effects, and there is no evidence of a standardized, fleet-wide “level-off procedure,” as summarized in Table 1.



Table 1. Departure level-off analysis summary. ICAO: International Civil Aviation Organization. KATL: Hartsfield-Jackson Atlanta International Airport, KDEN: Denver international Airport, KDTW: Detroit Metropolitan Wayne County Airport, KFLL: Fort Lauderdale-Hollywood International Airport, KJFK: John F. Kennedy International Airport, KLAX: Los Angeles International Airport, KMSP: Minneapolis-Saint Paul International Airport, KSEA: Seattle-Tacoma International Airport, KSLC: Salt Lake City International Airport, MMUN: Cancun International Airport.

Takeoff Airport ICAO Code	Flights with Level-Offs	Total Flights from Takeoff Airport	Rates
KATL	838	10,324	9.7%
KDTW	363	2,559	14.2%
KSEA	144	2,353	6.1%
KFLL	105	497	21.1%
KDEN	70	803	8.7%
KMSP	66	3,998	1.7%
MMUN	65	246	26.4%
KSLC	63	2,465	2.6%
KLAX	58	1,880	3.1%
KJFK	55	1,716	3.2%

In the context of validation, however, even these infrequent level-offs can have a disproportionate impact. Level-offs shift the altitude and distance at which acceleration begin and end are detected, causing anchors to fall outside the prescribed tolerance windows and generating outlier flags. This is especially relevant for profiles where level-offs occur later in the departure leg, compounding the effects of thrust derate and data noise on acceleration detection. Thus, there is a need to remove flights with level-offs from the analysis before clustering and validation is done.

Milestones
None.

Major Accomplishments
- Completed NUFP-based clustering of all FOQA A321-232 departures to the existing AEDT procedure/NADP library, producing cluster distributions for each airport and identifying the dominant procedures used in real-world operations.
- Extracted and classified anchors for thrust cutback, initial AB/AE, and final acceleration for all flights to support validation of the noise-based cluster assignments.
- Performed anchor and fuel-burn validation for each defined cluster, comparing the altitudes at which the anchors occur as well as the cumulative fuel burn at anchor locations between FPPs and their matched AEDT/NADP procedures to determine whether the NUFP-based assignments reflect operationally consistent behavior.
- Identified departures that cannot be represented by any existing AEDT/NADP procedure, based on anchor and fuel-burn mismatches, providing the basis for determining where new procedures may be required.
- Documented level-off behavior across the three airports, quantifying how often level-offs occur and assessing whether there is a need to define new procedures to account for them.

Publications
None.

Outreach Efforts
Participated in biweekly calls and biannual ASCENT meetings.

Awards
None.



Student Involvement

Graduate research assistants Ranya Almarzooqi, Vishnu Sankar Manivasakan, and Keletso Mmalane from the School of Aerospace Engineering participated in this task. They were involved with the generation of noise results, evaluation of clustering methods, and analysis of results.

Plans for Next Period

- Further analyze outliers for KDEN and KLAX to see if the same patterns that were seen for KATL occur.
- Study whether the outliers are occurring due to aircraft weights not being accurately represented in procedures (may need more AW variants) or if more thrust-derate settings are necessary as well (e.g., RT20, RT25, etc.).
- Revise validation thresholds to ensure only flights that require a new procedure definition are classified as outliers.
- Finalize analyses and develop recommendations for how additional departure profile could be modeled to enhance aviation environmental analysis with the AEDT.

Task 2 – Arrival Profile Modeling

Georgia Institute of Technology

Objectives

Currently, the AEDT implements arrival profiles using either specified fixed-point trajectories or manufacturer-provided procedures. The primary objective of Task 2 is to compare data from real-world flights to AEDT models to make recommendations that will allow the AEDT to better capture aircraft behaviors during arrival.

This year, the specific focuses of this task are (1) to develop and validate quantitative metrics to compare AEDT noise outputs with FOQA-derived fixed-point profiles, and (2) to investigate how variations in thrust, level-off height, and flap deployment affect the resulting noise contours. The end goal of this project is to provide recommendations regarding a subset of standardized AEDT arrival profiles which should be integrated into the system and what information those profiles should include.

Methodology

In the previous year, an evaluation of arrival trajectories was conducted to identify key level-off characteristics and quantify flap variations along descent paths. This analysis laid the foundation for the next phase of the study, which focused on understanding how configuration-driven variations such as flap deployment timing, thrust settings, and level-off altitudes translate into acoustic impacts in the AEDT. This year's work extends the investigation from trajectory and configuration modeling to noise outcome validation. Specifically, the study quantifies how well AEDT's standard arrival profiles capture real-world noise behavior observed in FOQA data and develops metrics to objectively measure these deviations.

For generating the FPPs, a large-scale analysis was performed using FOQA arrival data for A321-200 operations into KATL, Runway 26R, covering CY2023. A total of 3,030 FOQA arrival flights were processed through the AEDT version 3g Batch Report Run Tool to generate SEL noise contours. To handle this dataset efficiently, the jobs were divided into 13 chunks (12×234 flights and 1×222 flights), achieving roughly one-minute runtime per flight on the Batch Report Tool. This configuration improved throughput compared to prior single-job runs (~20 minutes/flight), enabling a comprehensive set of FOQA-based AEDT outputs for comparing metrics with the standard profile (see Table 2).

Table 2. Batch Tool Execution Summary.

No. of Jobs	~Time per Job (mins)	~Total Time
3,030 (Actual size)	18-20	38 days
1,000	7	5 days
500	1	8 hours
250	0.5 -0.75	2.5 hours

Quantitative Metrics

To assess the agreement between modeled and observed arrivals, several spatial similarity metrics were implemented:



- **Average Nearest Neighbor (ANN)**: Mean distance between the FOQA flight's noise contour and the standard (STD) AEDT contour along the ground track; a smaller score correlates to a closer match.
- **Hausdorff Distance**: Maximum contour separation; this metric emphasizes worst-case deviation. Because maximum noise deviation generally occurs over the ground track, reducing the dimensionality of the noise contours to the 1D ground track does not lose information for this metric.
- **Intersection over Union (IoU)**: Ratio of shared footprint area to total combined area (0–1 scale); as opposed to the first two, a higher score indicates a better overlap between two noise contours.
- **Percent Area Difference**: Relative footprint expansion or contraction versus the STD contour, with smaller values in magnitude corresponding to a closer match.
- **ΔSEL (FPP – STD)**: Pointwise difference in SEL values across the AEDT receptor grid, revealing localized regions of increased or decreased noise.

When selecting noise contours, the 75 dB SEL threshold was chosen as the lowest noise level of interest. A distribution of the Hausdorff-1D values used in this analysis is shown in Figure 14. Similarly, the distribution of ANN-1D values across all FOQA arrivals is shown in Figure 15. Together, the ANN and Hausdorff metrics form the backbone of this year's analysis. ANN capturing average conformity, and Hausdorff identifying localized anomalies such as isolated "thrust/noise islands." The ANN thresholds used for binning (0–5, 5–10, 10–20, and 20+ ft) were selected based on clear inflection points observed in the nonlinear relationship between ANN and Hausdorff distance. These breakpoints delineate natural groupings of nominal, moderate, and high-deviation arrivals and allow for consistent comparison across all noise-based performance metrics.

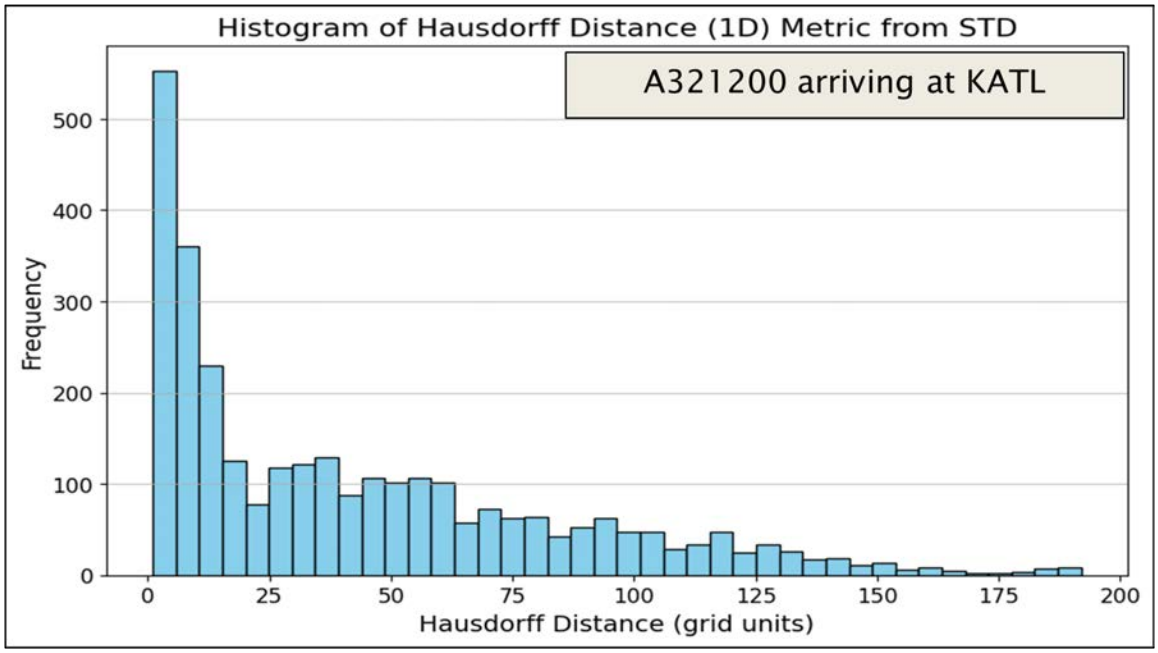


Figure 14. Distribution of Hausdorff distance (1D) from standard profile (STD) at Hartsfield-Jackson Atlanta International Airport (KATL).

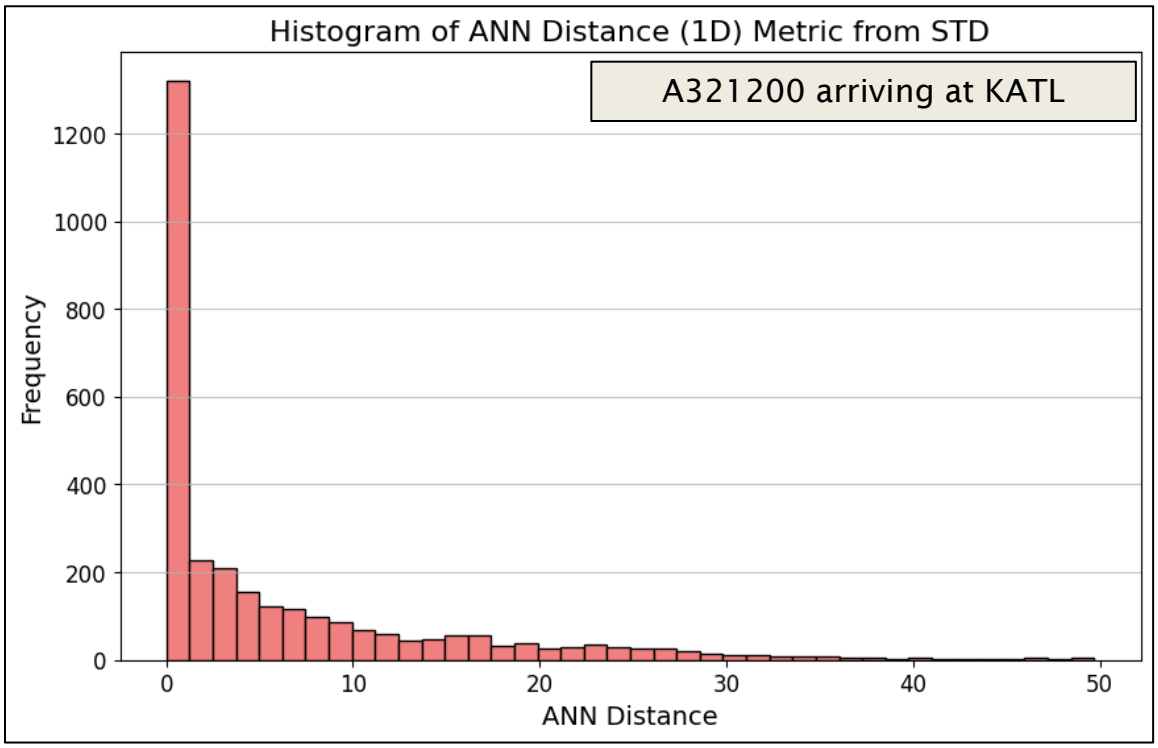


Figure 15. Distribution of ANN distance (1D) from standard profile (STD) at Hartsfield-Jackson Atlanta International Airport (KATL).

Analytical Workflow

The workflow for this year was designed to connect trajectory deviations directly to their noise footprints:

1. **Baseline Evaluation** – Compute AEDT noise contours for the standard arrival profile and compare them with FOQA-derived FPPs.
2. **Metric Binning** – Categorize flights by ANN distance into bins (0–5, 5–10, 10–20, 20+) to separate nominal versus anomalous operations.
3. **Noise Contour Analysis** – Evaluate footprint area, overlap, and ΔSEL distribution for each ANN bin across 75–95 dB SEL thresholds.
4. **Profile Recreation Experiments** – Modify key procedural parameters (level-off altitude, thrust mode, flap timing) in the AEDT to reproduce noise behavior seen in outlier FOQA flights.

The baseline comparison indicated that most FOQA flights align closely with the AEDT standard profile, with ANN scores <5 and Hausdorff <50, confirming strong conformity. The long right-tail of higher ANN values pinpointed a subset of non-standard arrivals requiring further evaluation.

Results & Discussion

Metric Correlation and Threshold Validation

The relationship between ANN-1D and Hausdorff-1D values for all FOQA arrivals is shown in Figure 16. A nonlinear correlation was observed between ANN and Hausdorff metrics: flights with high ANN distances generally exhibited high Hausdorff distances as well, though the sensitivity varied. Inflection points near ANN = 5, 10, and 20 validated the chosen binning scheme, distinguishing nominal, moderate, and highly deviating arrivals. For this analysis, both ANN-1D and Hausdorff-1D were computed using the 75 dB SEL contour, as this threshold corresponds to footprint extents of approximately 10–15 nmi that are most relevant for community noise exposure and reveal the clearest separation between standard and non-standard arrivals. The "1D" versions of these metrics quantify contour differences strictly along the centerline ground track, isolating along-track deviations without accounting for lateral dispersion.

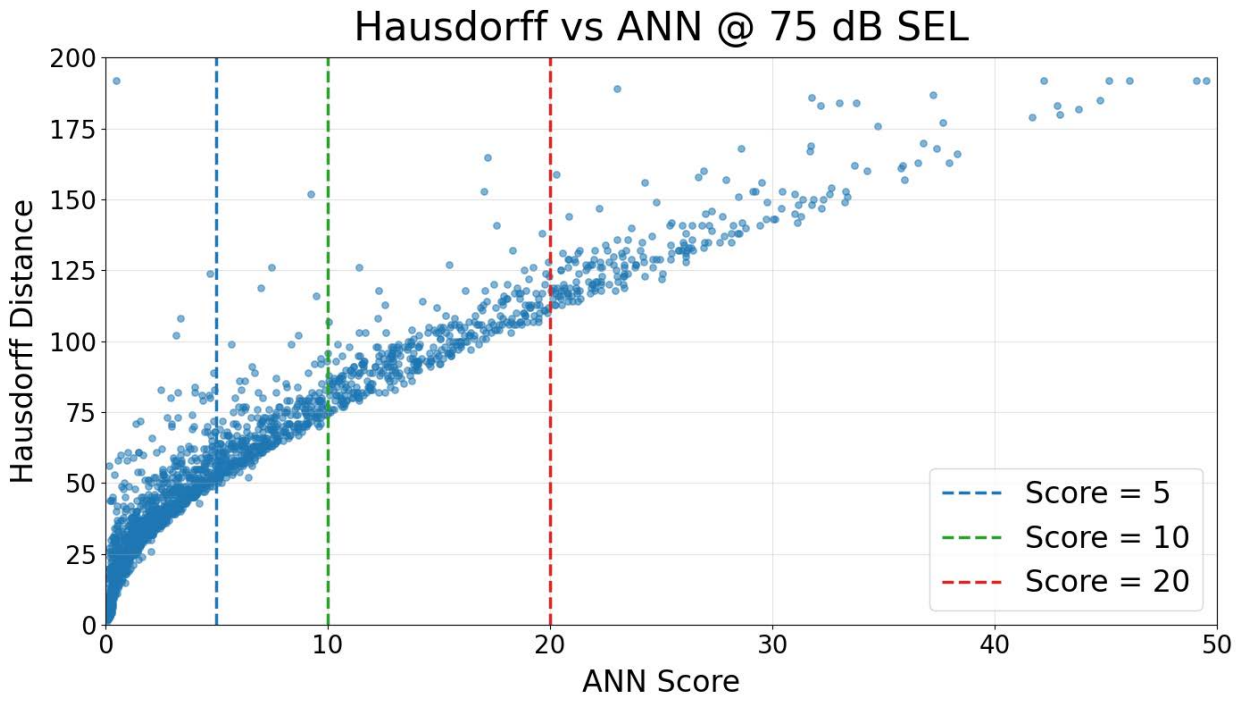


Figure 16. Hausdorff vs. Average Nearest Neighbor (ANN). SEL: sound exposure level.

Noise Footprint Trends

As the ANN score increased, flights exhibited systematically larger noise footprints and reduced spatial overlap with the standard contour. These trends are illustrated in Figure 17 and Figure 18, which show how IoU and percent area difference vary with SEL threshold for the 10–20 and 20+ ANN bins. At the 75 dB SEL threshold, flights in the 10–20 ANN bin showed roughly +80% footprint inflation, while those in the 20+ bin exceeded +130%. The IoU values correspondingly dropped from 0.75–0.8 for low-ANN cases to below 0.4 for the high-ANN group. At higher thresholds (85–90 dB), these differences narrowed, indicating that the most significant deviations occur in the outer, lower-noise regions of the footprint.

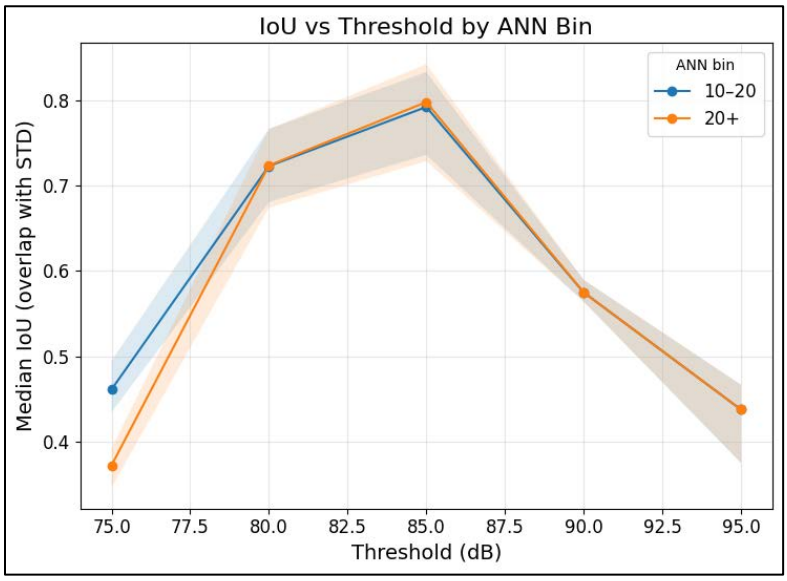


Figure 17. Intersection over Union (IoU) vs. threshold for A321-200 arrivals. ANN: Average Nearest Neighbor, STD: standard profile.

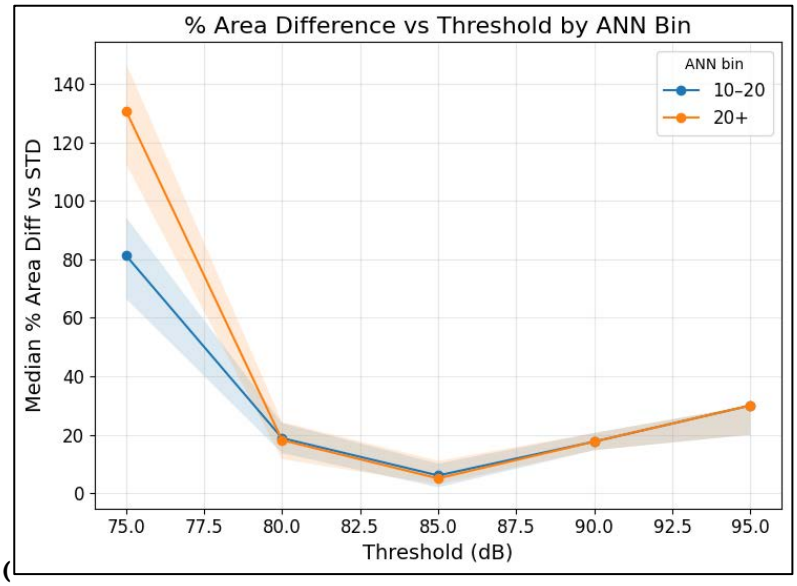


Figure 18. Percent area difference vs threshold for A321-200 arrivals. ANN: Average Nearest Neighbor, STD: standard profile.

Spatial ΔSEL Hotspots

To visualize how noise deviations manifest spatially, ΔSEL maps were averaged by ANN bin. These spatial noise deviation patterns are shown in Figure 19, Figure 20, Figure 21, and Figure 22 which illustrate the mean ΔSEL contours for the 0–5, 5–10, 10–20 and 20+ ANN bins respectively.

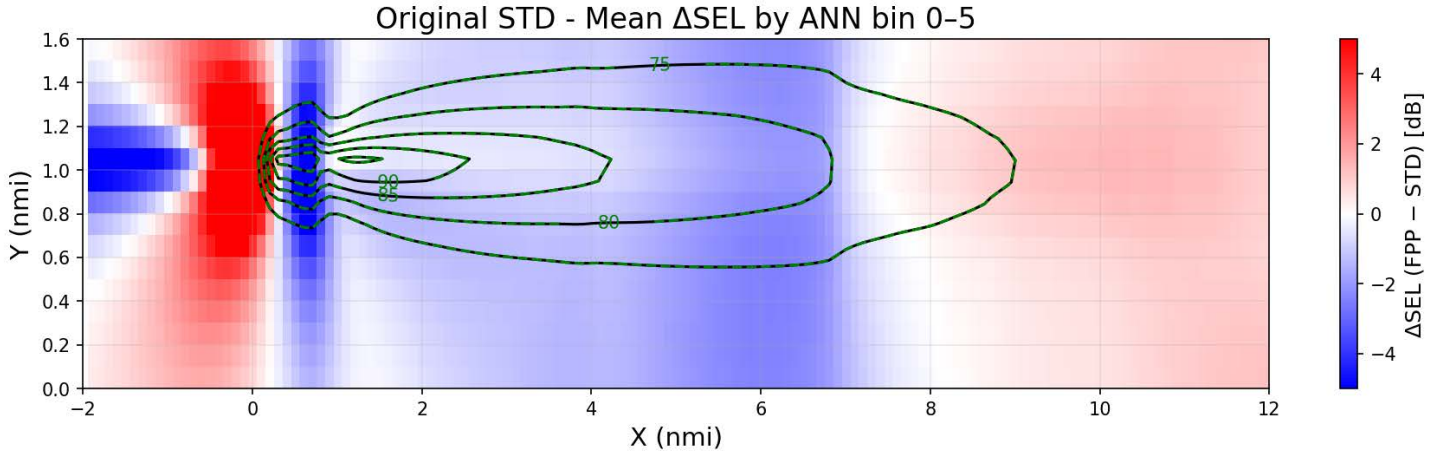


Figure 19. Mean ΔSEL for ANN 0–5 flights (FPP – STD). ANN: Average Nearest Neighbor, FPP: fixed point profile, SEL: sound exposure level, STD: standard profile.

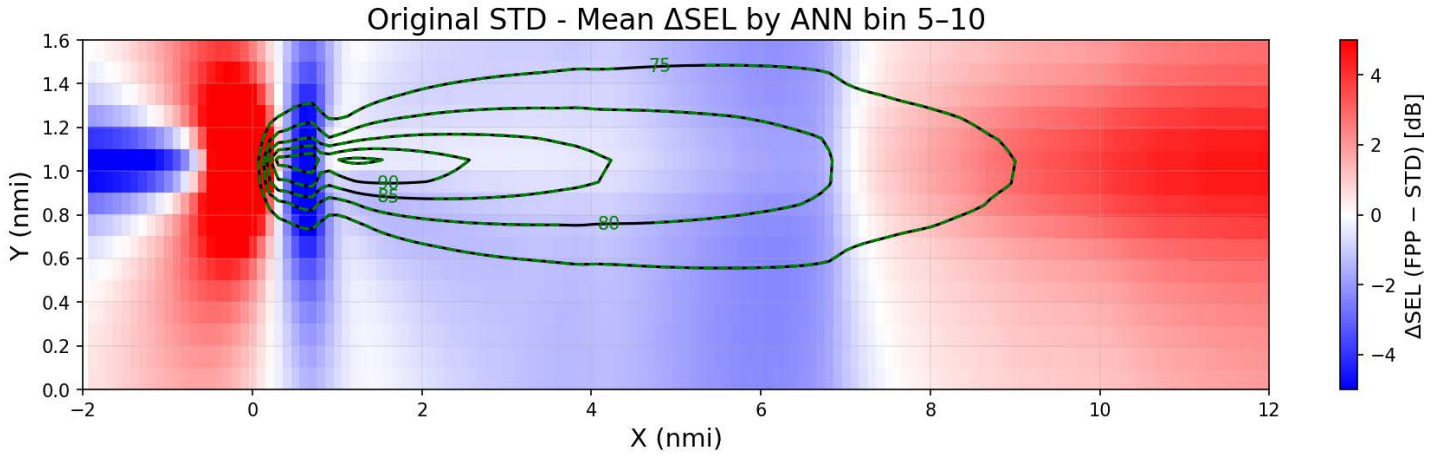


Figure 20. Mean ΔSEL for ANN 5–10 flights (FPP – STD). ANN: Average Nearest Neighbor, FPP: fixed point profile, SEL: sound exposure level, STD: standard profile.

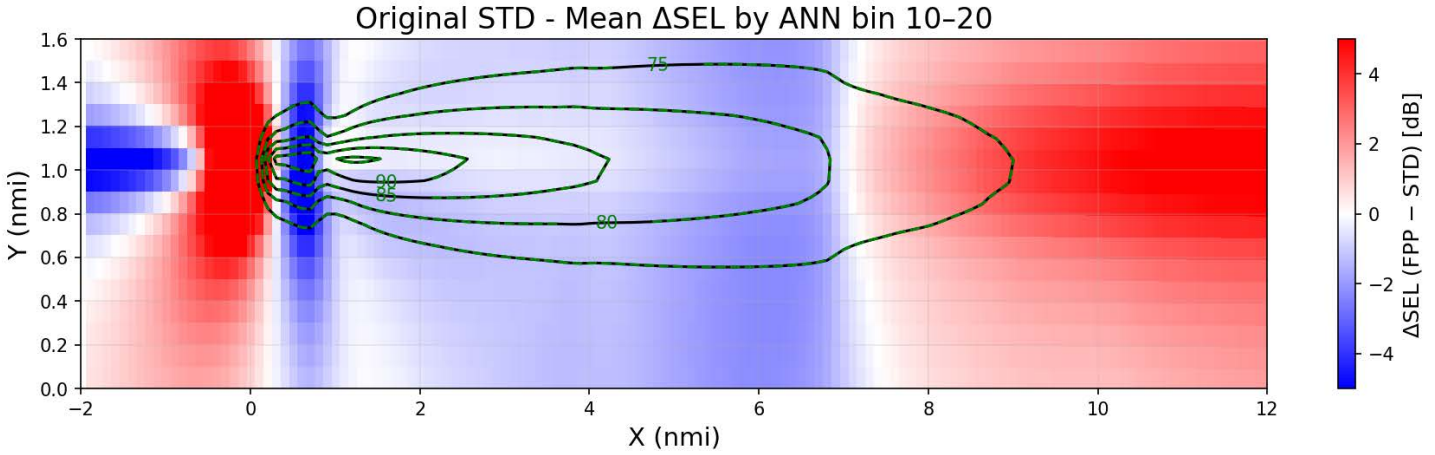


Figure 21. Mean ΔSEL for ANN 10–20 Flights (FPP – STD). ANN: Average Nearest Neighbor, FPP: fixed point profile, SEL: sound exposure level, STD: standard profile.

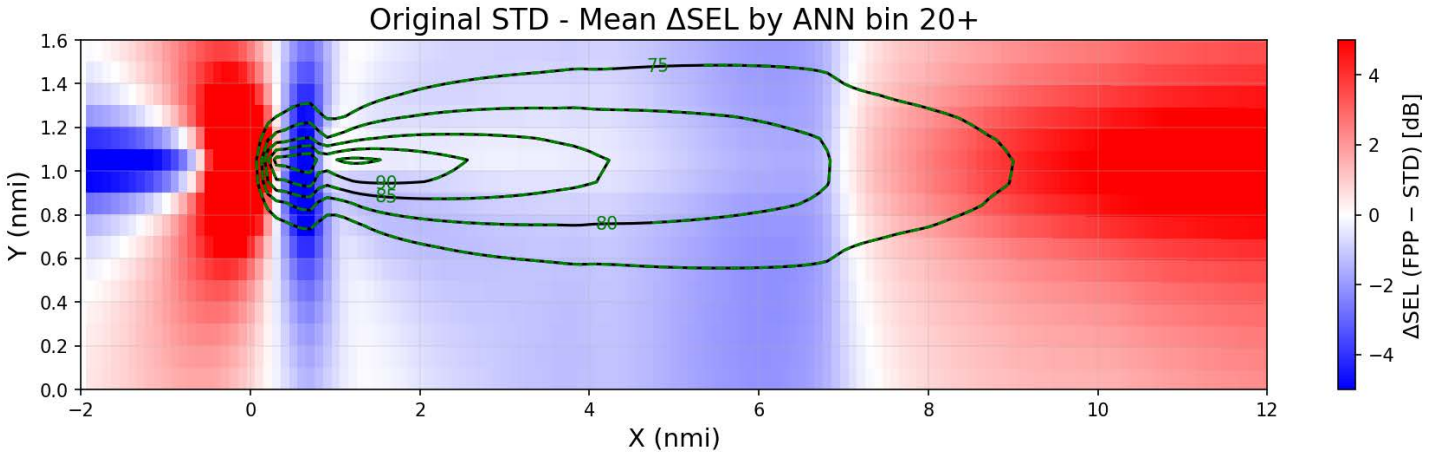


Figure 22. Mean ΔSEL for ANN 20+ Flights (FPP – STD). ANN: Average Nearest Neighbor, FPP: fixed point profile, SEL: sound exposure level, STD: standard profile.

Low-ANN flights (0–5) showed near-neutral behavior, with minor positive deviations near touchdown. Moderate-ANN bins (5–10 and 10–20) displayed progressively stronger upstream "hotspots," approximately 8–11 nautical miles from touchdown along the centerline, corresponding to level-off and deceleration regions. The highest-ANN group (20+) showed the most extensive and persistent positive ΔSEL band, confirming that these flights generate broader noise contours during the terminal descent.

Effect of Level-Off Altitude

Follow-up experiments adjusted the level-off altitude in the standard AEDT profile from 3,000 ft AFE to 2,000 ft AFE. This modification reduced the number of high-ANN outliers, particularly in the 20+ range, and yielded slightly lower Hausdorff extremes. The 2,000-ft STD thus better matched FOQA arrivals exhibiting low-altitude level-offs and stronger thrust applications. Conversely, 4000-ft level-offs showed near-perfect conformity (ANN < 5), consistent with smoother Continuous Descent Approaches (CDAs). These effects are illustrated in Figure 23, which compare altitude–distance descent trajectories for the original 3,000-ft standard profile and the modified 2,000-ft profile.

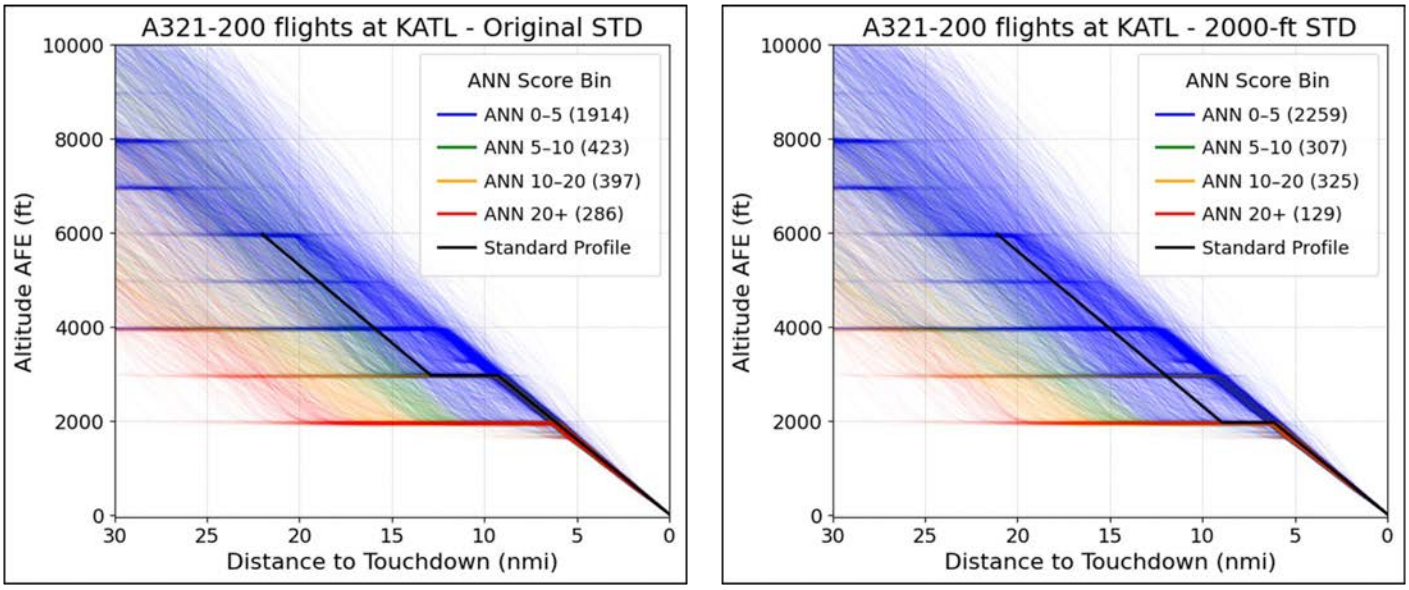


Figure 23. Trajectory plot by Average Nearest Neighbor (ANN) bin for original (left) and 2,000-ft modified (right) standard profile (STD) at Hartsfield-Jackson Atlanta International Airport (KATL).

Profile Perturbation and Noise Reproduction
To replicate noise "islands" observed in high-ANN flights, several perturbed profiles were simulated in the AEDT. Lowering airspeed during level-off (from ~250 kt to ~200 kt) and deploying flaps earlier reproduced the characteristic elongated 75 dB contours. These results suggest that noisier profiles are driven by early flap transitions and prolonged low-altitude level-offs, where sustained thrust produces elevated acoustic energy.
Across multiple case studies, the simulations confirmed that:

- **Low-speed, early-flap profiles** yield larger 75 dB footprints and higher ANN scores.
- **Higher-altitude, short level-offs** (≥4,000 ft) are acoustically benign and closely match AEDT's default model.
- **Intermediate cases (2,000–3,000 ft)** exhibit the most variability and drive the need for refined procedural modeling.

Overall, the analysis demonstrated that ANN and Hausdorff metrics can effectively characterize deviations between modeled and real-world noise footprints. Most arrivals are well captured by AEDT's standard procedures; however, specific subsets of flights–particularly those with low-altitude or extended level-offs and early flap deployment—produce significantly different and generally noisier signatures. Introducing modified profiles that account for these behaviors substantially improves contour alignment and reduces ANN deviations.

Milestones
None.

Major Accomplishments
None.

Publications
None.

Outreach Efforts
None.



Awards
None.

Student Involvement
Graduate research assistants, Anushka Moharir, and Hansen Lian from the School of Aerospace Engineering participated in this research. Anushka and Hansen were involved with the generation of noise results, exploration of various distance metrics, and analysis of results.

Plans for Next Period
- Refine metric thresholds and expand the perturbed profile library to include additional thrust and configuration variations.
- Quantify how each modified profile impacts overall contour statistics across multiple aircraft types. These results will support recommendations for new AEDT arrival procedures that better reflect real-world descent and configuration behavior.

Task 3 – Full-flight Modeling
Georgia Institute of Technology

Objectives
The objective of this study is to enhance the usability and analytical capabilities of full-flight modeling in the AEDT by developing an effective alternative to the existing sensor path method. While AEDT's sensor path remains the standard method, it is a high-fidelity and complex model, requiring heavy computation, and depends on detailed trajectory data that might not be accessible for large-scale analyses. This work aims to develop a simplified, statistically robust modeling framework that reduces dependence on high-resolution trajectory data while still delivering accurate gate-to-gate fuel burn and emissions estimates. The overall goal is to improve AEDT's capacity to support nationwide, data-driven assessments of flight performance within the National Airspace System (NAS).

In the previous year, we developed regression-based and machine learning models to estimate fuel consumption for both enroute and gate-to-gate operations across 16 representative city pairs. This research identified critical factors impacting fuel consumption, including aircraft attributes, flight operation variables, and relevant weather conditions. The results demonstrate that a data-driven modeling framework implemented in standalone Python® workflows can accurately estimate fuel burn, without requiring direct integration into the AEDT. The proposed methods serve as a complementary alternative to AEDT's sensor-path based approach and enable scalable fuel burn analyses outside the AEDT environment while using operationally relevant inputs.

Building on previous work that examined fuel burn modeling for enroute flight segments above 10,000 ft mean sea level (MSL), the current study refines and extends the research scope to focus on gate-to-gate fuel-burn prediction. This shift reflects the need to capture fuel consumption across all phases of flight, including surface operations and terminal-area maneuvers, which are not fully represented in enroute-only analyses. Using the CY2023 FOQA dataset, we investigated various approaches to improve the accuracy of fuel burn and emissions forecasts. To organize the analysis and display our findings clearly, the study is divided into three separate investigations.

1. Weather Integration Strategies

This investigation examines various methods of integrating Modern-Era Retrospective analysis for Research and Applications, Version 2 (MERRA-2) weather data, such as a baseline without weather, real-time atmospheric conditions, and monthly or seasonal climatological fields. It aims to identify which approach best enhances fuel-burn prediction for the initial 16 city pairs.

2. Operational and Directional Feature Enhancement

This study investigates the impact of additional operational variables, including takeoff weight and flight direction, on model accuracy and physical consistency. These variables help better represent wind effects and changes in fuel consumption caused by aircraft weight.

® Python is a registered trademark of Voxx International Corporation, Hauppauge, New York.

3. Large-Scale Application and Scalability Assessment

The final investigation applies the refined modeling approach to an expanded set of 86 city pairs with varied geographic and operational characteristics. Multiple algorithms, including Random Forest and Multilayer Perceptron (MLP), are employed to evaluate the scalability, prediction stability, and generalizability of the modeling framework.

Together, these three investigations establish a solid foundation for improving the AEDT's fuel-burn modeling capabilities and guiding future updates to its performance modeling framework.

The other side of this task builds upon and completes the initial clustering work by the team in 2024. The objective of the task is to analyze the performance of AEDT's sensor path-based modeling process, through a comparative study between representative 'core paths' for city pairs modeled in the AEDT, versus real-world flight data sourced from the CY2023 FOQA dataset. Secondary objectives for the study include developing and streamlining the workflow for modeling sensor path information in the AEDT, investigating bugs and issues with the modeling process, and providing recommendations for automating the process and solving any issues encountered. The overarching motivation behind this study is to set up an efficient workflow that can leverage the modeling of large-scale flight databases such as the NAS database in order to provide recommendations for future tool features and improvements.

Research Approach

Investigation 1. Weather Integration Strategies

Methodology

The initial study explored how various weather-representation strategies affect the accuracy of gate-to-gate fuel-burn predictions. Although the investigation focused on gate-to-gate fuel burn prediction, the weather integration methodology was applied only to the enroute phase of flight above 10,000 ft MSL. The objective was to identify a practical approach that improves model performance without adding extra data processing or computational burden, consistent with typical operational modeling limitations. The research analyzed CY23 FOQA flight data from 16 city pairs, encompassing 2,302 flights. Table 3 provides the FOQA flight counts per city pair, and Figure 24 illustrates the geographical distribution of these routes across the continental United States (U.S.), highlighting the range of operating conditions encompassed in the dataset.

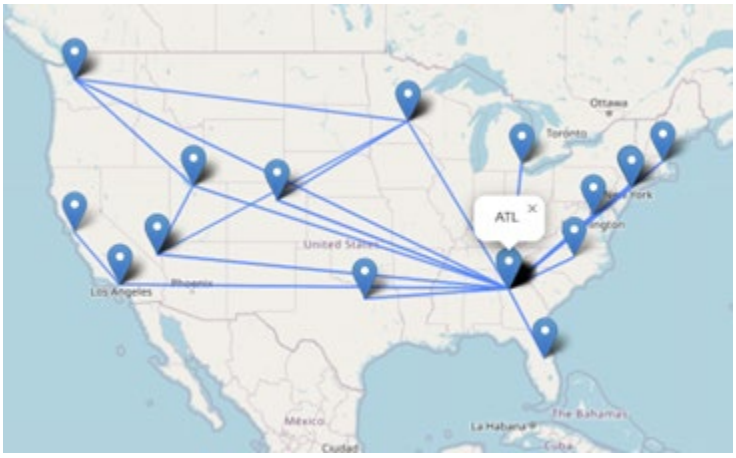


Figure 24. Visualization of 16 Origin-Destination (OD) pairs.



Table 3. Total flights selected from CY23 FOQA data for 16 city pairs. KATL: Hartsfield-Jackson Atlanta International Airport, KDCA: Ronald Reagan Washington National Airport, KJFK: John F. Kennedy International Airport, KLAS: Harry Ried International Airport, KLGA: LaGuardia Airport, KMSP: Minneapolis-Saint Paul International Airport, KSEA: Seattle-Tacoma International Airport, KSLC: Salt Lake City International Airport.

City Pair	Number of Flights	City Pair	Number of Flights
KATL-KDCA	163	KDCA-KATL	213
KATL-KJFK	72	KJFKKATL	59
KATL-KLAS	174	KLAS-KATL	160
KATL-KLGA	172	KLGA-KATL	279
KATL-KMSP	173	KMSP-KATL	147
KATL-KSEA	157	KSEA-KATL	127
KATL-KSLC	151	KSLC-KATL	129
KLAS-KSLC	68	KSLC-KLAS	58

Alternative Method 1 – Baseline (Aircraft and airport features only)
The baseline configuration relied exclusively on aircraft, airport, and basic flight-operation variables. No weather information was incorporated. This method required minimal preprocessing and served as the foundational reference for evaluating the added value of weather-based inputs in subsequent configurations. The features included in the baseline model are summarized in Table 4 below.

Table 4. Feature categories included in the baseline configuration. ICAO: International Civil Aviation Organization.

Category	Parameters
Airport	• Takeoff airport ICAO code • Takeoff runway • Landing airport ICAO code • Landing runway
Aircraft	• Aircraft category • Airframe • Engine type
Flight Operation	• Departure time • Season • Month • Azimuth • Flight direction • Flight time • Flight distance

Alternative Method 2 – Instantaneous MERRA-2 En-route Weather
The second method incorporated meteorological variables from instantaneous MERRA-2 data. Figure 25 illustrates the processing steps involved in obtaining weather data at each trajectory point. The process included three steps: (1) altitude interpolation, (2) spatial interpolation, and (3) temporal interpolation.

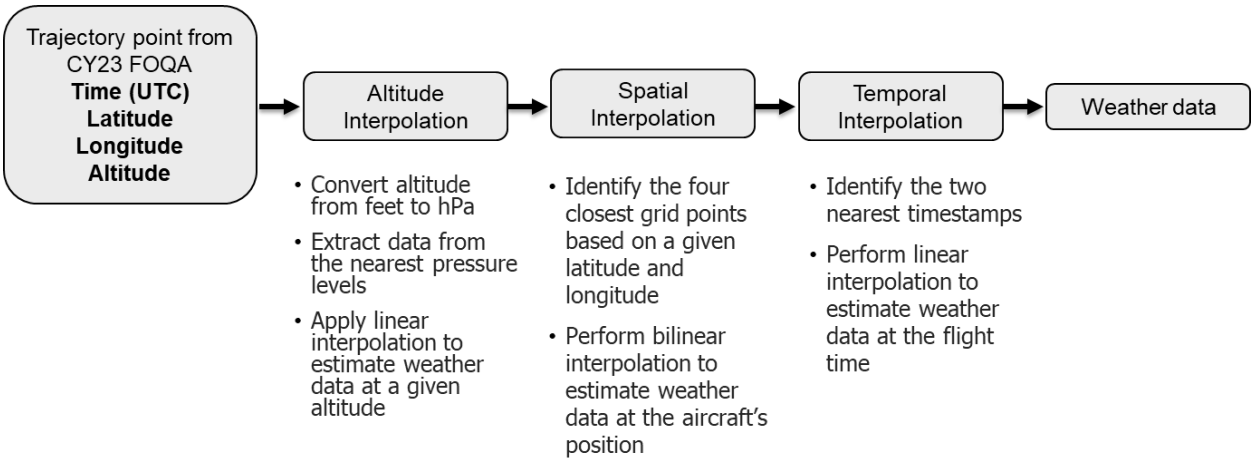


Figure 25. Workflow for obtaining instantaneous MERRA-2 weather at Flight Operations Quality Assurance (FOQA) trajectory points. CY: calendar year.

For each FOQA trajectory point, the aircraft's altitude in feet was converted to the corresponding pressure level in hectopascals. Weather variables from the nearest pressure surfaces were extracted, and linear interpolation was used to estimate the atmospheric conditions at the aircraft's exact altitude. Spatial interpolation was then performed by identifying the four closest MERRA-2 grid points based on latitude and longitude, applying bilinear interpolation to estimate weather conditions at the aircraft's horizontal position. Finally, temporal interpolation employed the two nearest MERRA-2 timestamps to calculate weather values at the precise time of flight.

Wind components and temperature were obtained for trajectory points above 10,000 ft MSL to accurately capture en-route atmospheric conditions. The interpolated data along each flight path were averaged to create a composite weather profile for each flight. This approach provided a clear, flight-specific perspective of the large-scale atmosphere, perfectly complementing the real-time weather method.

Alternative 3 - Monthly or Seasonal MERRA-2 Profiles
This method used monthly or seasonal averages from MERRA-2 to create a simplified model of enroute atmospheric conditions. For each origin–destination pair, a representative flight path was identified using a trajectory-clustering procedure applied to the FOQA data. The centroid trajectory from the most common cluster served as the standard route for that city pair.

Weather information was gathered only from the part of the representative trajectory above 10,000 ft MSL. Five sampling points were chosen along this enroute segment. At each point, monthly or seasonal averages of wind components and temperature were obtained from the MERRA-2 climatological fields. The five values were combined into a single climatological weather profile for each city pair.

This approach reduces data volume and preprocessing requirements compared with instantaneous weather retrieval. However, it does not capture day-specific atmospheric variability. The method therefore supports an assessment of the trade-off between simplified climatology-based inputs and the resulting changes in model performance.

In this study, our team implemented two models — (1) decision tree and (2) random forest — to predict aircraft fuel consumption and identify the most accurate predictor. Each model was evaluated using standard performance metrics, including mean absolute error (MAE), mean squared error (MSE), root mean squared error (RMSE), and the coefficient of determination (R^2).

MAE measures the average magnitude of errors between predicted and actual values, with lower values indicating more accurate predictions. MSE calculates the average of squared differences, where a lower value also signifies better performance. RMSE, the square root of MSE, offers an error value in the same unit as the target variable, aiding



interpretation. R^2 reflects how well the model explains variability in the target, with values closer to 1 indicating a better fit.

$$MAE = \frac{1}{n}\sum_{i=1}^{n}|Fuel\ Burn_{Actual} - Fuel\ Burn_{Predicted}| \quad \text{(Eq. 1)}$$

$$MSE = \frac{1}{n}\sum_{i=1}^{n}(Fuel\ Burn_{Actual} - Fuel\ Burn_{Predicted})^2 \quad \text{(Eq. 2)}$$

$$RMSE = \sqrt{MSE} \quad \text{(Eq. 3)}$$

As mentioned earlier, this study implemented two types of predictive models. The first is the decision tree, which effectively captures complex nonlinear relationships by iteratively splitting the data and making decisions at each node. This approach provides insights into the relative importance of each feature; however, decision trees are prone to overfitting, making them sensitive to variations in the training data.

The final model, the random forest, addresses this limitation by aggregating multiple decision trees, thereby reducing overfitting and enhancing generalization. By combining the outputs of many trees, random forests capture complex feature interactions, resulting in improved robustness and accuracy of predictions.

The dataset was partitioned into an 80% training set and a 20% testing set. In addition, five-fold cross-validation was applied within the training portion to assess model stability and ensure that performance estimates were not dependent on a single data split.

Results and Discussion

Investigation 1 examined how different methods of representing en-route weather affect gate-to-gate fuel-burn prediction. Four configurations were evaluated:

1. Operational features only
2. Instantaneous MERRA-2 averages
3. Monthly MERRA-2 averages
4. Seasonal MERRA-2 averages

Decision Tree and Random Forest models were applied consistently across all configurations to ensure that performance differences were due to the weather representation rather than the modeling technique.

Table 5 summarizes the Decision Tree performance across the four configurations. Incorporating instantaneous MERRA-2 weather reduced the MAE from 1.207 to 0.969 and reduced the RMSE from 1.927 to 1.832 compared with the operational-only baseline. The R^2 value increased from 0.957 to 0.961. Monthly and seasonal MERRA-2 averages resulted in MAE values of 1.029 and 1.035, respectively, and RMSE values of 1.981 and 1.863. These results show that the instantaneous weather method produced the lowest overall errors among the four configurations.

Table 5. Performance of Decision Tree fuel burn prediction models using different weather representation methods. MAE: mean absolute error, MERRA-2: Modern-Era Retrospective analysis for Research and Applications, Version 2, MSE: mean squared error, RMSE: root mean squared error, R^2: coefficient of determination.

Metric	Operational Feats	Avg. En-route Wx from Inst. MERRA2	Avg. En-route Wx from Monthly MERRA-2	Avg. En-route Wx from Seasonal MERRA-2
MAE	1.207	0.969	1.029	1.035
MSE	3.878	3.435	3.982	3.519
RMSE	1,927	1.832	1.981	1.863
R^2	0.957	0.961	0.955	0.960

Figure 26 shows the actual and predicted fuel-burn values and the corresponding residuals. The red dashed line indicates the condition in which the predicted value equals the observed value. Most points in the actual-versus-predicted panel lie

close to this line for lower and moderate fuel-burn values. Points begin to show a greater vertical spread when the actual fuel burn exceeds approximately 60,000 lb In the residual panel, most values are near zero, and larger residuals occur at higher fuel-burn levels. Some flights have residuals exceeding 20,000 lb.

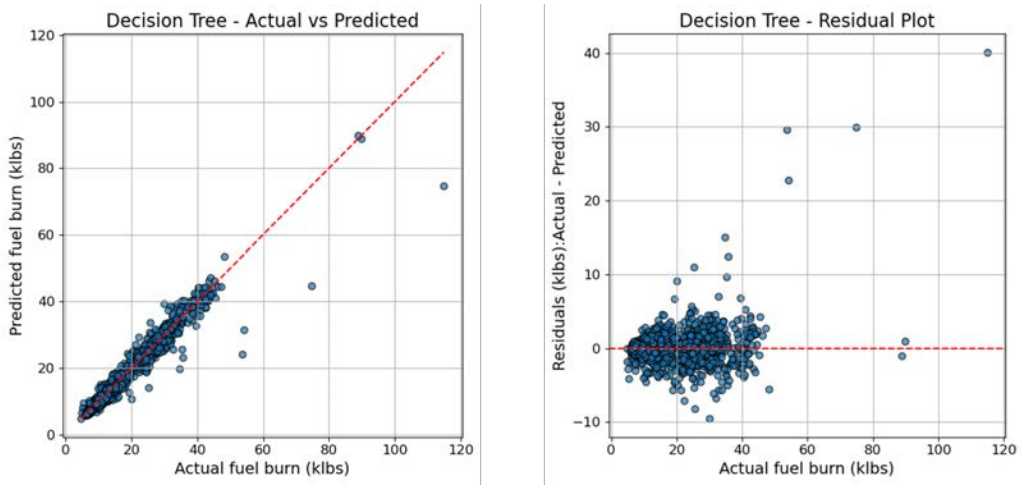


Figure 26. Decision Tree model performance for gate-to-gate fuel-burn prediction (16 city pairs).

Table 6 summarizes the Random Forest performance across the four configurations. The lowest MAE value was 0.701 and occurred when instantaneous MERRA-2 en-route weather was used. This configuration also produced the lowest RMSE value at 1.536. The operational-features-only configuration produced an MAE of 0.786 and an RMSE of 1.566. The monthly and seasonal MERRA-2 averages yielded MAE values of 0.792 and 0.808, respectively, and RMSE values of 1.582 and 1.684. The highest R^2 value was 0.974 for the operational-features-only configuration, followed closely by 0.972 for the instantaneous weather case.

Table 6. Performance of Random Forest fuel burn prediction models using different weather representation methods. MAE: mean absolute error, MERRA-2: Modern-Era Retrospective analysis for Research and Applications, Version 2, MSE: mean squared error, RMSE: root mean squared error, R^2: coefficient of determination.

Metric	Operational Feats	Avg. En-route Wx from Inst. MERRA-2	Avg. En-route Wx from Monthly MERRA-2	Avg. En-route Wx from Seasonal MERRA-2
MAE	0.786	0.701	0.792	0.808
MSE	2.734	2.577	2.798	3.372
RMSE	1.566	1.536	1.582	1.684
R^2	0.974	0.972	0.970	0.964

Figure 27 shows the actual and predicted fuel-burn values and the associated residuals. The Random Forest predictions are tightly clustered along this line for most flights, with a narrower vertical spread compared with the Decision Tree results. The residual plot shows a concentrated distribution around zero for lower and moderate fuel-burn values. A smaller number of flights exhibit large positive residuals, with several exceeding 20,000 pounds.

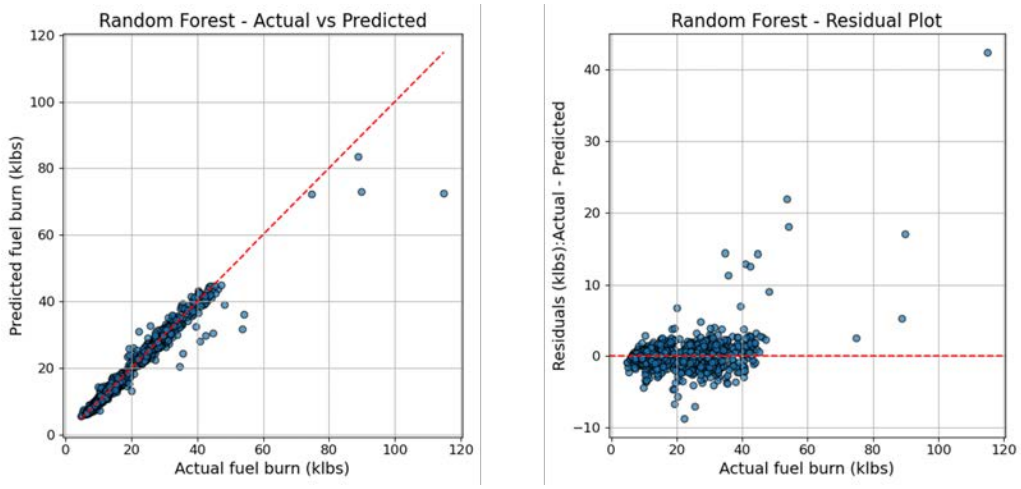


Figure 27. Random Forest model performance for gate-to-gate fuel-burn prediction (16 city pairs).

In all configurations, incorporating instantaneous MERRA-2 weather data reduced MAE and RMSE relative to the baseline that used only operational data. Monthly and seasonal averages from MERRA-2 yielded error levels similar to the baseline, offering no extra benefit. These findings suggest that only the instantaneous weather inputs significantly contributed to lowering prediction errors.

Investigation 2: Operational and Directional Feature Enhancement

Methodology

This investigation examined how two operational factors, aircraft takeoff weight and flight direction, affect the accuracy of gate-to-gate fuel-burn predictions. The analysis used the same weather-integrated framework as Method 2 in Investigation 1, which incorporated instantaneous MERRA-2 en-route weather data. The objective was to evaluate whether adding these operational variables improves prediction accuracy beyond what is obtained using aircraft and weather variables alone.

Two modifications were applied to the baseline configuration:

1. Aircraft takeoff weight: Aircraft takeoff weight was obtained from the FOQA dataset and represents the weight recorded for each flight at takeoff. Because takeoff weight affects the thrust and fuel required across all phases of flight, including this variable, allows the models to represent fuel-burn differences associated with variations in aircraft mass.
2. Flight direction classification: Flight direction was determined by comparing the longitudinal positions of the origin and destination airports for each city pair. Flights ending east of the departure airport were classified as eastbound, and flights ending to the west were classified as westbound. This classification provides a straightforward way to separate flights operating in opposite directions along the same route, allowing wind-related differences between the two directions to be evaluated.

In this investigation, the same modeling framework and evaluation metrics used in Investigation 1 were applied to assess the impact of the additional operational variables. Decision tree and random forest models were trained using the expanded feature set, and their performance was evaluated using MAE, MSE, RMSE, and R^2.

Results and Discussion

This initial analysis was conducted for 16 city pairs, which was later expanded to 86 city pairs in Investigation 3.

The inclusion of aircraft takeoff weight improved prediction accuracy in both models. For the Decision Tree, MAE decreased from 0.969 to 0.882, and RMSE decreased from 1.832 to 1.747 (Table 7). For the Random Forest model, MAE decreased from 0.701 to 0.607, and RMSE decreased from 1.536 to 1.300 (Table 8). In both models, the R^2 values increased slightly. These results indicate that adding takeoff weight consistently reduced prediction errors relative to the configuration without this variable.



Table 7. Fuel burn prediction performance of Decision Tree models with and without aircraft takeoff weight. MAE: mean absolute error, MSE: mean squared error, RMSE: root mean squared error, R^2: coefficient of determination.

Metric	Without Takeoff Weight	With Takeoff Weight
MAE	0.969	0.882
MSE	3.435	3.261
RMSE	1.832	1.747
R^2	0.961	0.963

Table 8. Fuel burn prediction performance of Random Forest models with and without aircraft takeoff weight. MAE: mean absolute error, MSE: mean squared error, RMSE: root mean squared error, R^2: coefficient of determination.

Metric	Without Takeoff Weight	With Takeoff Weight
MAE	0.701	0.607
MSE	2.577	1.950
RMSE	1.536	1.300
R^2	0.972	0.979

As shown in Table 9 and Table 10, flight direction resulted in measurable differences in prediction accuracy for both models. For the Decision Tree, the MAE values for eastbound and westbound flights were 0.899 and 0.929, compared with 0.882 for all directions. The corresponding RMSE values were 1.620 for eastbound flights and 1.806 for westbound flights. For the Random Forest model, the MAE values were 0.596 for eastbound flights and 0.671 for westbound flights, compared with 0.607 for the combined dataset. The RMSE values were 1.301 for eastbound flights and 1.548 for westbound flights. These results indicate that eastbound flights generally exhibited lower error values than westbound flights in both modeling approaches.

Table 9. Fuel burn prediction performance of Decision Tree models by flight direction. MAE: mean absolute error, MSE: mean squared error, RMSE: root mean squared error, R^2: coefficient of determination.

Metric	All Flight Directions	Eastbound	Westbound
MAE	0.882	0.899	0.929
MSE	3.261	3.367	3.701
RMSE	1.747	1.620	1.806
R^2	0.963	0.954	0.968

Table 10. Fuel burn prediction performance of Decision Tree models by flight direction. MAE: mean absolute error, MSE: mean squared error, RMSE: root mean squared error, R^2: coefficient of determination.

Metric	All Flight Directions	Eastbound	Westbound
MAE	0.607	0.596	0.671
MSE	1.950	2.322	3.080
RMSE	1.300	1.301	1.548
R^2	0.979	0.969	0.975

This study evaluated the influence of aircraft takeoff weight and flight direction on gate-to-gate fuel-burn prediction accuracy using the same modeling framework as Investigation 1. Adding the takeoff weight variable reduced prediction

errors for both the Decision Tree and Random Forest models, resulting in lower MAE and RMSE values compared to the configuration without this variable. Flight direction also affected error levels, producing different MAE and RMSE values for eastbound and westbound flights in both models. However, training direction-specific models did not yield an overall improvement in prediction accuracy relative to the combined-direction model. In the Random Forest case, the eastbound subset showed slightly lower errors; however, this reflects the properties of that subset rather than enhanced model performance. Overall, the results indicate that takeoff weight provides a clear contribution to accuracy, while separating models by flight direction does not provide a predictive benefit.

Investigation 3: Large-Scale Application and Scalability Assessment

Methodology

This investigation assessed how well the fuel-burn prediction framework generalizes when applied to a larger and more diverse set of operations. The dataset was expanded from 16 to 86 city pairs by adding routes in order of available flight counts, resulting in approximately 11,300 FOQA flights. The expanded network introduced additional variation in the atmospheric and geographic conditions represented in the dataset. All model configurations used the instantaneous MERRA-2 en-route weather variables defined in Method 2 of Investigation 1 and incorporated aircraft takeoff weight to maintain consistency with the enhanced feature set. Figure 28 illustrates the distribution of the 86 city pairs across major U.S. corridors, highlighting the increased range of operating conditions captured in the expanded dataset.

Two predictive modeling methods were evaluated: Random Forest and a Multilayer Perceptron (MLP). Random Forest was selected as the primary model because it demonstrated stronger performance than the other methods tested in the earlier investigations. Both models used the complete feature set developed in Investigation 2, which included aircraft type, FOQA-derived takeoff weight, aircraft construction year, flight direction, airport characteristics, and averaged en-route MERRA-2 weather variables.

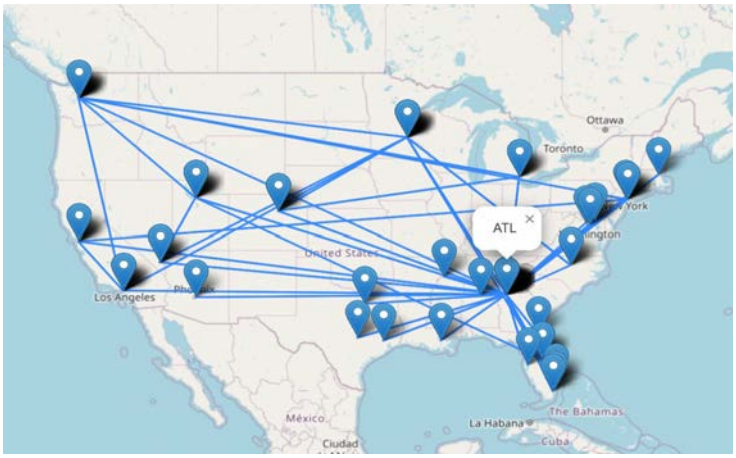


Figure 28. Visualization of 86 Origin-Destination (OD) pairs.

An MLP model was also implemented to examine whether a neural-network approach could represent nonlinear relationships among operational variables and atmospheric conditions that the Random Forest could not capture. The network consisted of two hidden layers with 64 and 32 nodes using rectified linear activation and a linear output layer. All numerical features were standardized before training. The MLP used a 70/15/15 train–validation–test split to allow independent assessment of hyperparameter tuning and final generalization performance.

Results and Discussion

The expansion from 16 to 86 city pairs improved the performance of the Random Forest model. As shown in Table 11, the MAE decreased from 0.607 to 0.474, and the RMSE decreased from 1.300 to 0.887. The R^2 value increased from 0.979 to 0.988. The actual-versus-predicted plot shows that most predictions fall close to the line of perfect agreement, with larger deviations appearing primarily at higher fuel-burn values. The corresponding residuals are centered near zero, with greater spread for flights with higher fuel-burn values.



Table 11. Fuel burn prediction performance with expanded city pairs and an added Multilayer Perceptron (MLP) model. MAE: mean absolute error, MSE: mean squared error, OD: Origin-Destination, RMSE: root mean squared error, R^2: coefficient of determination.

Metric	Random Forest 16 OD pairs	Random Forest 86 OD pairs	MLP 86 OD pairs
MAE	0.607	0.474	0.442
MSE	1.950	0.807	0.477
RMSE	1.300	0.887	0.691
R^2	0.979	0.988	0.993

The MLP model was evaluated only on the expanded 86-route dataset and produced the lowest overall error values among the models tested. The MAE and RMSE were 0.442 and 0.691, and the R^2 value was 0.993. The actual-versus-predicted plot shows close alignment with the reference line across the full fuel-burn range, and the residuals exhibit less dispersion than those from the Random Forest model (shown in Figure 29).

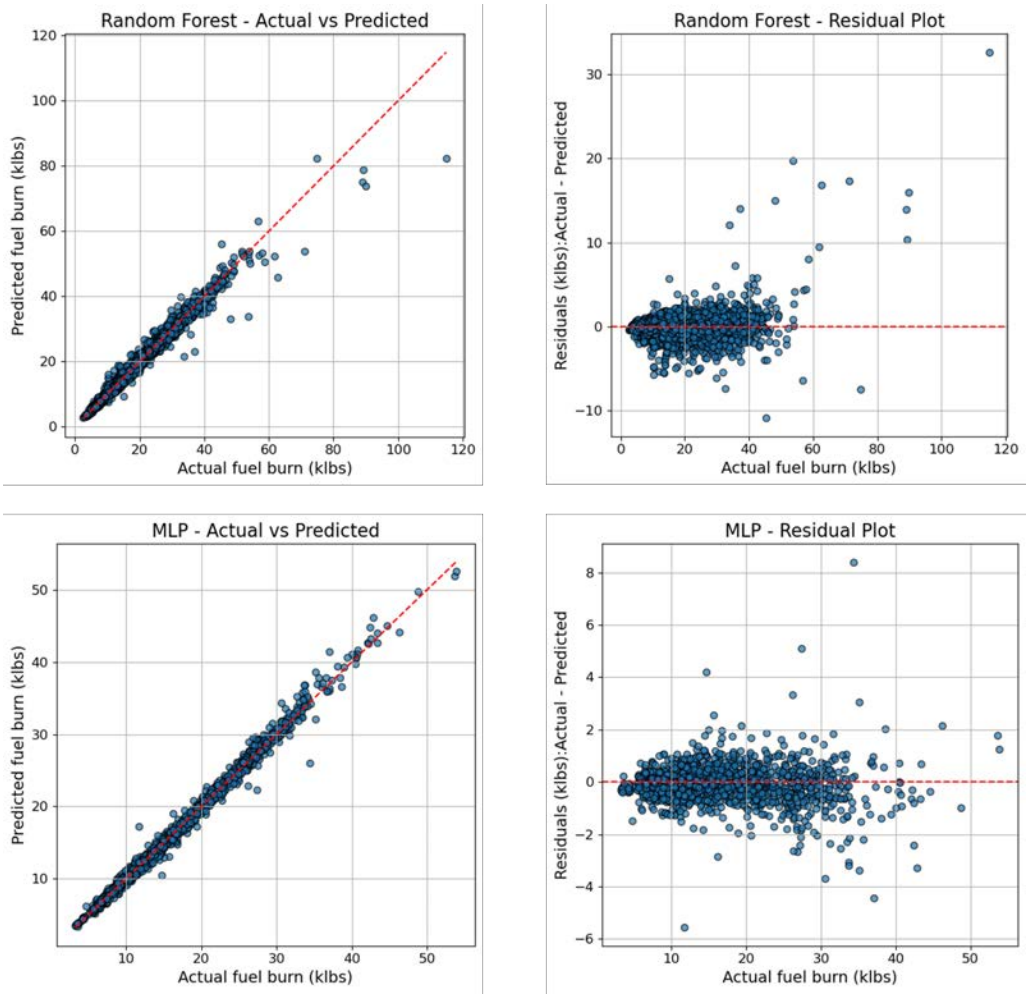


Figure 29. Multilayer Perceptron (MLP) and Random Forest models performance for gate-to-gate fuel-burn prediction (86 city pairs).



Overall, the results indicate that expanding the dataset enhanced the accuracy of the Random Forest model, and that the MLP model achieved the highest accuracy within the expanded 86-route configuration.

Investigation 4: Fuel Burn Analysis in AEDT Using Clustered Core Paths and Real-World Flight Data

Methodology

This study utilizes the AEDT 3e public release version 174.0.15710.1 and real-world full flight data provided by an airline partner, which forms part of the CY2023 FOQA dataset. As the entire FOQA dataset consists of over 50,000 individual flights, a total of 40 city pairs were chosen from the dataset for the purposes of this study based on flight frequency, industry inputs, and national importance. The 40 city pairs account for about 7,200 flights; these are described in Table 12. A flowchart summarizing the workflow followed by the team is shown in Figure 30.

Table 12. Total flights selected from FOQA data for selected city pairs. KATL: Hartsfield-Jackson Atlanta International Airport, KLAS: Harry Ried International Airport (Las Vegas, Nevada): KLGA: LaGuardia Airport (Elmhurst, New York), KMSP: Minneapolis-Saint Paul International Airport, KSEA: Seattle-Tacoma International Airport, KSLC: Salt Lake City International Airport, KJFK: John F. Kennedy International Airport (Queens, New York), KDCA: Ronald Reagan Washington International Airport (Arlington, Virginia), KRDU: Raleigh-Durham International Airport, KMCO: Orlando International Airport, KBOS: Boston Logan International Airport, KLAX: Los Angeles International Airport, KDEN: Denver International Airport, KDTW: Detroit Metropolitan Wayne County Airport, KDFW: Dallas Fort Worth International Airport, KSFO: San Francisco International Airport.

City Pair	Number of Flights	City Pair	Number of Flights	Great-Circle Distance (nmi)
KATL-KLAS	196	KLAS-KATL	169	1518
KATL-KLGA	175	KLGA-KATL	283	662
KATL-KMSP	191	KMSP-KATL	169	788
KATL-KSEA	192	KSEA-KATL	153	1896
KATL-KSLC	157	KSLC-KATL	141	1382
KLAS-KSLC	89	KSLC-KLAS	81	320
KATL-KJFK	103	KJFK-KATL	95	660
KATL-KDCA	163	KDCA-KATL	215	475
KATL-KRDU	274	KRDU-KATL	315	309
KATL-KMCO	306	KMCO-KATL	252	351
KATL-KBOS	147	KBOS-KATL	226	822
KATL-KLAX	152	KLAX-KATL	221	1691
KATL-KDEN	312	KDEN-KATL	215	1042
KATL-KDTW	165	KDTW-KATL	163	517
KATL-KDFW	170	KDFW-KATL	195	636
KMSP-KDEN	204	KDEN-KMSP	147	591
KSEA-KMSP	168	KMSP-KSEA	145	1216
KLAX-KSFO	157	KSFO-KLAX	116	293
KSEA-KSLC	161	KSLC-KSEA	135	598
KMSP-KLAS	156	KLAS-KMSP	130	1129

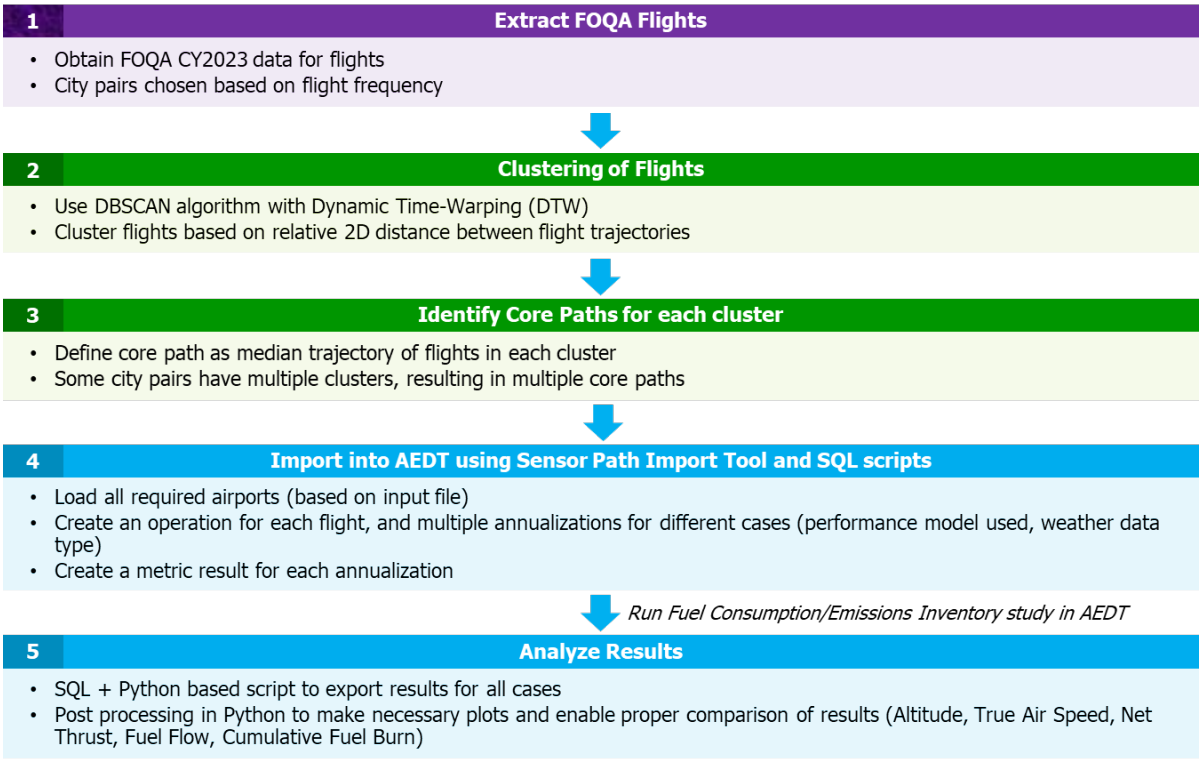


Figure 30. Flowchart summarizing the runway-to-runway fuel burn analysis process workflow. 2D: two-dimensional, CY: calendar year, FOQA: Flight Operations Quality Assurance, SQL: Structured Query Language.

All usable flight data from the chosen city pairs are extracted and properly formatted using a Python script written by the team. Any outlying flights (i.e., flights that return to their departure airport, or flights with invalid or corrupted data points) are rejected. Parameters extracted include flight trajectory information, airspeed, groundspeed, airframe and engine information, etc. Distance matrices are created out of the saved trajectory information of all flights for each city pair and saved in a high-efficiency binary format suitable for handling large amounts of numerical data. These distance matrices incorporate Dynamic Time-Warping, in order to properly and accurately calculate the relative two dimensional distance between two sets of coordinates belonging to different flights. The pre-computing of distance matrices significantly helps optimize clustering speed.

Once distance matrices are created, a clustering workflow developed by the team is run. The clustering workflow is based on the Density-Based Spatial Clustering of Applications with Noise (DBSCAN) algorithm, which is useful for clustering datasets such as trajectories. While the Hierarchical DBSCAN algorithm was used in the initial work done by the team in 2024, DBSCAN is chosen for this study as more granular control over clustering performance is possible with it. The algorithm clusters flight trajectories per city pair using the pre-computed distance matrices. Two runs of the algorithm are run. First, an iterative run that goes through combinations of compatible clustering parameters that are used to control the clustering performance (eps and min_samples). Eps is iterated from 0 to 200, and the min_samples are iterated from 2 to 20, covering all the possible combinations of both. The clusters generated by the first run are compared using two metrics, their R^2 value and their Davies-Bouldin score, to determine the optimal combination of parameters for each city pair. Once optimized parameters are decided, a second run of the clustering algorithm is performed to generate the final clusters for all city pairs. While it is noticed that many city pairs have a single general flight route dominating resulting in one major cluster, certain city pairs may have flights flying in one of multiple routes, leading to distinct clusters for those city pairs. In this case, if one route outweighs the other in terms of flights, the other is discarded. However, if the clusters are comparable in their flight frequency, they are all considered.



From the chosen cluster(s), the FOQA flight closest to the median flight trajectory within the cluster is selected as the 'core path,' which is essentially the representative flight path for a given city pair. As mentioned above, because of multiple clusters being chosen for certain city pairs, they may also have multiple core paths. Once determined, flight information for these core paths is extracted, reformatted and saved as two files, that will be required as inputs for the Safety Performance Indicator (SPI) tool in the AEDT. These two files are:

1. An 'operations' file, which contains information about the flight's wheels-off and wheels-on times, departure and arrival airports, aircraft, and AEDT-specific equipment ID.
2. A 'trajectory' file, which contains a sequential time series of the entire flight path and parameters, from departure runway to arrival runway. Parameters include latitude, longitude, pressure and Global Positioning System altitudes, true airspeed, ground track distance and timestamp.

An important aspect of these input files is the EquipID value for each flight, which controls the specific airframe and engine variant that will be used by the AEDT during the modeling process. The AEDT can contain multiple airframe and engine variants for a single aircraft type. Without any EquipID specified in the SPI input files, the AEDT may use a default airframe and engine variant, which may not exactly be the same configuration as the real-world flight, and is found to lead to inaccurate comparisons. Thus, it is important to specify an EquipID that is the closest match to the actual aircraft flown during a given flight. This is done by looking up the tail number of the FOQA flights within the FAA registry website and cross-referencing the specific airframe and engine type with the available options in the AEDT equipment database.

Once input files are created for all core path flights, a new study is created in the AEDT. All airports of interest are added into the study, after which the flights are imported using the SPI tool and the input files.

As this is a comparative study, four alternative configurations of the AEDT are considered in order to get an all-encompassing basis, including choices in both performance and weather models used by the AEDT for modeling. The performance models considered are Base of Aircraft Data (BADA) 3 and BADA 4; the weather models considered are AEDT's built-in average airport weather and high-resolution weather data imported from the National Aeronautics and Space Administration's MERRA-2 dataset. Individual operation groups, annualizations and emissions inventory cases are created for the four configurations. Once created, the cases are run in the AEDT, and results are exported as comma separated values (CSV) files for post-processing and further analysis.

Automation Efforts for Batch Report Tool

Large portions of the AEDT modeling workflow were automated to manage the scale of flights evaluated in the study. The Batch Report Tool was first considered as a potential end-to-end automation solution, since it can generate model runs and export results without manual intervention. However, during initial testing of the version available for AEDT 3e, all flight cases were automatically executed using BADA 3, regardless of the performance-model settings specified by the user. After working with Subject Matter Experts (SME) to identify the underlying cause, it became clear that this version of the tool relied on a fixed internal configuration that ignored study-specific settings and defaulted to BADA 3. Because accurate comparison across BADA 3 and BADA 4 was central to this work, relying on the Batch Report Tool was not feasible.

To address this, the team developed an alternative automation workflow (Figure 31) directly within the AEDT using Structured Query Language (SQL) scripting. The scripts automatically added airports to the study, created operation groups and annualizations, and generated four modeling cases per flight: BADA 3 with airport weather, BADA 3 with MERRA-2, BADA 4 with airport weather, and BADA 4 with MERRA-2. This allowed all performance-model and weather-model combinations to run consistently for every trajectory.

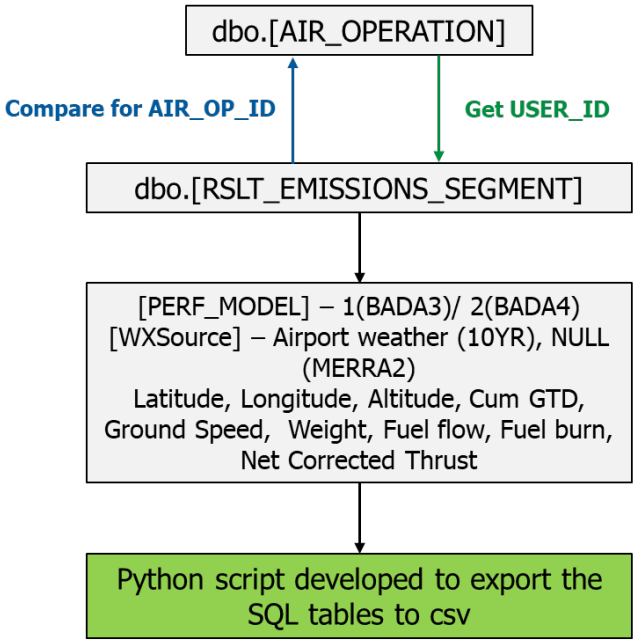


Figure 31. Workflow used to automate the bulk processing and export AEDT results. BADA: Base of Aircraft Data, CSV: comma separate values, FID: Flight ID, GTD: ground track distance, MERRA-2: OD: Origin-Destination, SQL: Structured Query Language.

A custom Python script was then written to extract modeled segment-level results from the SQL database and convert them into CSV files for post-processing, ensuring that flight ID, OD pair, weather source, and performance model were associated properly with each result. This end-to-end workflow enabled reproducible and efficient processing of all the flight cases without relying on the Batch Report Tool.

Results and Discussion

The modeled trajectories generated from the SPI tool were imported into the AEDT and evaluated using both BADA 3 and BADA 4 performance models with MERRA-2 and airport weather datasets. Because FOQA paths contain high-resolution time histories, the team applied a controlled reduction in data frequency before modeling so that the AEDT could process the flights without numerical instability. All analyses used the same filtered input paths, ensuring that the comparison across FOQA, BADA 3, and BADA 4 reflected differences in the performance models and weather assumptions rather than differences in trajectory fidelity.

The cumulative fuel burn is compared between the generated FOQA core paths and the same core paths modeled in the AEDT. The SPI tool was used to import the core paths, after which a fuel consumption study is run, using BADA 3 and BADA 4 models and both the average airport and MERRA-2 weather data. The cumulative fuel burn is computed for the modeled flights in the AEDT, subtracting the taxi-out and taxi-in phases.

As seen in Figure 32, the clustering algorithm does a satisfactory job in identifying grouped flight trajectories and generates clusters based on them. Proceeding on to inspecting the cumulative fuel burn for each city pair, Table 13 shows a comparison of the cumulative fuel burn computed by the AEDT and the fuel burn from the FOQA core path flight data for each city pair.

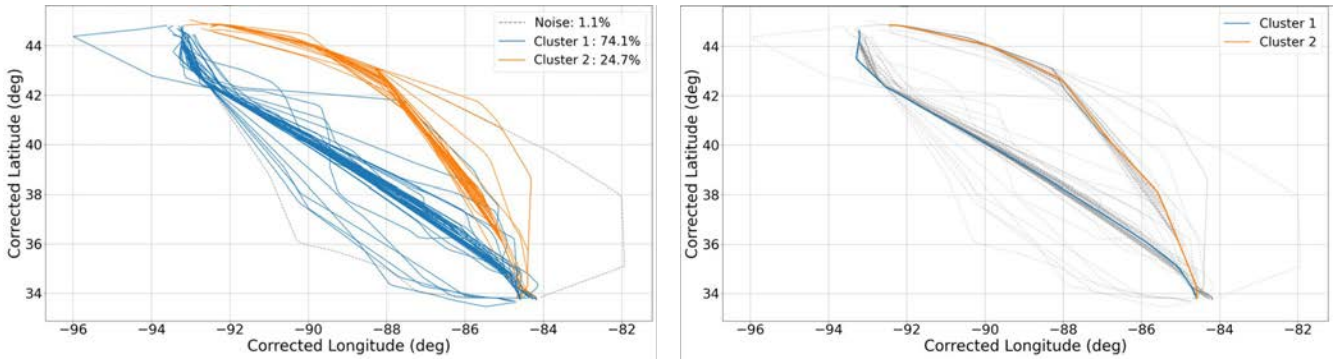


Figure 32. Clusters generated for Hartsfield-Jackson Atlanta International Airport (KATL)- Minneapolis-Saint Paul International Airport (KMSP) (left); chosen core path for the city pair (right).

Table 13. Comparison of cumulative fuel burn between FOQA data and AEDT output for selected city pairs. MERRA refers to the fuel burn calculations done with the MERRA-2 weather data, whereas APT is an identifier indicating the fuel burn calculations using average airport weather data in the AEDT. BADA: Base of Aircraft Data, FOQA: Flight Operations Quality Assurance, GT: Georgia Tech, KATL: Hartsfield-Jackson Atlanta International Airport, KBOS: Boston Logan International Airport, KDEN: Denver International Airport, KDFW: Dallas Fort Worth International Airport, KDTW: Detroit Metropolitan Wayne County Airport, KLAS: Harry Ried International Airport (Las Vegas, Nevada): KLAX: Los Angeles International Airport, KLGA: LaGuardia Airport (Elmhurst, New York), KMCO: Orlando International Airport, KMSP: Minneapolis-Saint Paul International Airport, KRDU: Raleigh-Durham International Airport, KSEA: Seattle-Tacoma International Airport, KSFO: San Francisco International Airport, KSLC: Salt Lake City International Airport, MERRA: Modern-Era Retrospective analysis for Research and Applications, N/A: not applicable.

				BADA 4				BADA 3			
GT Flight ID	**Aircraft Type**	**City Pair**	**Total Fuel Burn FOQA (lb)**	Total Fuel Burn - MERRA (lb)	Total Fuel Burn - APT (lb)	% Error MERRA	% Error APT Weather	Total Fuel Burn - MERRA (lb)	Total Fuel Burn - APT (lb)	% Error MERRA	% Error APT Weather
GT2409424	A319-100	KSFO-KLAX	5,249	4,986	5,236	5.02%	0.25%	5,612	6,003	-6.92%	-14.37%
GT2449334	A319-110	KLAX-KSFO	5,195	4,837	4,894	6.89%	5.79%	5,533	5,587	-6.51%	-7.55%
GT2438990	A320-200	KSEA-KSLC	9,789	9,253	9,501	5.47%	2.93%	9,904	10,557	-1.18%	-7.85%
GT2400565	A321-200	KBOS-KATL	15,283	14,583	13,891	4.58%	9.11%	16,262	15.151	-6.41%	0.86%
GT2406987		KDFW-KATL	10,350	10,099	11,897	2.43%	-14.94%	10,962	12,962	-5.91%	-25.24%
GT2407502		KATL-KDFW	12,423	12,216	11,635	1.67%	6.35%	13,034	12,244	-4.92%	1.45%
GT2414166		KATL-KBOS	13,685	13,376	15,009	2.25%	-9.68%	13,800	15,878	-0.85%	-16.03%
GT2419953		KATL-KDEN	19,092	18,265	16,557	4.34%	13.28%	20,901	18,444	-9.47%	3.39%



				BADA 4				BADA 3			
GT Flight ID	Aircraft Type	City Pair	Total Fuel Burn FOQA (lb)	Total Fuel Burn - MERRA (lb)	Total Fuel Burn - APT (lb)	% Error MERRA	% Error APT Weather	Total Fuel Burn - MERRA (lb)	Total Fuel Burn - APT (lb)	% Error MERRA	% Error APT Weather
GT2425557		KMSP-KLAS	19,788	20,289	18,117	-2.53%	8.44%	20,289	19,424	-2.53%	1.84%
GT2427137		KATL-KRDU	7,921	7,840	7,786	1.02%	1.71%	8,850	8,908	-11.72%	-12.46%
GT2440699		KDEN-KATL	15,061	15,109	16,852	-0.32%	-11.89%	16,011	17,830	-6.30%	-18.38%
GT2441139		KMSP-KDEN	11,034	10,874	10,696	1.45%	3.06%	11,764	11,519	-6.61%	-4.40%
GT2447364		KATL-KLAX	26,959	26,417	26,755	2.01%	0.76%	27,697	28,390	-2.74%	-5.31%
GT2448788		KDFW-KATL	11,739	11,164	12,306	4.90%	-4.83%	11,739	12,999	0.00%	-10.74%
GT2407293	A321-232	KLAS-KSLC	7,470	8,062	7,263	-7.92%	2.77%	8,062	8,496	-7.92%	-13.73%
GT2421526		KATL-KLAS	26,165	25,464	25,153	2.68%	3.87%	27,236	26,243	-4.09%	-0.30%
GT2421991		KATL-KSLC	28,700	26,963	22,782	6.05%	20.62%	29,870	24,612	-4.08%	14.24%
GT2424237		KATL-KLGA	12,375	12,177	13,160	1.60%	-6.34%	12,948	14,525	-4.63%	-17.37%
GT2425148		KSLC-KATL	19,655	19,953	22,840	-1.52%	-16.20%	20,187	23,698	-2.71%	-20.57%
GT2428735		KATL-KSLC	24,656	24,574	24,320	0.33%	1.36%	24,622	24,408	0.14%	1.01%
GT2429097		KMSP-KATL	14,918	14,860	15,225	0.39%	-2.06%	15,366	15,269	-3.00%	-2.35%
GT2440383		KLGA-KATL	12,039	11,975	12,312	0.53%	-2.27%	12,790	13,189	-6.24%	-9.55%
GT2446243		KSLC-KATL	20,896	20,728	23,967	0.81%	-14.70%	20,734	23,243	0.78%	-11.23%
GT2419261		KDEN-KATL	12,780	12,913	15,020	-1.04%	-17.52%	15,796	17,468	-23.59%	-36.68%
GT2439124		KDEN-KMSP	8,271	8,048	9,755	2.69%	-17.94%	10,402	12,052	-25.76%	-45.71%
GT2410840	B737-800	KSEA-KATL	26,396	25,967	28,412	1.63%	-7.64%	22,998	26,975	12.87%	-2.19%
GT2415788		KATL-KMSP	14,058	13,748	12,971	2.20%	7.73%	13,792	12,583	1.89%	10.49%
GT2423030		KLAS-KSLC	5,522	5,529	5,767	-0.12%	-4.43%	5,411	5,797	2.02%	-4.99%



				BADA 4				BADA 3			
GT Flight ID	Aircraft Type	City Pair	Total Fuel Burn FOQA (lb)	Total Fuel Burn - MERRA (lb)	Total Fuel Burn - APT (lb)	% Error MERRA	% Error APT Weather	Total Fuel Burn - MERRA (lb)	Total Fuel Burn - APT (lb)	% Error MERRA	% Error APT Weather
GT2423371		KSLC-KLAS	6,301	6,343	6,341	-0.68%	-0.65%	6,040	6,030	4.13%	4.30%
GT2434309		KATL-KMSP	14,571	14,331	12,926	1.65%	11.29%	13,988	12,081	4.00%	17.09%
GT2439960		KATL-KSEA	29,081	29,154	28,602	-0.25%	1.65%	27,299	27,293	6.13%	6.15%
GT2442148		KSLC-KLAS	5,932	5,935	6,074	-0.05%	-2.39%	5,597	5,869	5.64%	1.06%
GT2402954	B737-900	KLAS-KMSP	17,739	17,190	16,959	3.09%	4.4%	16,408	15,769	7.5%	11.1%
GT2404403		KSEA-KMSP	16,760	15,237	17,438	9.09%	-4.04%	15,528	18,593	7.35%	-10.94%
GT2409132		KSEA-KMSP	16,706	15,179	16,758	9.15%	-0.31%	15,319	17,324	8.31%	-3.70%
GT2443552		KMSP-KSEA	18,590	17,796	16,774	4.27%	9.77%	17,796	17,146	4.27%	7.77%
GT2447664		KDTW-KATL	9,959	9,174	8,557	7.88%	14.08%	9,674	8,730	2.86%	12.34%
GT2449664		KSLC-KSEA	10,445	9,747	9,507	6.69%	8.99%	10,167	9,821	2.67%	5.98%
GT2404615	B757-200	KATL-KDTW	11,324	10,765	11,135	4.94%	1.67%	10,744	11,192	5.13%	1.17%
GT2447376		KRDU-KATL	7,967	7,828	7,442	1.74%	6.59%	7,776	7,309	2.40%	8.26%
GT2447839		KATL-KMCO	8,416	8,458	8,716	-0.50%	-3.56%	7,905	8,367	6.07%	0.58%
GT2417499	B757-300	KATL-KSEA	38,179	39,578	39,781	-3.66%	-4.19%	N/A	N/A	N/A	N/A
GT2437635		KLAS-KATL	29,157	30,150	32,084	-3.41%	-10.04%	N/A	N/A	N/A	N/A
GT2434848		KMCO-KATL	10,435	11,371	10,033	-8.97%	3.85%	N/A	N/A	N/A	N/A

Across the evaluated flights, the AEDT-modeled fuel burn shows a consistent pattern of acceptable deviation from FOQA values, with performance depending on both the aircraft type and weather source. BADA 4 generally tracks FOQA fuel burn more closely than BADA 3, which tends to under- or over-estimate consumption depending on the route. BADA 4 showed the closest overall agreement, especially when paired with MERRA-2, which tended to minimize bias across climb, cruise, and descent segments. BADA 3 performed acceptably for most short- and medium-haul routes but displayed larger deviations for flights where strong meteorological gradients played a role. MERRA-2 based runs consistently show lower error magnitudes than the APT weather cases, although certain routes with strong winds or altitude profile mismatches show larger negative biases, especially for long-haul segments such as KDEN–KATL and KDEN–KMSP. In several short-haul pairs, including KSLC–KLAS and KLAS–KSLC, the modeled fuel aligns closely with FOQA, with errors often below 1%. Larger

discrepancies appear for flights with greater vertical variability or complex meteorological conditions, where APT weather occasionally produces over-predictions exceeding 10%. Overall, the comparison indicates that the AEDT combined with BADA 4 and MERRA provides the most stable agreement with FOQA data, while still exhibiting route-specific deviations that highlight the sensitivity to weather and climb–descent behavior.

The cumulative-fuel plots (Figure 33 and Figure 34) illustrate this behavior clearly: the AEDT tracks FOQA well at low altitudes, while cruise-phase differences accumulate gradually, leading to over- or under-estimation depending on the weather source. MERRA-2 usually produced smaller overall errors than airport weather, where several long-range flights showed persistent negative biases tied to missing instantaneous local weather information.

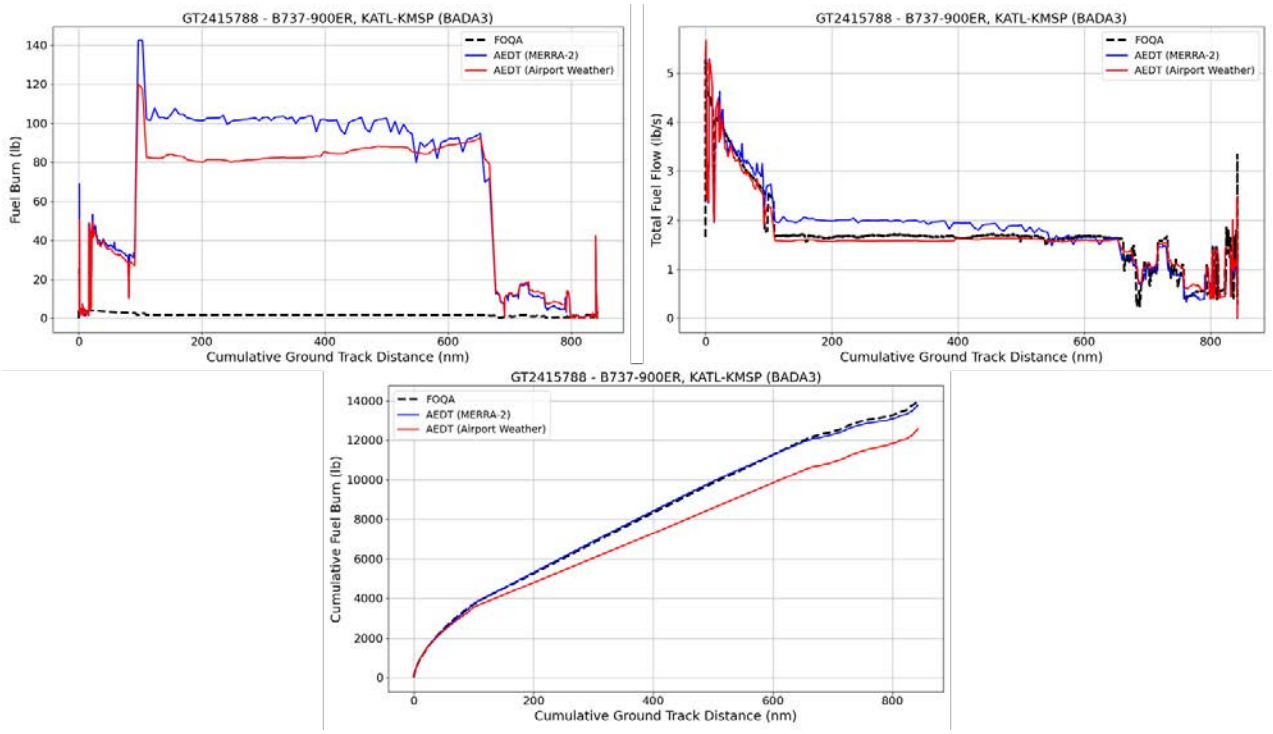


Figure 33. Fuel-burn and fuel-flow comparison for flight GT2415788 (B737-900ER, Hartsfield-Jackson Atlanta International Airport [KATL]– Minneapolis-Saint Paul International Airport [KMSP]) modeled in the AEDT using the Base of Aircraft Data (BADA) 3 performance model. FOQA: Flight Operations Quality Assurance.

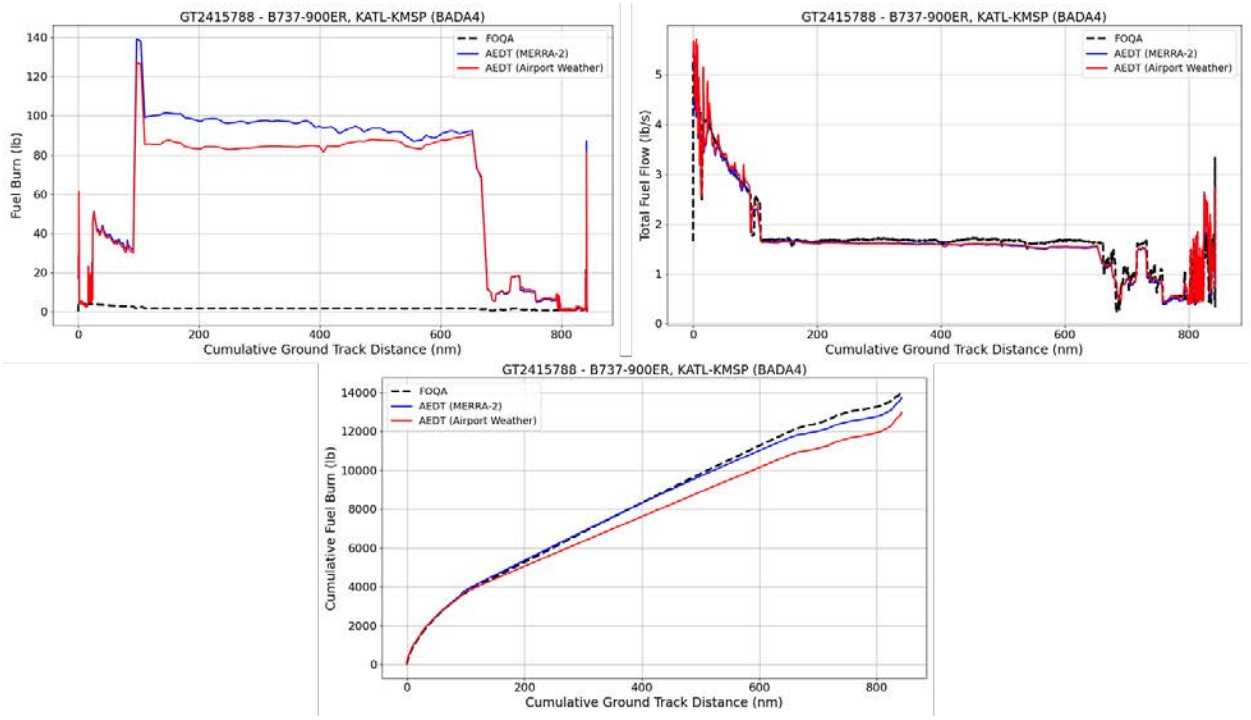


Figure 34. Fuel-burn and fuel-flow comparison for flight GT2415788 (B737-900ER, Hartsfield-Jackson Atlanta International Airport [KATL]– Minneapolis-Saint Paul International Airport [KMSP]) modeled using the Base of Aircraft Data (BADA) 4 performance model.

The representative case for the B737-900ER (KATL–KMSP) (Figure 33 and Figure 34) show how both models capture major performance features. In both the figures, the top-left image shows instantaneous fuel burn along the cumulative ground-track distance for FOQA, AEDT with MERRA-2 weather, and AEDT with airport weather. The top-right image presents the corresponding total fuel-flow profiles. The bottom image shows cumulative fuel burn, illustrating how differences in cruise-level fuel flow and weather inputs propagate over the full flight. The AEDT with MERRA-2 tracks FOQA more closely than the airport-weather case, though both capture the major climb, cruise, and descent features. The AEDT reproduces FOQA's climb-spike, stabilizes through cruise, and follows the same curvature in cumulative burn, even with reduced data resolution. BADA 4 narrows the gap further and maintains closer alignment with FOQA fuel-flow rates through the cruise segment, while BADA 3 shows a slightly larger spread. Overall, the results show that the AEDT combined with BADA 4 and MERRA-2 provides the most consistent agreement with FOQA, and that model-to-FOQA differences are driven more by route-specific atmospheric conditions and thrust modeling than by trajectory preprocessing.

SPI Tool Issues Reported

During the modeling process, several limitations in the SPI tool and its interaction with the AEDT were identified. These issues affected how FOQA trajectories could be imported and how thrust and fuel-burn behavior were represented during simulation. Each issue and the corresponding mitigation strategy are summarized below.

- Trajectory Size Limitation in SPI Imports: The SPI tool was unable to import FOQA trajectories containing more than roughly ten thousand points. Several flights in the dataset exceeded this threshold because FOQA operates at a one-second resolution throughout the mission. When these large files were passed to the AEDT, the import process failed before modeling could begin.
- Negative Thrust Values in BADA 4 Cruise and Descent: When full-resolution FOQA data (after reducing the points to be below 10,000) are input in the SPI tool, the AEDT consistently produced highly negative thrust values during cruise and parts of descent for BADA 4 cases. This behavior did not match FOQA and is not physically meaningful for commercial aircraft operating in steady cruise.



Cause Identified: The AEDT has difficulty processing extremely high-resolution (1 Hz) input, especially when paired with BADA 4, which uses a more detailed thrust model. Small fluctuations in altitude and ground speed at high resolution can produce unstable thrust estimates.

Mitigation applied: The team introduced a controlled down-sampling routine to reduce trajectory resolution while preserving high-value segments. Points below 10,000 ft were retained at full resolution to maintain climb and final-approach fidelity. Points between 10,000 and 30,000 ft were kept at 12-s intervals, and cruise-level points above 30000 ft were sampled at 60-s intervals. After the trajectory sampling was reduced, negative thrust values in cruise disappeared. Some negative values continued to appear in the descent phase, but these were isolated, moderate in magnitude, and did not affect cumulative fuel-burn results. The comparison of this reduced sample with the original is shown in Figure 35.

- Limitations of BADA 3 for Certain Aircraft Types: B757-300 and B767-400 flights could not be modeled using BADA 3 because corresponding performance models do not exist within that version of the database. These aircraft were therefore excluded from BADA 3 comparisons.
- Takeoff-Weight Adjustments Not Reflected in BADA 3: Adjusting aircraft takeoff weight had no effect on BADA 3 fuel-burn results. This is because BADA 3 does not incorporate takeoff weight into its thrust or drag formulations.
- Manual Assignment of Equipment IDs: The SPI tool requires each input trajectory to be linked to a BADA aircraft model via an equipment ID. This required manual editing of input file for all the flights (as mentioned in the Methodology section).

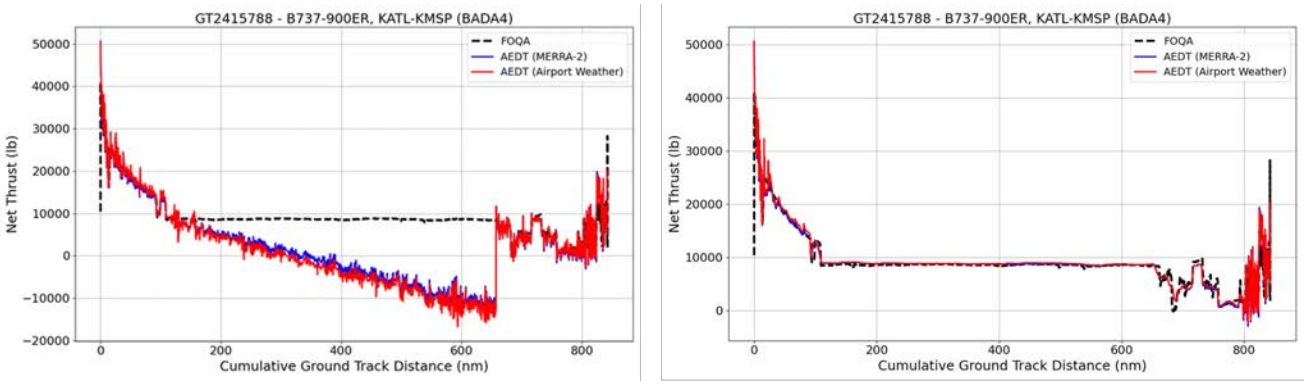


Figure 35. Net-thrust comparison for flight GT2415788 (B737-900ER, Hartsfield-Jackson Atlanta International Airport [KATL]– Minneapolis-Saint Paul International Airport [KMSP]) modeled with Base of Aircraft Data (BADA) 4. The left image shows results using full-resolution (1Hz) FOQA input. The right image shows the same flight after applying reduced-resolution trajectory sampling.

Milestones

None.

Major Accomplishments

- Conducted a correlation analysis of en-route fuel burn using real-world flight data, including the TTD and FOQA datasets.
- Developed linear regression/machine learning models to predict fuel burn using airport and aircraft performance features.

Publications

None.

Outreach Efforts

None.



Awards
None.

Student Involvement
Graduate research assistants, Hyungu Choi, Nitya Maruthuvakudi Venkatram, and Yash Vinod from the School of Aerospace Engineering participated in this task. Hyungu was involved with the creation of surrogate models for fuel burn prediction. Nitya and Yash performed the analysis for the clustered core path generation.

Plans for Next Period
Documentation and closeout of work performed under Task 3.

Task 4 – System Testing and Evaluation of AEDT
Georgia Institute of Technology

Objective
To provide the best possible environmental impact modeling capabilities in the AEDT, the FAA Office of Environment and Energy (OEE) continues to develop the AEDT by improving existing modeling methods and data and adding new functionalities. The FAA OEE seeks an independent effort in system testing to evaluate the accuracy, functionality, and capabilities of the AEDT, and support future model development. The objective of this task is to provide the FAA with high-quality systematic testing and evaluation of the capabilities of the AEDT, and to identify gaps in the tools' functionality and areas for further development.

Research Approach
Modeling Noise with Mixed Ground Types, Terrain, and Manmade Structures
New Mixed Ground Types, Terrain, and Manmade Structures (MGT/S) features, which include capabilities for enhanced terrain shielding, creation of various manmade structures and land cover definition, are being implemented for a future release of the AEDT. Thus, testing for these features commenced with focus primarily towards proper functioning of the features in terms of expected results and usability. Additionally, feature runtime was investigated, and user feedback was given in order to improve the aforementioned capabilities.

The structural creation feature allows for generation of building rows, individual buildings, and sound barriers, each of which was utilized individually and in combination in order to capture noise reflection and diffraction effects. For the study, several annualizations were created for modeling arrival and departure operations for the Brainerd Lakes Regional Airport (KBRD) in Brainerd, Minnesota (see Figures 36, 37, and 38). The annualizations included various structural combinations with and without land cover and terrain data.

The results showed that accuracy was only impacted by land cover data. The various structure types individually and in concert with each other without land cover data showed no difference in the shape of the noise contours, whereas inclusion of land cover data resulted in substantial differences for the noise contours. One of the tests included a large building far from the runway and showed an issue with the 25 dB contour being inside of the building rather than outside like all of the other structural tests without land cover. This finding was reported and was investigated further outside of the testing phase.

Runtime was investigated by examining start and end times for each case within the AEDT study logs. Findings showed that cases in which land cover was incorporated resulted in higher runtimes. Quantity of structures had little effect on runtime across cases; however, some variability still exists for runtimes within the same annualization. As in, if a case was run multiple times, different runtimes were shown. All findings were reported and backup files and logs were delivered as part of the results package.

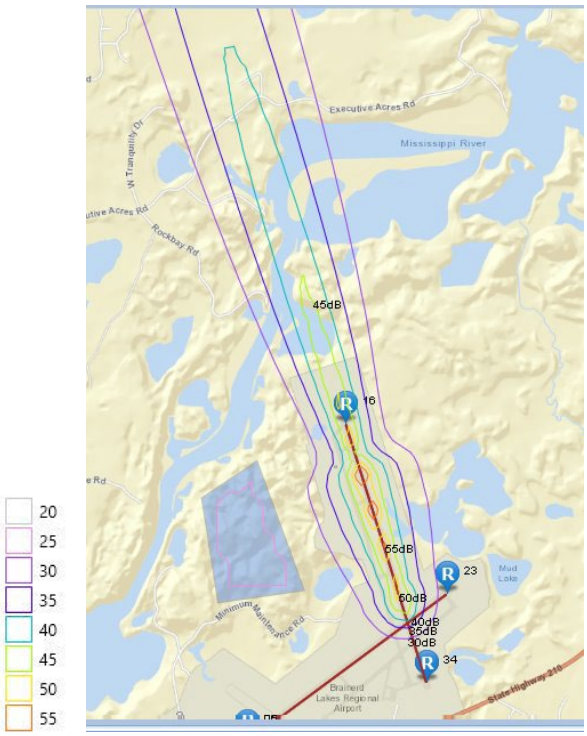


Figure 36. Large building far from runway (no land cover) at Brainerd Lakes Regional Airport.

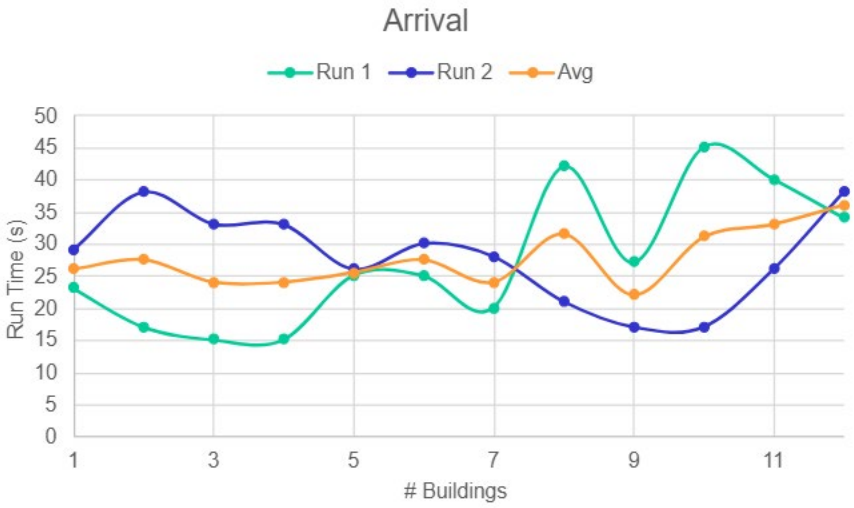


Figure 37. Runtime for arrival operations vs. building quantity.

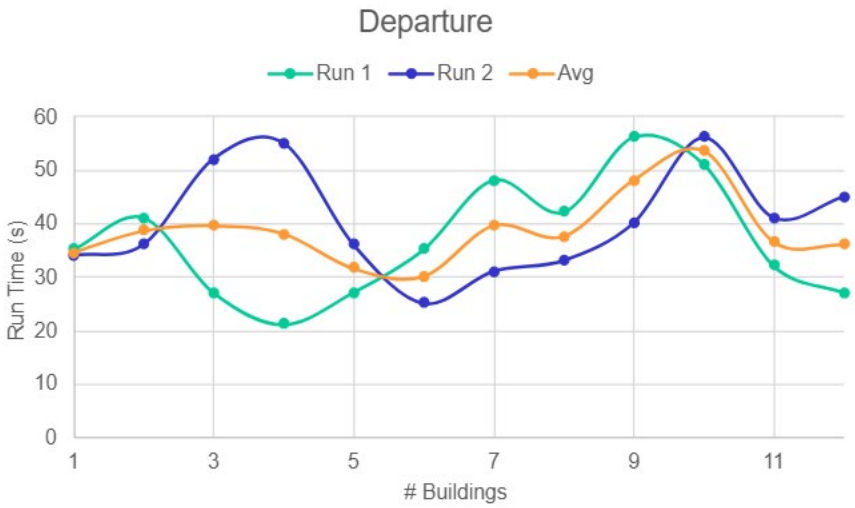


Figure 38. Runtime for departure operations vs. building quantity.

Supersonic Aircraft Modeling Testing
New SST aircraft modeling capabilities were implemented into the AEDT which required testing to ensure proper functionality of said features. The test consisted of six airport pairs with runway-to-runway operations and supersonic aircraft definitions. A user guide was provided with steps to follow in order to reproduce initial testing results and verify proper functioning of each step in the testing process.

One of the issues seen during the testing was in the SPI file import of the airport pair AEDT Standard Input File (ASIF) files in step 8 and its sub-steps. Partial sensor import was achievable in step 8.2 only after first changing the anpAircraftID in the provided .xml files. Prior to this, "unable to parse data" or "bad data integrity" errors would arise. Changing the anpAircraftID to be consistent with what was established in the GUI for the supersonic aircraft definition solved the partial sensor import issue for all airport pairs except for the Dubai International Airport (OMDB) - Suvarnabhumi Airport (VTBS) pair. This airport pair had a separate issue where two different airport codes were present in the SQL definition for one of the airports. By going in and deleting the older airport code, the problem was resolved. The SPI tool import was still an issue so proceeding was only possible by restoring the provided backup study with all sensor path operations already imported.

Other minor issues were documentation-related, such as step 9 of the document being misplaced due to the fact that the "tracks" option doesn't show up until a metric result has been defined. Another issue was that operation groups must be established prior to partial sensor path importing in step 8.2 for proper functioning. This information was missing from the documentation, and thus a recommendation to include this information was given. The final recommendation given was to create default airport settings for heavily used airports and airport pairs for enhanced ease of use when conducting studies.

Milestones
None.

Major Accomplishments
None.

Publications
None.

Outreach Efforts
None.

Awards
None.

Student Involvement
Graduate research assistants, Santusht Sairam and Fahraan Badruddin from the School of Aerospace Engineering participated in this task. Santusht and Fahraan were involved with ideation and modeling of test cases, analysis of results, and creation of any relevant bug reports.

Plans for Next Period
Continue system testing efforts to support ongoing AEDT development.

Task 5 – Supersonic Transport Modeling in the Aviation Environmental Design Tool
Georgia Institute of Technology

Objectives
The SST modeling task has two primary objectives:

1. Develop a predictive model for the propulsion system, encompassing thrust, fuel flow, engine dimensions, weight, and noise generation, and additionally accounting for variations in Mach number, altitude, and throttle setting, to enable comprehensive analysis of performance metrics such as fuel burn, gross weight, takeoff field length, and environmental factors including noise and emission.
2. Generate parametric drag polar models for the optimized vehicle that capture aerodynamic performance across the entire flight envelope as a function of Mach number, altitude, and lift coefficient.

Research Approach
Building on the ASCENT SST surrogate-model development implemented previously, the same end-to-end modeling workflow has been retained for this term's extension. The earlier study focused on validating regression-based propulsion (fuel flow) and aerodynamic (drag coefficient) models against Flight Optimization System (FLOPS) for six long-range international routes, and demonstrated that the methodology with continuous neural-network-based fuel-flow models and Total Energy Method (TEM)-based thrust estimation substantially reduced prediction errors, with final fuel-burn deviations remaining within approximately 6% across all evaluated origin-destination pairs. The combined method, which integrates the updated fuel-flow surrogate, TEM-based thrust estimation, and piecewise aerodynamic regression with flight-phase-specific logic (including dedicated descent thrust handling) is as shown in Figure 39.

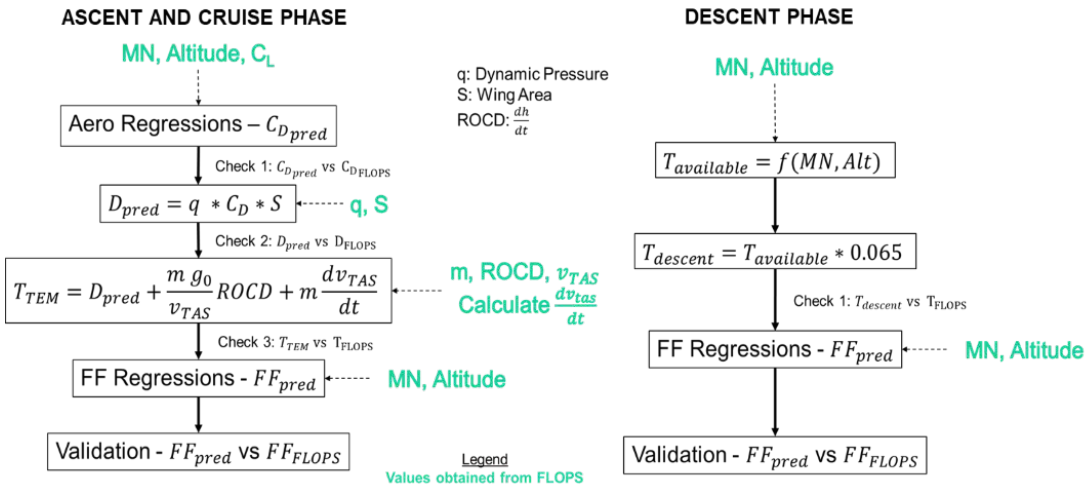


Figure 39. Modeling approach for ascent, cruise, and descent phases.

A brief summary of the implementation logic is as below:

1. **Fuel-Flow Regression Model:** Neural-network surrogate (2-layer Gaussian, 10 neurons each, LR = 0.01), trained on engine-deck data and validated against route-specific FLOPS outputs.
2. **Thrust Estimation Logic**: TEM formulation used to compute thrust directly from climb/descent energy balance and drag regressions.
3. **Aerodynamic Regression Model**: Drag coefficient modeled through regime-specific Mach–C_L sub-domains using cardinal grids and bi-quadratic interpolation, removing previous domain discontinuity artifacts.
4. **Descent-Phase Special Handling:** Thrust available predicted via polynomial regression with fixed idle-thrust factor applied, replacing TEM during descent to prevent over-prediction at low thrust conditions.

Because the foundational methodology has already been verified and documented, the current work focuses exclusively on the new route evaluation, applying the same modeling pipeline with no codebase or logic alterations. Trajectory discretization, weight propagation, altitude-Mach scheduling, and detailed takeoff and landing profiles followed the same implementation assumptions described in the earlier report. As before, detailed takeoff was modeled up to 15,000 ft and detailed landing from 3,333 ft to touchdown to ensure smooth physical continuity into and out of the surrogate-modeled cruise segment. FLOPS mission results were used as the validation reference for both total mission fuel burn as well as point-wise fuel-flow and thrust behavior along the ground-track distance.

A new city pair has been evaluated between KJFK and KLAX. Unlike the previously studied intercontinental missions, this route represents a domestic transcontinental scenario. In order to investigate performance trade-offs between design performance intent and practical regulatory compliance, each direction was modeled under two distinct cruise conditions as shown in Table 14.

Table 14. Modeling cases for SST route between John F. Kennedy International Airport (KJFK) and Los Angeles International Airport (KLAX).

Case	Direction	Cruise Mach	Motivation
A	KJFK → KLAX	1.70	Demonstrates peak design mission performance
B	KJFK → KLAX	1.15	Demonstrates regulatory-compliant domestic operation
C	KLAX → KJFK	1.70	Design Mach under prevailing tailwind conditions
D	KLAX → KJFK	1.15	Regulatory-compliant eastbound mission

In the previous phase of this study, the Supersonic Transport Route Tool (SSTRT) was used to optimize the mission routes by balancing time savings against fuel burn using a tunable weighting parameter α. That optimization framework allowed for over-water supersonic segments whenever possible to satisfy regulatory limits. The SSTRT therefore generated custom mission trajectories for each origin-destination pair, and those trajectories fed into the fuel-flow surrogate modeling workflow described earlier.

In the present phase, because the selected test route (KJFK–KLAX, bidirectional) flies entirely over continental landmass, supersonic cruise is not allowed under current FAA/ICAO regulations. As a result, no route optimization was performed, and the reference trajectory was defined using the Great Circle Distance (GCD). These routes are as shown in Figure 40. The Latitude-longitude for the FPPs are interpolated using the Great Circle path,



Figure 40. Route Visualizations - KJFK→KLAX (left) KLAX→KJFK (right).

Results and Discussion

The overall mission-level error, as shown in Table 15, remains within acceptable limits for both conditions, consistent with previous results. The surrogate appears slightly optimistic for Mach 1.7 and slightly conservative for Mach 1.15, but both remain within the target error window (< 3%). These errors are calculated without ignoring the duplicate points between the flight segments. FLOPS is path independent (directionally) and uses only the distance between the OD pair (GCD in this case) and airport latitude-longitude coordinates.

Table 15. Total fuel burn predictions comparison. FLOPS: Flight Optimization System, KJFK: John F. Kennedy International Airport, KLAX: Los Angeles International Airport.

Route	Actual (lbm)	FLOPS-Calculated (lbm)	% Error	Predicted (lbm)	% Error
KJFK ↔ KLAX (M1.7)	66,491.00	66,185.91	0.46%	65,566.38	1.39%
KJFK ↔ KLAX (M1.15)	70,868.00	70,526.18	0.48%	72,827.00	−2.76%

Plots of error in thrust and fuel-flow rate versus distance (Figure 41) indicate that all non-transient points remain below approximately 8% error. Outliers occur only at (1) the first data point, and (2) a duplicated point between segments associated with continuity (an artifact of FLOPS) (as can be seen the altitude plot on Figure 42).

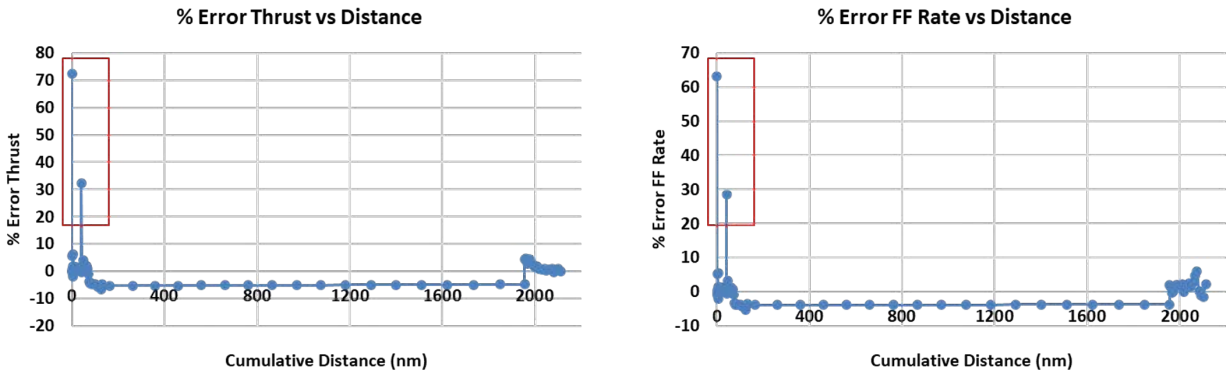


Figure 41. Percent error thrust (left) and percent error fuel flow (FF) rate (right) vs. ground track distance (nmi).

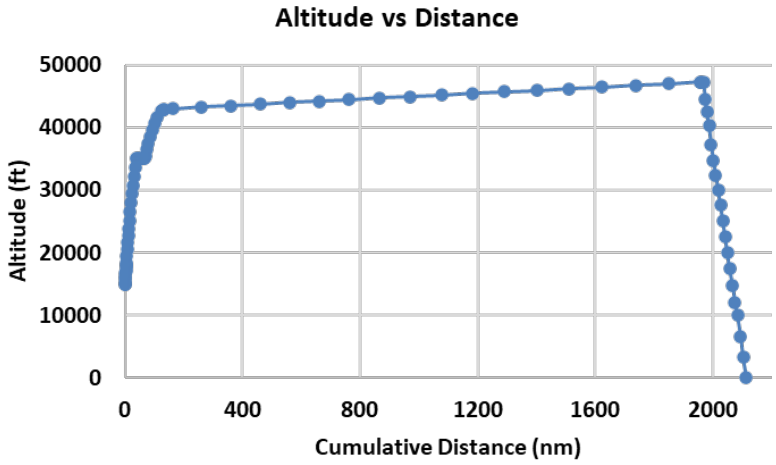


Figure 42. Altitude (ft) vs. ground track distance (nmi).

Histograms comparing raw versus de-duplicated error (Figure 43) confirm that other than the first point, the duplicate point, all other points have error lower than 8%.

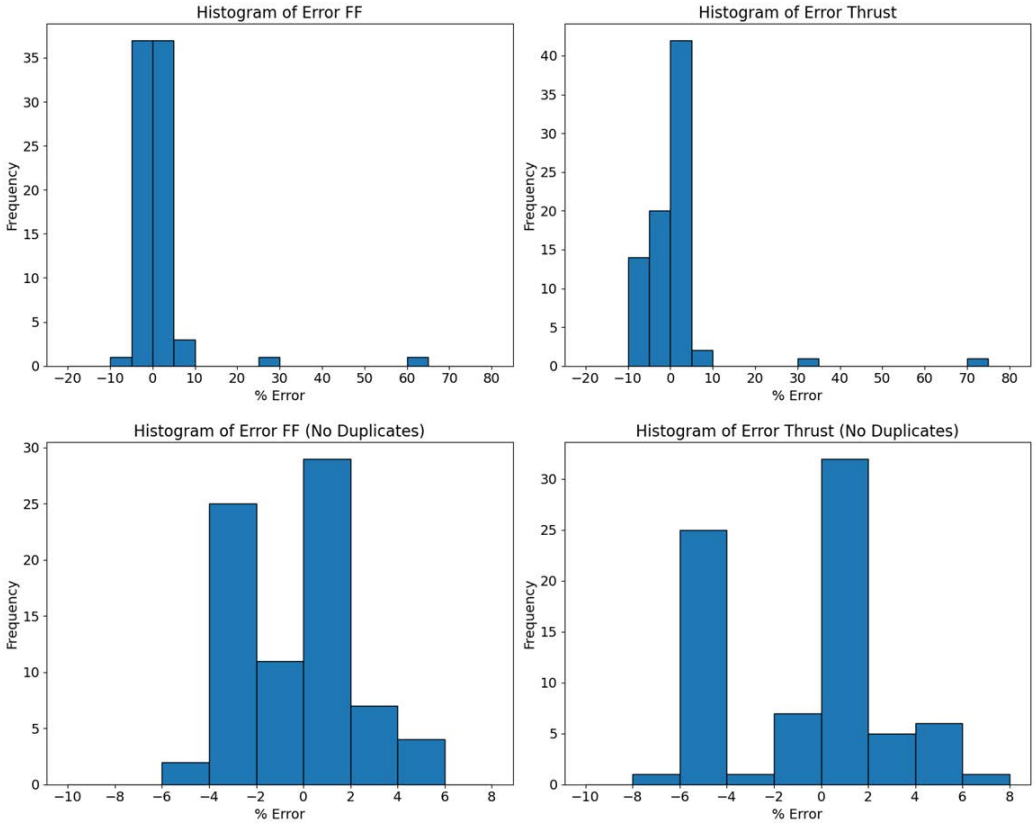


Figure 43. Raw and de-duplicated error histograms for fuel flow (FF) rate and thrust.

Detailed Takeoff and Landing Segments

Takeoff transition to the cruise mission matched closely, demonstrating good continuity between FPP and regression-based segments (Figure 44). Differences in detailed landing segments (Figure 45) are attributed to configuration modeling differences in FLOPS. FLOPS detailed landing assumes gear and full flaps from transition altitude, whereas the sizing run retains near-cruise aerodynamic configuration, leading to temporary true airspeed divergence. This behavior is consistent with earlier findings and stems from FLOPS internal modeling rather than the surrogate itself.

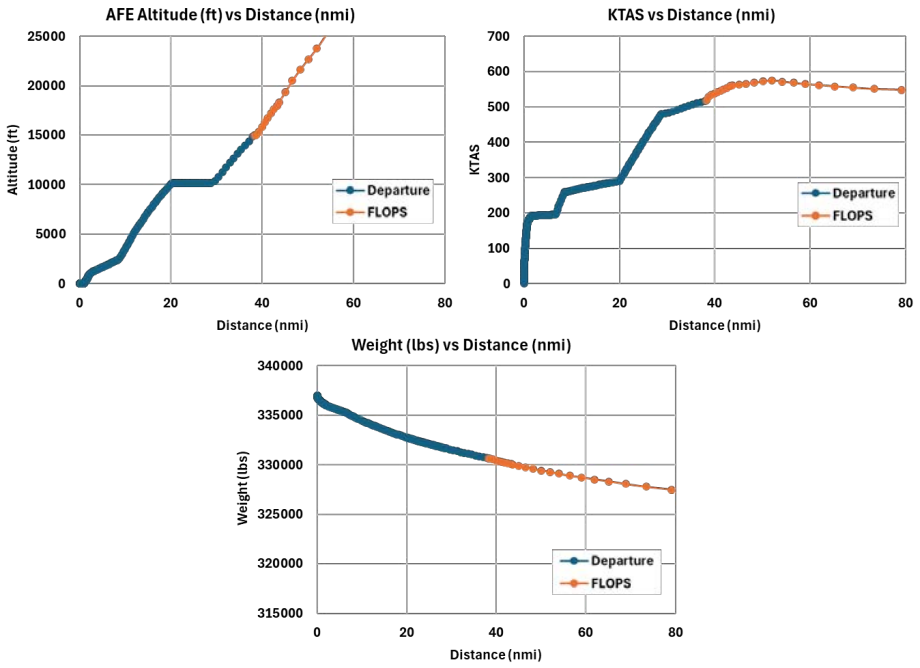


Figure 44. Detailed take-off segments (FPP) till 15,000 ft above field elevation (AFE). KTAS: knots true airspeed, FLOPS: Flight Optimization System.

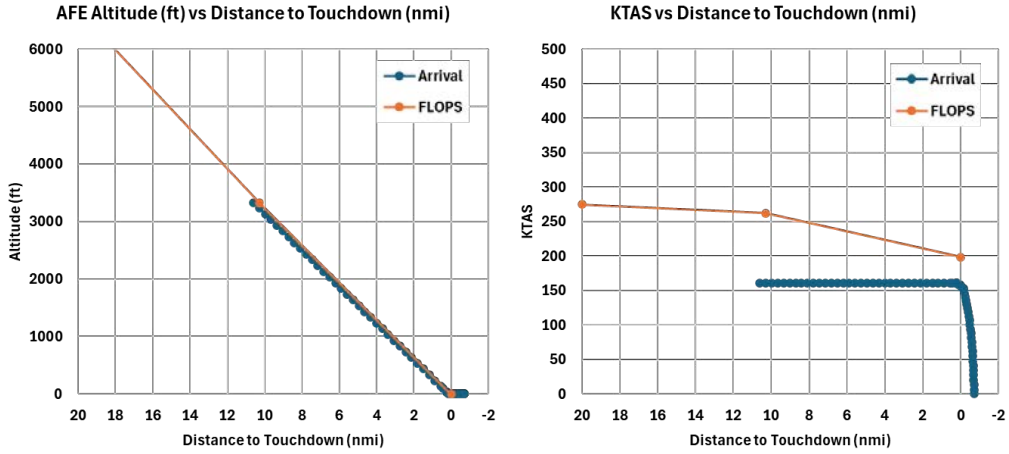


Figure 45. Detailed landing segment (FPP) from 3,333 ft above field elevation (AFE). KTAS: knots true airspeed.

To conclude, the surrogate-based fuel-flow modeling approach continues to demonstrate robust predictive behavior even when applied to land-constrained. Mission-level fuel burn accuracy remained within ±3%, and point-wise error remained below ±8% outside initialization transients.

Milestones

None.



Major Accomplishments
Complete Data Package Handover

Publications
None.

Outreach Efforts
Participated in biweekly calls and attended biannual ASCENT meetings.

Awards
None.

Student Involvement
Graduate research assistant, Nitya Maruthuvakudi Venkatram from the School of Aerospace Engineering participated in this research. Nitya was involved with the generation of the propulsion and aero models, modeling of test cases, and analysis of results.

Plans for Next Period
None.



Project 055 Noise Generation and Propagation from Advanced Combustors

Georgia Institute of Technology
RTX Technology Research Center

Project Lead Investigator

Timothy Lieuwen
Professor
Daniel Guggenheim School of Aerospace Engineering
Georgia Institute of Technology
270 Ferst Drive (M/C 0150)
Atlanta, GA 30332-0150
404-894-3041
tim.lieuwen@aerospace.gatech.edu

University Participants

Georgia Institute of Technology (Georgia Tech or GT)

- P.I.s: Prof. Timothy Lieuwen, Prof. Suresh Menon, Dr. Vishal Acharya, Dr. Benjamin Emerson
- FAA Award Number: 13-C-AJFE-GIT-058
- Period of Performance: February 5, 2020, to December 31, 2026
- Tasks:
  1. GT Experiments: This task addresses the measurements from experiments that will be performed at Georgia Tech. The task involves coordination between the teams to develop and define the aerodynamic design of a rich-quench-lean (RQL), quick quench, lean burn combustor for this study. This task is led by Tim Lieuwen with support from Ben Emerson and David Wu.
  2. GT Simulations: This task includes simulating the experiment at RTRC, with a focus on the pre-combustion flow dynamics, flame dynamics, and post-combustion dynamics of pressure and entropy disturbances. This task is led by Suresh Menon.
  3. GT Reduced-Order Modeling: This task consists of creating a reduced-order model (ROM) framework for the unsteady response of the flame and the generation of entropy disturbances due to unsteady heat release. This task is led by Vishal Acharya.

RTX Technology Research Center (RTRC)

- P.I.s: Dr. Jeffrey Mendoza, Dr. Duane McCormick, Dr. Julian Winkler, Dr. Lance Smith
- FAA Award Number: 13-C-AJFE-GIT-058 (subaward through Georgia Tech)
- Period of Performance: February 5, 2020, to December 31, 2026
- Tasks:
  4. RTRC Facility Development: This task addresses the design of experiments that will be performed at RTRC. The task involves coordination between the teams to develop and define the aerodynamic design of an RQL combustor for this study. This task is led by Jeffrey Mendoza, Lance Smith, and Duane McCormick.
  5. RTRC Post-Combustion Modeling: This task consists of both post-processing and simulation efforts. First, the post-combustion simulation data from the simulation of the Georgia Tech experiment are mined to investigate the dynamics of entropy fluctuations and their transport. Next, simulations are used to model noise propagation in the post-combustion architecture of the engine. The simulations are split across the different sections: nozzle, turbine, and far-field. This task is led by Jeffrey Mendoza and Julian Winkler.

Project Funding Level

Federal Aviation Administration (FAA) Funding: $4,999,984 (Georgia Tech: $3,000,343; RTRC: $1,999,641)



Cost-Share Funding: $4,772,851 (Georgia Tech: $2,773,210 from Airspace Engineering (AE) school; RTRC: $1,999,641 from company funds)
Total Funding: $9,772,835

Investigation Team

Georgia Institute of Technology

Prof. Tim Lieuwen, (P.I.), Lead P.I. responsible for overseeing all tasks; specifically, he leads the Georgia Tech experiments and design in Tasks 1 and 2, along with Prof. Steinberg. In addition, he co-leads the modeling tasks in Task 1 for pre-combustion, flame response, and post-combustion modeling, along with Dr. Acharya.

Prof. Suresh Menon, (co-P.I.), Responsible for simulations of the Georgia Tech experiment.

Dr. Vishal Acharya, (co-P.I.; Principal Research Engineer), Responsible for all modeling tasks for pre-combustion, combustion, and post-combustion physics, along with Professor Lieuwen. In addition, as an administrative coordinator, he is responsible for general project management, such as project deliverables, group meetings, and interfacing with the FAA project manager.

Dr. Benjamin Emerson, (co-P.I.; Principal Research Engineer), Responsible for designing and maintaining experimental facilities, as well as experimental operations and management, and graduate students' safety.

Dr. Achyut Panchal, (Research Engineer), Simulation of the Georgia Tech experiment.

Sungyoung Ha, (graduate student), Lead experimentalist on the Georgia Tech rig.

Parth Patki, (graduate student), Working on hydrodynamics modeling subtask (pre-combustion disturbances).

Guru Charan Ganesh, (graduate student), Working on the entropy dynamics modeling subtask (post-combustion disturbances).

Leo M. Kastenberg (graduate student), Working on analysis of large eddy simulation (LES) results and responsible for setting new simulations (until July 2025).

Sathvik Gujjati (graduate student), Working on analysis of large eddy simulation (LES) results and responsible for setting new simulations (since August 2025).

RTX Technology Research Center

Dr. Jeffrey Mendoza, (P.I.; Technical Fellow Acoustics), Leads the RTRC team and oversees its contributions to the project. He leads the subtasks related to modeling, measurements, and simulation for post-combustion disturbances, nozzle interactions, turbine interactions, and far-field sound propagation.

Dr. Lance Smith, (co-P.I.; Technical Fellow Combustion), Conducting design and measurements of the RTRC experiment. He collaborates closely with the Georgia Tech team to ensure similarities between both experiment setups.

Dr. Duane McCormick, (co-P.I.; Principal Research Engineer), Conducting design and measurements of the RTRC experiment as well as finite-element calculations in the design process.

Dr. Julian Winkler, (co-P.I.), Responsible for the simulation tasks at RTRC and focuses on post-combustion disturbances, nozzle interactions, turbine interactions, and far-field sound propagation.

Dr. Jordan Snyder, conducting design, measurements, and data processing using tunable diode laser absorption spectroscopy and chemiluminescence in the RTRC combustor rig.

Dr. Kenji Homma, Responsible for far-field sound propagation simulations.

Dr. Aaron Reimann, Responsible for ROM and high-fidelity (HiFi) modeling of the propagation of direct and indirect noise sources through the turbine nozzle and supports the far-field sound propagation simulations.

Dr. Sudarshan Koushik, Responsible for post-processing the Georgia Tech LES data to model post-combustion disturbances.

Project Overview

The objective of this project is to develop and validate physics-based design tools that can predict noise production mechanisms and their relative dominance and ultimately reduce the noise output of future engines. The motivation for this project stems from recent and future advances in aircraft engine technology. High-bypass engine technology has significantly reduced the traditionally dominant engine noise sources, namely fan and jet exhaust noise. Noise generated in the combustor has become a dominant source of engine noise for future advanced aircraft designs. In addition, as combustors evolve to increase efficiency and decrease pollutant emissions, methods for predicting and mitigating combustion noise have severely lagged, and legacy methods are insufficient to predict noise from next-generation combustors. This drawback has motivated the objective of this project, which addresses the critical need for physics-based

design tools. The resultant understanding of noise generation and propagation, along with validated noise prediction tools, will enable more rapid and cost-effective designs of low-noise engines for future aircraft.

The project objectives will be achieved through a program of cooperative experiments, high-fidelity simulations, and physics-based ROM. The physical processes involved are tightly coupled and directly determine the project tasks, as shown in Figure 1.

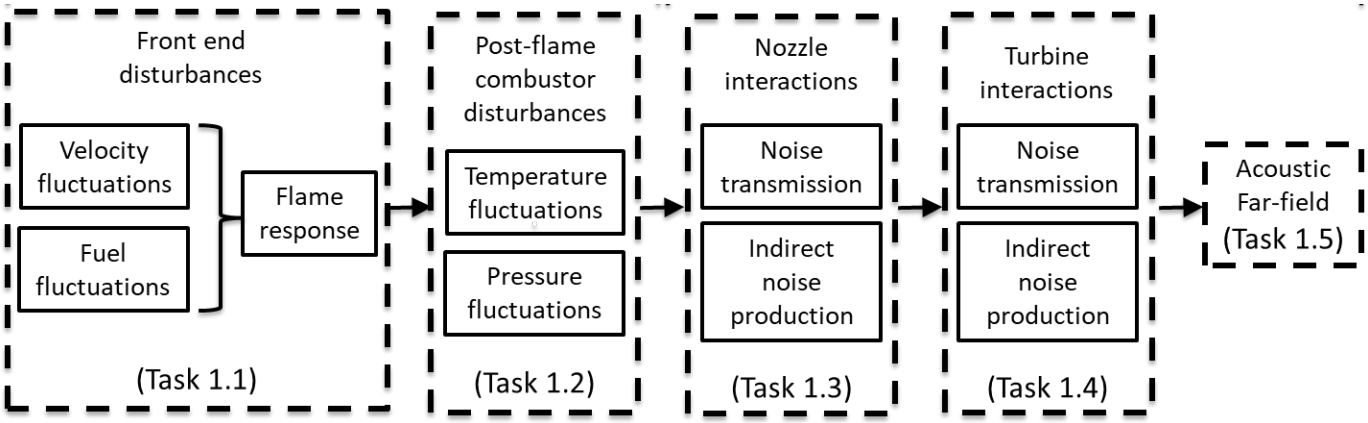


Figure 1. Diagram showing physical processes and project tasks for noise generation.

The physics of noise generation begins with source disturbances upstream of the combustion zone, which involve unsteady dynamics in the flow and incoming fuel (spray), followed by the response of the combustion zone (flame) to these upstream disturbances. The fluctuations in the unsteady heat release led to the generation of pressure and entropy fluctuations. These fluctuations propagate further downstream in the combustor, interact with the nozzle and turbine, and eventually lead to far-field sound generation. Given the complex interplay of unsteady physics in the various parts of the engine, developing a ROM is challenging.

An important goal of this project is to generate high-quality reference data from both measurements and validated high-fidelity simulations, including measurements of the flow, spray, and flame unsteadiness in the head end of the combustor. Subsequently, the secondary combustion zone is characterized. The generation of entropy and pressure disturbances is then characterized by measurements of temperature and pressure fluctuations, followed by measurements of noise reflection and transmission through the turbine and nozzle section, and sound measurements in the far field. The measurements are accompanied by LES and finite-element simulations that are validated against the measurements. Collectively, these data are generated across a range of operating parameters and provide a source database for the modeling task.

The main goal of this project is to develop a robust design tool that can predict noise at operating points for which prior measurements or data are unavailable. To achieve this goal, two major tasks are necessary. First, ROM and frameworks must be developed for various aspects of the engine architecture: flow/spray models, flame response models, entropy generation models, entropy propagation models, nozzle interaction models, turbine interaction models, and far-field noise generation models. The ROM for each of these aspects involves simplifications and assumptions that are validated against the source database. The validation study and iterative improvement of model predictions serve as the second task to achieve this goal.

In this report, the efforts of both teams, Georgia Tech and RTRC, are summarized from October 2024 to September 2025. The efforts primarily include Georgia Tech rig setups to ascertain the coherence of pressure and heat release fluctuations in both open and ducted flames. The RTRC rig was used to study the effect of tonal noise through a combination of measurements and finite element method (FEM) simulations. In addition, progress was made in hydrodynamics modeling, direct noise modeling and entropy noise modeling.

Task 1 – GT Experiments

Georgia Institute of Technology

Objective

The Georgia Tech experimental team has performed detailed studies on heat release – pressure coherence using the open flame rig developed in the previous period. With some modifications, high quality data have been obtained which allowed a systematical study on coherence, both confirming prior model predictions and highlighting new areas of study. The experiment was further expanded to a ducted configuration, which also supplemented modelling studies performed in the previous period.

Research Approach

Experimental Rig and Methods

The turbulent Bunsen burner that was constructed in the previous period was used in this period as well, with a few upgrades to the diagnostics. To reiterate, the burner is a piloted Bunsen burner using a blend of methane and air which are metered and controlled independently through critical orifices. A muffler and turbulence generator prior to the nozzle mitigates upstream flow noise, particularly from the orifices, and gives some control over the turbulence intensity. Acoustic data were taken through a PCB® Piezotronics 378B02 free-field microphone. A Photron® FASTCAM SA-Z1 high speed camera paired with a Lambert™ HiCATT intensifier was used to take high speed images of the flame, and three Thorlabs® PMM01 photomultiplier tubes were used to obtain global chemiluminescence intensity measurements. The configuration of the rig and diagnostics are shown in Figure 2.

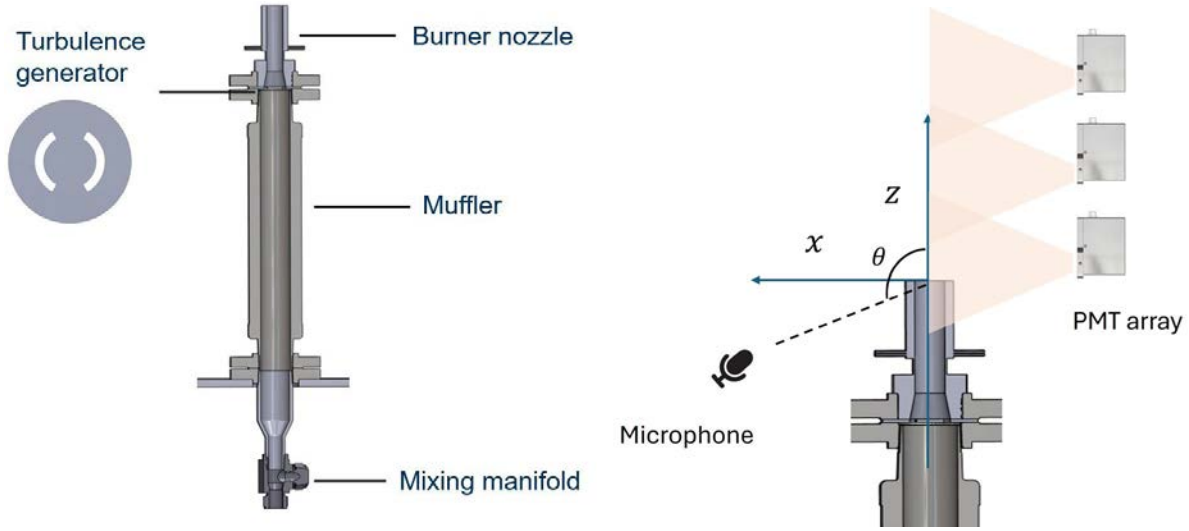


Figure 2. Cross section of experimental apparatus (left) and schematic of diagnostics (right). PMT: photomultiplier tube.

In the previous period, it was determined that the noise in photomultiplier tube (PMT) measurements limited the ability to resolve coherence at higher frequencies. Several modifications and efforts were made to improve the quality of PMT measurements. First, the filter was replaced with an edgepass filter with a nominal transmission window of 400 nm – 444 nm. This relatively wider bandwidth allows a stronger signal mainly composed of CH* emissions and the hydrocarbon continuum which is predominantly CO_2* emissions. While there are some differences in the characteristics of CH* and CO_2* emissions, the correlation between the heat release rate and chemiluminescence is expected to be high for the flame used

® PCB is a registered trademark of PCB Piezotronics, Inc., Depew, New York.
® Photron is a registered trademark of Photron Limited, Tokyo, Japan.
™ Lambert instruments is a trademark of Tibidabo Scientific Industries, Madison, Connecticut.
® Thorlabs is a registered trademark of Thorlabs, Inc., Newton, New Jersey.

in this study. Additional care was taken to minimize external lighting by coordinating with facility management to turn off the facility lights during testing and conducting experiments at night after sunset. To further minimize the effect of emergency lights that could not be turned off and reflections, a black background was installed.

The improvement of signal through these methods is shown in Figure 3, where the coherence between two PMT measurements with the same viewing window is shown for a benchmark case. It is difficult to estimate the noise floor in PMT signals with background measurements as PMT noise not only includes a background component but also shot noise which scales with the input signal. By taking the coherence between two PMT measurements which have the same viewing window, it is possible to estimate the effect of all noise sources and establish an upper limit on the measurable coherence. The coherence limit is increased with each improvement effort, and eventually there is no drop in coherence due to PMT measurement noise up to approximately 1kHz.

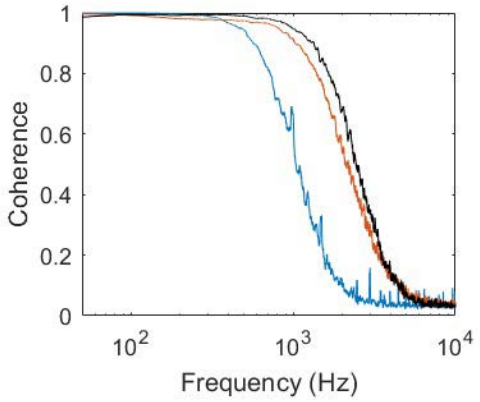


Figure 3. Coherence of two PMT measurements with the new filter (blue), also with the facility lights off (orange), and with the backdrop (black).

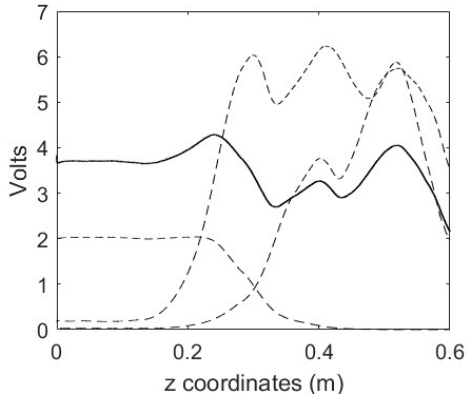


Figure 4. Spatial transfer function of individual PMTs shown by a dashed line and corrected spatial transfer function of the PMT array shown by a solid line.

It is also important to ensure that the PMT viewing window covers the entire flame to capture the global chemiluminescence. While it is desired to place the PMT close to the flame as possible to maximize signal intensity, this also limits the viewing window of the PMT. To find a balance between this tradeoff, three PMTs were arranged in a vertical array as shown in Figure 2 to allow sufficient coverage while also maintaining proximity to the flame. The spatial transfer function of each PMT was calculated by translating a constant point light source. Then the coefficients were calculated



where a linear sum of the PMT signals will yield a constant spatial transfer function. The global chemiluminescence intensity was calculated by summing the PMT signals according to this correction. This process is shown in Figure 4.

To measure coherence and its roll-off characteristics, it is desirable for the flame to have broadband characteristics, to be well anchored so that it does not lift off, and to have an appropriately long flame length such that good measurement accuracy is achieved for a wide range of κL_f values, where κ is the acoustic wavenumber and L_f is the flame length. The operating conditions shown in Table 1 were selected to achieve such conditions. Cases A indicates cases without the turbulence generator and Cases B are cases with the turbulence generator.

Table 1. Operating conditions for experiment.

Label	Air flow rate (g/s)	Fuel flow rate (g/s)	Average nozzle velocity (m/s)	Equivalence Ratio	R_e (×10⁴)	$L_{f_{90}}$ (cm)
A1, B1	14.8	1.05	20.2	1.23	3.85	26.6, 32.7
A2, B2	14.4	1.14	19.9	1.36	3.79	39.5, 38.5
A3, B3	15.2	1.22	21.0	1.38	4.00	38.2, 38.0
A4	11.1	0.81	15.1	1.26	2.88	29.6
A5	11.1	0.64	14.7	1.00	2.82	16.0
B4	8.8	0.60	11.9	1.18	2.28	26.7
B5	6.0	0.41	8.2	1.18	1.56	18.3
A6*, B6*	14.8	0.89 - 1.46	19.8- 21.0	1.04 - 1.70	3.78 - 4.00	--
B7*	8.8	0.56 - 0.97	11.8- 12.7	1.10 - 1.90	2.26 - 2.42	--
B8*	1.8	0.40 - 0.81	15.2 - 19.7	3.88 - 7.88	2.50 - 3.20	--

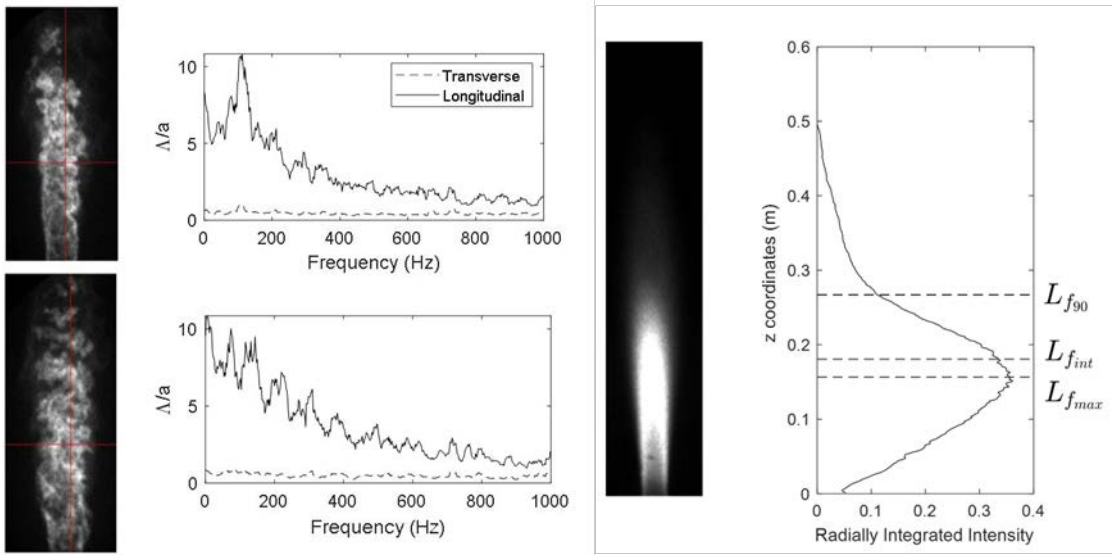


Figure 5. Normalized flame correlation length calculated from high-speed images for Cases A1 (upper left) and B1 (lower left), and mean chemiluminescence image and axial heat release rate distribution (right).



High speed camera images were used to calculate the flame correlation length, and mean images were used to derive the flame length. The flame correlation length is a key parameter that describes the spatiotemporal statistics of the heat release, which is defined as $\Lambda(x, e_r) = \int_0^\infty \frac{2}{\pi^{1/2}} \frac{|\langle q_v(x) q_v(x+r) \rangle|}{\langle q_v(x)^2 \rangle} dr$. Figure 5 shows how these images are processed. The correlation length in the longitudinal (along the flow) direction is greater than the transverse direction, showing the convective nature of the flame. It should be noted that model results predict that a correlation length variation in this range has an insignificant effect on coherence. The flame length is determined from the mean chemiluminescence image and radially integrated axial chemiluminescence intensity.

Results

In both theoretical and preliminary experimental studies performed in the previous period identified the parameters that govern the coherence between the globally integrated heat release rate and acoustic pressure fluctuations to be (1) the acoustic compactness described as κL_f which is the relative size of the flame to the acoustic wavelength, (2) the flame correlation length which describes the spatiotemporal statistics of the heat release, (3) the location of the observer, and iv) the flame geometry. Results can be interpreted in this context. Figure 6 shows the measured coherence and model predictions for Cases A1, A2, A3, and A5. These cases vary in flame length, which are mainly controlled by the equivalence ratio. The microphone is positioned at the coordinates $(x, y) = (0.2\,m, -0.2\,m)$. First, for Cases A1 and A5, excellent agreement between the measured results and model is observed. Consistent with results from the previous period, measured coherence trend towards unity at lower frequencies (i.e., the acoustically compact limit) as expected for a direct noise dominant system. Furthermore, the coherence roll-off is also extremely well predicted, validating the distributed monopole model which describes the acoustical noncompactness effect on coherence. For very rich conditions including Cases A2 and A3, while the roll-off trend is well predicted, some divergence from the model is observed, most notably the coherence at low frequencies asymptote to a value less than unity. It is believed that this is due to imperfect correlation between the unsteady heat release rate and chemiluminescence intensity associated with non-premixed flames.

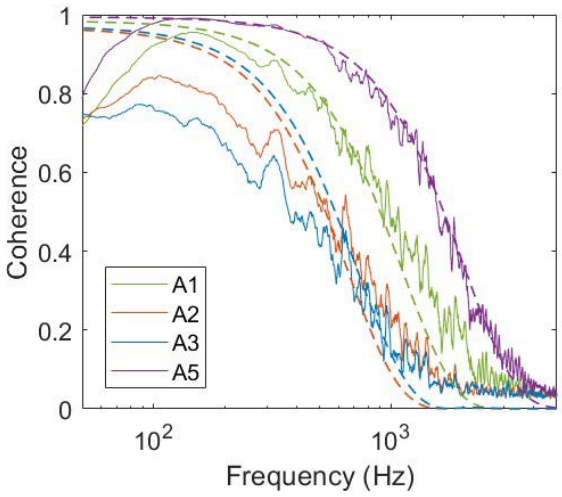


Figure 6. Measured coherence (solid) and model predictions (dashed) for Cases A1, A2, A3, and A5.

Since coherence roll-off is predicted to be a purely geometric phenomenon due to the distributed monopole nature of the source, it is possible to expect a universal form when normalized against the flame length. In Figure 7, an overlay of all test conditions is plotted. When normalized by the maximum coherence to account for the reduction in coherence associated with rich flames and plotted against the acoustic compactness factor κL_f, the plots collapse reasonably well, confirming predictions. Slight variance is expected as the axial heat release rate distribution for different operating conditions is not perfectly self-similar and thus not captured entirely within a single flame length. Comparing different definitions of the flame length, it was shown that $L_{f_{90}}$, which is defined as where 90% of the chemiluminescence intensity is observed, and $L_{f_{int}}$, which represents how spread out the distribution is and defined as $L_{f_{int}} = 3\int \left| z - L_{f_{max}} \right| Q dz / \int Q dz$, yields a good collapse. On the other hand, $L_{f_{max}}$ which is the location of the maximum axial heat release, performed



poorly, showing that it does not well represent the distribution of the axial heat release. Since some applications use $L_{f_{max}}$ or a similar definition for the flame length such as in $n-\tau$ type thermoacoustic instabilities, it is important to note how the flame length is defined for proper analysis.

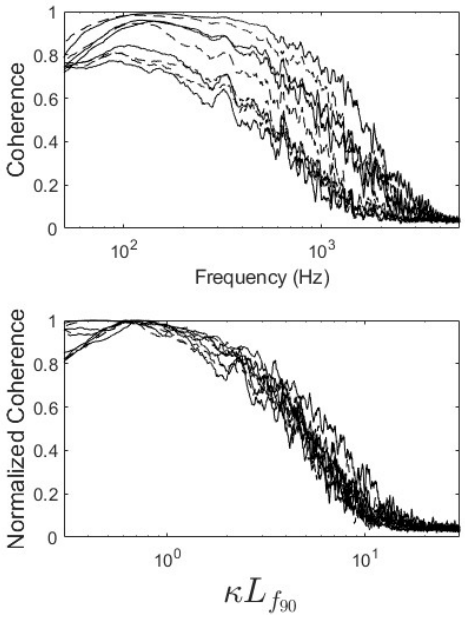


Figure 7. Overlay of coherence measured from all conditions (shown at top) and normalized coherence plotted against the acoustic compactness $\kappa L_{f_{90}}$ (shown at bottom).

As coherence roll-off is governed by the geometric relationship between the flame and observer, the observer location is also an important parameter of coherence. Previously, it was predicted that coherence is minimum along the primary dimension of the flame (i.e., for a long flame, the coherence is minimum along the centerline and vice versa). This is confirmed in Figure 8, where the normalized coherence for Case A3 is shown for different microphone locations. This effect is most prominent for long flames, hence Case A3 was chosen despite the necessity of normalization. As the microphone is moved to the side of the flame, coherence is increased, following model predictions. Deviations at the rightmost angle are due to the coherence roll off occurring at higher frequencies than what can be detected due to PMT measurement limitations. These results clearly show the role of observer location, especially angle, on coherence.

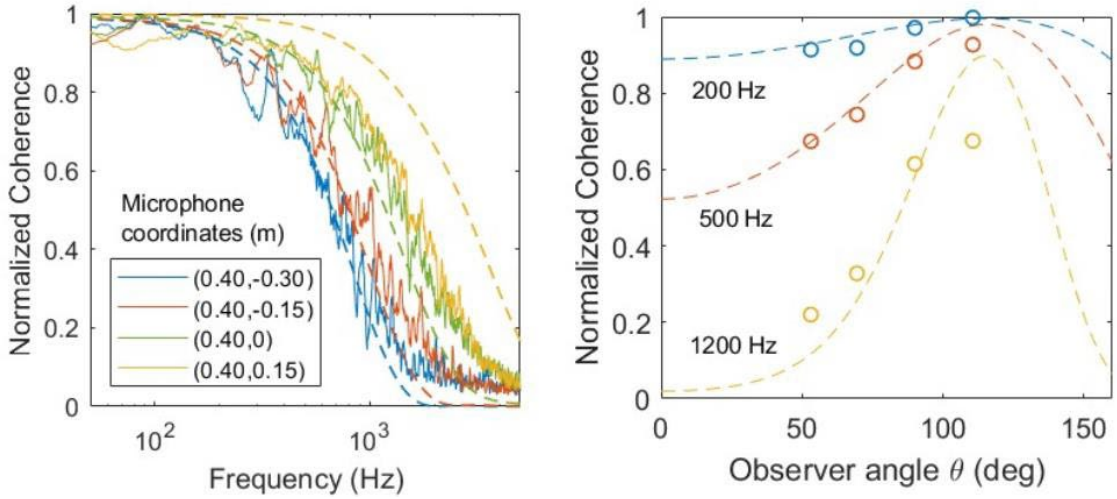


Figure 8. Normalized coherence measured at different microphone locations for Case A3 (left) and data plotted against the observer angle (right).

Having discussed the non-unity coherence at low frequencies for rich cases, further experiments were performed to investigate. Figure 9 shows the maximum coherence for Cases A6*, B6*, B7*, and B8* as a function of equivalence ratio. The phenomenon of a rapid decline of maximum coherence over a range of $\phi = 1.3 - 1.5$ followed by a plateau is observed across all cases tested. As this is not predicted by the distributed source model which agrees with other experimental results, it can be inferred that this phenomenon is not from the relationship between the unsteady heat release and acoustic pressure fluctuations. It is thought that the relationship between chemiluminescence intensity and heat release fluctuations are fundamentally different between premixed and non-premixed flames, and the coherence between the chemiluminescence and unsteady heat release is reduced as the non-premixed portion of the flame becomes significant. This also motivates a novel diagnostic method. As the coherence between the unsteady heat release rate and acoustic pressure is understood through this study, it is possible to gain insight into the relationship between chemiluminescence emissions and the heat release rate through coherence measurements. This is a point that deserves further study.

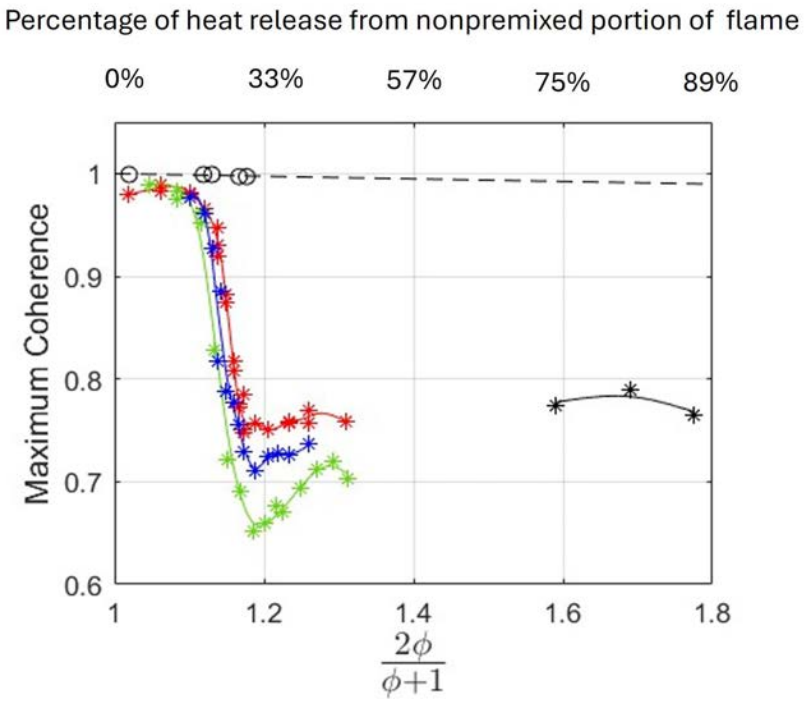


Figure 9. Maximum coherence across all frequencies, measured at various equivalence ratios. Red = A6*, $\frac{u'}{\bar{U}} \approx 8.5\%$, Blue = B6*, $\frac{u'}{\bar{U}} \approx 12.3\%$, Green = B7*, $\frac{u'}{\bar{U}} \approx 10.0\%$, Black = B8*, $\frac{u'}{\bar{U}} \approx 5.5\%$. Dashed line = extrapolated model prediction for maximum coherence.

Ducted configuration

The open flame experiment was equipped with a duct to verify new model predictions. The configuration is shown in Figure 10. In most practical applications, the flame is in an enclosed environment. Therefore, it is of interest to predict how coherence behaves in such a configuration. In the previous period, a two-dimensional (2D) model was developed to predict the effect of a duct based on the source image method. This model was also extended to a three-dimensional (3D) square duct. Figure 11 shows the coherence measured from microphone position 1 for the condition corresponding to Case A1. Model predictions, which were corrected to properly consider the increased speed of sound due to heating, show that the duct makes the coherence roll-off steeper, but also predicts a peak that appears after the initial decline. It is important to note that this peak is independent from the resonant duct modes and is caused by interference pattern-like effects from duct reflections. Indeed, the experimental results closely match such predictions, validating the image source model.

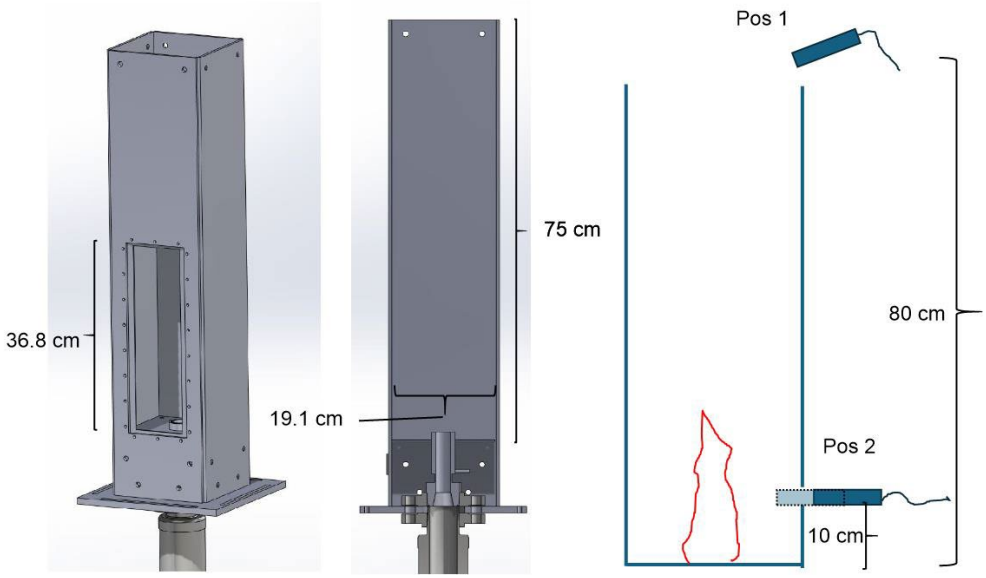


Figure 10. Ducted configuration of experiment.

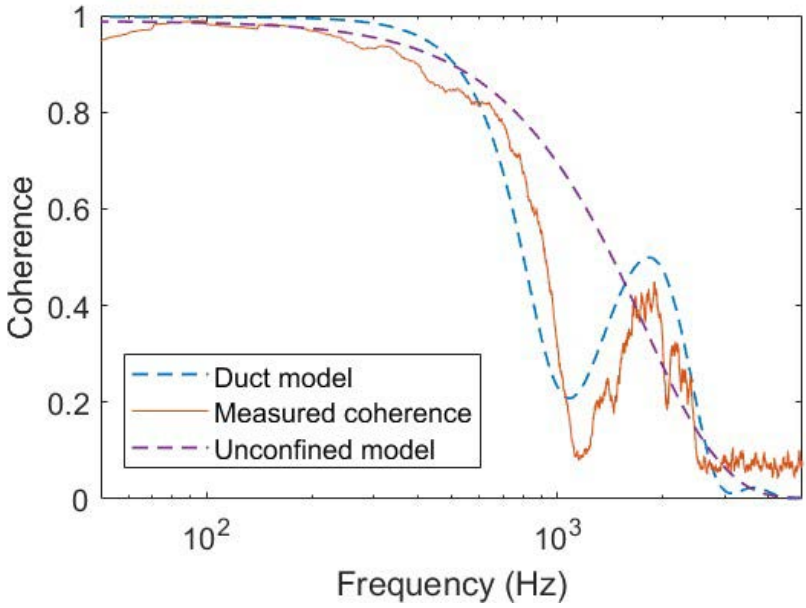


Figure 11. Coherence from microphone position 1, Case A1, for the ducted experiment.

Milestones

- Performed systematic study of coherence on open flame rig which was improved from the last period.
- Performed ducted studies on modified rig.

Major Accomplishments

- Made improvements on the rig and performed a systematic study on chemiluminescence-pressure coherence which successfully validated modeling efforts made in the previous period.



- Successfully implemented ducted configuration to open flame rig and validated model results.

Publications

Ha, S & Lieuwen, T. (2025). Direct combustion noise: Nearfield and non-compactness influences on pressure–heat release coherence, *Combustion and Flame,* Vol. 138, 113811.

Outreach Efforts

None.

Awards

None.

Student Involvement

Graduate student Sungyoung Ha is the lead experimentalist on the Georgia Tech rig.

Plans for Next Period

Dr. Ha graduated with his PhD Thesis in July 2025. Following his graduation, the work on this experiment will be continued in the next funding cycle.

Task 2 – GT Simulations

Georgia Institute of Technology

Objectives

Compressible multiphase reactive LES of the experimental rig are conducted under this sub-task to support the mechanistic understanding and ROM development for tonal noise. The computational configuration is a modification of the previous configuration used for the broadband noise program with a longer distance between the aft-end of the combustor and the choke point and a Variable Resonance Acoustic Screening Capability (VRASC) tube. The VRASC tube excites a tone, and this setup can then be used to evaluate strategies to mitigate the tone. The simulations are to be considered under three conditions. The baseline condition employs the same operating pressure, fuel-air-ratio (FAR), and air temperature (T3) as the previous match point from the broadband program. A higher-pressure condition is then simulated to match the RTRC experimental campaign for validation. Finally, a different combination of T3 and FAR is to be considered to evaluate the effect of modified mixing and combustion on the tone. Multiple time-dependent 3D snapshots are saved from LES and will be transferred to the RTRC and Georgia Tech ROM teams with sample post-processing scripts.

Research Approach

Solver Details

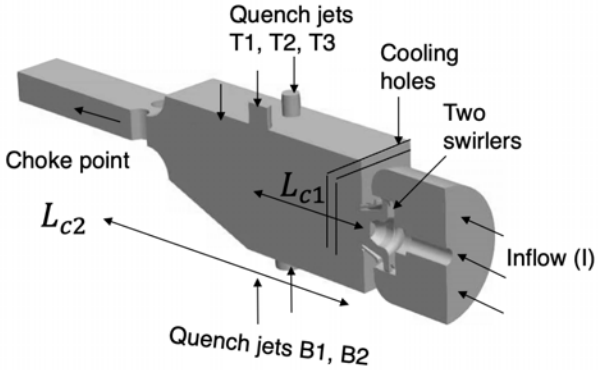
A fully compressible Eulerian finite-volume formulation for the gas phase and a Lagrangian formulation for the liquid phase are used in this study. An eddy-viscosity approach with a one-equation subgrid kinetic energy (k_{sgs}) model is used for the closure of gas-phase subgrid-scale fluxes. Because regions in which turbulence is not well established may exist in the plenum or outflow duct, the k_{sgs}-equation coefficients are set to constant values rather than being dynamically computed. Subgrid dispersion for spray particles is modeled with a stochastic separated flow model. Modeling of dense spray, corresponding compressible volume blockage effects, and breakup are also available, as we have previously shown, but these conditions are not considered herein; instead, a dilute injection of spray is considered. A well-established secondary breakup model based on Kelvin–Helmholtz instability is used.

The combustion is modeled via a finite-rate kinetics approach, by using a two-step, six-species mechanism for kerosene. Subgrid closure for turbulent combustion is provided by a simplified partially stirred reactor model, wherein the mixing time (τ_m) is computed locally by using k_{sgs}, and the chemical time (τ_c) is precomputed for the operating conditions from laminar premixed flame solutions under stoichiometric conditions. Further details about our modeling approach can be found in our recent works and are not repeated herein, for brevity.

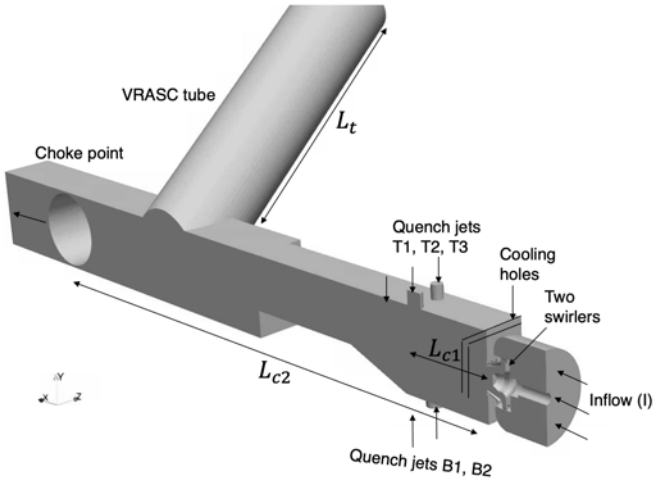
The LES equations are solved at Georgia Tech using the in-house solver LESLIE. LESLIE is a well-established multi-block, structured, fully compressible finite-volume solver. A hybrid second-order central and third-order upwind method is used

for the gas-phase evolution. A fourth-order Runge–Kutta solver is used for solving the Lagrangian equations. For computational efficiency, instead of tracking individual Lagrangian particles, the particles are grouped together in "parcels," which are tracked in a Lagrangian manner. A particle-per-parcel value of 8 is used in this work, which has been shown to provide a good balance between accuracy and efficiency for gas-turbine combustor LES.

The current version of the Georgia Tech compressible solver contains three parts: (1) CFDPreProc, (2) LESLIE, and (3) CFDPostProc. CFDPreProc is a pre-processor that can perform functions such as creating a grid and setting boundary conditions. LESLIE is a core compressible solver that conducts multi-phase reactive LES. The latest LESLIE code (improved during the Year 2 efforts) outputs 3D snapshots of conservative variables that are directly solved for in our compressible framework, including the density, momentum, total energy, and partial densities. Primitive variables remain required for the computation of noise-related quantities; therefore, CFDPostProc computational fluid dynamics (CFD) post-processing software is used to read the conservative variable-based 3D snapshots and compute additional primitive quantities. This code is provided to the RTRC and Georgia Tech ROM teams along with the 3D snapshots. The conservative variables form an exclusive and exhaustive set of variables; therefore, all other quantities can be computed from this set.



Computational configuration for LES, Original configuration



Computational configuration for LES, New configuration

Figure 12. Computational configurations for LES. Original configuration used for broadband program (shown in the top). New configuration with Variable Resonance Acoustic Screening Capability (VRASC) tube for tonal noise studies (shown in the bottom). Key features and corresponding boundary conditions are shown.



Computational Configuration

The computational configurations are shown in Figure 12. Both the original configuration used for the broadband program and the new configuration with the VRASC tube are shown. The flow from the inlet plenum enters the combustion chamber via two concentric swirlers (one axial and one radial). After the reaction zone, three quench jets on the top, and two on the bottom, are available to reduce the temperature. In addition, multiple small cooling holes are present on the bulkhead (or faceplate) to decrease the wall temperature. The flow exits the outflow duct through either the choked jail bars (original configuration) or a cylindrical choke point that is at a much longer distance after the combustor and with the VRASC tube in between (new configuration). The region between the bulkhead and the quench jets is where most of the heat release occurs and its length is denoted as L_{c1}. This part of the geometry is the same between the original and the new configurations. The distance between the bulkhead and the choke point is denoted as L_{c2}. It is approximately 2.5 times longer for the new configuration compared to the original configuration. The length of the VRASC tube is fixed and denoted here as L_t. This matches the reference value from the experiments.

All gas-phase inlet boundary conditions (ahead of the inlet plenum [I] and dilution holes [T1, T2, T3, B1, and B2]) specify a constant mass flow rate based on experimental inputs and are modeled with a characteristic Navier–Stokes boundary condition. The mass flow rate for the main inflow (I) is set as 25.0% of the total air flow rate. The total mass flow rate through the top (T1, T2, and T3) or bottom (B1 and B2) quench jet holes is 31.2% of the total. The cooling holes on the bulkhead are not resolved; therefore, they are modeled as a porous boundary condition. The mass flow rate specified through these cooling holes is 12.5% of the total. The incoming air is at T3=673.3K. The flow at the computational outflow (O) is always supersonic and extrapolation boundary conditions are used for it. No waves are expected to travel upstream into the combustor chamber from this region, because the flow is choked.

The fuel is injected as Lagrangian spray droplets in a stochastic manner with two concentric injectors. The total fuel mass flow rate is chosen to impose a global FAR of 0.025 and a global equivalence ratio of 0.37. The fuel mass flow rate through the primary injector is 25.8% of the total and through the secondary injector is 74.2% of the total. In the absence of any experimental measurements for this injector, a log-normal size distribution with Sauter mean diameter 55 μm is injected. A secondary breakup model based on Kelvin–Helmholtz instability is used that breaks the injected droplets into smaller droplets through a physics-based approach on its own. These modeling choices are like the previous gas-turbine LES. The primary injector is modeled as a solid cone injector with a 60° angle; the secondary injector surrounds the primary injector and is modeled as a hollow cone injector with 90° and 120° inner and outer angles, respectively. The injection temperature of the liquid fuel is 330K, and the velocities are set to 25 m/s. This dilute injection occurs 1 mm downstream of the actual injector plate. This injection procedure is empirical but could be improved in the future, based on experimental insights.

The multi-block structured grids for both the original and new configuration have approximately 6.8 million cells and grid clustering is applied to the near region of the shear flow from the swirler and exit plenum. For handling geometrical complexities, up to eight multi-block structure grids are generated with hanging nodes, which are stitched together via an interpolation technique of the same order as the numerical scheme used. Shear layers are resolved with 10–15 points across, and the swirlers have 10 or more points along their span, in agreement with previous LES. The LES solver is parallelized, and the simulations are run on 512 cores. The flow-through time of the combustor is estimated are $t_{flow} = L_{c1}/U_{bulk}$, where U_{bulk} is an approximate bulk flow velocity in the combustor. Since the combustor configuration and the bulk flow velocities are the same across all tests, a reference frequency for normalization is defined as $f_0 = 1/t_{flow}$. For all simulations, the initial transients are neglected for at least the first two flow-through times or until the chamber pressure and volume-integrated heat release rate (HRR) stabilize. The statistics are then collected over at least ten additional flow-through times. A simulation for a single flow-through time uses 11,605 central processing unit (CPU) hours on Georgia Tech's supercomputing cluster (Partnership for an Advanced Computing Environment-Phoenix) with Intel® Ivy-bridge i7 processors.

The comparison here considers three operating conditions. These are listed in Table 2. Case-0 refers to the match point from the previous broadband program with the old configuration that used jail bar for flow choking. The LES results at these conditions were validated against the experimental measurements in the past. Case-1 retains the same operating pressure, FAR, and T3 as Case-0, but uses the new geometry with the VRASC tube. Case-2 keeps the T3, FAR, and geometry the same as Case-1 but raises the chamber pressure by 1.4 times to match the RTRC experiments. The increased chamber pressure is achieved by keeping the same geometry and choking area but proportionately increasing all the mass

® Intel is a registered trademark of Intel Corporation, Santa Clara, California.



flow rates (fuel and air). An additional test, Case-3, is also being considered with modified FAR and T3. Further details and results for this will be provided in the next reporting period. All simulations are run with the same solver and model choices. Throughout this report, the chamber pressure of Case-0 is referred to as the reference pressure p_0 and is used to normalize all the results.

Table 2. List of simulated operating conditions.

Case	Normalized Pressure	FAR, T3	Geometry
Case-0 (Match point)	1.0	Ref. values	Jail bar choking
Case-1	1.0	Ref. values	VRASC tube
Case-2	1.4	Ref. values	VRASC tube

The LES captures unsteady turbulent combustion. The predicted temperature field at a representative instance is shown in Figure 13 for reference. As expected for a typical swirl-stabilized combustor, it shows a wrinkled flame structure with hot center and corner recirculation zones. The flow cools down upon mixing with the quench jets. Further quantification of this process is provided in the next sections. For demonstrating the sufficiency of the LES grid, the turbulent kinetic energy (TKE) is computed at a representative point in the shear layer, as shown in Figure 13, and the results capture the inertial subrange over more than a decade. This result has been confirmed at other points within the combustor (i.e., cooling jets, swirling shear layer, etc.), but these data are not shown herein, for brevity.

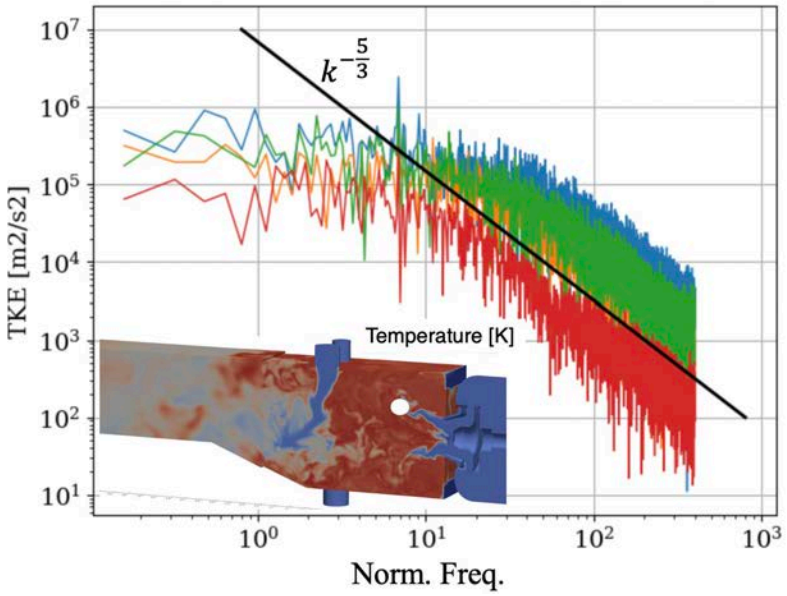


Figure 13. Turbulence and flame interaction in combustor: Predicted unsteady temperature field at a representative instance is shown in the sub-figure. Turbulent kinetic energy (TKE) spectrum at a representative point in the shear layer shows at least a decade of inertial range turbulence.

Pressure Dynamics

A key metrics for LES validation and combustion noise analysis is the pressure spectra or the sound pressure level (SPL) at a fixed probe location. The previous results for Case-0 matched the Georgia Tech experimental measurements in terms of the SPL broadband decay rate and peak locations and magnitude. For a probe located on the ramp after the quench jets, and the LES results predicted the decay of pressure spectra between f/f_0 4.8 and 16 and peaks near f/f_0 6.4 and 20.8. The peak at f/f_0=20.8 was shown to correspond to the first longitudinal acoustic mode. Further details on this validation exercise can be found in the previous reports and are not repeated here.

The current comparison between the different cases is for a probe placed on the bulkhead. The results for Case-0, Case-1, and Case-2 are compared in Figure 14. Unlike Case-0, which showed a broadband spectrum, the addition of the VRASC tube in Case-1 and Case-2 clearly enhances a much stronger tonal behavior. Two frequencies of interest are f/f_0=6.8 and 18.8. The latter is the strongest tone for Case-1 (reference pressure), and former is the strongest tone for Case-2 (higher pressure). Both tones are present in both configurations but with different relative strengths.

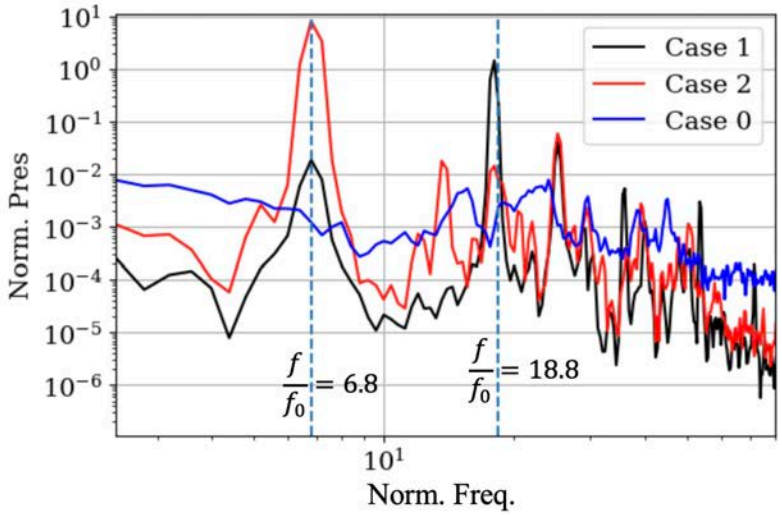


Figure 14. Pressure spectra from LES at a point on the bulkhead. Some notable frequencies are shown as vertical lines.

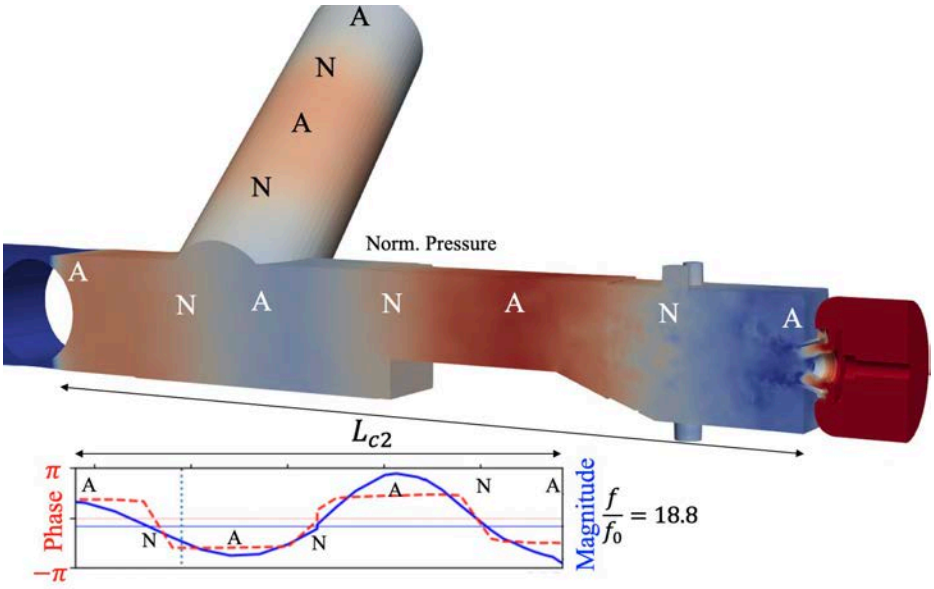


Figure 15. Case 1, Instantaneous pressure contours (shown in the top), phase and magnitude of pressure signal along the center (shown in the bottom). Corresponding pressure nodes (N) and anti-nodes (A) are also noted.

To further evaluate the nature of these tones, the pressure dynamics in the system is further analyzed through a phase-magnitude analysis. Corresponding results for Case-1 and Case-2 are shown in Figure 15 and Figure 16 respectively. 3D contours of instantaneous normalized pressure are also shown for reference. Case-1 showed the strongest tone at



f/f_0=18.8 and therefore the phase-magnitude analysis for Case-1 is at this frequency. The results confirm a longitudinal acoustic mode that is also coupled with the VRASC tube, and which shows the phase switching at the nodes and zero or largest magnitude at the nodes or the anti-nodes, respectively. The identified pressure node and anti-nodes are also noted in the 3D picture for reference.

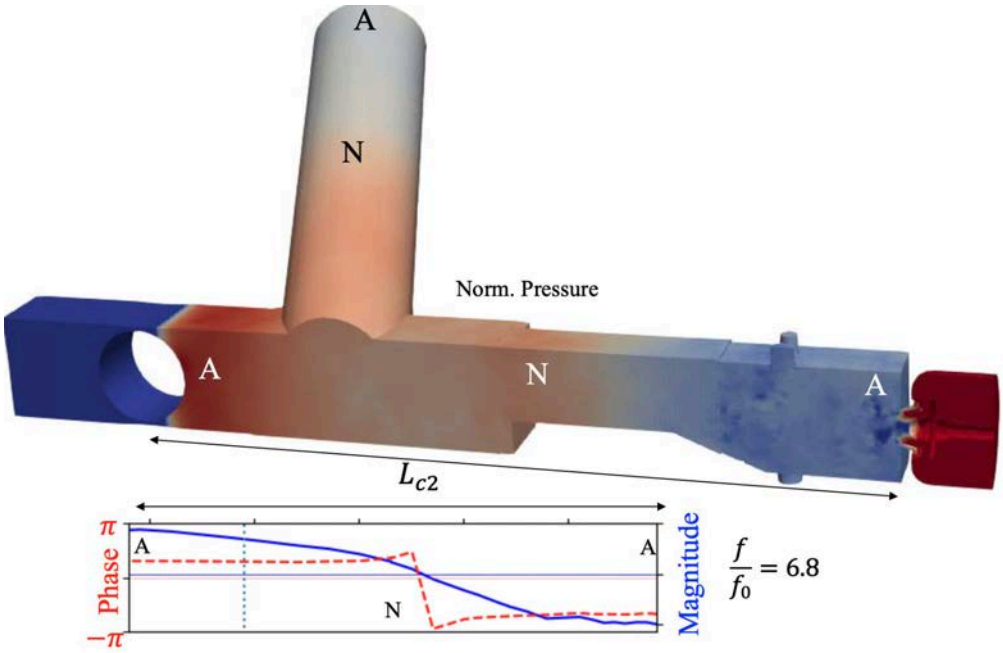


Figure 16. Case 2, Instantaneous pressure contours (shown in the top) and phase and magnitude of pressure signal along the center axis (shown in the bottom). Corresponding pressure nodes (N) and anti-nodes (A) are also noted.

A similar analysis for case-2 is also conducted at f/f_0=6.8 as shown in Figure 16. This is a lower order acoustic mode with only two nodes in the entire configuration, but it has a much stronger magnitude compared to Case-1 as confirmed from the pressure spectra. The phase-magnitude analysis is also conducted at other frequencies for both cases, and the results show that the 6.8 and 18.8 modes are present in both Case-1 and Case-2 but only one of them is activated depending on the operating pressure. The reasons for this are discussed in the next section. It is also noted that the mode shape and frequency for Case-2 is qualitatively consistent with the experimental observations from RTRC, but a one-to-one comparison is not conducted yet. This will be considered in the future as experimental data become accessible.

Heat Release Rate Dynamics

Unsteady HRR data are crucial for mechanistic understanding of combustion tones or ROM development. The overall burning is expected to occur in the swirling shear layers as the incoming droplets disperse, vaporize, and burn while interacting with a hot recirculation zone. In the past, for Case-0, the time-averaged and line-of-sight heat release rate from LES was compared against OH* chemiluminescence data from the Georgia Tech experiments for validation. These results showed a reasonable match in terms of the flame structure. The new results for Case-1 and Case-2 are shown in Figure 17. A qualitatively similar flame shape is observed for both the new configurations although there are significant quantitative differences between Case-1 and Case-2. The flame in Case-2 (higher pressure) is much longer along the combustor axis while the transverse extent is the same. A comparison with experimental measurements will be considered in the future as data become available. As shown later, the combustion in both Case-1 and Case-2 is actively coupled with a longitudinal acoustic mode but at different frequencies and this is the cause of the observed differences.

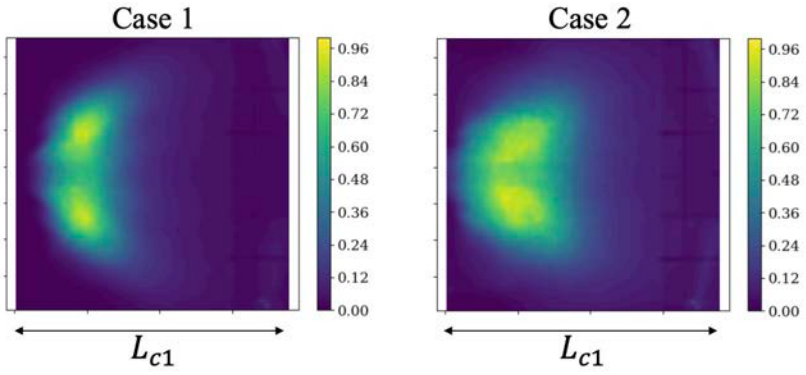


Figure 17. Case 1 (left) and Case 2 (right) time-averaged and line-of-sight averaged heat release rate contours.

The time-averaged view of the heat release does not provide any information about the dynamical features of the flame, which is necessary for understanding combustion noise mechanisms. Power spectral density (PSD) of volume-averaged HRR is shown in Figure **18**. These results show that HRR dynamics is coupled with the previously discussed pressure dynamics. Both Case-1 and Case-2 show strong peaks in the HRR spectra at f/f_0=18.8 and 6.8, respectively. Unlike the pressure, where both f/f_0=18.8 and 6.8 were present for both cases with different magnitudes, the HRR spectra only shows a frequency corresponding to the most dominant mode. This suggests that even though both the acoustic modes are present in the combustor, only one of them is activated and coupled with heat release and combustion. The HRR spectra does show a presence of harmonics of f/f_0=18.8 of 6.8 near approximately f/f_0=37.6 and 17.6 for Case-1 and Case-2, respectively.

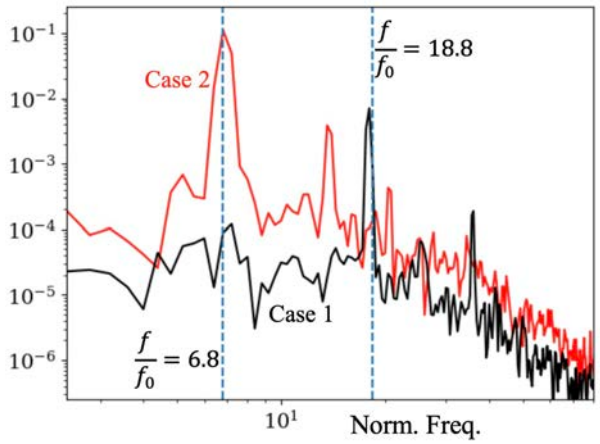


Figure 18. Spectra of volume averaged normalized heat release rate (HRR). Notable frequencies are shown as vertical lines.

The dynamical flame structures are further analyzed using a Proper Orthogonal Decomposition (POD) analysis of the 3D heat release rate. The first four most energetic modes and spectra of their mode coefficients are shown in Figure 19. Additional modes with a lower energy are also analyzed but not shown here. The spectral behavior of the first two mode coefficients clearly shows the presence of the activated 16.8 (for Case-1) and 8.8 (Case-2) modes and their harmonics. The shapes of both these modes show primarily a longitudinal variation suggesting a coupling with the longitudinal acoustic waves. The spectra of higher order mode coefficients show a nearly broadband behavior. Furthermore, even though there are qualitative similarities between the mode shapes of Case-1 and Case-2, clear quantitative differences are noticeable. This may suggest that a POD based reduced order model developed for Case-1 may not be applicable to Case-2 which

operates at a higher pressure, activates a different thermoacoustic mode, and results in quantitatively different POD modes.

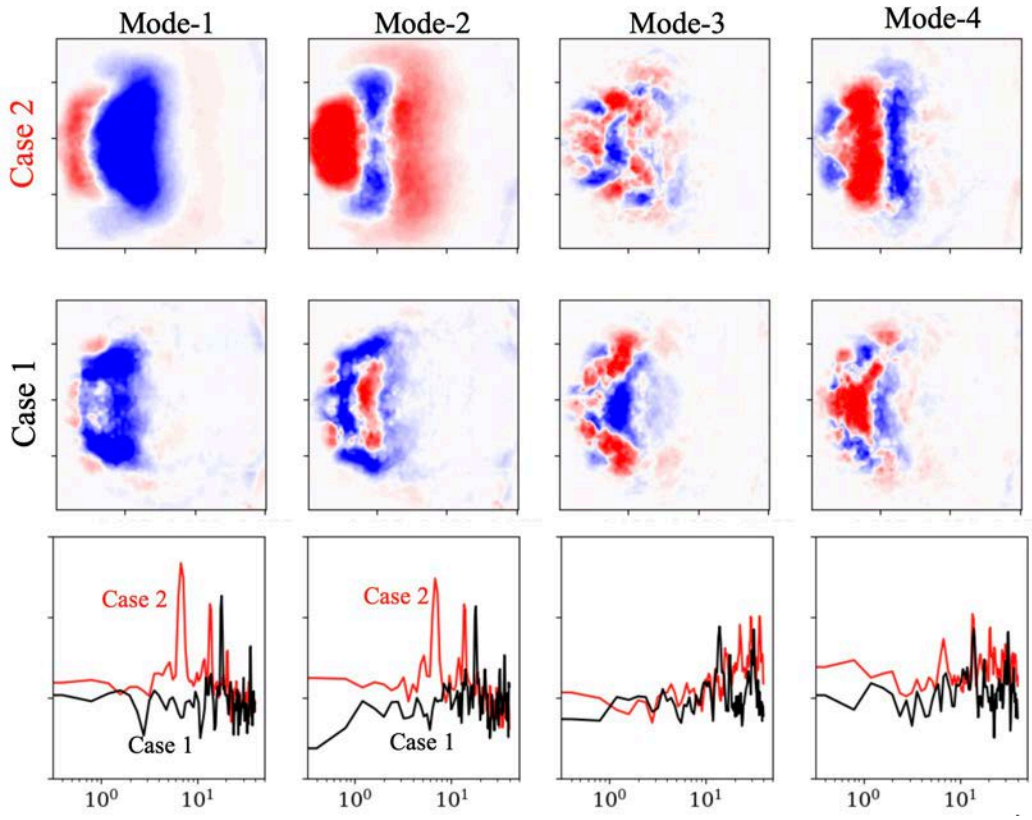


Figure 19. Proper Orthogonal Decompositions of normalized HRR: The shapes of first four most energetic modes are shown for Case-1 (top row) and Case-2 (middle row). The POD analysis is conducted using three-dimensional snapshots, but the mode shapes shown here are spanwise averaged to highlight the differences. The spectral signature of mode coefficients is also shown for Case-1 and Case-2 (bottom row).

A reliable way of identifying thermoacoustic instabilities is the Rayleigh Integral Criterion (RI). This is defined as the volume integral $\int_V p'q'$, where p' is the pressure perturbation and q' is the heat release perturbation. This criterion evaluates if the pressure and the heat release rate oscillations are in-phase or out-of-phase. The in-phase oscillations result in RI>0 and they would suggest a growing or limit-cycle thermoacoustic instability. On the other hand, RI<0 would suggest a damping thermoacoustic instability. The PSD of the RI identifies the frequencies where this coupling is happening, and these results are shown in Figure 20 for both Case-1 and Case-2. The results show that the thermoacoustic coupling is in general stronger for the higher-pressure configuration Case-2 and occurs at f/f_0 =8.8. On the other hand, the coupling for Case-1 occurs at f/f_0 =18.8. These results confirm that f/f_0 =8.8 (for Case-2) and f/f_0 =16.8 (for Case-1) are thermoacoustic instabilities operating in a limit-cycle. All the other frequency peaks of the RI in Figure 20 correspond to either harmonics or sub-harmonics of these dominant frequencies.

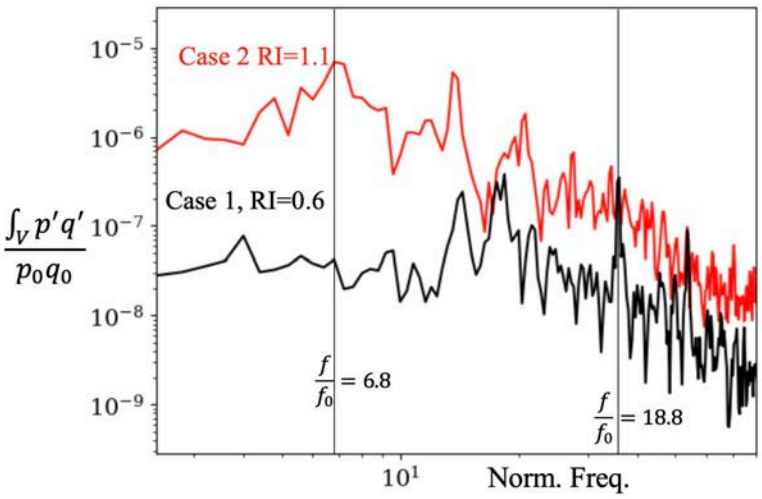


Figure 20. Power spectral density of normalized Rayleigh Integral Criterion (RI) is compared between Case-1 and Case-2. The time-averaged values of RI are noted for both cases. Some notable frequencies are shown as vertical lines.

Data Output and Transfer
The simulations output 3D snapshots of conservative variables. The output frequency of these outputs is f/f_0 =80 and at least 1,000 such snapshots are output for each case over the span of at least 10 flow-through times. The snapshots are collected only after the initial transients for the first two flow-through times have been neglected. A single 3D snapshot is approximately 1 GB in size. The CFDPostProc software and sample post-processing scripts can (a) compute primitive quantities, such as pressure, temperature, density, and reaction rates, (b) compute derivatives, (c) compute time-averaged quantities, and (d) interpolate data onto another rectangular grid from these files.

In addition to the 3D gas-phase snapshots, the Lagrangian data of the parcel are saved at the same frequency and are available for computing the spray droplet statistics. A post-processing script that translates the Lagrangian quantities onto a Eulerian grid via filtering is also available and provided to other teams. A single droplet snapshot is approximately 50 MB in size.

Because the 3D gas-phase snapshots are large, they could not be collected at higher frequencies. However, the simulation collects high-frequency data at f/f_0 =800 for approximately 200 probe points distributed throughout the computational domain. These points are uniformly placed along the *x*/*y*/*z* directions within the combustor, through the nozzle, and within the exit plenum. These data can be used for accurately computing the frequency characteristics of the system.

Finally, although time-averaged statistics (i.e., mean, root mean square [RMS]) can be computed by using the output 3D snapshots, fine-grained time averaging is also conducted within the code, and the mean and RMS primitive quantities are output for the entire 3D domain. These quantities include primitive variables, such as velocity, temperature, pressure, density, species mass fractions, and reaction rates. The size of a single time-averaged file is ~4 GB.

Milestones

- Conducted LES of the new experimental configuration with a VRASC tube for tonal noise predictions.
- The results show a clear presence of limit-cycle thermoacoustic instability. The frequency depends on the operating pressure and is qualitatively consistent with experimental observations.
- Multiple time-dependent 3D snapshots are collected for each operating condition to be provided to the ROM development teams with relevant post-processing scripts.

Major Accomplishments

Grid modifications and additional LES were conducted in Year-5 to study tonal combustion noise. The predictions show a limit-cycle combustion instability a qualitatively consistent behavior with the experiments. The oscillation frequency depends on the operating pressure.

Publications

Kastenberg, L. M., Panchal, A., & Menon, S. (2025). Direct and Indirect Combustion Noise Prediction in a Rich-Quench-Lean Combustor Using a Large Eddy Simulation. *AIAA SciTech Forum*, AIAA 2025-2489.

Outreach Efforts

None.

Awards

None.

Student Involvement

- Graduate student Leo Kastenberg graduated with a master's degree with thesis in August 2025. He worked on detailed validation of the LES results using POD and developing post-processing scripts for 3D snapshots, entropy processing, and direct and indirect noise identification.
- Graduate student Sathvik Gujjati, who is pursuing a master's degree with thesis, is currently working on grid refinement studies and will conduct LES at additional conditions in the future.

Plans for Next Period

- Consider a detailed validation of the new LES predictions against the experimental measurements if data become available. The comparison will use pressure probe and Chemiluminescence data.
- Conduct additional LES with modified FAR and T3 to study the effect of mixing and combustion on tonal noise. These conditions will be chosen consistently with the experimental campaign.
- Transfer all results and 3D snapshots to the ROM development team with relevant post-processing scripts.

Task 3 – GT Reduced-Order Modeling

Georgia Institute of Technology

Objective

The overarching objective of this task is to create quick-action ROMs to accurately predict various aspects of noise generation mechanisms that are then collectively fed into a design tool for noise prediction. The specific objective of the Georgia Tech ROM task focuses on the head-end physics in the architecture, namely the flow and spray dynamics, flame dynamics, and generation of entropy disturbances by the flame. The spray/flow dynamics feed into the flame dynamics, thus causing direct combustion noise. The flame dynamics also results in entropy disturbances, which in turn lead to indirect combustion noise at the nozzle. The flame response modeling and the model for the generation of entropy disturbances are provided as inputs to the post-combustion models that will be developed by RTRC. Depending on the prediction results obtained from the RTRC models, these head-end models will be iteratively refined.

Research Approach

In this reporting period, our team focused on tasks pertaining to hydrodynamics, coherence and entropy generation. Each of these tasks are detailed in their respective subsections below.

Hydrodynamics Modeling

In this reporting period, the hydrodynamics framework was extended to perform validation strategies for the swirling jet global stability analysis. Swirling flows usually result in unsteady hydrodynamic structures that can couple with acoustics. Thus, modeling and predicting the hydrodynamic structures arising from swirling jets is a key challenge, particularly in the presence of combustion, because these structures can interact with and perturb the flame. As discussed in the previous yearly report, global hydrodynamic stability predicts stable and unstable vortical modes of a time-averaged flow field. However, the instantaneous LES time snapshots of velocity fields can be used to detect coherent structures of the spatio-temporal flow field using data-driven modal decompositions.

For this study, space-only POD was used to separate the instantaneous velocity fields $u'(\boldsymbol{x},t)$ into deterministic spatial functions $\boldsymbol{\Phi_k}(\boldsymbol{x})$ and their modulating time coefficients $a_k(t)$:

$$u'(x,t) = u(x,t) - \bar{u}(x) = \sum_{k=1}^{\infty} a_k(t)\Phi_k(x) \quad \text{(Eq. 1)}$$

The mean-subtracted, planar velocity fluctuations at each time snapshot are then arranged as a column vectors and stacked side-by-side, forming the snapshot data matrix with m spatial points and n time snapshots.

$$U = \begin{bmatrix} u'(x_1,t_1) & u'(x_1,t_2) & \cdots & u'(x_1,t_n) \\ u'(x_2,t_1) & u'(x_2,t_2) & \cdots & u'(x_2,t_n) \\ \vdots & \vdots & \ddots & \vdots \\ u'(x_m,t_1) & u'(x_m,t_2) & \cdots & u'(x_m,t_n) \end{bmatrix} \quad \text{(Eq. 2)}$$

An economy-sized singular value decomposition (SVD) or $\mathbf{U} = \Phi\Sigma\Psi^T$ provides the POD modes and coefficients of the unsteady spatio-temporal data. Snapshot POD orders the modes according to their turbulent kinetic energy (TKE) when the input data consist of constant-density velocity fluctuations. The contribution of the k^{th} mode to total TKE is given by the σ_k or the diagonal elements of the matrix Σ:

$$E_k = \frac{\sigma_k^2}{\mathrm{Tr}(\Sigma)} = \frac{\sigma_k^2}{\sum_{k=1}^{min(m,n)} \sigma_k^2} \quad \text{(Eq. 3)}$$

Instantaneous $n = 1{,}473$ time snapshots with a time step of $\Delta t = 0.1$ ms or sampling frequency of $f_s = 10$ kHz are interpolated on a center line slice with 128×128 spatial grid points. Figure 21 displays an instantaneous axial velocity snapshot of this sliced dataset on the 128×128 spatial mesh.

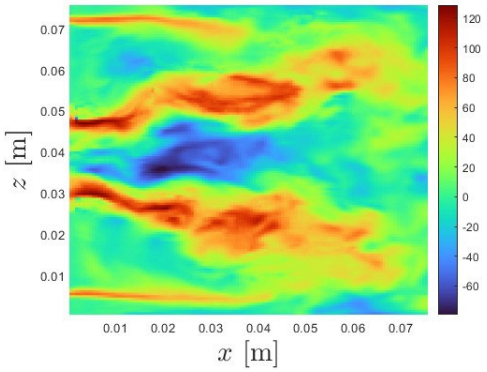


Figure 21. Instantaneous snapshot of axial velocity along center-line plane.

After application of POD to the instantaneous data, Figure 22 shows the spectrum of leading POD modes and their respective contribution to the total TKE. POD mode 1 accounts for approximately 10 percent of total turbulent kinetic energy present in the planar velocity flow field. Modes 2 and 3 each contain approximately half of the energy of the leading mode, while the energy in subsequent modes slowly decreases. The cumulative percent contribution to TKE shows the smooth and slow convergence of the POD spectrum, which is typical for turbulent shear flows.

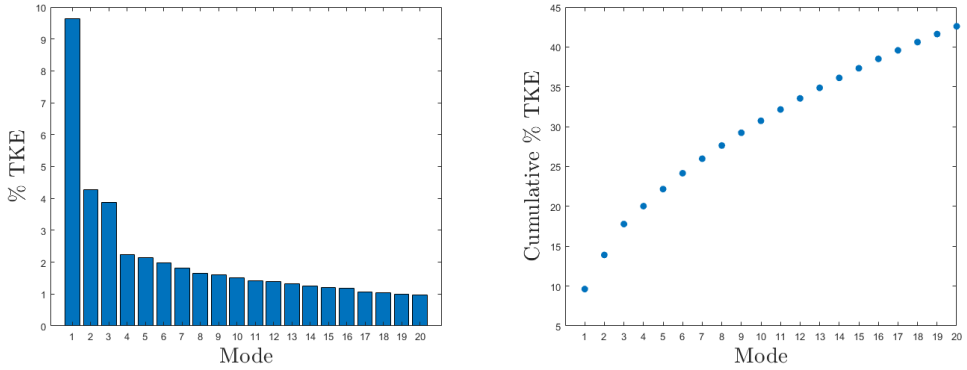


Figure 22. Individual and cumulative TKE distributions for leading POD modes.

Figure 23 shows the leading 12 POD modes, accounting for approximately 35% of TKE. The spatial mode shapes are displayed using the out of plane vorticity computed from the planar velocities of the POD modes. Planar velocity streamlines are overlaid to indicate vortex shedding structures in the domain. The highly energetic Mode 1 represents a shear-layer flapping mode, while Modes 2, 3 and 4 display distinct large length-scale out-of-plane vortical structures. These structures indicate sinuous modes, in which shear layer vorticity coalesces anti-symmetrically. Modes 5-8 contain a mix of both small length-scale and large length-scale vortex structures but display varicose behavior, in which shear layer vorticity coalesces symmetrically about the centerline. Lastly, Modes 9-12 are dominated by several smaller scale shear layer vortices shedding in the nozzle near-field with an anti-symmetric sinuous shedding fashion.

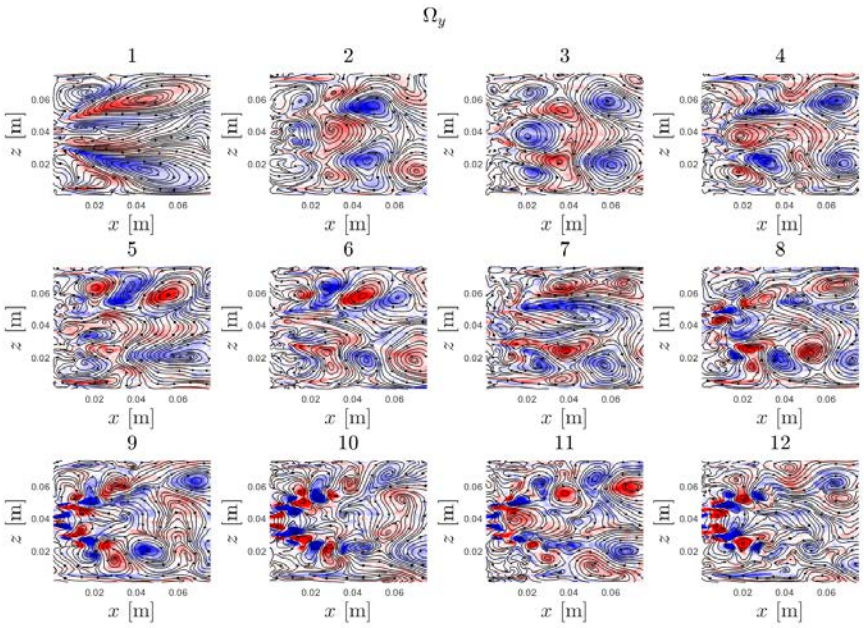


Figure 23. Leading center-line planar vorticity of leading POD mode shapes.

To understand the behavior of the modes in frequency space, window-averaged Welch's method is used to compute an estimate of the PSD by dividing the time coefficients of the leading POD modes into overlapping segments. Figure 24 displays the PSD amplitude of the leading modes in frequency space. Modes 2 and 3 display a broadband peak around 0.6

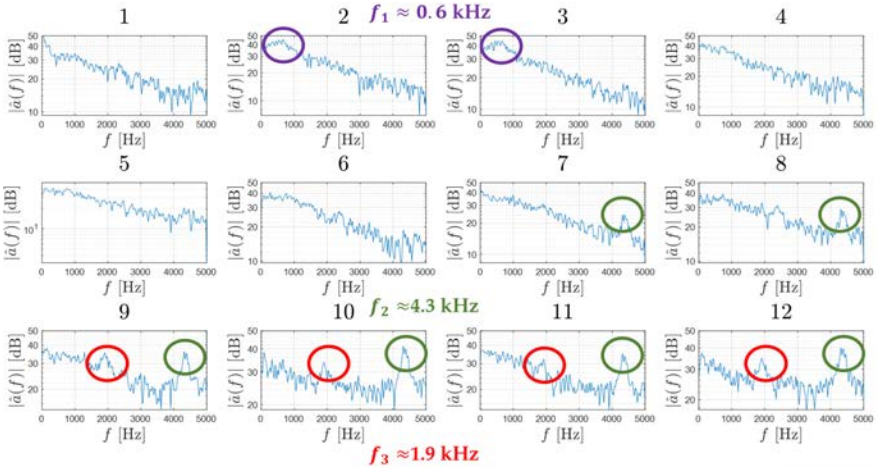


Figure 24. Power spectral density amplitude of time coefficients of leading POD modes.

The results from snapshot POD indicate that the high-energy POD modes capture inner and outer shear layer structures from the instantaneous data. Furthermore, there exists a large length-scale, lower-temporal frequency pattern dominating the downstream region, while a shorter length-scale, higher-frequency pattern is evident in the near-nozzle region. However, many of these features appear to be split over several POD modes as some of the POD modes appear to capture a noticeable mixture of these different vortex patterns. This is evident by both the spatial patterns and the multi-peak PSD spectra. A secondary validation study using advanced modal decomposition techniques such as spectral proper orthogonal decomposition and dynamic mode decomposition can be conducted to better identify spatially correlated features with different temporal behavior.

Modeling *p'-q'* Correlation/Coherence

The objective of this task is to study the correlation between the HRR measured by chemiluminescence and the generated noise, specifically direct noise. Through modeling and comparison with experimental data, it is possible to understand the governing physics behind coherence and extend results to any hypothetical flame configuration. Throughout the last several periods, an analytical model was successfully developed to study the effects of acoustic noncompactness and nearfield effects on the *p'-q'* coherence of an open flame. It demonstrated how these effects could act to lower coherence even in the case of a direct noise dominant system. Recent results in the GT Experimental task verified these findings, enabling predictions for future configurations.

In the previous period, the open flame model was extended to a 2D ducted configuration to study the effect of confinement. In this period, this 2D model was expanded to a 3D square duct for comparison with experimental data. To restate the approach, in the previous analytical model has shown that the parameters that govern coherence were identified as (1) the normalized flame correlation length $\frac{\Lambda}{a}$, (2) the "compactness factor" $\frac{a}{\lambda}$, (3) the distance of the observer $\frac{R}{a}$, and (4) the flame aspect ratio $\frac{L_f}{a}$. Starting from the linear wave equation:

$$\frac{\partial^2 p'(x,t)}{\partial t^2} - c_u^2 \nabla \cdot \left(\frac{\rho_u}{\rho_0} \nabla p'(x,t)\right) = (\gamma - 1)\frac{\partial q'(x,t)}{\partial t} \quad \text{(Eq. 4)}$$

The Fourier transformed solution can be written as:

$$p'(x_0,\omega) = \frac{-i\omega(\gamma-1)}{4\pi c_u^2} \oint q'(x_s,t) G(x_s,x_0,\omega) dS \quad \text{(Eq. 5)}$$



where $\boldsymbol{G}(x_s,\ x_0)$ is the Green's function for a source at x_s and the observer at x_0. From here on the Fourier transformed variables are considered. In the free field, it is well known that Green's function takes the form:

$$G(x_s, x_0, \omega) = \begin{cases} \frac{e^{ik|x_s - x_0|}}{|x_s - x_0|} & \text{3D freefield} \\ \frac{i}{4} H_0^{(1)}\left(\frac{2\pi|x_s - x_0|}{\lambda}\right) & \text{2D freefield} \end{cases} \quad \text{(Eq. 6)}$$

where $H_0^{(1)}$ is the Hankel function of the first kind of the zeroth order. Then, it is possible to write the auto spectra of the acoustic pressure G_{pp}, the global HRR G_{QQ}, and the cross spectra G_{Qp} as:

$$G_{QQ} = \iint q'(x_{s_1})\, q'^{*}(x_{s_2}) ds_1 ds_2 \quad \text{(Eq. 7)}$$

$$G_{pp} = \frac{\omega^2(\gamma-1)^2}{16\pi^2 c_u^4} \iint q'(x_{s_1})\, q'^{*}(x_{s_2}) G(x_{s_1}, x_0) G^{*}(x_{s_2}, x_0) ds_1 ds_2 \quad \text{(Eq. 8)}$$

$$G_{Qp} = \frac{i\omega(\gamma-1)}{4\pi c_u^2} \iint q'(x_{s_1})\, q'^{*}(x_{s_2}) G^{*}(x_{s_2}, x_0) ds_1 ds_2 \quad \text{(Eq. 9)}$$

Previously, the Green's function was developed for a 2D duct using the method of image sources. The same principle applies to a 3D square duct, where the image source now considers reflections from all surroundings as shown in Figure 25. The resulting Green's function is expressed as:

$$G(x_0, y) = \sum_{n=0}^{N} \sum_{n_x=0}^{n} \sum_{n_y=0}^{n-n_x} \left[\frac{exp\left(\frac{-2\pi i|y^n - x_0|}{\lambda}\right)}{|y^n - x_0|} + \frac{exp\left(\frac{-2\pi i|y^{*n} - x_0|}{\lambda}\right)}{|y^{*n} - x_0|} \right] \quad \text{(Eq. 10)}$$

where if $y^n = (y_x^n, y_y^n, y_z)$, $y^{*n} = (y_x^n, y_y^n, -y_z)$,

$$y_x^n = \begin{cases} \pm 2n_x r - y_x, n_x\ is\ odd \\ \pm 2n_x r + y_x, n_x\ is\ even \end{cases}$$
$$y_y^n = \begin{cases} \pm 2n_y r - y_y, n_x\ is\ odd \\ \pm 2n_y r + y_y, n_x\ is\ even \end{cases}.$$

Results and comparison with experimental results are discussed in the GT experimental task section.

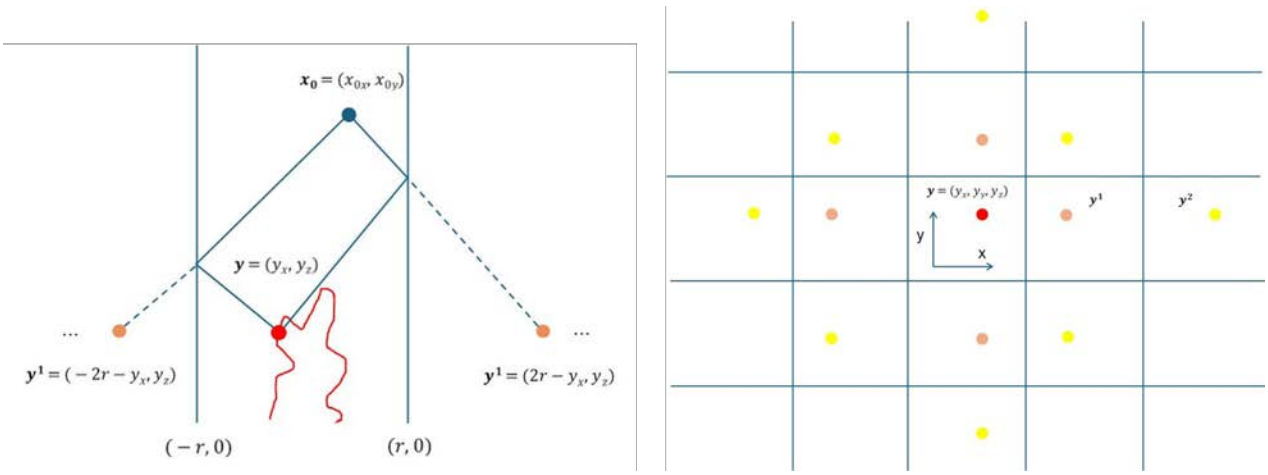


Figure 25. Illustration of the image source method for a 2D duct (left) and 3D duct viewed from above (right).



Analysis of Entropy Production Mechanisms

The objective of this task is to identify the dominant source terms in entropy production for accurate and flexible modeling of indirect combustion noise analysis of premixed and non-premixed flames. Prior work by our team on premixed flames has convincingly shown that fluctuations in heat-release dominate entropic fluctuations and hence indirect noise. However, in the case of non-premixed flames, where diffusion processes control the evolution and dynamics of the flame, the model requires rigorous analysis on other potential sources of entropy. In this reporting period, we have extended our entropy budget analysis framework to capture differential diffusion effects of species on entropy production due to mass diffusion. In our previous analysis, we were able to convincingly show the dominant effects of mass diffusion on producing significant amounts of entropy in a non-premixed turbulent flame (Sandia-D) and further analyzed the sensitivity of various production terms to operating conditions. Based on the feedback we received from our SciTech 2025 presentation, we have removed the problematic unity Lewis number, constant as well as equal mass diffusivities for all the species assumptions and thus incorporated the kinetic theory model in the calculations of species' diffusion coefficients. The mathematical formulation is presented below, and the preliminary results are discussed.

The governing equation of entropy transport in reacting, multicomponent flows is derived from the principles of energy conservation and the fundamental Gibbs relation as shown below:

$$\rho T \frac{Ds}{Dt} = -\nabla \cdot \vec{q} + \bar{\tau} : \nabla \vec{u} - \rho \sum_{i=1}^{N_s} D_i \nabla Y_i \cdot \vec{F_i} - \sum_{i=1}^{N_s} \mu_i \left(\dot{\omega}_i + \nabla \cdot (\rho D_i \nabla Y_i) \right) \quad \text{(Eq. 11)}$$

where ρ is density, T is temperature, $\bar{\tau}$ is the shear stress tensor and is modeled using Stokes' hypothesis, $\vec{u}$ is the velocity, D_i and Y_i is the laminar diffusion coefficient and mass fraction of species i, $\vec{F_i}$ is the body force per mass acting on species i, μ_i is the chemical potential of species i, $\dot{\omega}_i$ is the species production rate due to chemical reaction and $\frac{D}{Dt}$ is the substantial derivative. The heat flux vector $\vec{q}$ is given by:

$$\vec{q} = -k\nabla T + \quad \rho \sum_{i=1}^{N_s} h_i Y_i \vec{u}_{D,i} + R_u T \sum_{i=1}^{N_s} \sum_{j=1}^{N_s} \frac{X_j D_{T,i}}{W_i D_{ij}} \left(\vec{u}_{D,i} - \vec{u}_{D,j} \right) + \vec{q}_{rad} \quad \text{(Eq. 12)}$$

where h_i is the specific enthalpy of species i, $\vec{u}_{D,i}$is the diffusion velocity of species i, $D_{T,i}$ is the thermal diffusion co-efficient and D_{ij} is the binary mass diffusion coefficient of species i in otherwise pure j, $\vec{q}_{rad}$ is heat transfer due to radiation. The chemical reaction term $-\sum_{i=1}^{N_s} \mu_i \dot{\omega}_i$ can be further expanded as:

$$-\sum_{i=1}^{N_s} \mu_i \dot{\omega}_i = -\sum_{i=1}^{N_s} h_{f,i}^0 \dot{\omega}_i - \sum_{i=1}^{N_s} \dot{\omega}_i \int_{T_0}^{T} c_{p,i}\, dT + \sum_{i=1}^{N_s} T s_i \dot{\omega}_i = \dot{q} - \sum_{i=1}^{N_s} \dot{\omega}_i \int_{T_0}^{T} c_{p,i}\, dT + \sum_{i=1}^{N_s} T s_i \dot{\omega}_i \quad \text{(Eq. 13)}$$

where $\dot{q}$ is the HRR, $\sum_{i=1}^{N_s} \dot{\omega}_i \int_{T_0}^{T} c_{p,i}\, dT$ is the sensible enthalpy change of species i due to chemistry and $\sum_{i=1}^{N_s} T s_i \dot{\omega}_i$ is the partial entropy term.

The source terms on the right-hand side of Equation 11 represent entropy production due to heat flux, compressibility effects, body force, and chemical reactions respectively. Further, from the expansion of the heat flux vector, entropy is produced due to Fourier's heat conduction, enthalpy transport, full multicomponent diffusion, and radiation, respectively. Moreover, chemical reaction term represents the combined entropy generation due to heat release, sensible enthalpy changes, and partial entropy through species production/consumption. In the current extended framework, a simplified form of transport equation (Equation 11) is still considered by making a few assumptions in the context of low subsonic turbulent reacting flows. Assuming that the heat flux is driven purely due to heat conduction, only the first term on the right-hand side of Equation 12 is considered. For low subsonic flows, i.e., $M \ll 1$, compressibility effects are neglected and thus retaining only the viscous dissipation term. Second order diffusion effects such as Soret and Dufour diffusion are negligible in turbulence dominated flows and thus are neglected. In this extended model, the mass diffusion term is represented by Fickian diffusion, and the mass diffusion coefficients are calculated from kinetic theory, enabling us the riddance of unity Lewis number assumption. The diffusive mass flux is modeled using the mixture-averaged approach as:

$$J_i^{\alpha} = -\rho D_{\alpha,m} \nabla Y_{\alpha} \quad \text{(Eq. 14)}$$

Where Y_{α} is the mass fraction of species α, and the mixture-averaged diffusion coefficient $D_{\alpha,m}$ is defined as:

$$D_{\alpha,m} = \frac{1-X_\alpha}{\sum_{j\neq\alpha}\frac{X_j}{D_{\alpha,j}}} \quad \text{(Eq. 15)}$$

From Chapman-Enskog model for species diffusivity, the binary diffusion coefficient $D_{\alpha j}$ is calculated as follows:

$$D_{\alpha j} = \frac{3\kappa_B T\sqrt{\frac{4\pi\kappa_B T}{M_{\alpha j}}}}{16P\pi\sigma_{\alpha j}^2\Omega_D(T^*)} \quad \text{(Eq. 16)}$$

Incorporating the above assumptions and model changes, the resulting simplified entropy transport equation analyzed in this study is given as follows:

$$\frac{\partial\rho s}{\partial t} + \frac{\partial\rho u_i s}{\partial x_i} = \frac{\partial^2 s}{\partial x_i^2} + \frac{1}{T}\tau_{ij}\frac{\partial u_i}{\partial x_j} - \frac{\rho}{T}\sum_{\alpha=1}^{N_s}\mu_\alpha S_\alpha - \sum_{\alpha=1}^{N_s} J_i^\alpha \frac{R_\alpha}{X_\alpha}\frac{\partial X_\alpha}{\partial x_i} + \frac{\kappa}{T^2}\frac{\partial T}{\partial x_i}\frac{\partial T}{\partial x_i} \quad \text{(Eq. 17)}$$

In this simplified form of transport equation, the first term on the right-hand side represents the diffusion of entropy while the rest of the terms represent the volumetric entropy production rate due to viscous dissipation, heat conduction, mass diffusion, and chemical reaction, respectively.

To test this model, we have performed large eddy simulations on the Sandia-D flame like our prior work.
The computational domain of dimensions $100\ \ d_j \times 100\ \ d_j \times 105\ \ d_j$, where d_j is the jet-diameter of 7.2 mm, is used for the Sandia-D flame as shown in Figure 26.

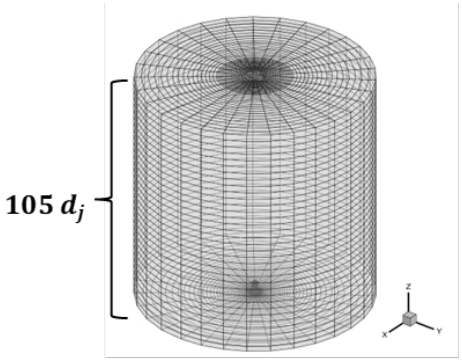


Figure 26. Computational domain of the Sandia-D flame.

As the flame is unconfined, the co-flow inlet of air spans $48\ d_j$ on either side of the jet-inlet. The length of the burner is $5\ d_j$ measured upstream of the jet exit as shown in Figure 26. The flame is stabilized by defining a pilot mixture of hot products of ethyne-air mixture at equivalence ratio of 0.77, spanning $2.5\ \mathrm{d_j}$. The summary of the boundary conditions is provided in Table 3.



Table 3. Boundary conditions of the baseline Sandia-D flame.

Condition	Jet	Pilot	Co-flow
Velocity (m/s)	49.6	11.4	0.9
Temperature (K)	294	1880	291
Pressure (atm)	0.993	0.993	0.993
Y_{CH_4}	0.156	0	0
Y_{O_2}	0.197	0.054	0.233
Y_{CO_2}	0	0.11	0
Y_{H_2O}	0	0.0942	0
Y_{CO}	0	4×10^{-3}	0
φ	2.38	0.77	0

The simulation for Sandia-D flame was performed using Ansys® Fluent 2024 R1 solver. The Wall adapting local eddy-viscosity (WALE) model is used for closure of the sub filter unresolved source terms in the LES equations. Detailed chemistry with pure finite rate effects has been used for modelling the chemical reactions for the Sandia-D flame. The chemical mechanism consists of 16 species and 41 reactions. Species transport model with Stiff Chemistry solver has been used to solve the species' conservation equations. Further, to isolate the pure transport effects, no turbulence-chemistry interaction was modeled. The equations are discretized using a cell-centered finite volume co-located pressure-based segregated solver. The pressure-velocity coupling is achieved using a SIMPLEC predictor-corrector algorithm. The numerical scheme is second-order accurate in space, and a bounded second-order implicit scheme is used for transient formulation. For accurate prediction of the material properties of the species, temperature dependent models like piecewise-polynomial and Sutherland formulations are used for computing specific heat and viscosity, respectively. Mass diffusivity is modeled using the kinetic theory model. Mixing law models are used for calculating the mixture-averaged properties. The entropic source-terms were calculated using a user-defined scalar formulation by treating the production of entropy as a passive scalar in the solution. Additionally, the source terms were volumed averaged locally to filter out the spatial fluctuations. For the transient calculation of both the flames, the Courant-Friedrichs-Lewy (CFL) value of 0.8 was maintained with the time-step size of 25 μs. The simulation was first run for 10 flowthroughs to wash out initial transient effects, after which statistical data were collected for an additional 15 flowthroughs for the final analysis.

First, the qualitative representations of entropy production in the Sandia-D flame due to different sources are discussed, Figure 27 shows the qualitative trends of time-averaged volumetric entropy production rates due to viscous dissipation, heat conduction, mass diffusion, and chemical reaction respectively at the center-plane. Consistent with the trends we have observed previously, the effects of viscous dissipation and heat conduction are highly negligible as seen from the orders of magnitude differences with the effects of mass diffusion and chemical reaction, respectively. The effects of mass diffusion and chemical reaction are still the dominant sources of entropy production rates. Species' concentration gradients drive mass diffusion and as the overall effect is summed over all the species, the resulting entropy production is significant. It can also be seen that as the flame grows downstream, forming an over-ventilated flame eventually, the regions of intense species production/consumption increase, thus resulting in wider species radial gradient profiles, and larger entropy production rates. Chemical reaction term is dominated by the species' production rates, and the associated entropy production rates are significant around the flame region. Moreover, as the overall effect is summed over all the species' production/consumption rates, the resulting entropy production is significant. The absolute magnitude of the mass diffusion contribution is higher than that of the chemical reaction, indicating the shortcomings of our previous model. The spatial profiles of integrated production rates across the flame are presented and contrasted with the results from the previous model next.

® Ansys is a registered trademark of Ansys, Inc., Canonsburg, Pennsylvania.

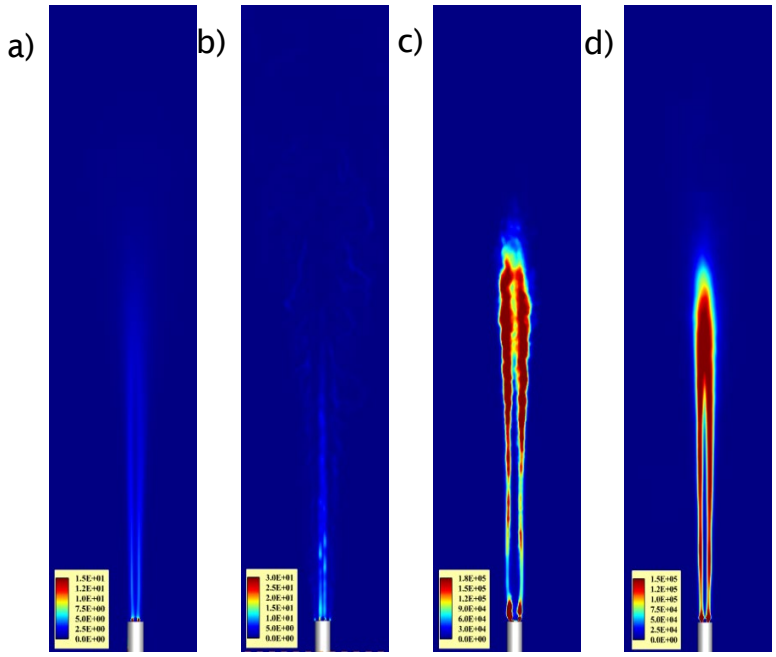


Figure 27. Qualitative representation of entropy production rates (J/K/m^3-s) in the center-plane (x=0) due to (a) viscous dissipation, (b) heat conduction, (c) mass diffusion, and (d) chemical reaction.

Figure 28 shows the integrated entropy production rate distribution due to various sources across the flame. As expected, the integrated entropy production due to viscous dissipation (blue line) and heat conduction (green line) are negligible across the flame. However, the updated mass diffusion term (solid black dots) appears to produce significant amounts of entropy, dominating the effect of chemical reactions (solid red line). This is a very significant observation in the context of indirect noise, as strong differential diffusion effects can lead to strong entropic fluctuations.

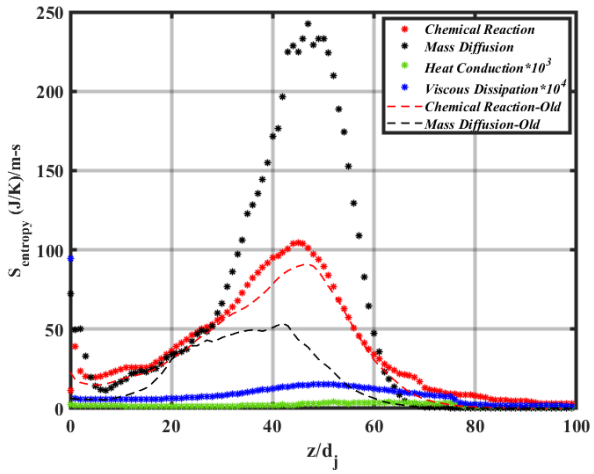


Figure 28. Spatial distribution of integrated mean entropy production rates (J/K/m-s) across the flame. Dashed lines correspond to results from the previous model.



Next, we are planning to rigorously analyze the sensitivity of these different source terms for various conditions using the canonical flame set-ups. Since the calculations involve computations of several gradients, a grid sensitivity analysis will be performed to verify the above observations. Additionally, the entropy budget analysis will be performed on an industrial-scale combustor configuration at elevated conditions to ascertain the trends observed from canonical flame configuration simulations.

Milestones

- Test validation strategies for global stability modeling by implementation of data-driven POD techniques.
- Extended p-q coherence study to 3D square ducts.
- Improved analysis of entropy budget completed based on relaxing earlier assumptions.

Major Accomplishments

Unsteady, spatio-temporal LES data were used by the hydrodynamics team to evaluate leading POD hydrodynamic modes including their dynamical frequencies and mode-shapes. Coherence modeling study showed differences in considering a 3D configuration versus 2D configuration. Entropy budget analysis framework can now consider more detailed molecular transport models.

Publications

Published Conference Proceedings

Patki, P. A., Ek, H., Acharya, V., & Emerson, B. L. (2025, March 16-19). *Reduced order modeling and validation of hydrodynamic modes of reacting, swirling jets.* 14th U.S. National Combustion Meeting, Boston, Massachusetts.

Ganesh, G.C., Ansari, N., Orsino, S., Xia, Y., & Acharya, V. (2025, January). *Analysis of Entropy Production Mechanisms in Turbulent Diffusion Flames.* AIAA SciTech Forum 2025, Orlando, Florida.

Outreach Efforts

None.

Awards

None.

Student Involvement

- Graduate student Parth Patki worked on the hydrodynamic stability task under the mentoring of Ben Emerson.
- Graduate student Sungyoung Ha worked on the coherence modeling task under the mentoring of Vishal Acharya and Tim Lieuwen.
- Graduate student Guru Charan Ganesh worked on the entropy generation task under the mentoring of Vishal Acharya.

Plans for Next Period

- Use RTRC tone campaign data for addition to flame response modeling validation.
- Consider advanced modal decomposition techniques for improved secondary validation and improvement of Tri-Global model from previous year with conclusions of the primary validation study.
- Build reduced order modeling for entropy noise based on findings from current reporting period.

Task 4 – Facility Development

RTX Technologies Research Center

Objective

The objective of this task is to provide machine learning data for combustion instability over range of configurations and operating conditions.

Research Approach

The combustor rig for the tone campaign test is shown in Figure 29 (left) together with the original test arrangement that was used for the broadband noise campaign (right). The tone campaign rig was achieved by removing the jail bars section, replaced with a constant area section. The VRASC section with a variable length side branch and variable elliptic choke was installed downstream of the combustion section. The side branch length of the VRASC tube varied by the plunger location.

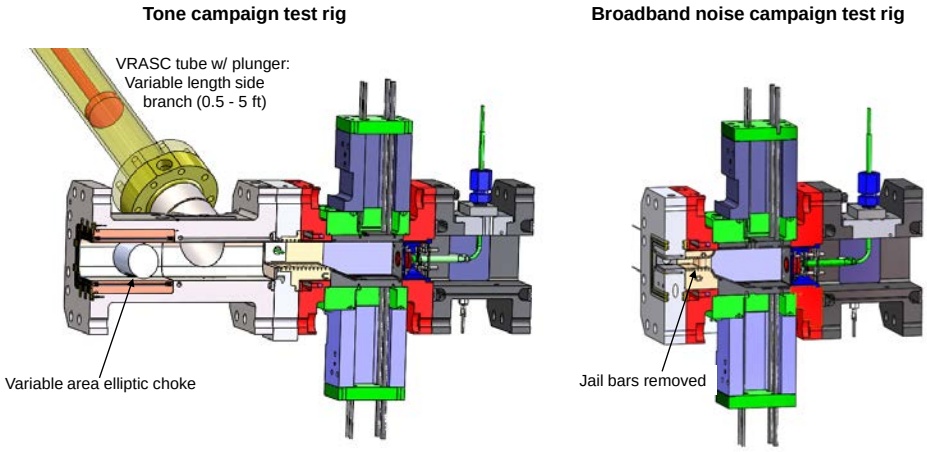


Figure 29. Test combustor rig for tone campaign vs original ASCENT combustor rig for broadband noise.

The dynamic instrumentation is shown in Figure 30 which consists of three diagnostics:

1. A photodiode sensor that captures a focused, time resolved chemiluminescence (OH*) signal of the unsteady combustion, which is a surrogate of the Unsteady Heat Release (UHR), and is used to compute Rayliegh gain,
2. Dynamic pressure tap array for wave decomposition and estimate of indirect noise, and
3. A dual thermocouple (dual TC) for temperature fluctuations downstream of the combustion.

In addition, several other locations (e.g., bulkhead) were instrumented for dynamic pressure, the bulkhead and other locations are illustrated in the figure on the right side of Figure 30.

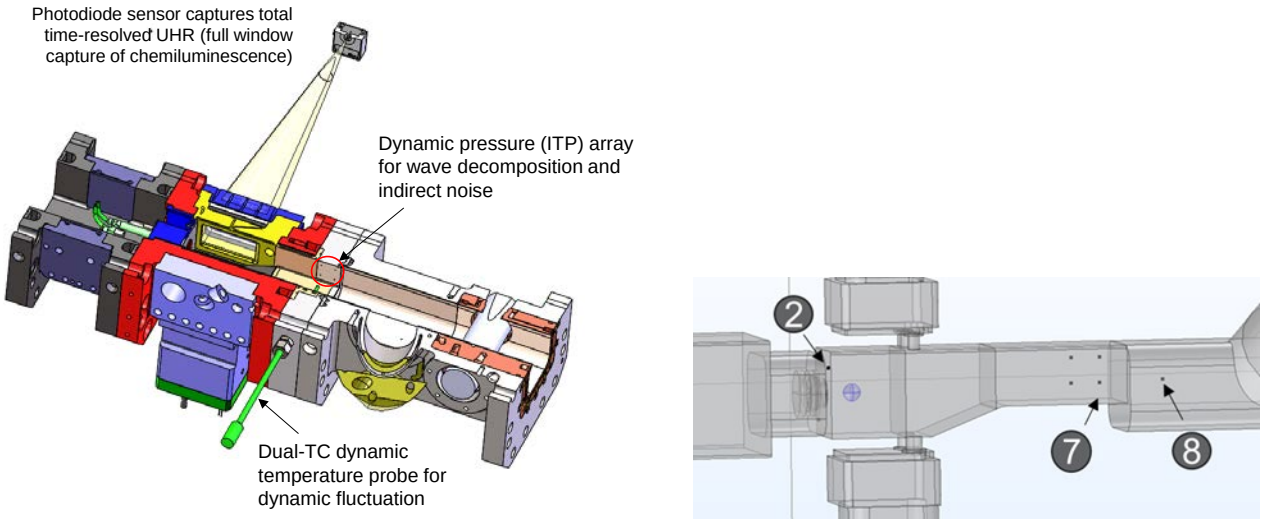


Figure 30. Dynamic instrumentation for test rig shown using the CAD drawing on the left and using the COMSOL Multiphysics model setup on the right.

The immersion of the fuel nozzle in the swirler (air-fuel mixer) was variable for this test campaign. Three immersions were tested and are shown in Figure 31.

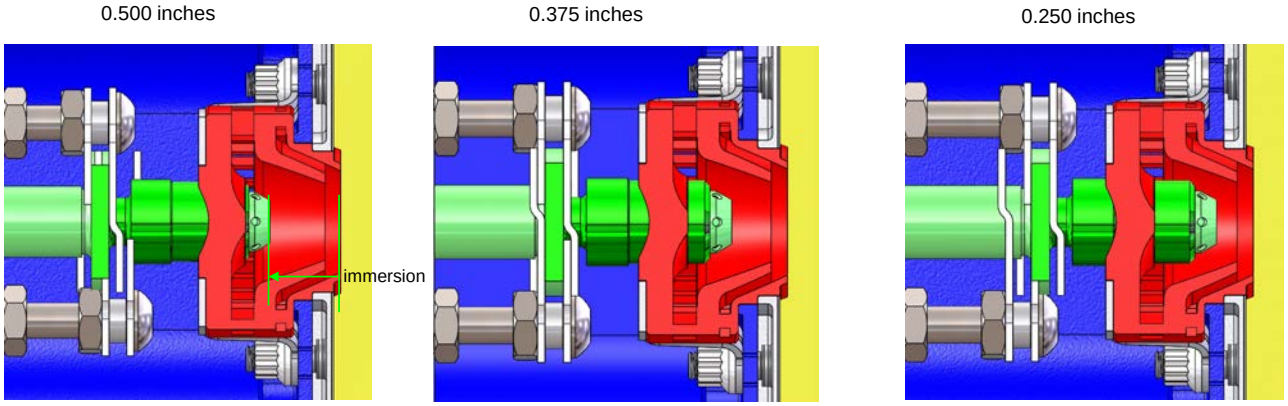


Figure 31. Fuel mixer configurations tested.

The test matrix focused on approach and ground Idle conditions. The target conditions are shown in Figure 32. Due to very high combustion dynamics (i.e., high pressure fluctuations), the initial two test days had limited conditions acquired because of concerns with rig health.



		Data Point Number	
Immersion	**0.25**	**0.5**	**0.375**
Description	**6/30/25**	**7/7/25**	**7/11/25**
Apprch: Cycle Pt. @ Cycle Cond.	**6**	**4**	**6**
Apprch: FARtot_+1up	**8**	**8**	**8**
Apprch: FARtot_+2up	**10**	**10**	**10**
Apprch: FARtot_+3up (HOT TCs)	**14**	**14**	
Apprch: FARtot_-1down	**16**	**16**	**12**
Apprch: Cycle Pt. @ T3 = 600 F	**18**	**22**	**18**
Apprch: FARtot_+1up	**20**	**24**	**16**
Apprch: FARtot_+3up	**26**	**26**	**14**
Apprch: FARtot_+4up (HOT TCs)		**28**	
Apprch: Cycle Pt. @ T3 = 500 F		**30**	**20**
Apprch: FARtot_+1up		**32**	**22**
Apprch: FARtot_+3up			
Apprch: FARtot_+4up			
Apprch: FARtot_+5up (HOT TCs)			
App Pt. @ T3=500 F, FAR+1, 20pph			**24**
Apprch: 500F, FAR+1, 40pph_Pilot			**26**
Apprch: 500F, FAR+1, 60pph_Pilot			**28**
Apprch: 500F, FAR+1, 80pph_Pilot			
App Pt. @ T3 = 500 F, FAR+1, 28/46			**30**
Apprch: 500F, FAR+1, 30/44=SwBH/Q			**32**
Apprch: 500F, FAR+1, 32/42=SwBH/Q			**34**
G-Idle: Cycle Pt.			**44**
G-Idle: FARtot_2			**42**
G-Idle: FARtot_3			**40**
G-Idle: FARtot_4			**38**
G-Idle: FARtot_5			**36**

Figure 32. Test matrix.

For each data point, dynamic data were acquired in a continuous manner as the VRASC plunger was swept from one end of its range to the other end (stoke range: 6 to 54 in.) over the course of 190 s. A typical combustion dynamic pressure response is shown in Figure 33 in terms of a spectrogram in plunger stroke vs frequency. As can be seen in the figure, the combustion instability tracks along the longitudinal modes (i.e., standing wave between bulkhead [BH] and plunger face) over a frequency range, in this case from 570 -720 Hz. As the plunger proceeds to longer stroke positions, the instability will jump from a lower longitudinal mode to the next higher mode to maintain this frequency range, thus identifying the dynamic characteristic of the fuel mixer. To characterize the response for a given immersion and operation point, the peak dynamic pressure and associated frequency are identified which is shown by the black circle in the spectrogram, location just above 600 Hz and the 20 in Stroke position. The specific value of peak-to-peak dynamic pressure and frequency are listed in the figure title.

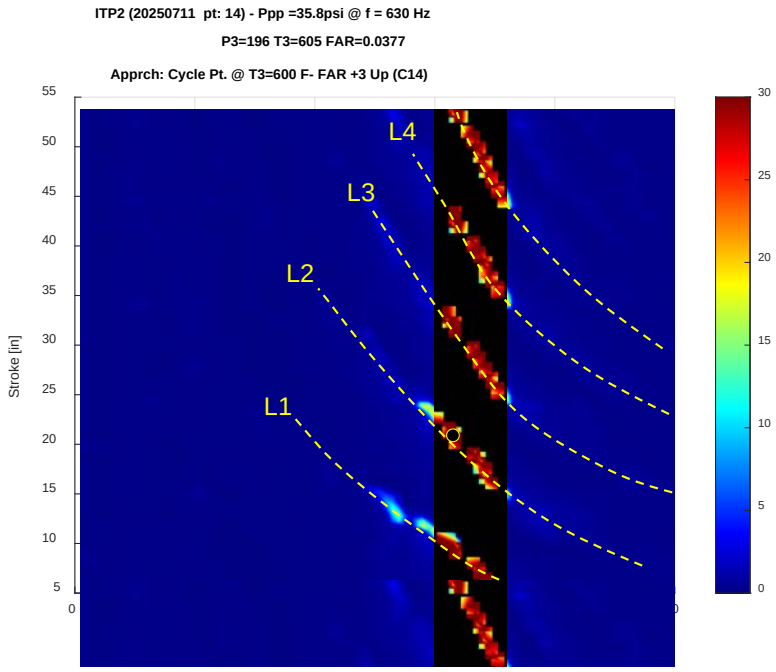


Figure 33. Typical dynamic pressure spectrogram for one operational condition. FAR: fuel-air ratio.

Figure 34 plots a summary of the peak response data versus FAR sweeps and the bulkhead pressure sensor. The top row is the pressure amplitude (half peak-to-peak value) and bottom row is the associated frequency. The cycle condition is listed at the top of each column, and the immersion configuration is identified by the symbol color.

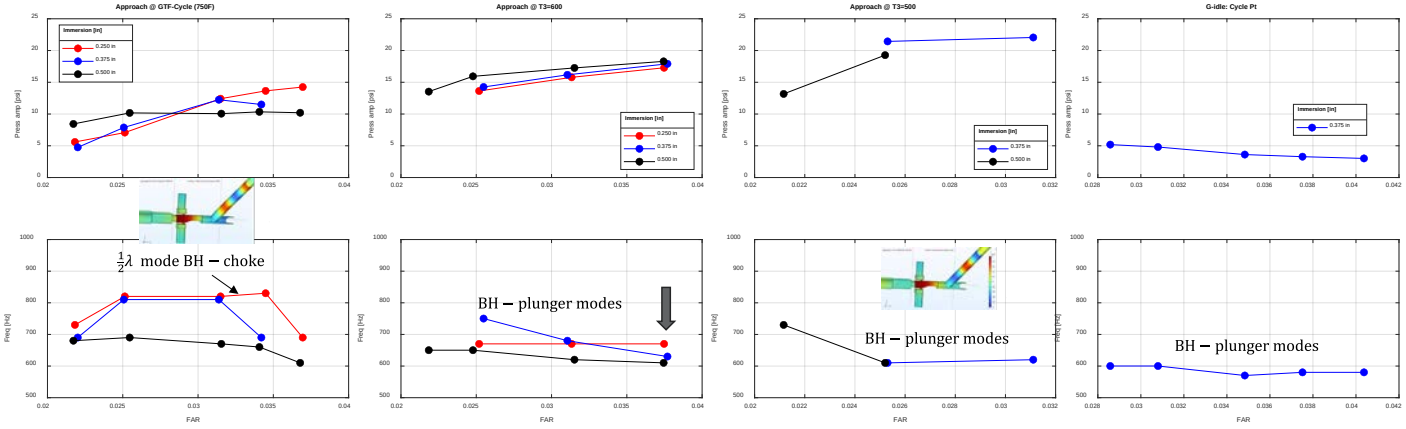


Figure 34. Summary of peak dynamic pressure and associated frequency.

As noted on the frequency plots, for five points (see Approach @ GTF-cycle [750°F]), the frequency is associated with a BH-choke half wave-length mode. For this mode, the BH-plunger and BH-choke modes are matching which causes (as the modeling shows) the acoustic pressure generated by a given combustor unsteadiness to be the largest here, making the attraction to instability much greater than the BH-plunger mode alone. Hence, these responses are of limited interest since they limit the range of the frequency response. More specifically, the bands of response shown in Figure 33, are mainly vertical along the 800 Hz frequency.

For the Approach @ T3=600°F conditions, the data here provide the more comparative assessment of the three immersion configurations. Unlike previous experience with more engine relevant fuel mixers that show great sensitivity to immersion, the results here do not. This is attribution to the large Acd (effective flow area) of the current fuel mixer and the limited number of outer flow passages (2). For the detailed dynamic analysis of Rayliegh gain and indirect noise estimation, the effort was focused on these conditions as identified in the figure.

For the detailed dynamic analysis, a good finite-element analysis (FEA) model is needed. The model domain and applied temperatures (mainly based on measured operating conditions together with adiabatic flame model) is shown in **Figure 35**. The primary data-matching parameter is the temperature of gas at the plunger face which was found to depend on stroke position.

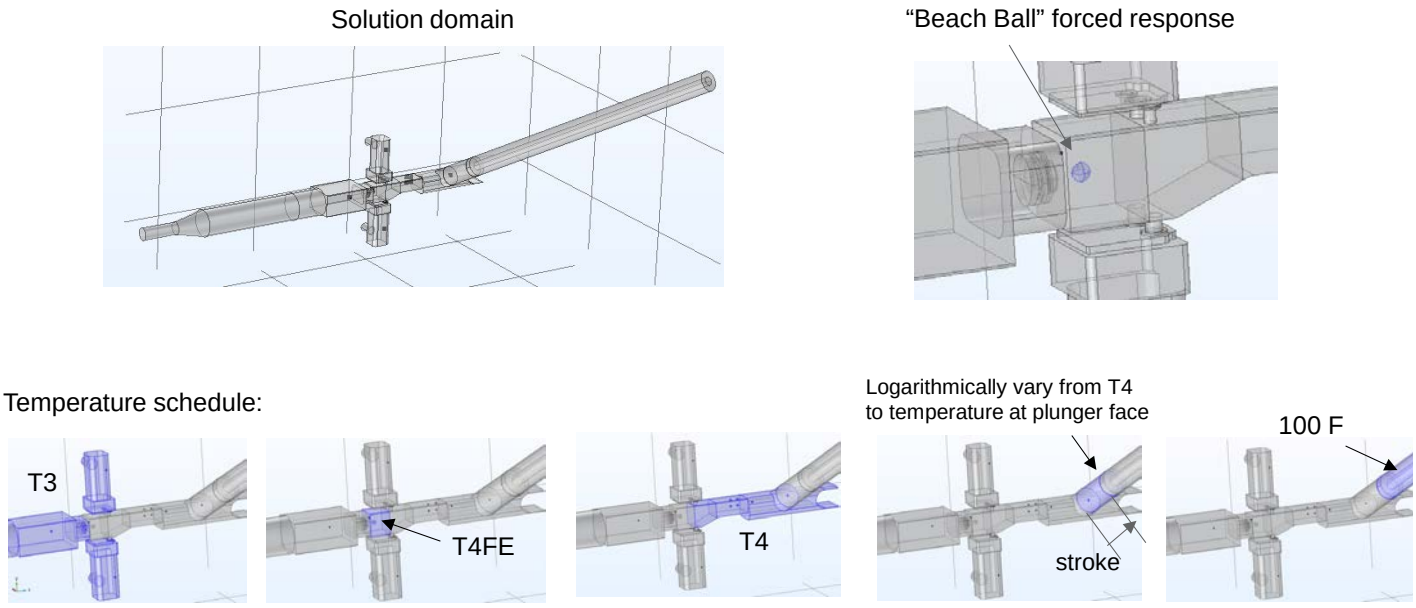


Figure 35. Finite element acoustic model using pressure-acoustics solver in COMSOL Multiphysics software.

The validation comparison of model vs data is shown in Figure 36 which compares the pressure ratio from a combustor aft dynamic pressure position (#8) to the BH (#2). Comparison is very good, capturing the BH-plunger longitudinal modes as well as the modes behind the "leaky" plunger. Quantifying line plots also confirm excellent data matching.

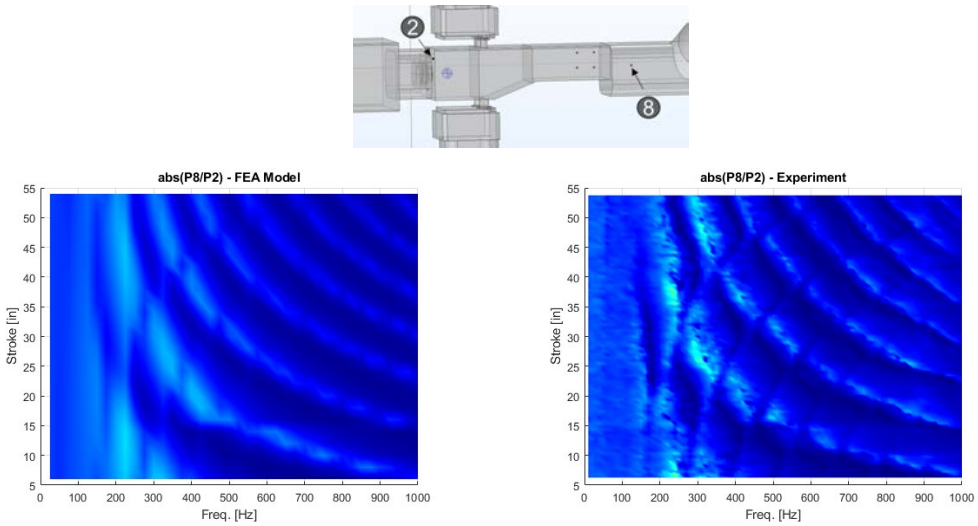


Figure 36. Comparison of data vs. model for full stroke variation.

Rayliegh gain was computed using the Eigenvalues from the FEA combined with the measure unsteady chemiluminescence. Rayliegh gain is shown in the approximate acoustic equation shown in Figure 37 (η = normalized dynamic pressure and ψ is the acoustic mode shape) and is the driving mechanism of combustion instability.

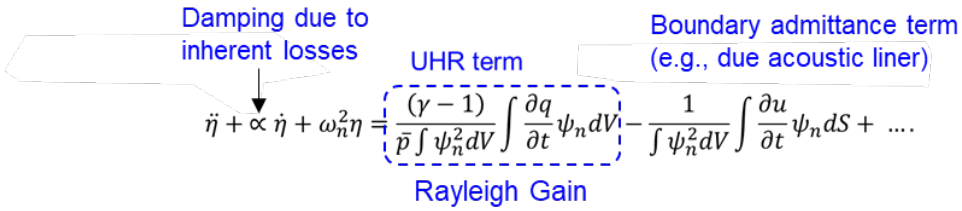


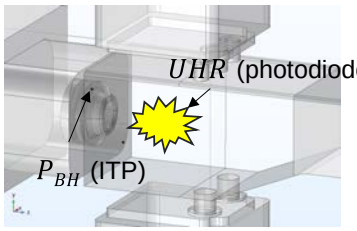
Figure 37. Rayliegh gain equation.

In a first attempt to characterize the Rayliegh gain vs plunger location, a FEA model was developed in COMSOL Multiphysics software to integrate the UHR with the acoustic modes. Figure 38 shows graphically the outline of the approach.

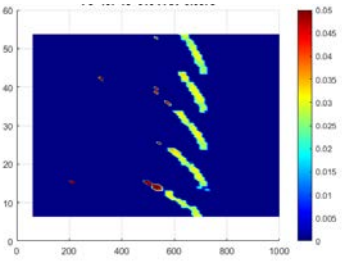


unsteady heat release (UHR) / pressure = $uhrTF = \frac{UHR}{P_{BH}} = func(f, Lplunger)$

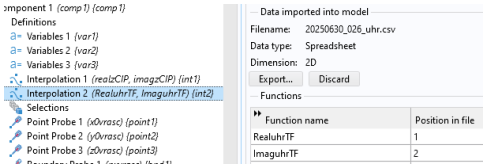
uhrTF experimental arrangement



uhrTF Magnitude map



Read uhrTF lookup table into COMSOL



Compute UHR for each mode and integrate p*UHR over combustion volume = Rayleigh Gain

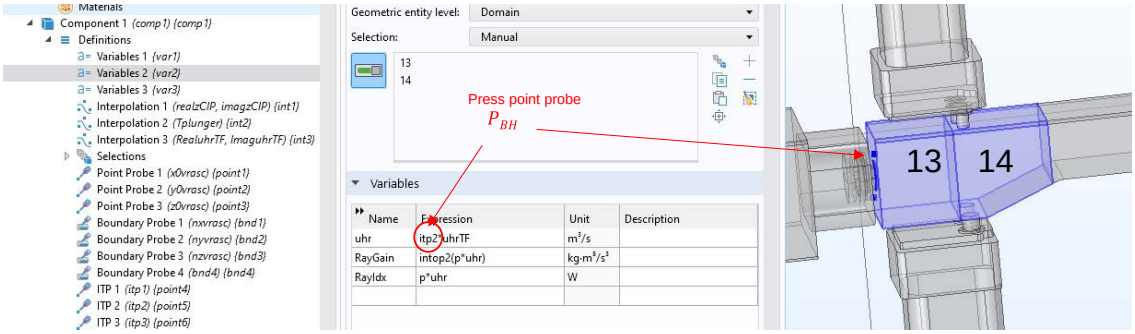


Figure 38. Approach to estimate Rayliegh gain from chemiluminescence data and FEA model.

Before showing the Rayliegh gain results, it is helpful to understand the modal content in the test rig. With the FEA model, the Eigenvalues were computed at half-inch increments of the plunger location. Approximate 20 were found around the band of interest (200-1,000 Hz). Shown in Figure 39 (left plot) is all the Eigenvalues that were discovered. To sort out the ones of interest, the volume-averaged mode shape (Λ) in the blue domain (combustion zone) was computed (color of dot). By picking a limit of Λ of 0.5, the modes of interest in the combustion zone are easily identified (right-hand plot). The gray lines are hand-faired lines from plots on the left which track the modes behind the plunger. The impact of these modes is visible in the right-hand plot.

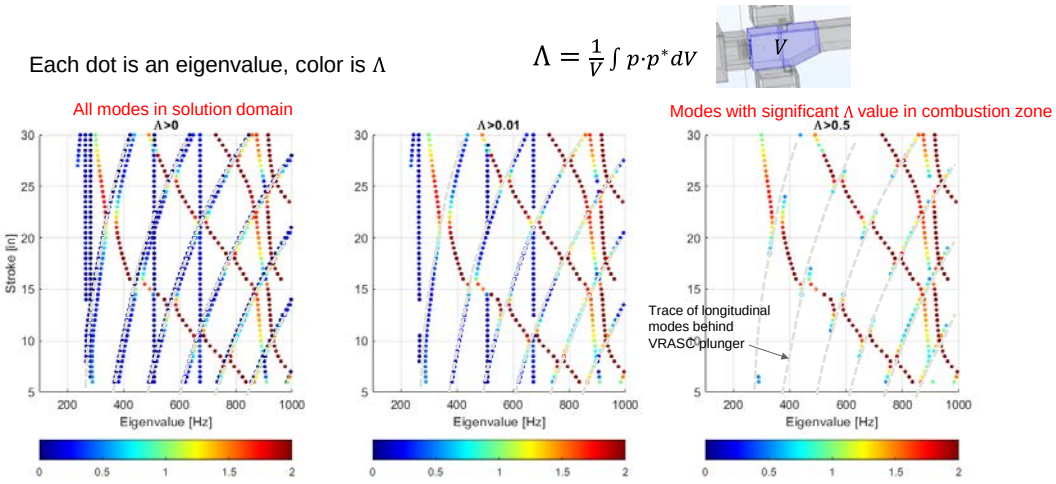


Figure 39. Acoustic Eigenvalues (dots) for one operating condition for full stroke variation and volume averaged mode shape in combustion region (Λ=color).

Figure 40 shows the Rayleigh gain results for the three immersion cases for the approach condition (T3=600 F), FAR excursion. The plots below show the modes with $\Lambda > 0.5$ colorized by the magnitude of the Rayliegh gain. The deeper the color red is, the greater the gain and hence the dynamic pressure. These results are consistent with the trending of measured dynamic pressure (increased immersion increases the dynamic pressure amplitude and lowers the associated frequency. This analysis represents a first for the VRASC tone rig and is a valuable tool to assess future fuel mixer investigations.

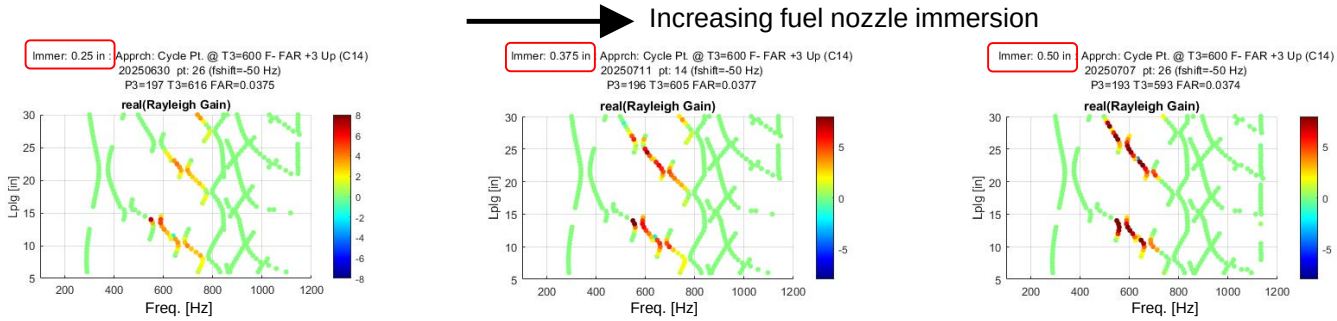


Figure 40. Rayleigh Gain maps verses immersion.

Figure 41 shows the result of the indirect noise estimate. This approach has been described in previous annual reports. In brief, when entropy/temperature fluctuation from the combustion process convect downstream through the choke, noise is generated that travel both downstream and upstream. Using the dynamic pressure array shown in Figure 30, the acoustics can be decomposed into downstream (A component) and upstream traveling (B component). By comparing the Bexp component from the test with the Bmodel component from the FEA (with does not contain indirect noise), the indirect noise can be estimated from the difference, Bexp-Bmodel. For the same conditions shown in Figure 40 for the Rayliegh gain, the estimated indirect noise spectrogram are shown in Figure 41. These results are consistent with the measured dynamic pressure data in that increased immersion corresponds with increased noise. Also interesting is the spottiness at lower frequencies suggesting temperature fluctuation in this band that is more significant for the larger immersion. This is in fact the observation from the temperature measurements (not shown).

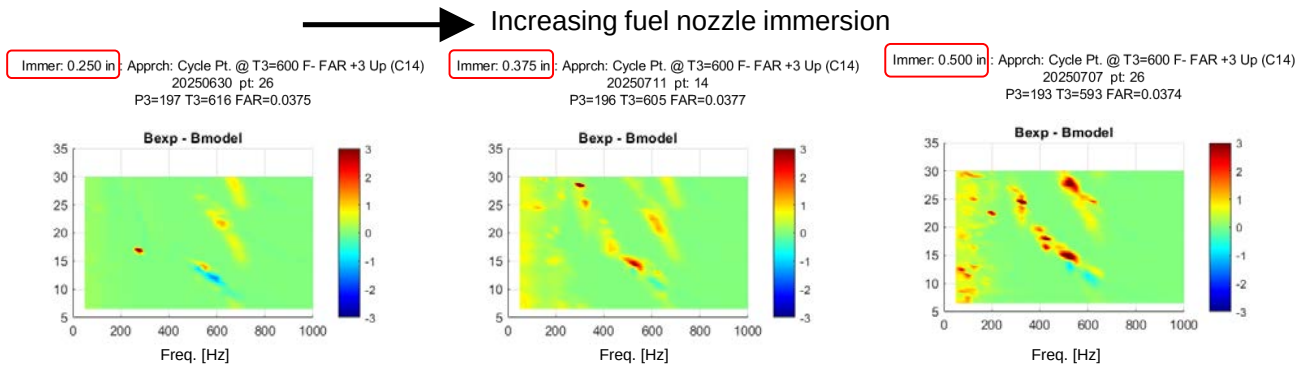


Figure 41. Estimated indirect noise variation with immersion.

In summary, though sensitivity to immersion in this campaign was less than expected, three new diagnostic techniques (Rayliegh gain, indirect noise, and d/s temperature fluctuations) for combustion tone studies have been developed and shown to be consist with observed dynamic pressure trending and should be a useful tool for future tone investigations. The Rayliegh gain estimation will be further refined and developed in the next phase of funding. Results shown here show great promise as a diagnostic tool. The following summarizes accomplishments and next steps for this effort.

Milestones

- Completed Year 1 Tone Prominence Program, RTRC main task a rig test identifying tone instabilities.
- Obtained initial GT rig LES results identifying peak mode at frequency consistent with rig test.

Major Accomplishments

- Demonstrated new VRASC rig diagnostics for dynamic analysis: dynamic exit temperature mapping, indirect noise mapping, UHR, and Rayleigh gain mapping.

Publications

None.

Outreach Efforts

None.

Awards

None.

Student Involvement

None.

Plans for Next Period

- Further develop Rayleigh gain analysis (integration of UHR and acoustic modes) as current development shows much promise (planned next phase, Year 2)
- Year 2 proposed, waiting for FAA to award.
  - Continue initial validation of GT LES with RTRC data (Y1),
  - Match rig LES and data at multiple rig test conditions (Y2),
  - Refine stability analysis (Y2), leverage LES/test for ML to define HRR ROM (Y2), Initiate analysis for design low tone design (Y2).
  - This program, when completed, will provide insight into instability challenges (prediction and mitigate) and a framework for propagating tones through the turbine and into the far field for noise.



Project 056 Turbine Cooling Through Additive Manufacturing

The Pennsylvania State University

Project Lead Investigator

Reid A. Berdanier
Associate Professor
Department of Mechanical Engineering
The Pennsylvania State University
NARCO Building, CATO Park, Room 148
3127 Research Drive
State College, PA 16801
(814) 863-3972
rberdanier@psu.edu

University Participants

The Pennsylvania State University (Penn State)

- P.I.s: Prof. Reid A. Berdanier, Prof. Stephen Lynch, Prof. Karen Thole
- FAA Award Number: 13-C-AJFE-PSU-126
- Period of Performance: February 5, 2020, to September 30, 2026
- Tasks:
  1. Manufacture and test existing FAA Continuous Lower Energy, Emissions, and Noise (CLEEN) II blade designs.
  2. Design new double-wall cooling technologies.
  3. Manufacture and test new double-wall cooling designs for linear cascade.
  4. Manufacture and Test AM NExT Blades with Varying Roughness
  5. Develop Correlations for Realistic Turbine Roughness

Project Funding Level

The Federal Aviation Administration (FAA) has provided $1,800,000 of funding to date. In-kind cost-sharing of $1,800,000 has been provided by Pratt & Whitney ($1,500,000), and Penn State ($300,000).

Investigation Team

Prof. Reid A. Berdanier, All Tasks
Prof. Karen A. Thole (co-P.I.), All Tasks
Prof. Stephen Lynch (co-P.I.), Tasks 2, 3, and 5
Assoc. Res. Prof. Michael Barringer, (staff scientist), Task 1 and 4
Asst. Res. Prof. Matthew Meier, (staff scientist), Task 1 and 4
Scott Fishbone, (project manager, departed), Task 1
Justin Brumberg (staff scientist), Task 1 and 4
Tom Houck (project manager), Task 1 and 4
Jeremiah Bunch, (laboratory technician), Task 1 and 4
Liam Boyd, (graduate student, graduated), Tasks 2 and 3
Nicholas Gailey, (graduate student, graduated), Task 1
Ethan Bonn, (graduate student), Task 1
Abigail Altland, (graduate student), Task 5
Matthew Stuber, (graduate student), Task 5
Benjamin Bizzak, (graduate student), Task 4

Project Overview

Gains in the cooling performance of cooled turbine airfoils directly affect the efficiency and durability (lifetime) of turbine engines and therefore are the subject of substantial development. Currently, many cooling designs for turbine airfoils use complex micro-channels placed within the wall of the airfoil to extract heat—a design known as double-wall cooling. However, the geometric complexities (and thus the effectiveness) of the micro-channels are limited by the current design space available through the use of conventional investment casting and core tooling methods to manufacture relatively small intricate internal cooling features. This project will investigate potential thermal performance and aerodynamic efficiency improvements made possible by exploring the expanded cooling design space opportunities by directly fabricating complex cooling geometries with three-dimensional laser powder bed fusion (L-PBF), a commonly used metal-based additive manufacturing (AM) method. L-PBF AM has begun to find many uses in the gas turbine industry, particularly because of the new design space enabled by this new fabrication method. However, the ability to manufacture high-efficiency, intricate, complex double-wall cooling airfoils design concepts is unknown. This research would generate some of the first thermal performance data at engine-relevant conditions comparing traditional cast airfoils to advanced airfoils manufactured through L-PBF AM. Understanding the potential of new innovative geometric heat transfer cooling design features coupled with unique airfoil cooling configurations will serve as an important guide for future investments in advanced manufacturing and cooling design technologies.

Task 1 – Manufacture and Test Existing FAA CLEEN II Blade Designs

The Pennsylvania State University

Objective

The objectives of this task are to measure the as-manufactured shape of FAA CLEEN II turbine blade airfoils with X-ray computed tomography (CT), and to use that information to fabricate additively manufactured copies for direct comparison at the rotating turbine facility at Penn State. The outcomes of this effort will be to (a) provide a direct back-to-back comparison of cast versus additively manufactured airfoils, (b) identify the unknown challenges in creating double-wall designs via AM and translating them into cast parts for commercialization, and (c) learn about and document the design, fabrication, and testing of additive blades that will spin at engine-relevant conditions.

Research Approach

AM Blade Inspections and Testing Preparation

Testing of the FAA CLEEN II blade designs has been completed within the Steady Thermal Aero Research Turbine (START) rig. A low, mid, and high blade coolant flow rate was achieved over the test campaign. CT scans and blue light scans of an ideal geometric FAA CLEEN II cast blade were used to generate a solid model for the manufacturing of the AM blade set. Infrared (IR) images were taken of every blade while rotating at 10,000+ rpm and initial observations were summarized in previous reports. The detailed analysis to understand the specific impact of AM versus cast blade performance is continuing, and those results are summarized in the current report.

Additional post-test coolant flow studies were conducted to better understand how much coolant was being supplied to specific sections of the blade. Figure 1 illustrates the flow parameter apparatus and measured data normalized by the maximum flow parameter across a representative range of pressure ratios for the trailing edge slots only. This was conducted by blocking all cooling holes and the tip region, while also blocking the inlet to all coolant feed channels except the one feeding the trailing edge slots, as shown in Figure 1a. The blades were then pressed into a custom-made gasket that sealed the root of the blade while a flowmeter measured the supplied pressure, temperature, and mass flow rate below the root. Figure 1b shows the cast blades have a greater flow parameter compared to the AM blades, where a greater flow parameter corresponds to more mass flow being supplied through the blades. This observation initially supports fundamental expectations that AM roughness will add to the pressure drop behavior and limit flow capacity.

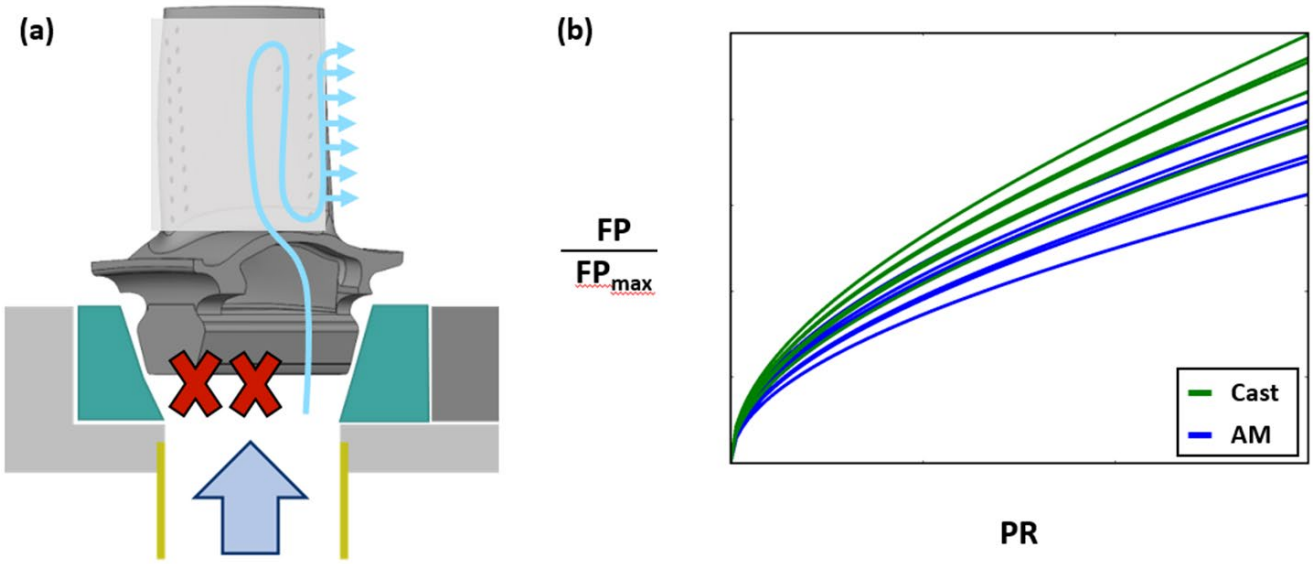


Figure 1. (a) Custom flow parameter apparatus representing trailing edge slot flow measurements (b) Post operation flow parameter measurements of the trailing edge slots for a subset of the turbine blade wheel. AM: additive manufacturing, FP: flow parameter, PR: pressure ratio.

It is important to understand how specific cooling flow rates compare to the measured overall cooling effectiveness (ϕ). The region to be analyzed on the pressure side was chosen to be upstream of the cooling hole row and over the internal trailing edge serpentine passage only, as shown in Figure 2a. Data comparing $\overline{\overline{\phi}}$ to flow parameter are shown in Figure 2b as three distinct groups for each blade manufacturing type corresponding to the three flow conditions measured within START. Differences within a blade group are expected due to manufacturing defects as shown by the separation between the datapoints. Any shift along a calculated polynomial curve fit is assumed to be due to the change in flow rate, while vertical shifts in thermal performance are due to internal geometric differences. When further analyzing these results, CT scans will be used to better determine which geometric changes impacted the blade surface temperatures.

Due to the AM blades having the same design as a singular cast blade, it is expected that the AM blades should have similar cooling performance for similar mass flow rate to that particular blade. However, it is important to understand how the whole group of manufactured blades performs as well. The polynomial curve fit for each blade was used to predict the thermal performance at a set flow parameter to provide similar flow rate comparisons between the two manufacturing types, as shown in Figure 2c. These data show larger variations in thermal performance for the AM blades, which could be caused by the manufacturing process. Again, CT scans and additional flow measurements will provide information on internal defects, i.e., internal cooling channel breakthroughs, internal rib geometries, and blade thickness, all of which have an impact on the surface temperature of the blade. This investigation is ongoing and is expected to advance further during the next reporting period.

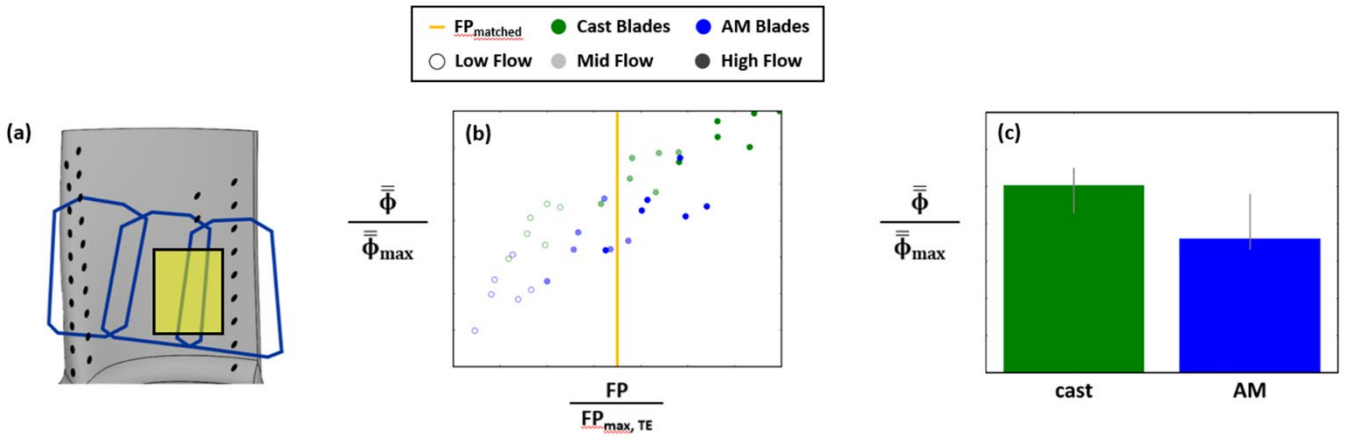


Figure 2. (a) Area-averaged region of interest on the pressure side of the blade, selected to compare (b) the measured post operation flow rate through the blade to the surface temperature and (c) the predicted normalized overall effectiveness at a target FP. AM: additive manufacturing, FP: flow parameter.

CT scans were analyzed to gather information about the blade's material thickness. Seven distinct locations along the blade's surface were measured between three cast blades and three AM blades. Shown in Figure 3 is measured wall thickness normalized by wall thickness design intent at a single span height along the blade's surface. It is important to note that the design intent wall thickness for cast blades was the FAA CLEEN II design, while the design intent wall thickness for AM blades was the solid model generated from the CT scans and blue light scans of the ideal geometric FAA CLEEN II blade as previously described. AM blades show less variability in wall thickness across the entire surface of the blades analyzed, which is expected due to the manufacturing process. Knowing the wall thicknesses between cast and AM blades is vital in understanding the exact thermal resistance felt by the blade material, which will help determine the specific impact thickness has on the measured cooling performances.

Initial thermal differences were discussed in the quarter (Q)1 fiscal year (FY)25 report by linking mass flow rate to area averaged effectiveness, which showed that the AM blades underflowed the cast blades, in addition to underperforming thermally. However, it was found that all the blades had internal kiss-ins which allowed coolant to leak between internal passages. This means that the partial flow parameters measured are not the same between bench flow tests and START rig tests. Therefore, a new thermal assessment has been conducted, which takes set span ϕ surface wraps along the entire blade, as shown in Figure 4 (high flow test condition only). The range of AM and cast blades, regions of blue and green, are bounded by their respective max and min values measured at the span indicated by the yellow line across the blade cartoon. The orange line represents the thermal performance of the cast blade that was used to generate the solid model for the manufacturing of the AM blade set. It can be noticed that the AM blades pressure side trailing edge generally has lower thermal performance when compared to cast blade set. But, when shifting from the trailing edge to the leading edge, the AM blades are observed to have greater thermal performance relative to the cast blades. This shift is directly due to the internal kiss-ins and slight design differences between the cast and AM blades, which caused the AM blade leading-edge region to have greater mass flow rate, thus driving temperatures lower.

Determining the wall thickness measurements impact on the IR thermal measurements requires a one-dimensional nodal network of resistances. Equation 1 relates the IR measured temperatures (left hand side) to the rearranged nodal network (right hand side).

$$\frac{T_{mgp}-T_s}{T_{mgp}-T_c} = \phi = \frac{\frac{1}{h_e}}{\frac{1}{h_e}+\frac{t_{wall}}{k_{material}}+\frac{1}{h_i}} = \frac{R_1}{R_1+R_2+R_3} \quad \text{(Eq. 1)}$$

T_{mgp} and T_c are circumferential temperature measurements taken from the main gas path and blade cooling flow path respectively, while T_s is the measured blade surface temperature. The external and internal convection coefficients are

represented by h_e and h_i and the specific blade material thermal conductivity is $k_{material}$. It is desired to understand which resistance- R_1, R_2, or R_3- is the primary driver of the measured thermal difference. With known wall thickness at discrete locations along the blade, and thermal measurements at those same locations, IR measurements can be related to R_2. Figure 5 shows the averaged cooling performance at the discrete locations used for thickness measurements plotted against the averaged wall thickness at the same location. Tracking regions that had similar wall thickness differences between the AM and cast blades- -28% (triangle), -10% (square), and 85% (right facing triangle)-there is no noticeable trend between these shapes. This indicates that the wall thickness does have an impact on measured surface temperatures but is not the primary driver of thermal differences measured between cast and AM blades.

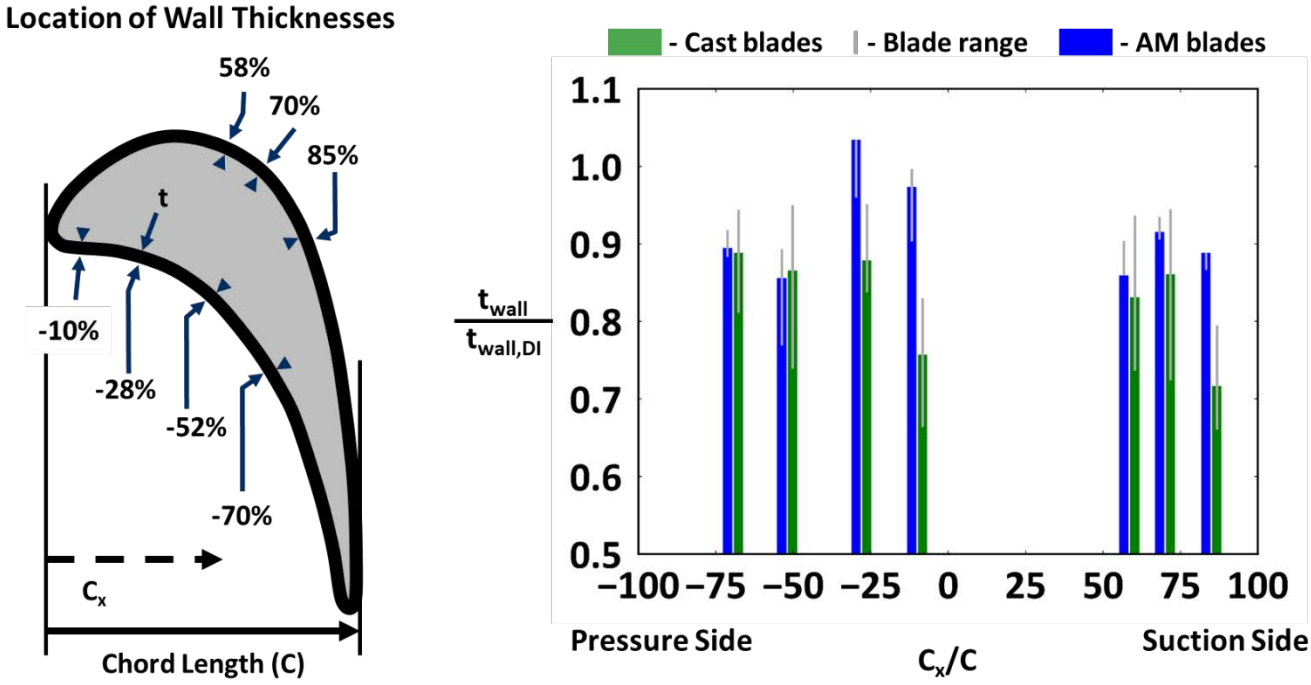


Figure 3. Blade wall thickness at seven distinct locations along the pressure side and suction side of the blade.

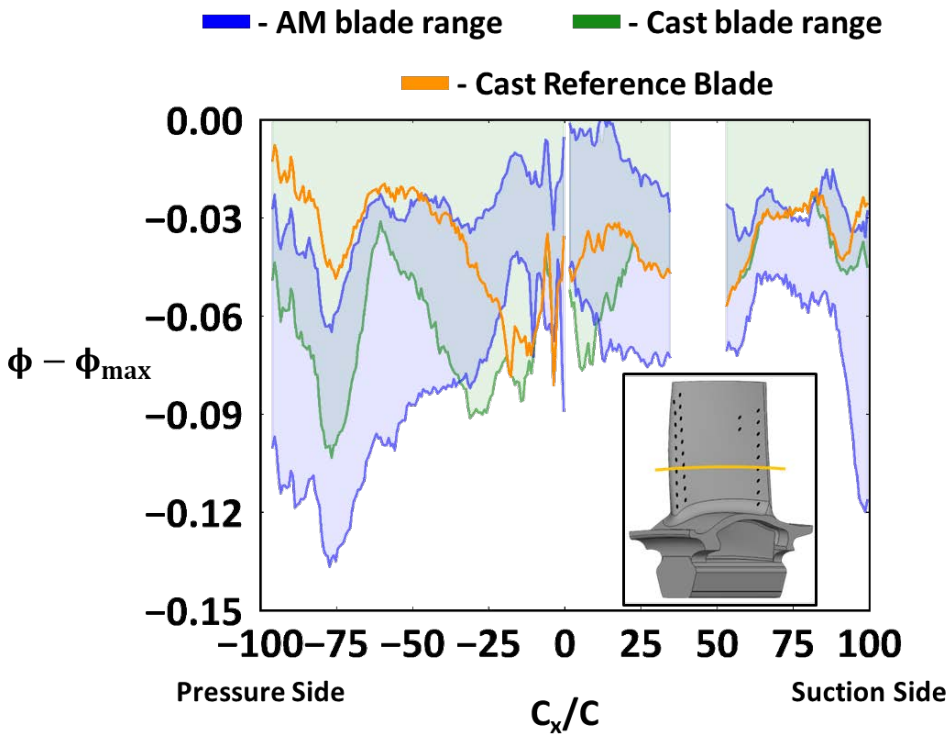


Figure 4. Blade cooling performance at the high flow test condition for a set span height across the entire surface of the airfoil. AM: additive manufacturing, C: chord length.

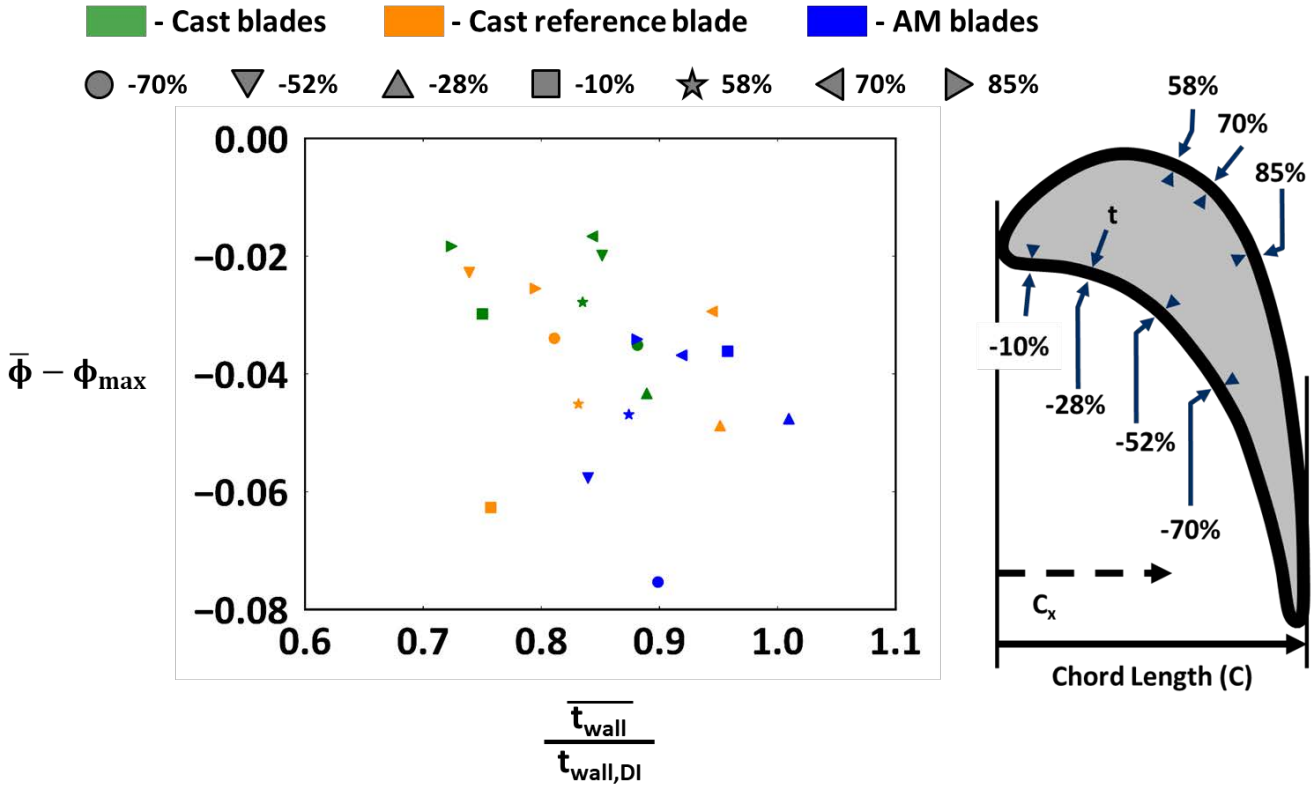


Figure 5. Averaged thermal performance compared to average wall thickness at seven discrete locations for a set span height. AM: additive manufacturing.

Future analysis is planned to understand how the other resistances, R_1 and R_3, impact cooling performance. It is known that AM produces rougher internal surfaces, which could enhance heat transfer and impact pressure loss through cooling channels. It is expected that the internal cooling coefficient will have the largest impact on blade surface temperatures based on preliminary calculations using simplified geometries. To help verify this prediction, Nusselt number surface roughness augmentations will be applied to calculated cooling performances, which will be directly compared to the measured cooling performances.

Following initial data analysis reported in prior quarterly reports, continued analysis was performed in Q3 FY25 to evaluate the cast versus AM comparison of CLEEN II blade designs. Figure 6a and 6b show an illustration of the external cooling features of the blades, along with the print direction used for this study for the AM blade set. Both the cast and AM blade sets comprised rib turbulated leading-edge cavity and serpentine cooling channels, internal impingement slots between the serpentine channels, and a trailing edge pin-fin array. Also shown in Figure 6c is an illustrated internal cooling passage that includes V-shaped rib turbulators. It is important to note that the internal cooling passage only has turbulators within the airfoil portion of the blade, location 3 in Figure 6c; there were no turbulators in the root portion of the blade that supplies the blade coolant, location 1 in Figure 6c. The region located between non-turbulated inlet portion of the blade and the turbulated airfoil portion of the blade is referred to throughout this section as location 2, shown in Figure 6c.

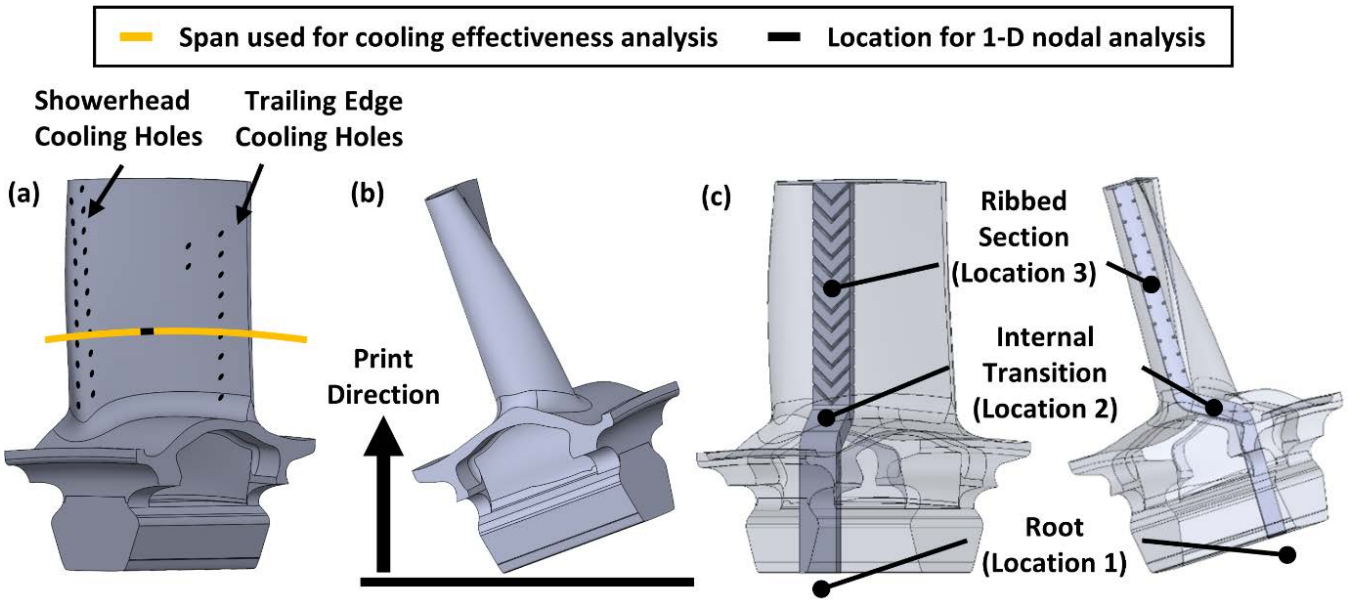


Figure 6. Graphical representations of an engine scale turbine blade with a generic internal cooling channel and external cooling hole locations. Also shown is the print direction used for the AM blade set and the specific span used for cooling effectiveness surface wraps, one-dimensional (1D) nodal network analyses, and predictive surface temperature analysis. Turbine blade geometries are for illustrative purposes only.

Using the spatially-resolved IR measurements, data were extracted for a fixed span location depicted in Figure 6a to compare cast and AM blades. Figure 7 shows the temperature distributions for both blade set ranges, with the AM blade set in blue and the cast blade set in green in terms of a non-dimensional $\Delta\phi$ value. Different from the analysis shown in Q2 FY25 report, Figure 7 evaluates the difference between the AM blade relative to the cast reference blade. Comparisons were made by normalizing the non-dimensional temperature data by that of the cast reference blade such that the orange line shows the datum. For this study, ϕ was defined using the cooling temperature located at location 1 and is shown by Equation 2. The main gas path temperature, T_∞, and coolant temperature, $T_{c,1}$, used in this chapter was in the relative reference frame. It was also important to distinguish T_c within this section was different from the coolant temperature discussed later in this section and therefore was marked with a location 1 indicator. All ϕ values, however, presented in this section are calculated using the root coolant temperature from location 1 and are also marked accordingly with a location 1 indicator, with the cast reference blade referred to as $\phi_{1,\mathrm{ref}}$ throughout this chapter.

$$\phi_1 = \frac{T_\infty - T_s}{T_\infty - T_{c,1}} \quad \text{(Eq. 2)}$$

The general shape of cooling performance between the cast and AM blades was similar along the whole surface except around C_x/C = -65% shown in Figure 4. In this region, the cast blades converged toward the cast reference blade, and then immediately diverged towards the trailing edge, C_x/C = -100%. This was a result of the internal impingement slots located between the serpentine passages. CT scans of this region of both blade sets revealed that the AM impingement slots had large downskin dross formations partially blocking the impingement passage. With the internal walls conducting heat from one side of the blade to the other, reduced cooling means less ability to convect heat out of the internal wall. However, there only appears to be a local impact due to the impingement slots, with the overall range of performance for the cast blade set matching the overall range of the AM blade set just downstream at C_x/C = -75%.

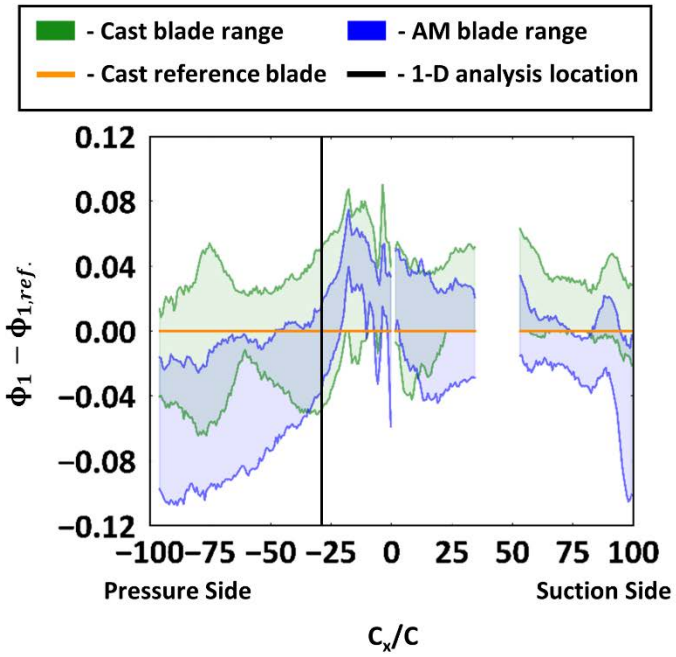


Figure 7. Blade cooling effectiveness ranges normalized by the AM design intent blade's cooling performance. AM: additive manufacturing, C: chord length.

The coolant temperature, $T_{c,3}$, was calculated using a discretized energy balance method for each manufacturing method, respectively. For this calculation, internal wall temperatures were required at three discrete locations – the root of the blade at location 1, where the internal passage transitions from smooth to a rib turbulated wall as shown in Figure 6c at location 2, and at 30% span as shown in Figure 6a at location 3. The surface temperatures at the blade root were calculated from isentropic flow relations converting cooling flow supply conditions to the relative frame of reference as the flow was swirled and onboarded to the blade disk. For this analysis, it was assumed that the coolant temperature at the blade root was equal to the surface temperatures at the blade root. IR images and external wall heat flux predictions were used to calculate the internal wall temperature at both the transition region and 30% span, locations 2 and 3, respectively. Using a discretized energy balance method for the two regions of the blade, smooth and rib-turbulated, and a linear internal wall temperature heat up, the coolant for the AM blades was calculated to be hotter at location 3 compared to the cast blades. This was expected due to the AM roughness throughout the full channel, including the region without ribs, within the blade. Equation 3 provides a non-dimensional comparison of the coolant heat up internally. The calculated difference of internal heat up was $\theta_{AM} - \theta_{cast}$ = -0.049. This result meant that the AM blade set had 5% less coolant potential than the cast blade set at location 3 with respect to the internal cooling temperatures.

$$\theta = \frac{T_\infty - T_{c,3}}{T_\infty - T_{c,1}} \quad \text{(Eq. 3)}$$

Recall that ϕ_1 is calculated using the location 1 coolant temperature, $T_{c,1}$, but the one-dimensional (1D) network utilizes the coolant temperature at location 3, $T_{c,3}$. The increase of calculated surface temperature for the AM blade set only when using the calculated cast coolant temperature, $T_{c,3,cast}$, compared to using the hotter calculated AM coolant temperature, $T_{c,3,AM}$, was a 4.5% decrease in ϕ_1. When the appropriate calculated coolant temperatures and literature driven correlations were used, the cast blades had a deviation of $\phi_{1,calculated} - \phi_{1,measured}$ = -0.002 on average, while the AM blades showed $\phi_{1,calculated} - \phi_{1,measured}$ = 0.006 on average. Both calculated surface temperatures were within measurement uncertainties. This analysis shows the importance of accounting for the additional roughness of the AM channel in closing the loop of understanding the thermal performance of AM and cast blades.



The 1D analysis provided a method for understanding the applicability of previously reported literature correlations derived in lower TRL facilities for use in a gas turbine blade analysis. While this analysis showed similar calculated ϕ_1 values to that of the measured ϕ_1 values, it was highly dependent on existing literature correlations and predicted data for location 2 on the blades surface. The limitations of this analysis were highlighted when the 1D network was applied to a region of the blade where no existing temperatures or correlations were available. This finding suggested that the entire blades surface temperature is needed to properly account for location 2 internal wall temperature, either measured or predicted. Also, ensuring internal convection correlations are acquired for geometries that match the end desired turbine blade product is essential for proper internal heat up analysis, which in turn means proper cooling effectiveness calculations.

Task 2 – Design New Double-wall Cooling Technologies

The Pennsylvania State University

Objective

The objective of this task is to develop novel double-wall cooling designs that feature the microchannel concepts being explored in the literature and which can be achieved via AM. The designs will be generated with advice from Pratt & Whitney, so that the concepts can be leveraged for commercialization. The designs will be packaged into cascade test articles that will be measured in the high-speed linear cascade at Penn State with IR thermography.

Research Approach

Design of Linear Cascade Test Articles

This task was completed in 2022 with final delivery of all high-speed cascade test articles to Penn State.

Task 3 – Manufacture and Test Novel Double-wall Cooling Designs for Linear Cascade

The Pennsylvania State University

Objective

The objective of this task is to measure the performance of the AM microchannels in the linear cascade airfoil and rank the performance of the novel geometries. This process includes measuring the pressure drop and the surface temperature of the airfoils with the novel microchannel geometries. Subsequent evaluation is conducted through computational fluid dynamics (CFD) investigations of the performance to understand physics and predictive capabilities of modern design tools.

Research Approach

Experimental Testing of Linear Cascade Hardware

This subtask was completed in 2024 and reported in a previous annual report. Blades were tested at a range of exit Mach and Reynolds numbers, with different amounts of internal cooling flow, and surface temperatures were measured using a calibrated infrared camera.

Computational Simulation of Linear Cascade Hardware

This task involved computational simulations of experimentally tested microchannel cooling designs from prior cascade tests. The goal of this task was to determine the accuracy of design-level conjugate CFD to predict the performance of the novel microchannel designs. To do this, a computational model of the single test blade was generated. Figure 8 shows the computational domain, with periodic sidewalls to simulate the periodic conditions of the high-speed linear cascade. The inlet of the domain was prescribed with stagnation pressure and temperature conditions from the experiments, and the outlet of the domain was prescribed with a static pressure also from the experiments to achieve the desired exit Mach number. The airfoil (cartoon shown due to proprietary nature of the actual airfoil design) had cooling channels based on the design intent of the various microchannel designs. The coolant inlet mass flow and temperature conditions were specified at the base of the airfoil to match test conditions. To conduct a conjugate analysis (prediction of metal temperature in the CFD), the domain included both the fluid volume inside the microchannels and around the blade but





also the solid domain of the blade material, connected by an interface that matches temperature and heat flux. All other walls (top endwall, bottom endwall) were specified as adiabatic and no-slip.

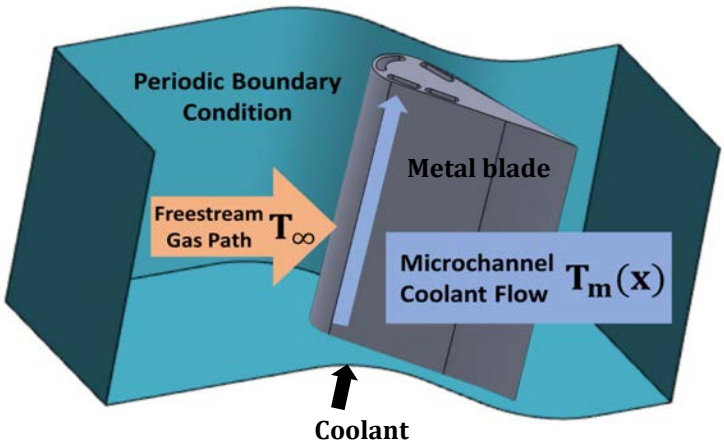


Figure 8. Computational domain for conjugate computational fluid dynamics analysis of microchannel cooled blade.

The solution approach was a steady Reynolds Averaged Navier Stokes (RANS) simulation in STAR CCM+,®[1] an industry standard design code. The fluid domain was modeled as an ideal gas with Sutherland's law for viscosity and thermal conductivity, and the solid domain was modeled as Inconel with constant thermal conductivity based on typical values for Inconel® 718 (the material the blades were constructed from). A coupled solver (simultaneous solution of all conservation equations) with second-order accuracy was chosen. To ensure iterative convergence, residuals of conservation equations were tracked, as well as mass-averaged outlet total pressure and surface average blade outer surface temperature. In general, the solution was iterated for more than 4,000 iterations until the residuals stopped changing and the other monitors were constant to within 1%. Work in prior years of this project indicated the necessary mesh size to achieve grid convergence, with approximately 3.7M cells for the empty microchannel simulations, and 10.4M cells for microchannels with internal geometries.

Figure 9 shows a comparison of computationally predicted results for nondimensional surface temperature of the blade metal (also known as overall cooling effectiveness), compared to the same experimental cases, for high and low microchannel flow rates. The cartoon on the left indicates how the results are "unwrapped" around the surface of the blade so that both sides of the blade can be presented in the figure. The external conditions for these cases were fixed at an exit Mach of 0.81 and an exit Reynolds number of 340,000.

In comparing Figures 9a to 9b, the level of nondimensional cooling of the metal decreases as the coolant flow rate decreases from a Reynolds number of 20,000 to a Reynolds number of 6,000. This is expected, since the hot gas conditions are unchanging, but the internal cooling convection decreases with Reynolds number. When comparing the computational predictions to the experiment at a given Reynolds number, there is generally good agreement in the trends of cool regions located around microchannels (dark blue) and warm regions (orange colors) that are downstream of the microchannel cooled region. The good agreement in external metal surface temperature was somewhat unexpected since the CFD does not model the as-manufactured surface roughness of the empty microchannels, but the results here indicate that the surface roughness is not a significant contribution to internal convective heat transfer for these microchannels.

® SimCenter and STAR CCM+ are registered trademarks of Siemens Industry Software NV, Leuven, Belgium.
[1] SimCenter STAR CCM+ is a comprehensive engineering simulation software that uses CFD and multiphysics technology to help engineers design and optimize products across a wide range of industries.
® Inconel is a registered trademark of Huntington Alloys Corporation, Huntington, West Virginia.

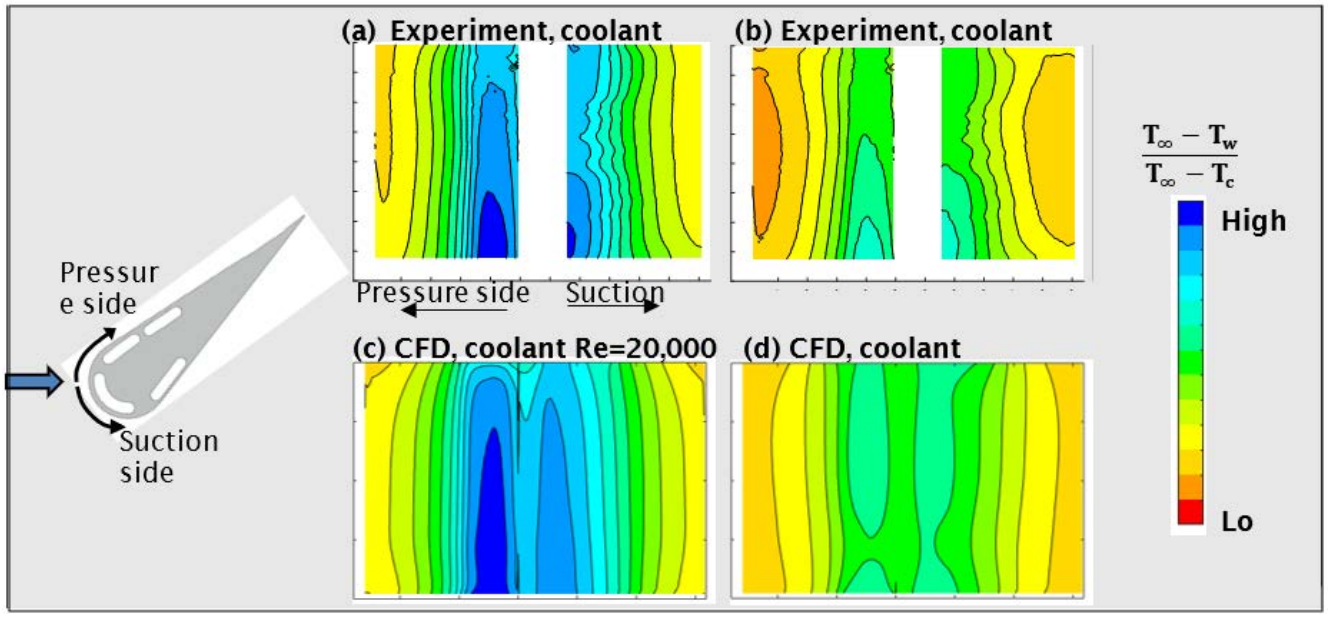


Figure 9. Comparison of experimentally measured nondimensional metal temperature (a,b) versus computationally predicted metal temperature (c,d) for high (Re=20,000) and low (Re=6,000) microchannel flow rates, for empty microchannels. CFD: computational fluid dynamics; Re: Reynolds number.

Other microchannels were also modeled in the conjugate CFD, including the w-rib design. Figure 10 shows a comparison of the experiment at a given coolant channel Reynolds number to the CFD at the same condition. Here, the CFD significantly overpredicts the cooling performance of the W-rib design, with a much cooler region (high overall cooling effectiveness) around the leading edge of the blade.

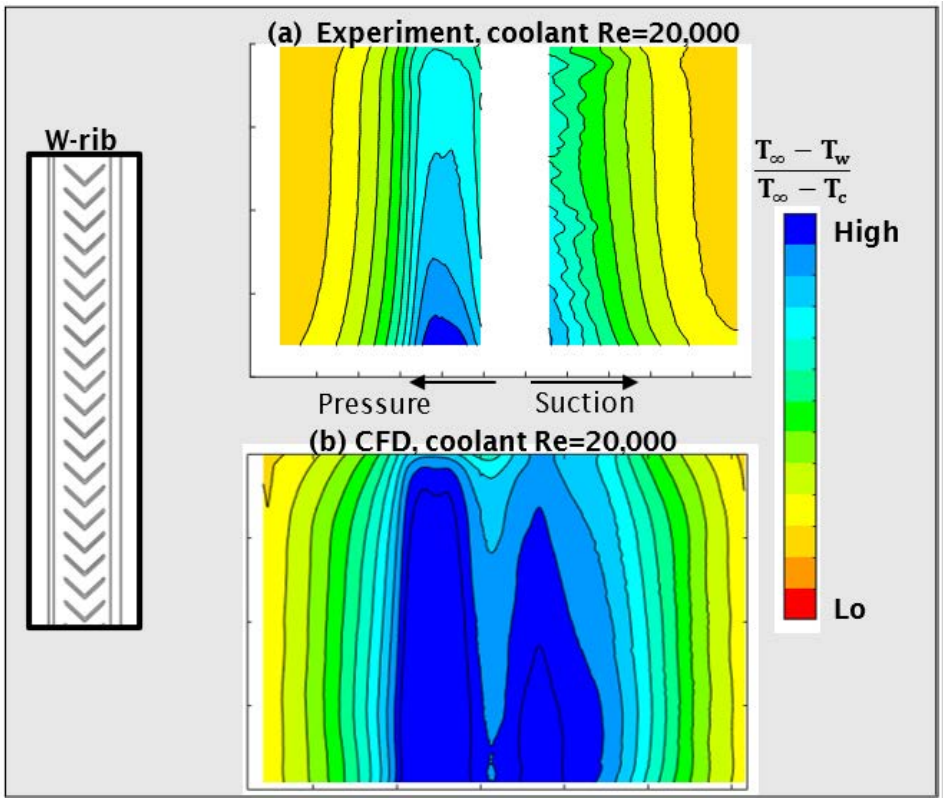


Figure 10. Comparison of experimentally measured nondimensional metal temperature (a) versus computationally predicted metal temperature (b) for a high coolant channel flowrate for a microchannel with W-ribs on the walls. CFD: computational fluid dynamics; Re: Reynolds number.

To understand this, analysis of CT scan results for the W-rib microchannel was conducted. Figure 11 compares a cross-section from the CT scan result to the design intent at that same location. For the CT scan analysis, a region identified as the rib protrusion from the surface (red) was isolated from the surrounding metal walls of the microchannel (green). When comparing to design intent, the sides of the as-manufactured rib are significantly rounded which likely reduces the sharp flow separations that normally occur around ribs. These separations are critical to the heat transfer performance of ribs, and it is quite likely that the as-manufactured geometry has reduced internal convective heat transfer, leading to warmer external metal temperature relative to the CFD.

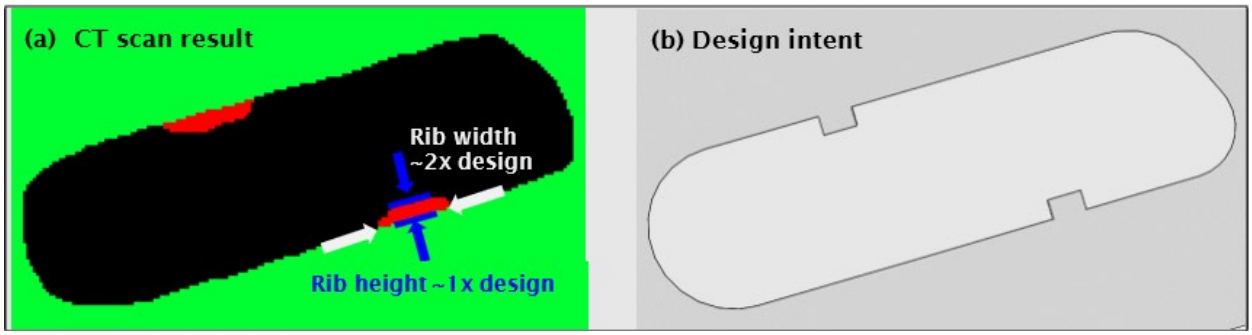


Figure 11. Comparison of computed tomography (CT) scan of an as-manufactured ribbed microchannel (a) to the design-intent shape (b) at a section in the middle of a microchannel.

Finally, conjugate CFD simulations were conducted of the microchannel with cylindrical pins that span between the inside and outside-facing walls of the microchannel. The resulting prediction of overall cooling effectiveness is shown in Figure 12, where the W-rib prediction is compared to the cylindrical pin prediction. In general, the overall cooling effectiveness is not significantly improved with cylindrical pins, despite their higher blockage of the microchannel. In fact, the pressure drop across the cylindrical pin microchannel is more than 12 times higher than for an empty microchannel, and more than 3 times higher than the pressure drop of the microchannel with W-ribs. This suggests that this type of design is not desirable since the pressure drop penalty is not offset by a significant improvement in cooling.

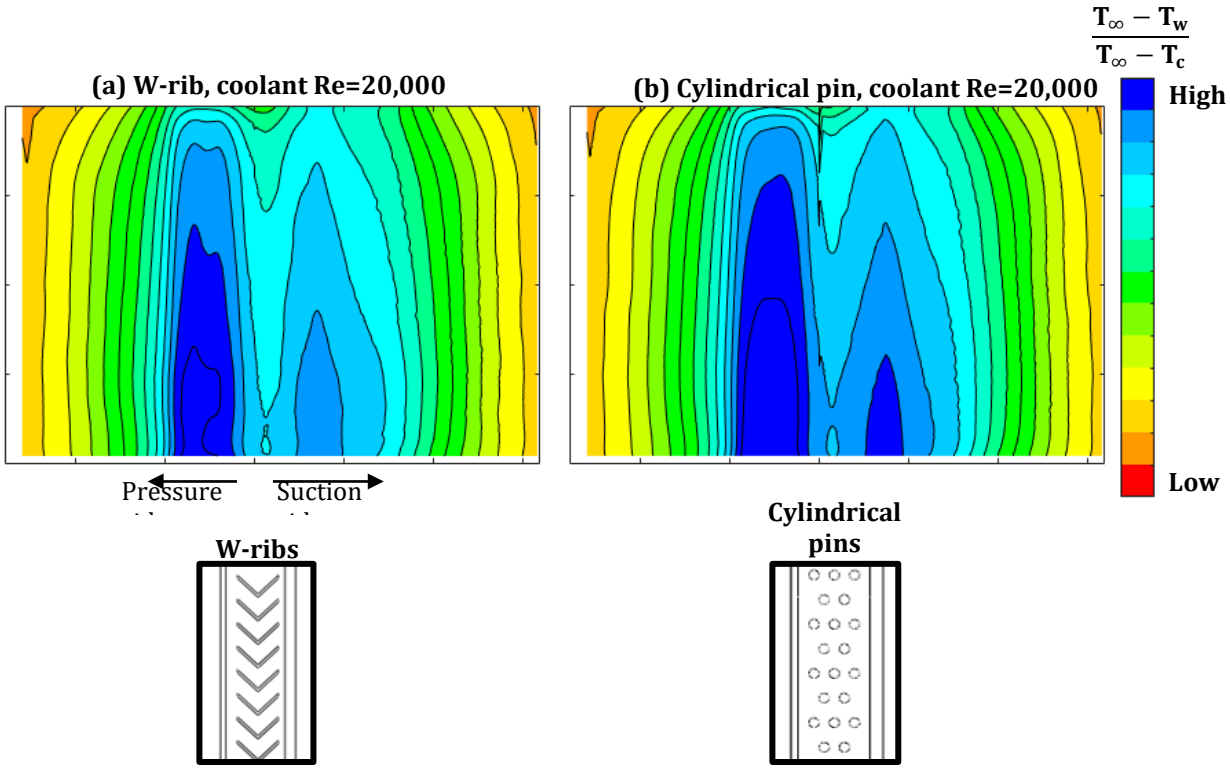


Figure 12. Comparison of overall cooling effectiveness prediction of W-rib design (a) to a cylindrical pin design (b) inside the microchannels.

Future work is investigating a modification to the W-rib cross section shape per observations of the as-manufactured design shown in Figure 11. This is being adjusted in the conjugate CFD so that new simulations can be run, to determine if the rib shape has a major impact on the overall cooling effectiveness.

Task 4 – Manufacture and Test AM NExT Blades with Varying Roughness

The Pennsylvania State University

Objective

The objective of this task is to quantify the impact of surface roughness for additively manufactured turbine blades. The START team will manufacture and evaluate a subset of turbine blades with methodical and controlled surface roughness levels. The specific roughness will be determined based on prior knowledge and informed by observations from fielded turbine engine hardware. Then, the roughness details will be applied to the National Experimental Turbine (NExT) blade geometry. Whereas prior work set out to understand differences strictly due to the roughness of the airfoil surfaces, this task will also evaluate the influence of roughness on the development of film cooling on the external surface of the airfoil. A combined approach evaluating external roughness levels with and without external film cooling will better differentiate

the connectivity between these effects. The subset of turbine blades will be assembled as a rainbow wheel, and the performance of the different roughness and cooling designs will be evaluated quantitatively using non-contact IR thermal imaging in the one-stage START facility.

Research Approach

A turbine "rainbow" test wheel has been designed to allow measurements of both cast Blades and AM Blades during the same experiment. This will ensure the test conditions are identical for the two different blade manufacturing processes, which will support understanding of the differences in manufacturing process on the heat transfer. The test wheel will also include different surface roughness levels on the printed blades, to help identify the impacts of internal cooling differences relative to external cooling differences. Figure 13 below shows a notional illustrative layout of the planned test wheel identifying blade configuration and surface roughness identified by color coordination.

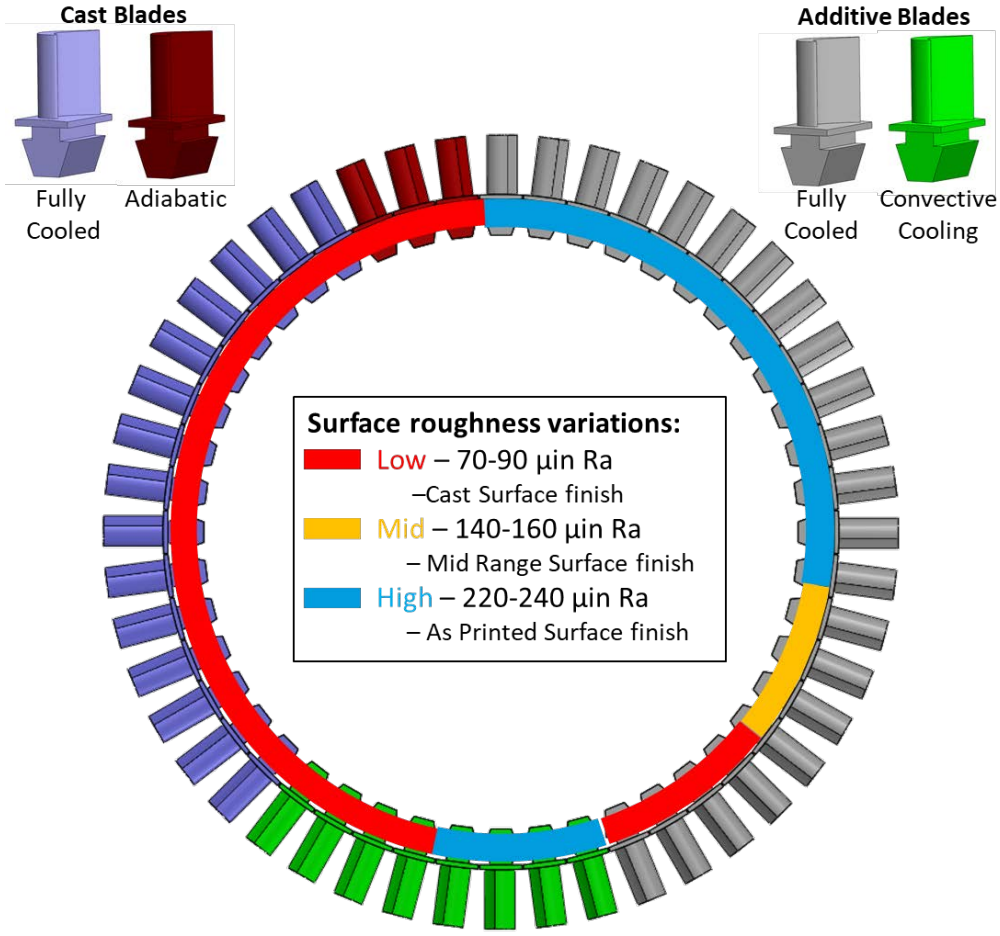


Figure 13. Example illustration of rainbow wheel configuration.

To facilitate modifying the printed blades to roughness levels equivalent to the cast blades, the cast blade surface roughness was measured using a surface roughness gage. The cast blade surface roughness average was determined to be an average of 80 µin Ra for these blades. The surface roughness of the as-printed blades was also measured using the surface roughness gage and determined to average 230 µin Ra—this value aligns with expectations and other measurements of as-printed AM components evaluated in prior programs. A subset of printed blades will have their surface roughness adjusted to align with the turbine test wheel configuration roughness plan, as demonstrated in

Figure 14. Following surface roughness modifications, the blades will transition to a vendor to have final hole configurations drilled as defined by the turbine test wheel configuration.

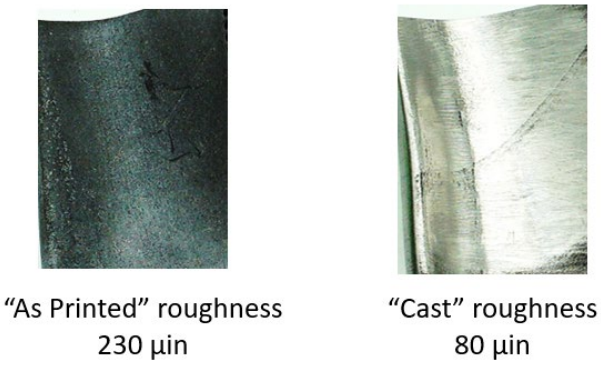


Figure 14. Additive manufacturing (AM) blade surface roughness comparison.

The configuration of the blades outlined in Figure 13 (cooled, convective, adiabatic) allows for more detailed understanding of the different aspects of the heat transfer occurring in the blades. The convective cooling configuration requires design work to ensure the convective blades have the appropriate internal flow characteristic. This design work is in progress and will enable final machining to be completed. The evaluation of external roughness on the behavior of film holes for AM turbine blades will be evaluated through testing in the START rig with a test schedule targeting a Q2 FY26 test window.

The rainbow wheel configuration that has been planned for this testing includes a convectively cooled blade configuration. The convectively cooled blade allows cooling flow to pass through the internal cooling channels of the blade and exit the blade without directly cooling the blade surface. This allows the internal cooling effectiveness to be studied. The design of the cooling flow exit features on the convective blades has been completed. The passage bleed holes sizes are established by matching the internal Reynolds numbers of each cooling passage with that of the film cooled blades thereby ensuring similar internal convective cooling characteristics between the two blade types. Figure 15 shows a cartoon of the cooling passages and their associated new bleed hole locations.

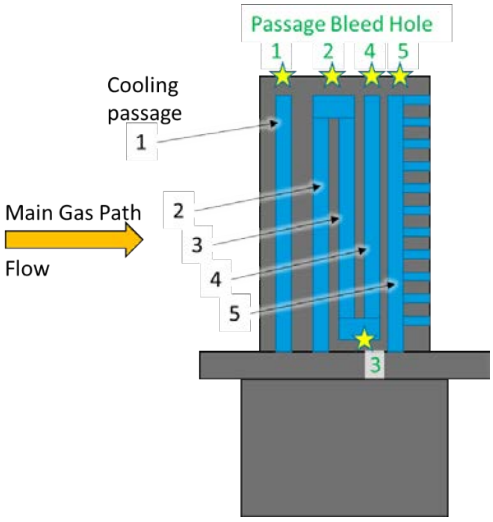


Figure 15. Convective Blade Cooling Bleed Holes.

For the external temperature of the blades to be determined using IR imaging, the surface of the blade has to be covered with a high emissivity coating. To understand the impact of the addition of this coating on surface roughness, a surface roughness comparator was coated using the same coating and technique that is used to coat the blades. Surface roughness measurements were taken before and after the coating was applied using a Taylor Hobson® Surtronic S-128 surface roughness tester. Figure 16 shows an image of the comparator plate taken post-paint. The green highlight boxes indicate the samples that were measured pre and post paint.

Coating the samples showed an impact on the surface roughness measurements from the applied coating. Table 1 shows that surface roughness less than ~100 Ra were made rougher, while surface roughness greater than ~100 were made less rough. The results of this test are driving additional studies to improve the coating process to reduce the impact on the surface roughness of the samples.

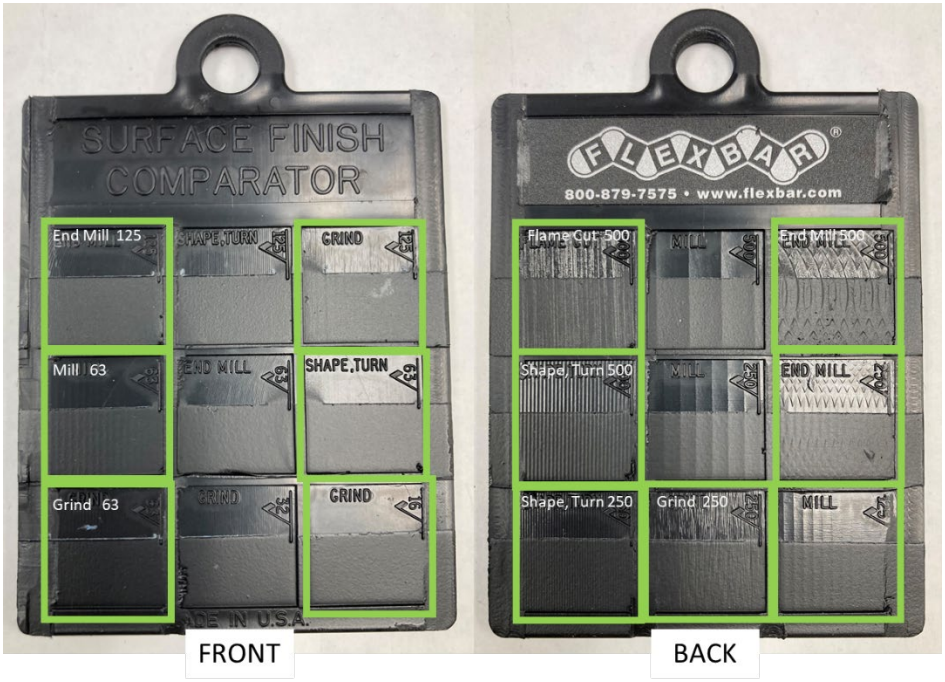


Figure 16. Comparator, Post-Paint.

®Taylor Hobson and Surtronic are registered trademarks of Taylor Hobson Limited, United Kingdom.



Table 1. Surface Roughness Measurements Pre- and Post-Paint.

Comparator Description	Ra [µin]	Pre-Paint	Post-Paint
Calibration Standard	236	240	240
Grind	16	20	43
Grind	63	37	63
Shape, Turn	63	40	37
Mill	63	30	43
Grind	125	57	67
End Mill	125	87	70
Mill	125	40	63
Grind	250	163	87
Shape, Turn	250	173	100
End Mill	250	83	63
Shape, Turn	500	253	160
End Mill	500	153	183
Flame Cut	500	247	177

Task 5 – Develop Correlations for Realistic Turbine Roughness

The Pennsylvania State University

Objective

The objective of this task is to evaluate the various roughness feature types using fielded engine parts to classify the various types of roughness levels and features. Experimental heat transfer measurements will be made on coupons with varied roughness scales and features based upon operational blades. AM coupons will be made to replicate those roughness types. It is important to note that having a fully metal coupon provides the needed boundary conditions for these heat transfer measurements of the convective heat transfer coefficients. As such, the approach of printing the three-dimensional (3D) coupons from metal is required rather than using the airfoils themselves. The printing also allows for a methodical approach whereby only the desired roughness scales are replicated thereby allowing for accurate correlations to be developed.

Research Approach

Using a laser microscope, optical scans were collected from three field-operated blades with different levels of deterioration to investigate degraded surface texture. On the pressure and suction sides, three scans were collected along the chord length at the upper midspan region of the blades. In addition, several scans were captured of the highly deteriorated regions near the leading edges including macroscale spallation and step-like features.

Rough surfaces are commonly characterized using the arithmetic mean height (S_a) which only quantifies average roughness magnitude. However, prior studies have shown that surface morphology and spatial orientation also influence aerothermal performance. To more comprehensively represent the surface roughness, a broader set of metrology parameters describing height, spatial structure, and shape were analyzed. The pressure sides of the blades displayed higher roughness magnitudes with more protruding deposition compared to the suction sides which had lower roughness magnitudes with more eroded features. The suction side roughness tended to have more directional textures along the flow direction. Regions near the leading edges and trailing edges were typically rougher compared to the mid chord regions.

To conduct heat transfer and pressure loss tests on these rough surfaces, the blade surface textures need to be replicated on flat plate test coupons. Because manufacturing microscale features is difficult, the first step was to evaluate 3D printing

resolution limits. Blade surface textures were replicated at-scale on flat plate test coupons with stereolithography (SLA) 3D printing. Figure 17 shows a height map of a blade surface next to its replicated 3D printed surface. Optical scans were also captured of the 3D printed surfaces to evaluate how closely replicated surfaces matched the original blade surfaces. Findings show that the SLA printer did not successfully resolve surface textures with small height magnitudes due to a minimum 25-micron layer thickness. Calculated metrology parameters deviated up to 2.5 times from the original blade surfaces. On the other hand, larger surface features at the meso- and macroscales, such as spallation pits, were better resolved. Metrology parameters for these replicated larger features closely matched on the real blade surfaces.

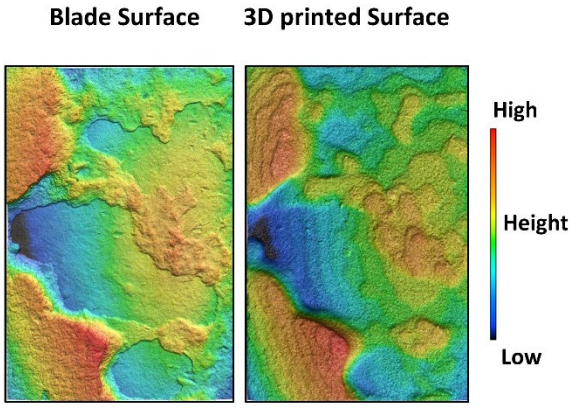


Figure 17. The high magnitude rough surface replicated using stereolithography three-dimensional (3D) printing.

Milestones

Milestone	Due date	Estimated date of completion	Actual date of completion	Status
Workplan	3/4/20	3/4/20	3/5/20	Completed
COE meeting 1	4/1/20	4/1/20		Cancelled
COE meeting 2	10/1/21	10/1/21	10/28–10/29/21	Completed
COE meeting 3	10/26/22	10/26/22	10/26–10/28/22	Completed
COE meeting 4	10/24/23	10/24/23	10/24/23	Completed
COE meeting 5	10/31/24	10/31/24	10/29-10/31/24	Completed
COE meeting 6	10/16/25	10/16/25	10/14-10/16/25	Completed
Annual report	12/31/25	12/31/25		
Project closeout	12/31/26	12/31/26		

Major Accomplishments

Following several years of planning and learning, significant learning continued this year under the project. In particular, data were collected from a second round of next-generation AM turbine blades for comparison with cast counterparts; AM NExT blades were manufactured and prepared for a rainbow wheel test program; and fundamental knowledge was gained in the impact of roughness for turbine heat transfer with applicability to fielded engine parts.

Publications

None.

Outreach Efforts

Research findings were presented throughout this review period as shown below.



Event	Date	Attendees
Bi-weekly calls	Every 2 weeks	Pratt & Whitney (PW) aerodynamics/durability engineers
Quarterly calls with turbine Original Equipment Manufacturers	Once per quarter	Industry partners: Solar, Siemens, Honeywell
National Aeronautics and Space Administration (NASA) university leadership initiative meeting	10/2/2024	NASA, FAA, PW, Collins, RTX Technology Research Center, Howard University, Georgia Institute of Technology
U.S. Department of Energy (DOE) National Experimental Turbine (NExT) annual review meeting	11/18/2024	DOE, NASA, PW, Solar, Siemens, Honeywell
Center of Excellence bi-annual meetings	1/30/2025 9/29/2025	Solar Turbine engineers
Research seminar visit	2/18/2025	Howmet Aerospace
Center of Excellence bi-annual meetings	12/9/2024 6/2/2025	PW aerodynamics/durability engineers and management

Awards

Dr. Reid Berdanier was elected as an Associate Fellow of the American Institute for Aeronautics and Astronautics (AIAA).
Dr. Karen Thole was awarded the 2025 Kate Gleason Award from the American Society of Mechanical Engineers (ASME).

Student Involvement

Nicholas Gailey was a PhD student who led the experimental analysis of AM turbine blades in the START rig. Nicholas completed his PhD in Summer 2025. Starting in September 2025, Nicholas is a turbine durability engineer at Pratt & Whitney.

Ethan Bonn, a PhD student, has been investigating AM turbine blade performance in the START rig since January 2025.

Benjamin Bizzak, a PhD student, has been participating in turbine blade preparation for Task 4 beginning Fall 2025.

Matthew Stuber, a MSME student, led the initial measurements of roughness for Task 5.

Abbigail Altland, a PhD Student, has led the detailed analysis of AM roughness effects for Task 5 beginning Fall 2025.

Plans for Next Period

- Conduct additional analysis of next-generation turbine blades manufactured through AM, supporting Task 1.
- Conduct further experimental and computational analysis of double-wall cooling designs in cascade performance, supporting Task 3.
- Build, test, and analysis of NExT turbine blades with AM roughness, supporting Task 4.
- Develop detailed roughness correlation models using available data, supporting Task 5.

Disclaimer

This research was funded by the FAA Office of Environment and Energy through ASCENT, the FAA Center of Excellence for Alternative Jet Fuels and the Environment, Project 056 through FAA Award Number 13-C-AJFE-PSU-126 under the supervision of Joshua Glottmann. Any opinions, findings, conclusions or recommendations expressed in this material are those of the authors and do not necessarily reflect the views of the FAA.



Project 057 Support for Supersonic Aircraft En-Route Noise Efforts in ICAO CAEP

The Pennsylvania State University

Project Lead Investigator

Victor W. Sparrow
United Technologies Corporation Professor of Acoustics
Graduate Program in Acoustics
The Pennsylvania State University
411 Engineering Collaborative Research and Education Building (ECoRE)
566 White Course Drive
University Park, PA 16802
814-865-6364
vws1@psu.edu

University Participants

The Pennsylvania State University (Penn State)

- P.I.: Professor Victor W. Sparrow
- FAA Award Number: 13-C-AJFE-PSU Amendments 55, 77, 86, 100, 115, 117, 122, and 127
- Period of Performance: February 5, 2020, to September 14, 2026
- Tasks:
  1. Procedures for sonic boom certification
  2. Assessing secondary sonic boom propagation
  3. Investigating seismic networks for measuring sonic booms

Project Funding Level

This project focuses on multiple tasks at Penn State and its subcontractors Farmingdale State University and RAC Consulting, LLC. The Federal Aviation Administration (FAA) funding to Penn State in 2025 was $400,000. Matching funds are expected to meet cost sharing on all tasks. In 2024, the FAA granted Penn State's request for reduced cost sharing to 25% of the total project costs. In-kind contributions have been pledged by Boom Supersonic ($120,000), Exosonic ($220,000 in 2024; however, Exosonic is ceasing operations, so this cost share is uncertain at the time of this writing), Gulfstream ($250,000), and Pivotal Supersonics (previously known as Global SST; $75,000).

Task 3, investigating seismic networks, is fully funded by the FAA in 2025. It should be noted that this task was initiated in 2023 and 2024 by the Project P.I. using funds from the United Technologies Corporation Professorship within the Penn State College of Engineering. Additionally, Task 3 start up support in previous years is gratefully acknowledged.

Investigation Team

The Pennsylvania State University

Prof. Victor W. Sparrow, (P.I.), Tasks 1, 2, and 3
Joshua Kapcsos, (Acoustics graduate research assistant), Task 1
Dr. Sampath Rathnayaka (Geosciences postdoctoral scholar), Task 3
Prof. Andrew Nyblade, (Geosciences professor), Task 3

Farmingdale State College, State University of New York (subrecipient of Penn State)

Kimberly A. Riegel, (Physics co-investigator), Tasks 2 and 3

RAC Consulting, LLC (RACC)

Robbie Cowart (Research scientist), Task 1



Boom Supersonic (industrial partner)
Michael Rybalko, Gus Silva, et al.

Gulfstream (industrial partner)
Brian Cook, Matthew Nickerson, Joe Gavin, Nick Ward, and Charles Etter

Pivotal Supersonic (previously known as Global SST; industrial partner)
Steve Ogg

Project Overview

Passenger aircraft development is on the verge of a true revolution. Companies such as Boom Supersonic, Gulfstream Aerospace Corporation, Lockheed Martin, Pivotal Supersonics, and others are reaching the point at which they can build and deliver to users aircraft capable of flying supersonically in an environmentally responsible way. This development will allow for decreased air transportation travel times, to the great benefit of society.

New supersonic aircraft must be certified as being sufficiently quiet to not excessively disturb the public. Preparation for such a certification process has been ongoing for several years in the FAA Office of Environment and Energy (AEE). Working with its international partners in the International Civil Aviation Organizations (ICAO)'s Committee for Aviation Environmental Protection (CAEP), the FAA has been laying the groundwork for certification standards. The FAA's efforts have been supported by both universities and other governmental agencies. Specifically, Penn State has supported the FAA/AEE through Projects 008 and 024 in the PARTNER Center of Excellence (COE) and more recently in ASCENT Projects 007, 041, and 042. Summaries of these research efforts can be found on the website ascent.aero. To date, a group of six candidate metrics for en route supersonic certification have been agreed upon in the CAEP's Working Group 1 (WG1) (Noise Technical) Supersonic Task Group (SSTG). Multiple schemes for certification have been generated. Several schemes have been eliminated from further consideration, and others are currently being evaluated for possible implementation. Procedures have been proposed for acquiring and processing ground measurement of the en route supersonic noise, but all possibilities remain under discussion. The extent to which atmospheric conditions will affect the measurements, and the requirements and roles of numerical simulations of the noise propagating from the aircraft to the ground are being considered. One particularly challenging aspect is the influence of the atmosphere in distorting the acoustic pressure signatures, owing to atmospheric turbulence, and the subsequent effects on the metric values. These gaps are only several of those that must be filled.

All these topics are being worked on, in a stepwise manner, in the FAA and in WG1's SSTG. Efforts in the completed ASCENT Project 041 have been aimed at supporting the FAA with technical expertise in the development of the certification procedures and gaining an initial understanding of secondary sonic booms. Secondary sonic booms, also known as over-the-top sonic booms, are the sound energy that travels upward at heights above the aircraft cruise altitude and lands at distant locations. Secondary sonic booms are the reason why the Concorde[1] was requested to transition from supersonic to subsonic speeds at substantial distances before entering the continental United States airspace. ASCENT Project 041 ended in early 2021, and ASCENT Project 057 is now in its sixth year. However, much work remains to be done, and efforts lasting several more years will be required to advance certification standards for supersonic aircraft.

In 2026 and beyond, continued support for supersonic aircraft noise efforts will be necessary for the FAA and its international partners to fill technical solution gaps and continue progressing toward certification procedures. Although other universities and industries will continue their focus on aircraft design and landing and takeoff studies, continued work on en route supersonic noise issues will be essential, because these issues remain the greatest barrier to the use of environmentally responsible supersonic aircraft. ASCENT Project 057 will support the ongoing activities in ICAO CAEP and their WG1 (Technical Noise), with a focus on establishing supersonic aircraft en route procedures and metrics for noise certification standards, and to support the interface with the ICAO Air Navigation Commission to address related noise issues.

In the 2020 through 2026 project period, the emphasis will be on continuing the research support for supersonic aircraft en route procedures, including the utilization of an agreed-upon reference-day atmosphere, the establishment of techniques for incorporating measurement data and simulations into a draft certification procedure, and the consideration

[1] The Concorde was a specifically designed aircraft for supersonic flight.



of off-design flight speed sonic booms, such as focus booms and acceleration booms. Support will also be provided for a more comprehensive analysis of the National Aeronautics and Space Administration (NASA) SonicBAT dataset and efforts in developing methods to remove the effects of atmospheric turbulence on measured acoustic pressure waveforms to support certification. The research in 2020 through 2026 will also need to consolidate and process the results of research from previous years on the topic of secondary sonic booms as a potential noise issue for the initial supersonic airplanes. This material will be of particular interest to ICAO's Air Navigation Commission because it could affect the operation of supersonic aircraft in the near term.

Task 1 – Procedures for Sonic Boom Certification

The Pennsylvania State University
RAC Consulting, LLC

Objectives

ASCENT Project 057 is a transition from ASCENT Project 041, *Identification of Noise Acceptance Onset for Noise Certification Standards of Supersonic Airplanes.* As national aviation authorities move toward developing noise certification standards for low-boom supersonic airplanes, several research gaps exist in areas including signature fidelity, metrics, metrics sensitivity to real-world atmospheric effects, and adjustments for reference conditions. The objective of Task 1 is to support the FAA in the development of technical standards for civil supersonic aircraft under the ICAO CAEP. This effort provides the FAA with technical noise expertise regarding the development of noise certification standards for future civil supersonic passenger aircraft, primarily in the area of en route noise (sonic boom) minimization and/or abatement.

Task 1 in ASCENT Project 057 focuses on research initiatives necessary to develop an overland supersonic en route noise certification standard. The objective is to improve the turbulence model in nonlinear propagation code KZKFourier by introducing atmospheric profiling and more realistic buoyancy- and shear-induced vector turbulence models. Additional work focuses on providing direct research support for ICAO/CAEP/WG1's SSTG and Procedures subgroup (PrSG) meetings and discussions.

Research Approach

Background

The KZKFourier propagation code is an augmentation of the Burgers equation into a Khokhlov–Zabolotskaya–Kuznetsov (KZK) propagation equation to include nonlinearity, diffraction, and absorption in directional sound beams, to simulate wind and temperature fluctuation effects of the atmospheric boundary layer (ABL), according to the Ostashev and Wilson (2015) model. During the 2019–2020 academic year, PCBoom 6.7.1.1 and KZKFourier were used above and within the atmospheric boundary layer, respectively, to simulate turbulence effects of atmospheric boundary layer heights of 268.2, 411.4, and 1026.7 m, corresponding to SonicBAT Flight 5 conditions. Information regarding this endeavor appears in the 2020 report for ASCENT Project 057. After propagating shaped boom signatures through 10 randomly generated atmospheres, the data were shared with the WG1/SSTG/PrSG, in which zero-padding and spiking artifacts were discovered near the beginnings and ends of certain ground signatures; the plots shown in the 2020 report did not span the entire retarded time domain of the ground waveform data. These artifacts were corrected in the 2020–2021 academic year, as described in the 2021 report for ASCENT Project 057. In the 2021–2022 academic year, Penn State expanded the shaped boom database to 20 realizations at NASA's request, conducted a parameter check on KZKFourier for boundary layer thicknesses, freezing temperatures, and turbulence parameters, conducted a grid refinement study on KZKFourier, and initiated a reference-day crosscheck with international members of the CAEP's WG1 (Noise Technical); these milestones are described in the 2022 report for ASCENT Project 057. The 2023 report for ASCENT Project 057 reviews an extension of the reference-day crosscheck to evaluate participant noise metrics, an investigation of the numerical interpolation methods of the KZKFourier solution, and the introduction of atmospheric profiling in KZKFourier, in which humidity was profiled in the molecular relaxation module for the first time. The 2024 report for ASCENT Project 057 highlights the initial research into introducing a ground-blocking methodology into KZKFourier, which was fully implemented in 2025.

It is important to include the effects of a realistic atmospheric profile during supersonic aircraft noise simulation. Atmospheric variables such as humidity, pressure, density, and temperature realistically vary by altitude. NASA requested Penn State investigate improving the atmospheric turbulence model in KZKFourier, which models the primary supersonic noise carpet with atmospheric turbulence included. The two types of vector turbulence modeled in KZKFourier are shear-



induced vector turbulence and buoyancy-induced vector turbulence, and as height-dependent ground blocking affects buoyancy, improving the modeling of both types of vector turbulence were the focus of the current project period.

Buoyancy-Induced Vector Turbulence Improvement

The original released version of KZKFourier does not consider the effect of the ground on the turbulent eddies in the atmospheric boundary layer; in reality, the proximity of the eddies to the ground affects their shape, as an eddy cannot penetrate the ground. While KZKFourier considers scalar (temperature) and both shear- and buoyancy-induced vector (wind) turbulence, height-dependent ground blocking affects only the buoyancy-induced vector turbulence. At the 186th meeting of the Acoustical Society of America in May 2024, Dr. D. Keith Wilson presented an equation (Wilson et al., 2024) to implement ground blocking by applying natural exponential factors to a two-dimensional cross spectrum (ϕ_{33}) between propagation heights, z_1 and z_2, and wavenumbers, κ_1 and κ_2 as follows:

$$\hat{\phi}_{33} = (\kappa_1, \kappa_2; z_1, z_2) = \phi_{33}(\kappa_1, \kappa_2; z_2 - z_1) - \phi^*_{33}(\kappa_1, \kappa_2; z_1)e^{-\kappa_\perp z_2} - \phi_{33}(\kappa_1, \kappa_2; z_2)e^{-\kappa_\perp z_1} + \phi_{33}(\kappa_1, \kappa_2; 0)e^{-\kappa_\perp (z_1+z_2)} \quad \text{(Eq. 1)}$$

Because KZKFourier uses a three-dimensional (3D) turbulence spectrum (E) as prescribed in *Acoustics in Moving Inhomogeneous Media* (Ostashev & Wilson, 2015) and not a two-dimensional (2D) cross spectrum as Wilson's ground blocking method requires, KZKFourier has now been modified to conciliate with the above exponential factors. Cotté and Blanc-Benon (2007) refer to a doctoral dissertation by Chevret (1994) that suggests the conversion factor from a 3D to 2D spectrum is $2\pi\kappa$. As shown in Figure 1, this conversion factor results in a spectrum that is similar to Wilson's 2D cross spectrum and factor of $4\pi\kappa^4/(\kappa_1^2 + \kappa_2^2)$ that returns E from a cross spectrum. Penn State has consequently used these conversion factors to modify the KZKFourier spectrum and implement the ground-blocking methodology in the C++ code.

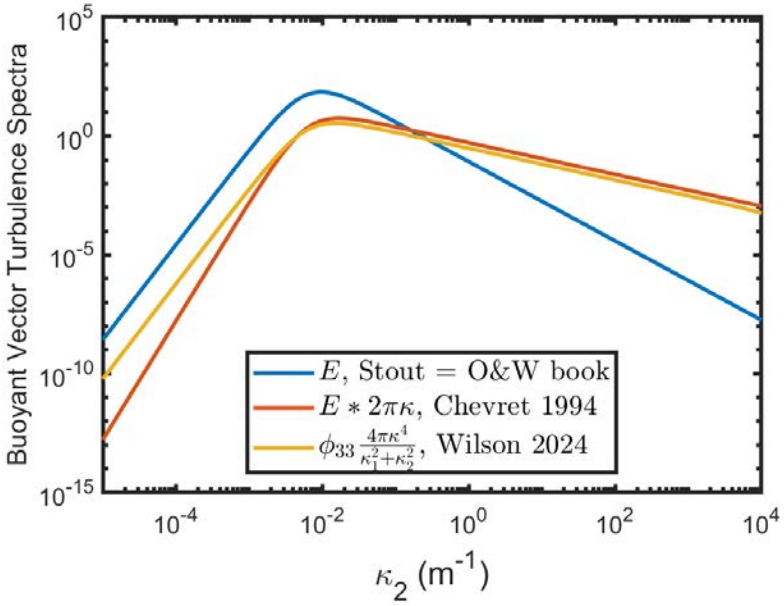


Figure 1. Buoyant vector turbulence spectra as it appears in three-dimensional E in KZKFourier, as multiplied by Chevret conversion factor to two-dimensional (2D), and as compared to a 2D cross spectrum ϕ_{33}.

PCBoom was used to propagate a C609 shaped boom, an early model of the NASA X-59 demonstrator, from a cruise altitude of 54 kilofeet to the top of the ABL, and the results were then fed into KZKFourier with and without ground blocking. After propagating the C609 shaped boom in KZKFourier through 1026.7 m and 268.224 m ABL heights with SonicBAT Flight 5 turbulence conditions, subtle differences were found in ground waveform distribution, but there was no difference to a hundredth of a decibel when comparing the ground-blocked results to the original unblocked results in average Perceived Level (PLdB) or Indoor Sonic Boom Annoyance Predictor (ISBAP) sound metrics. This may be due in part to the reliance of these metrics on overall waveform shape, which did not drastically change with the inclusion of ground



blocking. Additionally, at low wavenumbers, shear turbulence contributes to part of the total vector spectra affected by ground blocking, so ground blocking may be made insignificant by the shear vector turbulence effects during the addition of the buoyant and shear spectra for a total vector turbulence spectrum. Ultimately, ground blocking, which is greatest near the surface, affects only a very small portion of this scenario's total propagation from 54 kilofeet. These results were presented at NOISE-CON 2025 in Stowe, Vermont, and were subsequently published in the *Noise Control Engineering Journal* paper "Developments on ground blocking implementation in turbulence tool for sonic boom propagation" (Kapcsos & Sparrow, 2025).

Shear-Induced Vector Turbulence Improvement

While investigating the ground blocking implementation of buoyancy-induced vector turbulence, Dr. D. Keith Wilson brought to Penn State's attention that the original simplified distribution of shear-induced vector turbulence in KZKFourier that grows with increasing height is not realistic. To rectify this, KZKFourier needs to demarcate different regions of turbulence within the atmospheric boundary layer. Particularly, the surface layer needs to be considered, defined as the lower tenth of the ABL, which comes from the Monin-Obukhov length where buoyant production of turbulence meets shear production of turbulence; that is, with respect to vector turbulence, shear should dominate within the surface layer, and buoyancy should dominate above it. KZKFourier uses turbulent length scales based on Monin-Obukhov Similarity Theory (MOST), so the changes needed to make the surface layer more realistic can be applied to the code. After first trying a simple exponential decay of the shear spectrum itself above the surface layer as was presented in the Spring 2025 Noise and Operations Meeting, Penn State began to investigate the physical behavior of the parameters that determine the shear spectrum. The meteorological turbulence value that prescribes the variance of shear-induced vector turbulence σ_s is friction velocity u_* as $\sigma_s^2 = 3.0u_*^2$. Friction velocity is constant in the original version of KZKFourier, which is not realistic, allowing shear to grow with increasing height in the ABL and preventing buoyancy from dominating above the surface layer. More realistically, Garrat (1992) defines surface friction velocity u_{*_0} as

$$u_{*_0}^2 = -(\overline{u'w'})_0 \qquad \text{(Eq. 2)}$$

Here, mean field velocity components $\bar{u}$ and $\bar{w}$ are in the x and vertical directions, respectively, and the covariance $\overline{u'w'}$ is related to the turbulent flux of momentum. According to Wyngaard (2010), "$\overline{uw}$ decreases linearly to zero at the ABL top" in the convective boundary layer. The behavior of u_* should, therefore, be the square root of a linear decrease to zero with increasing height to the top of the ABL.

As seen in the revision of the shear spectrum in Figure 2, applying the square root of a linear decay with increasing height to friction velocity u_* in KZKFourier results in the eventual decay to zero of the shear turbulence spectrum at the top of the ABL, as the decay of u_* with increasing height eventually counteracts the growth of the shear length scale. For a C609 shaped boom in KZKFourier, less overall shear turbulence generally results in slightly increased average sound metrics, as less overall shear turbulence occurs with decayed friction velocity, smaller ABL heights, and lower turbulence strength. In the case of SonicBAT Flight 5 turbulence conditions and a 1026.7 m ABL, the average metrics increased on the order of approx. a tenth of a decibel when friction velocity decay was included in the code. However, large ABL heights with high turbulence can result in slightly decreased average sound metrics when friction velocity decay is included. The larger the ABL height and the stronger the shear turbulence strength, the more important it is to realistically decay friction velocity.

An additional work item in Task 1 is to more fully understand the role of background noise in potentially contaminating the recordings of en route supersonic signatures that will likely be one input to a certification procedure for supersonic flight. Those efforts regarding background noise processing are underway and will be reported upon in the next project period.

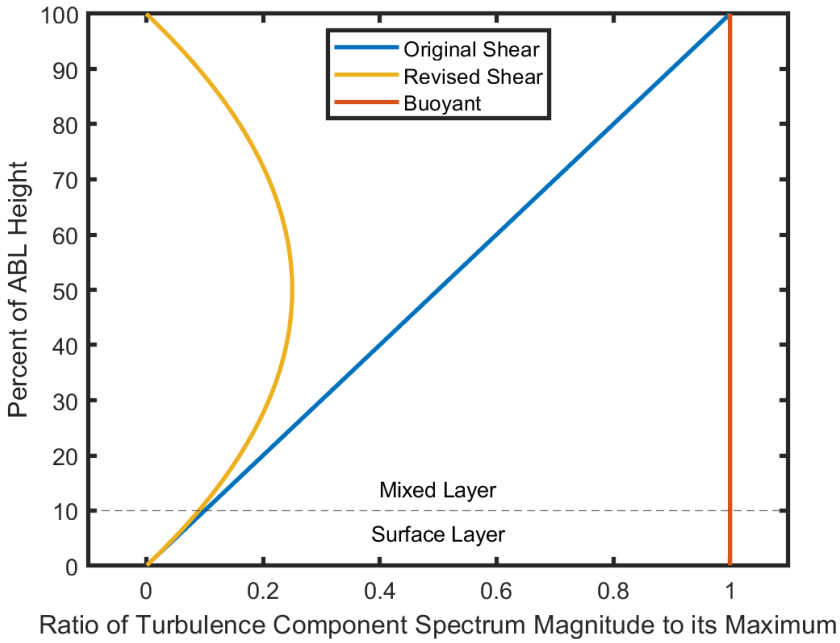


Figure 2. Shear vector turbulence spectra magnitude before and after applying the square root of a linear decay to friction velocity. Rather than growing with height, the revised shear vector turbulence begins to decay and reaches zero at the top of the atmospheric boundary layer.

Direct Support for CAEP/WG1 meetings

CAEP's WG1 on aircraft noise (technical) is responsible for aviation noise standards and recommended practices. ASCENT Project 057 research deliverables support WG1's SSTG tasks for supersonic en route/sonic boom noise standards. As described in the overview section, the SSTG's Procedures Subgroup concentrates on evaluating and implementing candidate noise certification schemes under consideration by WG1, supported by two smaller ad hoc groups. A Test Procedures ad hoc group (TPahg) is working to draft a set of proposed test procedures in concert with the Data Processing ad hoc group (DPahg) tasked to mature text for applying the candidate schemes. While much of the discussion and/or detailed results cannot be recorded due to the confidential nature of the ICAO-CAEP work, these paragraphs capture the essence of activities supporting the research.

During the current reporting period, teleconference coordination continued in the above-listed groups. RACC facilitated 10 virtual meetings in the fourth quarter of 2024, including a two-day virtual SSTG workshop in December 2024. Workshop topics centered around ongoing tasking and interface with the NASA Quesst project on its upcoming Phase 2 acoustic validation testing, a topic discussed over the most recent WG1 meetings. Data from Phase 2 are anticipated to be useful in evaluating the proposed test procedures and candidate noise certification schemes.

Early 2025 included a few teleconference meetings in preparation for the CAEP/13 meeting held in February. To date this year, RACC coordinated nearly 40 virtual meetings amongst the various groups in addition to supporting one virtual and two in-person WG1 meetings. During the second quarter 2025 (2Q25), in-person travel was accomplished to facilitate the SSTG session at WG1-1 in Aachen, Germany. The meeting included five technical papers covering research updates from the US, Europe, and Japan as well as progress reports and planning over the next 12 to 24 months. Research support into inflight and ground measurement techniques for low noise supersonic flight operations remains a priority topic, currently focused on the steady-state cruise flight condition as a starting point.

In addition to teleconference meetings, the third and fourth quarters included participation, both virtually and in person, for the WG1-2 and WG1-3 meetings to support SSTG sessions and facilitate ongoing discussion of key topics. Six technical papers were reviewed during the virtual WG1-2 and four papers at the in-person WG1-3 held in Phoenix, Arizona.

Unfortunately, NASA updates for WG1-3 were absent due to the United States government shutdown and employee furlough; however, a key event reported was the successful first flight of the X-59 research aircraft on October 28, 2025, just after the project period described here (see Figure 3). Another important note was the Japan Aerospace Exploration Agency (JAXA) Re-BooT flight research project update aimed at taking place in 2028. (ref. www.aero.jaxa.jp).



Figure 3. NASA X-59 First Flight (credit: www.lockheedmartin.com)

In addition to coordinating SSTG and its associated tasking, supersonic industry projects are monitored in support of ASCENT Project 057. During March 2024, Boom Supersonic conducted the first flight of its XB-1 flight test aircraft and continued to expand the flight envelope throughout the year (see Figure 4). In early 2025, the company conducted two supersonic test flights using the XB-1, one in January and the second in February before concluding its flight program and retiring the test aircraft. The flights consisted of multiple test points at flight speeds above Mach 1, demonstrating supersonic flight capability.



Figure 4. Boom Supersonic XB-1 (credit: www.boomsupersonic.com)

Milestones

- Made significant progress in improving the turbulence model in KZKFourier, beginning with the inclusion of uniform humidity profiling in its molecular relaxation module, a ground-blocking methodology to improve buoyancy-induced vector turbulence modeling, and currently a friction velocity decay to improve shear-induced vector turbulence modeling.



- Improved the realism of all vector turbulence components in KZKFourier, as the only types of vector turbulence in KZKFourier are buoyancy- and shear-induced.

Major Accomplishments

Considering the ground effects in buoyancy-induced vector turbulence spectra and surface layer behavior in shear-induced vector turbulence spectra will lead to more accurate sound metrics and annoyance predictions for NASA when they make comparisons to the data that will be obtained during the upcoming supersonic flights of their X-59 Quesst[1] aircraft.

Publications

Peer-Review Journal Publication

Kapcsos, J. L., & Sparrow, V. W. (2025). Developments on ground blocking implementation in turbulence tool for sonic boom propagation. *Noise Control Engineering Journal, 73(3)*, 407-412. https://doi.org/10.3397/1/377331

Outreach Efforts

None.

Awards

Joshua Kapcsos received a Student Paper Competition award for the paper presentation, "Developments on ground blocking implementation in turbulence tool for sonic boom propagation" given at the NOISE-CON 2025 meeting in Stowe, Vermont, on June 9, 2025.

Student Involvement

Joshua Kapcsos was the Penn State graduate research assistant who worked on ASCENT Project 057 during the 2024–2025 academic year.

Plans for Next Period

- Continue developing atmospheric profiling schemes in KZKFourier for other atmospheric quantities (e.g., temperature). The revised buoyancy- and shear-induced vector turbulence spectra will be used in KZKFourier simulations of various turbulence strengths and boundary layer heights to aid in the development of standards for civil supersonic aircraft.

Special Acknowledgment

Penn State would like to thank Dr. D. Keith Wilson for his recommendations on appropriate models of turbulence in the atmospheric boundary layer.

References

Bradley, K. A., Hobbs, C. M., Wilmer, C. B., Sparrow, V. W., Stout, T. A., Morgenstern, J. M., Underwood, K. H., Maglieri, D. J., Cowart, R. A., Collmar, M. T., Shen, H., & Blanc-Benon, P. (2020). *Sonic booms in atmospheric turbulence (SonicBAT): The influence of turbulence on shaped sonic booms* (NASA/CR–2020–220509). National Aeronautics and Space Administration, Armstrong Flight Research Center, Edwards, California.

Chevret, P. (1994). *Simulation numérique des effets de la turbulence sur la propagation du son dans l'atmosphère* (Publication No. 94-18) [Doctoral dissertation, L'école Centrale de Lyon]. Centre Acoustique. https://acoustique.ec-lyon.fr/publi/chevret_thesis.pdf

Cotté, B., & Blanc-Benon, P. (2007). Estimates of the relevant turbulent scales for acoustic propagation in an upward refracting atmosphere. *Acta Acustica United with Acustica, 93*, 944-958.

Davidson, P. A. (2015). *Turbulence: An Introduction for Scientists and Engineers* (2nd ed.). Oxford University Press, Oxford, United Kingdom.

Garrat, J. R. (1992). *The Atmospheric Boundary Layer*. Cambridge University Press, Cambridge, United Kingdom.

Kapcsos, J. L., & Sparrow, V. W. (2023). Progress update on inclusion of atmospheric profiling for sonic boom propagation through turbulence. *The Journal of the Acoustical Society of America*, *154*(4_supplement), A148.

Loubeau, A., Doebler, W., Wilson, S. R., Ballard, K., Coen, P. G., Naka, Y., Sparrow, V. W., Kapcsos, J. L., Page, J. A., Downs, R. S., Lemaire, S., & Liu, S. R. (2021). Developing certification procedures for quiet supersonic aircraft using shaped sonic boom predictions through atmospheric turbulence. *The Journal of the Acoustical Society of America, 149*(4_supplement), A102.

Maglieri, D. J., Bobbitt, P. J., Plotkin, K. J., Shepherd, K. P., Coen, P. G., & Richwine, D. M. (2014). *Sonic Boom: Six Decades of Research* (NASA/SP-2014-622). National Aeronautics and Space Administration, Langley Research Center, Hampton, Virginia.
Ostashev, V. E., & Wilson, D. K. (2015). *Acoustics in moving inhomogeneous media* (2nd ed.). CRC Press, Boca Raton, Florida.
Ostashev, V. E., Wilson, D. K., & Hart, C. R. (2023). Influence of ground blocking on the acoustic phase variance in a turbulent atmosphere. *The Journal of the Acoustical Society of America, 154*, 346-360.
Stout, T. (2018). *Simulation of n-wave and shaped supersonic signature turbulent variations* [Doctoral dissertation, Pennsylvania State University]. Pennsylvania State University. https://etda.libraries.psu.edu/catalog/15959tqs5346
Wilson, D. K., Ostashev, V. E., Hart, C. R., & Kamrath, M. J. (2024). Verifying turbulence models in the atmospheric boundary layer by acoustical means. *The Journal of the Acoustical Society of America, 155*(3_supplement), A200.
Wyngaard, J. C. (2010). *Turbulence in the Atmosphere.* Cambridge University Press, Cambridge, United Kingdom.

Task 2 – Assessing Secondary Sonic Boom Propagation

The Pennsylvania State University
Farmingdale State College, State University of New York

Research Approach

As described in previous project reports secondary sonic booms are those sound events which can occur when either: (1) [Type I] the upward traveling portion of a sonic boom bends back toward the ground and eventually reaches the ground or (2) [Type II] when the primary (downward) traveling sonic boom reflects from the surface and then refracts in the upper atmosphere and makes its way back to the ground a second time. Secondary sonic booms do not occur all the time, only when there is a strong upper atmospheric wind to aid the sound getting back to the ground, far in front of the aircraft. Because of the really long propagation paths, most of the high frequency energy dissipates due to atmospheric absorption. Therefore, if secondary sonic booms are heard, they sound like a low-frequency rumble, somewhat similar to the sound of distant thunder. Nevertheless, it is known that secondary sonic booms from Concorde can produce annoyance, as was reported by Rickley and Pierce (1980).

In previous work in ASCENT Project 057, secondary sonic booms were modeled from flights approaching the United States coastlines and around Edwards Air Force Base (EAFB) in Edwards, California. Using NASA's PCBoom program seems to work effectively for this modeling purpose, although the research team does not yet have any experimental evidence validating the PCBoom secondary boom predictions for amplitude and duration of the sounds. In previous studies the project team has investigated the reflection of the Type II ground-reflected secondary booms as well as the origin of the long-durations of secondary sonic booms which are on the order of 10-30 s. Each of these studies are pieces of the puzzle for us to more fully understand how secondary sonic booms are generated, propagated, and received by communities.

In the current project period, the research team focused on understanding the atmospheric conditions that can result in a Mach cutoff condition yielding secondary sonic booms. This condition is primarily dependent on Mach number and the atmospheric conditions below the aircraft. The team looked to see if these two conditions could be combined to produce both secondary sonic booms and Mach cut off.

As an initial case the team selected a previously modeled condition that resulted in secondary sonic booms. This was a steady flight at Mach 1.2 with a heading of 251 degrees approaching the eastern coastline. The aircraft altitude was 55,000 ft and the team started with a weather profile for New York City from August 2018 (see Figure 5). The lower atmospheric winds were then modified to determine if there could be a Mach cutoff condition as well.

The described atmospheric conditions resulted in secondary sonic booms and a Mach cut off condition with only very small changes to the original profile (see Figure 6). For this condition, the primary boom rays turns about 550 ft above the ground, so no primary/direct sonic boom is heard on the ground.

The team is now carrying out a parametric study to determine what are the conditions when Mach cutoff flight can create secondary sonic booms. The parameters to be varied include flight speed and altitude as well as the wind profiles. The plan is that the team's preliminary results will be discussed at the December 2025 joint meeting of the Acoustical Society of America and the Acoustical Society of Japan.

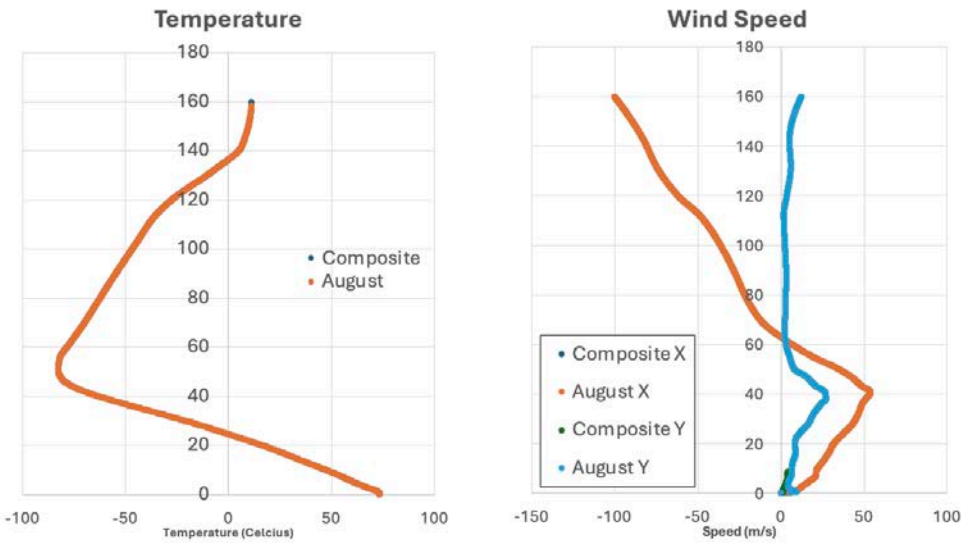


Figure 5. The atmospheric profiles result in both Mach cutoff and secondary sonic boom conditions compared to the unmodified August profiles.

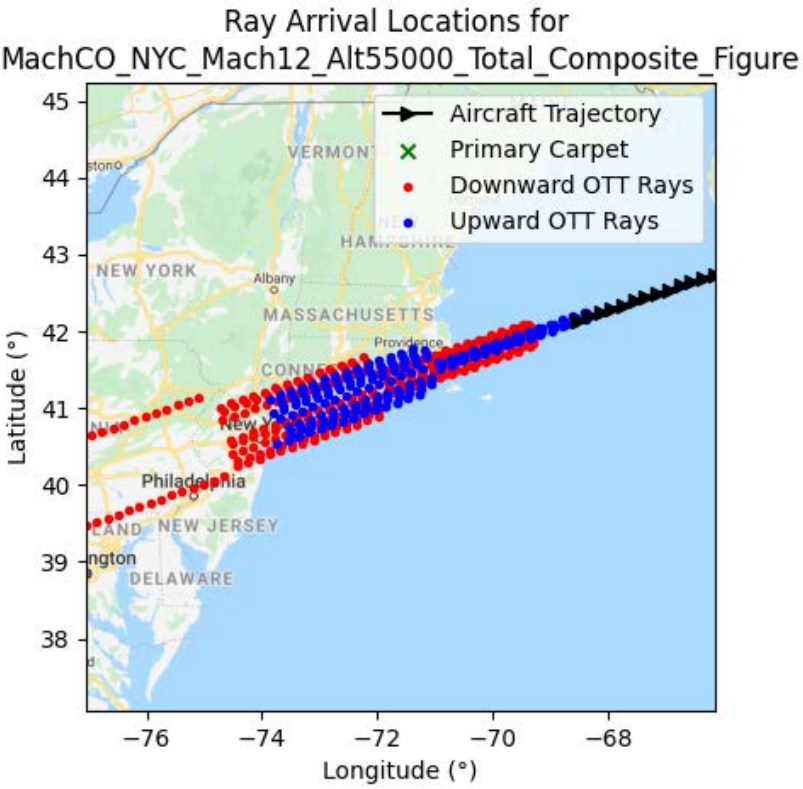


Figure 6. The resulting secondary sonic boom arrivals and no primary boom arrivals during an example Mach cutoff flight.



Milestone
N/A

Major Accomplishments
The project team has been shown that Mach cutoff flight can result in secondary sonic boom sounds, and our team believes that this is the first time that this has been demonstrated.

Publications
Conference Presentation

Sparrow, V. & Riegel, K. (2024, June 4-7). *Multipath interpretation of secondary sonic boom signatures* [Conference Presentation]. AIAA/CEAS Aeroacoustics Conference, Rome, Italy, AIAA-3187). https://doi.org/10.2514/6.2024-3187

Outreach Efforts
None.

Awards
None.

Student Involvement
None.

Plans for Next Period
- Continue the work exploring the parameter space for the occurrence of secondary booms during Mach cutoff flight, and report upon in a peer-reviewed journal.
- Participate in measurements of the test flights of the X-59 Quesst aircraft. The team aims to better understand whether secondary sonic booms are produced by X-59.

References
Rickley, E. & Pierce, A. (1980). *Detection and assessment of secondary sonic booms in New England* (Report No. FAA-AEE-80-22). Defense Technical Aviation Center, Fort Belvoir, Virginia.

Sparrow, V., & Riegel, K. (2023, September 11-15). The role of topography for secondary sonic boom reflection. *Proceedings of the Forum Acusticum 2023 - 10th Convention of the European Acoustics Association, EAA 2023,* Torino, Italy, 2221-3767. https://appfa2023.silsystem.solutions/atti/000361.pdf

Sparrow, V., & Riegel, K. (2024, June 4-7). *Multipath interpretation of secondary sonic boom signatures* [Conference presentation]. 30th AIAA/CEAS Aeroacoustics Conference, Rome, Italy, AIAA-3187. https://doi.org/10.2514/6.2024-3187

Task 3 – Investigating seismic networks for measuring sonic booms
The Pennsylvania State University
Farmingdale State College, State University of New York

Objective
The pressure signals from sonic booms, triggered by supersonic flights, will generate detectable ground motions along and across the land surface of the corresponding flight paths (Rickley & Pierce, 1980; Cates & Sturtevant, 2002). The long-range propagation of direct and indirect pressure wave signatures from the sonic booms is poorly understood due to the lack of precise sonic boom landing location predictions as well as better ground coverage of seismic stations which can detect the signals. The high-density seismic networks in southern California, which routinely detect sonic booms from supersonic flights (Cates & Sturtevant, 2002; Rathnayaka et al., 2023), provide a unique opportunity to study the areal extent of the boom signals and its' impact on U. S. population centers. In 2025, this work focused on investigating primary and secondary sonic boom signals recorded on seismic stations from four supersonic passes that occurred near EAFB, California, in 2005.

Research Approach

The sonic boom events used in this study were triggered on June 15, 2005, near EAFB, California, associated with the PARTNER (Partnership for AiR Transportation Noise and Emissions Reduction) Project 8 (LowBoom/NoBoom phase 1 project) field experiment (Sparrow, 2005). There were four supersonic passes, all of them were flown from east to west over EAFB at $M = 1.3$ or 1.4 at four different altitudes (9,753.6 m, 11,227.6 m, 12,192 m, and 13,716 m). The sonic booms were created by F-18 aircraft. The approximate event detection times correspond to 17 sonic boom events at a monitoring station (Latitude: 34.928, Longitude: -117.936) near EAFB (Table 1). The precise location and the time of boom initiations are not known. The sonic boom detection times, shown in Table 1, are from the PARTNER Project 8 annual report (Sparrow 2005).

Table 1. Summary of sonic booms detection time at the monitoring station, Edwards, California (Latitude: 34.928, Longitude: -117.936).

Boom ID	Pass Number	Mach Number (*M*)	Altitude (km)	Date	Event detection time (Coordinated Universal time-UTC)
1	1	1.3	9.7536	06/15/2005	13:13:37
2	1	1.4	11.228	06/15/2005	13:22:20*
3	1	1.4	12.192	06/15/2005	13:32:49
4	1	1.4	13.716	06/15/2005	13:41:42
5	2	1.3	9.7536	06/15/2005	13:49:08
6	2	1.4	11.228	06/15/2005	13:57:00*
7	2	1.4	12.192	06/15/2005	14:07:12
8	2	1.4	13.716	06/15/2005	14:17:51
9	2	1.4	11.228	06/15/2005	14:25:35
10	3	1.3	9.7536	06/15/2005	14:33:00
11	3	1.4	11.228	06/15/2005	14:40:20
12	3	1.4	12.192	06/15/2005	14:47:24
13	3	1.4	13.716	06/15/2005	14:57:00*
14	4	1.3	9.7536	06/15/2005	15:27:00
15	4	1.4	11.228	06/15/2005	15:37:00
16	4	1.4	12.192	06/15/2005	15:47:00
17	4	1.33	13.716	06/15/2005	15:54:00

*Detection time estimated based on seismic observations

Data and Methods

The seismic stations used in this study consist of 254 surface receivers which belong to the Northern California Seismic Network (NC), the Southern California Seismic Network (CI) and the US Transportable Array (TA) (Figure 7). All the stations consist of either single or three-component broadband seismometers with sample rates of 40 to 100 samples/s. Only vertical component ground motion data are used in this study. The seismic data used were provided by the Seismological facility for the Advancement of Geoscience (SAGE; https://ds.iris.edu/mda/), Northern California Earthquake Data Center (NCEDC; https://service.ncedc.org/fdsnws/dataselect/1/), and Southern California Earthquake Data Center (SCEDC; https://scedc.caltech.edu/data/waveform.html).

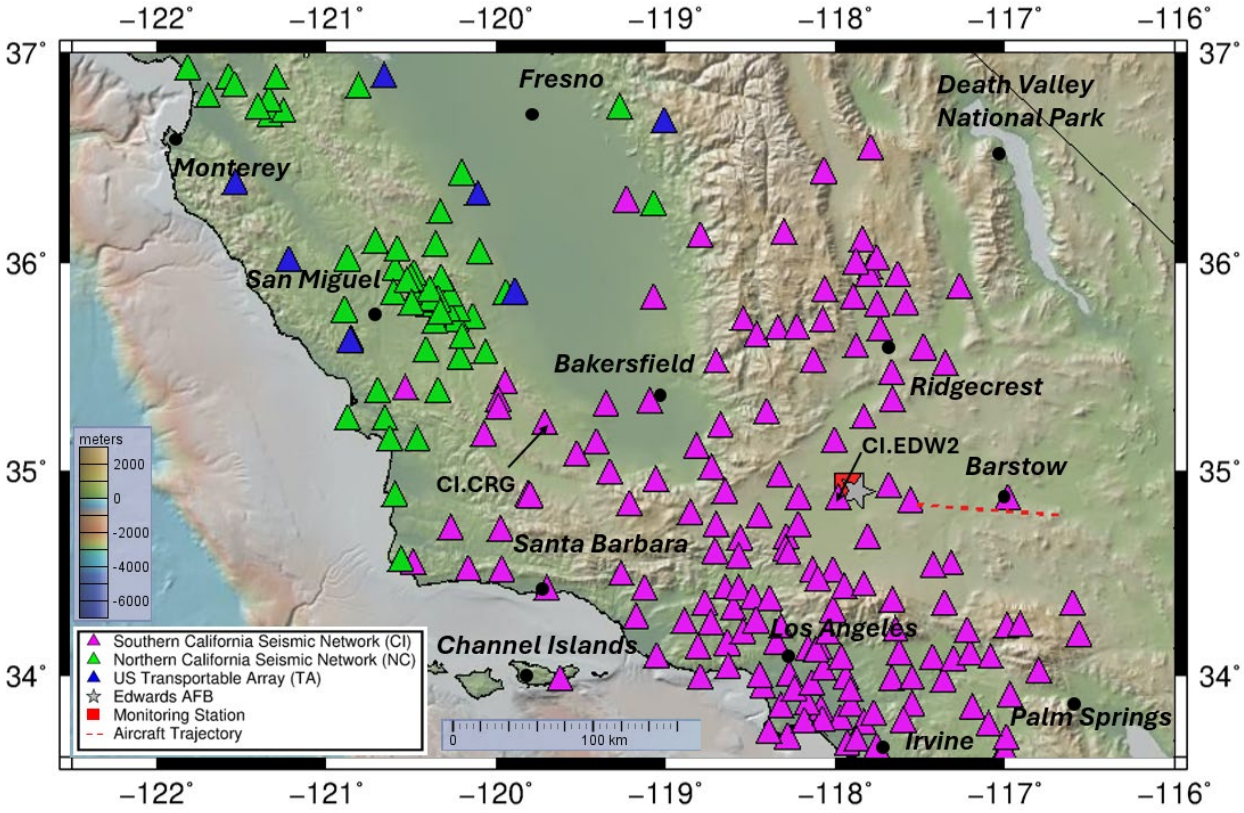


Figure 7. The distribution of seismic stations used in this study. The magenta, green and blue triangles represent instruments from the Sourthern California Seismic Network (CI), the Northern California Seismic Network (NC), and the US Transportable Array (TA), respectively. The gray star and red square show the locations of the Edwards Air Force Base and nearby sonic boom monitoring station, respectively. The red dashed line represents F-18 aircraft flight trajectories.

Instrument responses were deconvolved from the vertical ground velocity seismograms prior to converting them to ground displacement. The displacement seismograms for all boom events were windowed to begin 0 s prior to and few hundreds of seconds after the event time at the monitoring station (Table 1), ensuring recording of both the primary or secondary boom waves at all distance ranges. The windowed seismograms were then demeaned, detrended and tapered, and finally filtered at 1-20 Hz with four-pole two-pass Butterworth bandpass filters.

Using the seismograms, the primary and secondary boom events were detected through manual identification. For primary boom detection, event identification was performed by inspecting the seismograms for N-type wave signatures followed by a U-shaped wave, as illustrated in Figure 8a, at seismic stations located within a radius of ~ 100 km from EAFB where the primary carpet for the boom events is predicted to be seen. For secondary boom carpet detection, several template waveforms were chosen based on the infrasound microphone records published by Rickley and Pierce (1980) (type I and type II waves, Figure 8d). We then manually searched for secondary booms by visually comparing the template waveforms with seismograms for seismic stations located greater than 60 km from EAFB showing both type I and type II waves.

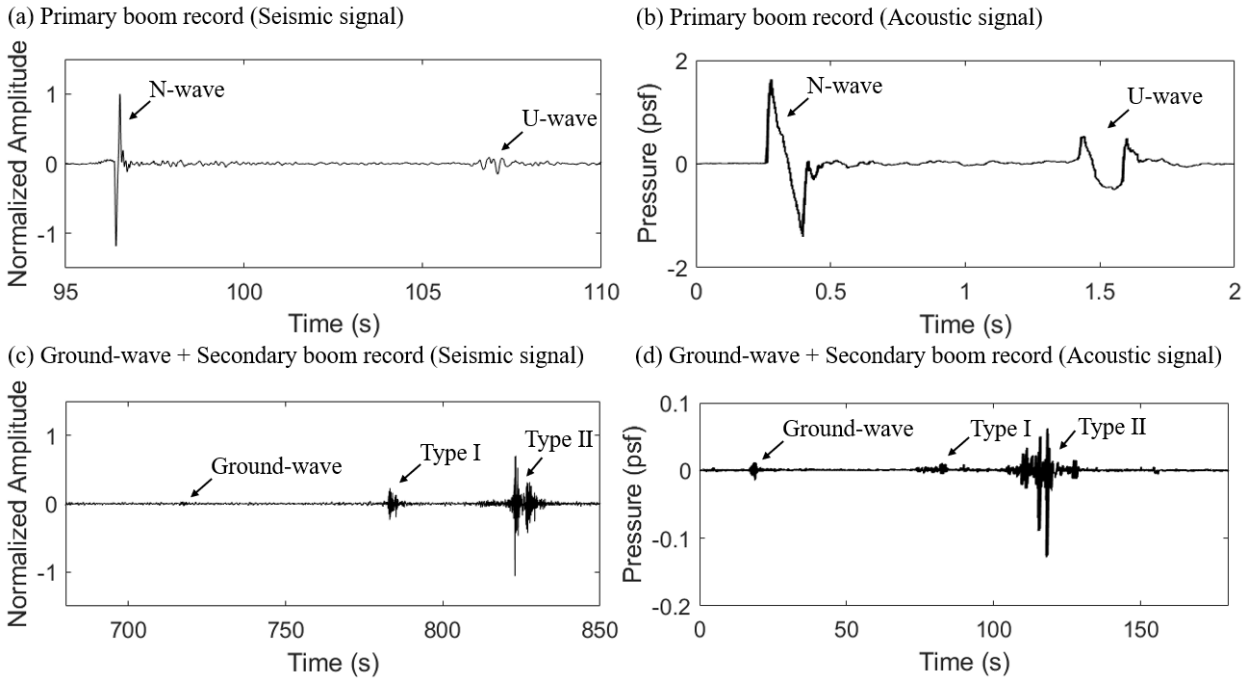


Figure 8. Primary (a,b) and secondary (c,d) sonic boom waves shown on displacement seismograms (left panel) and microphone records (right panel). (Left) The top (a) and bottom (c) seismograms are from boom number 3 recorded on station CI.EDW2 and boom number 4 recorded on station CI.CRG, respectively. Seismic station locations are shown in Figure 7. The starting time (i.e., 0 s) of each window corresponds to each of the sonic boom event detection times at the monitoring station. The waveforms are filtered at 1-20 Hz. Right: The top (b) and bottom (d) pressure traces are modified from the PARTNER project 8 annual report (Sparrow 2005) and Rickley and Pierce (1980), respectively.

Results

Seismograms illustrating primary and secondary sonic boom signatures are from the third boom event's first pass are shown in Figure 9 and Figure 10. It should be noted that the exact event origin time and location are not known, and so we have assumed all the events initiated near EAFB. Therefore, some arrivals plotted on Figure 9 and Figure 10 may show earlier or later arrivals than the minimum or maximum effective sound speeds of 0.2 km/s or 0.4 km/s, respectively. For all passes (Table 1), we note that primary and secondary boom signals are captured by the seismometers at distances up to ~55 km and ~100 - 250 km from EAFB, respectively. We further note that type II secondary sonic boom waves typically arrive about 30 to 50 s after the type I wave (Figure 10). Figure 11 shows the locations of stations that recorded primary and secondary booms for events 14-18 (Table 1), illustrating the spatial coverage of our results across southern California.

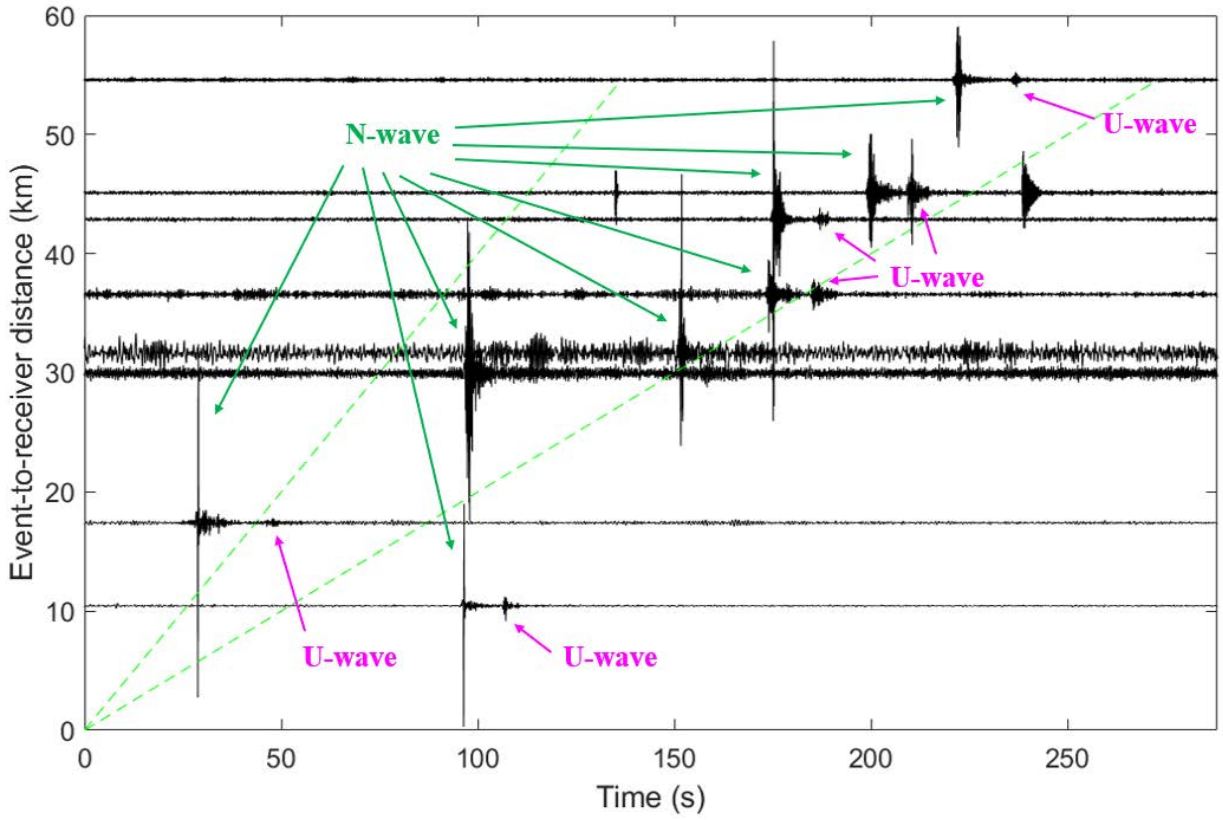


Figure 9. Displacement seismograms from seismic stations for the third boom event during first flight pass (Table 1) showing N and U-type waves (primary boom). Zero time corresponds to the sonic boom detection time at the monitoring station, and the green dashed lines shows velocities of 0.2 km/s to 0.4 km/s used to help identify primary sonic boom arrivals. The seismograms are filttered from 1 to 20 Hz.

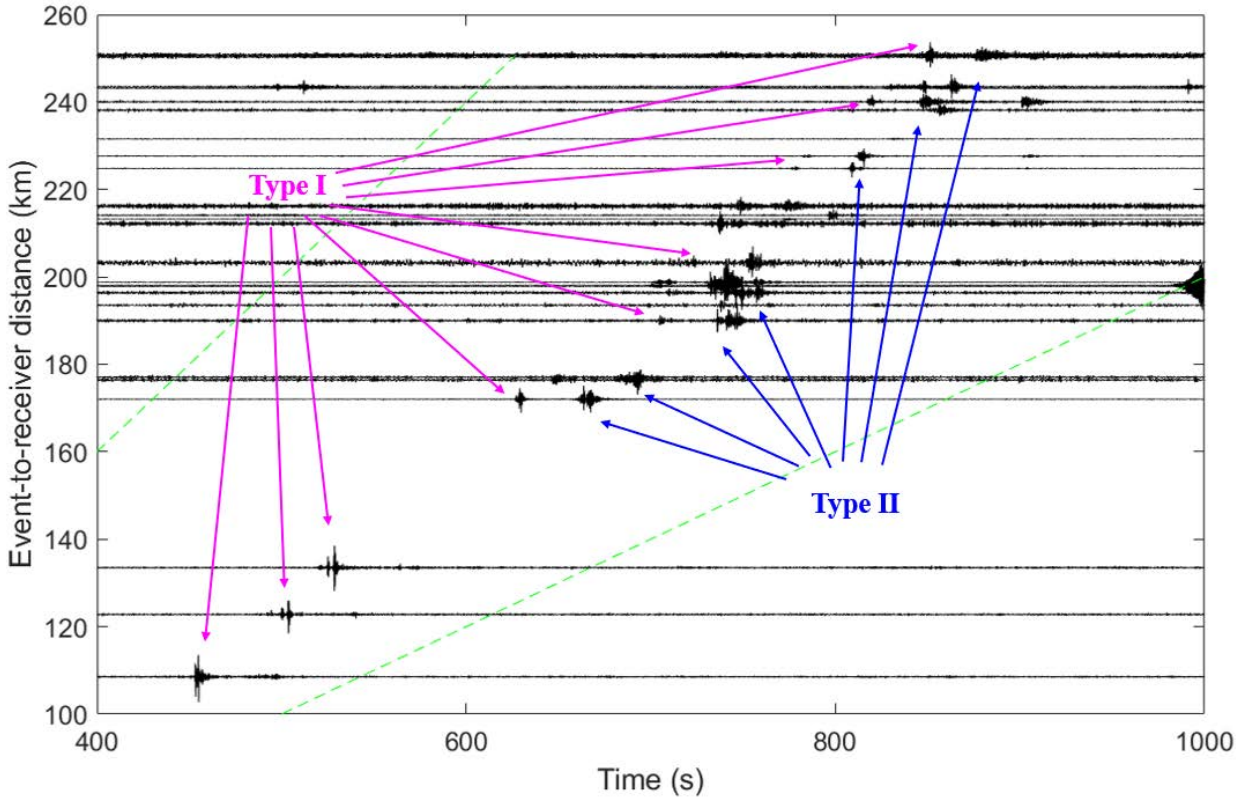


Figure 10. Displacement seismograms from seismic stations for the third boom event during the first flight pass (Table 1) showing type I and II waves (secondary boom). Zero time corresponds to the sonic boom detection time a the monitoring station, and the green dashed lines shows velocities of 0.2 km/s to 0.4 km/s used to help identify the boom arrivals. The seismograms are filtered from 1 to 20 Hz.

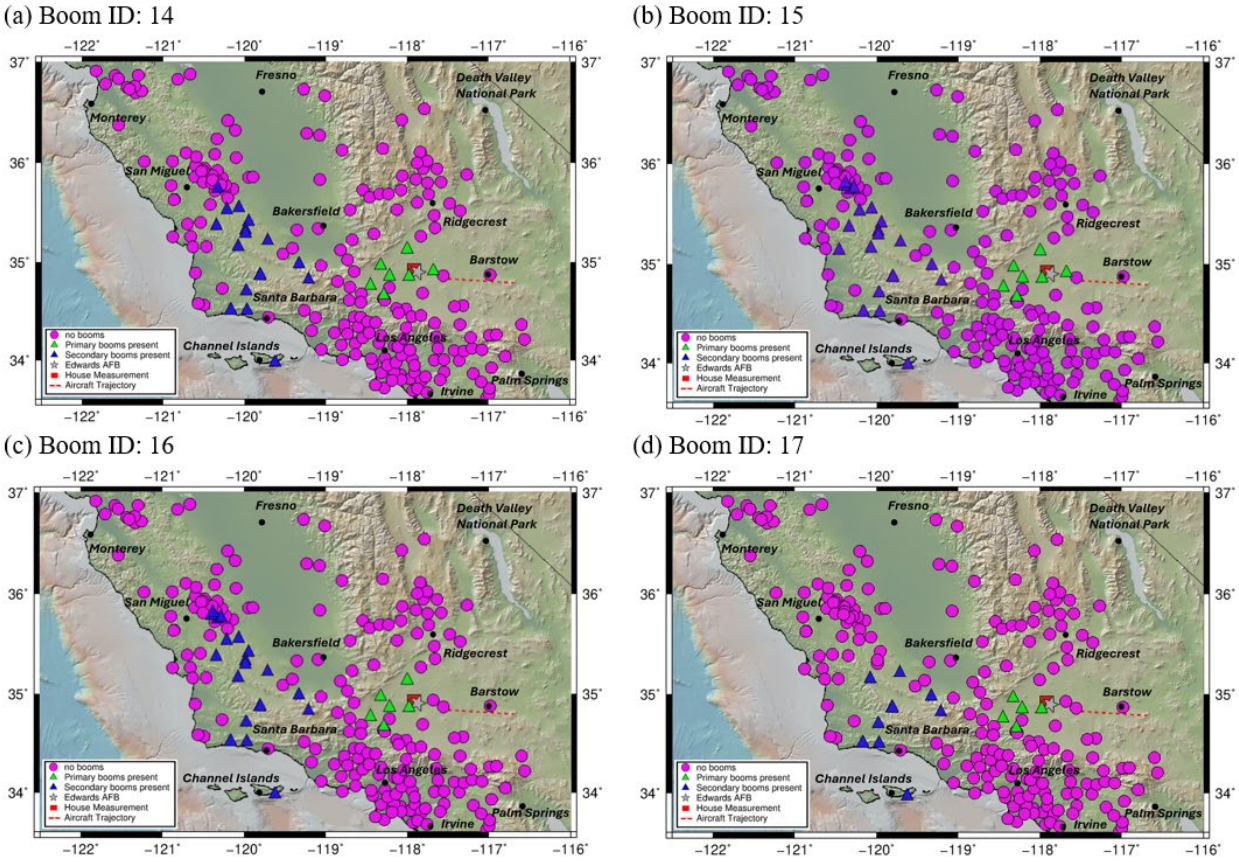


Figure 11. Maps showing primary and secondary boom event detections for boom events 14-17 (the fourth flight pass; Table 1). The green and blue triangles represent instruments with clearly recorded primary and secondary booms, respectively. The magenta circles show stations where the sonic booms were not clearly recorded. Other symbols are similar to Figure 7.

Summary

The goal of this work has been to explore the current capability of detecting primary and secondary sonic booms by seismic stations. The project is specifically aimed at identifying N-type and U-type waves from primary booms, and type I and type II waves from secondary booms recorded on seismic stations in southern California. The research team's results indicate that primary and secondary sonic booms were well recorded on seismic networks in 2005 in southern California over an area of ~ 5,000 km^2 and ~ 30,000 km^2, respectively. These results are consistent with findings previously reported by Cates and Sturtevant (2002) for primary booms. We also report the first seismic observations of secondary sonic booms. Thus, both primary and secondary sonic booms can be detected and classified using existing seismic networks.

Special Acknowledgments

The project team thanks NASA overall, particularly Edward Haering of the NASA Armstrong Flight Research Center, for providing flight info and tremendous support throughout this investigation.

Milestone

- Showed through the results of this study that seismic detection of primary and secondary booms from supersonic flights is possible using existing seismic networks.



Major Accomplishments

ASCENT Project 057 Task 3 extended knowledge of the recording capability of primary and secondary booms by existing seismic stations. The project can now continue identifying secondary booms to understand primary and secondary boom carpets.

Publications

Journal Publication of Presented Conference Abstract

Rathnayaka, S., Nyblade, A. A., Sparrow, V. W., & Riegel, K. A. (2023). Air show primary sonic boom across a Seismic network. *The Journal of the Acoustical Society of America, 154*(4). https://doi.org/10.1121/10.0023074

Outreach Efforts

None.

Awards

None.

Student Involvement

None.

Plans for Next Period

- Continue to work on identifying signatures for primary and secondary sonic booms from various supersonic passes, an essential step toward assessing community impact.
- Identify if secondary booms can be detected as part of NASA's X-59 phase II flight tests.

References

Cates, J. E., & Sturtevant, B. (2002). Seismic detection of sonic booms. *The Journal of the Acoustical Society of America*, *111*(1), 614-628. https://doi.org/10.1121/1.1413754

Rathnayaka, S., Nyblade, A. A., Sparrow, V. W., & Riegel, K. (2023). Air show primary sonic booms across a seismic network. *The Journal of the Acoustical Society of America*, *154*(4_supplement), A147-A147. https://doi.org/10.1121/10.0023074

Rickley, E. J., & Pierce, A. D. (1980). *Detection and assessment of secondary sonic booms in New England* (FAA-AEE-80- 22) Federal Aviation Administration. https://rosap.ntl.bts.gov/view/dot/8970/dot_8970_DS1.pdf

Sparrow, V. W. (2005). PARTNER Project 8: Sonic boom mitigation. *INTER-NOISE and NOISE-CON Congress and Conference Proceedings, NoiseCon05*, 267-274. https://ince.publisher.ingentaconnect.com/contentone/ince/incecp/2005/00002005/00000002/art00037#



Project 058 Improving Analysis Tools to Evaluate Higher-Altitude Aircraft Operations

Massachusetts Institute of Technology

Project Lead Investigator

P.I.: Dr. Raymond Speth
Principal Research Scientist
Associate Director, Laboratory for Aviation and the Environment
Massachusetts Institute of Technology
77 Massachusetts Ave, Building 33-322, Cambridge, MA 02139
speth@mit.edu

University Participants

Massachusetts Institute of Technology (MIT)

- P.I.: Dr. Raymond Speth
- FAA Award Number: 13-C-AJFE-MIT, Amendment Nos. 064, 089, 099, 115, 120, 128, 133, and 140
- Period of Performance: February 5, 2020, to January 20, 2026
- Tasks:
  1. Implement an improved temperature response model in Aviation Portfolio Management Tool – Impacts Climate (APMT-IC)
  2. Extend Goddard Earth Observing System (GEOS)-Chem sensitivities to regions with high current emission intensity
  3. Develop a reduced order model and parametrization of contrails for simplified climate models
  4. Conduct a robust comparison between current contrail models

Project Funding Level

The Federal Aviation Administration (FAA) provided $2,170,000 in funding and $2,170,000 were received in matching funds. Sources of match are approximately $383,094 from MIT, plus third-party in-kind contributions of $391,000 from NuFuels, LLC, and $127,000 from Savion Aerospace Corp., and $414,000 from Google, LLC, and $854,906 from Earth Force Technologies.

Investigation Team

Dr. Raymond Speth, (P.I.), All Tasks
Dr. Prakash Prashanth, All Tasks
Shreya Sharma, (graduate research assistant), Tasks 1-2
China Hagström, (graduate research assistant), Tasks 3-4

Project Overview

Future aircraft technologies may include aircraft operating at higher altitudes such as commercial supersonic aircraft and high-altitude, long-endurance (HALE) unmanned aerial vehicles, which offer the potential to become enablers for new use cases and business models in the aviation sector. However, the combustion emissions of these vehicles will have atmospheric impacts which differ from conventional subsonic aviation due to the higher altitudes of emission. Emissions at higher altitudes are associated with a different chemical environment, longer emission lifetimes, and greater distances over which the emissions will be transported. Furthermore, new developments in emissions impact estimation have enabled a more nuanced view of the environmental consequences of conventional aircraft activity. This includes the recognition that both their atmospheric impacts vary depending on the prevailing conditions of the emission and the time horizon of the assessment. In ASCENT Project 058, our team is working to quantify the environmental consequences of aviation emissions, incorporating information about altitude, location, and timing.



The current project goals are as follows:

(i) Develop and update operational tools capable of quantifying environmental impacts of aviation.
(ii) Improve global chemical transport model (GEOS-Chem) sensitivity analysis methods for enhanced resolution.
(iii) Develop a parametrization method for contrail models.
(iv) Investigate the dependence of aviation emissions impacts on non-aviation factors.

Task 1 – Implement an Improved Temperature Response Model in APMT-IC

Massachusetts Institute of Technology

Objective

The objective of this task it to align the APMT-IC with the state-of-the-art methods for deriving social cost of greenhouse gases, which includes various updates such as the surface temperature model, updated Equilibrium Climate Sensitivity and Transient Climate Response values (EPA, 2023)

Research Approach

We implement a three-box model for the temperature response following Cummins et al. (2020). The following formulation for a temperature model with k number of boxes is used:

$$C_1 \frac{dT_1}{dt} = F(t) - \kappa_1 T_1 - \kappa_2 (T_1 - T_2) + \xi(t)$$
$$C_2 \frac{dT_2}{dt} = \kappa_2 (T_1 - T_2) - \kappa_3 (T_2 - T_3)$$
$$\vdots$$
$$C_{k-1} \frac{dT_{k-1}}{dt} = \kappa_{k-1} (T_{k-2} - T_{k-1}) - \epsilon \kappa_k (T_{k-1} - T_k)$$
$$C_k \frac{dT_k}{dt} = \kappa_k (T_{k-1} - T_k)$$

Each box i has a temperature T_i and heat capacity C_i and is coupled to adjacent boxes above and below; heat transfer coefficients $\kappa_i > 0$ determine the strength of thermal coupling between boxes i and $i-1$. The heat transfer coefficient κ_k in the equation for box $k-1$ is multiplied by an efficacy factor $\varepsilon > 0$ to simulate variation in the effective strength of κ_1 during periods of transient (non-equilibrium) warming. The term $F(t)$ denotes radiative forcing measured at the top of the atmosphere and $\xi(t)$ is a stochastic disturbance. For a three-box model, the above equations can be simplified to write:

$$\dot{X}(t) = AX(t) + bF(t) \qquad \text{(Eq. 1)}$$

where X(t) is the vector of the temperature of the three boxes.

APMT-IC can now run three options to run the temperature-response model:

(i) The original two-box model.
(ii) An unconstrained three-box model: For this model, the distributions for the equilibrium climate sensitivity and transient climate response are as defined in Leach et al. (2021). These parameters are specified directly in the APMT-IC configuration file.
(iii) A constrained three-box model: Additionally, Leach et al. (2021) introduces a constrained formulation which ensures that the selected parameters result in a distribution similar enough to the historical temperature record. This constrained formulation only affects how the input parameter samples are selected, and not the mathematical formulation of the temperature model solver. For APMT-IC, these parameters are derived using the code from Leach et al. (2021).

Milestone

- Updated the temperature-response model in APMT-IC to a three-box model which incorporates the temperature change due to the atmosphere-ocean mixed layer, the shallow ocean layer, and the deep ocean layer which acts as a heat sink.



Publications
None.

Outreach Efforts
None.

Awards
None.

Student Involvement
The research and communication for this task were conducted primarily by Carla Grobler

Plans for Next Period
Short-term:

- Update other parts of the climate sub-module such as the time-varying carbon dioxide (CO_2) sinks, as modeled in FAIR (Leach et al., 2021).
- Update the damage functions in APMT-IC to incorporate more recent studies such as an updated social cost of carbon from Rennert et al. (2022).

Long-term:

- Use the harmonized version of the APMT-IC model to derive updated climate and air quality cost metrics, such as those published in Grobler et al. (2019)

References
EPA. (2023). *EPA Report on the Social Cost of Greenhouse Gases: Estimates Incorporating Recent Scientific Advances*. U.S. Environmental Protection Agency. https://www.epa.gov/system/files/documents/2023-12/epa_scghg_2023_report_final.pdf

Cummins, D. P., Stephenson, D. B., & Stott, P. A. (2020). Optimal Estimation of Stochastic Energy Balance Model Parameters. *Journal of Climate, 33*(18), 7909–7926, https://doi.org/10.1175/JCLI-D-19-0589.1.

Grobler et al., (2019) Marginal Climate and Air Quality Costs of Aviation Emissions. *Environmental Research Letters*, 14(11) https://doi.org/10.1088/1748-9326/ab4942

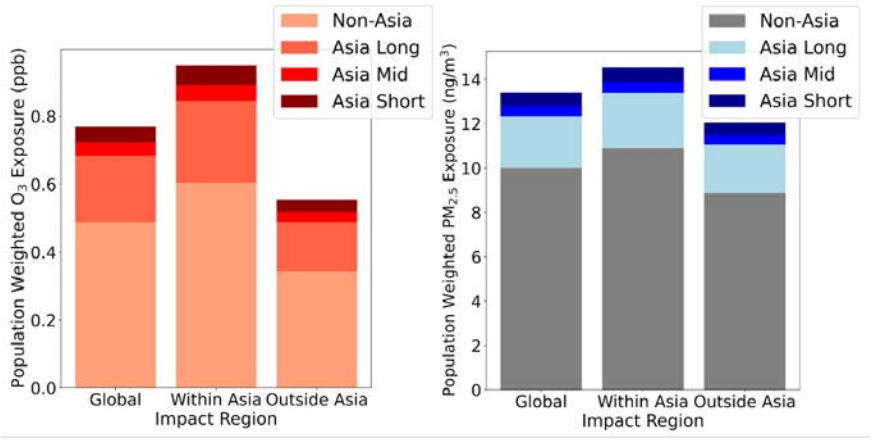
Leach, N. J., Jenkins, S., Nicholls, Z., Smith, C. J., Lynch, J., Cain, M., Walsh, T., Wu, B., Tsutsui, J., & Allen, M. R. (2021). FaIRv2. 0.0: a generalized impulse response model for climate uncertainty and future scenario exploration. *Geoscientific Model Development*, *14*(5), 3007-3036. https://doi.org/10.5194/gmd-14-3007-2021

Rennert, K., Errickson, F., Prest, B. C., Rennels, L., Newell, R. G., Pizer, W., Kingdon, C., Wingenroth, J., Cooke, R., Parthum, B., Smith, D., Cromar, K., Diaz, D., Moore, F. C., Müller, U. K., Plevin, R. J., Raftery, A. E., Ševčíková, H., Sheets, H., Stock, J. H., Tan, T., Watson, M., Wong, T. E., & Anthoff, D. (2022). Comprehensive evidence implies a higher social cost of CO2. *Nature*, *610*(7933), 687-692. https://doi.org/10.1038/s41586-022-05224-9

Task 2 – Extend GEOS-Chem Sensitivities to Regions with High Current Emission Intensity
Massachusetts Institute of Technology

Objective
The objective of this task is to extend the GEOS-Chem analysis by focusing on the specific high emission regions of South and East Asia. In addition, we evaluated the downstream air quality impacts in terms of population weighted exposure to ozone and Particulate Matter ($PM_{2.5}$), as well as the associated increase in mortalities. In addition to this, we hope to evaluate the sensitivities of these impacts to key routes and aircraft types.

Research Approach
The International Civil Aviation Organization (ICAO) air passenger forecasts predict the Asia Pacific region to account for almost half the total share of fuel burn in 2043 (this region in 2023 only accounted for about one third of the total aviation



fuel burn). For our analysis, this region is defined to be a combination of two groups of countries as defined by the world bank: (1) South Asia and (2) East Asia and Pacific. The traffic in this region was further divided into three mission sizes: short haul (<500 nmi), mid haul (>500 nmi to <2,000 nmi) and long haul (>2,000 nmi). The Aviation Emissions Inventory Code (AEIC) was used to generate the emissions inventories corresponding to each case.

GEOS-Chem High Performance (GCHP) simulations were run using these inventories and the change in surface concentration due to each case was evaluated along with the population distribution to obtain population-weighted exposure to ozone and PM2.5. This exposure was aggregated in the same regions (within the Asia set, outside the Asia set, global average) as presented in Figure 1.

Figure 1. Share of population weighted ozone and $PM_{2.5}$ exposure for flights outside the Asia set (non-Asia) and the share within the Asia set (short/mid/long haul) for flights in 2019.

The largest exposure was from the non-Asia flights, followed by long haul flights in Asia. For both ozone and $PM_{2.5}$, the population weighted exposure within Asia was greater than that outside Asia. This exposure was further normalized by the total amount of fuel burned occurring in each mission size, since different types of aircraft – widebody, narrowbody, regional jets – fly in these different mission classes. The resulting data are shown in Figure 2.

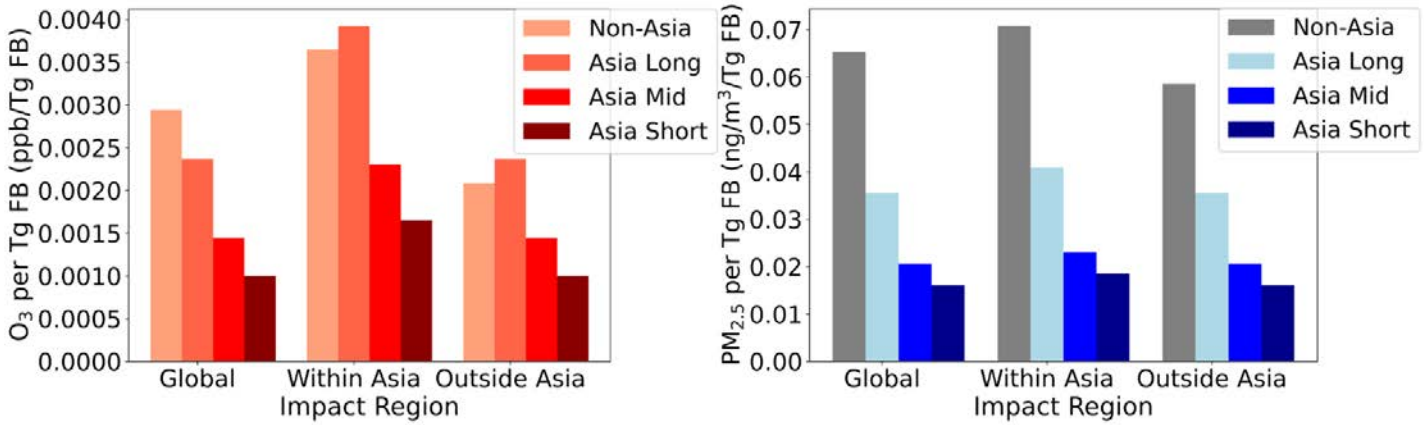


Figure 2. The relative population weighted ozone and $PM_{2.5}$ exposures per Tg fuel burn for flights outside the Asia set (non-Asia) and the share within the Asia set (short/mid/long haul) for flights in 2019.

When normalized by fuel burned, the non-Asia flights result in the highest exposure, and this trend is more prominent for $PM_{2.5}$ than ozone. We also find that long haul flights within Asia result in a relatively high ozone exposure within Asia.



Further, we use relative risk rates from epidemiological studies to estimate an increase in incidence rates of certain diseases like COPD, asthma, and upper respiratory infections. For ozone, we use the Turner et al. (2016) study which correlates the maximum daily 8-hour exposure to ozone, to negative health outcomes. For PM2.5, we use the GEMM (Burnett et al., 2018) meta-analysis, which is multi cohort study from 16 countries. We use data from the World Health Organization global burden of disease for this purpose. The countries with the five highest mortalities due to ozone are India, China, USA, Japan, and the UK, primarily due to high population density, and topology (ozone is more concentrated at higher altitudes). For $PM_{2.5}$, these are China, India, USA, Germany, and the UK due to similar reasons, along with a higher prevalence of precursor gases in these countries.

Milestones

For the high emission intensity region of South and East Asia, we now have the emissions inventory, the simulated changes in surface concentration of ozone and $PM_{2.5}$, along with the population weighted exposure and country-wise share of mortalities.

Publications

Shreya Sharma, Prakash Prashanth, Raymond Speth. Regional Differences in Surface Ozone and $PM_{2.5}$ due to Aviation in Growing Markets. ESS Open Archive. March 05, 2025. DOI: 10.22541/essoar.174120418.84924481/v1

Outreach Efforts

None.

Awards

None.

Student Involvement

The research and communication for this task were conducted primarily by MIT graduate research assistant Shreya Sharma.

Plans for Next Period

Short-term:

- Monetize the mortalities due to air quality degradation using a country-specific value of statistical life.
- Evaluate the climate impacts of these flight operations in terms of a temperature rise and use a damage function to evaluate the monetized cost.

Long-term:

- Extend a similar analysis to other global regions and different aircraft types and missions.

References

Burnett, R., Chen, H., Szyszkowicz, M., Fann, N., Hubbell, B., Pope III, C. A., ... & Spadaro, J. V. (2018). Global estimates of mortality associated with long-term exposure to outdoor fine particulate matter. Proceedings of the National Academy of Sciences, 115(38), 9592-9597.

Turner, M. C., Jerrett, M., Pope III, C. A., Krewski, D., Gapstur, S. M., Diver, W. R., ... & Burnett, R. T. (2016). Long-term ozone exposure and mortality in a large prospective study. American journal of respiratory and critical care medicine, 193(10), 1134-1142.

Task 3 - Develop a Reduced Order Model and Parametrization of Contrails for Simplified Climate Models

Massachusetts Institute of Technology

Objective

Contrail impacts are heavily influenced by their surrounding properties during and after formation. We find that current reanalysis estimates of the properties defining these ice supersaturated regions (ISSRs) are not in good agreement with experimental data. To quantify these effects, we compute upper and lower bounds of expected contrail radiative forcing impacts. We aim to develop reduced order models of high-resolution plume-based contrail models (Aircraft Plume

Chemistry, Emissions, and Microphysics Model [APCEMM]) and radiative transfer codes (libRadtran) which can then be used to understand the relative contribution of various uncertainty sources. Once completed, this method can be implemented as a fast surrogate for efficient contrail parametrizations in APMT-IC.

Research Approach

Consider an example case study for an initial ISSR condition *m,* where the initial ISSR condition is defined by the relative humidity with respect to ice (RH_i) and moist layer depth (MLD). This simulated ISSR state is static with the exception of the wind field. Assuming cruise conditions, pressure levels are considered constant within the ISSR. For a specific mission APCEMM produces a single contrail evolution. This model provides time-resolved ice water content (IWC) and contrail width estimates for the contrail lifetime in increments of 1 min.

The incorporation of uncertainty into this case study structure requires estimation of associated uncertainty with specific ISSR baseline initial condition pairings of RH_i and MLD. For an example case study with initial ISSR condition *m,* we perform multiple studies. Each study is identical except for the perturbations applied to the ISSR initial conditions. To perform these studies at lower computational cost we utilize the polynomial chaos expansion (PCE) method, a mathematical technique used to represent uncertain parameters in computational models by expanding them in terms of orthogonal polynomials. These polynomials are selected based on the probability distribution of the uncertain inputs, allowing for efficient approximation of complex stochastic systems. PCE is particularly effective for uncertainty quantification, as it provides a systematic way to propagate input uncertainties through a model while significantly reducing computational costs compared to traditional Monte Carlo methods. Additionally, PCE enables sensitivity analysis by identifying which input variables have the most influence on the model's output, thereby aiding in decision-making and optimization.

Preliminary Results

We run the surrogate for many initial conditions varying around the baseline initial conditions. The magnitude of the variations is based on the amount of uncertainty ascribed to the initial RH_i condition using the GRUAN/ERA5[1] average absolute difference. The time-resolved ice water content and contrail width results for each perturbed case study are then used as inputs to libRadtran. Each perturbed set of case studies results in an upper and lower bound estimate of the possible radiative forcing estimates for a contrail produced in an ISSR predicted by uncertain ERA5 meteorological parameters RH_i and MLD. The described workflow is shown in Figure 3. Repeating this methodology for additional ISSR initial conditions provides insights into the impacts of uncertainty in ERA5 provided initial conditions on contrail properties throughout its lifetime. The processes described above have been completed for a mean RH_i of 123% and a B737-800 with a CFM56 engine.

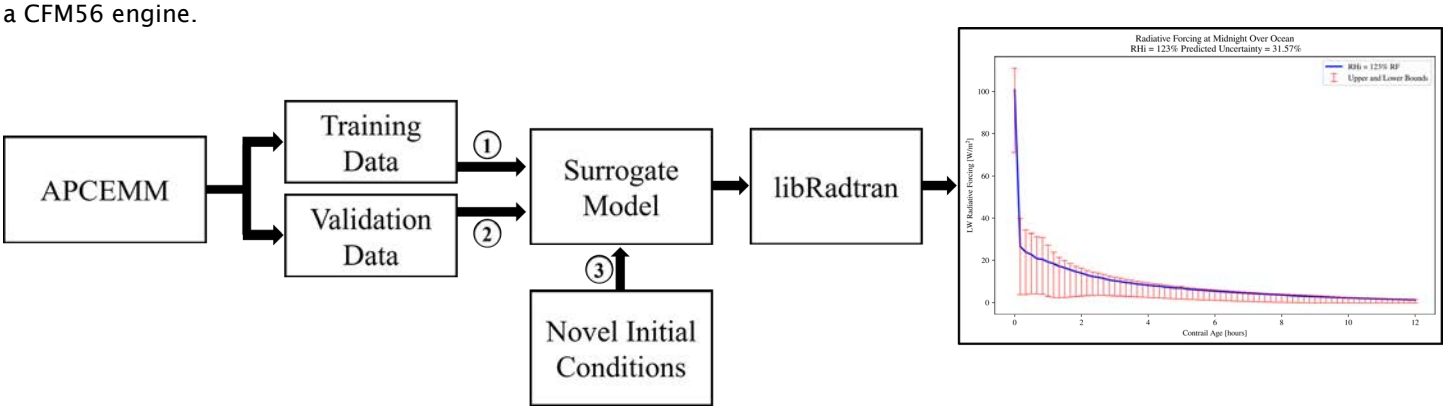


Figure 3. Workflow for training, validating, and utilizing a surrogate contrail model using polynomial chaos expansion (PCE) to produce an envelope of contrail radiative forcing based on uncertainty in the meteorological input data. APCEMM: Aircraft Plume Chemistry, Emissions, and Microphysics Model.

Milestones

[1] European Centre for Medium-Range Weather Forecasts (ECMWF) Reanalysis v5 (fifth generation ECMWF atmospheric reanalysis of the global climate). Produced by the Copernicus Climate Change Service (C3S) at ECMWF, it provides hourly, high-resolution (31km) global data on atmospheric, land, and ocean-wave variables from 1940 to the present.



Developed a fast surrogate model of APCEMM using non-intrusive polynomial chaos expansion to estimate internally limited contrail width and ice water content.

Major Accomplishments
Quantified the effects of uncertainty in APCEMM meteorological inputs on radiative forcing impacts estimates at every simulated contrail timestamp.

Publications
None.

Outreach Efforts
None.

Awards
None.

Student Involvement
The research and communication for this task were conducted primarily by MIT graduate research assistant, China G. Hagström.

Plans for Next Period
- Include moist layer depth as stochastic variable in addition to RH_i.
- Scale the reported emissions of additional engines to cruise.
- Complete surrogate training for an additional seven missions.
- Process additional surrogate outputs using the libRadtran ice cloud parametrization.
- Integrate tested surrogate model into APMT-IC.

References
None.

Task 4 – Conduct a Robust Comparison between Current Contrail Models
Massachusetts Institute of Technology

Objective
Multiple approaches to representing the property evolution of an equivalent contrail are required to satisfy computational constraints and fulfill a broad range of applications. The sensitivities of computed contrail properties to different parameterizations of the same phenomena are largely unknown and exacerbated by limited experimental data. We review the three most utilized contrail models, analyzing the differences in computed contrail properties for equivalent internally limited contrails under a variety of meteorological conditions. A contrail is defined as internally limited when the contrail ends because of internal ice evolution processes, rather than external meteorology evolving to no longer being contrail supporting (Schumann, 2016).

The models studied are the Contrail Cirrus Prediction (CoCiP) model, APCEMM, and large eddy simulations (LES) as described in Lewellen et al. (2014) parts one and two (Fritz et al., 2020; Lewellen, 2014; Lewellen et al., 2014; Schumann, 2012). Utilizing model-predicted contrail properties, comparisons of estimated radiative forcing values will be computed. Understanding the effects of different model approaches on contrail radiative forcing estimates will not only identify effective areas for model development but additionally provide recommendations for future best practices in model application, reducing uncertainty within the field.

Research Approach
The comparison of the models is based on available data from the 2014 Lewellen LES analyses (LLES). As such the meteorological and emissions conditions for APCEMM and CoCiP were chosen to match those of the LLES studies. The LLES



reports provide results for six reference contrail cases, defined by the combinations of two background relative humidities (130% and 110%) and three ambient temperatures (205 K, 218 K, and 225 K), all assuming a temperature lapse rate of 2.5 $km^{-1}K$. For each of these cases, LLES outputs are available for ice crystal number and ice mass as functions of time. Ice crystal radius distributions are reported for "cold and dry" (110% 205K) and "warm and moist" (130% 225K) cases for contrails aged 5 min to 12 hr. Contrail width and ice crystal surface area, which combined produce an estimate of integrated vertical optical depth (Lewellen, 2014), are reported for the "average" contrail condition (110% 218K). Each of these scenarios is recreated in APCEMM and CoCiP for direct comparison. We find differences in contrail properties across all cases, all contributing to differences in contrail radiative forcing. Preliminary results are described below.

Preliminary Results

CoCiP crystal number trends indicate that the model response is strongly affected by the initial available water content. This can be explained by the parametrization of the loss rate of ice crystal number. For a constant RH_i, as ambient temperatures warm the available moisture increases, and the equilibrium vapor pressure over ice increases as do diffusion rates, which increase the deposition rate of water onto ice. Crystal fall velocity and contrail depth both increase with crystal growth rate. This results in accelerated crystals losses and thereby shortens the contrail lifetime. When CoCiP's representative ice crystal falls into subsaturated air the contrail quickly disappears, underrepresenting the contrail lifetime.

APCEMM includes representations of multiple crystal sizes and allows for crystal stratification in a two-dimensional model, both of which lead to different loss functions. We find that larger crystals take up more water due to a reduced Kelvin effect and enhanced scavenging. As they grow their fall speed increases, allowing them to descend into new, moister air where smaller crystals reside. This process leaves behind smaller crystals in the original layer, which then compete less for the remaining water and therefore grow faster. However, when the contrail is ice water content limited, such as at 110% relative humidity, crystals do not grow and settle as rapidly as in the 130% case, resulting in longer lifetimes. Ice mass stays relatively constant for a period after initial water uptake, but at the expense of crystal number due to scavenging and coagulation. Additional mass is lost as a contrail ages and a subset of crystals begin interacting with subsaturated air.

The LLES approach uses similar mechanisms for ice evolution as APCEMM, presenting with similar ice mass and crystal number trends. In contrast to APCEMM the coupled aspect of temperature and velocity fields creates a buoyancy feedback loop. This may increase small crystals temporarily due to adiabatic heating resulting in more scavenging of small crystals to larger ones (Unterstrasser & Gierens, 2010). The LLES crystal radius tracking scheme may also over predict losses of small crystals, attributing losses to the Kelvin effect while also explicitly including a Kelvin effect term elsewhere. This may artificially inflate the concentration of larger crystals, reducing contrail lifetime estimates. Additionally, we see similar initial growth rates and trends to APCEMM, but lower total ice mass and faster mass loss. This mass loss may be attributed to the computational binning scheme used to track ice crystals, which does not conserve mass.

Through this analysis we contributed insights on mechanisms influencing contrail properties and lifetimes internal to the modeling approach chosen. We improved our understanding of individual model approaches to contrail dynamics and ice microphysics, and the associated downstream effects of resource-fidelity tradeoff decisions.

Milestones

- Performed the first inter-model comparison between CoCiP, APCEMM, and LLES for equivalent contrail initial conditions.

Major Accomplishments

- Analyzed and quantified impacts of model parametrization methodologies on computed radiative forcing values for internally limited equivalent contrail initial conditions under six bounding meteorological conditions.
- Provided previously unknown insights on mechanisms influencing contrail properties and lifetimes internal to the modeling approach chosen.
- Specifically improved understanding of individual model approaches to contrail dynamics and ice microphysics, and the associated downstream effects of computational resource-fidelity tradeoff decisions.

Publications

None.



Outreach Efforts
None.

Awards
None.

Student Involvement
The research and communication for this task were conducted primarily by MIT graduate research assistant, China G. Hagström.

Plans for Next Period
- Introduce radiative forcing post-processing of computed contrail optical and physical properties.
- Produce additional comparisons and sensitivity analyses of microphysical inputs for CoCiP and APCEMM.
- Publish this work in a peer reviewed journal.

References
Fritz, T., Eastham, S. D., Speth, R. L., & Barrett, S. R. H. (2020). The role of plume-scale processes in long-term impacts of aircraft emissions. *Atmospheric Chemistry and Physics, 20*(9), 5697–5727. https://doi.org/10.5194/acp-20-5697-2020

Lewellen, D. C., Meza, O., & Huebsch, W. W. (2014). Persistent contrails and contrail cirrus. Part I: Large-eddy simulations from inception to demise. *Journal of the Atmospheric Sciences, 71*(12). https://doi.org/10.1175/JAS-D-13-0316.1

Lewellen, D. C. (2014). Persistent contrails and contrail cirrus. Part II: Full lifetime behavior. *Journal of the Atmospheric Sciences, 71*(12). https://doi.org/10.1175/JAS-D-13-0317.1

Schumann, U. (2016). *The lifecycle and climate-impact of contrail cirrus*. European Planetary Science Congress 2016, EPSC2016-2385. https://ui.adsabs.harvard.edu/abs/2016EGUGA..18.2385S

Schumann, U. (2012). A contrail cirrus prediction model. *Geoscientific Model Development, 5*(3), 543–580. https://doi.org/10.5194/gmd-5-543-2012

Unterstrasser, S., & Gierens, K. (2010). Numerical simulations of contrail-to-cirrus transition – Part 1: An extensive parametric study. *Atmospheric Chemistry and Physics, 10*(4), 2017–2036. https://doi.org/10.5194/acp-10-2017-2010



Project 059(B) Jet Noise Modeling and Measurements to Support Reduced LTO Noise of Supersonic Aircraft Technology Development

Georgia Institute of Technology/Gulfstream Aerospace Corporation

Project Lead Investigator

Krishan K. Ahuja
Regents Professor
School of Aerospace Engineering
Georgia Institute of Technology
Atlanta, GA 30342
404-290-9873
Krish.Ahuja@ae.gatech.edu

University Participants

Georgia Institute of Technology (Georgia Tech)

- PI: Krishan K. Ahuja, Regents Professor
- FAA Award Number: 13-C-AJFE-GIT-060
- Period of Performance: June 5, 2020, to September 30, 2025
- Tasks:
  1. Consult with the Advisory Panel
  2. Define Nozzle Requirements and Design Tests
  3. Design and Fabricate a Baseline Nozzle
  4. Test Setup and Experimental Data Acquisition
  5. Data Dissemination
  6. Proposal for a Follow-on Efforts
  7. Reporting and Data Dissemination

Project Funding Level

This project received $750,000 from the Federal Aviation Administration (FAA) and $750,000 cost-sharing from Gulfstream Aerospace Corporation (GAC) for each of the three phases of this project. Total combined funding to date is $1.5M.

Investigation Team

Georgia Institute of Technology

Dr. Krishan Ahuja, PI, Georgia Tech
Dr. Jimmy Tai (Co-PI), Georgia Tech
Dr. Nicholas Breen, Co-Investigator and Lead Experimentalist, Georgia Tech Research Institute (GTRI)
Dr. Robert Funk, Experimentalist, GTRI
Jackson Larisch, Graduate Research Assistant, GTRI
David N. Ramsey, Graduate Research Assistant for portion of the program and subsequently a NSF Fellow working on fundamental issues related to the current project, Georgia Tech and since graduated, GTRI
Reagan Mayo, Graduate Research Assistant for portion of the program and since graduated, GTRI

Gulfstream Aerospace Corporation

Brian Cook (Gulfstream)

- Dr. Joseph Gavin (Gulfstream)



Project Overview

The overall goal of this project is to perform cost-effective supersonic transport (SST) jet noise research/technology experiments to enable low-, medium-, and high-fidelity jet noise prediction methods. The specific objective is to design the experiments in collaboration with industry, the National Aeronautics and Space Administration (NASA), Department of Defense (DOD), FAA, and modelers funded by the FAA to help develop improved jet noise prediction methods with reduced uncertainty and enable industry to design quieter supersonic jet engines with higher confidence regarding the noise that will be generated. In collaboration with GAC, Georgia Tech's industry partner on this project, a representative baseline nozzle design was selected for experiments at Georgia Tech. The data acquired consisted of far-field noise, high-speed flow visualization, source location, and detailed mean and unsteady flow measurements.

The experimental data acquired by Georgia Tech was provided to key stakeholders and other computational teams funded by FAA to validate their computational simulations to confirm that jet noise predictions using semi-empirical and computational modeling approaches can be reliably used for jet noise evaluation.

Task Objectives

This project had seven tasks, as listed below. These task titles are self-descriptive; however, a short objective statement and/or a summary of accomplishments are also provided for each task.

Task 1: Consult with the Advisory Panel
The objective of this task was to receive regular feedback from industry and NASA subject-matter experts (SME) in supersonic jet noise.

Task 2: Define Nozzle Requirements and Design Tests
The objective of this task was to define the nozzle requirements and design the experiments.

Task 3: Design and Fabricate a Baseline Nozzle
The objective of this task was to design and fabricate a baseline nozzle that meets the requirements defined in Task 2 above and is also suitable for the tests needed to meet the objectives of the overall program.

Task 4: Test Setup and Experimental Data Acquisition
The objective of this task was to get ready to conduct the tests and acquire and analyze the data

Task 5: Data Dissemination
The objective of this task is to stay in touch with the modelers being funded by FAA under ASCENT Project 059 and provide the project stakeholders with the nozzle design and both acoustic and flow data from the current project. The final model design has been shared with the modeling teams since November 2021. All Year 1 and 2 acoustic and particle imaging velocimetry (PIV) data, both for the unheated and heated-core conditions, have been shared with the modelers. Likewise, the flow visualization has been made available to the modelers.

Task 6: Proposal for a Follow-on Efforts
Each year a proposal for the following year was submitted and approved.

Task 7: Reporting and Data Dissemination
All Year 1-3 reports (annual and quarterly) were submitted on time.

Research Approach and Accomplishments

This project can be divided into two main parts: Years 1 & 2 were dedicated to studying the so-called Academic Nozzle (described below) and Year 3 was devoted to investigating the so-called Gulfstream® nozzle. The academic nozzle is a design created by the Georgia Tech Aerospace Systems Design Lab (ASDL) and the Gulfstream nozzle, like its namesake, is a design created by GAC. For both of these nozzles, various types of data were collected at a wide range of operating

® Gulfstream is a registered trademark of Gulfstream Aerospace Corporation, Savannah, Georgia

conditions and extraction ratios: acoustic spectra, flow data, PIV, flow visualization, and acoustic source locations. All of this data has been provided to aeroacoustics modelers for additional analysis and model development.

This report is divided into two large sections, each detailing the results for each of the two main parts of the effort described above.

Years 1 & 2 - the Academic Nozzle

Georgia Institute of Technology

Nozzle Design

The design of the baseline nozzle is shown in Figure 1. The baseline nozzle and tests were based on a paper engine design created by the Georgia Tech ASDL guided by ASCENT Project 010 on engine cycle selection for the Georgia Tech Medium SST jet (55 passenger class). For simplicity, it was decided that the Georgia Tech nozzle model tested under this project would not have a plug. For the purpose of calculating the area of the outer (secondary flow) duct, the annular areas of the paper engine were used to calculate the area of the secondary flow duct in GTRI's model nozzle facility. The GTRI model is a 0.045 scale of the paper engine. The model consists of the following parts: (1) the primary nozzle with the collar to avoid any anomalous flow effects due to any geometrical protrusions/recesses; (2) the secondary nozzle; (3) mixer ducts; and (4) the exhaust nozzle. A total of three mixer ducts were fabricated to allow for different mixing-duct length-to-nozzle-exit diameter ratios (L/D). The test model utilizes the coannular flow capabilities of the GTRI jet facilities. The primary and secondary flow streams converge into the mixer-duct and exhaust nozzle combination. The mixer-duct and exhaust nozzle combinations allow for four values of L/Ds, namely, 0.7 (exhaust nozzle mounted directly to the secondary nozzle), 1, 2, and 3. The jet stream is ultimately formed by the exhaust nozzle, which is a converging nozzle with geometry based on the converging section of the converging-diverging nozzle from the ASDL engine design.

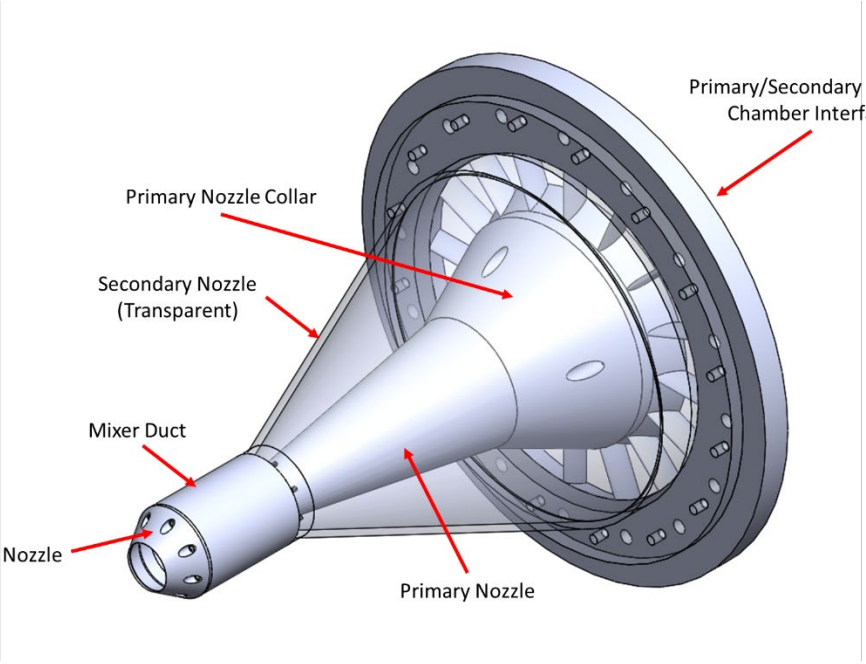


Figure 1. Year-1 experimental model design.

Acoustic Measurements

Facility Set-up and Testing Description

The test model was mounted in the GTRI Anechoic Jet-Facility for the acoustic data acquisition as seen in Figure 2. This facility is described in detail in Burrin et al. (1974), Burrin and Tanna (1979), and Ahuja (2003). Farfield microphones were



mounted on a polar arc at angles between 30° and 120° with respect to the jet axis in 10° increments. The upstream jet operating conditions were set by controlling the ratio of the total pressure to the ambient pressure (PR = p_t/p_a) for both the primary and secondary streams. The pressure ratios of both the primary and secondary streams varied between 1.12 and 1.89. The extraction ratio (ER = p_{t2}/p_{t1}) was also used as another parameter to define the secondary pressure ratio for a given primary stream pressure. This parameter was brought to our attention by the program partners and is of practical importance. Per insight from GAC and FAA, ERs between 1.00 and 1.07 are the most realistic conditions for a given PR_1. Additionally, the primary jet was operated under both unheated and heated conditions. In the unheated tests, the jet total temperature varied between 60°F and 70°F. For the heated testing, it was set nominally to 500°F. As a note, for the remainder of this program the pressure ratio, PR, will refer to the ratio between upstream total and ambient pressures. In addition to the acoustic measurements, the primary and secondary total pressure and temperature, the primary and secondary mass flow rates (measured at the control valve), and the ambient pressure, temperature, and relative humidity were measured.

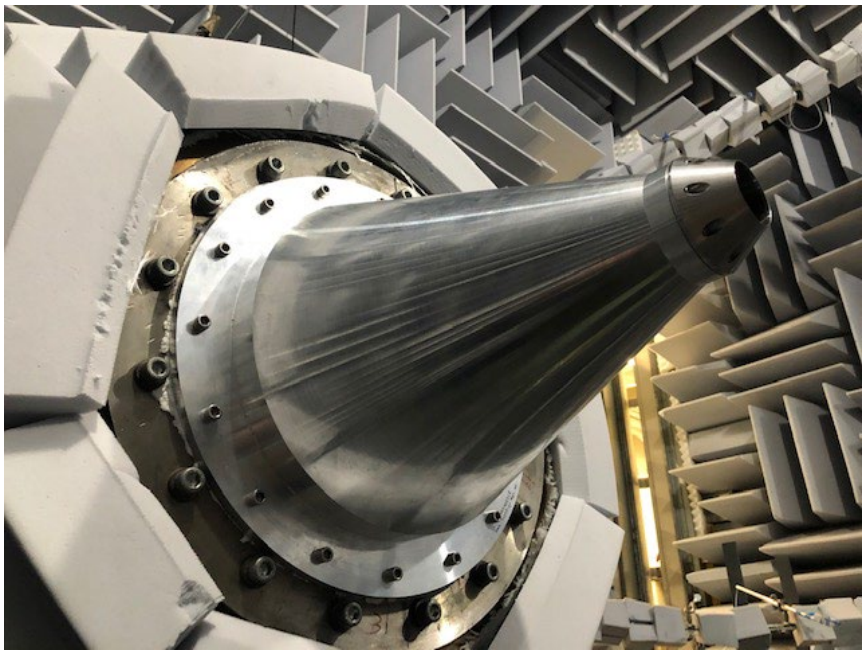


Figure 2. Project model set up in the GTRI Anechoic Jet Facility.

The microphones used for these measurements were Bruel and Kjaer (B&K) 4939 ¼-in. free-field microphones and were attached to B&K 2669 preamplifiers. The microphone-preamplifier combinations were connected to B&K 2960-A-0S4 Nexus conditioning amplifiers that, in addition to amplifying the signal, acted as the microphones' 200 mV power supply. The microphone signals were sampled at 204.8 kHz using National Instruments® PXIe-4499 modules. The acoustic pressure time histories were then processed into averaged sound pressure level (SPL) spectra using a window size of 6400 samples, 50% overlap, and a Hanning window. To render the data to lossless form for use by the modelers, the following corrections were applied to these SPL spectra: free-field response correction, windsock correction (if necessary), atmospheric attenuation, and distance. These corrections are described in detail in Karon and Ahuja (2016).

Acoustic Analysis

The following subsections detail the results acquired from acoustic measurements obtained using the baseline nozzle across a variety of operating conditions (including heated and unheated core flow) and mixing duct lengths. This analysis is categorized by the effects of extraction ratio, mixing-duct length, and core temperature. An additional analysis of noise produced by the dual-stream nozzle at extraction ratios of unity and just above unity – which are of most interest to the FAA and GAC – is provided. Much of the discussion here is expanded upon by Ramsey et. al. (2022a). The howling

® National Instruments is a registered trademark of National Instruments Corporation, Austin, Texas.

produced by this nozzle geometry at certain operating conditions is briefly discussed with references to more detailed published work.

Effect of changing the Extraction Ratio: Figure 3 shows the jet noise measurements for jet condition of ER = 1.1, 1.0, and 0.92 for the L_e/D_e = 0.7 configuration. It is noted that the ER = 1.1 and 0.92 are outside of the ER range advised to be of greater practical interest by the program partners, but the data is shown here because it was acquired as part of this program and validating the predictions by the modelers for these conditions would provide added confidence in their fidelity. As can be seen in Figure 3, the noise increases with increasing secondary pressure ratio. At lower frequencies (below ~3 kHz), the noise increased by about 1 dB as the secondary pressure ratio increases from 1.28 to 1.39 and from 1.39 to 1.52. At the higher frequencies, the noise increase is larger. As the secondary pressure ratio is increased from 1.28 to 1.39, the noise increases by as much as 3 dB, and when the secondary pressure ratio is increased from 1.39 to 1.52, the noise increases by as much as 5 dB. It will be shown later that if the extraction ratios are maintained close to unity, say up to 1.07, there is no noticeable change in SPLs at low frequencies and there is very little change at high frequencies.

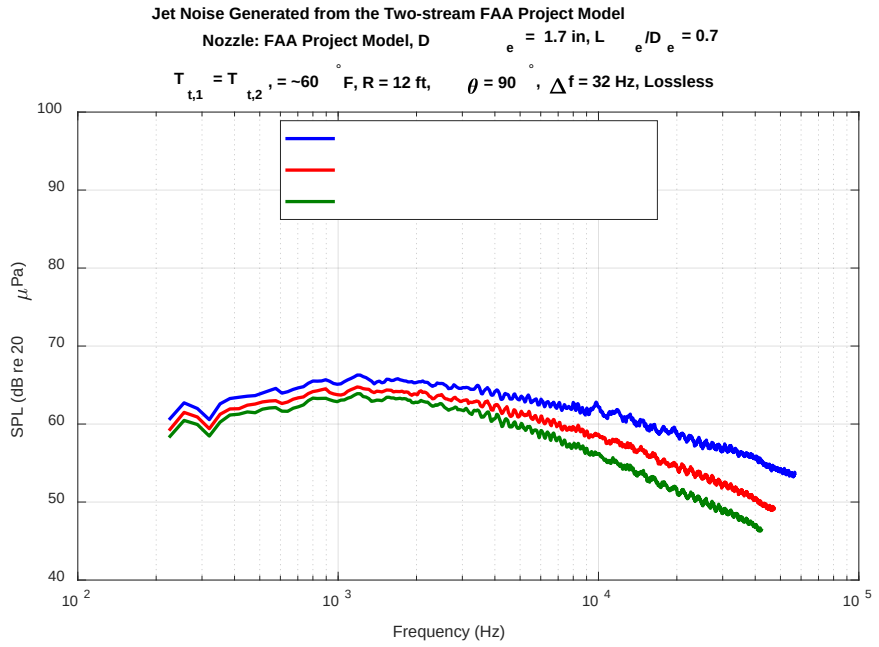


Figure 3. Typical jet noise spectra at extraction ratios of 1 and above and below 1 for the Le/De = 0.7 configuration. FAA: Federal Aviation Administration, SPL: sound pressure level.

Effect of increasing the mixing-duct length: Figure 4 shows the jet noise generated from the test model with primary and secondary pressure ratios both equal to 1.39 (ER = 1.0) with L_e/D_e varied between 0.7 and 3.0. As seen in the Figure 4, at frequencies below 7 kHz, the noise for the three conditions is the same. Above 7 kHz, there is a minor reduction in jet noise, of 1 dB at most. This indicates that increase in mixing-duct length does increase the mixing to a small degree, leading to reduced noise at high-frequencies.

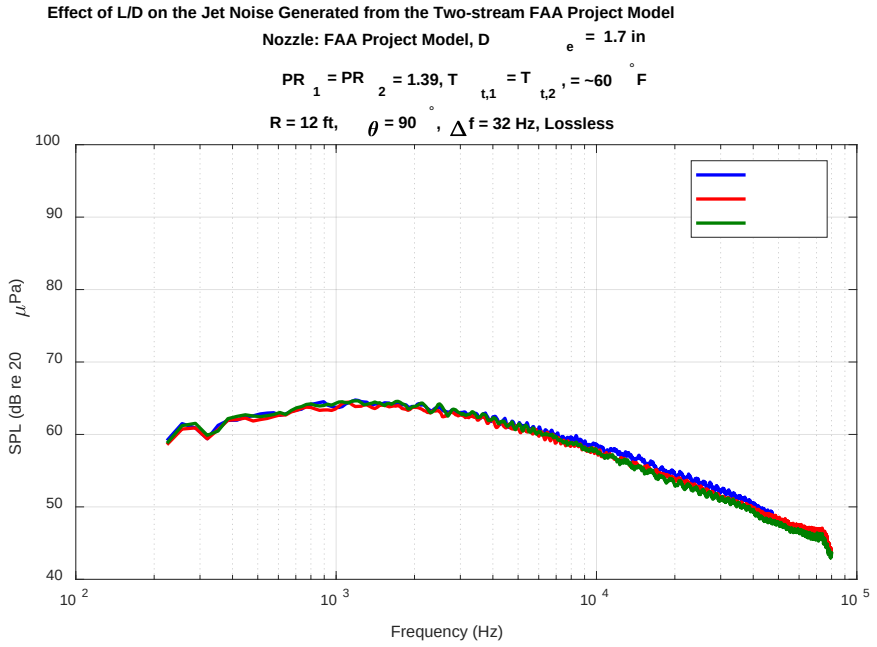


Figure 4. The effect of mixing-duct length on the jet noise produced by the test model. FAA: Federal Aviation Administration, SPL: sound pressure level.

Effect of increasing the primary jet temperature: Figure 5 shows the effect of increasing the primary nozzle total temperature for L_e/D_e of 0.7. The corresponding data for L_e/D_e of 3 appears in Figure 6. The unheated spectrum in both cases seems unaltered, but the spectrum for the larger L_e/D_e with the heated primary stream has somewhat lower SPLs at higher frequencies. For example, at a frequency of 50,000 Hz, the SPL for L_e/D_e = 0.7 is 51 dB and for L_e/D_e = 3, it is 47.4 dB. It may be an effect of reduced speed of the heated stream via mixing with the unheated secondary jet in the longer duct.

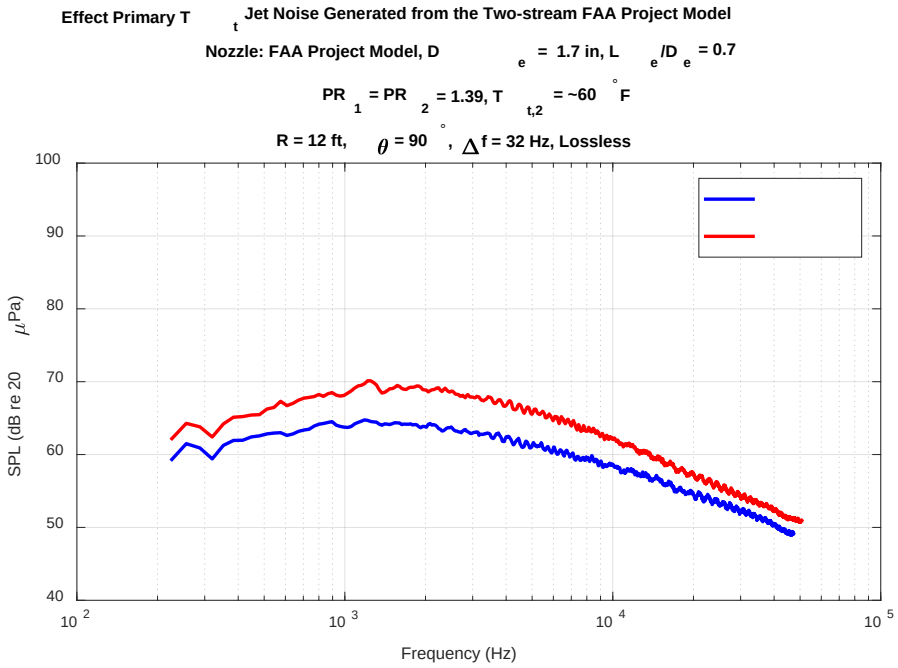


Figure 5. Effect of primary total temperature with the Le/De = 0.7 configuration. FAA: Federal Aviation Administration, SPL: sound pressure level.

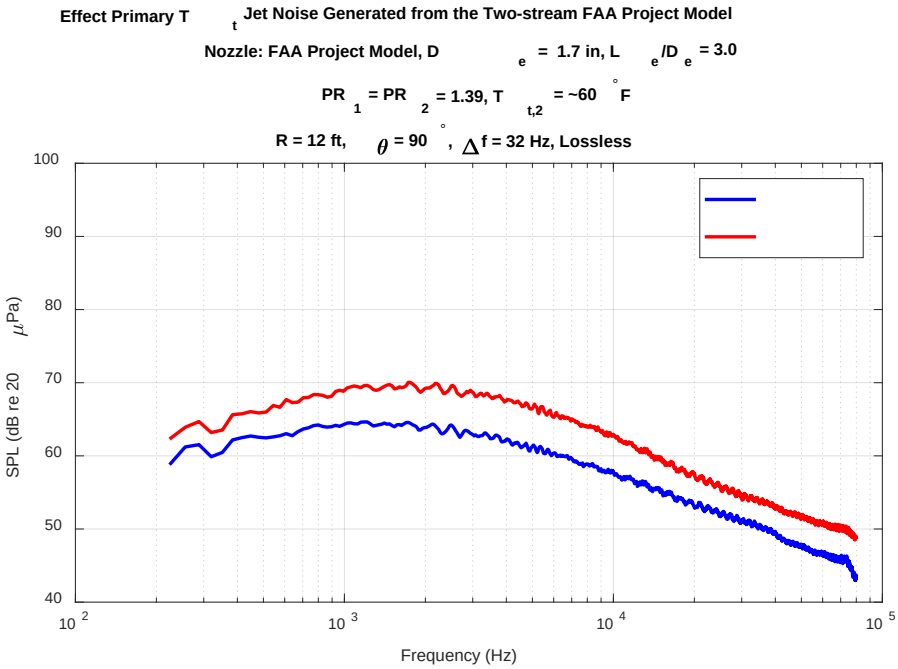


Figure 6. Effect of primary total temperature with the L_e/D_e = 3.0 configuration. FAA: Federal Aviation Administration, SPL: sound pressure level.



Detailed Analysis of Data at Extraction Ratios between 1 and 1.07: As mentioned above, FAA and GAC indicated that for mixed flow engines the extraction ratio between 1.00 and 1.07 are the most realistic. Acoustic measurements that focus on this extraction ratio range are presented here. Figure 7 shows the results of the small variations of extraction ratio for a PR_1 = 1.39. Figure 7 shows the results as the extraction ratio varies in 0.01 steps from 1.00 to 1.07 at a polar angle of 90°. Figure 7 also shows cases of L_e/D_e of 0.7 and 3.0 as well as cases of unheated core flow and the core flow heated to 500°F. Comparing Figures 7a and 7b as well as Figures 7c and 7d gives some insight into the effect of the heating the core flow. There are two main effects of heating the core flow: (1) the overall noise levels increase, which is a result of higher jet velocities in the case of the heated-core flow, and (2) the jet noise spectra show greater collapse across extraction ratios. To illustrate the first effect, for both L_e/D_e = 0.7 and 3.0 cases, as expected, the peak noise increases (by about 5 dB) as the core flow is heated to 500°F. This can be seen on comparing the spectra in Figures 7a and 7b for L_e/D_e = 0.7 and Figures 7c and 7d for L_e/D_e = 3.0. To illustrate the second effect (i.e., the effect of extraction ratio), for both L_e/D_e = 0.7 and 3.0 cases, for the unheated case, the change of extraction ratio has a minimal effect at low-frequencies and is of the order of 1 dB, but this spread increases to 5 dB at high-frequencies. This can be seen on comparing the spectra in Figure 7a and 7c for L_e/D_e = 0.7 for the unheated-core cases and Figure 7b and 7d for the heated-core cases. For the heated-core case, the spectra collapse below 8 kHz, and above 8 kHz all SPLs are within 2 dB. As a note, for the L_e/D_e = 3.0 case, the heated core flow shows very minimal variation in spectral levels. Observing the effect of the mixing duct length, for the unheated case, the spectral levels spread is reduced from a maximum of 5 dB for L_e/D_e = 0.7 to 3 dB for L_e/D_e = 3. For the heated core flow case, the spectral level spread does not change much as L_e/D_e = 0.7 is changed L_e/D_e = 3.0.

Ideally this analysis should be done by normalizing the SPLs and the frequency scales. Unfortunately, the normalizing parameters were not available at the time of this analysis.

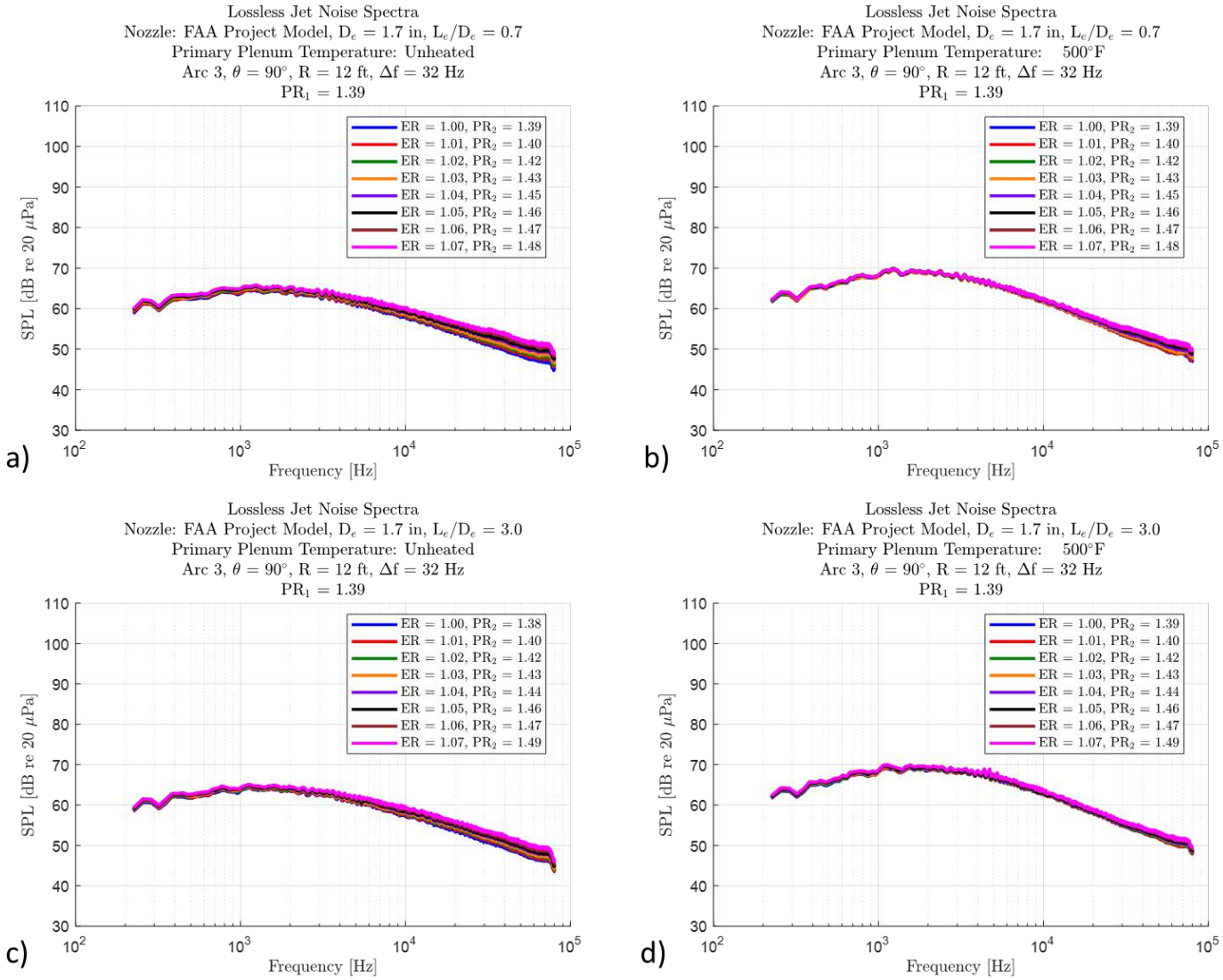


Figure 7. Example acoustic measurements for the small extraction ratio changes for PR1 = 1.39 at θ = 90°. (a) L_e/D_e = 0.7 and core flow unheated, (b) L_e/D_e = 0.7 and core flow heated to 500°F, (c) L_e/D_e = 3.0 and core flow unheated, and (d) L_e/D_e = 3.0 and core flow heated to 500°F. FAA: Federal Aviation Administration, SPL: sound pressure level.

Howling in an Internally Mixed Confluent Nozzle: At certain operating conditions high-intensity tones were observed in the jet noise measurements using the Year 1 baseline nozzle. The first set of operating conditions for which tones were observed were those with very low (well below unity) extraction ratios. The second set of operating conditions were those with high subsonic secondary-stream Mach numbers. Figure 8 shows the resulting tones created at these operating conditions and their effects on noise relative to an unheated, unity extraction ratio dual-stream jet, which is shown in red. It is seen that these tones are as much as 30 dB higher than the broadband jet noise for the same core jet operating pressure ratio (1.39 in this case) irrespective of whether the extraction ratio is below unity (the blue curve) or higher than unity (the green curve).

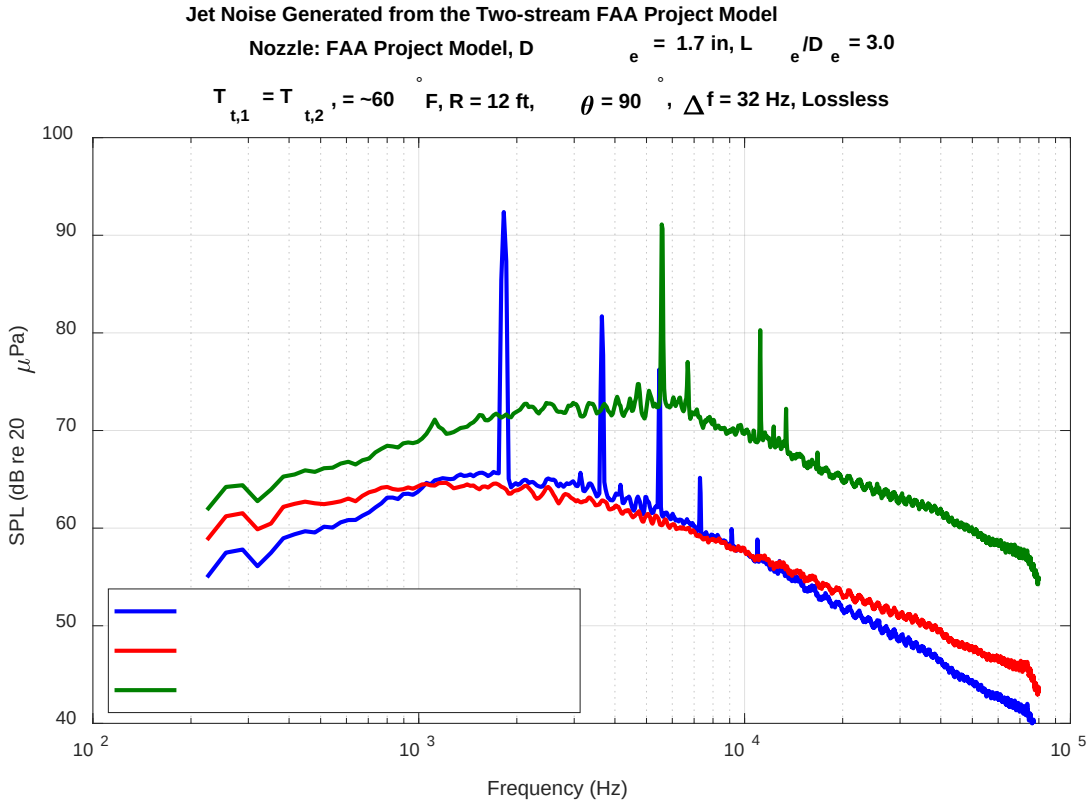


Figure 8. Jet noise measurements with pressure splits far from unity for the L_e/D_e = 3.0 configuration. FAA: Federal Aviation Administration, SPL: sound pressure level.

Extensive work (Ramsey et al., 2022b; Ramsey et al., 2023a; Ramsey et al., 2023b; Ramsey, 2024) has gone into understanding the mechanisms responsible for this howling, its impact on jet noise amplification and other related measurements, and methods to eliminate it. It was found that two distinct mechanisms were responsible for the howling. One of them, which occurs at low extraction ratios, is related to the impingement of the core jet shear layer on the exhaust nozzle lip (Ramsey et al., 2023a). The other, which occurs at high subsonic secondary Mach numbers, is related to periodic separation of the boundary layer near the exhaust nozzle exit as a result of an unsteady shockwave/boundary-layer interaction (Ramsey et al., 2023b). It was found that for either case, the feedback mechanism responsible can be weakened and the howling removed by using a suitably placed boundary layer trip. Figure 9 shows a boundary layer trip fashioned out of lock wire installed just upstream of the lip of the final exhaust nozzle, and the effect of this trip on the howling is demonstrated in Figure 10 showing the elimination of high-intensity tones and any broadband amplification.

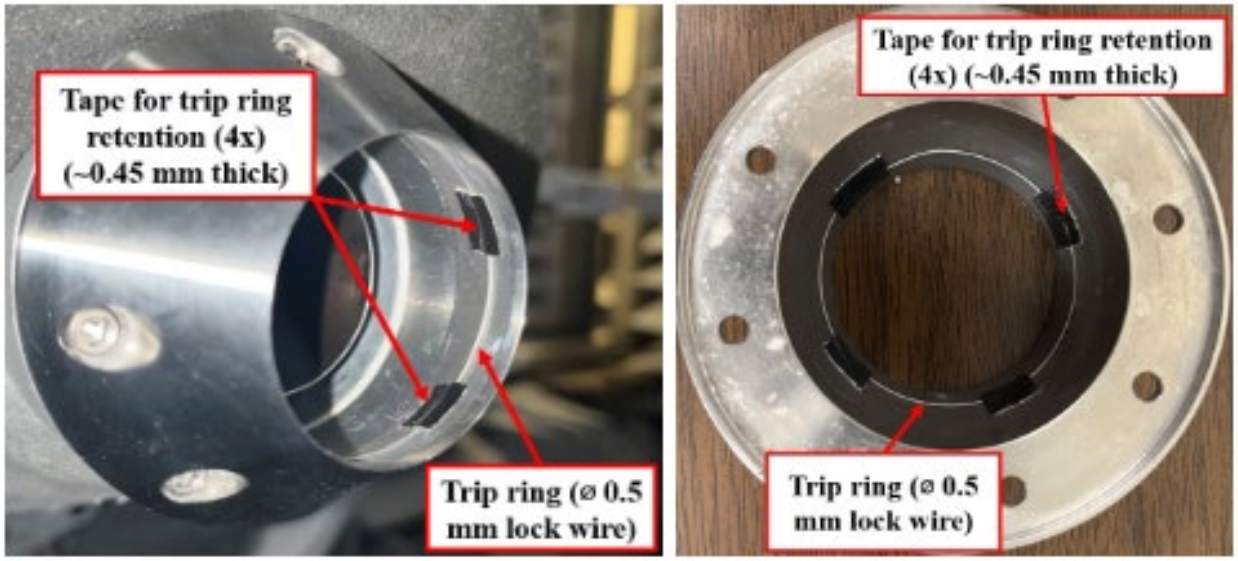


Figure 9. Boundary layer trip configurations: (a) view from exit and (b) view from upstream.

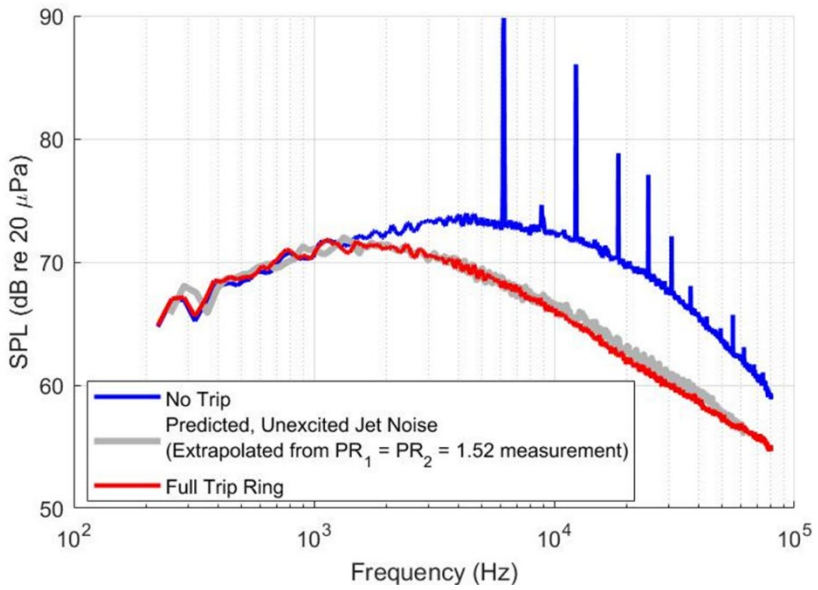


Figure 10. Effect of the boundary layer trip ring on the noise from a confluent nozzle. FAA Project Model, De = 1.7 in. and Le/De = 0.7. PR1 = 1.69, ER = 1.0, unheated, R = 12 ft, θ = 90°, Δf = 32 Hz, lossless. SPL: sound pressure level.

Effect of Tabs on the Noise Produced by the Confluent Nozzle: Before acquisition of more complex, lobed internal mixers from GAC as part of the Year 3 effort, a study was performed to determine the effects of using mechanical tabs, that are known to increase jet mixing, installed within the core nozzle as a simple forced mixer design. For this, two types of tab designs were used: (1) the smaller D-tabs shown in Figure 11a and the larger, and (2) the triangular delta tabs shown in Figure 11b. Figure 12 details how these tabs were installed within the core nozzle. Various configurations of the confluent nozzle equipped with tabs were tested. While a wide range of conditions were tested, the following results are presented

as typical results: PR_1 = 1.39 and ER = 1.0 and PR_1 = 1.39 and ER = 1.07. The tabs were tested with the confluent nozzle in both L_e/D_e = 0.7 and 3.0 configurations. It was observed during testing that the use of mechanical tabs – no matter how many – did not eliminate the howling. However, it is again noted that the howling can be eliminated through use of a simple boundary layer trip.

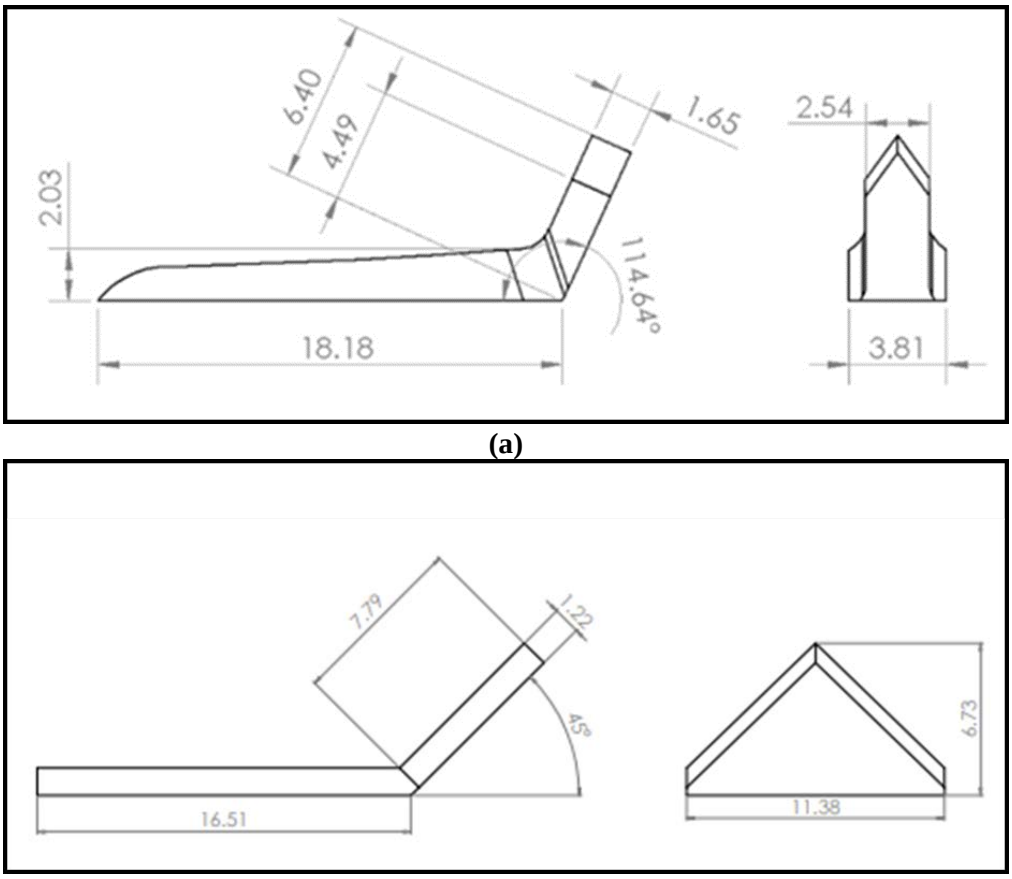


Figure 11. Design of the (a) D-tab and (b) delta tab (dimensions in mm).

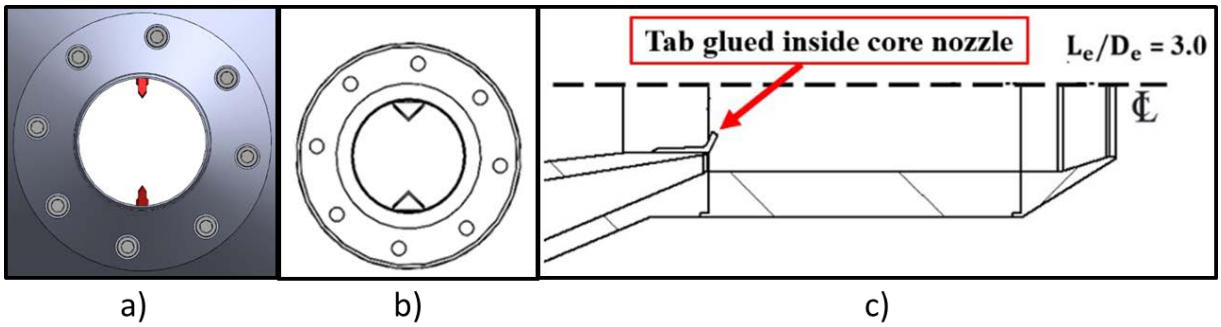


Figure 12. Tabs in the core nozzle: (a) D-tabs, (b) delta tabs, and (c) cross-sectional view of nozzle showing tab position.



Figures 13 and 14 show the effect on the jet noise produced by adding D-tabs to the core nozzle at the PR_1 = 1.39 and ER = 1.0, for mixing-duct lengths L_e/D_e = 0.7 and 3.0, respectively. As shown in Figures 13, the L_e/D_e = 0.7, no tab configuration has no appreciable effect on the noise. Similarly, as shown in Figure 14, for the L_e/D_e = 3.0, tabs irrespective of the number of tabs used, had no appreciable effect at low frequencies (the left of the spectral peak), but increasing the tab number to four and then to eight seems to increase the noise at higher frequencies. In particular, the noise at high frequencies is elevated by a maximum of 2 dB. These level increases begin at 20 kHz for the 4-tab case and at 7 kHz for the 8-tab case.

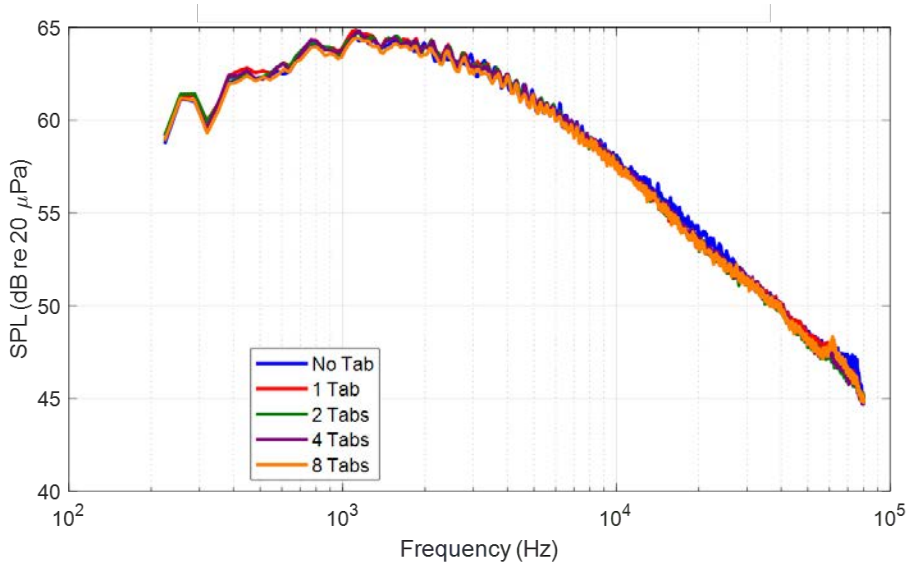


Figure 13. Effect of D-tabs on the noise from a confluent nozzle. FAA Project Model, D_e = 1.7 in. and L_e/D_e = 0.7. PR_1 = 1.39, ER = 1.0, unheated, R = 12 ft, θ = 90°, Δf = 32 Hz, lossless. SPL: sound pressure level.

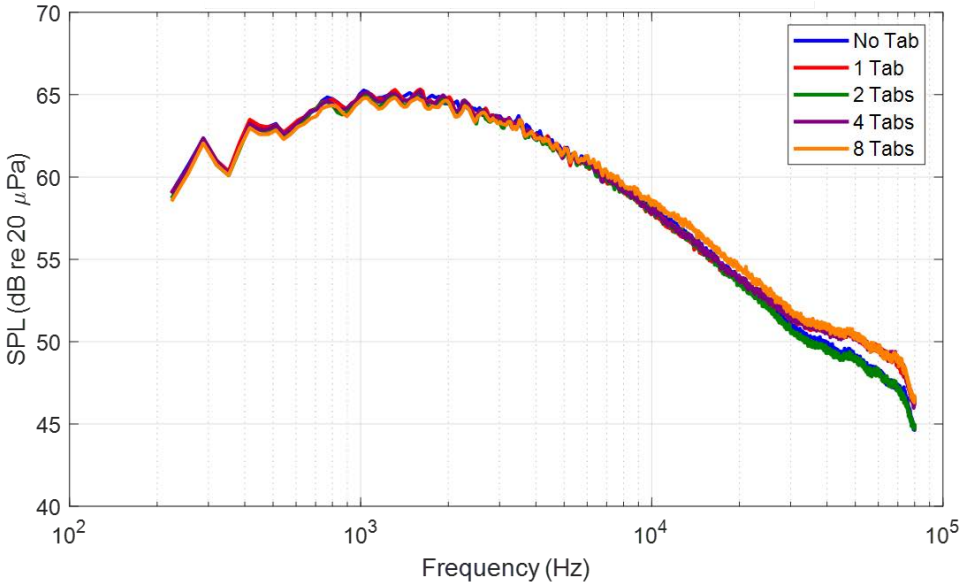


Figure 14. Effect of D-tabs on the noise from a confluent nozzle. FAA Project Model, D_e = 1.7 in. and L_e/D_e = 3.0. PR_1 = 1.39, ER = 1.0, unheated, R = 12 ft, θ = 90°, Δf = 32 Hz, lossless. SPL: sound pressure level.



The results shown in the last two figures were for an extraction ratio of unity. Figures 15 and 16 show the effect of the D-tabs on the noise produced by the confluent nozzle for PR_1 = 1.39 and ER =1.07 for L_e/D_e = 0.7 and 3.0 respectively. For both mixing duct lengths, the tabs do not seem to make substantial difference. The exception to this is the 1- and 2-tab configurations which generate a high-frequency tone for L_e/D_e = 0.7.

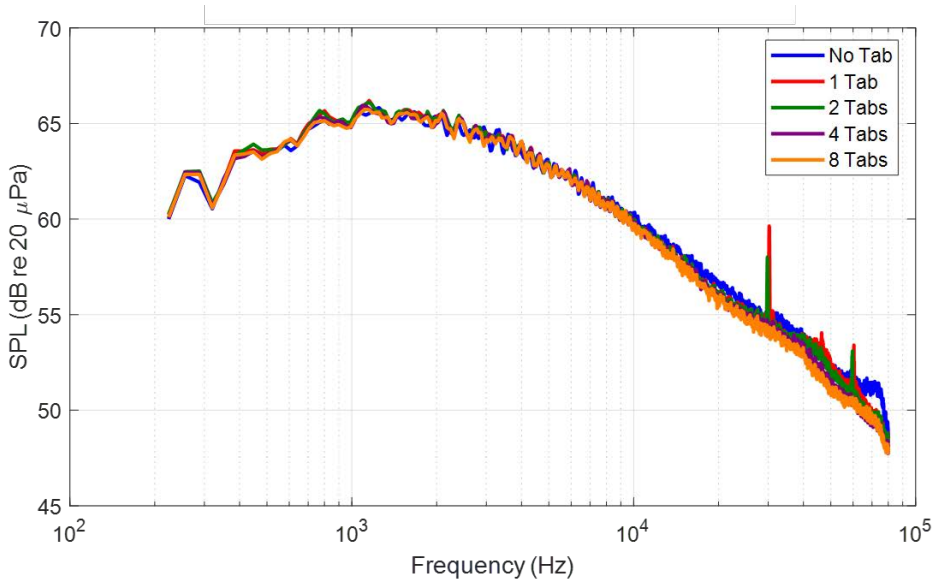


Figure 15. Effect of D-tabs on the noise from a confluent nozzle. FAA Project Model, De = 1.7 in. and Le/De = 0.7. PR1 = 1.39, ER = 1.07, unheated, R = 12 ft, θ = 90°, Δf = 32 Hz, lossless. SPL: sound pressure level.

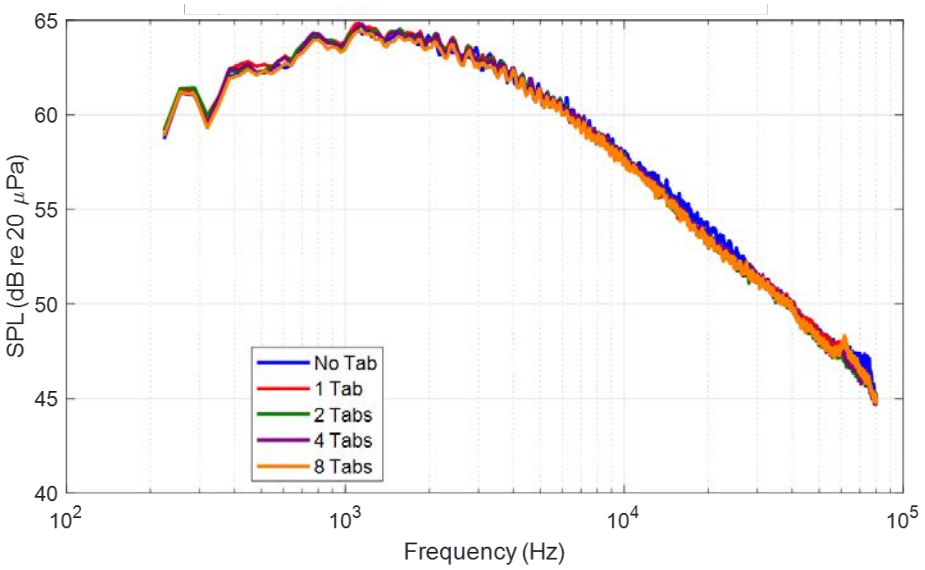


Figure 16. Effect of D-tabs on the noise from a confluent nozzle. FAA Project Model, De = 1.7 in. and Le/De = 3.0. PR1 = 1.39, ER = 1.07, unheated, R = 12 ft, θ = 90°, Δf = 32 Hz, lossless. SPL: sound pressure level.



The results shown indicate that for an internally mixed, dual-stream jet with an unheated core stream and near-unity extraction ratio, the use of tabs has little to no appreciable effect on the farfield noise. This same lack of effect is observed for the larger delta tabs as well and is also true even when using a lobed mixer nozzle as will be demonstrated later. When operating near unity extraction ratio with an unheated core stream, the core and bypass streams are nearly uniform, and there is little to no opportunity for any internal mixing which would otherwise change the farfield noise. In order for the tabs to create any appreciable change in the noise there must be a substantial difference in the two streams, either by operating at highly unrealistic extraction ratios or by heating the core stream. Figures 17 and Figure 18 show the effect of using two delta tabs on the jet noise spectra at PR_1 = 1.39, ER = 1.0, with a heated core flow ($T_{t,1} \approx 500°F$) at polar angles of 30° and 90°, respectively. The different colored curves denote acoustic measurements taken along polar arcs at different azimuths with respect to the installation of the tabs. As shown in Figures 17, at low polar observation angles the tabs reduce the level of peak jet noise by about 3 dB. Above about 6 kHz the tabs increase the noise by as much as 4 dB. A decrease in the level of peak jet noise at lower frequencies with an associated increase in higher frequency noise is typical of enhanced-mixing devices including lobed mixers (Mengle et al., 1997). Figure 19 shows the effect of the delta tabs across all polar angles and azimuths by showing the overall sound pressure level (OASPL). The dashed black line indicates noise measurements taken without the use of tabs to serve as a baseline. It is observed that the OASPLs decrease at lower polar observation angles where lower frequency noise is dominant and they increase at greater observation angles where lower frequency noise is less dominant.

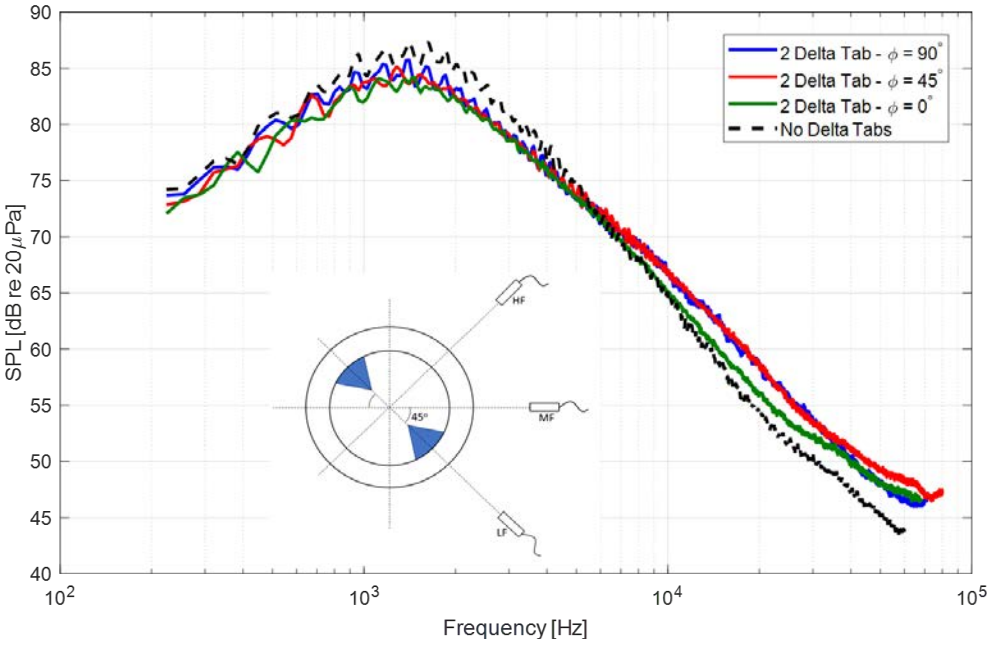


Figure 17. Effect of delta tabs on the noise from the confluent nozzle. De =1.7 in, Le/De = 0.7. PR1 = 1.39, ER = 1.00, Tt,1 = 500°F, Tt,2 = 60°F, R = 12 ft, θ = 30°, Δf = 32 Hz, lossless. SPL: sound pressure level.

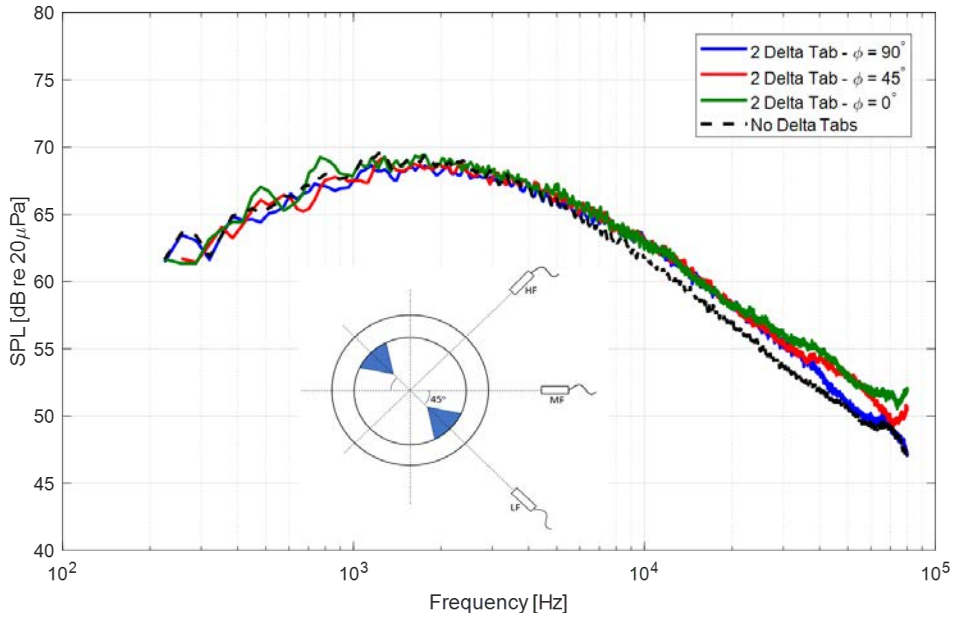


Figure 18. Effect of delta tabs on the noise from the confluent nozzle. De =1.7 in, Le/De = 0.7. PR1 = 1.39, ER = 1.00, Tt,1 = 500°F, Tt,2 = 60°F, R = 12 ft, θ = 90°, Δf = 32 Hz, lossless. SPL: sound pressure level.

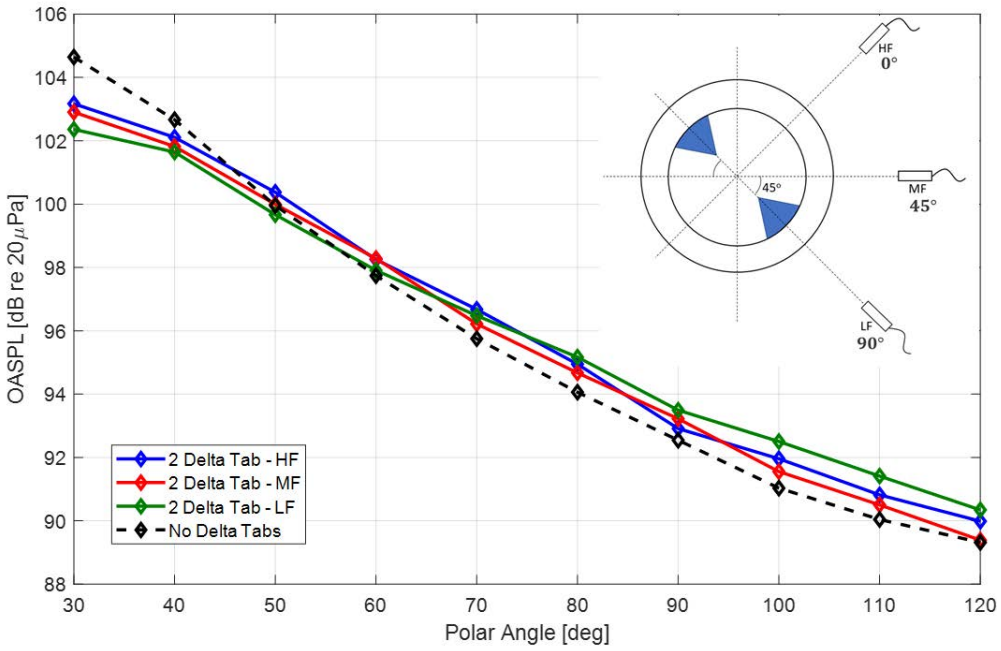


Figure 19. Effect of delta tabs on the noise from the confluent nozzle. De =1.7 in, Le/De = 0.7. PR1 = 1.39, ER = 1.00, Tt,1 = 500°F, Tt,2 = 60°F, R = 12 ft, Δf = 32 Hz, lossless. SPL: sound pressure level.

Particle Image Velocimetry Measurements

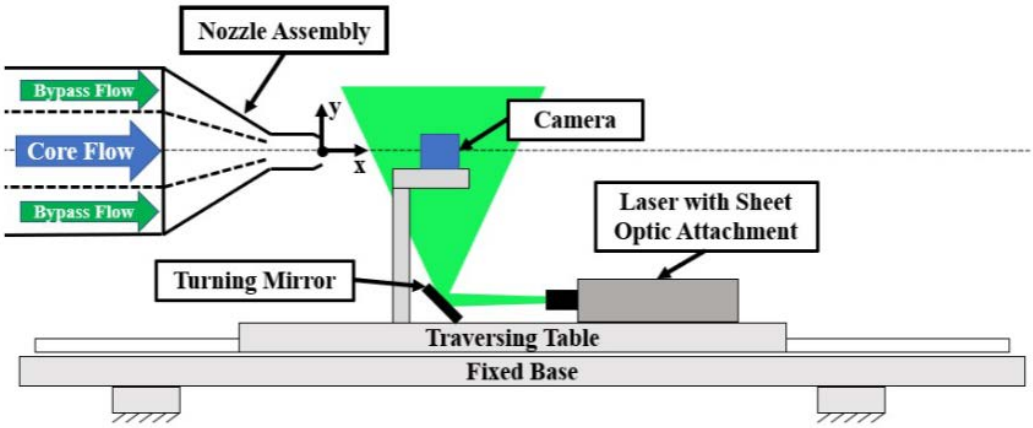
Facility Set-up and Testing Description

The PIV data was acquired in GTRI's Flow-Diagnostics Facility using a double-pulsed, two-dimensional (2D) PIV system. The details of GTRI's Flow-Diagnostics Facility were reported by Burrin et al. (1979), with salient details repeated here for completeness. The Flow-Diagnostics Facility is a sister facility to GTRI's Anechoic Jet Facility having identical plenum interfaces and identical plenum-to-nozzle area contraction ratios.

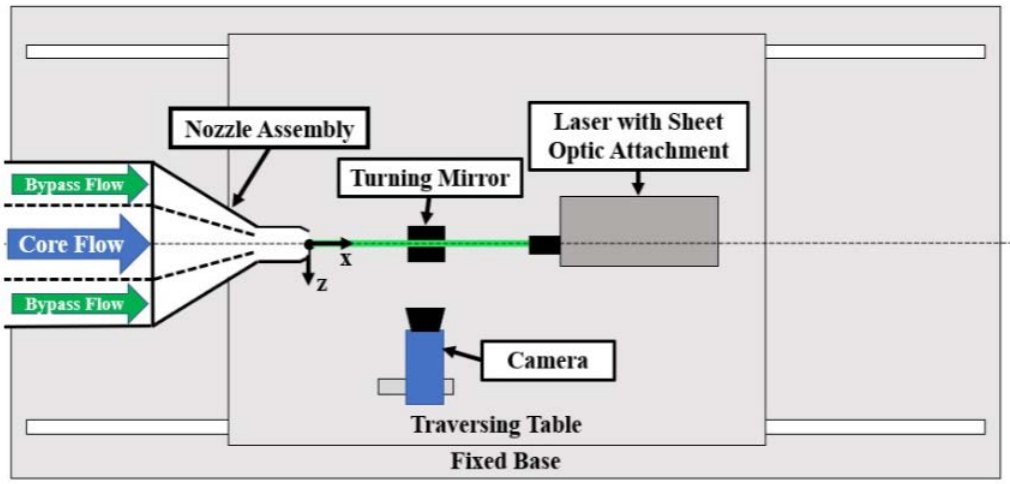
The PIV system is shown schematically in Figure 20. Figure 20a and Figure 20b show side-view and top-down-view schematics of this system, respectively. Figure 20c illustrates the camera's nominal field-of-view at each of the stations along the traverse. In selecting the time delay between image pairs, an optimization routine built into the DaVis software was used. The DaVis software is the LaVision™ proprietary PIV software that is used for the data acquisition and post-processing. This routine recommends a time delay between image pairs based in part on the peak Q-ratio (the ratio of highest and second highest correlation peak values) for several different time delays. A low Q-ratio indicates that a particle displacement cannot be accurately predicted from the correlation plane of a given image pair in a given interrogation window.

The measured instantaneous velocity fields may contain spurious velocity vectors. Spurious vectors are characterized by exceedingly large or small magnitudes and/or erroneous directions relative to the expected velocity vector field. Of course, as the expected vector field is not known a priori, criteria for identifying spurious vectors must be employed. In this work, spurious vectors are detected and rejected at two different stages of the data processing routine. First, the instantaneous velocity fields are screened in a processing stage referred to as vector post-processing. A filtering operation is used to detect and replace vectors that have a large deviation from their neighbors. This filtering operation is based on the framework of a dynamic mean value operator (Raffel et al., 2018). In particular, the filter was set to “strongly remove and iteratively replace" in the DaVis software – removing vectors that had a difference to the local mean outside of one standard deviation of the neighboring vectors before re-inserting vectors whose difference to the local mean is within two standard deviations of the neighboring vectors once the filter was applied. For vectors that failed to satisfy the criterion, the median of the neighbors was used to replace the vector. This filter was executed twice on each instantaneous velocity field. Further, a range of acceptable particle displacements was specified. Finally, any instantaneous vectors whose associated Q-ratio was less than 2.0 were deleted. The success of these vector post-processing operations in removing outliers without modifying the remainder of the velocity field is shown to be successful on a single, instantaneous velocity field in Figure 21. The top frame shows the result without the vector post-processing routine, and the bottom frame shows the same field with the vector post-processing routine executed – both of which use the same color scaling shown on the far right. This vector field is a measurement across the shear layer of the jet from the core nozzle in isolation operated at $\boldsymbol{M}_j$ = 0.58, unheated – with the jet flowing from left to right in the figure.

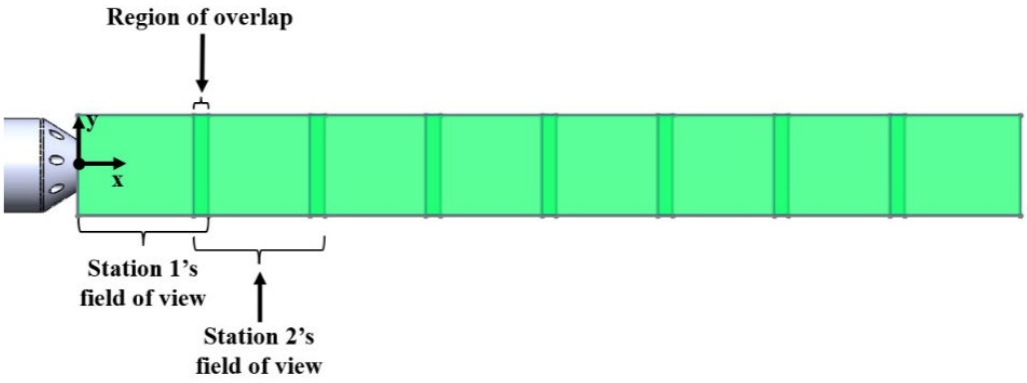
™ LaVision is a trademark of LaVision GmbH, Germany.



(a)



(b)



(c)

Figure 20. PIV system: (a) side view, (b), top-down view, and (c) multi-station acquisition scheme.

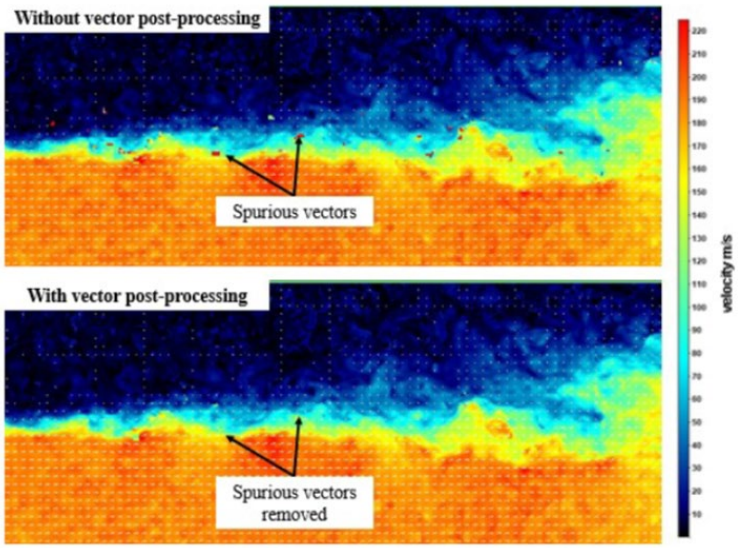


Figure 21. Success of vector post-processing in replacing spurious vectors. Both frames show same region of shear layer of jet from single nozzle in isolation, $M_j = 0.58$, unheated.

The ensemble averaging of the PIV measurements also includes applying Chauvenet's criterion for spurious vector (i.e., outlier) rejection. This only has an appreciable impact on the measurements of velocity fluctuation (i.e., turbulence intensity), with relatively small changes to the mean velocity measurements. Chauvenet's criterion was reported to be used by Bridges and Wernet (2011) and is a sample-size-dependent criterion that suggests thresholds outside of which values are unlikely to be sampled. If values are measured outside of these thresholds, the data are considered outliers. In each PIV interrogation window across all instantaneous velocity fields being ensemble averaged, Chauvenet's criterion is applied to each component of the measured velocity vectors. This criterion assumes that the measured velocities within each interrogation window are sampled from a Gaussian parent distribution. The reader astute in turbulent flows would likely dispute this assumption, and rightfully so. It is known that the turbulent velocities in a free shear layer are not always Gaussian distributed (as discussed in greater detail by Pope [2000]). In particular, the probability density function (PDF) of velocity at a point may have non-zero skewness – whereas a Gaussian distribution would have zero skewness. This potential criticism is acknowledged; however, a Gaussian PDF of velocities is not assumed aside from computing outlier rejection thresholds. Histograms of displacement in units of pixels as acquired using the PIV measurement system are presented in Figure 22. Figure 22 shows that the use of Chauvenet's criterion correctly flags obviously spurious vectors (at the tips of the red arrows) without wrongly flagging seemingly trustworthy vectors (based on their presence in a larger distribution of data). Displaying the displacement histogram with units of pixels serves the secondary purpose of providing evidence that the PIV measurements are not impacted by peak-locking effects. Were peak-locking present in the data, the displacement vectors would be biased toward integer displacement values (Raffel et al., 2018). Demonstrating this fact is vital to the integrity of the fluctuating velocity measurements produced, as Christensen (2004) showed that peak-locking may strongly impact second-order velocity statistics (i.e., the standard deviation of velocity reported in the present work).

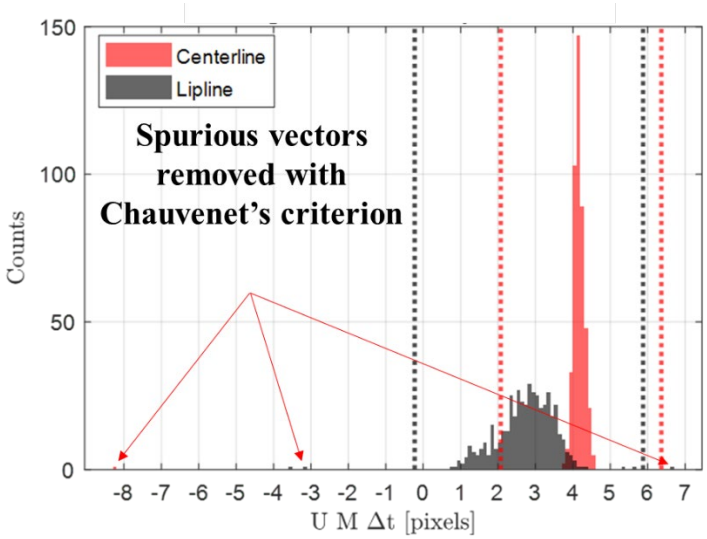


Figure 22. Histogram of axial displacement along lipline (x/D_e= 0.7, y/D_e=0.5, N=1500 image pairs) of jet from single nozzle (M_j = 0.58, unheated). Vertical lines show Chauvenet criterion boundaries.

Extensive care was taken to ensure that the measured PIV data were accurate and precise, including validating measurements against well-trusted, existing data provided in literature. Ahuja et al. (1982) acquired mean and unsteady velocity measurements of a jet produced by a convergent nozzle with an exit diameter of 2 in. (5.08 cm) in the GTRI Flow Diagnostics Facility using a laser doppler velocimetry (LDV) system. As shown by Bridges and Wernet (2011), the LDV data of Ahuja et al. (1982) and several other sources of published jet flow field measurements agree reasonably well when normalized. Thus, in the present work, agreement between flow-field measurements reported by Ahuja, et al. (1982) and a validation dataset acquired using the present work's PIV system (when both are presented in normalized form) is taken to provide a high degree of confidence in the PIV measurements. This relies, of course, on the accuracy of historical datasets. The 1.6-in. nozzle used here is shown in Figure 23a and the agreement between the validation dataset is shown in Figure 23b. This agreement is even better than before Chauvenet's criteria were implemented in the data processing routine.

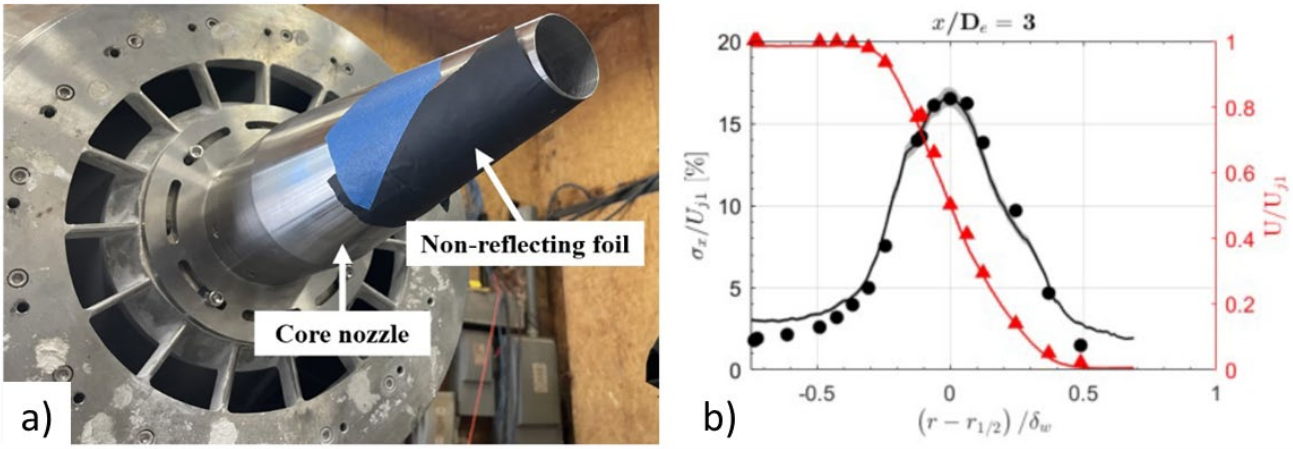


Figure 23. Validation dataset: (a) nozzle used and (b) agreement with dataset from Ahuja et al. (1982) (curves are PIV data, symbols are historical laser doppler velocimetry (LDV) data from Ahuja et al. [1982]).



Witze (1974) provided a model for the centerline velocity distribution of a compressible free jet, which was shown to agree well with experimental data. Bridges and Wernet (2011) used the potential core length obtained by the theory reported by Witze (1974) as a means to collapse PIV measurements acquired at different conditions. The "Witze model" (as it will be referred to hereafter) may be expressed as:

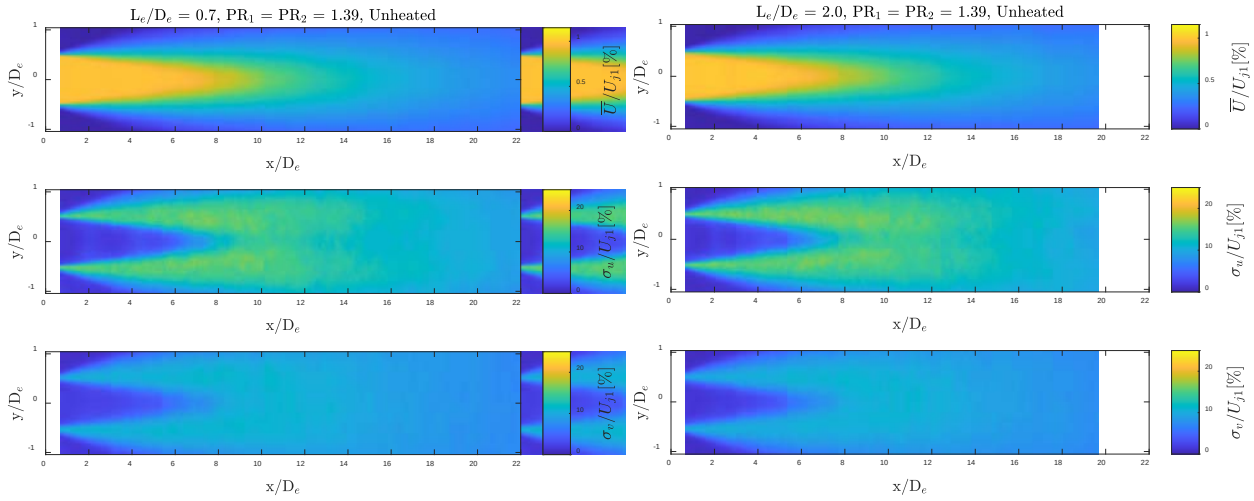
$$\bar{u}_c\left(\frac{x}{D_e}\right) = 1 - \exp\left(\frac{-1}{2\kappa\left(\frac{x}{D_e}\right)(\bar{\rho}_e)^{0.5} - X_c}\right) \quad \text{(Eq. 1)}$$

$$\kappa = 0.08\left(1 - 0.16M_j\right)(\bar{\rho}_e)^{-0.22} \quad \text{(Eq. 2)}$$

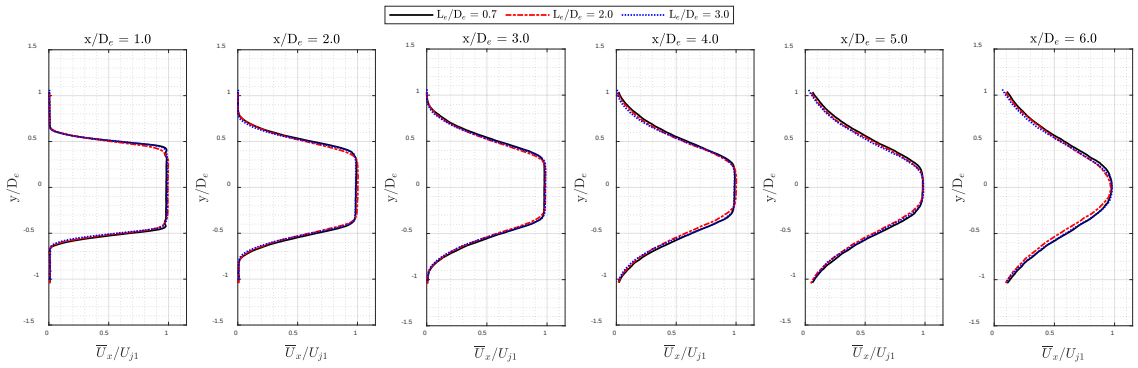
Here, $X_c = 0.70$, and the remaining parameters are defined in Witze's report.

PIV Analysis

Figure 24 shows typical jet flow fields at a lower pressure ratio ($PR_1 = PR_2 = 1.39$, unheated) where howling does not occur. The centerline mean velocity distribution of three different mixing-duct lengths with unity extraction ratio at $PR_1 = 1.39$ are shown in Figure 25 along with Witze's model. It can be seen that all curves agree reasonably well with Witze's model for the lower pressure ratio, regardless of mixing-duct length.



(a) **(b)**



(c)

(d)

Figure 24. Typical flow field of jet from confluent nozzle ($PR_1 = PR_2 = 1.39$, unheated) : (a) mean velocity, axial fluctuation intensity, and radial fluctuation intensity for $L_e/D_e = 0.7$, (b) mean velocity, axial fluctuation intensity, and radial fluctuation intensity for $L_e/D_e = 2.0$, (c) radial profiles of mean velocity near the nozzle exit for several mixing-duct lengths, and (d) radial profiles of axial fluctuation intensity near the nozzle exit for three mixing-duct lengths. N = 750 image pairs.

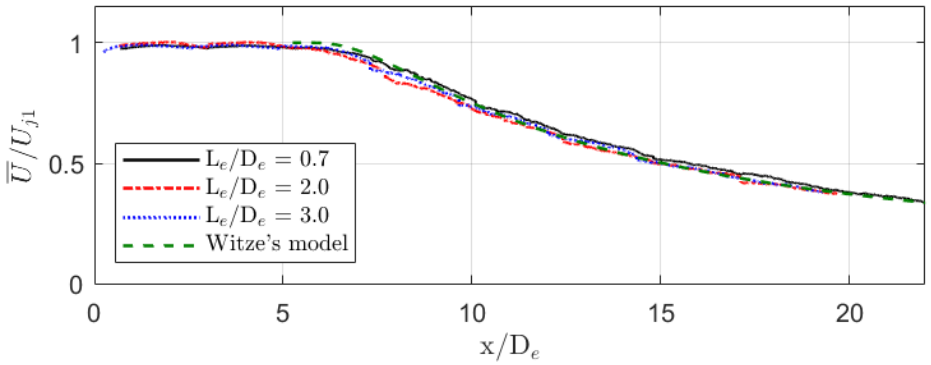


Figure 25. Centerline mean velocity distributions of typical flow field including Witze's model for single jet ($\boldsymbol{PR_1 = PR_2 = 1.39}$, unheated). N = 750 image pairs.

It is noted that there exists a mean axial velocity gradient close to the nozzle exit plane in Figure 25, and some explanations for this are offered. This phenomenon is believed to be a result of the contraction of the exhaust nozzle proximate to its exit plane. The contraction requires the fluid to turn radially inward near the upstream side of the exhaust nozzle and then to straighten out in a similar fashion near the exhaust nozzle exit plane. At these two locations, a force is required for the fluid to turn. Near the upstream side of the exhaust nozzle, the required force is supplied by the solid body of the nozzle. Near the exhaust nozzle exit plane, no solid body exists to supply the required force – it must instead come from the fluid itself in the form of a pressure gradient if the flow is to become approximately parallel as it exits the nozzle. The fluid near the center of the exhaust nozzle may supply the required pressure gradient if the fluid is at an elevated static pressure and thus has not yet reached its fully expanded velocity. Morris et al. (2010) measured a similar effect in the flow field produced by a single nozzle and also attributed this effect to the nozzle's convergence at the nozzle exit plane.

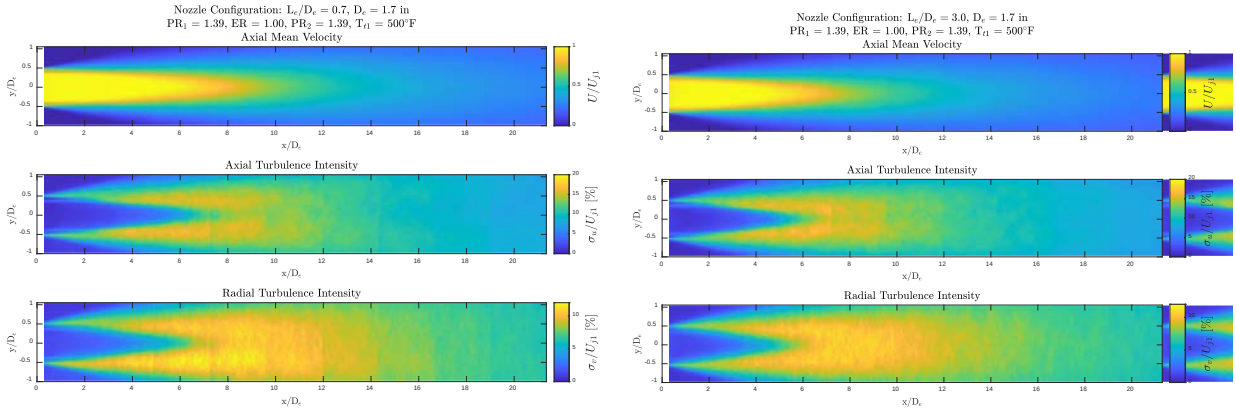
Six heated core conditions were selected for the confluent nozzle with both the shortest mixing-duct length ($L/D_e = 0.7$), and the longest mixing-duct length ($L/D_e = 3.0$). Only non-resonating conditions were chosen, as they are most useful to the modelers; these conditions are shown in Figure 26. Two conditions for each mixing-duct length are acquired with a high number of samples (750 samples) to allow for accurate turbulence measurements. These conditions are $PR_1 = PR_2 = 1.39$ and $PR_1 = 1.39, ER = 1.07$. For mean flow measurements, all other conditions are acquired at a lower number of samples (200), sufficient for capturing mean statistics of the flow.



Tt1 = 500 deg F		Primary Pressure Ratio, PR1			
		1.39 (M_{j1}=0.7)	1.52 (M_{j1}=0.8)	1.69 (M_{j1}=0.9)	1.89 (M_{j1}=1.0)
PR2	1.39 (M_{j2}=0.7)	ER = 1.00	ER = 0.91	ER = 0.82	ER = 0.73
	1.52 (M_{j2}=0.8)	ER = 1.10	ER = 1.00	ER = 0.90	ER = 0.91
	1.69 (M_{j2}=0.9)	ER = 1.22	ER = 1.11	ER = 1.00	ER = 1.89
	1.89 (M_{j2}=1.0)	ER = 1.36	ER = 1.24	ER = 1.12	ER = 1.00
ER	1.04	PR2 = 1.44			
	1.07	PR2 = 1.48			

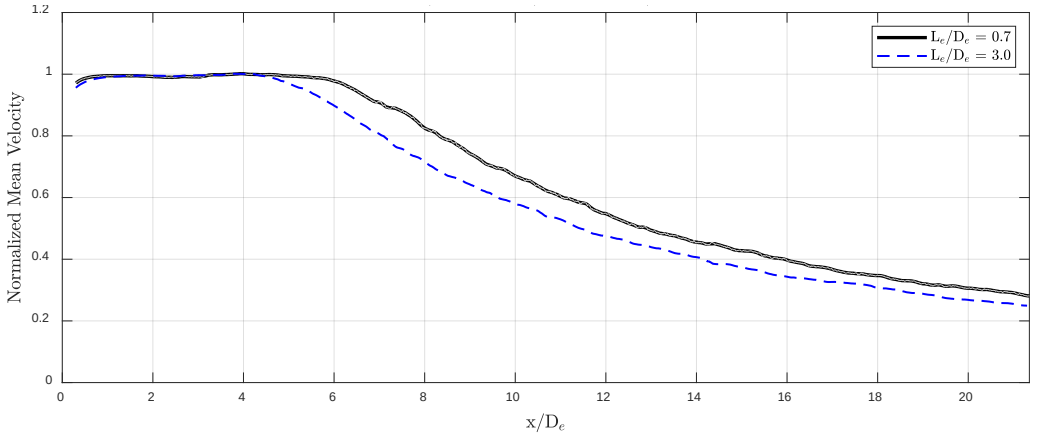
Figure 26. Data matrix for heated core PIV conditions. ER: extraction ratio, PR: pressure ratio.

Although data for a total of twelve flow conditions were gathered using PIV, results of only one condition for each mixing-duct length will be treated in detail below for the sake of brevity. In particular, the plots of the $PR_1 = PR_2 = 1.39$ heated condition will be discussed for the confluent nozzle with L_e/D_e = 0.7 and 3.0 mixing-duct lengths, since both mean and turbulent statistics are gathered for this condition. The 2D mean and turbulence intensity plots are shown in Figure 27. Note that a thin region near the nozzle exit has been masked off from the final PIV data to reject the effects of laser reflections off the nozzle. The length of this mask is from x/D_e = 0 to about 0.3-0.5 depending on the intensity of the reflections. Figure 28 shows comparisons of mean axial velocity and axial and radial turbulence intensities along the jet centerline for each mixing-duct length. Similarly, Figure 29 compares profiles of axial velocity and axial and radial turbulence intensities at various slices near the exhaust nozzle exit. Data for the L_e/D_e = 0.7 configuration are shown as solid black curves while those for L_e/D_e = 3.0 are shown as dashed blue curves.

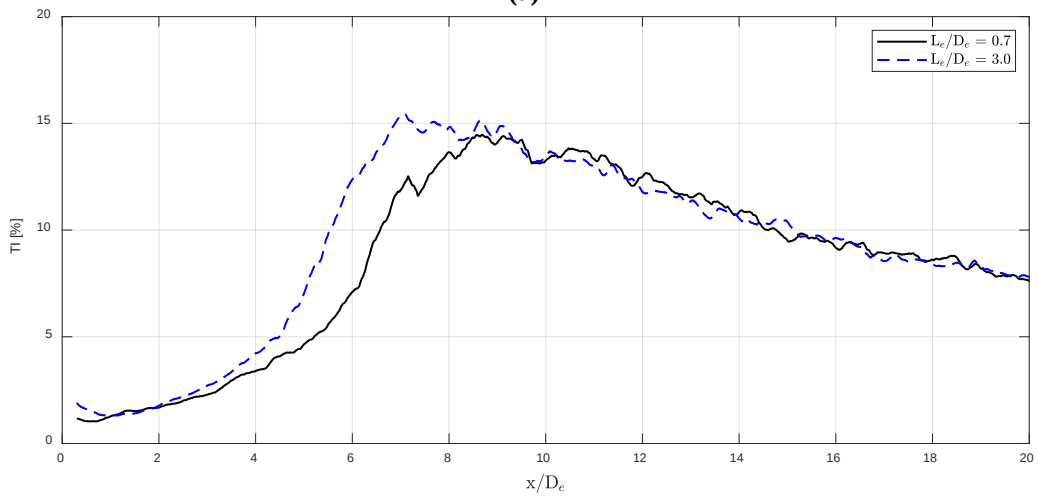


(a) **(b)**

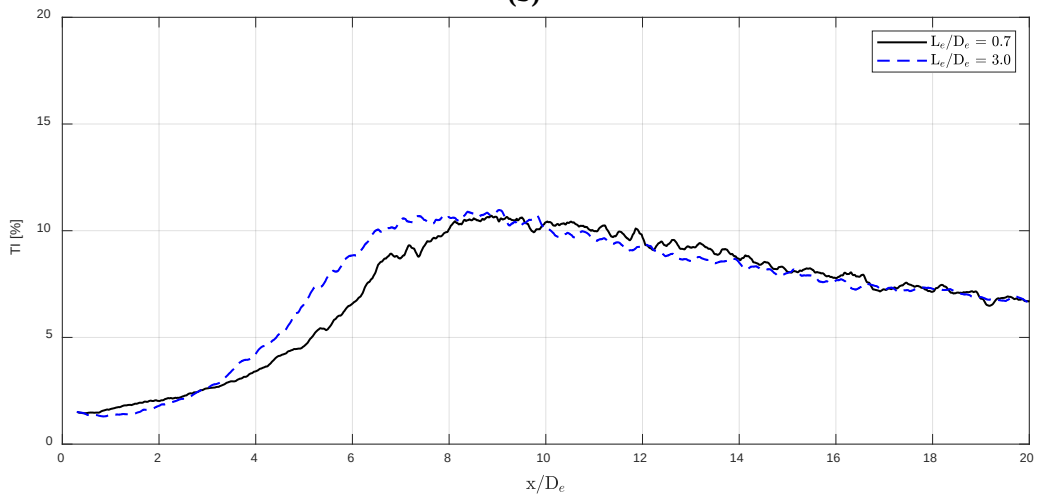
Figure 27. Two-dimensional mean and turbulence intensity plots. PR_1 = 1.39, PR_2 = 1.39, T_{t1} = 500°F, where (a) L_e/D_e = 0.7 and (b) L_e/D_e = 3.0, N = 750 image pairs.



(a)



(b)



(c)

Figure 28. Comparisons of centerline (a) mean axial velocity and (b) axial and c) radial turbulence intensities (TI) between mixing-duct lengths. PR_1 = 1.39, PR_2 = 1.39, T_{t1} = 500°F, L_e/D_e = 0.7 and L_e/D_e = 3.0, N = 750 image pairs.

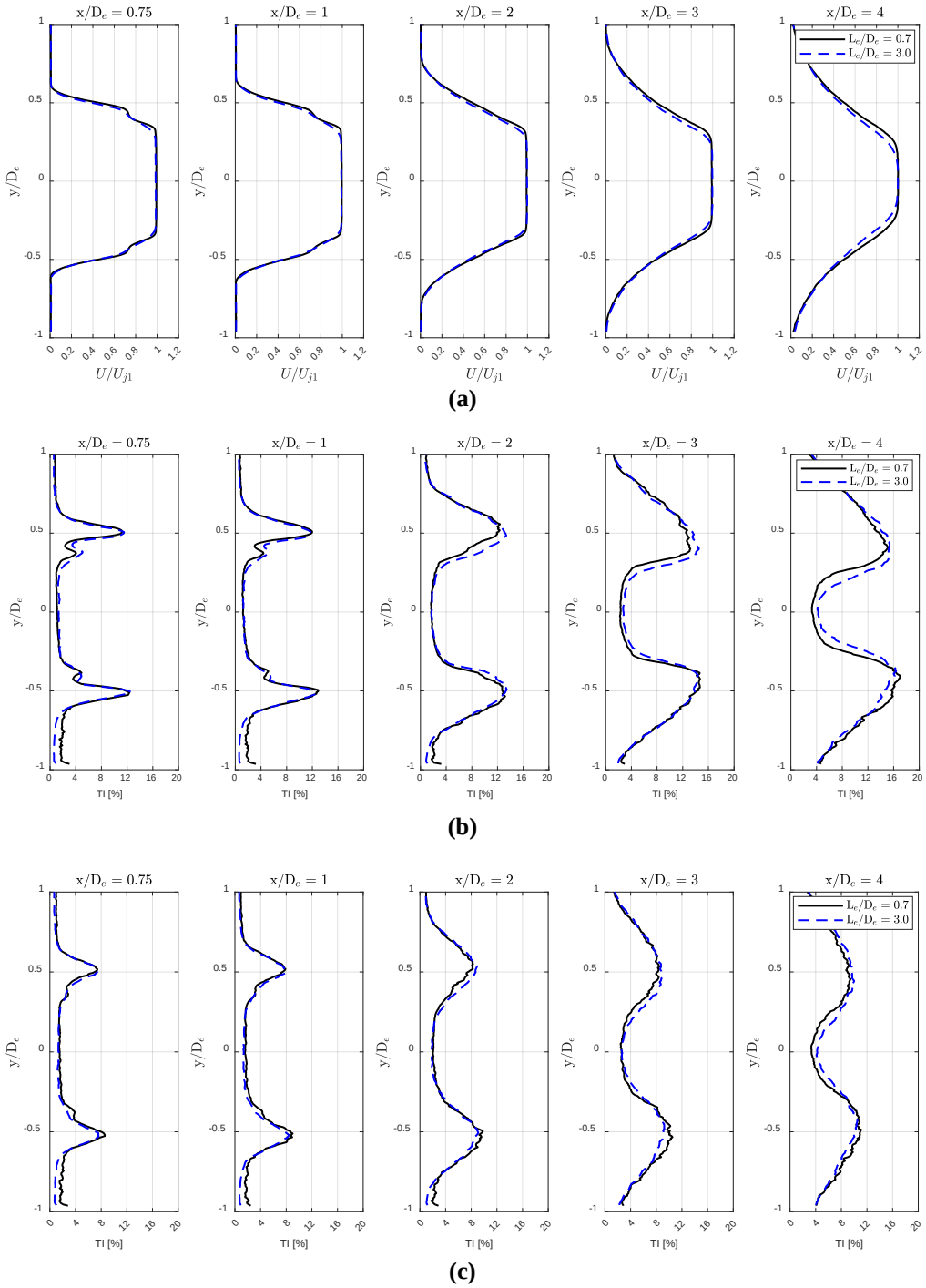


Figure 29. Comparisons of a) mean axial velocity and b) axial and c) radial turbulence intensity profiles between mixing-duct lengths at various x/D_e. PR_1 = 1.39, PR_2 = 1.39, T_{t1} = 500°F, L_e/D_e = 0.7 and L_e/D_e = 3.0, N = 750 image pairs.

With a heated core stream, there are observable differences in the flowfield from the internally mixed jet between the two mixing-duct lengths. The centerline velocity distribution in Figure 28a shows a decrease in the length of the potential core



of about one diameter when increasing the mixing-duct length from its shortest value of L_e/D_e = 0.7 to L_e/D_e = 3.0. This effect is also captured in the velocity profiles shown in Figure 29a as the profiles for the longer mixing-duct length seem to smoothen out slightly sooner as one traverses downstream.

High-Speed Schlieren Flow Visualization

Facility Set-up and Testing Description

GTRI's schlieren setup is shown in Figure 30. An arc lamp light source emits light that follows a z-shaped path along a series of mirrors and lenses. The light source is positioned at the focal point of the first parabolic mirror, sending collimated light into the test section (the horizontal region between the two parabolic mirrors). The second parabolic mirror focuses the light rays (now refracted by density gradients within the test section) to a focal point. At the appropriate focal point, a knife edge cutoff is positioned in one of two orientations: vertical (knife edge normal to jet axis) or horizontal (knife edge parallel to jet axis). These two knife edge orientations reveal axial and transverse density gradients in the test section, respectively. The light is then passed through a pair of refocusing lenses that allow the camera to be placed far from the jet, which may be heated, in order to protect the camera. The schlieren images are captured on a Vision Research Phantom® V2512 monochrome ultrahigh-speed camera, with a resolution of 1,280 x 800 pixels at 25,000 frames per second and with a 1 μs exposure time. The video files being released to modeling teams will be in the .AVI format, with 100 frames total at 20 frames per second. While only short, 100-frame videos are being released, 2,500 images were recorded at each condition and the longer duration measurements are available upon request.

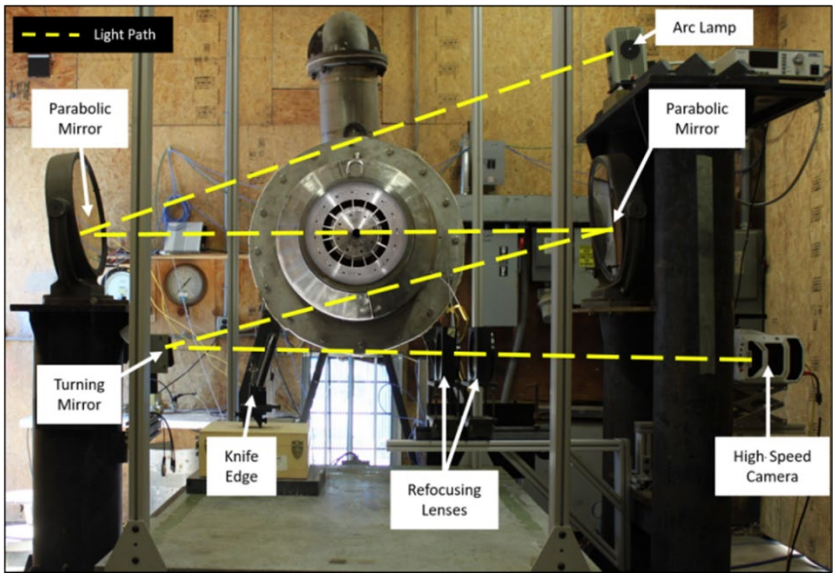
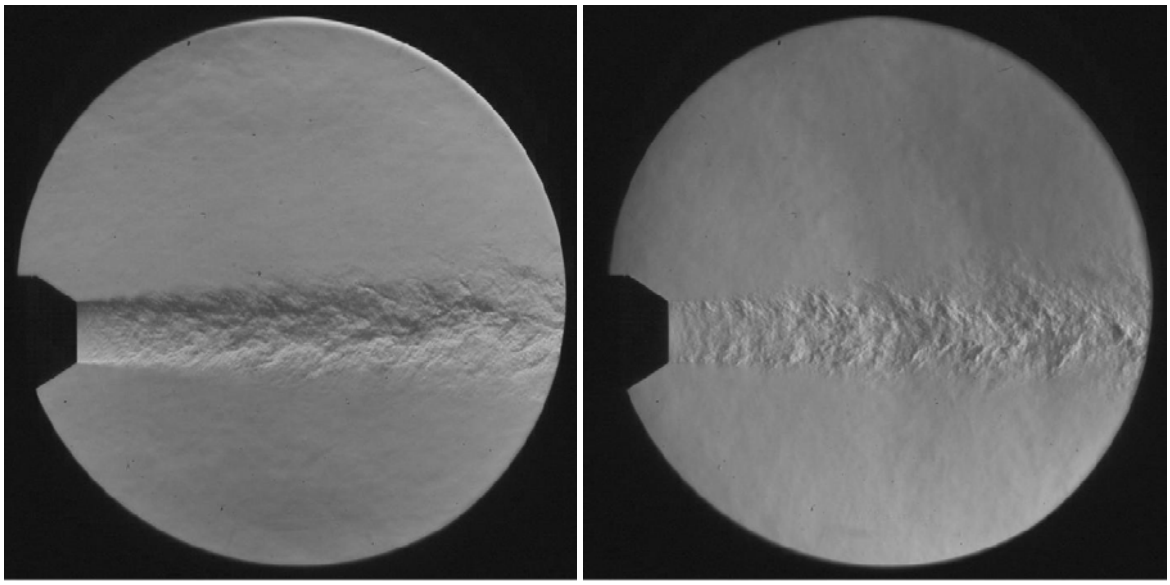


Figure 30. GTRI's Z-shaped schlieren setup (Ramsey et al., 2022b).

Schlieren Visualizations

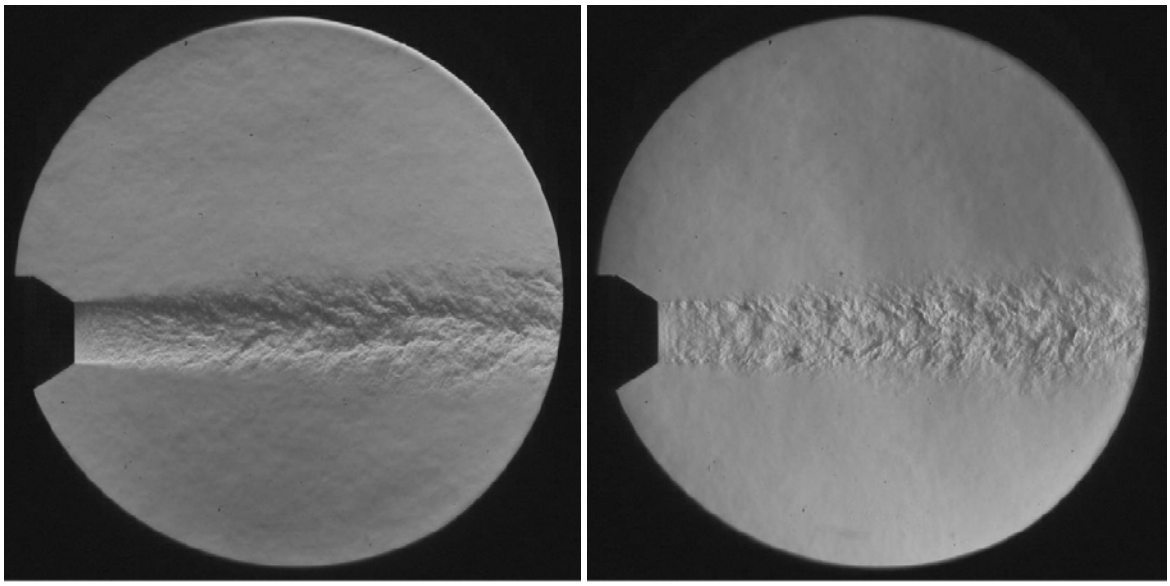
Representative schlieren snapshots are shown for the shortest mixing-duct length (L_e/D_e = 0.7) and ER = 1.00 in Figures 31 through 33, each of which shows both transverse and axial density gradients. As the pressure ratio (and thus its Reynolds number) is increased, the turbulent density gradients become more and more well-defined. This is expected for two reasons. First, turbulent velocity fluctuations and their associated stresses on the fluid increase with Mach number. Secondly, the smallest scales of turbulence decrease with increasing Reynolds number ($Re = U_j D_e/\nu$). Relatively small changes are caused to the apparent density gradients by increasing ER from 1.00 to 1.07 at the PR_1 = 1.39 condition, as shown in Figure 34. Similarly, little change is seen as ER is set to 1.10 (Figure 35). For the most part, the flow field at all of these conditions remains typical of turbulent jets.

® Phantom is a registered trademark of Vision Research, Inc., Wayne, New Jersey.



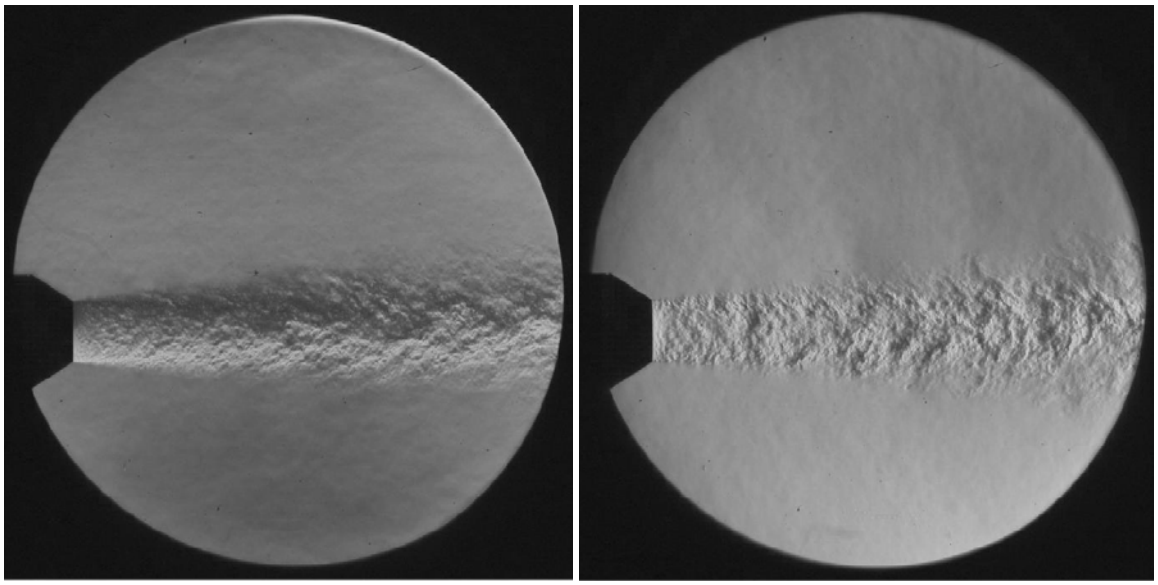
(a) **(b)**

Figure 31. Schlieren flow visualization of $L_e/D_e = 0.7$ at $PR_1 = 1.39$, $ER = 1.00$, $PR_2 = 1.39$, unheated configuration: (a) transverse density gradients and (b) axial density gradients.



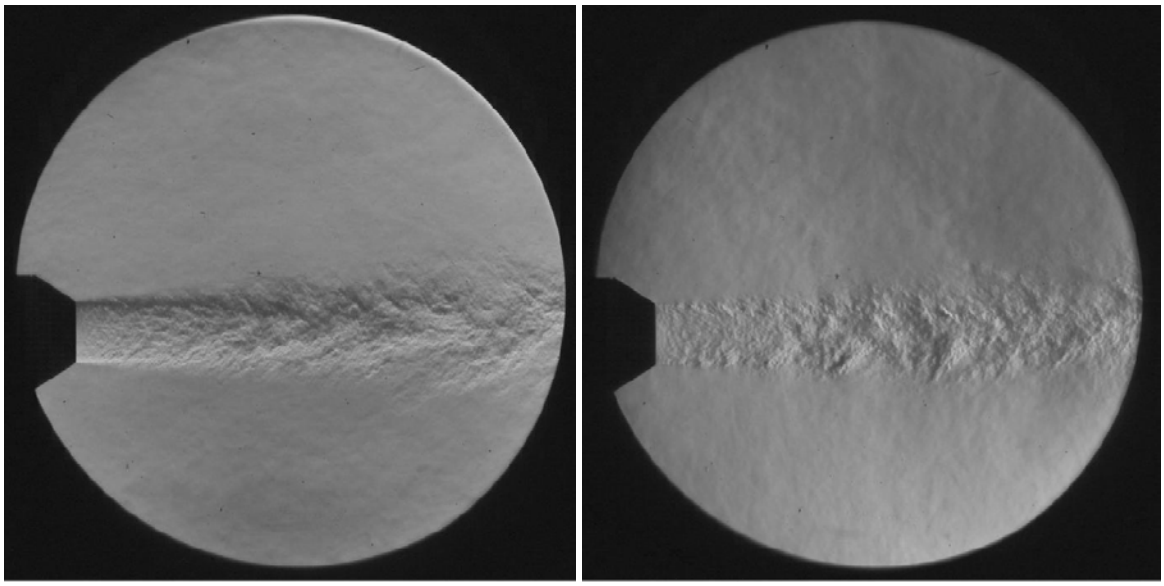
(a) **(b)**

Figure 32. Schlieren flow visualization of L_e/D_e = 0.7 at $PR_1 = 1.52$, $ER = 1.00$, $PR_2 = 1.52$ unheated configuration: (a) transverse density gradients and (b) axial density gradients.



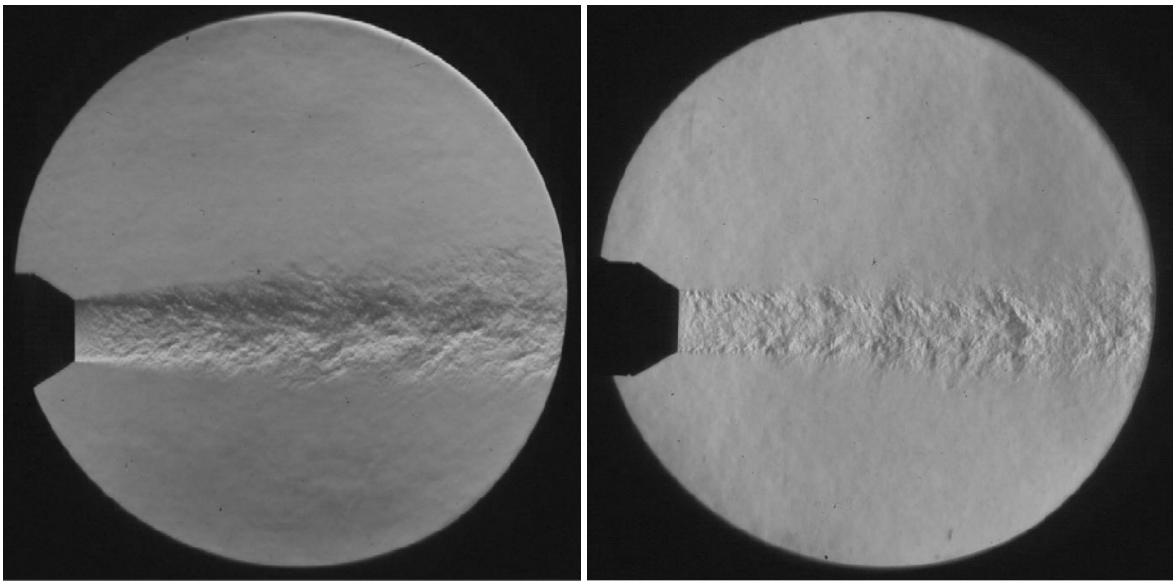
(a) **(b)**

Figure 33. Schlieren flow visualization of L_e/D_e = 0.7 at $PR_1 = 1.89, ER = 1.00, PR_2 = 1.89$, unheated configuration: (a) transverse density gradients and (b) axial density gradients.



(a) **(b)**

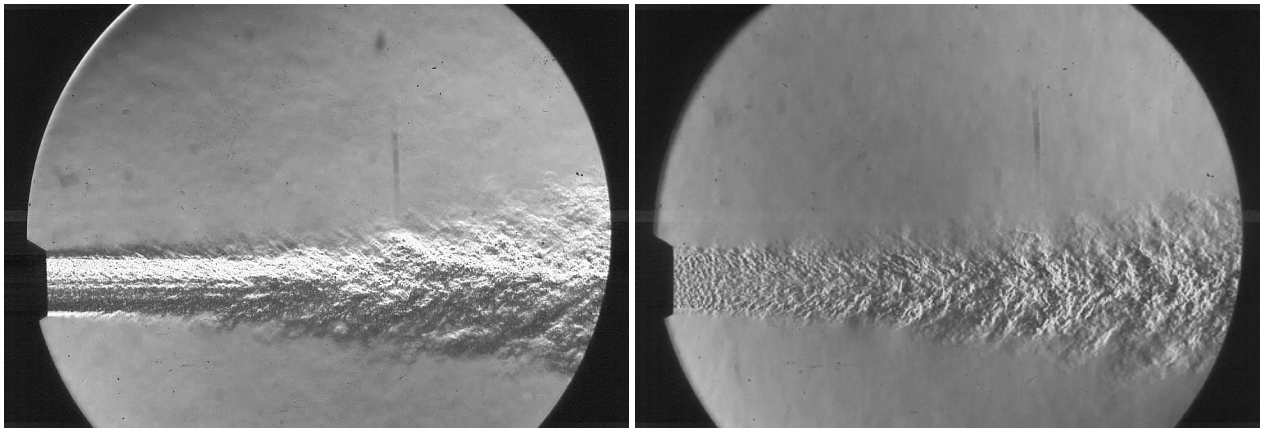
Figure 34. Schlieren flow visualization of L_e/D_e = 0.7 at $PR_1 = 1.39$, $ER = 1.07$, $PR_2 = 1.49$, unheated configuration: (a) transverse density gradients and (b) axial density gradients.



(a) **(b)**

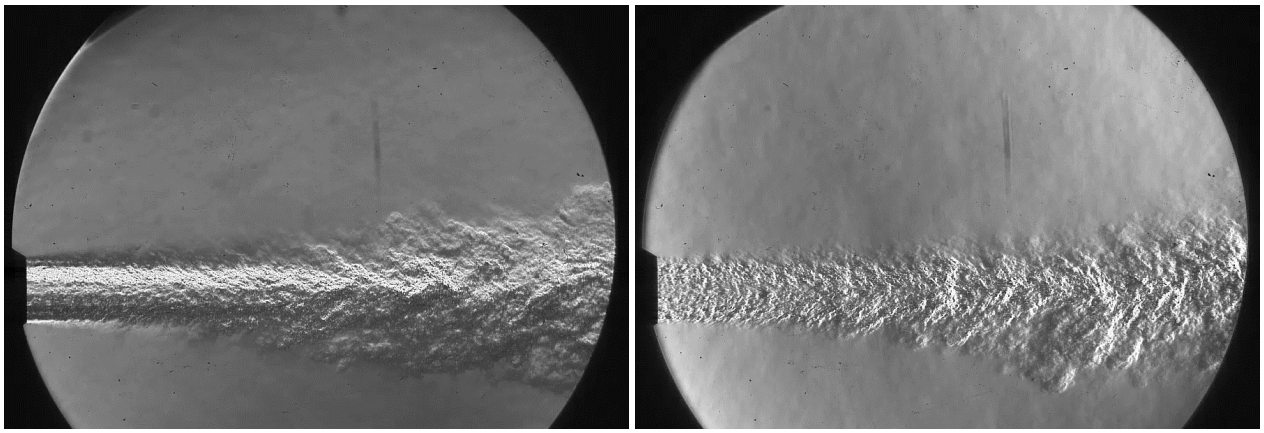
Figure 35. Schlieren flow visualization of $\boldsymbol{L_e/D_e = 0.7}$ at $\boldsymbol{PR_1 = 1.39}$, ER = 1.10, PR_2=1.52 unheated configuration: (a) transverse density gradients and (b) axial density gradients.

Time-resolved schlieren visualizations were recorded for each of the six heated core conditions identified in Figure 26 for both the shortest L_e/D_e = 0.7 and longest L_e/D_e = 3.0 mixing-duct lengths. The resulting visualizations acquired using both mixing-duct lengths are remarkably similar as seen by comparing Figures 36 and 37. This indicates that the noise of the two mixing-duct lengths will also remain largely unchanged as indeed noted in previous sections.



(a) **(b)**

Figure 36. Schlieren flow visualization of $\boldsymbol{L_e/D_e = 0.7}$ at $\boldsymbol{PR_1 = 1.39}$, $\boldsymbol{ER = 1.07}$, T_{t1} = 500°F configuration: (a) transverse density gradients and (b) axial density gradients. 1.5 μs exposure, f_s = 44 kHz



(a) **(b)**

Figure 37. Schlieren flow visualization of $\boldsymbol{L_e/D_e = 3.0}$ at $\boldsymbol{PR_1 = 1.39}$, $\boldsymbol{ER = 1.07}$, T_{t1} = 500°F configuration: (a) transverse density gradients and (b) axial density gradients. 1.5 µs exposure, f_s = 44 kHz.

These results are in agreement with the trends in the measured farfield noise of axisymmetric confluent nozzles reported by Ramsey et al. (2022a) – that is, the mixing-duct length of the nozzle has little effect on the noise and as such, there is little mixing accomplished upstream of the baseline exhaust nozzle exit in either case. For the sake of brevity, representative frames from only a single operating condition are shown. These visualizations look remarkably different when compared to those acquired with an unheated core stream. With an elevated core temperature, density gradients become more extreme, especially in the core-bypass shear layer as captured in Figures 36a and 37a. Additionally, compared to the unheated case, the plume width of the heated jets are broader, a commonly observed phenomenon reported in the literature.

Acoustic Source Location

Facility Set-up and Testing Description

Figure 38 shows the beamformer array mounted in the GTRI Flow Diagnostics Facility. The beamformer, developed by OptiNav™ for GTRI, consists of an array of 48 Earthworks Audio™ M30 microphones arranged in a spiral pattern emanating from the center of the beamformer resulting in an array approximately 3 ft across. It is an assembly of ¼-in. omnidirectional microphones with a flat free-field response from 5 Hz to 30 kHz with a peak input sound pressure level of 142 dB. The signals from the array of microphones are fed into three separate MOTU® Stage B16 digital mixers. They are then routed from each of these B16s to an Audio Video Bridging switch, which feeds the data to a MOTU timing unit. Analysis is performed using a Beamforming Interactive software package designed by OptiNav, primarily by using the "frequency sweep" option, which beamforms each band of the recorded one-twelfth octave spectra individually and records the resulting location for each frequency band. In some cases, multiple sources of comparable strength can exist, in which case multiple peak source locations are recorded and arranged in order of relative intensity. The choice of one-twelfth octave acts as a compromise between narrowband which results in an overwhelming number of data points leading to difficulties in comparing data and one-third octave which results in too few data points to accurately resolve trends in the data. For a more in-depth description of the beamformer and its uses at GTRI, the reader is directed to the works of Breen and Ahuja (2019, 2020) and Breen (2019).

™ OptiNav is a trademark of OptiNav, Inc., Bellevue, Washington.
™ Earthworks Audio is a trademark of Earthworks, Inc., Milford, New Hampshire.
® MOTU is a registered trademark of Mark of the Unicorn, Inc., Cambridge, Massachusetts.

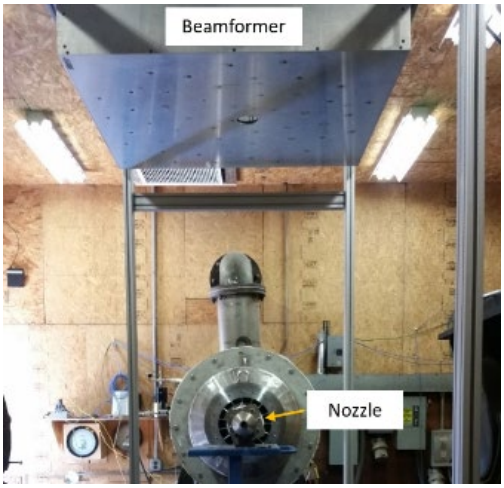


Figure 38. GTRI's acoustic beamforming setup (Breen & Ahuja, 2020).

Source Location Analysis

Acoustic source location data was acquired for the same six heated core conditions that were outlined in the text matrix shown in Figure 26 with both the shortest L_e/D_e = 0.7 and longest L_e/D_e = 3.0 mixing-duct lengths. Figure 39 shows an example of acoustic source-location data. In this plot, the streamwise location as measured from the exit of the final exhaust nozzle of the strongest source at a given frequency is plotted. This is done by computing a noise level contour for each frequency band and isolating the contour peak as the loudest source occurring in that band. The color of each data marker shows the strength of the source with bright yellow corresponding to peak jet noise. Note that the resolution of the array at low frequencies (below approximately 300 – 400 Hz) is rather poor. This is evidenced in the data as low-frequency sources suddenly move back upstream toward the nozzle exit. At higher frequencies where the beam width is very narrow, the beamformer is accurately able to discern the location of the contour peak versus its centroid. At lower frequencies the beam width is much wider, and as shown in Breen and Ahuja (2020) this results in an averaging of the source strength for the given frequency, shifting the peak location to the centroid of the contour. Frequencies in this range are, therefore, not shown in any subsequent source location plots in this report. All source location data is one-twelfth octave. Without a clear characteristic diameter and velocity needed to normalize the location and frequency, the data displayed here are not plotted against a non-dimensional frequency as typically found in the round-jet noise literature. In later sections when discussing source location results using the lobed internal mixer nozzles obtained from GAC, some attempts to collapse and compare data using a Strouhal number based both on the core-jet velocity U_{j1} and the theoretically fully-mixed velocity, U_{mix}, will be made.

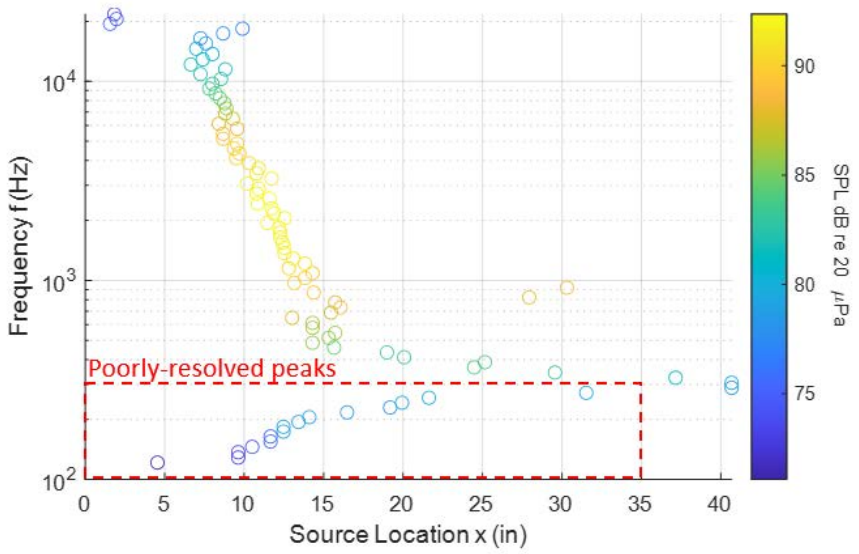


Figure 39. Source location of the Y1 GT dual-stream jet, L_e/D_e = 0.7. PR_1 = 1.39, ER = 1.07, T_{t1} = 500°F, one-twelfth octave band data. SPL: sound pressure level.

Higher-frequency noise sources are typically associated with the portion of the jet's shear layer closer to the nozzle exit where turbulent length scales are small. Enhanced levels of internal mixing would be characterized by movement of noise sources closer to the nozzle exit. For a rapidly-mixed, dual-stream jet (such as one produced through the use of a forced mixer), one might expect the source distribution to follow a steeper curve. This would be due to a more thoroughly mixed jet expanding faster once it has exited the nozzle, resulting in noise sources at all frequencies being measured as emanating from closer to the nozzle exit. A direct comparison between the results from the shortest and longest mixing-duct lengths shows a slight upstream shift of noise sources for the longer mixing-duct length: potentially evidence of enhanced mixing due to the longer mixing-duct length. Figures 40 through 42 below show the source locations for the shortest and longest mixing-duct lengths for three different heated conditions: one at unity extraction ratio and two slightly above unity (ER = 1.04 and 1.07). For all conditions, the noise sources move slightly closer to the nozzle exit as the mixing-duct length is increased, which would be expected of noise generated upstream of the nozzle exit associated with internal mixing. This effect is more pronounced for the unity extraction ratio case but is less pronounced as the secondary stream pressure ratio is increased. For the frequency range between 1 and 10 kHz, the sources move approximately 0.82 diameters upstream for the unity extraction ratio case, 0.27 diameters upstream for ER = 1.04, and 0.25 diameters upstream for ER = 1.07. The results shown in Figure 40 comparing the source distributions between the shortest and longest mixing-duct lengths at PR_1 = 1.39, PR_2 = 1.39, T_{t1} = 500°F are corroborated by the results obtained from PIV at the same condition shown in Figure 28a. That is, the nearly one-diameter upstream shift of noise sources when using the longest exhaust mixing-duct length is in part explained by the nearly one-diameter decrease in the length of the potential core.

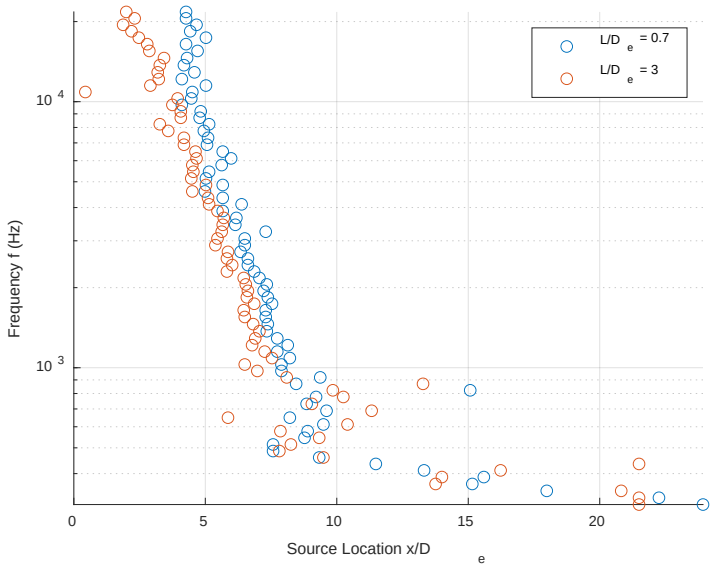


Figure 40. Comparison of source locations between L_e/D_e = 0.7 and 3.0. PR_1 = 1.39, PR_2 = 1.39, T_{t1} = 500°F,

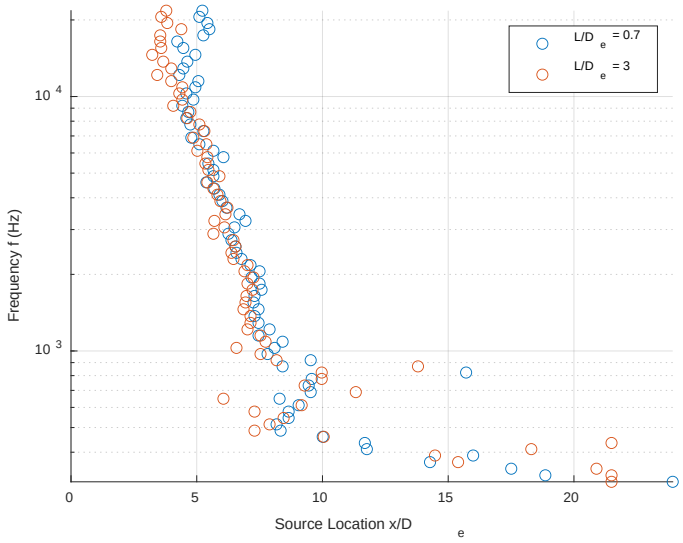


Figure 41. Comparison of source locations between L_e/D_e = 0.7 and 3.0. PR_1 = 1.39, ER = 1.04, T_{t1} = 500°F, one-twelfth octave band data.

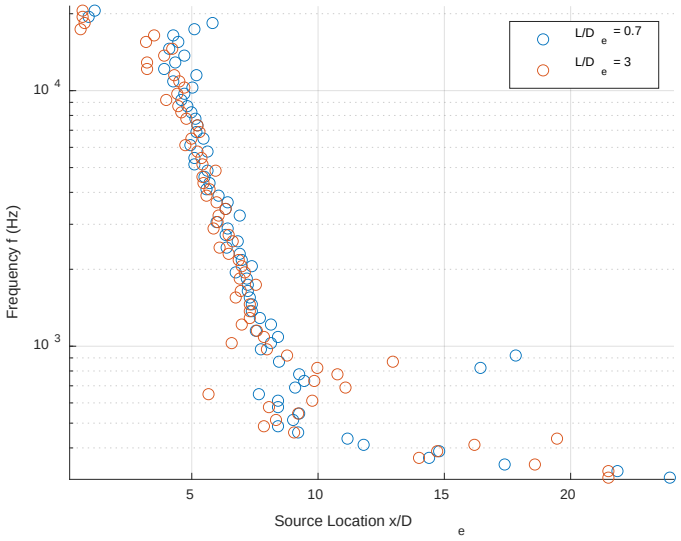


Figure 42. Comparison of source locations between L_e/D_e = 0.7 and 3.0. PR_1 = 1.39, ER = 1.07, T_{t1} = 500°F, one-twelfth octave band data.

Year – 3, the Gulfstream Nozzle

Nozzle Design

The third year of this project was devoted to designing, fabricating, installing and testing a set of nozzles that were physically different from those tested to date. They included a symmetrical nozzle and two forced mixers all of the same equivalent diameter and somewhat larger than those tested to date. The design of the dual-stream nozzles, assembly, and equivalent-diameter internal mixers are described in a recent paper by Clemens and Gavin (2024) of GAC. For a complete overview of the nozzle design and associated details, the reader is referred to this paper, though salient details will be reported here. The dual stream model obtained from GAC in April 2023 is designed for a bypass ratio of about 3.0, notably larger than that of the previous Year-1 academic nozzle designed by the ASDL. The assembly consists of a core duct, bypass duct, core nozzle, exhaust nozzle, and optional mixing-duct length spacers. The complete set of model parts is displayed in Figure 43.

The diameter or equivalent diameter of each primary nozzle is approximately D = 1.54 in., and the diameter of the final exhaust nozzle is D_e = 2.20 in. The diameter at the inlet of the mixing duct is D_{mix} = 2.80 in.



Figure 43. Model parts obtained from Gulfstream (Clemens & Gavin, 2024).

It is worth noting that unlike previously in which a single exhaust nozzle with length $L_e/D_e = 0.7$ was provided with spacers to increase the mixing-duct length to $L_e/D_e = 1.0$, 2.0, and 3.0, two distinct exhaust nozzles were designed For this study, the shorter $L_e/D_e = 0.7$ exhaust nozzle has a more rapidly convergent geometry than the $L_e/D_e = 1.0$ nozzle. In order to maintain uniform convergent geometry across nozzle configurations to isolate the effect of mixing-duct length alone, the $L_e/D_e = 1.0$ exhaust nozzle was used first in isolation to provide an $L_e/D_e = 1.0$. The exhaust mixing-duct length was then increased by attaching this nozzle to the end of one of two spacer ducts attached to the exit of the bypass duct. The nozzle at the end of the core duct is interchangeable, and Figure 43 shows the core duct and nozzle assembly using one of the two-lobed mixer nozzles provided.

All of the three core nozzles had the same exit area. Three-view diagrams of these nozzles taken from Clemens and Gavin (2024) are shown in Figure 44. The nozzle geometries consist of one baseline, axisymmetric nozzle and two lobed mixer nozzles, each with 10 lobes and 10 gullies. In all datasets corresponding to configurations using the axisymmetric mixer, the handle GAC23-AXI is used. The less aggressive of the two lobed mixers as shown in the center of Figure 44 is referred to as GAC23-SUN; while the more aggressive mixer with deeper lobes and gullies is referred to as GAC23-DAISY. For use in dual stream configurations a two-digit tag is included at the end of the configuration name to denote the mixing-duct length in tenths of L_e/D_e. For example, the handle GAC23-AXI-10 denotes a dual stream configuration using the baseline, axisymmetric core nozzle with an exhaust mixing-duct length of $L_e/D_e = 1.0$. The handle GAC23-SUN-00 would denote a dual stream configuration using the less aggressive SUN mixer with no exhaust nozzle but bypass flow still present. A single stream configuration using just the DAISY mixer nozzle alone with no bypass nozzle or secondary flow would be denoted as GAC23-DAISY. Figures 45 and 46 show various stages of the nozzle assembly installed in the GTRI anechoic chamber.

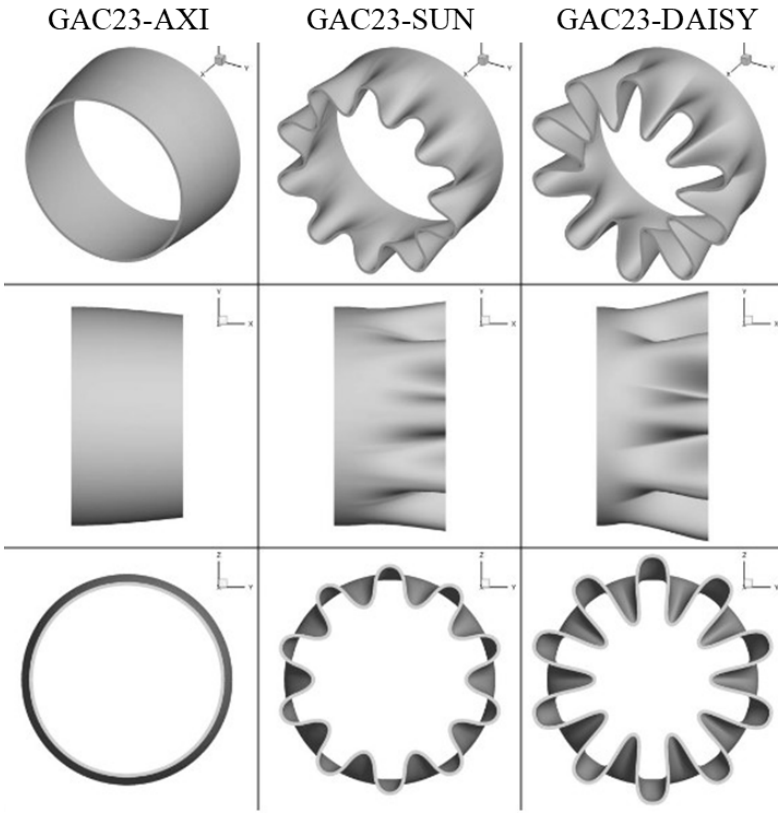


Figure 44. Three-view diagrams of core nozzles (Clemens & Gavin, 2024).

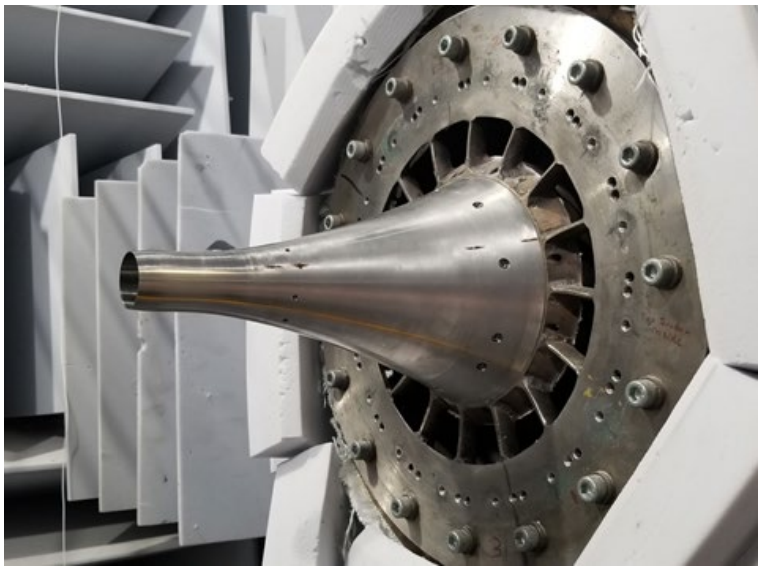


Figure 45. GAC primary nozzle with baseline axisymmetric nozzle (AXI) mixer installed in GTRI anechoic chamber.



(a) **(b)**

Figure 46. GAC nozzle assembly in GTRI static anechoic chamber with SUN internal mixer and bypass nozzle both (a) without exhaust nozzle and (b) with an exhaust nozzle of $L_e/D_e = 1.0$.

Single Stream Measurements

The acoustics and flowfields of jets issuing from lone lobed nozzles are complex in their own right even without the inclusion of secondary flow. In order to develop a more comprehensive understanding of the effects of lobed mixer nozzles on internally-mixed, dual-stream jets, it is important to first understand their behavior in isolation. As such, the same acoustic, PIV, schlieren, and source location measurements taken previously of dual-stream jets were acquired for each of the three core nozzles operated alone without any secondary nozzle or flow. The results discussed in the following sections highlight key characteristics of jets from the lobed nozzles that become important in dissecting their impact on the noise and flowfields of internally mixed jets. The facilities and methodologies by which these data were obtained are identical to those in previous sections and will not be repeated for the following sections.

Acoustic Measurements

Each of the three core nozzles – axisymmetric (AXI), SUN, and DAISY - were mounted in GTRI's anechoic chamber without the presence of the secondary duct (e.g., see Figure 45 showing the GAC23-AXI single stream configuration). Farfield acoustic measurements were taken along the same polar arcs as before with observation angles relative to the jet axis ranging from 30° to 110° in increments of 10°. During this testing, the jet Mach number M_j was varied from 0.5 to 1.0 in increments of 0.1 with the streams unheated ($T_{tj} \approx 60 - 70$°F). Figures 47 through 49 show the effect of both lobed nozzles on the noise produced by a single unheated jet at various observation angles. The effect of these mixers on the OASPL is shown in Figure 50. Data for the baseline, AXI nozzle is plotted in black, the SUN lobed nozzle is shown in blue, and the more aggressive DAISY lobed nozzle is shown in red. At the downstream polar observation angle $\theta = 30°$, the SUN mixer reduces jet noise at the peak frequency by approximately 5.5 dB while the DAISY mixer reduces it by about 10 dB relative to the AXI baseline. While more effective at reducing peak SPL, the DAISY mixer produces considerably more high-frequency noise. This is especially apparent at the sideline observation angle (Figure 49). This increase in high-frequency noise is less prevalent for the SUN mixer. A reduction in peak jet noise at the cost of enhanced higher frequency noise is to be expected of enhanced jet mixing devices. The callout at the bottom left of each figure is included to emphasize that the data are representative of the core nozzles operated in the single stream configuration. For reference, each core nozzle geometry is shown to the right of each figure with colored square boxes corresponding to the colors of their spectra on the plots.

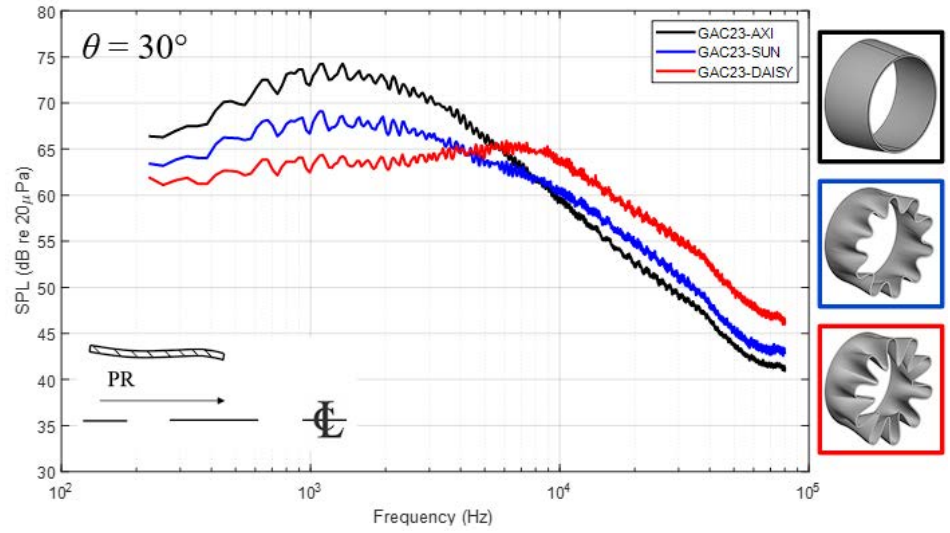


Figure 47. Effect of lobed nozzle on the noise from a single-stream jet. FAA GAC Project Model, D = 1.54 in. PR = 1.39 (M_j = 0.70), unheated, R = 12 ft, θ = 30°, Δf = 32 Hz, lossless.

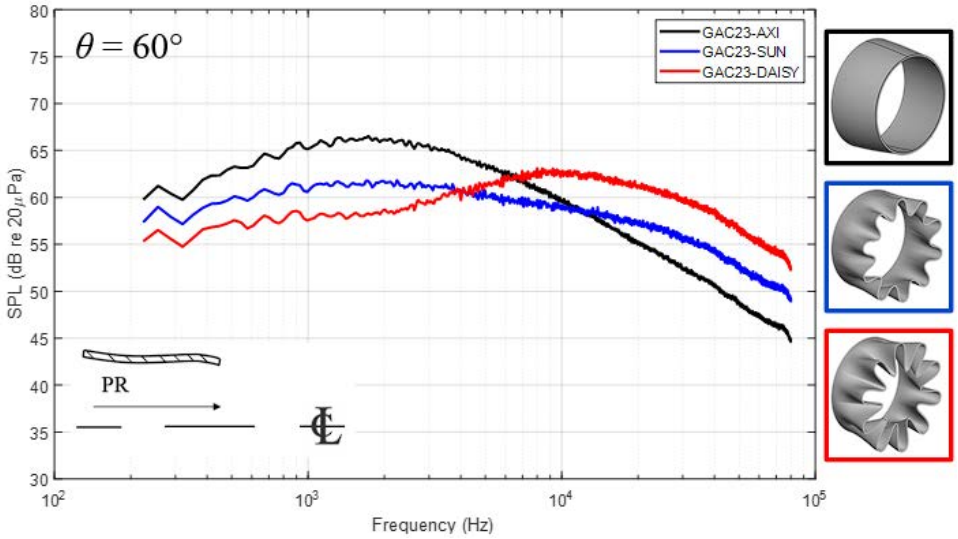


Figure 48. Effect of lobed nozzle on the noise from a single-stream jet. FAA GAC Project Model, D = 1.54 in. PR = 1.39 (M_j = 0.70), unheated, R = 12 ft, θ = 60°, Δf = 32 Hz, lossless.

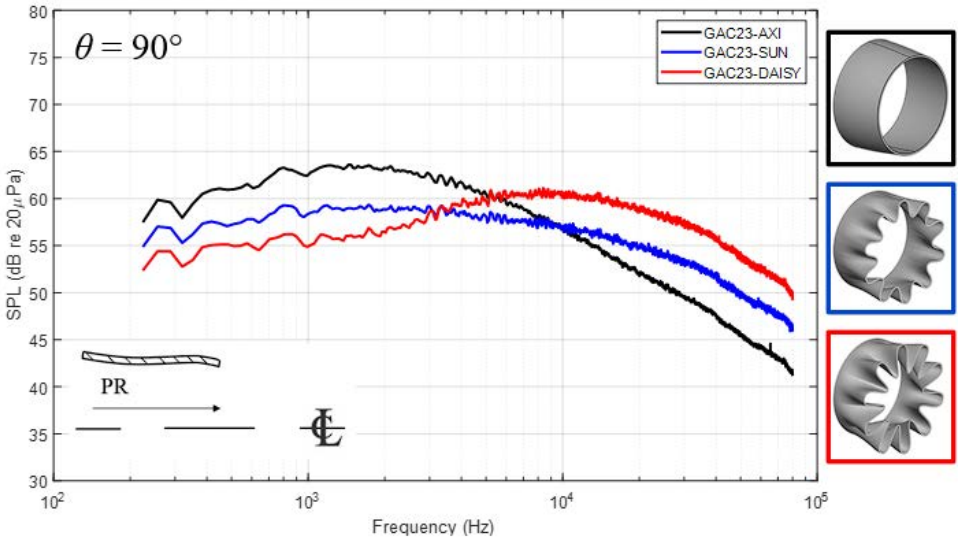


Figure 49. Effect of lobed nozzle on the noise from a single-stream jet. FAA GAC Project Model, D = 1.54 in. PR = 1.39 (M_j = 0.70), unheated, R = 12 ft, θ = 90°, Δf = 32 Hz, lossless.

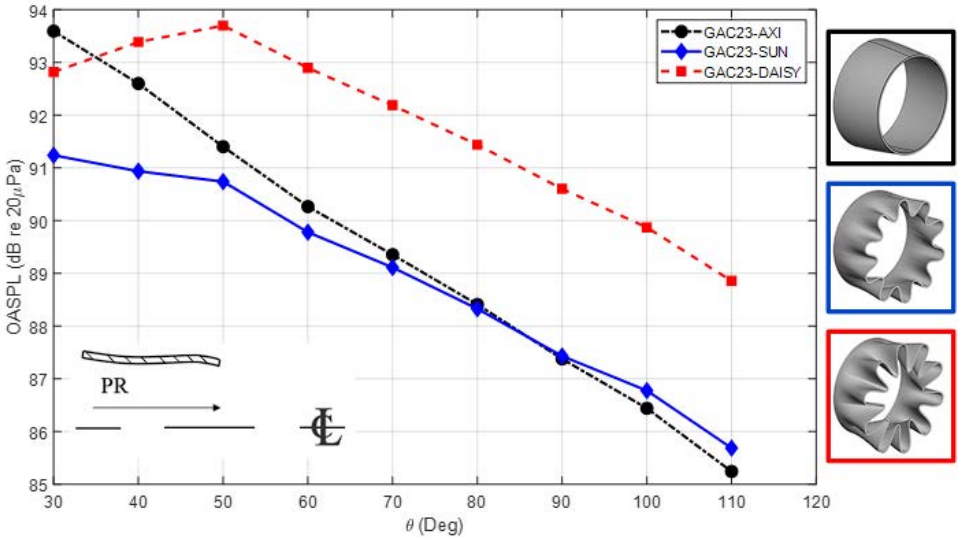


Figure 50. Effect of lobed nozzle on the overall noise from a single-stream jet. FAA GAC Project Model, D = 1.54 in. PR = 1.39 (M_j = 0.70), unheated, R = 12 ft, Δf = 32 Hz, lossless.

For the initial single stream testing with the lobed nozzles, all three polar arcs were employed to determine the directivity (if any) of jet noise produced by the lobed nozzles. Each arc was aligned differently relative to the orientations of the lobed as shown in Figure 51 which shows the alignment of the higher farfield (HF), middle farfield (MF) and lower farfield (LF) polar arcs relative to the lobes. Note that the lobed geometry shown is arbitrary and is not drawn to scale. As demonstrated in Figures 52 through 54 the farfield noise generated by these lobed nozzles at sideline angles is no more azimuthally dependent than that of the baseline AXI. This is also true for other polar observation angles.

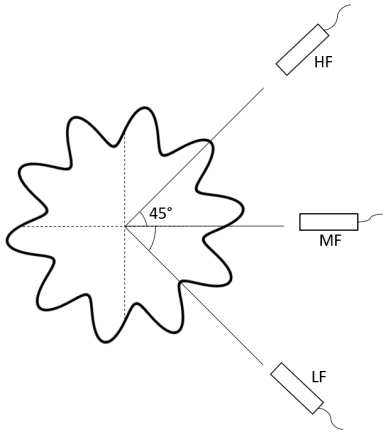


Figure 51. Microphone array orientation with respect to lobes.

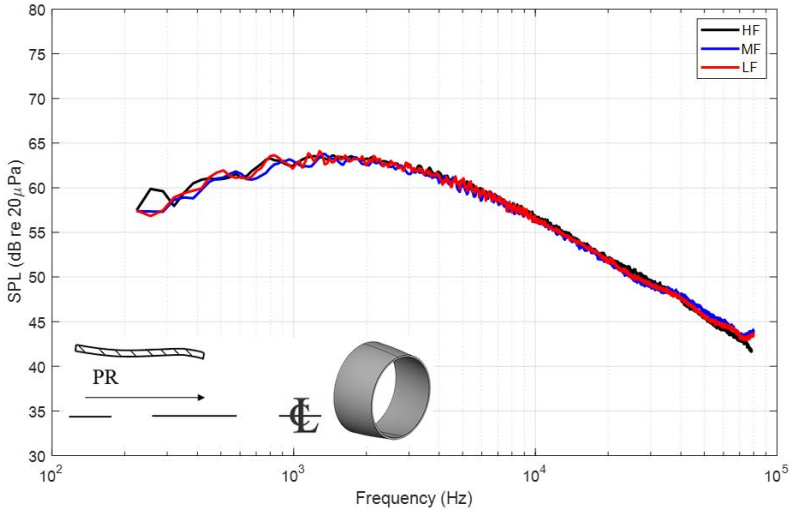


Figure 52. Azimuthal directivity of noise produced by axisymmetric (AXI) nozzle. FAA GAC Project Model, D = 1.54 in. PR = 1.39 (M_j = 0.70), unheated, R = 12 ft, θ = 90°, Δf = 32 Hz, lossless. HF: higher farfield, MF: middle farfield, LF: lower farfield, SPL: sound pressure level.

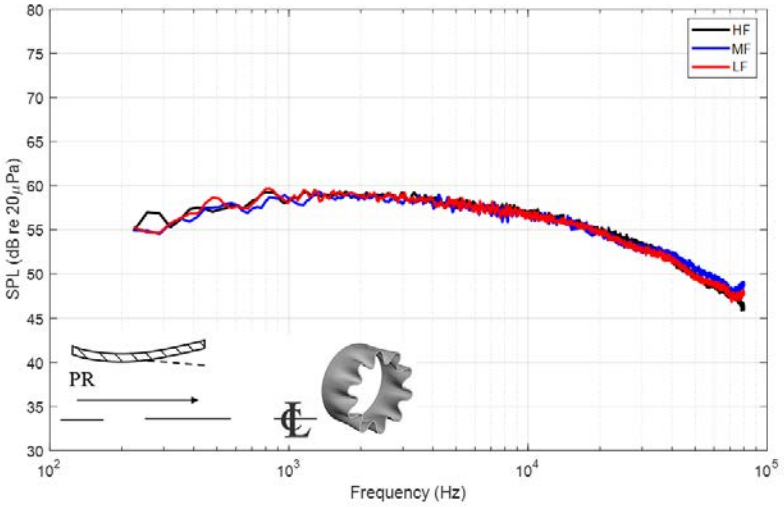


Figure 53. Azimuthal directivity of noise produced by SUN nozzle. FAA GAC Project Model, D = 1.54 in. PR = 1.39 (M_j = 0.70), unheated, R = 12 ft, θ = 90°, Δf = 32 Hz, lossless. HF: higher farfield, MF: middle farfield, LF: lower farfield, SPL: sound pressure level.

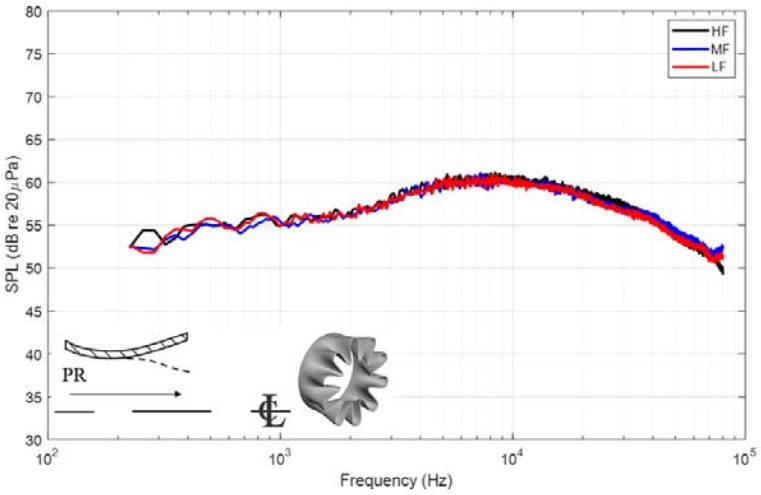


Figure 54. Azimuthal directivity of noise produced by DAISY nozzle. FAA GAC Project Model, D = 1.54 in. PR = 1.39 (M_j = 0.70), unheated, R = 12 ft, θ = 90°, Δf = 32 Hz, lossless. HF: higher farfield, MF: middle farfield, LF: lower farfield, SPL: sound pressure level.

The strong effect of the lobed mixers on jet noise observed at low polar angles (e.g., see Figure 47) suggests a stark difference in the nature of the large-scale turbulent structures between jets flowing from axisymmetric nozzles and those flowing from lobed mixer nozzles. This has become the focus of ongoing PhD student Larisch's thesis, which has revealed much about the nature of these lobed jets. One proposed model of jet noise given by the so-called two-source model by Tam et al. (1996, 2008) and Tam (2019) proposes that there are two distinct mechanisms by which jet noise is produced: one which pertains to large-scale turbulent structures (i.e., instability waves), which primarily radiates downstream to lower observation angles and one which pertains to fine-scale turbulent mixing, which radiates predominantly on the sideline. Tam et al. (1996, 2008) and Tam (2019) referred the source associated with the large-scale turbulence structures as the "F" spectrum and that associated with the fine-scale turbulence as the "G" spectrum. These labels are used in the following

figures also. The broadband noise produced by each component can be approximated using empirically-derived fits (Tam, 1996). Nance (2007), and Nance and Ahuja (2007, 2009) successfully showed that these two portions of jet noise can be isolated using a simple, coherence-based technique known as the three-microphone signal enhancement technique (Chung, 1977) by which the output power of a coherent signal at a given point may be separated from uncorrelated noise. An example of this decomposition is shown below in Figure 55 using the jet noise produced by the GAC23-AXI nozzle configuration at $PR = 1.69$ ($M_j = 0.90$), unheated at a polar observation angle of $\theta = 50°$. Here, the coherent portion of the jet noise spectrum is the component of noise associated with large-scale instability waves. A critical finding was made in that the jet noise spectra for the lobed mixer nozzles consist of a double-peaked coherent portion which can be closely approximated with two large-scale spectra as shown in Figure 56. The implications of this finding will become clearer in the following sections after we have presented the PIV and the source location data for the mixer nozzles.

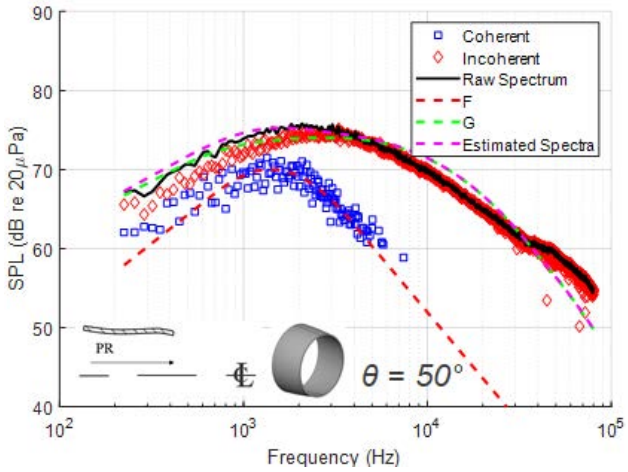


Figure 55. Estimated coherent and uncorrelated jet noise levels from axisymmetric nozzle measured at θ = 50° with fitted F and G similarity spectra. PR = 1.69, Tt ≈ 60°F, R = 12 ft, Δf = 32 Hz, lossless. SPL: sound pressure level.

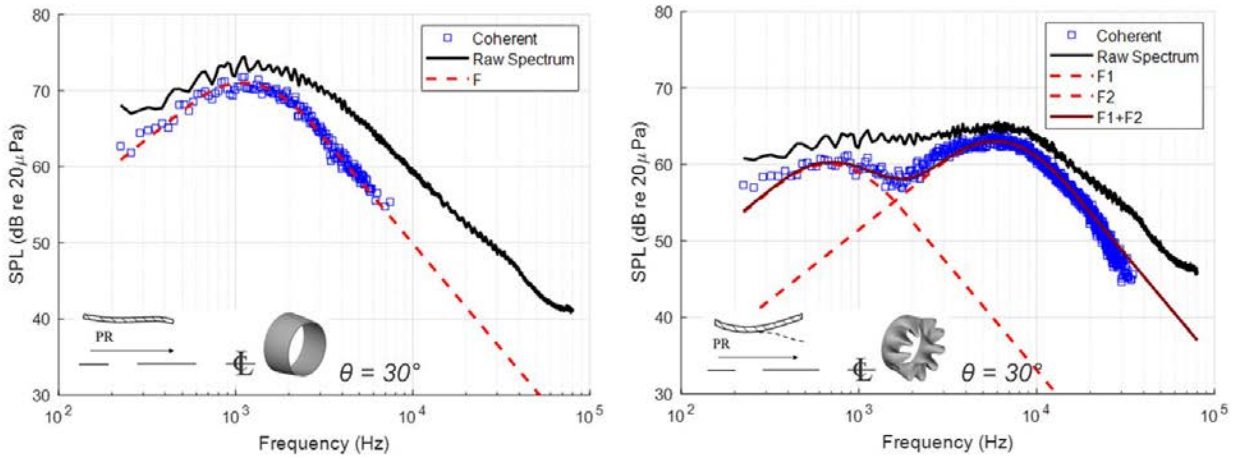


Figure 56. Estimated coherent jet noise levels from (a) axisymmetric and (b) lobed nozzles measured at θ = 30° with fitted *F* similarity spectra. PR = 1.39, $T_t \approx 60°F$, R = 12 ft, $\Delta f = 32$ Hz, lossless. SPL: sound pressure level.

PIV Measurements

PIV data were acquired in the same manner as before for each of the three primary nozzles at the same unheated conditions outlined in the previous section. A higher number of samples (N = 750) were acquired at two conditions - *PR* = 1.39 (M_j = 0.70) and *PR* = 1.69 (M_j = 0.90) – in order to accurately resolve turbulence statistics. Otherwise, a smaller sample size of N = 200 was sufficient to capture the mean flow. For the lobed nozzles, PIV data were acquired twice for each condition: once with the laser sheet aligned with lobes and once with the laser sheet aligned with gullies. As is to be expected from the differences seen in farfield noise, the flowfields of the lobed jets look wildly different from those of the axisymmetric nozzle. Figure 57 shows 2D plots of mean axial velocity, axial turbulence intensity, and radial turbulence intensity of the axisymmetric nozzle at *PR* = 1.69 and is not unlike those shown for the unity ER, unheated somewhat smaller axisymmetric jet in Figure 24a or Figure 24b.

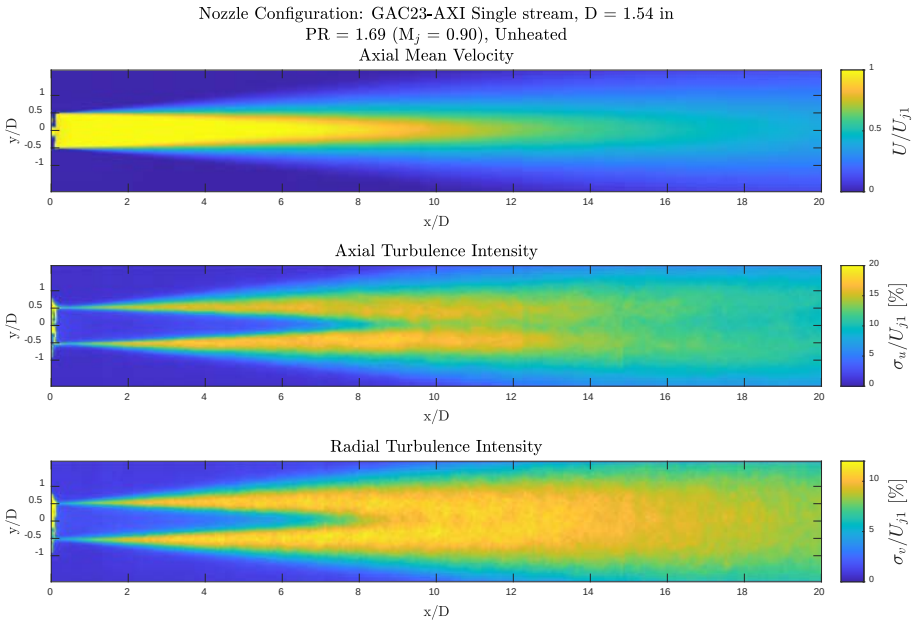


Figure 57. Two-dimensional mean velocity and turbulence intensity plots. GAC23-AXI configuration, *PR* = 1.69 (M_j = 0.90), unheated, N = 750 image pairs.

Figure 58 shows the same 2D plots but using the GAC23-DAISY configuration at *PR* = 1.39. Figure 58a shows measurements taken with the laser sheet aligned with lobes and Figure 58b shows those taken aligned with gullies. Very shortly downstream from the nozzle exit there exists a highly turbulent mixing region from an x/D of about 0.5 to 3. Beyond this region, the flowfield resembles that of a smaller, axisymmetric jet. A potential core still exists in the center as evidenced by the mean velocity plots but is shorter than that of the axisymmetric jet shown in Figure 57. A comparison of the centerline velocity distributions of the AXI and DAISY nozzles in Figure 59 reveals an approximately 40% reduction in the length of the potential core while the SUN mixer only slightly reduces the length of the potential core. After the mixing region, the centerline velocity of jets from both lobed nozzles decays following the distribution of the axisymmetric nozzle.

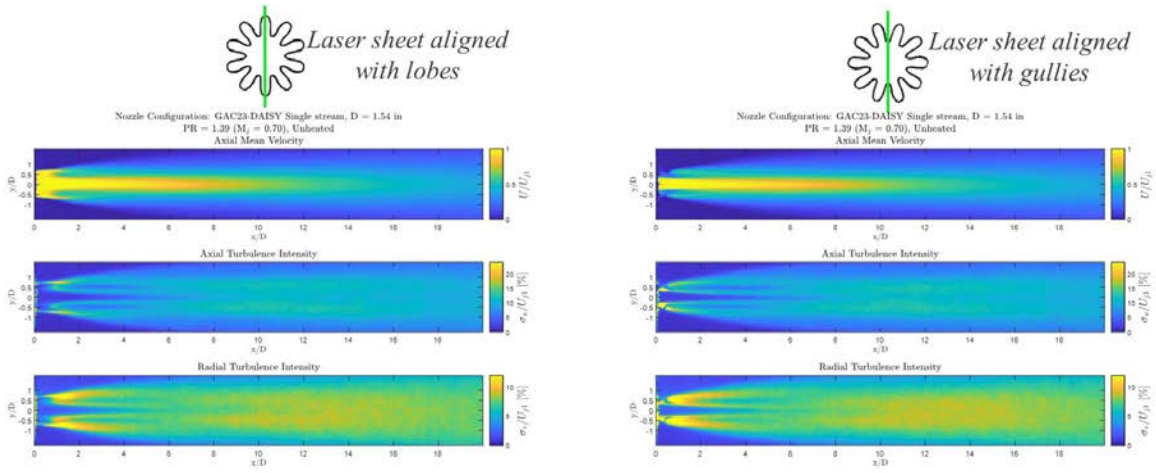


Figure 58. Two-dimensional mean velocity and turbulence intensity plots. GAC23-DAISY configuration (a) lobe aligned and (b) gully aligned. D = 1.54 in., *PR* = 1.39 (M_j = 0.70), unheated, N = 750 image pairs.

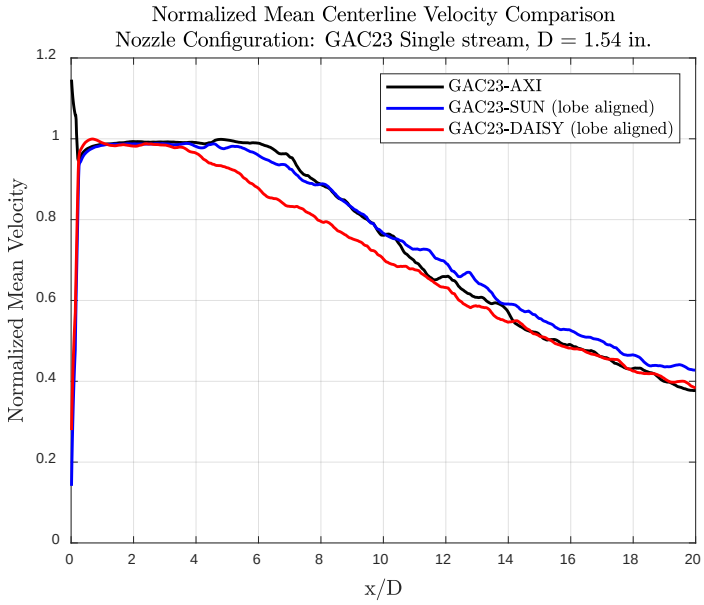


Figure 59. Centerline mean velocity distribution of jets from AXI, SUN, and DAISY nozzles. D = 1.54 in., *PR* = 1.53 (M_j = 0.80), unheated, N = 200 image pairs.

One remaining feature of note in the flowfield from the lobed nozzles is the existence of tiny potential cores issuing from the individual lobes. This can be observed upon close examination of the mean velocity field near the nozzle exit in Figure 58a wherein the laser sheet is aligned with the lobes. Just downstream of a lobe (at about y/D = 0.6 in the figure) one can see a streak of yellow which terminates around an axial position of x/D = 1.5. These tiny jets are better visualized in Figure 60, which shows profiles of mean axial velocity at various x/D near the nozzle. The curves in black are data taken with the laser sheet aligned with lobes while the curves in red are data taken with the laser sheet aligned with gullies. Outside the main potential core near the center of each profile there are peaks in axial velocity at about y/D = ±0.6 which

decay rapidly, disappearing into the shear layer about three diameters downstream from the nozzle exit. Interestingly, there are also local peaks in velocity at these same locations for the gully-aligned measurements. This may be due in part to entrainment of the flow downstream from a gully by adjacent flow issuing from lobes and may also be due to vortical flow from the lobes dumping axial momentum into the dead space downstream from a gully. This same observation is also made of the SUN nozzle.

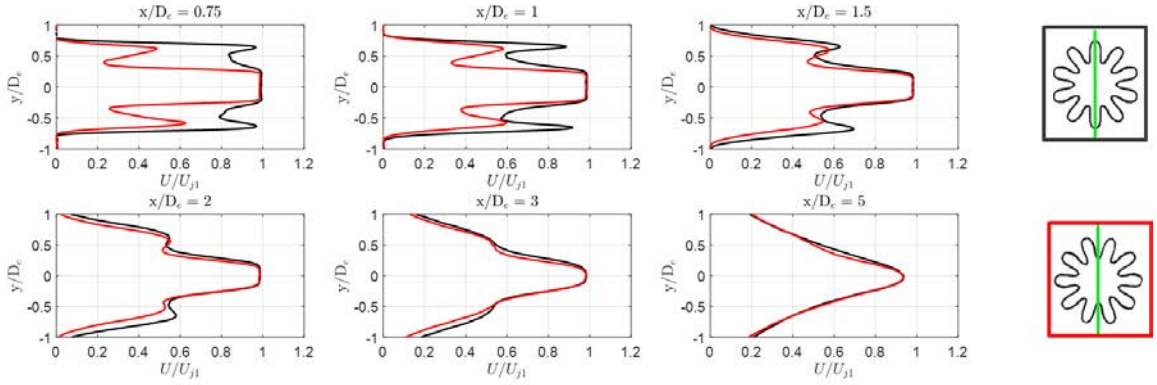


Figure 60. Profiles of mean axial velocity at various x/D. GAC23-DAISY configuration. Lobe aligned measurements shown in black and gully aligned measurements shown in red, D = 1.54 in., *PR* = 1.39 (M_j = 0.70), unheated, N = 750 image pairs.

Stereoscopic PIV measurements acquired as part of a separate research effort at GTRI capture this effect more clearly. The visualizations below are of flow from the SUN and DAISY nozzles captured in a plane perpendicular to the jet axis at an axial distance of x/D = 0.9. Note that the inclusion of these visualizations in the present context is mainly for illustrative purposes. There will be no quantitative treatment of these data in the present work. The key takeaway is the existence of 10 small jets – one for each lobe - which pinch off from the central flow. Knowledge of these features of the lobed nozzles is critical in discussion of their effects on jet noise and acoustic source distribution.

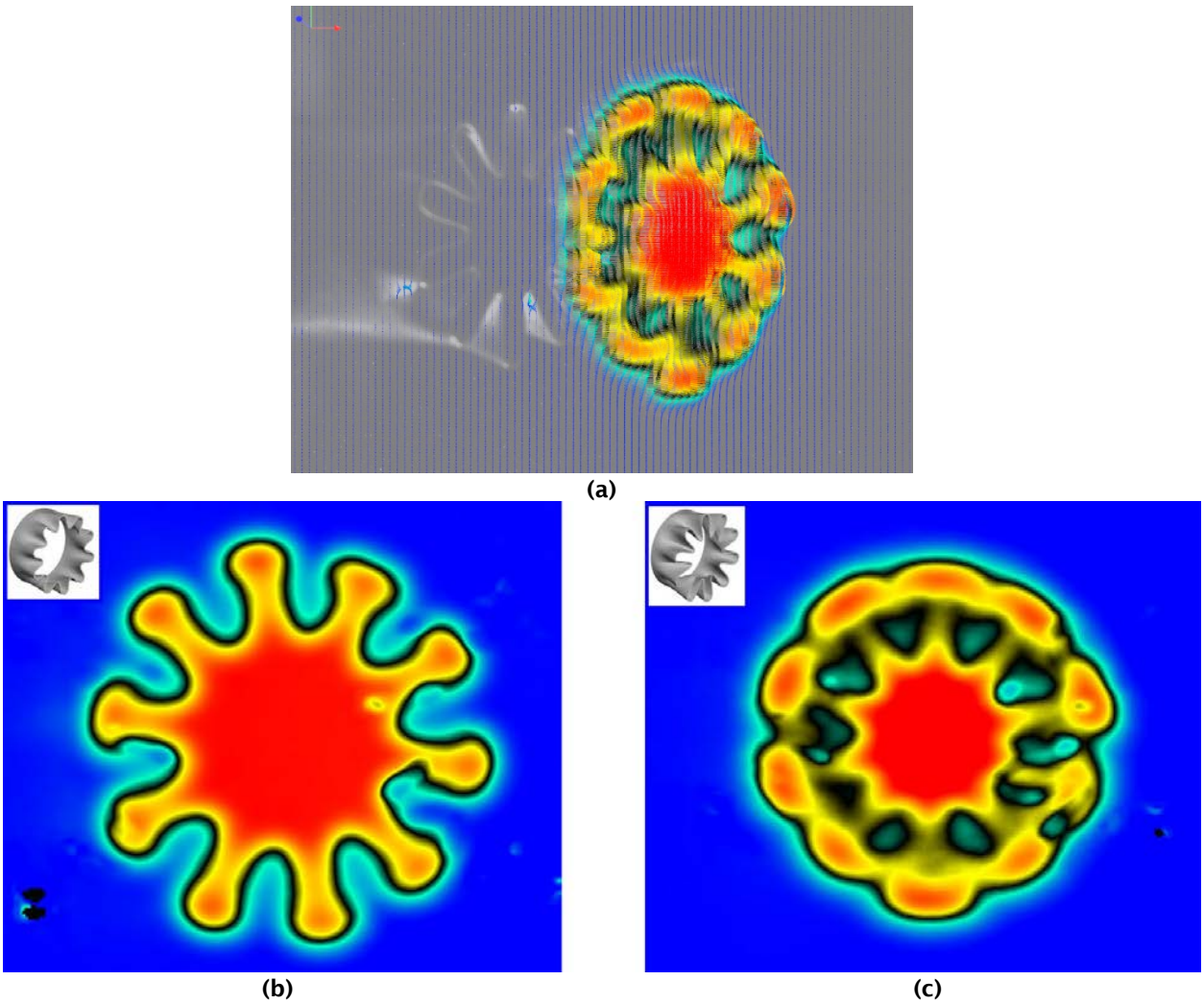


Figure 61. Example stereo-PIV visualizations showing the existence of jets from the lobes pinching off from the central flow, (a) image from one camera showing flow in relation to nozzle location, (b) flow from SUN nozzle and (c) flow from DAISY nozzle. M_j = 0.60, unheated. N = 750 image pairs.

Source Location Measurements

Source location data for each of the primary nozzle caps (AXI, SUN, and DAISY) were acquired without use of the secondary nozzle. For each primary nozzle, the jet was operated at a variety of unheated conditions with ideally-expanded jet Mach numbers (M_j) ranging from 0.5 to 1.0. The noise source distribution data from the AXI nozzle collapse based on a Strouhal number *St* formed using the exit diameter *D* (approximately 1.54 in.) and the fully-expanded jet velocity U_j as shown in Figure 62. Note that all source location data shown depict the locations of the peak noise source – as opposed to the centroid – for a given frequency. These data follow the typical pattern of a round nozzle and fit the empirical curve for the source distribution of a round jet found in jet noise literature (Breen & Ahuja, 2019).

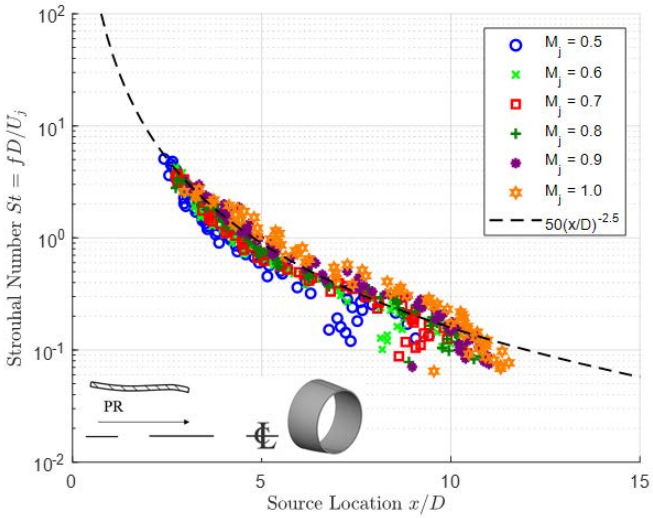


Figure 62. Source location of subsonic jet from AXI baseline nozzle. D = 1.54 in. Various M_j, unheated, one-twelfth octave band data.

The above experiment was then repeated using both lobed mixer nozzle designs, the results of which are shown in the Figures 63 and 64. It is observed that the rapid mixing region near the exit of the nozzle noted in the previous section produces a group of high-frequency noise sources, with the downstream portion (x/D from 7-15) of the noise source distribution loosely resembling that of an unmixed circular jet as shown above in Figure 62. As the jet Mach number is increased, these high-frequency sources seem to drift noticeably further downstream. These higher-frequency sources may in part be explained by the existence of the pinched jets found downstream of each lobe mentioned previously. These smaller jets would produce noise at much higher frequencies and terminate very rapidly which could explain the tight cluster of high-frequency noise sources seen in Figures 63 and 64.

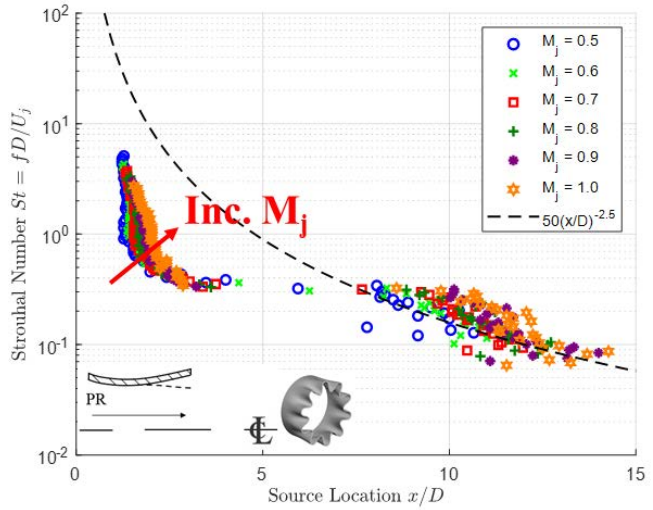


Figure 63. Source location of subsonic jet from SUN mixer nozzle. D = 1.54 in. Various M_j, unheated, one-twelfth octave.

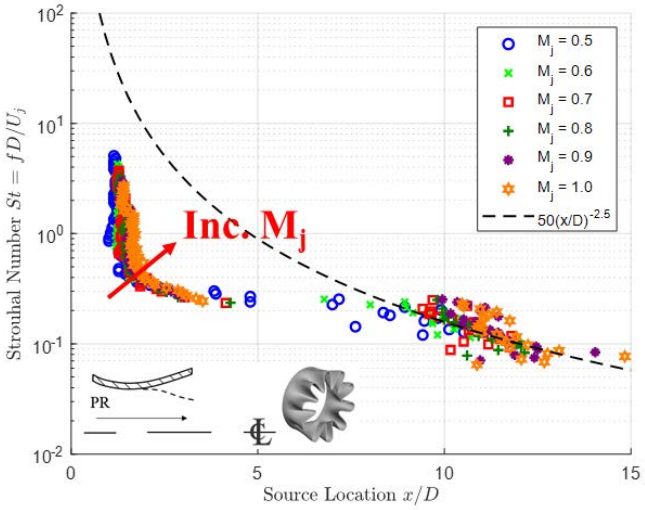


Figure 64. Source location of subsonic jet from DAISY mixer nozzle. D = 1.54 in. Various M_j, unheated, one-twelfth octave.

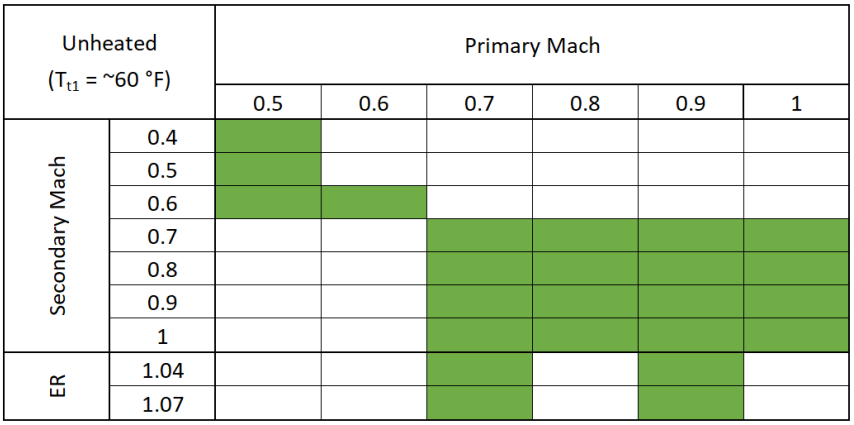
Now we can return to explain the double hump in Figure 56. Previous studies into jet noise reduction through mixing enhancement would suggest that fine-scale turbulent mixing is the dominant source of noise from a lobed jet, and that the noise produced by coherent large-scale structures is almost entirely suppressed. We have shown for the first time that for a forced lobed mixer nozzle this is not the case, and that there exists a second source of highly coherent, high-frequency noise not attributable to uncorrelated fine-scale turbulent mixing. Figure 56 shows the estimated coherent noise portions of the jet noise spectrum measured from a Mach 0.70 jet obtained through implementation of the three-microphone method for the round AXI and lobed SUN nozzles. Close to the jet axis the contribution to farfield noise from the coherent portion is substantial. Interestingly, we are able to recover two pronounced peaks in the coherent portion of jet noise measured from both lobed mixer nozzles. As evidenced by the dashed curves, the shape of this coherent noise spectrum may be precisely fit to the sum of two *F* spectra. These large-scale similarity spectra are each prescribed a peak amplitude *A* and frequency *f* such that their sum *F_1 + F_2* (obtained via dB addition) fits the estimated coherent noise portion via the method of least squares. To the authors' knowledge, this phenomenon has never been observed in existing jet noise literature and serves as the first concrete explanation for the increase in high-frequency jet noise produced by lobed jets.

Dual Stream Measurements

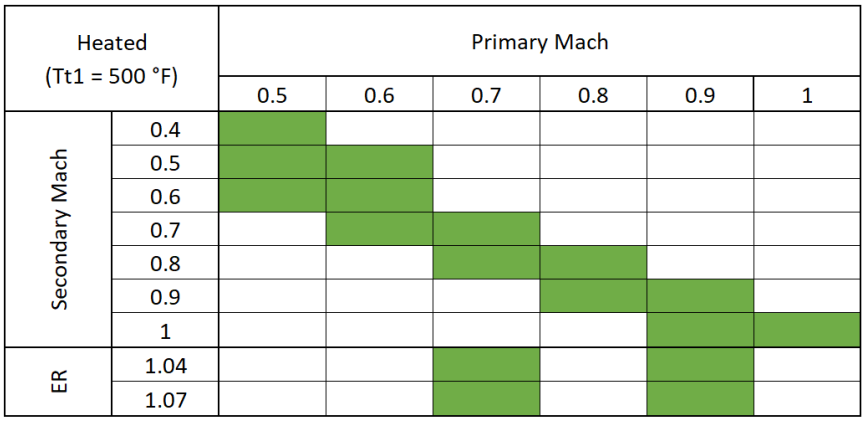
With the discussion of single stream measurements complete, the focus now changes to the discussion of results obtained using the Gulfstream models in dual stream configurations. All results presented from this point on involve the use of the secondary nozzle with bypass flow present. Testing was done with each of the three core nozzles and with two mixing-duct lengths: L_e/D_e = 1.0 and L_e/D_e = 3.0. It is again noted that while two exhaust nozzles were obtained from GAC – one with length L_e/D_e = 0.7 and one with length L_e/D_e = 1.0 – only the L_e/D_e = 1.0 nozzle with the less rapid convergent geometry was used.

Acoustic Measurements

Effect of lobed mixers: The conditions matrix for which dual stream measurements were taken with unheated and heated core flows are shown in Figures 65a and 65b, respectively.



(a)



(b)

Figure 65. Conditions matrices for (a) unheated and (b) heated core operating conditions. Green indicates an operating condition at which data was acquired.

The use of the forced mixers in conditions with an unheated primary stream fails to produce an appreciable reduction in jet noise, if any. Without a significant velocity and/or temperature difference between the core and bypass streams there is little-to-no internal mixing to take place that would reduce external jet noise. The spectra in Figure 66 show the jet noise measured at the ϑ = 90° sideline polar observation angle at the PR_1 = 1.39 (M_{j1} = 0.70), ER = 1.00, unheated operating condition. Similar to as was done previously, the jet noise spectrum corresponding to the dual stream configuration utilizing the axisymmetric core nozzle is shown as a black curve, while data taken using the SUN and DAISY nozzles are shown as blue and red curves respectively. The callout in the bottom left of the figure is meant to emphasize that the jet noise spectra shown are of a dual-stream, internally-mixed jet.

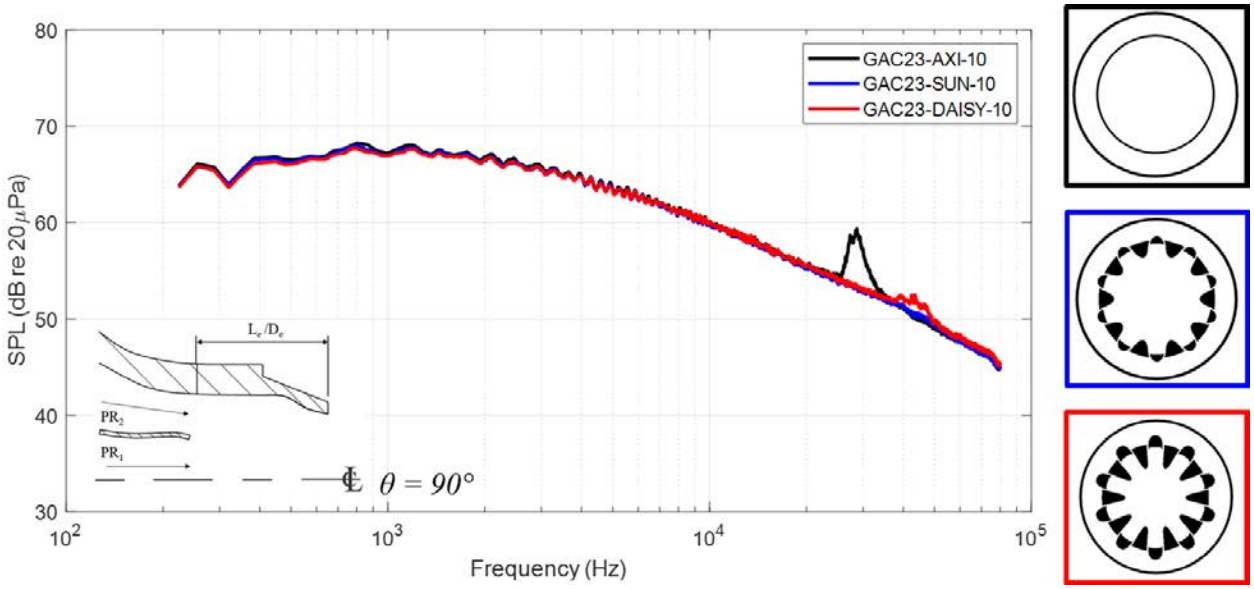
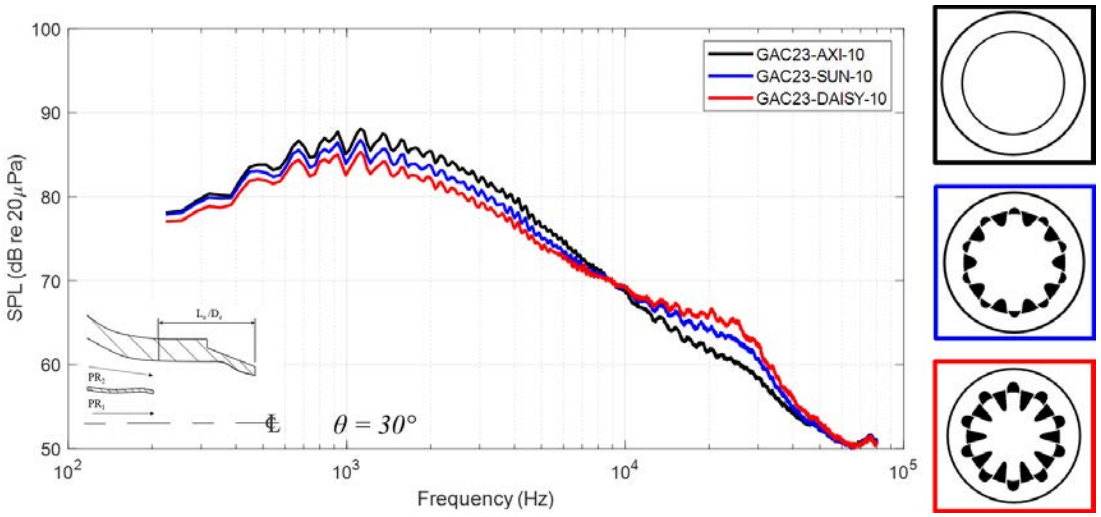


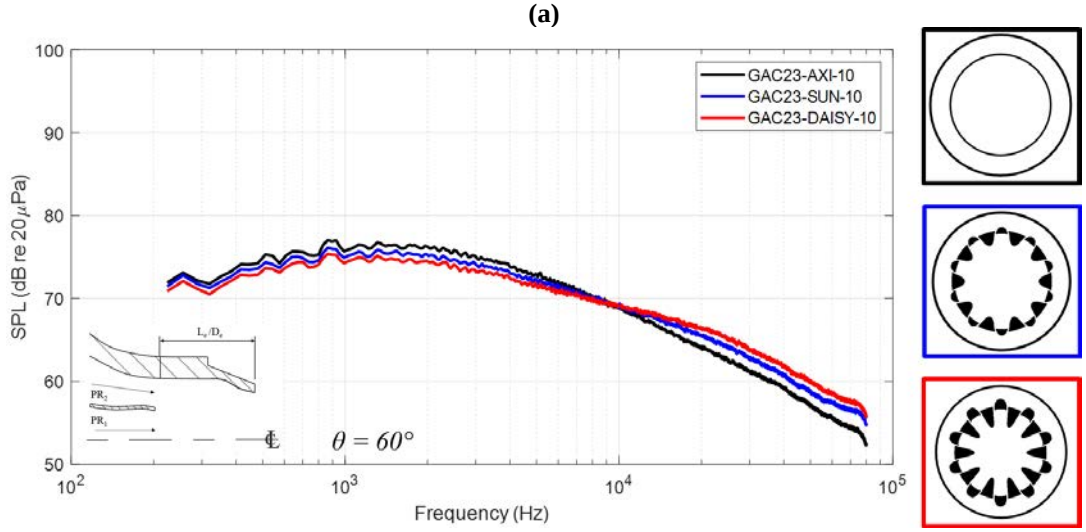
Figure 66. Noise generated from dual-stream, unheated jet from GAC project model at θ = 90° sideline polar observation angle. L_e/D_e = 1.0, PR_1 = 1.39, ER = 1.00, T_{t1} = 60°F, R = 12 ft, Δf = 32 Hz, lossless. SPL: sound pressure level.

While there is no change in the levels of external jet noise observed here, there is one noticeable difference in the spectra shown above. The high-frequency spectral hump observed in several jet noise spectra acquired thus far is hypothesized to be the acoustic signature of vortex shedding from the core nozzle lip, a phenomenon also observed in the Year-1 academic baseline nozzles. The Strouhal number, calculated from the velocity of the core nozzle exit obtained from isentropic relations, the core nozzle trailing edge thickness, and the peak frequency, aligns closely with the *St* = 0.2 trend observed in vortex shedding literature (Ramsey et al., 2022a). The cause of this shedding in dual-stream, model-scale nozzles and its associated noise is the subject of ongoing academic study by PhD student Larisch and recent PhD graduate Ramsey. At additional industry-relevant extraction ratios just above unity (e.g., ER = 1.04, 1.07) the farfield spectra are also nearly identical across the various mixers.

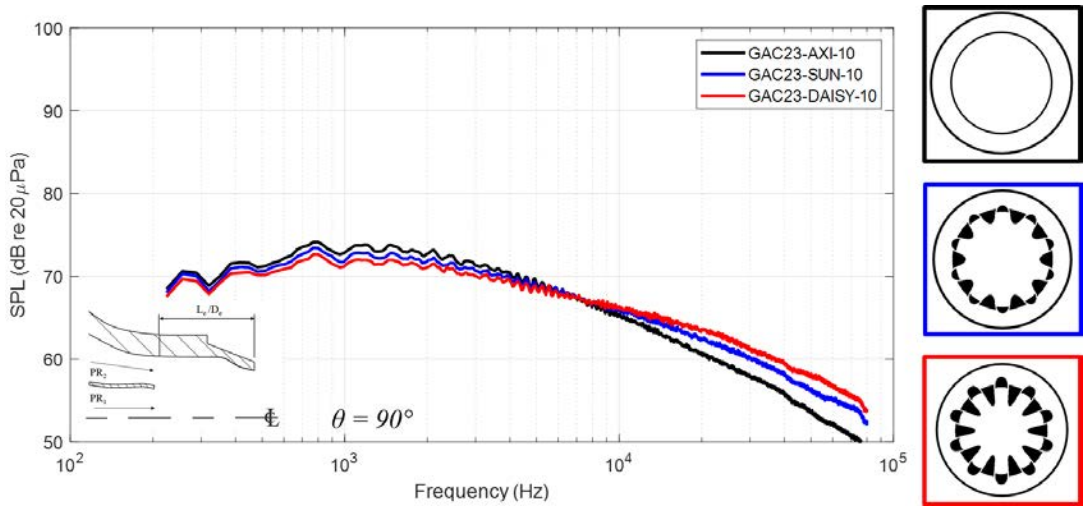
In order to observe any noticeable differences in the jet noise produced using the various nozzle caps for an unheated core stream, there must be a significant velocity difference between the two streams. The spectra in Figure 67 are taken from the most extreme unheated condition evaluated, namely, PR_1 = 1.89 (M_{j1} = 1.00), PR_2 = 1.39 (M_{j2} = 0.70), T_{t1} = ~60°F. Comparing the AXIS and SUN mixers, a decrease in peak jet noise of approximately 1.3 dB is observed at low polar angles (θ = 30°) and 0.7 dB at the sideline (θ = 90°). Likewise, comparing the AXIS and DAISY mixers yield similar results, with a decrease in peak jet noise of about 2.7 dB at low polar angles and 1.5 dB at the sideline. It is observed that the SUN mixer reduces the overall noise level by at most nearly 1.3 dB despite the increase in high-frequency noise at lower polar angles while the DAISY mixer shows a 2.2 dB reduction. The high-frequency, coherent noise sources observed in lobed jets are being investigated as part of PhD student Larisch's thesis to contribute to the understanding of noise suppression using forced mixers. As the observation angle shifts upstream, the noted decreases in peak jet noise are overtaken by the heightened levels of high-frequency noise due to enhanced mixing levels.


GAC23-AXI-10
GAC23-SUN-10
GAC23-DAISY-10
SPL (dB re 20 μPa)
Frequency (Hz)
θ = 30°

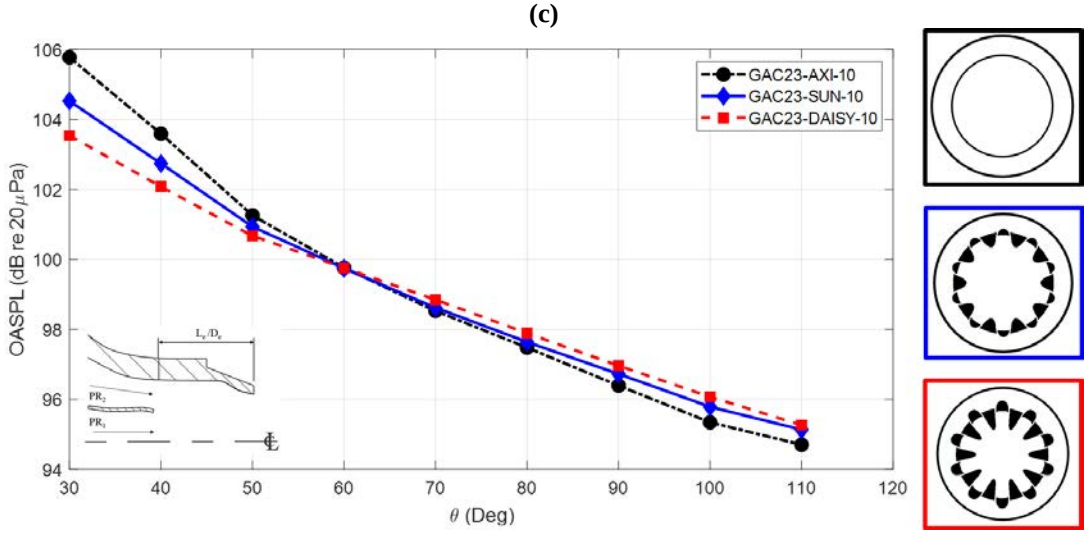
(a)


GAC23-AXI-10
GAC23-SUN-10
GAC23-DAISY-10
SPL (dB re 20 μPa)
Frequency (Hz)
θ = 60°

(b)



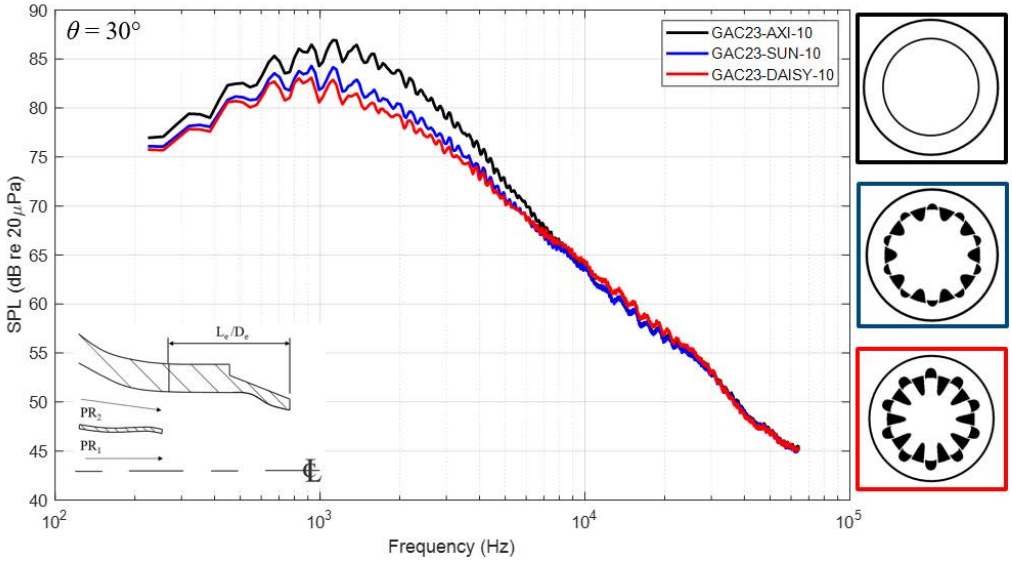
(c)



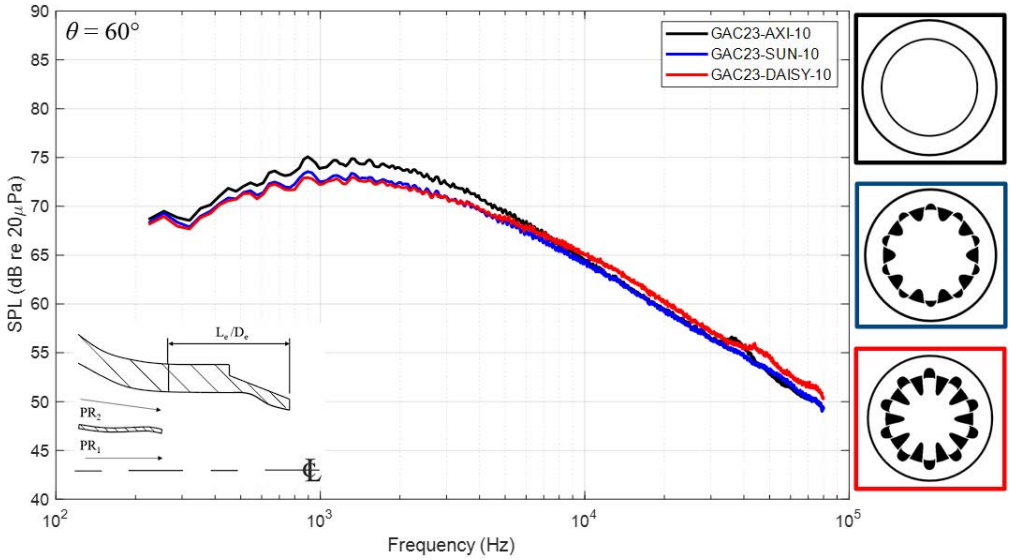
(d)

Figure 67. Noise generated from dual-stream, unheated jet from GAC project model at θ = (a) 30°, (b) 60°, and (c) 90° polar observation angles and (d) overall sound pressure level (OASPL). L_e/D_e = 1.0, PR_1 = 1.89, PR_2 = 1.39, T_{t1} = 60°F, R = 12 ft, Δf = 32 Hz, lossless. SPL: sound pressure level.

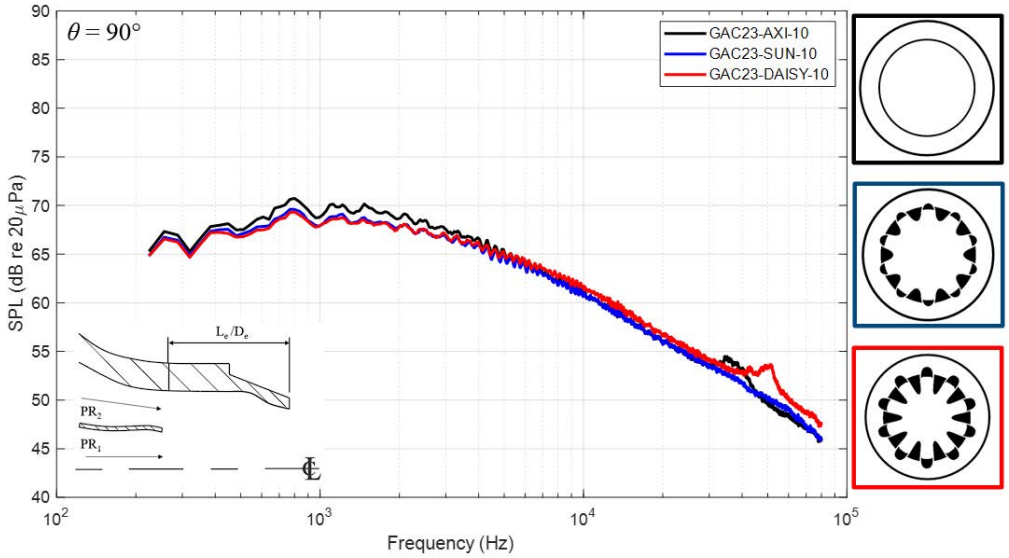
Shown in the figures below are representative jet noise spectra showing the effects of each of the lobed mixers on the noise from an internally mixed, dual-stream jet with a heated core stream. A consistent mixing-duct length of L_e/D_e = 1.0 is used to compare the jet noise of mixer nozzles with that of the axisymmetric nozzle. At the aft-most observation angle – the spectra for which are shown in Figure 68a - where the lobed mixers have the most impact, the SUN mixer reduces the level of jet noise at the peak frequency by approximately 2.6 dB relative to the baseline AXI for the condition shown (PR_1 = PR_2 = 1.39, M_{j1} = M_{j2} = 0.70). The more intense DAISY lobed mixer has deeper lobes and gullies and reduces the peak SPL by 3.7 dB. The sideline observation spectra shown in Figure 68c reveals a decrease in peak SPL of about 1.2 dB for each of the lobed mixers. A frequent characteristic of mixing-enhancement devices for dual-stream jets is a decrease in peak SPL at the cost of an increase in high-frequency noise. While the DAISY mixer performs better at decreasing jet noise at the peak frequency – especially at aft polar observation angles – there is a noticeable increase in high-frequency noise beyond about 8 kHz or so. However, the SUN mixer which provides similar noise reduction benefits at higher polar angles does not produce an increase in high-frequency jet noise relative to the axisymmetric baseline primary nozzle.


θ = 30°
GAC23-AXI-10
GAC23-SUN-10
GAC23-DAISY-10
SPL (dB re 20 μPa)
Frequency (Hz)
L_e/D_e
PR_2
PR_1

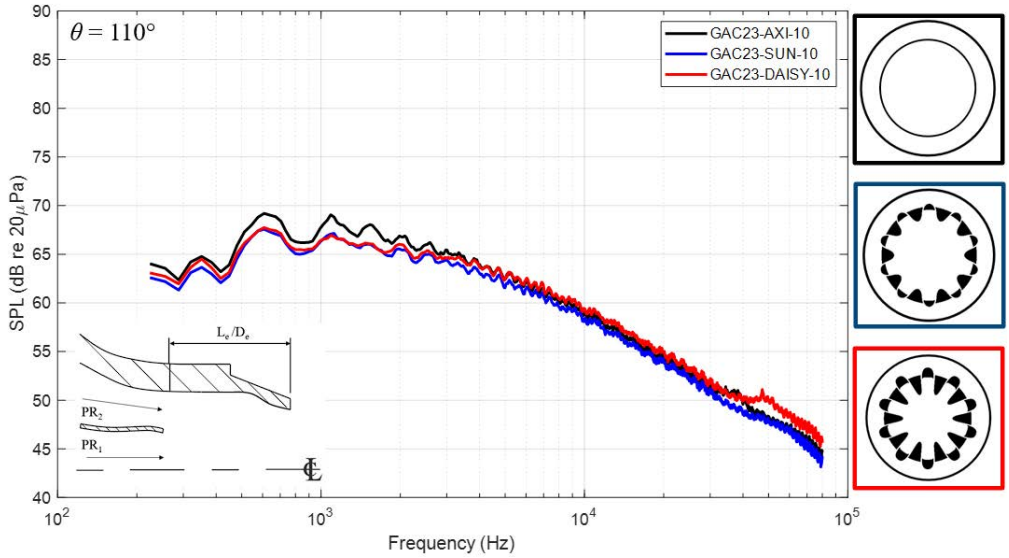
(a)


θ = 60°
GAC23-AXI-10
GAC23-SUN-10
GAC23-DAISY-10
SPL (dB re 20 μPa)
Frequency (Hz)
L_e/D_e
PR_2
PR_1

(b)



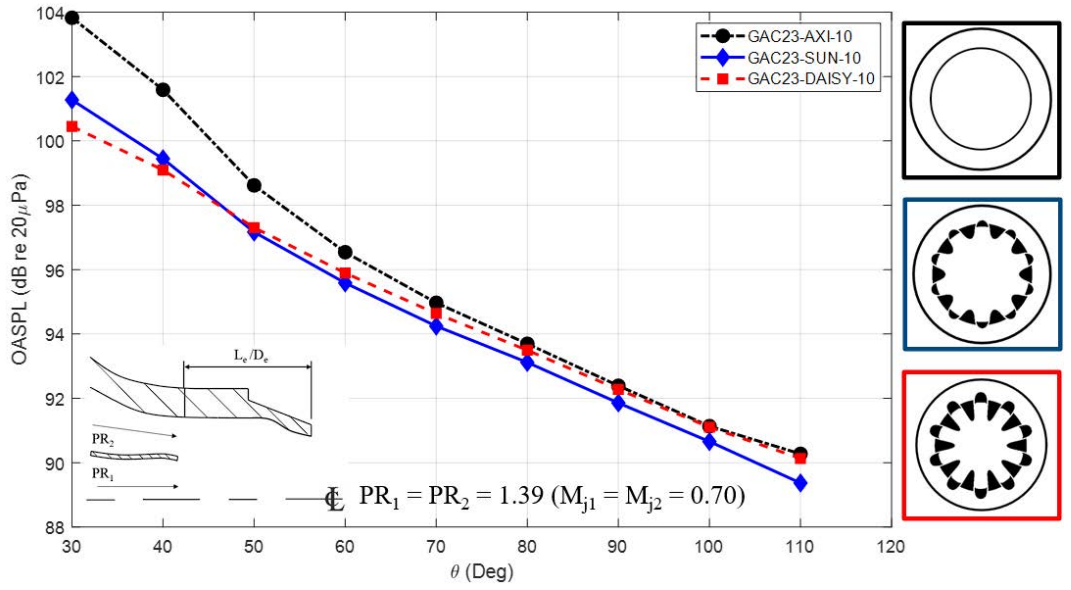
(c)



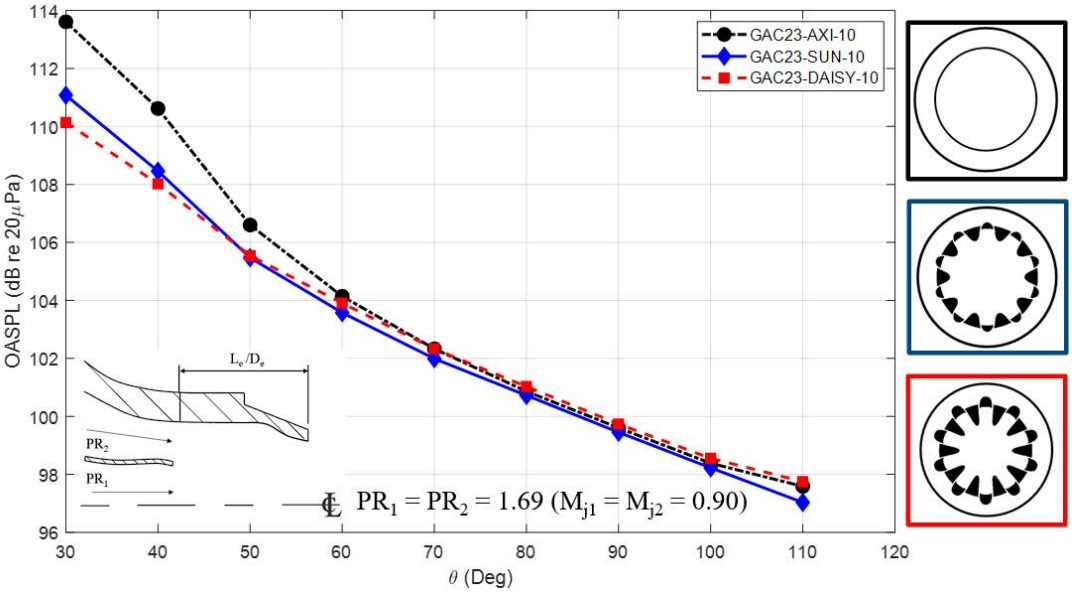
(d)

Figure 68. Effect of lobed nozzle on the noise from an internally mixed, dual-stream jet. FAA GAC Project Model, D_e = 2.20 in. L_e/D_e = 1.0, PR_1 = 1.39 (M_{j1} = 0.70), PR_2 = 1.39 (M_{j2} = 0.70), T_{t1} = 500°F, R = 12 ft, θ = a) 30°, b) 60°, c) 90°, d) 110°, Δf = 32 Hz, lossless. SPL: sound pressure level.

Overall noise level measurements (Figure 69) show the enhanced effect of the DAISY mixer at lower polar angles compared to the less-aggressive SUN mixer. For the lower pressure-ratio case shown in Figure 69a both mixers reduce or equate the overall noise level across all polar observation angles relative to the AXI baseline. At higher pressure-ratios (e.g., Figure 69b) it is observed that the SUN mixer maintains a decrease in overall noise everywhere but the excess high-frequency noise produced by the DAISY mixer leads to a slight increase in overall noise at sideline and upstream polar angles.



(a)

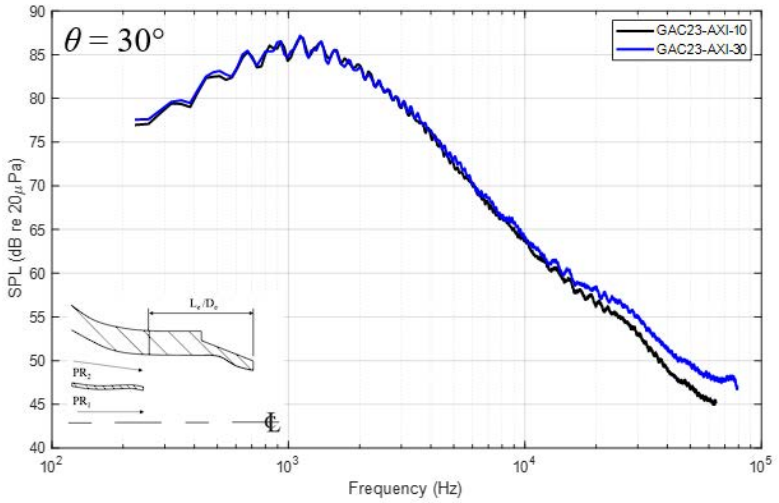


(b)

Figure 69. Effect of lobed nozzle on the overall noise from an internally mixed, dual-stream jet. FAA GAC Project Model, D_e = 2.20 in. L_e/D_e = 1.0, a) PR_1 = 1.39 (M_{j1} = 0.70), PR_2 = 1.39 (M_{j2} = 0.70) and b) PR_1 = 1.69 (M_{j1} = 0.90), PR_2 = 1.69 (M_{j2} = 0.90), T_{t1} = 500°F, R = 12 ft, Δf = 32 Hz, lossless. OASPL: overall sound pressure level.

Effect of increasing the mixing-duct length: The data shown above was restricted to L_e/D_e = 1.0. the effect of increasing the mixing duct length will now be discussed. Also, as there is little to no effect by the mixer nozzles on the noise produced by the dual stream jet with an unheated core, and since the effect of mixing-duct length on jet noise for an unheated core is treated in the discussion of the results from the Year-1 academic nozzle, only heated core results are presented and discussed here. The set of figures below show the effects of increasing the mixing-duct length for PR_1 = 1.39 (M_{j1} = 0.70), PR_2 = 1.39 (M_{j2} = 0.70), T_{t1} = 500°F condition. This, thus, refers to an extraction ratio of unity. The primary nozzle and polar

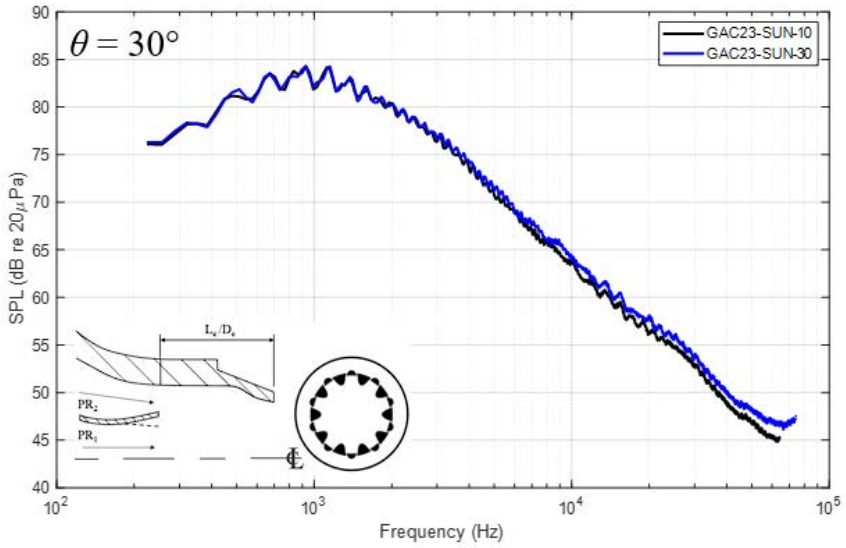
observation angle associated with each of the spectra are shown in the bottom left for reference. The black curves are representative of jet noise spectra taken from use of the shorter L_e/D_e = 1.0 mixing-duct length while the blue curves correspond to use of the longer, L_e/D_e = 3.0 mixing-duct length. Figure 70 shows a slight increase in noise at higher frequencies when using the AXI which is possibly representative of increased internal mixing. However, Figure 71 and Figure 72 show that this increase is not present when using the forced mixers SUN and DAISY. Previously it was observed that use of the SUN mixer nozzle reduced the overall noise level across all polar observation angles relative to the AXI baseline nozzle while the DAISY mixer produced approximately equal levels of overall noise at sideline and upstream polar angles due to the excess high-frequency noise resulting from enhanced mixing. However, through use of the longer mixing-duct length, both forced mixers decrease overall noise at all polar observation angles relative to the baseline core nozzle, an example of which is included below in Figure 73.



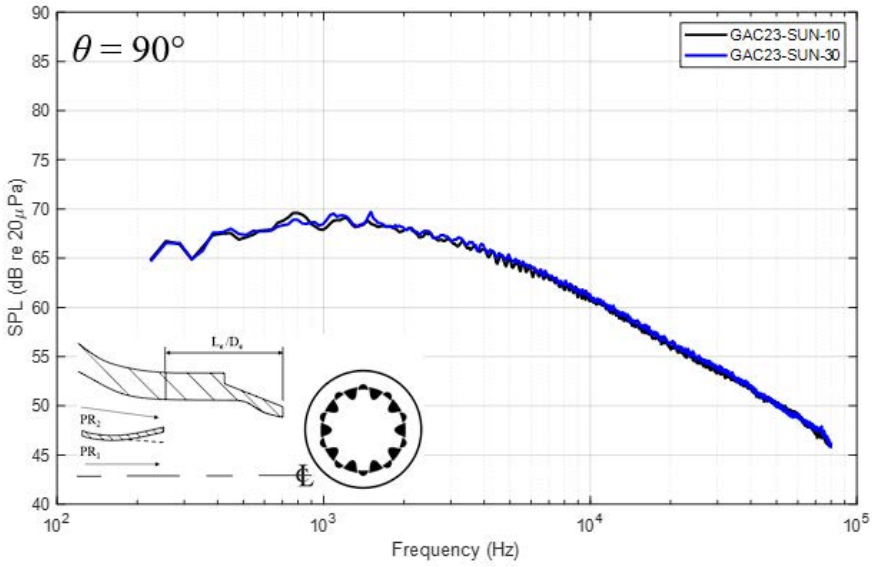
(a)

(b)

Figure 70. Effect of mixing-duct length on noise from an internally mixed, dual-stream jet with AXI mixer. FAA GAC Project Model, D_e = 2.20 in. PR_1 = 1.39 (M_{j1} = 0.70), PR_2 = 1.39 (M_{j2} = 0.70), T_{t1} = 500°F, R = 12 ft, θ = a) 30° and b) 90°, Δf = 32 Hz, lossless. SPL: sound pressure level.

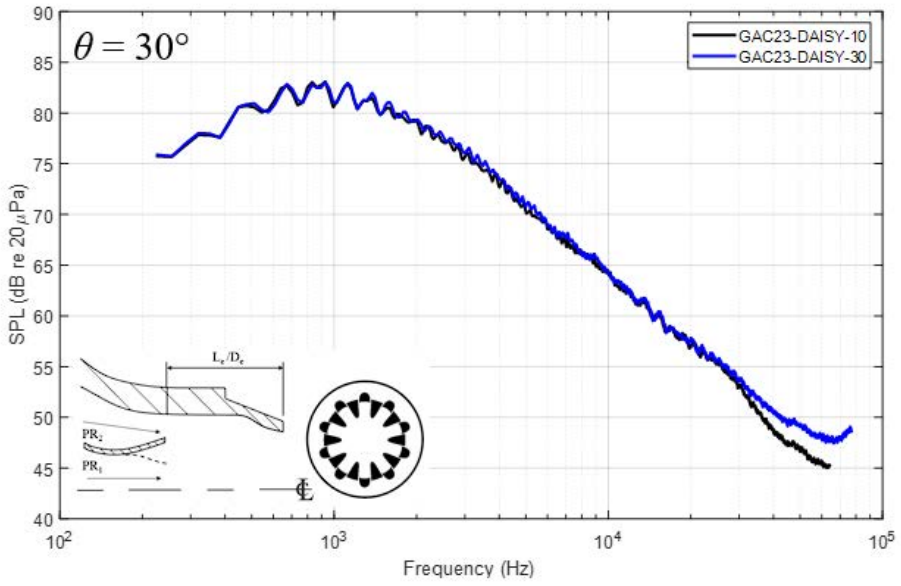


(a)

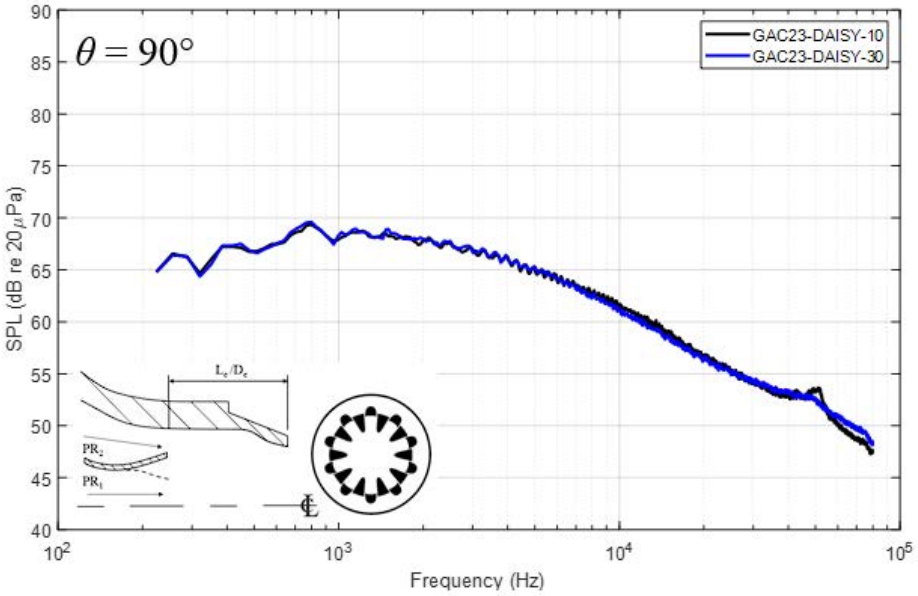


(b)

Figure 71. Effect of mixing-duct length on noise from an internally mixed, dual-stream jet with SUN mixer. FAA GAC Project Model, D_e = 2.20 in. PR_1 = 1.39 (M_{j1} = 0.70), PR_2 = 1.39 (M_{j2} = 0.70), T_{t1} = 500°F, R = 12 ft, θ = a) 30° and b) 90°, Δf = 32 Hz, lossless. SPL: sound pressure level.



(a)



(b)

Figure 72. Effect of mixing-duct length on noise from an internally mixed, dual-stream jet with DAISY mixer. FAA GAC Project Model, D_e = 2.20 in. PR_1 = 1.39 (M_{j1} = 0.70), PR_2 = 1.39 (M_{j2} = 0.70), T_{t1} = 500°F, R = 12 ft, θ = a) 30° and b) 90°, Δf = 32 Hz, lossless. SPL: sound pressure level.

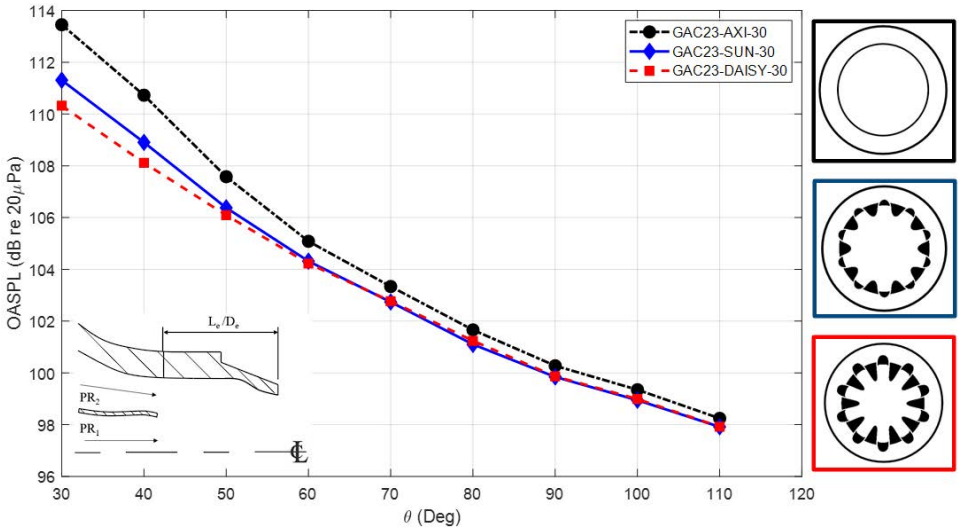


Figure 73. Effect of mixer nozzle on overall noise from an internally mixed, dual-stream jet. FAA GAC Project Model, D_e = 2.20 in. PR_1 = 1.69 (M_{j1} = 0.90), PR_2 = 1.69 (M_{j2} = 0.90), T_{t1} = 500°F, R = 12 ft, Δf = 32 Hz, lossless. SPL: sound pressure level.

PIV Measurements

Due to the intensely time-consuming process that goes into acquiring quality PIV data and large number of nozzle configurations, only a limited batch of dual stream PIV data were acquired with the most important conditions prioritized. High-resolution (i.e., N = 750 samples in order to properly resolve turbulence statistics) PIV measurements were taken for the GAC23-AXI-10 and GAC23-DAISY-10 configurations at each of the following operating conditions with both unheated and heated (T_{t1} = 500°F) core streams:

- PR_1 = 1.39 (M_{j1} = 0.70), PR_2 = 1.39 (M_{j2} = 0.70)
- PR_1 = 1.39 (M_{j1} = 0.70), ER = 1.07
- PR_1 = 1.69 (M_{j1} = 0.90), PR_2 = 1.69 (M_{j2} = 0.90)
- PR_1 = 1.69 (M_{j1} = 0.70), ER = 1.07

PIV data at some of these conditions has been collected for the GAC23-SUN-10 configuration. This data will continue to be taken independently in service of PhD student Larisch's individual research and may be revisited and supplied to modelers at a later date. Again, as there is little-to-no internal mixing was observed for an unheated core stream, only the results for the heated core stream will be presented and discussed. Shown below are various results taken from PIV measurements made of the GAC23-AXI-10 configuration at the PR_1 = 1.69 (M_{j1} = 0.90), PR_2 = 1.69 (M_{j2} = 0.90), T_{t1} = 500°F operating condition. Figure 74 shows the familiar 2D plots of mean axial velocity, axial turbulence intensity, and radial turbulence intensity. Note the much more visible bypass stream visible in the mean axial velocity plot as compared to the previous Year-1 academic nozzle (see Figure 27). One key difference between the Gulfstream models and the previous models is the heightened bypass ratio. This makes visualizations of the bypass stream in comparison to the core stream much easier, especially in schlieren visualizations which will be reviewed in the coming sections. Figure 75 shows profiles of axial velocity and turbulence intensities at various axial locations downstream from the final nozzle exit. Figure 76 shows centerline velocity and turbulence intensity distributions. These results are quite similar to those obtained for the Year-1 nozzle shown in Figure 28 and Figure 29.

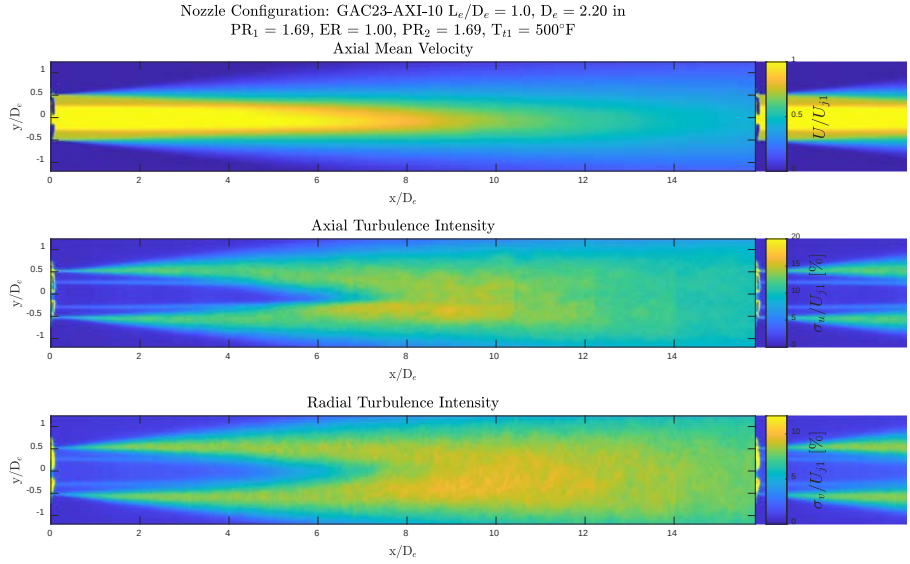
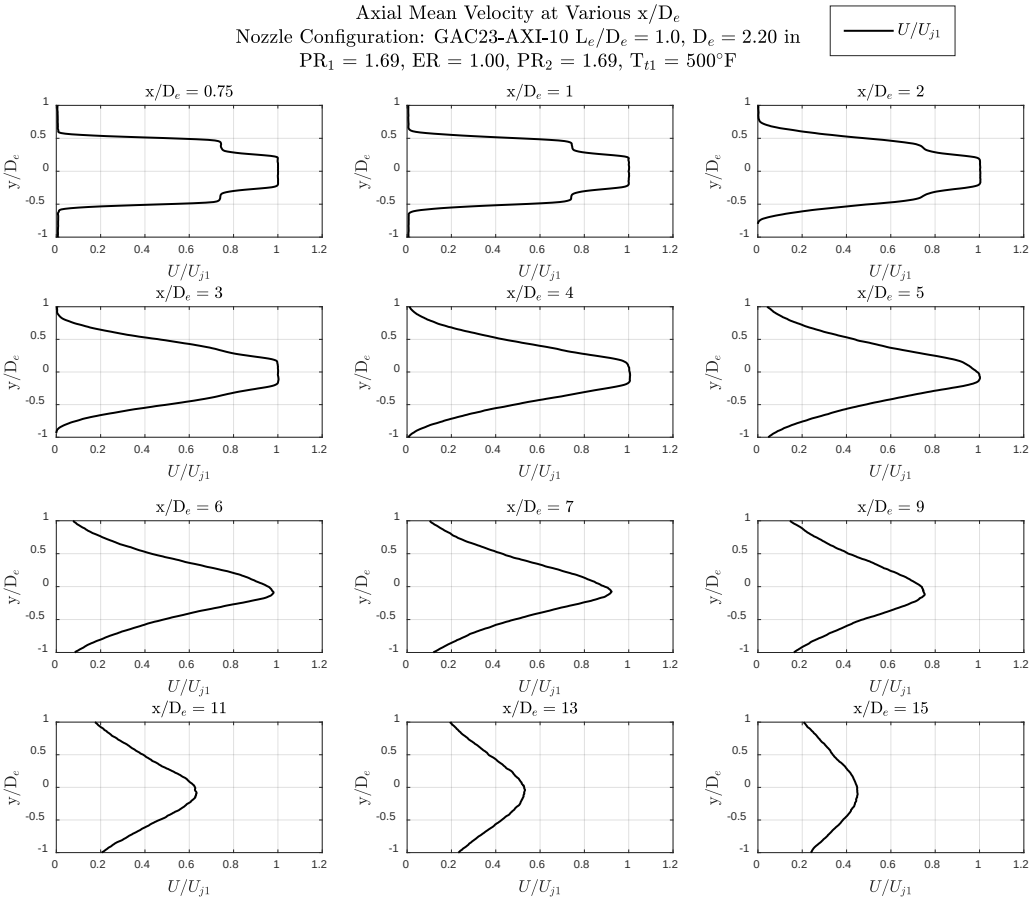
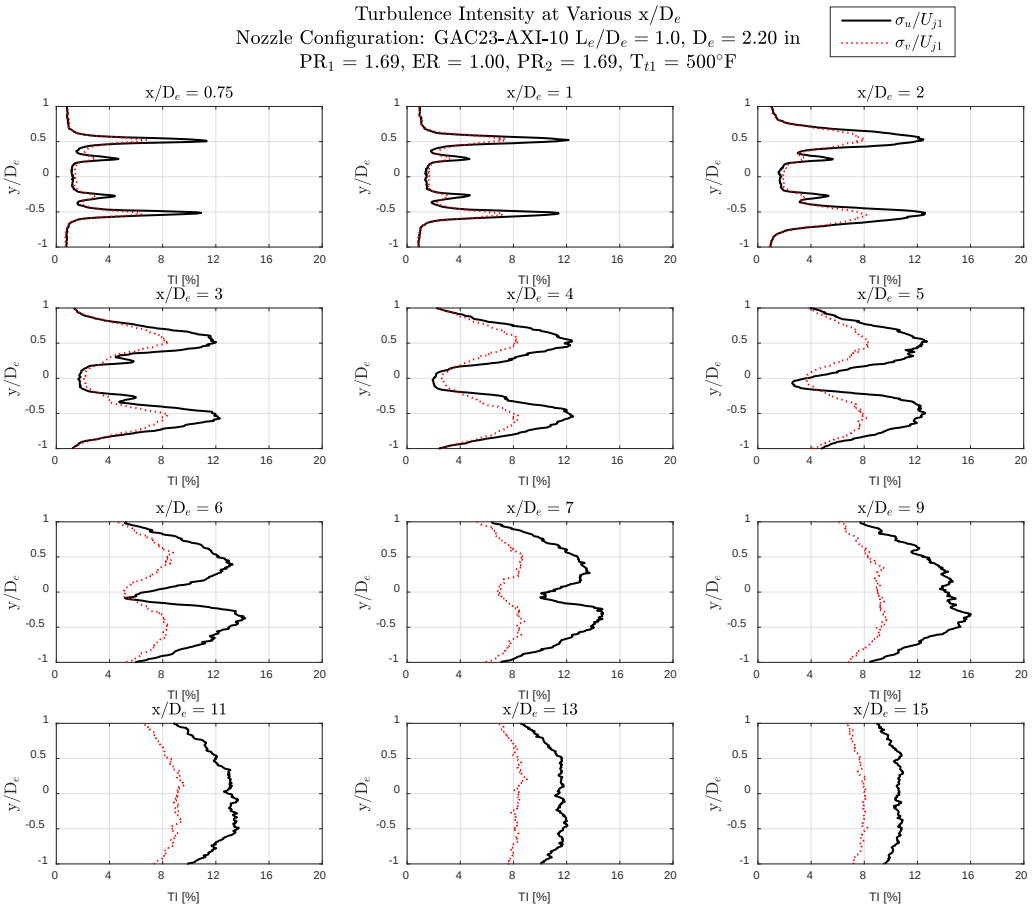


Figure 74. Two-dimensional mean and turbulence intensity plots. GAC23-AXI-10 configuration. PR_1 = 1.69, PR_2 = 1.69, T_{t1} = 500°F, L_e/D_e = 1.0, N = 750 image pairs.

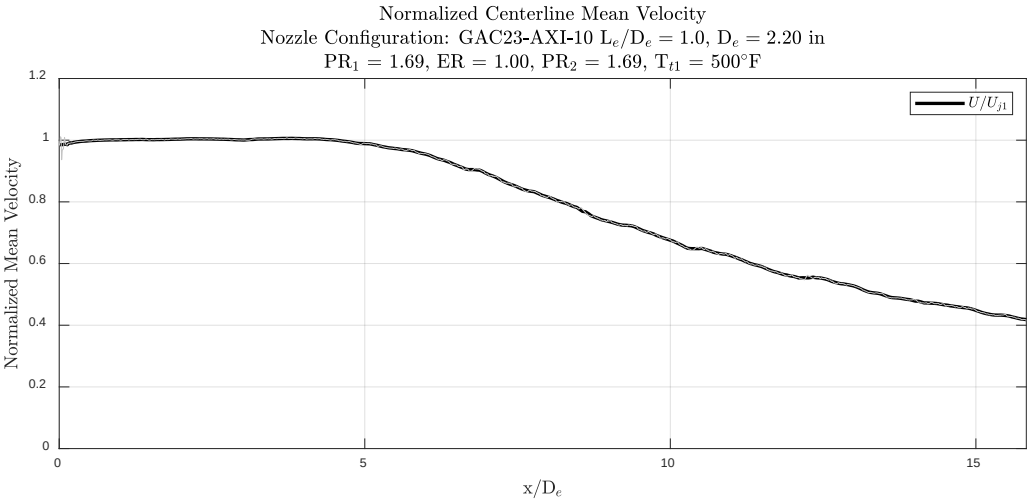

Axial Mean Velocity at Various x/D$_e$
Nozzle Configuration: GAC23-AXI-10 L$_e$/D$_e$ = 1.0, D$_e$ = 2.20 in
PR$_1$ = 1.69, ER = 1.00, PR$_2$ = 1.69, T$_{t1}$ = 500°F
U/U_{j1}
x/D$_e$ = 0.75
x/D$_e$ = 1
x/D$_e$ = 2
x/D$_e$ = 3
x/D$_e$ = 4
x/D$_e$ = 5
x/D$_e$ = 6
x/D$_e$ = 7
x/D$_e$ = 9
x/D$_e$ = 11
x/D$_e$ = 13
x/D$_e$ = 15
y/D$_e$
U/U_{j1}

(a)

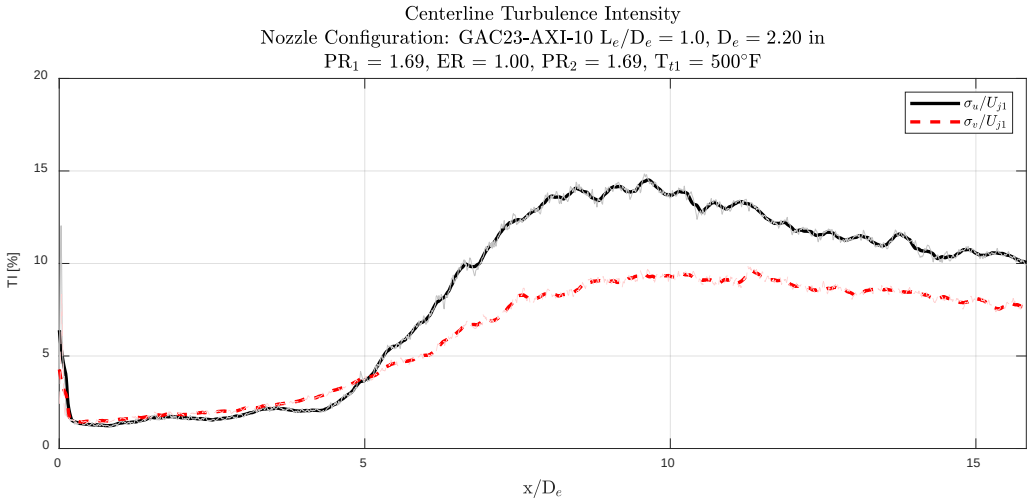


(b)

Figure 75. Profiles of (a) mean axial velocity and (b) turbulence intensities at various x/D$_e$. GAC23-AXI-10 configuration. PR_1 = 1.69, PR_2 = 1.69, T_{t1} = 500°F, L_e/D_e = 1.0, N = 750 image pairs.



(a)



(b)

Figure 76. Plots of centerline (a) axial velocity and (b) turbulence intensities (TI). GAC23-AXI-10 configuration. PR_1 = 1.69, PR_2 = 1.69, T_{t1} = 500°F, L_e/D_e = 1.0, N = 750 image pairs.

Below in Figure 77 are 2D plots of mean axial velocity and turbulence intensities at the same operating condition PR_1 = 1.69 (M_{j1} = 0.90), PR_2 = 1.69 (M_{j2} = 0.90), T_{t1} = 500°F with the DAISY internal lobed mixer (i.e., the GAC23-DAISY-10 configuration). Although the lobed nozzle is now buried within the secondary duct, it is still important to note that the laser sheet is aligned vertically with lobes (e.g., as in Figure 58a). Because of this, one can observe bright streaks of partially-mixed core flow just downstream from the nozzle exit near y/D$_e$ = ±0.4 in the axial velocity plot. The width of the remaining core jet is visibly much smaller than that from the GAC23-AXI-10 configuration shown in Figure 74 and the potential core seems to terminate quicker. Indeed, comparing the centerline velocity distributions between the two configurations shown in Figure 78, one can see an approximate 50% reduction in potential core length compared to the axisymmetric baseline.

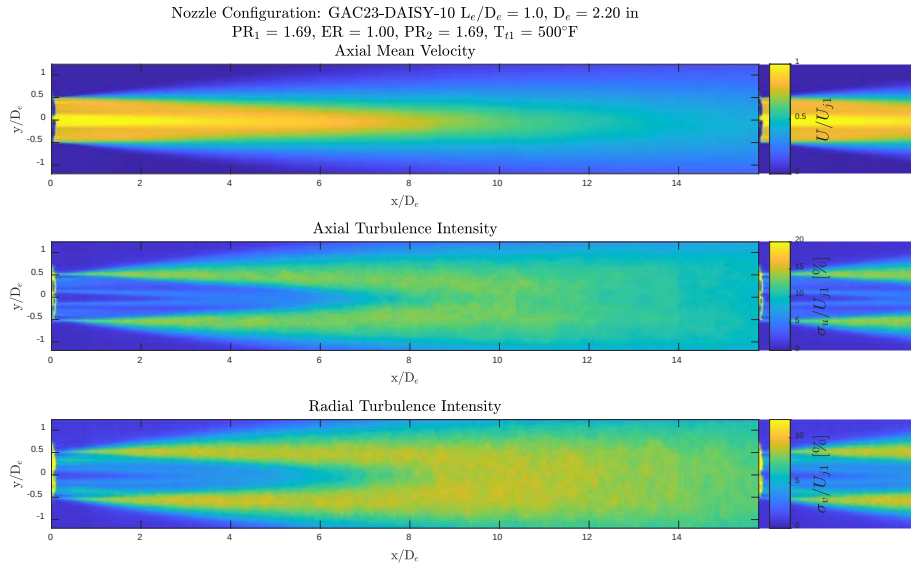


Figure 77. Two-dimensional mean and turbulence intensity plots. GAC23-AXI-10 configuration. PR_1 = 1.69, PR_2 = 1.69, T_{t1} = 500°F, L_e/D_e = 1.0, N = 750 image pairs.

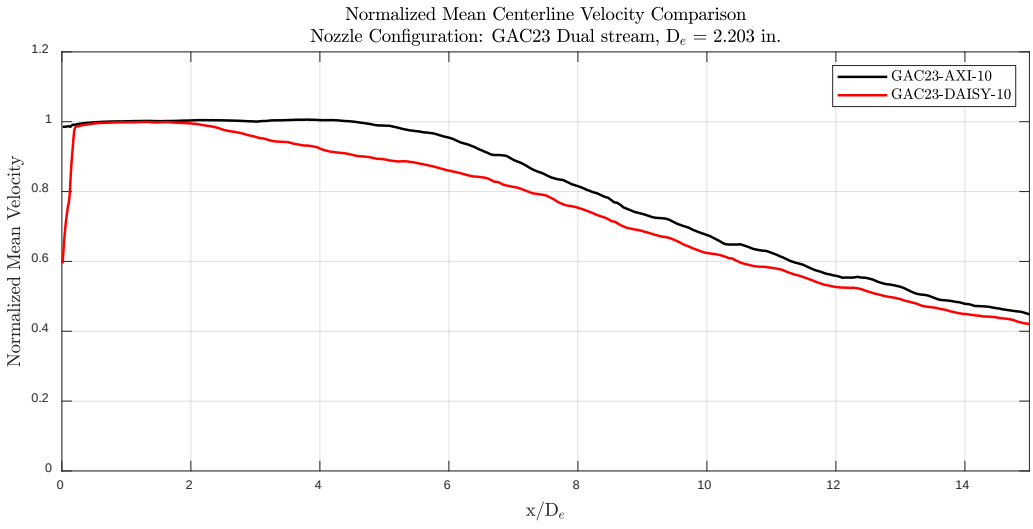


Figure 78. Comparison of centerline axial velocity distribution. GAC23-AXI-10 (black) and GAC23-DAISY-10 (red) configurations. PR_1 = 1.69, PR_2 = 1.69, T_{t1} = 500°F, L_e/D_e = 1.0, N = 750 image pairs.

To show a more direct comparison of the flowfields between the two configurations, mean velocity profiles at various axial stations for both the GAC23-AXI-10 and GAC23-DAISY-10 configurations are overlaid and shown in Figure 79.

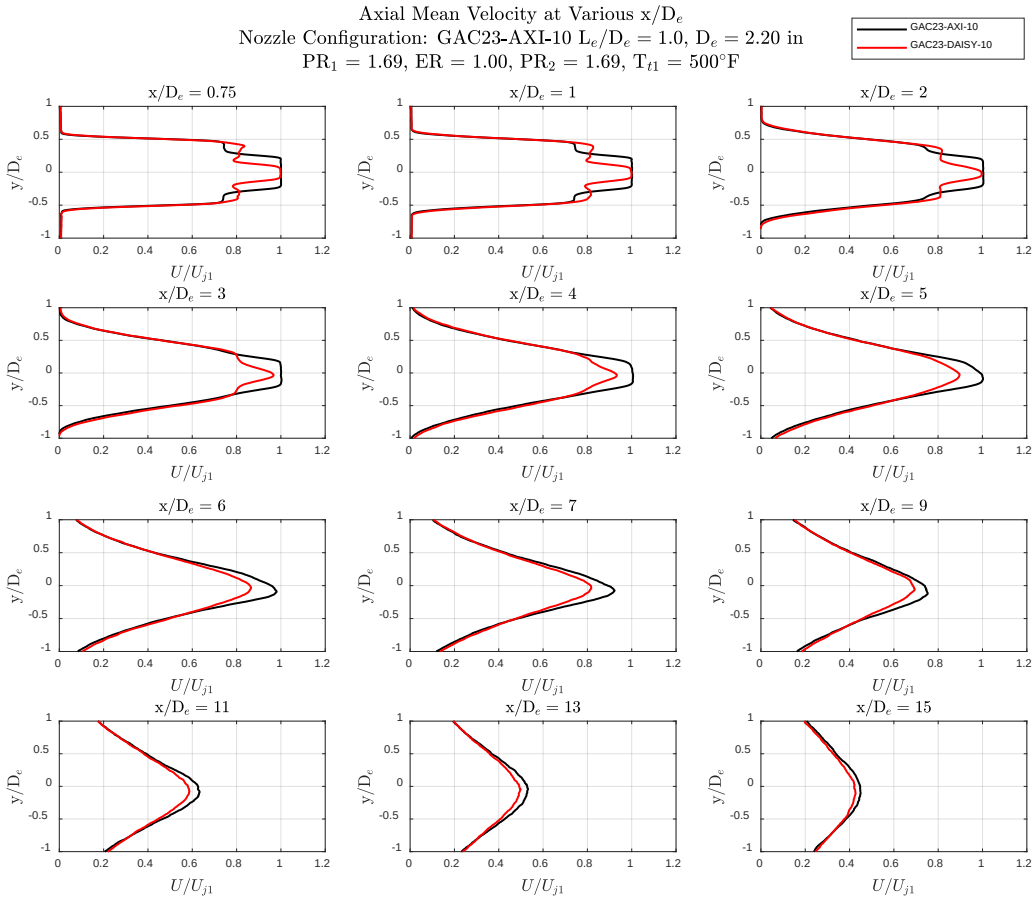


Figure 79. Profiles of mean axial velocity at various x/D_e. GAC23-AXI-10 (black) and GAC23-DAISY-10 (red) configurations. PR_1 = 1.69, PR_2 = 1.69, T_{t1} = 500°F, L_e/D_e = 1.0, N = 750 image pairs.

Schlieren Visualizations

High-speed schlieren flow visualizations were acquired simultaneously alongside acoustic source location measurements using the Z-type schlieren system in the GTRI Flow Diagnostics Facility at the set of heated core operated conditions shown in the matrix in Figure 65b. Schlieren and source location data was only acquired for heated core conditions due to the lack off effect by the lobed internal mixers on the farfield noise of the unheated jet. If it is desired, these unheated conditions could be revisited at a later date as part of extended work. All representative images shown visualize transverse density gradients in the flow ($\partial\rho/\partial y$). Time-resolved schlieren visualizations were captured at a rate of f_s = 51,000 frames per second. The qualitative results of these dynamic measurements are difficult to capture through single still images and as such sample results are included here with little discussion. Short, 200 frame videos will be made available to modeling teams with longer, 2,500-frame videos available upon request.

The set of images in Figure 80 show the effects of each primary nozzle cap (AXI, SUN, DAISY read from left to right) on the flow from a dual-stream jet operated at M_{j1} = 0.70, M_{j2} = 0.70, T_{t1} = 500°F with a common mixing-duct length of L_e/D_e = 1.0. The digits at the end of the nozzle configuration name above each image denote the mixing-duct length in tenths of L_e/D_e and are highlighted in red to assist in differentiating the figure from Figure 81 which shows the same results but for the longer mixing-duct length of L_e/D_e = 3.0. Orderly wave-like structures are still apparent in the flow downstream from the initial mixing region. These structures are somewhat visible in the right half of each image included in Figure 80, yet are much more easily discernible in the complete, time-resolved visualizations. Future experimental work may involve

attempting to reduce the presence of this instability by disrupting the boundary layers present on and inside the core nozzle – including when operating with the lobed mixers.

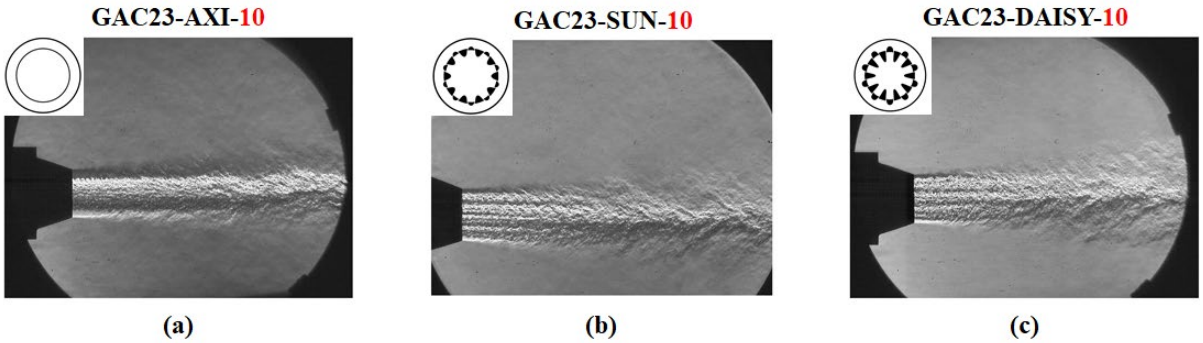


Figure 80. Instantaneous schlieren flow visualizations of dual-stream jet utilizing (a) AXI, (b) SUN, and (c) DAISY internal mixers. M_{j1} = 0.70, M_{j2} = 0.70, T_{t1} = 500°F. L_e/D_e = 1.0, D_e = 2.20 in. Sample rate f_s = 51,000 fps, 1.5 µs exposure.

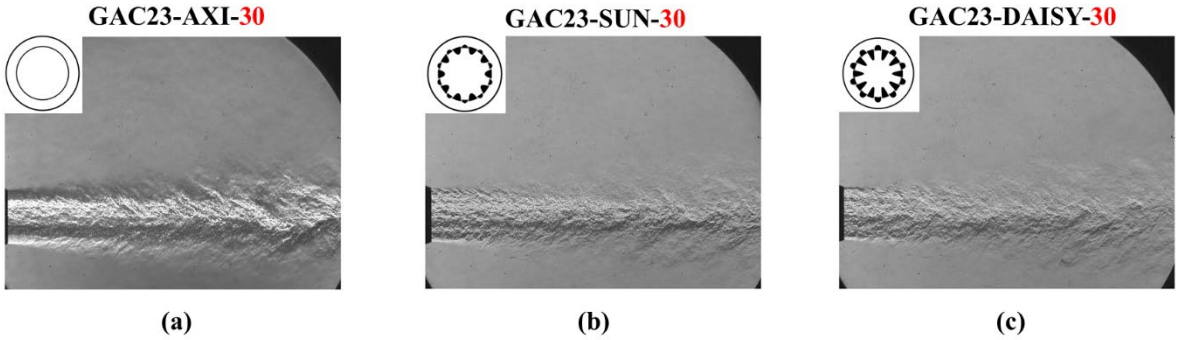


Figure 81. Instantaneous schlieren flow visualizations of dual-stream jet utilizing (a) AXI, (b) SUN, and (c) DAISY internal mixers. M_{j1} = 0.70, M_{j2} = 0.70, T_{t1} = 500°F. L_e/D_e = 3.0, D_e = 2.20 in. Sample rate f_s = 51,000 fps, 1.5 µs exposure.

Source Location Analysis

The effects of the different internal mixers on the distribution of noise sources of the dual stream are discussed first. Unless otherwise indicated, all source location data shown correspond to the location of peak noise for a given frequency; this is in contrast to that of some jet noise source location literature, which reports the centroid location of each frequency instead (Breen & Ahuja, 2020). Figure 82 and Figure 83 below show the effects of the lobed mixer nozzles on the source distribution of an internally-mixed, heated-core jet with a common mixing-duct length of L_e/D_e = 1.0 operated at an extraction ratio ER of unity. The origin of the x-axis is taken to be the exit of the final, exhaust nozzle. For reference, an empirical source distribution for a theoretically fully-mixed jet, with exit velocity U_{mix} (obtained using isentropic relations and enthalpy conservation) and diameter D_e, is provided as a dotted curve. The Strouhal number distribution for this reference curve is converted to frequency using the scale factor U_{mix}/D_e. The authors of this report decided against collapsing the measured data using a similar method as the proper characteristic length and velocity scales for these partially-mixed jets are not known. As such the source location data are displayed without normalization of the frequency axis. As observed in Figure 82 and Figure 83, there is a slight upstream shift in the distribution of higher-frequency noise sources (e.g., in Figure 82 greater than about 4 kHz) going from the axisymmetric internal mixer to each of the lobed mixers. Generally, the peak noise source distribution when using the AXI mixer (denoted in Figure 82 and Figure 83 as data markers with blue circles) is divided among two distinct regions. As the mixing of the dual-stream jet is enhanced through use of the lobed nozzles, the peak source location appears to follow a more uniform distribution. When comparing the two extremes – data taken from the AXI internal mixer in blue circles versus those of the DAISY mixer in red squares – the shape of the distribution when using the DAISY mixer approaches that of the empirical curve. The results are similar for both M_{j1} = 0.70, M_{j2} = 0.70, T_{t1} = 500°F (see Figure 82) and M_{j1} = 0.90, M_{j2} = 0.90, T_{t1} = 500°F (see Figure 83).

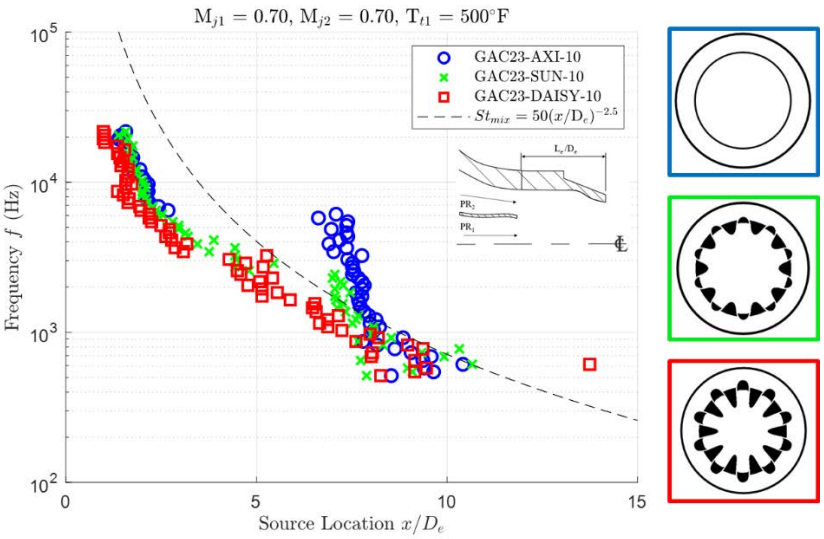


Figure 82. Effect of forced mixers on source location of dual-stream jet. L_e/D_e = 1.0, D_e = 2.20 in. M_{j1} = 0.70, M_{j2} = 0.70, T_{t1} = 500°F, one-twelfth octave.

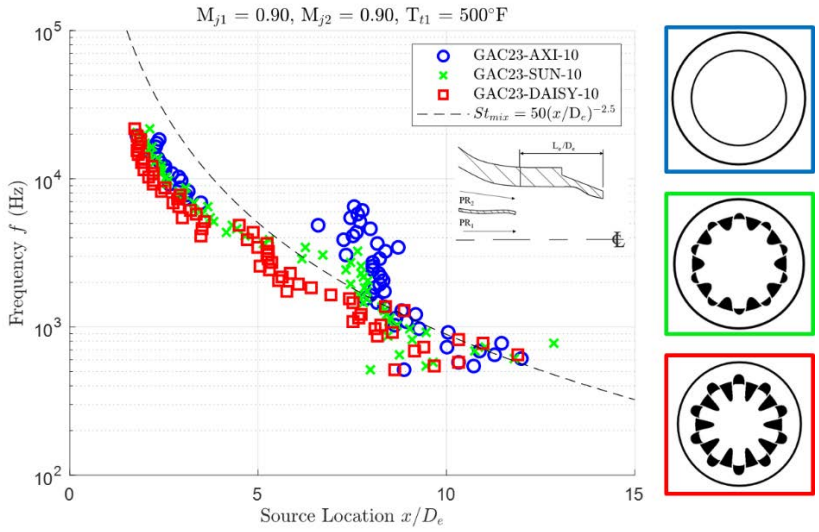


Figure 83. Effect of forced mixers on source location of dual-stream jet. L_e/D_e = 1.0, D_e = 2.20 in. M_{j1} = 0.90, M_{j2} = 0.90, T_{t1} = 500°F, one-twelfth octave.

Similar to Figure 82 and Figure 83, Figure 84 and Figure 85 show the effects of the internal mixers on the source distribution of the dual-stream jet but now with the longer mixing-duct length of L_e/D_e = 3.0. Once again, the dashed curve included in each figure represents the empirical source distribution of a fully-mixed jet. Unlike the shorter mixing-duct length data for L_e/D_e = 1.0 shown in Figure 82 and Figure 83, wherein use of the more aggressive DAISY mixer over the relatively mild SUN mixer yielded a slight upstream shift in the distribution of higher-frequency sources, Figure 84 and Figure 85 show next to no difference in the source distribution between configurations using the SUN versus DAISY internal mixers. The two distinct source location regions that occur for the AXI mixer for the L_e/D_e = 1.0 mixing-duct



lengths still occur for L_e/D_e = 3.0. For both mixing duct lengths, a cluster of many noise sources of frequencies in the range of 1000 – 7000 Hz seems to originate from a distance, x, of about $7D_e$ to $8D_e$. This effect is most prominent for the asymmetrical nozzle and appears to be located just downstream of the potential core of the final nozzle, which is typically about 6 diameters long. The extent of this effect reduces as additional mixing is introduced. For the SUN mixer, this effect is still present, although to a lesser extent. This effect is not as prominent for the DAISY mixer, which is expected to provide the most mixing. The precise reason for this clustering of sources still needs to be understood.

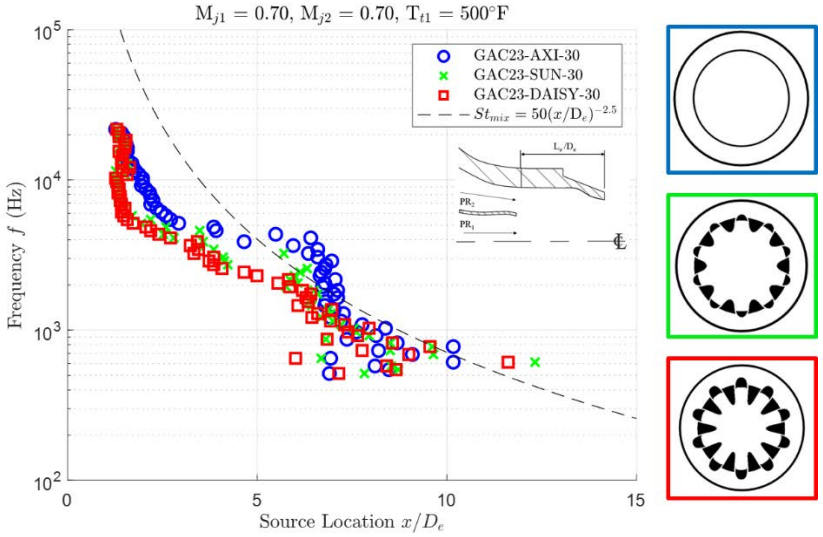


Figure 84. Effect of forced mixers on source location of dual-stream jet. L_e/D_e = 3.0, D_e = 2.20 in. M_{j1} = 0.70, M_{j2} = 0.70, T_{t1} = 500°F, one-twelfth octave.

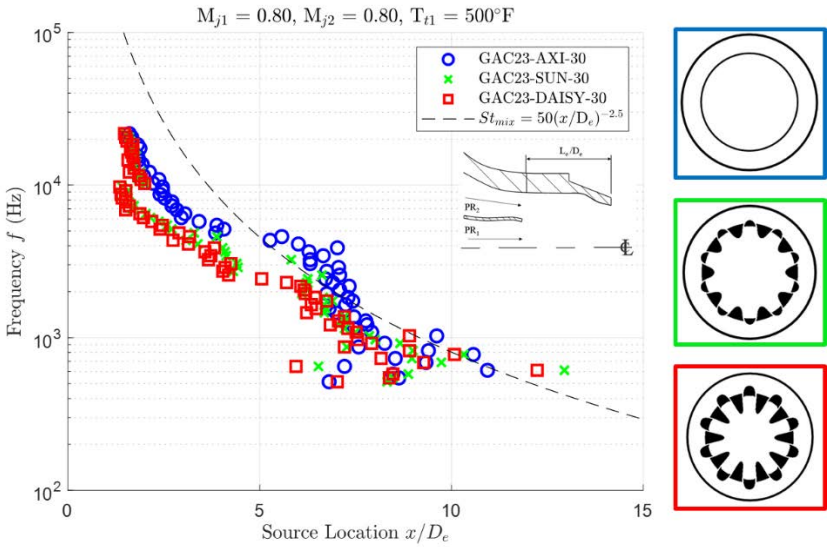


Figure 85. Effect of forced mixers on source location of dual-stream jet. L_e/D_e = 3.0, D_e = 2.20 in. M_{j1} = 0.80, M_{j2} = 0.80, T_{t1} = 500°F, one-twelfth octave.



Previously reported farfield acoustic data showed that increasing the mixing-duct length from L_e/D_e = 1.0 to 3.0 had little to no effect on the jet noise measured using the SUN and DAISY internal mixers. Similarly, this same increase in mixing-duct length has little to no effect on the source distribution of dual-stream jets using the SUN and DAISY internal mixers; however, there is a noticeable effect when using the axisymmetric baseline core nozzle. Figure 86 compares the peak noise source distribution between the two mixing-duct lengths for each of the three mixers. When using the SUN mixer (Figure 86b) there is a slight upstream movement in source distribution which is most apparent at mid-range (about 1 to 9 kHz) frequencies when comparing the shortest and longest mixing-duct lengths. This trend is not observable for the DAISY mixer (Figure 86c) where the data lay nearly on top of one another. This is not to say that the mixing-duct length of an internally-mixed jet using lobed mixers is a nonfactor. Rather, the nozzle length can have considerable effects on farfield noise measurements given the potentially substantial levels of mixing noise introduced by lobed internal mixers (see Mengle et al. [1997], Mengle [1999, 2000]). Future tests involving additional mixing-duct lengths and mixer designs may yield more thought-provoking results. When utilizing the baseline AXI mixer, increasing the mixing-duct length did have a consistent, observable effect on the source distribution.

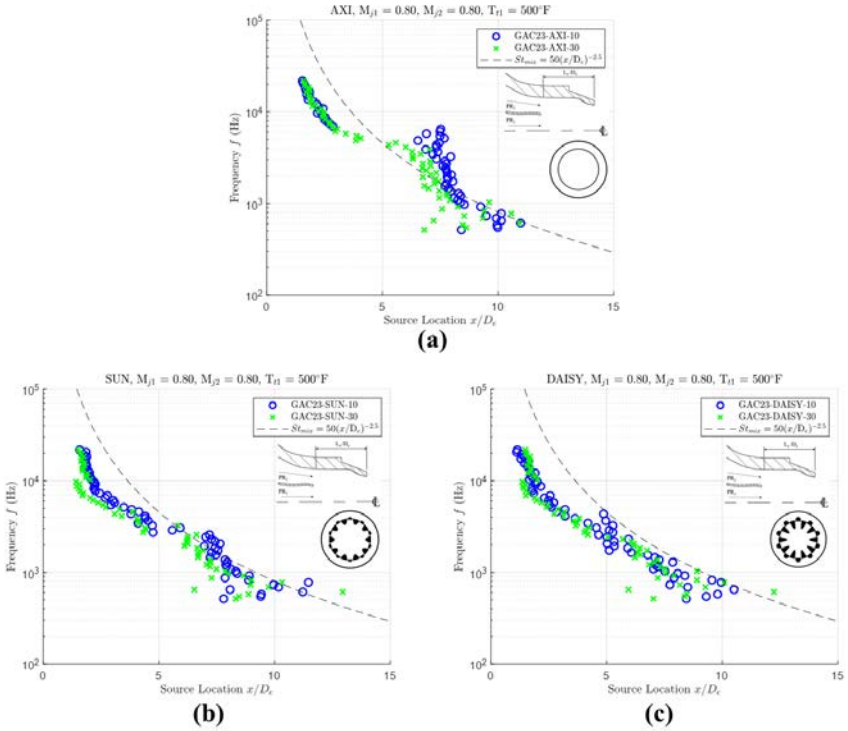


Figure 86. Effect of mixing-duct length on source location of dual-stream jet using (a) AXI (b) SUN and (c) DAISY internal mixers. D_e = 2.20 in. M_{j1} = 0.80, M_{j2} = 0.80, T_{t1} = 500°F, one-twelfth octave. (Blue circles: L_e/D_e = 1.0, Green crosses: L_e/D_e =3.0).

Increasing from the shortest to longest mixing-duct length has the most prominent effect on peak source distribution when using the axisymmetric internal mixer (Figure 86a) in which there is a substantial shift in the location of low-to-mid frequency noise sources toward the nozzle exit. In order to develop empirical relations for the source distribution of an internally-mixed, dual-stream jet, some initial attempts have been made to collapse the source location data across various operating conditions for a given nozzle geometry. Figure 87 shows the complete set of source location data for both GAC23-AXI-10 and GAC23-AXI-30 configurations collapsed using a Strouhal number based on the core-jet exit velocity U_{j1} and the exhaust nozzle exit diameter D_e – a normalization which had been shown in a past report to collapse the data from the GAC23-AXI-10 configuration reasonably well. We observe that the higher frequency content in the region close to the nozzle exit (x/D_e < 6) behaves generally the same between mixing-duct lengths, while the lower frequencies farther



downstream ($x/D_e > 6$) have shifted approximately one diameter upstream relative to the shorter mixing-duct length configuration.

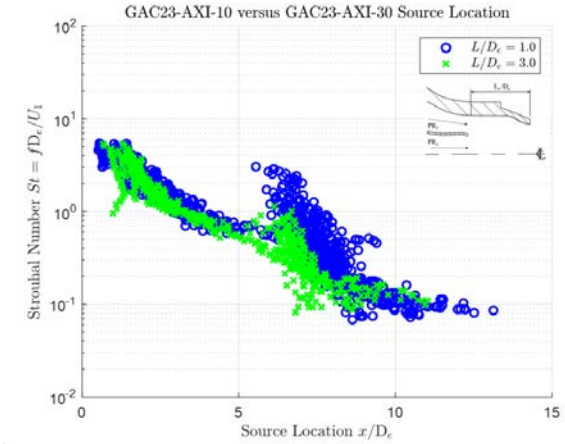


Figure 87. Effect of mixing-duct length on source location of dual-stream jet using AXI internal mixers. D_e = 2.20 in. Various M_{j1} and M_{j2}, T_{t1} = 500°F, one-twelfth octave.

Conclusions

The primary goal of the project was to conduct cost-effective SST jet noise experiments to support the development of low-, medium-, and high-fidelity jet noise prediction methods. This effort involved designing the experimental approach in collaboration with industry partners and federal agencies—including NASA, DOD, FAA, and FAA-funded modelers—to reduce uncertainty and inform the design of quieter supersonic jet engines. Working with GAC, Georgia Tech identified a representative baseline nozzle configuration for testing. The resulting dataset included far-field noise measurements, high-speed flow visualization, source localization, and detailed mean and unsteady flow measurements. GAC provided model-scale lobed mixer nozzles for testing unheated and heated flows at the same facility.

The experimental data from Georgia Tech was disseminated to key stakeholders and computational teams funded by FAA, validating semi-empirical and computational jet noise predictions.

Data were collected for both nozzles under various operating conditions and extraction ratios, including acoustic spectra, flow data, PIV, flow visualization, and acoustic source locations. This data was provided to aeroacoustics modelers for further analysis and model development.

Baseline Nozzle

- A substantial amount of far-field jet noise, PIV, schlieren, and source location data for various nozzle configurations was collected and analyzed.
- The experiments examined the effects of mixing-duct length, extraction ratio, and core temperature on noise and flow of jets from low-bypass annular confluent nozzle.
- For unheated jets, increased extraction ratio raised noise due to heightened bypass stream velocity.
- Short mixing-duct lengths produced this increase at higher frequencies.
- Long mixing-duct lengths distributed this increase across frequencies.
- Confluent nozzles experienced intense howling due to:
  - Impingement of the core-jet shear layer on the final nozzle exit when PR1 is greater than PR2.
  - Feedback loop created by periodic shock-induced boundary layer separation near the final nozzle exit at high subsonic secondary pressure ratios.
- Mitigation of howling was achievable with appropriate boundary layer trips.
- Mixing-duct length had minimal effect on far-field noise; however, dual-stream, heated-core confluent jets showed an upstream shift in low-frequency noise source distributions and a shortening of the potential core.



Forced Mixer Nozzle

- Lobed internal mixer nozzles had little impact on the far-field noise of unheated confluent jets.
- For unheated core streams and near-unity extraction ratios, minimal mixing was observed, resulting in little acoustic advantage.
- Effects on unheated jets occurred only with unrealistic pressure ratios, involving significant velocity differences between the two streams.
- For heated core streams, lobed internal mixers reduced noise at peak frequencies but increased noise at higher frequencies.
- These reductions were more pronounced closer to the jet axis.
- Increasing lobe penetration further reduced low-frequency noise but increased high-frequency noise.
- Lobed internal mixers decreased OASPL across all observation angles at industry-relevant conditions.
- PIV and schlieren measurements showed that internal mixer nozzles led to a rapid collapse of the jet potential core and thickening of the core-bypass mixing layer.
- Increased lobe penetration resulted in a more uniformly mixed jet at the exit of the mixing duct.
- Noise source distribution from dual-stream jets with lobed mixers resembled that of a theoretically "fully-mixed" jet.

PhD Student Jackson Larisch's Research Funded by This Project

- Investigated the effects of lobed nozzles on subsonic jet noise.
- Focused on lobed jets without bypass flow to isolate features of the lobed core flow.
- The highly vortical flow downstream from the lobed nozzle exit formed small 'jetlets.'
- Collapse of jetlets led to a dense distribution of high-frequency noise sources close to the nozzle exit.
- Jetlets acted as a new source of coherent, high-frequency noise, with a spectral shape similar to the large-scale universal similarity spectrum proposed by Tam et al.
- Reductions in low-frequency jet noise were attributed to the rapid collapse of the lobed jet potential core and shear layer thickening, which stabilized dominant instability waves and altered frequencies and growth rates of large-scale structures

References

Ahuja, K. (2003). Designing clean jet-noise facilities and making accurate jet-noise measurements. *International Journal of Aeroacoustics, 2*(3), 371-412. https://doi.org/10.1260/147547203322986188

Ahuja, K. K., Lepicovsky, J., Tam, C. K. W., Morris, P. J., & Burrin, R. H. (1982). *Tone-Excited Jet: Theory and Experiments* (NASA CR-3538). National Aeronautics and Space Administration. https://ntrs.nasa.gov/citations/19830004698

Breen, N. (2019). *Source Location of Subsonic and Supersonic Jets of Various Geometries via Acoustic Beamforming* [Doctoral dissertation, Georgia Institute of Technology].

Breen, N. P., & Ahuja, K. K. (2019, January). *Subsonic jet noise source location as a function of nozzle geometry* (AIAA 2019-0250). AIAA SciTech 2019 Forum. https://doi.org/10.2514/6.2019-0250

Breen, N. P., & Ahuja, K. K. (2020, June). *Limitations of acoustic beamforming for accurate jet noise source location* (AIAA 2020-2603). AIAA AVIATION 2020 FORUM. https://doi.org/10.2514/6.2020-2603

Bridges, J., & Wernet, M. P. (2011). *The NASA subsonic jet particle image velocimetry (PIV) dataset* (NASA TM-2011-216807). National Aeronautics and Space Administration. https://ntrs.nasa.gov/citations/20110023688

Burrin, R. H., Dean, P. D., & Tanna, H. K. (1974). A new anechoic facility for supersonic hot jet noise research at Lockheed-Georgia. *The Journal of the Acoustical Society of America, 55*(2), 400. https://doi.org/10.1121/1.3437223

Burrin, R., & Tanna, H. (1979). The Lockheed-Georgia coannular jet research facility. *The Journal of the Acoustical Society of America, 65*(S1), S44-S44. https://doi.org/10.1121/1.2017259

Christensen, K. T. (2004). The influence of peak-locking errors on turbulence statistics computed from PIV ensembles. *Experiments in Fluids, 36*(3), 484-497. https://doi.org/10.1007/s00348-003-0754-2

Chung, J. Y. (1977). Rejection of flow noise using a coherence function method. *Journal of the Acoustical Society of America*, 62(2), 388, 395. https://doi.org/10.1121/1.381537

Clemens, A. J., & Gavin, J. R. (2024). ASCENT 59: Aerodynamic Design of Nozzles and Mixers. *AIAA AVIATION Forum and ASCEND 2024*.

Karon, A. Z., & Ahuja, K. K. (2016). *Potential factors responsible for discrepancies in jet noise measurements of different studies* [Doctoral dissertation, Georgia Institute of Technology].

Mengle, V. (1999, May). Anomalous effect of nozzle length reduction on jet noise of forced mixers (AIAA 1999-1968). *5th AIAA/CEAS Aeroacoustics Conference and Exhibit*. https://doi.org/10.2514/6.1999-1968



Mengle, V. (2000, June). Optimization of lobe mixer geometry and nozzle length for minimum jet noise (AIAA 2000-1963). *6th Aeroacoustics Conference and Exhibit*. https://doi.org/10.2514/6.2000-1963

Mengle, V., Dalton, W., Bridges, J., & Boyd, K. (1997, May). Noise reduction with lobed mixers - Nozzle-length and free-jet speed effects (AIAA 1997-1682). *3rd AIAA/CEAS Aeroacoustics Conference*. https://doi.org/10.2514/6.1997-1682

Morris, P. J., & Zaman, K. B. M. Q. Z. (2010). Velocity Measurements in Jets with Application to Noise Source Modeling. *Journal of Sound and Vibration, 329*(4), 394 – 414. https://doi.org/10.1016/j.jsv.2009.09.024

Nance, D. K. (2007). *Separating contributions of small-scale turbulence, large-scale turbulence, and core noise from far-field exhaust noise measurements* [Doctoral dissertation, Georgia Institute of Technology].

Nance, D. K., & Ahuja, K. K. (2007, January). Limitations of the three-microphone signal enhancement technique," 45th AIAA Aerospace Sciences Meeting and Exhibit (AIAA 2007-441). *45th AIAA Aerospace Sciences Meeting and Exhibit*. https://doi.org/10.2514/6.2007-441

Nance, D. K., & Ahuja, K. K. (2009, May). Experimentally separating jet noise contribution of large-scale turbulence from that of small-scale turbulence (AIAA 2009-3213). *15th AIAA/CEAS Aeroacoustics Conference (30th AIAA Aeroacoustics Conference)*. https://doi.org/10.2514/6.2009-3213

Pope, S. B. (2000). *Turbulent flows*. Cambridge University Press. https://doi.org/10.1017/CBO9781316179475

Raffel, M., Willert, C. E., & Kompenhans, J. (2018). *Particle Image Velocimetry: A Practical Guide* (3rd Ed.). Springer International Publishing. https://doi.org/10.1007/978-3-319-68852-7

Ramsey, D. N. (2024). *Understanding and Preventing the Howling of a Model-Scale Internally Mixed Jet* [Doctoral dissertation, Georgia Institute of Technology]

Ramsey, D. N., Mayo, R., & Ahuja, K. (2023a, June). Howling in a Model-Scale Internally Mixed Confluent Nozzle Related to Excited Core-Jet Instability (AIAA 2023-3932). *AIAA AVIATION 2023 Forum*. https://doi.org/10.2514/6.2023-3932

Ramsey, D. N., Ahuja, K., & Gavin, J. (2023b, June). Howling in a Model-Scale Nozzle Related to Shock-Induced Boundary-Layer Separation at the Nozzle Exit (AIAA 2023-3933). *AIAA AVIATION 2023 Forum*. https://doi.org/10.2514/6.2023-3933

Ramsey, D. N., Karon, A. Z., Funk, R., & Ahuja, K. K. (2022a). Noise from Low-Bypass Confluent Nozzles: Mixing Length, Extraction Ratio, and Core Temperature Effects. *28th AIAA/CEAS Aeroacoustics 2022 Conference*.

Ramsey, D. N., Karon, A. Z., Funk, R., & Ahuja, K. K. (2022b). Self-Excited Jet from a Low-Bypass Confluent Nozzle at Unity Extraction Ratio. *28th AIAA/CEAS Aeroacoustics 2022 Conference*. https://doi.org/10.2514/6.2022-2864

Tam, C. K. W. (2019). A phenomenological approach to jet noise: The two-source model. *Philosophical Transactions of the Royal Society A: Mathematical, Physical and Engineering Sciences, 377*(2159). https://doi.org/10.1098/rsta.2019.0078

Tam, C. K. W., Golebiowski, M., & Seiner, J. M. (1996). On the two components of turbulent mixing noise from supersonic jets. *Proceedings of the 2nd AIAA/CEAS Aeroacoustics Conference*. https://doi.org/10.2514/6.1996-1716

Tam, C. K. W., Viswanathan, K., Ahuja, K. K., & Panda, J. (2008). The sources of jet noise: Experimental evidence. *Journal of Fluid Mechanics, 615*, 253 – 292. https://doi.org/10.1017/S0022112008003704

Witze, P. O. (1974). Centerline Velocity Decay of Compressible Free Jets. *AIAA Journal, 12*(4), 417 – 418. https://doi.org/10.2514/3.49262



Project 059(C) Modeling Supersonic Jet Noise Reduction with Global Resolvent Modes

University of Illinois Urbana-Champaign

Project Lead Investigator

Daniel J. Bodony
Blue Waters Professor of Aerospace Engineering
Associate Dean for Research and Graduate Programs
Grainger College of Engineering
University of Illinois Urbana-Champaign
306 C Talbot Labs
104 S. Wright St.
Urbana, IL 61801
217-244-3844
bodony@illinois.edu

University Participants

University of Illinois Urbana-Champaign (UIUC)

- P.I.: Dr. Daniel J. Bodony
- FAA Award Number: 13-C-AJFE-UI-031
- Period of Performance: October 1, 2023, to September 30, 2026
- Tasks:
  1. Establishment of industry-relevant low bypass ratio (BPR) engine parameters and acoustic assessment workflow with cost-sharing partner (completed)
  2. Automated Reynolds-averaged Navier–Stokes equation (RANS) predictions of jet exhaust (completed)
  3. Resolvent mode computation—primary and sensitivity (completed)
  4. Python® resolvent mode interpolation tool (completed)
  5. Python optimization tool for jet noise reduction (JNR) (version 1) (completed)
  6. Application of version 1 optimization tool on Georgia Institute of Technology Research Institute (GTRI) dual-stream nozzle (completed)
  7. Reformulation of resolvent modes by using local turbulent kinetic energy (in progress)
  8. Development and implementation of design parameter gradient direction for JNR (in progress)
  9. Application of version 2 optimization tool on GTRI dual-stream nozzle (paused)
  10. Application of version 1 optimization tool on Gulfstream®- and Boom®-relevant geometry (in progress)
  11. Collaboration with P.I.s for ASCENT Projects 010 and 047 (not yet started)

Project Funding Level

The Federal Aviation Administration (FAA) provided $199,999 in funding. In-kind cost-matching agreements were established with Gulfstream ($100,000; contact person: Dr. Brian Krupp [brian.krupp@gulfstream.com]) and with Boom ($50,000; contact person: Dr. Joe Salamone [joe.salamone@boom.aero]).

Investigation Team

University of Illinois Urbana-Champaign

Dr. Daniel Bodony (P.I.), Tasks 1, 3, and 11
Mr. Jay Woo (PhD student), Tasks 2, 3, 4, 5, 6, 8, and 9

® Python is a registered trademark of Python Software Foundation, Beaverton, Oregon.
® Gulfstream is a registered trademark of Gulfstream Aerospace Corporation, Savannah, Georgia
® Boom is a registered trademark of Boom Technology, Inc., Centennial, Colorado.



California Institute of Technology (Caltech)
Dr. Tim Colonius (subaward), Tasks 3, 7, and 11
Mr. Ethan Eichberger (PhD student), Tasks 3 and 7

Project Overview

This ASCENT project leverages recent research in global-resolvent-mode-based descriptions of jet turbulence and its associated noise to develop a physics-based tool for estimating the impact of JNR strategies on the takeoff noise of civil supersonic transports. The software tool will efficiently identify promising JNR technologies and will more precisely evaluate the noise impact of parametric variation in a specific JNR approach. The tool will be compatible with the fleet-scale evaluation codes Global and Regional Environmental Analysis Tool (GREAT; Georgia Institute of Technology) and Fleet Level Environmental Evaluation Tool (FLEET; Purdue University) developed in ASCENT Project 010 and integrated into the ASCENT Project 047 clean-sheet evaluation tool targeting civil supersonic transport.

The proposed research will create a multi-fidelity JNR tool that can operate in two modes: one mode for specific engine estimates and one mode for fleet-scale estimates, as discussed below.

JNR Evaluation for an Engine Mode
According to the RANS-provided mean flow for a specific engine, the global resolvent description of wavepackets and their sensitivity to mean flow variations will be computed. The solutions will provide estimates of the low-frequency radiated noise, and the sensitivity derivatives will estimate how the noise changes as a result of changes in the engine design, thus enabling JNR optimization.

Fleet-level Estimation Mode
The resolvent modes and their sensitivity derivatives for existing JNR strategies (e.g., chevrons or internal mixers) will be pre-computed for canonical jet exhaust profiles and flow conditions, compressed, and stored within an efficient data layout that can be quickly evaluated within FLEET, GREAT, and/or National Aeronautics and Space Administration (NASA) Aircraft Noise Prediction Program.

The Year 3 proposal was approved for funding with a period of performance of October 1, 2022, through December 31, 2023 (after a no-cost extension), and a budget of $199,999. The Year 2 statement of work included five tasks, listed above as Tasks 7–11, and rephrased from the prior year's annual report. The status of each task is indicated in parentheses. A Year 4 proposal was funded for $199,999 with a period of performance of January 1, 2024, through September 30, 2026 (after a no-cost extension).

Task 1 – Establish Industry-Relevant Low-BPR Engine Parameters and Acoustic Assessment Workflow with Cost-Sharing Partner [Completed]

University of Illinois at Urbana-Champaign

Objective

The objective of this task is to work with our cost-sharing partners to identify the anticipated range of characteristics of the low-BPR engines being considered for business-class civil supersonic transport. These parameters include, but are not limited to, diameter, BPR, mass flow rate, core and fan stream pressure ratios, core stream temperature ratio, thrust, nozzle configuration, plug designs, chevron designs, internal mixer designs, and afterburner design.

Research Approach

The research approach involves conducting face-to-face meetings and document exchange to obtain industry-relevant low-BPR engine parameters and acoustic assessment workflows.

Milestones

- Find a new candidate cost-sharing partner.
- Establish a nondisclosure agreement to initiate discussions.
- Exchange low-BPR engine parameters and acoustic assessment workflow.



Major Accomplishments
All milestones have been completed. A nondisclosure agreement between UIUC and Boom was signed in Year 2, and subsequent discussions led to Boom's partnership with $50,000 in-kind cost sharing for Year 3. The Boom commitment letter is attached. A cost-sharing agreement with Gulfstream was also established for $100,000 in-kind cost sharing. The Gulfstream letter is attached. In consultation with Dr. James Bridges at NASA Glenn Research Center, the "Plug20" family of nozzles (NASA TM-20210010291) was identified as relevant to industry. Downselecting the available nozzles will be the focus of the Year 4 effort, provided that it is funded.

Publications
None.

Outreach Efforts
None.

Awards
None.

Student Involvement
None.

Plans for Next Period
- Continued communication between UIUC and the principal contacts at Boom and Gulfstream, with focus on exchanging results, sharing data, and evaluating the UIUC-developed JNR workflow within each company's design process on the Plug20 nozzles. Of note, Dr. Joe Salamone left Boom and attempts to reconnect with Boom engineers have not yet been successful.

Task 2 – Automated RANS Predictions of Jet Exhaust [Completed]
University of Illinois at Urbana-Champaign

Objective
The objective of this task is to develop and verify an automated tool chain for using RANS methods to predict the jet exhaust plume from candidate near-sonic multi-stream jet nozzles.

Research Approach
Achieving JNR will require changes to the engine cycle and nozzle geometries. A Python-based software infrastructure is to be developed that takes parametrically defined computer-aided-design-based descriptions of nozzle geometries, automatically generates meshes and boundary conditions for the nozzle internal flow path and the external nozzle plume, initiates an open-source RANS solver, and curates the data.

Milestones
- Completed additional developments in computational fluid dynamics flow path.
- Verified RANS simulation results.
- Automated Python infrastructure.

Major Accomplishments
Milestone 1 has been completed and included subtasks such as adjusting the boundary conditions and increasing the computational domain of the mesh grid for each nozzle model. Post-processing calculations have also been developed to monitor properties of the nozzle exhaust and thereby characterize steady flow behavior. Milestone 2 has been completed, and included results obtained from post-processing that have been verified through comparison with a numerical solution based on quasi one-dimensional flow theory for mixed exhaust jet nozzles. Milestone 3 has been completed and included full automation of individual computational fluid dynamics processes.



Publications

Conference Proceedings

Woo, J., Murthy, S. R., & Bodony, D. J. (2024, January 8-12). Resolvent-based framework for jet noise reduction of a low-bypass ratio coannular nozzle (AIAA Paper 2024-2805). *AIAA SciTech 2024 Forum*. https://arc.aiaa.org/doi/10.2514/6.2024-2805

Dissertations and Theses

Woo, J. (2023). *Resolvent-based framework for jet noise reduction of a low-bypass ratio coannular nozzle* [Master's thesis, University of Illinois at Urbana-Champaign]. University of Illinois at Urbana-Champaign.

Outreach Efforts

None.

Awards

None.

Student Involvement

Jay Woo was responsible for developing the Python tool chain.

Plans for Next Period

None. This task is complete.

Task 3 – Resolvent Mode Computation—Primary and Sensitivity [Completed]

University of Illinois at Urbana-Champaign (lead) and California Institute of Technology

Objective

The objective of this task is to develop and verify a resolvent mode computation tool suitable for evaluating the JNR potential of candidate near-sonic multi-stream jet nozzles.

Research Approach

Achieving JNR will require changes to the engine cycle and nozzle geometries. Estimation of the JNR potential of candidate cycles and geometries will use resolvent mode descriptions of the coherent wavepacket-associated jet noise of the loudest sound sources. We denote the resolvent calculations that provide the input–gain–output modes of the resolvent operator $(i\omega - A)^{-1}$ as "primary," and we denote the changes in those modes due to changes in the jet nozzle geometry and engine cycle as "sensitivity." The resolvent operator requires knowledge of the linearized Navier–Stokes operator A generated for each nozzle and its exhaust plume, and a global mode computational infrastructure. The sensitivity of the resolvent input–gain–output modes requires knowledge of the change in A, e.g., δA, resulting from changes in the nozzle design and/or engine cycle.

Milestones

- Developed primary resolvent mode computation capability.
- Performed resolvent mode training data and fitting.
- Developed resolvent mode sensitivity computation capability.

Major Accomplishments

Milestone 1 has been completed and tested on single-stream subsonic and supersonic jets. Milestone 2 has been completed by using GTRI dual-stream jet data. Milestone 3 has been completed and validated by using GTRI dual-stream jet data.



Publications

Conference Proceedings

Woo, J., Murthy, S. R., & Bodony, D. J. (2024, January 8-12). Resolvent-based framework for jet noise reduction of a low-bypass ratio coannular nozzle (AIAA Paper 2024-2805). *AIAA SciTech 2024 Forum*. https://arc.aiaa.org/doi/10.2514/6.2024-2805

Dissertations and Theses

Pickering, E. (2021). *Resolvent Modeling of Turbulent Jets* [Doctoral dissertation, California Institute of University]. California Institute of University. doi:10.7907/szxb-f168. https://resolver.caltech.edu/CaltechTHESIS:03022021-005902351

Woo, J. (2023). *Resolvent-based framework for jet noise reduction of a low-bypass ratio coannular nozzle* [Master's thesis, University of Illinois at Urbana-Champaign]. University of Illinois at Urbana-Champaign.

Outreach Efforts

None.

Awards

None.

Student Involvement

Jay Woo is primarily responsible for running and applying the resolvent calculation and its sensitivity. Ethan Pickering was responsible for calibrating the primary resolvent mode computation and the preliminary training data and fitting tasks; he graduated and left Caltech. Ethan Eichberger is the current student, who learned from Liam Heidt and now leads global mode data-driven alignment.

Plans for Next Period

None. This task is complete.

Task 4 – Python Resolvent Mode Interpolation Tool [Completed]

University of Illinois at Urbana-Champaign (lead) and California Institute of Technology

Objective

The objective of this task is to develop and verify a Python-based interpolation tool for computing resolvent input–gain–output modes at nozzle geometry and/or engine cycles for which RANS data are unavailable but are near previously known input–gain–output modes from nearby nozzle geometries and/or engine cycles.

Research Approach

By using Kriging interpolation methods, a response surface-based interpolation approach will be developed to estimate resolvent input–gain–output modes for estimating the radiated noise from an engine geometry/engine cycle for which previously computed RANS data, linearized operators, and resolvent data are unavailable.

Milestones

- Identify candidate interpolation methods and downselect.
- Develop a Python tool to implement the interpolation method.
- Verify the Python tool.

Major Accomplishments

Milestones 1–3 have been completed: a Kriging method has been chosen, and an interpolation code has been developed and verified. Performance and accuracy comparisons between the interpolation tool and re-running the computational fluid dynamics and mode calculations suggest that the interpolation method is inferior.



Publications

Dissertations and Theses

Woo, J. (2023). *Resolvent-based framework for jet noise reduction of a low-bypass ratio coannular nozzle* [Master's thesis, University of Illinois at Urbana-Champaign]. University of Illinois at Urbana-Champaign.

Outreach Efforts

None.

Awards

None.

Student Involvement

Jay Woo was responsible for developing the Python tool chain.

Plans for Next Period

None. The resolvent-based interpolation tool will no longer be a focus of the work.

Task 5 – Python Optimization Tool for JNR [Completed]

University of Illinois at Urbana-Champaign (lead) and California Institute of Technology

Objective

The objective of this task is to develop and verify a Python-based optimization tool that searches the optimization space of the engine geometry/cycle, to identify design choices that improve JNR.

Research Approach

With gradient-informed optimization methods, an optimization approach will be developed for estimating JNR potential from a class of candidate engine geometries/cycles by using resolvent mode predictions of jet noise based on linearized operators described by RANS predictions of the jet exhaust plume.

Milestones

- Identify candidate optimization methods and downselect.
- Develop a Python tool to implement the optimization method.
- Verify the Python tool.

Major Accomplishments

Milestone 1 has been completed, and the conjugate gradient method was selected for the optimization. Milestones 2 and 3 are also complete.

Publications

Conference Proceedings

Woo, J., Murthy, S. R., & Bodony, D. J. (2024, January 8-12). Resolvent-based framework for jet noise reduction of a low-bypass ratio coannular nozzle (AIAA Paper 2024-2805). *AIAA SciTech 2024 Forum*. https://arc.aiaa.org/doi/10.2514/6.2024-2805

Dissertations and Theses

Woo, J. (2023). *Resolvent-based framework for jet noise reduction of a low-bypass ratio coannular nozzle* [Master's thesis, University of Illinois at Urbana-Champaign]. University of Illinois at Urbana-Champaign.

Outreach Efforts

None.



Awards
None.

Student Involvement
Jay Woo was responsible for implementing the optimization tool.

Plans for Next Period
None. This task is complete.

Task 6 – Application of Version 1 Optimization Tool on GTRI Dual-Stream Nozzle [Completed]
University of Illinois at Urbana-Champaign (lead) with California Institute of Technology

Objective
The objective of this task is to apply the Python-based tool developed in Tasks 2–5 to the GTRI dual-stream nozzle with extensible mixer duct lengths, to predict the quietest configuration.

Research Approach
The automated Python toolchain, starting with the moderate mixer duct length, will be applied to predict the mixer duct length that yields the quietest configuration. The predictions will be compared with the GTRI-measured acoustic field.

Milestones
- Select the GTRI operating condition of interest.
- Apply the optimization tool.
- Compare the predicted quiet configuration to the measured quiet configuration.

Major Accomplishments
Milestone 1 has been completed and was based on the conditions for which GTRI jet velocity particle image velocimetry (PIV) data and acoustic data are available. Milestone 2 has been applied, and optimization has been performed. Milestone 3 has been completed. Qualitative trends from the resolvent modes have been found to be consistent with the measured acoustic field.

Publications
Conference Proceedings
Woo, J., Murthy, S. R., & Bodony, D. J. (2024, January 8-12). Resolvent-based framework for jet noise reduction of a low-bypass ratio coannular nozzle (AIAA Paper 2024-2805). *AIAA SciTech 2024 Forum*. https://arc.aiaa.org/doi/10.2514/6.2024-2805

Dissertations and Theses
Woo, J. (2023). *Resolvent-based framework for jet noise reduction of a low-bypass ratio coannular nozzle* [Master's thesis, University of Illinois at Urbana-Champaign]. University of Illinois at Urbana-Champaign.

Outreach Efforts
None.

Awards
None.

Student Involvement
Jay Woo was responsible for applying version 1 of the optimization tool to the GTRI nozzle.



Plans for Next Period
None. This task is complete.

Task 7 – Reformulation of Resolvent Modes by Using Local Turbulent Kinetic Energy
California Institute of Technology

Objective
The objective of this task is to develop a means for the resolvent gain predictions to be internally calibrated by using information from the RANS-predicted flow-fields.

Research Approach
A calibrated reconstruction of the input–output modes from the resolvent formulation is used to estimate the jet's turbulent kinetic energy, as predicted by the RANS model.

Milestones
- Finalize the calibration formulation.
- Implement the calibration procedure.
- Verify the calibration procedure.

Major Accomplishments
Task 7 has been started. Initial results from Caltech showed a significant improvement in reconstructing the far-field acoustics using localized resolvent modes. The team is working on producing consistent resolvent responses which is essential for the training of the machine learning model. A wall-modeled large eddy simulation framework has been developed to produce high fidelity flow data for Milestones 1 and 3. Complete verification of the framework is ongoing with preliminary calculations showing promising performance.

Publications
None.

Outreach Efforts
None.

Awards
None.

Student Involvement
Ethan Eichberger and Jay Woo will be jointly responsible.

Plans for Next Period
Develop the new self-calibration formulation and apply it to Plug20 flow field data.

Task 8 – Development and Implementation of Design Parameter Gradient Direction for JNR
University of Illinois at Urbana-Champaign (lead) with California Institute of Technology

Objective
The objective of this task is to develop and verify an updated Python-based optimization tool based on version 1 that searches the optimization space of the engine geometry/cycle, to identify design choices that improve JNR.



Research Approach
Using gradient-informed optimization methods, we will develop an optimization approach for estimating JNR potential from a class of candidate engine geometries/cycles by using resolvent mode predictions of jet noise, on the basis of linearized operators described by RANS predictions of the jet exhaust plume.

Milestones
- Incorporated lessons-learned updates from version 1 of the Python toolchain into version 2.
- Verified implementation.

Major Accomplishments
Milestone 1 has been completed. Milestone 2 has been completed for a supersonic jet. The automated Python optimization tool is being applied to the GTRI dual-stream nozzle data.

Publications
Conference Proceedings
Murthy, S., & Bodony, D. J. (2023, June 12-16). Resolvent analysis based jet-noise-reduction of a biconical tactical jet nozzle (AIAA 2023-4518). *2023 AIAA Aviation Forum*. https://doi.org/10.2514/6.2023-4518

Dissertations and Theses
Woo, J. (2023). *Resolvent-based framework for jet noise reduction of a low-bypass ratio coannular nozzle* [Master's thesis, University of Illinois at Urbana-Champaign]. University of Illinois at Urbana-Champaign.

Outreach Efforts
None.

Awards
None.

Student Involvement
Jay Woo and Ethan Eichberger will be jointly responsible.

Plans for Next Period
Complete Milestone 2 on the Plug20 nozzle.

Task 9 – Application of Version 2 Optimization Tool on GTRI Dual-Stream Nozzle
University of Illinois at Urbana-Champaign (lead) with California Institute of Technology

Objective
The objective of this task is to apply version 2 of the Python-based tool developed in Tasks 2–5 to the GTRI dual-stream nozzle with extensible mixer duct lengths and predict the quietest configuration.

Research Approach
We will apply the automated Python toolchain, starting with the moderate mixer duct length, to predict the mixer duct length that yields the quietest configuration, then compare predictions with the GTRI-measured acoustic field.

Milestones
- Apply the optimization tool.
- Compare the predicted quiet configuration to the measured quiet configuration.



Major Accomplishments
Task 9 has been completed on the GTRI dual-stream nozzle but yielded null results because the nozzle design parameters (e.g., mixer length) were found not to change the far-field sound.

Publications
None.

Outreach Efforts
None.

Awards
None.

Student Involvement
Jay Woo will be responsible for applying version 2 of the optimization tool.

Plans for Next Period
Re-apply Task 9 to the Plug20 nozzles.

Task 10 – Application of Version 1 Optimization Tool on Gulfstream- and Boom-Relevant Geometry
University of Illinois at Urbana-Champaign

Objective
The objective of this task is to work with Gulfstream and Boom to apply version 1 of our optimization tool to a supersonic nozzle design relevant to Gulfstream and Boom. Performance, successes, and failures will be documented.

Research Approach
The results of version 1 of the Python optimization tool will be transitioned to Gulfstream and Boom for internal evaluation of the tool.

Milestones
- Developed and implemented a cost-sharing agreement with appropriate intellectual-property safeguards.
- Worked with Gulfstream and Boom engineers to identify cases of interest.
- Apply optimization code to Gulfstream and Boom cases of interest.

Major Accomplishments
Milestone 1 has been completed, and the letters of support from Gulfstream and Boom are included. Milestone 2 has been completed, and the NASA Plug20 configurations of Bridges et al. (NASA TM-20210010291) were selected. Milestone 3 has not yet been started.

Publications
None.

Outreach Efforts
None.

Awards
None.



Student Involvement
Jay Woo and P.I. Daniel Bodony will be jointly responsible.

Plans for Next Period
Begin Milestone 3.

Task 11 – Collaboration with P.I.s for ASCENT Projects 10 and 47
University of Illinois at Urbana-Champaign

Objective
The objective of this task is to collaborate with P.I.s on ASCENT Projects 010 and 047 to understand fleet-scale estimation needs and constraints and develop a prototype software interface that connects the engine-class tool from Task 3 to FLEET/GREAT.

Research Approach
We will discuss, document, and identify implementation possibilities for connecting version 1 (or version 2) of the JNR optimization tool within their project software tools.

Milestones
- Engage P.I.s on ASCENT Projects 10 and 47 to understand their goals, data, and software ecosystems.
- Identify possible means through which ASCENT Project 059C tools could be integrated ASCENT Projects 010 and 047 ecosystems.
- Re-engage ASCENT Projects 010 and 047 P.I.s to downselect the most promising integration path.

Major Accomplishments
This task has not yet been started.

Publications
None.

Outreach Efforts
None.

Awards
None.

Student Involvement
Jay Woo and P.I. Daniel Bodony will be jointly responsible.

Plans for Next Period
Begin Task 11.



Project 059(D) Physics-based Analyses and Modeling for Supersonic Aircraft Exhaust Noise

Stanford University

Project Lead Investigator

Sanjiva K. Lele
Professor
Department of Aeronautics & Astronautics
Stanford University
Stanford, CA 94305
Phone: (650) 723-7721
E-mail: lele@stanford.edu

University Participants

Stanford University (Stanford)

- P.I.s: Dr. Sanjiva K. Lele, Dr. Juan J. Alonso
- FAA Award Number: 13-C-AJFE-SU-024
- Period of Performance: September 30, 2023, to October 1, 2024
- Tasks:
  1. Develop and refine research plans in coordination with ASCENT Project 059 partners
  2. Perform large eddy simulation (LES)-based simulation, modeling, and validation of jet noise predictions
  3. Conduct Reynolds-averaged Navier–Stokes (RANS)-based simulation, modeling, and validation of jet noise predictions

Project Funding Level

This project receives $200,000 per year from the Federal Aviation Administration (FAA), in-kind matching from Stanford, and cost-share matching from Gulfstream Aerospace Corporation.

Investigation Team

Dr. Sanjiva K. Lele (P.I.; Department of Aeronautics and Astronautics)
Dr. Juan J. Alonso (P.I.; Department of Aeronautics and Astronautics)
Gao Jun Wu (PhD student; Department of Aeronautics and Astronautics)
Tejal Shanbhag (PhD student; Department of Aeronautics and Astronautics)
Kristen Matsuno (PhD student; Department of Mechanical Engineering)
Olivia Martin (PhD student; Department of Mechanical Engineering)

Project Overview

Improved methods for predicting and reducing noise for civil supersonic aircraft would be highly valued by the research and technology development community engaged in civil supersonic aircraft development. In addition to aircraft and engine companies, organizations such as the National Aeronautics and Space Administration (NASA), FAA, and the U.S. Department of Defense, and the research and technology community would also benefit from improved methods and tools. Supersonic jet noise tools with predictive capabilities can be used to design improved noise mitigation systems and to provide estimates of noise for certification studies.

This project involves the coordinated development of both low- and high-fidelity approaches for jet noise predictions for civil supersonic aircraft being considered in ASCENT and involves the tasks listed above. High-fidelity simulations of the jet exhaust flow and noise will be developed for a carefully selected subset of configurations and operating points being evaluated by the Georgia Institute of Technology (Georgia Tech) team. In parallel, RANS computations of a broader range



of configurations and operating conditions relevant for civil supersonic aircraft will be performed and used to develop improved jet noise source models and more accurate far-field noise propagation kernels. The noise source and noise propagation modeling will leverage high-fidelity simulation data and ongoing Georgia Tech experiments, as well as other noise and flow measurements available in the archival literature. Our goal is to understand the predictive quality of RANS-based noise prediction approaches with improved source and/or propagation models so that designers can better capture tradeoffs typical in the development of full civil supersonic aircraft configurations.

Task 1 – Develop and Refine Research Plans in Coordination with ASCENT Project 059 Partners

Stanford University

Objectives

The objective of this task is to design a simulation study that covers the range of operating conditions and nozzle configurations relevant for civil supersonic jet exhaust. The research plan must be inclusive of the current test plan from our experimental partner at Georgia Tech.

Research Approach

Planning involved discussions with ASCENT Project 059 partners and reaching out to external advisors at NASA and elsewhere in academia and industry. Based on these efforts, it was determined that the project should focus on axisymmetric dual-stream nozzles with an internal mixer and with the possibility of an internal and/or external nozzle plug. Our team has also searched for nozzle configurations and flow and noise measurement data in the archival literature that would be deemed relevant for civil supersonic aircraft and that could be used in the development of noise prediction methods. A comprehensive exploration indicated that the bulk of jet noise data including studies of noise reduction concepts were in the regime of moderate to high bypass ratios and were thus not particularly relevant for civil supersonic aircraft. While this affirmed the need for the planned laboratory measurement campaign by ASCENT Project 059 partner Georgia Tech, it also highlighted the need to use the most relevant data from the published literature to kickstart the modeling and simulation effort. Two specific datasets associated with jet noise tests at NASA Glenn Research Center were thus identified.

Georgia Tech Dual-Stream Nozzle

A coannular nozzle geometry with a variable-length mixing duct has been designed and is being evaluated extensively by the team at Georgia Tech. Following discussions among project collaborators and key stakeholders, a test matrix has been determined for the Year 1–2 experimental efforts. The jet Mach numbers for the two streams each vary between $M_j = 0.4$ and $M_j = 1.0$, and the length of the nozzle mixing duct can be adjusted to be 0.7, 1.0, 2.0, and 3.0 times the length of the nozzle diameter, $D_e = 1.7''$.

Bridges and Wernet Internal Mixer

Bridges and Wernet (2004) (at the NASA Glenn Research Center) reported flow and noise measurements for internally mixed two-stream nozzles with variations in the mixer duct length and mixer geometry. The operating conditions involve transonic and low supersonic jet exhaust velocity with a moderate bypass ratio. This configuration has also been used in previous RANS-based noise prediction studies by Rolls Royce® and Purdue University, along with a more recent LES study. Our team has been in touch with Rolls Royce and NASA regarding the nozzle geometry and measurement data. It is hoped that the geometry and data will become available in the future. This configuration is of interest to us because it is unique in providing both jet flow measurements and far-field noise for conditions relevant to civil supersonic flights.

Recent Jet Noise Measurements at NASA Glenn Research Center

As part of NASA's Commercial Supersonic Technology Project, under the Advanced Aero Vehicle Program, Dr. Bridges at NASA Glenn Research Center (Bridges, 2020) completed jet noise measurements on specially designed modular nozzle configurations at operating points selected to be relevant for commercial supersonic aircraft. Far-field acoustic measurements have been made available (Bridges et al., 2021), and particle image velocimetry (PIV) measurements of the jet have also been made available for select operating conditions (Bridges & Wernet, 2023). Our team is interested in

® Rolls Royce is a registered trademark of Rolls-Royce PLC, London, Great Britain.



exploring a selected subset of NASA's test matrix in our ASCENT Project 059 studies. Our team has obtained the computer-aided design (CAD) geometry for the nozzle and began early efforts in geometry cleaning and mesh generation.

Milestones

- Determined and followed the simulation plan (Years 1–2, complete).
- Studied the effects of mixing enhancement devices under heated jet conditions (Year 3, complete).
- Finalized and focused on trying to understand and improve noise discrepancies between the LES predictions and experimental measurements (Year 4).

Major Accomplishments

- Developed a research plan regarding the nozzle geometry and flow conditions to be studied. The plan includes both the experimental study by our partner at Georgia Tech and other relevant works from NASA Glenn Research Center.

Publications

None.

Outreach Efforts

Communication with researchers at NASA Glenn Research Center has been established, and ideas for collaboration have been exchanged.

Awards

None.

Student Involvement

Four graduate students have been involved in this part of ASCENT Project 059. G. Wu and K. Matsuno have conducted literature research on relevant jet experiments and simulations that involve similar flow conditions and nozzle mixing devices. T. Shanbhag has performed literature reviews on acoustic modeling of jet noise. K. Matsuno recently completed her Ph.D. O. Martin has joined the project and is helping with the simulations of the mixer nozzle.

Plans for Next Period

- Continue to refine our research plan according to ongoing discussions among teams of ASCENT Project 059.
- Select nozzle geometries with noise mitigation concepts that are of interest to industrial partners for the development of next-generation supersonic civil transport aircraft.

References

Bridges, J. E., & Wernet, M. P. (2004). *Cross-Stream PIV Measurements of Jets with Internal Lobed Mixers* (NASA/TM-2004-213206). National Aeronautics and Space Administration. https://ntrs.nasa.gov/citations/20040152075

Bridges, J. E. (2020). Personal Communication.

Bridges, J. E., Podboy, M. P., Gary, G., & Wernet, M. (2021). *Plug20 test report* (NASA/TM-20210010291). NASA Glenn Research Center. http://ntrs.nasa.gov/api/citations/20210010291/downloads/TM-20210010291.pdf

Bridges, J., & Wernet, M. P. (2023). *Plug20 test report: Particle image velocimetry (PIV) measurements* (NASA TM-20230006779). NASA Glenn Research Center. https://ntrs.nasa.gov/api/citations/20230006779/downloads/TM-20230006779.pdf

Task 2 – Perform LES-based Simulation, Modeling, and Validation of Jet Noise Predictions

Stanford University

Objectives

In collaboration with ASCENT partners in ASCENT Project 059, the objective of this task is to develop physics-based analyses for supersonic aircraft exhaust noise. The main goal of these analyses is to develop improved jet noise prediction

methods using a multi-fidelity approach. As part of the high-fidelity approach, LES will be conducted for a carefully selected set of configurations and operating points corresponding to tests conducted by the experimental team at Georgia Tech. The LES data will provide turbulence flow statistics and will be leveraged for acoustic source modeling.

Research Approach

In the past project year, efforts have been dedicated to high-fidelity modeling of the NASA Plug20 dual-stream nozzle with an internal plug and lobed mixer (configuration 122Am5pInt) and an internal plug and axisymmetric splitter (configuration 122Am0pInt), shown in Figure 1. LES and far-field acoustics modeling by the permeable Ffowcs Williams–Hawkings (FWH) formulation were performed using a compressible solver, CharLES, developed by Cascade Technologies (now part of Cadence Design Systems).

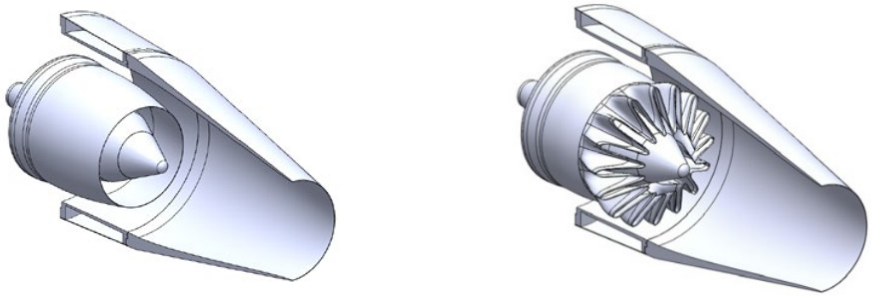


Figure 1. Detailed nozzle geometries. 122Am0pInt, confluent nozzle with an internal plug (left), 122Am5Int, confluent nozzle with an internal plug plus lobed mixer (right). Images obtained from Bridges et al. (2021).

In previous project years, configuration 122Am0pInt was tested at Setpoints 7 and 1183, and configuration 122Am5pInt was tested at Setpoint 1183. The LES-FWH far-field acoustic predictions for the 122Am0pInt nozzle showed good agreement with experimental measurements at Setpoint 7 across all polar angles. At Setpoint 1183, the LES–FWH results predicted downstream noise propagation accurately, but noise levels at upstream and sideline angles were substantially underpredicted. The 122Am5pInt nozzle LES-FWH results showed similar underprediction in the upstream and sideline angles, though the downstream noise was captured very well. In the current project year, we have run simulations at four new operating conditions in order to better diagnose these issues and understand where the LES-FWH method is performing well and where it is struggling. Table 1 summarizes the setpoints tested for nozzles 122Am0pInt and 122Am5pInt in the previous project years and the current project year (highlighted in gray). In the right-most columns of Table 1, the types of experimental measurements available at each operating condition (far-field acoustics/PIV) are listed. In the following, we examine the new simulation results and consider how they inform our understanding of the discrepancies between the LES and experimental data.



Table 1. Summary of the operating conditions (gray rows = current project year). FF: far-field, Nozzle Pressure Ratio (NPR):, PIV: particle image velocimetry.

Nozzle	Setpoint	NPR core	NPR bypass	NTR core	NTR bypass	flight stream M_f	Exp. FF acoustics Yes/No	Exp. PIV Yes/No
122Am0pInt	7	1.856	1.856	1	1	0.002	Y	Y
122Am0pInt	1183	1.8	1.8	2.9	1.20	0.3	Y	N
122Am0pInt	1183-FMESJ	1.8491	1.8491	1.606	1.606	0.3	N	N
122Am0pInt	4200	2.0	2.0	1.31	1.31	0.002	Y	Y
122Am0pInt	1200	2.0	2.0	3.25	1.2	0.002	Y	Y
122Am5pInt	1183	1.8	1.8	2.9	1.20	0.3	Y	N
122Am5pInt	1203	2.0	2.0	3.25	1.20	0.3	Y	Y
122Am5pInt	1233	2.3	2.3	3.25	1.25	0.3	Y	N

122Am0pInt – Dual-Stream Nozzle with Axisymmetric Splitter

For nozzle 122Am0pInt, additional simulations were run at Setpoint 4200 and 1200. Setpoint 4200 is similar to Setpoint 7 but introduces equal heating in the core and bypass streams. Setpoint 1200 has mismatched heating between streams similar to Setpoint 1183, but Setpoint 1183 has a Mach 0.3 flight stream and Setpoint 1200 does not have a flight stream. Figure 2 shows the far-field acoustic results from LES compared to experimental measurements for Setpoint 7 and Setpoint 4200. The LES results generally agree very well with the experiments across all polar angles, though there is slight overprediction of high-frequency noise at downstream angles and underprediction of broadband shock-associated noise (BBSAN) at upstream angles. The comparable outcomes at Setpoints 7 and 4200 indicate that equal heating of the streams does not introduce new physics that the LES is unable to capture. Figure 3 shows the far-field acoustics predicted at Setpoint 1200 compared to Setpoint 1183. At downstream angles, the LES predictions agree very well with the experimental measurements. However, at upstream and sideline angles, the LES underpredicts noise systematically across frequencies. The consistent underprediction in both operating conditions suggests that discrepancies between the LES and the experiments are unlikely to be caused by the Mach 0.3 flight stream. If we consider all operation conditions together (Sp7, Sp4200, Sp1200, Sp1183), we observe that the upstream and sideline discrepancies stem from the unequal heating of core/bypass streams, rather than heating more generally or the presence of the Mach 0.3 flight stream. These underpredictions are consistent in polar angle, frequency, and magnitude for the Setpoints 1183 and 1200.

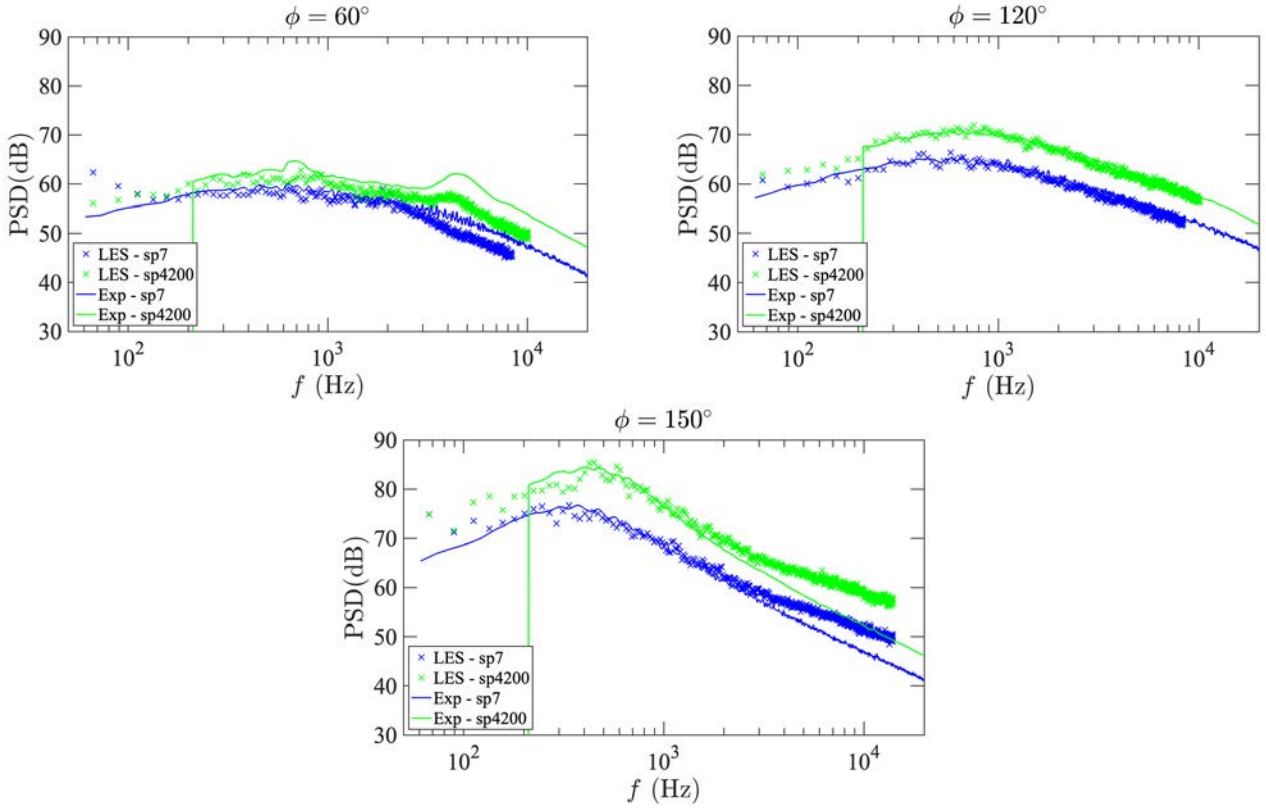


Figure 2. Far-field acoustics predictions for nozzle 122Am0pInt at Setpoint 7 (blue) and Setpoint 4200 (green) at polar angles $\phi = 60°, 120°, 150°$. Experimental data from Bridges et al. (2021). PSD: Power Spectral Density.

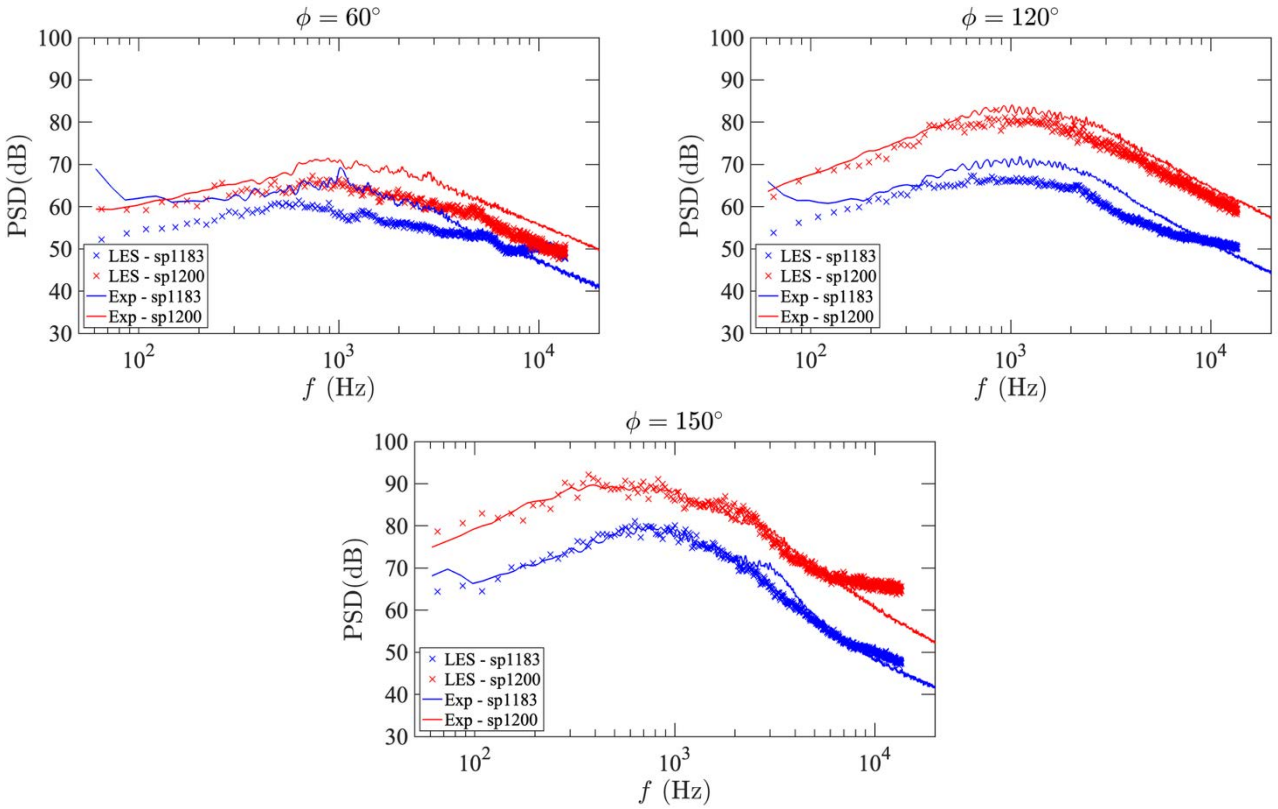
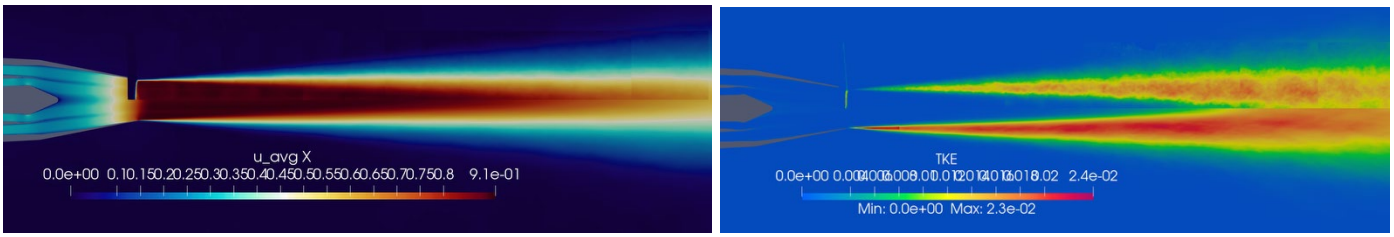
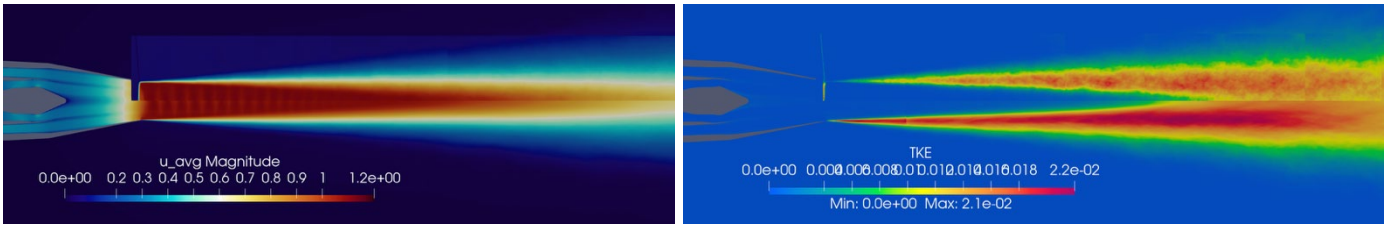


Figure 3. Far-field acoustics predictions for nozzle 122Am0pInt at Setpoint 1183 (blue) and Setpoint 1200 (red) at polar angles $\phi = 60°, 120°, 150°$. Experimental data from Bridges et al. (2021). PSD: Power Spectral Density.

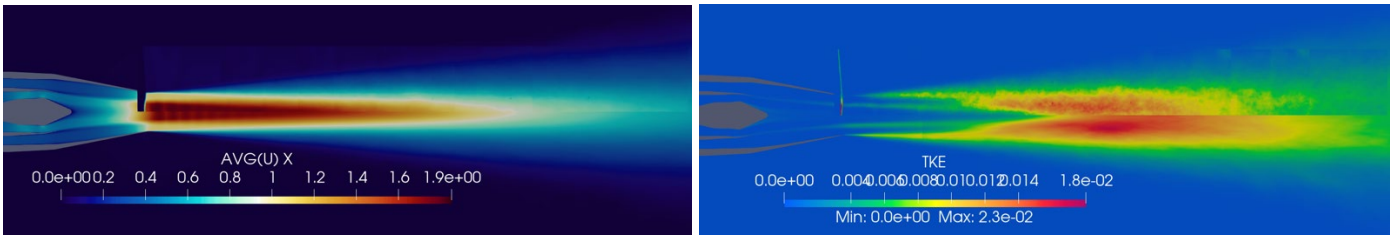
In Figure 4, mean streamwise velocity and turbulence kinetic energy (TKE) are compared between LES and PIV measurements at Setpoint 7, Setpoint 4200, and Setpoint 1200. The upper half of each figure outside the nozzle is the PIV field, and the bottom half of each figure is the LES. Across all three operating conditions, the mean velocity profiles agree very well between the LES and PIV. The flow exiting the nozzle and its development downstream is captured accurately in the LES. A weak shock-cell structure is observed at Setpoints 4200 and 1200 in both the LES and PIV measurements. The accurate representation of the base flow in the LES is consistent with our ability to capture the dominant downstream-radiated noise. TKE in the shear layer is overpredicted in the LES compared to the PIV, particularly in the upstream close to the nozzle exit. This suggests that the boundary layers inside the nozzle may be more turbulent in experiments than in the LES. For Setpoints 7 and 4200, this excess TKE in the shear layer may be linked to the high-frequency noise overprediction at downstream angles.



(a) Setpoint 7



(b) Setpoint 4200



(c) Setpoint 1200

Figure 4. Comparison of mean streamwise velocity (left column) and turbulence kinetic energy (TKE) (right column) from LES and experimental PIV measurements. For each figure, the upper portion downstream of the nozzle exit corresponds to the PIV field, and the lower portion corresponds to the LES.

122Am5pInt – Dual-Stream Nozzle with Lobed Mixer

For nozzle 122Am5pInt, additional simulations were run at Setpoint 1203 and Setpoint 1233. Setpoint 1203 was run in order to compare with available PIV measurements and assess whether underpredictions at Setpoint 1183 persistent across operating conditions. Setpoint 1233 was run to assess how the LES performs at much higher Mach numbers where BBSAN noise is significant. Figure 5 shows the far-field acoustics at Setpoint 1203 compared to Setpoint 1183. Very similar trends are observed as for nozzle 122Am0pInt at conditions with unequal heating between streams. The far-field noise is accurately captured by LES at downstream angles. However, at upstream and sideline angles, there is a systematic underprediction that is consistent across Setpoints 1183 and 1203. Figure 6 shows comparison between LES and PIV measurements at Setpoint 1203. Very good agreement is observed in both the mean streamwise velocity and TKE fields for this case. Figure 7 shows the far-field acoustic predictions at Setpoint 1233. Strong BBSAN is present for this case in the upstream direction. The LES captures the far-field acoustics well at downstream angles but underpredicts the broadband noise signal at upstream and sideline directions. The magnitude of the BBSAN hump is captured well in the LES, but it is shifted to lower a frequency range than experiments.

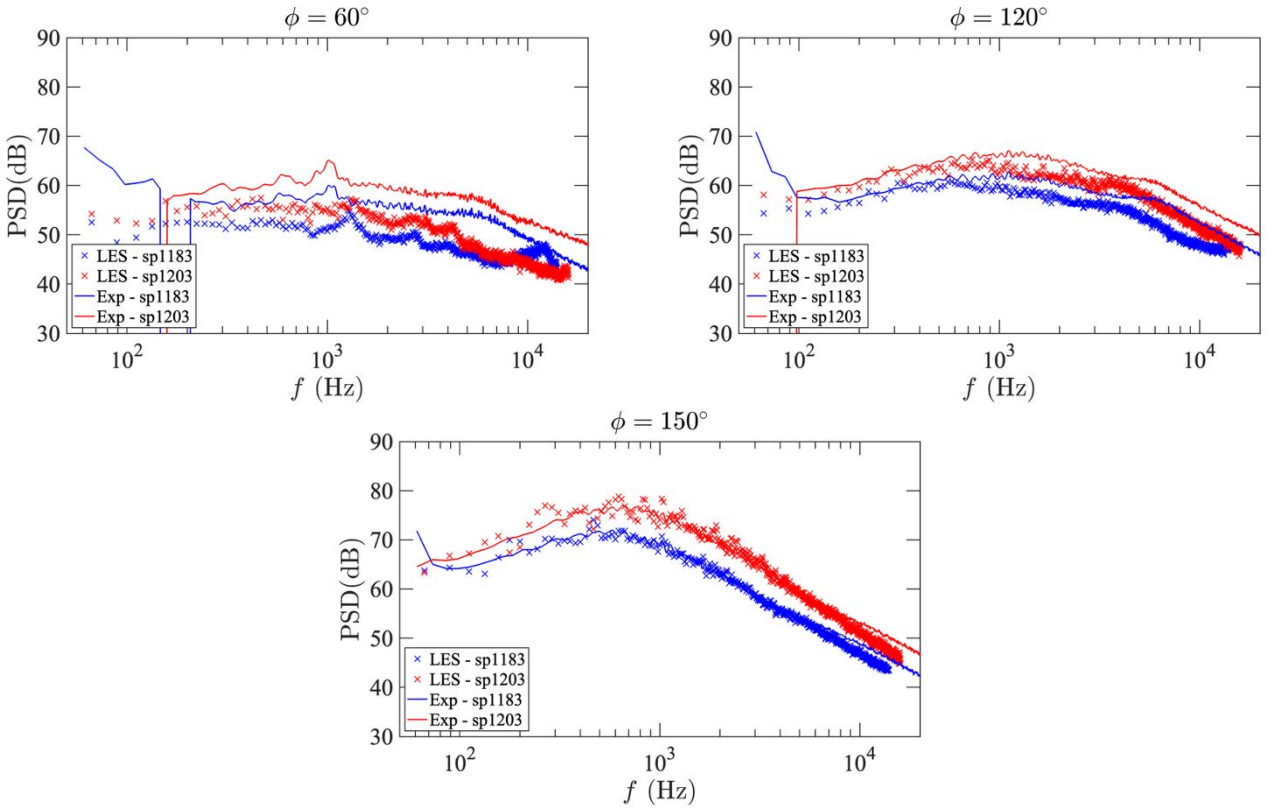


Figure 5. Far-field acoustics predictions for nozzle 122Am5pInt at Setpoint 1183 (blue) and Setpoint 1203 (red) at polar angles $\phi = 60°, 120°, 150°$. Experimental data from Bridges et al. (2021). PSD: Power Spectral Density.

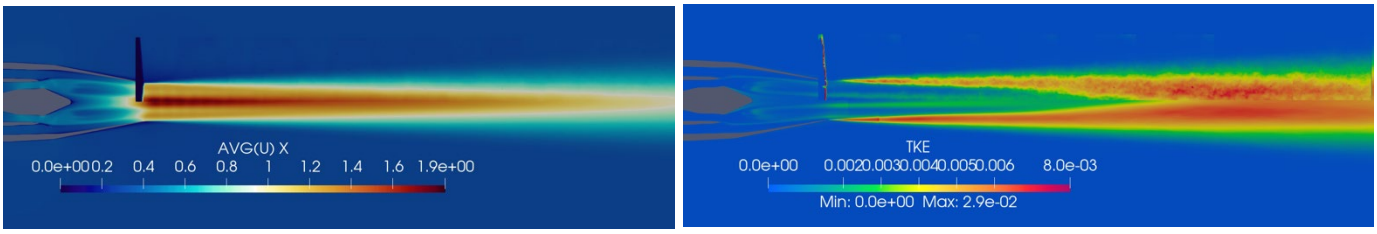


Figure 6. Comparison of mean streamwise velocity (left column) and turbulence kinetic energy (TKE) (right column) from LES and experimental PIV measurements at Setpoint 1203. For each figure, the upper portion downstream of the nozzle exit corresponds to the PIV field, and the lower portion corresponds to the LES.

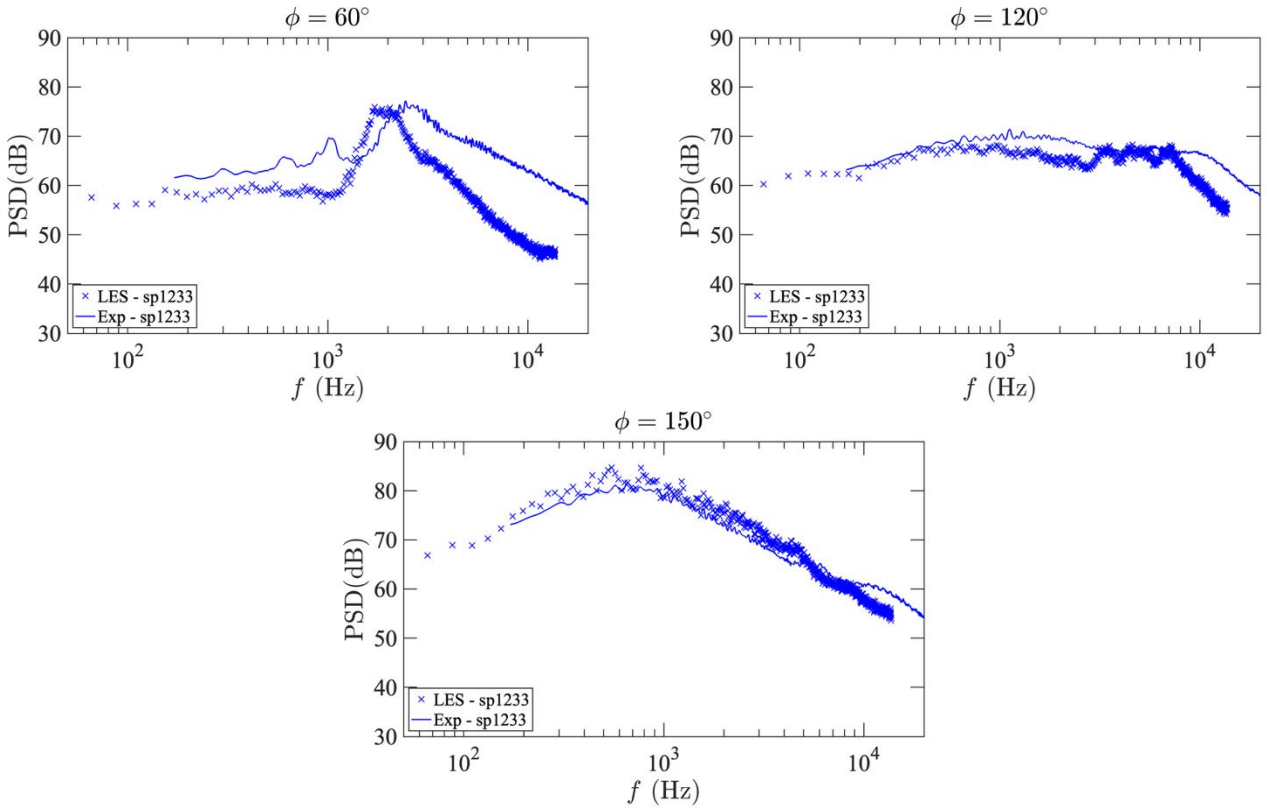


Figure 7. Far-field acoustics predictions for nozzle 122Am5pInt at Setpoint 1233 at polar angles $\phi = 60°, 120°, 150°$. Experimental data from Bridges et al. (2021). PSD: Power Spectral Density.

Conclusions from New Simulations

The new simulations performed for nozzles 122Am0pInt and 122Am5pInt show that the dominant downstream noise is accurately captured by LES across a wide variety of operating conditions (subsonic & supersonic, Mach 0.3 flight stream & no flight stream, equal heating and unequal heating between streams). These results also show that the noise underpredictions at upstream and sideline angles are consistent across all setpoints where there is unequal heating of core/bypass streams. Through comparison with PIV measurements, we confirm that the mean flow outside the nozzle is accurately captured in the LES for all setpoints. All of these results indicate that the missing noise sources contributing to upstream/sideline acoustics originate in the mixing region inside the nozzle.

In order to test the sensitivity of the upstream/sideline acoustics to the mesh resolution inside the nozzle, an additional simulation was run at Setpoint 1203 for the 122Am5pInt nozzle with 2x mesh coarsening throughout the inside of the nozzle ($\Delta x = 0.01D$ compared to $\Delta x = 0.005D$). Figure 8 shows the original mesh compared to the new coarsened mesh. The coarse mesh contained 150M cells, compared to 198M cells for the original mesh. Despite this large reduction in mesh count, no significant changes were observed in the far-field acoustics for the coarsened mesh compared to the original mesh at Setpoint 1203. This finding indicates that mesh resolution in the mixing region inside the nozzle is unlikely to be the source of the issue, and we can coarsen the mesh inside the nozzle by 50M cells without impacting the acoustic predictions. In future work, we plan to explore more modifications to model the flow inside the nozzle, such as the boundary layer treatment on the nozzle wall, the mixer, and the plug.

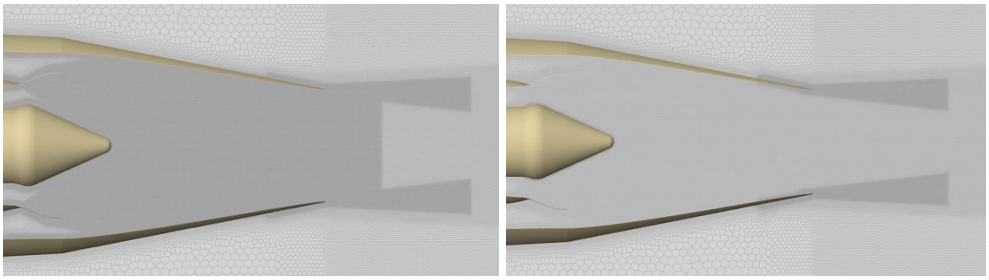


Figure 8. Original mesh inside the 122Am5pInt nozzle (left) and coarsened mesh (right). Dark gray regions indicate a mesh spacing of $\Delta x = 0.005D$.

Milestones

- Conducted LESs for test cases corresponding to the NASA Plug20 experiment for two different coaxial nozzles with an internal plug.
- Extended the LES database to include a variety of subsonic and supersonic operating conditions in order to more carefully identify where the LES is performing well and where it struggles to agree with experiments.
- Performed comparisons between LES flow fields and experimental PIV measurements for both NASA Plug20 nozzle configurations.

Major Accomplishments

- Made steady progress in the high-fidelity simulations of jet noise in accordance with the test plan established by our ASCENT Project 059 partners.
- Characterized discrepancies between LES and experimental far-field acoustics across a wide variety of operating conditions (subsonic & supersonic, flight stream & no flight stream, matched core/bypass heating & mismatched heating). Showed that the dominant downstream noise is predicted very well by the LES across all conditions tested.
- Identified that upstream and sideline noise underpredictions arise from mismatched heating between streams.
- Performed detailed comparison of LES flow fields to experimental PIV measurements. Confirmed that the LES accurately captures the mean flow fields across all operating conditions with available PIV.
- Examined sensitivity of far-field acoustics to mesh resolution inside the nozzle in the mixing region and identified potential for cost savings.

Publications

Doctoral Dissertation

Wu, G. J. (2024). *Towards quieter supersonic flight: a computational aeroacoustic study of high-speed jets* (Ch.4) [Doctoral dissertation, Stanford University]. Stanford University.

Conference Proceedings

Martin, O. G., Wu, G. J., & Lele, S. K. (2024, July 29-August 2). *Noise predictions of a dual-stream jet with forced internal mixing* [Conference paper]. AIAA Aviation Forum and ASCEND 2024, Las Vegas, Nevada.

Shanbhag, T. K., Zhou, B. Y., Ilario, C. R. S., & Alonso, J. J. (2024, January 8-12). *An AD framework for jet noise minimization using geometrical acoustics* [Conference paper]. AIAA SCITECH 2024 Forum, Orlando, Florida.

Shanbhag, T. K., Zhou, B. Y., Ilario, C. R. S., & Alonso, J. (2024, June 4-7). *Adjoint-based jet noise minimization using geometrical aeroacoustics* [Conference paper]. 30th AIAA/CEAS Aeroacoustics Conference, Rome Italy.

Shanbhang, T. K. (2024). *RANS-based methods for the prediction and reduction of jet noise* [Doctoral dissertation, Stanford University]. Stanford University.

Wu, G. J., Martin, O. G., & Lele, S. K. (2024, June 4-7). *Computational aeroacoustic study of coannular nozzles with internal mixing geometries at high transonic Mach numbers* [Conference paper]. 30th AIAA/CEAS Aeroacoustics Conference, Rome, Italy.

Outreach Efforts
Communication with ASCENT Project 059 partners and NASA scientists has been established. Deeper collaboration with the Georgia Tech experiments and with NASA scientists is expected as the project progresses further.

Awards
None.

Student Involvement
Two graduate students, G. Wu and O. Martin, participated in this task for Year 3. G. Wu has since graduated from Stanford.

Plans for Next Period
We plan to comprehensively explore the reasons for discrepancy between LES predictions and NASA data for the sideline and upstream observer locations. Grid refinement and coarsening and acoustic data-surface placement will be studied. We will also use more sophisticated data-decomposition methods to understand the role of upstream traveling modes in the generation of observed acoustic tones.

References
Bridges, J., & Wernet, M. P. (2023). Plug20 test report: particle image velocimetry (PIV) measurements (NASA TM-20230006779). NASA Glenn Research Center. https://ntrs.nasa.gov/api/citations/20230006779/downloads/TM-20230006779.pdf

Bridges, J. (2023, June 12-16). Diagnosing Noise Features of Internally Mixed, External Plug Exhaust Systems [Conference paper]. *AIAA AVIATION 2023 Forum*. https://doi.org/10.2514/6.2023-3210

Bridges, J. E., Podboy, M. P., Gary, G., & Wernet, M. (2021). Plug20 test report (NASA/TM-20210010291). NASA Glenn Research Center. http://ntrs.nasa.gov/api/citations/20210010291/downloads/TM-20210010291.pdf

Bridges, & Wernet. (2004). Cross-Stream PIV Measurements of Jets with Internal Lobed Mixers (NASA/TM-2004-213206). NASA Glenn Research Center. https://ntrs.nasa.gov/citations/20040152075

Stich et al. (2024). Noise Prediction of Multi-Stream Internally Mixed Jets with External and Internal Plugs Using Large-Eddy Simulation [Conference Paper]. *AIAA/CEAS Aeroacoustics Conference*, Rome Italy. https://arc.aiaa.org/doi/10.2514/6.2024-3377

Tanna, H. K., & Morris, P. J. (1985). The noise from normal-velocity-profile coannular jets. *Journal of Sound and Vibration, 98*(2), 213-234. https://doi.org/10.1016/0022-460X(85)90386-4

Tanna, H. K. (1980). Coannular jets—Are they really quiet and why? *Journal of Sound and Vibration, 72*(1), 97-118. https://doi.org/10.1016/0022-460X(80)90710-5

Wu, G. J., Martin, O. G., & Lele, S. K. (2024, June 4-7). Computational aeroacoustic study of coannular nozzles with internal mixing geometries at high transonic Mach numbers [Conference paper]. *30th AIAA/CEAS Aeroacoustics Conference*, Rome, Italy. https://arc.aiaa.org/doi/10.2514/6.2024-3198

Task 3 – Conduct RANS-Based Simulation, Modeling, and Validation of Jet Noise Predictions
Stanford University

Objectives
The objective of this task is a coordinated development of both low- and high-fidelity approaches for jet noise predictions. For the low-fidelity approach, RANS computations of a broader range of configurations and operating conditions relevant for civil supersonic aircraft will be performed and used to develop improved jet noise source models and more accurate far-field noise propagation kernels.

Research Approach
Turbulent Scales Modeling
The ASCENT Project 059D team is continuing work to model the turbulent length and time scales used in standard RANS-based acoustic source models. In previous work, our team studied the two-point fourth order velocity fluctuation correlation data extracted from LES databases of round jet simulations at Mach numbers of 0.5 and 0.9. In this research period, the same framework has been applied to extract the turbulent length and time scales at different points in the

hydrodynamic source-containing region from this unsteady flow data on the basis of two common frameworks used in high frequency modeling, assuming that the spatial and temporal components of these correlation functions are separable. The validity of the widely applied assumption that these turbulent scales may be assumed universally proportional to the dimensionally derived dissipation scales arising from RANS-based turbulent quantities is investigated. Our team has found that this assumption breaks down over the potential core, where in the context of both the source models studied, the length and time scales appear to be relatively constant (see Figure 9). In the case of the time scale, we find that the constant of proportionality is not in fact constant over space but may be well approximated by a simple radial weight function. Our proposed 'weighted scales' model offers improved predictive capability as compared with the baseline Ribner source model for an unseen jet case (see Figure 10). The similarity of both the length and time scale distributions between the two Mach numbers studied, supported by the experimental and numerical observations of previous authors, suggest that this type of prediction framework could be widely applicable across jet operating conditions (see Figure 11 and Figure 12). However, this assumption will require further verification. This could take the form of either repeating the type of 'scale extraction' analysis performed in the present work on a more extensive set of unsteady simulations or experimental measurements or testing the far field predictions of similar weighted scales models against other jet noise experiments.

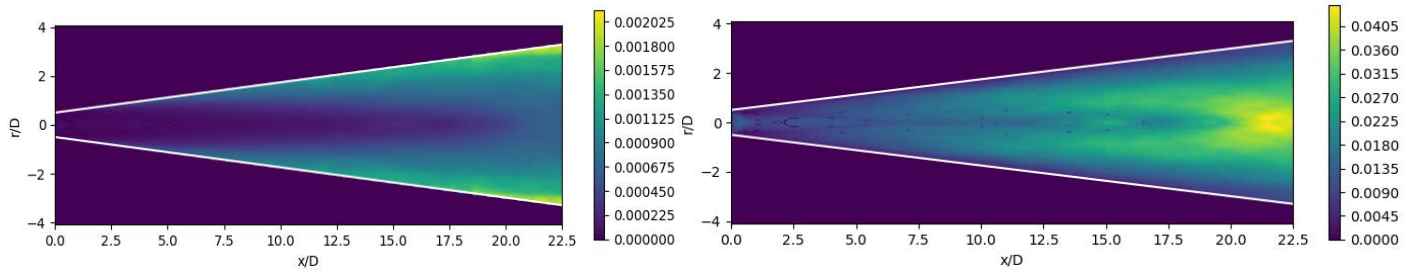


Figure 9. LES consistent scales for RANS modeling, time scale (left) and length scale (right).

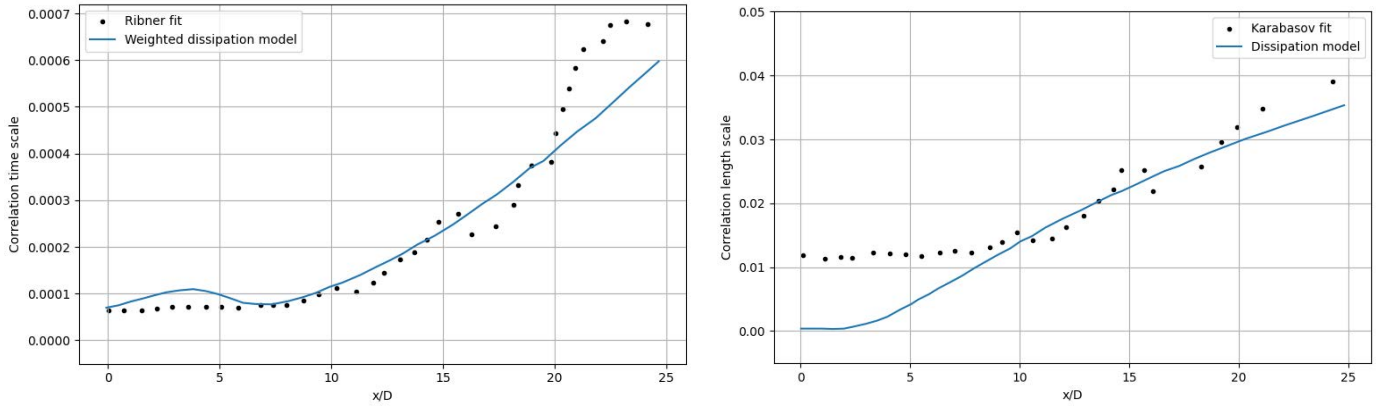


Figure 10. Comparison of fitted LES scales (symbols) and weighted dissipation model scales (line) along jet centerline based on Ribner fit (left) and Karabasov fit (right).

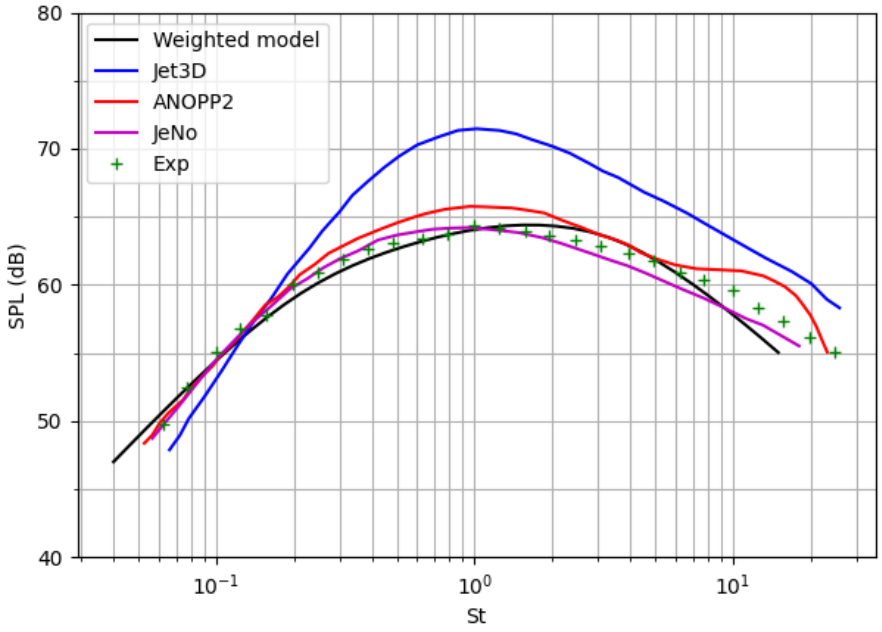


Figure 11. Convergent straight nozzle, M = 0.5: far field spectrum at r = 50.8D, θ = 90 deg.

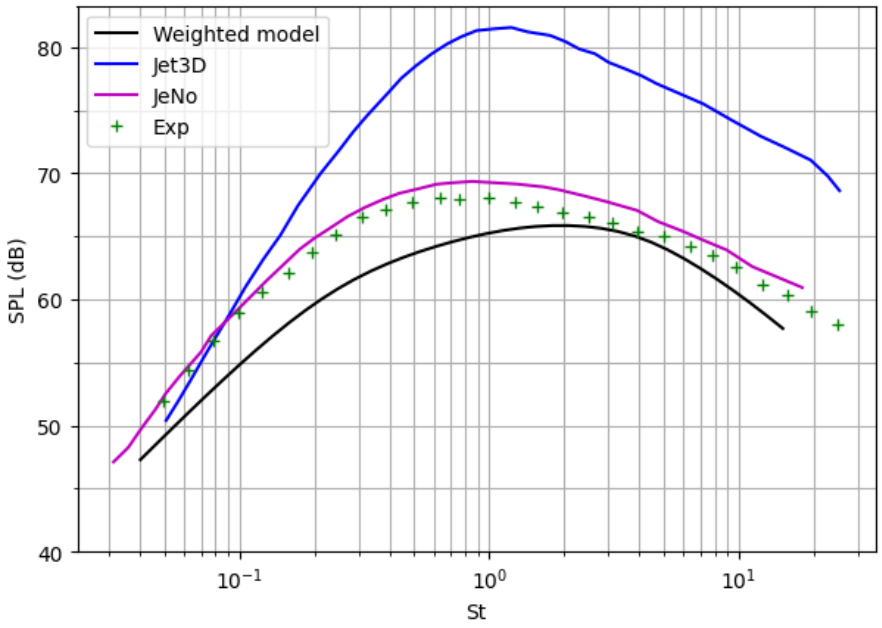


Figure 12. Convergent straight nozzle, M = 0.5: far field spectrum at r = 50.8D, θ = 50 deg.

Wavepacket Jitter Modeling

The ASCENT Project 059D team continued our effort towards modeling far field noise associated with the large-scale coherent structures in the jet flow. Our team proposed a predictive model form of the near field turbulent velocity fluctuation cross spectral density, based on a line source representation building upon the previous works of Crow, Mollo-

Christensen (1967), Cavalieri and Agarwal (2014). Resolvent analysis was used, augmented by a RANS-based eddy viscosity model, to deduce properties of the wavepacket spatial structure. This information was then used to reconstruct the cross-spectral density matrix (CSD), which is augmented with an explicit model of axial coherence decay along the wavepacket structure, observed experimentally as jitter. The coherence function used to represent the stochastic effects of jitter in the frequency domain is chosen to require minimal model parameter tuning, while offering an improved representation of the true CSD. The values of these parameters are selected, both based on LES conical nozzle round jet data at Mach number 0.5 and 0.9, and experimental measurements of far field acoustic directivity for round jets at subsonic Mach numbers between 0.4 and 0.9. In both cases, there is an observed linear scaling of the coherence length scale with wavelength (see Figure 13), supporting the hypothesis of this and previous works, that the wavepacket sources considered exhibit self-similar properties, not only in their spatial growth and decay but also in their streamwise coherence. However, while the LES-consistent parameters show this linearity between the coherence length and the acoustic wavelength, the experiment-consistent parameters suggest that the hydrodynamic wavelength is more relevant. The resulting global source model is demonstrated to be capable of low frequency noise prediction on a round jet test case at M = 0.9, and a promising degree of agreement with experimentally measured far field directivity profiles is obtained (see Figure 14 and Figure 15). With an unchanged parameter set, the model also has some preliminary applicability to supersonic jet cases, with minor modifications to the CSD construction methodology. Additional details on this work can be found in Shanbhag (2024).

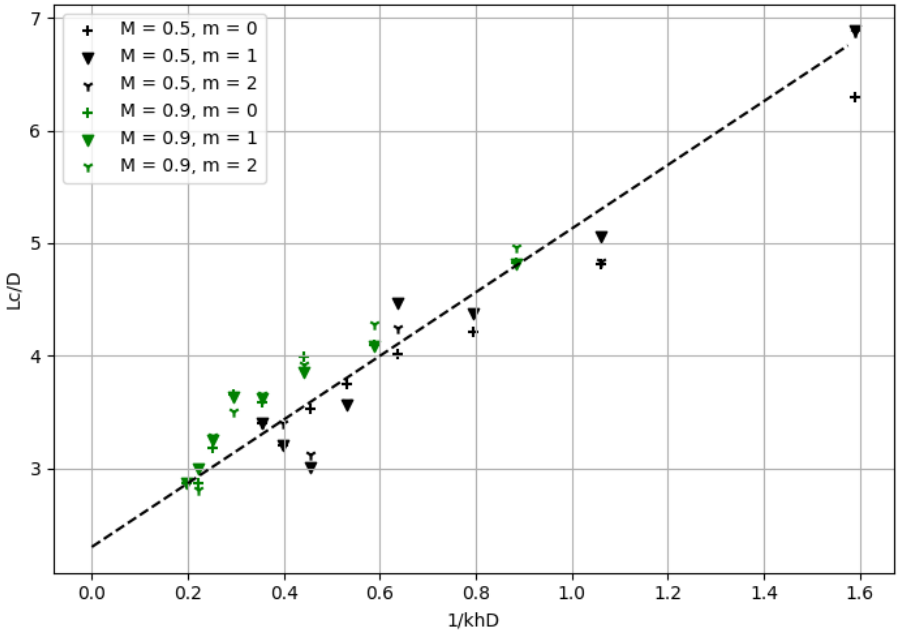


Figure 13. Optimal value of coherence length scale parameter Lc vs. acoustic wavelength 1/kh. Both length scales are normalized by nozzle diameter D

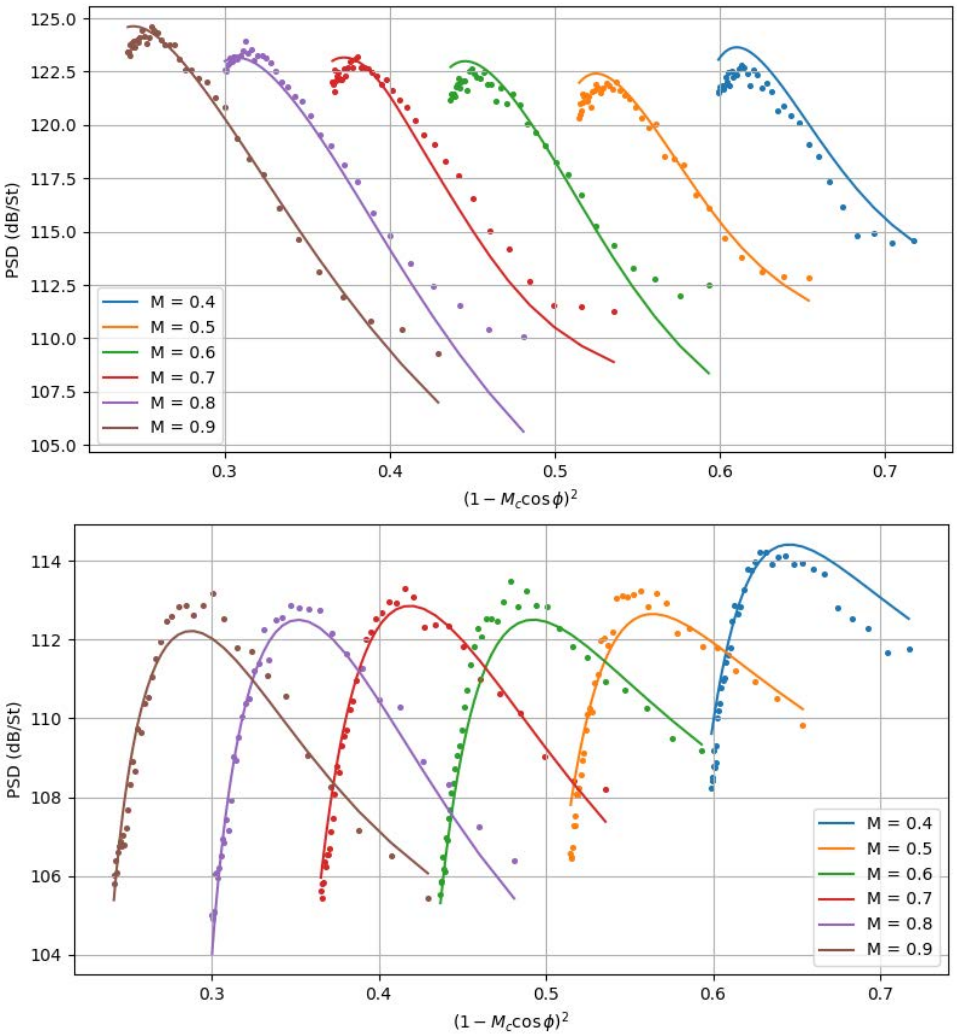


Figure 14. Predicted acoustic directivity for Poitiers jet compared against experimental measurements (Hasparyk et al., 2024) St = 0.2 (upper) and St = 0.6 (lower). PSD: Power Spectral Density. The polar angle ϕ is plotted on the horizontal axis in terms of the Doppler factor.

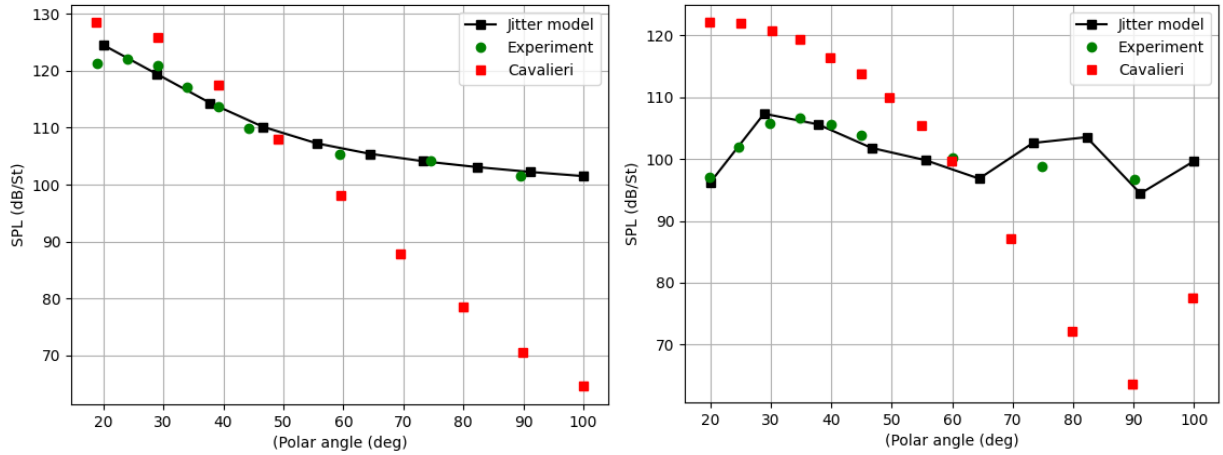


Figure 15. Comparison of M = 0.9 round jet directivity at St = 0.2 (left) and St = 0.75 (right). SPL: sound pressure level.

Given the relatively small amount of data used to select model parameters in this study, it will be important to repeat the model calibration in further work, using a greater variety of axisymmetric jet data across different Mach numbers and temperature ratios, to verify the trends that we observe. The recent experimental works of Hasparyk et al. (2024) have suggested that properly calibrated global source models proceeding along the lines in this work may be capable of shallow angle acoustic predictions accurate to within 1.5 dB of measured values, underlining the potential value of developing these methods further.

Adjoint (AD) Framework for Chevron Design Optimization

The ASCENT Project 059(D) team applied our previously developed framework for efficient adjoint-based design to the optimization of two baseline nozzle geometries. Our design framework allows the incorporation of realistic constraints on quantities such as thrust. The optimal designs produced show the capability of such a design framework to make significant noise reductions through minor geometric alterations. The alterations in geometry and flow field observed appear to be logically consistent with the conclusions drawn by the parametric design studies of previous authors looking to minimize jet noise through shear layer interference.

Figure 16 and Figure 17 show the results of a series of gradient-driven design iterations, beginning from the Poitiers round nozzle geometry. The results of two optimization problems are shown here: (1) the unconstrained problem, in which the computed nozzle thrust is allowed to vary freely, and (2) the constrained problem, in which thrust is maintained within 10% of the baseline value via incorporation of a penalty function. While this implementation does not guarantee satisfaction of the thrust constraint at every design iteration, the converged result of the optimization problem should satisfy the constraint exactly. The chosen design objective in both problems was the averaged SPL at St = 0.1, St = 0.3 and St = 1.0, computed over four equally azimuthally spaced sideline observers placed at r = 50D from the nozzle exit. It should also be noted that both problems were run under one additional constraint: the nozzle exit area was not permitted to increase beyond a certain point. This was found to be necessary during early design iterations, when the direction of the parameter gradient tended to open the nozzle exit - beyond a certain point this would result in the development of a choked throat and weak normal shock system. As an internal shock would be unacceptable to nozzle performance, this constraint was added to all design iterations and enforced via a backtracking line search along the computed gradient direction.

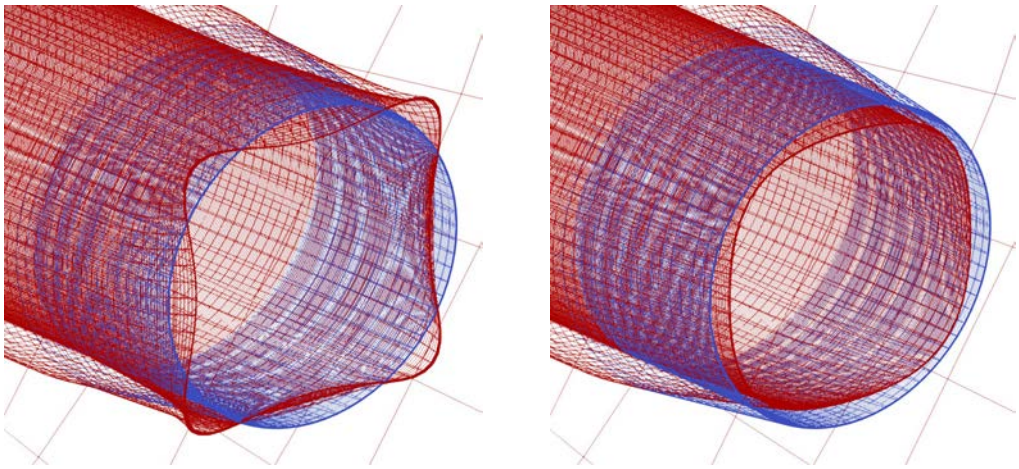


Figure 16. Poitiers jet optimization results: unconstrained (left) and constrained (right) cases.

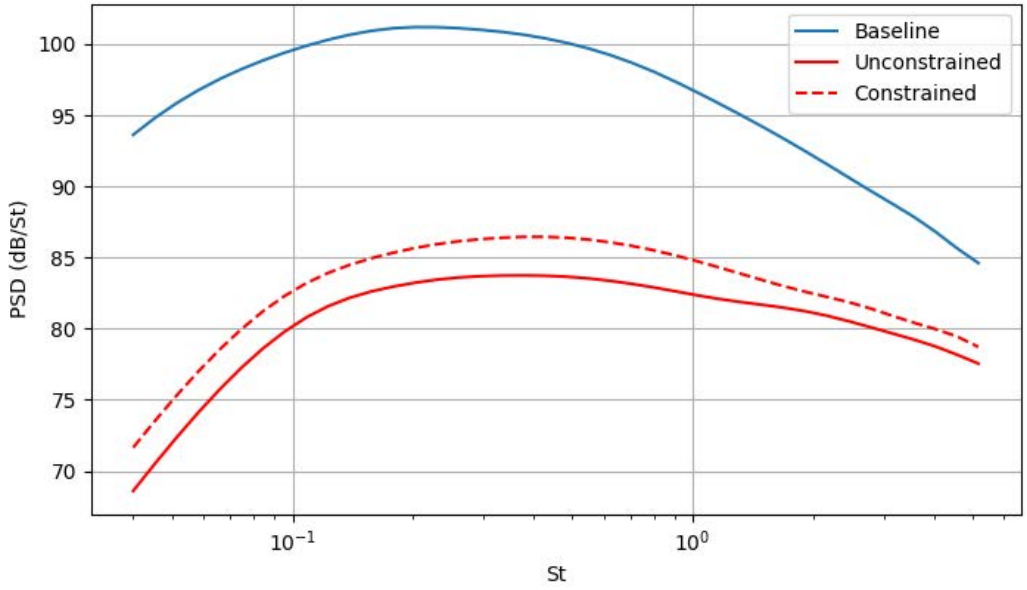


Figure 17. Baseline and optimized far field spectra for Poitiers optimization cases.

Comparing the two optimized geometries, both develop along similar lines. When prevented from simply expanding at the exit to reduce axial flow velocity, the nozzle instead develops an azimuthal radius asymmetry or 'waviness', similar to what is seen in a lobed mixer design. The amplitude of this waviness is significantly greater in the unconstrained case, whose geometry grows into something closer resembling lobes. The constrained case develops a squarer exit profile, whose final area is slightly contracted compared to the initial design point. Looking then at the relative performance of the two optimized geometries, the overall noise improvement in the constrained case is not much worse than that in the unconstrained case, with reductions of 12 dB and 15 dB, respectively. This suggests that while traversing this region of the design space, disruption of the shear layer, and the shape and amplitude of the associated turbulent kinetic energy field, via relatively small azimuthal variations has more impact on the far field noise than changes in the bulk axial velocity via exit area variations. It can also be seen that the single frequency noise objective monotonically reduces over both optimization problems, albeit to a lesser extent than the overall noise objective. This suggests that although the changes made during the design process have not resulted in crossover explicitly, they have resulted in an overall 'flattening' of the



spectrum, with the higher frequency part of the spectrum being raised in comparison to the low frequency part. This is illustrated clearly by the optimized geometry spectra plotted in Figure 17. In both cases, however, the nozzle 'squaring' that results in noise reduction also results in significant thrust deviation, corresponding to a loss of approximately 7% even in the constrained case. In a realistic optimization scenario, this would represent a design trade-off skewed too far in favor of noise reduction at the expense of propulsive performance. Repeating these optimizations with significantly tighter aerodynamic constraints will be important to demonstrate the real-world applicability of the method.

Considering the observed geometry changes in the context of existing design studies, there have been a number of investigations into the performance of similarly 'squared' or rectangular exit nozzles as compared to the round jet baseline. The conclusions of these studies have varied. The work of Tam and Zaman (2000) pointed out that beyond an initial region of evolution, both the flow field and radiated sound field associated with a square or rectangular jet is, “quite axisymmetric and practically the same as that of a circular jet.” In contrast, the experimental studies of Massey, Ahuja and Gaeta (2004), which examined unheated subsonic jets issuing from rectangular nozzles of varying aspect ratio, found that sideline Overall Sound Pressure Level (OASPL) was lowered for the rectangular geometries compared with the round baseline. Furthermore, this noise reduction effect was found to be more pronounced in lower AR rectangular exits, suggesting that an optimal geometry closer to a square is not unreasonable. The subsequent experiments of Bridges (2012) corroborated these observations and further noted that the non-square rectangular geometries result in an azimuthally varying effect on OASPL, whereby a reduction in noise was observed on the narrow side of the nozzle, but noise on the wide side was increased. It is possible that repeating this optimization problem without azimuthal averaging of the noise objective may therefore result in larger aspect ratio, narrowing in the direction of the chosen observer. Further work on this topic would include application of the framework to a greater range of baseline geometries, and investigation in detail the effects of different parameterizations of the geometry, and the outcomes of optimizing for multiple objectives.

Milestones

- Applied our modular implementation of the low-fidelity (RANS-based) acoustic prediction tool and AD-enabled adjoint design framework to two simple nozzle optimization problems.
- Extended our predictive model for the shallow-angle low-frequency component of jet noise based on resolvent analysis.

Major Accomplishments

- Demonstrated a simple predictive model of the acoustic line source CSD, using an eddy viscosity-augmented resolvent analysis to deduce coherent wavepacket structures in the hydrodynamic region of a jet, coupled with an explicit modified exponential function to account for the effects of axial coherence decay and the corresponding jitter. Preliminary predictions of far field noise using this model have shown reasonable agreement with experimental measurements.
- Demonstrated our AD-enabled framework for RANS-based jet noise minimization via a set of gradient-driven optimization steps on round and chevron baseline nozzle geometries. The resulting geometry changes are physically consistent with the conclusions of previous parametric study into the variation of nozzle geometries and jet flow fields for the purpose of noise reduction.

Publications

Shanbhag, T. K. (2024). *RANS-based methods for the prediction and reduction of jet noise* [Doctoral dissertation, Stanford University], Stanford University.

Outreach Efforts

None.

Awards

None.

Student Involvement

T. Shanbhag has led the efforts with geometrical acoustics, AD-enabled nozzle optimization, and wavepacket jitter modeling described for Task 3.



Plans for Next Period

None.

References

Bridges, J. (2012). Acoustic Measurements of Rectangular Nozzles with Bevel. *18th AIAA/CEAS Aeroacoustics Conference (33rd AIAA Aeroacoustics Conference)*.

Cavalieri, A. V. G., & Agarwal, A. (2014). Coherence decay and its impact on sound radiation by wavepackets. *Journal of Fluid Mechanics, 748*, 399–415. https://doi.org/10.1017/jfm.2014.186

Crow, S. C. (1972). Acoustic gain of a turbulent jet. *Annual Meeting of the APS Division of Fluid Dynamics*.

Crow, S. C., & Champagne, F.H. (1971). Orderly structure in jet turbulence. *Journal of Fluid Mechanics, 48*(3), 547–591.

Hasparyk, B., Jordan, P., Lesshafft, L., Pickering, E., & Colonius, T. (2024). Resolvent Modeling of Subsonic Jet Noise [Conference Paper]. *30th AIAA/CEAS Aeroacoustics Conference*. https://arc.aiaa.org/doi/10.2514/6.2024-3199

Hasparyk, B., Jordan, P., Martini, E., & Lesshafft, L. (2024). The Shape of Subsonic Jet Noise. *30th AIAA/CEAS Aeroacoustics Conference*. https://arc.aiaa.org/doi/10.2514/6.2024-3199

Massey, K., Ahuja, K., & Gaeta, R. (2004). Noise scaling for unheated low aspect ratio rectangular Jets [Conference Paper]. *10th AIAA/CEAS Aeroacoustics Conference*. https://arc.aiaa.org/doi/10.2514/6.2004-2946

Mollo-Christensen, E. (1967). Jet Noise and Shear Flow Instability Seen From an Experimenter's Viewpoint. *Journal of Applied Mechanics, 34*(1), 1–7. https://doi.org/10.1115/1.3607624

Tam, C. K. W., &. Zaman, K. B. M. Q. (2000). Subsonic jet noise from nonaxisymmetric and tabbed nozzles. *AIAA Journal*, *38*(4), 592–599. https://arc.aiaa.org/doi/10.2514/2.1029



Project 059(E) Moderate-fidelity Simulations for Efficient Modeling of Supersonic Aircraft Noise

The Pennsylvania State University

Project Lead Investigator

Philip Morris
Boeing/A.D. Welliver Professor Emeritus
Department of Aerospace Engineering
Pennsylvania State University
243 ECoRE Building
University Park, PA 16802
814-360-8681
pjm@psu.edu

University Participants

Pennsylvania State University (Penn State)

- P.I.s: Dr. Philip Morris (P.I.), Dr. Daning Huang (co-P.I.)
- FAA Award Number: 13-C-AJFE-GIT-070
- Period of Performance: January 1, 2025, to September 30, 2025
- Tasks:
  1. Coarse grid large eddy simulations (LES)
  2. Hybrid Reynolds-averaged Navier-Stokes (RANS) and acoustic analogy for noise predictions

Project Funding Level

The ASCENT Project 059E is funded at the following level: $100,000 from Federal Aviation Administration (FAA) and $100,000 in cost-sharing funding provided by Gulfstream Aerospace Corporation, a General Dynamics Company.

Investigation Team

Dr. Philip Morris (P.I.), All Tasks
Dr. Daning Huang (co-P.I.), All Tasks
Ms. Dana Mikkelsen (graduate student), All Tasks
Mr. Aravinth Sadagopan (graduate student), Computational fluid dynamics (CFD) tasks

Project Overview

The purpose of this project is to develop and assess efficient computational tools to simulate the flow and noise of civil supersonic aircraft engines.

The prediction of noise from supersonic jets, particularly when noise reduction devices are present, is a challenging computational task. Methods based on RANS solutions are relatively inexpensive to perform and provide satisfactory predictions of the average flow field, even for quite complicated geometries. The subsequent prediction of noise according to acoustic analogies is highly efficient but faces difficulties when the nozzle does not have simple axisymmetric geometry. Methods based on LESs provide considerably more information than those based on RANS methods about the unsteady flow and the noise generated. However, LESs are computationally expensive, particularly when the engine geometry is complex. This complexity is encountered in the case of nozzles with noise reduction devices, such as internal mixers. Noise predictions based on LES can be made quite efficiently by using the Ffowcs Williams and Hawkings (FW-H) acoustic analogy (Farassat & Succi, 1982; Ffowcs Williams & Hawkings, 1969), but long-time records are required to predict the noise radiated to far-field observers, thus adding additional expense to LES.



The approach in ASCENT Project 059E strikes a compromise between the accuracy and high computational cost of LES and the noise prediction limitations of RANS-based simulations. The RANS solution at the jet exit will be used as an initial condition for the external LES. This process will require the addition of some unsteady information based on linear instability modes. This approach will reduce the total computational cost because it removes much of the geometric complexity and the associated grid requirements for LES of the internal flow.

In addition, the LES-based predictions will be supplemented by more traditional acoustic analogy approaches based on RANS. As described below, the future research direction combines a RANS-based acoustic analogy approach for noise radiation to large angles to the jet downstream axis and a very coarse LES approach for noise radiation in the peak noise radiation direction.

If successful, ASCENT Project 059E will develop methods to predict the noise generated and radiated by civil supersonic aircraft engines. The developed tools should enable airframe and engine manufacturers to assess the noise impacts of engine design changes, and to determine whether the designs will meet current or anticipated noise certification requirements.

Major Accomplishments

The tasks for this project year included continued RANS simulations and LESs. The focus was on the Georgia Institute of Technology (Georgia Tech) dual-stream nozzle. LES simulations were performed at Gulfstream Aerospace, by using different grid resolutions to determine the flow resolution relative to different turbulent length scales. An acoustic analogy code was based on the Tam and Auriault (1999) model (Tam & Auriault, 1999) and integrated with output from the RANS simulations. Noise predictions with this method have been made for the Georgia Tech dual-stream nozzle and compared with measurements.

Task 1 – Coarse LES Simulations

Pennsylvania State University
Gulfstream Aerospace

Objectives

The goal of this task is to generate an LES using a coarse grid and then use the Ffowcs Williams-Hawkings acoustic analogy to predict the radiated noise. It is expected that the predicted noise radiation will only be reasonably accurate in the peak noise directions close to the jet downstream direction. As is noted below, trouble was found in generating the unsteady flow field prior to making noise predictions.

Research Approach

The case considered is described here. The nozzle exit is at 0.652336 m and diameter (D) is 0.0432 m. The complete nozzle is shown in Figure 1 for reference. The operating conditions are given in Table 1.

A steady-state RANS computation was performed for the nozzle configuration and grid shown in Figure 2. The mesh discretization involved 20 million finite volume (FV) cells with polyhedral cells and mesh adaptivity tailored to regions with high Mach number gradient. The objective was to resolve the shear layer at nozzle exit. The far field had cell size of 0.15 m and the nozzle wall had cells with size varying from 0.4 mm to 1 mm. A prism layer is specified on the nozzle wall to resolve the incoming boundary layer with thickness of 6 mm and 12 layers. The numerical scheme is detailed below. A stagnation inlet condition is specified for core and bypass inflow, and the far field is specified as freestream. The remainder of the surfaces are specified as wall with no-slip condition.

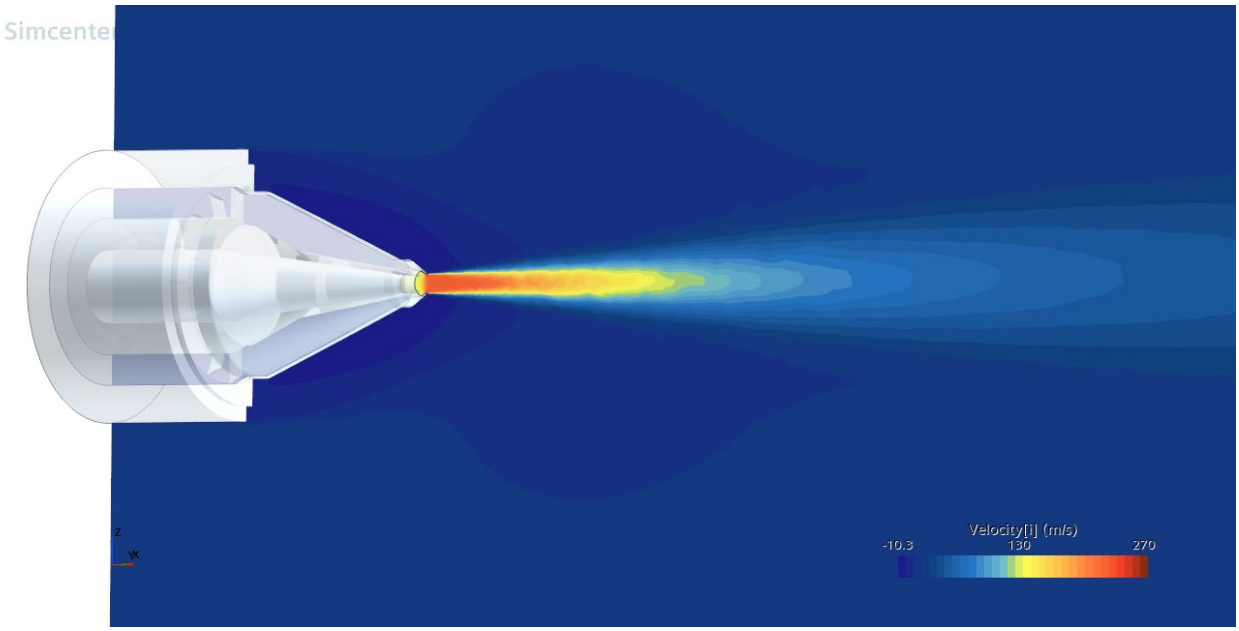


Figure 1. Geometry of jet nozzle exhaust in the present study. Velocity contour shown for NPR_1_39 case.

Table 1. Operating conditions for the dual stream nozzle.

Parameter	Core	Bypass
Nozzle pressure ratio, **NPR**	1.39	1.39
Nozzle temperature ratio, NTR	1	1
Total pressure, P_t	135219.98 Pa	135219.98 Pa
Total temperature, T_t	296.4433 K	296.4433 K
Jet Mach number, M	0.699	0.699
Velocity, **U**	230 m/s	230 m/s
Freestream		
Reference pressure, **P_{ref}**	97547 Pa	
Reference temperature, T_{ref}	295.45 K	
Initial Temperature, **T_i**	5.0e-4	

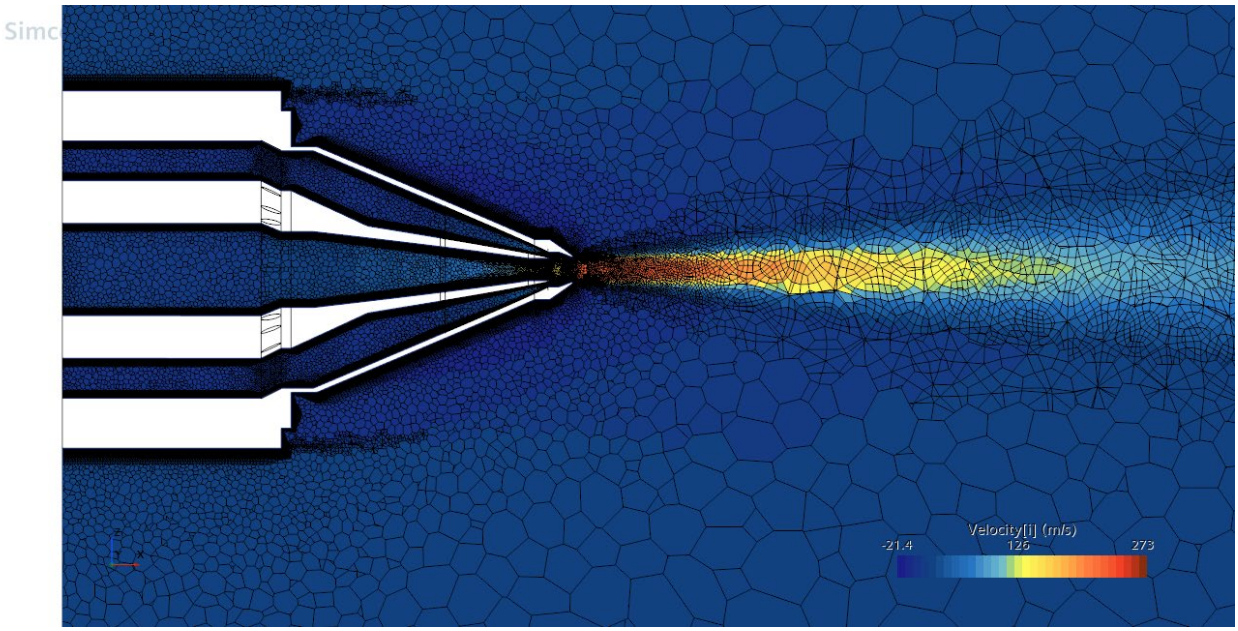


Figure 2. Jet nozzle configuration with the finite volume mesh. The Mach number contour corresponds to NPR_1_39 case.

Validation of the RANS with Experimental Results

The computational results were compared with the experimental particle imaging velocimetry measurements for the downstream section. Figure 3 compares the non-dimensionalized axial velocity with the experimental data at the centerline and lip line. It is observed that the predicted axial velocity at the core decreases at a faster rate than the experiment whereas it reasonably matches at the lip line. Figure 4 compares the axial velocity profiles downstream of the nozzle at different axial locations and the RANS predictions match with experimental data. Figure 5 provides a comparison of turbulent kinetic energy (left) and axial velocity (right) contours with the experiment.

A second order upwind scheme with AUSM+ inviscid flux was used for the RANS simulation. Diffusion is enabled at flow boundaries. To model turbulence, the $k-\omega$ shear stress transport (SST) (Menter) model was implemented with the assumption of ideal gas.

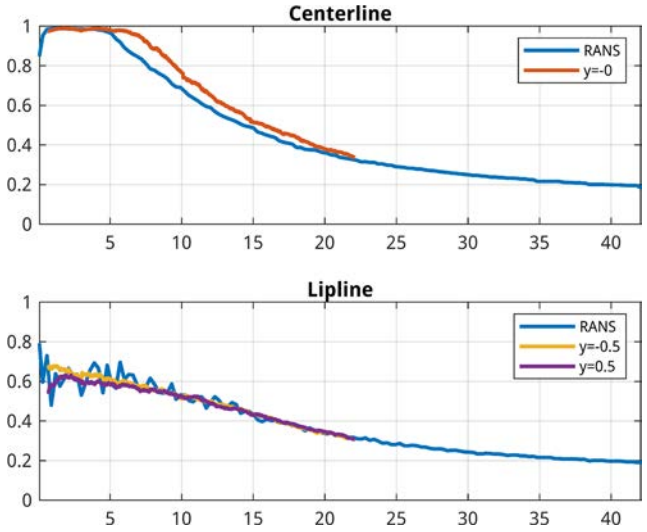


Figure 3. Comparison of non-dimensional axial velocity with the experimental data at centerline and lip line.

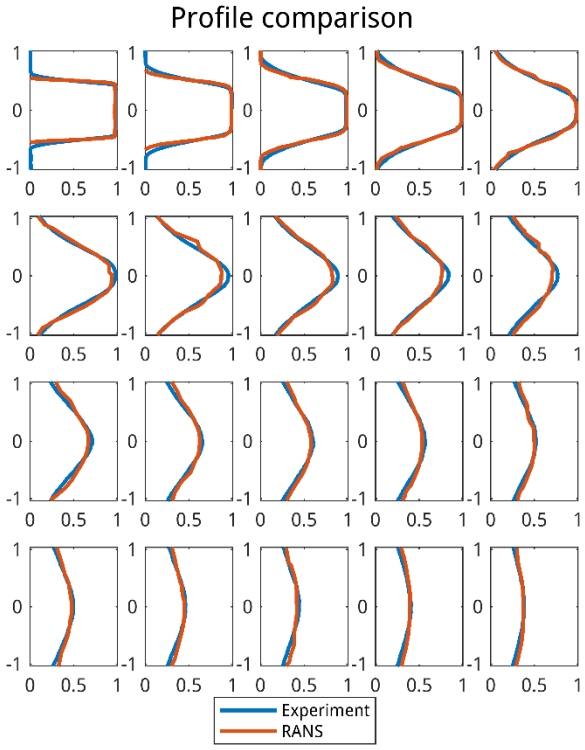


Figure 4. Comparison of axial velocity profiles downstream of the nozzle exit. x/D = 0 to 20 from top left to bottom right.

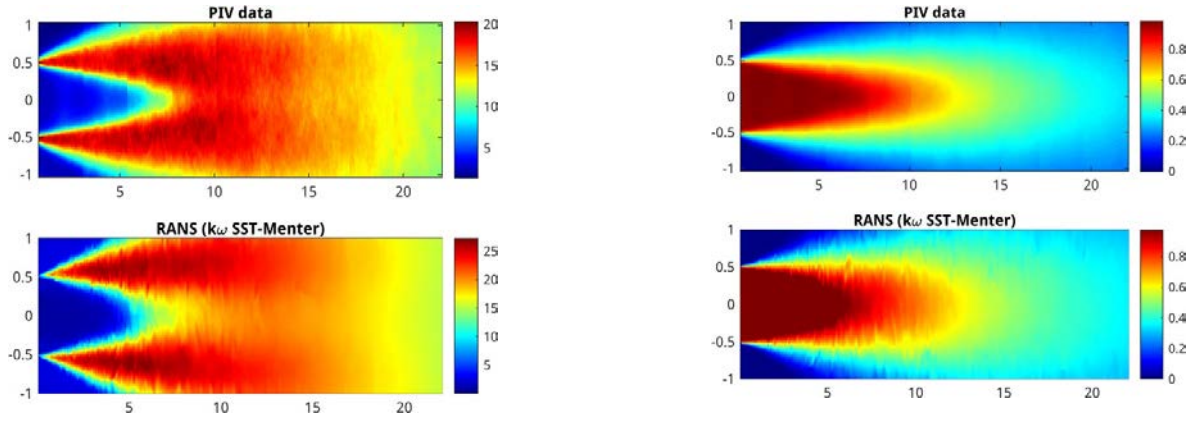


Figure 5. Comparison of turbulent kinetic energy (left) and axial velocity (right) contours with the experiment. Axis labels are x/D and y/D.

Unsteady Simulations

The next step was to compute the transient solution to characterize the shear layer instability behavior. An unsteady RANS with a second order finite difference (FD) temporal discretization, and a time step of 1.5e-4 s to resolve up to Strouhal number 5.0 failed to generate any shear layer instability.

The failure of RANS to compute shear layer instability led to the use of a coarse LES on a modified computational domain discretized using the unstructured polyhedral FV grid (see Figure 6). Most of the FV cells in the previous mesh were required to resolve the boundary layers inside the nozzle, therefore, to reduce the computational expenditure the flow field 0.02 m (x/D = 0.4651) downstream of the nozzle was used as the inlet for the modified computational domain.

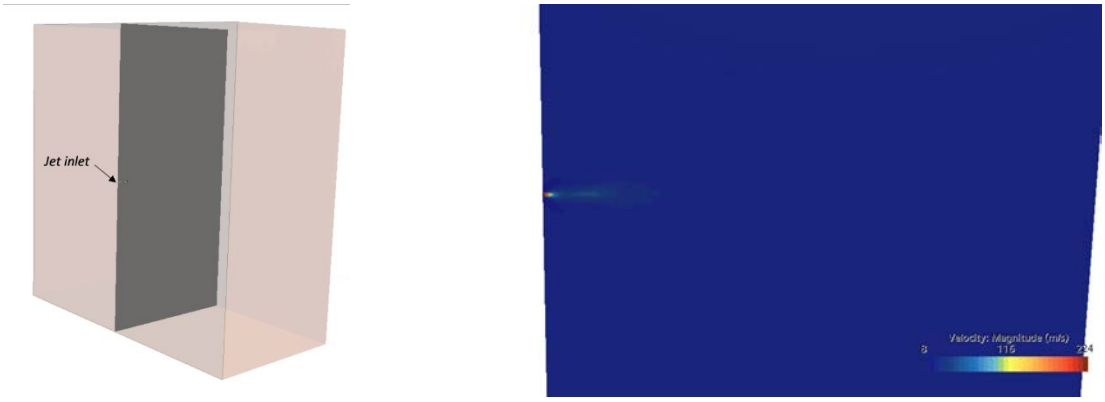


Figure 6. Computational domain of coarse large eddy simulations (LES) and initialized Reynolds-averaged Navier–Stokes (RANS) based solution.

The coarse LES domain was discretized with 3 million FV cells. The detail of the numerical scheme is given in below. Compared to the LES grid used in the fine grid simulations described in the last annual report, the selection of a cell size twice the original LES grid at the nozzle exit resulted in an unstructured mesh with 13 million cells. A bounded central scheme (second order with upwind blending factor of 0.15) with Roe inviscid flux was used for spatial discretization. The time step was $2.0^{e\text{-}6}$ s with a second order temporal discretization. The wall-adapting local eddy viscosity (WALE) sub grid scale model (C_w = 0.544; C_t = 3.5; kappa = 0.41) was implemented. For the fine grid LES, the spatial discretization used a trimmed mesh. The near wall resolution at the nozzle exit wall was 0.0004 m increasing to 0.024 m downstream of the

nozzle exit and then 0.001 m further downstream up to 0.42 m. This resulted in 42 million FV cells. The solution was initialized using steady state RANS, and then LES was implemented. A second order Central Difference scheme was used with turbulence modeled using the Dynamic Smagorinsky model with a filter width ratio of 2, and $C_t = 3.5$. A second order FD scheme discretized the temporal derivatives. Mach number contours for the fine grid LES are shown in Figure 7 for reference.

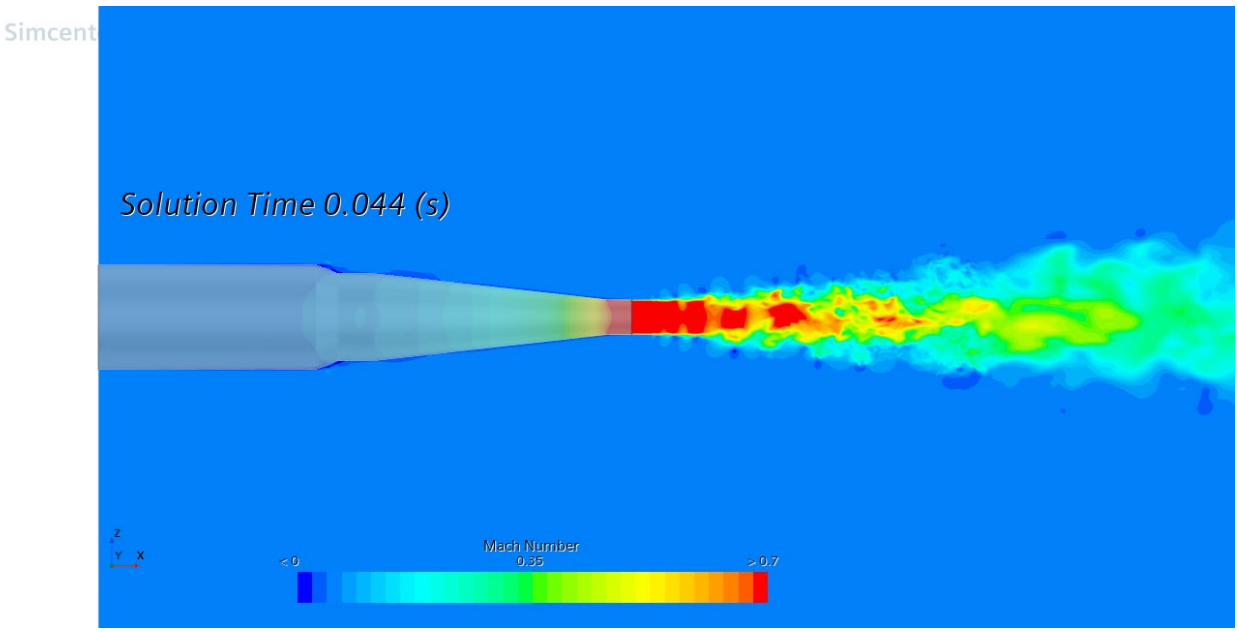


Figure 7. LES computation showing the Mach number contour.

Eigenfunction-based Forcing: Modal Analysis

Since coarse LES simulation failed to produce an unsteady behavior at the jet exit, eigenfunction-based small amplitude forcing at the inlet was used to generate shear layer instability in the coarse LES. A modal analysis of the shear layer profile using linear stability theory was performed 0.02 m downstream of the nozzle to include the low frequency modes. The velocity and temperature profiles were based on a hyperbolic tangent shape and fitted to the RANS-predicted profiles. These profiles of axial velocity, U and temperature, T are shown in Figure 8. The corresponding axial growth rates of the modes, based on linear stability theory (LST), are shown in Figure 9. The growth rate peaks at 2200 Hz, as shown in Figure 9. The corresponding mode shapes are shown in Figure 10.

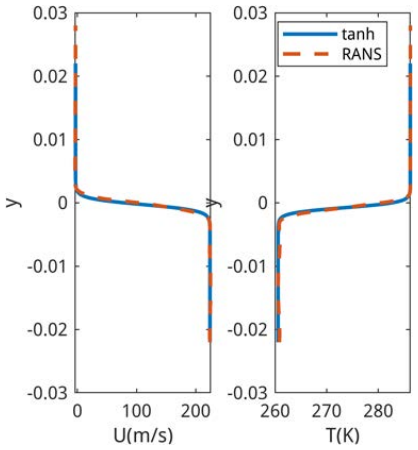


Figure 8. Comparison of hyperbolic tangent fit to the RANS simulations at 0.02 m downstream of the nozzle exit.



Figure 9. Growth rates of the shear layer instability from linear stability theory as a function of frequency and Strouhal number.

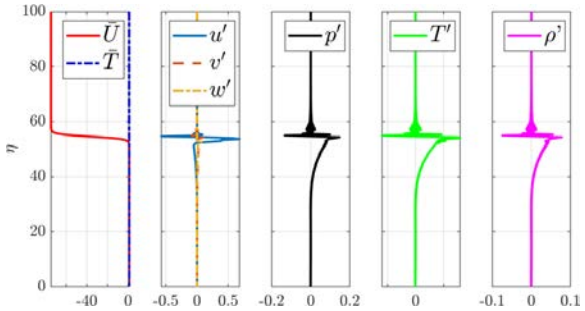


Figure 10. Kelvin-Helmholtz instability eigenfunctions computed from the linear stability analysis at 2200 Hz (St = 0.4) and axisymmetric mode.

The forcing at the jet exit was provided using a set of eigenfunctions at frequencies ranging from 500 to 3000 Hz with an interval of 500 Hz. The forcing set includes modes with angular wavenumbers varying from β = 0 to 2 with an interval of 0.25 for the same frequency range. Note that in this case, the spanwise wavenumber is approximated as angular wavenumber.



The forcing did result in unsteadiness in the jet's development, but not to the level of randomness seen in the fine LES simulations. This is seen in Figure 11 where the development of the forced jet (upper figure) is much slower than that of the unforced, fine LES case (lower figure).

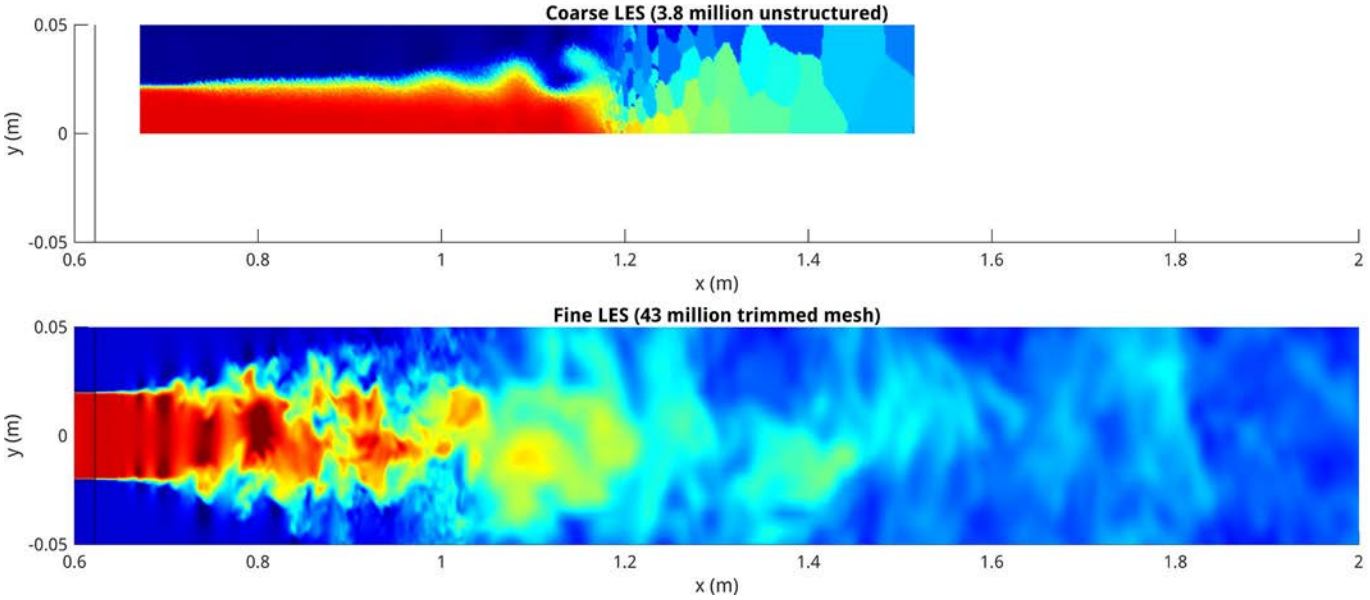


Figure 11. Comparison of initial jet development. Upper figure shows the excited jet case, and the lower figure shows the fine-grid LES simulation.

Task 2 - Hybrid RANS and LES Approach for Noise Efficient Predictions

Pennsylvania State University

Objective

The objective of this task is to develop a less computationally expensive approach. The basic concept and initial results were described in last year's annual ASCENT report. A summary and task progress are described below.

Research Approach

The idea arose from experimental results providing convincing evidence that jet noise consists of two characteristic source mechanisms. This was first proposed by Tam et al. (1996), who identified a small-scale similarity spectrum and a large-scale similarity spectrum. With these two spectral shapes, the radiated noise spectra of jets from a wide range of operating conditions could be matched very successfully. The original comparisons by Tam et al. (1996) were made for supersonic jets, but Viswanathan (2002) has shown that the same similarity spectra can be used to represent both subsonic and supersonic jet noise. A more recent overview of the "two-source model" has been given by Tam (2019). The two similarity spectra are shown in Figure 12.

Figure 13 shows how jet noise spectra at three polar angles can be decomposed into the two similarity spectra. At 90°, the full spectrum is described by the small-scale similarity spectrum. At 145°, both similarity spectra are required to match the full spectrum. Finally, at 165°, the large-scale similarity spectrum contributes almost completely to the full spectrum except for a possible contribution from the small-scale similarity spectrum at high Strouhal numbers. These examples are for an unheated $M_j = 0.51$ jet. For a higher Mach number, the large-scale similarity spectrum dominates over a wider-angle range. In addition, Tam and Zaman (2000) have shown that the same similarity spectrum can be used to represent the noise radiation to sideline directions for nozzles with tabs or rectangular nozzles, thus indicating that nozzle geometry has little influence on the noise radiation in these directions.

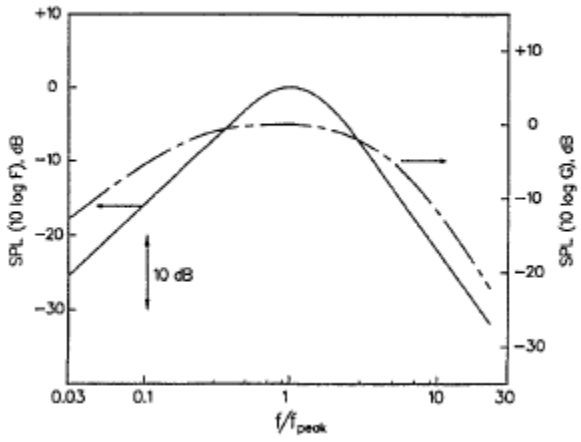


Figure 12. Similarity spectra for the two components of turbulent mixing noise. -------, large turbulent structures/instability wave noise; --- -- ---, fine scale turbulence noise.

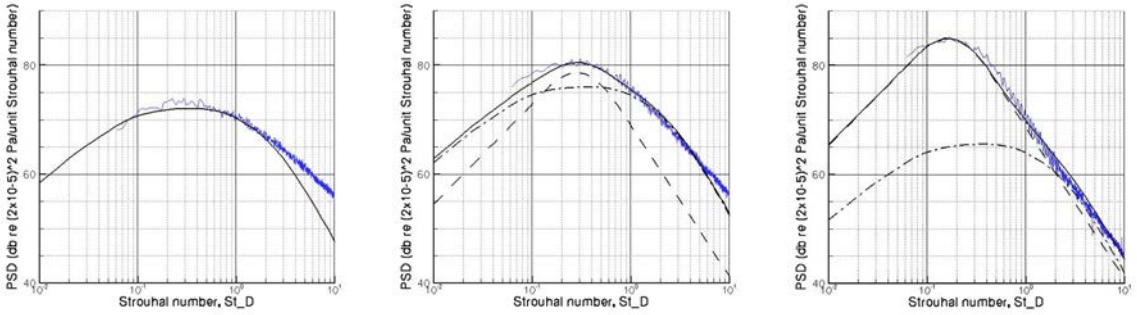


Figure 13. Demonstration of how the two similarity spectra can represent the full radiated noise spectrum at different polar angles: 90° (left), 145° (center), and 165° (right).

This behavior, particularly for the small-scale similarity spectrum, is similar to that displayed by the noise predictions using the Tam and Auriault (1999) prediction method for the noise from small-scale turbulence. Figure 13 shows predictions of jet noise from a convergent nozzle at the same acoustic Mach number of 0.875. One is unheated and has a static temperature ratio of 2.5.[1] The upper dataset is for the heated jet, and the lower set is for the unheated case. Predictions for three acoustic analogy models were performed by Gryazev et al. (2023). The models were those developed by Tam and Auriault (1999) and Khavaran and Bridges (2004), as well as the generalized acoustic analogy (GAA) by Goldstein and Leib (2008). The predictions for the Tam and Auriault model follow the trend seen in Figure 14, whereas the other models follow the experimental data more closely, because these models, particularly the GAA, attempt to model a non-isotropic source to represent noise radiation to large angles. The GAA model relies on LES to obtain the properties of the non-isotropic source, and whether the same properties would be retained if the geometry or complexity of the jet nozzle were different is unclear.

[1] These data were obtained as part of the Strategic Investment in Low-carbon Engine Tech program and were performed at QinetiQ.

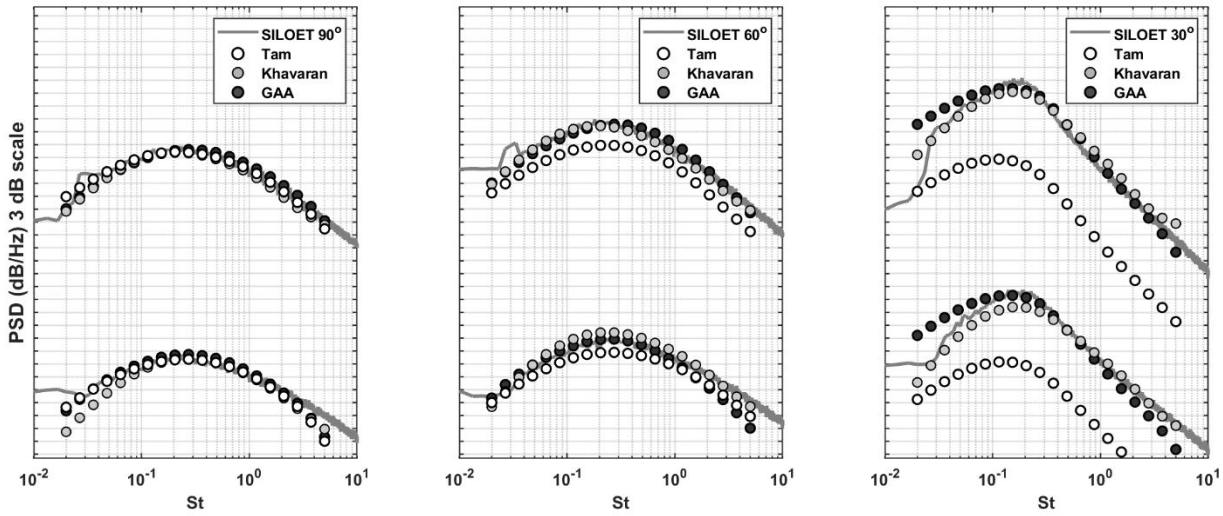


Figure 14. Noise spectra predictions of the cold (bottom) and hot (top) Strategic Investment in Low carbon Engine Technology (SILOET) jet, using the correlation scales based on the turbulent kinetic energy and dissipation rate reconstructed from RANS comparison.

These findings suggest that the Tam and Auriault (1999) model can represent the noise radiated by small-scale turbulence. The difference between the small-scale noise prediction and the full spectrum can be attributed to the contribution from the large-scale turbulence.

Due to time and personnel constraints no noise predictions using the acoustic analogy approach were completed. RANS predictions for several of the Georgia Tech experimental cases were performed as well as a RANS calculation for a rectangular jet; however, no noise predictions were made.

Awards

None.

Student Involvement

The Penn State team included one graduate research assistant, Dana Mikkelsen, who has been the lead on computational fluid dynamics simulations. During 2024, Dana Mikkelsen left Penn State to become a full-time employee of Gulfstream Aerospace. She graduated with Master of Science in Aerospace Engineering in December 2024. A senior graduate student, Mr. (now Dr.) Aravinth Sadagopan, provided computational support.

References

Farassat, F., & Succi, G. P. (1982). The prediction of helicopter rotor discrete frequency noise. *American Helicopter Society*, 497-507. https://api.semanticscholar.org/CorpusID:107210864

Ffowcs Williams, J., & Hawkings, D. L. (1969). Sound generation by turbulence and surfaces in arbitrary motion. *Philosophical Transactions for the Royal Society of London. Series A, Mathematical and Physical Sciences*,

Goldstein, M. E., & Leib, S. J. (2008). The aeroacoustics of slowly diverging supersonic jets. *Journal of Fluid Mechanics, 600*, 291-337.

Gryazev, V., Markesteijn, A. P., & Karabasov, S. A. (2023). Robustness of reduced-order jet noise models. *AIAA Journal, 61*(1), 315-328.

Khavaran, A., & Bridges, J. (2004, May 10-12). *Modelling of turbulence generated noise in jets* [Conference paper]. 10th AIAA/CEAS Aeroacoustics Conference, Manchester, Great Britain. https://doi.org/10.2514/6.2004-2983

Tam, C. K. (2019). A phenomenological approach to jet noise: the two-source model. *Philosophical Transactions of the Royal Society A, 377*(2159), 20190078.



Tam, C. K., & Auriault, L. (1999). Jet mixing noise from fine-scale turbulence. *AIAA journal, 37*(2), 145-153.

Tam, C., Golebiowski, M., & Seiner, J. (1996, May 6-8). *On the two components of turbulent mixing noise from supersonic jets* [Conference paper]. *Aeroacoustics conference*, State College, Pennsylvania. https://doi.org/10.2514/6.1996-1716

Tam, C. K., & Zaman, K. B. M. Q. (2000). Subsonic jet noise from nonaxisymmetric and tabbed nozzles. *AIAA journal, 38*(4), 592-599.

Viswanathan, K. (2002). Analysis of the two similarity components of turbulent mixing noise. *AIAA journal, 40*(9), 1735-1744.



Project 060 Analytical Methods for Expanding the AEDT Aircraft FLEET Database

Georgia Institute of Technology

Project Lead Investigator

Dimitri N. Mavris
Director, Aerospace Systems Design Laboratory
School of Aerospace Engineering
Georgia Institute of Technology
270 Ferst Drive, Mail Stop 0150
Atlanta, GA 30332-0150
404-894-1557
dimitri.mavris@ae.gatech.edu

University Participants

Georgia Institute of Technology (Georgia Tech)

- P.I.: Prof. Dimitri Mavris
- FAA Award Number: 13-C-AJFE-GIT-065
- Period of Performance: March 19, 2024, to September 30, 2025
- Task:
  1. Enhancement of the Aviation Environmental Design Tool (AEDT) Fleet database (Fleet dB)

Project Funding Level

The Federal Aviation Administration (FAA) funding for this project is $150,000 from March 19, 2024, to September 30, 2025. Georgia Tech has agreed to a total of $150,000 in matching funds.

Investigation Team

Dr. Dimitri Mavris (P.I.)
Dr. Michelle R. Kirby
Dr. Mayank Bendarkar, All Tasks
Dr. Ameya Behere, All Tasks
Bilal Mufti (graduate student)

Project Overview

The AEDT relies on aircraft noise and performance (ANP) data provided by aircraft manufacturers to support the calculation of aircraft trajectories and noise at receptors by using aircraft performance information and noise-power-distance relationships for specific aircraft/engine combinations. In the ANP/Base of Aircraft Data (BADA) workflow, ANP performance data are also used in the calculation of emissions inventories and air quality dispersion. However, not all aircraft in the fleet are represented in the ANP database. When ANP data are not available for a specific target engine/airframe combination, the AEDT uses a substitute aircraft from the ANP database to model the target aircraft by closely matching the certification noise characteristics and other performance parameters. However, a problematic issue is that the best substitute according to noise criteria does not always match the best substitute for emissions criteria. In addition, substitute aircraft do not capture the environmental benefits of newer aircraft with noise- and emissions-reduction technologies, thus resulting in overly conservative noise and emissions estimates.

The goal of this research is to increase the accuracy of AEDT noise and emissions modeling of aircraft not currently in the ANP database. Georgia Tech will identify, and review aircraft not currently modeled in the AEDT, and will collect information and necessary data to better understand the characteristics of these aircraft. Various statistical analysis



methods will be used to classify the aircraft into different types in terms of size, age, technologies, and other engine/airframe parameters. Quantitative and qualitative analytical methods will be identified and evaluated for each aircraft type, to develop ANP noise data for the aircraft. Validation data from certification data or airport planning documents will be gathered to validate the methods. After validation, the models will be applied to develop ANP and noise data for the aircraft. Finally, recommendations and guidelines will be developed for implementing the developed data in the AEDT, to expand the AEDT Fleet dB to include noise and performance data for aircraft currently not in the ANP database.

Task 1 - Enhancement of the AEDT Fleet Database

Georgia Institute of Technology

Objective

The objective of the last year of this research is to finalize the review of the AEDT Fleet dB entries for each unique equipment identifier, denoted as EQUIP_ID, and provide guidance to the AEDT development team on how to clean up the entries for more suitable noise and emissions modeling for stringency or inventory analysis.

Research Approach

Building upon the prior year approach to developing an ANP extension database, the final thrust of the research focused on finalizing the recommendations on erroneous EQUIP_ID entries in the Fleet dB. To accomplish this task, certification data from the FAA and the European Union Aviation Safety Agency (EASA) for each airframe and engine family. Certification data included the type certificate data sheet (TCDS), the EASA noise certification noise level database, and International Civil Aviation Organization's (ICAO) engine emissions databank (EEdB).

The methods used for matching the engine and airframe combinations comprised the following steps. In the ANP database, a total of 990 airframe/engine candidate combinations for noise data population were selected. The population procedure was started by selection of a specific airframe of interest (e.g., the Airbus A321-200 Series AIRFRAME_MODEL and "common aircraft name"). For that airframe, a specific engine, ENGINE_MODEL, among the different options available, was selected (e.g., the CFM56-5B3/2P). After the specific airframe/engine combination was defined, the same combination was searched and selected in the EASA certification noise level database. For matching to be performed, the selected airframe/engine combination in EASA database was required to be unique. To ensure this unique matching, a set of successive selection criteria was used involving the following sequence of steps:

1. Use the EASA TCDS to verify that the variants are actually on the airframe; use the EASA certification noise level database (e.g., Model Aircraft Database Jets) to cross-reference that the engine is certified for noise at the various maximum takeoff masses allowable (MTOM) as defined in the TCDS.
2. Use the EASA TCDS to verify that the engine emissions and thrust parameters in the ANP database are correct for the specific ENGINE_MODEL, as cross-referenced to the ICAO EEdB.
3. Identify and register identified differences by matching the ANP Equipment ID and EASA Record number.
4. For the certified airframe/engine combination in the EASA certification noise level database, select the maximum take-off weight (MTOW).
5. If no unique combination is obtained, proceed to select the maximum landing mass.
6. If the combination still has more than one option, the maximum cumulative noise level can be selected.
7. In cases in which multiple airframe/engine combinations have the same noise values, the first entry is selected.
8. Finally, if more than one combination remains after application of the preceding criteria, the most recent modification date for the data of the remaining combinations is selected. This modification date corresponds to the most recent date when the existing values for the selected combination were entered in the database.

The rationale underlying these selection criteria was to choose the most representative noise value of the airframe and engine combination selected. After a unique combination was found, the corresponding noise value was transferred from the EASA database to ANP extension database. To increase the number of combinations available for which noise values were obtained, engines with similar designation codes for some airframes were utilized. In this case, the criterion for selection was a direct comparison of the main parameters (bypass ratio, overall pressure ratio, and rated thrust) of the similar engines were selected. If the parameters were within 5% of each other, the combination was considered valid and was added to the ANP database. This process yielded data for less than 60% of the 990 unique EQUIP_IDs of interest. Upon further investigation of a unique EQUIP_ID entry for which noise data could not be established, erroneous and



questionable entries were identified when the ENGINE_MODEL was cross-referenced to FAA or EASA airframe TCDS. Four variables in the AEDT Fleet dB represent the proper entry in the flying fleet: AIRFRAME_MODEL, ACFT_DESCR, MANUF_DESC, and ENGINE_MODEL. In last year's research efforts, only a portion of these erroneous entries were documented, which was finalized in the current research.

Multiple teleconferences were held with the AEDT development team to walk through the recommendations for changes or removal of specific EQUIP_IDs to ensure a thorough understanding. The final ANP extension database and the compiled airframe and engine TCDS were also provided.

Milestone

- Developed a framework for identification of erroneous entries in the Fleet dB.

Major Accomplishments

- Finalized the ANP extension database and created additional certification database and provided to the AEDT development team at the Volpe National Transportation Systems Center.

Publications

None.

Outreach Efforts

None.

Awards

None.

Student Involvement

Bilal Mufti (graduate student): assisted in cross-checking of the Fleet dB with certification data and compiling that data from public sources.

Plans for Next Period

None. All tasks accomplished.

References

None.



Project 061 Noise Certification Streamlining

Georgia Institute of Technology

Project Lead Investigator

Prof. Dimitri N. Mavris
Director, Aerospace Systems Design Laboratory
School of Aerospace Engineering
Georgia Institute of Technology
Aerospace Systems Design Laboratory
Weber Space Science & Technology Building, Room 301A
275 Ferst Drive, NW, Atlanta, GA 30332
404-894-1557
dimitri.mavris@ae.gatech.edu

Dr. Michael Balchanos (co-P.I.)
Senior Research Engineer, Aerospace Systems Design Laboratory
School of Aerospace Engineering
Georgia Institute of Technology
Aerospace Systems Design Laboratory
Weber Space Science & Technology Building, Room 313B
275 Ferst Drive, NW, Atlanta, GA 30332
404-894-9799
michael.balchanos@asdl.gatech.edu

University Participants

Georgia Institute of Technology (Georgia Tech)

- P.I.s: Dr. Dimitri Mavris and Co-P.I.: Dr. Michael Balchanos
- FAA Award Number: 13-C-AJFE-GIT-066
- Period of Performance: October 1, 2024, to September 30, 2025
- Tasks:
  1. Define Model-Based Standard Framework.
  2. Develop a library of unmanned aircraft systems (UAS) and testing procedures
  3. Document and model noise testing and certification procedures based on existing practices
  4. Develop alternative procedures and assess their performance with existing tools (proof-of-concept)

Project Funding Level

The total amount of current funding from the Federal Aviation Administration (FAA) for ASCENT Project 061 is $250,000 for a 12-month period of performance. The Georgia Institute of Technology has agreed to a total of $83,333 in matching funds.

Investigation Team

Georgia Institute of Technology

Prof. Dimitri Mavris, (P.I.), Tasks 1-4
Dr. Michael Balchanos, (co-P.I.), Tasks 1-4
Dr. Adam Baker, (research engineer), Tasks 1-4
Dr. Jimmy Tai, (senior research engineer), Tasks 1-4
Dr. Evan Harrison, (research engineer II), Tasks 1-4
Balaji Ravikanti (graduate student), Tasks 1-4
Hussein Ali (graduate student), Tasks 1-4
Hajar Mali (graduate student), Tasks 1-4



Nathnael Geneti (graduate student), Tasks 1-4
Martin Poretti (graduate student), Tasks 1-4

All team members are affiliated with the Aerospace Systems Design laboratory (ASDL), under the School of Aerospace Engineering at Georgia Tech. Please refer to Figure 1 for a breakdown of the Georgia Tech ASDL Team.



Figure 1. ASCENT Project 061 Georgia Tech Aerospace Systems Design Laboratory (ASDL) team.

Past technical advisors who contributed to the tasks:

- **Mr. David Anvid**, Senior Research Engineer, provided guidance on best practices for noise certification testing, observed and articulated from an industry point of view.
- **Dr. Sehwan Oh**, postdoctoral researcher, focused on exploring current certification regulations, understanding their structure (i.e., hierarchy, associations, etc.) linked to Task 1, and providing input on the application of discrete event and agent-based methods as part of the efforts planned for Task 4.
- **Dr. Etienne Demers Bouchard,** postdoctoral researcher, focused on exploring process modeling methods from literature and formulating a canonical problem to assess the feasibility and applicability of various methods.

Former students who have contributed to the tasks:

- **Ms. Mika Xu,** a second-year Master of Science (MSc) student, contributed to the model-based systems engineering (MBSE) efforts for representing the UAS certification process in systems modeling language (SysML).
- **Mr. Rahul Rameshbabu,** a third year Doctor of Philosophy (PhD) student, supported activities in developing a parametric and interactive decision support tool.
- **Mr. Paul Wang,** a second-year PhD student, was involved in the formulation of a MBSE verification model for UAS.
- **Mr. Daewoon Kim,** a second-year MSc student, was leading the team's MBSE efforts for representing the baseline certification process in SysML.
- **Mr. Nathaniel Omoarebun,** a fifth-year PhD student, was supporting the team's MBSE efforts and SysML modeling activities.
- **Mr. Tyler Wills,** a second-year MSc student, was supporting the team's efforts in process improvement modeling (PIM) methods and process simulation.



- **Mr. Meric Taneri,** a second-year MSc student, was leading the team's efforts in PIM methods, stochastic process simulation (Markov chain Monte Carlo [MCMC]), and interactive visualization.
- **Ms. Shireen Datta,** an MSc student, supported efforts in documenting current procedures and exploring regulation-driven requirements, which are now included in the verification model.
- **Ms. Fatma Karsten,** a PhD student, worked on flight testing plan implementation and an effective perceived noise level (EPNL) calculation module within the MBSE verification model.
- **Mr. Arnaud Ballande**, an MSc student, worked on a process simulation capability for evaluating equivalent procedures under the PIM task.
- **Ms. Hayden Dean,** a PhD student, was instrumental in capturing and understanding current regulations and certification procedures, as dictated by the Certification Procedures for Products and Articles, 14 C.F.R. § 21 (2025), and Noise Standards: Aircraft Type and Airworthiness Certification, 14 C.F.R. § 36 (2025), as well as Advisory Circulars (AC) for Noise Standards: Aircraft Type and Airworthiness Certification, with a particular focus on AC 36-4D (FAA, 2017) and an emphasis on guidance instructions regarding flight testing for noise certification.
- **Ms. Domitille Commun,** a PhD student, worked on implementing a discrete event simulation (DES) model-based process simulation capability for the certification baseline.

Project Overview

Noise certification procedures (with their inclusion of equivalent procedures) have served aviation stakeholders (i.e., original equipment manufacturers [OEM], regulators, operators, airports, etc.) well since the 1960s. With new vehicle types and new technologies (including new entrants, digital technologies for airframes, propulsion, and measurements, etc.), it is necessary to critically examine the existing certification processes. Key features of current certification practices include equivalent procedures and supporting technology, which many OEMs utilize 14 C.F.R. § 36 (2025). Equivalent procedures are anticipated for both existing and new standards to further accommodate innovation in the future. The project objective is to examine current noise certification procedures and identify opportunities to streamline the noise certification process while recommending process updates and revised/new standards for building the flexibility needed to accommodate all air vehicle types. ASCENT Project 061 seeks to propose quantifiable process improvements and facilitate the application of traditional systems engineering and MBSE, while leveraging these methods for the management of regulatory requirements. To perform the proposed research under this effort, Georgia Tech has teamed with several industrial partners with extensive experience in noise certification. Each industrial partner brings expertise for different types of vehicles, such as large subsonic transports, propeller-driven small aircraft, and rotorcraft.

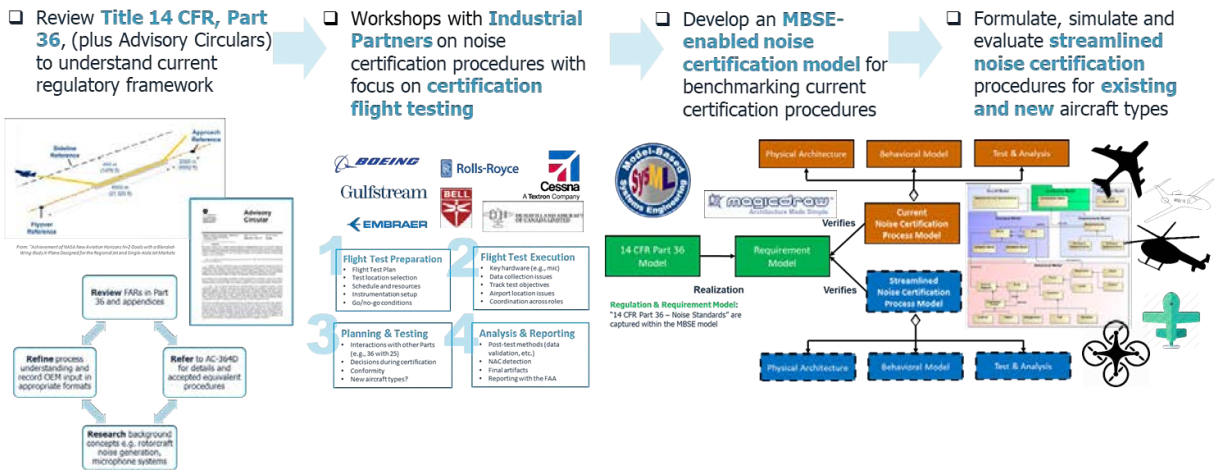


Figure 2. Roadmap toward a model-based framework for exploring current and streamlined noise certification.
AC: advisory circular; CFR: Code of Federal Regulations; FAR: Federal Acquisition Regulation; MBSE: model-based systems engineering; NAC: non-acoustical change; OEM: original equipment manufacturer.

The ASCENT Project 061 team is seeking to accomplish the following high-level goals:

- Identify opportunities for increased efficiency (by expediting steps and simplifying processes) and flexibility in current noise certification processes to accommodate multiple vehicle categories.



- Formulate and evaluate revised noise certification processes for current vehicle types and offer recommendations to the FAA (i.e., ACs for Part 36, AC 36-4D [FAA, 2017], etc.).
- Develop process modeling methods to enable quantitative assessments of noise certification.
- Facilitate the application of traditional systems engineering processes for complex systems and MBSE, leveraging these methods for the management of regulatory requirements.
- Leverage the technical expertise acquired in investigating and modeling noise regulatory frameworks and recommend procedures for certification testing and analysis to the FAA for small propeller-driven vehicles and UASs.

Overall ASCENT Project 061 Roadmap and Statement of Work

An overview of the ASCENT Project 061 roadmap toward goals and milestones is shown in Figure 3. The main goal is to provide recommendations to the FAA in the form of feasible equivalent procedures, supported by the latest technologies/hardware, as well as analysis techniques to support the certification of future air vehicle types. These recommendations should be accompanied by evidence that the suggested equivalent procedures are fully in compliance with ACs for Part 36 (FAA, 2017) and use case examples for future air vehicles (e.g., small propeller-driven aircraft and UASs). To implement this roadmap and achieve the targeted outcomes, the team will engage in four main tasks, along with the subtasks that have been prioritized for Year 5 of ASCENT Project 061. These tasks are summarized as follows:

- Task 1: Define Model-Based Standard Framework.
- Task 2: Develop a library of UAS and testing procedures.
- Task 3: Document and model noise testing and certification procedures based on existing practices.
- Task 4: Develop alternative procedures and assess their performance with existing tools (proof-of-concept).

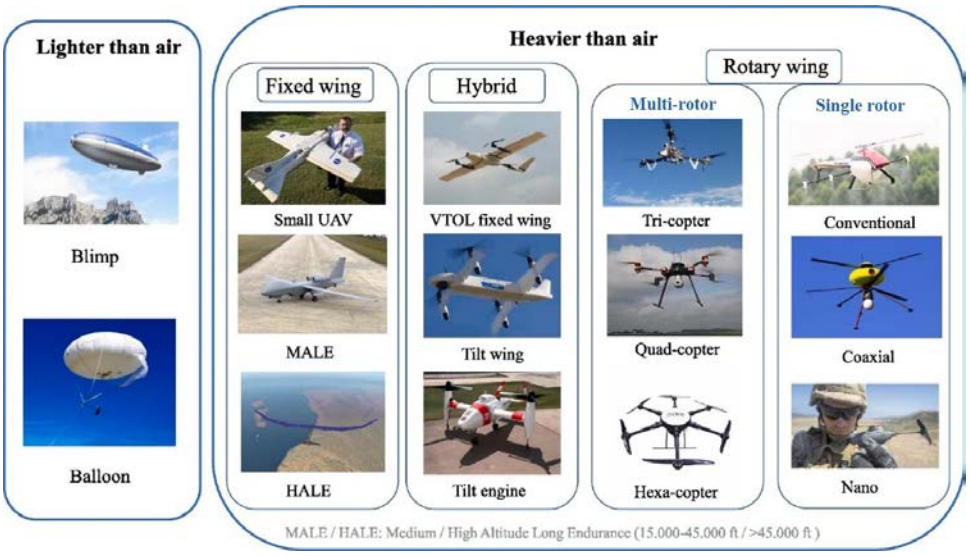


Figure 3. Overview of unmanned aerial system concepts. UAV: unmanned aerial vehicle; VTOL: vertical takeoff and landing.

General Direction for 2024-2025 (Year 5)

The FAA's Office of Environment and Energy (AEE) has suggested a timeframe for pivoting to UAS category certification as part of the year 4 effort (2023-2024). The main task for the Georgia Tech team is to investigate the feasibility and applicability of current ASCENT Project 061 models and analysis tools for exploring procedures and flight test planning to support noise certification of small propeller-driven UAS. To further align with the goals of the Committee on Aviation Environmental Protection (CAEP) Working Group 1 (WG1), the use of the ASCENT Project 061 model-based framework will be demonstrated for standard-setting problems, where decisions on noise standard formulation will be driven by criteria related to the effectiveness of certification rules, as well as the certification testing burden.



Looking ahead, the general direction emphasizes the demonstration of a **standard-setting framework for UAS and urban air mobility (UAM) vehicles** that enables the formulation and evaluation of standards meeting the criteria of being **environmentally beneficial, technically feasible, and economically viable**. This framework is expected to recommend a clear **demarcation between UAS and UAM categories** in terms of standard applicability, reference and test conditions, noise metrics, adjustments, measurement points, test profile procedures, and noise compliance limits. Establishing this structured distinction will ensure that future certification approaches remain scalable and appropriately tailored to the wide range of operational and design characteristics across these vehicle classes.

The above need is motivated by the primary issue with UAS certification, in that the spectrum of possible and available configurations covers a large class of aerial systems with completely different characteristics, as shown in Figure 3. It is assumed to be unlikely that UAS noise certification will be addressed as a "clean-sheet-of-paper" process. Multiple efforts are underway to establish guidance for noise certification similar to that for the transport category. The International Civil Aviation Organization (ICAO) is the recognized authority for developing and establishing a global baseline for noise standards and stringencies, and the harmonization of certification requirements among national airworthiness authorities remains desirable.

Goals and Technical Challenges

The high-level goals for this direction are to: (1) recommend testing procedures for UAS noise certification and, through the proposed methodology; and (2) ensure traceability between regulations, testing requirements, and certification procedures. As part of the planned capability demonstration for the model-based framework, the request for the Georgia Tech research team is to demonstrate the effectiveness of a standard-setting framework for UAS/UAM vehicles enabling the formulation and evaluation of standards that meet criteria of being environmentally beneficial, technically feasible, and economically viable.

Building on this foundation, the 2025 effort expands the scope to **demonstrate a comprehensive standard-setting framework for UAS/UAM vehicles** that directly supports the formulation and evaluation of certification standards meeting the criteria of **environmental benefit, technical feasibility, and economic viability**. This effort aligns with the broader international direction proposed in ICAO CAEP/Steering Group (SG) documentation (CAEP/SG.20221.WP.038.7), emphasizing harmonized and sustainable approaches to emerging aviation sectors.

The key challenges that have been identified and will be addressed by the Georgia Tech research team are as follows:

- There is currently a large spectrum of UAS designs and configurations under testing for production. As the FAA is preparing to release guidance for UAS noise certification, it is important to determine whether the MBSE-enabled method developed under ASCENT Project 061 is sufficiently flexible to accommodate UAS testing actions and to help establish a workflow that meets current and upcoming regulations.
- As there are currently no general regulations and the application of current certification procedures is on a case-by-case basis (e.g., recently completed certification framework for the Matternet® UAS), it is important to assess whether current testing procedures are effective for UASs.

Hence, the FAA is requesting that the ASCENT Project 061 team use the established framework to demonstrate its effectiveness in assisting the FAA through the assessment of Notice of Proposed Rulemaking (NPRM) plans, as these are being iterated before they become approved as part of the UAS noise certification standards.

As a starting point for the literature search, 14 CFR § 36 Appendices G and J are considered the only aircraft noise certification standards that might be applicable for noise certification of small, unmanned aircraft systems (sUAS) in the United States (U.S.), but a number of additional standards will be reviewed and included in formulating certification practices, including the following:

- ICAO Annex 16, Volume 1, Chapters 8, 10, 11, and 13
  - These are applicable to all fixed wing aircraft, rotorcraft, and tiltrotors below a maximum takeoff weight (MTOW) of 3,175 kg.
- NASA Ref. Publication 1258, *Aeroacoustics of Flight Vehicles: Theory and Practice* Volume 1 & 2, August 1991.
- ICAO CAEP Working Paper CAEP/SG.20221.WP.038.7, "UAS/UAM Standard-Setting Framework,"

® Matternet is a registered trademark of Matternet, Inc., Menlo Park, California.



Statement of Work/Task Definitions for UAS Noise Certification Research
Following the emphasized focus on UAS certification, the ASCENT Project 061 team further adjusted the statement of work (SOW) towards the development of use cases that address the FAA's needs for UAS noise certification. This SOW is based on the idea of integrating UAS certification goals into the model-based framework, which relies on an MBSE-based capture of the regulatory framework and PIM components. This development will entail the generation of multiple libraries that enable flexibility of use across a broader range of UAS configurations and support traceability between regulations, requirements, and elements of the library.

The tasks that have been implemented under the SOW are the following:

Task 1: Define Model-Based Standard Framework
- 1.1 Create a comprehensive noise standards database.
- 1.2 Breakdown the noise standards into logical elements.
- 1.3 Define a validation process for noise standards.

Task 2: Develop a library of UASs and testing procedures
- 2.1 Complete technical documentation of UAS configurations.
- 2.2 Complete technical documentation of UAS noise testing equipment.
- 2.3 Define UAS noise test plans.
- 2.4 Define possible simulation techniques.

Task 3: Develop a noise certification procedure based on existing practices
- 3.1 Transfer noise testing plans to the MBSE model.
- 3.2 Transfer noise testing data to the MBSE model.
- 3.3 Develop a full noise test plan.
- 3.4 Implement a validation process.

Task 4: Develop alternative procedures and assess their performance with existing tools
- 4.1 Develop alternative testing procedures using the elements library.
- 4.2 Transfer alternative procedures to the PIM.
- 4.3 Report on the performance of the alternative procedures.
- 4.4 Develop a proof-of-concept demonstration of the PIM capabilities.

Framework Demonstration Use Case for Standard Setting
As part of the framework capability demonstration, the ASCENT Project 061 team has scoped a problem that is specific to decision making for standard setting. In contrast to Tasks 1 to 4 listed above that mostly cover the development steps of the framework, the following tasks are specific to the demonstration exercise:

Task D.1: Define Model-Based Standard Framework
- Create a comprehensive database that synthesizes noise standards information from various sources including the FAA, European Union Aviation Safety Agency (EASA), and International Organization for Standardization (ISO).
- Analyze the existing standards to supplement a text-based definition of a standard by (1) identifying the categories of information necessary to sufficiently define a standard and then (2) use them to compare the existing standards.

Task D.2: Evaluate the Applicability of Existing Standards to UAS and UAM Vehicles
- Create a database of noise measurements (from publicly available test campaign data) for a variety of UAS/UAM configurations.
- Conduct a comparative analysis between UAS and UAM vehicles in terms of configuration, weight, operational altitudes, etc.
- Evaluate existing standards pertaining to prescribed test procedure altitude, speed, etc.
- Re-adjust and validate the standard framework once data for UAM vehicles are available.

Task D.3: Incorporate Process Complexity and Test Process Sensitivity Assessment to the Standard-Setting Framework
- Model and simulate the noise certification testing as a stochastic process.
- Quantify and assess the complexity level of the process using a set of complexity metrics.
- Identify trends related to the test conditions (i.e., altitude, speed, and weight).
- Conduct sensitivity analyses (e.g., histogram overlays and prediction profilers) to assess and compare different alternative processes.



Task D.4: Incorporate Economic Viability Assessment to the Standard-Setting Framework

- Conduct a time and cost analysis of the certification processes associated with the proposed standards to evaluate the overall economic impact on applicants to ensure the standards do not impose unnecessary economic burden.

Matrixing of Parallel ASCENT Project Efforts

Within the topic of UAS testing and certification for noise, there are currently three related, but unique, ASCENT research efforts (Figure 4):

- ASCENT Project 077: Measurements to Support Noise Certification for UAS/UAM Vehicles and Identify Noise Reduction (The Pennsylvania State University)
- ASCENT Project 009/094: Geospatially Driven Noise Estimation Module (Georgia Tech ASDL)
- ASCENT Project 061: Noise Certification Streamlining (Georgia Tech ASDL)

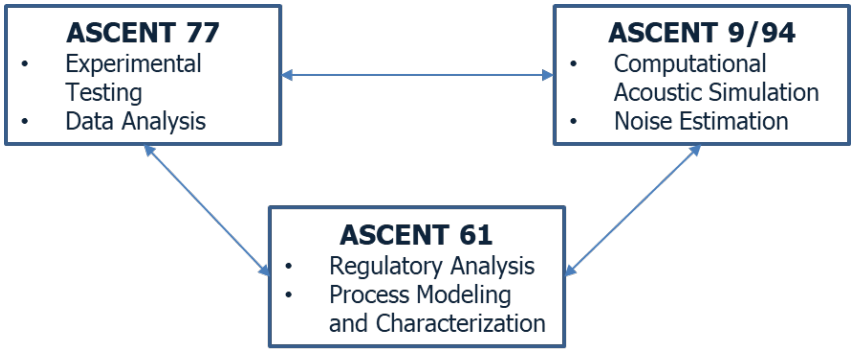


Figure 4. Coordination with parallel ASCENT work related to unmanned aerial system certification.

To preclude "mission creep" into other projects' remit and to leverage the work of the other ASCENT project teams, the ASCENT Project 061 team has been coordinating on a regular basis with ASCENT Project 077 and ASCENT Project 009/094 team members (as highlighted in Figure 4). The main collaboration areas are the following:

- ASCENT Project 077: Data sharing. Experimental test data provide real-world input for noise certification modeling. The results of the ASCENT Project 077 testing efforts provide a better understanding of the most significant parameters affecting UAS noise characteristics. The weighting of these parameters may influence modifications to the existing MBSE model.
  - Comparison of field geometry, test equipment, and basic flight profiles in addition to UAS configuration, weight, and vehicle performance
- ASCENT Project 009/094: Evaluation of possible vehicle operational environments and the practical impacts of noise profiles on the public. While the ASCENT Project 009/094 efforts do not provide direct technical data for MBSE modeling, these efforts do provide context for how noise level outputs from the certification process are applied to an operational environment.

Summary of Major Accomplishments to Date

The following accomplishments have been made to date for ASCENT Project 061:

- Performed a literature search and documented regulations and current testing standards for small UAS (14 CFR § 36 Appendix G, J, and H, and recent NPRMs)
- Completed the **architecting and implementation of a noise certification modeling and assessment framework** for transport and UAS category aircraft.
  - The traceable structure for UAS noise certification requirements uses the MBSE verification model developed for the transport category.
  - The MBSE framework can accommodate multiple UAS types and allows for process effectiveness and flexibility evaluation.
  - Finalized the model-based architecture and delineated key requirements across UAS standards for representation in the knowledge graph.
- Completed **development of the PIM**, which is a key enabling analysis module under the ASCENT Project 061 framework:



  - Developed and implemented metrics with the analysis.
  - Used stochastic Monte Carlo methods for capturing and simulating process uncertainties in the PIM.
  - Applied the PIM as a demonstration example for a typical plan for UAS noise testing to better capture the process and properly estimate the cost, staff, and time implications.
  - Calibrated the model using noise data provided by the 2021 Causey campaign (James et al., 2021).
- Formulated use cases aligned with the needs and recommendations provided by the OEM partners, with a focus on **exploring implications of alternative testing procedures on regulatory compliance.**
  - Focused on **process simplification** (e.g., lateral microphone placement or removal, if trusted analysis is used) for a set of scenarios and experiments.
  - Focused on exploring alternatives **for standard setting** for the overall framework demonstration.
- Reviewed and provided comparison of the UAM noise standards with the UAS standards for demarcation of categories.
- Developed a **visualization environment** in the JMP® software to support as a use case demonstrator and decision support environment.
- Published articles with the American Institute of Aeronautics and Astronautics (AIAA) for the SciTech 2025 and participated in the Quiet Drones Symposium 2024.

In the following sections, key contributions are highlighted, along with detailed descriptions of technical progress, research approaches, key milestones, and accomplishments for each task.

References

Certification Procedures for Products and Ports, 14 C.F.R. § 21 (2025). https://www.ecfr.gov/current/title-14/chapter-I/subchapter-C/part-21

FAA. (2017). *Advisory Circular 36-4D – Noise Standards: Aircraft Type and Airworthiness Certification*. Federal Aviation Administration. https://www.faa.gov/documentLibrary/media/Advisory_Circular/AC_36-4D.pdf

ICAO. (2018). Annex 16 to the Convention on International Civil Aviation: Environmental protection, Volume I – Aircraft noise (9th ed.). International Civil Aviation Organization.

Hubbard, H. H. (1991). *Aeroacoustics of Flight Vehicles: Theory and Practice,* Volume 1: Noise *Sources*. National Aeronautics and Space Administration. https://ntrs.nasa.gov/citations/19920001380

Hubbard, H. H. (1991). *Aeroacoustics of Flight Vehicles: Theory and Practice, Volume 2: Noise Control*. National Aeronautics and Space Administration. https://ntrs.nasa.gov/citations/19920005561

ICAO. (n.d., working paper). CAEP/SG.20221.WP.038.7 - UAS/UAM Standard-Setting Framework. Committee on Aviation Environmental Protection.

Task 1 - Define Model-Based Standard Framework

Georgia Institute of Technology

Objectives

In support of the main research objective of ASCENT Project 061 Task 1 focuses on examining current noise standards (Task 1.1) and benchmarking against current industry practices in how these standards are adopted and implemented (Tasks 1.2 and 1.3).

Task 1: Define model-based standard framework
- 1.1 Create a comprehensive noise standards database
- 1.2 Breakdown the noise standards into logical elements
- 1.3 Define a validation process for noise standards

Research Approach

Task 1.1 Create a Comprehensive Noise Standards Database

For Task 1.1, the main goal was to create a comprehensive database that synthesizes noise standards information from various sources including the FAA, EASA, and ISO. The task objective was to gain an understanding of current UAS and UAM noise standard frameworks in terms of their intent and structure. In particular, our team conducted a thorough

® JMP is a registered trademark of SAS Institute Inc., Cary, North Carolina.



literature review of noise standards for UAS and UAM vehicles that were issued by the FAA, EASA, and ISO. Figure 5 illustrates some of the existing standard references that were explored during this process. A traceable and manageable model-based environment is necessary to keep track of relationships and dependencies between all standards.

Along with the extensive review of existing noise standards, the research team aimed to obtain a fundamental understanding of the noise standard framework starting from the general regulatory intent which is to limit the annoyance to communities where UAS/UAM operate. The generation of standards that can successfully achieve this intent requires an understanding of how UAS/UAM vehicles produce noise and what are the key sound features that represent the human auditory system response. This fundamental understanding will provide the basis for understanding the noise measurement procedures and the choice of noise metrics in the existing noise standards as demonstrated in Figure 6.

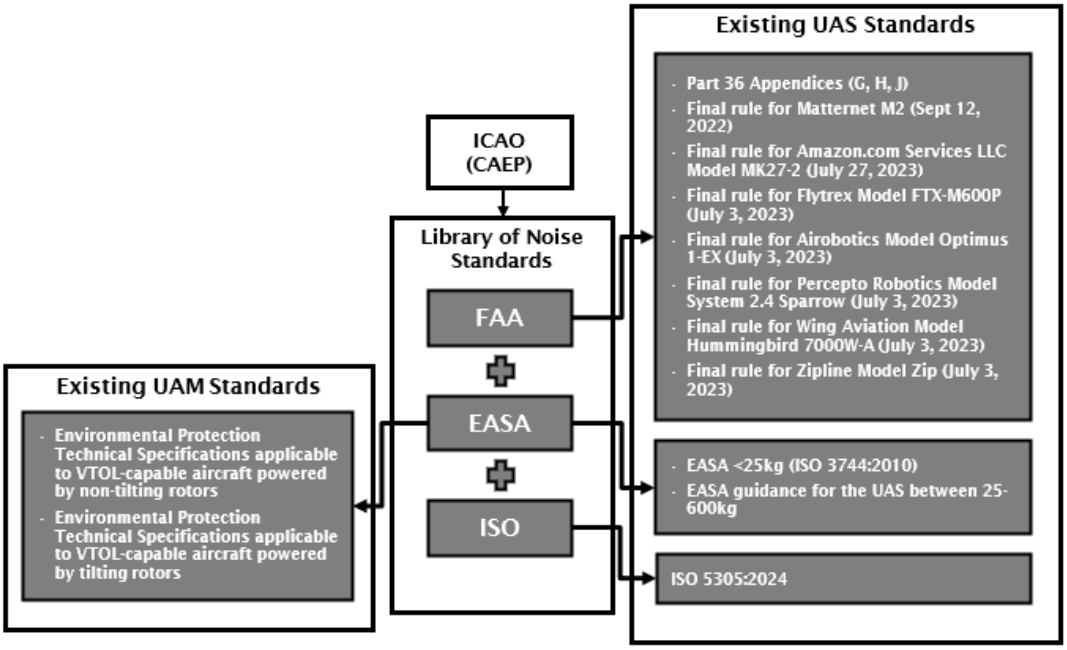


Figure 5. Existing noise standards frameworks. CAEP: Committee on Aviation Environmental Protection, EASA: European Union Aviation Safety Agency, FAA: Federal Aviation Administration, ICAO: International Civil Aviation Organization, ISO: International Organization for Standardization, VTOL: vertical takeoff and landing.

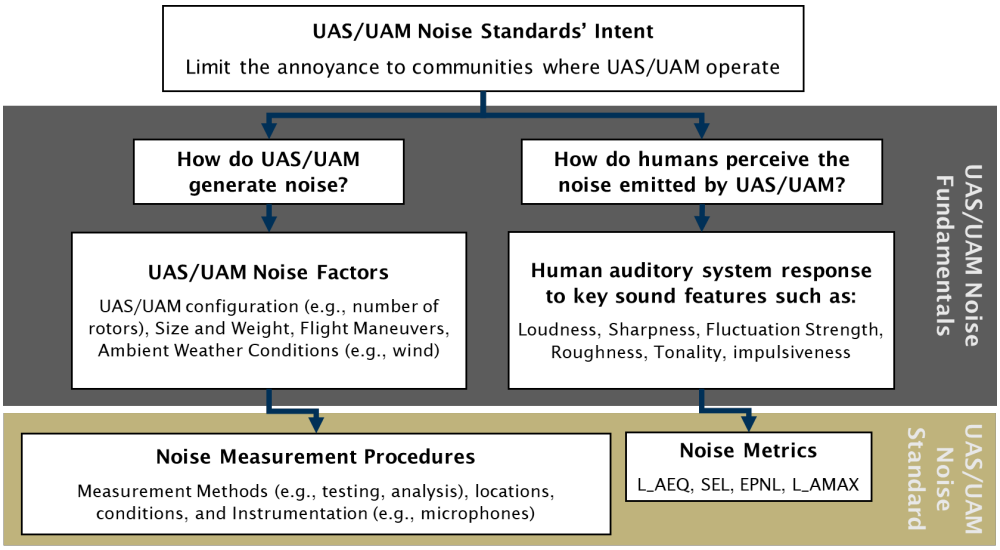


Figure 6. Noise standards intent, noise factors, key sound features and how they relate to the standards. UAM: urban air mobility, UAS: unmanned aircraft system.

Moreover, another motivating factor for creating the noise standards database is to examine the existing body of standards and identify the differences and similarities between them. Figure 7 illustrates a relationship diagram used to visually determine the different associations between the existing standards from different entities. This examination aims to produce two outcomes: (1) establishing a demarcation between UAS and UAM noise standards (as illustrated in Figure 8) and (2) enabling the identification of gaps within current UAS/UAM noise standards.

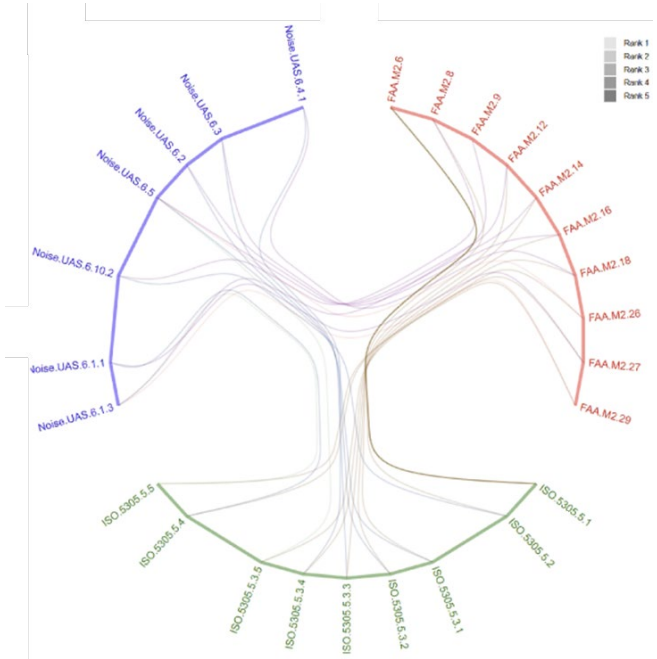


Figure 7. Relationship diagram showing the associations between the existing standards from different entities.

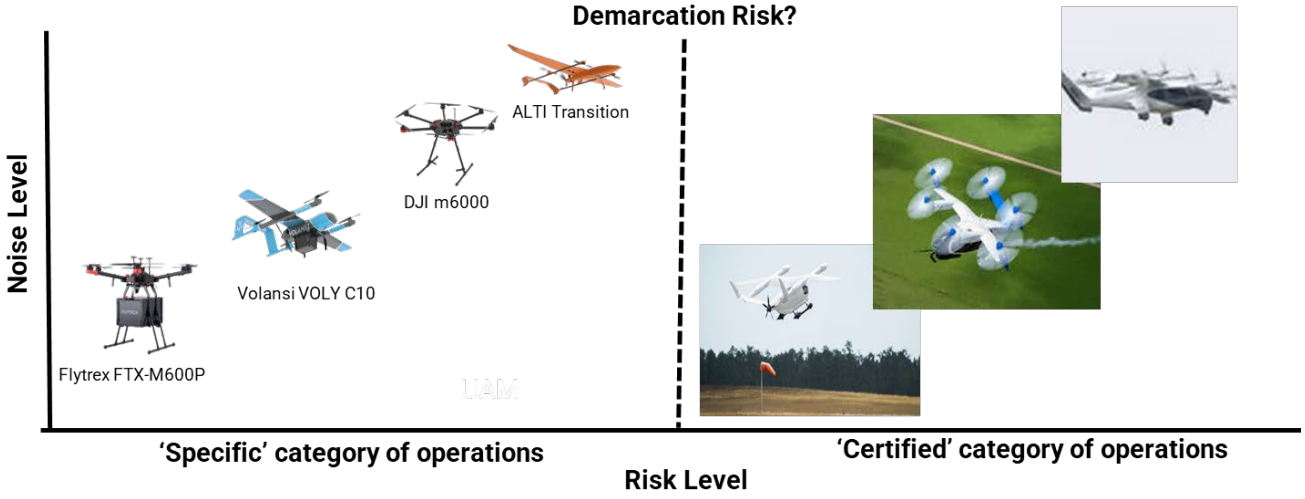


Figure 8. Demarcation between UAS and UAM noise standards.

To investigate the demarcation between the UAS and UAM noise standards, a case study considering the EASA's UAS and UAM noise standards was formulated by our team. By comparing the EASA's UAS Noise Measurement Guidelines and Environmental Protection Technical Specifications (EPTS) for vertical takeoff and landing (VTOL) capable aircraft as shown in Table 1. It is evident that weight cannot be considered as the demarcation parameter since the weight range of both frameworks overlap. Instead, the EASA uses "Risk" as a demarcation parameter between the UAS and UAM noise standards. In general, the EASA defines risk as the potential harm based on the environment, vehicle type, and nature of the operation (EASA, 2023). Higher risk operations require stricter regulations and certifications to ensure safety. Based on this definition, the EASA also provides three categories of risk:

1. Open (Low Risk): Drones are operated in visual line-of-sight under specific limits (e.g., weight, height), typically over nonpopulated areas, with no need for prior authorization (EASA, 2024a)
2. Specific (Low to Medium Risk): Requires an authorization due to higher risks (e.g., flying near people or complex environments) and needs an operational risk assessment (EASA, 2019)
3. Certified (High Risk): For the most dangerous operations (e.g., over urban areas or transporting people) where certification of both the drone and operator is mandatory (EASA, 2024b)

This delineation leads to trying to determine the influence of risk classification on the applicable noise standards. To this end, understanding the risk of annoyance to communities where UAS/UAM vehicles operate in terms of factors such as weight, configuration and concept of operations (CONOPS) is crucial to quantify risk, and thus produces a risk classification that can be mapped to applicable noise standards (i.e., noise metrics, test types, the number of microphones, etc.). The goal of this procedure is to propose proportional applicable noise standards corresponding to certain risk levels. Determining the proportionality of noise standards to the vehicle risk classification requires the evaluation of the Economic Viability (Economic Burden) of alternative noise standards in terms of time, cost, and process complexity.

One of the benefits of the outcome of Task 1.1 is that team members quickly became more knowledgeable of basics on noise standards in preparation for Task 1.2 (breakdown of standards) and were able to build a comprehensive MBSE representation (in SysML) of the current framework (see Task 3.1).

Task 1.2 Breakdown the Noise Standards into Logical Elements

Once a comprehensive database of existing noise standards has been established, the second step is to analyze existing standards to supplement a text-based definition of a standard. This is done by identifying the categories of information necessary to sufficiently define a standard and then use it to compare the existing standards. Our team aimed to demonstrate the flow of procedures, associations, and dependencies across the standard framework items. This was achieved by establishing a clear breakdown of noise standards in a proper structural arrangement as shown in Figure 9. This breakdown was inspired by the works of Bendarkar et al. (2023) and Fazal et al. (2022). Bendarkar et al. (2023)

provided a structural hierarchy of FAA regulations comprising four layers, (1) part, (2) subpart, (3) grouping, and (4) paragraph. Whereas Fazal et al. (2022) constructed a regulatory framework identifying three main categories of regulatory statements, (1) regulation requirement, (2) regulation context, and (3) regulation test.

Table 1. Comparison between the European Union Aviation Safety Agency (EASA) UAS Noise Measurement Guidelines and Environmental Protection Technical Specifications (EPTS) for VTOL capable aircraft (VCA).

	EASA EPTS applicable to VCA	EASA guidance for the UAS between 25-600kg
Weight Range	< 80,000 kg	25 kg – 600 kg
Prescribed Tests	Takeoff (TF), Approach (AP), Level Flyover (LF), Hover (H)	Level Flyover (LF), Hover (H)
Noise Metrics	EPNL (TF, AP, LF), L_AEQ (H)	SEL (LF), L_AEQ (H)
# of Microphones	3 (TF, AP, LF, H*), 9 (H) Inverted Ground Microphones	1 (LF, H) Inverted Ground Microphone
Noise Limits	87.0314 + 9.9673 log10 M (TF) 85.0314 + 9.9673 log10 M (LF) 90.0314 + 9.9673 log10 M (AP) in EPNdB	Not Applicable
# of runs	6 runs (TF, AP, LF, H)	6 runs (LF, H)

Breaking down standards into logical elements facilitates systematic comparison and helps to identify essential information needed to establish standards and ensure traceability. The breakdown in Figure 9 organizes standards into sections, paragraphs, and equations, ensuring clear and systematic representation. It also ensures uniformity, enabling diverse standards to seamlessly fit into a consistent framework. A breakdown was created for each of the noise standards gathered in the database.

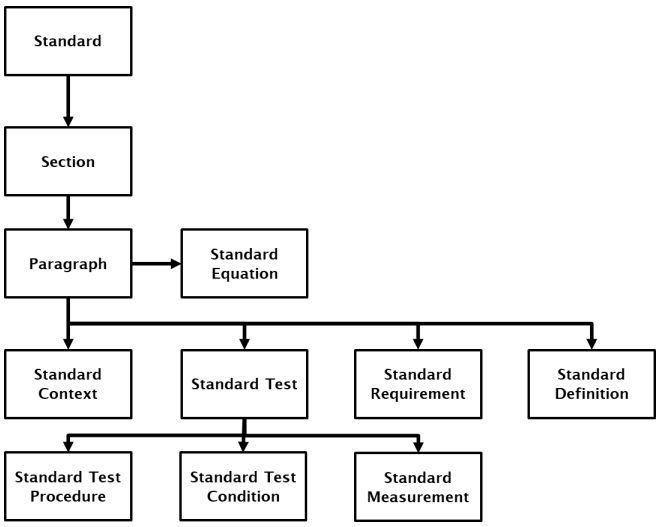


Figure 9. Standards breakdown and elements.

Establishing a breakdown of noise standards is a crucial first step in creating a model-based standards setting framework. As mentioned previously, one of the aims of the model is to provide a traceable and manageable model-based environment to keep track of relationships and dependencies between all the standards. In addition, the complexity of this process becomes apparent by examining the intricate networks created between standard framework items. The MBSE model can aid in nullifying this complexity by capturing the process of creating the certification plan in addition to other

supplementary domain knowledge within one model that is the singular source of truth. More information about the MBSE model's representation of the framework that was created in MagicDraw® is provided in Task 3.1.

A critical element of the standard breakdown is the standard requirement. Defining and maintaining a good set of requirements is vital for the successful design, development, and operation of systems, products, and processes. A requirement is defined as "a statement that identifies a system, product or process' characteristic or constraint, which is unambiguous, can be verified, and is deemed necessary for stakeholder acceptability" (International Council on Systems Engineering, 2006). "Good" requirements are those having attributes such as necessary, unique, unambiguous, clear, concise, complete, consistent, technically feasible/achievable/obtainable, traceable, measurable/quantifiable, verifiable (e.g., testable), able to be validated, operationally effective, and survivable and singular as outlined by the U.S. Department of Defense (DoD) *Systems Engineering Guidebook* (2022). In addition, requirements can vary in their type, which encompasses functional, nonfunctional, design, performance, certification, etc. (Firesmith, 2005).

The FAA Writing Standards provide a useful guide for defining the requirements to satisfy the desirable requirement attributes outlined by the DoD *Systems Engineering Guidebook* (2022) that are nonfunctional in nature (detailed in the Task 1.3). These standards include word choice such as using "must" instead of "shall," using short sentences and short paragraphs, limiting the use of abbreviations and acronyms, etc. (FAA, 2003). While converting the standards into requirements, the following considerations were taken (Kim et al., 2023):

- Not all standards needed to be converted into requirements.
- A single standard often needed to be broken down into multiple requirements. Conversely, multiple standards were sometimes merged into a single requirement.
- The standards do not always provide all the necessary information, so additional metrics and clarifying information were gathered from literature reviews and other noise standards related documents.

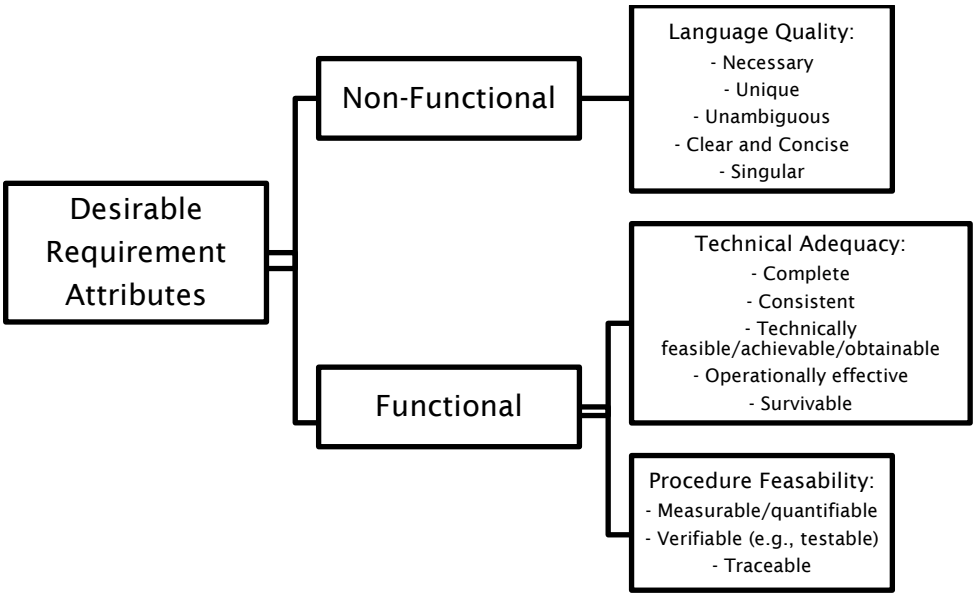


Figure 10. Attributes of desirable requirements.

Task 1.3 Define a validation process for noise standards.
Following the creation of a standards database and the breakdown of standards into their elements, it is imperative to verify noise standard requirements satisfy the desirable requirement attributes. The attributes can be classified into functional and nonfunctional categories, as illustrated in Figure 10. Functional attributes are concerned with the feasibility and technical adequacy of the requirements, whereas nonfunctional attributes are those concerned with language quality. Functional attributes require data for verification, unlike nonfunctional attributes. To this end, the standards requirements

® MagicDraw is a registered trademark of No Magic, Inc., Allen, Texas.



analysis process (outlined in Figure 11) provides a framework that allows for the verification of regulatory requirements' adherence to the desired requirement attributes. The outline indicates that once the requirements are defined, data need to be collected using flight testing data. Raw data are then processed by applying procedures such as correlating noise measurement data with position, calculating the required noise metrics (e.g., sound exposure level [SEL]), and applying the necessary data corrections (duration adjustments). The processed data are then used to verify the requirements. Additionally, the requirements can also be checked for functional attributes in the presence of available test data and experience. This is an iterative process, so there is a feedback element that allows for the refinement of the requirements such that it will satisfy the desired requirement features.

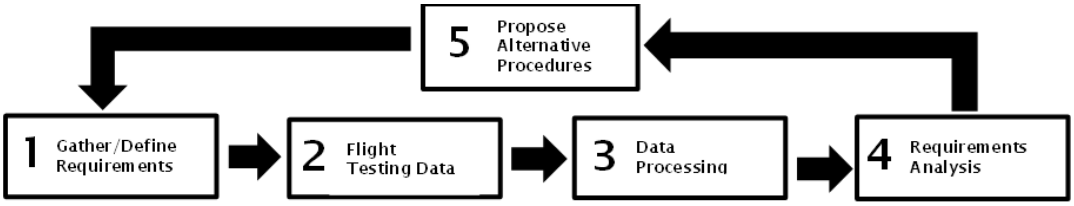


Figure 11. Noise standards requirements analysis process.

The iterative nature of the requirements analysis process dictates whether a standard requirement is deemed unsatisfactory or can be improved in terms of functional attributes; alternative standard requirements need to be proposed (as shown in Figure 11). These alternative requirements are meant to bridge the current gap that exists between current noise standards and UAS/UAM certification needs. Proposing alternative requirements will contribute to capturing the uniqueness of UAS/UAM vehicles while also addressing the challenges associated with their certification (i.e., operational and noise metric limitations). The proposed standards may include the use of different noise metrics, microphone setups, or additional flight tests that better capture the specific mission profile of UASs. Such suggestions could convert to opportunities for potential process streamlining if recommended practices are uncoordinated with current procedures.

The alternative standard requirements can be generated by identifying combinations in the morphological matrix shown in Table 2. The options provided by the matrix are surveyed from literature including FAA, EASA, and ISO noise standards.

Table 2. Noise standards morphological matrix.

Flight Test Profile	Flyover	Hover	Vertical Takeoff/Landing	Infrastructure Inspection	Maneuver
Microphone Type	Ground microphone	Inverted ground microphone	Elevated microphone on a tripod	Elevated microphone on a crane (high altitude)	-
Microphone Array Design	Linear (horizontal)	Circular	Vertical, elevated microphone array	-	-
Noise Measurement Metric	Sound exposure level (SEL)	A-Weighted maximum sound level (LAMAX)	Equivalent sound level (LAEQ)	Effective perceived noise level (EPNL)	-

The objective for generating alternative noise standards is to explore options for formulating a streamlined noise certification process. The following target objectives for streamlining the certification process are currently under consideration:

- Reduce the number of steps in the process, with anticipated savings in time and cost.
- Replace steps in analysis, data preparation, and post-processing with digital tools.
- Enhance automation on procedural tasks (e.g., data retrieval, queries, processing, and report generation).
- Simplify setup requirements to facilitate more test locations/weather windows.

In general, the process of assessing the alternative noise standards can be approached by conducting a series of tradeoff studies between alternative noise standards' technical feasibility and economic viability to find the best alternative in the design space illustrated in Figure 12. Technical feasibility or standard effectiveness can be interpreted as the standard's ability to capture UAS/UAM noise sources and their impact on communities. On the other hand, economic viability, also referred to as economic burden, evaluates the alternative standard time, cost, and complexity.

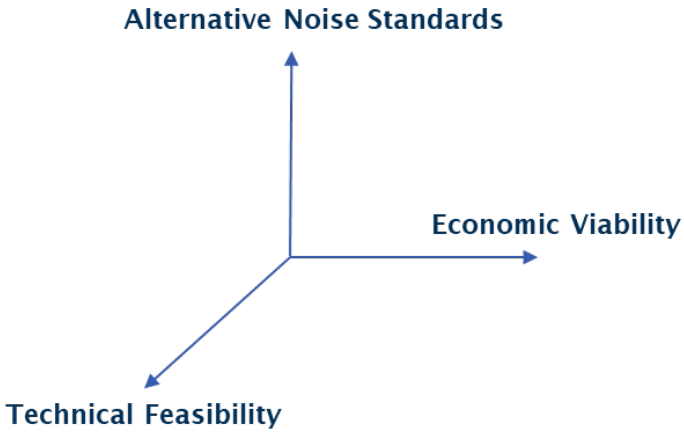


Figure 12. Alternative noise standards tradeoff space.

Along with the selection of the alternative noise standards of interest, the outcome of this exercise is to present certain use cases for which a feasibility demonstration of an equivalent procedure would be possible. This effort would require data for calibrating the standard-setting model against various UAS and UAM vehicle configurations. Additionally, this effort would require data to showcase quantifiable improvements against the process criteria listed above, while meeting the same noise standards constraints and requirements as the benchmarked certification procedure. The quantitative assessment, which will be supported under the PIM module developed under Task 4, is the main enabler for allowing an iterative process until process alternatives can meet the expectations for process streamlining and simplification.

As mentioned above, the existing connections and synergies with other ASCENT projects are expected to provide the resources needed to support the demonstration of this framework as a platform for evaluating equivalent procedures.

Milestones

Between October 2024 and September 2025, the following milestones were achieved:

- Completed the exploration and assessment of NPRM (86 FR 48281) (FAA, 2022), which presents only the noise certification basis for one new model of UAS seeking type certification, the Matternet® M2.
- Reviewed the recently approved remotely piloted aircraft (RPA) for noise certification of small UAS category vehicles.

Major Accomplishments

- Performed a literature search and documented regulations and current testing standards for small UAS.
- Defined a traceable structure for UAS noise certification requirements, using the MBSE verification model developed for the transport category.
- Published articles with AIAA SciTech 2025.

Publications

Published Conference Proceedings

Ali, H. E., Ravikanti, B., Balchanos, M. G., Harrison, E., & Mavris, D. (2025). MBSE Enabled Requirement Verification for a Traceable Regulatory Analysis Framework of UAS Noise Certification Standards. *AIAA SCITECH 2025 Forum* (p. 0367).



Mali, H., Geneti, N. F., Balchanos, M. G., Harrison, E., & Mavris, D. (2025). A Process Evaluation and Visualization Framework for Unmanned Aerial System (UAS) Noise Certification Testing. *AIAA SCITECH 2025 Forum* (p. 0368).
Balchanos, M., Ravikanti, B., Ali, H., Mali, H., D Harrison, E., & N Mavris, D. (2024, September 9-11). *A Regulatory Analysis and Process Improvement Decision Support Framework for Unmanned Aerial System (UAS) Noise Certification* [Conference presentation]. Quiet Drones 2024 Symposium, Manchester, United Kingdom.

Written Reports

Balchanos, M., Mavris, D. (2025). (Period ending December 2024) *ASCENT Quarterly Report, ASCENT Project 061 - Noise Certification Streamlining*. Award number 13-C-AJFE-GIT-066.
Balchanos, M., Mavris, D. (2025). (Period ending March 2025) *ASCENT Quarterly Report, ASCENT Project 061 - Noise Certification Streamlining*. Award number 13-C-AJFE-GIT-066.
Balchanos, M., Mavris, D. (2025). (Period ending June 2025) *ASCENT Quarterly Report, ASCENT Project 061 - Noise Certification Streamlining*. Award number 13-C-AJFE-GIT-066.
Balchanos, M., Mavris, D. (2025). (Period ending September 2025) *ASCENT Quarterly Report, ASCENT Project 061 - Noise Certification Streamlining*. Award number 13-C-AJFE-GIT-066.
Balchanos, M., Mavris, D. (2024). *Annual Report (period ending September 2024), ASCENT Project 061 - Noise Certification Streamlining*. Award number 13-C-AJFE-GIT-066.

Outreach Efforts

- Completed follow-up meetings with OEM partners for feedback on the certification model.
- Presented the model-based framework in two webinars.
- Completed a project overview and capability demonstration to the Volpe National Transportation Systems Center (Volpe) and requested information for model finetuning.
- Participated in conferences (2025 AIAA SciTech Forum and Quiet Drones 2024 Symposium).
- Participated in the FAA NEAT Series with an overview of ASCENT Project 061.
- Participated in the Spring 2025 ASCENT Meeting, where the team presented the latest research findings and final recommendations for standard setting.
- Interacted with the leadership of the ASTM F38 Committee and provided an overview of the A61 framework capabilities, per their request for collaboration with the ASCENT Project 061 team.

Awards

None.

Student Involvement

All participating graduate students have supported Task 1 activities by contributing to the literature, conducting ground research, and reviewing current regulations and FAA-instructed certification procedures. Recent efforts to document current regulations for UAS noise certification are currently led by Balaji Ravikanti.

Plans for Next Period

- Project ended on September 30, 2025.
- Publish peer-reviewed journal articles with *AIAA Journal* and AIAA SciTech.

References

Bendarkar, M. V., Harrison, E., Fields, T. M., Glinski, S., García, E., & Mavris, D. N. (2023). An Extended MBSE Framework for Regulatory Analysis of Aircraft Architectures. 2023 AIAA AVIATION. https://doi.org/10.2514/6.2023-3611
EASA. (2019, June 11). *Specific Category - Civil Drones | EASA*. European Union Aviation Safety Agency. https://www.easa.europa.eu/en/domains/drones-air-mobility/operating-drone/specific-category-civil-drones
EASA. (2023). *Environmental Protection Technical Specifications (Noise) Applicable to VTOL-Capable Aircraft Powered by Non-Tilting Rotors*. European Union Aviation Safety Agency. https://www.easa.europa.eu/en/downloads/139022/en
EASA. (2024a, July 10). *Open Category - Low Risk - Civil Drones | EASA*. European Union Aviation Safety Agency. https://www.easa.europa.eu/en/domains/drones-air-mobility/operating-drone/open-category-low-risk-civil-drones
EASA. (2024b). *Certified Category - Civil Drones | EASA*. European Union Aviation Safety Agency. https://www.easa.europa.eu/en/domains/drones-air-mobility/operating-drone/certified-category-civil-drones

Fazal, B., Glinski, S., Harrison, E., Fields, T. M., Bendarkar, M. V., García, E., & Mavris, D. N. (2022, June 29-July 1). *An MBSE Framework for Regulatory Modeling of Transport Category Airplanes*. AIAA AVIATION 2022 Forum, Chicago, Illinois, AIAA 2022-3256. https://doi.org/10.2514/6.2022-3256

FAA. (2003). *FAA Writing Standards*. Federal Aviation Administration. https://www.faa.gov/documentlibrary/media/order/branding_writing/order1000_36.pdf

Firesmith, D. (2005). Are your requirements complete? *The Journal of Object Technology, 4*(1), 27. https://doi.org/10.5381/jot.2005.4.1.c3

International Council on Systems Engineering. (2006). *Systems Engineering Handbook: A Guide for System Life Cycle Processes and Activities*, version 4.0, INCOSE-TP-2003-002-03. http://www.las.inpe.br/~perondi/21.06.2010/SEHandbookv3.pdf

Kim, D., Taneri, M., Omoarebun, E.N, Wills, T., Balchanos, M., & Mavris, D. (2023, January 23-27). *MBSE-Enabled System Verification and Process Improvement of Transport Aircraft Certification*. AIAA SciTech 2023 Forum, National Harbor, MD, AIAA 2023-1897. https://doi.org/10.2514/6.2023-1897

U.S. Department of Defense. (2022). *Systems Engineering Guidebook*. Office of the Under Secretary of Defense for Research and Engineering, Washington, D.C. https://ac.cto.mil/wpcontent/uploads/2022/02/Systems-Eng-Guidebook_Feb2022-Cleared-slp.pdf

Task 2 - Develop a Library of UAS and Testing Procedures

Georgia Institute of Technology

Objectives

Task 2: Develop a library of UAS and testing procedures
- 2.1 Complete technical documentation of UAS configurations
- 2.2 Complete technical documentation of UAS noise testing equipment
- 2.3 Define UAS noise test plans
- 2.4 Define possible simulation techniques

Research Approach

Task 2.1 Complete Technical Documentation of UAS Configurations

Research tasks on investigating and archiving technical documentation of UAS configurations, as well as recommended procedures for noise testing, started in July 2022. Due to the lack of historical data about the noise generated by most UAS models, the FAA is unable to provide generally applicable noise standards for UAS (FAA, 2021). This insufficiency in data is caused primarily by the novelty and variety of UAS, such that no clear categorization of the systems is currently established. Figure 13 illustrates this problem by listing some of the different UAS configurations currently available.

The aforementioned problem is exacerbated by the various mission profiles of UAS systems and their different operating environments (Kim, 2022). As an alternative measure, the FAA issues Rules of Particular Applicability (RPA) for applicants who wish to certify their product for noise (FAA, 2023). To achieve this, the FAA assumes that the fundamental physics of UAS operation and noise are scalable if UAS shares comparable characteristics with crewed aircraft. As a result, the current noise standards for crewed aircraft outlined in 14 CFR § 36 (2025) can be applied to UAS or extrapolated for testing lower-weight UAS at lower altitudes. An example of this is the “Noise Certification Standards: Matternet Model M2 Aircraft” (FAA, 2021), which is the first RPA establishing a noise certification basis for a single model of aircraft described only for the Matternet® Model M2 (FAA, 2021). These RPAs alongside the Volpe UAS Testing Campaign’s noise measurement reports have been valuable for documenting testing procedures and in identifying the most important technical challenges for UAS noise testing.

So far, depending on the availability of data, only multirotor UAS were encompassed within the scope of the provided analysis. This includes vehicles such as the Matternet Model M2, Tarot® X8, and Flytrex® FTX M600P. The three UASs are depicted in Figure 13. The Matternet Model M2 was issued the first RPA by the FAA in 2022; therefore, it was used for benchmarking efforts early in the pivot toward UAS from the transport category. Tarot X8 is employed by the ASCENT Project 077 team for their noise measurement testing campaigns. Thus, in collaboration with ASCENT Project 077, a

® Tarot is a registered trademark of Wenzhou Feiyue Aviation Technology Co., Ltd, Beijing, China.
® Flytrex is a registered trademark of Flytrex Aviation LTD, Tel Aviv, Israel.

dataset was obtained from the testing campaign and was used to investigate the noise generated by Tarot X8 within the scope of the benchmarked regulations. Finally, the Flytrex FTX M600P is the system under test (SUT) for the most recent case study under this project. Its noise certification standards were issued on July 3, 2023, and upon collaboration with the ASCENT Project 094 team, a dataset was obtained from the Causey Noise Measurement Testing Campaign that facilitated this case study. More details about the case study are provided in Task 4.



(a) Matternet® M2 (b) Tarot X8 (c) Flytrex® FTX M600P

Figure 13. Unmanned aerial systems (UAS) analyzed within this project.

Task 2.2 Complete Technical Documentation of UAS Noise Testing Equipment
Part of the motivation behind looking at RPAs and Volpe UAS noise measurement campaigns' reports, as well as collaborating with the ASCENT Project 077 team, is to generate technical documentation on UAS noise testing equipment. The equipment employed within a testing procedure includes everything from pressure sensors (i.e., microphones), to data recorders, weather data microstations, aircraft tracking systems, etc. This equipment will be supported by data measurement and collection software.

Microphones are the most critical element in noise testing. Figure 14 showcases three types of microphones that can be utilized during noise testing: (1) ground microphones, (2) inverted ground microphones, and (3) elevated microphones. Ground microphones, including the inverted ones, tend to minimize interference with directed or reflected sound, and reduce measurement uncertainty related to the microphone elevation; however, ground microphones tend to be more complex to set up and more costly than the elevated microphones. In contrast, elevated microphones are simpler to set up and less expensive, but elevated microphones suffer from interference with directed and reflected sound. All microphones utilized for noise measurement are outfitted with windscreens to ensure reliable acoustic measurements while minimizing noise due to weather variations (e.g., rain and wind) and birds.

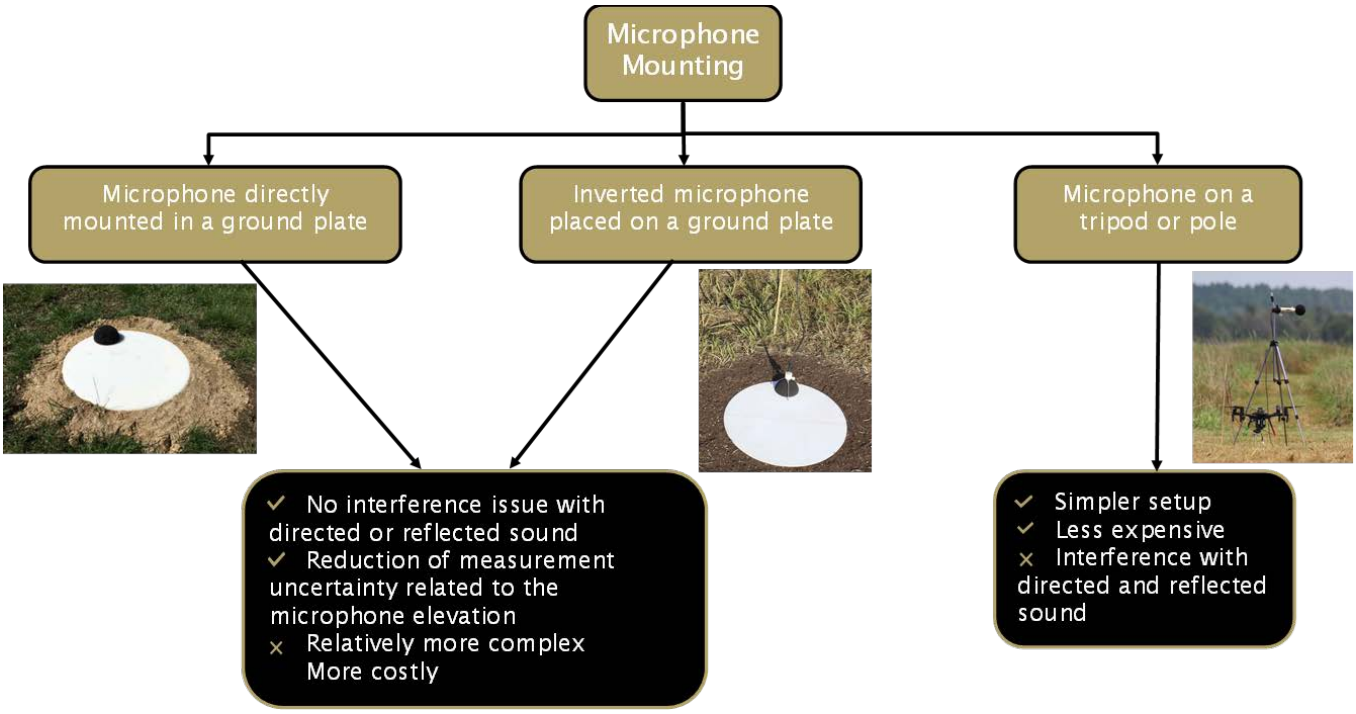


Figure 14. Microphone types and corresponding advantages and disadvantages.

The pressure fluctuations captured by the microphones are digitized via a data recorder. Data recorders are also used to power microphones and control the timing, synchronization, and data transfer between the input module and external host such as a computer. Moreover, meteorological conditions are continuously monitored during acoustic measurements. Weather data logging can be collected via weather microstations connected to anemometers and temperature/humidity sensors, as shown in Figure 15.



Figure 15. Anemometers for weather data acquisition equipment.

Time-space-position information for UASs within a noise testing procedure is captured by aircraft tracking systems such as the Survey and Tracking Apparatus for Research in Transportation (START) depicted in Figure 16. START is a tracking

system developed by Volpe "for the purpose of deriving precise positioning and timing information from UAS and other automated platforms" (James et al., 2021).

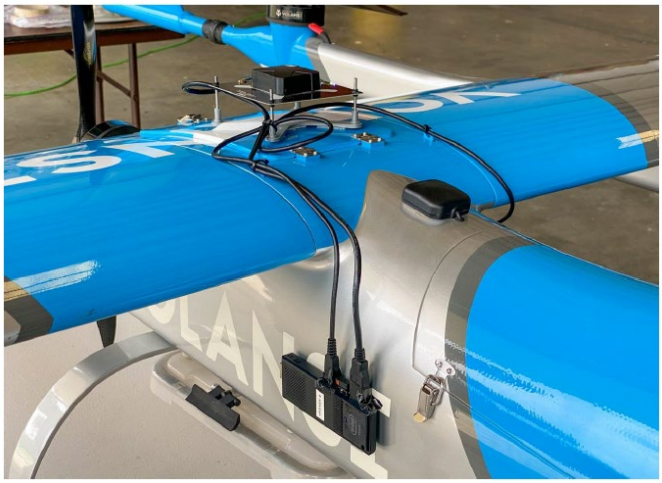


Figure 16. Survey and Tracking Apparatus for Research in Transportation (START) aircraft tracking system.

Task 2.3 Define UAS Noise Test Plans

Research tasks on investigating and archiving technical documentation of UASs, as well as recommended procedures for noise testing, started in July 2022. One of the key studies that the ASCENT Project 061 team has started to document, which has been valuable in identifying the most important technical challenges for UAS noise testing, is the document titled "Noise Measurement Report: Unconventional Aircraft" by the Choctaw Nation of Oklahoma (July 2019). The practice described for UAS noise testing took place on a grassland, which, taking the flight envelope into consideration, is not suitable due to the following reasons:

- Dense areas can have a different "perceived" noise.
- High altitudes and dense areas over buildings and hard surfaces can have different reflective behaviors.
- Within buildings, noise can be reflected, amplified, or attenuated.

Part of this grassroots effort in discovering the state of the art is the technical documentation on UAS noise testing equipment. By assessing testing procedures from a regulatory perspective, we can build some simple alternatives under the system verification model (Figure 17 shows examples). Finally, the UAS noise test plans must be defined and executed. Physical testing will not cease to exist, but simulation techniques are needed for testing process alternatives.

A major part of the study for this cycle involved gathering available experimental test data to aid in understanding both the sensitivity of noise metrics to flight test parameters or test setup parameters and the times and costs associated with various sub-steps of a noise testing procedure. Note that the experimental noise testing campaign is more rigorous in many ways compared with the certification noise testing procedures. This enabled us to compare various microphone locations, flight conditions, and metrics, which is not possible when limited to the data typically available from certification-type noise testing procedures.

The experimental test campaign whose data was extensively utilized in this cycle of the study was the Causey test campaign. The objective of the testing campaign was "to gather data on UAS noise emissions in compliance with the UAS noise regulations specified in 14 CFR § 135." Unlike other test campaigns, which may not be compliant with certification norms, the Causey campaign is explicitly meant to gather certification quality data. The report provides the acoustic measurements and resultant dataset. FAA, Volpe, and Blue Ridge Research and Consulting (BRRC) were the parties involved. Chris Hobbs (FAA) headed UAS flight operations, Robert Samiljan (Volpe) coordinated the vehicle tracking data collection, and Michael James (BRRC) managed the acoustic data collection.

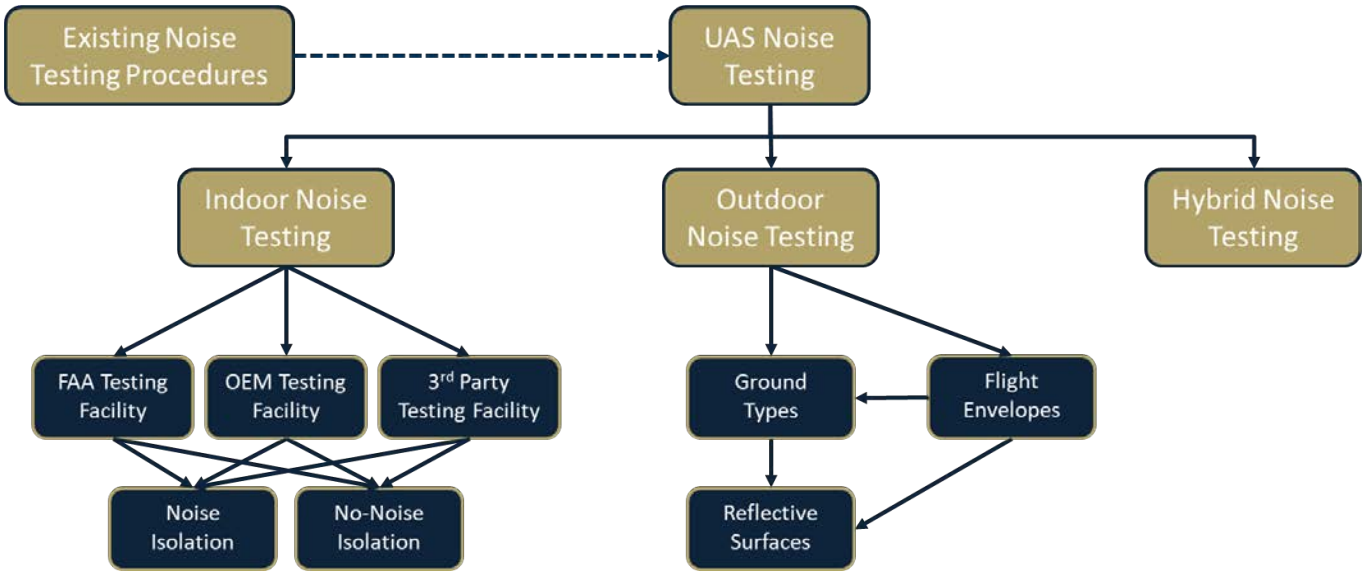


Figure 17. Alternative noise testing procedures for an unmanned aerial system (UAS). OEM: original equipment manufacturer.

Table 3 lists the empty and maximum weights of the test vehicles shown in Figure 18. Vehicles performed flyover and hover operations for multiple flight conditions. The weight of the Flytrex FTX-M600P is comparable to the Matternet M2 (for which there is an existing recent noise regulation linked in references), which has a MTOW of 29 lb, including a 4-lb payload. However, it is worth noting that the Flytrex FTX M600P is a hexacopter, whereas the Matternet M2 is a quadcopter. An RPA for the noise certification of Flytrex FTX-M600P was approved recently, alongside six other vehicles of the same class. Flight conditions are derived based on various combinations of weight, speed, and altitude. Three groups of "test points" were conducted (namely, level flyover operations; hover operations; and idle, takeoff, landing, or operational level flyover operations). The campaign took place from July 26 to July 29, 2021. Each day, a different vehicle underwent testing.

Table 3. Causey test campaign vehicle weights.

Weight	Flytrex FTX-M600P	Volansi® VOLY C10	DJI® m210
Empty (lb)	26.8	51.4	11.8
Max (lb)	33.4	55.0	-

® Volansi is a registered trademark of Volansi, Inc., Concord, California.



Figure 18. Test vehicles for Causey testing campaign.
From left to right, Flytrex FTX-M600P, Volansi VOLY C10 and DJI® m210.

An additional day of Flytrex FTX-M600P measurements was conducted to capture new test points and repeat two flyover test points to account for day-to-day variations. The goal was to complete six repeated test flights of each condition; however, some test points were repeated more than six times, as will be discussed in later sections.

Figure 19 illustrates the Causey testing campaign layout. This view is later used in the visualization environment that is to host all the key details of a test procedure to enable effective decision-making.

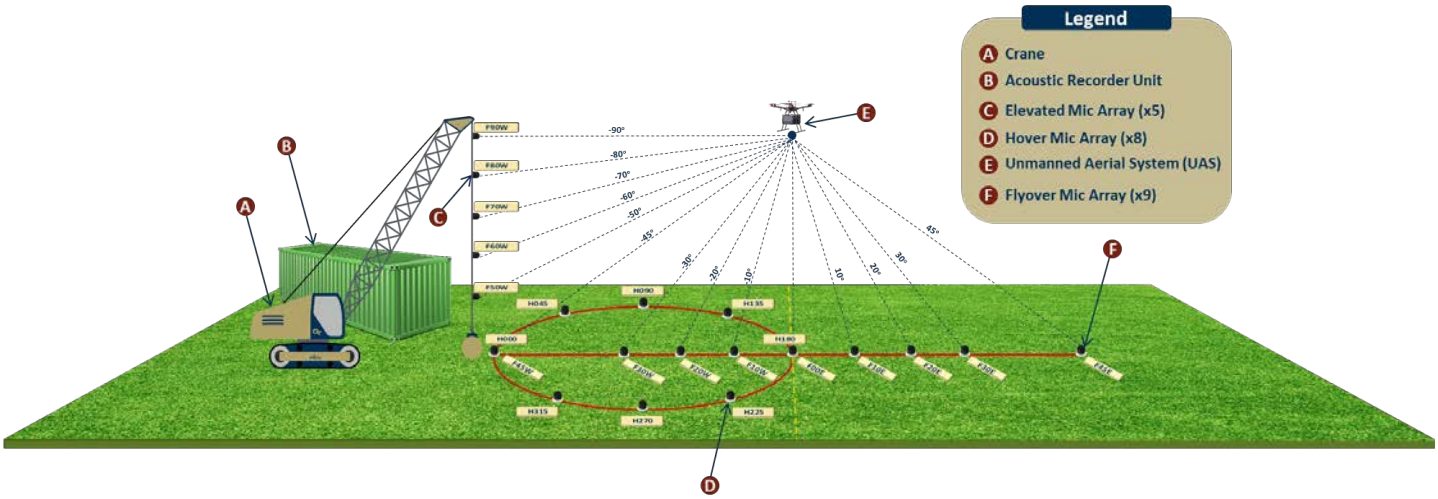


Figure 19. Causey test campaign concept of operations.

Task 2.4 Define Possible Simulation Techniques
Within the scope of this project, the MBSE model was used to assess current noise certification procedures. Typically, MBSE methods are used to represent a vehicle's lifecycle and enable the use of data and information as an integrated systems engineering approach. In the case of ASCENT Project 061, the product is a process architecture, within which current procedures will be assessed and equivalent procedures will be proposed, defined, implemented, and tested within this environment. The full MBSE model formulation for certification and implementation is shown in
Figure 20.

The validation process contains the steps needed to demonstrate that vehicle noise levels calculated from flight testing results are meeting requirements. Part of meeting the requirements is the instrumentation setup, which is implemented as a logical architecture within the model. A library of instrument model representations is also constructed, from which

® DJI is a registered trademark of SZ DJI Technology Company, LTD, Shenzhen, China.

alternative instrumentation lineups can be modeled. The latter feature is key, as this framework should allow for the evaluation of equivalent procedures (e.g., ground microphone placement). Other components of the verification model are the test procedures and the test report checklist, which are prototyped as activity diagrams in SysML, as well as the vehicle configurations represented as a state machine.

Completing the verification model is any applicable regulation text in the form of a SysML verification thread. With the verification model in place, the user can import any UAS model, perform the certification equivalent process by executing the verification model, and then generate a final report which would contain the instrument validation document and flight test plan. It is crucial that the overall framework be implemented in a highly modular fashion to obtain the needed flexibility for testing equivalent procedure alternatives and to accommodate a broader range of air vehicle designs and configurations. The SysML implementation currently comprises the following modules:

1. Requirement translation and constraints
2. Noise testing instrument architecture
3. Procedures, protocols, and behavior
4. SUT
5. System verification model overview
6. Auto-report generation and output to process evaluation model

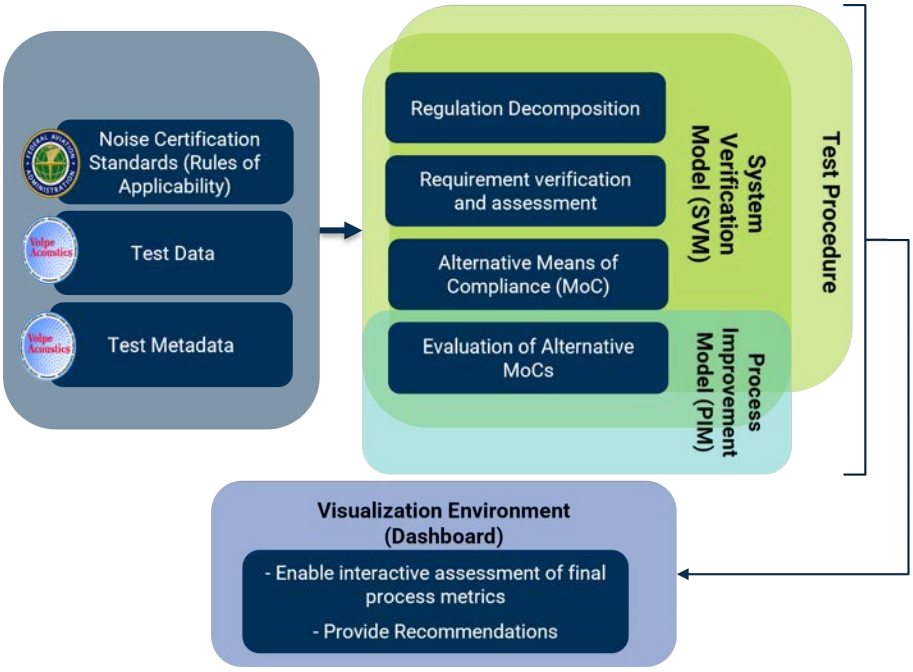


Figure 20. Model-based systems engineering (MBSE) verification model structure.

Event Process Modeling

With detailed guidance from the documents listed above, event-driven processes were defined and created within the certification model. Additions include modeling of the test-day acoustic collection process and test scenario event processes (i.e., flyover, hover).

Library Creation

A new task was identified to command the creation of libraries within the certification model, to allow for added flexibility and modularity. Current libraries include the aircraft library, microphone library, and data amplifier library. The SUT representation has been modified to allow for adaptability to various UAS types and configurations.



Aircraft Testing Environment

Another finalized improvement on the certification model is the modeling of the UAS test environment, including the flight test setup configuration. With input from documents such as RPAs and Volpe UAS noise measurement campaign reports, the model was updated and refined to include various instrumentation system architectures.

Noise Calculation

UAS noise certification only requires a flyover test, but noise certification also specifies a supplemental hover test to augment the process of collecting noise data that will inform the generation of generally applicable noise standards for UAS. The hover test, as described by the FAA in the noise certification standards for the Matternet M2, is a voluntary test that "will not be used to inform the applicant's airworthiness or type certification basis or be evaluated against any noise limits or regulatory criteria for noise certification purposes" (FAA, 2021). So far, UAS RPAs have described two noise metrics for noise measurements: (1) SEL for the flyover test and (2) equivalent sound level (L_{eq}) for the hover test (FAA, 2021).

1. **Sound Exposure Level:**
   SEL is an energy-averaged A-weighted sound level over a specified period of time or single event, with a reference duration of 1 s. SEL can be calculated using two methods, defined as follows (Bennett & Pearsons, 1981):

   1.1- Continuous time integration:

   $$L_{AE} = 10\log_{10}\left[\frac{\int_{t_1}^{t_2} 10^{\frac{L_A(t)}{10}} dt}{1\,sec}\right] \quad \text{(Eq. 1)}$$

   where t_1 and t_2 define the time interval, and $L_A(t)$ is the time function of A-weighted sound level during the time for $t_1 - t_2$.

   1.2- Temporal sampling:

   $$L_{AE} = 10\log_{10}\left[\sum_{i=1}^{n} 10^{\frac{L_A(i)}{10}} \Delta t\right] \quad \text{(Eq. 2)}$$

   where $L_A(t)$ is the instantaneous A-weighted sound level for the n^{th} sample, n is the number of samples taken during the observational period, and Δt is the time interval between samples.

   As mentioned previously, UAS RPAs prescribe the use of SEL for the flyover test, in which they specify that the integration time $t_2 - t_1$ in practice must not be less than the time interval during which $L_A(t)$ first rises to within 10 dB(A) of its maximum value (L_{Amax}) and last falls below 10 dB(A) of its maximum value. In addition, the regulations allow for the use of an integrating sound level meter to obtain L_{AE} directly rather than manually calculating L_{AE} (FAA, 2021).

2. **Equivalent Sound Level:**
   L_{eq} is the level of the A-weighted sound energy averaged over a specified period of time. Similar to L_{AE}, it can be calculated by two methods, defined as follows (Bennett & Pearsons, 1981):

   2.1- Continuous time integration:

   $$L_{eq} = 10\log_{10}\left[\frac{\int_{t_1}^{t_2} 10^{\frac{L_A(t)}{10}} dt}{t_2 - t_1}\right] \quad \text{(Eq. 3)}$$

   where t_1 and t_2 define the time interval, and $L_A(t)$ is the instantaneous A-weighted sound level.

   2.2-Temporal sampling:

   $$L_{eq} = 10\log_{10}\left[\frac{1}{n}\sum_{i=1}^{n} 10^{\frac{L_A(i)}{10}}\right] \quad \text{(Eq. 4)}$$



where $L_A(t)$ is the instantaneous A-weighted sound level for the n^{th} sample and n is the number of samples taken.

UAS RPAs prescribe the use of L_{eq} for hover tests only. Similar to L_{AE}, the regulations allow for the use of an integrating sound level meter to obtain L_{eq} directly rather than calculating it manually (FAA, 2021).

Before L_{AE} and L_{eq} are calculated, corrections must be applied to the measured data to account for uncertainties related to the measurement system, microphone and recording system used, background noise, actual flight path, and meteorological conditions present when the measurements were taken.

The use case described in Task 4 utilizes a Python® code to parse through the sound pressure time-history (audio) signals obtained from the Flytrex FTX M600P flyover and hover tests during the Causey UAS Acoustic Measurements campaign and calculate both L_{AE} and L_{eq} based on the equations above. Regarding the implementation of noise metric calculations, there is no option for directly performing such analyses within the SysML-based certification model. A possible solution is to create a function in Matlab® and then incorporate the analysis in the verification thread.

Milestones

- Reviewed UAS testing procedures from the literature.
- Obtained useful test data from collaborators.
- Established connections with OEMs and other research teams for further investigations.

Major Accomplishments

- Created scripts that are required to generate multiple noise metrics from raw frequency domain data.
- Documented UAS noise testing practices and processes.

Publications

Published Conference Proceedings

Ali, H. E., Ravikanti, B., Balchanos, M. G., Harrison, E., & Mavris, D. (2025). MBSE Enabled Requirement Verification for a Traceable Regulatory Analysis Framework of UAS Noise Certification Standards. *AIAA SCITECH 2025 Forum* (p. 0367).

Mali, H., Geneti, N. F., Balchanos, M. G., Harrison, E., & Mavris, D. (2025). A Process Evaluation and Visualization Framework for Unmanned Aerial System (UAS) Noise Certification Testing. *AIAA SCITECH 2025 Forum* (p. 0368).

Balchanos, M., Ravikanti, B., Ali, H., Mali, H., D Harrison, E., & N Mavris, D. (2024, September 9-11). *A Regulatory Analysis and Process Improvement Decision Support Framework for Unmanned Aerial System (UAS) Noise Certification* [Conference presentation]. Quiet Drones 2024 Symposium, Manchester, United Kingdom.

Outreach Efforts

- Provided full Year 4 performance review to the FAA AEE.
- Facilitated technical discussions and feedback provided by Volpe.
- Collaborated with the ASCENT Project 077, Dr. Eric Greenwood's research group, and Flytrex Aviation LTD.

Awards

None.

Student Involvement

All students participated in the collection and review of UAS noise testing practices and processes. Hussein Ali led the review of available noise testing data and the creation of scripts of noise metrics evaluation.

Plans for Next Period

- Project ended on September 30, 2025.

® Python is a registered trademark of Python Software Foundation, Beaverton, Oregon.
® Matlab is a registered trademark of The Mathworks Inc., Natick, Massachusetts.



- Publish peer-reviewed journal articles with *AIAA Journal* and AIAA SciTech.

References

Bennett, R., & Pearsons, K. (1981). *Handbook Of Aircraft Noise Metrics (CR-3406)*. National Aeronautics and Space Administration, N81-21871. https://ntrs.nasa.gov/api/citations/19810013341/downloads/19810013341.pdf

FAA. (2021). *Noise Certification Standards: Matternet Model M2 Aircraft*. Federal Aviation Administration. https://www.federalregister.gov/documents/2021/08/27/2021-17769/noise-certification-standards-matternet-model-m2-aircraft

FAA. x (2023). *Noise Certification of UAS/AAM using Rules of Particular Applicability.* Federal Aviation Administration. https://www.faa.gov/about/office_org/headquarters_offices/apl/aee/noise/uas_noise_certification

James, M., Salton, A., Downing, M., & Calton, M. (2021). *Causey UAS Acoustic Measurements*. Blue Ridge Research and Consulting, Asheville, North Carolina.

Kim, D., Karagoz, F., Datta, S., Balchanos, M., Anvid, D., Harrison, E., & Mavris, D. N. (2022). A Model Based Systems Engineering Approach to Streamlined Noise Certification of Transport-type Aircraft. *33rd Congress of International Council of the Aeronautical Sciences ICAS*, Stockholm, Sweden.

Noise Standards: Aircraft Type Certification, 14 C.F.R. § 36 (2025). https://www.ecfr.gov/current/title-14/chapter-I/subchapter-C/part-36

Read, D. R., Senzig, D. A., Cutler, C. J., Elmore, E., & He, H. (2020). *Noise Measurement Report: Unconventional aircraft - Choctaw Nation of Oklahoma: July 2019*. U.S. Department of Transportation, Volpe National Transportation System Center. https://rosap.ntl.bts.gov/view/dot/49647/dot_49647_DS1.pdf

Task 3 - Develop a Noise Certification Procedure Based on Existing Practices

Georgia Institute of Technology

Objectives

The focus of Task 3 is to develop an overall definition of a more flexible certification process and the evaluation criteria for determining that the procedure is more streamlined than the baseline. The pivot to a UAS focus is well aligned with the objectives of this task, where flexibility will be driven by the requirement for the MBSE model to accommodate a range of UAS configurations and payloads. Task 3 will build upon the capabilities of the integrated MBSE platform and leverage contributions from all other tasks. The following tasks will be conducted under Task 3:

Task 3: Develop a noise certification procedure based on existing practices
- 3.1. Transfer noise testing plans to the MBSE model
- 3.2. Transfer noise testing data to the MBSE model
- 3.3. Develop a full noise test plan
- 3.4. Implement a validation process

Research Approach

Tasks 3.1 and 3.2 Transfer Noise Testing Plans and Data to the MBSE Model

Task 3.1 seeks to define what is meant by a “flexible” process. One way to define the “flexible” process is to determine whether the introduction of a different vehicle configuration leads to many incompatibilities with the streamlined process under evaluation. For instance, it is important to assess how the UAS configuration affects the microphone technology and quantity needed and microphone placement in the testing facility. Task 3.1 will involve testing procedures and producing mapping compatibilities between vehicle configurations and testing procedures. A set of criteria and evaluation metrics is needed to assess the combinations of vehicle configuration, testing procedures, and uncertainty factors against regulatory-derived requirements, which will be implemented within the MBSE certification framework. Hence, a proposed set of flexibility criteria for the certification process could include the following considerations:

- Compatibility and applicability of equivalent procedures
  - Alternatives in the testing procedure should be accounted for in the model for verification (i.e., more microphones vs. more flight test points)
- Complexity (e.g., if a switch to another configuration requires more steps to setup) and additional instrumentation if a vehicle is more sensitive to variations in certain factors during testing.



- Sensitivity to weather and other aleatory uncertainties

The defined criteria will be tested and applied in other tasks; hence, this task is considered complete.

A regulation paragraph can contain both quantitative requirements and inspectional requirements. Quantitative requirements refer to those that contain numbers or a range of numbers to be met. Inspectional requirements usually do not contain numbers but ask the test procedure to follow the instructions or guidelines given in the paragraph. In the verification model, such paragraphs cannot be directly adopted but need functional breakdown. For quantifiable requirements, the subjects for which the quantified constraints are designed are identified and separated from each other for the convenience of validation. For an inspectional requirement, a straightforward number is not available to make constraints out of, but a simple 'yes' or 'no' test can be implemented to address the requirement. With the above modification logic, our team used the function of the requirement diagram in the MBSE model to delineate each requirement within each regulation paragraph. The requirements are constructed with several blocks in addition to the two archetypes mentioned above. Figure 21 shows the formal requirement breakdown process with the help of a requirement from the noise regulations of the Matternet M2. Table 4 above shows the mapping of the broken-down requirements to the test data which enables verification of the requirements.

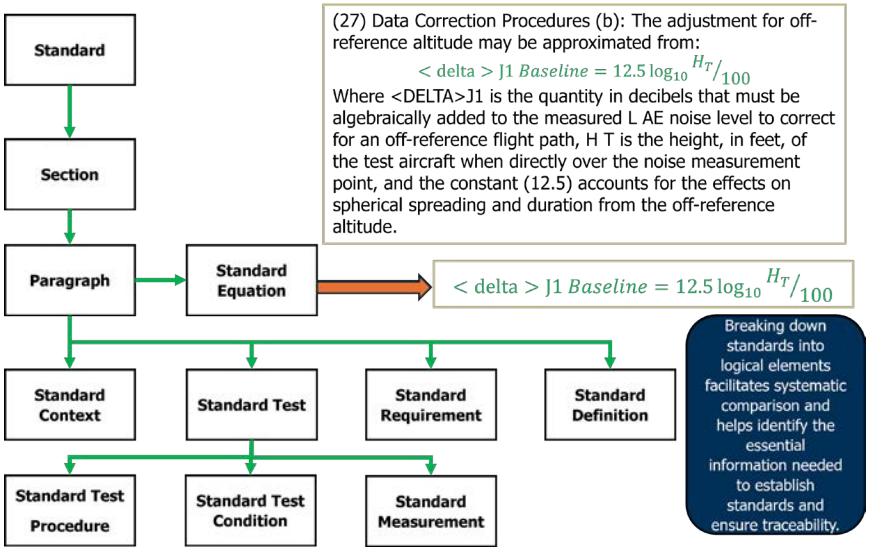


Figure 21. Requirements breakdown highlighting standard equation element.

Table 4. National instance table.

#	Name	lateral_distance	hover_height_0	lateral_distance	AGL_45	hover_height_9	radial_90
1	new_req_datapoint	3	4	1	2	7	2
2	new_req_datapoint1	3	3	1	1	2	1
3	new_req_datapoint2	2	3	3	4	4	4

Figure 22 and Figure 23 show the various standard elements that make up a requirement paragraph with the help of noise certification requirements of the Matternet M2. A standard equation element of requirement paragraphs enforces the usage of such equations for data correction/adjustment for consistency among all applicants and/or test runs. Similarly, a standard requirement is naturally a part of a requirement paragraph that spells out a metric and the corresponding threshold that needs to be met. In parallel with the requirement breakdown process, the compatibility of existing standards with the rapidly evolving UAS category vehicles is analyzed. This analysis helps assess alternative approaches

that could enhance the effectiveness of these standards. One such study targets the confidence interval requirement shown in Figure 22. Another study assessed the suitability of the duration adjustment equation highlighted in Figure 23.

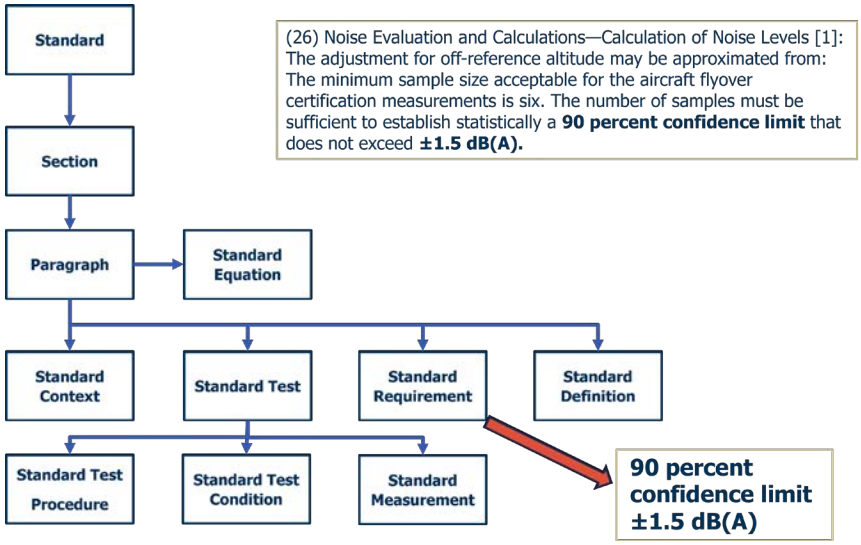


Figure 22. Requirements breakdown highlighting standard requirement element.

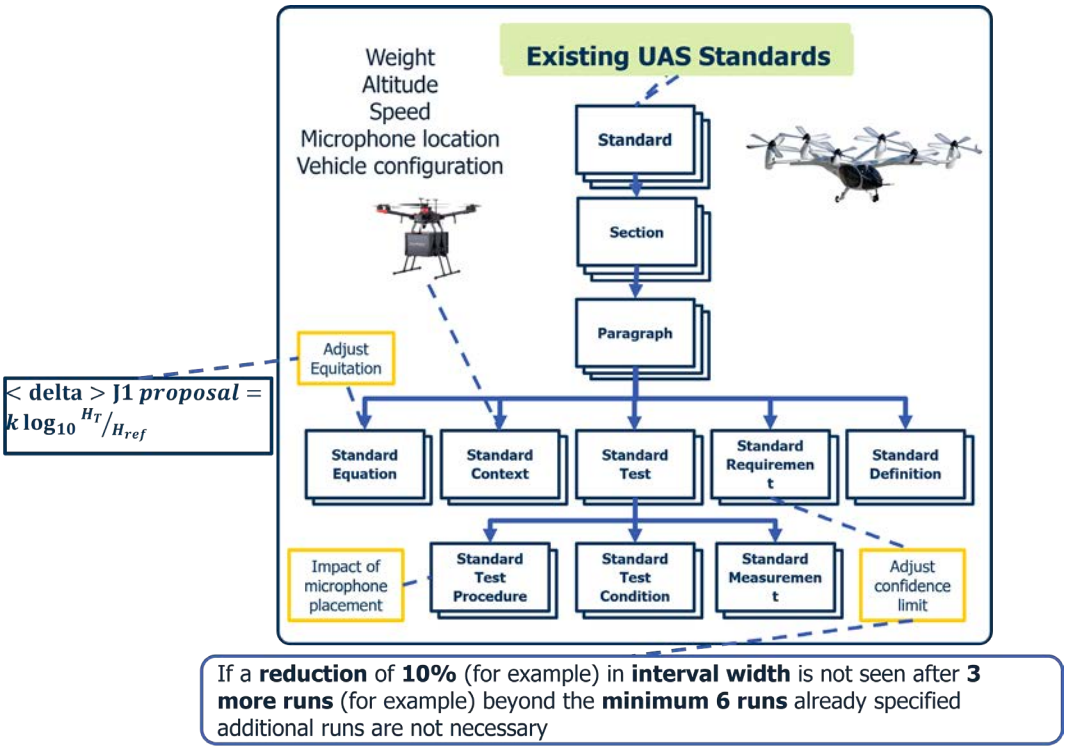


Figure 23. Model-based systems engineering certification framework version for unmanned aerial systems (UAS) to test category flexibility in equivalent certification procedures.

With the MBSE model, testing data can be validated against the requirements instantly after processing. For the convenience of the users, data should be populated in the form of an instance table shown in Table 4, aligning data to each corresponding constraint. The MBSE model validates data provided to each constraint instantly.

The workflow proposed is extended to an integrated framework for flexible assessment of the certification process and is expected to be reusable for a broader set of UAS configurations, as highlighted in Figure 23.

Task 3.3 Develop a Full Noise Test Plan

The certification framework for UASs developed under Task 3, and the use of the PIM completed under Task 4, allow our team to measure process flexibility, efficiency, complexity, and other figures of merit as part of comparing alternatives to the baseline. Framing this problem as a decision-making problem in this context, an "alternative" would be a version of the baseline certification process with a specific combination of a testing plan, instrumentation selection, and a setup for measurements and processing methods, as dictated by a possible equivalent procedure.

A typical flight test procedure can be divided into five major sections corresponding to four days of carrying out different activities or tasks, as shown in Figure 24. These sections are not necessarily carried out over consecutive days as any two sequential sections can be separated by days, if not months, depending on the testing campaign and the scheduling and planning of the parties involved.

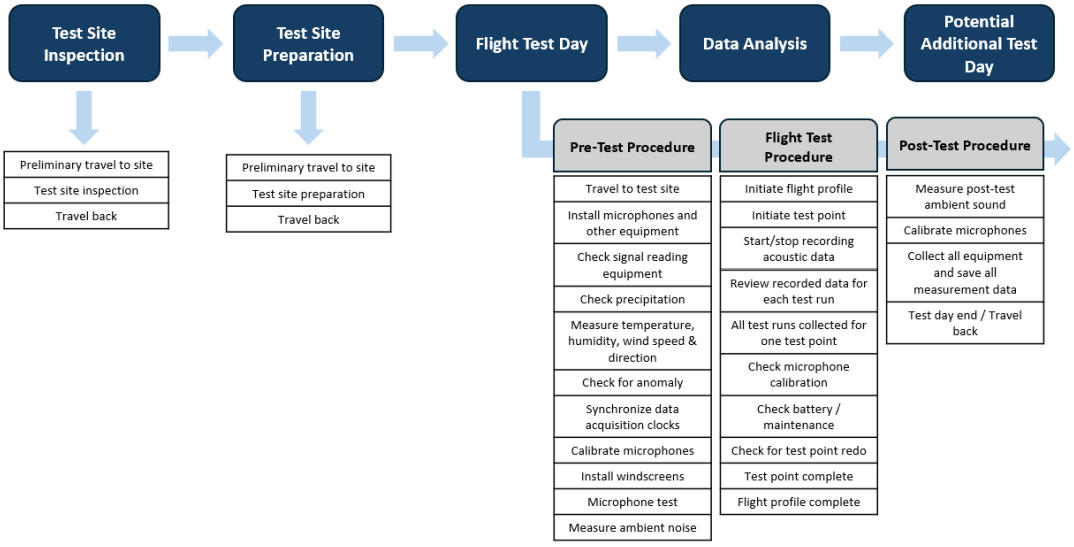


Figure 24. Outdoor noise testing procedure layout for unmanned aerial systems (UAS) noise measurements.

The flight test procedure can be described in the following steps (refer to Figure 24 for the detailed steps for each day of the testing process):

(1) Test Site Inspection. The team visits the potential test site to evaluate its suitability for conducting noise testing. This consists of assessment of the site location and surroundings in terms of proximity to noise-sensitive areas, weather conditions, and levels of background noise (e.g., traffic, birds, construction noise, or sound reflections off nearby buildings). The type of ground surface is also important as it could influence the noise measurement results. Common ground surfaces considered can include grass, concrete, asphalt, and open terrain. Grass tends to be the most preferred ground surface due to its ability to absorb sound and reduce sound reflections compared to hard surfaces; however, this requires the grass to be well maintained and free from tall vegetation. The elevation and uniformity of the ground surface are also crucial to avoid measurement inconsistencies. The overall site area is also evaluated by checking whether it can properly accommodate equipment installation, and distances and altitudes required for flight tests. Following this inspection, the test site is either approved, if deemed appropriate for the testing requirements, or denied, if it does not

meet certain criteria or would lead to test measurement complications or inconsistencies. The necessary permits for conducting UAS flights at the selected location and ensuring regulatory compliance are obtained.

(2) Test Site Preparation. Once the test site is approved and permits are obtained, a second visit to the test site is necessary to prepare the site prior to the actual flight test day. This consists of clearing the site of any obstacles or potential hazards, mowing grass, if needed, and marking the positions of microphones and other equipment installation. This requires having a clear flight plan for the specific flight paths, altitudes, and maneuvers to be performed by the UAS on the flight test day. The UAS to be flown is also inspected to ensure it is functioning properly prior to the flight test day.

(3) Flight Test Day. The flight test day can be delineated into three main action lists:

- Pre-test Procedure: All microphones, recording equipment, and other equipment are installed and deployed. Weather measurements are initiated, and microphones are calibrated and tested prior to the installation of windshields and measurement of ambient noise. Throughout this procedure, multiple checks are conducted to ensure proper functioning of all devices and adequate meteorological conditions for testing.
- Flight-test Procedure: Flight test profiles (i.e., flyover, hover, takeoff, and landing, etc.) are initiated. Within each flight profile, multiple test points can be conducted under different conditions including altitude, weight, and speed. To ensure the accuracy and reliability of measurements, each test point is repeated for a minimum of six test runs. After the completion of each test point, multiple checks are carried out to assess the need for microphone recalibration, maintenance, or battery changes for UASs, or a complete redo of the test point upon the detection of any anomalies or inconsistencies in the measurements.
- Post-test Procedure: Once all flight profiles are completed, the ambient sound is measured, the microphones are calibrated, all microphones and equipment are collected, and measurement data are saved.

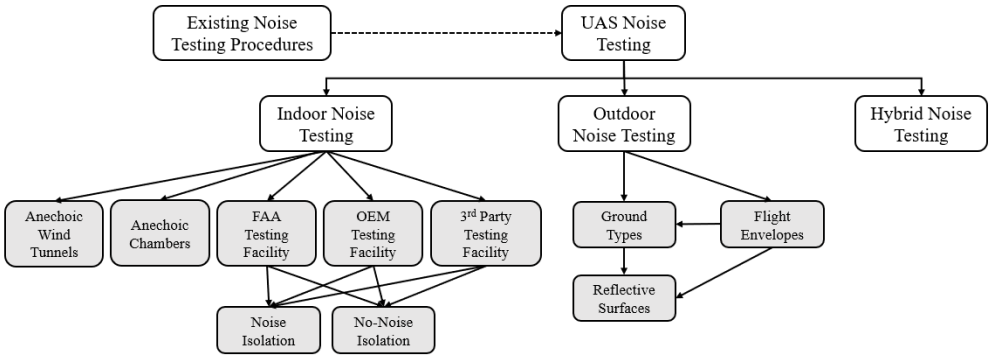


Figure 25. Noise testing types for unmanned aerial systems. FAA: Federal Aviation Administration, OEM: Original Equipment Manufacturer.

(4) Data Analysis. The data collected during the flight test day are postprocessed and analyzed. Raw measurements are translated in terms of noise metrics of interest, and any sources of inconsistency or interference with the measurements can be revealed. Consequently, the need for replacement or additional measurements is decided at this step.

(5) Potential Additional Test Day: Based on the results of the data analysis from the flight test, an additional flight test day might be necessary. This would either consist of a partial repeat of some test measurement points or a full flight retest if significant interference appears to have been present throughout the entire flight test day or throughout a major of the flight test.

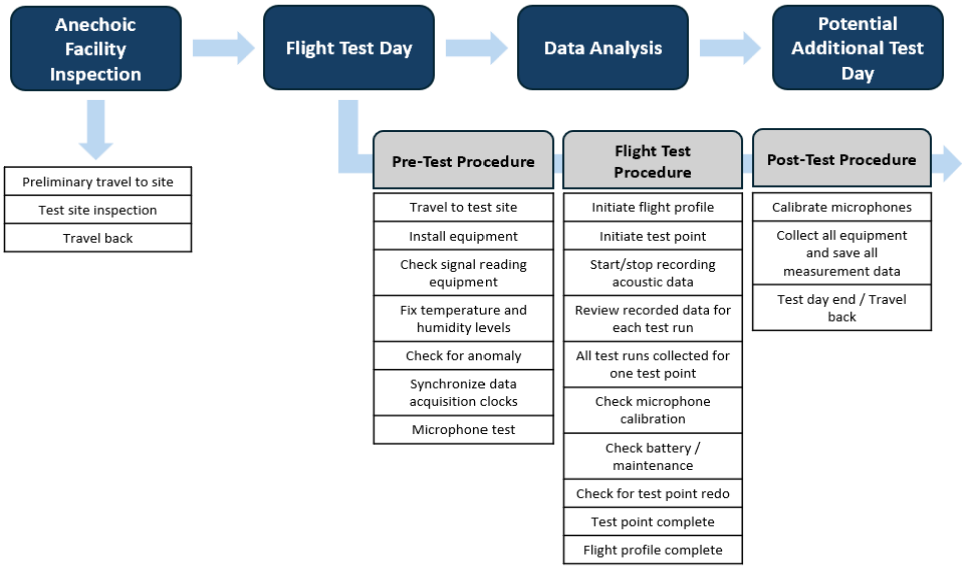


Figure 26. Indoor noise testing procedure layout for UAS noise measurements.

Similarly to the outdoor noise testing procedure for UASs described above, an indoor testing procedure can be formulated for UASs that can be tested in an enclosed space such as anechoic chambers or anechoic wind tunnels (Figure 25). The indoor testing consists of a smaller number of phases and steps considering the controlled nature of the testing environment which reduces the complexity of tasks to be carried out and increases the likelihood of measurements success due to the lack of weather or background noise interferences. Consequently, the corresponding procedure (Figure 26) does not require any travel for test-site preparation nor any continuous tracking of weather changes. Moreover, microphone installation and pre-calibration tasks are also eliminated as these are usually installed and calibrated beforehand by the facility. Additionally, the use of windscreens, previously needed for outdoor testing due to wind interference, is no longer essential.

After the model has been calibrated with inputs and parameter definitions that will be obtained from noise testing data resulting from ASCENT Projects 077 and 094, the model will rely on statistical analysis and an identification of process bottlenecks and showstoppers. Another set of metrics of interest will target the impact quantification of process complexities and will be used to indicate gaps and further drive certification process simplification using technologies and estimation methods (e.g., virtual sensing and instrumentation), where process steps could be reduced or eliminated.

As a means of facilitating a scenario-based parametric decision-making capability, the ASCENT Project 061 team has been developing an interactive visualization environment. Through the use of visual representations of the process and key analysis outputs, this environment serves as a user-friendly interface for requirement validation, exploration of process alternatives and their impacts, detection of process shortcomings and gaps, and ranking for the selection of test plans, instrumentation, and noise measurement data analysis against user-set criteria. The ranked alternatives are validated through an assessment of the equivalency for a procedure to standard regulatory practices. A notional representation of the final version of this environment is shown in Figure 27.

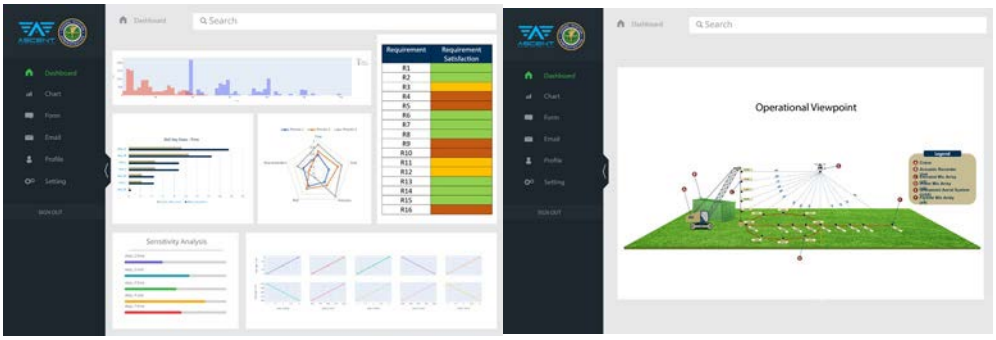


Figure 27. Graphical user interface for process specification.

As interactive dashboard development is often approached as a spiral development; the capabilities and features included in the current version are as follows:

- Histograms to visualize each metric of a given procedure. To compare procedures, it may be helpful to overlay the histograms for the respective procedures to visually compare time, cost, etc.
- Sensitivity plots to help select from alternative procedures to improve upon the current baseline. These sensitivities can indicate how robust an alternative is to unforeseen variability in the procedure steps in terms of time or cost it takes to complete the step. For example, how sensitive the overall cost improvement (with respect to the baseline) of an alternative is to the cost it takes to complete the alternatives' first step. This information can be presented to the decision maker in the form of a matrix of plots like the prediction profiler plot in the JMP statistical software.
- For multivariate and multicriteria problems, a spider chart (radar plot) is used to compare process alternatives against multiple criteria. This chart can help to drive the evaluation of all tested process alternatives and map the strengths and weaknesses of each alternative against the prioritized evaluation criteria.
- The highest ranked process as a chain of events to rank order key steps identified by the PIM in the order of importance for a given procedure.
- A requirements satisfaction section to present an assessment review of whether requirements are being met, which includes providing guidance toward the exploration of procedures and technologies that would help close any gaps and meet all requirements. In this part, the focus is on data analytics supported by the Monte Carlo process simulations using probabilistic inputs. Hence, the results are typically in the form of distributions for the metrics of interest, and allow for exporting means, median values, and cumulative distribution functions to assess whether constraints and requirements are being met.
- A high-level concept graphic (OV-1) charts to capture the physical representation of the test setup and easier communication with OEMs and decision makers as needed.

Using this visualization environment, decision makers can determine the feasibility of alternative procedures, compare alternatives relative to the baseline, and downselect between alternative procedures based on sensitivity to input values. On the actual model demonstrator, alternative procedures will be compared based on sensitivities. The sensitivity plots, along with the histograms and the complementary plots, will be used to select an alternative to the current baseline procedure that has the desired balance between mean performance, variability, and robustness in terms of relevant metrics such as overall time and cost of the procedures.

To enable the multicriteria, parametric, and interactive capability for rapid exploration of certification alternatives, the PIM, which executes a process simulation through Markov chains[1] and graph analysis, can allow probabilistic Monte Carlo simulations for investigating the limitations of each process alternative. This capability is primarily the focus of Task 4 and is presented in the following section (Figure 36 of the Task 4.1 Develop alternative testing procedures using the elements library) of this report.

[1] A Marcov chain, named after Andrey Markov, is a mathematical stochastic process (framework) for describing the sequence and/or states where transitions occur in a given state that are dependent on the probability of the state attained in the previous event and time elapsed (e.g., the probability that n+1th steps will be x depends only on the nth step, not the complete sequence of steps that came before n).

Task 3.4 Implement a Validation Process

A particular instance to illustrate the analysis of alternatives proposed is regulatory paragraph J36.205(b) of 14 CFR § 36, Appendix J, which prescribes the method of adjustment for test flight altitudes during flyover noise measurements that deviate from the reference altitude prescribed in the regulatory paragraph 14 CFR § 36 J36.3(c). Figure 28 (Figure 5 from Volpe test campaigns SEL Duration Adjustment Studies [Senzig et. al., 2018]) shows that the higher the test flight altitude deviation is from the reference altitude on which the correction curve is based, the higher the error is that results from the adjustment. The test campaigns by Volpe (Senzig et al., 2018) evaluated these errors by means of the difference in adjusted noise measurement values and actual noise measurement values at various altitudes. Referring to the morphological matrix discussed earlier (refer to Table 3; Task 1.3), an alternative procedure can emerge from any one of the procedural steps such as data processing methods, as in this particular use case. This again bolsters the need for a traceable platform that has the capability to conduct a holistic assessment of all potential certification bases.

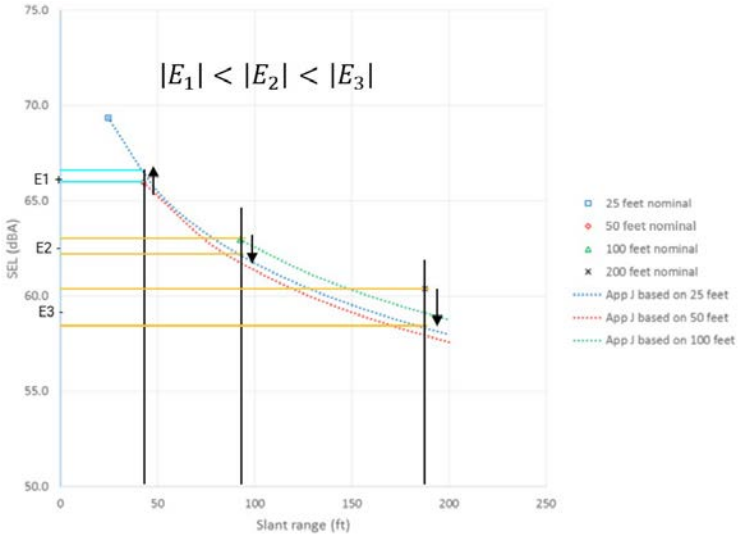


Figure 28. 14 CFR § 36 Appendix J duration adjustments applied to various altitudes (Figure 5 of SEL Duration Adjustment Studies [Senzig et. al., 2018]).

Figure 29 below shows the microphone array configuration employed by the Causey testing campaign (James et al., 2021) that generated data analyzed by the Cutler-Wood et al. (2022). The same experimental data were used to conduct the duration adjustment study discussed in this section in the context of analysis of alternatives.

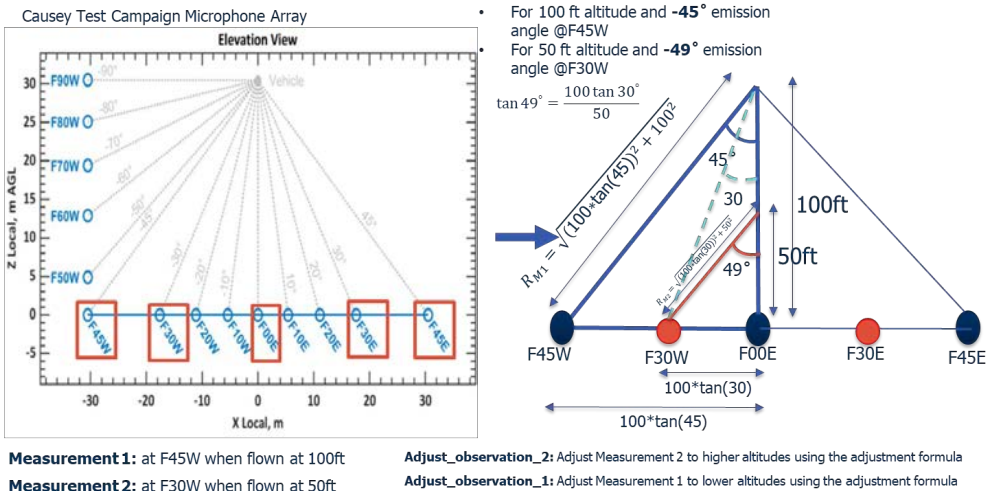


Figure 29. Causey microphone configuration and measurement nomenclature.

Each alternative procedure can have different ramifications on different paragraphs of a regulatory noise standard. Consider, for instance, the alternatives illustrated in Figure 30 for the duration adjustment equation. The variation of noise with respect to emission angles is represented using noise spheres in Cutler-Wood et al. (2022). To determine the utility of the proposed alternative in the context of the duration adjustment requirement alone, it is necessary to know the effects of emission angle and flight profile parameters such as hover flight altitude and weight of the vehicle on the variability in the measurement. It can be seen from Figure 30 that various fixed factor adjustments proposed do not necessarily guarantee a conservative adjustment of the true measurements to different altitudes. The fixed factor adjustments are specified in the RPA corresponding to the Matternet M2 (FAA, 2022), the other RPAs (FAA, 2023) issued by the FAA. Hence, as highlighted in Figure 23, it is worth considering vehicle specific k-factor adjustment regimen given the wide variety of configurations with varied noise generation and propagation characteristics emblematic of the UAS category.

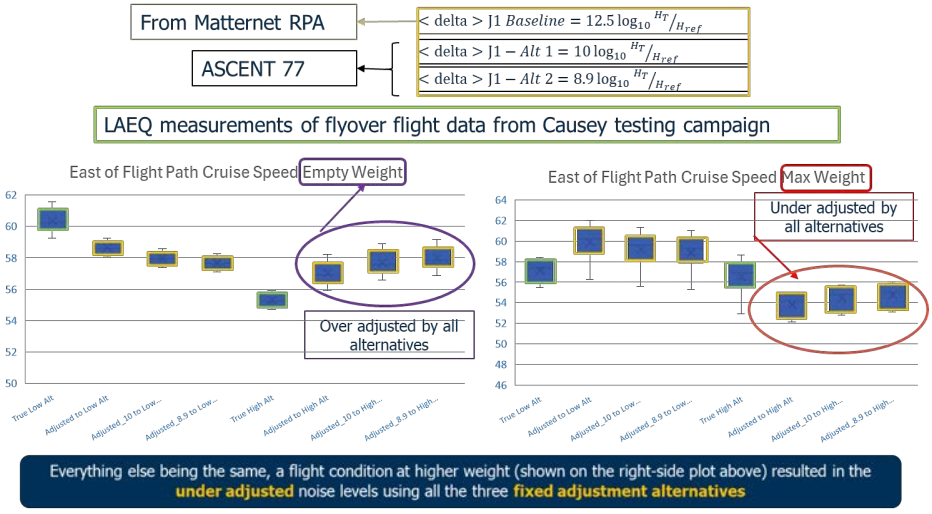


Figure 30. Application of the fixed factor duration adjustments to the noise measurements.

Figure 31 shows the microphone array configuration employed by the FAA and collaborating researchers (James et al., 2021) to acquire noise data necessary to understand the effects (Cutler-Wood et al., 2022). The vehicle deployed for the experimental campaign belongs to the small UAS category.

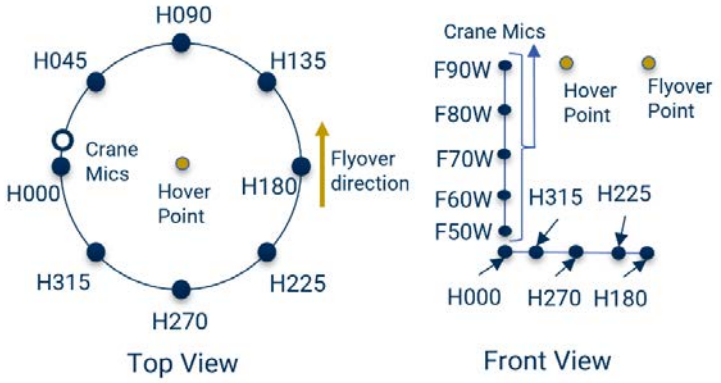


Figure 31. Experimental microphone array configuration (not to scale).

Experimental results consisted of higher-weight and lower-weight flights that were flown at an altitude of 100 ft and repeated five and six times, respectively. Our team evaluated the average confidence interval of SEL measurements of various subsets of a given number of repeats and plotted the results as shown in Figure 32. Figure 32 highlights the effect that vehicle weight has on variability in noise measurement. It can be observed that a higher weight configuration results in higher variability. Figure 32**,** however, does not illustrate a strict relationship in emission angle and weight, and further investigation may highlight the same. The ASCENT Project 061 team also observed that a greater number of runs is required to achieve a confidence interval limit of ± 1.5 dBA (SEL) at higher weight configuration. In view of this, it is proposed if a reduction of 10% (for example) in interval width is not seen after three additional runs (for example) beyond the minimum of six runs already specified, additional runs are not necessary, noting that further reduction variability may not be possible for the given combination vehicle configuration and test flight profile.

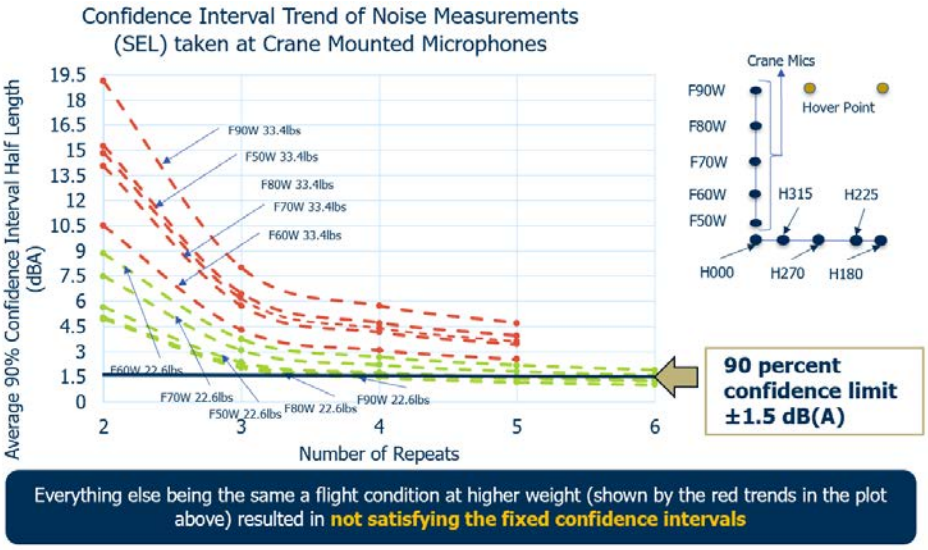


Figure 32. Effects of vehicle weight and emission angle on noise variability in hover flight. SEL: sound exposure level.



Figure 33 shows the average confidence interval trends for a flyover flight condition that was repeated the highest number of times. Although this flight condition is different from the hover flight condition, it highlights the trend of the average confidence interval of SEL over a higher number of runs. Hence, our team noted that although fewer microphones are required for the alternative method as shown in in the left panel plot of Figure 30, the number of repeats required to achieve the confidence interval limit make the alternative method, as shown in the right panel plot of Figure 30, preferable. Ultimately, to arrive at a decision, the costs and times of additional microphones and their setup need to be compared with those of additional flights.

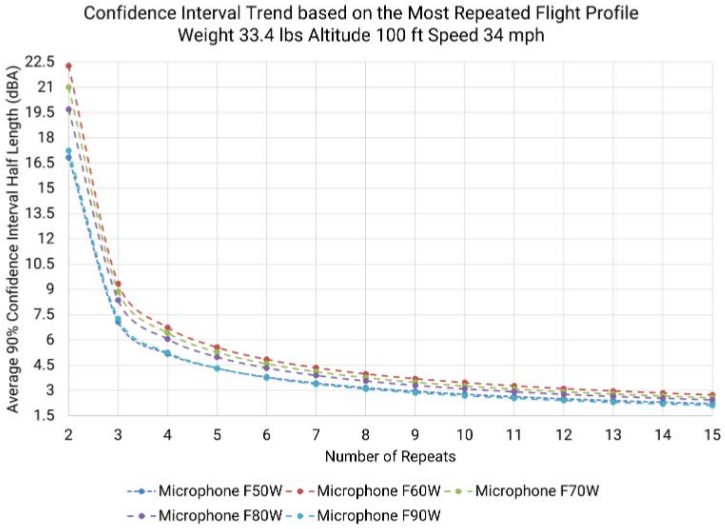


Figure 33. Effects of emission angle on noise variability in flyover flight.

Environmental Noise Impact Potential

As discussed under Task 1, the risk-based demarcation by the EASA takes operational parameters into consideration while demarking the noise standards. However, the design parameters such as design configuration and weight can enhance the demarcation exercise given their contribution to the Environmental Noise Impact Potential (ENIP). Framework in **Error! Reference source not found.** is proposed for the purpose of evaluating the same.

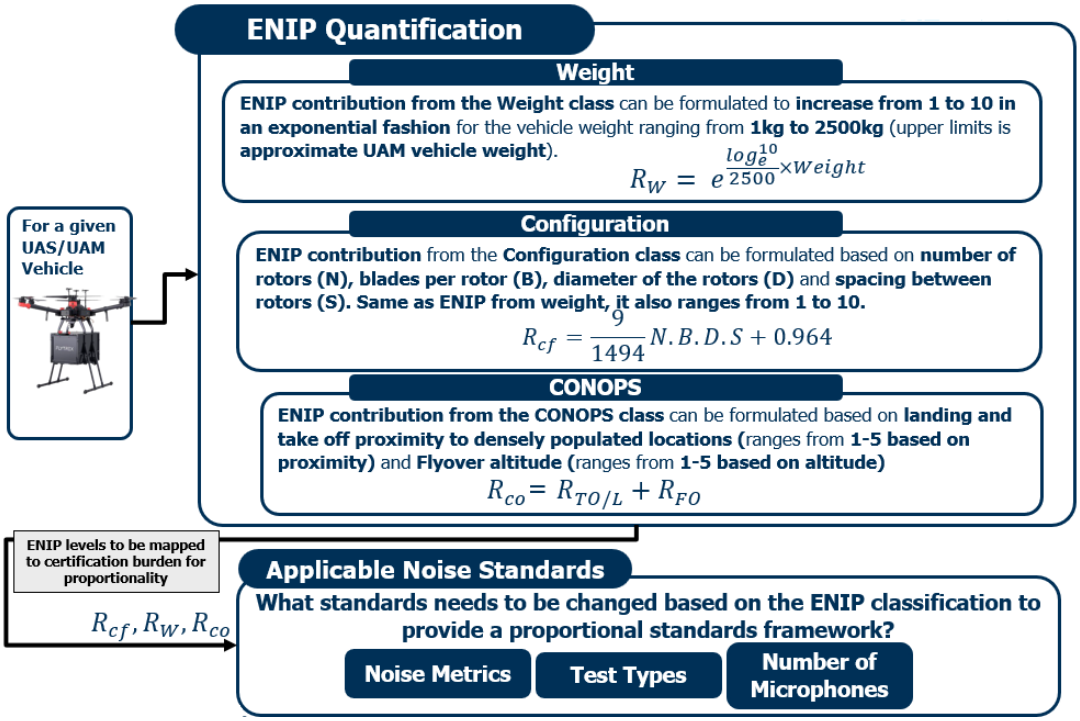


Figure 34. Environmental Noise Impact Potential (ENIP) Framework. CONOPS: configuration and concept of operations, UAM: urban air mobility, UAS: unmanned aircraft systems.

Engagement with ASTM F38

Advancing Standards and Transforming Markets (ASTM) working group F38 found the methodology proposed here for standards setting suitable for the FAA Part 108 Beyond Visual Line of Sight Operations (BVLOS) for commercial UAS operations noise certification. The committee members and the researchers on ASCENT Project 061 team met and discussed the collaboration opportunities to further effective rule making efforts. The meeting took place on August 21, 2025. The FAA proposed a rule on August 7, 2025 for scaling up the UAS BVLOS operations and integrating them into National Air Space safely. The commenting period on this proposed rule ended on October 6, 2025.

Milestones

See the milestones under Task 1.

Major Accomplishments

- Developed metrics and integrated the PIM under a parametric interactive decision support environment. The concept has been demonstrated through a minimum viable project exercise.
- Formulated and applied to the PIM to a typical plan for UAS noise testing.
- Conducted a preliminary analysis of noise measurement data and utilized resulting insights for requirement analysis.

Publications

Published Conference Proceedings

Ali, H. E., Ravikanti, B., Balchanos, M. G., Harrison, E., & Mavris, D. (2025). MBSE Enabled Requirement Verification for a Traceable Regulatory Analysis Framework of UAS Noise Certification Standards. AIAA SCITECH 2025 Forum (p. 0367).

Mali, H., Geneti, N. F., Balchanos, M. G., Harrison, E., & Mavris, D. (2025). A Process Evaluation and Visualization Framework for Unmanned Aerial System (UAS) Noise Certification Testing. *AIAA SCITECH 2025 Forum* (p. 0368).

Balchanos, M., Ravikanti, B., Ali, H., Mali, H., D Harrison, E., & N Mavris, D. (2024, September 9-11). *A Regulatory Analysis and Process Improvement Decision Support Framework for Unmanned Aerial System (UAS) Noise Certification* [Conference presentation]. Quiet Drones 2024 Symposium, Manchester, United Kingdom.

Awards
None.

Student Involvement
The full student team (Hussein Ali, Nathaniel Geneti, Hajar Mali, Martin Poretti and Balaji Ravikanti) has participated in brainstorming sessions toward formulating the integrated certification process assessment framework for UAS.

Plans for Next Period
- Project ended on September 30, 2025.
- Publish peer-reviewed journal articles with *AIAA Journal* and AIAA SciTech.

References
Cutler-Wood, C., Barzach, M., Hobbs, C. M., & Shirayama, S. (2022, June 27-30). *Estimating Unmanned Aircraft Takeoff Noise Using Hover* [Conference paper]. QUIET DRONES Second International e-Symposium, virtual. https://rosap.ntl.bts.gov/view/dot/64152

FAA. (2022). *Noise Certification Standards: Matternet Model M2 Aircraft*. Federal Aviation Administration. https://www.federalregister.gov/documents/2022/09/12/2022-19639/noise-certification-standards-matternet-model-m2-aircraft

FAA. (2023). *Noise Certification of UAS/AAM using Rules of Particular Applicability*. Federal Aviation Administration. https://www.faa.gov/about/office_org/headquarters_offices/apl/aee/noise/uas_noise_certification

James, M., Salton, A., Downing, M., & Calton, M. (2021). *Causey UAS Acoustic Measurements*. Blue Ridge Research and Consulting, Asheville, North Carolina.

Noise Standards: Aircraft Type and Airworthiness Certification, 14 C.F.R. § 36 (2023). https://www.ecfr.gov/current/title-14/chapter-I/subchapter-C/part-36

Senzig, D. A., Marsan, M., Cutler, C. J., & Read, D. R. (2018). *Sound Exposure Level Duration Adjustments in UAS Rotorcraft Noise Certification Tests*. U.S. Department of Transportation, Volpe National Transportation Systems Center. https://rosap.ntl.bts.gov/view/dot/37057

ASTM International. (2025). *Committee F38 on Unmanned Aircraft Systems*. ASTM Working Group F38. https://www.astm.org/membership-participation/technical-committees/committee-f38

Federal Register. (2025). *FAA Part 108 UAS BVLOS Proposed Rule: Normalizing Unmanned Aircraft Systems Beyond Visual Line of Sight Operations*. https://www.federalregister.gov/documents/2025/08/07/2025-14992/normalizing-unmanned-aircraft-systems-beyond-visual-line-of-sight-operations

Task 4 - Develop Alternative Procedures and Assess Their Performance with Existing Tools (Case Study)
Georgia Institute of Technology

Objectives
Task 4 seeks to explore options for evaluating noise certification within the MBSE certification framework. The purpose of this task is to allow a performance baseline to be established for current procedures and to allow for the evaluation and comparison of more flexible process alternatives as they are formulated within Tasks 2 and 3. The breakdown of tasks under Task 4 is as follows:

Task 4: Develop alternative procedures and assess their performance with existing tools
- 4.1 Develop alternative testing procedures using the elements library
- 4.2 Transfer alternative procedures to the PIM
- 4.3 Report on the performance of the alternative procedures
- 4.4 Develop a proof-of-concept demonstration of the PIM capabilities

Research Approach

The goal of Task 4 is to identify process modeling approaches for the purpose of simulating and evaluating the performance of a noise certification procedure. Task 4 delivers a solution that, in a broader sense, is referred to as the PIM. Tasks 4.1 to 4.3 focus on PIM implementation, whereas Task 4.4 integrates the PIM into the current MBSE framework. The PIM must analyze the process performance and interface with the verification model for completing steps regarding requirements and compliance. The PIM must also be flexible and reusable within the verification thread and must accommodate UAS configurations. An overview of the integrated verification thread and the PIMs is shown in Figure 35.

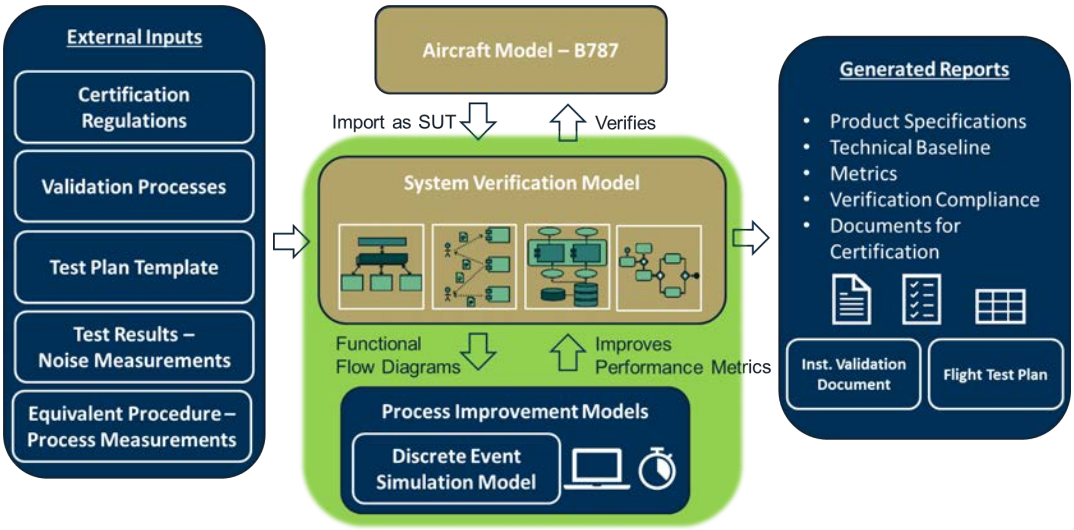


Figure 35. Integration of the process improvement model within the model-based systems engineering certification framework. SUT: system under test.

Task 4.1 Develop Alternative Testing Procedures Using the Elements Library

The team has completed a literature review on process modeling methods to enable process simulation. These methods are listed below:

- DES, where a clock tracks the duration of the transition between model states
- Agent-based simulation methods
- System dynamics
- MCMC simulation methods

These techniques are evaluated on the basis of their ability to capture and simulate actual industry-applied procedures, and to interface with the verification thread. For simulating a simple process that is representative of transport category certification, the DES modeling approach appears to be the most effective. To demonstrate feasibility, a proof-of-concept version was developed using the DES method in a Python-based environment. The chosen example covered the testing process for a flyover approach, as shown in Figure 36. The objective was to demonstrate that a process model, as defined in the MBSE framework, can be simulated using DES. With the MBSE model states imported, DES can track the clock and return time points at each event conclusion. The DES results are then fed back as input in turn updating the process diagram in the verification model, which then checks the process model against requirements and compliance.

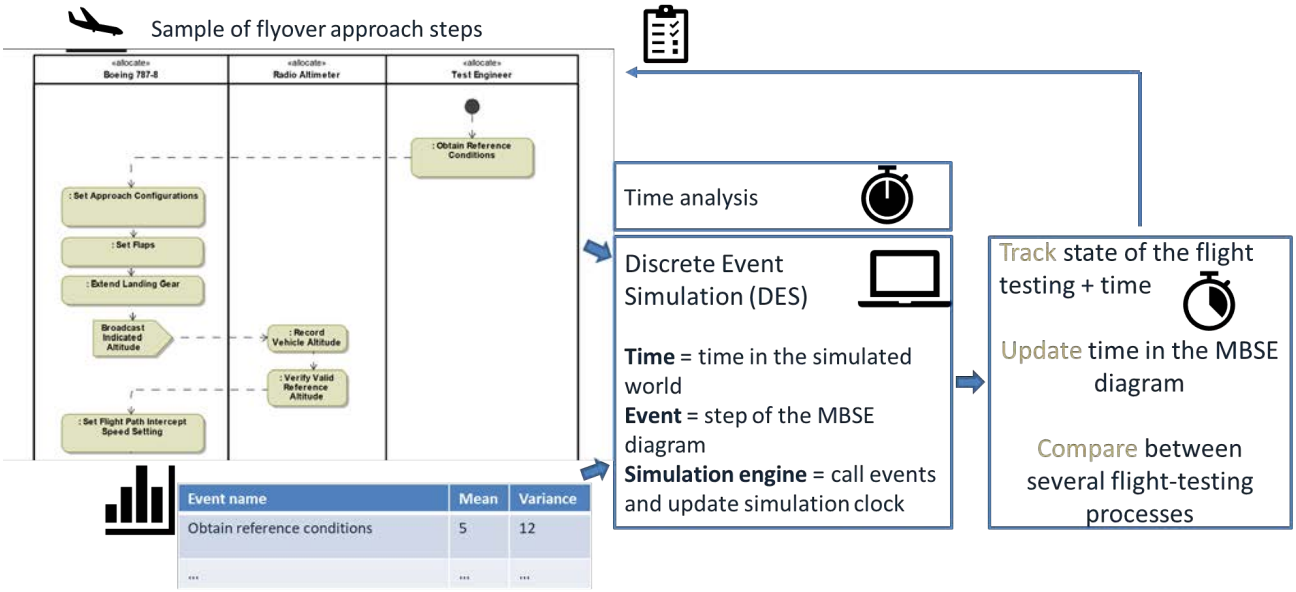


Figure 36. Discrete event simulation (DES) for a flyover approach. MBSE: model-based systems engineering.

However, because flight testing procedures are impacted by uncertainties, a different modeling approach is needed. To account for uncertainties, a probabilistic model using Markov chains has been developed to improve the accuracy of how interactions and emerging effects are captured. This approach is better suited to support use cases, with the objective of further process simplification, especially for flight testing portions, instrumentation setup, and measurement systems. This simplification could involve eliminating or replacing steps and potentially using advanced data-driven or physics-based modeling approaches as a substitute.

Because of the extension of DES to Markov chain approaches and the need for large samples, the ASCENT Project 061 team adopted the MCMC approach, where a Markov chain model is used to run a Monte Carlo study to collect sample runs, given an input probability matrix and stakeholder value function. Each run is associated with an incurred time, cost, and accuracy penalty. The output is provided in the form of activity diagrams and responses that are fed back to the verification model within the MBSE framework. Through the requirement model within the MBSE framework, the MCMC simulation data are imported to perform acceptance–rejection sampling, where each run (with its associated metric) is accepted or rejected by requirements/constraints within the verification model. The format of the MCMC simulation data follows the form of a step-by-step sequence (similar to a DES).

Summarizing the development of the PIM, the implementation path is shown in Figure 37, which illustrates the interface with the verification model. Using a similar flyover approach plan example as in Figure 36, the process model informs the PIM, which converts the flyover approach test into an executable simulation model. Based on the type of requirement test selected by the user, the appropriate response values, parametric settings for baseline values (i.e., time, cost, resources, disruption risks, accuracy penalty, etc.), and distributions for Monte Carlo simulations are chosen. The Monte Carlo simulation then generates the PIM metrics and prepares the dataset for verification.

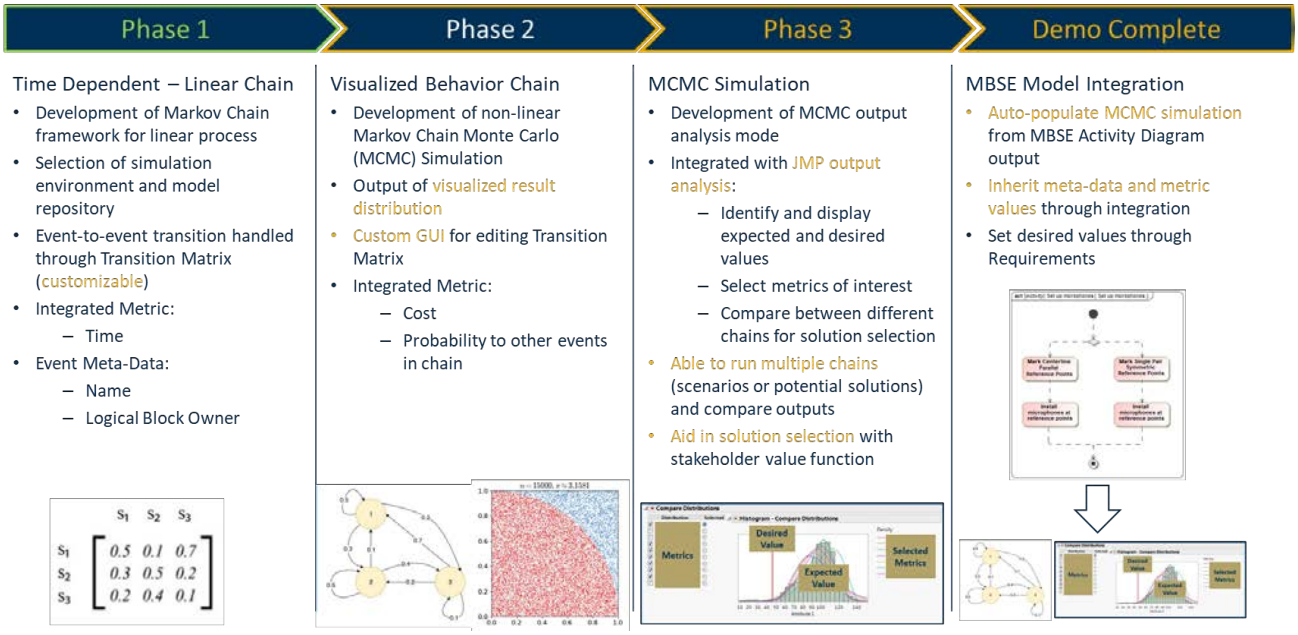


Figure 37. Functional development plan based on a process improvement model. GUI: graphical user interface, MBSE: model-based systems engineering, MCMC: Markov chain Monte Carlo.

For this task, the literature search, exploration of modeling options and selection, and proof-of-concept implementation are now completed.

Task 4.2 Transfer alternative procedures to the PIM.
With the PIM model now available in a flexible and customizable format, in Task 4.2 our team sought to expand the process simulation and analysis toward metrics that will link to use case objectives and process selection of improved alternatives.

The selected metrics should allow for a quantitative comparison of current and proposed streamlined noise certification process options. The updated list of identified metrics is as follows:

- Time: The schedule cost incurred to complete event.
- Cost: The budget cost incurred to complete event.
- P(Failure): The probability of repeating an event or reverting to a previous event (does incur time and cost [full or partial] in each occurrence).
- P(Success): The probability of moving out of the current event.
- Accuracy penalty: The impact on overall accuracy value for executing the event (does not incur an additional cost in each occurrence).
- Process complexity metrics: These metrics are one of the latest additions to the model and allow the model to capture the level of uncertainty and risks corresponding to a specific testing procedure. More complex procedures are highly susceptible to causing significant schedule and budget overruns.

The proposed integrated model uses a system verification model with external inputs, such as current certification regulations, validation processes, and test plan templates. This results in an interconnected model for the UAS, referred to as the SUT, which evaluates the validity of a certain certification procedure and generates alternative procedures suggesting one or a combination of modifications related to the utilized noise measurement metric, microphone type or array design, or flight profile (i.e., flyover, hover, vertical takeoff/landing, etc.). Figure 38 provides a general overview of the integrated structure of the system verification model, the PIM, and the visualization environment.

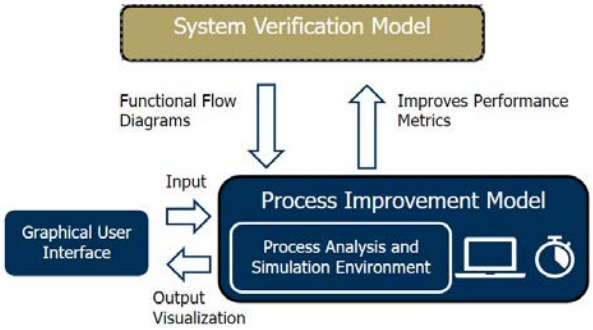


Figure 38. Integration of system verification model, process improvement modeling, and graphical interface.

In addition to the flight test procedure diagrams describing the sequence of events constituting the flight tests, different detailed reports can be generated as outputs of the system verification model. The PIM assesses the performance of the baseline flight test procedure and other alternative procedures in terms of overall time and cost. The PIM captures a typical noise testing process. Certain events within that process have feedback loops indicating that one event or a set of events is to be repeated due to the detection of anomalies or calibration issues. Hence, some events can have different outcomes and, depending on the likelihood of each outcome, the overall flight test sequence would differ and lead to a different overall time and cost of the entire process. This steers the focus toward a probabilistic modeling approach, in which it is desirable that each event exclusively depends on the previous event. Moreover, to properly account for uncertainty and risks in predictions and decision-making, it is crucial for these flight tests to be simulated multiple times. With all these elements taken into consideration, a suitable approach for modeling a flight test procedure is using a Markov chain. To maintain a simplified terminology for the PIM, the flight test procedures extracted from the system verification model are to be considered flight test processes and the events are to be referred to as steps.

The PIM implements a Matlab script incorporating the mathematical representation of the flight test process to be analyzed using Monte Carlo simulations. Two Microsoft® Excel® files are used as inputs to the script; the first file includes all the steps of the flight test process and the probabilities of occurrence of each outcome, and the second file contains the assigned time and cost values for each step.

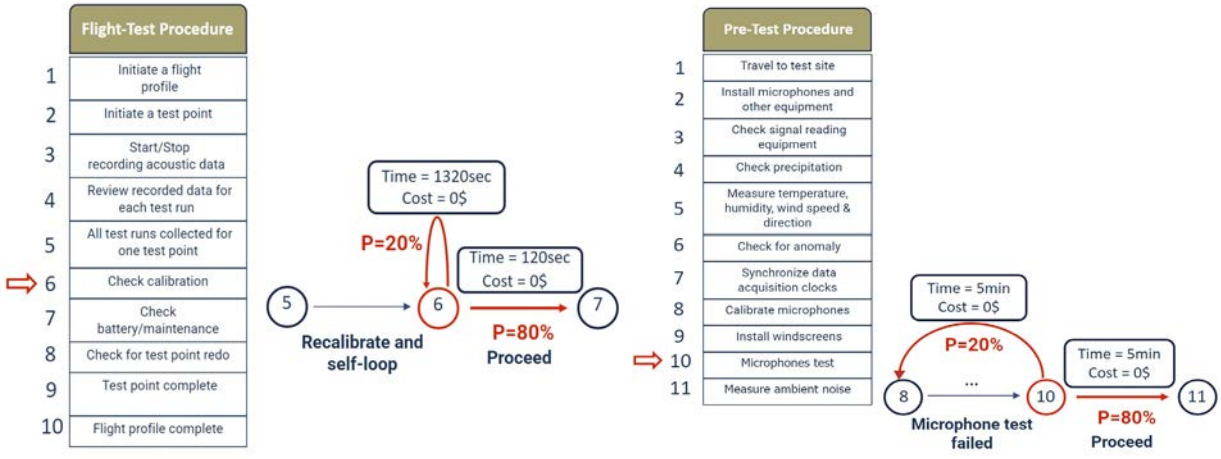


Figure 39. Example of self-loop (left figure) and feedback loop (right figure) within the noise testing process.

® Microsoft and Excel are registered trademarks of Microsoft Corporation in the United States and other countries.



As noise testing is captured as a stochastic process, most of the steps can lead to different outcomes depending on many factors, including human error, unstable weather conditions, equipment malfunction, unsatisfactory measurements, etc. These variations are modeled using feedback loops and self-loops in the Markov chain, in which the former represents the need to go back to a previous task in case an anomaly is detected, whereas the latter refers to the need to repeat the current task. Each potential outcome has a specific probability of occurrence assigned to it. Figure 39 portrays examples of a self-loop and a feedback loop within the process. In Figure 39, step 6 of the flight-test procedure consists of checking the calibration of the microphones after the completion of each test point. This step is crucial to avoid potential complications such as reducing confidence in the validity of noise test results, lacking a traceable chain of measurement standards, and impacting data comparability across multiple instruments. In this example, a probability of 20% is set for the need to recalibrate, which entails a longer time compared to the alternative outcome of not needing recalibration with 80% probability. Similarly, step 10 of the pre-test procedure consists of two potential outcomes for the microphone test; either the test fails, and the staff need to take the windscreens off, recalibrate the microphones, reinstall the windscreens and test again (probability of 20%), or the microphone test is successful (probability of 80%) and the following step is initiated.

In addition to evaluating the effectiveness and efficiency of different testing alternatives in terms of their resulting time and cost, capturing and understanding the complexity of the testing layout is also crucial as it helps identify improvement points within the process to better streamline it and reduce the uncertainty and error proneness related to it.

Two categories of metrics have been implemented to quantify the complexity level of a testing procedure; four metrics that are dependent only on the structure of the noise testing process, and one metric that is dependent on the outcome of the Monte Carlo simulations. This simulation-dependent metric is the Redundancy and Rework Index (RRI), and it indicates the percentage of steps in the process that are redundant or have been reworked, such as measurement repetitions or microphones' re-calibration. This metric highlights areas in the process where efficiency improvements might be necessary to reduce the uncertainty level related to those steps and minimize repetitions and corrections, as follows:

$$RRI = \frac{R}{T} \quad \text{(Eq. 5)}$$

where R is the number of repeated or reworked steps and T is the total number of steps.

RRI is computed for each Monte Carlo simulation. Since each of the 10,000 design of experiment (DoE) cases contains 10,000 Monte Carlo runs, the mean and standard deviation of RRI is calculated for each DoE case then calculated again over all cases to get a final mean RRI and standard deviation for the overall noise testing process. As for the process-dependent complexity metrics, these include:

- Cyclomatic Complexity (CC), which calculates the number of unique and independent paths (different sequence of nodes and edges) to go through the process such that full testing coverage is ensured, as follows:

  $$CC = E - N + 2P \quad \text{(Eq. 6)}$$

  where E is the number of edges, N is the number of process steps, and P is the number of connected components.

- Control Flow Complexity (CFC), which indicates how much decision-making and iteration is present within the process based on the control flow structure, as follows:

  $$CFC = D + L \quad \text{(Eq. 7)}$$

  where D is the number of steps with multiple potential paths and L is the number of feedback loops and self-loops.

- Decision Density (DD), which measures the concentration of decision points in the process (as shown in the following equation). A lower decision density value indicates fewer decision points leading to less uncertainty relative to the total number of steps. In contrast, a higher value would indicate the opposite.

  $$DD = \frac{D}{T} \quad \text{(Eq. 8)}$$



- Process Entropy (PE), which measures the unpredictability in the process flow. A high level of entropy indicates that there are many possible task outcomes(paths), making the process more complex and more difficult to predict. Lower entropy, however, means fewer paths, and a more structured and predictable process.

  For a step i with j potential paths:

$$\sum_{j=1}^{n} p_{ij} = 1 \quad \text{(Eq. 9)}$$

  where p_{ij} is the probability of occurrence of path j at step i.

  Process entropy for step i:

$$PE_I = -\sum_{j=1}^{n} p_{ij} \log(p_{ij}) \quad \text{(Eq. 10)}$$

  Overall process entropy:

$$PE = \sum_{i=1}^{m} PE_i = -\sum_{i=1}^{m} \sum_{j=1}^{n} p_{ij} \log(p_{ij}) \quad \text{(Eq. 11)}$$

Task 4.3 Report on the Performance of the Alternative Procedures

The objective of Task 4.3 is to produce a baseline of a noise certification procedure simulation and to propose a calibration step, as process data become available from ASCENT Project 061 partners. The analysis workflow for the PIM module is shown in Figure 40. The goal of the workflow within the PIM is to analyze the complexity of the process and to identify potential bottlenecks by assessing time, cost, and node/step criticalities. The workflow is completed in three basic steps:

1. **Definition of test data:** This step includes a test plan, setup, instrumentation and recording information, and sound pressure level measurement data.
2. **Process representation as an event chain through graph modeling:** In this step, the process is converted and represented as a weighted directed graph. Each node represents a step in the process, and the edges represent transitions between steps. The progression through the steps is represented by probabilities and parameters at each step.
3. **Execution of the MCMC algorithm:** The simulation starts from a node, and a "roll the dice" (i.e., generate a random number) function is performed. Depending on the outcome and the probability of each path, the algorithm selects the next node. A learning factor is utilized to update the probabilities of progressing through the steps (increased probability the second time).

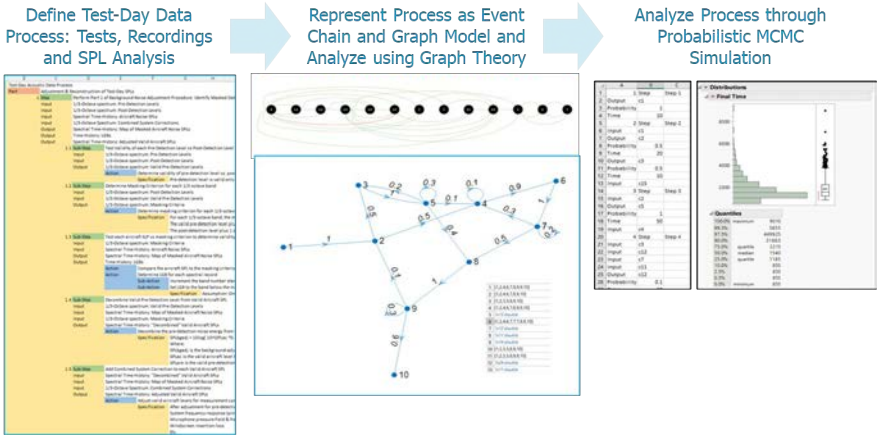


Figure 40. Analysis workflow based on the process improvement model. MCMC: Markov chain Monte Carlo; SPL: sound pressure level.

The analysis of different alternative procedures in noise flight testing relies on the evaluation of different performance criteria or metrics of interest to which the user may allocate different levels of importance. The outputs of this analysis heavily contribute to the decision-making alongside the regulatory adherence in which the requirements' satisfaction of each alternative procedure is evaluated. In the context of the suggested PIM, progression through the steps is associated with probabilities and parameters. Hence, tracking the propagation of these metrics of interest is enabled within the Monte Carlo simulations. Induced costs and time throughout the process are the focus of the current efforts. When combined with the sequencing of events of each process simulation, these outputs can provide insight into process complexity and induced risks and allow the anticipation of potential bottlenecks in the process.

Noise certification testing processes are represented using Markov chains within a probabilistic simulation environment. This approach relies on random variables, which are functions assigning real numbers to each potential outcome within the sample space of a random experiment. This approach also entails that every event solely depends on the previous event, thus preventing the propagation of uncertainties throughout the process. The entire process can be visualized using weighted directed graphs, in which every node represents a step within the noise testing process and the edges indicate the transitions between nodes. A valid representation of the certification testing process requires every node on the graph to be able to eventually reach the final step, thus ensuring process continuity by calculating the "connected components" in the graph. Figure 41 depicts the need to ensure continuity within the demonstrative process. The illustration on the left of Figure 41 depicts the demonstrative process in which step 7 cannot reach the final step; whereas the corrected Markov chain representation on the right of Figure 41 implements process continuity for each step.

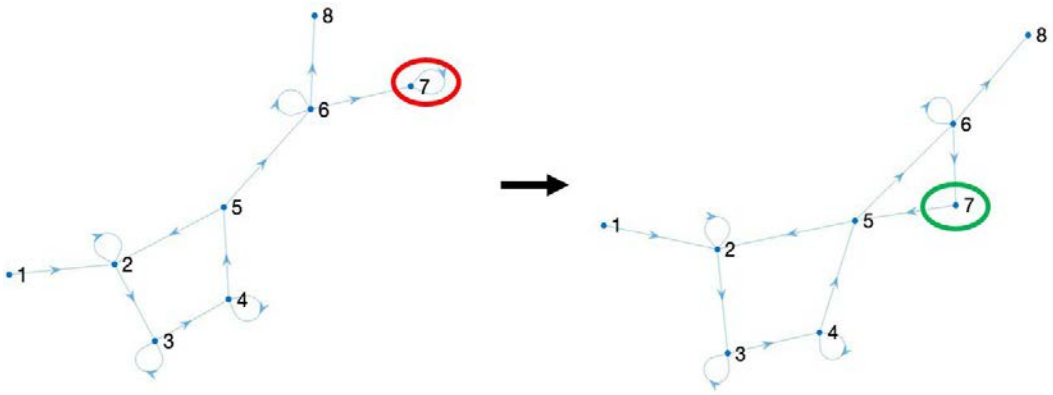


Figure 41. Illustration of process continuity in a sample flight test process.

Every edge of the Markov chain representation is assigned to a probability characterizing the likelihood of moving from one node to another, thus mapping different potential paths to be taken. The Monte Carlo method is implemented to achieve repeated random sampling during the simulation. This method generates a random number that is compared to the cumulative sum of the row corresponding to the current step of the transition matrix, which contains all potential probabilities connecting any two nodes. The next step is chosen once the random number is less than or equal to the smallest cumulative sum. Each Monte Carlo simulation follows a specific path that is dictated by the method. To achieve accurate estimates, the Monte Carlo simulation must be repeated multiple times by increasing the number of runs set within the Matlab script. This underlines an important trade-off between the accuracy of the results and the script execution time. In this work, the analysis was first exclusively targeting the most influential steps of the noise testing process as they will be the main sources of variation within the results. This approach allows for the reduction of computational time for PIM execution while ensuring the accuracy and reliability of the results. This can be accomplished by implementing PageRank centrality, which is a metric providing the average time spent at each node during a random process simulation. The average for each node is weighted according to the probabilities of reaching a node and the value of the associated parameter. These key (i.e., most influential) steps were varied in each simulation using DoEs. In addition to the identification of key steps, the code introduces the capability of detecting bottlenecks within the process, giving enough insight about steps susceptible to causing delays or complications within the process workflow.

Table 5. Identification of noise testing equipment and other expenses.

	Fixed Costs	Variable Costs
Equipment	Microphones	Batteries
	Windscreens	Personnel payment
	Weather sensors	
	Time-position tracker	
	Crane or poles (for elevated microphones)	
	Calibrators	
	Travel expenses	
	Test site rental	

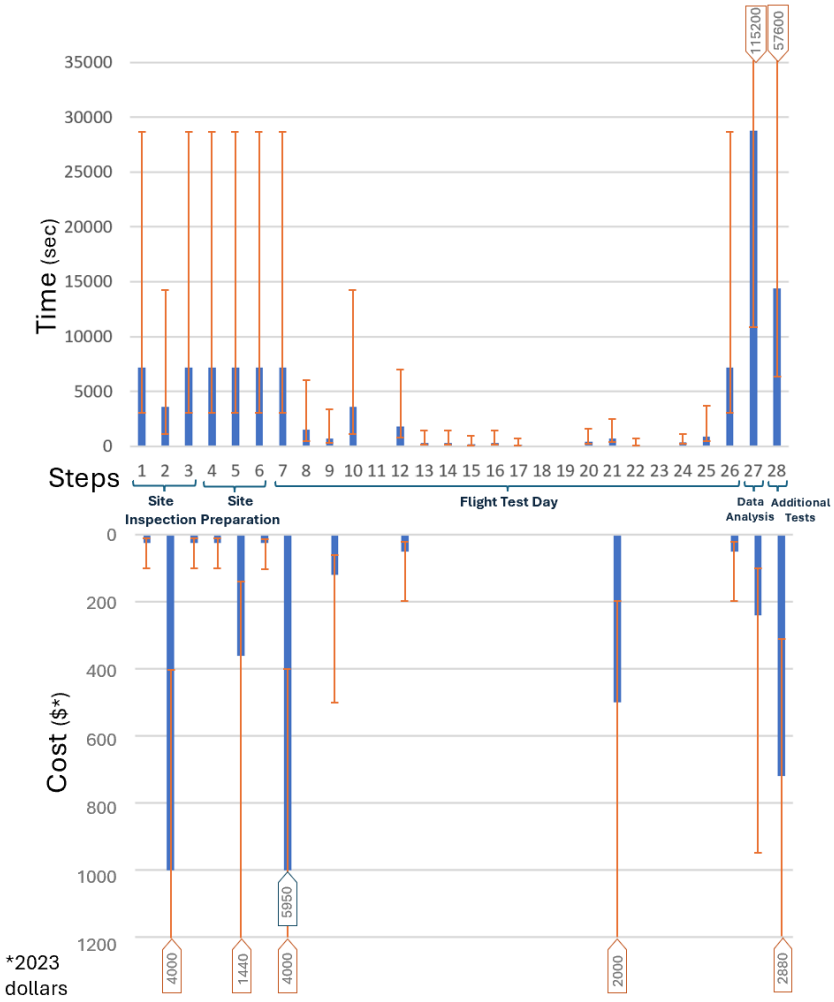


Figure 42. Time and cost estimates related to each noise testing phase and step.

As the model has been significantly expanded, the DoE is now conducted on all the steps of the process to enable a full analysis of the results and a comprehensive evaluation of testing alternatives. Furthermore, this approach allows us to explore a wide range of variables and assess their impact on the total time and cost of the noise testing process.
The inputs (i.e., individual times and costs) are now varied by multiplying the values by factors between [0.4, 4]. Figure 42 depicts the allocated time and cost to each step of the process with the hairline indicating the range of variation.
The baseline cost values have been estimated based on the list of equipment that has been used during the Causey Airport noise testing campaign. This served as a crucial starting point to formulate a more comprehensive list of equipment (Table 5) for which the prices have been either estimated or looked up online. The costs have been divided into two categories: (1) fixed costs consisting of all pieces of equipment, travel expenses, and rentals; and (2) variable costs such as the battery replacements for UAS or the personnel payment that depend on the duration of testing and/or the number of personnel. To generate this DoE, the Latin Hypercube Sampling (LHS) has been selected as the space-filling method of choice. Each process simulation has been conducted for the 10,000 DoE cases such that each case is repeated for 10,000 Monte Carlo runs.

The number of personnel available during each phase of testing can highly impact the time required to conduct certain tasks and eventually the total time of testing. Figure 43 showcases an example of the impact of the number of microphones and the number of personnel on the time needed to install the microphones. It has been assumed that one individual can install a single microphone in 5 min, and that one individual is always on standby as they could be carrying out a different task in parallel or supervising the installation process. In Figure 44, to help with the visualization of this plot, it has been broken down into two different plots such that the left plot displays the change in time with respect to the number of personnel for the installation of 10 microphones and the right plot shows the change in time with respect to the number of microphones for a total of six personnel members. For example, considering a total of 10 microphones and six personnel members are on site, only five members can participate in the installation process. The installation team would simultaneously install one microphone each then install the remaining five microphones, which requires a total duration of 10 min.

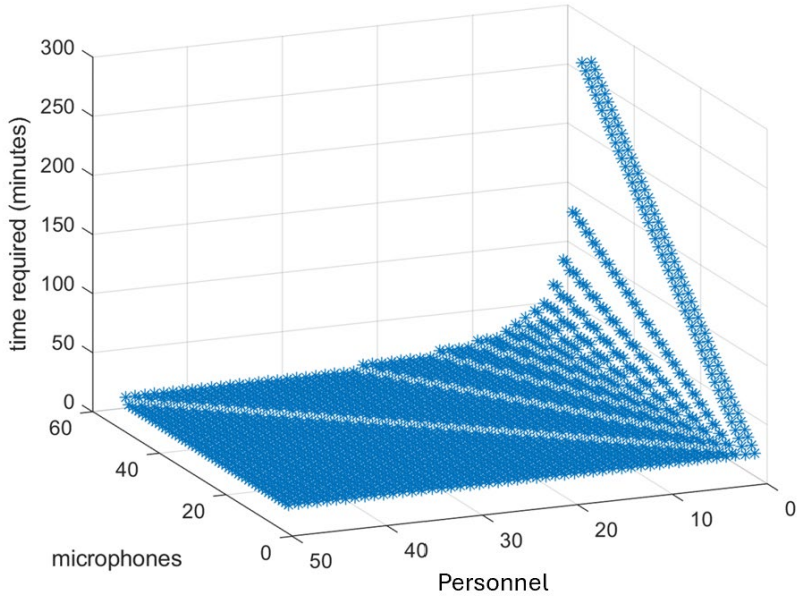


Figure 43. Three-dimensional plot of the impact of number of microphones and personnel variations on microphone installation time.

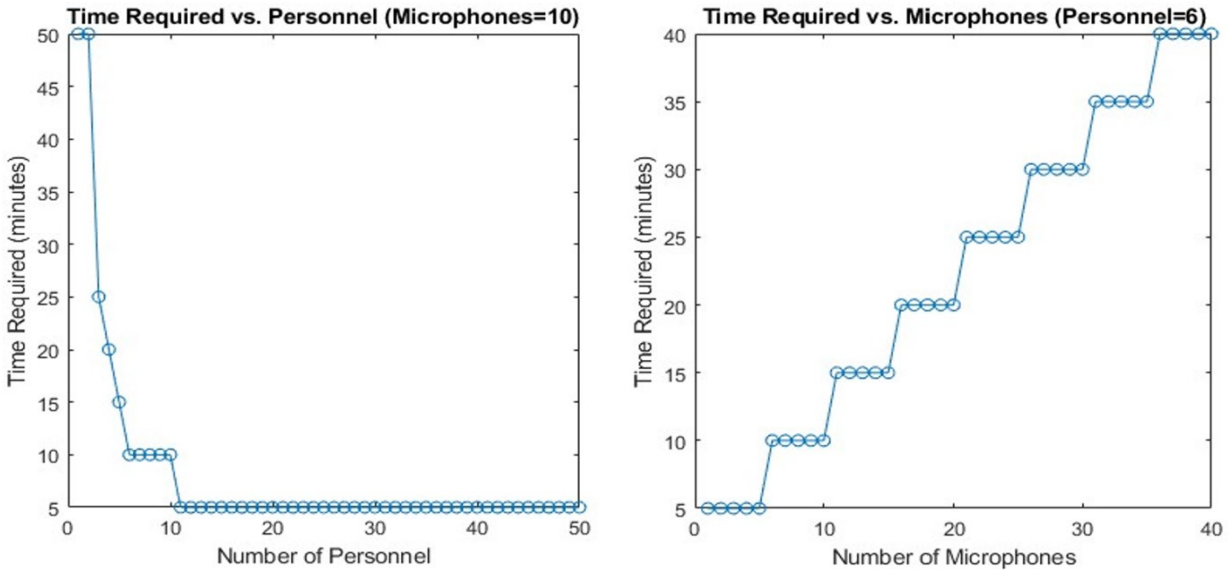


Figure 44. Two-dimensional projects of the impact of number of personnel on installation time of 10 microphones (left) and the impact of the number of microphones on equipment installation time for a team of six personnel (right).

The baseline process for the PIM exclusively considers a hover flight profile with three test points with a minimum of six runs per test point. Each test point refers to a test condition with a specific combination of weight, speed, and altitude. With the use of only one microphone, UASs will fly at three different locations relative to that microphone (Figure 45). The analysis is turned into a parametric analysis capable of automatically changing the types of flight profiles and number of test points based on a set of user-defined inputs without having to manually modify the values in the input files. This enables the modeling of any combination of flight procedures, thus capturing noise testing campaigns of any desired size. Other user-defined inputs apply to parameters that would simultaneously affect multiple steps of the process in different ways, such as the number of staff members, number of microphones, travel duration to the test site, etc. Manually assessing and incorporating the changes due to variation in these parameters can be very tedious, as many steps can be directly or indirectly affected. Thus, all the impacted steps are identified beforehand, and the effects are quantified and mathematically modeled in terms of time and cost consequences. Once the user identifies any combination of parameters, the code will automatically implement the corresponding changes to the time and cost values in the input file of the baseline process.

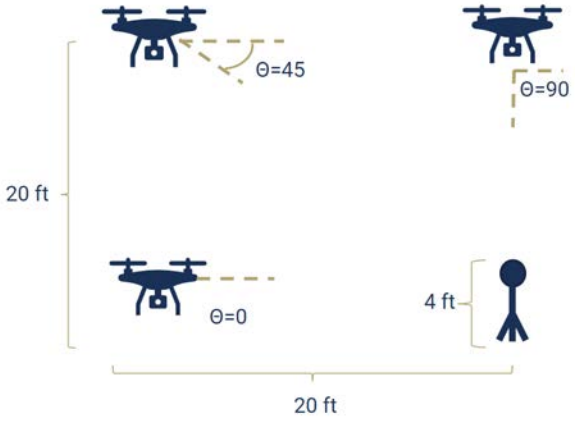


Figure 45. Baseline noise testing process (hover flight profile).

Calibration is an essential step for ensuring model accuracy and the validity of results and findings. This task requires a completed process simulation capability, which will be calibrated against a baseline that captures current certification testing plans and processing steps. The pivot to the UAS category has included plans to interface with ASCENT partners who can provide testing plans and noise datasets to be used as calibration data and overall process information. This task will be one of the key focus topics for the ASCENT Project 061 Year 3 activities. Scalability issues are bound to arise as this model is expanded to reflect the full verification thread; thus, the next step is to discuss options for data that ASCENT Project 061 partners could provide for further calibrating the model, according to the use cases of preference.

Task 4.4 Develop a Proof-of-Concept Demonstration of the PIM Capabilities
In a proof-of-concept demonstration of the complete certification process simulation capability within the PIM, the ASCENT Project 061 team has been formulating use case examples based on scenarios provided by OEM partners. For these examples, simulation runs are being executed to test modifications and proposed improvements over the baseline process. Under this task, a first demonstration of the PIM has been completed. For this example, the goal is to assess the impact of a simplified noise collection/analysis process for the Waco Aircraft® YMF-5 propeller aircraft.

The baseline (original) process was formulated within the PIM and executed using the best estimates for time and cost. The term "best" implies that our team had to rely on rationalized assumptions that were initially formulated by input from OEM partners. As this information could be of a sensitive nature for most OEMs, guidance was provided at a higher level, without any limitations on how the information would be distributed. Hence, for this example, a simplified process for flight segment testing is proposed, where a certain calculation is removed from the standard process. As shown in Figure 45, the simplified process removes step 18, the calculation of the second flight segment, while other steps were updated with new values to capture the updated process.

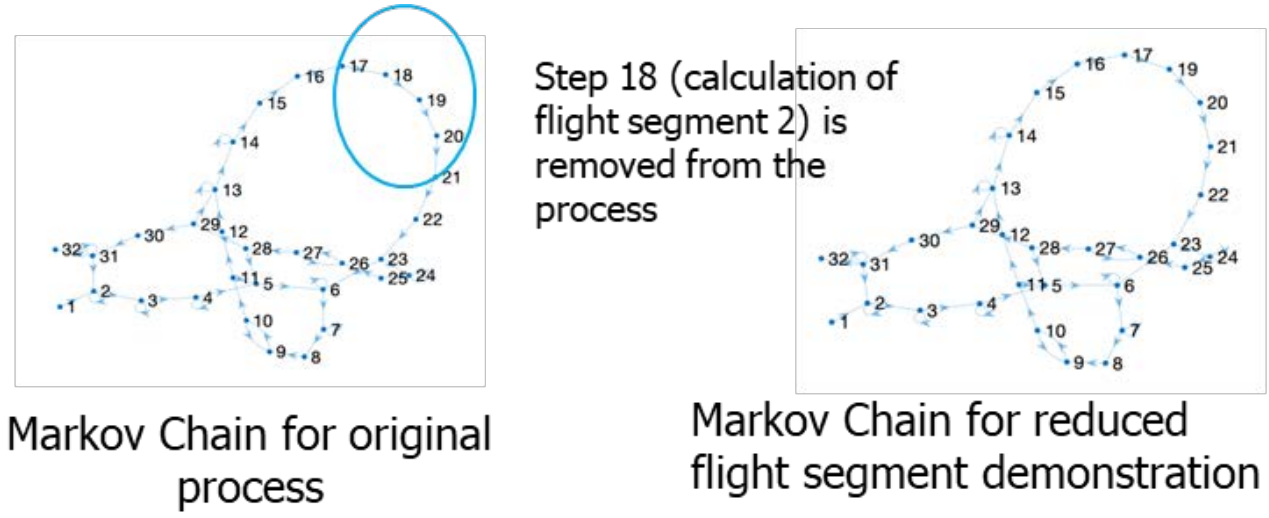


Figure 46. Process modification with step 18, the calculation of the second flight segment, is removed from the Markov chain flight-testing process.

A comparison of the two process alternatives is presented in Table 6. The results were obtained from an MCMC analysis and comparison between the baseline and simplified process. The PIM was able to quantify measurable savings in time and cost. In particular, the average process cost shows a reduction of 16%, and the average process time shows a decrease of 2%. The results are highlighted in Figure 47, where the Monte Carlo simulation data are plotted as distributions for the cost and time required for the process.

® Waco Aircraft is a registered trademark of Dimor Group Inc., Battlecreek, Michigan.

Table 6. Summary of cost ($) and time (hr) improvements.

		Mean
Original	**Cost($)**	166,770
	Time(hr)	155
Reduced Segments	**Cost($)**	140,430
	Time(hr)	151

With this fundamental example showcased under this task, the groundwork is set for scaling up the PIM to more comprehensive modifications, which would also include technology impact forecasting functions. As this practice will now be exclusive to the UAS category, the ASCENT Project 061 team's priorities are to investigate current noise testing plans and procedures and to be able to propose promising equivalent procedures.

Case Study 1

The FAA's Notice of Proposed Rulemaking (NPRM) for the Matternet Model M2 Aircraft (FAA, 2022a) outlines the use of a single microphone mounted on a tripod or pole, positioned 4 ft above the ground, for unmanned aircraft (UA) noise certification measurements. This proposed rule aims to streamline the process and reduce costs and workload by utilizing a single microphone. However, the possibility of using multiple microphones for hover noise testing was also explored to shorten testing time and enhance efficiency. Notably, the FAA is open to reviewing and approving multiple microphone configurations if deemed beneficial by the applicant. Consequently, a model-based approach is necessary to comprehensively evaluate and select between the proposed single-microphone setup and the alternative multiple-microphone configuration.

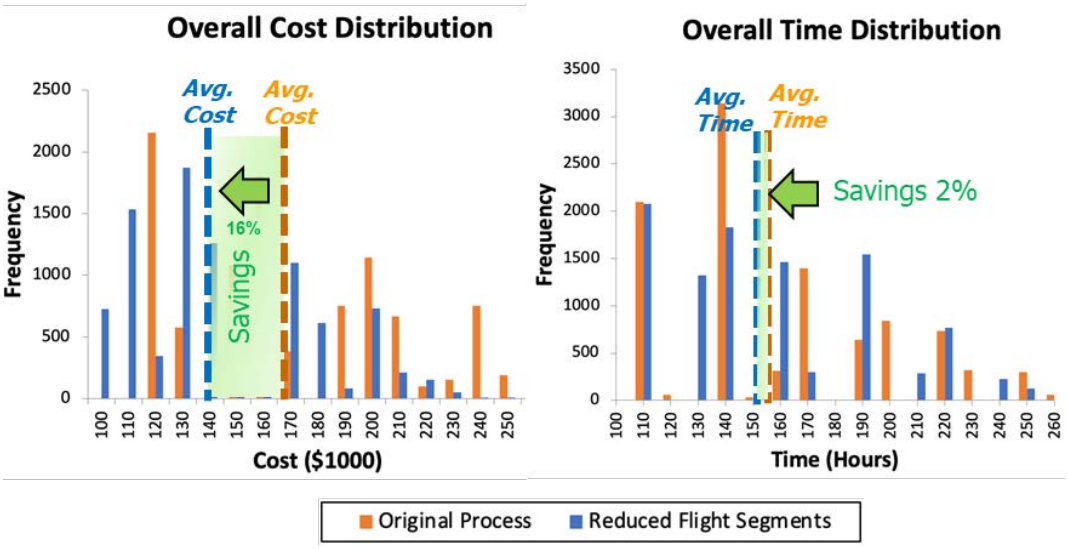


Figure 47. Execution of Markov-chain-based Monte Carlo analysis and comparison between the baseline and simplified process.

Following the adoption of rule for applicability for the Matternet M2 aircraft, the FAA introduced subsequent noise certification standards for other models, including the Flytrex FTX-M600P. In this section, the PIM capabilities are utilized to compare the single-microphone configuration (baseline process) with the multiple-microphone configuration (alternative

process) for a UA hover test, using the Flytrex FTX-M600P aircraft as a case study. According to the hover test conditions specified in paragraph 16, subparagraphs (b) through (e) of the Flytrex noise certification standards (FAA, 2023), the baseline configuration involves the aircraft hovering at three distinct spatial locations relative to the single microphone, as depicted in **Error! Reference source not found.**. Conversely, the alternative configuration uses three microphones, requiring the aircraft to hover at a single spatial location relative to these microphones, as shown in **Error! Reference source not found.**. A representation of the Markov Chain for both the baseline and alternative processes is provided in Figure 50.

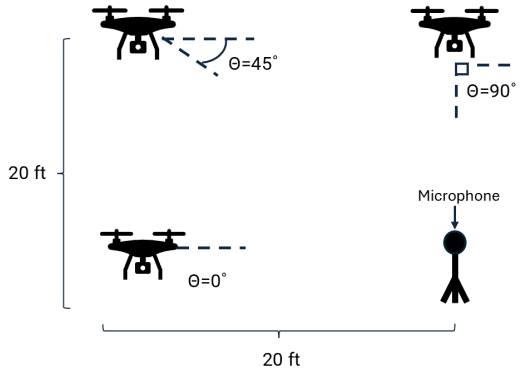


Figure 48. Microphone layout for the baseline process during the hover measurements.

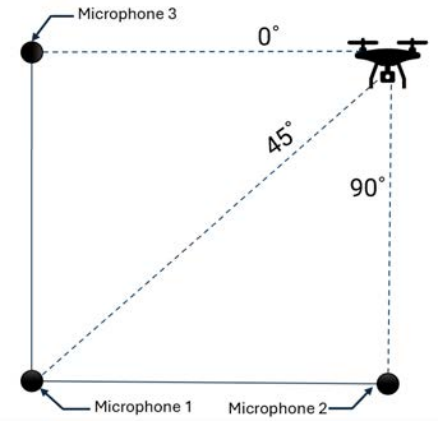


Figure 49. Microphone layout for the alternative process during the hover measurements.

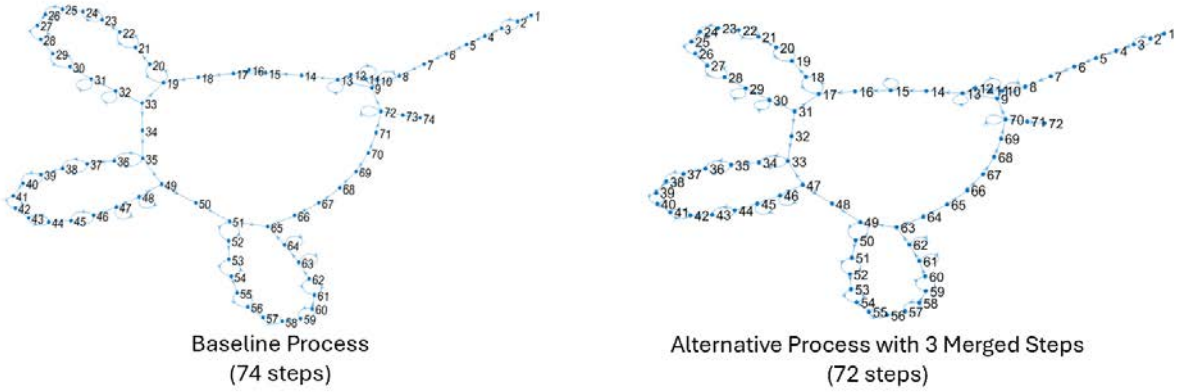


Figure 50. Markov Chain representation for the baseline process (left) and alternative process (right).

As outlined in the case study setup, a DoE consisting of 2,000 cases, each with 10,000 Monte Carlo simulations, was conducted. Process simulations for both the baseline and alternative configurations were performed to create a parametric, interactive decision-making environment. This environment enables the comprehensive comparison of test processes using various visualization techniques, including operational viewpoints, histogram overlays, and sensitivity analysis plots. This section provides an analysis of the process simulations for the baseline and alternative configurations for the Flytrex FTX-M600P case study, accompanied by visualizations to support interpretation of the results.

The operational viewpoint of the case study setup, shown in Figure 51, combines the schematic diagrams, providing a more realistic and comprehensive visual representation of the test setup. Following this, process simulations for both the baseline and alternative configurations were performed, producing key output metrics, specifically mean time and mean cost, for each case in the DoE. Histogram overlays were used to visually compare the two processes in terms of time and cost, as seen in **Error! Reference source not found.** and **Error! Reference source not found.**. These figures demonstrate that the baseline process results in both lower mean time and mean cost compared to the alternative process. The higher cost of the alternative process is expected due to the additional microphones, which incur extra costs for equipment, installation, and calibration.

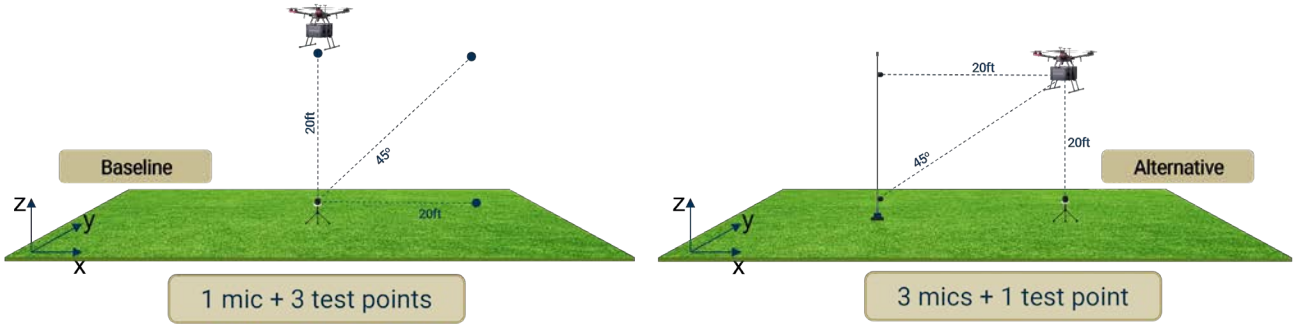


Figure 51. Operational viewpoint of baseline vs. alternative test set up for Flytrex FTX-M600P.

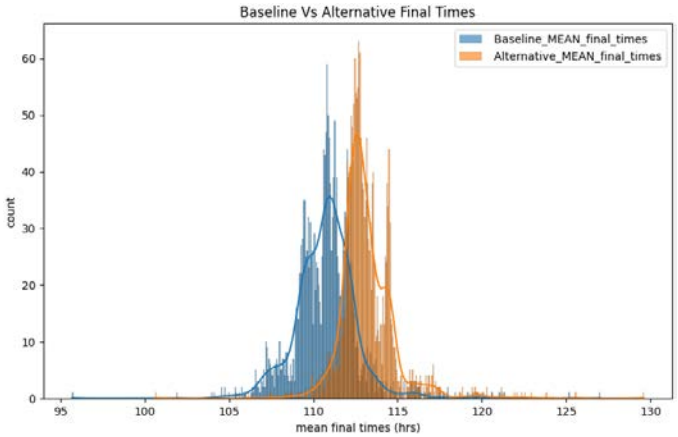


Figure 52. Baseline vs. alternative mean final times overlay.

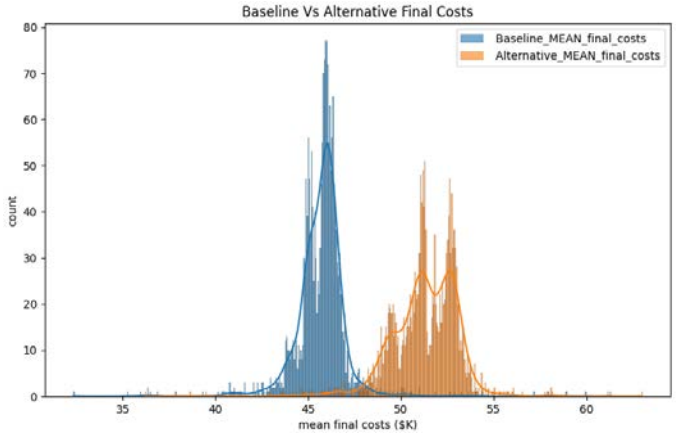


Figure 53. Baseline vs. alternative mean final costs overlay.

The time metric, however, exhibits more variability and is influenced by factors such as calibration time and the likelihood of test failures. Under the specific parameter values used in the model, the baseline process results in a shorter mean time. This indicates that the additional time required for microphone installation and calibration in the alternative process outweighs the time lost due to potential test failures. However, if the probability of test failure and the calibration time for a single microphone were increased, there could be cases where the alternative process proves more time efficient. In such cases, the single microphone in the baseline process would require repeated setup and calibration at various test points, extending the total test duration.

Histogram overlays provide a useful means of comparing baseline and alternative processes by visualizing the mean distributions of PIM outputs, such as time and cost. However, histogram overlays do not capture the variability of these metrics in relation to input parameters across different steps in the noise testing process. Understanding this variability is crucial for assessing a testing process's robustness to uncertainties. Tools like the JMP Prediction Profiler offer dynamic visualization capabilities, displaying relationships between input predictors (e.g., time or cost for specific testing steps) and output metrics. To enable interactive decision making, meta or surrogate models are needed to map input parameters to PIM outputs. However, the non-normal distribution observed in the Monte Carlo simulations necessitated the evaluation of various probability density functions (PDF) to replicate the data accurately. Among these, the log-normal distribution proved most suitable, demonstrating the closest match with minimal error, as shown in **Error! Reference source not**



found., and further validated by reconstructing the Monte Carlo distribution using random samples within the parameters of the log-normal PDF (i.e., μ, σ, and scale), as depicted in **Error! Reference source not found.**.

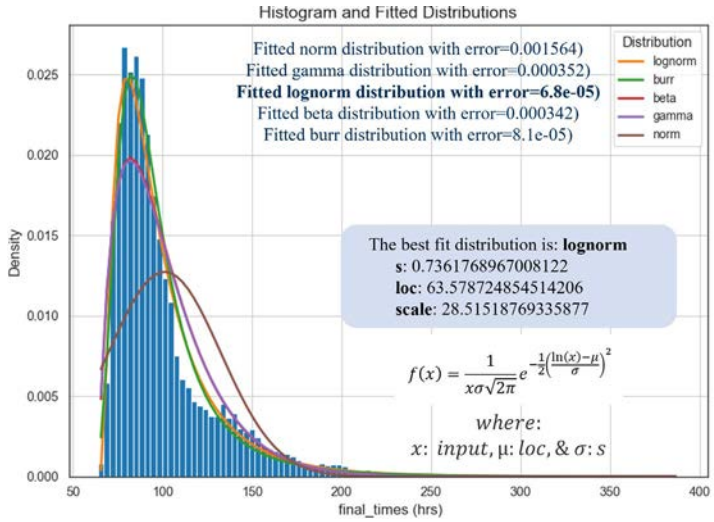


Figure 54. Sample Monte Carlo distribution of a single DoE case.

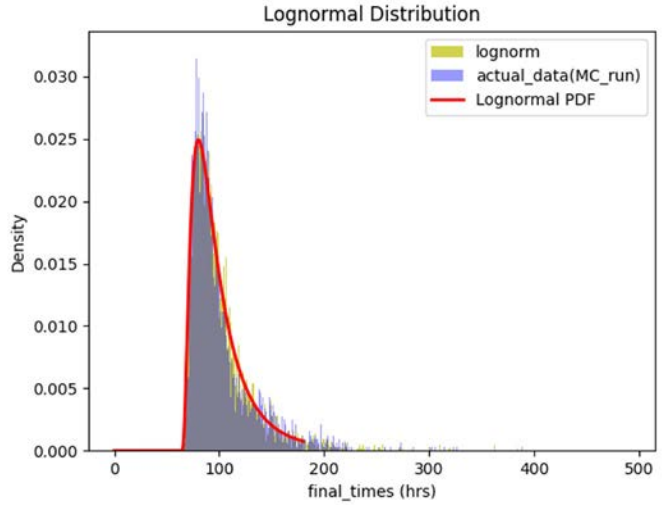


Figure 55. Actual vs. predicted Monte Carlo distribution fit using log-normal probability density functions (PDF).

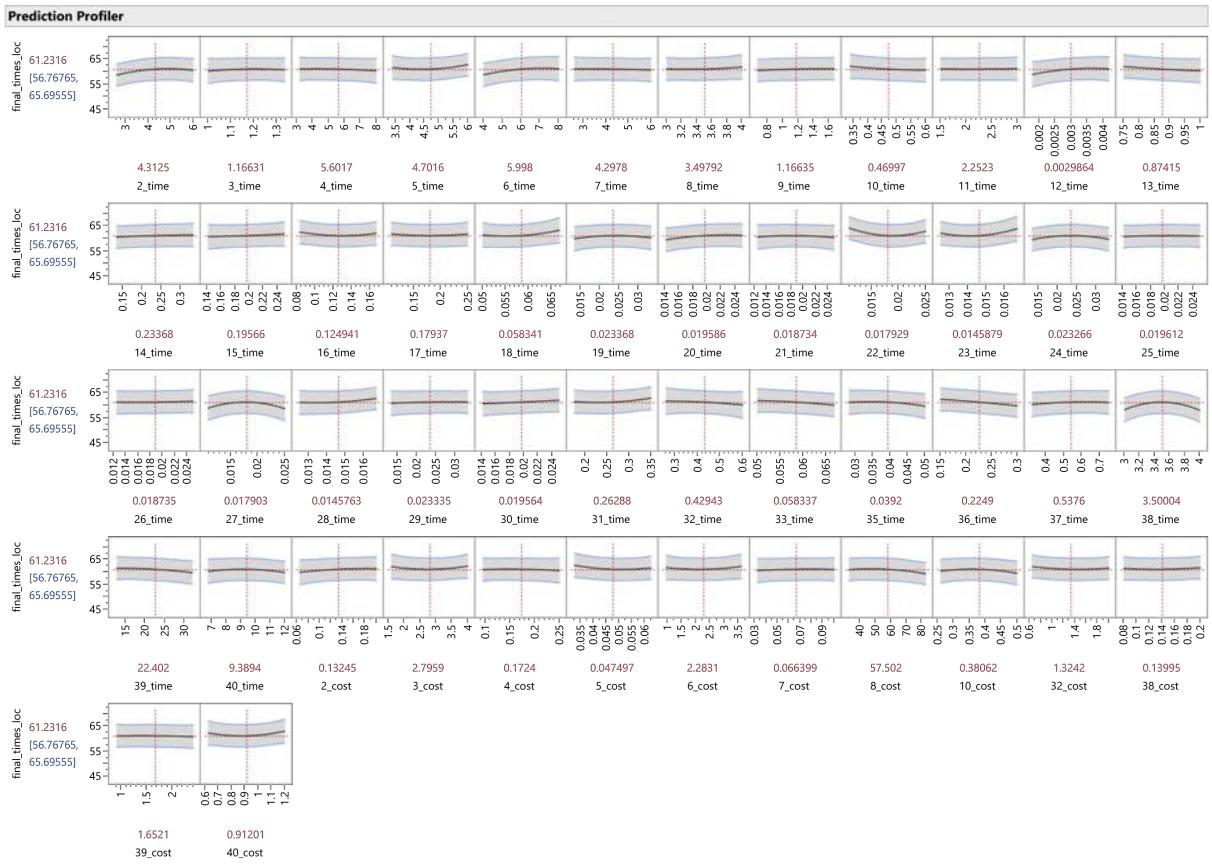


Figure 56. Prediction profiler plot of alternative process time generated using the JMP Prediction Profiler.

Using the log-normal PDF, calculations were performed for each case in the DoEs. The resulting parameters of the log-normal PDF served as output metrics and were instrumental in developing surrogate models. For instance, focusing on the μ (location) parameter for the time associated with the alternative process, Prediction Profiler plots were generated (Figure 56) to evaluate the sensitivity of this output metric to the time allocated for each step in the testing process. Analysis of the predictor variables within the model revealed that steps 36 and 12 were statistically significant in predicting the location parameter, prompting a deeper investigation into their influence. This analysis, illustrated in Figure 57, shows the impact of holding step 12 constant while varying the time for step 36. The results reveal a significant correlation, including a directional change, emphasizing the importance of these steps in influencing variability. While this study primarily examines the location parameter for time in the alternative process, similar insights can be extended to other parameters and metrics for both baseline and alternative processes.

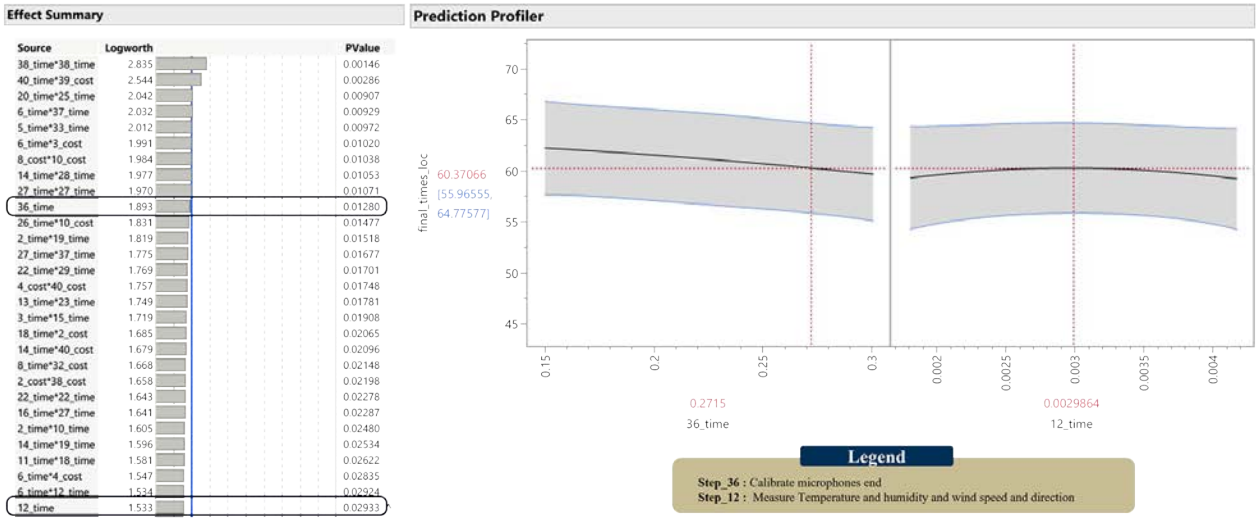


Figure 57. Key steps sensitivity plot generated using the JMP Prediction Profiler.

Case Study 2

The International Organization for Standardization provides detailed methodologies for measuring sound pressure levels in its ISO 3744 standard (ISO, 2010), which outlines microphone positioning, test point selection, and the number of test runs required for various flight profiles. Additionally, ISO 5305 (ISO, 2024) specifies configurations and microphone layouts for testing UASs in anechoic chambers or wind tunnels. EASA adopts a proportional, risk-based framework for UAS operations, classifying them into three categories: (1) open, (2) specific, and (3) certified. The EASA category, applicable to UAS with a maximum takeoff mass (MTOM) up to 600 kg (1323 lb), includes guidelines for noise emission assessments. EASA has also proposed noise assessment standards for air taxis under the EPTS, covering VTOL aircraft with tilting and nontilting rotors.

This section presents and analyzes results from the PIM for the second case study, which evaluates various testing procedures defined by existing standards and guidelines for UA and VTOL aircraft. To align with these regulatory standards, three models were developed for noise testing across different vehicle categories: (1) low risk indoor testing (UAS with MTOM ≤ 25 kg), (2) medium risk outdoor testing (25 kg < MTOM ≤ 600 kg), and (3) high risk outdoor testing (VTOL with 600 kg < MTOM ≤ 80,000 kg). The high-risk model for outdoor testing specifically addresses VTOL aircraft with tilting rotors. Table 7 summarizes the testing procedures from these guidelines, forming the basis for creating simulations to replicate certification noise testing and outlining the corresponding test runs for each category. To enable sensitivity analysis and account for cost and time uncertainties, the DoE excludes travel-related process steps, as their extended durations could disproportionately influence results. Only unique process steps are included as variables, with repetitive tasks represented by a single instance.

Table 7. Testing procedures set by existing standards and guidelines for UA and VTOL aircraft. EASA: European Union Aviation Safety Agency, ISO: International Organization for Standardization, MLW: maximum landing weight, MTOW: maximum takeoff weight, UAS: unmanned aircraft system, VTOL: vertical takeoff and landing.

Procedure Type	ISO 3744 (UAS ≤ 25kg)	EASA (UAS ≤ 600kg)	EASA (VTOL ≤ 80000kg)
Risk Level	Low Risk	Medium Risk	High Risk
Testing Type	Indoor Testing	Outdoor Testing	Outdoor Testing
Flight Profiles	Hover	Flyover - Hover	Takeoff - Approach - Hover - Flyover
Test Points	1 MTOW (hover)	1 MTOW + 1 ETOW (hover)	1 MTOW (takeoff) 1 MLW (approach) 1 MTOW (hover) 3 MTOW (flyover)
Test Runs	3 runs/test point	6 runs/test point	6 runs/test point
# of Microphones	10	1	9 total: 3 (takeoff- approach - flyover) 9 (hover)

The low-risk category indoor testing involves fewer tasks (27 steps yielding 32 variables, with 16 time and 16 cost variables) compared to outdoor procedures for medium-risk (146 steps yielding 44 variables) and high-risk (116 steps yielding 44 variables) categories. Notably, the medium risk outdoor testing procedure has slightly more steps due to the requirement to conduct tests at both maximum and empty takeoff mass, as outlined in Table 7.

A DoE with 10,000 cases was constructed, each case undergoing 10,000 Monte Carlo runs to account for the inherent variability in the simulation. The PIM was used to calculate the mean final time and cost for the testing procedures across all cases. Histograms of these outputs for the three categories are shown in **Error! Reference source not found.** and **Error! Reference source not found.**. From the overlay of mean final times, it is evident that low-risk indoor testing requires the least time due to its controlled environment and reduced uncertainties. Interestingly, while medium-risk outdoor testing includes more steps and variables than high-risk outdoor testing, the latter exhibits slightly longer mean final times across the DoE cases.

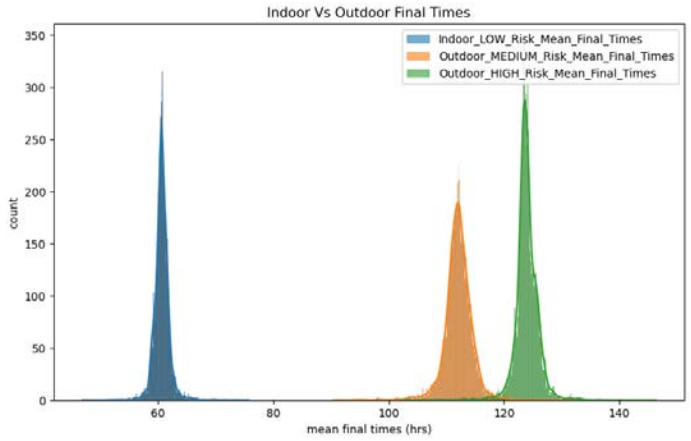


Figure 58. Indoor vs. outdoor testing final times overlay.

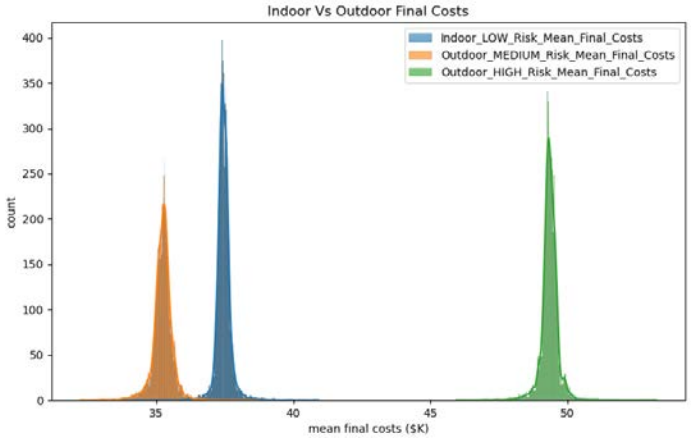


Figure 59. Indoor vs. outdoor testing final costs overlay.

In terms of costs, high-risk outdoor testing is the most expensive, driven by the need for nine microphones and multiple flight test profiles and test points. Surprisingly, medium-risk outdoor testing incurs slightly lower costs than low-risk indoor testing. This unexpected result is primarily due to the number of microphones utilized during each testing procedure.

Analyzing the complexity metrics of the three testing alternatives discussed earlier and applying the metrics outlined in Task 4.2 reveals that the low-risk indoor testing procedure consistently achieves the lowest scores across all metrics. This indicates it is the most efficient and least uncertain approach. The high-risk outdoor testing procedure ranks second, while the medium-risk outdoor testing procedure has the highest scores, making it the least efficient and most uncertain. Table 8 below summarizes the calculated complexity scores for each testing category.

Table 8. Process complexity scores of testing procedures.

Testing Procedure Type	Low Risk (ISO 3744)	Medium Risk (EASA)	High Risk (EASA)
# of Steps (N)	27	146	116
Cyclomatic Complexity	0.2321	0.2823	0.2735
Control Flow Complexity	0.2839	0.363	0.3534
Process Entropy	0.1441	0.2837	0.2732
Decision Density	0.4074	0.5342	0.5172
Overall Complexity	**0.1489**	**0.3336**	**0.3068**

Table 9 presents the overall time, cost, and complexity scores for the three testing procedures discussed, highlighting the relative difficulty of certification for each category. The low-risk indoor testing procedure stands out with the lowest overall time and complexity, making it the easiest option for certification. In contrast, the high-risk outdoor testing procedure has the highest time and cost, making certification more challenging.

Table 9. Overall time, cost and complexity of testing procedures.

	Low Risk (ISO3744)	Medium Risk (EASA)	High Risk (EASA)
Overall Time	60h 38min	112h 05min	123h 56min
Overall Cost	$37,459.83	$35,236.86	$49,353.97
Overall Complexity	0.1489	0.3336	0.3068

Lowest certification burden

Highest certification burden

Further Model Implementations

The earlier case studies demonstrated the ability of the Process Evaluation Model to evaluate and quantify the certification burden of various noise testing procedures, as defined by different regulatory standards, in terms of time, cost, complexity, and risks of schedule or budget overruns. In contrast, the next section explores the time and cost impacts of performing the same noise testing procedure under varying conditions. This analysis supports improved planning and resource management, including decisions regarding equipment, personnel, and test location selection. To illustrate the advantages of this capability, three use cases were developed, simulated, and analyzed.

(1) Alternative Testing Location and Weather Effects

Noise testing may be conducted at various locations, with the optimal test site depending on factors such as proximity, site area, ground type, background noise, and weather conditions. These factors significantly impact testing duration, overall expenses, measurement quality, and the likelihood of requiring an additional day to repeat measurements.
This use case compares two noise testing processes under different travel distances and weather conditions:

- **Baseline Process**: The test site is 2 hr away, with stable weather expected.
- **Alternative Process**: The test site is 40 min away, but weather conditions are less stable, with a higher likelihood of rain and strong winds.

While the alternative process reduces travel time and expenses, it increases the probability of adverse weather, leading to higher chances of test run rejections and additional test days for measurement repetitions. This presents a trade-off between travel-related time and costs and those associated with weather-impacted noise measurements.

To model these scenarios, travel time and costs, along with weather-related probabilities, were adjusted, and each process was simulated using 10,000 Monte Carlo runs to account for the inherent uncertainty. Table 10 summarizes the mean time and cost results, while Figure 60 and Figure 61 visualize the total time and cost distributions for each process, displaying a sample of 50 Monte Carlo runs for clarity. The results show that the alternative process incurs higher costs and nearly doubles the testing duration, indicating that shifting to a closer location with unstable weather is not advisable for this scenario.

Table 10. Mean time and mean cost (across 10,000 Monte Carlo runs) of the baseline process vs. the alternative process.

	Baseline process	Alternative Process
Average Time (h)	45.655	90.781
Average Cost ($)	18602.542	34600.877

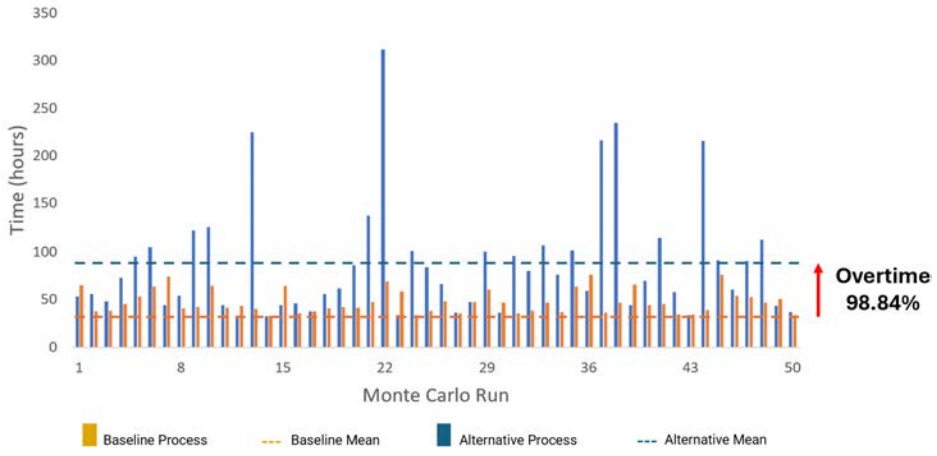


Figure 60. Total time (sample of 50 Monte Carlo runs) and mean time (10,000 Monte Carlo runs) between the baseline and alternative processes.

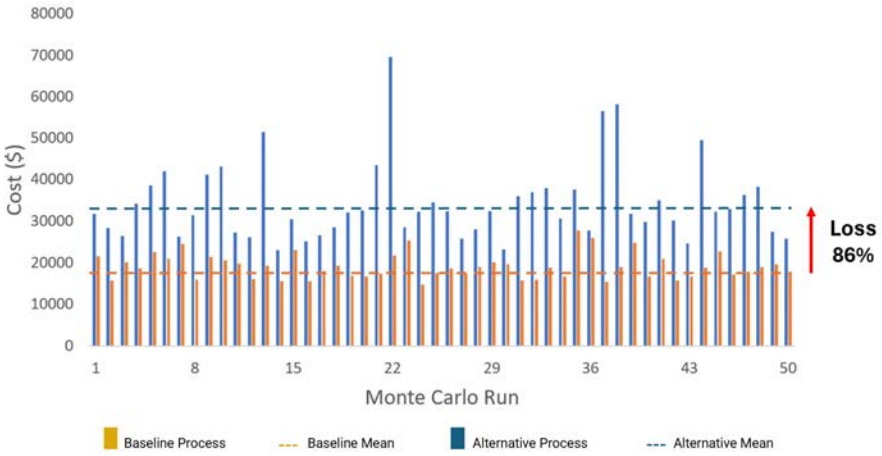


Figure 61. Total costs (sample of 50 Monte Carlo runs) and mean cost (10,000 Monte Carlo runs) of the baseline and alternative processes.

(2) Alternative Dispatching and Sequencing of Tasks

Parallel processing enables multiple tasks to be executed simultaneously, leading to a significant reduction in the overall noise testing time. This use case evaluates the impact of parallel processing by comparing two testing approaches:

- **Baseline Process**: All tasks are performed sequentially.
- **Alternative Process**: While some tasks depend on others and cannot be performed in parallel, and others involve uncertainty requiring separate handling to maintain accuracy, three specific tasks— (1) synchronizing data acquisition clocks, (2) calibrating microphones, and (3) installing windscreens—are executed simultaneously.

Figure 62 illustrates the Markov Chain representations of the baseline process, which includes 74 steps, and the alternative process, which reduces the total steps to 72 by merging three tasks for parallel execution. Table 11 outlines the mean time for each process, showing that the alternative process saves 2.25 hours, a 4.02% reduction in total testing time (as depicted in Figure 63).

This example demonstrates the potential for significant time savings through parallel task execution in noise testing, provided sufficient on-site personnel are available to optimize task allocation.

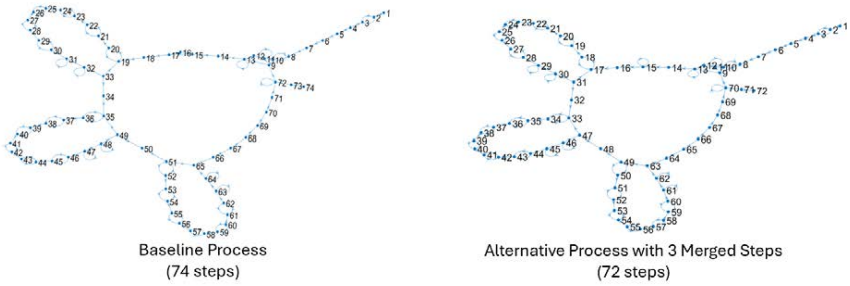


Figure 62. Markov Chain representation for the baseline process (left) and alternative process (right).



Table 11. Mean time (across 10000 Monte Carlo runs) of the baseline process vs. the alternative process.

	Baseline process	Alternative Process
Average Time (h)	55.798	53.554

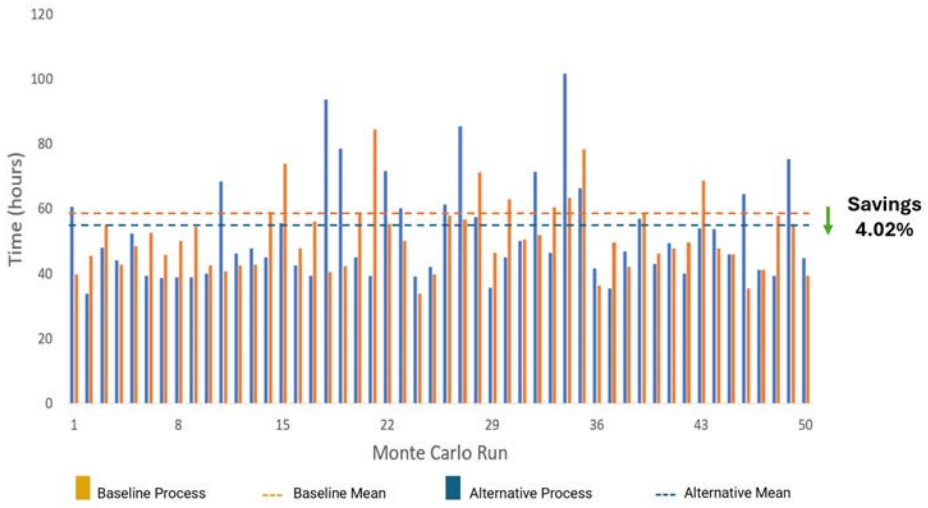


Figure 63. Total time (sample of 50 Monte Carlo runs) and mean time (10,000 Monte Carlo runs) of the baseline and alternative processes.

(3) Effects of Personnel Structure on Small Certification Testing vs. Large Testing Campaigns
Increasing the number of personnel may raise immediate payroll costs, but it can potentially shorten testing durations or enhance test quality, potentially reducing long-term expenses. This use case explores the effects of doubling the personnel assigned to each of the five phases of the noise testing process (Table 12). Two scenarios are modeled and analyzed: a standard noise certification process and a larger experimental noise testing campaign. The baseline personnel numbers are estimated for demonstration purposes, with user-defined inputs that the model adjusts automatically.

Table 12. Mean time (across 10,000 Monte Carlo runs) of the baseline process vs. the alternative.

Noise Testing Phase	Baseline process: Number of Personnel	Alternative Process: Number of Personnel
Site Inspection	2	4
Site Preparation	1	2
Flight Test Day	3	6
Data Analysis	1	2
Additional Test Day	2	4

Increasing the number of personnel reduces the time needed for site inspection, preparation, and the installation and calibration of equipment. However, it also raises travel and payroll expenses. With a larger team, parallel task execution is enhanced, leading to more efficient resource utilization, though this also adds complexity to the process. In the baseline certification scenario, a single microphone is used, whereas the larger campaign involves 21 microphones. Expanding the team reduces time for site setup and equipment calibration but increases costs for travel, wages, and equipment, particularly if elevated setups (e.g., poles or cranes) are required.



The results show that doubling personnel reduces total testing time by 12.19%, saving 5.67 hours. However, total costs increase by 45.15% (see Table 13, Figure 64, and Figure 65). While the alternative process achieves time savings, the higher personnel costs outweigh the benefits of reduced work time.

Table 13. Mean time and mean cost (across 10000 Monte Carlo runs) of the baseline process vs. the alternative process.

	Baseline process: Certification Testing	Alternative Process: Certification Testing	Baseline process: Large Experimental Campaign	Alternative process: Large Experimental Campaign
Average Time (h)	45.655	40.092	55.798	44.591
Average Cost ($)	18,602.54	27,001.99	47,955.98	56,273.50

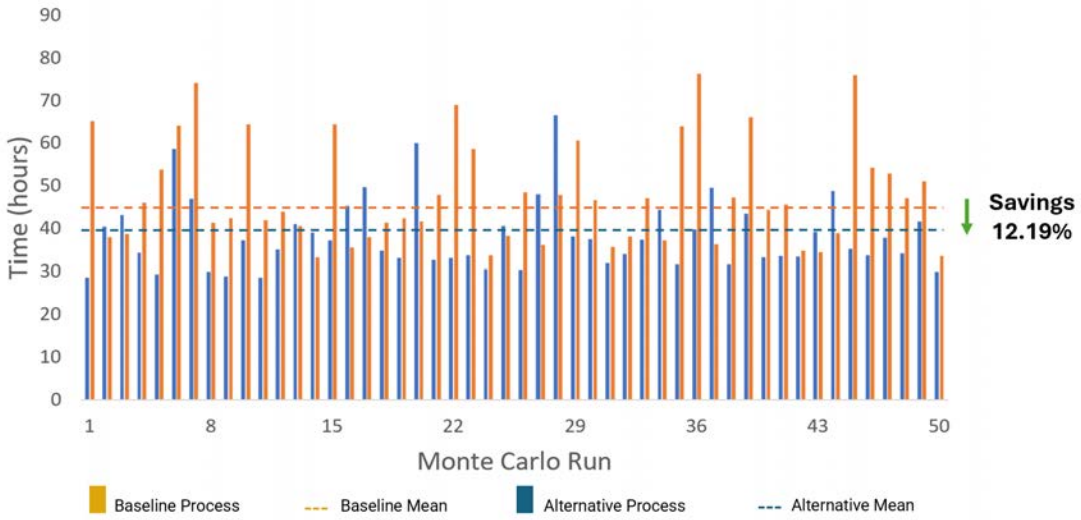


Figure 64. Total time (sample of 50 Monte Carlo runs) and mean time (10,000 Monte Carlo runs) between the baseline and alternative processes for certification testing.

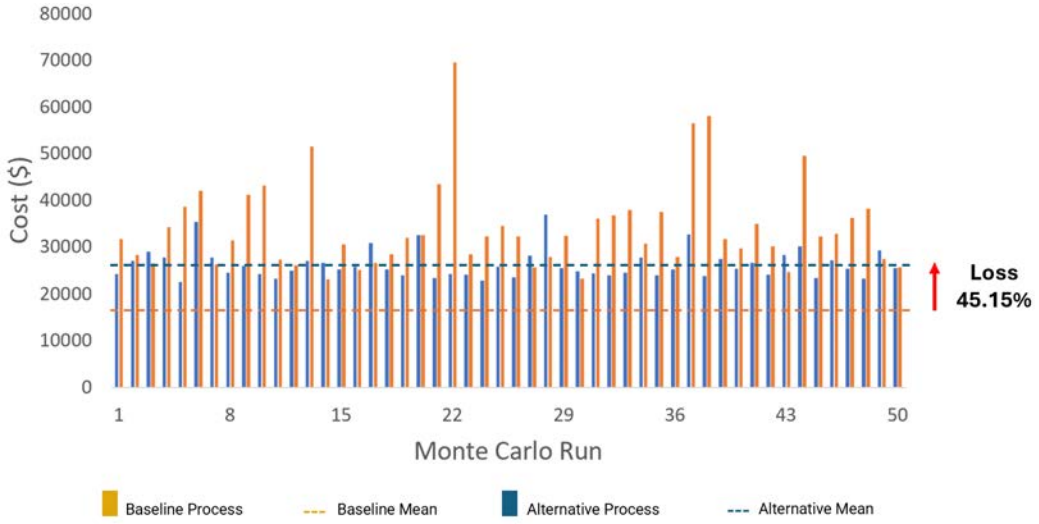


Figure 65. Total costs (sample of 50 Monte Carlo runs) and mean cost (10,000 Monte Carlo runs) of the baseline and alternative processes for certification testing.

Doubling the personnel team for a larger testing campaign results in a 20.09% reduction in time, significantly higher than the 4.02% savings observed for smaller certification testing (see Table 13 and Figure 66). Additionally, the financial loss is reduced to 17.34%, compared to 45.15% for certification testing (see Table 13 and Figure 67). The increased efficiency of additional personnel becomes more pronounced with the expansion of equipment, such as microphones, enabling more parallel task execution.

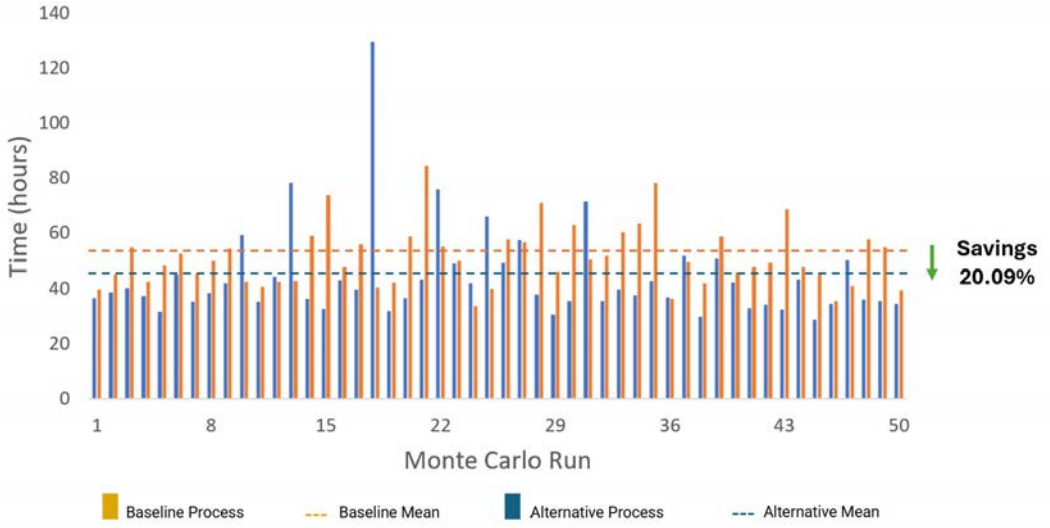


Figure 66. Total time (sample of 50 Monte Carlo runs) and mean time (10,000 Monte Carlo runs) between the baseline and alternative processes for experimental testing campaign.

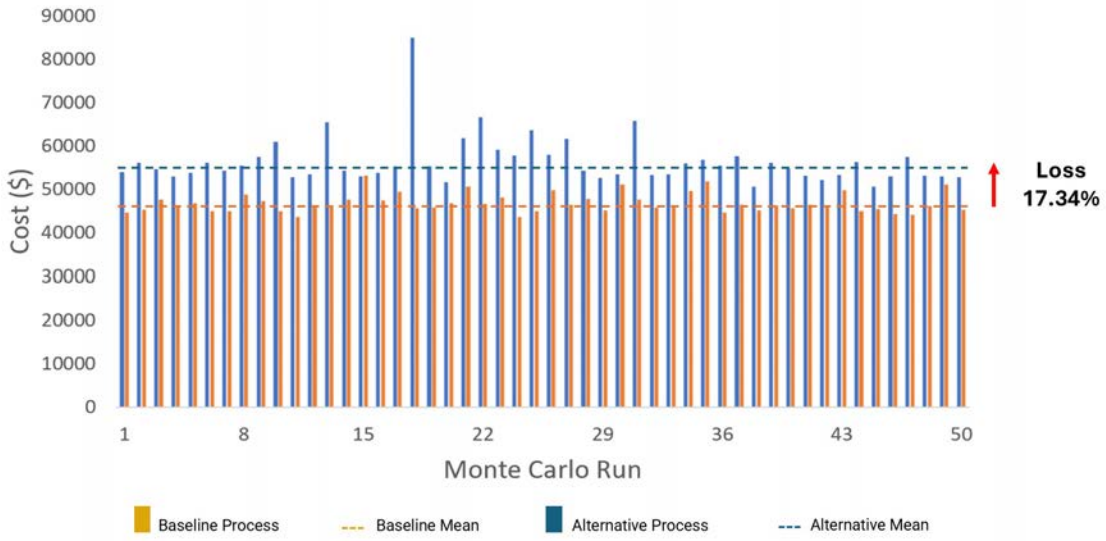


Figure 67. Total costs (sample of 50 Monte Carlo runs) and mean cost (10,000 Monte Carlo runs) of the baseline and alternative processes experimental testing campaign.

Milestones

Please refer to the milestones listed under Task 1.

Major Accomplishments

- Developed a small-scale PIM using DES as a deterministic modeling exercise.
- Developed a more comprehensive stochastic model using stochastic MCMC methods, formulated in a way that enables seamless integration into the verification thread within the MBSE framework.
- Defined a starting set of metrics as a working solution with a focus on process efficiency improvements.
- Designed approach for integrating the PIM with the verification model within the MBSE framework.
- Finalized PIM analysis workflow with the use of Monte Carlo simulation for Markov chain models of the certification testing process.
- Integrated workflow with the MBSE verification model.
- Obtained proof-of-concept use case for assessing the impact of process simplification through quantifiable outcomes, which has been supported by the current working version of the MCMC-enabled PIM module.
- Further improved and tuned the existing PIM with automation and parametrization of user-defined input data to make the model representative of any desired process.
- Applied the PIM to a typical plan for UAS noise testing to better capture the process and properly estimate the cost, staff, and time implications.

Publications

Published Conference Proceedings

Ali, H. E., Ravikanti, B., Balchanos, M. G., Harrison, E., & Mavris, D. (2025). MBSE Enabled Requirement Verification for a Traceable Regulatory Analysis Framework of UAS Noise Certification Standards. *AIAA SCITECH 2025 Forum* (p. 0367).

Mali, H., Geneti, N. F., Balchanos, M. G., Harrison, E., & Mavris, D. (2025). A Process Evaluation and Visualization Framework for Unmanned Aerial System (UAS) Noise Certification Testing. *AIAA SCITECH 2025 Forum* (p. 0368).

Balchanos, M., Ravikanti, B., Ali, H., Mali, H., D Harrison, E., & N Mavris, D. (2024, September 9-11). *A Regulatory Analysis and Process Improvement Decision Support Framework for Unmanned Aerial System (UAS) Noise Certification* [Conference presentation]. Quiet Drones 2024 Symposium, Manchester, United Kingdom.



Outreach Efforts

- Presented concepts to FAA and Volpe partners, who provided feedback on the tools and analysis methods.
- Participated in discussions with experts in the field with similar applications (i.e., process simulations for industrial systems, manufacturing, supply chains, etc.).

Awards

None.

Student Involvement

Although a small portion of the team has been leading the technical approach of PIM development, this task has involved the full team. Recent efforts to extend the PIM capabilities have been led by Hajar Mali, and the dashboard and visualization of results have been led by Nathnael Geneti.

Plans for Next Period

- Project ended on September 30, 2025.
- Publish peer-reviewed journal articles with *AIAA Journal* and AIAA SciTech.

References

FAA. (2022). *Noise Certification Standards: Matternet Model M2 Aircraft.* Federal Aviation Administration. https://www.federalregister.gov/documents/2022/09/12/2022-19639/noise-certification-standards-matternet-model-m2-aircraft

FAA. (2023). *Noise Certification Standards: Flytrex, Inc. Model FTX-M600P aircraft.* Federal Aviation Administration. https://www.faa.gov/media/31186

ISO. (2010). *Acoustics – Determination of sound power levels and sound energy levels of noise sources using sound pressure – Engineering methos for an essentially free field over a reflecting plane* (ISO Standard No. 3744:2010). International Organization for Standardization. https://www.iso.org/standard/52055.html

ISO. (2024). *Noise Measurements for UAS (unmanned aircraft systems) (ISO Standard 5305:2024. International Organization for Standardization.* https://www.iso.org/standard/81111.html

ASCENT Project 061 Year 5 Recap

The following key tasks and activities have been completed within the ASCENT Project 061 Year 5 performance period:

- Developed **a certification framework** to explore options for **standard setting** to support **noise certification of Emerging Technology Aircraft (ETA),**
- Demonstrated applicability of the current ASCENT Project 061 framework for noise certification of rotor or small propeller-driven UASs.
  - Formulated use cases that are aligned with needs and recommendations provided by OEM partners, with a focus on exploring implications of alternative testing procedures on regulatory compliance and highlighting the benefits of process simplification (e.g., lateral microphone placement/removal, if trusted analysis is used).
  - Provided a demonstration by assessing a simplified noise collection/analysis process.
- Developed **traceable and consistent methodology** to analyze Means of Compliance (MoC) alternatives for supporting rulemaking recommendations.
  - Model-based methods (e.g., MBSE) to **map regulatory-driven requirements to testing procedures.**
- Performed UAM noise **standards review** and **comparison with UAS standards for demarcation** of categories.
- Formulated **risk definitions and assessments**, based on various aspects of vehicle design and operational characteristics.
- Formulated **complexity-driven certification procedure modeling** using Markov Chains.
- Engaged in a **broader outreach of ASCENT Project 061** to the aviation community on noise certification, including:
  - Participation in ASCENT fall/spring meetings
  - Discussions with UAS OEMs
  - Publication of articles with AIAA and for the SciTech 2024/2025 meetings
- Provided **annual and quarterly reports**, available on the ASCENT Knowledge Services Network (KSN) database.
- Prepared peer reviewed publications for conferences, such as the AIAA SciTech 2025 and the Quiet Drones Symposium 2024.



Project 062 Noise Model Validation for AEDT

Georgia Institute of Technology
The Pennsylvania State University

Project Lead Investigators

Prof. Dimitri N. Mavris
Director, Aerospace Systems Design Laboratory
School of Aerospace Engineering
Georgia Institute of Technology
Mail Stop 0150
Atlanta, GA 30332-0150
404-894-1557
dimitri.mavris@ae.gatech.edu

Victor W. Sparrow
United Technologies Corporation Professor of Acoustics
Graduate Program in Acoustics
The Pennsylvania State University
411 Engineering Collaborative Research and Education Building (ECoRE)
566 White Course Drive
University Park, PA 16802
814-865-6364
vws1@psu.edu

University Participants

Georgia Institute of Technology (Georgia Tech)

- P.I.s: Prof. Dimitri N. Mavris, Dr. Michelle R. Kirby, and Dr. Mayank V. Bendarkar
- FAA Award Number: 13-C-AJFE-GIT Amendments 61, 82, 106, 125, 144, 160, and 164
- Period of Performance: September 27, 2021, to September 30, 2025
- Task:
  1. Noise modeling in the Aviation Environmental Design Tool (AEDT) with automation (Georgia Tech)

The Pennsylvania State University (**Penn State**)

- P.I.: Prof. Victor Sparrow
- FAA Award Number: 13-C-AJFE-PSU, Amendments 59, 83, 89, 106, 114, and 122
- Period of Performance: October 1, 2021, to September 30, 2025
- Task:
  2. Assessing the use of high-fidelity meteorological data in AEDT noise calculations (Penn State)

Project Funding Level

The project is funded by the Federal Aviation Administration (FAA) at the following levels: Georgia Tech: $235,000; Penn State: $140,000. Cost-sharing funding is described below.

Georgia Tech has agreed to a total of $235,000 in matching funds. This total includes salaries for the project director, research engineers, and graduate research assistants, as well as computing, financial, and administrative support, including meeting arrangements. Georgia Tech has also agreed to provide tuition remission for the students, paid for by state funds.

For Penn State, Spire Global is providing cost-sharing funds in the form of meteorological data and research support. The point of contact for this cost-sharing is Ms. Ashley O'Neil (703-853-8468; ashley.oneill@spire.com). Metropolitan



Washington Airports Authority is providing sound level meter data from Dulles International Airport (IAD) as in-kind cost-sharing; the point of contact is Mr. Mike Jeck (703-417-1204; michael.jeck@mwaa.com). Raleigh-Durham International Airport is providing sound level meter data from Raleigh-Durham International Airport (RDU) airport as in-kind cost-sharing; the point of contact is Mr. John Wiatrak (919-840-7748; john.wiatrak@rdu.com). Additional in-kind cost-sharing is being provided by the Penn State College of Engineering to meet the required matching of $140,000.

Investigation Team

Georgia Institute of Technology
- Prof. Dimitri N. Mavris, (P.I.)
- Dr. Michelle R. Kirby, (co-investigator)
- Dr. Mayank Bendarkar, (co-investigator)
- Dr. Ameya Behere (research faculty)
- Dr. Woong Je Sung (research faculty)
- Mr. Jirat Bhanpato, (research faculty)
- Humfrey Kimanya, (graduate student)
- Sonal Mehta, (graduate student)

The Pennsylvania State University
- Prof. Victor Sparrow, (P.I.)
- Pierce Hart, (postdoctoral scholar)

Project Overview

The focus of this project is to assess the accuracy of the AEDT in estimating noise in the vicinity of airports as well as further afield. The foundation of AEDT noise modeling is based on the Integrated Noise Modeling (INM) tool, which has undergone several validation and verification efforts in the past, specifically at the Denver International Airport (DEN), and has shown continual improvements in the agreement between modeling predictions and measurement data. During the development of the AEDT, multiple algorithm updates have occurred. This project seeks to quantify the new noise modeling capabilities through comparison with field measurement data from DEN and other airport monitoring systems. The research team will develop a detailed model validation plan, review the plan with the FAA for concurrence, execute the plan, and make recommendations for future AEDT development. The research, once completed, is expected to provide a noise model validation benchmark that can be used not only to respond to questions regarding AEDT noise prediction accuracy, but also to allow the tool development team to prioritize further development of modeling features and enhancements. The research team will also collaborate with Penn State on the assessment of the noise propagation assumptions and the use of higher-fidelity weather data.

Task 1 - Noise Modeling in AEDT With Automation

Georgia Institute of Technology

Objective

The objective of this task is to provide information on noise modeling data sources, AEDT assumptions, and automation capabilities developed for the current work. Improvements made to the AEDT input processing pipeline are described in full. The results generated for the bulk flight operations modeled, along with particular or aggregate insights are discussed. Additionally, a validation study to confirm input parameters for AEDT version transition from AEDT 3e to 3g was completed.

Research Approach

The research approach used for the present year mimics last year's approach applied to newer datasets to increase the size of the validation study (Mavris & Sparrow, 2023). Some important aspects of it are repeated here for completeness. Readers interested in the details are directed at prior annual reports (Mavris & Sparrow, 2023). The present work focuses on updates made to the framework and results from the 2021 datasets at Minneapolis-Saint Paul International Airport (MSP) and Seattle-Tacoma International Airport (SEA) airports.



The two essential elements in this modeling are (1) the data sources used during modeling and (2) the modeling assumptions and alternatives available for each assumption. It is worth noting that an improvement was made to the AEDT input processing pipeline to eliminate AEDT flight modeling errors that were experienced in previous years.

Data Sources Used
The main datasets relevant to this work include the flight operations data, airport noise event data, airport noise time-history data, and Automated Surface Observing Systems (ASOS) weather data, and are described below:

1. ***Flight Operational Quality Assurance (FOQA)*** data are recorded by the airline operating the flight. FOQA systems record large amounts of data at one recording per second (i.e., 1 Hz). The important elements of FOQA data in this report relate to the detailed time history of parameters such as altitude, speed, thrust, weight, configuration (i.e., flaps and gear), and so on, for each flight modeled in the AEDT. These flights consist of the Boeing® 717-200, 737-800, 737-900, 757-200, 757-300, and 777-200ER/LR, Airbus® A319-100 and A320-200, and Airbus 220 airframes.

2. ***Airport noise event data*** contain the following key parameters: a noise monitor identification (ID), noise monitor locations, sound exposure level (SEL), and the maximum, A-weighted sound level (L_{max}) metrics of associated noise events, the time of the noise event, and the flight operation correlated to the noise event. The flight ID and the time of closest approach in the noise monitor data allow flights to be matched to the appropriate flight from FOQA data, thereby matching the aircraft configuration and the time of the noise event with the noise metric value. The locations of the noise monitors are used in flight modeling within the AEDT. The noise monitor data are used as a benchmark comparison for noise results calculated by the AEDT.

3. ***Airport noise time-history data*** contain A-weighted equivalent noise levels (LAeq) (dB) that is measured by different noise monitors situated close to runways. These data are processed using an in-house visualization tool that couples associated noise levels perceived by noise monitors with flight trajectory on an interactive map. Noise event identification is conducted and on the back end, appropriate formulae are used to calculate SEL, the maximum, and L_{max} noise metrics. The formulae consider the distance to closest approach, speed of sound, air density, noise-event intervals, among others.

4. ***ASOS weather data*** contain meteorological observations collected by automated stations for forecasting purposes. This study employs the 5-min interval ASOS weather data at specific airports, obtained from the Iowa Environment Mesonet dataset of Iowa State University. Key parameters utilized in this study include temperature, wind speed and direction, and precipitation type.

The framework for modeling and automation developed in this report is independent of the data source used and will need to be modified only to account for the availability of parameters if other data sources are used. In this report, data used are obtained from flight operations SEA for 2021 in addition to detailed noise history for the same.

Modeling Assumptions and AEDT Capabilities
AEDT offers its users multiple modeling options for critical assumptions of performance and noise of a flight operation. A matrix of alternatives for these settings is shown in Table 1 for completeness. Although there are many possible modeling combinations, this project explores only those that are compatible with arrival and departure operations. The assumptions, limitations and compatible options are noted in the discussion of individual modeling options in previous year's annual reports.

® Boeing is a registered trademark of The Boeing Company, Seattle, Washington.
® Airbus is a registered trademark of Airbus Operations GmbH, Hamburg, Germany.



Table 1. Modeling Options on Aviation Environmental Design Tool (AEDT). ASOS: Automated Surface Observing Systems, FOQA: Flight Operational Quality Assurance, NPD: Noise Power Distance.

Assumption	AEDT Default	Option 2	Option 3	NPD: Option 4	Option 5
Procedure	Standard	FOQA	NADP1_1	NADP2_11	
Thrust	Full	FOQA	RT05	RT10	RT15
Weight	AEDT	FOQA	Alt Wt		
Ground Track	Airport Default	FOQA			
Weather	AEDT Standard	FOQA	ASOS	High Fidelity	
Surface	Soft	Hard			
Terrain	Flat	Actual			
Flaps	AEDT	FOQA			
Gear	AEDT	FOQA			
NPDs	AEDT	NPD+C			

AEDT Input Processing Improvements

This report utilizes an in-house procedure to convert real-world flight data in the form of FOQA into AEDT modeling inputs. These steps are developed to enhance quality of data and to reduce the high volume of bulk flight operations data prior to running on the AEDT (see Figure 1). These additional steps are an improvement to AEDT noise modeling methodology that was explained in former reports.

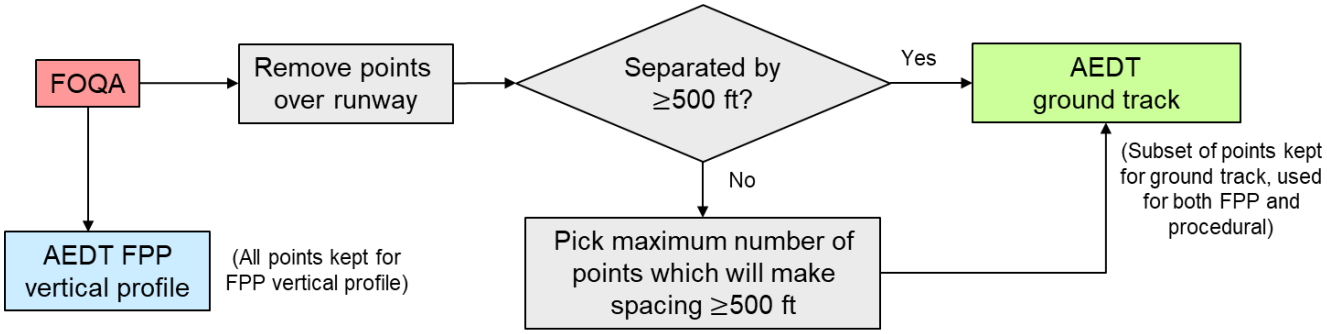


Figure 1. Aviation Environmental Design Tool (AEDT) Input Processing Pipeline.

In modeling ground tracks, the AEDT discards the first track point for departures and the last track point for arrivals, and numerical issues can arise if adjacent points are too closely spaced (e.g., bank-angle errors). Therefore, FOQA ground tracks must be pre-processed to avoid these issues while preserving the shape of the lateral profile. The input processing pipeline shown in Figure 1 performs this task. Track filtering distinguishes between "over-runway'" and "air"' points using a 500-ft lateral offset threshold. An example of this filtering for 2021 departures at SEA is shown in Figure 2.

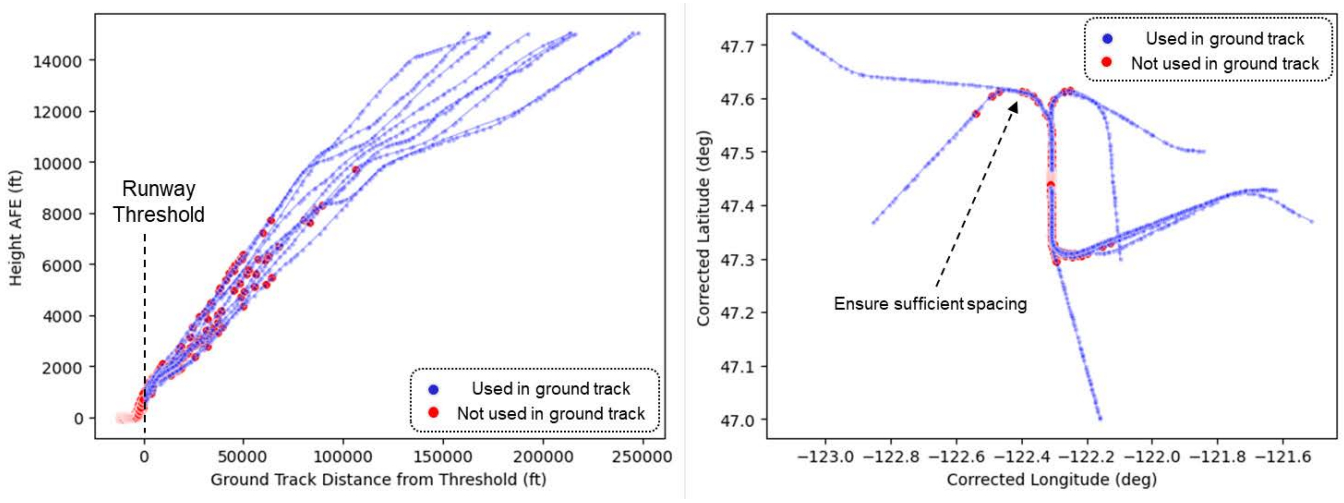


Figure 2. Example visualization for ground track filtering (SEA 2021 Departures). AFE: Above Field Elevation.

Raw FOQA data consist of points of elevation up to 15,000-ft above field elevation, recorded at 1 Hz. Such a high sampling rate is memory-intensive and impractical for modeling in the AEDT. As a result, an opportunity to reduce the number of datapoints for air segment and retain the shapes of trajectory and parameters of interest was found. An iterative end-point fit algorithm "Ramer-Douglas-Peucker" (RDP) (Douglas, Ramer) was modified and utilized in this procedure. The fundamental one-dimensional (1D) RDP algorithm (Figure 3 [left]) starts with just the end points of a trajectory, and forms piece-wise linear segments and recursively adds points from original trajectory until $d_{max} < \varepsilon$. The modification to the 1D trajectory RDP algorithm was made to use Euclidean distance to find d_{max} for N-D since raw FOQA data have at least 30 parameters. A select N target of parameters (Table 2) was identified and then normalized before computing the Euclidean distance between the piece-wise linear segments and the full data. It is noteworthy that applying the modified algorithm with all FOQA parameters would result in most points being kept which defeats the intention.

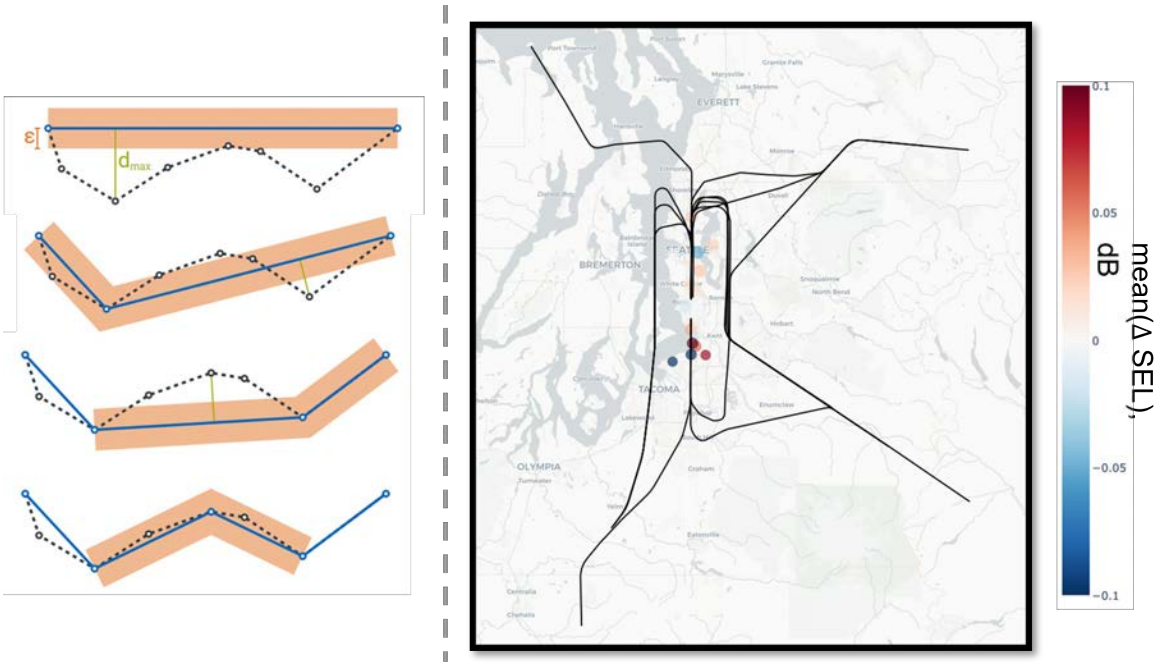


Figure 3. Ramer-Douglas-Peucker (RDP) algorithm (left) and down-sampled flights SEA 2021 arrivals (right).

Table 2. Target parameters for FOQA downsampling.

Corrected Latitude	Corrected Longitude	Ground Speed
Calibrated Airspeed	MSL Altitude	Corrected Thrust
Vertical Speed	Flap Position	Landing Gear Position

After down-sampling FOQA data, a sampling rate retaining about 45% of the total points on average for arriving flights contained enough flight information when modeled on AEDT. Figure 3 (right) shows that the difference in AEDT noise levels computed are within 0.1 dB compared to the Fixed-Point Profile (FPP) from raw FOQA data for a randomly selected set of flights at the noise receptors of SEA in 2021. This project utilizes down-sampled FOQA data as FPP and used as inputs in the AEDT.

To manage the large number of flight modeling combinations efficiently, an automation process consisting of pre-AEDT and post-AEDT stages is utilized. This stage is fully described in earlier reports as the procedure was not altered.

SEA 2021 – Validation of Aggregate Flight Modeling Results against Airport Noise History Data
Dashboard Development
The development of the dashboard was driven by the critical need to generate ground-truth noise measurement data by correlating flight trajectories with noise measurement time series. Because matching a specific portion of a flight trajectory to a segment of a noise time series is often characterized as an art rather than an exact science, the primary objective was to create an efficient, human-in-loop tool. This application allows analysts to identify and validate source flight and noise events segment pairs with high precision, bridging the gap between raw data collection and verified analysis.

The interface, shown in Figure 4, is designed to guide the user through a logical sequence of operations, beginning with the selection of a specific flight from monthly collections of arrival or departure flight data. Upon selection, the dashboard populates a flight metadata display with FOQA details. Central to the visualization is a three-dimensional (3D) map that renders the terrain, airport runway layout, the specific trajectory curve of the selected flight, and the locations of noise

monitoring stations. A time selector serves as the synchronization mechanism; as the user adjusts the time of flight, the aircraft's position on the 3D map updates immediately, simultaneously indicating the potential noise event interval across the time series plots of all monitoring stations. To facilitate detailed analysis, the dashboard presents noise time series data from all monitoring stations as time-vs-LAeq (dB) plots within the relevant flight window. These acoustic plots are juxtaposed with flight time series data, allowing the user to overlay selected FOQA metrics – such as aircraft flap position, airspeeds, or thrust – against the noise profile to investigate correlations. The user is provided with various controls to fine-tune the analysis, including settings for the noise event interval, the speed of sound used for propagation calculations, and variables for plot sizing. The core methodology for data association involves a systematic visual matching process. After the dashboard renders the 3D trajectory and corresponding noise time series for a finite pre-arrival or post-departure window, the user utilizes the time selector to identify a matching "peak" in a monitor's noise time series that aligns with a specific moment in the flight. The system dynamically calculates the distance and elevation angle between the aircraft and the station to help the user determine the relevancy of the candidate event. Once a match is confirmed, the user selects by clicking it, which automatically registers a comprehensive data row containing the flight and monitor IDs, start and end times, acoustic metrics such as SEL and L_{max}, and relative geometric or distance values.



Figure 4. Interactive dashboard (v5) to capture sound exposure level (SEL) and maximum, A-weighted sound level (L_{max}) from Seattle-Tacoma International Airport (SEA) noise time history data.

Technically, the dashboard is constructed as a standalone web application utilizing a standard JavaScript® and HTML framework. The implementation relies on a suite of specialized open-source libraries to handle the complex visualizations. D3.js is employed for all two-dimensional (2D) plotting of signal and flight data, while Mapbox® is utilized for the 3D geographic information system application programming interface to render terrain and base maps. Finally, Three.js handles the rendering of the aircraft models and the 3D flight trajectory visualization within the geospatial environment.

Methodology

The detailed methodology for comparing SEA 2021 aggregate flight modeling results in the AEDT against events capture using airport noise history data is summarized in Figure 5 below. We start by using FOQA data to model flight operations

® JavaScript is a registered trademark of Oracle America, Inc., Redwood Shores, California.
® Mapbox is a registered trademark of Mapbox, Inc., Washington, D.C.

in AEDT as described in the above subsection. After generating AEDT predictions, the next step is to utilize the noise history measurement data to calculate real-word noise metrics for validation. For SEA, the noise history data for calendar year 2021 obtained include detailed noise history in terms of noise levels LAeq (dB) that is measured by different noise monitors situated close to runways. These data are processed using an in-house visualization tool (shown in Figure 4 above) that couples associated noise levels measured by noise monitors with flight trajectory on an interactive map. This is described in detail in the above subsection on dashboard development. Using this, noise event identification is conducted. The formulae consider the distance to closest approach, speed of sound, air density, noise-event intervals, among others. All noise events with wind speeds greater than 10 knots, non-zero precipitation, elevation angles less than 20° will be discarded for the same reason stated under MSP 2021 results.

The two datasets are combined for further analysis. Some events were solely found in noise history analysis and were excluded from further study since the purpose of this analysis is to validate AEDT predictions. For events predicted in AEDT that were not recorded in the noise history analysis, the dashboard is reinvestigated to capture these noise events. This round of reinvestigation makes the approach robust to human errors, ensuring AEDT validation for all events predicted.

The final identified noise events are then used to calculate the ΔSEL between the two datasets. At this stage, any events with $\Delta SEL \geq 10$ dB are identified as outliers for the dataset and investigated for trends that might be causing high prediction errors. For the remaining dataset, trends are investigated to estimate prediction errors by modeling approach in AEDT, operation type, elevation angles, and aircraft type. Overall, this work is aimed at (1) assessing the accuracy of AEDT predictions for different modeling assumptions, against detailed noise history data, and (2) identifying outliers and any systematic biases in the matching between AEDT predictions and detailed noise-history data.

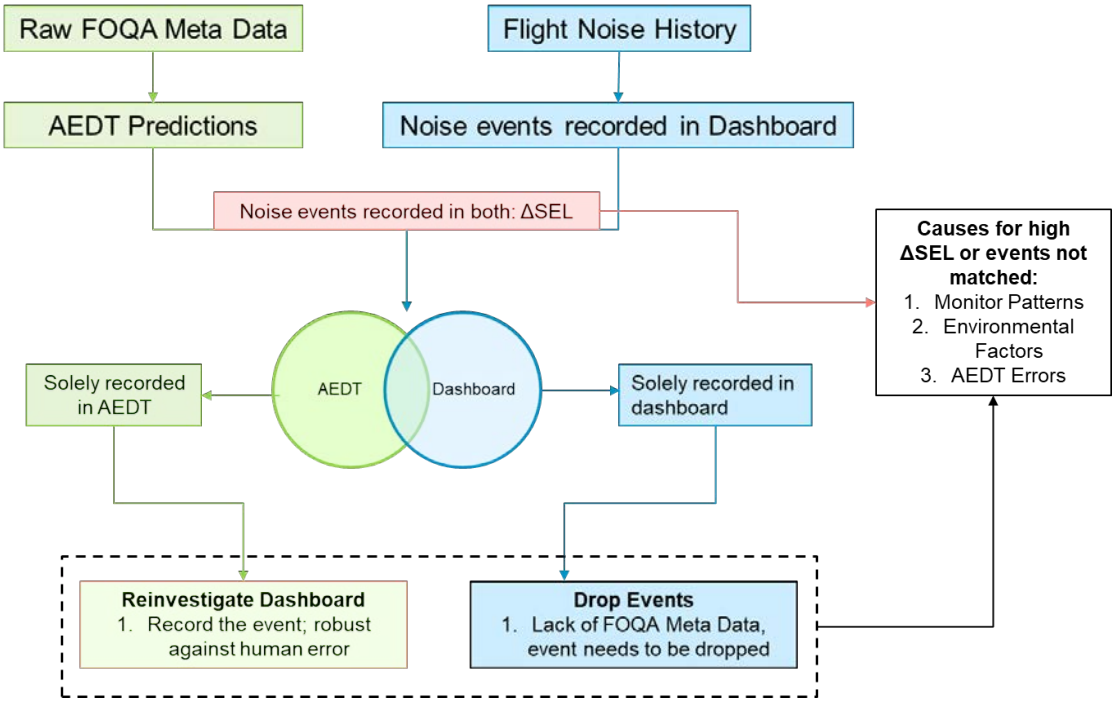


Figure 5. Methodology for comparing SEA 2021 aggregated flight modeling results in AEDT against airport noise history data.

Results

Using the methodology described above for which the results were also presented, flight and noise event data from both the AEDT predictions and measured noise histories were systematically processed and filtered to ensure data integrity. A total of 9,866 noise events were initially captured across both datasets. Of these, 3,882 events were excluded due to missing

AEDT predictions or FOQA metadata, and an additional 2,735 events were removed after applying standard quality filters, such as wind speed, precipitation, and elevation angle thresholds described above. Events with extreme discrepancies (Δ SEL ≥ |10| dB) accounted for 20 instances and were classified as outliers. After all filtering and validation steps, a total of 3,249 high-quality noise events were retained for SEA 2021, and a noise prediction error analysis was conducted.

Results for noise prediction error (ΔSEL) are shown, and the noise modeling accuracy is studied in different modeling options that are available in AEDT. ΔSEL levels are defined as $SEL_{predicted}$ – $SEL_{measured}$, where $SEL_{predicted}$ corresponds to AEDT predictions, and $SEL_{measured}$ corresponds to SEL calculated from the events captured in the noise-history dashboard. This offers more statistical insights into all noise computations. Of all AEDT modeling options, this report presents aggregate results that are categorized in terms of AEDT modeling profiles, elevation angles, and AEDT modeling airframes. Box plots were selected to explain all ΔSEL values. The distance between the whiskers on the plots indicate the interquartile range (IQR) with the upper whisker representing the 75th percentile while the lower one representing the 25th percentile. The maximum of the box is 1.5*IQR above 75th percentile and vice versa for minimum of the box. Ideally, the median of zero with a small spread (±3 dB) indicates that AEDT predictions are accurate with real-world data. It is important to note that the outliers were deliberately retained for the plots to permit examination of the complete distribution prior to outlier filtering in order to identify trends, if any, emerge in the outlier distribution.

Figure 6 compares ΔSEL levels that are compared for two different modeling approaches in the AEDT, Standard and FOQA. Standard profiles are generic, pre-defined flight trajectories provided within the AEDT based on assumed or average operational parameters. FOQA profiles by contrast are data driven and generated from actual flight operation data, thus reflecting real world performance. Overall, both FOQA and standard profiles show good agreement with measured noise history data, with median prediction errors lying within ±2 dB for both arrivals and departures. FOQA-based predictions exhibit slightly reduced bias and variability compared to standard profiles, suggesting that incorporating real flight performance data enhances model accuracy. Negative ΔSEL values indicate cases where the AEDT underpredicted measured noise levels, which is observed more in the case of arrival operations.

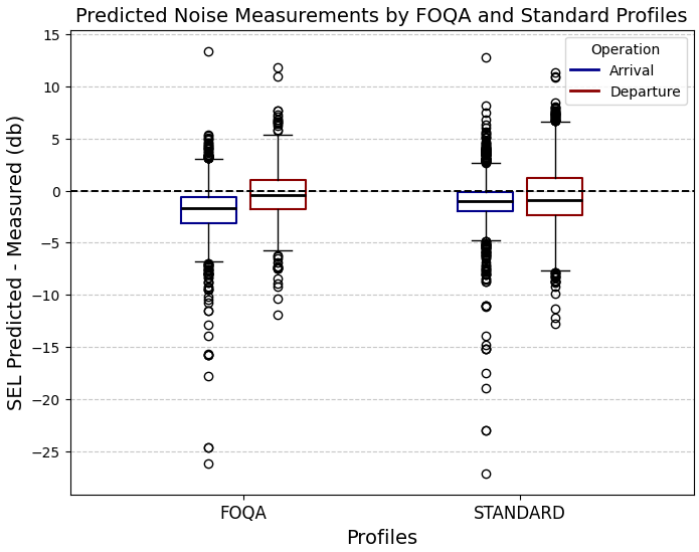


Figure 6. ΔSEL trends by profile type.

Figure 7 compares ΔSEL levels, defined as $SEL_{predicted}$ – $SEL_{measured}$, where $SEL_{predicted}$ corresponds to AEDT predictions, and $SEL_{measured}$ corresponds to SEL calculated from the events captured in the noise-history dashboard. ΔSEL levels are compared for two different modeling approaches in AEDT: Standard and FOQA, and clubbed by elevation angles. The results show systematic dependence of ΔSEL predictions on elevation angles. For elevation angles below 20°, both FOQA and standard profiles exhibit greater variability and underprediction of measured noise, for both arrivals and departures. These low-elevation events typically correspond to monitors located close to runways, where elevated background noise, ground

reflections, and operational variability can distort measurements. Consequently, such low-angle events were excluded from further analyses. For elevation angles ≥20°, prediction accuracy improves substantially, with median ΔSEL values generally within ±1 dB for both profile and operation types. This consistency indicates that after excluding near-runway monitors, AEDT predictions using FOQA and standard profiles perform within reasonable bounds of accuracy in estimating overall noise exposure.

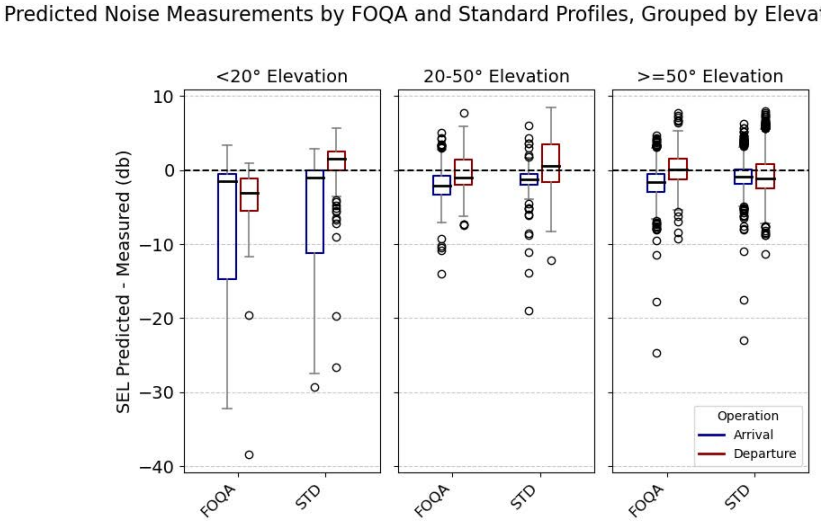


Figure 7. ΔSEL Trends by Elevation Angle.

Figure 8 compares ΔSEL levels, defined as $SEL_{predicted}$ – $SEL_{measured}$, where $SEL_{predicted}$ corresponds to AEDT predictions, and $SEL_{measured}$ corresponds to SEL calculated from the events captured in the noise-history dashboard. ΔSEL levels are compared for two different modeling approaches in the AEDT, Standard and FOQA, and grouped by aircraft type. Results show aircraft specific trends in prediction accuracy. A320 exhibits underprediction for departure operations, which is consistent with the results obtained from MSP 2021 modeling in a similar result in the previous year. The A220, which is modeled in the AEDT using the B737 Aircraft Noise and Performance (ANP) database entry due to the absence of dedicated ANP data, tends to overpredict noise levels. This likely reflects differences in airframe and engine characteristics between the two types. In contrast, B737 predictions, which use their native ANP data, show close agreement with measurements for both arrivals and departures. The B757 demonstrates good agreement when FOQA-based trajectories are used but exhibits noticeable underprediction under the standard profile configuration. Overall, these results highlight that AEDT prediction accuracy depends both on the fidelity of the underlying ANP data and on whether actual (FOQA-derived) or generic (standard) flight profiles are used.

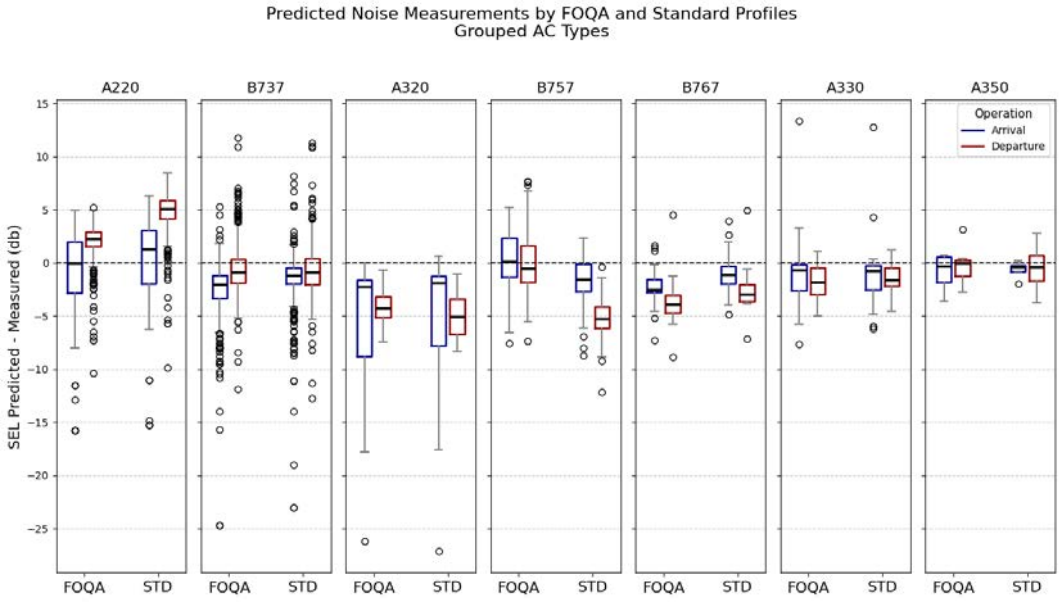


Figure 8. ΔSEL Trends by Airframe.

Figure 9 shows one example of an outlier (defined as ΔSEL ≥ |10|) in this validation study. As shown in this figure, the selected noise event does not exhibit the typical signature of an aircraft-related noise event but was nonetheless captured in AEDT predictions. This occurs because AEDT models the total noise contribution from aircraft overflight rather than filtering only for distinct, high-amplitude noise events. In this instance, a large slant distance between the aircraft and noise monitor resulted in a significant underprediction, with a ΔSEL of –17.97 dB. Across the full dataset of 3,449 matched noise events with filters applied, 20 such outliers were identified. Possible explanations include noise monitors positioned in areas with persistently high ambient noise, environmental conditions affecting measurement accuracy, or other untraceable anomalies. Despite thorough review, no consistent trend or operational pattern was observed among these outliers, indicating that these discrepancies are more likely due to random measurement variability than to systematic AEDT modeling bias.

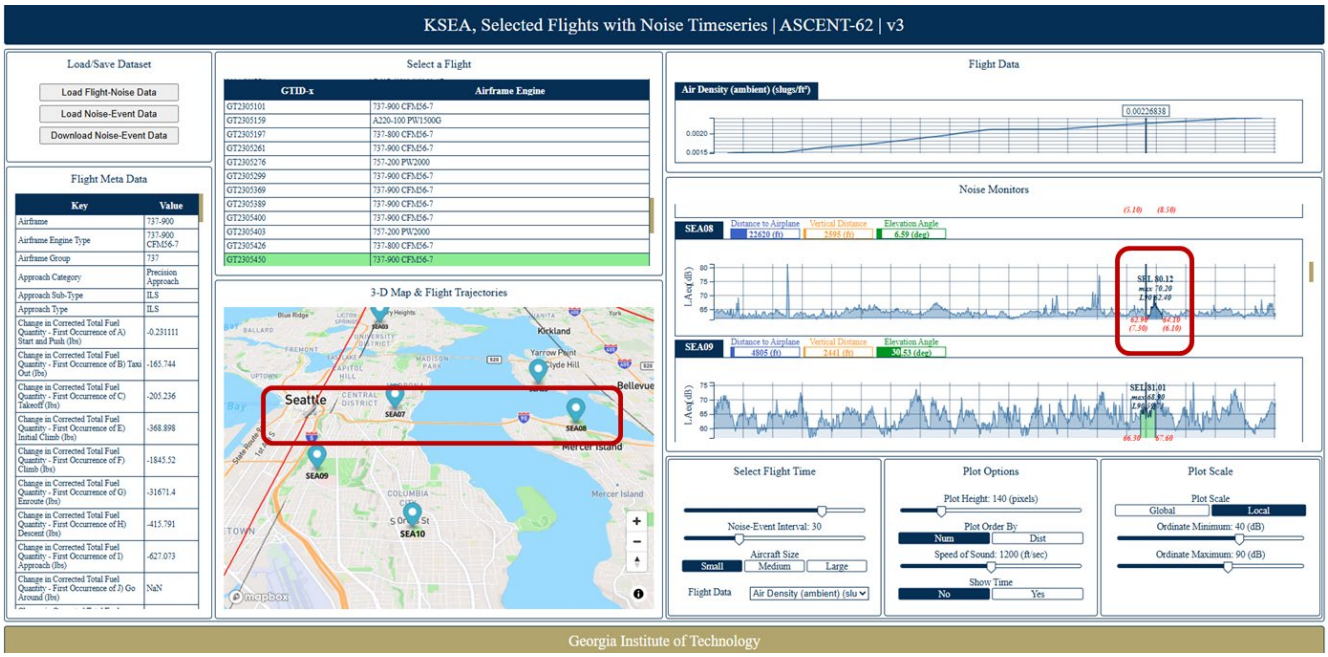


Figure 9. Visualization showing example outlier noise event.

SFO 2021 – Validation of Aggregate Flight Modeling Results against Airport Noise History Data

Data Processing

To support the validation of flight modeling results against historical data, specific datasets collected within the San Francisco International Airport (SFO) airspace during 2021 were targeted for incorporation. These datasets are comprised of LT6 files, which serve as collections of flight tracking data, and LN6 files, which contain pre-selected noise events described by relatively short time series histories and event-wise statistics. The data items and formats for these files are detailed in the ANOMS_8_LT6 Rosetta Stone documentation. Because these files constitute a novel form of flight and noise records when they are compared to the previous analyses, new data processing routines were required to correlate them effectively. However, the sheer volume of data spanning the entire year – including approximately 761,000 noise events and 3.8 million flight tracking points for arrivals and departures (to/from SFO) – rendered the exclusive use of the previously developed human-in-the-loop dashboard infeasible for pairing tasks.

In pursuit of a fully autonomous and quantitatively accurate matching process, a qualitative pilot matching workflow was developed this year, supported by necessary data processing routines and visual aids (as shown in Figure 10). One challenge was the requirement to juxtapose candidate noise events, which exhibit both statistical characteristics and time series history, directly onto the geospatial map alongside flight trajectory data. To facilitate this, the system moved away from conventional time series plots in favor of a station-centric pulsing visualization. This design choice enables an intuitive visual correlation between the aircraft's position and the variation of noise measurements across all monitoring stations, effectively replicating the visualization of seismic events or vibrations over a geographic area, but with the aircraft acting as a moving source.

The resulting dashboard successfully enables a comprehensive understanding of the relationship between the moving noise source (aircraft), derived from LT6 aircraft tracking positions, and candidate noise bursts identified in time-bounded LN6 noise time series, The interface, shown below, visualizes the matching process where arrival and departure tracks (red and blue lines) are correlated with station data. The established workflow now prioritizes performing automatic parings first, followed by validity spot checks using this dashboard to confirm the results for flight modeling analysis.

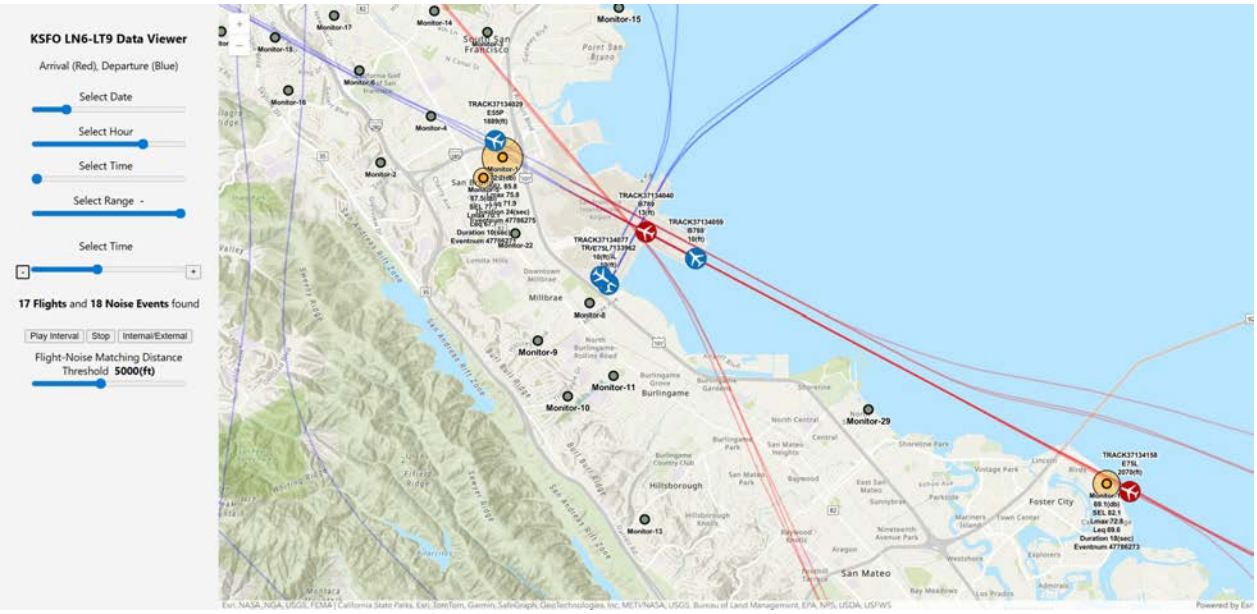


Figure 10. San Francisco International Airport (SFO) LN6-LT6 Data Viewer in action. Orange circles are paired noise bursts to closest aircraft.

AEDT 3e – 3g Transition and Verification

The AEDT version used in this research was initially 3e, released on May 9, 2022, and later upgraded to version 3g, released on August 24, 2024, for all subsequent analyses. It was important to confirm that all modeled flights in the year 2023 produced consistent results between the two versions since they used identical noise calculations. To ensure consistency between the two versions, a small verification study was conducted by randomly selecting flights—such as a 2023 departure from KRDU using the MODIFIED_AW_RT15 profile—and modeling them in both AEDT 3e and 3g with identical inputs. As expected, this produced matching results once settings were aligned (see Table 3).

During this verification, an initial discrepancy in noise results (Table 4) was traced to differences in the default decade-average Integrated Surface Database (ISD) weather databases used by each version: AEDT 3e relies on 2015–2024 data, while AEDT 3g uses 2014–2023 data (Table 3). Because the test flight operated in 2023, both weather datasets were technically appropriate but still yielded slightly different noise predictions due to the role of weather in AEDT's calculations, underscoring the importance of updating the AEDT 3g database to incorporate the most recent available weather data.

Table 3. Default decade average weather data for the AEDT versions on 28016001 – Raleigh-Durham Intl (KRDU).

Parameter	AEDT 3e	AEDT 3g
Decade average period	2015–2024	2014-2023
Temperature (°F)	61.3	61.64
Pressure (millibars)	1002.22	1002.14
Sea level pressure (mb)	1018.14	1018.05
Relative humidity (%)	68.87	68.36
Dew point (°F)	50.98	51.1
Wind speed (knots)	5.08	5.15



Table 4. Noise level discrepancies at Raleigh-Durham International Airport (RDU) receptors due to weather data differences.

		Exposure (SEL)			Maximum (LAMAX)		
Receptor ID	Receptor Name	AEDT 3e	AEDT 3g	Difference (3g-3e) dB	AEDT 3e	AEDT 3g	Difference (3g-3e) dB
1	KRDU_1	88.83	88.81	-0.02	79.45	79.43	-0.02
2	KRDU_2	82.93	92.91	-0.02	71.27	71.24	-0.03
3	KRDU_3	78.98	78.96	-0.02	67.77	67.75	-0.02
4	KRDU_4	60.66	60.62	-0.04	46.79	46.75	-0.04
5	KRDU_5	58.78	58.73	-0.05	44.83	44.79	-0.04
6	KRDU_6	61.23	61.19	-0.04	47.37	47.32	-0.05

Milestones
None.

Major Accomplishments
- Completed successful implementation of the AEDT automation pipeline for (a) modeling real-world flights in various settings and (b) extracting and visualizing results from noise modeling efforts.
- Successfully analyzed over 9800 noise events at SEA in 2021to generate validation results. Excluded noise events with wind speeds >10 knots, non-zero precipitation, elevation angles less than 20° and slant distances >7,000 ft to ensure high quality of results.
- Presented SEA and MSP 2021 (from previous year) results at 2025 ASCENT spring meeting.
- Completed AEDT modeling of 2023 flights at the following airports: SEA, MSP, SFO, IAD, and RDU. Further analysis of noise validation is in progress pending noise data from the airports.
- Coordinated with the Penn State team to provide AEDT performance data required for tasks relevant to high-fidelity weather modeling.
- Developed an interactive human-in-loop dashboard to process detailed airport noise-history data for SEA 2021. Events identified from this dashboard are used to validate SEA 2021 AEDT predictions.
- Developed an interactive automated dashboard for SFO 2021 events. Events identified from this dashboard will be used in upcoming efforts to validate SFO 2021 AEDT predictions.

Publications
Willitt, A., Bendarkar, M. V., Bhanpato, J., Kirby, M., Abelezele, S., & Mavris, D. N. (2024, January). Preliminary AEDT noise model validation using real-world data (AIAA 2024-2107). *AIAA SCITECH 2024 Forum*. https://doi.org/10.2514/6.2024-2107

Outreach Efforts
Held currently monthly (previously biweekly) calls with the FAA, the Volpe Center, and Airborne Tactical Advantage Company (ATAC) and participated in biennial ASCENT meetings.

Awards
None.

Student Involvement
Sonal Mehta and Humfrey Kimanya, students at Georga Tech, worked on noise modeling for 2021 and 2023 SEA, MSP, SFO, IAD and RDU, and data processing for 2021 SEA and MSP datasets that were modeled in the previous year.

Plans for Next Period
- Provide insights into the statistical significance of results at various noise monitoring stations at SFO, IAD, and RDU, for the years 2021 and 2023.



- Further develop the interactive dashboard containing the modeling results with all different settings combined for performing trade-off studies.
- Collaborate with Penn State to complete analysis of the impact of high-fidelity weather on noise predictions and measurement.

References

Douglas, D. H., & Peucker, T. K. (1973). Algorithms for the Reduction of the Number of Points Required to Represent a Digitized Line or its Caricature. *Cartographica, 10*(2), 1973, 112–122. https://doi.org/10.3138/FM57-6770-U75U-7727

Mavris, D. N., & Sparrow, V. W. (2023). Project 062 noise model validation for AEDT. In *ASCENT 2023 Annual Report*. https://s3.wp.wsu.edu/uploads/sites/2479/2024/04/ASCENT-Project-062-2023Annual-Report.pdf

Ramer, U. (1972). An iterative procedure for the polygonal approximation of plane curves. *Computer Graphics and Image Processing, 1*(3), 244–256. https://doi.org/10.1016/S0146-664X(72)80017-0

Willitt, A., Bendarkar, M. V., Bhanpato, J., Kirby, M., Abelezele, S., & Mavris, D. N. (2024, January 8-12). *Preliminary AEDT noise model validation using real-world data* [Conference presentation]. AIAA SciTech 2024 Forum. Orlando, Florida. https://doi.org/10.2514/6.2024-2107

Bibliography

Ahearn, M., Boeker, E., Gorshkov, S., Hansen, A., Hwang, S., Koopmann, J., Malwitz, A., Noel, G., Reherman, C. N., Senzig, D. A., et al. (2016). *Aviation Environmental Design Tool (AEDT) technical manual version 2c*. Federal Aviation Administration.

Alonso, J. J. (2022). Project 053 validation of low-exposure noise modeling by open-source data management and visualization systems integrated with AEDT. In *ASCENT 2022 Annual Report*. ASCENT. https://s3.wp.wsu.edu/uploads/sites/2479/2023/05/ASCENT-Project-053-2022-Annual-Report.pdf, last accessed 28 Dec 2025.

Behere, A., Bhanpato, J., Puranik, T. G., Kirby, M., & Mavris, D. N. (2021, January 11). *Data-driven approach to environmental impact assessment of real-world operations* [Conference presentation]. AIAA SciTech 2021 Forum, virtual. https://doi.org/10.2514/6.2021-0008

Behere, A., Isakson, L., Puranik, T. G., Li, Y., Kirby, M., & Mavris, D. (2020, June 15). *Aircraft landing and takeoff operations clustering for efficient environmental impact assessment* [Conference presentation]. AIAA Aviation 2020 Forum, virtual. https://doi.org/10.2514/6.2020-2583

Behere, A., Lim, D., Li, Y., Jin, Y.-C. D., Gao, Z., Kirby, M., & Mavris, D. N. (2020, January 6). *Sensitivity analysis of airport level environmental impacts to aircraft thrust, weight, and departure procedures* [Conference presentation]. AIAA SciTech 2020 Forum, Orlando, Florida. https://doi.org/10.2514/6.2020-1731

Behere, A., Rajaram, D., Puranik, T. G., Kirby, M., & Mavris, D. N. (2021). Reduced order modeling methods for aviation noise estimation. *Sustainability*, *13*(3), 1120. https://doi.org/10.3390/su13031120

Downing, J. M., Calton, M. F., Page, J. A., & Rochat, J. L. (2019). *Improving AEDT modeling for aircraft noise reflection and diffraction from terrain and manmade structures* (Tech. Rep. ACRP 02-79). Airport Cooperative Research Program.

Federal Aviation Administration. (n.d.) *Aviation Environmental Design Tool (AEDT).* https://aedt.faa.gov/

Forsyth, D. W. & Follet, J. I. (2006). *Improved airport noise modeling for high altitudes and flexible flight operations* (NASA/CR-2006-21451). National Aeronautics and Space Adminstration.

Gabrielian, A. B., Puranik, T. G., Bendarkar, M. V., Kirby, M., Mavris, D., & Monteiro, D. (2021a, August 2). *Noise model validation using real world operations data* [Conference presentation]. AIAA Aviation 2021 Forum, virtual. https://doi.org/10.2514/6.2021-2136

Gabrielian, A., Puranik, T., Bendarkar, M., Kirby, M., & Mavris, D. (2021b). Validation of the aviation environmental design tool's noise model using high fidelity weather. *INTER-NOISE and NOISE-CON Congress and Conference Proceedings*, *263*(2), 4810–4822. https://doi.org/10.3397/IN-2021-2846

Giladi, R., & Menachi, E. (2020). Validating aircraft noise models. *Proceedings, 59*(1). doi:10.3390/proceedings2020059012, URL https://www.mdpi.com/2504-3900/59/1/12.

Hastings, A. L. (2019). *Traffic Noise Model 3.0 - technical manual* (Tech. Rep. FHWA-HEP-20-012). U.S. Department of Transportation, Volpe National Transportation Systems Center.

Hobbs, C. M., Gurovich, Y. A., Boeker, E., Hasting, A., Rapoza, A., Page, J., Volpe, J. A., Airport Cooperative Research Program, Transportation Research Board, & National Academies of Sciences, Engineering, and Medicine.



(2017). *Improving AEDT noise modeling of mixed ground surfaces*. Transportation Research Board. https://doi.org/10.17226/24822

Jackson, D. C., Rindfleisch, T. C., and Alonso, J. J. (2021). A system for measurement and analysis of aircraft noise impacts. *Engineering Proceedings, 13*(1), doi:10.3390/engproc2021013006. https://www.mdpi.com/2673- 4591/13/1/6

Juniac, A. (2019). *IATA annual review 2018*. International Air Transport Association (IATA). https://www.iata.org/publications/Documents/iata-annual-review-2018.pdf

Lee, H., Madar, S., Sairam, S., Puranik, T. G., Payan, A. P., Kirby, M., Pinon, O. J., & Mavris, D. N. (2020). Critical parameter identification for safety events in commercial aviation using machine learning. *Aerospace*, *7*(6), 73. https://doi.org/10.3390/aerospace7060073

LeVine, M. J., Bernardo, J. E., Pfaender, H., Kirby, M., & Mavris, D. N. (2019). Demonstration of a framework for comparing aviation environmental impact mitigation strategies. *Journal of Aircraft*, *56*(3), 1116–1125. https://doi.org/10.2514/1.C035170

Lim, D., Behere, A., Jin, Y.-C. D., Li, Y., Kirby, M., Gao, Z., & Mavris, D. N. (2020, January 6*). Improved noise abatement departure procedure modeling for aviation environmental impact assessment* [Conference presentation]. AIAA SciTech 2020 Forum, Orlando, Florida. https://doi.org/10.2514/6.2020-1730

Mavris, D., Kirby, M., Lim, D., Li, Y., Pfaender, H., Levine, M., Brooks, J., Behere, A., Gao, Z., Chan Jin, Y., & Kim, J. (2018). *Project 045 takeoff/climb analysis to support AEDT APM development* (Tech. Rep.). ASCENT.

Mavris, D. (2019). *Project 043 noise power distance re-evaluation.* ASCENT. https://s3.wp.wsu.edu/uploads/sites/2479/2020/05/ASCENT-Project-043-2019-Annual-Report.pdf, last accessed 14 Dec 2025.

Mavris, D. N., & Sparrow, V. W. (2022). Project 062 noise model validation for AEDT. In *ASCENT 2022 Annual Report*. ASCENT. https://s3.wp.wsu.edu/uploads/sites/2479/2023/06/ASCENT-Project-062-2022-Annual-Report.pdf, last accessed 13th Nov 2023.

Monteiro, D. J., Prem, S., Kirby, M., & Mavris, D. N. (2018, January 8). *React: A rapid environmental impact on airport community tradeoff environment* [Conference paper]. 2018 AIAA Aerospace Sciences Meeting, Kissimmee, Florida. https://doi.org/10.2514/6.2018-0263

Page, J. A., Hobbs, C. M., Plotkin, K. J., & Stusnick, E. (2000). *Validation of aircraft noise prediction models at low levels of exposure* (NASA/CR-2000-210112). NASA. https://ntrs.nasa.gov/api/citations/20000068518/downloads/20000068518.pdf

Plotkin, K. J., Page, J. A., Gurovich, Y., Hobbs, C. M., et al. (2013). *Detailed weather and terrain analysis for aircraft noise modeling*. U.S. Department of Transportation, Volpe National Transportation Systems Center.

Puranik, T. G., & Mavris, D. N. (2018). Anomaly detection in general-aviation operations using energy metrics and flight-data records. *Journal of Aerospace Information Systems*, *15*(1), 22–36. https://doi.org/10.2514/1.I010582

Salgueiro, S., Thomas, J., Li, C., & Hansman, R. J. (2021, January 11). *Operational noise abatement through control of climb profile on departure* [Conference presentation]. AIAA SciTech 2021 Forum, virtual. https://doi.org/10.2514/6.2021-0007

Shaw, E., & Sparrow, V. (2022). Modeling acoustic impedance and atmospheric absorption around airports using high-fidelity weather data. *INTER-NOISE and NOISE-CON Congress and Conference Proceedings, 264*, 104–110, doi:10.3397/NC-2022-698.

Suder, K. (2012, July 30). *Overview of the NASA environmentally responsible aviation project's propulsion technology portfolio* [Conference paper]. 48th AIAA/ASME/SAE/ASEE Joint Propulsion Conference & Exhibit, Atlanta, Georgia. https://doi.org/10.2514/6.2012-4038

Thomas, J. L., & Hansman, R. J. (2019). Framework for analyzing aircraft community noise impacts of advanced operational flight procedures. *Journal of Aircraft*, *56*(4), 1407–1417. https://doi.org/10.2514/1.C035100

Yu, A., & Hansman, R. J. (2019, June 17). *Approach for representing the aircraft noise impacts of concentrated flight tracks* [Conference paper]. AIAA Aviation 2019 Forum, Dallas, Texas. https://doi.org/10.2514/6.2019-3186

Task 2 - Assessing the Use of High-fidelity Meteorological Data in AEDT Noise Calculations

The Pennsylvania State University

Objective

As an exploratory step, Penn State is investigating the possibility of incorporating high-fidelity meteorological data in AEDT noise calculations without modifying the noise model in the AEDT. The ultimate goal is to suggest enhancements to the AEDT that will enhance the predictive capability of AEDT's noise calculations with respect to real-world measurement data.

Research Approach

Penn State's overall approach was described in the 2024 annual report.

Application of Physics-based Noise Calculations to RDU

As mentioned in last year's ASCENT Project 062 annual report, Penn State has begun working with RDU. This is because RDU has a significant interest in sustainability practices, and they also have noise monitors. The monitors, at the time of this study, were located toward the ends of a singular main runway (see Figure 11).

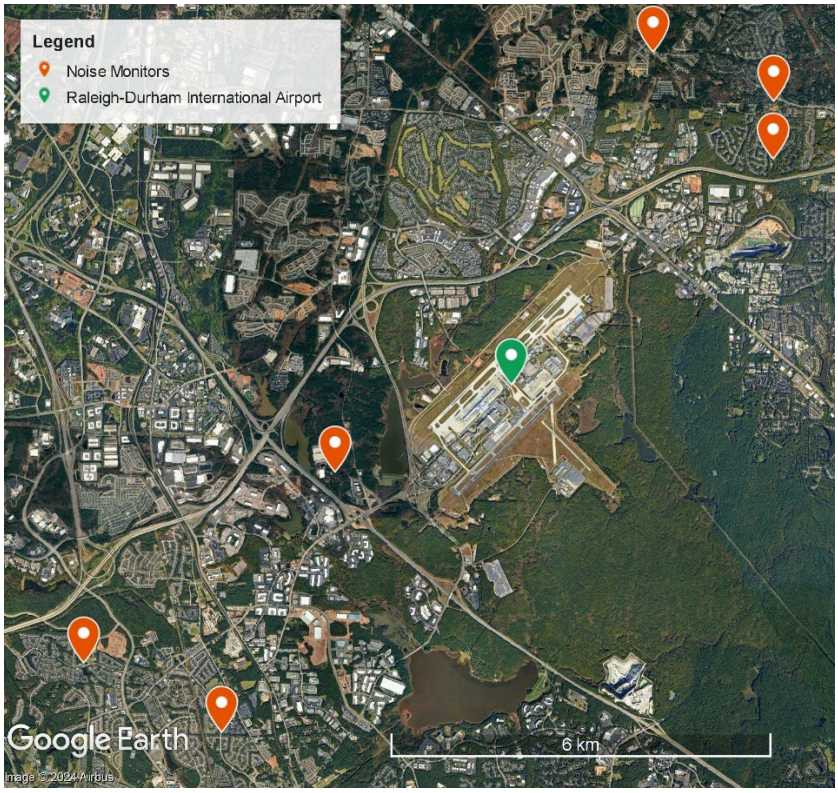


Figure 11. Locations of noise monitors around Raleigh-Durham International Airport.

Further, RDU is not near any large bodies of water, and this contrasts previously studied airports such as SFO. A long-term question is whether the presence of such large bodies of water can affect the accuracy of noise calculations, either with the AEDT or Penn State's physics-based ray-tracing noise calculation methodologies. It is hoped that by comparing across several airports that the question can be answered.

As a first go at analyzing the noise around RDU, noise monitor information was obtained from their noise office, and flight tracking data were obtained from an airline partner of Georgia Tech. Georgia Tech was able to sufficiently scrub the data of

identifiers so that it could be analyzed at Penn State, and Penn State thanks Georgia Tech for making this flight data available for this research.

As an initial exploration of the dataset, Penn State obtained the microphone data from January 2021. Correspondingly, the Penn State team received weather data and data for ten flights and AEDT outputs from Georgia Tech for the same time period. Seven of the flights were from 737-800 aircraft, and these flights have been analyzed.

One of the early flights in January 2021, a departure, is GT2300164. The flight is shown in Figure 12, where the upward triangle is RDU, and the circle symbols t_1, t_2, and t_3 show the location of the aircraft at 1, 2, and 3 minutes after departure, respectively.

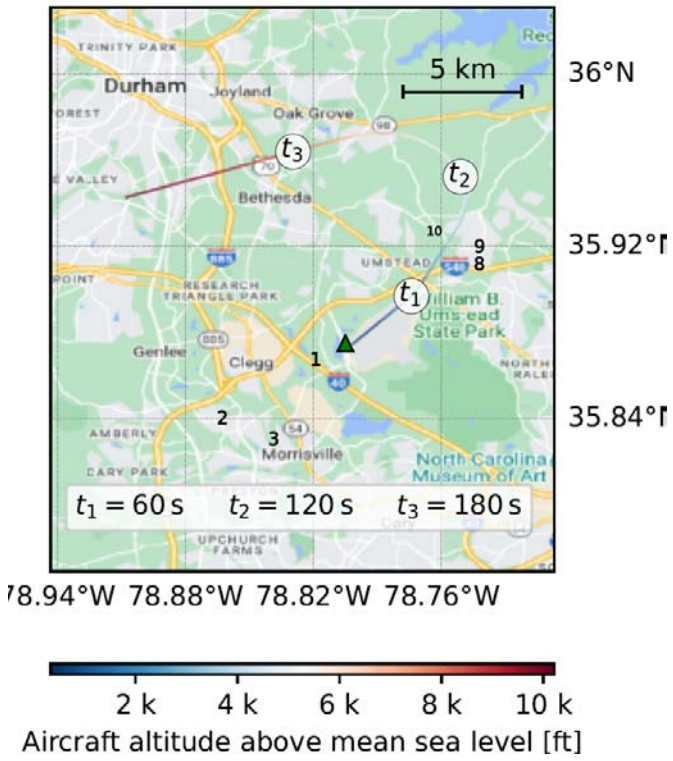


Figure 12. Departure of flight GT2300164 from Raleigh-Durham International Airport.

The weather on a notional day of flight GT2300164 varied considerably from the annual average weather assumed by the AEDT. These weather data are shown in Figure 13, and one can see this is a colder and dryer day than would be assumed in AEDT's annual average (shown with the red dashed lines). The AEDT does not include wind information in its noise calculation, so we will not include it in our physics-based calculations.

Table 5 shows the noise calculation results comparing the AEDT using its annual average atmosphere with the Penn State physics-based ray-tracing approach using an atmosphere with an average of the weather profiles on the day of GT2300164's departure. The in-house ray tracing assumes no refraction but does include altitude-dependent temperature and humidity, as an average over the weather at different times during a notional day of flight GT2300164. In this case, the LAmax (maximum, A-weighted sound level) values are quite close, and the SEL values vary only by about 1.5 dB. This is decent agreement between AEDT and the Penn State calculations, given all the uncertainties, particularly our not knowing the exact time of the flight.

Now we turn to a different case, a similar departure later in the month of January 2021, flight GT2301209, when the weather was particularly cold and dry in that portion of the month. Similar data processing shows AEDT and Penn State

noise calculations are much further apart, for both SEL and LAmax, on the order of 2 to 3 dB. In this case for flight GT2301209, the AEDT is overpredicting the noise levels in comparison to the physics-based approach.

Hence, during this project period shortened by funding delays, we have shown that there are noise calculation differences between the AEDT's approach and the Penn State physics-based straight ray tracing approach at the RDU airport. Sometimes SEL and LAmax metrics agree within a dB and other times they do not. This merits further research, and the Penn State team looks forward to analyzing both the RDU data in more detail and similar data from additional airports in the near future. It would also be helpful if such datasets contain a reasonable number of flights somewhat uniformly spread throughout the months of the year. This would make seasonal comparisons possible, such as comparing summer versus winter. Obtaining such results will allow us to provide FAA information that potentially could lead to impactful improvements in AEDT noise predictions.

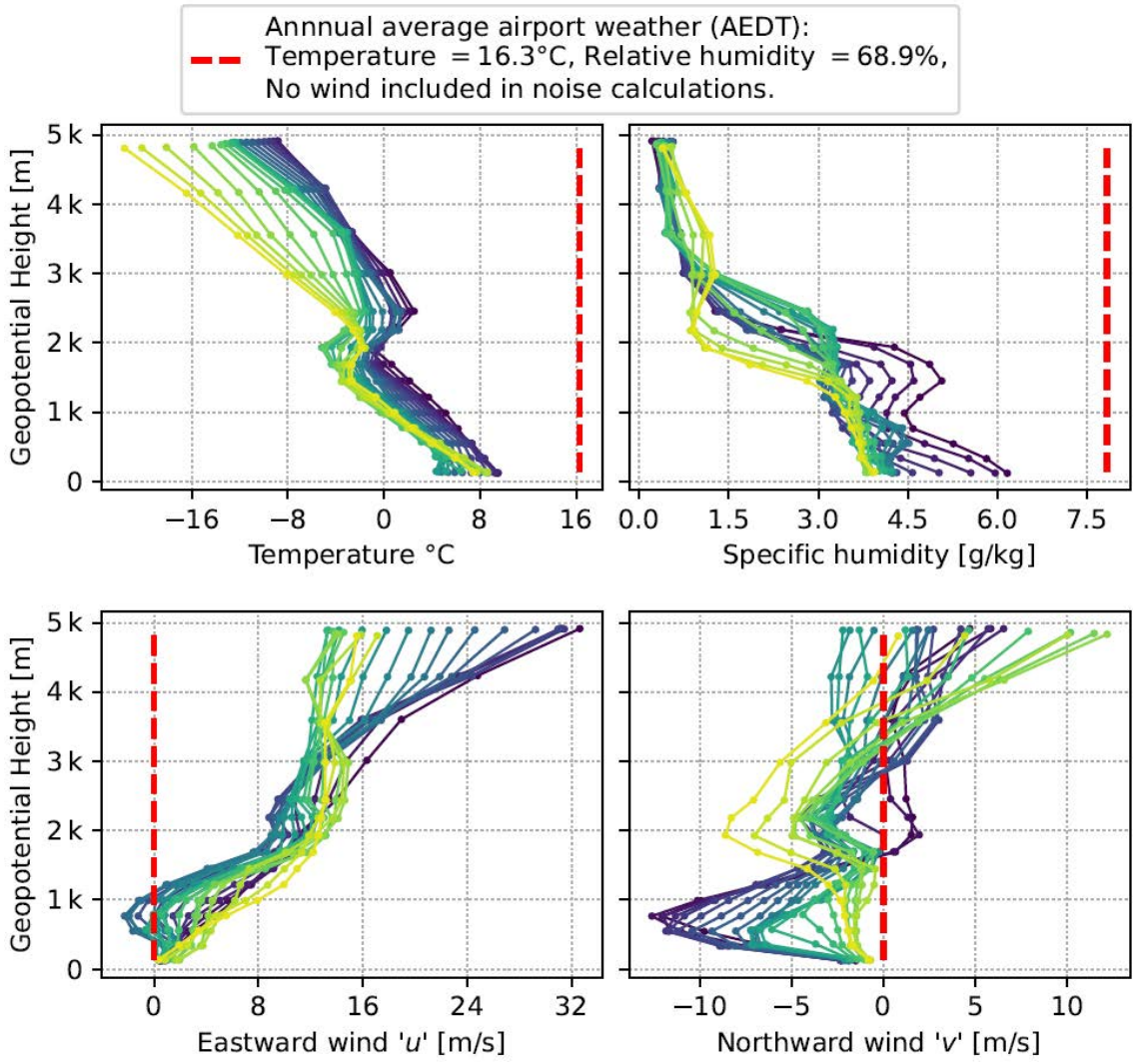


Figure 13. Weather data on the notional day of flight GT2300164 from Raleigh-Durham International Airport.



Table 5. Computed noise levels given by AEDT and Penn State's physics-based codes for flight GT2300164.

Sensor	AEDT		Ray Tracinig (Homo)	
	SEL	LAMAX	SEL	LAMAX
8	79.06	65.76	80.18	65.58
9	80.76	68.68	82.09	68.57
10	84.11	72.49	85.14	72.35

Milestones
None.

Major Accomplishments
None.

Publications
None.

Outreach Efforts
- Attended biweekly calls with the FAA and Georgia Tech.
- Participated in semiannual ASCENT meetings.

Awards
None.

Student Involvement
Harshal Patankar, a graduate student at Penn State, recently completed his Ph.D. work based on the ASCENT Project 040 research. ASCENT Project 040 was the predecessor to ASCENT Project 062. The in-house ray tracing approaches applied here were developed by Patankar. Pierce Hart, a post-doctoral scholar at Penn State, did all the heavy lifting during the current project period utilizing the Patankar codes and generating the results shown in this report.

Plans for Next Period
- Continue the analysis of RDU airport and expand such noise calculation comparisons to additional airports based on the availability of funding.

Special Acknowledgments
The contributions to ASCENT Project 062 by industrial partners Spire Global, Metropolitan Washington Airports Authority, and RDU were incredibly important for this project. Our research team gratefully acknowledges their essential and exemplary support to the Penn State research efforts described here.

References
Mavris, D. & Sparrow, V. (2021). Project 062 noise model validation for AEDT. In *ASCENT 2021 Annual Report*. ASCENT. https://s3.wp.wsu.edu/uploads/sites/2479/2022/10/ASCENT-Project-062-2021-Annual-Report.pdf

Mavris, D. & Sparrow, V. (2022). Project 062 noise model validation for AEDT. *In ASCENT 2022 Annual Report*. ASCENT. https://s3.wp.wsu.edu/uploads/sites/2479/2023/06/ASCENT-Project-062-2022-Annual-Report.pdf

Mavris, D. & Sparrow, V. (2023). Project 062 noise model validation for AEDT. *In ASCENT Project 2023 Annual Report*. ASCENT. https://s3.wp.wsu.edu/uploads/sites/2479/2024/04/ASCENT-Project-062-2023Annual-Report.pdf

Mavris, D. & Sparrow, V. (2024). Project 062 noise model validation for AEDT. *In ASCENT Project 2023 Annual Report*. ASCENT. https://s3.wp.wsu.edu/uploads/sites/2479/2025/06/ASCENT-Project-062-2024-Annual-Report.pdf



Project 064 Alternative Design Configurations to Meet Future Demand

Georgia Institute of Technology

Project Lead Investigator

Prof. Dimitri N. Mavris
Director, Aerospace Systems Design Laboratory
School of Aerospace Engineering
Georgia Institute of Technology
Atlanta, GA 30332-0150
404-894-1557
dimitri.mavris@ae.gatech.edu

Dr. Michelle Kirby
Chief, Civil Aviation Division
Aerospace Systems Design Laboratory
School of Aerospace Engineering
Georgia Institute of Technology
Atlanta, GA 30332-0150
404-385-2780
michelle.kirby@ae.gatech.edu

University Participants

Georgia Institute of Technology (Georgia Tech)

- P.I.s: Dr. Dimitri N. Mavris and Dr. Michelle Kirby
- FAA Award Number: 13-C-AJFE-GIT-062
- Period of Performance: September 30, 2023, to September 30, 2024
- Tasks:
    1. Improvement of Advanced Concept Aircraft (ACA) representation in Modeling and Databases Group (MDG)/Forecasting and Economic Analysis Support Group (FESG) models
    2. Alternative design approaches to meet demand.
    3. Exploring physics-based boundaries of the possible

Project Funding Level

The Federal Aviation Administration (FAA) provided $500,000 in funding, and Georgia Tech has agreed to a total of $500,000 in matching funds. This total includes salaries for the project director, research engineers, and graduate research assistants, as well as funds for computing, financial, and administrative support, including meeting arrangements. The Georgia Tech has also agreed to provide tuition remission for the students, paid from state funds.

Investigation Team

Prof. Dimitri N. Mavris, (P.I.), All Tasks
Dr. Michelle Kirby, (co-P.I.), All Tasks
Dr. Jon Gladin, (technical lead), All Tasks
Dr. Yu Cai, (technical lead), All Tasks
Dr. Jiacheng Xie, (technical lead), All Tasks
Mr. Yaw Tung Tan, (graduate student researcher), Task 1
Ms. Nina Kondur, (graduate student researcher), Task 1
Mr. Felipe Zurita, (graduate student researcher), Task 1



Mr. Tuna Ergan, (graduate student researcher), Task 2
Ms. Yutong Cheng, (graduate student researcher), Task 2
Mr. Nicholas Cocoves, (graduate student researcher), Task 2
Mr. Ty Mancao, (graduate student researcher), Task 2
Ms. Salma Benhissoune, (graduate student researcher), Task 2
Ms. Akshiti Parashar, (graduate student researcher), Tasks 2 and 3
Mr. Cem Kocer, (graduate student researcher), Task 3
Ms. Emmanuella Okonkwo, (graduate student researcher), Task 3

Project Overview

The purpose of ASCENT Project 064 is to improve upon the modeling approach used in the first two years of research and to provide insights or recommendations to the MDG regarding a more realistic approach to modeling ACA at the fleet level. In addition, the project will address alternative means of designing aircraft beyond the usual adoption of technologies with the payload and range capability of the existing fleet.

Task 1 - Improvement of ACA Representation in MDG/FESG Models

Georgia Institute of Technology

Objective

The objective of this task is to investigate potential opportunities for improving how ACAs are modeled within the fleet to benefit current analyses and probable future analyses. The traditional approach to modeling future aircraft types in the fleet has been to define a proxy aircraft that the new aircraft entering the fleet will replace and then establish a change in benefit. Although this process worked for evolutionary aircraft of the past, it does not work for ACAs, which may have markedly different performance behavior from that of conventional aircraft, such as different cruise altitudes and speeds or different range capabilities for the same seat class. To model an ACA within the MDG modeling tools, manufacturers would need to provide the necessary performance, emissions, and noise coefficients defined by Society of Automotive Engineers (SAE) Aerospace Information Report (AIR) 1845 and the Base Aircraft Data (BADA 3). Prior research in this area, specifically for a blended wing body (BWB), has shown limitations in the accuracy of these tools in capturing the expected performance.

Within the Environmental Design Space (EDS), algorithms exist to create the necessary performance, emissions, and noise coefficients needed by MDG's modeling tools. Although the coefficients can be determined, how the ACA actually flies within MDG tools may not be correct, and modifications to the framework may be required.

Building on these findings, the current objective is to enable ACA modelling and fleet assessment capability within the Aviation Environmental Design Tool (AEDT). Specifically, this year's work aims to establish and validate a data pipeline between EDS and AEDT to facilitate the transfer of ACA performance data. Once validated, the pipeline will be demonstrated by processing a BWB model developed in EDS, thus enabling ACA modeling capacity in AEDT.

Research Approach

This year's research focused on a deep-dive validation of the EDS-to-AEDT data pipeline, correcting engine modeling discrepancies, and beginning the integration of ACA models.

Step 1 – Tooling Development and Initial Discrepancy Investigation

To make future analyses more efficient, internal tools were developed to enable comparative assessments of ACA and conventional tube-and-wing aircraft models simulated in the EDS and AEDT. An Airbus® A320neo was selected as the Technology Reference Aircraft (TRA) to serve as a control case for validating connectivity and consistency between the EDS and AEDT. The TRA model was developed in EDS and calibrated using public domain data for the Airbus A320neo and Pratt & Whitney® PW1100G engine.

® Airbus is a registered trademark of Airbus Operations GmbH, Hamburg, Germany.
® Pratt & Whitney is a registered trademark of RTX Corporation, Farmington, Connecticut.

When comparing the TRA departure trajectories between EDS and AEDT, a discrepancy was observed in the climb gradient above 4000 ft above field elevation (AFE), as depicted in Figure 1, despite both tools applying the same cutback thrust setting. Initial investigations focused on identifying the source of this difference between EDS and AEDT takeoff performance models, with checks on aerodynamic drag performance, takeoff procedure implementation and weight.

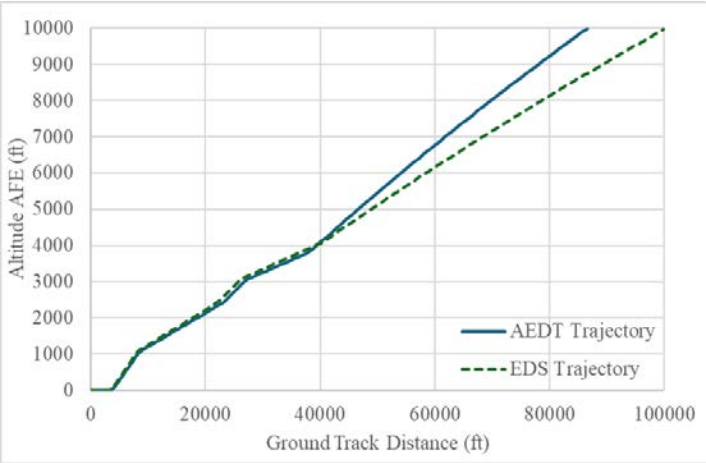


Figure 1. Trajectory discrepancy between Environmental Design Space (EDS) and Aviation Environmental Design Tool (AEDT). AFE: above field elevation.

Step 2 – Engine Model Refinement and Calibration

The root cause of the trajectory discrepancy was traced to a fundamental difference in thrust modeling between the two modeling environments:

- The EDS relies on a single lookup table (i.e., engine deck) of flight conditions, thrust, and fuel flow for all phases of flight. This model included a sharp transition from Maximum Takeoff (TO) thrust to Maximum Continuous (MCT) thrust at Mach 0.4, causing a sharp non-linear drop in thrust as depicted in Figure 2.
- The AEDT relies on different polynomials and models for different throttle settings. However, the sudden drop in maximum thrust due to the rating change is difficult for AEDT's polynomial-based thrust model to accurately capture, no matter how the coefficients are fitted, as seen in Figure 3. This created a significant thrust difference between the two models, ultimately causing the observed trajectory discrepancy.

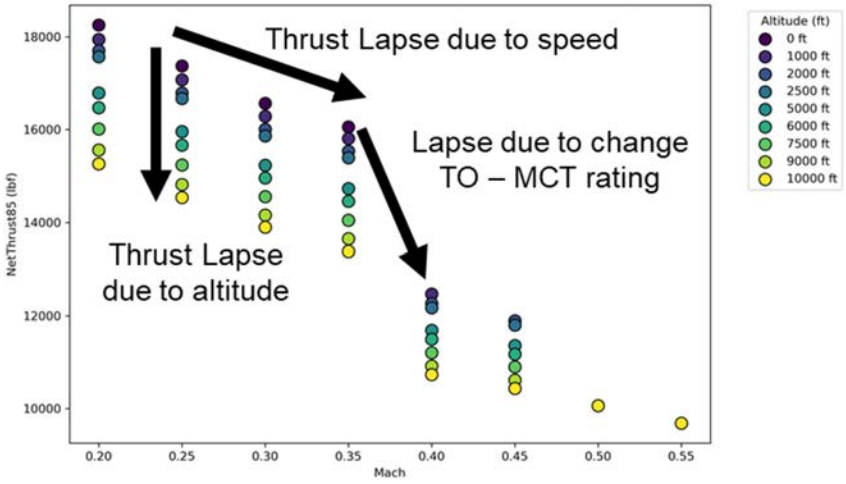


Figure 2. Non-linear drop in thrust due to the maximum thrust setting transition.

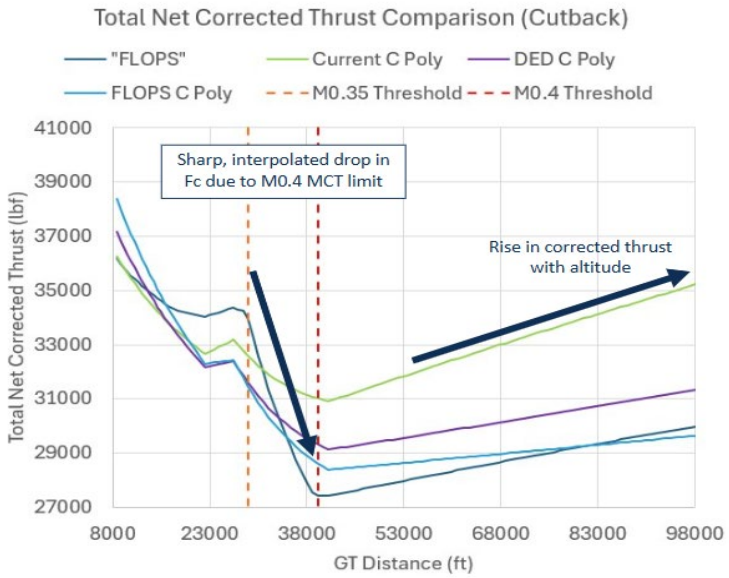


Figure 3. Difficulty in AEDT's polynomial-based model to capture thrust drop due to rating change at Mach (M) 0.4. FLOPS: Flight Optimization System.

A significant effort was made to resolve these thrust discrepancies between the models. This involved identifying and applying the corrections necessary to the climb power and rating modeling within EDS to produce a better fit using AEDT's aircraft nuclear propulsion jet thrust polynomial structure. Engine rating discrepancies were corrected in EDS by increasing the TO-MCT transition Mach number from 0.4 to 0.5 in EDS. This resolved thrust differences between the EDS engine deck and AEDT thrust polynomial models, enabling an improved polynomial fit. Figure 4 shows the improved thrust behavior after the fix. The main drawback of this method is that it may not fully represent real engine operating conditions, because the use of maximum takeoff thrust is typically limited to only a few minutes before transitioning to the MCT rating. However, because the departure procedure in this case applies an 85% thrust cutback rather than full power, this deviation from real operation is not expected to have a large impact on the overall results.

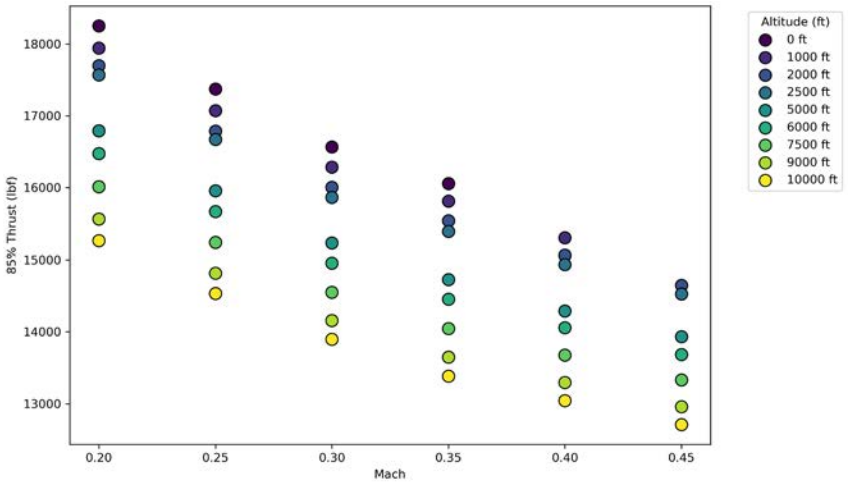


Figure 4. Thrust lapse after rating change set at Mach 0.5.

As part of this, the PW1133G-JM engine was re-calibrated in EDS to fix a thrust lapse issue, and a de-rated PW1129G-JM variant was developed for comparison with AEDT's A320neo BADA model. A new set of engine deck data was then generated using this modified rating structure for subsequent analysis.

Step 3: Trajectory Analysis

Following the thrust modeling refinement, the A320-271N model was simulated in both EDS and AEDT for the takeoff and landing phases to compare and check for consistent results. A set of 18 trajectories for the model was generated covering six stage lengths and three takeoff procedures. Figure 5 presents the takeoff comparison, showing altitude and net thrust versus ground track distance using a standard takeoff procedure and a mission range corresponding to stage length 1 (i.e.,350 nmi). The altitude profiles show a similar initial climb-out trajectory, but around 2,000 ft, the AEDT begins to overestimate thrust, causing an early constant speed climb. This creates a discrepancy in the final ground track distance, with the EDS model reaching 10,000 ft altitude at a ground distance of 4,144 ft after AEDT does. This deviation is primarily due to differences in physics modules and assumptions across the tools. The net thrust profiles show a much closer correlation, with a maximum deviation of only 9.5%. The takeoff trajectories are found to diverge beyond roughly 36,500 ft of ground track distance. As the trajectory deviation past 35,000 ft ground track distance has no effect on certification noise, this difference is considered to have a negligible effect on noise results. The final quantified weight and trajectory deviations across all 18 takeoff profiles are shown in Table 1 below.

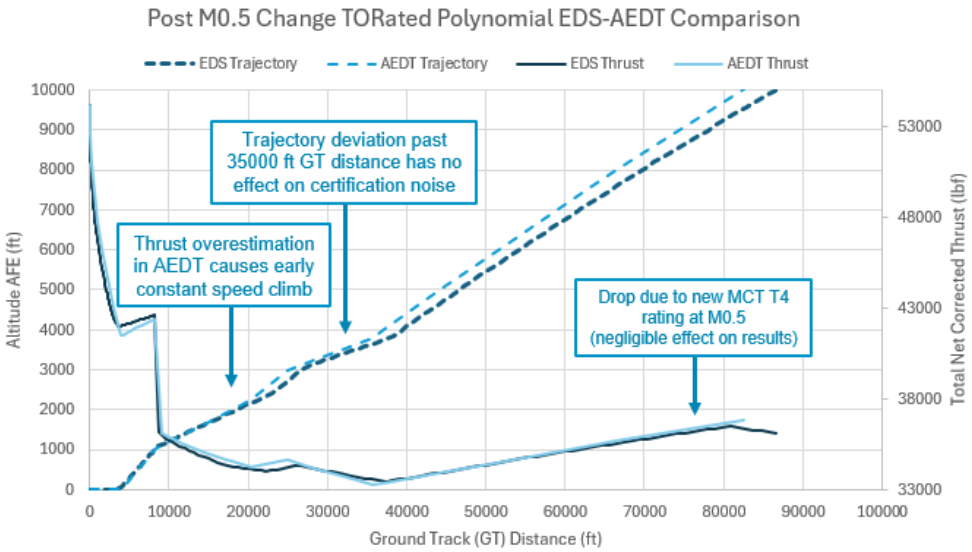


Figure 5. Takeoff trajectory comparison after thrust rating change. AEDT: Aviation Environmental Design Tool, AFE: above field elevation, EDS: Environmental Design Space, M: Mach.

Table 1. Departure trajectories comparison between EDS and AEDT. ICAO: International Civil Aviation Organization.

Stage length	Profile	Max altitude deviation (ft)	Initial weight difference (lb)	End-point weight difference (lb)	Final distance error (nmi)
1	STANDARD	463	1	2	0.682
1	ICAO A	501	1	9	0.742
1	ICAO B	469	1	6	0.691
2	STANDARD	458	2	4	0.706
2	ICAO A	489	2	10	0.761
2	ICAO B	448	2	5	0.682
3	STANDARD	456	2	5	0.725
3	ICAO A	484	2	13	0.785
3	ICAO B	426	2	6	0.684
4	STANDARD	520	2	17	0.898
4	ICAO A	503	2	15	0.874
4	ICAO B	408	2	8	0.73
5	STANDARD	564	2	29	1.068
5	ICAO A	526	2	26	1.014
5	ICAO B	401	2	10	0.767
6	STANDARD	567	3	32	1.093
6	ICAO A	540	3	35	1.053
6	ICAO B	404	3	11	0.793



An initial comparison of approach trajectories for Stage Length 1 was also completed. The landing comparison, shown in Figure 6, shows nearly identical trajectory plots for EDS and AEDT, but the thrust profiles show deviation. The AEDT assumes a specific reverse-thrust and braking procedure not modeled in EDS, leading to the large spike seen in the plot upon touchdown. Overall, this validation exercise demonstrates that the aerodynamic and propulsion characteristics of the EDS model are represented successfully within the AEDT.

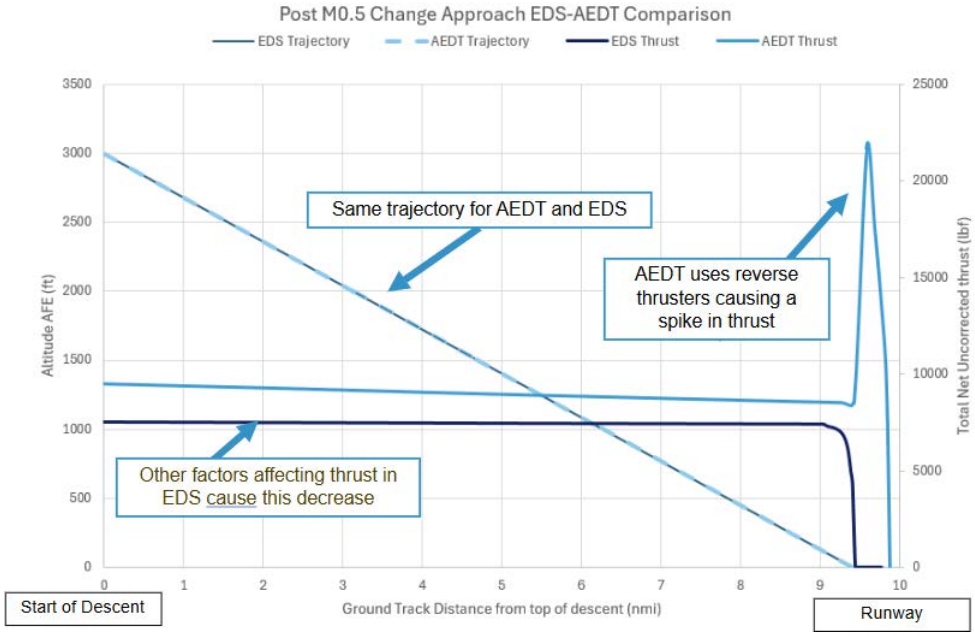


Figure 6. Approach trajectory comparison after thrust rating change. AEDT: Aviation Environmental Design Tool, AFE: above field elevation, EDS: Environmental Design Space, M: Mach.

Step 4: ACA Model Development

With the EDS-to-AEDT pipeline successfully validated, work commenced on modeling the target ACA. The ACA concept selected is a notional Blended Wing-Body (BWB) model, which was developed within the EDS framework by prior work in the lab. The model draws inspiration from JetZero®'s recent BWB concept. A three-view geometric layout of the ACA model generated in OpenVSP[1] is shown in Figure 7 below.

® JetZero is a registered trademark of Blended Wing Aircraft, Inc., Orange, California.

[1] OpenVSP is a parametric aircraft geometry tool. OpenVSP allows the user to create a 3D model of an aircraft defined by common engineering parameters. This model can be processed into formats suitable for engineering analysis. The predecessors to OpenVSP have been developed by J.R. Gloudemans and others for NASA since the early 1990's. On January 10, 2012. OpenVSP was released as an open-source project under the NASA Open-Source Agreement (NOSA) version 1.3.

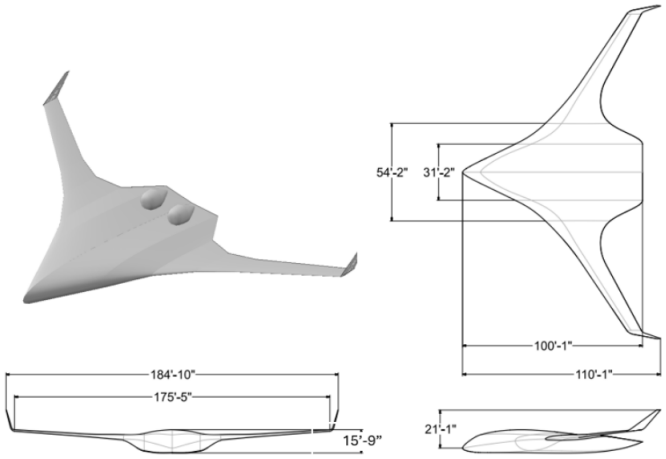


Figure 7. BWB model three-view layout.

The baseline geometry was aerodynamically optimized using a gradient-free approach along with high-fidelity computational fluid dynamics (CFD) analyses. The engine model used was derived from the current PW1133G geared turbofan and modified with an updated core and fan design to achieve a higher sea-level-static (SLS) thrust rating of approximately 43,000 lb. The notional engine model was developed using NPSS (Numerical Propulsion System Simulation) for cycle analysis and WATE++ for engine weights, based on the multi-point-design process. This 2030 variant features a larger fan, higher bypass and overall pressure ratios, and an improved lower thrust lapse rate, leading to lower specific fuel consumption and weight when compared to the baseline PW1133.

Some modifications were made to tailor the BWB model for the EDS-AEDT analysis. Specifically, the high-lift device deflections were revised to 12° for take-off flaps and 25° for landing flaps, and the aerodynamic performance inputs were adjusted with updated flap-induced drag increments to better capture the departure and approach segments effects rather than high-altitude and high-speed behaviors. A mission-level performance analysis was then conducted using the Flight Optimization System (FLOPS) tool, integrating the CFD-derived aerodynamic data and advanced propulsion model with an updated mission profile required for this analysis, as shown in Figure 8. The resulting key performance specifications for this mission are defined in Table 2.

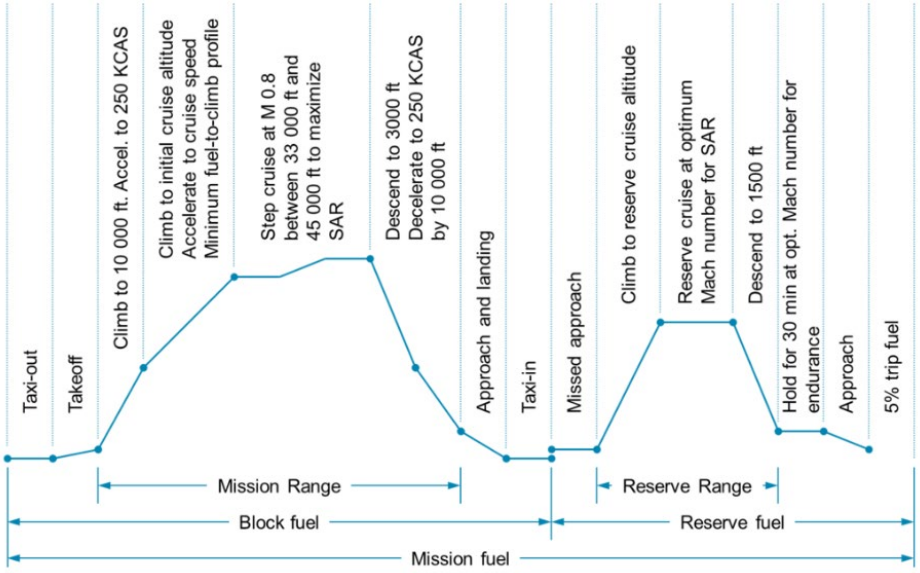


Figure 8. Mission profile of the ACA model. KCAS: Knots Calibrated Airspeed, M: Mach, SAR: specific air range.

Table 2. Key specifications of the ACA model with 2030 technologies infused PW1133G engine.

Parameter	Value	Unit
Design range	5000	nmi
Operational empty weight	143155	lb
Max takeoff weight	269987	lb
Max landing weight	209073	lb
Ramp weight	270415	lb
Design payload weight	56250	lb
Design fuel load	71010	lb
Thrust per engine	43000	lb
Wing loading	47.24	lbf/ft^2
Thrust to weight ratio	0.318	

Milestones

- Completed Step 1- Developed comparative analysis tooling and identified initial discrepancies.
- Completed Step 2 - Corrected engine rating and thrust modeling discrepancies, re-calibrated EDS engine models.
- Completed Step 3 - Generated and evaluated takeoff and approach profiles and quantified deviations.
- Step 4 in progress - Began development and refinement of the BWB ACA model.

Major Accomplishments

- Developed internal tooling to streamline and make future comparative analyses between EDS and AEDT models more efficient.
- Identified and corrected significant discrepancies in engine rating and thrust modeling between EDS and AEDT and successfully validated the pipeline by generating and evaluating 18 takeoff trajectories and approach profiles.



Publications

- Tan, Y. T., Kondur, N., Zurtia, F., Xie, J., Cai, Y., Kirby, M., & Mavris, D. (2026, June 8-12). *Development of Advanced Concept Aircraft Model in Aviation Environmental Design Tool*. Submitted to AIAA Aviation 2026 Forum.

Outreach Efforts

- Attended ASCENT meetings.

Awards

None.

Student Involvement

This task involves three graduate students: Yaw Tung Tan, Nina Kondur, and Felipe Zurita

Plans for Next Period

- Complete the current EDS runs for the BWB and once finalized, process this model through the validated data pipeline to generate the full set of AEDT performance, noise, and emissions coefficients.
- Replicate the trajectory analysis performed in Step 3 using the BWB model. A comprehensive set of departure and approach profiles will be run comparing both EDS and AEDT.
- Upon successful validation, the BWB model will be ready for use in the AEDT, fully enabling the new ACA modeling capability.

Task 2 - Alternative Design Approaches to Meet Demand

Georgia Institute of Technology

Objective

The objective of this task is to achieve, quantify, and enhance the potential efficiency of next-generation tube-and-wing large single-aisle vehicles and their fleet-wide operations through mission-based optimization enabled by the addition of operational design parameters as design variables. This goal is centered around not only reduced cruise Mach number and lowered design range as suggested by literature review, analysis of real-world operations, and prior work, but also around increased and variable passenger capacity. This variation of passenger capacity is to be enabled by a parametric fuselage sizing methodology, supporting vehicle-level trade-offs and maintaining same network-wide passenger flux with decreased operations. This work investigates how aircraft performance, vehicle-level fuel and noise emissions, and fleet-level environmental outcomes change when a clean-sheet single-aisle aircraft is sized and optimized simultaneously over sequential steps of future technology integration, fixed cruise speed, cruise speed optimization, laminar flow technology infusion, and finally coupled design range and payload capacity variation. These impacts are assessed with fleet-level simulations and comparisons to real-life data obtained from flown missions, as passenger demand evolves to imply a developing need for higher-capacity transports.

To support this objective, the EDS will be used to develop and optimize a family of next-generation single-aisle aircraft, modeling and incorporating technologies expected to achieve deployment readiness by 2035 targeting fuel burn and noise mitigation. The previously developed methodology to capture the natural laminar flow (NLF) aerodynamics and their impact will continue to be utilized, while simultaneously developing a brand-new payload-driven parametric fuselage sizing capability. These vehicles will be evaluated over a broad design space to characterize feasibility boundaries for each design and constraint, design variable impacts, trends which support the optimal design for each payload-range combination, and trade-offs among speed, range, and passenger capacity. The optimized vehicle set will then form the basis for the fleet-level impact study, where the associated reductions in fuel burn and emissions will be quantified. This fleet analysis will evaluate how shorter design ranges yield more efficient vehicles at the expense of reduced operational coverage, and how increased passenger capacity can lower the number of required operations. Particular emphasis will be placed on the fleet-level fuel-burn savings enabled by higher-capacity aircraft through operation count reduction, as well as on the resulting trade-offs between vehicle- and fleet-level outcomes.

The outcomes of this task are expected to first include the development and integration of a parametric and payload-driven fuselage sizing method. The payload-driven fuselage sizing method will enable a quantified understanding of the

impacts associated with the newly added variable of passenger count alongside other aspects of mission-based operational optimization, at both vehicle and fleet levels. Benefits, interdependencies, and trade-offs associated with this study aim to inform realistic performance targets as supported by technology development, production, and entry-into-service scenarios for future single-aisle aircraft. This group aims to refine previous work, further developing assumptions for market share evolution and impact of vehicles with different operational goals, environmental targets, and potential increased efficiency of next-generation conventional configurations.

Research Approach

The methodology applied in this research task builds upon the framework originally developed for the Long-Term CO_x Aspiration Goals (LTAG) study conducted by Committee on Aviation Environmental Protection (CAEP) in International Civil Aviation Organization (ICAO), which was conducted by Georgia Tech in support of the FAA, The present work extends that framework to incorporate (i) updated 2035 technology forecasts with a larger technology portfolio, (ii) improved fuselage sizing formulations that enable parametric variation in passenger capacity, and (iii) an expanded design space including variations in design range, cruise Mach number, and payload (passenger) capacity. These enhancements support a more comprehensive evaluation of how mission-optimized single-aisle aircraft affect vehicle-level performance and fleet-wide environmental and operational outcomes. The major steps of the analysis are summarized in Figure 9 and are described below.

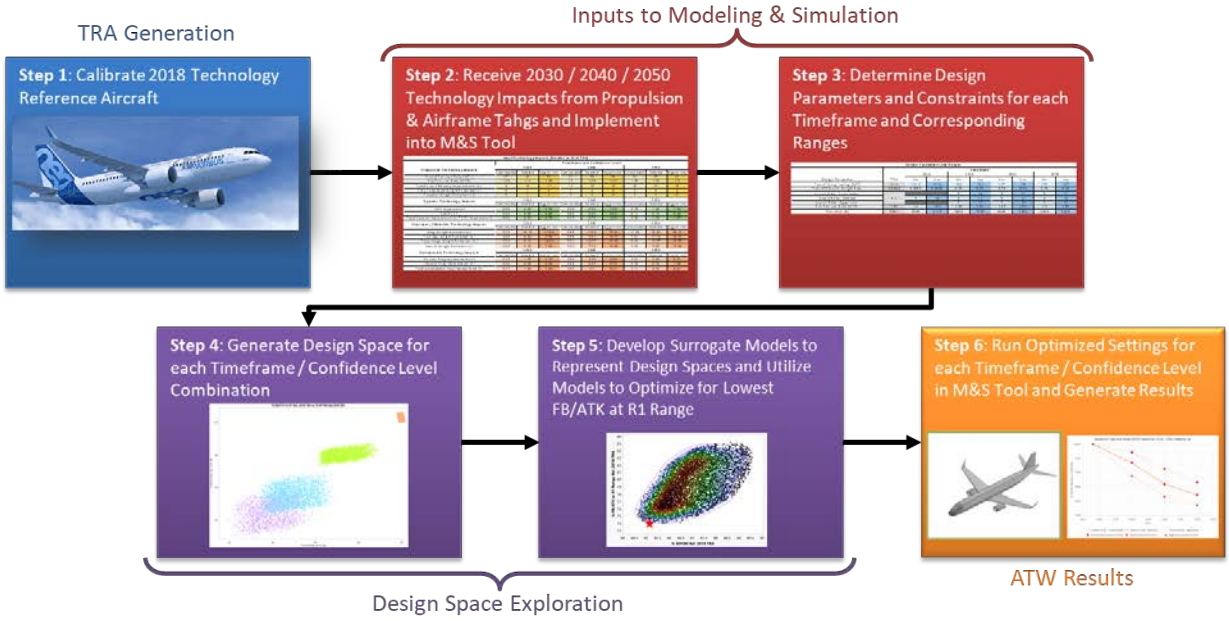


Figure 9. Long-term aspirational goal (LTAG) advanced tube and wing aircraft assessment method. ATW: Advanced Tube and Wing, FB/ATK: Fuel Burn per Available Tonne-Kilometer, M&S: modeling and simulation.

Step 1 - Technology Reference Aircraft Generation

The TRA represents the present-day state-of-the-art baseline against which the impacts of future technology and design changes are evaluated. As in prior work, a notional Airbus A320neo equipped with PW1127G geared turbofan engines is modeled in the EDS modeling and simulation environment, consistent with the 2018 narrow-body reference used during the LTAG study. Updates include refined calibrations of noise performance and takeoff/landing field lengths, while the key specifications are summarized in Table 3. Beyond being the vehicle-level reference point, the TRA also serves as the business-as-usual comparator for subsequent fleet-level analyses.



Table 3. Key design specifications of the TRA model.

Parameter	Unit	Value
Number of passengers	–	150
Design range	nm	3,420
Cruise Mach number	–	0.78
Maximum cruise altitude	ft	41,000
Maximum ramp weight	lb	175,047
Maximum sea-level static thrust	lb	2 × 27,080
Reference wing area	ft^2	1,341
Wingspan	ft	112.8
Takeoff field length	ft	6,619
Landing field length	ft	6,512

Step 2 - 2035 Technology Modeling

Consistent with the forecasts for the maturing airframe, propulsion, and noise reduction technologies, as well as the approximately two-decade service introduction cycles between generations of designs, the next-generation successor to the A320neo is assumed to enter service in 2035, incorporating technologies that have matured by this point. This date reflects the expected readiness of major aerodynamic, structural, propulsive, and acoustic technologies, justifying the engineering effort for a clean-sheet design. In addition, 2035 represents a plausible entry-in-service (EIS) date allowing propagation across the market to enable meeting international environmental goals such as net-zero 2050 initiatives. The 2035 technology portfolio draws from two sources: the ICAO LTAG Technology Subgroup Review, which provides 2030 and 2040 medium-confidence estimates for propulsion, structural, and aerodynamic technology impacts, and the ICAO Independent Expert Integrated Review (IEIR) Noise Technology Review, which provides predicted 2027 and 2037 noise mitigation impacts, both interpolated to obtain 2035 technology impacts. For a conservative estimation, only the moderate confidence of the LTAG and IEIR technology forecasts is utilized. The impacts of integrating technologies on the TRA model are summarized in Table 4. These impacts represent improvements in key design and performance parameters due to the expected evolution of technologies through research and development. The propulsion system of the 2035 design remains the geared turbofan engine, but along with the advanced cycle design, new engine components built with new materials and improved manufacturing processes are expected to improve overall engine efficiency and reduce engine weight. The structural technologies mainly include innovative composite materials and their associated manufacturing processes to decrease the weights of aircraft structural components. The drag reductions introduced by aerodynamic technologies are mainly due to the advanced aerodynamic shape optimization. Noise technologies focus on mitigating the airframe noise, particularly from high-lift devices and landing gears, as well as core and fan noise from engines.



Table 4. Impacts of 2035 technologies on the TRA model.

Technology Impact	Improvement
Engine core component weight	-3.00%
Fan efficiency	+0.95%
Low-pressure compressor (LPC) efficiency	+1.15%
High-pressure compressor (HPC) efficiency	+1.96%
High-pressure turbine (HPT) efficiency	+0.95%
Low-pressure turbine (LPT) efficiency	+1.21%
Reduction in small core efficiency losses	+13.50%
TSFC improvement from power extraction	-0.53%
Wing weight	-11.85%
Fuselage weight	-8.35%
Empennage weight	-9.52%
Nacelle weight	-6.25%
Lift-independent drag	-2.38%
Lift-dependent drag	-0.18%
Jet noise	-0.80%
Inlet noise	-2.39%
Fan discharge noise	-3.02%
Core (combustor) noise	-6.00%
Turbine noise	-2.00%
Landing gear noise	-3.60%
Trailing edge flap noise	-2.80%
Leading edge flap noise	-16.60%

Aside from the technologies listed above, the reduction of cruise speed also provides an opportunity for NLF technology integration. NLF reduces aircraft skin friction drag by shaping the airfoil to delay boundary layer transition from laminar to turbulent. When the cruise speed reduces from the transonic to subsonic regime, wave drag decreases, and skin friction drag becomes the dominating factor, creating a need to decrease skin friction drag for better aerodynamic efficiency. Simultaneously, a lower sweep angle may become feasible as wave drag decreases, which discourages crossflow instability and supports the implementation of NLF.

Instead of modeling the skin friction drag reduction due to the NLF as a constant, this research improves the NLF modeling approach of the LTAG study by incorporating additional influencing factors, including the Mach number, Reynolds number, and sweep angle. Specifically, in this task, the NLF is modeled using the flat plate approximation and analyzed using NASA's aircraft design tool FLOPS. The percentage of the laminar region on the wing surface is computed as the ratio between the transition Reynolds number and the local Reynolds numbers at different spanwise locations. The local Reynolds numbers are computed based on the altitude, Mach number, and local chord lengths, whereas the transition Reynolds number is determined by the leading-edge sweep angle using the crossflow instability and the Tollmien-Schlichting instability theories. The regions enclosed by control surfaces, behind the nacelles, and near the fuselage are assumed turbulent because of large disturbances.

The proposed NLF modeling method was applied to NASA's Common Research Model (CRM)-NLF model for validation. The calculated percentage of the laminar region on the wing was compared to the experimental result documented in the literature. Figure 10 shows the laminar area computed for the CRM-NLF model using the proposed method. The Mach

number and Reynolds number of the validation case are at 0.86 and 1.5×10^7, respectively. The upper surface laminar portion calculated by the proposed model is 55.6%, which closely aligns with the experimental result of 56.0%. The cruise lift-to-drag ratio improvement was also compared between two sides, with the proposed model result of 6.87% consistent with the experimental result of 6.81%.

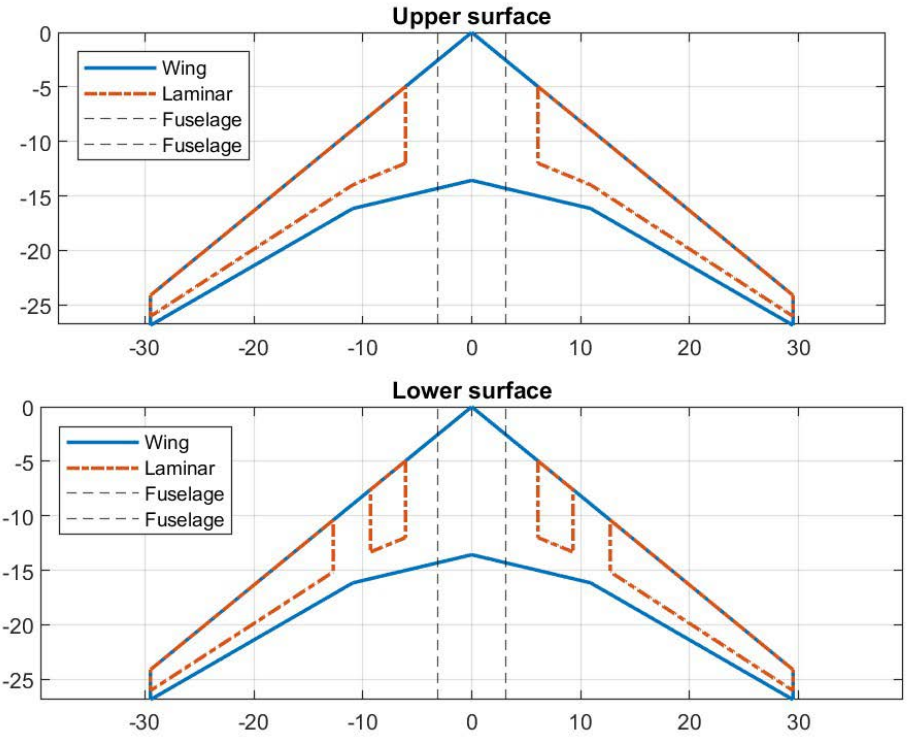


Figure 10. Laminar region on the wing surfaces of the Common Research Model-Natural Laminar Flow (CRM-NLF) model.

Step 3 – Fuselage and Cabin Sizing Method

To support the inclusion of passenger capacity as a design variable in the design space exploration for next-generation transports, a new fuselage sizing method with parametric variation of fuselage dimensions as a function of user-input payload capacity was required to replace the FLOPS methods constructed using legacy data. During this task, two new fuselage sizing methods were developed. The first mimicked the method used in FLOPS, estimating fuselage dimensions through a build-up of cabin elements based on physical dimensions called the Detailed-Layout Based Method, and a second, simplified, regressions-based model called the Data-Driven Direct Sizing Method. The first method reconstructs cabin geometry using physical dimensions and numbers of galleys, lavatories, doors, and effective joint lengths for all based on the number of passengers and number of seats abreast. While defining the seat pitch for the various classes ultimately helps with the prediction, the method is even able to assume default values and seat density, operating with a minimal number of inputs, requiring only counts of tourist and first-class passengers. Alternatively, the second method computes the counts of cabin elements after directly sizing the fuselage, and only for reference purposes. This data-driven method sizes the fuselage based on various regressions and relations between passenger compartment and fuselage dimensions with the passenger counts per class. While both methods have been made compatible with the modeling and simulation tool EDS, specifically through the input design of experiments, ultimately the latter method was selected due to its simplicity and lower computational cost. Regardless, both methods exhibited promising predictive performance, especially for the narrow-body passenger range between 130 and 270, with the percent error accuracy of both methods displayed in Figure 11 and Figure 12.

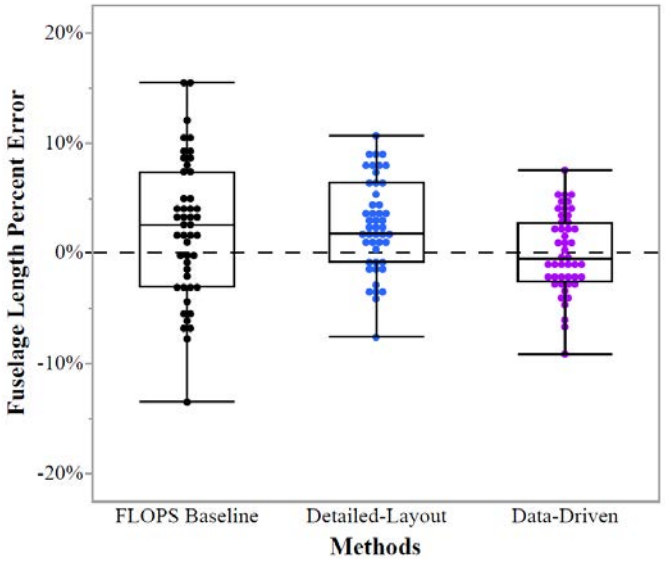


Figure 11. Comparison of fuselage length approximation between baseline and proposed methods. FLOPS: Flight Optimization System.

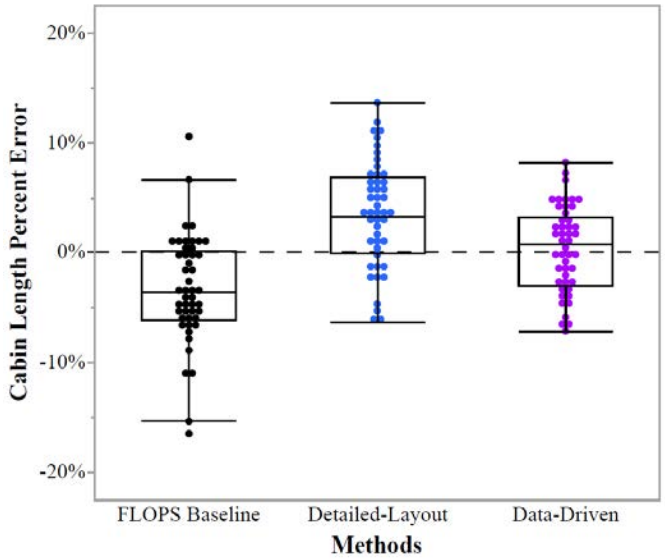


Figure 12. Comparison of cabin length estimation between baseline and proposed methods. FLOPS: Flight Optimization System.

Step 4 - Design Space Exploration

The design space of interest is constructed by the design variables and their associated ranges shown in Table 5. Aside from the variables used in the LTAG study, additional wing geometric parameters are added to the design space to maximize the benefits of reducing cruise speed and design range. The design objective is to minimize the block fuel of the design mission. The constraints considered in the optimization are summarized below:



- Takeoff field length at maximum takeoff weight (MTOW) and sea-level International Standard Atmosphere (ISA) condition no longer than 6,619 ft
- Landing field length at maximum landing weight and sea-level ISA condition no longer than 6,512 ft
- Wingspan no longer than 118 ft (Aircraft Design Group III)
- Excess fuel capacity for the design mission must be non-negative
- Fan diameter no greater than 86.04 ft
- Core size parameter no lower than 2.8 lb/s
- Maximum high-pressure compressor temperature no higher than 1,800° R

Table 5. Design variables and ranges. TRA: Technology Reference Aircraft.

Design Variable	Timeframe		
	TRA	2035	
		Minimum	Maximum
Design range (nm)	3,420	1,500	3,420
Cruise Mach number	0.78	0.70	0.80
Thrust-to-weight ratio	0.31	0.28	0.33
Wing loading (lb/ft^2)	131	128	134
Fan pressure ratio	1.52	1.375	1.55
Overall pressure ratio	45.8	41	51
Maximum turbine entry temperature (R)	3,360	3,334	3,519
Extraction Ratio	1.128	0.95	1.25
Wing aspect ratio	9.5	7.5	11.5
Wing taper ratio	0.19	0.15	0.25
Wing average thickness to chord	0.138	0.1	0.14
Wing quarter-chord sweep angle (°)	25.3	15	27

The first three constraints ensure the new aircraft maintains compatibility with all existing airport facilities. The fan diameter constraint ensures ground clearance of the nacelles. The last two constraints ensure the high-pressure compressor is manufacturable and its operating temperature does not exceed material temperature limits.

To sample the design space, nearly 20,000 DoE cases are generated using the design variables and their ranges listed in Table 4 by applying Box-Behnken and Face-Centered Central Composite designs to sample edge cases, with the Latin hypercube design applied for interior design space sampling. This DoE is run through the EDS design environment twice with two settings: (1) the NLF model disabled and (2) the NLF model activated, resulting in nearly 40,000 total cases. Based on the responses of the sampling cases, surrogate models are established between metrics of interest (i.e., design objective and constraints) and design variables using two-layer neural networks. To ensure that the established surrogate models are sufficiently accurate to replace true functions, multiple validation metrics are evaluated, including R^2, the root mean squared error, the actual versus predicted plot, and the residual versus predicted plot. Using these surrogate models, a set of constrained optimizations is performed to obtain optimal designs for varying scenarios, and these designs are then re-evaluated in EDS to determine fuel burn improvements.

Step 5 - Fleet-Level Impact Evaluation

The fleet analysis is performed using the in-house tool Global and Regional Environmental Aviation Trade-Off (GREAT). In GREAT, all aircraft are categorized into seat classes based on their passenger capacities. These seat classes include short thin haul (SHT), small regional jet (RJ-S), large regional jet (RJ-L), turboprop (TP), small single aisle (SSA), large single aisle (LSA), small twin aisle (STA), large twin aisle (LTA), and very large aircraft (VLA). The evaluation of the fleet composition depends on the retirement of old aircraft and subsequent replacement with new aircraft. Each seat class in GREAT is modeled using a retirement curve derived from historical data. Replacements are modeled using a structure matrix considering three aspects: (1) aircraft age, prioritizing the oldest units first, (2) mission capabilities, and (3) environmental feasibility. Meanwhile, the new aircraft's capabilities with respect to the design range, payload, and seat class must be equal to or greater than those of the previous aircraft that it is replacing. Finally, the fuel burn or emissions produced by this aircraft must be improved compared to those of the older aircraft. Figure 13 depicts the retirement and replacement algorithm used in GREAT.

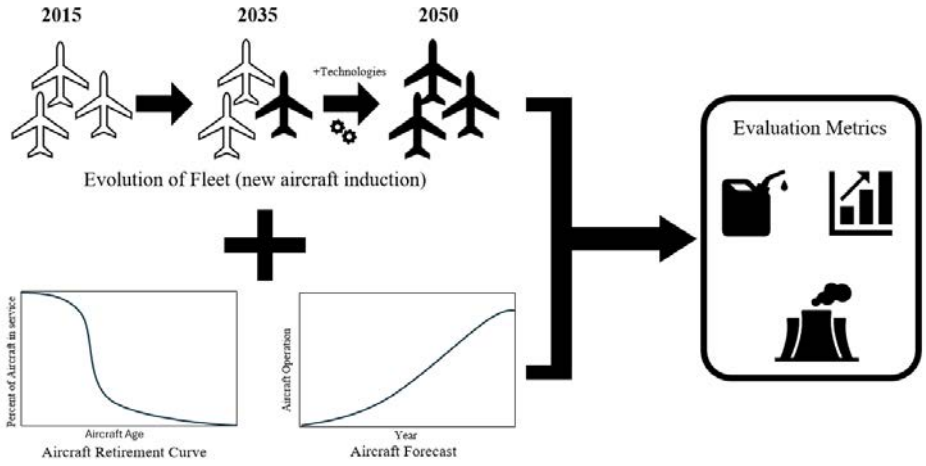


Figure 13. Retirement and replacement algorithm in GREAT.

The forecast model of the future flight demands integrated in GREAT is established based on the Boeing Commercial Market Outlook (CMO). As shown in Figure 14, this forecast model includes the COVID years and provides information on the forecasted recovery of air travel demand in post-COVID years. The black curve in the plot represents the growth in total operations from 2015 to 2050. Note that since the Boeing CMO only predicts the operations until 2041, the growth rates between 2041 and 2050 are based on extrapolation. The colored bars in Figure 14 denote the percentage of total operations covered by different classes of aircraft. For each class, the shaded bar represents the aircraft that are out of production, while the bright bar represents the aircraft that are still in production.

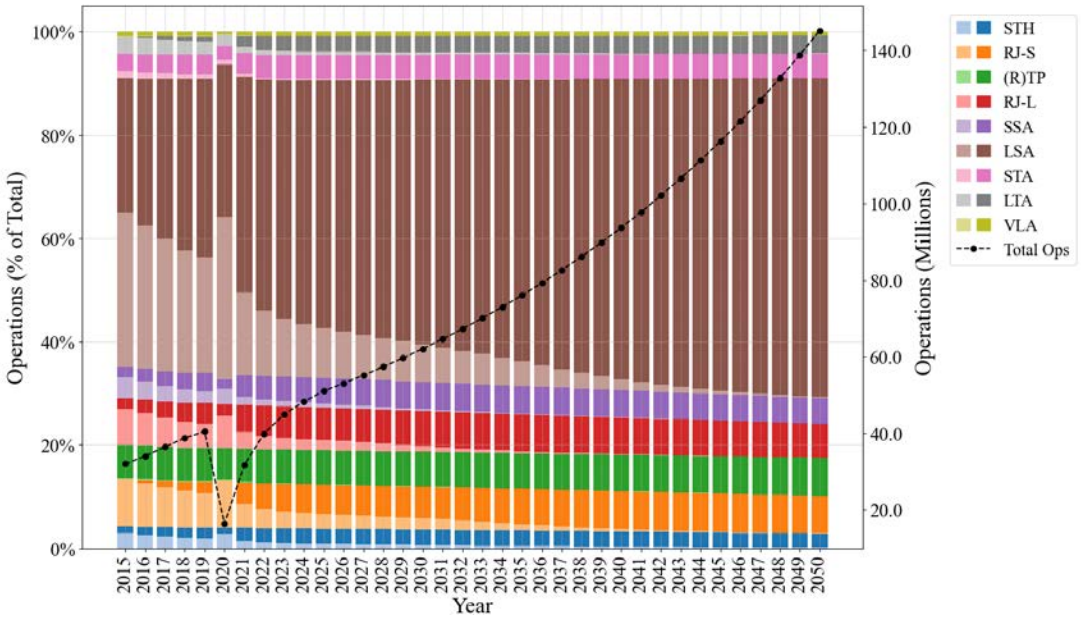


Figure 14. Commercial aviation growth forecast and business-as-usual scenario.

Although reducing the design range lowers an aircraft's fuel consumption due to a smaller vehicle size and lower thrust requirement, it also limits the set of missions the aircraft can serve. To assess how this constraint affects the fleet operation, this task performs a fleet analysis built upon the design space exploration results obtained from Step 4. Assuming the optimal designs with reduced design range, optimized cruise speed, and increased passenger capacity begin replacing the previous generation single-aisle aircraft in the current fleet starting from 2035, multiple fleet evolution scenarios are analyzed. To reflect a realistic EIS profile, a 6-year ramp-up schedule is applied, increasing the production share of the new vehicle from 0% to 100% between 2034 and 2039. This approach captures an initially slow rollout, accelerated production as manufacturing stabilizes, and tapers to full-scale class-wide production at full demand levels. Because the short-range optimized vehicles are unable to serve all mission ranges, longer missions within the same seat-class continue to be operated by the baseline TRA. As payload capacity is now a design variable in the vehicle optimization process, the fleet replacement logic is updated to reflect changes in the number of operations required to transport the same passenger demand. When aircraft with higher seating capacity enter the fleet, the required number of operations is reduced accordingly. Two adjustment approaches are applied, with the latter introducing a "penalty factor" to better represent operational realities, such as the occasional need for additional flights to satisfy the demand distribution across various hours of the day. These are:

- Option 1: Direct proportional scaling based solely on the ratio of the original to increased passenger capacity, preserving total transported passengers.

$$N_{\text{adj},1} = \frac{PAX_{\text{orig}}}{PAX_{\text{inc}}} N_{\text{orig}} \quad \text{(Eq. 1)}$$

- Option 2: A moderated adjustment that partially reverses the capacity-based scaling to account for operational realities such as variable load factors and scheduling flexibility.

$$N_{\text{adj},2} = N_{\text{adj},1}\left[1 + p\left(1 - \frac{PAX_{\text{orig}}}{PAX_{\text{inc}}}\right)\right] \quad \text{(Eq. 2)}$$

These adjusted operation counts directly modify the replacement percentages applied within GREAT. Higher-capacity aircraft receive lower replacement shares under both options, with Option 2 producing slightly higher values due to its more conservative treatment of operational efficiency gains. In this task, a baseline "business-as-usual" scenario is first established, followed by 50 scenarios using the optimized vehicles replacing the existing fleet, as summarized in Table 6.



In the baseline scenario, no newly designed aircraft is introduced, and the industry maintains production of existing vehicles with anticipated annual market and operations growth, intended to represent the current real-world situation. The scenario includes cases such as waiting until novel concept programs come to fruition or new vehicles arriving to the market with EIS dates following 2035. It could also represent new models being introduced in the fleet being less impactful. Fifty other scenarios were sketched to utilize the findings of the vehicle design study and its corresponding resultant optimized vehicle. The 51 scenarios are executed twice in GREAT, where the first execution uses Option 1 and the second uses Option 2 with a penalty factor of $p = 0.25$.

Table 6. Vehicle production and replacement scenarios of consideration. ATA: Advanced Technology Aircraft, LSA: large single aisle, SSA: small single aisle.

Scenario	Optimized Aircraft	Design Range (nm)	Replaced Aircraft Class
1	Business as usual		
2-6	ATA 1-5	1,500	LSA only
7-11	ATA 6-10	1,700	LSA only
12-15	ATA 11-14	2,000	LSA only
16-19	ATA 15-18	2,500	LSA only
20-23	ATA 19-22	3,000	LSA only
24-26	ATA 23-25	3,420	LSA only
27-31	ATA 1-5	1,500	LSA and SSA
32-36	ATA 6-10	1,700	LSA and SSA
37-40	ATA 11-14	2,000	LSA and SSA
41-44	ATA 15-18	2,500	LSA and SSA
45-48	ATA 19-22	3,000	LSA and SSA
49-51	ATA 23-25	3,420	LSA and SSA

The outputs from the tool include total operations conducted by that aircraft, annual distance covered, fuel burn, and carbon and nitrogen oxides (NO_x) emissions. To evaluate the global impact induced by the introduction of newly designed vehicles compared to the non-replacement scenario, these metrics are added up for the particular seat class and plotted against the time period in consideration.

Milestones

- Developed a fully parametric, payload-driven fuselage and cabin sizing methodology, replacing the legacy FLOPS formulations with two models: a data-driven direct estimation, and a physical dimensions-based detailed-layout buildup of components, scalable from smallest single-aisle to largest twin-aisle configurations.
- Validated the new fuselage sizing methodology using a comprehensive set of real aircraft data and comparing the performance with other legacy and modern tools with fuselage sizing capabilities, including FLOPS, SUAVE[2], Aviary/GASP[3], as well as established published regression-based sources like Roskam and Raymer, demonstrating improved accuracy and robustness across all classes.
- In the process of publishing a conference proceeding to 2026 SciTech titled "Rapid Fuselage and Cabin Sizing Method for Commercial Transport Aircraft Design," documenting the performance and results of the proposed fuselage and cabin sizing methods, alongside comparison with existing literature and tools.
- Completed identification, modeling, and infusion of 2035 propulsion, structural, aerodynamic, and acoustic technologies from ICAO LTAG and IEIR technology portfolios, as well as NLF aerodynamic model, achieving ATA model.

[2] SUAVE is a conceptual level aircraft design environment built with the ability to analyze and optimize both conventional and unconventional designs. SUAVE is a development of the Stanford Aerospace Design Lab.
[3] Aviary/GASP is NASA's aircraft analysis, design, and optimization tool.



- Performed a comprehensive design space exploration using EDS, densely sampling the design space with nearly 40,000 samples, obtaining responses of metrics and constraints of interest, followed by establishing high-accuracy neural net surrogate models to characterize the responses as functions of design variables, enabling optimization.
- Performed mission-based optimization across an array of payload-range design points, identifying feasible configurations, determining active constraints, and generating conceptual aircraft models for all viable combinations, while also re-performing past year setup, configuration, and results for crosscheck and validation.
- Investigated relaxation of constraints to obtain feasible designs across all design combinations.
- Developed setup and approach enhancements to the GREAT fleet analysis framework to accommodate variable passenger capacity and analysis of its influence on operations, replacements, and mission feasibility.
- Established and evaluated all-new fleet replacement scenarios, selected specifically to characterize distinct and joint effects of reduced range decreasing operational coverage and increasing passenger capacity transporting equal number of passengers in less operations, incorporating payload-dependent operations scaling, nonlinear fleet introduction ramp-up, and range-bounded mission assignments for range-limited vehicles.
- Visualized the results of vehicle and fleet-level analyses, displaying impacts across fuel burn, operations, noise, and comparing new optimized vehicles against business-as-usual baselines.
- In the process of publishing vehicle and fleet-level results as two separate but companion conference proceedings in 2026 Aviation, titled “Assessing Impacts of Design Range and Payload on Next-Generation Single-Aisle Transport Fuel Burn and Noise” and “Fleet-Level Assessment of Mission-Optimized Next-Generation Single-Aisle Aircraft with Varying Payload,” documenting the methodology, results, and implications.

Major Accomplishments

This task has delivered a two-part major accomplishment, with one part being the optimized 2035 single-aisle aircraft designs with reduced cruise speeds at multiple design ranges, and the other being fleet-level fuel burn impacts of introducing these optimized designs into fleet operations.

Part 1 - Vehicle-Level Assessment

Figure 15 illustrates the sequential reduction in block fuel achieved in each stage of the optimization process. Integration of 2035 LTAG technologies provides the single largest improvement, reducing fuel weight by about 12% for each range considered, as depicted by the blue bars. Fixed-speed optimization at a cruise speed of Mach 0.78 contributes further 7-8% block fuel reductions, as shown by the orange bars. Adding optimization of the cruise speed, shown by the gray bars, further reduces fuel consumption by approximately 2%. Lastly, the integration of NLF technologies and corresponding vehicle resizing, as seen in the purple bars, yields an additional block fuel reduction of about 6% across all the ranges analyzed.

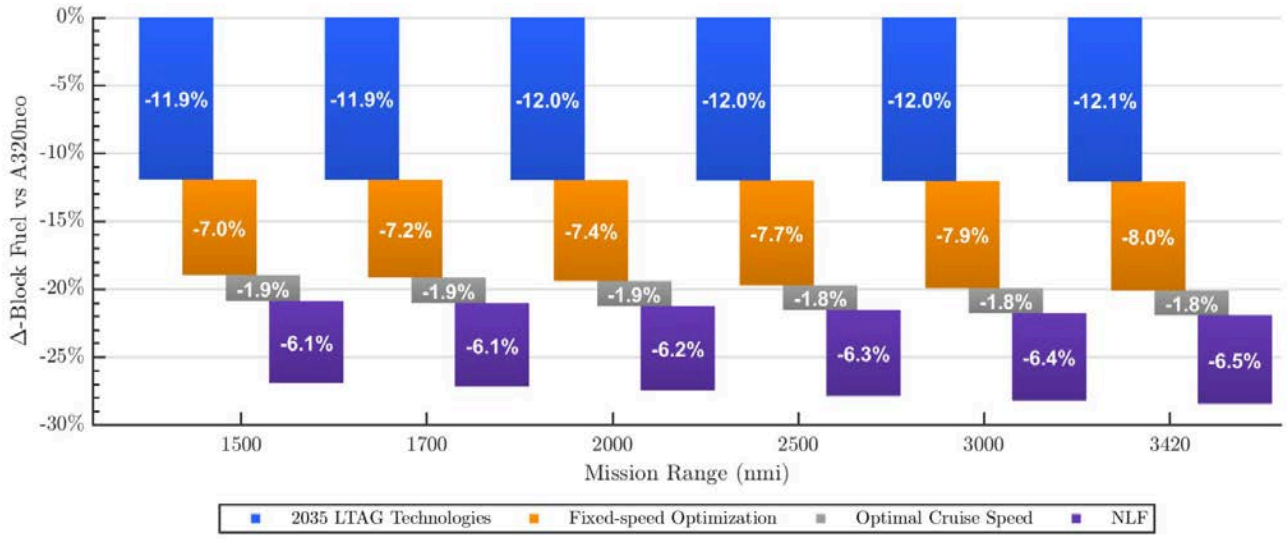


Figure 15. Block fuel reduction progression through sequential optimization process. LTAG: Long-term aspirational goal, NLF: natural laminar flow.

Figure 16 shows the resulting block fuel reductions across all range-payload combinations considered. Significant reductions of around 30% in block fuel weight are exhibited across all ranges for 150 passenger configurations, with the greatest reduction occurring with the lowest range of 1,500 nmi. The configurations at the upper limits of passenger capacity and range could not satisfy all design constraints and were subsequently omitted. Figure 17 presents the corresponding improvements in fuel-per-passenger-mile of optimized candidate vehicles; this figure was constructed to facilitate a direct comparison of the 150 passenger-3,420 nmi range TRA baseline with the final optimized vehicles. A region of desirability is displayed for combinations of increased passenger counts and reduced design ranges from that of the TRA baseline, with the greatest efficiency improvement of 35.8% shown by the 190 passenger-1,500 nmi model.

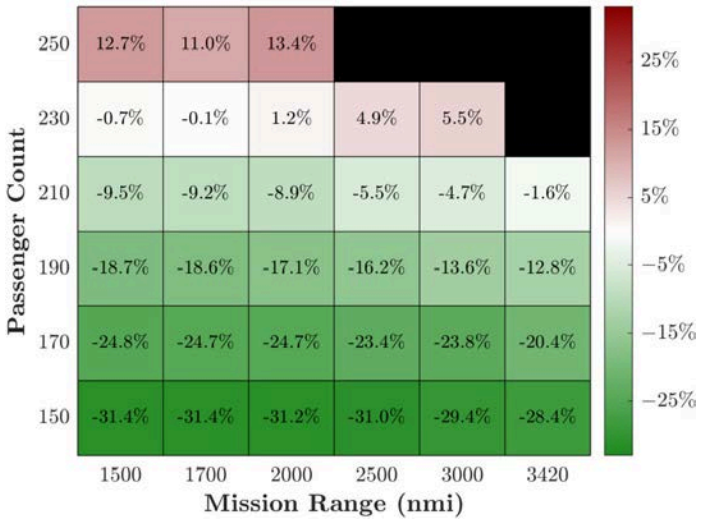


Figure 16. Block fuel reductions of optimized designs sized with respect to various combinations of design ranges and payloads compared to 150-pax TRA baseline.

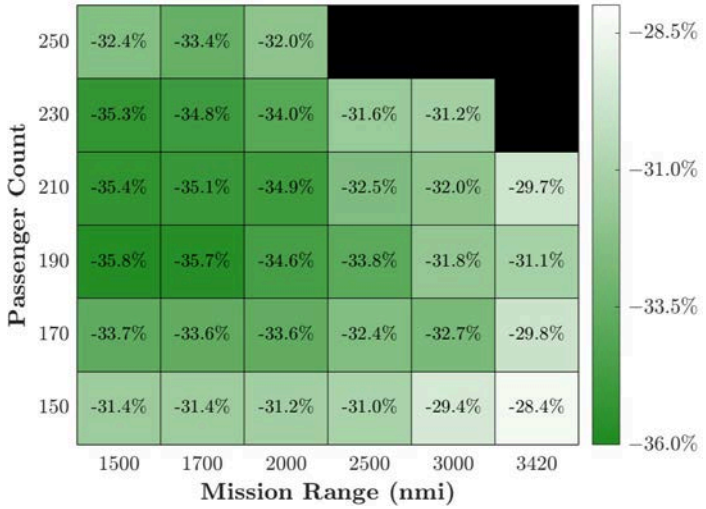


Figure 17. Fuel-per-passenger-nautical-mile reductions with respect to the 150-pax TRA baseline vehicle.

With a similar step-by-step optimization process, optimized vehicles for cumulative noise minimization were also produced. Figure 18 illustrates the cumulative noise reductions achieved, the greatest magnitude reduction stemming from integration of 2035 LTAG technologies, which reduce cumulative noise levels across the three certification recording locations by 9.0 effective perceived noise in decibels (EPNdB). Resizing the candidate vehicle with airframe and engine cycle design variables optimized reduces the cumulative noise by a further 6.4 EPNdB. Adding optimization of cruise speed alongside aircraft resizing delivers a more modest reduction of cumulative noise by 1.3 EPNdB, while NLF technology integration delivers a minute reduction of 0.1 EPNdB as turbulent airflow over lifting surfaces is deterred.

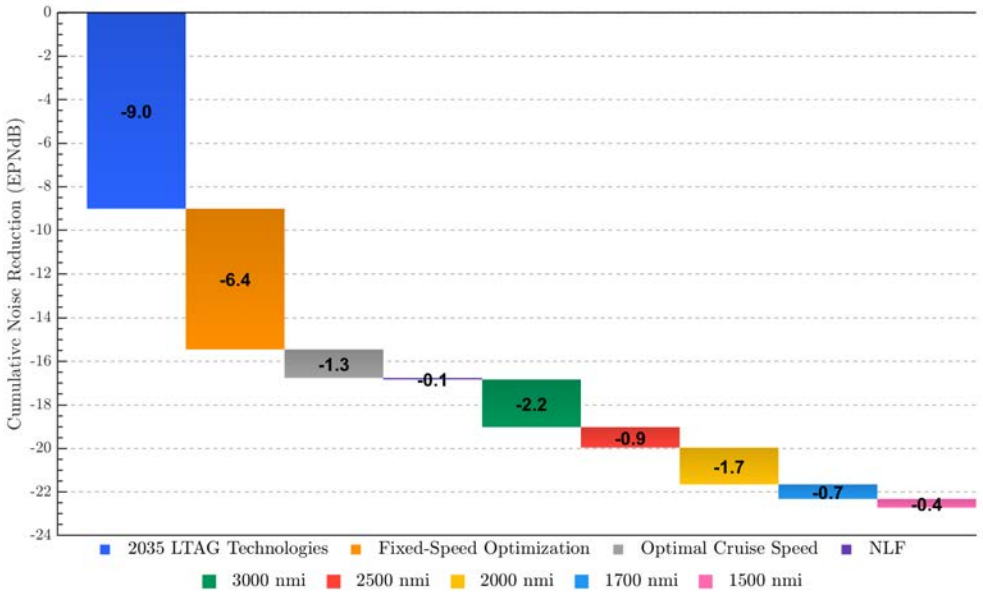


Figure 18. Cumulative noise reduction progression through sequential optimization process.

Part 2 - Fleet-Level Assessment

The 51 scenarios were executed twice, resulting in two sets of results corresponding to the two options of adjusting the number of operations. These options differ in whether a penalty factor is applied to simulate realistic daily schedule



demand. Option 1 represents an optimistic case in which the number of operations decreases directly in proportion to the increase in passenger capacity while maintaining baseline passenger flux. Alternatively, Option 2 includes a relatively harsh operations penalty, reflecting the operational reality that additional flights may be required to meet demand patterns, with the reality likely to fall between these scenarios. Figure 19 shows the implementation of Options 1 and 2 for increasing passenger count. The replacement percentages for 150-passenger aircraft align with the baseline as capacity remains unchanged. As passenger capacity increases, replacement percentages decrease relative to the baseline, but when Option 2 is enabled, some of the reduced replacement percentage is reverted, with the differential between Options 1 and 2 expanding as passenger capacity increases. The delta between the two options is 0% for 150 passenger configurations, about 5% for 175 passengers, and nearly 20% for the 250 passenger configurations. Option 1 yields lower replacement percentages, while option 2 produces slightly higher values by accounting for operational and scheduling needs.

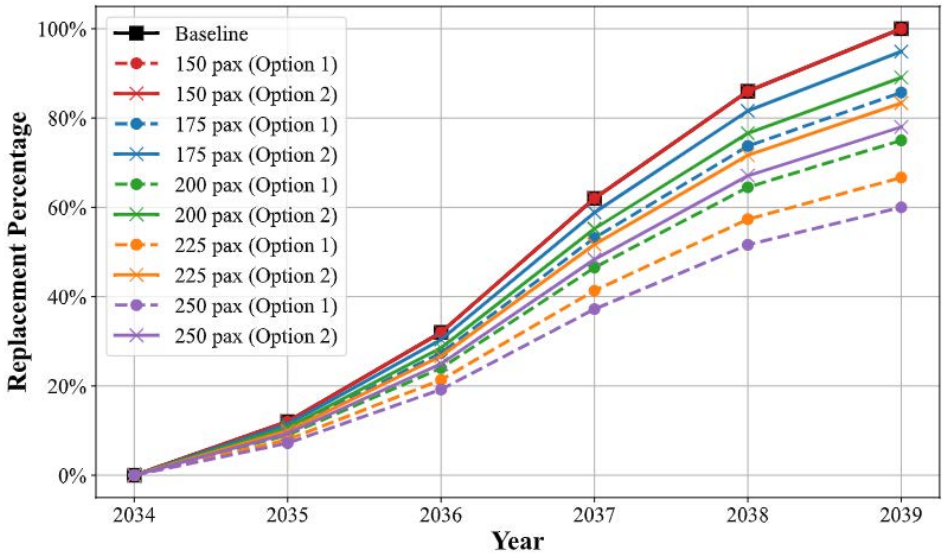


Figure 19. Operation replacement percentages for different passenger capacities.

The environmental benefits of introducing optimized aircraft to global fleets were evaluated through cumulative fuel-burn impacts for LSA, SSA, and global fleets across all replacement scenarios. The first set of figures portray the fuel burn changes when optimized vehicles replace only the LSA class. The second set portrays the changes when optimized vehicles replace both LSA and SSA classes, where the LSA fleet fuel burn changes are plotted with solid lines and the SSA fleet changes are plotted in dashed lines. The third set shows the global change for two replacement assumptions, with the solid lines representing only the LSA class being replaced, and the dashed lines showing both LSA and SSA classes being replaced.

In Figure 20 and Figure 21, two clear patterns are visible. The first is that the benefits of LSA-class fuel burn reduction, which would also be global as no other vehicle is being replaced, peak at 2,000 nmi for both the penalized and penalty-free options when passenger count is increased. The previous year's results showed that benefits for 2,000 nmi and 2,500 nmi vehicles were nearly identical, with the latter only slightly greater. However, those results were evaluated only at the 150-passenger size, included here as well. When passenger count is increased, the 2,000 nmi vehicle shows a greater benefit. With Option 1, the vehicle optimized for a 2,000 nmi and 200 passenger design mission shows the greatest benefit of about 16.8%. The second observation is that the penalty factor impacts the higher passenger capacity vehicles to a greater degree, and as the passenger count increases, the benefit loss deteriorates. At $p = 0.25$, this results in the new best-performing vehicle being optimized for a 2,000 nmi and 175 passenger design mission. When p increases, the passenger capacity of the optimal design lowers as the benefit of increasing passenger count diminishes, as the negative impact of operating a larger vehicle remains, while the benefit of operating fewer missions becomes less potent.

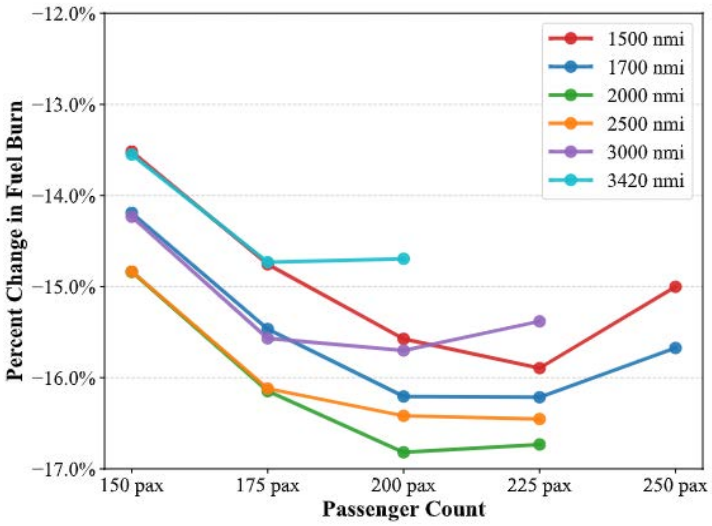


Figure 20. Cumulative LSA fleet fuel-burn reduction compared to the baseline scenario (Option 1, no penalty factor)

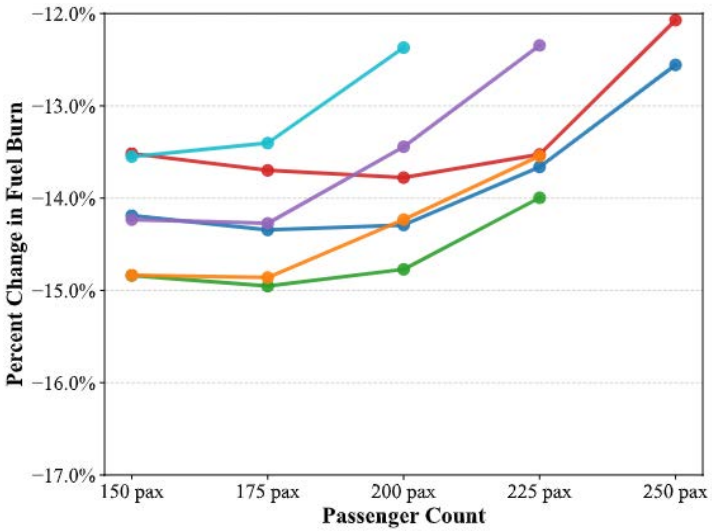


Figure 21. Cumulative LSA fleet fuel-burn reduction compared to the baseline scenario (Option 2, $p = 0.25$)

Then, when both LSA and SSA vehicles are replaced by the new designs, new insights arise from the impact within the SSA class and its differentiation from LSA trends, as shown in Figure 22 and Figure 23. As SSA vehicles are smaller than LSA vehicles, introducing higher-capacity designs yield an even stronger effect. Equal passenger flux can be met with substantially fewer operations, amplifying fleet-level benefits. Consequently, the best-performing optimized design shifts toward larger-capacity designs. In Figure 23, it can be seen that SSA-class benefits maximize with a passenger count of 225 for ranges of 1,500, 1,700, 2,000, and 2,500 nmi, with 1,500 nmi displaying the greatest improvement, achieving a nearly 22% SSA-class fuel burn reduction. However, this strong influence of payload capacity also increases the effect of the penalty factor. When the penalty factor is applied, the optimal point shifts significantly to the 175-passenger, 2,000-nmi design, indicating the greater operational penalties imposed on very high-capacity aircraft.

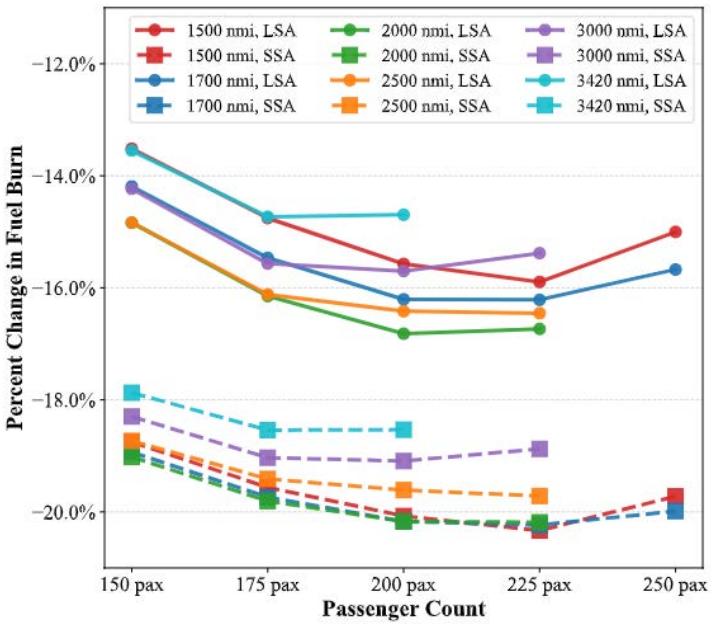


Figure 22. Cumulative large single aisle (LSA) and small single aisle (SSA) fleet fuel-burn reductions compared to baseline (Option 1, no penalty factor).

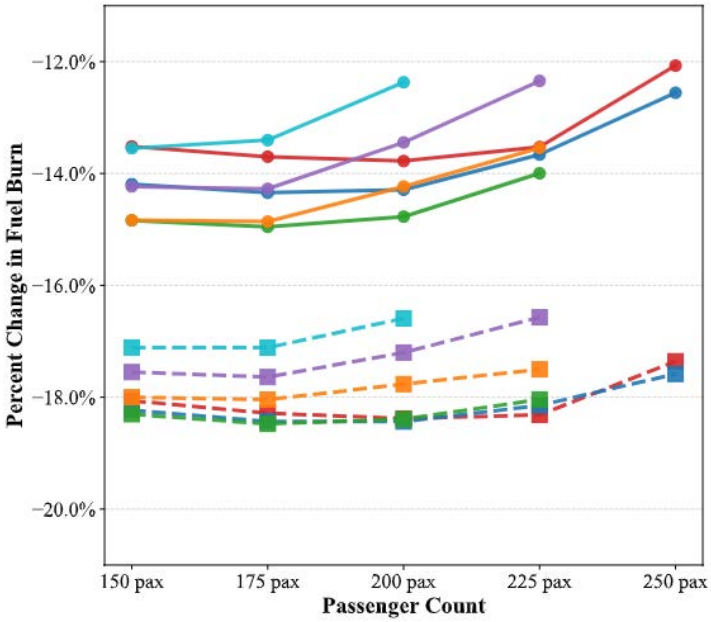


Figure 23. Cumulative large single aisle (LSA) and small single aisle (SSA) fleet fuel-burn reductions compared to baseline (Option 2, $p = 0.25$).

Lastly, the global fuel burn reduction is evaluated across all seat classes, comparing scenarios with and without SSA replacement and using both operational adjustment options. The results are provided in Figure 24 and Figure 25. Under



Option 1, the maximum fuel burn reduction is approximately 7.0% when replacing LSA aircraft only, and 7.6% when replacing both LSA and SSA, with the optimal point occurring at 200-passenger, 2,000-nmi vehicle. This outcome aligns with expectations. Although SSA benefits slightly more from higher-capacity designs, the LSA class dominates the market, so that global optimum closely follows the LSA trend. A similar pattern appears under Option 2, where the optimal design shifts to the 175-passenger, 2,000-nmi vehicles. This shift is again driven primarily by LSA class, while the imposed penalty factor reduces the overall benefit, yielding a maximum fuel burn reduction of about 6.8%.

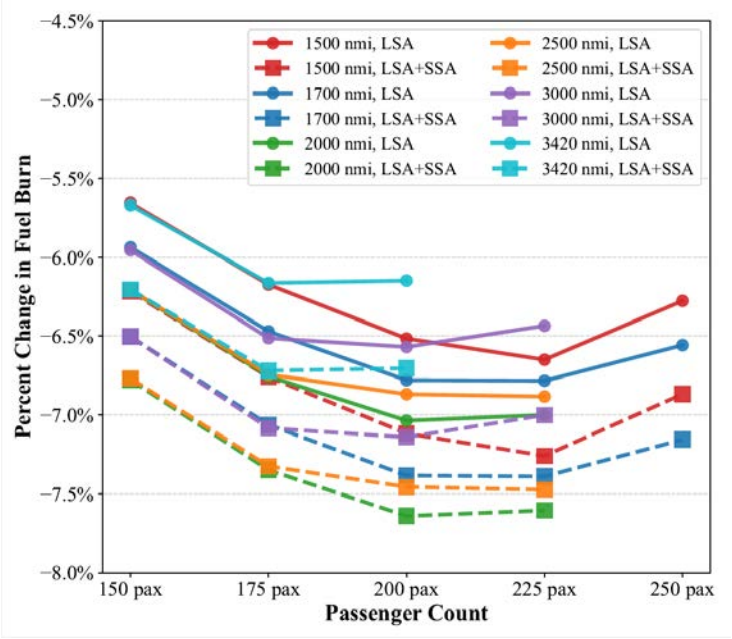


Figure 24. Global fuel burn reduction compared to baseline scenario (option 1, no penalty factor). LSA: large single aisle, SSA: small single aisle.

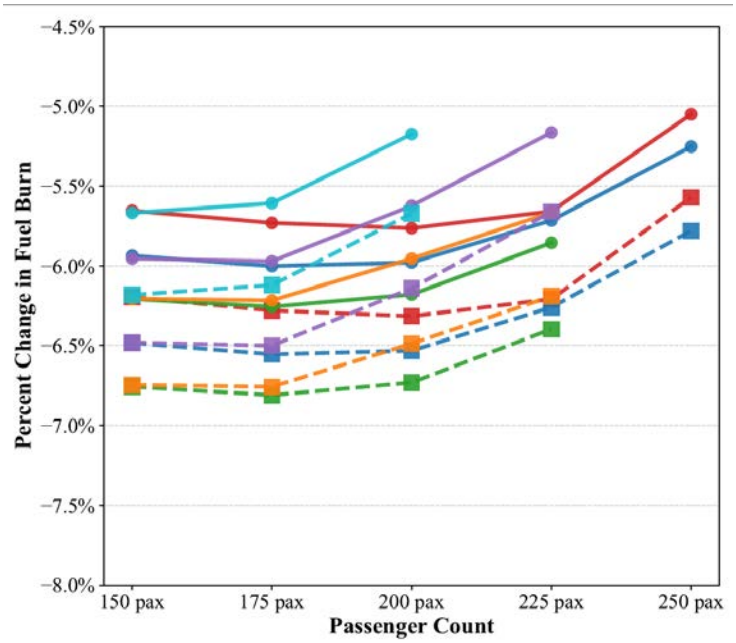


Figure 25. Global fuel burn reduction compared to baseline scenario (option 2, $p = 0.25$).). LSA: large single aisle, SSA: small single aisle.

Publications

Journal Article

Ergan, T., Parashar, A., Xie, J., Cai, Y., Kirby, M., Gladin, J., & Mavris, D. (in review). Design and Fleet-Level Assessment of Next-Generation Single-Aisle Aircraft with Reduced Range and Cruise Speed. Submitted to *Journal of Aircraft*.

Conference Proceedings

Cheng, Y., Ergan, T., Xie, J., Kirby, M., Gladin, J., & Mavris, D. (2026, June 8-12). *Fleet-Level Assessment of Mission-Optimized Next-Generation Single-Aisle Aircraft with Varying Payload*. Submitted to AIAA Aviation 2026 Forum.

Cocoves, N., Ergan, T., Benhissoune, S., Cai, Y., Gladin, J., & Mavris, D. (2026, June 8-12). *Assessing Impacts of Design Range and Payload on Next-Generation Single-Aisle Transport Fuel Burn and Noise*. Submitted to AIAA Aviation 2026 Forum

Cheng, Y., Ergan, T., Cocoves, N., Xie, J., Cai, Y., Kirby, M., and Mavris, D. (2026, January 12-16). *Rapid Fuselage and Cabin Sizing Method for Commercial Transport Aircraft Design*. Accepted in AIAA SciTech 2026 Forum. To be published.

Ergan, T., Parashar, A., Xie, J., Kirby, M., & Mavris, D. (2025, January). Fleet-level and global emissions impact analysis of mission-optimized next-generation single-aisle aircraft. *AIAA SciTech 2025 Forum*, AIAA 2025-2168. https://doi.org/10.2514/6.2025-2168

Patel, D., Ergan, T., Cai, Y., Gladin, J., & Mavris, D. (2025, January). Performance assessment and mission-based optimization for next-generation single-aisle aircraft conceptual design. *AIAA SciTech 2025 Forum*, AIAA 2025-0001. https://doi.org/10.2514/6.2025-0001

Outreach Efforts

- Attended ASCENT biannual meetings.
- Presented Performance assessment and mission-based optimization for next-generation single-aisle aircraft conceptual design and Fleet-level and global emissions impact analysis of mission-optimized next-generation single-aisle aircraft at the AIAA SciTech 2025 Forum, Orlando, Florida (January 6-10, 2025).

Awards

None.



Student Involvement

This task involved five graduate students: Tuna Ergan, Yutong Cheng, Nicholas Cocoves, Ty Mancao, and Salma Benhissoune.

Plans for Next Period

- Update the passenger capacity design points with smaller increments for a denser passenger-range combination array and re-performing both the vehicle-level and fleet-level analysis, as the limited feasibility for high passenger count-high range combinations a limit proper characterization of higher range and payload optima.
- Continue investigating relaxed constraints study, possibly as enabled by other sets of emerging technologies like folding wingtips eliminating wingspan as limiting constraint, with intention of achieving full feasibility across selected design points.
- Expand fleet-level analysis developments to allow comparisons of and across different novel and conventional architectures and configurations to support development-level trade-off studies.
- Investigate incorporation of fleet-level output metrics in the optimization study as part of work towards achieving fleet-informed vehicle design and optimization.

Task 3 - Exploring Physics-Based Boundaries of the Possible

Georgia Institute of Technology

Objective

The objective of this task is to examine the physics-based limitations of business-as-usual turbofan architecture. This type of study would aid the FAA in understanding the boundaries of the possible, rather than building from a baseline by applying specific individual technologies that benefit efficiency. Depending on any follow-on actions from the LTAG task group analyses, this task may also include the identification of barriers for future ACA and their propulsion systems, or additional supporting analysis.

Research Approach

Step 1 - Engine Materials

Advanced composite materials and improved manufacturing processes are expected to not only enable the engine components to sustain higher pressure ratios and temperatures but also reduce the overall engine weight. This task investigates engine materials that increase the maximum temperature limit and provide weight savings. These material technologies include ceramic matrix composite (CMC) vanes, CMC exhaust core nozzle, polymer matrix composites (PMC), 1,500°F hybrid disk, 1,500°F non-contacting seal, advanced polymer matrix disk, lightweight CMC liner, advanced thermal barrier coatings, advanced turbine alloys, PMCs, and NASA GRX-810.

Advancements in Environmental Barrier Coatings (EBC) have enhanced the durability of CMCs, allowing lightweight CMC liners to function effectively in high-temperature, high-stress environments up to 3,159°R (NASA, n.d.). The CMC exhaust core nozzles can operate at temperatures up to 1,960 R for oxide/oxide CMC (Heim et al., 2013a). This allows the engine to extract more energy from combustion. CMC vanes provide higher temperature capability than conventional high-pressure turbine (HPT) vanes. They can withstand higher temperatures of up to 3,160 R without the need for extensive cooling (Heim et al., 2013b).

The hybrid disk is a 15 µm grain size low-solvus, high-refractory (LSHR) superalloy bore, and a new NASA low density single (LDS) crystal rim superalloy. The materials are tailored to meet the structural requirements of a disk with increased maximum operating temperature of 1,500°F for future high 50+ OPR engines, compared to the current 1,300°F maximum operating temperature (Hathaway et al., 2013).

The advanced polymer matrix disk made of single crystal superalloys offers improved mechanical properties and higher temperature capabilities. This disk increases maximum high-pressure compressor (HPC) exit temperature to 1,400°F. The single crystal nickel based-superalloy of the disk rim will be bonded to the powder metallurgy disk alloy with 1,400-1,450°F temperature capability creating an advanced hybrid disk system with up to 1,500°F temperature capability (Misra, 2012).



The advanced thermal barrier coatings (TBC), typically ceramic-based, support higher turbine inlet temperatures. They reduce the need for excessive cooling air by increasing the allowable metal temperature of the HPT component by 300°F (Padture & Gell, 2003). Advanced TBC systems have demonstrated increased T4 max up to 3,002°F, which is far beyond the current state-of-the-art baseline Yttria-stabilized zirconia (ZrO_2-Y_2O_3) thermal barrier and Barium Strontium Aluminum Silicate (BSAS)/mullite+BSAS environmental barrier coating capabilities (Zhu et al., 2008).

The advanced turbine alloys are nickel-based superalloys that operate at higher temperatures while maintaining mechanical integrity, allowing for increased turbine inlet temperatures (TIT). Specifically, these superalloys increase maximum HPT and low-pressure turbine (LPT) vane and blade temperatures by approximately 90°R from their baseline temperature (MacKay et al., 2009; Nathal, 2009).

Polymer matrix composites offer weight reductions, specifically to fan blades. PMCs made with PMR-15 resin have been incorporated in the blades of military engines since they have a continuous use temperature between 550°F to 600°F (McDanels et al., 1986; Wei et al., 2024). RP-46 high temperature polymide resin is NASA's advanced alternative, initially capable of withstanding 371°C (700°F+), but Navy SBIR independent testing showed that it could withstand temperatures up to 2,300°F (Langley Research Center, 2009).

The NASA **G**lenn **R**esearch Center e**X**treme temperature alloy (GRX-810) was developed using Integrated Computational Materials Engineering (ICME). GRX-810 is an oxide dispersion strengthened (ODS) alloy designed for sustained use at 900-1,200°C with high strength and 100 times stress rupture capabilities (Gradl et al., 2024). GRX-810 can endure higher temperatures and stress and can last up to 2,500 times longer compared to other nickel-based alloys. It also has about four times the tensile strength before breaking and twice as resistant to oxidation damage when exposed to oxygen-rich environments at high temperatures (Newbacher, 2024).

As part of the materials evolution literature review, historical thermal trends were analyzed to understand how turbine inlet temperature (T4) has progressed across generations of civil and military gas turbine engines. Publicly available temperature data were obtained from numerous sources to (1) inform the calibration process for engines included in this study and (2) improve prediction accuracy for future propulsion systems by constraining T4 to physically realistic values. Incorporating these dataset-driven temperature bounds reduces the degrees of freedom in the calibration process, thereby preventing nonphysical cycle solutions and enabling more accurate models. Figure 26, adapted from Heidmann (2011), illustrates the increasing T4 capability enabled by advancements in materials and cooling technologies over the last century, providing a valuable reference for establishing credible thermal limits during engine model development.

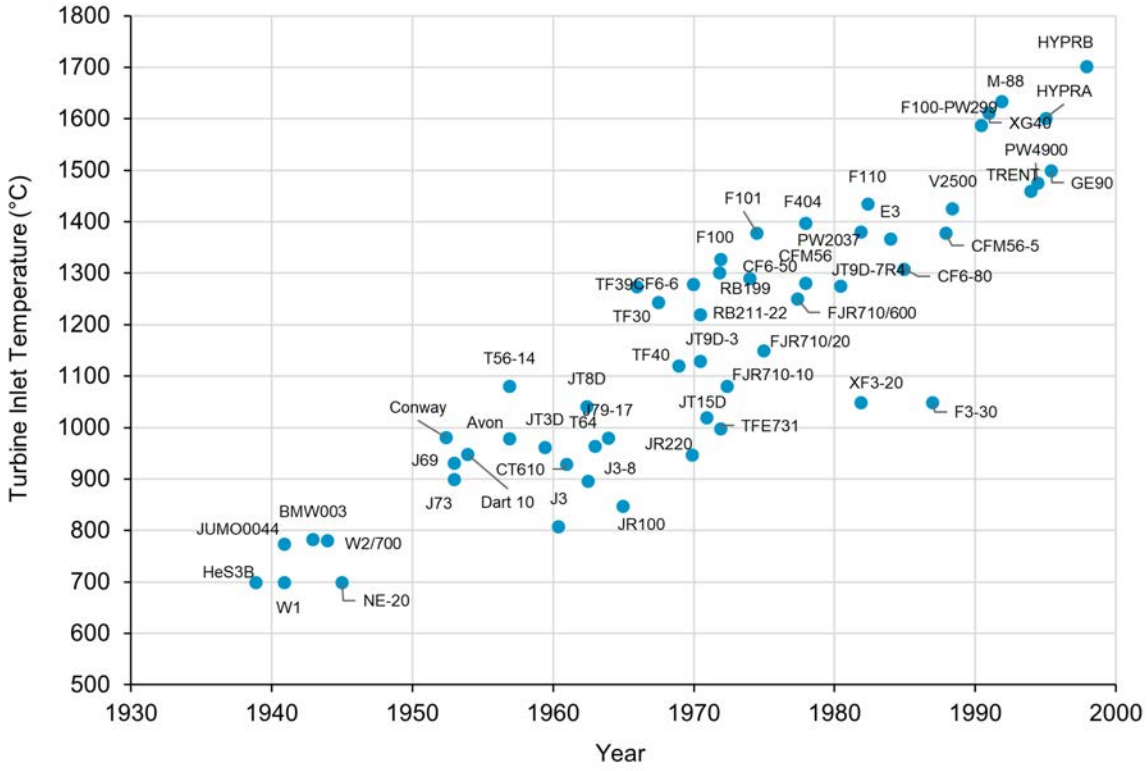


Figure 26. Engine thermal trends (turbine inlet temperature, T4).

To improve the accuracy of HPT blade temperature estimates, the evolution of material temperature capabilities was examined using data obtained from multiple published sources. The review covers historical and current turbine blade materials—including nickel-based superalloys, CMCs, titanium matrix composites, and PMCs as well as thermal and environmental coating systems. Figure 27, adapted from Misra et al. (2013), summarizes the progression of nickel-based superalloy temperature capability, highlighting the steady increase in allowable blade metal temperatures over time.

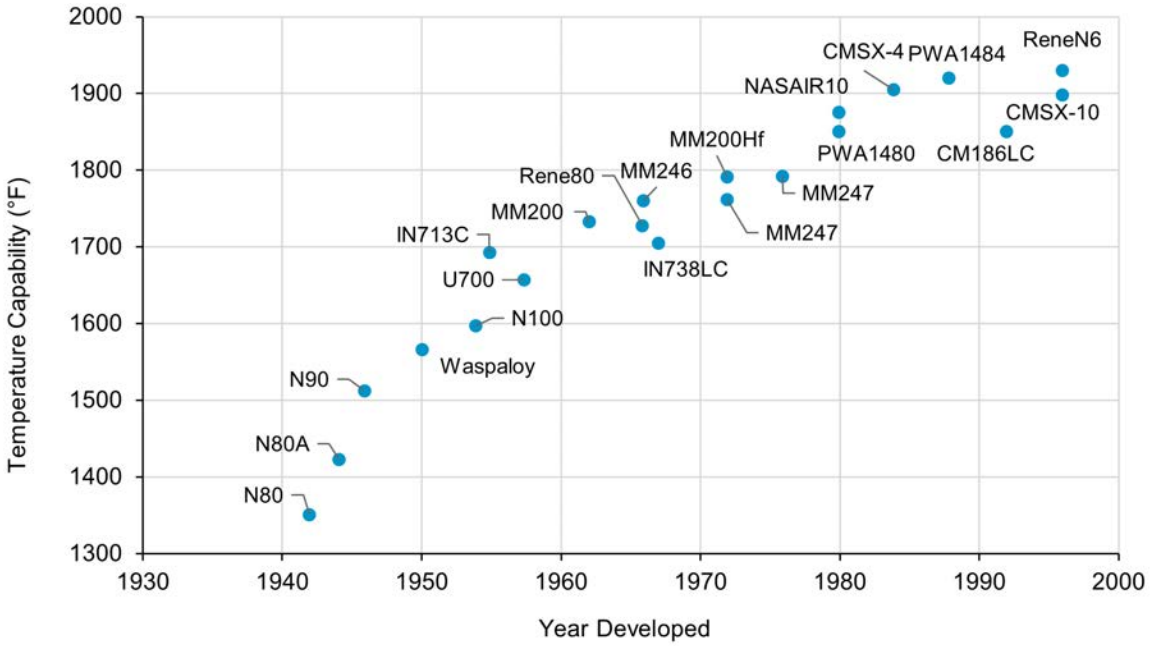


Figure 27. Temperature capabilities of nickel superalloys for turbine blade.

Step 2 - Engine Efficiency Improvement

With the advancement in engine design methods, engine materials, and engine manufacturing process, it is expected the thermal and propulsive efficiencies of gas turbine engines will be improved over the next few decades. To determine the possible performance boundary of the turbofan architecture, it is necessary to quantify the potential improvements in engine component efficiencies. The ICAO LTAG Report Appendix M3 Technology Subgroup Report (ICAO, 2022) provided a projection of efficiencies of engine core components in the years 2030, 2040, and 2050. The projection was made for different classes of aircraft, and for each class year, there are three levels of confidence: (1) conservative, (2) medium, and (3) aggressive. This task takes the 2050 aggressive prediction as the reference to maximize the improvements in core efficiencies to explore the boundary. Table 7 compares the efficiencies of engine components between the 2050 aggressive projection and the baseline Airbus A320neo model.

Table 7. Engine components' efficiencies. HPC: high-pressure compressor, HPT: high-pressure turbine, LPC: low-pressure compressor, LPT: low-pressure turbine).

Component	Baseline Airbus A320neo Engine Model	LTAG 2050 Aggressive Prediction	Improvement
Fan (adiabatic)	92.5%	93.4%	+0.9%
LPC (polytropic)	91.5%	93.3%	+1.8%
HPC (polytropic)	91.4%	93.3%	+1.9%
HPT (adiabatic)	89.0%	90.7%	+1.7%
LPT (adiabatic)	91.1%	93.1%	+2.0%

Propulsion technologies that contribute to advancement in engine design methods leading to improvement in engine component efficiencies include advanced compressors, advanced turbines, and active flow control integrated into the compressor and turbine. Advanced compressors and turbines are primarily designed to improve efficiency, performance, and durability using state-of-the-art materials, aerodynamics, and control mechanisms to achieve high-pressure ratios and



minimize energy losses. For the compressor, active flow control manages the boundary layer and reduces separation in both subsonic and supersonic conditions by adjusting the internal flow path. Pinto & G. (2024) demonstrated that active flow control techniques, such as tip injection, can improve the stall margin of compressors by 14.26% using a 0.3% total mass flow rate injection (Pinto & G, 2024). In a turbine, flow control increases loading and efficiency by injecting air around the turbine blades and near the end wall, in turn reducing the turbine stage count.

Step 3 - Small Core Size Effect

One contributing factor to the engine component efficiency is the core size effect. As the turbofan engine continues to strive for higher bypass ratios to promote propulsive efficiency, the core size is becoming smaller. Meanwhile, future airframe technologies will reduce the aircraft drag and the thrust required, encouraging smaller size engines for future aircraft. However, as the engine core becomes smaller, rotor tip clearance, knife-edge seal clearances, and edge thicknesses cannot be scaled down with the engine core size. All these non-scalable features introduce penalties to HPC efficiency. Figure 28, adopted from Evan et al. (2022), illustrates how HPC polytropic efficiency is affected by the engine core flow rate. The orange curve represents the current technology level, which is applied on the baseline A320neo model. The green curve is shifted from the orange curve by 25% improvement in HPC efficiency, as predicted by the LTAG study. This curve is utilized in the 2050 narrow-body aircraft engine model. The blue curve represents an ideal scenario where clearances can be scaled with the core size, which is used in a practical ideal engine model created in this task. All these curves are digitalized in EDS.

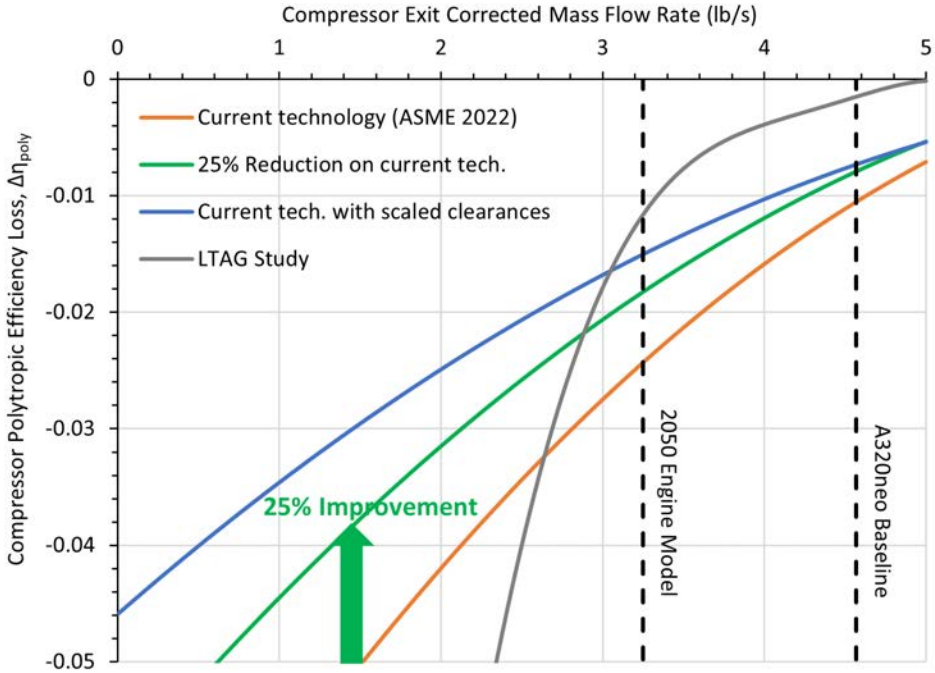


Figure 28. Engine core size effect on HPC.

Turbine size-effect losses were examined using publicly available studies on corrected mass-flow scaling and stage-level efficiency degradation. Data from Bettner's component arrangement studies and the more recent "Educated Guess" framework developed by the German Aerospace Center were obtained to characterize how HPT efficiency varies with turbine entry corrected mass flow rate. The Educated Guess study defines an efficiency envelope based on the Grieb coefficient (λ), from which stage-specific curves are selected, while the Bettner (1990) studies provide historical and projected technology trends. All curves were normalized using a reference large-core flow rate of 10 lbm/s and incorporated into EDS to model turbine size-effect penalties within the design loop. Figure 29 presents these turbine size-effect loss curves and illustrates how reductions in turbine core flow introduce measurable efficiency penalties.

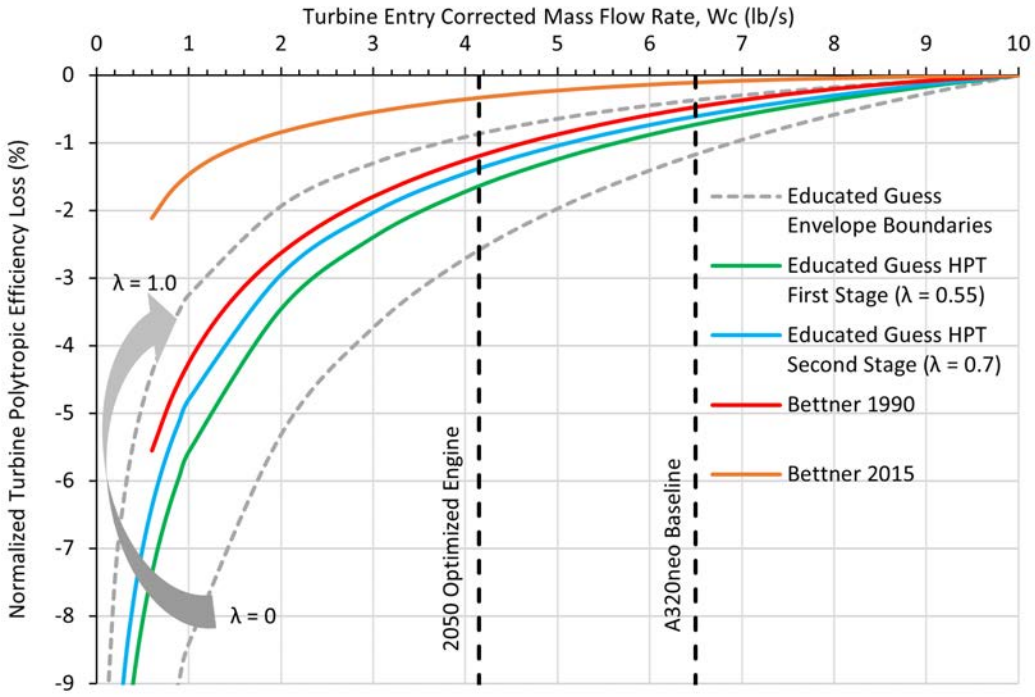


Figure 29. Engine core size effects on HPT.

Within the engine core, clearances can become significant during operation and allow more flow to bypass the blades. To meet the ICAO LTAG 2050 aggressive predictions for the compressor, implementing an active compressor clearance control mechanism can reduce clearance by adjusting the size of the casing. This would increase the compressor efficiency by reducing the amount of flow leakage up to 33% for a low-speed compressor cascade rig due to a Normal Synthetic Jet and Bae (2001). Active clearance control works by dynamically adjusting the position of the casing relative to the blade tip and maintains a certain clearance for each stage of the flight. For the turbine, an active clearance control would allow for dynamic tip clearance adjustments in response to thermal and mechanical deformations during engine operation. This would improve turbine efficiency by minimizing leakage losses while preventing blade-tip rubs. However, the efficiency improvements depend on actuator performance.

Step 4 - Aircraft Systems Impacts

Engine efficiency is also affected by the aircraft systems that consume pneumatic, hydraulic, electric, and mechanical power. These systems include but are not limited to environmental control system (ECS), ice protection system (IPS), aircraft control system, and avionic system. The pneumatic power is mainly provided by the bleed air extracted from the engine compressor. The hydraulic and electric power are mainly converted from the mechanical power extracted from the engine shaft. With the technological improvements in aircraft equipment systems and secondary power distribution systems, it is expected that less bleed air and power extractions will demand from the engine, improving the engine propulsive efficiency. The LTAG study predicted that the thrust-specific fuel consumption (TSFC) of the narrow-body aircraft engine at the aerodynamic design point would be reduced by 1.67% due to the improvements in bleed and power extraction, as listed in Table 8. Furthermore, enabled by the electrification of aircraft systems, bleed air from the engine compressor may not be needed. In the bleedless architecture, aircraft systems are mainly driven by the electric power converted from the mechanical power extracted from the engine shaft. Table 8 presents the engine TSFC improvement at different power extraction settings when the bleedless architecture is applied.



Table 8. Aircraft systems impact on engine TSFC.

Architecture	Bleed	Power extraction	TSFC change
Baseline A320neo	2	75	--
2050 engine model	1.25	50	-1.67%
Bleedless architecture	0	250	-2.57%
	0	225	-2.76%
	0	200	-2.96%

Step 5 - Engine Cycle Optimization
The implementation of engine cooling technologies has a direct impact on an engine cycle by lowering compressor exit temperature (T3) and increasing turbine inlet temperature (T4). Compressor intercoolers increase T3 max constraint by 50-60 K before the compressed air enters the combustion chamber. Cooled cooling technology enables the handling of high heat fluxes, critical for engines, avionics, and other components in modern aircraft. With its implementation, the HPC bleed air is cooled by around 4.44%, so that the turbine inlet temperature, T4, increases from 1,860 K to 1,910 K (Zhang et al., 2022). Active film cooling allows for higher turbine inlet temperatures, which exceed 1,900 K/3,420°R in modern engines by decreasing the convective heat transfer to the turbine components such as guide vane, blades, turbine casing, and exhaust nozzle (Acharya & Kanani, 2017). As mentioned in Step 5, advanced engine materials also impact the engine cycle. The 1,500°F hybrid disk allows for a 50+ overall pressure ratio (OPR), and the advanced TBC systems have demonstrated an increased T4 max up to 3,462°R.

To maximize the benefits of these engine technologies, the engine needs to be resized with optimal cycle parameters. In this task, the engine cycle parameters include bypass ratio (BPR), OPR, fan pressure ratio (FPR), high-pressure compressor pressure ratio (HPCPR), and turbine entry temperature (T4max). The optimization process follows the steps described in Task 2, where surrogate models are developed based on the responses of the DoE sample cases run through the EDS. The objective function is to minimize the fuel burn of the notional Airbus A320neo model at an economic mission. Table 9 presents the optimized cycle of the 2050 engine and compares it to the baseline model.

Table 9. Optimized engine cycle parameters.

Design Variable	Baseline Airbus A320neo Engine Model	Optimized 2050 Engine Cycle
BPR	11.6	14.5
OPR	45.8	61.0
FPR	1.52	1.45
HPCPR	17.0	17.5
T4max (R)	3091	3144

Step 6 - Fuel Burn Evaluation
The possible boundary of the turbofan engine is evaluated based on the aircraft-level fuel consumption at an economical mission that is most frequently flown by the narrow-body aircraft. With Steps 2 to 6 implemented sequentially, several engine models are established and integrated with the notional A320neo aircraft model. The fuel burn is evaluated at the 900-nm mission with the design payload. The fuel reductions due to efficiency improvement, size effect reduction, aircraft system architecture, engine weight, and engine cycle optimization are evaluated in a stepwise manner.

Milestones

- Finished literature review on turbofan engine efficiency, and the potential impacts of engine materials, engine cooling technologies, fan and inlet technologies, core size effects, and bleedless aircraft system architecture.
- Established 2050 narrow-body aircraft model based on the aggressive prediction made in the LTAG study.



- Created a practical ideal engine model by assuming scalable tip clearances, large-core efficiencies, and bleedless architecture on the 2050 engine model.

Major Accomplishments

The major accomplishments of this task include the evaluations of contributions of different engine technologies to the fuel burn efficiency when retrofitting the state-of-the-art aircraft with a new turbofan engine, as well as the development of a practical ideal engine model to explore the boundary of the turbofan architecture.

Figure 30 displays the reductions of the 900-nm mission block fuel when engine technologies are progressively applied to the notional PW-1127G engine. Note that the airframe is maintained as the notional A320neo model during the evaluation, while only the engine model is updated. The practical ideal engine shown in the last bar is established by assuming bleedless architecture with 200 hp power extraction and scalable tip clearances on top of the aggressive core efficiency improvement prediction, engine weight reduction, and the application of advanced engine materials. Overall, with all potential engine technologies applied and the idealized core size effect, the turbofan engine can reduce the fuel burn at the economical mission by 20.7% for the A320neo aircraft compared to the current technology level. It is seen that the core efficiency improvement has made the most significant contribution to the engine fuel efficiency, reducing the economical mission block fuel by 7.7%. Meanwhile, engine cycle optimization also has a considerable impact on the fuel burn reduction due to the increased OPR and T4max and decreased FPR.

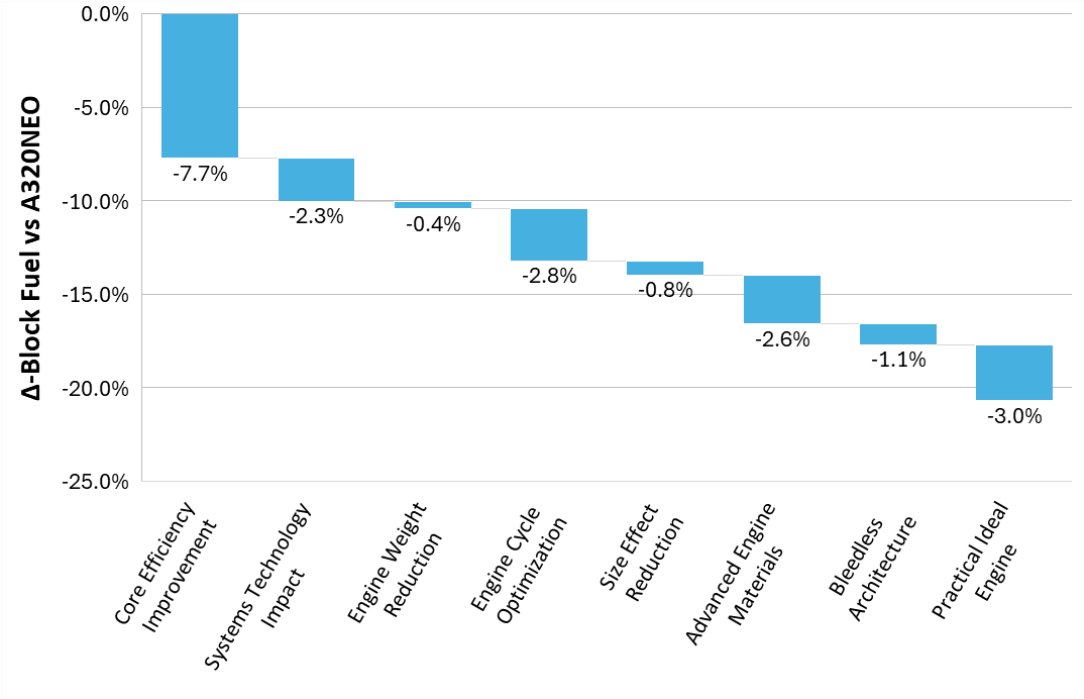


Figure 30. Potential block fuel reductions due to engine technologies.

Publications

None.

Outreach Efforts

- Attended ASCENT biannual meetings.

Awards

None.



Student Involvement

This task involves three graduate students: Cem Kocer, Emmanuella Okonkwo, and Akshiti Parashar

Plans for Next Period

- Add inlet, fan, and nozzle technologies from the FAA's Continuous Lower Energy, Emissions and Noise (CLEEN) Program and other literatures to the 2050 "practical" ideal turbofan engine model.
- Investigate the impact of engine core size on HPT efficiency.
- Develop a parametric model to quantify secondary power extraction and subsystem weights within a bleedless architecture.
- Introduce logistic regression as a data-driven method for predicting engine component polytropic efficiencies to investigate the physics-based limitations of existing and retired turbofan engines.

References

Acharya, S., Kanani, Y. (2017). Advances in Film Cooling Heat Transfer (Ch. 3, pp. 91–156). In *Advances in Heat Transfer*, (Vol. 49). Elsevier. https://doi.org/10.1016/bs.aiht.2017.10.001. Accessed 10 Mar. 2025.

Bettner, J. (1990, July). Component Arrangement Studies for an 8000 SHP Turboshaft High Technology Core. *26th Joint Propulsion Conference*, AIAA 1990-2398. https://doi.org/10.2514/6.1990-2398

Gradl, P. R., Tinker, D., Williams, B., Smith, T. M., & Kantzos, C. (2024, January). Extreme Temperature Additively Manufactured GRX-810 Alloy Development and Hot-fire Testing for Liquid Rocket Engines (AIAA-2024-0997). *2024 AIAA SciTech Forum*. https://doi.org/10.2514/6.2024-0997

Hathaway, M. D., Rosario, R. D., & Madavan, N. K. (2013). NASA Fixed Wing Project Propulsion Research and Technology Development Activities to Reduce Specific Energy Consumption. *49th AIAA/ASME/SAE/ASEE Joint Propulsion Conference*.

Heidmann, J. (2011*). Improving Engine Efficiency through Core Developments* [Conference presentation]. 49th AIAA Aerospace Sciences Meeting, American Institute of Aeronautics and Astronautics (AIAA), Orlando, Florida.

Heim, F. M., Halbig, M. C., & Salvatore, M. J. (2013a). *Evaluation of Ceramic Matrix Composite Technology for Aircraft Turbine Engine Applications* (NASA/TM-2013-10774). National Aeronautics and Space Administration, Glenn Research Center.

Heim, F. M., Halbig, M. C., & Salvatore, M. J. (2013b). *Ceramic Matrix Composite (CMC) Components for Aircraft Engines* (NASA/TM-2013-10774). National Aeronautics and Space Administration, Glenn Research Center.

ICAO. (2022). Report on the Feasibility of a Long-Term Aspirational Goal Appendix M3, Technology Subgroup Report. International Civil Aviation Organization.

Langley Research Center. (2009). *Polyimide/glass composite high-temperature insulation*. https://www.techbriefs.com/component/content/article/5002-lar-17321-1

MacKay, R., Gabb, T., Smialek, J., & Nathal, M. (2009). *Alloy Design Challenge: Development of Low Density Superalloys for Turbine Blade Applications* (NASA/TM-2009-215819). National Aeronautics and Space Administration.

McDanels, D. L., Serafini, T. T., & DiCarlo, J. A. (1986). Polymer, metal, and ceramic matrix composites for advanced aircraft engine applications. *Journal of materials for energy systems, 8*(1), 80-91.

Misra, A. K., & Greenbauer-Seng, L. A. (2013). Aerospace Propulsion and Power Materials and Structures Research at NASA Glenn Research Center. *Journal of Aerospace Engineering, 26*(2), 459–490. https://doi.org/10.1061/(ASCE)AS.1943-5525.0000325

Misra, K. (2012, October 15-18). *Durability Challenges for Next Generation of Gas Turbine Engine Materials* [Conference Paper]. AVT Symposium on Design, Modelling, Lifting and Validation of Advanced Materials in Extreme Military Environments, Biarritz, France.

NASA. (n.d.). *High-Temperature Environmental Barrier Coatings for SiC/SiC Ceramic Matrix Composites*. National Aeronautics and Space Administration, Technology Transfer Program, Patent LEW-TOPS-136. https://technology.nasa.gov/patent/lew-tops-136

Nathal, M. (2009). *High Temperature Turbine Materials*. 2009 Annual Meeting, Fundamental Aeronautics Program.

Newbacher, B. (2024). *NASA Licenses 3D-Printable Superalloy to Benefit US Economy*. National Aeronautics and Space Administration, Glenn Research Center.

Padture, N., & Gell, M. (2003). *Advanced Thermal Barrier Coatings for Industrial Gas Turbine Engines* (AGTSR Subcontract No. 00-01-SR081). Clemson University Research Foundation.

Pinto, P., & G, S. (2024). Performance Enhancement of an Axial Flow Compressor Using Active Flow Control Technique. *Cogent Engineering, 11*(1), 2380804. https://doi.org/10.1080/23311916.2024.2380804



Wei, Jiahui, Zhang, Y., Liu, Y., Wang, Y., Li, C., Sun, Z., Xu, H., Shao, H., Zhang, D., Zou, Q., Zhang, Q., Feng, J., Kong, W., Jiao, Y., & Chen, L. (2024). Advances in resin matrix composite fan blades for aircraft engines: a review. *Thin-Walled Structures, 202*, 112058. https://doi.org/10.1016/j.tws.2024.112058

Zhang, L., Xu, G., Liu, Q., Li, M., Dong, B., & Wen, J. (2022). Superiority Analysis of the Cooled Cooling Air Technology for Low-Grade Energy Utilization in Aircraft Engines. *Energy Conversion and Management, 252*, 115028.

Zhu, D., Miller, R., & Fox, D. (2008). *Thermal and Environmental Barrier Coating Development for Advanced Propulsion Engine Systems* (NASA/TM-2008-215040). National Aeronautics and Space Administration.



Project 065(A) Fuel Testing Approaches for Rapid Jet Fuel Prescreening

Washington State University

Project Lead Investigator

Joshua Heyne
Bioproducts, Sciences, and Engineering Laboratory Director, Associate Professor
School of Engineering and Applied Science
Washington State University
2710 Crimson Way, Richland, WA 99354
509-372-7461
joshua.heyne@wsu.edu

University Participants

Washington State University (WSU)

- P.I.: Joshua Heyne
- FAA Award Number: 13-C-AJFE-UD, Amendments 26, 31, 34, and 42
- Period of Performance: October 1, 2024, through September 30, 2025. Cost share is from the German Aerospace Center (DLR).
- Task:
  1. Prescreening of sustainable aviation fuels (SAF)

Investigation Team

Washington State University

Joshua Heyne (P.I.) Coordinates all team members (both ASCENT and non-ASCENT efforts) and communicated prescreening results with SAF producers.
Zhibin (Harrison) Yang (research assistant professor) Conducts Tier Alpha prediction and Tier Beta measurements.
Conor Faulhaber (PhD student) Conducts seal swell, sulfur, and nitrogen measurements
Patricia Garcia-Alfaro (undergraduate student) Conducts lubricity measurement.

Project Overview

The ASCENT Project 065A focuses on further developing the Tier Alpha and Tier Beta test methods, which can help minimize the fuel volume needed for testing and improve a fuel's potential for meeting ASTM approval criteria. Tier Alpha refers to low-volume analytical testing approaches (i.e., two-dimensional gas chromatography [GCxGC], nuclear magnetic resonance, and infrared analytical testing). Tier Beta tests focus on directly assessing the physical and chemical properties of a fuel rather than predicting properties from GCxGC methods.

Task 1 - Prescreening of Sustainable Aviation Fuels

Washington State University

Objective

The objective of this task is to develop a tiered prescreening process for new alternative jet fuels that uses low fuel volumes and will improve a fuel's potential to meet ASTM approval criteria. This work facilitates the flow of meaningful information to fuel producers when their production processes are at a low technology readiness level while simultaneously strengthening a producer's readiness for the approval process.



Research Approach

Previous annual reports summarized significant progress toward prescreening SAF candidates. The motivation, conceptual application, detailed description, and examples of this effort were described in publications in peer-reviewed journals in the first 18 months of this project. Prior to this report, the ASCENT Project 065A team has reported 18 publications. This report documents four additional peer-reviewed journal articles, published between October 1, 2024, and September 30, 2025. Citations for the articles are listed in the *Publications* section below and are provided as Appendices A-B:

- Paper 19 - "Freezing Point of Hydrocarbon Fuels from Single Species Concentrations" (Bell et al., 2025) in *ACS Energy & Fuels*. (Presented in Appendix A.)
- Paper 20 - "Upgrading of biocrude oil into sustainable aviation fuel using molybdenum carbide nanocatalysts" (Yu et al., 2025) in *Science Advances*. (This is collaboration, where WSU personnel are not the first author)
- Paper 21 - "Measurement of Spray Chamber Ignition Delay and Cetane Numbers for Aviation Turbine Fuels" (Luecke et al., 2025) in *Energy & Fuels*. (This is collaboration, where WSU personnel are not the first author)
- Paper 22 - "Geometric and Positional Isomer Effects on Ignition Behavior of Cycloalkanes: Implications for Sustainable Aviation Fuels" (Yang et al., 2025) in *ACS Energy & Fuels*. (Presented in Appendix B.)

Milestones

- Performed Tier Alpha testing a total of 470 times.
- Performed Tier Beta testing a total of 267 times.
- Determined the maximum blending ratio for 46 SAF candidates.

Major Accomplishments.

- Developed method to predict freezing points from single species concentrations resulting in one publication.
- Measured the derived cetane number in numerous fuels and mixtures resulting in one publication.
- Made many strides on improving aviation fuel blending rules, including a novel blending rule for distillation curves.
- Participated in numerous prescreening collaborations with groups at National Renewable Energy Laboratory (NREL), Massachusetts Institute of Technology (MIT), Pacific Northwest National Laboratory (PNNL), and other groups withing WSU.

Publications

Peer-reviewed Journal Publications

Bell, D. C., Boehm, R. C., & Heyne, J. S. (2025). Freezing Point of Hydrocarbon Fuels from Single Species Concentrations. *Energy and Fuels, 39*(9), 4221-4226. https://doi.org/10.1021/acs.energyfuels.4c06091

Luecke, J., Naser, N., Yang, Z., Heyne, J., & McCormick, R. L. (2025). Measurement of Spray Chamber Ignition Delay and Cetane Numbers for Aviation Turbine Fuels. *ACS Energt & Fuel, 39*(22), 10479-10487. https://doi.org/10.1021/acs.energyfuels.5c01350

Yang, Z., Faulhaber, C., Boehm, R. C., & Heyne, J. S. (2025). Geometric and Positional Isomer Effects on Ignition Behavior of Cycloalkanes: Implications for Sustainable Aviation Fuels. *ACS Energy & Fuel,* 39(38), 18641-18648. https://doi.org/10.1016/j.fuel.2024.133230

Yu, S., He, H., Summers, S., Yang, Z., Si, B., Gao, R., Song, A., Heyne, J. S., Zhang, Y., & Yang, H. (2025). Upgrading biocrude oil into sustainable aviation fuel using zeolite-supported iron-molybdenum carbide nanocatalysts. *Science Advances, 11*(26), 5777. https://doi.org/10.1126/sciadv.adu5777

Outreach Efforts

- Served as panel moderator for Chief Executive Officer (CEO) and Co-founder of Volaris, CEO and Founder of CleanJoule, Chief Sustainability Officer of Pratt & Whitney, and US SAF Ambassador (2025, July) for "Expansion and Security of Aviation Fuel Availability Globally," AIAA ASCEND, Las Vegas, Nevada. Sponsored travel.
- Presented at and participated in multiple relevant meetings, panels, and conferences.

Presentations

Heyne, G. (2024, September). *SAF Center at Paine Field* [Panel presentation]. 19th Annual Aerospace Summit, Aerospace Futures Alliance, Tacoma, Washington.

Heyne, G. (2024, September 16). Drop-in solutions to minimize aviation fuel sooting. International Civil Aviation Organization (ICAO) Symposium on non-CO_2 Aviation Emissions, Montréal, Canada. Sponsored travel.



Heyne, G. (2024, October). *Collaborating to Decarbonize Aviation* [Panel presentation]. Ohio State Sustainable Aviation Forum, Ohio State University – Columbus, Center of Aviation Studies. Sponsored travel.
Heyne, G. (2024, December). *Contrail Avoidance and Mitigation with Fuel Composition* [Meeting presentation]. Rocky Mountain Institute (RMI), Contrail Impact Task Force Meeting.
Heyne, G. (2025, August). *ART OF THE POSSIBLE: Shaping Cutting-Edge Economic Opportunity for Washington's Future!* [Panel presentation]. Washington Economic Development Association, Tacoma, Washington.

Awards
None

Student Involvement
- Conor Faulhaber (PhD student) has made many of the measurements discussed herein and commissioned some the test methods used.
- Patricia Garcia-Alfaro (undergraduate student) has contributed to the measurements discussed herein.

Plans for Next Period
- Expand testing to include numerous new testing equipment. These include combustion ion chromatography, coupled plasma–optical emission spectroscopy (ICP-OES), graphite furnace, and more.
- Publish trace polar molecules impact on lubricity in alternative jet fuel.
- Continue to develop our O-ring swell measurements to test the effects of low temperature on O-ring swell. This is in addition to the work we perform for fuel producers through Tier Alpha and Tier Beta.



APPENDIX A

Freezing Point of Hydrocarbon Fuels from Single Species Concentrations

Bell, D. C., Boehm, R. C., & Heyne, J. S. (2025). Freezing Point of Hydrocarbon Fuels from Single Species Concentrations. *Energy and Fuels, 39*(9), 4221-4226. https://doi.org/10.1021/acs.energyfuels.4c06091

Introduction

The freeze point of a petroleum-refined fuel has traditionally been regarded as a difficult property to predict with confidence. These challenges are amplified when applied to synthetic fuels. One of numerous factors contributing to this is that freezing point is very sensitive to hydrocarbon structure [1]. For example, 2-methylheptane has a freezing point below the measurement limit of the PAC 70Xi freezing point machine used in this experiment (<-88 °C) while a different C8H18 isomer, 2,2,3,3-tetramethylbutane is a solid at room temperature. This difference between their freeze points that is only attributable to structure makes methods relating hydrocarbon group type compositions to the bulk mixture freezing point unreliable. Compositional relationships from the literature have used n-alkane concentration, aromatic concentration, and distillation curve information among other properties to try to predict the freezing point, but these methods designed around petroleum-refined fuels have been ineffective when applied to alternative fuels [2,3]. Such fuels generally have similar ratios of isomers within groups, even as the group concentrations vary. Petroleum-refined fuels generally have 'smooth' carbon number distributions peaking at C11 or C12. They are primarily mixtures of n-alkanes, iso-alkanes, cyclo-alkanes, and alkyl-benzenes, made up of over 1000 different species. The specific species with the highest concentrations are almost always n-alkanes. N-Alkanes, especially high carbon number n-alkanes, have been identified qualitatively as the cause for high freezing point fuels, but this has not been translated into specific predictions [4–6].

For alternative fuels, the fuel composition can be dramatically different. For instance, many fuels are comprised of a single hydrocarbon family. Hydroprocessed Esters and Fatty Acids (HEFA) is primarily alkanes; Cycloparaffinic Kerosene (CPK-0), which is currently in the ASTM D4054 process, is composed of cycloalkanes; Synthetic Aromatic Kerosene (SAK) is only aromatics. Alternative fuels do not always have many species. Farnesane, the product of ASTM D7566 Annex A3, is composed of only one species, 2,6,10-trimethyldodecane. Iso-butanol-to-jet procedures effectively only produce two species in major quantities, 2,2,4,6,6-pentamethylheptane and 2,2,4,4,6,8,8-heptamethylnonane. These types of products necessitate a freeze point prediction model which can handle major differences in composition. In this work, we seek to develop a practical model based around the fundamental physics of freezing and mixing.

In 2022, Boehm et al. published a paper proposing a thermodynamically derived method of predicting the freezing point of a mixture [7]. One of the primary conclusions of this work is that freezing point is determined by the concentration of a single controlling species and the balance of the sample negligibly affects the freeze point. This results in another challenge observed in predicting the freezing point, that the blending rule is not linear because the relationship between freeze point and concentration is not linear and because the controlling species may differ from one fuel to another. The published empirical blending rules for freeze point prediction of blends of petroleum-refined fuels are not effective for blends of dissimilar solutions. This will be demonstrated in more detail in this paper. Alternatively, the experimental scope of Boehm et al. was limited to mixtures having a concentration of the freezing component greater than 10% by mole. Such concentrations are higher than any individual hydrocarbon in conventional jet fuel. Moreover, and in spite of being significantly simpler than a prior thermodynamically-derived model, [8] that model requires several thermodynamic property inputs such as enthalpy and entropy of fusion as well as liquid and solid phase heat capacities, which are not always readily available. Such absence of inputs makes it difficult to implement in fuel-property prediction models. Adding to this inconvenience, the Boehm model is an implicit function T=f(T,x) for which an iterative solution methodology is not always well-behaved.

Although the thermodynamic models [7,8] are impractical for complex fuel predictions, the fundamentals behind them are tractable for a simpler model. Boehm's model suggests that freezing point of a fuel is limited by the freezing point of only one molecule which implies we only need to identify and characterize that one species to get a freezing point prediction. For a given complex fuel sample, we only need to characterize the concentrations of species with high freezing points and we can apply the model to each of these species and logically select the maximum value from this set of interim predictions. Taking this a step further, we do not need to use a thermodynamic model at all to predict values. Because the



balance of the hydrocarbons in the mixture was deemed unimportant, the freeze point of species k, as a function of concentration of this species can be measured experimentally in blends with control hydrocarbons, and the resulting control curves can be used in place of the moderately complex thermodynamic model to explicitly relate freeze point of species k to its concentration in the mixture. GC×GC/FID-VUV is perfectly suited for determining concentration of individual species in complex mixtures [9]. All specific isomers with relatively large concentrations that have been seen before are included in the spectral database and will continue to grow as more species relevant to freeze point are identified.

In this work, we explore the above hypothesis expanding upon the work of Boehm et al. [7] to improve the scientific understanding of the impact of composition on freezing point. We will detail the problems associated with other freezing point models, evaluate the experimental control curve as a prediction method, and determine the accuracy of the conclusions made in Boehm et al. First, we present additional results reinforcing the theory of Boehm et al. by showing the freezing point of blends of two high freezing point species (n-tridecane and bicyclohexyl) result in a decrease in freezing point, a trait which will not be predicted in most other models. Next, we test C11-C17 n-alkanes in iso-octane to generate reference data predicting when each of these species will freeze in a mixture at various concentrations. We use these data to test the hypothesis when applied to synthetic fuels. Then, we perform tests to isolate the 2nd order effects of species interaction and blending. Finally, we leverage the results of this research to generate a 100% n-alkane fuel that passes the ASTM D1655 limit for freeze point.

Method

Principal Component Quantitation

Freezing point measurements of many hydrocarbon blends are discussed. Freezing point is measured using a Phase Technology PAC 70Xi: Cloud, Pour, and Freeze Point Analyzer, following the procedure described in ASTM D5972. The machine has a reporting resolution of 0.1 °C and can measure between -88 °C and 70 °C. 0.15 mL samples are injected into a metallic sample chamber with a reflective bottom surface which is used for reflecting light to measure diffusive light scattering. When an experiment is started, the temperature is decreased in the chamber at a rate of 15 ± 5 °C/min until the detected opacity exceeds a threshold suggesting that the sample is mostly solid. The system then begins to increase the temperature at a rate of 10 ± 0.5 °C/min. Freezing point, or more accurately melting point, is determined when the opacity returns to the original flat line observed while cooling. According to the Phase Technology product brochure, the rated reproducibility is ±0.8 °C.

In this work, tests are performed on complex fuel samples, single components, and mixtures. The complex fuel mixtures used in this work are all 'prescreening fuels' from the FAA ASCENT project 65a. The fuels are sourced from numerous fuel producers, national labs, and universities and include many different conversion pathways including hydrothermal liquefaction (HTL), HEFA, and alcohol-to-jet (ATJ). For mixtures, blending was performed by mass and converted to moles, accordingly. Most of the mixtures are using pure components where molecular weight is provided; for synthetic aromatic kerosene (SAK), the molecular weight is calculated from GCxGC data [9]. For the complex fuels, mole concentrations are measured using GCxGC-MS/FID performed by colleagues at University of Dayton Research Institute [10,11].

Results

Freezing Point Blend Rule Non-Linearity

For many applications, blending rules are desired for fuel properties. For many properties, a straight-forward scalar product between a concentration vector and a properties vector is sufficiently accurate for developing synthetic fuel assessments. The freezing point blend rule that was originally adopted by Yang et al. [12] for Tier α fuel pre-screening came from the work of Al Mulla et al. [3] (presented as the green line in Figure A-1) which utilizes a logarithmic transformation, but generally mimics a linear by volume blending rule. (Those authors claim a mean absolute error of 0.05 K for this model, but we are skeptical of this value.) The model fundamentally suggests that the addition of species with a higher freezing point than the starting mixture will increase the freezing point and vice versa. This concept strictly competes with the hypothesis of Boehm et al. This model was developed using results from blends of petroleum-based fuels. In petroleum fuels, the freezing component is almost certainly an n-alkane that is present in both mixtures. When the component that is determining the freezing point is not in both samples the model falls apart.

Boehm et al. utilized blends of relatively large concentrations (>10%) of high freezing point components (n-tridecane and bicyclohexyl) in complex fuels to support the theoretical assertions. These mixtures demonstrated that the fuel into which the freezing component is blended has little effect on the freezing point. However, in these tests, it was known that a high



freezing point component was being added to a mixture that was not expected to freeze. This work did not demonstrate the assertion that a mixture of two different solutions whose freeze points are controlled by different species can, when blended, result in a mixture with a lower freeze point than either of the preblended solutions. In Figure A-1, the freezing points of mixtures of bicyclohexyl in n-tridecane (gold line) are compared against the freezing points of bicyclohexyl (red line) and n-tridecane (blue line) in a solvent that we know will not freeze, iso-octane (2,2,4-trimethylpentane, freezing point = ~-110 ˚C). The freezing points of the neat hydrocarbons used in this work are included in Table A-1. The first observation is the difference between the green line representing the Al Mulla blending model prediction of the freezing point of the bicyclohexyl/tridecane blends compared to the experimental results of these blends. The freezing point of the blend is consistently lower than the prediction. Now, compare the experimental results of the tridecane/bicyclohexyl blends to the components individually blended in iso-octane. The freezing point of the blends closely track the greater of the blue and red lines. There is a bimodal response consistent with the hypothesis of Boehm et al.[7]. This plot emphasizes the issues with the Al Mulla blending rule and demonstrates the potential for a new method.

Table A-1. Freezing points of the pure hydrocarbons used in this study.

Name	Freeze Point, ˚C
nC8	-58
nC11	-25.5
nC12	-9.5
nC13	-5.3
nC14	5.8
nC15	9.9
nC16	18.1
nC17	21.9
Iso-octane	-108
bicyclohexyl	7.5

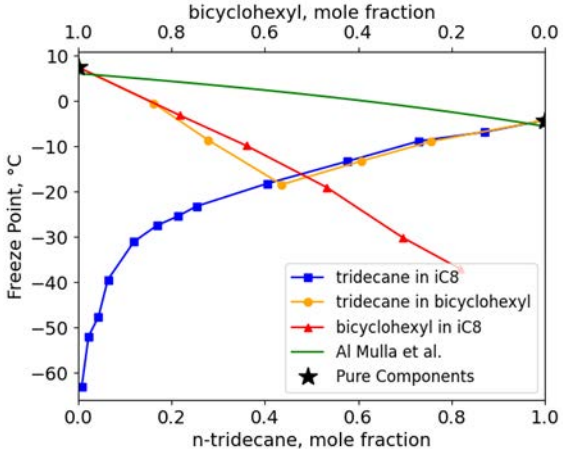


Figure A-1. Tridecane and bicyclohexyl blends are measured for freezing point and compared to the old freezing point blend rule. Additionally, 'control curves' of bicyclohexyl and tridecane in iso-octane are included to demonstrate that the freezing point of a tridecane limited mixture is the same whether it is blended in a high freezing point substance (bicyclohexyl) or a non-freezing component (iso-octane).

Data Driven Control Curve Model

n-Alkanes are known for their high freezing points and are often blamed when a fuel has a poor freezing point. This is supported by the numerous models correlating n-alkane concentration to freezing point [2,6]. Additionally, n-alkanes are typically the highest concentration single species in petroleum-refined fuels. The combination of them being high freezing point species and frequently in relatively high concentrations justify their selection as species to highlight during fuel screening. They are the focus of this research, but additional species could be included in a similar manner.

Equations A-1 – A-3 are the thermodynamically derived equations of Boehm et al.

$$T_{f,mix} = \max\left(T_{f,mix,i}(x_i, i)\right) \quad \text{(Eq. A-1)}$$

$$T_{f,mix,i} = \frac{\Delta H_{fusion,i} + x_i \times (Cp_{sol,i} - Cp_{liq,i}) \times (T_{f,i} - T_{f,mix,i})}{\Delta S_{fusion,i} + x_i \times (Cp_{sol,i} - Cp_{liq,i}) \times ln\left(\frac{T_{f,i}}{T_{f,mix,i}}\right) + \alpha \times \Delta S_{mixing}} \quad \text{(Eq. A-2)}$$

$$\Delta S_{mixing} = -R \times \frac{1}{X_j} \times \left[(1 - X_j) \times ln(1 - X_j) + X_j \times ln(X_j)\right] \quad \text{(Eq. A-3)}$$

Where T_f is freezing point temperature, 'x' is for mole fraction, subscript 'i' is for various species, H is enthalpy, S is entropy, Cp is heat capacity, and R is the ideal gas constant.

In this work, we suggest the replacement of Equations A-2 and A-3 with tabulated experimental results of species in a non-freezing solution (iso-octane). To execute this, we gather data for the freezing point of n-alkanes from n-undecane (C11) to n-heptadecane (C17) in a range of concentrations in iso-octane. The reported lines serve as control curves and represent when the various molar concentrations of these species will freeze in a more complex mixture. These control curves are plotted in Figure A-2. In Figure A-2, it is seen that the freezing point is linear with concentration on log scale. This feature allows for interpolation of the best fit line to determine the freezing point caused by a given species. One noteworthy result from this figure is that at a mole concentration of 0.2% n-hexadecane in iso-octane will fail the -40 ˚C specification limit for freezing point. This exemplifies why mixtures with n-alkanes, especially when associated with higher molecular weight, can have difficulty passing freezing point; very small quantities of n-hexadecane can have a major influence on freezing point. Another interesting observation is the similarity in the freezing point curves between even/odd pairs of n-alkanes (e.g., nC14 and nC15).

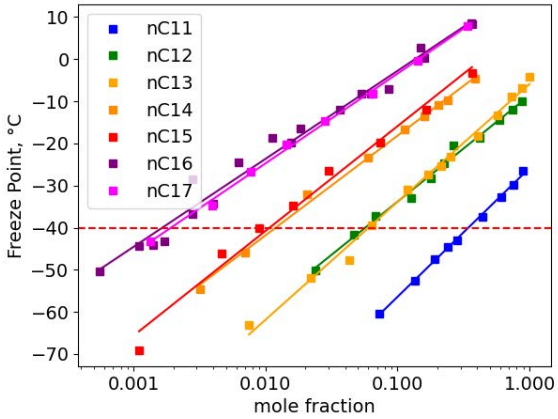


Figure A-2. Freezing point of various n-alkanes blended in a non-freezing control solvent (iso-octane). At a given concentration for any of these n-alkanes in a fuel, the point at which it will freeze in a fuel can be determined by interpolating between the reported data.



Freezing Point Prediction Accuracy

The freezing point of twenty-four sustainable aviation fuel candidates are predicted using the method described above. For consistency, all of the compositional information comes from GCxGC testing done by the University of Dayton Research Institute. The freezing point values were measured within the lab at Washington State University. The sustainable aviation fuel candidates are very diverse coming from various research pathways. Using the iso-octane control curves from Figure A-2 as the prediction, Figure A-3 shows the parity plot of the predicted and measured freezing points. The unity line is shown in black, and the best fit line is shown in blue. Interestingly, none of the predictions are lower than the measurement. This hints that blending with iso-octane represents an upper limit of the freeze point, which is counterintuitive. In these examples the lower freeze point 'solvent' results in a higher freezing point mixture, given the same concentration of the high-freeze-point solute. The predictions generally capture the trend well, but there is a consistent offset of about 12 ˚C. The best fit line is approximately horizontal to the unity line (slope=0.988). In addition to the freeze point experimental uncertainty, the greatest potential source of error is the quantification of the n-alkane concentrations. This prediction method is sensitive to slight changes in the limiting high-molecular-weight n-alkane concentration. There could also be errors associated with the measurement of the control curves which would propagate into these predictions as well. Moreover, it is entirely possible that the 12 ˚C offset is not indicative of an error with any of the model inputs, but rather with the assumption that the solvent characteristics such as the number of components, hydrocarbon types, density, or the presence of other solutes that may freeze at nearly the same temperature do not matter. In the next section we explore this question in more detail.

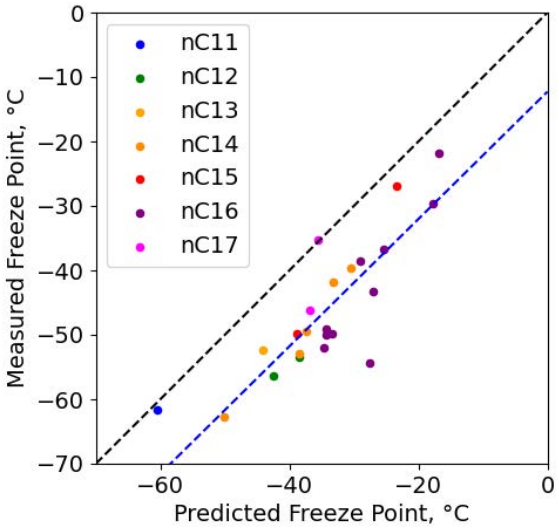


Figure A-3. Parity plot of predicted freezing points using the control curve approach compared to measured freezing points. The unity line is included in black, and a best fit line is included in blue. All of the predictions are higher than the measured freezing points.

Second Order Effects on Freezing Point

In Figure A-3, we see that the freezing point of specific species in a mixture is often lower than the freezing point of the same species in iso-octane. Affens et al. [13] observed that in ternary mixtures of n-tridecane, n-hexadecane and Isopar 150 (an isoparaffinic solvent), the freezing point at times decreased when both n-hexadecane and n-tridecane were present. These results were recreated in our lab using iso-octane in place of Isopar 150 with similar results, albeit to a lesser magnitude. The current results are shown in Figure A-4. These results suggest that the identity of components other than the first solute to freeze may have some impact on the freezing point of the solute. In this example, normal alkanes other hexadecane can depress the freeze point of hexadecane, from a 0.17% solution of hexadecane, by up to 12 ˚C depending on how much of the companion normal alkanes are present. However, the presence of a different solute (bicyclohexyl) that is predicted to freeze out of solution at nearly the same temperature as hexadecane is shown to have little impact on the freeze point of hexadecane.

Returning to the assumptions that fed into the simplified theory that is represented by Equation A-2, there are two convenient hypotheses to potentially explain the presence of a second order effect. One is that the entropy of mixing term may vary based on similarity of the solute with the remainder of the solution. The other is that of incomplete separation of molecular species between phases; meaning that perhaps the solid phase is not 100% hexadecane, but rather some solid-state, molecular-level mixture that is mostly hexadecane but partially n-tridecane and n-octane. Regardless of its cause, the magnitude of this second-order effect seems to plateau at 12 ˚C for 0.17% hexadecane solutions.

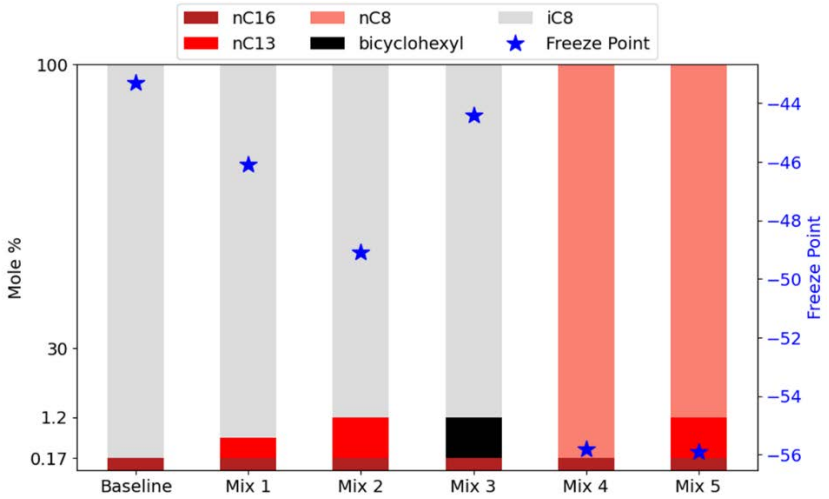


Figure A-4. Freezing points of 0.17% hexadecane in various mixtures. Composition is described by the color of the bar. NOTE: the sizes are not drawn to scale. The freezing point of each mixture is noted with the blue star. The baseline and mixtures 1 and 2 recreate the results of Affens et al.

We expanded on this analysis by exploring how different solutions impact the freezing point of the limiting component. Figure A-5 shows the freezing point of n-hexadecane when blended at various proportions into a variety of solvents. In each case the freezing point of hexadecane is linear with the log of its molar concentration. The highest of these curves is what we refer to as the first order effect, as we assume ethylbenzene has negligible impact on the purity of the freezing hexadecane and provides a bounding example for the entropy of mixing term (the α scalar) in Equation A-2. The magnitude of second order effect is the difference between the top (black, ethylbenzene) curve and any other curve. In this example, methylcyclohexane, dimethylcyclohexane, n-octane, SAK, and mixture of dodecane isomers each produce a second order effect with approximately the same magnitude, which is approximately 30% that of the first order effect, regardless of the hexadecane (solute) concentration. Pragmatically, the significance here is that both of these effects are always negative. Note: The reference solvent that is chosen to represent the first order effect may not always be truly bounding; however there is significant anecdotal evidence to suggest that complex solvents (such as jet fuels) will never have a less negative second order effect than any reasonably chosen reference solvent; a single-component hydrocarbon, dissimilar in size and type from the solute.

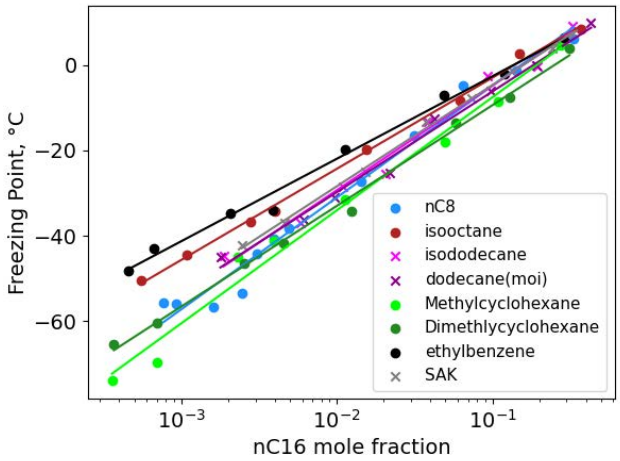


Figure A-5. Freezing point of n-hexadecane in various solvents. Solvents containing only one species are marked with circles and mixtures are marked with 'x's. n-Alkane and cycloalkane solvents result in a lower freeze point of nC16 than aromatic or iso-alkane solvents. The three complex mixtures (two different sets of mixtures of isomers of dodecane and Synthetic Aromatic Kerosene [SAK]) all resulted in very similar curves. The 'moi' after dodecane stands for 'mixture of isomers.'

100% n-Alkane Fuel

Fuels with large concentrations of n-alkanes are generally associated with higher freezing points. Eight of the nine models included in Wang et al.'s review of freezing point included concentration of n-alkanes as factors positively correlated with freezing point [2]. To reinforce one of the critical implications of this method that freezing point is not determined by group concentrations or bulk property characteristics, we created a 100% n-alkane fuel with comparable molecular weight to Jet A with a freezing point below the Jet A specification (-40 ˚C). This fuel is designed such that every n-alkane starting from nC16 and descending has approximately the concentration which would cause that species to freeze out in a mixture. The mole concentrations of the fuel blended are included in Table A-2. At these concentrations, all of the species between nC10 and nC16 would be expected to freeze in a solvent at approximately the same temperature (-40 ˚C). This mixture has an average molecular weight of 145 g/mol and has an ASTM D2887 simulated distillation curve shown in Figure A-6. This mixture was designed to emphasize the weaknesses of the empirical models based on petroleum-derived samples. Out of the 9 models shared in Wang et al., the closest prediction for the freezing point of this fuel is -12.7 ˚C; the measured freezing point is -40.7 ˚C. The model suggested here predicts -44.1 ˚C. Correlative methods fail to capture the physics which are controlling the freezing point which results in large errors when predicting the freezing point of fuels that are significantly different from those used in creating the model.

Table A-2. Mole percentages blended for the 100% n-alkane used in Figure A-6.

Molecule	Mole %
nC16	0.13%
nC15	0.91%
nC14	0.86%
nC13	4.40%
nC12	4.57%
nC11	25.71%
nC10	25.89%
nC9	37.52%

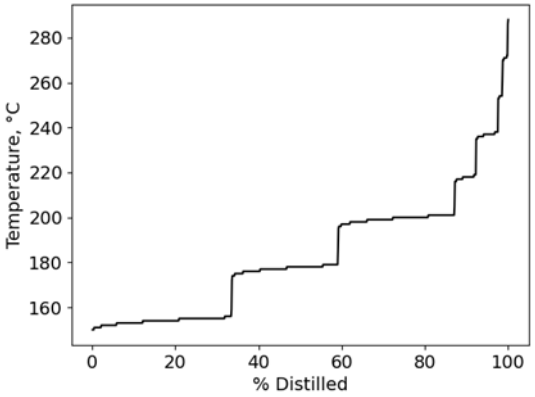


Figure A-6. ASTM D2887 Distillation Curve of a 100% n-alkane fuel.

Discussion

Aviation fuel freezing is primarily determined by the freeze point of a single component. Reducing the concentration of that component will lower the freezing point of the mixture unless another component begins to dominate freezing behavior. To a first order, this phenomenon can be predicted by accurately measuring the concentration of all plausibly limiting solutes in a given sample of an arbitrary hydrocarbon mixture. In petroleum-refined fuels, the limiting species is typically an n-alkane. These species are in high concentrations in petroleum and have high freezing points. Quantities as low as 0.5% of n-hexadecane can cause the fuel to be outside of the acceptable freeze point range for jet fuel regardless of the contents of the remainder of the fuel. For alternative fuels with more diverse and unique compositions, the n-alkanes will not always be the freeze-controlling species. Many alternative fuel candidates contain high concentrations of a single component. For these fuels, the structure of the most prevalent species will be important. Any species that shows up as a plausible freeze point controlling component can be identified using analytical chemistry approaches, including GC×GC-VUV. If not already available, this structural isomer identification would be augmented by the creation of new control curves specific to each of the plausible limiting isomers. Once those data are generated, the specific offending species can be identified and targeted for concentration reduction in future synthetic pathways.

Many species in petroleum-refined jet fuel, if isolated, would have a freezing point higher than the -40 ˚C limit (for Jet A) set in ASTM D1655. The same is true of synthetic blend components (SBC). Individually, the SBC must adhere to the requirements detailed in the annexes of ASTM D7566. The upper limit on the freezing point of SBC is also -40 ˚C which is overly restrictive unless the freezing point of the SBC happens to be governed by a high molecular weight, normal alkane, which is not the case for any of the eight synthetic pathways approved thus far. The results of this work suggest that the freezing point of all SBC/petroleum blends will be less than the freezing point of either one prior to mixing, and that limit for SBC should be applicable a blend of the SBC at its maximum allowed concentration with some reference solvent. However, a note of caution should be added, stating that a higher freezing point may be observed for SBC/petroleum blends if the petroleum component happens to contain a significant concentration of the same molecule that is controlling the freezing point of the neat SBC. Ultimately, the freezing point limit that is specified in ASTM D7566 Table 1 shall control the SBC/petroleum blend.

References

[1] Hall, C., Bell, D. C., Feldhausen, J., Rauch, B., & Heyne, J. (2024). Quantifying isomeric effects : A key factor in aviation fuel assessment and design. *Fuel, 357*,129912. https://doi.org/10.1016/j.fuel.2023.129912

[2] Wang, X., Jia, T., Pan, L., =Liu, Q., Fang, Y., Zou, J. J., & Zhang, X. (2021). Review on the Relationship Between Liquid Aerospace Fuel Composition and Their Physicochemical Properties. *Trans. Tianjin Univ., 27*, 87–109. https://doi.org/10.1007/s12209-020-00273-5

[3] Al Mulla, H.A., & Albahri, T. A. (2017). Predicting the properties of petroleum blends. *Pet. Sci. Technol., 35*, 775–782. https://doi.org/10.1080/10916466.2016.1277238



[4] Ervin, J. S., Zabarnick, S., Binns, E., Dieterle, G., Davis, D., & Obringer, C. (1999). Investigation of the use of JP-8+100 with cold flow enhancer additives as a low-cost replacement for JPTS. E*nergy and Fuels, 13*, 1246–1251. https://doi.org/10.1021/ef9901600

[5] Van Winkle, T. L., Affens, W. A., Beal, E. J., Mushrush, G. W., Hazlett, R. N., & Deguzman, J. (1987). Determination of liquid and solid phase composition in partially frozen middle distillate fuels. *Fuel, 66,* 890–896.

[6] Striebich, R. C., Motsinger, M. A., Rauch, M. E., Zabarnick, S., & Dewitt, M. (2005). Estimation of select specification tests for aviation turbine fuels using fast gas chromatography (GC). *Energy and Fuels, 19*, 2445–2454. https://doi.org/10.1021/ef050136o

[7] Boehm, R. C., Coburn, A. A., Yang, Z., Wanstall, C. T., & Heyne, J. S. (2022). Blend Prediction Model for the Freeze Point of Jet Fuel Range Hydrocarbons. *Energy & Fuels*. https://doi.org/10.1021/acs.energyfuels.2c0206

[8] Coutinho, J. A. P., Andersen, S. I., & Stenby, E. H. (1995). Evaluation of activity coefficient models in prediction of alkane solid-liquid equilibria. *Fluid Phase Equilib., 103*, 23–39. https://doi.org/10.1016/0378-3812(94)02600-6

[9] Feldhausen, J., Bell, D. C., Yang, Z., Faulhaber, C., Boehm, R., & Heyne, J. (2022). Synthetic aromatic kerosene property prediction improvements with isomer specific characterization via GCxGC and vacuum ultraviolet spectroscopy. *Fuel, 326*, 125002. https://doi.org/10.1016/j.fuel.2022.125002

[10] Johnson, K., Loegel, T., Metz, A., Wrzesinski, P., Shafer, L., Striebich, R., & West, Z. (2020). *Method for Detailed Hydrocarbon Analysis of Middle Distillate Fuels by Two-Dimensional Gas Chromatography*. NAVAIR Public Release 2020-361.

[11] Striebich, R. C., Shafer, L. M., Adams, R. K., West, Z. J., DeWitt, M. J., & Zabarnick, S. (2014). Hydrocarbon group-type analysis of petroleum-derived and synthetic fuels using two-dimensional gas chromatography. *Energy and Fuels, 28*, 5696–5706. https://doi.org/10.1021/ef500813x

[12] Yang, Z., Kosir, S., Stachler, R., Shafer, L., Anderson, C., & Heyne, J. S. (2021). A GC × GC Tier α combustor operability prescreening method for sustainable aviation fuel candidates. *Fuel, 292*, 1–9. https://doi.org/10.1016/j.fuel.2021.120345

[13] Affens, W. A., Hall, J. M., Holt, S., & Hazlett, R. N. (1984). Effect of composition on freezing points of model hydrocarbon fuels. *Fuel, 63*, 543–547. https://doi.org/10.1016/0016-2361(84)90294-1



APPENDIX B

Geometric and Positional Isomer Effects on Ignition Behavior of Cycloalkanes: Implications for Sustainable Aviation Fuels

Yang, Z., Faulhaber, C., Boehm, R. C., & Heyne, J. S. (2025). Geometric and Positional Isomer Effects on Ignition Behavior of Cycloalkanes: Implications for Sustainable Aviation Fuels. *ACS Energy & Fuel, 39*(38), 18641-18648. https://doi.org/10.1016/j.fuel.2024.133230

Introduction

The commercial aviation industry is facing mounting pressure to reduce greenhouse gas (GHG) emissions. In the United States, the Sustainable Aviation Fuel Grand Challenge has set ambitious goals: a 50% reduction in aviation-related GHG emissions and full substitution of fossil-based jet fuel with Sustainable Aviation Fuel (SAF) by 2050[1]. Similarly, the ReFuelEU Aviation Regulation mandates that SAF comprise at least 2% of jet fuel at EU airports by 2025, rising to 70% by 2050[2]. Achieving these targets requires not only scale-up of existing production but also the approval of new SAF production pathways. However, most currently certified ASTM D7566 pathways (e.g., A2 HEFA, A5 ATJ) primarily yield synthetic paraffinic kerosene (SPK), which consists almost entirely of n- and iso-alkanes. Although some pathways (e.g., A6 CHJ, A8 ATJ-SKA) can produce aromatic and cycloalkane components, their commercial-scale output remains limited.

There is growing interest in SAF candidates derived from novel feedstocks and conversion technologies, particularly those that produce predominantly aromatic and cycloalkane-rich fuels. Many of these are progressing through the ASTM D4054 approval process. However, due to limited research and historical uncertainty regarding cycloalkane behavior in combustion, original equipment manufacturers (OEMs) and regulatory bodies continue to limit the cycloalkane content within certain D7566 annexes and specifications. One key distinction between cycloalkanes and other hydrocarbon classes found in jet fuel (e.g., n- and iso-alkanes, aromatics) is the presence of cis-trans isomerism, also known as geometric isomerism. Although alkenes also exhibit geometric isomerism, their poor thermal stability renders them present only in trace amounts in conventional jet fuels and absent from all currently approved SAFs.

Ignition delay (ID) and derived cetane number (DCN) are key metrics used to characterize the combustion reactivity of liquid fuels[3,4]. Ignition delay is defined as the time between the start of fuel injection and the onset of significant combustion. DCN, a dimensionless quantity, is inversely related to ignition delay and serves as a standardized indicator of ignition quality. For aviation turbine fuels, maintaining DCN in the range of 35 to 60 is critical to ensure safe and efficient engine operation[5]. Fuels with excessively low DCN (i.e., long ignition delay) may increase the risk of lean blowout (LBO), particularly under high-altitude or low-load conditions[6]. Conversely, fuels with excessively high DCN (i.e., short ignition delay) may contribute to hardware durability issues, especially upstream of the primary reaction zone where large heat release is not anticipated by the hardware designers. As a result, understanding and controlling ignition delay behavior is essential for SAF certification and performance optimization.

The ignition behavior of hydrocarbons is strongly influenced by their molecular structure, particularly in the case of cyclic and branched alkanes. Cycloalkanes like DMCH are of growing interest in SAF formulations and surrogate development due to their abundance in lignin-derived fuels[7,8]. Dimethylcyclohexane (DMCH), with its multiple positional and geometric isomers, offers an ideal molecular platform to examine the structural sensitivity of fuel reactivity. However, their behavior during autoignition differs substantially from linear or branched alkanes. The cis-trans configuration, resulting from the rigid ring structure, modulates steric strain, radical stability, and low-temperature reaction pathways. For instance, cis-isomers tend to ignite more readily than trans-isomers, owing to reduced conformational strain and more favorable intramolecular hydrogen shift (1,5-H shift) mechanisms[9]. This trend is consistent across several cycloalkane systems, including decalin, where Heyne et al.[10] reported a significantly higher derived cetane number (DCN ≈ 41.6) for cis-decalin than trans-decalin (DCN ≈ 32.0) under identical IQT conditions. This trend is further supported by detailed structural and experimental analysis of decalin. Decalin exists as a fused bicyclic cycloalkane with two ring junction configurations: cis-decalin, where both hydrogens at the ring junctions are on the same face, and trans-decalin, where they are on opposite faces. The cis isomer adopts a more flexible conformation, which allows for enhanced low-temperature reactivity due to more favorable hydrogen abstraction and chain-branching pathways. In contrast, the trans isomer exhibits a more rigid structure with lower reactivity under similar conditions.



Beyond geometry, positional isomerism also plays an important role. Prior studies report that 1,2-DMCH exhibits significantly lower reactivity than 1,3-DMCH, attributed to steric hindrance around the methyl groups and fewer accessible β-scission pathways[11]. Experimental work by Kang et al.[12] and Yang & Wang[13] supports this trend, demonstrating that 1,3-isomers produce earlier low-temperature heat release and higher radical concentrations in motored engine studies and quantum kinetic calculations.

These structural effects are also reflected in DCN measurements. Using IQT, Jameel et al.[14] measured a DCN of 24 for 1,2-DMCH and 30.5 for 1,3-DMCH, supporting the view that increased substitution near the ring reduces reactivity. However, their study did not provide detailed characterization of isomer purity or cis-trans ratios, limiting interpretation of configurational effects. Similarly, Do et al.[15] investigated ring-opening reactions of 1,2- and 1,3-DMCH over iridium-based catalysts and predicted cetane numbers using artificial neural networks, obtaining CN = 22 for 1,2-DMCH and CN = 30 for 1,3-DMCH. These predicted and experimental values align well with the trend that increased substitution near the ring reduces reactivity, but also highlight the sensitivity of these metrics to both position and geometry of substituents.

A recent comprehensive study by Yang et al.[16] provided direct comparative insight into the oxidation kinetics of 1,2- and 1,3-DMCH using flow reactor experiments and detailed chemical kinetic modeling. Their work revealed that 1,2-DMCH exhibits stronger high-temperature reactivity, whereas 1,3-DMCH is more reactive under low-temperature conditions, particularly within the negative temperature coefficient (NTC) regime. Their study contributed validated kinetic sub-models for both isomers, yet did not differentiate cis- and trans- configurations, highlighting a critical gap in understanding the role of geometric isomerism in ignition behavior.

Other modeling efforts, such as those by Kubic[9], used group contribution methods and neural networks to predict DCNs across a wide molecular domain. These models confirmed that ring substitution, branching, and unsaturation consistently reduce cetane numbers, primarily through their inhibitory effects on early-stage radical formation and propagation. Additionally, Rosado-Reyes and Tsang[17] explored the isomerization kinetics of cis-1,2-DMCH in a single-pulse shock tube. Their findings showed unexpectedly slow cis-to-trans isomerization, suggesting kinetic bottlenecks due to steric hindrance in cyclic transition states.

Collectively, these findings emphasize the necessity of treating geometric and positional isomers as discrete species in kinetic models. Their differences are not merely of academic interest but bear significant implications for SAF performance metrics such as ignition delay, lean blowout risk, and nvPM emissions[18]. Despite growing understanding of DMCH oxidation chemistry, there remains a lack of experimental data that clearly isolates geometric isomerism effects under tightly controlled conditions. Many previous studies either used mixed isomer samples or did not specify isomeric purity, limiting mechanistic conclusions. As a result, detailed characterization of ignition delay and DCN as a function of cis-trans configuration remains an open research question.

In this work, we present a systematic investigation of the effect of geometric isomerism specifically cis vs. trans configurations—on the ignition delay of high-purity dimethylcyclohexane and decalin isomers. This study aims to fill a critical knowledge gap in surrogate fuel modeling and contribute to the broader understanding of how molecular structure dictates fuel performance in advanced combustion systems.

Materials and Methods

Reference Materials

All six configurations of DMCH and their mixtures were purchased for testing as shown in Table B-1. Some configurations of fuel were purchased twice to acquire different lot numbers and used for cross referencing.



Table B-1. Hydrocarbons used in this study, including source and purity.

Molecules	Purity	Lot number	Company
cis-1,2-dimethylcyclohexane	>98%	FIJ01-KU	TCI America
trans-1,2-dimethylcyclohexane	>99%	KRFHJ-QI	TCI America
cis-1,2-dimethylcyclohexane	>98%	FHA01-BN	TCI America
trans-1,2-dimethylcyclohexane	>99%	KRFHJ-BQ	TCI America
cis-1,3-dimethylcyclohexane	>99%	FB001-OX	TCI America
trans-1,3-dimethylcyclohexane	>95%	HD6TH-CM	TCI America
trans-1,3-dimethylcyclohexane	>98%	HD6TH-OK	TCI America
cis-1,4-dimethylcyclohexane	>98%	FHC01-NOJD	TCI America
trans-1,4-dimethylcyclohexane	>95%	G3HHM-US	TCI America
trans-1,4-dimethylcyclohexane	>95%	X7YKC-TT	TCI America
cis-decalin	>98%	TED3A-SN	TCI America
trans-decalin	>98%	7SQEF-LB	TCI America

Sample Preparation

As with any hydrocarbon-based fuel, prolonged exposure to atmospheric oxygen can lead to the formation of trace oxygenates and peroxides. These oxidative degradation products can significantly affect ignition delay measurements by altering fuel reactivity. To minimize these effects and ensure consistent sample quality, solid phase extraction (SPE) was employed to remove potential contaminants prior to testing. The material retained in the SPE trap was subsequently analyzed by gas chromatography–mass spectrometry (GC–MS), and representative oxygenated species are reported in the results section.

A Thermo Scientific HyperSep™ Silica SPE cartridge (1000 mg) was used for this process. The procedure was as follows. An initial 5 mL portion of the fuel sample was passed through the cartridge to precondition the column and then discarded. Subsequently, 25 mL of test fuel was passed through the cartridge under positive pressure to maintain a uniform collection rate. After extraction, the sample was filtered through a fine membrane (0.2 μm) to remove any residual sorbent particles. The cleaned sample was then used directly for ignition delay measurements in the IQT system.

Experimental Setup and Procedure

The ID and DCN measurements were conducted using a CFR Ignition Quality Tester (IQT-LM model) in accordance with ASTM D6890. Traditionally, approximately 150 mL of fuel was required to complete a DCN test, but the new IQT system acquired by Washington State University in 2024 includes manufacturer updates that significantly reduce the fuel volume needed. In this method, the fuel is injected into a heated, temperature-controlled constant-volume combustion chamber (CVCC) pre-charged with compressed air. Each injection triggers a compression ignition event, and the ignition delay defined as the time between the start of fuel injection and the onset of significant combustion is recorded. Each test consists of 15 pre-injections, used to condition the chamber and purge residual fuel, followed by 32 injections from which ignition delay values are averaged. An equation is used to correlate ID to CN using ASTM D613, resulting in a DCN. The Equation B-1 is used when ID ranges from 2.64 ms to 6.90 ms (75.1 DCN to 31.5 DCN).

$$DCN = 4.460 + 186.6/ID \quad \text{(Eq. B-1)}$$

The IQT is able to measure ID outside of this range; however the precision may be affected. When outside the ID range 2.64 ms to 6.90 ms, Equation B-2 should be used for the correlation of ID to DCN.

$$DCN = 83.99(ID - 1.512)^{(-0.658)} + 3.547 \quad \text{(Eq. B-2)}$$



It should be noted that the equation (B-1) and equation (B-2) are not equal at both end points (2.64 ms and 6.90 ms). However, the resolution of this discrepancy is outside the scope of this work. All measurements were calibrated following ASTM protocol using n-heptane (Haltermann solution, 99.86 vol%) with a measured ID of 3.78 ± 0.01 ms and methylcyclohexane (CFR Engine, purity unspecified) with an ID of 10.4 ± 0.5 ms. The charge air pressure was maintained at 310 psi, and the average charge air temperature was 582 ˚C.

Results and Discussion

Experimental Ignition Delay Measurements

Ignition delay measurements were conducted for all six isomers of DMCH and two isomers of decalin using the CFR IQT system, and the corresponding DCNs are summarized in Table B-2. Among the tested DMCH isomers, cis-1,3-DMCH exhibited the highest reactivity, with a DCN of 37.4, while cis-1,2-DMCH showed the lowest reactivity, with a DCN of 21.8. This represents a substantial difference of 15.6 DCN units among structurally similar isomers of DMCH, underscoring the significant influence of both positional and geometric isomerism on ignition behavior.

Table B-2. Ignition delay and DCN of pure compounds.

Compound	Ignition delay, ms	DCN
cis-1,2-DMCH	11.690	21.8
trans-1,2-DMCH	11.404	22.1
cis-1,3-DMCH	5.660	37.4
trans-1,3-DMCH	9.250	25.4
cis-1,4-DMCH	9.742	24.5
trans-1,4-DMCH	7.797	28.6
cis-decalin	5.062	41.3
trans-decalin	6.734	32.2

For the 1,2-substituted isomers, cis-1,2-DMCH and trans-1,2-DMCH yielded nearly identical DCNs of 21.8 and 22.1, respectively. This suggests that geometric isomerism has a negligible effect on ignition delay for 1,2-DMCH. This observation is consistent with values reported in the NREL Compendium of Experimental Cetane Numbers[19], which lists a DCN of 24.0 for a mixed 1,2-DMCH sample. In contrast, the effect of stereochemistry is most pronounced in the 1,3-substituted isomers. The DCN of cis-1,3-DMCH (37.4) is significantly higher than that of trans-1,3-DMCH (25.4), a difference of 12 DCN units. The DCN value of 30.5 reported in the NREL compendium for a mixed 1,3-DMCH sample falls between these two values, further supporting the sensitivity of ignition behavior to stereochemistry in this isomer group. For the 1,4-DMCH isomers, a moderate stereochemical effect is observed. The cis isomer exhibited a DCN of 24.5, whereas the trans isomer reached 28.6, resulting in a difference of 4.1 DCN units. When averaged across stereoisomers, the DCN trend by substitution position follows the order: 1,3-DMCH > 1,4-DMCH > 1,2-DMCH, indicating that positional isomerism also plays a significant role in ignition reactivity, independent of geometry. Figure B-1 summarizes DCN comparison among DMCH isomers.

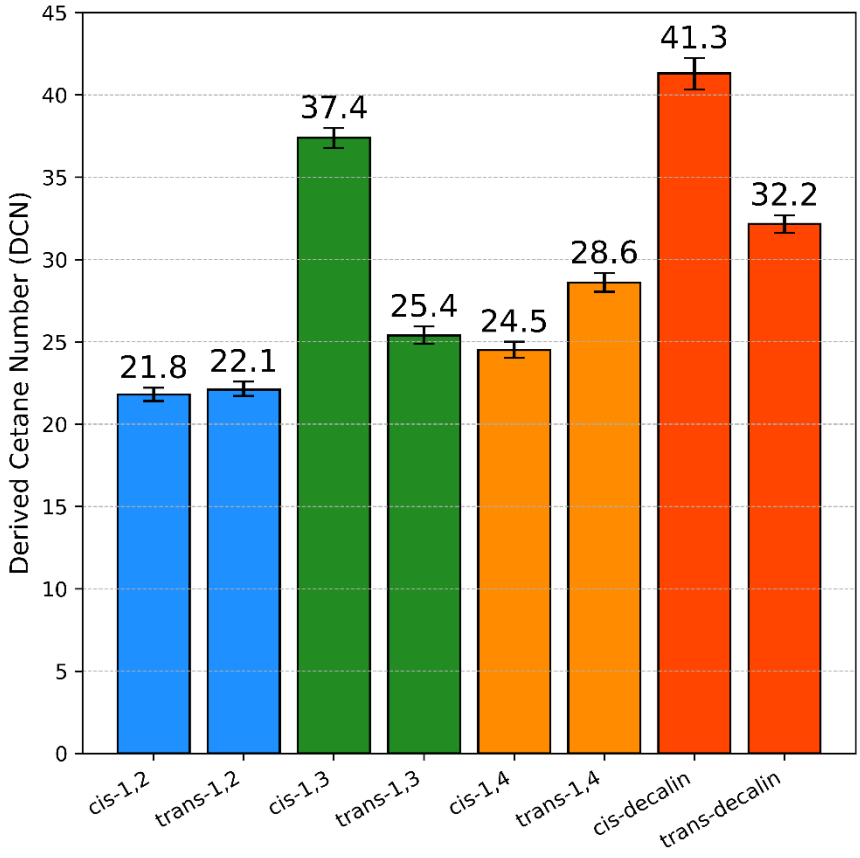


Figure B-1. DCN comparison among DMCH and decalin isomers.

To further validate the role of stereochemistry, cis- and trans-decalin were also evaluated under identical IQT conditions. Cis-decalin yielded a DCN of 41.3, while trans-decalin yielded 32.2—a difference of 9.1 DCN units. These results closely match those of Heyne et al.[10], who reported values of 41.6 and 32.0 for cis- and trans-decalin, respectively.

Possible Kinetic Explanation of DMCH Isomers

The observed variation in DCN among the isomers of DMCH reflects differences in molecular conformation and the corresponding impact on low-temperature oxidation kinetics. These effects are governed by the steric accessibility of hydrogen abstraction sites, the population and stability of reactive conformers, and the propensity for chain-branching pathways such as 1,5-H shifts and β-scission. Collectively, these parameters influence the onset and rate of exothermic radical chemistry that drives low-temperature heat release. The ignition behavior differences among DMCH isomers can be mechanistically explained by examining their molecular conformations, particularly the accessibility of hydrogen abstraction sites and the feasibility of intramolecular hydrogen shifts. Figure B-2 illustrates the most stable chair conformations of the six DMCH isomers, showing the relative positions of methyl groups and highlighting stereochemical effects that influence reactivity.

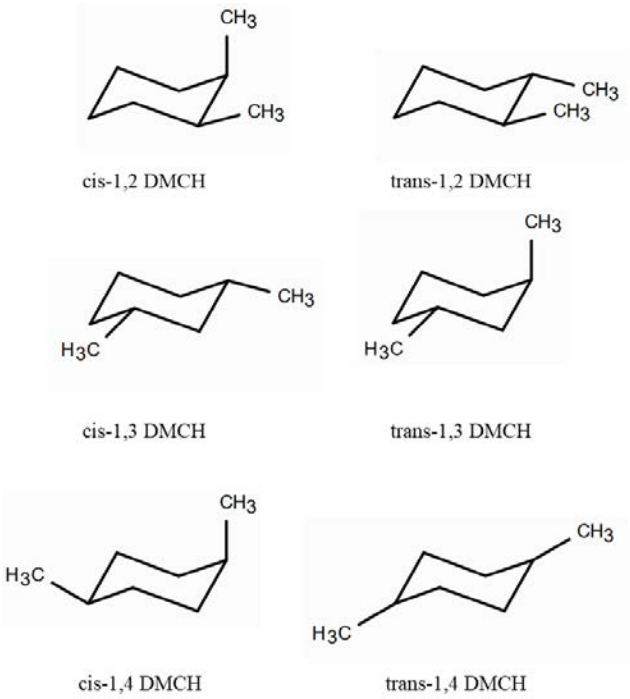


Figure B-2. Chair conformations of six DMCH isomers, highlighting the relative position and stereochemistry of the two methyl groups. Each structure represents the most stable conformer.

Both cis- and trans-1,2-DMCH exhibit similarly low DCNs (~22), indicating that positional substitution at adjacent carbon atoms (C1 and C2) significantly hinders reactivity regardless of stereochemistry. This behavior stems from severe steric congestion between the two methyl groups, which limits access to secondary axial hydrogens, the preferred sites for initial hydrogen abstraction by OH or O_2 radicals[20]. Quantum chemical studies confirm that these isomers predominantly occupy low-energy chair conformers with restricted conformational interconversion. In particular, Bian et al.[21] showed that inversion between conformers in cis-1,2-DMCH involves high energy barriers (>13 kcal/mol), and productive 1,5-H transfer is accessible only in rare, energetically disfavored geometries. Similarly, Sakurai et al.[22] found that radical cation fragmentation in 1,2-DMCH is stereoselective and limited, reinforcing the notion that conformational strain suppresses radical reactivity. Rossini and Pitzer[23] further support this conclusion with thermodynamic data: cis-1,2-DMCH has a higher enthalpy and lower entropy than its trans counterpart, reflecting its greater steric strain and reduced flexibility. Together, these findings indicate that 1,2-substitution locks the molecule into kinetically hindered conformations, reducing the formation of hydroperoxyalkyl radical (QOOH) and other chain-branching intermediates at low temperature.

In contrast, the 1,3-isomers show a pronounced stereochemical influence on DCN. The cis-1,3 isomer exhibits the highest DCN (37.4) of all isomers studied, while the trans form displays significantly lower reactivity (DCN = 25.4). Ab initio studies by Bian et al.[21] demonstrate that cis-1,3-DMCH favors low-energy conformers such as C13Cee, where both methyl groups occupy equatorial positions. This geometry is sterically favorable and facilitates intramolecular 1,5-hydrogen shifts via accessible transition states. At 500 K, the population of this conformer exceeds 99%, ensuring a high likelihood of radical isomerization and early OH regeneration through QOOH pathways. By contrast, trans-1,3-DMCH in its stable chair conformation must adopt an axial–equatorial (C13Cea) geometry due to the trans-1,3 substitution pattern. This configuration leads to more linear molecular geometries that are less favorable for internal hydrogen shift reactions, potentially delaying the onset of OH formation compared to the cis isomer. These conformers restrict chain-branching, delay low-temperature heat release, and result in a lower DCN. This stereochemical dependence on 1,5-H migration is consistent with prior kinetic models by Yang et al.[16], which identify H-shift rates and QOOH formation as sensitive to ring geometry and substituent orientation.



The 1,4-DMCH isomers fall between the extremes observed in 1,2- and 1,3-substitution. Both cis and trans forms exhibit intermediate DCNs, with only a modest difference between stereoisomers. In these structures, the methyl groups are positioned at para-positions, on opposite poles of the cyclohexane ring, which minimizes steric interference and preserves conformational flexibility. Quantum calculations show relatively low energy differences among conformers and lower inversion barriers, suggesting that both isomers maintain access to reactive geometries over a wide temperature range[24]. This pattern is supported by pyrolysis data from Gillespie et al.[25], who found that 1,4-DMCH readily undergoes radical fragmentation via ring hydrogen abstraction, consistent with the structural accessibility of reactive sites in these isomers.

These structure reactivity trends are reinforced by kinetic modeling and flow-reactor studies. Yang et al.[16] showed that 1,2-DMCH is more reactive at high temperatures, where ring-breaking dominates. While 1,3-DMCH exhibits enhanced reactivity under low-temperature conditions due to its propensity for H-migration and QOOH generation. Their sensitivity analyses confirmed that cis-isomers generally promote earlier formation of chain-branching intermediates, correlating with shorter ignition delays and higher DCN.

Temperature and Pressure Dependence of Decalin Isomers

To further investigate the mechanistic differences between cis- and trans-decalin in low temperature oxidation chemistry, a comprehensive series of ID measurements were conducted over a range of temperatures (400-620 ˚C) and pressure (250-350 psi). These conditions span the peroxy radical chemistry and hydrogen shift isomerization regime, allowing detailed investigation of conformational effects. During the temperature sweep, pressure was held constant at 310 psi, while the pressure sweep was performed at a fixed temperature of 450 ˚C, enabling isolated analysis of each variable's influence on ignition behavior.

Figure B-3 illustrates the pressure and temperature dependence of ID for cis- and trans-decalin. The top panel displays strong Arrhenius behavior, with high linearity for both cis- and trans-decalin (R^2 =0.992 and 0.992, respectively). Although both exhibit similar slopes, the cis isomer consistently displays shorter ID times across the entire temperature range studied. This indicates that the overall reactivity of cis-decalin is higher, likely due to greater accessibility of low-temperature chain-branching pathways, particularly below 550 ˚C, where RO_2 and QOOH intermediates play key roles[26-29]. As these reactions involve complex networks rather than single elementary steps, the observed differences in ID may reflect variations in the number or efficiency of reactive pathways available to each isomer, rather than differences in a single activation energy barrier.

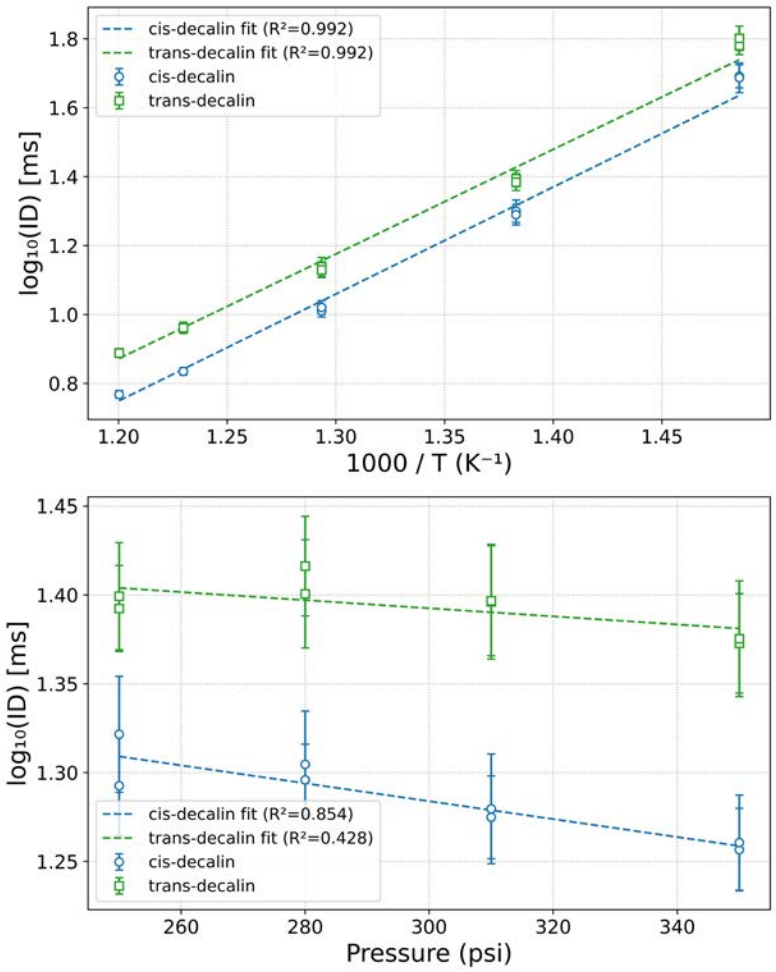


Figure B-3. Pressure and temperature dependence of ignition delay for cis- and trans-decalin. Data points represent duplicate measurements with error bars showing one standard deviation (SD). Each point is the mean of 32 injections; error bars are one SD across injections; two markers at a condition indicate independent duplicate tests. Dashed lines are linear fits to the logarithm of ignition delay, with coefficients of determination (R^2) included in the legend.

The bottom panel of Figure B-3 shows that cis-decalin also exhibits stronger pressure dependence (R^2 = 0.854), while trans-decalin shows weak sensitivity to pressure changes (R^2 = 0.428). This differential response implies that cis-decalin benefits significantly from pressure assisted stabilization of radical intermediates, which is consistent with unimolecular reaction pathways that involve third-body collisions[27,30].

Figure B-4 expands on these observations by directly comparing the ratio of ID (cis/trans-decalin) across temperature and pressure sweeps. In the top panel, the ID ratio decreases slightly with increasing temperature but remains below one across the full range. This reinforces the conclusion that cis-decalin is consistently more reactive, particularly at lower temperatures where peroxy radical isomerization dominates. The weak temperature dependence and low R^2 (0.006) indicate that the ratio of ignition delays between cis- and trans-decalin remains nearly constant across the studied temperature range. This supports the earlier observation that both isomers have similar apparent activation energies in this regime. Each point represents one of many pairwise combinations between individual cis- and trans- measurements, with error bars reflecting the propagated uncertainty from both isomers. The resulting scatter reflects real experimental variability while still preserving the overall trend.

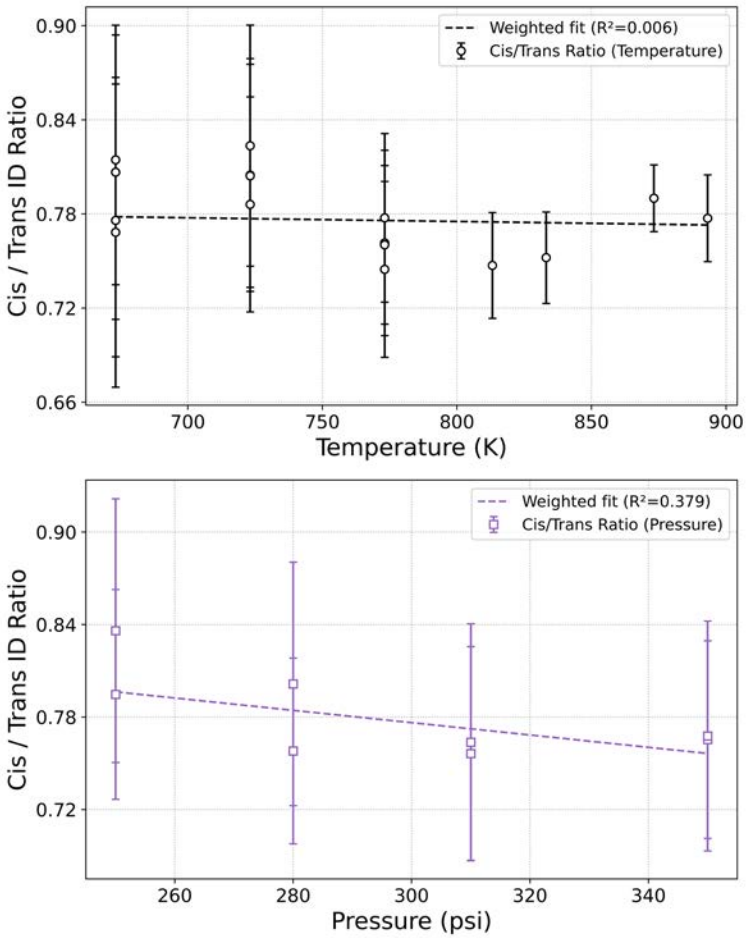


Figure B-4. Effect of temperature and pressure on cis/trans ignition delay ratio of decalin isomers. Data points represent ratios derived from independent replicate measurements of cis- and trans-decalin; error bars were propagated from the replicate standard deviations. Dashed lines show linear fits with R^2 reported in the legend.

In contrast, the bottom panel of Figure B-4 reveals a negative correlation between the ID ratio and pressure ($R^2 = 0.379$). This supports the interpretation that the pressure-enhanced reactivity of cis-decalin is not matched by trans-decalin, likely due to geometric constraints that limit efficient 1,6-H shift isomerization in the trans isomer. As pressure increases, the efficiency of pressure-dependent low-temperature pathways[27,30] (e.g., $RO_2 \rightleftharpoons QOOH$ and O_2QOOH formation) disproportionately benefits cis-decalin, driving the ratio lower. Figure B-5 illustrates a representative 1,5-H abstraction transition state in cis-decalin, where axial hydrogen accessibility supports faster QOOH formation under low-temperature and high-pressure conditions.

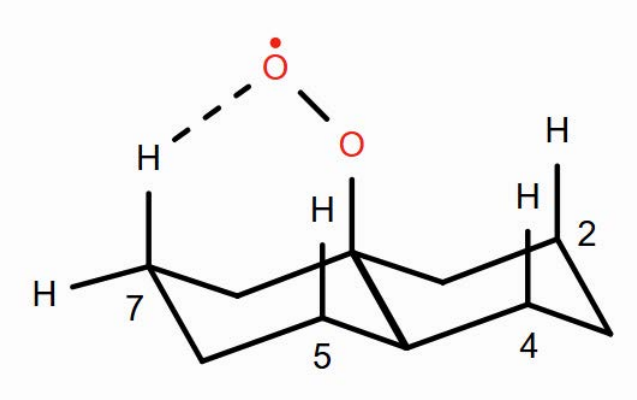


Figure B-5. Illustration of a 1,5-hydrogen abstraction transition state in cis-decalin. The axial hydrogen at the 7-position is abstracted by a peroxy radical (ROO·), initiating QOOH formation. The adjacent equatorial hydrogen and other abstractable sites are shown for reference. This geometry supports efficient low-temperature chain branching, consistent with the enhanced reactivity and pressure sensitivity observed experimentally. Adapted from Heyne et al.[10]

Taken together, the temperature and pressure dependence of ID in cis- vs. trans-decalin highlight the mechanistic role of H-shift pathways. The data support a scenario where 1,5-H shift isomerization in cis-decalin is more accessible and pressure-enhanced, whereas trans-decalin is constrained to slower or less pressure-responsive 1,6-H pathways. These insights clarify the structure-reactivity relationship and aid in modeling low-temperature oxidation behavior of bicyclic hydrocarbons. A full computational treatment of the isomer-dependent oxidation pathways lies beyond the scope of this work, but represents an important avenue for future study.

Polar Contaminant Effect on Ignition Delay

Trace polar species, particularly peroxides and oxygenates, are well known to accelerate low temperature combustion chemistry and reduce ID. These compounds can form during ambient storage through slow autoxidation of hydrocarbons in the presence of oxygen, and even at ppm levels, they can significantly bias DCN measurements by promoting radical generation and chain branching.

To assess this effect, each DMCH isomer was tested immediately upon opening (“as received”), then stored under ambient, light-protected conditions for 135 days in sealed amber bottles (although no purge using inert gas was performed). No further purification was applied prior to re-testing. Figure B-6 compares ID values before and after storage, with error bars representing standard deviations from 32 injections per test.

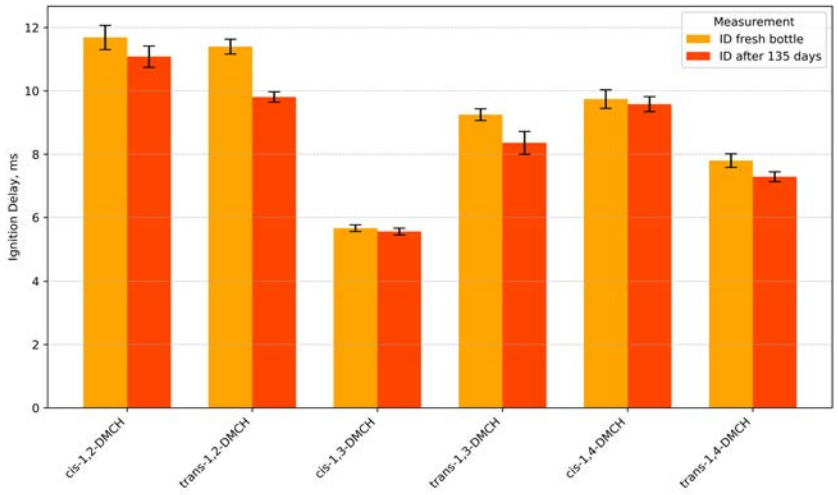


Figure B-6. Ignition delay comparison of DMCH isomers before and after 135 days of storage.

Among the DMCH isomers, trans-1,2-DMCH showed the most significant ID reduction from 11.40 ms to 9.81 ms, well beyond experimental uncertainty. Smaller but measurable decreases were also observed for trans-1,3-DMCH and trans-1,4-DMCH. In contrast, the cis isomers exhibited less change over time, indicating greater oxidative (storage) stability which is likely due to conformational constraints that hinder peroxide formation or radical propagation.

A similar trend was observed in trans-decalin, which initially showed an abnormally low ID of 5.33 ms (DCN = 39.5), inconsistent with literature values (≈32). Following SPE to remove polar contaminants, the ID increased to 6.73 ms (DCN = 32.2), aligning with prior reports and confirming that oxidative degradation had artificially enhanced the sample's reactivity. This validates both the susceptibility of trans-fused cycloalkanes to oxidative change and the efficacy of SPE purification.

GC-MS analysis of the SPE retained polar fraction from trans-decalin confirmed the presence of multiple oxygenated species, including ketones and hydroxylated decalin derivatives, further supporting the hypothesis that oxidative byproducts were responsible for the observed ID reductions. A full chromatogram, annotated peak identities, and mass spectra are provided in Supplemental Information (SI). It should be noted that while SPE GC-MS analysis is qualitative in nature, these results reinforce the need for careful fuel handling and purification when evaluating ignition properties particularly for fuels prone to peroxide formation. This is especially important for accurate kinetic model validation and experimental repeatability in surrogate fuel testing. The scope of this polar study is not to quantify the kinetics or concentrations of these impurities, but rather to alert the community to their potential impact on ignition measurements.

It should be noted that while the IQT provides a standardized and certification relevant platform for ignition delay and DCN determination, it does not capture the full range of autoignition behavior accessible with complementary equipment such as shock tubes or rapid compression machines. IQT measurements are most sensitive to mid temperature reactivity, whereas low-temperature chain branching and high-pressure kinetics are better resolved by other devices. Thus, while the present work emphasizes relative trends among isomers under ASTM D6890 conditions, a broader mechanistic picture will require integration with complementary methods in future studies. Although a comprehensive ab initio calculation/kinetic modeling of the isomer dependent oxidation network (conformers, H-abstraction sites, RO_2/QOOH isomerization, and pressure effects) would be valuable, it lies beyond the scope of this experimental study and would constitute a separate contribution. Here we focus on delivering an isomer-resolved, internally consistent IQT dataset under certification-relevant conditions (ASTM D6890), together with a literature based mechanistic context that can be used to benchmark and refine future models and surrogate fuel formulations.

Conclusion

Here, we investigated the impact of stereochemistry on the ID behavior of DMCH isomers. Among the isomers tested, cis-1,3-DMCH exhibited the highest reactivity, with a DCN of 37.4, while cis-1,2-DMCH was the least reactive, with a DCN of



21.8. The most pronounced stereochemical effect was observed between cis- and trans-1,3-DMCH, which showed a significant DCN difference of 12.0. In contrast, the effect was minimal for cis- and trans-1,2-DMCH, with only a 0.3 DCN difference. These variations are attributed to differences in molecular conformation, which directly influence low-temperature oxidation pathways and the formation of reactive intermediates during combustion.

To validate and extend these findings, cis- and trans-decalin were examined under a range of temperatures and pressures. Cis-decalin consistently exhibited faster ignition and stronger pressure sensitivity, consistent with its ability to access more favorable low-temperature chain-branching mechanisms (e.g., 1,5-H shift). The trans isomer, in contrast, was limited by conformational rigidity and exhibited weaker pressure dependence, likely due to inefficient 1,6-H isomerization. These results clarify the mechanistic basis for structure-reactivity trends among fused bicyclic hydrocarbons.

We also evaluated the impact of trace polar contaminants formed during ambient storage. Trans isomers, particularly trans-decalin, showed notable ignition delay reductions due to oxidative degradation. SPE and GC-MS confirmed the presence of oxygenated byproducts, such as ketones and hydroxylated species. These findings underscore the need for careful sample preparation to ensure accurate ignition property comparisons across isomer classes.

Taken together, these findings demonstrate that molecular stereochemistry and positional isomerism play critical roles in governing ignition behavior. This work deepens the mechanistic understanding of structure-reactivity relationships in cycloalkanes and offers valuable guidance for surrogate fuel formulation, SAF pathway evaluation, and chemical kinetic model development. Although this study focused on pure cis- and trans-cycloalkanes, such measurements are directly relevant to multi component SAF mixtures. Because DCN typically follows a linear by volume blending rule, accurate pure-component data expand the DCN database and support both hydrocarbon type analysis and quantitative structure property relationship (QSPR) modeling. These insights help address knowledge gaps on cycloalkanes and strengthen confidence in their role within sustainable aviation fuel blending strategies.

References

[1] US DOE. USDA, EPA, US Department of Transportation. (2022). *SAF Grand Challenge Roadmap*. https://www.energy.gov/eere/bioenergy/articles/sustainable-aviation-fuel-grand-challenge-roadmap-flight-plan-sustainable

[2] European Union. (2023). *Regulation - EU - 2023/2405 - EN - EUR-Lex*. https://eur-lex.europa.eu/eli/reg/2023/2405/oj

[3] Colket, M., & Heyne, J. (2021). *Fuel Effects on Operability of Aircraft Gas Turbine Combustors*. American Institute of Aeronautics and Astronautics, Inc., https://doi.org/10.2514/4.106040

[4] Luecke, J., Naser, N., Yang, Z., Heyne, J., & McCormick, R. L. (2025). Measurement of Spray Chamber Ignition Delay and Cetane Numbers for Aviation Turbine Fuels. *Energy and Fuels, 39*(22), 10479-10487. https://doi.org/10.1021/acs.energyfuels.5c01350

[5] ASTM International. (2022). *ASTMD4054: Standard Practice for Evaluation of New Aviation Turbine Fuels and Fuel Additives*. https://doi.org/10.1520/D4054-22

[6] Boehm, R. C., Colborn, J. G., & Heyne, J. S. (2021). Comparing Alternative Jet Fuel Dependencies Between Combustors of Different Size and Mixing Approaches. *Front. Energy Res. 9*, 440. https://doi.org/10.3389/FENRG.2021.701901

[7] Ruan, H., Qin, Y., Heyne, J., Gieleciak, R., Feng, M., & Yang, B. (2019). Chemical Compositions and Properties of Lignin-Based Jet Fuel Range Hydrocarbons. *Fuel, 256*, 115947. https://doi.org/10.1016/j.fuel.2019.115947

[8] Yang, Z., Xu, Z., Feng, M., Cort, J. R., Gieleciak, R., Heyne, J., & Yang, B. (2022). Lignin-Based Jet Fuel and Its Blending Effect with Conventional Jet Fuel. *Fuel, 321*, 124040. https://doi.org/10.1016/j.fuel.2022.124040

[9] Kubic, W. L. (2016). *A Group Contribution Method for Estimating Cetane and Octane Numbers*. https://doi.org/10.2172/1291241

[10] Heyne, J. S., Boehman, A. L., & Kirby, S. (2009). Autoignition Studies of Trans- and Cis-Decalin in an Ignition Quality Tester (IQT) and the Development of a High Thermal Stability Unifuel/Single Battlefield Fuel. *Energy and Fuels, 23*(12), 5879–5885. https://doi.org/10.1021/ef900715m

[11] Kang, D., Kirby, S., Agudelo, J., Lapuerta, M., Al-Qurashi, K., & Boehman, A. L. (2014). Combined Impact of Branching and Unsaturation on the Autoignition of Binary Blends in a Motored Engine. *Energy and Fuels, 28*(11), 7203–7215. https://doi.org/10.1021/ef501629p

[12] Kang, D., Lilik, G., Dillstrom, V., Agudelo, J., Lapuerta, M., Al-Qurashi, K., & Boehman, A. L. (2015). Impact of Branched Structures on Cycloalkane Ignition in a Motored Engine: Detailed Product and Conformational Analyses. *Combust. Flame, 162*(4), 877–892. https://doi.org/10.1016/j.combustflame.2014.09.009



[13] Yang, M., & Wang, J. (2024). Comprehensive Multipath Variational Kinetics Study on Hydrogen Abstraction Reactions from Three Typical Dimethylcyclohexane Isomers by Hydroxyl Radicals: From the Electronic Structure to Model Applications. *J. Phys. Chem. A, 128*(22), 4517–4531. https://doi.org/10.1021/acs.jpca.4c00480

[14] Abdul Jameel, A. G., Naser, N., Emwas, A. H., Dooley, S., & Sarathy, S. M. (2016). Predicting Fuel Ignition Quality Using 1H NMR Spectroscopy and Multiple Linear Regression. *Energy and Fuels, 30*(11), 9819–9835. https://doi.org/10.1021/acs.energyfuels.6b01690

[15] Do, P. T., Alvarez, W. E., & Resasco, D. E. (2006). Ring Opening of 1,2- and 1,3-Dimethylcyclohexane on Iridium Catalysts. *J. Catal., 238*(2), 477–488. https://doi.org/10.1016/j.jcat.2005.12.021

[16] Yang, M., Liang, Y., & Wang, J. (2025). A Comparative Experimental and Kinetic Modeling Study on the Oxidation Chemistry of 1,2- and 1,3-Dimethylcyclohexanes: Key Cyclic Components in Sustainable Biofuels and Fossil Fuels. *Fuel, 387*, 134417. https://doi.org/10.1016/j.fuel.2025.134417

[17] Rosado-Reyes, C. M., & Tsang, W. (2014). Isomerization of Cis-1,2-Dimethylcyclohexane in Single-Pulse Shock Tube Experiments. *J. Phys. Chem. A, 118*(36), 7707–7714. https://doi.org/10.1021/jp505305y

[18] Boehm, R. C., Yang, Z., & Heyne, J. S. (2022). Threshold Sooting Index of Sustainable Aviation Fuel Candidates from Composition Input Alone: Progress toward Uncertainty Quantification. *Energy & Fuels, 36*(4), 1916-1928. https://doi.org/10.1021/acs.energyfuels.1c03794

[19] Yanowitz, J., Ratcliff, M. A., Mccormick, R. L., Taylor, J. D., & Murphy, M. J. (2017). *Compendium of Experimental Cetane Numbers*. Golden.

[20] Klimkowski, V. J., Manning, J. P., & Schafer, L. (1985). Molecular Structures and Intramolecular Interactions in Dimethyl Cyclohexane Isomers. *J. Comput. Chem., 6*(6), 570–580.

[21] Bian, H., Ye, L., Li, J., Sun, J., Liang, T., Zhong, W., & Zhao, J. (2019). Impact of Conformational Structures on Primary Decomposition of Cis-1,2-Dimethylcyclohexyl Isomers: A Theoretical Study. Combust. *Flame, 205*, 193–205. https://doi.org/10.1016/j.combustflame.2019.04.024

[22] Sakurai, H., Shiotani, M., & Ichikawa, T. (1999). Hydrogen Molecule Detachment in Irradiated 1,2-Dimethyl Cyclohexane: Stereo-Selective Reaction. *Radiat. Phys. Chem., 54*(3), 235–240. https://doi.org/10.1016/S0969-806X(98)00257-6

[23] Rossini, F. D., & Pitzer, K. S. (1947). Relabeling of the Cis and Trans Isomers of 1,3-Dimethylcyclohexane. *Science, 105*(2738), 647. https://doi.org/10.1126/science.105.2738.647

[24] Bian, H., Zhang, Y., Wang, Y., Zhao, J., Ruan, X., & Li, J. (2021). Computational Study of Inversion-Topomerization Pathways in 1,3-Dimethylcyclohexane and 1,4-Dimethylcyclohexane: Ab Initio Conformational Analysis. *Int. J. Quantum Chem., 121*(11), 1–13. https://doi.org/10.1002/qua.26636

[25] Gillespie, H. M., Gowenlock, B. G., & Johnson, A. F. (1979). The Pyrolysis of Cyclic Hydrocarbons. Part 1. 1.4-Dimethylcyclohexane. *J. Chem. Soc. Perkin Trans., 2*, 317-324.

[26] Burke, U., Somers, K. P., O'Toole, P., Zinner, C. M., Marquet, N., Bourque, G., Petersen, E. L., Metcalfe, W. K., Serinyel, Z., & Curran, H. J. (2015). An Ignition Delay and Kinetic Modeling Study of Methane, Dimethyl Ether, and Their Mixtures at High Pressures. *Combust. Flame, 162*(2), 315–330. https://doi.org/10.1016/j.combustflame.2014.08.014

[27] Zádor, J., Taatjes, C. A., & Fernandes, R. X. (2011). Kinetics of Elementary Reactions in Low-Temperature Autoignition Chemistry. *Prog. Energy Combust. Sci., 37*(4), 371–421. https://doi.org/10.1016/j.pecs.2010.06.006

[28] Peeters, J., Nguyen, T. L., & Vereecken, L. (2009). HOx Radical Regeneration in the Oxidation of Isoprene. *Phys. Chem. Chem. Phys., 11*(28), 5935–5939. https://doi.org/10.1039/b908511d

[29] Westbrook, C. K., Pitz, W. J., Herbinet, O., Curran, H. J., & Silke, E. J. (2009). A Comprehensive Detailed Chemical Kinetic Reaction Mechanism for Combustion of N-Alkane Hydrocarbons from n-Octane to n-Hexadecane. *Combust. Flame, 156*(1), 181–199. https://doi.org/10.1016/j.combustflame.2008.07.014

[30] Glowacki, D. R., Wang, L., & Pilling, M. J. Evidence of Formation of Bicyclic Species in the Early Stages of Atmospheric Benzene Oxidation. *J. Phys. Chem. A, 113*(18), 5385–5396. https://doi.org/10.1021/jp9001466



Project 065(B) Fuel Testing Approaches for Rapid Jet Fuel Prescreening

University of Illinois at Urbana-Champaign

Project Lead Investigator

Tonghun Lee
Professor of Mechanical Science & Engineering
University of Illinois at Urbana-Champaign
1206 W. Green St., Urbana, IL 61801
517-290-8005
tonghun@illinois.edu

University Participants

University of Illinois at Urbana-Champaign (UIUC)

- P.I.: Professor Tonghun Lee
- FAA Award Number: 13-C-AJFE-UI-051
- Period of Performance: October 1, 2024, to September 30, 2025
- Tasks:
  1. Detailed Mixing and Chemistry Analysis for Lean Blowout (LBO) Evaluation
  2. Spray Characterization:
     a. Analytical Model Techniques for Characterizing Combusting Sprays
     b. Ignition Spray Measurements and Flame Propagation
     c. Alternative Fuel Reduced Order Modeling (ROM) of Breakup Dynamics

Project Funding Level

Federal Aviation Administration (FAA) funding level: $150,000
Cost Sharing: 100% matching funds provided by software license support from Converge, Inc.

Investigation Team

Prof. Tonghun Lee, (P.I.), All Tasks
Casey O'Brien, (graduate student), experimental efforts in characterizing the M1 combustor

Project Overview

This study is aimed at introducing a new compact test rig (Army research combustor [ARC] M1), developed with original equipment manufacturer (OEM) support within the National Jet Fuel Combustion Program (NJFCP), that can screen fundamental combustor behavior with much lower fuel volumes (approximately gallons) before tier 3 and 4 tests in the ASTM D4054 (ASTM, 2024) evaluation. In the NJFCP, the referee rig at the Air Force Research Laboratory (AFRL) was used as a foundational test rig for this goal. The M1 may have the potential to perform screening tasks at reduced fuel volumes (approximately gallons rather than hundreds of gallons) in a simplified and open architecture that can be readily shared and operated at different locations at a fraction of the cost. Both the Army Research Laboratory (ARL) and Argonne National Laboratory (ANL) have been and will be partners in the effort to fully characterize the M1 facility. If successful, these efforts will allow fuel providers and OEMs to conduct basic combustor tests by using an identical testing architecture and identical test conditions at multiple test locations, in contrast to the referee rig, which is housed in a secure government facility (i.e., AFRL). Tests in smaller test rigs can provide a platform for individual suppliers or researchers to independently evaluate their new fuels and to make predictions without requiring the use of one single facility. Over time, as test data are accumulated, the potential for test rigs, such as the M1 to predict actual tier 3 and 4 performances will increase, potentially reducing the burden of relying on capital-intensive ASTM rig and engine tests.

Background of the M1 Combustor
Under the FAA-funded NJFCP, the referee rig combustor at AFRL was used to determine the sensitivity of combustor performance parameters, such as LBO and ignition parameters, to the chemical composition of novel fuels. The results from this investigation were instrumental in establishing a relationship between fuel chemistry and its effects on combustor performance. Prof. Tonghun Lee's research group conducted a substantial portion of the laser and optical diagnostic work for the referee rig as part of the NJFCP, including quantitative-phase Doppler particle analysis, which provided key quantitative data for the simulation efforts.

Although the referee combustor used in the NJFCP program provides valuable information, a few key issues were identified. One issue is that the combustor requires hundreds of gallons of fuel to operate, which likely would not be available for many of the new sustainable aviation fuels (SAF) that would become available in the near future in the initial phase of production. The second issue is that the referee combustor lacks adequate optical access for diagnostics as a research combustor. Most significantly, it does not have windows on the top where laser beams can be inserted. Finally, the combustor itself is in a secure military facility (AFRL) and is not readily accessible to the general community. For these reasons, a smaller, compact, and less expensive option was needed; thus, the M1 combustor was developed with both the FAA and ARL (FAA NJFCP member). The M1 was designed as a joint effort between the University of Illinois and select OEMs who were involved with the referee combustor. The M1 combustor would run with moderately high-pressure air and would require a few gallons of fuel instead of hundreds of gallons. If this type of low-cost combustor can be well characterized, it can help prescreen SAFs as new fuels become available.

The dimensions and a magnified view of the M1 combustor are included in Figure 1. This combustor was built to be modular so that components can be easily switched out to suit the needs of different optical and laser diagnostics. The combustor includes four-sided optical access to allow for maximum flexibility in the diagnostics. The modular aspect was designed to allow us to transport the combustor easily to other locations for measurements, primarily because our team envisioned using x-ray imaging for fuel spray characterization at ANL as well as combustion characterization with velocity field and radical species measurements at UIUC. With this approach, the ASCENT Project 065(B) team can ensure that we are able to characterize the M1 combustor in an unprecedented way to enable wide adoption in the academic/industrial community as a test platform for new fuel blends. After this characterization is complete, the basic physics, dimensions, and operational envelope of the combustor will be openly shared with the academic and commercial sectors. This work is expected to provide a common platform not only for prescreening SAFs but also for performing other sustainability-related experiments involving novel fuels in a laboratory setting. It can also be noted that the combustor and surrounding hardware were designed specifically to be inexpensive (low flowrate requirements, lower pressure requirements, low fuel requirements on hardware) so that other labs could replicate this setup with reasonable resources.

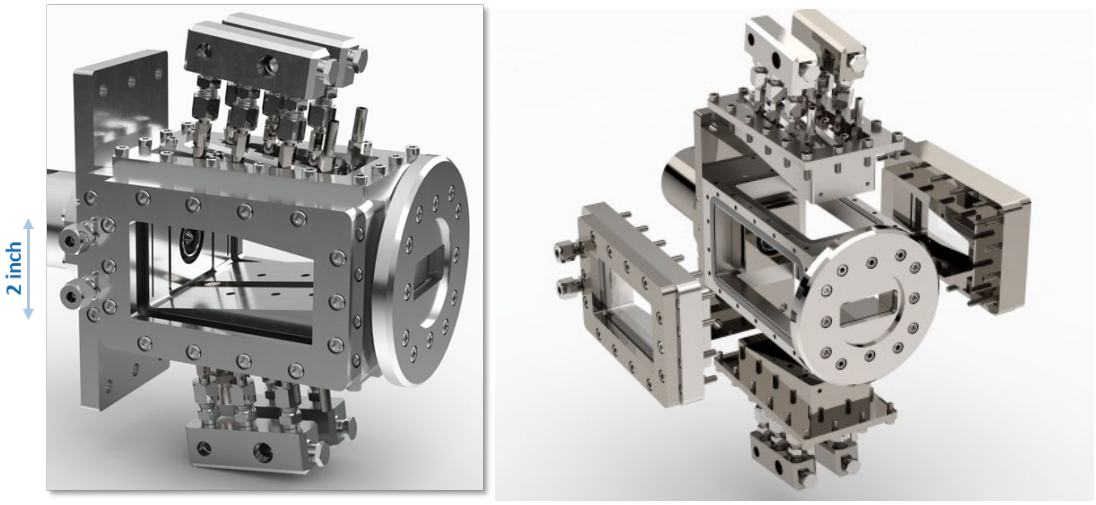


Figure 1. M1 combustor.

Task 1 – Detailed Mixing and Chemistry Analysis for LBO Evaluation

University of Illinois at Urbana-Champaign

Objectives

The main goal of this task is to find the direct causal link between fuel properties, in-flame fluid dynamics, and LBO performance. This work moves beyond simple correlation to determine why LBO behavior changes. A key objective is to determine if the flame structures, shear-layer instabilities, or heat release patterns are fundamentally different between the fuels, and if these differences can be used to predict LBO limits. To isolate these effects, LBO measurements are conducted on four fuels with wide-ranging properties at two combustor pressures. This pressure change is designed to force a transition from a physically dominated regime (where atomization and vaporization control LBO) to a chemically dominated one (where reaction kinetics are rate-limiting). By capturing this shift, it will be possible to pinpoint which specific fuel-driven dynamics are the limiting factors that control LBO under different conditions.

Research Approach

Previous research, including large-scale tests within the NJFCP, successfully characterized LBO performance and established strong correlations between bulk fuel properties and LBO limits. However, these studies were largely focused on macroscopic behavior and often lacked the high-speed diagnostics required to understand the underlying mechanisms. Critically, they could not sufficiently resolve the transient flame-flow interactions, turbulent mixing, and flame dynamics that immediately precede a blowout event.

This research approach is designed to fill that specific knowledge gap. We are shifting the focus from if a fuel property affects LBO to how it does so at a fundamental, physical level. To achieve this, we are employing simultaneous 10 kHz OH-planar laser induced fluorescence (PLIF) and particle image velocimetry (PIV) imaging in the M1 combustor. This approach provides the high-fidelity, time-resolved data necessary to capture the detailed gas flow dynamics (i.e., PIV) and instantaneous heat release structures (OH-PLIF). This rich dataset is specifically intended for analysis with advanced ROM techniques. By applying methods like proper orthogonal decomposition (POD) and, in the future, dynamic mode decomposition (DMD), we can identify and quantify the dominant dynamic instabilities and coherent structures within the flame, allowing us to connect these specific physical phenomena directly to the LBO event. This allows us to move beyond simple correlation and build a model of the causal dynamic mechanisms that govern LBO for different fuels.

Fuels for Lean Blowout Testing

In these experiments, four different fuels are tested in the M1 combustor to probe the effects of fuel properties on combustion behavior at these critical conditions. In addition to a reference fuel, the tested fuels consist of F-24 (comprising Jet A fuel and military-specific additives) and three fuels from the NJFCP with specific properties designed to probe the edges of the jet fuel operational envelope. Fuel C-1 has been developed with a low derived cetane number (DCN) and a relatively flat boiling curve. Fuel C-3 has been formulated to have a high viscosity, and fuel C-5 has been developed with an extremely flat boiling curve with respect to those of other fuels. Table 1 shows selected important parameters of each fuel for comparison, demonstrating some of the key features of the fuels chosen for testing.

Table 1. Comparison of key properties of the four tested fuels.

Fuel	Key features	Derived cetane number	Heat of combustion (MJ/kg)	H/C ratio	Stoichio-metric air/fuel ratio	Kinematic viscosity at 40°C (cSt)	Surface tension (dynes/cm)
F-24	Jet A with additives	48.6	43.2	1.94	14.70	1.36	23.6
C-1	Low cetane	17.1	43.8	2.18	15.03	1.53	21.0
C-3	High viscosity	47.0	43.3	1.97	14.65	1.78	24.2
C-5	Flat boiling	39.6	43.0	1.94	14.68	0.83	22.2

Previous Lean Blowout Results

A principal component analysis (PCA) was used to overcome multicollinearity in fuel properties, reducing them to three key components: physical dependence (PD), chemical dependence (CD), and droplet dependence (DD). These components were correlated with LBO data at two pressures, revealing a clear regime transition shown in Table 2 and Figure 2. At 2 atm, LBO



is physically dominated, with the LBO equivalence ratio (ϕ_{LBO}) correlating strongly with properties governing atomization and vaporization, specifically the 20% distillation temperature (T_{20}) and kinematic viscosity (ν). This was confirmed as the best-performing fuel, C-5, had low viscosity, while the worst-performing, C-3, had high viscosity. Increasing the pressure to 3 atm causes a distinct shift to a chemically dominated regime. At this pressure, the influence of physical properties diminishes, and the DCN becomes the most influential parameter. This transition occurs because the enhanced mixing and faster reaction kinetics at higher pressure mean that chemical reactivity (i.e., ignition delay), not atomization, becomes the rate-limiting step.

Table 2. Lean blowout (LBO) equivalence ratio (ϕ_{LBO}) correlation analysis with fuel properties for two pressures.

Noz	P (kPA)	TAFR (g/s)	ϕ_{LBO} (F-24)	ϕ_{LBO} (C-1)	ϕ_{LBO} (C-3)	ϕ_{LBO} (C-5)
A	203	65.07	0.173	0.167	0.188	0.147
B	203	65.07	0.104	0.104	0.106	0.097
C	203	65.07	0.149	0.133	0.157	0.125
B	304	92.18	0.066	0.084	0.065	0.064

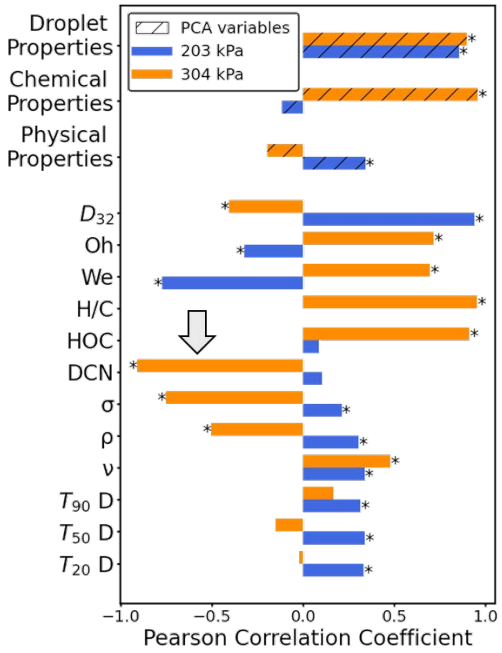


Figure 2. Lean blowout (LBO) equivalence ratio correlation analysis with fuel properties for two pressures.

Detailed Flame Mixing Characteristics

Detailed flame mixing characteristics for the four tested fuels were investigated using simultaneous 10 kHz OH-PLIF and PIV imaging. This approach allowed for the analysis of gas flow dynamics (PIV) alongside instantaneous heat release (OH-PLIF), a key indicator of combustion intensity. As shown in the average OH PLIF images (Figure 3), a clear differentiation in the flame structure and peak heat release location was observed among the fuels, despite similar average velocity fields across all four. Specifically, Fuel C-3, with its high viscosity, exhibited its peak heat release furthest downstream, followed sequentially by C-1, F-24, and C-5. This downstream shift of the flame front is almost directly correlated with the increasing kinematic viscosity of the fuels, confirming that physical properties significantly influence flame stabilization at these conditions.

Further insights into the dynamic behavior were gained by applying POD to both the PIV and PLIF fields. This method identifies the most energetic spatial structures (modes) within the data. By projecting the time-series onto these modes,

their temporal coefficients are extracted, allowing the energy contained within each dynamic mode to be quantified. This analysis revealed significant differences in the transient flow structures among the fuels. Notably, in some of the lower-energy POD modes (e.g., mode 3 for PIV and mode 4 for PLIF), the high-viscosity fuel C-3 displayed much more pronounced instabilities within the upper outer shear layer, an instability that was considerably weaker in the other fuels. Figure 4 visually highlights this localized, energetic instability in the C-3 fuel. While POD effectively identified these key spatial structures and provided a crucial link between fuel viscosity and flame dynamics, its energy-based nature is less suited for defining the complete time-evolving system. Therefore, future work will leverage advanced ROM techniques, such as DMD, to more fully characterize these complex, time-dependent dynamics.

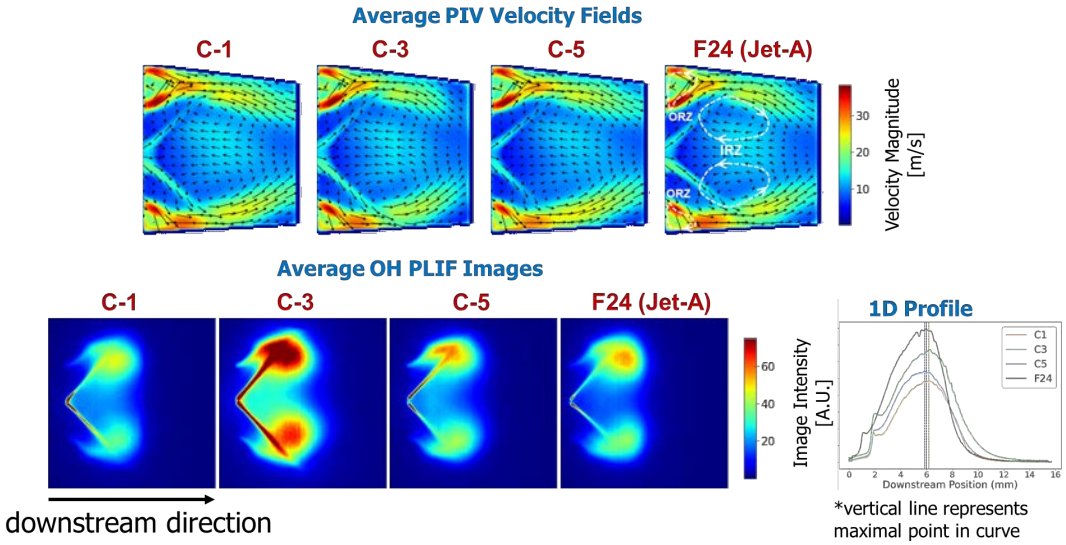


Figure 3. Average planar laser induced fluorescence (PLIF) particle image velocimetry (PIV) fields for four fuels.

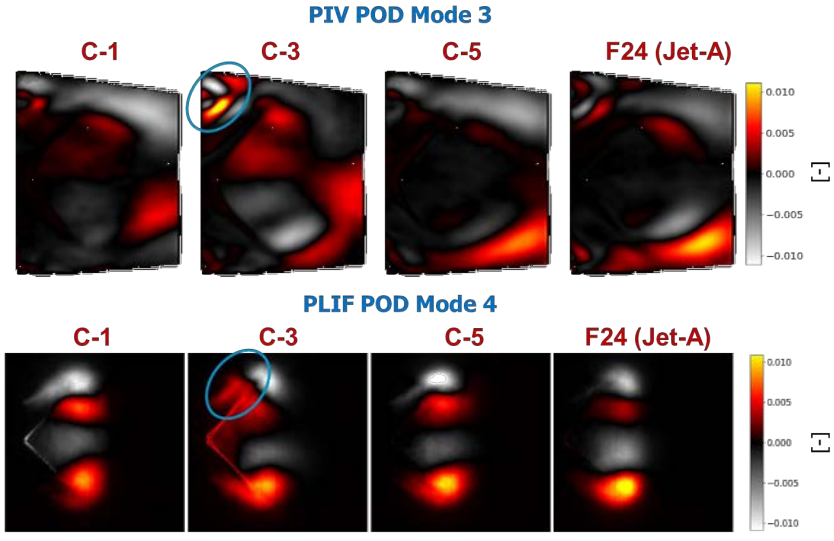


Figure 4. Lower energy modes identifying instabilities of planar laser induced fluorescence (PLIF) particle image velocimetry (PIV) through proper orthogonal decomposition (POD).

Milestones

- Processed the high-speed diagnostic data to identify the dominant spatial modes and dynamic structures (6 months).
- Established the direct link between the diagnostic findings and the performance data. This involved correlating the ROM-identified dynamic features (e.g., shear layer instability strength) and mean-flow structures (e.g., flame standoff distance) with the LBO limits (12 months).

Major Accomplishments

The major accomplishment of this investigation is the identification of the key causal mechanism linking fuel physical properties to LBO performance. This work has successfully moved beyond the correlations of previous studies by providing direct diagnostic evidence of how fuel properties fundamentally alter flame dynamics. The high-speed analysis revealed critical findings: average OH-PLIF fields show that high-viscosity fuels (e.g., fuel C-3) produce a longer flame standoff distance, pushing the primary heat release zone further downstream. The POD analysis then confirmed that this downstream flame position drives a pronounced hydrodynamic instability in the outer shear layer (Figure 4), a dynamic feature that was weak or absent in the other fuels. This instability is identified as the direct physical mechanism responsible for the degraded LBO performance of high-viscosity fuels.

Publications

Published Conference Proceedings

Dasgupta, D., & Som, S. (2024). Fuel property impact on lean blow out for sustainable aviation fuels in gas turbine combustors. *Proceedings of the ASME Turbo Expo 2024: Turbomachinery Technical Conference and Exposition. Volume 3A: Combustion, Fuels, and Emissions*, V03AT04A073, London, United Kingdom. https://doi.org/10.1115/GT2024-126789

Wood, E. J., Mayhew, E., Motily, A., Temme, J., Kweon, C. B., & Lee, T. (2021). Lean blowout dependence on fuel properties and combustion conditions in the ARC-M1 single-cup swirl combustor. AIAA 2021-0652. *AIAA Scitech 2021 Forum*. 0652. https://doi.org/10.2514/6.2021-0652

Outreach Efforts

All test data will be made accessible through https://altjetfuels.illinois.edu/.

Awards

None.

Student Involvement

Task 1 was primarily conducted by Casey O'Brien (PhD student).

Plans for Next Period

The primary focus for the next period will be to advance the ROM of the flame dynamics, moving beyond the spatial structure identification of POD. The high-speed OH-PLIF and PIV datasets will be analyzed using DMD. This analysis is central to extract the key spatiotemporal modes, their frequencies, and their growth/decay rates. The objective is to build a quantitative, dynamics-based model that directly links the amplitude and persistence of specific instabilities, such as the observed shear layer mode, to LBO performance.

This validated modeling framework will then be applied to an expanded set of alternative fuels. New tests will incorporate a wider range of fuel types, including hydroprocessed esters and fatty acids (HEFA), synthetic paraffinic kerosene (SPK), and alcohol-to-jet (ATJ) blends. This effort is not simply to expand the LBO database, but to test the generality of the identified mechanisms. This will provide a systematic framework to determine if the same controlling dynamics govern LBO for these new fuels or if their unique properties introduce different physical or chemical pathways to blowout.

Task 2 – Spray Characterization
Task 2a – Analytical Model Techniques for Characterizing Combusting Sprays

University of Illinois at Urbana-Champaign

Objectives

In this task, a novel, high-fidelity analytical framework is developed and validated to quantitatively characterize the primary breakup and spray dynamics in a combusting environment. This framework is necessary because traditional or single-point diagnostics are insufficient to resolve the complex, transient, and multi-scale physics of atomization, which is a rate-limiting step for fuel-air mixing. This work will combine high-speed X-ray phase contrast imaging (PCI) with a newly developed machine learning optical flow model, PC-Flow, to extract time-resolved velocity fields. The primary objectives are to (1) validate PC-Flow's performance and quantify its predictive uncertainty and (2) deploy this validated tool to establish new, physically-based metrics for spray characterization, including breakup time and sphericity evolution. By establishing this quantitative methodology, we provide the toolset required to isolate the physical properties (viscosity, surface tension, and volatility) of fuel variability on spray formation, which is essential for the subsequent ignition and fuel-comparison studies in Tasks 2b and 2c.

Research Approach

High-speed X-ray PCI was performed on the operating ARC-M1 combustor at stable combusting with a specific focus on the fuel spray immediately after exiting the nozzle. The experiments were performed using the X-ray white beam at ANL's Advanced Photon Source using beamline 7-BM. The ARC-M1 combustor was fitted with thin X-ray transparent Kapton windows to enable the beam to pass through the combustor. The technique allowed visualization of only the liquid fuel droplets in the combustor, enabled through a combination of X-ray absorption by the fuel and additional diffractions at the boundaries due to the density difference between the fuel and surrounding air. Figure 5 shows an image of important features of the ARC-M1 combustor as well as the imaging regions measured experimentally. The combustor conditions for the spray measurements were maintained at an inlet air temperature of 323 K and a combustor operating pressure of 1 atm. Two pressure drops across the combustor were tested. For the 26, 30, 35 g/min fuel flow rates, a 1.75% pressure drop was set, which resulted in 16.1 g/s main and 4.0 g/s dilution air flow rates. For the 37, 40, 45 g/min flow rates, a 3% pressure drop was set, resulting in 21.3 g/s main and 5.4 g/s dilution air flow rates. These specific pressure drops were selected to emulate the operating conditions of the referee rig, ensuring direct comparability between the two setups. Furthermore, relatively ambient conditions were utilized to establish a baseline dataset where the effects of pressure and inlet air temperature on droplet distribution are minimized.

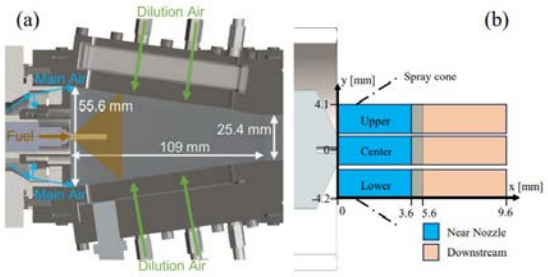


Figure 5. Schematics of (a) ARC-M1 combustor geometry and (b) imaging region.

We developed PC-Flow, an unsupervised machine learning optical flow model, to extract high-fidelity velocity fields from high-speed spray imaging. It builds on the UPFlow (state-of-the-art) architecture but integrates key modifications, including a new correlation volume, concatenated features to model flow dependencies, and an integrated attention mechanism. The UPFlow model performed best on publicly available synthetic datasets (KITTI 2012 & 2015) and consequently was chosen as baseline. The new design proved highly effective, demonstrating a 29.9% reduction in mean absolute error (MAE) compared to the original UPFlow baseline. Qualitatively, PC-Flow also produces less noisy velocity predictions that are well-localized to the liquid fuel structures shown in Figure 6. To ensure its suitability as an analytical instrument, we performed



a Lucas-Kanade-based uncertainty quantification (UQ). This validation confirmed that PC-Flow achieves sub-pixel average uncertainty for its velocity predictions shown in Figure 7, verifying its reliability for extracting quantitative physical data.

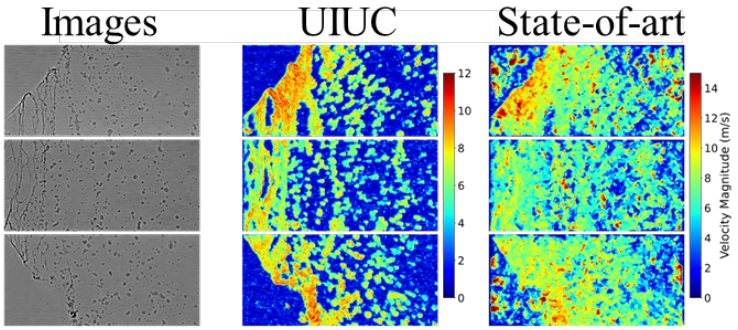


Figure 6. An example comparison of flow predictions: (a) raw images, (b) PC-Flow, and (c) UPFlow.

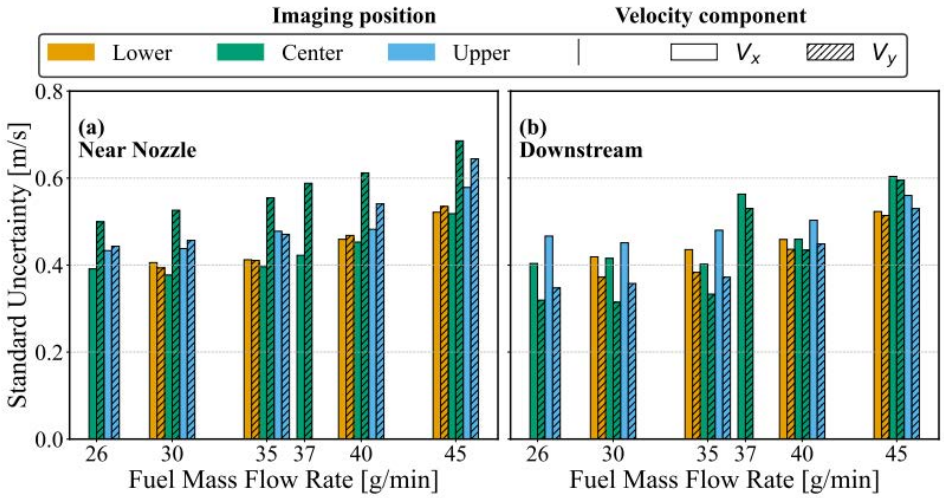


Figure 7. Average uncertainty estimation for multiple fuel flow rates and imaging positions: (a) near nozzle and (b) downstream.

Using this validated PC-Flow tool in conjunction with image binarization, we characterized the spray's primary breakup dynamics. A key parameter in any spray model is the primary breakup length (l_b), as this location (visualized in Figure 8[a]) defines the critical transition from a continuous liquid sheet to discrete droplets. This, in turn, sets the initial conditions for all downstream processes, including vaporization, fuel-air mixing, and subsequent combustion. We tracked the leading edge of the liquid sheet (Figure 8[b]) and found that l_b increases near linearly with the fuel flow rate. However, the velocity data from PC-Flow provided a much deeper insight: by calculating the characteristic breakup time ($\tau_b = l_b/V_x$), we found this value remained nearly constant. This strongly suggests that the leading edge breakup is governed by a fixed instability-driven rate, and the observed increase in length is primarily a transport-driven phenomenon where the faster-moving sheet simply travels further before it has time to disintegrate.

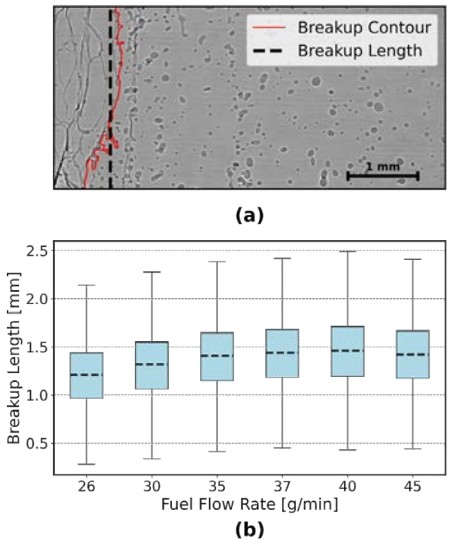


Figure 8. Breakup length estimation: (a) identification of the breakup point and (b) box plot of breakup length dispersion (dashed line indicates arithmetic mean, blue box indicates the interquartile range (Q1 to Q3), and vertical whiskers indicate the minimum and maximum values).

To understand the output of this breakup process, we analyzed the probability density functions (PDF) of velocity and droplet size, sampled at the breakup location (shown in Figure 9). This statistical approach is crucial because it moves beyond simple averages to capture the full operational range, which is essential for understanding spray consistency and the stochastic nature of ignition and other combustor tests. The velocity PDFs (Figure 9[a], Figure 9[b]) quantify the axial and transverse momentum being imparted to the new droplets, which governs their downstream penetration and mixing with the surrounding air. The droplet diameter PDF (Figure 9[c]) is a direct input for any vaporization or combustion model, as it defines the initial surface area available for heat and mass transfer.

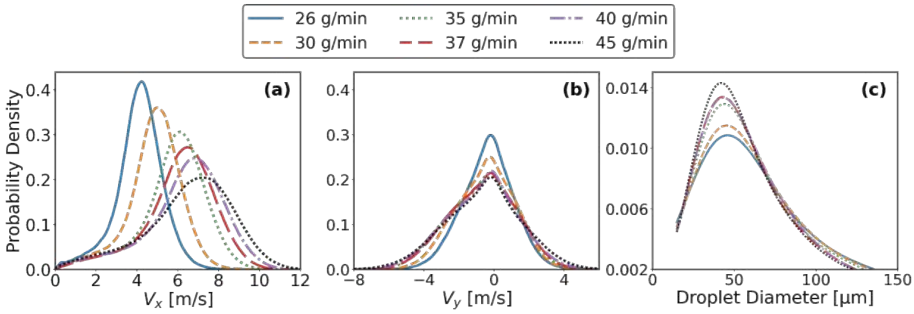


Figure 9. Probability density function at the breakup location of different fueling rates for (a) Vx, (b) Vy, and (c) droplet diameter.

Finally, we analyzed droplet sphericity as a function of downstream distance shown in Figure 10. This metric is critical for two primary reasons. First, many standard spray diagnostic techniques, such as phase doppler particle anemometry (PDPA), rely on the assumption of spherical droplets; our analysis directly quantifies where in the spray this assumption becomes valid (i.e., where sphericity approaches 1). This is vital for validating data used in certification. Second, the evolution of sphericity physically represents the spray's relaxation from chaotic, non-spherical liquid fragments into stable droplets, a process governed by the competition between aerodynamic shear (deforming the droplets) and surface tension (restoring them to spheres). We identified the inflection point of the sphericity curve as a new, physically meaningful metric that tracks the sheet's internal instability timescale (e.g., disintegration via perforation). This offers a powerful,



complementary perspective to the convective timescale captured by leading-edge tracking. Coupling this morphological data with PC-Flow's velocity data, we also discovered a slightly trimodal transverse velocity (V_y) distribution near the chaotic breakup region. This is a direct signature of the highly fluctuating motion inherent to atomization, which transitions to a more developed, smoother flow as the droplets stabilize downstream.

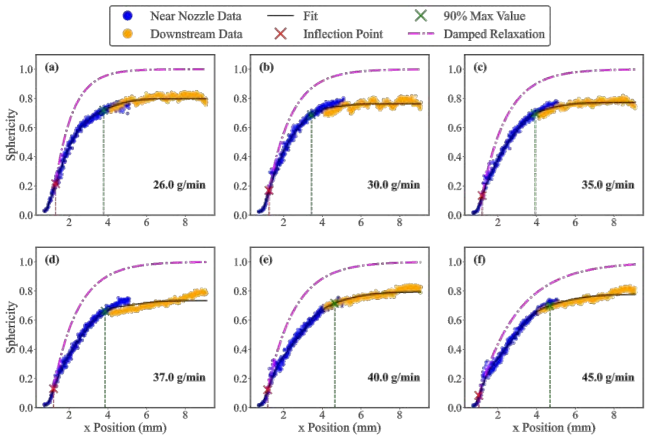


Figure 10. Sphericity curve along the streamwise direction: (a) 26 g/min, (b) 30 g/min, (c) 35 g/min, (d) 37 g/min, (e) 40 g/min, and (f) 45 g/min.

Task 2b – Ignition Spray Measurements and Flame Propagation

University of Illinois at Urbana–Champaign

Objectives

In this task, the transient spray dynamics governing gas turbine ignition and relight are investigated. This is a critical safety metric, as ignition is a stochastic process highly dependent on the local fuel droplet distribution at the spark kernel, particularly under low-load conditions. A knowledge gap persists in an in-situ quantification of the spray's response to the spark and subsequent flame. This study will use simultaneous high-speed X-ray PCI and broadband visible imaging to capture spark-droplet interactions and flame kernel propagation at relevant ignition conditions. The primary objective is to test the hypothesis that combustion itself alters the spray, by segregating and comparing spray statistics (e.g., D10 and D32) from pre-ignition (non-combusting) and post-ignition (combusting) sequences. We will determine whether preferential vaporization (D^2 law) is the dominant mechanism downstream and whether thermal feedback from the flame front alters primary atomization near the nozzle. Understanding this quantitative link between spray properties and ignition success is essential for evaluating the relight performance of future SAFs, which may possess different vaporization characteristics than conventional jet fuel.

Research Approach

Gas turbine ignition performance is a critical safety metric, particularly the ability to relight after a flame blowout, which can occur during low-load conditions like descent. Ignition is a stochastic process where a spark kernel's heat release must overcome local heat losses, a balance governed by the local droplet distribution and fuel-air mixture. Foundational research identified the quantity of fuel vapor from the spark as the critical factor. However, a knowledge gap persists regarding the transient dynamics of spark kernel interactions with liquid fuel droplets, particularly their vaporization. Resolving this interaction is crucial for low-temperature conditions where liquid-phase behavior dominates. This study investigates these transient phenomena in the ARC-M1 combustor at relevant low-load ignition conditions (25°C inlet air, atmospheric pressure). To capture the critical spark-droplet interactions, simultaneous broadband and high-speed X-ray PCI images are acquired. Both imaging systems are synchronized with a 4 Hz aviation spark igniter, with data acquisition commencing approximately 5.5 ms before each spark. This method yielded 750 broadband and 3,000 X-ray PCI images per sequence, enabling analysis of transient vaporization and kernel development. For statistical analysis, three pre-ignition and four spark sequences starting from ignition are consolidated, as depicted in Figure 11.

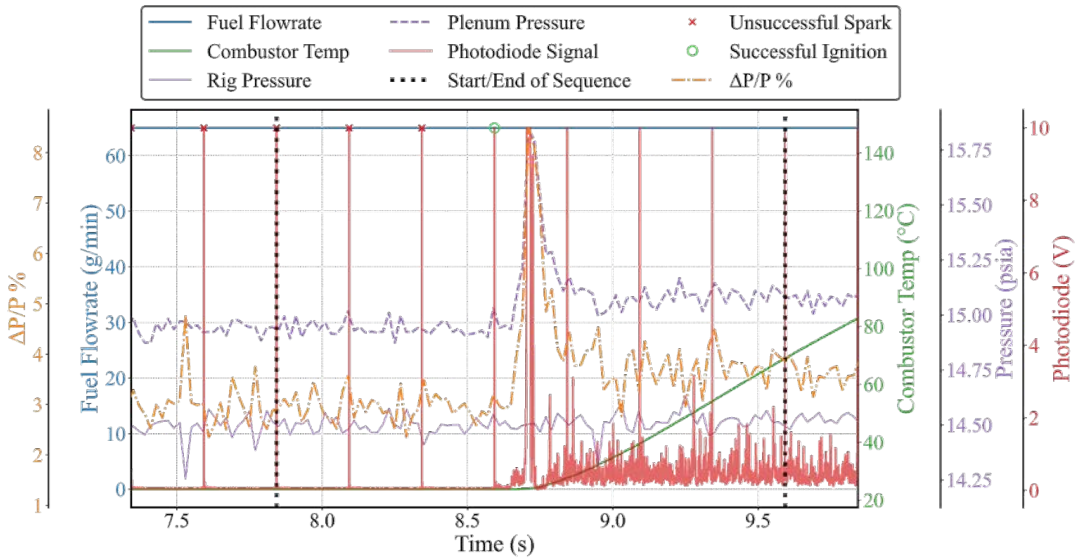


Figure 11. Temporal evolution of key metrics during sample ignition test at a fuel flowrate of 65 g/min. Recording sequence is highlighted with three sparks before ignition and four sparks starting from ignition.

Combusting vs Non-Combusting Statistical Comparison

Droplet size distributions significantly impact gas turbine engine performance. Different statistical moments of the distribution are required to fully characterize spray behavior. The general form for a droplet size diameter based on statistical moments is:

$$D_{xy} = \left[\frac{\sum n_i d_i^x}{\sum n_i d_i^y}\right]^{1/(x-y)}$$

where x and y define the moments and n_i is the number of particles with diameter d_i. The arithmetic mean, D_{10}, is the statistical mean of the number-weighted distribution. It represents the simple average diameter based on droplet count. Yet, the Sauter mean diameter D_{32}, which represents the diameter of a droplet with the same volume-to-surface-area ratio as the entire spray, is a standard metric used for correlating heat and mass transfer phenomena because these processes are highly dependent on total surface area.

To quantify discrete particle sizes, droplets were identified and extracted from each frame and then segregated into pre-combusting and post-combusting sequences. The raw histogram data were fitted to a truncated log-normal distribution, which provides a non-biased fit by accounting for droplets below the 10.8 μm X-ray detection limit. A log-normal distribution is physically appropriate, as droplet breakup is a multiplicative cascade process that trends toward this distribution via the central limit theorem. Figure 12 shows an example fit for both non-combusting and combusting sequences.

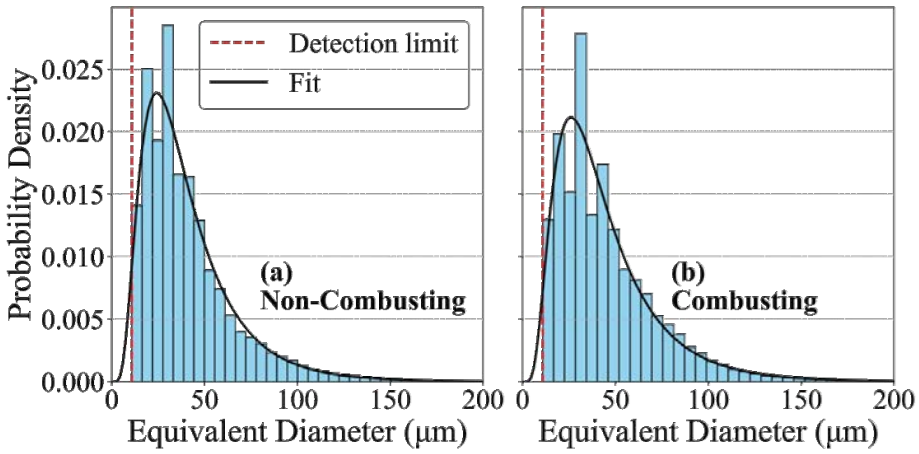


Figure 12. Histogram of measured droplet equivalent diameters with log-normal fitting: (a) non-combusting and (b) combusting.

To compare general trends, Figure 13 plots D10 and D32 for combusting and non-combusting cases. The data cover two configurations, near-nozzle (x=0 mm) and downstream (x=12 mm), and two different pressure-swirl nozzles (Nozzle A and Nozzle B). Nozzle A is the same as that used in Section 2a. At the downstream position (x=12 mm), the D32 is noticeably larger in the combusting case, while the D10 is simultaneously smaller. This combined trend is a strong indicator of preferential vaporization, consistent with the D^2 evaporation law. The smallest droplets, which have the highest surface-area-to-volume ratio, evaporate fastest. The decrease in D10 indicates that the increased vaporization is reducing the overall population, lowering the simple average diameter of all droplets. However, D32 becomes larger because it is now biased toward the remaining, larger droplets that dominate the spray's total surface area.

The near-nozzle position (x=0 mm) shows a more complex phenomenon, where both D10 and D32 are larger for the combusting case. At this position, there has been insufficient time for droplet evaporation to be the primary cause of this size increase. This implies that the combustion process itself is altering the primary atomization dynamics. Thermal feedback from the flame front to the liquid sheet, or modified aerodynamics from gas expansion, likely changes the liquid's breakup characteristics.

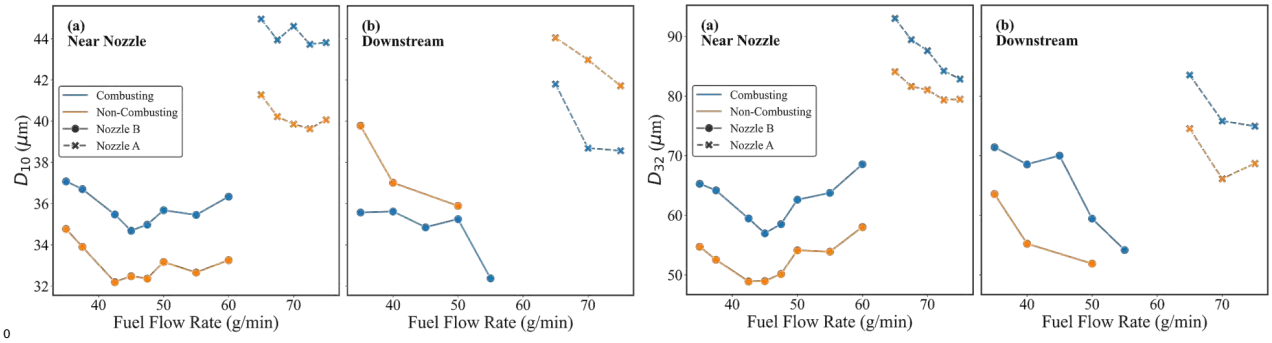


Figure 13. Mean diameter of fitted droplet distributions for non-combusting and combusting cases: (a) near nozzle and (b) downstream.

In addition to droplet distributions, the integrated behavior of flame propagation is analyzed. Flame propagation is captured via high-speed broadband visible imaging, and the flame extent is determined using a binarization scheme. Figure 14 summarizes the intensity-weighted centroid movement over time for unsuccessful (non-combusting) and successful (combusting) ignition events. For this analysis, time is normalized so that ignition occurs at t=0 seconds. In

unsuccessful cases, the centroid positions are scattered. In successful cases, this behavior transitions, with the centroid swirling and then attracting to a central region. Future analysis will focus on correlating the flame extent and propagation dynamics with local droplet properties.

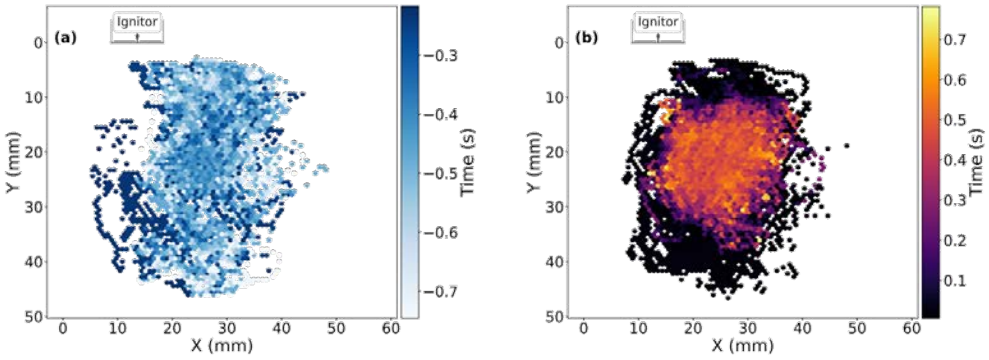


Figure 14. Flame kernel weighted centroid propagation: (a) non-combusting and (b) combusting.

Task 2c – Alternative Fuel Reduced Order Modeling of Breakup Dynamics

University of Illinois at Urbana-Champaign

Objectives

In this task, the impact of fuel property variability on primary atomization is directly investigated to accelerate the adoption of alternative fuels. The current ASTM D4054 certification process is a major bottleneck; developing "prescreening" tools that link fuel properties to spray performance is essential. This work will apply the validated analytical framework from Task 2a to a matrix of four fuels (F-24, C-1, C-3, C-5) selected for their wide-ranging physical properties (e.g., viscosity, distillation curve). We hypothesize that these properties create unique, quantifiable signatures in the spray's spatiotemporal velocity field. The primary objective is to use ROM, specifically DMD, to extract the dominant, low-dimensional physics from this high-dimensional data. This will provide a physically interpretable model that links specific fuel properties (like viscosity) to dominant breakup instabilities (e.g., spatial growth rates of DMD modes). This work represents a critical step toward creating a model-based prescreening methodology, reducing the reliance on large-scale, expensive testing for SAF certification.

Research Approach

ROM is an essential tool for quantifying dominant, translatable physics. Even in highly turbulent environments, ROMs can extract low-dimensional dynamics from seemingly random processes. This capability is critical for accelerating the adoption of alternative aviation fuels, which are necessary for sustainability and multi-fuel capability. Prescreening fuels by modeling their spray dynamics is therefore essential to reduce this cost and timeline. In smaller combustors, the time and length scales for atomization, vaporization, fuel-air mixing, and chemical reaction are shortened. Atomization and vaporization, in particular, become rate-limiting steps under unfavorable conditions, making spray behavior a key area of study.

Understanding the variance in spray dynamics across different fuels is therefore paramount. Classically, liquid sheet breakup is described via dispersion relations, where breakup is governed by the growth rate of the most unstable infinitesimal disturbance. However, this theory is difficult to validate experimentally, as it requires high-resolution spatiotemporal data. While some efforts have applied modal analysis to raw spray images of the liquid sheet (Leask et al., 2021; Jia et al., 2023; Kang et al., 2018; Kasmaiee et al., 2024), pixel intensity variance is not directly interpretable and does not necessarily correlate to physical motion or true variance. Therefore, it is more physically meaningful to pose the modal analysis in terms of the extracted velocity fields. Additionally, limited experimental work has investigated the effect of varying fuel properties on instability growth on the liquid sheet and breakup.



This analysis was accomplished using the optical flow model developed in Task 2a. Four different fuels with widely varying properties, shown in Table 1, are experimentally investigated: a baseline fuels F-24, C-1 (low cetane number), C-3 (high viscosity), and C-5 (low viscosity, flat boiling curve). Preliminary analysis on identical conditions to (Task 2a), but extended to these four fuels, indicates significant deviations in primary breakup length as identified by leading-edge contour tracking (Figure 15). Viscosity, a damping factor for deformation, appears to have a significant impact on breakup characteristics. Future work will involve using ROM to describe the breakup process. DMD is a promising methodology to coherently represent spatiotemporal information. This eigen decomposition technique has been applied to simulation data of spray breakup. Previous work suggests that temporal growth is not significantly meaningful in a pseudo-steady-state system. However, the spatial growth rates of individual modes may be a better indicator of instability. Preliminary dynamic mode decomposition of the four fuels shown in Figure 16 indicates spatial coherence in the axial direction indicating instabilities. Future work will investigate the DMD modeling technique for spray breakup prediction using this four-fuel dataset.

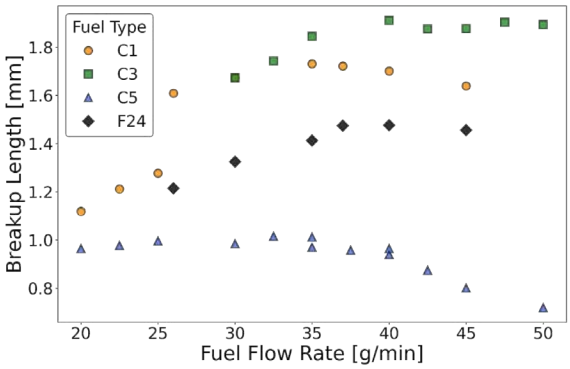


Figure 15. Primary breakup length of four fuels.

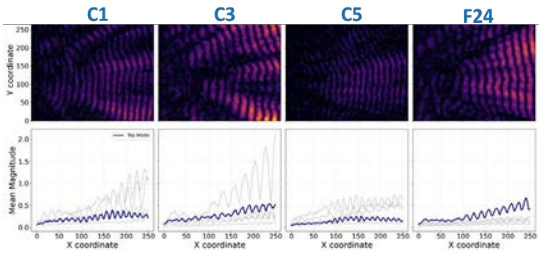


Figure 16. Dynamic mode decomposition spatial growth for four fuels.

Milestones

- Developed optical flow PC-Flow model with uncertainty quantification for spray velocimetry (3 months).
- Characterization of field parameters for primary and secondary atomization (breakup length, sphericity, size, and velocity distributions) (6 months).
- Analysis of ignition spray measurements (9 months).
- Application of DMD to extract spatiotemporal instabilities for four fuels (12 months).

Major Accomplishments

This research establishes a quantitative, mechanism-based framework for prescreening SAFs, addressing a key bottleneck in their certification. This is accomplished by moving beyond simple correlations to link fuel properties directly to in-situ spray dynamics under reacting conditions. First, a novel analytical tool, PC-Flow, was developed and validated to extract time-resolved velocity fields from combusting X-ray spray data, providing the necessary quantitative metrics (Task 2a). This framework was then applied to ignition, providing direct evidence that the combustion process itself actively alters



atomization and drives preferential vaporization, demonstrating that non-reacting spray data are insufficient for predicting performance (Task 2b). Finally, this validated methodology is now being applied to a matrix of fuels with diverse properties. By coupling these high-fidelity velocity fields with ROM (i.e., DMD), this work will produce a physically-interpretable, low-dimensional model that links specific fuel properties (e.g., viscosity) to quantifiable breakup instabilities (e.g., DMD spatial growth rates), forming the basis of a predictive prescreening tool for new SAFs (Task 2c).

Publications

Peer-Review Journal Articles

O'Brien, C. J., Kang, K., Wood, E. J., Yoon, J., Mayhew, E. K., Kastengren, A., Kweon, C. M., & Lee, T. (2026). Time-resolved spray characterization via unified optical flow and binarization technique. *Fuel, 407*(C), doi: 137433. https://doi.org/10.1016/j.fuel.2025.137433

Oh, J. H., Wood, E., Mayhew, E., Kastengren, A., & Lee, T. (2023). Sequence2Self: Self-supervised image sequence denoising of pixel-level spray breakup morphology. *Engineering Applications of Artificial Intelligence, 126*(B), doi: 106957. https://doi.org/10.1016/j.engappai.2023.106957

Outreach Efforts

All experimental spray breakup data, including high-speed videos, processed velocity fields, and droplet size distribution measurements, will be made publicly accessible via altjetfuels.illinois.edu.

Awards

None.

Student Involvement

This task has been primarily conducted by Casey O'Brien (PhD student).

Plans for Next Period

The primary focus for the next period will be to complete the ROM of the multi-fuel spray data, which is the core of Task 2c. The DMD analysis, which is still in a preliminary stage (Figure 16), will be fully investigated. The objective is to move from initial findings of spatial coherence to a robust, predictive model that quantitatively links specific fuel properties (like viscosity) to the spatial growth rates of the dominant breakup instabilities.

Concurrently, the ignition analysis from Task 2b will be finalized. This involves correlating the flame kernel propagation dynamics (from broadband imaging, Figure 14) with the local, time-resolved droplet statistics (from X-ray PCI, Figure 13). This final step will provide a quantitative link between the evolving flame front and its direct impact on the local spray properties, completing the multi-modal ignition study.

References

ASTM International. (2024). *ASTM D4054-24d: Standard Practice for Evaluation of New Aviation Turbine Fuels and Fuel Additives.* https://doi.org/10.1520/D4054-24

Leask, S., McDonell, V., & Samuelsen, S. (2021). Modal extraction of spatiotemporal atomization data using a deep convolutional Koopman network. *Physics of Fluids, 33.* https://doi.org/10.1063/5.0046177.80

Jia, B., Xie, L., Deng, X., He, B., Yang, L., & Fu, Q. (2023). Experimental study on the oscillatory Kelvin–Helmholtz instability of a planar liquid sheet in the presence of axial oscillating gas flow. *Journal of Fluid Mechanics, 959*, A18. https://doi.org/10.1017/jfm.2023.19.81

Kang, Z., Li, X., & Mao, X. (2018). Experimental investigation on the surface wave characteristics of conical liquid film. *Acta Astronautica, 149*, 15–24. https://doi.org/10.1016/j.actaastro. 2018.05.030

Kasmaiee, S., Tadjfar, M., Kasmaiee, S., & Ahmadi, G. (2024). Linear stability analysis of surface waves of liquid jet injected in transverse gas flow with different angles. *Theoretical and Computational Fluid Dynamics, 38*, 107–38. https://doi.org/10.1007/s00162-024-00685-2.79



Project 066 Evaluation of High-Thermal-Stability Fuels

Washington State University

Project Lead Investigator

Joshua Heyne
Bioproducts, Sciences, and Engineering Laboratory Director, Associate Professor
School of Engineering and Applied Science
Washington State University
2710 Crimson Way, Richland, WA 99354
(937) 229-5319
joshua.heyne@wsu.edu

University Participants

Washington State University (WSU)

- P.I.s: Assoc. Prof. Joshua Heyne and Assoc. Res. Prof. Randall Boehm
- FAA Award Number: 13-C-AJFE-WaSU-036
- Period of Performance: October 1, 2024, to September 30, 2025
- Tasks:
  1. Perform Jet Fuel Oxidation Tester (JFTOT) repeatability and reproducibility assessment
  2. Gain proficiency in analytical methods for trace impurities detection
  3. Develop methods for natural impurities amplification
  4. Establish a detailed experimental test plan for evaluating thermal stability
  5. Execute thermal stability test campaign

Project Funding Level

The Federal Aviation Administration (FAA) provided $350,000 in funding. Cost-sharing funding is provided by Air Company Holdings, Inc. ($350,000).

Investigation Team

Washington State University

Assoc. Prof. Joshua Heyne, (P.I.), All Tasks
Assoc. Res. Prof. Randall Boehm, (co-P.I.), All Tasks
Conor Faulhaber, (graduate research student), All Tasks

Project Overview

It has long been understood that increasing the reliance on jet fuel as a primary coolant for both the engine and the aircraft has significant performance and efficiency benefits relative to the use of air as a coolant (Bruening & Chang, 1999), but fuel degradation and coking at high temperatures restrict how much heat can be put into the fuel. In some military applications, the performance benefits are sufficiently large to justify the creation of specialty fuels such as JP7 and Jet Propellant Thermally Stable (JPTS), which can tolerate much higher temperatures than petroleum-derived Jet A or Jet A1 (JP8) fuels (Edwards, 2007). In land-based applications of gas turbines, weight is of little consequence; thus, the operations of waste heat recovery (WHR) for plant efficiency or the cooling of combustor inlet temperature for emission reductions can be accomplished in a wide variety of ways, all of which are impractical for flight because of their impact on the mass of the power plant. Nonetheless, these applications provide some common examples of how controlling the air temperature along its flow path through the engine can have a large impact on performance, durability, and energy efficiency (Wilfert et al., 2007). The flurry of works relating to fuel deoxygenation (Zabarnick et al., 2020) and other ways to decrease coking propensity and its impacts (Mancini et al., 2004) is largely motived at the sponsorship level by these benefits.



More recently, sustainable aviation fuels (SAF) have received much attention because they can contribute to high-priority geopolitical goals to diversify energy supply chains and reduce greenhouse gas emissions. Most of these efforts have focused on streamlining the evaluation and approval processes to use synthetic fuels at some blend ratio with petroleum-derived jet fuel to create a so-called drop-in fuel that can be used within existing infrastructure without objection from any stakeholders (Colket & Heyne, 2021). Additionally, there have been discussions regarding characteristics of synthetic blend components (e.g., low aromatics, high specific energy, and high thermal stability) that would make these components attractive to consider as potential specialty fuels (i.e., JPTS) or high-performance fuels. Kosir et al. (2020) published work highlighting the efficiency gain that could be realized by using fuels with high specific energy, via lower aircraft weight at take-off, with less mass to lift and hold against the force of gravity.

The weight of fuel uplifted to an aircraft, as necessary to complete its mission, is certainly an important component to consider in assessing the integrated engine/aircraft energy demand and efficiency. The energy efficiency of the engine is also expected to be influenced by other fuel properties, including the following:

- **Hydrogen/carbon (H/C) ratio:** Through its impact on combustor exhaust gas composition, this ratio has a small impact on the ratio of heat capacities (gamma), combustor exit temperature, and work extracted during expansion through the turbine, even when the total enthalpy created at the combustor is unchanged.
- **Viscosity:** Viscosity impacts the heat transfer coefficients, which determine how much waste heat is recovered by the fuel (coolant) and delivered back to the engine via the combustor.
- **Energy density:** Energy density, measured in joules per liter (J/L), impacts volumetric flow rates, which also impacts heat transfer coefficients.
- **Specific heat:** Specific heat also has some effect on heat transfer coefficients, but perhaps more importantly has a direct impact on the temperature rise in the fuel per unit of heat energy absorbed, which in turn may impact the coking rate.
- **Coking rate:** Also known as fuel thermal stability, the coking rate drives several high-level design decisions relating to the thermal management of an engine.

References

Bruening, G. B., & Chang, W. S. (1999). Cooled cooling air systems for turbine thermal management. *Proceedings of the ASME 1999 International Gas Turbine and Aeroengine Congress and Exhibition. Volume 3: Heat Transfer; Electric Power; Industrial and Cogeneration*, Indianapolis, Indiana. https://doi.org/10.1115/99-GT-014

Colket, M., & Heyne, J. (2021). *Fuel effects on operability of aircraft gas turbine combustors*. The American Institute of Aeronautics and Astronautics, Inc. https://doi.org/10.2514/4.106040

Edwards, T. (2007). Advancements in gas turbine fuels from 1943 to 2005. *Journal of Engineering for Gas Turbines and Power, 129*(1), 13–20. https://doi.org/10.1115/1.2364007

Kosir, S., Stachler, R., Heyne, J., & Hauck, F. (2020). High-performance jet fuel optimization and uncertainty analysis. *Fuel, 281*. https://doi.org/10.1016/j.fuel.2020.118718

Mancini, A. A., Ackerman, J. F., Richard, L. K., & Stowell, W. R. (2004). *Method and coating system for reducing carbonaceous deposits on surfaces exposed to hydrocarbon fuels at elevated temperatures* (6808816 B2). General Electric Company.

Wilfert, G., Sieber, J., Rolt, A., Baker, N., Touyeras, A., & Colantuoni, S. (2007). *New environmental friendly aero engine core concepts*. https://api.semanticscholar.org/CorpusID:73527508

Zabarnick, S., West, Z. J., Arts, A., Griesenbrock, M., & Wrzesinski, P. (2020). Studies of the impact of fuel deoxygenation on the formation of autoxidative deposits. *Energy Fuels, 34*, 13814–13821. https://doi.org/10.1021/acs.energyfuels.0c02603

Task 1 – Perform Jet Fuel Thermal Oxidation Tester Repeatability and Reproducibility Assessment

Washington State University

Objective

The objective of Task 1 is to establish the repeatability and reproducibility of the JFTOT measurement. Doing so will provide a foundation for determining the thermal stability impacts of varying SAF impurity profiles, begin to evaluate the

effectiveness of the current specification's trace impurity limits on reducing thermal stability risks for novel SAF, and explore the potential of improved thermal stability relative to conventional fuels.

Research Approach

The repeatability assessment was accomplished by performing 22 total JFTOT measurements over seven temperature settings on a conventional Jet A fuel ("Richland Jet A") sourced from a local airport. Other than varying temperature, tests were run under conditions abiding by the standard ASTM D3241 specifications (ASTM, 2023b) on Falex® 400 JFTOT. The JFTOT sample tubes (aluminum, Falex, Inc.) were rated for total deposit thickness using the ellipsometric method described in ASTM D3241 Annex 3 on a Falex 430 ellipsometric tube rater (ETR). The repeatability was also evaluated for the maximum differential pressure and total deposit volume metrics.

The portion of this task relating to reproducibility was completed via participation in the ASTM Intralaboratory Study (ILS) for the JFTOT experiment. Participation involved two measurements of a newly devised JFTOT Operational Validation Fluid from the ASTM D3241 Reference Fluid Task Force. Both Alcor and Falex brand JFTOT sample tubes were tested, and both measurements were run at 275°C, per the ILS instructions.

Results

1. Repeatability Measurements

Figure 1 presents the maximum deposit thickness and total deposit volume results of the repeatability measurements at 5˚C temperature intervals from 255˚C to 275˚C. The breakpoint of the Richland Jet A, or highest temperature at which the deposit remains below the 85nm max. deposit thickness specification limit, was found to be 265˚C. The maximum deposit thickness results show consistent standard deviation values between temperature settings through 270˚C, but increases drastically at 275˚C. The deposit volume results show a similar trend, but with the decrease in repeatability showing at 270˚C. With both metrics, there are lower deposition levels at 275˚C than 270˚C. This is a sign that the oxidation pathway may become oxygen-limited between these two temperatures. Overall, these metrics provide adequate repeatability for research purposes, with the maximum deposit thickness used in the specification showing a lower standard deviation when 5˚C above the breakpoint temperature.

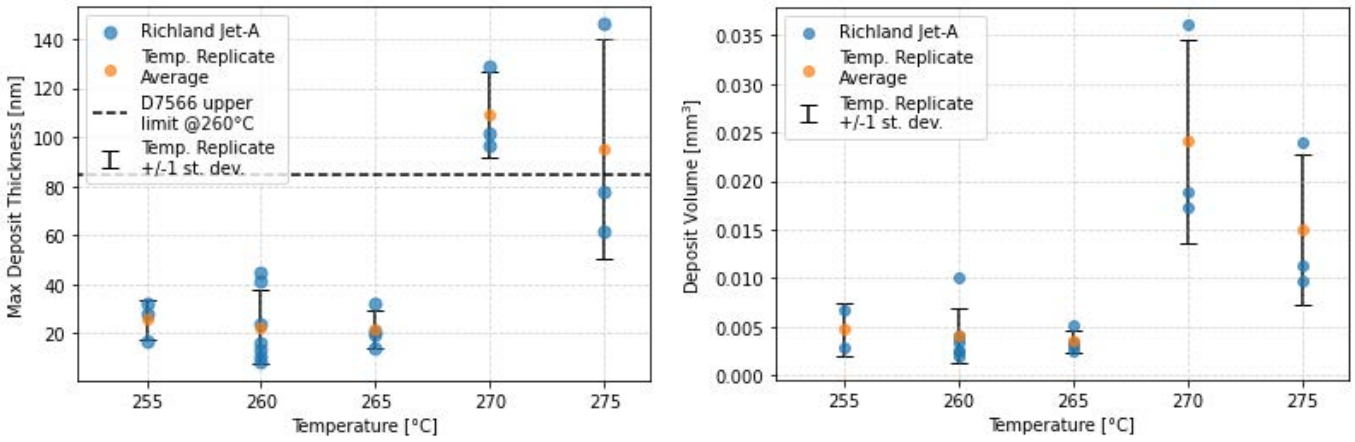


Figure 1. Repeatability measurement maximum deposit thickness (left) and total deposit volume (right) for Richland Jet A at 5˚C intervals from 255˚C to 275˚C.

A third metric recorded during JFTOT testing is the differential pressure (DP). This metric measures the pressure difference across the filter placed on the back end of the sample tube assembly, and is intended to account for insoluble oxidation products that, while not contributing to deposition, are an indicator of thermal oxidative instability. As these products are caught in the filter, the pressure drop increases. A DP greater than or equal to 25mmHg is considered a fail. The DP results for the repeatability measurements are found in Figure 2 below. Unusual oscillating behavior was found for the measurements at 255˚C and 260˚C, where the DP result indicated either 0 or 100mmHg. This poor repeatability makes it

® Falex is a registered trademark of Falex Corporation, Sugar Grove, Illinois.



difficult to use the DP data as a pass/fail metric, and given the sensitivity of the ETR compared to the visual tube rating (VTR) previously used in JFTOT research it appears that the deposit thickness is a more reliable metric to rate JFTOT tubes. Documentation of this behavior is important as the 25mmHg maximum DP remains in the ASTM specifications for jet fuels.

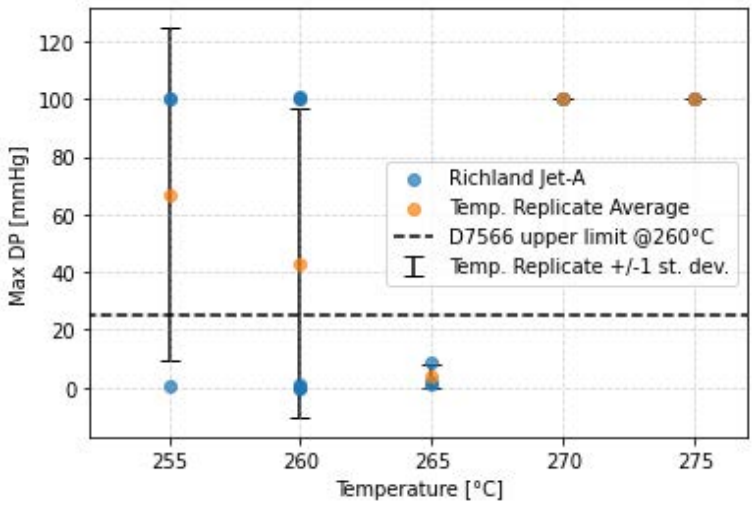


Figure 2. Repeatability measurement maximum differential pressure (DP) for Richland Jet A at 5˚C intervals from 255˚C to 275˚C.

2. Reproducibility Measurements

The results of the ILS are not yet published. The team at WSU was informed that the measurements produced as a part of this work were well within the reproducibility determined by the study.

3. Streaking Phenomenon

While performing breakpoint testing on a second batch of Jet A fuel ("Richland 2 Jet A") an unusual streaking phenomenon appeared on the ETR deposition profile of the JFTOT sample tubes tested at high temperature settings (≥350˚C) and persists for new tests <350˚C. The repeatable nature of this issue makes it relevant to the work relating to JFTOT repeatability in items 2 and 3 above. This section will chronologically report the discovery of the streaking phenomenon and attempted, but ultimately unsuccessful, mitigation strategies.

Figure 3 and the following two paragraphs present a summary of the testing leading to the tube streaking. A fuel's JFTOT breakpoint is determined by running a series of tests at different temperature settings to determine the highest temperature (+/- 5˚C) that a fuel will pass the 85nm maximum deposit thickness and 25mmHg DP spec limits. Richland 2 Jet A performed especially well for a conventional Jet A fuel during breakpoint testing, reporting maximum deposit thickness below 85nm at 330˚C (Figure 3, top left), well above the 260˚C requirement found in ASTM D1655 (ASTM, 2023a) for petroleum-derived Jet A fuel. This result was also suggested to be accurate by low total nitrogen and sulfur results, <0.5ppm and 48ppm, respectively. A similar result was seen at 325˚C (Figure 3, bottom left). Thus, breakpoint testing continued, and the next measurement was made at 350˚C.

At 350˚C (Figure 3, top center), an asymmetric deposit profile appeared. Interestingly, a separated streak appears upstream on the tube, separate from the primary ridge of deposits, and a gap in the primary ridge is present where the streak would fit. Since noisy data are known to occur in some JFTOT measurements and the deposits did not surpass the 85nm limit, this result was ignored initially, and breakpoint testing proceeded. At 380˚C (Figure 3, bottom center), a similar streak appeared upstream on the tube along with a corresponding gap in the primary deposit ridge. Because the primary ridge far exceeded the 85nm specification limit, breakpoint testing continued at a lower temperature. At 360˚C (Figure 3, top right), a similar result to the test at 350˚C occurred. At this point it was clear that the asymmetric streaking was repeatable. Suspecting high temperature impacts, a test was run at 325˚C. These results (Figure 3, bottom right) showed the same anomaly, indicating that some semi-permanent/permanent change had occurred to the instrument.

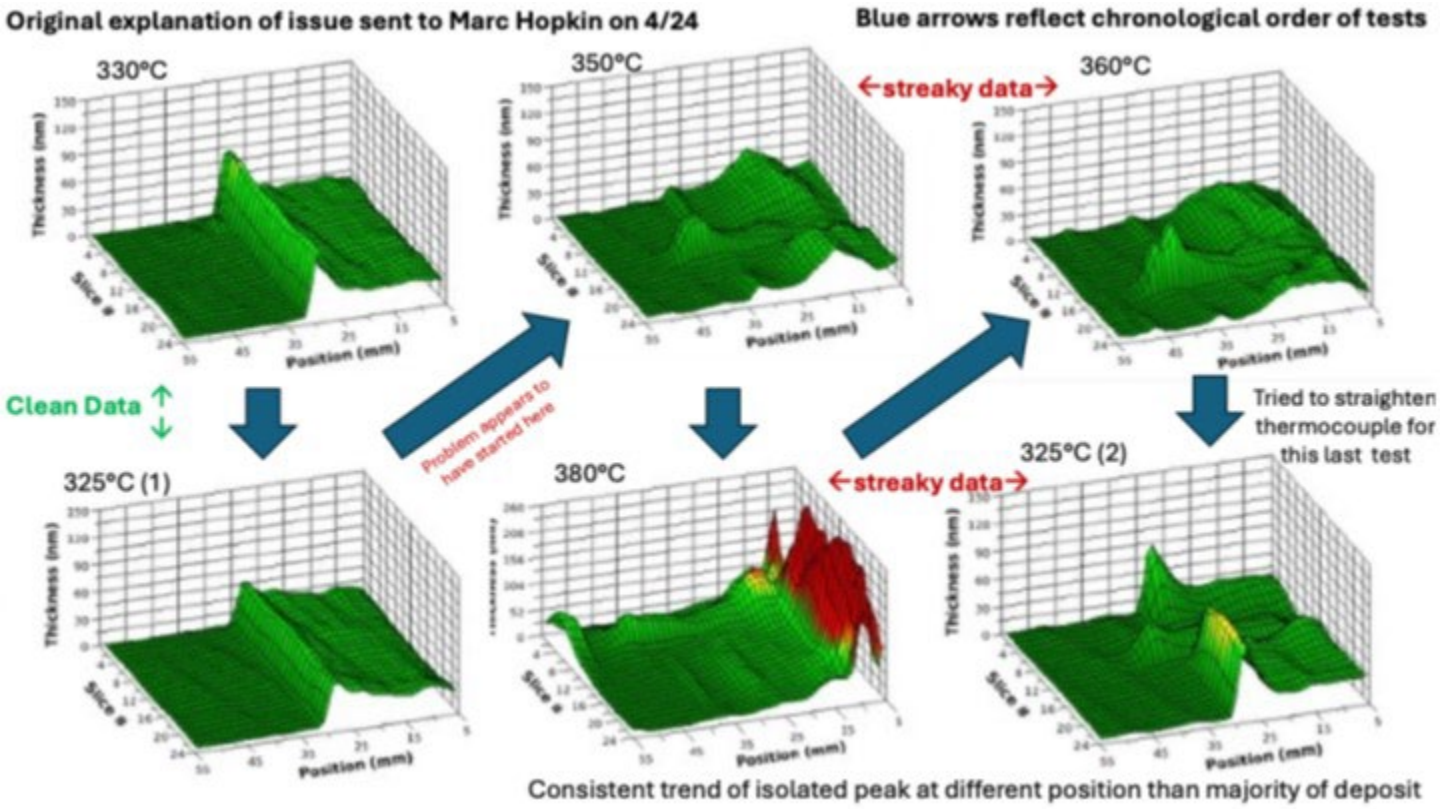


Figure 3. Chronological flowchart summary of streaking phenomenon on Jet Fuel Thermal Oxidation Tester (JFTOT) sample tubes with Richland 2 Jet A.

Once this issue was repeated at previously tested lower temperatures, the process towards reversing or mitigating this issue began. Table 1 contains the experimental variables considered and how we addressed potential problems with said variables. It is important to note that none of these attempts were successful, and the streaking persists at the time of this documentation. The team at WSU has also been in contact with Falex, Inc. (the instrument manufacturer) and George Wilson (retired, previously of Southwest Research Institute) who led the effort to develop the ASTM 3241 JFTOT method.



Table 1. JFTOT experimental variables and attempts to mitigate the asymmetrical streaking. All efforts have been unsuccessful at the time of this report.

JFTOT Experimental Variable	Mitigation Approach
Fuel	• 3 conventional fuels, 4 synthetic blend components (SBC) candidates
Test temperature	• 6 temperature settings
Flow rate	• 3 total flow rate settings: 1.5, 3 (default), and 6 mL/min
Sample tube	• Tube batch number varied • Pre-test uniformity verified in ETR
Sample tube thermocouple	• Thermocouple straightened and lengthwise position varied • Thermocouple replaced • Recalibrated. Both old and new calibration metrics are within recommended range
Sample tube assembly	• Assembly vigorously cleaned, purged between runs with 80/20 petroleum ether/toluene solvent blend • O-rings replaced each run • Entire assembly replaced
Bus bar cooling	• Refreshed with new coolant, removed air bubbles
Internal hardware	• Internal tubing accessed and cleaned • Pump visually inspected

To date since the first occurrence of the streaking, all tests exhibiting any noticeable amount of coking have also displayed the streaking behavior. The engineering team at the manufacturer, Falex, Inc., has not been able to provide a resolution. George Wilson's observation is that asymmetric flow is common in JFTOT tests, and that he sees no apparent problem in the streaking results. He also provided useful background information and resources, including the notion that the results above 330˚C are likely showing pyrolytic deposits, a far different reaction mechanism than thermal oxidative deposits typically observed by the JFTOT. Thoroughly investigating the streaking phenomenon became an obstacle to continued JFTOT testing (see Task 5) but was necessary to grasp the potential impacts of this on research efforts as well as documenting it as a repeatability risk for the broader community.

Milestone

- Developed understanding of test repeatability and reproducibility.

Major Accomplishments

None.

Publications

None.

Outreach Efforts

George Wilson (Southwest Research Institute, retired) and Falex, Inc., were contacted for feedback about the streaking phenomenon. While not able to resolve the issue, both provided useful feedback to investigate and/or rule out several potential causes, including fuel flow properties, thermal gradients, and additional maintenance procedures not performed during routine care of the instrument.

Awards
None.

Student Involvement
Conor Faulhaber, a PhD student at WSU, leads JFTOT-related experimental work for the lab including test planning, data organization, data analysis, instrument maintenance, and reporting results. Kaamel Sidiqi, an undergraduate at WSU, is trained on and runs the JFTOT experiment.

Plans for Next Period
Continue to monitor the streaking phenomenon. Assess repeatability of doped samples.

References
ASTM International. (2023a). *ASTM D1655-22a: Standard Specification for Aviation Turbine Fuels.* https://doi.org/10.1520/D1655-22A

ASTM International. (2023b). *ASTM D3241-23: Standard Test Method for Thermal Oxidation Stability of Aviation Turbine Fuels.* https://doi.org/10.1520/D3241-23

Task 2 – Gain Proficiency in Analytical Methods for Trace Impurities Detection
Washington State University

Objective
The objective of Task 2 is to become skilled in performing the experimental methods required to detect the trace impurities responsible for thermal oxidation in jet fuels. This task requires equipment installation, lab personnel training, and in-house method development to master the application of interest.

Research Approach
The main subject of this work was to detect fuel-bound sulfur, nitrogen, and oxygenated species in jet fuel, as well as trace metals. The following sub-sections detail the different analytical methods employed for each type of impurity.

Sulfur-Containing Compounds
Sulfur-containing compounds (SCC) are being detected with three different methods: ultraviolet fluorescence (UVF), inductively coupled plasma optical emission spectrometry (ICP-OES), and combustion ion chromatography (CIC). Multiple methods were developed for sulfur detection due to its prevalence in conventional jet fuel pathways and because, in addition to thermal stability, there is significant research interest in the quantification of parts-per-billion levels of sulfur for its impact on contrails: ice particle count and size distribution (Karcher, 1998). Comparisons of these methods to each other contributes to the evaluation of these methods and builds confidence in results near the detection limit.

1. Ultraviolet Fluorescence
The UVF system quantifies total sulfur by converting sulfur-containing compounds into sulfur dioxide (SO_2) in an oxygen-rich combustion environment. The generated SO_2 absorbs ultraviolet light in the 200–400 nm range and subsequently emits fluorescence (~330 nm) upon relaxation. This fluorescence is detected using a photomultiplier tube, and the resulting signal is integrated to calculate the total sulfur content of the original sample. The signal intensity is directly proportional to the sulfur concentration, allowing for quantitative analysis via linear regression of standard concentrations versus integrated signal area.

UVF results were benchmarked against ASTM D5453 (ASTM, 2025), a standard method for determining total sulfur in the range of 1.0 to 8000 mg/kg. ASTM D5453 is widely regarded for its ability to convert all sulfur species into SO_2, thereby minimizing matrix effects and enhancing accuracy. This method is preferred for regulatory compliance monitoring due to its high sensitivity and reliability, and is referenced in the jet fuel specifications, ASTM D1655 (ASTM, 2023a), D7566 (ASTM, 2024d), and D4054 (ASTM, 2024b), for this reason. For UVF sulfur detection, the WSU SAF Lab uses XPLORER-TS.® The

® XPLORER-TS is a registered trademark of TE Instruments, Houston, Texas.



instrument settings are as follows: 100 mL/min argon flow rate, 300 mL/min primary oxygen flow rate, 100 mL/min collision oxygen flow rate, 1000°C furnace temperature. The instrument is calibrated using eight internal standards of dibenzothiophene (98% purity) doped in n-dodecane (>99% purity) for three different sulfur content ranges: 0 – 100 mg/kg, 0 – 12 mg/kg, and a low-sulfur calibration from 0 – 1.58 mg/kg. Each calibration curve maintains $R^2 > 0.999$ (R^2: coefficient of determination).

2. Inductively Coupled Plasma Optical Emission Spectroscopy

ICP-OES is an analytical technique that uses a high-temperature plasma to excite atoms and ions, causing them to emit electromagnetic radiation at element-specific wavelengths. The intensity of this emitted light is directly proportional to the concentration of each element in the sample.

In a typical ICP-OES setup, the liquid sample is introduced via a nebulizer, which generates an aerosol that is carried by an argon gas stream into an argon plasma operating at approximately 10,000 K. Within the plasma, the sample components are atomized and excited. As the excited atoms and ions return to their ground state, they emit light at characteristic wavelengths. An optical system, typically equipped with a polychromator, disperses this light and measures the emission intensity at each relevant wavelength. These intensities are then correlated to elemental concentrations through calibration.

ASTM D7111 (ASTM, 2021) is a standard method developed to quantify trace levels of metallic elements in middle distillate fuels (e.g., diesel, kerosene, jet fuel). However, analyzing petroleum-based samples presents several analytical challenges. One major issue is the requirement for matrix-matched calibration standards—the calibration curve must be prepared using a solvent mixture that closely mimics the fuel sample matrix. Due to the complex and variable composition of fuel samples, creating a suitable matrix-matched standard is not straightforward.

The method also recommends the use of internal standards to correct for matrix effects and instrumental drift. However, care must be taken to avoid wavelength overlap, which can lead to spectral interference or false positives due to signal contributions from other elements. The hydrocarbon matrix can significantly influence signal behavior, either suppressing or enhancing emission intensities, further complicating quantitative analysis. Moreover, the volatility and flammability of the organic solvents used in sample preparation demand strict adherence to safety protocols.

To mitigate these challenges, ASTM D7111 outlines specific strategies, including the use of matrix-matched calibration standards, internal standardization for signal normalization, controlled sample introduction rates to maintain plasma stability and analytical precision. Although ICP-OES is traditionally applied to the quantification of metals under ASTM D7111, we have adapted this method for sulfur determination in organic fuel samples. This adaptation is motivated by several published studies that demonstrate the feasibility of ICP-OES for sulfur quantification in oil matrices, prompting us to validate this approach for our application.

The instrument settings for the WSU SAF Lab ICP-OES sulfur detection method are as follows: 181.669 nm wavelength, 0.61 L/min nebulizer flow, 12.0 L/min plasma flow, and 25% oxygen flow. A-solv, Agilent®'s commercial kerosene solvent, is used as the calibration solvent for matrix-matching purposes. This limits the ICP-OES analysis method's sensitivity, as A-solv contains some baseline sulfur content (~1mg/kg). Investigating other matrix-matched solvents with lower sulfur levels will be part of the future work with this instrument. The ICP-OES method was calibrated for sulfur measurement using two calibration curves produced with sulfur compounds doped into A-solv, one with dodecanethiol (0.25–50 mg/kg) and another with dibenzothiophene (0.27 – 9.3 mg/kg). Both curves demonstrated $R^2 > 0.999$

3. Combustion Ion Chromatography

The CIC method includes a combustion and sample introduction unit and an ion chromatography (IC) system. Sulfur in the sample is converted to sulfur oxides (SO_x) (mainly SO_2 and sulfur trioxide [SO_3]) in a high-temperature combustion furnace at approximately 1000°C in a pure oxygen atmosphere. The combustion gases are transferred into an absorption solution, typically a hydrogen peroxide solution where SO_2 and SO_3 dissolve to form sulfurous acid (H_2SO_3) and sulfuric acid (H_2SO_4) and sulfite ion (SO_3^{2-}) further oxidizes to sulfate (SO_4^{2-}). The aqueous containing anions such as sulfate is injected into an ion chromatography system. The IC column separates the ions based on their charge and size. The separated ions are detected using suppressed conductivity detection, a sensitive method that enhances signal by reducing background conductivity from the eluent.

® Agilent is a registered trademark of Agilent Technologies, Inc., Santa Clara, California.



The scope of ASTM D7359 (ASTM, 2023d), the standard method for halide and sulfur detection via CIC, is 0.1–10 ppm per element. For sub-ppm detection, special attention must be given to contamination control and system cleanliness. Our system was optimized by reducing sample injection (60uL) volume to minimize soot formation and extending measuring tubing (aqueous sampling, 200uL) to improve signal-to-noise ratio. The WSU SAF Lab method for CIC sulfur measurement uses the following conditions: 200 mL/min argon flow rate, 400 mL/min oxygen flow rate, 100 mL/min working standard argon flow rate, 8 mL absorption solution volume, Dionex® IonPac® AS19 250mm x 4mm ion chromatography column, 50mm x 4mm guard column, 20mM potassium hydroxide (KOH) eluent, and a 1.0 mL/min sample flow rate. Multiple calibration curves were developed and compared for the CIC using dodecanethiol, benzothiophene, dibenzothiophene, and di-tert-butyldisulfide doped in n-dodecane at concentrations ranging from 0 to 14ppm. While the slope and intercept for each dopant's curve varied slightly, all reported $R^2 > 0.999$.

4. Results

Table 2 below depicts the detection (i.e., limit of detection [LOD]) and quantification (i.e., limit of quantitation [LOQ]) limits determined for each of the sulfur quantification methods discussed. The results indicate that the UVF method exhibits slightly better sensitivity than the CIC method, with the ICP-OES method far behind the other methods. This is likely due to the need for matrix-matching calibration for the ICP-OES method, making it difficult to find a high-purity solvent to establish a low-sulfur baseline. In addition to having desirable sensitivity, the UVF method is also the simplest instrument to operate and maintain, making it the first choice for sulfur quantification efforts. Interestingly, the standard for this method, ASTM D5453, bounds the application of UVF to sulfur levels between 1.0 and 8,000 mg/kg. Thus, it was necessary to verify the sub-ppm UVF sulfur measurements with the CIC method. Additionally, the CIC method more directly measures sulfur content compared to the UVF method. Because the UVF detector captures signal across a range of UV wavelengths, overlapping UV signal from the hydrocarbon content making up over 99% of jet fuel samples can create a false sulfur signal that becomes significant for fuels with little sulfur content. The ion chromatography avoids this issue, as hydrocarbons will not elute with a sulfate ion peak. While it is a more complex experiment to run and maintain, this makes the CIC method a dependable choice for gaining confidence in low-sulfur measurements, including verifying the sulfur content in low-sulfur standards used to calibrate other experiments.

Table 2. Sulfur detection method limit of detection (LOD) and limit of quantitation (LOQ), determined by 3x and 10x, respectively, of the standard deviation of 7 instrument blanks.

Sulfur Detection Method	LOD [mg/kg]	LOQ [mg/kg]
UVF	0.024*	0.098*
ICP-OES	0.5	1.5
CIC	0.04	0.1

**Approximation based on the 0 – 12 mg/kg calibration curve. In practice LOD/LOQ is determined directly from signal area. Also, see discussion around Figure 5 for context surrounding these values.*

Figure 4 shows the results of a set of sulfur measurements on a set of Hydroprocessed Esters and Fatty Acids (HEFA) fuel samples used in a flight test, external to this project. The UVF and CIC results display good agreement across the range of samples, remaining within 5% relative standard deviation (RSD) of each other. Meanwhile, the ICP-OES results appear systematically lower than the other methods. Additionally, as shown by the black lines, the repeatability for the ICP-OES method exceeds 10% RSD while the UVF and CIC methods report values of 0.069 – 1.18% and 0.063 and 1.13% RSD, respectively. Both the agreement between UVF and CIC methodologies and the good repeatability at low sulfur concentrations confirm that they are more than suitable for the application of jet fuel sulfur quantification.

® Dionex and IonPac are registered trademarks of Dionex Corporation, Sunnyvale, California.

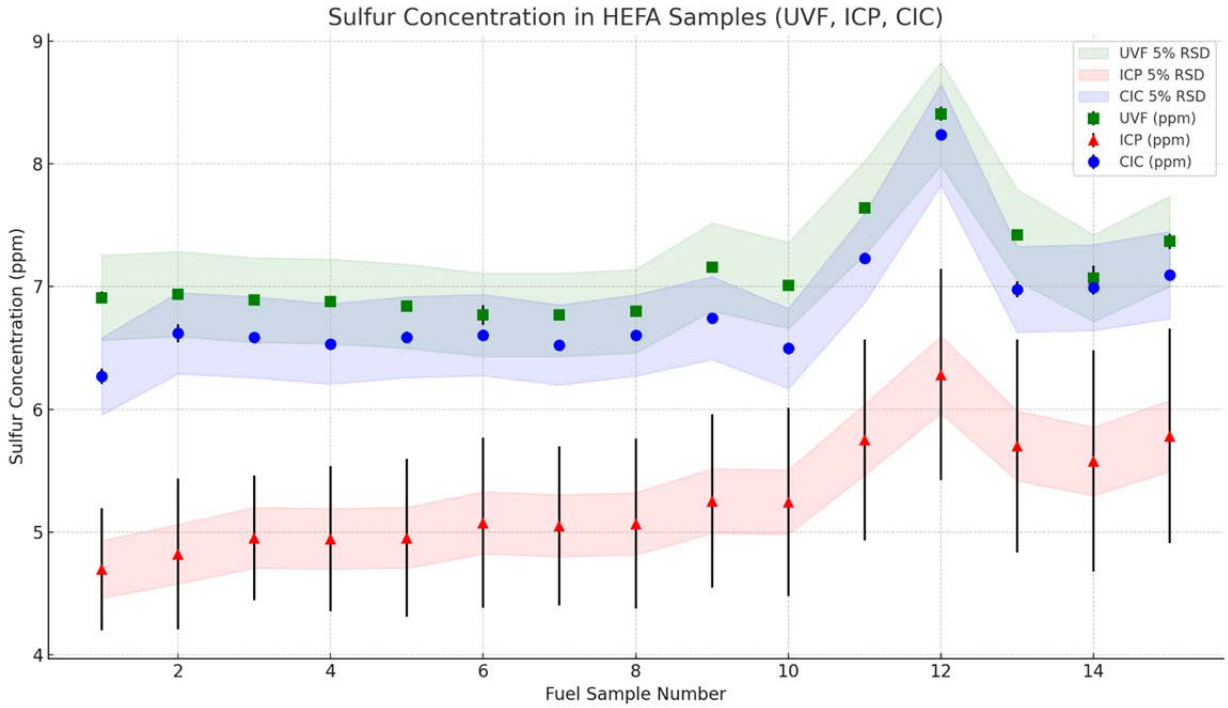


Figure 4. Ultraviolet fluorescence (UVF), inductively coupled plasma optical emission spectrometry (ICP-OES), and combustion ion chromatography (CIC) sulfur quantification results for 15 hydroprocessed esters and fatty acids (HEFA)-synthetic paraffinic kerosene (SPK) fuel samples. The shaded region reflects 5% relative standard deviation (RSD) for each test, and the black bars indicate the RSD of three replicate measurements on each sample.

After deeming the UVF and CIC methods suitable for jet fuel sulfur quantification, including sub-ppm-level detection, 6 SAFs with suspected low sulfur content were selected for testing. The results of this work are shown below in Figure 5. Here, the UVF measurements consistently overshoot those of the CIC method. This is suspected to be a result of the chemistry involved with each detection method, as mentioned before. At sub-ppm sulfur levels, the small amount overlapping ultraviolet wavelength from the bulk hydrocarbons become significant to the overall signal captured by the UVF detector. On the other hand, there is no hydrocarbon interference in the sulfate ion peak on the IC chromatograph, so the sulfur content is measured more directly than in the UVF method, and the result is consistently lower. Using the CIC method, the calibration blank n-dodecane can be analyzed for its baseline sulfur content, and the UVF calibration can then be adjusted. However, because the LOD and LOQ are derived from instrument blank values, they are not corrected in the UVF and ignore the impact of blank interference. Thus, the LOD and LOQ values for the UVF method in Table 2 likely overestimate the instruments sensitivity. The extent of this overestimation is yet to be determined and may also depend on the composition of the bulk hydrocarbon matrix. Still, its ease of use and good repeatability makes the UVF method a valuable tool for sulfur quantification.

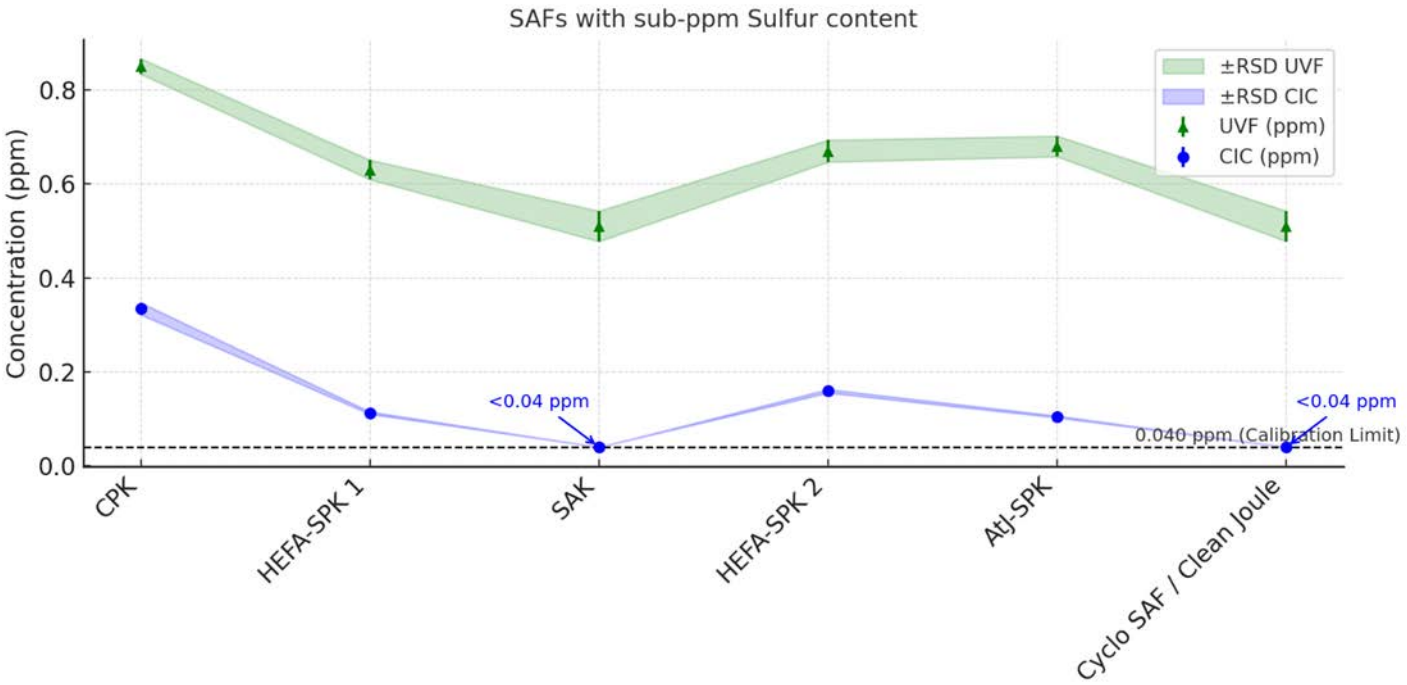


Figure 5. Low-sulfur measurement results from ultraviolet fluorescence (UVF) (green) and combustion ion chromatography (CIC) (blue) test methods. The shaded regions reflect the measured standard deviation for 3 replicates of each sample. Note that synthesized aromatic kerosene (SAK) and CycloSAF were measured below the CIC limit of detection of 0.04 mg/kg.

Mercaptan Sulfur

In addition to total sulfur content, mercaptan sulfur is also called out in the jet fuel specification. The WSU SAF Lab maintains the capability to run ASTM D3227 (ASTM, 2023b), a potentiometric method for quantifying mercaptan sulfur in jet fuel samples.

Nitrogen-Containing Compounds

Nitrogen-containing compounds (NCC) are quantified using 1-dimensional gas chromatography-nitrogen chemiluminescence detection (GC-NCD). The WSU SAF Lab runs this instrument as an adapted version of ASTM D4629 (ASTM, 2017), which sends the sample directly from the combustor to the detector rather than separating it through a gas chromatography (GC) column first. The added advantage of the GC-NCD is that individual nitrogen species can be evaluated on boiling point or polarity, depending on the type of column used. This can aid with further identification via solid-phase extraction (SPE) coupled with gas chromatography-mass spectrometry (GC-MS) that will be described in Task 3 of this document. After several iterations of method development using the work of Deese et al. (2020) as a starting point, Gaussian peak shapes and acceptable sensitivity were achieved. The resulting GC-NCD conditions can be found in Table 3.



Table 3. Gas chromatography-nitrogen chemiluminescence detection (GC-NCD) conditions determined via method development.

GC-NCD Variable	Setpoint
Inlet Temperature	300˚C
Inlet Pressure	3.3573 psi
Total Flow	20.6 mL/min
Septum Purge Flow	3 mL/min
Inlet Mode	Split
Split Ratio	10:1
Carrier Gas	Helium
Column	HP-5, 30m x 0.320mm x 0.250micron
Column Flow	1.6 mL/min
Column Pressure	3.3573 psi
Average Velocity	43.907 cm/sec
Holdup Time	1.1388 min
Oven Program	Start at 60˚C and hold 2 min. Ramp 25˚C/min to 160˚C hold 2.3min. Ramp 20˚C/min to 300˚C, no hold.
NCD Base Temperature	280˚C
NCD Burner Temperature	900˚C
Hydrogen Gas Flow	4 mL/min
Oxygen Gas Flow	8 mL/min

The NCD burner is fed with pure hydrogen (H_2) and oxygen (O_2), such that any nitric oxide (NO) produced is the result of the combustion of nitrogenated species in the sample. The nitrogen chemiluminescence method works by reacting NO with generated ozone, resulting in excited nitrogen dioxide (NO_2^*). When this returns to its ground state NO_2, the emitted red/infrared light is detected and can be directly related to the nitrogen content in the sample. However, similar to the UVF method for sulfur detection, the bulk hydrocarbon content of the fuel can contribute to some overlapping light emission that is captured by the detector. According to Agilent, the ratio of carbon signal to that of a nitrogen compound is $1{:}10^7$, meaning that there can be noticeable interference depending on the hydrocarbon matrix and the amount of individual nitrogen compounds. To probe this, GC-NCD calibration curves were produced using several purchased nitrogen compounds doped individually in a number of low-boiling point solvents, including n-hexane, isopropyl alcohol, and acetone. It was found that calibration curves were consistent between nitrogen compounds and solvents as long as coelution did not take place. An example of one of these calibration curves is found in Figure 6 below.

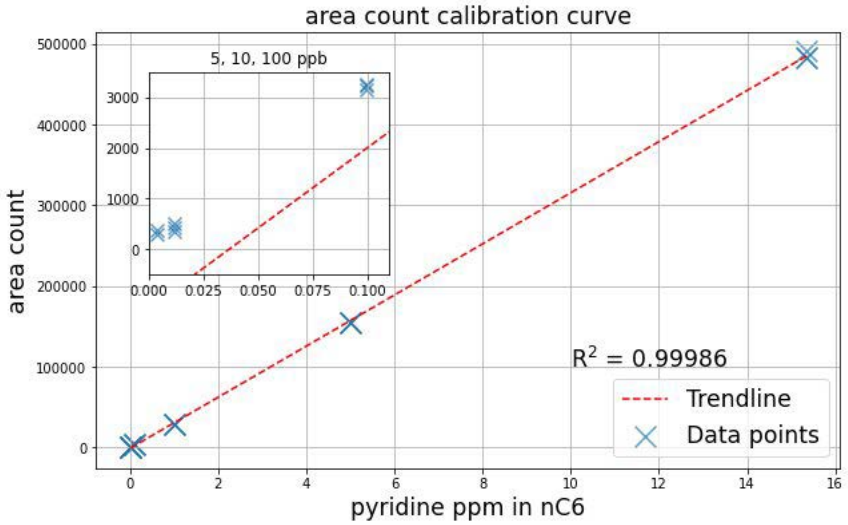


Figure 6. Gas chromatography-nitrogen chemiluminescence detection (GC-NCD) calibration curve with pyridine doped in n-hexane. This graph is one of several calibration curves produced during method development and may not reflect the exact curve used to calculate nitrogen content.

While it did not prove to cause significant issues for calibration, the interfering carbon signal was found to cause some baseline-related problems with more complex fuels. Figure 7 below shows a zoomed-in portion of overlapping GC-NCD chromatograms from fuels sampled sequentially in a continuous run process as hydrodenitrification (HDN) were increased over time. Calling attention to the signal at approximately 2.145 min retention time, these peaks are roughly Gaussian and noticeably decrease in size with each sampling. This indicates that these are likely true nitrogen peaks given the context known about the samples. Comparatively, the "peaks" prior to the 2.145 min mark are misshapen and appear to remain consistent between samplings. With knowledge of the HDN process, the WSU SAF Lab was able to determine that these "peaks" are actually the interfering signal from the bulk hydrocarbon species at high concentration in the fuel. Since the HDN targets nitrogen species, this part of the signal remains the same between samplings. This was an important discovery for the team, as the sequentially sampled fuels allowed for the overlaid comparison. In most GC-NCD use cases, there is little reference outside of rough peak shape to determine whether or not a small peak is an NCC or some carbon interference. One way to circumvent this, which takes additional fuel volume, is to perform solid-phase extraction to amplify the true polar NCC peaks away from the baseline. This method is discussed in Task 3. Additionally, changing column type to a mid-polar phase may help to isolate the non-polar carbon signal to one end of the chromatogram that can be ignored during analysis. Investigating this is part of the next steps in progressing the GC-NCD method.



Figure 7. Overlaid and cropped gas chromatography-nitrogen chemiluminescence detection (GC-NCD) chromatograms for fuels sampled sequentially during a continuous run experiment where HDN levels were increased over time.

Oxygen-Containing Compounds

The ASTM D3242 (ASTM, 2023c) potentiometric method for acidity measures total acidity but, by inference, it is reasonable to assign all of the acidity to carboxylic acids. Similarly, peroxides are detected via the ASTM D3703 (ASTM, 2024a) potentiometric method. Esters can be measured via ASTM D7871 (ASTM, 2023c) which employs infrared (IR)



spectroscopy to interrogate the carbonyl stretch of effluent passing through a high-pressure liquid chromatographer. Alcohol and ethers are harder to characterize. Lastly, impurities amplification methods have been found to be useful for oxygen-containing compounds (OCC) identification via solid phase extraction and gas chromatography-mass spectrometry (SPE-GC-MS). This is described in detail in Task 3 below. All of these strategies have been developed and utilized in the WSU SAF Lab for jet fuel analysis.

Olefins
Along with polar OCCs, olefins are also able to be quantified via ASTM D1319 (ASTM, 2020a). Additionally, WSU SAF Lab personnel are trained in the ASTM D2710 test method (ASTM, 2020b) for Bromine index, a method for evaluating olefin content in jet fuels.

Trace metals
Trace metals are quantified via ICP-OES according to ASTM D7111. This method is the same as that of sulfur detection with the same instrument but largely avoids the matrix-matching issue that was previously discussed. The A-solv matrix has little-to-no baseline metals content, which provides better sensitivity when calibrating on trace metals standards. The improved sensitivity allows for detection down to the specification limit of 0.1 mg/kg for 22 metals listed in ASTM D7566.

Amongst the metals regulated by jet fuel specifications, copper is known as a significant thermal stability risk for fuels. For that reason, it is further limited to 20 ppb in novel jet fuel pathways going through ASTM D4054 evaluation. The WSU SAF Lab personnel have been trained to operate a graphite furnace-atomic absorption spectrometer for the detection of copper at parts-per-billion levels via the ASTM D6732 method (ASTM, 2024c).

Milestones

- Gained at least some proficiency in execution of the experiments necessary to characterize all of the most common or important impurities that may be found in sustainable or petroleum jet fuel components.
- Advanced the state-of-the-art measurement capability for ultra-low levels of sulfur in jet fuels.

Major Accomplishments

None.

Publications

None published. Journal article evaluating the three sulfur detection methods is in progress. Submission to ACS *Precision Chemistry* Journal is expected in Spring 2026.

Outreach Efforts

None.

Awards

None.

Student Involvement

Conor Faulhaber, a graduate student at WSU, leads the development of the nitrogen and sulfur detection methods and is involved in the reporting of this material. Kaamel Sidiqi, an undergraduate at WSU, is trained on and operates the GC-NCD and UVF sulfur instruments and assists with data organization for these tests. Patricia Garcia-Alfaro, another undergraduate at WSU, is trained on and operates the CIC sulfur instrument. She also developed a standard operating procedure for the CIC method.

Plans for Next Period

- Complete a publication on low-sulfur detection methods.
- Improve the GC-NCD method for fuels resulting in a noisy baseline.

References

ASTM International. (2017). *ASTM D4629-17: Standard Test Method for Trace Nitrogen in Liquid Hydrocarbons by Syringe/Inlet Oxidative Combustion and Chemiluminescence Detection.* https://doi.org/10.1520/D4629-17

ASTM International. (2020a). *ASTM D1319-20a: Standard Test Method for Hydrocarbon Types in Liquid Petroleum Products by Fluorescent Indicator Adsorption.* https://doi.org/10.1520/D1319-20A
ASTM International. (2020b). *ASTM D2710-20: Standard Test Method for Bromine Index of Petroleum Hydrocarbons by Electrometric Titration*, PA May 1, 2020. https://doi.org/10.1520/D2710-20
ASTM International. (2021). *ASTM D7111-16 (Reapproved 2021): Standard Test Method for Determination of Trace Elements in Middle Distillate Fuels by Inductively Coupled Plasma Atomic Emission Spectrometry.* https://doi.org/10.1520/D7111-16R21
ASTM International. (2023a). *ASTM D1655-22a: Standard Specification for Aviation Turbine Fuels.* https://doi.org/10.1520/D1655-22A
ASTM International. (2023b). *ASTM D3227-23: Standard Test Method for (Thiol Mercaptan) Sulfur in Gasoline, Kerosine, Aviation Turbine, and Distillate Fuels (Potentiometric Method).* https://doi.org/10.1520/D3227-23
ASTM International. (2023c). *ASTM D3242-23: Standard Test Method for Acidity in Aviation Turbine Fuel.* https://doi.org/10.1520/D3242-23
ASTM International. (2023d). *ASTM D7359-23: Standard Test Method for Total Fluorine, Chlorine, and Sulfur in Aromatics Hydrocarbons and Their Mixtures by Oxidative Pyrohydrolytic Combustion followed by Ion Chromatography Detection (Combustion Ion Chromatography-CIC).* https://doi.org/10.1520/D7359-23
ASTM International. (2023e). *ASTM D7871-23: Standard Test Method for Analysis of Cyclohexane by Gas Chromatography (Effective Carbon Number).* https://doi.org/10.1520/D7871-23
ASTM International. (2024a). *ASTM D3703-18 (Reapproved 2024): Standard Test Method for Hydroperoxide Number of Aviation Turbine Fuels, Gasoline, and Diesel Fuels.* https://doi.org/10.1520/D3703-18R24
ASTM International. (2024b). *ASTM D4054-24d: Standard Practice for Evaluation of New Aviation Turbine Fuels and Fuel Additives.* https://doi.org/10.1520/D4054-24
ASTM International. (2024c). *ASTM D6732-04 (Reapproved 2020): Standard Test Method for Determination of Copper in Jet Fuels by Graphite Furnace Atomic Absorption Spectrometry.* https://doi.org/10.1520/D6732-04R20
ASTM International. (2024d). *ASTM D7566-24d: Standard Specification for Aviation Turbine Fuel Containing Synthesized Hydrocarbons.* https://doi.org/10.1520/D7566-24D
ASTM International. (2025). *ASTM D5453-25: Standard Test Method for Determination of Total Sulfur in Light Hydrocarbons, Spark Ignition Engine Fuel, Diesel Engine Fuel, and Engine Oil by Ultraviolet Fluorescence.* https://doi.org/10.1520/D5453-25
Deese, R.D., Morris, R.E., Romanczyk, M., Metz, A.E., Loegel, T.N. (2020). Nitrogen Compound Characterization in Fuels by Multidimensional Gas Chromatography. *Journal of Visualized Experiments, 159.* https://doi.org/10.3791/60883
Karcher, B. (1998). On the potential importance of sulfur-induced activation of soot particles in nascent jet aircraft exhaust plumes. *Atmospheric Research, 46*, 293 – 305. https://doi.org/10.1016/S0169-8095(97)00070-7

Task 3 – Develop Methods for Natural Impurities Amplification

Washington State University

Objective

The objective of Task 3 is to experimentally increase the concentration of the natural impurities of a jet fuel, conventional or synthetic, into a polar extract. The reason for this is twofold. First, the increased concentration of trace impurities improves the resolution of peaks in GC-MS analysis for the purposes of identification. Second, a polar extract isolated from the solvent used for extraction allows for doping studies using the natural impurities profile of the fuel. Doing so for thermal stability, as will be discussed in Tasks 4 and 5, may provide more relevant information compared to that of doping studies with individual molecules on the extent of refining required to meet thermal stability standards. If isolation from the extracting solvent is a problem, the improved identification capabilities with the extracted impurities better inform future doping studies with cocktails of purchased impurities made to approximate naturally occurring impurities.

Research Approach

To accomplish this goal, a common fuel analysis technique known as solid-phase extraction (SPE) was employed to separate the polar impurities of a fuel from the bulk hydrocarbon matrix (Link et al., 2005 & 2007). Previous work on this project performed liquid-liquid extraction on fuels using methanol to achieve the same goal. However, after experience with that method, the removal of large quantities of methanol proved difficult and the isolation of trace impurities as discussed in Task 2 from the aromatic fraction of the fuel is easier under SPE. For this reason, the work in this period of performance was dedicated towards refining the SPE methodology.

SPE works in a 4-step process outlined in Figure 8 below. The SPE is performed by the WSU SAF Lab using a 6mL, 500mg silica bed Thermo Fisher Scientific® Hypersep® cartridge. First, the cartridge is conditioned using 5 mL of n-heptane. This homogenizes the silica bed and washes out any loose particulates. Then, the sample is introduced. Depending on the impurity concentration in the sample, anywhere from 5 to 50 mL of sample may be needed to achieve adequate resolution in GC-MS analysis. Next, the remainder of the non-polar hydrocarbons in the sample are washed out of the silica bed using n-heptane while the polar impurities stick to the silica. An example of this can be seen on the right side of Figure 7, where oxidation products in a trans-decalin sample are seen as a thin dark line in the silica bed. Up to two times the amount of sample is needed in n-heptane to wash out the aromatic content of fuels, as these molecules are slightly polar and can be difficult to remove from the silica bed. Lastly, the polar analytes are eluted using a methanol rinse and are collected into a vial for further analysis. A volume of 1-2 mL methanol, depending on sample impurity concentration, is ideal to maintain a high concentration of polars in the extract for the best possible resolution.

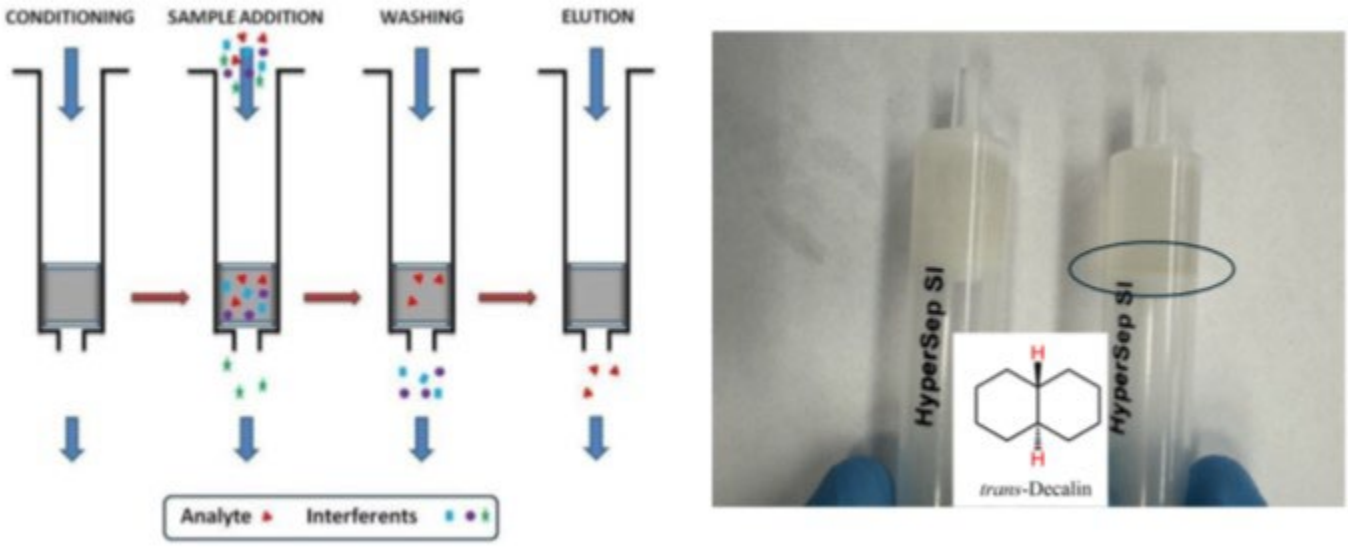


Figure 8. Graphical description of the SPE process (left) and a comparison of two SPE cartridges (right) with the left cartridge representing a clean, conditioned silica bed and the right showing the oxidation products of an aged trans-decalin sample as a dark line in the silica bed (circled).

For a separate ongoing project, ignition delay measurements taken with the aged trans-decalin sample were inconsistent with literature values, and oxidation was suspected as the culprit (Yang et al., 2025). SPE was performed to “clean” the trans-decalin sample, and the polar extract was analyzed in the GC-MS for validation of this procedure. Figure 9 below features the GC-MS chromatogram of said extract shown on the right side of Figure 8. The primary peak was identified as trans-decalin, as expected. Further along the x-axis, smaller peaks of oxidized derivatives of trans-decalin were identified in the MS Library, indicating that polars had been successfully extracted from the sample. To reinforce this result, the ignition delay result for the cleaned trans-decalin sample was consistent with literature data.

® Thermo Fisher Scientific and Hypersep are registered trademarks of Thermo Fisher Scientific, Inc., Waltham, Massachusetts.

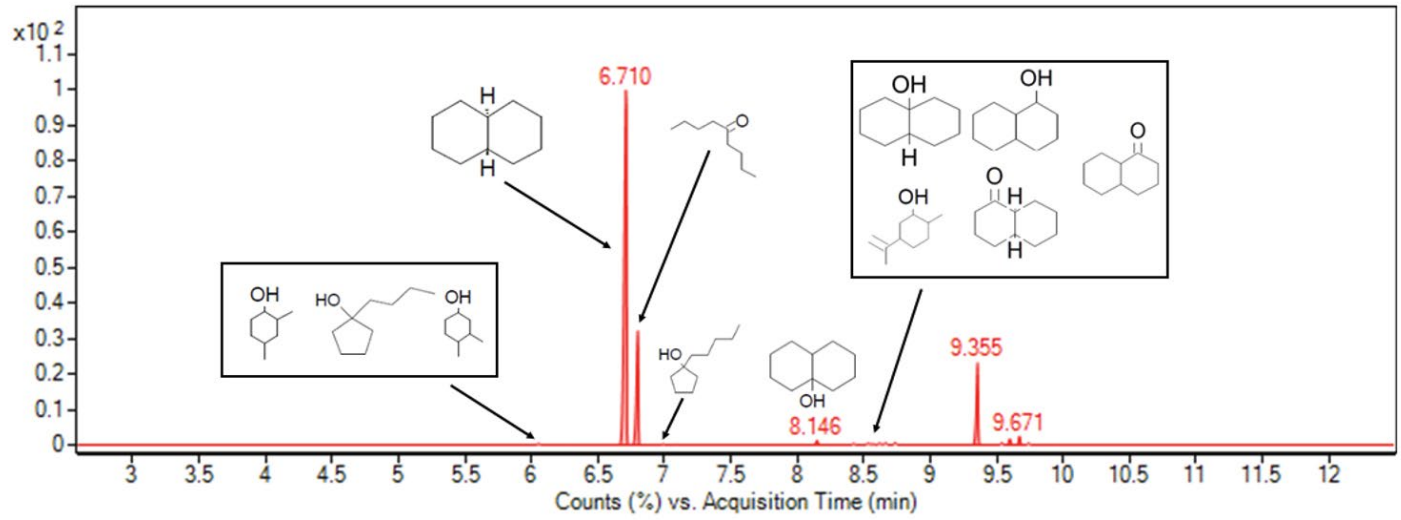


Figure 9. GC-MS chromatogram of aged trans-decalin solid-phase extraction (SPE) extract. Callouts show molecular structure of peaks identified in the MS Library.

Figure 10 provides an example of further application of this method. This time, rather than a neat molecule, SPE was performed on a complex SAF candidate to determine its polar impurity profile. On the left is the bulk hydrocarbon distribution of this fuel, and on the right is the GC-MS result of the SPE extract. The peaks in the GC-MS chromatogram were identified as mostly phenolic compounds, which are known to impact thermal stability in fuels (Link et al., 2005). For this synthetic fuel, the impurity profile is very specific. However, for more complex pathways, including conventional petroleum fuels, the impurity profile is broader and can cause difficulties in identification efforts. This can be seen in Figure 11, where the significant number of overlapping peaks indicates poorer separation and results in poor matches in the MS Library. Future work on this method may include adjusting GC-MS hardware and/or method programming to improve separation. Additionally, while not shown here, the plethora of impurities quantification tools outlined in Task 2 can help to characterize these SPE extracts.

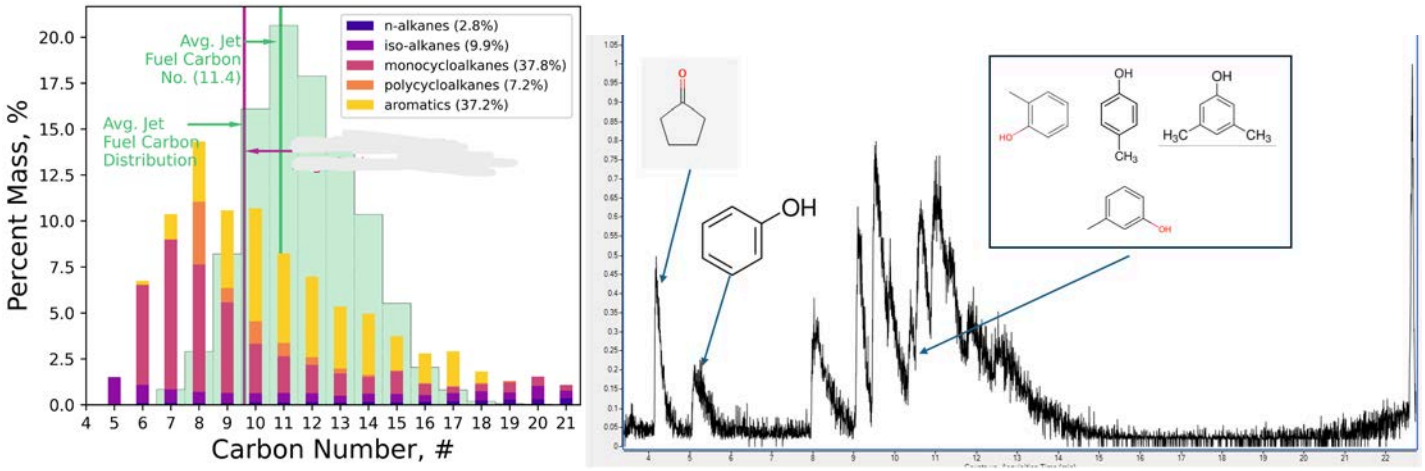


Figure 10. Bulk hydrocarbon distribution of a complex SAF candidate (left) and SPE extract of the same fuel (right)

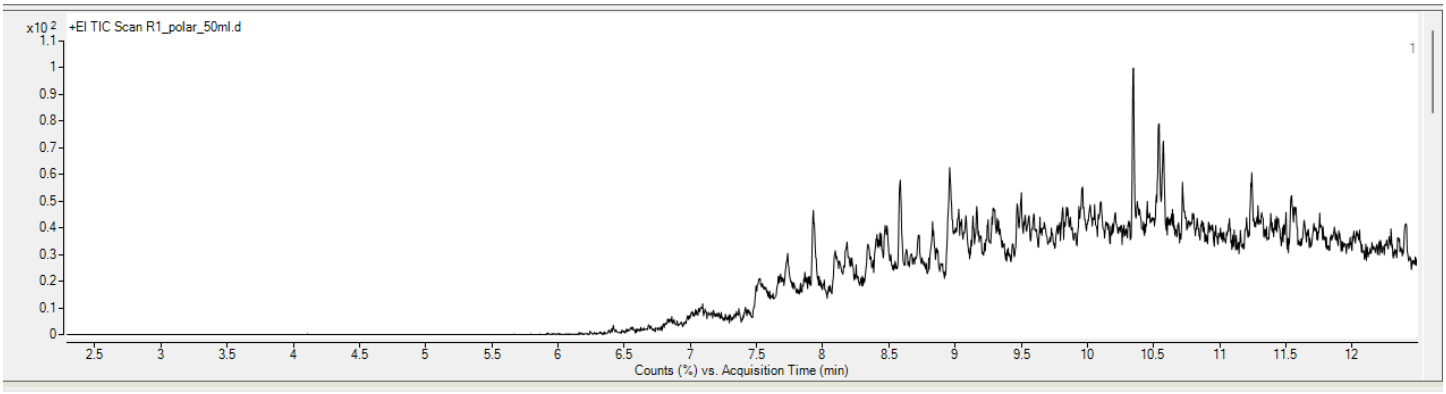


Figure 11. GC-MS chromatogram from conventional Jet A SPE extract.

Milestone
Isolated the polar fraction of real fuel samples from hydrocarbon matrix sufficiently well to identify several individual species.

Major Accomplishments
None.

Publications
None.

Outreach Efforts
None.

Awards
Conor Faulhaber, Distinguished Graduate Research Program (DGRP) appointment, Pacific Northwest National Laboratory (PNNL).

Student Involvement
Conor Faulhaber, a graduate student at WSU, worked with Research Faculty Zhibin Yang to develop this method capability, and leads its application towards the thermal stability project.

Plans for Next Period
- Improve GC-MS analysis for better identification of extracted polars.
- Scale-up the SPE method to larger volume suitable for doping studies.

References
Link, D. D., Baltrus, J. P., & Zandhuis, P., Hreha, D. C. (2005). Extraction, separation, and identification of polar oxygen species in jet fuel. *Energy and Fuels, 19*(4), 1693–1698. https://doi.org/10.1021/ef040095q

Link, D. D., Baltrus, J. P., & Zandhuis, P. (2007). Isolation and identification of nitrogen species in jet fuel and diesel fuel. *Energy & Fuels, 21*(3), 1575–1581. https://doi.org/10.1021/ef060451q

Yang, Z., Faulhaber, C., Boehm, R., Heyne, J. (2025). Geometric and Positional Isomer Effects on Ignition Behavior of Cycloalkanes: Implications for Sustainable Aviation Fuels. *Energy & Fuels, 39*(38), 18641–18648. https://doi.org/10.1021/acs.energyfuels.5c03856



Task 4 – Establish a Detailed Experimental Test Plan to Evaluate Thermal Stability

Washington State University

Objective

The objective of Task 4 is to outline in detail the approach to the thermal stability test campaign, including a description of how the required fuel volumes will be procured. The purpose of this test campaign is to evaluate the impact of natural polars from conventional fuel and PNNL's hydrothermal liquefaction (HtL) SAF candidate on thermal stability. Thermal stability will be measured using the JFTOT method outlined in Task 1.

Research Approach

The test plan is broken into two parts: baseline tests and design of experiment (DoE). The purpose of the baseline tests is to establish the thermal stability of the primary test fuels, a conventional Jet A fuel and a 10%v blend of HtL in the same Jet A fuel. HtL blending component volume limitations are the primary constraint in this test plan. While it is desirable to perform JFTOT testing on neat HtL, it is unlikely WSU SAF Lab will receive sufficient sample. On that note, it is worthwhile to mention that each JFTOT test requires approximately 600mL of fuel sample to be completed, and two to three replicates are desired due to the repeatability of the measurements, as shown in Task 1.

The test plan outlines the levels of impurities to be doped into each fuel, the nature of these dopants (nitrogen/sulfur levels, fuel source, etc.), and the temperatures to perform testing. The goal in this portion of the experimental design is to perform duplicate measurements at each level of JFTOT testing, while having spare fuel to test a third replicate if large variation is observed for a set of duplicates. The details of this test planned are outlined in Table 4.

Table 4. Thermal stability test campaign design of experiment.

Fuel	JFTOT Temperature [°C]	Dopant from polar extract of Jet A	Dopant from cocktail simulating polar extract of HtL	Number of Replicates	HtL SBC Volume [L]
Baseline Tests					
Conventional Jet A	TBD (higher value)[1]	n/a	n/a	3	0
	TBD (lower value)[2]	n/a	n/a	3	0
HtL SAF/Jet-A 10/90 blend	Lower value	n/a	n/a	2	0.12
	Higher value	n/a	n/a	2	0.12
Impurity Concentration Derivatives					
HtL SAF/Jet-A 10/90 blend	TBD (lower value)[1]	High	High	2	0.12
	Lower value	Low	High	2	0.12
	Lower value	High	Low	2	0.12
	Higher value	High	High	2	0.12
	Higher value	Low	High	2	0.12
	Higher value	High	Low	2	0.12

[1] The higher test temperature shall not exceed the breakpoint of the petroleum fuel by more than 10 C and shall be at least as high as its breakpoint temperature. This set of tests shall be done first

[2] The lower test temperature shall produce at least one localized tube deposit of at least 60 nm when the most contaminated sample is tested but not more than 30 nm when the petroleum jet fuel sample is tested. In doing these trial-and-error experiments, a surrogate will be used to represent every aspect of the HtL to preserve HtL volume for the derivative study. The maximum levels of dopant concentration may be adjusted to ensure the lower test temperature satisfies both criteria.

JFTOT: jet fuel oxidation tester; HtL: hydrothermal liquefaction; SAF: sustainable aviation fuel; SBC: synthetic blend components; TBD: to be determined



Several levels of the test plan, including temperature, dopant composition, and dopant concentration, are still to be finalized. The footnotes on Table 4 address the upper and lower test temperatures. In order to get meaningful results, it is desired for the baseline Jet A fuel test at the higher temperature to reside near the Jet A fuel breakpoint. If temperature is too high the reaction could be driven to completion too quickly, meaning the deposition thickness could be driven more by dissolved oxygen concentration and/or deposit oxygen concentration than fuel quality. If lower test temperature is too low, then it will not be possible to measure the impact of fuel quality diversity. While the preliminary trial-and-error runs that are necessary to establish the upper and lower test temperature will require some reference petroleum jet fuel and some amount of a surrogate that represents the HtL synthetic blend components (SBC), neither of these materials are volume-limited within the context of this test matrix.

Dopant composition will be determined by the impurity amplification and characterization efforts outlined in Tasks 2 and 3. It is expected that the HtL extraction will define a dopant that is high in nitrogen. To preserve HtL volume for JFTOT testing, a surrogate (cocktail) that represents its polar extract will be created based on a recipe made from GC-MS characterization of the actual polar extract. The polar extract of the petroleum Jet A fuel is expected to be relatively high in sulfur content. Since we are not limited by the available volume of our reference petroleum fuel, its polar extracts can be collected until we have enough volume to satisfy the demand of the test plan. Testing these dopants at elevated levels in varying ratios in the HtL-Jet A blend will provide insight towards the impact of interactions between these two types of impurities on thermal stability, building on previous research (Zabarnick et al., 2019).

The two levels of dopant concentration shall be approximately one times (low) or three times (high) that of the blending component with which it is associated. For example, the low dopant level for the polars of the reference petroleum fuel will be created by extracting 540 ml of reference jet fuel, which would then be used to spike an untreated aliquot of 540 ml of the reference fuel. To complete a single test point with high dopant from the reference petroleum fuel will require approximately 2,160 ml of petroleum fuel (540 for the sample) and 60 ml of HtL SBC.

Fuel Procurement
HtL samples for this test plan will be procured from the PNNL team led by Huamin Wang. Conventional Jet A fuel will be procured from a local airport.

Milestones

- Completed the thermal stability test campaign design of experiment as outlined in Table 4 above.
- Developed contingency plans should the proposed plan run into further sample volume limitations.

Major Accomplishments

None.

Publications

None.

Outreach Efforts

Collaboration with the PNNL HtL team for procurement of their HtL SAF.

Awards

None.

Student Involvement

Conor Faulhaber, a graduate student at WSU, leads the HtL characterization effort within the WSU SAF Lab and acts as a liaison between PNNL and WSU on this project. He also is responsible for sourcing the Jet A from the local airport for this work, and aids in reporting on this task.

Plans for Next Period

Determine the exact temperature and doping levels for this task prior to executing the test plan. This will finalize the work for this task.



References

Zabarnick, S., West, Z. J., Schafer, L. M., Mueller, S. S., Striebich, R. C. (2019). Studies of the Role of Heteroatomic Species in Jet Fuel Thermal Stability: Model Fuel Mixtures and Real Fuels. *Energy & Fuels, 33*, 8557–8565. https://doi.org/10.1021/acs.energyfuels.9b02345

Task 5 – Execute Thermal Stability Test Campaign

Washington State University

Objective

The objective of Task 5 is to execute the test campaign outlined in Task 4 and provide full analysis of the results.

Research Approach

This test campaign will begin as soon as Tasks 1, 2, 3, and 4 are complete. Each of the first three tasks have proven to be more time consuming than originally envisioned, but we are now confident that they will be done within 6 months. From Task 1, the repeated asymmetrical streaking occurrence took a significant amount of time and resources to investigate, troubleshoot, and document to a point where the team felt comfortable moving forward with further JFTOT testing despite the occurrence of the streaking. During Task 2, the use of multiple sulfur methods to investigate low-sulfur detection required training and work on two additional, more complicated instruments than the UVF method and necessitated that the methods remain consistent with each other. Using the CIC method to probe the true LOD and LOQ of the UVF method made all three method development efforts interdependent. The GC-NCD also went through several different hardware configurations before its final state, requiring significant time for planning and site visits from technicians on top of method development. Task 3 and 4 both went roughly as planned, but Task 3 saw small challenges in the development of GC-MS techniques to characterize the amplified polars. A small obstacle with Task 4 was reassessing the amount of fuel that the PNNL HtL team would be able to provide.

Milestones

None.

Major Accomplishments

None.

Publications

None.

Outreach Efforts

None.

Awards

None.

Student Involvement

Conor Faulhaber, a graduate student at WSU, is responsible for leading the lab work associated with executing this experimental campaign. He is assisted by Kaamel Sidiqi, an undergraduate at WSU.

Plans for Next Period

Follow through on completing Task 5.

References

Not applicable.



Project 067 Impact of Fuel Heating on Combustion Performance and Lean Combustion Characterization

Purdue University

Project Lead Investigators

Robert P. Lucht
Ralph and Bettye Bailey Distinguished Professor of Combustion
School of Mechanical Engineering
500 Allison Road
Purdue University
West Lafayette, IN 47907-2014
765-714-6020
Lucht@purdue.edu

Carson D. Slabaugh
Associate Professor
School of Aeronautics and Astronautics
500 Allison Road
Purdue University
West Lafayette, IN 47907-2014
765-494-3256
cslabau@purdue.edu

University Participants

Purdue University

- P.I.s: Dr. Robert P. Lucht and Dr. Carson D. Slabaugh
- FAA Award Number: 13-C-AJFE-PU-038
- Period of Performance: October 1, 2020, to September 30, 2024
- Task:
  1. Investigate the effects of fuel heating on combustion performance and products for aviation gas turbines

Project Funding Level

The ASCENT Project 067 was funded by the Federal Aviation Administration (FAA) at the level of $250,000 for the project period from June 5, 2020, to June 4, 2021; an additional $250,000 for the time period from June 5, 2021, to September 30, 2022; an additional $250,000 for the time period from October 1, 2022, to September 30, 2023; and an additional $200,000 was approved for the project period of October 1, 2023, to September 30, 2024. A no-cost extension of this funding period is now in place. The required cost-sharing 1:1 match of $950,000 was provided by Purdue University.

Investigation Team

Prof. Robert P. Lucht (P.I.)
Prof. Carson D. Slabaugh, (co-P.I.)
Ben Murdock, Zander Hodge, Tristan Shahin, and Keaton Koenig (graduate students), Responsible for the design of system components, such as the fuel heating system, and will be responsible for executing test operations.
Dr. Rohan Gejji, Research Engineer, Help graduate students with their design projects and supervising test operations.
Dr. Theodore Johnson, Current Program Manager
Dr. Bahman Habibzadeh, Program Manager from October 1, 2023, to June 30, 2025
Dr. Prem Lobo, Program Manager from October 1, 2022, to September 30, 2023

Project Overview

The goal of this project is to evaluate the effects of heating jet fuel before injection in an aviation gas turbine combustor on combustion efficiency, pollutant formation, and dynamics. In an aircraft engine, heat that would otherwise be wasted can be directed into the fuel to increase its sensible enthalpy before injection. Thermochemistry dictates that this increase in sensible enthalpy must lead to lower fuel consumption for a given combustor exit temperature. However, the effects of elevated fuel temperature on combustion performance characteristics (e.g., the fuel spray pattern, spatial distribution of reaction zones, pollutants, and combustion dynamics) are not yet well understood. The ASCENT Project 067 team will perform experiments with heated fuels by using a piloted, partially premixed fuel injector located in an optically accessible combustor. This process will allow us to apply advanced laser diagnostic techniques to compare the behavior of the combustor at different fuel temperatures over a wide range of operating conditions.

The platform for the planned experiments is the Combustion Rig for Advanced Diagnostics (COMRAD). The test rig (Figure 1) is designed to operate at steady-state conditions with thermal power as high as 8 MW, inlet air pressure (P_3) as high as 4.0 MPa, and inlet air temperature (T_3) as high as 1,000 K. To facilitate operation at these conditions, the test article is made of aviation-grade alloys and is thoroughly water cooled, and the inner windows are film cooled with heated nitrogen. Before this project, extensive testing with ambient-temperature fuels was performed in this test rig, with a focus on 5- and 10-kHz particle image velocimetry (PIV) measurements in the downstream boundary condition window section, and 50- and 100-kHz PIV measurements in the flame zone.

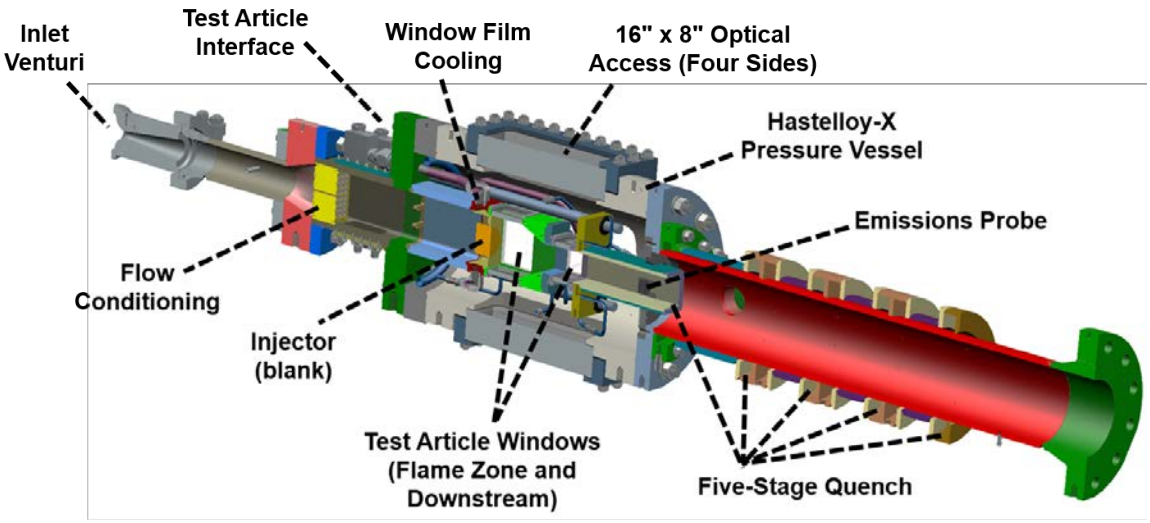


Figure 1. Schematic diagram of COMRAD.

Task 1 - Investigate the Effects of Fuel Heating on Combustion Performance and Products for Aviation Gas Turbines

Purdue University

Objective

The goal of this project is to determine the effects of fuel heating on the performance of aviation gas turbines. Fuel heating can potentially lead to higher efficiency but can also lead to changes in the fuel distribution pattern and in the locations of reaction zones in the combustor. These changes may also affect pollutant formation and combustion dynamics during engine operation. The ASCENT Project 067 team will perform experiments using heated fuels and measure the fuel distributions, reaction zone distributions, pollutants, and combustion dynamics at a range of fuel temperatures from near room temperature to above the supercritical temperatures for hydrocarbon fuels.

Research Approach

Our team will perform experiments with heated fuels by using a piloted, partially premixed fuel injector located in an optically accessible combustor. This experimental system will allow us to apply advanced laser diagnostic techniques to compare the behavior of the combustor at different fuel temperatures over a wide range of operating conditions. These advanced diagnostic techniques include fuel planar laser-induced fluorescence (PLIF) imaging to monitor fuel distribution patterns, hydroxyl (OH) radical PLIF (OH PLIF) imaging to monitor reaction zones, PIV to measure the flow fields, and laser-induced incandescence (LII) imaging to monitor spatially resolved soot volume fractions. We will also measure combustion products with probe sampling and will use pressure transducers to measure combustion dynamics.

Facility Overview

COMRAD is supplied by facility fluid systems including heated air, heated nitrogen, high-pressure water, and liquid jet fuel. Three types of liquid jet fuel were used separately for this work: (a) Jet A fuel, (b) Shell® gas-to-liquids (GTL) GS190, a Fischer-Tropsch synthetic paraffinic kerosene (FT-SPK), and (c) World Energy® hydroprocessed esters and fatty acids (HEFA). The rig features a piloted swirl injector (shown schematically in Figure 2) housed inside a duct within a large-windowed pressure vessel enabling optical access to the entire flame from four sides. Figure 3 shows a diagram of the test rig. Combustion air is supplied to the test article at 755 K and up to 20 bar. After it is metered, the air passes through a flow conditioner and into the air plenum, which supplies both the pilot and main sections of the injector.

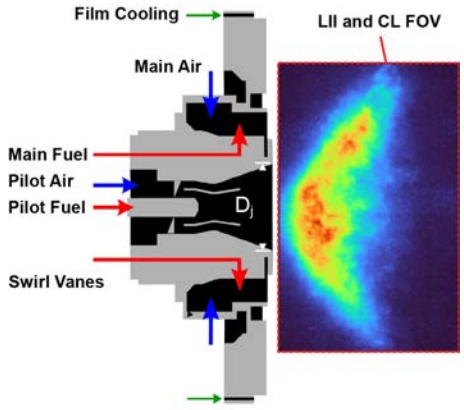


Figure 2. Schematic diagram of the injector indicating reactant flow routing. The laser-induced incandescence (LII) and OH* chemiluminescence (CL) fields of view (FOV) are also shown.

® Shell is a registered trademark of Shell Trademark Management B.V., The Hague, The Netherlands.
® World Energy is a registered trademark of World Management Group LLC, Boston, Massachusetts.

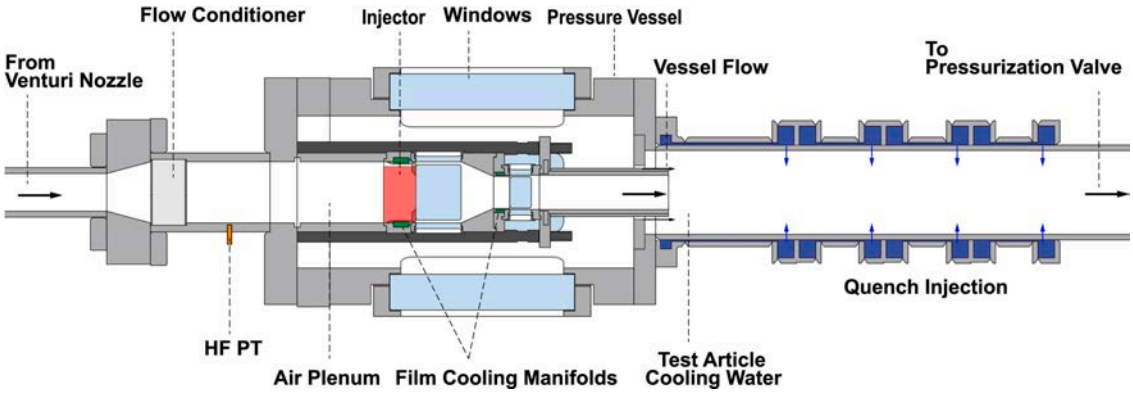


Figure 3. Schematic diagram of the combustor.

Liquid jet fuel is supplied to the injector at temperatures as high as 590 K by an 81-kW fuel heater. The fuel heater (Figure 4) comprises a stack of copper blocks with 20 cartridge heaters inserted into each block. Fuel flows in stainless steel tubes through three independent circuits, two pilot circuits, and one main circuit. The mass flow rates in each circuit are measured with Coriolis flow meters. In the fuel heater, the stainless-steel tubes are clamped between each pair of copper blocks before being delivered to the test rig. The temperature of the fuel is monitored both in the fuel heater (to ensure that no phase change is encountered) and immediately upstream of the injector. Fuel passes through approximately 50 cm of trace-heated tubing from the heater to the test rig. The tubing is air-jacketed within the test rig to inhibit heat transfer from the heated air before the injector is reached. To prevent coking in the fuel lines at high fuel temperatures, the fuel tank is sparged with nitrogen for 30 minutes before use to remove dissolved oxygen, and the tank ullage is purged with nitrogen during the experiment. A dissolved oxygen sensor (Mettler Toledo® Inpro 6850i) is used to ensure that the levels of dissolved oxygen remain below 0.2% of the fully saturated level during the experiment. An inert gas purge circuit is used to prevent the collection of stagnant fuel in the heater and the tubing to the experiment when fuel is not flowing to the experiment. This purge displaces the fuel to a collection tank through a bypass circuit and counter-flow heat exchanger that cools the fuel temperature to ambient temperature with water as the heat transfer medium.

® Mettler Toledo is a registered trademark of Mettler-Toledo GmbH, Greifensee, Switzerland.

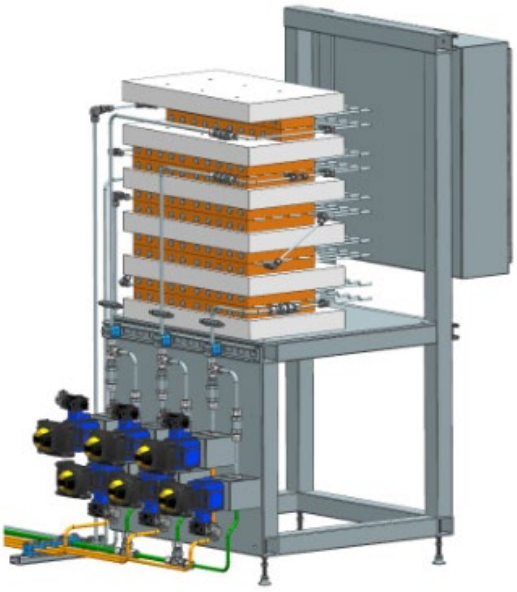


Figure 4. Fuel heater.

At the injector, fuel is injected into two co-swirling flows of air separated by a bluff body. The inner flow forms the pilot flame, and the outer flow forms the main flame, where most of the fuel is burned. The fuel flow rates to the pilot and main circuits are separate to enable independent control of the fuel/air ratio in each part of the flame. The pilot flame is operated at a higher fuel/air ratio than the main flame, allowing the main flame to stabilize as the pilot products mix with the main reactants. The main reactant stream is assumed to be partially premixed when it reaches the flame, but the pilot flame is mostly non-premixed.

The flame zone is contained by a rectangular duct with a height/width ratio of approximately 1.4. Fused quartz windows are installed on each side of the duct to enable imaging of the flame. These windows are film cooled with heated nitrogen at approximately 590 K to lessen the thermal load created by the flame. The film cooling flow rate is independently controlled but is set to a constant fraction of the combustion air flow rate. The duct then contracts vertically to a height/width ratio of approximately 0.75. Downstream of this contraction, another windowed section is present. A separate supply of heated air flows through the pressure vessel at the same pressure as the combustor, and this flow merges with the test article flow in a pipe, where water is radially injected into the flow to cool it. An electrically actuated butterfly valve is installed at the exit of the flow path to back-pressurize the combustor. The inner duct is coated with a thermal barrier coating and cooled by internal water channels. This cooling water is directed into the flow at the exit of the inner duct.

Heated air and nitrogen sources are metered with sonic Venturi nozzles, high-pressure water is metered with cavitating Venturi nozzles, and jet fuel is metered with Coriolis flow meters. The test rig is equipped with pressure transducers (GE® PMP50E6) and K-type thermocouples (Omega® GKMQSS-062G) for flow metering and in several different locations throughout the flow path. These instruments are sampled at 100 Hz to monitor the operating conditions, and a National Instruments® LabVIEW virtual instrument is used to display measured values and send commands to pneumatically and electrically actuated valves in the test cell. The relative uncertainties of calculated mass flow rates have been determined to

® GE is a registered trademark of General Electric Company, Schenectady, New York.
® Omega is a register trademark of Omega Engineering, Inc., Stamford, Connecticut.
® National Instruments is a registered trademark of National Instruments Corporation, Austin, Texas.



be below 0.83% for gases and below 0.10% for liquid fuel according to the Kline–McClintock[1] method, with a 95% confidence interval. A high-frequency pressure transducer (Kulite® WCT312M-70BARA) is installed in the air plenum to monitor acoustic oscillations.

During testing operations in Spring 2024, a facility water softener failure resulted in damage to the water-cooled portions of the test article. The damage to the exhaust duct of the combustor was severe and the cost of the repair was more than $50,000. Because this failure was a facility issue, Purdue University insurance rather than the FAA project paid for the repair, but the exhaust duct had to be refabricated, and it took over 6 months to complete that fabrication. The experiment repair was completed in early Spring 2025, allowing testing to resume.

Laser-Induced Incandescence Overview

LII is an in-situ method for determining soot levels in a combustion flow field. The diagnostic was first applied to a lab scale laminar diffusion flame (Yale burner) to validate the accuracy of the experimental setup and then used to investigate soot formation for both rich and lean dome operation in COMRAD. Comparison of soot levels between several different fuels has begun with noticeable decrease in signal for synthetic fuels lacking aromatics such as World Energy HEFA across all operating conditions. LII measurements provide valuable information of the spatial locations for particulate formation in the combustor flow field. GE Aerospace is very interested in the types and number of particulates that are in the combustor exhaust.

Two-dimensional LII measurements can be obtained in a flame by using a laser sheet that passes through a plane of interest and measuring the incandescence signal with a camera. Comparative soot volume fraction measurements can be determined by gating the detection device around the entire incandescence signal.

A Quanta-Ray® Pro-290 Nd:YAG laser is used to generate a 1064 nm beam at a frequency of 10 Hz. Using an excitation wavelength of 1064 nm reduces poly-aromatic hydrocarbon (PAH) laser-induced fluorescence (LIF) and excitation of diatomic carbon (C_2) molecules. The beam is attenuated to the desired power with a half-wave plate and a thin-film polarizer allowing for a max of 240mJ down to as low as 8.5mJ. A set of cylindrical lenses (f = -50, +300) is used to expand the beam in a vertical direction and collimate it. Two horizontal cylindrical focusing lenses (f = +150) are then used to focus the beam into a sheet with a variable focal length. The focal point of the laser sheet is aligned with the center line of the injector. For the experiments in the gas turbine combustor, the sheet is 48.49 mm wide and 0.53 mm thick at the focal point. The sheet is introduced to the experiment from above, perpendicular to the injector's face. The sheet is aligned with the center of the injector while ensuring vertical alignment using a reflected beam. A diagram of the setup used for the COMRAD testing is shown in Figure 5.

[1] The Kline-McClintock Method is used to determine the uncertainty of a calculation given certain measurements and the tolerances on those measurements. The method defines the uncertainty as a range where the true value lies in.

® Kulite is a registered trademark of Kulite Semiconductor Products, Inc., Leonia, New Jersey.

® Quanta-Ray is a registered trademark of Newport Corporation, Irvine, California.

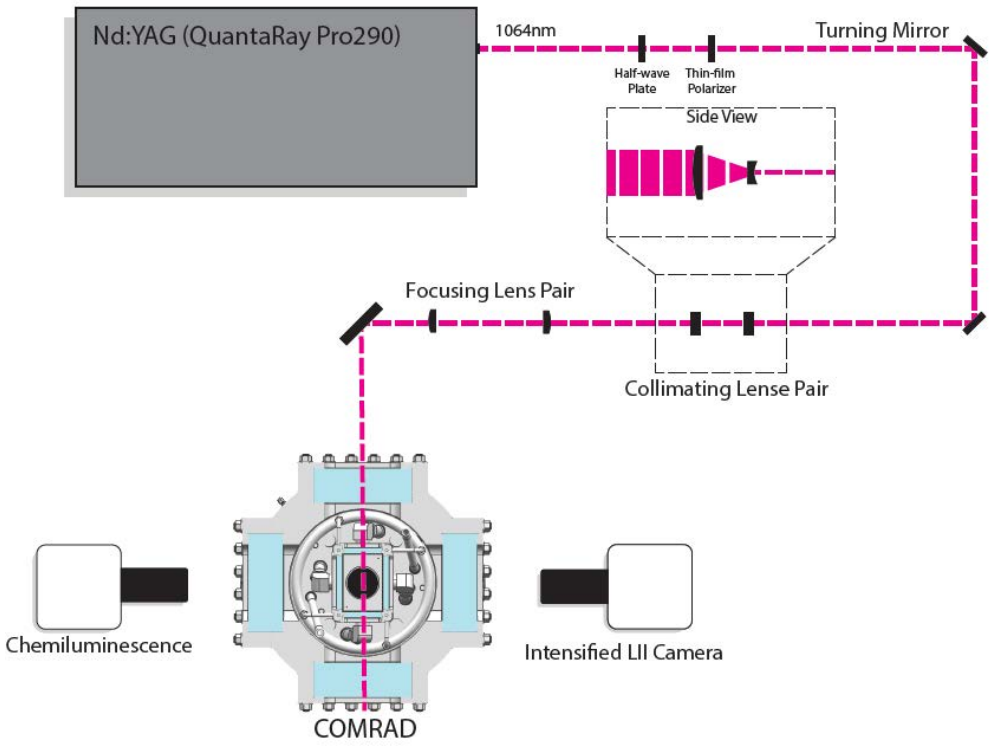


Figure 5. Schematic diagram of the LII diagnostic system for measurements in COMRAD.

An intensified ultrahigh-speed complementary metal-oxide-semiconductor (CMOS) camera (Phantom® TMX and Lambert™ High-speed Intensified Camera Attachment [HiCatt]) measures the LII signal emitted from soot within the flame. A gate time of 250 ns is used to capture the incandescence with the arrival of the laser occurring approximately 50 ns after the beginning of the gate. The camera was equipped with a 50 mm lens to achieve the desired spatial resolution. A bandpass filter centered at 450 nm with a 20 nm bandwidth isolates the LII signal at a wavelength with negligible interference from C_2 chemiluminescence. A shortpass filter with a cut-off wavelength of 900 nm is used to block any scattered 1064 nm laser light from reaching the camera.

Time-Resolved LII Model

Prior to attempting LII measurements in the COMRAD test rig last year, our team performed LII experiments in a well-characterized sooting laminar diffusion flame. This allowed us to optimize experimental parameters such as the details of the time gate for the detection of the LII signal and also allowed us to develop data analysis methods. Another consideration for performing these measurements in the Yale burner is that we were using the infrared 1064-nm out of the Q-switched Nd:YAG laser, a beam that presents significant eye hazards. Our team wanted to gain experience with working this beam prior to attempting alignment in the test cell for the COMRAD experiments.

Measurements collected in the Yale burner included both time-integrated and time-resolved LII. Time-integrated measurements allow for the extraction of relative soot volume fraction and time-resolved measurements enable primary particle size measurements. We have previously performed time-integrated measurements in the gas turbine combustor. Time-resolved measurements require detection devices with sufficiently high repetition rates to resolve a single signals decay. The LII signal intensity is a function of three major variables, primary particle diameter, number of particles in an agglomeration, and temperature of the particles, as shown in Equation 1.

® Phantom is a registered trademark of Vision Research, Inc., Wayne, New Jersey.
™ Lambert is a trademark of Lambert Instruments, Netherlands.



Equation 1. LII signal intensity.

$$S_{LII} = f(d_p, N_p, T) = \frac{8\,\pi^3\,d_p^3\,N_p\,h\,c^2\,E(m)}{\lambda_c^6\left[exp\left(\frac{hc}{\lambda_c k_B T}\right) - 1\right]}$$

Temperature of the solid soot particles must be accurately modeled to predict LII signal, which is dependent on the heat transfer mechanisms removing heat following the rapid laser heating event. This includes conduction to adjacent particles and the gas environment, sublimation of solid particles to the gas phase, and thermal radiation to the background. The net change in internal energy is related to the particle temperature as shown in Equation 2.

Equation 2. Change in internal energy.

$$\frac{dU_{Internal}}{dt} = \frac{\pi}{6} d_p^3 N_P \rho_s c_s \frac{dT}{dt}$$

These fundamental equations are combined with chemical equilibrium calculations to develop a versatile representative molecular kinetic model. This model employs an ethylene-air reaction mechanism to compare to the work of Liu et al. (2006) and an n-Dodecane kinetic mechanism for Jet A fuel combustion. The n-Dodecane model uses an average chemical composition representative of the gas turbine rig bulk conditions. Figure 6 shows the resulting soot particle temperature and LII signal intensity as a function of time for each model. The primary particle size, number of particles in an agglomeration, and pressure are held constant at 30 nm, 200, and 1 MPa respectively. Each model reaches a peak soot particle temperature of just over 3000 K, with the resulting temperature decay occuring faster for the heavier hydrocarbon model. This results in a more rapid LII signal intensity decay as well, though the variation is subtle. The LII signal intensity decay time is much shorter at this elevated pressure condition (150 ns) compared to the previous work in the atmospheric diffusion flame (1500 ns). While single-point detection devices are capable of acquiring sufficient datapoints to reconstruct a decay of 150 ns, two-dimensional detector arrays that enable time-resolved (TiRe)-LII imaging are limited to a period of 100 ns between datapoints.

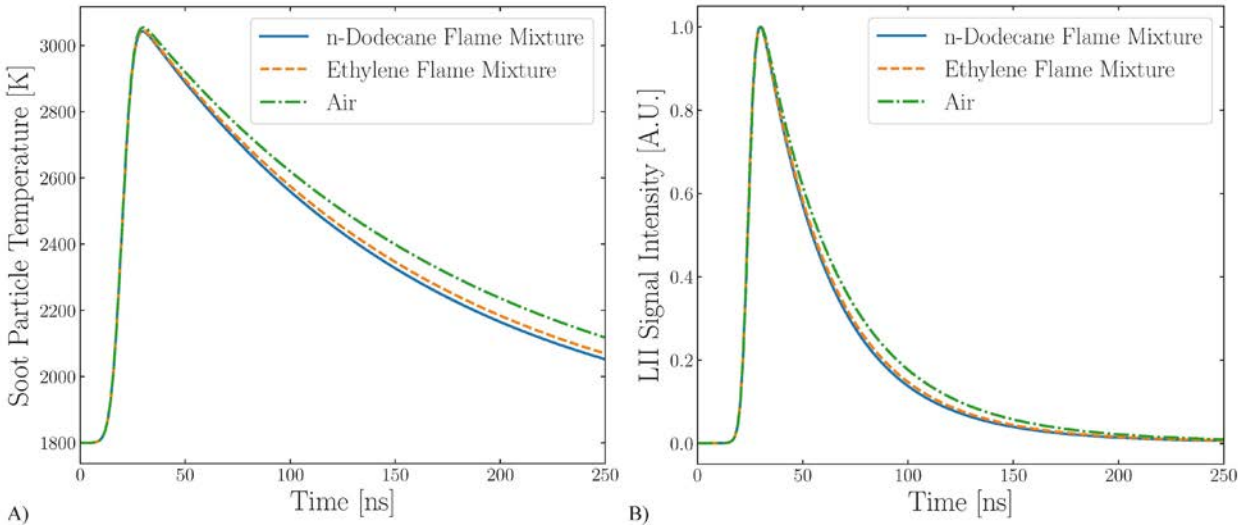


Figure 6. Two graphs showing (a) simulated particle temperature and (b) normalized LII signal.



LII Measurements in COMRAD

The filter stack does not completely isolate the LII signal, as shown in Figure 7(a). To account for this, the collection system is operating at 250 kHz, a much higher repetition rate than the 10 Hz excitation laser. This allows capture of a background frame 4 us prior to the laser introduction to the experiment (Figure 7[b]). At these conditions, this sufficiently freezes motion to perform a background subtraction. The resulting corrected image is shown in Figure 7(c).

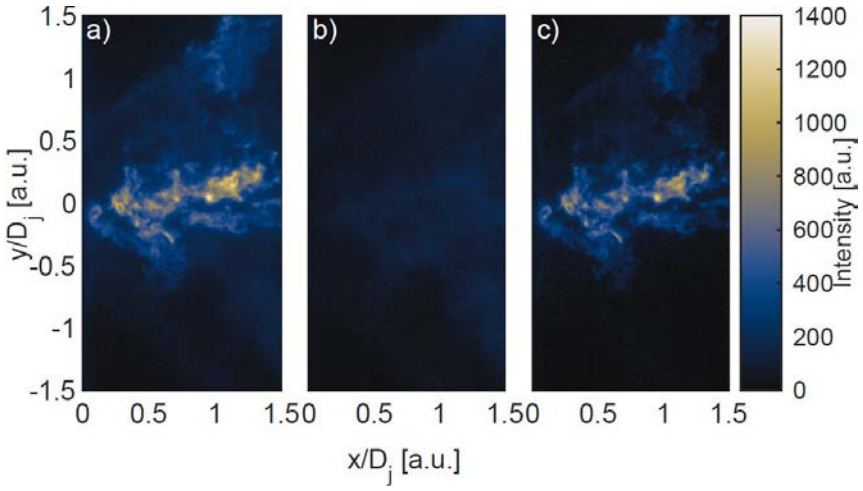


Figure 7. Three images illustrating LII signal processing: (a) LII signal image, (b) Background image taken 4 us prior, and (c) Resulting background subtracted LII signal.

Pilot Only Operation

Soot formation in pilot only operation of current generation combustors is of particular interest due to its use during landing approaches at airports. Studies by Mueller et al. (2025) determined non-volatile particulate matter (nvPM) concentrations surrounding airports can be primarily correlated with arrival aircraft. To investigate this in the optically-accessible combustor, conditions such as inlet air flowrate and temperature, equivalence ratio, and dome pressure drop are held constant. The primary variables investigated are supplied fuel temperature and fuel type (Jet A or World Energy HEFA fuels). Resulting average LII signals from pilot operation with Jet A fuel from 311 to 472 K fuel temperatures are shown in Figure 8. Throughout each fuel temperature, the majority of the LII signal is located along the vertical centerline of the combustor. The pilot element is centered at a y/D_j of 0, which is locally rich for this pilot-only condition. As fuel temperature increases, the bulk intensity of soot volume fraction decreases. At the 472 K condition, the average signal is approximately half the value at the ambient fuel temperature condition. This may be a combination of two factors. Increasing fuel temperature decreases the evaporation timescale, which has been previously shown to dampen combustion instabilities. Reducing evaporation timescales allows for longer residence times for chemical kinetics processes. Soot particles may be consumed, which is supported by the shortening of the most intense regions of soot volume fraction. The increased sensible enthalpy of the fuel may also raise the flame temperature slightly, which results in an increase in the critical sooting equivalence ratio for most hydrocarbons. A higher flame temperature would reduce the quantity of carbon available for soot formation as it is instead converted to carbon dioxide (CO_2).

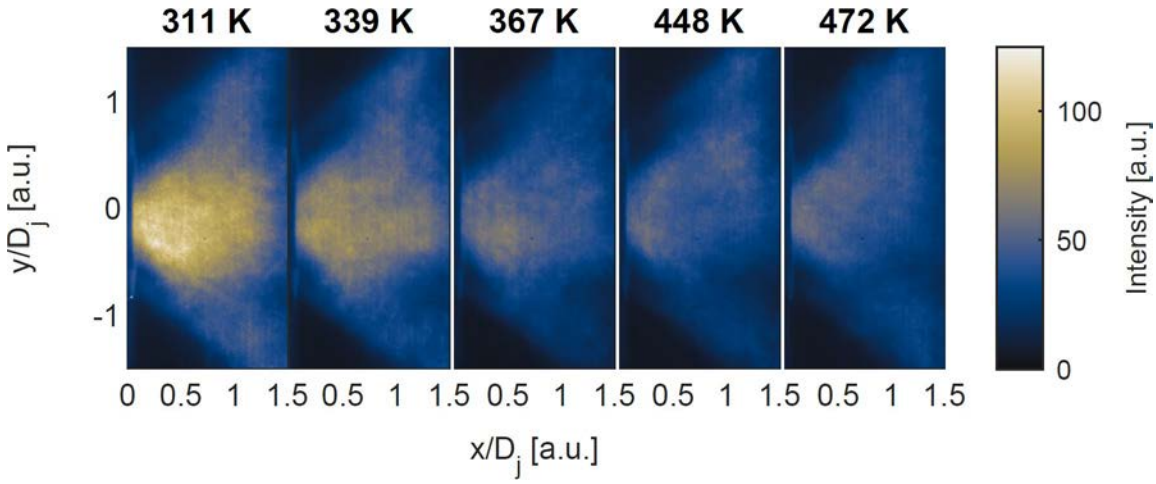


Figure 8. Results of time-averaged LII signals from Jet A fuel for pilot-only operation. The inlet fuel temperature is listed above each image.

Experiments were performed using the World Energy HEFA fuel at the same pilot operation conditions, shown in Figure 9. The color scale in this figure is approximately one-quarter of that in Figure 8, highlighting the distinct difference due to a lack of aromatics in this fuel. As fuel temperature is increased, there is not a significant variation in LII signal intensity. This suggests the mechanism responsible for the decrease in signal for the Jet A fuel measurements is related to the aromatic content. There is not a significant variation in soot formation structure as the HEFA fuel temperature is increased, along the centerline it remains relatively uniform. If soot is in fact being consumed as a function of flame temperature, this mechanism is not active for the neat HEFA fuel.

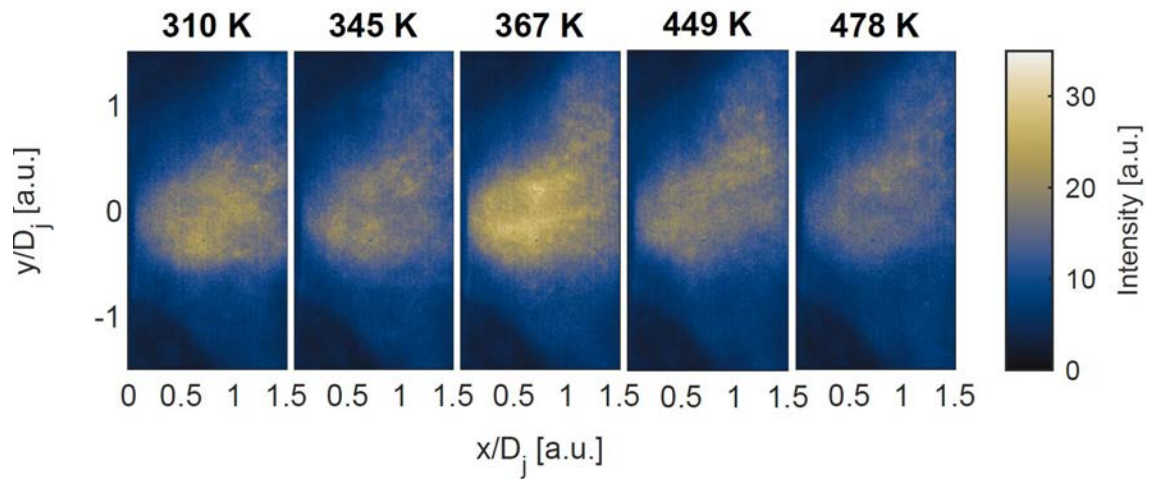


Figure 9. Results of time-averaged LII signals from HEFA fuel for pilot-only operation. The inlet fuel temperature is listed above each image.

Development of Ultrahigh Speed Nitric Oxide Planar-Laser Induced Fluorescence

Previous work done on this project utilized extractive gas sampling measurements to investigate combustion product variations as a function of fuel temperature. Nitric oxide (NO) was found to increase by a factor of two as fuel temperature was increased from 366 K to 589 K. To further investigate this NO increase, we have developed an ultrahigh speed NO planar-laser induced fluorescence (NO PLIF) diagnostic. The optical system is shown in Figure 10. A burst-mode laser operating at 100 kHz provides the necessary energy at 355 nm to pump an optical parametric oscillator (OPO), which

converts the 355 nm light to a 622 nm signal. An idler diode laser operating at 851 nm spectrally narrows the signal leaving the OPO. A portion of the 355 nm beam is routed around the OPO to be used in a sum-frequency generation process with the 622 nm light. The resulting beam at 226 nm is tuned to excite the P1(23.5) line in the NO A-X(0,0) band.

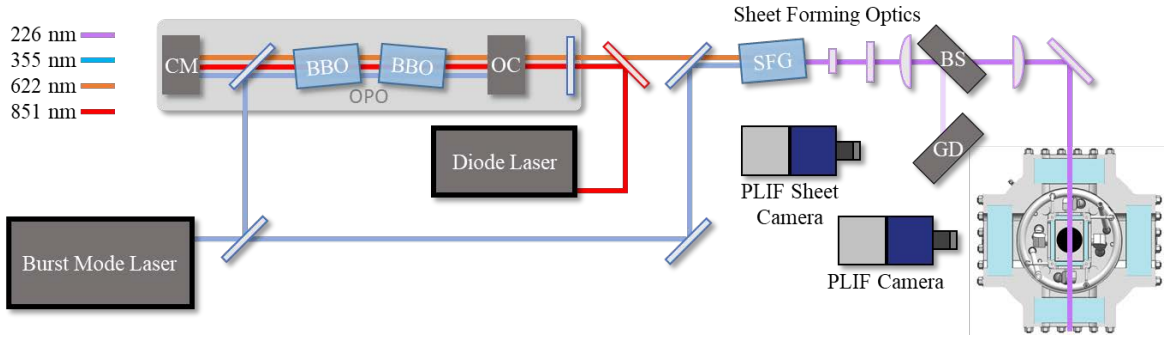


Figure 10. NO PLIF diagnostic system.

A heated, high-pressure gas cell was used to contain up to 8000 ppm of NO for verification of excitation wavelength, necessary pulse energy, and a detection limit of approximately 100 ppm. Signal was verified at up to 0.5 MPa and 670 K. Prior to implementation into the gas turbine combustor, new windows made of fused silica are necessary to transmit the excitation laser and image the NO fluorescence.

Small-volume Fuel Delivery System

PAHs are known to be an immediate precursor to soot. In petroleum-based jet fuels, the aromatic content of approximately 17% significantly increases nvPM formation compared to neat synthetic paraffinic kerosene (SPK) fuels. To investigate the sensitivity of aromatic content on soot formation, we would like to blend either synthetic aromatic kerosene or petroleum-based aromatics into neat SPK. Current ASTM D7566 standards (ASTM, 2022) allow variations in aromatic content from 8-25%v/v for Jet A fuel, and up to 50% blending of HEFA SPK. Due to the extremely limited quantity of synthetic aromatic kerosene (SAK) and the large quantity of fuel necessary for testing in our gas turbine combustor, it is necessary to develop a small-volume fuel delivery system. This system would allow us to expand our testing matrix to investigate the bounds of ASTM D7566 for both aromatic addition and fuel blending, and influence of fuel temperature.

A schematic diagram of the small volume fuel delivery system is shown in Figure 11. The bulk fuel (shown as HEFA SPK) is delivered from the bulk storage tank utilizing a mechanical pump. This is the same system currently used for operations. The small volume fuel (shown as SAK) is delivered using a piston accumulator system. Tank level is monitored using a linear encoder to provide piston location feedback. This allows pressurization of the fuel using a volume of gas, and more importantly rapid flow control for the small volume fuel. This will drastically reduce small volume fuel consumption rate. This liquid flowrate is metered using a cavitating Venturi nozzle.

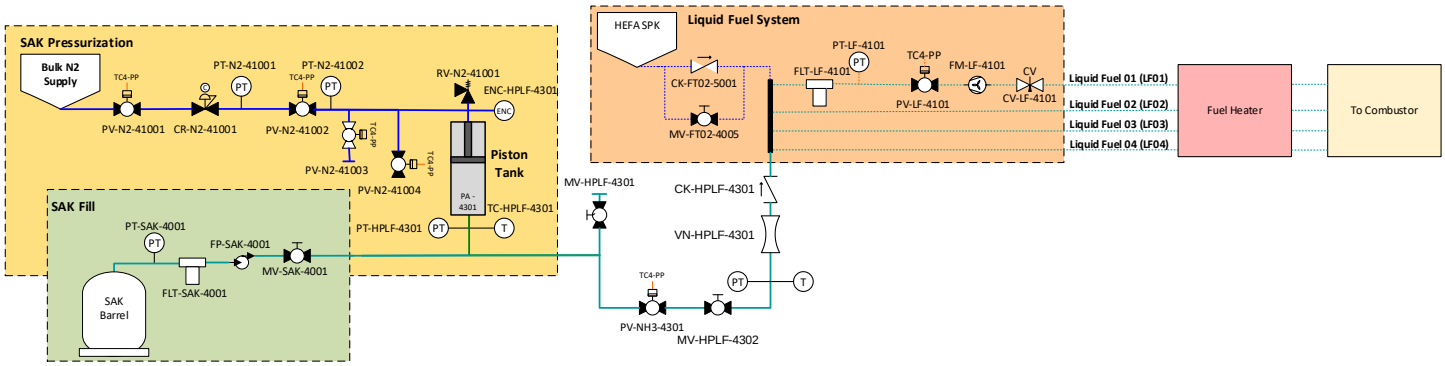


Figure 11. Schematic diagram of the small volume fuel delivery system.



Milestones

- Completed the full-scale facility reconfiguration in the test cell housing this experiment allowing for the continued operation of the COMRAD test rig.
- Applied the previously developed LII system for the measurement of soot formation and oxidation processes in the combustion zone to COMRAD. Measurements were taken in the combustor utilizing Jet A fuel and synthetic aviation turbine fuel (SATF) (World Energy HEFA) at a variety of inlet fuel temperatures.
- Procured significant quantities of SAK for testing in COMRAD. This SAK will be mixed into SPK to match the aromatic content using a piston accumulator fuel delivery system.

Major Accomplishments

- Continued our development of LII for determining soot levels in our combustion flow.
- Developed a time-resolved LII model for extracting primary particle size, which was applied to the lab-scale calibration flame and compared to potential high-pressure combustor operating conditions.
- Testing in COMRAD was performed with Jet A fuel and SATF (World Energy HEFA) for a range of fuel temperatures at a pressure of 1.0 MPa with LII measurements.
- Developed an ultrahigh speed NO-PLIF diagnostic capability, demonstrating imaging of NO in a heated gas cell at 100 kHz.

Publications

Peer-Reviewed Journal Publications

Hodge, A. J., Shahin, T. T., Gejji, R. M., Philo, J. J., Lucht, R. P., & Slabaugh, C. D. (2025). Fuel temperature effects on combustion stability of a high-pressure liquid-fueled swirl flame. *Journal of Propulsion and Power, 41*(1), 53-63. https://doi.org/10.2514/1.B39592

McDonald, C. T., Shahin, T. T., Philo, J. J., Gejji, R. M., Fish, D. D., Slabaugh, C. D., & Lucht, R. P. (2025). Combustion product measurements in a liquid-fueled aviation gas turbine combustor with heated fuels. *ASME Journal of Engineering for Gas Turbines and Power, to be submitted.*

Philo, J. J., Shahin, T. T., McDonald, C. T., Gejji, R. M., Lucht, R. P., & Slabaugh, C. D. (2023). Effect of fuel temperature on the structure of a high-pressure liquid-fueled swirl flame, *Fuel, 354*. 129142. https://doi.org/10.1016/j.fuel.2023.129142

Published Conference Proceedings

McLean, T. N., Koenig, K. C., Murdock, B. K., Shahin, T. T., Hodge, A. J., Gejji, R. M., Slabaugh, C. D., & Lucht, R. P. (2025, January 6-10). *Laser-induced incandescence measurements in a high-pressure swirl-stabilized flame* [Conference presentation]. AIAA SciTech 2025 Forum, Orlando, Florida. https://doi.org/10.2514/6.2025-1580

Hodge, A., Shahin, T., McLean, T., Gejji, R., Lucht, R., & Slabaugh, C. (2024, January 8-12). *Fuel temperature effects on combustion stability of a high-pressure liquid-fueled swirl flame* [Conference presentation]. AIAA SciTech 2024 Forum, Orlando, Florida. https://doi.org/10.2514/6.2024-1241

McDonald, C. T., Philo, J. J., Shahin, T. T., Gejji, R., Slabaugh, C. D., & Lucht, R. P. (2021, August 9). *Effect of fuel temperature on emissions and structure of a swirl-stabilized flame* [Conference presentation]. AIAA Propulsion and Energy 2021 Forum, virtual. https://doi.org/10.2514/6.2021-3480

Outreach Efforts

None.

Awards

Professor Lucht was the recipient of the **2025 Propellants and Combustion Award** from the American Institute of Aeronautics and Astronautics. The citation reads "For numerous contributions to combustion, propulsion, and power generation through innovative development of advanced laser diagnostics and applying them to practical energy systems."

Student Involvement

Three PhD students (Tristan Shahin, Ben Murdock, and Zander Hodge) are currently working on the project. John Philo graduated in March 2022 with his PhD after working on the project and is currently employed at Blue Origin. Colin McDonald graduated in September 2022 with his MS degree and accepted a position with Astra (Merced, California), where he is responsible for setting up a new rocket engine test facility. Thomas McLean graduated in May 2024 with his MS



degree after working on the project and is currently attending U.S. Air Force Flight School. Keaton Koenig graduated in May 2025 with his MS after working on the project. Tristan Shahin defended his PhD dissertation in October 2025 after working on the project.

The project provides outstanding research experiences for the graduate students, including the design of system components for, and the operation of, a sophisticated aviation gas turbine combustion test rig, as well as application of advanced laser diagnostic methods for measurements in this test rig. As noted above, the graduate students have been responsible for designing system components, such as the fuel heating system, and for executing test operations.

Plans for Next Period

The focus for the next period of this project will be a detailed comparison of a selected SATF with a well-characterized petroleum-based fuel, Jet A or fuel A2 from the National Jet Fuel Combustion Program. The SATF will be a mixture of SPK and SAK, and the composition will be selected in consultation with other FAA ASCENT researchers and our collaborators at GE Aerospace. The nominal SATF composition is expected to be 92% SPK (World Energy HEFA) and 8% SAK (single-ring aromatic compounds from Virent®). SATFs with SAK contents as low as 4% and as high as 30% will also be investigated, depending on the availability of supplies from Virent. We may also explore petroleum-based single-ring aromatic compounds if we cannot obtain enough SAK from Virent.

We plan to expand our operational test matrix to include conditions of significant interest to GE Aerospace. Thus far in our test program, the relative equivalence ratios for the pilot and main have been fixed. GE Aerospace is interested in expanding the test matrix to investigate the effect of varying equivalence ratios in the main and pilot on hot fuel effects, especially as it relates to nitrogen oxides (NO_x) formation. Along these same lines, pilot-only operation is of significant interest. We will also explore the effects of fuel heating for rich dome operation, implemented by supplying sufficient fuel in the streams to create a globally rich mixture.

Additionally, LII will be used to further investigate soot formation measurements taken in lean dome operation. Additional funding will allow us to expand the operational test matrix to include conditions with higher pilot to main fuel, globally rich conditions, and further fuel composition blends. The LII measurements will provide valuable information of the spatial locations for particulate formation in the combustor flow field for engines using both conventional Jet A fuel and a variety of SATFs. We are also interested in both nonvolatile and volatile particulate formation. GE Aerospace has shown considerable interest in the types and number of particulates that are in the combustor exhaust. Further experimentation with differing laser sheet location and increased laser repetition rate are both of considerable interest to gain further special and temporal resolution. The effects of passing through the turbine on nvPM particulates are not well understood. In addition to LII, the NO PLIF diagnostic system will be applied with PIV to probe the flow field for selected operating conditions.

References

ASTM International. (2022). *ASTM D7566-22: Standard Specification for Aviation Turbine Fuel Containing Synthesized Hydrocarbons*. https://doi.org/10.1520/D7566-22

Liu, F., Daun, K. J., Snelling, D. R., & Smallwood, G. J. (2006). Heat conduction from a spherical nano-particle: status of modeling heat conduction in laser-induced incandescence. *Applied Physics, 83*, 355–382. https://doi.org/10.1007/s00340-006-2194-1

Mueller, S. C., Patil, P., Levy, J. I., Hudda, N., Durant, J. L., Gause, E. L., van Loenen, B. D., Bermudez, M., Geddes, J. A., & Lane, K. J. (2025). Quantifying Aviation-Related Contributions to Ambient Ultrafine Particle Number Concentrations Using Interpretable Machine Learning. *Environmental Science & Technology, 59*(37), 19942–19952. https://doi.org/10.1021/acs.est.5c07989

® Virent is a registered trademark of Virent, Inc., Madison, Wisconsin.



Project 068 Combustor Wall Cooling with Dirt Mitigation

The Pennsylvania State University

Project Lead Investigator

Reid A. Berdanier
Associate Professor
Department of Mechanical Engineering
The Pennsylvania State University
NARCO Building, CATO Park, Room 148
3127 Research Drive
State College, PA. 16801
(814) 863-3972
rberdanier@psu.edu

University Participants

The Pennsylvania State University (Penn State or PSU)

- P.I.s: Prof. Karen Thole, Prof. Reid A. Berdanier, Dr. Michael Barringer, Prof. Stephen Lynch
- FAA Award Number: 13-C-AJFE-PSU-128
- Period of Performance: June 5, 2020, to September 30, 2026
- Tasks:
  1. Manufacturing and testing of combustor liner cooling concepts with small coupons
  2. Testing of scaled models of optimal cooling concepts
  3. Profile simulator for the Steady Thermal Aero Research Turbine (START)

Project Funding Level

For the entire 5-year effort ASCENT Project 068 received $1,400,000 Federal Aviation Administration (FAA) funding, and matching funds of $1,400,000 were provided by Pratt & Whitney ($1,250,000), University of Michigan (U-M) ($100,000) and PSU ($50,000).

Investigation Team

Prof. Reid A. Berdanier (P.I.), Management, reporting, and oversight of all technical tasks
Prof. Karen A. Thole (co-P.I.), Management, reporting, and oversight of all technical tasks
Prof. Stephen Lynch (co-P.I.), Management, reporting, and oversight of all technical tasks
Assoc. Res. Prof. Michael Barringer (research advisor), Task 3
Scott Fishbone (project manager, departed), Tasks 1-3
Tom Houck (project manager), Tasks 1-3
Kyle McFerran (graduate student, PSU, graduated), Tasks 1 and 2
Chad Schaeffer (graduate student, PSU, graduated), Task 3
Fabrizzio Vega (graduate student, U-M), Task 2
Peyton Boudinot (graduate student, U-M), Task 2
Dan Strobel (graduate student, PSU), Task 3
Benjamin Bizzak (graduate student, PSU), Task 3

Project Overview

A critical issue related to the current operation of gas turbines is the ingestion of dirt and other fine particles that lead to dirt buildup and reduced cooling of hot section components, such as the liner walls of the combustion chamber. With increasing need to fly in dirty environments, the criticality of operations in dirty environments is increasing. Modern gas turbine engines typically use a double-walled combustor liner with impingement and effusion cooling technologies, whereby impingement cooling enhances the backside internal cooling, and effusion cooling creates a protective film of

coolant along the external liner walls. Dirt accumulation on the internal and external surfaces severely diminishes the heat transfer capability of these cooling designs. This study also investigates the development of a combustor profile simulator upstream of the START test turbine. Combustor profiles affect turbine performance and durability. As combustor designs evolve, particularly the liner cooling technologies, understanding the impacts on the turbine is important. This study investigates practical designs applied to combustor walls to decrease dirt accumulation and also explores the development of a profile simulator that can replicate relevant temperature and pressure profiles at elevated turbulence levels upstream of a test turbine.

Task 2 – Testing of Scaled Models of Optimal Cooling Concepts

The Pennsylvania State University

Objective

The objective of this task is to produce an effective cooling design for combustor walls that is insensitive to dirt accumulation at existing or lower coolant flow rates. Various parameters such as dirt deposition, flow behavior, and heat transfer effectiveness will be investigated and quantified to compare the efficiency of candidate designs. Improved understanding of the underlying reasons for dirt sensitivity and deposition behavior is also being sought. During this past year, the ASCENT Project 068 team took two primary approaches to the problem: (1) identify the impact of dirt deposition on the cooling performance of a typical double-wall combustor liner and (2) identify a novel geometry to replace the double-wall liner design with a triple-wall combustor liner.

Research Approach

Considering size constraints due to material availability, designs for new combustor liner walls were created and are presented in Figures 1, 2, and 3. In total ten combustion liner walls were designed, including two effusion plates and eight impingement plates. In total there are four diameters of impingement holes, namely D = 0.025, 0.06, 0.09, and 0.125 in., each with two versions of differing wall spacings.



Figure 1. Third-wall impingement plate, with an impingement hole diameter of 0.06 in.

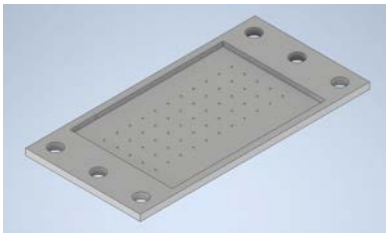


Figure 2. Second-wall impingement plate, with an impingement hole diameter of 0.025 in.

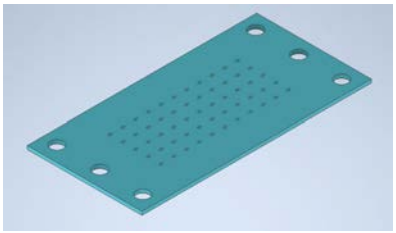


Figure 3. First-wall effusion plate, with an effusion hole diameter of 0.033 in. at an angle of 30°.

Additionally, a new concept for the impingement and effusion hole patterns was created. The previously used hole alignment is presented in Figure 4, black representing the impingement holes on the second wall, red the impingement holes on the third wall, and blue the effusion holes on the first wall. This design features effusion holes laterally and longitudinally offset from the second-wall impingement holes and the third wall impingement holes centered between four second-wall impingement holes. The new design, shown in Figure 5, centers the effusion holes between two adjacent second-wall and two adjacent third-wall impingement holes.

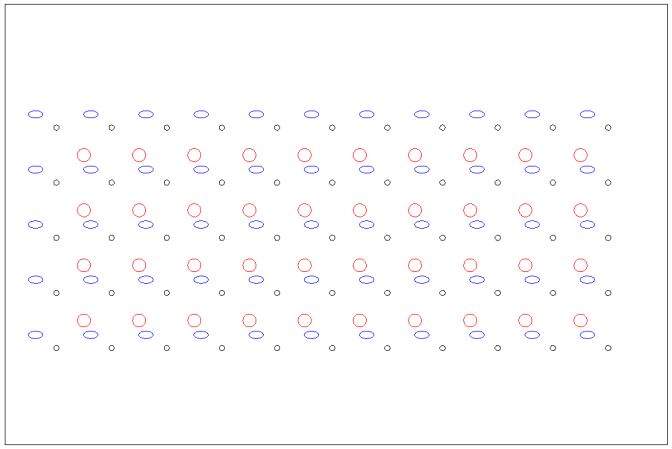


Figure 4. Previously used effusion (blue) and impingement (red, black) hole pattern.

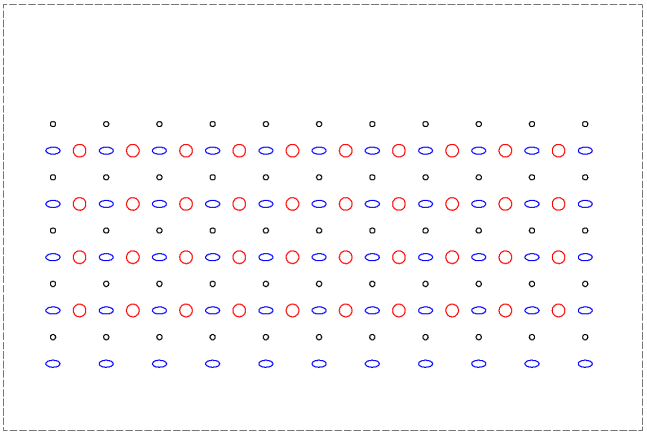


Figure 5. New effusion (blue) and impingement (red, black) hole pattern.



Compilation of Test Matrix

A plan for tests to be conducted at the room- and at the high-temperature test facilities was devised for the original and new hole patterns, as seen in Table 1 and Table 2, respectively. The test matrix for the original hole pattern features previously done hole double- and triple-wall tests, with novel tests for this design being changes in the wall to wall spacing to hole diameter ($\frac{H}{D}$) ratio alternates between 3 and 10. All tests presented in the test matrix for the new hole pattern will be new.

It should be stated that even previously performed room-temperature tests will be repeated at the new U-M facility (i.e., all tests in both matrices will be performed at both temperatures).

Table 1. Test matrix for original hole pattern.

	Wall #0	Wall #1	Wall #2
Double Wall Tests	-	Imp-025-3	Eff-033c0
	-	Imp-025-10	Eff-033c0
Triple Wall Tests	Imp-125-10	Imp-025-3	Eff-033c0
	Imp-090-10	Imp-025-10	Eff-033c0
	Imp-060-10	Imp-025-3	Eff-033c0
	Imp-125-3	Imp-025-10	Eff-033c0
	Imp-090-3	Imp-025-3	Eff-033c0
	Imp-060-3	Imp-025-10	Eff-033c0

Imp-**DDD**-**HH**
DDD ➔ Hole diameter ($\frac{1}{1000}$ths inches)
HH ➔ $\frac{H}{D}$, ratio of plate spacing above to hole diameter

Eff-**DDDs**
DDD ➔ Hole diameter ($\frac{1}{1000}$ths inches)
s ➔ Hole geometry, c: cylindrical

Table 2. Test matrix for new hole pattern.

	Wall #0	Wall #1	Wall #2
Double Wall Tests	-	Imp-025-3	Eff-033c1
	-	Imp-025-10	Eff-033c1
Triple Wall Tests	Imp-125-10	Imp-025-3	Eff-033c1
	Imp-090-10	Imp-025-10	Eff-033c1
	Imp-060-10	Imp-025-3	Eff-033c1
	Imp-125-3	Imp-025-10	Eff-033c1
	Imp-090-3	Imp-025-3	Eff-033c1
	Imp-060-3	Imp-025-10	Eff-033c1

Imp-**DDD**-**HH**
DDD ➔ Hole diameter ($\frac{1}{1000}$ths inches)
HH ➔ $\frac{H}{D}$, ratio of plate spacing above to hole diameter

Eff-**DDDs**
DDD ➔ Hole diameter ($\frac{1}{1000}$ths inches)
s ➔ Hole geometry, c: cylindrical

Construction of Test Facility

The design of the test rig has been completed, a diagram for which is presented in Figure 6. Like the previous rig, this one will be slug-feeding dirt samples into the system.

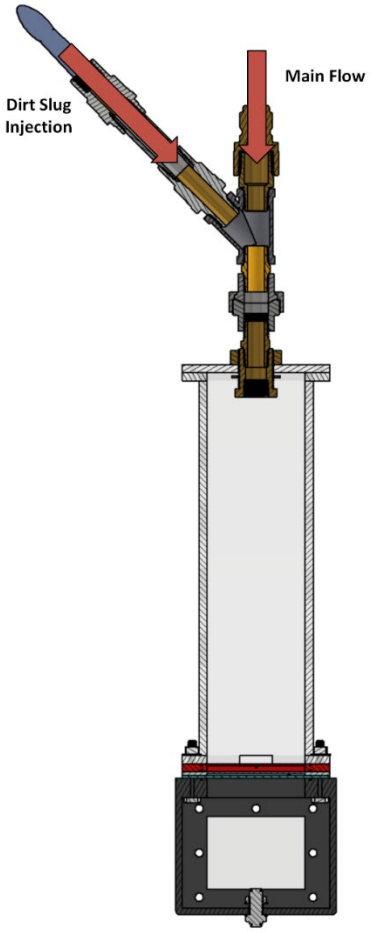


Figure 6. Cross-sectional view of the new U-M dirt rig.

Finally, the as-built flow control plumbing circuit is shown in Figure 7. An Alicat® mass flow controller regulates the flow rate to maintain a constant pressure ratio (PR) of 1.045 across the test section. The mass flow that the controller is set to is updated by the LabVIEW code via a Proportional-Integral-Derivative (PID) system, the process variable being the PR calculated from pressures measured by transducers.

The room-temperature dirt deposition facility at U-M, shown in Figure 8, serves to study the effects of dirt deposition in cooling geometries found within the combustor liner of gas turbines. A test coupon emulating the walls of a combustor liner is composed of stacked impingement and effusion plates. The facility features a slug feed system for injecting dirt into the main flow path. During a typical deposition experiment, a nominal mass of dirt is split into three slugs of equal mass and are sequentially fed into the system. Pressure taps are located at various locations throughout the facility for measuring the coolant air pressure (P_{0C}), pressures between subsequent effusion/impingement plates (P_1, P_2), and the pressure at the exit of the test coupon (P_∞).

® Alicat is a registered trademark of Alicat Scientific, Inc., Tucson, Arizona.



Figure 7. As-built flow control plumbing at U-M.

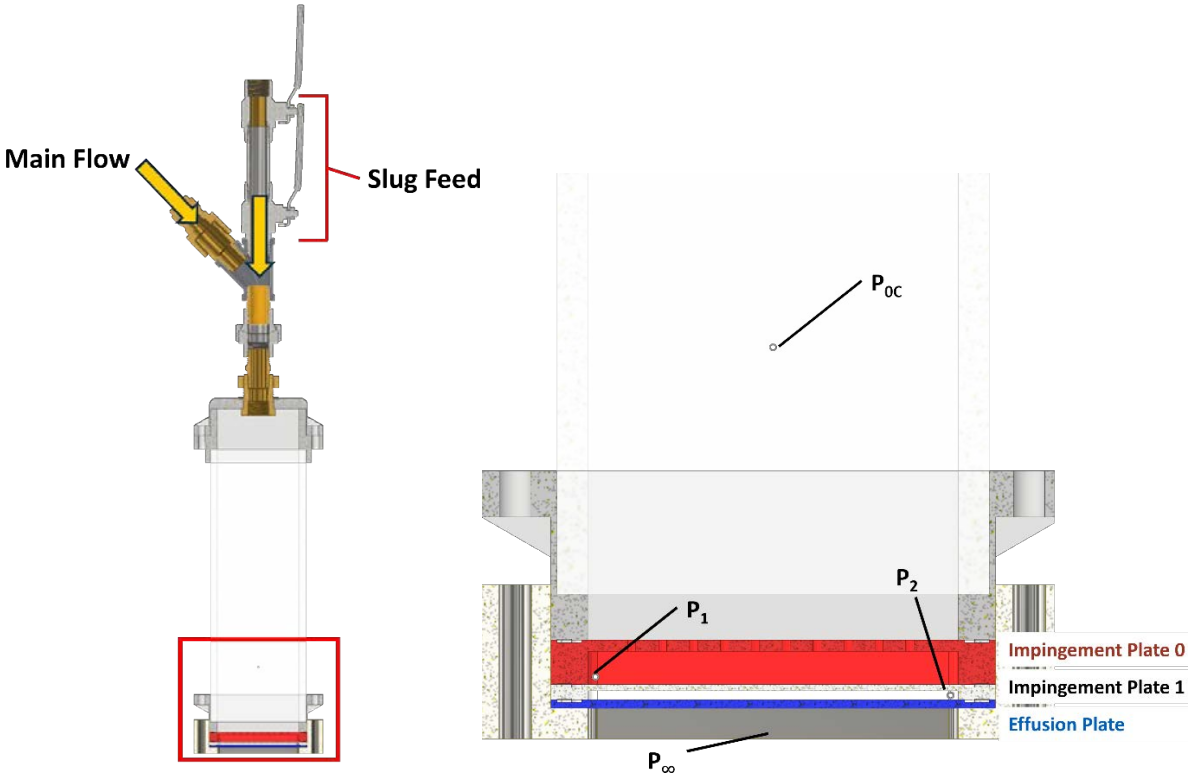


Figure 8. Overview of room-temperature dirt deposition testing facility (left). Cross sectional view of test coupon in testing facility (right).



An absolute pressure transducer measures the pressure of the supply air (P_{Supply}), a differential pressure transducer measures the pressure drop from the air supply to the plenum (ΔP_0), and a second differential pressure transducer with ±0.08% best straight line accuracy measures the pressure drop across the test section (ΔP_{Total}). As per Equation 1, the PR across the test section is dynamically calculated during experiments. A PID controller, using PR as the process variable, maintains a constant PR = 1.045 across the test section by adjusting the mass flow rate of coolant air ($\dot{m}$).

The flow parameter (FP), defined in Equation 2, is also monitored during testing and serves to quantify the flow through the test section. To maintain consistency with previous studies, the metering section of the FP is the "Imp1" plate, with the number of holes (N) and hole diameter (D_1) corresponding to "Imp1." For this particular double-wall geometry, the dependence of the FP with PR under clean conditions (i.e., no dirt injection) is depicted in Figure 9. The FP measured at the start of each experiment, prior to dirt injection, is compared to this baseline curve to make sure that no blockages remain from previous tests.

$$PR = \frac{P_{0C}}{P_{\infty}} = \frac{P_{supply} - \Delta P_0}{P_{supply} - \Delta P_0 - \Delta P_{total}} \quad \text{(Eq. 1)}$$

$$FP = \frac{4\dot{m}\sqrt{RT_{0C}}}{\pi P_{0C} N D_1^2} \quad \text{(Eq. 2)}$$

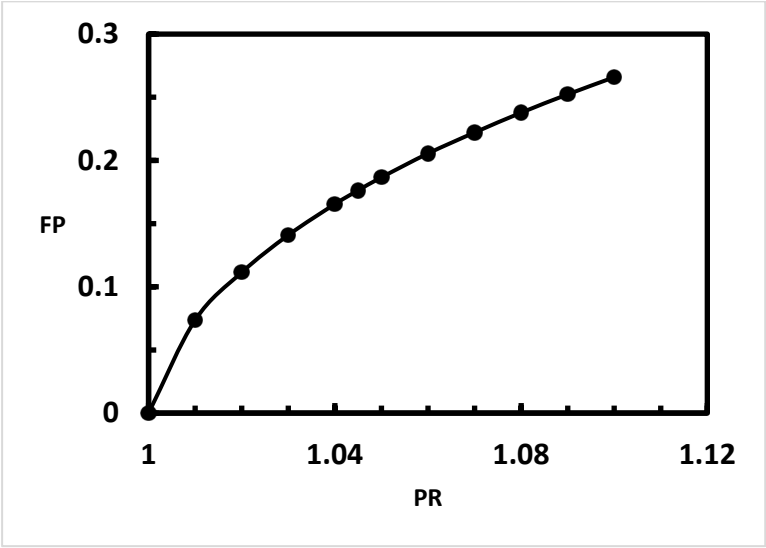
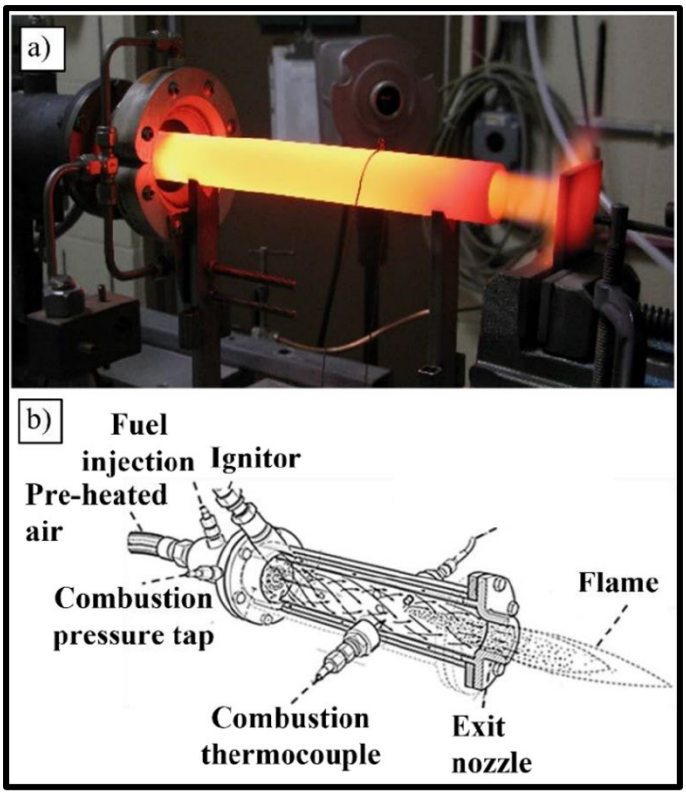


Figure 9. Baseline clean flow parameter (FP) as a function of pressure ratio (PR) for the baseline double-wall geometry.

In collaboration with researchers at the National Aeronautics and Space Administration (NASA) Glenn Research Center (GRC), a facility has been constructed to study deposition within combustor liners at high temperatures. Of particular interest in these experiments is to investigate the enhanced deposition mitigation provided by the addition of a third combustor liner wall. NASA GRC houses a Mach 0.3 burner rig, shown in Figure 10, and is used to simulate the high-temperature conditions within a combustor.



Stokes, J. L. & Presby, M. J. (2024)

Figure 10. (a) The burner rig during operation, heating up a sample. (b) A drawing of the burner rig labeling key components.

A top-down view of the testing rig is shown in Figure 11. Test coupons made up of stacked impingement and effusion plates are used to simulate the walls of a combustor liner and are housed in a stainless-steel enclosure. The enclosure serves to create an airtight seal between adjacent plates by pressing the plates together. Pre-heated particle-laden air is fed into the backside of the enclosure, passes through the test coupon, and exits out of the effusion holes on the other side. An inline heater brings the absolute temperature of the cooling air, T_{0c}, to half of the effusion plate surface temperature (TS). A thermocouple provides the coolant temperature to a furnace controller that regulates the power output of the inline heater to achieve the desired coolant temperature.

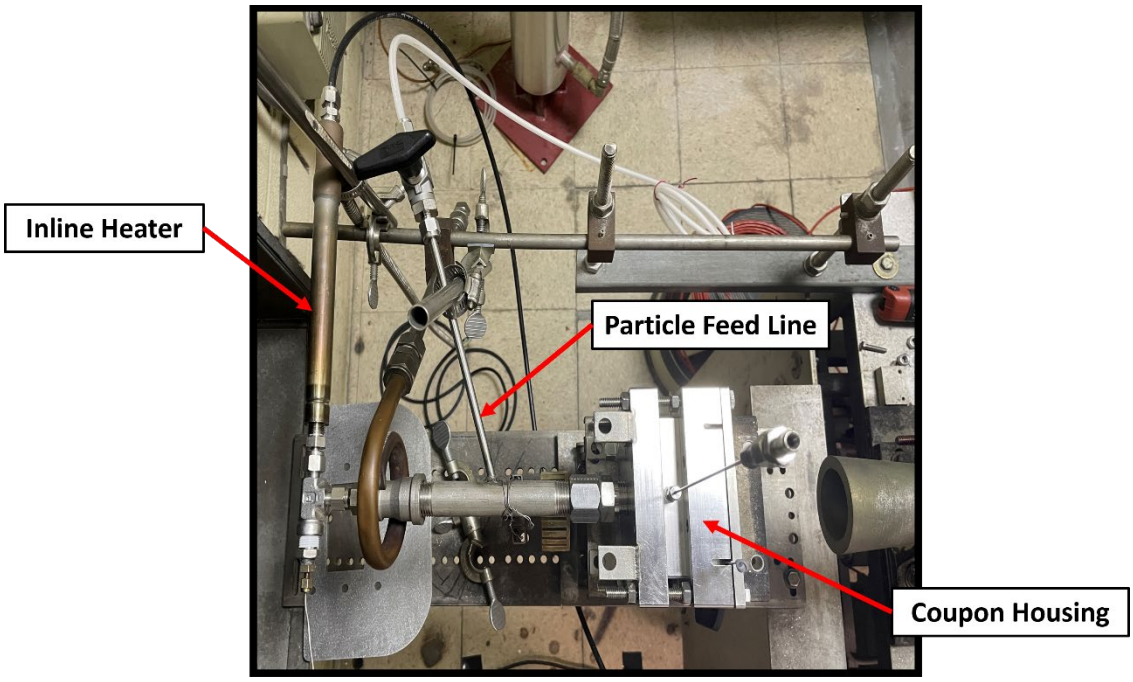


Figure 11. Top-down view of the testing rig.

The burner nozzle was aimed at the combustor side (downstream) of the effusion wall, as seen in Figure 12, with the flame produced having the capability of creating hot side surface temperatures on the effusion wall of up to 1,200°C. At the start of each experiment, the fuel-air ratio for the burner is modified until the desired T_s is reached at steady state. A pyrometer monitors T_s at the center of the effusion wall.

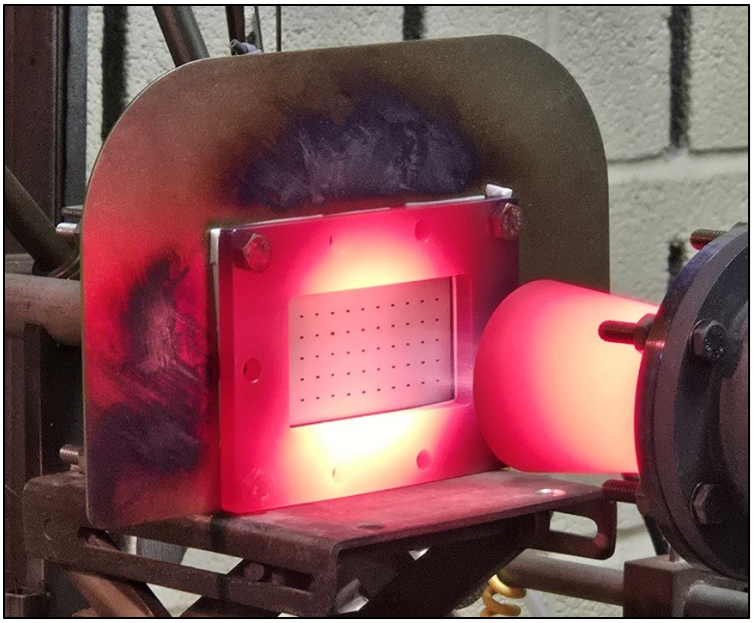


Figure 12. The high-temperature testing facility during operation. An effusion plate (center) is exposed to a flame that is seen coming out of the burner nozzle (right).



A total of four unique test cases are performed varying in combustor liner geometry. The different test cases are presented in Table 3. The combustor liner geometry varies in the number of walls (double- or triple-wall) and in the diameter of the impingement holes on the third wall (D_0). A constant PR of 1.045 is maintained across the liner for each test case.

Table 3. Testing conditions for high-temperature deposition experiments.

	Testing Conditions			Geometry		
	T_s [˚C]	T_{0C} [˚C]	PR [-]	D_0 [in]	D_1 [in]	D_2 [in]
Combustor Liner Geometry	1200	463	1.045	0.060	0.025	0.033
	1200	463	1.045	0.090	0.025	0.033
	1200	463	1.045	0.125	0.025	0.033
	1200	463	1.045	-	0.025	0.033

A thermal barrier coating (TBC) composed of yttria-stabilized zirconia was applied onto all the effusion plates via the process of Plasma Spray-Physical Vapor Deposition (PS-PVD). The average coating thickness for each of the three plates is around 120 microns. As shown in Figure 13, the TBC inadvertently deposited on the inside of the effusion holes. Since this is a common occurrence in effusion plates coated and used by industry, the holes were not cleared out following the coating process.



Figure 13. A hole on an effusion plate coated in yttria-stabilized zirconia thermal barrier coating.

Throughout every test, the PR across the test coupon (PR), defined as the ratio of coolant pressure immediately upstream (P_{0C}) to that immediately downstream, is maintained constant at PR = 1.045. Because the test coupon vents to atmosphere, the pressure immediately downstream to it is taken to be the absolute ambient pressure (P_∞) for which a barometer inside the burner rig cell is referenced at the start of every test. An OMEGA 2.5 psi differential pressure transducer measures the drop in pressure of the coolant across the test coupon (ΔP_{Total}). The PR is calculated in terms of P_∞ and ΔP_{Total} as per Equation 3.

$$PR = \frac{P_{0C}}{P_\infty} = 1 + \frac{\Delta P_{total}}{P_\infty} \quad \text{(Eq. 3)}$$



Building supply compressed air serves as the coolant in these series of tests and is regulated throughout their duration by a mass flow controller (250 SLPM Flow Controller, Alicat Scientific, Inc.) such that a PR=1.045 is maintained across the test coupon. After passing through the mass flow controller, the air is heated to the desired coolant temperature (T_{0C}) using a 750W inline heater, the temperature of which is measured with a type-K thermocouple placed at the outlet of the heater. To maintain a constant T_{0C}, a temperature controller regulates the power output of the heater. All piping downstream to the inline heater is insulated with mineral wool.

The coolant flow was seeded with AFRL-05 (Air Force Research Laboratory) particles which is primarily made up of gypsum and quartz and has a mean particle diameter of 1.2μm with a 0-3μm size distribution. Dust feed was accomplished via a slug injection system where a discrete quantity of dirt was fired into the coolant flow. Prior to use in testing, dirt samples were passed through a fine wire mesh to break up agglomerations and subsequently dehumidified by baking in an oven.

Prior to and after deposition, the mass of each impingement and effusion plate that made up the test coupon was individually measured. The difference between corresponding measurements indicated the mass of dirt that deposited on the n^{th} layer (m_n). The primary method for comparing dirt deposition across liner geometries was through the capture efficiency (η_c) presented in Equation 4. The capture efficiency of the n^{th} layer is defined as the ratio of m_n to the total dirt which deposited on layers downstream to the first impingement plate (m_t). Because the double-walled configuration has only one impingement plate, by definition its capture efficiency is always 100%, whereas for a triple-wall configuration the capture efficiencies for the middle impingement and the effusion plates both sum to 100%.

$$\eta_c = \frac{m_n}{m_t} * 100 \qquad \text{(Eq. 4)}$$

Capture efficiencies for the baseline double-wall design and the best performing triple-wall design are presented for T_s = 1,200°C and for room temperature conditions in Figure 14. Under high temperature conditions, the presented triple-wall design is shown to reduce dirt deposition on the effusion wall by 63%. These results agree with those by McFerran et al. (2025) who reported an 87% reduction of deposition on the effusion wall using the same combustor liner design. It is well known that deposition is more likely to occur at higher temperatures, which explains the smaller reduction seen under high temperature conditions. Both room- and high- temperature results support the idea that the addition of an impingement wall to the commonly seen double-wall configuration will significantly reduce deposition on the effusion wall.

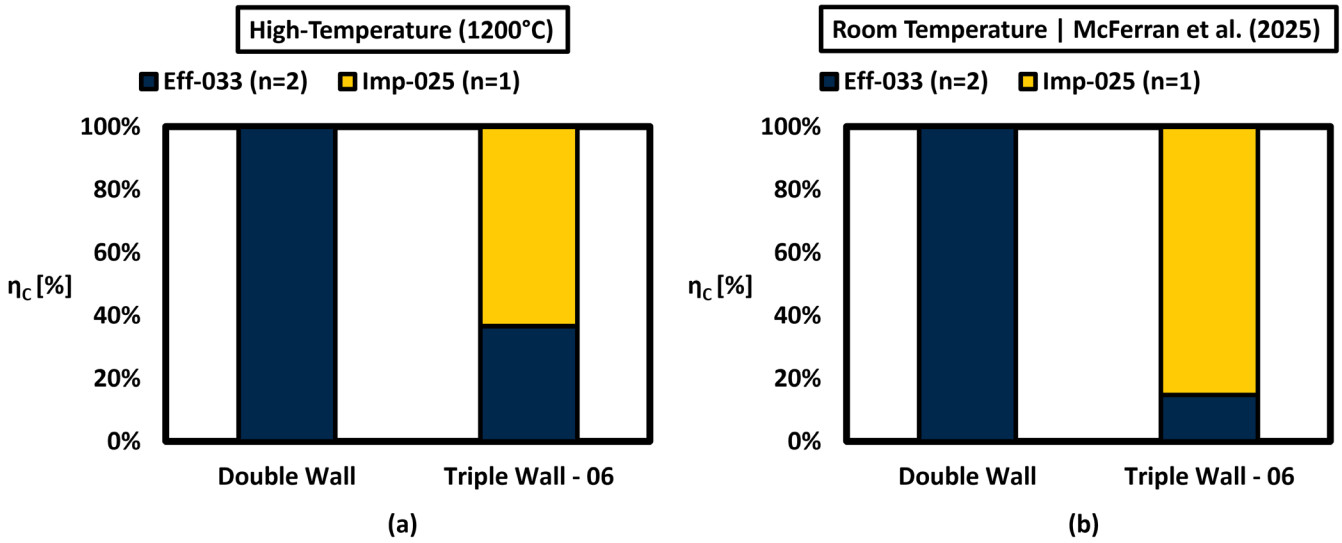


Figure 14. Dirt capture efficiencies for the double-wall configuration and triple-wall configuration, with Imp-060 (n=0), for (a) high effusion wall surface temperature and (b) room temperature conditions.

An optical profilometer was used to take three-dimensional scans of resulting dirt depositions after every test. The lateral average of the height profiles for the middle three columns of dirt mounds on the effusion wall is presented for the double- and triple-wall configurations in Figure 15. For both cases, the mounds form in the stagnation region of the

impingement jets from the plate immediately upstream to the effusion wall. Also, in agreement with the capture efficiency results, the lateral average of deposit heights is smaller when using a triple wall over a double-wall configuration indicative of a reduction in deposition on the effusion wall.

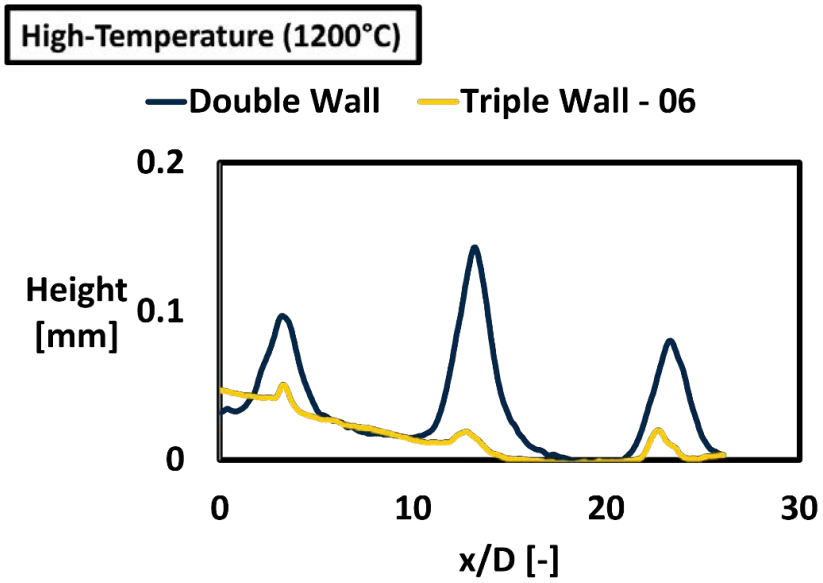


Figure 15. Lateral average deposit heights on the effusion wall for double- and triple-wall liner geometries.

Task 3 – Profile Simulator for START

The Pennsylvania State University

Objectives

The objectives of this task are to (1) develop and integrate a non-reacting profile simulator to be placed upstream of the START test turbine and (2) understand the impacts of a range of temperature and pressure profiles, representative of current and future combustors, on turbine efficiency and durability.

Background

A combustor profile simulator was designed and is being implemented into the START rig upstream of the turbine test section. Previous reports include a summary of the simulator design, results of initial computational fluid dynamics (CFD) simulations, and the CFD Design of Experiments (DOE) sensitivity analysis. The primary hardware components of the simulator have completed the manufacturing process. During the current reporting period, work was performed to procure all remaining parts that are needed for experimentally testing the simulator, such as the 360° traverse components, flow valves, flow meters, and general instrumentation. An instrumentation plan was developed to establish (1) a bill of materials for the instruments and sensors, (2) details related to instrumentation installation and placement, and (3) details related to egress of sensor tubes and wires. The instrumentation includes temperature, pressure, and flow measurement devices placed throughout the simulator device to control experimental operation settings that enable the simulator to produce the target profiles. In addition, these measurement instruments help aid in CFD validation by providing accurate experimental data that can be compared back to computational predictions.

Computational Simulations of the Profile Simulator

Recall from previous reports, the design target profiles for the new profile simulator include a radial center-peaked, outer diameter (OD) peaked, inner diameter (ID) peaked, and a flat uniform profile. The profile results from the CFD DOE study that best matched the design targets are plotted in Figure 16 and are designated as “Center-Peaked,” “ID-Peaked,” “OD-Peaked,” and “Uniform.” These four target profiles are representative of the engine profiles that were collected from

literature and are also shown. The shaded gray region in Figure 16 represents the full range of profiles produced by the CFD study.

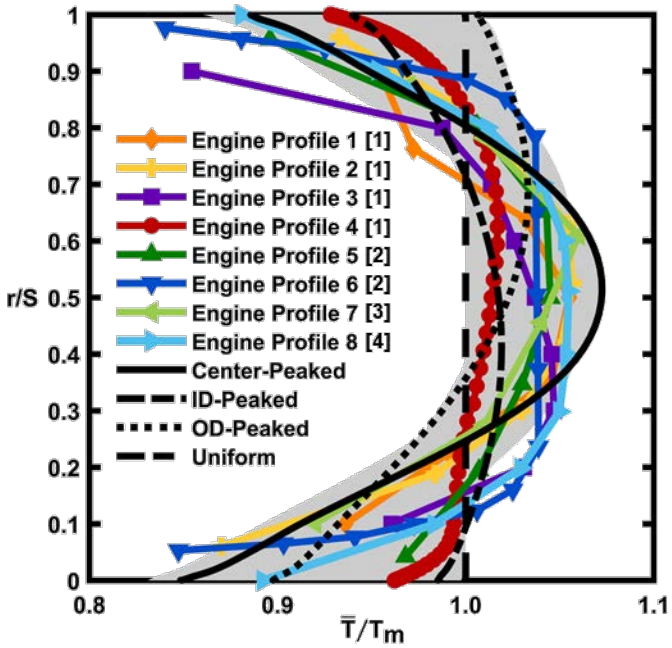


Figure 16. Range of non-dimensional total temperature profiles generated from the CFD DOE, plotted versus radial span location and compared to original equipment manufacturer (OEM) engine combustors (Schaeffer, 2025). ID: inner diameter, OD: outer diameter.

One reason for the selection of the four target profiles was to allow the target profiles to be studied using experiments and a higher fidelity computational model. It was previously determined in literature that the Reynolds-averaged Navier Stokes (RANS) model provides a good prediction of the flow physics, such as jet penetration depth and bulk-averaged velocities, but Large Eddy Simulation (LES) modeling is needed to accurately capture the turbulence created by the intense mixing process of the dilution jets. Understanding how well the RANS simulations predict the temperature profiles is important in determining the viability of using RANS as a predictor for the various flow and geometry configurations in which the profile simulator can be operated. The center-peaked profile was selected as the preliminary case to perform the LES modeling used in this study.

Before transitioning the simulator computations over to LES, a more in-depth RANS simulation was completed that included the domain regions defined by the simulator's upstream strut, profile plate, and downstream turbine vane. An in-depth discussion about the combustor simulator RANS simulation was included in previous reports but a summary of the additional geometry add-ons is provided here as a reminder. The turbine vane used is from the Penn State National Experimental Turbine (NExT) geometry. This updated CFD domain can be seen in Figure 17, with the axial location of the turbine inlet traverse rakes marked in green and the axial location of the vane leading edge (LE) marked in blue. The perforated profile plate acts to reduce the air pressure to enable proper injection of the dilution and effusion flows into the central chamber. The profile plate is interchangeable and contains an engineered perforated pattern that facilitates the desired air mass flow distribution throughout the simulator. In addition to creating a pressure loss, the profile plate is used to reduce the aerodynamic wake effect of the strut's presence in the main flow and to create a uniform flow field entering the central chamber. The struts act as a passageway to distribute cooling air to the inner diameter annulus flow paths and to structurally support the inner hardware components.

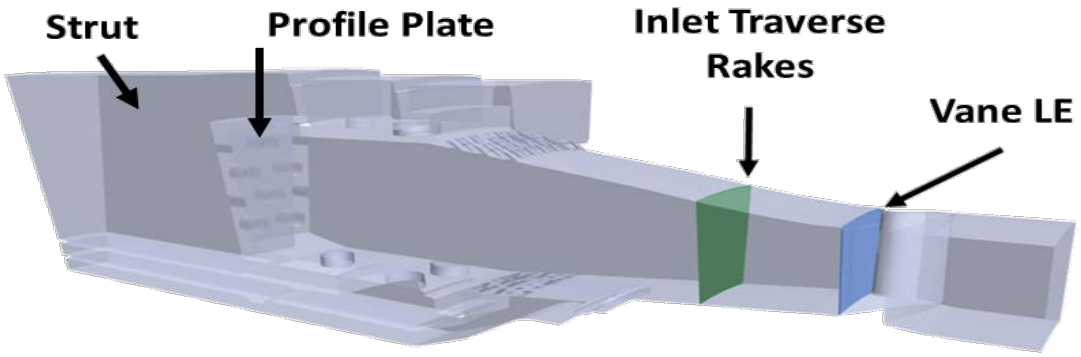


Figure 17. Combustor simulator computational fluid dynamics (CFD) domain including the upstream strut region, profile plate, and downstream turbine vane (Penn State National Experimental Turbine [NExT]). LE: leading edge.

The findings of the RANS simulation are explained in detail in a previous report. With the RANS simulation completed, the transition process from RANS to LES began during the current reporting period. The mesh used for the initial LES simulation was the same mesh that was used for the RANS simulation. The grid resolution for the LES was assessed and selectively refined by evaluating the amount of the turbulent kinetic energy (TKE) that has been resolved to that of the total amount of TKE in a given cell. This ratio is defined as M, as shown in Equation 5.

$$M = \frac{TKE_{resolved}}{TKE_{resolved}+TKE_{sub\ grid\ scale}} \quad \text{(Eq. 5)}$$

The variable $TKE_{sub\ grid\ scale}$ is provided as a field function in the simulation software STAR-CCM+, but $TKE_{resolved}$ is calculated through the unsteady time traces of the velocity field, by summing up the square of each root mean square of the three velocity components and dividing by 2, as shown in Equation 6.

$$TKE_{resolved} = \frac{1}{2}\left(u'_{rms}{}^2 + v'_{rms}{}^2 + w'_{rms}{}^2\right) \quad \text{(Eq. 6)}$$

From literature, Pope (2000) proposed a guideline for performing LES in which he suggested that ideally, $\overline{M} \geq 0.8$, where $\overline{M}$ is defined as the volumetric average of M over the domain. The LES was initialized from the RANS computational grid and solution. An appropriate timestep was determined after the LES solution had been initialized and so that the convective Courant number was never greater than unity. The M criterion was assessed after one flow field time and was determined to need extra refinement in the central chamber, in the approach flow plenums, and in the profile plate region. A flow field time is defined by dividing the total domain length by the volume-average axial velocity as calculated from the RANS simulation. Since the mesh was determined to be under-refined, the domain was re-meshed and evolved through several meshing iterations until the volume average M in the regions of interest were above the $\overline{M} \geq 0.8$ guideline. The mesh cross-section shown in Figure 18a corresponds to a mid-passage plane and was the selected mesh to proceed with the LES because the mesh met the M criterion guideline. Figure 18b shows contour levels of the M criterion within the mid-passage plane of the domain. It can be seen in the regions of interest, particularly the dilution holes, effusion holes, and the central chamber the M criterion is above 0.8. This mesh that was selected for the LES has a volume average M criterion of 0.96.

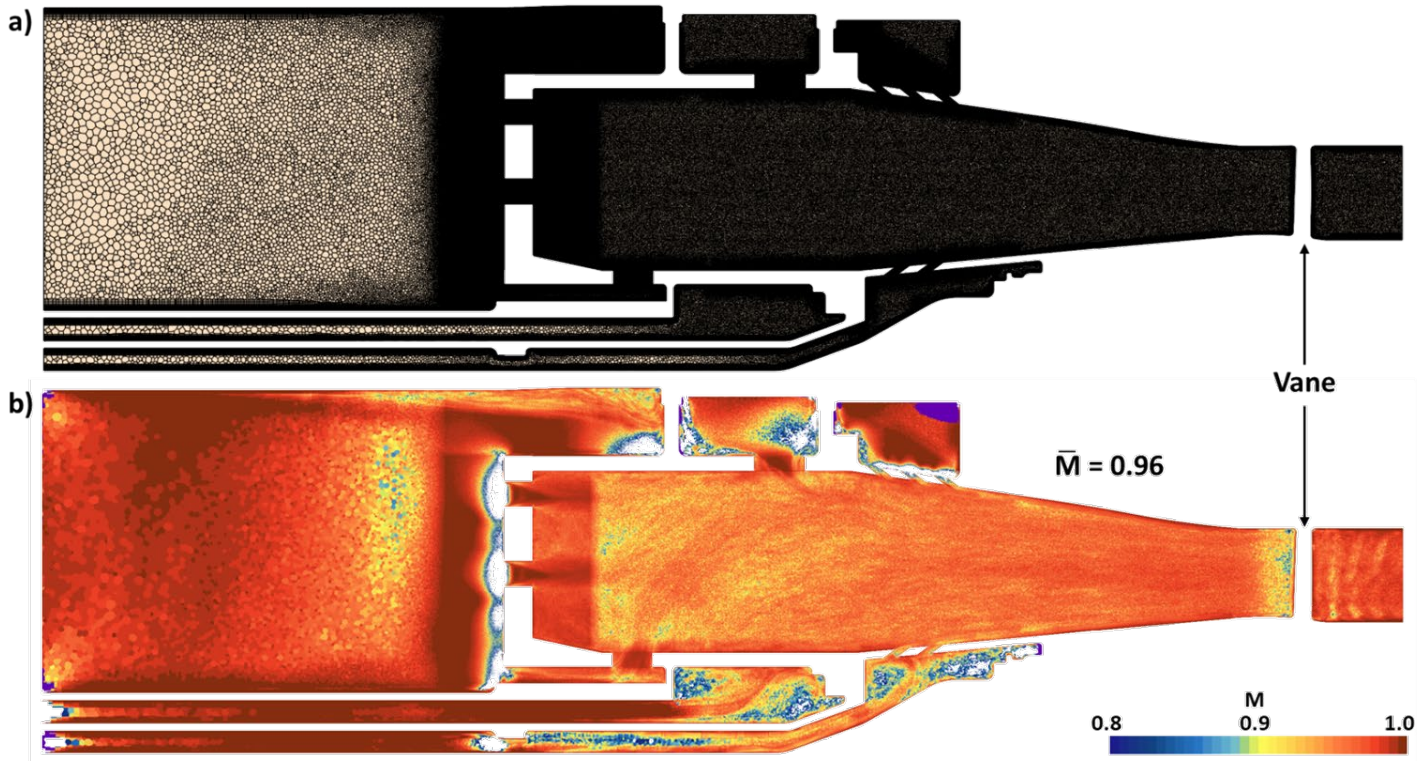


Figure 18. Mid-passage cross-section of the combustor simulator computational fluid dynamics (CFD) Large Eddy Simulation (LES) including (a) mesh domain with extra refinement in high shear zones and coarser regions that are at slow air velocity and (b) M criterion after one flow field time.

The LES was run for a total of seven flow field times, with the first three to ensure at the start of time-averaging the simulation is considered statistically stationary. The LES was time-averaged over four flow-field times ensuring high resolution of the unsteady behavior created by the dilution and effusion flows. Upon the completion of the simulator LES, an analysis was performed that focused on the flow and thermal fields. A comparison was made between the CFD DOE RANS "Center-Peaked" profile, the "more complex" RANS simulation, and the LES simulation radial total temperature profiles to see the prediction capability of RANS compared to the higher fidelity LES. Further analysis included how the LES model predicted temperature and velocity streamwise contours. A deep dive into the hot streaks that exist and were predicted by the LES was important to analyze as well. The hot streaks are known to cause degradation issues on the downstream turbine components and knowing how dilution holes can be used to mix out the hotspots is important. Finally, since LES is known to be better at predicting turbulence over RANS, an analysis focused on turbulence levels was completed.

Computational Simulations of the Shrager Study

Recall the intent as explained in previous reports was to first validate the modeling methods for running both RANS and LES simulations. To validate the modeling methods, both RANS and LES simulations were run that used the same combustor liner geometry as reported by Shrager et al. (2019a). After the computational simulations were completed, a comparison between the predicted RANS and LES flow field and the experimental measurements taken by Shrager was completed. The outward facing effusion hole geometry as seen in Figure 19 was the selected test case for validation, which includes the highest dilution jet momentum flux ratio of I = 30 and a low freestream turbulence intensity of TI = 0.5%.

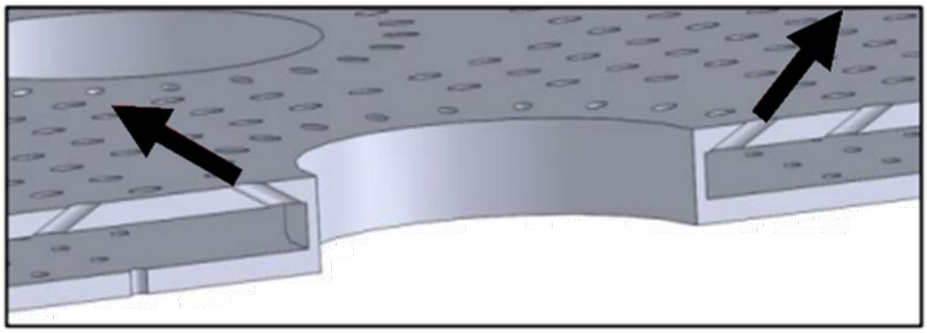


Figure 19. The combustor liner geometry used in the experimental study by Shrager et al. (2019a) showing the large dilution hole with surrounding effusion holes pointing radially outward, that was also used in the current computatonal simulations to validate modeling methodology.

In general, the turbulence levels were underpredicted for five of the six turbulence models that were evaluated. The five turbulence models included the realizable k-ε, the k-ω Menter shear stress transport, the elliptic blending Reynolds stress, the linear pressure strain Reynolds stress, and the incompressible realizable k-ε models. The only model that overpredicted the turbulence intensity was the standard k-ε model. The realizable k-ε model is the same RANS turbulence model that was used in the simulations of the combustor profile simulator. The computational predictions showed that the incompressible turbulence model matched well with the realizable k-ε turbulence model. Overall, the realizable k-ε model compared the best to the experimental results. Figure 20 shows the six different RANS models that were selected and compared to the experimental results collected by Shrager et al.(2019a).

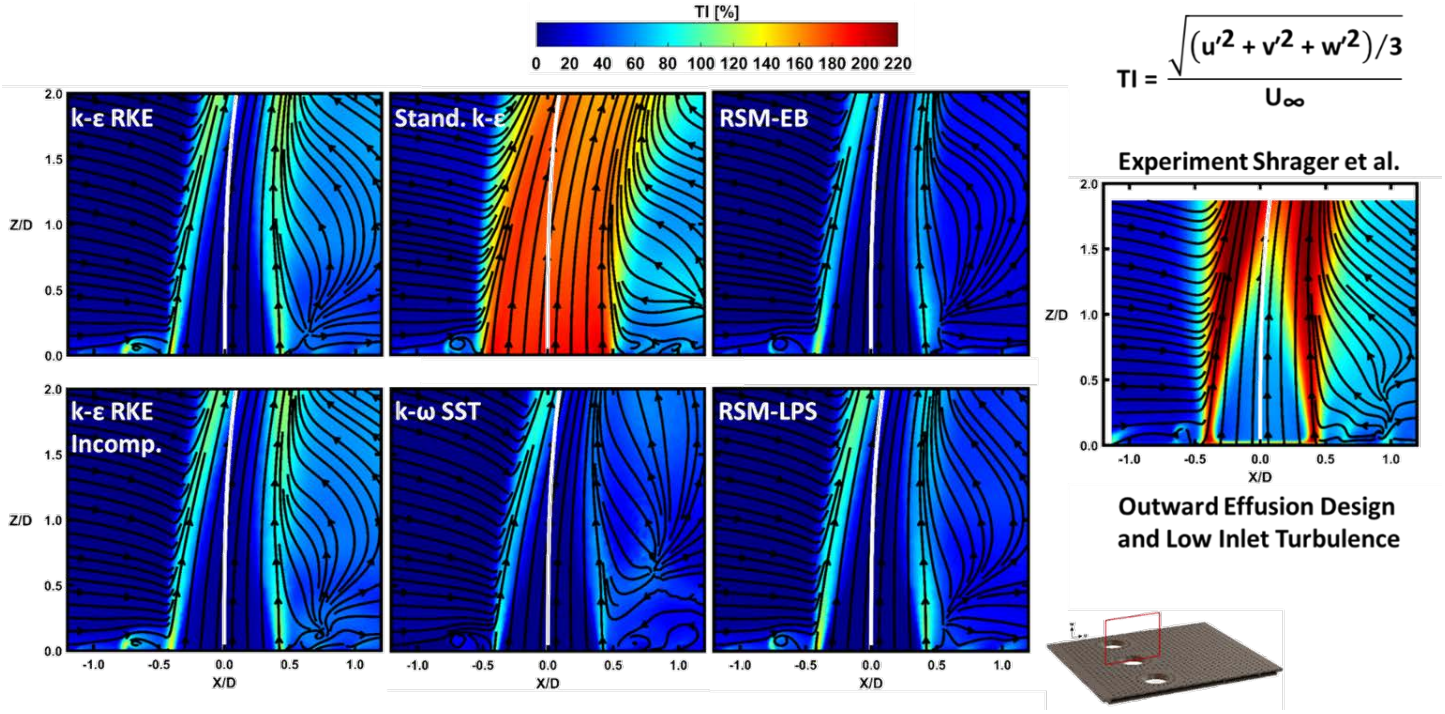


Figure 20. Turbulence intensity contours aligned with the centerline of the central dilution jet comparing six Reynolds-averaged Navier Stokes (RANS) turbulence models of the dilution flow, including k-ε realizable k-e (RKE), standard k-ε, k-ω Shear Stress Transport (SST), EB-RSM (Remote Sensor Module), LPS-RSM, incompressible k-ε RKE, to Shrager's experimentally measured results. TI: turbulence intensity.

Figure 21 shows the results from both the RANS and LES models, including colored streamlines in Figure 21A and contour plots of turbulence intensity levels with streamlines in Figure 21B. The selected RANS model for comparison is the realizable k-e (RKE) model. In Figure 21A the streamlines colored green correspond to the dilution flow, while streamlines colored red correspond to the effusion flow and streamlines colored blue correspond to near-dilution hole effusion flow. Streamlines are shown from the center of each effusion hole, where some of the effusion flow is shown to be entrained up into the dilution flow and mixes with the outer shear layers of the dilution jet. Both the RANS and LES results show this entrainment process, but the LES predicts more entrainment in the region downstream of the dilution hole, which in turn influences the downstream temperature profile shape. In Figure 21B the LES results showed better turbulence predictions than the RANS model compared to the experiment, but both models still slightly underpredicted dilution jet penetration as shown by the white line defined by the Lefebvre correlation.

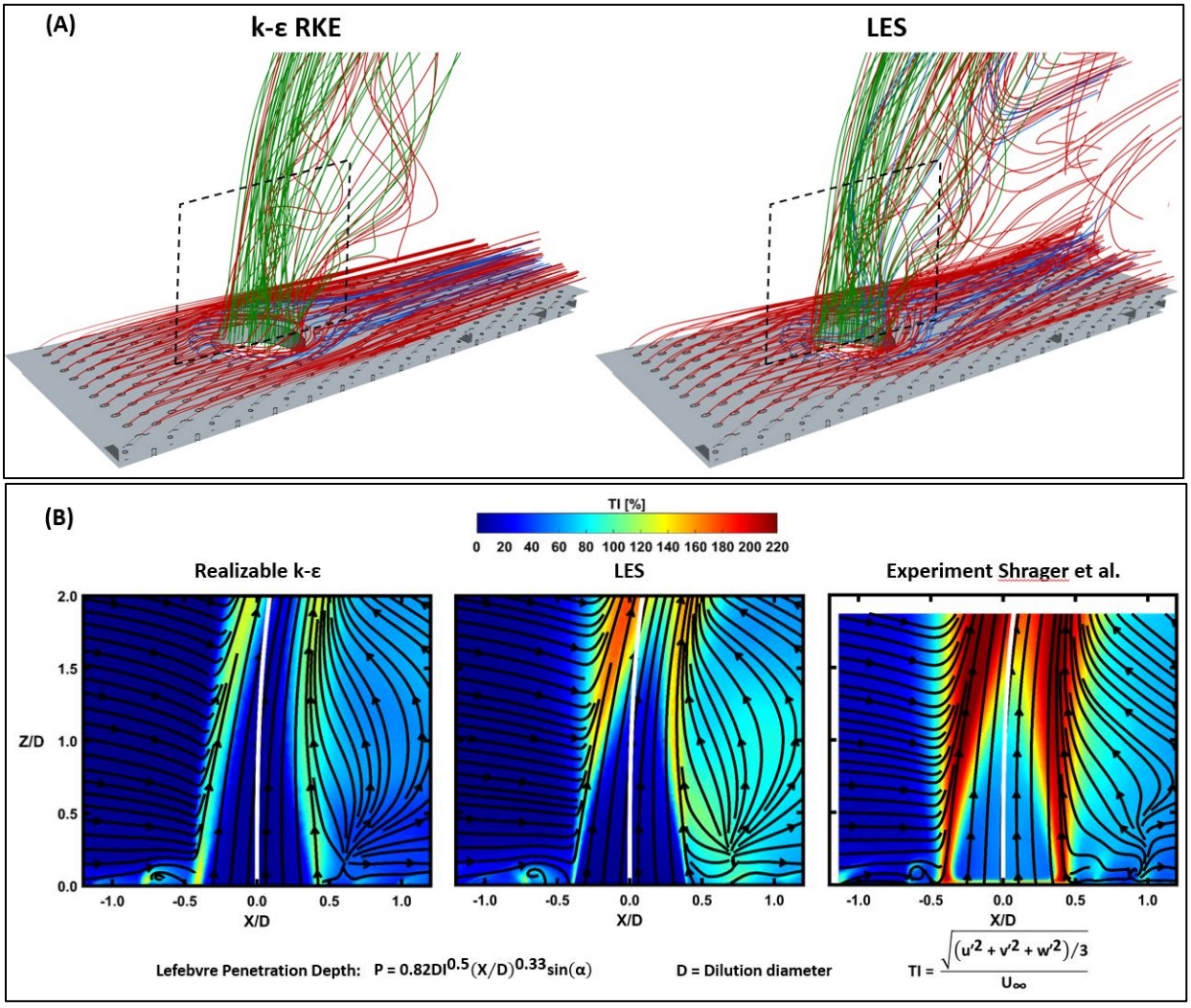


Figure 21. Current computational simulation results from Reynolds-averaged Navier Stokes (RANS) and large eddy simulation (LES) performed at Penn State Steady Thermal Aero Research Turbine (START) compared to previous experimental data from Shrager et al. (2019a) all using the same combustor liner panel geometry with effusion cooling and dilution flow. Results illustrated in (A) show streamlines color coded to the effusion flow (red), near-dilution hole effusion flow (blue), and dilution flow (green). Results illustrated in (B) show contours of turbulence intensity within the dashed planar region passing through the dilution hole. RKE: realizable k-e, TI: turbulence intensity.

To help facilitate experimental testing of the combustor profile simulator within the PSU START rig, specific rig hardware components were pursued for duplicate manufacturing. Figure 22 shows a cross-section drawing of the combustor profile simulator highlighting two rig regions in which hardware manufacturing was pursued to enable the simulator hardware assembly to become a single independent module. These specific hardware components included a forward bulkhead and a cooling air manifold. Once manufactured, these two components will be installed into the combustor profile simulator assembly to quickly support turbine testing with or without the simulator depending on the test goals.

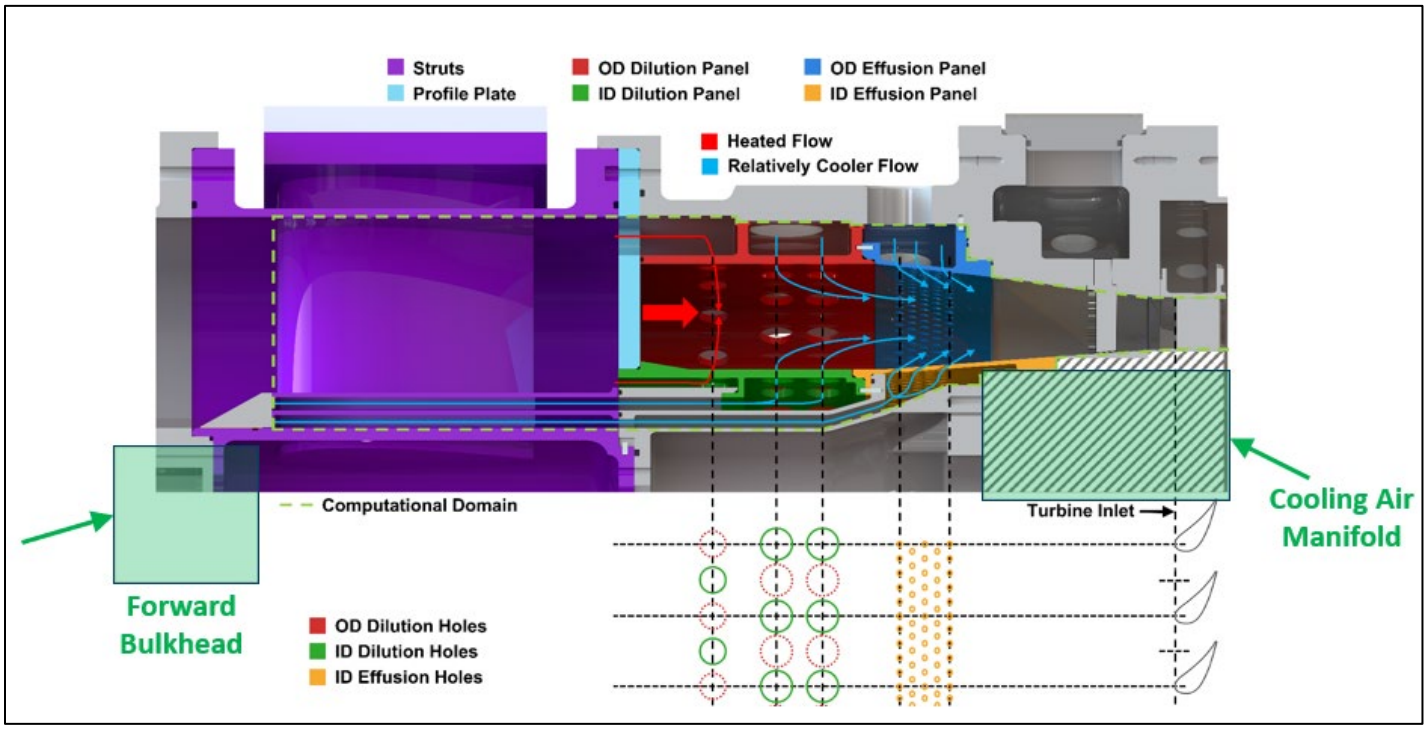


Figure 22. Cross-section drawing of the combustor profile simulator indicating key design features and two highlighted green regions in which hardware manufacturing was pursued to enable the simulator hardware assembly to become a single independent module. ID: inner diameter, OD: outer diameter.

The LES computational modeling of the combustor profile simulator was also completed for the center-peaked target profile case. A total of seven flow through times were completed with the last four flow through times being time averaged. One flow through time is the duration that a particle on average takes to travel from the inlet to the exit of the domain. The mesh grid resolution was assessed and refined by evaluating the ratio of turbulent kinetic energy resolved relative to the total amount of kinetic energy in a given cell. Figure 23 shows a contour plot of its distribution throughout the simulator domain, which contains over 200 million cells. Most of the domain shown in Figure 23 indicates the turbulence to be well resolved above M > 80%, with only a few minor regions to be under resolved including just upstream of the profile plate and areas within the plenums that do not significantly affect the flow and thermal fields within the central chamber of the combustor profile simulator.

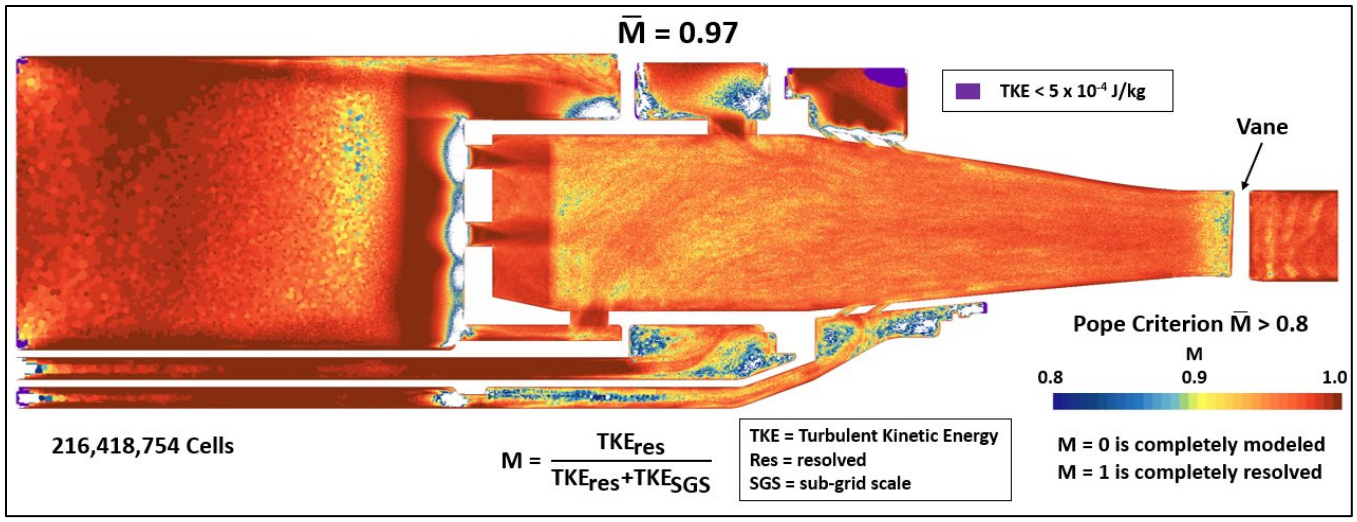


Figure 23. Time-averaged large eddy simulation (LES) contour plot of the turbulence M criterion within the vane mid-passage plane showing successfully resolved turbulence between the ranges of 80% to 100%.

Flow streamlines were also generated from the LES results and are shown in Figure 24. The streamlines are associated with the dilution and effusion flow within the center chamber and were used to illustrate and better understand the fluid mechanics behavior of the individual flow field components. The first-row dilution flow on the OD side of the central chamber is colored red, while the ID side is colored green. Recall, the second-row dilution was not used for the current study. The third-row dilution flow on the OD side is colored yellow, while on the ID side is colored light blue. The liner effusion flow on the OD side is colored dark blue, while on the ID side is colored orange. The streamline trajectories illustrate that the first-row dilution flow penetrates deep into the central chamber freestream and ultimately migrates to a radial height region at the simulator exit plane mostly towards mid-span as intended. The ID effusion and OD effusion flows remain relatively close to their respective liner walls also as intended. The third-row dilution flow on the ID and OD sides penetrate into the central chamber from their respective liner walls a smaller distance than the first row and contributes to the exit temperature profile shape in the radial height regions between mid-span and the near-walls also as intended.

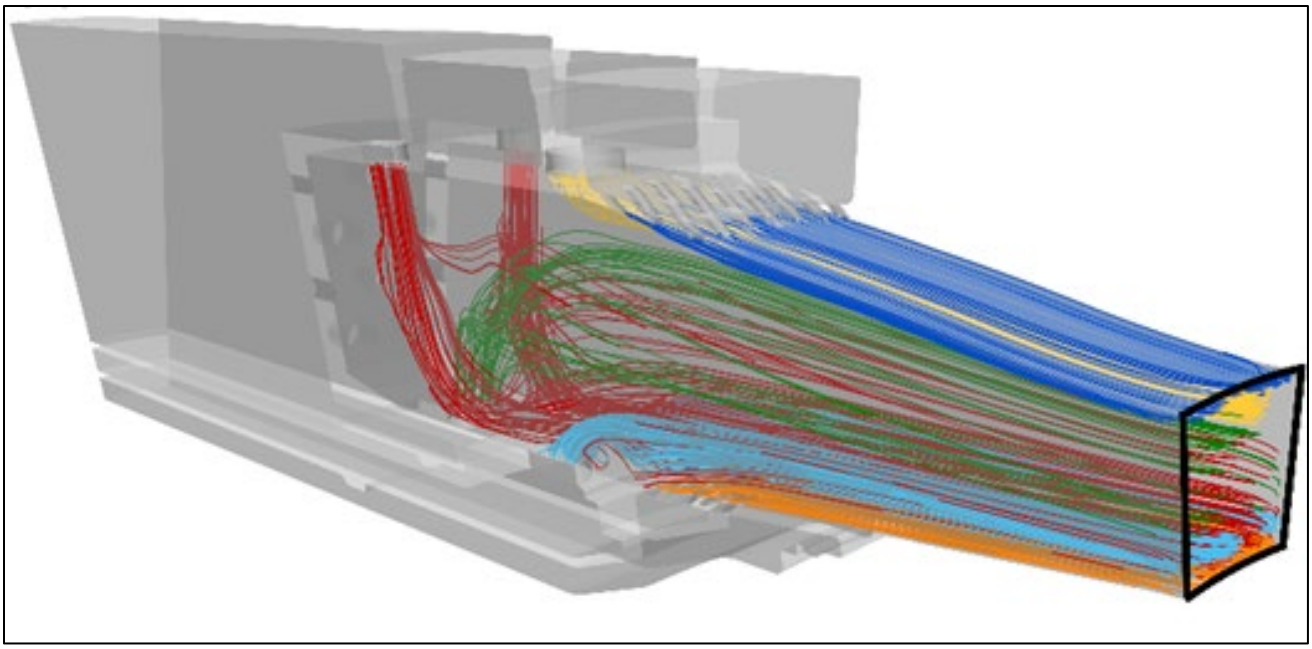


Figure 24. Time averaged large eddy simulation (LES) streamlines within the combustor simulator for the center-peaked target profile.

A new publication was completed on these comparisons (see products section), and a summary of the new paper was made into a poster that was presented at the American Society of Mechanical Engineers (ASME) Turbo Expo 2025. LES computational simulations of the combustor simulator were also completed during the current reporting period including high fidelity predictions of the flow and thermal fields based on the "Center-Peaked" profile configuration. A second new publication was also completed that focuses on the combustor simulator LES methodology and results (see products section). The PhD student working on this aspect of the project wrote two new publications related to the research work and successfully passed his final PhD defense enabling their graduation.

Finally, during the current reporting period, a series of grommet inserts shown in Figure 25 were designed to enable different dilution hole diameters to be used and studied. The threaded inserts act as bushings to change the hole diameter size, and the insertion tool acts as a spanner socket wrench to fasten the insert into the threaded dilution holes. Pricing to manufacture the grommet inserts and tooling was also obtained to pursue manufacturing.

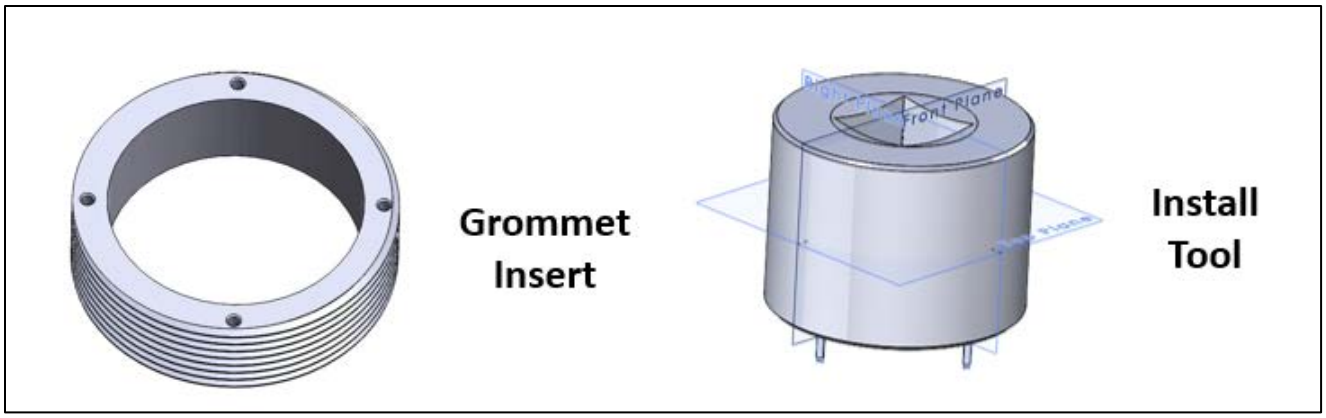


Figure 25. Drawings of an example threaded grommet insert and installation tool that will enable different dilution hole sizes to be installed and studied within the combustor profile simulator.

To help facilitate experimental testing of the combustor profile simulator within the PSU START rig in 2026, specific rig hardware components completed manufacturing. Figure 26 shows a cross-section drawing of the combustor profile simulator highlighting in green the hardware that completed manufacturing helping to enable the simulator hardware assembly to become a single independent module. The hardware highlighted in yellow was assembled and then machined to ensure design intent positional tolerances are met for the hardware closest to the turbine.

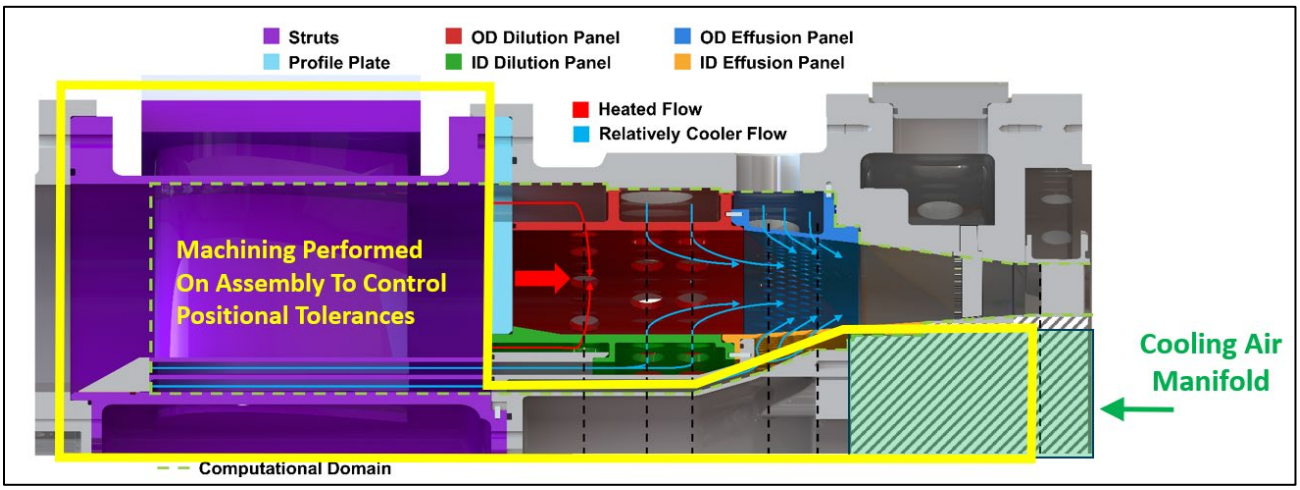


Figure 26. Cross-section drawing of the combustor profile simulator indicating two highlighted regions in which hardware manufacturing was completed to help enable the simulator hardware assembly to become a single independent module and accurately align with the turbine hardware. ID: inner diameter, OD: outer diameter.

The profile plate shown in cyan blue within Figure 26 was originally designed and manufactured to produce the "Center-Peaked" target profile exiting the combustor simulator and entering the test turbine. This profile plate hardware component is shown in Figure 27 and includes a perforation pattern (not shown) that is specific to the target turbine inlet profile. Efforts began to design and manufacture additional profile plates for the other target profiles shown in Figure 27 referenced within the red box.

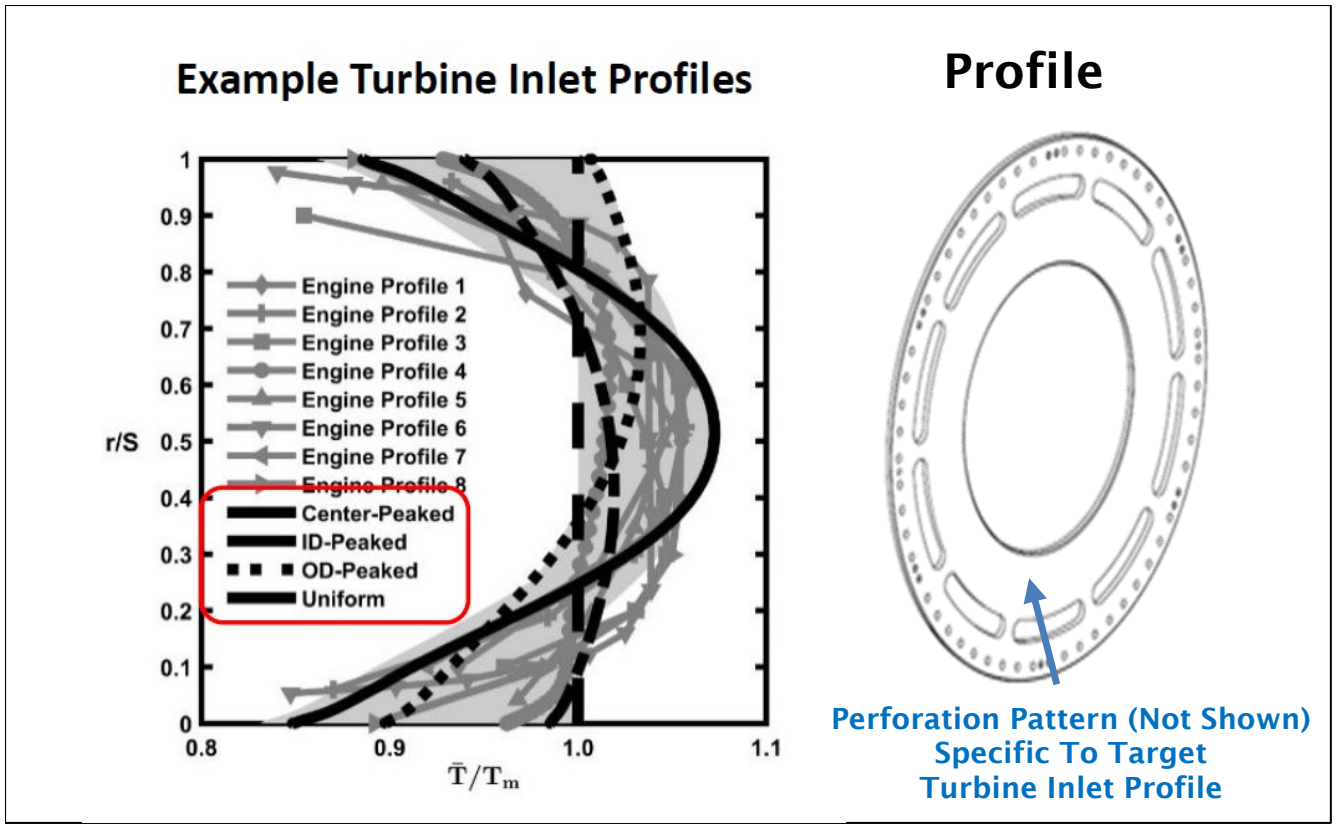


Figure 27. Drawing of the profile plate located at the inlet of the combustor simulator central chamber that is designed with a perforation pattern specific to the target turbine inlet profile. ID: inner diameter, OD: outer diameter.

Finally, during the current reporting period trial assembly work continued for the complete 360° traverse system that is located at the exit of the combustor simulator shown in Figure 28. This traverse system includes a series of rake probes that enable the flow temperature and pressure exiting the simulator and entering the test turbine to be spatially measured around the full annulus. Planning was also initiated for integrating the instrumentation shown within the combustor simulator assembly.

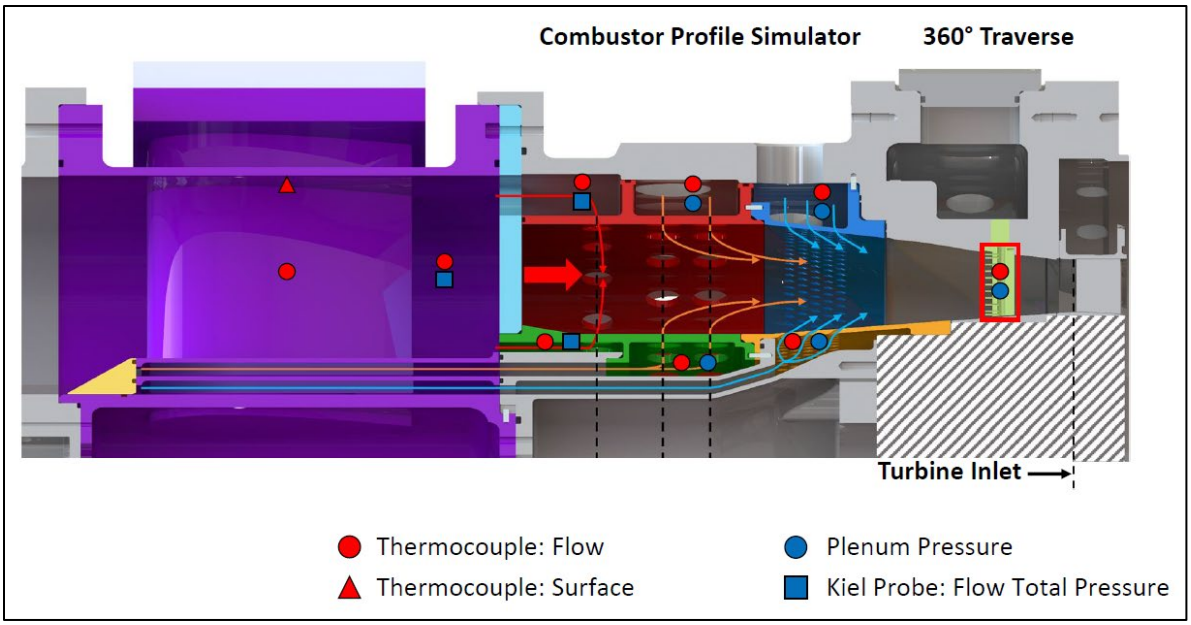


Figure 28. The traverse system at the combustor simulator exit will be used to measure the spatial profiles of temperature and pressure entering the turbine, while the instrumentation within the combustor simulator will be used to evaluate the simulator performance and for comparing to model predictions.

Milestones

Milestone	Completion Date	Status
Workplan	03/5/2020	Completed
COE Meeting 1	10/29/2021 - 10/29/2021	Completed
COE Meeting 2	10/26/2022 - 10/28/2022	Completed
COE Meeting 3	10/24/2023	Completed
COE Meeting 4	10/29/2024 - 10/31/2024	Completed
COE Meeting 5	10/14/2025 – 10/16/2025	Completed
Annual Report	12/31/2025	Completed

Major Accomplishments

- Successfully demonstrated improved dirt management for combustor liners through the implementation of a triple-wall cooling design. (Task 2)
- Completed manufacturing of the combustor profile simulator. In addition, more detailed computational predictions of the flowfield to meet the needs of the START facility have been completed including the higher fidelity LES simulations. (Task 3)

Publications

McFerran, K., Thole, K. A., & Lynch, S. P. (2025). Dirt ingestion impacts on cooling within a double-walled combustor liner. *ASME Journal of Turbomachinery, 147*(8), 081019. https://doi.org/10.1115/1.4067464

McFerran, K., Thole, K. A., Lynch, S. P., Boardman, G., Lundgreen, R., Kramer, S., and Joshi, D., (2025), "A Novel Approach to Dirt Mitigation for Combustor Walls," ASME Turbo Expo 2025. https://doi.org/10.1115/GT2025-154071

Schaeffer, C. B., Barringer, M. D., Lynch, S. P., & Thole, K. A. (2025). Influence of dilution and effusion flows in generating variable inlet profiles for a high-pressure turbine. *ASME Journal of Turbomachinery, 147*(3), 031003. https://doi.org/10.1115/1.4066560

Schaeffer, C., Barringer, M., Lynch, S., & Thole, K. (2025, June 15-19). *Comparison of Predicted and Measured Combustor-Relevant Flow Fields* [Poster presentation]. ASME Turbo Expo 2025, Memphis, Tennessee.

Schaeffer, C., Barringer, M., Lynch, S., & Thole, K. (2025, under review) Comparison of Predicted and Measured Combustor-Relevant Flow Fields. *Journal of Turbomachinery*.

Schaeffer, C., Barringer, M., & Thole, K. (2026, June 15-19). *Large Eddy Simulation of a Non-Reacting Profile Simulator for the First-Stage Vane* [Abstract accepted]. ASME Turbo Expo 2026, Milan, Italy.

Outreach Efforts

- Presented periodically to Pratt & Whitney through this joint collaboration.
- Presented the combustor simulator concept to the U.S. Department of Energy, Siemens Energy, Honeywell, and Pratt & Whitney. Industry partners are very supportive of this direction and provide guidance.

Awards

- Dr. Reid Berdanier was elected as an Associate Fellow of the American Institute for Aeronautics and Astronautics (AIAA).
- Dr. Karen Thole was awarded the 2025 Kate Gleason Award from ASME.

Student Involvement

- Chad Schaeffer was a PhD student at Penn State University who led the combustor simulator design effort at Penn State. Chad successfully defended his PhD in August 2025.
- Fabrizzio Vega is a PhD student at the University of Michigan. Fabrizzio completed an internship at NASA Glenn Research Center during Summer 2025, where he performed high-temperature experiments for triple-wall combustor liner samples.
- Dan Strobel (MSME, PSU), Benjamin Bizzak (PhD, PSU) are new graduate students starting Fall 2025 contributing to combustor simulator work at Penn State.
- Peyton Boudinot (U-M) is a new graduate student working on triple-wall combustor liner tests. Peyton was recruited to graduate school following a summer Research Experience for Undergraduates program in the START Lab at Penn State.

Plans for Next Period

- Optimize the multi-wall combustor liner design and evaluate associated heat transfer performance benefits.
- Integrate the profile simulator into the START rig and perform experimental testing.

References

McFerran, K., Thole, K. A., & Lynch, S. P. (2025). Dirt ingestion impacts on cooling within a double-walled combustor liner. *ASME Journal of Turbomachinery, 147*(8), 081019. https://doi.org/10.1115/1.4067464

Schaeffer, C. B., Barringer, M. D., Lynch, S. P., & Thole, K. A. (2025). Influence of dilution and effusion flows in generating variable inlet profiles for a high-pressure turbine. *ASME Journal of Turbomachinery, 147*(3), 031003. https://doi.org/10.1115/1.4066560

Shrager, A. C., Thole, K. A., & Mongillo, D. (2019a). Effects of effusion cooling pattern near the dilution hole for a double-walled combustor liner—Part 1: overall effectiveness measurements. *ASME Journal of Engineering for Gas Turbines and Power, 141*(1), 011022.

Shrager, A. C., Thole, K. A., & Mongillo, D. (2019b). Effects of effusion cooling pattern near the dilution hole for a double-walled combustor liner—Part II: Flowfield measurements. *ASME Journal of Engineering for Gas Turbines and Power, 141*(1), 011023. https://doi.org/10.1115/1.4041153

Disclaimer

This research was funded by the U.S. Federal Aviation Administration Office of Environment and Energy through ASCENT, the FAA Center of Excellence for Alternative Jet Fuels and the Environment, Project 068 through FAA Award Number 13-C-AJFE-PSU-128 under the supervision of Joshua Glottmann. Any opinions, findings, conclusions or recommendations expressed in this material are those of the authors and do not necessarily reflect the views of the FAA.



Project 069 Transitioning a Research nvPM Mass Calibration Procedure to Operations

Missouri University of Science and Technology, Aerodyne Research Inc., & U.S. Air Force Arnold Engineering Development Center

Project Lead Investigator

Philip D. Whitefield
Professor Emeritus of Chemistry
Department of Chemistry
Missouri University of Science and Technology
400 W 11th Street, Rolla, MO 65409
573-465-7876
pwhite@mst.edu

University Participants

Missouri University of Science and Technology (MS&T)

- P.I.: Prof. Philip D. Whitefield
- FAA Award Number: 13-C-AJFE-MST, Amendments 014, 020, and 023
- Period of Performance: June 5, 2020, to January 31, 2026
- Task:
  1. Investigate the validity of the centrifugal particle mass analyzer mass calibration research approach for non-volatile particulate matter certification measurement systems

Project Funding Level

Project	Funding	Matching	Source
13-C-AJFE-MST; Amendment 014	$846,707.00	$846,707.00	EMPA letter
13-C-AJFE-MST; Amendment 020	$100,853.00	$100,853.00	FOCA letter
13-C-AJFE-MST; Amendment 023	$99,999.00	$99,999.00	GE letter

Investigation Team

Missouri University of Science and Technology
Prof. Philip Whitefield, (P.I.)
Steven Achterberg, (research technician)
William Satterfield, research technician

Aerodyne Research, Inc. (ARI)
Dr. Richard Miake-Lye, (subcontractor)

Arnold Engineering Development Center (AEDC)
Dr. Robert Howard, (subcontractor)

Project Overview

This project is designed to investigate the validity of the centrifugal particle mass analyzer (CPMA) mass calibration research approach. The assessment will extend across all non-volatile particulate matter (nvPM) mass ranges encountered during certification tests. The primary goal will be the successful transitioning of the research methods to operations. The project will begin with a laboratory assessment leading to dedicated turbine engines as the test sources at the United

States (U.S.) Air Force (USAF) AEDC. The challenge mass devices for calibration (micro-soot sensor [MSS], laser-induced incandescence monitor, and cavity attenuated phase shift monitor) will be provided by the North American Reference nvPM Measurement System, together with the CPMA and other necessary instruments, such as a DMS500 particulate analyzer, and aerosol mass spectrometer.

Task 1 – Investigate the Validity of the Centrifugal Particle Mass Analyzer Mass Calibration Research Approach for Non-volatile Particulate Matter Certification Measurement Systems

Missouri University of Science and Technology

Objectives

The objectives of this task are to acquire the components of a CPMA-based mass calibration system similar to that described in Society of Automotive Engineers (SAE) E31 discussion paper DP-32 (presented by Dr. G. Smallwood) from the annual SAE E31 committee meeting on June 17–21, 2019, in Saclay, France, assemble the system, and evaluate its performance.

Research Approach

Subtask 1.1 (Completed)

Acquire the components of a CPMA-based mass calibration system similar to that described in SAE E31 discussion paper DP-32 (presented by Dr. G. Smallwood) from the annual committee meeting on June 17–21, 2019, in Saclay, France. The CPMA-based system has also been referred to as the CPMA-Electrometer Reference Mass Standard (CERMS).

Subtask 1.2 (Completed)

Assemble and test the CPMA-based mass calibration system's performance at MS&T's laboratories, by using a miniature combustion aerosol standard (Minicast) as the nvPM generation source (Figure 1). Compare the laboratory performance of the MS&T CPMA-based mass calibration system with that of two highly similar systems owned and operated by the University of Alberta and the Canadian National Research Council (NRC).

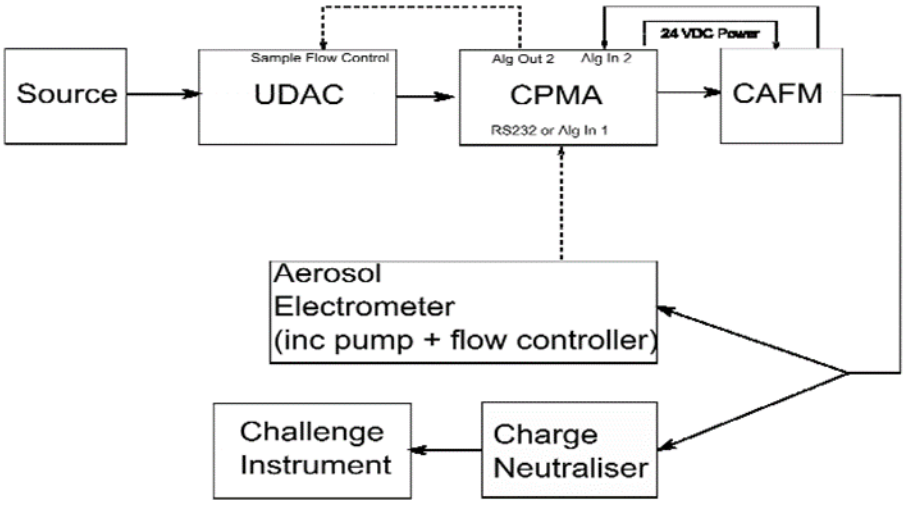


Figure 1. Schematic diagram of the CPMA-based mass calibration system.

Subtask 1.3 (Completed)

Investigate the validity of the CPMA mass calibration research approach across all nvPM mass ranges encountered during certification tests, to successfully transition the methods to operations.



Subtask 1.3a (Completed)
Deploy (transport and install) the North American Reference System, including the CPMA-based mass calibration system and ancillary diagnostic suite, with the USAF's AVL® nvPM measurement system and the two Canadian CPMA systems, at engine testing facilities at Arnold Air Force Base in Tennessee, which will include the J85 turbojet and a gas-turbine-based "start cart" as nvPM sources.

Subtask 1.3b (Completed)
Evaluate the performance of the three CPMA-based mass calibration systems, surveying across all mass ranges by using the start cart as the nvPM source; compare these results with concomitant mass calibration data acquired with SAE E-31 elemental carbon/organic carbon (EC/OC)-based mass calibration methods.

Subtask 1.3c (Completed)
Demonstrate the performance with an nvPM emissions test on the J85 engine, with calibration including standard EC/OC analysis, as well as the CPMA-based calibration system described in DP-32.

Subtask 1.3d (Completed)
Decouple the diagnostic suites from the Arnold Air Force Base engine facilities and transport them back to Missouri and Massachusetts.

Subtask 1.4 (Completed)
Analyze and interpret the data gathered in Subtasks 1.2 and 1.3.

Subtask 1.5 (Completed in 2025)
Prepare and deliver a final report.

Milestone
Published a comprehensive paper in the peer-reviewed literature describing (1) the assessment and (2) the conclusions and recommendations arising from the assessment.

Major Accomplishments
Published a comprehensive paper in *Aerosol Science and Technology*, "Quantification of the repeatability and reproducibility of the CPMA-electrometer reference mass standard for in-situ calibration of mass concentration aerosol instruments."

Publications
Peer Reviewed Journal Publication

Mehri, R., Nishida, R. T., Sipkens, T. A., Smallwood, G. J., Corbin, J. C., Whitefield, P., Achterberg, S., Miake-Lye, R. C., Nault, B. A., Howard, R., & Olfert, J. S. (2025). Quantification of the repeatability and reproducibility of the CPMA-electrometer reference mass standard for in-situ calibration of mass concentration aerosol instruments. *Aerosol Science and Technology, 60*(3), 230-244. https://doi.org/10.1080/02786826.2025.2568694

Outreach Efforts
Comprehensive peer-reviewed paper published.

Awards
None.

Student Involvement
None.

Plans for Next Period
There are no plans for the next period. The project ended in 2025.

® AVL is a registered trademark of AVL List GMBH, Graz, Austria.



ASCENT Project 069 Draft Final Report

The final report for ASCENT Project 069 is comprised of two parts, first a comprehensive publication describing the assessment study (see above) and second a list of conclusions and recommendations for future assessment studies developed by the ASCENT Project 069 research team and summarized as follows:

The ASCENT Project 069 team is comprised of the following team members:

- The ASCENT Project 069-funded research was led by P.I. Phil Whitefield (MS&T), and Co P.I.s Rick Miake Lye (ARI) and Robert Howard (AEDC). They were supported by Klaus Woelk, Steven Achterberg, Max Trueblood, Dave Satterfield (MS&T), and Ben Naught (ARI)
- The NRC Canada team was led by P.I. Greg Smallwood, supported by Rym Mehri and Brett Smith
- The University of Alberta team was led by P.I. Jason Olfert, supported by Robert Nishida
- The U.S. Environmental Protection Agency (EPA) team was led by Robert Giannelli, supported by John Kinsey, Jeff Stevens, Samuel Johnson, and David Kittelson.

An anticipated outcome of this study, "Transitioning A Research nvPM Mass Calibration Procedure to Operations," was to demonstrate that the CERMS system was a field-deployable, user-friendly, low-cost mass calibration system for nvPM measurements during engine emissions certifications. Based on the CERMS in its current state of development and in consideration of the results of this study, the ASCENT Project 069 team believes the CERMS has demonstrated potential to reduce the uncertainty associated with the current reference for mass concentration instruments (EC) but does not fully satisfy the desired operational criteria due to some issues that were observed. Additionally, calibration with a CERMS should be done by a competent laboratory. As a result, the team recommends that a follow-on evaluation study is justified in addressing the unresolved issues described in this report.

It is important to note that using the CERMS is fundamentally different from the traditional calibration method. In the CERMS, the principle is to provide a stream of particles of known mass concentration. Whereas the traditional calibration requires a concurrent measurement of EC to establish the concentration of particles from the calibration source.

In terms of assessing the reproducibility of CERMS, the uncertainties in this study indicate that it may be capable of lowering the uncertainty associated with the calibration of the mass concentration instruments. This uncertainty could be significantly reduced if the recommendations to minimize the bias between CPMAs are investigated.

Future experiments should include using different particulate matter measurement techniques in similar configurations (including the aerosol mass spectrometer [AMS]), to investigate if the CERMS system, dilution, and/or other aspects not considered here, lead to the losses of the volatile particulate matter.

Although some of the issues encountered by the ASCENT Project 069 team are a result of instrument limitations (penetration through the instruments and hence low concentration), further studies are recommended to address the issues encountered during this study. These recommended future studies would have the following objectives.

- Objective 1: Reduce the reproducibility uncertainty. The reproducibility for CERMS was largely attributed to the CPMA reproducibility, such that reducing the CPMA uncertainty will have a direct impact on reducing the CERMS uncertainty. The CPMA response could be potentially traceably calibrated using certified reference material (CRM) particles of a known narrow mass distribution.
- Objective 2: Understand the impact of particle conditioning on CERMS. Simultaneous characterization of the particles (using different laboratory and engine sources) upstream and downstream of the CPMA would be informative to understand the effect of the CPMA classification (in time) on the particle composition, with and without the use of a catalytic stripper.
- Objective 3: Increase the CERMS output mass concentration. Determine the influence of the CPMA model (Mk I or Mk II) on the classified particles and penetration through the instrument. Investigate the use of high transmission efficiency chargers in place of the Unipolar Diffusion Aerosol Charger (UDAC).
- Objective 4: Optimize CERMS set point determination. Address the shift in the UDAC charging efficiency in time or changes in the experimental setup.
- Objective 5: Determine performance of CERMS under realistic calibration conditions. Compare CERMS and thermal-optical analysis in the context of a calibration as intended with a gas turbine source across a representative concentration range. This will require a direct comparison of the EC to the electrometer, without any other



instruments, and may result in low concentrations on the filter used for EC analysis due to shorter acquisition periods.

It is recommended that future experiments should use low sulfur jet fuel to avoid poisoning of the catalytic stripper.



Project 070 Reduction of nvPM Emissions from Aero-Engine Fuel Injectors

Georgia Institute of Technology

Project Lead Investigator

Wenting Sun
Professor
School of Aerospace Engineering
Georgia Institute of Technology
270 Ferst Drive, Atlanta, GA 30332
404-894-0524
wenting.sun@aerospace.gatech.edu

University Participants

Georgia Institute of Technology (Georgia Tech)

- P.I.: Dr. Wenting Sun
- FAA Award Number: 13-C-AJFE-GIT-080
- Period of Performance: October 01, 2024, to September 30, 2025
- Tasks:
  1. Spray characterization and measurement of non-volatile particulate matter (nvPM) formation of Jet-A and sustainable aviation fuel (SAF)
  2. Design of a new single piece additively manufactured combustor

Project Funding Level

The total amount of funding from the Federal Aviation Administration (FAA) is $1,500,000. The funding match includes $1,350,000 from Georgia Tech and $150,000 from Honeywell.®

Investigation Team

Georgia Institute of Technology

Dr. Wenting Sun, (P.I.), Task 1,2
Adam Steinberg, (co-P.I.), Task 1
Ellen Yi Chen, (co-P.I.), Task 1
Shawn Wehe, (research engineer), Task 1,2
Rahul Vishwanath, (postdoctoral fellow), Task 1,2
Eric Douglas, (graduate student), Task 1
Harshit Dhayal, (graduate student), Task 1
Adhav Arulanandan, (graduate student), Task 1
Andrew Fan, (graduate student), Task 1

Honeywell, Inc

Rudy Dudebout, (co-P.I), Task 2
Alejandro Torres, (co-P.I.), Task 2
Fang Xu, (co-P.I.), Task 2

® Honeywell is a registered trademark of Honeywell International, Inc., Charlotte, New Jersey.



Project Overview

Reducing nvPM from gas turbine engines is essential for improving air quality and decreasing the environmental impact of aviation. However, predicting and controlling nvPM remains a challenge because of the complicated physical and chemical processes at play. The proposed research will characterize the fuel spray and nvPM formation for optimizing the design of an aeronautical gas turbine fuel injector to reduce nvPM at flight-relevant conditions. In this project, we developed a sector combustor containing three fuel injectors. The sector combustor is a generic rich-quench-lean (RQL) jet engine combustor equipped with the actual fuel injectors used in Honeywell's auxiliary power unit (APU). The combustor was fabricated through three-dimensional (3D) printing, and the fuel injectors are directly provided by Honeywell. The combustor and high-pressure system were detailed in a previous report and are presented briefly in the next section. The research focus of this year is on conducting an experimental campaign to characterize fuel spray, drop-size, measure nvPM volume fraction distribution in the primary zone of the combustor, and obtain nvPM and gas emissions at the exhaust section of the combustor. The performance of combustion in the rich region along with the particulate and gas emissions at the exhaust dictates the overall performance and efficiency of the combustor, and therefore it is the focus of research of this project.

Task 1 – Spray Characterization and Measurement of nvPM Formation

Georgia Institute of Technology

Objectives

The objectives of Task 1 include the following:

1.1 Obtain drop-size distribution for spray injectors using phase doppler particle anemometry (PDPA).
1.2 Characterize spray breakup and spray penetration using Mie scattering.
1.3 Measure and quantify the nvPM mass concentrations at the exit of the combustor.

The above tasks are performed over a broad range of conditions for Jet-A fuel and SAF (hydroprocessed esters and fatty acids synthetic paraffinic kerosene [HEFA-SPK]), respectively.

Research Approach

In this year, droplet-size distributions are obtained to characterize liquid fuel spray using phase doppler particle anemometry (PDPA) at a larger set of operating pressure, and inlet preheat temperature in both reacting and non-reacting conditions. ***This is the first such measurement performed in a three-sector combustor housed in a pressure vessel due to its unconventional configuration.*** Simultaneously droplet Mie scattering is performed to characterize spray breakup and penetration for the same conditions as the PDPA measurements. Additionally, quantitative soot volume fractions along with soot particle diameter measurements are being performed using two-color laser-induced incandescence (LII) and a GHz camera at different operating conditions. Both these measurements are performed using Jet-A fuel and SAF to compare the combustion characteristics of both the fuels and their blends. The SAF employed in this study is the HEFA from World Energy.® Results are presented below in corresponding sections. At the exit of the combustor, nvPM mass concentrations are obtained using a photo-acoustic based micro soot sensor measurement system from AVL Test Systems, Inc. (AVL), by mounting the probe at the combustor exhaust.

Subtask 1.1: Obtain Drop-size Distribution for Spray Injectors Using Phase doppler Particle Anemometry

PDPA utilizes the light scattering interferometry technique wherein interference signals are created by two intersecting laser beams in a small measurement volume of interest. As individual particles/droplets move through this volume, a shift in the frequency of scattered light is detected which is proportional to the particle velocity. Additionally, there is a phase shift in the detected interference signal which is proportional to the size of the particle. Hence, simultaneous information on particle velocity and size can be obtained with high spatial and temporal accuracy using this technique. For environments with high spatial and temporal variations in density, the technique suffers from beam steering, giving rise to low signal to noise ratios.

For measuring droplet sizes, PDPA requires off-axis scattering angles in the range of 30° to 70°. This presents a challenge for confined combustors housed in pressure vessels wherein such scattering angles are not available. To overcome this difficulty, a creative mirror system has been proposed and mounted inside the pressure vessel to obtain scattering angles

® World Energy is a registered trademark of World Management Group, LLC, Boston, Massachusetts.



up to 40º in the plane of measurement. The PDPA system (from Dantec Dynamics, Inc.) consists of a diode-pumped solid state (DPSS) laser transmitter capable of emitting a pair of 1000 mW, 561 nm laser beams, with each beam frequency shifted by 40 MHz using a Bragg cell. Although the system can operate with two pairs of laser beams at 532 nm and 561 nm, only one pair is utilized for droplet-size measurements. The laser beam pair is then sent into a transmitter probe (from TSI, Inc.) through fiber optic cables, where a lens having a focal length of 61 cm is used to focus the two beams into the sample measurement volume. The phase-shifted light scattered from the droplet in the small measurement volume is then collected by a receiver module through two mirrors placed and aligned such that the collection angle of the scattered light is approximately 40º. The collected light passes through a three slit mask mounted onto the receiver, where the light through each of the slits is focused separately and transmitted through fiber optical cables into the BSA (Burst Spectrum Analyzer). The analyzer can measure signal bursts at frequencies up to 400 kHz and subsequently produce instantaneous drop-size distributions.

The combustor wall (liner) includes three Honeywell aircraft swirl injectors on the dome face, representing typical multiple sectors of an aeroengine combustor, as illustrated in Figure 1b. The combustion liner has four fused quartz windows on top provide visual access to the rich-burn and lean-burn regions. The mirror system is mounted onto the inner face of the quartz vessel window flange as shown Figure 1a. It consists of two mirrors, with the first mirror having a 7.5 cm diameter clear aperture and the second mirror having a 15 cm by 10 cm rectangular area. They are aligned together to collect the scattered light from the droplets and focus onto the PDPA receiver module. The entire mirror system mount is made of stainless steel to minimize material deformation from high temperature air flowing through the vessel. The measurement region was restricted to a 5 cm by 5 cm area on left-hand side of the central nozzle as shown in Figure 1a, due to the constraints on the current PDPA and mirror system.

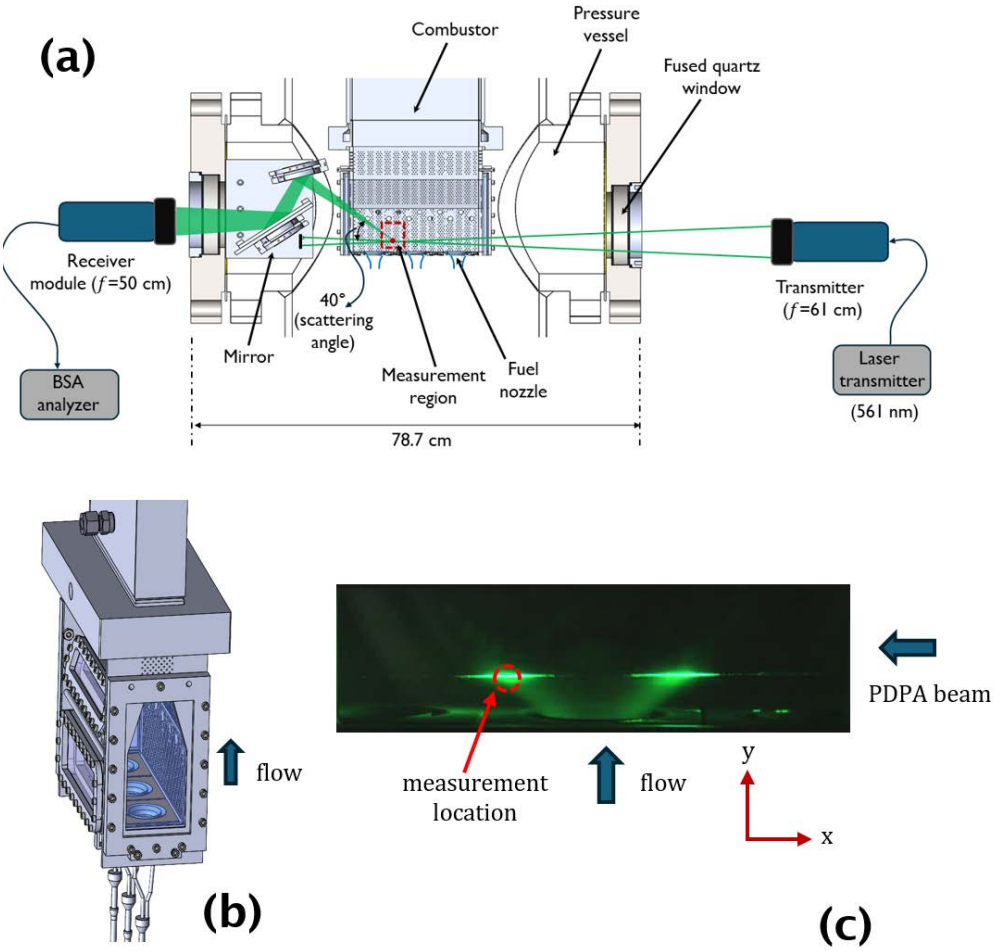


Figure 1. (a) Schematic of the phase doppler particle anemometry (PDPA) setup showing the two-mirror configuration to obtain required scattering angles in a confined vessel for the depicted measurement region. (b) View of the combustor depicting the three fuel nozzles and quartz windows for optical access. (c) Raw image of Mie scattering from the central injector spray along with the PDPA laser beam oriented in the vertical plane (perpendicular to the flow direction) passing through the spray.

Experiments are performed at both cold flow and reacting flow conditions to study the effect of combustion environment on droplet vaporization and subsequent drop-size. In all cases, only the central injector is operated so that the droplets do not cover the combustor windows which will affect PDPA measurements, especially in cold-flow conditions. The test conditions included five operating pressures (14.7 psig, 35.3 psig, 58.8 psig, 85.3 psig, and 120 psig) and four preheat temperatures (450 K, 540 K, 600 K, and 660 K), with a global equivalence ratio of 0.264 for both Jet-A and SAF fuels. It is to be noted that since the combustor is run on a RQL concept, the local equivalence ratios in the rich-burn region immediately downstream of the nozzles may vary from 1.22 to 1.45, depending on the global equivalence ratio. Although only the central injector is utilized while operating the combustor for PDPA measurements, the local equivalence ratio for that injector should remain the same.

At every spatial location, a total of 10,000 instantaneous measurements were made for all cases. But in certain conditions where the signal to noise ratio was slightly poor, the total measurement counts reduced. Nonetheless, the frequency distributions were repeatable for all conditions. The current fuel injectors utilized in this study are pre-filming air blast type assisted with surrounding swirl air for jet breakup. Figure 2 shows the number frequency distributions at a given spatial location for non-reacting Jet-A fuel spray at different operating pressures and preheat temperatures. The droplet



diameters are typically in a broad range of 1-100 μm at most locations, although the maximum frequencies are within the small range of 10-40 μm suggesting good atomization at these operating conditions. It is to be noted that the present PDPA system can detect droplets only in the range of 0.1-170 μm based on the slit size and mask used on the receiver module. As seen from the frequency distributions, this range was sufficient to cover the entire spray as the probability of detecting droplets larger than 150 μm was almost negligible. Due to the right skewed nature of the number frequency distributions, the Sauter mean diameter (SMD) values will tend to shift towards larger diameters, but the peak diameters are always lower. With increasing preheat, the droplet diameter distributions tend to shift towards smaller diameters at a given operating pressure. A similar trend is also seen for increasing pressure at a given preheat. This is clearer from the SMD values shown in Figure 3 for all spatial locations.

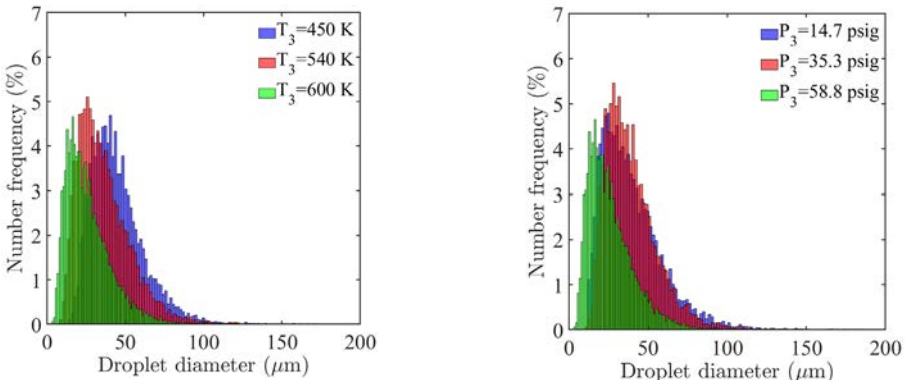


Figure 2. Comparison of number frequency distributions for Jet-A fuel at non-reacting conditions at spatial location *x*=25 mm, *y*=10 mm. (left) varying preheat at 58.8 psig pressure (right) varying pressure at 600 K preheat temperature.

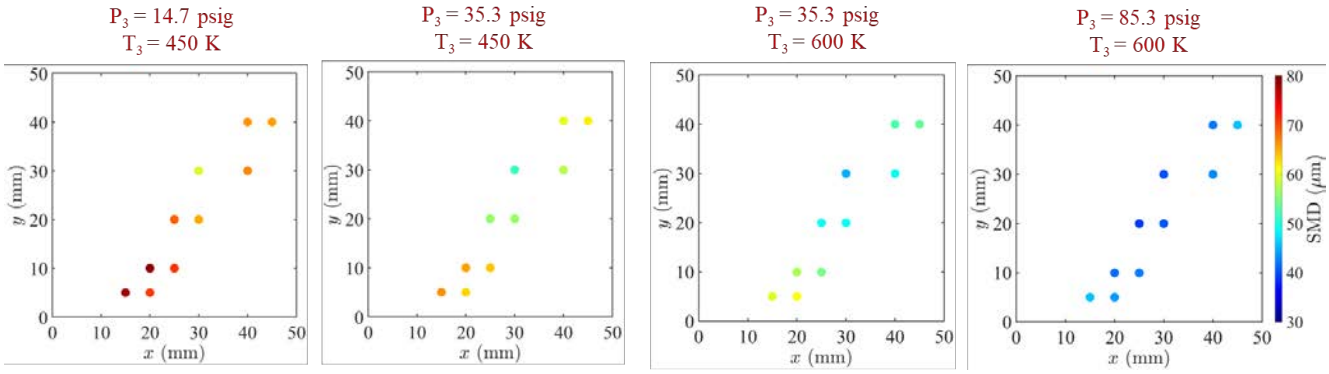


Figure 3. Spatial variation of Sauter mean diameter (SMD) values for non-reacting Jet-A fuel spray at different operating conditions.

It can be seen from the results shown in Figure 3, that the SMD values of the droplets generally reduces with increasing axial distance downstream of the injector along the spray cone as the swirling air assists in secondary atomization of the spray. Another reason for the decrease of SMD along the flow direction is vaporization of the droplets while flowing downstream. Apart from the general trend of decreasing diameters with increasing downstream distance, there are trends observed with different pressures and preheat temperatures. With increasing operating pressure, the SMD decreases for a given location and preheat temperature. This is due to the increase in Reynolds number of surrounding air causing larger relative velocities between the liquid and gas phase, thereby inducing faster primary breakup of liquid jet and subsequent smaller droplets. The amount of reduction is highly dependent on the Reynolds number range or the operating pressure. The reduction in SMD due to increasing preheat for surrounding air is due to droplets being able to evaporate faster as they travel downstream of the fuel nozzle. Compared to the low pressure conditions, the mean SMD values have decreased

by more than two times when the combustor is operated at 85.3 psig pressure at a preheat of 600 K (see Figure 4). Our results suggest that measurements and characterization need to be conducted at practical engine operating conditions.

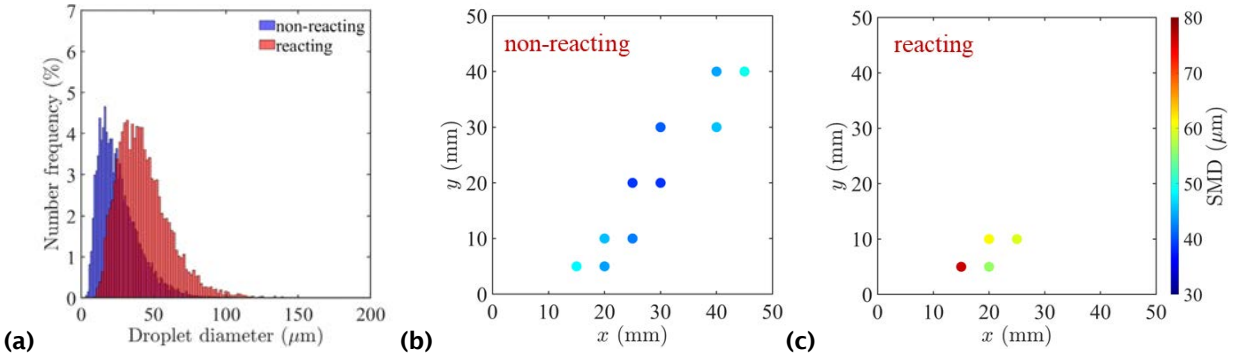


Figure 4. (a) Comparison of droplet diameters for Jet-A fuel at reacting and non-reacting conditions with 58.8 psig pressure and 600 K preheat temperature (a) number frequency distributions for locations *x*=25 mm, *y*=10 mm (b) Sauter mean diameter (SMD) at non-reacting conditions (c) SMD at reacting conditions.

To study the effect of reacting conditions on the spray, measurements were performed with the same PDPA configuration at the same operating conditions. It is to be noted that the current combustor operates liquid spray flames that produce large amounts of soot, especially in the primary zone of the combustor. Laser extinction can be very high in these regions leading to an overall drop in signal to noise ratio. To avoid this, the measurement region is confined to a small region 10- to 20 mm downstream of the dump plane within the spray cone. This region is largely devoid of soot, apart from small fluctuations in the flame where soot/flame can be entrained into these regions. A total of four measurements points (matching the non-reacting conditions) were possible for all the reacting conditions. The number frequency distributions for non-reacting and reacting conditions are compared in Figure 4 for Jet-A fuel at 58.8 psig pressure, and 600 K preheat for a given spatial location. For the reacting case, the distributions seem to shift towards larger diameters for all locations. This is counter-intuitive in the sense that reaction/flame should help the droplets evaporate faster adding to the preheat leading to smaller droplets. The plots in Figure 4 suggests that the smaller droplets not only evaporate faster but are almost non-existent, leaving only the larger droplets being detected. Hence, it is very possible that the SMD values are considerably higher in the reacting cases as compared to the non-reacting cases owing to the disappearance of small droplets which are vaporized promptly. An increase in almost 20 to 30 μm is observed for SMD in reacting cases compared to their non-reacting counterparts. This change was consistently observed for all cases at the same spatial location and operating conditions. Additionally, these distribution changes also provide information on the number of smaller diameter droplets available in reacting cases at any downstream location. It is worth mentioning that the signal to noise ratio was much lower in reacting cases at the same measurement location due to laser extinction as the laser beam passes through the flame/spray regions from the side nozzles before reaching the measurement zone.

The second part of the measurements involved utilizing SAF for the measurements at the same conditions as Jet-A fuel. The SAF used here is a HEFA-based fuel with almost negligible amount of aromatic content in it. Since the availability of SAF is limited at the current scenario due to production/supply issues, blending sustainable fuels with neat Jet-A fuel is considered a viable option. Due to small changes in physical and chemical properties of these blended fuels as compared to their neat counterparts, their spray and combustion characteristics are still not well known. Hence, measurements were also performed at the same locations by blending the neat fuels in 50-50% by volume. Figure 5 shows the comparison in number frequency distributions between Jet-A fuel and SAF in the non-reacting case for the same operating conditions. It is seen that the SAF spray produces slightly smaller droplets compared to Jet-A fuel, giving a smaller SMD value. But this difference is almost negligible in non-reacting cases. This is mostly due to the changes in physical properties of the two different fuels. The SAF utilized in this study has approximately 10% lower surface tension as compared to Jet-A fuel. Reduction in surface tension helps in formation of new surface areas promoting droplet/jet breakup, thereby creating smaller droplets. This can also be looked at in terms of the Weber number which is inversely proportional to the surface tension force. Higher the Weber number, better is the atomization quality of the liquid spray. The variation in SMD values at different operating conditions followed similar trends as Jet-A fuel at all the measurement locations.

For reacting cases, the difference in droplet diameters is slightly more pronounced as compared to the non-reacting case. This is apparent from Figure 6, where the distributions shift towards smaller diameters as we shift from neat Jet A fuel to neat SAF. Also, at temperatures above 100° C, the vapor pressure of SAF is approximately 5% higher than Jet-A fuel which can contribute to better vaporization and smaller droplets. The effect of vapor pressure seems to be more prominently observed in reacting conditions where temperatures are much higher than in non-reacting conditions. In the present study, physical properties such as surface tension, viscosity and density for the 50-50 blend generally lie in between their neat fuel properties. Hence, their behavior in spray breakup and atomization is expected to occur in the same trend.

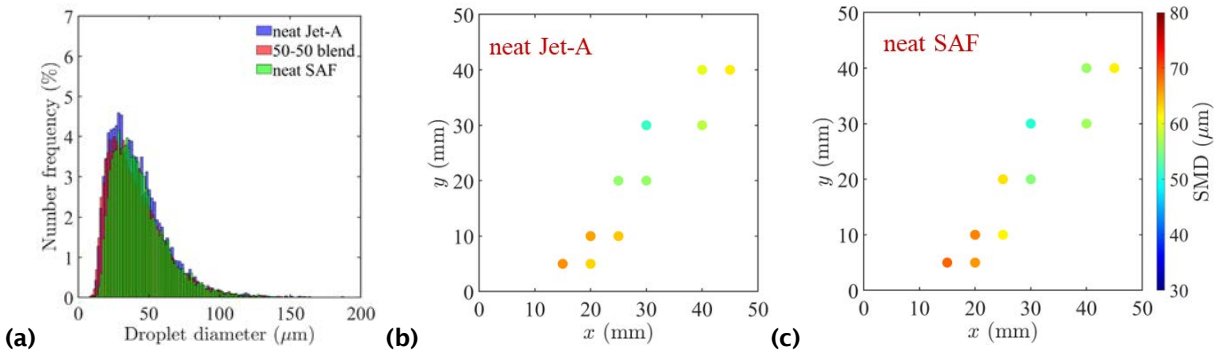


Figure 5. Comparison of droplet diameters for Jet-A fuel and sustainable aviation fuel (SAF) at non-reacting conditions with 35.3 psig pressure and 450 K preheat temperature for locations (a) *x*=25 mm, *y*=10 mm (b) neat Jet-A fuel, non-reacting (c) neat SAF, non-reacting. SMD: Sauter mean diameter.

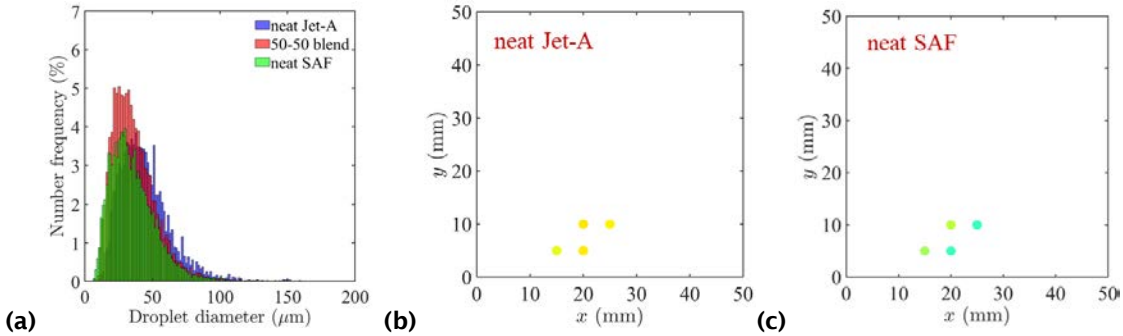


Figure 6. Comparison of droplet diameters for Jet-A fuel and sustainable aviation fuel (SAF) at reacting conditions with 35.3 psig pressure and 600 K preheat temperature for locations (a) *x*=25 mm, *y*=10 mm (b) neat Jet-A fuel, reacting (c) neat SAF, reacting.

Subtask 1.2: Characterize Spray Breakup and Spray Penetration Using Mie Scattering

To study the breakup characteristics of the fuel spray and obtain global spray parameters such as spray penetration and spray cone angles, droplet Mie scattering is performed for both non-reacting and reacting conditions at different operating conditions. Mie scattering is performed using a Nd:YAG laser (Mesa™-PIV) emitting 532 nm beam at the rate of 5kHz. The laser beam is shaped into a thin sheet of dimensions 50 mm x 0.5 mm using a combination of cylindrical lenses and passed through the primary zone of the combustor where fuel spray exists. The resulting scattering signal from the droplets is collected using a high-speed camera (Photron® SA-Z), equipped with a 100 mm camera lens (Tokina,® f/#=4.0) and 532 nm bandpass filter to avoid flame radiation. For obtaining global properties of the spray, a total of 5,000 images were averaged over time and subsequently post-processed to remove any background signal.

™ Mesa is a trademark of Amplitude Holding, France.
® Photron is a registered trademark of Photron Limited, Tokyo, Japan.
® Tokina is a registered trademark of Kenko Tokina Co., Ltd., Tokyo, Japan.

Figure 7 shows the time-averaged Mie scattering images for Jet-A fuel at both non-reacting and reacting conditions. With varying pressures, the spray penetration seems to reduce at the same preheat temperatures of 600 K. From the PDPA results, it was observed that the averaged droplet diameters reduced considerably with increasing pressure.

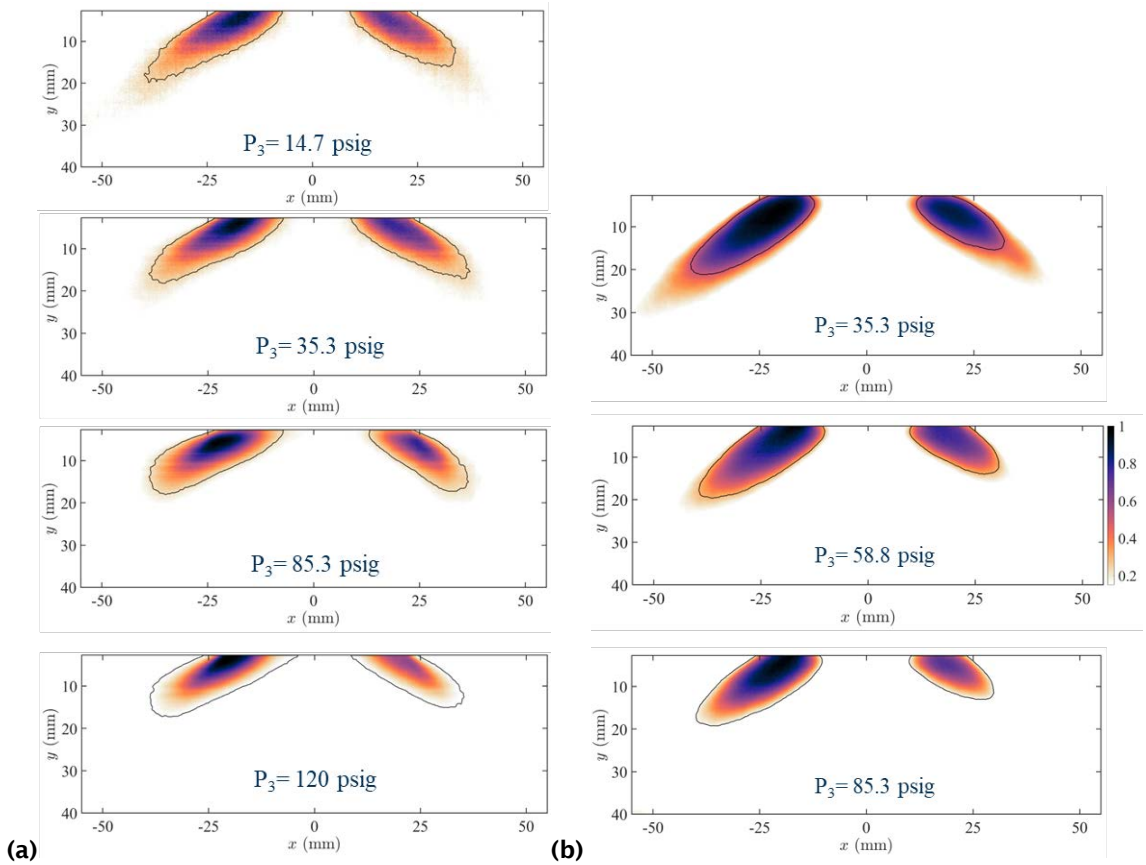


Figure 7. Comparison of averaged Mie scattering images with varying pressures for Jet-A spray at 600 K preheat. (a) Non-reacting conditions. (b) Reacting conditions. The color bar represents the relative density of droplets.

Hence, more smaller droplets are present in the flow which may evaporate faster at higher preheat leading to low Mie scattering signals as compared to larger diameter signals close to the injector exit. For reacting conditions, similar patterns in spray penetration are observed with increasing pressure. The intensities are slightly higher compared to non-reacting spray as much of the smaller droplets are vaporized faster in reacting conditions. Due to this, the Mie scattering signal from the larger droplets tends to be higher over larger spatial regions. This is very apparent from images in Figure 7b as compared to the images in Figure 7a. The spray cone angles do not seem to vary significantly and is seen to be nearly independent of operating pressure. More data are available for SAF and their blends, which is currently under processing.

Subtask 1.3: Measure and Quantify the nvPM Mass Concentrations at the Exit of the Combustor

The nvPM mass concentration measurements at the exit of the combustor are important as they provide the overall performance of the combustor in terms of emissions and combustion efficiency. The measurements in the current study are collected utilizing a commercial micro soot sensor system from AVL, which can measure particle mass concentrations at a given spatial location outside the combustor. The system works based on the photoacoustic measuring principle. With this measurement method, the sample gas with strongly absorbing soot particulates, is exposed to modulated light. The periodical warming and cooling and the resulting expansion and contraction of the carrier gas can be regarded as a sound wave and detected by means of microphones.

The soot sensor probe is equipped with temperature compensation to account for thermal deposition of nvPM particles in the sampling line due to cooling. The entire sampling line is heated, and constant temperature is maintained to avoid any major soot deposition and aggregate formation. The system can also be equipped with a pressure reduction unit for operation in pressurized environments. Since the current measurements are performed at the exit of the combustor exhaust, downstream of the choke, so pressure reduction unit was not necessary. The system is able to continuously measure the nvPM mass concentrations at a max data rate of 10 Hz by maintaining a constant internal acoustic cell temperature. At high gas temperatures exceeding 700 ºC or at high mass concentrations (above 150 mg/m^3), dilution air can be mixed to the sample gas which reduces the temperature/concentrations to operate the system within its limits. Figure 8 shows the AVL micro soot sensor system and its probe placement for measurements at the combustor exit, downstream of the exhaust choke.

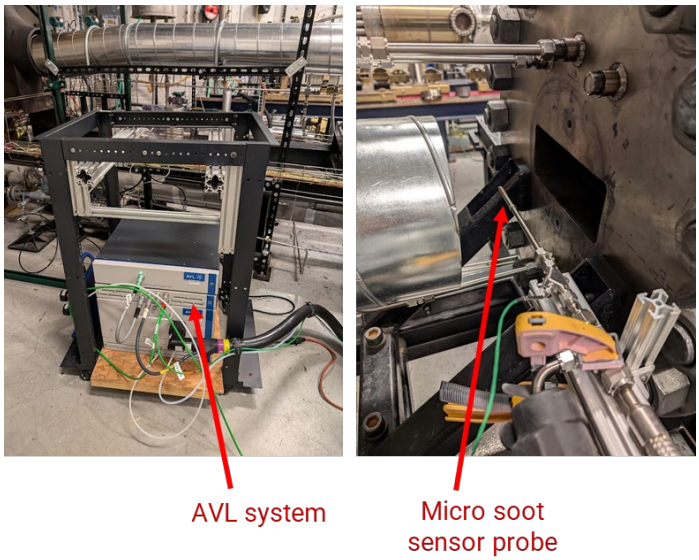


Figure 8. The AVL Test Systems, Inc. (AVL), micro soot sensor system with the probe attached and placed at the exit of the combustor exhaust outside the pressure vessel.

The current measurements are performed with all three injectors running at various operating pressures and two preheat temperatures with a fixed equivalence ratio for both Jet-A fuel and SAF. The dilution ratio of 3 was sufficient to maintain the probe temperature below 700 ºC for continuous operation. The results are finally compensated for both the temperature compensation at the probe inlet and dilution ratio. The probe is mounted perpendicular to the flow direction at the exit of the pressure vessel. The downstream distance of the probe from the combustor dump plane is close to 92 cm.

The soot concentration measurements over time for 35.3 psig pressure and 540 K preheat with Jet-A fuel is shown in Figure 9a. The values remain nearly constant over time, indicating steady combustion, with minor peaks appearing instantaneously where large soot aggregates may have gathered at a small spatial location. Nonetheless, the overall measurement values can be considered steady over time. In addition, the concentration measured at the probe is compensated for dilution gas and temperature correction. Since the dilution ratio in the current measurements is 3, the concentrations increase by three times after the correction. Figure 9b shows the variation of soot concentrations with pressure for different neat fuels at two different preheats. The concentrations seem to have pressure scaling that is similar to the results predicted inside the primary zone of the combustor. This suggests that the nvPM volume fractions in the primary zone of the combustor can be correlated to the final exhaust mass concentrations. This will give a good overall picture of the combustor performance in terms of nvPM formation and subsequent oxidation downstream of the combustor zone. SAF produces much lesser soot concentrations compared to Jet-A fuel at the same operating conditions. This is expected since the SAF utilized in the current study has negligible amount of romantic content reducing the tendency for soot formation. Additionally, for a given fuel and pressure, the concentrations are slightly lower for 600 K preheat as compared to 540 K preheat. Increasing preheat aids in vaporizing fuel droplets faster, improving mixing and



combustion efficiency, reducing soot formation. Also, higher preheat increases oxidation processes, thus reducing final particle concentrations as the combustion gases move along the exhaust section. Once the nvPM volume fractions are obtained in the combustor using laser induced incandescence, these results can be compared and correlated in detail.

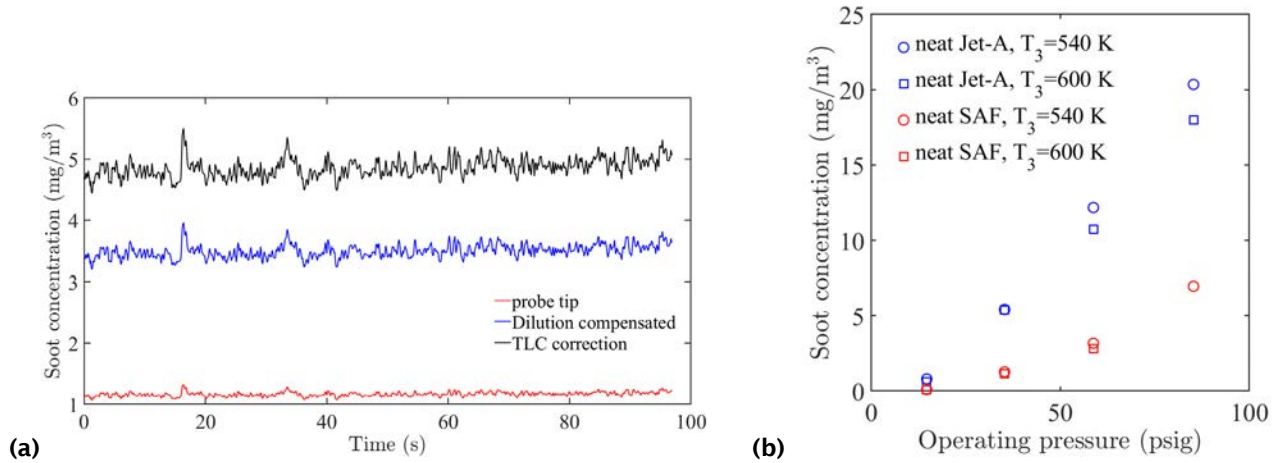


Figure 9. (a) Soot concentrations measured over time for Jet-A fuel at 35.3 psig pressure and 540 K preheat temperature. The measured concentrations at the probe and the final dilution and temperature compensated (TLC) values are provided. (b) Variation of soot concentrations with operating pressure for neat Jet-A fuel and SAF.

Milestone

- Conducted systematic PDPA, Mie scattering and exhaust nvPM mass concentration measurements at different combustor operating conditions with Jet-A fuel and SAF, respectively.

Major Accomplishments

- Spatially resolved droplet size measurements in a confined sector combustor using PDPA for Jet-A fuel and SAF were conducted.
- Conducted droplet Mie scattering measurements at high data rates up to 5 kHz to study droplet breakup and global spray characteristics for Jet-A fuel and SAF in both non-reacting and reacting conditions.
- Compared the differences between Jet-A fuel and SAF in terms of nvPM formation at the exhaust at different operating pressures through probe measurements using a micro soot sensor.

Publications

Conference Presentations

Juergensmeyer, J., Miller, J., Bond, R., Mcgrath, R., Wehe, S., Sun, W., Mazumdar, Y. C., & Steinberg, A. (2025, June 16–20). Measurement of Particulate Matter and Its Oxidation in a Multi-Sector Rich-Quench-Lean Combustor. *Proceedings of the ASME Turbo Expo 2025: Turbomachinery Technical Conference and Exposition*. Memphis, Tennessee. https://doi.org/10.1115/GT2025-153181

Vishwanath, R., Douglas, E., Wehe, S., Mazumdar, Y. C., Steinberg, A., & Sun, W. (2026). *Spray measurements in a sector combustor operating with conventional and sustainable fuels at elevated conditions*. Submitted to ASME Turbo Expo 2026.

Vishwanath, R., Bibik, O., Olimid, D., Douglas, E., Wehe, S., Mazumdar, Y. C., Steinberg, A., & Sun, W. (2025, January 6-10). Drop-size measurements using phase doppler particle anemometry in a confined high-pressure sector combustor (AIAA 2025-1519). *AIAA SCITECH 2025 Forum*, Orlando, Florida. https://doi.org/10.2514/6.2025-1519

Outreach Efforts

None.

Awards

Wenting Sun: Hiroshi Tsuji Early Career Researcher Award, 2023. The Combustion Institute (recognizes early career researchers who have demonstrated excellence in fundamental or applied combustion science and have achieved a significant advancement in their field within four to ten years of completing a doctoral degree or equivalents.)

Wenting Sun: AIAA Associate Fellow, 2023

Adam Steinberg: Fellow of the Combustion Institute, 2023

Student Involvement

This task involves four graduate students (Eric Douglas, Harsh Dhayal, Adhav Arulanandan, Andrew Fan). Eric Douglas worked on OH-LIF (OH radical Laser Induced Fluorescence) related measurements. Harsh Dhayal and Adhav Arulanandan worked on sampling probe design. Harsh Dhayal and Andrew Fan worked on DMA (Differential Mobility Analyzer) setup and characterization.

Plans for Next Period

- Conduct PDPA, two-color LII and OH-PLIF measurements in a new combustor configuration for Jet-A, SAF and their blends at a large range of operating conditions. Currently, detailed combustor design and comprehensive thermal stress analysis are completed.

Task 2 – Design of a New Single Piece Additively Manufactured Combustor

Georgia Institute of Technology and Honeywell

Objective

The objective of this task is to develop a new sector combustor with three compact dual-tip fuel injectors and optical access. This will be an improved version of the previous liner, wherein the entire combustor will be additively manufactured as a single piece using Haynes 282.® This combustor will be operated under high-pressure and high-temperature conditions to replicate real engine conditions. This sector combustor will be used as a test bed to characterize the formation and oxidation of nvPM.

Research Approach

The sector combustor is initially modeled using computer-aided design (CAD) by adopting the geometry of a typical annular combustor, wherein three sectors of an annular combustor is unwrapped into a straight geometry to simplify the mechanical design and allow for optical access. The combustor will consist of effusion holes to cool down the combustor surface and maintain metal temperature limits, quench holes downstream of the primary combustion zone, optical windows on three sides, and fuel injector assembly (see Figure 10). Subsequent mechanical stress and thermal stress analysis is performed at maximum load to understand the mechanical performance and integrity of the combustor liner during continuous operation. To analyze flow patterns, spray and nvPM formation, computational fluid dynamics (CFD) analysis is performed at various operating conditions to optimize the combustor design and predict combustor performance.

® Haynes 282 is a registered trademark of Haynes International, Inc., Kokomo, Indiana.

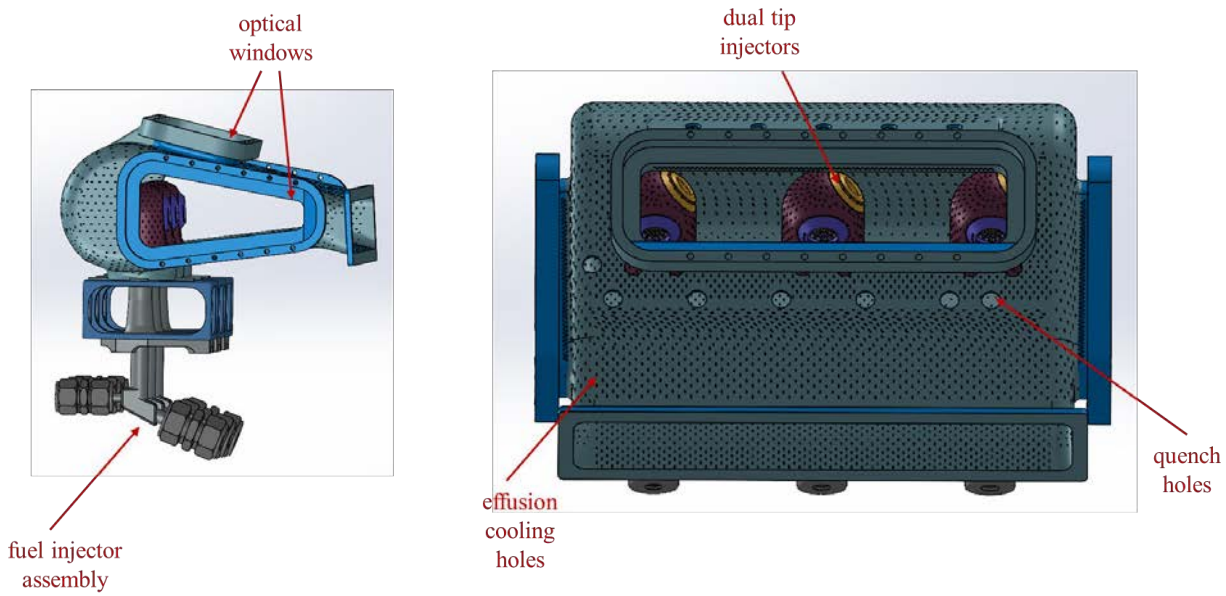


Figure 10. CAD design of the sector combustor with fuel injector assembly.

The CAD design and assembly of the new combustor design is shown in Figure 10. The effusion hole and quench hole pattern is optimized using CFD approach to obtain uniform temperature pattern across the combustor surface and avoid hot spots and non-uniform thermal expansion. The optical windows on either side of the combustor allow for laser-based diagnostics. Each window is equipped with film air channels to shield the quartz windows from sooting gases and cool down the surface. The top window is designed such that additional air can be provided and controlled to avoid soot build up at high soot load operating conditions. This is a major improvement from the previous combustor design where soot buildup was one of the major issues.

The thermal-mechanical CFD predictions involved steady state thermal analysis, along with combined thermal and pressure load analysis. The steady state thermal analysis revealed hot and cold side temperatures throughout the combustor surface as shown in Figure 11. This included convective and radiative heat flux predictions that would be seen at full load conditions. The results revealed that the maximum temperatures were within the temperature limits of Haynes 282 at the max operating pressures. Hot spots obtained from initial CFD predictions are eliminated by optimizing the cooling hole patterns and positioning of quench holes through several iterations.

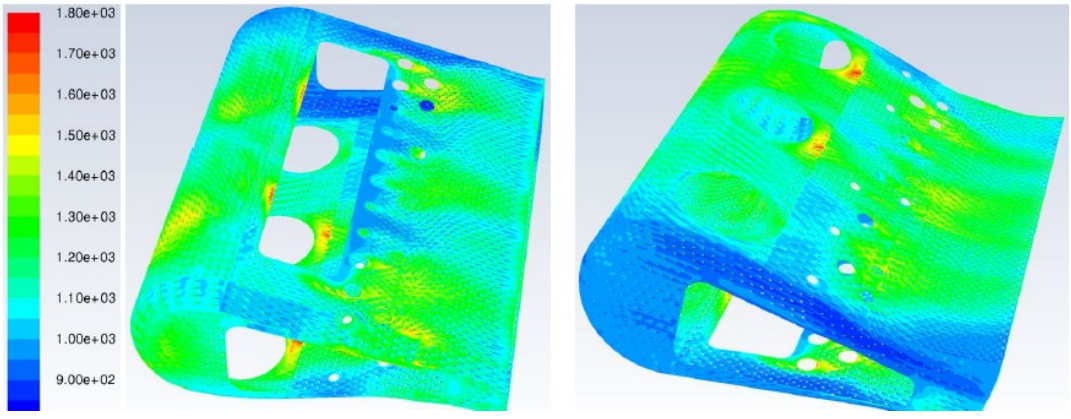


Figure 11. Steady state thermal analysis using CFD for the combustor.

Thermal loading analysis is performed based on the temperature variations obtained from the steady state thermal results wherein temperatures variation from 870°F to 1,750°F is assumed to occur at different locations over the combustor surface. This is done by assuming fixed boundaries at the combustor exit flange as it will be attached to the exhaust section and making the dome and the entire liner as the displacement boundary. The predicted stress values were below the material yield strength. In addition, pressure loading is added to this analysis to account for the pressure drop seen across the combustor during the operation. The peak stresses near the quench holes and window brackets were reduced over several iterations to minimize the overall stress. All the boundary conditions experienced by the combustor is applied during the overall analysis.

Once the combustor mechanical design is finalized, subsequent CFD analysis is performed at both non-reacting and reacting conditions to gather information on spray patterns, flame temperatures and nvPM formation within the combustor. Figure 12 shows the reacting flow predictions including spray pattern and penetration downstream of the injectors before combustion. The colored contours reveal nvPM volume fractions at 100 psig operating condition. These results will help in predicting soot formation sensitivity to pressure and fuel air ratios. It also helps in designing the combustor dimensions accurately to obtain reasonable temperature distribution on the liner surface and avoid soot deposition on the combustor windows before it can be manufactured for experiments. The results obtained will be later compared to optical diagnostic measurements to help in improving the numerical models and guide new fuel injector designs.

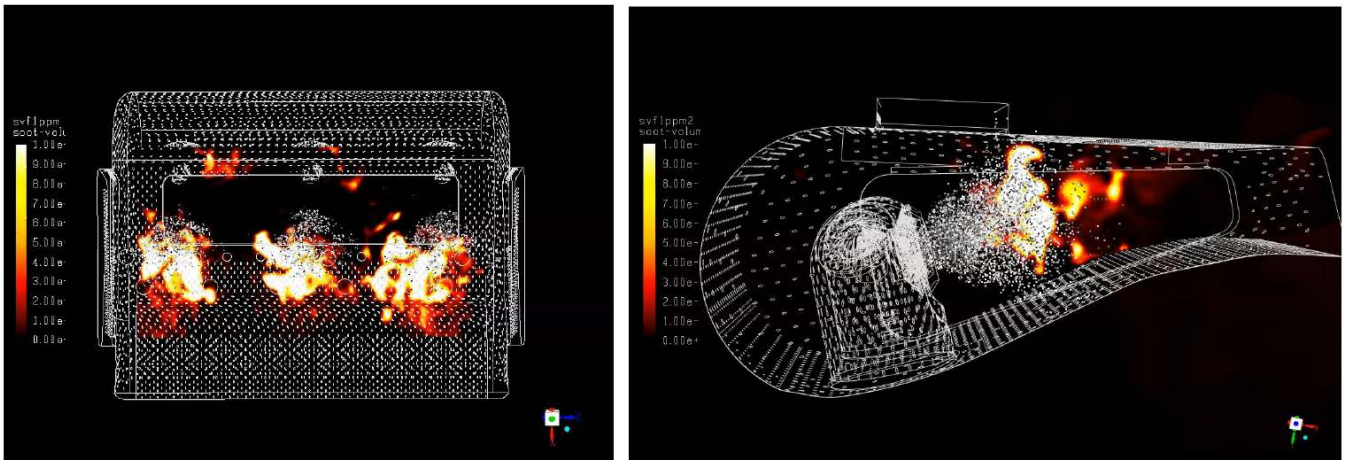


Figure 12. Spray pattern and soot formation prediction using CFD approach at 100 psig operating condition with three injectors spraying jet fuel.

Milestone
This task was completed in April 2025.

Publications
None.

Outreach Efforts
None.

Awards
None.

Involvement
Honeywell performed the overall CFD analysis and mechanical design. Georgia Tech assisted in designing the final combustor configuration to integrate with the pressure vessel, optimize the combustor window dimensions and placement for performing optical diagnostics, and provide required instrumentation ports.



Plans for Next Period

- Perform spray and nvPM measurements in the newly built single piece additively manufactured combustors having dual tip injectors.
- Undertake experiments over a wide range of engine operating conditions aligning with Honeywell auxiliary power unit.



Project 071 Predictive Simulation of nvPM Emissions in Aircraft Combustors

Georgia Institute of Technology

Project Lead Investigator

Suresh Menon
Professor at the School of Aerospace Engineering
Georgia Institute of Technology
270 Ferst Drive, Atlanta, GA 30332-0150
404-894-9126
suresh.menon@aerospace.gatech.edu

University Participants

Georgia Institute of Technology (GT)

- P.I.: Prof. Suresh Menon
- FAA Award Number: 13-C-AJFE-GIT-067
- Period of Performance: October 1, 2020, to September 30, 2025
- Tasks:
  1. Kinetic Modeling: Develop kinetic models to predict fuel decomposition and soot precursor polycyclic aromatic hydrocarbon (PAH) pathways in representative sooting fuels
  2. Nucleation Modeling: Develop reduced incipient particle nucleation rates according to PAH dimerization rates from molecular dynamics (MD) simulations
  3. Surface Growth and Aggregation Modeling: Develop a blended reaction-transport-limited growth model of soot particle aggregation
  4. Large eddy simulation (LES) of soot formation within canonical flames, strategy to upscale the soot formation to resolve LES scales, integrate the updated rates in the global soot models, and apply them to predict soot formation in complex rich-quench-lean configuration

Project Funding Level

The current project was funded initially for a 3-year effort (July 2020 to September 2023), with a request of $500,000 per year from ASCENT (per year). An additional request for no-cost extension was approved for the remainder of the term till September 2025. Cost-sharing is provided as follows.

- GT provides cost-sharing for its share of $150,000 per year. The GT point of contact (POC) is Kevin Ellis (kevin.ellis@aerospace.gatech.edu).
- Raytheon Technologies Research Center (RTRC) provided cost-sharing of $250,000 per year. Dr. Colket is a consultant on this project with many years of experience in soot modeling. The RTRC POC is John LaSpada (LaSpadJW@RTRC.utc.com).
- University of Michigan (UM) provides cost-sharing in the amount of $100,000 per year. The UM POC is Alexandra Thebaud (thealexi@umich.edu).

Investigation Team

Georgia Institute of Technology

Prof. Suresh Menon, GT: (P.I.), Task 4
Mr. Shubham Karpe, GT: (Student), Task 4

Raytheon Technologies Research Center

Dr. Miad Yazdani, (co-P.I.), Task 3
Dr. Steve Zeppieri, (co-P.I.), Task 1
Dr. Meredith Colket, (co-investigator), Task 3

University of Michigan
Prof. Angela Violi, (co-P.I.), Task 2

Project Overview

This project aimed to establish a new multiscale framework for predicting soot formation in both canonical and practically relevant sooting flames. A hierarchy of first-principles simulation methods was employed to capture the multiscale physics governing the formation and transport of non-volatile particulate matter (nvPM, commonly referred to as soot). The work specifically targeted several empirical elements that traditionally limit soot modeling fidelity, for example, uncertainties in particle inception models, the roles of key precursor species in nucleation, assumptions regarding particle morphology and their effects on surface growth, sensitivities to particle size distribution, and the use of ad hoc coagulation and coalescence formulations. To address these challenges, the state-of-the-art modeling tools are developed and a systematic coupling of these tools in a multiscale, multiphysics manner is established. Hence, this approach provides insights into establishing new predictive abilities by integrating these capabilities. The final objective of this work demonstrated the capabilities of this approach to modeling the soot physics in realistic gas turbine combustor for which the experiments are being conducted under Federal Aviation Administration (FAA) ASCENT Project 070.

The multiscale and multiphysics layers of collaborations among the cost-sharing groups are summarized in Figure 1 and Figure 2 and briefly described herein. In Year 1 and 2 efforts, at Georgia Tech, the method of moment-based soot model is first established using canonical studies of ethylene fuels and key inputs for improvements are identified by investigating the sensitivity of soot predictions to different modeling components. These conditions are then provided to other collaborative groups for establishing their modeling approaches. Specifically, the kinetics group at RTRC compared different gas-phase kinetics in predicting important soot precursor species. These efforts primarily resulted in the development of detailed gas-phase kinetic mechanism that was provided to UM. In the UM study, the propensity of gas-phase species to form dimers (considered the building blocks of soot inception) under flame conditions was studied using MD simulations. A unique approach based on machine learning was developed that can be potentially extended to any relevant sooting fuel to obtain the inception rates that can be provided to post-inception growth modeling. At RTRC, Monte Carlo (MC) simulations approach was established using jet-fueled lean direct injection (LDI) combustor data simulated at GT to understand the fractal growth of soot aggregates. At Georgia Tech, the modular moment-based soot modeling was established to assemble the above inputs it. Additionally, standalone linear eddy mixing (LEM-MOM) approach was established to upscale the soot source rates at LES level scales.

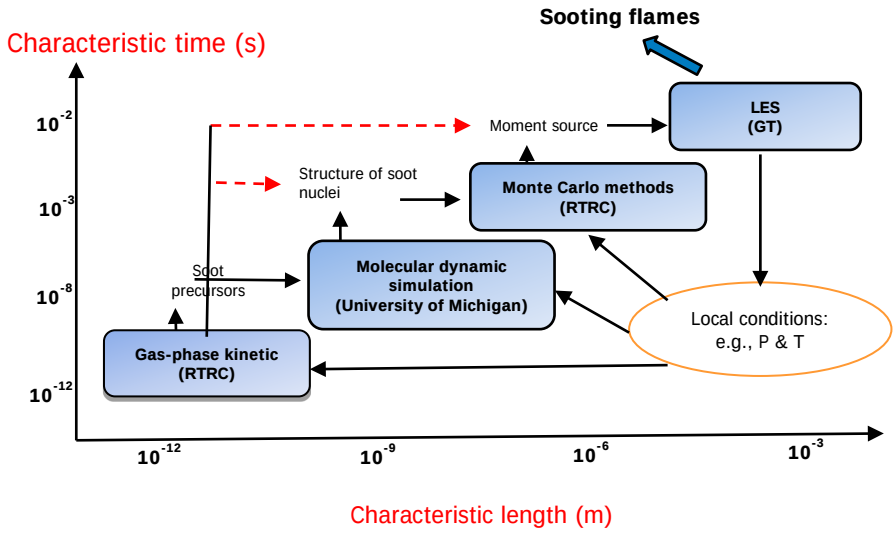


Figure 1. Multiscale collaborative efforts to improve non-volatile particulate matter (nvPM; soot) predictions. LES: large eddy simulation, GT: Georgia Institute of Technology, RTRC: Raytheon Technologies Research Center.

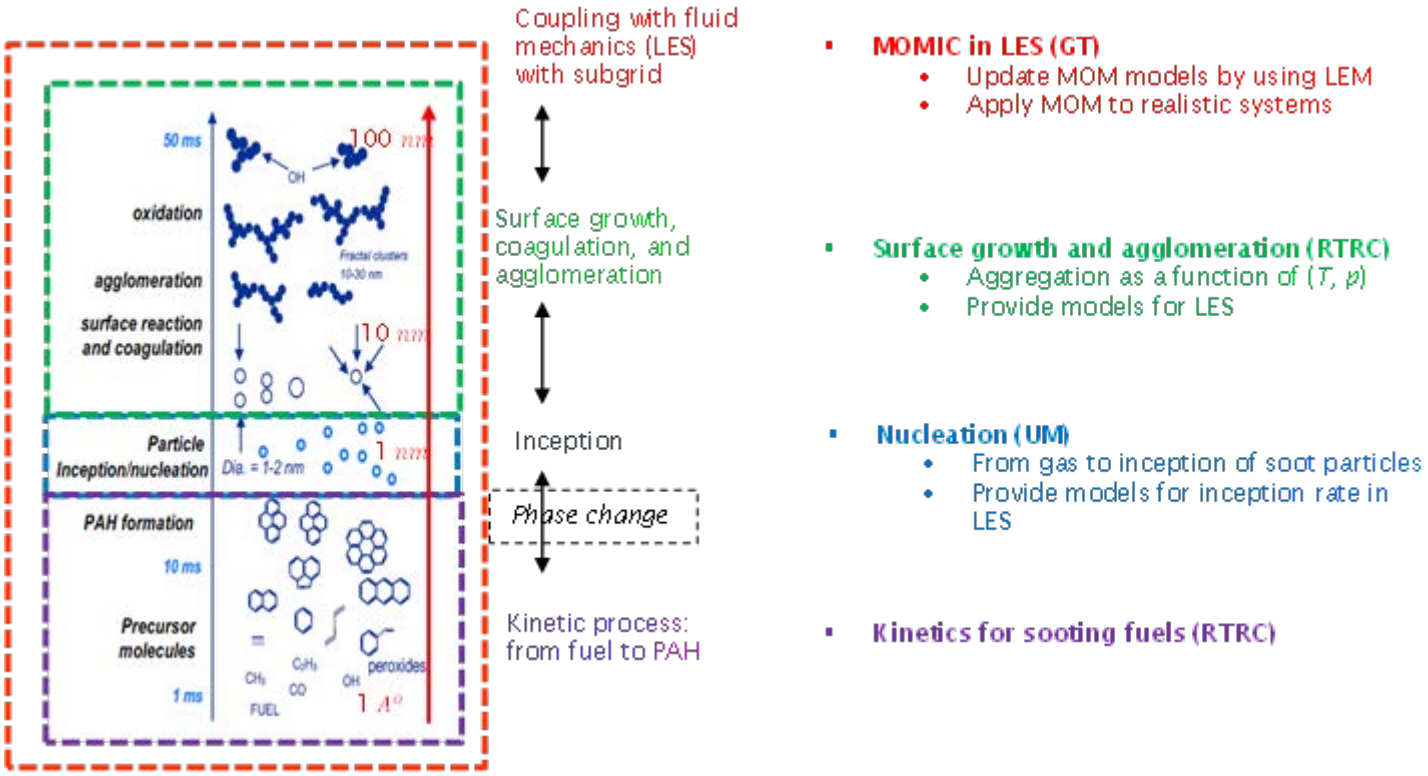


Figure 2. Multiscale collaborative efforts to improve non-volatile particulate matter (nvPM; soot) predictions. LES: large eddy simulation, GT: Georgia Institute of Technology, MOMIC: method of moments with interpolative closure, PAH: polyaromatic hydrocarbons, RTRC: Raytheon Technologies Research Center, UM: University of Michigan.

In the Year-3 and NCE efforts, this established collaborative approach is extended to study soot evolution in a realistic single sector Rich-Burn Quick-Mix Lean-Burn (RQL) model combustor operated using conventional jet fuels. At first, LES studies at GT conducted non-sooting simulations of this rig to generate a useful parametric space as representative conditions to be used in different modeling components of the collaborative partners. The kinetics activities at RTRC resulted in the development of a 210-species detailed mechanism with formation of PAH species till five aromatic rings. The molecular dynamics-based studies identified key soot precursors and the rates of formation of soot nuclei under RQL combustion-relevant conditions and formed a semi-empirical modified expression of soot nucleation using benzopyrene (A_4R_5). This nucleation rate was provided to GT to update the source terms associated with nucleation processes in the method of moment-based soot model, and the information on the structures of these soot nuclei was also provided to RTRC for modeling surface growth and aggregation processes along the streamlines of RQL combustor. At GT, LES studies soot formation from RQL combustor under two operating conditions were performed using a reduced gas-phase kinetic mechanism with PAH formation pathways till naphthalene. Due to the heavy computational cost incurred during the simulations even with the reduced gas-phase kinetics, the coupled soot model inputs were not directly used in the LES. Rather using the baseline LES data, a predictive computational fluid dynamics (CFD)-Chemical Reactor Network (CRN) strategy was adopted to construct a reduced reactor network model and is then used to understand the relative effects of incorporating detailed kinetics and inception model obtained as inputs from multi-scale collaborative studies.

Task 1 – Kinetic Modeling

Raytheon Technologies Research Center

Objective

The objective of this task is to develop a chemical kinetic model of parent fuel decomposition and oxidation reactions, with a special focus on fuel rich chemistry, to enable the accurate evolution of PAH/soot precursor formation and incipient soot particle formation.

Milestone(s)

- Develop a detailed kinetic mechanism with PAH pathways for ethylene and jet fuels.
- Formulate a semi-empirical soot model for coupling with CFD.

Research Approach

The schematic in Figure 3 shows the coupling among the LES, nucleation, and kinetic activities focused on during this project, where T, P, and ϕ represent the temperature, pressure, and equivalence ratio of the surrounding gas phase, respectively. For ethylene fuels, the conditions corresponding to well-stirred reactors (Brown et al., 1998), laminar premixed flames in international sooting flame workshop were used as a baseline, whereas for the jet fuels, the non-sooting simulations conducted using LES were used to map the local ranges of conditions witnessed in the combustor. Based on the developed gas phase kinetics, information about the key precursor PAH species is passed to the nucleation modeling activities at university of Michigan and the detailed kinetics is provided to GT.

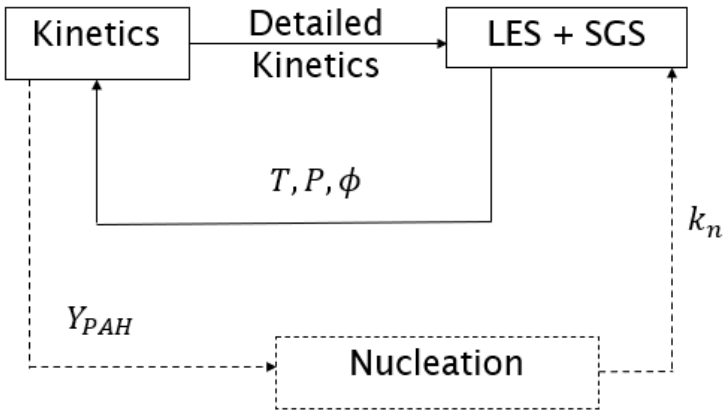


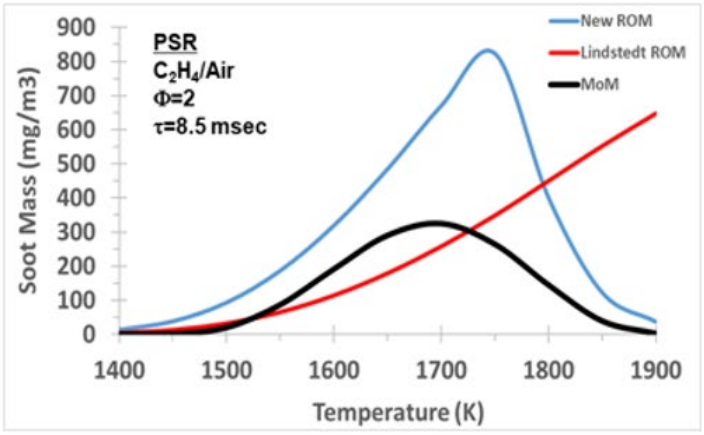
Figure 3. Coupling of large eddy simulation (LES)–kinetic activities. PAH: polyaromatic hydrocarbon, SGS: subgrid-scale.

The Year 1 activities mainly focused on kinetic model development of ethylene fuel to establish the methodology. The set of detailed chemical mechanisms at GT were extended here to include a comprehensive list as below: Appel-Bockhorn-Frenklach (101 species/544 reactions), Wang-Frenklach (99 species/533 reactions), National Jet Fuels Combustion Program (NJFCP) Foundational Chemistry sub model with Strategic Environmental Research and Development Program (SERDP) PAH reactions (166 species/504 reactions), NJFCP Foundational Chemistry sub model with King Abdullah University of Science and Technology (KAUST) PAH reactions (168 species/818 reactions), Full ARAMCO®-KAUST C_4 mechanism (581 species/3,037 reactions), CRECK Natural Gas mechanism (114 species/1,999 reactions), University of Connecticut (UCONN) (Lu) Skeletal ethylene (C_2H_4) mechanism (33 species/206 reactions). The Lu skeletal mechanism serves as a proxy for the reduced 19 species ethylene mechanism currently used at GT, because both mechanisms derive from the same fully detailed mechanism. These models were benchmarked against published ethylene datasets for comparative analysis against both experimental data and relative performance against the various models.

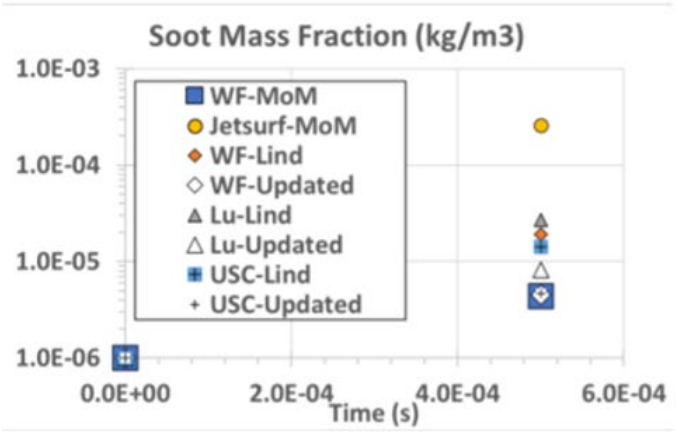
® ARAMCO is a registered trademark of Saudi Arabian Oil Company, Dhahran, Saudi Arabia.



The skeletal mechanism from T. Lu has been used to optimize the global soot kinetic model. The Lindstedt 4-step soot model consists of nucleation step based on acetylene (C_2H_2) precursor, soot surface growths based on C_2H_2, soot oxidation via hydroxide (OH) and dioxygen (O_2). The perfectly stirred reactor (PSR) studies are conducted using Chemkin® to optimize the coefficient [pre-exponential factor, minimum C atoms to form soot nuclei, Activation energy (E_a/R)] to develop a new soot kinetic model. Th results of soot evolution with PSR studies for a wide range of temperature conditions, using the Lindstedt soot model, method of moments in Chemkin and the improved kinetic model are demonstrated in Figure 4a. The improved kinetic model can predict trends very well (specifically the reduced rates and soot mass fractions at elevated temperature) consistent with Chemkin Method of Moments (MOM), as opposed to Lindstedt model. The updated model is also coupled with other detailed kinetics to predict the variations in soot mass fractions and results are displayed in Figure 4b. It can be seen that predictions of soot mass fractions from the updated soot kinetics coupled with different mechanisms are consistent. The small discrepancy lies with the uncertainty in predictions of C_2H_2 mass fractions which acts as soot precursor.



(a) Improved soot kinetic over range of temperature



(b) Updated soot kinetic model with detailed mechanisms

Figure 4. Assessment of the improved soot kinetic model at Raytheon Technologies Research Center (RTRC). MOM: Method of Moments, PSR: perfectly stirred reactor.

The later efforts were focused on the completion and assessment of chemical kinetics models coupled to PAH formation for logistic (Jet-A) fuels. In summary, the HyChem (Hybrid Chemistry) (Wang et al., 2018) method was used, in which semi-empirical reactions treat the parent fuel decomposition process to the relevant intermediate hydrocarbon species, and the so-called SERDP technique, in which compositions of several surrogate hydrocarbon species are formulated that capture the bulk properties of the fuel of interest (for example, Jet-A fuel would be considered a binary blend of *n*-dodecane and *m*-xylene). The HyChem model was coupled with both the SERDP and KAUST PAH-chemistry (Selvaraj et al., 2016) models for analysis and the SERDP model was coupled with the SERDP PAH-chemistry model. Finally, the California Institute of Technology (Caltech)-mech (Blanquart et al., 2009) model was appended with the HyChem model to incorporate additional reactions related to the decomposition of Jet-A fuels. The overall layout of the workflow adopted in this effort is highlighted in Figure 5. This assessment is carried out using a perfectly stirred reactor configuration where a mixture of Jet-A (assumed as 77% nC12, 23% *m*-xylene)/air is subjected to the following conditions *P*: 1-5.8 atm, τ_{res}: 1-25 msec, ϕ : 0.5–5.5, T: 1,400–2,300K which were based on local conditions obtained from non-sooting simulations of RQL combustor at GT.

® Chemkin is a registered trademark of Ansys, Inc., Canonsburg, Pennsylvania.

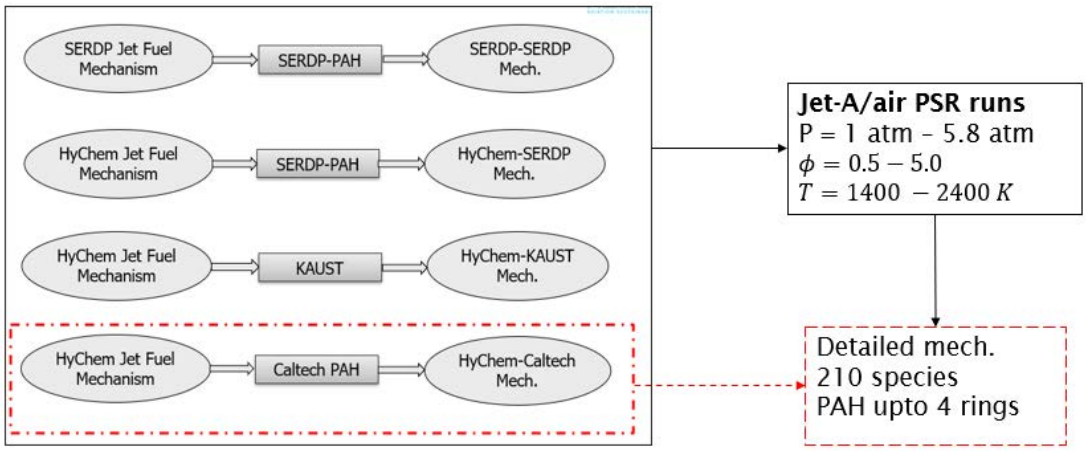
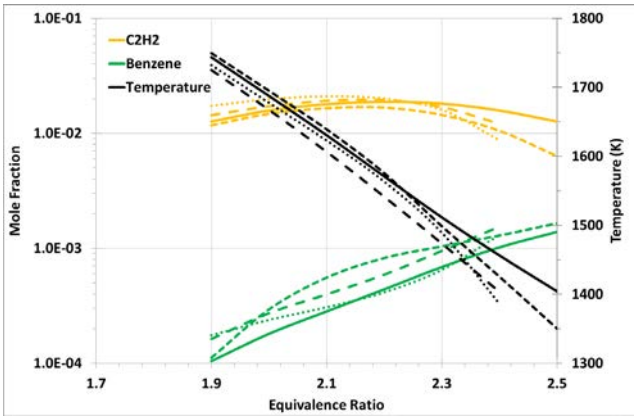
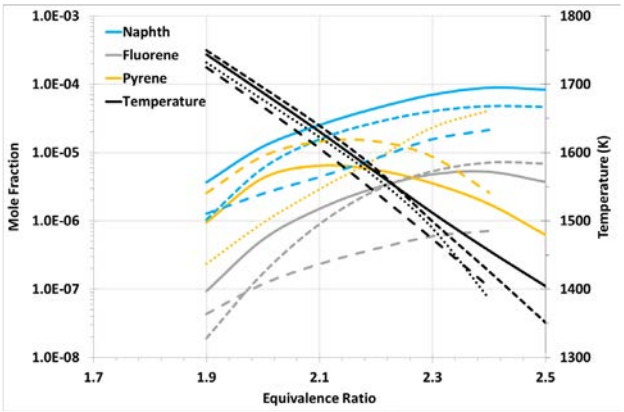


Figure 5. Assessment of detailed gas-phase chemical mechanisms, the red dashes depict the final delivered gas phase kinetics through Raytheon Technologies Research Center (RTRC) kinetic activities. PAH: polyaromatic hydrocarbon, PSR: perfectly stirred reactor.

The key outcomes of kinetic activities are discussed briefly here. The results obtained from the assessment of all detailed gas phase mechanisms are provided in Figure 6. As can be seen from Figure 6a, overall predictions of temperature are similar for all mechanisms. Some visible differences arise in the range of higher equivalence ratios. The benzene (C_6H_6) profiles and acetylene (C_2H_2) profiles are in qualitative agreement among mechanisms except the Pitsch mechanism (Langer et al., 2023), which must be investigated further. Encouragingly, both the HyChem models and the Caltech-mech model have an overall satisfactory agreement.



(a) Comparison of major precursor species



(b) Comparison of heavier PAH species

Solid:	Caltech Mech
Dash:	Pitsch et al.
Dot:	Hychem/Kaust Mech.
Long Dash:	Hychem/SERDP Mech.

Figure 6. Assessments of key soot relevant characteristics among different detailed mechanisms.



The nucleation studies at UM required addressing the formation of heavier PAH species which play a critical role in the inception of soot particles. In this regard, a comparison of major PAH species that are used in the state-of-the-art nucleation models was conducted across a range of conditions. Such an assessment for key species such as naphthalene ($C_{10}H_8$), fluorene ($C_{13}H_{10}$), and pyrene ($C_{16}H_{10}$) is provided in Figure 6b. The results suggest a wider spread of PAH species among all four mechanisms that may be crucial in predicting the early nucleation stages of soot formation in large-scale simulations. The Pitsch mechanism was relatively new and required further assessment. Keeping this in mind, further analysis is presented here for comparing predictions of soot formation for ethene using Wang-Frenklach, HyChem-KAUST, HyChem-SERDP and Caltech-mech with particulate matter reduced order model (PM-ROM) model (optimized rates for Lindstedt soot model) described earlier. The RTRC formulation extends the original premise by adding benzene as key PM forming species, the hydroxyl radical as another oxidation species and the utilizes a double Arrhenius rate expression for both the inception and surface growth processes that enables the model to capture the well-known and experimentally observed “soot bell” concentration profile with respect to temperature.

Figure 7 suggests that the soot concentration levels at range of temperature from Wang-Frenklach, HyChem SERDP and Caltech-mech show similar behavior in terms of bell-shaped dependency on temperature. The HyChem-KAUST predictions are qualitatively very different compared to the other three mechanisms. In terms of quantitative analysis, HyChem-SERDP mechanism underpredicts soot levels by a factor of 1.5 at higher equivalence ratios than Wang-Frenklach mechanism. Similarly, the Caltech-mech overpredicts soot levels by a factor of 1.5-2 when its predictions are compared with Wang-Frenklach mechanism.

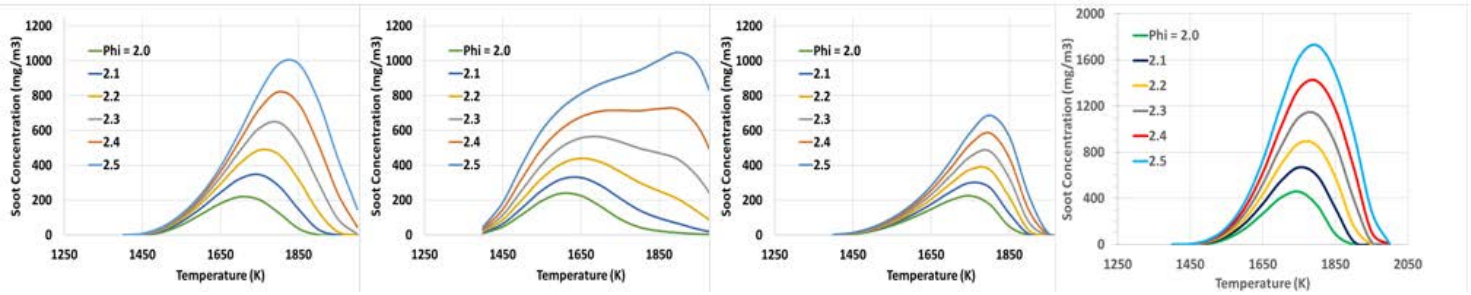


Figure 7. Comparison of soot volume fractions for different gas phase mechanisms: WF, HyChem-KAUST, HyChem-SERDP, Caltech-mech from left to right.

In the next set of activities, predictions are compared by changing the fuel to Jet-A fuels under the same operating conditions investigated for ethene fuels mentioned above. The HyChem-KAUST, HyChem-SERDP and Caltech-mech mechanisms are assessed against each other. As can be seen from Figure 8, the predictions from Caltech-mech and HyChem-KAUST agree with each other quantitatively. However, HyChem-KAUST predicts two peaks in soot levels whereas Caltech-mech predicts only one peak and bell-shaped dependency. This qualitative bell shaped one peak trend is also visible in the predictions of HyChem-SERDP; however, the quantitative magnitude is factor of 3 lower than Caltech-mech and HyChem-KAUST mechanism.

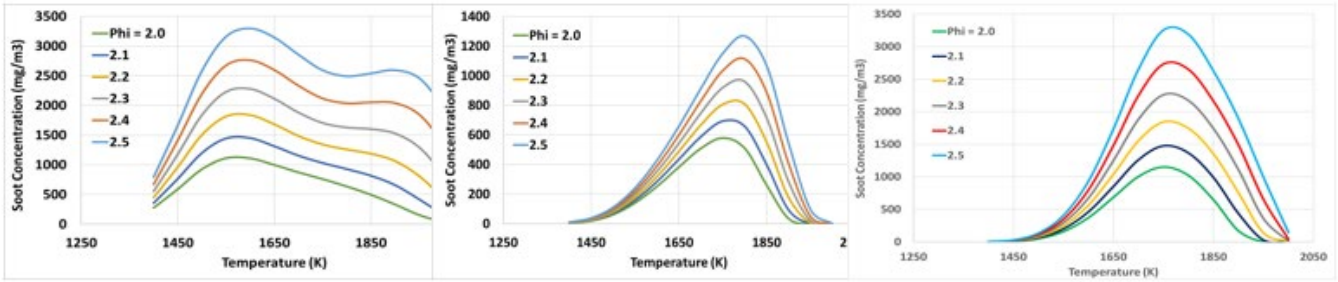


Figure 8. Comparison of soot volume fractions for different gas phase mechanisms: HyChem-KAUST, HyChem-SERDP, Caltech-mech from left to right.



With the analysis of the ethene/air and Jet-A/air simulations combined for the same reactor conditions, considering the trends as well as quantitative levels of soot predictions, Caltech-mech seems to be the best mechanism and is used to derive the final 210 species detailed mechanism, provided later to GT and UM for their modeling activities.

Finally, to conclude upon the final piece of kinetic activities at RTRC, the PM-ROM model is further optimized of rates for the Lindstedt soot model with the newly developed 210 species detailed mechanism. "Soot bell" concentration profile with respect to temperature. As the objective was to generate a higher fidelity PM-ROM model, a numerical shooting fitting procedure was used to establish rate coefficients that enabled the PM-ROM model to identically match the soot concentration levels generated via detailed kinetic analysis coupled with moment-based soot calculations. In the most recently developed PM-ROM, the reduced model was calibrated against PSR calculations at the elevated pressure (5.8 atm) and air temperature (600K) conditions of RQL combustor operation. The nominal reactor residence time for these calculations was 5 ms, and the fuel-air equivalence ratio spanned from 1.8 to 2.5. The detailed mechanism used was the previously discussed HyChem-Caltech mechanism. The agreement between the soot concentrations generated via detailed kinetics and MOM and the PM-ROM are shown in Figure 9, indicating quite good agreement.

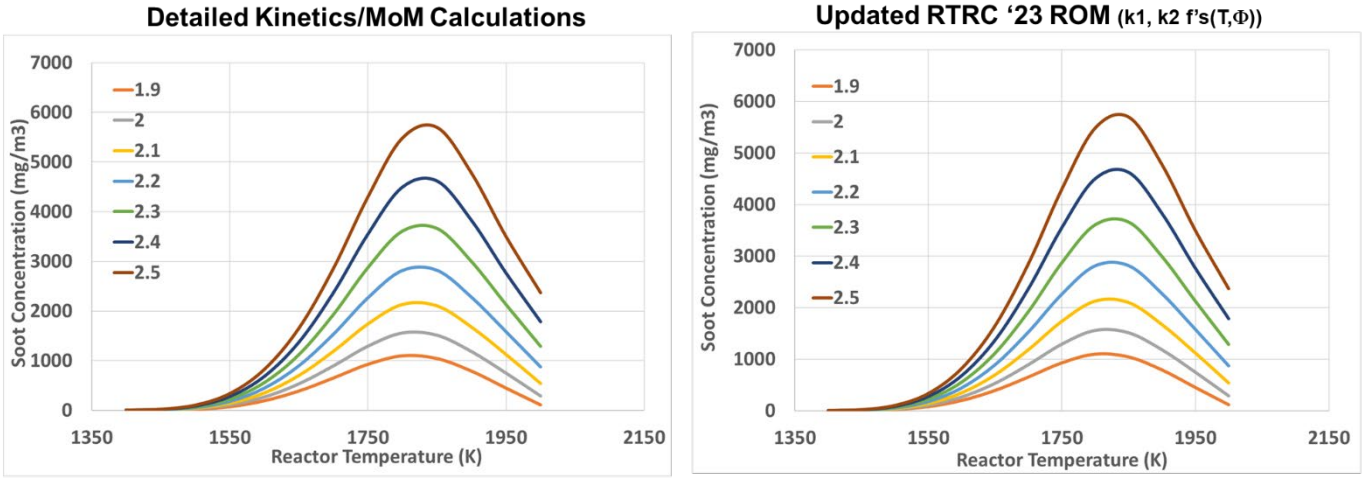


Figure 9. Comparison of soot concentrations generated from the two modeling approaches listed at nominal rich-burn quick-mix lean-burn (RQL) combustor conditions. MOM: method of moments, PSR: perfectly stirred reactor, PM-ROM: , RTRC: Raytheon Technologies Research Center.

Recognizing that two-dimensional (2D) (i.e., temperature and equivalence ratio) correlation may not be computationally efficient, the developed rate correlations were reduced to one-dimensional (1D) as follows. The developed rate expression equivalence ratio dependencies were averaged over the range, yielded rate constants that were functions only of temperature. The average rate expressions for nucleation and surface growth processes are shown in Figure 10.

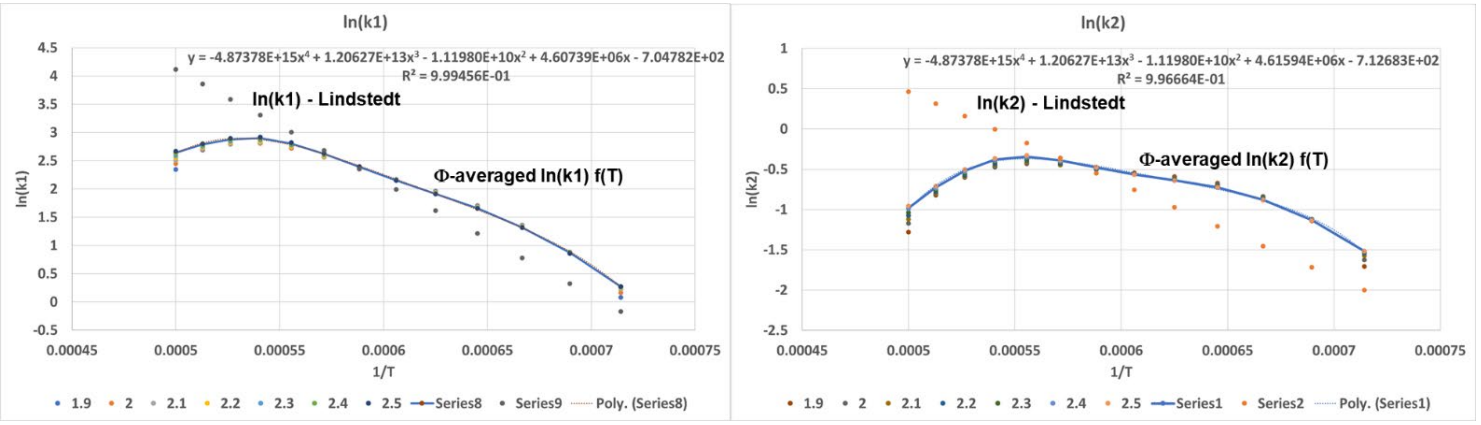
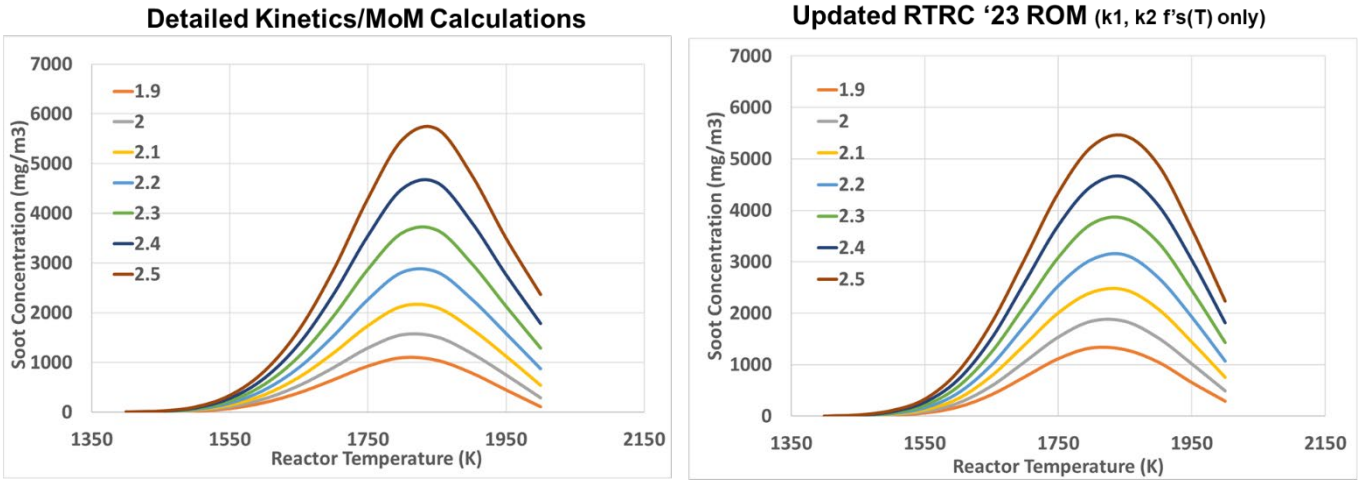


Figure 10. Fuel-air mixture averaged kinetic rate expressions for nucleation (Left) and surface growth (Right) for use in the PM-ROM Tool.

With this new temperature only rate expression, the soot concentration outputs associated with the PSR simulations were then computed and compared against the original detailed chemistry/MOM calculations. This comparison is shown in Figure 11. As can be seen in Figure 11, there is a slight decrease and slight increase in the fuel rich and lean, respectively, conditions, but overall, the concentration values are in good agreement with the detailed data.



PSR Settings: Jet-A/Air, P: 5.8 atm, τ_{res}: ~5 msec, Φ: 1.9-2.5, Air Inlet T: 600 K, Reactor Temp's: 1400-2000 K

Figure 11. Comparison of soot concentrations generated from the two modeling approaches listed at nominal rich-burn quick-mix lean-burn (RQL) combustor conditions. MOM: Method of Moments, PSR: perfectly stirred reactor, PM-ROM: RTRC: Raytheon Technologies Research Center.

Major Accomplishments

- Developed a detailed jet-fuel kinetic mechanism (210 species) and delivered to GT.
- Formulated a two-equation, four-step PM-ROM soot model as an improvement over the Lindstedt model, enabling closer agreement with detailed MOM-based predictions.



Publications
None.

Outreach Efforts
None.

Awards
None.

Student Involvement
None.

Plans for Next Period
None.

Task 2 – Nucleation Modeling
University of Michigan

Objective
The objective of this task is to develop models for nanoparticle inception, a critical step in predicting emissions. This effort bridges the work on gas-phase chemistry (RTRC) with the model for particle growth (RTRC) and provides inputs for the moment model (GT) and growth models (RTRC) using atomistic simulations.

Milestone(s)
- Developed a reduced nanoparticle inception model based on dimerization of PAH species.

Research Approach
Current models for particle inception are unable to reproduce a variety of experimental data, including molecular structure. This work aims at developing a predictive model for particle inception that can provide accurate chemical and physical growth pathways for PAHs. Molecular dynamics simulations are used to study the collisions of PAHs and the formation of aromatic dimers leading to soot inception. These atomistic simulations coupled with advanced sampling techniques are used to study the collisions of PAHs.

Free energy calculations provide information on the effect of chemical structure and shape on the tendency to form nuclei. After collaboration with RTRC, PAHs that are critical to inception are identified. A pool of aromatic compounds such as pyrene, benzopyrene, coronene, ovalene, circumcoronene are selected. Initially, some preliminary studies for free energy calculations are conducted at temperatures of 500K and 1,000K. As can be seen from Figure 12, at lower temperatures all PAHs seem to be forming dimers even though it is more favorable for higher PAHs to form a dimer. However, at higher temperature of 1,000K (typical of flame temperature conditions), only higher PAHs have tendency to form dimers. This suggests nucleation model from traditional pyrene precursors fails to participate in the actual soot inception processes.

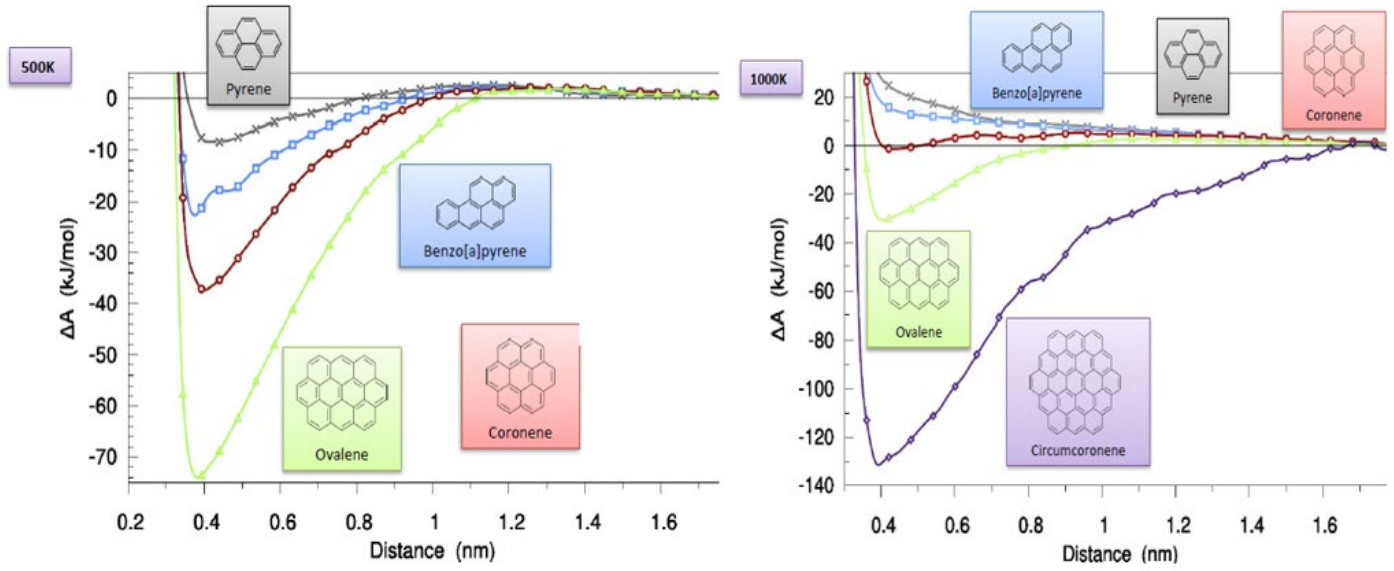


Figure 12. Free Energy calculations of polycyclic aromatic hydrocarbons (PAHs) as function of temperature.

The initial pool of PAH species is later extended to include atomistic simulations of higher PAH species that also include oxygen. Figure 13 shows the structures of gas-phase compounds considered in this study and the results for their homo-dimerization propensity. The data points are broadly clustered in three groups. The first, composed of compounds I.C (462 u), I.D (462 u), and I.E (460 u), which have the same mass and O/C ratios (0.125), and are less stable than I.A (448 u) and I.B (472 u), which constitute the second group. This difference indicates that the presence of oxygen slightly destabilizes the dimers, an effect possibly caused by the increased repulsive electrostatic interactions of oxygenated molecules compared to pure aromatic hydrocarbons. The third group is formed by I.F (402 u), I.G (452 u), and I.H (502 u), which are less likely to dimerize than the other two groups. The low dimer stability of the third group can be due to the presence of a sigma bond, which introduces an internal rotatable bond that interferes with the formation of clusters. A few points can be drawn from this study. First, the details of the structure of the species that nucleate cannot be ignored. It has been suggested that the mounting evidence of the presence of five-membered rings, aliphatic side chains, and oxygenated groups in soot precursors, does not change the nucleation mechanism that leads to soot formation. Our results, both pertaining to the dimerization propensity and the change in free energy barriers between monomers and dimers, which directly relates to the kinetic rates of dimerization, show otherwise. Second, the effects of shape, presence of oxygen, mass, and rotatable bonds are tightly intertwined, and have different importance as well as diverse temperature dependencies, although, they are all dominated by entropic effects at high temperatures. The presence of oxygen affects the dimer propensity, by reducing the molecular cohesion due to electrostatic repulsion although, it should be noted that the force field employed in this study cannot capture the effect of molecular polarizability.

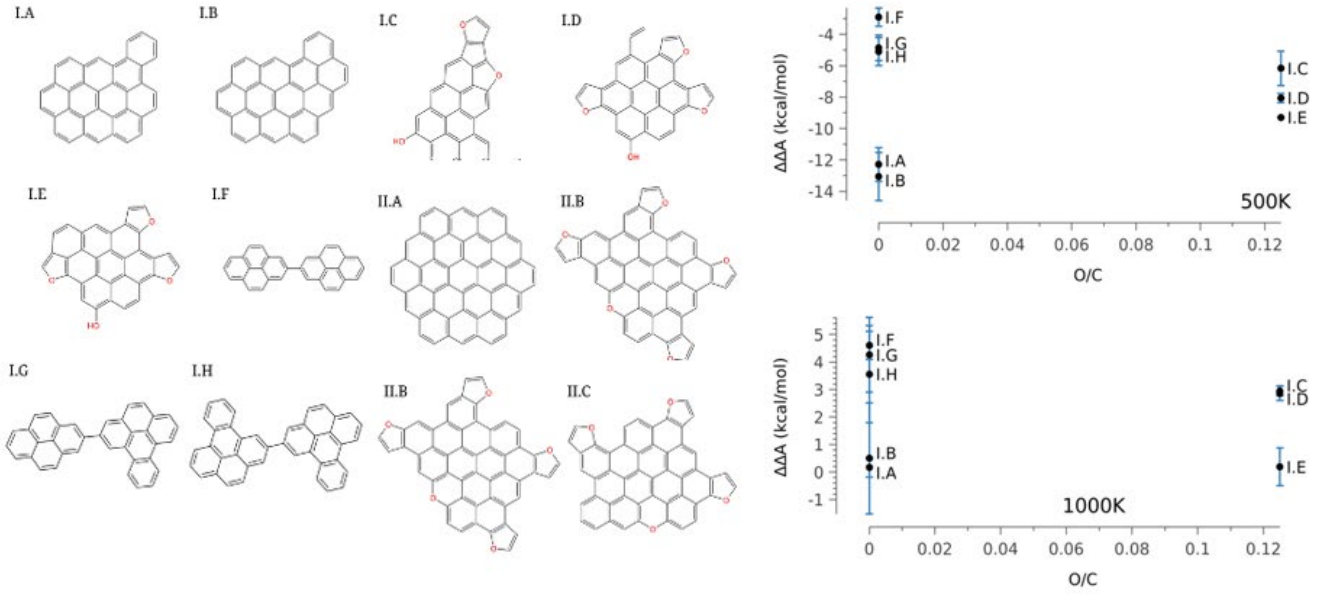


Figure 13. Structural formula of gas-phase compounds (left) and homo-dimerization propensity at 500K and 1,000K as a function of their oxygen/carbon ratio.

In the next task, we focused on machine learning algorithms with the goal of leveraging this technique to predict dimerization propensity of various polycyclic aromatic compounds (PAC). While molecular dynamics simulations can provide this information for specific dimer pairs, it is not feasible to extend this to all potential dimer components. With millions of different PACs observed in even simple flames, it is too costly to compute this information for all possible PACs, especially when accounting for the combinations of hetero dimerization between different PAC molecules. Recently, machine learning has shown potential to learn complex quantitative relationships between PAC properties and predict the energy difference between the monomer and dimer state for an arbitrary pair of PACs with minimal computational cost. However, the approach only considered thermodynamic energy differences at a single temperature and therefore is insufficient to predict the energy barriers needed to derive kinetic rates.

As a first step, we perform numerous Meta dynamics molecular dynamics simulations to calculate the dimer energy barrier for a large dataset of PACs at multiple temperatures. This value is critical in characterizing the kinetic stability of the PAC dimer, and in conjunction with equilibrium data can provide a comprehensive description of forward and reverse barriers and rates in the dimerization process. Molecular dynamics simulations enhanced by Meta dynamics were used to reproduce the free energy landscape of the dimerization process as a function of the center-of-mass (COM) distance. To define the chemical space, a wide set of PACs was considered, as reported in the last report, which broadly reproduces the sizes, shapes, and functional groups observed in flame systems. In order to describe PAC chemistry, we compute a set of 312 descriptors for each molecule. These descriptors capture properties such as mass, atomic ratios such as carbon-hydrogen ratio, and counts of specific subgroups such as aromatic rings. From our simulations, we obtain 315 unique energy barriers between the monomer and dimer states. Generally, we observe the same qualitative relationships with size and temperature. All else being equal, free energy barriers tend to increase with mass as Van der Waal's and electrostatic interactions become stronger and decrease with temperature as entropic effects increase in importance. It is important to note, however, that these two parameters are insufficient to describe all differences observed in the energy barrier and a quantitative trend cannot accurately be derived solely from these two values. Different machine learning (ML) algorithms were explored while still running molecular dynamic simulations. Figure 14 below shows our target ML algorithm.

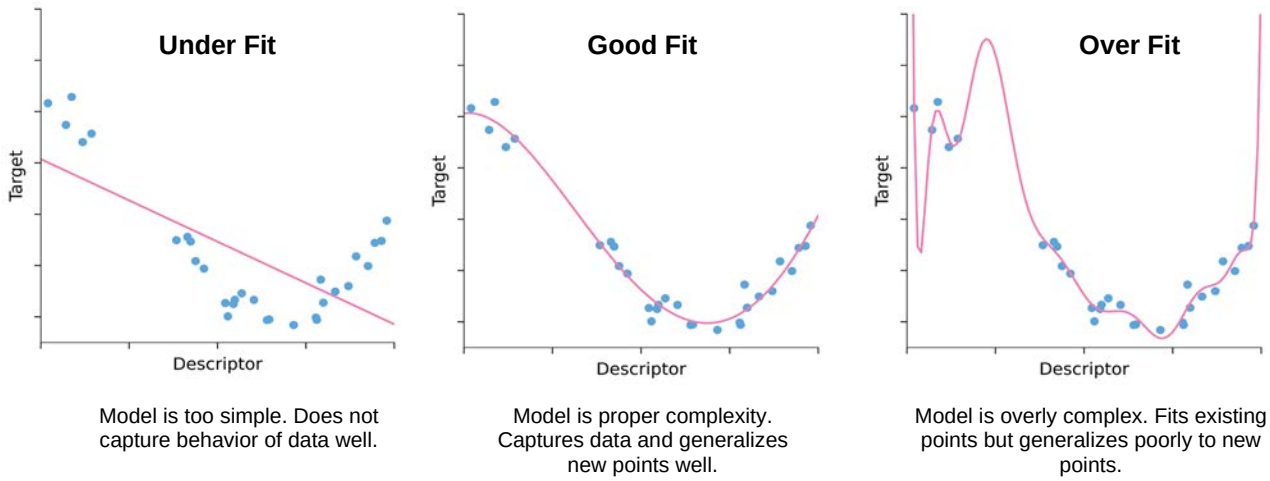


Figure 14. Evaluation of machine learning algorithms.

In order to analyze the complex space, we resort to machine learning with good fit models. Before training our machine learning model, we eliminated similar features by removing any feature with a variance of zero and any feature with a Pearson correlation greater than 0.95. To build a predictive model for the formation efficiency (FE) of aggregation, we applied the Lasso method as it allows for high accuracy and often interpretable predictions. Lasso is a supervised machine learning regression model that minimizes a loss function. It uses the least absolute shrinkage and selection operator, has been applied successfully to make interpretable pre-dictions in chemical problems as it eliminates extraneous features and only selects a smaller sub-set of properties needed to make predictions.

Our model outperforms existing physical dimerization models present in the literature. We compared our results, including the test on a restricted dataset with no data leakage, with three additional models. One advantage of Lasso is its ability to provide a degree of interpretability towards the aspects that control prediction, as it sets coefficients of unused features to zero. Thus, by analyzing which features the Lasso model retains, we can gain a sense of which molecular properties are important for predicting the FE of dimer aggregation. Of note, while some of the molecular properties discussed below resemble quantities that have been used in the past to predict the aggregation propensity, they are not generally interchangeable with those found in literature. Overall, across all 105 folds of cross validations, the model selects a nearly identical set of 10 features. If we exclude these top features, no other feature is selected in more than four folds and as such we will not discuss them. Broadly, the top features can be divided into three groups of properties that are important for PAC dimerization: size, shape, and presence of specific chemical groups.

The first class of properties are extrinsic properties that are broadly related to the size of the molecule. Specifically, the algorithm selected the number of aromatic rings, the number of carbons not connected to a hydrogen, the number of tessellations containing four carbons, the number of tessellations with three carbons and a hydrogen, and the number of six-membered rings. Figure 15 below shows that the FE of dimerization is strongly related to the (harmonic) average number of aromatic rings in the dimer (Pearson coefficient of −0.8397 and Spearman coefficient of 0.8719). This result agrees with the general observation that PACs will often cluster in lateral stacks, and the interaction strength between PACs is closely related to their number of aromatic rings. Among the molecular descriptors in this class, the number of aromatic rings is the feature that has the highest correlation with the FE (more than the number of six membered rings, for example), but it is crucial to note that, by itself, it is not sufficient to fully capture the physical dimerization. A linear fit of the FE as a function of the total number of aromatic rings produces predictions model with a root mean square error (RMSE) of 15.6 kJ mol−1 and a mean absolute error (MAE) of 11.3 kJ mol−1, which has a significantly larger error than our model and is (not coincidentally) comparable to using only the mass as a descriptor. Some features in this group encode size with molecular shape information. One such example is the number of internal carbon atoms, defined as the aromatic carbon atoms that are not bonded to H atoms. As most of the molecules in the dataset are highly peri condensed hydrocarbons, these PACs will have a greater percentage of internal carbons than catacondensed PACs.

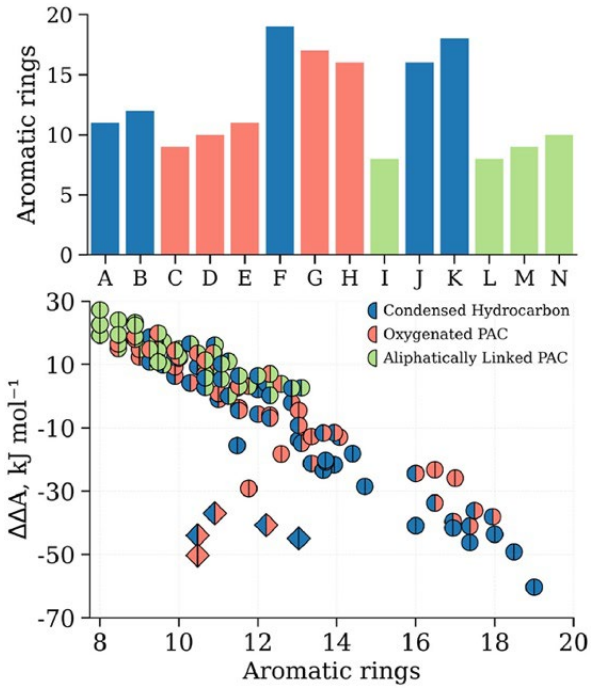


Figure 15. Relationship between the number of aromatic rings and dimerization FE. Top: Number of aromatic rings associated with each dimer. Bottom: Aggregation propensity compared to average number of aromatic rings in the dimer. PAC: polycyclic aromatic compound.

The success of such ML-based predictions in predicting free-energy barriers (ΔA) is shown in Figure 16. Moreover, Lasso regularization in the ML model helped us to extract critical features of importance by providing valuable insights regarding their influence on the dimerization ability of PAHs. Detailed discussions regarding these results were already provided in our previous annual efforts and hence are not repeated here for brevity.

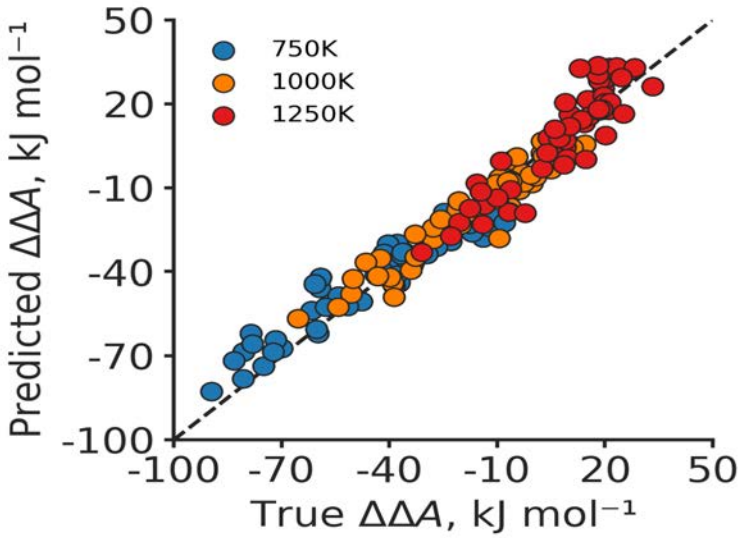


Figure 16. ML-assisted free-energy barrier analysis across a range of conditions.



In recent efforts, we closely collaborated with RTRC kinetics to identify PAH species available in the gas phase mechanism. A reduced nanoparticle inception model was then developed using our framework. The model used information on the PAH species benzopyrene (A_4R_5). The optimized rate constant can be approximated as shown in Equation 1.

$$k_f \left(\frac{L}{mol.s}\right) = \text{A T exp -} \left(\frac{G_f}{RT}\right) \quad \text{(Eq. 1)}$$

In this equation, the preexponential factor (A) is obtained as 2.0837×10^{10} 1/K/s, whereas the activation free energy is computed as

$$G_f \text{ (kJ/mol)} = g_o + g_1 T + g_2 T^2 \quad \text{(Eq. 2)}$$

g_o, g_1, and g_2 are the constants with respective uncertainty as noted below.

$$\begin{aligned} g_o &= \text{-4.12147} \quad \text{+/- 0.4233} \quad (10.27\%) \\ g_1 &= 0.101723 \quad \text{+/- 0.001069} \quad (1.051\%) \\ g_2 &= \text{5.55181e-06 +/- 5.515e-07} \quad (9.935\%) \end{aligned} \quad \text{(Eq. 3)}$$

Finally, this information is provided to the models described in Task 3 for MC simulations of post-inception growth as well as the nucleation rate expression in the moment-based soot model at GT.

Major Accomplishments

- Established a machine-learning-enabled MD framework, providing a reusable approach for future studies involving fuel-chemistry-dependent soot formation under relevant flame conditions.
- Developed a reduced nanoparticle inception model based on benzopyrene (A_4R_5) for coupling with both MC simulations and the moment-based soot model at GT for RQL combustor-relevant conditions.

Publications

Peer-Reviewed Journal Publications

Baranwal, M., Saldinger, J. C., Kim, D., Elvati, P., Hero, A. O., & Violi, A. (2024). SPIN: A data-driven model to reduce large chemical reaction networks. *Fuel*, *367*, 131299.

Di Liddo, L., Saldinger, J. C., Jadidi, M., Elvati, P., Violi, A., & Dworkin, S. B. (2022). Exploring soot inception rate with stochastic modelling and machine learning. *Combustion & Flame, 258,* 112375.

He, T., Kim, D., Dillstrom, T., Cai, K., Zhang, P., Liu, C., He, X., Wang, Z. & Violi, A. (2021). Oxidation of 2,6-dimethylheptane at low temperature: Kinetic modeling and experimental study. *Fuel*, 287, 119220.

Kim, D., & Violi, A. (2021). On the importance of species selection for the formulation of fuel surrogates. *Proceedings of the Combustion Institute, 38*(4), 5615-5624.

Kim, D., & Violi, A. (2022). Uncertainty-based weight determination for surrogate optimization. *Combustion and Flame, 237*, 111850.

Saldinger, J. C., Elvati, P., & Violi, A. (2021). Stochastic and network analysis of polycyclic aromatic growth in a coflow diffusion flame. *Physical Chemistry Chemical Physics, 23*(7), 4326-4333.

Saldinger, J.C., Elvati, P., & Violi, A. (2023). A machine learning framework to predict the aggregation of polycyclic aromatic compounds. *Proceedings of the Combustion Institute*, 39(1),1009-1017.

Saldinger, J. C., Elvati, P., Alrawi, K., & Violi, A. (2024). Predicting aggregation rates of polycyclic aromatics through machine learning. *Fuel*, *364*, 131031.

Shao, C., Wang, Q., Zhang, W., Bennett, A., Li, Y., Guo, J., Im, H. G., Roberts, W. L., Violi, A. & Sarathy, S. M. (2023). Elucidating the polycyclic aromatic hydrocarbons involved in soot inception. *Communications Chemistry*, *6*(1), 223.

Shi, X., Wang, Q., & Violi, A. (2021). Reaction pathways for the formation of five-membered rings onto polyaromatic hydrocarbon framework. *Fuel*, 283, 119023.

Wang, Q., Saldinger, J. C., Elvati, P., & Violi, A. (2021). Molecular structures in flames: A comparison between SNapS2 and recent AFM results. *Proceedings of the Combustion Institute, 38*(1), 1133-1141.

Outreach Efforts

None.

Awards
None.

Student Involvement
One PhD student, J. Saldinger, contributed to this work.

Plans for Next Period
None.

Task 3 – Surface Growth and Aggregation Modeling
Raytheon Technologies Research Center

Objective
The objective of this task is to develop a physics-based framework for the prediction of soot particle growth after the inception process. The growth consists of agglomeration due to collisions between the primary particles and surface growth as a result of direct deposition of the precursors on the aggregate. The final aggregate fractal structure and its temporal evolution as a function of local conditions are of interest. This model provides the morphology characteristics of soot aggregates.

Milestone(s)
- Formulate a one-way coupled methodology to study fractal growth of soot particles along the conditions inside the combustor.

Research Approach
Soot particles from nucleation stages undergo various surface growth processes and form primary particles. These primary particles are spherical in nature and typically formed in the diameter range of 1-10 nm. The studies conducted under this effort will bridge the gap between formation of primary particles and their transformation into fractal aggregates through processes of surface growth and aggregation. Experimentally it is witnessed that structures of these soot particles are dependent on the local conditions (e.g., φ). These surface growth processes can occur because of heterogenous reactions of gas-phase precursors on solid soot particle surfaces (reaction limited growth) or through transport of soot precursors in high-speed flames (transport limited growth). Majority of growth models only account for reaction limited growth, ignore transport limited growth as well as cluster-cluster interactions which are important in aggregate formation. In this work, information on background gas-phase species contributing to soot particles (Kinetics RTRC) and the structure of initial soot nuclei (MD studies from Michigan) and the local conditions (Pressure, Temperature, equivalence ratio, diffusion of precursors) is merged to understand the fundamental processes contributing to formation of large soot aggregates. The transport limited growth is modelled through phase-field formulation.

At first, a blended model for transition from reaction limited growth to transport limited growth is achieved. As shown in Figure 17, the current model can predict the transition from fractal shape to spherical morphology of soot particles with increasing equivalence ratio. Anisotropy of aggregates and their fractal dimensions are two important factors that determine the shape of soot aggregates formed. The sensitivity of these aggregates with background equivalence ratio and the primary particle number density after nucleation is studied.

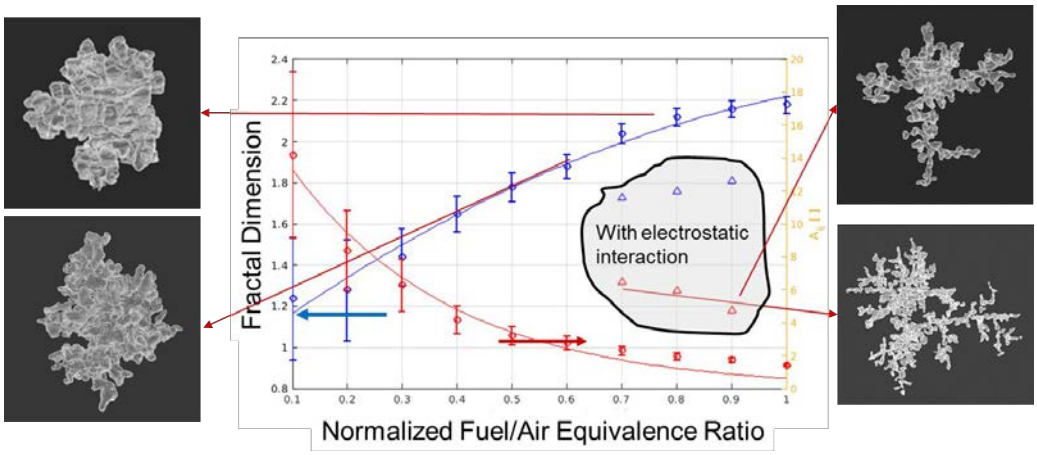


Figure 17. Phase field simulations to predict the aggregate structures.

The coupling between the growth framework being developed at RTRC with MD simulations from UM and the LES study at GT is briefly highlighted in Figure 18. The growth module takes the number density and size distribution of incipient soot particles from nucleation as an input and tracks the growth of such particles along the statistically averaged path lines, which have varying background LES conditions in form of temperature (*T*), pressure (*P*) and local equivalence ratio (ϕ), as detailed below. The output from such studies in the form of the parametrized fractal dimension (D_f) will be fed back into the LES-method of moment soot approach.

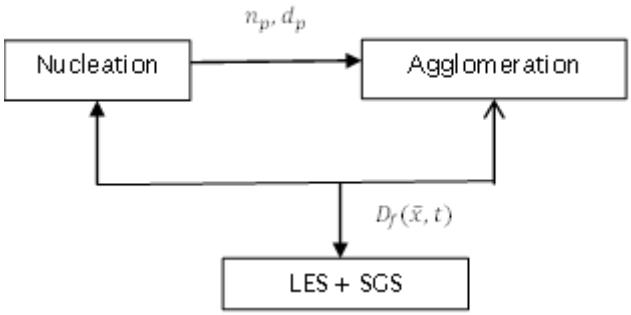


Figure 18. Post-inception growth of soot particles (LES-RTRC-UM coupling). LES: large eddy simulation, SGS: subgrid-scale.

The developed post-inception growth model described in previous annual effort has shown to capture the effect of different operating conditions on the growth characteristics of the particles, including size and morphology. The parametric exercise of this model, however, could become computationally prohibitive if one is to sweep over a range of operating parameters and combinations therein. A path line-sampling approach was proposed (schematic in Figure 19) where the full flow-field (obtained by the LES) is represented through statically sampled path lines over which the operating conditions would be time-variant. For example, the temperature and fuel/air ratio would evolve over the course of time as a particle moves from the injector towards the exit of the combustor. This time-history is then provided to the growth model where the variation of particle characteristics will be solved over the course of this timeframe for each individual path-line histogram (example output shown in Figure 20). This information can then be fed back into the LES with time-space mapping through the path line coordinates and nearest-point interpolation to provide full spatial representation of growth information which is then used in the moment soot approach. This approach effectively reduces the computational overhead of the growth model to a dozen simulations (assuming that this number of path lines is sufficient to properly sample the combustor flow field) compared to potentially hundreds in the conventional parametric approach. One should note that this is considered a one-way coupling approach where it is assumed that the macroscopic changes in the flow-

field due to the interaction with the soot-particle transport have negligible impact on the growth characteristics of the particles.

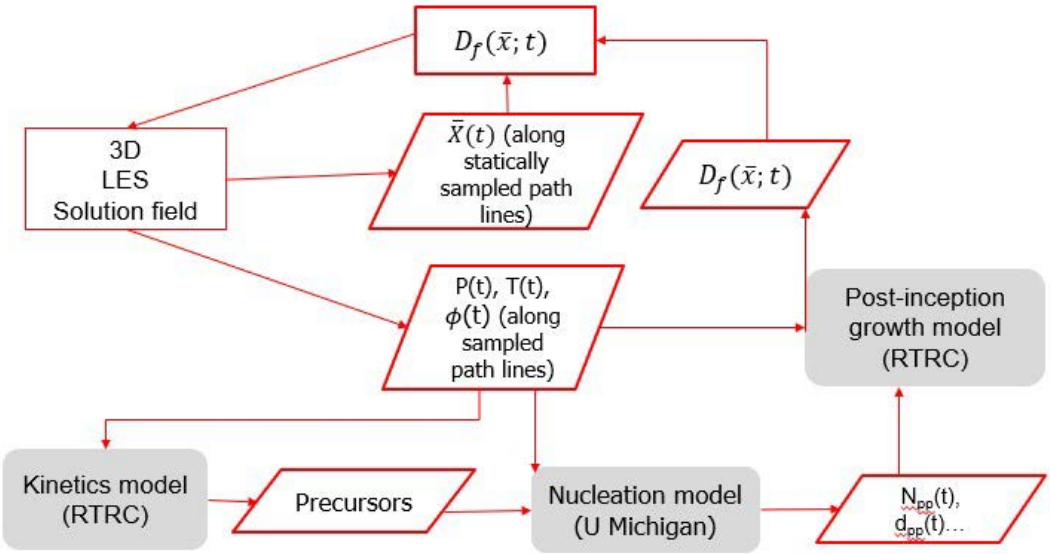


Figure 19. One way coupled strategy for growth of soot particles. LES: large eddy simulation, RTRC: Raytheon Technologies Research Center.

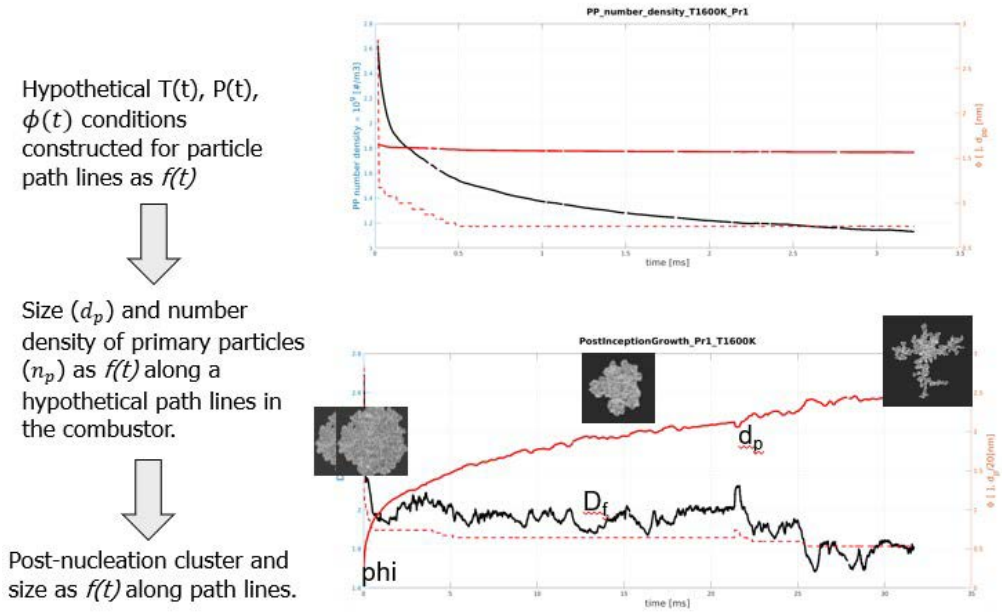


Figure 20. Demonstration of one-way coupled strategy along hypothetical large eddy simulation (LES) path-line.



To establish this methodology, the post inception growth modeling framework and the coupling therein to the LES framework is demonstrated for the solution of National Aeronautics and Space Administration (NASA)-LDI geometry for which LES solution was obtained from GT. The information along statistically sampled path lines is provided to the post-inception model which then solves the evolution of the soot clusters along those path lines. In order to get a sense of primary particle size and number density, a classical nucleation theory was used which takes the following form.

$$N_0(t) = [M(t)] \exp\left(-\frac{\Delta G_0(t)}{kT}\right) \quad \text{(Eq. 4)}$$

It is worth noting that this formulation or terms therein is eventually replaced by the solution of the molecular dynamics simulation. An example of primary particle number density along one of the path lines in the rig is shown in Figure 21. Figure 22 shows the evolution of soot particle characteristics (fractal dimension and average size) along two of the path lines inside the combustor.

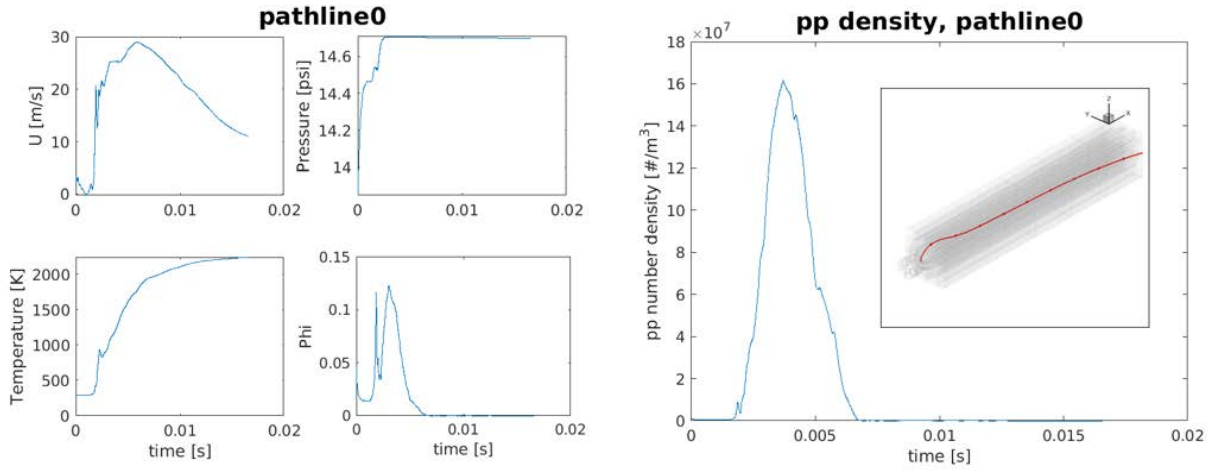


Figure 21. Variation of flow parameters along one path line in the combustor (left) and calculated primary particle number density using classical nucleation theory (right).

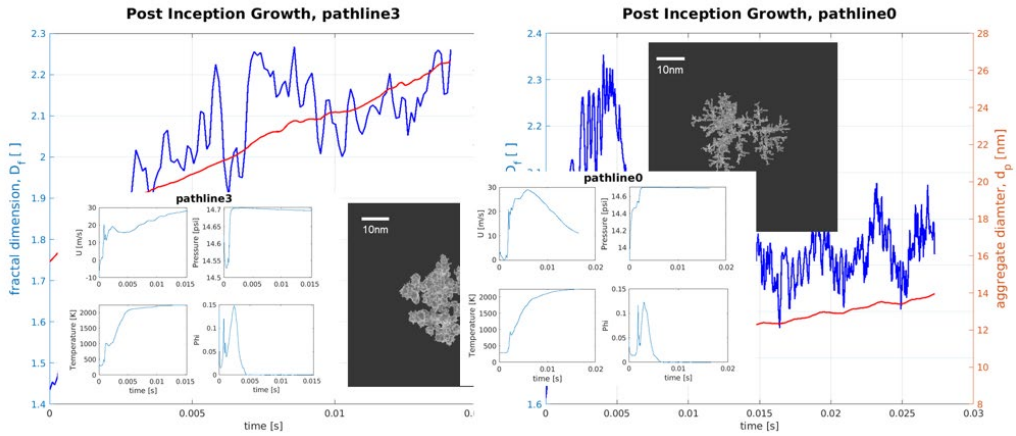


Figure 22. Evolution of soot particle characteristics along two path lines within the lean direct injection (LDI) combustor.

The demonstration along with the NASA LDI combustor provided confidence to use the framework for RQL combustor as highlighted in Figure 23.

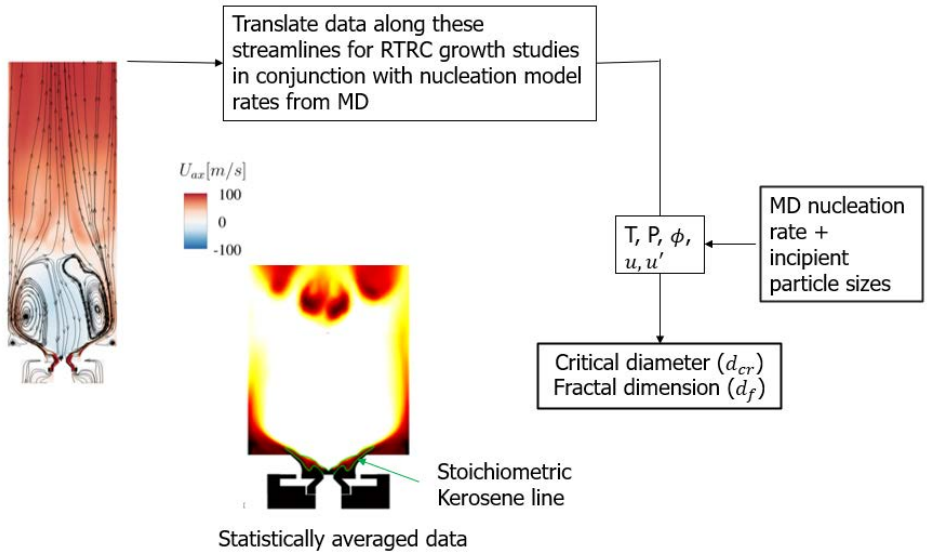


Figure 23. One-way coupled data along the rich-burn quick-mix lean-burn (RQL) computational fluid dynamics (CFD) Streamlines. MD: molecular dynamics, RTRC: Raytheon Technologies Research Center.

A parametric graph was generated to understand variation of fractal dimension (D_f) as a function of local mixture stoichiometry and the temperature conditions at different residence time available for soot particles to grow (see Figure 24). This coarse information was provided to GT in order to investigate its effects on the global soot output from moment models.

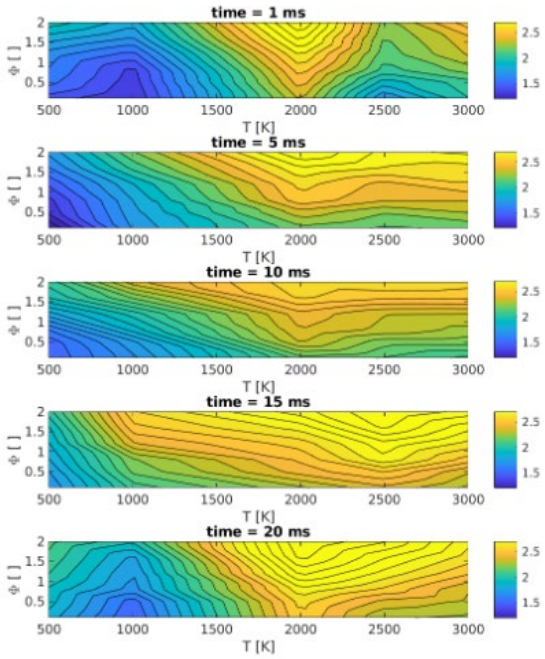


Figure 24. Fractal dimension as a function of parametric background conditions in rich-burn quick-mix lean-burn (RQL).

Major Accomplishments

Established one-way coupled methodology to study fractal growth of soot particles along the conditions inside the combustor.

Publications

None.

Task 4 – Large-Eddy Simulation

Georgia Institute of Technology

Objective

The objective of this task is to establish the soot modeling capabilities, use it within a physics-informed LES framework to model soot formation in turbulent reacting configurations, focusing on both canonical and complex settings, and eventually couple the inputs from Task 1-3 in the soot model to demonstrate the framework's ability and sensitivity to predict soot formation in a spray combustor of practical relevance.

Milestone(s)

- Develop and establish an LES–MOM methodology for sooting simulations of canonical and complex flames.
- Integrate components developed in Tasks 1–3 into the MOM soot framework and evaluate their relative impact against the baseline model.

Research Approach

LES studies of turbulent sooting problems are challenging because of the multiscale nature of soot inception, coagulation, and surface growth that must be modeled in a highly turbulent and reactive environment, typically in a complex combustor. Most prior studies have focused on global models that approximate small-scale physics. Consequently, many available models account for the underlying physics. In contrast, simulations require some approximations, because the computational resources will never meet the simulation requirements. In the current effort, we balance contributing to the



prediction of soot formation physics in a realistic gas turbine combustor with the need to obtain high-fidelity, reliable predictions by using advanced models. To achieve this goal, we leverage our past LES capability with baseline soot models. The original method of moments with interpolative closure (MOMIC) model (Frenklach, 2002) is also reapproximated to three-equation moment-based model (Nmira et al., 2023) to account for the key components of aggregate formation. The capabilities of implemented framework within LES are demonstrated in a range of canonical and complex sooting flames. Additionally, a multiscale LEM based strategy is established to upscale the small-scale soot processes towards the resolved LES scales and demonstrated in a 1D turbulent premixed flame simulation. However, coupling all these inputs in a fully resolved LES is computationally prohibitive especially in the final RQL spray sooting flame simulation, and hence a reduced order modeling approach based on reactor network modeling is utilized to compare the predictive capabilities of the model components assembled through Task 1- Task 3.

4.1 Modeling Framework

The full set of compressible reacting multispecies Navier–Stokes equations cannot be solved directly, because a direct numerical simulation is not feasible for practical applications. For LES, the large-scale flow features are resolved, and subgrid modeling is used for the smaller scales. The LES governing equations for a reacting sooting spray flame are obtained by filtering the compressible form of Navier-Stokes equations using a low-pass filter with a cut-off length equal to the grid size (Δ).

$$
\begin{aligned}
&\frac{\partial \bar{\rho}}{\partial t} + \frac{\partial}{\partial x_i}(\bar{\rho}\,\tilde{u_\iota}) = \tilde{\dot{\rho}_s} \\
&\frac{\partial}{\partial t}(\bar{\rho}\,\tilde{u_\iota}) + \frac{\partial}{\partial x_j}\left(\bar{\rho}\,\tilde{u_\iota}\,\tilde{u_j} + \bar{P}\,\delta_{ij} - \overline{\tau_{\iota j}} + \tau_{ij}^{sgs}\right) = \widetilde{F_{s,\iota}} \\
&\qquad\qquad \frac{\partial}{\partial t}\left(\bar{\rho}\,\tilde{E}\right) + \frac{\partial}{\partial x_j}\left[\left(\bar{\rho}\,\tilde{E} + \bar{P}\right)\tilde{u_\iota} + \bar{q_\iota} - \tilde{u_j}\,\overline{\tau_{\iota j}} + H_i^{sgs} + \sigma_i^{sgs}\right] = \widetilde{\dot{Q}_s} + \widetilde{\dot{Q}_R} \\
&\frac{\partial}{\partial t}\left(\bar{\rho}\,\widetilde{Y_k}\right) + \frac{\partial}{\partial x_j}\left[\bar{\rho}\,\widetilde{Y_k}\,\tilde{u_j} - \bar{\rho}\,\overline{D_k}\,\frac{\partial \widetilde{Y_k}}{\partial x_j} + \Phi_{j,k}^{sgs} + \Theta_{jk}^{sgs}\right] = \bar{\rho}\,\widetilde{\dot{w}_k} + \widetilde{\dot{S}_{s,k}} \\
&\qquad \frac{\partial}{\partial t}\left(\bar{\rho}\,\tilde{Y}_{soot}\right) + \frac{\partial}{\partial x_j}\left[\bar{\rho}\,\tilde{Y}_{soot}\,\tilde{u_j} - \bar{\rho}\,\overline{D}_{soot}\,\frac{\partial\,\tilde{Y}_{soot}}{\partial x_j} + \widetilde{V_T}_{soot}\,\tilde{Y}_{soot} + \Phi_{j,k,soot}^{sgs} + \Theta_{jk,soot}^{sgs}\right] = \bar{\rho}\,\tilde{\dot{w}}_{soot} \\
&\qquad\qquad \frac{\partial}{\partial t}\left(\bar{\rho}\,\widetilde{M_k}\right) + \frac{\partial}{\partial x_j}\left[\bar{\rho}\,\widetilde{M_k}\,\tilde{u_j} - \bar{\rho}\,\overline{D}_{soot}\,\frac{\partial\,\widetilde{M_k}}{\partial x_j} + \widetilde{V_T}\,\widetilde{M_k} + \Psi_{j,k}^{sgs} + \Omega_{j,k}^{sgs}\right] = \bar{\rho}\,\tilde{\dot{M}}_k \\
&\frac{\partial}{\partial t}\left(\bar{\rho} k^{sgs}\right) + \frac{\partial}{\partial x_i}\left(\bar{\rho}\,\tilde{u}_i k^{sgs}\right) = -\tau_{ij}^{sgs}\frac{\partial\,\tilde{u}_i}{\partial x_j} - C_\epsilon\,\bar{\rho}\,\frac{k^{sgs\frac{3}{2}}}{\bar{\Delta}} + \frac{\partial}{\partial x_i}\left(\frac{\bar{\rho}\nu_T}{\mathrm{Pr}}\frac{\partial k^{sgs}}{\partial x_i}\right)
\end{aligned}
\qquad \text{(Eq. 5)}
$$

In the above equations, $\bar{\rho}$ is the filtered mass density, $\tilde{u}_i$ is the filtered velocity vector, $\bar{p}$ is the filtered pressure determined from the equation of state, $\overline{\tau_{ij}}$ is the filtered viscous stress, $\tilde{E}$ is the resolved energy per unit mass, $\bar{q}_i$ is the heat flux vector, $\tilde{Y}_k$, $\tilde{Y}_s$ are the gas-phase and soot mass fractions, and $\widetilde{M}_k$ is the filtered soot moment. The gas-phase governing equations contain source terms due to the Lagrangian dispersed phase ($\widetilde{\dot{\rho}_s}, \tilde{\dot{F}}_{s,i}, \widetilde{\dot{Q}_{s,\iota}}, \tilde{\dot{S}}_{s,k}$). Further information about the overall modeling can be found elsewhere (Panchal and Menon, 2022; Patel and Menon, 2008). $\widetilde{\dot{Q}_R} = \Sigma_\alpha 4\,\sigma\kappa_\alpha\left(\tilde{T}^4 - \widetilde{T_o}^4\right) + 4\,\sigma\kappa_{soot}\,\tilde{T}^4$ is the radiative heat loss term (Guo et al., 2004) in which κ_α is the Planck-mean absorption coefficient for gas-phase species $\alpha \in [CH_4, CO_2, H_2O, CO]$ and κ_{soot} is computed as $\kappa_{soot} = C_{soot}\,\tilde{f_v}\,\tilde{T}/4\sigma$, where C_{soot} is the soot radiation model constant assumed as 3.334 x 10^{-4} W/m3K5, f_v is the soot volume fraction. Contributions from subgrid radiation fluctuations in the radiative heat source terms are neglected presently. The terms $\widetilde{\dot{w}}_k$ represents the production rates of gas-phase species obtained using finite-rate chemistry approach which also includes the PAH species. The term $\widetilde{\dot{w}}_{soot}$ represents the production rate for soot consistent with the moment rate M1 (discussed later). The term D_{soot} associated with diffusion of soot is typically neglected. The thermophoretic term represented by $\tilde{V}_T$ is also neglected due to its overall lower contribution in turbulent flames.

The subgrid scale viscous stress tensor terms are modeled using local dynamic kinetic energy model (LDKM) (Menon & Kim, 1996). The subgrid enthalpy flux is modeled using eddy viscosity and a gradient assumption where turbulent Prandtl number (Pr_t) is assumed as unity. The subgrid diffusion of species is again also modeled using gradient-diffusion hypothesis with unity turbulent Schmidt number. A similar gradient-diffusion hypothesis ($\Phi_{j,k,soot}^{sgs}, \Psi_{j,k}^{sgs}$) is used for subgrid diffusion of soot scalar flux with a turbulent Schmidt number of 0.7. An additional challenge associated with turbulent combustion is the modeling of subgrid turbulence chemistry interaction terms unresolved on the LES grid. In the current



work, Partially stirred reactor based closure model is used in which the mixing time (τ_m) is calculated locally as $\tau_m = \sqrt{\tau_p \tau}_K$ where τ_p is the time scale of the largest eddy relevant for the mixing of the sub-grid and is computed as $\tau_p = \frac{\Delta}{\sqrt{2k_{sgs}/3}}$ and τ_K is the time scale relevant for the Kolmogorov length scale $\tau_K = \sqrt{\nu/\epsilon_{sgs}}$ where ϵ_{sgs} here represent the dissipation rate. Furthermore, the chemical time scale (τ_c) is computed using the laminar premixed flame thickness (δ_L) and flame speed (S_L) at stoichiometry. Once the relevant time scales are estimated, the filtered reaction source terms $\widetilde{\omega}_k$ are computed using filtered variables as $\widetilde{\omega}_k \approx \frac{\tau_m}{\tau_m+\tau_c}\, \dot{\omega}(\tilde{T}, \tilde{P}, \tilde{Y}_1.\tilde{Y}_2, \ldots., \tilde{Y}_k)$. This modeling approach has yielded satisfactory results in the past for referee rig simulations (Panchal & Menon, 2022) involving similar complexity to the current work. Modeling soot formation using LES presents additional difficulty associated with subfilter soot dynamics. In the current work, multiscale linear-eddy mixing based model is demonstrated to account for subgrid-turbulence-chemistry interactions in a 1D simulation. However, using this model within the subgrid of LES is computationally prohibitive especially for PAH-based MOM models and hence it is only demonstrated in a standalone manner. The subgrid effects are neglected for the present RQL simulations; however, they can be activated with enough computational resources. As the focus of the current work is soot modeling, the relevant formulation of baseline soot models is discussed. Figure 25 shows the key components of moment-based soot modeling.

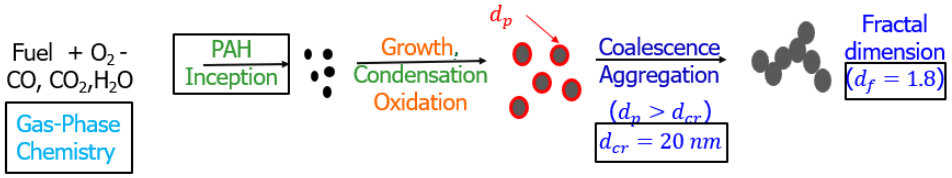


Figure 25. Key components of moment-based soot model. PAH: polyaromatic hydrocarbon.

The first component of the overall soot modeling is based on the gas-phase mechanisms that describe the oxidation of real fuel resulting in the formation of major product species such as CO_2 and H_2O along with key soot precursor species such as PAHs, C_2H_2, OH, etc. The baseline soot models employed in this work are based on MOMIC formulation (Frenklach, 2002). The MOMIC approach involves solving moment equations in two limiting conditions. In the coalescent limit where the soot particles are assumed to conserve the spherical shape after collision, the six moments are used where the equation of r-th moment M_r are solved in either the subgrid or in the resolved space along with the LES equations. A general form is $\frac{dM_r}{dt} = R_r + C_r + S_r + F_{M_r}$. r = 0,1,2,3,…,5 where M is the moment of the soot particle size distribution function (PSDF), and R, C, S, and F are respectively source terms due to nucleation, coagulation (in the coalescence limit), surface growth, and subgrid turbulent mixing contributions to the r-th moment equation. When soot particles exceed a certain size limit (dcr), the particles start to form chain-like aggregate structures of fractal dimensions (D_f = 1.8). The above equations are added with three other set of aggregate moments denoted by P_r with its own source terms, and their effects are included in the source terms of M_r i.e., aggregate rates, growth rates, coagulation rates in the non-coalescent limit resulting in total of nine moments. One key issue with these higher-order moments is that they can take very large or low exponents that can numerically explode. In such scenarios preserving the monotonicity of the original moments can become numerically cumbersome, especially important in logarithmic interpolative closures. Hence, in the present work, these nine moment formulations are converted to three moment formulation (Nmira et al., 2023), much easier to couple with CFD, where the particles are assumed to be monodisperse facilitating their numerical treatment in a more robust manner. This assumption has minor effects in comparison to other sources of chemical uncertainties on the overall predictions as discussed later. In this the zeroth moment, M_0, represents the number density (N_D) of the soot aggregates, the first moment (M_1) represents the soot mass concentration (Ycs), and the second moment represents the number density of the primary particle (N_{ps}). These moments are then later used to compute key global properties of engineering interests such as soot volume fraction ($f_v = M_1/\rho_s$), mean particle diameter $d_p = \left(\frac{6Y_{cs}}{\pi\rho_s N_{ps}}\right)^{1/3}$, mean number of primary particles per aggregate $n_p = \frac{N_{ps}}{N_D}$, and area density $A_s = \pi d_{ps}^2 N_{ps}$. The soot density ρ_s is assumed to be constant at 1,850 kg/m^3.



A brief description of kinetics models used to compute the corresponding source terms is provided here. Mainly two different soot kinetics models are available.

In the Lindstedt model (Leung et al., 1991), nucleation is assumed to occur via acetylene gas phase species. An empirical relation is used to correlate nucleation rate with acetylene concentration. A similar empirical relation is used to account for surface growth due to acetylene concentration. Oxidation is accounted for by the rate of expression involving O_2 oxidation. This kinetic model implemented within the MOMIC code and has been used within the subgrid LEM to simulate soot formation from turbulent premixed and non-premixed flames (El-Asrag et al., 2007; El-Asrag & Menon, 2009). A PM-ROM (discussed in Task 1) is an improvement in the rate coefficients of this model to better match with detailed PAH-based soot model (discussed next) and is also implemented in the modeling suite.

To account for detailed physics of soot formation processes rather than empirical relations involved in Lindstedt model, soot kinetic models that rely on PAH-inception and detailed growth pathways are also implemented. For three-dimensional (3D) LES, using detailed gas-phase kinetics with pathways for heavier PAHs till seven rings are not feasible computationally, and thus the reduced gas-phase mechanisms are considered which tracks growth of PAH formation only until naphthalene (A_2). However, higher PAH species such as pyrene (A_4), or benzopyrene (A_4R_5) can also be used in the same framework as long as they are part of reduced gas-phase chemistry. These PAH dimers are assumed to contribute to both nucleation and condensation processes. The PAH dimers resulting in nucleation are assumed to have a sticking efficiency γ_{PAH} and can be provided as an input to the code. Surface growth and oxidation reactions are assumed to occur using H-abstraction-C-addition mechanism. Soot particles are assumed to grow spherically until they reach a critical primary particle diameter (d_{cr}) of 10 nm beyond which they begin to form aggregates with a fractal dimension (D_f) of 1.8. Coagulation of soot particles is modeled across all three regimes free molecular, transitional, and continuum. Both the d_{cr} and D_f are provided as an input option to these models such that they can be changed following the aggregation characteristics obtained through MC studies in Task 3.

4.2 Verification and Sensitivity of Standalone Soot Models

Comparison of Zero-Dimensional (0D) PSR Simulation Framework

In these test cases, the soot models developed in the present work are evaluated using numerical simulations of 0D PSR configurations, for which reference data are available (Brown et al., 1998) using the MOMIC approach (see Figure 26). The operating conditions correspond to an ethylene–air premixed mixture at equivalence ratio ϕ = 2.5, temperatures ranging from 1,500–2,000K, and a reactor residence time of 8.5 ms. Three different soot kinetics models are investigated: (1) the MOMIC approach with Leung and Lindstedt (LL) soot kinetics (Leung et al., 1991), (2) the MOMIC model with PAH-based soot kinetics, and (3) a monodisperse (MONO) formulation of MOMIC. A detailed 99-species Wang–Frenklach ethylene–air mechanism (Wang & Frenklach, 1997) is employed to account for PAH formation pathways up to pyrene, and soot inception is assumed to occur via pyrene dimerization.

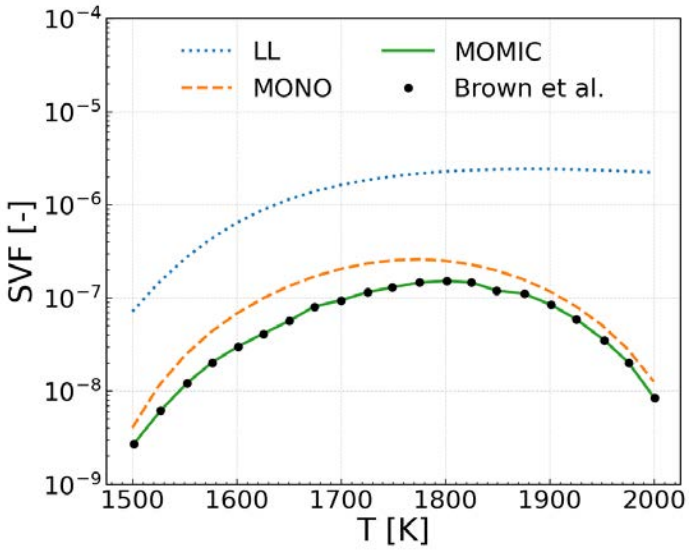


Figure 26. Comparison of the present soot models with zero-dimensional (0D) perfectly stirred reactor (PSR) simulations (Brown et al., 1998). LL: Leung and Lindstedt, MONO: monodisperse, MOMIC: method of moments with interpolative closure.

The LL-based MOMIC model fails to capture the characteristic bell-shaped dependence of soot volume fraction on temperature within the studied range, and it overpredicts soot levels by approximately an order of magnitude compared to the baseline MOMIC–PAH model. The reformulated monodisperse model closely matches the baseline MOMIC results, with only minimal deviations arising from the assumption of Monodispersity, whereas the MOMIC model successfully reproduces the reported data.

Sensitivity of Soot Modeling Components Using International Sooting Flame Workshop Data

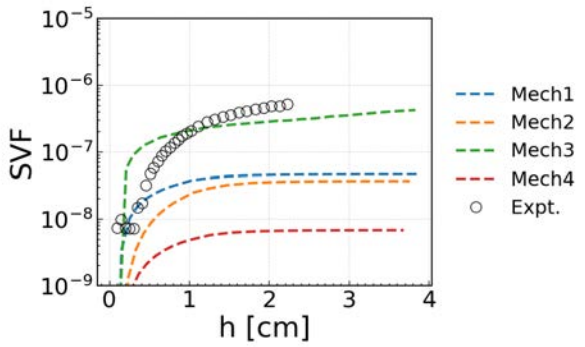
As noted earlier in Figure 25, soot modeling is highly sensitive to several key components, including the underlying gas-phase chemistry, nucleation pathways, and post-inception aggregation processes. In this section, burner-stabilized laminar premixed ethylene–air flames at $\phi = 2.33$ are used to assess the sensitivity of the soot model to these components. Experimental data are obtained from the International Sooting Flame Workshop (Menon et al., 2007). The experimentally measured temperature profiles are directly imposed in Cantera[1] during simulations; thus, radiative heat-loss modeling is not required. For these assessments, the monodisperse version of the soot model is employed, and only one modeling component is varied at a time to systematically isolate its effect. To reiterate, the baseline soot model uses a three-moment formulation with pyrene-based nucleation, hydrogen-abstraction-C_2H_2-addition (HACA)-based surface growth and oxidation, and coalescent coagulation followed by aggregate formation once the primary particle diameter exceeds a critical value of 27.5 nm.

First, the influence of gas-phase chemistry is examined using four well-established kinetic mechanisms from literature. While the soot predictions obtained using the Slavinskaya mechanism (Slavinskaya & Frank, 2009) appear encouraging, the intent here is not to evaluate the absolute accuracy of each mechanism, but to quantify the relative variation in soot levels arising from changes in gas-phase chemistry. These variations strongly affect the predicted pyrene concentrations—the assumed soot precursor in this model (also emphasized in Task 1)—and lead to order-of-magnitude differences in soot volume fraction, as shown in Figure 27a.

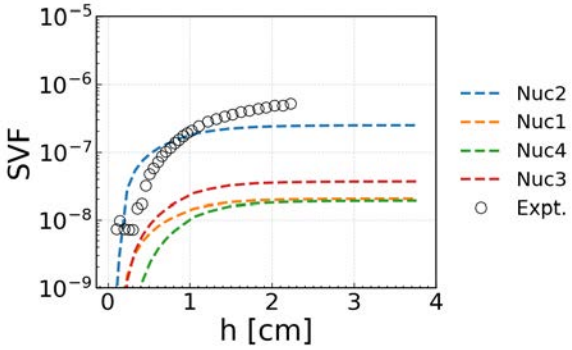
The effect of nucleation modeling is evaluated while keeping the gas-phase mechanism Caltech mechanism [also inferred as robust mechanism in RTRC Task 1 activities] and other soot sub-models fixed. The simplest nucleation approach uses

[1] Cantera is an open-source suite of tools for problems involving chemical kinetics, thermodynamics, and transport processes. Cantera is a sponsored project of NumFOCUS®, a 501(c) nonprofit charity in the United States. NumFOCUS is a registered trademark of NumFOCUS, Inc., Austin, Texas.

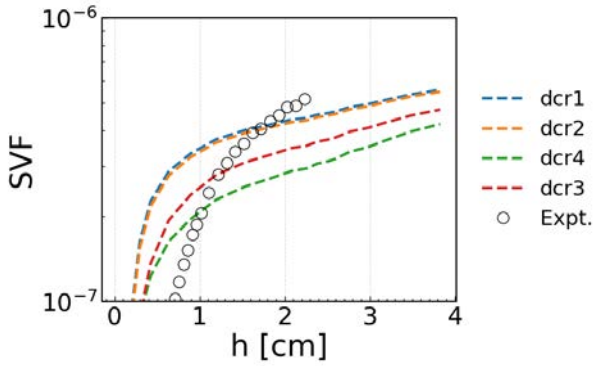
the semi-empirical acetylene-based expression of Leung and Lindstedt, whereas the PAH-based formulations assume inception via naphthalene and pyrene pathways (with the capability to include heavier PAHs up to A7, discussed in Task 2, when supported by the gas-phase mechanism). For the pyrene-based models, the dimerization efficiency (γ_{A_4}) is also varied. As shown in Figure 27b, the choice of nucleation pathway and dimerization efficiency has an impact comparable in magnitude to the gas-phase mechanism variations, underscoring the need for accurate representations of PAH concentrations and their dimerization chemistry.



(a) Effects of gas-phase mechanism
Mech 1: ABF, 2001
Mech 2: CalTech, 2009
Mech 3: Slavinskaya, 2009
Mech 4: WF, 1999



(b) Effects of nucleation mechanism
Nuc 1: C_2H_2-based
Nuc 2: Naphthalene-based ($\gamma_{A_2} = 1.0$)
Nuc 3: Naphthalene-based ($\gamma_{A_4} = 1.0$)
Nuc 4: Pyrene-based ($\gamma_4 = 0.025$)



(c) Effects of variation in transition from coalescence to aggregation
dcr1 : 1 nm, **dcr2** : 5 nm, **dcr3** : 10 nm, **dcr4** : 27.5 nm

Figure 27. Illustrations of sensitivities of soot predictions to gas-phase kinetics, nucleation models, and the aggregation parameters using Internation Sooting Flame-target Bunsen burner stabilized laminar premixed flame.

Finally, the effect of varying the aggregation transition criterion (d_{cr}) is examined. Decreasing d_{cr} leads to earlier formation of aggregate structures, which increases the effective surface area available for surface reactions, resulting in higher soot volume fractions. However, these effects are smaller relative to the variations caused by gas-phase kinetics and nucleation modeling. Although surface growth contributes significantly to soot mass addition, the corresponding HACA kinetics are not varied here due to broad agreement in the literature, with remaining uncertainties discussed later.



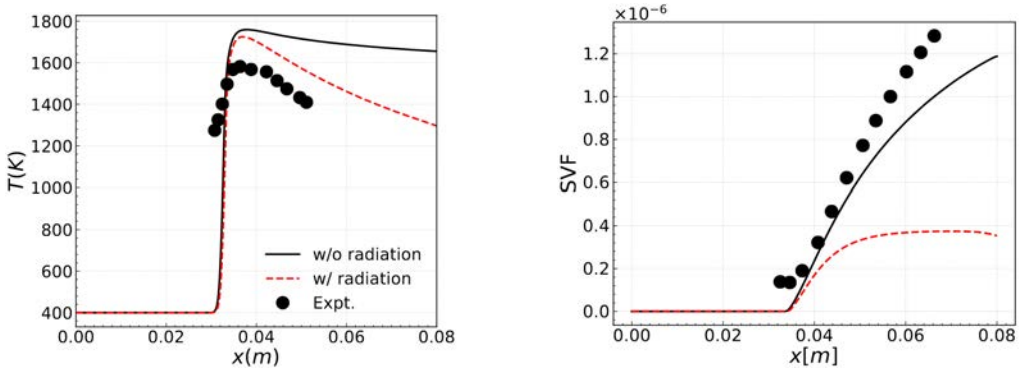
Overall, these analyses highlight the strong sensitivity of soot formation to the selected gas-phase mechanism, nucleation chemistry, and aggregation physics. The soot modeling framework developed in this project is modular, allowing new or modified sub-models to be incorporated easily. This soot modeling suite is subsequently integrated into the in-house compressible LES solver LESLIE.

4.3 Modeling Canonical Soot Formation with LESLIE

The verified standalone soot modeling frameworks are coupled with the in-house compressible flow solver LESLIE and then used to investigate soot formation in a range of canonical flame configurations. As the accurate description of PAH species requires detailed mechanism of O(100) species, making their direct integration in 3D LES is computationally prohibitive. To mitigate these challenges, often tabulated strategies have been preferred in literature. Although such approach is computationally efficient, their assumptions of equilibrium chemistry and nature of tabulation remain questionable in spray flames due to partial premixing, product-reactant mixing, and the interactions of wide spatial and temporal scales of soot with turbulence. Finite-rate-chemistry LES, on the other hand, can account for such shortcomings; however, they become computationally intractable, especially for sooting simulations where details of PAHs have to be included. Therefore, to make these simulations feasible, few approximations are necessary. Specifically, to conduct these simulations, reduced gas-phase mechanisms are used that track the growth of PAH species till naphthalene.

Verification in Laminar Premixed Flames

The implemented soot modeling framework, integrated with reduced gas-phase chemistry (Bisetti et al., 2012), is verified against experimental data for a canonical premixed ethylene–air flame. A rich laminar premixed flame (Menon et al., 2007) at $\phi = 2.64$ is simulated under two conditions: (1) with radiation modeling and (2) without radiation modeling. As shown in Figure 28b, numerically predicted soot volume fractions exhibit reasonable agreement with experimental measurements. Furthermore, the complex dependence of soot formation on temperature (see Figure 28a) is evident: when radiation is included, at lower temperatures, soot levels are lower, suggesting consistency with lower temperatures of soot-bell curve.



(a) (b)

Figure 28. Comprison of (a) temperature and (b) soot volume fraction predictions in lamiar premixed ethylene-air flames with and without radiation. Expt. represents experimental data by Menon et al., 2007.

2D Mixing Layers from Jet-A Fuel

In this section, 2D calculations of temporal mixing layer with gasified Jet-A fuel are performed. A representative 2D strip (width H = 15 mm) of Jet-A fuel (diluted with 85 % N_2 by volume) is surrounded with air (21 % O_2 and 79 % N_2 in volume), as shown in Figure 29. The rectangular computational domain is around 94 mm long in a direction parallel (horizontal) to the fuel strip and 105 mm wide in a direction perpendicular to the fuel strip. Both the oxidizer and the fuel strip are atmospheric pressure. The air stream is preheated to 800K to increase resistance of the flame to extinction induced by the strain. The computational domain is discretized in a uniform mesh with total 1,048,576 cells (1,024x1,024), which corresponds to the minimum grid spacing of $\Delta x = \Delta y = 91.5$ micron. This resolution is equivalent to the resolutions of direct numerical simulations (DNS) studies. Characteristic non-reflecting outflow boundary conditions are imposed in a direction perpendicular to the fuel strip (vertical) and periodic boundary conditions are applied in the other direction. The fuel strip moves to the right at a velocity of 8.74 m/s while the air co-flow moves in the opposite direction with the same



speed. For initialization, the temperature and species mass fractions are taken from a flamelet and mapped from mixture fraction space onto the crosswise direction using a mixture fraction profile.

$$z(y) = \frac{1}{2}\left[\mathrm{erf}\left(\frac{\frac{1}{2}\delta + y}{\sqrt{2\sigma_1^2}}\right) + \mathrm{erf}\left(\frac{\frac{1}{2}\delta - y}{\sqrt{2\sigma_1^2}}\right)\right] \quad \text{(Eq. 6)}$$

Here, y represents the spatial location in a perpendicular direction, the parameter δ controls the width of fuel strip and the slope parameter σ_1 controls the slope of the profile. The values of these parameters were taken as 7.5 mm and 1.8. The simulations are conducted using the 62 species reduced chemical kinetics model for Jet-A fuel developed under NJFCP.

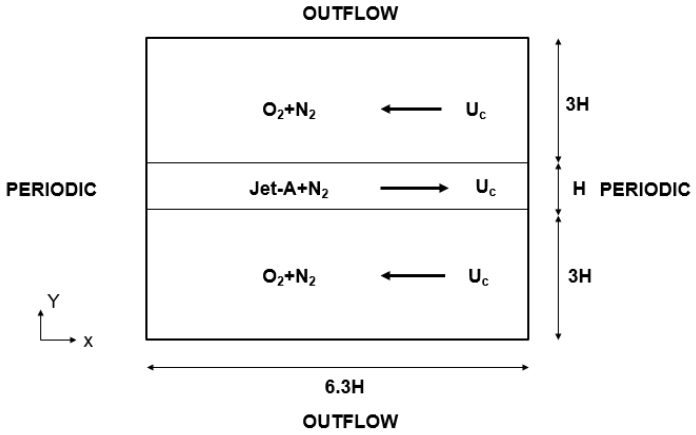


Figure 29. Schematic of temporal mixing layer of Jet-A fuel.

Figure 30 shows the contours of evolution of soot number density overlapping with isolines of temperature. The mixing layer grows with time, and the simulations are continued till time reaches 20 ms, when large structure forms. As can be seen, the growth of shear layers causes the wrinkling of the flame. The soot number density follows closely with the pyrene formation zones in the non-premixed flames as the nucleation process is assumed to occur through pyrene dimerization. Figure 31 shows the average profiles of u velocity normalized with $U_{o,}$ number density of soot particles formed and soot mass fractions profiles. The quantitative magnitudes of soot mass fraction (~10^{-4}) as well as the number density (~10^{12} 1/cm^3) match well with the values reported in Atilli et al. (2014), whereas the soot models in their studies were different than the one used in the present work.

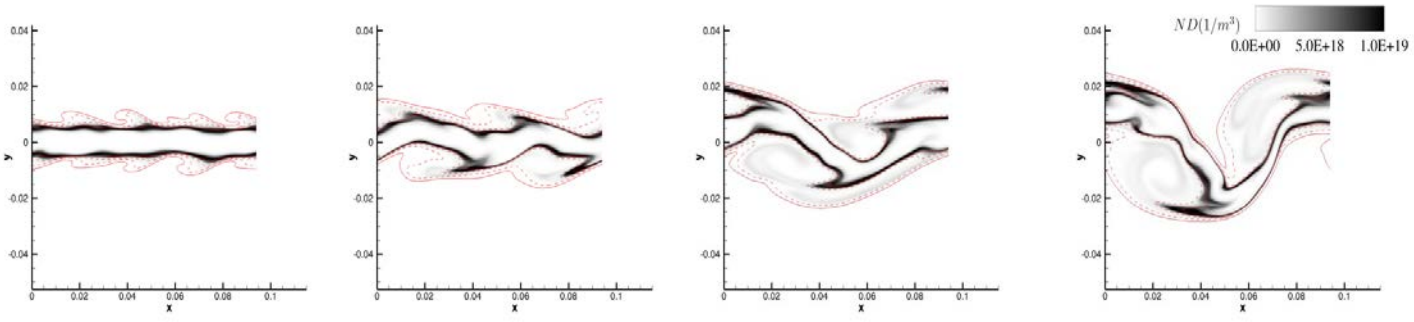


Figure 30. Contours of soot evolution overlayed with isolines of temperature T=1600K (----) and T=2000K (—).

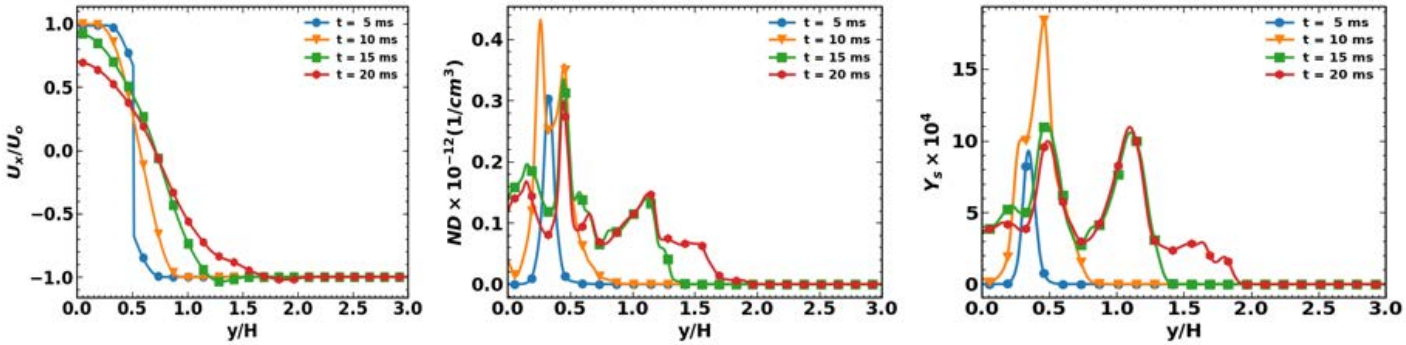


Figure 31. Spatially averaged profiles of velocity, soot number density and soot mass fractions.

3D LES of Gas-Phase Turbulent Premixed Flame Propagation (TPF)

We performed 3D calculations of turbulent premixed flames of gasified Jet-A2 fuel as a final investigation case. The schematic for the configuration is shown in Figure 32. Specifically, the laminar premixed flames investigated in the earlier section are superimposed on top of the isotropic turbulence field such that the flame turbulence interactions fall in a thin reaction zone $\left(\frac{u'}{S_l} = 10 \,\&\, \frac{l}{\delta_f} = 6.2\right)$ where, u' represents the turbulence intensity, S_l represents the laminar flame speed, l represents the turbulent length scale and δ_f is the flame thickness. The grid resolution is 96x96x96 for a physical domain of 15x15x15 mm. Characteristic inflow-outflow conditions are applied in the streamwise direction whereas periodicity is applied in the cross-streamwise and spanwise direction. The initial turbulence field is generated using a well-developed DNS simulation of isotopic turbulence in the same periodic domain and then filtered back to the LES grid. Fuel kinetics is based on the same 41-species skeletal mechanism developed by T. Lu and coworkers at the University of Connecticut. To model the unresolved subgrid stresses, we employ a well-established LDKM. Additionally, we use the partially stirred reactor (PaSR) model to incorporate the effects of turbulence-chemistry interactions due to unresolved subgrid interactions between chemistry and turbulence. All the simulations are conducted using Georgia Tech's super-computing cluster (PACE-phoenix) with Intel® Ivy-bridge i7 processors.

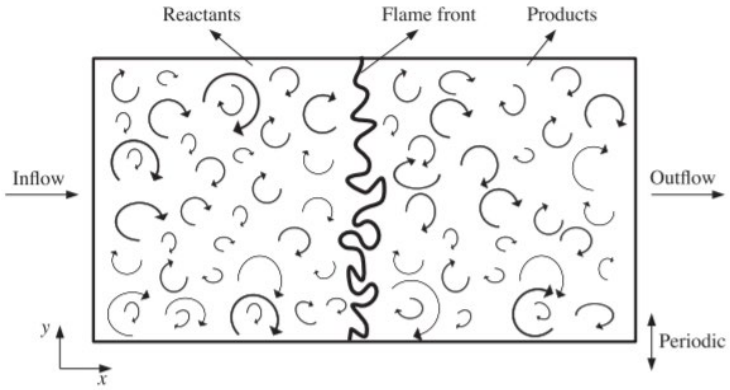


Figure 32. Schematic of the turbulent premixed flame.

Figure 33 shows the inflow and outflow vorticity contours as well as the wrinkling of the initially planar surface due to background turbulence. The overall qualitative zones of soot nucleation, growth, and oxidation behind the flame are shown in Figure 34. Moreover, as highlighted by the maximum contour lines of nucleation, surface growth, and oxidation

® Intel is a registered trademark of Intel Corporation, Santa Clara, California.

processes, the processes occur very close to each other in a thin zone; however, their relative magnitudes may differ significantly.

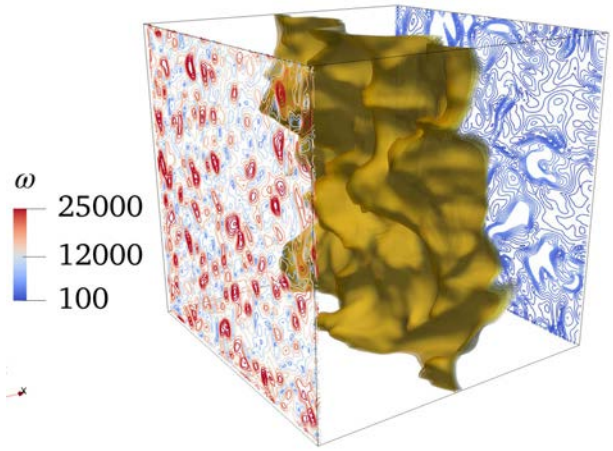


Figure 33. Vorticity magnitude (s^{-1}) at the inflow and outflow planes along with wrinkled flame surface.

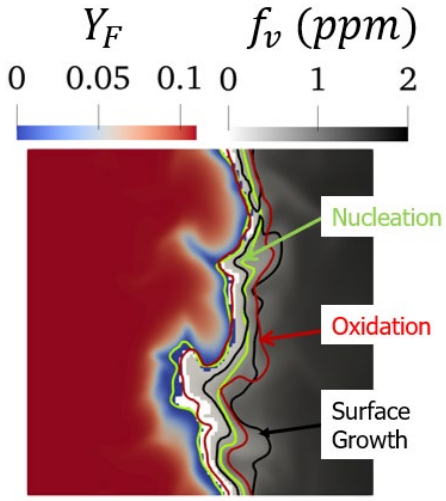


Figure 34. Consumption of gas phase fuel (left) formed soot levels (right) superimposed with contour lines of soot sub-processes in a turbulent premixed flame.

4.4 Upscaling the Soot Sources Using the Linear Eddy Mixing (LEM) Strategy

As shown schematically in Figure 35, the soot scalar fields in the above formulation are transported on the LES grid (LES-MOM). The central challenge, however, lies in accurately determining the soot source terms in an LES context. These sub-processes occur at subgrid scales, and the baseline source-term expressions are derived under quasi-steady assumptions, which are not directly valid in turbulent flows with strong spatial and temporal fluctuations. Therefore, the objective of this work is to develop a methodology, guided by high-fidelity, first-principles studies, to account for the multiscale evolution of soot source terms in turbulent environments. This provides a physically justified basis for incorporating soot models within LES frameworks.

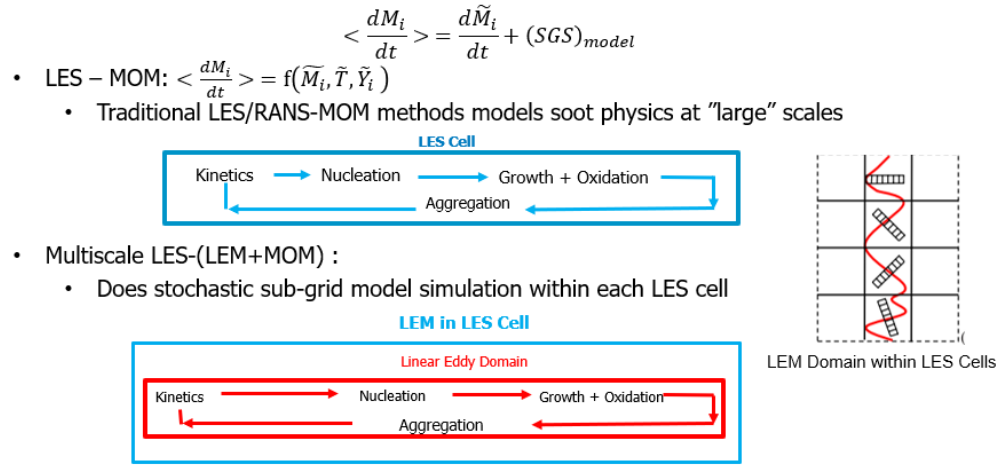


Figure 35. Mixing based sub-filter soot scales. LEM: Linear Eddy Mixing, LES: large eddy simulation, MOM: method of moment, RANS: Reynolds-averaged Navier–Stokes.

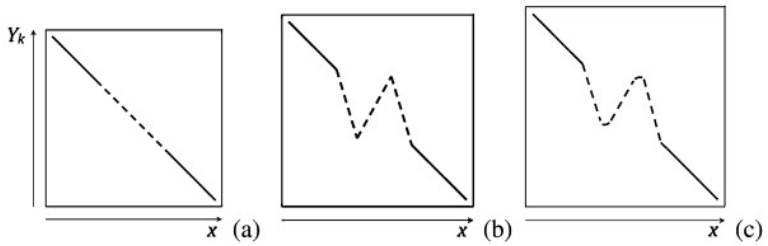
To address this, we employed a standalone 1D LEM model (Srinivasan & Menon, 2014). Previous studies have used the combined LES+LEM–MOM approach (El Asrag et al., 2007) with a reduced 19-species gas-phase mechanism, which limits soot kinetics to simplified Lindstedt-type formulations. However, detailed PAH chemistry involves approximately 60 species and is inherently stiff; thus, in this work, the focus is placed on standalone LEM+MOM simulations to examine subgrid-scale turbulent mixing effects in premixed jet flames at two rich equivalence ratios and across different turbulence Reynolds numbers. The 1D nature of the LEM framework enables the use of a more detailed reduced jet-fuel mechanism, allowing PAH growth to be tracked up to pyrene. In this study, a 62-species reduced mechanism is employed, permitting nucleation modeling based on pyrene dimerization.

The standalone LEM model which has been used to simulate high Karlovitz number non-sooting turbulent flames in the past (Sreenivasan & Menon, 2014). It solves temperature evolution and species evolution through reaction-diffusion equations and is now coupled with additional soot moment scalars as represented mathematically below:

$$\begin{aligned}
\frac{\partial Y_k}{\partial t} &= F_{k,stir} - \frac{1}{\rho}\frac{\partial}{\partial s}(\rho Y_k V_k) + \frac{\dot{\omega_k} W_k}{\rho} \quad k = 1, \dots, N_g \\
\frac{\partial T}{\partial t} &= F_{T,stir} - \frac{1}{\bar{c_p}} \Sigma_{k=1}^{N} c_{p,k} Y_k V_k \frac{\partial T}{\partial s} + \frac{1}{\rho\,\bar{c_p}} \frac{\partial}{\partial s}\left(\bar{\kappa}\frac{\partial T}{\partial s}\right) - \frac{1}{\rho\,\bar{c_p}} \Sigma_{k=1}^{N} (h_k\, \dot{\omega}_k\, W_k) \\
\frac{\partial M_r}{\partial t} &= F_{M_r,stir} + \dot{\omega}_{M_r} \quad r = 0,1,2,3,4,5
\end{aligned} \qquad \text{(Eq. 7)}$$

Here ρ represents the two phase density, N_g denote the total number of gas phase species, $F_{k,\,stir}$ is the term for stirring for species mass fraction, M_r represents the soot moments, $F_{M_r,stirr}$ is the stirring for moment terms, $Y_k, h_k, \dot{\omega}_k, \dot{\omega}_{M_r}$ represent the mass fraction, enthalpy, reaction rate of the k_{th} species and r_{th} moment, $W_k, c_{p,k}, V_k$ denote the k_{th} species molecular weight, specific heat at constant pressure and diffusion velocity.

The turbulent effects are modelled using the triplet mapping procedure which rearranges the scalar field by the motion of an eddy. This approach has shown to reproduce the turbulent diffusion associated with high Re inertial range turbulence. The evolution of the scalar field within the LEM domain is shown in Figure 36.



(a) Initial Scalar Field (b) After Triplet Mapping (c) after reaction-diffusion

Figure 36. Evolution of scalar field within linear eddy mixing (LEM) domain.

In this, the eddy size (l) is chosen from a turbulent PDF $f(l)$

$$f(l) = \frac{\frac{5}{3}l^{-\frac{8}{3}}}{\left(\eta_e^{-\frac{5}{3}} - l_o^{-\frac{5}{3}}\right)} \quad where\ \eta_e = N_n l_o Re^{-\frac{3}{4}} \qquad \text{(Eq. 8)}$$

The frequency of the stirring operations is estimated as

$$\lambda = \frac{54}{5}\left(\frac{\nu Re}{c_\lambda l_o^3}\right)\left[\frac{\left(\left(\frac{l_0}{\eta}\right)^{\frac{5}{3}} - 1\right)}{1-\left(\frac{\eta_e}{l_0}\right)^{\frac{4}{3}}}\right] \qquad \text{(Eq. 9)}$$

Where η_e is the kolmogorv length scale, l_o is the integral length scale, Re_t is the turbulent Reynolds number and c_λ, N_n are the model constants. Based on the above two parameters, the eddy location is randomly selected from the permissible locations in the domain. The length of the 1D LEM domain is 25 mm, and the smallest grid size is 1μm. The laminar flame properties such as flame thickness ($\boldsymbol{\delta^o_{L,max}} = \frac{\nu}{S_l^o}$) and flame speed ($\boldsymbol{S_l^o}$) are provided in Table 1.

Table 1. Laminar flame properties of Jet-A fuel.

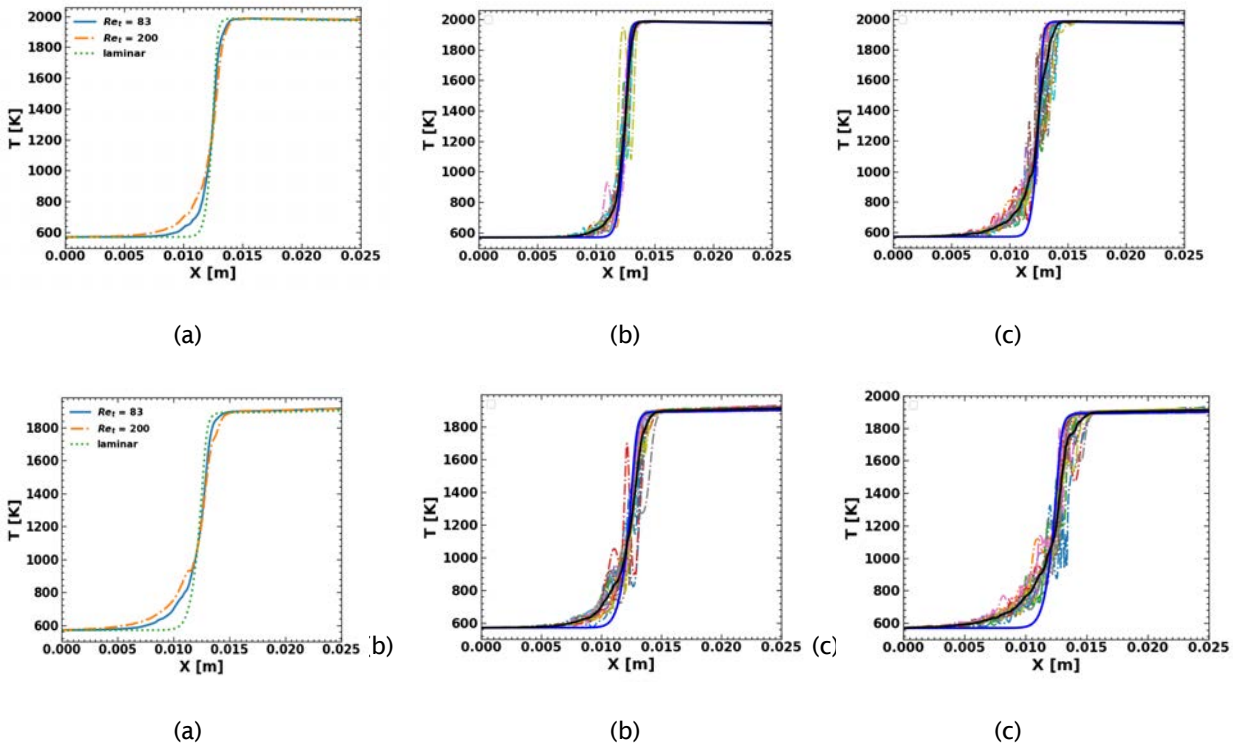
$\boldsymbol{\phi}$	$\boldsymbol{S_L^o}$ (m/s)	$\boldsymbol{\delta^o_{L,max}}$ (mm)	$\boldsymbol{\delta_T^0}$ (mm)
1.8	0.227	0.179	0.957
2.0	0.164	0.243	1.18

The turbulent cases simulated using LEM-MOM are given in Table 2. l_o represents the integral length scale, u' denotes the turbulence intensity; turbulent Reynolds number is defined as $Re_t = \frac{u' l_o}{\nu}$, Kolmogorov length scale is estimated as $\eta \sim l_o Re_t^{-3/4}$and Karlovitz Number is calculated as $Ka = \sqrt{\frac{\left(\frac{u'}{S_l^o}\right)^3 \delta_L^o}{l_o}}$. Since LEM-MOMIC is a stochastic model, the statistical averages over the 10,000 instantaneous snapshots are taken to obtain averaged flame profiles.

Table 2. Simulation parameters at different turbulent conditions.

Case	$\boldsymbol{\phi}$	$\boldsymbol{u'/S_L}$	$\boldsymbol{Re_t}$	$\boldsymbol{l_o}$ (mm)	$\boldsymbol{\eta}$ ($\boldsymbol{\mu}$m)	Ka
1A	1.8	10	83	2.0	72.8	9.46
1B	1.8	25	200	2.0	36.3	38.36
2A	2.0	10	83	1.9	91.1	11.02
2B	2.0	25	200	1.9	45.4	43.57

Figure 37 shows how the structure of flame changes because of isotropic 1D model turbulence by tracking the profiles of temperature. The thickening of flame with increasing Karlovitz number (Ka) is observed.



- (a) (b) (c)

Figure 37. (a) Averaged profiles of temperature at laminar conditions, Re_t = 83 and Re_t= 200, (b) Representative instantaneous snapshots of temperature demonstrating action of eddies at Re_t = 83, and (c) Representative instantaneous snapshots of temperature demonstrating action of eddies at Re_t = 200. The top three figures present results for ϕ=1.8 while the bottom three figures show results for ϕ=2.0.

The main idea behind the current work is to understand the effects of turbulence due to different equivalence ratios as well as different turbulent conditions. The following Figure 38 shows how spatial variations of soot volume fraction and number density profiles occur. As expected, the rich flame shows more sooting behavior. For example, at $\phi = 2.0$ soot volume fraction levels are roughly four times more than that at $\phi = 1.8$. A similar effect is also observed on the soot number density profiles. The turbulence also seems to have a profound effect on the emissions levels. With increasing levels of turbulence, the levels as well as the initiation of soot formation seem to be affected. For example, at $\phi = 1.8$ the maximum soot volume fraction rises from 0.015 ppm to 0.025 ppm. Similarly, the initiation of soot inception also occurs earlier with increasing turbulence. The temperature profile suggests that the preheat zone thickens with increasing Re_t, and hence the pyrene formation as well as the soot inception due to pyrene (A_4) occurs earlier. To understand the physics of soot formation due to MOMIC model, we looked at the various source terms due to nucleation, coagulation and surface growth normalized with their maximum values to identify their locations of dominance behind the flame. A comparison of their locations is provided in Figure 39. The plot shows the competition between the nucleation, coagulation, and surface growth zones behind the flame in laminar and turbulent conditions. All these profiles are statistically averaged for stochastic comparison. The coagulation zone (CG) closely follows the nucleation (Nuc) zone. The combined effect of surface growth and oxidation is more dominant post nucleation.

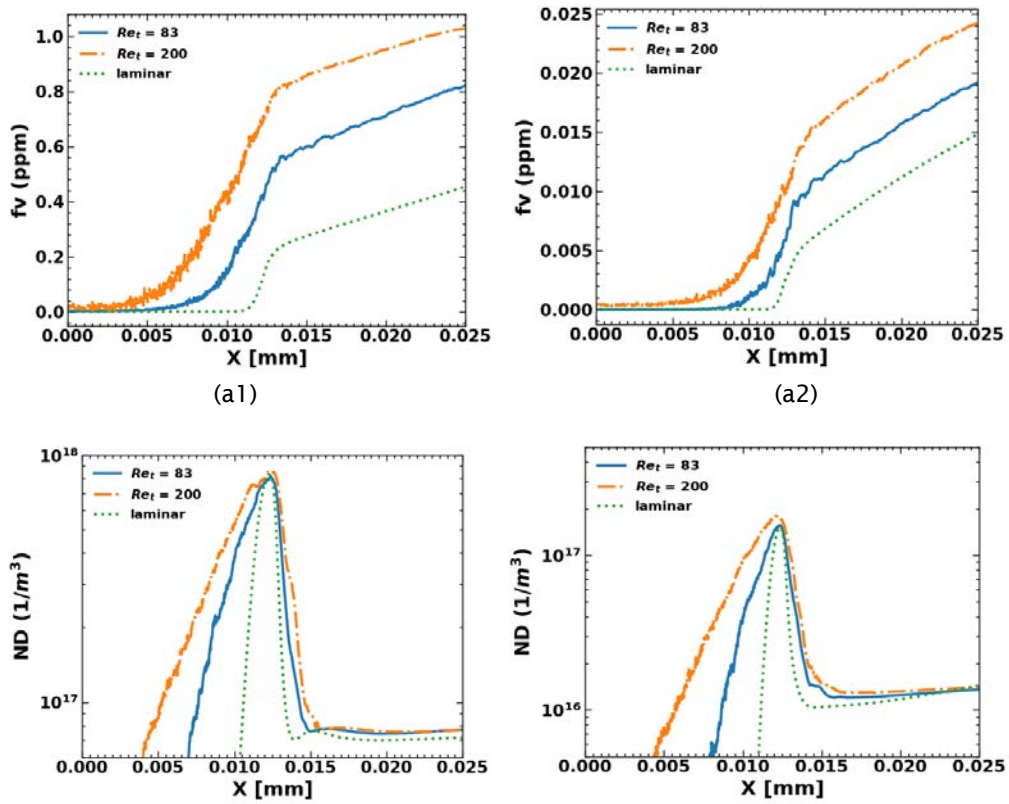


Figure 38. Comparison of soot volume fraction at laminar and turbulent conditions (a1) and (a2). Comparison of soot number density at laminar and turbulent conditions (b1) and (b2).

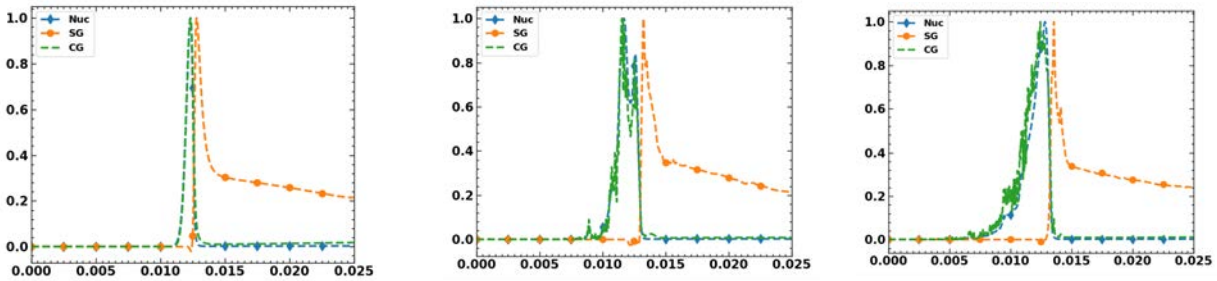


Figure 39. Normalized nucleation (Nuc), coagulation (CG) and surface growth (SG) source terms.

The comparison of nucleation and surface growth terms is shown in Figure 40 for $\phi = 1.8$. The surface growth adds more soot mass compared to nucleation under laminar as well as turbulent conditions. The surface growth source terms are further analyzed to understand contributions from surface growth due to C_2H_2 additions and surface oxidations due to O_2



and OH and are shown in Figure 41 for $\phi = 1.8$. The soot mass addition due to C_2H_2 is almost three times more dominant than O_2 and OH radicals. The oxidation by OH molecules is four times higher than the O_2 molecule.

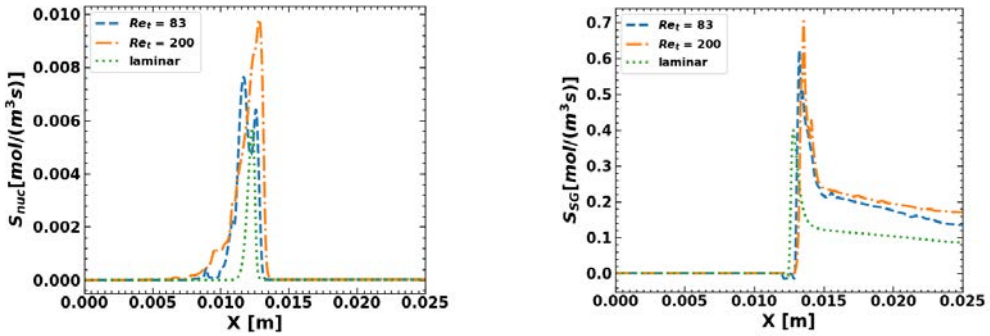


Figure 40. Comparison of contribution from nucleation and surface growth.

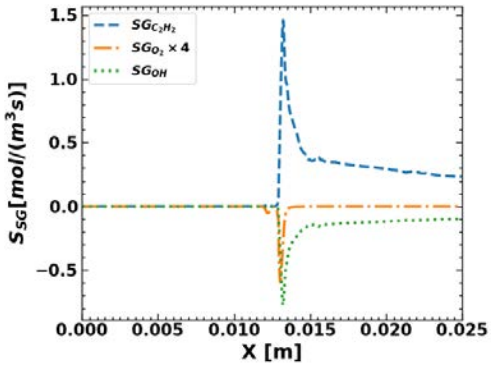


Figure 41. Comparison of contribution from C_2H_2, O_2, and OH for soot surface growth and oxidation.

4.4 Coupling RTRC PM-ROM within Soot Models at GT

In this section, we specifically focused on coupling the RTRC PM-ROM model within our soot modeling framework. We specifically look at the propagation of a laminar flame through a rich premixed gas phase mixture under combustor-relevant conditions. The physics of soot formation in this scenario is depicted in the schematic shown in Figure 42. Using this setup, we compared baseline Lindstedt model with RTRC PM-ROM and also the role of aggregation models in the post-flame environment. In this configuration, a premixed reactant mixture enters the 1D domain from the left side and burns at the flame front. Due to an insufficient amount of oxidizer, the fuel-rich mixture cannot completely combust, leading to the decomposition of leftover fuel into soot. Various stages of soot formation occur behind the flame. Immediately after the flame front, influenced by the kinetic model, nucleation, surface growth, and oxidation processes initiate the formation of soot, which continues to aggregate as it progresses downstream.

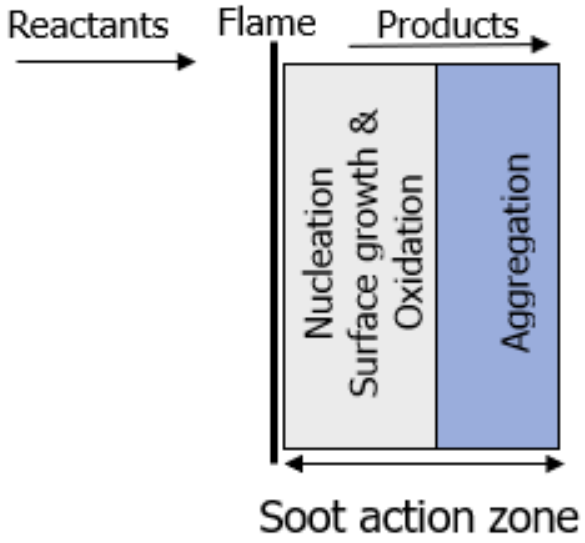


Figure 42. Schematic of Laminar Premixed Flame.

As illustrated in Figure 43, the PM-ROM model predicts slightly less soot accumulation than the Lindstedt model (similar to the observations in Task 1 at RTRC). We also explored the sensitivity of incorporating an aggregation model, which helps characterize the structure of soot aggregates forming behind the flame, as depicted in Figure 44. The baseline model posits that aggregation effects commence once the primary particle reaches a critical diameter of 27 nm, with a fractal dimension of 1.8. Incorporating the aggregation model enhances the rate of particle coagulation, leading to a decrease in soot aggregate density. However, as aggregation increases the overall surface area available for soot reactions, it consequently raises the soot volume fraction. The aggregation model specifically influences the sizes of the particles formed behind the flame; without it, the model predicts large, spherical particles, whereas with aggregation, a cluster of soot aggregates composed of primary spherical particles is predicted.

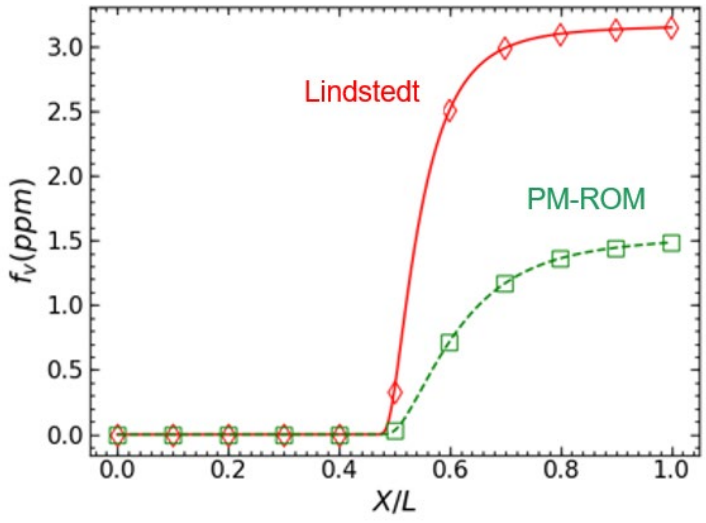


Figure 43. Soot volume fraction behind the laminar flame.

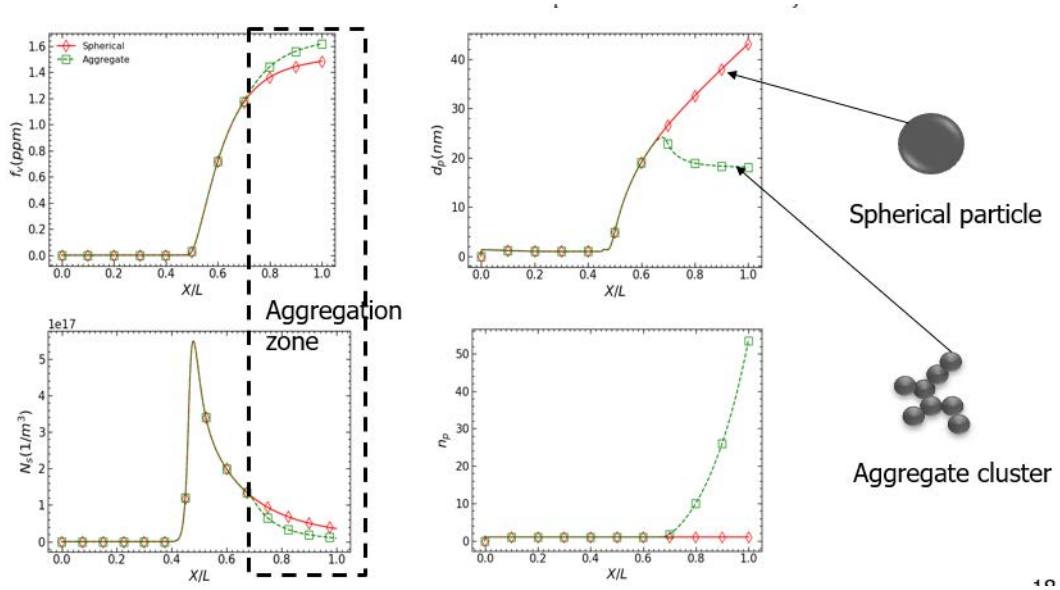
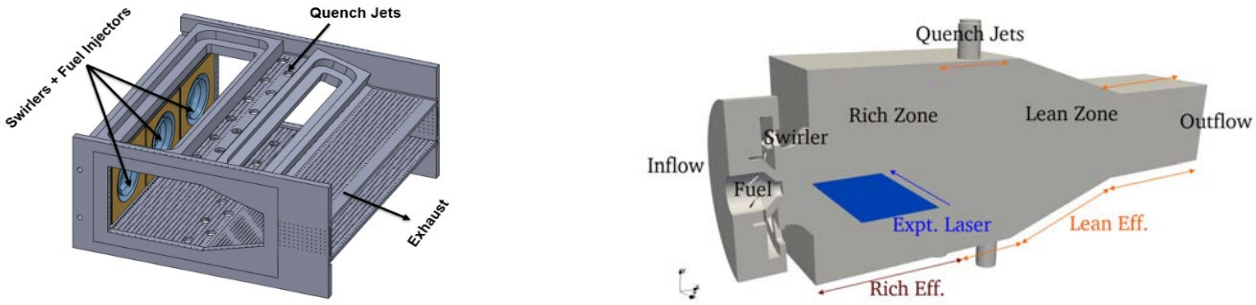


Figure 44. Aggregate characteristics of non-volatile particulate matter (nvPM) formed behind the flame.

4.4 Apply Moment Soot Models at GT to RQL Spray Flames

In the remainder of the project work, the modeling framework is applied to study soot formation in a realistic RQL spray combustor. The computer-aided design (CAD) model of the rig investigated in the Year 3 effort is shown in Figure 45a. The RQL burner simulated in GT is a subsection (only one swirler) and is represented in Figure 45b.



(a) Three-swirler RQL experimental rig (b) Model single-injector combustor with periodic BC

Figure 45. Computational aspects of the sector rich-burn quick-mix lean-burn (RQL) rig investigated in the current work.

In summary, the computational domain from the inlet plenum to the outlet duct is considered. The overall components of the combustor consist of the swirler, fuel injector, quench jets, effusion surfaces, and the outlet duct. The main combustor has the primary rich zone from the dump plane to the quench jets and the secondary lean burn zone post-quench jets. The overall combustor operates at a pressure of 6.8 atm and the preheated air at a temperature of 600K is supplied through different inlets such as the primary inflow, quench jets, and the effusion holes along the walls of the rich primary and lean secondary zones of the combustor. We have primarily investigated two cases corresponding to lower fuel-air ratio (case A, $\phi_g = 0.12$) and higher fuel-air ratio (case B, $\phi_g = 0.2$).

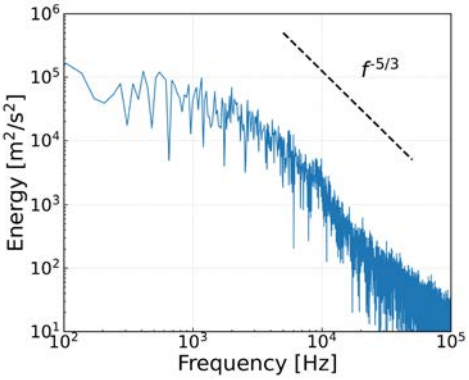


Figure 46. Current grid demonstrates Turbulent Kinetic Energy cascade over two orders of magnitude scales.

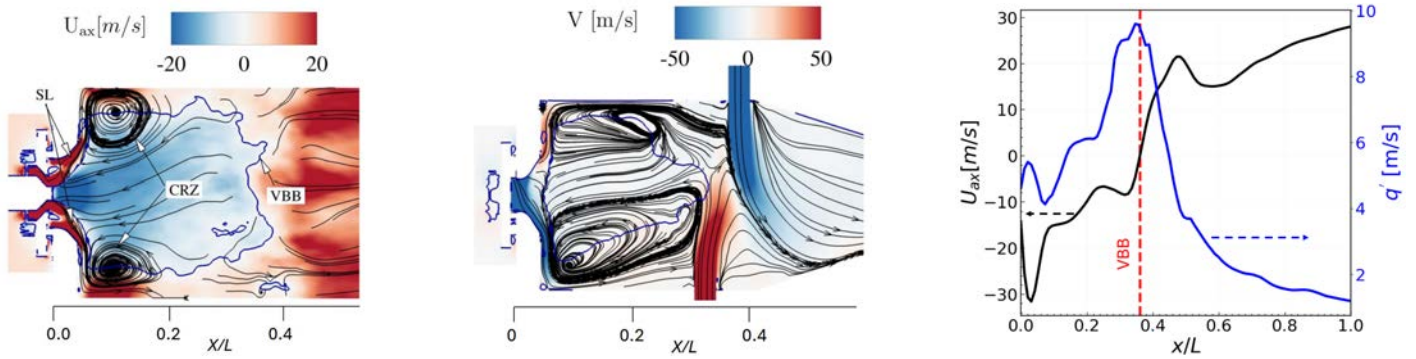
The computational domain is discretized using 6.3 million finite-volume cells. A multi-block structured grid with hanging nodes is generated to handle the geometric complexities of the combustor. Shear layers are resolved with minimum grid points of 0.25 mm - 0.7 mm consistent with previous LES simulations (Panchal & Menon, 2022). Swirlers have 10 points along their span. The grid quality is on average above 0.9 with a minimum value of 0.7 mainly near dilution jets and geometrically complex swirled regions. The stretching ratio of 1.01 is applied on average with a maximum value of 1.2 near the outlet channel and the inlet plenum where no complex physics occurs. The kinetic energy spectra, as shown in Figure 46, demonstrates that the current grid captures 5/3rd energy cascade typically observed in turbulent flows.

The parts that are stitched together with hanging nodes use an interpolation scheme of the same order of accuracy as the numerical scheme. The geometry is further split into 5,141 blocks. Characteristic-based constant mass inflow boundary conditions are used at the primary inflow as well as inflow for quench jets. Periodic boundary conditions are used in the z-direction (spanwise-direction) as the current work focuses only on the single section of the multi-sector grid. At the outflow, the domain is extended by 30% of the combustor length, and a relaxing sponge boundary condition is applied. Small effusion holes are present throughout the walls in the primary and secondary zones of the combustor for wall cooling. Such holes are difficult to resolve in LES and hence are modeled using an effusion boundary condition. The air split for the combustor is 18% from the dome face (resulting in the equivalence ratios of 0.66 and 1.14 in the primary zone of the combustor), 44% from the two rows of quench holes, 7% from effusion cooling holes in the rich-burn region, and 19% for the effusion cooling holes in the lean-burn, taper, and exhaust regions.

In the current work, the numerical scheme for the gas phase is of second-order accuracy in time while a hybrid scheme for spatial discretization is employed, which dynamically switches between a second order-accurate MacCormack central scheme and a third order-accurate Monotone Upstream-centered Schemes for Conservation Laws (MUSCL) scheme. A fourth order-accurate Runge-Kutta method for time integration is used for the Lagrangian phase.

Due to the absence of corresponding experimental data, the non-reacting flow features are only qualitatively illustrated in Figure 47 and discussed here. The radial swirlers generate a strong swirling motion with a swirl number of approximately 1.6 near the combustor dump plane, which exceeds the critical threshold (typically 0.6 for such flows). This high swirl intensity induces a recirculating region downstream, known as the vortex breakdown bubble (VBB), marked by the solid blue line in Figure 47(a,b). The VBB arises primarily from an adverse pressure gradient and is characterized by a region of negative axial velocity, as seen in the centerline velocity profile (Figure 47c). This recirculation gives rise to toroidal central recirculation zones (CRZ) adjacent to the high-shear layers. Qualitatively the non-reacting field exhibits various regimes typical of swirling flows.

Figure 47c also denotes the length of VBB about 0.36 times the overall combustor length from the dump plane. Additionally, obtained turbulence intensity ($q' = \frac{1}{3}\sqrt{u_{x,rms}'^2 + u_{y,rms}'^2 + u_{z,rms}'^2}$) suggests that peak turbulence intensity increase in magnitude with peaks near the edge of VBB and then decreases in magnitude along the length of the combustor. The recirculation zones are also observed to be asymmetric (see Figure 47b) due to two main reasons. First, the dilution jets are arranged along the top and bottom walls of the combustor in a zigzag pattern, resulting in inherently asymmetric



(a) (b) (c)

Figure 47. Swirling flow features showing the presence if recirculating zones in the region of interest.

Liquid fuel is injected from the swirled fuel nozzle, and the surrounding high-speed air assists the injected fuel atomization. Such liquid fuel goes through a primary and secondary breakup before the droplets are small enough to vaporize and burn. However, it is not practical to resolve such near-injector dynamics of atomization and since the goal here is primarily to study overall soot formation in the primary zone, Lagrangian point particles are injected downstream of the actual injector with an assumed log-normal distribution. Such assumptions behind the treatment of spray can certainly have an impact on the soot formation but as per our knowledge, have not been investigated in literature yet. The qualitative features of this spray flame are shown in Figure 48.

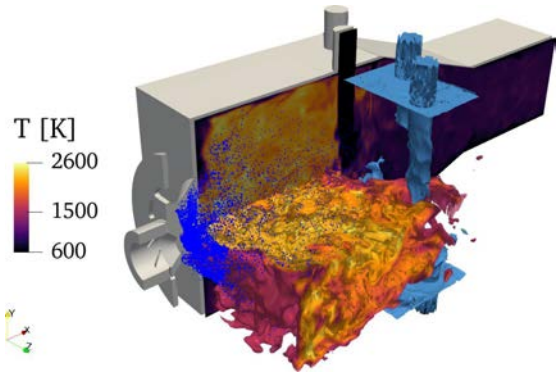


Figure 48. Qualitative visualization of spray droplets (blue color), quench jets (sky-blue isosurfaces) and temperature field iso-surfaces as well as slice through center of dilution jets.

Under identical operating conditions, with variations only in the fuel injection flow rates, case A and case B exhibited approximately 0.065 million and 0.11 million droplets, respectively, after reaching a quasi-steady state. The comparisons of unsteady flame temperature (top halves) and OH species fields (bottom halves) resulting from the combustion of vaporized fuel are shown in Figure 49. The overall combustion behavior shows qualitative similarities in both cases. As shown by the temperature contours, the central region (the recirculating region of the VBB) is hot in both cases. This recirculation promotes further vaporization of the incoming spray and acts as an aerodynamic flame holder. Additionally, both the contours of OH species and temperature are highly wrinkled due to interactions with background turbulence. The OH concentrations field shows local extinction spots, which are also observed in other swirl-stabilized spray flames. The

secondary zone is relatively cold compared to the primary zone, due to the sudden mixing of the quench jet air with the hot products from the primary zone. Despite these qualitative similarities, notable differences are also observed. First, the temperature in the primary zone of the combustor is higher in case B compared to case A. This trend persists in the secondary zone of the combustor post-quench jets. A similar pattern is evident in the unsteady OH field, where case B showed denser OH radical concentrations in the primary zone than case A.

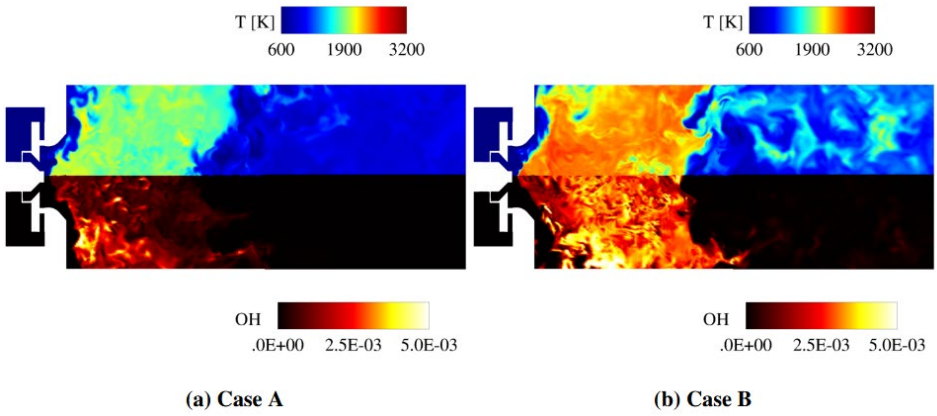


Figure 49. Reacting flow-field comparison of temperature and OH-mass fraction between the investigated cases.

The instantaneous and time-averaged soot presence are compared against the experimental visualizations, as shown in Figure 50, for the two fuel-air ratios investigated in this work. The top set of experimental images shows the LII signals captured by a Shimadzu HPV-X2 high-speed camera using a Spectra-Physics® Quanta-Ray® Pro-250 Nd:YAG laser. Due to the sensitivity of soot estimations to measurement techniques and the modeling uncertainties in soot processes, achieving accurate quantitative validation of LES soot predictions against experiments is challenging, and hence normalized locations of soot presence are compared between the two cases. First, the overall soot formation increases from case A to case B, consistent with experimental observations. For case A, the central recirculating region, is almost completely devoid of soot. Soot seems to be mainly concentrated along the shear layers. On the contrary, a significant soot presence is observed in case B and shows better spatial alignment with the experimental results. There is a slight discrepancy in the transverse location of peak soot on the left side and an overall underprediction of soot downstream of X > 0.02 m compared to experimental observations. However, such discrepancies have also been observed in gas-phase RQL sooting flames, even with state-of-the-art soot modeling. Nevertheless, based on qualitative visual comparisons, the overall influence of the equivalence ratio on soot formation appears to be reasonably captured in the simulations, which was the primary objective of the current analysis. The underlying mechanism behind these observations is analyzed by comparing further the distribution of different soot processes involved in the soot formation and destruction.

® Spectra-Physics and Quanta-Ray are registered trademarks of Newport Corporation, Irvine, California.

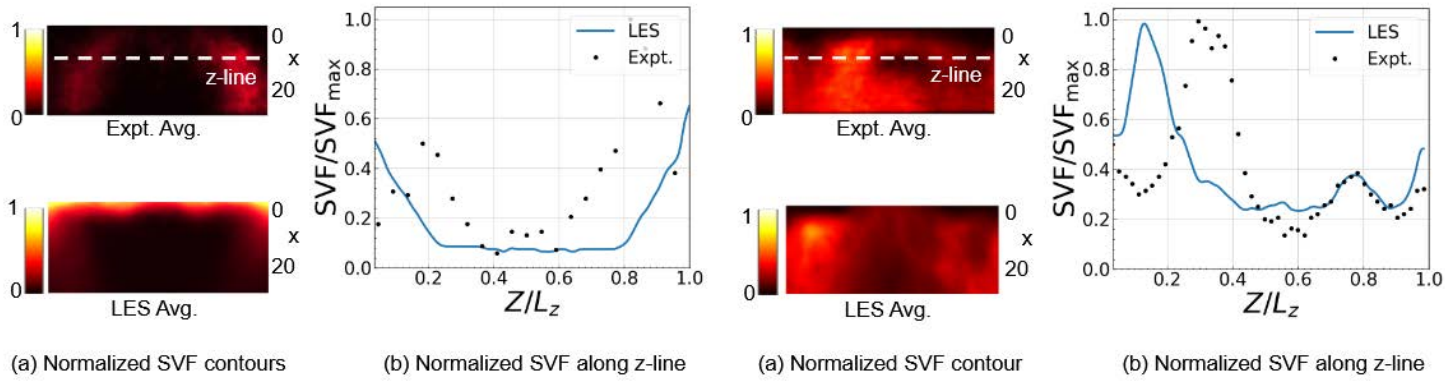


Figure 50. Soot volume fraction field is compared with the experimental data for Case A and Case B.

Figure 51 compares the time-averaged spatial distributions of the nucleation, surface growth, condensation, and oxidation source terms for both operating conditions, as these processes collectively determine the evolution of the soot. Contours of the source-term magnitudes are included to highlight the quantitative differences between the two cases. In addition, Figure 52 presents the mass fractions of key soot precursor species to compare their relative availability for the underlying soot formation and oxidation pathways. Soot inception (Figure 51a) occurs near the fuel injector, where the fuel-air mixture is very rich, and dense pockets of A2 exist (Figure 52b). This nucleation persists along the shear layers, though its intensity decreases as the fuel-air mixing progresses. Condensation closely follows nucleation, exhibiting a similar trend due to the involvement of the same PAH species in both processes. Quantitative comparisons of isolines from Figure 51a and Figure 51c reveal that both nucleation and condensation processes are higher in case B than in case A due to overall higher PAH species formed. In addition, for case A, as shown in Figure 51b, surface growth source terms are very low compared to case B. Especially, the surface growth begins immediately after the onset of inception zones, and its influence is only confined along the shear layers. This behavior is associated with the overall low concentrations of C_2H_2 as shown in Figure 52c. Moreover, the soot particles formed undergo oxidation and hence show less tendency to intermittently trap in recirculation zones at lower global fuel-air ratio. A similar mechanism is initially observed in case B, where surface growth and oxidation processes start following the inception and condensation zones. However, the overall magnitudes of surface growth in Figure 51b are higher in case B than in case A, consistent with elevated concentrations of C_2H_2. This sustained growth persists not only along the shear layers but also within the inner recirculation zones, where longer residence times further promote soot growth. The increased surface area resulting from surface growth, combined with the dense presence of oxidizer, leads to higher oxidation rates further downstream from the combustor dump plane, primarily within the primary zone. These observations suggest that soot formation in the primary zone is dominated by surface kinetics rather than inception.

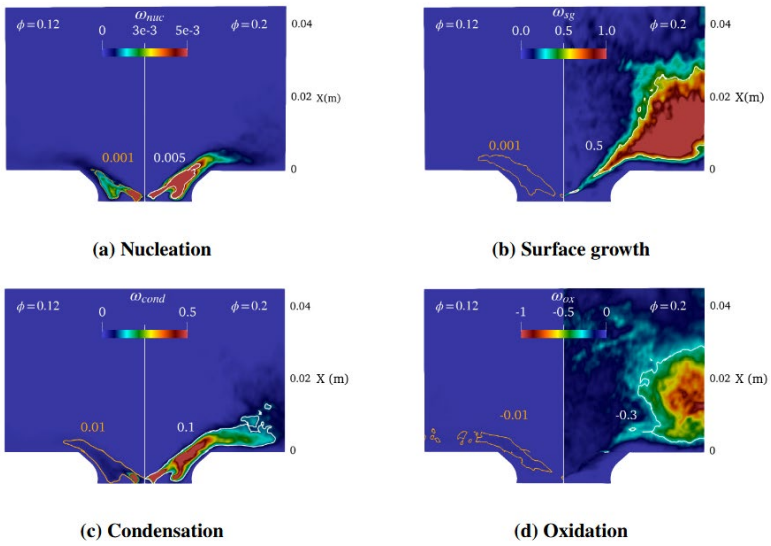


Figure 51. Comparative assessment of time-averaged soot source terms (kg/m3.s) between case A (left half) and case B (right half). Lines represent the order of magnitude of source terms for respective cases.

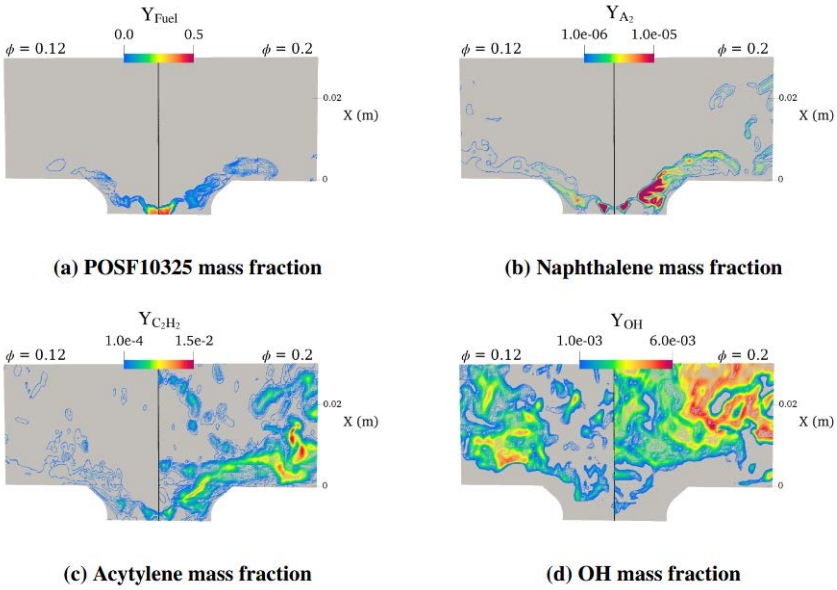


Figure 52. Comparative distribution of vaporized fuel (a) and key precursor species (b), (c), and (d) involved in soot formation reactions for the two investigated cases: case A (left half) and case B (right half).

4.5 Modeling Coupled Detailed Kinetics in the Soot Model

The systematic investigation of kinetic and nucleation model effects is computationally expensive to perform within the full 3D LES. Therefore, in the current work, a CRN model is employed in which the hydrodynamic field is assumed frozen, and only the effects of chemistry are solved by constructing a network of reactors that are connected via mass flow controllers.

Since the overall computational field is not solved, the CRN model is computationally cheaper when compared with the full 3D LES simulation. For example, in the current work, a full 3D LES solution took approximately 100,000 CPU hours on 12000 MPI processors to simulate one flow through time on the Intel Ivy bridge i7 cluster, whereas the CRN model required only 0.1 CPU hour on a single processor to get a qualitative predictive effect. A verified CRN model for exhaust NOx and CO emission predictions based on GE®-CF6-80C2 RQL engine optimization is used here as a reference as shown in Figure 53. This CRN model is refined further to better capture the soot evolution in the primary zone of the combustor. The nozzle and primary zones are discretized using six different PSR whereas the post-quench jet zone is modeled using the plug flow reactor (PFR). The conditions for these reactors are averaged from the LES. The gas-phase chemistry and the soot model are kept consistent between the two.

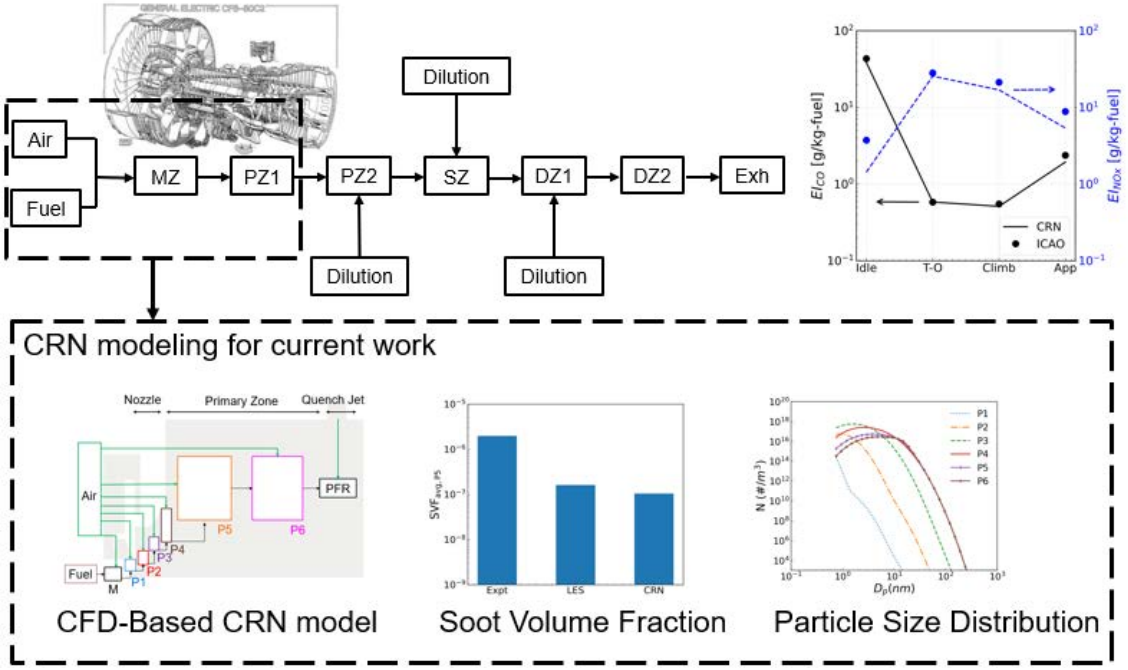


Figure 53. Chemical Reactor Networks (CRN) modeling framework employed in the current work. The top figures show CRN model predictions for rich-burn quick-mix lean-burn (RQL) combustors against the International Civil Aviation Organization (ICAO) emission databank. The bottom figures show a refinement of this CRN model for the primary zone of the RQL combustor investigated in this work. CFD: computational fluid dynamics.

We also exploited the capabilities of the CRN model coupled with Dakota (Figure 54 for overall framework) to perform a comprehensive uncertainty analysis of its predictions (Karpe & Menon, 2025). This analysis aimed to understand the response of the baseline soot model to input uncertainties through forward uncertainty quantification (UQ) analysis, while sensitivity analysis was performed to assess the relative contribution of each process to the overall predictive uncertainties. Here, the results of the local sensitivity analysis, which are more relevant to the current work, are reported.

® General Electric is a registered trademark of General Electric Company, Evendale, Ohio.

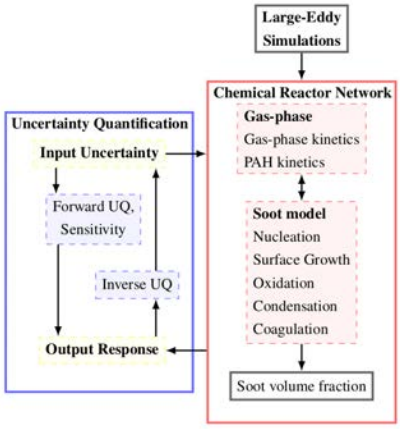


Figure 54. Uncertainty analysis framework to investigate modeling sensitivities of baseline soot model. UQ: uncertainty quantification.

As can be seen from Figure 55, normalized local sensitivity indices are plotted first. Such indices generally provide an intuitive representation of how local perturbations in the baseline rates influence the overall soot formation or depletion. The positive value of such an index suggests that an increase in the baseline rate of the process promotes soot formation, whereas the negative value implies it contributes to soot depletion. The local sensitivity analysis reveals the nucleation, growth, and condensation process consistently show positive sensitivity indices, whereas the oxidation has a negative local index. Coagulation appears to have a marginal impact on the total soot mass. Furthermore, if we compare the trends of these reactors, the P3 reactor, located upstream of the primary zone, showed the highest sensitivity to PAH-based processes. In contrast, further downstream, P4-P6 reactors display stronger sensitivity to the growth and oxidation processes.

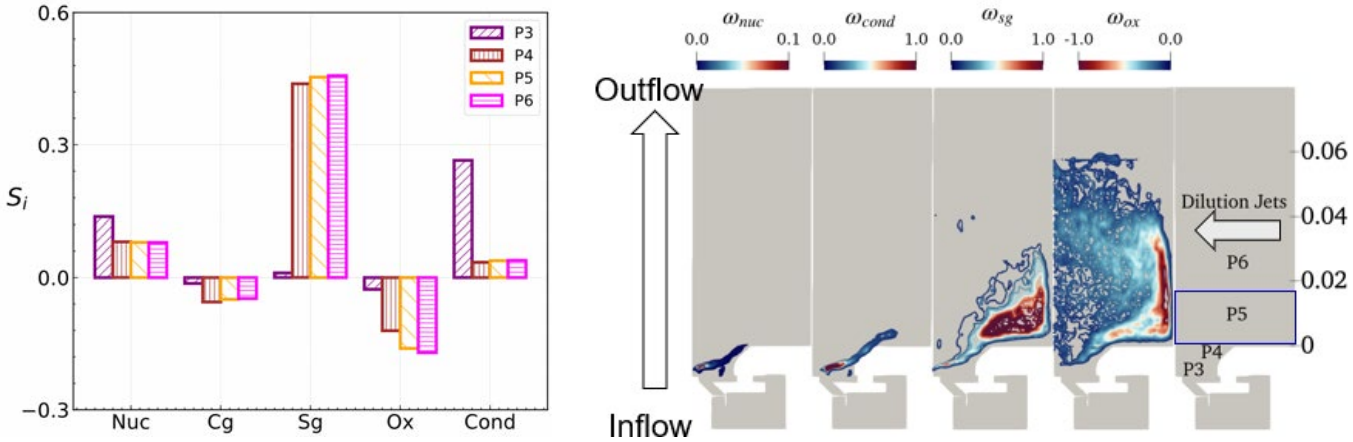


Figure 55. (a) Influence of soot subprocesses in different reactors using the uncertainty quantification-Chemical Reactor Network (UQ-CRN) framework. (b) Presence of these processes from large eddy simulation (LES) highlighting the consistency between the both. Overall the relative dominance of each of the soot processes is tracked along the spatial extent of the combustor.

These findings are further supported by visualizing the presence of these processes in different zones of the combustor. As can be seen, the nucleation and condensation processes influence a localized region within the nozzle, primarily along the shear layers, while the growth and oxidation processes are more prominent in the primary zone of the combustor. This suggests that these nanoparticles form in the shear layer and undergo further growth as they are transported in the inner

recirculation zone of the primary zone. Within the primary zone, the influence of oxidation is observed to increase, and this possibly occurs due to the enhanced mixing of the primary zone-rich mixture with cold air entering through the dilution jets, gradually making the mixture lean.

Finally, this local influence of different processes is used in the next part of the work to understand the effects of changing the gas-phase chemistry, nucleation models, and growth kinetics at these reactors (for example, the rates of nucleation and condensation processes in the P3 reactor, whereas growth and oxidation processes in the P5 reactor) and overall soot predictions in the P5 reactor. The following sections present a brief account of such effects.

First, the effects of gas-phase kinetics on overall predictions are assessed by varying the gas-phase mechanisms. The three different mechanisms investigated in this work are listed in Table 3. The skeletal mechanism by Gallen (2023), was also used in the LES simulations, while the second mechanism, developed by Wang et al. (2018), combines the HyChem mechanism with the KAUST mechanism. The third mechanism, referred to as the RTRC mechanism, was developed through collaborations with the RTRC kinetics group and integrates the HyChem mechanism with the CalTech-Force mechanism. Although the detailed gas-phase mechanisms provide a wide range of PAH species that can be considered for nucleation, to isolate the effects of the gas-phase kinetics, the same soot model—namely, the baseline soot model—is coupled with all three mechanisms. These effects are presented in Figure 56.

Table 3. Different gas-phase kinetics mechanisms investigated in this work.

Mechanism	# of species	PAH Mechanism
Gallen	45	Bisetti
Wang	210	KAUST
RTRC	222	Caltech

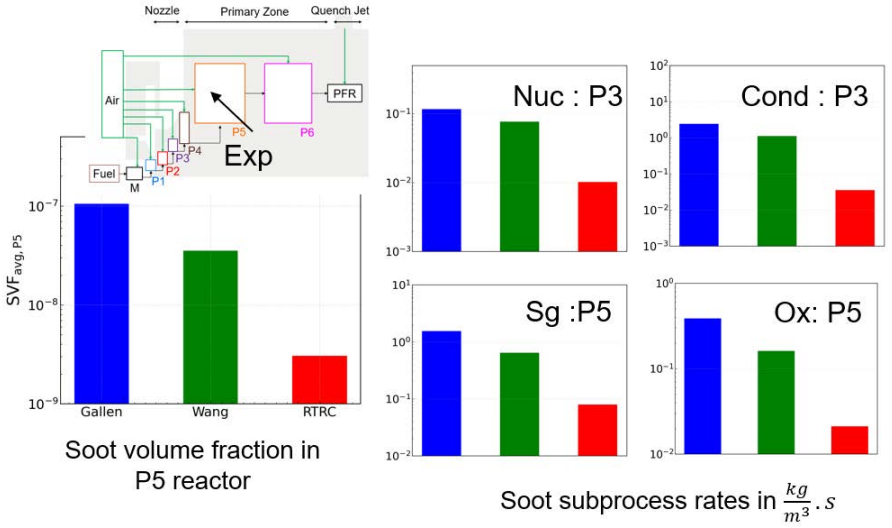


Figure 56. Effects of detailed gas phase mechanism on primary zone soot predictions of rich-burn quick-mix lean-burn (RQL) system.

As seen in Figure 56, both detailed mechanisms generally predict slightly lower soot levels compared to the skeletal Gallen mechanism. The Wang detailed mechanism still shows reasonable agreement with the Gallen mechanism, whereas the RTRC mechanism predicts soot concentrations approximately an order of magnitude lower than those predicted by the other two mechanisms. This discrepancy is likely due to the lower concentrations of soot precursor species predicted by the detailed mechanisms, resulting from the enhanced breakdown of C_2H_2 and naphthalene into heavier PAH species. This



trend is evident from the peak rates of the individual processes responsible for soot formation and oxidation. In particular, the RTRC mechanism predicts condensation and growth rates approximately an order of magnitude lower than those predicted by the other detailed and reduced mechanisms. These results suggest that soot predictions are highly sensitive to the choice of gas-phase kinetics, as the mechanism directly influences the individual process rates through species concentrations.

The use of a detailed gas-phase mechanism also enables the investigation of various nucleation models, particularly those involving heavier PAH species beyond naphthalene. In this work, five such nucleation models are examined, as summarized in Table 4. The first two models are based on nucleation involving naphthalene (A_2). In general, PAH species form stable dimers through collisions, which are characterized by an efficiency parameter (γ_{PAH}). These two models explore the influence of incorporating this efficiency parameter. In the first model, the sticking coefficient for naphthalene collisions follows the value recommended by Blanquart et al. (2009), whereas in the second model, the sticking efficiency is assumed to be unity. The next set of models involves nucleation based on pyrene. Lastly, the M5 model incorporates inputs from nucleation studies conducted at UM. As the parameters in this model have already been calibrated to account for sticking efficiency, no additional variation in this parameter is investigated.

Table 4. Different nucleation mechanisms investigated in this work.

-	PAH	γ_{PAH}
M1	Naphthalene (A_2)	0.0011
M2	Naphthalene (A_2)	1.0
M3	Pyrene (A_4)	0.025
M4	Pyrene (A_4)	1.0
M5	Benzo-pyrene (A_4R_5)	1.0

As shown in Figure 57, the incorporation of nucleation effects can significantly influence soot predictions. Generally, the naphthalene-based model predicts higher overall soot levels compared to the pyrene-based models, primarily due to the lower concentrations of pyrene relative to naphthalene. Furthermore, since nucleation is the initial step in the soot formation process, variations at this stage can have a substantial impact on the subsequent processes. To further investigate this, the peak source rates of condensation, surface growth, and oxidation are also plotted. Increased nucleation rates typically result in a greater number of incipient soot particles, thereby enhancing subsequent condensation, growth, and oxidation processes through the increased availability of surface area. Since the overall rates of nucleation are generally smaller than those of growth and condensation, the influence of nucleation is primarily indirect, exerted through its effect on subsequent processes rather than by directly contributing to soot mass.

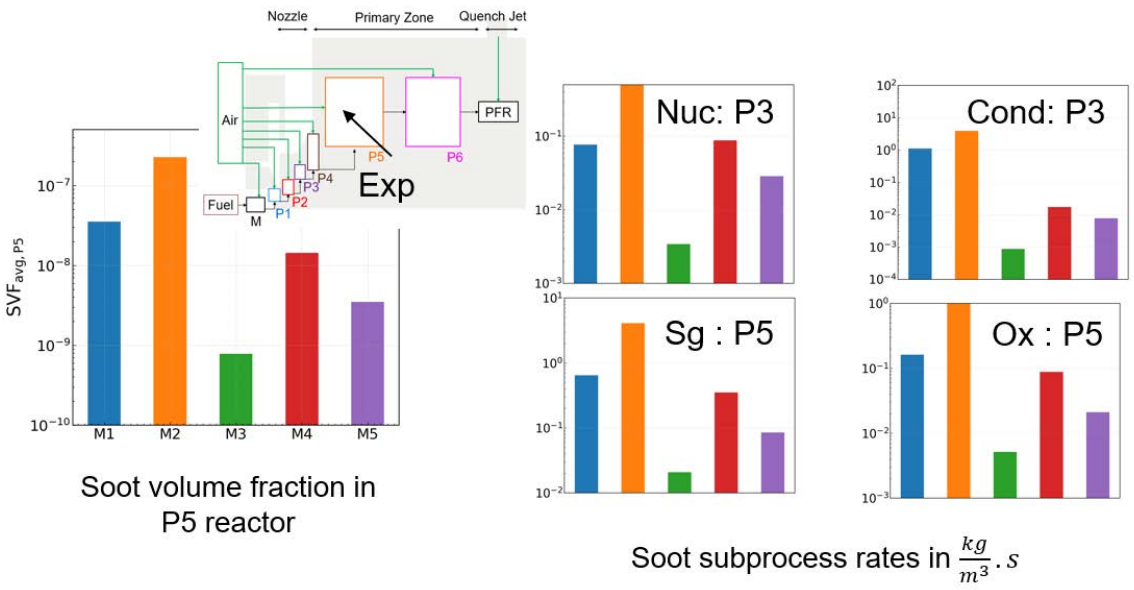


Figure 57. Effects of different nucleation mechanisms (M5 represents the nucleation mechanism obtained from the University of Michigan) on primary zone soot predictions of rich-burn quick-mix lean-burn (RQL) system.

After understanding the effects of the gas-phase kinetics and nucleation model, the effects of growth modeling are systematically investigated by changing the growth kinetics. For consistency, the baseline soot model is kept where nucleation is assumed to occur via naphthalene dimerization whereas the reduced gas-phase kinetics is used. In the current work, three different growth kinetics models are investigated: (1) Kazakov et al. (1995), (2) Appel et al. (2000), and (3) Blanquart et al. (2009). From the overall soot volume fractions predicted for P5 reactors, it seems that the surface growth reaction mechanism plays a vital role. The Kazakov mechanism produced the least soot volume fractions whereas the Blanquart mechanism predicted the highest soot volume fractions with the Appel-Bockhorn-Frenklach (ABF) mechanism in between. To delineate these effects further, the source rates of these processes at their respective peak locations are also compared. As can be seen from Figure 58, as expected, the nucleation and condensation processes didn't have much influence on such variation in surface growth kinetics as they occur before the surface growth effects start dominating. The major influence of varying surface growth kinetics is observed on the surface source rates in the P5 reactor. At the same time, the Blanquart mechanism also predicted slightly lower oxidation rates as compared to the Kazakov and ABF mechanisms, further enhancing soot formation.

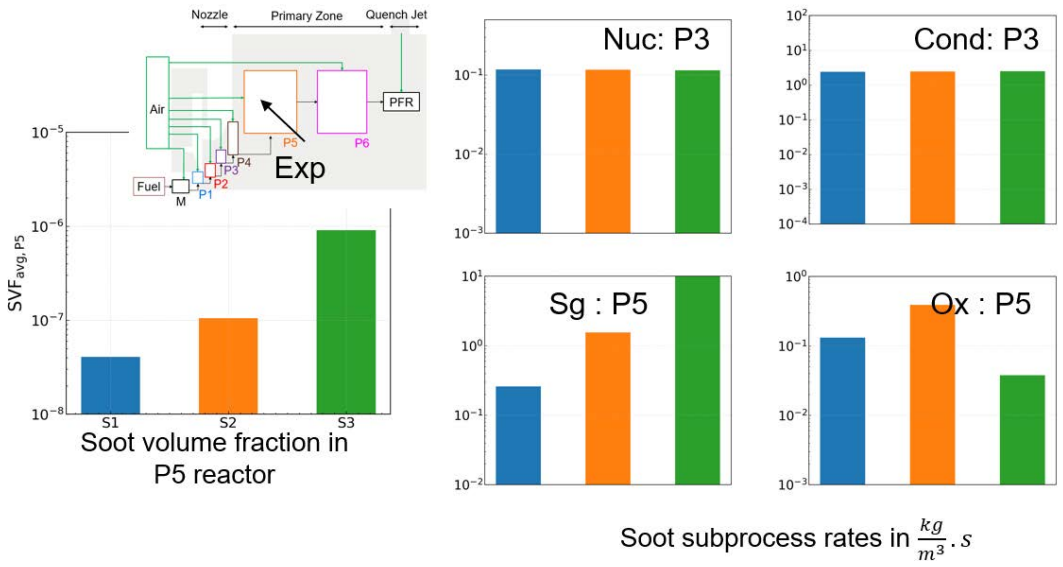


Figure 58. Effects of varying growth kinetics on primary zone soot predictions of rich-burn quick-mix lean-burn (RQL) system.

Major Accomplishments

- Established the baseline MOM-based soot modeling framework, both in standalone form and integrated within LES for canonical flame configurations.
- Quantified the sensitivity of soot predictions (soot volume fraction) to gas-phase kinetics, nucleation models, and aggregation parameters, and shared these findings with collaborative partners.
- Developed a standalone LEM-based strategy to upscale soot source terms for use at LES-resolved turbulence scales.
- Performed LES simulations of a sooting RQL spray combustor at two operating conditions and compared results against FAA ASCENT Project 070 data.
- Incorporated detailed gas-phase kinetics from RTRC and the nucleation model from UM into the MOM soot framework and evaluated their effects relative to variations of the baseline soot models.

Publications

Peer-Reviewed Journal Publications

Karpe, S., & Menon, S. (2022). Numerical Simulations of Soot Formation in Turbulent Premixed Flames of Jet Fuels. *75th Annual Meeting of the APS Division of Fluid Dynamics, 67*(19).

Karpe, S., & Menon, S. (2025). Modeling uncertainties in primary zones soot predictions for rich-quench-lean combustion system. *Proceedings of Combustion Institute, 41*, 105805.

Presentations

Karpe, S., & Menon, S. (2023, January). Model Simulations of Soot Formation due to PAH Kinetics from Mixing Layers of Jet-A Fuels. (AIAA-2023-2690). *AIAA SciTech 2023 Forum*, National Harbor, Maryland.

Karpe, S., & Menon, S. (2025, January). Large-Eddy Simulations of Soot Formation and Dispersion in Rich-Burn Quick-Mix Lean-Burn (RQL) Spray Combustor (AIAA-2025-2484). *AIAA SciTech 2025 Forum*, Orlando, Florida.

Karpe, S., & Menon, S. (2026). Large-Eddy Simulations of dilution jet effects on rich-quench-lean spray flame. *AIAA SciTech 2026 Forum*.

Outreach Efforts

None.



Awards
None.

Student Involvement
One PhD student, S. Karpe, was involved in this work.

Plans for Next Period
None.

References

Appel, J., Bockhorn, H., & Frenklach, M. (2000). Kinetic modeling of soot formation with detailed chemistry and physics: Laminar premixed flames of C2 hydrocarbons. *Combustion and Flame*, *121*(1-2), 122-136.

Attili, A., Bisetti, F., Mueller, M. E., & Pitsch, H. (2014). Formation, growth, and transport of soot in a three-dimensional turbulent non-premixed jet flame. *Combustion and flame*, *161*(7), 1849-1865.

Bisetti, F., Blanquart, G., Mueller, M. E., & Pitsch, H. (2012). On the formation and early evolution of soot in turbulent nonpremixed flames. *Combustion and Flame*, *159*(1), 317-335.

Blanquart, G., Pepiot-Desjardins, P., & Pitsch, H. (2009). Chemical mechanism for high temperature combustion of engine relevant fuels with emphasis on soot precursors. *Combustion and Flame*, *156*(3), 588-607.

Brown, N.J., Revzan, K.L., & Frenklach, M. (1998). Detailed kinetic modeling of soot formation in ethylene/air mixtures reacting in a perfectly stirred reactor. Symp*osium (International) on Combustion, 27*, 1573–1580.

El-Asrag, H., & Menon, S. (2009). Large eddy simulation of soot formation in a turbulent non-premixed jet flame. *Combustion and Flame, 156*(2), 385–395.

El-Asrag, H., Lu, T., Law, C. K., & Menon, S. (2007). Simulation of soot formation in turbulent premixed flames. *Combustion and Flame, 150*(1-2), 108–126.

Frenklach, M. (2002). Method of moments with interpolative closure. *Chemical Engineering Science, 57*(12), 2229–2239.

Gallen, L., Riber, E., & Cuenot, B. (2023). Investigation of soot formation in turbulent spray flame burning real fuel. *Combustion and flame*, *258*, 112621.

Guo, H., Liu, F., & Smallwood, G. J. (2004). Soot and NO formation in counterflow ethylene/oxygen/nitrogen diffusion flames. *Combustion Theory and Modelling*, *8*(3), 475

Karpe, S. B., & Menon, S. (2025). Modeling uncertainties in primary zone soot predictions for a rich-quench-lean combustion system. *Proceedings of the Combustion Institute*, *41*, 105805.

Kazakov, A., Wang, H., & Frenklach, M. (1995). Detailed modeling of soot formation in laminar premixed ethylene flames at a pressure of 10 bar. *Combustion and Flame*, *100*(1-2), 111-120.

Langer, R., Mao, Q., & Pitsch, H. (2023). A detailed kinetic model for aromatics formation from small hydrocarbon and gasoline surrogate fuel combustion. *Combustion and Flame, 258*, 112574.

Leung, K. M., Lindstedt, R. P., & Jones, W. P. (1991). A simplified reaction mechanism for soot formation in non-premixed flames. *Combustion and Flame, 87*(3-4), 289–305.

Menon, A. V., Lee, S. Y., Linevsky, M. J., Litzinger, T. A., & Santoro, R. J. (2007). Addition of NO2 to a laminar premixed ethylene–air flame: Effect on soot formation. *Proceedings of the Combustion Institute*, *31*(1), 593-601

Menon, S., & Ranjan, R. (2016). Spray Combustion in Swirling Flow (Ch. 12). In *Coarse-Grained Simulation and Turbulent Mixing*. Cambridge University Press.

Menon, S., & Kim, W. (1996, January). High Reynolds number flow simulations using the localized dynamic subgrid-scale model (AIAA 1996-425). *34th Aerospace Sciences Meeting and Exhibit*, Reno, Nevada.

Nmira, F., Bouffard, A., & Consalvi, J. L. (2023). Flamelet/transported PDF simulations of ethylene/air jet turbulent non-premixed flame using a three-equation PAH-based soot production model. *Combustion Theory and Modelling*, *27*(6), 820–851

Panchal, A., & Menon, S. (2022). Large eddy simulation of fuel sensitivity in a realistic spray combustor II. Lean blowout analysis. *Combustion and Flame*, *240*, 112161

Patel, N., & Menon, S. (2008). Simulation of spray–turbulence–flame interactions in a lean direct injection combustor. *Combustion and Flame*, *153*(1-2), 228-257

Selvaraj, P., Arias, P. G., Lee, B. J., Im, H. G., Wang, Y., Gao, Y., Park, S., Sarathy, S. M., Lu, T., & Chung, S. H. (2016). A computational study of ethylene–air sooting flames: Effects of large polycyclic aromatic hydrocarbons. *Combustion and Flame*, *163*, 427-436

Slavinskaya, N. A., & Frank, P. (2009). A modelling study of aromatic soot precursors formation in laminar methane and ethene flames. *Combustion and Flame*, *156*(9), 1705-1722



Srinivasan, S., & Menon, S. (2014). Linear eddy mixing model studies of high Karlovitz number turbulent premixed flames.*Flow, turbulence, and combustion*, *93*, 189-219

Wang, H., and Frenklach, M. (1997). A detailed kinetic modeling study of aromatics formation in laminar premixed acetylene and ethylene flames. *Combustion Flame, 110*(1–2), 173–221

Wang, H., Xu, R., Wang, K., Bowman, C. T., Hanson, R. K., Davidson, D. F., Brezinsky, K. and Egolfopoulos, F. N. (2018) A physics-based approach to modeling real-fuel combustion chemistry-I. Evidence from experiments, and thermodynamic, chemical kinetic and statistical considerations *Combustion and Flame, 193,* 502-519



Project 072 Aircraft Noise Exposure and Market Outcomes in the United States

Massachusetts Institute of Technology

Project Lead Investigators

R. John Hansman
T. Wilson Professor of Aeronautics & Astronautics
Department of Aeronautics & Astronautics
Massachusetts Institute of Technology
77 Massachusetts Avenue, 33-303
Cambridge, MA 02139
617-253-2271
rjhans@mit.edu

Christopher R. Knittel
George P. Shultz Professor of Applied Economics
Sloan School of Management
Massachusetts Institute of Technology
77 Massachusetts Avenue, E62-527
Cambridge, MA 02139
617-324-0015
knittel@mit.edu

Florian Allroggen
Principal Research Scientist
Department of Aeronautics and Astronautics
Massachusetts Institute of Technology
77 Massachusetts Avenue, 33-328
Cambridge, MA 02139
617-715-4472
fallrogg@mit.edu

University Participants

Massachusetts Institute of Technology (MIT)

- P.I.: Prof R. John Hansman
- FAA Award Number: 13-C-AJFE-MIT, Amendment Nos. 075, 081, 094, 111, 115, 130, and 143
- Period of Performance: August 11, 2020, to August 31, 2027
- Tasks (tasks listed below are general project tasks; reporting includes the period from October 1, 2024, to September 30, 2025):
  1. Literature review (not reported; completed during past reporting periods)
  2. Empirical identification strategy and scope of dataset (not reported; completed during past reporting periods)
  3. Calculation of noise impact metrics (not reported, completed during past reporting periods)
  4. Cleaning and aggregation of housing transaction dataset (not reported; completed during past reporting periods)
  5. Descriptive analysis of dataset (not reported; completed during past reporting periods)
  6. Empirical analysis of house prices and underlying market effects
  7. Analysis of noise exposure patterns



Project Funding Level

$1,080,000 FAA funding and $1,080,000 matching funds. Sources of match are approximately $236,300 from MIT, plus 3rd party in-kind contributions of $519,000 from NuFuels LLC, and $79,000 from Savion Aerospace Corp., and $245,700 from Earth Force Technologies.

Investigation Team

Prof. R. John Hansman, (P.I.), all tasks
Prof. Christopher R. Knittel, (co-P.I.), Tasks 1, 2, 4, 5, and 6
Dr. Florian Allroggen, (co-P.I.), all Tasks
Dr. Jasdeep Mandia, (postdoctoral associate), Tasks 4 and 6
Juju Wang, (graduate student), Tasks 3, 5, 6, and 7

Project Overview

As enplanements at United States (U.S.) airports have increased by almost 50% over the past two decades, the number of Americans exposed to substantial levels of aircraft noise has decreased. However, considerable concerns regarding aircraft noise remain in some airport communities. This project leverages revealed preference approaches to infer the "implicit price" of aircraft noise exposure from market outcomes in U.S. airport communities. More specifically, the research team quantifies the capitalized disutility associated with aircraft noise exposure through analyzing the empirical relationship between aircraft noise exposure and transaction values for residential properties in communities surrounding U.S. airports. The project leverages potential changes in noise exposure associated with quasi-experimental settings (e.g., the opening of new runways or changes in arrival and departure paths) to empirically identify potential effects on house prices. The results provide insight into the average impacts of noise exposure on residential property values, while also assessing dynamic adjustment processes and potential heterogeneities in revealed preferences, by targeting factors such as time, location, or noise exposure patterns.

Task 6 – Empirical Analysis of House Prices and Underlying Market Effects

Massachusetts Institute of Technology

Objectives

This task explores the impact of noise exposure on house prices to quantify the revealed preference for noise exposure. Under previous periods of performance, initial results for communities surrounding Boston Logan Airport, Seattle-Tacoma International Airport (SEA), and Chicago O'Hare International Airport (ORD) were derived.

During this reporting period, one objective of this task was to understand the underlying mechanisms behind such housing market responses. We started analyzing whether noise exposure changes may alter the prevalence of households to stay in, move into, or move out of a neighborhood. Because such behaviors directly affect supply and demand in housing markets, the analysis can help us validate and understand the causes of the potential housing price impacts discussed during previous reporting periods.

During this reporting period, the analysis focused on communities surrounding Boston Logan International Airport (BOS) to develop the analysis framework.

Research Approach

We combine household-level demographic and movement data with modeled aircraft noise exposure from the Aviation Environmental Design Tool (AEDT). Noise data are available for 2011 and 2016. For years in-between, we used the (preliminary) assumption that noise levels stayed constant within the pre-period (2011–2013) and post-period (2016–2019). Each property is matched to the nearest 0.25 nautical mile noise grid cell. The data used for BOS are shown in Figure 1.



(a) (b)

Figure 1. (a) Red dots show the points of the noise grid and green dots show the location of the households. Each household is spatially matched to the nearest noise grid, which assigns them to the noise exposure under different time periods. (b) Noise exposure changes from 2011 to 2016 at Boston Logan International Airport.

Household data were collected from Data Axle® (InfoUSA). The dataset follows millions of U.S. households each year. Each household has a unique identifier that allows us to track residential mobility and neighborhood composition over time. Table 1 summarizes key variables from the Data Axle household database, including unique identifiers, demographic characteristics, address information, and geographic coordinates used to link households to census tracts and modeled noise exposure grids.

Table 1. Selected variables from the Data Axle household database. The variables capture household demographics, property characteristics, and geospatial identifiers that enable linkage to census tracts and modeled noise exposure grids.

Category	Variable	Description
Household Attributes	FAMILYID	Unique 12-digit household identifier used to track families across years
	HEAD_HH_AGE_CODE	Age of household head or individual
	MARITAL_STATUS	Modeled likelihood that the head of household is married
	CHILDREN_IND	Indicates presence of children in the household.
	WEALTH_FINDER_SCORE	Modeled prediction of household wealth level
	PPI_DIV_1000	Estimated purchasing power index adjusted for local cost of living.
Household & Property Attributes	ADDRESS	Complete address of the property
	LATITUDE/LONGITUDE	Geographic coordinates of the household location
	LENGTH_OF_RESIDENCE	Number of years at current address.
	OWNER_RENTER_STATUS	Indicates whether the household owns or rents its home.
	FIND_DIV_1000	Estimated annual household income (in $1,000s).

The analysis uses panel regressions with multiple levels of spatial controls. We start with county-year and tract-year effects and plan to add town-year effects for finer spatial detail. These models are designed to empirically isolate how changes in noise relate to changes in household flows.

® Data Axle is a registered trademark of Data Axle, Inc., Dallas, Texas.

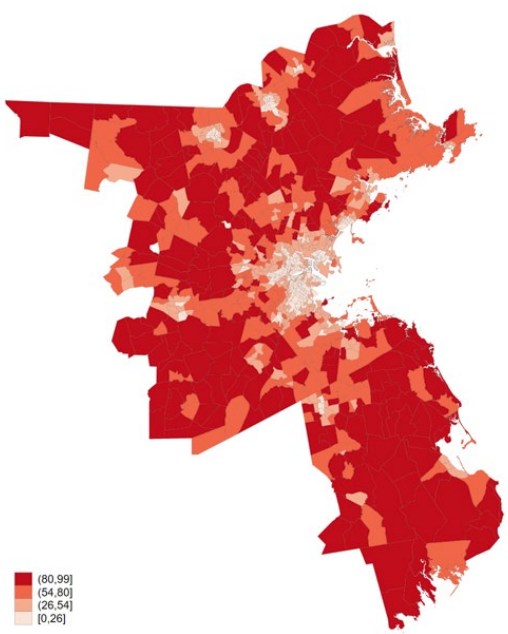
Milestones

- Created tract-level measures of stay, move-in, and move-out rates for Essex, Middlesex, Nantucket, Norfolk, and Suffolk counties.
- Matched over 6,400 AEDT noise grid points to property data in a 25 by 25-mile area around Boston Logan.
- Built baseline regression models with tract and county-year controls.

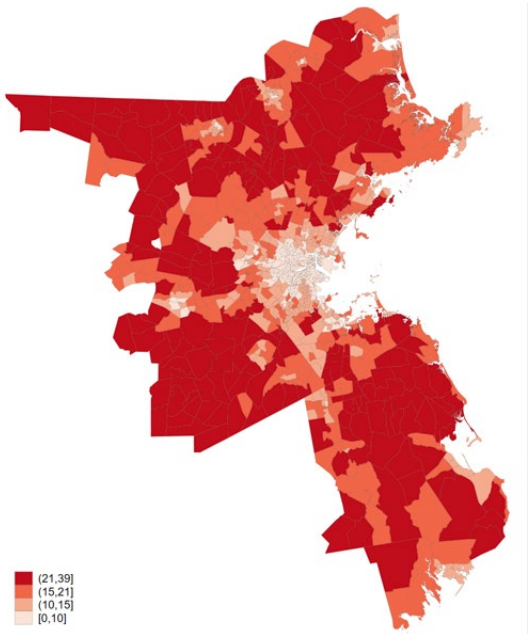
Major Accomplishments

We first explored the spatial variation in household characteristics that may influence moving patterns. We plotted the spatial distribution of key neighborhood attributes using the Data Axle household data for 2012. Figure 2 illustrates this variation across five counties surrounding BOS—Essex, Middlesex, Norfolk, Plymouth, and Suffolk. Panel (a) shows the share of homeowners, panel (b) shows the share of households with children, panel (c) shows the share of households where the head of household is aged 65 or older, and panel (d) shows the median length of residence.

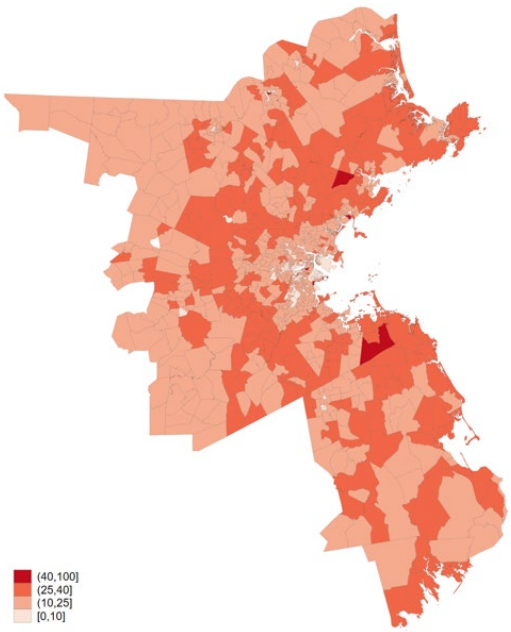
Urban tracts in Boston and Cambridge tend to have lower homeownership rates, fewer families with children, and shorter median years of residence. These areas tend to attract younger, more mobile populations who are often renters and early in their housing or career cycles. This pattern likely corresponds to a lower stay rate, as reflected in the shorter residential tenure. In contrast, suburban tracts surrounding the city show the opposite pattern: higher ownership rates, more families with children, and older household heads. These areas are characterized by longer residence durations and greater neighborhood stability, reflecting both life-cycle factors and the prevalence of owner-occupied housing. The differences between urban and suburban areas highlight how demographic composition and housing market structure can shape observed mobility rates even before accounting for noise exposure.



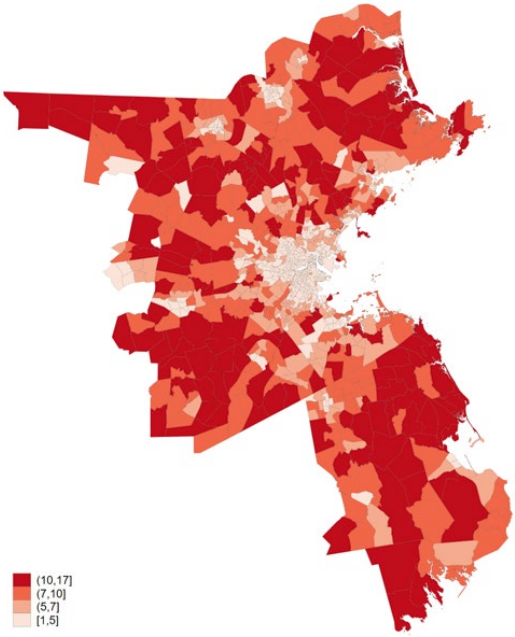
(a) share of households that are homeowners



(b) share of households with children



(c) share of households where the head of household is aged 65 or older



(d) the median length (years) of residence.

Figure 2. Spatial variation in household demographics across the Boston metropolitan area (2012) Panel (a) percentage of households that are homeowners; panel (b) share of households with children; panel (c) share of households where the head of household is aged 65 or older; panel (d) median length of residence among households

We then estimated the relationship between aircraft noise exposure and household mobility using a panel regression at the census tract-year level. Specifically, we modeled the tract-level move-in rate as a function of average noise exposure and

fixed effects for tracts and years. The inclusion of tract fixed effects accounts for time-invariant differences across neighborhoods, such as location, long-term housing characteristics, or baseline demographics. The year-fixed effects control for common shocks affecting all tracts in a given year, such as macroeconomic conditions or policy changes. Preliminary results for the Boston Logan Airport area suggest that higher noise exposure is associated with modest declines in move-in rates, indicating that noise may influence neighborhood attractiveness and residential sorting patterns.

Publications

Working Paper

Allroggen, F., Knittel, C. R., Hansman, R. J., Li, J., Wan, X., & Wang, J. (2025). *Planes Overhead: How Airplane Noise Impacts Home Values* (No. w34431). National Bureau of Economic Research. https://doi.org/10.3386/w34431

Outreach Efforts

The research team presented during the ASCENT Spring and Fall meetings.

Awards

None.

Student Involvement

Juju Wang (PhD Student)

Plans for Next Period

Finalize our pilot analysis for Boston Logan airport and then roll out the framework to SEA, ORD, and other airports.

Task 7 – Analysis of Noise Exposure Patterns

Massachusetts Institute of Technology

Objective

The objective of this task is to analyze spatial patterns of aircraft noise exposure across 22 major U.S. airports and the profiles of exposed communities.

Research Approach (Data and Method)

The empirical work leveraged the following data:

- Flight-track data: Threaded Track (2019).
- Demographics: American Community Survey 5-year (2019).
- Noise metrics: Average Daily N60 (number of overflights > 60 dBA per day) and day-night noise level (DNL).

Noise exposure was modeled using flight-track data for the year 2019 and the AEDT Fast model (see year 2021 report). This Fast model uses AEDT outputs for various aircraft types to set up a noise lookup table. It then applies the noise-power-distance curves from the AEDT to obtain accurate noise data for specific flight tracks. The noise contours were geospatially linked to demographic and population data taken from American Community Survey data to identify where and how noise affects communities. We then explored patterns and trends in exposure intensity and spatial concentration across multiple airports.

Milestones

- Modeled noise data for 22 airports using 2019 flight track data.
- Created geospatial database linking noise metrics (Average Daily N60, DNL) to population data.
- Produced comparative exposure maps showing variation across airports.
- Identified key approach patterns and exposure gradients near arrival/departure corridors.

Major Accomplishments

The results of our analysis show that noise exposure patterns differ by airport, reflecting differences in operational layouts and navigational procedures. For example, airports with concentrated arrival paths show more localized high-noise zones, while airports with dispersed operations have spatially larger, moderate exposure areas. By way of example, we compared

flight operations and noise exposure patterns for LaGuardia Airport (LGA) and SEA (see Figure 3). The top panels display aircraft movements, where red lines represent departure paths and blue lines represent arrivals. As shown, SEA flight paths are more concentrated, with both departures and arrivals aligned along a north-south axis. In contrast, there are different corridors for take-off from and landing into LGA which, over time, spreads departures and arrivals in several directions. Contours of noise exposure (Average Daily N60) are subsequently concentrated along the axes for SEA, whereas the contours for LGA show less concentrated patterns.

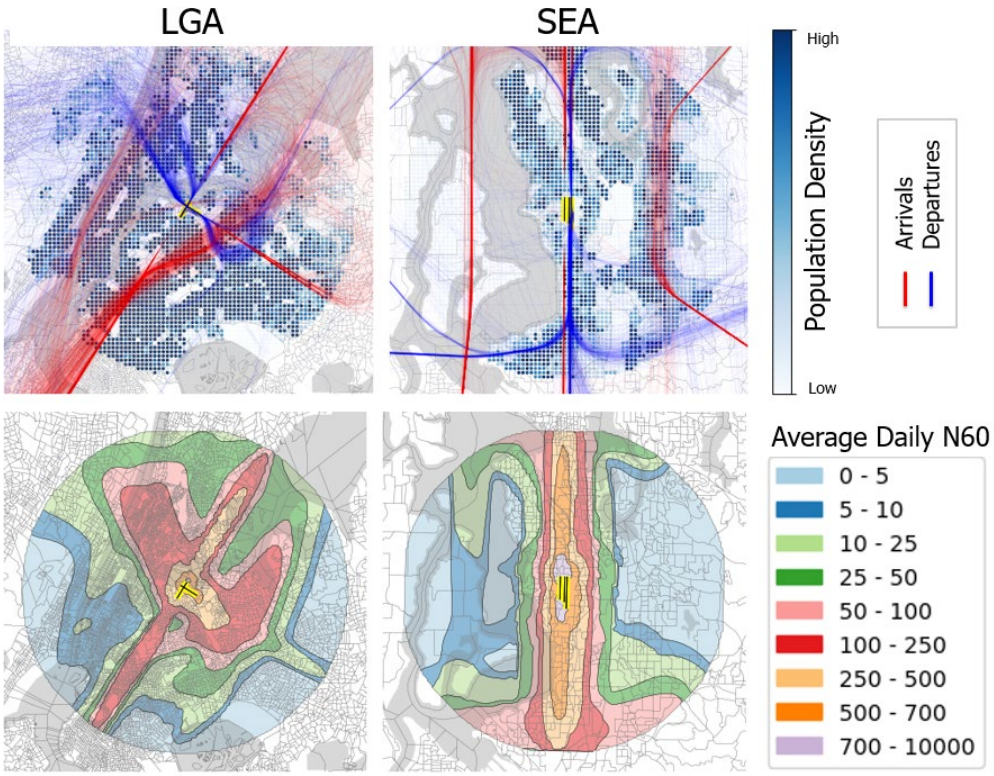


Figure 3. Flight Paths and noise exposure (Average Daily N60) at LaGuardia Airport (LGA) and Seattle-Tacoma International Airport (SEA). The top panels show aircraft arrival (red) and departure (blue) paths overlaid on population density. The bottom panels show modeled Average Daily N60, representing the number of overflights above 60 dBA per day.

Figure 4 illustrates how different airports in this study compare in noise exposure. The number of person-noise events (overflights over 60dBA averaged over 2019) is shown in Figure 4a. The metric captures both the scale of airport operations and the density of nearby population. LGA shows the highest average daily person-noise events among all airports in the sample. More generally, airports with the highest surrounding population and most operations tend to have the highest number of person-noise events. The result subsequently reflects not only LGA's high volume of operations but also its location within a densely populated urban area. Other large airports such as Los Angeles International Airport (LAX) and ORD also record high noise-population interactions. In Figure 4b, we show how noise exposure is distributed within communities surrounding airports, using the N60 metric. The x-axis shows the population sorted from least to most noise exposure, the y-axis shows the average daily N60 values. The total number of flights and population for each airport is also shown as a plotted point. For most airports, the curve rises steeply near the right tail, indicating that a relatively small portion of the population experiences high noise exposure.

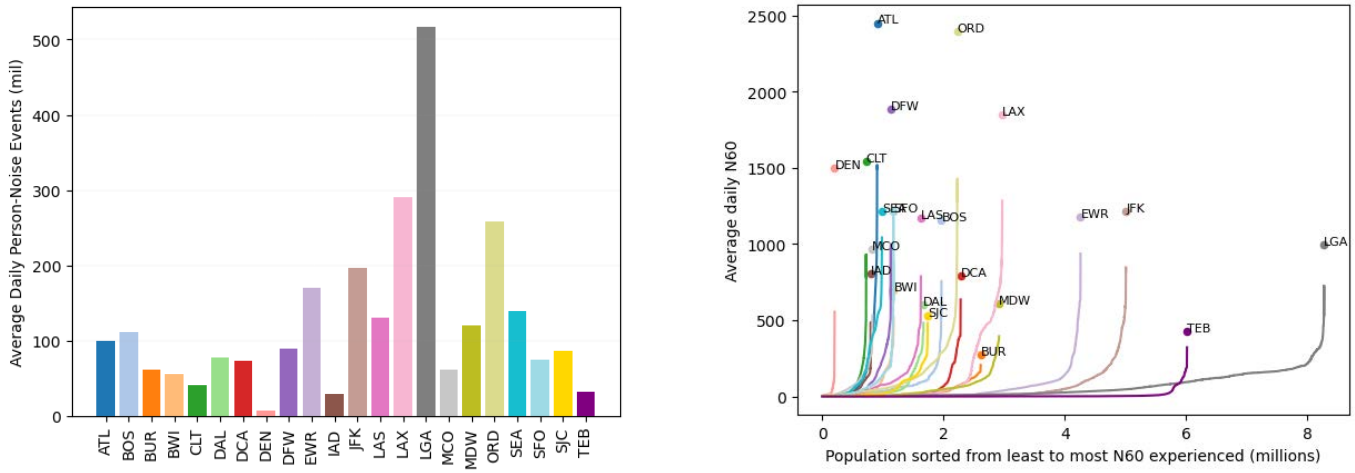


Figure 4. Comparison of noise exposure across airports: (a) shows the average daily person-noise events (millions) for each airport in 2019, while panel (b) plots the distribution of average daily N60 exposure, with population sorted from least to most exposed.

Publications
Dissertation thesis of Dr. Juju Wang, to be made available by MIT.

Outreach Efforts
The research team presented during the ASCENT Spring and Fall meetings in 2025.

Awards
None.

Student Involvement
Juju Wang (PhD Student) conducted research under this task. She graduated with a PhD in the summer of 2025.

Plans for Next Period
Publish results.



Project 073 Fuel Composition Impact on Combustor Durability

University of Dayton Research Institute

Project Lead Investigator

Scott Stouffer
Group Leader, Combustion Group, Fuels and Combustion Division
University of Dayton Research Institute
300 College Park, Dayton, OH 45469-0043
937-255-7277
Scott.Stouffer@udri.udayton.edu

University Participants

University of Dayton Research Institute

- P.I.: Scott Stouffer, PhD, PE
- FAA Award Number: 13-C-AJFE-UD, Amendment 029
- Period of Performance: August 11, 2020, to September 30, 2021
- Period of Performance: August 10, 2021, to February 10, 2022: Amendment 036
- Period of Performance: October 1, 2021, to September 30, 2022: Amendment 040
- Period of Performance: October 1, 2022, to September 30, 2023: Amendment 044
- Period of Performance: October 1, 2023, to September 2025: Amendment 54
- Task:
  1. Perform radiation measurements of various fuel types in the referee combustor to evaluate the effect of fuel composition on combustor liner lifetime

Project Funding Level

Amendment	Funding
Amendment No. 029	$299,148
Amendment No. 040	$199,865
Amendment No. 044	$200,000
Amendment No. 054	$130,000
Total	$829,013

Investigation Team

Dr. Scott Stouffer, (P.I.), project direction
Mr. Tyler Hendershott, (research engineer), combustor operations
Dr. Jeff Monfort, (research engineer), radiation measurements
Mr. Harry Grieselhuber, (technician), combustor testing
Ms. Elizabeth Koetter, Student Intern

Project Overview

In this study, the effects of fuel chemical composition on radiative heat transfer and the resulting combustor liner lifetime will be evaluated. Alternative fuels contain ratios of hydrocarbon types that may substantially differ from those in familiar petroleum-based fuels. In petroleum-based fuels, higher aromatic levels are known to contribute to greater particulate matter loading radiative heat transfer and reduced combustor liner lifetimes. Consequently, aromatic compounds are



limited to 25 vol% in the ASTM D1655 (ASTM International, 2023) jet fuel specification. Some candidate alternative fuels contain synthetically produced aromatic compounds and cycloparaffins, which must be evaluated for their radiative heat transfer characteristics. The measurements collected in this project will provide insights into the effects of fuel type on liner lifetime. Several fuel types will be investigated, including a synthetic aromatic kerosene, a baseline Jet A fuel, and a fuel high in cycloparaffins. Diagnostic methods to be used in the investigation include the measurement of wall and gas temperatures, and the use of infrared (IR) cameras and radiometers.

Task 1 – Perform Radiation Measurements of Various Fuel Types in the Referee Combustor to Evaluate the Effect of Fuel Composition on Combustor Liner Lifetime

University of Dayton Research Institute

Objective

The objective of this task is to provide insights into the effect of fuel type on engine combustor liner lifetime. The study conducted under this task will ensure that candidate drop-in fuels will perform satisfactorily in jet engines and will not increase the need for engine maintenance or decrease flight safety. The findings of this study may also indicate which fuel composition changes may reduce radiative heat transfer and therefore increase combustor liner lifetime.

Research Approach

Fuel chemical composition is well known to strongly affect soot formation, smoke production, and radiative heat flux in gas turbine combustors (Chin & Lefebvre, 1990). Studies of petroleum-based fuels with varying levels of aromatic levels have indicated that these properties increase with the overall content of aromatic species. Other parameters such as hydrogen content, hydrogen/carbon ratio, and smoke point have also been correlated with liner temperatures, but the effects of individual types of aromatic species have not been well studied. Candidate alternative fuels may meet the overall limits for aromatic species but may contain individual species or mixtures of species that are markedly different from those in petroleum-derived fuels. Radiation heat transfer to combustor liners is a major issue affecting the durability and operational envelope of gas turbine engines. Radiation can cause high heat fluxes, thus resulting in localized heating, hotspots, and high thermal gradients along and across the liner. Increases in liner temperature can decrease liner durability (Gleason & Bahr, 1980). Intense heating can cause problems with low cycle fatigue, cracking, and buckling of the liner and, in extreme cases, localized melting of the liner. The combustor walls can be convectively cooled by effusion or film cooling; however, film cooling typically imposes a cycle performance penalty, along with elevated levels of carbon monoxide (CO) and unburnt hydrocarbons, particularly at low power settings. Because of concerns regarding the effects of fuel type on radiation, the radiant heat flux is considered a figure of merit by aircraft engine original equipment manufacturers in the evaluation of alternative fuels for aircraft use (Colket et al., 2017).

The radiation from a gas turbine flame has two main components: (a) "non-luminous" radiation from product gases, such as carbon dioxide (CO_2), H_2O, and CO, and (b) luminous radiation from non-volatile particulate matter (principally soot).

Non-luminous radiation corresponds to the IR region and has a spectral distribution, whereas the luminous radiation is broadband, and a fraction of the radiation appears at visible wavelengths. Typically, as the pressure is increased, the luminous radiation from soot particles becomes the dominant source of heat flux to the liner walls. Whereas the convective component of the wall heat transfer depends on the fluid dynamics and gas temperature distribution near the walls, the peak radiant fluxes are related to the combinations of high-temperature gas and non-volatile particulate matter.

The emissivity of the combustion gases is typically related in an expression such as:

$$\epsilon_g = 1 - exp\left[-aPL(ql)^{0.5}T_g^{-1.5}\right] \quad \text{(Eq. 1)}$$

where ϵ_g= emissivity of the combustion gases (non-dimensional)
P = gas pressure in kPa
l = characteristic length factor, which is a function of combustor geometry
T_g = gas temperature in K
q = fuel-to-air ratio



L = luminosity factor

The luminosity factor is set to 1 for gaseous emissivity. For sooting flames associated with liquid aviation fuels, the luminosity is greater than 1 and can be correlated with the fuel composition. Several relations between luminosity and fuel type have been reported in the literature (Lefebvre, 1999; Naegeli & Moses, 1980; Clark, 1982). In general, the luminosity factor has been found to decrease with increasing hydrogen/carbon ratio and decreasing aromatic content of the fuel. Other correlations in the literature have addressed the correlations with smoke point and naphthalene content. Although IR has been used as a diagnostic tool in basic flame experiments (Rankin et al., 2012), very little work using multiple radiometers and/or planar measurements of IR emissions in practical combustors has been reported in the literature. The referee rig combustor is ideal for assessing radiation heat transfer because the walls are heavily cooled—a condition that tends to suppress the convective component and thus the background radiant heating from opposing walls, so that the wall heat transfer is primarily from the flame radiation.

The referee rig combustor was developed to conduct experimental combustion research. Highlights of previous contributions to the evaluation of alternative fuels include the following:

1. Experimental measurements of lean blowout (LBO) for fuels at conditions of interest to original equipment manufacturers and the National Jet Fuels Combustion Program, which have resulted in the unexpected finding of a high correlation between the derived cetane number and the LBO limit.
2. Experimental measurements of boundary conditions for the combustor, including air flow splits to support numerical combustion modeling efforts.
3. Development of cold air and cold fuel capabilities for the facility, to enable atmospheric cold start ignition experiments to be conducted over a range of conditions.
4. Further extension of the facility's ability to allow altitude relight experiments to be conducted with a range of fuels at simulated altitudes of 25,000 ft.
5. Examination of the effects of heated fuels on combustion characteristics and emissions.

The work with the referee rig combustor has yielded publications that detail cold start ignition (Hendershott et al., 2018), ignition at elevated temperatures (Stouffer et al., 2017), LBO characteristics (Corporan et al., 2017; Esclapez et al., 2017; Colborn et al., 2020), particulate and gaseous emissions (Corporan et al., 2017), acoustic response (Monfort et al., 2017), flow through the liner effusion passages (Erdmann et al., 2017; Briones et al., 2017), spray characteristics (Mayhew et al., 2017), and altitude relight (Stouffer et al., 2020; Stouffer et al., 2021).

Milestones

Milestone	Planned Due Date
Provided test plan	December 1, 2020
Conducted initial instrumentation experiments	September 2022
Perform detailed testing for a range of fuels	April 1, 2026
Complete final report	September 30, 2026

Major Accomplishments

The experimental research facility used for the combustion experiments, which is owned by the United States Air Force Research Laboratory (AFRL), was unavailable during the past year for this program because of issues with construction programs and other AFRL programs that had priority over the past year. Experiments are expected to resume in spring 2026. During the past year, the ASCENT Project 073 team was able to make progress with the analysis of data from the previous year these results are discussed below.

The fuels that were studied in the previous year are briefly described here to provide context for the discussion to follow. The fuels for the experiments are listed in Table 1 which shows a top-level breakdown of the chemical constituents. The fuels are listed in order of increasing total aromatic fraction. The Fischer Tropsch (FT) fuel is a low aromatic fuel consisting mainly of iso-paraffins. The A2 fuel is a "middle of the road" Jet A fuel studied extensively in the National Jet Fuels Combustion Program. A 50% blend of the A2/FT fuel was also considered to examine the effect of lowering the aromatic content of Jet A fuel. A mixture of synthetic aromatic kerosene (SAK) and Jet Propellant-8 (JP8) fuels was also studied, this fuel contained more than twice the number of single ring aromatic compounds (alkybenzenes) but lower



levels of diaromatics, and cycloaromatics. A final blend of aromatic compounds (30% volume) mixed with FT (70%) fuel was created to examine the effect of high levels of both total aromatics and diaromatic compounds on soot and radiation.

Table 1. Properties of the fuels studied.

	Volume %								Empirical Formula		
	Aromatics				Paraffins						
Fuel	Total Alkylbenzenes	Total Diaromatics	Total Cycloaromatics	Total Aromatics	Total Isoparaffins	Total n-paraffins	Total Cycloparaffins	Total Paraffins	C	H	MW
Fisher Tropsch (FT)	0.37	0.02	0.13	0.51	94.31	0.32	4.87	99.49	10.80	23.50	153.2
50% FT/50& Jet A	6.10	0.93	1.47	8.50	62.88	10.77	17.85	91.51	11.10	22.74	156.1
Jet A (A2)	11.84	1.84	2.81	16.49	31.46	21.23	30.83	83.52	11.40	22.10	159.0
JP8/SAK Blend	23.36	0.62	1.35	25.33	33.62	23.18	17.87	74.67	10.50	19.90	146.0
70% FT/30% Aromatic Blend	24.50	3.73	1.92	30.15	66.21	0.23	3.41	69.85	10.48	19.56	145.5

Analysis of Experimental Results

The observed limitations surrounding the transmission of long-wavelength radiation through the quartz side windows highlight the need for an alternate solution by which the relevant properties of interest could be established. Previous work has suggested that there is a fuel sensitivity realized by the relative distribution within the combustor of the high-temperature regions. The limited number of surface thermocouples does not afford the required spatial resolution necessary for effective analysis. A proof-of concept exercise was conducted to evaluate the feasibility of using images collected with the near IR camera to calculate an apparent temperature distribution from the soot within the combustor, using only shorter-wavelength data.

For a given fuel and a given condition, there is a clear difference between the captured images as a function of wavelength. Figure 1 shows a series of time-averaged, long-duration images, each corrected for the various acquisition parameters, for each of the five wavelengths of interest.

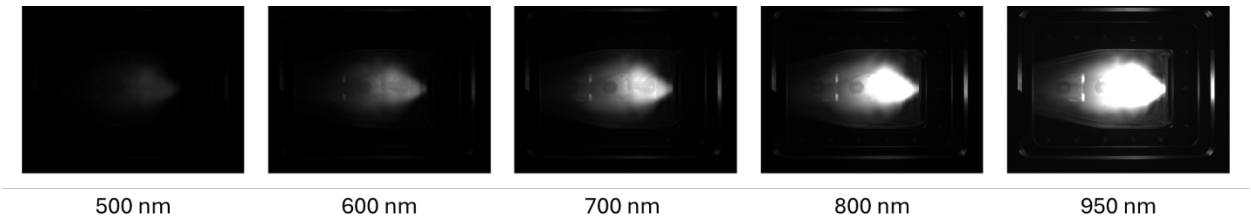


Figure 1. Images for A2 fuel vs. wavelength.

The differences, both in terms of absolute intensity and relative shape, suggest that there is a link between the temperature observed at a given location (pixel) and the ratio between the signals at that location for multiple

wavelengths. To model this temperature-based link, the assumption is made that the radiation-emitting particles within the combustor act as blackbodies. Figure 2 shows a series of blackbody curves over a range of temperatures between 300 K and 3,000 K. Over the range of temperatures and wavelengths, each curve is monotonically increasing, with no overlap between the traces, indicating that if given a pair of known wavelengths, the ratio between the emissive power at those two wavelengths can be traced back to a single temperature.

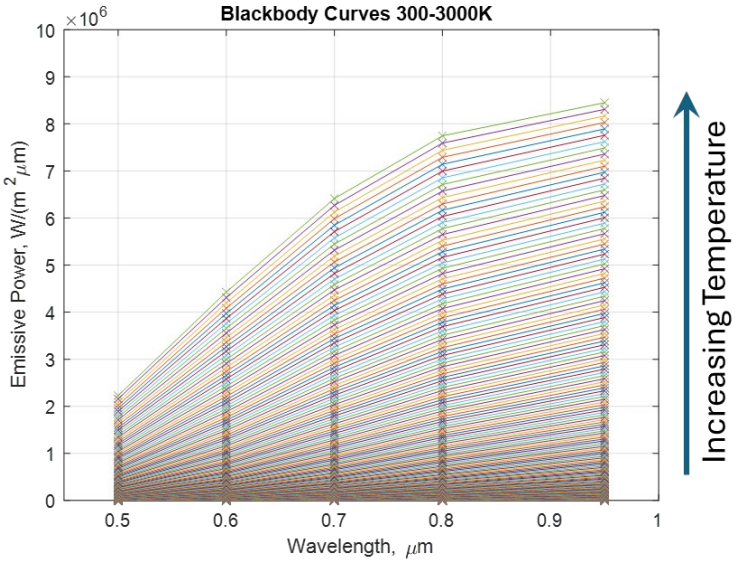


Figure 2. Graph of Blackbody radiation curves.

A multi-column lookup table was generated, which links the ratios of each pair of wavelengths to the modeled blackbody temperature. The lookup table is then applied to ratio maps, which are calculated on a pixel-by-pixel basis for each of the wavelength pairs and the time-averaged images. Figure 3 shows the results of the applied temperature-based correlations for a single fuel at a single condition, for each of the wavelength pairs.

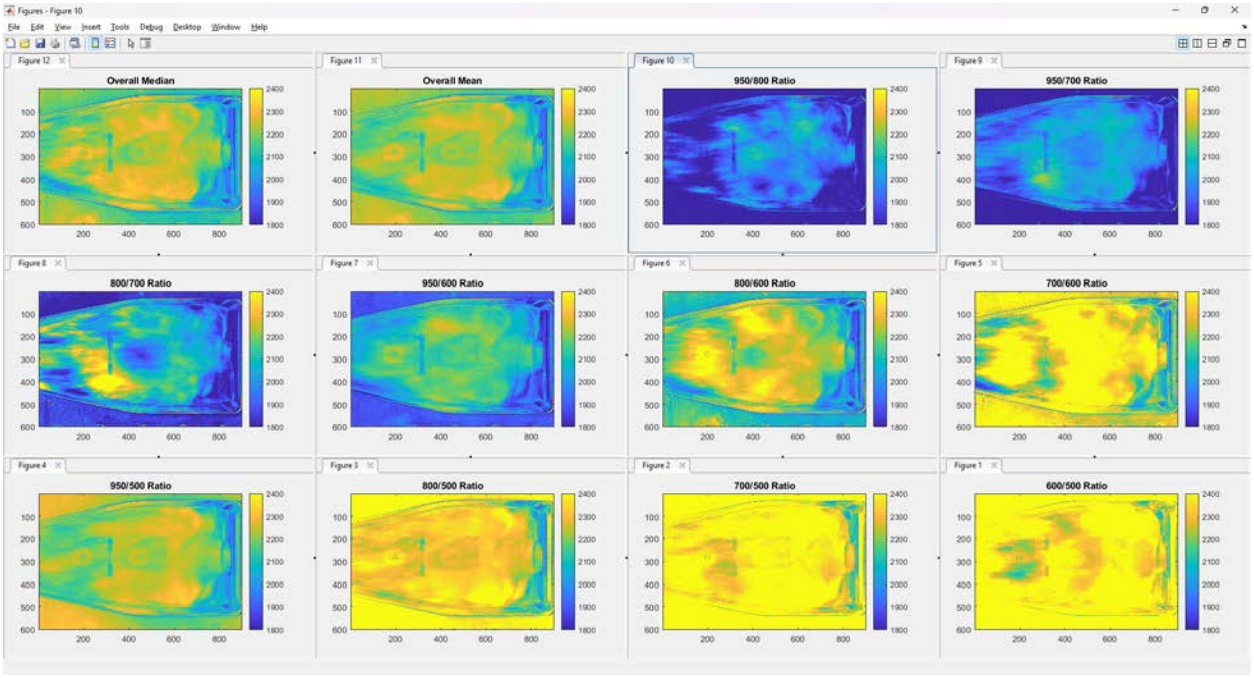


Figure 3. Calculated Pairwise Temperature fits based on a blackbody assumption from a near infrared camera.

Literature on the subject suggests that the quality of the correlation is very dependent on the wavelengths selected. Improved quality is usually achieved via the selection of wavelengths at the long end of the spectrum, with a moderate sized difference between the two chosen wavelengths. This advice seems to hold true in this case, with the flame features being most identifiable in the 950/800, 950/700, and 800/700 nanometer pairs. A limitation noted with this average-based approach is that the non-linearities associated with the lookup table result in significant uncertainty in the correlated temperature values. An improved approach utilizes multiple pairs of individual images, with the averaging process applied to the resulting temperature maps. Figure 4 shows the results of such an approach, using the 950 and 700 nanometer data, across the same range of conditions evaluated via other means.

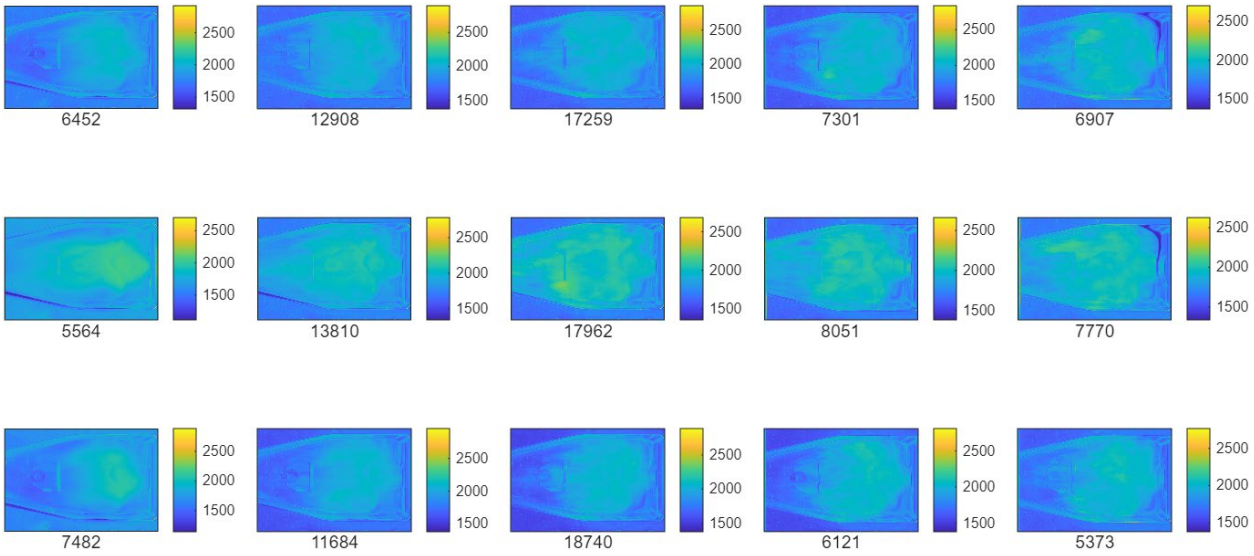


Figure 4. Calculated Temperature fits based on a blackbody assumption using multiple pairs of images from the near infrared camera.

The results here suggest that some condition and fuel sensitivity might be identifiable, but that the image pairs need to be collected simultaneously, and over a long enough duration to mitigate the effects of any experimental uncertainty, and the dynamic nature of the moving flame. Further work is underway to develop a method by which images can be collected simultaneously for a chosen pair of wavelengths. The approach requires the use of two cameras, and an algorithm by which the slight perspective differences between the two can be corrected.

Previous efforts had shown that the spatially-integrated intensities collected within the image data correlated quite strongly with parameters such as fuel aromatic content, equivalence ratio, and combustor mass flow. A sample of such data is shown in Figure 5. The image data had also shown, in a qualitative sense, that the relative locations of the high-intensity regions shift as functions of the same parameters.

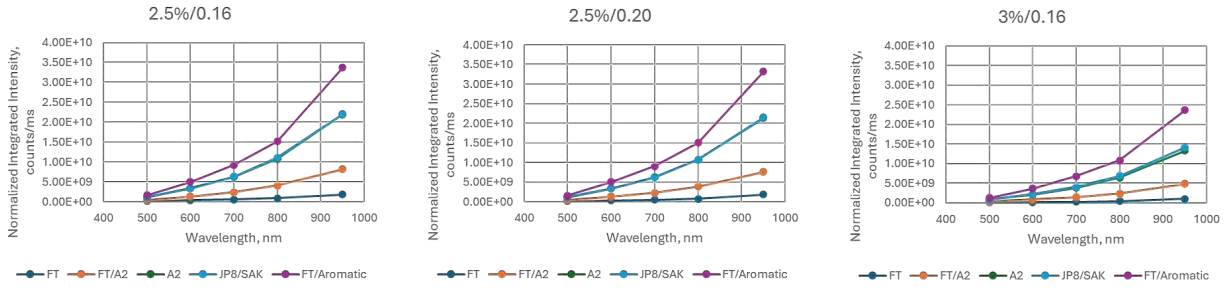


Figure 5. Three graphs showing Spatially and Temporally Integrated radiation for each of the fuels.

The overall integrated radiation intensity measured in the near infrared (950 nm) was compared side by side with the measured total particle number count at the exit of the combustor in Figure 6. The results show a strong relation between the particle concentration at the exit of the combustor and the total radiation measured by the camera.

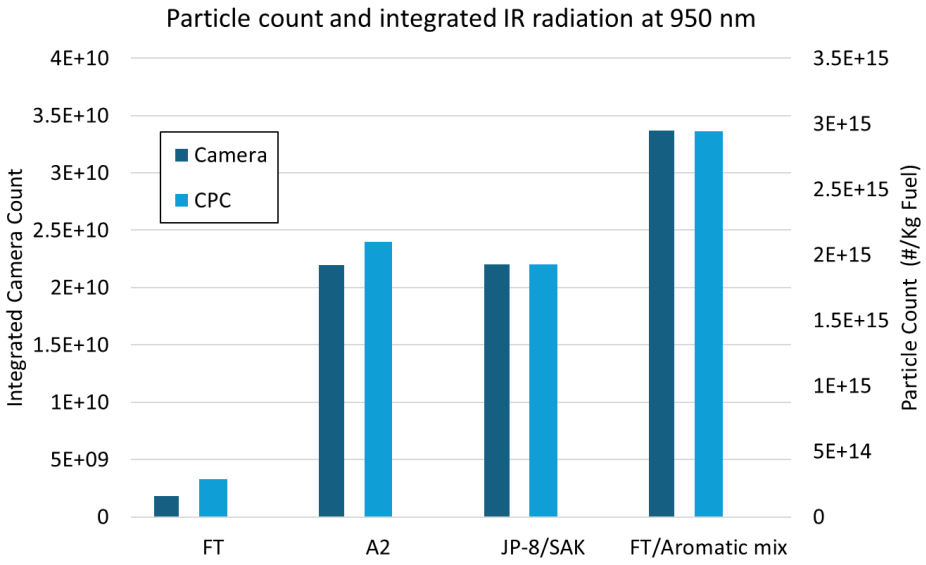


Figure 6. Graph of particle count at combustor exit and integrated IR radiation at 950 nm.

Further analysis on the spectrally-filtered emission data has been conducted, with the intent of being able to add some quantitative basis for comparisons of relative locations, and to link the data collected via the near IR camera to the radiometer output. Given that the radiometers are located within the field of view of the camera, it can be assumed that certain portions of the resultant images should correlate with the total radiation signals collected via the radiometers, at least within the range of wavelengths available. For reference the radiometer locations are shown in Figure 7 so that R1 corresponds to the location of the upstream radiometer near the dome and R2 corresponds to the location of the radiometer at the mid combustor. The camera signal at each radiometer location was integrated in a 1-in. diameter circle centered on the radiometer locations for each wavelength using five filters. The integrated signal from these locations is assumed to represent the regions at the combustor midplane which are most impactful on the radiometer signals, when considering their relatively wide cone angles, and the complicated geometry related to their fields of view.

The results are shown in Figure 8 which shows the ratio of the spatially integrated radiation from the camera at the upstream radiometer location divided by that at the mid combustor location, denoted as the R1/R2 ratio. Note that for all of the points shown the upstream radiation level is higher than that at the downstream side. The difference in this ratio is more pronounced for the lower equivalence ratio cases (R1/R2 is higher for the $\phi = 0.16$ case) because for the higher equivalence ratio cases the flame extends over a larger portion of the combustor. Moreover, there appears to be a clear upward trend in the intensity ratios, indicating an increased importance of the near-dome region as a function of increased aromatic content. The combination of these observations leads to the conclusion that the increased aromatic content has two effects: it serves to increase the overall intensity and sooting propensity, and that it will preferentially locate the highest intensity regions within a relatively small area at the upstream portion of the combustor.

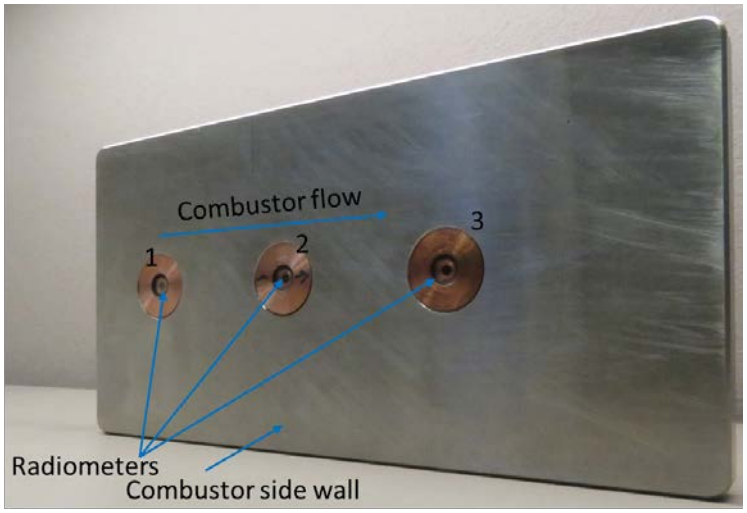


Figure 7. Combustor radiometer section.

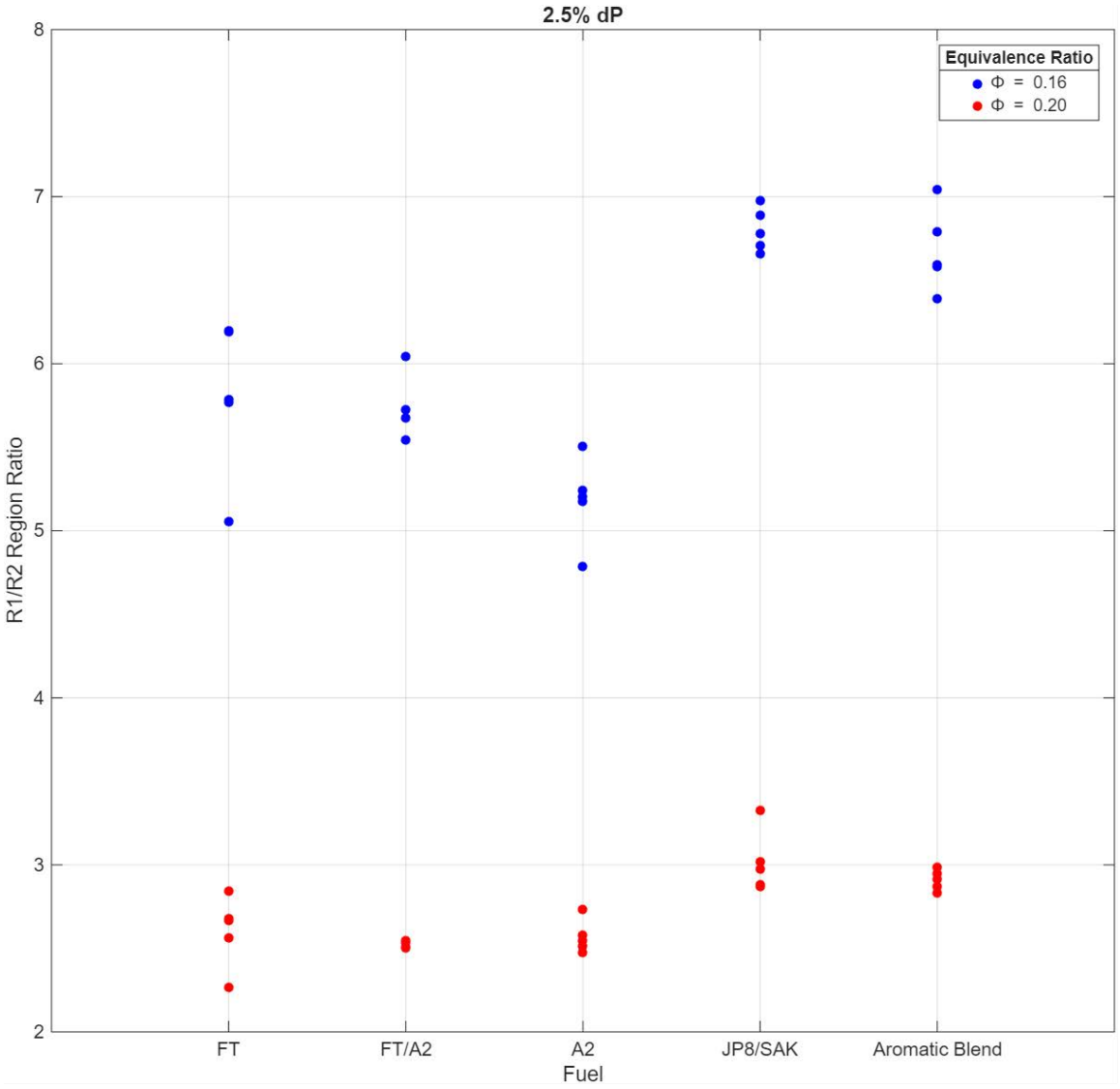


Figure 8. Ratio of the spatially and temporally integrated signal at the upstream (R1) and downstream (R2) radiometer locations.

The plan for the next series of experiments is to conduct the experiment at different pressures to allow further insight into the relative contributions of gaseous and particulate radiation. Planned instrumentation will include near infrared and infrared imaging. For the infrared images, further spectral filtering of the IR images will be explored to allow separation of the effects of radiation from gases and particulates.

Publications

None.

Outreach Efforts

As part of this work, a parallel modeling effort has been started by the National Aeronautics and Space Administration (NASA) Glenn Research Center. Our contribution so far has been to provide boundary conditions to the NASA team, who



will use the data from this effort to validate combustion models of the Referee Combustor that incorporate radiation calculations within the computational fluid dynamics framework.

Awards
None.

Student Involvement
An undergraduate student intern (Elizabeth Koetter) has started to work with the ASCENT Project 073 team and will be working with us through the spring.

Plans for Next Period
Conduct future tests are at higher pressures and consider high cycloparaffin fuels. It is thought that at the test conditions, the radiation from soot, while showing a strong relation to fuel type, does not overwhelm the gaseous component of the radiation, resulting lower fuel differences in the broad-spectrum radiation detected by the radiometer. The radiating gases (CO_2, H_2O, and CO) are expected to be similar for a given temperature and pressure condition for all the fuels. The ratio between particulate (soot) and gaseous radiation is expected to change as pressure increases.

References

ASTM International. (2023). *ASTM D1655-25a: Standard Specification for Aviation Turbine Fuels*. https://doi.org/10.1520/D1655-25A

Briones, A. M., Stouffer, S., Vogiatzis, K., & Rankin, B. A. (2017, January 9). *Effects of liner cooling momentum on combustor performance* [Conference publication]. 55th AIAA Aerospace Sciences Meeting, Grapevine, Texas. https://doi.org/10.2514/6.2017-0781

Clark, J. A. (1982). Fuel property effects on radiation intensities in a gas turbine combustor. *AIAA Journal*, *20*(2), 274–281. https://doi.org/10.2514/3.7908

Chin, J. S., & Lefebvre, A. H. (1990). Influence of fuel composition on flame radiation in gas turbine combustors. *Journal of Propulsion and Power*, *6*(4), 497–503. https://doi.org/10.2514/3.25462

Colborn, J., Heyne, J. S., Hendershott, T. H., Stouffer, S. D., Peiffer, E., & Corporan, E. (2020, January 6). *Fuel and operating condition effects on lean blowout in a swirl-stabilized single-cup combustor* [Conference publication]. *AIAA Scitech 2020 Forum*, Orlando, Florida. https://doi.org/10.2514/6.2020-1883

Colket, M., Heyne, J., Rumizen, M., Gupta, M., Edwards, T., Roquemore, W., Andac, G., Boehm, R., Lovett, J., Williams, R., Condevaux, J., Turner, D., Rizk, N., Tishkoff, J., Li, C., Moder, J., Friend, D., & Sankaran, V. (2017). Overview of the National Jet Fuels Combustion Program. *AIAA Journal*, 55(4), 1087-1104. https://doi-org/10.2514/1J055361

Corporan, E., Edwards, J. T., Stouffer, S., DeWitt, M., West, Z., Klingshirn, C., & Bruening, C. (2017, January 9*). Impacts of fuel properties on combustor performance, operability and emissions characteristics* [Conference publication]. 55thAIAA Aerospace Sciences Meeting, Grapevine, Texas. https://doi.org/10.2514/6.2017-0380

Erdmann, T. J., Burrus, D. L., Briones, A. M., Stouffer, S. D., Rankin, B. A., & Caswell, A. W. (2017, June 26-30). Experimental and computational characterization of flow rates in a multiple-passage gas turbine combustor swirler. *Proceedings of the ASME Turbo Expo 2017: Turbomachinery Technical Conference and Exposition. Volume 4B: Combustion, Fuels and Emissions,* Charlotte, North Carolina. V04BT04A076. https://doi.org/10.1115/GT2017-65252

Esclapez, L., Ma, P. C., Mayhew, E., Xu, R., Stouffer, S., Lee, T., Wang, H., & Ihme, M. (2017). Fuel effects on lean blow-out in a realistic gas turbine combustor. *Combustion and Flame*, *181*, 82–99.

Gleason, G. C. & Bahr, D. W. (1980, March 10-13). Fuel property effects on life characteristics of aircraft turbine engine combustors. *Proceedings of the ASME 1980 International Gas Turbine Conference and Products Show. Volume 1A: General*, New Orleans, Louisiana. 80-GT-55. https://doi.org/10.1115/80-GT-55

Hendershott, T. H., Stouffer, S., Monfort, J. R., Diemer, J., Busby, K., Corporan, E., Wrzesinski, P., & Caswell, A. W. (2018, January 8). *Ignition of conventional and alternative fuel at low temperatures in a single-cup swirl-stabilized combustor* [Conference publication]. 2018 AIAA Aerospace Sciences Meeting, Kissimmee, Florida. https://doi.org/10.2514/6.2018-1422

Lefebvre, A. H. (1999). *Gas turbine combustion* (2nd Ed.), Taylor and Francis, Philadelphia.

Mayhew, E., Mitsingas, C. M., McGann, B., Hendershott, T., Stouffer, S., Wrzesinski, P., Caswell, A. W., & Lee, T. (2017, January 9). *Spray characteristics and flame structure of jet and alternative jet fuels* [Conference publication]. 55th AIAA Aerospace Sciences Meeting, Grapevine, Texas. https://doi.org/10.2514/6.2017-0148

Monfort, J. R., Stouffer, S., Hendershott, T., Wrzesinski, P., Foley, W., & Rein, K. D. (2017, January 9). *Evaluating combustion instability in a swirl-stabilized combustor using simultaneous pressure, temperature, and chemiluminescense*

measurements at high repetition rates [Conference publication]. 55th AIAA Aerospace Sciences Meeting, Grapevine, Texas. https://doi.org/10.2514/6.2017-1101

Naegeli, D. W. & Moses, C. A. (1980, Mar 10-13). Effects of fuel properties on soot formation in gas turbine engines. *Proceedings of the ASME 1980 International Gas Turbine Conference and Products Show. Volume 1A: General*, New Orleans, Louisiana. https://doi.org/10.1115/80-GT-62

Rankin, B. A., Blunck, D. L., Katta, V. R., Stouffer, S. D., & Gore, J. P. (2012). Experimental and computational infrared imaging of bluff body stabilized laminar diffusion flames. *Combustion and Flame*, *159*(9), 2841–2843. https://doi.org/10.1016/j.combustflame.2012.03.022

Stouffer, S. D., Hendershott, T. H., Colborn, J., Monfort, J. R., Corporan, E., Wrzesinski, P., & Caswell, A. (2020, January 6). *Fuel effects on altitude relight performance of a swirl cup combustor* [Conference publication]. AIAA Scitech 2020 Forum, Orlando, Florida. https://doi.org/10.2514/6.2020-1882

Stouffer, S., Hendershott, T., Monfort, J. R., Diemer, J., Corporan, E., Wrzesinski, P., & Caswell, A. W. (2017, January 9). *Lean blowout and ignition characteristics of conventional and surrogate fuels measured in a swirl stabilized combustor* [Conference publication]. 55th AIAA Aerospace Sciences Meeting, Grapevine, Texas. https://doi.org/10.2514/6.2017-1954

Stouffer, S. D., Hendershott, T. H., Boehm, R., Lovett, J. (2021). Chapter 4: The referee rig combustor. In *Fuel effects on operability of gas turbine combustors*. The American Institute of Aeronautics and Astronautics, Inc. https://doi.org/10.2514/4.106040



Project 075 Improved Engine Fan Broadband Noise Prediction Capabilities

Boston University & Raytheon Technologies Research Center

Project Lead Investigator

Sheryl Grace
Associate Professor
Mechanical Engineering
Boston University
110 Cummington Mall, Boston, MA 02215
617-353-7364
sgrace@bu.edu

University Participants

Boston University (BU)

- P.I.: Sheryl Grace – Associate Professor, Mechanical Engineering
- FAA Award Number: 13-C-AJFE-BU Amendment 022
- Period of Performance: November 1, 2023, to October 30, 2024
- Tasks:
  1. Fan-wake surrogate model creation
  2. Improved low-order model
  3. Rig test planning

Project Funding Level

Year 4 Funding (March 18, 2024, to September 30, 2025):
Federal Aviation Administration (FAA): $201,044 total ($105,286 to BU, $95,758 to Raytheon Technologies Research Center [RTRC])
Matching Funds: $201,044 from BU (datasets, AeroAcoustics Research Consortium [AARC] previous funding, faculty time)

Year 5 Funding (December 3, 2024, to July 31, 2026):
FAA:$219,979 total ($25,000 to BU, $194,980 to RTRC)
Matching Funds: $110,161 from BU (datasets, AARC previous funding, faculty time), $109,819 from RTRC (Pratt & Whitney [P&W] effort)

Investigation Team

Boston University

Sheryl Grace (PD/P.I.), Tasks 1, 2 & 3
Nuo Li, graduate researcher (PhD), Tasks 1 & 2
Ronald Chambergo, undergraduate researcher, Tasks 2
Oliver Zajac, undergraduate researcher, Task 2

Raytheon Technologies Research Center

Jeff Mendoza (Co-PD/P.I.), Tasks 1, 2 & 3
Craig Aaron Reimann, Tasks 2 & 3
Julian Winkler, Tasks 1, 2 & 3
Dmytro Voytovych, Task 1
Dustin Frohnapfel, Task 3
Matt Kennedy, Task 3

Project Overview

The noise signature of contemporary turbofan engines is dominated by fan noise, both tonal and broadband. Accepted methods for predicting the tonal noise have existed for many years. Furthermore, engine designers have methods for controlling or treating tonal noise. This is much more challenging for broadband noise. Thus, it is clear that further reductions in engine noise will require accurate prediction methods for the broadband noise to enable design decisions. Interaction noise from the fan-stage is a dominant broadband mechanism in a modern high bypass engine and is created by the interaction of the turbulence in the fan wakes with the fan exit guide vanes (FEGV). This project leverages prior development of low-order models for the prediction of fan broadband interaction noise. Gaps in the low-order approach are addressed based on knowledge gained from computation and experimentation. In particular, a method for determining the inflow into the stator via a machine learning (ML) algorithm is being developed. The low-order method will also be validated against full- and rig-scale data and appropriate development undertaken based on the findings.

Task 1 - Fan-wake Surrogate Model Creation

Boston University

Objective

The objective of this task is to build a surrogate model using ML that will work with performance level unsteady Reynolds-Averaged Navier-Stokes (URANS) to specify the mean flow, turbulent kinetic energy, and turbulent length scale at locations along the helical fan-wake path.

Research Approach

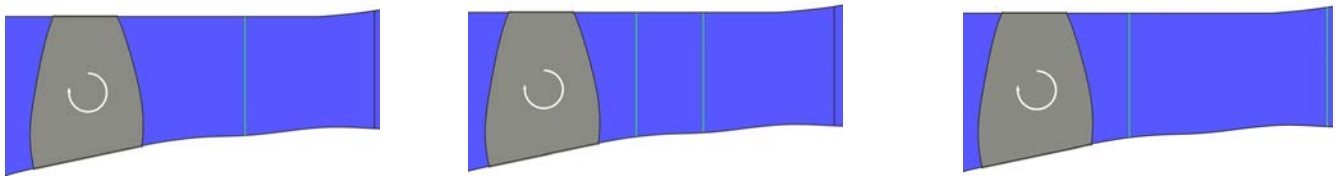
Subtask 1.1&2: Development of Autoencoder & Development of Decoder

The ML was applied to this problem in Years 4 & 5 of the ASCENT Project 075 and our team continued to use the decoder part of a neural network. Four wake flow parameters are learned in the region downstream of the fan. The mean flow axial and circumferential velocities and the turbulent kinetic energy and turbulence length scale are learned using a two-dimensional (2D) Convolution Neural Network (CNN). In the 2D method, the data are made of axial slices of the wake flow.

TensorFlow® is used for the ML and is integrated into a Python® wrapper. In Years 4 & 5, the CNN method was further tested. The large fan dataset obtained previously from collaborators at the Institut Supérieur de l'Aéronautique et de l'Espace (ISAE-Supaero) in Toulouse, France was the basis for these studies. Initial results for the ML outcomes for this set of fans were presented at the 2025 American Institute of Aeronautics and Astronautics (AIAA) Aviation conference.

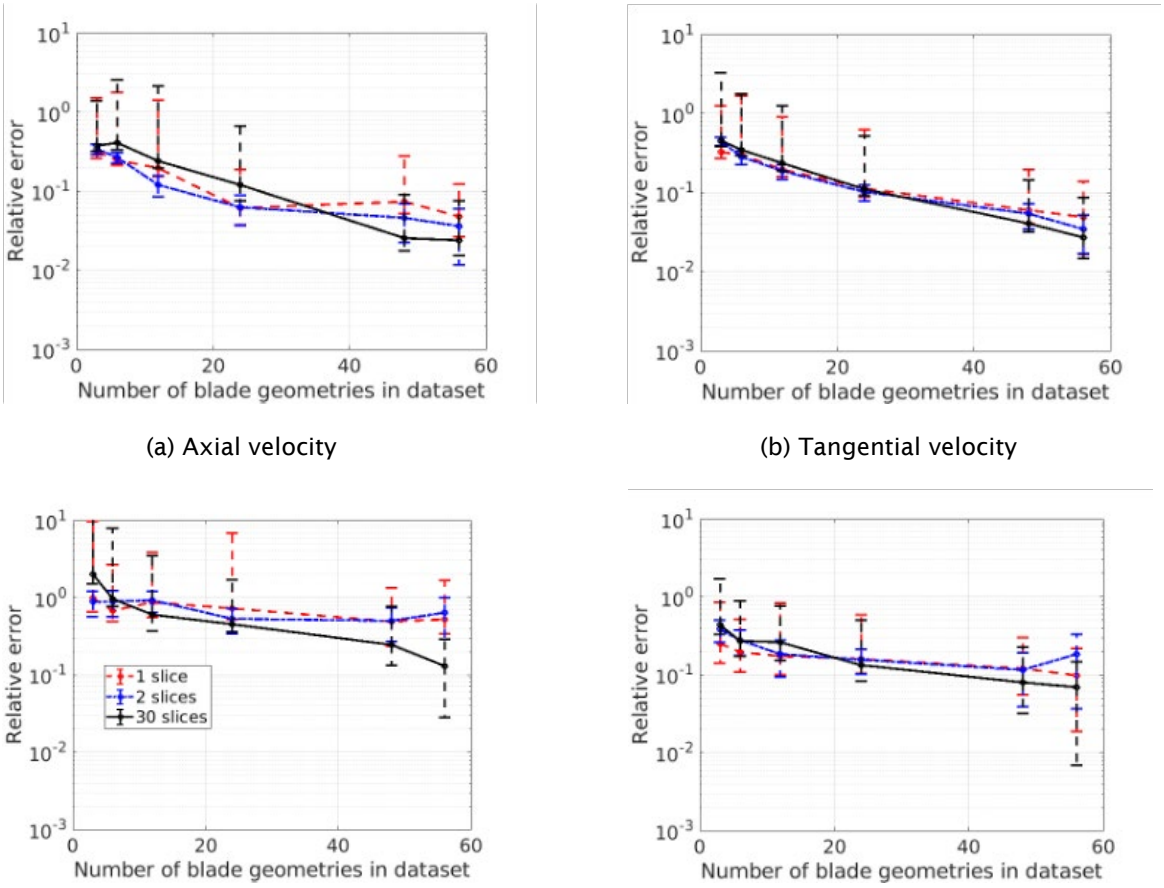
Next, the ISAE database was used to determine how the number of fans included in the database and the number of axial slices used downstream of each fan affects the ML. The different variations for the number of slices are shown in Figure 1. For each of the flow variables learned, the error between the ML prediction of three target fans not included in the database and the Reynolds-Averaged Navier-Stokes (RANS) determined wake for each of the three test fans were computed. Figure 2 shows the results for the prediction error of the slice at x = 0.129m. Not surprisingly, the error decreases as more fans are used in the database. However, at around 40 fans, the error is acceptable. It is also noted that one of the test fans is an outlier in terms of its geometry. This makes the prediction of it based on the fans in the database, an extrapolation, which is not expected to work well. When the predicted results are used in the low-order method to obtain the noise prediction, the results for the extrapolated cases are not good (see Figure 3). In terms of the number of axial slices, 1, 2, or 30 perform very similarly, except that the error bars are much smaller when more slices are used. As such, at this time, we still use a large number of axial slices to create the database.

® TensorFlow is a registered trademark of Google LLC, Mountain View, California. TensorFlow is a software library for ML and artificial intelligence that is used across a range of tasks, but mainly for training and inference of neural networks.
® Python is a registered trademark of Python Software Foundation, Beaverton, Oregon.



(a) 1 slice at x = 0.129m (b) 2 slices at x = 0.08 & 0.129 m (c) 30 slices between x = 0.08 & 0.2449m

Figure 1. Different axial slice numbers for testing the machine learning.



(a) Axial velocity (b) Tangential velocity

(c) TKE (d) Lengthscale

Figure 2. Effect of number of fans and number of axial flow slices included in the machine learning (ML) database, on the accuracy of the prediction: (a) axial velocity, (b) tangential velocity, (c) turbulent kinetic energy (TKE), and (d) lengthscale.

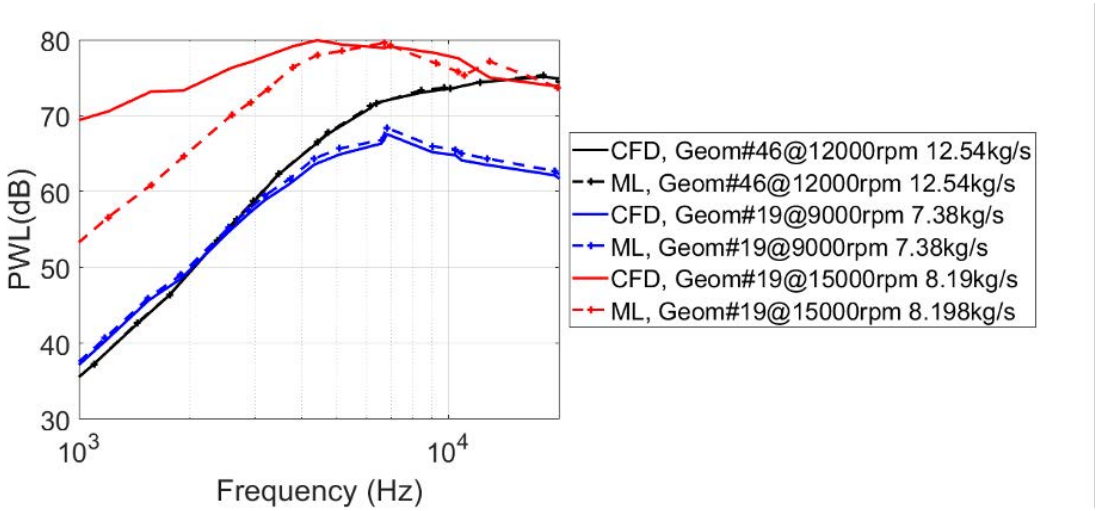


Figure 3. Exhaust power level for three different test fan geometries (from the Institut Supérieur de l'Aéronautique et de l'Espace [ISAE] cases) that were not used in the database. The same stator is used to complete the fan stage for each case. The low order acoustic method has been used with fan wake parameters from Reynolds-Averaged Navier-Stokes (RANS) (solid line) & fan wake parameters from machine learning (ML) prediction (dashed). CFD: computational fluid dynamics. PWL: sound power level.

Another modification to the ML method was also tested. A data wrapping method was tested. The goal was to allow the database to have arbitrary fan blade position and potentially improve inclusion of different fan blade counts. It was determined that the method did not improve the ML. It underscored that it is important to set up the axial slices such that the fans are positioned in their passage similarly. This often requires rotation (addition of a set angle) which does not impede the initial database setup greatly.

Subtask 1.3: Identification & Creation of Training Data

The focus of Years 4 & 5 was *Subtask 1.3b: Creation of additional training data.* The large dataset obtained from collaborators at ISAE-Supaero in Toulouse, France, continued to be a focus as discussed in the previous section. Two other geometries were also identified: the advanced ducted propulsor (ADP) whose geometry and accompanying rig test data are available from the National Aeronautics and Space Administration (NASA), and the ECL5 fan stage which has a very recent large eddy simulation (LES) completed on it. RANS simulations for both geometries are currently being developed so that they can be included in the database. These geometries were sought because they have differing blade counts than the fans in our current databases. The ability to predict fan wakes for a wide variety of fans with different blade counts has not been demonstrated yet.

The BU PhD student Nuo Li learned and thoroughly tested the Cadence® Fidelity® Fine Turbo[1] software. Multiple discoveries for best practices when running this code for the simulation of a fan and its wake as well as a full fan-stage were made. In particular, best practice for creating the grid (wake aligned) and turbulence model choice (Mentor's shear stress transport - SST) were discerned. Unfortunately, there was no turbulence model that gave as good as results as the United Technologies Computational Fluid Dynamics (UTCFD) code did for the approach case. Still, if the database is developed consistently the ML can still be assessed. Hence, currently, UTCFD and Cadence computed cases are not mixed in the database. Also, it was determined that because ISAE was not interested in the wake evolution when they performed the RANS for the fans in their database, the results did not match those obtained using our best practices. Therefore, the PhD student reran the RANS for all of the ISAE cases using the new best practices and then performed the ML.

® Cadence and Fidelity are registered trademarks of Cadence Design Systems, Inc., San Jose, California.
[1] Cadence Fidelity Fine Turbo is a computational fluid dynamics (CFD) platform specifically designed to optimize the power and efficiency of turbomachinery designs.



Subtask 1.4: Application of Surrogate Model to Relevant Fan Geometries
As discussed above, the CNN ML predictions were applied to the ISAE database of 59 fans. These fans were created by morphing aspects of several existing fans. In this sense, they have relevant features. The two newly acquired fan geometries: ADP and ECL5 will next be used to determine how well ML can predict these relevant fan geometries.

Milestones
- Validated and refined the ML surrogate model.
- Improved the ML model and applied the model to a new database with success.

Major Accomplishments
- Tested modifications to the 2D CNN models for fan wake parameter prediction.
- Fully tested and created a workflow for using the Cadence Fine Turbo software to provide a method for creating and analyzing additional fans in the future. Used it to rerun all of the ISAE cases.
- Demonstrated fast, downstream broadband noise prediction for a fan stage.

Publications
Li, N., & Grace, S. M. (2025). Low-Order, Data-Driven Method for Analysis of Impact of Fan Design on Fan Stage Broadband Interaction Noise (AIAA 2025-3650). *AIAA AVIATION 2025 Forum*, Las Vegas, Nevada.

Outreach Efforts
- Presented (undergraduate student) at the BU Undergraduate Research Symposium, October 17, 2025.
- Presented at the 2025 AIAA Aviation Forum, July 20, 2025, Las Vegas, Nevada.

Awards
None.

Student Involvement
Nuo Li, graduate researcher (PhD) developed the ML and adopted and fully tested the Cadence Fine Turbo solver. He also modified and tested the new ML input strategies. Ronald Chambergo and Oliver Zajac, the undergraduate researchers, worked with the Cadence software to perform some of the fan RANS simulations and they worked with a fan blade design tool, parablade, to support the creation of new fan blades for inclusion in the database.

Plans for Next Period
- Continue refinement and validation of the ML surrogate model.
- Develop and add additional fans to the database.

Task 2 - Improvement of Low-order Model
Boston University
Raytheon Technologies Research Center

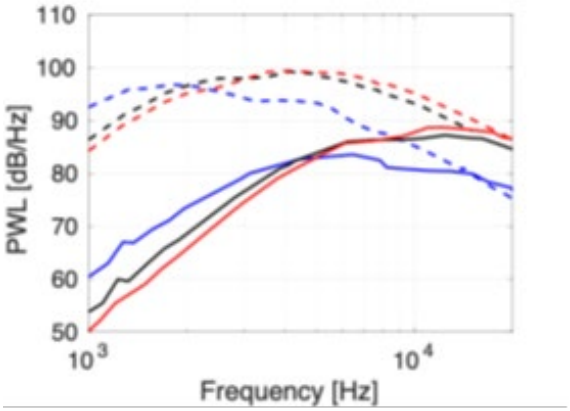
Objective
The objective of this task is to validate the low-order method against full-scale test data and adjust the low-order method as needed. The existing low-order methods are regularly applied to the source diagnostics test (SDT) cases and as such have been well validated against this test, which represents one scaled fan and multiple FEGV configurations.

Research Approach
Subtask 2.1: Ability to Predict Full-Scale Results
Great progress was made in Years 4 and 5 on this subtask. An initial check had been run previously using RTRC-generated RANS data for the FAA Continuous Lower Energy, Emission and Noise (CLEEN) Program I rig and full-scale rotor geometries. To perform the full-scale predictions, the Boston University Rotor-Stator Interaction (BU-RSI) code was updated so that the integrals carried out during the simulation had appropriate limits still as these do change with frequency and the frequency range of interest for the full-scale engine is different than for the rig. Once the low-order method was shown to converge properly, we used the normal method for extracting the low-order method inputs from the RANS data and

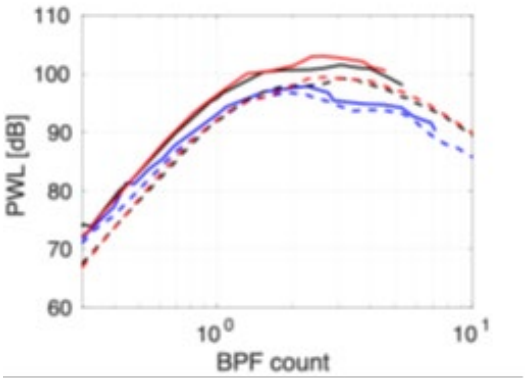


created the predictions. RTRC made comparisons with the expected results and noted that the results were not acceptable. Over this past year, we revisited this issue.

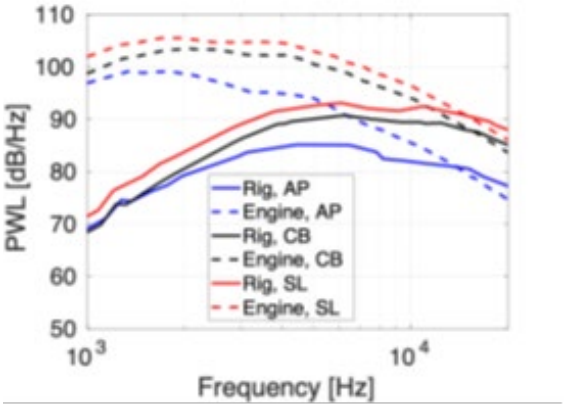
First, we created our own full scale SDT geometry. We performed our own RANS simulations for the rig and full scale SDT geometries and explored how the fan wake flow parameters varied from rig to full scale. We compared this variation to the variation seen in the CLEEN I RANS results and realized that the CLEEN I RANS results were not correct. Using the SDT case, we verified that there is a scaling of the acoustic power with the geometry change. That is, if the geometry from rig to full scale increases by a factor of X, then the acoustic power scales with an exponent of X. This scaling is not perfect because the boundary layer on the fan plays a large role in creating the fan wake parameters of interest changes as the Reynolds number changes. This affects the turbulence intensity and length scale in the wake slightly altering what would otherwise be a perfect geometric scaling. Figure 4 shows the relevant results for the SDT case. The predictions were obtained using two different methods for determining the turbulence length scale. First, Pope's method which combines the turbulence parameters via : $\Lambda_k = \frac{0.043}{0.09}\frac{\sqrt{TKE}}{\omega}$. Second, the wake width, L_w, at half depth is determined and then the length scale is set to: $\Lambda_w = 0.21\, L_w$. We note that, near the hub and tip of the FEGV, the flow is not wake like. In these regions, one cannot fit a Gaussian to the wake profile in order to define the wake width. Therefore, a Gaussian fit error is defined and when it is more than 7% no value is computed. Currently, the radial locations where the wake is well defined are simply stretched onto the entire hub-to-tip extent in order to have a length scale value at every radial location. The predictions vary slightly when the different methods are applied to obtain the input to the low-order calculation. However, they are consistent in their application to the rig and full-scale cases.



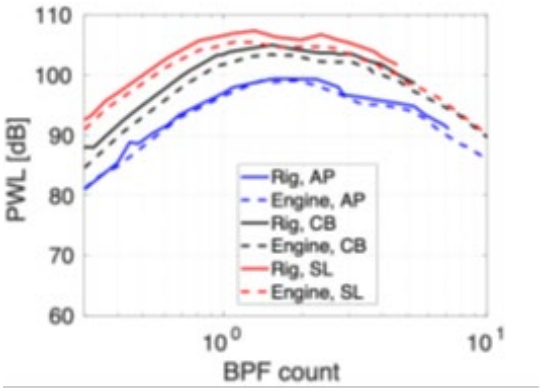
(a) Pope k-w based lengthscale; actual



(b) Pope k-w based lengthscale; scaled



(c) Wake based length scale: actual



(d) Wake-based length scale; scaled

Figure 4. Exhaust sound power for source diagnostics test (SDT) rig and full scale (three times larger) at three operating points as predicted using the low-order method using input computed with Cadence Fine Turbo. Left: actual sound pressure level (PWL) spectra. Right: full scale fan stage results scaled by geometry factor and plotted against blade passage frequency. Top: length scale computed from turbulence parameters using Pope's method. Bottom: length scale computed based on wake width.

It was determined that using Pope's method for determining the length scale from the turbulence model parameters in the RANS, does not work when the UTCFD is applied to the CLEEN I rig and full-scale cases. We wrote a brief summary report about the length scale issue (included as Appendix A). Even though the full-scale case was rerun using different turbulent parameter inputs, which improved the RANS result, it still does not give the expected length scale. As such, we switched to using the wake width method for defining the length scale. We showed that this method is far more robust for defining the length scale from the UTCFD results. The predicted sound pressure level (PWL) spectra with the rig values scaled by the geometric multiplier are shown in Figure 5 plotted against the blade passing frequency count. The geometric scaling is a bit less accurate for the CLEEN I, implying that the Reynolds number effects are stronger. This is still being investigated. A full scaling formula that includes both the geometric and Reynolds number effects is being sought.

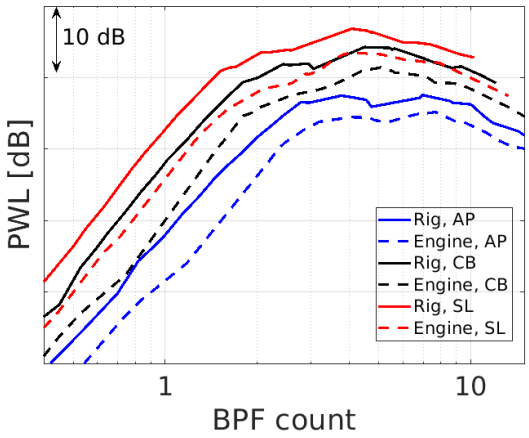


Figure 5. Exhaust sound power for Continuous Lower Energy, Emission and Noise (CLEEN) I rig results scaled up three times and full-scale results both plotted against blade passage frequency at three operating points as predicted using the low-order method with input computed via United Technologies Computational Fluid Dynamics (UTCFD). Wake width-based length scale. BPF: blade passage frequency, PWL: sound power level.

After a journal article submission came back from review. There were some comments that led to further investigation concerning the results reported last year about the effect of moving the FEGV in fan-stage broadband interaction noise. Further studies were run that indeed solidified the low-order prediction results. Moving the FEGV does not significantly affect the performance of the fan-stage for the cases considered and only changes the broadband noise by 1-2 dB. The differences between the predictions using BU-RSI and Hanson's method, which differ on whether the noise is increasing or staying the same is still not completely understood.

The low-order method was used to perform a preliminary assessment of the effect of having a bifurcation and a pylon downstream of the fan-stage. The new rig is similar to the CLEEN I rig but slightly larger. The first question that was addressed was whether the pylon and bifurcation add significant noise to the full-stage geometry. The wake information downstream of the FEGV was estimated and used as input to a BU-RSI type simulation where the mean flow has no tangential component and the flow interacts with only one vane – either the pylon or the bifurcation. This is more like the reaction of a single airfoil to unsteady disturbances versus a cascade. The response was still based on flat plate theory even though the pylon's cross section is a very thick airfoil. The acoustic propagation downstream still assumes propagation in a full annulus whereas the pylon splits the annulus. Previous studies showed that whether the annulus is split or not does not change the total power, it just shifted the modes a bit. Therefore, we believed this assumption was reasonable to get a first look at the effect on sound power. The results when adding the contributions from both the pylon and bifurcation show that their effect will be small as shown in Figure 6. The pylon and bifurcation raise the level of the broadband by up to 5 dB in the low frequency range. The change is expected to be negligible beyond the second blade pass frequency.

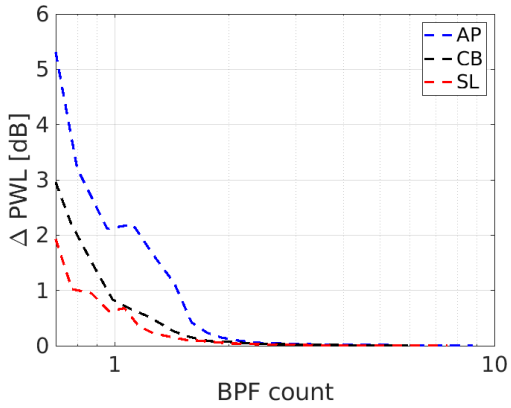


Figure 6. Difference in exhaust sound pressure level (PWL) for the Continuous Lower Energy, Emission and Noise (CLEEN) I fan stage without and with downstream pylon and bifurcation. BFP: blade passage frequency.

The second analysis was done in support of a fan alone test that was originally being planned. The question again was how fan-alone broadband noise would change with the presence of the bifurcation and pylon. However, it was discerned that because for the fan-alone case, the flow will not be well aligned with the pylon. The separation that will occur on the pylon will give rise to broadband self-noise which may be on the same order as the interaction broadband noise. Without more information about the actual geometry and ability to estimate the separation, this calculation could not be completed.

Subtask 2.2: Inclusion of Tip Flow Impact on the Low-Order Model and *Subtask 2.3: Inclusion of Inflow Distortion Impact on the Low-Order Model* were discussed previously (in Year 2).

Milestones

- Validate the low-order model for rig and full-scale applicability.
- Improve low-order model.

Major Accomplishments

- Developed best practices for using Cadence Fine Turbo for these simulations.
- Acquired enough information and developed full-scale SDT fan in order to validate that the low-order model works well for full scale as well as rig size fan stages.
- Analyzed some cases that will be of interest for the upcoming rig test.

Publications

Li, N., Winkler, J., Reinmann, C. A., Mendoza, J., & Grace, S. M. (2024). On the Use of a Low-Order Model for Rig and Full-Scale Turbofan Broadband Noise Predictions. *Being developed for the AIAA/CEAS Aeroacoustics Conference (2026).*

Outreach Efforts

None.

Awards

None.

Student Involvement

Nuo Li, graduate researcher (PhD), worked on the low-order model.

Plans for Next Period

- Further validation of the full-scale broadband noise predictions.
- Package the BU-RSI code and ML for distribution.

Task 3 - Rig Test Preparation

Raytheon Technologies Research Center

Objectives

The objectives of this task are to perform experiments in the RTRC Acoustic Research Tunnel (ART) to: (a) acquire key aerodynamic and acoustic data to support the validation of low-order and mid- (RANS) to high- (VLES, LBM Very Large Eddy Simulation, Lattice Boltzmann Method) fidelity computational fluid dynamics (CFD) models, and (b) assess the noise trends and scaling laws of different fan stages.

Research Approach

The rig being designed is a scaled version of the P&W fan rig from the FAA CLEEN I program. Thus, the rig will include a modern fan, but the flow path will focus solely on the bypass, thus eliminating the need for a core. The configurations that are planned include the P&W baseline design, as was previously evaluated at NASA. While it was anticipated that either a rotor-alone (no FEGV) configuration or a shifted FEGV configuration might be part of this test, the available funding will only cover testing of the baseline configuration.

The rig and measurement methods are fully designed as shown in Figure 7. The flow measurement probe setup was designed to capture radial length scale, which has not been measured previously in the fan-stage gap. The two-probe setup is novel and can be deployed at two different locations axially in the gap.

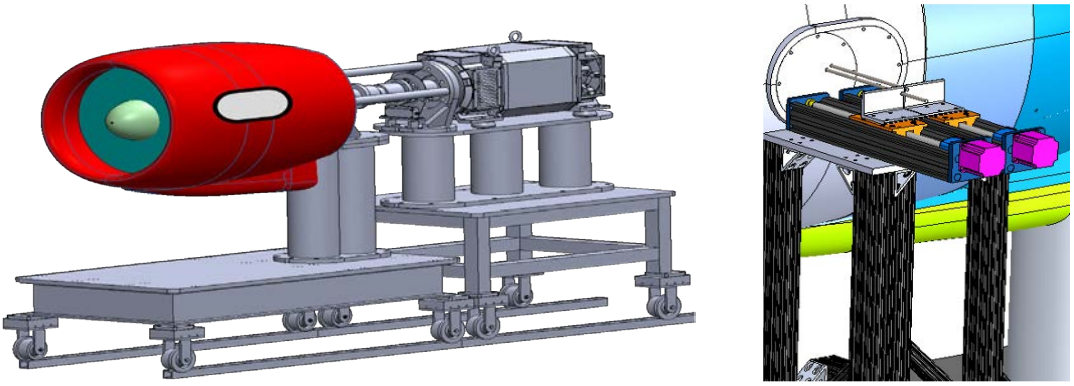


Figure 7. Raytheon Technologies Research Center (RTRC) rig design (left) and two hot-wire probe design (right).

As Year 5 concludes, the rig should be complete and ready for testing. The Gantt chart for the project in Figure 8 shows the best estimate for completion of the tests. The tests will now take place in early 2026.

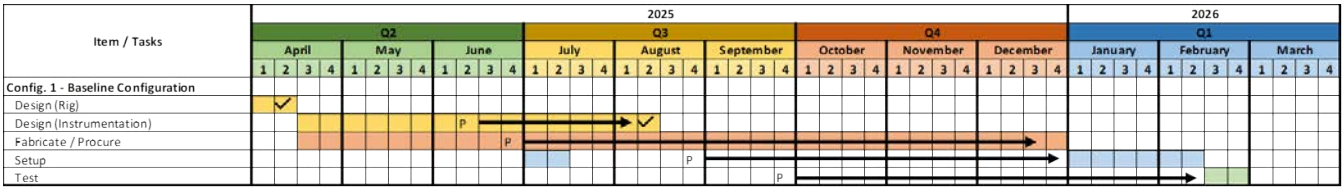


Figure 8. Raytheon Technologies Research Center (RTRC) rig development and test schedule.

Milestone

Design the rig test.

Major Accomplishments

- Participated in multiple meetings between RTRC/BU and P&W to determine the exact test capabilities.
- Completion of the probe design.



- Sourced all of the parts.
- Initial set up of the rig – parts that have arrived.

Publications
None.

Outreach Efforts
None.

Awards
None.

Student Involvement
None.

Plans for Next Period
- Test rig shakedown.
- Complete rig testing.

Appendix A

A Study in Why Lengthscale is a Difficulty in Broadband Modeling

Boston University
Authors: Sheryl Grace and Nuo Li
September 9, 2025

Introduction

This report details salient points related to length scale estimation applied to the flow solutions obtained from two computational fluid dynamics (CFD) solvers: United Technologies Computational Fluid Dynamics (UTCFD) and Cadence® Fidelity® Turbo. UTCFD utilizes the Ni-scheme based on Lax-Wendroff (Lax & Wendroff, 1960). A turbulence model based on Wilcox's $k-\omega$ with a vorticity source term is applied (Wilcox, 1988, 2006). Fidelity Turbo uses the Jameson–Schmidt–Turkel (JST) scheme (Jameson, et al., 1981). The Wilcox k–ω model is implemented but it has numerical instability issues and does not perform well. The Menter Shear Stress Transport (SST) model (Menter, 2003) was suggested by the developers. As such, the Fidelity Turbo simulations currently utilize the SST turbulence model. Table A-1 shows which solvers have been applied to which fan geometries in this study.

Table A-1. Solver applied to the fan geometry. CLEEN: Continuous Lower Energy, Emission and Noise, SDT: Source Diagnostics Test, UTCFD: United Technologies Computational Fluid Dynamics.

Solver	Fan Geometry
SDT rig scale	UTCFD, Fidelity Turbo
SDT full size	Fidelity Turbo
CLEEN rig scale	UTCFD
CLEEN full size	UTCFD

The UTCFD simulations were run by Julian Winkler (Raytheon Technologies Research Center [RTRC]), and the solution files were transmitted to Boston University (BU). We only have the flow values downstream of the fan. We do not have the Continuous Lower Energy, Emission and Noise (CLEEN) geometry and cannot repeat any of the simulations using Fidelity Turbo to check for consistency.

Length Scale Estimation

There are two main methods that have been considered for estimating the turbulent length scale in this work.

Pope's method: $\Lambda_k = \frac{0.043}{0.09}\frac{\sqrt{TKE}}{\omega}$ (Eq. A-1)

Wake width based: $\Lambda_w = 0.21 L_w$ (Eq. A-2)

L_w is obtained by fitting the turbulent kinetic energy (TKE) on the passage with a Gaussian function as shown in Figure A-1.

$$TKE(r,\theta) = TKE_b(r) + TKE_\omega(r)e^{-(\frac{\theta}{2\sigma})^2} \quad \text{(Eq. A-3)}$$

and then $L_w = 2\sqrt{2ln2\sigma}$

® Cadence and Fidelity are registered trademarks of Cadence Design Systems, Inc., San Jose, California.

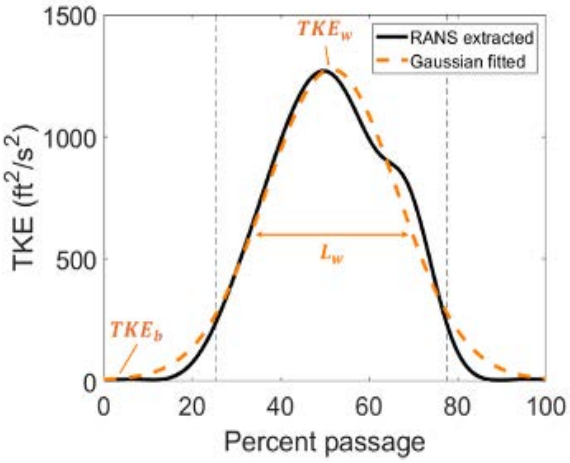


Figure A-**1.** Typical Gaussian fit to turbulent kinetic energy (TKE) on passage at given spanwise location. RANS: Reynolds-Averaged Navier-Stokes.

Pope's method requires a decision on how the averaging on the passage will be conducted. The averaging can be done in many ways. Two methods are compared here: (1) identify average values of turbulence kinetic energy *(TKE)* and ω separately on the passage at each radial location and then form Λ_k, this is denoted by "Λ_k avg k,ω" in Figure A-2, or (2) identify a value of $\Lambda_{k\vartheta}$ at every point on the passage and then average to get Λ_k, this method is denoted by "Λ_k" in Figure A-2. These methods give different outcomes depending on the wake shape of k and ω. When the source diagnostics test (SDT) cases were originally run using the flow solution from UTCFD, it was determined that a best match to the experimentally calculated integral length scale was obtained when the latter method of computing $\Lambda_{k\vartheta}$ at every point and then averaging to get Λ_k provided the better prediction. Hence, this method has been used moving forward.

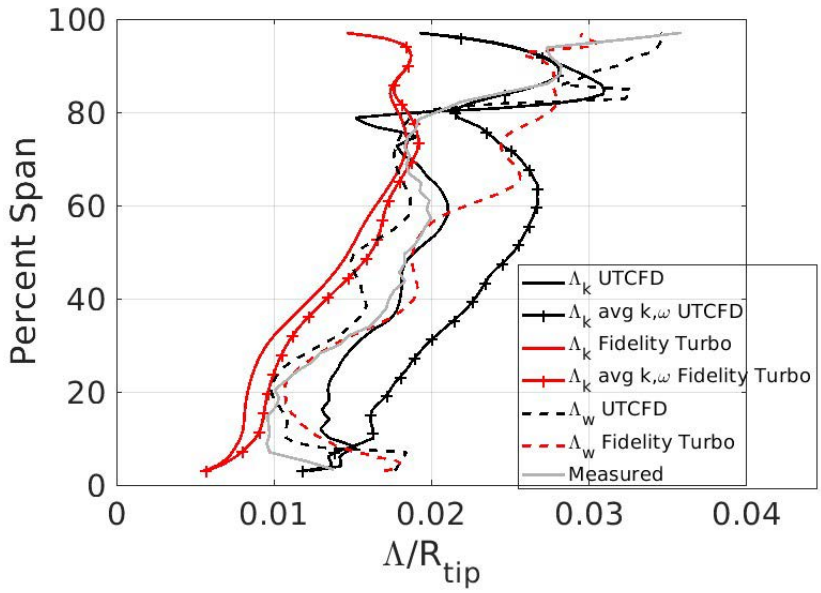


Figure A-2. Source diagnostics test (SDT) approach. Comparison of different methods for obtaining length scale applied to the flow solutions from the two solvers. UTCFD: United Technologies Computational Fluid Dynamics.



Results from the simulation of the SDT approach case show that the wake width method gives much more similar results between the UTCFD and Fidelity Turbo outcomes (dashed lines in Figure A-2) than the length scale based on Pope's method (i.e., the $k-\omega$ enhance and SST model outcomes).

It is noted from the ACAT1 report (Kissner et al., 2020) that many others have shown that the Pope-based length scale predictions can vary greatly depending on the solver and turbulence model. Many others have reported that the SST turbulence model leads to low Pope-based length scale values compared to Wilcox and this is clearly seen here.

Length Scale for Rig and Full-scale Engines

We created our own SDT full size engine by scaling the SDT geometry uniformly in every direction by a factor of 3. The rotations per minute (RPM) and mass flow are scaled in a way that $\frac{RPM_{Rig}}{RPM_{Engine}} = 3$ and $\frac{\dot{m}_{Engine}}{\dot{m}_{Rig}} = 3^2$.

We used the Fidelity Turbo solver to compute the flow field for both the rig and engine scaled fans. The length scale computed using the two methods are different, but both behave similarly. The length scale for the rig is smaller than the engine length scale by a factor equal to ~3 for both the Pope and wake width methods. This can be seen in Figure A-3.

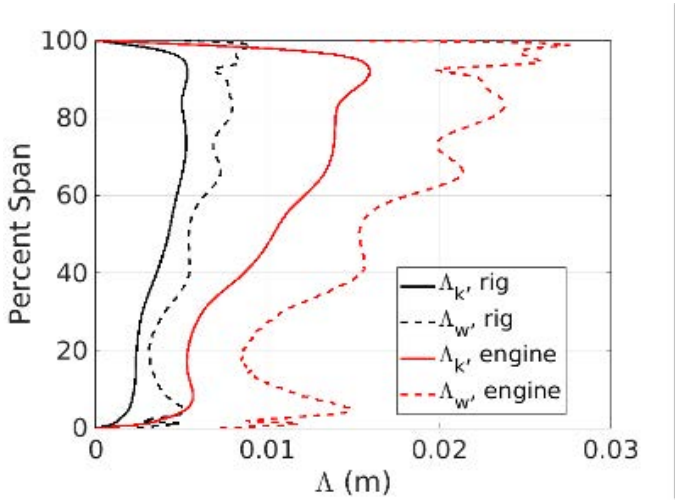
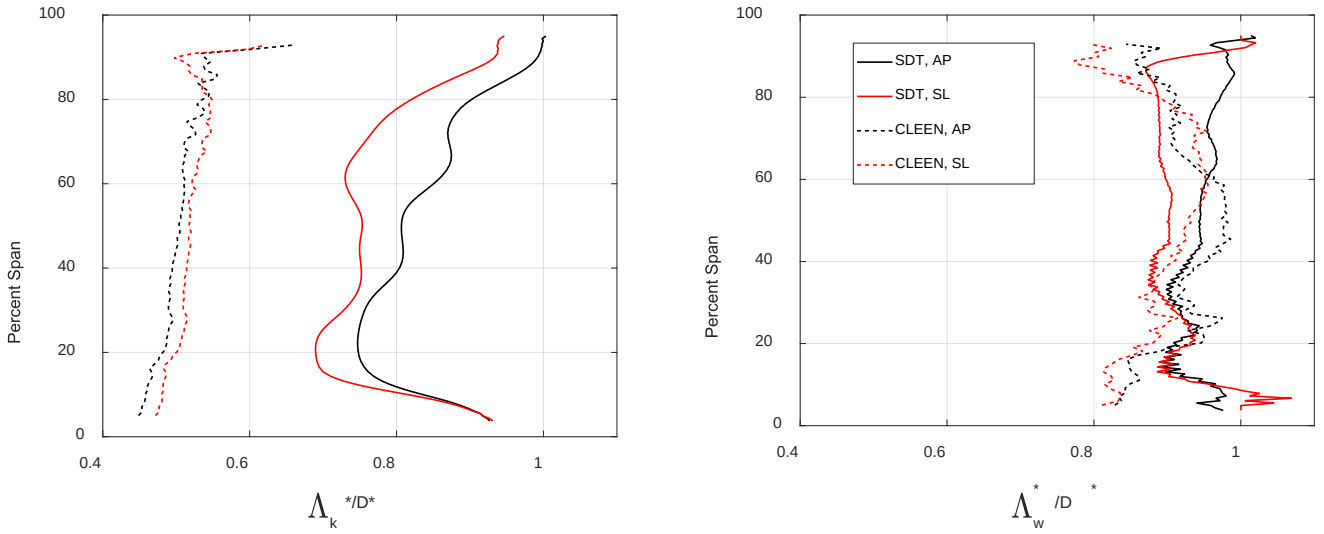


Figure A-3. Source Diagnostic Test (SDT) at approach speed. Comparison of two different methods for obtaining length scale. Based on Fidelity Turbo inputs.

The UTCFD results that were provided to us for the CLEEN rig and full-scale engines were used to compute the length scale. The outcomes indicate that the Pope method may be no longer valid, as we expect that the length scale for the full-size engine to be roughly proportional to the size of the fan. This is not true when Pope's method is used to obtain the length scale from the CLEEN UTCFD results. However, they are true when the wake-width method is used. To show this, we defined a decay coefficient for both Pope-based length scale and wake-width-based length scale. This is shown in Figure A-4, where the superscript $*$ indicates ratio between engine and rig (i.e., $\Lambda^*_\omega = \Lambda^*_{\omega,Engine}/\Lambda^*_{\omega,Rig}$, note that $\Lambda^*_\omega = L^*_\omega$), and D is the diameter. This plot shows how turbulence length scale changes with respect to geometry.



(a) Pope's $k-\omega$ method

(b) Wake-width method

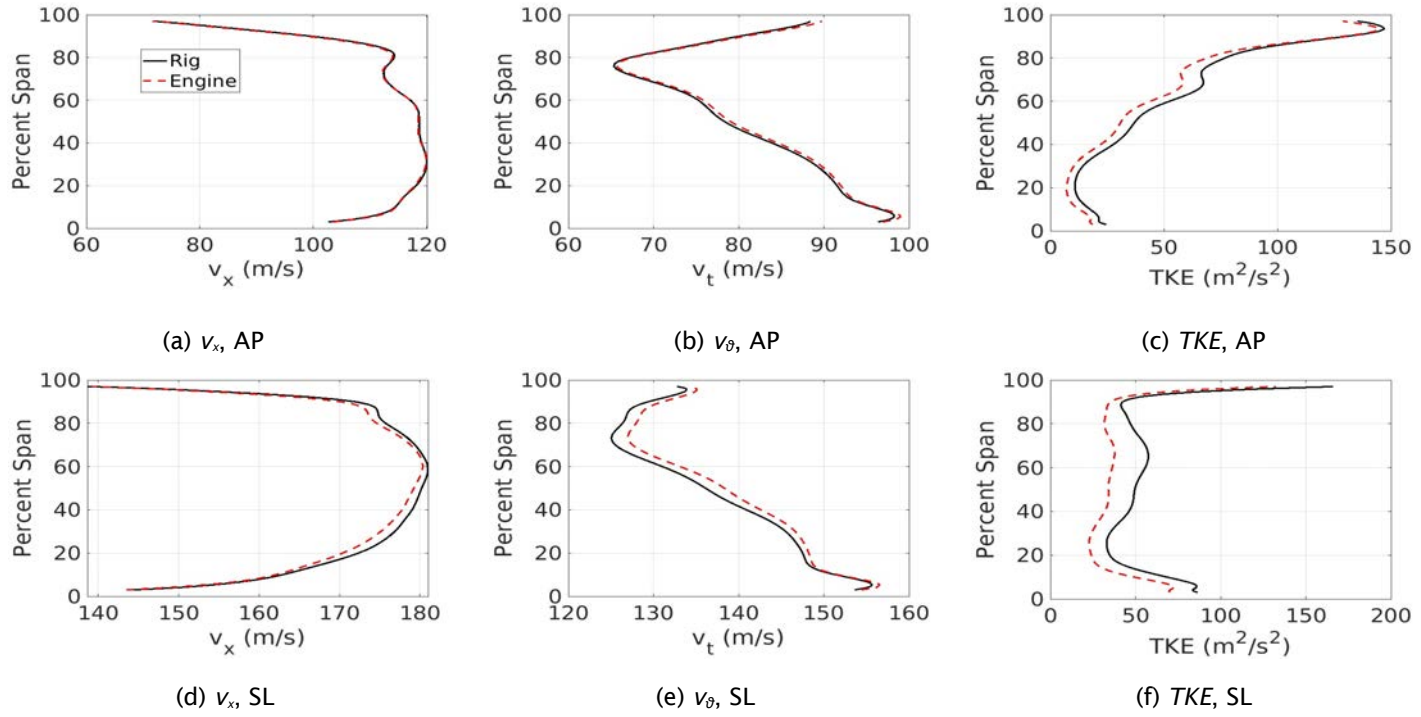
Figure A-4. Influence of engine scale on mean flow extracted near fan exit guide vanes (FEGV) leading edge. CLEEN: Continuous Lower Energy, Emission and Noise, SDT: Source Diagnostics Test.

In Figure A-4, the solid lines compare the SDT length scales, which show rather similar trends for Λ_k and Λ_w, with coefficients slightly less than 1 and decrease at higher speed. The CLEEN geometry denoted by dashed lines on the other hand, shows much smaller values for Λ_k^* , while Λ_ω^* show similar aforementioned trend.

The exact reason behind the unreliable Pope-based length scale is unclear. However, we noted that the difference is mainly driven by the background values, where the specific turbulence dissipation rate does not scale proportionally to the geometry.

Other Input Parameters

The low-order broadband noise method relies on other input parameters besides the length scale. These include the axial and tangential mean flow values and TKE. Figure A-5 shows the results for the SDT at approach and sideline. Again, the larger fan was obtained by simply multiplying the original geometry by 3.0. Importantly, the TKE for the full engine is slightly less than the TKE for the rig and this is more pronounced for the sideline case. The mean axial and tangential flows are very closely aligned because the operating points were chosen to be identically scaled as the geometry scaled, which leads to identical relative flow at the blade leading edge.

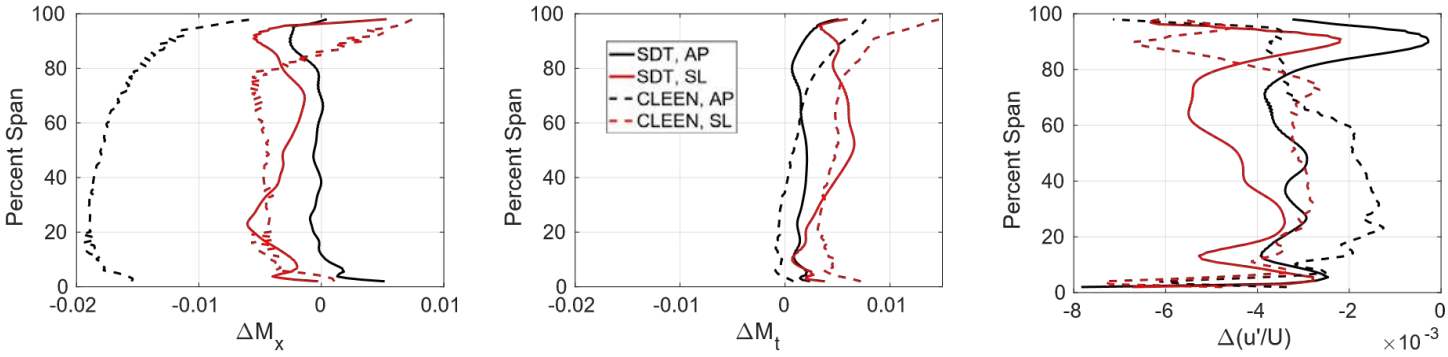


(a) v_x, AP (b) v_ϑ, AP (c) *TKE*, AP

(d) v_x, SL (e) v_ϑ, SL (f) *TKE*, SL

Figure A-5. SDT rig and full-scale engine flow inputs. Based on Fidelity Turbo inputs. TKE: turbulence kinetic energy.

Figure A-6 shows the difference in mean flow between engine and rig. The CLEEN cases show similar trends to the SDT cases, except at the approach speed which operating point does not scale exactly with geometry. The biggest differences between the behavior of these flow parameters as the engine size changes from rig to full for the CLEEN occurs in the axial velocity at approach which is much lower for the full engine. The turbulence intensity (TI) for $\dot{u}/U$ behaves similarly to what we see in TKE from the Fidelity Turbo run of the SDT engine at two scales. The full-engine TKE is lower than the rig and this is more pronounced for the sideline case.



(a) Axial Mach number (b) Tangential Mach number (c) Turbulence intensity

Figure A-6. Difference in inflow extracted near FEGV leading edge, (a) axial Mach number, (b) tangential Mach number, and (c) turbulence intensity. CLEEN: Continuous Lower Energy, Emission and Noise, SDT: Source Diagnostics Test.

Noise outcomes

The results we presented originally for the CLEEN rig and engine used the Pope-based method for determining the length scale. As shown in the previous section, this method is not reliable. As such, new simulations were run using the wake width-based method for determining the length scale. This analysis was done also for the SDT rig and full engine that we created.

Starting with the SDT where the geometry and RPM are identically scaled, Figure A-7 shows the spectra for the three operating points for the rig and full-scale engines. The full-scale values are then scaled by a power of 3 and the frequency is scaled based on the blade passage frequency (BPF). The results using both the Pope and wake-width methods are shown. The scaling performs a bit better for the wake-based method; however, the power 3 scaling works for approach and not as well for cutback and sideline.

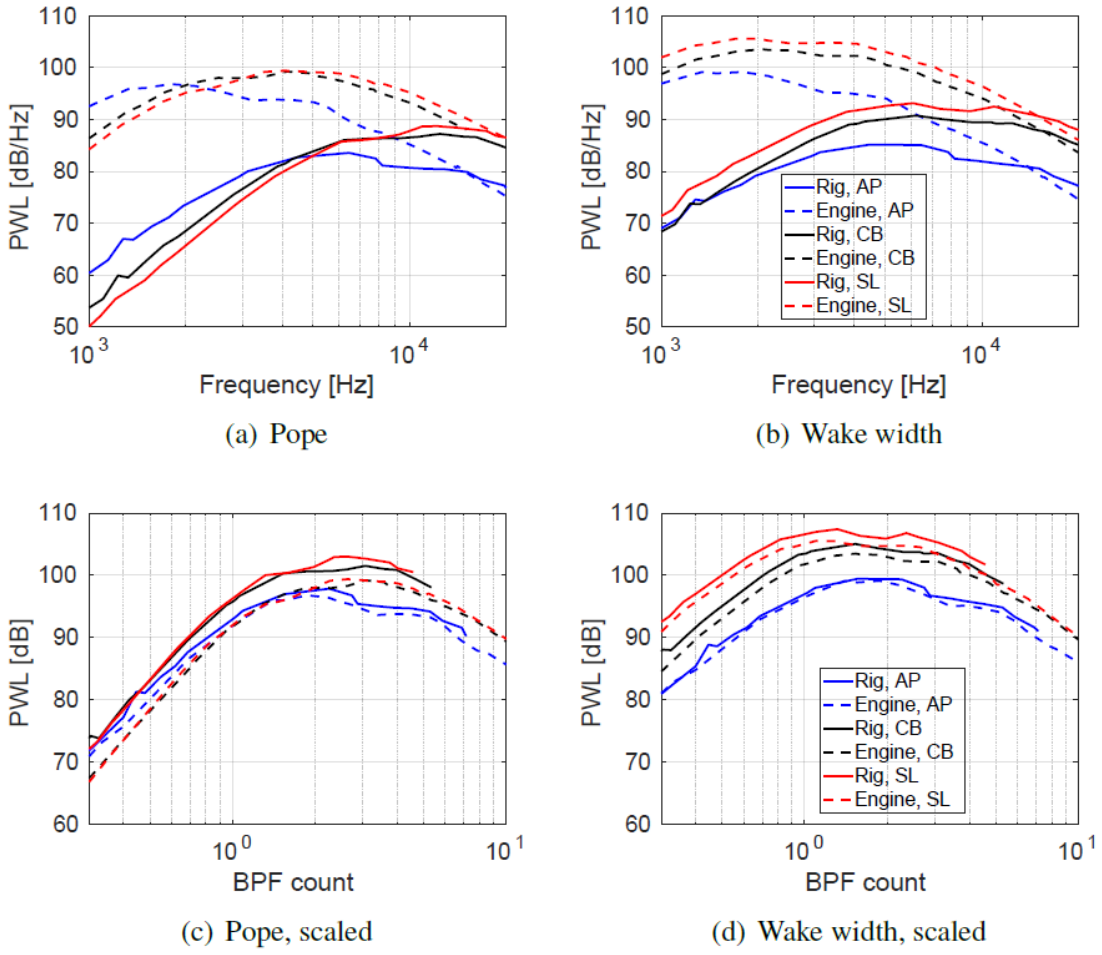


Figure A-7. SDT spectra rig and full scale. Based on Fidelity Turbo inputs. Pope length scale (left). wake width length scale (right). Based on Fidelity Turbo inputs. BPF: blade passage frequency, PWL: sound pressure level.

For the CLEEN, we will show the Pope based outcomes in Figure A-8 (a) but know these cannot be correct. They were our original results, and one can see how much the difference between engine and rig spectra amplitude changed (see

Figure A-8 [b]). The scaling of the spectra amplitude by the third power of the diameter ratio works better when the wake width method is used.

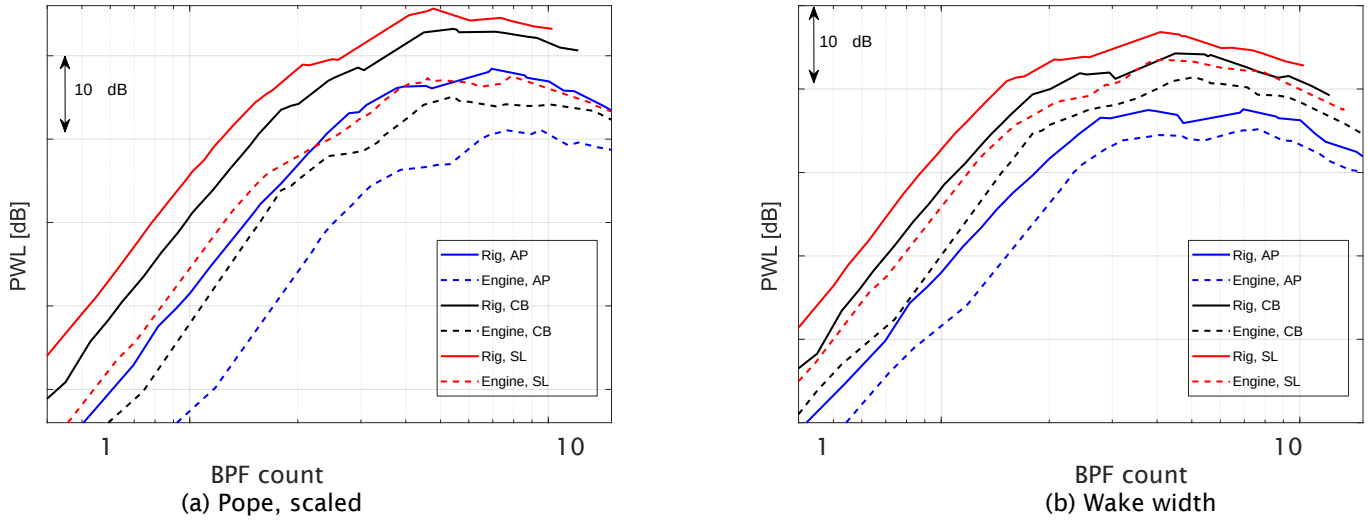


Figure A-8. CLEEN spectra rig and full scale. Based on Fidelity Turbo inputs. (a) Pope length scale and (b) wake-width length scale. United Technologies Computational Fluid Dynamics (UTCFD). BPF: blade passage frequency, PWL: sound pressure level.

References

Jameson, A., Schmidt, W., & Turkel, E. (1981). Numerical solution of the Euler equations by finite volume methods using Runge-Kutta time-stepping schemes. AIAA Journal, 19(9), 1127–1135.

Kissner, C., Guérin, S., Seeler, P., Billson, M., Chaitanya,P., et al. (2020). ACAT1 Benchmark of RANS-Informed Analytical Methods for Fan Broadband Noise Prediction-Part I-Influence of the RANS Simulation. Acoustics, 2(3):539-578. ⟨10.3390/acoustics2030029⟩. ⟨hal-03829160⟩

Lax, P. D., & Wendroff, B. (1960). Systems of conservation laws. Communications on Pure and Applied Mathematics, 13(2), 217–237.

Menter, F. R. (2003). Zonal two equation k-ω turbulence models for aerodynamic flows. Progress in Aerospace Sciences, 32(4), 271–327.

Wilcox, D. C. (1988). Reassessment of the scale-determining equation for advanced turbulence models. AIAA Journal, 26(11), 1299–1310.

Wilcox, D. C. (2006). Turbulence modeling for CFD (3rd ed.). DCW Industries.



Project 077 Measurements to Support Noise Certification for UAS and UAM Vehicles and Identify Noise Reduction Opportunities

The Pennsylvania State University

Project Lead Investigator

Eric Greenwood
Associate Professor of Aerospace Engineering
Department of Aerospace Engineering
The Pennsylvania State University
422 ECoRE Building T
556 White Course Drive
University Park, PA 16802
814-863-9712
eric.greenwood@psu.edu

University Participants

The Pennsylvania State University (Penn State or PSU)

- P.I.: Eric Greenwood, Assistant Professor of Aerospace Engineering
- FAA Award Number: 13-C-AJFE-PSU-112
- Period of Performance: March 15, 2024, to September 30, 2026
- Tasks:
  1. Computational predictions of unmanned aircraft system (UAS) noise
  2. Microphone array design using computational modeling
  3. Development and testing of a reconfigurable multirotor UAS
  4. UAS noise measurement and analysis
  5. Development of a source separation process (SSP) for distributed propulsion vehicles
  6. Noise reduction through synchrophasing
  7. Improved air-data system integration and calibration

Project Funding Level

The Federal Aviation Administration (FAA) provided $500,000 in funding. Cost sharing funds of $495,933 were received from Beta Technologies for labor, flight test support, and technical data.

Investigation Team

Eric Greenwood (P.I.), All Tasks
Kenneth S. Brentner (co-P.I.), Tasks 1, 2 and 7
Eric N. Johnson (co-P.I.), Tasks 2 and 5
Vítor T. Valente (senior personnel), Tasks 2, 3, 4, 6, and 7
Joel Rachaprolu (graduate research assistant), Tasks 4, 5, and 7
Rupak Chaudhary (graduate research assistant), Tasks 1, 2, 4, 6 and 7
EzzEldin ElSharkawy (graduate research assistant), Tasks 4 and 7

Project Overview

Measurement techniques for conventional propeller-driven aircraft and rotorcraft are well established. These techniques typically assume that the acoustic state of the vehicle does not change over the duration of a steady-state pass over a microphone or microphone array. UAS and urban air mobility (UAM) platforms violate the steadiness assumption used in



the measurement and modeling of conventional aircraft noise. Rotor or propeller states, such as the rotational speed or blade pitch angle, vary continuously and independently as the vehicle control system responds to atmospheric perturbations. Many of these vehicles use distributed propulsion systems, in which the rotors or propellers are not locked in phase. When multiple rotors or propellers operate at similar blade passing frequencies, coherent addition of the tonal noise results in lobes of acoustic radiation that are tightly focused in certain directions. As the phase relationships between the rotors change over time, the directionality of these lobes varies. Consequently, the noise cannot be modeled as a single stationary source, and no two flight passes will result in the same noise radiation pattern on the ground. Moreover, because numerous possible combinations of control inputs can result in the same flight condition, unique mapping of the overall flight condition of the vehicle to a corresponding acoustic state is no longer present. This project is aimed at developing noise measurement techniques and data analysis methods that can reduce this variability, thereby allowing for repeatable characterization of UAS and UAM noise.

Task 1 – Computational Predictions of UAS Noise

The Pennsylvania State University

Objectives

The objective of this task is to understand the noise characteristics of small multirotor vehicles in hover and level flight and to support the field measurement planning, testing method development and noise data collection. The task focuses on the X8 UAS configuration developed during the previous year of this project. The X8 configuration has four rotor support arms, each of which supports two rotors driven by separate electric motors in a coaxial arrangement. This octocopter configuration is commonly used in modern drones and relevant to applications such as package delivery. The rotors on each arm may be operated in either co- or counter-rotating pairs. Another objective of this task is to evaluate the acoustic characteristics of Penn State's X8 octocopter when operating in either co- or counter-rotating configurations prior to acoustic measurements in the field.

Research Approach

The Penn State Noise Prediction System (NPS) was used to predict the noise characteristics of co- and counter-rotating octocopter configurations. Although flight acoustic measurements have not yet been performed for these configurations, these predictions are being used to guide the design of future experimental maneuvers. Since experimental data for the X8 are not yet available, the simulation approach was validated against previously collected acoustic measurements of similar co- and counter- rotating rotors pairs obtained in Penn State's flow through anechoic chamber under a separate National Aeronautics and Space Administration (NASA)-supported project.

Milestones

- Model the co- and counter-rotating octocopter configurations in the Penn State NPS.
- Validate the predicted noise using previously obtained measurements of coaxial rotor acoustics.
- Use the noise predictions to study the noise characteristics of each configuration and inform the design of future experimental procedures.

Major Accomplishments

A model of the large reconfigurable UAS X8 has been developed by using the Penn State NPS. The NPS, described by Figure 1, is a simulation architecture consisting of three subsystems: (1) PSU Distributed Electric Propulsion Simulator (PSUDEPSim), (2) the Comprehensive Hierarchical Aeromechanics Rotorcraft Model (CHARM), and (3) PSU-WOPWOP. PSUDEPSim is a flight simulation model for multirotor aircraft developed at Penn State. PSUDEPSim is used to compute the aircraft's flight state as it undergoes steady or maneuvering flight. PSUDEPSim can be coupled to a higher-fidelity aerodynamics model to capture the effects of interactions among components of the aircraft, such as the rotors. In the Penn State NPS, PSUDEPSim is coupled with CHARM to form DEPSim. CHARM, developed by Continuum Dynamics, Inc., is a rotorcraft comprehensive analysis platform including a higher-order free vortex rotor wake method and a panel method for aerodynamic bodies and surfaces, such as the fuselage and wings of UAM aircraft. In addition to providing aerodynamic data in DEPSim for flight dynamic simulation, CHARM produces high-resolution rotor airloads for input into aeroacoustic propagation tools, such as PSU-WOPWOP. PSU-WOPWOP is a general-purpose Ffowcs Williams–Hawkings equation solver that uses Farassat's formulation 1A for tonal noise prediction. Broadband noise, specifically airfoil self-noise, is predicted using the semiempirical Brooks, Pope, and Marcolini (BPM) model. PSU-WOPWOP uses the time-dependent data (e.g.,

geometry, motion, sectional airloads, and angle of attack) generated from CHARM as inputs to compute the noise at any number of observers on the ground or moving with the aircraft.

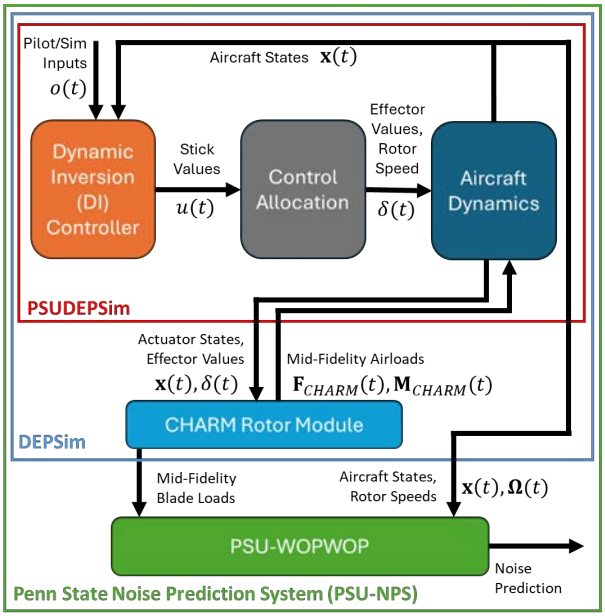


Figure 1. Overview of the different components of the PSU-NPS. CHARM: Comprehensive Hierarchical Aeromechanics Rotorcraft Model, DEPSim: Distributed Electric Propulsion Simulator.

Figure 2 represents the layout of the large reconfigurable UAS developed by Penn State in a X8 configuration. The rotor diameter is 0.71 m, and the vehicle weight is 159 N. The front of the vehicle is aligned with the x-axis. For the current study, the X8 flies in an "X" configuration, with two rotors toward the front of the vehicle.

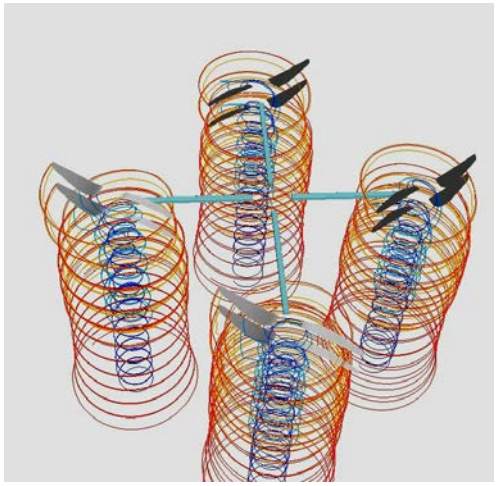


Figure 2. Computational model of X8 with wake during hover.

To validate the results of X8 using the Penn State NPS, a frequency-domain comparison was performed for the two stacked rotors operating in co- and counter-rotating configurations. The predicted acoustic spectra in hover were compared against previously acquired data for a 0.46 m diameter rotor operating at 4,600 rotations per minute (RPM) with combined thrust



of 48 N. Figure 3 compares the 1/3-octave spectra for co- and counter-rotating stacked rotors separated with a vertical distance between the rotors of 20% of one rotor radius. A phase control system was used during the experiment to maintain a rotor-to-rotor phase offset of $\psi_r = 0°$. For the co-rotating configuration, this results in the upper and lower rotor blades being stacked directly over one another. For the counter-rotating configuration, the blades cross over one another at the same position every revolution. Measurements were obtained from a microphone positioned at a distance (d) of 2 m from the rotors and an elevation angle (ϕ) of $-28°$ below the rotor plane.

Figure 3a presents the measured and predicted spectra for the co-rotating configuration. The model predicts the lower-frequency (mostly tonal) contribution levels reasonably well but overpredicts the noise levels between 1 kHz and 5 kHz. Figure 3b presents the spectra for the counter-rotating configuration. Here, the lower-frequency contribution agrees well with the experiment, but the model underpredicts the higher-frequency components, particularly from 5 to 10 kHz. Note that in both cases, a shaft order (1/rev) tone is present in the measured data due to test stand vibrations and imbalances between the rotor blades; these effects are not modeled in the simulations.

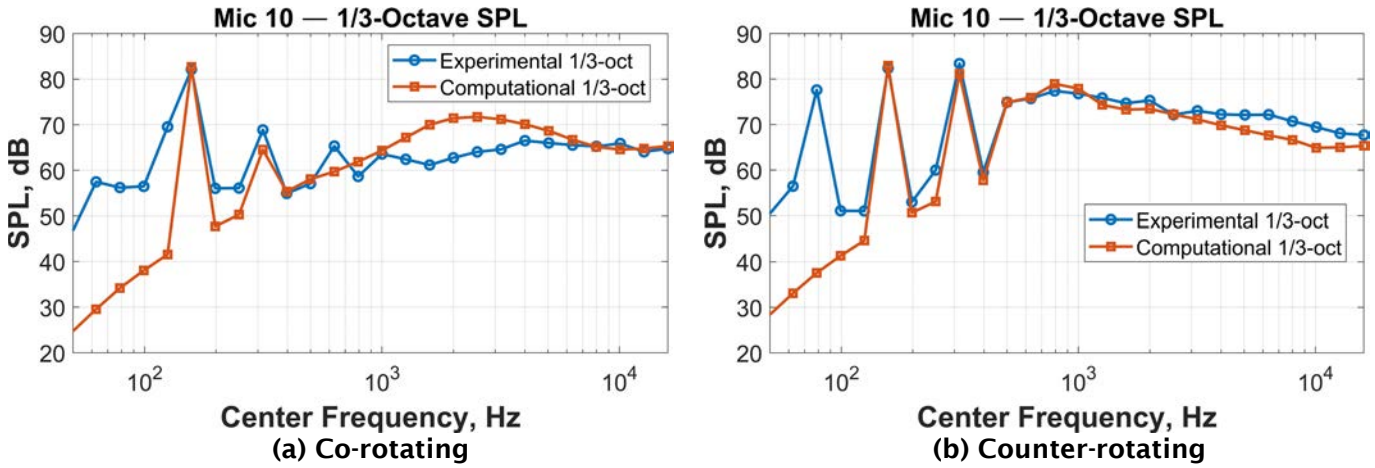
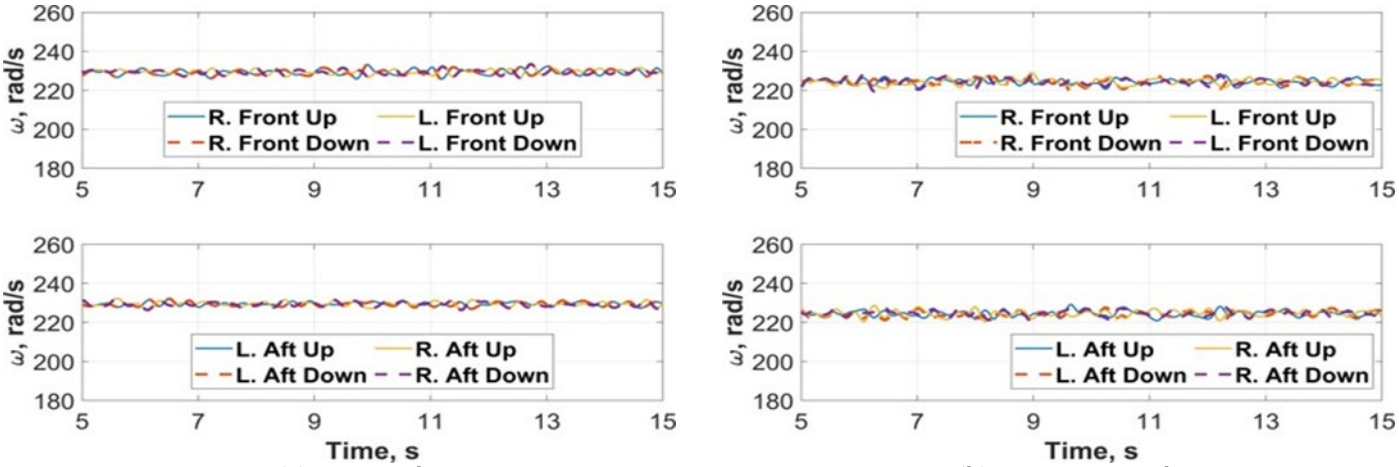


Figure 3. 1/3-octave spectra comparison of stacked rotors, (a) co-rotating and (b) counter-rotating, with zero phase offset, separated by 0.2R, with the microphone positioned at $d = 80$ in and $\phi = -28°$ (below the rotor plane)

The X8 vehicle was trimmed to produce 155 N thrust to hover in both the co-rotating and counter-rotating configurations. The phase offset between rotors is again held at zero. Figure 4 shows that the co-rotating rotors operate at a slightly higher RPM, but in both configurations the eight rotors maintain closely grouped RPMs, indicating consistent thrust distribution during hover.



(a) Co-rotating (b) Counter-rotating

Figure 4. Comparison of rotor revolutions per minute (RPM) during hover for an X8 configuration with (a) co-rotating and (b) counter-rotating rotors.

Figure 5a shows the vertical-force variation with azimuth $\left(\frac{dF_z}{d\psi}\right)$ for the co-rotating configuration in hover, where the small fluctuations indicate weak rotor–rotor interaction. Figure 5b, in contrast, shows the counter-rotating case, where the loading variations are larger and more irregular, demonstrating stronger wake-induced interaction across the rotor disk.



(a) X8 Co-rotating (b) X8 Counter-rotating

Figure 5. Variations in vertical force with respect to azimuth $\left(\frac{dF_z}{d\psi}\right)$ during hover in rotor disk, (a) X8 co-rotating and (b) X8 counter-rotating.

Figure 6 shows the tonal acoustic pressure time histories for the co-rotating and counter-rotating configurations. The counter-rotating configuration exhibits strong impulsive interaction noise, arising from intensified rotor-rotor interactions. In contrast, the co-rotating configuration shows smoother and lower-amplitude pressure fluctuations, indicating weaker aerodynamic interactions and reduced impulsive content.

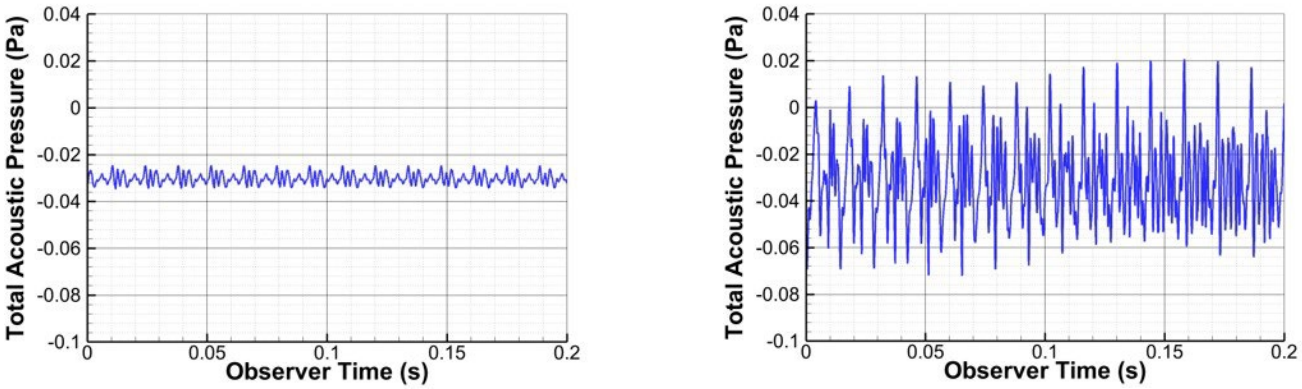


Figure 6. Acoustic pressure time-history comparison of (a) X8 co-rotating and (b) counter-rotating configurations for an observer positioned at d = 20R in and ϕ = -80° (below the rotor plane).

Publications

Chaudhary, R., Valente, V., Mukherjee, B., Jue, A., Brentner, K., S., & Greenwood, E. (2024, May 7-9). *Understanding Takeoff and Landing Noise for Small Multirotor Vehicles* [Conference paper]. Vertical Flight Society's 80th Annual Forum & Technology Display, Montreal, Canada. https://doi.org/10.4050/F-0080-2024-1157

Outreach Efforts

The investigation team holds monthly meetings with FAA and an external advisory board consisting of a dozen interested parties from government and industry.

Awards

None.

Student Involvement

PhD student Rupak Chaudhary is the primary person responsible for conducting UAS noise predictions by using the Penn State NPS (DEPSim/CHARM/PSU-WOPWOP). These predictions include the flight dynamics of the vehicle based on the DEPSim multirotor flight simulation code, including the variation in rotor RPM required to perform the maneuver. The resulting acoustic predictions are compared with experimental data from both outdoor acoustic flight test measurements and laboratory experiments conducted under controlled conditions.

Plans for Next Period

- Conduct simulations for different maneuvers that are representative of multirotor aircraft operations to comprehensively study the generated noise and inform the development of UAS noise measurement techniques.
- Examine additional cases with varied rotor phase offsets to assess how configuration changes influence the vehicle's radiated noise.

Task 2 – Microphone Array Design Using Computational Modeling

The Pennsylvania State University

Objective

To design a microphone array, informed by computational modeling, to capture near-instantaneous noise radiation from multirotor UAS/UAM vehicles. The flight state of these vehicles changes over time, which makes it difficult to characterize the directionality of the noise using conventional measurement approaches. The proposed "snapshot" array is intended to

resolve these time-varying noise characteristics by measuring noise across a wide range of emission angles over a short time interval.

Research Approach

The Penn State NPS was used to evaluate and design microphone array layouts. The selected maneuver was first simulated with a high-density observer grid to generate a detailed acoustic noise hemisphere. The number of observers was then reduced to match the available microphone count, and their positions were optimized to reproduce the same hemispherical noise features with a sparse array. Finally, the selected microphone locations on the hemisphere were projected onto the ground to establish the physical snapshot array geometry.

Milestones

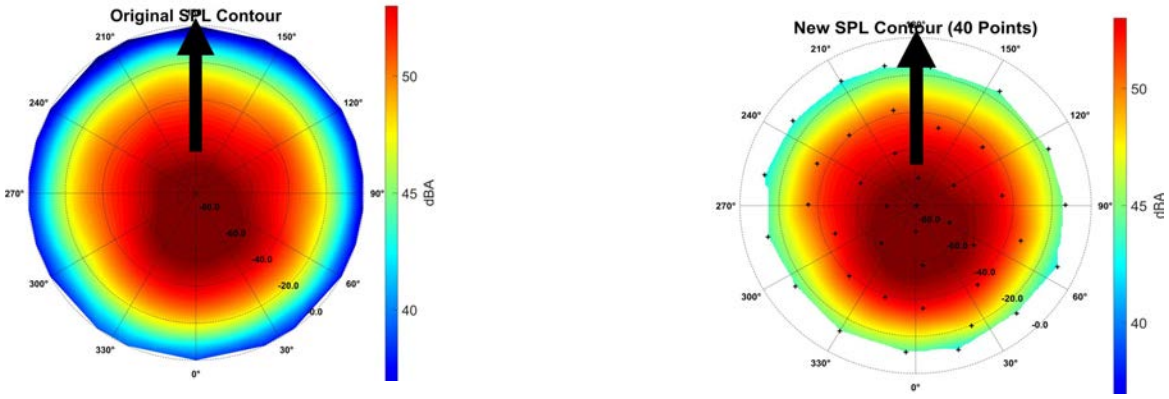
- Generate high-resolution noise hemispheres using NPS.
- Design and optimize a snapshot microphone array.
- Project microphone array to the ground and validate the layout.

Major Accomplishments

Noise hemispheres are traditionally generated using a linear microphone array placed perpendicular to the vehicle flight path. As the aircraft flies over the line of microphones, acoustic data are captured at multiple azimuth and elevation angles, allowing a hemispherical noise map to be reconstructed. This approach works well when the vehicle behaves as a steady-state acoustic source, e.g., for a conventional aircraft flying at constant speed and attitude. However, this assumption breaks down for UAS and UAM vehicles, whose attitudes, thrust levels, and operating states change rapidly—especially during transient maneuvers such as climbs, descents, and accelerations. These time-varying states produce corresponding changes in the emitted noise, making a steady-state linear array reconstruction less accurate.

To address this limitation, a snapshot array methodology is employed. A snapshot array captures acoustic data simultaneously from many angles over a short time window, effectively "freezing" the vehicle at a specific moment. By treating the vehicle as a stationary source only for the duration of this short window, the snapshot approach provides a near-instantaneous noise hemisphere suitable for analyzing transient or maneuvering flight conditions.

A descent maneuver with a flight-path angle of $\gamma = -15°$ and a vehicle speed of 10 mph was simulated in PSU-NPS using the PSU reconfigurable hexacopter model. The original noise hemisphere for this maneuver was generated using a high-resolution grid of 933 observer locations (Figure 7a). To match the density of the experimental microphone layout, a second noise hemisphere was reconstructed using only 40 observer positions using k-mean clustering method to represent a number of microphones that could practically be deployed in the field. Cubic interpolation was applied to these 40 points to produce a continuous sound pressure level (SPL) contour (Figure 7b). As shown in Figure 7, the reduced-observer contour retains the primary directivity characteristics of the original high-resolution hemisphere.



(a) Full resolution (b) Reduced observers

Figure 7. Stereographic projection of lower noise hemisphere of radius 50R during descent maneuver γ=-15° and vehicle speed of 10 mph, at (a) full resolution and with (b) reduced observers.



To experimentally support snapshot-array noise reconstruction, a ground array of 23 microphones was deployed (Figure 8). Twenty microphones were arranged to cover half of a hemispherical surface, providing angular resolution across a wider elevation angle. Three additional microphones were placed to evaluate left-right symmetry. A separate seven-microphone linear array was also deployed to capture propagation characteristics along the flyover direction which will be used to study difference. All acoustic flyovers are planned to be conducted at a nominal altitude of 50 ft above the center of the array.



(a) Plan view **(b) Google Earth view of actual field deployment**

Figure 8. Snapshot microphone array, (a) plan view and (b) Google Earth® view of actual field deployement.

Publications

None.

Outreach Efforts

The investigation team holds monthly meetings with FAA and an external advisory board consisting of a dozen interested parties from government and industry.

Awards

None.

Student Involvement

PhD student Rupak Chaudhary is the primary person responsible for designing the snapshot microphone array. Dr. Vítor T. Valente provided guidance and mentorship throughout the development of the snapshot microphone array.

Plans for Next Period

- Conduct acoustic flight tests for both steady maneuvers—such as hover and level flight—and transient maneuvers, including climb, descent, and turning flight,
- Use the snapshot microphone array to capture near-instantaneous acoustic hemispheres during these operating conditions.

® Google Earth is a registered trademark of Google LLC, Mountain View, California.

Task 3 – Development and Testing of a Reconfigurable Multirotor UAS

The Pennsylvania State University

Objectives

The objectives of this task are (a) to design and develop a multirotor UAS research vehicle that can be easily reconfigured, and (b) to study the acoustic effects of different UAS vehicle configurations and their influence on the noise measurement and data processing approaches developed in this project.

Research Approach

Small and large reconfigurable multirotor UAS aircraft architectures were developed in previous years of the project, with the smaller vehicle serving as a testbed for design concepts that were later integrated into the larger, more capable aircraft. Ground tests and several flight tests of the UAS were conducted prior to acoustic data collection to support the development of the aircraft systems. One focus of these tests was validated upgrades intended to improve the reliability of the telemetry and on-board data recording systems of the aircraft systems prior to acoustic data collection flights. Onboard instrumentation includes a real-time kinematic Differential Global Positioning System (DGPS), an inertial measurement unit, individual rotor RPM and phase measurements, and an air-data system including measurements of outside air temperature, static pressure, humidity, and ultrasonic measurements of true airspeed. Two large multirotor are available, one in a hexacopter configuration and another in an X8 configuration (quad with coaxial set up).

Milestones

- Identify acoustically significant configuration changes to be made on the vehicle.
- Complete initial design of the vehicle and selection of sensors.
- Design control system.
- Perform ground and flight testing.

Major Accomplishments

Two major tasks were performed within the current period: (a) weight optimization and (b) improvements in the onboard recording of the states.

Weight Optimization

As additional sensors were installed on the vehicles, vehicle's endurance per battery charging cycle decreased, which limited the number of flights that could be completed in a single day. To address this issue, a weight-reduction effort was carried out on both platforms, focusing mainly on structural components and supports for the sensor suite. After this work, the Hexa reached a final system weight of 30.9 lb, and the X8 reached 32.4 lb, reflecting the gains from simplifying structures and reducing unnecessary mass. Each vehicle includes the required radio control (RC) system, with Global Positioning System (GPS) added as needed, for a combined weight of 0.8 lb. Depending on the mission, the Li560 and Wx150 sensors may also be installed, adding 4.7 lb (when both used). These updates help balance structural weight, control hardware, and sensor payloads so that the vehicles can achieve better endurance and more efficient operations.

Onboard Recording of States

A new sensor-recording system has been introduced to capture detailed information from each motor or rotor during flight. Main parameters being logged include raw RPM, raw rotor azimuth angle, motor current and voltage, and input percentage command. This implementation relies on updated motor firmware that communicates through the Controller Area Network (CAN) bus, allowing the system to decode two dedicated messages for logging. Data acquisition is handled by a Raspberry Pi 4 equipped with a CAN bus hat and running custom C++ software. Parameters such as the number of motors, their rotation direction, and the desired read or save rates can be adjusted through an external configuration file, eliminating the need to recompile the code. A complementary Python® tool supports quick verification in the field. Each motor transmits data at 100 Hz (configurable in the firmware), although overall throughput is constrained by baudrate limits, allowing approximately 173 Hz total on the Hexa and 130 Hz on the X8. The system writes data to file at 1 Hz and remains agnostic to vehicle layout, currently supporting up to twenty motors.

® Python is a registered trademark of Python Software Foundation, Beaverton, Oregon.



Publications
None.

Outreach Efforts
The investigation team holds monthly meetings with FAA and an external advisory board consisting of a dozen interested parties from government and industry. Technical data regarding the reconfigurable multirotor UAS have been shared with investigators from the National Research Council Canada, the Georgia Institute of Technology, the University of Salford, Texas A&M University, and the NASA Langley Research Center. Discussions are ongoing regarding potential opportunities for collaboration.

Awards
None.

Student Involvement
Dr. Vítor T. Valente is primarily responsible for the design, assembly, and configuration of the UAS.

Plans for Next Period
- Maintain all these systems.
- Make improvements where necessary to add additional sensors.

Task 4 – UAS Noise Measurement and Analysis
The Pennsylvania State University

Objective
The objective of this task is to conduct an acoustic flight test campaign to collect noise data for a variety of UAS vehicles under a variety of operating conditions and configurations.

Research Approach
Acoustic measurements of a flying UAS were conducted at the Mid-State Regional Airport (KPSB), surrounded by the Moshannon State Forest and Black Moshannon State Park near Philipsburg, Pennsylvania. Noise measurements were made for the large reconfigurable research UAS described in the previous tasks. The vehicle was flown through a range of operating conditions, including hover, forward flight at several speeds, climb and descent, yaw and maneuvers for calibration of the weather system onboard. For all maneuvers, the aircraft was flown at different altitudes, from near ground level up to 400 ft above ground level, to evaluate the ability to scale UAS noise levels measured at one flight altitude to another. Acoustic measurements were made with Penn State's networked, battery-powered, and field-deployable acoustic data acquisition system capable of sampling at a frequency up to 125 kHz at 24-bit resolution with subsample accurate (within 200 ns) GPS time synchronization across all nodes. A microphone array was designed to capture both spatial and temporal variations in the radiated noise. Weather instrumentation was also deployed, including measurements of wind speed, direction, temperature, pressure, and humidity, both on the vehicle and at ground level near the ground control station. The weather station used at ground level is the same make and model of the one mounted on the vehicle.

Milestones
- Collect a baseline acoustic, performance, and meteorological dataset of UAS noise measurements
- Analyze the data to quantify and understand the variability in UAS noise.

Major Accomplishments
The major accomplishments were performed during this evaluation period.

Flight Testing
Due to varies reasons beyond the control of the team, relatively few flight tests were conducted in 2025. The ones that happen were mostly related to the air-data system calibration already described in previous reports. The team expects to resume flight testing in new campaigns as the weather allows.



Data Analysis
In a different effort, the data analysis process was uniformized in terms of creating the packet structure to facilitate post-processing analysis. The software used was Matlab.® The current supported flight conditions are:

- H - Hover
- HW - Hover with added weight
- AD - Ascent/Descent
- FF - Forward flight
- FFW - Forward flight with added weight
- WCAL - Weather station calibration
- XFLY - X or + pattern for weather data collection
- YAW - Yaw maneuver on top of a specific microphone

Each condition filename (or flight) is accompanied by "_XXX.mat" where XXX is a number. For example, H_134.mat represents the data from a hover test with number 134. The specifics of this flight (e.g., date, time of the day, altitude set points, etc.) will be in a test matrix from the day when the flight happened and should be provided separated from the .mat itself.

The structure includes onboard flight data from the flight controller (PX4), data from the weather station at ground level (WX150), data from weather station onboard (WX150 and LI560), onboard recording of the states of the motors (custom) and general information about the test. Each variable (onboard log or microphone recording) has their own time vector since the sampling frequency is not always the same among different sources. However, all data are synchronized to the same Coordinated Universal Time (UTC) time reference.

A function was created to process a .mat file pointed by the user generating a set of default plots. It uses user inputs to select a file and from there multiple plots are generated. They include:

- Latitude x Longitude of a flight in a geomap with microphone locations
- North x East x Altitude of a flight in a three-dimensional (3D) plot with microphone locations
- Attitude timeseries
- Altitude timeseries
- Velocity timeseries
- Pressure time series of selected microphones
- SPL time series of selected microphones

User may select more than one microphone to be plotted. By using the file structure above, the user can implement their own functions for a more in-depth/specific results.

A different script was also created to allow for splitting an original file into many by visually selecting points of interest. The result of this second script is a set of segments, using the same file structure, separated by the points the user selected. This allows for the selection of specific sections of each flight.

Publications
None.

Outreach Efforts
The investigation team holds monthly meetings with FAA and an external advisory board consisting of a dozen interested parties from government and industry. Data collected for UAS under this task may also be provided to collaborators at the University of Salford and the NASA Langley Research Center to enable psychoacoustic evaluations of UAS noise by using their auralization and human participant testing capabilities.

Awards
None.

® Matlab is a registered trademark of The MathWorks, Inc., Natick, Massachusetts.



Student Involvement

Dr. Vítor T. Valente, PhD students Joel Rachaprolu and Rupak Chaudhary, conducted acoustic flight testing of the large reconfigurable UAS and participated in analysis of the measured data.

Plans for Next Period

Resume and expand flight testing campaigns to evaluate different vehicle configurations as well as microphone array configurations.

Task 5 – Development of a Source Separation Process for Distributed Propulsion Vehicles

The Pennsylvania State University

Objective

The objective of this task is to develop a process for separating the noise generated by rotors or propellers at non-constant, but potentially similar, RPM values from flyover measurements of UAS and UAM vehicles. By separating noise generated from each rotor, it will be possible to develop a more repeatable characterization of the noise of the entire aircraft.

Research Approach

The SSP was developed in this task is a two-step process that combines a time-domain de-Dopplerization procedure and Vold–Kalman order tracking filter. This approach will de-Dopplerize the acoustic measurements and separate the individual rotor noise components, with the capability to extract time-varying impulsive noise. Performing this source separation in the specified time domain will enable the application of a wide range of post-processing techniques in both the time and frequency domains. Each step of the SSP was verified on computational and experimental/flight test data to assess the performance. Acoustic analysis with the SSP components was also performed, in which individual steps of the SSP were isolated and applied to different datasets. This process was applied to the Bell® 430 helicopter and was extended to separate the tonal noise generated by individual rotors of the large reconfigurable UAS in the previous reporting period. During this period, the approach was additionally applied to simulated data to allow the accuracy of the approach in separating the individual rotor noise components to be quantified.

The flowchart in Figure 9 outlines the steps of the approach used to quantify the accuracy of the SSP. First, a computational setup is used to predict the noise generated by the hexacopter modelled in simulation using the framework described in Task 1 based on the aircraft developed and then built in Task 3.

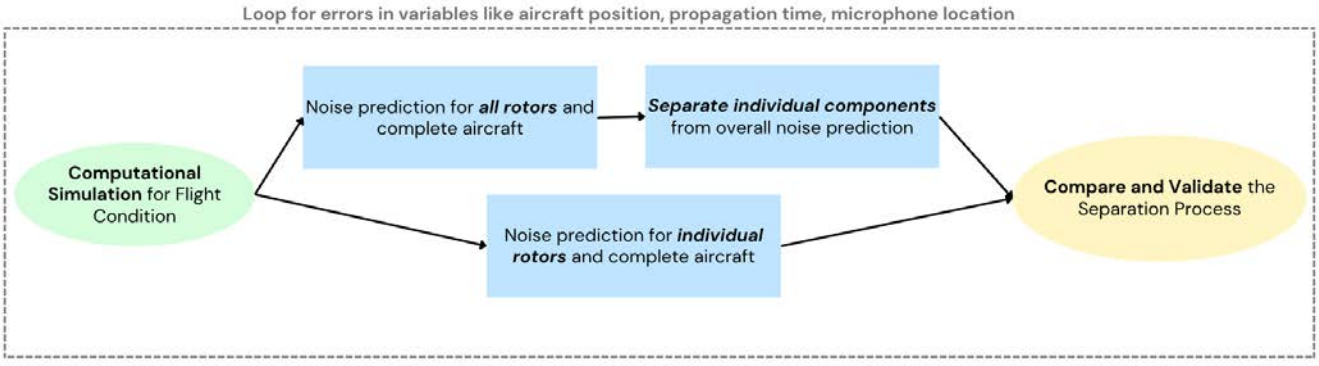


Figure 9. Outline of the approach used to quantify the accuracy of source separation process (SSP).

® Bell is a registered trademark of Textron Innovations Inc., Providence, Rhode Island.



First, noise is predicted for entire aircraft with all six rotors using the computational setup and then separated into individual components using the SSP. Second, noise is predicted for each rotor individually with the same computational setup as the previous predictions. Then, the separated noise components are compared to the "true" predicted components to reveal the accuracy of the separation. This approach and results for a test hover test case are presented in the accomplishments section.

Milestones

- Develop an SSP for stationary acoustic measurements.
- Implement a de-Dopplerization approach to convert non-stationary measurements to a stationary frame.
- Apply the process to simulated and measured data to evaluate the effectiveness of the separation.
- Apply the process to multirotor aircraft acoustic measurements to extract acoustic components for each rotor.
- Study the accuracy of the SSP to separate individual rotor components.

Major Accomplishments

The results of SSP on hover are provided in this section. The approach was applied to forward flight, with similar results. Figure 10 shows the rotor speed histories during hover. The six rotors maintain nearly constant speeds, with only minor fluctuations induced by the flight control system as it stabilizes the vehicle against small disturbances. In this case, data from a microphone under the aircraft are used for the analysis.

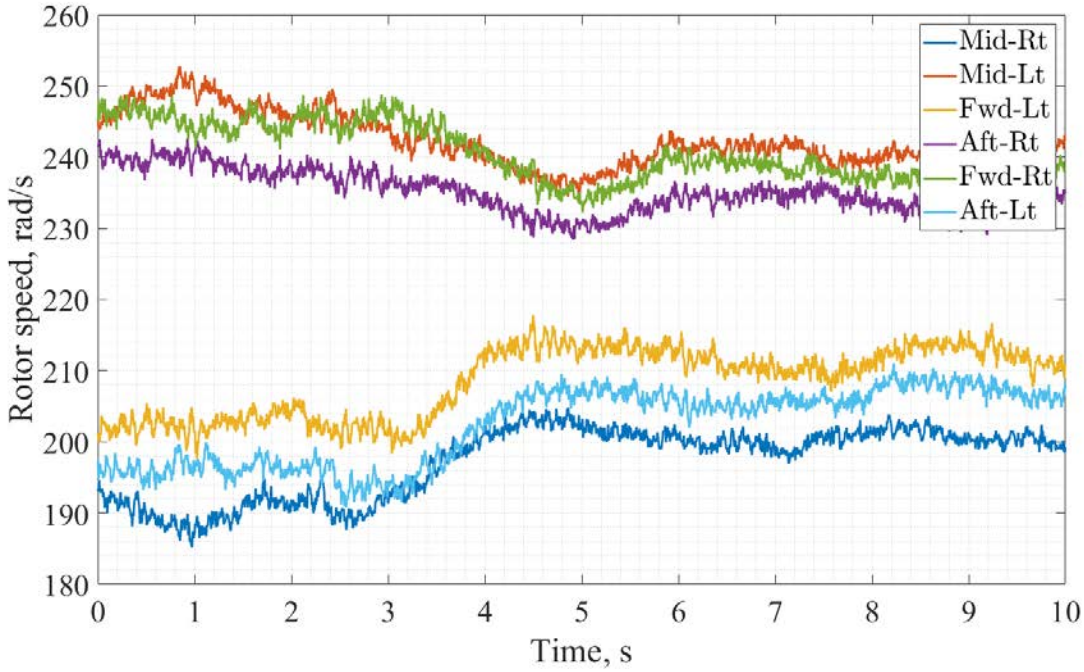


Figure 10. Rotor rotations per minute (RPM) time history in hover case.

Using the aircraft with the rotor speeds shown in Figure 10, the separation was performed on the noise prediction (see Figure 11). The separation was performed for the first 15 harmonics of the rotor blade passing frequencies. During this period, the aircraft was fairly stable, and we can see that each of the rotor has a distinct pulse shape with respect to each other. This reveals distinct noise features of each of the rotors.

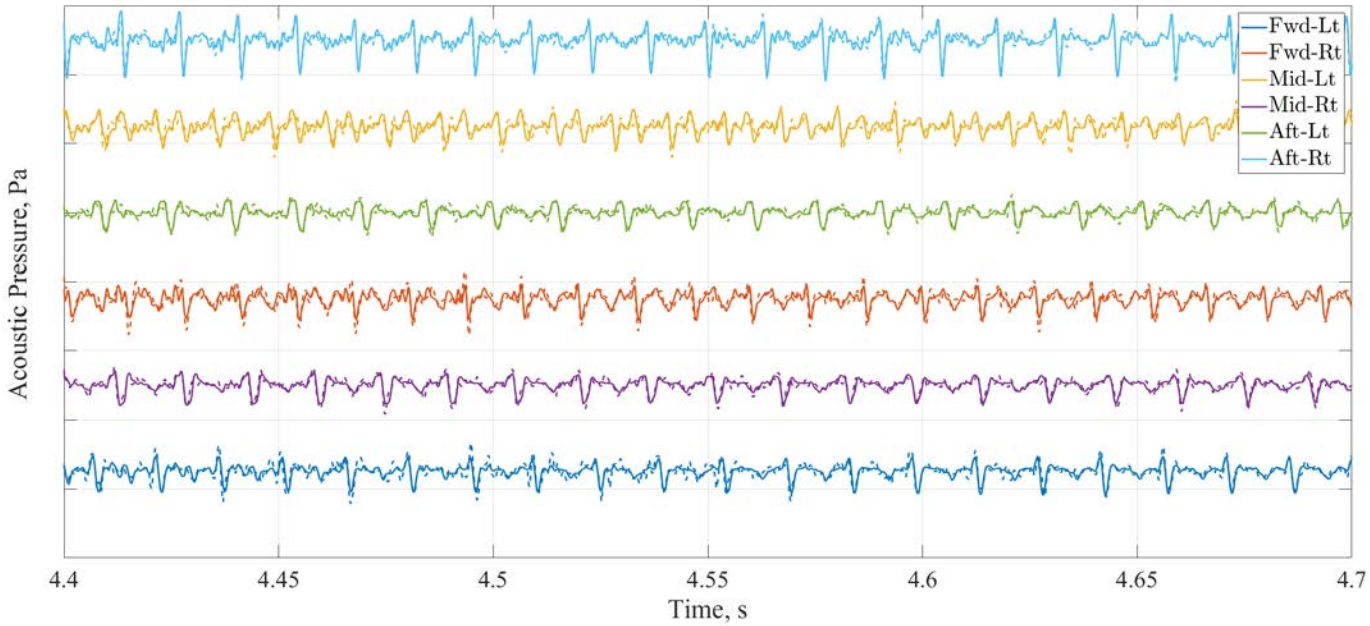


Figure 11. Separated components of all the six individual rotors using the source separation process (SSP) for the hexacopter data.

In addition to that, in Figure 11, the solid line is the separated component, and the dotted line is the predicted component for each rotor. During the time period shown, the separated component is quite close to the predicted component reassuring the separation is accurate. To take a closer look, if we plot a shorter time period in the same formation as a traditional placement of rotors in a hexacopter, the distinction would be much clearer.

Figure 12 is the separated acoustic pressure time series pulse shaped for each individual signal arranged according to rotor placement in a hexacopter. The distinctions between each of the rotors are clear, as well as the agreement with the predicted acoustic pressures. It is clear that the separation is accurate in the time domain, following this, a frequency domain plot for the same time period is shown in Figure 12.

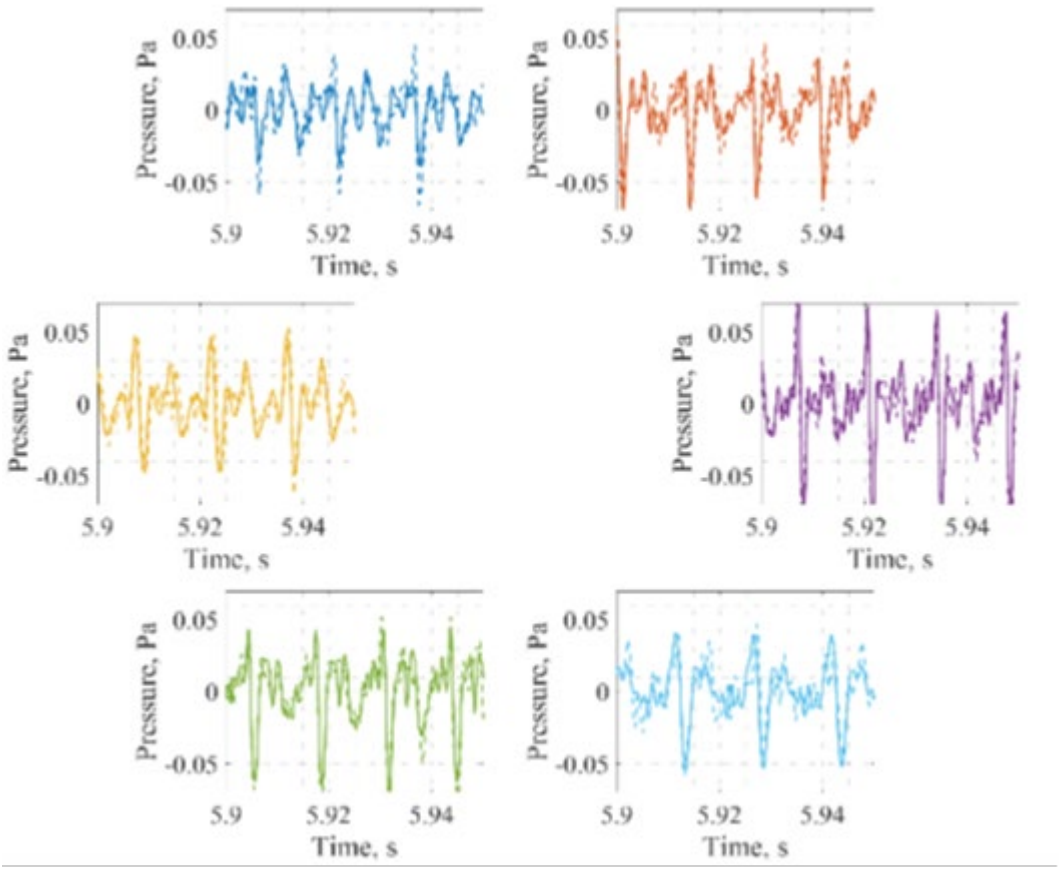


Figure 12. Separated acoustic pressure time series signals for each rotor on the aircraft over a short time window arranged in a hex-format.

The spectra shown in Figure 13 is for the same time period as the acoustic pressure time series as the signals shown in Figure 12. In the frequency domain, looking at the tonal content of the separated and the predicted signals, it is evident that the SSP can accurately separate the individual rotor tonal noise contributions.

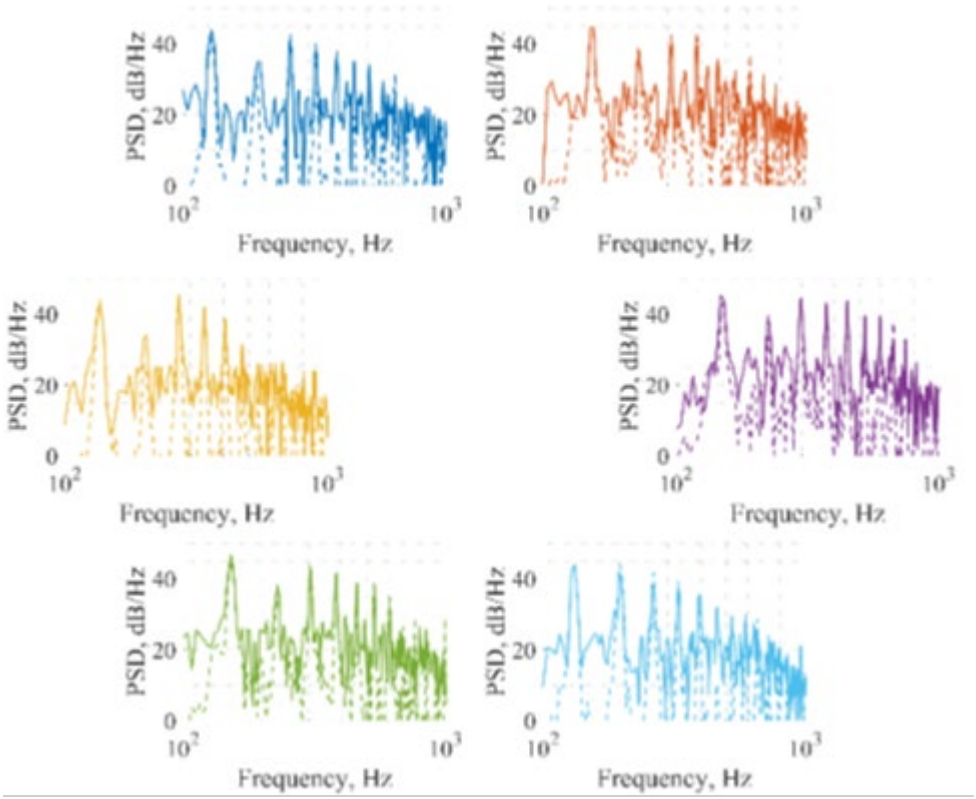


Figure 13. Separated spectra for each rotor for the same time period as the time series signals arranged in a hex-format.

Publications

Rachaprolu, J., & Greenwood, E. (2024). Helicopter Noise Source Separation using an Order Tracking Filter. *Journal of the American Helicopter Society*. https://doi.org/10.4050/JAHS.69.012006

Rachaprolu, J., Valente, V. T., ElSharkawy, E., & Greenwood, E. (2024, May). *Multirotor Noise Source Separation and Characterization from Ground-Based Acoustic Measurements* [Conference presentation]. Vertical Flight Society Forum 80, Montreal, Canada.

Outreach Efforts

The investigation team holds monthly meetings with FAA and an external advisory board consisting of a dozen interested parties from government and industry. The SSP developed under this task has been provided to Blue Ridge Research and Consulting, which has applied the method to isolate noise generated by an Urban Air Mobility vehicle.

Awards

Joel Rachaprolu was awarded the Vertical Flight Foundation Scholarship award.

Student Involvement

PhD Student Joel Rachaprolu developed and tested the SSP with experimental measurements of helicopter and multirotor data, and has now been extended to demonstrate the accuracy with hexacopter data.

Plans for Next Period

All major milestones for the task have been completed. However, in the next period, the SSP will be applied to a wider range of conditions to validate its accuracy. Improvements will be made, as necessary, to increase the robustness of the process for future use on multirotor vehicles.



Task 6 – Noise Reduction through Synchrophasing

The Pennsylvania State University

Objective

The objective of this task is to develop and experimentally validate an active noise reduction approach for multirotor aircraft based on phase synchronization of the rotors.

Research Approach

A fully electronic rotor phase control scheme was developed for a hexacopter small UAS (sUAS) designed and built at Penn State. The process begins by characterizing the acoustics of each rotor of the vehicle by using an acoustic array installed in Penn State's flow-through anechoic chamber. These acoustic signals were processed to allow the results to be generalized to any other far-field observer location. An optimization approach was then applied to identify the rotor phase combinations that reduce the noise of the vehicle at one or more observer locations. An electronic phase controller was then used to maintain the target phase relationships between the rotors, and the radiated noise of the entire vehicle was measured and assessed.

Milestones

- Adapt an electronic phase control method to a fixed wing UAS.
- Validate electronic phase control method in free flight.

Major Accomplishments

An off-the-shelf fixed wing airplane was acquired and modified to allow the installation of multiple motors on the wing. The phase control method, previously used in a multirotor electric vertical take-off and landing (eVTOL), was modified to account for the differences in the geometry of the vehicle being used.

Experimental approach

This section presents the approach followed to develop and demonstrate a synchrophasing strategy on a fixed wing distributed electric propulsion (DEP) aircraft configuration. The noise control method is based on previous work and is intended to control the directionality of the radiated noise by modifying the relative propeller phases, thereby influencing the tonal components of the acoustic field. Synchrophasing methodology includes three main steps: acoustic characterization of the propellers, optimization for the set of phases achieving the desired noise control target, and implementation of phase controller itself.

For this work, the first step was performed using the CHARM in combination with PSU-WOPWOP. CHARM provides a mid-fidelity framework for predicting the aerodynamics of rotor- and propeller-driven aircraft, employing a panel-based method for the representation of airframe aerodynamics. PSU-WOPWOP is a general-purpose aeroacoustics solver, implementing Farassat's Formulation 1A of the Ffowcs Williams–Hawkings equation. Time-resolved data generated by CHARM Standalone serve as inputs to PSU-WOPWOP for the computation of the associated acoustic fields.

For each propeller on the aircraft, the average acoustic pressure over one propeller revolution was generated using CHARM and PSU-WOPWOP, considering the expected operating conditions of the propeller. Assuming linear superposition of the propeller waveforms, an optimization is conducted to minimize the average mean square pressure across a subset of observers by adjusting the set of relative phases. By minimizing the sum of the mean-squared pressures, the average SPL is also reduced in that region. Conversely, the sum of the mean-squared pressures can be maximized to determine the phase combinations that will increase the SPL in the target region. The phase controller constitutes the final stage of the noise attenuation strategy. Its function is to regulate the relative phase of each rotor with respect to a virtual reference, which depends on the rotor's instantaneous phase, the target phase offset, and its rotational speed.

Vehicle Configuration

The vehicle to be used in this work is a modified Pilatus® PC6 remote-controlled aircraft. The basic specifications of the original aircraft are presented in Table 1 below.

® Pilatus is a registered trademark of Pilatus Aircraft Ltd., Stans, Switzerland

Table 1. Original aircraft characteristics.

Characteristic	Value
Model Scale	1/6
Wingspan	107.0 in.
Length	78.7 in.
Empty Weight	310.4 oz
Material	Balsa and Plywood

In its original form, the vehicle is designed for a single 20-in. by 8-in. propeller attached on the nose. Modifications were made to both wings and fuselage to include a distributed electric propulsion system with eight Vertiq® 4006 770 kV motors with APC® 10-in. by 10-in. propellers in both clockwise (CW) and counterclockwise (CCW) rotation configurations. The avionics include an onboard computer, an inertial measurement unit, and a GPS unit. A picture of the current status of the vehicle is shown in Figure 14 with dimensions given from the centerline of the fuselage.

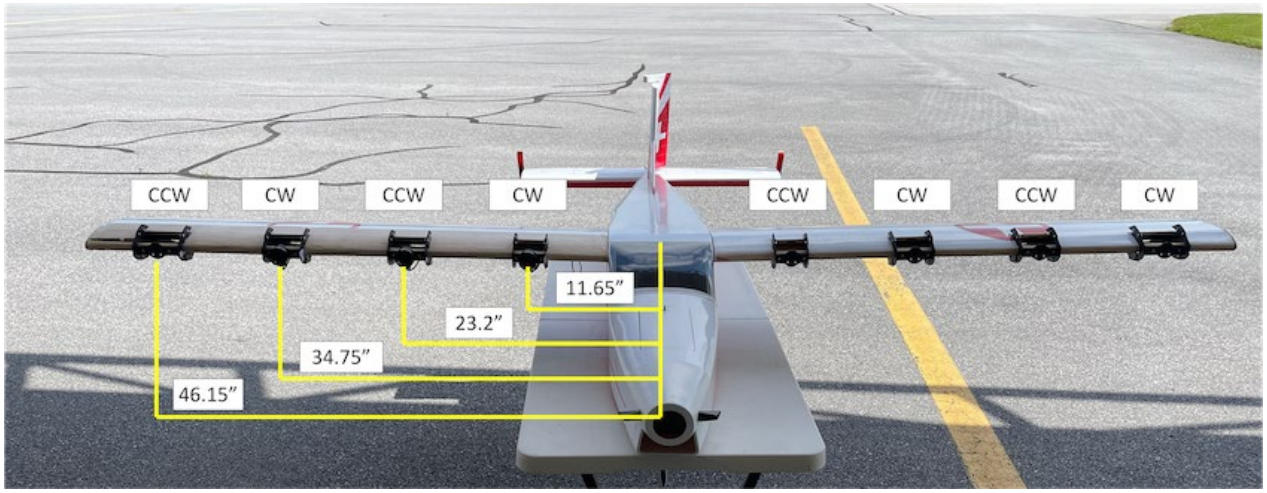


Figure 14. Modified Pilatus PC-6 model with a synchrophasing distributed electric propulsion (DEP) system. The direction of rotation of the propellers is indicated as in the picture.

Simulations were performed comparing performance data available for the selected propeller versus the original propeller suggested for the unmodified vehicle design. Figure 15 below presents the result of these simulations, showing that for an expected range of model velocity around 60 mph, the combination of eight smaller propellers will provide higher power and thrust in comparison to the original propeller. The difference of 20%-30% also accounts for performance losses given the change from one propeller to eight propellers set up. The target set point for the group of motors for angular velocity is 9,000 RPM, which corresponds to slightly less than 50% of the motor capabilities. The original motor set point for the comparison was at 7,000 RPM, which corresponds to approximately 60% of the suggested motor for the model without modifications.

® Vertiq is a registered trademark of Iqinetics Technologies Inc., Philadelphia, Pennsylvania.
® APC is a registered trademark of Landing Products, Inc., Woodland, California.

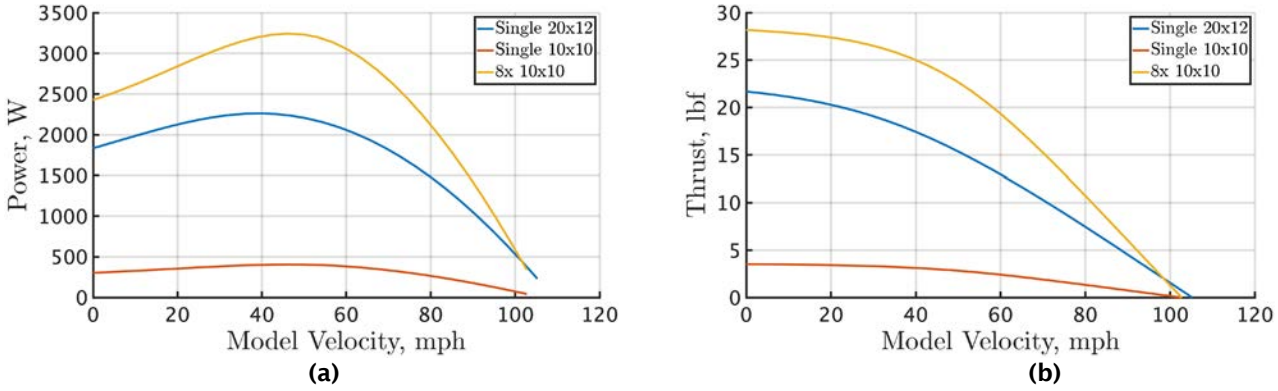


Figure 15. Simulation comparing the originally suggested blade with the newly selected blade, model velocity versus (a) power and (b) thrust.

Microphone Array Configuration

The proposed location is shown in Figure 16 The center microphone (Mic 6) is directly underneath the vehicle path (blue line). On each side, five microphones are spaced at successively increasing 9° increments of elevation angle, considering the target flying altitude of 100 ft. The last microphone on each side (Mic 11 and Mic 1) is placed at 100 ft from the centerline of the array, providing similar sideline angles for later analysis. This microphone array provides a ±45° sideline angle measurement region under the target flight path.

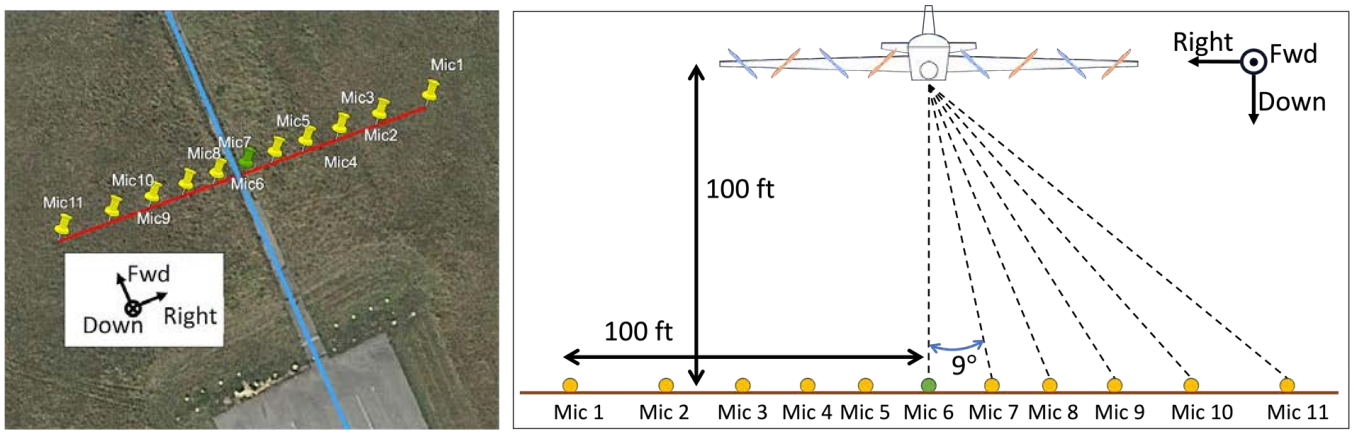


Figure 16. Proposed microphone array configuration with eleven inverted microphones and relative vehicle flight path. Vehicle and microphone spacing are not at scale.

Preliminary Results

Based on the selected propeller and the prescribed operating condition (~9,000 RPM at ~ 60mph), the time-averaged acoustic pressure over a single revolution was evaluated using PSU-NPS. The PSU-NPS framework couples mid-fidelity aerodynamic modeling through CHARM with acoustic predictions using PSU-WOPWOP. This integrated approach enables an accurate prediction of the noise from the rotorcraft across various flight regimes.

The predicted acoustic signals were subsequently employed as input to an optimization procedure, wherein three different sets of simulated observers were analyzed:

- Symmetric distribution directly beneath: A set of observers distributed beneath the vehicle along a ±20° arc centered on the fuselage axis.



- Asymmetric wide-angle distribution beneath right wing: A set of observers ranging from directly beneath the vehicle to 50° arc to one side.
- Sparse wide-angle distribution: A set of observers sparse in a semicircular span beneath the vehicle.

The prediction for the symmetric and asymmetric observer distributions, assuming the vehicle is located directly above the microphone 6 in the microphone array, is illustrated in Figure 17a and Figure 17b, respectively. This prediction accounts exclusively for the tonal component and highlights the overall SPL, as well as the expected attenuation and amplification, due to a different set of relative phases, at and around the specified frequency. The optimal case corresponds to a condition of attenuation, whereas the pessimal case is associated with amplification. This result demonstrates the expected attenuation and amplification obtained through the imposed relative phase distributions, while also evidencing the capability to tailor the radiated noise directivity by appropriately selecting the governing solution. Furthermore, for the symmetric distribution, the results indicate that destructive interference at an elevation of -90° yields an attenuation of approximately 20 dB, whereas constructive interference at the same elevation produces an amplification of about 10 dB, both with reference to the expected incoherent level. For the asymmetric distribution, similar analysis yields an average difference of approximately 18 dB from the pessimal to the optimal case. The optimization process aims to minimize or maximize the SPL within the entire target region; however, the resulting set of phase combinations may produce varying acoustic performance across that region due to differences in the overall phase interaction.

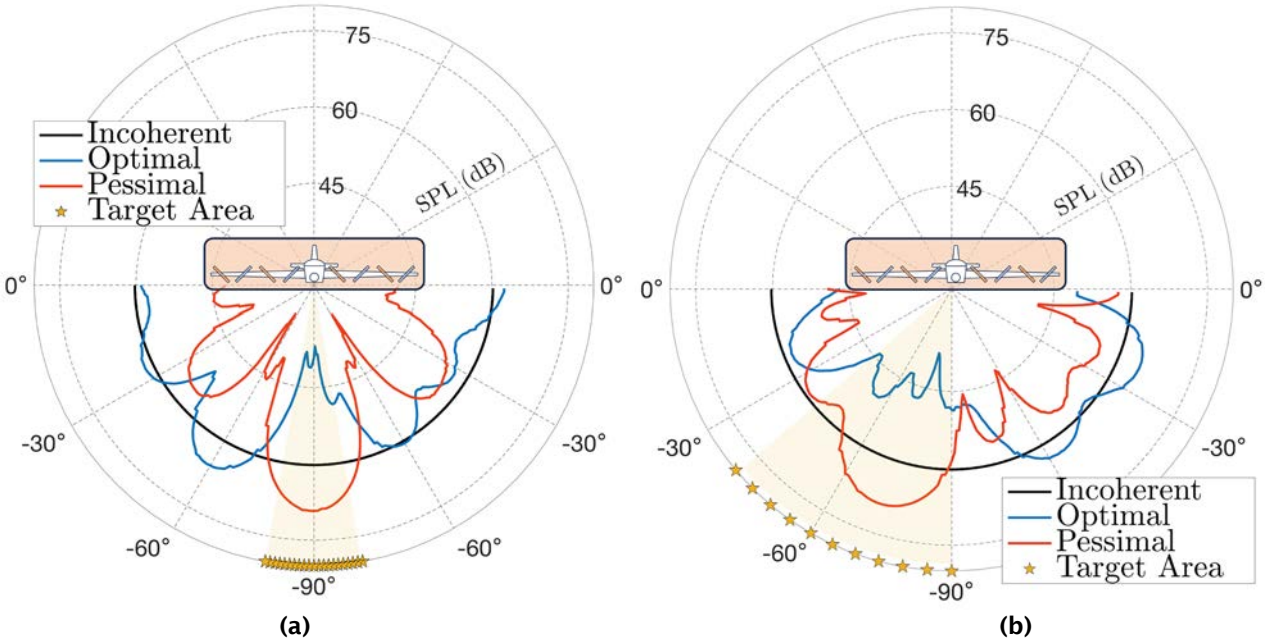


Figure 17. Prediction slice for the cases with (a) symmetric and (b) asymmetric observer distributions, covering a different set of elevation angles beneath the vehicle.

In addition, using the same set of relative phases for the symmetric observer distribution, Figure 18a and Figure 18b show the stereographic projections of the lower noise hemisphere for the optimal and pessimal cases, respectively, as obtained from CHARM and PSU-WOPWOP when applying the fixed-phase solution determined by the optimization algorithm.

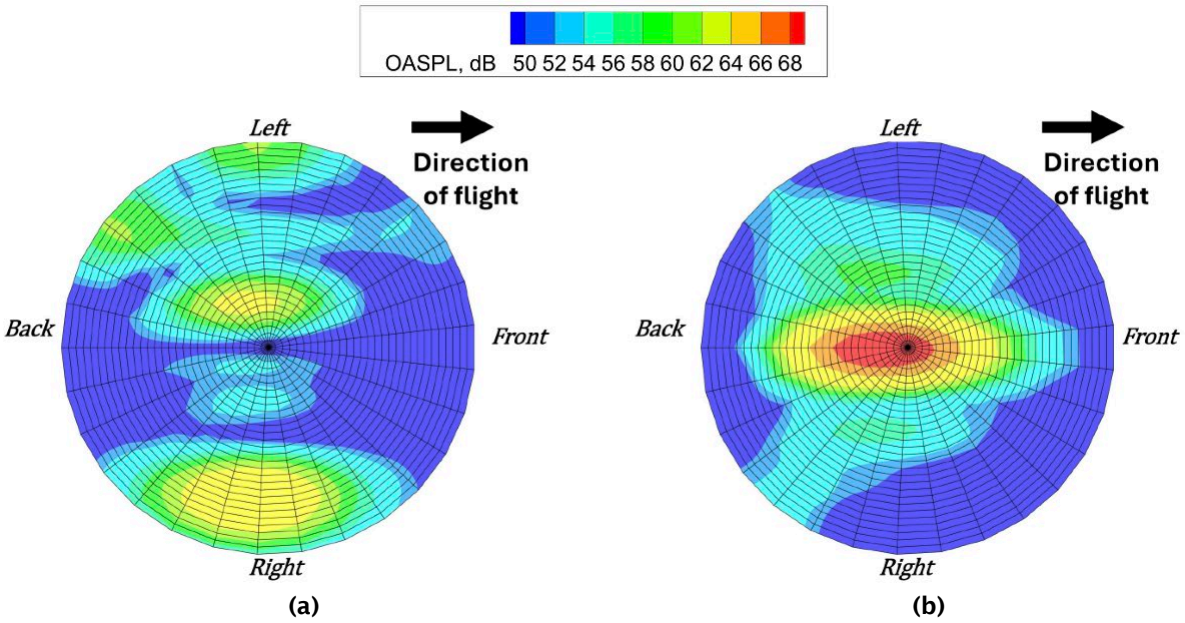


Figure 18. Projection of the lower noise hemisphere, where the center indicates directly below the vehicle and the outer edge corresponds to the vehicle plane. Acoustic predictions from CHARM and PSU-WOPWOP are shown for the optimal (a) and pessimal (b) phase combinations of the symmetric distribution case.

PSU-WOPWOP was also used to investigate a larger observer region to assess the acoustic footprint over an extended area. In this configuration, the vehicle approaches from a distant location, passes directly over the microphone array, and then continues beyond it by an equivalent distance, ensuring symmetry in the flight path relative to the measurement grid. The acoustic impact at the observer locations is quantified using the SEL, which incorporates both the amplitude and duration of the noise event.

The result of SEL analysis versus the lateral distance from the center of the array is presented in Figure 19a and Figure 19b. The first shows the comparison between optimal and pessimal cases for the symmetrical observer distribution case studied, while the second shows the comparison between the optimal condition for all three cases studied.

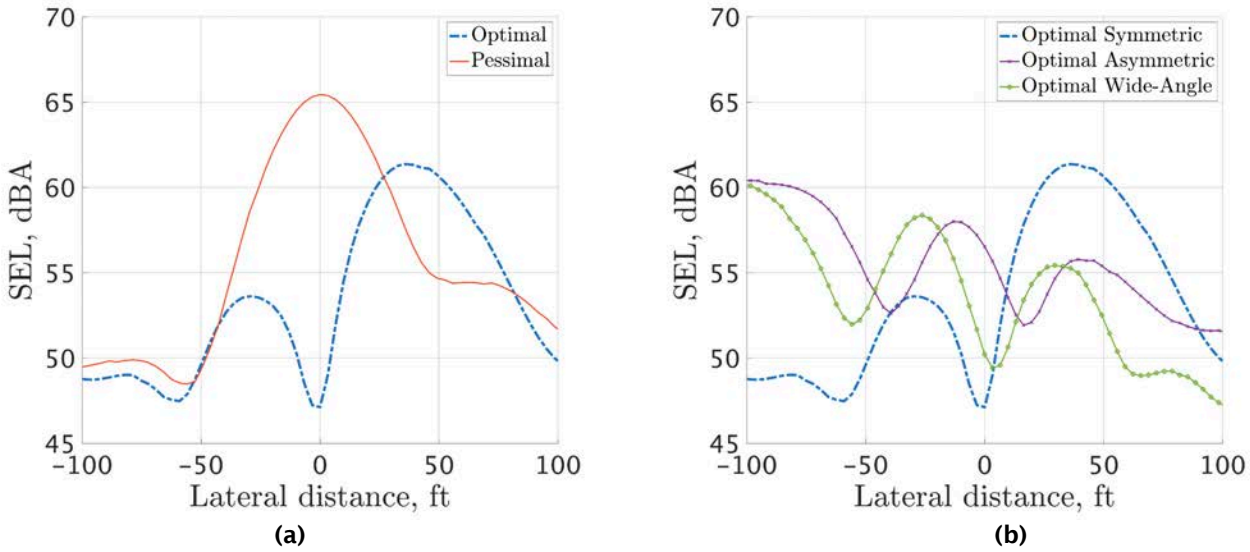


Figure 19. Predicted sound exposure level (SEL) variation over lateral distance for the (a) symmetric distribution and (b) all three cases.

Publications

Valente, V. T., Greenwood, E., & Johnson, E. N. (2025). An Experimental Evaluation of an Electronic Rotor Phase Synchronization System for Multirotor Aircraft Noise Control. *Journal of American Helicopter Society, 70*(4). https://doi.org/10.4050/JAHS.70.042008

Valente, V. T., Greenwood, E., & Johnson, E. N. (2026). Multirotor Noise Control using Synchrophasing Under Nonstationary Conditions. *Journal of Sound and Vibration, 629*. https://doi.org/10.1016/j.jsv.2026.119673

Valente, V. T., Chaudhary, R., Greenwood, E., Johnson, E. N., & Brentner, K.S. (2026, May 26-29). Predictions and Measurements of Noise Control via Synchophasing for a Fixed Wing Distributed Electric Propulsion Aircraft in Free Flight [Abstract submitted]. 32nd AIAA/CEAS Aeroacoustics Conference, Brussels, Belgium.

Outreach Efforts

The investigation team holds monthly meetings with FAA and an external advisory board consisting of a dozen interested parties from government and industry.

Awards

None.

Student Involvement

Dr. Vítor T. Valente was responsible for preparing the vehicle setup and adapting the method (both hardware and software). Ph.D. candidate Rupak Chaudhary was responsible for the simulation using CHARM and PSUWOPWOP for generation of pressure time series of the selected propeller and noise hemisphere analysis.

Plans for Next Period

The vehicle has been fully assembled; however, flight testing has not yet been conducted. The installation of avionics systems is currently underway, and ground-based tests are being performed to verify the synchrophasing performance. Preliminary simulation results indicate promising capabilities in terms of both attenuation and amplification of the overall sound pressure level. Furthermore, additional simulations are in progress to evaluate the sound exposure level as a supplementary performance metric. For next term, flight testing is expected to happen along with the analysis and presentation of the results in a conference.

Task 7 – Improved Air Data System Integration and Calibration

The Pennsylvania State University

Objective

The objective of this task is to integrate and characterize a new high frequency air-data system—transitioning from the previously used Airmar® 150 WX to the LI-COR® LI-560—on the large reconfigurable UAS platform. This includes calibrating the LI-560 for inflow and installation effects, validating the accuracy and consistency of the calibration results, and utilizing the improved air-data measurements to better understand the influence of ambient wind on multirotor UAS noise measurements.

Research Approach

A review of prior research was conducted to identify a practical air-data solution for multirotor UAS. Conventional pitot systems are unsuitable for these platforms due to low speeds, variable attitudes, and disturbed inflow. Earlier work on multirotor atmospheric sampling relied on sonic-anemometer weather stations, and these showed good agreement with tower and Light Detection and Ranging (LIDAR) measurements in hover. In transitioning from the Airmar 150 WX to the LI-560 TriSonica® Sphere, the LI-560 offered several advantages: true 3D wind-vector measurement, higher sampling rate capability, lower weight, and reduced flow obstruction—making it better suited for measuring inflow around small UAS and for future installation-effect characterization. Although prior studies focused mainly on hover, installation effects during forward flight remain largely unquantified and motivated development of this system.

To address this gap, the LI-560 TriSonica Sphere–based air-data system was integrated into the reconfigurable UAS platform to provide higher frequency 3D wind measurements, temperature, acoustic speed and static pressure. All data are time synchronized using an independent GPS. A custom Raspberry Pi–based logger was developed to record high-rate data to a compact binary file, along with a parallel 1 Hz ASCII summary. A separate post-processing script converts the binary logs into comma-separated value (CSV) and generates diagnostic plots. The LI-560 and electronics were mounted on an elevated structure to minimize rotor-induced inflow.

Milestones

- Develop a robust data-logging architecture using Python.
- Validate sensor functionality and GPS synchronization.
- Conduct Wind-tunnel testing to characterize baseline sensor performance.
- Integrate the LI-560 air-data system as a standalone system on the reconfigurable UAS.

Major Accomplishments

A new air-data system was developed by integrating the LI-560 module with a Raspberry Pi–based data logger and a GPS receiver to ensure alignment with vehicle state information. Wind-tunnel tests were conducted to characterize baseline sensor performance. Planned work includes GPS-assisted upwind–downwind calibration flights, and full characterization of installation effects on the UAS. The integrated system already supports analysis of how wind and airspeed influence multirotor noise during flyover tests, enhancing understanding of UAS noise behavior under varying atmospheric conditions.

Figure 20 shows the wind speed variation over time. The weather station was placed inside the wind tunnel, and wind speed was measured at several throttle settings. At each setting, the throttle was held for approximately 3 mins before being increased to the next level. Wind speed was also measured using two reference methods: (1) a Venturi meter and (2) a static pitot probe.

® Airmar is a registered trademark of Airmar Technology Corporation, Milford, New Hampshire.
® LI-COR and TriSonica are registered trademarks of Li-Cor, Inc., Lincoln, Nebraska.

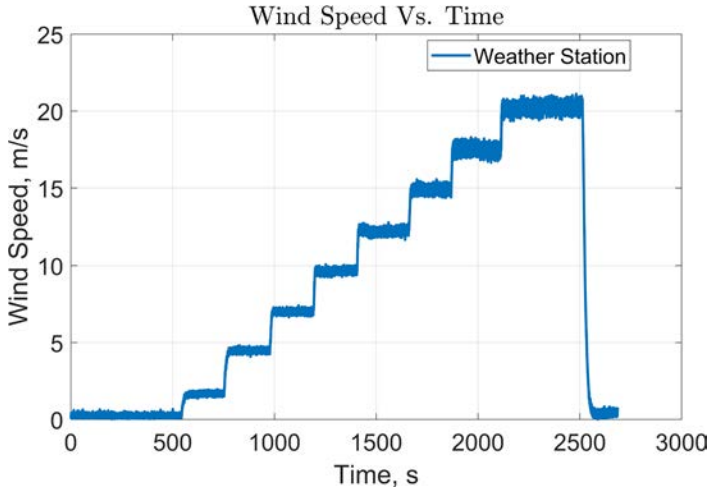


Figure 20. Wind speed time history during test inside wind tunnel.

Figure 21 shows the average wind speed at different throttle settings measured by the weather station, the Venturi meter, and the static pitot probe. The observed error ranges from 3–7%, with a maximum error of 7% occurring at approximately 15 m/s.

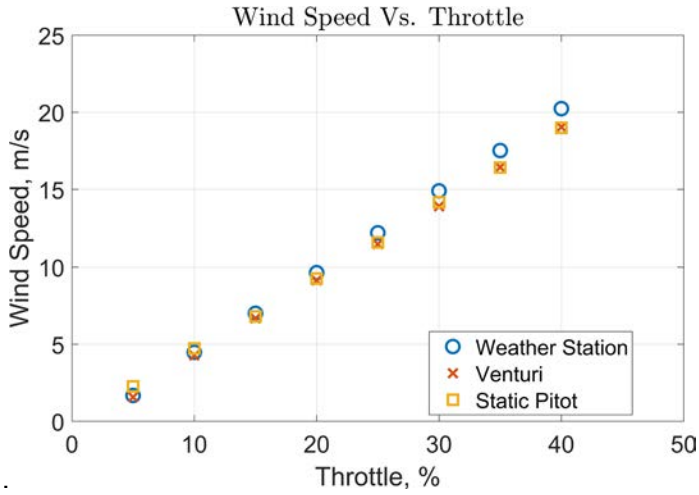


Figure 21. Wind speed at different throttle settings.

Figure 22 shows the wind-speed time history during the throttle-ramp test. The measured trend agrees well with the venturi reference, with discrepancies appearing at higher speeds and a maximum error of approximately 5%.

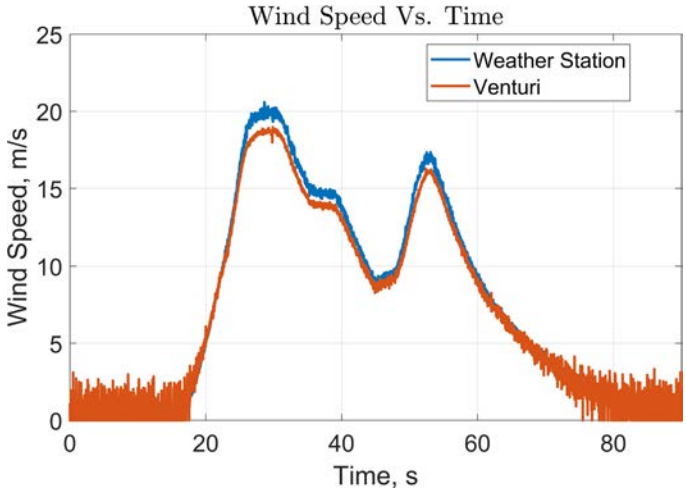


Figure 22. Wind speed time history during ramped throttle.

Figure 23 shows the PSU-hexacopter with the LI-560 TriSonica weather station installed. The sensor is mounted approximately 1 ft above the top plate and about 1.7 ft above the rotor plane. The system is standalone and can be easily removed and installed on the PSU octocopter as needed.



Figure 23. Weather station installed in PSU-hexacopter.

Publications

ElSharkawy, E., Valente, V. T., Rachaprolu, J. S., & Greenwood, E. (2024, July 29 – August 2). *Calibration of an Air Data System for Small Multirotor Aircraft* [Conference Presentation]. AIAA AVIATION FORUM AND ASCEND 2024 (AIAA 2024-4393). Las Vegas, Nevada. https://doi.org/10.2514/6.2024-4393

ElSharkaway, E., Valente V. T., Rachaprolu, J. S., & Greenwood, E. (2024, September 9-11). *Effect of Wind on Multirotor UAS Noise Measurements* [Conference presentation]. QuietDrones 2024 Symposium, Manchester, United Kingdom. https://doi.org/10.17866/rd.salford.27886245.v1

Outreach Efforts

The investigation team holds monthly meetings with FAA and an external advisory board consisting of a dozen interested parties from government and industry.

Awards

None.



Student Involvement

PhD candidate Rupak Chaudhary has been responsible for the development, programming, and analysis of the data produced by the onboard air-data system. Dr. Vitor Valente has provided guidance and mentorship throughout the development of the air-data system.

Plans for Next Period

- Conduct tests to build trust in the air-data system calibration methods.
- Use the calibrated sensor to conduct wind profile measurements at different heights and spatial locations throughout the test site. These data will be correlated to ground-based meteorological measurements.
- Correlate measured air and meteorological data to the aircraft flight state and acoustic data to better understand the effects of environmental conditions on noise generation and propagation.



Project 078 Contrail Avoidance Decision Support and Evaluation

Massachusetts Institute of Technology

Project Lead Investigator

Ian A. Waitz
Professor of Aeronautics and Astronautics
Vice President for Research
Massachusetts Institute of Technology
77 Massachusetts Ave, Building 3-240, Cambridge, MA 02139
(617) 253-0218
iaw@mit.edu

University Participants

Massachusetts Institute of Technology (MIT)

- P.I.: Prof. Ian Waitz
- FAA Award Number: 13-C-AJFE-MIT, Amendment Nos. 086, 100, 115, 125, 128, 133, 139, and 143
- Period of Performance: October 1, 2021, to August 31, 2027
- Tasks:
  1. Contrail Forecast Module
  2. Contrail Identification Module
  3. Contrail Observability Module

Project Funding Level

The Federal Aviation Administration (FAA) provided $2,250,000 in funding and $2,250,000 was received in matching funds. The sources of matching funding are approximately $333,100 from MIT, plus third-party in-kind contributions of $469,000 from Savion Aerospace Corp., and $463,000 from Google, LLC, and $984,900 from Earth Force Technologies.

Investigation Team

Prof. Ian Waitz (P.I.), All Tasks
Dr. Prakash Prashanth (co-PI), All Tasks
Dr. Florian Allroggen (co-investigator), All Tasks
Dr. Raymond Speth (co-investigator), All Tasks
Marlene V Euchenhofer (graduate student), Tasks 1, 3
Olivier Ng'weno Kigotho (graduate student), Tasks 1, 2
Louis Robion (graduate student), Tasks 2

Project Overview

Condensation trails (contrails) are the line-shaped ice clouds that form behind aircraft. These contrails and subsequent contrail cirrus are thought to account for around half of the climate warming attributable to aviation. Contrail avoidance through vertical flight path changes is estimated to cause fuel burn penalties at the few percent level. As such, it is a potentially cost-effective way to mitigate aviation's climate impacts. However, contrail avoidance has not been demonstrated at scale, and a comprehensive toolset to support the approach has not been developed. The goal of this project is to create a contrail avoidance decision support and evaluation tool that can be trialed to optimize and evaluate the benefits, costs, and practicality of contrail avoidance. In addition, subject to agreement with industry partners, our team will seek to test contrail avoidance in a way that has no negative implications for air traffic control or safety.



This project aims to satisfy four specific objectives: (1) to develop the capabilities necessary to predict the formation and impacts of contrails from a given flight, (2) to evaluate the financial costs and environmental benefits of deviating from that path to avoid a contrail, including uncertainty, (3) to integrate these capabilities into an operational tool that can provide near-real-time estimate of the costs and benefits of a contrail avoidance action, informed by automated, coordinated observational analysis and modeling, and (4) to evaluate the effectiveness of these tools in a safe, scientifically sound real-world experiment.

The objectives outlined above will be met through a work program that comprises the following tasks:

1. Contrail forecast module
2. Contrail identification module
3. Contrail observability module

The following tasks will be included under future periods of performance (i.e., not funded through current submission) but provide an outlook for follow-on work in future project years.

4. Airline and air traffic control integration
5. Contrail radiative impacts analysis
6. Experiment evaluation module

What follows in this document is a description of the tasks, including research progress and next steps.

Task 1 - Contrail Forecast Module

Massachusetts Institute of Technology

Objective

The objective of this task is to develop a contrail forecast module that predicts the likelihood of persistent contrail-forming conditions in the hours before the flight, and in real time during a flight. This is intended to allow airlines to decide ahead of time to consider whether flights should use contrail avoidance, to file flight plans accounting for the best estimated cruise altitude, and to adjust in real time (subject to pilot workload and air traffic control constraints).

Research Approach

Development of the MIT Contrail Avoidance Support Tool and MIT Contrail Avoidance Support Tool-Board

The MIT Contrail Avoidance Support Tool (MCAST) Board has been enhanced with new features that further the research use of the tool. A new calendar view has been developed that shows the contrail coverage over the year (as detected by the machine learning model) along with higher resolution Visible Infrared Imaging Radiometer Suite (VIIRS) satellite imagery. Additionally, an improved contrail detection model has been tested and deployed on MCAST board. Furthermore, to support ongoing efforts to attribute flights to contrails, an efficient flight data assimilation framework has been developed.

Development of Contrail-Flight Matching Algorithms

Matching contrails to the flights which formed them is a necessary component for verifying a contrail avoidance strategy's effectiveness. It provides a quantitative measure, on a per flight basis, of the change in contrail length due to an avoidance action based on a given contrail-forming region forecast. It can also be used to complement these forecasts by providing additional altitude information about the detected contrails; for a contrail matched to a given flight, Automatic Dependent Surveillance-Broadcast (ADS-B) data provide the altitude of the contrail at the time it was created, an approach we investigate further in Task 2. Two flight-attribution algorithms have been developed under ASCENT Project 078. The first one, described in a previous report and in Barbosa (2024) matches contrail segments to flight segments, while the second one, the Contrail Attributor and Tracker (CAT) takes a different approach by analyzing contrail masks to match contrails to flights waypoints.

Barbosa (2024) Algorithm

This section details the updates to the flight-attribution algorithm described in Barbosa (2024). Broadly, it matches contrails identified automatically on satellite imagery to discretized and advected aircraft trajectories derived from ADS-B data and numerical weather prediction. The matching process considers lateral and heading distances to pair flight segments and linearized contrails.



The algorithm has since been improved with regards to computational performance resulting in runtime reduction of 10 to 100 times for larger scenes by only considering flight segments within a certain relevant distance from each contrail segment before initiating the pairwise comparison in lateral and heading distance, respectively to determine potential flight matches.

The attribution accuracy of the algorithm has further been improved by considering the match likelihoods for all flight segments of an individual flight to a contrail, rather than looking at the match likelihood of each flight segment individually. This allowed us to also rank all considered flights regarding whether they might have formed a certain contrail and to express the likelihood for each flight.

Accuracy is evaluated on a dataset of manual labels of contrail-flight attribution pairs where some pairs were labeled in several subsequent time steps. The size of the 1980 manual contrail-flight attributions dataset was increased from 1,980 to 2,571 since the last reporting period. Though instrument limitations and labeler errors can sometimes lead to misattributions, this dataset is used as the basis of algorithm performance comparisons.

Moving from an attribution on a per-flight segment basis to a per-flight basis resulted in an increase of 3 percentage points in accuracy of the attribution output compared to our manual attributions. For this dataset, the algorithm's most likely flight match now agrees with the manually attributed flight for 79.8% of the contrails. The probability of identifying the correct contrail-forming flight increases to 93.9% and 95.6% when considering the top three and top five most likely flights, respectively.

Contrail Attributor and Tracker

The CAT is a new algorithm designed to explicitly consider the temporal evolution of contrails and uncertainty in wind advection through a probabilistic framework. In addition, it also accounts for the waypoint level uncertainty by computing for each flight waypoint the probability that it formed a contrail. This is necessary to accurately capture the horizontal extents of contrail forming regions.

The CAT differs from existing contrail attribution algorithms (Barbosa et al., 2024, Chevallier et al., 2023, Geraedts et al., 2024, Sarna et al., 2025) by focusing on attributing the new contrails in each satellite image instead of solving the entire attribution problem at each timestep. By doing so, the CAT effectively declutters images and limits match candidates to new contrails and recent flights waypoints, limiting the accumulation of advection error due to uncertain wind data. The CAT is intended to be run over multiple consecutive timesteps, allowing the algorithm to build knowledge of the scene by attributing contrails and flights incrementally.

In practice, the filtering process at a timestep T involves three steps. First, the contrail masks corresponding to the previous timestep are warped with the numerical weather prediction winds serving as a prior to where we expect existing contrails to be on the image at T. Second, these warped masks are aggregated by a Bayesian filter, the output of which is a new contrail mask where each pixel encodes the likelihood of it being a contrail pixel. Finally, the filtered mask from T-1 to T is subtracted to the masks at T to identify newly formed contrails. This approach enables the CAT to isolate newly formed contrails from those that were present in previous frames while the Bayesian filter handles the case where the segmentation of the contrail is noisy and the contrails flicker in and out between frames.

The matching process consists of Bayesian updates, where the posterior from the previous time step naturally informs the prior for the next, so each update simply incorporates the latest evidence. An intermediate step is necessary to take into account the uncertainty of tracking contrails between frames since contrails might split or merge over time. The prior for next step is therefore a weighted average of the posterior from previous steps based on the likelihood that the contrail in the current frame is a particular contrail in the previous frame. This process makes attribution temporally consistent, computationally efficient, and well-suited to real-time contrail avoidance.

The new contrail-flight matching algorithm is now complete and is ready to be tested and compared to our existing algorithm by using the synthetically generated contrails in Task 2. Figure 1 shows the outputs of the new contrail-flight attribution algorithm.

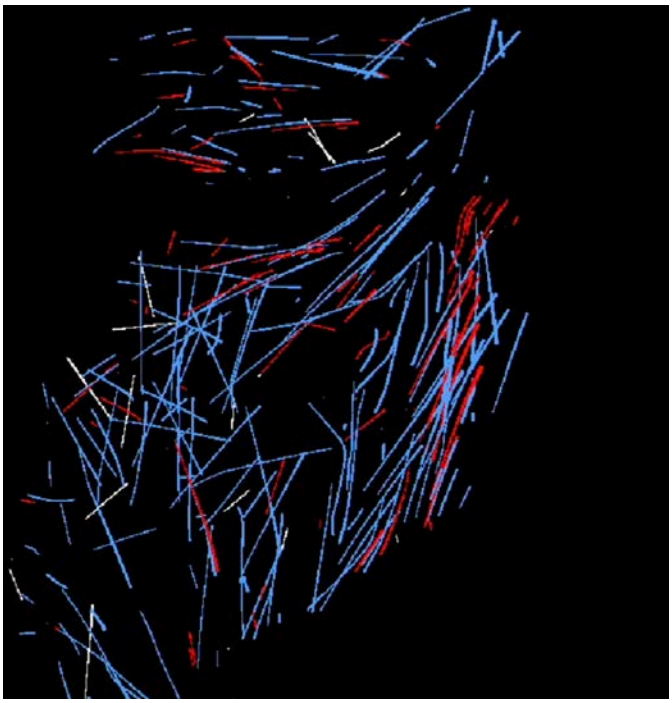


Figure 1. Outputs of the new contrail-flight attribution algorithm. Blue contrails correspond to those with a correct top match while red contrails have an incorrect top match. White features represent contrails for which the algorithm could not find a good fit and are therefore left unattributed.

Updates to the Aircraft Plume Chemistry, Emissions, and Microphysics Model (APCEMM)
APCEMM has been updated to allow users to bypass its early plume simulation, enabling users to directly input ice crystal number and size distribution to initialize the mature plume evolution model. By decoupling the early and mature plume models, this facilitates inter-model comparisons undertaken in ASCENT Project 058. This work also enables the initialization of APCEMM from in-situ measurements collected during the 2023 Boeing® ecoDemonstrator campaign which will be used to validate and constrain the model.

Milestone

- Expanded dataset of manual attributions.
- Created the new contrail-flight matching algorithm, now ready to be tested on synthetic contrails in Task 2.

Major Accomplishments

Improved attribution algorithm performance in both speed and accuracy and established a “ranking” of potential contrail-forming flights.

Publications

None.

Outreach Efforts

Presented at the ASCENT Spring Meeting 2025, online.

Awards

None.

® Boeing is a registered trademark of The Boeing Company, Seattle, Washington.



Student Involvement

The research and communication for this task were conducted primarily by MIT graduate research assistants, Marlene V. Euchenhofer, Olivier Ng'weno Kigotho, and Louis Robion.

Plans for Next Period

Conduct a canonical sensitivity study of the two attribution algorithms performance under different scenarios (i.e., flight density, errors in advection data, etc.).

References

Barbosa, M. P. (2024). *Relationship between synoptic scale meteorology, aircraft parameters, and observable contrails* [Master's Thesis. Massachusetts Institute of Technology]. Massachusetts Institute of Technology.

Chevallier, R., Shapiro, M., Engberg, Z., Soler, M., and Delahaye, D. (2023). Linear Contrails Detection, Tracking and Matching with Aircraft Using Geostationary Satellite and Air Traffic Data. *Aerospace*, *10*(7), 578.

Geraedts et al. (2024).

Meijer, V. R., Kulik, L., Eastham, S. D., Allroggen, F., Speth, R. L., Karaman, S., & Barrett, S. R. (2022). Contrail coverage over the United States before and during the COVID-19 pandemic. *Environmental Research Letters*, *17*(3), 034039.

Sarna, A., Meijer, V., Chevallier, R., Duncan, A., McConnaughay, K., Geraedts, S., McCloskey, K. (2025). Benchmarking and improving algorithms for attributing satellite-observed contrails to flights. *Atmospheric Measurement Techniques*, 18, 3495–3532.

Task 2 - Contrail Identification Module

Massachusetts Institute of Technology

Objective

The objective of this task is to develop a real-time contrail identification module that locates contrails both horizontally and vertically.

This module will be necessary to evaluate whether avoidance has been successful. Furthermore, this module will enable contrail forecasting approaches that are based on contrail detections, and that might prove to be more reliable for shorter lead times than approaches based on numerical weather forecasts. The initial version will use Geostationary Operational Environmental Satellite (GOES) satellite observations combined with an MIT-developed (under National Aeronautics and Space Administration sponsorship) deep learning approach to identify contrails from space. Future developments could add other satellite products and ground and other observations.

Research Approach

New Contrail Height Estimation Approach

The ASCENT Project 078 team's previous height estimate approach was purely based on remote sensing and relied on the radiances of pixels that our model identifies as part of a contrail. Using the radiances of all available wavelengths, an altitude probability distribution is calculated for each pixel (Meijer, 2024). Currently, the mean of this distribution is used to retrieve the altitude of the contrail pixel. During the assessment of our computing pipeline, our team identified that this approach was not sufficiently accurate for our operational purposes – potentially due to temperature variations in the upper troposphere being too small to provide sufficient information to distinguish nearby altitudes.

Therefore, the ASCENT Project 078 team decided that a new approach to estimate the altitude of detected contrails is required. Our team attributes contrails to flights and takes advantage of the flights' known altitude to estimate the altitude of the contrails. This approach was updated to also estimate the latitude and longitude of the contract-forming region using the new contrail-flight matching algorithm. Given that the new algorithm outputs the likelihood a contrail was formed at any given point along the flights' trajectory, the set of all flights can be interpolated using a radial basis function to estimate both the height and horizontal extents of contrail likely regions.

Synthetic Contrail Imagery

Quantifying the performance of contrail-flight attribution algorithms requires an evaluation dataset where contrails and their associated flights are known. While a human labeled dataset was developed at MIT and used to quantify attribution performance in Barbosa (2024), it remains limited in number of samples and is subject to human error. The following work



was initially developed to create a synthetic dataset of contrail geometries and masks where we directly simulate which flight forms which contrail, in support of the flight attribution tasks.

This approach is scalable and is not prone to matching error, given that by construction, we know all contrail-flight pairs. It comes with associated contrail modeling and numerical weather predictions limitations, but the contrail masks serve as an appropriate test dataset for attribution purposes. The methods described here for mask generation are similar to the ones in Sarna et al. (2025) though they were developed independently.

With a systematic approach to simulating contrail masks (see Figure 2), we can go a step further and generate synthetic satellite observations of contrails. We do so by explicitly solving the radiative transfer problem using the Community Radiative Transfer Model (CRTM, Johnson et al., 2023) which directly models the radiative signature of the contrail in the visible to near infra-red bands as measured by a satellite sensor. The simulated responses are effectively synthetic contrail images, and they can be compared directly to observations informing our understanding of our abilities in contrail forecasting, and modeling:

- Forecasting: to what extent can the modeled contrail forming regions appearing in synthetic images reproduce observations? What does this imply on historical and future estimates of contrail radiative forcing?
- Modeling: when are contrail process models able to reproduce observed contrail radiative properties? This is particularly interesting in the later phases of contrail lifetime as this is where most radiative impacts occur. Satellite imagers are the primary source of observations in that phase, and this method allows for direct comparison of modeling with satellite radiances.

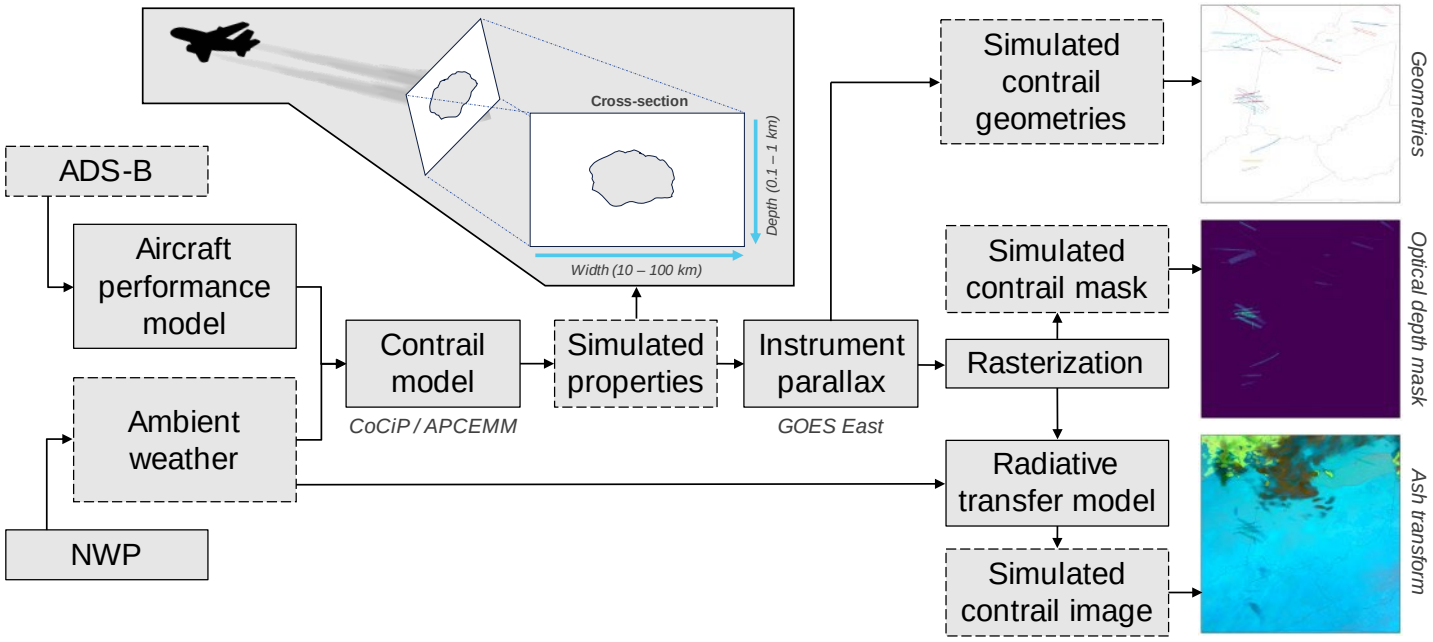


Figure 2. Model diagram detailing processing steps from Automatic Dependent Surveillance-Broadcast (ADS-B) data to synthetic contrail images. Ambient weather is taken from numerical weather prediction (NWP) and used both for contrail modeling and background weather for the radiative transfer simulation. In addition to accounting for sensor specific radiative response, the synthetic images also account for the sensor's viewing geometry by modeling the parallax correction and instrument's image grid. The example here is for Geostationary Operational Environmental Satellite (GOES)-16 Advanced Baseline Imager (ABI), but Community Radiative Transfer Model (CRTM) supports most existing satellite sensors. APCEMM: Aircraft Plume Chemistry, Emissions, and Microphysics Model, CoCiP: Contrail Cirrus Prediction.

Currently, synthetic contrail images can be generated with contrails simulated with ERA5[1] meteorology and Contrail Cirrus Prediction (CoCiP) (Schumann, 2012), using its *pycontrails* (Shapiro et al., 2025) implementation. We aim to extend this to contrails simulated by APCEMM (Fritz et al., 2020) as well as High-Resolution Rapid Refresh (HRRR) for meteorology. Weather data for the non-contrail background can be from ERA5 or HRRR. This flexibility allows us to compare the ability of the entire system, numerical weather prediction (NWP) data and contrail model, to match observed radiative properties. Existing approaches to generate synthetic contrail datasets either are not physics-based (Lee & Yoo, 2025) or do not explicitly simulate the satellite response (Chevallier et al., 2023, Sarna et al., 2025).

Preliminary simulations combining CoCiP and ERA5 data as well as HRRR for the background are presented in Figure 3. Using different NWPs for contrail and background simulations leads to inconsistent humidity fields and will be changed in the future. The simulation results below are for illustration purposes.

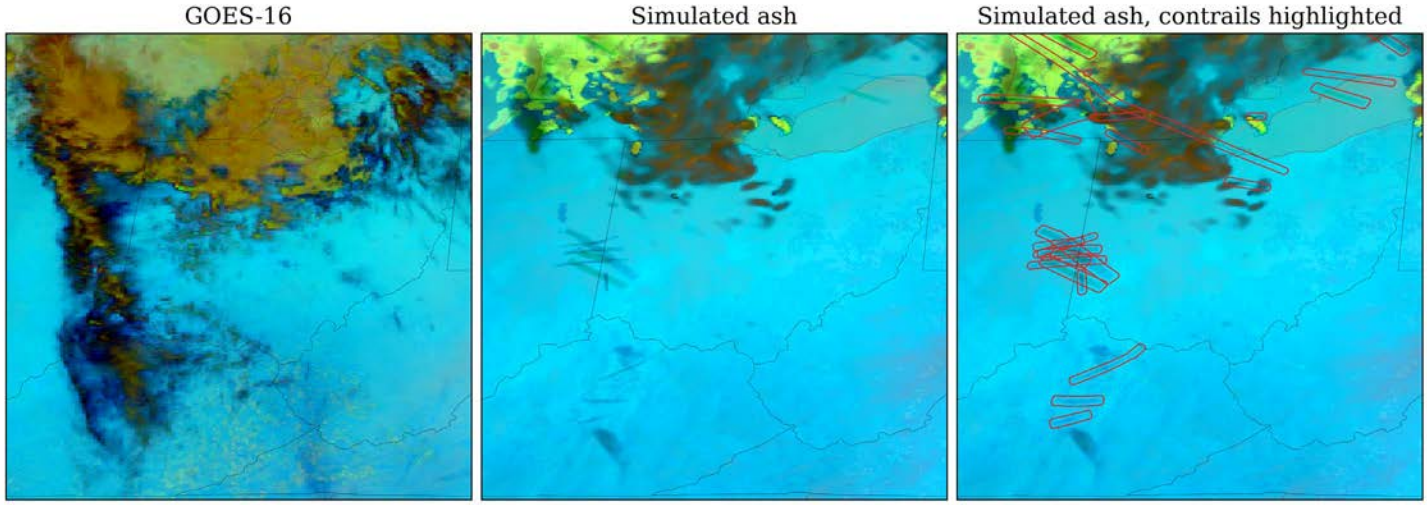


Figure 3. Synthetic images of contrails for Geostationary Operational Environmental Satellite (GOES)-16 at 2024-07-02T21:00Z over Ohio. Left: Ash-like transform of GOES-16 Advanced Baseline Imager (ABI) image. Middle and right: Simulated contrails using CoCiP and ERA5 meteorology, with background conditions taken from HRRR data.

Figure 3 shows that NWP predictions disagree with observations both for background cloud placement (thick brown cirrus clouds here) as well as contrails. This is significant for contrail climate impacts because those are dependent on the presence of other clouds below or above the contrail. This also provides insights into the observability of contrails: simulated contrails over Lake Erie are difficult for a human to distinguish from the background even though they are over clear sky. While we do not expect modeling to be able to reproduce individual contrail instances, this framework allows us to test this hypothesis and expand it to contrail cluster level statistics.

Milestone

Developed a framework that simulates contrails, their geometries and synthetic satellite contrail images enabling new comparisons of modeling to satellite observations.

Major Accomplishments

Generated physics-based synthetic satellite contrail images.

Publications

None.

[1] European Centre for Medium-Range Weather Forecasts (ECMWF) Reanalysis v5 (fifth generation ECMWF atmospheric reanalysis of the global climate). Produced by the Copernicus Climate Change Service (C3S) at ECMWF, it provides hourly, high-resolution (31km) global data on atmospheric, land, and ocean-wave variables from 1940 to the present.



Outreach Efforts
None.

Awards
None.

Student Involvement
The research and communication for this task were conducted primarily by MIT graduate research assistants, Olivier Ng'weno Kigotho and Louis Robion.

Plans for Next Period
- Implement contrail simulations using HRRR data.
- Implement contrail simulation using APCEMM.
- Benchmark altitude predictions from the output of the altitude estimation algorithm.

References
Barbosa, M. P. (2024). *Relationship between synoptic scale meteorology, aircraft parameters, and observable contrails* [Master's Thesis. Massachusetts Institute of Technology]. Massachusetts Institute of Technology.

Chevallier, R., Shapiro, M., Engberg, Z., Soler, M., and Delahaye, D. (2023). Linear Contrails Detection, Tracking and Matching with Aircraft Using Geostationary Satellite and Air Traffic Data. *Aerospace*, *10*(7), 578.

Fritz, T. M., Eastham, S. D., Speth, R. L., & Barrett, S. R. (2020). The role of plume-scale processes in long-term impacts of aircraft emissions. *Atmospheric Chemistry and Physics*, *20*(9), 5697-5727.

Johnson, B. T., C. Dang, P. Stegmann, Q. Liu, I. Moradi, and T. Auligne, (2023). The Community Radiative Transfer Model (CRTM): Community-Focused Collaborative Model Development Accelerating Research to Operations. *Bulletin of the American Meteorological Society*, 104, E1817–E1830.

Lee, Y., and Yoo, J. (2025) Improving Contrail Detection via Diffusion-Based Data Augmentation Framework. *ICLR 2025 Workshop on Tackling Climate Change with Machine Learning*.

Meijer, V. R. (2024). *Satellite-based analysis and forecast evaluation of aviation contrails* [Doctoral dissertation, Massachusetts Institute of Technology]. Massachusetts Institute of Technology.

Sarna, A., Meijer, V., Chevallier, R., Duncan, A., McConnaughay, K., Geraedts, S., McCloskey, K. (2025). Benchmarking and improving algorithms for attributing satellite-observed contrails to flights. *Atmospheric Measurement Techniques*, 18, 3495–3532.

Schumann, U. (2012). A contrail cirrus prediction model, *Geoscientific Model Development,* 5, 543–580.

Shapiro, M., Engberg, Z., Teoh, R., Stettler, M., Dean, T., Abbott., T. (2025). pycontrails: Python library for modeling aviation climate impacts (v0.59.0). *Zenodo*.

Task 3 - Contrail Observability Module
Massachusetts Institute of Technology

Objective
The objective of this task is to assess the limitations of the sensing platform used and to develop an understanding for how this quantitatively affects our capabilities in performing and measuring successful operational contrail avoidance. Furthermore, this module aims to provide insights into the practical observability implications of contrails on satellite imagery. While recent work (Driver et al., 2024) investigated the resolution-based observability limitations of remote sensing for satellite detection using synthetic data of linear contrails over clear sky ocean background, there is a need for a systematic analysis using real satellite imagery and a larger breadth of scenarios. The ASCENT Project 078 team has therefore generated a comparison dataset of contrails identified on infrared imagery from two different satellite imagers with different spatial resolutions and will eventually open source the data to support the research efforts of the broader scientific community.

Research Approach

Contrail Observability Limitations

Our now-casting pipeline currently fully relies on imagery from the Advanced Baseline Imager (ABI) onboard the geostationary satellite GOES-16. The platform's continental United States (CONUS) product covers the full contiguous United States (U.S.) and has a temporal resolution of one image every five minutes, making it operationally feasible for our approach. However, the limited spatial resolution of the images (2 to 3 km per pixel) is a limitation that can result in a previously not quantified number of unobserved contrails. This partially results from an observability lag, i.e., contrails do not appear on the imagery right after formation but only once they have grown wide enough relative to the remote sensing instruments spatial resolution. Further, some contrails might not be observable at any point throughout their life due to not reaching a critical width or optical depth, or by not being distinct enough from the background. In either of these cases, our method could miss clusters or regions of contrails due to limited spatial resolution and thus not initiate deviations where they might be necessary.

Quantification Approach

We generated a dataset up manually labeled (and manually checked by a second trained labeled) contrails in infrared imagery of 12 scenes over the contiguous U.S. For each scene, we labeled one image from VIIRS, an instrument that is currently onboard three satellites in the low Earth orbit (NOAA-20, NOAA-21, SUOMI NPP) and one image from GOES-16 ABI. The polar orbits of the VIIRS-carrying satellites, however, limit use to two overpasses over the U.S. per satellite per day (not allowing for continuous real-time observations), as well as coverage of maximum half the contiguous U.S. Therefore, our team cannot use the imagery from VIIRS for our nowcasting pipeline, but it allows us to assess resolution-based contrail observability limitations by comparing images between GOES-ABI and VIIRS when data from the latter are available. VIIRS, while also being an imperfect imager and not representing "ground truth," generates images at a spatial resolution at a factor 3.5 times higher and serves as the benchmark for this comparison.

The contrail labels on the VIIRS and the ABI images for each of the 12 scenes were then analyzed to determine observation limitations of ABI with respect to VIIRS.

Results

The ASCENT Project 078 team found that on average over all scenes, ABI captures only about 20% of all contrails and only about half of the total contrail length observable from VIIRS (higher resolution). Figure 4 presents parity plots for the two metrics where each marker represents one scene and with the scene's metric for VIIRS on the x-axis and for ABI on the y-axis. We found that VIIRS captures significantly more short contrails. These could become observable in subsequent ABI frames, once they spread enough to meet a certain width. Further, we assume that VIIRS also allows us to identify my non-persistent contrails which will likely not appear on ABI at all but are also expected to be of negligible climate impact.

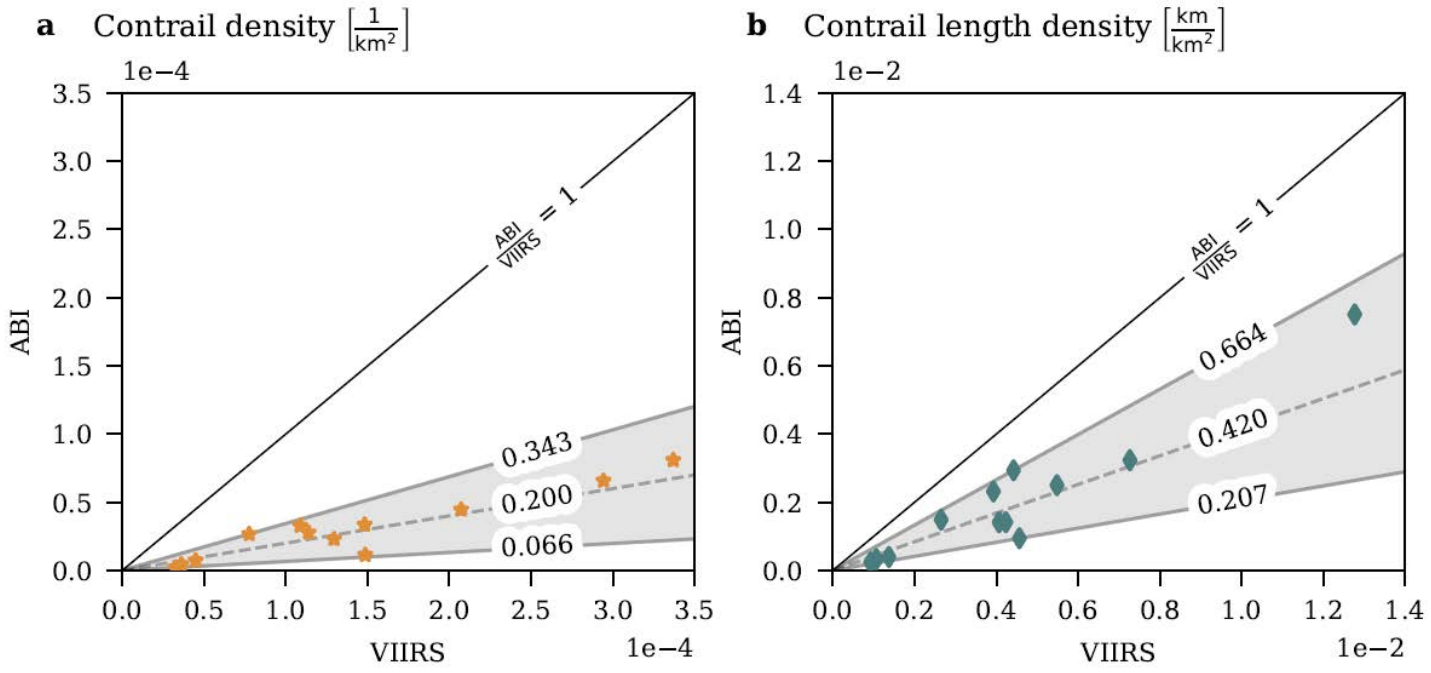


Figure 4. Comparison of (a) contrail density (number of contrails per unit area) and (b) contrail length density (total contrail length per unit area) for each of the 12 scenes in the dataset. The slope of the line through each point represents the ABI/VIIRS ratio, where a value of 1 would represent equality. The solid grey lines represent the minimum and maximum ratios, respectively. The dashed lines indicate the average ratio over all scenes.

We further found that contrail widths determined from ABI contrail observations represent and overestimate compared to higher resolution labels and subsequently an overestimate in individual contrail area. In some cases, this overestimate can result in a contrail cover that exceeds the value derived from the up to five-times as many contrails observed with VIIRS.

Our work highlights limitations for contrail observations from geostationary satellite imagers, but we point out that the high temporal resolution and large spatial coverage of these imagers is what makes them the key provider of observational data for observation-based contrail avoidance. We see an opportunity in combining observational data from multiple sensors to address some of these shortcomings and to gain a more comprehensive dataset of contrail observations and contrail evolution.

Milestone

Generated a dataset with manual labels of several thousand contrails in infrared imagery from VIIRS and ABI.

Major Accomplishments

Quantified the number of missed contrail observations for ABI in comparison to a higher resolution imager (VIIRS).

Outreach Efforts

The research progress was presented at the Fall ASCENT meeting 2025, in Alexandria, Virginia.

Publications

Euchenhofer, M. V. (2025). *An investigation into contrail observability from different satellite platforms* [Master's thesis, Massachusetts Institute of Technology]. Massachusetts Institute of Technology. https://hdl.handle.net/1721.1/162925

Euchenhofer, M. V., Prashanth, P., Parke, S. A., Eastham, S. D., & Waitz, I. A. (2025). Contrail observation limitations using geostationary satellites. *Geophysical Research Letters, 52*, e2025GL118386. https://doi.org/10.1029/2025GL118386

Awards
None.

Student Involvement
The research and communication for this task were conducted primarily by MIT graduate research assistant, Marlene V. Euchenhofer.

Plans for Next Period
Publish the dataset on Zenodo after acceptance of the above manuscript.

References
Driver, O. G. A., Stettler, M. E. J., & Gryspeerdt, E. (2024). *Factors limiting contrail detection in satellite imagery* (p. 1-28). EGUsphere. https://egusphere.copernicus.org/preprints/2024/egusphere-2024-2198/



Project 079 Novel Noise Liner Development Enabled by Advanced Manufacturing

The Pennsylvania State University
RTX Technology Research Center
Altair Engineering
Cornerstone Research Group

Project Lead Investigator

Nicholas Meisel
Associate Professor
School of Engineering Design and Innovation
The Pennsylvania State University
University Park, PA 16802
nam20@psu.edu

University Participants

The Pennsylvania State University (Penn State)

- P.I.: Nicholas Meisel, Associate Professor of Engineering Design
- FAA Award Number: 13-C-AJFE-PSU-079
- Reporting Period: October 1, 2024, to September 30, 2025
- Tasks:
  1. Identifying Sensitivity of Acoustic Liner Performance to Key Design Variables
  2. Establishing Systematic Approach to Identify and Account for Manufacturing Error
  3. Automating the Generation of Acoustic Lattice Meshes

Project Funding Level

The ASCENT Project 079 received $1,200,000 from the Federal Aviation Administration (FAA) with match from Penn State ($110,000), RTX Technology Research Center ($450,000), Altair Engineering ($400,000), and Cornerstone Research Group ($240,000).

Investigation Team

The Pennsylvania State University

Nicholas Meisel (P.I.), Project management, task coordination, and student advising
Allison Beese (co-P.I.), Student advising, Tasks 1 and 2
Eric Greenwood (co-P.I.), Student advising, Task 1
Alden Packer (graduate student; PhD), Task 1
Joeseph Windows (graduate student, MS), Task 2

RTX Technology Research Center (RTRC)

Jeff Mendoza (P.I.), Project coordination and management at RTRC
Julian Winkler (co-P.I.), Acoustic analysis and evaluation as part of Task 1
Aaron Reimann (co-P.I.), Acoustic analysis and evaluation as part of Task 1
Kenji Homma (investigator), Acoustic analysis and evaluation as part of Task 1
Paul Braunwart (investigator), Acoustic analysis and evaluation as part of Task 1

Altair Engineering (Altair)

Eric Nelson (P.I.), Manufacturability accommodation as part of Task 2



Cornerstone Research Group (CRG)
Akiva Wernick (P.I.), Direct mesh generation as a part of Task 3

Project Overview

Penn State in collaboration with industrial partners, RTRC, Altair, and CRG, along with government collaborator, the National Aeronautics and Space Administration (NASA) Langley Research Center (LaRC), will help the FAA develop and advance innovative engine acoustic liner technology to meet the demands of low noise for future aircraft. Specifically, the team will develop and demonstrate a method to rapidly design, manufacture, and evaluate novel structures that enhance noise attenuation in aircraft engines. Analysis and experimental testing will be used to characterize the effect of lattice topology, geometry, and features size to attenuate noise while ensuring the manufacturability of these complex structures in different materials. Advanced manufacturing technologies will be used to enable rapid design-build-test cycles for liner development, including assessment of structural integrity and acoustic performance. Promising engine liner designs and their performance will be documented to aid future advancements in aircraft engine noise reduction.

The overall project approach includes the following steps:

1. Establish a set of acoustic requirements for future aircraft engine designs.
2. Design and analyze lattice-based acoustic liners using advanced software tools.
3. Perform rapid, iterative prototyping and testing to identify promising designs and materials.
4. Conduct detailed assessments of manufacturability.
5. Perform acoustic and structural evaluations of novel liners in collaboration with NASA LaRC.
6. Document results and archive data for the FAA.

Task 1 – Sensitivity of Acoustic Liner Performance to Key Design Variables

The Pennsylvania State University, RTX Technology Research Center

Objective

The objective of this task is to identify the sensitivity of the additive manufacturing (AM) acoustic liner designs to changes in key design parameters. This sensitivity will be compared against traditional honeycomb-shaped liners.

Research Approach

To verify the viability of triply periodic minimal surface (TPMS) lattice-based acoustic liners, they were compared against traditional single degree-of-freedom (SDOF) and double degree-of-freedom (DDOF) liners. Allowing for an equal comparison, both categories of liners were first optimized using the same target objective, that of maximizing acoustic absorption in defined frequency ranges. The design optimization process that was used was created through the unification of necessary pieces of software that performed the functions of parameterizing the design variables for the acoustic liner concepts, modeling the geometries, simulating the acoustics physics, and analyzing the response objectives.

Parameterization of Design Variables

For SDOF, DDOF, and TPMS based liners alike, optimization requires that the available design variables be parameterized and given bounds within which to explore. For each liner type, and subsequent construction, there are changes to the design that can impact the acoustic response of the liner. For all liner types in this study, the total depth or thickness of the liner was capped at 1.5 in. or 38.1 mm, to compare the performances of the lattices when similarly constrained. The design parameters of the facesheet were also given equal constraints across all lattice types.

The SDOF acoustic liner has four main design variables, shown in Figure 1. Three of the parameters correspond to properties of the perforated facesheet, percent open area (POA), facesheet thickness, t, and perforation diameter, d. To eliminate the possibility of the POA and perforation diameter requiring a non-whole number of perforations, the number of perforations was used as a design variable, and the POA was calculated from the number of perforations multiplied by the area of a single perforation, all divided by the total area of a cell. That POA value was then used in modeling. The depth of the honeycomb core, D, pertains to the honeycomb core itself, and is a critical parameter for resonating liners, like the SDOF. Varying the depth of the liner adjusts the frequency where the most absorption will occur, with deeper liners corresponding to lower frequency absorption. The facesheet parameters also affect the acoustic response by creating resistive losses through friction in the perforations. DDOF acoustic liners maintain the same design variables as the SDOF liner, but the added intermediate septum introduces additional variables that can be altered to achieve higher acoustic

absorbing performance. Like the facesheet in the SDOF, the DDOF facesheet also causes acoustic energy losses through friction within the perforations. This is added to by the perforations in the intermediate septum. The lowest frequency response of the DDOF liner is still driven by the total depth, as with the SDOF; however the septum can cause additional ranges of high absorption. This dividing septum has thickness, t_s, and variable permeability properties, such as percent open area, POA_s, and perforation diameter, d_s. The depth of the septum within the honeycomb core, D_s, can be varied as well, yielding in total three additional design variables. Figure 1 shows the honeycomb core liner with the additional septum related design variables included.

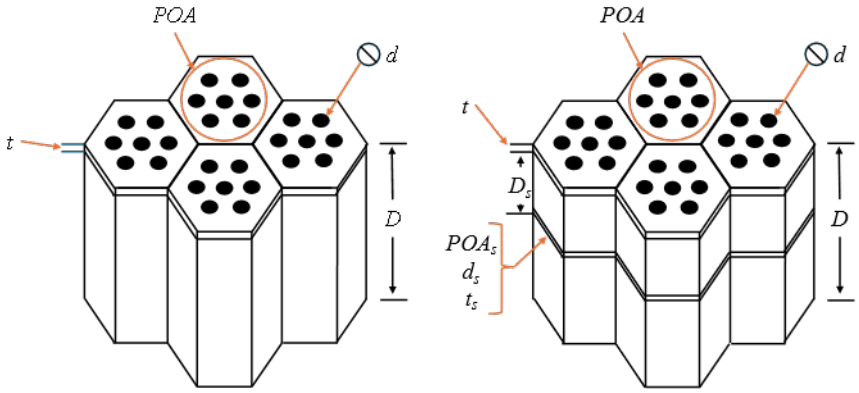


Figure 1. Single degree-of-freedom (SDOF) and double degree-of-freedom (DDOF) liner designs with relevant design variables: liner depth (D), facesheet thickness (t), facesheet perforation diameter (d), percent open area (POA), septum depth (D_s), and percent open area and perforation diameter of the septum (POA_s and d_s).

Instead of a cavity with variable depth, TPMS lattice structures encompass a complex pair of channels with unique tortuous paths that are controlled by specific design variables. The design variables used in this study are general to all TPMS lattices, but the lattice types of Schwarz P and Diamond were selected for exploration and comparison with the SDOF and DDOF. Schwarz P was selected for the study based on the research team's previous preliminary investigations, while the Diamond lattice was selected for its high levels of internal tortuosity. The first group of design parameters is the variability of unit cell size. This allows us to adjust the size of individual unit cells in three directions, X Y, and Z, effectively stretching or compressing the cells of the lattice in those directions (see Figure 2). These variables can also be scaled uniformly to vary the overall size of the unit cell. Due to the symmetry inherent in normal incidence testing, the unit cell size in X and Y were coupled, and the samples were modeled in a 1x1xn stack of cells. The total depth of the sample was determined by the height of the cells (Z) multiplied by another design variable, the total number of cells in the Z-direction. These design variables modify the internal volumes of the lattices, potentially causing variations in the resonating effects of the geometry.

Control of the levelset or iso-surface offset of TPMS lattices allows for the offsetting of material from the surface midplane to either side of the surface. This effect is shown in Figure 2 for both the Schwarz P and Diamond lattices. TPMS lattices split a region into two non-intersecting sub-regions. Changes in levelset varies the volumes of the two sub-regions, expanding one while contracting the other, promoting a unique acoustic response in each region. These two subregions can be broadly differentiated as the endo-region and the exo-region. In this study, levelset was defined twice, once at the facesheet and once at the backplate. This causes a functional grading effect of the levelset, where cells of the lattice in the Z-direction can have different levelset values.

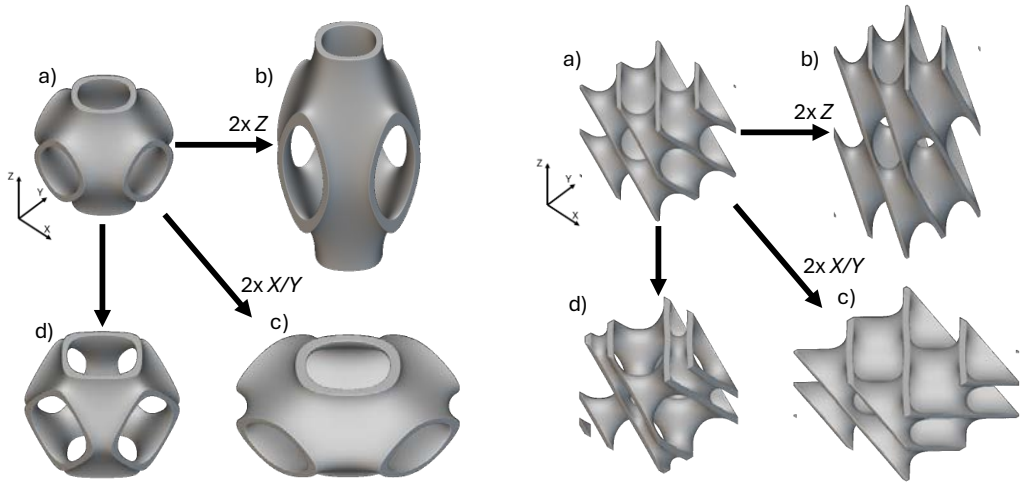


Figure 2. Triply periodic minimal surface (TPMS) lattice variations from the basic unit cell (a) for the Schwarz P and Diamond lattices (left and right, respectively), (b) change in Z height, (c) change in X/Y width, and (d) change in levelset.

The additional benefit of the presence of the two sub-regions is that a unique facesheet can be applied to each region separately. In this way, each region essentially acts as its own acoustic liner, leading to the possibility of wider ranges of high absorption. For both the endo and the exo-regions, the design variables of perforation diameter and number of perforations can be defined uniquely. Examples of the facesheet over Schwarz P and Diamond unit cells are shown in Figure 3. Variation of the facesheet thickness is consistent between the two regions to avoid off-setting either the top of the facesheet or the back of the lattice. This configuration leads to five design variables for the TPMS facesheet alone, in addition to the five variables from the lattice core geometry. A summary of the available design variables associated with each liner in the current study provided in Table 1.

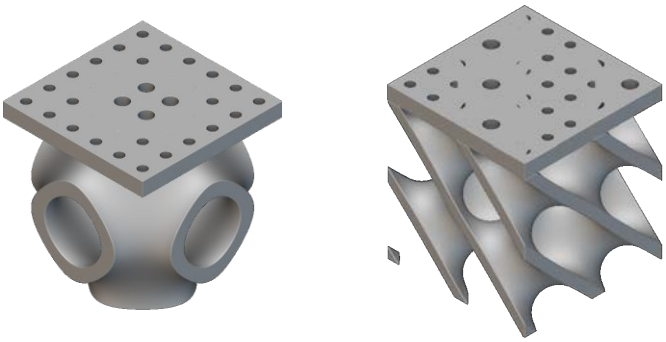


Figure 3. Facesheet depictions for the Schwarz P (left) and Diamond (right) triply periodic minimal surface (TPMS) lattice geometries. For these examples, the endo-region has a larger perforation diameter than the exo-region.



Table 1. Design variables of the single degree-of-freedom (SDOF), double degree-of-freedom (DDOF), and triply periodic minimal surface (TPMS) acoustic liners.

SDOF	DDOF	TPMS
# of Facesheet Perforations **Perforation Diameter**	# of Facesheet Perforations Perforation Diameter	X/Y Unit Cell Size Z Unit Cell Size
Facesheet Thickness **Liner Depth**	Facesheet Thickness Liner Diameter	Z: # of Cells Level set (Facesheet)
	# of Septum Perforations	Level set (Backplate)
	Septum Perforation Diameter Septum Thickness	Facesheet Thickness Endo Perforation Diameter
	Septum Depth	# of Endo Perforations Exo Perforation Diameter
		# of Exo Perforations

Geometry Modeling and Acoustic Simulation

The next step in the process is to represent the liner geometry in a way that we can parameterize the important geometric components and calculate the acoustic performance. For the SDOF and DDOF acoustic liners, the Zwikker-Kosten Transmission Line (ZKTL) method was used to model geometry and predict acoustic performance. In this method, each section of the liner is represented by a transmission matrix, including both cavities and perforated sheets. For modeling of the perforated sheets, the flow resistance is calculated using the lumped element model or two parameter model, shown in Equation 1. In this equation, ζ represents the impedance, ϑ represents the acoustic resistance (linear and nonlinear), and χ represents the acoustic reactance of the facesheet. It is referred to as the two-parameter model because it breaks the acoustic resistance into two terms: the linear and the non-linear resistance. This model is suitable for calculating the acoustic response of SDOF acoustic liners directly, but it was implemented into the ZKTL code in order to be robust enough to also predict DDOF performance.

$$\zeta = \theta + i\chi = \theta_{lin} + \theta_{nonlin} + i\chi_{fs} \quad \text{(Eq. 1)}$$

The tradeoff of exploring higher complexity geometries is that analytical solutions often do not exist to model the physics present in these structures. Because of this, a numerical approach is necessary. First, the acoustic liner structure must be modeled in computer aided design (CAD) software, then a mesh will be applied to the geometry, and a numerical simulation of the physics will be applied to the mesh. For the TPMS acoustic liners, an implicit geometry CAD software, nTopology, was used to generate the lattice geometries. As an implicit geometry software tool, nTopology is able to model mathematically defined functions and efficiently represent and export the complex lattice geometry. The lattice geometry files from nTopology were then imported into COMSOL Multiphysics® software (COMSOL). Additionally, select SDOF and DDOF designs were modeled in CAD and simulated in COMSOL for verification of the previously discussed analytical approach. Geometry generation of liner designs was performed on local desktop machines, but COMSOL was run on a cluster computing cloud service through Penn State. The pressure acoustics COMSOL library was used to apply the necessary boundary conditions for modeling acoustic performance. All walls in the model were treated as hard wall boundaries, and a perforated plate boundary condition representing a perforated facesheet was used to reduce the computation time caused by attempting to mesh such small features as the facesheet perforations. The facesheet design variables were imported into the study and applied to this boundary condition. A physics-defined mesh was used, which automatically adjusts the element size according to the physics being simulated. The acoustic response is solved across a prescribed frequency range of 300 to 3,400 Hz, which are the lower and upper bound of viable frequencies of typical normal incidence tube experimental testing. After the acoustic data are gathered, the response objectives are extracted for performance characterization.

The two main pieces of information that are output from both numerical and analytical acoustic modeling are acoustic resistance, ϑ, and reactance, χ. For every tested frequency, these values describe the resistance to sound flow due to friction and heat, and to inertia of the medium, respectively. Those two quantities can be used to calculate the acoustic

® COMSOL Multiphysics is a registered trademark of Comsol AB, Stockholm, Sweden.



absorption coefficient, α, which is the response objective used in the optimizations. Acoustic absorption coefficient is calculated as follows for normal incident acoustics.

$$\alpha = \frac{4\theta}{(1+\theta)^2+\chi^2} \quad \text{(Eq. 2)}$$

The acoustic absorption coefficient is an efficient performance metric, providing a value between zero (complete reflection) and one (complete absorption) for each frequency. When plotted, the result is an acoustic absorption curve. When calculating acoustic absorption for an acoustic liner design, the result is a series of absorption values for every frequency in the range that is tested. This poses difficulty when comparing the performance between two or more liners because it becomes inefficient to compare the absorption at every frequency. The most efficient metric would be a single scalar value to describe the general performance of the acoustic absorption coefficient in the desired frequency range. The method used to provide this metric is to integrate the absorption coefficient curve over a predetermined bandwidth, yielding a single value describing the absorption performance. This can be done for both the entire sample bandwidth as well as smaller sub-bands. Where our simulations tested over a frequency range of 300 to 3,400 Hz, the absorption objectives of broadband (300 to 3,400 Hz), low band (300 to 1,300 Hz), mid band (1,300 to 2,300 Hz), and high band (2,300 to 3,400 Hz) were used in four distinct optimizations.

Optimization Approach

With design and simulation capabilities established and demonstrated, the optimization process was run through the design exploration and automation software, Altair HyperStudy.® HyperStudy was used as the interface for parameterizing the design variables of the liner geometries and creating the design exploration routine. It was linked to nTopology and was able to autonomously generate TPMS acoustic liner designs. However, due to the use of COMSOL being used on a remote server, direct automation between HyperStudy and COMSOL was not available. Therefore, large, spacing-filling design of experiments (DOE) were established to generate many TPMS lattice geometries at once. Then, all the designs were uploaded to the COMSOL server where a batch script automation process was set up to iteratively simulate each design. When all designs were simulated, the acoustic results were imported back into HyperStudy for analysis.

The traditional liners followed the same optimization approach as the TPMS designs, with the exception of the geometry and physics being modeled in a python script instead of nTopology and COMSOL. Not needing the same computational power as the finite element solver, the ZKTL python script was run for the entire DOE on a local desktop machine, and results were imported immediately back into HyperStudy. Verification using the COMSOL method was performed on select samples to ensure that the ZKTL code and initial search were providing usable results. The verification showed that the ZKTL script was accurate at low frequencies, but diverged slightly at higher frequencies, underpredicting the acoustic absorption. Because this underprediction was consistent across all samples, the ZKTL method was used to identify an estimation of acoustic performance, while COMSOL provided a higher fidelity solution.

Results and Discussion

Using the described process, SDOF, DDOF, Schwarz P, and Diamond acoustic liners were optimized for acoustic absorption in four target frequency bandwidths: (1) broadband (300 to 3,400 Hz), (2) low band (300 to 1,300 Hz), (3) mid band (1,300 to 2,300 Hz), and (4) high band (2,300 to 3,400 Hz). DOE datasets were created for both TPMS-based liners, Schwarz P and Diamond, and traditional liners, SDOF and DDOF. 500 samples were generated for each TPMS-based liner and each traditional liner, from which the top performing designs would be selected for each lattice type. The simulation of each batch of lattice samples was done over the course of several days on the Penn State cluster computer due to the approximately 10-min solution time for each sample. The ZKTL code for the traditional liners was much faster, solving all 500 samples in approximately 10 min on a local machine. Using the design exploration dashboard from previous work, the liner design concepts, with accompanying performance metrics, were sorted according to the response objectives of acoustic absorption over various frequency bandwidths. For each response objective and each liner type, the liner concept with the highest performance was identified.

For the traditional liners, after the highest performing liner designs were identified, they were modeled and simulated in COMSOL for verification. The coplotted ZKTL and COMSOL results are shown in Figure 4. The results of the two simulation methods predict similar trends in the absorption coefficient curves, though at frequencies greater than 1,600 Hz, the COMSOL solution predicts higher absorption. This is less evident in the SDOF designs, which align very well in all cases

® HyperStudy is a registered trademark of Altair Engineering, Inc., Troy, Michigan.

except for the high band target. Because the COMSOL solution comes from a higher fidelity solver than the ZKTL solution, the comparisons with the TPMS liners were made using the COMSOL results. This also helps to ensure consistency within analysis and optimization.

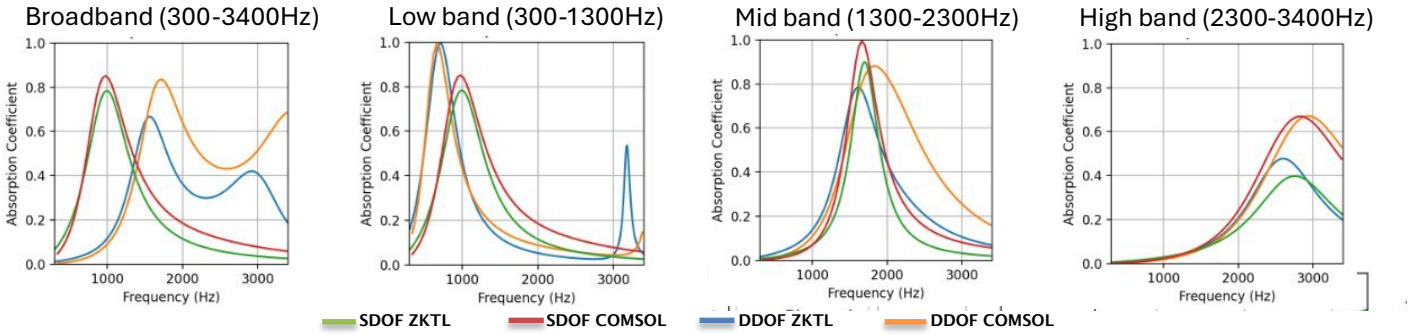


Figure 4. Single degree-of-freedom (SDOF) and double degree-of-freedom (DDOF) samples compared using Zwikker-Kosten Transmission Line (ZKTL) and COMSOL solutions.

When looking at the images of the generated, optimized liner designs in the design exploration dashboard, trends were more easily noted in the SDOF and DDOF liner types than in the TPMS designs. For example, the trend for traditional liners total thickness (depth for the SDOF and the sum of two depths for the DDOF) led to deeper liners being better adapted to low frequencies and shorter liners being better adapted to high frequencies. However, a more nuanced assessment was revealed using a sensitivity analysis. The sensitivity analysis on the DOE results from the SDOF and DDOF liners showed that the facesheet parameters, perforation diameter and the number of perforations, had some of the greatest impact across all target frequency bandwidths. Perforation diameter of the facesheet (as opposed to the septum) was consistently one of the most impactful design variables for the traditional liners. The facesheet was also highly impactful in the TPMS liner response, though the key design parameter differed between the Diamond and Schwarz P. For the Diamond lattice, the number of perforations in both the endo and exo regions were highly impactful; the perforation diameters remained important, but *X/Y* unit cell size and number of stacked unit cells were more impactful across all target ranges. The two most impactful design variables for the Schwarz P liners were the exo region facesheet perforation diameter and number of perforations. This makes intuitive sense because the structure of the Schwarz P unit cell already restricts the available open area of the endo region. For both Schwarz P and Diamond, in the high band target bandwidth, the number of stacked unit cells was the most impactful design parameter. Because the number of cells directly influenced the total height of the liner, and high frequency absorption favors shorter channels, this design parameter was critical for the high band regime.

With trends in the lattice geometry noted, the comparison results for liner performance are shown in Figure 5, where for each target frequency range, acoustic absorption coefficient is compared for the four liner types. In each of the target frequency bands, the TPMS acoustic liners had similar or better performance than the traditional liners; for example, in the broadband regime, the DDOF response value was 933 Hz while the Schwarz P design had the value of 1,372 Hz. For the broadband target, SDOF peaked at a lower frequency than DDOF, Schwarz P, or Diamond; however, the absorption of the DDOF and TPMS designs acted across a wider frequency range, with the Schwarz P design showing the widest band. The low band target showed comparable results for all four liner types, all very high absorption coefficients at a peak frequency around 900 Hz. The mid band target also showed a cluster where all liners peaked around 1,850 Hz, except the Schwarz P design also had an additional absorption peak at lower frequencies. Finally, in the high frequency target band, the TPMS designs showed higher absorption than the traditional liners.

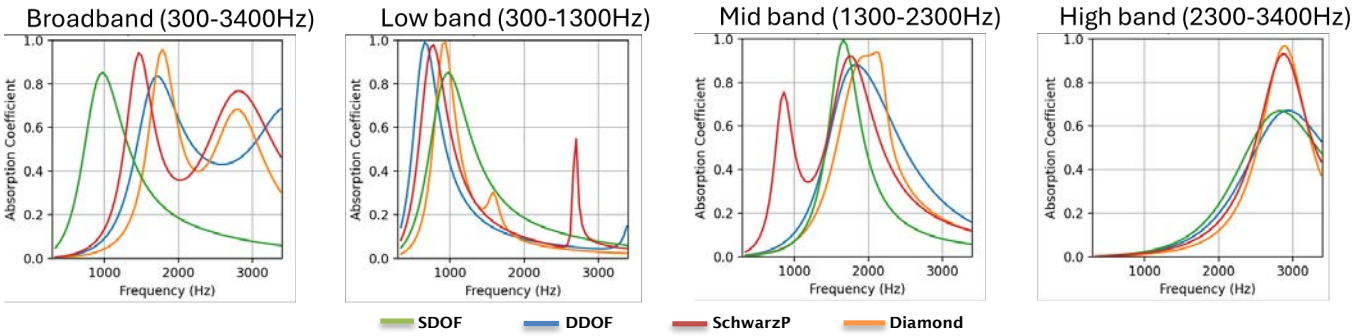


Figure 5. Acoustic absorption coefficient plots comparing four acoustic liner types, across four target frequency bands.

In the four target frequency ranges, the SDOF and DDOF acoustic liner types converged on designs that yielded similar performance. The intermediate perforated septum in the DDOF liner should produce a higher performance liner; however, all liners were subject to a maximum thickness constraint, which may have impeded the DDOF from taking full advantage of the perforated septum. Looking at the liner the total depth of all the liners (displayed in Table 2), the Schwarz P and Diamond acoustic liners required less height than the traditional liners to achieve competitive low and broadband acoustic absorption performance. This suggests that using greater design freedom, such as with AM enabled TPMS lattice acoustic liners, performance of traditional acoustic liners can be matched, while requiring less volume within the nacelle.

Table 2. Depth (mm) across all candidate liner types. DDOF: double degree-of-freedom; SDOF: single degree-of-freedom.

Liner Type	Broadband Depth (mm)	Low Band (mm)	Mid Band (mm)	High Band (mm)
SDOF	36.0	36.0	7.3	11.0
DDOF	21.4	37.0	36.6	14.5
Schwarz P	11.9	27.1	16.0	12.5
Diamond	11.6	18.7	13.0	9.5

The absorption curves of the Diamond and Schwarz P liners show two peaks in all target ranges except the high band. In the broadband regime, the DDOF design mounts to what would be an additional peak, but that peak is out of range. In the DDOF, the second peak is achieved through the perforated septum and the resonating effects of having two depths (from facesheet to septum, and from facesheet to backplate) creates two peaks. Due to the total depth constraint, the second peak is often out of the test range. For the TPMS lattices, there is only one depth to the structure, though the path is potentially more tortuous. The second peak, in the case of these lattices, comes from the endo and exo regions. The facesheets over the two regions, in addition to differences in the internal channel, create an additional peak. Because the depth is constant, the second peak is largely controlled by the facesheet parameters, so the two peaks are able to appear closer together. This is likely the cause of the mid band Diamond lattice behavior, where the peak plateaus before descending. This is a useful phenomenon when trying to absorb noise are two frequencies that are in close proximity to one another.

Milestones

- Demonstrated the use of the HyperStudy dashboard across traditional and TPMS liners.
- Cemented the benefits of TPMS liners in acoustic absorption.
- Initialized sensitivity study of TPMS liners, to be further expanded in-depth.

Major Accomplishments

- Applied theoretical and computational analysis to SDOF and DDOF liner specimens.
- Compared computational performance of optimized TPMS liners against traditional liners.
- Identified performance advantages of TPMS liners, especially as related to required liner thickness.

Publications

Packer, A., Reimann, C. A., Winkler, J., Homma, K., Mendoza, J., Greenwood, E., Manahan, M., & Meisel, N. A. (2025) Evaluating the Performance of Novel TPMS-Based Acoustic Liner Designs Suitable for Additive Manufacturing. *Proceedings of the Annual International Solid Freeform Fabrication Symposium*, in press.

Outreach Efforts

None.

Awards

None.

Student Involvement

One graduate student was involved in this task. Alden Packer, a PhD student in mechanical engineering who worked closely with RTRC to refine the modeling and sensitivity analysis of the acoustic liners.

Plans for Next Period

Focus on validating this sensitivity in experimental specimens with initial design sensitivity identified at the computational level. This will enable a robust understanding of the design science underpinning the creation of high-performing acoustic liners via AM.

Task 2 – Systematic Approach to Identify/Account for Manufacturing Error

The Pennsylvania State University, Altair Engineering

Objective

The objective of this task is to identify, measure, and account for the presence of manufacturing variations and defects in TPMS liners created via vat photopolymerization AM.

Research Approach

This section explores a pipeline for rapid cost-efficient analysis of defects and stochastic errors in manufactured acoustic liners without the need for extensive resources involved in current inspection methods like x-ray computed tomography (XCT). The method is designed to screen for surface level defect and dimensional accuracy but is not intended for full three-dimensional (3D) part inspection. It uses a combination of manual measurements and image processing tools to find the average manufactured deviation in the printed liners. From these measurements, approximate distributions can be found for the printed variation of the liner design variables.

Overview of Liner Design and Manufacturing

To allow for the removal of excess resin in the lattice core of the acoustic liner used in this paper, the liner is printed as two pieces and assembled after printing. The two parts are referred to as the liner casing and the liner core as shown in Figure 6. The liner casing acts as the housing for the liner core to slot into. The liner core consists of a TPMS Schwarz-P lattice structure connected to a perforated face sheet. A Schwarz-P lattice is chosen because it was found to have promising acoustic performance during preliminary tests. The liner core is modeled using nTop for the lattice structure and SOLIDWORKS® for the perforated face sheet. nTop requires lattice design parameters for both the overall bulk structure and the individual unit cell being tessellated throughout space. The design parameters of the bulk lattice are primarily dictated by the acoustic testing rig (in this case a normal incidence tube) since the active area of the liner needs to align with the active area of the test rig. The unit cell and face sheet design parameters can be varied based on the desired performance of the liner and are the main drivers behind the acoustic performance of the specimen. The face sheet is designed to be a flat solid sheet with a user specified perforation pattern that aligns with the lattice underneath. Once the face sheet is designed in SOLIDWORKS, it is exported as a Parasolid and imported into nTop where it is attached to the top of the lattice to form a single implicit body. The single body is then exported as a .3MF mesh for manufacturing.

® SOLIDWORKS is a registered trademark of Dassault Systemes Solidworks Corporation, Waltham, Massachusetts.

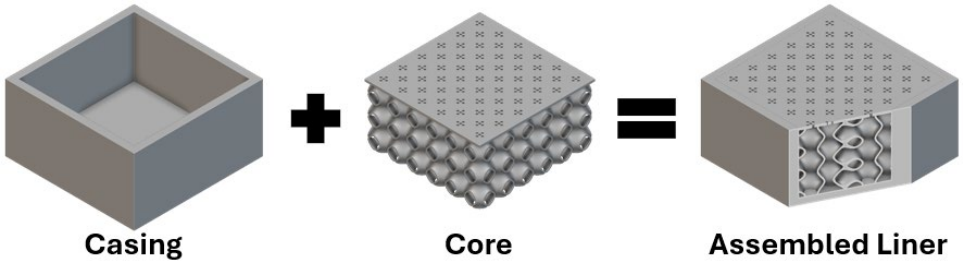


Figure 6. Acoustic Sample Design.

The liner core is printed on a Form 4® resin printer which uses masked stereolithography (MSLA). The core is prepped by importing the mesh in PreForm® where it is carefully oriented with a 20° tilt about the y-axis, supported, and sliced for printing. For acoustic purposes, the liner is required to be printed in a rigid material. The chosen resin also needs to be opaque so that the features of the part are visible for image detection. To ensure proper resin evacuation after printing, the part is washed once upside down and once right-side up in a FormWash™ station. With the excess resin removed, the part is cured in a FormCure™ station. Support material is then removed from the part, and it is ready for inspection.

Manual Measurement Method

The inspection pipeline in this report focuses on capturing stochastic variability through a combination of both manual measurements and two-dimensional image inspection. One of the most limiting factors with this approach is that, since a significant portion of the lattice in the liner core is enclosed by the outermost layer of Schwarz-P lattice cells and the face sheet, it is not possible to measure the internal lattice structure. Because of this, assessment must be based on the assumption that measurements from the external lattice bulbs and face sheet are representative of the entire liner core. Unfortunately, this assumption limits the accuracy of the measurement approach since there is no easy way to verify that the internal bulbs of the lattice share the same geometry as the outer surfaces.

There are several design variables that define the acoustic liner core and impact the acoustic properties. The overall length and width of the core are dictated by the testing apparatus and are not included as a design variable since they are considered fixed. The face sheet is defined by thickness, perforation diameter, and POA. The lattice is defined by a unit cell size, a wall thickness, and an isovalue. Measurements that can be taken manually using digital calipers (NEIKO® 01407A) include the face sheet thickness, the unit cell size, and the wall thickness as shown in Figure 7. The face sheet thickness is measured around the edge of the face sheet where the lattice bulbs join the face sheet and in between two lattice bulbs. The unit cell size is found by measuring the distance from the edge of a wall on one cell to the same edge on an adjacent cell. The wall thickness is found by measuring thickness of the walls at the pore openings. To account for the different print resolutions in the X-Y and Z directions on the Form 4 printer, the cell size and wall thickness measurements are grouped based on their orientation and location. Measurements taken on the sides (3 by 9 unit cell planes) along the length are considered “side length measurements” while measurements taken along the depth of the sides are considered “side depth measurements.” Additionally, measurements from the cells making up the 6x6 bottom of the core, defined as “bottom length measurements,” are kept separate due to the increased number of support structures that get attached to the bottom during printing. The removal process of such support material may cause bumps, chips, or cracks in the walls of the lattice which can affect the quality of the measurements around the locations where support structures are attached. Due to the 20° tilt used for manufacturing the sample, x-, y-, and x-axis of the printed core do not perfectly align with the axes of the printer; however, the X-Y and Z dimensions of the core should still be primarily impacted by the corresponding X-Y and Z resolutions of the printer.

® Form 4 is a registered trademark of Formlabs Inc., Somerville, Massachusetts.
® Preform is a registered trademark of Formlabs Inc., Somerville, Massachusetts.
™ FormWash is a trademark of Formlabs Inc., Somerville, Massachusetts.
™ FormCure is a trademark of Formlabs Inc., Somerville, Massachusetts.
® NEIKO is a registered trademark of Ridgerock Tools, Inc., Corona, California.

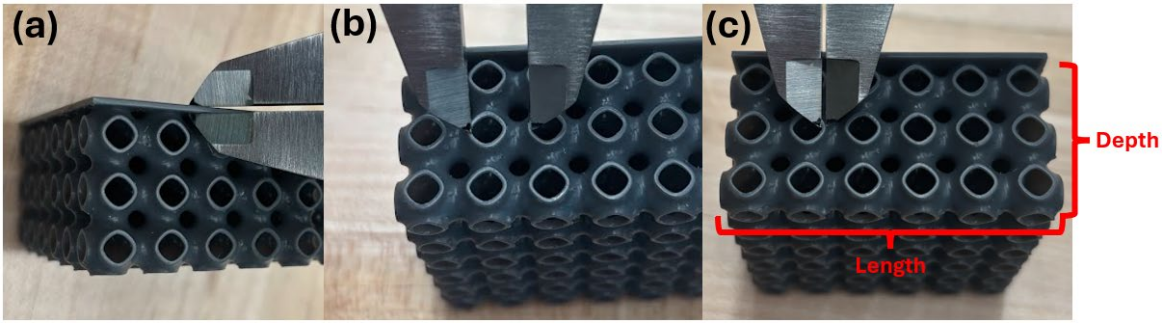


Figure 7. Measurement technique for (a) the face sheet thickness, (b) the unit cell size, and (c) the wall thickness.

In addition to parameters that are measured manually, the perforation diameter, POA, and isovalue are also measured. Since these parameters are too small to accurately measure with standard digital calipers, they are instead measured using a combination of several image processing tools. To accomplish this, it is necessary to first capture images of the sample from multiple views; this can be accomplished using a standard Apple® iPhone® 15 back camera to photograph the face sheet, sides, and bottom of the liner core. The images are then imported into Adobe® Lightroom® where a lens correction is applied (Apple iPhone 15 back camera 5.96mm f/1.6) and the image is cropped to remove the excess background around the liner core. Additionally, perspective correction is applied to address any camera tilt and remove the remaining pin cushion distortion, bringing all the opposing edges parallel to each other. This process results in images of the core where the exposed sides match the physical part as much as possible. After editing, the images can be used for inspection. To capture the perforation diameters and POA, the face sheet image is imported into the analysis tool ImageJ. The measurement scale is set, and the image is further cropped to only capture the area of the face sheet where the perforations are found. The image is then thresholded up to the point immediately before any of the perforations start to fade away. After removing any noise in the image due to artifacts such as layer lines, ImageJ's particle analysis tool is used to capture the individual areas of the face sheet perforations. Since the perforations in the face sheet are not perfectly circular, the effective diameter is estimated using their area. In some cases, excess resin or other contaminants can cause perforations to become partially blocked. Additionally, some of the residual noise particles in the image may be detected as very small areas. To remove the impact of the blockages and noise particles, any estimated diameter less than 80% of the nominal design diameter is removed from the data. This process yields a dataset of as-printed estimated perforation diameters. To estimate the POA, the area of all the particles in the thresholded image are combined and divided by the total measured area of the face sheet.

The final value to measure is the isovalue. The main purpose of the isovalue is to control the volume ratio between the endo and exo void channels. This means that the isovalue also controls the ratio of cross-sectional area between the two channels. Unfortunately, since the isovalue is a somewhat arbitrary constant when defining lattice geometry, measuring it can be difficult. For a Schwarz-P lattice, changing the isovalue changes the cross-sectional area ratio between the endo and exo pores as shown in Figure 8. To find the ideal relationship between the isovalue and the cross-sectional area ratio of the pores, images of nTop models at different isovalues are carefully thresholded, cropped, and cleaned so that the area ratio of the pores, in pixels, can be used to establish a correlation with the isovalues. With this relationship, the as manufactured isovalue can be estimated by finding the ratios of the endo and exo pores in the printed core. First, the edited images of the core sides and bottom are run through a Canny edge detection algorithm. This is necessary because the threshold function of ImageJ cannot accurately capture the lattice pores due to the uneven lighting in the images. Unwanted edges inside of pore areas are then removed and any small gaps in the pore edges are closed. Area ratios are then captured between each endo and corresponding exo pore. Finally, the as manufactured isovalues are determined based off the isovalue/area relationship established previously.

® Apple and iPhone are registered trademarks of Apple Inc., Cupertino, California.
® Adobe and Lightroom are registered trademarks of Adobe Inc., San Jose, California.

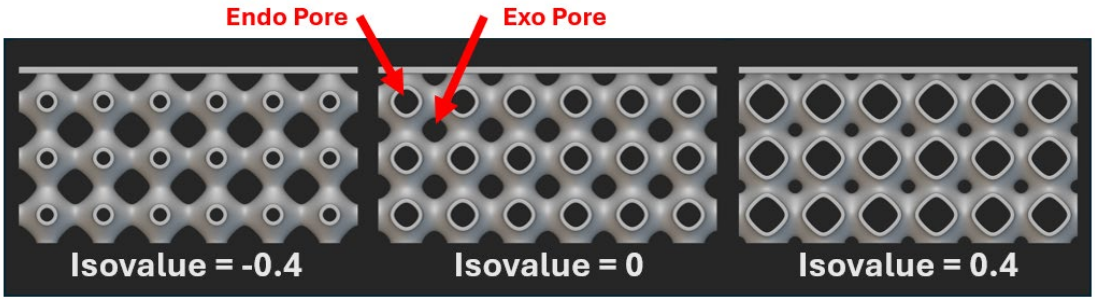


Figure 8. The effect of the isovalue on the cross-sectional area of the endo and exo lattice pores.

To capture the manufacturing deviation from the nominal design, each of the design variables is measured to find the average manufactured value and the standard deviation when possible. Crucially, several of these design parameters can be measured in multiple locations to create distributions that can be visually interpreted through the use of histograms or other means. A summary of each measured parameter is provided in Table 3. While the proposed approach intends to be systematic and as consistent as possible, some of the measurement techniques can still be somewhat subjective in nature. For example, due to uneven lighting, the user may be required to make a judgement call for what degree to threshold the face sheet perforation images. Face sheet perforation measurements could be verified using a second measure such as a pin gauge. The use of the calipers can also cause slight variations in the measured data. Since the calipers are harder than the resin, increasing the clamping pressure can compress the resin leading to smaller measured thickness values. The unit cell size measurements can also vary since the user has to do their best to properly align the calipers to the pore edges of the unit cell pores. Finally, the editing conducted on the photo could lead to changes in the interpretation of the printed geometry which could reflect in the final data.

Table 3. An overview of the parameters measured for a Schwarz-P liner core.

Measurement Tool	Parameter	Measurement Technique
Digital calipers	Face Sheet Thickness	Measure the thickness around the edge of the face sheet.
	Unit Cell Size	Measure the offset unit cell size by finding the distance from the pore edge of one cell to the corresponding pore edge of an adjacent cell.
	Wall Thickness	Measure the wall thickness around the exposed lattice pore edges.
Image processing and analysis	Perforation Diameter	Threshold images of the face sheet so that only the perforations are visible and then batch measure the areas of the perforations. Use the areas to estimate the effective diameter of each perforation.
	Percent open area	Threshold images of the face sheet so that only the perforations are visible and then find the total area of the perforations. Divide the total perforation area by the total area of the face sheet.
	Isovalue	Use edge detection to capture clean edges of the endo and exo lattice pores. Find the cross-sectional area ratio between the corresponding endo and exo pores. Convert the ratios to isovalues using an isovalue vs. area ratio relationship calculated from the ideal model.

Test Liner Core Design

The first step in demonstrating the defect detection pipeline was to develop a representative acoustic liner core. The core used for this case study was designed with both a length and width of 50.8 mm based on a normal incidence tube to be used for later testing. While these dimensions are not a focus of our error identification, they will be important for measuring the manufactured POA of the sample. The parameters used to design the face sheet included a face sheet thickness of 1 mm, perforation diameter of 0.8 mm, and a POA of 5.94% which was dictated by the perforation pattern of the face sheet. The TPMS Schwarz-P lattice was designed with a uniform wall thickness of 0.6 mm, unit cell size of approximately 8.47 mm, and an isovalue of 0.2. The final printed core is shown in Figure 9 both with and without supports

attached. The core was printed in Form Tough 2000 resin at a layer height of 0.05 mm. It was then washed in the Form Wash upside-down for 10 min and right-side up for 10 min. Finally, it was cured in the Form Cure at the standard time and temperature for the Tough 2000 resin.

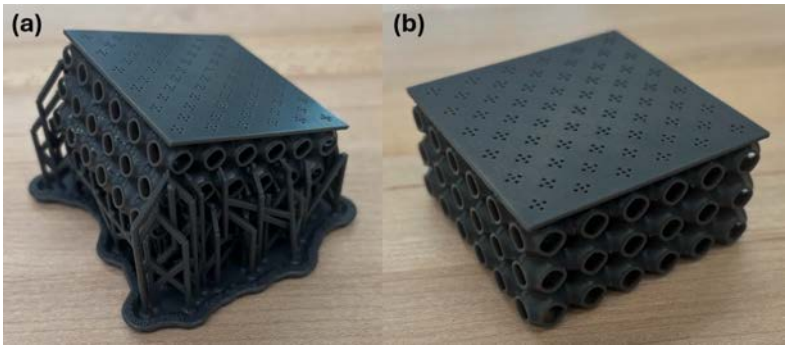


Figure 9. (a) The printed liner core with supports and (b) the printed liner core without supports.

Manual Measurement Pipeline Execution

Using the representative liner core, the manual measurement pipeline was executed. The first stage was to gather the measurements that were found using calipers. The face sheet thickness was measured 12 times for a total of 48 measurements. On each side, six measurements were aligned with the endo pores of the lattice, and the remaining six measurements were aligned with the exo pores. During this process, it was found that the face sheet thickness where the lattice connected to the face sheet was slightly thicker than the thickness aligned with the exo pores. This was most likely due to small amounts of excess resin that gathered around the connection points leading to small fillets instead of sharp edges. The unit cell size was measured in the side length, side depth, and bottom length orientations as shown in Figure 10. Based on the geometry of the lattice, a total of 60 measurements were captured for the side length orientation, 48 for the side depth orientation, and 60 for the bottom length orientation. The last measured variable was the wall thickness of the lattice. Figure 10 also shows how these measurements were collected similar to the cell size, with 144 measurements captured for each of the three orientations.

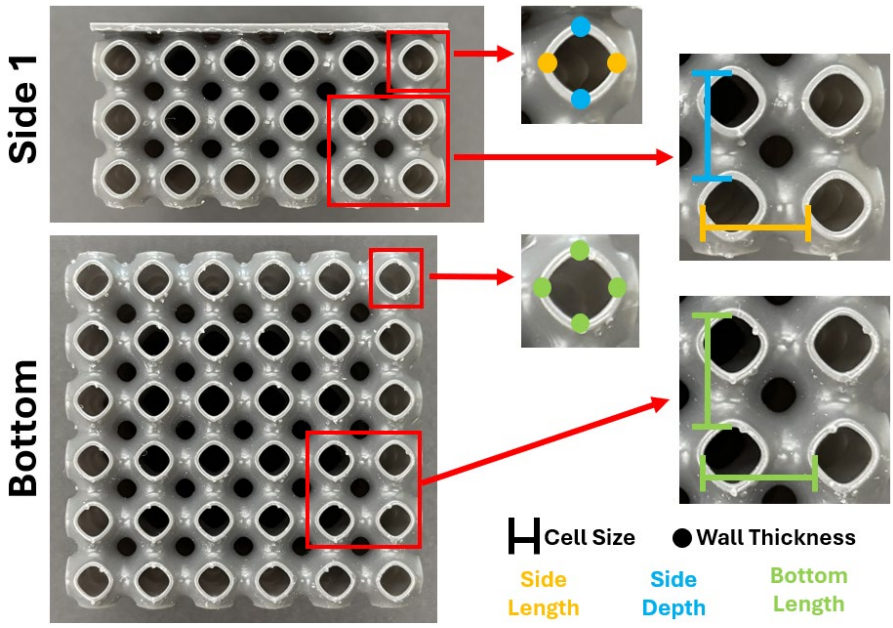


Figure 10. Measurement locations and directions for each cell size and wall thickness orientation.

Once the face sheet thickness, cell size, and wall thickness had been measured with calipers, the rest of the measurements were found using image processing tools, starting with perforation diameters. Figure 11 shows a comparison between the original image opened in ImageJ and the thresholded image used for the area estimations on the perforations. Using the thresholded image, particle analysis yielded 459 area measurements. The effective diameters of the particles were found by converting the areas to diameters using simple circle geometry. In some perforations, small flakes can be seen partially blocking the openings. This was suspected to be small contaminants from the shared Form Wash which got stuck during the wash process. The flakes caused some of the perforations to appear partially blocked or split into multiple sections in the thresholded image. After removing the diameters of both noise particles and significantly blocked/split perforations, the data were reduced to 297 effective diameters. The particle analysis also outputs a total area which was used as the total open area of the face sheet. By dividing the open area by the as-printed cross-sectional area of the face sheet, found by measuring the length and width of the face sheet, which was 51.3 mm and 50.03 mm respectively, the manufactured POA was found.

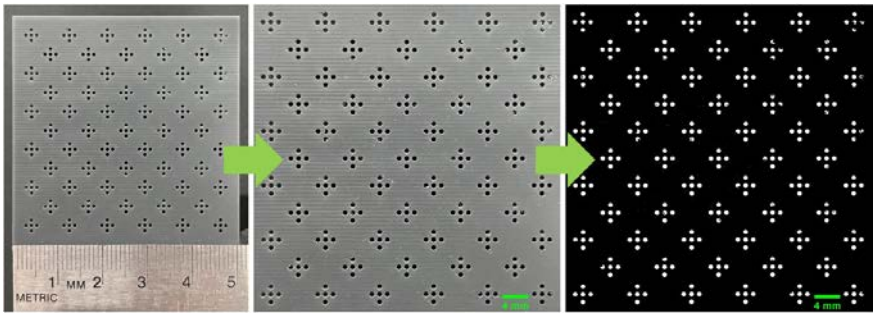


Figure 11. Facesheet image preparation for perforation area measurements.

The final design parameter measured was the isovalue. Images of the sides and bottom of the sample were run through the Canny edge detection software and cleaned in ImageJ so that a section of the endo and exo pore areas could be measured in terms of pixels as shown in Figure 12. The endo pore area was then divided by the exo pore area to find the ratio between the two and could then be related to an isovalue. Through a similar measurement technique of the ideal nTop model at several different isovalues, the relationship was found between the endo/exo pore area ratio and the isovalue. This relationship was then used to convert the manufactured pore ratios into isovalues. By analyzing each of the sides and the bottom of the sample, a total of 65 pore area ratios, and thus isovalues, were measured.

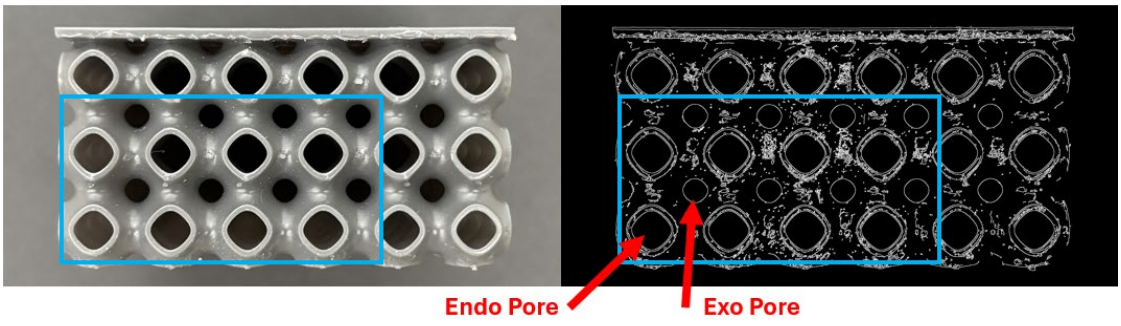


Figure 12. Conversion of lattice to binary edges for the purpose of measuring the areas of the endo and exo pores outlined in blue.

All of the collected data were used to find the average, standard deviation, minimum, and maximum values for each design variable as shown in Table 4. As can be seen, every design variable except perforation diameter and POA was found to be slightly oversized on average. This shows that most of the design variables would need to be undersized before printing in order to achieve the correct nominal dimensions in the manufactured part. Conversely, the perforation diameter and POA would need to be slightly oversized before printing. In the event that visual inspection of the distributions of the data is needed, the collected raw data can also be used to create histograms for several design variables.



Table 4. Summary of design parameter measurements.

Parameter	Nominal	Average	Standard Deviation	Minimum	Maximum
Face Sheet Thickness	1 mm	1.17 mm	0.05 mm	1.09 mm	1.29 mm
Unit Cell Size (Side Length)	8.47 mm	8.51 mm	0.04 mm	8.43 mm	8.61 mm
Unit Cell Size (Side Depth)	8.47 mm	8.51 mm	0.05 mm	8.42 mm	8.59 mm
Unit Cell Size (Bottom Length)	8.47 mm	8.50 mm	0.04 mm	8.42 mm	8.59 mm
Wall Thickness (Side Length)	0.6 mm	0.64 mm	0.03 mm	0.55 mm	0.71 mm
Wall Thickness (Side Depth)	0.6 mm	0.73 mm	0.05 mm	0.64 mm	0.87 mm
Wall Thickness (Bottom Length)	0.6 mm	0.63 mm	0.04 mm	0.55 mm	0.72 mm
Perforation Diameter	0.8 mm	0.69 mm	0.02 mm	0.64 mm	0.72 mm
Percent Open Area (POA)	5.94%	4.26%	N/A	N/A	N/A
Isovalue	0.2	0.201	0.003	0.192 mm	0.207 mm

Milestones

- Established a method for identifying geometric variations in as-manufactured TPMS lattice structures.
- Demonstrated the use of manual measurements to capture liner variation.
- Specified an approach to formulate error distributions in a way that can later be integrated with HyperStudy.

Major Accomplishments

- Quantified the presence of oversized/undersized features in manufactured TPMS liners.
- Measured a range of different design parameters through the use of manual calipers.
- Identified the need to account for both predictable build error and stochastic build error.

Publications

Windows, J., Packer, A., Nelson, E., Chowaniec, J., Mendoza, J., Reimann, C. A., Winkler, J., Homma, K., & Meisel, N. A. (2025). Identification of Stochastic Manufacturing Defects Within Additively Manufactured Acoustic Liners. *Proceedings of the Annual International Solid Freeform Fabrication Symposium*, in press.

Outreach Efforts

None.

Awards

None.

Student Involvement

Joseph Windows, an MS student in mechanical engineering, was involved in this task. He worked to identify key manufacturability challenges and determine a systematic way by which to measure and account for them in the design of the TPMS liner structures.

Plans for Next Period

- Using the systematic approach developed in this period, combine the measured findings with HyperStudy to predict acoustic performance variation based on the likelihood of stochastic error in manufactured specimens.
- Augment the measurement process using Rapidminer® machine learning software.

® Rapidminer is a registered trademark of Rapidminer, Inc., Troy, Michigan.

Task 3 – Automating the Generation of Acoustic Lattice Meshes

The Pennsylvania State University, Cornerstone Research Group

Objective

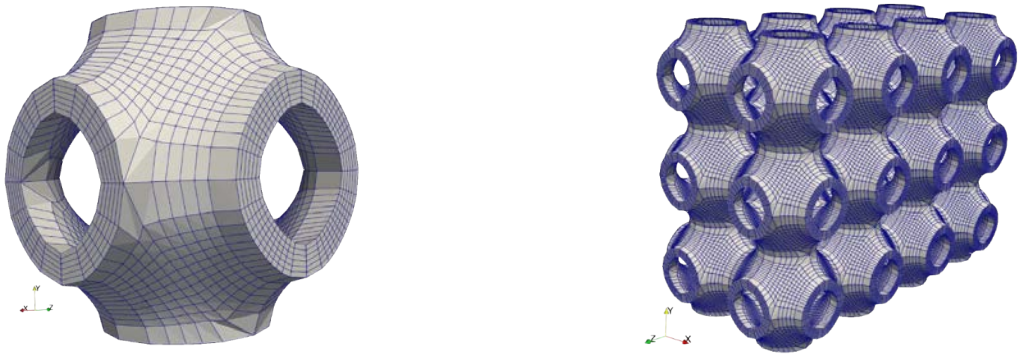
The objective of this task is to develop a tool which is capable of generating mesh structures for TPMS lattice geometries that will be integrated into the acoustic modeling procedure used in Task 1.

Research Approach

Through efforts in this task, CRG has developed a workflow for the existing acoustic modeling and analysis pipeline that will allow the user to generate a multi-cell lattice structure using the Schwarz P TPMS geometry. The workflow is outlined as follows:

Step 1. User will generate a user input file.
Step 2. Code will read in the user input file.
Step 3. Code will generate the core of a single cell TPMS structure by solving the TPMS equation at the core.
Step 4. Code will generate a thickness for a single cell by computing the core's surface normal and extrapolating the nodes outward from the core.
Step 5. Code will copy the single cell throughout the region to form the multi-cell structure.
Step 6. Code will export the single and multi-cell structures as either surface or volume mesh formats depending on the user inputs.

Currently the code is capable of generating the solid domain for a multi-cell Schwarz P TPMS structure. The overall lattice is then generated to fit within a 3D rectangular domain based on the user input parameters. The meshing algorithm itself takes advantage of the structured equation defining the TPMS geometry and is capable of generating eight structured meshes representing the eight octants of a single cell. The algorithm then stitches the eight regions to generate the single cell. At the time of this report, the user can control the approximate number of nodes making up a single cell, the sizing of a single cell, and the number of cells within each lattice structure. Figure 13 displays an example of a uniform Schwarz P lattice structure with a single-cell structure and a multi-cell structure. CRG's code can export the mesh representing the lattice structure into four formats: (1) NASTRAN, (2) Tecplot, (3) PLY, and (4) STL. The NASTRAN and Tecplot formats are volume mesh formats that can be used for computational fluid dynamics (CFD) or finite element analysis. The PLY and STL are surface mesh formats which can be used for applications such as additive manufacturing.



a) Single-cell structure b) Multi-cell structure

Figure 13. Single and multi-cell structures of the Schwarz P solid domain geometry generated by CRG's code.

In the latest version of the meshing tool, CRG has implemented an algorithm to generate the fluid domain of the Schwarz P structure for CFD and acoustic modeling. CRG initially utilized a similar approach to that of the solid domain generation; however the mesh quality was generally weaker, and bugs existed that prevented the mesh from being read into the modeling tool, COMSOL. Illustrations of the mesh are shown in Figure 14. CRG is currently implementing an incremental insertion algorithm that meets the Delauney criteria which helps maximize the quality of a given mesh using tetrahedrons. CRG has implemented a version of the incremental insertion algorithm in a code written for another tool developed by CRG. Modifications are being performed to the code to handle the Schwarz P TPMS geometry.

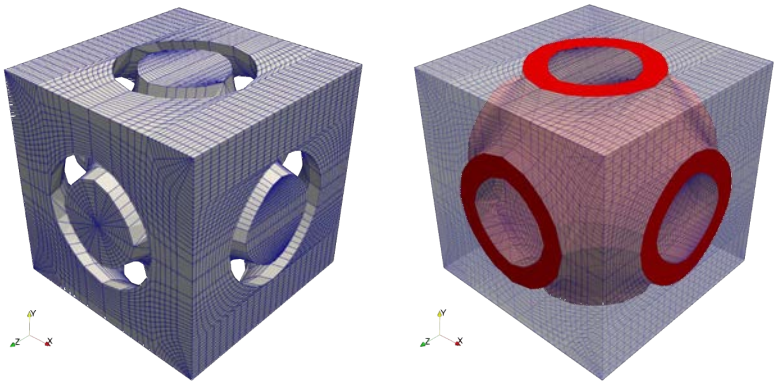


Figure 14. Single-cell structures of the Schwarz P fluid domain geometry generated by CRG's code.

In the meantime, CRG has generated and provided Penn State with a licensed executable of an alpha version of the code that can be run on the university computer systems. The provided alpha version is only capable of generating the solid domain of the mesh and only includes the four mesh formats described above as export options. Penn State has successfully generated and imported a NASTRAN version of the mesh into COMSOL using the provided code.

Milestones

- Demonstrated the use of direct mesh modeling to generate multi-cell solid TPMS domains.
- Established a method to export the generated meshes for use in existing acoustic simulation.

Major Accomplishments

- Created a tool capable of generating both solid and fluid domains suitable for acoustic analysis.

Publications

None

Outreach Efforts

None.

Awards

None.

Student Involvement

None

Plans for Next Period

- Continue to work on improving the implementation of the fluid domain generation for the Schwarz P TPMS geometry.
- Once a reasonable fluid domain is generated, send a sample mesh over to Penn State in the NASTRAN format to verify that it can be read into their version of COMSOL.
- Initiate the expansion of the code to generate the fluid domain representation of a multi-cellular Schwarz P geometry.
- Exported the multi-cellular geometry in a suitable format such as NASTRAN and provided to Penn State for testing in COMSOL.



Project 080(A) Hydrogen and Power-to-Liquid Concepts for Sustainable Aviation Fuel Production

Washington State University

Project Lead Investigators

Manuel Garcia-Perez
Professor and Chair
Biological Systems Engineering Department
Washington State University
PO Box 646120, Pullman, WA 99164-6120
509-335-7758
mgarcia-perez@wsu.edu

Michael P. Wolcott
Regents Professor
Department of Civil & Environmental Engineering
Washington State University
PO Box 642910, Pullman, WA 99164-2910
509-335-6392
wolcott@wsu.edu

University Participants

Washington State University (WSU)

- P.I.s: Prof. Manuel Garcia-Perez, Prof. Michael P. Wolcott
- FAA Award Number: 13-C-AJFE-WaSU-031
- Period of Performance: October 1, 2023, to September 30, 2024
- Tasks:
  1. Evaluate the strengths and weaknesses of hydrogen production and power-to-liquid (PtL) concepts in the United States
  2. Co-location and incorporation of hydrogen technologies into existing sustainable aviation fuel (SAF) production and infrastructure
  3. Evolution of SAF production pathways to integrate alternative hydrogen and carbon sources

Project Funding Level

The ASCENT Project 080 received $450,000 in Federal Aviation Administration (FAA) funding and $450,000 in matching funds. State-committed graduate school contributions for PhD students and faculty time for Michael Wolcott, Manuel Garcia-Perez, Xiao Zhang, and Su Ha contribute to the cost share. WSU funding is reported for this reporting period.

Investigation Team

Washington State University

Prof. Manuel Garcia-Perez (P.I.), Tasks 1, 2, 3, and 4
Prof. Michael P. Wolcott (P.I.), Tasks 1, 2, 3, and 4
Prof. Xiao Zhang (Co-PI), Tasks 3 and 4
Prof. Su Ha (Co-PI), Tasks 1, 3, and 4
Dr. Jonathan Male (Co-P.I.), Tasks 1, 2, 3, and 4
Kristin Brandt (adjoint faculty), Tasks 1, 2, and 3
Aidan Garcia (research associate), Tasks 2 and 3
Valentina Sierra (graduate research assistant/post doctoral fellow), Tasks 1 and 2
Brandon Lewis (graduate research assistant) Task 3



Collaborating Researchers

Corinne Drennan, Pacific Northwest National Laboratory (PNNL)

Project Overview

The aviation industry is under pressure to reduce its greenhouse gas (GHG) emissions. SAFs are considered a promising approach for achieving the sector's GHG emissions reduction targets. To date, no comprehensive assessment exists for analyzing how different carbon, hydrogen, and energy sources can be combined with different conversion processes to produce SAF with high GHG emission reductions and low costs. The goals of this project are to (a) evaluate the strengths and weaknesses of hydrogen production concepts, (b) assess the cost and environmental impacts of these hydrogen sources on existing SAF technologies (c) synthesize this information to guide the development of new technologies using novel hydrogen and energy sources, and (d) assess how hydrogen can be utilized more efficiently within SAF synthesis and hydrotreatment. This research will enable the identification of new pathways to optimize SAF production for maximum GHG reductions with minimal fuel costs.

Approved SAF pathways commonly use photosynthesis-derived carbon from sugars, lignocellulosic materials, or lipids. Some SAF technologies that are currently being investigated include those based on hydro-processed ester and fatty acid synthetic paraffinic kerosene (HEFA-SPK), Fischer–Tropsch (FT) synthetic paraffinic kerosene (FT-SPK), Fischer–Tropsch synthetic kerosene with aromatics (FT-SKA), synthesized iso-paraffins (SIP), Virent® BioForming synthesized aromatic kerosene, hydrodeoxygenation synthesized kerosene, catalytic hydro-thermolysis, alcohol-to-jet (ATJ) fuel, hydropyrolysis (Shell® IH2®), fast pyrolysis, and hydro-processed depolymerized cellulosic jet fuel. The jet fuels produced from eight paths (FT-SPK, HEFA-SPK, SIP, FT-SKA, ATJ, catalytic hydro-thermolysis, and HEFA) (ASTM International, 2024a) and by co-processing lipids and FT biocrude in refineries (ASTM International, 2024b) are now approved by ASTM International (formerly known as the American Society for Testing Materials) for use in commercial aircraft. Although these processes can result in substantial GHG reductions, their production costs are still substantially higher than those of conventional jet fuels derived from petroleum distillation ($0.88–$3.86/L) (Tanzil et al., 2021).

Previous studies have shown that the quality of the carbon source determines the SAF yield. Although lignocellulosic materials are ten times cheaper than lipids (on a mass basis), the latter's quality as a carbon source makes triglyceride-derived fuels much cheaper (two to five times) than those derived from cellulose, hemicellulose, or lignin (Tanzil et al., 2021). Carbon in organic matrices containing a higher level of oxygen, nitrogen, and sulfur is more challenging to convert to jet fuel because of the penalties associated with the removal of oxygen, nitrogen, and sulfur, a process that typically consumes hydrogen. Carbon in polymeric molecules is also more challenging to convert to jet fuel because it requires costly molecular weight reduction technologies and often lacks selectivity to the targeted jet fuel cut. Carbon in the form of aliphatic molecules can be more easily converted to jet fuel than carbon as aromatics, which have a higher tendency to form coke. Carbon sources such as carbon dioxide (CO_2), biomass, coal, petroleum, and municipal solid waste (MSW) must be thoroughly investigated as feedstocks for SAF production. Because carbon is the most abundant element in jet fuel, high fuel yields can only be achieved in processes with high carbon conversion efficiencies.

Most technologies that produce SAF consumed large amounts of hydrogen, ranging from 2 mass percent of the fuel produced for ATJ (Snowden-Swan et al., 2017) to 11-12 mass percent for pyrolysis (Brandt et al., 2022). Although hydrogen can currently be produced using clean electricity from wind and solar farms, most hydrogen is currently produced through steam methane reforming (SMR) (which is associated with significant CO_2 emissions) due to its low production cost. Commonly considered paths for hydrogen production include (a) steam and dry reforming, partial oxidation or electrochemical reforming of (oxygenated) hydrocarbons, (b) low-temperature water electrolysis, (c) plasma arc decomposition, (d) water thermolysis, (e) thermochemical water splitting, (f) thermochemical conversion of biomass (biomass gasification and biofuel reforming), (g) photovoltaic electrolysis, photocatalysis, and photochemical methods, (h) dark fermentation, (i) high-temperature water electrolysis, (j) hybrid thermochemical cycles, (k) coal and petroleum gasification, (l) MSW gasification, (m) fossil fuel reforming, (n) biophotolysis and photo-fermentation, (o) artificial photosynthesis, and (p) photo-electrolysis (Dincer & Acar, 2015). One goal of this project is to evaluate the strengths and

® Virent is a registered trademark of Virent, Inc., Madison, Wisconsin.
® Shell is a registered trademark of Shell Trademark Management B.V., The Hague, The Netherlands.
® IH² is a registered trademark of Gas Technology Institute, Des Plaines, Illinois.



weaknesses of hydrogen production concepts, determine how they can be integrated with existing infrastructure to produce cheap green hydrogen, and identify the potential impact of these technologies in producing SAF.

In some biomass and waste conversion processes, CO_2 and methane (CH_4) are produced as a side product or as the starting material. To meet SAF specifications, hydrogen will be needed to hydrogenate alkenes and hydrotreat oxygenates. Utilizing waste CO_2 and CH_4 can increase the amount of carbon obtained from resources in the SAF while reducing emissions. This can be done in conjunction with hydrogen production with a lower carbon intensity. Our analysis will examine the trade-offs between enhanced carbon utilization, the effects of increased renewable energy use, the need for stability in the grid and energy storage, access to lower-carbon-intensity (or even the carbon negative) hydrogen against positive impacts on environmental indicators, the cost impact of such changes, and technology uncertainty in emerging science and engineering.

References

ASTM International. (2024a). *ASTM D7566-24D - Standard Specification for Aviation Turbine Fuel Containing Synthesized Hydrocarbons*. https://doi.org/10.1520/D7566-24D

ASTM International. (2024b). *ASTM D1655-24A - Standard Specification for Aviation Turbine Fuel*. https://doi.org/10.1520/D1655-24A

Brandt, K., Tanzil, A. H., Martinez-Valencia, L., Garcia-Perez, M., & Wolcott, M. P. (2022). *Pyrolysis techno-economic analysis* (v. 2.2). Washington State University. https://doi.org/10.7273/000002563

Dincer, I., & Acar, C. (2015). Review and evaluation of hydrogen production methods for better sustainability. *International Journal of Hydrogen Energy*, *40*(34), 11094–11111. https://doi.org/10.1016/j.ijhydene.2014.12.035

Snowden-Swan, L. J., Zhu, Y., Bearden, M. D., Seiple, T. E., Jones, S. B., Schmidt, A. J., Billing, J. M., Hallen, R. T., Hart, T. R., Liu, J., Albrecht, K. O., Fox, S. P., Maupin, G. D., & Elliott, D. C. (2017). *Conceptual biorefinery design and research targeted for 2022: Hydrothermal liquefaction processing of wet waste to fuels* (p. 1-40). Pacific Northwest National Laboratory, 27186. https://www.osti.gov/servlets/purl/1415710

Tanzil, A. H., Brandt, K., Wolcott, M., Zhang, X., & Garcia-Perez, M. (2021). Strategic assessment of sustainable aviation fuel production technologies: Yield improvement and cost reduction opportunities. *Biomass and Bioenergy*, *145*, 105942. https://doi.org/10.1016/j.biombioe.2020.105942

Task 1 - Evaluate the Strengths and Weaknesses of Hydrogen and PtL Concepts in the United States

Washington State University

Objectives

The objective of this task is to perform a literature review and develop design cases for hydrogen and PtL concepts.

Research Approach

In this task, the ASCENT Project 080 team will identify areas that require more research and development to reduce technology uncertainty. Specifically, our team analyzed six technologies for hydrogen production: (a) steam reforming, (b) dry reforming, (c) water electrolysis, (d) gasification of carbonaceous materials (biomass, coal, bitumen, and MSW) (with steam and CO_2), (e) thermal decomposition of hydrocarbons (methane pyrolysis with capture and use of solid carbon), and (f) fossil fuel reforming. This task is being conducted by WSU and PNNL and started during 2022. The main goal of this task is to build design cases for each of these hydrogen production technologies (i.e., mass and energy balances, and techno-economic analyses [TEA]) and identify the strengths and weaknesses of each technology studied. A team of hydrogen production experts from WSU and PNNL meets monthly with a PhD student and post-doctoral associate from WSU to guide them in the literature review and in the creation of a road map for constructing design cases and identifying the opportunities and challenges for each of the technologies studied.

Milestones

- Completed a literature review for hydrogen production within the context of SAF technologies.
- Developed design cases of standalone hydrogen production technologies.
- Obtained minimum selling price, carbon intensity (CI), and abatement cost (AC) results for all hydrogen technology design cases.

Major Accomplishments

- Completed a literature review on the TEAs of hydrogen production technologies (low and high-pressure gasification, steam reforming, methane partial oxidation, autothermal oxidation, methane pyrolysis, and low- and high-temperature water electrolysis). Figure 1 summarizes the environmental and economic performance of all hydrogen technologies examined, except for electrolytic hydrogen. Electrolysis is sensitive to the cost and CI of power available, which is explored more fully in the submitted manuscript.

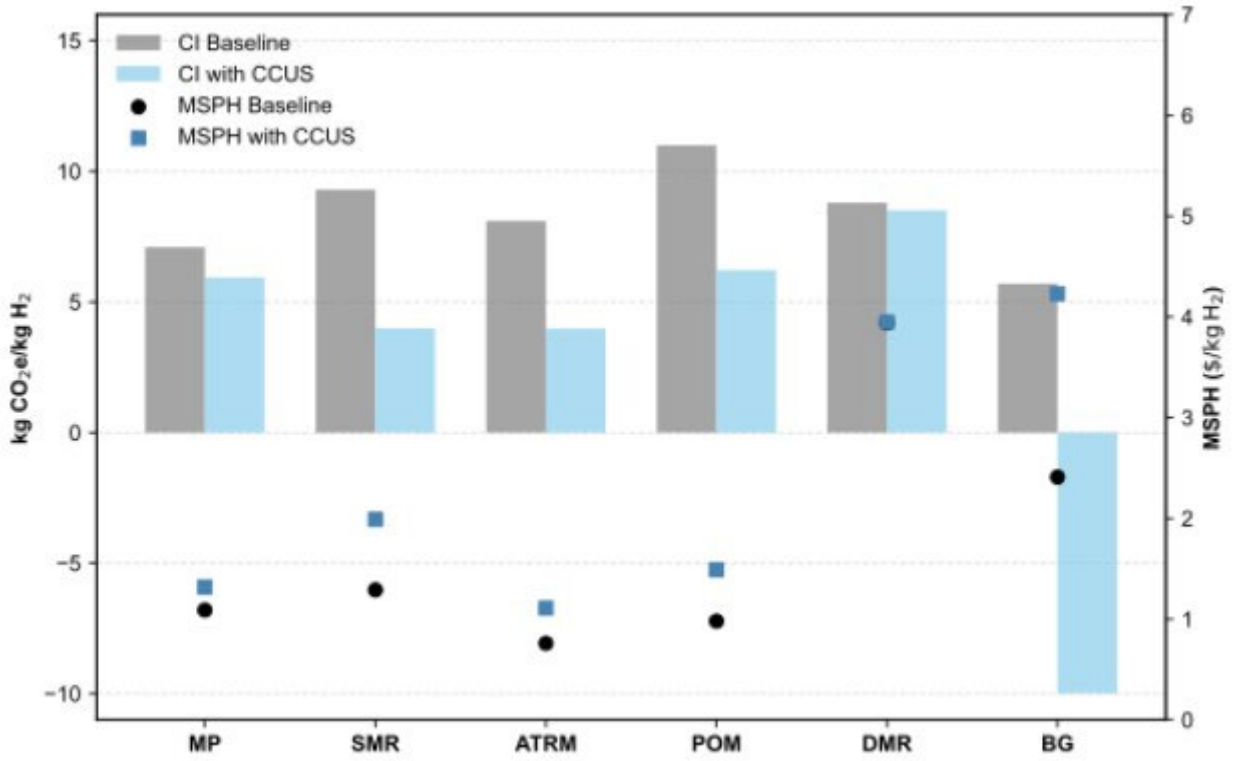


Figure 1. Minimum selling price and CI of representative hydrogen technologies. CI: carbon intensity; CCUS: carbon capture, utilization, and storage; MSPH: minimum selling price of hydrogen.

- Developed standardized design cases to estimate hydrogen production costs for each of the technologies studied. These cases will provide a harmonized set of process models, TEA, and lifecycle analysis (LCA) results for future studies utilizing hydrogen from various sources, and they have already proved useful as reference values for Tasks 2 and 3.
- Expanded TEAs to include monetary policy, including support from the Inflation Reduction Act that was modified in the One Big Beautiful Bill Act. Specifically, the credits for the production of clean hydrogen (45V) and the credit for CO_2 capture and sequestration (45Q).
- Updated the methodology for our TEA to a cost of equity (COE) model during this project. This methodology represents a more realistic assessment of the risk and profits assumed by investors.

Publication

Peer-Reviewed Journal Publication

Sierra, V., Wolcott, M., Zhang, X., Ha, S., Male, J., Garcia, A., Brandt, K., Garcia-Perez, M., Drennan, C., & Holladay, J. (Under review). *Evaluating Hydrogen Production Through Techno-Economic, Carbon Intensity, and Policy Perspectives in the U.S.* Pending submission.



Presentations

Sierra-Jimenez, V., Brandt, K., Wolcott, M., Male, J., Garcia-Perez, M. (2024, November 20-21). *Hydrogen Production Techno-economic and Carbon Intensity Insights for a Sustainable Energy Transition in the U.S.* [Poster presentation]. Re+CHARGE H_2 Conference (PNWH2 Hub), Seattle, Washington.

Garcia, A., Sierra-Jimenez, V., Garcia-Perez, M. (2025, October 15) *Hydrogen and Power-to-Liquid Concepts for Sustainable Aviation Fuel Production* [Poster presentation]. ASCENT 2025 Fall Meeting, Alexandria, Virginia.

Outreach Efforts

- Presented results at the ASCENT 2025 Fall Meeting in Alexandria, Virginia.

Student Involvement

Valentina Sierra, a graduate student majoring in biological systems engineering at WSU, performed the literature review of hydrogen production technologies and the role that hydrogen has in SAF production. Sierra has graduated and is continuing work on this project as a post doctoral fellow.

Plans for Next Period

- Publish the revised hydrogen production manuscript and the standardized TEAs.

Task 2 – Evaluate the Effect of Emerging Hydrogen Sources on Existing SAF Production Technologies

Washington State University

Objective

The goal of this task is to estimate the cost and emissions-reduction potential of different hydrogen sources for SAF production. A harmonized set of techno-economic and lifecycle assessments will determine the minimum selling price (MSP) and CI of different SAF technologies as a function of hydrogen cost and CI. While LCA and TEA do exist for these SAF technologies, their assumed source of hydrogen varies between studies and is usually fixed (De Jong et al., 2017; Tanzil et al., 2021). Harmonized abatement cost data will allow stakeholders to make better decisions about which SAF technologies will benefit from investments in hydrogen technical improvements or infrastructure. It will also indicate which SAF technologies reduce emissions most effectively when paired with a given hydrogen technology.

Research Approach

In this task, the ASCENT Project 080 team will use hydrogen cost and CI data from Task 1 to determine their effect on existing SAF technologies - namely power-to-liquid (PtL), HEFA, pyrolysis-hydrotreatment (PH), ATJ, and gasification Fischer-Tröpsch (GFT). Each of these technologies will be evaluated by TEA and LCA to determine minimum selling prices and CIs of the resultant fuels. Abatement costs will be compared within individual technologies to determine the benefits of hydrogen technical improvements, while comparison of abatement cost between technologies will determine which are most effective under various hydrogen costs and CIs.

Milestones

- Developed a gasification TEA that allows the purchase of supplemental hydrogen and production of power.
- Conducted lifecycle assessments of technologies listed above as a function of hydrogen CI.
- Classified all processes analyzed according to the fraction of biomass oxygen they remove in the form of water (to link them with our stoichiometric models in Task 3).

Major Accomplishments

We have compiled the results above into a first draft on the effect of hydrogen sources on SAF technologies. Figure 2 shows the range of abatement costs achieved by six SAF technologies under a range of hydrogen costs and CIs. Notably, the abatement cost of HEFA is lowest with fossil hydrogen sources. PtL achieves a distinct abatement cost optimum with electrolytic hydrogen, which is expected given its exorbitant hydrogen consumption. The remaining stover-consuming technologies are relatively insensitive to the hydrogen source. Despite individual technologies being insensitive to hydrogen price, differing hydrogen cost and CI may still favor one or the other, with key implications for which SAF

technologies will perform best with a given hydrogen source. Figure 3 illustrates a composite abatement cost of all stover-consuming SAF technologies, constructed by selecting the technology of lowest abatement cost for each combination of hydrogen cost and CI. This reveals the SAF technology favored by each hydrogen technology, all of which fall within the region for which gasification Fischer-Tropsch is the optimal technology. This indicates that current and emerging hydrogen technologies still favor the use of hydrogen-independent SAF production for carbon abatement, despite its low yields and high fuel cost. However, projections for hydrogen cost may favor pyrolysis-hydrotreatment. These results are explained further in our forthcoming manuscript.

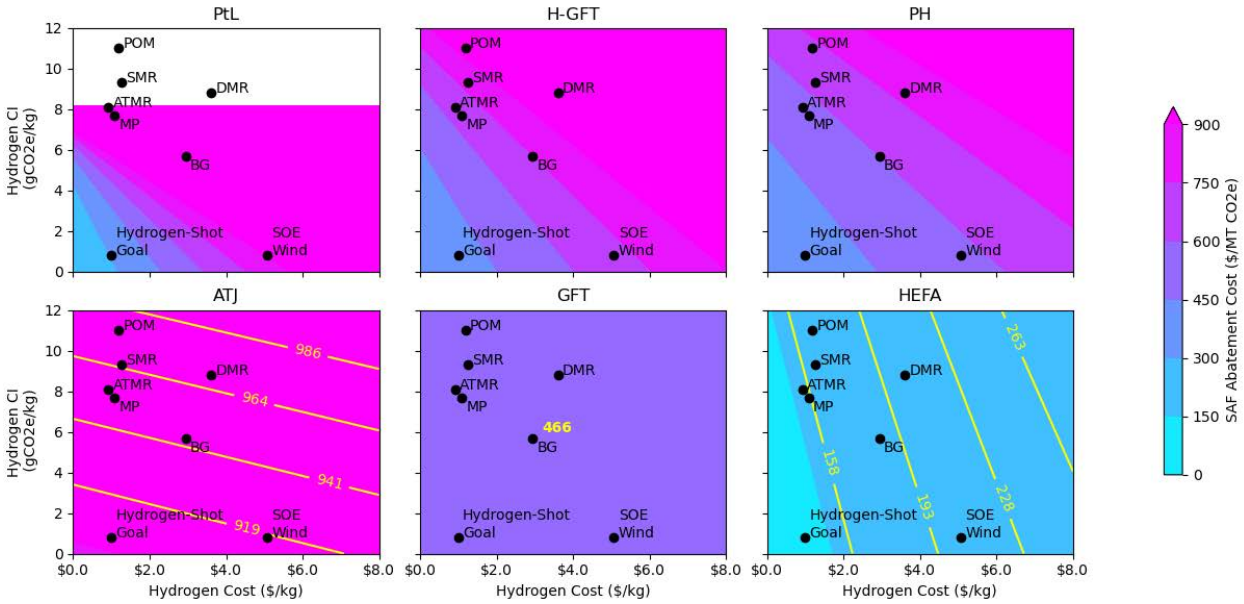


Figure 2. Abatement cost of SAF technologies as a function of hydrogen cost and carbon intensity (CI). Black dots represent hydrogen sources, while yellow lines provide additional detail for fuel abatement costs. ATJ: alcohol-to-jet; GFT: gasification Fischer-Tröpsch; H-GFT: Hydrogen-enhanced Gasification Fischer-Tropsch; HEFA: hydro-processed ester and fatty acid; PH: pyrolysis-hydrotreatment; and PtL: power-to-liquid.

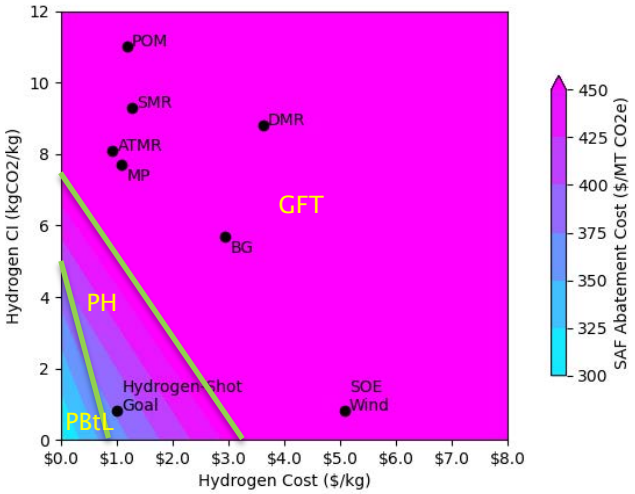


Figure 3. Lowest abatement cost technologies for stover conversion to SAF as a function of hydrogen price and carbon intensity (CI). Black dots represent hydrogen sources, while yellow lines illustrate the transition between different favorable technologies. GFT: gasification Fischer-Tröpsch; and PBtl: power- and biomass-to-liquid.

Publications

Presentations

Garcia, A., Sierra-Jimenez, V., Garcia-Perez, M. (2025, October 15) *Hydrogen and Power-to-Liquid Concepts for Sustainable Aviation Fuel Production* [Poster presentation]. ASCENT 2025 Fall Meeting, Alexandria, Virginia.

Garcia, A., Sierra-Jimenez, V., Garcia-Perez, M. (2024, October 15-16) *Screening and Optimization of Sustainable Aviation Fuel (SAF) Technologies in an Evolving Hydrogen Market* [Poster presentation]. Northwest Bioenergy Summit, Spokane, Washington.

Outreach Efforts

Presented preliminary results from this study at the 2024 Northwest Bioenergy Summit and Ascent 2025 Fall meetings.

Awards

None.

Student Involvement

None.

Plans for Next Period

Complete revision of the draft manuscript and publish results.

References

De Jong, S., Antonissen, K., Hoefnagels, R., Lonza, L., Wang, M., Faaij, A., & Junginger, M. (2017). Life-cycle analysis of greenhouse gas emissions from renewable jet fuel production. *Biotechnology for Biofuels, 10*(1), 64. https://doi.org/10.1186/s13068-017-0739-7

Tanzil, A. H., Brandt, K., Wolcott, M., Zhang, X., & Garcia-Perez, M. (2021). Strategic assessment of sustainable aviation fuel production technologies: Yield improvement and cost reduction opportunities. *Biomass and Bioenergy*, *145*. https://doi.org/10.1016/j.biombioe.2020.105942

Task 3 – Evaluate Potential for Integration of Hydrogen and Power into SAF Production

Washington State University

Objective

The objective of this task is to identify new pathways to optimize SAF production for maximum GHG reductions with minimal fuel costs.

Research Approach

This task involves both a theoretical and an applied approach. The theoretical subtask uses heuristic models to explore broader trends in SAF production using simplified SAF process models that expel oxygen in the form of CO_2, H_2O, and dioxygen (O_2), as well as the potential for hydrogen inclusion in a simplified gasification model (Garcia et al., 2024). Hydrogen data from Task 1 were used to determine which processes are favored by different hydrogen sources MSP, CI, and abatement cost data from these processes will provide data about more general trends in SAF production. This approach was also used to evaluate the effect of plastic co-feeding and char production on these idealized SAF processes, to understand the effect of consuming and sequestering fossil carbon on SAF abatement costs (Garcia et al., 2024).

In the second subtask, our team will evaluate the integration and co-location of these technologies with the new hydrogen production technologies discussed in Task 1. Using guidance from the previous subtask, we will develop explicit process models, TEAs, and complete LCAs to determine the economic and environmental impacts of different process modifications on SAF production. These include the introduction of power at different points in a gasification process (whether as supplemental heat during gasification or supplemental electrolytic hydrogen).

Milestones

- Developed a heuristic correlation to estimate fuel MSP without explicit equipment costing.
- Developed three purely stoichiometric mass balances to estimate the effect of deoxygenation method (e.g., oxygen removal as O_2, H_2O, or CO_2) on production cost and CI under various hydrogen costs and CIs.
- Used our cost heuristic to evaluate the effect of many hydrogen production technologies on a simplified gasification model. The introduction of technical constraints for a simplified oxygen gasification model yielded a tipping point of about 2.75 $/kg hydrogen. An assessment of this simplified gasification model with different oxidizers (O_2, steam, and CO_2) indicated that current gasification technologies (O_2, steam) do not justify its inclusion in these simplified cases.
- Analyzed biomass gasification technologies for more detailed optimization. We concluded that existing technologies for the conversion of biomass into syngas are limited by very low carbon conversion efficiencies. To achieve carbon conversion efficiencies close to 100%, the introduction of outside hydrogen and energy is necessary. While low-temperature gasification technologies have higher cold-gas efficiencies, the use of existing high-temperature gasification technologies may allow for better yields and heat integration with hydrogen technologies through reactive quenching by reverse water gas shift (Hillestad et al., 2018). Syngas cleaning methods must also be optimized accordingly (de Oliveira et al., 2023).
- Developed preliminary models for gasification control, integrated electrolysis, and direct heating cases. Our base-case is modelled on the results of Swanson (Swanson et al., 2010). Preliminary results indicate that introduction of power to gasifier may be more efficient than electrolysis.
- Expanded our gasification TEA to include methanol production for product diversification (Tan et al., 2015)

Major Accomplishments

The ASCENT Project 080 team has learned that the most critical factor governing production cost is fuel yield, which is directly related to carbon conversion efficiency (Tanzil et al, 2021). At 79% carbon conversion (Swanson et al., 2010), gasification outcompetes the 72% and 32% conversion achieved by PH (Jones et al., 2009a) and ATJ (Humbird et al., 2011) for lignocellulosic feedstocks. It's ability to process MSW (Jones et al., 2009b) and synthesize a variety of end products (Tan et al., 2015) makes it a good candidate for development. However, an overall mass and energy balance shows that typical gasification systems are energy- and hydrogen-deficient, requiring the oxidation of carbon that could otherwise go to fuel. This is typically accomplished by introducing oxygen to the gasifier to release necessary energy for conversion, while using water to oxidize carbon monoxide (CO) in the produced syngas and evolve additional hydrogen through the



water-gas-shift reaction (Swanson et al., 2010). This creates an opportunity to supplement hydrogen and energy from outside the system (e.g., via the low-temperature or high-temperature water electrolysis) maximizing the carbon available for fuel production and removing additional oxygen in the form of water (Garcia et al., 2024). The high temperatures required for gasification also leave syngas with an energy content higher than that of the fuel produced; therefore, nearly one-third of the system's energy is released as heat (Lange, 2007). Heat integration is critical to maximizing the economic viability of technologies producing a syngas intermediate and may provide additional opportunities for integration with hydrogen production technologies (Dossow et al., 2024; Hillestad et al., 2018). Because hydrogen must be produced externally to maximize fuel production yields, hydrogen production technologies and their potential synergisms with SAF production must be carefully studied to develop optimized systems.

For this purpose, our team has produced a holistic analysis of the hydrogen market's effect on the potential of oxygen, steam, and CO_2 gasification technologies. This overall analysis was then integrated with the hydrogen production technologies examined in Task 1 to forecast which pathways will become favorable as the hydrogen market evolves. We have also produced a Microsoft® Excel®-based model that accounts for both stoichiometric and thermodynamic constraints in fuel production from biomass. This tool has not been utilized but could theoretically be updated and deployed for the testing of basic process optimization. Our extended Lange model has been placed into a Python® module that allows the calculation of economics for simple stoichiometric processes. We can easily extend this model to accept generalized user inputs, if needed for public outreach. Through this analysis, our team was able to determine a tipping point of 2.50 $/kg for the inclusion of hydrogen in stoichiometric SAF production processes. Without the availability of hydrogen below this price, removal of biogenic oxygen in the form of CO_2 is more cost effective than removal in the form of water for the stoichiometric models evaluated. The results of this holistic analysis have been published in *ACS Energy and Fuels* (Garcia et al., 2024). These results are currently being evaluated in more detail using standard techno-economic and lifecycle methods.

Publications

Peer-Reviewed Journal Publication

Garcia, A., Sierra-Jimenez, V., Brandt, K., Martinez-Valencia, L. P., Wolcott, M., Male, J., & Garcia-Perez, M. (2024). Holistic methodology to guide the evolution of sustainable aviation fuel production technologies. *Energy & Fuels, 38*(18), 17706–17716. https://doi.org/10.1021/acs.energyfuels.4c02795

Presentations

Alroggen, F., Garcia, A., (2025, April 23-24). *ASCENT Project 80: Hydrogen and Power-to-Liquid Concepts for SAF Production* [Conference presentation]. ASCENT Spring Meeting, Knoxville, Tennessee.

Garcia-Perez, M., Garcia, A., & Wolcott, M. (2024, October 2-4). Holistic methodology to guide the evolution of sustainable aviation fuel production technologies [Conference presentation]. Sustainable Aviation Futures, North America, Houston, Texas.

Outreach Efforts

Presented our results at the Spring 2024 and Fall 2024 ASCENT meetings in Hawai'i and Alexandria, Virginia, respectively.

Student Involvement

Valentina Sierra (PhD student-graduated), Brandon Lewis (PhD student), Aidan Garcia (research associate), and Robert Macias (research associate) contributed to this task.

Plans for Next Period

- Extend TEA and LCA analysis to new gasification models.
- Use these results to determine the effectiveness of power use in electrolysis or direct heating of gasification.

® Microsoft and Excel are registered trademarks of Microsoft Corporation in the United States and other countries.
® Python is a registered trademark of Python Software Foundation, Beaverton, Oregon.



References

de Oliveira, Diego C., Lora, E. E. S., Venturini, O. J., Maya, D. M. Y., & Garcia-Perez, M. (2023). Gas cleaning systems for integrating biomass gasification with Fischer-Tropsch synthesis-A review of impurity removal processes and their sequences. *Renewable and Sustainable Energy Reviews, 172*. https://doi.org/10.1016/j.rser.2022.113047

Dossow, M., Klüh, D., Umeki, K., Gaderer, M., Spliethoff, H., & Fendt, S. (2024). Electrification of gasification-based biomass-to-X processes – a critical review and in-depth assessment. *Energy & Environmental Science*, *17*(3), 925–973. https://doi.org/10.1039/D3EE02876C

Garcia, A., Sierra-Jimenez, V., Brandt, K., Martinez-Valencia, L. P., Wolcott, M., Male, J., & Garcia-Perez, M. (2024). Holistic Methodology to Guide the Evolution of Sustainable Aviation Fuel Production Technologies. *Energy & Fuels*, *38*(18), 17706–17716. https://doi.org/10.1021/acs.energyfuels.4c02795

Hillestad, M., Ostadi, M., Serrano, G. D. A., Rytter, E., Austbø, B., Pharoah, J. G., & Burheim, O. S. (2018). Improving carbon efficiency and profitability of the biomass to liquid process with hydrogen from renewable power. *Fuel, 234*, 1431–1451. https://doi.org/10.1016/j.fuel.2018.08.004.

Humbird, D., Davis, R., Tao, L., Kinchin, C., Hsu, D., Aden, A., Scheon, P., Lukas, J., Olthof, B., Worley, M., Sexton, D., & Dudgeon, D. (2011). *Process Design and Economics for Biochemical Conversion of Lignocellulosic Biomass to Ethanol: Dilute-Acid Pretreatment and Enzymatic Hydrolysis of Corn Stover*. National Renewable Energy Laboratory, US Department of Energy, Golden, Colorado. https://doi.org/10.2172/1013269

Jones, S. B., Valkenburg, C., Walton, C. W, Elliott, D. C., Holladay, J. E., Stevens, D. J., Kinchin, C., & Czernik, S. (2009a). *Production of Gasoline and Diesel from Biom.ass via Fast Pyrolysis, Hydrotreating and Hydrocracking: A Design Case* (No. PNNL-18284). Pacific Northwest National Laboratory, Richland, Washington. https://www.pnnl.gov/main/publications/external/technical_reports/PNNL-18284.pdf

Jones, S. B., Zhu, Y., & Valkenburg, C. (2009b). *Municipal Solid Waste (MSW) to Liquid Fuels Synthesis, Volume 2: A Techno-economic Evaluation of the Production of Mixed Alcohols* (No. PNNL-18482). https://doi.org/10.2172/962845

Lange, J. P. (2016). Catalysis for biorefineries-performance criteria for industrial operation. *Catalysis Science and Technology, 6*(13), 4759–4767. https://doi.org/10.1039/c6cy00431h

Lange, J.-P. (2007), Lignocellulose conversion: an introduction to chemistry, process and economics. *Biofuels, Bioprod. Bioref.*, 1: 39-48. https://doi.org/10.1002/bbb.7

Swanson, R. M., Satrio, J. A., & Brown, R. C. (2010). *Techno-economic analysis of biofuels production based on gasification* (No. NREL/TP-6A20-46587). National Renewable Energy Laboratory, US Department of Energy, Golden, Colorado. https://www.nrel.gov/docs/fy11osti/46587.pdf

Tan, E. C. D., Talmadge, M., Dutta, A., Hensley, J., Schaidle, J., & Biddy, M. (2015). *Process design and economics for the conversion of lignocellulosic biomass to hydrocarbons via indirect liquefaction. Thermochemical research pathway to high-octane gasoline blendstock through methanol/dimethyl ether intermediates* (No. NREL/TP-5100-62402). National Renewable Energy Laboratory, US Department of Energy, Golden, Colorado. https://www.nrel.gov/docs/fy15osti/62402.pdf

Tanzil, A. H., Brandt, K., Wolcott, M., Zhang, X., & Garcia-Perez, M. (2021). Strategic assessment of sustainable aviation fuel production technologies: Yield improvement and cost reduction opportunities. *Biomass and Bioenergy*, *145*. https://doi.org/10.1016/j.biombioe.2020.105942

Task 4 – Improvement of Hydrogen Efficiency in Hydrotreatment and Synthesis

Washington State University

Objective

In this task, our team will study how hydrogen is used in hydrotreatment steps. Hydrogen utilization for SAF production typically occurs in a hydrotreatment step that varies depending on the technology (Tanzil et al., 2021; Han et al., 2019). This step can proceed from a simple hydrogenation, hydrodeoxygenation, hydrocracking, or all of them together, depending on the technology (Han et al., 2019). Especially troublesome is the hydrotreatment of oligomers and materials with a high tendency to form coke (Han et al., 2019). A more detailed understanding of the mechanisms at play will allow for supplemental hydrogen to be used more effectively.



Research Approach

In addition, we will develop a detailed phenomenological mathematical model for the hydrotreatment step of the HEFA and fast pyrolysis pathways, which the team will then use to study potential strategies to reduce hydrogen consumption during SAF production (Chen et al., 2019; Plazas-González et al., 2018). This type of model requires a detailed description of the chemical composition of the feedstock, the reaction mechanism, and associated kinetics (Gutiérrez-Antonio et al., 2018; Talib Jarullah, 2011; Boesen, 2011; Jeništová et al., 2017; Tieuli et al., 2019; Hachemi & Murzin, 2018). The modeling work will complement studies in batch and continuous hydrotreatment reactors with different catalysts to validate the mathematical model.

Milestones

- Conducted an investigation of hydrogen efficiency in hydrotreatment, which began in January 2023 with a literature review of catalytic hydrotreatment reactions.
- Began development of atomistic models of hydrotreatment processes and a description of pyrolysis oils in terms of representative compounds.
- Began hydrotreatment trials of coconut oil and used cooking oil mixtures to maximize SAF yields.
- Began trials of co-hydrotreatment of coconut oil and kerosene to simulate hydrotreatment in existing refinery infrastructure.

Major Accomplishments

We have made progress on a literature review on pyrolysis oils hydrotreatment reactions and a preliminary atomistic model of pyrolysis oil molecules catalytic hydrodeoxygenation.

Publications

Peer-Reviewed Journal Publication

Denson, M. D., Manrique, R., Olarte, M., & Garcia-Perez, M. (2024). *Co-hydrotreatment of Bio-oil and Waste Cooking Oil to Produce Transportation Fuels*. Energy & Fuels, 38(8), 6982–6991. https://doi.org/10.1021/acs.energyfuels.3c05176

Dissertation

Denson, M. (2023). *Contributions to understanding oligomeric sugars derived from biomass pyrolysis* [Doctoral dissertation], Washington State University. Washington State University.

Outreach Efforts

None.

Student Involvement

Melba Denson, a PhD student at WSU, has contributed applied and theoretical hydrotreatment work to this task as part of her thesis. Rona Landoy and Emmanuel Villaruel (Visiting Master's students) are also contributing to this step.

Plans for Next Period

This work was planned for the extended period of performance for the project. As additional funding was not received, we will focus on delivering on previous tasks and do not plan to continue this one.

References

Boesen, R. R. (2011). *Investigation and modelling of diesel hydrotreating reactions* [Doctoral dissertation, Technical University of Denmark]. Technical University of Denmark. https://backend.orbit.dtu.dk/ws/portalfiles/portal/6470295/Thesis+Rasmus+R.+Boesen+2010+final.pdf

Chen, Z., Feng, S., Zhang, L., Shi, Q., Xu, Z., Zhao, S., & Xu, C. (2019). Molecular-level kinetic modelling of fluid catalytic cracking slurry oil hydrotreating. *Chemical Engineering Science*, *195*, 619–630. https://doi.org/10.1016/j.ces.2018.10.007

Gutiérrez-Antonio, C., Soria Ornelas, M. L., Gómez-Castro, F. I., & Hernández, S. (2018). Intensification of the hydrotreating process to produce renewable aviation fuel through reactive distillation. *Chemical Engineering and Processing - Process Intensification*, *124*, 122–130. https://doi.org/10.1016/j.cep.2017.12.009



Han, Y., Gholizadeh, M., Tran, C.-C., Kaliaguine, S., Li, C.-Z., Olarte, M., & Garcia-Perez, M. (2019). Hydrotreatment of pyrolysis bio-oil: A review. *Fuel Processing Technology*, *195*. https://doi.org/10.1016/j.fuproc.2019.106140

Hachemi, I., & Murzin, D. Yu. (2018). Kinetic modeling of fatty acid methyl esters and triglycerides hydrodeoxygenation over nickel and palladium catalysts. *Chemical Engineering Journal*, *334*, 2201–2207. https://doi.org/10.1016/j.cej.2017.11.153

Jenišťová, K., Hachemi, I., Mäki-Arvela, P., Kumar, N., Peurla, M., Čapek, L., Wärnå, J., & Murzin, D. Y. (2017). Hydrodeoxygenation of stearic acid and tall oil fatty acids over Ni-alumina catalysts: Influence of reaction parameters and kinetic modelling. *Chemical Engineering Journal*, *316*, 401–409. https://doi.org/10.1016/j.cej.2017.01.117

Plazas-González, M., Guerrero-Fajardo, C. A., & Sodré, J. R. (2018). Modelling and simulation of hydrotreating of palm oil components to obtain green diesel. *Journal of Cleaner Production*, *184*, 301–308. https://doi.org/10.1016/j.jclepro.2018.02.275

Talib Jarullah, A. (2011). *Kinetic parameters estimating hydrotreating reactions in trickle bed reactor (TBR) via pilot plant experiments; Optimal design and operation of an industrial TBR with heat integration and economic evaluation* [Doctoral. dissertation, University of Bradford]. University of Bradford. https://bradscholars.brad.ac.uk/bitstreams/01cfae05-bc0d-4a5e-9611-a465899e3e13/download

Tanzil, A. H., Brandt, K., Wolcott, M., Zhang, X., & Garcia-Perez, M. (2021). Strategic assessment of sustainable aviation fuel production technologies: Yield improvement and cost reduction opportunities. *Biomass and Bioenergy*, *145*. https://doi.org/10.1016/j.biombioe.2020.105942

Tieuli, S., Mäki-Arvela, P., Peurla, M., Eränen, K., Wärnå, J., Cruciani, G., Menegazzo, F., Murzin, D. Y., & Signoretto, M. (2019). Hydrodeoxygenation of isoeugenol over Ni-SBA-15: Kinetics and modelling. *Applied Catalysis A: General*, *580*, 1–10. https://doi.org/10.1016/j.apcata.2019.04.028



Project 080(B) Hydrogen and Power-to-Liquid Concepts for Sustainable Aviation Fuel Production

Massachusetts Institute of Technology

Project Lead Investigators

Florian Allroggen
Principal Research Scientist
Laboratory for Aviation and the Environment
Massachusetts Institute of Technology
77 Massachusetts Ave, Building 33-328
Cambridge, MA 02139
617-715-4472
fallrogg@mit.edu

University Participants

Massachusetts Institute of Technology (MIT)

- P.I.: Dr. Florian Allroggen
- FAA Award Number: 13-C-AJFE-MIT, Amendment Nos. 091, 101, 115, 124, 128, 133, 136, and 143
- Period of Performance: October 1, 2021, to August 31, 2027
- Tasks (during current reporting period, October 1, 2024, to September 30, 2025):
  4. Develop methods for assessing the economic and environmental impacts of promising sustainable aviation fuel (SAF) production pathways
  5. Apply models to analyze the economic and environmental footprint of SAF production pathways
  6. Analyze the prospects of direct air capture (DAC) of atmospheric carbon dioxide (CO_2) to provide a carbon source for SAF production

  Note: additional tasks to be reported separately by Washington State University

Project Funding Level

The Federal Aviation Administration (FAA) provided $950,000 in funding; $950,000 matching funds were committed. Sources of matching funds are approximately $264,100 from MIT, plus third-party in-kind contributions of $101,000 from Savion Aerospace Corp., $213,000 from NuFuels LLC, and $371,900 from Earth Force Technologies.

Investigation Team

Florian Allroggen (P.I.), Tasks 4, 5, and 6
Niamh Keogh (Research Scientist), Tasks 4, 5 and 6
Tae Joong Park (graduate research assistant), Tasks 4 and 5
Tara Housen (graduate research assistant), Task 6

Project Overview

The aviation industry is under pressure to diversify its energy supply. The use of SAF is considered one of the most promising approaches to meet the industry's targets. To date, no comprehensive assessment exists which analyzes how different carbon sources, hydrogen sources, and conversion processes can be combined to make SAF with lowest costs and highest benefits. The goals of this research project are to (1) evaluate the strengths and weaknesses of hydrogen production and power-to-liquid (PtL) concepts in comparison to current SAF production pathways, (2) assess how hydrogen production and PtL production can be integrated with existing production and distribution infrastructure, and (3) analyze the effects these technologies could have on the current production of SAF (e.g., impacts, cost). The MIT team has focused on assessments of how existing SAF pathways can be optimized from an impact perspective, including costs. The team primarily investigates electrification of SAF production as a possible evolution path.

Task 4 - Develop Methods for Assessing the Impacts of Promising SAF Production Pathways

Massachusetts Institute of Technology

Objective

The objective of this task is to define a method for assessing the economic and environmental impacts of promising fuel production pathways. For this purpose, the ASCENT Project 080(B) team developed techno-economic assessment (TEA) and life-cycle assessment (LCA) models. The TEA model calculates the minimum selling price of a specific fuel. The LCA model computes its atmospheric impacts. Because the exact process layout and process characteristics (e.g., mass and energy balances, capital expenditures, operating expenditures) of novel fuel production pathways are subject to uncertainty, sensitivity studies will be conducted. Through this approach, we obtain insights into the range of impacts associated with electrified SAF production pathways.

Research Approach

Electrification of SAF production can be seen as a spectrum in terms of electricity use, where conventional SAF and PtL use the least and most electricity, respectively. Electricity-enhanced fuels are another class of fuel production process which fits in between the two endpoints. Such electricity-enhanced SAF production processes use up to ten times more electricity than conventional SAF per unit energy of fuel output but require up to 81% less electricity than PtL. The modeling chain used to explore the impacts of electrifying the conventional SAF production process is outlined using three feedstock and fuel conversion combinations (hence referred to as pathways). These pathways are corn grain ethanol-to-jet (ETJ), hydroprocessed esters and fatty acids (HEFA) soybean, and HEFA tallow. The team reconstructed the process specifications utilizing data from the calculation of United States (U.S.)-based LCA values for each pathway under the Carbon Offsetting and Reduction Scheme for International Aviation (CORSIA) (ICAO, 2022). These process models are based on older versions of the Greenhouse gases, Regulated Emissions, and Energy use in Technologies (GREET®) model. More specifically, the team used the GREET 2022 (Rev. 1) (Argonne National Laboratory, 2022a), GREET 2022 Aviation module (Argonne National Laboratory, 2022b), and International Civil Aviation Organization (ICAO)-GREET 2019 (Argonne National Laboratory, 2022c) to reconstruct the processes. The replicated baseline impact values are 3–8 g carbon dioxide equivalent (CO_2e)/MJ lower than the respective CORSIA values, largely due to assumed efficiency improvements since the original CORSIA analyses; the remaining differences are attributable to a variety of smaller changes in more recent versions of GREET vs. older GREET versions.

Figure 1 shows the electrification strategies used for this study. All direct combustion of carbonaceous fuels in the primary supply chain are replaced with onshore wind electricity with battery storage, inclusive of embodied emissions (15.7 g CO_2e/kWh) (Argonne National Laboratory, 2022a). Embodied emissions of electricity refer to emissions from the material sourcing, component manufacturing, construction, maintenance, and decommissioning of the power generation facility. This includes all heating energy used in natural gas (NG), liquefied petroleum gas, diesel, residual oil, coal, biomass, and landfill gas boilers (Argonne National Laboratory, 2022a) being substituted with resistance heating electric boilers (Engineer Live, 2021). All existing electricity use from the U.S. grid is replaced with onshore wind electricity with battery storage. In farming, off-road equipment (tractors) (Lagnelöv et al., 2021), irrigation units (Husker Power Products, 2023), pumps (Honda, 2023), and generators powered by diesel, gasoline, and NG are replaced with equivalent electric units (U.S. Department of Energy, 2023). For material inputs such as fertilizer, herbicide, and insecticide use, where there is no direct combustion in the primary jet fuel supply chain, the secondary supply chain (i.e., inputs into fertilizer production) is electrified. This includes ammonia (NH_3) produced from electrolytic hydrogen (H_2), electrified transportation of inputs (battery trucks [Tesla Semi, 2023], rail [Popovich et al., 2021], and NH_3 fuel cell–powered ocean tankers and barges [Korberg et al., 2021]), and electrified off-road mining equipment (battery trucks [Henrio et al., 2023] for phosphoric rock hauling for monoammonium phosphate [$NH_4H_2PO_4$]). H_2 from proton exchange membrane (PEM) electrolysis powered by wind replaces H_2 from steam methane reforming in the HEFA process. Carbon capture and sequestration (CCS) is deployed for the biogenic CO_2 released during the ethanol (EtOH) fermentation process. Feedstock, intermediates, and jet fuel transport and distribution are also electrified; the aforementioned vehicle electrification strategies are applied accordingly. No mode change is assumed.

® GREET is a registered trademark of the U.S. Department of Energy.

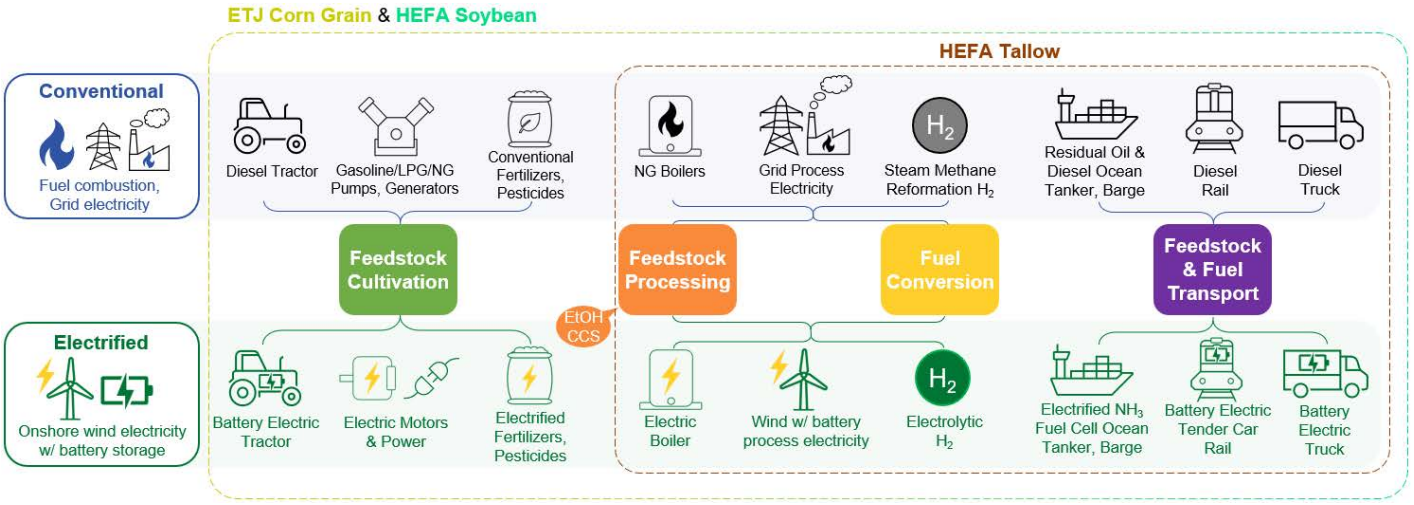


Figure 1. Strategies for reducing the impact of the ethanol-to-jet (ETJ) corn grain, hydroprocessed esters and fatty acids (HEFA) soybean, and HEFA tallow pathways, using electrification. Electrolytic hydrogen is produced via proton exchange membrane (PEM) (low temperature) electrolyzer from onshore wind electricity with battery storage, replacing "gray" electrolytic hydrogen (H_2) from steam methane reformation using natural gas (NG). Note: this is a simplified schematic, not an exhaustive analysis of every element of the lifecycle assessment. LPG: liquefied petroleum gas.

Milestone

- Presented the updated modeling approach to the FAA and other stakeholders.
- The methodology has been documented in a paper draft which will be submitted for publication.

Major Accomplishment

The focus of this year's efforts was on understanding how this method can be expanded to other pathways. The team aimed to select pathways which would provide the most insight into optimizing conventional SAF via electrification and appropriately apply the previously developed electrification method to these pathways (HEFA soybean, HEFA tallow).

Publications

A paper outlining the methods and process modifications is in preparation.

Outreach Efforts

Presented at the ASCENT Spring 2025 Meeting and a poster presentation at the ASCENT Fall 2025 meeting.

Student Involvement

During the reporting period, TJ Park (MIT graduate student) worked on this task. The student developed the structure to analyze electrified variants of existing SAF pathways. This included data gathering from the literature for energy, emissions, and cost data of electrified alternatives to SAF production steps and subsequent adaptation for use in LCAs and TEAs. The student also reconstructed existing LCA and TEA models to replicate baseline values and modified the models to suit the electrification study.

Plans for Next Period

Publish the methods and data for this task.

References

Argonne National Laboratory. (2022a). *GREET: The greenhouse gases, regulated emissions, and energy use in Transportation Model*. U.S. Department of Energy. https://www.energy.gov/eere/bioenergy/articles/greet-greenhouse-gases-regulated-emissions-and-energy-use-transportation

Argonne National Laboratory. (2022b*). Energy systems and infrastructure analysis – GREET aviation module.* https://greet.es.anl.gov/greet_aviation
Argonne National Laboratory (2022c). *ICAO-GREET model*. https://greet.anl.gov/greet_icao
Engineer Live. (2021, December 10). *The move to electric boilers*. Engineer Live. https://www.engineerlive.com/node/20952
Henrio, M., van der Ende, O., Motta, G., & Ray, R. K. (2023). *Mining electrification could double their electricity demand*. McKinsey & Company. https://www.mckinsey.com/industries/metals-and-mining/our-insights/electrifying-mines-could-double-their-electricity-demand
Honda. (2023). *Honda IGX800 engine*. https://www.hastingshonda.co.nz/power-equipment/honda-igx800/
Husker Power Products. (2023). *NGE 14.6L spec sheet*. Husker Power Products. https://www.huskerpowerproducts.com/assets/site/specsheets/irrigation/psi-14.6l-nglpg-specsheet.pdf
ICAO. (2022). *CORSIA eligible fuels – life cycle assessment methodology (CORSIA supporting document)*. International Civil Aviation Organization (ICAO), Montreal, Canada. https://www.icao.int/environmental-protection/CORSIA/Documents/CORSIA_Eligible_Fuels/CORSIA_Supporting_Document_CORSIA%20Eligible%20Fuels_LCA_Methodology_V5.pdf
Korberg, A. D., Brynolf, S., Grahn, M., & Skov, I. R. (2021). Techno-economic assessment of advanced fuels and propulsion systems in future fossil-free ships. *Renewable and Sustainable Energy Reviews*, *142*. https://doi.org/10.1016/j.rser.2021.110861
Lagnelöv, O., Dhillon, S., Larsson, G., Nilsson, D., Larsolle, A., & Hansson, P.-A. (2021). Cost analysis of autonomous battery electric field tractors in agriculture. *Biosystems Engineering*, *204*, 358–376. https://doi.org/10.1016/j.biosystemseng.2021.02.005
Popovich, N. D., Rajagopal, D., Tasar, E., & Phadke, A. (2021). Economic, environmental and grid-resilience benefits of converting diesel trains to battery-electric. *Nature Energy*, *6*(11), 1017–1025. https://doi.org/10.1038/s41560-021-00915-5
U.S. Department of Energy. (2023). *Determining electric motor load and efficiency.* https://www.energy.gov/eere/amo/articles/determining-electric-motor-load-and-efficiency
Tesla. (2023). *Tesla Semi*. https://www.tesla.com/semi

Task 5 - Analyze the Footprint of SAF Production Pathways

Massachusetts Institute of Technology

Objective

The objective of this task is to provide harmonized assessments of different SAF pathways. During the reporting period, the ASCENT Project 080(B) team analyzed the implications of different measures, including using renewable electricity and hydrogen, in selected CORSIA-eligible SAF pathways. In addition, the costs of these strategies and the impact abatement costs were calculated to provide a holistic view of the impacts associated with SAF electrification.

Research Approach

Figure 2a shows the impact reduction potential of electrifying the ETJ corn grain, HEFA soybean, and HEFA tallow SAF pathways. Differences in GREET 2011 and 2022 (Argonne National Laboratory, 2022), partially attributed to decreases in methane (CH_4) impact factors in newer NG boilers and efficiency improvements throughout the process, result in new baselines of 82.7 g CO_2e/MJ, 62.9 g CO_2e/MJ, and 18.9 g CO_2e/MJ, for ETJ corn grain, HEFA soybean, and HEFA tallow, respectively. All reduction measures considered (see Figure 1), the lifecycle impact of the electrified ETJ corn grain, HEFA soybean, and HEFA tallow fuel are estimated at 16.8 g CO_2e/MJ (82% reduction), 37.1 g CO_2e/MJ (44% reduction), and 1.2 g CO_2e/MJ (95% reduction), respectively. For ETJ corn grain and HEFA soybean, the remaining impacts include those from farming (corn: 9.8 g CO_2e/MJ, soybean: 11.4 g CO_2e/MJ) - the majority of which is attributed to nitrous oxide (N_2O) emissions from nitrogen fertilizer use in the soil with direct mitigation options currently in an experimental phase (Itakura et al., 2013) - and induced land use change (ILUC) emissions (25.1 g CO_2e/MJ). There may be reduction opportunities with cover crops, double cropping, and sustainable land management practices which remain an area of research. HEFA tallow has a 95% reduction in greenhouse gas (GHG) emissions, as there are no remaining emissions, given that tallow is considered a byproduct of the animal slaughtering process, and thus the feedstock cultivation stage is outside the system boundary of the LCA.



Figure 2b shows the cost changes associated with the electrification strategies. For ETJ corn grain, the two largest impact reduction mechanisms, CCS in corn fermentation and electric heat for jet upgrading, incur the largest cost increases. In total, there is a 34% cost penalty ($0.55/L) for implementing electrification throughout the ETJ corn grain supply chain. However, the fuel after electrification qualifies for SAF and H_2 credits. If 40B (SAF) and 45V (H_2) tax credits are assumed to be directly applied without amortization, the new minimum selling price (MSP) after credits is 16% higher than the baseline, with the credits partially mitigating the cost increases associated with electrification. For HEFA soybean, electrically produced farm chemicals add the most cost to the fuel MSP, due to the complexity of the existing supply chain for phosphate fertilizer production. The HEFA soybean fuel MSP increases 24% due to electrification, while the SAF and H_2 credits reduce the cost penalty of electrification to 7% over the HEFA soybean baseline. For HEFA tallow, electrified rendering is the measure with the highest cost impact, and the fuel MSP rises 22% with all electrification measures implemented. The SAF and H_2 credits apply to both the baseline and electrified HEFA tallow pathway, and electrification can reduce the fuel MSP by 14%.

Figure 2c shows the abatement costs of each electrification step applied independently, and a value for the electrified fuel with all steps applied. Since the CORSIA default LCA value for the U.S. corn ETJ process is above that of fossil jet, there is no impact abatement; thus, there is no associated abatement cost. Instead, the updated GREET value (Argonne National Laboratory, 2022) is used as the basis for calculating the baseline abatement costs. Every electrification method results in a reduction of abatement cost. This shows that the reduced impact outweighs the cost increase from electrification. For HEFA soybean, not every electrification strategy results in an abatement cost reduction. For example, the cost increase from utilizing electrified fertilizers outweighs the associated impact reductions, resulting in an abatement cost increase. However, with electrification of the entire supply chain, the abatement cost is reduced 34% from the baseline, and by 49% after credits. Abatement cost for electrified HEFA tallow SAF increases 16% from the baseline, as the impact of the baseline is already low, and thus the maximum possible impact reduction is limited, compared to the cost increase from electrification.

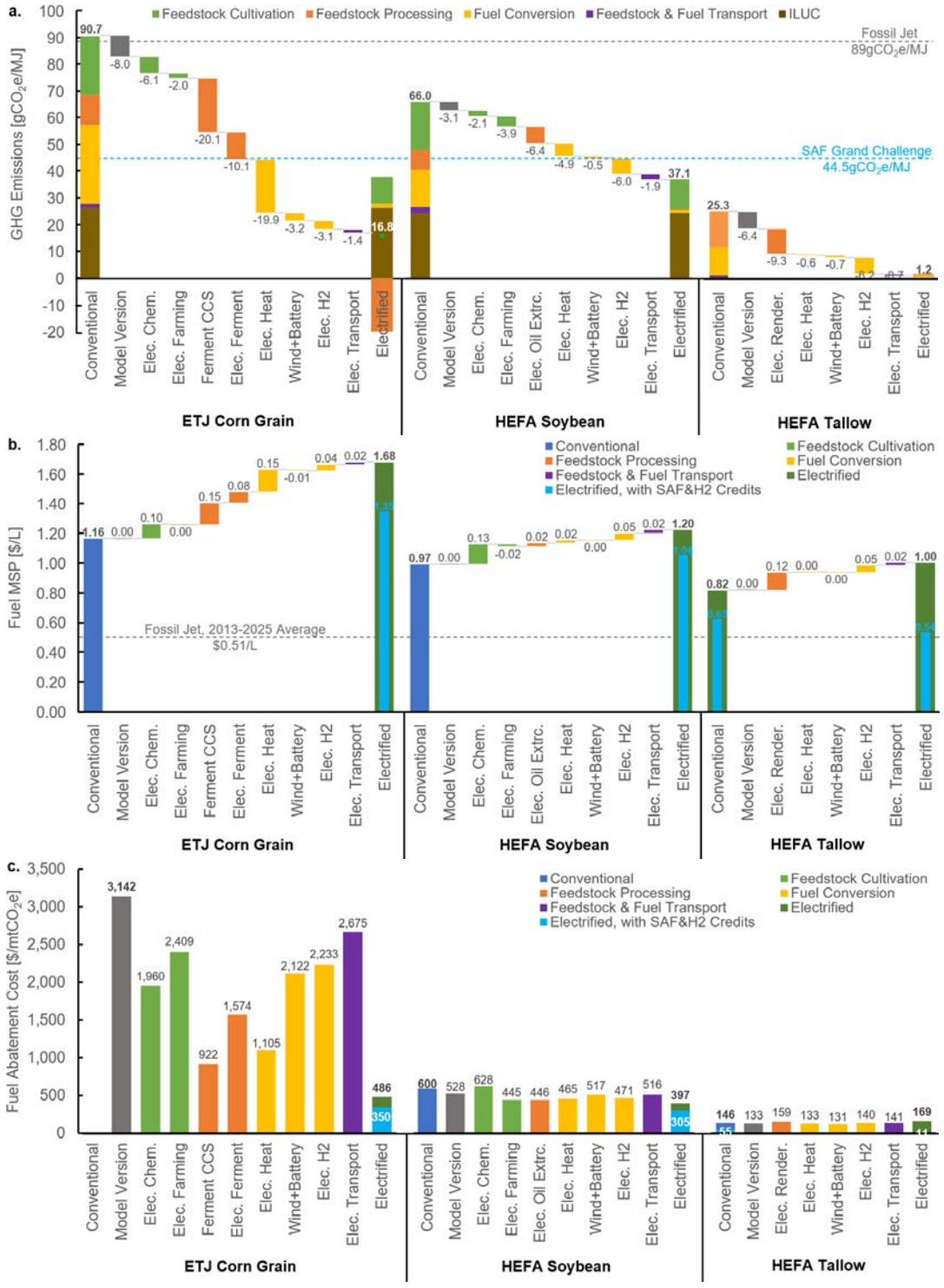


Figure 2. (a) Greenhouse gas (GHG) emissions reduction potential jet fuel supply chain from ethanol-to-jet (ETJ) corn grain, hydroprocessed esters and fatty acids (HEFA) soybean, HEFA tallow via electrification. (b) Minimum selling price (MSP) impacts from fuel electrification, in $2017USD/L. (c) Abatement cost of electrification strategies. Model Ver.: differences in

calculation of CORSIA U.S. baseline value using GREET 2022 (Argonne National Laboratory, 2022); Elec. Farming: electrified farming, including equipment, fertilizer, input material transport; Ferment CCS: Carbon capture and sequestration (CCS) of biogenic carbon dioxide (CO_2) from ethanol fermentation; Elec. Ferment: electrified fermentation, including resistance heating; Elec. Heat: electric heating; Wind+Battery: onshore wind electricity with battery storage replacing U.S. grid electricity in fuel conversion; Elec. H2: electrolytic proton exchange membrane H2; Elec. Trans: battery electric trucks, rail, and ammonia fuel cell powered ocean tankers and barges; Elec. Oil Extr.: electrified oil extraction, including resistance heating; Elec. Render.: electrified tallow rendering, including resistance heating; ILUC: induced land use change (remains constant); SAF: sustainable aviation fuel.

Milestone
Finalized the analysis.

Major Accomplishment
Summarized results and prepared for publication.

Publications
A paper summarizing the results is currently under preparation.

Outreach Efforts
Presented results during the Spring and Fall 2025 ASCENT meetings.

Student Involvement
During the reporting period, TJ Park (MIT graduate student) worked on this task. The student performed the LCA and TEA of the baseline and electrified ETJ corn grain, HEFA soybean, and HEFA tallow pathways for SAF production. The student calculated the change in abatement cost for each electrification strategy applied independently, as well as all strategies combined. The student included the impact of SAF and hydrogen credits on the minimum selling price and abatement cost of the fully electrified processes.

Plans for Next Period
Publish the results for this task.

References
Argonne National Laboratory. (2022). *GREET: The greenhouse gases, regulated emissions, and energy use in Transportation Model*. U.S. Department of Energy. https://www.energy.gov/eere/bioenergy/articles/greet-greenhouse-gases-regulated-emissions-and-energy-use-transportation

Argonne National Laboratory. (2011). *GREET: The greenhouse gases, regulated emissions, and energy use in Transportation Model*. U.S. Department of Energy.

Itakura, M., Uchida, Y., Akiyama, H., Hoshino, Y. T., Shimomura, Y., Morimoto, S., Tago, K., Wang, Y., Hayakawa, C., Uetake, Y., Sánchez, C., Eda, S., Hayatsu, M., & Minamisawa, K. (2013). Mitigation of nitrous oxide emissions from soils by Bradyrhizobium japonicum inoculation. *Nature Climate Change*, *3*(3), 208–212. https://doi.org/10.1038/nclimate1734



Task 6 - Analyze the Prospects of Direct Air Capture of Atmospheric CO_2 to Provide a Carbon Source for SAF Production

Massachusetts Institute of Technology

Objectives

The objective of this task is to evaluate the current and future costs of liquid and solid DAC through component-based learning curves. These projections were utilized to compare two pathways for decarbonization of aviation with DAC: (1) DAC with carbon capture and sequestration (DACCS) to offset emissions from continued use of fossil Jet A fuel, and (2) production of PtL fuels with DAC as a carbon source. The economic and environmental impact of these pathways were evaluated under various technology and cost assumptions in the near-term and long-term.

Milestone

- Finalized the results as described in the report for the previous period of performance.
- Finalized a paper and submitted for publication.

Major Accomplishments

Submitted paper for publication.

Publications

Housen, T., (2024). *Climate impact analysis of direct air capture deployment* [Master's thesis, Massachusetts Institute of Technology]. MIT Libraries. https://hdl.handle.net/1721.1/155419

Outreach Efforts

None.

Student Involvement

None.

Plans for Next Period

None.



Project 082(A) CAEP Stringency Analysis Modeling

Georgia Institute of Technology

Project Lead Investigators

Prof. Dimitri N. Mavris
Director, Aerospace Systems Design Laboratory (ASDL)
School of Aerospace Engineering
270 Ferst Dr, Mail Stop 0150
Georgia Institute of Technology
Atlanta, GA 30332-0150
404-894-1557
dimitri.mavris@ae.gatech.edu

Dr. Michelle Kirby
Chief, Civil Aviation Division
Aerospace Systems Design Laboratory
School of Aerospace Engineering
270 Ferst Dr, Mail Stop 0150
Georgia Institute of Technology
Atlanta, GA 30332-0150
404-385-2780
michelle.kirby@ae.gatech.edu

University Participants

Georgia Institute of Technology (Georgia Tech)

- P.I.s: Dr. Dimitri N. Mavris, Dr. Michelle Kirby
- FAA Award Number: 13-C-AJFE-GIT-117
- Period of Performance: September 21, 2022, to March 31, 2025
- Task:
  1. Development of Future Aviation Technology Portfolio for Trends Analysis

Project Funding Level

The Federal Aviation Administration (FAA) provided $514,500 in funding, and Georgia Tech has agreed to a total of $514,500 in matching funds. This total includes salaries for the project director, research engineers, and graduate research assistants, as well as funds for computing, financial, and administrative support, including meeting arrangements. Georgia Tech has also agreed to provide tuition remission for the students, paid from state funds.

Investigation Team

Prof. Dimitri N. Mavris (P.I.), Task 1
Dr. Michelle Kirby (co-P.I.), Task 1
Dr. Holger Pfaender (research engineer), Task 1
Dr. Jiacheng Xie (research engineer), Task 1
Mr. Srikanth Tindivanam Varadharajan (graduate researcher), Task 1
Mr. Kevin Florian (graduate researcher), Task 1

Project Overview

This project has provided technical support to the FAA for the assessment of the 13th cycle of the International Civil Aviation Organization's (ICAO) Committee on Aviation Environmental Protection (CAEP/13) stringency analysis, including cost estimates of various stringency options (SO). Prior CAEP stringency analysis included a cost-benefit assessment of



different scenarios on the basis of outdated information and relied on industry subject-matter input. This project has enhanced and updated the assumptions, on the basis of a quantitative assessment of technological benefits and the costs associated with achieving those benefits. The results will provide the FAA with a data-driven process for decision making, including the interdependencies between fuel burn and noise, as well as the costs associated with their mitigation.

Task 1 – Development of Future Aviation Technology Portfolio for Trends Analysis

Georgia Institute of Technology

Objective

During this period of performance, the CAEP/13 analysis support had finalized and focus turned towards preparation for the CAEP/14 trends analysis. As such, the objective of this task to prepare for the next cycle is to synthesize technology assessments from multiple academia and industry studies in recent years and develop a unified technology portfolio for predicting future aircraft performance improvements to support the trends analysis. ASDL at Georgia Tech has conducted numerous technology studies for the FAA, National Aeronautics and Space Administration (NASA), and other entities over the years. Each study employed different scopes, assumptions, methodologies, reference aircraft, resulting in diverse technology characterization across analyses. These inconsistencies arise from various approaches. For example, ICAO's Long Term Aspirational Goals (LTAG) (ICAO, 2022) and Independent Expert Integrated Review (IEIR) (ICAO, 2017) follow a top-down methodology using aggregated technology "buckets" representing combined effects across time frames 2030-2050, while NASA's Advanced Air Transport Technology (AATT) (Georgia Tech, 2019) uses a bottom-up approach evaluating individual technologies. Discrepancies between LTAG and IEIR include varying levels of conservative assumptions.

The goal of this task is to create a consolidated technology database providing comprehensive and consistent technology assessments for any stakeholder, including the FAA and NASA. This database will incorporate overlapping technologies identified across LTAG, IEIR and AATT with updated findings from recent academic and industry publications post 2020, ensuring the database reflects current technology predictions along with technology readiness levels (TRL) and compatibility assessments.

Research Approach

The first step was to establish a correlation between the overlapping LTAG and IEIR technologies' impact prediction values. This information would help identify how each one of them approached future prediction and assist in implementing a similar approach for this task. Once the overlapping technologies between IEIR & LTAG were identified, they were also matched with similar technologies in the AATT report. These were documented to be worked on first. Then these technologies were consolidated into subgroups of technologies such as aerodynamics, structures, composites, and propulsion.

A comprehensive literature review was conducted focusing on individual technologies with the highest impacts. The review targeted publications from official and reputable sources specifically documenting improvements since 2020. Technologies from AATT were reviewed and incorporated into expanding the library. For each technology, recent findings were documented and compared against previous claims from LTAG, IEIR, and AATT, with emphasis on quantifying performance impacts and corresponding implementation in Georgia Tech's Environmental Design Space (EDS) tool. For each technology in the consolidated library, the team documented estimated years to TRL level 9, quantified performance impacts, and identified technological incompatibilities. The database structure is set up such that it supports both bottom-up and top-down technology assessments, ensuring its impact can be applied across different aircraft types, classes, and project requirements.

Aerodynamic Technologies

Aerodynamic technologies aim to decrease aircraft drag and noise. Aerodynamic technologies and their impact play a significant role in predicting the future fleet of aircraft. Current review classifies aero technologies broadly into two categories based on the type of drag they reduce and how they achieve improvement in aerodynamic efficiency.

The technologies that correspond to reducing the viscous drag are riblets, natural laminar flow control, excrescence reduction, and hybrid laminar flow control.



a. Riblets: Riblets are small rectangular fences that create spanwise viscous forces acting on the turbulent boundary layer to reduce drag. This technology is incompatible with morphing surfaces and select advanced composite technologies.
b. Natural laminar flow control (NLFC): NLFC attempts to increase the region of laminar flow through airfoil design, thereby decreasing wing skin friction drag. Incompatible with DRE and Hybrid Laminar Flow Control (HLFC).
c. Hybrid laminar flow control (HLFC): HLFC is an active technique that uses suction to delay airflow transition from laminar to turbulent, improving aerodynamic efficiency. Incompatible with DRE, and some composite technologies influence the performance of HLFC.
d. Excrescence drag reduction: Excrescence drag reduction refers to all surface imperfections and irregularities leading to a significant source of airframe drag. This technology has interactions with NLFC, HLFC, and riblets technologies.

Table 1 summarizes the evolution of key drag reduction technologies, comparing original impact claims with recent studies findings. Riblets, initially projected to achieve 5-8% skin friction drag reduction with 2-3% total drag reduction (Walsh, 1986; Viswanath, 2002; El-Samni et al., 2007; Bushnell & Hefner, 1990), now demonstrates 4-9.9% skin friction reduction but only a 0.8% total drag reduction (Cornish, 2024; Smith & Yagle, 2025). Natural laminar flow control, originally had the capacity to maintain up to 70% laminar flow with suction (Joslin, 1998), and recent flight demonstration validated through flight test puts its around 50% laminar flow over the wing (Gibson et al., 2021). For hybrid laminar flow control with suction device positioned at 15% chord achieves 50-60% laminar flow (Green, 2008) and recent studies shows that this technology additionally delivers up to 4% reduction in fuel consumption (Clean Aviation, 2023). Excrescence drag reduction technologies was aimed at reducing the 15-24% of profile drag caused due to surface imperfections, which accounted for 8-12% of cruise drag (Kundu et al., 1998), now achieves a fuel burn reduction of 1-5% (Pfeiffer & Lednicer, 2014; Hue & Molton, 2020; Cretin et al., 2024).

Table 1. Aerodynamic technology aircraft drag results comparison.

Technology	Original Impact	Recent study
Riblets	5-8% skin friction drag reduction (Walsh, 1986) 2-3% total drag reduction (Viswanath, 2002; El-Samni et al., 2007; Bushnell & Hefner, 1990)	4-9.9% skin friction drag reduction (Cornish, 2024) 0.8% total drag reduction (Smith & Yagle, 2025)
Natural Laminar Flow Control	Up to 70% laminar flow on certain wings with suction (Joslin, 1998)	Flight test demonstrated natural laminar flow over 50% of the wing (Gibson et al., 2021) Aero shape optimization showed a 10% reduction in total drag (Husain et al., 2024)
Hybrid Laminar Flow Control	Suction device placed at 15% of the chord typically yields 50-60% laminar flow (Green, 2008)	Up to 4% reduction in fuel consumption (Clean Aviation, 2023)
Excrescence Drag Reduction	Surface imperfections account for 15-24% of profile drag, or 8-12% of cruise drag (Kundu et al., 1998)	Cruise fuel burn reductions of up to 1-5% (Pfeiffer & Lednicer, 2014; Hue & Molton, 2020; Cretin et al., 2024)

Another set of aerodynamic technologies that contribute to improvement to aerodynamic performance is Adaptive Aeroelastic Wing Shape Control. Current and future-generation aircraft wing technologies are moving towards lightweight, flexible, high-aspect-ratio wing designs. Flexible high-aspect ratio wings reduce off-design drag, gust sensitivities, and flutter risk. Adaptive aeroelastic wing shape control is the dynamic adjustment of a wing's shape during flight to optimize its aerodynamic performance, which maximizes aerodynamic efficiency by maintaining optimal lift-to-drag (L/D) ratio throughout the flight.

a. Variable-camber continuous trailing-edge flap (VCCTEF): VCCTEF provides continuous control surfaces with reduced drag compared to traditional control surfaces, as they allow for active wing shaping and eliminate gaps between control surfaces. These systems minimize drag during cruise and off-design by adjusting the camber of the wing. Recent studies found cruise drag reduction of 1-5% (Reist et al., 2022) and total drag reduction of up to 8.4% (Nguyen et al., 2019; Ting et al., 2018). This technology is incompatible with cruise slotted flap, continuous distributed control surface.



b. Adaptive wing variable camber: This technology alters the wing geometry in real-time to improve aerodynamic performance in different flight conditions, mostly applied to trailing-edge wing shapes. 5% increase in aerodynamic efficiency is expected (Pecora, 2021). This technology is incompatible with continuously distributed control surfaces and slotted flaps.
c. Advanced winglets: These wingtip devices are designed to reduce induced drag by weakening wingtip vortices, with up to 6.1% L/D improvement leading to a 3-5% fuel saving (Segui et al., 2021). Incompatible with certain active control surfaces.
d. Morphing wing: These are shape-adaptive wing structures that modify geometry in-flight (camber, twist, span) to optimize aerodynamic efficiency at each flight phase with seamless shape transitions. They are expected to reduce drag by 3-10% (Cumming et al., 2016; Giuliani et al., 2022), reduce fuel burn by 5-7% (Cumming et al., 2016; Pecora, 2021), and reduction in wing structural weight and approach noise is also expected (Giuliani et al., 2022). Morphing wings are incompatible with wingtip devices and highly rigid structures, and they interact with advanced composites.

Structure/Composite Technologies
Structural technologies help decrease aircraft operating empty weight. Composite technologies reduce aircraft structural weight by using materials such as fiber metal laminates, glass fiber, and other materials that can replace traditional metallic materials such as aluminum. Composite structures can be applied to smaller elements, such as elevators, as well as complex structures, like entire wings and fuselage sections.

a. Damage-arresting stitched composites: This technology integrates skins, stiffeners, and joints into condensed composites using stitching, which arrests delamination and improves damage tolerance for a 32-47% increase in flexural improvements with optimized stitch angles (Alaziz et al., 2024). This technology is incompatible with continuous distributed control surfaces.
b. Tow-steered composites: Tow-steered composite ply can be oriented along the curvilinear structure direction compared to straight-fiber laminates, thereby reducing the need for overlap, reducing overall weight with wing weight reduction of 6.3-14% for high aspect wing (Brooks et al., 2017) and fuel burn reduction of 0.4-2.4% (Brooks et al., 2020; Brooks et al., 2017; Stodieck et al., 2017). They are incompatible with damage-arresting stitched composites, unitized metallic structures, and advanced sandwich composites.
c. Advanced load alleviation: Load alleviation on the wings aims to reduce structural requirements by lowering root bending moments by actively using flight control surfaces to counter the bending moment induced by maneuvers or gusts. Advantages include reduced wing weight by reducing the material used to support bending moments, fuel burn reduction between 11 and 13.3% (Breitenstein et al., 2024; Xu & Kroo, 2014), and drag reduction up to 1.8% (Krengel, 2022). This technology requires a fly-by-wire control system, and when combined with laminar flow technology, fuel burn reduction increases notably (Xu & Kroo, 2014).
d. Active structural control: This flight control technology integrates actuators and sensors into an aircraft's wing structure to actively manipulate structural responses. Active structural control enables flexible wings, which enables lighter structures and higher aerodynamic efficiencies. Also, it supports active flutter suppression and gust load alleviation. It achieves a wing weight reduction of 10-20% (Stalla et al., 2024; Takarics et al., 2020) and 1-5% fuel burn reduction (Toffol et al., 2024). It is possibly incompatible with VCCTEF for trailing-edge flap.
e. Advanced sandwich composites: These composites are a structural technology consisting of two thin composite face plates and a lightweight core. The face plates resist in-plane and bending loads, while the core resists transverse forces. Advantages include 5-10% airframe weight reduction depending on the sandwich composite technology. It is incompatible with damage-arresting stitched composites, unitized metallic structures, and tow-steered composites.

Milestones

- Established a correlation between LTAG and IEIR technology impact predictions and identified discrepancies.
- Consolidated technologies mentioned in LTAG, IEIR, and AATT into one database.
- Completed review of aerodynamic technologies and structural technologies that were found common across all three reports.
- Reviewed additional technologies from AATT that were related to core technologies but were not explicitly mentioned either in LTAG not IEIR.



Major Accomplishments

- Reviewed and documented a total of eight aerodynamic technologies, ranging from Riblets, HLFC, and NLFC to Advanced Wing Shape Control technologies that lead to improving aerodynamic performance. These technologies were explored in detail with publications in recent times to reflect newer findings and enable better future aircraft models.
- Reviewed a total of five structural technologies that would help lower the operating weight of the aircraft, either through lighter composite materials, reducing loads carried by the wing, or active control surfaces.

Publications

None.

Outreach Efforts

Attended ASCENT meetings.

Awards

None.

Student Involvement

This task involves two graduate students, Srikanth Tindivanam Varadharajan and Kevin Florian.

Plans for Next Period

- Complete the remaining set of composite technologies. Once all composite technologies have been identified, create a compatibility matrix that accounts for incompatibility between different composite technologies.
- Review other subgroups of technologies under systems integration and flight control.
- Review folding wing tip technology and derive a regression model for wing weight penalty as a function of wing fold location. Use this model to work with Task 2 to explore their infeasible case with relaxed constraints for wingspan.
- Collaborate with Task 3 to add propulsion technology to the database.

References

Alaziz, R., Saha, S., & Sullivan, R. W. (2024). Effects of 3D Periodic Stitch Patterns on-the-flexural-properties-of-polymer-matrix-composite, in *AIAA SCITECH 2024 Forum* (AIAA 2024-2082), Orlando, Florida. https://doi.org/10.2514/6.2024-2082

Breitenstein, C., Müller, J., Hillebrand, M., Woidt, M., Haupt, M., & Radespiel, R. (2024). Fluid–Structure Coupled Analysis of Maneuver Load Alleviation on a Large Transport Aircraft. *Journal of Aircraft, 61*(4), 1247–1261. https://doi.org/10.2514/1.C037648

Brooks, T. R., Kennedy, G., & Martins, J. R. R. A. (2017). High-fidelity Multipoint Aerostructural Optimization of a High Aspect Ratio Tow-steered Composite Wing. In *58th AIAA/ASCE/AHS/ASC Structures, Structural Dynamics, and Materials Conference* (AIAA 2017-1350), Grapevine, Texas. https://doi.org/10.2514/6.2017-1350

Brooks, T. R., Martins, J. R. R. A., & Kennedy, G. J. (2020). Aerostructural Tradeoffs for Tow-Steered Composite Wings. *Journal of Aircraft, 57*(5). https://doi.org/10.2514/1.C035699

Bushnell, D., & Hefner, J. N. (1990). *Viscous drag reduction in boundary layers* (Vol. 123). American Institute of Aeronautics and Astronautics. https://doi.org/10.2514/4.865978

Clean Aviation. (2023). Hybrid Laminar Flow Control on Tails & Wing. https://clean-aviation.eu/research-and-innovation/clean-sky-2/clean-sky-2-achievement-report/clean-sky-2s-key-achievements/hybrid-laminar-flow-control-on-tails-wing#:~:text=The%20technical%20foundations%20for%20high%2Dperformance,future%20transport%20aircraft%20was%20established

Cornish, I. (2024). Exploring hierarchical nested riblet technology for reducing turbulent drag. *Scilight, 2024*(42). https://doi.org/10.1063/10.0032498

Cretin, A., Molton, P., & Defréville, F. (2024). Surface roughness effects on transonic aircraft performance: Experimental/numerical comparisons. *Aerospace Science and Technology, 146*, 109275. https://doi.org/10.1016/j.ast.2024.109507



Cumming, S. B., Smith, M. S., Ali, A., Bui, T. T., Ellsworth, J., & Garcia, C. A. (2016). Aerodynamic flight-test results for the Adaptive Compliant Trailing Edge. In *AIAA Atmospheric Flight Mechanics Conference* (AIAA 2016-3855), Washington, D.C. https://doi.org/10.2514/6.2016-3855

El-Samni, O. A., Chun, H. H., & Yoon, H. S. (2007). Drag reduction of turbulent flow over thin rectangular riblets. *International Journal of Engineering Science, 45*(2-8), 436-454. https://doi.org/10.1016/j.ijengsci.2007.03.002

Georgia Tech. (2019). *Advanced Air Transportation Technologies Project Final Report* (No. NASA/CR-2019-220395). Georgia Institute of Technology, Atlanta, Georgia.

Gibson, T., Soucheleau, B., & Rogers, N. (2021, September 6-10). BLADE - Natural Laminar Flow Flight Testing. In *32nd Congress of the International Council of the Aeronatical Sciences*, Shanghai, China.

Giuliani, M., Dimino, I., Ameduri, S., & Pecora, R. (2022). Status and perspectives of commercial aircraft morphing. *Biomimetics, 7*(1), 11. https://doi.org/10.3390/biomimetics7010011?urlappend=%3Futm_source%3Dresearchgate.net%26utm_medium%3Darticle

Green, J. (2008). Laminar flow control – back to the future? In *AIAA 38th Fluid Dynamics Conference and Exhibit* (AIAA 2008-3738), Seattle, Washington. https://doi.org/10.2514/6.2008-3738

Hue, D., & Molton, P. (2020). Turbulent drag induced by low surface roughness at transonic speeds: Experimental/numerical comparisons. *Physics of Fluids, 32*(12), 125111. https://doi.org/10.1063/1.5143068

Husain, F., Simmons, I., & Zingg, D. (2024). Application of Aerodynamic Shape Optimization to Swept Natural Laminar Flow Wings. In *AIAA AVIATION FORUM AND ASCEND 2024 (*AIAA 2024-3507), Las Vegas, Nevada. https://doi.org/10.2514/6.2024-3507

ICAO. (2017). *ICAO Independent Expert Integrated Technology Goals Assessment and Review for Engines and Aircraft.* Committee on Aviation Environmental Protection (CAEP), International Civil Aviation Organization, Montreal, Quebec.

ICAO. (2022). *Report on the Feasibility of a Long-Term Aspirational Goal, Appendix M3, Technology Subgroup Report.* International Civil Aviation Organization, Montreal, Quebec. https://www.icao.int/sites/default/files/sp-files/environmental-protection/LTAG/Documents/ICAO_LTAG_Report_AppendixM3.pdf

Joslin, R. D. (1998). *Overview of Laminar Flow Control* (No. NASA/TP-1998-208705). NASA Langley Research Center, Hampton, Virginia. https://ntrs.nasa.gov/api/citations/19980232017/downloads/19980232017.pdf

Krengel, M. D. (2022). Effects of Wing Elasticity and Basic Load Alleviation on Conceptual Aircraft Designs. In *AIAA SCITECH 2022 Forum* (AIAA 2022-0126), San Diego, California. https://doi.org/10.2514/6.2022-0126

Kundu, A. K., Watterson, J., Raghunathan, S. (2012). A Multi-Disciplinary Study of Aircraft Aerodynamic Surface Smoothness Requirements to Reduce Operating Cost. In *7th AIAA/USAF/NASA/ISSMO Symposium on Multidisciplinary Analysis and Optimization*, St. Louis, Missouri. https://doi.org/10.2514/6.1998-4874

Nguyen, N., Cramer, N., Hashemi, K. E., Drew, M., Wise, R., Boskovick, J., Precup, N., Mundt, T., Livne, E. (2019). Real-Time Adaptive Drag Minimization Wind Tunnel Investigation of a Flexible Wing with Variable-Camber Continuous Trailing-Edge Flap System. In *AIAA Aviation 2019 Forum* (AIAA-2019-3156), Dallas, Texas. https://doi.org/10.2514/6.2019-3156

Pecora, R. (2021). Morphing wing flaps for large civil aircraft: Evolution of a smart technology across the Clean Sky program. *Chinese Journal of Aeronautics, 34*(7), 13-28. https://doi.org/10.1016/j.cja.2020.08.004

Pfeiffer, J. A., & Lednicer, D. A. (2014). A study of airplane excrescence drag. In *14th AIAA Aviation Technology, Integration, and Operations Conference* (AIAA 2014-2866), Atlanta, Georgia. https://doi.org/10.2514/6.2014-2866

Reist, T. A., Koo, D., & Zingg, D. W. (2022). Aircraft Cruise Drag Reduction Through Variable Camber Using Existing Control Surfaces. *Journal of Aircraft, 59*(6). https://doi.org/10.2514/1.C036754

Segui, M., Abel, A., Botez, R. M., & Ceruti, A. (2021). New aerodynamic studies of an adaptive winglet application on the Bombardier CRJ700. *Biomimetics, 6*(4), 54. https://doi.org/10.3390/biomimetics6040054

Smith, B. R., & Yagle, P. (2025). RANS Turbulence Model for Drag Reducing Riblets and Its Predictions for Aerodynamic Applications. In *AIAA SCITECH 2025 Forum* (p. 0044). https://doi.org/10.2514/6.2025-0044

Stalla, F., Kaufmann, D., Krüger, W. R., & Reimer, L. (2024). Wind Tunnel Testing of an Active Gust Load Alleviation System for Flexible Wings. In *AIAA Scitech 2024 Forum,* Orlando, Florida.

Stodieck, O., Cooper, J. E., Weaver, P. M., & Kealy, P. (2017). Aeroelastic Tailoring of a Representative Wing Box Using Tow-Steered Composites. *Journal of Aircraft, 55*(4). https://doi.org/10.2514/1.J055364

Takarics, B., Petres, Z., Abraham, S., Vanek, B., & Molnar, L. (2020). Active Flutter Suppression Flight Control Design for the FLEXOP Demonstrator Aircraft. *IFAC-PapersOnLine, 53*(2).

Ting, E., Chaparro, D., Nguyen, N., & Fujiwara, G. E. C. (2018). Optimization of Variable-Camber Continuous Trailing-Edge Flap Configuration for Drag Reduction. *Journal of Aircraft, 55*(6). https://doi.org/10.2514/1.C034810



Toffol, F., Lanz, M., Rozhdestvensky, K. V., et al. (2024). Comparative Analysis of Gust Load Alleviation via Active Control and Passive Folding Wingtips for UHARW Aircraft. In *AIAA AVIATION Forum and ASCEND 2024,* Las Vegas, Nevada.

Viswanath, P. R. (2002). Aircraft viscous drag reduction using riblets. *Progress in Aerospace Sciences, 38*(6-7), 571-600. https://doi.org/10.1016/S0376-0421(02)00048-9

Walsh, M. J. (1986, December). Riblets for aircraft skin-friction reduction. In *Langley Symposium on Aerodynamics*, Volume 1. NASA Langley Research Center, Hampton, Virginia. https://ntrs.nasa.gov/api/citations/19880005573/downloads/19880005573.pdf

Xu, J., & Kroo, I. (2014). Aircraft Design with Active Load Alleviation and Natural Laminar Flow. *Journal of Aircraft, 51*(5). https://doi.org/10.2514/1.C032402



Project 082(B) Integrated Noise and CO_2 Standard Setting Analysis

Massachusetts Institute of Technology

Project Lead Investigator

Raymond L. Speth
Senior Research Scientist
Department of Aeronautics & Astronautics
Massachusetts Institute of Technology
77 Massachusetts Ave, Building 33-316
Cambridge, MA 02139
617-253-1516
speth@mit.edu

University Participants

Massachusetts Institute of Technology (MIT)

- P.I.: Dr. Raymond L. Speth
- FAA Award Number: 13-C-AJFE-MIT, Amendment Nos. 095, 102, 115, 119, 133, and 143
- Period of Performance: June 14, 2022, to August 31, 2027 (with the exception of funding and cost-sharing information, this report covers the period from October 1, 2024, to September 30, 2025)
- Tasks:
  1. Engagement in CAEP policy revisions
  2. Development of an aircraft conceptual design tool for policy analysis
  3. Aircraft design and impacts studies

Project Funding Level

ASCENT Project 082(B) has received $1,400,000 Federal Aviation Administration (FAA) funding and $1,400,000 matching funds. Sources of matching funds are approximately $185,200 from MIT, plus third-party in-kind contributions of $274,000 from Savion Aerospace Corp., and $532,000 from NuFuels, LLC, and $408,800 from Earth Force Technologies.

Investigation Team

Dr. Raymond L. Speth (P.I.), Tasks 1, 2, & 3
Dr. Prakash Prashanth (co-investigator), Tasks 2 & 3
Dr. Jayant Sabnis (co-investigator), Task 1
Jonas J. Gonzalez (PhD student), Tasks 1 & 2
Aditeya Shukla (PhD student), Tasks 2 & 3

Project Overview

To evaluate the economic reasonableness of proposed aircraft environmental standards, the International Civil Aviation Organization's (ICAO) Committee on Aviation Environmental Protection (CAEP) requires tools for assessing the impacts of technologies and design changes intended to control aircraft noise and emissions, and for evaluating the costs of implementing such changes to aircraft and engine designs. Existing methods used to support decision-making in previous CAEP stringencies do not represent modern aircraft and propulsion designs and technologies. The goal of this project is to develop new tools that address the shortcomings of the previous methods, in support of CAEP/13 and CAEP/14 stringency analyses.



Task 1 – Engagement in CAEP Policy Revisions

Massachusetts Institute of Technology

Objective

A primary contribution of this project is continued support of the United States Research Team (USRT) for CAEP and its constituent Working Groups (WG). This support includes technical review, studies, and proposals that inform the WG's stringency analyses, and is intended to provide accurate assessments of commercial aviation's technological capability for rulemaking. This reporting period spanned the conclusion of CAEP/13 (Integrated Dual Stringency [IDS] of noise and fuel burn) and the initiation of CAEP/14 (nitrogen oxide stringency).

Research Approach

The inputs provided to the stringency analysis are intended to modify its technology and policy assumptions. These inputs include examination of existing aircraft technology, presentation of historical trends, and technical analyses of aircraft and engines. Specific to this reporting period, proposals were put forth for (i) the stringency analysis's analytical space and limit line options as follows from extensive analysis of the Engine and Emissions Data Bank and (ii) the types of anticipated technology responses as follows from an engine cycle design demonstration highlighting the sensitivity of emissions of nitrogen oxides (NO_x) to engine pressure ratio (OPR).

Milestones

- CAEP/13 Conclusion
  - Contributed to and reviewed the IDS final report. The decisions from the CAEP/13 meeting will be reflected in updates to ICAO Annex 16, Volumes I and III.
- CAEP/14 Initiation
  - Prepared proposals to be presented at the WG3/3 meeting advocating for (1) analyzing a broad analytical space that enables reduced OPR-scaling in the limit lines, and (2) flexibility in the technology assumptions for OPR of engines designed in response to new emissions limits. These proposals would enable a robust reflection of the capabilities of current and near-future engine technologies.

Publications

None.

Outreach Efforts

- Presented the analyses to the US CAEP participants and WG members to collect feedback during regular teleconferences.
- Submitted analysis proposals for consideration and adoption during quarterly in-person WG3 meetings.

Awards

None.

Student Involvement

MIT Graduate student, Jonas J. Gonzalez, conducted and presented part of the analyses presented in this work to CAEP WGs.

Plans for Next Period

- Apply lessons learned and methods developed during the CAEP/13 stringency process to contribute to emissions standards being updated during CAEP/14.
- Develop additional analyses as input to the technology response process.



Task 2 – Development of an Aircraft Conceptual Design Tool for Policy Analysis

Massachusetts Institute of Technology

Objective

The goal of this task is to enhance the capability of our Julia[1]-based aircraft conceptual design software, Transport Aircraft System Optimization in Julia (TASOPT.jl), to incorporate new disciplines and components, including noise analysis and optimization. The objective is to use this tool to estimate the sensitivities of design changes to the engine, structures, and aerodynamics on metrics of performance, such as fuel burn, emission of NO_x, and certification noise.

Research Approach

Development of TASOPT.jl during the reporting period centered around two thrusts: (i) component model enhancement and (ii) enhancing user-accessibility and transparency. While the former supports enhanced fidelity and expanded applicability, the latter focus is essential for the long-term development of TASOPT.jl and its future use in CAEP.

New model capabilities include support for interpolated compressor maps, a simplistic specific-fuel-consumption-based engine model, ducted fan modelling (for electrified propulsion architectures), and landing gear geometry modelling. To enable integration with the Python Noise Assessment (pyNA) model, aerodynamic performance models are being extended and validated to cover landing-takeoff operations (LTO) in with higher fidelity. A review of the "basket" of relevant technology insertions to be modelled was also initiated to guide this thrust in the future.

Documentation was written about the new capabilities as part of the accessibility thrust. Beyond this, user-friendly data structures were introduced and integrated through the codebase, along with developer-friendly interfaces that simplify the integration of novel component models. Additional enhancements include miscellaneous documentation updates and expansions, new user-facing functions for common analyses (e.g., payload-range), plotting utilities, and various bug patches.

Milestones

A paper describing TASOPT.jl was accepted to the *Journal of Open Source Software (JOSS)*.

Publications

Prashanth, P., Gomez-Vega, N., He, S., Shukla, A., Gonzalez, J. J., Bobadilla, D. S., Lee, K., Ranjan, P., Zahid, S. S., Abel, J., Drela, M., & Speth, R. (2025). TASOPT.jl: A Julia package for conceptual commercial transport aircraft design. *Journal of Open Source Software, 10*(113), 8521. https://doi.org/10.21105/joss.08521

Outreach Efforts

Continued publication of updates to TASOPT.jl on GitHub (github.com/MIT-LAE/TASOPT.jl).

Awards

None.

Student Involvement

MIT graduate students, Jonas J. Gonzalez and Aditeya Shukla, were engaged in code development and documentation.

Plans for Next Period

- Continue to expand TASOPT.jl functionality and documentation toward its application as a transparent source of data in the CAEP tech response process. Development focus is pulled toward engine modelling and NO_x by the current CAEP cycle. Noise prediction also continues to be a development target, though it awaits integration of aerodynamic performance modelling for LTO operations.

[1] Julia is a high-performance, open-source, general purpose programming language designed for scientific computing, machine learning, and data mining.



- Benchmark the included baseline models against trusted performance data of existing aircraft of varying sizes. This will all for the accuracy of the current models to be characterized, and a metric to be established for further model improvement.

Task 3 – Aircraft Design and Impacts Studies

Massachusetts Institute of Technology

Objectives

The objectives of this task are to (1) analyze the environmental impact of near-future technology insertions across three aircraft subsystems: propulsion, structures, and aerodynamics, (2) quantify the climate and air quality impacts resulting from purely fuel efficiency driven design and optimization, and (3) assess and compare results across three aircraft categories—narrow body, wide body, and regional jet—to understand technology effects across different baseline aircraft and operational profiles.

Research Approach

- Defined technology insertion scenarios across propulsion (engine upgrades), structures (advanced materials for primary structures), and aerodynamics (drag reduction improvements) for each aircraft category.
- Developed integrated assessment framework to insert technology, design and optimize aircraft and then evaluate multiple environmental impact pathways from emissions such as carbon dioxide (CO_2), NO_x, sulfur oxides (SO_x), etc.
- Used monetization of environmental impacts to estimate present day values of future environmental damages and compare climate impacts, air quality impacts, and economic trade-offs between different technologies.

Milestones

- Established that fuel efficiency improvements alone do not serve as a reliable proxy for overall environmental impact reduction, revealing important trade-offs between climate and air quality effects.
- Quantified that engine upgrades, while improving fuel efficiency through higher pressure ratios, generally increase NO_x emissions and negatively affect air quality unless paired with other technologies that provide substantial fuel burn reductions.
- Demonstrated that structural material improvements offer environmental benefits comparable to engine upgrades on a net present value basis, with reduced operating weight leading to decreased fuel consumption and lower NO_x emissions across all aircraft categories.

Publications

Shukla, A., Prashanth, P., & Speth, R. L. (2025, July). Impact of Efficiency-Driven Aircraft Technology Improvements on Climate and Air Quality (AIAA 2025-3502). *AIAA AVIATION FORUM AND ASCEND 2025*. https://doi.org/10.2514/6.2025-3502

Outreach Efforts

Presented at the AIAA AVIATION Conference in Las Vegas, Nevada in July 2025 during the technical session “Aircraft Operational and System Studies.”

Awards

None.

Student Involvement

This work was primarily conducted by MIT graduate student Aditeya Shukla.

Plans for Next Period

Expand on the existing work, which is based on optimizing aircraft for minimum mission fuel consumption, to consider alternative optimization targets that include environmental impacts. Analysis of these results will help to understand design decisions and policies that can lead to reduced environmental impacts while avoiding significant fuel consumption and cost trade-offs.



Project 083 NO_x Cruise/Climb Metric System Development

Massachusetts Institute of Technology

Project Lead Investigator

Raymond L. Speth
Principal Research Scientist
Department of Aeronautics & Astronautics
Massachusetts Institute of Technology
77 Massachusetts Ave
Building 33-310
Cambridge, MA 02139
617-253-1516
speth@mit.edu

University Participants

Massachusetts Institute of Technology (MIT)

- P.I.: Dr. Raymond L. Speth
- FAA Award Number: 13-C-AJFE-MIT, Amendment Nos. 103, 115, 117, 133, 137, and 143
- Period of Performance: September 19, 2022, to August 31, 2027 (reporting here with the exception of funding level and cost-sharing only for the period October 1, 2024, to September 30, 2025)
- Tasks:
  1. Evaluation of cruise nitrogen oxides (NO_x) dependence on pressure ratio
  2. Assessment of Boeing Fuel Flow Method 2's accuracy for modern engines

Project Funding Level

The Federal Aviation Administration (FAA) provided $900,000 in funding and $900,000 in matching funds were received. Sources of matching funds are approximately $129,500 from MIT, plus third-party in-kind contributions of $250,000 from NuFuels LLC, and $520,500 from Earth Force Technologies.

Investigation Team

Dr. Raymond L. Speth (P.I.), All Tasks
Sarah Reider (graduate student), Task 1
Wyatt Giroux (graduate student), Task 2

Project Overview

The International Civil Aviation Organization (ICAO) is responsible for setting emissions standards for aircraft engines to limit the environmental impacts of these emissions. To limit the impacts of aviation emissions, the FAA's Office of Environment and Energy is working with the ICAO Committee on Aviation Environmental Protection (CAEP) to consider updated emissions standards for aircraft engines by using metrics relevant to the full-flight emissions of these species, rather than only those emissions occurring during a standard landing and takeoff (LTO) cycle. Emissions standards set by ICAO will influence the development of future engine technologies, thus resulting in a reduction of emissions from future aircraft engines, and consequently improved human health and reduced environmental impacts. To this end, the FAA needs to understand and quantify how current and future standards may impact aviation emissions in the United States and worldwide, and how changes in these emissions may affect the environment and human health.

The objective of this project is to provide support for FAA decision-making related to potential certification standards that control emissions during cruise and climb, in addition to the current standards for LTO. The project includes analyses important for understanding the costs and benefits of both current standards and policies that may be proposed in the future. By providing a rational, scientific basis for decisions regarding the implementation of emissions standards, this



project contributes to an efficient implementation process and provides industry with regulatory certainty. The analyses provided in this project will allow the FAA to identify policy proposals that serve the national interest and advocate for those policies within the ICAO.

Task 1 – Evaluation of Cruise NO_x Dependence on Pressure Ratio

Massachusetts Institute of Technology

Objective

The objective of this task was to assess the uncertainty associated with marginal social costs of NO_x and carbon dioxide (CO_2) and their implications for a potential cruise NO_x standard.

Research Approach

The basis of this task involved developing a modelling framework for estimating uncertainty in monetized environmental cost for full-flight missions. The Transport Aircraft System OPTimization (TASOPT) aircraft design tool (Prashanth et al., 2025) was used to estimate aircraft/engine performance on a mission level for representative narrow-body (NB), wide-body (WB), and regional jets (RJ) at a range of engine overall pressure ratio (OPR) values. This was combined with NO_x emissions characteristic curves derived from Engine Emissions Databank (EEDB) (ICAO, 2024) to obtain the average mission nitrogen oxide emission index ($EI(NO_x)$). Conventional Jet-A fuel was assumed to be used, resulting in constant $EI(CO_2)$. The Aviation Climate and Air Quality Impacts (ACAI) framework (Kim, 2023) was used to estimate marginal cost distributions for NO_x and CO_2 based on a 2019 global aviation emissions inventory generated by the Aviation Emissions Inventory Code (AEIC) (Simone et al., 2013) with Official Airline Guide (OAG) data. The impulse-normalized cost for each species given sampled marginal costs was then estimated using the marginal costs, thrust specific fuel consumption, and emissions indices for each species.

A Monte-Carlo simulation was performed using the cost distributions from ACAI to evaluate the cost response of potential cruise NO_x standards. Specifically, scenarios where a single capped value is placed on NO_x was considered. This was performed for each aircraft type for several NO_x characteristic curves representing both rich-quench-lean (RQL) and staged lean burn combustors. The examined caps were specified in terms of $EI(NO_x)$ at the climb out (C/O) LTO point as a surrogate for cruise values. Cap values between 15 g/kg and 34 g/kg were examined. In cases where the total cost did increase, the marginal cost of CO_2 was generally found to be extremely high ($\gtrsim 0.45$ \$/kg) and the probability of increased total cost reaches a maximum of around 14% for the most stringent limits considered. The OPR changes required for each engine/aircraft to meet the corresponding cap value are shown in Figure 1.

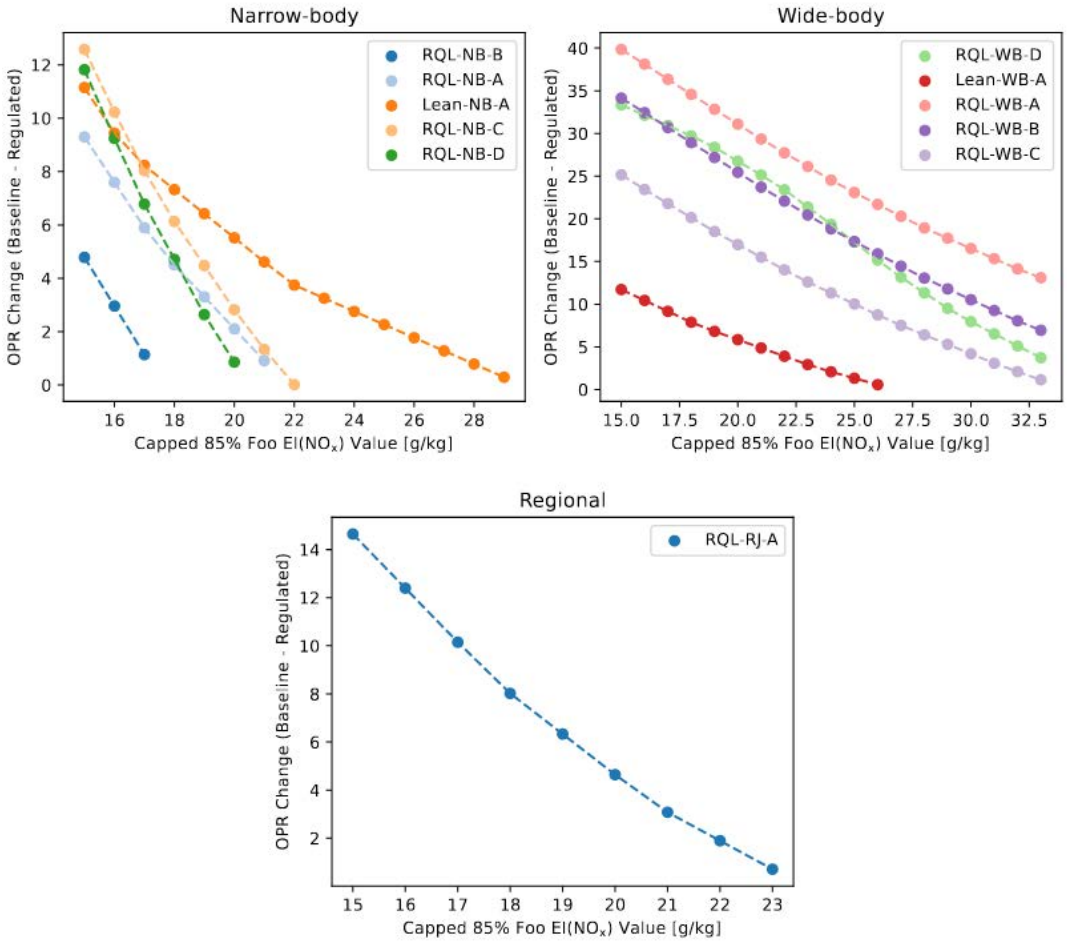


Figure 1. Change in overall pressure ratio (OPR) relative to baseline vs. cap values for each aircraft/engine combination examined. EI (NOx): nitrogen oxide emission index, NB: narrow-body, RJ: regional jet, RQL: rich-quench-lean, WB: wide-body.

Milestone

Documented the completed analysis in a master's thesis (Reider, 2025).

Major Accomplishments

The analysis demonstrated that even given uncertainty in monetized emissions models, it remains cost effective on an environmental basis to place caps on cruise NO_x. The changes in OPR required to meet aforementioned caps were also determined.

Publications

Reider, S. (2025). *Stochastic Methods for Setting Effective Aviation NO_x Policies* [Master's thesis, Massachusetts Institute of Technology]. MIT Libraries. https://dspace.mit.edu/handle/1721.1/163033

Outreach Efforts

None.



Awards
None.

Student Involvement
Graduate student Sarah Reider conducted the analyses and presented the work to the FAA.

Plans for Next Period
This task is complete.

References
ICAO. (2024). *ICAO Aircraft Engine Emissions Databank* (v30). International Civil Aviation Organization. https://www.easa.europa.eu/domains/environment/icao-aircraft-engine-emissions-databank

Kim, J. (2023). *Sensitivity of the ozone layer, climate, and public health to changes in the location of aviation emissions* [Master's thesis, Massachusetts Institute of Technology]. MIT Libraries. https://dspace.mit.edu/handle/1721.1/150205

Prashanth, P., Gomez-Vega, N., He, S., Shukla, A., Gonzalez, J. J., Bobadilla, D. S., Lee, K., Ranjan, P., Zahid, S. S., Abel, J., Drela, M., & Speth, R. (2025). TASOPT.jl: A Julia package for conceptual commercial transport aircraft design. *Journal of Open Source Software*, 10(113), 8521. https://doi.org/10.21105/joss.08521

Reider, S. (2025). *Stochastic Methods for Setting Effective Aviation NO_x Policies*. Massachusetts Institute of Technology.

Simone, N. W., Stettler, M. E. J., & Barrett, S. R. H. (2013). Rapid estimation of global civil aviation emissions with uncertainty quantification. *Transportation Research Part D: Transport and Environment, 25*, 33–41. https://doi.org/10.1016/j.trd.2013.07.001

Task 2 – Assessment of Boeing Fuel Flow Method 2's Accuracy for Modern Engines

Massachusetts Institute of Technology

Objective
The objective of this task was to ensure the Boeing® Fuel Flow Method 2 (BFFM2) is continuing to provide accurate estimates of cruise emissions given evolutions in modern engine technology since the method's development in 2006.

Research Approach
During work on cruise/climb NOx stringency assessment, numerous inconsistencies were identified in the derivation of BFFM2 (DuBois & Paynter, 2006). While many were relatively minor, two of the key assumptions of the method were determined to not follow well-understood engine cycle physics. These assumptions are made based on matching combustor inlet conditions between the evaluation point at altitude (alt) and a known point at reference sea-level static (SLS) conditions. Namely, the combustor inlet temperature is assumed to be equal ($T_{t3,alt} = T_{t3,sls}$) to ensure similarity in chemistry conditions. To ensure this, BFFM2 defines the equivalent SLS fuel flow where this condition should be met:

$$\dot{m}_{f,\text{equiv}} = \dot{m}_{f,\text{alt}} \frac{\theta_{\text{amb}}^{3.8}}{\delta_{\text{amb}}} e^{0.2M_0^2} \quad \text{(Eq. 1)}$$

In the derivation of this equivalent fuel flow, the two core assumptions under suspicion are (1) equal combustor exit temperature, $T_{t4,alt} = T_{t4,sls}$, and (2) equal corrected mass flow per unit area at combustor inlet, $D(M_{3,alt}) = D(M_{3,sls})$. The former would require equal fuel-air ratio (FAR) between the two operation points. However, this condition does not generally hold, with FAR varying significantly between sea level and altitude conditions.

The second assumption requires equal corrected flow per unit area at the combustor inlet. Corrected flow per unit area is defined as

® Boeing is a registered trademark of The Boeing Company, Seattle, Washington.

$$\frac{\dot{m}\sqrt{RT_t}}{p_t A\sqrt{\gamma}} = D(M) = M\left(1+\frac{\gamma-1}{2}M^2\right)^{-\frac{\gamma+1}{2(\gamma-1)}} \quad \text{(Eq. 2)}$$

Corrected mass flow per unit area is expressible as a function of only Mach number, another non-dimensional group. As such, it is subject to the same issue identified in the equal exit temperature assumption.

To quantify the error in these assumptions and the overall method, TASOPT (Prashanth et al., 2025) was used to determine an altitude, Mach number, and thrust schedule for a notional narrow-body aircraft. Notional narrow-body engine designs sized at 124 kN thrust were generated using the Numerical Propulsion System Simulation tool (Jones, 2007) for a range of design variables including design altitude, Mach number, and thrust, as well as component efficiencies. Each design was optimized for minimum design-point thrust-specific fuel consumption (TSFC) by varying pressure ratios, fan diameter, and turbine inlet temperature. These engines were then run through the operation schedule determined by TASOPT as well as a sweep of SLS thrust values. Using these two datasets, the point where T_{t3} matches between operation and SLS was found and the altitude and SLS values of T_{t4} and $D(M)$ were obtained. Figure 2 shows the resulting sensitivity of error in the T_{t4} assumption to the design variables, while Figure 3 shows the sensitivity for the corrected mass flow assumption. The error was time-averaged across the mission flown.

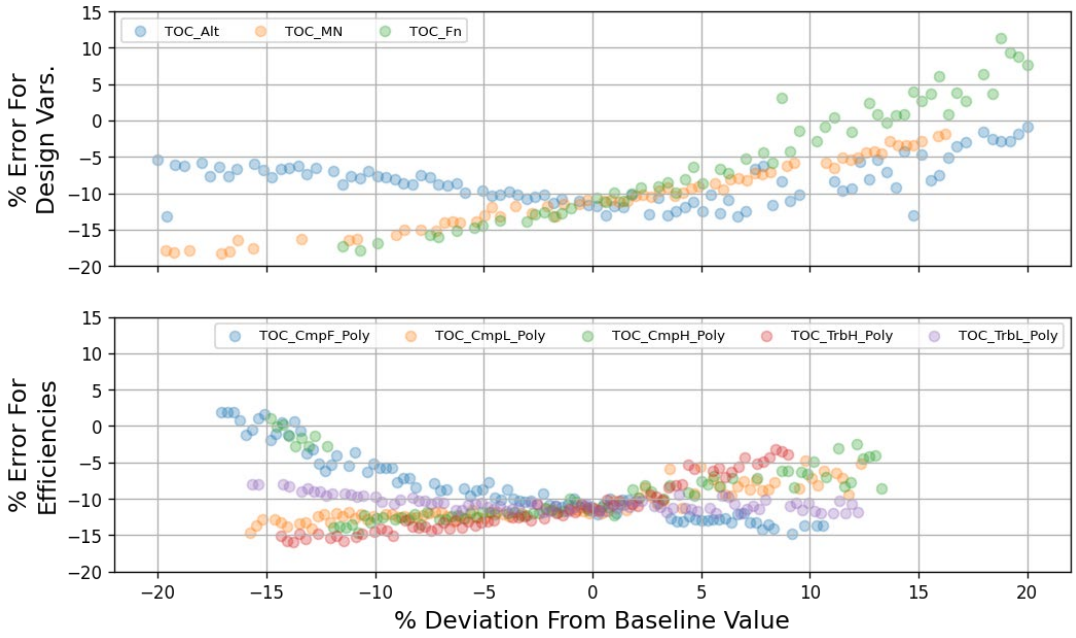


Figure 2. Time-weighted percentage error in the equal T_{t4} assumption as design variables deviate from baseline values. Higher percentage error indicates $T_{t4,alt} > T_{t4,sls}$.

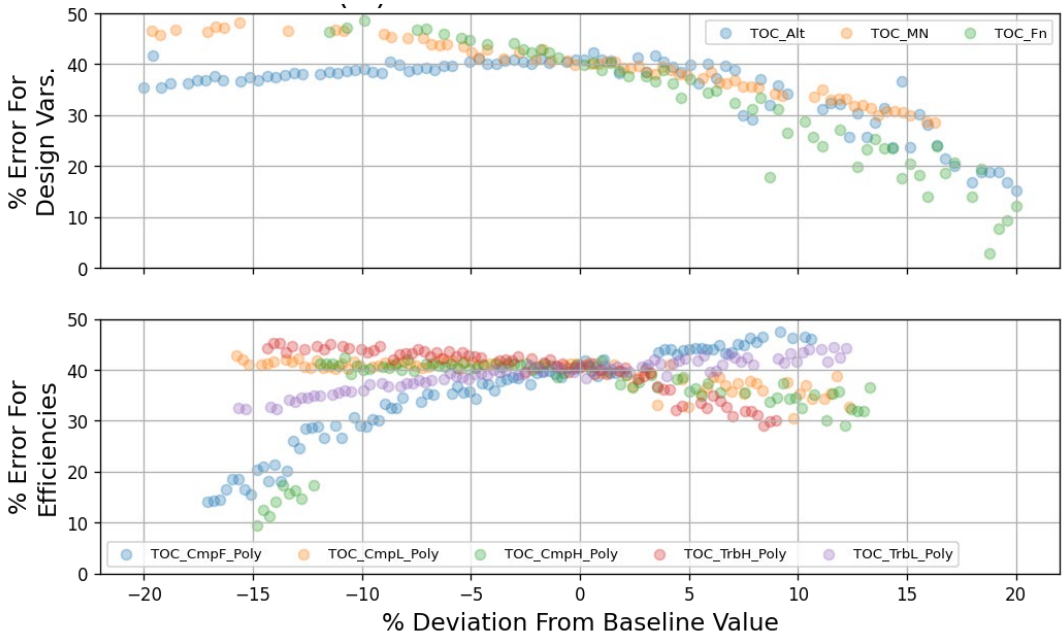


Figure 3. Time-weighted percentage error in the equal $D(M_3)$ assumption as design variables deviate from baseline values. Higher percentage error indicates $D(M_{3,alt}) > D(M_{3,sls})$.

The percentage error in assumptions was found to be consistent across a wide range of design variable values, only approaching zero for extreme cases.

Milestone
Presented the assumption error at the CAEP14-WG3/2 meeting while the analysis of the EI(NO_x) error will be presented at the upcoming CAEP14-WG3/3 meeting.

Major Accomplishments
This work demonstrates that BFFM2 maybe overpredicting cruise NO_x emissions relative to our approximations of proprietary models. This error is derived from the lack of physics-based assumptions in BFFM2's derivation.

Publications
None.

Outreach Efforts
Presented at the CAEP/14-WG3/2-ECTG meeting (June 23-27, 2025).

Awards
None.

Student Involvement
Graduate student, Wyatt Giroux, conducted the analyses and presented the work to the FAA and CAEP WG3.

Plans for Next Period
- Assess the effect of these model assumptions on mission NO_x emissions.
- Formulate a method to replace/improve BFFM2 and test this method against exiting models. The new model will attempt to use principles of non-dimensional analysis to establish a scaling relation between OPR and $\dot{m}_f$ given



publicly reported rated thrust, fuel flow, and OPR. This can then be used to obtain an improved estimate of the SLS fuel flow rate that matches the altitude T_{t3}.

References

DuBois, D., & Paynter, G. C. (2006). "Fuel Flow Method2" for Estimating Aircraft Emissions. *SAE Transactions*, *115*, 1–14. http://www.jstor.org/stable/44657657

Jones, S. M. (2007). An Introduction to Thermodynamic Performance Analysis of Aircraft Gas Turbine Engine Cycles Using the Numerical Propulsion System Simulation Code (NASA/TM-2007-214690). National Aeronautics and Space Administration. https://ntrs.nasa.gov/citations/20070018165

Prashanth, P., Gomez-Vega, N., He, S., Shukla, A., Gonzalez, J. J., Bobadilla, D. S., Lee, K., Ranjan, P., Zahid, S. S., Abel, J., Drela, M., & Speth, R. (2025). TASOPT.jl: A Julia package for conceptual commercial transport aircraft design. *Journal of Open Source Software, 10*(113), 8521. https://doi.org/10.21105/joss.08521



Project 084 Noise Modeling of Advanced Air Mobility Flight Vehicles

Massachusetts Institute of Technology

Project Lead Investigators

R. John Hansman
T. Wilson Professor of Aeronautics & Astronautics
Department of Aeronautics & Astronautics
Massachusetts Institute of Technology
Room 33-303
77 Massachusetts Ave
Cambridge, MA 02139
617-253-2271
rjhans@mit.edu

Jacqueline Huynh
Assistant Professor of Mechanical and Aerospace Engineering
4212 Engineering Gateway
Irvine, CA 92697
949-824-3561
huynhlj@uci.edu

University Participants

Massachusetts Institute of Technology (MIT)

- P.I.: Prof. R. John Hansman
- FAA Award Number: 13-C-AJFE-MIT, Amendment Nos. 112, 115, 131, and 143
- Period of Performance: January 1, 2023, to August 31, 2027
- Tasks:
  1. Identify target advanced air mobility (AAM) vehicle configurations for noise model development
  2. Identify noise modeling gaps for selected AAM configurations and operations
  3. Develop physics-based noise and flight profile model for representative AAM vehicles
  4. Incorporate noise results for representative AAM vehicles with the Aviation Environmental Design Tool (AEDT)
  5. Expand methods to additional vehicle sets
  6. Evaluate implications for noise mitigation and low-noise operations for AAM vehicles

University of California Irvine (UCI)

- P.I.: Prof. Jacqueline Huynh
- Award Number: MIT Subaward Purchase Order No. 883753
- Period of Performance: January 1, 2023, to September 30, 2026
- Tasks:
  1. Identify target AAM vehicle configurations for noise model development
  2. Identify noise modeling gaps for selected AAM configurations and operations
  3. Develop physics-based noise and flight profile model for representative AAM vehicles
  4. Incorporate noise results for representative AAM vehicles with the AEDT
  5. Expand methods to additional vehicle sets
  6. Evaluate implications for noise mitigation and low-noise operations for AAM vehicles



Project Funding Level

The Federal Aviation Administration (FAA) provided $615,000 in funding and $615,000 matching funds were received. Sources for matching funds are approximately $123,100 from MIT, and $44,900 from subrecipient U.C. Irvine, and $447,000 from Electra.aero, Inc (Electra).

Investigation Team

Massachusetts Institute of Technology

Prof. R. John Hansman (P.I.), Tasks 1-6
Brandon Hadfield (graduate student), Tasks 1-6

University of California Irvine

Prof. Jacqueline Huynh (P.I.), Tasks 1-6
Victoria Pellerito (graduate student), Tasks 1-6
Nathan Yeung (graduate student), Tasks 1-6

Project Overview

This project develops first-principles noise models of urban air mobility (UAM) and AAM vehicle configurations to make community noise predictions of these aircraft flying at various operating states. Estimated noise levels from these models will be used to develop methods needed for a UAM/AAM-compatible the AEDT to make preliminary noise estimates of these vehicles. Conventional aircraft configuration noise levels at both the source and procedural levels have been examined extensively in projects such as ASCENT Projects 011, 023, and 044. This project aims to expand upon this work for UAM/AAM. Various vehicle configurations are currently under consideration for feasibility for use in UAM and AAM operations, including short takeoff and landing (STOL) configurations, tilt-rotor vertical takeoff and landing (VTOL), and lift-plus-cruise (LPC)-VTOL configurations, each of which has unique sources and operating modes. Thus, targets of opportunity are identified to estimate the noise levels and develop AEDT compatibility for these vehicles and operating modes. The work will be expanded to generalized AAM operations, and the models developed will be used to make preliminary noise footprint estimates for a variety of configurations. The goals of the project are thus to:

- Develop methods to model the noise levels at the source and due to different operations of UAM and AAM vehicle configurations.
- Develop methods needed for a UAM/AAM-compatible AEDT, to make preliminary noise estimates of AAM vehicles.

Task 1 – Identify Target AAM Vehicle Configurations for Noise Model Development

Massachusetts Institute of Technology
University of California Irvine

Objective

The objective of this task is to determine target AAM vehicle configurations for development of the noise model. Various AAM configurations are under consideration in industry, such as STOL, as well as VTOL vehicles including tilt-rotor VTOLs. Various AAM vehicles across industry will be examined to determine which will be the most relevant for developing the noise modeling method. From this examination, one or more representative vehicles will be chosen as a focus in the initial noise modeling effort.

Research Approach

- Research candidate AAM configurations currently being proposed by the top industry contenders, such as Joby Aviation,® Wisk Aero (Wisk®), and Electra.
- Gather specifications and representative flight profile definitions for selected representative vehicle configurations needed for noise model development.

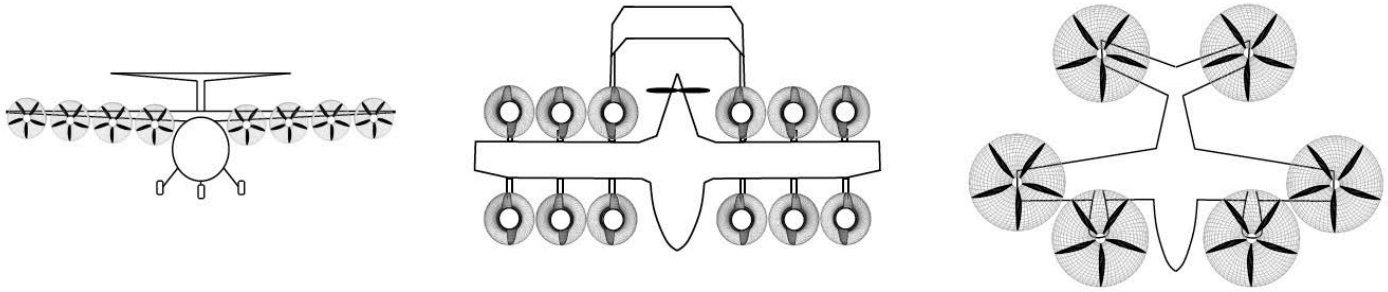
® Joby Aviation is a registered trademark of Joby Aero, Inc., Santa Cruz, California.
® Wisk is a registered trademark of Wisk Aero, LLC, Mountain View, California.

Milestones

- Selected three vehicle configurations for noise model development.
- Determined the geometry and performance specifications for vehicle configurations for noise model development from published resources and from discussions with industry.

Major Accomplishments

The research team identified three AAM vehicle configurations for the initial noise modeling development. In Figure 1, the vehicles examined include (a) a blown-flap STOL vehicle, (b) a lift-plus-cruise VTOL vehicle, and (c) a tilt-rotor VTOL vehicle.



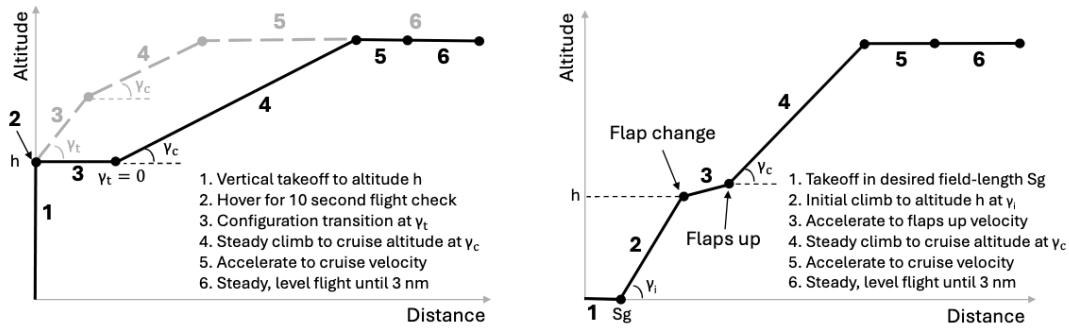
(a) Blown-Flap STOL (b) LPC-VTOL (c) Tilt-Rotor VTOL

Figure 1. Selected AAM vehicle configurations for noise model development: (a) blown-flap short takeoff and landing (STOL), (b) lift-plus-cruise vertical takeoff and landing (LPC-VTOL), (c) tilt-rotor VTOL.

For the purposes of modeling representative operations and noise models, an aircraft performance model that sizes and determines the off-design performance conditions of rotors for these vehicles was developed by using the XROTOR[1] blade element momentum model. Given design conditions such as the weight and required thrust of the representative vehicles, the ASCENT Project 084 team sized sample propellers for each of the vehicles to determine representative noise levels. For each of the vehicles selected, our team determined opportunities to obtain noise data for validation of the noise modeling done in Task 3. Electra provided data for the blown-flap STOL vehicle, Wisk provided data for the lift plus cruise vehicle, and published data from Joby Aviation were available for the tilt-rotor vehicle.

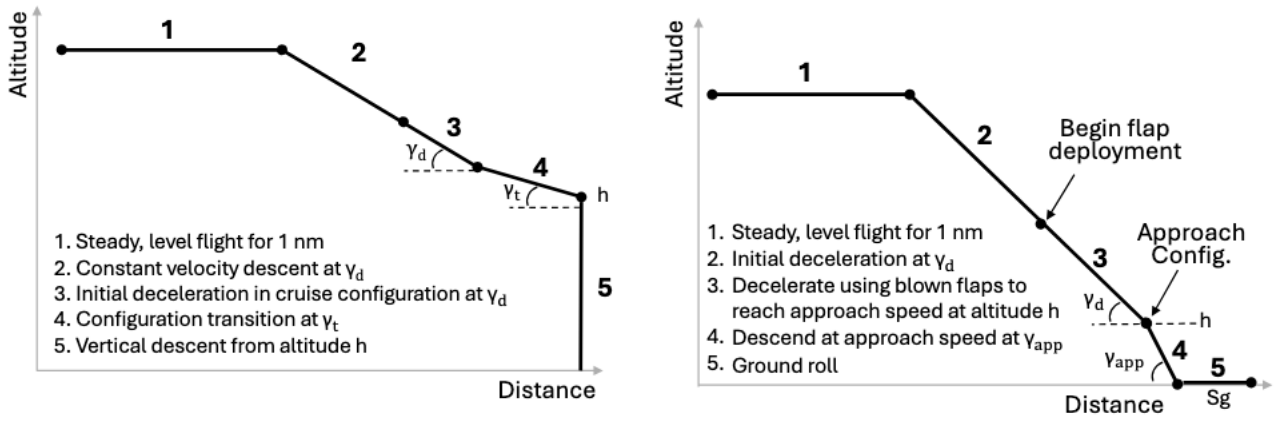
Depending on the type of vehicle, representative departure operations (Figure 2) and approach operations (Figure 3) for each were conceptualized.

[1] XROTOR is an interactive program for the design and analysis of ducted and free-tip propellors and windmills



(a) eVTOL (b) eSTOL

Figure 2. Example departure control strategy for electric vertical take-off and landing (eVTOL) and electric short take-off and landing (eSTOL) AAM aircraft.



(a) eVTOL (b) eSTOL

Figure 3. Example approach control strategy for electric vertical take-off and landing (eVTOL) and electric short take-off and landing (eSTOL) AAM aircraft.

Publications

None.

Outreach Efforts

- Presented at biannual ASCENT Advisory Board meetings.
- Presented the project to engineers at Wisk.
- Collaborated with Electra to gather noise data for a full scale blown-flap STOL aircraft.
- Collaborated with Wisk to receive sample noise data for a full-scale lift plus cruise aircraft.
- Participated in weekly teleconferences and meetings with FAA Technical Monitor.

Awards

None.



Student Involvement

Graduate students have been involved in all aspects of this research, in terms of analysis, documentation, and presentation. These students conducted the research in selecting vehicles, and defining the representative vehicles used for Tasks 2 and 3 of the research goals.

Plans for Next Period

The primary objective for this task was met with the selection and development of specifications for representative vehicles to use for initial noise model development. As the project continues, opportunities to consider other vehicle configurations and flight procedures that will enrich the noise model development efforts will be considered, particularly via additional industry collaboration. Representative flight operations for each vehicle will continue to be analyzed.

Task 2 – Identify Noise Modeling Gaps for Selected AAM Configurations and Operations

Massachusetts Institute of Technology
University of California Irvine

Objective

The objective of this task is to identify noise modeling gaps for selected AAM configurations and operations. According to the target AAM vehicle configuration to focus the noise model in effort on in Task 1, in Task 2, current gaps in noise modeling that must be addressed to formulate the noise modeling method for AAM vehicles will be identified. The noise modeling literature will be consulted, and the effort will leverage collaboration with the National Aeronautics and Space Administration (NASA) UAM and AAM work as appropriate. Noise sources most likely to dominate for different configurations and operations will also be identified. The task will focus primarily on the target vehicles identified Task 1, while considering additional gaps for other vehicle configurations on an ongoing basis.

Research Approach

- Examine the configurations and potential operating procedures of the AAM vehicles determined in Task 1 via performance modeling and consultation with industry.
- Research potential noise sources from the AAM vehicles and determine modeling approaches of the current state-of-the-art noise models.

Milestones

- Identified specific cases for the tilt-VTOL vehicle where noise modeling gaps are influential in predicted noise.
- Examined potential noise modeling operations for each of the three vehicle configurations from Task 1.
- Identified gaps in noise modeling, according to the three vehicle configurations from Task 1.

Major Accomplishments

The AAM vehicles examined in Task 1 feature unique sources of noise stemming from different numbers of rotors and their placements, which interact with one another and with the airframe. These features were examined during this task, and the noise levels the ASCENT Project 084 team modeled in Task 3 were compared to the available noise data from industry. The tilt-VTOL vehicle's noise directivity changes with the tilt of the rotor; the LPC vehicle has varied rotor sizes; and the blown-flap STOL vehicle features noise levels arising from the blown lift. The operating procedures for each of these vehicles also varies and must be considered in the noise modeling. For example, the tilt-VTOL vehicle and LPC vehicle can operate in both vertical and forward flight conditions and must feature transition modes. In addition, the blown-flap STOL vehicle has different flight path angles depending on the flap setting and amount of blowing, thus making the flight profile and produced noise levels a coupled system.

For each of the vehicles, noise was modeled in Task 3 and compared to the available data for each of these vehicles as described in the accomplishments for Task 1. The results indicate that modeling noise using a simple uniform inflow model results in reasonably close results compared to the validation data (within 1-3 dB) for steady state conditions for the tilt rotor, lift plus cruise, and STOL vehicle. Furthermore, the noise output of the tilt-VTOL vehicle is found to be particularly sensitive to the powerplant condition during transition. Given that standard noise modeling tools like the AEDT are suited for a helicopter or traditional airplane models, but not something in between, this represents a notable gap.



This gap has motivated deeper investigation into the loading of each of the rotors during conditions with cross flow or potential rotor-wake interactions which is described in more detail in the accomplishments for Task 3.

Multiple non-axial inflow conditions were identified based on the flight profiles created for the vehicles described in Task 1. These are summarized in the following three main effects: crossflow, rotor-wake interaction, and rotor-wing interaction (Figure 4). Crossflow describes a non-axial velocity component that occurs when the inflow velocity vector is not normal to the disk plane of the propulsor. This velocity component cyclically alters the effective angles of attack, affecting flow separation, thrust, and potentially creating higher noise levels due to unsteady blade loading. This phenomenon primarily affects the tilt-VTOL and LPC vehicles during the transition segments between vertical and horizonal flight. Rotor-Rotor interaction describes effects of a forward propulsor's wake on the inflow of a rear propulsor. This phenomenon potentially increases the overall propulsor noise though unsteady loading and turbulent inflow of rear propellers and is affects the tilt-VTOL and LPC vehicles due to the overlapping propulsor wake during forward flight. Rotor-Wing interaction describes the change in propulsor inflow due to a propeller in the nearfield of the wing. The presence of a wing has the possibility of affecting the potential field of the upstream propulsor, the propulsor affecting the potential field of the wing, and the turbulent wake of the propulsor creating viscous interactions with the wing. This phenomenon has the potential to increase noise primarily affects the blown-flap STOL vehicle.

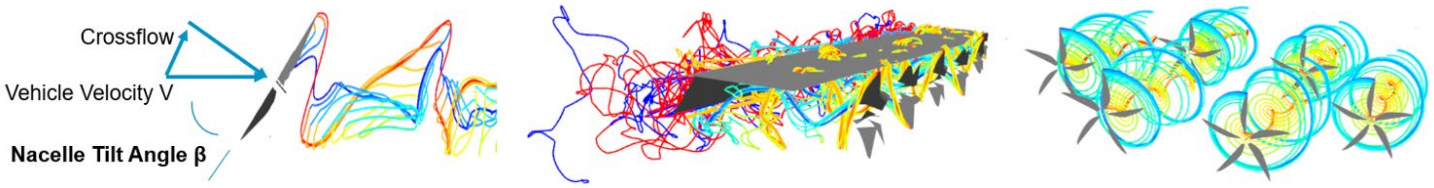


Figure 4. Illustration flow filaments in conditions of non-axial crossflow, rotor-wing interaction, and rotor-wake interaction (left to right).

Publications
None.

Outreach Efforts
- Presented at the biannual ASCENT Advisory Board meetings.
- Collaborated with Wisk to understand the noise profile of their new V6 vehicle.
- Participated in weekly teleconferences and meetings with FAA Technical Monitor.

Awards
None.

Student Involvement
Graduate students have been involved in all aspects of this research, in terms of analysis, documentation, and presentation. These students conducted the research in determining noise modeling gaps for Task 3 of the research goals.

Plans for Next Period
As the project continues, our team will continue seeking industry collaboration opportunities to share concepts for AAM vehicle flight operations. As we examine additional vehicles of interest for the project, gaps in noise modeling and operation design will continue to be documented.

Task 3 – Develop Physics-Based Noise and Flight Profile Model for Representative AAM Vehicles

Massachusetts Institute of Technology
University of California Irvine

Objective

The objective of this task is to develop a physics-based noise and flight profile model for representative AAM vehicles. A first-principles modeling method for the flight profiles and noise of the target AAM vehicle configurations identified in Tasks 1 and 2 will be developed, with the ability to make community noise predictions for these aircraft flying at different operating states. Component-based noise models for the key sources identified in Tasks 1 and 2 will be developed primarily from the methods in the NASA Aircraft Noise Prediction Program 2 (ANOPP2). As data become available, the noise source models will be validated. More complex sources, such as propulsion-airframe interaction noise, may be modeled with external computational fluid dynamics tools such as Comprehensive Hierarchical Aeromechanics Rotorcraft Model (CHARM), and the results will be incorporated into ANOPP2 as needed. In addition, a first-principles flight profile generator applicable to the target AAM vehicle configuration from Tasks 1 and 2 will be developed and incorporated into the noise model. Noise at a variety of velocities, flight path angles, and operating modes will be estimated to construct noise-operation mode-distance curves to adapt the data to the AEDT. In this process, the operational drivers with the greatest impact on varying the vehicle noise levels will be identified, to determine which modes should be focused on when forming the curves. The potential to expand the noise modeling to other vehicle configurations will be considered on an ongoing basis.

Research Approach

- Develop a method to model the noise of flight operations of representative AAM vehicles.
- Use methods to generate noise-operation mode-distance curves to adapt noise results on the AEDT to determine operational drivers with the greatest impact.

Milestones

- Gained significant refinements to AAM flight condition modeling enable investigation of wider range of trajectories.
- Evaluated sensitivity to the source noise hemisphere, allowing for significant speedup and creation of a hemisphere database.
- Performed investigation of tilt-VTOL condition range to show that noise is highly sensitive to flight condition during configuration transition.

Major Accomplishments

Significant refinement to the method for flight condition generation was made in the past year for all of the AAM vehicles identified in Task 1. The refined method was implemented first on the tilt-VTOL vehicle, which enabled analysis of the noise effects of a wider range of the vehicle operating space. Specifically, the capability to define vehicle trajectories by desired physical parameters, such as vehicle flight path angles, airspeeds, or altitudes was built into the simulation loop for generating flight conditions. This capability was enabled by applying closed-loop control systems to determine control inputs which would result in a pilotable version of the desired flight trajectory. To ensure the forces required were physical, the blade element momentum theory propellor design tool XROTOR was used to ensure the required shaft power did not exceed the design maximum.

A significant library of source noise hemispheres at various conditions was generated in the past year using ANOPP2 allowing the noise effects of new flight conditions to be simulated efficiently. A major speedup was achieved by conducting a sensitivity study between the resolution of the source noise hemisphere and the final ground-propagated noise, which found that reducing the resolution by approximately 13 times resulted in differences on the ground of only 1 – 3 dB on average. A representation of the results of this analysis for a reference flight trajectory is visualized in Figure 5. This reduction in resolution resulted in an approximately 40-fold time savings for hemisphere generation, allowing for a larger set of conditions to be simulated.

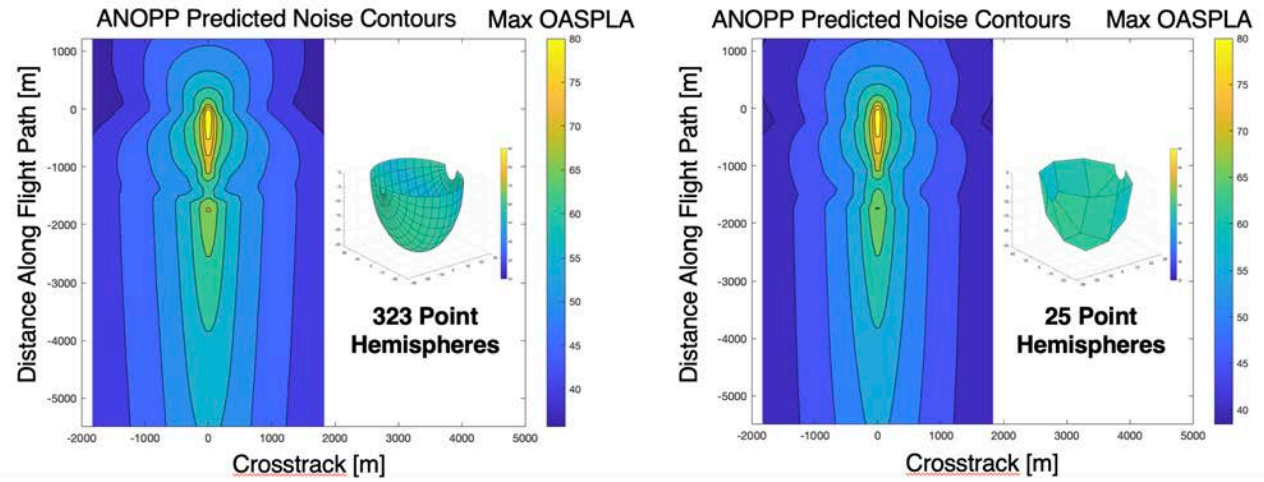


Figure 5. Visualization of propagated maximum noise results for a reference trajectory with different source noise hemisphere resolution. The left contour mapping was generated using dense hemispheres, right contour mapping was generated using coarse hemispheres. Differences are generally within 1 - 3 dBA. ANOPP: Aircraft Noise Prediction Program, OASPLA: Overall Sound Pressure Level, A-weighted.

With refinements to the flight condition generation and noise hemisphere library, a wider array of operations were investigated using the updated analysis framework outlined in Figure 6. An initial finding is that the maximum noise contour from a tilt-VTOL vehicle operation is particularly sensitive to the vehicle condition during the configuration transition phase. Upon investigation this was related to increased, un-modeled crossflow when flying with rotors at nonstandard angles. This effect has motivated ongoing and future work to better capture the crossflow effects on rotor disc loading, and subsequent source noise.

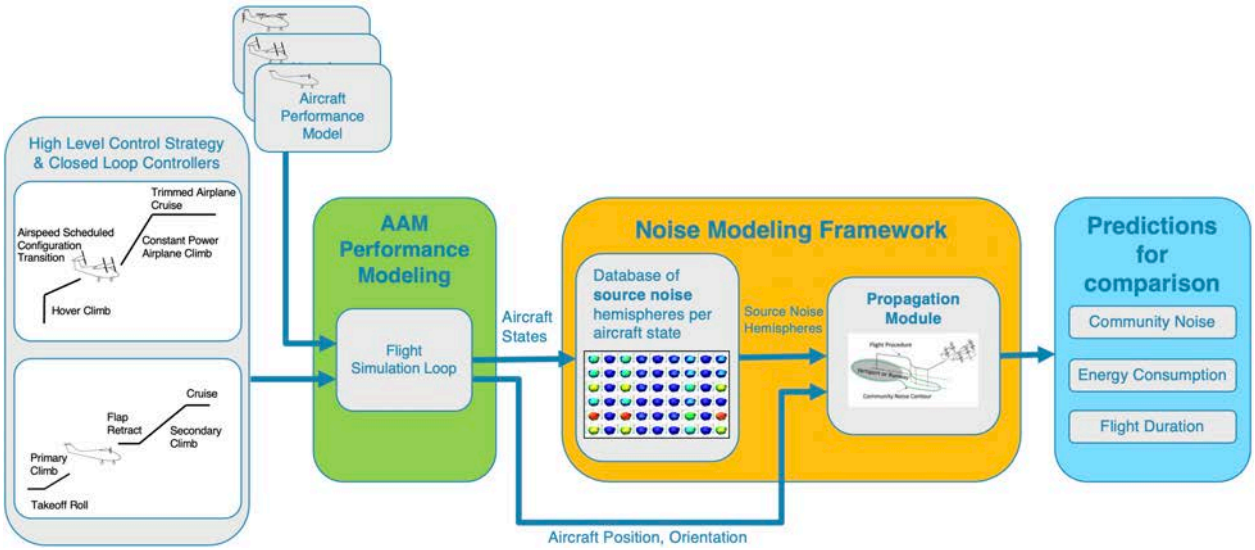


Figure 6. Updated analysis framework for AAM noise prediction and analysis. Flight conditions are generated from simulation from a high-level control strategy, a set of closed loop controllers to maintain the strategy, and an aircraft performance model. Conditions are then matched to appropriate source noise hemispheres from database and propagated to the ground to generate resulting noise contours.

The AAM vehicles described in Task 1 were modeled while operating in regions of potential inflow complications, defined in Task 2, using CHARM. This was done to establish a range of expected noise impact while operating in these more complicated flight regimes. To study crossflow effects, the tilt-VTOL rotor was modeled in various angles nacelle tilt and was found to have an approximate 15 dB increase in noise over 45 degrees of rotor tilt. The required power also increased with increasing crossflow which was consistent with experimental results found in literature. Modeling these results in ANOPP2's ABEAT, which can also account for crossflow, revealed similar noise results. For rotor-rotor interaction, two tilt-VTOL rotors were modeled in various configurations of overlap (Figure 7) found in the Tilt-VTOL during cruise. Noise results indicate a slight increase of less than 1 dB for the full overlap case compared to a two-rotor case with no overlap in the same conditions. These results were also consistent with experimental results found in literature.

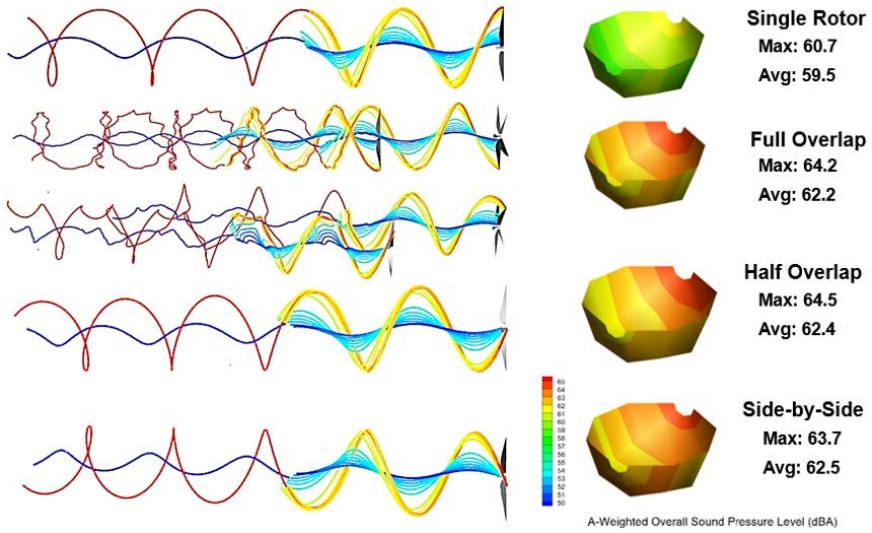


Figure 7. Illustrations of various conditions of rotor-rotor overlap and the resulting noise hemispheres. Results are shown in Overall Sound Pressure Level, A-weighted (OASPLA).

To study the noise effects of rotor-wing interaction, the STOL vehicle propellers were modeled with a wing in various flap conditions in CHARM to represent cruise and landing conditions (Figure 8). Experimental results in literature indicate that wing-rotor interaction noise is greatest when the vertical separation distance is less than one propeller radius apart and outside this range, the effect diminishes rapidly. The representative STOL vehicle showed noise results consistent with these findings with an average increase of 8 dB with the addition of a wing compared to results of the propellers alone.

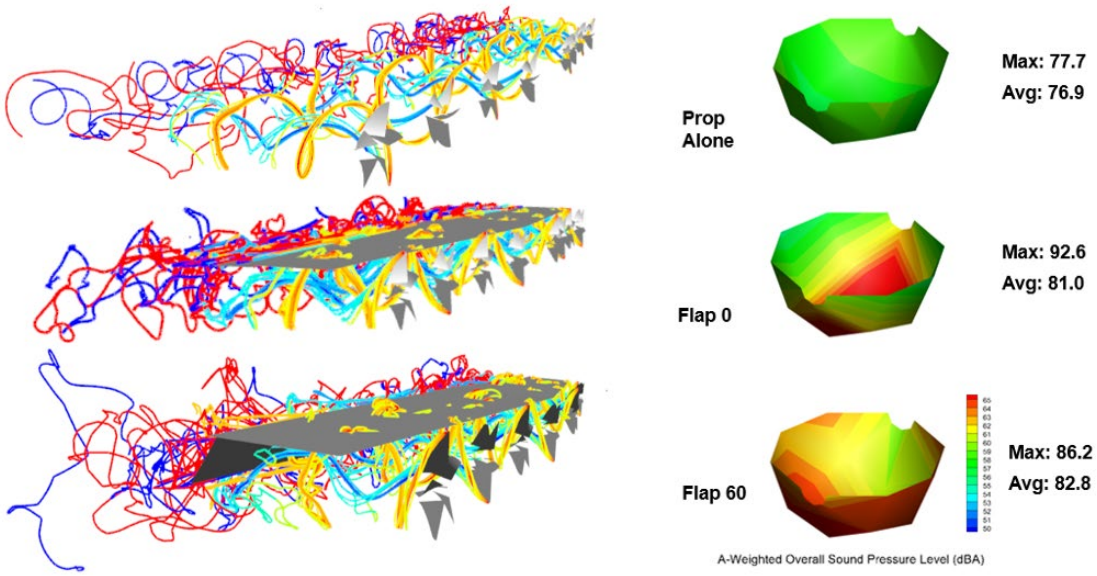


Figure 8. Illustration of rotor-wing interaction modeling using the STOL vehicle and wing. The resulting noise hemispheres are shown in Overall Sound Pressure Level, A-weighted (OASPLA).

Publications

Gonzalez, V. (2025). *A Methodology for Integrating Vehicle Performance into Traffic Flow Management Analysis for AAM Airspace Integration* [Doctoral Dissertation, University of California, Irvine]. California Digital Library. https://escholarship.org/content/qt3sb9w403/qt3sb9w403.pdf

Pellerito, V., Yeung, N., Huynh, j., & Hansman, R. J. (2025). Impact of flight trajectory design on performance and noise for AAM aircraft. *AIAA Journal of Aircraft*, 1-16. https://doi.org/10.2514/1.C038248

Outreach Efforts

- Presented at the biannual ASCENT Advisory Board meetings.
- Collaborated with Wisk to validate assumptions regarding the expected flight profile of their new V6, tilt-VTOL vehicle.
- Participated in weekly teleconferences and meetings with FAA Technical Monitor.

Awards

None.

Student Involvement

Graduate students have been involved in all aspects of this research, in terms of analysis, documentation, and presentation. These students conducted the research formulating the overall framework.

Plans for Next Period

In the upcoming period the aerodynamic effects leading to noise sensitivity during configuration transition will be modeled in more depth, both using updated versions of ANOPP2, and the more sophisticated CHARM model. The model outputs will be compared to understand what level of simplification is acceptable to retain the necessary model accuracy for tools like the AEDT. The investigation of more flight conditions will be extended to the other reference vehicle architectures. The opportunity to minimize noise exposure by changing flight procedures will also be explored. Opportunities for noise validation via industry collaborations will also be conducted on an ongoing basis.



Task 4 – Incorporate Noise Results for Representative AAM Vehicles with the Aviation Environmental Design Tool

Massachusetts Institute of Technology
University of California, Irvine

Objective

The objective of this task is to incorporate noise results for representative AAM vehicles in the AEDT. Based on the results of Tasks 1, 2, and 3, an appropriate approach to model the representative vehicle in the AEDT will be determined. The existing AEDT structure will be evaluated, and operating modes necessary for the representative vehicle configuration will be identified. The noise estimates from Task 3 as a function of flight procedure characteristics will be incorporated into the AEDT. Preliminary modeling of AEDT-compatible vehicles and flight procedures will be performed as a test. In addition, the use of this technique to evaluate the noise impact of AAM of flight procedures will be examined.

Research Approach

- Evaluate the existing AEDT structure to determine operating modes necessary for the representative AAM vehicle configurations.
- Perform initial modeling of AEDT compatible vehicles and flight procedures.

Milestones

- Developed a process to determine the variety of operations that will be relevant to include in the AEDT for modeling AAM vehicles using a control strategy.
- Modeled a matrix of STOL operations and noise to determine how various factors impact noise.

Major Accomplishments

The process to determine the variety of operations that will be relevant to include in the AEDT for modeling AAM vehicles involves simulating viable operations for different takeoff and landing segments. This process is based on the flight profile and noise modeling development and validation efforts from Task 3. Preliminary examples of this for different tilt rotor segments have been done.

Publications

None.

Outreach Efforts

- Participated in weekly teleconferences and meetings with FAA Technical Monitor.
- Presented at the biannual ASCENT Advisory Board meetings.

Awards

None.

Student Involvement

Graduate students have been involved in all aspects of this research, in terms of analysis, documentation, and presentation.

Plans for Next Period

The process to determine the variety of operations that will be relevant to include in the AEDT for modeling AAM vehicles will continue to be developed to simulate different performance states for each of the vehicles that our team will be assessing, particularly for vehicles where cross flow is expected during the flight. The current AEDT structure will be examined to determine its suitability for assessing AAM noise operations in its current state and identify gaps in the modeling approaches. Our team will consult with technical experts at the Volpe National Transportation Systems Center regarding the existing AEDT structure.



Task 5 – Expand Methods to Additional Vehicle Sets

Massachusetts Institute of Technology
University of California Irvine

Objective

The objective of this task will be to expand the methods developed in Tasks 3 and 4 to more complex vehicles featuring additional noise components that have not yet addressed the initial target vehicle configuration. In collaboration with FAA Technical Monitors, the noise model will be updated to incorporate these noise levels and demonstrate their utilization in the AEDT, as was done in Task 4.

Research Approach

- Determine complex candidate vehicle sets via examination of current common vehicle configurations being proposed in industry.
- Update noise modeling methods by using advanced analysis approaches or noise data.

Milestones

Discussed with Wisk about their V6 tilt-rotor vehicle.

Major Accomplishments

Made a plan to incorporate Wisk's V6 vehicle into our database.

Publications

None.

Outreach Efforts

- Participated in weekly teleconferences and meetings with FAA Technical Monitor.
- Presented at the biannual ASCENT Advisory Board meetings.
- Collaborated with Wisk about their new V6, tilt-VTOL vehicle.

Awards

None.

Student Involvement

Graduate students have been involved in all aspects of this research, in terms of analysis, documentation, and presentation.

Plans for Next Period

We will incorporate Wisk's V6 vehicle noise and operations into our database. Opportunities for gathering noise data that can be used for validation and the assessment of more complex noise sources beyond the initial modeling framework developed in Task 3 will be determined on an ongoing basis.

Task 6 – Evaluate Implications for Noise Mitigation and Low-Noise Operations for AAM Vehicles

Massachusetts Institute of Technology
University of California Irvine

Objective

The objective of this task will be to determine implications for noise mitigation and low-noise operations for AAM vehicles. The development of the AEDT for the study of AAM vehicle noise is likely to yield implications for noise mitigation and low-noise operations of AAM vehicles. These implications, along with the AAM-compatible AEDT tool, will allow future research teams to continue to use the AEDT to assess AAM vehicle noise. Implications for the development of low-noise procedures



for AAM will also be evaluated. The results of the previous tasks have the potential to indicate the need for additional noise model development and validation. Validation of the noise models or flight procedures as data become available will be the goals of future research efforts.

Research Approach

- Assess the noise of candidate vehicles performing several advanced flight procedures.
- Determine low-noise operations and flight procedure design for different candidate vehicles that can be assessed in the AEDT.

Milestones

Process to model many flight operations using a control strategy for each vehicle is in development.

Major Accomplishments

- Determined sample control strategies for the tilt-rotor vehicle based on a speed schedule during transition.
- Determined an alternative control strategy using constant power and used it to assess tilt rotor noise during transition.

Publications

None.

Outreach Efforts

- Participated in weekly teleconferences and meetings with FAA Technical Monitor.
- Presented at the biannual ASCENT Advisory Board meetings.

Awards

None.

Student Involvement

Graduate students have been involved in all aspects of this research, in terms of analysis, documentation, and presentation.

Plans for Next Period

After examination of the noise of the representative vehicles operating in multiple operating conditions, the flight procedures and noise operations resulting in the lowest noise levels will be documented. This process is ongoing for the different vehicles.



Project 085 Strategies for Improving En-Route Fuel Efficiency

Georgia Institute of Technology

Project Lead Investigator

Professor Dimitri N. Mavris
Director, Aerospace Systems Design Laboratory
School of Aerospace Engineering
Georgia Institute of Technology
Phone: (404) 894-1557
Fax: (404) 894-6596
Email: dimitri.mavris@ae.gatech.edu

University Participants

Georgia Institute of Technology (Georgia Tech)

- P.I.s: Dr. Dimitri N. Mavris, Dr. Michelle Kirby
- FAA Award Number: 13-C-AJFE-GIT-161
- Period of Performance: March 19, 2024, to September 30, 2025
- Tasks:
  1. Development of a path optimization algorithm and use case examples
  2. Speed Control and Vectoring Identification
  3. Fuel Burn Surrogate Modeling
  4. Fleet-wide Speed Control Strategy

Project Funding Level

Georgia Tech has received $400,000 in funding from the Federal Aviation Administration (FAA) for this project. In terms of cost-share details, Georgia Tech has agreed to a total of $400,000 in matching funds. This total includes salaries for the project director, research engineers, and graduate research assistants, as well as computing, financial, and administrative support, including meeting arrangements. Georgia Tech has also agreed to provide tuition remission for the students, paid for by state funds.

Investigation Team

Prof. Dimitri N. Mavris, (P.I.), Tasks 1-4
Dr. Michelle Kirby, (co-Investigator), Tasks 1-4
Dr. Ameya Behere, (research faculty), Tasks 1-4
Dr. Holger Pfaender (research faculty), Tasks 1-4
Dr. Cedric Justin (research faculty), Tasks 1-4
Mr. Jirat Bhanpato, (research faculty), Tasks 1-4
Jouwairia Ahabchane (graduate student), Tasks 2
Titien Berberian (graduate student), Tasks 1
Jacob Hawkins (graduate student), Tasks 1
Ghizlane Jari (graduate student), Tasks 3
Yasser Moumtaz (graduate student), Tasks 4
Vishva Rana (graduate student), Tasks 2



Project Overview

In the face of anticipated increased aviation demand for the future, multiple avenues exist to achieve system-wide fuel efficiency including aircraft and engine technologies, operational improvements, and policy measures. This research project focuses on the strategies of near and long-term operational improvements (OIs) and quantify their impact on reducing the aviation fuel efficiency, with specific focus on en-route efficiency. The anticipated outcomes for the FAA are a series of recommended strategies for improving the en-route fuel efficiency of aviation.

Task 1 - Development of a Path Optimization Algorithm and Use Case Example

Georgia Institute of Technology

Objectives

The objective of this task is to develop a flight trajectory path optimization algorithm that can measure the amount of fuel a flight would save by implementing speed control to avoid some of the delays spent in holding patterns or vectoring that occurs during system disruptions or high-volume activity. This is done by combining Flight Operations Quality Assurance (FOQA) data with fuel burn surrogate models to get an estimation of the fuel savings. Currently, the focus is on the holding pattern identification task as a primary use case for using speed control during cruise to avoid inefficient flight in holding patterns, with future plans to include vectoring.

Research Approach

Compared to the path optimization algorithm presented in last year's annual report, the new path optimization algorithm has many upgrades. Most of the improvements come from using FOQA data as the basis of the simulation. Last year's algorithm sought to find a path between two points that would minimize the amount of fuel used by the aircraft. While this algorithm was useful, it was difficult to draw conclusions about how to best modify an aircraft's speed to avoid burning fuel in a holding pattern. To fix this issue, a new type of path optimization algorithm was created. This new algorithm simulates how the total amount of fuel an aircraft uses would change if the aircraft slowed down to avoid at least a portion of a holding pattern. By using FOQA data from a real flight as its starting point, the algorithm can test how speed control would affect fuel usage in real life scenarios and provide recommendations for how aircraft in certain situations should modify their speed to save fuel.

Path Optimization Algorithm

To quantify the potential fuel savings available to a flight, a simulation environment was created that helps assess what would happen if a flight were to implement speed control tactics. Results are compared to the baseline FOQA data from the real flight. This simulation uses the fuel burn surrogate models discussed in Task 3 to estimate the amount of fuel that would be saved by implementing speed control at different speeds for different durations.

Before the simulation is run, the holding pattern detection algorithm, discussed in Task 2, is run on each FOQA flight and the information on any holding patterns is stored in a database for that given flight. Once a flight has been identified as having experienced a hold, its information can be passed on to the path optimization algorithm for further analysis. Now that the flights with holds have been identified, the cases run on each flight need to be defined. To define a set of cases to run for a flight, the Mach numbers flown at during speed control and the percentages of the hold to absorb must be specified. The user has the option to provide specific Mach numbers and absorption percentages to test, or they can leave these fields blank and the simulation will instead use default values. If no Mach numbers are provided, the simulation will select a default set of Mach numbers that depends on the airframe. The simulation then pulls information on the length of the hold and how much fuel was used during the hold from the database created by the holding pattern detection algorithm using a flight identification number, denoted as flight ID. The flight ID is also used to get additional metadata on the flight, such as which airframe and engine combination was used. Information on the airframe and engines is then used to select which fuel burn surrogate model to use for calculating the new fuel flow values when speed control is implemented. Once the general flight information has been collected, a Design of Experiments (DoE) is used to vary the time to absorb and Mach number ranges (either those provided by the user or the default values if none were provided) and running each possible combination in the trajectory simulator. The code is parallelized so that each case can be run simultaneously, which reduces the overall run time. The speed improvement provided by this parallelization of the code is



limited by how many processes a computer can execute at once. For example, if the simulation runs 32 cases on a computer that can run 8 processes at once, it will run the cases in four batches of eight cases.
For each case in the DoE, the trajectory simulator tries to determine when speed control should start to absorb the requested amount of time by flying at the requested Mach number for that specific DoE case. Using latitudes and longitudes listed in the FOQA data, the simulation can determine how far the aircraft moved during each timestep throughout all of cruise. Next, the ground speed of the aircraft, as it travels from point to point, is calculated. To ensure this calculation is accurate, the wind conditions need to be accounted for. How the wind conditions affect the ground speed, as well as definitions for all relevant variable abbreviations, is shown in Figure 1.

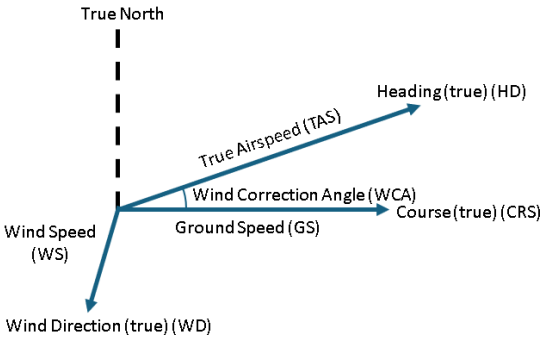


Figure 1. A graphical representation of the values used in the ground speed calculation.

Because the wind and aircraft are not guaranteed to be moving in the same direction, the heading of the aircraft and its course will not be aligned. This difference is accounted for by the wind correction angle, which can be found using Equation 1:

$$\sin WCA = \frac{WS}{TAS}\sin(WD - CRS) \quad \text{(Eq. 1)}$$

Once the wind correction angle is known, the ground speed can be calculated using Equation 2:

$$GS = TAS\sqrt{1 - (\sin WCA)^2} - WS\cos(WD - CRS) \quad \text{(Eq. 2)}$$

With the distances between each point and the new ground speeds known, the amount of time it would take to travel between each point while implementing speed control can be calculated by dividing the distances by the ground speeds. The amount of time absorbed at each timestep can then be calculated by subtracting the original amount of time taken to move between points from these new times.

Now that the amount of time absorbed at each location is known, the location where speed control should start can be identified. This can be done by taking the individual absorption times and summing them up starting from the end of the cruise phase and working backwards. The summation continues until the total absorbed time reaches the requested absorption time. At this point, the time at which speed control should start is recorded. If the summation reaches the beginning of the cruise phase before the total absorbed time reaches the requested absorption time, this means that the flight is not long enough to absorb the requested amount of time at the requested Mach number. If this occurs, the simulation will end the case by producing an error message explaining that that case is not feasible.

Once the starting point of speed control is identified, the amount of fuel used during speed control can be calculated. In order to calculate the fuel flow, the altitude, air temperature, gross weight, Mach number, rate of climb, and Mach change over a 20-sec period must be known. Almost all these values can be acquired from the FOQA data. Only the gross weight is unknown because the weight of the aircraft at any point in the flight is a function of all the instantaneous fuel flows before that point. This contradiction can be solved by creating an iteration scheme to converge on the correct gross weight. By using the gross weight listed in the FOQA data as an initial estimate, it is possible to calculate an initial estimate of the instantaneous fuel flows throughout the entire speed control phase. Using these estimated fuel flows, the gross weight estimate can be updated. This process can then be repeated until the gross weights converge, which means that the gross



weights supplied to the surrogate models match the gross weight we would calculate using the fuel flows provided by the surrogates. The update to the weight estimate is given by Equation 3:

$$\overrightarrow{W_{n+1}} = W_{n,0} - \vec{f}(\overrightarrow{W_n}, \dots) \quad \text{(Eq. 3)}$$

where $\vec{W}$ is the weight of the aircraft at each timestep from the start of speed control to the end of cruise and $\vec{f}$ is the amount of fuel used from the start of speed control to each timestep. The simulation then stops iterating on the weight estimate once Equation 4 is satisfied:

$$\max(\|\overrightarrow{W_{n+1}} - \overrightarrow{W_n}\|) < \varepsilon \quad \text{(Eq. 4)}$$

where ε is a small number. While it would be simpler to iterate through each time step and calculate each instantaneous fuel flow sequentially, this method is much more efficient because it only requires a handful of iterations to converge as opposed to the hundreds or thousands of time steps that would need to be iterated through.

Once the fuel calculations are completed, the simulation is done. All that remains is to output a handful of measures of effectiveness for the case that determine how feasible and useful absorbing that much of the hold at that Mach number would be. Examples of some of the measures of effectiveness that are calculated and stored include speed control duration and net fuel savings. Net fuel savings is a crucial measure of effectiveness because it quantifies how much fuel would be saved by implementing speed control. This metric is calculated by comparing the amount of extra fuel used in cruise to the amount of fuel saved by avoiding part of the holding pattern. When making this calculation, it is assumed that the fuel flow during the holding pattern was constant, so the total amount of fuel saved is proportional to the percentage of the holding pattern that was avoided. To calculate the net fuel savings, Equation 5:

$$\Delta F = \frac{F_{Hold} T_{Abs}}{T_{Hold}} - (F_{Cruise,SC} - F_{Cruise,O}) \quad \text{(Eq. 5)}$$

where ΔF is the net fuel savings, F_{Hold} is the amount of fuel that was burned during the hold, T_{Abs} is the amount of time absorbed by speed control, T_{Hold} is the duration of the hold, $F_{Cruise,SC}$ is the amount of fuel burned during cruise when speed control is implemented, and $F_{Cruise,O}$ is the amount of fuel originally burned during cruise. The other important metric is speed control duration, which determines how much lookahead time for a hold is required to implement that combination of absorbed hold time at the specified Mach number. Even if a case can provide a large fuel benefit, it may require too long of a look ahead time to be practical. A process diagram that summarizes the overall logic of the path algorithm is included in Figure 2.

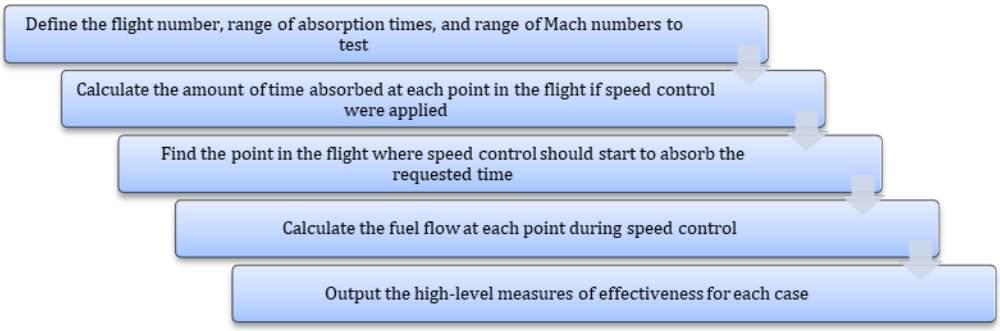


Figure 2. Process diagram for the path optimization algorithm

Reducing the Algorithm's Runtime

The 2024 version of the trajectory simulator was not optimized for execution time. This limitation poses challenges to analyzing a large number of flights and multiple strategies were implemented to significantly reduce the trajectory simulator's runtime. The first step taken to reduce the runtime was to only simulate the speed control portion of the flight as opposed to the entire cruise phase. The calculations were then optimized by vectorizing them. The 2024 version of the

code iterated through each point in the flight sequentially and calculated the state of the aircraft at each of these points individually. To improve efficiency, these equations controlling the aircraft's state were modified to perform these calculations on vectors. This allows all state calculations for the entire speed control phase to be combined into one set of function calls, which significantly improves the performance of the simulation. Logic was also added to discard cases where it is not feasible to absorb the requested time at the requested speed during the cruise phase, which keeps the algorithm from wasting simulation time on impractical cases.

The runtime has improved for the new path optimization algorithm compared to the 2024 version is listed in Table 1. Overall, the various code optimization strategies have produced a 98% reduction in the runtime. This faster runtime will make it significantly easier to analyze all the flights available in the FOQA data and also extend to a system level assessment with a very large number of flights to simulate.

Table 1. Runtime comparisons for the 2024 and 2025 versions of the path algorithm.

GT Flight ID	Cases	2024 Version Runtime (minutes)	2025 Version Runtime (minutes)
GT2437319	20	24	0.5
GT2417663	25	35.5	0.6

Use Case Example

Once the simulation is completed, the environment produces contour plots that show how each case is performed. Using Once the simulation is completed, the simulation produces contour plots that show how each case performed. Using these graphs, it is possible to draw conclusions about the possible benefits of applying speed control to that flight. As an example, consider a Boeing® 767-400ER flight from Los Angeles International Airport (KLAX), Los Angeles, California to John F. Kennedy International Airport (KJFK), New York, New York that encountered a hold. The entire flight path of the flight is depicted in Figure 3, while a zoomed in view on the descent phase that shows the holding pattern the aircraft experienced is depicted in Figure 4. The aircraft spent 3.9 hr in cruise at an average speed of Mach 0.797 before entering a holding pattern during its descent. This holding pattern lasted approximately 24 min and burned 3,575 lb of fuel.

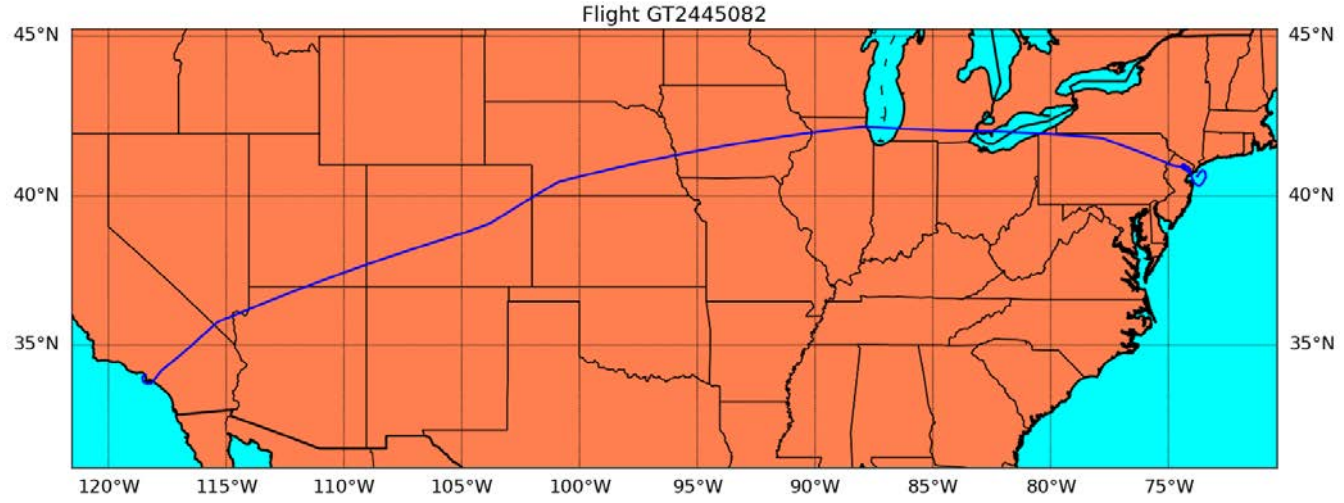


Figure 3. Flight path for the flight from Los Angeles to New York City

® Boeing is a registered trademark of The Boeing Company, Seattle, Washington.

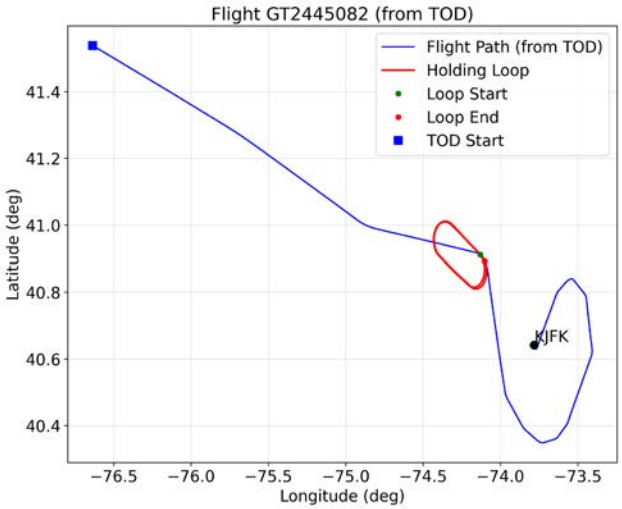


Figure 4. The descent phase of the flight with the holding pattern highlighted.

By applying the path optimization algorithm to this flight, the potential fuel burn benefits available if this flight had implemented speed control can be quantified. The net fuel savings calculated by the path optimization algorithm for a range of speed control Mach numbers and absorption times are shown in Figure 5 as a contour plot. The case that saves the most fuel occurs when the aircraft absorbs 6 min of the hold by slowing down to Mach 0.76 to save 860 lb of fuel in the upper left corner of the contour plot, but there are many other cases that would result in fuel savings. In general, cases with more fuel savings occur at high absorption times and low Mach numbers. This trend occurs because at low absorption times, the amount of fuel the aircraft avoids burning in the holding pattern is smaller compared to high absorption times. Meanwhile, at higher Mach numbers, the aircraft must implement speed control for longer, which negates the fuel savings that would be seen by avoiding the holding pattern because the aircraft has to fly at a Mach number with a higher fuel flow compared to the original cruise for a longer time. Some of these high Mach number cases are not even feasible because the required duration for speed control would exceed the cruise duration for that flight.

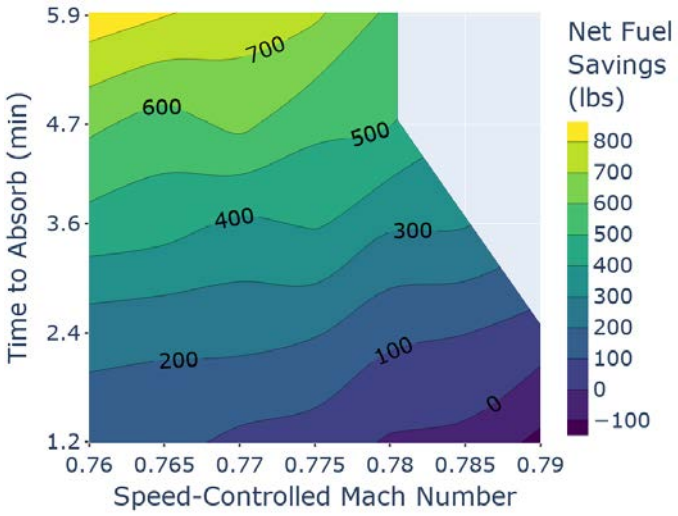


Figure 5. Net fuel savings for a 767-400ER flight from Los Angeles to New York City.

To ensure that these fuel savings are also practical to achieve, the required speed control duration of these cases must also be examined. A contour plot of the speed control durations for the tested cases is depicted in Figure 6. The case that



saves the most fuel requires 2.5 hr of lookahead time to implement, which is usually too much time for there to be sufficient warning for a holding event. If that amount of time is not available, one of the other cases in the DoE that requires less lookahead time could be selected and still provide some fuel savings. For example, as part of Task 2, approximately one-third of flights in the FOQA flight data experienced a hold with a lookahead time of at least 40 min. With 40 min of lookahead time, cross-referencing the time to absorb in Figure 5 to the speed control duration in Figure 6 shows that absorbing approximately 2 min of a hold by flying at Mach 0.76 will take 40 min and save approximately 180 lb of fuel.

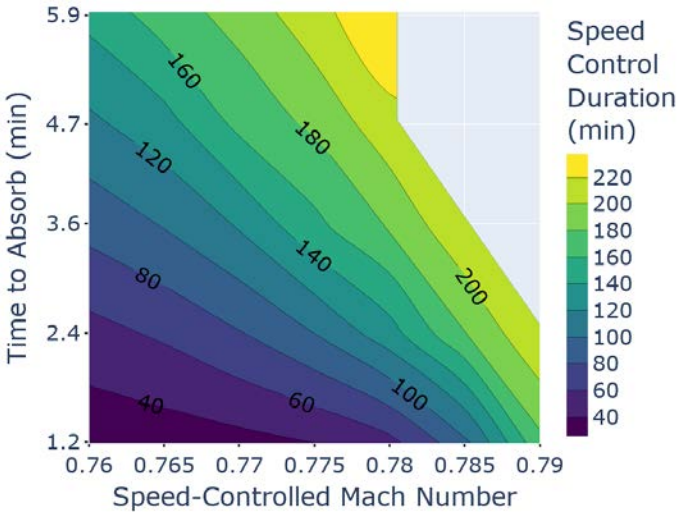


Figure 6. Speed control durations for a 767-400ER flight from Los Angeles to New York City.

These kinds of tradeoffs between lookahead time and net fuel savings highlight the importance of considering a flight's specific situation when making speed control recommendations. Depending on the situation, some flights will have more lookahead time and be able to achieve greater fuel savings than other flights. For example, a narrowbody on a short to medium haul flight distance will always have less potential to benefit from speed control than a widebody aircraft on an international flight because it will always have a limited lookahead time. The situation becomes even more complex when considering how multiple flights affected by the same holding event should act, as will be discussed in Task 4. Regardless, this example shows that saving hundreds of pounds of fuel on a single flight is possible and could lead to significant fleet-wide savings if more widely implemented.

Milestones

- Identified holding patterns in both FOQA and threaded track (TT) flights in 2023.
- Developed a path optimization algorithm for a trajectory simulator that uses FOQA data as a baseline to compare the effects of speed control to quantify fuel burn benefits and assessed a number of FOQA flights.

Major Accomplishments

- Successfully implemented a path optimization algorithm that can quantify how much fuel a flight would save if speed control were implemented. This trajectory simulator will assist in determining how often speed control can be used to save fuel and will be used to inform the fleet-wide speed control strategies discussed in Task 4.
- Optimized the path optimization algorithm to significantly reduce its runtime, which will make it much easier to acquire all of the fuel savings data needed to create fleet-wide speed control strategies.

Publications

None.

Outreach Efforts

Participated in ASCENT biannual meetings.

Awards
None.

Student Involvement
- Titien Berberian (graduate student) created the 2024 version of the path algorithm.
- Jacob Hawkins (graduate student) created the 2025 version of the path algorithm.

Plans for Next Period
- Use the path optimization algorithm to analyze all flights with available FOQA data and store the resulting fuel savings metrics in a database. This database could then be used as the training basis for a surrogate model that produces an expected fuel savings for a given set of speed control parameters.
- Modify the path optimization algorithm to accept threaded track data, which would allow many more flights to be analyzed.

References
None.

Task 2 – Speed Control, Holding Patterns and Vectoring
Georgia Institute of Technology

Objective
The objective of this task is to leverage FOQA data to understand how delays are currently or could be absorbed en-route and in terminal airspace through speed control, holding patterns and vectoring. For speed control, the goal is to use speed change analysis to uncover speed control events within the 50,000 FOQA flights and to characterize when an intentional cruise Mach adjustment occurs in cruise. For holding patterns, the work focuses on finalizing and applying a refined holding detection methodology across TT data to quantify when holding occurs, identify holding stacks, and determine the look-ahead time for potential early cruise speed control application. For vectoring, the initial work centers on developing a methodology for identifying air traffic control (ATC) vectoring events in terminal airspace and quantifying the additional time and fuel burn induced by vectoring.

Research Approach
This section presents the research approaches for speed control, holding patterns, and vectoring while outlining the methodology and methods used in this task.

Speed Control Detection
Changepoint (CP) analysis was applied to cruise-phase flight data to systematically identify speed-control events, which includes instances where the aircraft may have intentionally altered Mach number to meet flow-management objectives or manipulate estimated time of arrival (ETA). The motivation behind this approach is that manually reviewing thousands of flights for subtle speed shifts from a visual perspective in a plot of Mach number versus ground distance is inefficient, subjective, and inconsistent. By holding altitude constant and jointly examining related parameters, specifically turbulence, the algorithm distinguishes between intentional speed-control maneuvers and natural fluctuations in response to atmospheric effects. Instead of individually and visually identifying flights for potential speed control events, an algorithm incorporating changepoint analysis was developed and applied to all flights of interest. The full detection pipeline, from raw flight data preprocessing through changepoint filtering and classification, is depicted in Figure 7 and each step will be discussed further.

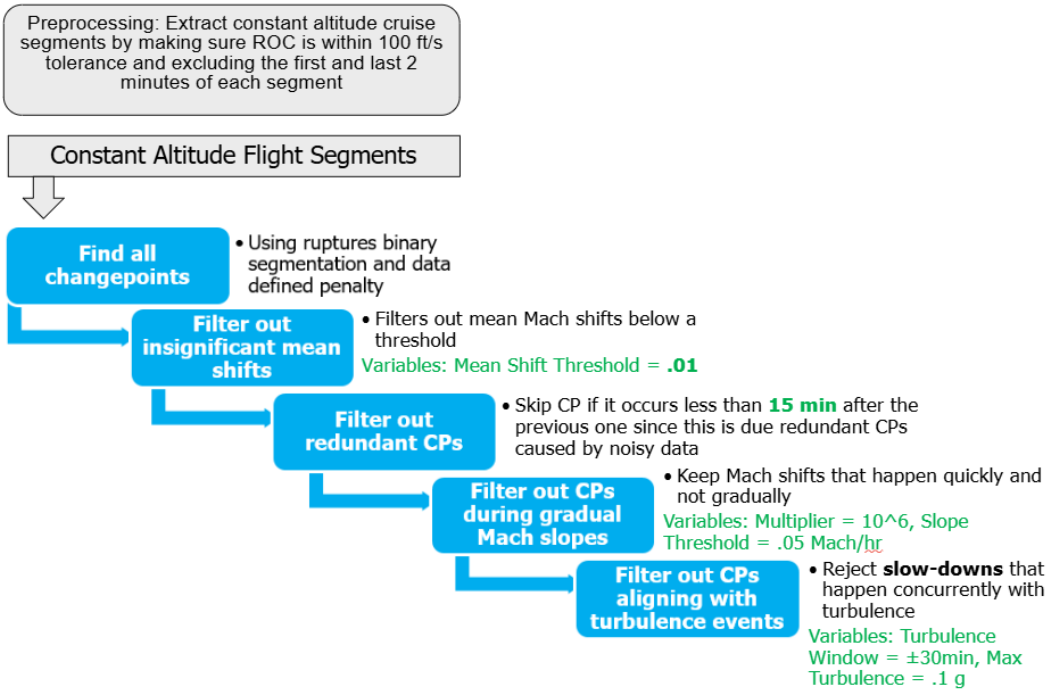


Figure 7. Changepoint (CP) analysis algorithm process.: Rate of Climb (ROC)

Data Preparation

Changepoint analysis is a family of statistical methods that identify locations in typically time series data where underlying properties such as mean level change (Aminikhanghahi & Cook, 2017). In this study, changepoint analysis is used to determine shifts in mean Mach level in FOQA flight time series data. The changepoint algorithm begins by segmenting each flight into constant-altitude cruise portions. To avoid large changes in Mach number or acceleration and deceleration behavior in transient flight phases from steady and level flight, the first and last 2 min of each segment are excluded. Within each valid cruise section, the Python library ruptures is used to perform CP detection, applying the binary segmentation algorithm with a data-defined penalty to detect changes in the mean Mach number (Truong et al., 2018). Binary segmentation iteratively finds the most significant single changepoint in a segment, splits the series at that location, and then repeats the procedure on the resulting sub-segments, yielding multiple changepoints in long time series (Fryzlewicz, 2014). This produces raw CPs representing any statistically significant shift in mean Mach number. However, many of these events are operationally insignificant, redundant, or gradual trends rather than discrete speed-control actions. For example, many speed shifts are gradual over time, indicating that this is not a pilot-induced or deliberate attempt to change speeds, but rather due to autothrottles or flight management systems. Therefore, a multi-stage filtering sequence was implemented to refine the CP set.

Algorithm Filtering

The first filter removes insignificant mean shifts by applying a threshold—mean Mach changes below 0.01 are discarded. This mean shift threshold (MST) variable acts as a sensitivity knob to how many CPs are kept from the large amount that are initially detected using ruptures' binary segmentation. The CP detection with various threshold values is depicted in Figure 8. The value 0.01 was picked to grasp as many significant shifts as possible while excluding CPs detected due to noisy data. The second filter removes redundant CPs caused by noisy data, skipping any CP that occurs within 15 min of a previous one. An example of a case where one CP would be filtered out is shown in Figure 9 below, where multiple CPs are detected next to each other. The third filter targets CPs that result from gradual Mach drifts rather than abrupt operational decisions. Using a slope-based criterion (with a slope threshold of 0.05 Mach/hr and a large multiplier to emphasize rapid changes), only sharp, sudden Mach shifts are retained. This ensures that the algorithm isolates discrete actions rather than slow trends. An example of these kinds of CPs is shown in Figure 10, which are filtered out.

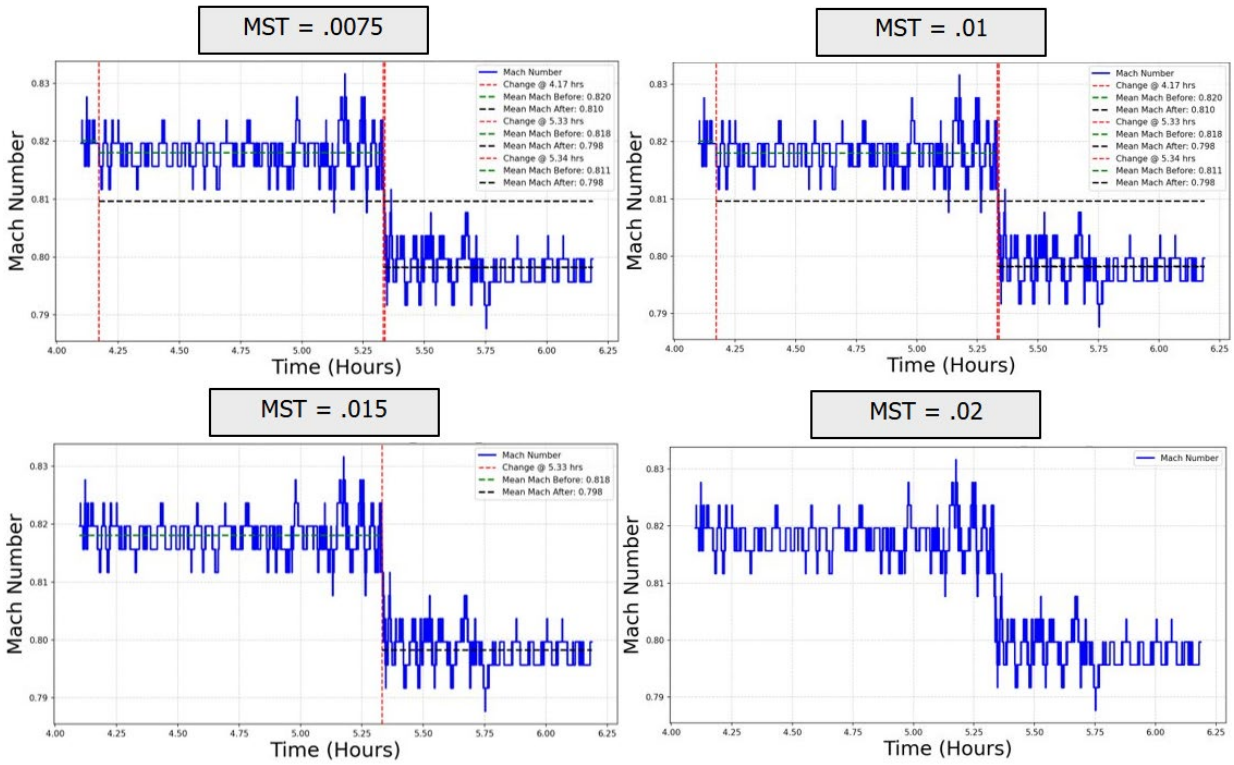


Figure 8. Sensitivity of changepoint (CP) analysis to various mean shift thresholds.

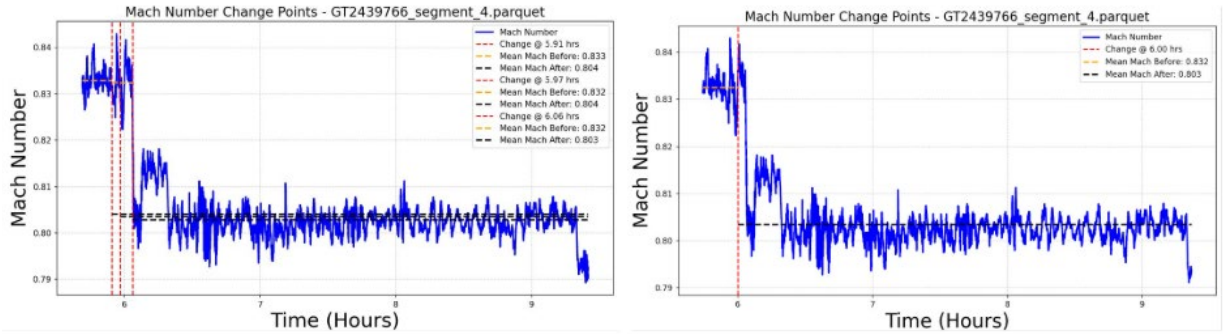


Figure 9. Segment with redundant changepoints (CPs).

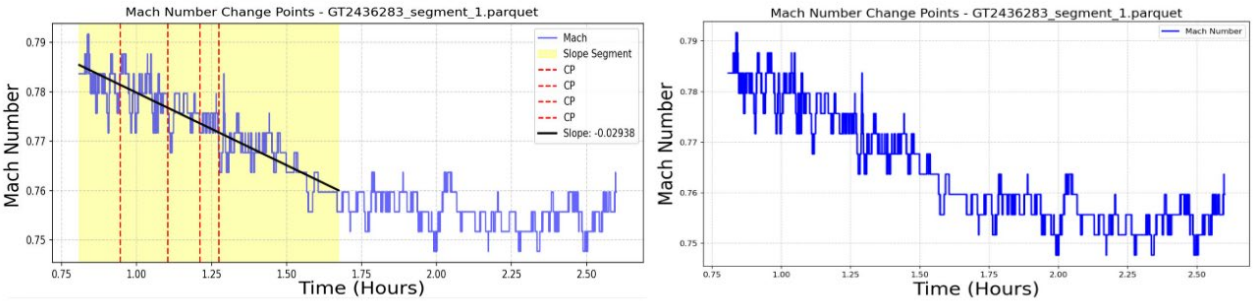


Figure 10. Segment with gradual changepoints (CP) Turbulence Filtering.

A final filter incorporates turbulence. Turbulence can cause passenger discomfort and structural loads that can be mitigated via slowdowns during cruise, rather than speed-ups, and altitude changes. To capture the speed change mitigation approach, the algorithm first classifies each CP as either a Mach increase or decrease. The turbulence filter uses a ±30-min time window, and a maximum turbulence threshold of 0.1 g is applied only to slow-down CPs. Having a window around the CP is important since turbulence and the speed change may not align exactly. This 0.1 g value is derived from subject matter experts from major commercial airlines. A turbulence value of 0.1g is considered a mild turbulence event but may still cause enough discomfort to prompt pilots to slow down. Any slow-down coinciding with a turbulence event is rejected as non-intentional but related to an atmospheric cause. Speed-ups are left unfiltered, since turbulence should not lead the flight crew to speed up. Through this series of filters, the algorithm isolates high-confidence CPs that represent meaningful, likely intentional speed-control maneuvers. The results of these modifications and their impact on CP identification are presented in subsequent analyses.

Speed Control Results and Discussion

As an example for the Airbus® A350-900 airframe, almost 20% of flights potentially use speed control. Out of 510 flights analyzed, there are 100 flights with at least one or more changepoints as shown in Figure 11. The total number of speed control events, which only included slowdowns, for each widebody airframe, is shown in Figure 12. The total number of medium and long-haul widebody flights that had speed control event is 2,922 of the 50,000 FOQA flights. The results show that speed control seems to be already practiced by some airlines. Thus, absorbing terminal delays via lower cruise speeds is an operationally promising path to improve en-route fuel efficiency. System-wide implementation may yield significant benefits and can be determined by considering the fuel burn impact of flights utilizing speed control and flights utilizing holding or vectoring. The results of this investigation provide clarity on the frequency of speed control used in the fleet currently and insights for parallel efforts such as the simulation of speed control events in place of holding.

® Airbus is a registered trademark of Airbus Operations GmbH, Hamburg, Germany.

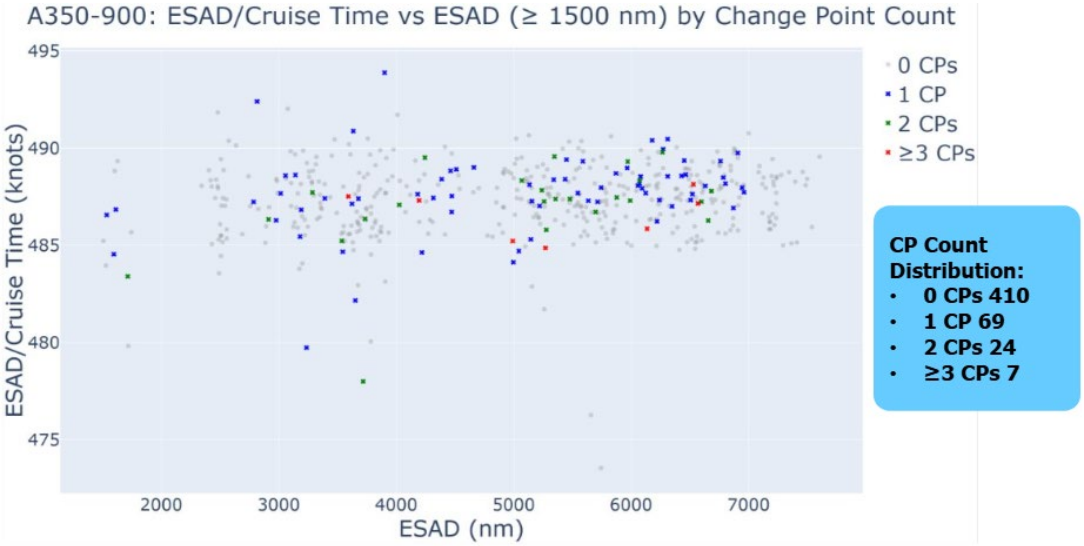


Figure 11. Changepoint (CP) breakdown for the A350-900. ESAD: equivalent still air distance.

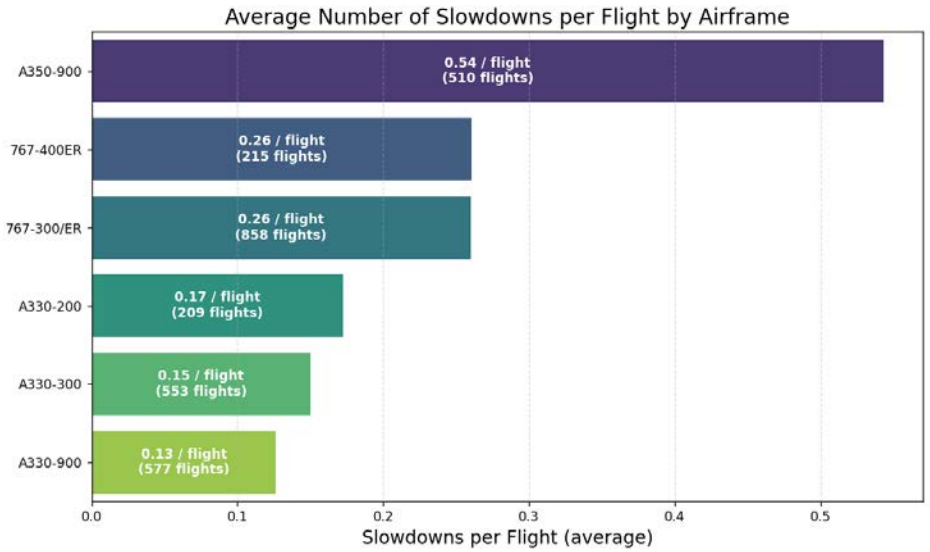


Figure 12. Slow-down breakdown for each widebody airframe identified with algorithm.

Summary and Observations of the Speed Control Detection Algorithm

The changepoint-based speed control detection algorithm provides a systematic and data-driven method for identifying intentional cruise-phase Mach changes across the entire FOQA dataset. By leveraging statistical CP detection, multi-stage filtering, and turbulence screening, the algorithm detects only those Mach shifts that are operationally meaningful, while removing noise, redundant detections, and unintentional shifts. The resulting dataset represents a set of potential speed-control events that can likely be attributed to flight crew decision-making.

Several observations can be made from these results. First, speed control seems to already be in practice by a sizeable portion of the fleet. Focusing on long-haul widebody flights, approximately 20% of A350-900 flights in the sample exhibited at least one potential speed-control event and nearly 3,000 events were detected across all long-haul widebody flights examined. Also, the average number of slowdowns per 100 flights for the A350-900 is 54, the most significant out

of all widebody airframes. This analysis plays a crucial role in the broader investigation of how terminal area delays can be absorbed upstream in the trajectory to reduce the reliance on holding patterns and vectoring. The results quantify the prevalence of speed-control already used across the fleet, establishing a baseline against which holding and vectoring can be evaluated. The detected events can be integrated into fuel burn models to estimate the potential system-wide benefit of shifting some delay absorption from holding to speed control. The CP dataset informs parallel simulation efforts by providing realistic speed-control magnitudes, durations, and start times. These parameters help improve overall simulation fidelity and insights for modeling and comparison of the different alternative delay management strategies being explored.

Holding Pattern Detection in Threaded Track Data

The detection of holding patterns in TT data builds upon the methodology established in last year's report that focused on the FOQA flights, with several refinements implemented to improve accuracy and exclude go-arounds from the analysis. TT data required additional processing steps compared to FOQA since it does not contain flight phase labels. A fuzzy logic (Junzi et al., 2017) phase identification method was implemented to classify each point in a TT flight as climb, cruise, descent or level using membership functions based on altitude, vertical speed and true air speed. This approach was chosen because fuzzy logic provides a continuous membership-based representation of flight behavior which is well suited to TT data because it avoids hard thresholds and reduces misclassification in regions where climb, level and descent characteristics overlap. Compared to rule-based classification methods, fuzzy logic is more robust to noise and avoids misclassifying brief fluctuations in vertical speed which ensures a more reliable phased identification compared to threshold-based methods. This step ensures that every segment of the TT trajectory is classified into the correct flight phase, allowing the holding detection to be selectively applied to the cruise and descent phases of flight where holding patterns occur. Once the top of descent (ToD) is identified, a go-around detection logic flags flights having a transition from descent to a sustained climb or level-off at low altitude, and those flights are removed before the holding pattern detection algorithm is applied. An example of the fuzzy logic method and the go-around detection applied to a TT flight is shown in Figure 13 where the different phases of flight are categorized along with a go-around. After this filtering, the same geometric self-intersection logic developed previously for FOQA data is applied to the TT flights. An example of this approach is shown in Figure 14, where a FOQA flight with holding pattern in red along with the surrounding TT holds in blue arriving at Hartsfield-Jackson Atlanta International Airport (KATL) are displayed within a 100-nautical-mile radius.

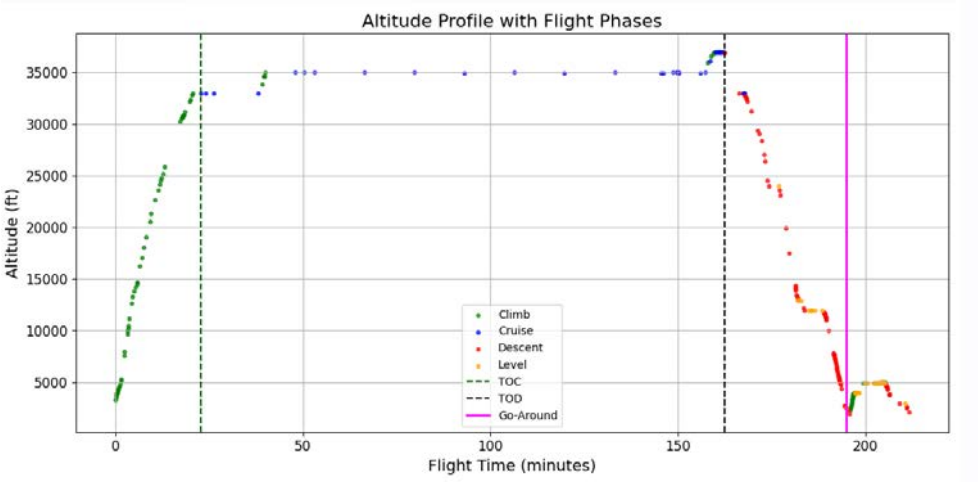


Figure 13. Example of top of descent (ToD) and go-around detection for a threaded track (TT) flight. ToC: top of climb.

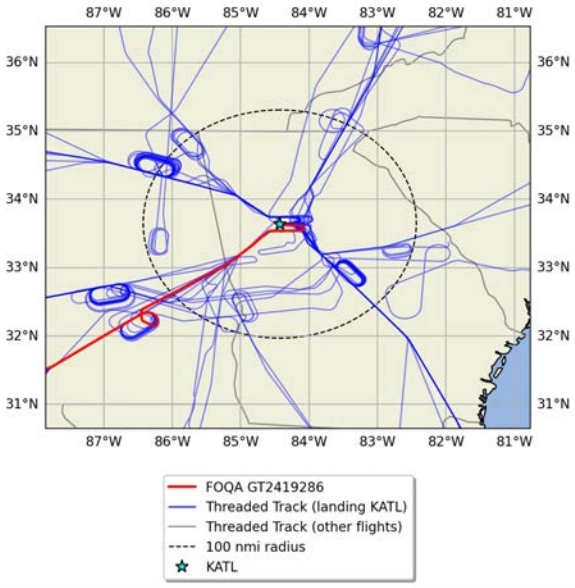


Figure 14. Example of Flight Operations Quality Assurance (FOQA) and threaded track (TT) holding patterns at Hartsfield-Jackson Atlanta International Airport (KATL).

Identifying Holding Stacks and Look-ahead Time

The identification of the holding stack shows how early the holding event becomes visible in the surrounding traffic environment and whether there is sufficient time for cruise speed control implementation to absorb a part or all of the holding pattern. Once the FOQA holdings are isolated, TT data are used to examine the surrounding traffic around the landing airport. The analysis begins with a ±30-min query window to identify TT flights holding within a 100-nmi radius centered around the landing airport. The window is then expanded in a 30-min increment on each side until no additional TT holding is identified. This iterative expansion reveals the holding stack which is defined by the earliest and latest TT holds around the FOQA holding event. This analysis considers FOQA and TT flights with holding patterns detected both in cruise and descent. The relative timing between the onset of the holding stack and the moment the FOQA aircraft enters holding provides a direct measure of the look-ahead time, which indicates whether speed control could be applied early enough to absorb part or all of the hold to potentially save fuel. An example of a holding stack is shown in Figure 15, where each TT hold is plotted relative to the FOQA hold start time. The pink shaded region represents the holding stack window, and the look-ahead time is measured from the earliest TT hold to the FOQA hold start.

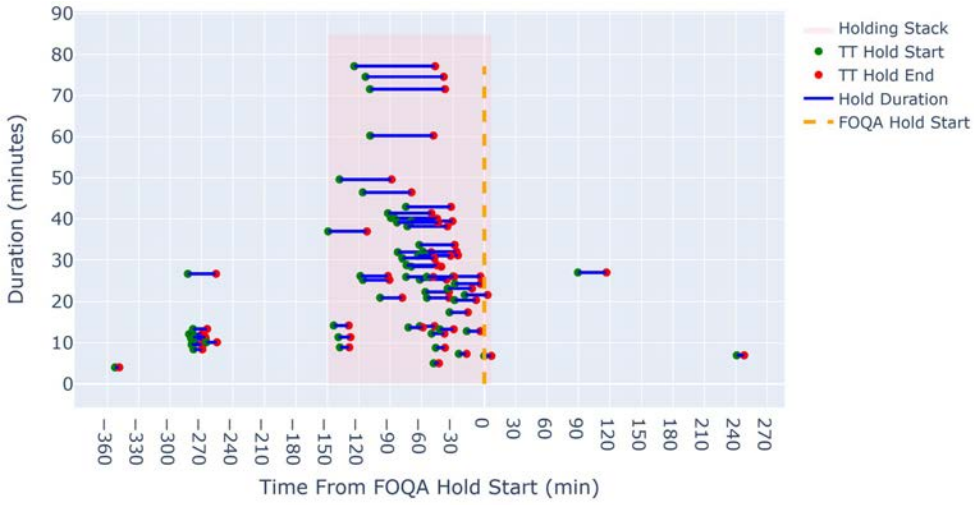


Figure 15. Holding stack of a Flight Operations Quality Assurance (FOQA) flight. TT: threaded track.

The distribution of FOQA flights across holding stack categories is shown in Figure 16. A total of 540 FOQA flights joined an ongoing holding stack, meaning the look ahead time was greater than zero minutes. Among these, 213 flights joined the stack at least 40 min after its formation, providing substantial opportunities for cruise phase speed control application. An additional 116 FOQA flights were the first aircraft to initiate the stack producing zero look-ahead time. Another subset of flights, totaling 202, exhibited isolated FOQA holds, and an additional set of 129 flights could not be evaluated due to the absence of TT data for international destinations. If this analysis is broadened by lowering the look-ahead time from 40 to 20 min, the set of eligible flights for speed control simulation expands. Under this threshold, the number of flights joining the stack at least 20 min after its formation is 350.

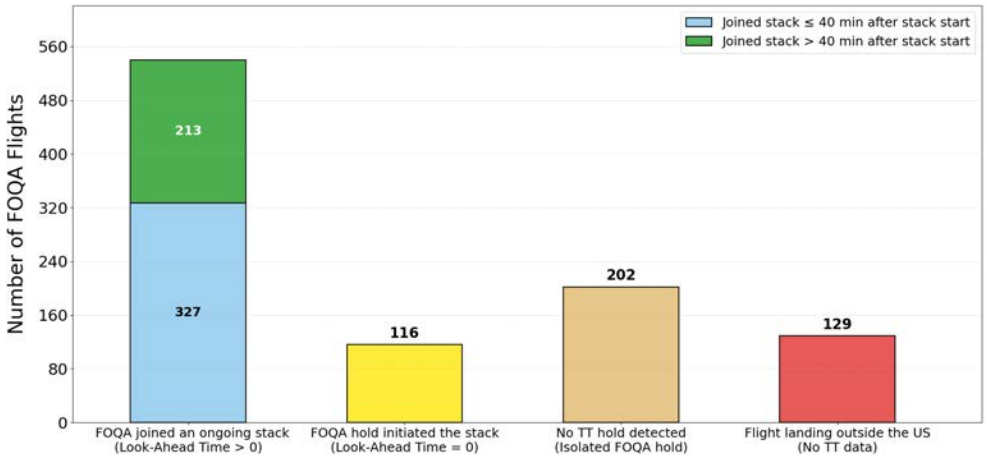


Figure 16. Flight Operations Quality Assurance (FOQA) flights holding stack analysis for 40 min look-ahead time. TT: threaded track.

Flight of Interest for Speed Control Simulation

To determine which FOQA flights represent strong candidates for speed control simulation, the analysis integrates three sources of data: (1) meteorological aerodrome report (METAR) weather observations (ISU, n.d.), (2) on time performance (OTP) (DOT, n.d.), and (3) FAA Air Traffic Control System Command Center Advisories (ATCSCC) (FAA, n.d.). The objective is to identify cases where moderate or severe weather conditions and congestion lead to holding stack formation with

sufficient look-ahead time to implement speed control. METAR data provide a time-resolved view of weather evolution leading to each holding event. Seven weather scenarios are considered in this analysis: heavy precipitation, low visibility below 1 statute mile and low ceiling below 200 ft above ground level, thunderstorms accompanied by lightning and precipitation, freezing rain and ice, moderate to heavy snow, gusty winds exceeding 30 kt, and dense fog. OTP data complement this by classifying record delay minutes into five categories of which Extreme Weather and National Aviation System (NAS) are the most relevant for holding events. Extreme Weather captures severe conditions that restrict safe operations while NAS delays include delays from moderate weather conditions, reduced arrival capacity and congestion. FAA ATCSCCs provide a record of flow management actions issued during the holding events such as ground delay programs, ground stops and arrival delay programs.

A flight is considered a strong candidate for speed control simulation when these three data sources, collectively, indicate a holding stack that was initiated due to predictable or progressively deteriorating weather conditions and when the TT data reveal sufficient look-ahead time before FOQA aircraft enters holding. The overall process for identifying flights of interest for speed control simulation is summarized in Figure 17. The holding detecting algorithm first isolates FOQA flights with holding patterns then matches each FOQA flight with its associated domestic TT flights and identifies holds within this set of TT flights. The earliest and latest TT holds identify the holding stack start and end and the FOQA entry time relative to stack start provides the look-ahead time. Flights with look-ahead time greater than 20 min are then retained for further analysis. The second part of the analysis is to identify the potential holding causes. FOQA flights are matched with domestic TT flights in the same stack to retrieve their OTP delay categories. NAS and extreme weather delays are then extracted and METAR data are analyzed to distinguish between congestion-driven and weather-driven events. Relevant ATCSCC advisories associated with the holding stack window are also collected to determine whether the holding stack contributed to airport congestion and the associated impacting conditions. This analysis identified 169 FOQA flights of interest for speed control simulation, with the potential to leverage the associated TT holds to further expand the cases for fuel savings analysis.

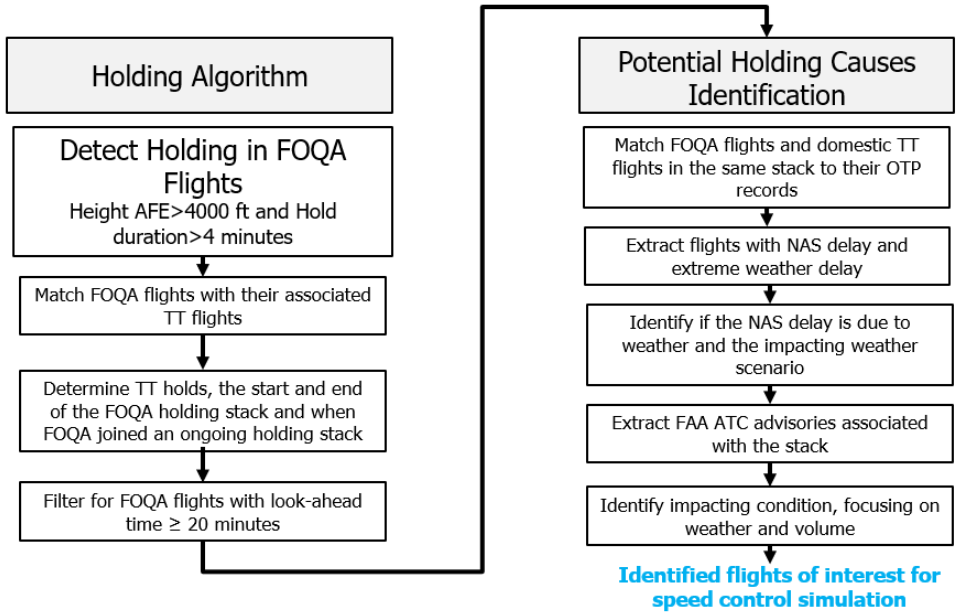


Figure 17. Identifying flights for speed control simulation process. AFE: above field elevation, FOQA: Flight Operations Quality Assurance, NAS: National Aviation System, OTP: on time performance, TT: threaded track.

Example of a Flight of Interest for Speed Control Simulation

After defining the criteria used to identify FOQA flights suitable for speed control simulation through the combined analysis of METAR weather, OTP data, and FAA ATCSCC advisories, an example helps demonstrate how these inputs come



together in an operational context. The following analysis shows an A321 flight originating from KLAX and landing at KATL that entered a holding stack driven by progressively deteriorating weather conditions. METAR observations, presented in Table 2, show early signs of convective development including distant lightning appearing roughly 30 min after the first TT hold, followed by increases in wind gusts, heavy rain and formation of cumulonimbus clouds. Cloud ceilings gradually lowered, and visibility reduced as conditions deteriorated. A summary of METAR abbreviations referenced in this analysis is provided in Table 3. The operational impact of these conditions for the same period is reflected in the OTP records, which indicate 126 min of total arrival delay, of which 101 min were attributed to NAS delay which is consistent with moderate weather or congestion at the landing airport. This delay is further reinforced by showing that the ATCSCC issued a ground delay program at KATL during the same window citing weather and specifically thunderstorms as the impacting weather condition as depicted in Figure 18. Taken together, the METAR, OTP and ATCSSC advisory data collectively provide consistent evidence that the holding stack was driven by approaching convective weather and was formed early enough to support an application of early speed control during cruise.

Table 2. METAR data before and during the holding stack window (ISU, n.d.).

Time relative to start of Holding Stack (HH:MM)	Wind Direction	Wind Speed	Gust	Visibility	Precipitation	Cloud Layer 1	Height 1	Lightning/ Thunderstorm
- 01:00	190°	18 kt	33 kt	8 SM	None	FEW	2900 ft	None
- 00:45	Variable	20 kt	-	9 SM	None	SCT	3100 ft	None
- 00:30	Variable	18 kt	26 kt	9 SM	None	SCT	3100 ft	None
- 00:15	210°	22 kt	28 kt	9 SM	None	BKN	3700 ft	None
Start of Stack	200°	20 kt	30 kt	9 SM	None	SCT	3500 ft	None
+ 00:15	-	19kt	30kt	9 SM	None	BKN	3500 ft	None
+ 00:30	-	18kt	24kt	10 SM	None	SCT	3500 ft	LTG DSNT NW
+ 00:45	210°	19kt	34kt	10 SM	None	SCT	3900 ft	LTG DSNT N
+ 01:00	200°	21kt	28kt	10 SM	None	SCT	3700 ft	LTG DSNT N AND SW
+01:15	270°	-	31kt	5 SM	-RA	SCT	2000 ft	LTG DSNT NE AND SW
+01:30	270°	15kt	22kt	2.5 SM	+RA BR	SCT	1300 ft	LTG DSNT N
+01:45	260°	9 kt	-	7 SM	-RA	FEW	2500 ft	LTG DSNT, TS NE-SE
+02:00	260°	9 kt	14 kt	10 SM	None	FEW	2500 ft	LTG DSNT, CB DSNT
+02:15	260°	10 kt	-	10 SM	None	FEW	2500 ft	LTG DSNT, CB DSNT
+02:30	260°	8 kt	-	10 SM	None	FEW	2500 ft	LTG DSNT, CB DSNT
+02:45	260°	8 kt	-	10 SM	None	FEW	2500 ft	LTG DSNT, CB DSNT
End of Stack +02:50	260°	7 kt	-	10 SM	None	BKN	4500 ft	LTG DSNT, CB DSNT



Table 3. METAR abbreviation guide.

Category	Code	Meaning
Precipitation	-RA	light rain
	+RA	heavy rain
	BR	mist
Lightning or Thunderstorm	DSNT	distant
	LTG	lightning
	TS	thunderstorm
Cloud Layer	FEW	few clouds
	SCT	scattered clouds
	BKN	broken clouds
	CB	cumulonimbus (cloud associated with thunderstorms)

ATCSCC Advisory

ATCSCC ADVZY XXX **ATL/ZTL** XX/XX/XXXX **CDM GROUND DELAY PROGRAM**

MESSAGE: CTL ELEMENT: ATL
ELEMENT T
ADL TIME: +2h39min from start of stack
DELAY ASSIGNMENT MODE: UDP
ARRIVALS ESTIMATED FOR: +1h55min to +3h49 min from start of stack
CUMULATIVE PROGRAM PERIOD: +1h55min to +3h49min from start of stack
PROGRAM RATE: 60
FLT INCL: CONTIGUOUS US DEP CARRIER DAL ONLY
DEP SCOPE: (1STTIER) ZTL ZDC ZHU ZJX ZME ZID
CANADIAN DEP ARPTS INCLUDED: NONE
DELAY ASSIGNMENT TABLE APPLIES TO: ZTL
MAXIMUM DELAY: 136
AVERAGE DELAY: 47
IMPACTING CONDITION: WEATHER / THUNDERSTORMS
COMMENTS: DAL AND DAL SUBS ONLY. RATE 60. SCOPE 1ST TIER. PLEASE APPLY EDCTS.

EFFECTIVE TIME: +2h31min to +4h49min from start of stack

SIGNATURE: +2h33min from start of stack

Figure 18. Air Traffic Control System Command Center Advisories (ATCSCC) ground delay program advisory at Hartsfield-Jackson Atlanta International Airport (KATL) (FAA, n.d.).

Summary and Observations of the Holding Detection Algorithm

The holding detection methodology developed in this effort builds upon and extends the approach established in last year's report. The geometric self-intersection logic for FOQA data has been adapted for TT data through the addition of fuzzy logic phase identification, which enables accurate classification of flight phases. This step removes flights with go-arounds and ensures that the holding detection is only applied during cruise and descent phases where holding patterns occur. Once holdings are identified, TT data are used to examine surrounding traffic and identify holding stacks through an iterative query expansion that captures the earliest and latest TT holds around each FOQA event. The relative timing between the onset of the holding stack and the instance the FOQA aircraft enters holding provides the look-ahead time, which indicates whether speed control could be applied early enough during cruise to absorb part or all the hold. The integration of METAR weather observations, OTP delay records and ATCSCC advisories provide insight into what caused each holding event and allows the selection of flights where the holding stack formed due to foreseeable conditions. This methodology has been validated through application to the dataset and has demonstrated reliable results in identifying holding events, holding stacks and the cause behind the stack formation.



The outputs of this analysis directly support two subsequent tasks in the project. For Task 1, the identified flights of interest provide realistic cases for trajectory evaluation of speed control strategies, with the look-ahead time serving as the key input for determining how early speed control can be initiated and how much of the hold can be absorbed during cruise. Based on the distribution of FOQA flights across holding stack categories, an average look-ahead time of approximately 40 min represents a practical threshold for identifying cases where meaningful fuel benefits from cruise speed control become achievable, with longer cruise segments providing more opportunity for speed reductions and therefore greater fuel savings. This suggests that the primary candidates for speed control are wide-body on long-haul routes and narrow-body aircraft operating cross-continental flights. For Task 4, this methodology enables fleet-wide analysis by identifying all flights entering a holding stack at a given airport, along with their associated look-ahead times, to quantify fuel benefits achievable through coordinated speed control across all affected flights.

Vectoring Identification

Vectoring often occurs when arriving traffic flight plans must be changed due to congestion and weather disruptions to slow down the arrival rate at the destination airport. Vectoring is the navigational guidance that ATC provides to aircraft through instructions on heading, altitude, or speed, causing aircraft to deviate from their nominal arrival paths (SKYbrary Aviation Safety, n.d.). Instead of placing aircraft into holding patterns, controllers use vectoring, such as prolonged downwind legs or zigzagging, to absorb delay and maintain required spacing (Erzberger et al., 2016; FAA, 2026b). However, vectoring can be difficult to detect in trajectory data (Zhang et al., 2022). Challenges include separating vectoring from deviations driven by the choice of original flight plans filed, by weather, or by turbulence and uncovering vectored flights from variations in FOQA metrics. Additionally, differentiating between flights vectored for sequencing or weather and flights vectored due to arrival airport congestion poses a significant challenge. To address these challenges, the initial work is currently assessing various analytical techniques that might be best suited for detecting vectoring in FOQA data, leading to exploration of two potential approaches: a machine learning approach and a clustering-based trajectory analysis method. Given the infancy of the machine-learning approach research, this report focuses on the preliminary results derived from the clustering approach.

Data Preparation for FOQA Calendar Year 2023 and Arrival Routes

Data preparation used FOQA arrival trajectories from calendar year (CY) 2023 along with the corresponding FAA standard terminal arrival (STAR) procedures obtained from the FAA National Airspace System Resources (NASR) database (FAA, 2026a). The STAR data were collected to serve as reference paths for identifying potential ATC vectoring events. When an aircraft follows a particular STAR and then deviates significantly from the published route, this deviation may indicate vectoring by ATC. By comparing FOQA trajectories against published STAR routes, deviations from expected paths can be detected and flagged for further analysis. Flights with holding patterns were removed using the holding pattern detection algorithm, and flights were filtered from top of descent onward to focus on terminal areas as a first step in this analysis before expanding to en-route detection. For the STAR routes, the most recent waypoint information and route segments were selected based on effective dates, as defined by the FAA. The STAR entries for the airport were filtered, their codes identified, and the associated segments collected. The STAR waypoints were then combined with their location data so the routes could be traced and used as reference paths when comparing against FOQA trajectories. An example of 2023 STAR routes for KATL airport is shown in Figure 19.

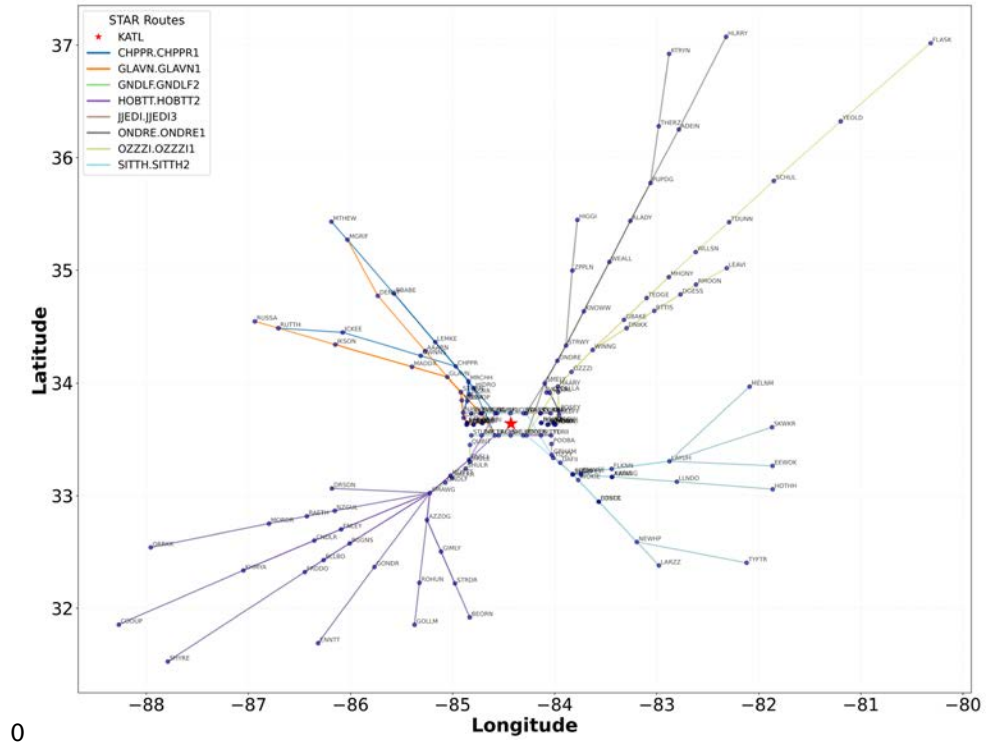


Figure 19. Example of 2023 standard terminal arrival (STAR) routes configuration for Hartsfield-Jackson Atlanta International Airport (KATL).

Machine Learning Approach for Vectoring Identification

The objective is to use machine learning (ML) techniques to characterize ATC vectoring as the first step towards detecting and classifying vectoring events in FOQA data. From the identification of vectoring events, fuel burn impacts due to vectoring can be quantified. The One-Class Support Vector Machine (OC-SVM) is an anomaly detection method that learns the boundary to separating "normal" data from outliers. The OC-SVM approach is trained only with “normal” data, meaning it learns what the typical flight behavior looks like, and anything that deviates significantly is considered an anomaly. For vectoring detection, OC-SVM is fed flight trajectories, determines the regions of data that are "normal," and identifies any deviation from this normal behavior as a vectoring event.

One-Class Support Vector Machine for Vectoring Detection

The OC-SVM, a machine learning technique used in anomaly detection, will be used to detect vectoring events within the flight data (Basora et al., 2019; Guo et al., 2022). In this analysis, the en-route and terminal phases are considered separately due to differing trajectory flows. The en-route phase is characterized by high variability in flows due to flexibility in flight plans, while the terminal phase has lower variability because of sequencing and approach requirements. The initial focus is on detecting vectoring events within the terminal/approach area. The process starts with building a planned route for one airport’s arrivals from FOQA flights and STAR data. Then the deviations along each flight, in terms of cross-track distance compared to the “reference route,” will be computed. Next, the OC-SVM will be trained using these computed deviations. Finally, this OC-SVM will be used to detect vectoring events as consecutive anomaly seconds exceeding a predefined threshold (e.g., 20 sec). The analysis can be expanded to all flights by looking at the arrivals of all airports in the FOQA and TT data to obtain system-wide insights.

Clustering Approach for Vectoring Identification

A clustering approach is used to group arrival trajectories based on how similar their lateral shapes are, where lateral shapes refer to the horizontal path of the aircraft as projected on the ground. The method relies on the Ordering Points to Identify the Clustering Structure (OPTICS) algorithm (Scikit Learn, 2025), which identifies clusters at different density levels



and does not require choosing the number of clusters in advance. The key parameters used are xi, which controls how clusters are separated, and min_samples, which sets the minimum number of flights needed to form a cluster. To compare the shapes of different trajectories, dynamic time warping (DTW) (DTAIDistance, n.d.) is used to measure the similarity between trajectories. DTW is a time series alignment technique that computes the optimal match between two sequences of different lengths or speeds, which makes it well suited for comparing FOQA flights that vary in duration and speed. These parameters provide a way to group flights with similar patterns and identify where deviations occur. To evaluate how the model is performing and the quality of the clusters, silhouette scores are calculated. This metric measures how similar a trajectory is to others in its own cluster compared to trajectories in neighboring clusters, with values ranging from -1 to 1, where higher values indicate well separated clusters.

Clustering Use Case and Preliminary Results

The clustering approach was applied to a two-week set of arrival trajectories into KATL to assess how well the method separates standard arrival flows from trajectories that diverge from the published STAR procedures. Each trajectory was trimmed from top of descent onward before being compared using DTW. An OPTICS parameter sweep over a range of xi and min_samples values was performed, and the silhouette score was used to identify the best parameter values. The configuration that yielded the highest silhouette score was min_samples = 35 and xi = 0.03, with a score of 0.704. This configuration revealed four primary arrival clusters that aligned closely with the STAR routes, as shown in Figure 20, indicating that the method can reasonably capture the dominant flow structure. A substantial fraction of flights was classified as noise, which suggests that additional feature refinement is needed to more reliably isolate vectoring. Overall, the two-week KATL use case demonstrates that clustering provides a useful first step toward identifying trajectories that diverge from expected arrival paths.

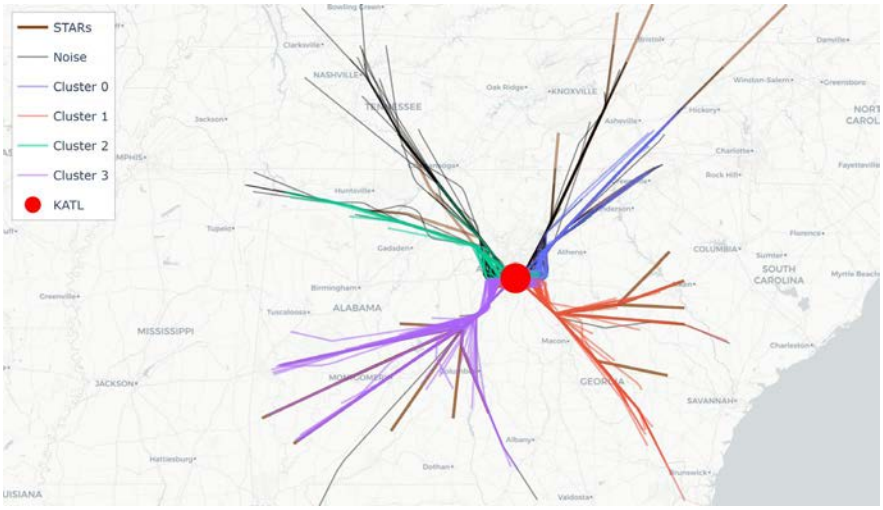


Figure 20. Clustering analysis on Hartsfield-Jackson Atlanta International Airport (KATL) arrivals (two-week period).

Milestones

- Completed speed control detection algorithm and analysis on all widebody 2023 FOQA flights.
- Extended holding pattern detection methodology from FOQA data to TT data.
- Developed an iterative query expansion method to identify holding stacks and calculate look-ahead time calculation for each FOQA flight relative to stack formation.
- Identified flights of interest for speed control simulation.

Major Accomplishments

- Implemented fuzzy logic phase identification to classify flight phases in TT data and remove go-arounds from the analysis.
- Integrated METAR weather observations, OTP delay records and ATCSCC advisories to determine the cause behind holding stack formation.



- Established a look-ahead time of approximately 40 min as a practical threshold for achieving meaningful fuel benefits from cruise speed control.
- Completed speed control algorithm to identify speed control events in the FOQA data.
- Obtained speed control results and performed analysis for 2023 widebody FOQA data.
- Created algorithm to support OC-SVM by assigning each flight its own terminal reference route using STAR data.
- Implemented the first version of the clustering methodology, including DTW similarity computation, and OPTICS clustering.
- Produced the first clustering results for a two-week KATL arrival dataset, identifying four dominant arrival patterns aligned with STAR routes.

Publications

None.

Outreach Efforts

Participated in ASCENT biannual meetings.

Awards

None.

Student Involvement

- Jouwairia Ahabchane (graduate student) created the holding pattern detection algorithm, analyzed the holding events and implemented the vectoring detection using clustering approach
- Vishva Rana (graduate student) worked on the changepoint detection algorithm to identify speed control events and vectoring detection utilizing one-class support vector machine

Plans for Next Period

- Assign each 2023 flight with its own STAR to create a list of “reference routes” for every flight.
- Calculate the deviations between these flights and their respective STARs.
- Train and use the OC-SVM to detect vectoring events.
- Assign STAR procedures to each cluster to better understand how arrival flows relate to published routes and to refine cluster interpretation.
- Incorporate STAR deviation metrics into the clustering analysis, expanding the feature set beyond lateral trajectory shape to help reduce noise.
- Identify vectored flights by combining clustering results with STAR deviation measures and quantify the additional time and fuel burn associated with ATC vectoring.
- Compare the two analytical approaches, the machine-learning method and the clustering-based trajectory analysis, to determine which more reliably identifies vectoring behavior.
- Expand the use case to TT data at a single airport, specifically KATL.

References

Aminikhanghahi, S. & Cook, D. J. (2017). A survey of methods for time series change point detection. Knowledge and Information Systems, 51, 339–367. https://doi.org/10.1007/s10115-016-0987-z

Basora, L., Olive, X., & Dubot, T. (2019). Recent Advances in Anomaly Detection Methods Applied to Aviation. *Aerospace, 6*(117). https://doi.org/10.3390/aerospace6110117

DOT. (n.d.). *On-Time Performance (OTP) data* [Data set]. U.S. Department of Transportation, Bureau of Transportation Statistics.

DTAIDistance, (n.d.). *Dynamic Time Warping (DTW) — usage documentation.* https://dtaidistance.readthedocs.io/en/latest/usage/dtw.html

Erzberger, H., Nikoleris, T., Paielli, R. A., & Chu, YC. (2016). Algorithms for Control of Arrival and Departure Traffic in Terminal Airspace. Proceedings of the Institution of Mechanical Engineers Part G Journal of Aerospace Engineering, 230(9), 1762-1779. https://doi.org//10.1177/0954410016629499

FAA. (n.d.). *Advisory Database Form.* Federal Aviation Administration. https://www.fly.faa.gov/adv/advAdvisoryForm



FAA. (2026a). 28 Day NASR Subscription. Federal Aviation Administration. https://www.faa.gov/air_traffic/flight_info/aeronav/aero_data/NASR_Subscription/
FAA. (2026b). Section 4. ATC Clearances and Aircraft Separation (Ch. 4). In *Aeronautical Information Manual* (Chg. 2). Federal Aviation Administration. https://www.faa.gov/air_traffic/publications/atpubs/aim_html/index.html
Fryzlewicz, P. (2014). Wild binary segmentation for multiple change-point detection. Annals of Statistics, 42(6), 2243–2281. https://10.1214/14/AOS1245
Guo, Z., Yin, C., Zeng, W., Tan, X., & Bao, J. (2022). Data-Driven Method for Detecting Flight Trajectory Deviation Anomaly, *Journal of Aerospace Information Systems*, 19(12), 799–810. https://doi.org/10.2514/1.I011124
ISU. (n.d.). Iowa Environmental Mesonet. Iowa State University. https://mesonet.agron.iastate.edu/request/download.phtml
Junzi, S., Ellerbroek, J., & Hoekstra, J. (2017). Flight extraction and phase identification for large automatic dependent surveillance–broadcast datasets. *Journal of aerospace information systems,* 14(10), 566-572. https://doi.org/10.2514/1.I010520
Scikit Learn. (2025). *OPTICS Clustering Algorithm Documentation*. https://scikit-learn.org/stable/modules/generated/sklearn.cluster.OPTICS.html
SKYbrary Aviation Safety. (2025). Basic Controller Techniques: Vectoring | SKYbrary Aviation Safety. https://skybrary.aero/articles/basic-controller-techniques-vectoring
Truong, Oudre, L., & Vayatis, N. (2018). *ruptures: change point detection in Python*. arXiv:1801.00826 (eprint). https://doi.org/10.48550/arXiv.1801.00826
Zhang, S., Zhang, Y., Tay, T., & Shankar, J. (2022). Learning-based Aircraft Trajectory Analysis Tool for Holding and Vectoring Identification with ADS-B Data. *2022 IEEE 25th International Conference on Intelligent Transportation Systems* (ITSC), Macau, China (pp. 1100-1105). https://10.1109/ITSC55140.2022.9921823

Task 3 - Fuel Burn Surrogate Modeling

Georgia Institute of Technology

Objective

The primary objective of this task is to develop a capability to predict fuel flow any time within a flight profile. This granular prediction capability is essential for accurately quantifying the potential fuel benefits derived from optimized flight trajectories. By enabling the evaluation of fuel flow at any given point, this research supports the assessment of en-route speed control to maximize fuel efficiency.

Research Approach

Data Preparation

The study utilized a massive dataset comprising 50,000 FOQA flights from 2023, spanning both widebody (e.g., A350, B767) and narrow-body (e.g., A321, B737) aircraft categories. A flight segmentation algorithm was developed to partition flight data into distinct main flight phases: climb, cruise, cruise step-climbs, and descent. The analysis placed a specific focus on the cruise segment which is defined as the period between top of climb (ToC) and ToD capturing both steady altitude phases and step climbs (i.e., high rate of climb and altitude jumps). To ensure data quality and remove high-frequency noise, a 1-min moving average smoothing technique was applied to critical variables, including mean sea level (MSL) altitude, temperature, corrected gross weight, Mach number, and total fuel flow. Following this, the processed segments were concatenated by aircraft type to form a unified training dataset.

Modeling Methodology

The modeling framework evolved from the previous tree-based approach to a regularized polynomial regression architecture, balancing predictive performance with physical interpretability. While previously, the tree-based models that used XGBOOST (XGBoost Developers, 2025) demonstrated higher accuracy, it functioned as a black box model and produced counterintuitive, non-smooth, relationships between the key model features. To address this, the current methodology shifted to a regularized least squares regression using a third-degree polynomial model. This approach provides the general polynomial equation used in making the fuel flow predictions, and it ensures smooth physical behavior between the model features. The polynomial model framework was used in building fuel flow models for all aircraft in the FOQA data. Within this framework, a comparative assessment was conducted between Elastic Net (Truong et al., 2018) (optimizing both alpha and the L1/L2 ratio) and L1 regularization (Least Absolute Shrinkage and Selection Operator) (LASSO) (Scikit-learn, n.d.). While Elastic Net regularization constrained coefficients magnitudes, it yielded lower

predictive accuracy compared to the L1 approach. Consequently, the LASSO technique was selected for model architecture (Scikit Learn, n.d.).

The modeling process was grounded in feature selection and pre-processing protocol (see Figure 21). To ensure model stability and exclude sensor anomalies or extreme outliers, the training data were trimmed to strictly include values between the 5th and 96th percentiles. The core feature set defined for the cruise phase included best available MSL altitude (ft), outside air temperature (°C), corrected gross weight (lb), calculated Mach, and a temporal feature, Mach change over 20 s as an acceleration proxy, to capture transient speed effects. For step climb segments, this feature set was augmented with rate of climb, with fuel flow total (lb/hr) serving as the target response variable for all models. These features served as inputs to the LASSO framework. By applying L1 regularization, the model automatically performed feature selection, isolating the most significant polynomial terms and shrinking redundant terms to zero. To validate the model's robustness, a comprehensive cross-validation strategy was employed. This process involved iteratively splitting the data into training and validation subsets to ensure that the selected hyperparameters and polynomial terms generalize well to unseen data, rather than overfitting specific trajectory characteristics found in the training set. This training methodology was batch-applied consistently across all airframes in the dataset, ensuring a standardized modeling approach while producing a unique, optimized coefficient set for each specific aircraft type depending on their fuel flow behavior.

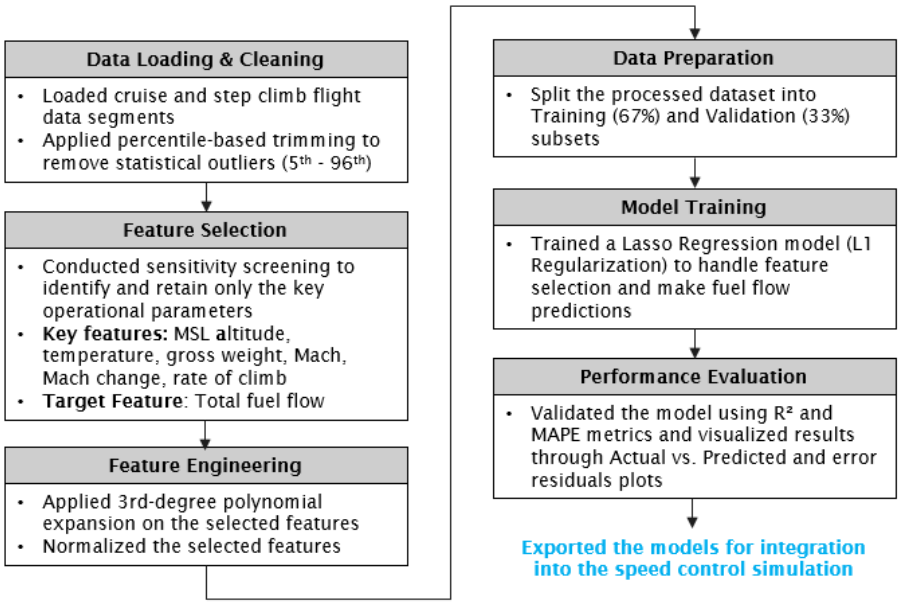


Figure 21. Surrogate model building process. MAPE: mean absolute percent error, MSL: mean sea level.

Models Validation

The validation assessment relied on a segmented analysis to evaluate model fidelity across distinct flight regimes. To assess model accuracy, performance metrics such as mean absolute percent error (MAPE) and R^2 were calculated separately for steady-state cruise and step-climb phases. The comprehensive breakdown of the analyzed fleet, including specific engine configurations, valid Mach ranges, and the volume of flight data for each airframe is listed in Table 4. Notably, the number of available flights varies across the fleet, a factor that directly influences the data density available for training and validation. Despite this variance, the surrogate models were validated across diverse operational profiles. The table lists the aggregate validation metrics for both flight phases, providing the numerical basis for the comparative analysis presented in the subsequent figures.

A side-by-side comparison of model performance across the fleet for both steady cruise and step climb phases is depicted in Figures 22 and 23. The steady cruise models consistently outperform the step climb models, maintaining error rate below 2.5% as shown in Figure 22. However, (R^2) shows that several airframes, particularly narrowbodies such as the 757-300 exhibit significantly higher R^2 values for step climb despite having high error rates, this potentially stems from the



variance in the target variable in the step climb model, conversely, the low variance in target value for the steady-state cruise model makes achieving a high R^2 challenging as seen in Figure 23. This suggests that the achieved batch processing of all airframes using one modeling framework may not be ideal; segmentation strategies by tail number or different modeling techniques might be required to harmonize the accuracy metrics across the different flight phases. Current investigations are exploring advanced mitigation strategies, such as refined smoothing techniques and the previously mentioned segmentation techniques, to better isolate these transient behaviors and improve prediction accuracy for both phase models.

The validation residuals and actual-by-predicted results for a wide-body aircraft cruise segment are depicted in Figure 25. The data cover a typical operational cruise envelope, spanning fuel flow rates from approximately 10,500 lb/hr to 13,500 lb/hr. Across this range, the percentage error is primarily bound between -5% and +5%, with a MAPE of 1.84% and R^2 of 0.84.

Table 4. Comprehensive summary of the analyzed fleet parameters and validation metrics for cruise and Step Climb (SC) phases. FOQA: Flight Operations Quality Assurance, MAPE: mean absolute percent error.

Airframe with Engine Type	FOQA Flight Count	Cruise Mach Range	Cruise R^2	Cruise MAPE	SC R^2	SC MAPE
A350-900 Trent 1000	675	0.79 - 0.87	0.80	2.42%	0.85	3.37%
A330-900 Trent 7000	598	0.76 - 0.83	0.71	2.44%	0.79	3.28%
A330-300-CF6-80	311	0.78 - 0.83	0.75	2.11%	0.72	3.68%
A330-300 PW4000-100	450	0.78 - 0.83	0.76	2.02%	0.84	3.46%
A330-200 PW4000-100	232	0.78 - 0.83	0.77	2.09%	0.84	3.52%
A321-200 PW1100G	2173	0.74 - 0.79	0.66	1.89%	0.82	5.32%
A321-200 CFM56-5B-C	10271	0.74 - 0.80	0.58	2.06%	0.85	5.19%
A320-200 CFM56-5A	4665	0.74 - 0.80	0.54	2.13%	0.71	5.36%
A319-100 CFM56-5A	4100	0.75 - 0.80	0.59	2.07%	0.64	5.61%
A220-300 PW1500G	915	0.75 - 0.79	0.59	2.28%	0.71	4.85%
A220-100 PW1500G	1768	0.75 - 0.80	0.59	2.32%	0.75	5.19%
767-400/ER CF6-80	244	0.76 - 0.83	0.84	1.83%	0.87	3.45%
767-300/ER CF6-80	297	0.78 - 0.83	0.78	1.85%	0.85	3.58%
767-300/ER PW4000-94	773	0.76 - 0.83	0.78	2.01%	0.84	3.59%
757-300 PW2000	701	0.75 - 0.82	0.53	2.19%	0.88	4.51%
757-200 PW2000	5438	0.76 - 0.81	0.61	2.63%	0.76	6.02%
737-900 CFM56-7	9371	0.75 - 0.80	0.69	1.75%	0.89	4.62%
737-800 CFM56-7	3236	0.73 - 0.80	0.63	2.03%	0.88	4.92%
717-200 BR715	3706	0.70 - 0.78	0.61	1.90%	0.63	4.32%

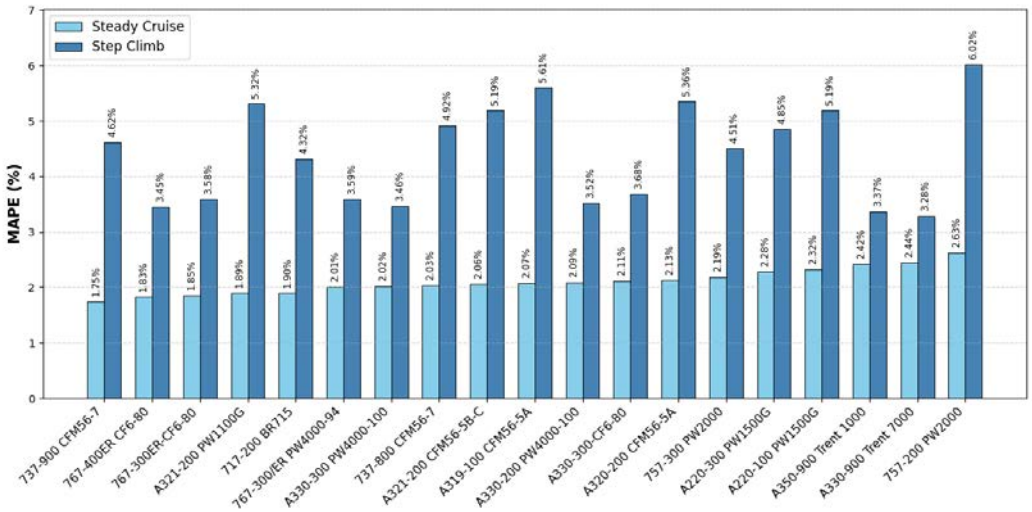


Figure 22. Comparative distribution of mean absolute percent error (MAPE) across the analyzed fleet for step cruise and step climb (SC) phases.

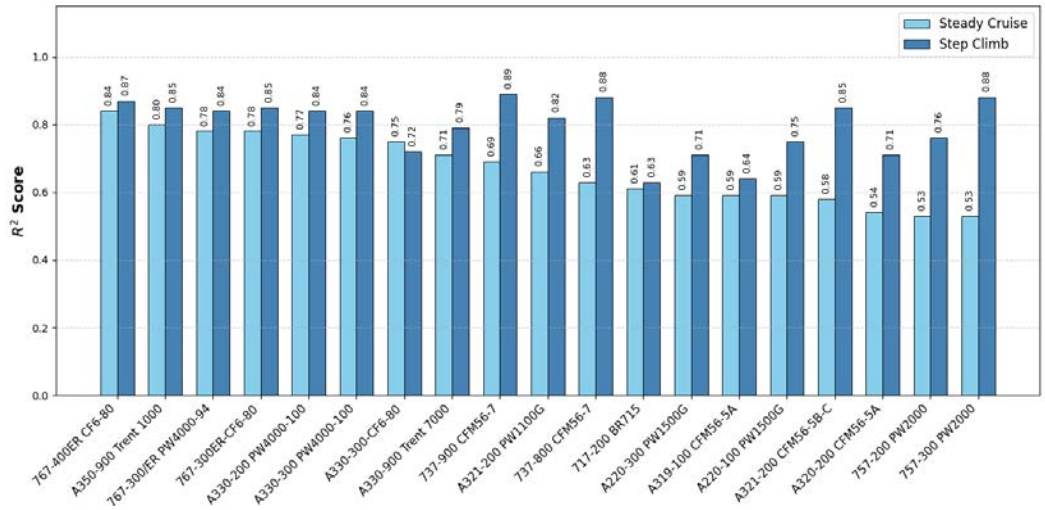


Figure 23. Comparative distribution of R^2 across the analyzed fleet for steady cruise and step climb (SC) phases.

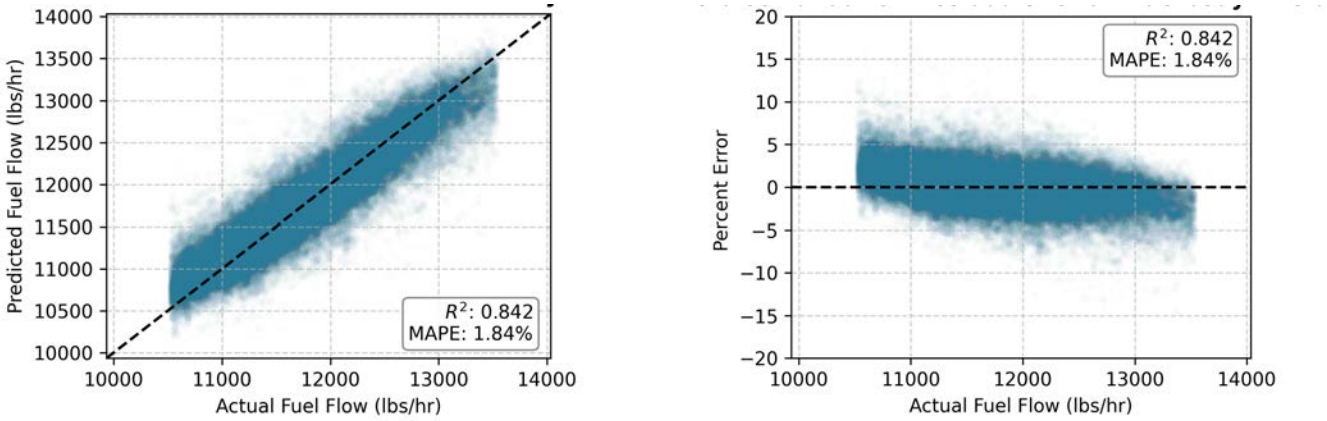


Figure 24. Wide-body aircraft actual by predicted (left) and percentage error residuals (right) of fuel flow prediction. MAPE: mean absolute percent error.

Milestones

- Developed surrogate models for all aircraft in the FOQA fleet for cruise and step-climb phases.

Major Accomplishments

- Successfully developed LASSO-regularized polynomial models that achieved a fleet-wide MAPE of approximately 2.1% during steady-state cruise (ranging from 1.75% to 2.63% by airframe). This validates the surrogate model's ability to provide predictions of fuel consumption under standard operating conditions.
- Demonstrated that these current surrogates operate orders of magnitude faster in simulation compared to previously attempted modeling techniques, this speed is critical for enabling large-scale fleet analysis and optimization.

Publications

None.

Outreach Efforts

Participated in ASCENT biannual meetings.

Awards

None.

Student Involvement

Ghizlane Jari (graduate student) was responsible for all elements of this task of creating fuel flow surrogate models

Plans for Next Period

The research roadmap for the upcoming period centers on the refinement of the existing surrogate framework. A primary objective is to enhance the model's handling of dynamic segments, specifically step climbs, to reduce prediction error. Concurrently, the research scope will expand to potentially include the development and validation of surrogate models for remaining flight phases.

References

Scikit Learn. (n.d.). *Lasso*. https://scikit-learn.org/stable/modules/generated/sklearn.linear_model.Lasso.html
Scikit-learn. (n.d.). *ElasticNet*. https://scikit-learn.org/stable/modules/generated/sklearn.linear_model.ElasticNet.html
Truong, Oudre, L., & Vayatis, N. (2018). *ruptures: change point detection in Python*. arXiv:1801.00826 (eprint). https://doi.org/10.48550/arXiv.1801.00826

XGBoost Developers. (2025). *XGBoost Documentation — xgboost 3.1.1 documentation*. (2025). https://xgboost.readthedocs.io/en/stable/

Task 4 – Fleet-wide speed control strategy

Objective

The objective of this task is to develop an initial fleet-wide speed control strategy to maximize total fuel savings while respecting various operational constraints. This effort builds upon the single-flight analyses by extending the methodology developed to a fleet-wide scope. To achieve this, TT data are needed to augment the available FOQA data to capture all the flights by all airlines that might be impacted by predictable delays and that might benefit from some speed control tactics. Therefore, this task aims to generalize the quantification of fuel savings from single flights to all flights impacted by delay-inducing events.

Research Approach

In tasks highlighted previously, a simulation is developed to estimate fuel burn on a trajectory: a trajectory described in FOQA data is used as a baseline trajectory and speed control tactics are then investigated to see how much fuel could be saved by selecting a lower cruise speed and thus absorbing some of the time that would otherwise be spent in holding patterns. The trajectory simulation runs cases at different Mach numbers and for different amounts of absorbed time. It then outputs the fuel savings for each case alongside the duration of the speed control slow-down and the amount of fuel saved. This task aims to expand the single flight analysis to a system-wide analysis. While the holding pattern detection algorithm helped identify FOQA flights with holding patterns for which the simulation can be leveraged, this represents neither an event-wide assessment nor a system-wide assessment of fuel burn benefits as many other flights are also impacted and could benefit from slowing down early. A more comprehensive database of flights needs to be used, and the research team decided to augment the FOQA data with TT data. For example, for a severe weather event at an arrival airport, aircraft will enter holding patterns such as the ones depicted in Figure 25, where the aircraft in green represent flights for which the research team has FOQA data, while the other aircraft depicted in black have TT data. This task is an initial attempt to quantify a system level disruption event at a single airport and is in its infancy stage of formulation for the current effort.

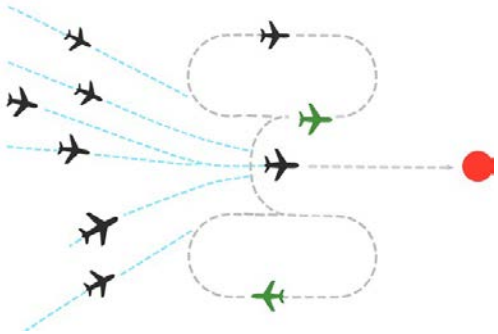


Figure 25. Multiple flights arriving at airport with a holding event due to severe weather.

Data Preparation

To carry out an event-wide or system-wide assessment, TT data are used to account for most of the air traffic coming into an airport where some disruption is first detected in the FOQA data. However, two challenges arise when using TT data. First, unlike FOQA data, which were limited to the fleet of aircraft operated by one major air carrier that provided the data, this is not inclusive of all aircraft types that operate on any given day. Hence, the surrogate models of aircraft fuel flow created in Task 3 do not cover the entire fleet of aircraft that may be impacted by terminal delays. Assumptions must be made for the initial system-wide assessment, and aircraft that are deemed similar will use the same fuel burn surrogate models. The fuel flow surrogates models are currently limited to a subset of narrow and wide-body aircraft and do not include turboprops, regional jets, business jets, and other general aviation aircraft. For instance, the A350-900 surrogate model could be used as a proxy to represent the fuel burn of a B787-10. Second, TT data are not as *parameter-rich* as FOQA data and a few parameters essential to estimate fuel flow are not available, as listed in Table 5. Indeed, TT data are



essentially a reconstructed continuous flight path that is processed, sequenced, and cleaned. However, it is missing environmental information such as wind direction, wind speed, outside air temperature, as well as operational parameters such as aircraft gross weight and Mach number. As a result, data pre-processing is needed to synthesize some of these parameters.

Table 5. Comparison of Flight Operations Quality Assurance (FOQA) data and threaded track (TT) data.

Category	FOQA	Threaded Track
Trajectory data	Sampled at 1Hz: Time, Latitude, Longitude, Altitude, True air speed, Ground speed and Heading	Non-uniformly sampled with up to 500s between entries, Latitude, Longitude, Altitude, True air speed and Ground speed
Aircraft/Engine data	Gross weight, fuel flow total, Total fuel used (all engines)	N/A
Environmental data	Wind speed, Wind direction, Drift angle, Air temperature and Headwind	N/A

To augment the TT data with the missing parameters needed for the fuel flow surrogates, several assumptions are initially made. First, all flights are modeled under zero wind conditions and standard atmospheric conditions In addition, the gross weight of the aircraft must be estimated. This is a challenging task as the aircraft gross weight in the TT data is unknown for each aircraft type flight. As such, approximation is needed based on using the weight of aircraft with similar capabilities and with similar remaining distances to fly based on the FOQA data and fuel flow surrogates developed in Task 3. This approach assumes that aircraft of similar sizes with similar distances to cover until their destination will statistically have similar gross weights. Although this is a simplifying assumption, it is likely reasonable first step to understand the system's behavior. FOQA data are leveraged to generate this surrogate model by regressing aircraft's gross weight against the remaining distance to destination for each subfleet of aircraft. These assumptions serve the first iteration, with future refinements that will include more realistic wind conditions.

Methodology

This initial framing of the methodology aims to investigate the fuel-saving potential of fleet wide speed control strategies while respecting operational requirements such as arrival sequencing and arrival times to the airport with a holding event. Several research questions arise as the team is formulating an approach for the assessment at a single airport for a single day. To understand the complexity of the problem, an example of weather disruption at KATL was investigated based on the holding detection analysis of the FOQA and TT data in Task 2. Flights arriving at KATL for a day in 2023 and entering a holding pattern to build a holding stack are listed in Table 6, where the FOQA flight is highlighted in green. As evident, there is a diversity of aircraft types, when a flight entered the holding stack, the starting and ending altitude of the first holding loop (although multiple may exist for a given flight), the duration of that loop, and the look ahead time.



Table 6. A stack of flights arriving at Hartsfield-Jackson Atlanta International Airport (KATL) and entering holding patterns due to severe weather.

c	Departure Airport	Arrival Airport	Loop 1 Start Altitude (ft)	Loop 1 End Altitude (ft)	Loop 1 Duration (min)	Look Ahead Time (min)
B752	KORF	KATL	8,048	4,037	31.1	0
B739	KSTL	KATL	6,530	5,027	16.1	3.42
B752	TIST	KATL	25,000	24,974	27.1	12.52
A320	MMMY	KATL	20,986	18,000	45.2	15.82
A20N	KTPA	KATL	33,002	33,000	42.7	20.68
A319	KDAL	KATL	22,000	22,003	39.9	25.48
A321	KDFW	KATL	24,839	21,002	34.9	27.12
A321	KDEN	KATL	27,934	24,000	27.6	36.45
B739	KSEA	KATL	26,268	24,999	23.4	42.30
A321	KOMA	KATL	34,000	29,000	48.4	43.52
B744	KORD	KATL	32,720	31,000	34.1	49.60
B763	SBGR	KATL	37,000	36,000	29.2	51.35
B738	TISX	KATL	35,000	35,000	21.9	53.90
A21N	KBOS	KATL	28,000	28,000	22	72.25
B739	MYNN	KATL	17,996	11,919	10.3	77.18
B739	KSFO	KATL	20,995	14,011	27.2	113.30
A21N	KDEN	KATL	24,006	20,511	23.6	119.82
B752	MGGT	KATL	23,714	21,000	17.6	120.20
B39M	KSEA	KATL	21,000	16,956	18.6	121.60
B739	MSLP	KATL	22,000	21,000	6.5	123.82
B738	KCOS	KATL	26,000	16,228	20.4	125.90
B752	MMUN	KATL	28,000	21,000	18.8	132.80
B739	TNCB	KATL	30,470	12,861	15.3	135.32
A359	RKSI	KATL	32,004	26,110	10.6	135.45
B752	KBZN	KATL	33,000	24,003	13.8	140.90
B739	MRLB	KATL	25,980	24,006	7.4	145.00
B752	KSNA	KATL	27835	23136	9.6	152.12
B752	TJSJ	KATL	29771	14920	10.6	156.50

This example raises several research questions to approach the methodology formulation. First, given the large variation in look ahead and duration of the first loop time, which flights have sufficient time during cruise to absorb the delay. Not all flights have the same look ahead time, nor total cruise time nor duration of the hold. Additionally, the sequence at which a flight enters and exits the stack is important to maintain the landing order, since the current research effort scope does not model airport landing capacity. Hence, how can that flight exit time of a holding stack be maintained. Depending on the specific aircraft type, average cruise speed, and length of cruise, how much time can be absorbed? And lastly, how can the absorption be distributed across the stack of flight to gain the most fuel savings from a system perspective? There exist numerous strategies that could be evaluated. At the extreme lower bound of fuel savings, all flights would go into the



hold as it was, and no fuel savings would exist. At the other end, each individual flight would independently apply speed control, if feasible during cruise.

Bounding the problem in this way allows the identification of minimum and maximum levels of delay absorption that are operationally feasible, recognizing that many possible strategies exist between these two extremes. For instance, one strategy could be targeted at aircraft with highest fuel burn, prioritizing speed control for aircraft in the stack that fits that criteria. However, before exploring a range of operationally feasible tactics, examining the lower and upper bounds defines the outer limits of what is achievable. At the upper bound, each aircraft absorbs its individual optimal amount of delay, maximizing fuel savings but potentially altering the arrival times and disregarding arrival sequence in Atlanta. Therefore, flights with a longer look-ahead would absorb more of their terminal delays than others. This could, however, change the sequencing of flights exiting the holding pattern and lead to fairness issues. At the lower bound, all aircraft absorb the same amount of delay based on the flight with the shortest available look-ahead time. This preserves sequencing order and arrival times but restricts the achievable fuel benefits. In this case, fairness is not violated as the order aircraft leave the holding pattern remains unchanged at the cost of absorbing less delay. Quantifying these two limits provides the basis for developing operationally feasible tactics. Ultimately, the goal is to design practical, scalable speed-control strategies that deliver fleet-wide fuel benefits while respecting real-world constraints.

Milestones
None.

Major Accomplishments
Initial framing of the approach to assess an airport level speed control strategy to absorb delay.

Publications
None.

Outreach Efforts
Participated in ASCENT biannual meetings.

Awards
None.

Student Involvement
Yasser Moumtaz (graduate student) was responsible for all elements of enhancing Threaded Track data to resemble FOQA and enable fleet-wide analysis

Plans for Next Period
- Develop surrogate models for gross weight estimation from FOQA data.
- Map the TT aircraft types to the FOQA fuel flow surrogates.
- Execute a test case example for the upper and lower bounds.



Project 086 Study on the Use of Broadband Sounds to Mitigate Sleep Disruption Due to Aircraft Noise

University of Pennsylvania

Project Lead Investigator

Mathias Basner, MD, PhD, MSc
Professor of Psychiatry
Department of Psychiatry
University of Pennsylvania
1019 Blockley Hall, 423 Guardian Dr.
Philadelphia, PA 19104-6021
215-573-5866
basner@pennmedicine.upenn.edu

University Participants

University of Pennsylvania (UPenn)

- P.I.: Prof. Mathias Basner
- FAA Award Number: 13-C-AJFE-UPENN, Amendment No. 015
- Period of Performance: October 1, 2024, to September 30, 2025
- Task:
  1. Complete data analysis

Project Funding Level

Project funding support from the Federal Aviation Administration (FAA) for the Year 2 award (January 1, 2024, to December 31, 2024) for this 2-year project totals $520,700. The cost-sharing requirement for this project is met by our international collaborators at the German Aerospace Center (DLR) and at St. George's University of London. Since January 1, 2025, the project has been in a no-cost extension that was extended once until September 30, 2026.

Investigation Team

University of Pennsylvania

Mathias Basner, MD, PhD, MSc (P.I.), All Tasks
Christopher Jones, PhD (co-investigator), All Tasks
Matthew Kayser, MD, PhD (co-investigator), Task 1
Haochang Shou, PhD (statistician), Task 2
Quy Cao, MS (statistician), Task 2
Michel Carlin (other professional), All Tasks
Adrian Ecker (other professional), All Tasks
Sierra Park-Chavar (other professional), All Tasks
Victoria Schneller (research assistant), All Tasks
Sinead Walsh (research assistant), All Tasks

Civil Aerospace Medical Institute (CAMI)

Hilary Uyhelji, PhD, PMP (co-investigator), All Tasks

Project Overview

Sound insulation of bedrooms is expensive and is typically provided only to residents living near an airport. The goal of this project is to investigate the effects of different types of aviation noise (AN) on sleep under controlled laboratory conditions, and to determine whether some of the sleep-disturbing effects can be mitigated by introduction of pink noise



(PN) into the bedroom or by wearing earplugs (EP). The study will be performed in the Chronobiology Isolation Laboratory at the Hospital of the University of Pennsylvania. This newly constructed facility includes four acoustically isolated bedrooms and a high-fidelity sound system.

Objectives

- Investigate the following hypotheses on the whole night level:
  - AN disturbs sleep and reduces time spent in slow wave sleep + rapid eye movement sleep.
    AN vs. control
  - PN mitigates the negative effects of AN in a dose-dependent manner.
    AN + 50-dBA PN (PN50) vs. AN + 40-dBA PN (PN40) vs. AN
  - EPs mitigate the negative effects of AN.
    AN + EPs vs. AN
  - PN promotes sleep.
    PN50 vs. control
- Investigate the following hypotheses on the event-related level:
  - Various types of AN differ in their awakening potential.
  - The masking effects of PN differ by AN type.
  - PN masks meaningful sounds (e.g., fire alarm or baby crying).

Research Approach

Study Design

The sleep of 24 participants will be monitored through polysomnography (PSG) over seven consecutive nights in groups of four participants. After an adaptation night, participants will be exposed to the following conditions:

1. Control night without noise and without EPs (control)
2. AN only
3. PN50
4. AN + EPs
5. AN + PN40
6. AN + PN50

Our team will investigate participants in six groups of four participants each. Each participant in a given group will be exposed to the same condition in each study night. Each group will receive the six exposure conditions in a randomized and balanced fashion, according to the randomization table below (see Table 1). Of note, in this randomization paradigm, each exposure appears in each position exactly once and is preceded by each other exposure exactly once (letters A–F will be randomly assigned to exposure conditions 1–6 listed above):

Table 1. Randomization of exposure conditions for the sleep research study using PSG.

Group	Night 1	Night 2	Night 3	Night 4	Night 5	Night 6	Night 7
1	Adaptation	A	B	C	D	E	F
2	Adaptation	B	D	A	F	C	E
3	Adaptation	C	A	E	B	F	D
4	Adaptation	D	F	B	E	A	C
5	Adaptation	E	C	F	A	D	B
6	Adaptation	F	E	D	C	B	A

Measurements During Sleep

Participants' sleep will be measured polysomnographically with the Prodigy® system, which includes electroencephalography with frontal electrodes only, electrooculography, and electromyography. Data will be transmitted wirelessly to a bedside tablet. The tablet will also record sound pressure levels to help synchronize the polysomnographic

® Prodigy is a registered trademark of Younes Medical Technologies, Winnipeg, Manitoba, Canada.



and acoustic data. Participants will also wear a Bittium Faros™ device that measures the electrocardiogram (1 kHz) and body movements (25 Hz).

Noise Exposure

The AN night will consist of 93 noise events with maximum sound pressure levels (i.e., $L_{AS,\,max}$ of 45, 55, or 65 dB), including noise from jet engine aircraft, helicopters, drones, low sonic booms, rail, and road traffic. The jet engine, and road and rail noise events will be identical to events used in a prior study at the DLR and another study on broadband sounds on sleep performed by collaborator Dr. Michael Smith in Sweden, thus enabling direct comparison with those studies. Our team will choose several events within each noise level category and repeatedly play those events back. Each aircraft noise event is played back three times at three different maximum sound pressure levels (45, 55, and 65 dBA) for a total of nine times. Because of the limited sample size, playing every event back only once would not provide sufficient data for averaging. An alarm sound and the sound of a baby crying will also be included because a potential caveat of using EPs/PN is that meaningful sounds may be missed. The sequence and spacing of noise events will be identical within a study group but different across study groups. Noise scenarios will be preprogrammed and will start 15 min after the lights are turned off (PN playback will start immediately after lights out). The lights are planned to be turned off at 11:00 p.m. and turned on at 7:00 a.m. for an 8-hour sleep opportunity.

Evening and Morning Procedures

Participants will arrive at the laboratory at approximately 7:00 p.m. and will be able to leave the laboratory at approximately 9:00 a.m. Because our noise exposures can affect sleep and impair recuperation to some degree, participants will be informed in the consent form that they should not operate heavy machinery during the study. A taxi will also be offered for participants who would otherwise use a car to travel to the Chronobiology Isolation Laboratory. Snacks will be provided in the evening and a light breakfast in the morning. Participants will be able to shower in the morning (after all tests) if they wish.

In the evening (before bed) and in the morning (after waking up), the following will be conducted:

1. Blood draw (for untargeted messenger ribonucleic acid [mRNA] analyses expected to be performed by the FAA CAMI, morning only)
2. Completion of a survey asking participants about the previous day (evening survey) or the previous night (morning survey)
3. Cognition test battery (10 cognitive tests)
4. Driving simulator task
5. Hearing test (up to 16 kHz)
6. Blood pressure and heart rate variability measurements

The four participants of a group will be rotated through the six tasks. Each participant will perform the different tasks always in the same order.

Participant Recruitment

Participants will be screened on two occasions. The first screening will include blood draws with drug screening, electrocardiography, and a hearing test. Participants will receive a pulse oximeter, which they will return at the second screening. At the second screening, participants will be familiarized with the cognitive tests and the driving simulator. They will also receive an actigraph that they will wear in the week before the start of their study run. They will be asked to adhere to a sleep schedule of 11:00 p.m. to 7:00 a.m. to the extent possible in the week before participation. We plan to conduct a seventh backup study run if participants drop out during the first six study runs.

Study inclusion criteria:

- Age between 21 and 50 years
- Absence of psychological/psychiatric conditions precluding participation
- Body mass index < 35 kg/m^2
- Self-reported regular sleep schedule; ability to maintain sleep schedule during the course of the study

™ Bittium Faros is a trademark of Bittium Oyj, Oulu, Finland.



- Self-reported sleep duration of 6–8.5 hours per night (verified by six workdays of ambulatory sleep monitoring with wrist actigraphy and daily logs)
- Ability to read and write in English
- Full vaccination against, or recovery from, COVID-19

Study exclusion criteria:

- Hearing loss > 25 dB in any frequency band up to 8 kHz
- History of neurological, psychiatric, or other medical conditions precluding participation
- Current mania or psychosis
- Current depression, according to the Beck Depression Inventory (Beck et al., 1996)
- Excessive alcohol or drug use in the past year, on the basis of history and urine toxicology screening
- Excessive alcohol intake (≥ 21 drinks per week) or binge alcohol consumption (more than five drinks per day)
- Excessive caffeine consumption (> 650 mg/day from all caffeinated drinks regularly absorbed during the day)
- Current use of cigarettes/tobacco, or nicotine replacement therapy (those nicotine-free for 30 days will be included)
- Body mass index ≥ 35 kg/m^2
- Acute, chronic, or debilitating medical conditions, major axis I psychiatric illness, according to history, physical examination, blood and urine chemistry, and complete blood count
- Self-reported history of recurrent seizures or epilepsy or a history of medical conditions that could increase the chance of seizure (e.g., stroke, aneurysm, brain surgery, or structural brain lesion)
- Cardiovascular, neurological, gastrointestinal, or musculoskeletal problems that preclude participation
- Major controlled or uncontrolled medical conditions, such as congestive heart failure, neuromuscular disease, renal failure, cancer, chronic obstructive pulmonary disease, respiratory failure or insufficiency, cardiac arrhythmia, or a need for oxygen therapy (as determined by self-report)
- Current night, swing, split, or rotating shift work
- Current use, or use of within the prior month, of a prescription or over-the-counter sleep medication or stimulant; use of psychoactive medication (based on self-report and review by a study clinician)
- Pregnancy or current breastfeeding
- Prior history or diagnosis of any sleep disorder including obstructive sleep apnea (Apnea-Hypopnea Index ≥15 events/hour) from ambulatory or in-laboratory PSG; restless legs syndrome or periodic limb movement disorder; insomnia; parasomnia; high risk of obstructive sleep apnea, according to the STOP-BANG Questionnaire ("yes" on at least four of eight questions); high risk of restless legs syndrome, according to the Cambridge-Hopkins Screening questionnaire; or high risk of insomnia, according to the Insomnia Severity Index (score of 22 or higher)
- Self-reported severe contact dermatitis, or allergy to silicone, nickel, or silver
- Planned travel across more than one time zone up to one month before and/or during the anticipated study period
- Intentional naps during the week
- Habitual use of broadband noise to facilitate sleep

Endpoints and Power Considerations

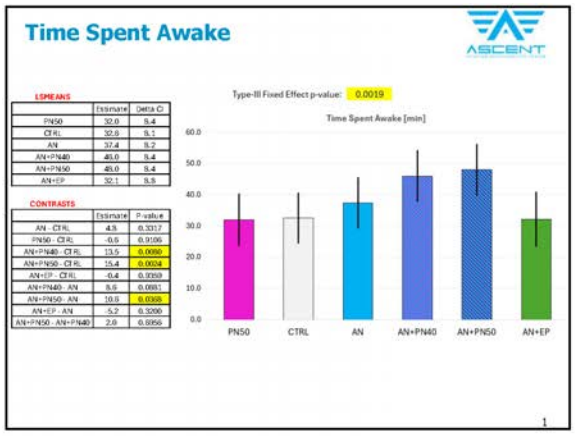
The primary outcome of the study is time spent in slow wave sleep plus rapid eye movement sleep during an 8-hour sleep opportunity (11:00 p.m. to 7:00 a.m.). Our team will investigate several other outcomes related to the entire night (e.g., sleep efficiency or wake after sleep onset); to outcomes before and after sleep (e.g., cognitive performance and driving); or to individual noise events (e.g., event-related analysis).

All power calculations were conducted in the Power Analysis & Sample Size (PASS) (Version 21; NCSS, 2021), by assuming a 5% type I error rate and using two-sided hypothesis tests. The data collected in the AIRORA study (Study on the effects of Air, Road, and Rail traffic noise on sleep), performed at DLR, was used to inform power calculations. With a proposed sample size of 24 participants, our team expects to have at least 80% power to detect a medium effect size of 0.60 for the mitigation effect of PN on our primary outcome due to aviation noise.

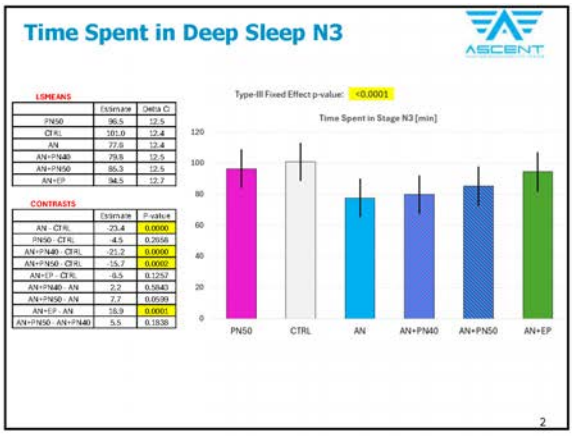
Key Findings

Key findings of the first study are shown in Figure 1. In a dose-dependent fashion, time spent awake was longer and time spent in rapid eye movement (REM) sleep was shorter in nights with aircraft noise and pink noise, while time spent in deep

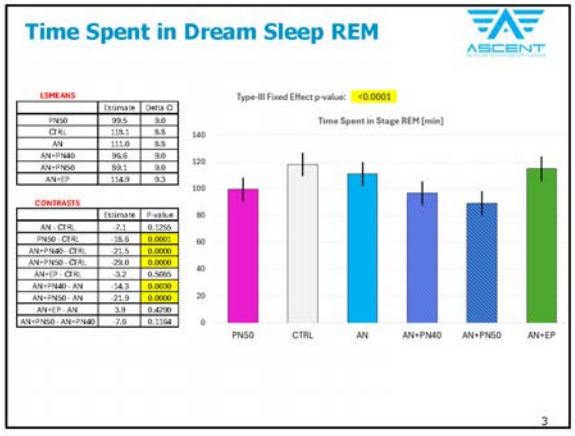
sleep stage N3 was longer and sleep fragmentation during noise events was lower in nights with aircraft noise and pink noise. Thus, pink noise improved some aspects of sleep while it worsened other aspects.



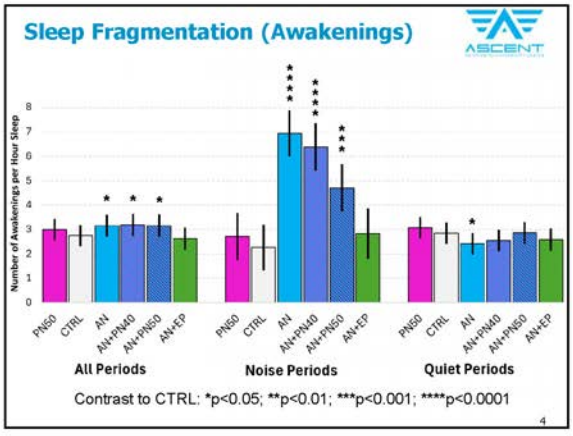
1



2



3



4

Figure 1. Polysomnography findings of the first study. (1) Time spent awake was significantly higher in aircraft noise plus pink noise at 40 dBA (AN+PN40) nights and aircraft noise plus pink noise at 50 dBA (AN+PN50) nights compared to noise-free control nights (CTRL). Time spent awake was not significantly different for the aircraft noise only night (AN), the pink noise at 50 dBA night (PN50), or the aircraft noise plus earplugs (AN+EP) night relative to CTRL. (2) Time spent in deep sleep stage N3 was significantly lower in AN, AN+PN40, and AN+PN50 nights relative to CTRL. It was slightly longer in AN+PN40 and AN+PN50 nights relative to AN, albeit not statistically significantly. (3) Time spent in rapid eye movement (REM) sleep was significantly lower in all nights containing pink noise relative to CTRL. It was also significantly lower in AN+PN40 and AN+PN50 relative to AN. (4) Pink noise at 40 dBA and 50 dBA were able to mitigate some of the effects of aircraft noise on sleep fragmentation measured by awakenings (Noise Periods).

The different aircraft noise events and alarm sounds differentially affected sleep, and that they were also differentially mitigated by pink noise (see Figure 2).

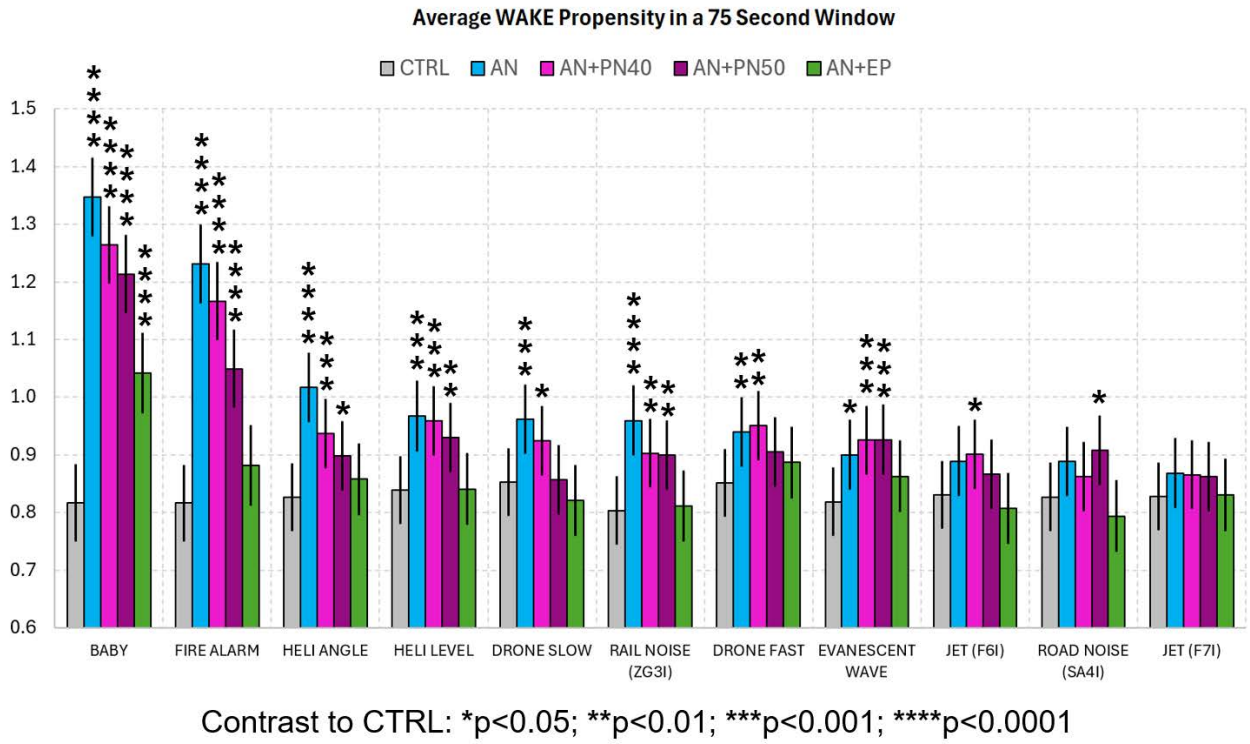


Figure 2. Effects of different noise sources on wake propensity adjusting for maximum sound pressure level. Wake propensity decreased in the following order: crying baby, fire alarm, helicopter noise, drone noise, low boom noise (evanescent wave), and jet noise. CTRL: control night (sham events); AN: aircraft noise only night; AN+PN40: aircraft noise plus pink noise at 40 dBA; AN+PN50: aircraft noise plus pink noise at 50 dBA; AN+EP: aircraft noise plus earplugs

Milestones

- Finalized data analysis in July 2025 (except for mRNA analysis, which is still ongoing).
- Submitted first scientific manuscript.

Major Accomplishments

- Enrolled a total of 27 subjects in the study, three of whom withdrew early from the study. Partial data of one subject withdrawing early can still be used for analysis. Thus, complete data of n=24 participants and partial data of n=1 participant will be used for data analysis (planned total was n=24).
- Analyzed all study data. mRNA data were initially analyzed by CAMI. We are currently performing an in-depth analysis of the mRNA data with UPenn collaborators. These analyses are still ongoing.

Publications

One manuscript was submitted to the journal *Sleep*. Two more manuscripts are in preparation.

Outreach Efforts

A press release for the first manuscript is in preparation and was shared with the FAA project manager.

Awards

None.



Student Involvement

Six temporary undergraduate or post-baccalaureate student workers have supported participant screening and data acquisition in the sleep laboratory.

Plans for Next Period

- Finalize mRNA analysis.
- Generate report.

References

Beck, A.T., Steer, R.A., Ball, R., & Ranieri, W.F. (1996). Comparison of Beck Depression Inventories-IA and -II in psychiatric outpatients. *Journal of Personality Assessment*, 67(3):588-597.

NCSS. (2021). *Power Analysis & Sample Size* (Version 21) [Computer software]. https://www.ncss.com/download/pass/updates/pass-2021/



Project 088 A Method for Rapidly Assessing Jet Fuel Compatibility with Non-Metallic Materials

University of Dayton Research Institute

Project Lead Investigator

John Graham, PhD
Distinguished Research Engineer
Sealants and Elastomeric Materials Address, Nonstructural Materials Division
University of Dayton Research Institute
1700 S. Patterson Blvd. Dayton, OH 45459
937-229-2807
John.Graham@udri.udayton.edu

Project Co-Lead Investigator

Gina Roesch, PhD
Research Chemist
Sealants and Elastomeric Materials Address, Nonstructural Materials Division
University of Dayton Research Institute
1700 S. Patterson Blvd. Dayton, OH 45459
937-229-3488
Gina.Roesch@udri.udayton.edu

University Participants

University of Dayton Research Institute (UDRI)

- P.I.s: John Graham and Gina Roesch
- FAA Award Number: 13-C-AJFE-UD
- Period of Performance: February 01, 2023, to September 30, 2025
- Tasks:
  1. Material Selection and Acquisition
  2. Detailed Fuel Composition
  3. Volume Swell
  4. Analysis of Absorbed Fuels
  5. Statistical Analysis
  6. Multiple Regression Modelling
  7. Reporting

Project Funding Level

The Federal Aviation Administration (FAA) provided $350,000 for ASCENT Project 088. The funds from the FAA were matched by several cost-sharing partners including Global Bioenergies, The Boeing Company, General Electric (GE) Aviation, National Research Council (NRC) Canada, Lanzatech, Neste, Shell, and IHI Corporation. In the fall of 2023, UDRI submitted a proposal for Phase II funding for Project 088. The FAA provided an additional $350,000 for ASCENT Project 088 Phase II. The same cost share partners were used for Phases I and II. In 2024, a no cost time extension (NCTE) was granted for Phase II testing due to the extended soak time required to execute Phase I testing.

Investigation Team

Dr. John Graham, PhD (P.I.), performs aspects of all parts of Project 088 from ideation, data acquisition, data analysis and reporting, as well as is the primary lead on statistical analysis and modeling of the data.

Dr. Gina Roesch, PhD (Co-P.I.), performs data acquisition and analysis as well as all project briefings.



Barbara Miller (Sealants and Elastomer Group Leader) oversees all technical outputs and controls the financial aspects of ASCENT Project 088.
Mary Galaska (technician) acquires analytical measurements including but not limited to volume swell and gas chromatography–mass spectrometry in support of ASCENT Project 088.
Wesley Waldron (technician) assists in the mechanical testing of the materials used in ASCENT Project 088.
Bradley Swindall (technician) assists in mechanical and physical property testing of the materials used in ASCENT Project 088.

Phase I Testing - Project Overview

The goal of ASCENT Project 088 is to create a prescreening method to assess whether a given synthetic aviation turbine fuel (SATF) is a good candidate for the rigorous fuel certification process established in ASTM D4054 (ASTM International, 2022). As an evaluation method, ASTM D4054 is time-consuming (turnaround times of months to years) and expensive process. In addition, material costs and fuel quantities are substantial barriers to entry for original equipment manufacturers (OEMs) to submit candidate fuels. As a result, ASCENT Project 088 was proposed and designed to develop a low-cost, small-sample-volume method to assess fuel interactions for the list of non-metallic materials proposed for material compatibility testing in ASTM D4054. The advantage of the approach proposed in ASCENT Project 088 is that it is less expensive, has a faster turnaround time (weeks), and requires smaller sample volumes (<250 ml). To keep the requirements to a minimum, the ASCENT Project 088 team chose volume swell as the physical property of interest. In tandem with volume swell experiments, gas chromatography mass spectrometry (GC-MS) will be used to quantify the interaction and exchange between fuels and materials. Using these two techniques as the foundation, statistical models will be generated to predict SATF compatibility with non-metallic materials given the known material response in conventional Jet A. Additionally, the experimental data gathered in ASCENT Project 088 can be used as a method to down select the extensive list suggested in ASTM D4054 (ASTM International, 2022).

ASCENT Project 088 involves two crucial deliverables. The first is the creation of a reference dataset by using a population of Jet A fuels gathered from ten sites across the continental United States (CONUS). This sample of 12 Jet A fuels represents the population of Jet A fuels currently in-service. Using these conventional Jet A fuels, ASCENT Project 088 will study and characterize how the materials on the ASTM D4054 Non-metallic Short List (Annex A3) interact with the current Jet A fuel population thus providing information on how today's non-metallic materials respond when exposed to Jet A fuel. The second deliverable for ASCENT Project 088 is a set of statistical models. The data points gathered for non-metallic materials and the known composition of the Jet A fuels will be used to build statistical models utilizing key class fractions as fitting parameters. Both single and multivariate models will be explored. At the end of ASCENT Project 088, the models generated can be used to compare SATF non-metallic responses in light of the same material's response to conventional Jet A fuels.

References

ASTM International. (2022). ASTM D4054-22L: Standard Practice for Evaluation of New Aviation Turbine Fuels and Fuel Additives. https://store.astm.org/d4054-22.html

Task 1 – Material Selection and Acquisition

University of Dayton Research Institute

Objective

The objective of this task is to select the list of non-metallic materials to evaluate in the survey of Jet A fuels, request quotations, and purchase all necessary materials for the project.

Research Approach

The 12 fuels were selected from a stock of 93 fuels obtained from 10 geographically dispersed locations across the CONUS. One fuel was selected from each of the 10 locations, and the fuels with the highest and lowest percentages of aromatic compounds were also selected for a total of 12 sample Jet A fuels.



Milestones
A survey of Jet A fuels was acquired from various locations across the CONUS so that the population could be considered a statistical representation of fuels being flown at the time of the study. This suite of Jet A fuels includes a variety of compositions (i.e., low aromatic compounds, high aromatic compounds, etc.). Additionally, all materials of interest have been acquired.

Major Accomplishments
Task 1 was completed during the 2024 calendar year.

Publications
None.

Outreach Efforts
None.

Awards
None.

Student Involvement
None.

Plans for Next Period
None. Task 1 is complete.

Task 2 – Detailed Fuel Composition
University of Dayton Research Institute

Objective
The objective of this task is to provide a detailed chemical analysis of current, in-service Jet A fuels. To achieve this objective, a survey of Jet A fuels was gathered from across the CONUS and characterized using two-dimensional gas chromatography (GCxGC) to determine the fuel composition against which future candidate SATFs can be compared.

Research Approach
The approach to evaluate the selection of the 12 Jet A fuels involved GCxGC, with emphasis placed on a selected set of class fractions known to play a role in the volume swell of non-metallic materials. Table 1 shows the class fractions of interest for ASCENT Project 088. Additionally, GCxGC analysis and simulated distillation curves were provided for each of the 12 fuels.

Table 1. Fuel Composition by GCxGC.

Class	Class Fraction
Aromatics	Alkyl benzenes
	Diaromatics (Naphthalenes, Biphenyls, etc.)
	Cycloaromatics (Indans, Tetralins, etc.)
Paraffins	iso-paraffins
	n-paraffins
	Monocycloparaffins
	Dicycloparaffins
	Tricycloparaffins

Milestone
Task 2 was completed during the 2024 calendar year.

Major Accomplishments
None.

Publications
None.

Outreach Efforts
None.

Awards
None.

Student Involvement
None.

Plans for Next Period
Task 2 is complete. The GCxGC data will be used for the remainder of the project, to understand material compatibility with the reference fuels and, in the future, with candidate SATFs.

Task 3 – Volume Swell
University of Dayton Research Institute

Objective
Task 3 is the mission-critical task of ASCENT Project 088 as it provides the experimental data for the selected representative physical property, the volume swell of each material in the ASTM D4054 Non-metallic Short List in each of the 12 Jet A fuels selected in Task 2.

Research Approach
Experimental Approach
Volume swell was chosen as the keystone physical property for ASCENT Project 088 because it captures the overall exchange of components between the material and the fuel. In order to use small material and fuel volumes for the prescreening method, UDRI will utilize a custom technique to measure the volume swell of materials in fuel/fluid called optical dilatometry. Optical dilatometry uses sample sizes on the order of millimeters and fuel volumes of less than 5 mL per test. Task 3 hinges on using optical dilatometry to measure the volume swell of all the materials in the ASTM D4054 Non-metallic Short List in the candidate Jet A fuels selected in Task 2.

Figure 1 shows a schematic of an optical dilatometer on the left and an example system on the right. Up to four small samples are placed in an optical cell with 3–5 mL of test fluid at room temperature (approximately 75°F). The vial is placed on an optical stage that is lit form above with a light-emitting-diode (LED) strip. Below the optical cell is a digital camera and lens setup. The camera photographs the materials every 10 s for the first 3 min and then every 10 min for the remainder of the experiment. The length of the swelling experiments is variable. For ASCENT Project 088, the duration of the soak was chosen to be 160 hours such that an equilibrium or near-equilibrium state was reached for each material.

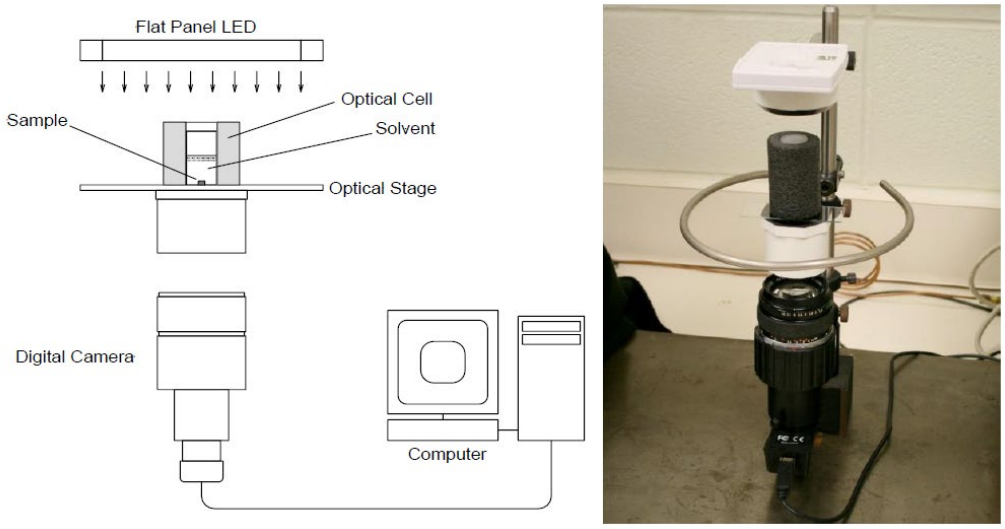


Figure 1. Schematic (left) and photograph (right) of an optical dilatometer.

Data Processing

When the exposure is complete, the images are analyzed via ImageJ, a software program used to extract the cross-sectional area of each of the samples. Assuming isotropic swelling of the material, the two-dimensional (2D) area from the image can be extrapolated to a three-dimensional (3D) volume for each sample over the duration of the experiment. The final volume swell is recorded as an average of the material areas at and around the 160-hour mark.

Figure 2 shows a summary of the results of Task 3. Figure 2 shows the average volume swell of each material in the ASTM D4054 Non-metallic Short List in all 12 Jet A fuels used in ASCENT Project 088. Two major conclusions arise from Figure 2. The first being that the duration of exposure (160 hours) was enough for all materials to reach equilibrium or near-equilibrium states. This is evidenced by the flatlining of the volume swell curves of each material at 160 hours. The second conclusion is that only 6 of the 34 materials tested showed a significant response to fuel exposure. In the context of ASCENT Project 088, significant fuel response is considered any average volume swell that is greater than 3%. Back-calculating from a 3D volume swell to a linear swell, a 3% change in volume corresponds to a 1% change in linear swell. A 1% linear swell was deemed acceptable because it is unlikely for major leaks to occur when there is a less than 1% change in the linear swell of the material. The materials that swelled more than 3% via volume swell are named in Figure 2. Figure 2 serves as one potential method in which the experimental results of ASCENT Project 088 can be used to down select the ASTM D4054 Non-metallic Materials Short List when testing compatibility with candidate SATFs. Specifically, if materials that are responsive and change as a result of fuel exposure to Jet A fuel are within the same statistical range pass compatibility testing, it is likely that materials that do not response to conventional Jet A fuel will also pass compatibility tests.

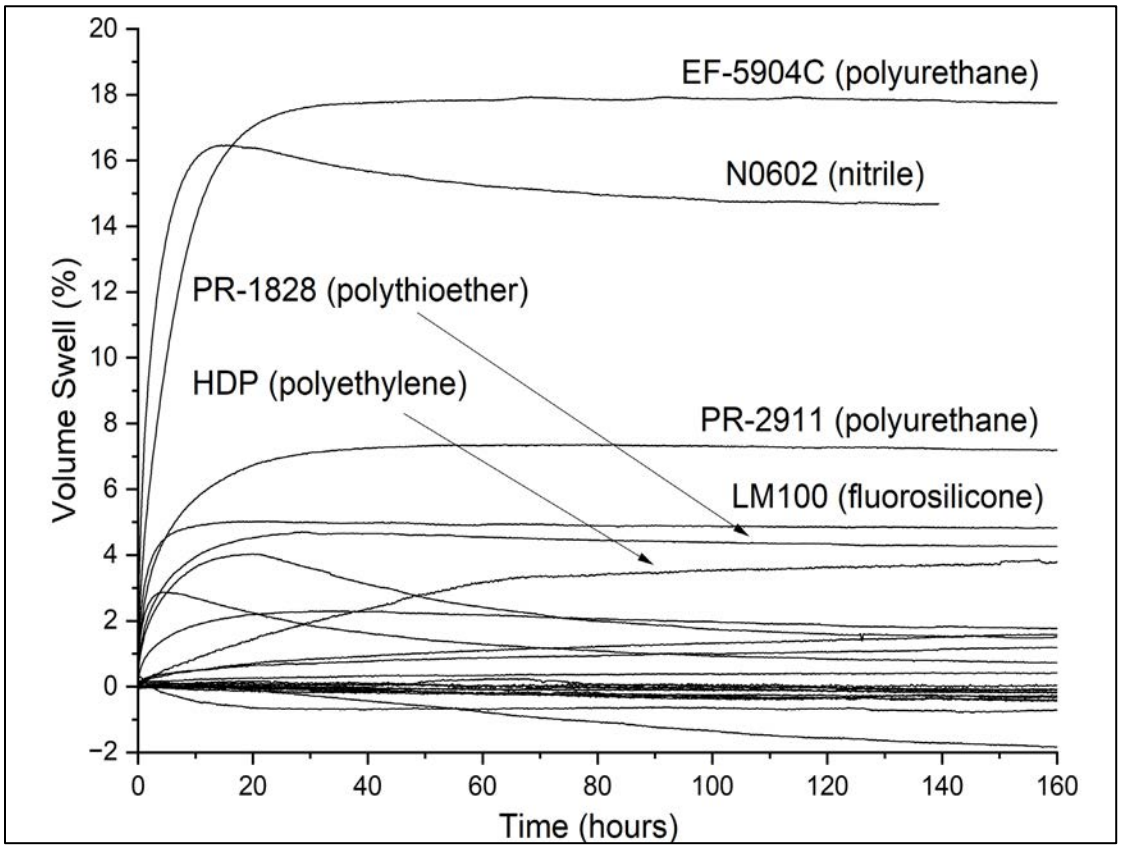


Figure 2. Task 3 summary graph showing the volume swell of all the materials in the ASTM D4054 Non-metallic Short List tested in triplicate in all 12 Jet A fuels selected in Task 2.

Milestones
Task 3 was completed during the previous calendar year.

Major Accomplishments
None.

Publications
None.

Outreach Efforts
None.

Awards
None.

Student Involvement
None.

Plans for Next Period
None. Task 3 is complete.



Task 4 – Analysis of Absorbed Fuels

University of Dayton Research Institute

Objectives

Task 4 is included to complement the results of Task 3 and gain a fundamental understanding of how the materials and fuels interact with one another throughout the exposure period. Task 3 can be described as the "what," i.e., what happens to a material when it is exposed to fuel and Task 4 is the "why," i.e., why the material does or does not swell. To study what causes the swelling (or lack thereof), gas chromatography mass spectrometry (GC-MS) will be used. GC-MS is a technique that identifies which, if any, of the selected class fractions are absorbed into the material from the fuel and/or what parts of the material are extracted into the fuel. The class fractions of interest are listed in Table 2 and were selected based on previous studies of material interactions with fuels. They were also based on the GCxGC analysis such that several of the class fractions quantified in Task 2 could be utilized here as well. Of note in Table 2, the class fraction labeled "naphthalenes" encompasses all alkyl naphthalene species. Alkyl naphthalenes usually consist of but are not limited to methyl or ethyl groups ($-CH_3$ or $-CH_2CH_3$) across different carbons in the aromatic structure.

Table 2. Class fractions investigated via GC-MS.

Class	Class Fraction
Aromatics	Alkyl benzenes
	Diaromatics (Naphthalenes, Biphenyls, etc.)
	Cycloaromatics (Indans, Tetralins, etc.)
Paraffins	iso-paraffins
	n-paraffins
	Monocycloparaffins
	Dicycloparaffins
	Tricycloparaffins

Research Approach

Experimental Approach

GC-MS is performed with an Agilent® 7890A gas chromatograph equipped with an Agilent 5975C VL Mass Selective Detector (MSD). The sample preparation for the material is as follows:

1. Remove aged samples from fuel, and pat dry three times with laboratory wipes to remove any fuel residing on the outside of the material (i.e., not absorbed by the material).
2. Place one piece of test material in a 1.5-ml GC vial with 1 ml methylene chloride (MeCl).
3. Repeat steps 1 and 2 with a second aged test material from the sample vial.
4. Place the samples sitting in solvent (MeCl) on the autosampler and run under UDRI's standard method/temperature ramp.
5. After GC-MS analysis is complete, decant the residual solvent and dry the test material and vial in an oven for 30 min using a predetermined heating cycle.
6. Remove and weigh the dried test material. Record the final weight of the sample for quantitative analysis.

Steps 1–4 should be repeated for the sample Jet A fuels (1 µL of fuel in 1 ml of MeCl) to quantitatively compare the material's ability to extract from the fuel (and vice versa).

Data Analysis

Data analysis for Task 4 consists of integrating the area under the curve of each peak present in the overall chromatogram (total ion chromatogram [TIC]) and the extracted ion chromatograms (EICs) for the representative class fractions.

® Agilent is a registered trademark of Agilent Technologies, Inc., Santa Clara, California.

Integration is performed using Agilent ChemStation® Analysis software and Agilent MassHunter,® both via manual integration methods. The area under each curve for TICs and EICs are exported to another software program in which partition coefficients (K_{pf}) are calculated. The K_{pf}, the ratio of a class fraction in the polymer relative to its concentration in the neat fuel, is the metric used to summarize the interaction between the non-metallic material and the surveyed Jet A fuels. Figure 3 provides a visual representation of the two-way exchange that occurs between the material extracting from the fuel and the fuel extracting from the material. The bottom panel of Figure 3 shows the test fuel (sample Jet A), and the top panel shows the absorbed fuel in a sample O-ring (AMS-P-5315). The ratio of the two spectra shows that the material only absorbed a fraction of the fuel components because it has a lower overall signal response.

As shown on the left side of Figure 3, K_{pf} values can fall into three regions. A $K_{pf} < 1$ indicates that the material is resistant to the class fraction of interest. A $K_{pf} > 1$ indicates that the material absorbs or extracts a substantial portion of the class fraction of interest. Finally, a $K_{pf} = \sim 1$ indicates relatively equal exchange in material and fuel. The K_{pf} values calculated for the materials can be used to predict the swelling behavior of fuels with similar class fractions in the future.

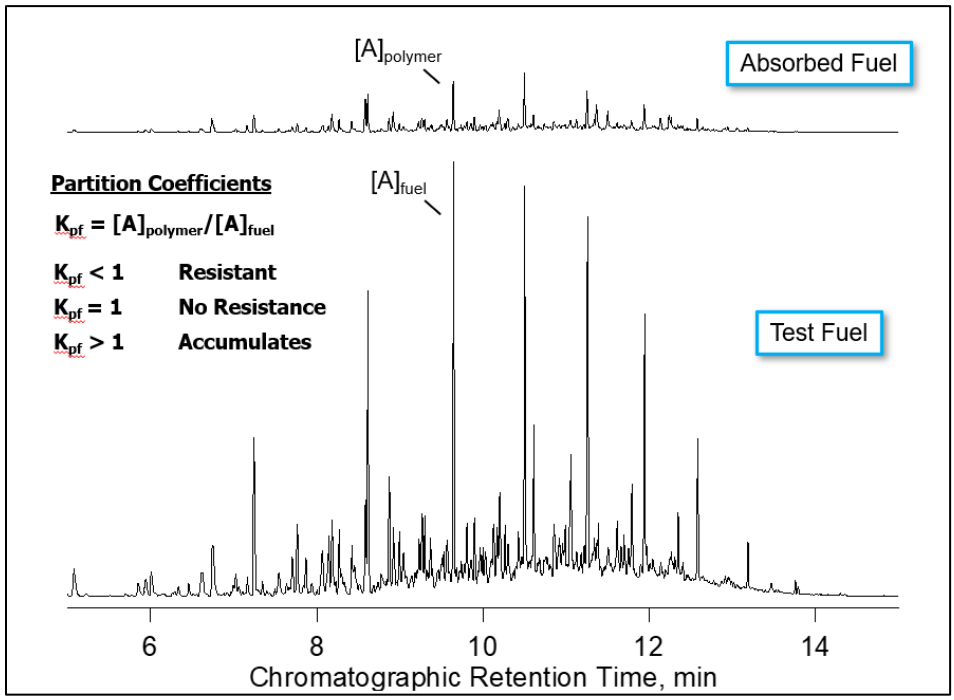


Figure 3. Absorbed fuel analysis via GC-MS. This technique is used to compare a neat polymer (AMS-P-5315), the reference fuel (Jet A) and the exchange between the fuel and material during the volume swell experiment.

Table 3 and Table 4 contrast experimental K_{pf} values associated with O-rings and Films found in the ASTM D4054 Non-metallic Short List. These two examples show a stark contrast in experimental partition coefficients and, by extension, starkly different responses to fuel exposure. In Table 3, AMS-P-5315 (Table 3, Column 1) has K_{pf} values that are all greater than 0.10 with some values even nearing 1.0. On the other hand, Kapton (Table 4, Column 3) showed so little response to fuel exposure that it could not be quantified via GC-MS, which is approximately a 10 ppm technique. This result is confirmed by the low volume swell experimentally determined in Task 3 (0.02% volume swell). A more quantitative example compares AMS-P-5315 and polyethylene (Table 4, Column 2). Even the most readily absorbed class fraction (the naphthalenes), had experimental K_{pf} value of 0.21 indicating that approximately less than 1/5 of the class fraction was absorbed into the material. The large K_{pf} values in AMS-P-5315 (large values relative to high-density polyethylene (HDP) and many other non-metallic species in the ASTM D4054 Non-metallic Short List) indicate that AMS-P-5315 responds to all class

® ChemStation is a registered trademark of Agilent Technologies, Inc., Santa Clara, California.
® MassHunter is a registered trademark of Agilent Technologies, Inc., Santa Clara, California.



fractions in a significant amount relative to other materials. Comparing materials, both within a material class and externally between material classes, demonstrates the power of Task 4's quantitative approach to material-fuel interactions. The quantitative approach enhances the understanding of what class fractions play a role in volume swell, lifetime, hardness and other physical and mechanical properties of materials.

Table 3. Experimental K_{pf} values for all O-rings across sample Jet A fuels.

Class	AMS-P-5315	AMS25988	AMS7276	AMS83485
Fraction	N0602	LM100	V0747	VM125
Overall	0.17	0.04	0.01	0.02
n,i-Paraffins	0.12	0.04	0.01	0.01
Cycloparaffins	0.15	0.04	0.01	0.01
Alkyl Benzenes (C10 Bz)	0.37	0.09	0.03	0.07
Naphthalene	0.94	0.16	0.07	0.17
Naphthalenes (C11 & 12)	0.60	0.09	0.03	0.09

Table 4. Experimental K_{pf} values for all films across sample Jet A fuels. High-density polyethylene (HDP) is below the detection limit (bdl).

Class	Nylon	Polyethylene	Kapton
Fraction	Dupont Zytel 101	HDP	UPILEX
Overall	bdl	0.10	bdl
n,i-Paraffins	bdl	0.09	bdl
Cycloparaffins	bdl	0.14	bdl
Alkyl Benzenes (C10 Bz)	bdl	0.20	bdl
Naphthalene	bdl	0.31	bdl
Naphthalenes (C11 & 12)	bdl	0.21	bdl

Milestones
During the 2025 calendar year, all GC-MS analysis was completed and vetted by Dr. Graham and Dr. Roesch.

Major Accomplishments
Task 4 was completed.

Publications
None.

Outreach Efforts
None.

Awards
None.

Student Involvement
None.

Plans for Next Period
None. Task 4 is complete.

Task 5 – Statistical Analysis

University of Dayton Research Institute

Objective

The primary objective of this task is to explore if there is a correlation between the volume swell of a given material and the aromatic content of the fuels to which it was exposed. To achieve this objective, the volume swell data will be fit with a linear model against the aromatic content of the fuels, thus providing a line of fit in which experimental data points of candidate SATFs can be plotted and referenced against. This fit, along with the associated confidence and prediction intervals, will be the primary point of comparison used to evaluate the viability of future SATF candidates.

Research Approach

In Task 5, linear statistical models were created correlating the swell of each material to the aromatic content of the 12 Jet A fuels used in this study. Figure 4 is a sample single-variable model (AMS-P-5315). Each single variable model was generated using Statistical Analysis System (SAS®) software. As shown in Figure 4 for AMS-P-5315, both the visual/graphical representation and the numerical model (equation of fit) are provided. The equation of fit for each material produces three key variables: (1) the slope of the line, (2) the intercept, and (3) the coefficient of determination. The slope of the line of fit describes if the average volume swell is a function of the aromatic content of the fuel. The intercept of the linear model represents the estimated volume swell for a Jet A fuel with 0% aromatics in the fuel. This is a useful data point given that many candidate SATFs could have little to no aromatic content. Lastly, the coefficient of determination, the R^2 value, describes the strength of correlation between the measured aromatic content of the fuel and the volume swell. All these parameters contribute to the overall understanding of the aromatic content of the fuel's effect on a given material in the ASTM D4054 Non-metallic Short List.

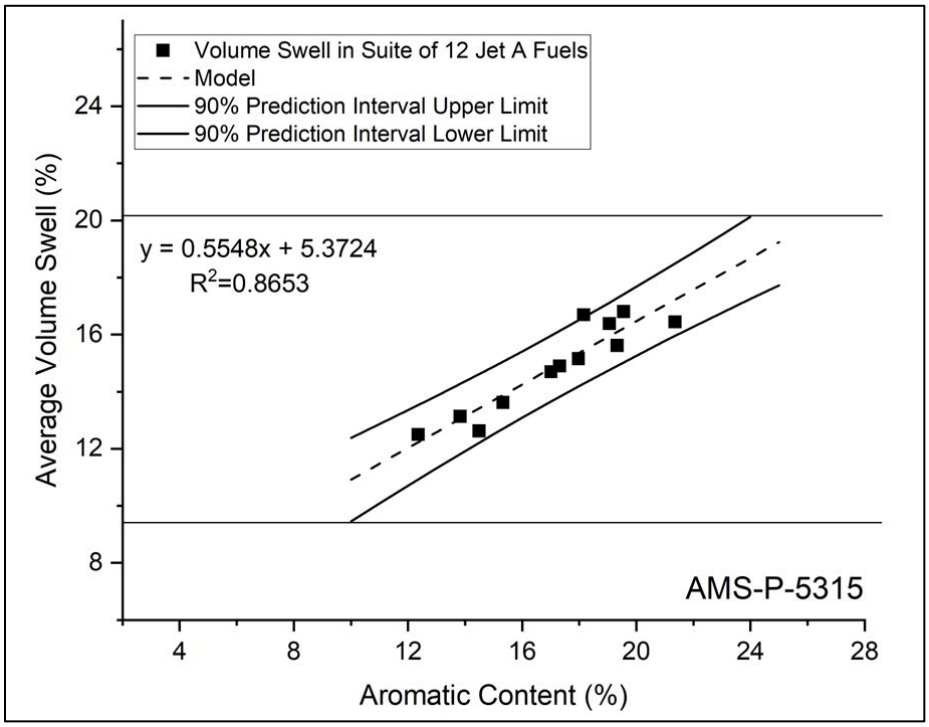


Figure 4. Single variable linear model describing the volume swell of AMS-P-5315 as a function of the aromatic content of Jet A fuels.

® SAS is a registered trademark of SAS Institute, Inc., Cary, North Carolina.

In addition to the key outcomes described above, SAS also generates a 90% prediction interval for the data. The 90% prediction interval is distinct from a traditional confidence interval in that it describes individual fuels within a larger population and is not based solely on the mean value of the 12 sample fuels used in this study. Producing and graphing prediction intervals is a key aspect of Project 88 because it contextualizes each material response with 90% of ***all*** in-service Jet A fuels being flown at the time of the study. Essentially, the prediction intervals for each material describe the response of the material to 90% of all Jet A fuels used today and thus depicts the field as it stands in 2024/2025.
Figure 5 shows an example of how to use one of the single variable models generated in Task 5 of ASCENT Project 088. Specifically, Figure 5 shows the volume swell observed for the material as a function of the aromatic content in a candidate SATF (blue) and a 50:50 blend of the candidate SATF and Jet A (red) superimposed on the Task 5 model. As is seen, the neat SATF (blue) falls outside of the prediction interval generated for the material in Jet A. A data point falling outside of the statistical range of the material in Jet A fuel does not imply that the candidate SATF is not compatible with the material. It simply means that the material will see a condition which it has not seen in service before. It also does not indicate that the candidate SATF will fail full-scale material compatibility testing. It is simply an indication that the material responds differently. Often, further investigation is necessary to determine if this is an issue or simply a difference. Ultimately, this information helps inform OEMs as to how their products interact with materials relative to that material's response in conventional Jet A fuel. The second observation – and somewhat of a comfort to a potential OEM - is that the 50:50 blend falls within the predicted range of Jet A-material compatibility. P088 investigators suggest that 50:50 blends be run alongside the neat SATF so that fuels more akin to ASTM D7566 (ASTM International, 2022) regulations are also tested. This approach simply gives OEMs an additional data point helping them to make data-informed decisions.

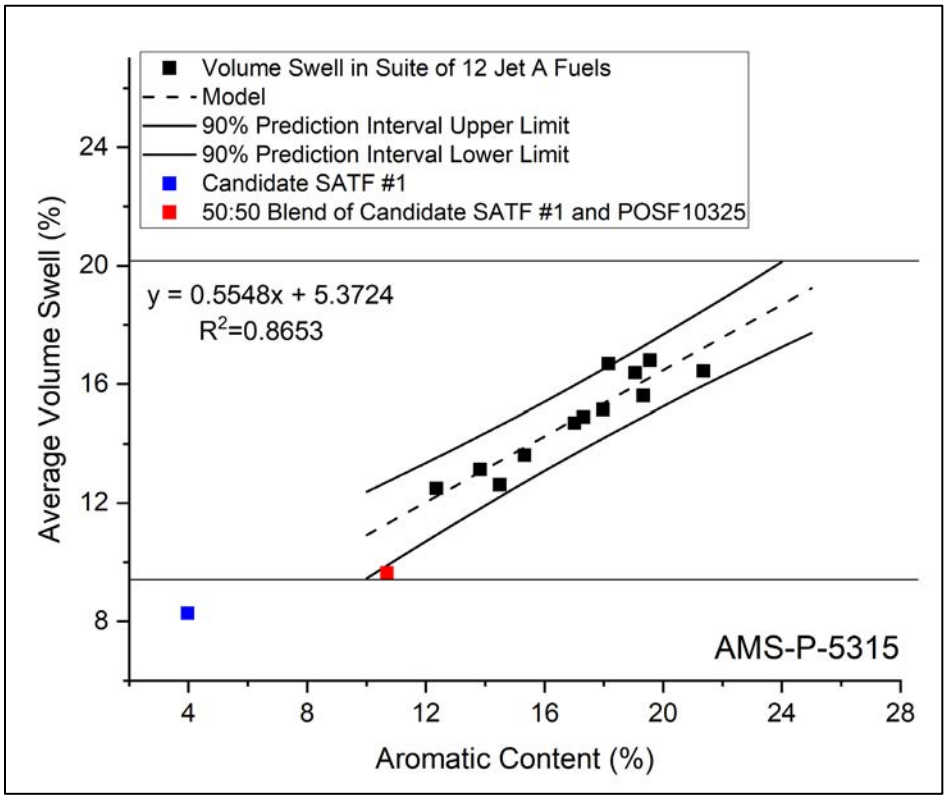


Figure 5. Single variable linear model demonstrating how a candidate SATF (blue) and a 50:50 blend of the candidate SATF and Jet A fuel (red) fall with respect to AMS-P-5315 in 90% of all in-service Jet A fuels.

Lastly, the results of Task 5 can be used to generate informative graphics for OEMs based on specific fuel components. Today, many material compatibility questions revolve around the concentration of aromatics in synthetic fuels because aromatics are known to contribute to the volume swell. To address this question, Figure 6 (below) shows one way of visualizing the experimental data produced by Task 5 to address the previous question. Because the coefficient of



determination defines the 'goodness' of the linear model, the materials that have high swelling character and high coefficients of determination would be of main interest for a fuel producer that is concerned about their low or no aromatic fuel being compatible with a non-metallic material that would normally only see Jet A fuels. The top right quadrant of Figure 6 shows materials who exhibited significant volume swell (greater than 3% swell) ***and*** volume swell that positively correlated to the aromatic content of Jet A fuels (R^2 value greater than 0.5). OEMs now have the option to make data-based decisions on what materials to test if aromatic content is the most important variable. The results of Figure 6 suggest a matrix that potentially decreases from 36 materials to 4. Not only is this a data-backed decision, but it saves time and costs for OEMs with specific questions related to fuel composition and material compatibility.

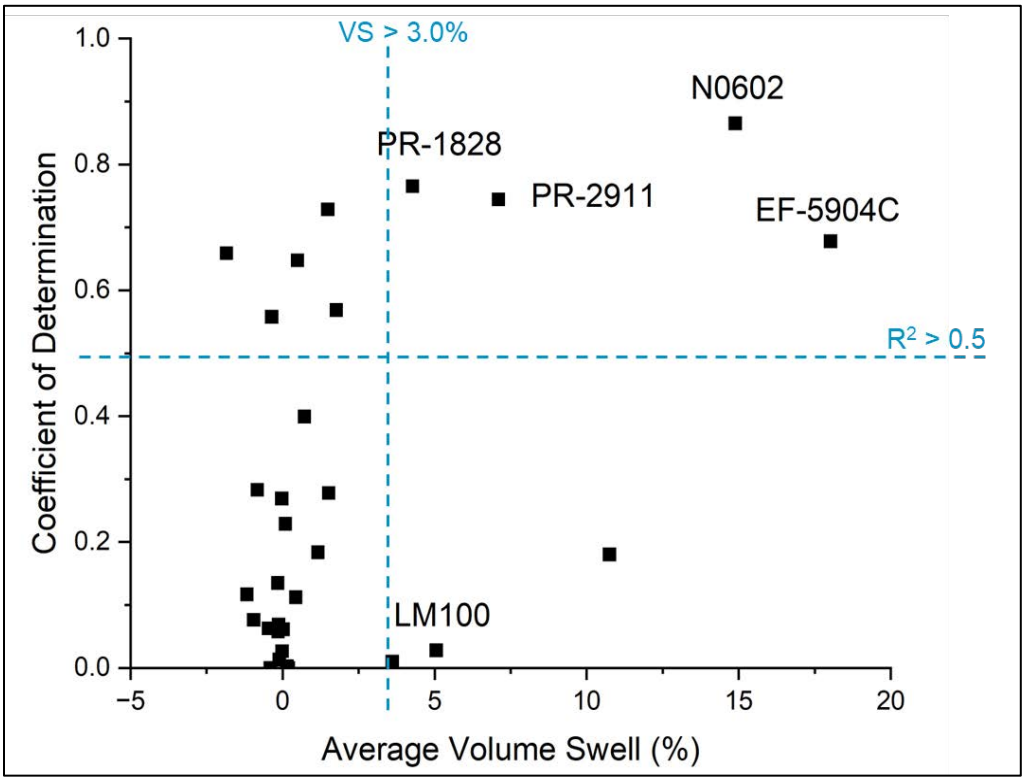


Figure 6. Average volume swell as a function of the coefficient of determination for the single variable model for all materials on the ASTM D4054 Non-metallic Short List.

Milestones

Task 5 was completed during the 2025 calendar year.

Major Accomplishments

The statistical models created in Task 5 will achieve one of the primary goals of implementing ASCENT Project 088 as a prescreening method. First, Task 5 summarizes the results of Task 3, volume swell, and graphs them as a function of the aromatic content of the 12 Jet A fuels used in this study. These models and the resulting data analysis approaches will help OEMs determine how their fuel compares to the current, in-service, safe-to-fly fuels currently in the fleet.

Publications

None.

Outreach Efforts

None.



Awards
None.

Student Involvement
None.

Plans for Next Period
None. Task 5 is complete.

Reference
ASTM International. (2022). ASTM D 7566-21: Standard Specification for Aviation Turbine Fuel Containing Synthesized Hydrocarbons. https://doi.org/10.1520/D7566-21

Task 6 – Multiple Regression Modeling
University of Dayton Research Institute

Objective
The objective of Task 6 is to expand on the single-variable correlations generated in Task 5. In Task 6, multi-variate models will be created to understand in more depth the influence of the fuel composition on volume swell (as opposed to just the impact of the aromatic content). Task 6 will utilize the experimental volume swell results (Task 3) as well as the partition coefficients generated in Task 4. These models aim to provide a more holistic picture of material and fuel interactions.

Research Approach
Task 6 will combine the results of Task 2 and Task 3 to create a more robust predictive model. The model will relate the measured fuel composition (Task 2) and the measured volume swell (Task 3) via a multiple regression linear model. The model will be fit to Equation 1:

$$\text{Volume Swell} = \sum_{i=1}^{n} ki[Ai] \qquad \text{(Eq. 1)}$$

where *ki* is the regression coefficient for a given component or class fraction, *i* is the class fraction, and *[Ai]* is the concentration of the component or class fraction *i*. The regression coefficient is calculated using Equation 2:

$$\text{Regression coefficient} = \frac{\text{Percentage volume swell of material in fuel}}{\text{Percentage concentration of class fraction in fuel}} \qquad \text{(Eq. 2)}$$

for all class fractions, *n,* which will be used in the model. In ASCENT Project 088, the class fractions of interest are normal and iso-paraffins, cycloparaffins, alkyl benzenes, diaromatic compounds, and cycloaromatic compounds (Table 2). In addition to fitting the class fractions from the HTA, the model will include a term to account for the average molecular weight because molecular weight of the fuel impacts the volume swell. This aspect will be an essential component enabling extension of the model to the candidate SATFs in the future that are also likely to have different chemical compositions than traditional Jet A fuels.

Table 5 shows the coefficients generated for the full Task 6 model for a sample material (AMS-P-5315). Upon initial glance, the coefficients make little physical sense. Upon verification of the source code, it was determined that indeed the multi-variate model was a good *predictive tool* and that the coefficients provided the correct fuel compositions when the model was run in reverse. However, Dr. Graham wanted a tool that was more *interpretable* for OEMs and researchers. Therefore, an intermediate model was created in Task 6. The intermediate model decreased the number of independent variables and therefore gave the model more degrees of freedom. By removing the mean molecular weight and making the n,i-paraffins an implicit parameter, the model became far less constrained, and the outputs were far more reasonable. Table 6 shows the coefficients generated for the intermediate model for the same sample material (AMS-P-5315).



Table 5. Full model volume swell coefficients for AMS-P-5315 at 75°F in Jet A fuels.

Model Coefficients (%/%)					Average M.W.	Intercept	R^2
Aromatics			Paraffins				
Alkyl-	Cyclo-	Di-	n, i-	Cyclo-	%/(g/mol)	%v/v	Value
-1.891	-2.045	-1.605	-2.530	-2.452	-0.159	279.951	0.950

Table 6. Full model volume swell coefficients for AMS-P-5315 at 75°F in Jet A fuels.

Model Coefficients, %/%				Intercept	R^2
Aromatics			Paraffins		
Alkyl-	**Cyclo-**	**Di-**	**Cyclo-**	**%v/v**	**Value**
0.698	0.386	0.250	0.081	1.974	0.919

Milestones
During the previous reporting period, Task 6 full and intermediate models were completed for all 36 materials.

Major Accomplishments
Task 6 expands ASCENT Project 088's prescreening toolkit for SATF and Jet A fuel compatibility with non-metallic materials beyond the singular contributions of the aromatics to volume swell. The model built in Task 6 will incorporate the effects of selected class fractions on volume swell both in terms of concentration and molecular structure. In the long term, the model in Task 6 will help OEMs understand the impact of individual class fraction on individual non-metallic materials. On a fuel-design level, the model will provide OEMs with numbers indicating which class fractions play the greatest role in a material's swell, thus informing the design of future SATFs.

Publications
None.

Outreach Efforts
None.

Awards
None.

Student Involvement
None.

Plans for Next Period
None. Task 6 is complete.

Task 7 – Reporting
University of Dayton Research Institute

Objective
The objective of this task is to document and report the results of ASCENT Project 088 in both quarterly and annual reports. Additionally, at the end of ASCENT Project 088, the results will be compiled into a final report and shared with the FAA.

Research Approach
None.

Milestones
During the previous reporting period, the first half of the Phase I report was completed. Tasks 1-3 were fully vetted and reported on. Additionally, all figures and graphics were made for Tasks 4-6.

Major Accomplishments
Dr. Gina Roesch provided status updates for ASCENT Project 088 at the Spring SATF Meeting in Knoxville, Tennessee, and the Fall ASCENT Meeting in Alexandria, Virginia.

Publications
None.

Outreach Efforts
None.

Awards
None.

Student Involvement
None.

Plans for Next Period
The remaining part of Task 7 involves completion of the Phase I report. The report is projected to be completed by mid-February of 2026. The final report will then be reviewed by the FAA and UDRI will make edits as requested.

Phase II Testing - Project Overview
The goal of Phase II of ASCENT Project 088 is to narrow the list of materials studied and expand the set of fuels used to begin to describe how specific materials respond to synthetic aviation turbine fuels (SATFs). In Phase I, O-ring seals continually came up as high-swelling or high-responding materials (see Figure 2). Furthermore, the field continues to document O-ring seals as the most common locations for leaks in modern aircraft systems. This is especially true when testing new, synthetic fuels as a result of the different chemistry between synthetic fuels and conventional jet fuels. Therefore, Phase II will narrow the material investigation from all 36 materials in the Annex A3 list to 4 O-ring seal materials. The four seal materials will be tested in not only Jet A as the reference fuel, but a SATF and a 50:50 blend of the Jet A:SATF. This test matrix will improve upon the dataset generated in Phase I which depicted the state of material and jet fuel compatibility as it is today by beginning to characterize and understand what the state of material compatibility could be if SATFs are used interchangeably with conventional jet fuels.

Because there is interest in SATF compatibility with respect to Jet A fuel, Phase II will begin with an evaluation of the volume swell of the candidate seal materials in the SATF and 50:50 blend to compare and contrast the material response to the experimental results of Phase I. The bulk of Phase II testing, however, will focus on determining the engineering performance properties of seals in conventional versus synthetic jet fuels. Two key metrics will be measured: (1) the compression set and (2) sealing pressure. Compression set is a well-known performance metric for seal lifetimes and sealing pressure characterizes the conditions under which leaks will or will not occur. These metrics will be measured in a variety of scenarios including neat fuels and switch-loading between Jet A fuel and SATFs/SATFs blends. By experimentally determining the seal performance in SATFs, Phase II will provide OEMs with critical information on how or if material performance is affected when SATFs are substituted for traditional jet fuels.

Phase II brings two major advantages to the previous body of work executed in Phase I. First, it includes the study of the SATFs and, critically, switch-loading scenarios between SATFs and conventional Jet A fuel. This is of great interest to the community because of the differences in swelling character of common materials in conventional and synthetic jet fuels due to the difference in fuel composition. Second, Phase II expands from studying analytical properties of interest – the volume swell – to measuring actual engineering metrics for seal performance. With a narrow focus on seals and the



inclusion of SATFs of interest, Phase II aims to generate information to inform airframe and fuel OEMs on the critical aspects of fuel switching as it relates to material compatibility.

Task 1 – Material Selection & Acquisition

University of Dayton Research Institute

Objective

The objective of this task is to determine the appropriate materials and fuels to execute the test plan and provide the best possible data to the FAA.

Research Approach

The research approach for Task 1 involved evaluating Phase I data to elucidate which materials were of most interest to study in Phase II testing. Additionally, UDRI talked with FAA project managers (PMs) and other OEMs to gather information on which SATFs and associated synthetic blending components to investigate based on industrial and gubernatorial relevance.

Milestones

Task 1 was 75% completed during the 2025 calendar year.

Major Accomplishments

All materials for ASCENT Project 088 Phase II were acquired, and the fuels of interest were decided upon. Four O-rings spanning three material chemistries were chosen (nitrile rubber, fluorosilicone, fluorocarbon and low temperature fluorocarbon). A standard Jet A fuel and a Hydroprocessed Esters and Fatty Acids Synthetic Paraffinic Kerosene (HEFA-SPK) were chosen as the candidate fuels for testing. It was also decided that a 50:50 blend of Jet A:HEFA-SPK should be used to model a true candidate SATF given the blending rules dictated in ASTM D7566. Finally, both the neat Jet A fuel and neat HEFA-SPK were characterized via GCxGC for detailed information on bulk hydrocarbon type analysis.

Publications

None.

Outreach Efforts

None.

Awards

None.

Student Involvement

None.

Plans for Next Period

During the next reporting period, the remaining amounts of the HEFA-SPK will be acquired for testing.

Task 2 – Volume Swell & Switch-loading

University of Dayton Research Institute

Objective

The objective of this task is to measure the fuel-material interaction via volume swell in both static (single-fuel) and switch-loading conditions. To measure the volume swell, optical dilatometry will be used. All four seal materials will be exposed to four different fuel scenarios: (1) neat Jet A fuel, (2) neat HEFA, (3) a 50:50 blend of Jet A:HEFA-SPK and, finally, (4) the switch-loading scenario. All static soaks will be two weeks long. Switch loading will occur been Jet A fuel and neat HEFA for all four materials at a switching cadence of every two weeks for a minimum of 26 weeks.

Research Approach

For detailed information on optical dilatometry and static fuel soaks, please refer to Task 3 in the Phase I report. Here, the technique of optical dilatometry as applied to switch-loading will be discussed.

To perform switch-loading experiments via optical dilatometry, no change in hardware is necessary (see Figure 1). In lieu of multiple specimens being tested at one time, one singular 1 mm thick O-ring cross section is placed in the center of the glass vial with 3-5 mL of fuel 1. The first exposure proceeds as a normal optical dilatometry experiment with images acquired every 10 seconds during the first exposure period and every 10 mins during the second exposure period. It is of great importance to note that there was procedural change in the timings for optical dilatometry experiments between Phase I and Phase II. In Phase II, the first exposure period is 30 mins as opposed to the previous 3 mins used in Phase I. Overall volume swell is still taken as an average at the end of testing, so there is no concern about the comparability of datasets. At the end of the 2-week exposure period, a new test vial is prepared with fuel 2. Once the new test vial is setup, the sample is removed from fuel 1 and dabbed dry at least three times with a KimWipe™ to remove excess fuel on the outside of the sample. The sample is then placed in the new vial with fuel 2 and the experiment exposure proceeds as normal. This procedure can be done as many times as desired. With respect to data processing, there are only two differences. First, each fuel exposure uses the extrapolated time-zero area from the very first exposure to fuel 1 as the reference area. Second, for all the last and first data points between switches, the volume swell values are adjusted (normally averaged) so that the progression between datasets is smooth. A sample showing the volume swell of a material switching between JP-8 fuel and an iso-paraffinic kerosene (IPK) is in Figure 7 below.

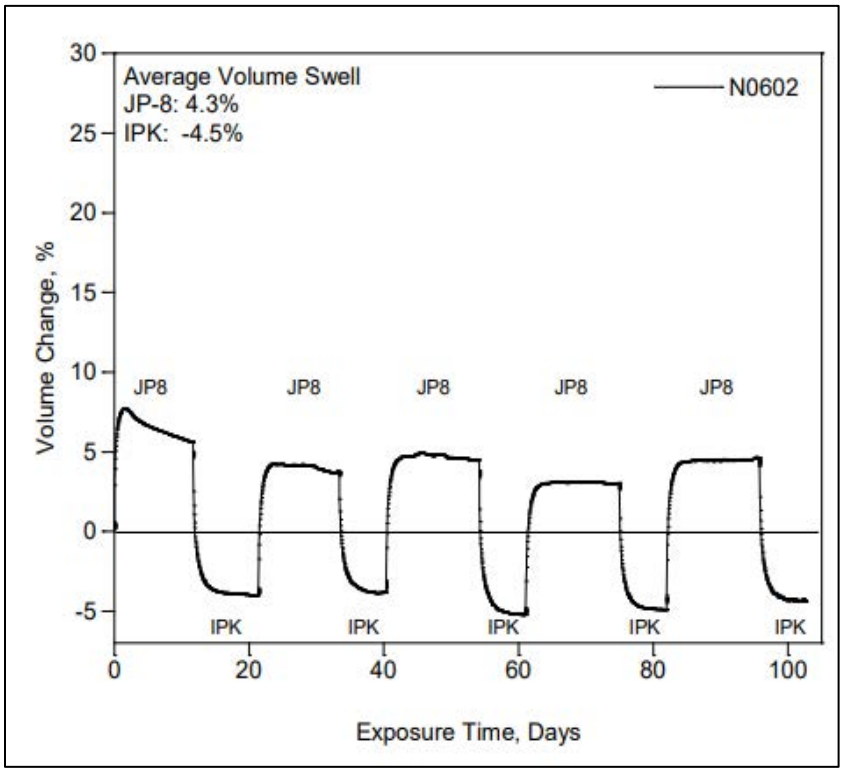


Figure 7. Switch-loading volume swell profile for AMS-P-5315 material switching between JP-8 fuel and an iso-paraffinic kerosene (IPK).

™ Kimwipe is a trademark of Ansell Healthcare Products LLC, Iselin, New Jersey.



Milestones
During the previous reporting period, all static, two-week fuel soaks were completed for all four materials. Additionally, long-term switch-loading soaks for each material in duplicate were started and will have completed 18 weeks of exposure by January 01, 2026.

Major Accomplishments
One of the major accomplishments achieved throughout the previous reporting period was experimental determination of the volume swell of each of the four materials in each neat fuel and the 50:50 blend. This information will be used to complement the data taken in Phase I of ASCENT Project 088.

Publications
None.

Outreach Efforts
None.

Awards
None.

Student Involvement
None.

Plans for Next Period
The plans for the next reporting period are to complete the long-term switch loading soaks and perform appropriate data analysis for both static and switch-loading volume swell experiments.

Task 3 – Compression and Switch-loading
University of Dayton Research Institute

Objective
The objective of this task is to measure the compression set of O-rings in model face seals under switch-loading conditions. Compression set was chosen as the measurement of interest because it is a good indicator of the proverbial age of an O-ring. In Phase II, UDRI-designed model face seal fixtures will be used to better simulate in-service conditions (i.e., in a gland as opposed to free-floating). Ultimately, the compression set data will be used in conjunction with the Task 2 volume swell data to better strengthen the link between volume swell measurements and seal performance.

Research Approach
Compression set, by definition, is a measure of an elastomeric material's ability or inability to return to its original dimensions after being exposed to various conditions (Parker O-ring Handbook, 2001). In Task 3, the compression set of all four O-ring materials in each fuel will be measured using UDRI's model face seal glands. The face seal glands, shown in Figure 8, are often referred to as compression set fixtures. UDRI's compression set fixtures were custom designed to mimic a 25% compressed gland for standard 2-214 O-rings. The small, modifiable-in-height stack can be easily placed in fuels or fluids. Fluid access is achieved via a channel and opening in the middle which can be best seen in the two stacks on the far right of Figure 8. The fixtures can also be placed at temperature, adding yet another opportunity to more closely imitate in-service conditions for these materials.

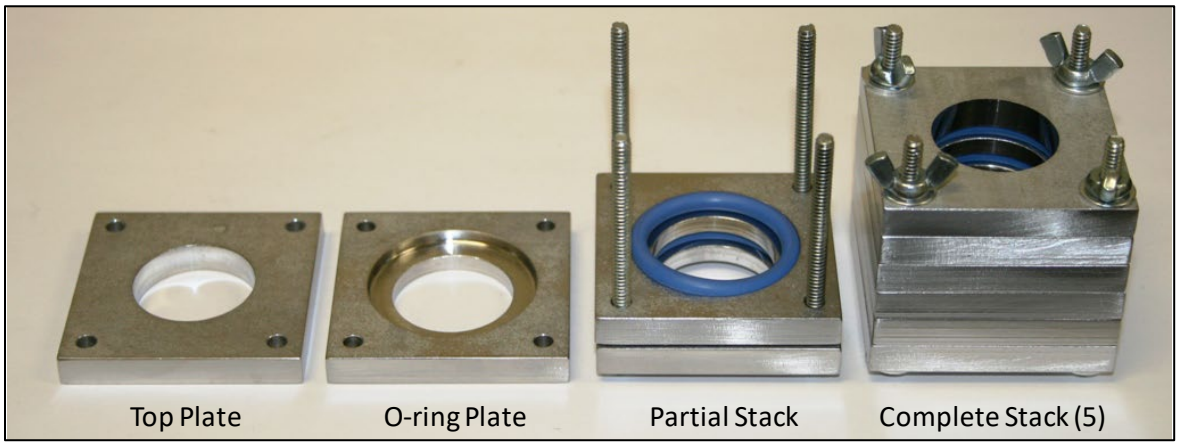


Figure 8. UDRI compression set fixtures used to age O-ring materials under nominal 25% compression. The stacks can be placed in fuel and at elevated temperatures to accelerate the aging of O-ring materials.

To conduct compression set measurements, the O-rings are removed from the fixtures, and the thickness is measured at three points around the O-ring. Once the measurements have been made, the O-rings are reinstalled in the fixtures, the compression is applied by tightening the wingnuts, and the stack is returned to the previous exposure conditions. Once completed, the compression set measurements will be combined with the volume swell measurements (Task 2) to investigate the correlation between volume swell and seal performance.

Milestones

During the previous year, compression set measurements were started for all four O-ring materials in Jet A fuel at 160°F. As of January 01, 2026, the O-rings will have been in compression set testing for approximately 16 weeks. Compression set measurements are being made and recorded on a two-week basis.

Major Accomplishments

Data sheets, policies and procedures were put in place in UDRI's Sealants and Elastomers Lab for full-scale compression set testing at elevated temperatures.

Publications

None.

Outreach Efforts

None.

Awards

None.

Student Involvement

None.

Plans for Next Period

During the next reporting period, full-scale compression set testing at elevated temperature will be conducted in the other soak scenarios. Also, the UDRI researchers will examine Tasks 2 and 3 datasets to determine the correlation between volume swell and seal performance.

Task 4 – Real-time Measurement of Sealing Force & Pressure During Switch-loading

University of Dayton Research Institute

Objective

The objective of this task is to bridge the gap between analytical measurements and engineering performance metrics. Specifically, Task 4 will involve measuring how and if the sealing pressure of an O-ring changes when the fuel is switched from a conventional Jet A fuel to the candidate SATF. The final step in Task 4 will be to determine the minimum sealing pressure required to prevent fuel leaks in the model face seals.

Research Approach

The research approach for Task 4 involves obtaining two critical experimental variables that will be used to calculate the sealing pressure of the material. First, the sealing force of the O-ring must be measured as function of time in dry, wet and changing fuel environments. This measurement is made using a modified Elastocon® compressive stress relaxometer (CSR). In short, a CSR measures the sealing force required to maintain the applied compression from a load cell (the value of which is set by the operator). In order to understand the change as a result of fuel exposure, the CSR was equipped with fuel lines as shown in Figure 9. The leftmost image in Figure 9 shows the bottom gland and fuel inlets. The glands used to hold the O-rings are the same dimensions as the glands used to hold O-rings in the UDRI compression set fixtures (Figure 8). The right side of Figure 9 shows the bottom gland in the CSR configured to run sealing force tests (load cell not shown). Second, the area over which the force is applied must be measured. To make this measurement, Dr. John Graham designed an optical cell that consists of the same bottom gland used on the CSR and compression set fixtures, but instead of a flat platen on top, the gland is topped with a thick glass window providing optical access. Critically, the compression applied by the glass window can be varied by placing metal shims of various thicknesses between the gland and the window. Thus, the area of the contact band of an O-ring can be measured at various compressions and fuel exposures. A camera and lens setup are placed directly above the glass window to acquire real-time information on how the area of the contact band changes. ImageJ is used to measure the area of the contact band with distances in the image calibrated based on known distances in the gland/fixture.



Figure 9. O-ring flow cell equipped with fuel lines (left) and the flow cell installed in the compressive stress relaxometer (CSR) (right).

The modified CSR and the optical flow cells are equipped to measure O-ring the sealing force whether in their dry, as-received forms or O-rings after they have been conditioned using elevated temperature, fuel/fluid exposure, etc. The sealing force from the CSR and the area of the contact band as a function of applied compression will be used to determine the sealing pressure of O-rings in each scenario (Equation 3). The most informative scenario is expected to be the change in sealing pressure under switch-loading conditions. These results can be correlated to the change in volume swell (Task 2) and compression set (Task 3). Once or if leaking conditions are calculated, the model face seals with optical access can be

® Elastocon is a registered trademark of Elastocon AB, Sweden.



pressurized up to 60 psi to determine if a leak will occur. This measurement will add yet another engineering metric by which we can understand the impact of fuel switching on various in-service conditions as we move towards implementing SATF in the field.

$$Sealing\ Pressure = \frac{Sealing\ force\ required\ to\ maintain\ O{-}ring\ compression}{Area\ of\ the\ contact\ band\ of\ the\ O{-}ring} \quad \text{(Eq. 3)}$$

Lastly, UDRI has a suite of flexible fuel couplings that were – at one time – actual flight hardware. Figure 10 shows the fuel couplings which house up to four candidate O-rings. The fuel couplings can be filled with fuel and, similar to the compression set fixtures, can undergo accelerated aging at temperature. Given the information gathered in Tasks 2, 3 and 4, these fuel couplings can be aged to a given compression set and then tested for fuel leaks. The use of flight hardware will provide the most realistic results to the FAA and OEMs on the lifetime of seals under switch-loading conditions.

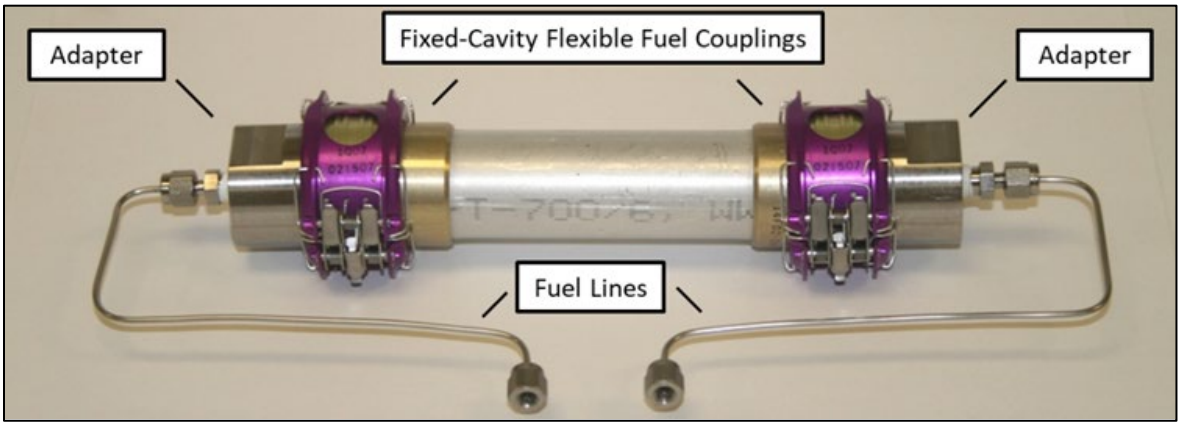


Figure 10. Flexible fuel couplings equipped to be a closed, fuel-filled system for accelerated O-ring agings.

Milestones

UDRI experimentally measured and reported on the sealing pressure of all four materials in their dry, as-received state using the optical cells and the Elastocon® CSR.

Major Accomplishments

During the 2025 calendar year, the CSR was set up for sealing force measurements and four optical cells for imaging contact bands were created. This setup equips UDRI to execute one full material investigation at a time and will increase the efficiency of the overall data collection process.

Publications

None.

Outreach Efforts

None.

Awards

None.

Student Involvement

None.

® Elastocon is a registered trademark of Elastocon AB, Sweden.



Plans for Next Period
During the next reporting period, UDRI will finish the plumbing of the modified CSR and optical cells so that fuel can be pumped through the instruments. Then, all O-ring materials will be characterized upon initial fuel wetting with Jet A fuel. After understanding the change in the sealing pressure as a result of exposure to Jet A, the investigation of changes in the sealing pressure under switch loading conditions will begin.

Task 5 – OEM Engagement
University of Dayton Research Institute

Objective
The objective of this task is to ensure that the materials and experiments are relevant to the real-world use of SATFs for OEMs, maintainers and the FAA.

Research Approach
The research approach to ensuring that Phase II is relevant for OEMs, maintainers and the FAA is establishing clear and regular communication. Communication can be in the form of updated results and meeting presentations, or less formal discussions based on observations in the field. Ultimately, ASCENT Project 088 hopes to obtain information not only on the experimental approach and results, but real-world examples of O-rings that have leaked when fuel was switched from Jet A to a SATF or SATF blends.

Milestones
This year, many SATF companies (Global Energies, Montana Renewables, etc.) were reached out to for fuel samples. In the end, the ASCENT SATF Repository was used to obtain a preliminary 1L of HEFA-SPK for testing.

Major Accomplishments
None.

Publications
None.

Outreach Efforts
The Fall Meeting was used as an opportunity to connect and build relationships between UDRI with ASCENT Industry partners, specifically fuel OEMs.

Awards
None.

Student Involvement
None.

Plans for Next Period
During the next reporting period, UDRI will make further efforts to contact and connect with both fuel and materials OEMs. UDRI will continue to leverage FAA PMs and FAA ASCENT meetings to get quality facetime with supporting partners who are already invested in the ASCENT program.

Task 6 – Reporting
University of Dayton Research Institute

Objective
The objective of this task is to properly document and analyze all the results of ASCENT Project 088 Phase II.



Research Approach
None.

Milestones
None.

Major Accomplishments
None.

Publications
None.

Outreach Efforts
None.

Awards
None.

Student Involvement
None.

Plans for Next Period
During the next period, reporting will begin for Phase II by means of collecting, organizing and processing all the data collected in Tasks 1-5.



Project 089 Characterization of Compositional Effects on the Dielectric Constant

University of Dayton Research Institute

Project Lead Investigator

Zachary West, PhD
Principal Research Engineer
Group Leader, Fuel Science
University of Dayton
300 College Park
Dayton, OH 45458
937-255-4062
zachary.west@udri.udayton.edu

University Participants

University of Dayton Research Institute (UDRI)

- P.I.: Zachary West, PhD
- FAA Award Number: 13-C-AJFE-UD, Amendment 056
- Period of Performance: January 1, 2025, to December 31, 2025
- Task:
  1. Measurement of dielectric constant and density

Project Funding Level

Amendment	Funding
Amendment No. 47	$499,999.67
Amendment No. 53	$110,607.00
Total	$610,606.67

Investigation Team

Dr. Zachary West (P.I.)
Shane Kosir (Staff Scientist)
Dr. William H. Steinecker (Staff Scientist)
Taylor Nicely (Undergraduate Student)
CJ Nesbit (Undergraduate Student)

Project Overview

Aircraft fuel tanks use capacitive gauges to determine fuel capacities during flight. Two crucial fuel properties, the dielectric constant and density, are used to calculate fuel volume from the response determined from the concentric, cylindrical gauging sensors. In recent years, the airframe original equipment manufacturers (OEM) have closely monitored the behavior of the dielectric constant (also referred to as relative permittivity) of candidate synthetic aviation turbine fuels (SATF), sometimes referred to as sustainable aviation fuels (SAF), because small changes in this property can result in atypical fuel tank gauging. This project involves measuring the behavior of fuel dielectric constants over a range of temperatures and fuel blends, by using a new dielectric constant instrument. While previous efforts (Kosir et al., 2024) focused on bulk hydrocarbon composition effects on dielectric constant, the current effort focuses primarily on the effects of trace polar species, including additives and incidental materials.

Task 1 – Measurement of Dielectric Constant and Density

University of Dayton Research Institute

Objective

The objective of this effort is to study the effect of trace polar species on jet fuel dielectric constant. An additional focus is the development of a dielectric constant blending rule that can be used by fuel producers, researchers, and other interested parties. This effort extends on previous work that focused on the effects of bulk composition on jet fuel dielectric constant.

Research Approach

The approach of this program is to measure the behavior of fuel dielectric constants over a range of temperatures and fuel blends, by using the Stanhope-Seta® JetDC instrument. UDRI purchased and commissioned the JetDC, which meets the requirements of specification *IP 638: Determination of relative permittivity (dielectric constant) of aviation fuels, small scale automated temperature scanning method* (Energy Institute, 2023). Previously, measurements were taken for conventional petroleum-based jet fuels and SATFs conforming to ASTM D7566 (ASTM International, 2022), reflecting a range of bulk hydrocarbon compositions. A major finding was that the bulk hydrocarbon composition influenced the dielectric constant, with the Clausius-Mossotti (CM) slope (historically used by airframe OEMs for fuel gauging) varying significantly with aromatic content (Kosir et al., 2024). This effort builds on the previous effort by focusing on additives and impurities common in jet fuel. Three approved additives were studied: fuel system icing inhibitor (FSII), corrosion inhibitor/lubricity improver (CI/LI), and static dissipator additive (SDA). The allowable concentration ranges for CI/LI, FSII, and SDA per ASTM D1655 (ASTM International, 2024) are 0.07 to 0.15 vol%, 0 to 23 mg/L, and 0 to 5 mg/L (after field reblending), respectively. A preliminary attempt was also made to study the effect of water contamination on jet fuel dielectric constant. Water concentration was measured using a Mettler Toledo® C30S Karl Fischer coulometer following the ASTM D6304 (ASTM International, 2025). Dielectric constant data for polar species from this effort, as well as bulk hydrocarbon data from the previous effort, are being compiled to validate a volume fraction dielectric constant blending rule. Future efforts will investigate dielectric constant models trained using linear solvation energy relationships (LSERs) as inputs to provide a deeper understanding of what governs the dielectric constant.

Research Results and Discussion

Figure 1 shows dielectric constant at 20˚C versus FSII concentration for FSII in Jet A (POSF 10325, left), FSII in *n*-heptane (middle), and FSII in toluene (right). *n*-heptane and toluene were selected as representative solvents representing the paraffinic and aromatic extremes of jet fuel. The repeatability from IP 638 (Energy Institute, 2023) is indicated as error bars, which was relatively small for all three blends compared to the measured dielectric constant values. Linear regression of dielectric constant versus FSII concentration produced R^2 values >0.99 for all three blends, indicating that the effect on dielectric constant is linear with volume at the FSII concentrations studied. The dielectric constant increased by 0.5% for all three blends at the maximum allowable FSII concentration of 0.15 vol% compared to the neat fuels/solvents. This increase will be discussed in the next paragraph.

® Seta is a registered trademark of Stanhope-Seta Limited, United Kingdom.
® Mettler Toledo is a registered trademark of Mettler-Toledo GMBH, Greifensee, Germany.

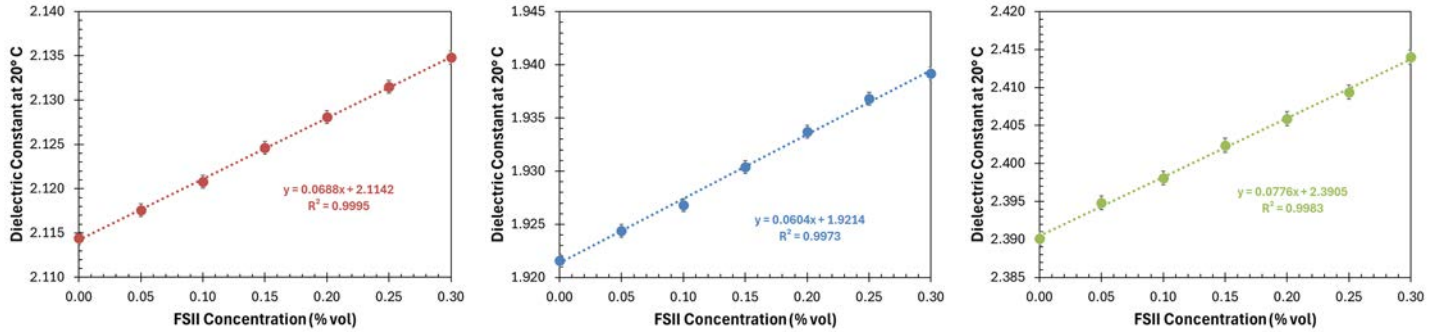


Figure 1. Dielectric constant at 20°C vs. fuel system icing inhibitor (FSII) concentration for FSII in Jet A (left), FSII in *n*-heptane (middle), and FSII in toluene (right).

Figure 2 shows the FSII results plotted over conventional fuel distributions from Aeronautical Radio, Inc. (ARINC) Report 611-1 (Aeronautical Radio, Inc., 1999), Coordinating Research Council (CRC) Report 647 (Hadaller & Johnson, 2006), and AV-33-22 (Kosir et al., 2025). These plots were made to contextualize the effects of FSII relative to bulk hydrocarbon composition. To calculate the CM slope and intercept, CM plots of the form $(K-1)/\rho$ versus $(K-1)$ were constructed for Jet A fuel, *n*-heptane, and toluene over a temperature range of 0-40°C. Linear regression was then done to generate the CM slope and intercept, which capture the effect of temperature on the dielectric constant and density in tandem. The CM slope has been shown to provide meaningful distinction between aromatics and *n*-/*iso*-/cycloalkanes, while the CM intercept further differentiates between *n*-/*iso*-alkanes and cycloalkanes (Yang et al., 2025). For all three blends, increasing FSII concentration systematically shifts the CM slope-intercept position along a well-defined linear path. For the FSII/Jet A fuel blend, the trajectory stays within the bounds of the ARINC/CRC contours, confirming that the observed dielectric constant variation remains representative of fuels already in circulation. It is possible that if the starting fuel were positioned further to the right, the addition of FSII could result in a shift outside the conventional experience range. Neat *n*-heptane is positioned at the outer ARINC/CRC contour, but higher FSII concentrations of 0.15-0.30 vol% result in outlier CM behavior. Toluene differs from the FSII/Jet A fuel and FSII/*n*-heptane blends in that the data fell entirely outside the conventional fuel experience range. The FSII/toluene blend has the tightest clustering of the three FSII blends, indicating smaller changes per concentration step.

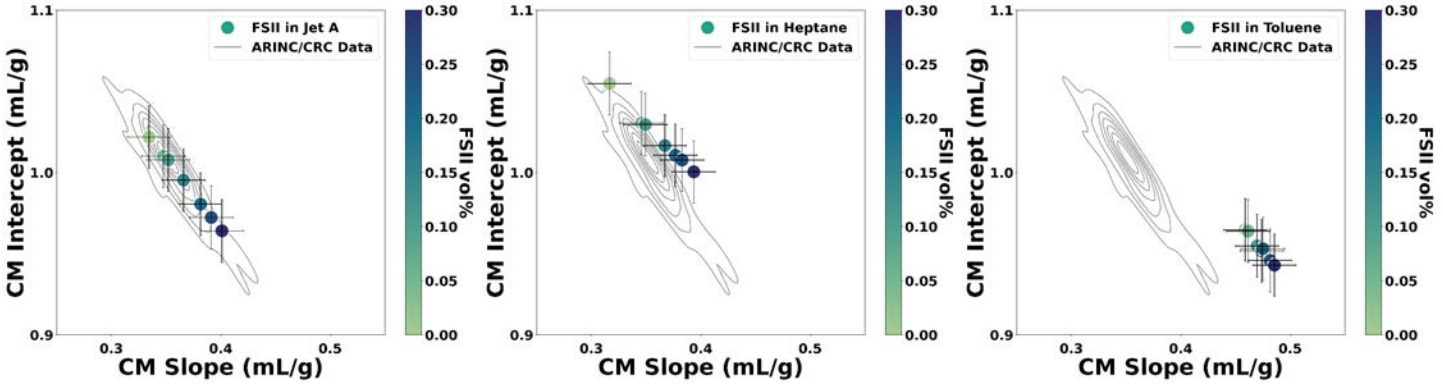


Figure 2. Clausius-Mossotti (CM) slope vs. intercept for fuel system icing inhibitor (FSII) in Jet A fuel (left), FSII in *n*-heptane (middle), and FSII in toluene (right). Colored markers represent data from this effort, with color intensity corresponding to FSII concentration. Error bars reflect measurement uncertainty per IP 638 (Energy Institute, 2023). Black contour lines represent conventional fuel dielectric constant distributions from ARINC Report 611-1 (Aeronautical Radio, Inc., 1999), CRC Report 647 (Hadaller & Johnson, 2006), and AV-33-22 (Kosir et al., 2025).



Dielectric constant measurements for blends of Jet A fuel with either CI/LI at 23 mg/L or SDA at 5 mg/L additive are shown in Figure 3. As show in Figure 3, there is no significant change in the measured dielectric constant due to inclusion of either additive. Due to the insensitivity at preliminary levels, measurements were not taken at additional concentrations.

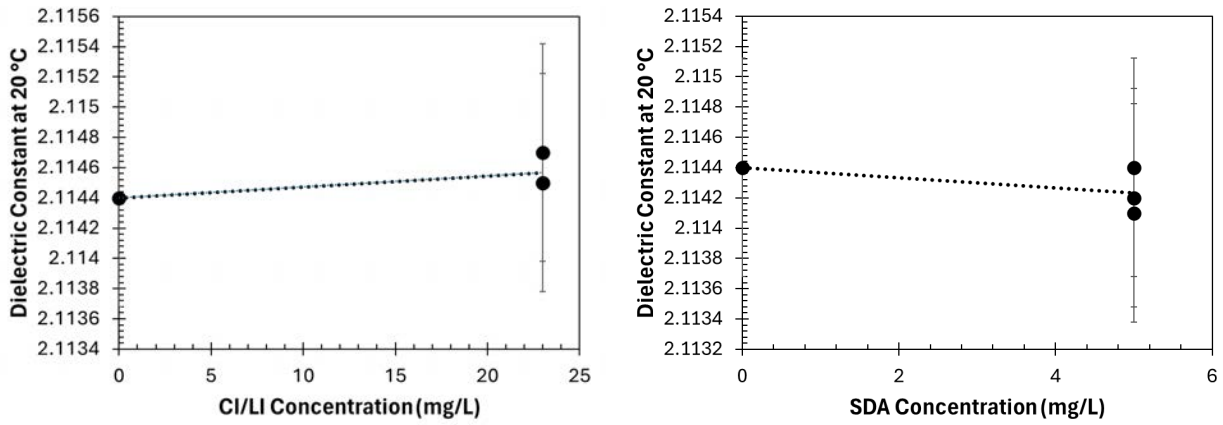


Figure 3. Dielectric constant at 20°C versus additive concentration for corrosion inhibitor/lubricity improver (CI/LI) in Jet A fuel (left) and static dissipator additive (SDA) in Jet A fuel (right).

A blending rule is explored here as a practical extension of this work for fuel producers, researchers, and other interested parties. The blending rule is shown in Equation 1. Here, ε_{blend} is the predicted dielectric constant of the blend, v_i is the volume fraction of blend component i, ε_i is the dielectric constant of blend component i, and n is the number of components in the blend. In the case of the binary blends explored here, $n = 2$. Previous work validated both a volume fraction and a polarizability blending rule using 40 mixtures of neat molecules and fuels (Yang et al., 2025). The species used were hydrocarbons (i.e., *n*-alkanes, *iso*-alkanes, cycloalkanes, and aromatics). The blending rule effort here builds on Yang et al. by validating Equation 1 using polar species. Because the JetDC is limited to a dielectric constant measurement range of 1.000-2.500, values for FSII, isopropyl alcohol (IPA), and aniline were pulled from the literature.

$$\varepsilon_{blend} = \sum_{i=1}^{n}(v_i \times \varepsilon_i) \quad \text{(Eq. 1)}$$

Figure 4 shows parity plots of dielectric constant predictions (using the volumetric blend rule) and measurements at 20°C for blends of hydrocarbons with polar components and complex hydrocarbons. While Figure 5 shows relative error for dielectric constant predicted using the volume fraction blending rule versus the concentration of blend component #1 (e.g., concentration of FSII in FSII/Jet A fuel blend). Polar blends from this effort are shown on the left, and synthetic blend components (SBC) from a previous effort are shown on the right. Errors were positive in both plots, which means that Equation 1 tended to overpredict the dielectric constant. Prediction errors for polar species increased in a linear manner from left to right, indicating a systematic bias. Errors for the FSII blends were ≤ 0.7% in the allowable FSII range of 0.07-0.15 vol%. This makes the volume fraction blending rule a promising tool for interested users. Errors for FSII, IPA, and aniline in *n*-heptane generally become significant at concentrations ≥ 1 vol%. However, these concentrations are unlikely in a real-world fuel and would likely cause other operational issues.

As shown on the right of Figure 5, dielectric constant predictions were made for binary blends from the previous effort (Kosir et al., 2024) using to further validate the volume fraction blending rule. These data consisted of three SBC/Jet A fuel blends, three binary SBC blends, and three neat molecule/Jet A fuel blends. The specific SBCs used were alcohol-to-jet-synthetic paraffinic kerosene (ATJ-SPK), cycloparaffinic kerosene (CPK), hydroprocessed esters and fatty acids-synthetic paraffinic kerosene (HEFA-SPK), and synthetic aromatic kerosene (SAK). The blending rule proved to be effective, with a maximum relative error of 0.5% for decalin. The relative error changed linearly with concentration for four of the blends. However, the relative error for the SAK/Jet A and CPK/SAK blends had a nonmonotonic trend, reaching a maximum at the 50/50 blend ratio.

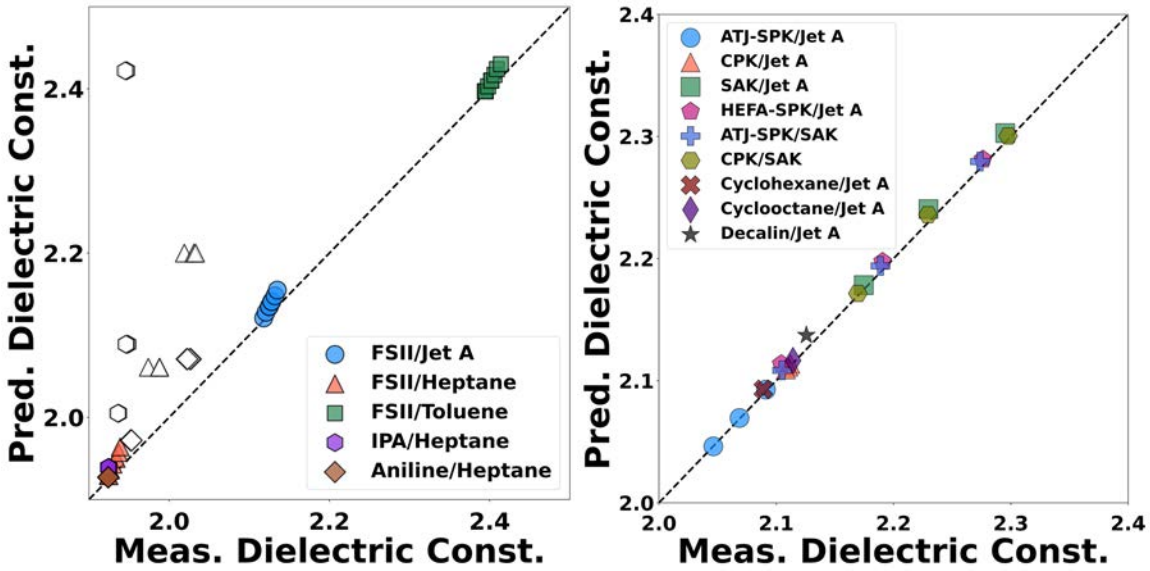


Figure 4. Parity plots of predicted versus measured dielectric constants at 20°C for polar/hydrocarbon mixtures (left) and cd complex hydrocarbon mixtures (right); polar species blended at greater than 0.3 vol% are filled white on the left plot.

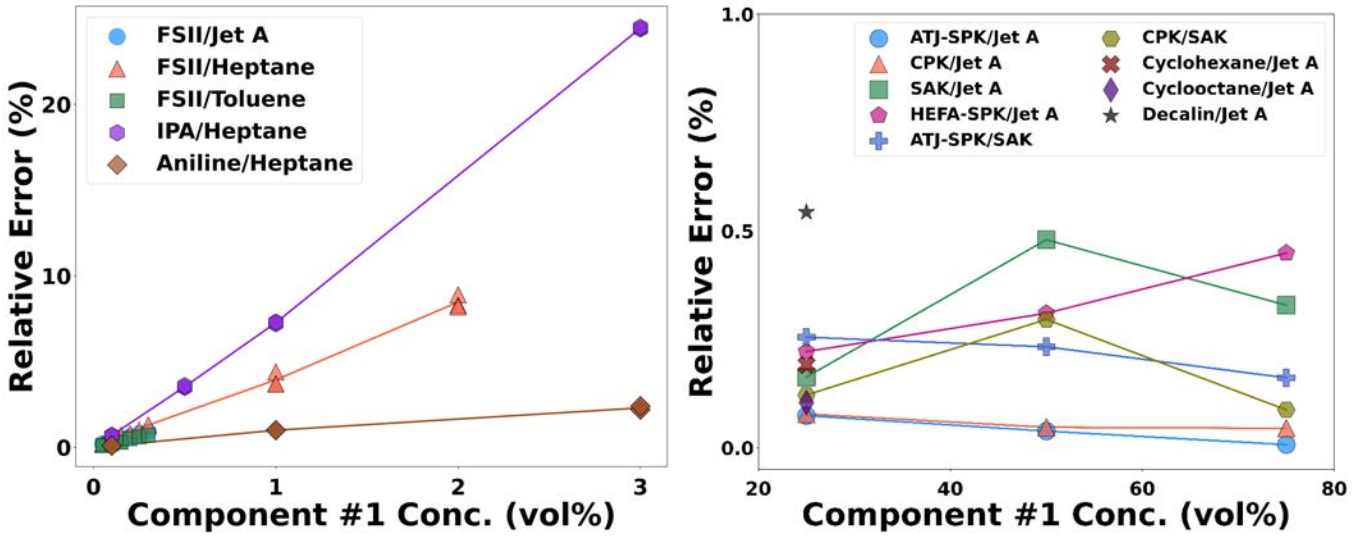


Figure 5. Validation of volume fraction blending rule at 20°C for blends containing polar species (left, current effort) and complex hydrocarbon mixtures (right, data from Kosir et al., 2024).

Milestones

- Acquired and commissioned the JetDC instrument.
- Participated in the interlaboratory study (ILS) and measurements of dielectric and density on fuel/SBC blends.
- Presented our work at two major international conferences, and published journal publication of major findings.

Major Accomplishments

- Published peer reviewed journal publication in *Energy & Fuels*.



- Presented our work at two major international fuels conferences: 2024 CRC Aviation Committee Meeting and 18th International Conference on Stability, Handling, and Use of Liquid Fuels (September 2024).

Publications

Peer-Reviewed Journal Publications

Kosir, S., Landsaw, A., Steinecker, W. H., West, Z. J., & Zabarnick, S. (2024). Synthetic blend component study: the effects of hydrocarbon composition on aviation fuel dielectric constant. *Energy & Fuels, 38*(17), 16451—16457, https://doi.org/10.1021/acs.energyfuels.4c02342

Nicely, T., Nesbit, C. J., Kosir, S., Steinecker, W. H., & West, Z. (In process). Influence of Additives and Impurities on the Dielectric Properties of Jet Fuel. *Energy & Fuels.*

Conference Presentations

Kosir, A., Landsaw, A., West, Z., & Zabarnick, S. (2024, September 8-12). *Synthetic blend component study: the effects of hydrocarbon composition on aviation fuel dielectric constant* [Conference presentation]. 18th International Conference on Stability, Handling and Use of Liquid Fuels, Louisville, Kentucky.

Kosir, S., Landsaw, A., West, Z., & Zabarnick, S. (2024, April 29 - May 2). *Composition effects on the dielectric constant for blends of aviation fuel synthetic blend components (SBCs)* [Conference presentation]. 2024 CRC Aviation Committee Meeting, Alexandria, Virginia.

Outreach Efforts

A presentation was made at the ASCENT Spring 2024 meeting, and a poster was presented at the Fall 2024 ASCENT meeting. Presentations were also made at the 2024 CRC Aviation Committee Meeting and the 18th International Conference on Stability, Handling and Use of Liquid Fuels; both meetings were well attended by aviation fuels industry experts (from OEMs and producers). The goal of these meetings is to receive feedback from industry experts on future steps to enable this work to most effectively contribute to the approval of new SAF candidates.

Awards

- Dr. Steven Zabarnick, ASTM D02 Award of Excellence, December 2023

Student Involvement

- Undergraduate student, Taylor Nicely, was responsible for taking dielectric constant measurements. She also presented a poster for her work on this project at an undergraduate chemical engineering research symposium hosted by the Ohio State University.
- Undergraduate student, CJ Nesbit, was responsible for taking dielectric constant and water content measurements. He was also awarded the Ohio Space Grant Consortium (OSGC) undergraduate STEM scholarship for his work on this project.

Plans for Next Period

- Report on impacts of trace water on the dielectric constant.
- Further develop model predictions to include LSER based models.
- Draft final report and second journal publication.

References

Aeronautical Radio, Inc. (1999). *Guidance for the design and installation of fuel quantity systems (ARINC Report 611-1).* https://img.antpedia.com/standard/files/pdfs_ora/20230613/ARINC/ARINC%20REPORT%20611-1-1999.pdf

ASTM International. (2024). *ASTM D1655-24b: Standard specification for aviation turbine fuels.* https://doi.org/10.1520/D1655-24B

ASTM International. (2025). *ASTM D6304-25: Standard test method for determination of water in petroleum products, lubricating oils, and additives by coulometric Karl Fischer titration.* https://doi.org/10.1520/D6304-25

ASTM International. (2022). *ASTM D7566-22a: Standard specification for aviation turbine fuel containing synthesized hydrocarbons.* https://doi.org/10.1520/D7566-22A

Energy Institute. (2023). *IP 638: Determination of relative permittivity (dielectric constant) of aviation fuels, small scale automated temperature scanning method.*



Hadaller, O. J., & Johnson, J. M. (2006). *World Fuel Sampling Program* (CRC Report No. 647), Coordinating Research Council, Inc. https://crcao.org/wp-content/uploads/2025/07/CRC-647.pdf

Kosir, S., Landsaw, A., Steinecker, W. H., West, Z. J., & Zabarnick, S. (2024). Synthetic blend component study: the effects of hydrocarbon composition on aviation fuel dielectric constant. *Energy & Fuels, 38*(17), 16451—16457, https://doi.org/10.1021/acs.energyfuels.4c02342

Kosir, S., Arts, A. M., Nicely, T., Nesbit, C. J., Mueller, S., Landsaw, A., Baker, M., Brown, L., Thompson, J., Anderson, C., Shafer, L., Steinecker, W. H., Zabarnick, S., & West, Z. J. (2025). *World Jet Fuel Survey Part 1: 2023-2024* (AV-33-22). Coordinating Research Council, Atlanta, Georgia.

Yang, Z., Bell, D. C., Boehm, R., Marques, P. F., Boze, J. A., Kosilkin, I. V., & Heyne (2025). Assessing the effect of composition on dielectric constant of sustainable aviation fuel. *Fuel, 380*. https://doi.org/10.1016/j.fuel.2024.133230



Project 090 World Fuel Survey

University of Dayton Research Institute

Project Lead Investigator

Zachary West, PhD
Principal Research Engineer
Group Leader, Fuel Science
University of Dayton
300 College Park
Dayton, OH 45458
937-255-4062
zachary.west@udri.udayton.edu

University Participants

University of Dayton Research Institute (UDRI)

- P.I.: Zachary West, PhD
- FAA award number: 13-C-AJFE-UD
- Overall Period of Performance: January 1, 2023, to September 30, 2025
- Tasks:
  - Period of Performance: January 1, 2023, to December 31, 2023; Amendment No. 048
    1. Conduct a survey of commercial jet fuels and develop a modern technical dataset for relevant fuel samples
  - Period of Performance: September 22, 2023, to September 30, 2024; Amendment No. 049
    - No-Cost Extension
  - Period of Performance: March 19, 2024, to March 18, 2025; Amendment No. 051
  - Period of Performance: September 23, 2024, to September 30, 2025; Amendment No. 057
    - No-Cost Extension
  - Period of Performance: September 30, 2025, to September 30, 2026; Amendment No. 063
    - No-Cost Extension

Project Funding Level

Amendment	Funding
Amendment No. 048	$749,886.56
Amendment No. 051	$999,998.00
Total	**$1,749,884.56**

In-kind cost sharing has been obtained from the following organizations. Additional cost-sharing will be obtained from fuel refineries for the cost of fuel samples and testing services.

Organization	Amount	Year
Marathon Petroleum Corporation	$30,120	2023
ASG Analytik-Service AG	$9,357	2024
Total	**$39,477**	

Investigation Team

Dr. Zachary West (P.I.)
Carlie Anderson (staff scientist)



Dr. Amanda Arts (staff scientist)
Dr. Joseph Gord (staff scientist)
Shane Kosir (staff scientist)
Susan Mueller (staff scientist)
Linda Shafer (staff scientist)
Dr. Willie Steinecker (staff scientist)
CJ Nesbit (undergraduate student)
Taylor Nicely (undergraduate student)
Maria Baker (other professional)
Lisa Brown (other professional)
Jim Thompson (other professional)

Project Overview

Jet fuel is defined by a robust physicochemical and performance specification; however, the exact chemical composition is variable and depends on numerous market factors, such as petroleum crude sources, production/refinery techniques, and impacts from transportation/handling in the fungible fuel system. As the United States and other countries are accelerating the pace of fuel certification (via the ASTM D4054 standard practice [ASTM International, 2022]) and production of synthetic aviation turbine fuels (SATF) to include sustainable aviation fuels (SAF), having a robust and representative set of data for comparison is critically important to the safe adoption of SATF/SAF fuels. Almost two decades have passed since the last major survey of commercial jet fuels (CRC Report No. 647, 2006 [Hadaller & Johnson, 2006]); therefore, this project aims to collect a contemporary set of representative jet fuel samples and conduct both specification and non-specification testing on the subject samples. The results of this survey will be used to inform how to accelerate SAF adoption in the market.

Task 1 – Conduct a Survey of Commercial World Jet Fuels

University of Dayton Research Institute

Objectives

The objectives of this task are to (1) secure relevant jet fuel samples directly from refineries around the world, (2) analyze the fuel samples to create a robust set of physicochemical and property technical data, and (3) make the test data available to the aviation fuels community, to enhance and expedite decisions regarding current and future SATF/SAF compositional requirements.

Research Approach

Our research approach has been two-fold where the first part involved collecting industry stakeholder interest/feedback and building partnerships with fuel refiners. The second portion of the project has involved the development and execution of the process shown in Figure 1. The execution of the process includes soliciting fuel samples from refiners, coordinating the shipping and handling of the samples to UDRI, subjecting fuel samples to testing at both UDRI and other vetted contracted laboratories, and reporting test data through partnerships with both the Coordinating Research Council (CRC) and Volpe National Transportation System Center (Volpe Center).

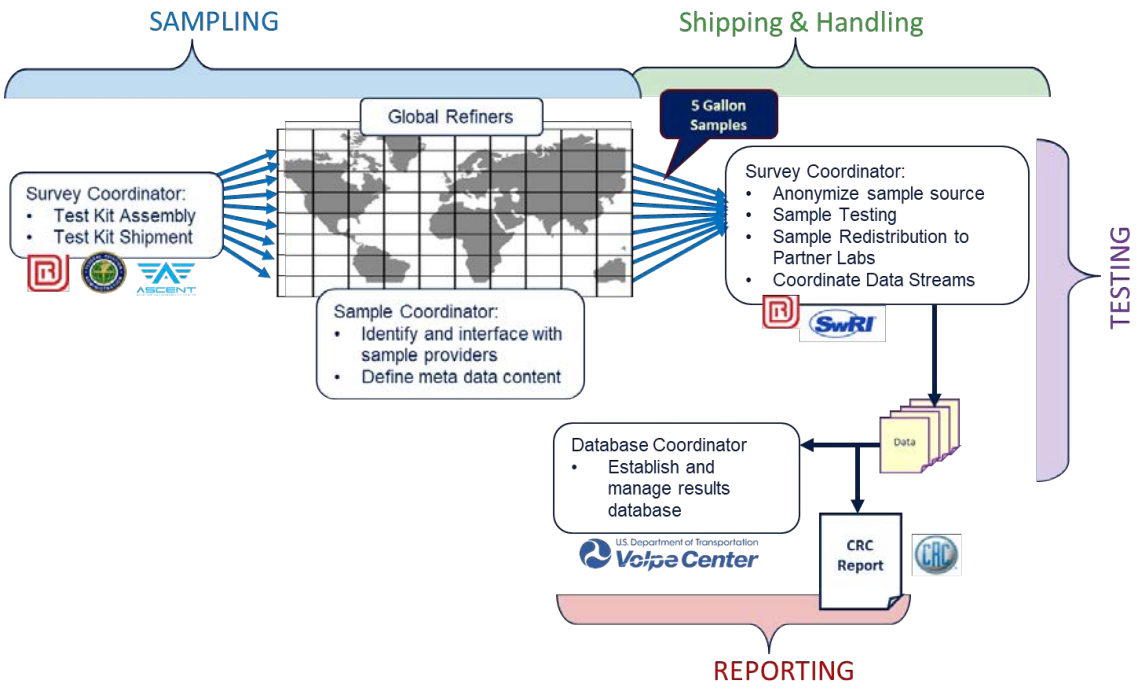


Figure 1. Schematic representation of the world jet fuel survey process.

Solicitation of Samples

Targeted email solicitations requesting samples of 5 gal were sent to our fuel producer partners. After obtaining positive responses, UDRI sent sampling kits and instructions to fuel producers to submit samples along with certificates of analysis. The ASCENT Project 090 team have received a total of 54 jet fuel samples as of December 10, 2025, which represents over 151 million US gallons of product (as self-reported by refiner batch volumes). The first 38 of these samples will be included in the first-year (Part 1) data reporting with the CRC and Volpe Center. Our team is actively soliciting additional samples to increase the total observed sample population and increase both the depth and breadth of the dataset. We have been working with Concawe in Europe over the past few months to procure an additional 15 samples by late first quarter in 2026.

Table 1 and Table 2 show fuel counts by continent for the Part 1 (2023-2024) and current Part 2 (2024-present) fuels, respectively. Although the number of fuels received during Year 2 decreased, the global distribution of samples is geographically more diverse, with contributions for Asia and South America.

Table 1. Part 1 Jet Fuel Samples (Collected from 2023-2024).

Continent of Origin	Fuel Count	Total Batch Volume (US MGal)
North America	28	71
Europe	9	27
Asia	1	8



Table 2. Part 2 Jet Fuel Samples (Collected from 2024-Present).

Continent of Origin	Fuel Count	Total Batch Volume (US MGal)
North America	4	4
Europe	3	8
Asia	7	29
South America	2	5

Testing

In addition to the refiner's reported specification data (i.e., Refiner's Certificate of Quality [RCQ]), fuels are being subjected to 27 chemical, physical, and performance tests (Table 3). Testing is being performed at both UDRI and Southwest Research Institute (SwRI).

Table 3. Fit-for-Purpose Test List.

Property	Test Method
Detailed Hydrocarbon Type	UDRI FCM-101; FED-STD-791, Method 7508
Aromatics, saturates, and olefins	ASTM D1319
Hydrogen content	ASTM D3701
Polars	UDRI FCM-102
Inorganic compounds: N, total, and basic	ASTM D4629
Trace Metals	UDRI FC-M-107
Distillation	ASTM D86
Simulated distillation	ASTM D2887
Thermal stability, breakpoint	ASTM D3241
Thermal stability, QCM	ASTM D7739
Lubricity	ASTM D5001
Viscosity vs. temperature	ASTM D7042
Specific heat vs. temperature	ASTM E2716
Density vs. temperature	ASTM D4052
Surface tension vs. temperature	ASTM D1331
Isentropic bulk modulus vs. temperature and pressure	FED-STD-791, Method 7507
Thermal conductivity vs. temperature	ASTM D7896
Water solubility vs. temperature	Modified ASTM D6304
Air solubility (oxygen/nitrogen)	UDRI FCM-103
True vapor pressure vs. temperature	ASTM D6378
Refractive index (nD20)	UDRI In-House
Derived cetane number	ASTM D6890
Indicated cetane number	ASTM D8183
Dielectric constant vs. density	IP 638
Autoignition temperature	ASTM E659
Hot surface ignition temperature	ISO 20823

Reporting

UDRI has anonymized all the test data before reporting, to protect fuel producers' commercial interests. The ASCENT Project 090 team is working with the Volpe Center to establish an online database to archive test data. 225 lines of Python® code was written to unpivot the data for the database. Our team also intends to report the test data in a CRC report (CRC AV-33-22 [Kosir et al., 2025]). The report has undergone three rounds of revision, with an anticipated publication date around December 2025/January 2026. Some of the rebuttal edits include:

- Addition of a section for the certificate of analysis (CoA) data
- Documentation of specific instrumentation and methods used
- Inclusion of method precision when available
- Addition of antioxidant concentration to the dataset where available from the CoA

Figure 2 shows acidity values from the Part 1 data report as an example of CoA data reporting. The top histogram (blue) depicts Jet A fuels, and the bottom histogram (red) shows Jet A-1 fuels. The histograms generally mirror each other, with a significant number of fuels falling in the 0-0.005 mg KOH/g bin. Two Jet A-1 fuels had acidity greater than the Defence Standard maximum limit of 0.015 mg KOH/g but within the ASTM D1655 (ASTM International, 2023) limit of 0.10 mg KOH/g. Similar histograms are shown in CRC AV-33-22 for 20 properties taken from the CoA data.

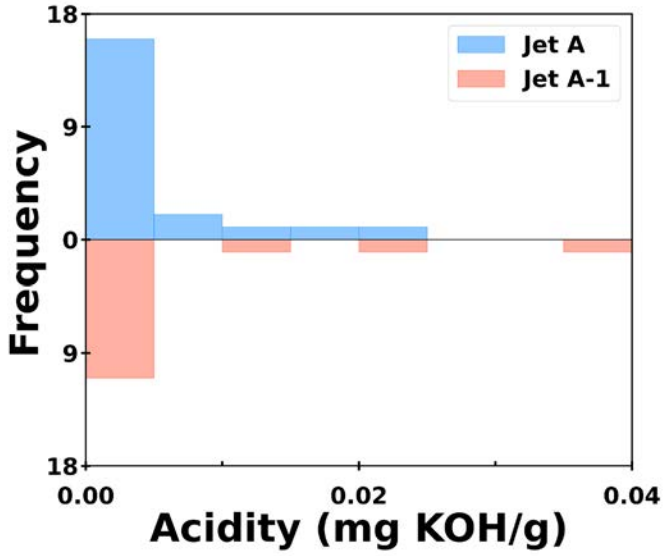


Figure 2. Comparison of Jet A fuel and Jet A-1 fuel acidity data taken from the certificates of analysis (CoA) contained in CRC AV-33-22 (in press).

Figure 3 shows a parity plot (left) and model coefficients (right) for an initial boiling point (IBP) model trained using partial least squares (PLS) regression with two-dimensional gas chromatography (GCxGC) hydrocarbon type data as its input. This is an example of a composition-to-property (C2P) model. In total, 19 C2P models were trained and included in CRC AV-33-22. The models serve a few roles: (1) they provide an indication of how well the measured properties correlate with existing fuel composition measurement techniques, (2) when the model performance is good, the model coefficients provide insight into fuel chemistry, and (3) when the model performance is poor, the models indicate that experimental method development and/or more advanced modeling techniques are required. In the case of the initial boiling point model the normalized root mean squared error (NRMSE) is low at 1.9%. Since the model demonstrates good correlation, the model coefficients can more confidently be assigned chemical meaning. That is to say, the model coefficients indicate that the lowest carbon numbers, in each class, contribute to lower IBP values, which makes intuitive sense. This same technique is applied to other properties, e.g., dielectric constant, that might not have as obvious chemical correlations.

® Python is a registered trademark of Python Software Foundation, Beaverton, Oregon.

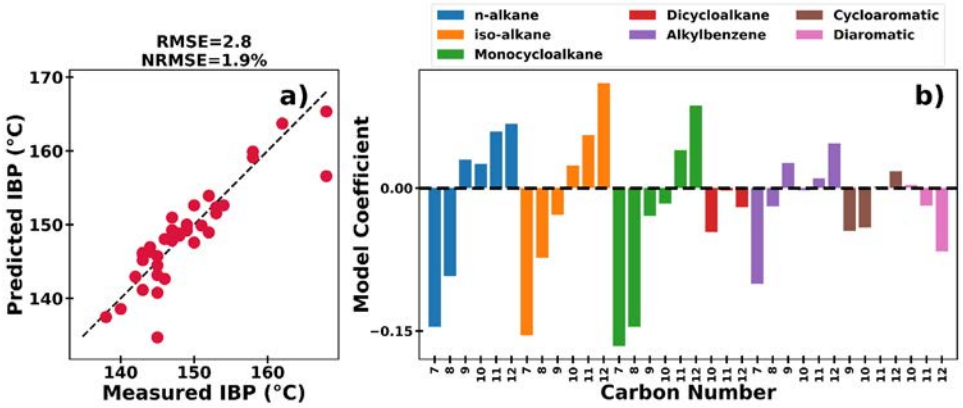


Figure 3. (a) Partial least squares (PLS) initial boiling point predictions made using two-dimensional gas chromatography (GCxGC) hydrocarbon type data as training features. (b) Model coefficients for the initial boiling point model. IBP: initial boiling point.

ASTM D4054 Plots

Eleven figures have been developed to update the existing figures in ASTM D4054 Annex A1: "Basis of Engine and Airplane Manufacturers' Experience." These figures have been created using data from CRC Report 647, CRC AV-33-22, and other sources when available. Figure 4 shows the typical viscosity characteristics of jet fuel from CRC Report 647 and CRC AV-33-22 (91 fuels in total). Boxes represent the interquartile range (IQR), and whiskers represent the non-outlier range. The horizontal bars in the boxes represent median values. As expected, the viscosity median and IQR increases exponentially as temperature decreases. A task force was created by Dr. Zach West at the December 2025 ASTM D02.0J meeting to investigate updating the Annex A1 figures in ASTM D4054. The preliminary timeline is to host a task force meeting in the first quarter of 2026 to solicit feedback, with the potential to ballot updated figures by the June 2026 ASTM meeting.

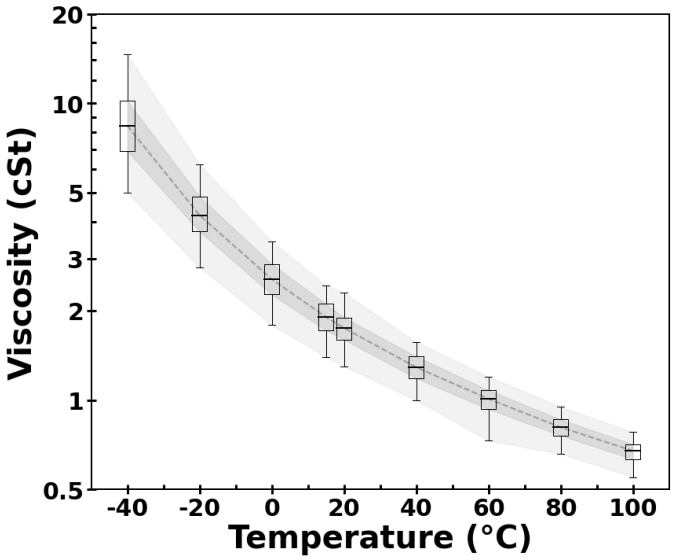


Figure 4. Typical viscosity characteristics of jet fuel. Data was pulled from CRC Report 647 (ASTM D455, measured at -40, -20, and 20°C) and CRC AV-33-22 (ASTM D7042 [ASTM 2025], measured at all depicted temperatures).



Milestones

The original project proposal indicated that sample testing would be completed by July 1, 2023, and a final report and analysis would be complete by September 30, 2023. However, this timeline failed to account for fuel producer schedules to provide samples and the time required for outside/sub-contracted testing services. That said, the Part 1 data report (to be published circa December 2025) will be delivered to the aviation fuels community at a faster pace than other, less detailed survey data (e.g., CRC Project AV-18-18/19 contains data from 2018-2019 and was published in April 2025), especially considering the level of effort to stand up the new processes. It is recommended to continue data collection and reporting with the current, active processes while it is operating at high efficiency. It is anticipated that Part 2 data will be reported by December 2026.

Major Accomplishments

- Received 54 jet fuel samples to date, which represent over 151 million US gallons of product (as self-reported by the refinery batch volumes).
- Presented the ASCENT Project 090 preliminary data at two major, international jet fuel conferences.
- Drafted the Part 1 report, which is expected to be published by December 2025/January 2026.

Publications

West, Z. (2024, April 29-May 2). *World jet fuel survey* [Conference presentation]. 2024 CRC Aviation Committee Meeting, Alexandria, Virginia.

Kosir, S., & West, Z. (2024, September 8-12). *World jet fuel survey (preliminary results)* [Poster presentation]. 18th International Conference on Stability, Handling and Use of Liquid Fuels (IASH 2024), Louisville, Kentucky.

Kosir, S., Arts, A. M., Nicely, T., Nesbit, C. J., Mueller, S., Landsaw, A., Baker, M., Brown, L., Thompson, J., Anderson, C., Shafer, L., Steinecker, W. H., Zabarnick, S., & West, Z. J. (2025). *World Jet Fuel Survey Part 1: 2023-2024* (CRC AV-33-22). Coordinating Research Council (CRC), Atlanta, Georgia. In press.

Outreach Efforts

The ASCENT Project 090 activities were presented at the spring and fall ASCENT semi-annual meetings in 2024 and 2025. Additionally, the project has been briefed at the following conferences and meetings:

- CRC Aviation Committee Meeting, Alexandria, Virginia, April 29 – May 2, 2024
- ASTM International D02.0J Sub-committee meeting, Anaheim, California, December 11, 2024
- OEM Technical Review Panel meeting, online #74, September 3, 2024
- 18th International Conference on Stability, Handling and Use of Liquid Fuels (IASH), Louisville, Kentucky, September 8-12, 2024
- UK MoD Aviation Fuels Committee Meeting, Manchester, United Kingdom, March 18-19, 2025
- ASTM International D02.0J Sub-committee meeting, Brussels, Belgium, April 9, 2025
- CRC Aviation Committee Meeting, Dayton, Ohio, April 28 – May 1, 2025
- International Air Transport Association (IATA), Aviation Energy Forum, Mexico City, Mexico, November 19, 2025
- ASTM International D02.0J Sub-committee meeting, Houston, Texas, December 10, 2025

Awards

None.

Student Involvement

Two undergraduate chemical engineering students that have been involved with the preparation of samples for solid phase extraction, GCxGC with tandem flame ionization detection and mass spectrometry detection analysis for polar organic compounds (UDRI FC-M-102) and investigating simulated distillation data analysis techniques.

Plans for Next Period

- Continue to solicit samples from fuel producers.
- Collect test data in earnest (i.e., fit-for-purpose property data).
- Prepare to report Part 2 data.



References

ASTM International. (2022). *ASTM D4054-22: Standard practice for evaluation of new aviation turbine fuels and fuel additives*. https://doi.org/10.1520/D4054-22

ASTM International. (2023). *ASTM D86-23ae1: Standard test method for distillation of petroleum products and liquid fuels at atmospheric pressure*. https://doi.org/10.1520/D0086-23AE01

ASTM International. (2023). *ASTM D1655-22a: Standard Specification for Aviation Turbine Fuels*. https://doi.org/10.1520/D1655-22A

ASTM International. (2025). ASTM D7042-21a: Standard Test Method for Dynamic Viscosity and Density of Liquids by Stabinger Viscometer (and the Calculation of Kinematic Viscosity). https://doi.org/10.1520/D7042-21A

Hadaller, O. J., Johnson, J. M. (2006). *World Fuel Sampling Program* (CRC Report 647). Coordinating Research Council, Inc., Alpharetta, Georgia. https://crcao.org/wp-content/uploads/2025/07/CRC-647.pdf



Project 091(B) Environmental Impacts of High-altitude and Space Vehicle Emissions

University of Illinois at Urbana-Champaign

Project Lead Investigator

Dr. Donald Wuebbles
Department of Atmospheric Sciences
University of Illinois
105 S. Gregory Street
Urbana, IL 61801
217-244-1568
wuebbles@illinois.edu

University Participants

University of Illinois at Urbana-Champaign

- P.I.: Dr. Donald Wuebbles
- FAA Award Number: 13-C-AJFE-UI-048
- Period of Performance: January 1, 2024, to September 30, 2025 (partial year; project started January 1, 2023)
- Tasks:
  1. Examine the environmental impacts of technologies related to scenarios for extensive potential use of high-altitude vehicles, including rockets, and their associated emissions by mid-century
  2. Coordinate with Massachusetts Institute of Technology (MIT) and Aerospace Corporation in these studies

Project Funding Level

Project funding support from the Federal Aviation Administration (FAA) over this time period was approximately $175,000; an additional $175,000 of in-kind matching support was provided by the University of Illinois.

Investigation Team

Dr. Donald Wuebbles (P.I.), project oversight

Swarnali Sanyal and Rachana Pradhan (postdoctoral associates), conducting studies and performing analyses with the Community Earth System Model Whole Atmosphere Community Climate Model (WACCM), a three-dimensional atmospheric climate-chemistry model including the whole atmosphere.

Project Overview

This project uses state-of-the-art modeling capabilities for atmospheric physics and chemistry processes in association with expert analysis to develop an assessment of the potential impacts of rockets (i.e., high-altitude and space vehicle emissions) on the global environment, specifically the compositions of gases and particles in the global atmosphere (troposphere, stratosphere, mesosphere, and above) and the resultant potential impacts on the Earth's climate. These analyses are useful for policymakers to understand the potential effects of projected rocket emissions on the environment.



Task 1 – Revisiting High-Speed Civil Transports and Their Potential Effects on Ozone and Climate

University of Illinois at Urbana-Champaign

Objectives

Numerical models of the Earth's physics and chemistry system that fully represent atmospheric processes from the ground to the top of the mesosphere (and above), to further improve understanding and evaluation of the environmental impacts of technologies related to scenarios for extensive potential use of high-altitude vehicles, including rockets, and their associated emissions by mid-century (approximately the year 2050). The aim, in coordination with the FAA, Aerospace Corporation (which will develop the rocket emission scenarios), and Massachusetts Institute of Technology (MIT) (which will also use its global modeling capabilities) is to further assess the state of understanding of potential high-altitude and space vehicle emissions on the global environment, and to publish these analyses in major science journals.

Research Approach

The study uses the state-of-the-art WACCM model that is part of the range of models within the Community Earth System Model (CESM), developed through community-coordinated efforts by the National Center for Atmospheric Research (NCAR). The version of the WACCM model used here has 66 layers from the ground to above the mesosphere and provides a comprehensive treatment of tropospheric and stratospheric (and above) chemical processes. WACCM is one of the most advanced models worldwide for studying atmospheric processes and one of the few with a complete representation of stratospheric and mesospheric processes and higher; for example, it is one of very few models to represent the quasi-biennial oscillation that is important to stratospheric ozone. It has a comprehensive treatment of gas phase, particle based and heterogeneous chemistry. This model extends higher in the atmosphere than any other atmospheric model in existence except for another version of this model that goes even higher (to be considered for later studies, but it is computationally very expensive). Therefore, the model used here is ideal for studying the environmental impacts from rockets.

Results and Discussion

Emissions from rockets and their effects on stratospheric ozone have been a subject of research since the 1970s (e.g., Prather et al., 1990; Harris & Wuebbles, 2014; Dallas et al., 2020). However, research in this area has comprised largely incomplete evaluations and has relied on poorly understood emission assumptions. A major need exists for assessment of the state of the science for understanding the environmental impacts according to the most up-to-date understanding of the potential future annual rocket emissions over the coming decades. Below, the existing research is summarized relating to such emissions.

More satellites have been launched into low Earth orbit during the past few years than during the previous 60 years, as a result of a combination of larger rockets and higher launch rates. Most of this growth has come from kerosene-fueled rockets, from which black carbon (BC) emissions have doubled in the past four years (Miraux, 2022). Emissions from solid fuel rockets have increased only slightly. Hydrazine-fueled rocket launches have decreased during this period, because of propellant toxicity concerns. Hydrogen-fueled launches have been constant but have represented only a small fraction of all launches. Methane-fueled rockets in advance testing are expected to play a major role in the future, although the rate at which methane would replace existing rocket fuel is uncertain.

Rocket propulsion systems typically combine the exhausts from several of the four primary propellant types (by fuel: kerosene, ammonium perchlorate, hydrazine, and hydrogen). Mixed rocket emissions into the stratosphere are mostly (>90% of approximately 8 Gg/yr) a combination of carbon dioxide (CO_2), carbon monoxide (CO), H_2O, and hydroxide (OH); the exact amounts vary, depending on propellant and altitude. None of these major emission components significantly affect stratospheric ozone, even at implausibly higher launch rates (Larson et al., 2017). Nitrogen oxide emissions (<1%) from some rocket types can affect ozone (Ross et al., 2004), although to a lesser degree than solid fuel chlorine emissions.

Direct ozone loss caused by chlorine emissions (0.2 Gg/yr) from solid fuel rockets is well understood. Models agree on the amount and distribution (Voigt et al., 2013). Alumina emissions from solid fueled rockets (0.4 Gg/yr) cause ozone loss through heterogeneous chlorine-involving Cl_y activation reactions; the importance of these reactions are less well bounded because of uncertainties in the alumina surface area density, the extent of sulfate coating, and reaction coefficients (Danilin et al., 2003). In situ plume data suggest that ozone loss from alumina might be larger than that from chlorine (Danilin et al., 2001).



Indirect ozone loss caused by the absorption and scattering of solar radiation by rocket BC and alumina particles in the stratosphere has not yet been investigated. General principles of stratospheric processes suggest that rocket BC and alumina increase heating rates and temperatures in the stratosphere, and cause ozone loss (Lee et al., 2021). Linear scaling of solid aerosol climate mitigation models and models of rocket BC emissions (Maloney, 2022) suggest that the ozone loss from rocket BC and alumina stratospheric heating is comparable to that from chlorine emissions (Weisenstein et al., 2015).

Hydrogen-fueled projected space travel has been estimated to enhance stratospheric water by as much as 9%, thus leading to a potential 20% increase in polar stratospheric clouds in both hemispheres (Larson et al., 2017). An even larger effect of hydrogen-based space travel may arise from the expected increases in stratospheric nitrogen oxides, which, combined with hydrogen oxide (HO_x) cycle perturbations, leads to a 0.5% loss of the globally averaged ozone column, with column losses in the polar regions exceeding 2%.

New space technologies, such as large low Earth orbit constellations and active removal of space debris, dispose of derelict spacecraft into the middle atmosphere. The effects of stratospheric aerosols generated by destruction of space debris during reentry is a new area of research (Boley & Byers, 2021). Reentry vaporization and lower mesosphere particle production and sedimentation are a source of stratospheric particles likely to exceed present-day launches by 2030 (Boley & Byers, 2021). Very little is known regarding the composition, sizes, and steady-state distribution of reentry particles, or their possible impact on stratospheric ozone.

Three scenarios have been developed through our coordination with ASCENT Project 091A at MIT. These scenarios for 4,000 launches per year projected to occur annually by 2050 were evaluated with the WACCM model. These scenarios correspond to assuming the use of (1) fossil fuel, (2) methane fuel, and (3) hydrogen fuel. A series of meetings has been jointly held with MIT and Aerospace Corporation over the past project year towards not only developing the scenarios, but also to coordinate the modeling studies done with WACCM and with the MIT model. Our team is coordinating with MIT to evaluate the results from the model calculations and to complete a joint journal paper.

Milestones

- Completed analyses for the modeling studies for the three scenarios. The University of Illinois runs are fine and will be the basis of a journal paper. The MIT runs were shown to have an error in the upper boundary conditions that affected interpretation of their findings.
- Completed a journal paper currently being reviewed by the authors – being submitted to the journal

These studies will provide important context for further studies of rocket use projections, which our team will be examining next.

Publications

Kulkarni, R., Sanyal, S., Ma, C. Z., McDonald, H., Speth, R. L., Ross, M., & Wuebbles, D. J. (2025). Effects of Potential Future Emissions from Different Rocket Fuel Types on Climate and Stratospheric Ozone. *AGU Advances*, submitted.

Outreach Efforts

- Presented at ASCENT Meetings in October 2024 and May 2025.
- Presented at the FAA Aviation Emissions Characterization (AEC) Roadmap meeting in October 2024 and May 2025.
- Participated in biweekly meetings with the project manager.
- Participated in monthly International Civil Aviation Organization (ICAO) Impacts and Science Group (ISG) meetings (Dr. Wuebbles).

Student Involvement

Two postdoctoral associates, Swarnali Sanyal and Rachana Pradhan, were responsible for the analyses and modeling studies within the project, and for leading the preparation of the journal article.

Plans for Next Period

- Revise paper based on reviewer comments and complete journal publication of the paper.
- Complete development of additional scenarios to examine potential rocket launch issues and key questions to enhance understanding of the envelope (range) of potential impacts on ozone and climate from such vehicles. Complete modeling studies for these new scenarios.



References

Boley, A. C., & Byers, M. (2021). Satellite mega-constellations create risks in Low Earth Orbit, the atmosphere and on Earth. *Scientific Reports, 11*(1), 10642. https://doi.org/10.1038/s41598-021-89909-7

Dallas, J. A., Raval, S., Alvarez Gaitan, J. P., Saydam, S., & Dempster, A. G. (2020). The environmental impact of emissions from space launches: A comprehensive review. *Journal of Cleaner Production, 255*, 120209. https://www.sciencedirect.com/science/article/pii/S0959652620302560

Danilin, M. Y., Popp, P. J., Herman, R. L., Ko, M. K. W., Ross, M. N., Kolb, C. E., Fahey, D. W., Avallone, L. M., Toohey, D. W., Ridley, B. A., Schmid, O., Wilson, J. C., Baumgardner, D. G., Friedl, R. R., Thompson, T. L., & Reeves, J. M. (2003). Quantifying uptake of HNO_3 and H2O by alumina particles in Athena-2 rocket plume. *Journal of Geophysical Research: Atmospheres, 108*(D4). https://agupubs.onlinelibrary.wiley.com/doi/abs/10.1029/2002JD002601

Danilin, M. Y., Shia, R.-L., Ko, M. K. W., Weisenstein, D. K., Sze, N. D., Lamb, J. J., Smith, T. W., Lohn, P. D., & Prather, M. J. (2001). Global stratospheric effects of the alumina emissions by solid-fueled rocket motors. *Journal of Geophysical Research: Atmospheres, 106*(D12), 12727-12738. https://agupubs.onlinelibrary.wiley.com/doi/abs/10.1029/2001JD900022

Harris, N. R. P., & Wuebbles, D. J. (Eds.). (2014). *Chapter 5 in Scientific Assessment of Ozone Depletion: 2014, Scenarios and information for policymakers* (Vol. Global Ozone Research and Monitoring Project – Report No. 55). World Meteorological Organization, Geneva, Switzerland.

Larson, E. J. L., Portmann, R. W., Rosenlof, K. H., Fahey, D. W., Daniel, J. S., & Ross, M. N. (2017). Global atmospheric response to emissions from a proposed reusable space launch system. *Earth's Future, 5*(1), 37-48. https://agupubs.onlinelibrary.wiley.com/doi/abs/10.1002/2016EF000399

Lee, W. R., MacMartin, D. G., Visioni, D., & Kravitz, B. (2021). High-Latitude Stratospheric Aerosol Geoengineering Can Be More Effective if Injection Is Limited to Spring. *Geophysical Research Letters, 48*(9), e2021GL092696. https://agupubs.onlinelibrary.wiley.com/doi/abs/10.1029/2021GL092696

Maloney, C., Portmann, R. W., Ross, M. N., & Rosenlof, K. H. (2022). The Climate and Ozone Impacts of Black Carbon Emissions from Global Rocket Launches. *Journal of Geophysical Research: Atmospheres, 127*(12). https://doi.org/10.1029/2021JD036373

Miraux, L. (2022). Environmental limits to the space sector's growth. *Science of The Total Environment, 806*, 150862. https://www.sciencedirect.com/science/article/pii/S0048969721059404

Prather, M. J., García, M. M., Douglass, A. R., Jackman, C. H., Ko, M. K. W., & Sze, N. D. (1990). The space shuttle's impact on the stratosphere. *Journal of Geophysical Research: Atmospheres, 95*(D11), 18583-18590. https://agupubs.onlinelibrary.wiley.com/doi/abs/10.1029/JD095iD11p18583

Ross, M. N., Danilin, M. Y., Weisenstein, D. K., & Ko, M. K. W. (2004). Ozone depletion caused by NO and H_2O emissions from hydrazine-fueled rockets. *Journal of Geophysical Research: Atmospheres, 109*(D21). https://agupubs.onlinelibrary.wiley.com/doi/abs/10.1029/2003JD004370

Voigt, C., Schlager, H., Stock, P., Curtius, J., Mann, G. W., Pöschl, U., and Schäfer, M. (2103) Impact of rocket exhaust on atmospheric chemistry and climate. Geophysical Research Letters, 40, 12, 2970–2975.

Weisenstein, D. K., Keith, D. W., & Dykema, J. A. (2015). Solar geoengineering using solid aerosol in the stratosphere. *Atmospheric Chemistry and Physics, 15*(20), 11835-11859. https://acp.copernicus.org/articles/15/11835/2015/



Project 092 Advanced Two-stage Turbine Rig Development

The Pennsylvania State University

Project Lead Investigator

Reid A. Berdanier
Associate Professor
Department of Mechanical Engineering
The Pennsylvania State University
START Lab, 3127 Research Drive
State College, PA 16801
814- 863-3972
rberdanier@psu.edu

University Participants

The Pennsylvania State University (Penn State)

- P.I.: Dr. Reid A. Berdanier
- FAA Award Number: 13-C-AJFE-PSU-125
- Period of Performance: January 1, 2023, to September 30, 2026
- Tasks:
  1. Oversee new turbine rig design
  2. Design motor generator to dissipate the turbine power
  3. Order remaining air compressor components and complete manufacturing

Project Funding Level

For the three-year effort, the Federal Aviation Administration (FAA) provided $5,900,000 and matching funds of $6,150,000 were provided by Pratt & Whitney® and Penn State.

Investigation Team

Reid A. Berdanier (P.I.), Management, reporting, and oversight of all technical tasks
Assoc. Res. Prof. Michael Barringer (co-PI), Research Advisor, Tasks 1-3
Karen Thole, Affiliate Professor, Tasks 1-3
Tom Houck, Project Manager, Tasks 1-3
Justin Brumberg, Research Engineer, Tasks 1-3
Jeremiah Bunch, Engineering Technician, Tasks 1-3
Asst. Res. Prof. Matthew Meier, Research Engineer, Tasks 1-3

Project Overview

This project will significantly advance the efficiency levels of small-core gas turbines relevant to current engines, as well as future propulsion architectures such as hybrid electric propulsion systems for large single- and twin-aisle aircraft. The motivation for this research is aimed at reducing the carbon footprint of aviation through increasing turbine thermal efficiency, while maintaining or even improving component durability. This project will expand the infrastructure and research scope of the Steady Thermal Aero Research Turbine (START) Lab at Penn State, in which a two-stage, small-core, test turbine will be designed, manufactured, commissioned, and put to use in acquiring the necessary data to meet the proposed goal. The new infrastructure will be referred to as START⁺. The proposed expansion will result in a research

® Pratt & Whitney is a registered trademark of RTX Corporation, Farmington, Connecticut.

turbine facility like no other in the world and will situate turbine research in the United States (U.S.) at the leading edge in efficiency improvement and emissions reduction for future propulsion applications.

Task 1 – Oversee New Turbine Rig Design

The Pennsylvania State University

Objectives

The objectives of this task include (1) overseeing the design of the new START⁺ turbine rig and laboratory expansion, (2) integrating the entire facility by having the mechanical engineering firm work with the building design firm to layout piping, building penetrations, supports, and ensure proper access for lab personnel, (3) ensuring the new compressors and test turbine can be appropriately accommodated in the new laboratory building, and (4) beginning the preliminary design of the rig layout, and confirming with Pratt & Whitney the entire scope of the test turbine.

In the oversight of the design of the new START turbine rig and laboratory expansions, this objective includes pursuing the selection of a turbine engineering firm by interviewing multiple firms and creating a request for quotation, to enable selection of the firm that best meets the cost, schedule, and quality requirements of the program. The construction of the new building (which is funded by the Penn State and Pratt & Whitney cost share) is required to meet the research objectives of this project since the current START Lab does not have enough space for the new START⁺ two-stage turbine rig and compressors. The new START⁺ building expansion will add more than 10,000 ft^2 of space to the START Lab to house the new research equipment, rig, and turbine.

Research Approach

During the current reporting period, design proposals were received and reviewed by Penn State from multiple engineering design firms to perform the main design work on the START⁺ turbine integration plan. Upon reviewing all proposals for acceptable cost, schedule, and design content, the engineering design firm Belcan was selected. This turbine integration plan includes the design firm working closely with both the START team and Pratt & Whitney to perform the detailed design of the hardware components that define the primary test section of the new two-stage turbine rig. The design scope for the START⁺ turbine test section is shown in Figure 1.

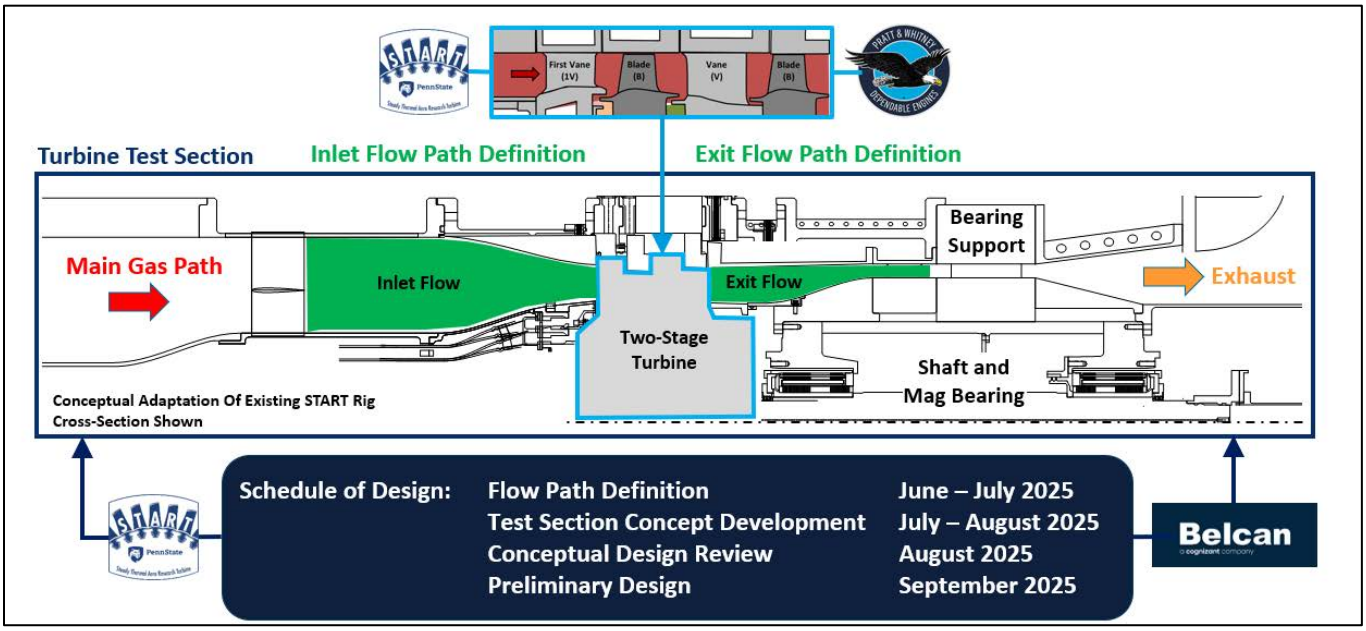


Figure 1. Design work status and schedule for the START⁺ two-stage turbine test section.



The hardware interface control plan that was presented in the previous reporting period is summarized briefly here. The two-stage turbine hardware design including the airfoils, disks, cover plates, and fasteners will be sourced by Pratt & Whitney directly from one of their current production aircraft engines. Pratt & Whitney, in conjunction with the selected design firm, Belcan, are responsible for designing any modifications to enable the engine hardware to be installed and operated within the START+ turbine test section. The hardware components that define the outer casing walls, inner flow path walls, rotor shaft and bearing system, and the bearing support structure are the responsibility of the START research group and Belcan.

The Penn State START team worked with Pratt & Whitney to complete a design kick-off meeting in December 2024 related to the hardware interface control plan. This meeting included several team members from START and Pratt & Whitney to begin review of the hardware components described above.

Following the kick-off meeting, weekly meetings were scheduled to review status of the design work. The conceptual instrumentation plan was progressed into a detailed instrumentation plan that is currently in progress covering the entire turbine test section. Additional design review meetings were held during the current reporting period between START and Pratt & Whitney to refine the key learning parameters associated with the research objectives for aerodynamics, durability, efficiency, and secondary flow systems. These meetings included the Penn State START team as well as managers and design engineers from Pratt & Whitney.

Special consideration was given to design options that enable all the two-stage turbine hardware to be frequently assembled and disassembled to and from the shaft. Since the intent of the new two-stage turbine rig is to conduct research, the frequent assembly and disassembly is an important consideration in the design process to provide access for turbine vane and blade airfoil design changes, as compared to an in-service gas turbine engine that remains fully assembled during its use in the field. The progress of the design work was presented during a June 2025 on-site meeting at the Penn State START facility for our annual Pratt & Whitney Center of Excellence partnership. This meeting included the Penn State START team as well as senior managers and design engineers from Pratt & Whitney. The conceptual instrumentation plan progressed into a detailed instrumentation plan that is currently in progress covering the entire turbine test section.

Belcan's design of the turbine test section started with a project kick-off in March 2025. A design requirements document was created by the START team and was provided to Belcan, which outlined the purpose and key design requirements for the new turbine test section. Design details incorporated into the document included the target turbine operating conditions, design ownership responsibilities, hardware interfaces, and instrumentation needs. During the current reporting period, START and Belcan began the conceptual design process which included a review of several 'lessons learned' from designing the existing single stage START turbine rig. The conceptual design work also included generating an initial geometry layout of the primary air flow path (main gas path) extending from upstream of the turbine to downstream of the turbine. Preliminary definition of instrumentation locations and quantities were also assessed to characterize measurement capabilities. Design work progressed in quarter (Q)2 to further develop the stationary hardware components that comprise the upstream part of the turbine test section in Figure 1 and the outer diameter casing pieces. The upstream part of the turbine test section includes the upstream settling chamber, the inner diameter core pieces that include the cooling air delivery system, and the strut section that physically connects the inner diameter core pieces to the outer diameter casing pieces. Concepts for the cooling air delivery system were also designed during this reporting period including cooling path quantities, locations, and egress routes.

A detailed conceptual instrumentation plan was also developed in Q3 associated with the complete turbine test section shown in Figure 1. This detailed conceptual instrumentation plan includes measurement locations, probe types, probe quantities, and probe wire and tube egress paths to fully characterize the two-stage turbine performance.

Belcan, the Penn State START team, and Pratt & Whitney held a conceptual design review meeting in August 2025. The meeting was successful in enabling the design to progress into the preliminary design phase. A review meeting for the preliminary design will take place in the timeframe of November 2025 that will cover an end-to-end engineering review of the complete turbine test section. A detailed design review will take place in the timeframe of January 2026. The goal is to enable manufacturing from January through the summer of 2026.

The design of the START+ rig air piping and equipment integration to be located upstream and downstream of the turbine test section are the responsibility of the Penn State START team and the design firm Burns & McDonnell (BMCD). Penn State

initiated a purchase order with BMCD to perform the detailed design phase of the work. Their scope includes detail design to integrate major equipment systems including the compressors, combustor, air piping network, turbine test section, dynamometer, and outdoor cooling yard.

Figure 2 shows the detailed design work that the Penn State START team conducted with BMCD regarding the layout of the large air compressors and outdoor cooling yard equipment. A set of high priority design tasks were developed to enable an efficient progression from the preliminary design phase into the current detailed design phase. These specific design tasks focused on the air piping network, cooling piping network, physical supports and foundations, electrical and utility connections. The equipment installation and their integration will take place in the latter half of 2026 as originally planned.

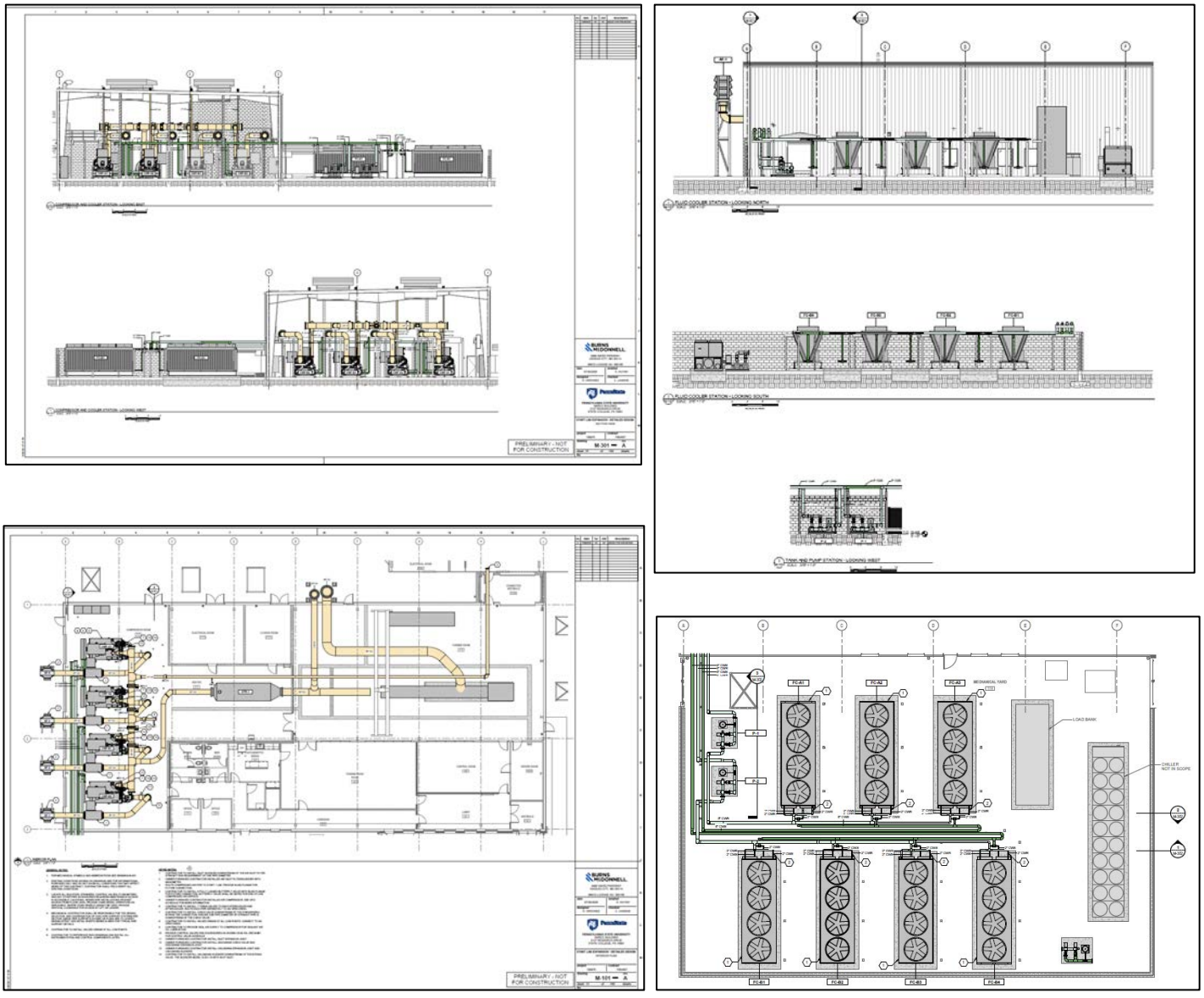


Figure 2. Drawing examples of the detailed design work for the major equipment system integration.

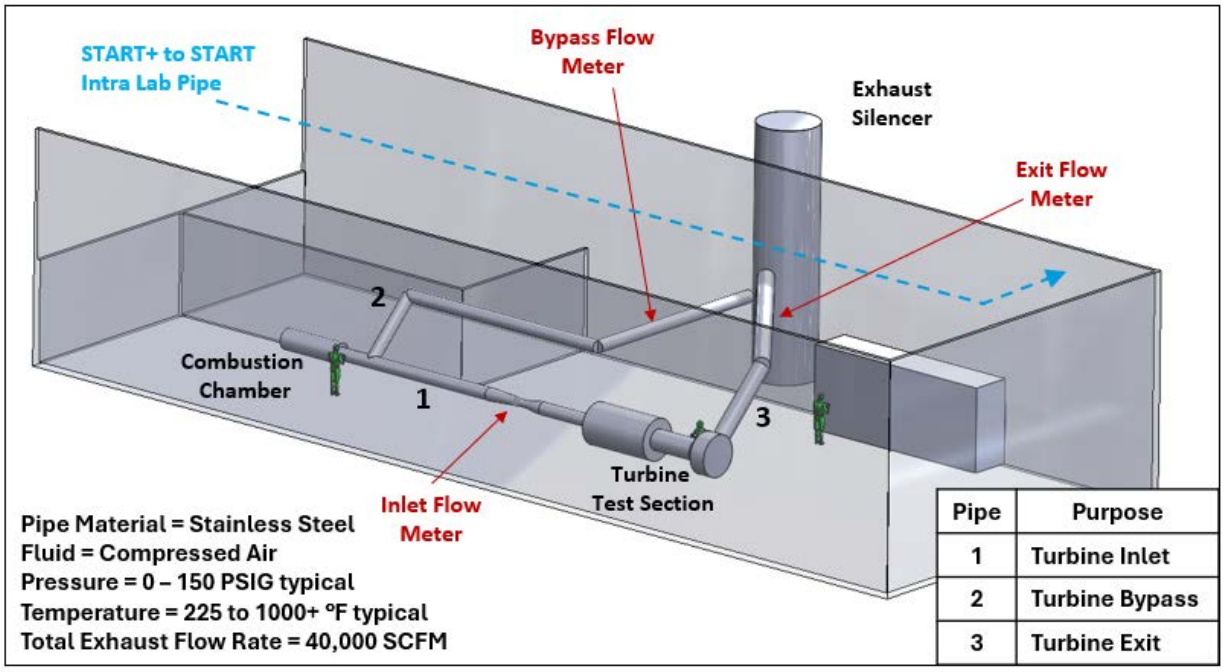


Figure 3. Drawing showing the concept equipment layout within the turbine room. START: Steady Thermal Aero Research Turbine.

Construction on the main building and cooling yard began at the new START+ facility property site in June of 2025. Figure 4 shows photographs of the construction zone before (June 2025) and during the construction work (July through September 2025). The construction work has recently focused on installing the building foundation that includes a facility wide concrete slab on grade, and isolated concrete block foundations for select major equipment systems. The steel support beams, exterior walls, and roof system are planned for installation during the timeframe of October and November 2025. At time of writing this report a significant completion of the steel support beams was achieved. The detailed design and construction of the START⁺ laboratory addition is funded by other project partners to support this work.



Figure 4. Photographs show the construction zone in progress for the START⁺ building expansion that will house the two-stage turbine rig and facility.

Task 2 – Design Motor Generator to Dissipate the Turbine Power

The Pennsylvania State University

Objectives

The objectives of this task are to create a request for quotation for a motor generator system to dissipate the turbine power, review all bids, and select the company that best meets the cost, schedule, and quality requirements of the program. Collaborate with the selected vendor to develop manufacturing drawings so the turbine and motor generator system layout can be completed.

Research Approach

As noted in the previous annual report, the START research group selected the company ACS to provide a dynamometer motor generator solution to dissipate the two-stage turbine power. The ACS proposal met all technical requirements and was cheaper than other vendor sales quotes. The purchase order from Penn State to ACS was successfully completed to have ACS perform the detailed engineering phase of the complete dynamometer system including the alternating current (AC) motor generator, gear box, oil system, variable frequency drive (VFD), and load bank, all of which are needed to dissipate the turbine power. Preliminary costs and timeline schedules associated with procuring each piece of the dynamometer system equipment noted above were then obtained from multiple vendors and reviewed. Two of the five vendors provided equipment solutions that were reasonably aligned with the project budget and schedule, while the other three vendor solutions were well above the available project budget.

The START team worked with ACS to size a 4,500-horsepower motor generator solution that can absorb the operating conditions of the START+ turbine. Specifically, two options were discussed and identified to support the operation of the dynamometer system. The two options for the method of operation include (1) a non-regenerative power mode and (2) a regenerative power mode. The first optional method includes a dissipative electrical load bank that is sized for the full 4,500 horsepower of the AC motor generator, in which all power being absorbed from the turbine by the VFD drive is electrically directed and dissipated into the outdoor load bank system. The second optional method includes a much smaller-sized load bank, in which most (or all) power being absorbed from the turbine by the VFD drive is directed back into the facility electrical switchgear system for medium voltage (4,160 V) that supports the electrical operation of the four large air compressors. The second option essentially recycles the power absorbed from the turbine and sends the power back to operate the air compressors, with any residual power being offloaded to the smaller-sized load bank. The electrical infrastructure design required to support both options was determined and provided to Penn State. At the time of writing this report, the START research group is preparing to present the two options to university administrators for evaluation to determine which of the two options will be acceptable and pursued.

The dynamometer system will mostly be used to absorb the power that is produced by the two-stage turbine during research testing. In some instances, while preparing for research testing, the dynamometer VFD system will be used to supply power to the AC motor in order to rotate the turbine shaft at relatively slow speeds (approximately 0 – 1000 rpm) without air flow. This infrequent style of operation in supplying power to drive the turbine shaft will be focused mainly on (1) confirming rotor dynamic balancing of the turbine rotating hardware assembly and (2) inspecting the operability and functionality of instrumentation sensors mounted on the test turbine. The START research team worked with ACS to confirm that this low-speed style of operation is suitable for the various equipment.

Work continued into Q2 with a focus on the preliminary design of the system components including component selection, sizing, and vendor pricing. The primary components include the large AC motor generator, VFD system, gearbox, high and low speed drivelines, electrical load bank, riser support structure, and cooling systems. Identifying the primary instrumentation and electronics controls logic necessary for safely operating the dynamometer system with the new START+ test turbine was also performed. A preliminary design review was then held in February of 2025 that summarized all identified components and their specifications. The START team then held preliminary internal meetings to begin preparations for procuring the large AC motor generator and VFD drive system.

Design of the dynamometer system was completed in Q3, and a detail design review meeting was held including Penn State START and ACS. A solid model drawing of the dynamometer system is shown in Figure 5 including the AC motor generator, gearbox, shaft drivelines, and support table system. A separate image is also shown of the VFD that will be used to control the AC motor generator. Purchase orders for long-lead items including the AC motor generator and VFD have been coordinated, and purchase order preparations for the remaining shorter lead-time equipment items are in

progress. The remaining equipment includes the gearbox system, a central electronic controller and computer system, a hydraulic oil skid, and a thermal conditioning coolant system.

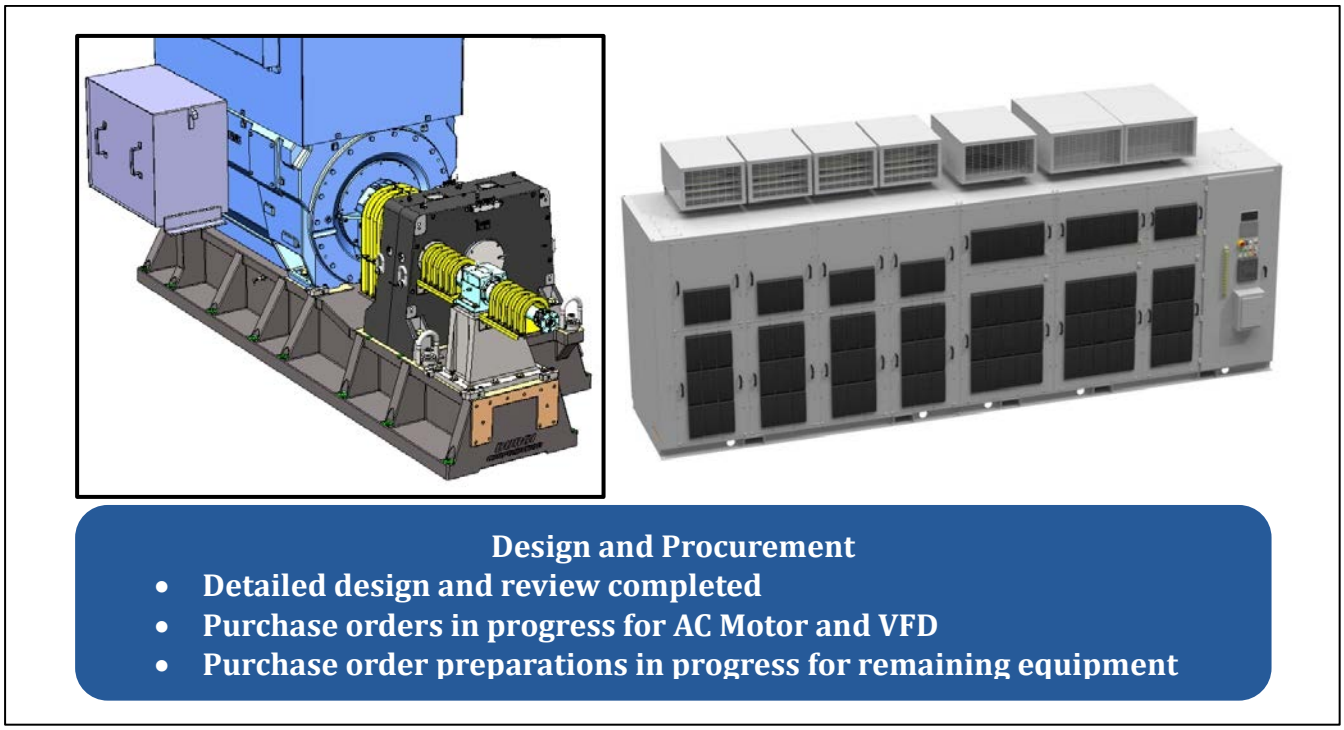


Figure 5. Drawing of the alternating current (AC) motor generator, gearbox, shaft drivelines, and variable frequency drive (VFD).

Recently, options were investigated for mounting the equipment system to a steel bed plate as shown in Figure 6 that is rigidly embedded into an isolated concrete foundation. During the current reporting period, the purchase of the equipment was divided into two separate acquisitions including one for the AC motor generator and VFD, and a second for the gearbox and subsystem equipment. The delivery estimate for all the equipment is in the latter half of 2026 corresponding to building occupancy.

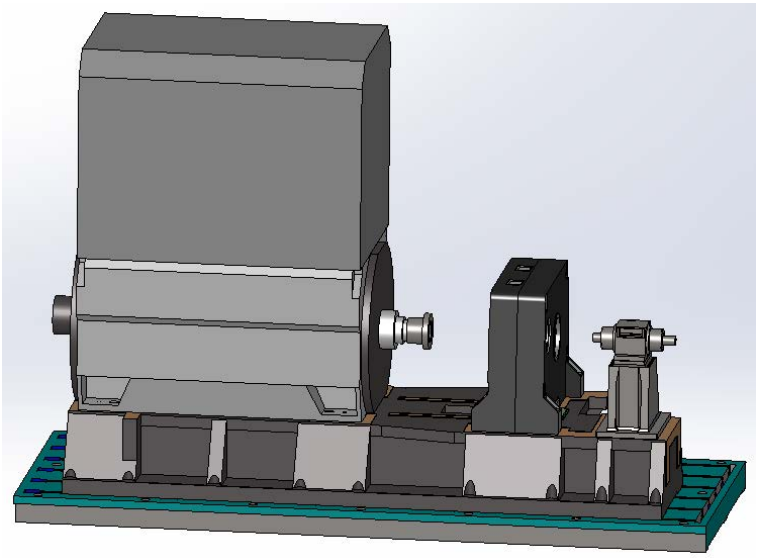


Figure 6. Drawing of the primary dynamometer equipment anchored to a steel foundation.

Task 3 – Order Remaining Air Compressor Components and Complete Manufacturing.

The Pennsylvania State University

Objectives

The objectives of this task are to (1) review manufacturing quality documents related to the compressor starters, VFD layout, cooler general arrangement drawings, and manufacturing reports, as well as to resolve non-conformances and approve final inspection reports, (2) attend factory performance testing and ensure the compressors meet all of the quoted performance metrics, review testing data such as hydrotests, flow, and pressure results, and (3) oversee the installation of equipment in START⁺ to ensure the compressors fit on their anchor bolts, are grouted in to place per the compressor vendor's requirements, and all lifting requirements are met.

Research Approach

The START team successfully processed a purchase order for the compressors. Manufacturing has continued as planned and the manufacturing of the outdoor cooler fan banks has been completed and delivered. Delivery of the air compressors and their accessories is still scheduled to coincide with the new START⁺ laboratory occupancy in mid-2026. A summary of the air compressor systems is provided in Table 1.



Table 1. Summary of the START⁺ Compressor Designs. START: Steady Thermal Aero Research Turbine.

Compressor Specification	Existing START	START⁺
Compressor Stages	2	3
Total Horsepower	3000	9000
Flow Rate per Unit	12 lbm/s	10 - 11 lbm/s
Discharge Pressure	60-80 psia	125 psia, 165 psia
Discharge Temperature	225°F	225°F, 110°F
Number of Compressors	2	2 + 2 = 4
Number of Outdoor Fluid Coolers	2	7

Turbine Main Gas Path Flow
Turbine Cooling Air Flow + Supplemental Flow

As noted in Task 2, the dynamometer system has completed the detailed design phase and procurement of the equipment items is in progress. Purchase orders for long-lead items are being processed this November, with mid- and short-lead items being purchased in 2026.

Conceptual design work on the bearing system was performed with the vendor Synchrony during the current reporting period. A design requirements document was created by the START team and was provided to Synchrony, which outlined the goals, objectives, and key design requirements for the new turbine bearing system. The requirements included the turbine shaft operating speed range, physical design space, and rotor dynamics analysis. The magnetic bearing system progressed to the preliminary design phase. Continuing meetings are being held with the bearing vendor to review design topics including rotor dynamics analysis, bearing physical sizes, and load capacities.

The combustion heater also continued to progress through its design phase into detailed design. During the current reporting period, weekly meetings continued with the combustor vendor. The design of the combustor system has been developed to include process and instrumentation diagrams, preliminary chamber drawings, and the natural gas delivery stand. The delivery of the complete combustion system is still on track for delivery to coincide with the new START⁺ laboratory occupancy in mid-2026.

As noted in Task 1, design work is continuing for the complete network of air piping, valves, and the exhaust silencer system.

The chiller system has been delivered to the new START⁺ facility site. This chiller will enable future operation of delivering cooling air to the test turbine down to 40°F. A status summary of all major equipment systems is shown within Figure 7 for the current reporting period.

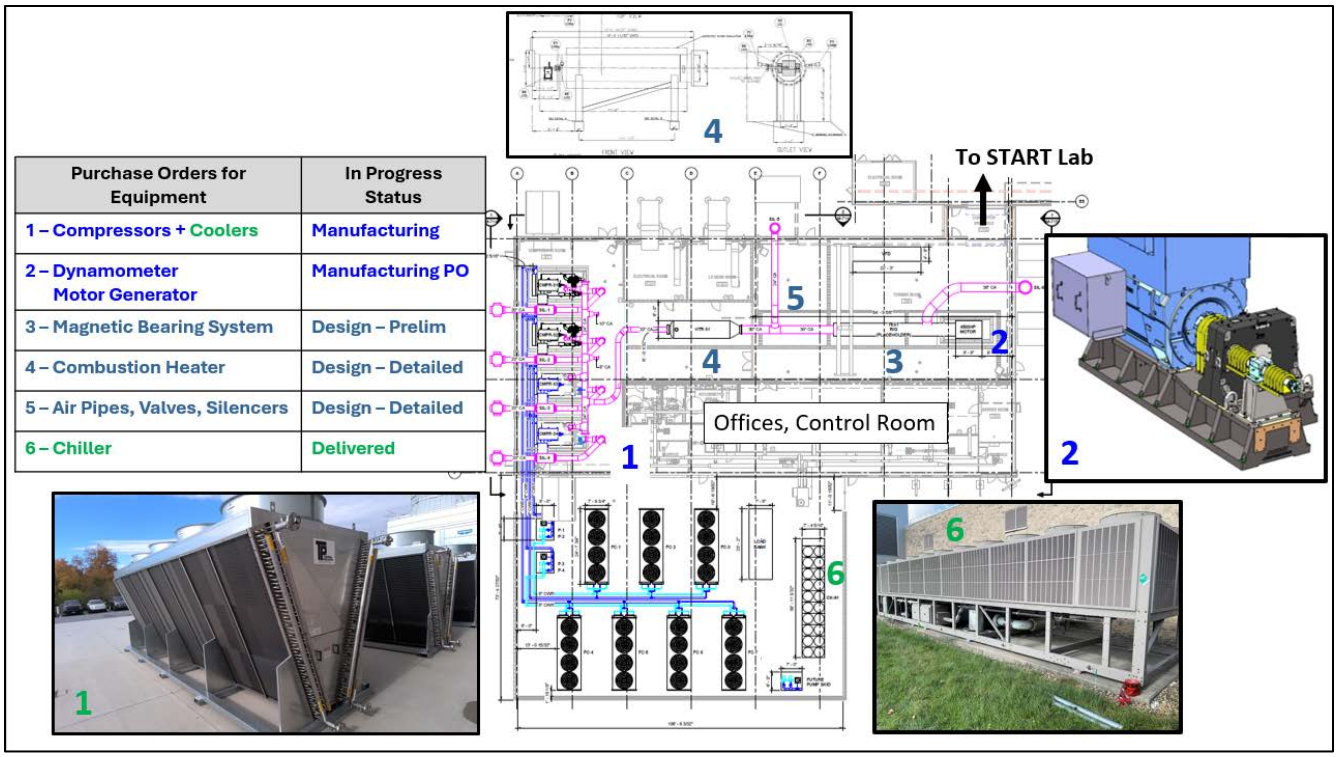


Figure 7. Status summary of the main equipment systems. START: Steady Thermal Aero Research Turbine.

Milestones

Milestone	Vendor	Completion Date
Dynamometer Design Purchase Order	ACS	November 5, 2024
Magnetic Bearing System Purchase Order	Synchrony	December 19, 2024
Turbine Test Section Purchase Order	Belcan	February 27, 2025
Building Contractor Selected	Poole Anderson	March 20, 2025
Construction Kickoff Meeting	Poole Anderson	April 17, 2025
Combustion Heater Purchase Order	Alstam	April 21, 2025
Building Construction Started	Poole Anderson	June 25, 2025
Air Pipes, Valves, Silencers Design Purchase Order	Burns & McDonnell	August 8, 2025
Coolers Delivered	F.S. Compression	November 12, 2025
Dynamometer Procurement	ACS/Innomotics	Pending

Major Accomplishments

Penn State completed the open-bid process for construction companies to submit their proposal packages. Penn State reviewed all proposals and issued an official contract for the construction work to begin in the next reporting period. Poole Anderson began work in June of 2025, with a projected completion date of May 2026.

Design proposals were received and reviewed by Penn State from multiple engineering design firms to perform the main design work on the START⁺ turbine integration plan. Upon reviewing all proposals for acceptable cost, schedule, and design content, the engineering firm Belcan was selected. Penn State START team held a kick-off meeting with Belcan for



the new turbine rig design work that focused on a review of the project goals, objectives, requirements, and schedule. A design requirements document was created by the START team and was provided to Belcan, which outlined the purpose and key design requirements for the new turbine test section. START and Belcan began the conceptual design process. START staff continues to hold weekly meetings with Belcan in preparation for a preliminary design review this to held in December 2025.

The Penn State START team also worked with Pratt & Whitney to complete a design kick-off meeting related to the two-stage turbine design and integration plan. This meeting included several team members from START and Pratt & Whitney to begin review of the turbine hardware components. Weekly meetings are currently being held including START and Pratt & Whitney to identify and design specific geometry changes required to enable the engine hardware to be installed within the new START^{+} rig.

Penn State submitted a purchase order to BMCD to perform the detailed design phase of the air piping and equipment integration to be located upstream and downstream of the turbine test section. The detailed design to integrate these major equipment systems is now in progress. A concept equipment layout within the new turbine room was also completed including the air piping, turbine test section components, and supporting equipment. Weekly meetings are currently in progress.

A vendor was selected for the combustion heater. After reviewing proposals from multiple vendors, Alstam was selected for design and manufacturing. Biweekly meetings are currently underway. A preliminary design review meeting has been completed. Delivery is anticipated for February 2026.

A purchase order was issued to ACS to perform the detailed engineering phase of the complete dynamometer system to dissipate the turbine power. The detailed design of the dynamometer system was completed, and a detail design review meeting was held including Penn State START and ACS. Purchase orders for long lead-time items including the AC motor generator and VFD were coordinated, and purchase order preparations began for the remaining shorter lead-time equipment items. Long-lead item purchase orders are anticipated for November 2025.

The manufacturing of the compressors continued as planned, and the manufacturing of the outdoor cooler fan banks was completed and delivered. Procurement of the dynamometer system equipment is in progress. The magnetic bearing system continued progress through its preliminary design phase. The combustion heater also continued to progress through its design phase into detailed design.

Publications

None.

Outreach Efforts

Dr. Reid Berdanier presented updates on this project to gas turbine industry representatives from Pratt & Whitney, Solar Turbines, Siemens Energy, Honeywell Aerospace, Mitsubishi Heavy Industries, GE Aerospace, GE Vernova, EPRI, Howmet Aerospace, IHI Corporation, Baker Hughes, Collins Aerospace, and more. Similarly updates for U.S. government agencies were shared to the Department of Energy, National Aeronautics and Space Administration, Office of Naval Research, Air Force Research Laboratory, and National Science Foundation.

Awards

Dr. Reid Berdanier was elected as an Associate Fellow of the American Institute for Aeronautics and Astronautics (AIAA).
Dr. Karen Thole was awarded the 2025 Kate Gleason Award from the American Society of Mechanical Engineers (ASME).

Student Involvement

Although no formal student support was included in this project for this reporting year, the students in the START Lab are provided regular updates on the status of this project through weekly team meetings.

Plans for Next Period

- Oversee and complete construction of the new START^{+} laboratory building addition.
- Continue working with Pratt & Whitney and Belcan to complete the integration design of the two-stage turbine and primary test section.



- Continue working with BMCD to complete the detailed design of the rig air piping and equipment integration.
- Integrate major equipment, including industrial compressors and associate subsystems.
- Begin procurement of test section hardware for a two-stage turbine.
- Execute purchase orders for motor/generator and associated electrical systems.

Disclaimer

This research was funded by the U.S. Federal Aviation Administration Office of Environment and Energy through ASCENT, the FAA Center of Excellence for Alternative Jet Fuels and the Environment, Project 092 through FAA Award Number 13-C-AJFE-PSU-125 under the supervision of Joshua Glottmann. Any opinions, findings, conclusions or recommendations expressed in this material are those of the authors and do not necessarily reflect the views of the FAA.



Project 093(A) Collaborative Research Network for Global SAF Supply Chain Development

Massachusetts Institute of Technology

Project Lead Investigators

Dr. Florian Allroggen
Principal Research Scientist
Laboratory for Aviation and the Environment
Massachusetts Institute of Technology
77 Massachusetts Ave, Building 33-328
Cambridge, MA 02139
617-715-4472
fallrogg@mit.edu

Dr. Raymond L. Speth
Senior Research Scientist
Department of Aeronautics & Astronautics
Massachusetts Institute of Technology
77 Massachusetts Ave, Building 33-316
Cambridge, MA 02139
617-253-1516
speth@mit.edu

University Participants

Massachusetts Institute of Technology (MIT)

- P.I.: Dr. Raymond Speth
- FAA Award Number: 13-C-AJFE-MIT, Amendment Nos. 114, 115, 118, 133, and 143
- Period of Performance: January 1, 2023, to August 31, 2027
- Tasks (for reporting period October 1, 2024, to November 30, 2025):
  1. Assess global biomass availability for sustainable aviation fuel (SAF) production
  2. SAF supply chain design for Africa, with specific focus on sub-Saharan Africa
  3. Facilitate a network for capability building for global SAF supply chain development
  4. Support knowledge sharing and coordination across ASCENT Project 093 universities

Hasselt University (UHasselt, through subaward from MIT)

- P.I.(s): Prof. Robert Malina
- FAA Award Number: MIT Subaward Purchase Order No. 855522
- Period of Performance: September 1, 2016 to September 30, 2026 (based on no cost extension in process)
- Tasks (for reporting period October 1, 2024, to November 30, 2025):
  1. *(omitted, led by MIT)*
  2. SAF supply chain design for Africa, with specific focus on sub-Saharan Africa
  3. Facilitate a network for capability building for global SAF supply chain development
  4. Support knowledge sharing and coordination across ASCENT Project 093 universities

Project Funding Level

The Federal Aviation Administration (FAA) provided $1,150,000 in funding and $1,150,000 matching funds were received. Sources of matching fund are approximately $90,000 from MIT, plus third-party in-kind contributions of $1,060,000 from Earth Force Technologies.



Investigation Team

Dr. Raymond L. Speth, Principal Investigator (MIT), all tasks
Dr. Florian Allroggen, Principal Investigator (MIT), all tasks
Prof. Robert Malina, Principal Investigator (UHasselt), all UHasselt tasks
Dr. Niamh Keogh, Co-Investigator (MIT), Tasks 1 and 3
Dr. Alessandro Martulli. Postdoctoral Associate, Task 3
Dr. Sumit Maharjan, Postdoctoral Associate, Task 2
Francis Mwangi, Graduate Research Assistant (UHasselt). Task 2 and 3
Dr. Teshome Deressa, Graduate Research Assistant (UHasselt), Task 3
Andy Eskenazi, Graduate Research Assistant (MIT), Task 1

Project Overview

Large-scale production of SAF around the globe is needed to meet aviation's ambitious goals to scale up alternative energy sources. Production scale-up will require identification of waste feedstocks and land for energy crop cultivation, sustainable farming and land use practices, and investments in conversion capacity as well as fuel and feedstock logistics. Access to data, expertise, and capital remains a major roadblock towards successfully creating these supply chains around the globe. Under ASCENT Project 093, MIT aims to (1) assess global biomass availability, broken down by region, and the associated potential for SAF production with current and improved conversion technologies, (2) analyze opportunities and roadblocks for supply chain designs, specifically focusing on sub-Saharan Africa, (3) share supply chain designs and feedstock availability assessments with other members of the ASCENT Project 093 team, and (4) facilitate a network of academics around the globe to support capacity building for SAF production.

Task 1 – Assess Global Biomass Availability for SAF Production

Massachusetts Institute of Technology

Objective

The objective of this task is to assess biomass availability for producing bio-based aviation fuels in different world regions. The biomass feedstock could originate from two sources: (1) yield growth or land use expansion, as modeled from current and future land use patterns, considering competing demands for land from agriculture and other uses, and (2) waste and residue streams, such as agricultural residues, forestry residues, animal manure, and municipal solid waste (MSW). Initial work under this project focused on the former, while research during the current reporting period focused on the latter.

Research Approach

Residual biomass is an attractive feedstock for SAF production due to its low cost and the lack of competition for additional land. The bioenergy potentials of waste and residue feedstocks can be quantified using a framework of cascading energy potential categories, as shown in Figure 1 (see also report for previous reporting period). The *Theoretical Potential* refers to the maximum amount of residues that are produced; the *Technical Potential* is the quantity of residues (energy equivalent) that could be collected after considering harvesting equipment limitations; the *Sustainable Potential* represents the residual biomass that could be collected ensuring that soil health is maintained (i.e., primarily by keeping the amount of carbon in the soil constant). The combination of the *Technical Potential* and *Sustainable Potential* results in the *Technical Sustainable Potential*, which satisfies both technical and environmental limitations. Finally, the *Available Potential,* represents the amount of residue that is available for fuel conversion after accounting for competing uses, such as for cooking or animal feed. MIT efforts over the past 2 years have sought to (I) create a standard approach for stochastically computing the five energy potentials for 173 residue types, (2) extend the results to a 2,160-by-4,320 map grid for each residue type, and (3) evaluate the logistical challenges of using the residues.

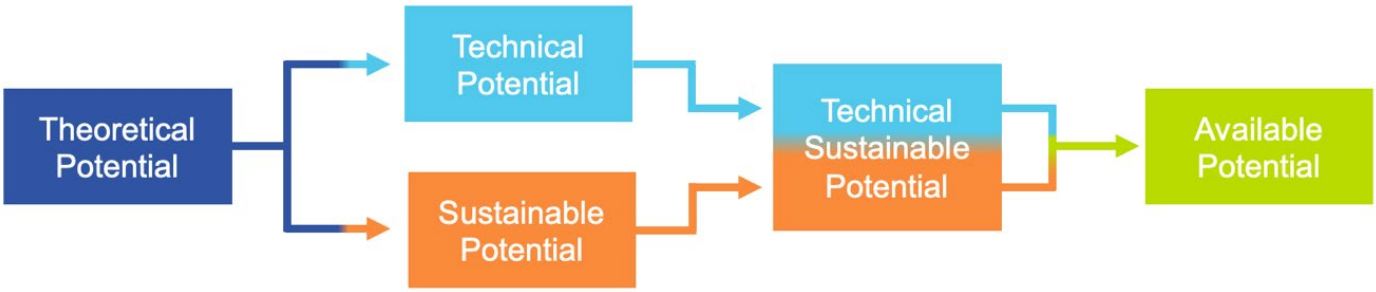


Figure 1. Five categories of energy potentials.

Modeling energy potentials requires a set of parameters. In the case of crop residues, these include (1) the residue-to-product ratio (RPR) (i.e., the amount of residue generated per unit of crop produced), (2) the technical recoverability ratio (TRR) (i.e., the percentage of residues that can be collected with typical harvesting machinery), (3) the sustainable removal ratio (SRR) (i.e., the percentage of residues that can be collected while being able to maintain soil health), (4) the technical sustainable removal ratio (TSRR) (i.e., the minimum between TRR and SRR), and (5) the residue availability ratio (RAR) (i.e., the percentage of residues available after considering competing uses). For this study, these parameters are obtained from a literature review. The literature review revealed substantial variation in some of these parameters. For example, for corn, we find that the RPR ratio (amount of stover per kilogram of grain) varies between 1.4 to 2.55. Given the unknown nature of the "true" value, probability distributions were constructed across the 173 residue types, using the literature estimates. We then obtained distributions of the energy potentials via Monte Carlo simulations.

Preliminary results are shown in Figure 2. The findings are two-fold. First, the imposition of constraints across the potential categories decreases the energy potentials. However, these impacts differ between constraints and feedstocks. For example, in the case of crop residues, enforcing ecological criteria produces the largest drop in potential, due to substantial residue requirements to preserve soil properties. In contrast, in the case of forestry residues and animal manure, the biggest drop is seen with the imposition of the technical constraints, due to the difficulties in waste and residue collection (e.g., manure in pastureland). Second, across each potential category, there is significant uncertainty about the "true" expected potential.

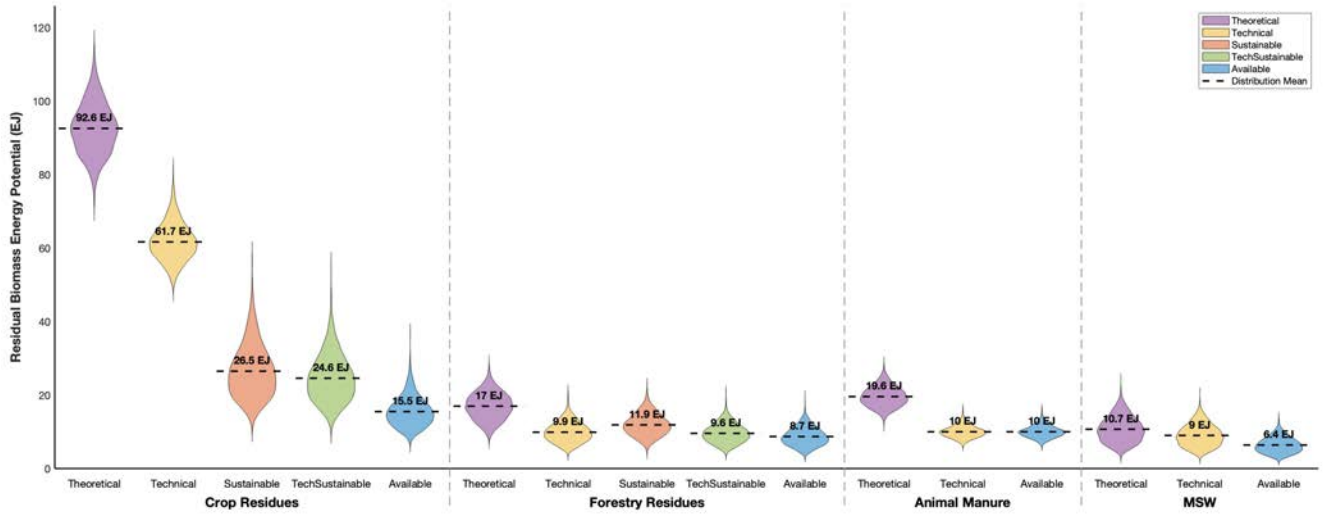


Figure 2. Stochastic evaluation of the energy potentials, considering 173 different residual biomass types.

The mean available potential is mapped in a gridded world map in Figure 3. We find that while some regions have high density of available waste and residue feedstock (including the United States), some regions possess low density in

available potentials (e.g., northern Alaska). This raises the question whether such low-density potentials are suitable for advanced energy conversion purposes. The answer to this question depends on whether it is possible to form clusters of sufficient scale (i.e., enough to support the establishment of a biorefinery) within reasonable collection distance (e.g., transporting the residues up to 100 km).

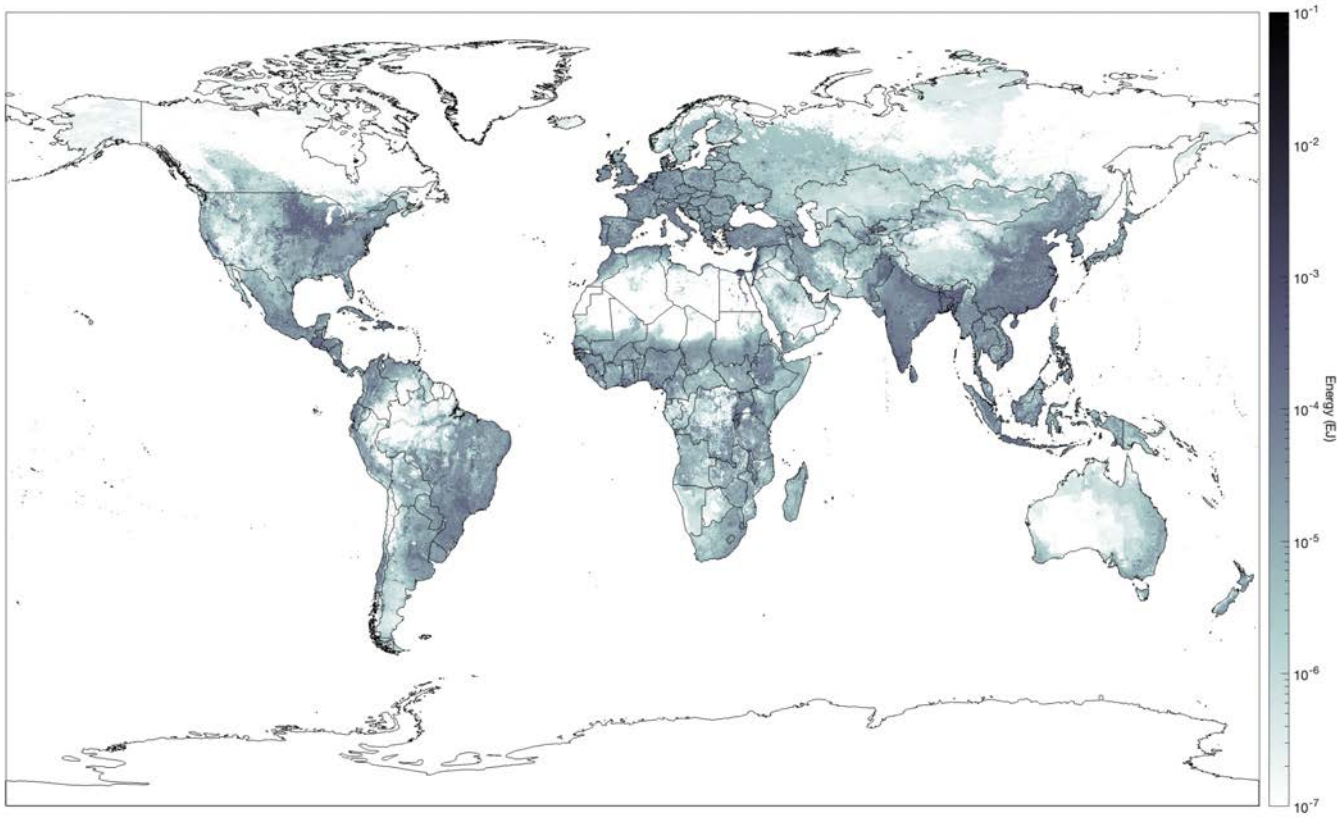


Figure 3. Global distribution of the available energy potential stemming from crop residue production to the 0.1-degree resolution.

To assess such aggregation concerns, we introduce the processable potential. It assesses whether there is sufficient bioenergy potential in surrounding cells with which the available potential in a specific cell can be combined to meet the input requirements of a conversion facility. However, processability also depends on the type of feedstocks, as it is important to ensure that feedstocks can be processed jointly. For this purpose, we collapsed the 173 residue types into three categories, according to their suitability for processing using anaerobic digestion (AD), fermentation, or thermochemical processes. In the initial analysis, we used a 10,000 TJ minimum cluster threshold and a 100 km maximum collection distance. While the stochastic analysis had found a mean available potential of 40.6 EJ across all the residue types (after the imposition of technical, sustainable, and competing use constraints), the processability requirement reduced this potential to 29.7 EJ.

Milestones

- Developed a standardized methodology for evaluating the energy potential from waste streams stochastically via Monte Carlo simulations.
- Pioneered a new metric to evaluate the processability of residues, based on cluster scale and collection distance constraints, as well as residue aggregation.



Major Accomplishments

- Completed the evaluation of the global available and processable energy potential for 173 different residue types.
- Produced a database of 173 maps on a 2,160-by-4,320 resolution, each corresponding to a residue type, across three scenarios (pessimistic, mean, optimistic), containing their available potential.

Publications

A paper summarizing the approach and results is under preparation.

Outreach Efforts

- Presented the results at the ASCENT Spring 2025 Meeting.
- Presented the results at the International Conference on Sustainable Aviation Research (ICSAR) 2025.
- Presentation to the ASCENT Fuels group in October 2025.
- Presentation at the Boeing Cascade conference.

Awards

None.

Student Involvement

Andy Eskenazi (MIT graduate student) conducted the research under the supervision of the PI.

Plans for Next Period

- Submit papers documenting the results.
- Attempt extension to energy cropping.

Task 2 – SAF Supply Chain Design for Africa, with Specific Focus on Sub-Saharan Africa

Massachusetts Institute of Technology
University of Hasselt

Objectives

The objectives of this task are (1) to study the current hurdles for the development of a local SAF industry in Africa, (2) to develop science-driven advice to help overcome these hurdles, and (3) to help kick-start the SAF industry in Africa. For this purpose, our team has developed an understanding of the current economic, social, environmental, technological, logistical, and legal hurdles for SAF development in Africa. We then create quantitative assessments of supply chain designs that leverage the specific opportunity space on the African continent. This entails (techno-) economic assessments and environmental lifecycle assessments of selected supply chain designs, and the inclusion of regulatory and policy considerations.

During the current reporting period, this task focused on working with local partners in Kenya to advance supply chain development.

Research Approach

A set of frameworks were developed and applied for the Kenyan context, which informed the SAF Steering meeting held in Mombasa in October 2024, and the third “High-Level Meeting on SAF Development and Deployment” held in May 2025 in Naivasha, Kenya (see Task 3). The team is also supporting the organization of the next Steering Committee Workshop, to be held in November 2025 in Nairobi, Kenya. The workshop will evaluate the progress made by the SAF Steering Committee. Importantly, the techno-economic study on the Mombasa refinery (International Civil Aviation Organization [ICAO] funding) and the fueling the Africa Flight study (World Bank) will be presented to the delegates. In addition, participants will discuss the next steps in developing a SAF financing mechanism.



Finalization of Green Premium Study for Kenya
During the reporting period, the analysis on the green premium allocation of SAF production in Kenya (see past reporting period) was reviewed and finalized for journal publication.

Socio-economic Contribution of SAF Refinery in Kenya
During the report period, the team supported the development of a draft concept to understand the economic impacts of establishing a SAF refinery in Kenya. More specifically, UHasselt efforts over the past year have sought to create a standard approach for measuring the economic benefits by supporting the study on the assessment of the Kenya petroleum refinery.

Development of SAF Strategy and ROADMAP for Kenya
The team supported the development of the SAF Strategy for Kenya (roadmap). Specifically, the team helped develop the first draft strategy and helped incorporate the comments submitted during the 4th Steering Committee Meeting.

Milestones

- Presented the first set of techno-economic analyses and stakeholder mappings during the Second Meeting of the National SAF Steering Committee on October 3-4, 2024, in Mombasa, Kenya.
- Co-organized, participated in, and contributed to the 3rd SAF Steering Committee Meeting held from 19-21st May 2025.
- Contributed to the African Civil Aviation Commission (AFCAC)/African Union/Common Market for Eastern and Southern Africa SAF Policy guideline workshop held from August 26-28, 2025, in Harare, Zimbabwe.
- Contributed to the development of a SAF strategy and roadmap for Kenya.
- Co-organized, participated in, and contributed to the fourth SAF workshop to be held from November 25-27, 2025, in Nairobi.
- Provided input to and review for the Technical Assessment of the old Kenya Petroleum refinery supported by the ICAO. The study was completed in September 2025.

Major Accomplishments

- Briefed the results from the green premium coverage analysis for Kenya during the second meeting of the National SAF Steering Committee on October 3-4, 2024, in Mombasa, Kenya.
- Supported organization of two workshops to build a SAF strategy and roadmap for Kenya.
- Participated in and contributed to the African SAF initiative under AFCAC.
- Helped secure funding for the SAF Technical Assessment of the Old Kenya Petroleum refinery.
- Contributed to the Energy Policy that has the SAF Policy subsection in the new policy 2025-2034.

Publications

Paper on the green premium study is under preparation.

Outreach Efforts

- Presented the results of initial analyses during the 2nd meeting of the National SAF Steering Committee on October 3-4, 2024, in Mombasa, Kenya.
- Presented the results of initial analyses during the 3rd meeting of the National SAF Steering Committee on May 19-21, 2025, in Naivasha, Kenya.
- Presented a summary of the efforts during the ASCENT Spring 2025 and Fall 2024 meetings.
- Co-organized and helped conduct SAF Steering Committee Meetings in Kenya.

Awards

None.

Student Involvement

Francis Mwangi (UHasselt graduate student) was involved in this task.



Plans for Next Period

- Further refine the analyses for Kenya.

Task 3 – Facilitate a Network for Capability Building for Global SAF Supply Chain Development

Massachusetts Institute of Technology
University of Hasselt

Objective

The objective of this task is to interface with partners to build the skills, expertise, and capacities needed for scaling up SAF development and deployment around the globe. During the current reporting period, the focus of this task was to deepen ties with external partners in support of advancing SAF development in Kenya.

Research Approach

To meet the goals of this task, the MIT/UHasselt team followed three approaches: (1) Capability building in Kenya, (2) developing a structure for capability building within the ASCENT Project 093, and (3) country workshops on SAF development in sub-Saharan Africa. During this reporting period, the first and third approach were emphasized. Specifically, the team continues to support stakeholders in Kenya in building capacity and knowledge to develop a SAF roadmap for Kenya and to build SAF production capacity in Kenya. To achieve this, the team supported the Kenyan Civil Aviation Authority (KCAA) in the running a National Steering Committee. Three MIT and UHasselt team members are members of the National Steering Committee and continue to support organization of meetings.

During the current reporting period, three key meetings were supported: (1) the second Meeting of the National SAF Steering Committee in October 2024, (2) third SAF Steering Committee Meeting in May 2025, and (3) fourth SAF workshop in November 2025. These meetings brought together key governmental and private stakeholders to work on issues such as feedstock sourcing and sustainability certification, plant financing, SAF policy, and fuel blending and certification. In support of these activities, the team fostered a network of supporting international stakeholders, including the KCAA, the Deutsche Gesellschaft für Internationale Zusammenarbeit (giz), the World Bank, the European Union Aviation Safety Agency (EASA), and ICAO.

Major Accomplishments

Co-organized (MIT/UHasselt team) three SAF events in Kenya.

Publications

None.

Outreach Efforts

- Co-organized three SAF workshops.
- Presented a summary of the efforts during the ASCENT Spring 2025 meeting.

Awards

None.

Student Involvement

Francis Mwangi and Teshome Deressa (UHasselt graduate students) supported coordination and implementation of the work.

Plans for Next Period

Continue to support efforts in Kenya as needed.



Task 4 - Support Knowledge Sharing and Coordination Across all ASCENT Project 093 Universities

Massachusetts Institute of Technology
University of Hasselt

Objective

The objective of this task is to share best practices and coordinate efforts with other ASCENT Project 093 universities (Washington State University and University of Hawaii). The sharing of approaches minimizes duplication of ASCENT Project 093 universities' work on similar topics and can help develop transferable approaches for stakeholder engagement across various geographical regions.

Research Approach

The MIT/UHasselt team participated in regular ASCENT Project 093 coordination teleconferences, which served as a venue to discuss progress in the various geographies and to learn about the activities of other ASCENT Project 093 universities.

Milestones

- Shared progress in Kenya.
- Shared global feedstock availability assessment.

Major Accomplishments

Developed and delivered a joint course on the fundamentals of SAF to a first cohort in November 2023.

Publications

None.

Outreach Efforts

Ongoing coordination between ASCENT Project 093 teams.

Awards

None.

Student Involvement

Andy Eskenazi (MIT) and Francis Mwangi (UHasselt) participated in knowledge sharing.

Plans for Next Period

Continue engagement in regular teleconferences and the development and delivery of the SAF lecture series.



Project 093(B) Collaborative Research Network for Global Sustainable Aviation Fuel Supply Chain Development

University of Hawai‘i

Project Lead Investigator

Scott Q. Turn
Researcher
Hawai‘i Natural Energy Institute
University of Hawai‘i
1680 East-West Rd., POST 109
Honolulu, HI 96822
808-956-2346
sturn@hawaii.edu

University Participants

University of Hawai‘i (UH)

- P.I.: Scott Q. Turn, Researcher
- FAA Award Number: 13-C-AJFE-UH, Amendment 020
- Period of Performance: January 1, 2023, to December 31, 2023
- Tasks:
  1. Establish a collaborative research network for sustainable aviation fuel supply chain development in southeast Asia
     - 1.1 Identify partner universities (and other entities) in the southeast Asian region
     - 1.2 Organize and conduct a sustainable aviation fuel supply chain workshop in Southeast Asia
     - 1.2 Develop a plan for an education and exchange program with collaborating universities in Southeast Asia and with ASCENT Project 093 universities

- FAA Award Number: 13-C-AJFE-UH, Amendment 024
- Period of Performance: March 19, 2024, to September 30, 2026
- Tasks:
  2. Collaborative research network for sustainable aviation fuel supply chain development in southeast Asia
     - 2.1 Develop sustainable aviation fuel research themes of common interest for Association of Southeast Asian Nations countries
     - 2.2 Hold sustainable aviation fuel supply chain workshop in Indonesia

Project Funding Level

Under Federal Aviation Administration (FAA) Award Number 13-C-AJFE-UH, Amendment 020, the ASCENT Project 093(B) Collaborative Research Network for Global sustainable aviation fuel (SAF) Supply Chain Development received $250,000 in funding from the FAA and cost-share funding of $250,000 from UH.

Under FAA Award Number 13-C-AJFE-UH, Amendment 024, the ASCENT Project 093(B) Collaborative Research Network for Global SAF Supply Chain Development received $250,000 in funding from the FAA and cost-share funding of $250,000 from UH.

Investigation Team

University of Hawai‘i

Dr. Scott Turn (P.I.; Hawai‘i Natural Energy Institute)
Dr. Quang-Vu Bach (assistant researcher; Hawai‘i Natural Energy Institute)
Dr. Elmar Villota (postdoctoral fellow, Hawai‘i Natural Energy Institute)



Other Lead Personnel

Washington State University
Prof. Manuel Garcia-Perez (co-P.I.)
Michael Wolcott (P.I.)

Volpe National Transportation Systems Center
Kristin Lewis (P.I. and principal technical advisor)

Massachusetts Institute of Technology
Florian Allroggen (P.I. and research Scientist)

Project Overview

UH will engage universities (and other entities) in southeast (SE) Asian countries and develop collaborative research programs focused on SAF supply chains. These activities will identify information shortfalls and generate fundamental data necessary for the design of engineered SAF production systems. Research activities will include supporting analyses related to the assessment of available feedstocks, supply chains, infrastructure needs, and stakeholder engagement. Planned activities under the program include support of research projects, workshops, and student and researcher exchanges.

The key objectives for this project are as follows:

- Establish a collaborative research network for SAF supply chain development in SE Asia.
- Provide technical support to other ASCENT Project 093 universities and partner activities for which tropical feedstocks are relevant.

Task 1 – Establish a Collaborative Research Network for Sustainable Aviation Fuel Supply Chain Development in Southeast Asia

University of Hawai‘i

Objectives

This task includes three subtasks:

- Subtask 1.1 Identify partner universities (and other entities) in the SE Asian region
- Subtask 1.2 Organize and conduct a SAF supply chain workshop in SE Asia
- Subtask 1.3 Develop a plan for an education and exchange program with collaborating universities in SE Asia and with ASCENT Project 093 universities

Research Approach

UH has led the tropical regional supply chain effort under ASCENT Project 001 since 2015. Activities under this effort have focused on tropical energy crops and agriprocessing residues and urban residues as candidate feedstocks for SAF production. This experience forms the basis for the development of SE Asian SAF supply chains.

Background

Regional supply chain development is informed by crop-science-based evaluations of plants for feedstock production, analyses of crop production potential based on geographic information systems, development of advanced feedstock processing and conversion systems, assessments of the compatibility of biomass and bioderived products with existing infrastructure and logistical resources, and evaluations of biomass-based energy systems based on life cycle and economic approaches. The results of past efforts have provided a baseline of information to be accessed and built upon in developing scenarios of future SAF production along regional supply chains in Hawai‘i and the tropics. Pretreatment and conversion options for materials from potential SAF feedstock crops in the tropics are shown in Figure 1.

In August 2017, the Hawai‘i Natural Energy Institute at UH initiated efforts under a five-year grant from the Office of Naval Research for the Asia Pacific Regional Energy System Assessment. The objective of this 5-year grant was to develop comprehensive energy system assessments that include strategy, policy, regulation, technology options, demonstrations, implementation plans, and training for energy system transitions in select locations throughout the Asia-Pacific region, based on the specific requirements or needs of the targeted jurisdictions and strategic alliances. The first 3 years of this



program laid a firm foundation for continued success built upon the development of solid partnerships with national, regional, and local jurisdictions as well as private and public stakeholders, including utility companies, universities, and other research and international aid and development entities. Relationships developed in SE Asia (i.e., Thailand, Indonesia, and Vietnam) through the Asia Pacific Regional Energy System Assessment were leveraged to facilitate the ASCENT Project 093(B) global supply chain development effort. The Association of Southeast Asian Nations (ASEAN) includes the countries of Brunei Darussalam, Cambodia, Indonesia, Lao PDR, Malaysia, Myanmar, Philippines, Singapore, Thailand, and Vietnam. Universities (and other entities) from ASEAN countries, with the exception of Cambodia and Myanmar, were the initial target participant group in the collaborative research network for SAF supply chain development in SE Asia under this ASCENT project.

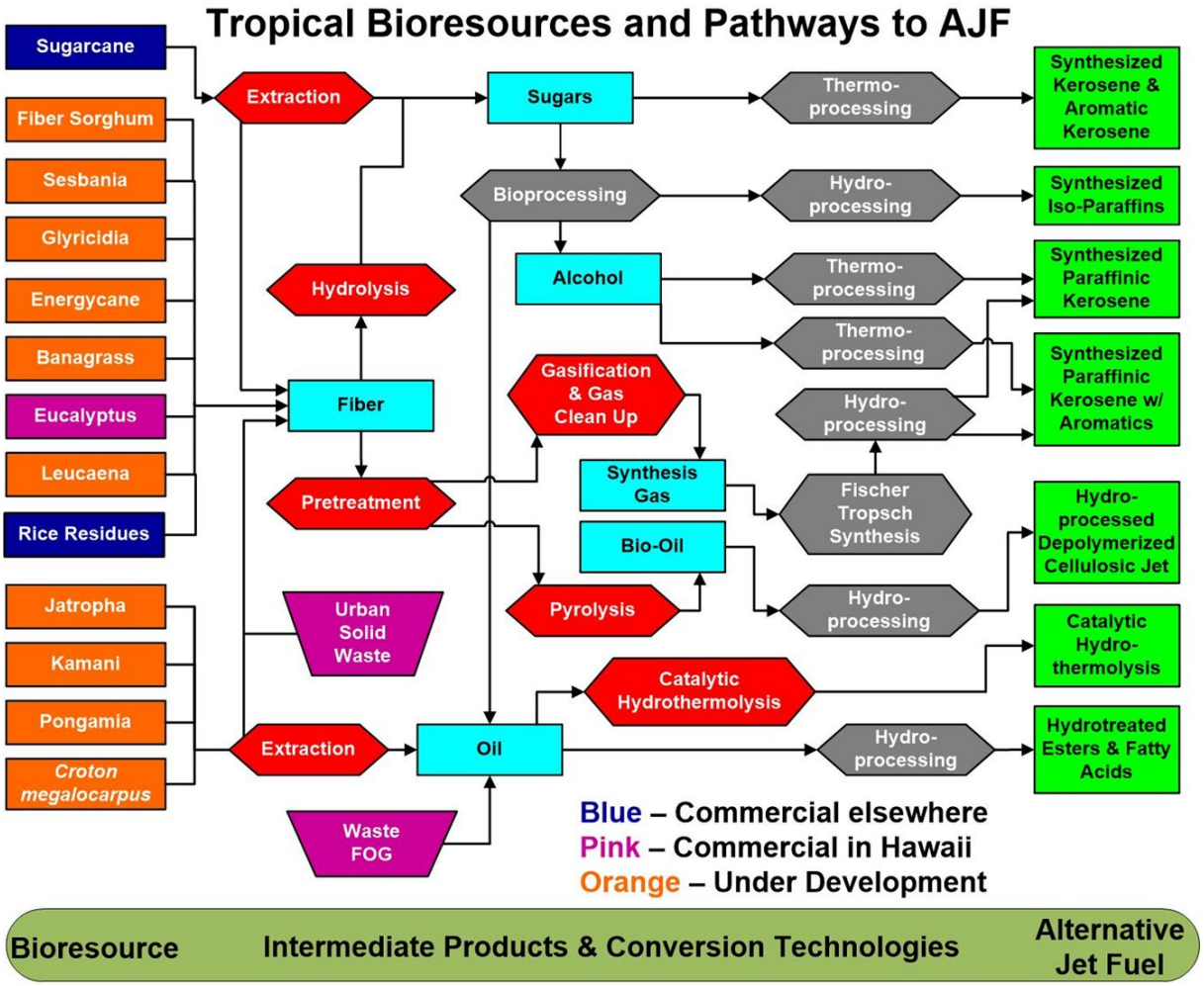


Figure 1. Tropical bioresources and pathways to alternative jet fuel (AFJ)/SAF. FOG: fats, oils, and greases.

Subtasks 1.1 and 1.2

Activities conducted to accomplish Subtasks 1.1 and 1.2 were coordinated in planning the SAF supply chain workshop held in Bangkok in May 2023. The workshop was coordinated with the United States (U.S.) Trade and Development Agency (Commerce Department) as part of their effort to support the SAF business development of U.S. companies in the region. Thailand's National Energy Technology Center and Chiang Mai Rajabhat University were instrumental in the planning process, providing contacts at universities and government agencies throughout the ASEAN region. Staff from the U.S. Embassy in Bangkok and FAA Asia Pacific Office at the U.S. Embassy in Singapore supported workshop planning by contacting and coordinating with government agencies across the region.



The archival literature was reviewed to identify universities and entities from ASEAN countries with either ongoing SAF-related development activities or prior work in biomass resource assessment or biomass supply chains. Based on the results, researchers from 13 universities across the region (i.e., Philippines, Indonesia, Thailand, Vietnam, Malaysia, and Brunei) were contacted to assess interest in workshop participation. Twelve researchers from seven universities attended the SAF workshop in Bangkok, Thailand.

The workshop objectives were as follows:

- Connect stakeholders.
- Foster collaboration.
- Drive innovation in the adoption of SAF.

The FAA-supported section of the workshop was held on May 22–23, 2023, at the Conrad Hotel in Bangkok, Thailand. More than 100 attendees from eight countries participated in the workshop (see Figure 2). Participants self-identified their organization's place in the SAF value chain, as shown in Figure 3.

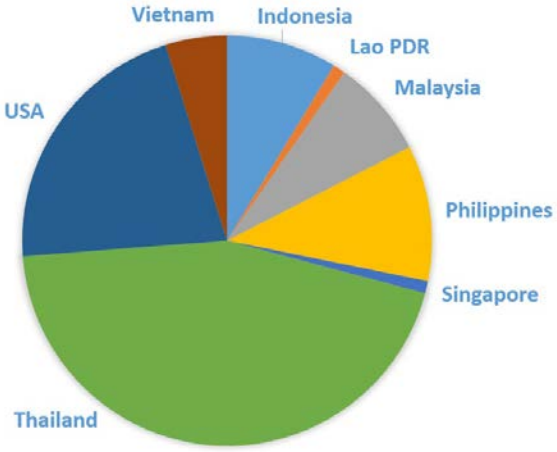


Figure 2. Country of origin of participants at the sustainable aviation fuel workshop.

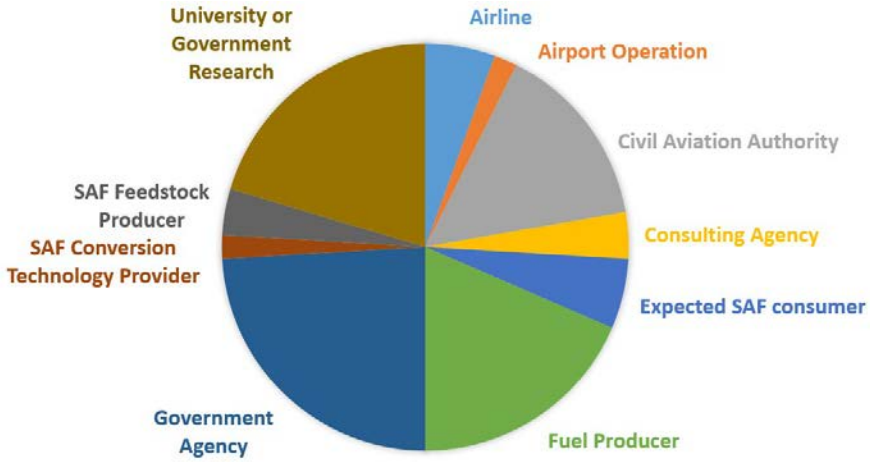


Figure 3. Organizations of sustainable aviation fuel (SAF) workshop attendees.



The two days of the workshop were organized as shown below:

Day 1, Morning
- Workshop overview and introduction
- Keynote address: International Civilian Aviation Organization
- Civil aviation authority perspectives
- Energy policy perspectives on SAF

Day 1, Afternoon
- Panel on SAF production: Upstream considerations/logistics
- Update on the Commercial Aviation Alternative Fuels Initiative
- Summary and close out of Day 1

Day 2, Morning
- Recap from Day 1
- Keynote address: SAF sustainability criteria
- Agricultural industry: Feedstocks for SAF production
- Airport fuel system operator perspectives

Day 2, Afternoon
- University research in support of SAF development
- Panel discussion: Way forward
- Summary and close out of Day 2

Participants who gave presentations were provided with five motivational prompts:
- Tell us about your organization (e.g., private/public, size, authority, etc.).
- What role will your organization play in the transition to SAF use in your country?
- How will your organization plan for the expanded use of SAF?
- What barriers will need to be overcome for SAF deployment in your country?
- What tools and resources are needed to overcome those barriers?

Workshop participants identified common themes that need to be addressed across the region, as summarized below:
- Sustainable funding models and strategies are needed for the aviation industry's transition to SAF.
- There is a lack of discussion on sustainability and economic viability of feedstocks.
- Investments in research and development are required to diversify feedstock options and promote sustainable alternatives that do not compete with food supplies.
- Infrastructure development is crucial for the production, storage, and distribution of SAF.

Workshop recommendations included the following:
- Explore and establish supporting policy (e.g., the use of incentives and carbon credits) to promote SAF production and adoption.
- Raise awareness and develop education initiatives to inform stakeholders, including the public, about the benefits and importance of SAF.

Participant feedback identified the sessions on civil aviation authorities' perspectives, energy policy perspectives on SAF, and the agricultural industry feedstocks for SAF production as the most useful.

Subtask 1.3
A meeting was held with the Dean of Education Programs and the Deputy Director of Research Programs at the East-West Center (www.eastwestcenter.org) adjacent to the UH campus. The purpose of the meeting was to inform the Dean and Deputy Director about ASCENT Project 093(B) goals and activities and to explore opportunities to integrate East-West Center educational and research networks and infrastructure with the ASCENT Project 093(B) goals of recruiting and educating SE Asian postdoctoral fellows and visiting scholars. UH faculty members that are actively engaged in research on ecosystem services and transportation networks have been recruited as mentors for the ASCENT Project 093(B)-supported postdoctoral fellows and visiting scholars.



Milestones

- Identified partner universities for the SAF research network.
- Selected a venue and support organizations for the SE Asia SAF workshop.
- Held the SAF supply chain workshop in SE Asia.

Major Accomplishments

The major accomplishment of the project was holding the highly successful SAF supply chain workshop in Bangkok, Thailand, on May 22–23, 2023. The workshop established ASCENT Project 093(B) as a leader in supporting the development of global SAF supply chains in the ASEAN region. Participants expressed great interest in FAA support for a similar workshop in 2024.

Publications

None.

Outreach Efforts

Organizing and conducting the SAF supply chain workshop in Bangkok, Thailand, provided outreach and education to the SAF supply chain stakeholder community. Presentations were made by Dr. Prem Lobo and Dr. Scott Turn during the workshop. Electronic communications were made with all the workshop participants, either directly or through in-country partners.

A presentation describing the workshop, its goals, and its outcomes was presented at the 3rd ASEAN International Conference on Energy and Environment held in Bali, Indonesia, on August 23–25, 2023.

Awards

None.

Student Involvement

None.

Plans for Next Period

This task is complete.

Task 2 –Collaborative Research Network for SAF Supply Chain Development in SE Asia

University of Hawai'i

Objectives

This task includes two subtasks:

- Subtask 2.1 Develop SAF research themes of common interest for ASEAN countries
- Subtask 2.2 Hold SAF supply chain development workshop in Indonesia

Research Approach

Subtasks 2.1. and 2.2

A snapshot of jet fuel consumption and development plants for SAF in SE Asia is shown in Figure 4. Across the region, annual jet fuel consumption approaches 25 million metric tonnes. Planned and operating SAF annual production capacity is less than 3 million metric tonnes.

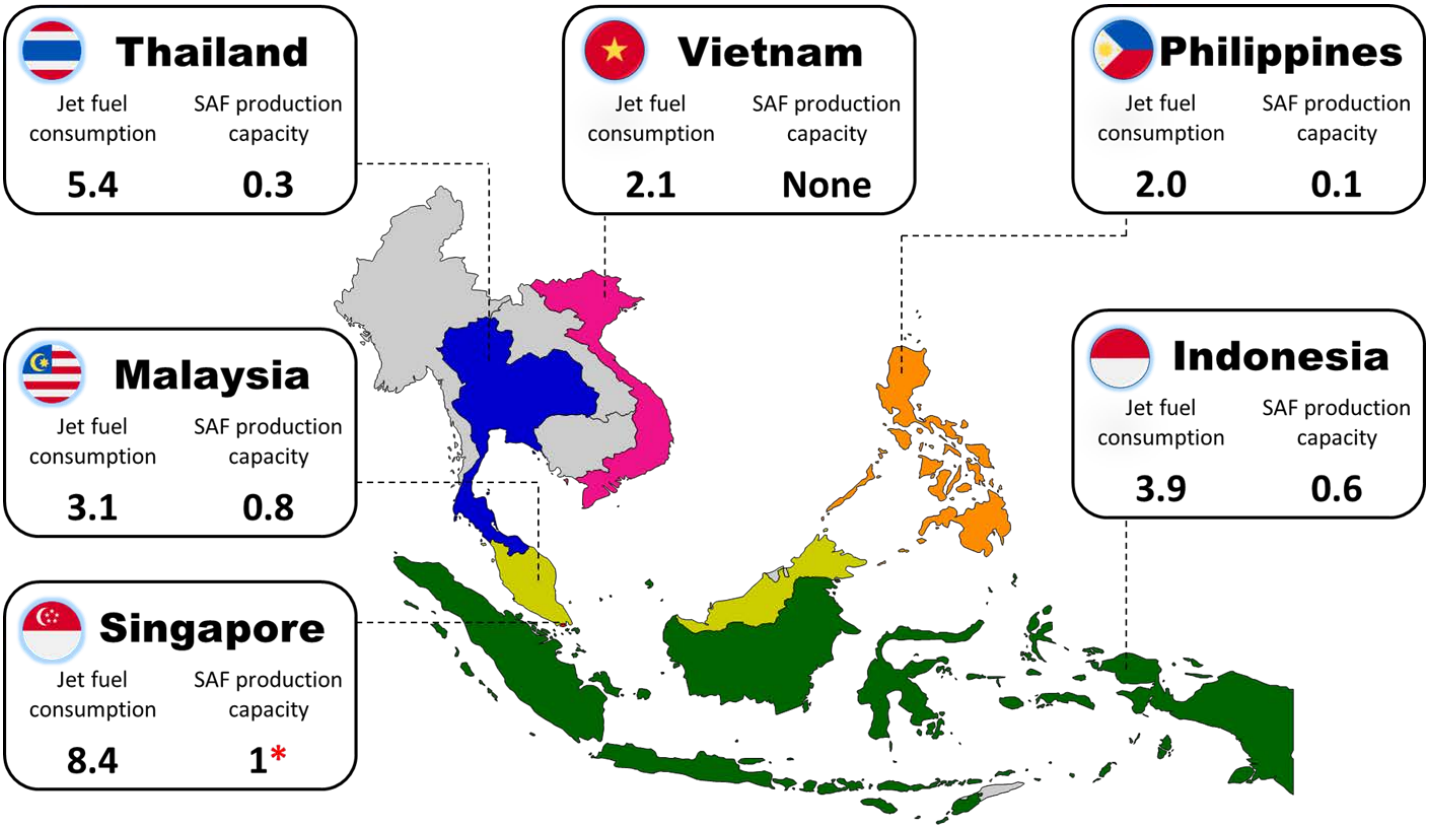


Figure 4. Summary of jet fuel consumption (U.S. Energy Information Administration, 2019) and planned sustainable aviation fuel (SAF) production capacity (Argus Media, 2024) in southeast Asia (* facility currently in operation). Units = million metric tonnes.

The SAF supply chain development workshop was organized and held on July 10-12, 2024, in Bali, Indonesia, to support and coordinate ongoing SAF development activities across the region. The workshop was co-organized by the FAA through ASCENT, the Indonesian Directorate General for Civilian Aviation, the Energy Technology Center of Thailand, and UH.

The workshop registered 95 participants from Malaysia, Indonesia, Philippines, Thailand, Singapore, Vietnam, the U.S., and the European Union and included representatives from agricultural commodity groups, airlines, airport operations, civil aviation authorities, consulting groups, fuel producers, government energy and transportation agencies, SAF conversion technology providers, feedstock producers, university and research organizations, and aircraft manufacturers. Data on attendees and their organization are presented in Figure 5 and Figure 6, respectively.

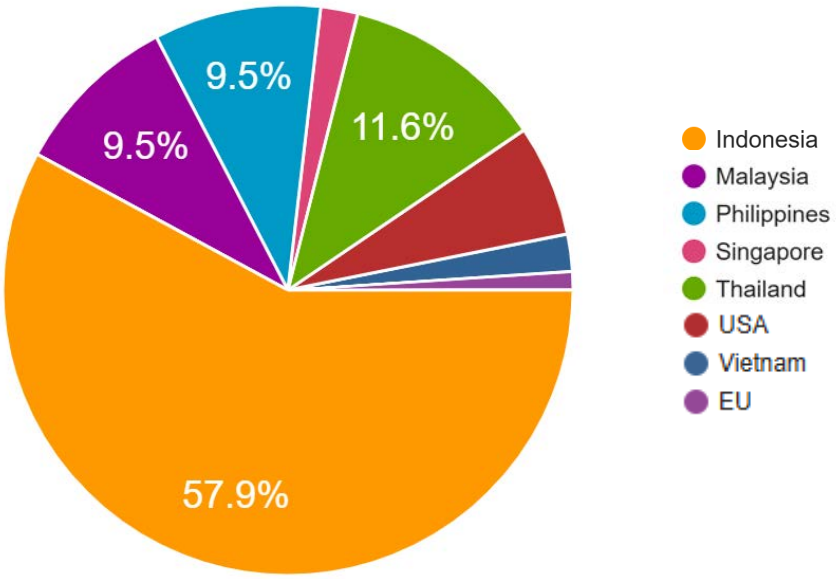


Figure 5. Country of origin of participants at the 2024 sustainable aviation fuel workshop in Bali.

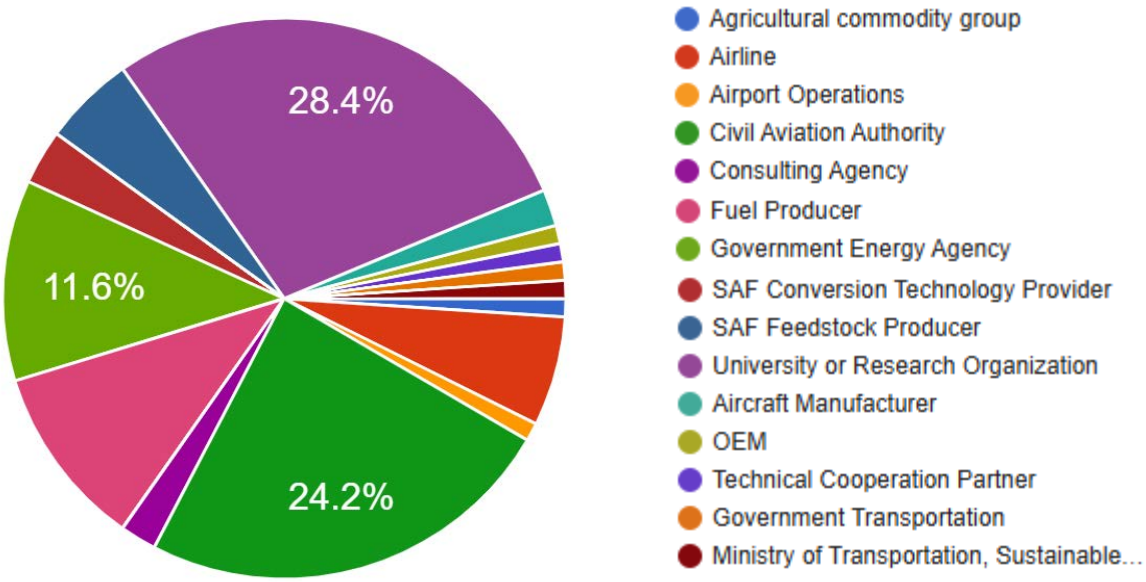


Figure 6. Organizations of sustainable aviation fuel (SAF) 2024 workshop attendees.

The workshop agenda included sessions on perspectives of civil aviation authorities, energy policy, SAF fuels/airports/airplanes, airline perspectives, feedstocks, feedstocks production and logistics, SAF conversion technologies, climate finance, SAF policy development, and university research. The first two days of the workshop were organized as shown below:



Day 1, Morning
- Workshop overview and introduction
- Civil aviation authority perspectives

Day 1, Afternoon
- Energy policy perspectives on SAF
- SAF Fuels: Airports and Airplanes
- Airline Perspectives on SAF
- Summary and close out of Day 1

Day 2, Morning
- Recap from Day 1
- Keynote address: Feedstocks for SAF: The Realm of Possibilities
- SAF Feedstocks: Production and Logistics
- SAF Conversion A-Z

Day 2, Afternoon
- Keynote: Climate Finance Options for SAF
- Development of SAF Policy
- University Research Activities
- Summary and close out of Day 2

Participants who gave presentations were provided with five motivational prompts:
- Tell us about your organization (e.g., private/public, size, authority, etc.).
- What role will your organization play in the transition to SAF use in your country?
- How will your organization plan for the expanded use of SAF?
- What barriers will need to be overcome for SAF deployment in your country?
- What tools and resources are needed to overcome those barriers?

An evaluation of workshop effectiveness was provided by 50 attendees who participated in an exit survey on the workshop content and organization. Participants found sessions on feedstock production and logistics, SAF policy development, energy policy, and SAF conversion technologies to be the most useful, demonstrating the value of an inter-agency approach to moving the SAF agenda forward.

The survey also queried participants on important research questions that needed to be addressed in order to advance SAF production in the region. Suggestions coalesced around common themes of (1) feedstock diversification and supply chains, (2) conversion technology advancement, and (3) environmental/sustainability certification. Cross cutting themes included funding, finance, and long term economic, social and environmental impacts of SAF implementation/utilization. This information was used as motivation in a four-hour session for university and research organization participants where they were encouraged to workshop on (1) specific research questions to include in a proposal, (2) funding sources, and (3) approaches to collaboration between their organizations for proposal development.

Central Luzon State University (CLSU) in the Philippines is undertaking a national biomass resource assessment in support of SAF development efforts. Dr. Elmar Villota, a postdoctoral fellow at UH, is coordinating with CLSU faculty and staff to serve as a resource person. Results from the draft report will be presented to Philippines Department of Energy staff in the fourth quarter of 2025.

UH personnel have initiated a study to quantify the occurrence of non-standard coconut in post-harvest supply chains. The Philippines would be the initial study area and contacts in Indonesia have been made to gauge interest there.

Milestones

- Identified partner universities for the SAF research network.
- Held the SAF supply chain workshop in SE Asia. This effort required identifying co-organizer groups for the SAF workshop in Bali, Indonesia, finalizing the workshop terms of reference, selecting and contracting a venue for the workshop and support organizations, and holding the SAF supply chain workshop in SE Asia.



Major Accomplishments

The major accomplishment of the project was holding the highly successful SAF supply chain workshop in Bali, Indonesia, on July 10-11, 2024. The workshop established ASCENT Project 093(B) as a leader in supporting the development of global SAF supply chains in the ASEAN region. Participants expressed great interest in FAA support for a similar workshop in 2025.

Publications

None.

Outreach Efforts

Organizing and conducting the SAF supply chain workshop in Bali, Indonesia, provided outreach and education to the SAF supply chain stakeholder community. Electronic communications were made with all the workshop participants, either directly or through in-country partners.

- Presented (Dr. Manuel Garcia-Perez and Dr. Scott Turn) information on SAF production and ASCENT global engagement to students from Taylor University in Malaysia at the request of the U.S. Grains Council on October 13, 2023.
- Presented two lectures (February 15 and May 16, 2024) as part of the ASCENT Project 093b Latin America training course organized by Washington State University.
- Presented on ASCENT Project 093b activities at the ASCENT review meetings in Honolulu, Hawai‘i (April 2024) and Alexandria, Virginia (October 2024).
- Participated (Dr. Scott Turn) in the Asia Pacific Air Transport Forum in Bali, Indonesia, and attended the release of Indonesia’s SAF road map at the Bali Airshow in September 2024.
- Held meetings with the Indonesian Directorate General for Civil Aviation (January, July, and September 2024) to discuss SAF development in the region and preparation and timelines for the release of Indonesia’s SAF road map.
- Participated in the 2025 Philippines SAF Forum #1 and subsequent feedstock availability working group meetings on agricultural residues and non-standard coconut, February 28 to March 4, 2025.
- Visited Universitas Sumatera Utara (USU) in Medan, Indonesia and Hasanuddin University (UNHAS) in Makassar, Indonesia during the week of April 14, 2025, accompanied by Dr. Wendy Aritenang, the Senior Technical Advisor to the Indonesian Directorate General for Civil Aviation. Visit focused on common interests in *Aleurites moluccanus*, a tree species that bears a nut containing 60% oil.
- Participated in the 1st Philippine SAF Policy Development Roundtable Discussion on June 23, 2025. This meeting included stakeholders from the Philippines government, agricultural commodity producers, airlines, and petroleum refiners. UH made a presentation entitled, "Stakeholder Needs: Building the SAF Ecosystem."
- Presented on ASCENT Project 093b activities at the ASCENT review meetings in Knoxville, Tennessee (April 2025).
- Participated in the My Aero Sustainable Aviation APAC Symposium in Kuala Lumpur. Meetings with personnel from Petronas, the Malaysian oil company, indicated that they remain interested in partnering with UH/FAA to co-host future SAF workshops for southeast Asia in Malaysia. (July 2025)
- Attended the southeast Asia SAF Forum, "From Waste to Wings: Thailand's Role in Sustainable Aviation Fuel (SAF)," in Bangkok, Thailand and made a presentation entitled, "SAF Perspectives in ASEAN." (July 2025)
- Initiated a study to quantify the occurrence of non-standard coconut in post-harvest supply chains. The Philippines would be the initial study area and contacts in Indonesia have been made to gauge interest there.

Awards

None.

Student Involvement

None.

Plans for Next Period

- Draft and submit a manuscript for publication in the journal *IOP Sustainability Science and Technology.* A report was prepared describing the 2024 workshop in Bali, Indonesia, and detailing its outcomes. This report will be used to draft the manuscript.
- Pursue a study to quantify the occurrence of non-standard coconut in post-harvest supply chains. The Philippines would be the initial study area and contacts in Indonesia have been made to gauge interest there.



- Explore interests in establishing core values of carbon intensity for SAF produced from *Aleurites moluccanus*. Participants from Indonesia and Hawai'i will be the initial focus group.
- Continue efforts to develop regional projects for southeast Asian universities currently involved with SAF development work.

References

Argus Media, 2024. Global SAF Map. https://view.argusmedia.com/global-saf-capacity-map.html

U.S. Energy Information Administration, 2019. International Energy Statistics. https://www.eia.gov/international/data/world



Project 093(C) Collaborative Research Network for Global Sustainable Aviation Fuel Supply Chain Development: Latin America and Caribbean Case

Washington State University

Project Lead Investigators

Manuel Garcia-Perez
Professor and Chair
Biological Systems Engineering Department
Washington State University
LJ Smith, Room 205, PO Box 646120
Pullman, WA 99164-6120
509-335-7758
mgarcia-perez@wsu.edu

Michael P. Wolcott
Regents Professor
Department of Civil & Environmental Engineering
Washington State University
PO Box 642910
Pullman, WA 99164-2910
509-335-6392
wolcott@wsu.edu

University Participants

Washington State University (WSU)

- P.I.s: Manuel Garcia-Perez and Michael P. Wolcott
- FAA Award Number: 13-C-AJFE-WaSU-037
- Period of Performance: October 30, 2024, to October 30, 2025
- Tasks:
  1. Create working groups in each Latin America and Caribbean (LAC) country involved in this project
  2. Conduct the design and analysis of sustainable aviation fuel (SAF) supply chains in each of the LAC countries involved in this project
  3. Create training modules/courses and graduate programs to train students

Project Funding Level

This project has received so far $656,586 in Federal Aviation Administration (FAA) funding and $656,586 in matching funds to WSU. Faculty time for Michael Wolcott, Manuel Garcia-Perez, Erik Jessup, Allyson Beall King, and Hanwu Lei contributes to the cost share. WSU funding is reported for the reporting period.

Investigation Team

Washington State University

Manuel Garcia-Perez (P.I.), Tasks 1, 2, and 3
Michael Wolcott (P.I.), Task 1
Hanwu Lei (co-P.I.), Task 3
Kristin Brandt (co-P.I.), Tasks 2 and 3
Lina Martinez (research staff), Tasks 1, 2, and 3
Dane Camenzind (research staff), Tasks 2 and 3



Allyson Beall King (research staff), Tasks 2 and 3
Eric Jessup (research staff), Tasks 2 and 3
Claudia Marcella Valderrama (graduate research assistant), Tasks 2 and 3
Raul Perez Mena (graduate research assistant) Tasks 1, 2, and 3
Paulina Echeverria Paredes (graduate research assistant) Tasks 1, 2, and 3
Robert Macias (graduate research assistant), Task 3

Volpe National Transportation Systems Center (Volpe)
Kristin Lewis (co-P.I.), Tasks 2 and 3

Project Overview

SAFs offer the potential to reduce the net environmental impact of aviation-related emissions while enhancing United States (U.S.) energy security and diversifying energy supplies. As a result, these technologies are receiving considerable attention from policymakers, industry, and academia. Most importantly, SAF has been included in the International Civil Aviation Organization (ICAO)'s Carbon Offsetting and Reduction Scheme for International Aviation (CORSIA), which aims to reduce carbon dioxide (CO_2) emissions of international aviation above 85% of year-2019 levels. Using SAF, aircraft operators can reduce their offsetting requirements using the reduced CORSIA values of CO_2 emissions from SAF using their well-to-wake lifecycle greenhouse gas (GHG) emissions (including credits for biogenic carbon emissions during combustion).

Significant progress has been made over the past decade in assessing the economic and environmental properties of SAFs. This includes studies that have fostered our general understanding of life cycle analysis (LCA) (e.g., Stratton et al., 2010). In addition, work has focused on the economic and environmental properties of specific pathways, including jet fuel produced from hydroprocessed esters and fatty acids (HEFA) (Pearlson et al., 2013; Olcay et al., 2013; Seber et al., 2014; Stratton et al., 2011), from Fischer-Tropsch (FT) pathways (Stratton et al., 2011; Suresh et al., 2018; Suresh, 2016), and from biomass-derived sugars using a variety of chemical and biological techniques (Bond et al., 2014; Staples et al., 2014; Winchester et al., 2015). Most recently, Monte Carlo approaches have been systematically introduced for quantifying uncertainty and stochasticity in LCA and techno-economic analysis (TEA) (Bann et al., 2017; Oriakhi, 2020; Sureshet al., 2018; Suresh, 2016; Yao et al., 2017).

A suite of decision-support tools for assessing SAF supply chains has been developed within ASCENT Project 001. These tools can be used to assess the economics of SAF production, the optimization of SAF supply chain logistics, and the configuration of supply chains to consider both the sale of the fuel commodity and the commensurate environmental benefits. This suite of tools has been widely applied within regions of the U.S. and has potential for use internationally. Of particular interest is understanding feedstock availability and financial considerations for delineating both the minimum selling price and capital investment requirements for SAF production in regions outside the U.S. This project has the potential to benefit our understanding of the worldwide production of SAF to inform ICAO.

ASCENT Project 001 has made progress in harmonizing TEAs across technology pathways and feedstock selections for both technical and financial assumptions. Five SAF production pathways have been completed and are publicly available TEAs: HEFA, alcohol to jet (ATJ), FT, pyrolysis, and catalytic hydro thermolysis (CH) (Brandt et al., 2021a, 2021b, 2021c, 2022a, 2022b). These TEAs have been used extensively in work within ASCENT and for ICAO Committee on Aviation Environmental Protection (CAEP) analyses. As part of the ICAO tasks, the TEAs were updated to allow for regional variables to be changed based on global location. These include local consumable prices such as feedstock and electricity, as well as equipment capital costs and labor. Location-specific financial assumptions, including tax rate, inflation rate, and terms of loans, are also customizable. With expertise from Latin American colleagues, these TEAs can be rapidly deployed for use in member countries.

The process for siting facilities consists of two steps: (1) generating an initial set of candidates, and (2) using mixed integer optimization to select facilities from the candidate locations. The candidate generation phase uses geospatial data to evaluate a location's compatibility with specific facility types. The optimization phase allows for the locations of facilities to be found that result in systemwide minimum costs for a specific set of variables, like fuel cost, tariffs, and feedstock availability. Batch processing allows for the rapid iteration of variables so that a supply chain's sensitivity can be evaluated in different scenarios. During the past decades, Latin America has grown its bioethanol and biodiesel production. Brazil, Argentina, and Colombia have the largest production of biofuel in the region (IEA, 2021). In addition, the LAC region is



classified as a high-potential area for producing energy crops (Acharya & Perez-Pena, 2020; Trindale et al., 2019). Currently, interest in the production and consumption of SAF has spiked in the region. Omega Green is the first renewable diesel and SAF project under construction in Paraguay, with Brazilian investment (ECB Group, 2021). The project started in 2023 and is still under construction. Legal framework and initiatives to produce or import SAF are being initiated in the Dominican Republic, Mexico, Costa Rica, and Colombia (Argus, 2021). LATAM, a South American airline with main hubs in Chile, Peru, Brazil, and Colombia, plans to use 5% SAF for its operations by 2030, favoring producers throughout South America (LATAM, 2022). To date, no comprehensive assessment exists of the potential for SAF production in Latin America.

During Year 2, our team focused on four countries in Latin America and the Caribbean: (1) Colombia, (2) Dominican Republic, (3) Ecuador and (4) Costa Rica. So far, we have conducted literature reviews on biomass and SAF-related publications and existing infrastructure for each of these four countries. The study of Colombia has been socialized with the Colombian stakeholders and is now published. We are now socializing our literature reviews with our stake holders from Ecuador and Dominican Republic. The literature review of Costa Rica is still under internal review. These literature reviews are being used as a supporting source of information to create the SAF roadmaps in these countries.

The overall objectives of this project are to: (1) create working groups in each of the LAC focus countries involved in this project that will work directly with the students on the development of SAF supply chains, (2) design and analyze SAF supply chains in the LAC region, and (3) create training modules, courses, and graduate programs to train students and stakeholders in Latin America and the Caribbean on the design and analysis of SAF production and supply chains.

References

Acharya, R. N., & Perez-Pena, R. (2020). Role of comparative advantage in biofuel policy adoption in Latin America. *Sustainability*, *12*(4), 1411. https://doi.org/10.3390/su12041411

Argus. (2021, August 31). *Jet Fuel Insights: The move to SAF in Latin America*. https://www.argusmedia.com/en/blog/2021/august/31/podcast-jet-fuel-insights-the-move-to-saf-in-latin-america

Bann, S. J., Malina, R., Staples, M. D., Suresh, P., Pearlson, M., Tyner, W. E., Hileman, J. I., & Barrett, S. (2017). The costs of production of alternative jet fuel: A harmonized stochastic assessment. *Bioresource technology*, *227*, 179-187. https://doi.org/10.1016/j.biortech.2016.12.032

Bond, J. Q., Upadhye, A. A., Olcay, H., Tompsett, G. A., Jae, J., Xing, R., Alonso, D. M., Wang, D., Zhang, T., Kumar, R., Foster, A., Sen. S. M., Maravelias, C. T., Malina, R., Barrett, S. R. H., Lobo, R., Wyman, C. E., Dumesic, J. A., & Huber, G. W. (2014). Production of renewable jet fuel range alkanes and commodity chemicals from integrated catalytic processing of biomass. *Energy & Environmental Science*, *7*(4), 1500-1523. https://doi.org/10.1039/C3EE43846E

Brandt, K., Tanzil, A. H., Martinez-Valencia, L., Garcia-Perez, M., & Wolcott, M. P. (2022a). *Pyrolysis techno-economic analysis* (v. 2.1). Washington State University. https://doi.org/10.7273/000002563

Brandt, K., Eswaran, S., Subramaniam, S., Zhang, X., & Wolcott, M.P. (2022b). *Catalytic Hydrothermolysis techno-economic analysis* (v. 2.1). Washington State University. https://doi.org/10.7273/000002564

Brandt, K., Tanzil, A. H., Martinez-Valencia, L., Garcia-Perez, M., Wolcott, M. P. (2021a). *Hydroprocessed esters and fatty acids techno-economic analysis* (v. 2.1). Washington State University. https://doi.org/10.7273/000001460

Brandt, K., Geleynse, S., Martinez-Valencia, L., Zhang, X., Garcia-Perez, M., & Wolcott, M. P. (2021b). *Alcohol to jet techno-economic analysis* (v. 2.1). Washington State University. https://doi.org/10.7273/000001461

Brandt, K., Tanzil, A. H., Martinez-Valencia, L., Garcia-Perez, M., & Wolcott, M. P. (2021c). *Fischer Tropsch techno-economic analysis* (v. 2.1). Washington State University. https://doi.org/10.7273/000001459

ECB Group. (2021). *Omega Green*. https://www.ecbgroup.com.br/en/group/bsbios-paraguay/omega-green

IEA. (2021, December). *Renewables 2021: Analysis and forecast to 2026*. International Energy Agency. https://iea.blob.core.windows.net/assets/5ae32253-7409-4f9a-a91d-1493ffb9777a/Renewables2021-Analysisandforecastto2026.pdf

https://bradscholars.brad.ac.uk/bitstreams/01cfae05-bc0d-4a5e-9611-a465899e3e13

LATAM. (2022, April 6). *LATAM seeks to reach 5% sustainable fuel use by 2030, favoring producers throughout South America*. LATAM Airlines. https://www.latamairlines.com/us/en/press-room/releases/latam-sustainable-aviation-fuel

Olcay, H., Seber, G., & Malina, R. (2013). *Life Cycle Analysis for Fully-Synthetic Jet Fuel Production*. MIT Support for Honeywell Continuous Lower Energy, Emissions and Noise (CLEEN) Technologies Development, Report to the FAA.

Oriakhi, U. M. (2020). *A stochastic life cycle and greenhouse gas abatement cost assessment of renewable drop-in fuels* (Doctoral dissertation, Massachusetts Institute of Technology). Massachusetts Institute of Technology. https://hdl.handle.net/1721.1/127738

Pearlson, M., Wollersheim, C., & Hileman, J. (2013). A techno-economic review of hydroprocessed renewable esters and fatty acids for jet fuel production. *Biofuels, Bioproducts and Biorefining*, *7*(1), 89-96. https://doi.org/10.1002/bbb.1378

Seber, G., Malina, R., Pearlson, M., Olcay, H., Hileman, J., & Barrett, S. (2014). Environmental and economic assessment of producing hydroprocessed jet and diesel fuel from waste oils and tallow. *Biomass and Bioenergy, 67*, 108-118. https://doi.org/10.1016/j.biombioe.2014.04.024

Staples, M. D., Malina, R., Olcay, H., Pearlson, M. N., Hileman, J. I., Boies, A., & Barrett, S. R. (2014). Lifecycle greenhouse gas footprint and minimum selling price of renewable diesel and jet fuel from fermentation and advanced fermentation production technologies. *Energy & Environmental Science*, *7*(5), 1545-1554. https://doi.org/10.1039/C3EE43655A

Stratton, R., Wong, H. M., & Hileman, J. (2010). *Life cycle greenhouse gas emissions from alternative jet fuels* (No. PARTNER-COE-2010-001). Partnership for Air Transportation Noise and Emissions Reduction.

Stratton, R. W., Wong, H. M., & Hileman, J. I. (2011). Quantifying variability in life cycle greenhouse gas inventories of alternative middle distillate transportation fuels. *Environmental science & technology*, *45*(10), 4637-4644. https://doi.org/10.1021/es102597f

Suresh, P., Malina, R., Staples, M. D., Lizin, S., Olcay, H., Blazy, D., Pearlson, M. N., & Barrett, S. R. (2018). Life cycle greenhouse gas emissions and costs of production of diesel and jet fuel from municipal solid waste. *Environmental science & technology*, *52*(21), 12055-12065. https://doi.org/10.1021/acs.est.7b04277

Suresh, P. (2016). *Environmental and economic assessment of alternative jet fuel derived from municipal solid waste* (Master's thesis, Massachusetts Institute of Technology). Massachusetts Institute of Technology. http://hdl.handle.net/1721.1/105567

Trindade, S. C., Nogueira, L. A. H., & Souza, G. M. (2019). Relevance of LACAf biofuels for global sustainability. *Biofuels*, 1-11. https://doi.org/10.1080/17597269.2019.1679566

Winchester, N., Malina, R., Staples, M. D., & Barrett, S. R. (2015). The impact of advanced biofuels on aviation emissions and operations in the US. *Energy Economics*, *49*, 482-491. https://doi.org/10.1016/j.eneco.2015.03.024

Yao, G., Staples, M. D., Malina, R., & Tyner, W. E. (2017). Stochastic techno-economic analysis of alcohol-to-jet fuel production. *Biotechnology for Biofuels*, *10*(18), 1-13. https://doi.org/10.1186/s13068-017-0702-7

Task 1 - Create Working Groups in Each of the LAC Countries Involved in This Project

Washington State University

Objective

The objective of this task is to engage with stakeholders from Ecuador, Dominican Republic, Costa Rica, and Colombia.

Research Approach

Under Task 1, the team has been working with groups in each of the LAC countries involved in this project. For Colombia, Dominican Republic, and Ecuador, we took advantages of activities in these countries. Last year, we expanded our work to cover Costa Rica. A new graduate student from Costa Rica (Rayman Angulo Gutierrez) joined our research program in January 2025. We are in contact with stakeholders in all these countries.

Milestone

- Started work on this task in January 2023 and continued work through 2025.

Major Accomplishments

We are working with active working groups in Colombia, Dominican Republic, Ecuador, and Costa Rica. The first workshop was hosted by ASCENT Project 093 by WSU in Bogota, Colombia, on March 15, 2024, with 37 attendees with diverse and covered industries, universities, and the government. In 2024 and 2025, technical support was provided to the Colombian Civil Aviation Authority (Aerocivil) on the Colombian SAF round map. The group in the Dominican Republic is formed by academic partners coordinated by the Ministry of Higher Education and the existing SAF round table coordinated by (Instituto Dominicano de Aviacion Civil (IDAC). Students participated in the "Second meeting: Sustainable Aviation Fuels," organized by the IDAC. Raul Perez presented the preliminary results of the overview for this country. All the students presented preliminary results from a dynamic systems analysis of four SAF production pathways. Universities and



industries mainly form the working group from Ecuador. We are working to attract more industries (especially EP Petroecuador) and more government agencies. In the case of Costa Rica, we have made our first contacts and have recruited a graduate student to work on this project with their civil authority.

Publications
None.

Outreach Efforts
- Participated (Raul Perez, Marcela Valderrama, Paulina Echeverria, and Micaela Peralta) in the "Second meeting: Sustainable Aviation Fuels," organized by the Sustainable Development Directorate of the IDAC in March 2025. Raul Perez presented the preliminary results of the overview for this country. All the students presented the preliminary results of a dynamic systems analysis for four SAF production pathways.
- Participated (Manuel Garcia-Perez) in the Latin American and Caribbean Air Transport Association (ALTA) Fuel and Sustainability Conference organized in the Dominican Republic in March 2025.
- Participated (Marcela Valderrama, a student from Colombia) in the event "Impact of SAF in the Supply Chain of the Fuel" organized by the Civil Aeronautics of that country. The results of the "SAF production in Colombia: opportunities and challenges" and the ASCENT TEA were referenced in the study.
- Held meetings with experts and stakeholders in Colombia, Dominican Republic, and Ecuador to validate the system dynamics models.

Student Involvement
- Claudia Marcela Valderrama (Colombian) has supported the Colombian working group communications since January 2023.
- Raul Perez, a Dominican Republic student who started his graduate studies on January 1, 2024, has supported the Dominican Republic working group communications.
- Paulina Echeverria and Micaela Peralta, Ecuadorian students who started their graduate studies on January 1, 2024, are in contact with stakeholders in their countries.

Plans for Next Period
- Continue supporting our stakeholders and participating in conferences that are relevant to them.

Task 2 - Conduct the Design and Analysis of SAF Supply Chains in Each of the LAC Countries Involved in the Project
Washington State University

Objective
The objective of this task is to develop system dynamic models to study the potential to produce SAF via HEFA, ATJ, municipal solid waste to SAF and energy crops to jet. These models will be used to study the number of plants that can be built in the Dominican Republic, Costa Rica, Ecuador, and Colombia, depending on the level of incentives. Once the number of plants has been identified, we will use Freight and Fuel Transportation Optimization (FTOT) to identify the optimal location.

Research Approach
Under Task 2, we conduct the design and analysis of SAF supply chains in each of the focus countries in LAC. In these studies, we will try to answer the following questions: (1) what LCA values for the feedstock and sustainability criteria compliance should be used, (2) what public policies the countries should develop to grow the production of SAF in Latin America, and (3) how should the design supply chain and sitting of facilities be conducted.

Milestone
- Started this task in January 2023 and continued working on this task through 2025.



Major Accomplishments

The students, Raul Perez, Paulina Echeverria, and Micalea Peralta, have completed writing the reports for the Dominican Republic and Ecuador; both documents are under review for publication in the WSU repository. The first draft of the Dominican Republic report was shared with stakeholders in March 2025. The Ecuadorian first draft report has been completed. The student, Rayman Angulo, has completed writing the report for Costa Rica, and the first draft has been shared with stakeholders in October 2025.

All the students are now developing system dynamics models to describe the effect of incentives on the number of HEFA, ATJ, pyrolysis, and gasification/FT fuel plants in the region. Students have presented the base case system dynamics models for the four main pathways: ATJ using sugarcane-derived ethanol, HEFA using used cooking oil and palm oil, FT using municipal solid waste, and pyrolysis of energy crops, as work in progress in the 2025 International System Dynamics Conference in Boston, Massachusetts. Four papers are currently in preparation, each focusing on the system dynamics base case for one of the four technologies being evaluated for SAF production. These papers will present the general modeling frameworks developed for each technology and explore a series of "what-if" scenarios to assess their performance, interactions, and potential contributions to the overall SAF production system. Two papers have been completed, one for the ATJ pathway and the other for the HEFA pathway and are now under review.

An econometric model has been developed to evaluate the impact of SAF prices on airfare and passenger demand, based on data from Colombia, Costa Rica, Dominican Republic, and Ecuador to the U.S., including ticket prices, fuel consumption, fuel prices, occupancy rates, load factors, and tourism statistics.

Volpe started to work with our Colombian partners, introducing the road network and running an initial proof of concept for the biodiesel supply chain. The biodiesel supply chain includes crude palm oil extraction, biodiesel production, and truck distribution to the main blending facilities listed by the Energy and Mines Ministry. Information regarding pipelines was provided to Volpe so they could initiate runs focused on SAF scenarios. The base cases of the FTOT tool are currently being tested for the HEFA and ATJ technologies in Colombia, Dominican Republic, and Ecuador, respectively.

Publications

Written Report

Martinez-Valencia, L., & Valderrama-Rios, C. (2024). *Sustainable Aviation Fuel Production in Colombia: Opportunities and Challenges*. Washington State University. https://doi.org/https://doi.org/10.7273/000006281

Outreach Efforts

We are working with Volpe to implement a FTOT proof of concept, focusing first on a road-only network. This model maps Colombia's road system, mills, biorefineries, and blending sites for the palm oil biodiesel supply chain.

Continuous meetings with experts and stakeholders in Colombia, the Dominican Republic, and Ecuador have been held to validate the system dynamics models.

- Meeting with Jairo Alfonso Cordero, Consultant, Government of Colombia, June 17, 2025
- Meeting with Juan Japa, Farmer, Sugarcane Industry, Dominican Republic, June 25, 2025
- Meeting with Monica Cuellar, New Business Manager, Fedepalma Colombia, July 1 & August 21, 2025
- Meeting with Carlos León, Manager, APALE Ecuador, July 8 & August 22, 2025
- Meeting with José Nuñez, Consultant, Government of the Dominican Republic, July 3, 2025
- Meeting with Professors, Universidad San Francisco de Quito, Ecuador, August 20, 2025
- Meeting with Rodrigo Gallegos, Executive Director, Aprograsec Ecuador, August 20, 2025
- Meeting with Yessica Castro, Daniel Galván, and Juan Japa, Experts, Government, and Academia, Dominican Republic, August 28, 2025
- Meeting with Jairo Salcedo, External Consultant, BioD Colombia, September 15, 2025

Awards

None.



Student Involvement

Claudia Marcela Valderrama (Colombia) is working on this task. Paulina Echeverria Paredes (Ecuador), Micaela Peralta (Ecuador), and Raul Perez Mena (Dominican Republic) started their graduate studies on January 1, 2024. Rayman Angulo (Costa Rica) started the PhD program in January 2025.

Plans for Next Period

- Continue working with Volpe to refine the base case scenario for the supply chain in Colombia using FTOT, focusing on optimizing the existing biodiesel supply chain, including biodiesel conversion and blending facilities.
- Continue to develop System Dynamics models for the main SAF technologies and use FTOT for each country, which will be used in the analysis of the potential to grow the industry in the different regions.
- Complete a final report for the Dominican Republic and a revised version of the report on the Ecuadorian Overview to be socialized with our stakeholders.

Task 3 - Creating Training Modules, a Course, and Graduate Programs for Training Students

Washington State University

Objective

The objective of this task is to create a year-long training program to introduce the stakeholders to the design of SAF supply chain, as well as a master's program.

Research Approach

Under Task 3, the team created training modules, a course, and graduate programs for the preparation of personnel involved in the design of SAF production supply chains. The training started with students from Latin America. The methodologies and tools developed as part of ASCENT Project 001 that are being used in the design of supply chains in the U.S. are being used to do similar work in Latin America. Our training materials included: (1) methodologies for the creation of waste biomass feedstock databases, geographic information systems (GIS), and facility siting (leaders: Michael Wolcott, Dane Camenzind, and Kristin Lewis); (2) supply chain configurations to capitalize on sale of the fuel commodity and valorizing environmental services (leaders: Lina Martinez, Michael Wolcott, Allyson Beall King); (3) logistics optimization (leaders: Eric Jessup, Dane Camenzind); and (4) SAF production technologies (mass and energy Balances [Aspen], TEA, and LCA) (leaders: Kristin Brandt, Manuel Garcia-Perez, Hanwu Lei). These training materials evolved into courses that will be offered as part of certificates and a master's program currently under review by the WSU faculty senate (Hanwu Lei).

Milestone

- Started work on this task in January 2023 and continued work through 2025.

Major Accomplishments

We made progress in the professional master's program and associated courses. The WSU Department of Biological Systems Engineering submitted the curriculum design for a master's program in sustainable aviation fuel production to the WSU Faculty Senate. To complete this program, students must complete two common classes, seven courses, and a capstone project. The common courses are: Sustainable Aviation Fuels Technology, Feedstock Assessment, and SAF Law, Policies, and Regulations. Students can obtain three certificates that, when combined, result in a master's degree. The first certificate, in SAF production technologies, comprises three courses: Biomass Conversion Technologies, SAF TEA, and Financing and Investment in Renewable Electricity and Hydrogen. The second certificate, in SAF law, policies, and systems view, includes three courses: LCA, Supply Chain Analysis and Optimization, and Systems Dynamics. The final certificate, in SAF fuel qualification, consists of two courses. This will be the first professional master program in the world and will start in September 2026. The first two courses for the master's program have been developed. Students collaborated to prepare the material and information for the SAF 501 Biomass Conversion Technologies and SAF 502 Sustainable Aviation Fuels Technology courses.



Publications
None.

Outreach Efforts
The master's program offer has been socialized with partners in Latin America.

Student Involvement
Claudia Marcela Valderrama, Raul Perez, Paulina Echeverria, Micaela Peralta, and Rayman Angulo were invited to participate in the development of the master's program.

Plans for Next Period
- Hold additional workshops with international organizations to enhance stakeholder engagement in Colombia, the Dominican Republic, Costa Rica, and Ecuador.
- Continue working with the WSU Senate to secure approval for our master's program and to develop new courses, aiming to start in September 2026.



Project 094 Probabilistic Unmanned Aircraft System (UAS) Trajectory and Noise Estimation Tool

Georgia Institute of Technology

Project Lead Investigators

Prof. Dimitri N. Mavris
Director, Aerospace Systems Design Laboratory
School of Aerospace Engineering
Georgia Institute of Technology
Phone: (404) 894-1557
Fax: (404) 894-6596
Email: dimitri.mavris@ae.gatech.edu

Dr. Holger Pfaender
Aerospace Systems Design Laboratory
School of Aerospace Engineering
Georgia Institute of Technology
Phone: (404) 385-2786
Fax: (404) 894-6596
Email: holger.pfaender@ae.gatech.edu

University Participants

Georgia Institute of Technology (Georgia Tech)

- P.I.s: Dr. Dimitri N. Mavris (P.I.), Dr. Holger Pfaender (Co-P.I.)
- FAA Award Number: 13-C-AJFE-GIT-143
- Period of Performance: January 1, 2025, to December 31, 2025
- Tasks:
  1. Investigate and Implement Modeling Improvements
  2. Extend Sources of Uncertainty
  3. Extension to urban air mobility (UAM) operations
  4. Case Study Leveraging Previously Developed Methodologies
  5. Coordination with Federal Aviation Administration (FAA) and Volpe National Transportation Systems Center (Volpe)
  6. Documentation

Project Funding Level

The ASCENT Project 094 is funded by the FAA at the following levels: Georgia Tech ($335,000).

Georgia Tech has agreed to a total of $335,000 in matching funds. This total includes salaries for the project director, research engineers, and graduate research assistants and for computing, financial, and administrative support, including meeting arrangements. Georgia Tech has also agreed to provide tuition remission for students whose tuition is paid via state funds.

Investigation Team

Georgia Institute of Technology

Dimitri N. Mavris (P.I.)
Holger Pfaender (co-P.I.), Tasks 1-6
Raphaël Gautier (research faculty), Tasks 1-6
Jiacheng “Albert” Xie (research faculty), Tasks 1-6



Nada Himdi (graduate student), Tasks 1, 2, and 5
Venkat Sai Chinta (graduate student), Task 1
Zhiyao “Echo” Song (graduate student), Task 3
Kumanan Srinivasan (graduate student), Task 3
Lloyd Teta (graduate student), Tasks 1, 2, and 5
Xi Wang (graduate student), Task 3

Project Overview

Context and Motivation

The unmanned aircraft system (UAS) market is expected to grow rapidly in coming years, with projections estimating the civil UAS market at $121 billion in the next decade. Multiple operators are currently developing and testing various concepts of operations that fall within the umbrella of UAM, with the two main use cases being drone delivery and electric-vertical takeoff and landing (eVTOL) air taxis. Like traditional aircraft operations, these novel concepts are expected to have an impact on the environment in which they operate, particularly regarding noise. Just as noise assessments of traditional commercial and general aviation fixed wing and rotary aircraft operations are completed today, similar noise assessments for UAM operations will be necessary.

Problem Definition

UAM operations bring unique requirements. First, UAM operations are expected to be denser than current general or commercial aviation operations, possibly by orders of magnitude. Thus, a noise assessment method should be able to manage large vehicle densities. Second, UAM vehicles are expected to be smaller and therefore quieter (e.g., small drones for deliveries or helicopter-sized vehicles for eVTOL air taxis, benefiting from novel electric propulsion systems). As a result, the noise footprint of such vehicles is expected to be more localized. Therefore, noise exposure levels should be estimated with sufficient resolution. Third, instead of primarily following fixed trajectories dictated by approach and departure routes around airports, UAM vehicles are expected to operate point-to-point within populated areas. Departure and arrival locations are expected to vary from day to day; delivery drones may depart from warehouses and deliver goods to different customers every day, and eVTOL air taxis may allow their customers to be picked up and dropped off all around an urban area. Thus, a noise assessment method should be flexible enough to accommodate changing flight paths, and the resulting noise assessment should account for the variability introduced by these changes.

Research Objective

The objective of this research is to develop a novel noise estimation method/tool that supports the computation of noise resulting from the stochastic operation of UAS and other upcoming vehicle concepts with irregular locations and operations in large numbers.

Task 1 – Investigate and Implement Modeling Improvements

Georgia Institute of Technology

Objective

The objective of this task is to identify and implement improvements to the noise-modeling workflow that enhance both realism and computational efficiency. The work focuses on examining key components of the current modeling process, including input variability, operational assumptions, and data-handling methods, and introducing refinements that improve the accuracy and robustness of predicted noise exposure. This involves evaluating alternative statistical and computational techniques, streamlining the representation of operational data, and integrating modeling approaches that better capture the spatial and temporal characteristics of UAS and UAM activities. The overall goal is to produce a more efficient and reliable framework capable of generating consistent noise results across a wide range of operational conditions.

Research Approach

This section lays out the developed modeling and simulation framework and briefly discusses each step of the process. Representative results for each step are presented in the section devoted to Task 4, “Case Study Leveraging Previously Developed Methodologies.”



Overview of Modeling and Simulation Framework

The overall workflow, illustrated in Figure 1, consists of four sequential stages that link operational modeling with noise assessment. The first two stages determine where flights may occur and how frequently they are expected, while the remaining stages evaluate their noise impact. In the first stage, feasible paths between staging locations and customers are identified using a path-planning algorithm that accounts for vehicle range, obstacles, and restricted airspace, yielding a set of potential flights with optimized routes. The second stage assigns each identified flight a probability based on spatial variations in demand and the presence of multiple operators. Using input noise source data, the third stage simulates single-event noise by converting planned paths into three-dimensional (3D) trajectories and propagating directional noise at each time step to obtain standard noise metrics. Finally, daily noise metrics are computed by selecting flights according to their assigned probabilities and aggregating their previously computed noise fields within a single day.

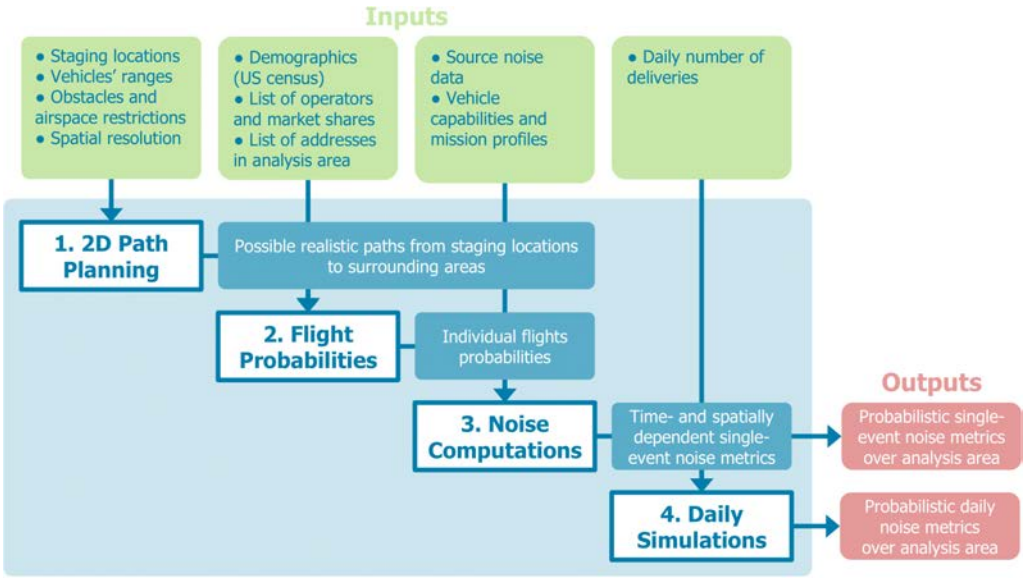


Figure 1. Refined workflow of drone delivery noise assessment.

Flight Path Planning

The first step of the workflow consists of identifying all feasible flights that may occur within the study area, given the locations of staging sites, vehicle range constraints, and the spatial distribution of customers. Straight-line navigation at a fixed altitude is insufficient in dense urban environments, where buildings, restricted airspace, and other obstacles must be avoided. A dedicated path-planning strategy is therefore required to produce realistic routes while maintaining computational efficiency. To balance these considerations, a two-step trajectory-generation process is employed: a two-dimensional track is first computed, and a fixed vertical profile is later applied when forming the full 3D trajectory for noise assessment.

Graph-based methods were identified as suitable due to their deterministic behavior and ease of implementation. The A⋆ algorithm (Hart et al., 1968) yields optimal grid-based paths but often produces pixelated trajectories unless smoothed. Its extension, Theta⋆ (Daniel et al., 2010), provides more realistic paths by allowing straight segments between non-adjacent cells when the line of sight is unobstructed, resulting in minor deviations from optimality that are acceptable for this application. Applying A⋆ or Theta⋆ to every origin–destination pair, however, becomes computationally prohibitive in large urban regions with hundreds of thousands of customer locations.

The adopted approach therefore relies on a modified Dijkstra algorithm (Dijkstra, 1959) augmented with Theta⋆-style line-of-sight checks implemented through a ray-tracing method (Amanatides & Woo, 1987). This formulation makes it possible to compute all reachable paths from each staging location in a single run, terminating once further cells would require exceeding vehicle range. The line-of-sight operation represents the dominant computational cost and is optimized using a Cython implementation. All feasible paths are stored in a database, enabling efficient retrieval of the appropriate two-dimensional track for any customer within range.

Flight Probability Calculation

Once all feasible flights and their corresponding paths are identified, the next step is to assign a probability to each of them so that the variability of drone delivery operations can be represented probabilistically. This requires estimating how likely each address is to place an order and then distributing this probability across the flights that can serve it.

Demand is treated in relative terms in order to capture how the likelihood of placing an order varies geographically. Since no dedicated drone-delivery demand model is available, the probability of online shopping is used as a proxy (Aller & Pahwa, 2020). The modeled shopping behavior using the multinomial logit formulation:

$$p(k|X) = \frac{e^{\beta_k X}}{1+\sum_{i=1}^{4} e^{\beta_i X}} \quad \text{(Eq. 1)}$$

where X represents demographic characteristics and k indexes four shopping categories: no shopping (k = 1), in-store shopping only (k = 2), online shopping only (k = 3), and both in-store and online shopping (k = 4). The probability of placing an online order is obtained by summing the two categories that involve online purchasing. Census demographic histograms are then used to aggregate these individual probabilities at the census-tract level:

$$p(o|a \in A_t) = \sum_{X \in C_t} \big(p(k=3|X) + p(k=4|X)\big) \times p(X) \quad \text{(Eq. 2)}$$

All addresses within tract t are assigned this same value. The resulting tract-level probabilities are normalized across all tracts so that the per-address probabilities sum to one:

$$p(a|o, a \in A_t) = \frac{p(o|a \in A_t)}{\sum_{\tau \in T} p(o|a \in A_\tau) \times \#(A_\tau)} \quad \text{(Eq. 3)}$$

After determining the order probability for each address, this value is subdivided among the flights capable of reaching the destination. If several operators can serve the address, the probability is divided among them using user-provided market shares, renormalized to include only operators with feasible paths. For a given operator, its share is further split among staging locations within range. A user-defined fraction is assigned to the closest staging location, and the remainder is evenly divided among the others.

The probability of an individual flight is the product of the address-level probability and the operator and staging-location components along its corresponding branch in the decomposition shown in Figure 2.

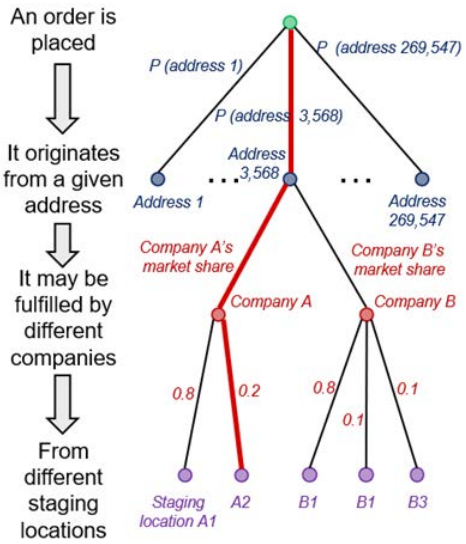


Figure 2. Tree diagram summarizing the process used to determine individual flights' probabilities.

Single-Event Simulation

1. Noise Propagation Model

The noise associated with each flight is evaluated using a propagation model consistent with the Society of Automotive Engineers' (SAE) ARP5534 standard (SAE, 2013). The 3D trajectory is first discretized in time, and the position of the vehicle at each timestep is mapped onto a rectilinear grid of virtual receivers covering the study area. A pre-processing procedure determines the maximum distance beyond which the propagated sound level is negligible. This allows the model to restrict computations to receivers located within the range of acoustic relevance.

At every timestep, the distance and 3D emission angles between the vehicle and each relevant receiver are calculated. These angles determine which element of the vehicle's directional noise sphere is selected for that position in the trajectory. The selected spectrum is propagated to the receiver on a frequency-band basis following the procedures defined in ARP5534, and the resulting band levels are combined using A-weighting to produce instantaneous sound pressure levels. The independence of individual flights enables the noise-propagation calculations to be executed in parallel.

2. UAS Noise Source Modeling

The noise source sphere is a required input for noise propagation using the ASCENT Project 094 tool. Previously, the tool utilized a single noise source sphere on all flight phases and flight conditions. This is not realistic for the drone delivery application which is sensitive to varying flight conditions.

In the following, we discuss the generation of four distinct noise source sphere data for different (a) flight phases, (b) weights, (c) speeds, and (d) altitudes.

The four considered flight phases are hover, takeoff, cruise, and landing. The altitude was categorized as low (~35 ft above ground level [AGL]), medium (~90 ft AGL), and high (200 ft AGL). For the weight, the maximum and empty weights are respectively considered to represent the drone with and without the payload.

Generating noise source data for UAS relies on three analysis tools. The first two are from Volpe: (1) the Advanced Acoustics Model (AAM) and (2) the Acoustic Repropagation Technique (ART). The third is an in-house sound sphere post-processing tool. The noise-sphere generation process is described thereafter.

Atmospheric conditions, microphone locations, and flight trajectories used in the Causey Airport measurements are first input into AAM. Using time- and geometric-based analyses, AAM calculates the propagation physics and geometric relationship between the noise source (UAS aircraft) and microphones. AAM then outputs a time-history file that includes the mapped relationship on a sphere for each trajectory point.

ART uses microphone measurement data, aircraft specifications, and the time-history file generated by AAM as inputs to generate the vehicle's noise source data. This noise sphere is obtained by applying the propagation corrections from AAM to the measured microphone spectral time histories. These histories are then mapped into a 3D spectral source description, stored as a NetCDF file. Figure 3 illustrates an example of a generated noise sphere visualized in Tecplot.®

® Tecplot is a registered trademark of Tecplot, Inc., Bellevue, Washington.

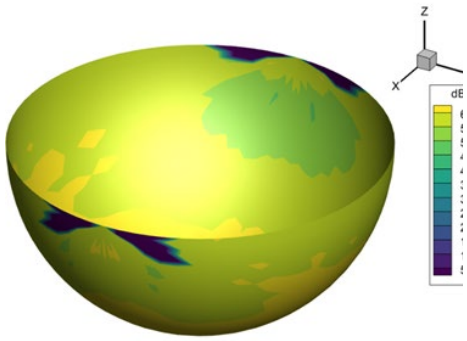


Figure 3. Example of a generated noise sphere.

3. Output Of Noise Propagation

The propagation model yields, for each flight, a time series of A-weighted sound levels at all receivers located within the propagation radius. These time histories reflect the directional source noise selected at each time step based on the vehicle's position, attitude, and flight phase. Integrating the received levels over the duration of the trajectory produces standard single-event noise metrics such as $L_{A,eq}$ and $L_{A,max}$. The complete set of receiver values forms the spatial noise footprint associated with that flight.

Probability-weighted results may also be constructed at the single-event level by combining the noise output of each flight with its previously computed flight probability. This enables the formation of probability distributions for single-event noise metrics across all feasible flights. These distributions characterize the variability in noise outcomes resulting from differences in routing, receiver geometry, and operational demand patterns.

Daily Simulation

The daily simulation models all delivery flights within a day to assess the overall noise exposure. Daily simulations are carried out by sampling flights according to their probability distribution. The total number of flights happening within a day is a user input, such that studies can be carried out for different envisioned daily volumes. Flights are then distributed within the day, and the results of the noise propagation step are leveraged, now accounting for the fact that the noise of multiple flights may be perceived by a virtual receiver at any given time step. The noise sources associated with the different vehicles are assumed to be uncorrelated, such that their noise energy can be summed. Alternate noise metrics, such as the day-night average sound level (DNL), can be computed from the outcome of daily simulations. The daily simulation is further discussed in additional detail in the section devoted to Task 2, "Extend Sources of Uncertainty."

Milestones

- Completed the workflow for path generation, flight-probability assignment, and single-event noise propagation.
- Integrated phase-specific noise spheres and ARP5534-based propagation into the ASCENT Project 094 tool.
- Validated distance/angle calculations and noise-sphere interpolation against AAM outputs.

Major Accomplishments

- Generated realistic obstacle-avoiding paths and assigned probabilities to all feasible flights.
- Implemented single-event noise simulation using directional noise spheres.
- Refined the model by adding reflected sound and adjusting propagation timing to improve agreement with AAM.

Plans for Next Period

- Introduce a step that precomputes noise for each flight phase and reuses it across time steps.
- Replace per-step propagation with fast lookups to reduce database size and improve runtime.



References

Aller, M., & Pahwa, A. (2020). Evaluating the environmental impacts of online shopping: A behavioral and transportation approach. *Transportation Research Part D: Transport and Environment, 80*. https://doi.org/10.1016/j.trd.2020.102223

Amanatides, J., & Woo, A. (1987). A fast voxel traversal algorithm for ray tracing. *Eurographics*, 3–10. https://doi.org/10.2312/EGTP.19871000

Center, V. (2020). *Advanced Acoustic Model (AAM) Technical Reference and User's Guide.* U.S. Department of Transportation.

Committee, A. R. (2024). *Census Data Manifest 2019–2023*. Atlanta Regional Commission. https://opendata.atlantaregional.com/pages/census-data-arc

Community, T. S. (2019). *scipy.spatial.distance.cdist — Reference Guide*. SciPy.org. https://docs.scipy.org/doc//scipy-1.3.2/reference/generated/scipy.spatial.distance.cdist.html

Community, T. S. (2023). *scipy.interpolate.interp1d — Manual*. SciPy.org. https://docs.scipy.org/doc/scipy/reference/generated/scipy.interpolate.interp1d.html

Daniel, K., Nash, A., Koenig, S., & Felner, A. (2010). Theta*: Any-angle path planning on grids. *Journal of Artificial Intelligence Research, 39*(1), 533–579.

Developers, S.-L. (2023). *Linear Models — User Guide*. Scikit Learn. https://scikit-learn.org/stable/modules/linear_model.html

Developers, S.-L. (2023). *Neural Network Models (Supervised) — User Guide*. Scikit Learn. https://scikit-learn.org/stable/modules/neural_networks_supervised.html

Dijkstra, E. W. (1959). A note on two problems in connexion with graphs. *Numerische Mathematik*, 1, 269–271. https://doi.org/10.1007/BF01386390

Hart, P. E., Nilsson, N. J., & Raphael, B. (1968). A formal basis for the heuristic determination of minimum cost paths. *IEEE Transactions on Systems Science and Cybernetics, 4*(2). https://doi.org/10.1109/TSSC.1968.300136

Heutschi, K., Ott, B., Nussbaumer, T., & Wellig, P. (2021). Virtual microphone signals of flying drones. *NATO STO MSG-SET-183 Specialists' Meeting on Drone Detectability* (pp. 27–29).

Hofferth, S., Flood, S. M., & Sobek, M. (2017). *American Time Use Survey Data Extract System: Version 2.6*. University of Maryland / University of Minnesota.

Jha, A. a. (2022). Urban Air Mobility: A preliminary case study for Chicago and Atlanta. *2022 IEEE/AIAA Transportation Electrification Conference and Electric Aircraft Technologies Symposium (ITEC+EATS)*, (pp. 300-306).

SAE. (2013). *Application of Pure-Tone Atmospheric Absorption Losses to One-Third Octave-Band Data (ARP5534).* SAE International.

Task 2 – Extend Sources of Uncertainty

Georgia Institute of Technology

Objectives

The objective of this task is to quantify uncertainty in the cumulative daily UAS noise exposure by incorporating variability in flight selection, scheduling, and service times. Current methods often analyze single flight events in isolation, which fails to capture the realistic noise environment where a receiver experiences multiple, overlapping events. Therefore, this research aims to develop a Monte Carlo simulation framework that models a full day of operations to produce probabilistic noise metrics, rather than deterministic point estimates.

Research Approach

During a typical day, a receiver location experiences multiple flight events due to outbounds and inbounds flight, potentially from different drones serving various customers and from different warehouses. To quantify the cumulative noise exposure from these concurrent events, a daily simulation model is required. This step utilizes the precomputed results from the previous stages: (1) a list of all possible flights identified, (2) their corresponding probability of occurrence for each path, and (3) the pre-computed time-series sound pressure level (SPL) noise footprints for every flight at every receiver. The overall daily simulation process is illustrated in Figure 4.

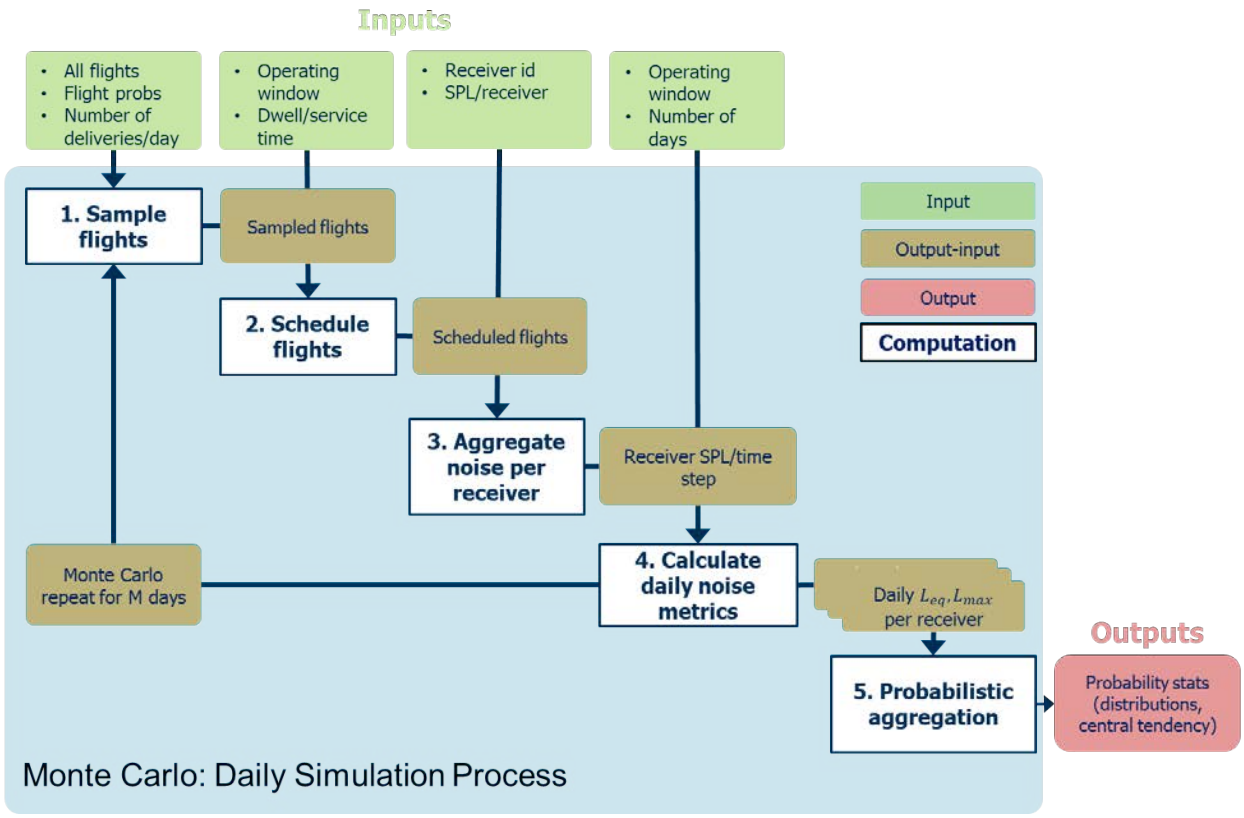


Figure 4. Implementation of the daily simulation process.

Single Day Simulation

The simulation process begins with the definition of the total number of flights occurring within a day, denoted as N. This parameter provides flexibility to analyze different daily operational volume scenarios. The computation of daily metrics follows a four-step process:

1. **Sample Flights:** The simulation samples N flights from the list of all possible paths. This sampling is weighted by each path's probability of occurrence. The draw is performed randomly with replacement to ensure that each sampled flight is independent and retains its original probability. The random sampling with replacement portrays the real world, demand driven characteristic of drone delivery operations where high-demand (high-probability) flight paths are likely to be used multiple times per day. That means high probability flights are likely to be sampled more than low probability flights.
2. **Schedule Flights:** Each of the N sampled flights is assigned a random departure time. These times are drawn from a uniform distribution over the defined operational window for the day, e.g., 8:00 a.m. to 10:00 p.m.
3. **Aggregate Noise:** Instead of recalculating noise propagation, the simulation leverages the pre-computed SPL time-series data. For a given receiver, the process accounts for the fact that noise from multiple flights may be perceived at any given time step. It offsets the SPL time-history of each sampled flight according to its random departure time. When flight events concurrently impact a specific receiver, the simulation aggregates the **acoustic energies** (a linear quantity) over the duration of the day to build a total, cumulative time-history of the noise footprint.
4. **Calculate Metrics:** From this aggregated daily time-history, the simulation calculates the primary daily noise metrics. These include (1) Maximum A-weighted Sound level, ($L_{max,day}$) which is the highest sound pressure level experienced at a particular time during the day and (2) Equivalent Continuous Sound Level ($L_{eq,day}$), which is the average exposure over operational window. Alternate metrics, such as DNL, time above threshold (TAT) can be computed from the outcome of daily simulations. This capability enables the exploration of metrics beyond peak loudness because a persistent drone presence may be more disturbing than a single loud flyover.



Monte Carlo Simulation

The daily simulation process described above is inherently stochastic. The output metrics $L_{max,day}$ and $L_{eq,day}$ are not fixed, deterministic values. They are the result of a system governed by random variables. There are two primary sources of this operational uncertainty:

1. **Path Selection Uncertainty:** It is unknown *which* of the thousands of possible flight paths will be used at any given time. The simulation models this by sampling flights based on their probability, to reflect day-to-day variability in customer demand.
2. **Scheduling Uncertainty:** It is unknown *when* each of those N flights will occur. The simulation models this by assigning random departure times within the operational window to mimic the unpredictable timing of individual orders.

The combination of these two factors creates a third, emergent source of uncertainty: *concurrency uncertainty*. On one simulated day, multiple flights may, by chance, have start times that cause their noise to overlap at a single receiver, leading to a high $L_{max,day}$. On another simulated day, those same flights might be spaced far apart, resulting in a lower $L_{max,day}$. Because the output is dependent on these random interactions, it is not possible to calculate a single, "correct" answer. The goal is to understand the *full range* of possible outcomes and their likelihood. This requires a method designed to solve problems using random sampling.

To address this stochastic system, this research employs the Monte Carlo simulation method. A Monte Carlo simulation is a computational technique that relies on repeated random sampling to obtain numerical results (Kissell, 2021). It is an ideal method for analyzing a complex system, like this one, where the interactions of random variables are too complex to be modeled by a simple equation. In this context, the four-step daily simulation process (sample, schedule, aggregate, calculate) is treated as a single "experiment" or "trial." The Monte Carlo simulation framework repeats this experiment M times, where M is a large, user-defined number of days. For each of the M iterations, a new set of N flights is sampled and a new set of random departure times are assigned. This mimics a new, unique, and plausible operational day of drone delivery.

Probabilistic Output

The final output of this M day simulation is a *probability distribution* for the daily noise metrics at each receiver. The simulation generates a list of M different $L_{max,day}$ and $L_{eq,day}$ values. The day-to-day variation of the daily metrics can be visualized as a histogram (an example is given in Figure 14 as part of the discussion of the notional results obtained for the Atlanta case study) and analyzed statistically to determine:

- The *mean* (the expected average exposure)
- The *median* (the 50th percentile, or "typical" day)
- The *95th percentile* (a "high noise" day, often used for policy and community impact assessment)

Milestones

- Completed initial implementation of the Monte Carlo simulation framework for daily noise analysis.
- Integrated pre-computed noise footprints (from Step 3) and flight probabilities (from Step 2) into the daily simulation environment.

Major Accomplishments

- Integrated flight sampling, random scheduling, and SPL aggregation into a repeatable simulation loop.
- Executed a preliminary large-scale test simulating 1000 operational days with 1,000 daily sampled flights per day.

Publications

None.

Outreach Efforts

None.

Awards

None.



Student Involvement
None.

Plans for Next Period
- Refine flight scheduling logic: Incorporate return flight and service/dwell times to increase operational realism.
- Improve computational efficiency through lookup SPL table caching and heading quantization to allow for large-scale simulations.
- Extend analysis from single point receivers to area wide spatial metrics (e.g., contour mapping) and new exposure metrics (e.g., time above threshold)

References
Kissell, R. L. (2021). Chapter 8 - Nonlinear Regression Models. In *Algorithmic Trading Methods* (2nd ed., pp. 197–219). Academic Press.

Task 3 – Extension to UAM Operations
Georgia Institute of Technology

Objectives
The objective of this task is to extend the current methodology to UAM operations. The preliminary phase is focused on defining a representative use case, specifically addressing the selection of a suitable location, identifying airspace constraints and the concept of operations.

Research Approach
Concept of Operation
UAM is rapidly transitioning from a futuristic concept to a near-term reality, propelled by technological advancements. Commercial UAM initiatives, ranging from conceptual design to full-scale flight-testing and active pursuit of regulatory certification, are maturing quickly. Companies have announced commercial plans for air taxi services on high-demand metropolitan routes (e.g., city centers to airports). Specifically, Archer Aviation plans airport shuttles and air mobility networks in the San Francisco Bay Area, Los Angeles, and New York. Wisk Aero® is targeting Houston, Los Angeles, and Miami. Joby Aviation® has announced plans for Los Angeles and New York.

On the academic side, many studies have been conducted to analyze UAM feasibility. A preliminary feasibility study for urban air mobility services in Chicago and Atlanta, by integrating eVTOL aircraft performance models (like the Joby® S4 and Lilium 7-seater) with a derived travel demand model based on commuter survey data was conducted (Jha, 2022). The analysis compares a potential UAM service against ground transportation, emphasizing that the viability and success of UAM hinges on meeting this projected travel demand by overcoming technical constraints, developing a necessary network of specialized infrastructure (vertiports), and achieving community acceptance to realize projected travel time reductions.

A study of the placement of UAM vertiports accounting for land use planning in the San Francisco Bay Area has also been conducted (Wei et al., 2023). It focuses on case studies in urban San Francisco, suburban San Jose, and exurban Livermore. The study establishes a systematic framework for vertiport site selection using a geographic information systems (GIS) suitability analysis. The core methodology employs a set of stakeholder-informed parameters categorized by safety, access, and equity, which are prioritized differently across the distinct geographic settings to determine site suitability. The goal is to provide planners with a replicable, cost-effective approach to identify suitable parcels and offer recommendations to integrate UAM network planning and land use regulations.

An analysis of optimal infrastructure placement for UAM air taxi services in New York City was conducted using a three-phased, data-driven approach (Senthilnathan et al., 2025). The research first uses the Clustering LARge Applications (CLARA) algorithm to identify a set of candidate vertiport and vertistop locations. Subsequently, an integrated genetic algorithm (GA)-simulation model is employed to select the most strategic final locations based on key operational metrics.

® Wisk Aero is a registered trademark of Wisk Aero, LLC, Mountain View, California.
® Joby and Joby Aviation are registered trademarks of Joby Aero, Inc., Santa Cruz, California.



These metrics prioritize factors such as minimizing rental cost, maximizing population coverage, ensuring favorable road facility access, and optimizing routing performance measures like customer waiting time, with the overarching goal of minimizing overall customer travel time within the air taxi system.

In addition to academic studies and industrial initiatives, work has also been done on the regulatory side. In the FAA's UAM Concept of Operations (Fontaine, 2023), a "crawl-walk-run" approach is outlined to operational maturation based on increasing tempo and complexity.

- Crawl Phase (Initial): New certified aircraft will operate under current regulatory frameworks and existing air traffic services (ATS) and routes, with the pilot in command onboard.
- Walk Phase (Intermediate): New regulations will accommodate a higher operational tempo, introducing UAM corridors that may not require traditional air traffic controller services, and allowing for preliminary remote pilot in command operations.
- Run Phase (Mature/Future): This high-tempo phase envisions new operational rules, a complex network of UAM corridors, and highly automated aircraft operating in a cooperative service environment called "extensible traffic management" (xTM).

The FAA's Advanced Air Mobility Implementation Plan targets achieving integrated AAM operations in the United States by 2028. Initial operations in the "crawl" phase are expected to be piloted and operated under the existing regulatory environment. Aircraft will fly under visual flight rules (VFR) using existing VFR constructs or specific chartered routes. Air traffic control (ATC) will provide services as needed, and operations will primarily use existing, modified airports and heliports.

Use Case Selection

To establish a consistent foundation for UAM demand modeling and vertiport network development, a comprehensive literature review was conducted across existing metropolitan use cases in New York, Chicago, Atlanta, and the San Francisco Bay Area. These prior studies provide insight into how bounding boxes are defined, how vertiport sites are selected, what vehicle types are assumed, and what methodological frameworks are used for demand estimation and infrastructure planning.

Based on the comparative assessment of these studies and considering regional airspace complexity, multimodal connectivity, zoning constraints, and the availability of high-quality operational data, the San Francisco Bay Area is selected as a representative use case due to its unique combination of dense urban development, complex airspace structure, and strong regional demand for high-capacity mobility solutions (see Table 1).



Table 1. Comparison of preceding studies on urban air mobility (UAM) network design for use case selection. ACS: American Community Survey, CLARA: Clustering LARge Applications, eVTOL: electric vertical take-off and landing, GIS: geographic information system, LODES: LEHD Origin-Destination Employment Statistics

City	Bounding area	Objective	Vertiport Selection	Vehicle Type	Technical Approach	Methodology Used
New York (NY)	Varied (high-density clusters)	Demand estimated using NY city taxi trip data, requiring ≥40% travel-time saving	Population density, access to transport, rental cost	Joby S4, Archer Midnight	Piloted eVTOL, high-density vertiport integration	CLARA Clustering, Genetic Algorithm (GA)
Chicago	50 mi × 50 mi	Derived from commute-time and congestion models using ACS LODES data	Commute time, income-based demand	Archer Midnight	Piloted eVTOL, infrastructure adaptation to helipads	GIS-based demand modeling, commute-time optimization
Atlanta	30 mi × 30 mi	Same as Chicago	Commute time, income-based demand	Joby S4, Wisk Cora	Mixed piloted + autonomous eVTOL models	GIS-based demand modeling, commute-time optimization
San Francisco (SF)	SF Bay Area	Multi-modal integration focusing on zoning and accessibility to transit	Land availability, zoning laws, demand clusters	Wisk Cora, Joby S4	Focus on autonomy (Wisk) and piloted ops (Joby)	GIS for vertiport site selection

Airspace Constraints

The San Francisco Bay Area contains one of the most complex and highly constrained terminal airspace environments in the United States. The region is shaped by the overlapping controlled airspace associated with San Francisco International Airport (KSFO), Oakland International Airport (KOAK), San Jose International Airport (KSJC), and numerous surrounding general-aviation airports. The KSFO Class B airspace imposes the highest level of control, requiring explicit ATC clearance and strict compliance with published transition instructions. The Class C airspace surrounding KOAK and KSJC requires two-way radio communication and transponder to always use. Although some outer segments may allow limited maneuvering, transitions generally follow established VFR procedures and ATC instructions. Several Class D airports, including Hayward (KHWD), Palo Alto (KPAO), and Reid-Hillview (KRHV), add additional altitude limits and localized traffic-pattern constraints. For modeling simplicity in this study, Class D regions are treated as uncontrolled airspace areas.

Guidance from the FAA's AAM Implementation Plan indicates that near-term eVTOL operations should rely on existing VFR and helicopter routes, while dedicated AAM corridors and special flight procedures are expected to emerge later. As a result, identifying workable transition procedures through Class B and Class C structures is a necessary step before generating feasible eVTOL flight paths. These airspace constraints directly affect allowable routing, transition altitudes, and the width of operational corridors throughout the Bay Area case study.

Transition procedures in the San Francisco Bay Area are derived by combining published VFR helicopter routes with data-driven analyses of historical flight-track patterns. Controlled airspaces around KSFO (Class B), KOAK (Class C), and KSJC (Class C) impose distinct altitude and lateral constraints that shape the feasible corridors for eVTOL operations. To identify representative transition paths, more than 40,000 piston-aircraft and helicopter tracks between 500 and 4000 ft mean sea level were clustered using the HDBSCAN algorithm (Campello et al., 2013). HDBSCAN is a clustering algorithm that identifies and separates groups of points or trajectories based on density, grouping flight paths where they naturally



concentrate and treating scattered or infrequent tracks as noise. Unlike parametric methods like K-Means, HDBSCAN identifies clusters without requiring a pre-specified number of groups. HDBSCAN improves traditional density-based methods by organizing data into a hierarchical structure, extracting clusters based on their stability over varying distance thresholds. All these features enable it to adapt to local variations in traffic density and capture clusters of arbitrary shape, making it effective for identifying the complex flight-track patterns found in congested airspace. Departure and arrival of trajectories were removed to isolate lateral transit behavior within each terminal area.

For the KSFO Class B inner circle, clustering reveals two primary transition patterns: (1) a San Francisco Bay Shore routing that follows the US-101 corridor and maintains separation from the 1,500–4,000 ft protected sectors and (2) a Pacific transition that remains offshore and merges eastbound near the coastline. In the KOAK Class C airspace, an outer "free fly" region exists north of the Bay Bridge below 3,000 ft, while the inner circle exhibits well-defined transitions, including the Coliseum routing and a Runway 30 parallel segment used to maintain lateral separation from airport operations.

Within the KSJC Class C inner circle, clustered tracks show a consistent mid-field crossing at approximately 2,000 ft and a fan-shaped set of pathways bounded by VPEMB, VPRPU, US-101, and I-680. These corridors aligned with helicopter practices and were further validated through consultations with local flight instructors. The resulting transition procedures provide structured, altitude-aware guidance for routing eVTOL trajectories through each controlled airspace while respecting existing ATC practices.

Validation against Aviation Environmental Design Tool

The objective of this subtask is to validate the in-house noise analysis tool (ASCENT Project 094 approach) using a National Aeronautics and Space Administration (NASA) UAM study conducted using the Aviation Environmental Design Tool (AEDT) (Rizzi & Rafaelof, 2023). Given the unique operational and acoustic characteristics of UAM vehicles, the study aims to overcome limitations in existing AEDT frameworks by generating noise-power-distance (NPD) data based on advanced simulation tools like NASA's Aircraft Noise Prediction Program (ANOPP2). The research focuses on segmenting point-to-point UAM operations into distinct departure, overflight, and approach phases, comparing noise exposure levels for fixed-wing, helicopter, and hybrid modeling approaches. The input data provided by the NASA UAM study group, along with the data generated by the AEDT, are utilized to replicate the study within the ASCENT Project 094 tool. This implementation serves as a critical component of the validation study, ensuring consistency and accuracy in noise modeling methodologies.

The validation process comprises two primary steps. The first step involves replicating the NASA UAM study within the AEDT, utilizing the input data provided by the NASA acoustics team. The output generated by the AEDT plays a crucial role in the second step of the validation process. In this step, the NASA UAM study is implemented within the ASCENT Project 094 tool, leveraging both the input data from NASA and the processed data from the AEDT. This phase requires extensive parsing and integration of multiple data files into the ASCENT Project 094 environment to ensure accurate and reliable implementation.

The discrepancies between AEDT and ASCENT Project 094 stem primarily from the fundamental differences in their noise modeling approaches, namely, AEDT's use of NPD curves versus ASCENT Project 094's use of noise spheres. Earlier observations from debug studies highlighted that AEDT's noise decay model behaves differently, particularly due to its method of computing slant range using the perpendicular distance from the closest point of approach. In contrast, ASCNET Project 094 applies the inverse square law, using the Euclidean distance between the source and the receiver at each time step. Further analyses revealed that AEDT's noise fraction adjustment introduces variability in the segment-wise contributions to the event-level sound exposure level (SEL). This adjustment was found to be highly sensitive to segment length, contributing to the uneven distribution of acoustic energy across the trajectory. Further differences arise from the treatment of source directivity: the AEDT uses lateral interpolation and extrapolation based on fixed azimuthal angles, producing broader, more diffuse contours, while ASCENT Project 094's full directivity model yields sharper, more localized noise regions. Across all analyses, a consistent trend was observed: ASCENT Project 094 tends to overpredict in takeoff and landing zones, while underpredicting during level flyover. However, the majority of undertrack deviations remain within 2–3 dBA, suggesting a reasonable level of agreement between the two tools under cruise conditions.

Milestones

- Conducted comprehensive review of academic literature and industrial plans regarding UAM deployment.
- Down selected the use case as the eVTOL transportation at the San Francisco Bay Area.



- Identified potential vertiport sites at the San Francisco Bay Area based on existing airports and preceding GIS-based UAM flight demand studies.
- Applied clustering algorithms to extract representative transition corridors from flight track data.
- Generated Origin-Destination pairs using performance-based mission-range criteria, producing a realistic set of eVTOL mission candidates.
- Formulated integrated obstacle zones, altitude bands, and transition areas for use in path-planning simulations.
- Implemented the NASA UAM case study within the ASCENT Project 094 tool, incorporating the input data, provided noise spheres and performance data reproduced from the original NASA acoustics study.
- Identified and analyzed discrepancies between ASCENT Project 094 and the AEDT, using diagnostic reports and detailed debug procedures to isolate sources of deviation between the two models.
- Performed an in-depth comparative assessment of the AEDT and ASCENT Project 094 noise propagation methodologies, outlining the key conceptual and computational differences that drive variation in their predictions.

Major Accomplishments

- Demonstrated a data-driven methodology for extracting operationally feasible transition paths from real flight-track data within constrained Class B and C airspaces.
- Integrated geometric airspace structures, local operating practices, and historical behavior into a unified transition-modeling framework.
- Established a reproducible workflow for mapping eVTOL routes that respect FAA-defined airspace layers and locally validated transition behaviors.
- Implemented and validated the NASA UAM case study within the ASCENT Project 094 tool.
- Completed a comprehensive diagnostic and comparative assessment of ASCENT Project 094 and the AEDT, identifying and examining the key sources of deviation.

Publications

None.

Outreach Efforts

None.

Awards

None.

Student Involvement

None.

Plans for Next Period

- Implement path planning algorithm to generate trajectories for use case study.
- Generate UAM travel demand for the designated study area.
- Generate altitude profiles and 3D trajectories for representative missions.
- Begin integration of noise-prediction workflows using trajectory outputs.
- Enhance the noise modeling capabilities in the ASCENT Project 094, with a particular focus on improving reflection and ground impedance modeling.

References

Wei, W., Rohrmeier, K., Martinez, T., Winans, M., & Park, H. (2023). *Land Use Analysis on Vertiports Based on a Case Study of the San Francisco Bay Area* (No. 23-13). San Jose State University. College of Business. Mineta Transportation Institute.

Senthilnathan, V. P., Singaravelu, M., Rajendran, S., & Srinivas, S. (2025). A clustering-metaheuristic-simulation approach to determine air taxi operating site location. *Transportation Research Interdisciplinary Perspectives*, 29, 101330.

Fontaine, P. (2023). Urban air mobility (UAM) concept of operations. Federal Aviation Administration, 800.

Campello, R. J., Moulavi, D., & Sander, J. (2013, April). Density-based clustering based on hierarchical density estimates. In *Pacific-Asia conference on knowledge discovery and data mining* (pp. 160-172). Berlin, Heidelberg: Springer Berlin Heidelberg.

Jha, A. a. (2022). Urban Air Mobility: A preliminary case study for Chicago and Atlanta. *2022 IEEE/AIAA Transportation Electrification Conference and Electric Aircraft Technologies Symposium (ITEC+EATS)*, (pp. 300-306).

Rizzi, S. A., & Rafaelof, M. (2023). On the modeling of UAM aircraft community noise in AEDT helicopter mode. *AIAA Aviation 2023 Forum.*

Task 4 – Case Study Leveraging Previously Developed Methodologies

Georgia Institute of Technology

Objectives

The Atlanta drone-delivery use case is introduced to illustrate the methodology developed in Task 1. This notional scenario provides a realistic urban context in which staging locations, customer addresses, and operational constraints are defined, allowing the full workflow—trajectory generation, demand-based probability estimation, and noise propagation setup—to be demonstrated on a representative environment. The results shown in the following sections reflect the application of this methodology to this specific test case.

Research Approach

Grid Definition

The notional setup is shown in Figure 5, where six staging locations are distributed between two operators (displayed in red and purple). The shaded discs represent nominal vehicle ranges of 5 km and 10 km. These discs provide only an approximate visualization of feasible operations, since obstacle avoidance is not yet considered and the true reachable areas will be smaller. The study area is defined as the union of these discs, expanded by a buffer chosen so that noise propagation is evaluated out to the distance where the maximum source level drops below a threshold of 30 dBA.

Once the study area is defined, residential addresses located within its boundaries are loaded, as illustrated in Figure 6. These addresses form the potential delivery destinations corresponding to the staging locations in Figure 6. The address distribution is non-uniform, and some regions contain few or no identifiable homes. This reflects limitations in the availability of public address data; because residential address lists are not openly released, data were manually collected through county offices. The spatial variability in address density influences the distribution of feasible flights and the resulting noise metrics.

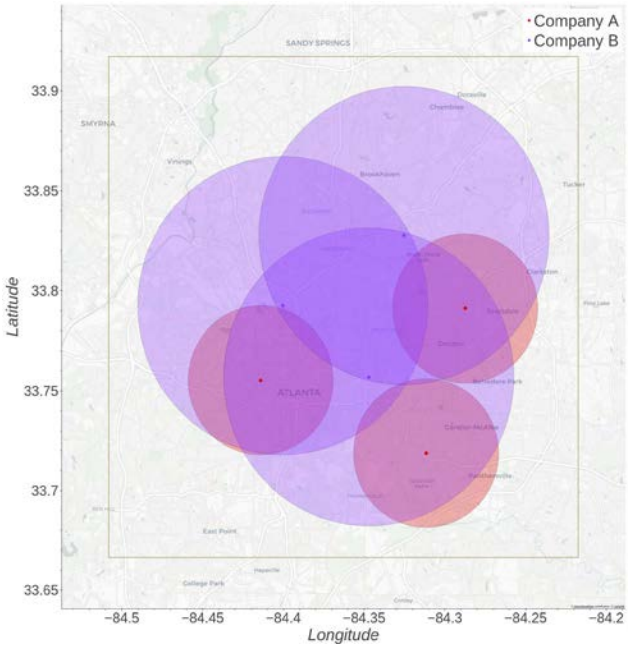


Figure 5. Map of the notional Atlanta use case showing six staging locations (red and purple).

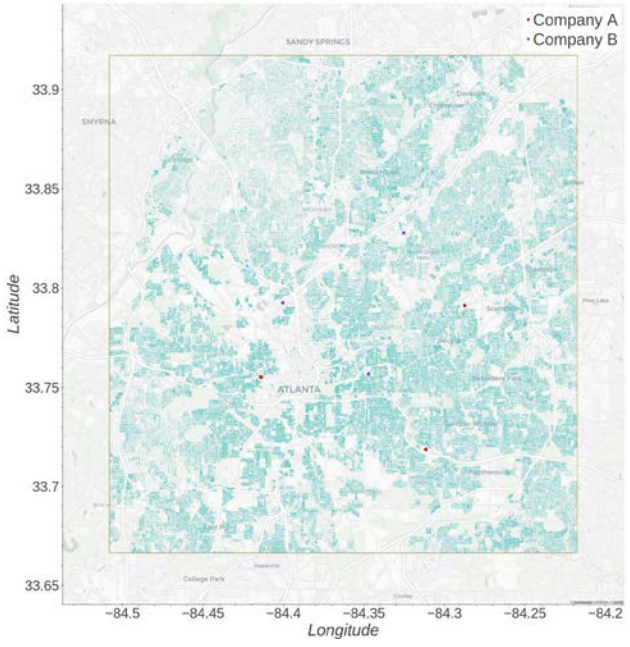


Figure 6. Scatter plot of the addresses loaded for the notional Atlanta use case.

Two-dimensional Flight Path Generation

The first stage generates paths between each staging location and the set of addresses while accounting for local obstacles. Two types of obstacles are included in this use case: (1) city parks, which some operators avoid, and (2) structures listed in the FAA obstacles database. These areas are rasterized onto the planning grid and treated as no-fly



regions. A subset of the resulting two-dimensional (2D) paths is shown in Figure 7, using colors corresponding to each operator. Only a limited sample of paths is displayed for clarity, as the full dataset includes roughly 300,000 destinations. Parks and FAA obstacles appear in green and dark blue, respectively, and the planned trajectories avoid both types of restricted areas. The modified Dijkstra-based routing method used here produces piecewise straight paths whenever unobstructed line-of-sight exists and remains computationally efficient. For example, computing all reachable paths for a single staging location with a 10 km range and a 50 ft grid resolution (about 430,000 cells) requires approximately 90 seconds on a laptop equipped with an Intel® Core i7-1370P processor. All computed paths are stored as waypoint sequences for use in subsequent steps.

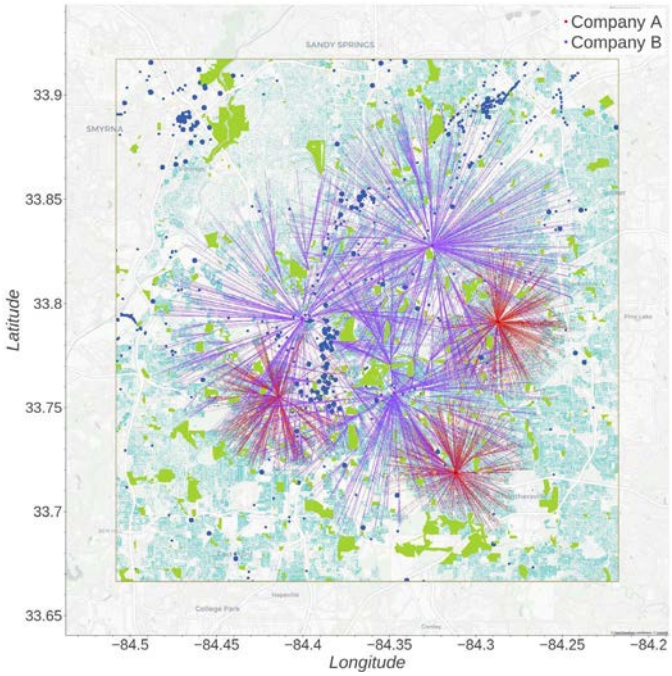


Figure 7. Subset of 2D tracks from the six staging locations to nearby customer addresses.

Flight Probability Calculation

After all feasible flights have been generated, the next step is to assign a probability to each flight. This is achieved by combining a spatial demand estimate with the operational reachability derived earlier. The address-level demand probabilities are shown in Figure 8, where each point is colored according to its estimated likelihood of placing an online order within a day. Since Census demographic information is defined at the tract level, all addresses within the same tract share the same probability value, producing the clearly delineated colored regions visible in Figure 8. These values are used only in a relative sense within the overall probability calculation.

Figure 9 highlights how many operators and staging locations can reach each address. Some addresses are served by only one staging location, while others fall within overlapping operational regions of one or more operators. These patterns reinforce the need for the hierarchical probability decomposition previously described, ensuring that the final flight probabilities reflect both demand distribution and operational accessibility.

® Intel is a registered trademark of the Intel Corporation, Santa Clara, California.

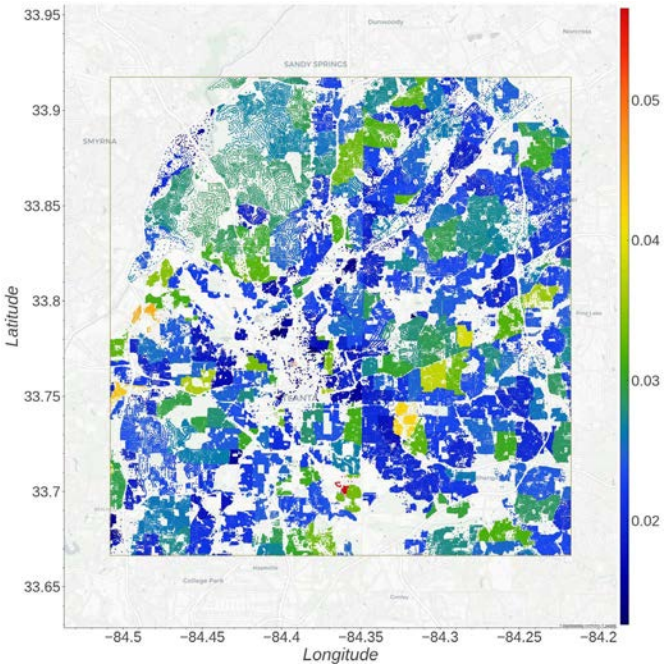


Figure 8. Scatter plot of addresses colored by daily order probability (lowest probabilities shown in blue, highest in red).

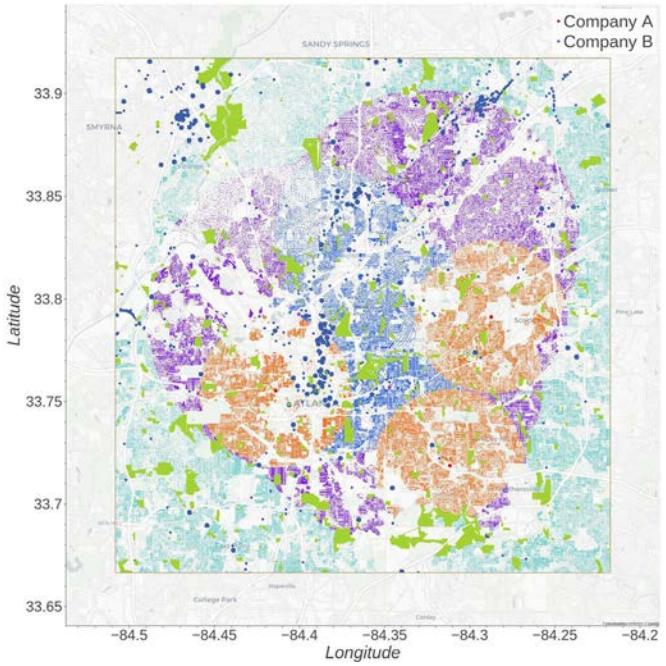


Figure 9. Scatter plot of addresses colored by how many companies and staging locations can serve them.



Single-Event Simulation Results

For a given flight, the stored 3D trajectory provides the vehicle's position at every timestep. Noise propagation is then carried out only to receivers lying within a 2 km radius of the path. These receivers correspond to the centers of the spatial grid cells. For each vehicle position, the distance and angular coordinates relative to each receiver are computed, and the appropriate noise sphere is selected based on the vehicle's instantaneous altitude and mission phase. Distinct noise spheres are used for the delivery leg (maximum weight) and for the return leg (empty weight), and phase transitions—such as climb, level flyover, or descent—are determined directly from altitude thresholds.

Taking the representative path shown in Figure 10 as an example, the receivers lying within the propagation radius are first identified. These receivers constitute the set to which source noise is propagated during the entire event. The resulting maximum A-weighted level, $L_{A,\max}$, is shown in Figure 11. This metric captures, for each receiver, the highest sound level experienced at any point along the flight. The contour clearly highlights the union of receivers contributing to the footprint, as well as the overall spatial extent of the event.

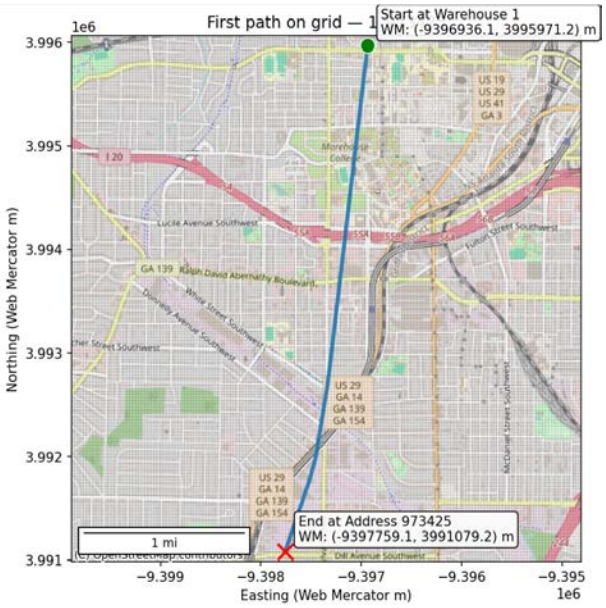


Figure 10. Selected two-dimensional path between a staging location and a customer address.

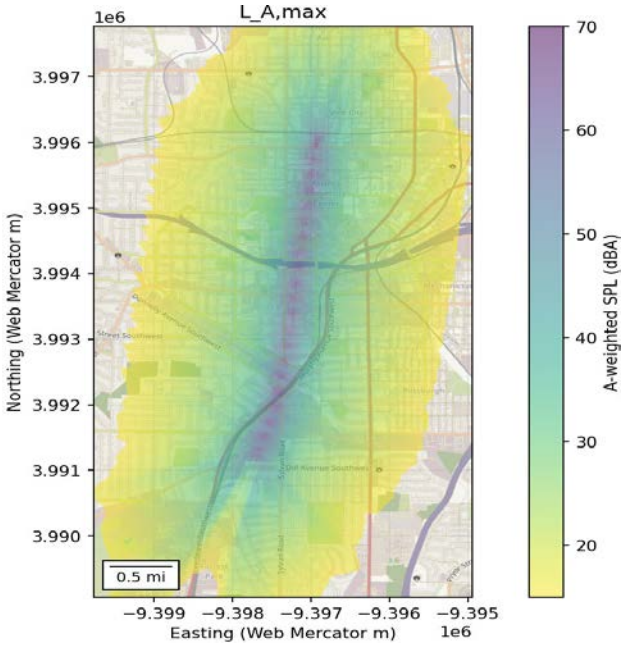


Figure 11. Single event, $L_{A,max}$, footprint of the selected two-dimensional path.

In addition to the $L_{A,\max}$ contour, it is also informative to examine the acoustic field at specific instants along the trajectory. Figure 12 and Figure 13 show the instantaneous A-weighted sound level for the delivery and return legs, respectively. In this example, the receivers located beneath the vehicle record approximately 61.7 dBA during the delivery leg and about 58.9 dBA during the return leg, reflecting the difference in vehicle mass. These instantaneous contours complement the $L_{A,\max}$ results by depicting the footprint at a particular moment during the flight.

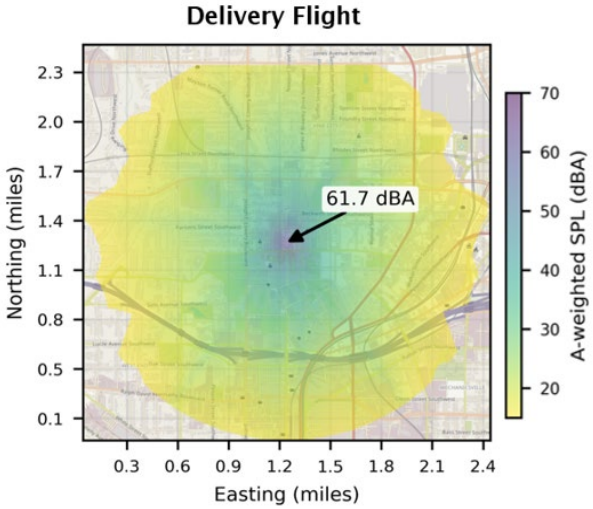


Figure 12. Instantaneous A-weighted sound pressure level (SPL) for the delivery leg.

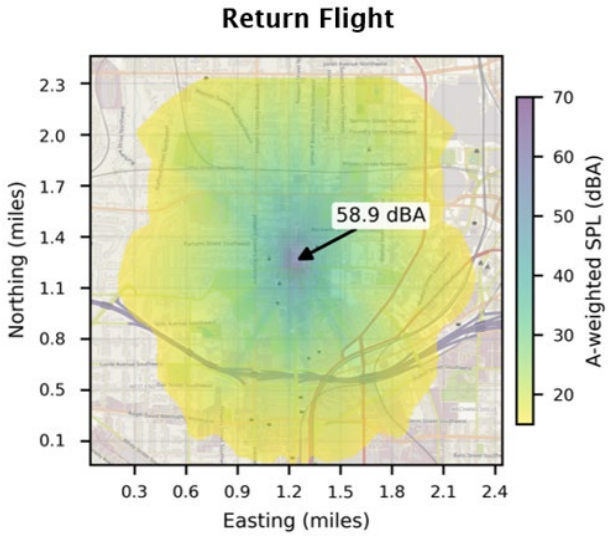


Figure 13. Instantaneous A-weighted sound pressure level (SPL) for the return leg.

Daily Simulation Results

The Monte Carlo is based on daily simulation that was implemented on a notional test case that has 1,877 candidate flights. Each simulated day samples 1,000 flights from this set based on their probabilities. The study repeats the daily simulation for 1,000 days. The simulation successfully generated probability distributions (histograms Figure 14) for both $L_{max,day}$ and $L_{eq,day}$.

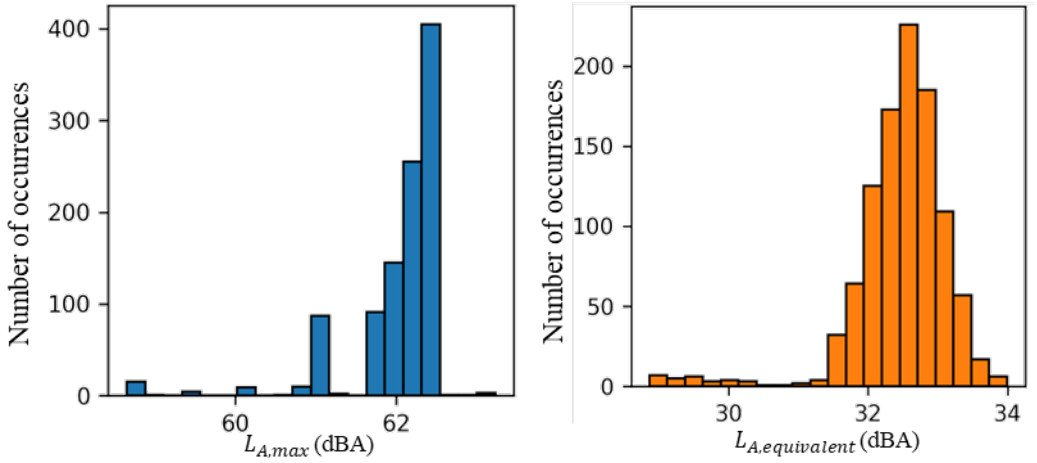


Figure 14. Notional results for a representative receiver.

As shown in the results for this receiver, this approach allows us to move beyond single-number estimates. Instead of one value, statistical measures like the mean and variance can be computed. The Monte Carlo simulation output provides a much richer understanding of the expected noise exposure and its variability, and this is essential for community noise assessment.

Milestones

- Established the Atlanta use case by defining staging locations, loading customer addresses, and initializing the study area for trajectory generation and noise analysis.



- Completed the full set of 2D flight paths for all feasible staging-location–to-address pairs and stored the resulting waypoint sequences for later noise propagation.
- Generated the complete set of flight probabilities using tract-level demand estimates and operator/staging-location reachability, producing probability values for every feasible flight.
- Verified the acoustic energy summation process to ensure accurate handling of overlapping flight events and correct conversion between linear energy and decibel metrics.

Major Accomplishments

- Established a simulation environment for UAS fleet operational noise assessment with demand model, flight trajectory optimization, and noise propagation integrated.
- Validated the noise computation module by comparing propagation results to AAM/ART using Causey UAS measurement data.
- Generated probabilistic distributions for $L_{eq,day}$ and $L_{max,day}$ metrics to quantify daily noise variability.

Publications

None.

Outreach Efforts

None.

Awards

None.

Student Involvement

None.

Plans for Next Period

- Reduce computational and storage demands for the single-event simulation database created for daily simulations for the UAS task.
- Visualize uncertainty and spatial distribution with contour maps for the UAS community noise exposure metrics.



Project 095 Assessment of Fuel Cells for Powering Modern Business Jets

Georgia Institute of Technology

Project Lead Investigator

Professor Dimitri N. Mavris
Director, Aerospace Systems Design Laboratory
School of Aerospace Engineering
Georgia Institute of Technology
Phone: (404) 894-1557
Fax: (404) 894-6596
Email: dimitri.mavris@ae.gatech.edu

University Participants

Georgia Institute of Technology (Georgia Tech)

- P.I.: Dr. Dimitri N. Mavris
- FAA Award Number: 13-C-AJFE-GIT-158
- Period of Performance: March 19, 2024, to September 30, 2025
- Tasks:
  1. Developing a baseline vehicle model of the Gulfstream G280 aircraft
  2. Creating an off-line Proton Exchange Membrane Fuel Cell (PEMFC) system model that incorporates all aspects of fuel cell systems
  3. Integrating PEMFC model into the baseline aircraft model and conduct a trade study to identify promising opportunities for fuel cells to displace traditional systems

Project Funding Level

This research was funded by the Federal Aviation Administration (FAA) Office of Environment and Energy through ASCENT, the FAA Center of Excellence for Alternative Jet Fuels and the Environment, Project 095 through FAA Award Number 13-C-AJFE-GIT-A95 under the supervision of Joshua Glottmann. Any opinions, findings, conclusions or recommendations expressed in this material are those of the authors and do not necessarily reflect the views of the FAA.

The FAA provided $200,000 in funding to Georgia Tech. Georgia Tech has secured in-kind cost share from both Gulfstream and Honeywell in the amount of $100,000, respectively, totally $200,000.

Investigation Team

Dr. Dimitri Mavris, Georgia Tech, Principal Investigator
Dr. Jimmy C. Tai, Georgia Tech, Co-Principal Investigator
Mr. Berkay Terzi, Graduate Student Researcher, Georgia Tech (Task 2 and 3)
Mr. Jeremy Decroix, Graduate Student Researcher, Georgia Tech (Task 1, 2 and 3)
Mr. Leo Wattebled, Graduate Student Researcher, Georgia Tech (Task 2 and 3)
Mr. Axel Jazzini, Graduate Student Researcher, Georgia Tech (Task 2 and 3)

Project Overview

The purpose of this research project is to identify opportunities for utilizing fuel cells on regional jet class aircraft to displace traditional power systems and reduce the total fossil fuel consumption of these vehicles. Fuel cell modeling and simulation will be performed for integration alongside an appropriate regional jet aircraft model.

Task 1 – Developing a Baseline Vehicle Model

Georgia Institute of Technology

Objective

The objective of Task 1 is to model and calibrate a notional Gulfstream® G280 aircraft model powered by a notional HTF7250G engine model and a GTCP36-150 auxiliary power unit (APU). The modeling and simulation environment used for this task is the Environmental Design Space (EDS). The notional aircraft model is calibrated against publicly available data.

Research Approach

The notional G280 aircraft calibration process is performed using EDS and the results are validated against public available data from Gulfstream and the European Union Aviation Safety Agency (EASA) (EASA, 2020).

EDS is an aircraft modeling and simulation environment developed by Georgia Tech and based on validated National Aeronautics and Space Administration (NASA) software tools, e.g., FLight Optimization System (FLOPS), Weight Estimation for Turbine Engines (WATE++), and Numerical Propulsion System Simulation (NPSS) (refer to Figure 1). EDS was used to develop physics-based model of the G280 aircraft (see Figure 2), so that a parametric approach can be used to evaluate the effects of various design parameters. Built on the NPSS object-oriented framework, EDS supports automated data exchange between modules, allowing for comprehensive analysis of engine architectures and airframe configurations, including multi-design point cycle designs. The comprehensive suite of software tools which comprise EDS are integrated and designed to enable a thorough assessment of the environmental impacts associated with aviation.

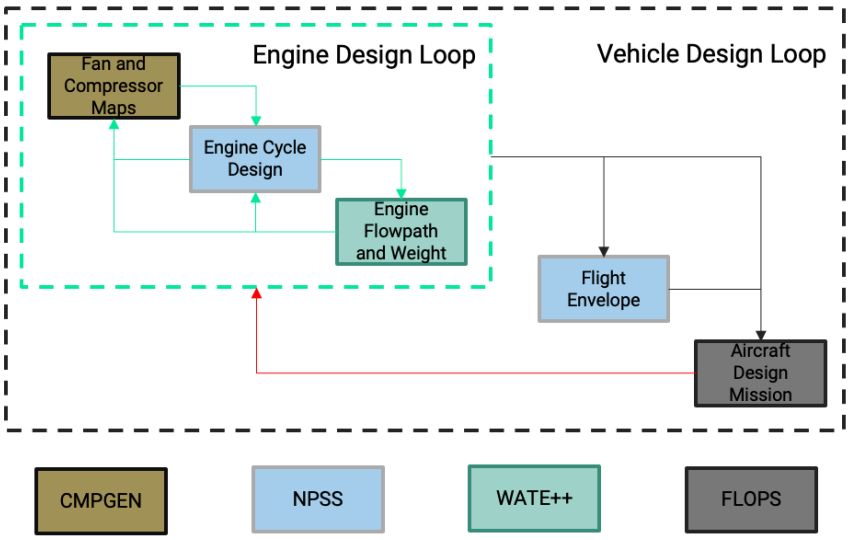


Figure 1. Environmental design space vehicle design loop. FLOPS: FLight Optimization System; NPSS: Numerical Propulsion System Simulation; and WATE++: Weight Estimation for Turbine Engines.

® Gulfstream is a registered trademark of Gulfstream Aerospace Corporation, Savannah, Georgia



Figure 2. Gulfstream G280 business jet.

The Gulfstream G280 is a super mid-size business jet designed and manufactured jointly by United States (U.S.)-based Gulfstream Aerospace and Israel Aerospace Industries. The G280 is equipped with two Honeywell® HTF7250G engines with a rated takeoff thrust of 7,624 lbf each. The notional HTF7250G mixed flow turbofan engine model was sized using the multi design point (MDP) methodology and calibrated using International Civil Aviation Organization (ICAO) databank to match the thrust-specific fuel consumption (TSFC) at four different sea level static (SLS) uninstalled points: take-off, climb-out, approach and idle. The results of the very close calibration are shown in Figure 3.

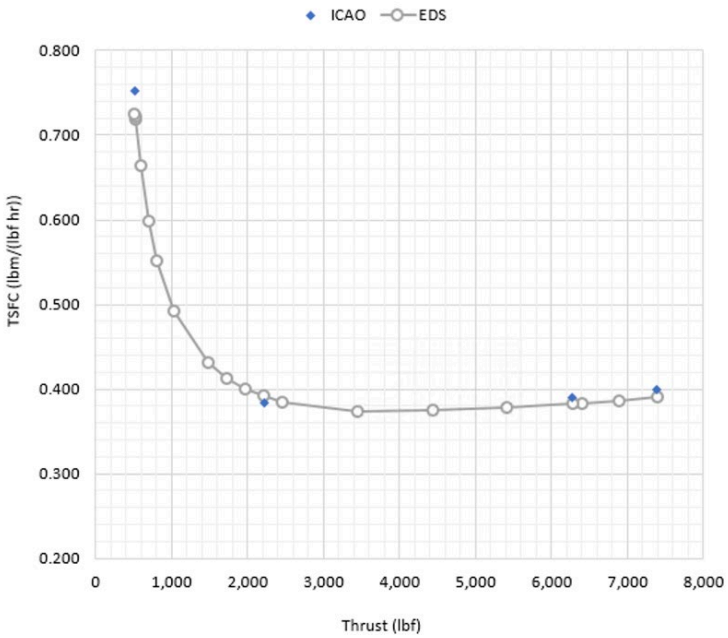


Figure 3. Environmental Design Space (EDS) HTF7250G engine calibration using International Civil Aviation Organization (ICAO) databank.

The APU being displaced onboard of the aircraft during this research effort is the GTCP36-150. Figure 4 outlines the key performance data for the GTCP36-150. It has a single-stage centrifugal compressor and a single-stage radial turbine architecture. Its weight varies between 125 lb (51 kg) and 168 lb (76 kg) depending on the standard and high flow rates. With the integration of a k-factor of 2.2, the group weight value of 370 lb (168 kg) can be obtained. The rated horsepower can go up to 40kVA (59 F, SL) and the bleed airflow goes up to 70lb/min (59 F, SL). The rotor speed ranges from 58,737 to 62,000 rpm with a maximum operating altitude of 20,000 ft (Honeywell, 2008).

® Honeywell is a registered trademark of Honeywell International, Inc., in the United States and other countries.



Key Performance Data

Weight:	125 – 168lbs
Digital Control Weight:	6lbs
Basic Spec:	FAA TSO-C77a Category 1 (Essential)
Rated Horsepower:	Up to 40kVA, 59F, SL
Bleed Airflow:	Up to 70lb/min, 59F, SL
Rated EGT:	1230F
Rotor Speed:	58,737 – 62,000 rpm

Figure 4. APU GTCP36-150 characteristics (Honeywell, 2008). EGT: exhaust gas temperature.

The role of the APU is to provide electrical and pneumatic power to the aircraft during the ground operations while the engines are turned off. Its role can also be to start the main engines. After the main engines start, the APU system is turned off. In case of an engine failure, the APU will be turned on after an emergency descent under 20,000 ft. For on the ground operations, if the APU is running for an hour, assuming a fuel consumption of 231 lb/hr (104 kg/hr) it will consume 231 lb (105 kg) of fuel before the taxi out segment.

Using the previous technical specification of the G280 found in Tables 1 and 2 and leveraging the engine deck of the notional HTF7250G mixed flow turbofan engine model, the notional G280 model was calibrated by performing a mission analysis with the FLOPS software. FLOPS takes the statistical weights fractions of each subsystem on the aircraft as input, the geometry of the aircraft from the computer aided design three-dimensional view rendering and the payload and range values.

Table 1. G280 aircraft specifications.

G280 Aircraft Specifications	
Overall Wingspan	63 ft
Fuselage Length	66.8 ft
Fuselage Height	11.2 ft
Fuselage Width	7.9 ft
Passenger Compartment Length	25.8 ft
Maximum operating Mach number	0.85
Long Range Cruise Mach Number	0.8
Maximum Cruise Altitude	45,000 ft
Maximum Range	3,600 nmi
Passenger	4
Crew Member	2



Table 2. Notional G280 model detailed weight breakdown. EDS: Environmental Design Space.

Mass Breakdown	Reference (lb)	EDS Results (lb/kg)	Error (%)
Auxiliary Power Unit	252 (114)	252 (114)	0
Operating Empty Weight	24,150 (10,954)	24,151 (10,955)	0.004
Maximum Payload	1,000 (454)	1,000 (454)	0
Mission Fuel Weight	14,600 (6,622)	14,601 (6,623)	0.007
Ramp Weight	39,750 (18,030)	39,752 (18,031)	0.005
Taxi Out Fuel	150 (68)	151 (68)	0.67
Maximum Takeoff Weight	39,600 (17,962)	39,601 (17,963)	0.003
Design Landing Weight	32,700 (14,832)	32,703 (14,834)	0.009

The baseline calibration was performed using the maximum payload (1,000 lb/454 kg) and the maximum mission fuel weight (14,600 lb/6,622 kg) for the maximum range (3,600 nmi) with a reserve mission of 30 minutes at 10,000 ft. A cruise climb schedule was implemented. The results of the calibration show a very close percentage error for the aggregated weights as indicated in Table 2.

Milestones
- Performed calibration of the notional HTF7250G engine model.
- Performed calibration of the notional G280 aircraft model.

Major Accomplishments
Performed the notional baseline aircraft model of the G280 super mid-size business jet which allowed for the integration of the PEMFC system impact.

Publications
None.

Outreach Efforts
- Scheduled and participated in monthly meetings with Gulfstream, Honeywell, and FAA to guide this research effort.
- Attended ASCENT biannual meetings.

Awards
None.

Student Involvement
This task involves one graduate student, Jeremy Decroix (PhD candidate). He is in charge of the notional HTF7250-G engine model and the G280 notional baseline aircraft model calibration against publicly available data.

Plans for Next Period
Continue to refine the mission schedule used for the calibration to make sure the integration of the PEM fuel cell system is accurate.

Task 2 – Creating Off-line PEMFC System Model
Georgia Institute of Technology

Objective
The objective of this task is to develop a comprehensive modeling and simulation environment for fuel cells, with potential application in the target aircraft. After evaluating traditional power system alternatives for APUs, Solid Oxide Fuel Cells



(SOFCs) and Proton Exchange Membrane Fuel Cells (PEMFCs) emerge as the most promising options (Daggett et al., 2003). Given PEMFCs' lower operating temperature, high efficiency, and their power output profiles that align with the typical power demands of business jets, PEMFCs are considered the preferable option for APU applications in business jets. Therefore, the modeling and simulation environment developed in this task will focus on PEMFC technology.

Research Approach

Designing a novel power system for an aircraft demands a comprehensive understanding of both onboard power sources and aircraft system-level power demands. In conventional aircraft, gas turbine engines generate electrical power via generators connected to the engine spools and supply bleed air for the environmental control system (ECS). Additionally, traditional APUs provide electrical power and bleed air during ground operations, engine start-up, and in certain emergency scenarios. For a fuel cell system to feasibly replace a gas turbine APU, it must at least fulfill all these operational requirements which are namely, supplying electrical power to onboard subsystems, delivering pressurized air for the ECS, and supporting engine start-up without relying on ground power units.

Although a fuel cell system can be sized to meet the original requirements of a conventional APU, an alternative approach involves adjusting these requirements to better align with the benefits offered by emerging aircraft systems. This strategy serves as a step toward achieving a More Electric Aircraft. In this configuration, the fuel cell system is designed to supply continuous electrical power and pressurized air to the ECS throughout the entire flight, rather than being limited to ground operations and emergency situations. By enabling these capabilities, the approach aims to reduce Jet-A fuel consumption and lower overall emissions by eliminating the need for customer bleed air and shaft power extraction from the main engines.

To successfully replace the gas turbine APU with a fuel cell system under a revised mission profile, the system must operate reliably across a wide range of environmental conditions, including hot- and cold-day ground operations, takeoff, and high-altitude flight. For instance, during hot-day scenarios, the ambient air drawn into the cooling ducts by fans may reach such high temperatures that the temperature differential between the air and the fuel cell stack becomes minimal. This necessitates a significantly larger volume of cooling air, often exceeding the capacity of conventional ducting systems. In such cases, advanced cooling cycles may be required to meet thermal management demands (Bargal et al., 2020). In contrast, during cold-day operations, the primary challenge becomes preheating the intake air before it enters the fuel cell stack to maintain optimal performance.

The capability to operate at high altitudes presents significant challenges for the proposed fuel cell system, primarily due to the low ambient pressure at such elevations. For air-breathing fuel cells, reduced pressure directly impacts performance by lowering the open-circuit voltage (Willich et al., 2014), as shown in the Nernst equation through the partial pressure of hydrogen. Additionally, low pressure adversely affects activation and concentration overpotentials and indirectly increases ohmic overpotential (Willich et al., 2024). Therefore, incorporating compression elements upstream of the fuel cell is essential to ensure efficient performance at high altitudes. However, these compression components require power to operate and to achieve a self-sustained fuel cell system, this power should be supplied by the fuel cell stacks themselves.

Modeling the stack-level performance of a low-temperature PEMFC alone is insufficient for making informed aircraft-level design decisions, especially during the early stages of conceptual development. This is primarily because the balance of plant (BoP) components in a low-temperature PEMFC system (e.g., compressors, pumps, and thermal management subsystems) are significant electrical consumers. These components contribute to the parasitic power load, directly impacting the system’s net electrical output available to serve onboard loads such as avionics, galleys, and other aircraft subsystems. Therefore, a complete system-level model that includes both the fuel cell stack and auxiliary components is essential to establish a robust, parametric simulation environment.

The proposed PEMFC system is designed to replace the conventional gas turbine APU while ensuring continuous and reliable power delivery to all aircraft subsystems throughout the flight, in accordance with the defined sizing mission. The overall aircraft system architecture is illustrated in Figure 5. The BoP for the fuel cell system can be divided into three primary subsystems: the air supply system, the fuel conditioning system, and auxiliary components.

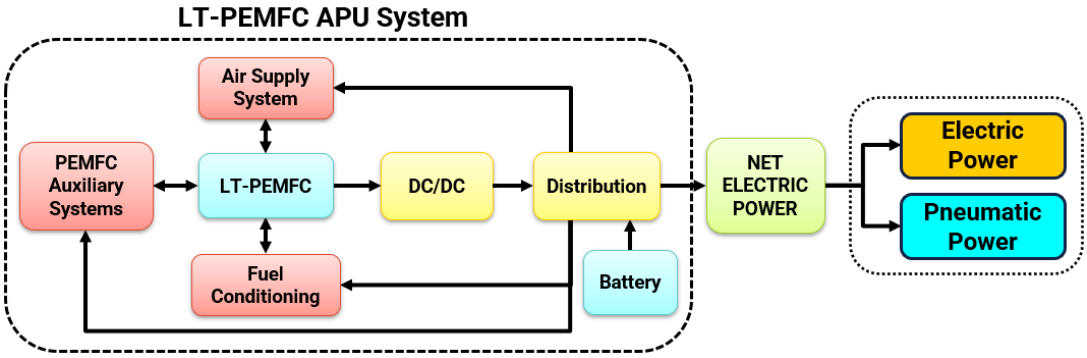


Figure 5. General overview of the proposed power system. APU: auxiliary power unit, LT-PEMFC: Low-Temperature Proton Exchange Membrane Fuel Cells, and DC: direct current.

One of the main objectives of this task is to quantify the parasitic power demands, or in other words, the power requirements of the auxiliary components in the PEMFC system. As illustrated in Figure 5, the power sources for the auxiliary components include both the PEMFC stack and a parallel battery. The battery serves as an additional power source to assist the fuel cell stack during rapid transients in power demand, periods of high-power demand, or emergency situations. The outputs of the proposed system include direct current (DC) electrical power for use in aircraft subsystems and pressurized air for the aircraft's ECS.

The air supply subsystem is responsible for delivering the required mass flow of air at the appropriate pressure and temperature to the PEMFC stacks. The fuel conditioning subsystem regulates the flow of hydrogen to the stacks, ensuring optimal electrochemical performance. The auxiliary subsystem includes supporting components such as heat exchangers for thermal management, as well as controllers, valves, and various monitoring devices. The net electrical output of the system, after accounting for parasitic power consumption by auxiliary subsystems, is available to supply the aircraft's electrical loads and to generate pneumatic power for the ECS.

The mechanical system architecture, illustrated in Figure 6, is designed to ensure reliable operation of the PEMFC under a wide range of flight conditions, including high-altitude environments where ambient air pressure and density are significantly reduced. In such scenarios, ambient air must first be compressed to meet the stack's pressure requirements. This compression process raises the air temperature above the optimal operating range for the fuel cell, necessitating the use of a heat exchanger to cool the air before it enters the stack. Subsequently, a humidifier adjusts the humidity of the air, utilizing the system's by-product water to meet the fuel cell's specific moisture requirements.

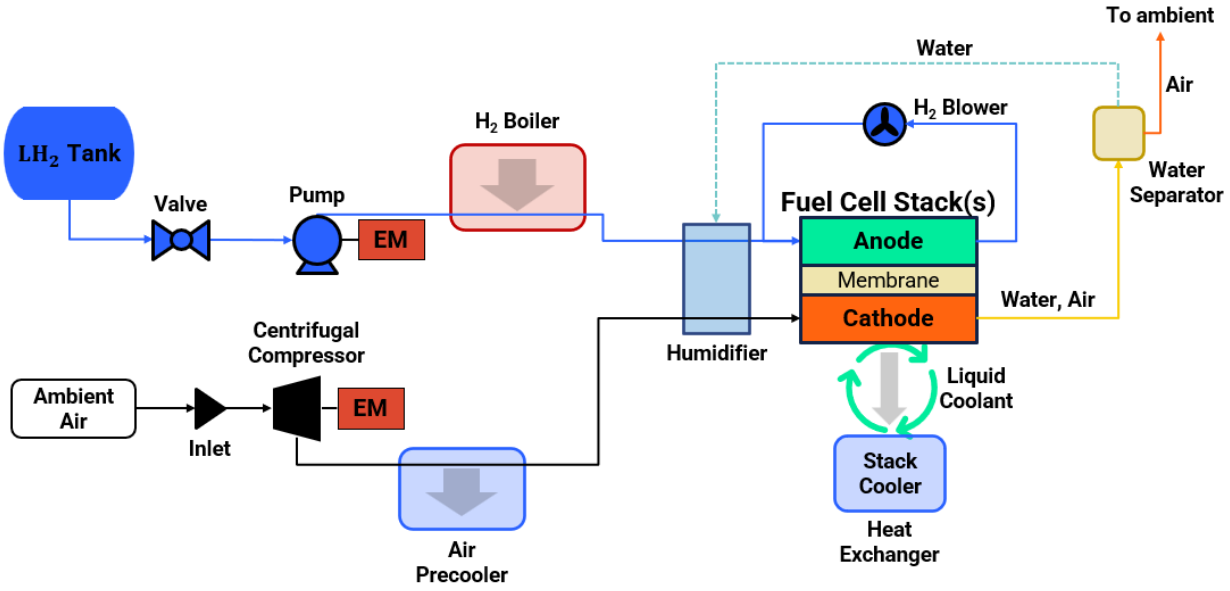


Figure 6. Fuel cell system architecture.

PEMFCs require high-purity hydrogen, as they are highly sensitive to contaminants. While hydrogen can be stored in either gaseous or liquid form, liquid hydrogen is often preferred due to its superior gravimetric energy density. However, storing cryogenic hydrogen onboard presents thermal and mechanical challenges. The storage tank must be designed to minimize heat ingress from the environment. Before delivery to the stack, the liquid hydrogen is gasified and heated to the required temperature using heat exchangers. Because of the low mass flow rates involved, pressurization is achieved using micropumps. Any excess hydrogen is recirculated back into the system via a blower to improve efficiency and maintain consistent fuel supply.

Inside the PEMFC stack, the electrochemical reaction is exothermic, generating substantial heat energy. To maintain the stack within its optimal operating temperature range, typically between 20°C and 90°C, a closed-loop single-phase liquid cooling system is used. This system includes a liquid-cycle heat exchanger that effectively dissipates the waste heat, ensuring stable and efficient stack performance under varying operational conditions.

As shown in Figure 5, the pneumatic power, i.e., the compressed air supplied to the ECS, is one of the two outputs of the new APU system. In aircraft, the ECS is responsible for maintaining a safe and comfortable cabin environment by regulating pressure, temperature, and humidity. Traditionally, engine bleed air serves as the primary airflow source for the ECS. The system typically includes two pneumatic air conditioning kits, commonly referred to as packs, which manage core air conditioning and distribution functions. A schematic of this traditional configuration is shown in Figure 7.

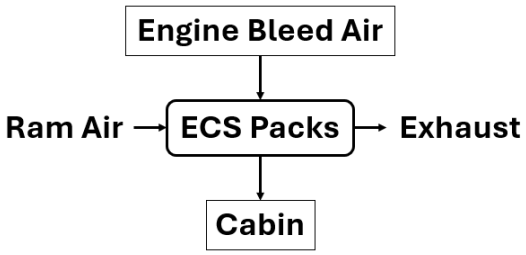


Figure 7. Conventional environmental control system (ECS) schematic (Cai, 2023).



As this project investigates the transition toward more electric aircraft architecture, electrifying the ECS using power supplied by a fuel cell system offers a promising opportunity to reduce Jet-A fuel consumption by minimizing reliance on engine bleed air. Therefore, accurately quantifying the power consumption, as well as other key parameters (e.g., weight and ram airflow) of the electrical environmental control system (eECS) is essential for the proper sizing of the fuel cell system. To accomplish this, defining the new eECS architecture is a key step. The cabin air compressor system consisting of centrifugal compressors and their associated drive mechanisms represents one of the major modifications to the ECS and serves as a primary power consumer. A general schematic of the eECS configuration is presented in Figure 8. Furthermore, trade-off studies can be conducted on the packs, which currently exhibit low efficiencies (Rosero et al., 2007), to evaluate their weight and performance for electrified applications, especially considering that the new cabin air compressor system may deliver cooler, lower-pressure air compared to traditional engine bleed air.

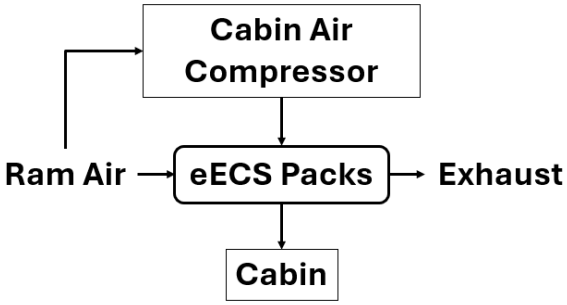


Figure 8. Electrical environmental control system (eECS) schematic (Cai, 2023).

When updating the aircraft's ECS, several key requirements must be met to ensure mission suitability. According to FAA regulations, the minimum airflow that must be supplied to the cabin is 0.55 lb/min per passenger (FAA, 1996). In addition to meeting this constraint, the system must deliver sufficient mass flow to refresh the cabin air within a defined time interval while maintaining a steady cabin temperature by effectively removing the internal heat load.

The modeling of the proposed system is carried out in the NPSS environment. NPSS is an object-oriented simulation platform primarily developed for modeling gas turbine engine cycles, but its modular structure also enables broader applications. The software provides a library of built-in components while offering flexibility to define custom elements and user-defined functions. This adaptability, combined with its robust numerical solver and support for multiple thermodynamic property packages, makes NPSS a powerful environment for system-level modeling. Its capability to simulate both on-design and off-design performance scenarios is particularly valuable for this study, as it supports accurate component sizing and performance assessment, which are key requirements for establishing a reliable parametric simulation framework. The fuel cell modeling process is divided into five main steps.

Step 1: Baseline Flight Mission Definition and Design Point Selection
Sizing a fuel cell system, including hydrogen storage and cabin air compressors, to continuously supply electrical power to aircraft subsystems and pressurized air to the eECS throughout the flight requires a well-defined aircraft mission, which must include a detailed profile of the electrical power requirements of the onboard systems. Although aircraft power demand profiles can sometimes be obtained directly from manufacturers, the study by Voth et al. (2024) presents a methodology to estimate the electrical power requirements of several aircraft subsystems. Additionally, a pack model incorporating the selected thermal conditioning strategy for the eECS must be included to determine air demand and the corresponding power consumption across the ground, flight, and reserve phases of the mission. A generic altitude profile for the baseline aircraft, which is considered in the sizing process, is shown in Figure 9. The flight mission is critical in determining the design point of the new system and in properly sizing the liquid hydrogen (LH_2) tank. For the design point of this project, the maximum possible altitude is selected, where the air density will be lowest for the given flight mission.

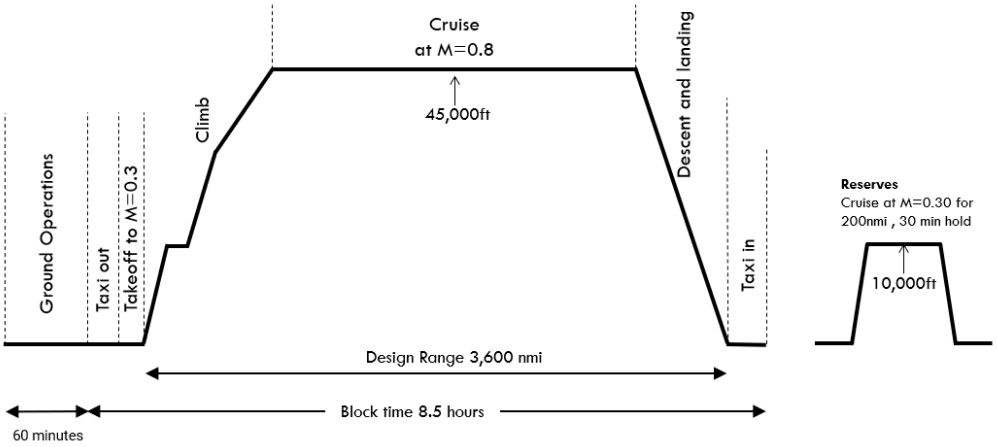


Figure 9. Baseline flight mission summary.

Step 2: PEMFC Stack Sizing

Fuel cell modeling approaches span from zero-dimensional to three-dimensional frameworks, with increasing fidelity and computational complexity. For early-stage aircraft design and system-level analysis, zero-dimensional and one-dimensional models are typically favored, as they provide sufficient accuracy with lower computational cost. In this project, a zero-dimensional empirical electrochemical model of a PEMFC is adopted, informed by various established references.

This model incorporates the three main voltage losses—activation, ohmic, and concentration—that reduce the actual output voltage from the theoretical maximum. The analysis begins by calculating the reversible cell voltage using the Nernst equation, which is a function of the stack temperature and the partial pressures of hydrogen, oxygen and water vapor. This reversible voltage represents the ideal open-circuit potential under given conditions. However, real-world performance is reduced due to inherent electrochemical and physical limitations (O'Hayre et al., 2016).

$$E_{rev} = E^{\circ} + \frac{\Delta \hat{s}}{nF}(T - T_0) - \frac{RT}{nF}\ln\left(\frac{p_{H_2O}}{p_{H_2} \cdot p_{O_2}^2}\right) \quad \text{(Eq. 1)}$$

The first category of voltage loss is activation loss, which dominates at low current densities. It is associated with the energy required to initiate electrochemical reactions at the anode and cathode. This loss is described using a modified form of the Tafel equation (O'Hayre et al., 2016):

$$E_{act} = -\frac{RT}{\alpha n_e F}\ln(i_0) + \frac{RT}{\alpha n_e F}\ln(i + i_{leak}) \quad \text{(Eq. 2)}$$

The second major source of voltage loss is the ohmic loss, which arises from resistance to charge transport within the fuel cell. This resistance primarily stems from proton transport through the polymer electrolyte membrane. The associated voltage drop is calculated using the area-specific resistance (ASR) of the membrane, which encapsulates the resistivity of the membrane as a function of its thickness, surface area, and proton conductivity (O'Hayre et al., 2016):

$$E_{ohm} = i \cdot ASR_{ohmic} \quad \text{(Eq. 3)}$$

The third loss mechanism is the concentration loss, which becomes prominent at high current densities. This loss results from limitations in mass transport, particularly the depletion of reactants near the catalyst layer or the accumulation of products that impede further reactions. As the fuel cell approaches its limiting current density, the reactant concentrations at the electrode surface tend towards zero, leading to a sharp increase in loss. The concentration overpotential is modeled by (O'Hayre et al., 2016):

$$E_{conc} = \left(1 + \frac{1}{\alpha}\right)\frac{RT}{n_e F}\ln\left(\frac{i_L}{i_L - (i + i_{leak})}\right) = \mathrm{C} \cdot \ln\left(\frac{i_L}{i_L - (i + i_{leak})}\right) \quad \text{(Eq. 4)}$$



By summing the activation, ohmic, and concentration losses and subtracting them from the reversible voltage, the effective output voltage of the PEMFC can be estimated as follows. This equation forms the foundation for assessing the performance of each cell in the stack.

$$E_{cell} = E_{rev} - (E_{act} + E_{ohm} + E_{conc}) \quad \text{(Eq. 5)}$$

Although this model is relatively simple, it depends heavily on design constants outlined in the governing equations. Datta (2021) provides these key constants across different pressure levels, as presented in Table 3. The same study also offers correction factors to account for variations in operating stack temperature and humidity, enabling more accurate modeling under diverse conditions.

Table 3. Model parameters used in PEMFC simulation (Datta, 2021). ASR: area-specific ohmic resistance.

Pressure	1 atm	2 atm	3 atm	4 atm
$i_{0,C}$	10^{-4}	10^{-4}	10^{-4}	10^{-4}
α_C	0.15	0.155	0.155	0.16
$i_{0,A}$	0.1	0.1	0.1	0.1
α_A	0.5	0.5	0.5	0.5
$i_L\ (A/cm^2)$	0.73	1.0	1.1	1.23
$i_{leak}\ (A/cm^2)$	0.01	0.01	0.01	0.01
$C\ (V)$	0.08	0.08	0.08	0.12
$ASR_{ohmic}\ (\Omega\ cm^2)$	0.12	0.115	0.1	0.06

To achieve the required electrical power output, individual fuel cells are connected in series to form a stack, thereby increasing the overall voltage. The total number of cells is determined based on the target stack and individual cell voltages, while the required membrane area is calculated from the desired stack-level current density. Under off-design conditions, although the physical dimensions of the stack (i.e., number of cells and membrane area) remain fixed, its performance varies with changes in aircraft altitude and speed. In addition to electrical power, fuel cell stacks produce waste heat, which can be repurposed for various onboard functions. Accurately quantifying this waste heat is critical for TMS sizing and is dependent on both cell efficiency and electrical power output.

$$Waste\ Heat = \left(\frac{1}{v} - 1\right) \times PWR_{cell} \quad \text{(Eq. 6)}$$

where v is the cell efficiency and PWR_{cell} is the electrical power generated by the cell.

To estimate the stack weight, Datta (2021) provides a detailed approach that accounts for individual sub-components. Alternatively, a simplified estimation can be made using a specific power-based method, in which the maximum stack power is divided by a representative specific power value. The Fuel Cell Roadmap report (Aerospace Technology Institute, 2022), prepared for FlyZero project, outlines specific power targets for future years. However, due to the relatively low Technology Readiness Level (TRL) of the system, there is considerable uncertainty in these values. To address this, confidence intervals should be established to capture the range of possible outcomes. Using the latter method, the fuel cell stack weight is estimated by dividing the maximum stack power—although potentially outside the typical operating range, as illustrated in the polarization curve in Figure 10, by an assumed specific power value.

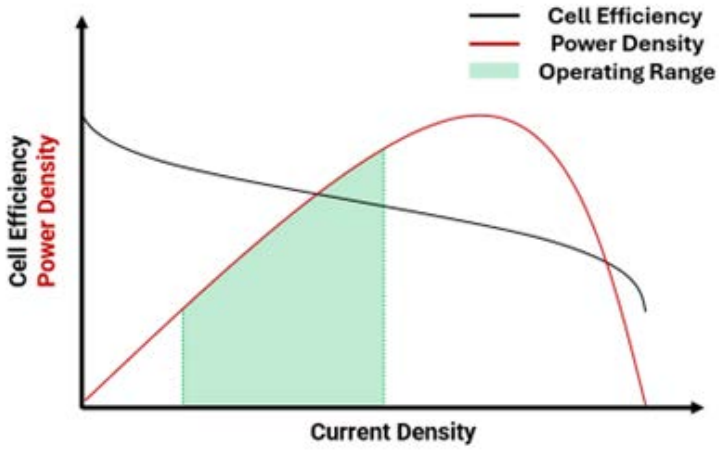


Figure 10. Cell efficiency and power density versus current density.

Step 3: Balance of Plant Sizing and Modeling
As illustrated in the fuel cell system architecture, the system comprises several auxiliary components, including pressure-boosting elements such as compressors and pumps. The fuel cell compressor and hydrogen micropump requirements are determined by the pressure and flow rate demands of the fuel cell stack at the selected design point. The most critical design condition corresponds to the maximum operating altitude of the baseline aircraft. From the stack perspective, specifying the stack design pressure and temperature is essential, as these parameters directly influence the compressor pressure ratios and overall stack performance.

The power requirement for the air compressor is calculated using the following relation with compressor efficiency. The total enthalpy rise and power without any bleed across the compressor is given by:

$$h_{t,out} = h_{t,in} \times \left[1 + \frac{\left(\Pi_{cmp}^{\frac{\gamma-1}{\gamma}} - 1\right)}{\eta_{\mathrm{cmp}}}\right] \quad \text{(Eq. 7)}$$

$$PWR_{cmp} = \dot{W}_{cmp} \times \left(h_{t,in} - h_{t,out}\right) \quad \text{(Eq. 8)}$$

where $\Pi = \frac{\mathrm{p_{t,out}}}{p_{t,in}}$ is the total pressure ratio across the compressor, $\dot{W}_{cmp}$ is the mass flow rate through the compressor, and γ is the specific heat ratio of air.

To accurately quantify the power consumption of the cabin air compressor system, which comprises multi-stage centrifugal compressors, an electric motor, and associated components required for motor operation, in the eECS, additional system details must be defined. As proposed by Tagge et al. (1985), the system may be configured with three cabin air compressors: two dedicated to normal operation and one serving as a redundant unit for emergency situations. The overall system architecture is illustrated in Figure 11. Depending on the number of packs implemented, the total number of compressors, as well as the allocation between operational and backup units, may vary.

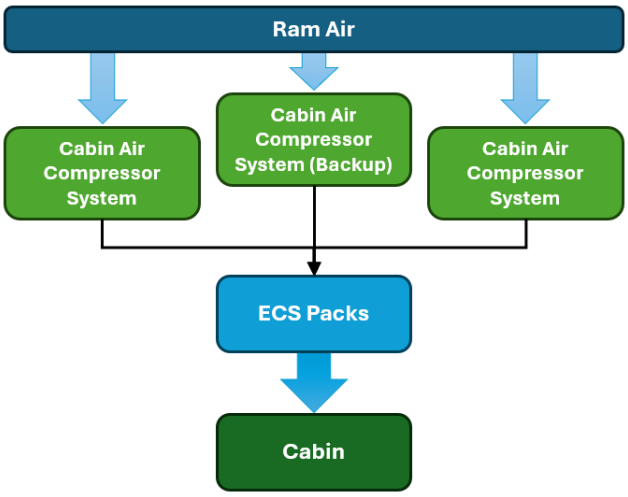


Figure 11. Overall electric environmental control system (eECS) system architecture.

Tagge et al. (1985) also presented several system configurations in their study, each employing a different thermal conditioning method, namely, air-cycle, vapor-cycle, and air-cycle with heat exchanger cooling. The selected thermal conditioning approach significantly influences the discharge pressure requirements of the cabin air compressors, which in turn directly impacts their power consumption, as illustrated in Figure 12. For instance, implementing a vapor-cycle system can lead to substantial reductions in compressor power consumption due to its lower discharge pressure requirement. However, since this approach alters the thermal management architecture, its broader implications must be carefully evaluated through detailed system-level analysis to ensure overall performance and integration benefits.

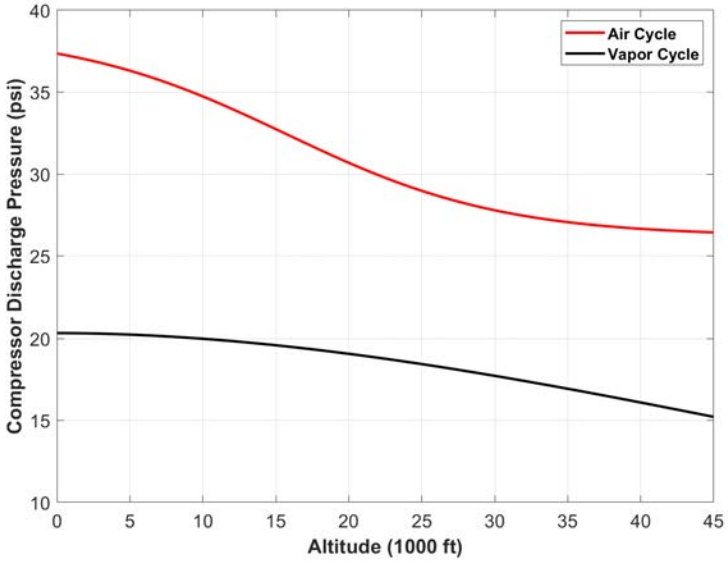


Figure 12. Required discharge pressure of cabin air compressors as a function of altitude (Tagge et al.,1985).

Another important consideration for the turbomachinery is the weight estimation for each of the components. In the case of this study, centrifugal compressors are selected over axial compressors. Indeed, axial compressors are known for higher efficiency and handling larger mass flows and thus will be privileged for big jet engines applications. Centrifugal



compressors, on the other hand, have higher compression per stage, are more compact and are easy to maintain (Campbell & Talbert, 1945). Therefore, they are more suited in the case of this study.

To estimate the weight of the ECS and fuel cell compressors, the needed inputs for both are the maximum required mass flow rate as well as the maximum pressure ratio. These values can be obtained through the modeling and simulation environment previously described. They are then compared to the values of existing compressors from manufacturers' databases available online and a suitable solution is determined, and the weight of the selected industrial solution is used.

With a similar approach, the design pressure ratio for the hydrogen pump is estimated by considering liquid hydrogen tank pressure and pressure losses across the hydrogen boiler to ensure that hydrogen is delivered to the stack at the required pressure. The hydrogen pump shaft power is then calculated as the product of the volumetric flow rate and the pressure difference, divided by the pump's hydraulic efficiency, representing the hydraulic power requirement:

$$PWR_{pump} = \frac{Q \times \Delta P}{\eta_{pump}} \quad \text{(Eq. 9)}$$

Efficiencies are critical factors in calculating the performance of both compressors and pumps. Performance maps, sourced either from manufacturers or derived from semi-empirical models in turbomachinery literature, are used to evaluate these components under off-design conditions. These maps are then scaled according to the specified on-design efficiency to estimate power requirements during off-design operation.

For the hydrogen pump, the choice to use a micropump is made. Indeed, the required hydrogen mass flow rate required by the stack will remain very low. The exact value can be determined in the modeling and simulation environment that was developed for this study. The weight estimation is then obtained by following the exact same methodology as for the ECS and fuel cell compressors. Manufacturers databases are analyzed, and the weight of a suitable industrial solution is used.

Another important BoP subsystem is the electrical components, which include but are not limited to electric motors, power converters, and batteries. Among these components, electric motors serve as the backbone of fuel cell systems, converting electrical power generated by the fuel cell into mechanical power to drive key components such as compressors. Depending on system requirements, various motor types can be employed, including brushless DC motors (MicroPump, Inc., 2025) and permanent magnet synchronous motors (Rotrex Fuel Cell Compressors, 2025). Motor sizing is based on the mechanical power demands of the fuel cell system and accounts for the projected design efficiency. Pastra et al. (2022) provide efficiency and specific power projections for electric motors in future years, which are used as reference points. Once the motor is sized, shaft power output is evaluated using an efficiency map derived from industrial motor data, scaled to reflect the chosen design-point efficiency.

Alongside electric motors, power converters play a crucial role in the electrical BoP by ensuring that the electrical power from the fuel cell is properly conditioned to meet the voltage and current requirements of the system. For example, a DC-DC converter is required to regulate the output voltage of the fuel cell stack to match the bus voltage, which is determined primarily by the aircraft subsystem requirements and the battery voltage. This converter ensures stable and consistent DC output. Additionally, since electric motors within the fuel cell system require alternating current (AC) input, DC-AC inverters are employed to convert the regulated DC voltage into AC. Similar to electric motors, the design efficiency of these power electronics components is critical. Hall et al. (2022) provide projections for future years, including efficiency targets and specific power values, which inform the sizing and performance assessment of these devices.

In the proposed system architecture, the secondary energy storage device, the battery, plays a critical role in supporting the fuel cell system by fulfilling several essential functions. At startup, it supplies electrical power to the balance-of-plant components, such as electric motors driving the compressors and temperature regulation units for air and hydrogen, enabling the system to initiate autonomously without external power. Once the PEMFC stack generates sufficient power to cover parasitic loads and provide a net output to aircraft subsystems, the battery can be deactivated. Additionally, due to the inherently slow dynamic response of fuel cell systems to transient power demands, the battery also acts as a buffer to manage power fluctuations, ensure consistent system output, and supplement the fuel cell during peak load conditions (Smith et al., 2021). In this setup, the fuel cell is sized to meet average power requirements, while the battery handles dynamic variations. Future projections for battery specific energy and associated confidence intervals are provided by Tiede et al. (2022), offering valuable input for long-term planning.



The water management system is designed to control the fuel cell's humidity, which directly affects the membrane's resistance. Therefore, the humidity levels of fuel cell must be carefully controlled throughout the flight mission, regardless of environmental conditions. To maintain appropriate humidity levels, the system may utilize the by-product water generated during fuel cell operation, enabling a more self-sustained configuration. This water can be collected via a water separator and subsequently directed to the humidifier, while any excess water can be expelled into the atmosphere.

Various types of humidification systems are available for fuel cell applications, with membrane humidifiers and enthalpy wheels being the primary options (Chang et al., 2018). Since enthalpy wheels require electrical power to operate, membrane humidifiers are generally considered a more efficient solution for this application.

For weight estimation of the humidification system, industrial data can be used to develop a simple parametric model. For example, Schröder et al. (2021) estimate the weight of a membrane-type humidifier based on the dry air mass flow rate that supplied to the stacks, using a value of 82.353 kg/(kg/s of dry air). The weight of the water separator is typically negligible compared to that of the humidifier, as indicated by the industrial supplier (MANN+HUMMEL, n.d.).

Step 4: Liquid Hydrogen Tank Sizing
After sizing all components of the fuel cell system and finalizing the design, the total hydrogen fuel required for the complete sizing mission, including reserve segments, is calculated. Based on this estimated total hydrogen consumption, the hydrogen storage tank is sized. It is assumed that a single storage tank is placed within the fuselage, designed as a cylindrical vessel with 2:1 semi-ellipsoidal heads. Due to the significantly higher ambient temperature in the fuselage compared to the cryogenic storage temperature of liquid hydrogen, a constant inward heat flux occurs during flight. This heat is absorbed by both the liquid and gaseous hydrogen, accelerating the boil-off phenomenon. To mitigate hydrogen losses, the tank is equipped with an insulation jacket. For the sizing process, the choice of tank and insulation material is critical, as both heat transfer characteristics and structural weight must be carefully balanced. In a study conducted by Johnson et al. (2024), candidate tank materials such as aluminum alloy Al 5083 (a metallic option) and Cycom® 5320 (a composite material), along with various insulation materials, were evaluated. Among these, the combination of Cycom 5320 with a Quest® vacuum insulation jacket provided the best performance in terms of thermal insulation and overall weight efficiency. The material properties of these materials are summarized in Table 4.

Table 4. Material properties for hydrogen tank design (Johnson et al., 2024).

Properties of Cycom5320		Properties of Quest Vacuum Jacket	
Property	**Value**	**Property**	**Value**
Yield Stress [psi]	190,000	Density [kg/m^3]	0.0
Density [kg/m^3]	1,310	Surface Area Density [kg/m^2]	2.0
Thermal Conductivity [W/(mK)]	0.167	Thermal Conductivity [W/(mK)]	2.1E-4

To preserve the current cabin layout, the fuel cell system and its BoP is placed in the tail cone. Since this system will occupy more space than the traditional APU, elongating the cabin has been identified as the most viable option. This modification will be factored into the aircraft-level analysis.

Step 5: Thermal Management System Sizing and Modeling
The thermal management system (TMS) plays a critical role in conditioning hydrogen and air to meet the temperature requirements of the PEMFC under operational conditions. The proposed TMS architecture (see Figure 6) includes three key heat exchangers, each serving a distinct function, and whose modeling approach is detailed in subsequent sections. First, a hydrogen boiler is used to bring liquid hydrogen to the working conditions of the PEMFC. To size the hydrogen boiler responsible for heating cryogenic hydrogen to the steady-state temperature required by the PEMFC, we assume an initial shell-and-tube heat exchanger geometry. Unlike TMS architectures in previous studies (Link et al., 2022), which rely on hot compressed air for hydrogen preheating, this method is not viable in our case during ground operations and low altitudes, where compressed air lacks sufficient thermal energy. Consequently, several heat sources were investigated in this study. The first one is to use bleed air, yet, in order to maintain engine performance this alternative was discarded. Alternatively,

® Cycom is a registered trademark of Syensqo SA/NV, Brussels, Belgium.
® Quest is a registered trademark of Quest Thermal Group, LLC, Arvada, Colorado.



the heat up of cryogenic hydrogen to gas hydrogen could be performed by electric heaters alone, alimented by the PEMFC, yet this alternative increases the load on the PEMFC and increases the weight of the overall PEMFC subsystems. Consequently, the most viable alternative consists on using warm air from the stack heat exchanger for an initial heat up of the cryogenic hydrogen and adjusting the final temperature of gas hydrogen using electric heater (see Figure 13). Figure 14 depicts in blue the final hydrogen temperature after applying the first heat up and the red line depicts the required power to adjust the hydrogen temperature to the working temperature of the PEMFC through the mission.

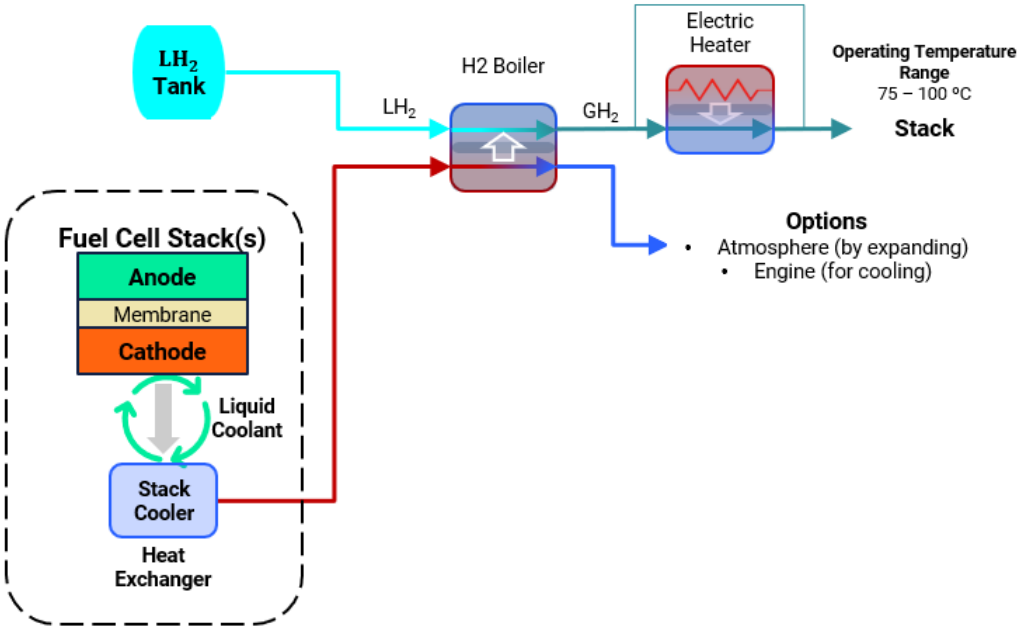


Figure 13. Hydrogen boiler architecture. H_2: hydrogen, LH_2: liquid hydrogen.

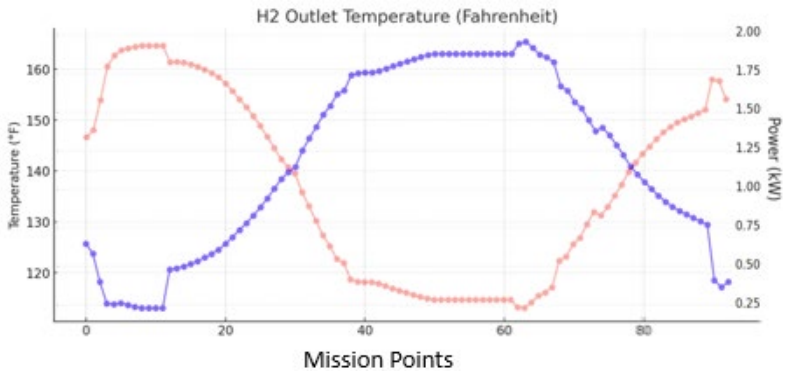


Figure 14. Hydrogen (H_2) temperature and required electric power for full heat up.

The sizing methodology is based on the effectiveness– number of transfer units (NTU) method. A thermal scaling parameter, referred to as the k factor, is applied to the initial geometry and dynamically updated at each iteration to rescale the heat exchanger. This iterative process continues until the hydrogen outlet temperature matches the PEMFC stack's target operating condition, ensuring effective thermal integration of the cryogenic hydrogen loop.



The second heat exchanger conditions the compressed air to bring it to the required PEMFC steady temperature. Many methods can be used to efficiently extract the waste heat of the PEMFC such as air cooling, heat spreaders or liquid cooling. Yet, for high waste heat (superior to 10kW), liquid cooling is a more efficient method (Baroutaji et al., 2021), consequently this method was considered in the current TMS architecture. The liquid cooling heat exchanger for the PEMFC stack is modeled as a finned flat tube exchanger, designed to manage the thermal load generated during PEMFC operation. The sizing process uses the effectiveness–NTU method in an iterative framework (Brooks & Mavris, 2021). Specifically, two pairs of dependent and independent variables are considered (see Table 5). As previously, the $k\ factor$ is dynamically updated in each iteration to rescale the heat exchanger geometry, starting from an initial assumed cube of 10 in. per side. Because the liquid coolant circuit operates in a closed loop, the target outlet temperature of the coolant is precomputed to match the inlet temperature, ensuring thermal equilibrium and effective heat rejection. Once convergence on the effectiveness and geometry is achieved, the solver computes the necessary ram air flow rate to meet the cooling requirement, ensuring the PEMFC stack operates within its designated temperature range for performance and durability. The algorithm used to size the PEMFC stack liquid heat exchanger is outlined in Table 6. The hot ram air exiting the heat exchanger will then be expelled and create a Meredith effect, where the exhausted hot air will provide an additional thrust (Frey et al., 2025). In order to integrate the air precooler in the global NPSS code, the modeling approach selected is presented in Figure 15. A bypass must be implemented to avoid an error from the solver. Indeed, during descent, the flow rate density increases and there is a limit altitude beneath which the mass flow rate is more than enough to cool down at 176°F. The NPSS solver tries to reduce the flow rate to meet the targeted temperature by giving negative values to the fan velocity. This leads to an error. The solution is therefore a bypass architecture with fixed rotating velocity for the fan and variation of bypass ratio.

Table 5. Considered dependent-independent variables.

Dependent Variable	Independent Variable
k_{factor}	Target effectiveness
Ram Air Flow Rate	Liquid Coolant Outlet Temperature

Table 6. Iterative sizing algorithm for liquid-cooled proton exchange membrane fuel cell (PEMFC) heat exchanger.

Step	Description
1	Initialize geometry
2	Compute required incoming liquid temperature around the PEMFC to ensure steady stack temperature
3	repeat
4	Initialize ram air flow rate
5	repeat
6	Initialize (k_{factor})
7	repeat
8	Initialize guess for air and liquid side temperatures
9	Compute liquid and air side characteristics using the effectiveness–NTU method
10	Update (k_{factor})
11	until the effectiveness converges to the target
12	Update Hydrogen outlet temperature
13	until outlet Hydrogen temperature is at the stack steady temperature

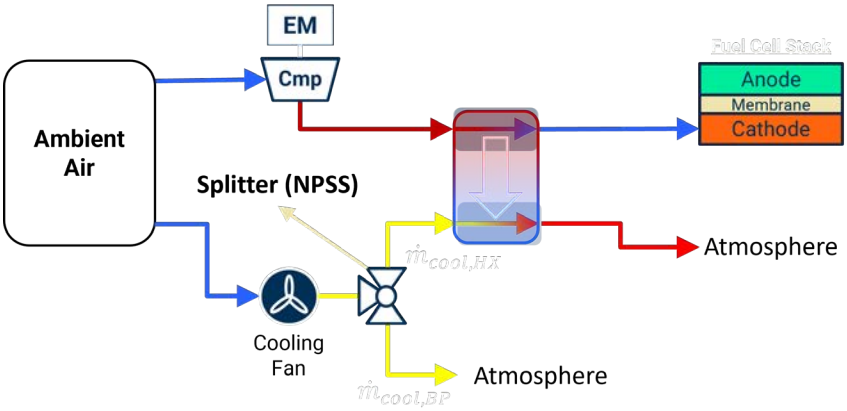


Figure 15. Air precooler modeling approach.

Finally, a third heat exchanger maintains the PEMFC stack temperature within safe operational limits to ensure system stability and fuel cell longevity. The air-air heat exchanger, also called air precooler, is used to cool down the compressed air to the operating temperature of the PEMFC stack. Several options can be considered to cool down the compressed air. First, hydrogen could be used as a liquid medium to remove the compressed air heat. Indeed, the hydrogen temperature is very low before the hydrogen boiler. This method has a double benefit: it cools down the air and heats up hydrogen. Thus, the hydrogen boiler can be downsized as the temperature raise needed is less important. It can ultimately lead to weight saving for the total system. However, this methodology presents a major drawback as the hydrogen mass flow rate is very low and probably not enough to achieve the required heat rejection. Another option would be to use hydrogen as a heat sink in addition to the air from ram air channels (Quaium et al., 2022). Yet this solution exacerbates the complexity of the architecture of the thermal management system. The most promising option would be to exploit only the ram air as the coolant medium and is further assessed below. In this solution, the air precooler receives hot pressurized air from the compressor outlet and uses ram air as a medium to extract the heat. The geometry used to model this heat exchanger is a finned flat tube exchanger, designed to manage the thermal load generated during the pressurization of ram air by the compressor. As for the PEMFC air-liquid heat exchanger, the sizing process uses the effectiveness–NTU method (Navarro & Cabezas-Gómez, 2006) in an iterative framework. The architecture of the system and the sizing methodology used are also similar to the PEMFC heat exchanger. The exact same pairs of dependent and independent variables are considered. Indeed, a *k factor* is implemented to match targeted effectiveness, and the ram air mass flow rate is varied to reach the correct temperature at the outlet of the heat exchanger (i.e., the stack temperature). The *k factor* is dynamically updated at each iteration to rescale the heat exchanger geometry, starting from an initial assumed cube of 20 in. per side. Once convergence on the effectiveness and geometry is achieved, the solver varies the ram air mass flow rate until the cooling requirement is satisfied. The new temperature of the compressed air at the outlet of the heat exchanger is recomputed at each iteration while ensuring thermal equilibrium and effective heat rejection. Finally, the necessary ram air flow rate to reach the steady stack temperature at the inlet of the stack is outputted. This ensures once again that the PEMFC stack operates within its designated temperature range for performance and durability.

Milestones

- Imported the flight mission defined in EDS, used for aircraft sizing, into the NPSS environment. The manufacturer has also provided the average electrical power and bleed air requirements for each flight phase of the baseline aircraft. Step 1 has been completed.
- Established the fuel cell stack element for use in the NPSS environment, with both on-design and off-design capabilities. Step 2 has been completed.
- Established the fuel cell elements and their connections within the NPSS environment, and implemented weight-estimation models. Ongoing work focuses on refining the weight-estimation models to account for changes in the aircraft ducting system, such as additional air intakes, ducts, and nozzles. Step 3 is in progress.
- Implemented a cryogenic tank sizing function with the capability to handle several material types into the model. Step 4 has been completed.
- Developed thermal management system models and integrated the models into the NPSS environment and tested the models. Additional design alternatives are currently being explored. Step 5 is in progress.



Major Accomplishments

- Added all major BoP components to a single modeling and simulation environment, tested, and used the components to create a suitable performance table for the aircraft mission analysis tool.
- Conducted a literature review, and identified the projected specific power and energy of the system's electrical components to support estimation of the system weight for the target year.

Publications

Terzi, B., Decroix, J., Wattebled, L. A., Jazzini, A. S., Tai, J. C., & Mavris, D. (2025). Modeling Methodology for PEM Fuel Cells as Auxiliary Power Units in Aircraft Applications. In *AIAA AVIATION FORUM AND ASCEND 2025* (p. 3373).

Outreach Efforts

- Scheduled and participated in monthly meetings with Gulfstream, Honeywell, and FAA to guide this research effort.
- Attended ASCENT biannual meetings.

Awards

None.

Student Involvement

This task involves four graduate students: Berkay Terzi (Ph.D. candidate), who worked on fuel cell stack modeling and integration of fuel cell components into the modeling environment; Jeremy Decroix (Ph.D. candidate), who worked on hydrogen tank sizing; Leo Wattebled (M.S. candidate), who worked on hydrogen preheater modeling; and Axel Jazzini (M.S. candidate) worked on compressor weight estimation and air precooler modeling.

Plans for Next Period

- Refine some weight estimation models which are used in Task 2.
- Integrate the off-line PEMFC code into the EDS environment to enable seamless data transformation between them and centralize control from a single hub.

Task 3 – Integrating Vehicle & PEMFC Models & Conducting Trade Studies

Georgia Institute of Technology

Objective

The objective of Task 3 is to integrate the offline PEMFC code developed under Task 2 with the EDS environment to perform aircraft-level assessments and conduct feasibility studies for the proposed fuel-cell system.

Research Approach

As described in Task 2, the proposed fuel-cell system must satisfy three primary objectives: (1) supplying electrical power to aircraft subsystems, (2) providing pressurized air for the ECS, and (3) enabling independent engine start without external power sources. In the baseline aircraft, the conventional gas-turbine APU fulfills these requirements by delivering backup AC power up to 20,000 feet, supplying in-flight bleed air for air-conditioning up to 15,000 feet, and providing pneumatic power for engine start. These functions are achieved through extracting of shaft power and bleed air from the engine compressor (Honeywell, 2008).

In the proposed architecture, however, the fuel-cell system will supply continuous electrical power and pressurized air for the ECS throughout the entire flight, thereby reducing Jet-A fuel consumption and overall emissions. In Task 3, the fuel-cell system weight will be estimated using the modeling environment developed in Task 2, and aircraft-level weight-balance implications will be assessed in EDS. The overarching objective is to perform these analyses within a unified modeling and simulation framework. Using this simulation framework will also streamline the process and enable possible parametric studies.

Step 1: PEMFC System Weight Estimation

One of the main parameters for sizing a PEMFC system to meet target performance is the power demand of the aircraft subsystems. Because business-jet designs vary more widely than those of commercial transport aircraft, the subsystem

power demand which is provided directly by the manufacturer rather than estimated using generalized equations will be used for sizing the system.

The power demand of the electric ECS is another key factor in the sizing process. Since this project focuses on fuel cells, the ECS packs themselves will not be modeled; instead, their power consumption will be included within the overall aircraft subsystem loads. However, the cabin air compressors and their driving electric motors will be sized to deliver the required discharge pressure while providing the necessary fresh-air flow rate to the cabin. Their resulting power consumption will be quantified and will play a significant role in the overall sizing process. The selection of the thermal-conditioning pack cycle type, as shown in Figure 12, is also an important consideration, since discharge pressure directly influences power consumption. Based on aircraft manufacturer feedback, the discharge pressure associated with the preferred thermal-conditioning pack will be used.

Once system performance, including parasitic power consumption, has been defined, the weights and volumes of the components must be estimated for aircraft-level assessment. Because implementing such a system is a long-term effort, technology-projection studies are required to establish future assumptions for component-specific power, volume, and efficiency. Several references provided in Task 2 already contain useful projected specific-power data for certain components (Aerospace Technology Institute, 2022; Pastra et al., 2022; Hall et al., 2022; Tiede et al., 2022; Schröder et al., 2021). Having projected values across multiple future time horizons also enables identification of the breakeven point at which the fuel-cell system becomes competitive in terms of weight. Ongoing work includes expanding the set of technology-assumption studies and identifying current industry manufacturers of fuel cells and fuel-cell components. In parallel, the system layout will also be defined to support accurate estimation of ducting and cable weights, as well as any internal or external modifications to the aircraft required to integrate the system into the aircraft.

Step 2: Aircraft Level Assessment of the New System

For seamless integration of the PEMFC modeling environment into EDS, a performance table is generated by running the model in off-design mode at each point in the flight envelope. This table contains the hydrogen consumption rate, ram drag, and the thrust produced by the expansion of warm, pressurized air. However, the aircraft mission analysis software FLOPS cannot simultaneously utilize two engine decks within the same mission segment. In this study, both the conventional engine deck and the PEMFC performance table are required to conduct the analysis. To address this limitation, a combined engine deck is created by merging the conventional engine deck with the PEMFC performance table, following the process outlined in Figure 16.

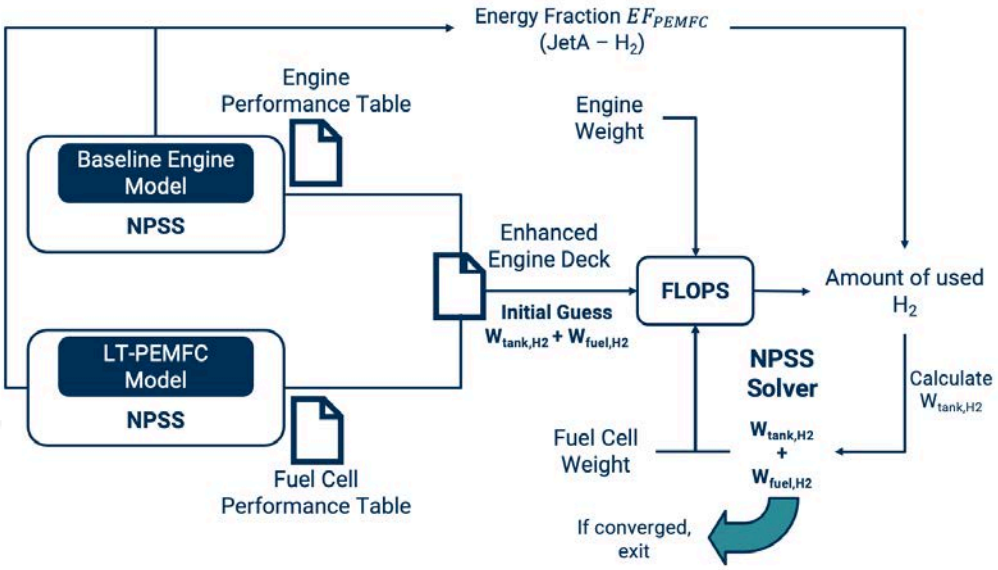


Figure 16. Aircraft modeling environment integration process.



The following performance metrics are modified to account for hydrogen consumption, PEMFC-generated thrust and the drag penalty introduced by the PEMFC system integration:

$$\dot{m}_{Fuel} = \dot{m}_{kerosene} + \dot{m}_{hydrogen} \quad \text{(Eq. 10)}$$

$$F_g = F_{g,Engine} + F_{g,PEMFC} \quad \text{(Eq. 11)}$$

$$D_{ram} = D_{ram,Engine} + D_{ram,PEMFC} \quad \text{(Eq. 12)}$$

$$TSFC = \frac{\dot{m}_{kerosene}+\dot{m}_{hydrogen}}{(F_{g,Engine}+F_{g,PEMFC})-(D_{ram,Engine}+D_{ram,PEMFC})} \quad \text{(Eq. 13)}$$

To track the relative usage of kerosene and hydrogen throughout the mission the energy fraction (EF) metric is defined as:

$$EF = \frac{\dot{m}_{hydrogen}}{\dot{m}_{kerosene}+\dot{m}_{hydrogen}} \quad \text{(Eq. 14)}$$

The resulting combined dataset is then imported into FLOPS within the EDS environment to enable accurate mission analysis and determine the required liquid hydrogen tank capacity.

In designing a new aircraft power system, it is also essential to consider emergency scenarios that require redundancy. In the proposed configuration, the fuel cell system serves as the primary power source under the revised mission profile. However, one of the original engine-mounted generators may be retained—potentially in a downsized form—to provide a backup power source in the event of a fuel-cell system failure. This ensures continued electrical power supply to critical subsystems, thereby maintaining operational safety and system reliability.

To support a fair comparison against the PEMFC-powered configuration, the notional calibrated aircraft baseline is additionally resized to reflect the fuel consumption that would result if the conventional APU were operated throughout the entire mission. This produces a more representative reference configuration, since the PEMFC system is designed to supply electrical power and bleed air to the ECS continuously for the full mission duration.

For the aircraft-level system assessment, two evaluation pathways are considered. The first is a retrofit analysis, in which the aircraft geometry remains unchanged; in this case, the comparison can be conducted under either fixed-payload or fixed-range assumptions. The second pathway is a resize analysis, where the fuselage is extended to accommodate PEMFC subsystem integration—most notably the cryogenic hydrogen tank. Across both approaches, key metrics such as weight penalties or benefits, fuel savings, emissions reductions, and payload–range impacts are systematically tracked to quantify the overall aircraft-level performance of PEMFC integration.

Milestone

Ran two modeling and simulation environments separately to generate interim results, and to demonstrate their usefulness. Once the fuel cell model is finalized, efforts will be focused on integrating these environments. Steps 1 and 2 are in progress.

Major Accomplishments

Examined the weight effects at the aircraft level are examined using the interim results from the fuel cell sizing tool.

Outreach Efforts

- Scheduled and participated in monthly meetings with Gulfstream, Honeywell, and FAA to guide this research effort.
- Attended ASCENT biannual meetings.

Publications

None.



Awards
None.

Student Involvement
This task involves two graduate students: Berkay Terzi (Ph.D. candidate), who worked on the PEMFC system weight estimation; Jeremy Decroix (Ph.D. candidate), who worked on the aircraft modeling environment integration process and the aircraft system-level performance assessment.

Plans for Next Period
- Integrate the off-line PEMFC code into the EDS environment to enable seamless data transformation between them and centralize control from a single hub.
- Conduct more comprehensive design studies by expanding the design space following the integration of the two environments.
- Evaluate the volumetric impact of the new system on the aircraft.

References

Aerospace Technology Institute. (2022). Fuel Cells Roadmap Report (FZO-PPN-COM-0033). https://www.ati.org.uk/wp-content/uploads/2022/03/FZO-PPN-COM-0033-Fuel-Cells-Roadmap-Report.pdf

Bargal, M. H., Abdelkareem, M. A., Tao, Q., Li, J., Shi, J., & Wang, Y. (2020). Liquid Cooling Techniques in Proton Exchange Membrane Fuel Cell Stacks: A Detailed Survey. Alexandria Engineering Journal, 59(2), 635–655. https://doi.org/10.1016/j.aej.2020.02.005

Baroutaji, A., Arjunan, A., Ramadan, M., Robinson, J., Alaswad, A., Abdelkareem, M. A., & Olabi, A.-G. (2021). Advancements and prospects of thermal management and waste heat recovery of PEMFC. *International Journal of Thermofluids, 9*, 100064. https://doi.org/10.1016/j.ijft.2021.100064

Brooks, J., & Mavris, D. N. (2021). Compact heat exchanger sizing and weight estimation. In *AIAA Propulsion and Energy 2021 Forum* (p. 3711). https://doi.org/10.2514/6.2021-3711

Cai, Y. (2023). Multi-mission sizing and analysis framework for aircraft and subsystem architectures with electrified propulsion systems [Doctoral dissertation, Georgia Institute of Technology].

Campbell, K., & Talbert, J. E. (1945). *Some advantages and limitations of centrifugal and axial aircraft compressors," SAE Transactions* (pp. 607–620). SAE Technical Paper 450224. https://doi.org/10.4271/450224

Chang, Y., Qin, Y., Yin, Y., Zhang, J., & Li, X. (2018). Humidification Strategy for Polymer Electrolyte Membrane Fuel Cells–A Review. *Applied energy, 230*, 643–662. https://doi.org/10.1016/j.apenergy.2018.08.125

Daggett, D., Eelman, S., & Kristiansson, G. (2003). Fuel cell APU. In *AIAA International Air and Space Symposium and Exposition: The Next 100 Years* (p. 2660).

Datta, A. (2021). PEM Fuel Cell Model for Conceptual Design of Hydrogen eVTOL Aircraft. National Aeronautics and Space Administration. https://ntrs.nasa.gov/citations/20210000284

EASA. (2020). *Type Certificate Data Sheet No. EASA.IM.A.348 for Gulfstream G280*. European Union Aviation Safety Agency. https://www.easa.europa.eu/en/document-library/type-certificates/noise/easaima348-gulfstream-lp-g280

FAA. (1996). AC 25-20 - Pressurization, Ventilation and Oxygen Systems Assessment for Subsonic Flight Including High Altitude Operation. Federal Aviation Administration. https://www.faa.gov/regulations_policies/advisory_circulars/index.cfm/go/document.information/documentid/22648

Frey, A. C., Stonham, J., Bosak, D., Sangan, C. M., & Pountney, O. J. (2025). Radiators in fuel cell powered aircraft: the effect of heat rejection on drag. *Applied Thermal Engineering, 274*, 126697. https://doi.org/10.1016/j.applthermaleng.2025.126697

Hall, C., Pastra, C. L., Burrell, A., Gladin, J., & Mavris, D. N. (2022). Projecting Power Converter Specific Power through 2050 for Aerospace Applications. *2022 IEEE/AIAA Transportation Electrification Conference and Electric Aircraft Technologies Symposium (ITEC+EATS)*, Anaheim, California (pp. 760–765). https://doi.org/10.1109/ITEC53557.2022.9813991

Honeywell. (n.d.). *Honeywell 36-150 Ported Shroud APU, Redimec*. https://www.redimec.com.ar/contenido/productos/pdf/1425325504_1.pdf (accessed November 21, 2024)

Johnson, W., Baltman, E., & Koci, F. (2024). Assessment of Insulation Systems for Aircraft Liquid Hydrogen Tanks. *IOP Conference Series: Materials Science and Engineering, 1301*, 012062. https://doi.org/10.1088/1757-899X/1301/1/012062



Link, A., Ludowicy, J., & Staggat, M. (2022, September 4-9). Assessment of a serial cooling concept for htpem fuel cell systems for aviation applications [Conference paper]. 33rd Congress of the International Council of the Aeronautical Sciences – ICAS 2022, Stockholm, Sweden. https://elib.dlr.de/188369/1/ICAS2022_0456_paper.pdf

MANN+HUMMEL. (n.d.). Water Separator- Fuel Cells. https://shop.mann-hummel.com/en/e-mobility/fuel-cells 1231/water-separator.html (accessed May 14, 2025).

MicroPump, Inc. (2025). EagleDrive DEE/LE. https://micropump.com/products/drives/eagledrive-deele?language_code=en, 2025

Navarro, H. A., & Cabezas-Gómez, L. C. (2006). Effectiveness-NTU computation with a mathematical model for cross-flow heat exchangers. *Brazilian Journal of Chemical Engineering, 24*(04), 509-521.

O'Hayre, R., Cha, S.-W., Colella, W., & Prinz, F. B. (2016). *Fuel Cell Fundamentals*. John Wiley & Sons. https://doi.org/10.1002/9781119191766

Pastra, C. L., Hall, C., Cinar, G., Gladin, J., & Mavris, D. N. (2022). Specific Power and Efficiency Projections of Electric Machines and Circuit Protection Exploration for Aircraft Applications. *2022 IEEE/AIAA Transportation Electrification Conference and Electric Aircraft Technologies Symposium (ITEC+EATS)*, Anaheim, California (pp. 766–771). https://doi.org/10.1109/ITEC53557.2022.9813927

Quaium, F., Bielsky, T., & Thielecke, F. (2022). *Fuel Cell Cooling System Design for Hydrogen-Powered Concept Aircraft*. Deutsche Gesellschaft für Luft- und Raumfahrt - Lilienthal-Oberth e.V. (Text). https://doi.org/10.25967/570127

Rosero, J., Ortega, J., Aldabas, E., & Romeral, L. (2007). Moving towards a more electric aircraft. *IEEE Aerospace and Electronic Systems Magazine, 22*(3), 3–9. https://doi.org/10.1109/MAES.2007.340500

Rotrex Fuel Cell Compressors. (2025). Fuel Cell Compressors. https://rotrex-fuel-cell-compressor.com/fuel-cell-compressors/

Schröder, M., Becker, F., Kallo, J., & Gentner, C. (2021). Optimal operating conditions of PEM fuel cells in commercial aircraft. *International Journal of Hydrogen Energy, 46*(66), 33218–33240. https://doi.org/10.1016/j.ijhydene.2021.07.099

Smith, P. J., Bennett, W. R., Jakupca, I. J., Gilligan, R. P., & Edwards, L. G. (2021). *Proton Exchange Membrane Fuel Cell Transient Load Response*. National Aeronautics and Space Administration. https://ntrs.nasa.gov/citations/20210018094

Tagge, G., Irish, L., & Bailey, A. R. (1985). *Systems study for an Integrated Digital-Electric Aircraft (IDEA).* National Aeronautics and Space Administration. https://ntrs.nasa.gov/citations/19850007405

Tiede, B., O'Meara, C., & Jansen, R. (2022). Battery key performance projections based on historical trends and chemistries," *2022 IEEE/AIAA Transportation Electrification Conference and Electric Aircraft Technologies Symposium (ITEC+EATS)*, Anaheim, California (pp. 754–759). https://doi.org/10.1109/ITEC53557. 2022.9814008

Voth, V., Lübbe, S. M., & Bertram, O. (2024). Estimating Aircraft Power Requirements: A Study of Electrical Power Demand Across Various Aircraft Models and Flight Phases. *Aerospace, 11*(12), 958. https://doi.org/10.3390/aerospace11120958

Willich, C., Tomaszewski, A., Henke, M., Friedrich, K. A., & Kallo, J. (2014). Temperature effect due to internal reforming in pressurized SOFC. *Journal of The Electrochemical Society, 161*(5), F674. https://doi.org/10.1149/2.075405jes

Willich, C., Frank, D., Graf, T., Wazlawik, S., Brandao, S., & Bauer, C. (2024). High-Altitude Operation of a Commercial 100 kW PEMFuel Cell System. Energies, 17(24), 6903. https://doi.org/10.3390/en17246309



Project 096 Future Transportation System Opportunities and Constraints

Georgia Institute of Technology

Project Lead Investigator

Principal Investigator:
Professor Dimitri N. Mavris
Director, Aerospace Systems Design Laboratory
School of Aerospace Engineering
Georgia Institute of Technology
Phone: (404) 894-1557
Fax: (404) 894-6596
Email: dimitri.mavris@ae.gatech.edu

Co-P.I.:
Dr. Holger Pfaender
Aerospace Systems Design Laboratory
School of Aerospace Engineering
Georgia Institute of Technology
Phone: (404) 385-2786
Fax: (404) 894-6596
Email: holger.pfaender@ae.gatech.edu

University Participants

Georgia Institute of Technology (Georgia Tech)

- P.I.s: Dr. Dimitri N. Mavris, Dr. Holger Pfaender
- FAA Award Number: 13-C-AJFE-GIT-159
- Period of Performance: October 1, 2024, to September 30, 2025
- Tasks:
  1. Develop Background Scenarios
  2. Commercial Aviation
  3. Non-traditional Vehicle Scenarios
  4. Regional Passenger Demand Estimation
  5. Vehicle Technology Specific Scenarios
  6. Coordination with FAA
  7. Documentation

Project Funding Level

This research was funded by the Federal Aviation Administration (FAA) Office of Environment and Energy through ASCENT, the FAA Center of Excellence for Alternative Jet Fuels and the Environment, Project 096, through FAA Award Number 13-C-AJFE-GIT-159 under the supervision of Joshua Glottmann. Any opinions, findings, conclusions or recommendations expressed in this material are those of the authors and do not necessarily reflect the views of the FAA.

This project is funded at the following levels: Georgia Tech ($800,000). Georgia Tech has agreed to a total of $800,000 in matching funds for a two-year period of performance. This total includes salaries for the project director, research engineers, and graduate research assistants and for computing, financial, and administrative support, including meeting arrangements. The institute has also agreed to provide tuition remission for students whose tuition is paid via state funds.



Investigation Team

Georgia Institute of Technology

Dimitri Mavris (P.I.), Tasks 1-7
Holger Pfaender (co-P.I.), Tasks 1-7
Raphaël Gautier (research faculty), Tasks 1-7
Cedric Justin (research faculty), Tasks 1-7
Paul Boyer (graduate student), Tasks 1-7
Cristobal Garces (graduate student), Tasks 4, 6, 7
Lensa Alemu (graduate student), Tasks 3-6
Autumn Edwards (graduate student), Tasks 1-6
Anass Jari (graduate student), Task 4, 6, 7
Yilin Deng (graduate student), Tasks 1-6
Xi Wang (graduate student), Tasks 1-6
Hans Leung (graduate student), Tasks 1-6

Project Overview

The primary objective of this research project is to support the FAA in modeling and assessing the potential future evolution of the next generation aircraft fleet while supporting the FAA Office of Environment and Energy goals and objectives. Research under this project will consist of three integrated focus areas: (1) developing a set of harmonized scenarios investigating what the air transportation system will look like in 2050, 2075, or 2100, (2) modeling advanced aircraft technologies and advanced vehicles expected to enter the fleet through 2100, and (3) performing vehicle and fleet level assessments based on input from the FAA and the results of (1) and (2).

Task 1 – Develop Background Scenarios

Georgia Institute of Technology

Objectives

The study will begin with a comprehensive literature review to provide an overview of the current state of the aviation industry and identify the challenges facing the sector. The research will also potentially include interviews with aviation experts, policymakers, and industry leaders to gain insights into the industry's current state and future direction. This review will be used to define macroeconomic and general technological advancements expected during this extended time horizon to 2100.

Research Approach

Literature Review

A review of the aviation sector's impacts on global carbon dioxide (CO_2) emissions is presented in the Sixth Assessment Report (AR6) of the Intergovernmental Panel on Climate Change (IPCC) prepared by Working Group (WG)-III. The review emphasizes that around 65% of the sector's emissions are from international flights, with total emissions in 2018 adding to about 1 gigaton (Gt) of CO_2. The research focuses on the alarming acceleration of emission rates, which increased by 2.5% annually over the previous 20 years to almost 4% annually between 2010 and 2018. The study examines the net warming effects of aviation's CO_2 and non-CO_2 emissions, such as water vapor, soot, sulfur dioxide, and nitrogen oxides (NO_x).

Since net-zero emissions are a requisite for 1.5° scenarios, it calls for sweeping transformations in both technology and fuel types. It also asserts current technological advances, like blended wing body aircraft that could deliver about 10% fuel savings, will not be able to offset projected emissions growth due to their slow introduction into the market. The AR6 IPCC report also examines operational inefficiencies and potential improvements, including finding that better air traffic control could reduce emissions by 13% globally by the year 2050. It points to major uncertainties about non-CO_2 impacts of liquid hydrogen powered aircraft and suggests a move toward high-speed rail as a practical substitute for regional travel, which could significantly lower the demand for short-haul flights (Guivarch et al., 2022).

The process for generation of scenarios is a major component of the IPCC AR6 reports, involving collaboration between the IPCC's working groups to combine socio-economic storylines with environmental impacts. This comprehensive approach to



scenario planning has been explained in the report, showing how socio-economic data are used with climate simulations to yield accurate and relevant policy scenarios (IPCC, 2023).

The report presents mid- to long-term projections through 2050 to illustrate how technology and infrastructure improvements could reduce aviation emissions, discusses hybrid modelling approaches used to project developments in the sector, and describes the top-down/bottom-up hybrid approach it uses which captures a wide range of drivers. It also rates potential mitigation pathways across three levels of concern based on a multidimensional feasibility framework that considers their transformative impact and feasibility, providing a systematic method for measuring the efficacy of different policymaking and technological approaches in addressing climate impacts from aviation (Lee et al., 2021).

To gain an understanding of how one of the models used by IPCC works, the Global Change Analysis Model (GCAM) was studied. GCAM integrates environmental, economic, and energy systems to forecast global future scenarios effectively. GCAM calculates transportation service demand using a sophisticated formula that includes variables such as per-capita gross domestic product (GDP), service price, population, and elasticity measures, which enables the prediction of future transportation needs under various socio-economic conditions.

More details in GCAM (discussing competition between different transportation subsectors, technology share, and time value of transport) also show how the model handles competition. The cost calculation method for alternative transportation technologies is also overly broad with respect to fuel price, vehicle fuel intensity factors, non-fuel costs and load factors (Joint Global Change Research Institute, 2024).

Another aviation model designed to quantify environmental and economic impacts of policies related to the emission reduction is the Aviation Emissions and Evaluation of Reduction Options Modelling System (AERO-MS). The AERO-MS is a framework built to provide a comprehensive quantitative system analysis of the present and future air transport system with special emphasis on assessing emissions from aircraft engines. The AERO-MS evaluates the downstream effect of policy change-related impact on supply-side costs, which in turn affects demand for air travel. The system evaluates global emissions under different emission mitigation scenarios, incorporating responses from all key stakeholders, including supply (airlines), demand (consumers), and policy sector (governments and manufacturers).

The AERO-MS has five linked modules: (1) the Unified Database, Airport Technology Model (ATEC), (2) Air Transportation Demand Module (ADEM), (3) Aviation Cost Module (ACOS), (4) Flights and Emissions Modules (FLEM), and (5) the Direct Economic Impacts Module (DECI). Together, these modules provide complementary perspectives on developments in the aviation system, with the DECI offering detailed assessments of volumes of air transport traffic, airline revenues and fleet and flight activity—all according to data from the other modules (European Commission, 2004).

The model organizes its analysis according to three scenarios: (1) the base scenario, which demonstrates what would happen in a business as usual global air transportation system, (2) the datum scenario, consisting of projections for technical and economic progress that continue with no policy changes, and (3) the forecast situation which inspects the impacts of various policy alternatives. The comparison of alternative mitigation policy measures against a common baseline enables the AERO-MS to provide high-resolution projections of future states, making the assessments applicable to real-world policy evaluation and subsequent efforts at mitigation with robust estimates.

In general, the AERO-MS is an important and necessary tool to better understand and predict the consequences of policy and technology changes in the aviation sector (European Union Aviation Safety Agency, 2009).

In addition to these models, trend projection is an important part of aviation forecasting. Trend projection is a process of making educated predictions of the future by using the known past as a basis. This approach necessitates in-depth knowledge of a large number of factors that affect the predicted outcomes. Trend projection should consider the consistency and variability of the main economic indicators, the technological advances, and the demographic changes.

To effectively project trends, the focus needs to dive into the inner structure and reasoning behind each variable. This requires examining how GDP, population, and technological advancement interacted with aviation demand in the past and how these can be projected to affect industry in the future under different conditions. For instance, when GDP is stable, air travel demand may be more predictably rising; whereas, when the economy is unstable, travel behavior can become more challenging to predict.



Apart from that, long-term forecasting should also take into consideration the probable occurrences of disturbances that can cause the trends to break. These disturbances might include, for instance, recent breakthroughs in aircraft technologies that would cut down the operation costs or new regulations that make flight operations difficult. In a like manner, there can be a massive geopolitical incident or a significant economic crisis that will highly affect the market conditions, which in turn would force changes in the trend projections. Besides, the forecast changes must be capable of bending if the baseline ideas turn out to be different than expected or if future circumstances exhibit unexpected behavioral changes. This versatility guarantees the survival of the methodology over time and its high predictive capability as to the strategic decisions of the aviation sector. The skill of recalibrating forecasts in the face of new developments or adaptations in the underlying assumptions is key for the accuracy and credibility of long-term aviation forecasts (Ashford et al., 2011).

Given the importance of trend projections, understanding the underlying assumptions in any forecast becomes important. The FAA forecast implements both optimistic and pessimistic scenarios to consider changes in national and global economic markets, which requires flexibility in bringing in the effects of various uncertainties that might impact the aviation sector, such as the economic recession or geopolitical conflicts (FAA, 2020).

The FAA's forecasting methodology is based on economic data and assumptions from IHS Markit® Economics. The data are divided into data, such as the Consumer Price Index (CPI) and unemployment rates, to form baseline, optimistic, and pessimistic economic scenarios. The scenarios typically do not consider factors such as recessions, changes in consumer behavior, and the overall economic effect of international conflicts.

Among the specific data sources utilized in the FAA forecast are the historical data from the Bureau of Labor Statistics (BLS) and Bureau of Economic Analysis (BEA) including forecasts from IHS Markit. These sources provide economic information that the FAA uses to make economic assumptions which, in turn, guides forecasts of future domestic aviation demands (FAA, 2023).

Milestones

- Examined the scenarios in the studies covered in Task 1 for how they include aviation and the emissions estimates.
- Identified how aviation is integrated into global change analysis models, including their links to the global economy and emissions impacts.

Major Accomplishments

The research team identified potential data sources for the development of very long-term trends. The IPCC scenarios are still a benchmark for climate analyses and therefore are useful in identifying the circumstances aviation will have to operate in. In addition, the scenarios for the 7th Assessment Cycle are currently under development. The research team therefore anticipates that this project will be able to assimilate data produced for this purpose.

Publications

None.

Outreach Efforts

- Presented at biannual ASCENT Advisory meetings.
- Participated in biweekly teleconferences with the FAA Technical Monitor.

Awards

None.

Student Involvement

Graduate students have been involved in the research of the background scenarios. This includes documentation and presentation of their findings. The students conducted research into how global change scenarios include or at least are connected to aviation-specific scenarios.

® IHS Markit is a registered trademark of S&P Global Limited, in the United States and other countries.



Plans for Next Period

Consider opportunities to enrich the development efforts to connect aviation scenarios to high level global change scenarios including modeling efforts to cover a wide range of plausible outcomes of aviation sector scenarios.

References

Ashford, N. J., Mumayiz, S., & Wright, P. H. (2011). *Airport Engineering: Planning, Design, and Development of 21st Century Airports* (4th ed.). John Wiley & Sons, Hoboken, New Jersey.

European Commission. (2004, November 19). *Aviation Emissions and Evaluation of Reduction Options Modelling System (AERO-MS), Policy Model Inventory*. Joint Research Centre. https://web.jrc.ec.europa.eu/policy-model-inventory/explore/models/model-aero-ms

European Union Aviation Safety Agency. (2009). *SAVE - Study on Aviation and Economic Modelling - Final Report*. European Union Aviation Safety Agency, 2009/OP15. https://www.easa.europa.eu/en/document-library/research-reports/easa2009op15

FAA. (2020). *FAA U.S. Passenger Airline Forecasts, Fiscal Years 2020-2040* (v1.1.). Federal Aviation Administration

FAA. (2023). *FAA Aerospace Forecast Fiscal Years 2023–2043 - Appendix A: Alternative Forecast Scenarios*. Federal Aviation Administration. https://www.faa.gov/sites/faa.gov/files/FY%202023-2043%20Full%20Forecast%20Document%20and%20Tables_0.pdf

Guivarch, C., Kriegler, E., Portugal-Pereira, J., Bosetti, V., Edmonds, J., Fischedick, M., Havlík, P., Jaramillo, P., Krey, V., Lecocq, F., Lucena, A., Meinshausen, M., Mirasgedis, S., O'Neill, B., Peters, G. P., Rogelj, J., Rose, S., Saheb, Y., Strbac, G., Hammer Strømman, A., van Vuuren, D. P., & Zhou, N., (2022). Annex III: Scenarios and modelling methods. In: *IPCC 2022: Climate Change 2022: Mitigation of Climate Change. Contribution of Working Group III to the Sixth Assessment Report of the Intergovernmental Panel on Climate Change.* Eds. Shukla, A.R., Skea, J., Slade, R., Al Khourdajie, A., van Diemen, R., McCollum, D., Pathak, M., & Some, S., pp. 1842-1908 Cambridge, United Kingom and New York, New York, United States: Cambridge University Press. https://doi.org/10.1017/9781009157926.022

IPCC. (2023). *Climate Change 2023: Synthesis Report. Contribution of Working Groups I, II and III to the Sixth Assessment Report of the Intergovernmental Panel on Climate Change* [Core Writing Team, H. Lee and J. Romero (eds.)]. Intergovernmental Panel on Climate Change, Geneva, Switzerland, pp. 184. https://doi.org/1010.59327/IPCC/AR6-9789291691647

Joint Global Change Research Institute. (2024). *GCAM v7.1 Documentation: Demand for Energy*. https://jgcri.github.io/gcam-doc/demand_energy.html

Lee, J.-Y., Marotzke, J., Bala, G., Cao, L., Corti, S., Dunne, J. P., Engelbrecht, F., Fischer, E., Fyfe, J. C., Jones, C., Maycock, A., Mutemi, J., Ndiaye, O., Panickal, S., & Zhou, T. (2021). Future Global Climate: Scenario-Based Projections and NearTerm Information. In: *Climate Change 2021: The Physical Science Basis. Contribution of Working Group I to the Sixth Assessment Report of the Intergovernmental Panel on Climate Change.* 'Eds.' Masson-Delmotte, V., Zhai, P., Pirani, A., Connors, S. L., Péan, C., Berger, S., Caud, N., Chen, Y., Goldfarb, L., Gomis, M. I., Huang, M., Leitzell, K., Lonnoy, E., Matthews, J. B. R., Maycock, T. K., Waterfield, T., Yelekçi, O., Yu, R., & Zhou, B. Cambridge University Press, Cambridge, United Kingdom and New York, New York, pp. 553–672. https://doi.org/10.1017/9781009157896.006

Task 2 – Commercial Aviation

Georgia Institute of Technology

Objectives

This task includes the extension of existing commercial aviation forecasts with long-term trends to the year 2100. Additionally, this task will address potential vehicle and operational changes that could have larger scale effects on airline operating models. For example, reducing cruise Mach numbers to allow more efficient vehicles to operate could require significant airline schedule changes. A transition to smaller vehicle sizes and more direct service would also require significant route and schedule changes, which will also be among the potential changes to commercial aviation considered in this task.



Research Approach

The rapid technology estimation tools developed under prior PARTNER and ASCENT projects (Projects 010, 011, etc.) (FAA ASCENT, 2020) are being examined for how they could allow categorizing into smaller, well organized and tested components that can be used to quickly explore commercial aviation and emissions estimates for future years.

Enplanements and Passenger Flow Modeling

Using FAA T-100 All Carrier Segment Data (FAA, 2024) and the terminal area forecast (TAF) (FAA, 2024), the team developed a workflow to estimate current and future passenger volumes between airport pairs. The process includes:

- Extracting domestic segments from T-100 operations data.
- Reading TAF enplanements definitions across multiple subtypes (mainline, commuter, air taxi, United States (U.S.) and foreign international categories.
- Calculating base-year (2023) and forecast-year (2033) passengers for each airport.
- Applying TAF-derived growth factors to extrapolate future flows.
- Removing airport identifiers not included in the TAF dataset to ensure consistency.

A case study between Newark, New Jersey (Newark Liberty International Airport [EWR]) and Richmond, Virginia (Richmond International Airport [RIC]) was used in the monthly presentations to validate the methodology. Six airlines operated on the route in 2023, with passenger counts projected to grow from 74,968 in 2023 to 111,242 in 2033 based on TAF growth assumptions.

Terminal Area Forecast + Fleet Toolkit Integration

To support long-horizon commercial aviation analysis, the research team is loading the full 2024 TAF into a developing Fleet Toolkit built using existing libraries to handle user interaction. This includes:

- Airport metadata (i.e., location, region, identifiers)
- Enplanements
- Arrivals and departures (e.g., itinerant, local, civil, and military)
- Based aircraft counts
- Terminal Radar Approach Control activity levels

Initial visualizations and interactive components have been prototyped, demonstrating the ability to map traffic activity and airport operations using TAF data. These components will later support integrated CO_2 emissions and fuel-use projections.

Technology-Specific Fleet Evolution and Environmental Impact Assessment

Overview

In the initial part of this task the development of a route-level fleet evolution and environmental impact assessment framework designed to evaluate the long-term effects of emerging aircraft technologies across the U.S. domestic network. The framework models how advanced aircraft, such as the hybrid-electric aircraft (HEA), hydrogen-fueled aircraft, transonic truss-braced wing (TTBW) (Wells et al., 2024), and blended wing body (BWB) (Ahuja et al., 2024) configurations, propagate across origin–destination (OD) pairs as demand evolves over time. The methodology integrates forecasted operational activity, technology-specific performance models, survivorship behavior, and logistic adoption dynamics to quantify annual changes in fleet composition, fuel burn, and emissions through 2050.

Methodology

Data Integration

The assessment integrates three main datasets: (1) base-year OD operations, aircraft families, and distances from the T-100 Domestic Segment dataset, (2) future airport-level operations from the FAA TAF covering 2024 to 2050, and (3) technology-specific fuel burn and emissions coefficients obtained from the Global and Regional Environmental Assessment Trade (GREAT)-Airport Noise Grid Integration Method (ANGIM) environmental modeling framework. Airport identifiers, which appear in mixed formats (FAA location identifiers, International Air Transport Association), were standardized to International Civil Aviation Organization (ICAO) codes to improve OD matching.

OD-Level Operational Forecasting

Future OD matrices are generated using an iterative Fratar algorithm in which airport-level growth factors, computed as the ratio of future to base-year departures are applied until row and column totals match TAF-provided values within a 0.6% convergence threshold. These OD forecasts replace historical GREAT inputs so that technology adoption is driven by realistic demand patterns. Each OD pair functions as a yearly control volume whose required operations must be met



through a balance of surviving aircraft, replacements, and demand-driven growth. Survivorship curves determine how many aircraft remain in service, while logistic adoption parameters and seat-class distributions govern the entry of advanced technologies. Fuel burn and NO_x emissions for each aircraft family are evaluated using calibrated quadratic stage-length models, with coefficients sourced from National Aeronautics and Space Administration (NASA) system studies, FAA Continuous Lower Energy, Emissions and Noise (CLEEN) datasets, and reference aircraft calibrations, and route-year totals are obtained by multiplying intensity values by annual operations and stage length.

Output

The Interactive framework produces comprehensive annual outputs and projections for every domestic origin–destination pair, including route-level operations, distance flown, and technology penetration across conventional, TTBW, HEA, hydrogen fueled, and BWB aircraft from 2024 to 2050. Fuel burn and NO_x emissions are calculated for each technology category using quadratic stage-length models. Fleet turnover is tracked through survivors, replacements, and growth-driven additions, offering a clear view of how advanced technologies displace legacy aircraft over time. All results are delivered in multi-indexed tables indexed by year, origin ICAO, destination ICAO, and technology type, supporting integration with GREAT-ANGIM and FAA environmental assessments. Scenario-level summaries allow comparison across different adoption pathways and modeling assumptions, enabling long-range evaluation of fleet evolution, environmental impacts, and operational trends under alternative futures.

Units Management

Given the scope of the projects, datasets are sourced from multiple disciplines, which have different unit conventions when storing data. For one, it is not uncommon that datasets related to climate science use metric unit system whereas datasets related to U.S. aviation often employ imperial unit system. As the studies continue to expand, it is anticipated that an increasing number of datasets will be used. Thus, a unit conversion system was needed to provide a clean interface for defining and converting units.

To address this need, a proposed solution is the implementation of Pint, a Python® unit conversion library that enables arithmetic operations between numerical values and conversion to and from different units. In addition to conversion between common units, unit conversion for aviation-specific units, such as between available seat miles (ASM) and available seat kilometers (ASK), was also added to the library.

Milestone

Examine the scenarios in the studies covered in Task 1 for how these scenarios include aviation and the emissions estimates.

Major Accomplishments

The team made progress on establishing reference datasets like the well published forecasts. In addition, initial mockups of this capability have progressed to the prototyping phase.

Publications

None.

Outreach Efforts

- Presented at biannual ASCENT Advisory meetings.
- Participated in biweekly teleconferences with the FAA Technical Monitor.

Awards

None.

Student Involvement

The students have undergone training to familiarize themselves with the existing tools and their heritage.

® Python is a registered trademark of Python Software Foundation, Beaverton, Oregon.



Plans for Next Period
Quickly move to a functional prototype so that its usefulness can be evaluated and expanded from there.

References

FAA. (2024). *Terminal Area Forecast (TAF): Fiscal Years 2024–2044. U.S. Department of Transportation*. Federal Aviation Administration. https://www.faa.gov/data_research/aviation/taf

FAA. (2024). Air Carrier Activity Information System (ACAIS) – T-100 Segment and Market Data. U.S. Department of Transportation, Federal Aviation Administration. https://www.transportation.gov/policy/aviation-policy/airline-data

Lee, D. S., Fahey, D. W., Showron, A., Allen, M. R., Burkhardt, U., Chen, Q., Doherty, S. J., Freeman, S., Forster, P. M., Fuglestvedt, J., Gettelman, A., De León, Lim, L. L., Lund, M. T., Millar, R J., Owen, B., Penner, J. E., Pitari, G., Prather, M. J., Sausen, R., & Wilcox, L. J. (2021). The Contribution of Global Aviation to Anthropogenic Climate Forcing for 2000 to 2018. *Atmospheric Environment, 244*. https://doi.org/10.1016/j.atmosenv.2020.117834

ICAO. (2022). *Report on the Feasibility of a Long-term Aspirational Goal LTAG) for International Civil Aviation CO_2 Emission Reductions, Appendix M5 Fuels Sub Group Report*. International Civil Aviation Organization Committee on Aviation Environmental Protection. https://www.icao.int/sites/default/files/sp-files/environmental-protection/LTAG/Documents/ICAO_LTAG_Report_AppendixM5.pdf

Ahuja, J., Perron, C., Bermudez Rivera, R., Tai, J., & Mavris, D. (2024). *Performance Comparison of the Blended Wing Body and Tube-and-Wing Configurations*. Aerospace Systems Design Laboratory, Daniel Guggenheim School of Aerospace Engineering, Georgia Institute of Technology, Atlanta, Georgia. https://www.icas.org/icas_archive/icas2024/data/papers/icas2024_1296_paper.pdf

Wells, D., Gatlin, G., June, J., & Marien, T. (2024). *NASA Transonic Truss-Braced Wing Studies*. National Aeronautics and Space Administration. https://ntrs.nasa.gov/citations/20240007120

FAA ASCENT. (2020). *ASCENT Project 011 Rapid Fleet-Wide Environmental Assessment Capability*. Federal Aviation Administration Center of Excellence for Alternative. Jet Fuels and Environment.

Task 3 – Non-traditional Vehicle Scenarios
Georgia Institute of Technology

Objective
Several new vehicles with capabilities that are completely different from conventional commercial airlines are expected to enter service and potentially become widely adopted. For this reason, traditional airline demand projections are not appropriate and are also not able to define future projections of these vehicles.

For example, intra-regional air travel in the U.S. is an economically challenging endeavor as the demand on any given route is minor compared to inter-regional travel which typically consists of flights to, from, and between large hub airports connecting these regions. Given the limited demand and shorter ranges, regional aircraft serving these intra-regional markets tend to be smaller, which leads to direct operating costs amortized over a smaller number of passenger seat-miles compared to larger aircraft. Regional aircraft usually have lower daily average utilization owing to the time spent on the ground in between flights. This increases the significance of fixed costs which are amortized over fewer passenger seat-miles. Short-range missions also result in more takeoffs and landings on average for each flight hour. Proportionally more time is thus spent during takeoff and climb, where power settings are high, and more takeoffs and landings are performed. This increases the wear and tear on the aircraft structure. All this tends to increase the maintenance costs and therefore the operating costs of regional air transportation.

The core of this research effort and its objective is to generate an optimized operational model to allow the construction of a potential future state of aviation where new types of mobility are enabled by highly efficient vehicles.

Research Approach
This task tries to connect the conventional commercial business models with new types of operation also supported by the results of Task 4.

Milestone
None. Not started yet.



Major Accomplishments
None. Not started yet.

Publications
None.

Outreach Efforts
None. Not started yet.

Awards
None.

Student Involvement
Student researchers will be involved in all aspects of this task.

Plans for Next Period
Determine the specific scope of this task in collaboration with FAA Technical Monitors.

Task 4 – Regional Passenger Demand Estimation
Georgia Institute of Technology

Objective
Regional aviation in the United States has seen a significant decline, with many routes left abandoned due to a multitude of challenges. The objective of this task is to assess the feasibility of revitalizing regional aviation by forecasting passenger demand using more advanced modeling techniques under various macroeconomic and energy price scenarios.

Research Approach
To model regional aviation demand effectively, this task was divided into two interconnected parts:

1. Creating scenarios to evaluate the impact of different effects on current aircraft configurations and estimate change of aviation demand from the baseline scenario, including:
    a. Operating cost breakdown
    b. Categorization and evaluation of impacts on direct operating costs (DOC)
    c. Technology impacts
    d. Energy impacts
    e. Operations impact
    f. Scenarios generation
2. Investigation and evaluation of demand models to:
    a. Explore forecasting methods, including statistical time-series methods such as auto-regressive integrated moving average (ARIMA) and machine learning/deep-learning techniques (ML/DL).
    b. Seek models that can incorporate both internal and external factors.

Modeling Techniques
Air travel demand forecasting is an important task for understanding and planning the future of any aviation system. The choice of an appropriate forecasting model is heavily dependent on the type of factors and goals of the forecast itself. In the case of modeling the demand for regional aviation, historical data are sparse. Additionally, regional aviation is influenced by advancements in technology and the fluctuation of energy prices. Recent advancements in ML and DL have motivated many researchers to explore the applicability of these techniques to aviation-related problems such as forecasting passenger demand (Zachariah et al., 2023). The ability of ML and DL to learn complex patterns and incorporate high-dimensional data offers the potential to create more accurate and robust forecasting models.
Figure 1 shows a breakdown of common techniques to forecast passenger demand.

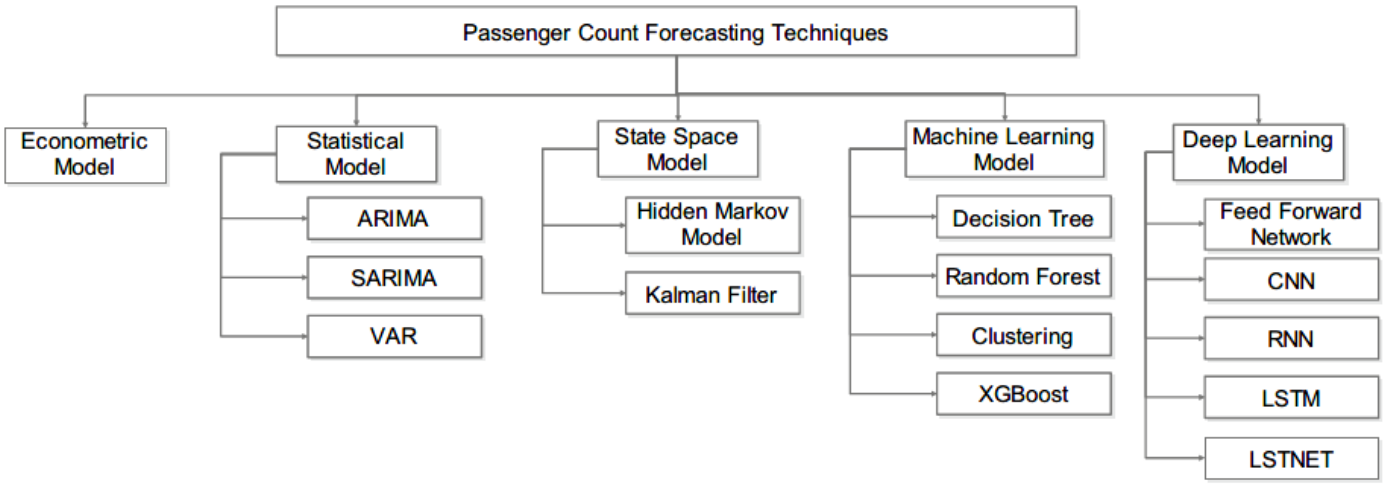


Figure 1. Aviation demand forecasting techniques.

Time-series forecasting is used to predict future trends based on historical data that are observed over regular intervals, much in an analogous way to econometric models. However, these models can be specifically designed to analyze and forecast data points ordered sequentially over time. A pure time-series forecasting method for aviation has increased challenges associated with the increased uncertainty and irregularity of air passenger movement. Two popular and well-known statistical time-series models are the ARIMA and seasonal auto-regressive integrated moving average (SARIMA) models. ARIMA and SARIMA both rely on linear assumptions between data points and thus limit their ability to accurately forecast high dimensional and nonlinear behavior as commonly found forecasting passenger demand. These models are typically used in hybridized models since alone, they often have poor performance at long time horizons (Kanavos et al., 2021).

ML provides a powerful framework for addressing the challenges of forecasting regional passenger demand. Unlike traditional models, ML techniques excel at identifying nonlinear relationships and dependencies between variables, making them more suitable to handle the complexity of factors influencing demand. Additionally, with the decrease in computational cost and increase of memory capacity, ML methods have already been utilized to solve real-world problems (Kanavos et al., 2021). Additionally, ML techniques are more flexible and adaptable to varying scenarios such as shifts in energy price or macroeconomic conditions. Most ML techniques work primarily with cross-sectional data but may be used in hybrid models to boost performance in forecasting by better relating macroeconomic factors to demand.

DL is a subcategory of ML that is based on iterative learning from the method's own error. DL is nonlinear by its very nature and, thus, is capable of modeling highly complex and nonlinear time-series data. Additionally, DL models can receive both time-series and cross-sectional data to capture patterns between variables automatically (Do et al., 2020). However, DL is much more computation intensive than ML methods and requires more resources and time to model with an additional tendency to overfit data. Long short-term memory (LSTM) models are a type of recurrent neural network (RNN) that solves many faults of RNN-based models: long-term dependency problem and vanishing gradient problem which occurs during backpropagation (Do et al., 2020). This allows the model to capture long-term effects on demand from factors such as population and GDP.

Hybrid models combine the strengths of multiple modeling approaches and balance each other's shortcomings. By integrating more traditional methods such as basic econometric or time-series methods (i.e., SARIMA) with more modern techniques like ML and DL, hybrid models can capture both simple and complex behaviors in the data. Hybrid models typically are a combination of statistical+ML, statistical+DL, and ML+DL. One side of the hybrid model can analyze the linear trends and seasonality while the ML or DL portion can account for the more complex relationships and interactions between diverse variables.



The performance of various forecasting techniques in predicting aviation demand varies significantly, as shown in Table 1. Hybrid models outperformed single method forecasting approaches. However, these models have primarily been evaluated for short- to medium-term forecasts. Although their effectiveness for long-term forecasting remains untested, their strong performance in shorter timeframes suggests they could be adapted successfully for long-term forecasting problems.

Table 1. Comparison of aviation demand models.

Model Description	Mean Absolute Percentage Errors (MAPE)
Random Forest (RF)	6.76%
Deep Neural Network	7.98%
Particle Swarm Optimization Support Vector Regression (PSO-SVR)	2.38%
Seasonal Auto-Regressive Integrated Moving Average (SARIMA)-SVR Passenger Traffic Volume	2.31%
Regression+SVM Model	5.07%
Long Short-Term Memory (LSTM)	4.00%

Model Description
The model type chosen to model demand will be an LSTM. LSTMs are composed of forget gates, input gates, output gates, and an internal state (cell memory). The vanilla LSTM cell is pictured in Figure 2.

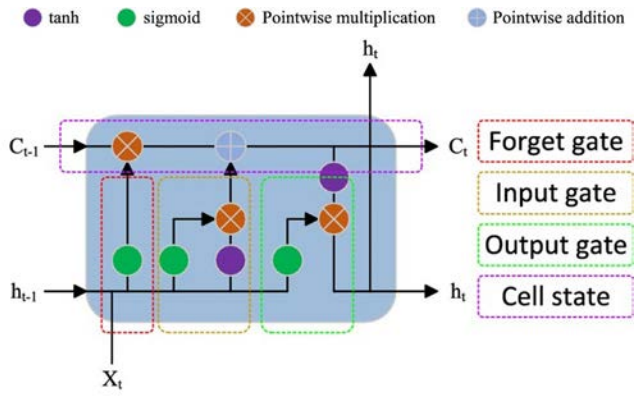


Figure 2. Long short-term memory cell (image from Dai et al. [2025]).

The structure of an LSTM as summarized by Abbasimehr et al. (2020):
X_t: The input value
h_{t-1} & h_t: The output value at time points t and $t-1$
C_{t-1} & C_t: The cell states at points t and $t-1$

The forget gate uses the current input (X_t) and previous output (h_{t-1}) to compute the information that will be stored in the cell state (C_{t-1}) using some activation function. Similar gating operations govern the update of new information and the generation of the output (h_t).

For this work, the demand model employs three LSTM layers, each with different hyperparameters and activation functions that are tuned with a large design of experiments. The LSTM's internal memory structure allows it to incorporate information across time horizons, which is essential in modeling long-term behavior.

Dataset Description
The model inputs consist of:



- Monthly domestic revenue passenger miles (RPM) in millions
- Real gross domestic product (RGDP) in trillions of 2024 USD
- Population in millions
- Crisis indicators (Boolean variables) for major disruptive events, including COVID-19, the September 11, 2001, attacks, and additional periods of significant financial distress

The dataset spans January 1990 through December 2024. RPM values are retrieved from the T-100 Segment dataset. Historical RGDP and population data are retrieved from the Federal Reserve Bank of St. Louis, Missouri. The first six months of these inputs are shown in Table 2.

Because future aviation demand depends strongly on past demand, the model incorporates lagged RPM values when generation predictions. This means the model's own prior output is used as an input in subsequent steps. In this way, the LSTM functions as an auto-regression model, using historical demand trends and economic indicators to forecast future domestic RPM.

The model needs dedicated training and validation datasets to evaluate forecasting performance. In typical time-series applications, the first ~70% of the data are used for training and the remaining ~30% for validation. However, the COVID-19 pandemic caused unprecedented disruptions in aviation demand that do not resemble any previous historical patterns. Using a traditional chronological split would prevent the model from learning COVID-related dynamics, which could lead to overly optimistic forecasting behavior.

Table 2. Sample of model inputs. RPM: revenue passenger miles, RGDP: real gross domestic product.

Date	RPM	RGDP	POPULATION	COVID	SEPT11	Financial Crisis
1/1/1990	25160794	12.85089	248.743	0	0	0
2/1/1990	24360423	12.85089	248.92	0	0	0
3/1/1990	29337299	12.85089	249.146	0	0	0
4/1/1990	27630792	12.89754	249.436	0	0	0
5/1/1990	27536900	12.89754	249.707	0	0	0
6/1/1990	29945449	12.89754	249.99	0	0	0

To address this, the historical dataset was divided into three disjoint training/validation segments, ensuring that the model encounters a mix of pre-crisis, crisis-adjacent, and post-crises behavior during training. A visual representation of the segments, as well as the deseasonalized trend of the domestic RPM is shown in Figure 3.

Training periods:
- 1990-2003
- 2005-2012
- 2018-2022

Validation periods:
- 2004
- 2013-2017
- 2023-2024

To ensure consistency across variables and to support stable model training, all input features were scaled prior to modeling. The RPM data are scaled relative to the first month's reported RPM value, which serves as a reference anchor. GDP and population inputs were scaled using a min-max normalization, allowing each feature to occupy a comparable numerical range despite significant differences in magnitude. This normalization process prevents any single variable from dominating the learning process solely because of its scale and facilitates more accurate interpretation of model performance.

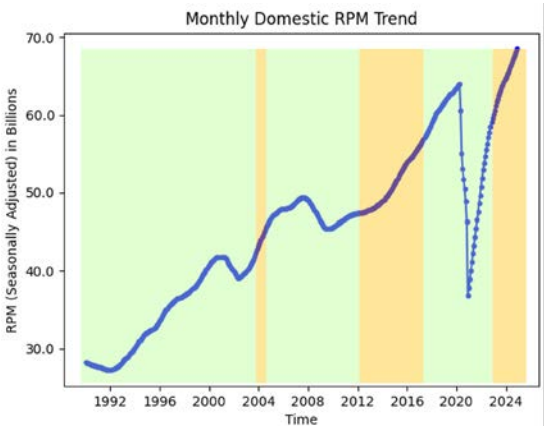


Figure 3. Training/validation segments on domestic revenue passenger miles (RPM).

Modeling Results and Validation

A backcasting approach on the historical data will be used to validate the selected forecasting model. Backcasting involves applying the model to the historical dataset, where actual results are already available. Backcasting is a widely used method for validating forecasting models, providing a benchmark for how well the model can replicate real-world outcomes. By comparing the model's predictions against these known values, performance parameters such as normalized root mean square error (NRMSE) and coefficient of determination (R^2) can be calculated. Additionally, the evaluation of the model's residuals will indicate if the trained model is overfitting on the data. These performance parameters quantitatively assess a model's accuracy, consistency, and ability to generalize, allowing for a more objective evaluation of the chosen model.

As mentioned beforehand, a large design of experiments was used to tune the hyperparameters of the model in order to achieve the best performance. Table 3 summarizes the top three cases with the highest NRMSE and R^2 values, while **Figure 4** shows their corresponding results graphically. In each plot, the dotted line represents the model's prediction on the validation set for that specific case.

Table 3. Top performing cases. NRMSE: normalized root mean square error, R^2: normalized root mean square error.

Case	Train NRMSE	Train R^2	Validation NMRSE	Test R^2
2126	0.0530	0.965	0.0602	0.939
1845	0.0396	0.981	0.0621	0.935
1032	0.0760	0.928	0.0664	0.926

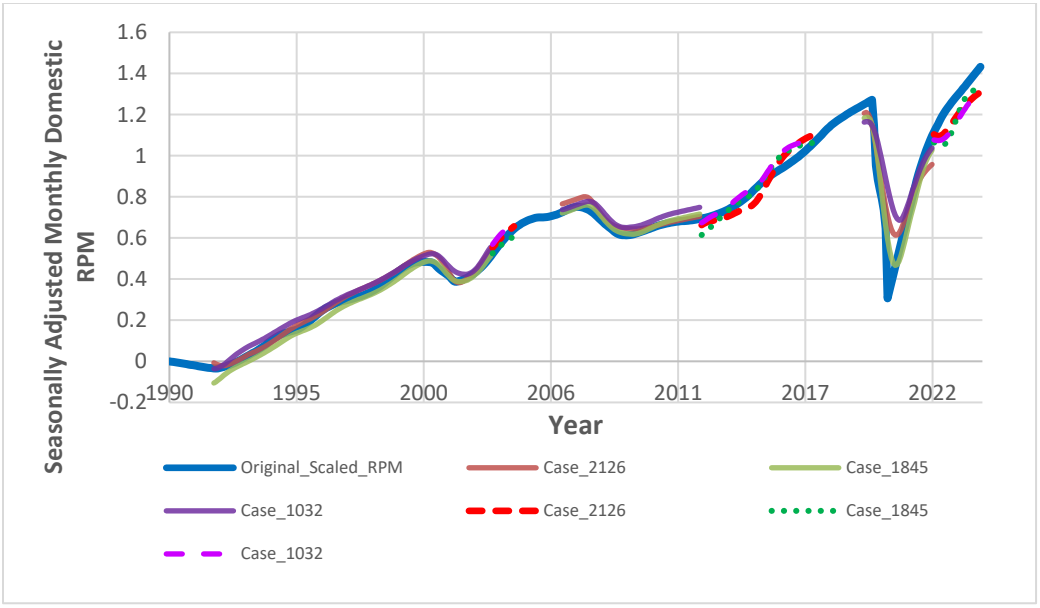


Figure 4. Model's performance on historical data.

It is important to note that for each training period, the model requires an initial sequence of historical observations to initialize its internal memory state before generating predictions. As a result, the first several timesteps of each training prediction window do not appear in Figure 4 and Figure 5. These initial values are used to "warm up" the LSTM's state and are not included in the reported performance metrics. Expanding this initialization window can improve the performance of the validation predictions for the tradeoff of less training data. For this disjointed training/validation segmented configuration, two years' worth of data were decided to be the ideal minimum before significant loss of data occurs. Also, recall that the y-axis (RPM) is scaled relative to first month's reported RPM value.

Figure 5 shows the training residuals of the model. Although the residuals may appear poor at first glance, much of this behavior is driven by the highly irregular demand patterns during the COVID-19 pandemic. This is especially apparent when examining the residuals over time as shown in the second subplot in Figure 5.

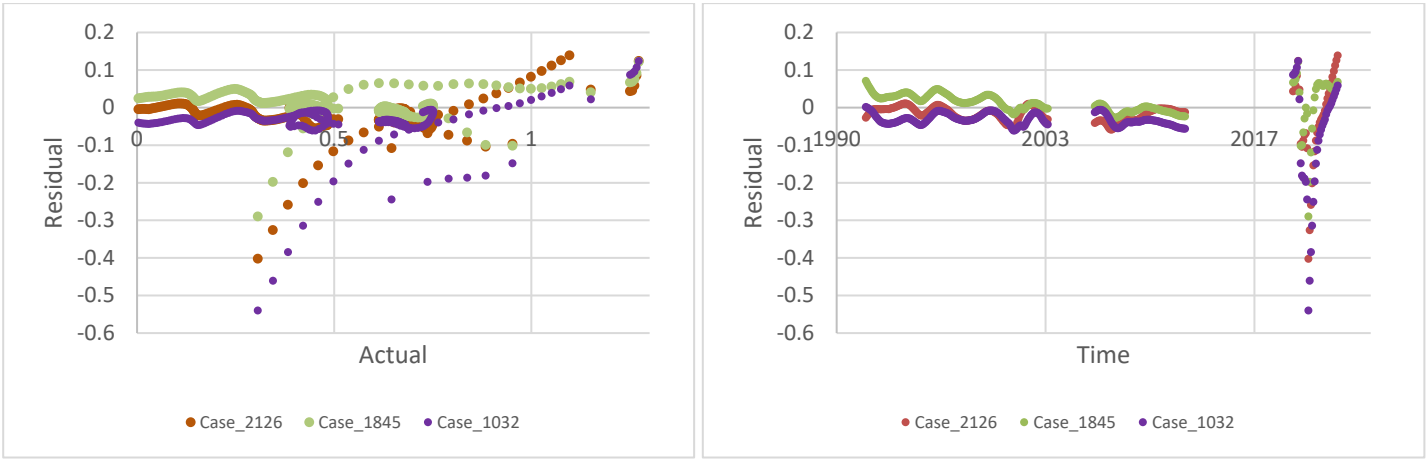


Figure 5. Training residual plots.

Model Forecast

Figure 6 shows the long-term forecasts generated from the top-performing model configurations. Up to 2045, the forecasts remained relatively consistent across all cases. Beyond this point, however, the projections begin to diverge substantially. The most optimistic case (Case 1845) predicts continued growth through the end of the century, while the more pessimistic case (Case 2126) shows demand flattening by approximately 2075. This widening spread reflects growing model uncertainty at long time-horizons and highlights the sensitivity of the LSTM to historical patterns that may not extend cleanly into the future.

Because these forecasts diverge so dramatically, it is challenging to select a single trajectory as the most representative. External benchmarks, such as the Boeing or Airbus market outlooks, can provide helpful reference points, but these industry forecasts only extend to 2044. Likewise, the FAA domestic market forecast terminates in 2045. Beyond this year, these existing forecasts offer little guidance for narrowing the model's long-term behavior.

To address this issue, future work may explore implementing a hybrid modeling architecture in order to stabilize long-range predictions. One potential approach would involve training one model exclusively on pre-COVID historical data to capture long-term structural trends. A second model will be trained to account for anomalous behavior related to COVID-19. Then, these two models will be combined to form a single predictive model capable of predicting other COVID-like events in the future. This hybrid approach will also have the benefit of allowing the model to retain more data in memory when making future predictions, which may lead to a more stabilized realistic forecast.

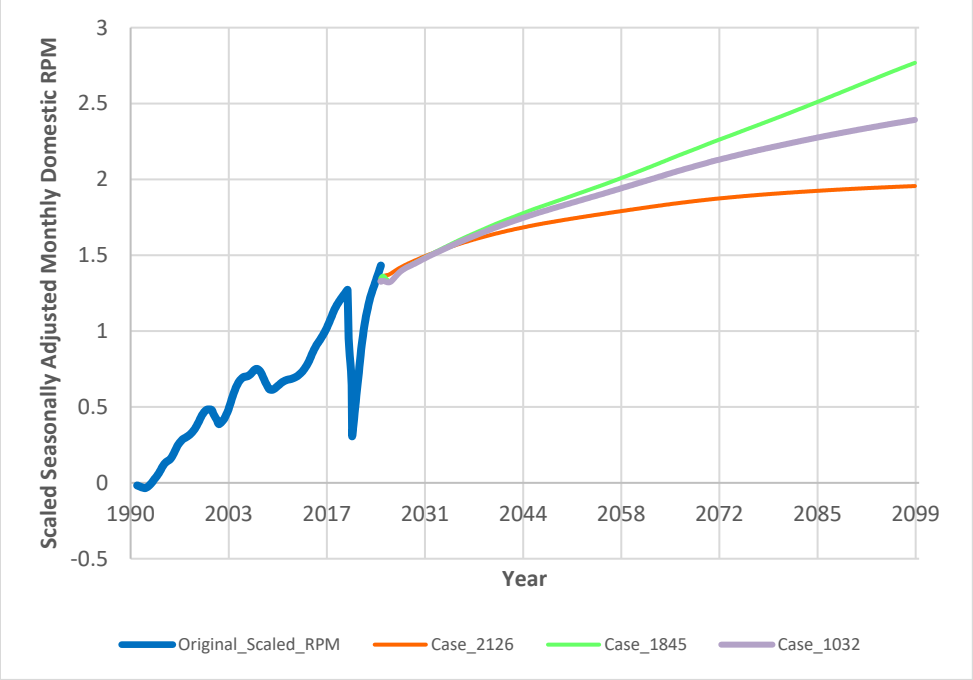


Figure 6. Model's forecasts of demand.

Scenario Analysis

Given the gradual change in commercial aviation to hub and spoke operations as well as other factors, the regional aviation sector has seen a decrease in attractivity which is estimated to be reversed given an introduction of technologies that can revitalize the sector with newer and more efficient configurations. These configurations may enable lower emissions and noise within urban areas. However, the inclusion of modern technologies that prompt new configurations makes it hard to predict what future configurations would be flown in 2050, 2075, and 2100. Therefore, there is a need to find a modeling approach for new emerging configurations.



Operating Cost Breakdown

To forecast different scenarios for future aviation demand, it is imperative to assess the pricing strategies that airlines use to generate "airfare" or "ticket prices" since it is one of the most important socio-economic factors behind air travel demand (Clark, 2017). The pricing system used by airlines currently is summarized in Revenue Management Systems (RMS), which enables airlines to maximize revenue by using multiple pricing strategies such as dynamic pricing, route-based pricing, and more. These pricing strategies are often a mix of three main pricing principles as laid out by Lesgourgues and Malavolti (2023):

- Cost-based pricing
- Demand-based pricing
- Service-based pricing

Cost-based pricing refers to a system of pricing in which the airline sets its prices equal to the marginal cost of producing an incremental unit of output. This practice is one of the theoretically optimal conditions of "perfectly competitive" markets. Demand-based pricing is based on consumers' "willingness to pay," as defined by the price–demand curve in each origin-destination market. Finally, service-based pricing refers to differences in the quality of services (and, in turn, in terms of the cost of providing these services) as a basis for pricing (Belobaba et al., 2009). For the scope of this task, the ASCENT Project 096 team will be using a cost-based model to derive the airfares set by the airlines in the future since other pricing principles require access to more data and more complex models that are not within the scope of this task. To use the cost-based pricing principle, our team will lay out a few assumptions such as a fixed marginal cost across all airlines which will in turn disregard pricing based on services and time of purchase of tickets.

The use of cost-based pricing principles causes us to investigate costs related to airline operations and more specifically direct operating cost, which is the cost related to the operations of the aircraft. The direct operating cost is usually expressed as a function of block hours to normalize the data collected from large and small fleets, long and short flights, and so on. To only consider the direct operating cost of airlines to predict future airfare, it is assumed that the indirect operating cost of airlines would not contribute to the airfare and thus is assumed to be constant. The direct operating cost can be further broken into two categories: (1) fixed direct operating cost and (2) variable direct operating cost. Fixed direct operating cost refers to operating cost components that are expenses directly tied to operating the aircraft but do not vary significantly with flight hours or distance flown. Variable operating cost refers to expenses directly tied to operating the aircraft and which vary with flight activity. Therefore, in order to further investigate the impact of effects on the direct operating cost, the focus is on the variable direct operating cost and the assumption that effects do not impact the fixed direct operating cost.

The literature review revealed that there are two main approaches to direct operating cost estimation. Both approach methodologies use historical data to a certain extent. The first approach, mean-based methodologies, use large datasets of reported direct operating cost broken down by component. The direct operating cost is categorized by aircraft category or by engine configuration and by using the mean of the cases selected from the datasets. The second approach uses historical data of the operating cost of certain aircraft, and performance and general data about the aircraft such as maximum takeoff weight to create a regression curve linking both variables and is thereby able to predict the direct operating cost of an aircraft given its general information.

For the task, our team will use the mean-based methodology to determine the direct operation cost breakdown by component for the respective aircraft categories within regional aviation as well as what might become part of regional aviation in the future due to effects.

When discussing effects that can impact the direct operating cost, the different advancements in other scientific fields as well as aviation that can directly decrease the cost associated with fuel, crew, and maintenance as defined in FAA (2024) are discussed.

Categorization and Evaluation of Impacts on DOC

The consideration of effects that can impact the future direct operating cost of aircraft is something that other research papers have tangentially explored (ICAO, 2022; Air Transport Action Group, 2021). ICAO (2022), for example, explores how different effects impact the CO_2 emissions of aircraft to meet future environmental aspirational goals. The report categorizes these effects into three main categories: (1) operations, (2) technologies, and (3) fuels. Operations effects are defined by opportunities for reducing costs and improving energy efficiency by improving the way existing aircraft operate. Technologies effects pertain to the development of evolutionary aircraft and engine technology such as



incremental improvements of established architectures, development of novel aircraft concepts, and significant changes at the propulsion level. Fuels effects refer to the development of fuels and new energy carriers that can lead to decrease in fuel cost. Our team will use the same categorization to refer to the different impacts on the direct operating cost with a slight modification to the nomenclature referring to fuels, which will be rather referred to as energy, to better encapsulate a wider range of energy carriers that can be considered in the long future under the assumption that some future aircraft configurations may not rely on fuel to operate.

Technology Impacts
The technologies that have been considered have been carefully selected as potential implementations in future configurations of aircraft due to their impact on the performance of the aircraft as well as their readiness level. The technologies are divided into the following categories:

- Aerodynamics and flight controls
  - Outboard Horizontal Stabilizers: Placing stabilizers further outboard leads to a 20% reduction in fuel consumption via improved trim efficiency (Dae & Nomenclature, n.d.)
  - Ducted Fans: Enclosed propellers increase airflow over the wing, practical during takeoff and landing operations (Jedamski et al., 2023)
- Operations and maintenance
  - Predictive Maintenance: Use of data and sensors to forecast component failures, reducing unplanned downtime and lowering maintenance costs by 25-30%
  - Simplified Vehicle Operations: Easier-to-fly designs lower pilot workload and training needs. Assuming reduction in pilot recurrent training time by 50% reduces crew cost by 1-41% annually.
- Powertrain efficiency
  - Hybrid Powertrain: Combines conventional and electric systems, leading to approximately 15% reduction in energy use (Zhang et al., 2018)
  - (Dae & Nomenclature, n.d.) Distributed Propulsion: Multiple small motors spread across the airframe improve efficiency, achieving up to 10% energy block reduction(Dae & Nomenclature, n.d.)
  - Electric Powertrain: Battery-powered electric motors drive propellers or ducted fans, reducing energy costs by up to 70% (Zhang et al., 2018)
- Structures and materials
  - Composite Technologies: Use of advanced composite materials yields in a weight reduction and savings of 2.8% (Cai et al., 2022)
  - Advanced Sandwich Composites: Lightweight layered materials contributing to 2.4% savings (Cai et al., 2022)
  - Out-of-Autoclave Composite Fabrication: Alternative to traditional curing processes with 0.2% improvement (Cai et al., 2022)
  - Lightweight Cabin Furnishings: Reduces interior weight, offering 0.5% savings (Cai et al., 2022)
  - Flexible Skins: Adaptive surfaces that reduce drag or support morphing wings; savings of 1.1% (Cai et al., 2022)
  - Variable-Camber Trailing-Edge Flap: Morphing flaps improve aerodynamics, saving 0.6% (Cai et al., 2022)
  - Natural Laminar Flow (NLF): Surface shaping that delays transition to turbulence, reducing drag and offering fuel block reduction of 10.8% (Cai et al., 2022); Catalano et al., 2020)

The infusion of technologies in future aircraft configurations would enable improvements in terms of performance. Given that certain technologies that have widely developed over the last century have reached their limits in terms of improvements, there is a need for a paradigm shift to enable more growth in the aviation industry. The technology sectors that would benefit the most from a paradigm shift would be the sectors that have a wide application of similar products such as the powertrain sector for which turbofans have been the standard choice despite their low efficiency compared to other powertrain configurations. One of the rapidly emerging technological advancements that could drive progress in the aerospace sector is the development of electric vehicles, which enables the use of electric powertrains in aircraft, resulting in higher efficiency and lower emissions. This is one of many examples of how a paradigm shift can impact future aircraft configuration, and thus, impact aviation demand.

Nine-passenger Aircraft Future Technology Selection
By 2050, the nine-passenger sub-fleet is expected to adopt key technologies that will reduce energy use and simplify operations. Battery-powered electric motors and ducted fans will enable short-range flights with up to a 75% reduction in energy costs. This move supports sustainable and low-cost operations. Electric propulsion will also slightly decrease the operating empty weight (OEW) by eliminating complex engine parts. Additionally, simpler vehicle operations from



automation and fly-by-wire systems will reduce pilot workload and training hours by about 50%, leading to a 1 to 2% annual decrease in crew costs. Predictive maintenance driven by data analysis will further lower maintenance costs by optimizing parts replacement, minimizing aircraft downtime, and creating a more cost-effective and reliable operation.

By 2075, this same nine-passenger fleet is expected to benefit from further improvements in distributed electric propulsion and aerodynamic redesign. Distributed propulsion systems will enhance load distribution and thrust efficiency, resulting in an additional 10% reduction in energy use compared to earlier electric setups. Adding outboard horizontal stabilizers will improve aerodynamic stability and efficiency, contributing to a further 20% reduction in fuel or energy use. These aerodynamic and propulsion upgrades, along with the established predictive maintenance and electric powertrain technologies, will significantly cut direct operating costs, particularly energy and maintenance expenses, making the nine-passenger fleet a leading option for short-haul, low-cost regional travel by 2075.

19-passenger Aircraft Future Technology Selection:
For the 19-passenger sub-fleet, changes by 2050 will focus on enhancing both structure and propulsion. New composite technologies like sandwich structures (2.3%), out-of-autoclave fabrication (0.2%), and riblets (1.7%) will together provide about a 7% reduction in drag and weight, boosting overall efficiency. The introduction of hybrid-electric powertrains will lead to a notable 15% drop in energy costs. Natural laminar flow (8.7%) and reducing excrescence drag (0.3%) will also improve aerodynamic performance. Operationally, easier vehicle operations will reduce annual training hours by 50% resulting in a 2% decrease in crew costs, while predictive maintenance will cut maintenance expenses by up to 25%. Together, these technologies will improve the sub-fleet's energy efficiency, lower maintenance, and crew costs, and enhance lifecycle sustainability.

Looking ahead to 2075, the 19-passenger sub-fleet is set to reach even greater efficiency through electric propulsion and distributed systems, combined with outboard horizontal stabilizers. These technologies will collectively produce up to a 10% additional reduction in energy use and a 20% decrease in fuel consumption, making this sub-fleet a state-of-the-art hybrid-electric platform for medium-range routes in a sustainable way. A shift to single-pilot operations will decrease crew costs by 41%, marking a substantial change in operational economics. By 2075, these advancements in propulsion, aerodynamics, and operations will yield cumulative benefits across energy, crew, and maintenance costs, establishing the 19-passenger sub-fleet as a standard for efficient regional air travel well into the future.

50-passenger Aircraft Future Technology Selection
By 2050, the 50-passenger sub-fleet will combine electric propulsion, ducted fan systems, and predictive maintenance. It will adopt new technologies from smaller regional aircraft for larger-capacity operations. Battery-powered electric motors will make these aircraft ideal for short-haul routes, reducing energy costs by up to 35% compared to traditional regional jets or turboprops. Ducted fans will improve propulsive efficiency and slightly decrease OEW by eliminating heavy turbine assemblies. Furthermore, simpler vehicle operations and updated cockpit interfaces will lower pilot workload, cutting training hours by about 50% and reducing crew-related costs by 1 to 2% each year. The predictive maintenance systems, backed by constant data monitoring, will cut maintenance costs through improved component replacement and reduced downtime, enhancing overall fleet reliability and cost efficiency.

By 2075, the 50-passenger sub-fleet will become an extremely efficient regional platform powered by advanced electric powertrain technologies, distributed propulsion designs, and well-optimized flight deck layouts that ease pilot burden. The improved cockpit and dashboard systems will make flight management simpler, allowing one pilot to fly the aircraft safely and effectively while keeping operational backup through smart systems and streamlined controls. This change will lead to a 41% drop in crew costs, representing one of the biggest improvements in the fleet's operating economics. At the same time, innovations in distributed propulsion and next-generation energy storage will allow for another 10 to 15% reduction in energy use, further cutting DOC. When combined with ongoing progress in lightweight structures and predictive maintenance, the 50-passenger fleet will secure significant savings in energy, crew, and maintenance costs establishing itself as a leading example of efficient, sustainable, and economically improved regional air transport by 2075.

Future Aircraft Energy Consumption
The analysis starts with figuring out the power needed to keep the plane flying steadily. This depends on the aircraft's weight, speed, and how well it moves through the air. The lift-to-drag ratio and overall propulsive efficiency are key factors in determining the energy needed for a specific operating condition.

$$\eta_{propulsive} = \eta_{motor} \times \eta_{power_{converters}} \times \eta_{propeller} \quad \text{(Eq. 1)}$$



We calculate the overall propulsive efficiency by looking at how well the motor, power converters, and propeller work together. This shows how energy changes from electrical input to useful thrust.

$$P_{required} = \frac{Weight \times Velocity}{L/D \times \eta_{pr}} \quad \text{(Eq. 2)}$$

$$Energy\ Consumed_{kwh} = Power_{required} \times Energy\ Price \quad \text{(Eq. 3)}$$

Finally, we estimate the total energy consumption by multiplying the required power by the energy price. This helps us understand the operational energy cost for the chosen flight condition. It also allows us to compare different propulsion system setups or assess how improvements in efficiency affect energy spending.

Figure 7 outlines the future aircraft energy consumption and efficiency. Table 4 provides the physics-based modeling results compared to literature simulation results for energy consumption and the cost of energy per block hour use in validation of the electric model. Table 5 outlines the direct operating costs for fuel and oil, maintenance, and crew costs per block hour for the three passenger fleets evaluated. Table 6 provides a cost comparison for direct, indirect, and total operating costs for 2023, 2050, and 2075 for the three passenger fleets evaluated.

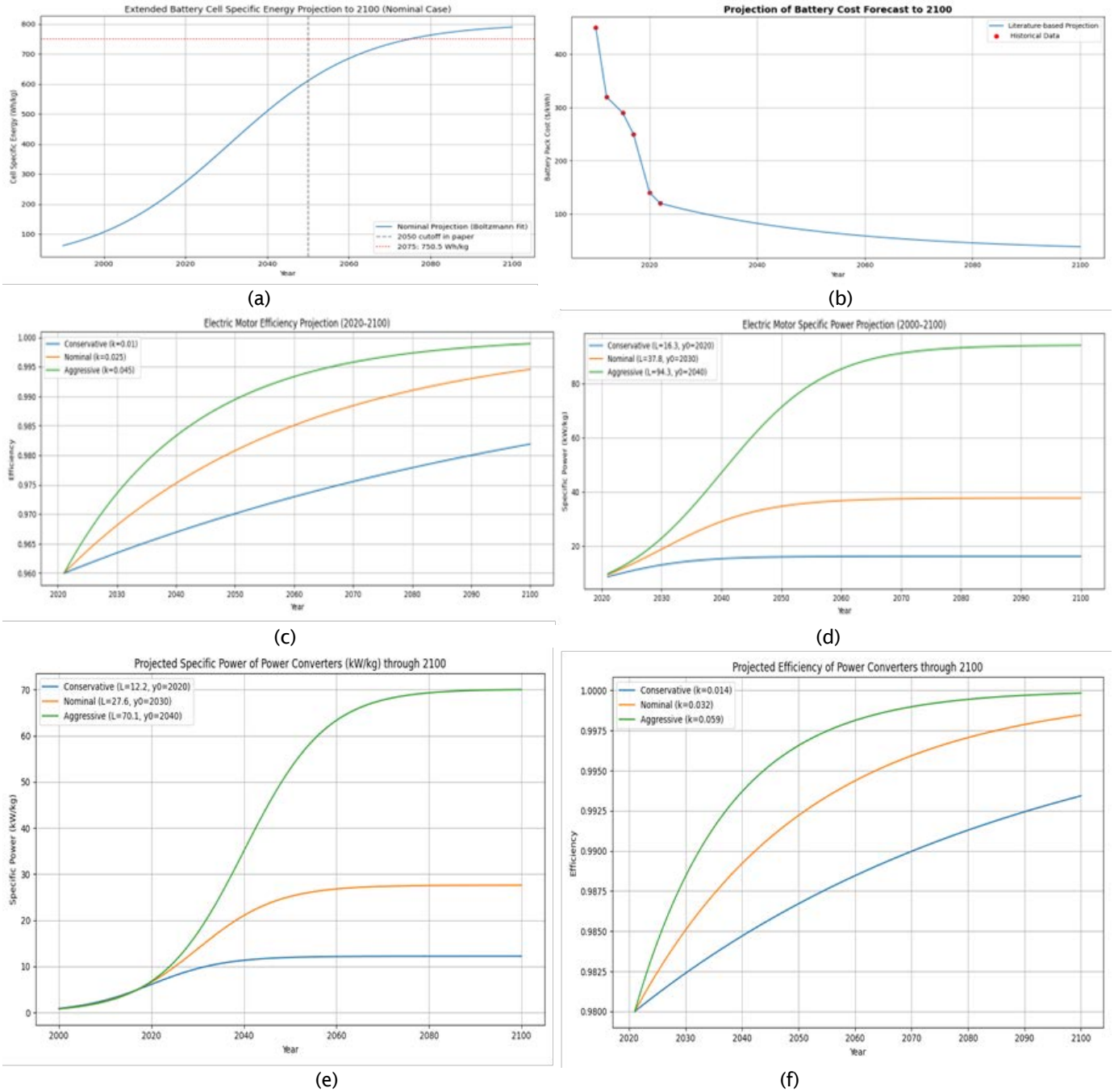


Figure 7. Future aircraft energy consumption and efficiency: (a) extended battery cell-specific energy (nominal case), (b) forecast of projection of battery costs, (c) future projection of electric motor efficiency, (d) future projection of electric motor-specific power, (e) projected specific power of power converters (kW/kg, and (f) projected efficiency of power converters through.



Table 4. Physics-based model results compared to literature simulation results.

Electric Model Validation	Physics Equations	Simulation Results
Energy Consumed per block hour (kwh)	356.2	367
Cost of Energy per block hour ($ 2023)	51	53

Table 5. Direct operating cost variable components for each sub-fleet per timeline.

Fleet	Cost Components	2023	2050	2075
9 pax: Cessna 208	Fuel and oil cost ($/BH)	227	42	32
	Maintenance cost per block hour ($/BH)	186	140	140
	Crew cost ($/BH)	116	133	112
19 pax: Cessna 408	Fuel and oil cost ($/BH)	776	534	319
	Maintenance cost per block hour ($/BH)	423	296	205
	Crew cost ($/BH)	177	173	104
50 pax: ATR 42-600	Fuel and oil cost ($/BH)	993	661	661
	Maintenance cost per block hour ($/BH)	627	439	439
	Crew cost ($/BH)	258	255	152

Table 6. Direct operating costs (DOC), indirect operating costs (IOC), and total operating costs (TOC) for each sub-fleet per timeline.

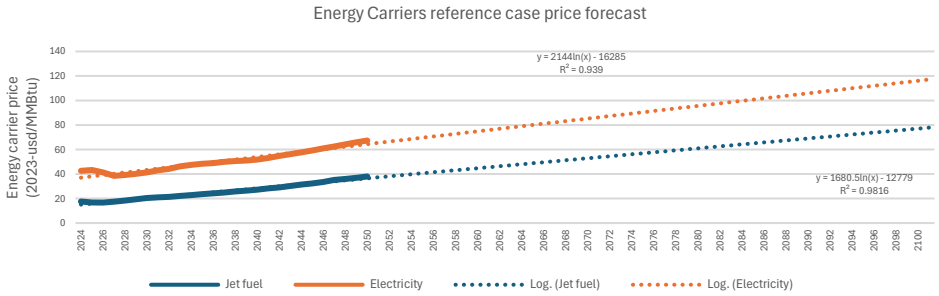
Fleet	Cost Components	2023	2050	2075
9 pax : Cessna 208	DOC	$ 649	$ 562	$ 558
	IOC	$ 649	$ 555	$ 555
	TOC	$ 1,298	$ 1,117	$ 1,113
19 pax : Cessna 408	DOC	$ 1,690	$ 1,472	$ 1,327
	IOC	$ 1,690	$ 1,457	$ 1,323
	TOC	$ 3,381	$ 2,929	$ 2,650
50 pax : ATR 42-500	DOC	$ 2,061	$ 1,871	$ 1,391
	IOC	$ 2,061	$ 1,856	$ 1,387
	TOC	$ 4,121	$ 3,727	$ 2,778

Energy Carriers: Jet-A, Electricity Forecast to 2100

The forecast of energy carrier prices was extended beyond the U.S. Energy Information Administration's (EIA) Annual Energy Outlook (AEO) 2050 projections by applying a time series regression model to the historical and projected data.



Using the EIA's long-term baseline as the foundation, the model extrapolated future trends in jet fuel and electricity prices through 2100. A logarithmic regression was selected to capture the diminishing rate of price increase over time, reflecting the stabilizing behavior observed in long-term energy markets. Figure 8 provides a reference case forecast for energy carriers for jet fuel and electricity.



$Fuel\ price = 1689.5\ ln(years) - 12779$ for jet fuel (2023-USD/MMBtu)
$Electricity\ price = 2144\ ln(years) - 16286$ for electricity (2023-USD/MMBtu)

Figure 8. Reference case price forecast for energy carriers.

The resulting fitted equations yielded high coefficients of determination (R^2 = 0.9616 and R^2 = 0.939, respectively), indicating strong model accuracy and goodness of fit. These metrics confirm that the extended forecast maintains statistical consistency with the EIA reference case, providing a credible outlook for long-term energy cost evolution.

Regional Market Demand Model Generation

The chosen demand model framework builds on a long history of research focused on modeling how travelers choose their modes of transportation. Traditionally, these models have used detailed utility-based methods, which evaluate the appeal of each transport option based on traveler characteristics like income, value of travel time, or trip purpose, along with specific attributes of the modes, such as cost, comfort, and service frequency. However, previous studies have shown that adjusting complex utility functions with many variables often requires a lot of survey data, which can be tough to gather. To solve this problem, the current model uses a simplified but effective approach based on the generalized cost of travel (GCT) (Roy et al., 2023). The GCT combines two main parts: (1) the monetary cost of a trip and (2) the opportunity cost of the time spent traveling. This provides a unified measure that reflects both the financial and time aspects of a traveler's decision-making.

$$GC_m = C_m + VT \times T_m \quad \text{(Eq. 4)}$$

$$U_{car} = \alpha \times GC_{car} + \epsilon \quad \text{(Eq. 5)}$$

$$U_{air} = \alpha \times GC_{air} + \beta + \epsilon \quad \text{(Eq. 6)}$$

This generalized cost approach allows for clear and data-efficient estimation of travel preferences while still being realistic compared to more complicated utility-based models. By using publicly available wage data from the U.S. Bureau of Labor Statistics, the model figures out the value of time by averaging the median hourly wages across the states of departure and arrival. When applied to comparison scenarios from 2008 and 2040, the GCT-based demand model shows its ability to measure how regional air mobility services affect traveler behavior (Justin et al., 2021).

$$P_{air} = \frac{1}{1+e^{\alpha \times (GC_{car} - GC_{air}) - \beta}} \quad \text{(Eq. 7)}$$

Specifically, the decrease in GCT for air travel, resulting from shorter door-to-door times due to more regional airports, implies that air travel becomes more attractive and competitive compared to ground options. This ability to capture changing travel dynamics in a straightforward, understandable way makes the GCT-based demand model a strong choice for predicting future mobility patterns and evaluating the potential uptake of new air travel services.

Figure 9 outlines the Terminal Area Forecast for air, automobiles, and railways extended from 2040 to 2100. Figure 10 shows a diagram of the proposed framework to generate a future demand model.

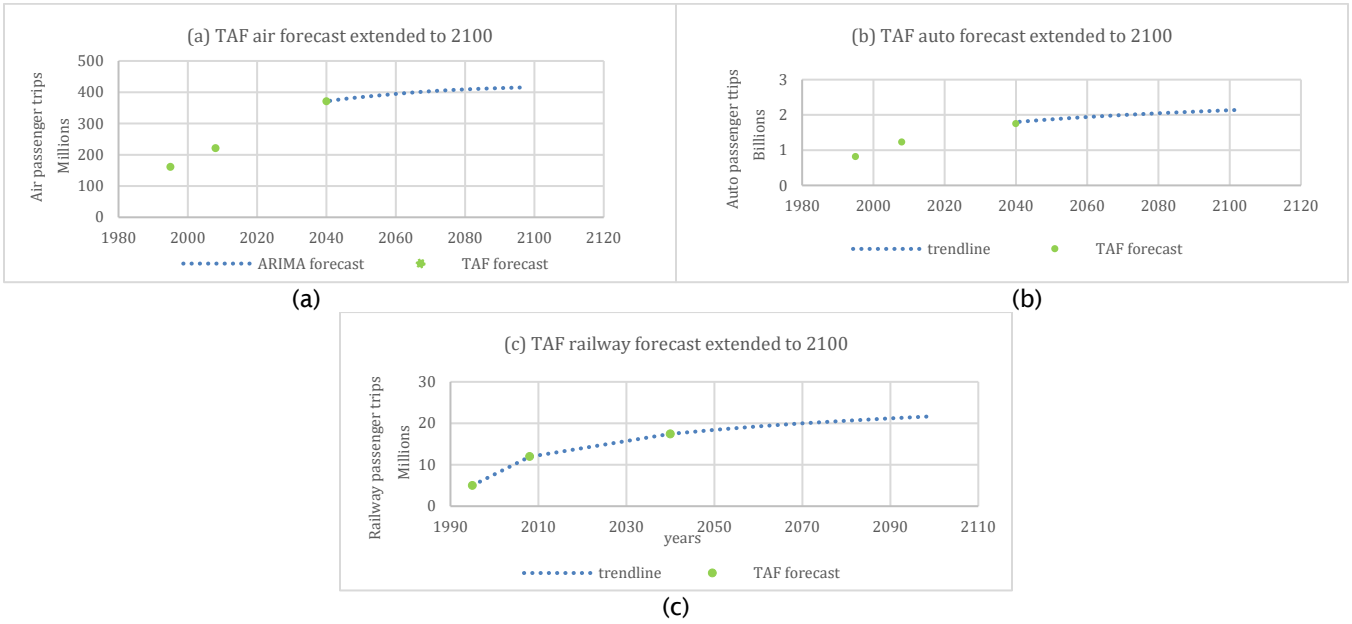


Figure 9. Annual passenger trips forecast extended from 2040 to 2100 for three modes of transportation (a) air, (b) business automobile, and (c) passenger railway.

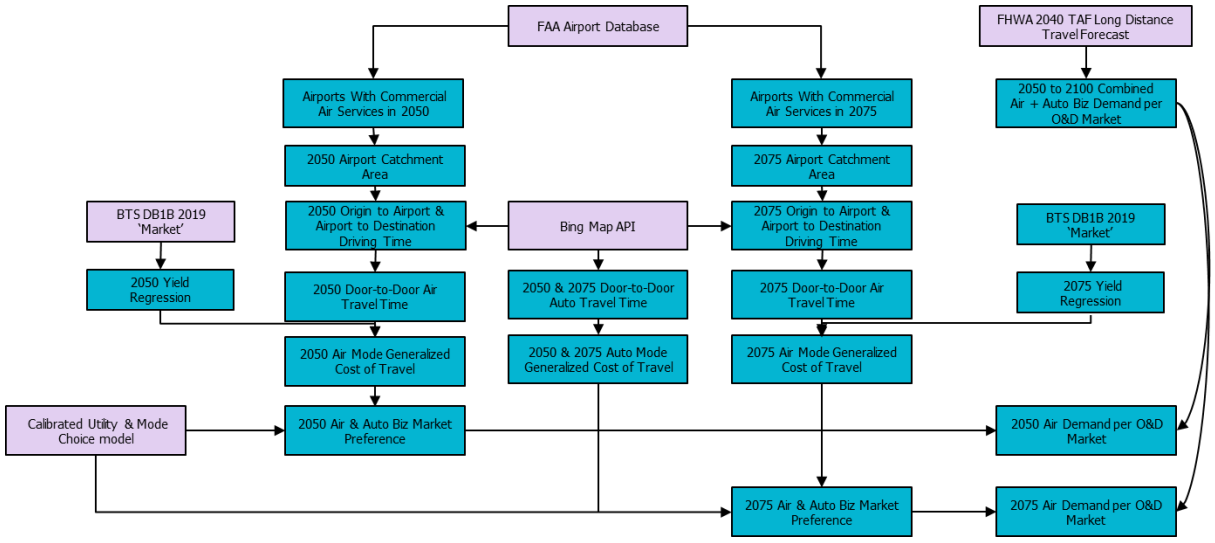


Figure 10. Proposed framework to generate a future demand model.

Milestones

- Created demand model and demand forecasts.
- Investigated use cases of various forecasting models.
- Evaluated different operating cost prediction methodologies.



- Examined the technologies to evaluate their impact on operating cost for scenarios generation.
- Generated surrogates of aircraft costs with respect to flow distance for each sub-fleet and timeline
- Generated an approach for scenarios based on traveler demand elasticities.
- Identified and prepared the required datasets for the demand model framework.

Major Accomplishments
None.

Publications
None.

Outreach Efforts
None.

Awards
None.

Student Involvement
Graduate students are actively participating in research.

Plans for Next Period
Continued Model Evaluation
As discussed previously, a modeling method was selected and evaluated. However, further improvement is still warranted. During the writing of this report, it has become apparent that a hybrid modeling architecture might offer a more effective way to handle the structural disruptions introduced by COVID-19 data. This may become especially useful in stabilizing long-term forecasts.

Modeling Modes of Transportation
For the mode of choice modeling, the next steps include implementation of a railway model that depicts future plans envisioned by the federal railway administration which include high speed railways between megaregions in the US mainland as well as a complete modeling of the rail network using a generalized cost of travel mode. Coupling the railway model with the already developed Air and Automobile models will enable direct analysis of traveler preferences for 2050 and 2075 given the introduction of novel technologies using a fleet assignment and scheduling module predict future demand for different airports as well as the needed infrastructure to handle these novel aircrafts in the United States.

Scenario Generation
The mean-based methodology will be used to generate a direct operating cost breakdown for the respective aircraft categories that is to be assessed. A range of impacts from the different technologies on the aircraft performances will be created, which will then be used to generate the scenarios.

References
Justin, C. Y., Payan, A. P., & Mavris, D. N. (2021, August). Demand modeling and operations optimization for advanced regional air mobility. In AIAA AVIATION 2021 Forum. https://doi.org/10.2514/6.2021-3179

Abbasimehr, H., Shabani, M., & Yousefi, M. (2020). An optimized model using LSTM network for demand forecasting. *Computers & Industrial Engineering, 143*, https://doi.org/10.1016/j.cie.2020.106435

Air Transport Action Group. (2021). *Waypoint 2050* (2nd ed.). https://aviationbenefits.org/media/167417/w2050_v2021_27sept_full.pdf

Belobaba, P., Odoni, A., & Barnhart, C. (Eds.). (2009). *The global airline industry*. John Wiley & Sons.

Cai, Y., Xie, J., Cinar, G., & Mavris, D. N. (2022). Advanced 2030 Turboprop Aircraft Modeling for the Electrified Powertrain Flight Demonstration Program. *2022 IEEE Transportation Electrification Conference and Expo, ITEC 2022*, 664–669. https://doi.org/10.1109/ITEC53557.2022.9813858

Catalano, P., De Rosa, D., Mele, B., Tognaccini, R., & Moens, F. (2020). Performance improvements of a regional aircraft by riblets and natural laminar flow. *Journal of Aircraft*, *57*(1), 29–40. https://doi.org/10.2514/1.C035445



Clark, P. (2017). *Buying the Big Jets: Fleet Planning for Airlines* (3rd ed.). Routledge. https://doi.org/10.4324/9781315570662

Dae, H., & Nomenclature, I. (n.d.). *Progress in Distributed Electric Propulsion Vehicles and Technologies*.

Dai, ZQ., Li, J., Cao, YJ., & Zhang, YX. (2025). SALSTM: Segmented self-attention long short-term memory for long-term forecasting. *Journal of Supercomputing, 81*(115). https://doi.org/10.1007/s11227-024-06493-z

Do, Q. H., Lo, S. K., Chen, J. F., Le, C. L., & Anh, L. H. (2020). Forecasting air passenger demand: A comparison of LSTM and SARIMA. *Journal of Computer Science, 16*(7), 1063–1084. https://doi.org/10.3844/jcssp.2020.1063.1084

FAA. (2024). *Economic values for FAA investment and regulatory decisions*, *Section 4: Aircraft Operating costs*. Federal Aviation Administration. https://www.faa.gov/regulations_policies/policy_guidance/benefit_cost/econ-value-section-4-op-costs.pdf

ICAO. (2022). *Report on the feasibility of a long-term aspirational goal (LTAG) for international civil aviation CO_2 emission reductions*. International Civil Aviation Organization (ICAO), Committee On Aviation Environmental Protection (CAEP). https://www.icao.int/environmental-protection/LTAG/Documents/REPORT%20ON%20THE%20FEASIBILITY%20OF%20A%20LONG-TERM%20ASPIRATIONAL%20GOAL_en.pdf

Jedamski, D., Lakshminarayan, V., Ahuja, V., Alvarez, E. J., & Moore, M. (2023). Distributed Electric Propulsion and Vehicle Integration with Ducted Fans. *AIAA Aviation and Aeronautics Forum and Exposition, AIAA AVIATION Forum 2023*. https://doi.org/10.2514/6.2023-3455

Kanavos, A., Kounelis, F., Iliadis, L., & Makris, C. (2021). Deep learning models for forecasting aviation demand time series. *Neural Computing and Applications, 33*, 16329–16343. https://doi.org/10.1007/s00521-021-06232-y

Lesgourgues, A., & Malavolti, E. (2023). Social cost of airline delays: Assessment by the use of revenue management data. *Transportation Research Part A: Policy and Practice, 170*. https://doi.org/10.1016/j.tra.2023.103613

Roy, S., Herniczek, M. T. K., German, B. J., & Garrow, L. A. (2021). User base estimation methodology for a business airport shuttle air taxi service. Journal of Air Transportation, 29(2), 69–79.Zachariah, R. A., Sharma, S., & Kumar, V. (2023). Systematic review of passenger demand forecasting in aviation industry. Multimedia Tools and Applications, 82, 46483–46519. https://doi.org/10.1007/s11042-023-15552-1

Zhang, X., Bowman, C. L., O'Connell, T. C., & Haran, K. S. (2018). Large electric machines for aircraft electric propulsion. *IET Electric Power Applications, 12*(6), 767–779. https://doi.org/10.1049/iet-epa.2017.0639

Task 5 – Vehicle Technology Specific Scenarios

Georgia Institute of Technology

Objectives

This task aims to capture the implications of vehicle-specific technology and their potentially required infrastructure changes. This is intended to cover the adoption of electric or fuel cell aircraft as well as the potential large-scale adoption of sustainable aviation fuel and hydrogen vehicles. Combined with the results of Tasks 1, 2, 3, and 4, this will define combined scenarios that bring the various aspects of demand, operational changes, and new vehicle-specific changes together in new scenarios for aviation.

This year we developed an analytical dashboard for evaluating ground charging infrastructure requirements across the U.S. domestic airport network. The tool addresses a gap in existing aviation infrastructure planning: how to size and deploy charging systems for HEA as this technology moves toward commercial deployment.

The dashboard uses actual operational data—flight schedules, turnaround times, and route-level energy consumption—to estimate charging demand at individual airports. Rather than relying on simplified assumptions about average daily usage, we model charging requirements at the hourly level using January 2023 on-time performance data matched with physics-based energy consumption estimates for turboprop and turbofan routes.

Research Approach

- Narrow down the potential options in coordination with the FAA and industry.
- Perform initial tests of how the vehicle technologies intersect with the overall modeling framework.
- Study and estimate the infrastructure needed to generate the required electricity using renewable energy, particularly wind and solar energy. One of the scenarios currently being developed is if majority of the passenger's



transportation part of commercial aviation is flown by hybrid-electric aircraft. For this scenario, it is reasonable to assume additional infrastructure would be required to supply sufficient electrical energy to charge the aircraft.

Data Integration
We work with three primary data sources. The Bureau of Transportation Statistics T-100 dataset provides route-level traffic volumes and operational patterns. FAA Aerospace Forecast domestic RPM projections scale these baseline figures through 2045. On-time performance records give us actual arrival and departure timestamps, which we use to construct realistic charging schedules rather than assuming uniform distribution throughout the day.

Energy consumption per route comes from surrogate models that account for distance, payload, and aircraft market (turboprop vs. turbofan). These models estimate both fuel burn and electrical energy requirements under hybrid-electric operation. The key assumption—that all charging occurs at departure airports—simplifies the analysis but captures the dominant infrastructure burden. Destination charging would redistribute demand but not eliminate it.

Charging Window Calculations
A critical parameter is the usable charging window. Aircraft do not arrive and immediately plug in, nor do they charge until the instant of pushback. We define the usable turnaround time as:

$$Usable\ TAT\ =\ Actual\ TAT\ \times\ (1\ -\ \alpha) \quad \text{(Eq. 8)}$$

where α represents non-charging buffer time (default 0.20, or 20% of turnaround). This accounts for deplaning, servicing, boarding, and the practical reality that chargers are not connected for the full ground time.

Required charging power follows directly:

$$P_required\ =\ Energy_needed\ /\ Usable_time \quad \text{(Eq. 9)}$$

This gives us the minimum charger rating needed to replenish the battery within available time. Flights where this exceeds installed charger capacity are flagged as infeasible under current operational constraints.

Charging Model
The dashboard implements both a simplified linear charging model and a more realistic constant current-constant voltage (CC-CV) model. The linear model assumes constant power delivery throughout the charging session—charge delivered is simply power multiplied by time. This works for rough estimates but overstates charging capability.

The CC-CV model reflects actual lithium-ion battery behavior. It charges at constant current until reaching approximately 80% state of charge, then transitions to constant voltage with declining current. This transition matters: a charger rated at 600 kW delivers 600 kW through most of the charge cycle but tapers off as the battery approaches full. Our implementation uses HEA battery specifications (396 kWh total capacity, 317 kWh usable from 20-100% state of charge) and shows that the CC-CV physics can reduce effective charging by 15-40% compared to linear assumptions for longer sessions.

Dashboard Structure
The tool comprises six analytical pages, each addressing various aspects of infrastructure planning:

Page 1: Route Explorer provides an interactive map for examining individual origin-destination pairs. Users select airports to view route distance, traffic volume, aircraft types, and per-mission energy requirements (see Figure 11). Growth projections through 2045 are displayed based on FAA domestic RPM forecasts. This is useful for understanding specific route characteristics and identifying high-priority corridors.

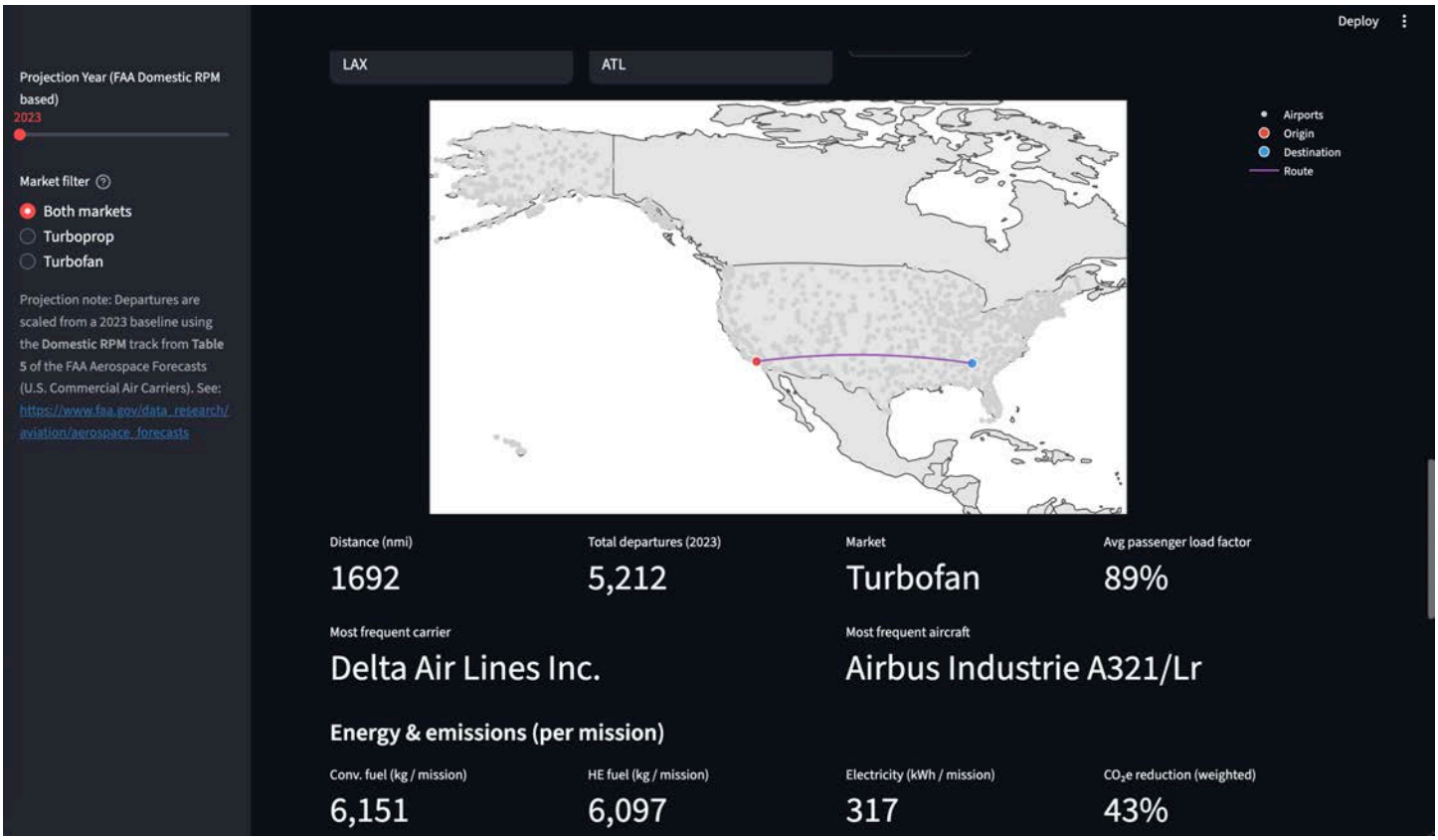


Figure 11. Tab 1 route explorer (from Los Angeles International Airport to Atlanta International Airport).

Page 2: Geographic Energy Demand maps total annual electricity consumption and average required energy per mission across airports (see Figure 12, Figure 13, and Figure 14). The visualizations help identify geographic clusters of charging demand and show which airports face the highest per-flight energy requirements. Filters allow focusing on airports above specified departure thresholds and separate analysis of turboprop versus turbofan markets.

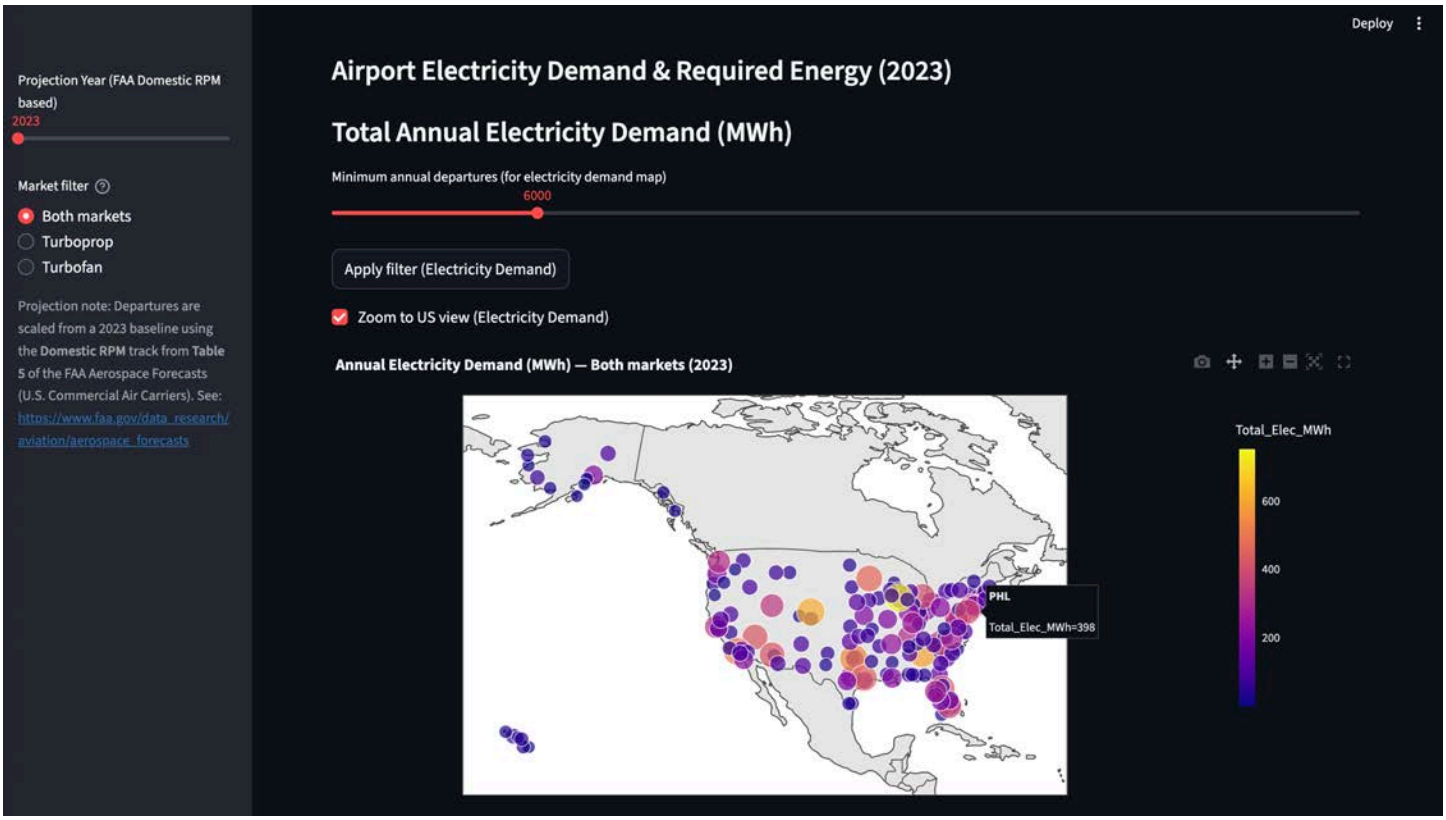


Figure 12. Tab 2 annual electricity demand by airport.

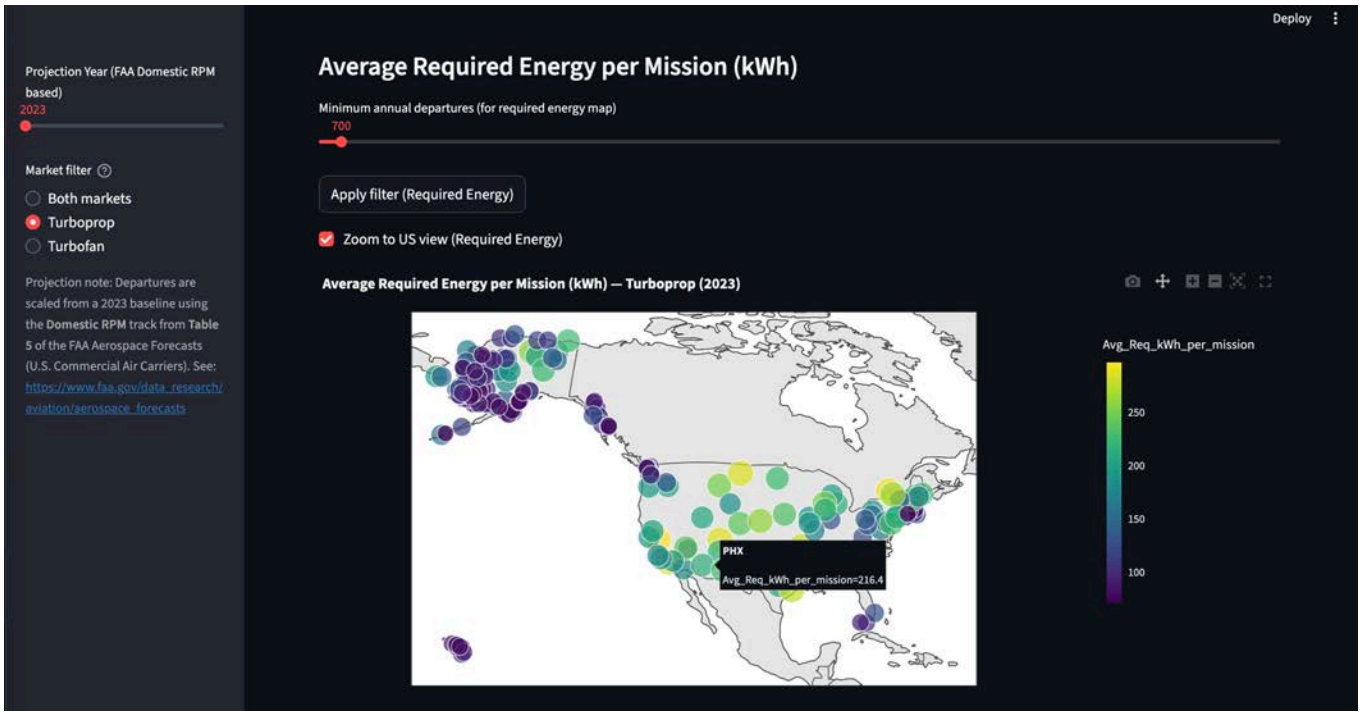


Figure 13. Tab 2 average electricity demand by airport (turboprop only).

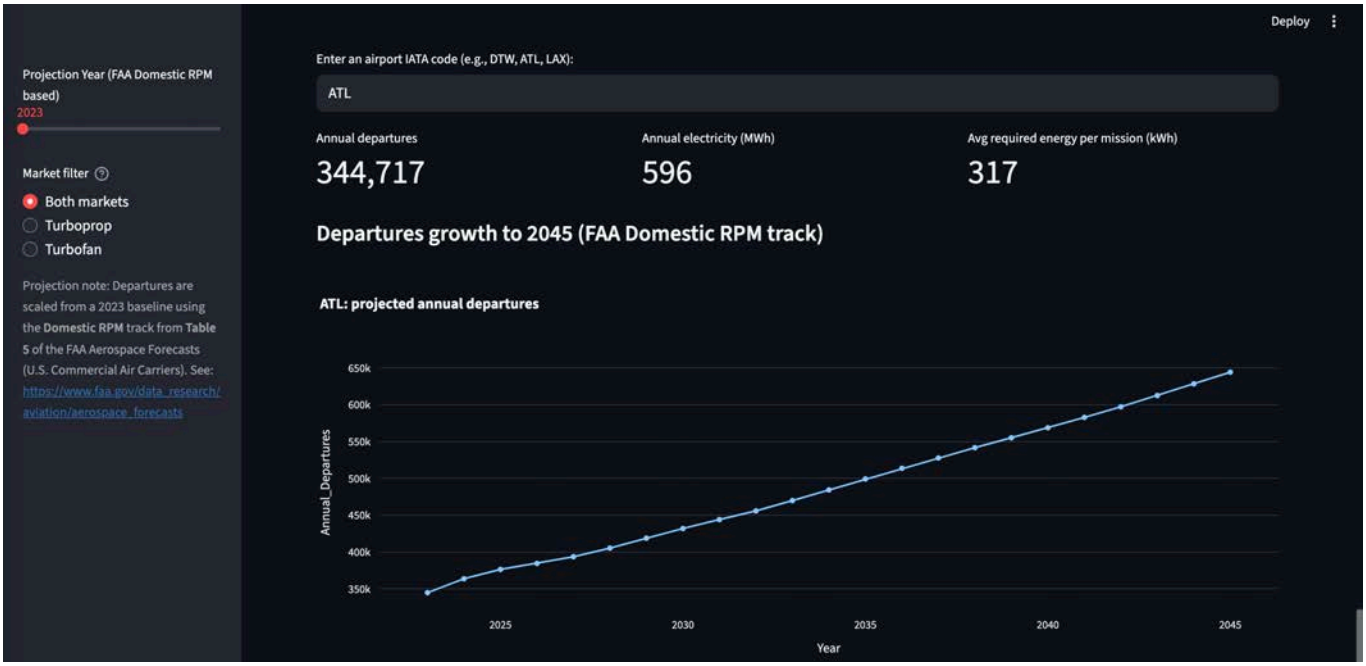


Figure 14. Tab 2 airport explorer (for Atlanta International Airport [AT]) displaying the projected departures growth to 2045 (Federal Aviation Administration [FAA] Domestic revenue passenger-mile [RPM] track).



Page 3: Charge Availability vs. Requirement compares what can be delivered (charger power × turnaround time) against what is needed (mission energy requirement) on a per-airport basis. This reveals where standard turnaround times are sufficient for charging and where they are not. The analysis is parametric in charger rating, allowing quick assessment of how increasing charger power affects feasibility.

Page 4: Required Charging Rate calculates the minimum charger power needed at each airport given typical turnaround times and energy requirements. This inverts the usual question: instead of asking "can we charge with 300 kW chargers," it asks "what charger power do we actually need here?" The answers vary substantially by airport due to differences in typical route distances and turnaround times.

Page 5: Charging Facility Sizing performs date-aware analysis using individual flight records (see Figure 15 and Figure 16). This is the most detailed method. We track each flight's charging session from arrival through departure, accounting for actual timestamps and calculating hourly load profiles and port concurrency. The analysis supports two scenarios:

- Power-based sizing*:* Determines charger count from peak hourly load divided by charger rating and diversity factor. Different charger ratings yield different port counts.
- Make-up charging scenario*:* Assumes each flight occupies a port for its entire usable turnaround window, regardless of charger power. Required ports equal the peak number of simultaneous charging sessions. This is conservative but reflects operational realities where aircraft positions are fixed.

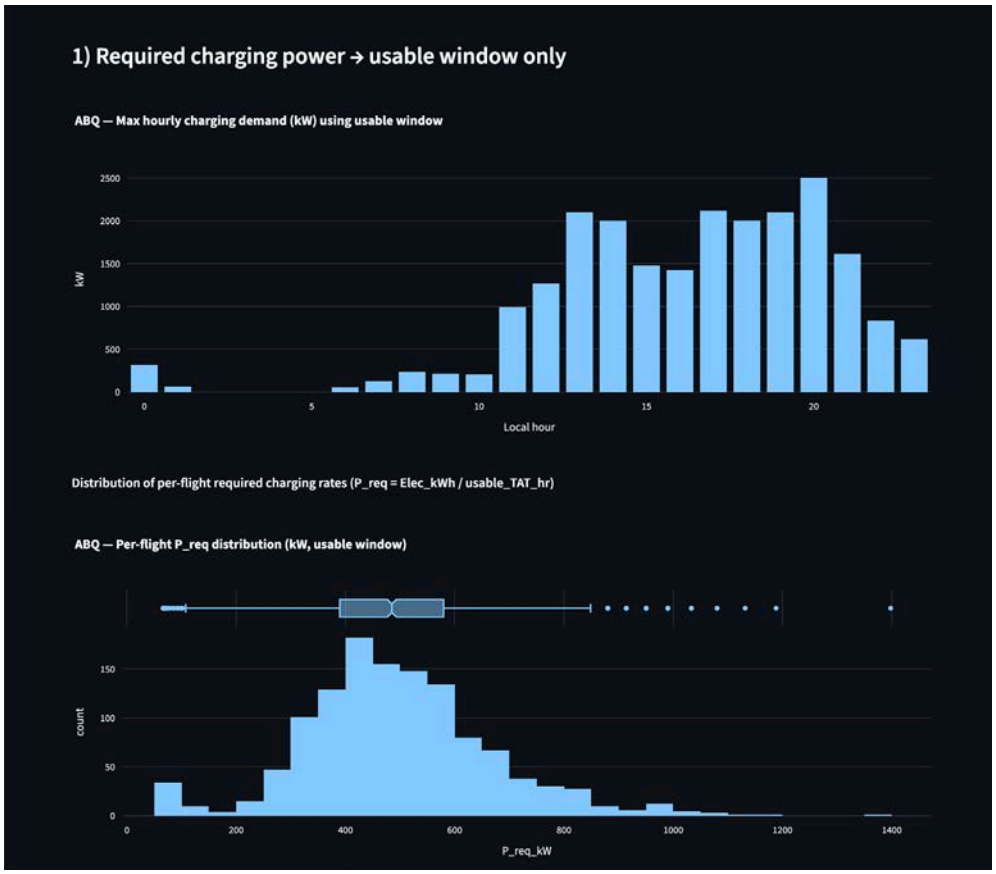


Figure 15. Tab 5 scenario 1 (for Albuquerque International Sunport [ABQ]).



Figure 16. Tab 5 scenario 2 (for Detroit Metropolitan Wayne County Airport [DTW]).



The per-flight analysis also includes feasibility assessment. For each flight and charger rating, we compare energy that can be delivered against energy required. Infeasible flights are those that cannot fully charge within available time. The dashboard reports not just feasibility rates but also the additional turnaround time needed to make infeasible flights feasible. This quantifies the operational impact: if 15% of flights need an extra 25 minutes of ground time on average, which has real implications for schedule design and aircraft utilization.

Milestone

Identified the specific technologies and scenarios that will be covered under this task in collaboration with the FAA.

Key Capabilities and Findings

The dashboard reveals several important patterns. First, required charging rates vary more by typical route structure than by absolute traffic volume. An airport handling many short routes might need only 150-300 kW chargers, while one serving longer turbofan routes might require 600+ kW even with comparable departure counts. We have extended the charger rating range to 1,200 kW to capture potential future high-power installations.

Second, turnaround time is often the binding constraint, not charger power. Increasing charger power from 300 to 600 kW helps, but if typical turnaround times are 40-50 minutes, even 600 kW is not enough for longer routes. Some route-airport combinations are fundamentally infeasible without operational changes—longer ground times, mid-route charging, or reduced payload.

Third, the CC-CV charging physics matter for accurate planning. Linear models consistently overestimate charging capability. For an airport where the CC-CV model shows 85% flight feasibility at 450 kW, a linear model might show 95% feasibility—a difference of hundreds of missed flights per year. Infrastructure sized based on linear assumptions will underperform.

Fourth, hourly demand profiles are not uniform. Morning and evening banks at hub airports create sharp peaks in charging load. Schedule-aware analysis shows these peaks can be 2-3× higher than assumptions based on spreading daily energy evenly across hours. This affects both the number of chargers needed and the electrical service capacity required from the grid.

Applications and Limitations

We have used the dashboard internally for several analyses. One examined Atlanta (ATL) in detail, showing that with 300 kW chargers approximately 60-70% of turboprop flights are feasible under current turnaround constraints, but this drops substantially for turbofan operations. Increasing to 600 kW improves feasibility but still leaves 20-30% of flights requiring operational adjustments.

Another analysis compared schedule-aware versus averaged facility sizing across top 20 airports by electricity demand. Schedule-aware methods consistently require 15-25% more chargers due to actual peaking patterns versus smoothed averages. This is not a flaw in either method, it reflects the difference between detailed operational realism and simplified planning estimates.

The tool has clear limitations. It assumes all charging occurs at departure airports, ignoring potential destination charging that could reduce departure-side infrastructure needs. It uses January 2023 schedules, which may not represent seasonal variations or post-pandemic traffic patterns. The energy consumption models are surrogate estimates, not actual aircraft performance data. Battery specifications assume a single standardized HEA design, when in reality different manufacturers will have different battery systems.

The FAA RPM scaling is a rough projection method. It assumes traffic growth scales all routes proportionally, when in reality growth patterns will vary by region and route type. The 20% non-charging buffer is based on judgment rather than time-motion studies of actual ground operations. These assumptions are defensible for system-level planning but would need refinement for actual infrastructure deployment.

Major Accomplishments

These vehicle-specific analyses will be integrated with the conventional aviation and the long-term scenarios from Tasks 1, 2, and 3. The goal is to show how certain technologies could help or hinder the adoption of certain types of vehicles.



The dashboard provides a data-driven foundation for evaluating HEA charging infrastructure needs. It translates abstract questions about electrification feasibility into concrete engineering requirements: how many chargers, what power ratings, what electrical service, at which airports. The analysis shows that universal answers do not exist—requirements vary substantially by location, route mix, and operational constraints.

The tool's value is not in providing definitive answers but in enabling systematic evaluation of alternatives. How does feasibility change at 450 vs. 600 kW? What happens if we accept 10% infeasible flights? Which airports should be prioritized? These are answerable questions, and the dashboard provides the analytical framework to answer them with realistic operational constraints and physics-based charging models.

Publications
None.

Outreach Efforts
None.

Awards
None.

Student Involvement
The graduate students that are part of this project will conduct most of this research under faculty supervision and with feedback from project management and other stakeholders.

Plans for Next Period
Consider specific technologies to enable new types of vehicles to be commercially and environmentally successful based on the results of Task 3.

Future Development
Several extensions would add value. Integration with grid capacity data would help identify locations where electrical infrastructure may be limiting. Weather impacts on charging (temperature effects on battery performance) are not currently modeled. Economic analysis—capital costs, electricity costs, revenue impacts of extended turnarounds—would help prioritize investments.

The per-flight analysis could be extended beyond single airports to network-wide assessment, though computational costs increase substantially. Machine learning models might identify patterns in which flights are most likely to face charging constraints, helping prioritize operational solutions. Integration with aircraft scheduling optimization could explore how modifying turnaround times or aircraft rotations might improve charging feasibility.

We are also considering support for mixed charger deployments—a hub might have both 300 kW chargers for short routes and 600+ kW chargers for longer flights. This would require matching flights to charger types, adding complexity but reflecting probable real-world deployments.

As hybrid electric aircraft move from concept to certification to entry into service, infrastructure planning needs to move in parallel. This dashboard represents one approach to that planning—imperfect, assumption-dependent, but grounded in real schedules and honest physics.



Project 097 FAST-Tech System Level Assessment

Georgia Institute of Technology

Project Lead Investigator

Principal Investigator:
Professor Dimitri N. Mavris
Director, Aerospace Systems Design Laboratory
School of Aerospace Engineering
Georgia Institute of Technology
Phone: (404) 894-1557
Fax: (404) 894-6596
Email: dimitri.mavris@ae.gatech.edu

University Participants

Georgia Institute of Technology (Georgia Tech)

- P.I.(s): Dr. Dimitri N. Mavris
- FAA Award Number: 13-C-AJFE-GIT-155
- Period of Performance: October 1, 2024, to December 31, 2025
- Tasks:
  1. Fueling Aviation's Sustainable Transition (FAST)-Tech Fleet Benefit Assessment Problem Formulation
  2. Initializing Modeling of FAST-Tech Aircraft Technologies and Advanced Configurations

Project Funding Level

The Federal Aviation Administration (FAA) provided $250,000 in funding to Georgia Tech. Georgia Tech has agreed to a total of $250,000 in matching funds. This total includes salaries for the project director and research engineers, as well as funding for computing, financial, and administrative support, including meeting arrangements. Georgia Tech has also agreed to provide tuition remission for students, paid from state funds.

Investigation Team

P.I.: Prof. Dimitri Mavris
Co-P.I.: Dr. Jimmy Tai
Program Manager: Brennan Stewart
Supporting Engineers: Srujal Patel and Dr. Zhimin Liu
Students: Joao De Azevedo, Kavya Krishnan, Alexandre Masset, Clementin Leron, Benjamin Bashtovoi, Byron Chang, Saisruthi Bandla, Paul Dumont, and Naomi Michael

Project Overview

The objective of this research project is to support the FAA by independently modeling and assessing the technologies that are being developed under the FAST Program. This will involve direct coordination and data sharing with FAST-funded companies to accurately model the environmental benefits of these technologies at the vehicle and fleet levels.

Georgia Tech was previously selected to perform all system-level assessments for the Continuous Lower Energy, Emissions and Noise (CLEEN) program under Partnership for Air Transportation Noise and Emission Reduction (PARTNER) Project 036, ASCENT Project 010, and ASCENT Project 037. As a result, Georgia Tech is in a unique position from both the technical and programmatic standpoints to perform system level assessments for the FAST Program. From a technical perspective, Georgia Tech has significantly enhanced the Environmental Design Space (EDS) over the past 5 years to incorporate advanced, adaptive, and operational technologies targeting fuel burn and emissions.



The goal of this work is to conduct fleet-level assessments for aircraft representative of future "in-service" systems. To accomplish this goal, Georgia Tech requires system-level EDS models using a combination of both FAST Technologies and other public domain technologies and defining assumptions for future fleet scenarios. To expedite this study, Georgia Tech will leverage previously created EDS models, public technologies sets, and future fleet scenarios from Georgia Tech's work on ASCENT Project 037, in combination with the technology models created for the FAST technologies funded under ASCENT Project 097. This approach will allow Georgia Tech to complete the FAST fleet assessment quicker and for less cost than if Georgia Tech were to redevelop these assumptions using ASCENT Project 097 funds.

Work conducted during this period of performance focused on reviewing which assumptions ASCENT Project 097 would utilize from Georgia Tech's ASCENT Project 037 program and assessing Georgia Tech's capabilities of modeling FAST technologies and performing background research on the technology concept. In the previous year of performance, Georgia Tech had selected a fleet assessment methodology and a base year case from Georgia Tech's ASCENT Project 037. However, as Georgia Tech has become more familiar with technology set which is to be evaluated for the FAST Tech program, Georgia Tech recognized that significant edits will be required to the framework used in ASCENT Project 037. This is due FAST technologies being developed to support multiple fuel types and the introduction of novel vehicle architecture, while ASCENT 037 is focused around traditional tube and wing aircraft fueled by Jet A. Georgia Tech does have experience with these concepts in other programs such as our support of National Aeronautics and Space Administration (NASA) Electrified Powertrain Flight Demonstration, some work will be required to implement these changes. However, Georgia Tech's working effort for this year primarily focuses on Modeling of FAST-Tech Aircraft Technologies and Advanced Configurations. Georgia Tech was able to initiate Non-Disclosure Agreements (NDA) with the majority of FAST contractors whose technologies will be models as part of the Fleet assessment, and thus heavy emphasis for this year was place on the initial modeling work based on FAA FAST Tech contractor inputs.

Next year's work will focus on continuation of modeling of FAST-Tech Technologies, construction of vehicle models for Advanced Configurations, and adapting the Fleet Analysis assumptions for the set of architecture developed to access FAST Technologies.

Milestones

The major milestones and their planned due dates are listed below:

Task No.	Milestone	Planned Due Date
1	FAST-Tech Fleet Benefit Assessment Problem Formulation	December 31, 2025
2	Initialize Modeling of FAST-Tech Aircraft Technologies and Advanced Configurations	December 31, 2025

Major Accomplishments

- Established NDAs and held kickoffs held with nearly all FAST Tech contractors.
- Initiated modeling work for over half of the contractors.
- Completed preliminary models for select contractors.

Task 1 - FAST-Tech Fleet Benefit Assessment Problem Formulation

Georgia Institute of Technology

Objective

The objective of this task is to align the assumptions used in this FAST fleet benefit assessment with the most relevant assumptions used across similar recent assessments performed by Georgia Tech.

Research Approach

Georgia Tech has provided fleet benefit assessments regarding fuel burn, nitrogen oxides (NO_x) emissions, and noise in a number of previous research efforts. Learnings from these previous fleet benefit assessments will set the starting point for this assessment. The FAA is interested not only in the effects of individual FAST technologies, but also the impact of combining various FAST and other public domain technologies across vehicle size classes. The fleet benefit assessment will be updated to match the most relevant assumptions constraining the FAST program in conjunction with the FAA.



Georgia Tech and the FAA have agreed that methodology used in ASCENT Project 037 will serve as a useful starting point for the methodology for the FAST fleet benefit assessment (Mavris et al., 2023). Figure 1 shows an overview of the methodology for the FAST-Tech fleet benefits assessment based on the fleet assessment methodology used in ASCENT Project 037. The public set of technologies used in ASCENT Project 037 will also serve as the basis for the non-FAST technologies which will be infused into the mid- and far-term generations of aircraft analyzed in the FAST fleet benefits assessment.

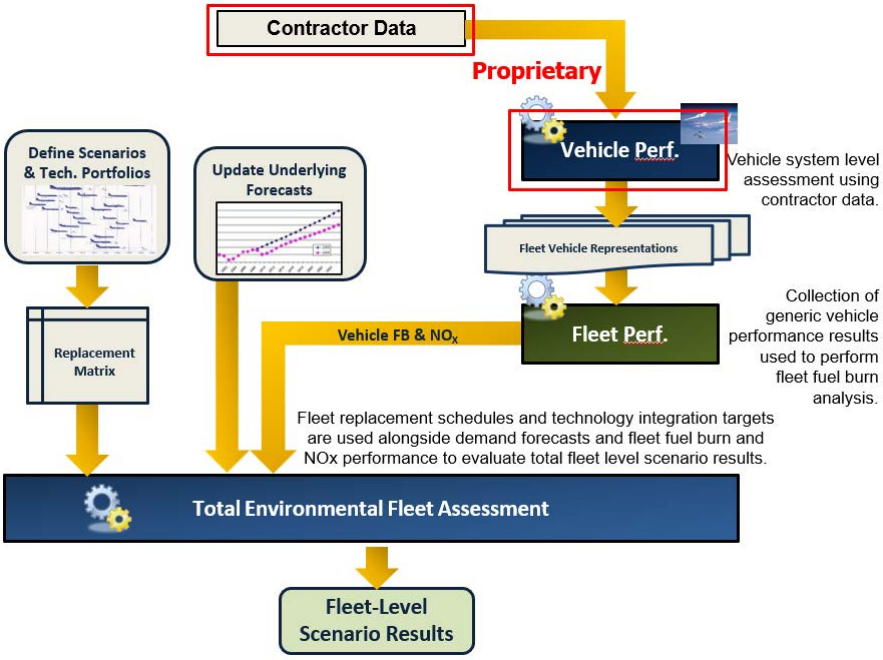


Figure 1. FAST Fleet Assessment Initial Methodology Overview. FB: Fuel Burn, NO_x: nitrogen oxides.

However, this methodology does not currently account for comparisons between multiple fuel types, (as necessitated by the list of technologies funded by the FAST program), nor does it currently consider the introduction of novel vehicle architectures. These are problems which Georgia Tech research teams have addressed in the past, such as work in support of NASA's Electrified Powertrain Flight Demonstration program, but it will take effort to adapt out fleet assessment methodology to those changes. However, Task 2 has been prioritized over this task during the performance period of this report.

Task 2 - Initialize Modeling of FAST-Tech Aircraft Technologies and Advanced Configurations

Georgia Institute of Technology

Objectives

The objective of this task is to estimate the impact of FAST relevant technologies at the vehicle-system level, each of these technologies must be modeled regarding their impacts to aircraft fuel burn and emissions using EDS.

Research Approach

To complete the FAST fleet benefit assessment outlined in Task 1, Georgia Tech must develop aircraft representative of future "in-service" systems, utilizing the technologies funded by FAST. Two necessary steps to accomplish the modeling of these future "in-service" systems are modeling all FAST technology in EDS and ensuring that new vehicle architectures are included in EDS modeling space. Once these tasks are completed, Georgia Tech will be able to develop the representative models of the future "in-service" systems and perform the fleet-level benefit assessment outlined in Task 1.



Table 1 shows the status of the modeling effort regarding each of the FAST relevant technologies. The FAA announced the awards for the FAST contracts in August 2024, (FAA, 2024), and Georgia Tech was authorized to begin initiating NDA discussions with each of the contractors in December 2024. As the initial FAA announcement of the awards of the FAST contracts is currently unavailable online, additional references for each award have been provided, (Businesswire, 2024, Heart Aerospace, 2024, Marquand, 2024, SAF Path, 2024, USASpending, 2025, Warwick, 2024, and ZeroAvia, 2024).

Throughout the period of performance, Georgia Tech was able to complete NDA discussions with nearly all FAST contractors. Georgia Tech was able to begin the technology modeling process with select contractors (Georgia Tech did not have resources to work with all contractors simultaneously) and finished preliminary modeling with some of the contractors. Table 1 provides a brief overview of the contractors Georgia Tech plans to work with and a description of their technologies.

Table 1. FAST Technologies and Their Modeling Status. CO_2: carbon dioxide, NAS: National Airspace System.

Contractor	Technology
Green Taxi, Inc.	Green Taxi Electric Taxi (eTaxi) system for Embraer E-175 Aircraft
JetZero, Inc.	Blended Wing body Lightweight Composite Structures
Honeywell International Inc.	Sustainable Electrified Aircraft Power
APiJET, LLC	Optimizing Flight Routes using Real-Time Operating Constraints for Maximum Reduction of CO_2 Emissions via Scalable Ground-Based Software
Heart Aerospace Inc.	Total Hybrid Electric Management and Integration System
University of Michigan	Expanding Flight Operations-based Low Emissions Technologies: Fleet-wide and NAS-wide Arrival Flow Optimizer
ZeroAvia Federal, Inc.	Project Hydrogen Aircraft Engine Zero Emission Leap
Otto Aviation Group, LLC	Wind-Tunnel Testing of a Transonic Aircraft with a Fully Integrated Slotted, Natural Laminar-Flow Wing
Wright Electric Inc.	Ultra-High Energy Battery

In the previous annual report, Georgia Tech provided insight into how each of the technologies might be modeled under Georgia Tech's current modeling capabilities based on publicly available information on each of these technologies. This insight was provided before Georgia Tech initiated discussions with each contractor under an NDA. Now that discussions have taken on a proprietary nature, Georgia Tech will not be able to publicly disclose the details of any of these modeling efforts.

Publications

Conference Presentation

Stewart, B., Tai, J., Mavris, D. (2025, October 16). *FAST-Tech System Level Assessment* [Conference presentation]. ASCENT Fall Meeting 2025, Alexandria, Virginia.

Outreach Efforts

Georgia Tech presented the current status of Fleet Assessment plans for the FAST Program as part of the ASCENT Fall Meeting in Alexandria, Virginia on October 16, 2025, to a mixed audience of industry, academia, and government representatives.

Awards

None.



Student Involvement

Nine graduate students have been funded by the effort: Joao De Azevedo, Kavya Krishnan, Byron Chang, Benjamin Bashtovoi, and Saisruthi Bandla are PhD students, and the remaining four students, Alexandre Masset, Clementin Leron, Paul Dumont, and Naomi Michael, are master's students.

Plans for Next Period

- Continue modeling of FAST-Tech Technologies.
- Construct vehicle models for Advanced Configurations, which are needed to access each technology.
- Adapt the Fleet Analysis assumptions for the set of architecture developed to access FAST Technologies.

References

Businesswire. (2024). *Wright Selected for $3.34M Award From FAA FAST for Ultra-Lightweight Batteries.* Businesswire https://www.businesswire.com/news/home/20240819989681/en/Wright-Selected-for-%243.34M-Award-From-FAA-FAST-for-Ultra-Lightweight-Batteries

FAA. (2024). *Fueling Aviation's Sustainable Transition (FAST) Grants.* Federal Aviation Administration. https://www.faa.gov/general/fueling-aviations-sustainable-transition-fast-grants

Heart Aerospace. (2024). *Heart Aerospace Awarded $4.1 Million in FAA FAST Grant to Advance Electric Aviation in the U.S.* Heart Aerospace. https://heartaerospace.com/newsroom/heart-aerospace-awarded-4-1-million-in-faa-fast-grant-to-advance-electric-aviation-in-the-u-s/

Mavris, D., Tai, J., & Brooks, J. (2023). *Project 037 CLEEN II System-level Assessment.* Washington State University. https://s3.wp.wsu.edu/uploads/sites/2479/2024/08/2023-ASCENT-Annual-Report.pdf

Marquand, Yves L. (2024). *Heart, JetZero and others awarded FAA FAST grants.* Revolution.Aero. *https://www.revolution.aero/news/2024/08/16/heart-jetzero-and-others-awarded-faa-fast-grants/*

Otto Aerospace. (2024). *Otto Aerospace Awarded $7 Million FAA Grant to Advance Transonic Laminar Flow Technology for Sustainable Aviation. https://ottoaerospace.com/news/otto-aviation-awarded-7-million-faa-grant/*

SAF Path. (2024). *Meet the Recipients of the FAA FAST Grants: Pioneering the Future of Sustainable Aviation.* SAF Path. *https://safpath.com/saf-insight/meet-the-recipients-of-the-faa-fast-grants-pioneering-the-future-of-sustainable-aviation/*

USASpending. (2025). *20.115 | Fueling Aviation's Sustainable Transition via Sustainable Aviation Fuels (FAST-SAF) and Low-Emissions Aviation Technologies (FAST-Tech) Grant.* USASpending.Gov *https://www.usaspending.gov*

Warwick, Graham. (2024). *FAA's FAST Grants Support SAF Buildup, Low-Emission Technologies.* Aviation Week. *https://aviationweek.com/air-transport/safety-ops-regulation/faas-fast-grants-support-saf-buildup-low-emission-technologies*

ZeroAvia. (2024). *Federal Aviation Administration Awards ZeroAvia $4.2 Million US Federal Grant to Advance Electric Propulsion for Clean Aviation.* ZeroAvia. *https://zeroavia.com/federal-aviation-administration-awards-zeroavia-4-2-million-us-federal-grant-to-advance-electric-propulsion-for-clean-aviation/*

Project 098 Low Emissions Lean Pre-Mixed Pre-Vaporized Combustion Technology for Subsonic Civil Transport

Georgia Institute of Technology

Project Lead Investigator

Adam Steinberg
Professor
School of Aerospace Engineering
Georgia Institute of Technology
Phone: (404) 897-1130
E-mail: adam.steinberg@gatech.edu

University Participants

Georgia Institute of Technology

- P.I.: Dr. Adam Steinberg
- FAA Award Number: 13-C-AJFE-GIT-150
- Period of Performance: March 19, 2024, to December 31, 2026
- Tasks:
  1. Experimental Measurement of Emissions, Lean Operation Limits, Spray, and Flame Structure
  2. Computational Fluid Dynamics (CFD) Simulations of LPP Combustor

Project Funding Level

Federal Aviation Administration (FAA): $1,000,000
Georgia Institute of Technology (Georgia Tech): $486,000
General Electric (GE) Aerospace Research: $514,000

Investigation Team

Dr. Adam Steinberg (Georgia Institute of Technology [GT], PD/PI)
Dr. Ellen Mazumdar (GT, Co-PI)
Dr. Joseph Oefelein (GT, Co-PI)
Dr. Jerry Seitzman (GT, Co-PI)
Mr. Arihant Jain (GT, PhD student)
Mr. Alexander Stevens (GT, PhD student)
Ms. Ijeoma Obi (GT, MS student)
Ms. Jananee Dhanasekaran (GT, MS student)
Dr. Krishna Venkatesan (GE Research [GER], Co-PI)
Dr. Victor Salazar (GER, Co-PI)
Dr. John Hong (GER)
Ms. Sydney Borrello (GER)

Project Overview

Lean premixed prevaporized (LPP) combustion is a key enabling technology to further reduce nitrogen oxides (NO_x) and non-volatile particulate matter (nvPM) emissions from aeronautical gas turbine engines. However, achieving practical LPP combustion is challenging due to the need to rapidly vaporize and mix fuel, stabilize LPP flames across a wide operating envelope, and prevent unwanted combustion dynamics. Furthermore, the ability of current design methodologies to predict the operability and emissions of these combustors is unproven. Previous work during ASCENT Project 074 demonstrated positive results for an LPP combustor configuration at the conditions found in engines for supersonic transport aircraft and encouraged further exploration at conditions relevant for the conventional subsonic fleet (Jain et al.,

2026; Passarelli et al., 2024). Hence, ASCENT Project 098 is characterizing the emissions and operability of an updated LPP combustor at key operating points for such subsonic aircraft engines, including low power (i.e., idle and taxi), cruise, and approach. It also is developing measurement techniques needed to study high-power (i.e., takeoff and climb) conditions that are challenging for LPP combustors. The high-quality experimental data at relevant conditions are being coupled with the development and validation of CFD simulations and reduced order models. These activities form a key first step in the development of both the LPP combustor technology and validated design tools for subsonic aircraft engine conditions.

Task 1 – Experimental Measurement of Emissions, Lean Operation Limits, Spray, and Flame Structure

Georgia Institute of Technology
GE Aerospace

Objectives

The objectives of this task under the current project scope are to:

- Redesign and optimize the ASCENT Project 074 LPP combustor geometry to have a pilot system that is more relevant for subsonic aircraft engines.
- Fabricate and commission this new combustor.
- Experimentally test the combustor at conditions representing idle, taxi, approach, and cruise to establish emissions levels and blow-off limits.
- Collect data using optical diagnostics with which to validate large eddy simulations (LES) and better understand the combustor.
- Develop and demonstrate novel measurement techniques that can be applied under high-power conditions (takeoff, climb) for studies in future years.

Research Approach

Experiments have been performed in the same basic test article as used for Experimental Campaign 2 in ASCENT Project 074 (see Figure 1) (Jain et al., 2026), with some facility and premixer modifications to accommodate the different operating conditions for subsonic aircraft engines compared to supersonic aircraft.

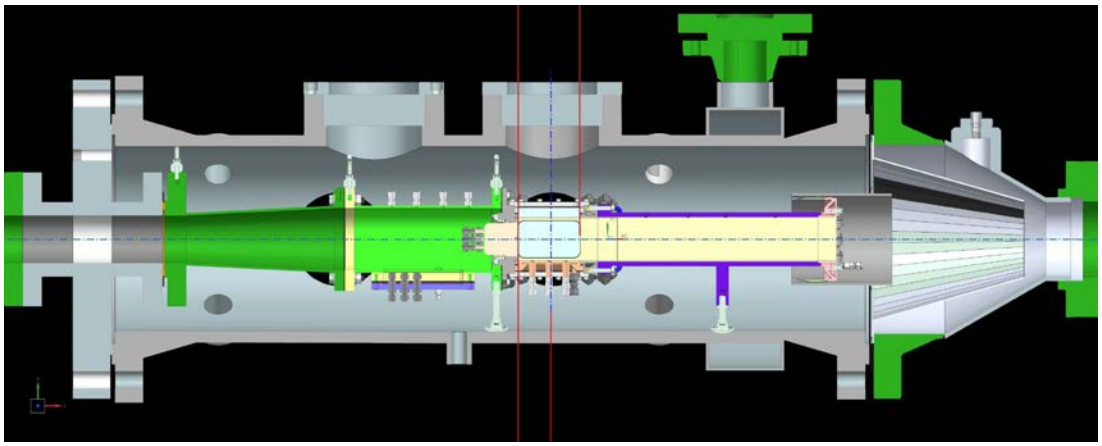


Figure 1. Conceptual schematic of experimental test article.

The FAA ASCENT Project 098 builds upon the success of the mixer technology developed during the ASCENT Project 007 for supersonic cruise conditions. However, the potential impact of LPP combustion on the future commercial subsonic aircraft fleet is much larger. Combustors for subsonic aircraft engines experience quite different air inflow pressures (p_3) and temperatures (T_3), which affect the performance of LPP combustion. Although the ASCENT Project 074 mixer achieved low emissions, its pilot design was relatively simple as it was based on a commercial pressure swirl atomizer employed as a placeholder pilot to ignite the main. Fuel atomization by this pilot is expected to be suboptimal. Therefore, to improve



pilot fuel atomization and further reduce emissions, a key aspect of the ASCENT Project 098 is to improve the pilot design of the ASCENT Project 074 mixer by integrating a contemporary pilot.

Detailed design and trade studies for the ASCENT Project 098 pilot and mixer were performed using CFD; they are described in more detail under Task 2. Once designed, the mixer was three-dimensionally (3D) printed, and conventional heat treatment and post machined processes were performed. A thermal barrier coating was applied to the aft face of the mixer. Once all the manufacturing processes were completed, the mixer was flow checked and finally released for testing.

Two mixers, manufactured by two different 3D printed vendors, were tested in the rig show in Figure 1 using the measurement techniques described below. A skeletal test matrix is provided in Table 1. Note that the overall test matrix involved approximately 30 test points, including variations of other operating parameters, which are not described in detail here. Both mixers performed as expected at the various operating conditions and the observations were consistent with their specific designs.

This experimental campaign occurred from August to October 2025. The measurement techniques described below were transported from Georgia Tech (Atlanta, Georgia) to GE Aerospace Research (Niskayuna, New York). Georgia Tech students were present at GE Aerospace® Research throughout the campaign to setup and conduct the measurements, alongside GE scientific and technical staff who operated the combustor facility. Note that only preliminary results are included below since the experimental campaign ended after the reporting period. Analysis of the data is ongoing. The combustor currently is being installed in a different test cell at GE to measure pollutant emissions.

Table 1. Test Matrix. FAR: Federal Aviation Regulations.

Parameter	Measurements
p_3 [psia]	110 & 200
T_3 [°F]	450, 550 & 650
Mixer FAR [-]	0.045, 0.050 & 0.055

Optical Diagnostics Measurements

To determine operability limits and examine flame and spray structure, a suite of state-of-the-art optical diagnostics techniques were deployed during the experimental campaign. These included hydroxyl (OH) planar laser induced fluorescence (PLIF), OH* and CH* chemiluminescence (CL), high magnification shadowgraphy, and fuel droplet Mie scattering (Jain et al., 2026). The diagnostics setup is schematically shown in Figure 2 and Figure 3.

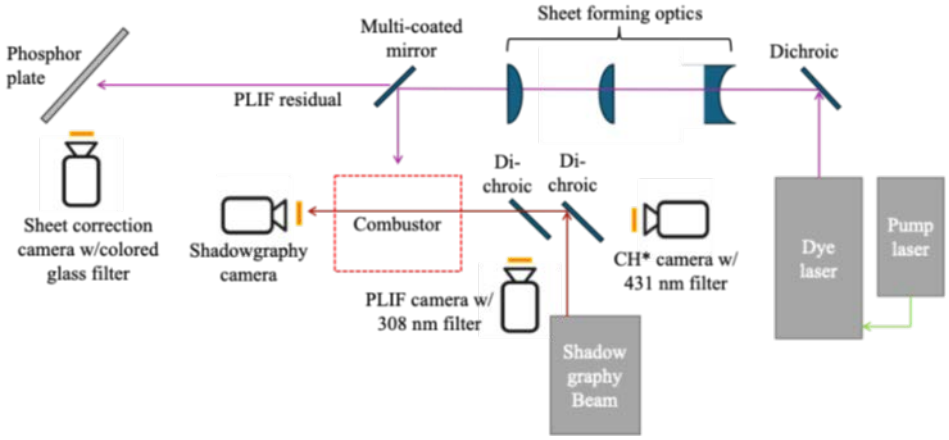


Figure 2. Simplified diagnostics schematic with shadowgraphy implemented. PLIF: planar laser induced fluorescence.

® GE Aerospace is a registered trademark of the General Electric Company, Evendale, Ohio.

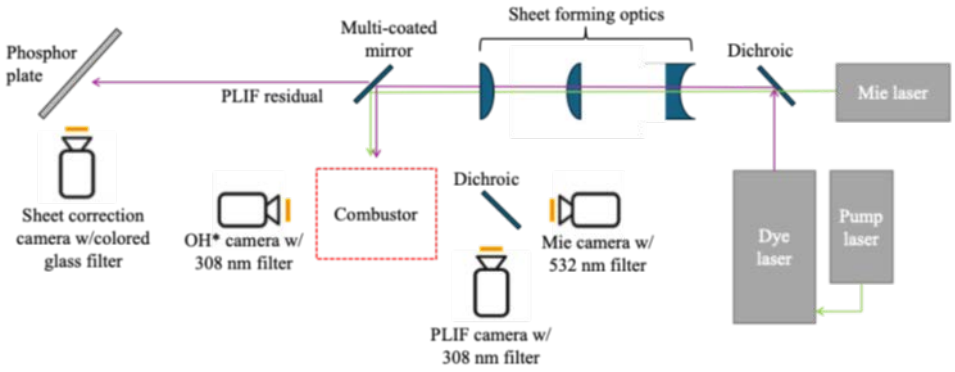


Figure 3. Simplified optical schematic with Mie scattering implemented.

In OH PLIF, a laser is used to excite OH radicals and their subsequent fluorescence is captured using an intensified camera. The OH PLIF system used here employed an Nd:YAG laser (Quantel® Q-Smart 850, 532 nm, 10 Hz, 300 mJ per pulse) to pump a tunable dye laser (Sirah PrecisionScan,™ Rhodamine 6G). The dye laser output at approximately 568 nm was frequency-doubled to yield an ultraviolet (UV) pulse with energy of approximately 21 mJ. The dye laser output was tuned to excite the Q1(9) transition of OH near 283.9 nm. To select, monitor, and tune the laser line, a reference laminar flame burner was used.

Images were recorded using a 308±10 nm filter, UV objective lens (Cercolens,™ 100 mm), and an sCMOS intensified camera (Andor™ iStar, gate time of 150 ns). The camera recorded 1,000 frames per test point with a projected pixel size of 40 μm. As shown in Figure 2 and Figure 3, the residual laser sheet that did not get reflected into the test section was impinged on a phosphor-coated plate placed after the final mirror. The resultant phosphorescence was imaged by a camera (FLIR Blackfly®) with a colored glass filter. These images were used to correct the PLIF data for shot-to-shot variation in laser sheet profile and intensity.

OH* and CH* CL images were recorded at 10 kHz using a high-speed camera (Photron® SA-5) coupled to an image intensifier (Invisible® Vision UVi 2550-10, gate time of 20 μs). The camera recorded 15,068 frames (1.5068 s) per test point. CH* images were recorded using a 431±10 nm filter and objective lens (DC Nikkor®, 105 mm), while the OH* images used a 308±10 nm filter and UV objective lens (Cercolens, 100 mm). Note that either OH* or CH* data were collected on a given test day (not both). During the first half of the test campaign, fuel droplet shadowgraph imaging was implemented and iteratively optimized (described below). Because the shadowgraph optical configuration occupied had particular optical access and layout requirements, CH* chemiluminescence was collected during these early runs, as shown in Figure 2.

To identify droplets within the combustor, shadowgraphy first was attempted with a high-speed light-emitting diode (LED) and parabolic mirror setup shown in Figure 4a. First, the 385 nm wavelength light from the LED source (Lightspeed hpls-36dd18b) is collimated through a lens. Then the dichroic mirror reflects the light through the combustor and into the mirror system. The light first hits an 80 mm elliptical mirror and then is reflected into the 304 mm parabolic mirror, after which it is reflected into the other identical parabolic mirror that focuses it on another 80 mm elliptical mirror and finally into the camera. Attached to the camera is a 280 nm ±10 nm filter to block out any flame luminosity.

® Quantel is a registered trademark of Lumibird, Lannion, France.
™ PrecisionScan is a trademark of Sirah Lasertechnik GmbH, Grevenbroich, Germany.
™ Cercolens is a trademark of Cerco, France.
™ Andor is a trademark of Oxford Instruments, United Kingdom.
® Blackfly is a registered trademark of Teledyne FLIR, LLC, Treasure Oaks, California.
® Photron is a registered trademark of Photron Limited, Tokyo, Japan.
® Invisible is a registered trademark of Invisible Vision Ltd., United Kingdom.
® DC Nikkor is a registered trademark of Nikon Corporation, Tokyo, Japan.

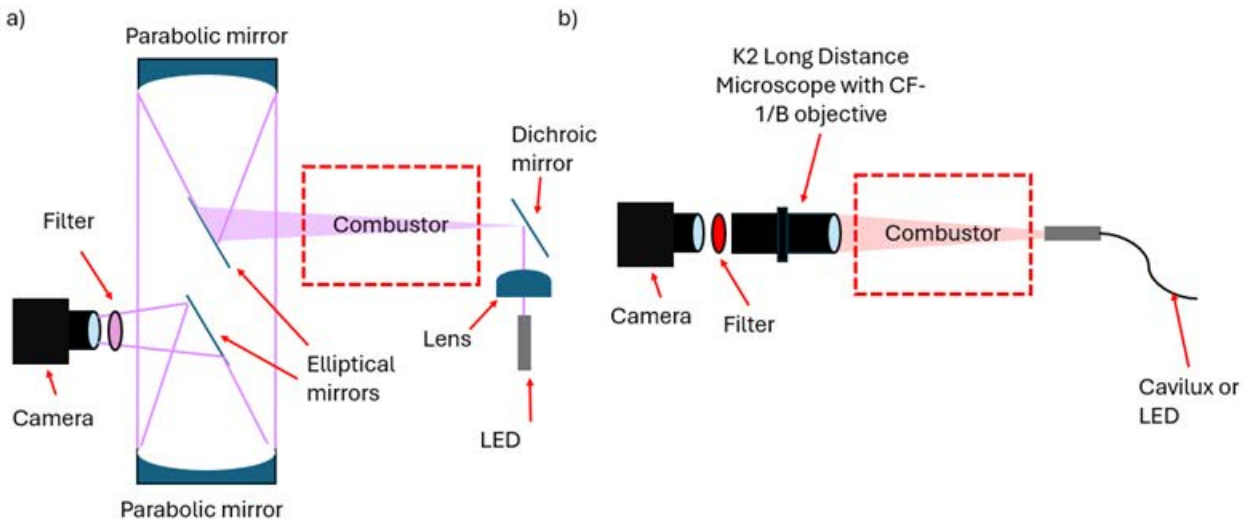


Figure 4. (a) Shadowgraphy system with mirrors and Lightspeed Technologies™ light emitting diode (LED) and (b) shadowgraphy system with the K2 long distance microscope with the CF-1/b and Cavilux® Smart UHS laser or the Lightspeed Technologies LED.

Unfortunately, this setup was unable to gather the light necessary to identify the droplets in the flame. A source of signal attenuation was from the center light rays being blocked by the elliptical mirror. The mirror system was designed to only see the diffraction pattern from the droplets and lost the center rays, accounting for most of the light. To capture the central light rays, the long-distance microscope system (Infinity K2 with the CF-1/B objective) was switched in place of the mirrors as shown in Figure 4b. However, the light captured on the camera was still insufficient to identify the droplets in the spray. When compared to the mirror system, the long-distance microscope had more light on the camera sensor, but the LED either had to be on for too long (leading to droplet smearing) or the light would not be bright enough to resolve the droplets. To resolve this issue a spoiled cavity laser system (Cavilux Smart UHS) was substituted in place of the LED, as also shown in Figure 4b. This system was able to identify some droplets in the flow at low temperature operating conditions.

As described above, modifications to the shadowgraph system were implemented during the test campaign. During the periods when the shadowgraph system was being modified, available optical table space and dichroic mirror arrangements allowed the diagnostics suite to be reconfigured, as shown in Figure 3. In this configuration, laser Mie scattering measurements were collected to characterize the fuel spray and the chemiluminescence system was transitioned to measure OH* instead of CH*.

Mie scattering used the output of an Nd:YAG laser (Quantel Evergreen EVG00200, 532 nm, 10 Hz, 160 mJ/pulse) to assess the fuel spray qualitatively. The Mie scattering beam path utilized the same optics as the OH PLIF system, enabling coincident laser sheets. Mie scattering images were isolated on a different camera (Andor Zyla) using a dichroic mirror, 532±10 nm bandpass filter, and objective lens (DC Nikkor, 105 mm). For each test point, 1,000 frames were collected at an exposure of 9.24 μs. An external pulse generator was used to synchronize the Mie and OH PLIF images.

A critical aspect of understanding the combustor's performance is understanding how the pilot flame interacts with the LPP main flames. Unraveling such interactions requires measurements to be made in multiple planes between the pilot centerline and the outer annulus of the main flames. To examine multiple planes, the sheet-forming optics, final multicoated mirror, and cameras were placed on remotely controlled translation stages. This allowed the laser sheet to be traversed across the combustor while keeping the images in focus. Images are captured at eight different planes ranging from the pilot centerline to the outer edge of the combustor for each operating condition. These measurements allow the

™ Lightspeed Technologies is a registered trademark of Lightspeed Technologies, Inc., Campbell, California.
® Cavilux is a registered trademark of Cavitar Ltd., Finland.

development of the main and pilot flames to be mapped relative across the full combustor width, capturing the spatial extent of pilot's influence under different operating regimes. The approximate range of the laser sheet traverse and location of the shadowgraphy beam with reference to the dome face are shown in Figure 5.

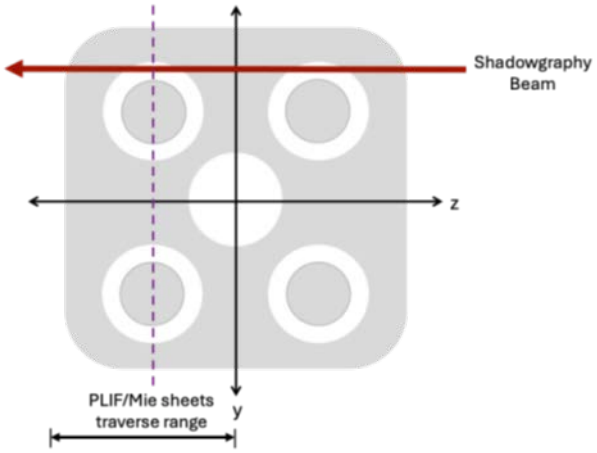


Figure 5. Dome face schematic, aft looking forward. PLIF: planar laser induced fluorescence.

In addition to the "conventional" diagnostic suite, an experimental fiber optic coupled spectrally resolved CL measurement technique was deployed as a demonstration for future high-power measurements in optically inaccessible combustor configurations. The top window in the combustion liner was replaced with a water-cooled blank. Four gold-coated multimode optical fibers (NA = 0.12, 200 μm pure fused silica core, Molex Polymicro®) were directly mounted via high-temperature epoxy to the blank. The gold-coated fibers can survive operating temperatures up to 973K, preventing damage as they are routed outside of the pressure vessel and coupled to a fiber bundle (Thorlabs® 1-to-4, linear, NA = 0.22). Light from the fiber bundle is captured by a spectrograph (Andor Shamrock 303i, 600 l/mm grating, 500 nm blaze) and imaged by a charge-coupled device (CCD) camera (Andor iDus 420A-BU).

The four fibers are positioned along the centerline of one of the main flames at varying axial distances from the dome face. Light collected by the four fibers is relayed to the spectrograph entrance slit and imaged simultaneously onto the CCD sensor using a custom relay-imaging system. In this configuration, the fiber outputs are vertically stacked so that each fiber occupies a distinct and confined region of the detector's vertical pixel array. This arrangement allows all four spectral signals to be recorded concurrently on a single camera exposure while preserving spatial separation between channels. Figure 6 shows a schematic of the positioning of the fibers in the combustor and the subsequent relay imaging system.

® Polymicro is a registered trademark of Molex, LLC, Lisle, Illinois.
® Thorlabs is a registered trademark of Thorlabs, Inc., Newton, New Jersey.

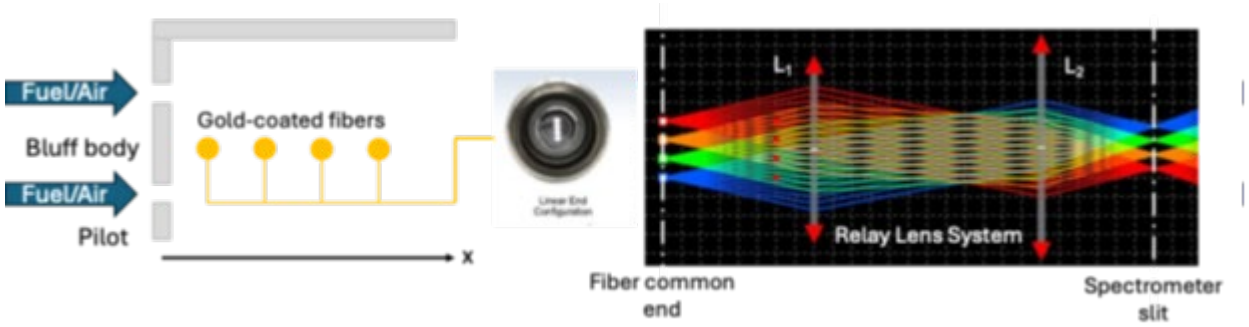


Figure 6. Spectrally resolved fiber optic coupled chemiluminescence schematic. Left: Approximate fiber axial position in combustor (side view). Right: Relay lens imaging system from fiber bundle to spectrometer. For visualization, each fiber is shown as a different color.

Optical Diagnostics Results

Figure 7 shows sample OH* chemiluminescence images for an attached and blown-off condition. The attached case on the left shows clear signal in the recirculation zone of both bluff bodies. Comparatively, the blown-off case shows no signal, as indicated by the red box in the figure. While OH* CL is a line-of-sight-integrated diagnostic method, and it is possible that one (or more) mains blow off while the others remain attached, it is a suitable diagnostic for identifying global blow off conditions. A systematic analysis of all the operating conditions identified the blow-off conditions as listed in Table 2. Across all cases where the pilot remained stably attached, the global lean blowoff boundary was dictated mainly by inlet temperature and global Federal Aviation Regulations (FAR), showing little dependence on pilot equivalence ratio. Conditions became pilot-limited only when the pilot neared its own lean extinction threshold, at which point further reductions in global FAR were not achievable.

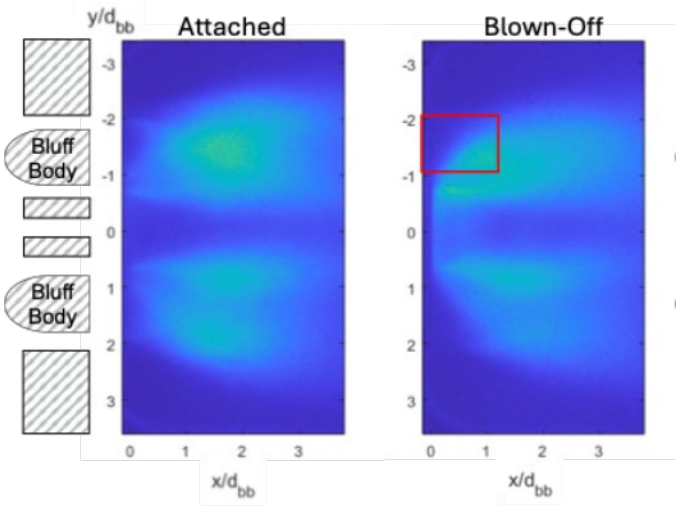


Figure 7. Sample mean OH* chemiluminescence images for attached cases (left) and blown-off cases (right).



Table 2. Lean Blowoff Conditions.

T_3 (F)	Φ_{pilot}	Φ_{mains}	Blown Off?
650	Low	0.69	No
650	Medium	0.65	No
650	High	0.59	No
550	Low	0.69	Could not reach condition
550	Medium	0.65	Yes
550	High	0.59	Yes
450	Low	0.78	Could not reach condition
450	Medium	0.74	Yes
450	High	0.68	Yes

Figure 8 shows sample temporal mean PLIF images for an attached case at the pilot and main centerline. The raw images show a region of high signal at $1 \lesssim x/d_{bb} \lesssim 2$, which corresponds to a region of high beam energy intensity. To correct for these nonuniformities, the shot-for-shot beam correction is applied to the raw images, creating a relatively more uniform distribution seen on the right for each set of images. Nonetheless, the beam profile corrected images along the means centerline show significant signal along the reactant jets, indicating strong fuel-PLIF crosstalk from the aromatic content in Jet-A. Indeed, mean Mie scattering images show unvaporized droplets entering the combustor, even at the highest T_3 conditions. Therefore, as images are further processed, overlayed mean Mie scattering images will be used to guide PLIF interpretation.

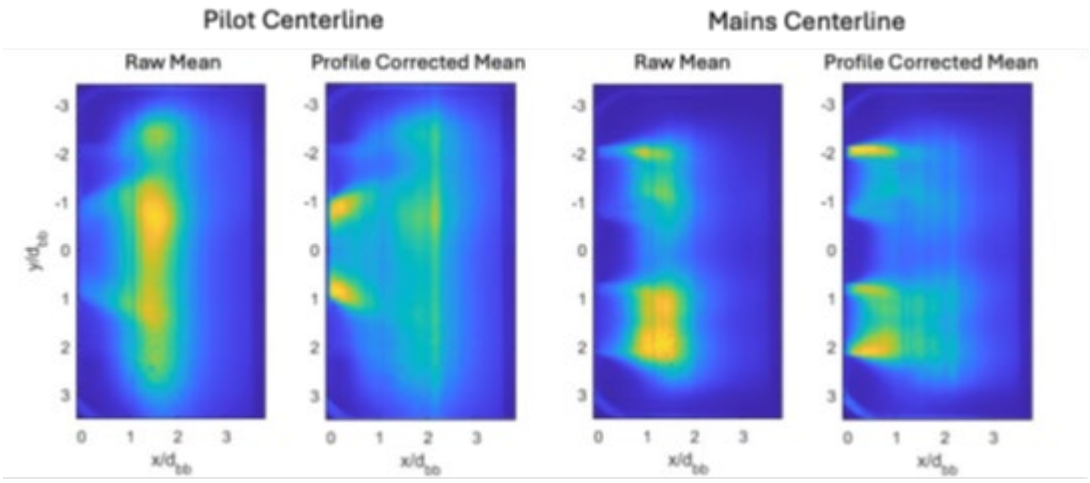


Figure 8. Sample temporal mean PLIF images along the pilot and main centerline. The left images in each set are the raw mean, and the right are beam profile corrected.

Figure 9 shows the combustor-facing side of the water-cooled window blank into which the fiber optics were mounted. The fiber locations are shown via the red arrows, although the holes are too small to see, as the fiber diameter with cladding and coating is 250 μm. The spectrometer was unable to capture any signal, likely because of the soot coating the blank and blocking any light. However, the epoxy held the fibers in place, and they did not become dislodged during testing. Therefore, future testing will benefit from an effusion cooled liner that provides a protective boundary layer of air for the fibers.



Figure 9. Combustor blank with mounted fiber optics after testing.

Shadowgraphy was able to identify droplets in the combustor at a low temperature. Figure 10 shows some of these droplets. As data processing continues droplet statistics may be able to be identified.

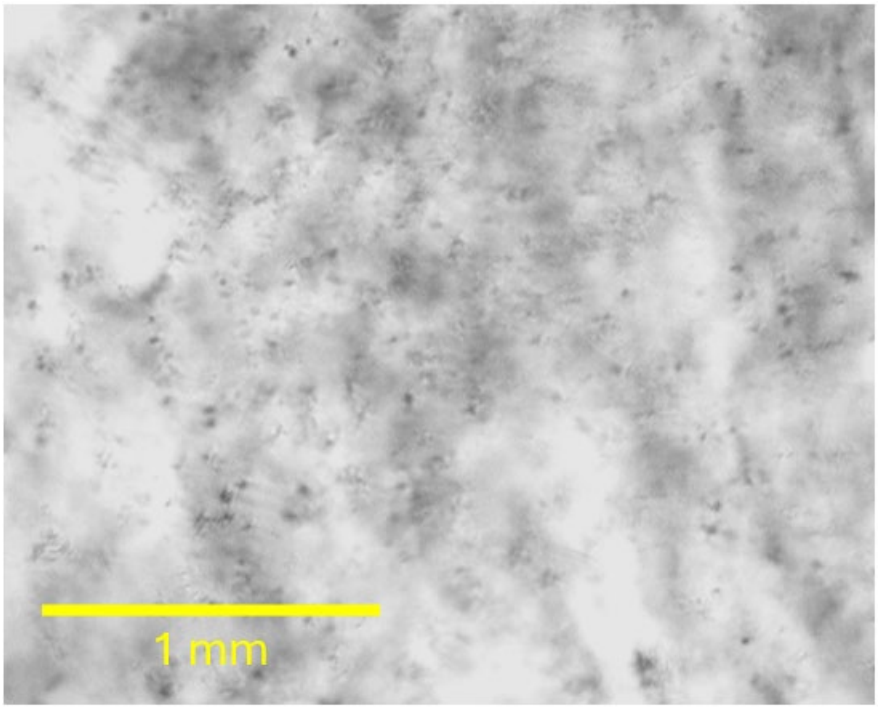


Figure 10. Sample image of droplets in the combustor.

Milestones

- Redesigned mixer and pilot for subsonic aircraft conditions.
- Fabricated combustor hardware, including mixer, pilot, liner, and window blank.
- Designed and optimized optical diagnostic configuration for multiple-simultaneous measurements.
- Successfully executed experimental campaign 1; data acquired across a range of conditions.
- Assess and improved novel fiber-coupled and shadowgraph techniques.

Major Accomplishments

- Acquired C=critical data on LPP combustor operation.

Publications
None.

Outreach Efforts
None.

Awards
Ari Jain received the AIAA Martin Summerfield Graduate Student Award.

Student Involvement
- Arihant Jain (PhD Student) – Laser induced fluorescence measurements, chemiluminescence measurements, overall optical layout, experimental execution, data post-processing and analysis.
- Alexander Stevens (PhD Student) – Shadowgraph measurements, Mie scattering measurements, experimental execution, data post-processing and analysis.
- Ijeoma Obi (MS Student, Graduated) – Shadowgraph measurements, Mie scattering measurements, experimental execution, data post-processing and analysis.
- Jananee Dhanasekaran (MS Student, Graduated) – Image segmentation for fluorescence measurements.

Plans for Next Period
- Analyze optical data from Experimental Campaign 1 to understand and characterize LPP combustor.
- Execute an experimental campaign to measure pollutant emissions from the combustor.
- Further advanced diagnostics, particularly fiber-coupled diagnostics needed for high-power conditions.

References
Jain, A., Obi, I. M., Salazar, V., Kodali, M., Venkatesan, K., Mazumdar, Y. C., & Steinberg, A. M. (2026). Characterization of a Lean Premixed Prevaporized Combustor with Conventional and Sustainable Fuel. *AIAA Journal*, 64(2), 767-779. https://doi.org/10.2514/1.J065617

Passarelli, M. L., Wonfor, S. E., Zheng, A. X., Mazumdar, Y. C., Steinberg, A. M., Bower, H., Hong, J., Venkatesan, K. (2024, June 24-28). Blowoff Characteristics of a Bluff-Body Stabilized, Multi-Element, Lean Premixed Pre-Vaporized Combustor for Supersonic Transport Applications. *Proceedings of the ASME Turbo Expo 2024: Turbomachinery Technical Conference and Exposition. Volume 3B: Combustion, Fuels, and Emissions,* London, United Kingdom.

Task 2 – CFD Simulations of Combustor Operation and Emissions
Georgia Institute of Technology
GE Aerospace

Objective
The objective of this task under the current project scope is to perform CFD simulations of the LPP combustor to both aid in optimizing the combustor design and develop/validate best practices for simulating LPP combustors.

Research Approach
GE Aerospace has performed CFD simulations of the combustor test article. The solvers are being exercised to determine to what degree key processes can be represented both predictively and affordably. The central objective is to systematically establish a validated system of models for treatment of the device relevant processes emulated by the experimental rig. A major goal is to explore the ability of engineering-standard models to predict the trends observed as part of the experimental campaign and provide parametric analysis that provides additional insights with high levels of confidence. This validation effort will proceed during the upcoming performance period based on the data obtained in Task 1.

During the past reporting period, the CFD was leveraged to help redesign the ASCENT Project 074 geometry for the ASCENT Project 098 conditions (i.e., for subsonic aircraft engines). A legacy GE Aerospace pilot geometry was scaled via CFD to fit within the geometry constraints of the ASCENT Project 074 mixer while still meeting target aerodynamic design metrics. Select aero and combustion CFD iterations were performed by the GE CFD team to achieve the final design. The

pilot integration also necessitated additional cooling and flow area changes that were not present in the original mixer. Thus, air assisted cooling for the pilot and dome was needed. Next, the CFD effort focused on modeling the full combustor using the newly designed mixer (see Figure 11). Both non-reacting and reacting runs were performed.

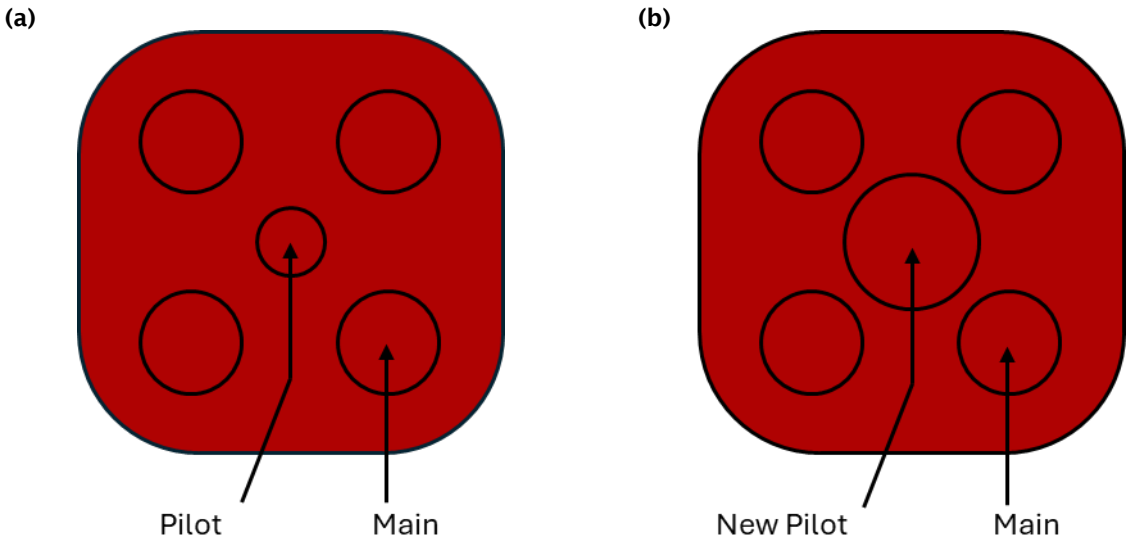


Figure 11. Schematic showing the pilot differences between mixers: (a) ASCENT Project 074 and (b) ASCENT Project 098.

A nominal condition of $T_3 = 1000$ F and P_3=350 psia was selected for the CFD simulations. These conditions would eventually be matched during testing. The non-reacting CFD simulations were performed to check that the main flow fields look similar to the baseline mixer and within design experience and expectations and ensure the mixer modifications perform as expected (see Figure 12). Next, the CFD modeling focused on reacting conditions, where both pilot-only, and pilot-with-mains operation modes were modeled. Fuel distribution, velocity and temperature maps were used to evaluate the performance of the mixer (see Figure 13). The CFD results were satisfactory for both operation modes and subsequent effort was focused on structural analysis.

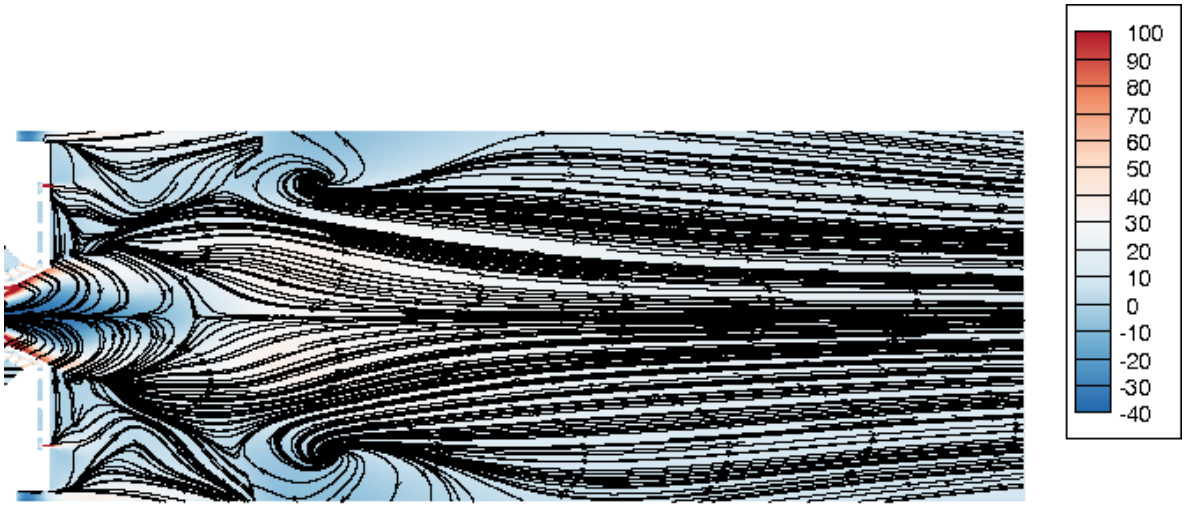


Figure 12. Streamlines showing key recirculation zones inside the combustor.

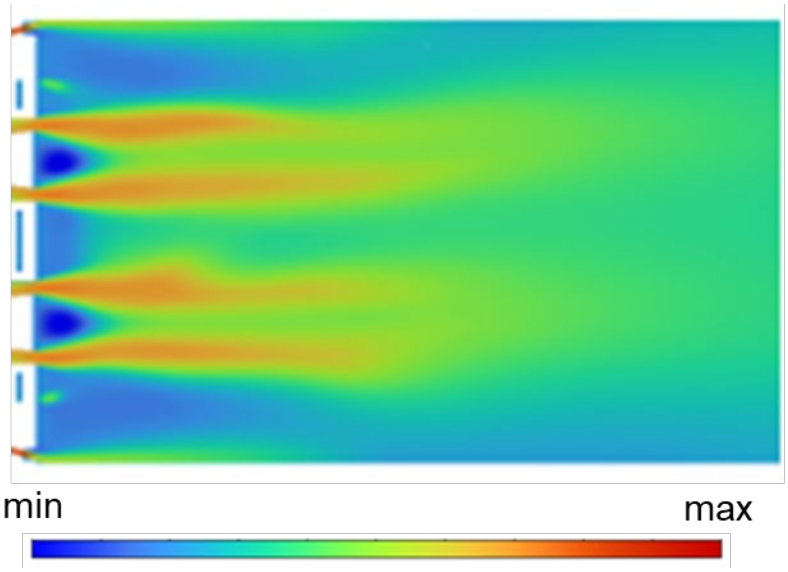


Figure 13. Axial velocities in the near dome region.

To meet the durability requirements at the higher pressure and temperature operating conditions and the inclusion of cooling flow features within the new mixer, the GE team performed a detailed thermal and structural analysis. The structural analysis relies on the input of temperature maps of the part to be analyzed. Thus, using a combination of CFD and GE Aerospace design tools, the necessary pressure and temperature and boundary conditions were provided to the thermal and structural model. The analysis was performed at conditions with pilot-only and pilot-with-mains modes. The first study highlighted regions that needed further optimization and locations needing increased dome cooling. Subsequent analysis after design update were deemed satisfactory after which the model was released for manufacturing.

Milestone

- Completed non-reacting CFD simulations for flow-field design and assessment.
- Completed reacting CFD simulations for assessment of fuel, flow, and temperature fields.
- Released a design for fabrication.

Major Accomplishments

Predicted CFD basic combustor behavior with sufficient fidelity for design.

Publications

None.

Outreach Efforts

None.

Awards

None.

Student Involvement

Arihant Jain (PhD Student) – Compilation of validation data, design consultations.

Plans for Next Period

Perform and validate LES of LPP combustor.



Project 099 Conceptual Analysis of Cryogenic Hydrogen Distribution to Airports

Washington State University

Project Lead Investigator

Jacob Leachman
Professor and HYPER Laboratory Director
School of Mechanical & Materials Engineering
Washington State University
Pullman, WA 99164
509-335-7711
Jacob.leachman@wsu.edu

University Participants

Washington State University (WSU)

- P.I.: Dr. Jacob Leachman
- FAA Award Number: 13-C-AJFE-WaSU-050
- Period of Performance: September 18, 2024, to September 17, 2025
- Tasks:
  1. Contribute to the State of the Technology Analysis considering current efficiencies, realistic 5-year efficiencies, and ideal/limiting efficiencies
  2. Site Selection Analysis to supplement/complement the ongoing National Laboratory of the Rockies (NLR) study
  3. Cryogenic hydrogen effects on demand modeling
  4. Cryogenic hydrogen fueling analysis including needs for technology development
  5. Cryogenic hydrogen infrastructure sizing estimates
  6. Cryogenic hydrogen infrastructure safety analysis

Project Funding Level

The Federal Aviation Administration (FAA) provided $199,910 in funding. Airbus Americas is the cost share partner, partnering with NLR for the previous infrastructure study and investing over $1M in WSU's HYPER Laboratory over the last couple years.

Investigation Team

Jacob Leachman, PI, Washington State University (WSU)
Kazunori Nagasawa, co-PI, National Laboratory of the Rockies (NLR)
Kyle Appel, Research Scientist, Washington State University – Responsible for conducting the research under all tasks
Justin Bracci, Hydrogen Delivery Scenario Analysis Model (HDSAM) modeling, National Renewable Energy Laboratory – Conducted HDSAM modeling under Tasks 2 and 3

Project Overview

This project partners with an existing project funded by the FAA at the NLR to analyze gaseous hydrogen delivery to airports. The goal of this project is to add corresponding cryogenic hydrogen infrastructure analysis to a previous study conducted at the NLR. This previous study, sponsored by the FAA, investigated hydrogen implementation at the Seattle-Tacoma Internation Airport (SEA), Portland International Airport (PDX), San Francisco International Airport (SFO), and Los Angeles International Airport (LAX), primarily focusing on gaseous hydrogen delivery and conducting technoeconomic, emissions, safety, and job analysis. NLR, WSU, and FAA agreed to this ASCENT project to complement the previous study by evaluating cryogenic hydrogen implementation. The following specific objectives were pursued:



1. Contribute to the State of the Technology Analysis by reviewing conceptual hydrogen delivery pathways to airports including liquid hydrogen tankers, trains, and liquid and or cryogenic gaseous pipelines. The analysis considered current efficiencies, realistic achievable efficiencies for technologies developed in the next five years, and ideal/limiting efficiencies.
2. Site Selection Analysis for suitability to cryogenic hydrogen deliveries. The site selection analysis was limited to no more than three sites from the current NLR study for ease of comparison. The analysis applied the realistic technology delivery pathways identified in the prior objective to the sites with information to supplement/complement the ongoing NLR study.
3. Cryogenic hydrogen effects on demand modeling. This considered the effects of boil-off and transfer losses of cryogenic hydrogen and the effects on demand.
4. Cryogenic hydrogen fueling analysis including needs for technology development. This objective considered needs for cryogenic technology development and interviewed key industrial players to verify the technology development needs.
5. Cryogenic hydrogen infrastructure sizing estimates. This objective considered differences in sizing/scaling of cryogenic hydrogen infrastructure for refueling stations relative to gaseous hydrogen and applying these to airport infrastructure.
6. Cryogenic hydrogen infrastructure safety analysis relevant to codes and standards. WSU considered the American Institute of Aeronautics and Astronautics (AIAA) and the National Fire Protection Association (NFPA) hydrogen safety codes specific to cryogenic hydrogen for setback and other safety requirements.

Task 1 – Contribute to the State of the Technology Analysis Considering Current Efficiencies, Realistic 5-year Efficiencies, and Ideal/Limiting Efficiencies

Washington State University

Objective

The objective of this task is to contribute to the State of the Technology Analysis by reviewing conceptual hydrogen delivery pathways to airports including liquid hydrogen tankers, trains, and liquid and or cryogenic gaseous pipelines. The analysis considered current efficiencies, realistic achievable efficiencies for technologies developed in the next five years, and ideal/limiting efficiencies.

Research Approach

An investigation into the state of cryogenic hydrogen technology was conducted through a literature review, exploring conceptual hydrogen delivery pathways for airports. Table 1 was created to compare the conceptual pathways discussed in previous studies. Based on the results of the literature review, delivery pathways of liquid hydrogen (LH_2) ships, rails, and cryogenic/cryo-compressed pipelines should be analyzed in Task 2.

Table 1. Previous hydrogen delivery pathway studies found in the literature.

Author	Year	Airport	LH_2 Ship	LH_2 Train	LH_2 Truck	Cryo-Pipeline	Onsite Liquefaction
Brewer [1]	1975	San Francisco	×	✓	✓	✓	✓
Boeing and Nasa [2]	1976	O'Hare	×	×	×	×	✓
Alder [3]	1987	Zurich	×	×	×	×	✓
Gretz [4]	1994	Conceptual	✓	×	×	×	×
Sefain [5]	2006	Conceptual	×	×	×	✓	✓
Stadler [6]	2014	Conceptual	✓	×	✓	×	×
Amy [7]	2019	Conceptual	×	×	×	×	✓



Author	Year	Airport	LH_2 Ship	LH_2 Train	LH_2 Truck	Cryo-Pipeline	Onsite Liquefaction
Clean Sky 2 JU and FCH 2 JU [8]	2020	Conceptual	×	×	✓	×	✓
Marksel [9]	2020	Tromso	×	×	✓	×	✓
ATI-ACI [10]	2021	Conceptual	×	×	✓	✓	✓
Alexandrou [11]	2022	Toulouse Blagnac	×	×	✓	×	✓
Hoelzen [12]	2022	Conceptual	✓	×	✓	×	✓
Degirmenci [13]	2023	Conceptual	✓	✓	✓	✓	✓
Dijk [14]	2024	Rotterdam	✓	×	✓	×	✓

Relevant metrics for current, 5-year, and limiting efficiencies for cryogenic hydrogen technologies were recorded as part of the literature review. Efficiencies are defined differently for storage, liquefaction, or cryo-compression. For hydrogen storage efficiency is defined by boil-off losses, which is hydrogen unutilized due to venting or transfers. This is also associated with a heat leak entering the tank that causes a normal background boil-off rate. The efficiency for hydrogen liquefaction is defined by the energy required to liquefy one kilogram of hydrogen, expressed as the Specific Energy Consumption (SEC) in kWh/kg. Cryo-compressed hydrogen efficiency can be measured by SEC required to compress and cool the hydrogen or by heat loss of the pipeline. These metrics are used in Task 2 to predict the levelized cost of hydrogen (LCOH) for each conceptual pathway with the advancement of technologies and scaling. The metrics are shown in Table 2.

Table 2. Current, 5-year, and limiting efficiencies for truck, rail, marine, cryo-compressed pipelines, and onsite liquefaction.

	Truck	Rail	Marine	Onsite Liquefier	Cryo-compressed pipeline
Current Losses	3.0 wt% [15]	1.0 wt% [16]	1.0 wt% [16]	-	-
5-year Losses	0.3 wt% [16]	0.3 wt% [16]	0.3 wt% [16]	-	-
Limiting Losses	0 %	0 %	0 %	-	-
Current Power Requirement	-	-	-	12.3 kWh/kg [17]	6.42 kWh/kg [18]
5-year Power Requirement	-	-	-	6.7 kWh/kg [17,19]	5.62 kWh/kg [18]
Limiting Power Requirement	-	-	-	2.98 kWh/kg [20]	-
Current Heat Leak to Fluid	300-400 W	300-400 W	300-400 W	-	1.0 W/m [21]
5-year Heat Leak to Fluid	126-168 W [22]	126-168 W [22]	126-168 W [22]	-	0.42 W/m [22]
Limiting Heat Leak to Fluid	0 W	0 W	0 W	-	0 W/m

Milestone

This task is complete and documented in a draft NLR report.



Major Accomplishments
Literature revealed with analyzed conceptual cryogenic hydrogen delivery pathways and estimated efficiency metrics for current, 5-year, and limiting cryogenic hydrogen technologies.

Publications
This work is included in a final report detailing all the studies to be published in cooperation with NLR.

Outreach Efforts
Presented at the spring and fall ASCENT meetings in 2025.

Awards
None.

Student Involvement
None.

Plans for Next Period
None. The scope of work will be completed in December 2025 with an NLR report in progress for publication.

References

[1] Brewer G.D., Morris RE, Lange RH, Moore JW. LH2 Airport Requirements Study. 1975 Jan.
[2] Boeing, NASA. A N EXPLORATORY STUDY TO DETERMINE THE INTEGRATED TECHNOLOGICAL AIR TRANSPORTATION SYSTEM GROUND REQUIREMENTS OF LIQUID-HYDROGEN-FUELED SUBSONIC, LONG-HAUL CIVIL AIR TRANSPORTS NATIONAL AERONAUTICS AND SPACE ADMINISTRATION. 1976.
[3] Alder H. Hydrogen in air transportation. Feasibility study for Zurich airport, Switzerland. Int J Hydrogen Energy. 1987;12(8):571–85.
[4] Gretz J, Drolet B, Kluyskens D, Sandmann F, Ullmann OI. Status of the Hydro-Hydrogen Pilot Project (EQHHPP). Vol. 19. 1994.
[5] Sefain MJ. Hydrogen Aircraft Concepts & Ground Support. Cranfield University; 2000.
[6] Stadler P, Caliandro P, Leonardi C, Van Herle J. Cost evaluation of large scale hydrogen production for the aviation industry. Master Semester Project. 2014;
[7] Amy C, Kunycky A. Hydrogen as a Renewable Energy Carrier for Commercial Aircraft. 2019; Available from: https://www.researchgate.net/publication/336551230
[8] Clean Sky 2, Fuel Cells and Hydrogen 2 JU. Hydrogen-powered aviation. 2020;
[9] Marksel M, Brdnik Prapotnik A, Kamnik R, Hanžič K, Letnik T, Božičnik S, Rok Kamnik Ds, Katja Hanžič Ds, Stanislav Božičnik Ds. Adaptation of Airport Infrastructure for Operation of ICE-Hybrid and Fuel-Cell Aircraft. 2000.
[10] ACI-ATI. Integration of Hydrogen Aircraft into the Air Transport System. 2021.
[11] Alexandrou S. Comparative Analysis of On-site vs Off-site green-Hydrogen Value Chain Scenarios to cover projected Aviation demand A case for Toulouse Blagnac Airport in France. KTH School of Industrial Engineering and Management; 2022.
[12] Hoelzen J, Flohr M, Silberhorn D, Mangold J, Bensmann A, Hanke-Rauschenbach R. H2-powered aviation at airports – Design and economics of LH2 refueling systems. Energy Conversion and Management: X. 2022 May 1;14.
[13] Degirmenci H, Uludag A, Ekici S, Hikmet Karakoc T. Analyzing the hydrogen supply chain for airports: Evaluating environmental impact, cost, sustainability, viability, and safety in various scenarios for implementation. Energy Convers Manag. 2023 Oct 1;293.
[14] Dijk D, Ebrahim H, Jooss Y, Bodal EF, Hjorth I. Integrating liquid hydrogen infrastructure at airports: Conclusions from an ecosystem approach at Rotterdam The Hague Airport. 2024 Apr.
[15] Zhang F, Zhao P, Niu M, Maddy J. The survey of key technologies in hydrogen energy storage. Int J Hydrogen Energy. 2016 Sep 7;41(33):14535–52.
[16] Borsboom-Hanson T, Patlolla SR, Herrera OE, Mérida W. Point-to-point transportation: The economics of hydrogen export. Int J Hydrogen Energy. 2022 Aug 29;47(74):31541–50.
[17] Al Ghafri SZ, Munro S, Cardella U, Funke T, Notardonato W, Trusler JPM, … May EF. Hydrogen liquefaction: a review of the fundamental physics, engineering practice and future opportunities. Vol. 15, Energy and Environmental Science. Royal Society of Chemistry; 2022. p. 2690–731.

[18] Wang H, Zhao Y, Dong X, Yang J, Guo H, Gong M. Thermodynamic analysis of low-temperature and high-pressure (cryo-compressed) hydrogen storage processes cooled by mixed-refrigerants. Int J Hydrogen Energy. 2022 Aug 5;47(67):28932–44.
[19] Zhang T, Uratani J, Huang Y, Xu L, Griffiths S, Ding Y. Hydrogen liquefaction and storage: Recent progress and perspectives. Vol. 176, Renewable and Sustainable Energy Reviews. Elsevier Ltd; 2023.
[20] Valenti G, MacChi E, Brioschi S. The influence of the thermodynamic model of equilibrium-hydrogen on the simulation of its liquefaction. Int J Hydrogen Energy. 2012 Jul;37(14):10779–88.
[21] Demaco. Vacuum Insulated Transfer Lines (VIP). 2025.
[22] Yin L, Yang H, Ju Y. Review on the key technologies and future development of insulation structure for liquid hydrogen storage tanks. Vol. 57, International Journal of Hydrogen Energy. Elsevier Ltd; 2024. p. 1302–15.

Task 2 – Site Selection Analysis to Supplement/Complement the Ongoing NLR Study

Washington State University, National Laboratory of the Rockies

Objective

The objective of this task is to perform site selection analysis for suitability to cryogenic hydrogen deliveries. The site selection analysis was limited to no more than three sites from the previous NLR study for ease of comparison. The analysis applied the realistic technology delivery pathways identified in the prior objective to the sites with information to supplement/complement the ongoing NLR study.

Research Approach

HDSAM[1] is used to estimate the LCOH for the hydrogen delivery pathways. The technoeconomic analysis was conducted by Justin Bracci (NLR) utilizing the pathways, assumptions, and metrics generated in Task 1. The analysis includes conceptual pathways to deliver cryogenic hydrogen to the SEA, PDX, SFO, and LAX independent of location. Truck tanker and gaseous pipeline pathways assume hydrogen production and liquefaction is 50 km from any one of the airports. The rail tanker pathway assumes production and liquefaction are 1,000 km from the airport with last mile trucking from a rail spike near the airport. The ocean tanker pathways assume production and liquefaction are 10,000 km from the airport with last mile trucking from a marine port to the airport. In the analysis different station throughput capacities are used, evaluating the effect of scale on dispensing cost. The effect of technology advancement is analyzed utilizing the metrics of current, 5-year, and limiting efficiencies. The results of the analysis are shown in Figure 1 with 80% utilization and throughput capacity of 6, 12, and 24 metric tonnes per day (MTPD) for all delivery pathways. LCOH is shown on the y-axis and delivery method on the x-axis. Based on the assumptions made, the plot shows that delivering LH_2 via truck tankers currently yields the lowest LCOH, with onsite production and liquefaction as a close second lowest. For both the 5-year estimate and limiting efficiencies, the LCOH from rail and ocean tankers is less than that of truck tankers.

[1] https://hdsam.es.anl.gov/index.php?content=hdsam

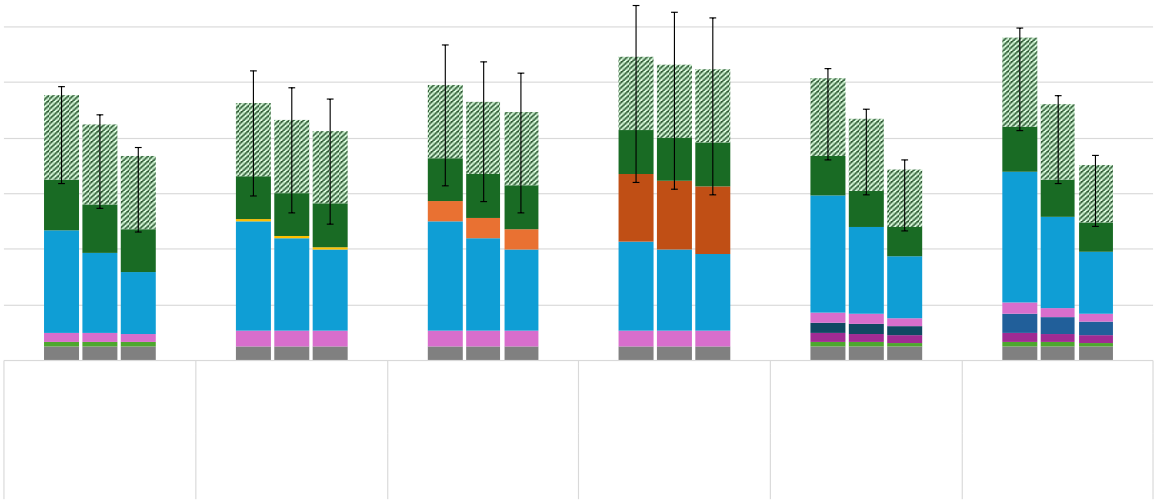


Figure 1. Results of Task 2 showing six delivery methods for LH_2, 80% utilization of the refueling station, and current/5-year/limiting losses and efficiencies.

Milestones
This task is complete.

Major Accomplishments
Levelized the cost of hydrogen estimates obtained via modeling in HDSAM by Justin Bracci and various altered assumptions and delivery pathway development. Effects of future technological development and scaling of LH_2 usage on LCOH are included.

Publications
This work is included in a final report detailing all the studies to be published in cooperation with NLR.

Outreach Efforts
Presented at the spring and fall ASCENT meetings in 2025.

Awards
None.

Student Involvement
None.

Plans for Next Period
None. The scope of work will be completed in December 2025 with an NLR report in progress for publication.

Task 3 – Cryogenic Hydrogen Effects on Demand Modeling
Washington State University

Objective
The objective of this task is to identify the cryogenic hydrogen effects on demand modeling. This considered the effects of boil-off and transfer losses of cryogenic hydrogen and the effects on demand.

Research Approach

Using HDSAM, sensitivity studies are conducted evaluating the effect of boil-off and transfer losses, SEC of liquefaction, and capital cost of liquefaction plants on LCOH. The results are shown in Table 3.

Table 3. Sensitivity analysis on the levelized cost of hydrogen (LCOH) with different boil-off and liquefaction parameters for liquid hydrogen (LH_2). SEC: Specific Energy Consumption.

Scenario #	Delivery Method	Altered parameter	Parameter % change	LCOH % change	LCOH % / Input %
3.1	LH2 Truck Tanker	Liquefier SEC	-45.53	-7.28	0.160
3.1	LH2 Truck Tanker	Liquefier capital cost	-9.99	-2.20	0.220
3.1	LH2 Truck Tanker	LH2 unloading losses	-23.08	-2.98	0.129
3.1	LH2 Truck Tanker	Truck LH2 boil-off rate	-66.67	-0.69	0.010
3.5	LH2 Rail Tanker	LH2 unloading losses	-23.08	-5.69	0.247
3.5	LH2 Rail Tanker	Rail LH2 boil-off rate	-70.00	-0.51	0.007
3.6	LH2 Marine Tanker	LH2 unloading losses	-23.08	-5.78	0.250
3.6	LH2 Marine Tanker	Marine LH2 boil-off rate	-70.00	-8.04	0.115

Additionally, a numerical model which was previously validated and used to predict boil-off losses for in-service LH_2 tanks, was used to predict the number of tanks required to supply airport throughput. The model was used to evaluate single spherical tanks that would only be refilled once per day, sized to fit the airport throughput capacities of 6, 12, and 24 MTPD. Vertical or horizontal cylindrical tanks were also modeled using 2-12 tanks in a storage system. The total losses and number of times the tanks required refilling over a 6-day period were predicted. Losses and number of fills are shown below in Figure 2 for horizontally oriented tanks.

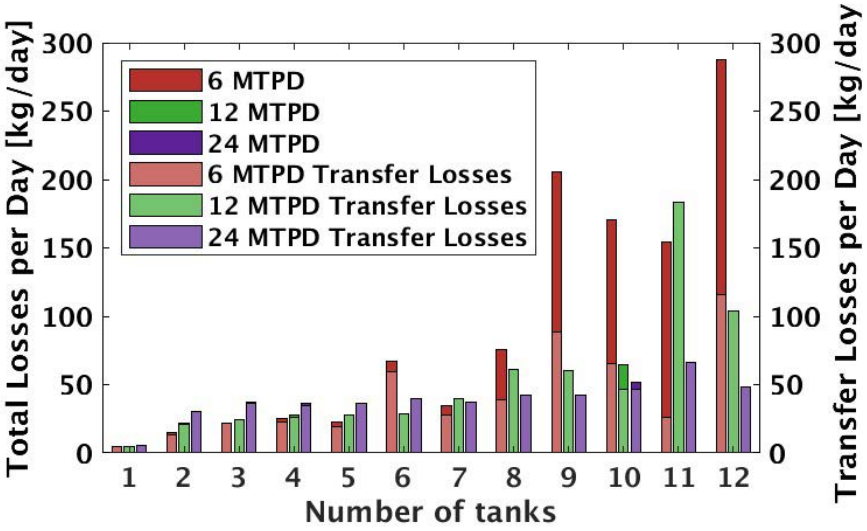


Figure 2. Average daily boil-off losses for a varied number of horizontal tanks for Cases 3.1-3.6 scenarios with 6, 12, and 24 metric tonnes per day (MTPD) refueling capacity.

Milestones

This objective is complete.



Major Accomplishments
The sensitivity of the LCOH is evaluated by altering boil-off and transfer losses, liquefaction SEC, and liquefaction capital cost for scenarios 3.1, 3.5, and 3.6. Hydrogen losses and tank filling requirements are predicted by a numerical model.

Publications
This work is included in a final report detailing all the studies to be published in cooperation with NLR.

Outreach Efforts
Presented at the spring and fall ASCENT meetings in 2025.

Awards
None.

Student Involvement
None.

Plans for Next Period
None. The scope of work will be completed in December 2025 with an NLR report in progress for publication.

Task 4 – Cryogenic Hydrogen Fueling Analysis Including Needs for Technology Development
Washington State University

Objective
The objective of this task is to perform cryogenic hydrogen fueling analysis including needs for technology development. This objective considers needs for cryogenic technology development and during this task, key industrial players were interviewed to verify the technology development needs.

Research Approach
Analysis of current liquid hydrogen refueling technologies was conducted through literature review. Several technologies were identified that require advancement before commercial use in airports.

- High efficiency hydrogen production
- High efficiency cooling technologies
- Boil-off management systems
- LH_2 pumps
- LH_2 hydrant systems
- Mobile refuelers
- Mobile refueler safety devices
- Standardized refueling procedures

Industry partners including ZeroAvia, Airbus, and Joby Aviation were interviewed for their perspective on the technological advancement needed for LH_2 implementation. As part of this interview, a new list containing technological advancements industry believes is needed was created.

- LH_2 transportation and logistics
- Boil-off gas capture
- Liquefaction technologies
- Operational study of interim LH_2 integration
- Pumps and heat exchangers for refueling control
- Zero venting transfer line chill down
- Refueler sizing
- Advanced leak detection
- Easily manageable transfer lines



- Onsite production and liquefaction efficiency
- Hydrogen vent stack burn-off
- Standardized refueling components
- LH_2 storage tank materials and designs

Milestones
This objective is complete.

Major Accomplishments
Several technologies have been identified by industry for improvement to enable LH_2 integration with airport infrastructure.

Publications
This work is included in a final report detailing all the studies to be published in cooperation with NLR.

Outreach Efforts
Presented at the spring and fall ASCENT meetings in 2025.

Awards
None.

Student Involvement
None.

Plans for Next Period
None. The scope of work will be completed in December 2025 with an NLR report in progress for publication.

Task 5 – Cryogenic Hydrogen Infrastructure Sizing Estimates
Washington State University

Objective
The objective of this task is to complete cryogenic hydrogen infrastructure sizing estimates. This objective considered differences in sizing/scaling of cryogenic hydrogen infrastructure for refueling stations relative to gaseous hydrogen and applying these to airport infrastructure.

Research Approach
Using the estimated number of tanks required for 6, 12, and 24 MTPD throughput capacity, the space required for storage is estimated. This estimation requires use of the NFPA-2 hydrogen codes and local Washington and California state codes for the minimum distance between LH_2 storage tanks. Setback distances are included for the tanks. Three example layouts for LH_2 storage tanks are shown in Figure 3 with horizontal tanks arrayed in one or two rows or as vertical tanks. The spatial requirement for singular spherical tanks or equivalent gaseous hydrogen storage tubes was also estimated. Table 4 shows the comparison of the different hydrogen storage methods.

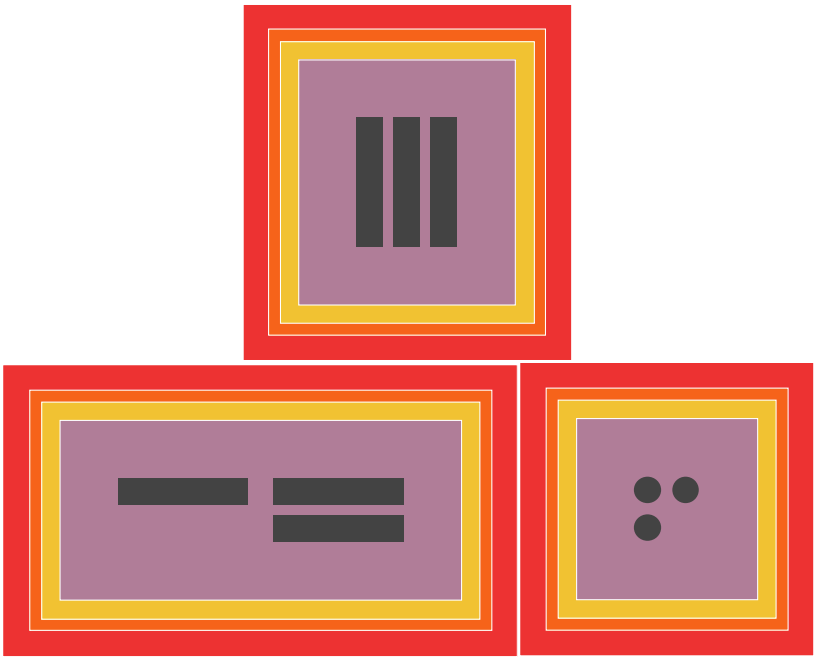


Figure 3. Single row of horizontal LH_2 tanks (top), two rows of horizontal LH_2 tanks (bottom left), two rows of vertical LH_2 tanks (bottom right).

Table 4. Spatial estimate for 6, 12, and 24 metric tonnes per day (MTPD) throughput with different LH_2 storage options. GH_2: gaseous hydrogen.

Refueling Capacity	One Spherical LH_2	Horizontal One/Two Line LH_2	Vertical LH_2	GH_2 Tube Array
6 MTPD	1397 m^2	2017 m^2/2567 m^2	1459 m^2	2380 m^2
12 MTPD	1533 m^2	2710 m^2/2896 m^2	1646 m^2	4369 m^2
24 MTPD	1695 m^2	3861 m^2/3877 m^2	2433 m^2	6750 m^2

Milestones
This objective is complete.

Major Accomplishments
Spatial requirements for multiple LH_2 tank configurations and one array for gaseous hydrogen (GH_2) have been estimated as shown in Table 4.

Publications
This work is included in a final report detailing all the studies to be published in cooperation with NLR.

Outreach Efforts
Presented at the spring and fall ASCENT meetings in 2025.

Awards
None.



Student Involvement
None.

Plans for Next Period
None. The scope of work will be completed in December 2025 with an NLR report in progress for publication.

Task 6 – Cryogenic Hydrogen Infrastructure Safety Analysis
Washington State University

Objective
The objective of this task is to perform cryogenic hydrogen infrastructure safety analysis relevant to codes and standards. WSU considered the AIAA and NFPA hydrogen safety codes specific to cryogenic hydrogen for setback and other safety requirements.

Research Approach
Setback distance analysis was conducted as part of Task 5 to evaluate infrastructure required for LH_2 implementation at airports. Extensive safety analysis was conducted in the previous NLR report. The final report published with NLR may consider the following potential safety analyses:

- Excess fuel reserves
- Additional space required for LH_2 pumps, plumbing, and vaporizers
- A high-level overview of explosion distancing
- Needs for LH_2 aircraft fueling with passengers aboard
- Latest activities in LH_2 codes and standards

Milestones
This objective will be completed in December 2025.

Major Accomplishments
Spatial requirements are estimated and include NFPA-2 guidelines for LH_2 storage tank setbacks.

Publications
This work is included in a final report detailing all the studies to be published in cooperation with NLR.

Outreach Efforts
Presented at the spring and fall ASCENT meetings in 2025.

Awards
None.

Student Involvement
None.

Plans for Next Period
None. The scope of work will be completed in December 2025 with an NLR report in progress for publication.

Summary and Recommendations for Future Research
This study partnered with NLR to analyze conceptual liquid hydrogen delivery scenarios to airports, expanding on a prior study completed by NLR for gaseous hydrogen distribution. SEA, PDX, SFO, and LAX were considered for refueling of liquid hydrogen aircraft at 6, 12, and 24 MTPD. Several new conceptual delivery pathways were considered that had not previously been analyzed in the literature. Modifications were made to the HDSAM tool developed by the U.S. Department of Energy for uniform comparison between pathways. A recently developed boil-off model was adapted to analyze losses from on-site storage and filling for various numbers and configurations of on-site tanks. An industrial survey for



technology development needs was conducted, identifying high-efficiency hydrogen production and cooling technologies as the primary needs. A safety codes analysis completed for the NLR gaseous hydrogen study was extended to liquid hydrogen.

Several opportunities for technology advancement were identified during this program and warrant consideration for future research. High-efficiency cooling technologies to maintain liquid hydrogen in a sub-cooled state to eliminate boil-off would increase technology performance and reduce losses for all pathways considered. These cooling technologies, also known as cryocoolers, reduce losses from any cryogenic fuel (hydrogen or natural gas) and have yet to be comprehensively surveyed for terrestrial applications to determine a design specification, including price points, capacities, and efficiencies.



Project 100 U.S.-Canada SAF Supply Chain Analysis

Washington State University

Project Lead Investigator

Michael P. Wolcott
Regents Professor
Department of Civil & Environmental Engineering
Washington State University
PO Box 642910
Pullman, WA 99164-2910
509-335-6392
wolcott@wsu.edu

University Participants

Washington State University (WSU)

- P.I.s: Michael P. Wolcott, Regents Professor; Kristin Brandt, Adjoint Faculty
- FAA Award Number: 13-C-AJFE-WaSU-051
- Period of Performance: September 18, 2024, to September 17, 2025
- Tasks:
  1. Quantify Regional Demand
  2. Lipid Feedstock Assessment
  3. Potential Regional Production
  4. State, Provincial and Federal Policy Support
  5. Carbon Intensity (CI) Valuation by Policy
  6. Baseline Freight and Fuel Transportation Optimization Tool (FTOT) Supply Chain Analyses
  7. Shared Infrastructure Review

Project Funding Level

This project has received $200,000 in Federal Aviation Administration (FAA) funding over its lifetime, $200,000 in corporate matching funds for cost share from Boeing Environmental Sustainability division.

Investigation Team

Washington State University

Prof. Michael Wolcott (P.I.)
Kristin Brandt (co-P.I.) – Tasks 1, 2, 3, 4, 5, 7
Dane Camenzind (staff engineer) – Task 2
Lina Pilar Martinez Valencia (postdoctoral research associate) – Tasks 4, 5

Collaborating Researchers

University of British Columbia

Jack Saddler
Susan van Dyk – Tasks 1, 3, 5

U.S. Department of Transportation Volpe Center (Volpe)

Kristin C. Lewis – Tasks 6, 7
Kevin Zhang – Tasks 6, 7
Peter Wilke – Tasks 6, 7

Joint Cascadia Airports – Tasks 1, 4
Seattle-Tacoma International Airport
Stephanie Meyn, Sandra Kilroy
Portland International Airport
Jennifer Bies
Vancouver International Airport
Wendy Avis

Project Overview

This project builds on the historically strong trade partnership between the United States (U.S.) and Canada for both agricultural and energy products (Canada Energy Regulator, 2025; Government of Canada, 2025; U.S. Energy Information Administration, 2023; USDA, 2025a). Data was compiled to support initial supply chain analyses that model potential sustainable aviation fuel (SAF) production and use among the U.S. and Canada, building on tools and information from the regional supply chain analyses completed as part of ASCENT Project 001. These tools were used to assess potential SAF production and consumption locations utilizing compiled data detailing feedstock volume and location, announced potential and operational SAF production facilities, existing transportation networks, and governmental policies.

This first project year focused on the largest airports in the primary region, denoted Cascadia and defined as Oregon (OR), Washington (WA), and British Columbia (BC) (Figure 1). Those airports include Portland International Airport (PDX), Seattle-Tacoma International Airport (SEA), and Vancouver International Airport (YVR). The near-term (2030) goals are likely to be met by SAF made using lipid feedstocks with hydroprocessed esters and fatty acids (HEFA) as the conversion technology. HEFA is mature technology, although it is deployed to manufacture renewable diesel (RD) on a larger scale than for SAF. No other technology has been successful at multiple commercial-scale facilities. Potential feedstock sources were considered for the U.S. and Canada. The primary region was extended for potential SAF production options to the expanded region (Figure 1).



Figure 1. Primary and expanded study regions.



Progress made on the project was shared at a stakeholder meeting in July 2025. Attendees included corporate partners (airlines, renewable fuel producers, petroleum refiners, original equipment manufacturers [OEM]), airport representatives, state, provincial, and federal government employees, and University of British Columbia researchers. Attendees provided feedback on work completed to date and suggested next steps. Follow-up meetings allowed for additional information sharing.

Task 1 – Quantify Regional Demand

Washington State University
University of British Columbia

Objective

The objective of this task is to quantify the Jet A/Jet A-1 fuel and SAF demand at the three major Cascadia airports. PDX, SEA, and YVR. Additional airports could be included in future work.

Research Approach

A review of public information was completed, including conversations with airport representatives, to determine the conventional Jet A/Jet A-1 fuel use and SAF goals at each of the three primary airports. SEA has recent public information; PDX and YVR values were provided by airport representatives (Port of Seattle, 2024). SAF demand was estimated for each airport as a portion of the Jet A/Jet A-1fuel consumption follows:

1. PDX – 10% to align with U.S. SAF Grand Challenge (U.S. Department of Energy et al., 2021)
2. SEA – 10% per SEA goal for 2028 and aligning with U.S. SAF Grand Challenge (U.S. Department of Energy et al., 2021; Port of Seattle, 2024)
3. YVR – 3% per BC mandate up to 10% per Canadian federal aspirational goal (British Columbia, 2024; Government of Canada, 2022)

Additional information was collected on the fuel delivery methods for each airport for use in supply chain analyses. Expansion beyond the initial airports is being explored to determine a more complete regional demand value.

Major Accomplishments

The Jet A/Jet A-1 fuel consumption and estimated SAF demand for 2030 were estimated and existing fuel delivery systems were collated (Table 1).

Table 1. Current fuel delivery method, Jet A/Jet A-1 fuel consumption, and 2030 estimated SAF demand. PDX: Portland International Airport, SEA: Seattle-Tacoma International Airport, YVR: Vancouver International Airport.

Airport	Current Fuel Delivery	Jet A/Jet A-1 Fuel Consumption (BLY)	2030 Estimated SAF Demand (BLY)
PDX	Pipeline and barge	0.8	0.08
SEA	Pipeline, limited ability to use trucks	2.3-3.0	0.2-0.3
YVR	Pipeline, rail, truck, barge	1.8	0.05-0.2
TOTAL	-	4.9-5.6	0.3-0.6

Task 2 – Lipid Feedstock Assessment

Washington State University
University of British Columbia

Objectives

The objectives of this task are to assess the lipid feedstocks within the U.S. and Canada, including imports and exports, and to geolocate lipid volumes for use in supply chain analyses. Lipid feedstocks assessed for SAF production include oilseed oils, animal fats (beef tallow, pig fat, poultry fat), and used cooking oil (UCO). These feedstocks are energy dense,

and the conversion process has a high yield, making them inexpensive to transport. For this reason, lipids were quantified and geolocated for the entire U.S. and Canada. Imported lipids were quantified but have not been geolocated.

Research Approach

Oilseed production, primarily canola in Canada and soybeans in the U.S. and the subsequent processing to oil at geolocated and scaled crushing facilities were determined. Animal fat production was estimated using public resources and geolocated at slaughterhouse locations. UCO was determined using a per capita estimation. These sources were combined to generate the total supply (Figure 2).

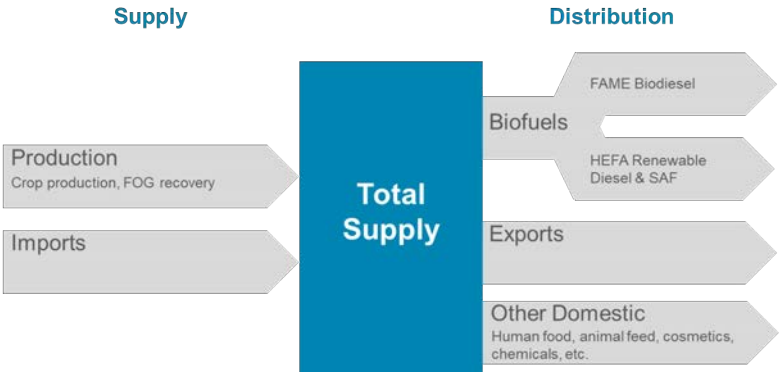


Figure 2. Components considered in U.S. and Canada lipid feedstock inventory.

Oilseed crushing facilities were identified, geolocated, and described according to type and volume of seeds processed using public sources as possible. Crushers were eliminated from the potential feedstock value if public information stated that the oil produced is specifically for food, seeds are not soy or canola oil, are organic, or if the facility is idled/closed/closing or co-located with an operational renewable fuel facility. For Canada, seed capacity was available for all fourteen identified crushers with a total annual output of 4.8 million tons. The survey for the U.S. resulted in 63 operational facilities with five more under construction. The operational U.S. facilities have a nameplate annual capacity of 11.2 million tons. The crushers that are under construction add an additional 0.8 million tons per year. Two-thirds of the U.S. facilities have public crush capacities. The sum of these values was subtracted from the total U.S. volume. The remainder was divided evenly among the facilities without public scale information. The oil production at each crusher was calculated using average oil yields (wt/wt) for soybeans and canola of 17.8% and 42.1%, respectively (USSEC, 2025; Secchi, 2023).

Animal fat production was estimated by creating fat production coefficients that relate total animal fat production in the U.S. to total meat production and/or total head slaughtered in the U.S. for beef, pork, chicken, and turkey (USDA, 2024a; USDA, 2025b; USDA, 2025c; USDA, 2025d; USDA, 2025e). The U.S. and Canada have similar livestock systems, thus it was assumed that the same coefficients are applicable in both countries. Animal fat production was then calculated for facilities that have known slaughter capacities. For facilities with unknown slaughter capacities, the remaining production capacity was divided evenly among facilities on a state or provincial basis. In 2023, the U.S. and Canada produced 4.3 and 0.44 million tons of animal fats, respectively.

UCO was determined by applying a production coefficient of 6.3 kg/year/capita to all locations with a minimum population of 100,000. This estimate aligns with the domestically produced UCO for consumption and trade in the U.S. (United States Census Bureau, 2025; U.S. Energy Information Administration, 2025). However, there are currently no comprehensive inventories of UCO produced within the U.S. so this should be considered an estimate. The quantity of UCO was collated on a county (U.S.) or census division (Canada) level and geolocated at the population-weighted centroid of the census (U.S.) or dissemination (Canada) blocks (Table 2, Figure 3).



Table 2. U.S. and Canada geographies used in collating and geolocating estimated UCO volumes.

Country	Primary Geography	Splitting Geography	Geography for Centroid Calculation
U.S.	urban areas	counties	census blocks
Canada	population centres	census divisions	dissemination blocks

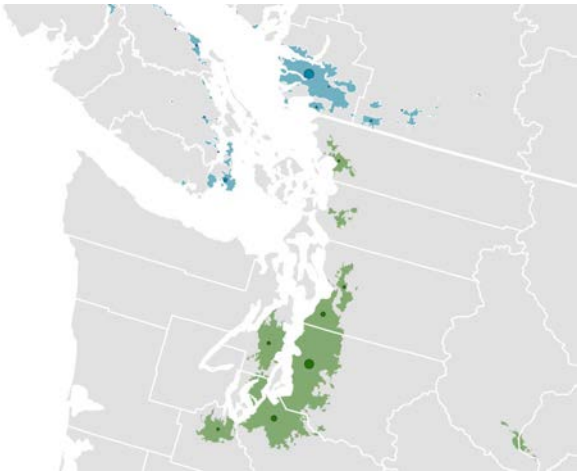


Figure 3. Visualization of the method used for geolocating used cooking oil (UCO) based on minimum population and population centers.

Major Accomplishments

U.S. and Canadian lipid feedstocks were quantified and geolocated for use by the Volpe team in FTOT. The map in Figure 4 includes shaded areas of U.S. and Canada representing canola and soybean cropland. In addition, the location and scale of existing crushing facilities are shown as scaled circles. Of note is that only one crushing facility is located inside of the primary region. The map in Figure 5 shows the location and scale of large slaughterhouses separated by beef, pork and poultry. Figure 6 shows the estimated quantity of UCO produced in each county (U.S.) or census division (Canada).

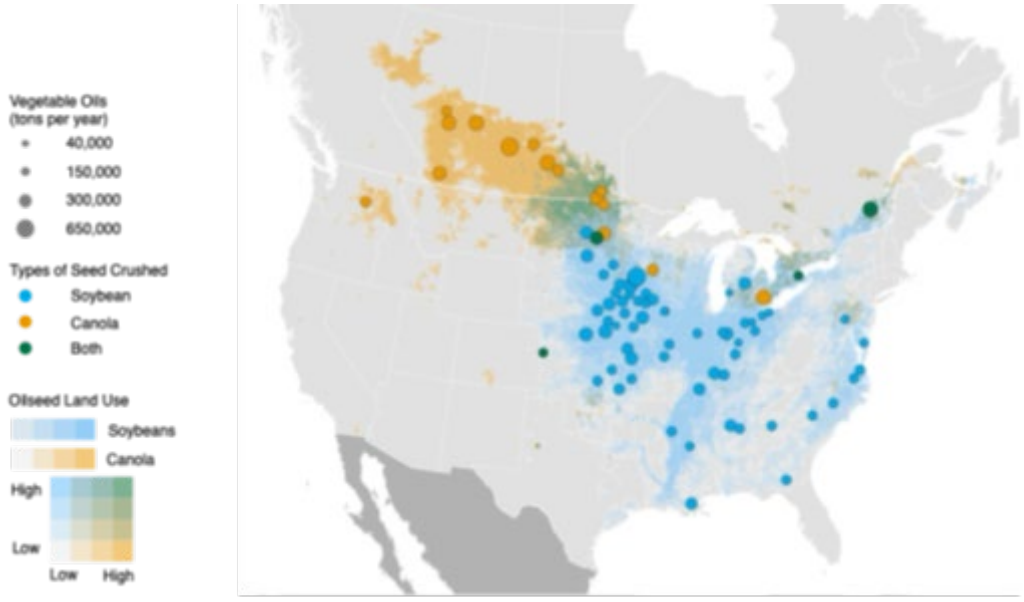


Figure 4. U.S. and Canada soybean and canola cropland (2023) and crushing facilities (2025) scaled to annual seed oil output.

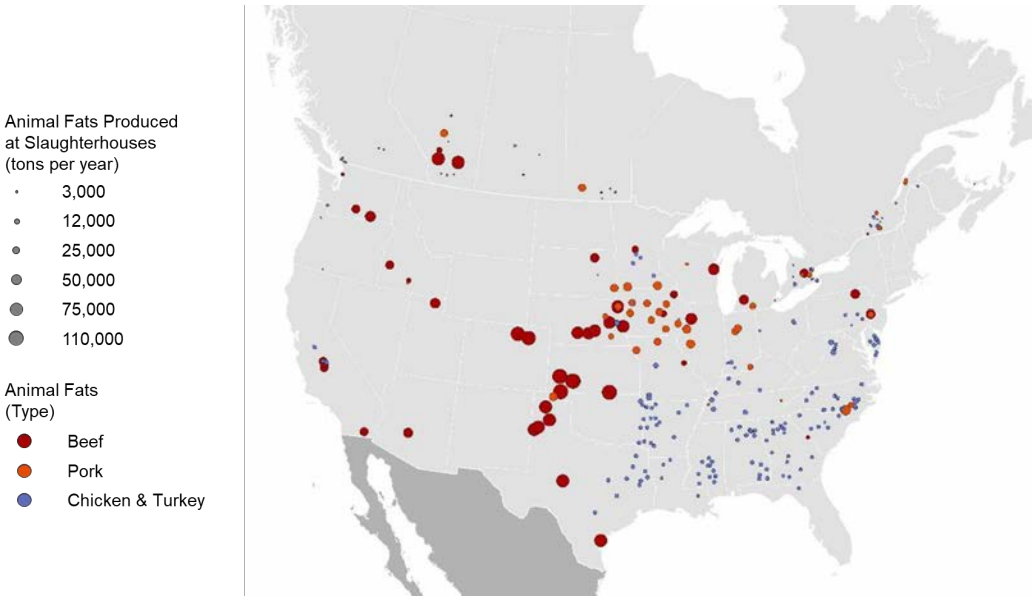


Figure 5. 2025 annual U.S. and Canada production of animal fat (beef, pork and poultry) located at slaughterhouses.



Figure 6. Estimated 2024 Annual UCO production in U.S. and Canada for locations with a population of at least 100,000.

Total lipid supply establishes an upper limit of SAF potential. However other uses like human food, animal feed, other biofuels, chemical processing, and exports compete for the same feedstocks. Figure 7 illustrates current uses divided into renewable fuels, exports and other domestic consumption and separated by country. Figure 8 shows the relative impact of U.S. and Canadian trade rose from 2018 to 2023. Canadian exports of lipids to the U.S. reached a peak in 2023 with 64% of the total Canadian supply was exported to the U.S., which corresponds to 13% of the U.S. supply.

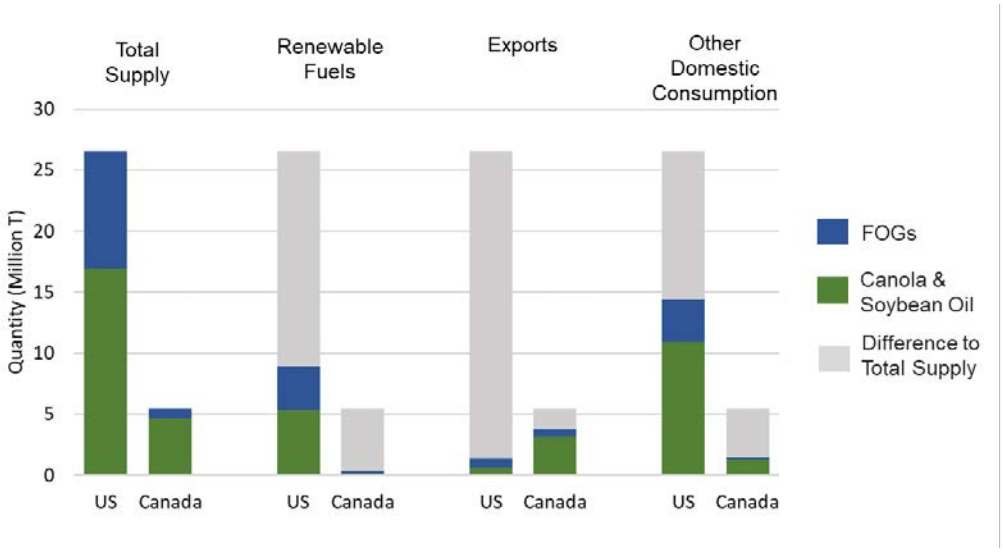


Figure 7. Annual U.S. and Canada lipid supply, biofuel use, exports and other domestic consumption (Canada Meat Council, 2024; Danielson, 2023; Danielson, 2024; GlobalData, 2023; Government of Canada, 2024; United States Census Bureau, 2025; U.S. Energy Information Administration, 2025; Statistics Canada, 2024; Statistics Canada, 2025; USDA, 2023; USDA, 2024a; USDA, 2024b; USDA; 2024c; USDA, 2025b; USDA, 2025d). FOGs: Fats, Oils, and Greases.

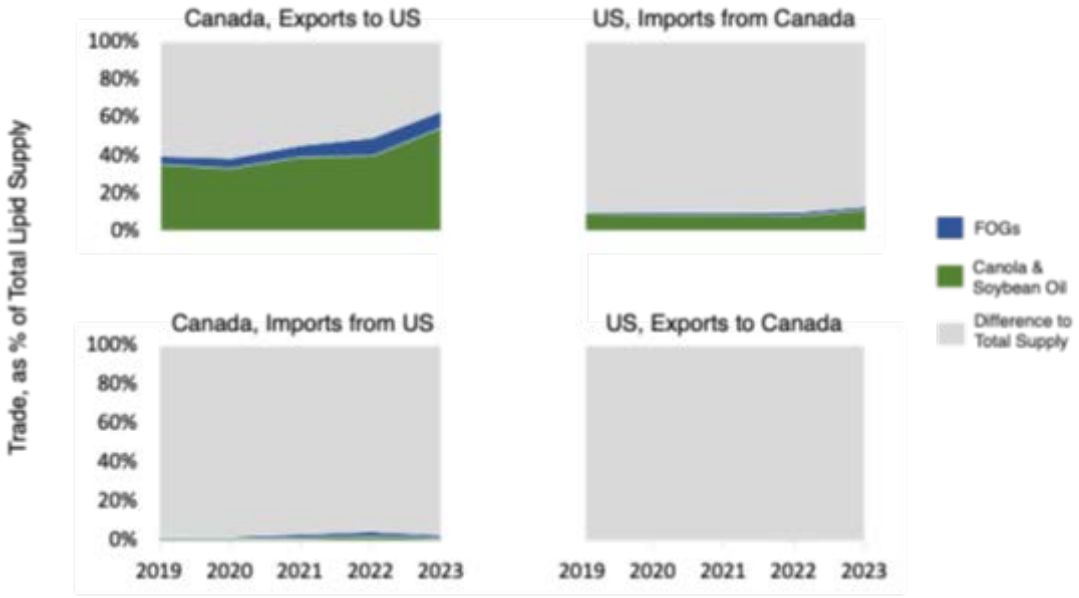


Figure 8. U.S. and Canada trade summary for lipids (2019-2023) (Canada Meat Council, 2024; Danielson, 2023; Danielson, 2024; GlobalData, 2023; Government of Canada, 2024; United States Census Bureau, 2025; U.S. Energy Information Administration, 2025; Statistics Canada, 2024; Statistics Canada, 2025; USDA, 2023; USDA, 2024a; USDA, 2024b; USDA; 2024c; USDA, 2025b; USDA, 2025d).

Task 3 – Potential Regional Production

Washington State University
University of British Columbia

Objectives

The objective of this task is to compile a list of regional facilities that produce or could potentially produce SAF. The potential SAF production in the expanded region was determined from a list of operational, under construction and planned facilities. Additional potential volume from co-processing at petroleum refineries was also assessed.

Research Approach

Utilize the U.S. and global databases of potential SAF production from ASCENT Project 001A and public petroleum refinery information to identify, scale, and geolocate current and potential SAF production.

Major Accomplishments

Primary and extended region facilities were identified, verified, scale determined, and located (Table 3, Table 4). The facilities listed must have public records of location, scale, start-up date, and either use HEFA or co-processing to produce renewable fuels. Existing petroleum refineries could be used to co-process lipids with crude oil or converted renewable fuels. It is important to note that not all of these refineries have expressed interest in renewable fuel production. In addition, petroleum refineries that produce only asphalt, road oil, and/or heavy oils were not included.

The potential SAF production volume at biorefineries is either the publicly stated volume or an estimate calculated using the SAF distillate cut from the ASCENT HEFA Techno-Economic Analysis (TEA) (Brandt et al., 2021). The total lipid demand was back calculated using the ASCENT HEFA TEA yield and the announced fuel production volume. For the petroleum refineries, it was assumed that each refinery would co-process the maximum feedstock fraction allowed by ASTM D1655 (ASTM International, 2023), i.e. 5%. The SAF volume was then calculated after accounting for loss of biogenic carbon, yield, total non-fuel products, and the average Jet A/Jet A-1 fuel cut of 10% at U.S. refineries (Brandt et al., 2026).



Capital costs were estimated using a combination of public announcements and the ASCENT HEFA TEA (Brandt et al., 2021). Co-processing costs were calculated following the methodology defined in Brandt et al. (2026). Costs will be used in future FTOT scenarios as part of the decision matrix in modelling the order that new capacity could come online.

Table 3. Announced and operational renewable fuel facilities in the primary and expanded region that have the potential to produce sustainable aviation fuel (SAF).

Company	Country	Location	Estimated Potential SAF Production (MLY)	Estimated Lipid Demand (t/y)
Parkland	Canada	Burnaby, BC	10	364,000
Tidewater Renewables*	Canada	Prince George, BC	25	42,000
Tidewater Renewables*	Canada	Prince George, BC	207	344,000
GETI	Canada	Calgary, AB	207	344,000
Imperial Oil	Canada	Edmonton, AB	100	913,000
BP America	U.S.	Blaine, WA	10	228,000
NEXT Renewable Fuels	U.S.	Clatskanie, OR	1249	2,074,000
XCF Global Capital	U.S.	Reno, NV	102	170,000
Edgewood	U.S.	Clark County, NV	250	415,000
Montana Renewables*	U.S.	Great Falls, MT	114	484,000
Montana Renewables*	U.S.	Great Falls, MT	511	657,000
Marathon/Neste	U.S.	Contra Costa County, CA	1532	2,544,000
Phillips 66	U.S.	Rodeo, CA	1666	2,766,000
Aemetis	U.S.	Riverbank, CA	45	82,000
Kern Energy	U.S.	Bakersfield, CA	4.8	110,000

*locations have multiple projects and/or potential expansion plans.



Table 4. Primary and expanded region petroleum refineries that could potentially choose to add or expand co-processing to produce sustainable aviation fuel (SAF).

Company	Country	Location	Estimated Potential SAF Production (MLY)	Estimated Lipid Demand (t/y)
Tidewater Midstream	Canada	Prince George, BC	2.2	26,000
Suncor	Canada	Edmonton, AB	27	321,000
Shell	Canada	Edmonton, AB	21	249,000
NWR Sturgeon	Canada	Redwater, AB	15	176,000
BP Americas (expand to 5%)	U.S.	Blaine, WA	36	550,000
Sinclair	U.S.	Anacortes, WA	28	328,000
Marathon	U.S.	Anacortes, WA	22	262,000
Phillips 66	U.S.	Ferndale, WA	19	231,000
Par Pacific	U.S.	Tacoma, WA	8	92,000
Phillips 66	U.S.	Billings, MT	11	128,000
Par Pacific	U.S.	Billings, MT	12	139,000
CHS	U.S.	Laurel, MT	11	132,000
Calumet	U.S.	Great Falls, MT	0.3	4,000
Chevron	U.S.	Richmond, CA	45	539,000
PBF Energy	U.S.	Martinez, CA	29	344,000
Valero	U.S.	Benicia, CA	27	319,000
San Joaquin	U.S.	Bakersfield, CA	3	33,000

The total feedstock required to meet the demands for the facilities listed in Table 3 is 11.5 million t/yr with an additional 3.9 million t/yr if the refineries in Table 4 are included. While this is less than the total feedstock determined in Task 2, it is unlikely that the available lipids would fully cover these after considering biofuel demands from other regions and demands from other sectors. It should be noted that the regional SAF demand is less than 10% of the volume included in Table 3.

Task 4 – State, Provincial and Federal Policy Support

Washington State University

Objectives

The objective of this task is to update U.S. policy in the ASCENT U.S. Policy Applicability and Value Estimation Tool and expand tool to include federal Canadian and BC policies (Brandt et al., 2025).

Research Approach

The U.S. tool was updated with new California CI targets, changes to the Clean Fuel Production Credit (45Z) based on the One Big Beautiful Bill Act (OBBBA), and market values. The tool also includes the U.S. Renewable Fuel Standard (RFS), Oregon's Clean Fuel Program (CFP) and Washington's Clean Fuel Regulation (CFR). Canadian Clean Fuel Regulation (CFR) and the BC Low Carbon Fuel Standard (LCFS) were added to the policy tool. This tool will be published to the WSU repository concurrent with a peer-reviewed paper that is under internal review.



Major Accomplishments

Tool updates and expansion needed to determine disparate policy support that can be used in future FTOT runs were completed. In addition, the stakeholder meeting provided guidance on valuing the BC low carbon jet fuel incentive program (LCJFIP). For HEFA, the value of this incentive is 0.75 CAD/liter (YVR, 2025). However, the funds for this incentive are based on the BC Low Carbon Fuel Standard (LFCS) credit value and the number of credits used to fund it. This information is not public, but industrial partners estimated that it would be paid at approximately 10-25%. This is a result of on the policy funding each liter of fuel equally combined with the expected underfunding compared to the demand.

Task 5 – CI Valuation by Policy

Washington State University

Objectives

The objective of this task is to quantify and compare fuel CI values using policy-specific values (from GREET®, GHGenius, etc.). Each policy has a unique methodology to calculate the CI of the fuel, which is used to determine the estimated monetary value. The differences in the policies need to be understood and CI values identified to allow for future supply chain analyses that will include the impact of disparate policies.

Research Approach

The life cycle assessment (LCA) methodology used to calculate CI for each applicable policy within the primary region was reviewed. Public CI values were collated to allow for value estimation.

Major Accomplishments

Table 5 lists the policies selected for use in supply chain analyses in the primary region. Future supply chain analyses will likely include production and markets outside of this region and additional policies will be assessed, for example California's LCFS.

Table 5. Summary of major policy attributes of policies in the primary region. BC: British Columbia, CI: carbon intensity, CFP: Clean Fuel Program, CFR: Clean Fuel Regulation, ILUC: indirect land use change, LCFS: Low Carbon Fuel Standard, LCJFIP: low carbon jet fuel incentive program, OR: Oregon, RFS: Renewable Fuel Standard, WA: Washington.

Jurisdiction	Policy	Volume Target	CI Target	ILUC	Support	Penalty	Jet Specified
Canada							
Federal	CFR	X	X	Risk	X	X	
Province	BC LCFS	X	X		X	X	X
Province	BC LCJFIP		Follows BC LCFS	Follows BC LCFS	X		X
U.S.							
Federal	45Z		X		X		
Federal	RFS	X	X	X	X	X	
State	OR CFP, WA CFR		X	X	X	X	

The CI for canola oil, calculated for each policy using the corresponding LCA tool/methodology is listed in Table 6. For CFR, BC LCFS, OR CFP and WA CFR, the CI was compared to the average target CI for 2025-2030 to calculate the number of credits earned. All policies except 45Z and BC LCJFIP are market based and historical medians were used from 2025 (January-August), except for CFR which used 2024 data as it is the most recent publicly available.

® GREET (Greenhouse gases, Regulated Emissions, and Energy use in Technologies) is a registered trademark of the U.S. Department of Energy.



Table 6. Canola oil carbon intensity (CI) and estimated SAF policy value for selected primary region policies. BC: British Columbia, CFP: Clean Fuel Program, CFR: Clean Fuel Regulation, ILUC: indirect land use change, LCFS: Low Carbon Fuel Standard, LCJFIP: low carbon jet fuel incentive program, OR: Oregon, RFS: Renewable Fuel Standard, USD: United States dollar, WA: Washington.

Value	CFR	BC LCFS	BC LCJFIP[a]	45Z[b]	RFS	OR CFP	WA CFR
CI (g CO_2e/MJ)	42.2	35.5	35.5	20.1	32.0	55.0	55.1
USD/liter	0.18	0.33	0.15[c]	0.16	0.29	0.05	0.03

[a] policy in effect through 2026, [b] policy in effect through 2029, [c] value is assumed to be 25% of policy max for conversion technology, set per stakeholder feedback.

Task 6 – Baseline FTOT Supply Chain Analyses

U.S. Department of Transportation Volpe Center

Objectives

The objective of this task is to complete baseline FTOT supply chain analyses for the U.S. alone, Canada alone and joint U.S. and Canada without constraints.

Research Approach

Expand FTOT to include Canadian roads, rail, pipelines and barge routes.

Major Accomplishments

The Volpe FTOT team completed three baseline runs representing the technical potential for delivery of SAF to YVR, SEA, PDX, and San Francisco International Airport (SFO) given the feedstock assessment and existing/current operating infrastructure noted in Tasks 1-3. California feedstock supply, refinery infrastructure, and SAF demand at SFO were incorporated due to the relative efficiency of production and cost-effective transportation options to the primary region. The FTOT-optimal supply chains for a U.S.-Canada combined scenario were compared to the U.S. only and Canada only scenarios. Preliminary results were presented to project stakeholders. After the stakeholder event Canadian intermodal facilities were added to the FTOT North American multimodal network to better reflect existing infrastructure.

Task 7 – Shared Infrastructure Review

Washington State University

Objectives

The objective of this task is to determine if additional infrastructure is needed to promote SAF use in the primary region and if shared infrastructure will benefit SAF utilization.

Research Approach

Use supply chain analysis results to identify shared infrastructure locations.

Major Accomplishments

For the baseline U.S.-Canada supply chain analyses which encompass the expanded region, all fuel was produced and blended in California and did not require additional infrastructure. These baseline runs did not include needed constraints to feedstock availability and policy was not incorporated. Future work with this additional information is likely to produce disparate results that could demonstrate a need for infrastructure within the primary region.



All Tasks

Publications
None.

Outreach Efforts
- BC Smart – Vancouver, BC, Canada, February 2025
- ASCENT spring meeting – Knoxville, Tennessee, April 2025
- Stakeholder Meeting and follow-ups – online, July 2025

Awards
None.

Student Involvement
None.

Plans for Next Period
- Expand demand for additional primary and secondary region airports.
- Evaluate feedstock reductions based on realistic assumptions regarding lipid availability.
- Complete shared infrastructure review.
- Hold stakeholder review meeting.

References

ASTM International. (2023). *ASTM D1655-23a - Standard Specification for Aviation Turbine Fuels*. https://www.astm.org/workitem-wk88158

Brandt, K., Martinez Valencia, L., Camenzind, D., & Wolcott, M. (2025). *U.S. Policy Applicability and Value Estimation Tool* (v.2). Washington State University. https://doi.org/10.7273/000007300

Brandt, K., Martinez-Valencia, L., Camenzind, D., Martulli, A., Malina, R., Allroggen, F., & Wolcott, M. (2026). Pragmatic assessment of meeting the 2030 U.S. sustainable aviation fuel goal. *Biomass Bioenergy, 206*. https://doi.org/10.1016/j.biombioe.2025.108516

Brandt, K., Tanzil, A. H., Martinez-Valencia, L., GARCIA-PEREZ, M., & Wolcott, M. P. (2021). *Hydroprocessed esters and fatty acids techno-economic analysis* (v.3.1). Washington State University. https://doi.org/10.7273/000001460

British Columbia. (2024). *LCFS Requirements, British Columbia*. https://www2.gov.bc.ca/gov/content/industry/electricity-alternative-energy/transportation-energies/renewable-low-carbon-fuels/requirements

Canada Energy Regulator. (2025). *Market Snapshot: Overview of 2024 Canada-U.S. Energy Trade*. https://www.cer-rec.gc.ca/en/data-analysis/energy-markets/market-snapshots/2025/market-snapshot-overview-of-2024-canada-us-energy-trade.html

Canada Meat Council. (2024). *Industry Resources Archive*. https://cmc-cvc.com/industry/industry-resources-archive/

Danielson, E. (2023). *Biofuels Annual, Ottawa*. U.S. Department of Agriculture, Foreign Agriculture Service. https://apps.fas.usda.gov/newgainapi/api/Report/DownloadReportByFileName?fileName=Biofuels%20Annual_Ottawa_Canada_CA2023-0030.pdf

Danielson, E. (2024). *Oilseeds and Products Animal, Ottawa*. U.S. Department of Agriculture, Foreign Agriculture Service. https://apps.fas.usda.gov/newgainapi/api/Report/DownloadReportByFileName?fileName=Oilseeds%20and%20Products%20Annual_Ottawa_Canada_CA2024-0008.pdf

GlobalData. (2023). *UCO Supply Outlook*. https://cleanfuels.org/wp-content/uploads/GlobalData_UCO-Supply-Outlook_Sep2023.pdf

Government of Canada. (2022). *Canada's Aviation Climate Action Plan 2022-2030*. https://tc.canada.ca/en/corporate-services/policies/canada-s-aviation-climate-action-plan

Government of Canada. (2024). *Supply comparison by species between Canada and the United States*. https://agriculture.canada.ca/en/sector/animal-industry/red-meat-and-livestock-market-information/supply-comparison-species-between-canada-and-united-states



Government of Canada. (2025). *Canada-United States agriculture and agri-food trade in 2024*. https://agriculture.canada.ca/en/international-trade/agriculture-and-agri-food-trade-between-canada-and-united-states/canada-united-states-agriculture-and-agri-food-trade-2024

Port of Seattle. (2024). *Sustainable Aviation Fuels, Port of Seattle*. https://www.portseattle.org/page/sustainable-aviation-fuels#:~:text=The%20Port's%20goals%20are%20ambitious,produced%20locally%20from%20sustainable%20sources

Secchi, M. A., Fernandez, J. A., Stamm, M. J., Durrett, T., Prasad, P. V. V., Messina, C. D., & Ciampitti, I. A. (2023). Effects of heat and drought on canola (Brassica napus L.) yield, oil, and protein: A meta-analysis. *Field Crops Research, 293*. https://doi.org/10.1016/j.fcr.2023.108848

Statistics Canada. (2024). *Number of cattle, by class and farm type (x1,000), Table: 32-10-0130-01*. https://www150.statcan.gc.ca/t1/tbl1/en/tv.action?pid=3210013001

Statistics Canada. (2025). *Canadian International Merchandise Trade Web Application*. https://www150.statcan.gc.ca/n1/pub/71-607-x/71-607-x2021004-eng.htm

U.S. Department of Energy, U.S. Department of Transportation, U.S. Department of Agriculture, U.S. Environmental Protection Agency. (2021). *SAF Grand Challenge Roadmap: Flight Plan for Sustainable Aviation Fuel*. https://www.energy.gov/sites/default/files/2022-09/beto-saf-gc-roadmap-report-sept-2022.pdf

U.S. Energy Information Administration. (2023). *Higher energy prices push United States energy trade with Canada to a record-high value*. https://www.cer-rec.gc.ca/en/data-analysis/energy-markets/market-snapshots/2025/market-snapshot-overview-of-2024-canada-us-energy-trade.html

U.S. Energy Information Administration. (2025). *Monthly Biofuels Capacity and Feedstocks Update, Petroleum & Other Liquids*. https://www.eia.gov/biofuels/update/

United States Census Bureau. (2025). *USA Trade Online*. https://usatrade.census.gov/

USDA. (2023). *Grain Crushings and Co-Products Production 2022 Summary*. U.S. Department of Energy. https://downloads.usda.library.cornell.edu/usda-esmis/files/v979v304g/sq87d9947/3n205h555/cagcan23.pdf

USDA. (2024a). *United States and Canadian Hogs*. U.S. Department of Agriculture, National Agricultural Statistics Service, National Agricultural Statistics Service. https://esmis.nal.usda.gov/sites/default/release-files/7h149p85x/xd07jf68t/dv141f23z/usch0324.pdf

USDA. (2024b). *Oil Crops Yearbook*. U.S. Department of Agriculture, Economic Research Service. https://www.ers.usda.gov/data-products/oil-crops-yearbook/

USDA. (2024c). *Feed Grains Database - Feed Yearbook: Report Tables*. U.S. Department of Agriculture, Economic Research Service. https://www.ers.usda.gov/data-products/feed-grains-database/feed-grains-yearbook-tables

USDA. (2025a). *USMCA, Canada, & Mexico - Canada: Trade & FDI*. U.S. Department of Agriculture, Economic Research Service https://www.ers.usda.gov/topics/international-markets-us-trade/countries-regions/usmca-canada-mexico/canada-trade-fdi#:~:text=Canada%20is%20a%20major%20participant,Agreement%20(NAFTA)%20in%201994

USDA. (2025b). *Fats and Oils: Oilseed Crushings, Production, Consumption and Stocks*. U.S. Department of Agriculture, National Agricultural Statistics Service. https://esmis.nal.usda.gov/publication/fats-and-oils-oilseed-crushings-production-consumption-and-stocks

USDA. (2025c). *Livestock Slaughter Annual Summary*. U.S. Department of Agriculture, National Agricultural Statistics Service. https://esmis.nal.usda.gov/publication/livestock-slaughter-annual-summary

USDA. (2025d). *United States and Canadian Cattle*. U.S. Department of Agriculture, National Agricultural Statistics Service. https://esmis.nal.usda.gov/publication/united-states-and-canadian-cattle

USDA. (2025e). *Poultry Slaughter Annual Summary*. U.S. Department of Agriculture, National Agricultural Statistics Service. https://esmis.nal.usda.gov/publication/poultry-slaughter-annual-summary

USSEC. (2025). *Conversion Table*. U.S. Soybean Export Council. https://ussec.org/buyer-tools/conversion-table/

YVR. (2025). *Low Carbon Jet Fuel*. https://www.yvr.ca/en/about-yvr/environment/low-carbon-jet-fuel



Project 101 Sustainable Aviation Fuel Repository

Washington State University

Project Lead Investigator

Joshua Heyne
Bioproducts, Sciences, and Engineering Laboratory Director, Associate Professor
School of Engineering and Applied Science
2710 Crimson Way, Richland, WA 99354
(937) 229-5319
joshua.heyne@wsu.edu

University Participants

Washington State University (WSU)

- P.I.: Dr. Joshua Heyne
- FAA Award Number: 13-C-AJFE-WaSU-043
- Period of Performance: March 15, 2025, to September 30, 2025
- Tasks:
  1. Investigating detailed needs and requirements of a sustainable aviation fuel (SAF) Repository
  2. Procuring SAF and conventional fuel samples for testing
  3. Testing procured samples for reference data to be leveraged by other partners
  4. Developing a data management protocol for sharing and distributing data
  5. Distributing fuel samples and data to partners per Federal Aviation Administration (FAA) prioritization

Project Funding Level

The ASCENT Project 101 received $2,000,000 from the FAA and cost sharing funding. In-kind cost share funding has been provided by Trinity College Dublin ($1,965,000), Woodward ($35,000), and the state of Washington ($1,200,000).

Investigation Team

Dr. Joshua Steven Heyne, P.I., Washington State University
Dr. Randall Boehm, Co-investigator, Washington State University
Dr. Tim Edwards (retired U.S. Air Force Research Laboratory), Consultant
Dr. Zhibin (Harrison) Yang, Assistant Research Professor, Washington State University
Conor Faulhaber, graduate student, Washington State University
Patricia Garcia-Alfaro, Washington State University
Kaamel Sidiqi, undergraduate student, Washington State University

Project Overview

This project will serve to acquire, distribute, test, and document SAF and other reference conventional fuel samples. At present, accessing SAF samples is costly for the FAA and difficult for many research groups. Private, federal, and public research entities have issues collecting relevant SAF samples for testing. The lack of access inhibits progress in SAF research. Concurrently, procuring SAF materials is costlier for the FAA as samples are charged the full overhead rates, and individual acquisitions do not benefit from economies of scale. Fuel samples after acquisition will be tested for critical properties and then distributed to labs, per the preference of the FAA. A small portion of the acquired fuels will be retained for posterity and additional testing if anomalous observations are made.



Task 1 – Investigating Detailed Needs and Requirements of a SAF Repository

Washington State University

Objective

The objective of this task is to investigate detailed needs and requirements of a SAF Repository. SAF is currently produced using novel feedstocks and conversion technologies. The combination of these novel feedstocks and conversion technologies results in unique chemical compositions and physical properties in sustainable aviation fuel. As a result, the blend ratios for approved sustainable aviation fuel pathways vary between 5% and 50% as of October 30, 2025, and work is on-going to qualify SAF pathways at 100%. However, now, the limited blend ratios are the result of the unique properties and compositions of SAF relative to fossil fuel. For example, ASTM D7566 (ASTM International, 2024), the standard for synthetic aviation turbine fuel blend components, includes several annexes that have no aromatic content in the final product. The lack of aromatic content in the final product means that certain properties, such as seal swelling and dielectric constant, are outside of the experience range of 100% fossil fuels. This deviation is pronounced in the case of aromatics, but other more subtle deviations can also occur. For example, SAFs may be composed of only one or two molecules, as in the case of the iso-butanol to jet and Annex A3 in ASTM D7566. These compositions are very different from fossil jet fuel and, as a result, are not considered anything close to a conventional petroleum fuel and hence required blending with conventional petroleum jet fuel before use.

Subtle and dramatic differences in composition can have substantial impacts on many safety and operability aspects. For example, changes in isomeric structure can impact a wide range of properties relevant to aviation. Properties like viscosity, for instance, can be increased substantially with changes in catalyst technologies, which is allowed under current ASTM D7566 definitions. While there are no known issues with allowable blends or the current regulatory framework, it is critical to understand the scientific underpinnings of the impact of compositional variance on all aspects related to aviation fuel impacts on engines, infrastructure, aircraft, humans, and the environment. This task, investigating detailed needs and requirements of a sustainable aviation fuel repository, aims to identify the following characteristics required to assist in understanding the following compositional impacts:

- Types of fuels or synthetic blend components needed
- Volumes of each needed fossil-synthetic blend component
- Number and type of fossil jet fuels for use as reference materials
- Number of entities that are needed to support this project
- Facilities needed to support activities SAF testing and research
- Forecasting future fuels and requirements several years in advance

Research Approach

Types of Fuels or Synthetic Blend Components Needed

There are three categories of fuels or synthetic blend components needed. The first category is benchmark conventional fuels. Conventional or petroleum-based fuels are needed to establish baseline experience ranges in various experimental architectures. Current aviation systems operate effectively, safely, and consistently on conventional fuels. However, all petroleum-based aviation fuels are not all the same. There are deviations across petroleum-based fuels in terms of their densities, viscosities, compositions, contaminants, etc. As a result, it is important to acquire several different petroleum-based fuels for testing in relevant architecture and configurations. Historically, three main petroleum-based fuels have been used for baselining. Under the National Jet Fuels Combustion Program (NJFCP) (Colket & Heyne, 2021), these fuels were defined as Category A fuels: Jet A-1, A-2, and A-3. These three fuels were selected based on their combustor operability characteristics, namely their ability to resist or trigger lean blowout and ignite under altitude conditions. Jet A-1 fuel was selected to be the easiest to ignite and have the lowest lean blowout limit, making it a best-case fuel. Jet A-2 fuel was selected to be an "average" fuel, with properties similar to the average fossil fuel that aircraft in the United States (U.S.) were burning in 2014. The third fuel, Jet A-3, was selected to be a "worst-case" fuel, with the poorest ignition and lean blowout characteristics relative to most conventional fuels used in the U.S. Under this funded activity, the team has sought to acquire these Category A fuels from the U.S. Air Force Research Lab and gather additional fuels from other refineries in the U.S. To the investigation team's knowledge, there are still some volumes of Category A fuels remaining; however, the available quantity of these fuels is not sufficient to meet the needs of the FAA SAF repository project. The team will therefore need to identify and acquire a new batch of reference fuel with properties matched as closely as practical with those acquired during the NJFCP.



The second category of reference fuels sought under the SAF repository project are approved or candidate synthetic blend components. Currently, there are eight annexes under ASTM D7566 that detail the quality control requirements of these materials. Some annexes, e.g., Annex A2, pertain to a product (hydro-processed esters and fatty acids [HEFA]) made by multiple producers. For example, Montana Renewables in Great Falls, Montana, and Neste in Porvoo, Finland, both produce synthetic blend components leveraging the ASTM D7566 Annex A2 pathway. Annex A5 pertains to the production of SAF from alcohols through dehydration, oligomerization, hydrogenation, and fractionation. Lanzajet produces and sells products leveraging this pathway. Several other annexes, A3, A6, A7, and A8 are not currently leveraged by any commercial activity, while annexes A1 and A4 pertain to a Fischer-Tropsch process that usually employs coal as a feedstock. In addition to these eight approved pathways, there are many SAF candidate pathways that are currently undergoing ASTM qualification or working towards entering the ASTM qualification process, ASTM D4054 (ASTM International, 2022). The investigators have identified several institutions and products from these synthetic fuel routes.

The last broad category of synthetic blend components this program has sought to procure are solvents or other hydrocarbon materials that are not currently used as commercial fuels or being produced as an approved ASTM D7566 pathway. Historically, programs have leveraged aromatic solvents such as aromatic (ARO) 100 and ARO 150. Furthermore, there are other solvents, such as NORPAR™ and ISOPAR®, which can be prepared to develop critical blends for testing various features or properties of aviation hardware.

Finally, under the NJFCP, combinations of all these categories were at times blended together to form mixtures that would stress-test various theories related to aircraft operability. These blends were collectively referred to as Category C fuels. Table 1 documents a range of fuels that have been selected based on the criteria above for inclusion in the repository.

Table 1. List of high interest materials for procurement under the repository project.

Category and motivation	Fuel description	Notes	POSF ID	Reason for Inclusion
SAF, emissions	HEFA (ASTM D7566 Annex A2)	Current producers: World Energy,® Montana Renewables, and Neste®	-	-
SAF	ATJ (ethanol) (ASTM D7566 Annex A5)	Lanzatech Global, Inc.	-	-
SAF	ATJ (isobutanol) (NJFCP C-1) (ASTM D7566 Annex A5)	Gevo® or Global Bioenergies	Gevo: 11498 etc.	Historical, low cetane, narrow boiling
SAF	Power to liquids (Air Company)	In development toward ASTM D4054	-	-
Petroleum, operability	NJFCP A-2 "average" jet fuel, also used for blending	-	10325, Jet A (also 4658)	Baseline for combustor operability testing
Petroleum, operability	NJFCP A-3 worst case jet fuel	-	10289, JP-5	High viscosity, high flash
Petroleum, operability	NJFCP A-1 best case jet fuel	-	10264, JP-8	Low viscosity, low (but >38˚C) flash
Petroleum, operability	New average Jet A fuel, also used for blending	-	-	-
Petroleum, operability	High flash JP-5 POSF 10370?	-	10376	70˚C flash

™ NORPAR is a trademark of Exxon Mobil Corporation, Spring, Texas.
® ISOPAR is a registered trademark of Exxon Mobil Corporation, Spring, Texas.



Category and motivation	Fuel description	Notes	POSF ID	Reason for Inclusion
SAF, emissions	Virent, Inc.,® SAK	Single-ring aromatics	12924, 13349, 13350	General Electric CLEEN II, 100% SAF flights by United and Virgin Atlantic
SAF	CleanJoule LLC,® CycloSAF	1,4 dimethyloctane	-	-
SAF	Alder® Renewables pyrolysis pathways to Alder Renewable Crude (ARC) and Alder Pyrolytic Sugars (APS)	In development toward ASTM D4054	-	-
SAF	Visolis, Inc.	In development toward ASTM D4054		-
SAF historical	Amyris, Inc.,® fully synthetic	Contains farnesane, limonane, isopropyl methyl benzene	-	-
Operability	NJFCP C-8 (JRF-3)	-	12936	25% aromatic, maximum sulfur
SAF historical	Swedish Biofuels® ATJ SKA	ASTM D7566 Annex A8	12924, 7691	-
"SAF" historical	Sasol Ltd. IPK CTL	31 DCN, in production (coal)	7629	Baseline property data
"SAF" historical	Syntroleum Corp. S-8 or Rentech, Inc., GTL	GTL, a typical F-T product similar to HEFA	5018	Baseline property data
SAF historical	KiOR, Inc., HDCJ	Lignocellulosic pyrolysis, aromatic blend component (dormant)	-	-
SAF historical	Applied Research Associates CHJ	Aromatic-containing SAF, ASTM D7566 Annex A6	8455, 13676	-
SAF historical	IHI Corp. Bio-SPK	ASTM D7566 Annex A7	-	-
SAF historical	Shell International Ltd. CPK-0	High cyclo, on hold	-	-
SAF historical	Virent, Inc., HDO SK	High cyclo, on hold	8535	-
SAF historical	Honeywell International, Inc., UOP camelina HEFA	-	10301	-
SAF historical	Dynamic Fuels LLC, HEFA mixed fats	-	7635	-
SAF historical	Amyris, Inc., farnesane (DSH-76)	Trimethyl dodecane	12398	-
Operability	NJFCP C-2	-	12223, 11813	Asymmetric boiling range



Category and motivation	Fuel description	Notes	POSF ID	Reason for Inclusion
Operability	NJFCP C-3	-	12341, 12363	Maximum viscosity
Operability	NJFCP C-4	-	12344, 12489	Low cetane, broad boiling
Operability	NJFCP C-5	-	12345, 12713, 12789, 12816	Flat/narrow boiling range
Operability	NJFCP C-7	-	12925, 12969, 12973	Maximum cycloparaffins
Operability	NJFCP C-9	-	12933, 12968	Maximum cetane

ATJ = alcohol-to-jet
CHJ = Catalytic Hydrothermolysis jet
CLEEN = continuous lower energy, emissions and noise
CPK-0 = cycloparaffinic Kerosene
CTL = coal-to-liquids
DCN = derived cetane number
DSH = direct sugar to hydrocarbon
GTL = gas-to-liquids
HDCJ = hydroprocessed depolymerized cellulosic jet
HDO = hydrodeoxygenation
HEFA = hydroprocessed esters and fatty acids
IPK = iso-paraffinic kerosene
JRF = jet reference fluid
NJFCP = National Jet Fuels Combustion Program
UOP = Universal Oil Products
POSF = U.S. Air Force Research Laboratory fuel identification number prefix
SAF = sustainable aviation fuel
SAK = synthesized aromatic kerosene
SKA = synthetic kerosene with aromatics
SK = synthetic kerosene
SPK = synthetic paraffinic kerosene

ASTM International. (2022). *ASTM D7566-22: Standard specification for aviation turbine fuel containing synthesized hydrocarbons.* https://www.astm.org/d7566-22.html
ASTM International. (2022). *ASTM D4054-22: Standard practice for evaluation of new aviation turbine fuels and fuel additives.* https://www.astm.org/d7566-22.html

®World Energy is a registered trademark of World Management Group, LLC, Boston, Massachusetts.
®Neste is a registered trademark of Neste Oyj, Espoo, Finland.
®Gevo is a registered trademark of Gevo, Inc., Englewood, Colorado.
®Virent is a registered trademark of Virent, Inc., Madison, Wisconsin.
®CleanJoule is a registered trademark of CleanJoule, LLC, Salt Lake City, Utah.
®Alder is a registered trademark of Alder Energy, LLC, Washington, D.C.
®Amyris is a registered trademark of Amyris, Inc., Emeryville, California.
®General Electric is a registered trademark of General Electric Company, Schenectady, New York.
®Swedish Biofuels is a registered trademark of Swedish Biofuels AB, Stockholm, Sweden.
®Sasol is a registered trademark of Sasol Limited, Gauteng, South Africa.
®Syntroleum is a registered trademark of Emerging Fuels Technology, Inc., Tulsa, Oklahoma.
®Shell is a registered trademark of Shell Trademark Management B.V., The Hague, The Netherlands.
®Honeywell is a registered trademark of Honeywell International, Inc., Charlotte, New Jersey.
™Dynamic Fuels is a trademark of Dynamic Fuels, LLC, Springdale, Arkansas.

Facilities and Volumes of Each Needed Petroleum and Synthetic Blend Component

The volumes of each desired synthetic blend component were investigated based on the product availability, research needs, and storage availability. Two storage facilities have been identified to support the SAF repository project. One facility on campus at WSU is able to store 55-gal drum containers. The second facility, which is under development at Seattle Paine Field International Airport (hereinafter called Paine Field) in Snohomish County, Washington, can store tens of thousands of gallons of material. Finally, volumes needed for short-term distribution and use, have also been investigated and leveraged as will be reported later. Plans are underway to procure up to 55 gal of each of the materials reported in Table 1. Ideally, the facility at WSU would be able to accommodate all of these procurements. Material volumes to be stored at Paine Field have emphasized large volumes with relatively limited number of samples. Nine above-ground fuel tanks with a combined capacity of 50,000 gallons are in the process of being specified for request for bid to be sent out by Snohomish county. The volume stored at Paine Field would be able to support ASCENT projects and other global efforts in a manner that is substantial, and beyond current capabilities anywhere else in the world.



Number and Type of Petroleum Jet Fuels for Use as Reference Materials
After consideration, there are additional motivations to procure new reference materials composed of fossil hydrocarbons (beyond NJFCP A-1, A-2, and A-3) for this project. A key motivation for procuring new petroleum-based reference fuels is that the existing Category A fuels—originally obtained over a decade ago—are nearly depleted. Replacing these diminishing stocks with updated standards is essential for ongoing and future research needs. Towards this end, several fuel suppliers have been contacted to source additional reference petroleum fuels. To date no additional fuels have been identified with certainty, this remains an ongoing subtask. Upon installation of the above-ground tanks at Paine Field, it is anticipated that selection of the supplier for reference petroleum jet fuel will be completed within a few weeks.

Number of Entities that Could be Supported Under this Project
Domestic and international entities have been identified as potential users or entities that could be supported as a result of this project. Domestically, 16 ASCENT universities/principal investigators and 36 total entities or principal investigators have been identified as potential users of the repository project. Internationally, entities have queried for samples to be purchased and shipped to their locations. The major benefit of the repository project is that many experiments can study and explore the same fuel composition producing a key uncertainty in comparing results from numerous studies.

The facilities mentioned herein are sufficient to support the vast majority of programs domestically and internationally researching the compositional the property impacts of novel synthetic blend components on operability, emissions, various forms of compatibility, human health, and the environment. Unfortunately, current forecasts for large-scale flight and emissions campaigns, which require tens of thousands of gallons per campaign, are outside the scope of possibility for the two currently pursued facilities. This means that while many lower volume tests performed at ASCENT universities routinely can be supported sufficiently, years-long investigations on the impacts of composition on emissions and the environment will not be able to be supported by the size of facilities envisioned at present.

Milestones

- Developed a short list of candidate materials for storage in the SAF repository.
- Worked with ASCENT stakeholders to identify compositional and volume interests for testing.

Major Accomplishments

- Developed a short list of candidate materials for storage in the SAF repository.
  - Candidate materials identified sought in the next federal fiscal year.
- Worked with ASCENT stakeholders to identify compositional and volume interests for testing.
  - Materials will be distributed more broadly once they are acquired in sufficient volumes quality.

Publications

None.

Outreach Efforts

In support of defining the repository's technical and capacity requirements, the ASCENT Project 101 team engaged multiple ASCENT principal investigators to learn about their specific demands for fuel volumes, compositional preferences, and testing frequencies. Our team also collaborated closely with original equipment manufacturer (OEM) partners—such as Gulfstream,® Airbus,® Pratt & Whitney,® World Energy®, Montana Renewables™, and CleanJoule®—to align the repository's capabilities with industry goals. These interactions, along with presentations at the Coordinating Research Council (CRC) aviation fuels meeting and the Commercial Aviation Alternative Fuels Initiative (CAAFI) webinar, helped refine our understanding of what a comprehensive SAF repository should encompass.

® Gulfstream is a registered trademark of Gulfstream Aerospace Corporation, Savannah, Georgia
® Airbus is a registered trademark of Airbus Operations GmbH, Hamburg, Germany.
® Pratt & Whitney is a registered trademark of RTX Corporation, Farmington, Connecticut.
® World Energy is a registered trademark of World Management Group, LLC, Boston, Massachusetts
™ Montana Renewables is a trademark of Montana Renewables LLC, Great Falls, Montana.
® CleanJoule is a registered trademark of CleanJoule, LLC, Salt Lake City, Utah.



Awards
Joshua Steven Heyne, American Chemical Society (ACS) Energy & Fuels, Rising Star

Student Involvement
None.

Plans for Next Period
Continue to add additional details and solicit feedback from stakeholders.

References
ASTM International. (2022). *ASTM D4054-22: Standard practice for evaluation of new aviation turbine fuels and fuel additives*. https://doi.org/10.1520/D4054-22

ASTM International. (2024). *ASTM D7566-24: Standard specification for aviation turbine fuel containing synthesized hydrocarbons*. https://doi.org/10.1520/D7566-24

Colket, M., & Heyne, J. (2021). *Fuel Effects on Operability of Aircraft Gas Turbine Combustors: Progress in Astronautics and Aeronautics*. The American Institute of Aeronautics and Astronautics, Inc. https://doi.org/10.2514/4.10604

Task 2 – Procuring SAF and Conventional Fuel Samples for Testing
Washington State University

Objective
The objective of this task is to procure SAF and conventional fuel samples for testing under various ASCENT projects. Given the wide array of petroleum jet fuel producers, approved SAF producers, novel SAF producers, and manufacturers of relevant solvents for blend studies, it's essential to continually monitor the availability and changes in properties and compositions these producers offer. These variations can occur even over time at a given facility due to changes in production technology or feedstock.

To ensure quality and consistency, our team aims to:
- Gather certificates of analysis from various producers at different points in time to verify that the materials are consistent and are suitable for our research needs.
- Balance costs, availability, and desirability in terms of properties and compositions when procuring samples, ensuring we obtain high-quality materials within budget constraints.
- Identify cost-effective alternatives, such as contracting with petroleum fuel producers or solvent vendors who can provide products similar to expected SAF products.
- Monitor availability and property changes in producers' offerings on an annual or more frequent basis to support critical ASCENT projects.

Research Approach
Our approach involves collaborating with producers of sustainable fuels, conventional fuels, and solvent manufacturers to purchase and distribute the necessary materials. Our team will work closely with these suppliers to identify sources that meet the specific property and composition requirements for our research. This includes reviewing certificates of analysis and assessing the consistency of their products over time. By maintaining relationships with multiple producers, we ensure a reliable supply of samples for testing and blend studies.

Milestones
- Acquired reference HEFA fuel from Montana Renewables.
- Sampled and analyzed fuel that is planned for a test campaign; now postponed to commence in spring 2026.

Major Accomplishments
- Procured test volumes and distributed them to a research partner's test location for evaluation, ensuring that the necessary materials were available for timely testing.
- Established a procurement process that balances cost, availability, and quality, allowing for the acquisition of samples that meet research requirements without exceeding budget constraints.



- Supported for research initiatives enabling researchers to conduct fuel blend studies and other tests by providing appropriate samples sourced from various producers, thereby supporting the overall objectives of the ASCENT projects.

Publications
None.

Outreach Efforts
To streamline the procurement of various SAF and conventional fuel samples, our team proactively contacted ASCENT principal investigators to ascertain their project-specific requirements around fuel volumes, composition, and testing schedules. We also worked with the U.S. Navy, U.S. Air Force, and OEMs, such as Gulfstream, Airbus, Pratt & Whitney, World Energy, Montana Renewables, Monument Chemical,® CleanJoule, and World Kinect® (World Fuel Services) to ensure the correct types of fuel were sourced and supplied for research or operational needs. Our team presented at the CRC aviation fuels meeting and other technical conferences with a spotlight on sustainable aviation, further facilitating the sharing of procurement insights and best practices with a broader community.

Awards
None.

Student Involvement
None.

Plans for Next Period
- Support similar emissions campaign measurements.
- Procure additional materials for storage and distribution within the repository at WSU and Paine Field.

Task 3 – Testing Procured Samples for Reference Data to be Leveraged by Other Partners
Washington State University

Objectives
The objectives of this task are to (1) measure and disseminate standard reference data on materials associated with the repository project, (2) establish the extent of contamination from residual conventional fuels mixing with SAF in fuel storage tanks, and (3) provide reference test data to research partners to understand the variance in SAFs, specifically regarding sulfur content.

The success of the repository project critically depends on accurately measuring and disseminating standard reference data on materials associated with SAFs, reference petroleum fuels, hydrocarbon solvents, and blends of all these materials. SAFs can exhibit substantial variance in properties and compositions—from one ASTM D7566 (ASTM International, 2024) annex to another, and even within the same feedstock and process due to catalyst aging. For example, sulfur content plays a significant role in catalyzing contrail formation and persistent aviation-induced cloudiness, which contribute to the radiative forcing associated with aviation. Therefore, providing reliable data on sulfur content and other properties is essential for research partners and the broader scientific community.

Research Approach
Recognizing that sulfur is a key component that catalyzes contrail formation and persistent aviation-induced cloudiness, we aimed to understand how even minimal sulfur levels could have a significant environmental impact. During this period of performance, this task has focused on furtherance of sulfur measurement capabilities, advancing the limit of quantification to levels near 1 ppm. Our efforts are centered around cross-method validation including ultraviolet fluorescence (ASTM D5453 [ASTM International, 2025a]), inductively coupled plasma – optical emission spectroscopy

® Monument Chemical is a registered trademark of Monument Chemical, LLC, Indianapolis, Indiana.
® World Kinect is a registered trademark of World Kinect Corporation, Miami, Florida.



(ASTM D7111 [ASTM International, 2025b]), and especially, combustion ion chromatography (ASTM D7359 basis [ASTM International, 2023]).

Concurrently, we continue to document other important properties such as dielectric constant and seal swell to fill critical needs as indicated by OEM stakeholders. Further tests were performed by distributing HEFA material to Stanford University and the University of Dayton Research Institute for ASCENT-funded research. Under all these programs, our team also measured standard reference properties for the HEFA materials. These data are being prepared for public dissemination in accordance with FAA guidance.

Milestones

- Received and analyzed dozens of HEFA samples for sulfur content, establishing a thorough sampling process across the supply chain to trace sulfur introduction.
- Fostered collaborations with key partners, including Gulfstream, University of Dayton Research Institute, and Stanford University.

Major Accomplishments

- Procured and distributed HEFA samples with the necessary cleanliness to validate low-sulfur concentration measurements.
- Prepared data for public dissemination per FAA guidance, contributing to broader industry knowledge and efforts to mitigate environmental impacts.

Publications

None.

Outreach Efforts

To optimize our testing protocols and capture critical reference data, the ASCENT Project 101 team reached out to ASCENT principal investigators, confirming the volumes and compositional attributes they require for meaningful analysis. Our team also coordinated with OEMs—Gulfstream, Airbus, Pratt & Whitney, World Energy, Montana Renewables, Monument Chemicals, CleanJoule, and World Kinect (World Fuel Services) —to integrate feedback on how test results could support engine performance and emissions evaluations.

Our work on low sulfur measurement capabilities has been presented at conferences including International Conference on Sustainable Aviation Research, SAF End-User Meeting hosted by Sandia National Laboratory, and we are in the process of preparing a journal article for scholarly review.

In parallel, our team engaged with Aerodyne® and other FAA program managers to clarify property measurement requirements that benefit broader SAF repository projects. For example, we discussed detection limits for total sulfur in HEFA blends—a key parameter for understanding contrail formation—and identified additional property measurements needed to address emerging research questions. By showcasing our testing objectives and methodologies at CRC aviation fuels meetings and other technical conferences (mentioned above), we fostered open discussion on these measurement needs, ensuring our approach remains aligned with the latest stakeholder and industry requirements.

Awards

- Joshua Steven Heyne - ACS Energy & Fuels, Rising Star

Student Involvement

- Conor Faulhaber is leading the effort to publish our work on low sulfur quantification methodology.
- Patricia Garcia-Alfaro is assisting with our lab's commissioning and standardization of the combustion ion chromatography method.
- Kaamel Sidiqi is assisting with ultraviolet fluorescence (UVF) sulfur data collection and organization.

® Aerodyne is a registered trademark of Aerodyne Research, Inc., Billerica, Massachusetts.



Plans for Next Period

- Support similar research activities with other partners. Specifically, our team is looking to support a greater number of low-volume SAF requirements at partner institutions as well as at least two large-scale emissions campaigns.
- Publish journal article on low sulfur measurement capabilities.

References

ASTM International. (2023). *ASTM D7359-18: Standard Test Method for Total Fluorine, Chlorine and Sulfur in Aromatic Hydrocarbons and Their Mixtures by Oxidative Pyrohydrolytic Combustion followed by Ion Chromatography Detection (Combustion Ion Chromatography-CIC).* https://doi.org/10.1520/D7359-18

ASTM International. (2024). *ASTM D7566-24: Standard specification for aviation turbine fuel containing synthesized hydrocarbons.* https://dol.org/10.1520/D7566-24

ASTM International. (2025a). *ASTM D5453-24: Standard Test Method for Determination of Total Sulfur in Light Hydrocarbons, Spark Ignition Engine Fuel, Diesel Engine Fuel, and Engine Oil by Ultraviolet Fluorescence.* https://doi.org/10.1520/D5453-24

ASTM International. (2025b). *ASTM D7111-16: Standard Test Method for Determination of Trace Elements in Middle Distillate Fuels by Inductively Coupled Plasma Atomic Emission Spectrometry (ICP-AES).* https://doi.org/10.1520/D7111-16R21

Task 4 – Developing a Data Management Protocol for Sharing and Distributing Data

Washington State University

Objectives

Building upon the experience gained from ASCENT Project 065A the ASCENT Project 101 team aims to enhance our processes for the SAF repository project. The objectives for this task are to:

- Develop a Comprehensive Suite of Tests: Create and document a suite of tests specific to the SAF repository project, tailored to support airframers and engine companies in designing experiments for large-scale emissions tests.
- Collect and Database Property Data: Gather and systematically record property data and compositional information for all materials received under the repository project.
- Leverage U.S. Department of Transportation (DOT) Resources: Collaborate with the developing resource within DOT, as recommended by the FAA, to enhance our data collection and analysis capabilities.
- Support Critical Research Needs: Focus on properties like sulfur content, trace metals, thermal stability, and other critical measurements not commonly emphasized in previous projects.

Research Approach

The ASCENT Project 101 team is leveraging the robust, consistent, and streamlined processes established under ASCENT Project 065A for collecting and documenting relevant properties and compositions of aviation fuels. This existing system has been effectively utilized for materials processed under the repository project, including samples from Pratt & Whitney, Montana Renewables, and those distributed to Stanford University and the University of Dayton Research Institute.

Recognizing the different requirements of the SAF repository project, our team is developing a new suite of tests that may differ from those used in ASCENT Project 065A. Specifically, we are incorporating tests for properties such as sulfur content—which is of high importance for the repository project but not commonly measured under ASCENT Project 065A. Additional tests include, but are not limited to:

- Trace metals analysis
- Thermal stability (JFTOT®) tests
- Heat capacity measurements
- Dielectric constant measurements

® JFTOT is a registered trademark of Petroleum Analyzer Company, L.P., Housten, Texas. JFTOT is a globally recognized standard for jet fuel thermal oxidation testing.



These tests are critical for supporting airframers and engine companies as they design experiments for large-scale emissions tests. A comprehensive list of properties that has begun to be documented will be included for each material received.

Moving forward, our team plans to leverage the developing resource within DOT, as suggested by the FAA, during the next period of performance. This collaboration will enhance our ability to collect, analyze, and disseminate critical fuel property data.

Milestones

- Collected and databased property data and compositional information for all materials received under the repository project.
- Began developing and documenting a full list of properties and tests specific to the SAF repository project.
- Applied the established processes from ASCENT Project 065A to streamline data collection and documentation efforts for the repository project.
- Initiated plans to collaborate with DOT's developing resource, setting the stage for enhanced capabilities in the next performance period.

Major Accomplishments

- Established a robust and streamlined process for gathering and documenting aviation fuel properties, tailored to the needs of the SAF repository project.
- Developed a suite of tests focusing on critical properties such as sulfur content, trace metals, and thermal stability, which are essential for large-scale emissions testing.
- Provided vital property data to support airframers and engine companies in designing experiments, thereby facilitating advancements in emissions testing and environmental impact assessments.
- Positioned the project to leverage new tools and methodologies by preparing to collaborate with DOT's developing resource, as recommended by the FAA.

Publications

None.

Outreach Efforts

In designing our data management framework, the ASCENT Project 101 team consulted multiple ASCENT principal investigators to gauge the types of data they collect (e.g., compositional or performance) and how frequently they need updates. This feedback, along with guidance from OEM partners ensured the protocol would support both research and operational analytics. Our team presented at conferences including International Conference on Sustainable Aviation Research (ICSAR), CRC Aviation Fuels meeting, and SAF End-User Meeting hosted by Sandia National Laboratory and we participated in OEM-led task forces and meetings on drop-in fully synthetic aviation fuel and 100% paraffinic aviation fuel. These engagements allowed us to share draft data standards and solicit feedback for a more robust, user-oriented database system.

Awards

- Joshua Steven Heyne, ACS Energy & Fuels, Rising Star

Student Involvement

- Conor Faulhaber supported database upkeep and development and presented research findings pertaining to dielectric constant at ICSAR.
- Patricia Garcia-Alfaro is helping to measure fuel and other hydrocarbon fluids lubricity.
- Kaamel Sidiq is helping with JFTOT thermal stability measurements.

Plans for Next Period

- Await FAA guidance to enable our team to put our research data into databases.



Task 5 – Distributing Fuel Samples and Data to Partners per FAA Prioritization

Washington State University

Objectives

Distributing fuel samples is one of the most critical steps in the FAA SAF Repository project. The objectives of this task are to:

- Provide Appropriate Fuel Samples: Distribute relevant fuel samples—including neat SAFs, SAF candidates, reference fossil fuel materials, solvent materials, and blends—to partner institutions per the FAA's priority.
- Support Diverse Research Needs: Enable testing for operability, compatibility, emissions, human health impacts, and environmental impacts by ensuring that partner institutions receive fuel samples suited to their specific experimental hardware and testing motivations.
- Enhance Collaboration: Facilitate effective collaboration by matching partner institutions with the correct SAF repository materials, both within and outside of the ASCENT program.

Research Approach

Introduction

Distributing fuel samples is a critical component of the FAA SAF Repository project. The effectiveness of this task depends on matching partner institutions with fuel samples that meet their specific research needs. Partner institutions, both within and outside of the ASCENT program, receive reference materials from the repository. These materials may include neat SAFs, SAF candidates, reference fossil fuel materials, solvent materials, and blends of these hydrocarbon mixtures. These test materials enable experiments related to operability, compatibility, emissions, human health impacts, and environmental impacts.

Research Partner Material Requirements

The materials distributed need to align with partner experimental hardware and testing objectives. For example:

- Operability Testing: Institutions focusing on fuel operability in different hardware require fuel samples that reflect the operational conditions and stresses their equipment might encounter.
- Emissions and Environmental Impact Studies: Researchers examining emissions or performance metrics related to human health and the environment may require fuels with specific combustion characteristics or constituents.
- Flight Condition Testing: Facilities conducting tests under flight conditions require fuels that perform reliably and safely in those environments.

By understanding these specific needs, candidate materials are paired to the institution with the appropriate SAF repository material.

Material Selection and Preparation

Based on the needs assessment, our team selects and prepares the fuel samples for distribution. This process includes:

- Reviewing Repository Inventory: Evaluating available materials in the repository, including their properties, compositions, and suitability for the intended research.
- Custom Blending: Creating blends of fuels or adding specific additives when necessary to meet the precise needs of the partner institution.
- Quality Assurance: Verifying that all fuel samples meet the required quality standards and specifications before distribution.

Distribution Process

The distribution process is managed to comply with safety regulations and to maintain the integrity of the fuel samples. Materials are shipped with qualified hazardous material distribution entities such as FedEx,® UPS,®,and World Kinect. Steps of the distribution process include:

- Documentation: Preparing detailed documentation for each fuel sample, including certificates of analysis, safety data sheets, and handling instructions.

® FedEx is a registered trademark of Federal Express Corporation, Memphis, Tennessee.
® UPS is a registered trademark of United Parcel Service of America, Inc., Atlanta, Georgia.



- Packaging: Using appropriate containers and packaging materials to protect the fuel samples during transit.
- Logistics Coordination: Arranging transportation while adhering to all relevant regulations concerning the shipment of hazardous materials.

Distribution Recipients
Over this period of performance, materials were distributed to the following institutions:
- Standford University
- University of Dayton Research Institute

Data Sharing
In addition to physical fuel samples, our team provides data packages that include:
- Property Measurements: Information on fuel properties such as density, viscosity, sulfur content, and more.
- Compositional Analysis: Data on the chemical makeup of the fuels to assist partners in their analyses.

Conclusion
By assessing partner needs, selecting suitable materials, and managing the distribution process, our team has aimed to ensure that each research institution receives fuel samples appropriate for their specific projects. This approach supports the objectives of the SAF Repository project, facilitates research across multiple domains, and aligns with the FAA's priorities to advance the understanding and adoption of sustainable aviation fuels.

Milestones
- Distributed samples to support two research projects; One led by Standford University, the other led by the University of Dayton Research Institute.
- Coordinated with producers by requesting additional materials to expand the repository's offerings and better meet partner needs.

Major Accomplishments
- Enabled critical research to occur at the University of Dayton Research Institute and Stanford University.

Publications
None.

Outreach Efforts
To efficiently supply partners with the fuels and data they need, the ASCENT Project 101 team contacted a range of ASCENT principal investigators to ascertain their project timelines, fuel needs, and preferred reporting formats. We continued collaborating with OEMs such as Gulfstream, Airbus, Pratt & Whitney, World Energy, Montana Renewables, Monument Chemicals, and CleanJoule to align sample distribution with ongoing testing programs. By participating in the International Conference on Sustainable Aviation Research, the CRC Aviation Fuels meeting, task forces and meetings on drop-in fully synthetic aviation fuel and 100% paraffinic aviation fuel, we demonstrated the distribution processes, addressed questions about sample integrity, and highlighted the broader benefits of a centralized, FAA-prioritized repository.

Awards
- Joshua Steven Heyne - ACS Energy & Fuels, Rising Star

Student Involvement
- Conor Faulhaber distributed, analyzed, and provided experimental context for thermal stability and UVF sulfur data.

Plans for Next Period
- Expand Sample Distribution to Additional Partners: Engage with more partner institutions, both within and outside of ASCENT per FAA guidance, to assess their specific fuel sample needs. We aim to provide appropriate materials from the repository to support their research projects.



- Process and Distribute New Materials: Upon receiving additional materials from various producers, we will incorporate these fuels into the repository. These new materials will be made available to partner institutions whose research requires specific fuel properties.



Project 102 Assessment on Contrail Formation via Combustion of SAF

University of Illinois at Urbana-Champaign

Project Lead Investigator

Tonghun Lee
Professor of Mechanical Science & Engineering
University of Illinois at Urbana-Champaign
1206 W. Green St., Urbana, IL 61801
517-290-8005
tonghun@illinois.edu

University Participants

University of Illinois at Urbana-Champaign (UIUC)

- P.I.: Professor Tonghun Lee
- FAA Award Number: 13-C-AJFE-UI-053
- Period of Performance: October 1, 2024, to September 30, 2025
- Tasks:
  1. Development of Environmental Test Chamber Platform
  2. Development of Laboratory Scale Soot Generator
  3. Characterization of Aviation Soot

Project Funding Level

Federal Aviation Administration (FAA) funding level: $250,000
Cost sharing: 100% match provided by software license support from Converge, Inc.

Investigation Team

Prof. Tonghun Lee, (P.I.), All tasks
Sungho Hwang (graduate student), experimental efforts in designing and characterizing the combustor used in soot production.
Connor Malley (graduate student), experimental efforts in designing and characterizing the environmental chamber.
Anson Regi (graduate student), experimental efforts in instrumentation analysis of soot.

Project Overview

This study seeks to develop an environmental testing chamber to allow for the experimental creation and analysis of condensation trails (contrails) in a consistent and repeatable laboratory environment. The goals of this chamber will be to (1) understand the physics of contrail formation using advanced laser and optical diagnostics and potentially develop novel diagnostic methods for contrail characterization, (2) investigate contrail formation for fuels, including sustainable aviation fuels (SAF), and (3) integrate test data with both environmental modeling teams and flight-based tests. This study is done in collaboration with the Sandia National Laboratory (Livermore) where Dr. Lee is affiliated with the Sandia Faculty Loan Program.

Contrails are mainly composed of water (in the form of ice crystals) and contain a nucleus of soot particles. There is a major gap of knowledge in our understanding of the fundamental physics of contrail formation at the molecular level, but in certain supersaturate environments, contrails can form and then persist until they develop into high altitude cloud formations, which can impact the temperature of the Earth's atmosphere through radiative forcing. Due to this reflection of thermal radiation from the Earth's surface, it is believed that contrails contribute to greater than half of aviation's climate impact, the other portions being impacted by carbon dioxide (CO_2) and other greenhouse gases. This chamber aims at



studying these various factors of contrails to better inform efforts to mitigate contrail formation through flight path adjustment, improving engine technologies, and characterizing contrail development for SAFs to better predict the impact of fuel composition.

This project involves four main design considerations: (1) the environmental testing chamber, (2) the soot generating combustor, (3) soot particle parameters, and (4) the laser/optical diagnostic design. The environmental chamber is used to control the relevant conditions of contrail development in an optically accessible environment. The chamber consists of a co-flow section prior to the chamber where humidity and temperature are controlled for incoming air/soot mixtures. This is done using a chiller and heat exchanger, which cools both the chamber walls and the incoming air flow. Attached upstream of the chamber is a vacuum pump exhaust assembly that will control the pressure levels within the chamber and help regulate air speed throughout the system. The intended diagnostics systems consist of Rayleigh scattering for soot density and ice crystal formation, infrared (IR) spectroscopy absorption and optics for soot composition and water-content, and laser induced incandescence for soot diameters along with other non-in situ methods such as transition electron microscopy (TEM), elemental-to-total carbon (EC/TC) analysis, and mobility diameter analysis.

Task 1 – Development of Environmental Test Chamber Platform

University of Illinois at Urbana-Champaign

Objective

The objective of this task is to develop a test chamber. This involves defining the thermodynamic operating ranges for temperature, pressure, humidity, and air speed that are relevant to contrail formation. Once defined, the thermodynamic operating ranges inform the design of the chamber itself, and the cooling, co-flow, and exhaust systems being utilized to control the relevant thermodynamic properties, which will then be assembled.

Research Approach

The purpose of this study is to provide a controllable laboratory method for contrail formation and analysis to better inform environmental modeling of contrails and to corroborate and prevent the extensive need for expensive/difficult in-situ methods directly involving aircraft (e.g., chase planes). This is conducted by developing a controllable environmental chamber in which sample soot and cold air flow through with diagnostic access through chamber viewports and soot sample collection methods. This task is completed by utilizing a cooling co-flow upstream of the chamber and a vacuum exhaust system downstream of the chamber. The primary concern of the chamber system is the control of pressure, temperature, humidity, and air speed. The relevant formation physics of the contrails are collected using laser/optical diagnostics utilizing both in situ (through the viewports) and non-in-situ (collected soot particulate matter) methods. The properties that will be measured are soot density, soot diameter, soot composition, particle porosity, ice crystal growth, and temperature gradients within the flow as heat is transferred to create the ice crystals.

Environmental Test Chamber

The environmental test chamber is designed to mimic high atmospheric conditions in a controlled laboratory environment. It will do this through a co-flow and vacuum exhaust control system. Table 1 outlines the relevant operational ranges of the chamber. Pressure within the chamber will be able to range from 1 bar to near vacuum conditions with the standard experimental range being 0.2-0.5 bar. The temperature will have an ultimate range of 200-300K with the standard experimental range being 217K to 250K. This represents an atmospheric range of sea-level conditions to the tropopause. The maximum water content within the chamber will be roughly 1,000 ppm with the intent being able to create a supersaturated region with respect to water within the chamber. The system has the ability to add water content through wet air injections but for most experiments the water produced from combustion of the burner should be enough to create supersaturation and therefore contrails. The internal environment will be a pressure-controlled air/nitrogen gas environment with the air acting as the source for additional water content when needed. In general, internal cooling of the chamber will utilize air flow through a heat exchanger. This is due to limited supply of nitrogen through gas cylinders while filtered building air is effectively infinite. The maximum flow rate throughout the entire system will be 10 g/s with a maximum velocity of roughly 1.9 m/s. Normal experimental speeds will be significantly lower with the intent of producing the maximum residence time of 9 s with speeds as low as 0.1 m/s. The atmosphere within the system will be composed of air and nitrogen gas with soot included during operation.

Table 1. Environmental Test Chamber Operational Conditions.

Parameter	Range
Pressure	0.01-1 bar
Temperature	200-300 K
Maximum Water Content	~1000 ppm
Maximum Flow Rate	10 g/s
Maximum Chamber Speed	1.9 m/s
Maximum Residence Time	~9 s
Chamber Atmosphere	Air/N_2

The chamber design is shown in Figure 1. The chamber is double-walled stainless steel with coolant running between the walls to maintain the wall temperature to levels seen in the co-flow entering the chamber. It is roughly 13.5 in. in diameter and 35 in. tall. The inner wall has a 10-in. outer diameter while the outer wall has a 10.5-in. outer diameter. The chamber has four larger optical windows (21.75 in. by 1.75 in.) that are double-paned to allow their interior to be vacuum pumped to prevent condensation. One pair of these windows is made of Corning® 7980 fused silica, and the other pair is TSC-3 fused quartz to allow for varying spectrum transmission options for laser diagnostics. Between the windows there are twelve 2.75-in. ConFlat (CF) ports and eight 1.33-in. CF ports to allow for specialty windows or sensors. The bottom of the chamber (not shown) has six to eight equidistant holes, which the co-flow will be pumped through, centered around a smaller hole where the sample exhaust from the combustor is injected. The top of the chamber has an exhaust port that will connect to an Edwards® nES220 vacuum pump that will serve as the air speed and pressure control for the chamber. Both the top and the bottom ports are attached to 12-in. CF flanges.

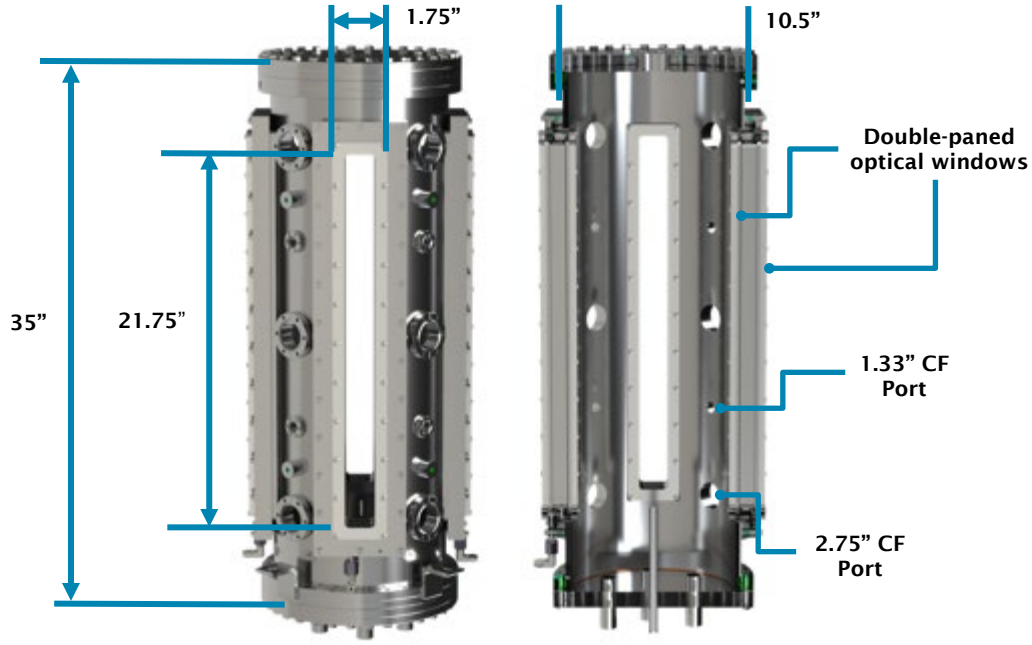


Figure 1. Environmental Test Chamber Design.

® Corning and HPFS are registered trademarks of Corning Incorporated, Corning, New York.
® Edwards is a registered trademark of Edwards Limited, Burgess Hill, United Kingdom.



Figure 2 summarizes the control system in its entirety. The co-flow system outputs "hot" air and nitrogen into a heat exchanger which cools down the flow before it enters the testing chamber. The heat exchanger uses cold TMC HFE-347 coolant fluid from a Thermonics® water-cooled chiller. The chiller has a temperature range of -80°C to +25°C with a cooling capacity of 1,800W at -80°C. It has an 8-gallons-per-minute (50 psi at 60 Hz) pump and relies on 480V, three-phase power. A portion of this coolant is siphoned off prior to the external heat exchanger to be supplied into the interior of the double-walls to decrease the chamber wall temperature. The "hot" fluid from the heat exchanger and the chamber walls are then combined again before being pumped into the chiller to be cooled again by the in-house water system. After the chamber is the exhaust vacuum system. This system includes an inline heater, control valve panel, and a vacuum pump. The inline heater is a TEMPCO® circulation heater with 6,000 W heating and a control range of 60° to 250°F. The heater raises the temperature of the exhaust from the chamber to prevent the vacuum pump from cold conditions. The control valve panel is composed of a major ball valve and two smaller needle valves. The ball valve acts as the evacuation control and is used during the chamber cooling phase and general pressure-down of the chamber. The needle valves then act as the flow rate controls during experimentation by limiting the pull of the pump in the chamber to control the flow speed. The vacuum pump is an Edwards® nES220 single stage rotary vane pump with an ultimate vacuum of 0.08 mbar and pumping speeds of 125 cfm. This pump is what brings the chamber down to experimental pressures. The last major section of the experimental platform is the soot generating combustor which burns liquid aviation fuel and sends portions of the soot to the chamber and to a diffusion dryer for soot instrumentation.

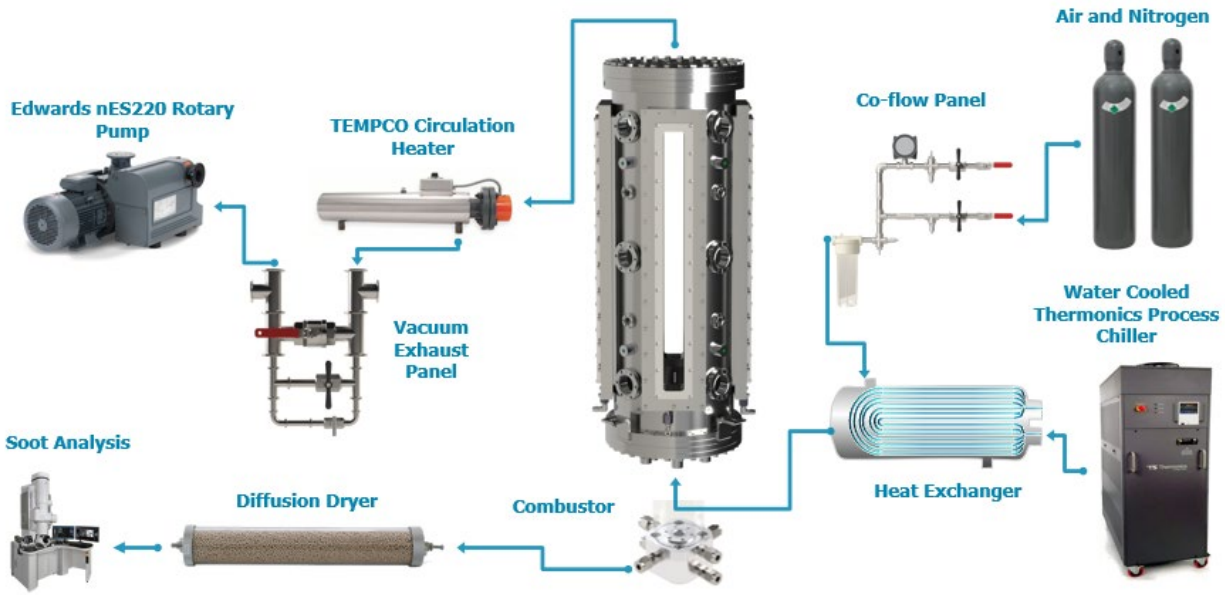


Figure 2. Control system overview.

The final portion of the chamber design is a smaller chamber shown in Figure 3. This chamber is roughly 6 in. in diameter and 16 in. in height. This chamber would focus exclusively on the initial nucleation of soot for contrails and have the advantage of shorter cooling times with the drawback of shorter residence times. It was designed with the intention of even faster experimentation for focused areas and for easier transportation with the intent of utilizing it to take experimental data using instrumentation at national laboratories that we may not have direct access to. The new chamber would have roughly 27% of the internal volume and 27% the internal surface area of the larger chamber and would have roughly half the residence time. It is expected to drop the 3-hr required cooling time of the larger chamber to roughly 1 to 1.5 hr of cooling time depending on coolant flow rates within the interior of the walls.

® Thermonics is a registered trademark of Temptronic Corporation, Mansfield, Massachusetts.
® TEMPCO is a registered trademark of TEMPCO Electric Heater Corporation, Wood Dale, Illinois.
® Edwards is a registered trademark of Edwards Limited, Burgess Hill, England.

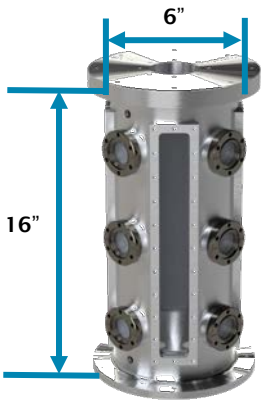


Figure 3. Small experimental chamber design.

Task 2 – Development of Laboratory Scale Soot Generator

University of Illinois at Urbana-Champaign

Objectives

The objective of this task is to develop a soot generating combustor for liquid aviation fuel. This combustor is designed to evaporate and burn such fuel in varying ways with the intent of modulating soot parameters. By modulating such parameters, specific physical and chemical considerations may be explored within the contrail chamber to determine the impact of soot parameters on ice crystal nucleation. The soot parameters of interest are primary particle diameter, mobility diameter, EC/TC ratio, and porosity. This starts with an objective of stabilizing and characterizing the flame to ensure consistency in soot production.

Research Approach

The soot particulate matter (PM) is provided to the chamber through the burning of liquid aviation fuel in a fully characterized soot generator. The generator has the primary goal of controlling PM sizes and maintaining a relatively uniform PM size of roughly 10-30 nm in diameter. It also has the goal of developing soot that can mimic the EC/TC ratio of aviation-derived soot, which has a value of roughly 0.75-0.8. Other relevant soot parameters that may be researched are mobility diameter and porosity. To confirm the ability of the soot generator to create soot of varying features, multiple fuels are tested and different equivalence ratios, mixing speeds, and mixing geometry. Stability and efficiency of the combustor is studied through oscillation observations, carbon monoxide (CO) emission index, and hydroxyl radical (OH*) chemiluminescence.

Combustor Design

The combustor has been completed and is shown in Figure 4 below. It is made of aluminum and is modular to allow for iterative designing. Its main components are the gas ports for air, nitrogen, and methane gas, an interior cavity, a pilot flame ring, and a quartz tube for soot collection and flame stability. The gas ports are 1/4-in. npt to 1/8-in. Swagelok® tubing. The output for the pilot flame is composed of two concentric rings of 0.04 in. diameter holes. The combustor is roughly 60 mm in width, and the fuel exhaust is 12 nm in diameter. Fuel is injected with a 1.6 mm inner diameter tube. The combustor is 2.36 in. wide in a square shape at its further edges with rounded corners with a radius of 0.59 in. The height of the combustor is 1.57 in. without the pilot flame plate and 1.75 in. with the pilot flame plate. The three modular components of the combustor are secured with four 18-8 stainless steel socket head screws, and the different components are sealed from fuel leaks using o-rings. The pilot flame plate is secured to the top of the modular combustor using six 18-8 stainless steel hex drive flat head screws. The combustor is secured to a raised aluminum breadboard with two M5 screws to allow fuel to be evaporated and injected underneath the combustor. This evaporation is done using either a Bronkhorst evaporation unit or an insulated inline heater. The internal geometry is shown in Figure 5.

® Swagelok is a registered trademark of Swagelok Company, Solon, Ohio.

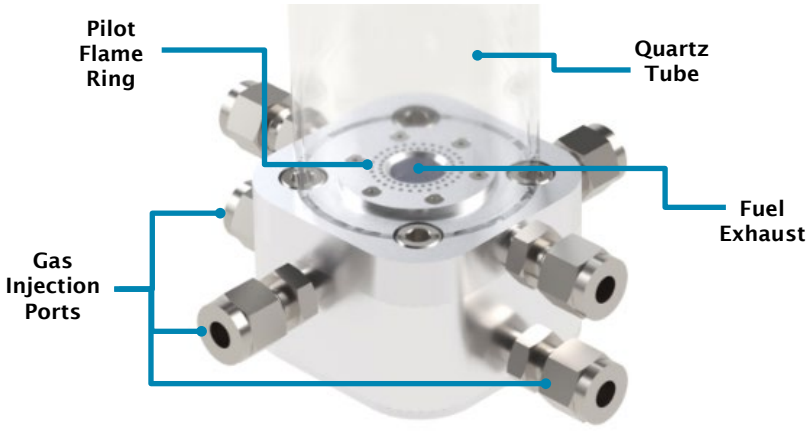


Figure 4. Soot-generating combustor.

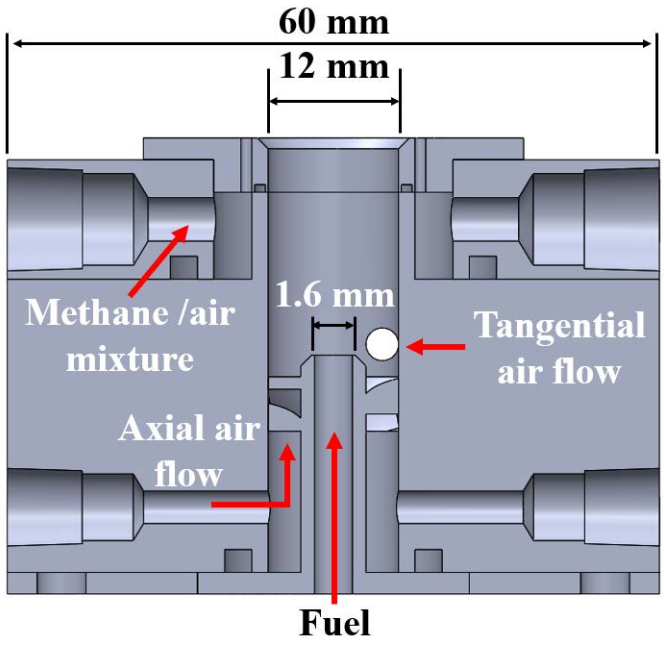


Figure 5. Combustor internal geometry.

The internal geometry of the combustor is composed of fueling sections, the mixing cavity, and the inner bodies. Axial air enters parallel to the injected fuel stream and provides the bulk of the upwards momentum to the flow. Tangential air is injected directly above the fuel at off-axis locations to provide swirl mixing to the flow within the mixing cavity. Methane and air are mixed outside of the combustor and injected into the top where they exit through a ring of miniature injection ports where it is ignited by a lighter during experimentation. A summary of the external injection scheme is shown in Figure 6.

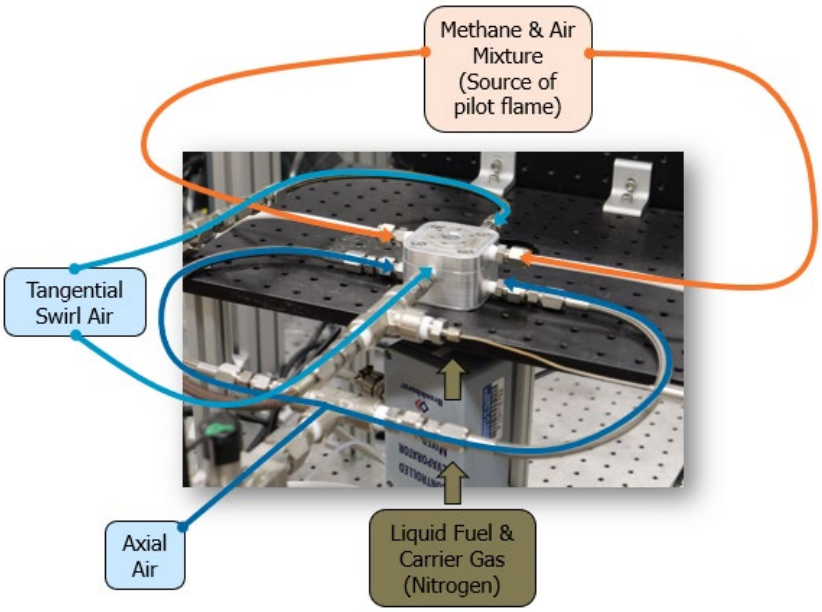


Figure 6. Combustor experimental platform.

The combustor experimental platform is summarized. It is important to note that liquid aviation fuel is evaporated within a Bronkhorst evaporation unit before being carried by nitrogen gas to be injected into the mixing cavity of the soot generating combustor. Different inner bodies are also utilized within the interior of the combustor to modify the momentum of the axial air injection with the intent of producing different mixing environments within the mixing cavity. These inner bodies are shown in Figure 7.

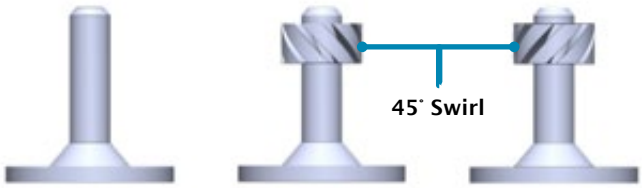


Figure 7. Combustor inner bodies.

There are three inner bodies of interest. The first is the straight body, which is the base case that adds no change to the axial air flow. The second is the uni-flow body, which adds swirling momentum to the axial air flow in the same rotational direction as the tangential air flow. The last is the counter-flow body, which swirls the axial air flow in a counter rotating pattern relative to the tangential flow, providing the highest level of mixing within the combustor cavity while also reducing the net momentum of the swirl. The inner bodies are all made of three-dimensional printed stainless steel from Protolabs Inc.

Combustor Characterization

The combustor was tested for flame stability and combustion efficiency. The goal was to define the conditions which influenced the stability of the flames as this was thought to have an impact on the uniformity of the soot production. There was also an interest in the efficiency of the combustor based on the different inner bodies. One of the primary methods used to stabilize the flame was heating of the injected air lines. It was believed that heated air would reduce the chances of fuel recondensing and decrease temperature gradients within the gas mixture of the cavity. The results of this are shown in Figure 8 below. Oscillation was determined visually based on fluctuation in the maximum height of the flame. Flames



that rapidly cut their heights in half in cycles were deemed oscillatory. The evaporation temperature of the fuel was modulated along with the temperature of the injected air to determine the impacts on the flame stability. When using the straight body, it was found that oscillation was experienced when the evaporations temperature was greater than the air temperature. For the two swirling inner bodies, oscillation only occurred when the evaporation temperature was greater than 433.15 K for all air temperatures tested. This demonstrated that for the straight body, increased air temperature improved stability, and for the swirlers the stability is dependent solely on the fuel evaporation temperature.

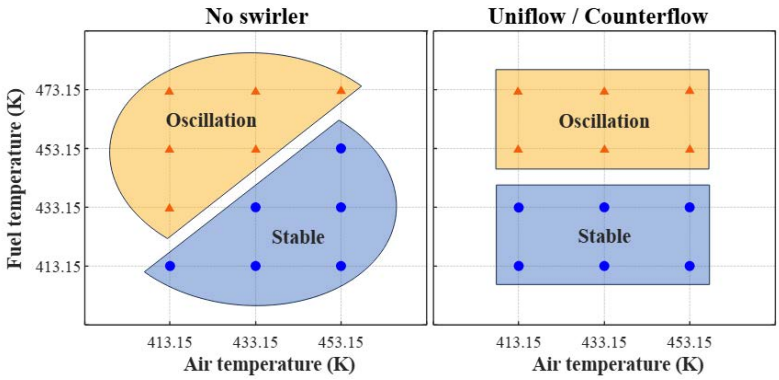


Figure 8. Impact of temperature on flame oscillation.

Combustion efficiency was determined to understand the mixing triggered by the various inner bodies and the effective production of soot. It was defined through the emission index of CO gas (grams of CO per kg of fuel) using an MRU™ AMPRO plus combustion and emission analyzer placed above the flame. The results are shown in Figure 9. Within Figure 9, "F1" represents the straight body, "F2" the uni-flow body, and "F3" the counter-flow body. The emission indexes were studied for lean flames as they were expected to best represent turbine combustion with regards to primary particle diameter. There was no trend with the straight body, but it was about an order of magnitude greater in values than the swirler bodies with the range of 20-25 g/kg. The swirlers saw roughly the same values with emission index decreasing as the equivalence ratio approached stoichiometric. This indicated that the swirlers increased mixing in the combustor as expected. As a result, it would be expected that the combustor would produce less soot when utilizing those bodies for the same equivalence ratios compared to the straight body.

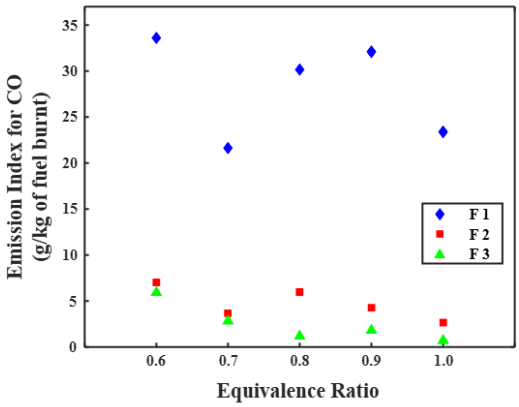


Figure 9. Emission Index for carbon dioxide (CO).

™ MRU is a trademark of MRU Instruments, Inc., Humble, Texas.

The final method of characterization for the combustor was OH* chemiluminescence imaging. Representative snapshots for each inner body are shown in Figure 10. This provided a qualitative indication of the location of the flame front and heat release zone. This gives a general sense of how well mixed the gases in the flame are, and therefore how efficient the combustion is. The emitted light of OH* molecules were collected using a band pass filter (310 nm) attached to a Cerco 100 mm ultraviolet (UV) lens (f/2.8). A HighSpeed IRO (LaVision®) UV intensifier was used in conjunction with a FASTCAM SA5 (Photron®) to collect the images. From left to right, (a) is the straight body, (b) is the uni-flow body, and (3) is the counter-flow body. The straight body had OH* molecules along the bottom and sides of the flame structure, which suggested that the air did not penetrate the fuel jet significantly, resulting in insufficient mixing. The uni-flow body had OH* molecules throughout the entire flame, indicating even mixing and heat release relative to the straight body. Lastly, the counter-flow body showed a similar level of mixing to the uni-flow body but with more vibrant emission. This suggested increased turbulence that resulted in a higher heat release and mixing compared to both the straight and the uni-flow bodies.

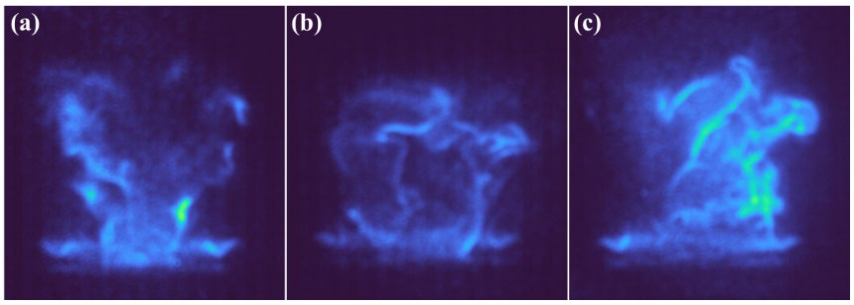


Figure 10. Hydroxyl radical chemiluminescence imaging. From left to right, (a) is the straight body, (b) is the uni-flow body, and (3) is the counter-flow body.

Task 3 – Characterization of Aviation Soot

University of Illinois at Urbana-Champaign

Objectives

The objective of this task is to characterize the soot parameters of soot derived from burning aviation fuel. The first tests burnt Jet-A fuel (properties shown in Table 2) to be used as a reference point, while later tests will focus on alcohol-to-jet (ATJ) and CycloSAF. The parameters of interest are primary particle diameter, EC/TC ratio, mobility diameter, and porosity.

Research Approach

The soot from these experiments is analyzed through a JEOL® 1200 transmission electron microscope (TEM) and a Sunset® carbon aerosol analyzer. After a stable flame is created for a desired equivalence ratio and inner body, soot is collected through a port within the quartz tube. A pump pulls soot from above the flame through this port into insulated lines that lead to a diffusion dryer filled with activated alumina desiccant beads to remove any water moisture from the stream. The soot is then collected onto a quartz filter where it can be weighed by a Thermo Cahn C-31 microbalance. The soot is then transferred to a copper grid for TEM or placed directly into an organic and elemental carbon analyzer utilizing the NIOSH 930 protocol.

® LaVision is a registered trademark of LaVision GmbH, Gottingen, Germany.
® Photron is a registered trademark of Photron Limited, Tokyo, Japan.
® JOEL is a registered trademark of JEOL LTD., Tokyo, Japan.
® Sunset is a registered trademark of Sunset Laboratory Incorporated, Beaverton, Oregon.



Table 2. Jet-A 10325 Fuel Information.

Parameter	Range	Chemical Compound	Percent
CAS # (Kerosine)	8008-20-6	alkylbenzenes	12.90%
CAS # (Naphthalene)	91-20-3	diaromatics	2.33%
Freezing Point (°C)	-56 to -39	cycloaromatics	3.28%
Boiling Range (°C)	134 to 294	n-parafins	19.98%
Flash Point (°C)	42-62	iso-parafins	29.69%
Flammability in air (%)	0.4-5.0	monocycloparaffins	25.07%
Relative Density	0.7-0.82	dicycloparaffins	6.55%

Soot Characterization

Figure 11 shows representative images of soot particles for primary particle diameter (PPD) measurements imaged using a JEOL JEM-2100 TEM. Only some preliminary images have been taken so far. One measured sample so far is from the uni-flow inner body with a burner equivalence ratio (EQ) of 2 for Jet-A fuel. The mean PPD for this soot taken from roughly 50 particle measurements was 19.2 nm with a standard deviation of 3.32 nm. Another sample was taken from the straight body with an EQ of 1.4. The mean PPD was 20.04 nm with a standard deviation of 3.53 nm. The last condition studied to this date was the straight body with an EQ of 2. The mean diameter of this sample was 20.81 nm with a standard deviation of 5.06 nm. This is promising as it is representative of the expected 20-50 nm range for aviation soot with minimal variation in soot size.

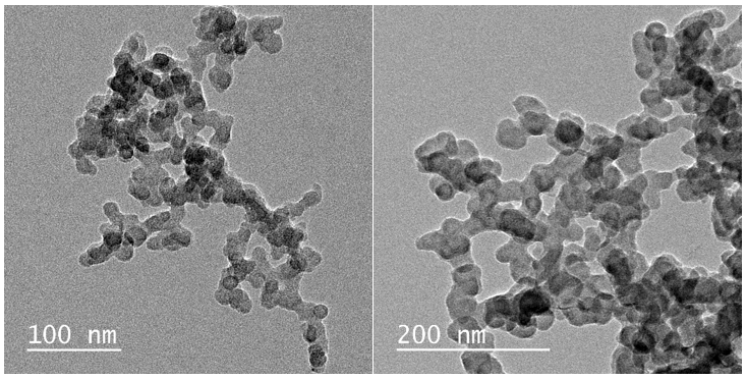


Figure 11. Example transition electron microscopy (TEM) images for Jet-A fuel.

Figure 12 presents the soot mass production per minute for varying EQs of Jet-A fuel. For the uni-flow and counter-flow bodies the mass production increases with EQ up to EQ = 3. From there, both bodies experience a drop before the counter-flow continues to increase at EQ = 4. The production for the straight body was too inconsistent but shows a general trend of increasing with EQ. It is theorized that the inconsistencies seen within this data are caused by the fixed sampling height of the collection port along the quartz tube. Because the sampling port is at a fixed height of roughly 8 in. above the combustor, it is possible that different flame heights with changing EQ is leading to different amounts of soot being collected. Lower heights may be losing too much soot to the open atmosphere above the tube as it has more time to spread to the edges of the tube and out the top. Too high flames may also be causing too much soot to be collected as the flame may be interacting with gases and soot inside the collection port causing reburn and reoxidation or even prevent soot from being collected as it is released from the flame above the collection port. An adjustable port will be designed.

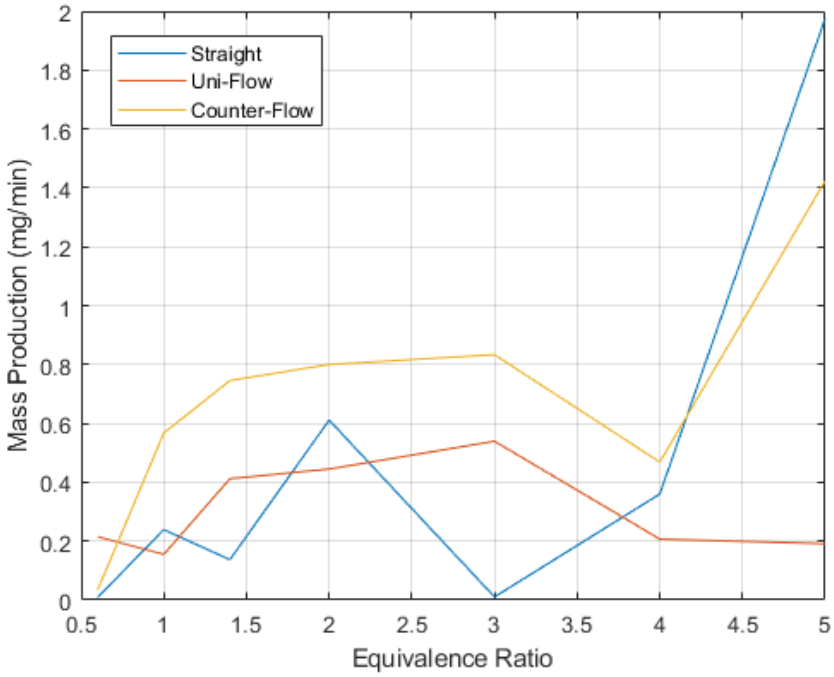


Figure 12. Soot mass production for Jet-A fuel.

Figure 13 shows the EC/TC data for varying EQ of Jet-A fuel. An increase in EC/TC is expected with increase in EQ. This held true for the straight and counter-flow bodies until EQ = 2 where the EC/TC ratio proceeded to drop. For the uni-flow body, this held true until EQ = 1.4 and then occurred again after EQ = 3. It is believed that the deviation from the expected trends also resulted in this case from the fixed height of the collection port. Soot collected from taller flames may be collected from within the flame itself and as a result lack the needed exposure to oxygen from the ambient atmospheric air need for the oxidation to mature the soot. However, there seems to be a consistent trend of dropping EC/TC ratio after a peak point and this may be the result of the methodology of the burns. These experiments modified the air flow rates and kept the fuel flow rates fixed for the rich conditions to preserve fuel and because there was a limit to fuel supply due to the diameter of the fuel injection. This not only impacts the mixing as the Reynolds number changes with change in air momentum but also means there is less overall air within the quartz system. This means that for richer conditions there may not be enough oxygen within the quartz tube to properly oxidize the soot as expected. It is recommended that both an adjustable collection port be implemented along with modulating fuel rates while keeping air rates the same.

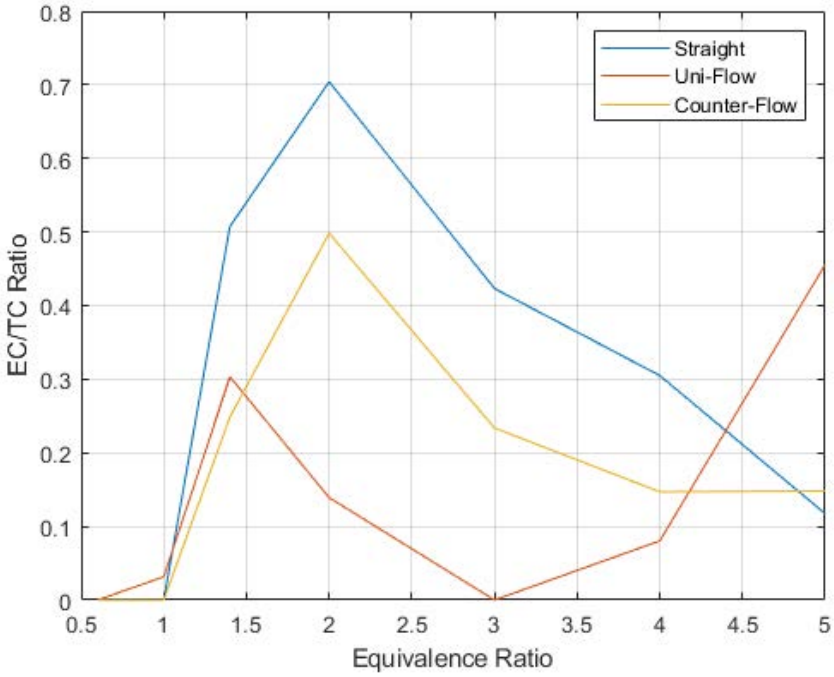


Figure 13. Soot EC/TC Ratio for Jet-A fuel.

Milestones

- Finished manufacturing of the chamber and control systems (at 3 months).
- Finished design and manufacturing of the laboratory-scale soot generating combustor (at 6 months).
- Finished characterizing the stability of Jet-A fueled flames and began to characterize ATJ, CycloSAF, and hydro-processed renewable jet (HRJ) fuel flames (at 9 months).
- Finished analyzing primary particle diameters, soot mass production, and EC/TC ratio for varying equivalence ratios of a Jet-A flame (at 12 months).

Major Accomplishments

The most important accomplishment to date is the establishment of a partnership with the Sandia National Laboratory (Livermore), of which Dr. Lee is now an employee. The Sandia National Laboratory has already developed their own contrail chamber, and with their advisement, we have been able to properly identify operation goals and methods to explore in the development of our own chamber. We have finished development and stability characterization of our own laboratory-scale soot generating combustor that burns liquid aviation fuel and are in the process of characterizing the soot production.

Publications

None.

Outreach Efforts

All test data will be made accessible through https://altjetfuels.illinois.edu/.

Awards

None.



Student Involvement

This project was conducted by PhD student, Sungho Hwang, who is developing the combustor for the chamber; PhD student, Connor Malley, who is developing the chamber and stabilizing the flame; and master's student, Anson Regi, who is developing the soot diagnostic systems.

Plans for Next Period

Our plan for the next period is to fully characterize the limits of the soot production for the combustor. This involves finishing the data for primary particle diameter and EC/TC while also collecting new data on mobility diameter and porosity for Jet-A. This will be done by modulating the equivalence ratios and inner bodies of the combustor. We also intend to collect data for ATJ, HRJ, and CycloSAF fuels. For the contrail chamber, characterization will consist of confirming operational environmental ranges for temperature, pressure, humidity, and air speed. After both characterization tasks are complete, the ASCENT Project 102 team will develop a test plan and perform our first attempt at creating a contrail in a controlled experimental environment utilizing generic fuel (e.g., Jet-A fuel). This will involve using our laser/optical diagnostics to gather data on soot density, diameter, composition, and ice crystal growth.

Project 103 Pareto Efficient SAF Yield and Blending

Washington State University

Project Lead Investigator

Joshua Heyne
Bioproducts, Sciences, and Engineering Laboratory Director, Associate Professor
School of Engineering and Applied Science
2710 Crimson Way, Richland, WA 99354
(937) 229-5319
joshua.heyne@wsu.edu

University Participants

Washington State University

- P.I.: Dr. Joshua Heyne
- FAA Award Number: 13-C-AJFE-WaSU-044
- Period of Performance: October 01, 2024, to September 30, 2025
- Tasks:
  1. Distillation optimization tool and procedure improvement
  2. Vapor pressure measurement for sustainable aviation fuel (SAF)

Project Funding Level

The Federal Aviation Administration (FAA) provided $350,000 in funding; cost sharing is provided by Air Company ($200,000) and Trinity College Dublin ($150,000).

Investigation Team

Washington State University

Joshua Heyne (P.I.), Coordinating all team members (both ASCENT and non-ASCENT efforts) and communicating distillation results with SAF producers.
Randall Boehm, Research Engineer, Overseeing the project and providing guidance.
Zhibin (Harrison) Yang, Research Engineer, Conducting distillation optimization and property measurements.
Alexander Kelly (Ph.D. student), Conducting distillation and modeling.

Project Overview

The ASCENT Project 103 supports the conversion of pilot-scale bio-crude samples into plausible aviation fuel blend components, up to 100%, with the balance coming from a petroleum distillate. For non-selective sustainable aviation fuels production processes, the product stream could contain species ranging from as few as five to many (>26) carbon atoms per molecule (distillation range, 36°C to greater than 450°C), which is broader than the jet fuel range. In these cases, distillation can be used to separate the product stream into fractions, where the monetary value of each fraction varies based on contemporary policies, and the properties of that fraction. While this is essentially the same process as petroleum refining, the population distribution of different molecular species within a given distillation cut could be markedly different depending on the pathway, and composition differences result in significant property differences.



Task 1 – Distillation Optimization Tool and Procedure Improvement

Washington State University

Objectives

The objectives of this task are intended to improve the current distillation optimization tool, Jet Fuel Blend Optimizer (JudO), and procedures associated with distillation processes to improve yield for a given SAF candidate while keeping the properties within the specification limits.

Research Approach

Introduction

Volatility properties of jet fuels are known to have some impact on the safe operation of aircraft. As such, certain representative properties are specified in governing specifications such as ASTM D1655 (ASTM International, 2023), DEF STAN 91-091(Ministry of Defence, 2025), and GB/T 6539-1997 (State Bureau of Technical Supervision, 1997). The flash point relates to aircraft-level fire safety. The initial boiling point relates to fuel pump cavitation and fuel control instabilities that could be caused by two-phase flow. The temperature at which 10% of petroleum-derived jet fuel (T10) has vaporized is correlated with engine ignition characteristics. During thermal soak-back after a jet engine is shut off, the vapor pressure inside the closed circuit from the fuel metering unit to the fuel nozzle valves could exceed the valve cracking pressure and lead to fuel burping into the fuel nozzles where it can bake until it turns to coke. A similar phenomenon can happen during part-power operation, when some fuel circuits are turned off (called staging). The dry-out rate of passively purged, staged fuel circuits, similar to droplet evaporation rates, depends on the mass transfer rate, vapor pressure and liquid-phase surface area. Finally, the end point of the distillation is correlated with combustor coking and unburned hydrocarbon emissions. None of these relationships are one-to-one. Moreover, the above listing of operating concerns that could potentially be impacted by fuel properties is not exhaustive. Indeed, an exhaustive list of potential concerns is not generally known (Colket & Heyne, 2021). Motivated by such known and unknown factors, two volatility properties, (T50–T10) and (T90–T10), where the subscript refers to the volume fraction distilled, were added as “extended requirements” in the quality specification, ASTM D7566 (ASTM International, 2022a), governing aviation turbine fuels containing synthesized hydrocarbons.

Specifically, the rate of evaporation across a plurality of temperature, convective, and dwell time conditions is directly related to potential operating concerns. Unlike measure temperature (Tn), the vapor pressure (P_{vap}) of fuel droplets or sheets is directly proportional to their evaporation rate under all operating conditions. The importance of this is recognized by the community, and as such, the vapor pressure as a function of temperature is listed as a Tier 2 property in ASTM D4054 (ASTM International, 2023). While maintaining an approximate match to a family of P_{vap} versus temperature curves derived from a representative survey of petroleum-derived jet fuels is a prudent goal for developers of SAF or other fuels with synthetic components, it is neither sufficient nor necessary in all circumstances.

SAF and synthetic blending components (SBC) are considered mid-term solutions to help decarbonize the aviation sector by 2050 (IATA, 2025). The term SAF is primarily used in policy and regulatory contexts, whereas SBC is the corresponding technical term used in fuel qualification standards. Currently, SBCs are limited up to 50% by volume when blended with conventional jet fuel, because some pathways (e.g., hydroprocessed esters and fatty acids synthetic paraffinic kerosene) lack certain hydrocarbon classes such as aromatics, which are necessary for elastomer swelling and ensuring proper fuel system performance. To overcome this limitation and enable 100% synthetic ‘drop-in’ jet fuels, the aviation community is exploring blending multiple ASTM D7566 annexes. However, original equipment manufacturers (OEM), prioritizing safety and reliability, have emphasized the need to evaluate ASTM D4054 Tier 2 or fit-for-purpose (FFP) properties to ensure that fully synthetic fuels meet operational requirements. Measuring all FFP properties experimentally is costly and often beyond the capabilities of many refineries. As a result, the ability to accurately predict FFP properties, particularly volatility and vapor pressure, has become a high priority within the fuel community, as it would accelerate certification, enable higher SAF blend limits, and ultimately support aviation decarbonization efforts.

The chemical (and, to a lesser extent, transport) properties of fuel vapor vary throughout the evaporation time scale, and so do the volatility properties of the liquid that have yet to evaporate. Chemical properties (represented by the derived cetane number, radical index, threshold sooting index, etc.) play an important role in lean blowout, non-volatile particulate matter (nvPM) emissions and the rate of heat release during combustion, indicating a potential impact on combustion dynamics, combustor temperature distribution and combustion efficiency, for example. The composition of the remaining liquid, in tandem with the temperature at its interface with air, determines its vapor pressure and hence its evaporation



rate for the relevant transport conditions. All these variances are hereafter referred to as preferential evaporation in this article.

Property models that neglect to track changes in liquid-phase composition throughout the evaporation time scale sacrifice the capability to directly capture the impact of preferential evaporation. However, through correlation with specific points on the ASTM D86 (ASTM International, 2024a) distillation curve, some indirect capturing of preferential evaporation may occur, provided that the relative population distribution of each type of hydrocarbon in the boiling sample is similar to the database of fuel samples from which the model was built. Mendes et al. (2017) published a regression model to predict the Reid vapor pressure (P_{vap} at 37.8°C) of conventional gasoline based on its ASTM D86 distillation curve. Two groups (Cooper et al., 1995; Flecher et al., 1997) published separate regression models built from Raman spectrographic data to predict Reid vapor pressure and octane numbers of petroleum fuels. Flumignan et al. (2008) built a regression model built from chromatographic data to predict the density, distillation curve and octane numbers of Brazilian gasoline, while Côcco et al. (2005) used chromatographic data of 25 samples to build an artificial neural network model to predict the density, distillation curve and Reid vapor pressure of Brazilian gasoline. It is unknown whether any of these models capture the impact of preferential evaporation, even for petroleum-derived gasoline, or whether any are valid for jet fuel range hydrocarbons.

Other notable examples of simulated ASTM D86 distillation curves include ASTM D2887 (ASTM International, 2024b) (which employs chromatographic data) and the work of Mondragon and Ouchi (1984) (which employs thermogravimetric data). The intense interest around this task is a testimonial to its value, which appears to be rooted in the reduction in sample volume required to determine properties that are controlled by some quality specification. Not only do such models neglect to directly capture the impact of preferential vaporization, but they offer little value to efforts, such as those described by Miller et al. (2022), to maximize biomass in SAF by optimal selection of distillation fractions or other refinement processes of the synthetic blend component. Furthermore, such models, barring a simulation of the base data, do still necessitate some mass of representative sample to obtain the input data.

Within the so-called tier-α suite of property models published by Yang et al. (2021), vapor pressure is calculated by Dalton's Law, with partial pressured calculated by Raoult's Law, and simulated D86 distillation is carried out by incremental mass extraction per the composition of the simulated vapor phase. Miller et al. (2022) now execute simulated distillation using this same approach and have observed significant error in the prediction of T90. Such error could stem from distillation assumptions (e.g., the number of theoretical plates), inaccurate composition input or propagated errors in components' vapor pressures.

In a provocative article published in 1995, Hawkes (1995) proclaimed that Raoult's Law is deceptive, which is somewhat interesting in that Wilson's model of activity coefficients was introduced in 1964 (Wilson, 1964), and it was already common by then, in some circles, to use activity coefficients to scale the partial pressures that are predicted by Raoult's Law to arrive at a more accurate description of the vapor–liquid-phase equilibrium. By 1975, the unsettling fact that vapor–liquid equilibrium data were needed to determine one or more of the parameters used in the Wilson model (and several of its off-shoots) was addressed by Fredenslund et al. (1975) by relating these terms to groups (e.g., >C<, -CH_3, aromatic CH, etc.) that are contained in all molecules where the contributions from each group were determined by fitting to vapor–liquid equilibrium data for a variety of binary mixtures, which in theory would permanently establish these contributions so they could be used without modification for other molecules and mixtures that were not part of the original database. This model is called the UNIFAC (UNIQUAC Functional-group Activity Coefficients) model and is included in publicly available software such as Aspen Plus, DWSIM, and ChemCAD. It is simple enough to be implemented within a spreadsheet such as Microsoft® Excel®, which is what we did to enable comparisons with the new model presented in this work. This spreadsheet is included in the Supplementary Materials, entitled, "UNIFAC Vapor Pressures." Yet more fundamental models based on intermolecular potentials (RGEMC) (Lisal et al., 1999) or simulated osmotic pressure (OMD) (Crozier & Rowley, 2002) are available in molecular dynamics software such as LAMMPS, while Reference Fluid Thermodynamic and Transport Properties Database (REFPROP) (Lemmon et al., 2013) employs mixing rules to develop an equation of state for the mixture (Kunz & Wagner, 2012) from which many properties can be calculated, including vapor pressure.

Here, our goal is to evaluate simpler corrections to Raoult's Law as fuels comprise thousands of different molecules, and simulated fuel distillations may require several thousand determinations of the vapor–liquid equilibrium. Among these thousands of molecules, only seven carbon types are significantly represented; four aliphatic carbon types (-CH_3, -CH_2-,

® Microsoft and Excel are registered trademarks of Microsoft Corporation in the United States and other countries.



>CH- and >C<) and three aromatic carbon types (protonated aromatic carbon, substituted aromatic carbon and bridgehead aromatic carbon). Within UNIFAC, four terms are used to represent the four aliphatic carbon types, and two terms are used to represent aromatic carbon, protonated or not protonated. In contrast, we are not distinguishing between carbon types or molecular structure. Rather, we acknowledge that every molecule is forced into an environment determined by the liquid mixture's Gibbs energy minima, which differs significantly from that of pure liquids and is the root cause of a non-zero heat of mixing. While the magnitude of the heat of mixing is approximately 500 times less than the magnitude of the heat of vaporization, we postulate that enthalpy difference can have a significant impact on the vapor pressure of each liquid mixture component. The main effect on the heat of mixing of jet fuel-range hydrocarbons is the mole fraction, not molecular structure, so here we develop a model framework that is based exclusively on mole fractions as input and a tuning database of binary mixture vapor pressures where the (much) more volatile component is present at mole fractions ranging from 0.01 to 0.09. Over this range of mole fractions, the traditional activity coefficient approach to correcting Raoult's Law is not validated to the best of the authors' knowledge.

The approach we considered is described below. Then, we describe the materials, test conditions and testing methodology used to support determination of the adjustable parameters of this modeling approach, and the derivation of empirically based correction. Validation of the resulting model is accomplished by comparing modeled vapor–liquid equilibrium systems with experimental measurements. Finally, a summary of the major findings of this study is presented in the "Results" and "Conclusions" sections.

Theory

Background

The earliest model of vapor pressure can be traced back to Clapeyron (1834), nearly 190 years ago. Since then, many model refinements have been published, starting with Clausius (1850), who published the form that is found in many current physical or general chemistry textbooks. These models relate the vapor pressure of a liquid to its latent heat of vaporization (ΔH_{vap}) and imply that ($\Delta H_{vap}/R$) equals the slope of $\ln(P_{vap})$ versus inverse temperature $(1/T)$. Interestingly, the general form of this model can also be derived from kinetic theory, although it was originally conceived entirely from fundamental principles of thermodynamics. Trouton (1884) shared a recognition that the entropy of vaporization at the ambient pressure of most liquids is approximately the same, 87.3 $J{\cdot}K^{-1}{\cdot}mol^{-1}$, which implies that ΔH_{vap} is directly proportional to the normal boiling point.

By definition, the vapor pressure of a substance is the pressure at which the rate of adsorption of gaseous molecules that strike the surface of a liquid equals the rate of desorption of molecules from the surface of that liquid. The evaporation rate is the difference between the rate of desorption and the rate of adsorption and goes to zero at equilibrium. Theoretically, the rate of desorption of any component in a liquid mixture could be limited by the diffusion of volatile molecules to the surface or by the fundamental process of desorption.

As accommodated by Antoine (1888) semiempirical correction to the vapor pressure model, the activation energies of whatever steps control the rate of desorption in pure materials are not generally equal to ΔH_{vap} as, by definition, ΔH_{vap} is the enthalpy difference between the liquid and gaseous phases of the material. The activation energy is coincidentally nearly equal to ΔH_{vap} in many systems. However, the desorption process could occur in multiple steps, and the activation energy governing the rate of each step is, more likely than not, greater than the energy difference between the two geometrical configurations that define the step. In other words, even for pure materials, the slope of $\ln(P_{vap})$ versus inverse temperature $(1/T)$ could be higher or lower than ΔH_{vap}.

As recognized by Antoine (1888) and many authors since then Poling et al. (2001), $\ln(P_{vap})$ is not exactly linear with $(1/T)$, which suggests that the rate limiting steps in the desorption process are influenced by the bulk change in molar volume as temperature varies. In other words, it matters how many first or second nearest neighbors to a desorbing molecule are vacant. By extension, it should also matter how many first or second nearest neighbors are heterogeneous molecules. To estimate the order of magnitude of this effect, we compare the heat of mixing, which is approximately 25 J/mol (Lundberg, 1964) for jet fuel-range hydrocarbons, to the heat of vaporization of a representative fuel molecule, n-dodecane, which is 44,000 J/mol. While the heat of mixing has a small (<0.1%) impact on the heat of vaporization, its impact on the desorption rate is approximately 0.6% at the normal boiling temperature of n-dodecane. Intuitively, this impact increases as the mole fraction decreases because molecules of this mixture component are progressively less likely to have homogeneous neighbors as the mole fraction decreases.



For a more fundamental description of the relationship between the molecular arrangements in the condensed phase and the mobility of molecules or vacancies within the condensed phase, the reader is referred to Gaudin and Ma (2020). Briefly, in the condensed phase (the liquid), the desorbing molecule from a mixture sometimes originates (departs) from a shallower (potential energy surface) well than it would if it were not mixed with heterogeneous molecules, but essentially never originates from a deeper well. This is because optimal molecular packing in the condensed phase occurs when all the molecules are the same size and solutes are essentially forced into a packing arrangement that is determined by the solvent. The corresponding transition state, however, is less impacted by the mixture-induced geometric distortions of the condensed-phase lattice. This results in a lower effective activation energy. Quantifying this energy difference from first principles would be very difficult. Instead, we simply acknowledge that it should be lower and dependent on the mole fraction and use measured vapor pressures to gage its magnitude.

Raoult's Law, in combination with a somewhat modified version of the Clausius–Clapeyron equation, is reproduced here as Equation 1, where x_i is the mole fraction, P_{ref} is 1 atm, $T_{ref,i}$ is the normal boiling point of pure component *i* and the remaining term is expanded below. The activation energy ($E_{a,i}$) varies with temperature and the actual vapor pressure of pure component *i* according to Equation 2, such that Equation 1 returns a correct vapor pressure at all temperatures, within the range of the data, when the mole fraction is unity. Pragmatically, an Antoine equation or a Wagner (1973) equation is used to represent discrete ($T, P_{vap,i}$) data points continuously, for each pure component. A spline is used to represent $E_{a,i}$ over the range of temperature ±5°C from the normal boiling point.

$$P_{vap,i} = x_i * P_{ref} * \exp\left[\left(E_{a,i} \,/\, T_{ref,i}\right) * \left(1 - \left(T_{ref,i} \,/\, T\right)\right] \right. \quad \text{(Eq. 1)}$$

$$E_{a,i} = \ln\left(\frac{P_{vap,i}}{P_{ref}}\right) / \left[\left(1 \,/\, T_{ref,i}\right) - (1 \,/\, T) \right] \quad \text{(Eq. 2)}$$

The reason why Equation 1 fails to accurately represent the actual partial pressure of component *i* in the vapor phase ($P_{vap,i}$) is not just because $E_{a,i}$ varies as the identity of nearest neighbors changes but also because the reference temperature ($T_{ref,i}$, the temperature at which $P_{vap,i} = x_i * 1$ atm) varies as the effective surface area of the ith component, its concentration, varies. The desorption rate scales with the mole fraction (surface coverage) while the adsorption rate does not. In other words, both ($E_{a,i}$) and ($T_{ref,i}$) are concentration-dependent but the conventional approach to remediate the failure of Raoult's Law is to maintain each of these terms as constant and instead scale the resulting partial pressure by an activity coefficient, which depends not only on the identity of the *i*th component but also on its concentration, the temperature of the system and the identity and concentration of every other component in the mixture. Here, we evaluate simpler ways to make this correction.

Data Reduction Strategy

We consider replacing ($E_{a,i}$) and/or either or both occurrences of ($T_{ref,i}$) in Equation 1 with a simple, parameterized function of the mole fraction, the exact form of which is to be determined, for the purpose of minimizing the root mean square error (RMSE) of the predicted vapor pressure relative to the measured vapor pressure. These variants of Equation 1 are expressed here as Equations 3a through 3d. Ultimately, one (or none) of these equations will be recommended for the vapor pressure, evaporation rate and distillation simulation of complex fuels. For comparison, the activity coefficient approach is represented by the UNIFAC model.

$$P_{vap,i} = x_i * P_{ref} * \exp\left[\left(E_{a,i} \,/\, T_{ref,i}\right) * \left(1 - (A(x_i) / T)\right] \right. \quad \text{(Eq. 3a)}$$

$$P_{vap,i} = x_i * P_{ref} * \exp\left[\left(B(x_i) \,/\, T_{ref,i}\right) * \left(1 - \left(T_{ref,i} \,/\, T\right)\right] \right. \quad \text{(Eq. 3b)}$$

$$P_{vap,i} = x_i * P_{ref} * \exp\left[\left(E_{a,i} \,/\, C(x_i)\right) * \left(1 - (C(x_i) \,/\, T)\right] \right. \quad \text{(Eq. 3c)}$$

$$P_{vap,i} = x_i * P_{ref} * \exp\left[(B(x_i) \,/\, C(x_i)) * \left(1 - (C(x_i) \,/\, T)\right] \right. \quad \text{(Eq. 3d)}$$

In these equations, $A(x_i)$ and $C(x_i)$ are scaled reference temperatures, while $B(x_i)$ is a scaled activation energy. Two functional forms of the scale factor were tried for each term, where s is adjusted to minimize the RMSE. The trial 1 scale factor provided a lower RMSE in every case.



$$Trial\ 1\ scaling: A(x), C(x) = T_{ref}^{0} * \ (1 + s - s * x_i) \text{ or } B(x) = E_a^0 * \ (1 + s - s * x_i) \quad \text{(Eq. 4a)}$$

$$Trial\ 2\ scaling: A(x), C(x) = T_{ref}^{0} * (1 - s/1.001 + \ s/(x_i + 0.001) \text{ or}$$
$$B(x) = E_a^0 * (1 - s/1.001 + \ s/(x_i + 0.001) \quad \text{(Eq. 4b)}$$

The same value of s applies to all three components, n-pentane, toluene and n-dodecane, as well as (conceptually) every component in jet fuel. A different value of s was determined for each model ([3a] through [3d]). For model (3d), two separate tuning parameters were derived, (1) for $B(x_i)$ and (2) for $C(x_i)$), and not surprisingly, this model provided the lowest RMSE of the set. Relative to the UNIFAC modeling scheme, this modeling approach sacrifices dependencies on component identity (differences in interaction energies, molecular shape and size) in favor of simplicity and generality. It also potentially gains an ability to elegantly capture some of the composition-specific temperature dependencies through its linkage to the Clausius–Clapeyron equation and the best available, temperature-dependent component data.

Reference Model (UNIFAC) Description

The UNIFAC model is described in detail by Fredenslund et al. (1975) and is one of several derivatives of earlier models of activity coefficients. In this model, the activity coefficient of component *i* is assumed to be a product of two terms: (1) the combinatorial term and (2) the residual term.

The log of the combinatorial term is then estimated by the sum of four more terms, involving six different terms, one of which is the mole fraction of component *i*, and another of which is a modeling constant set equal to 10. The four remaining terms are different arithmetic combinations of mole fractions, van der Waals volumes, and van der Waals surface areas of every component in the mixture.

The log of the residual term is the sum, over all groups (-CH_3, etc.) in the mixture, of the difference between two new terms, where one of these relates to the group's contribution in the mixture and the other relates to the group's contribution in pure component *i*. The same expression is used to define each of the 'new' terms. The independent paraments in this expression include the van der Waals surface area of each group, as well as the group fraction (analogous to the mole fraction), and it involves a group interaction parameter. A large set of group interaction parameters was determined by Fredenslund et al. (1975) through a non-linear, least squares data reduction scheme, where vapor–liquid (and liquid–liquid) equilibrium data of binary systems from 200 different sources were used as the foundational database.

The molecules used in this work comprise four groups: -CH_3, -CH_2-, arCH and arC-CH_3. The methyl group of toluene is combined with the aromatic carbon that it is bound to, and this pair is treated as one group. All four of these groups contribute uniquely to the van der Waals volume and surface area calculations, but for the purpose of interaction parameters, the methyl and ethyl groups are considered identical. However, the interaction terms (a) are not symmetric so $a_{mn} \neq a_{nm}$, meaning that we have to consider six interaction terms rather than three. A compilation of the values used in this work is provided in Table 1. The spreadsheet used to compile all of the arithmetic combinations of these parameters is provided in the Supplementary Material, entitled "UNIFAC Vapor Pressures."

Table 1. Fundamental UNIFAC parameters used in this work.

Molecular Group	vdW Volume	vdW Surface Area	a_{12}	a_{21}
-CH_3	0.9011	0.848	-	-
-CH_2-	0.6744	0.540	-	-
arCH	0.5313	0.400	-	-
arC-CH_3	1.2663	0.968	-	-
CH_2 :: arCH	-	-	32.08	15.26
CH_2 :: arC-CH_3	-	-	26.78	−15.84
arCH :: arC-CH_3	-	-	167.0	−146.8



Comparative Summary of Pressure Models

A number of different models applicable to pressure have already been mentioned in this manuscript (summarized in Table 2), and these are merely representative of a much larger population of models that we segregate into three intersecting purposes. Vapor pressure models of pure compounds (i.e., Clausius–Clapeyron, Antoine, Wagner) describe the relationship between the temperature of the system and its vapor pressure, where the gas and liquid phases are in equilibrium. The algebraically simplest of these, the Clausius–Clapeyron equation, is derived from fundamental theory and contains no empirically tuned parameters to correct for assumptions made in its derivation. The Antoine and Wagner equations leverage the fundamental relationship that vapor pressure is exponentially related to the inverse of temperature but use empirically tuned parameters to extend the applicable temperature and pressure range of the model, where the Wagner model extends applicability well into the supercritical region, beyond the critical temperature (T_{cr}) and critical pressure (P_{cr}). The Antoine and Wagner equations, via their reliance on measured pressures and temperatures, necessarily account for real gas deviation from ideal gas behavior. The simplest of all equations of state is the ideal gas law, but it applies only to gases with weak intermolecular force fields with a mean free path much larger than the molecular diameter. Several other equations of state similarly apply only to gases but with allowance, through empirically tuned parameters, for intermolecular attractions/repulsions and molecular volume. Some of the more sophisticated equations of state can also be used for characterizing the boundary (in pressure, temperature coordinates) between the gas and liquid phases, which is an alternative way of saying, "the vapor pressure curve." Most of these models were developed for pure materials but can be extended to mixtures. For example, Opacich et al. (2019) used measured data to fit an Antoine equation for each jet fuel within scope in order to characterize its vapor pressure across a broad temperature range. Rauch (2017) made a systematic accuracy assessment for alternative aviation fuel evaporation models, which included an examination of fuel surrogates and simple vapor pressure models. In another approach, blending rules can be applied to the tuning parameters used in equations of state, with the complication that heterogeneous intermolecular interaction terms require measured data to determine their values. In both of these examples, the necessity for some measured data to build (or refine) the model severely restricts their scope of applicability.

For Raoult's Law, the model captures the two main effects that contribute to the vapor pressure of a liquid mixture; namely the set of liquid-phase mole fractions and the set of the vapor pressures of each corresponding liquid component, but it is not as accurate as required for many applications. Among the early attempts to improve Raoult's Law, Wilson (1964) introduced a scaling term (activity coefficient) that ultimately required some measured data pertaining to the mixture of scope to empirically derive parameters used in their model and predict activity coefficients. This approach, whether or not it yielded a more robust model than a mixture-specific Antoine (or Wagner) equation, suffers from a similar restriction on its scope of applicability for the same reason; measured data pertaining to the liquid of scope are required to finish constructing the model. The UNIFAC model eliminated the need for mixture-specific measurements to finish the model. However, its accuracy is not great, and it is more complex than desired for some applications. This work combines Raoult's Law with a generalized form of the Clausius–Clapeyron equation, yielding a simple algebraic equation that depends on two tuned parameters that are applicable to all aliphatic and aromatic hydrocarbons, the set of liquid-phase mole fractions, the vapor pressures of each component of the mixture and their normal boiling points.



Table 2. Summary of pressure models mentioned in this work.

Model	Mathematical Form	Comment	System	Complexity
Clausius–Clapeyron	$d(lnP)/d(\frac{1}{T}) = \Delta H_{vap}/R$	Explains temperature dependence	Pure liquids	Very low
Antoine	$lnP = f(T)$	Three empirically tuned parameters	Pure liquids	Low
Wagner	$\ln(\frac{P}{P_{cr}}) = f(T/T_{cr})$	Four empirically tuned parameters	Pure liquids	Low
Equation of State	Many versions from Van der Waals to Span–Wagner		Gases, but extendable	High
Raoult's Law	$P_i(T) = x_{i,liq} * P_i^0(T)$	Fundamental	Liquid mixtures	Very low
Wilson	$P_i(T) = a_i * x_{i,liq} * P_i^0(T)$	Tunable activity coefficient (a_i)	Specific liquid mixtures	Data required
UNIFAC	$P_i(T) = a_i * x_{i,liq} * P_i^0(T)$	Activity coefficient found from standard inputs	Liquid mixtures	Moderate
This Work	$P_i(T) = x_{i,liq} * P_i^0(T, x_{i,liq})$	Integrated Clausius–Clapeyron to introduce dependence on mole fraction	Liquid mixtures	Low

Materials and Methods

Vapor Pressure Measurement

The Eravap device, manufactured by Eralytics, was used to measure vapor pressure of liquid samples. The device employs factory-installed software to control sample volume, fill temperature and sample temperature as per user-selected test methodology. We considered the ASTM D6378 (ASTM International, 2022b) triple-point expansion method, as well as the Eralytics® LowVP (low vapor pressure) module. For both methods, the sample is pulled into the measuring cell (see Figure 1) via an actuated piston. A pre-set number of rinse cycles are used to saturate the gas in the measuring cell with sample vapor. Upon conclusion of this conditioning operation, the piston is positioned to a depth corresponding to a chamber volume equal to 4 mL. The suction created by moving the piston up to a depth corresponding to 5 mL is responsible for pulling 1 mL of liquid sample into the measuring cell. During the filling process, sensed pressure is monitored to flag potential filling errors. Once the sensed pressure is found to be within 5 kPa of the (air-only) ambient pressure, which was recorded prior to rinsing, a second timer (t_2) is activated, and the first timer (t_1) is stopped. The first timer starts upon opening the inlet valve (see Figure 1) to the sample. In the controller module, called ASTM D6378, the inlet valve is closed when $t_2 = t_1/3$.

The ASTM D6378 module employs four pre-set volumes (the smallest being 4 mL), which are created by moving the piston within the sealed measuring cell (see Figure 1). The slope of pressure (P) multiplied by volume (V) versus V at constant temperature (T) is the vapor pressure of the sample at that temperature. The total number of moles, as well as the number of sample moles, is determined from the ideal gas law, using total pressure and vapor pressure, respectively, as inputs. The number of moles of air is the difference between these two determined quantities. The Eralytics LowVP module differs from the ASTM D6378 module in several ways. Notable differences include longer fill times achieved by decreasing the pressure variation from ±5 kPa to a lower value (~±0.15 kPa), implementing a degassing procedure to rid the liquid phase of any trapped bubbles and executing a triple expansion at a temperature higher than the test temperature to determine the number of moles of air in the sealed measuring cell. For further description of this method, readers are referred to the Eralytics User Manual for the Eravap device.

® Eralytics is a registered trademark of Eralytics GmbH, Austria.

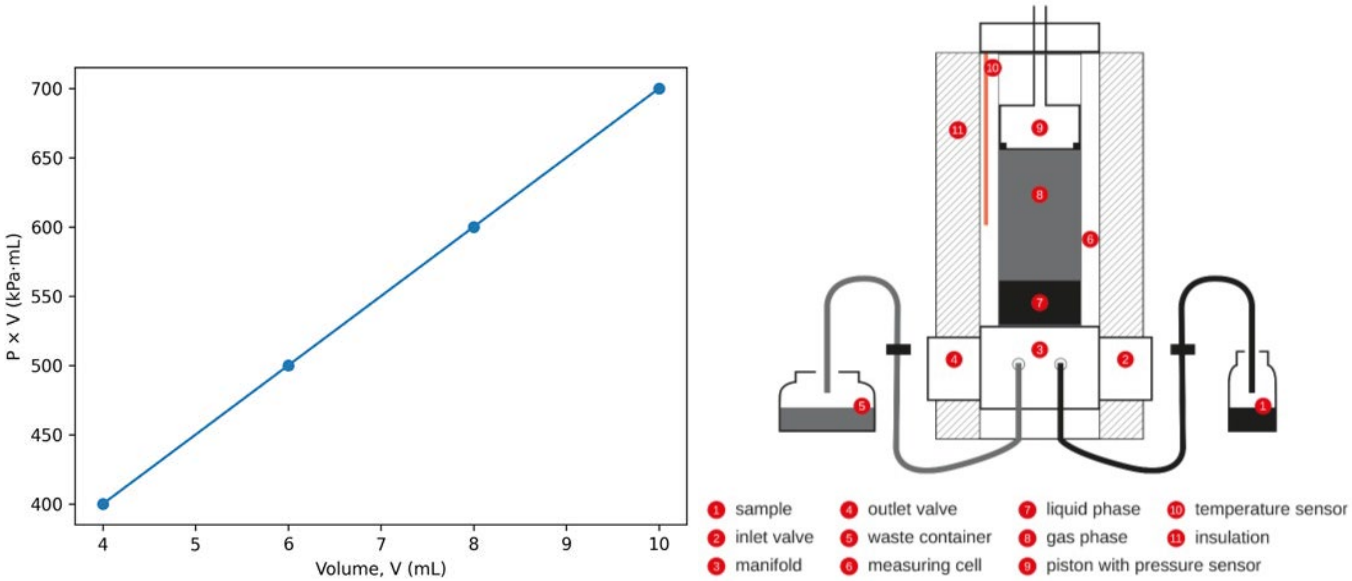


Figure 1. Illustrative ASTM D6378 slope of pressure (P) multiplied by volume (V) vs. V at constant temperature (T) (left), and instrument cross-section (right). Image taken from the Eralytics User Manual for the Eravap device, which is commercially available.

For three pure solvents, n-pentane, toluene and n-decane, the indicated vapor pressure as a function of temperature was compared to reference data published by the National Institute of Standards and Technology (NIST; Linstrom & Mallard, 2001). When using the ASTM D6378 module, we found discrepancies of ±1.5 kPa, which is much higher than desired for this work. For this reason, we selected the Eralytics LowVP module for all vapor pressure determinations reported here. According to Eralytics, this method has a repeatability of ±0.15 kPa for all samples at temperatures between -20°C and 120°C, with a vapor pressure between 1.0 kPa and 1000 kPa. Our observations are consistent with the quoted repeatability value.

Materials and Temperatures

The solvents listed in Table 3 were used to make a variety of mixtures containing 0–10%$_{mol}$ of light components. The heaviest component (n-dodecane or n-tetradecane) used in two- or three-component mixtures was present at higher concentration.



Table 3. Materials used in hydrocarbon mixtures. TCD: Trinity College Dublin; WSU: Washington State University.

Name	Normal Boiling Point, °C [29]	Supplier	Purity (%)
n-pentane	36.0	Thermo Scientific	99
cyclohexane	80.8	Fisher Scientific	99.8
n-heptane*	98.4	Alpha Aesar	99
Isooctane	99.2	Sigma Aldrich	99.5
Toluene	110.6	Thermo Scientific	99.7
ethylbenzene*	136.2	Thermo Scientific	99
o-xylene	143.8	TCI	98
n-nonane*	150.6	Thermo Scientific	99
n-propylbenzene*	158.8	Alpha Aesar	98
n-decane*	174.1	Thermo Scientific	99
n-dodecane (TCD)	216.3	Thermo Scientific	99
n-dodecane (WSU)*	216.3	Thermo Scientific	99
n-tridecane*	233.8	TCI	99
n-tetradecane	249.8	Thermo Scientific	99

*These seven materials were part of a 10-component mixture that was distilled as part of this project. The data pertaining to that distillation are available by request to the correspondence author.

Binary mixtures of n-pentane or toluene in n-dodecane, each at four different blending ratios and heated to 70° or 100°C, were used to determine the tuning parameter(s), c. Both sets of binary mixtures included 0.04, 0.06 and 0.09 mole fractions of the lighter component, while the n-pentane/n-dodecane set also included one mixture with a 0.02 mole fraction of n-pentane, and the toluene/n-dodecane set also included one mixture with a 0.06 mole fraction of toluene. A significant difference in volatility was deliberately chosen to minimize the impact of errors stemming from the vapor–liquid equilibrium of the solvent, focusing instead on a single volatile component at low mole fractions. For example, the liquid mixture containing 0.04 mole fraction toluene produces a vapor at 100°C that consists of at least 60% toluene, with wide variation depending on which model is used to predict the component vapor pressures.

Ternary mixtures of n-pentane, toluene and n-dodecane were used as a first level of model validation. In these mixtures, the mole fractions of toluene and n-pentane were made equal to each other: 0.01, 0.04, 0.07 and 0.09. At minimum, the model developed in this work should predict the vapor pressure of these mixtures at 70 and 100°C more accurately than any of the general models, regardless of its relative simplicity, because its parameters were trained specifically on n-pentane and toluene data. Extension of this model to higher temperatures, corresponding to the ambient-pressure bubble points, is somewhat more stressful, but each of the models considered in detail here employ the same vapor pressure curves of the pure components, so even here, the model developed in this work should be more accurate than Raoult's Law and the correction to it based on UNIFAC-determined activity coefficients.

Ternary mixtures, (cyclohexane, o-xylene, n-tetradecane) and (isooctane, o-xylene, n-tetradecane), were used to evaluate the generality of the model. In one experiment, the pot temperature of a mixture made from 2.55 g of cyclohexane, 2.56 g of o-xylene and 44.99 g of n-tetradecane was compared with the modeled liquid temperature of a system for which 0 or 1.0%$_{vol}$ of the liquid is assumed to have vaporized, but to be present in the reflux apparatus (Figure 2) above the surface of the boiling liquid and below the condenser. In another experiment, 100 mL of a mixture made from A (10.36 g of cyclohexane, 10.04 g of o-xylene and 90.93 g of n-tetradecane) or B (10.02 g of isooctane, 10.01 g of o-xylene and 79.96 g of n-tetradecane) was distilled according to the method described as ASTM D86. A brief description of this experiment is provided in the section below under the "Distillations" heading.

Finally, data were extracted from the work of Hung et al. (2024). Although none of the 90 (T, P) vapor–liquid equilibrium points they measured satisfy our predetermined filter criteria, the dataset serves as a valuable benchmark for assessing



how our model performs when applied to systems clearly outside the training set's range. For the record, our predetermined filter criteria were non-associated components, *a <0.10* mole fraction of the volatile component(s), which we call solute, *a >100K* difference between the solute and solvent's normal boiling points, and a mixture vapor pressure between 1.5 and 101.3 kPa. Their study involved five sets of binary mixtures involving n-nonane, n-octane, methylcyclohexane and methylcyclopentane and three fixed temperatures (120°, 160°, 200°C). We selected the points at 120°C to minimize the confounding effects of real gas behavior, as model (3d) does not address heterogeneous intermolecular attractions/repulsions in the gas phase. Three older datasets by different authors were also evaluated, but the data contained in those reports, relative to Raoult's Law predictions, showed deviations much different from our observations, leading us to question whether we properly understand the experiment they conducted.

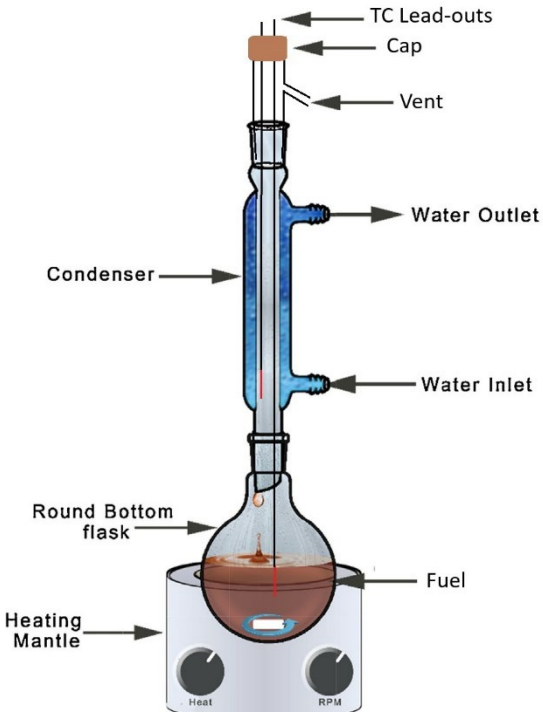


Figure 2. Apparatus used for reflux experiment.

Reflux Experiment

The glassware shown in Figure 2 was used to measure the liquid temperature of a boiling mixture. Type K thermocouples (±2.2°C) were used to measure temperature. Fifty milliliters of a cyclohexane/o-xylene/tetradecane mixture were inserted into the 100 mL round-bottom flask and heated until a steady-state reflux was established. Ordinary tap water was used as the coolant, fed through the condenser sleeve from the bottom port upward, through the top port. Negligible pot temperature (lower thermocouple) variation was observed as the heat flux (vigorousness of the boil) varied. However, the condensate temperature (upper thermocouple) varied significantly with heat flux, with subtle changes in its vertical position. For this reason, the upper thermocouple temperature is not reported here, although it was used to verify internal coherence. For the purpose of comparing the measured liquid (pot) temperature with the theoretical bubble point of the liquid mixture, the dynamic holdup was approximated to contain the equivalent of $1\%_{vol}$ of the sample, or 0.5 mL at reference (lab) temperature. The theoretical temperature corresponding to $1\%_{v}$ distilled was compared with the measured pot temperature. Additionally, the measured temperature corresponding to the first visual observation of bubbles was recorded, as well as the bubble point, as predicted by the vapor pressure model. In this way, there is a band represented for both the measured and modeled temperatures.

Distillation

Distillations were carried out with the apparatus shown in Figure 3, achieving a collection rate of 1.5–3.0 mL/min from 5% distilled to 50% distilled, which is lower than the requirement stated in ASTM D86 (4–5 mL/min). As a consequence, the degree of separation attained in this set-up is likely somewhat higher than is typical of apparatuses used in conjunction with ASTM D86. The vertical placement of the thermocouple junction is controlled by its sub-assembly, which fits into the ground-glass fitting at the top of the column. Its depth was determined from prior work, manually tuned to reproduce the distillation curve determined with a commercial apparatus conforming fully to the specifications of ASTM D86. The condenser arm is water-cooled, and the collection cylinder is bathed in quiescent air at ambient temperature and pressure. The only vent in the distillation apparatus is at the exit of the condenser arm. Heat is applied via an electrically controlled hot-plate to the bottom of a 125 mL round-bottom flask, which is filled initially with 100 mL of sample. The dimensions of the distillation column, condenser and collection cylinder (100 mL, graduated) are similar to those of the corresponding pieces as specified in ASTM D86. No fractionating media is present in the column.

The volume of dynamic holdup (which includes all mass, liquid or vapor that is not present as liquid in the pot or collection cylinder) varies with the temperature gradient (Ferris & Rothamer, 2016) between the bubble point of the liquid phase (in the pot) and the dew point of the vapor phase at the inflection point in the condenser arm, as well at the heat flux applied to the bottom of the round-bottom flask. By adjusting the heating rate periodically to maintain a distillate collection rate of 1.5 to 3.0 mL/min, the variation in dynamic holdup throughout the course of the distillation is reduced. The dynamic holdup volume is the largest source of mismatch between the recorded distillation curve temperatures (Tn) and the actual distillate temperature throughout a distillation. It can be anywhere from 0.5 to 10 mL, depending on sample composition (Ferris et al., 2016), but is more commonly approximately 2.6 mL.



Figure 3. Apparatus used for distillations.



Larger dynamic holdup volumes suggest a higher degree of fractionation, because liquid that forms upstream of the inflection point on the condenser arm will drain toward the heat and re-vaporize (whether fully or partially) prior to blending back into the pot. Bounding assumptions of one or two theoretical plates of separation are assumed here for the purpose of comparing modeled distillations with measured distillation curves and distillate compositions. The theoretically estimated temperatures should be consistently higher than the measured temperatures (Tn) if they accurately reflect the actual temperature of a system with n $\%_v$ 'not-in-pot,' which includes dynamic holdup volume and collection volume, instead of n $\%_v$ collected.

The fraction distilled is defined as the volume of distillate collected, divided by the volume of sample charge, which is 100 mL. The temperature can be monitored throughout the distillation, although usually the operator will only record the temperature at pre-determined distillate volumes. For example, at 10$\%_v$ distilled, the operator may record T10 if 10$\%_v$ is a pre-determined test point. In this work, the operator has recorded four points for distillation of the ternary mixture (T5, T10, T15 and T20). Specific to this work, a 0.2 mL sample of distillate was pipetted from the collection cylinder at each of the scheduled test points for the purpose of characterizing its composition via two-dimensional gas chromatography (GCxGC)/flame ionization detector (FID). The composition of distillate is not subject to errors introduced by the dynamic holdup. To minimize distillate sample inhomogeneity, the material in the graduated cylinder was swirled and agitated by pulsing with five pipette volumes prior to each collection, and to minimize the risk of evaporative loss from the sample, it was immediately transferred to the gas chromatograph. The sampled volumes were not compensated for later collections, meaning the actual collected distillate volume at the second test point, for example, was 0.2 mL greater than indicated by the test point schedule, which consistently referenced the volume of material in the graduated cylinder.

Distillate Composition Analyses

The composition of each distillate was determined by two-dimensional gas chromatography with an in-series FID, according the method described originally by Striebich et al. (2014) and later by Trinklein et al. (2020). In these experiments, the composition determination was particularly simple because the samples were made of just three highly pure components that eluted over easily distinguished time/time domains.

One micro-liter of undiluted sample was injected into the head of the gas chromatograph. The integrated FID response corresponds to the mass of each component that elutes over the user-defined time domain of the integration. Since all masses are determined, and the identity of all species are known in advance, the corresponding mass, mole or volume fractions of each component can be readily determined.

Modeled Distillation

Idealized one-plate and two-plate distillations were completed for each experimentally distilled mixture and each vapor pressure model (this work and Raoult's Law). The initial condition is 100 mL of a test mixture of a known composition at ambient temperature and pressure (P_{amb}), from which total moles are determined. This mixture is heated (or cooled) in increments of 0.001K until its vapor pressure reaches (P_{amb} ± 0.001) kPa. At that point, for one-plate distillations, 0.1$\%_{mol}$ of material, with its composition determined by the modeled vapor phase, is removed from the system. The dew point of this drop is determined by cooling (or heating) the vapor in increments of 0.001K until a liquid of that composition produces a vapor pressure of (P_{amb} ± 0.001) kPa. For two-plate distillations, two vapor-phase compositions are tracked. The first one (the higher-temperature one) is determined by the temperature and composition of material in the pot; and the second one (the lower-temperature one) is determined by the temperature and composition of the first drop. The second bubble point temperature is equal to the first dew point temperature. This temperature, along with the composition of the first drop (as well as the first vapor phase), determines the composition of the second phase. At this point, for two-plate distillations, 0.1$\%_{mol}$ of material, with its composition determined by the second modeled vapor phase, is removed from the system. The dew point of this (second) drop is determined by cooling (or heating) the vapor in increments of 0.001K until a liquid of that composition produces a vapor pressure of (P_{amb} ± 0.001) kPa. In each case the modeled (final) dew point is compared with experimentally measured condensate temperatures.

To model a significant span of the distillation curve, this process is repeated up to 1,000 steps, with an incremental reduction in liquid in the pot at each step. To avoid numerical issues that are likely to arise somewhere (between 950 and 1,000 steps) as the quantity of material being extracted becomes significant relative to the total material left in the system, we stop the numerical distillations at 950 steps. The (first) bubble point temperature, (final) dew point temperature and composition of the extracted drop are recorded at each step. The fully mixed distillate composition is also updated at each step.



Results

Tuning Vapor Pressure Models

The mixtures of n-pentane in n-dodecane and toluene in n-dodecane were used to represent the vapor pressure of an aliphatic or aromatic solute dissolved in a hydrocarbon solvent. A large volatility difference between the solute and solvent was chosen so that the composition of the vapor phase would be predominantly one component, the solute, even as the solute mole fraction in the liquid phase was taken down to 0.02 (n-pentane) or 0.04 (toluene). Thus, the confounding impact of solvent vapor pressure was minimized. Table 4 documents the normal boiling points and the Antoine coefficients for each of these three materials, where the Antoine equation was used to obtain the values of $P_{vap,i}$ that were used in Equation 2. The singularity (in Equation 2) that occurs when the temperature equals the normal boiling point does not arise at the tuning stage of this work because only test temperatures (70° and 100°C) not equal to the normal boiling point of any component were selected. Two values of temperature were chosen, effectively decoupling variation in $E_{a,i}$ from normal boiling point variation. A mix of aliphatic and aromatic hydrocarbons (one each) was deliberately selected because the entropy of vaporization, which effectively relates to the normal boiling point temperature and the heat of vaporization, is somewhat different for each; approximately 86.5 and 72.5 J/mol/K for alkanes and aromatics, respectively. Our intent here is to model each in the same way and to assess the error introduced by neglecting this difference. For reference, the approximate entropies of vaporization of cycloalkanes and alkenes are 85.0 and 82.5 J/mol/K, respectively, within the bounds of the representatives chosen for this work.

Table 4. Antoine coefficients of selected materials: $\log_{10}(P) = A - B\,/(T + C)$.

Material	nBP (°C)	A	B (K)	C (K)
n-pentane	36.0	3.9892	1070.617	−40.454
toluene	110.6	4.0783	1343.9	−53.77
n-dodecane	216.3	4.10549	1625.928	−92.839
cyclohexane	80.8	3.96988	1203.526	−50.287
o-xylene	143.8	4.12928	1478.244	−59.076
n-tetradecane	249.8	4.13735	1739.623	−105.616
isooctane	99.2	3.9368	1257.8	−52.42

For the n-pentane/n-dodecane mixtures, vapor pressure data were recorded for mixtures with 2, 4, 6 and 9%$_{mol}$ n-pentane at 70° and 100°C. For the toluene/n-dodecane mixtures, vapor pressure data were recorded for mixtures with 4, 6, 8 and 9%$_{mol}$ toluene at 70° and 100°C. These 16 data points were used to train the models. Figure 4 displays the best fit for each of the models defined in Equations 3a–3d. The toluene/n-dodecane data are confined to panel (a) and the n-pentane/n-dodecane data are confined to panel (b). The motivation for showing all of these fits is to underscore the improvement offered by the second tuning parameter. For model (3d), the root mean square and mean absolute errors are 0.35 and 0.25 kPa, respectively, substantially better than any of the single-parameter models. More importantly, for model (3d), the error is split evenly between each of the four groupings of data, resulting in a mean error of just 0.09 kPa and a mean absolute relative error (MARE) of 3.5%. In contrast, the errors of the single-parameter models are heavily skewed toward the toluene/n-dodecane mixtures, while a temperature-dependent pattern is also apparent. The tuned values of *s*, applicable to model (3d), are reported in Equations 5 and 6.

$$\mathrm{C}(x_i) = T^0_{ref,i}\,(1.0154 - 0.0154 \times x_i) \qquad \text{(Eq. 5)}$$

$$\mathrm{B}(x_i) = E^0_{a,i}\,(0.77275 + 0.22725 \times x_i) \qquad \text{(Eq. 6)}$$

A comparison of model (3d) with other global models, UNIFAC and Raoult, is displayed in Figure 5. Surprisingly to these authors, the zero-parameter Raoult's Law misrepresents the n-pentane/n-dodecane vapor pressures at 100°C by a whopping 22% to 60%, while it essentially matches the toluene/n-dodecane vapor pressures at 100°C. Across the 16 points, its MARE is 26.6%. Compared with the 100°C data, at 70°C, Raoult's Law predictions decrease relative to the data for both sets of mixtures, which is a characteristic shared by the UNIFAC model predictions. The "corrections" to Raoult's Law offered by the UNIFAC activity coefficients scale the vapor pressures of the toluene/n-dodecane mixtures (activity



coefficients > 1) to higher values, which drives it in the wrong direction at 100°C and the right direction at 70°C. For the n-pentane/n-dodecane mixtures, the UNIFAC model (activity coefficients < 1) scales Raoult's Law vapor pressures to lower values, which is closer to the data at both 70° and 100°C, but still wrong by up to 31% at 100°C for the mixture containing 9.0%$_{mol}$ n-heptane. Across the 16 points, its MARE is 12.6%. Clearly, the two-parameter model developed here shows greater promise than the activity coefficient approach represented here by the UNIFAC model, which has a total of seven tuned parameters that are applicable to these mixtures.

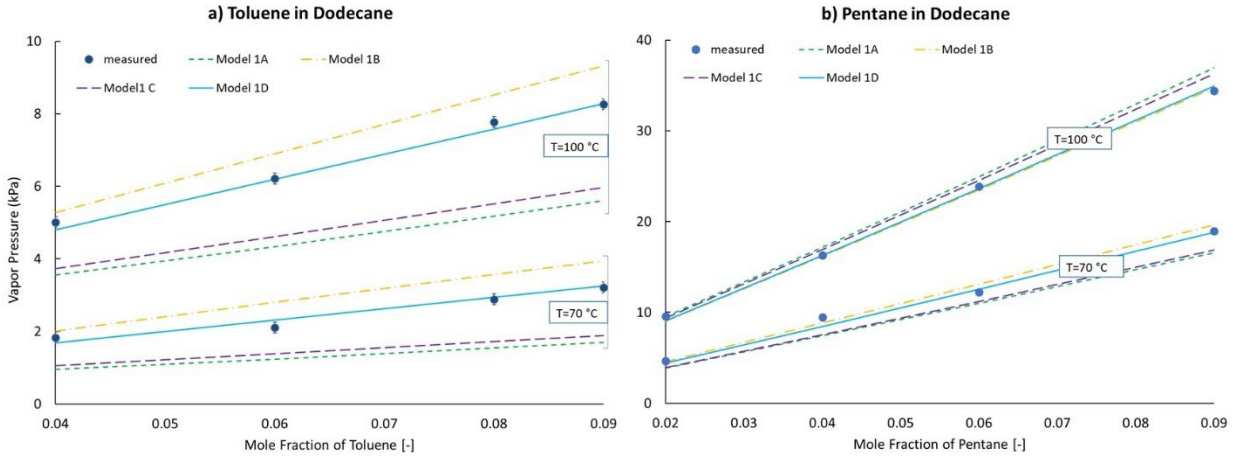


Figure 4. Vapor pressure model tuning results. Filled symbols correspond to measurements. Curves correspond to model predictions.

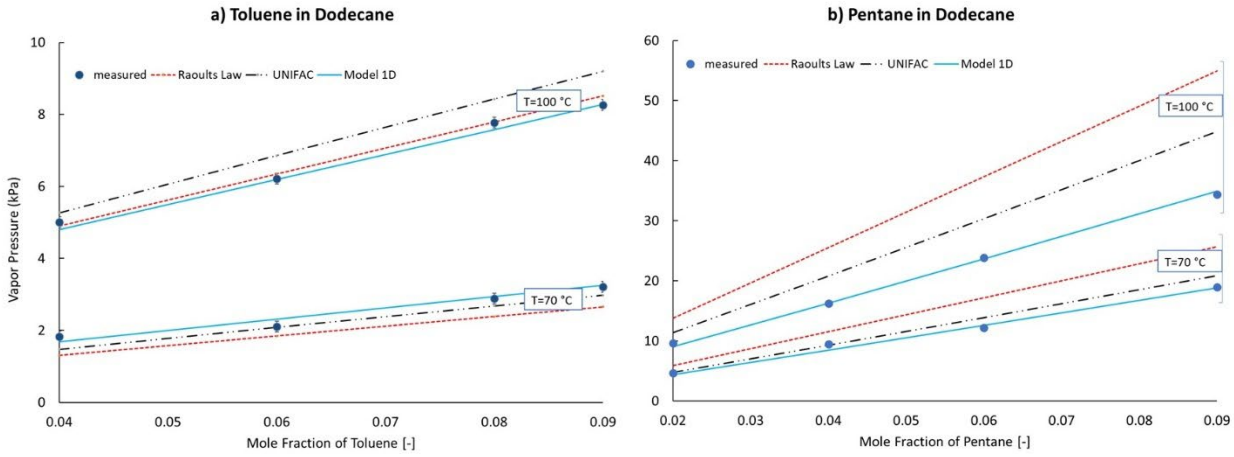


Figure 5. Tuned vapor pressure model comparisons. Filled symbols correspond to measurements. Curves correspond to model predictions.

Modeled Vapor Pressure Validation

The first level of validation discussed is to compare predictions to measurements of systems under slightly different conditions compared with the tuning dataset. Here we use ternary mixtures of n-pentane, toluene and n-dodecane. For convenience of reporting, the mole factions of toluene and n-pentane were prepared equal to each other. According to Raoult's Law and model (3d), the vapor pressure of this mixture should be essentially the sum of the vapor pressures of



the respective binary mixtures, because these models do not consider potential differences between components of differing identities, and the slight reduction in n-dodecane's contribution to the total vapor pressure is small, because its vapor pressure is much lower than those of n-pentane and toluene. In contrast, the activity coefficients of the UNIFAC model are impacted by the identities of the other components. For example, at 9%$_{mol}$, the activity coefficient of n-pentane is 0.811 at 70°C for the binary mixture and 0.837 for the ternary mixture. Very astute readers may be able to see the effect of this difference by comparing Figure 5 and Figure 6, as the UNIFAC model is slightly more wrong for the ternary mixture than the binary mixture at this temperature, even though it gets the vapor pressure of toluene right at this temperature. Comparison to the equation-of-state (EOS) model (Kunz & Wagner, 2012) used in REFPROP (Lemmon et al., 2013), which lacks key features relevant to complex mixtures such a fuels, reveals several notable observations. Although exaggerated relative to the measured vapor pressure curves, the EOS model predicts some curvature to the vapor pressure as a function of the mole fraction, whereas this characteristic of model (3d) (clearly present based on Equations 5 and 6) is not visibly apparent on the viewing scales of Figures 4–6. The temperature dependence of the EOS model brings it closer to the measured values at 100°C than at 70°C, which may not be surprising, because the critical temperature is a focal point within that model's framework. Most surprising to the authors, however, was the magnitude of the errors afforded by this model in spite of its complexity and specificity to these three materials. In numerical summary, the MAREs of model (3d), Raoult's Law, UNIFAC and REFPROP are 44.6%, 24.3%, 33.6%, and 5.5%, respectively. Only model (3d) has a lower mean relative error (MRE) magnitude (5.1%) than MARE.

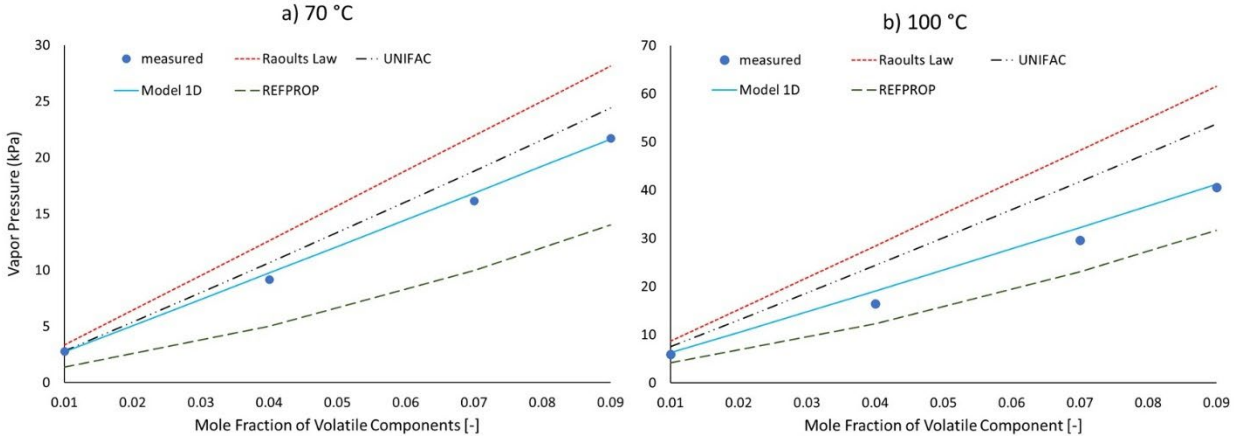


Figure 6. Measured and predicted vapor pressures of ternary mixture. Filled symbols correspond to measurements. Curves correspond to model predictions.

The next level of validation is to introduce a greater variety of materials and temperatures, resulting in vapor pressure up to ambient pressure. One simple way to obtain this data is to measure the temperature of a refluxing mixture. The temperature of the liquid phase is easy to get right, and the pressure is the barometric pressure of the lab, but the composition of the liquid phase is somewhat confounded because some mass of sample exists as dynamic holdup; vapor or condensed vapor that has not yet fallen back into the pot. In Figure 7, we show the measured reflux temperature of a mixture of o-xylene (8.6%$_{mol}$), cyclohexane (10.8%$_{mol}$) and tetradecane (80.6%$_{mol}$) in comparison with the predicted bubble point resulting from model (3d), Raoult's Law and the UNIFAC model. To account for the uncertainty of the liquid-phase composition, predictions corresponding to 0 and 1%$_{vol}$ are reported. The measured temperatures correspond to the moment when the first bubble was observed (bottom) and the moment it reached a steady-state temperature (top). For each of the models, the $P_{vap,i}$ term in Equation 2 was represented by an Antoine equation, with coefficients as documented in Table 4. As is quite evident from Figure 7, model (3d) predicts a normal boiling point and refluxing temperature, in far better agreement with the measured values than Raoult's Law or the UNIFAC model. While none of the models predict the measured result to within the ±2.2°C reproducibility of the thermocouple, the vapor pressure predicted by model (3d) at the lower edge of the measured temperature uncertainty band is just 11% higher than lab pressure, much closer than the other models. The liquid phase composition of 1%$_{vol}$ distilled for both model (3d) and UNIFAC reflux temperatures (upper) was based on model (3d), and one theoretical plate was assumed since no removal of material was occurring in this system.

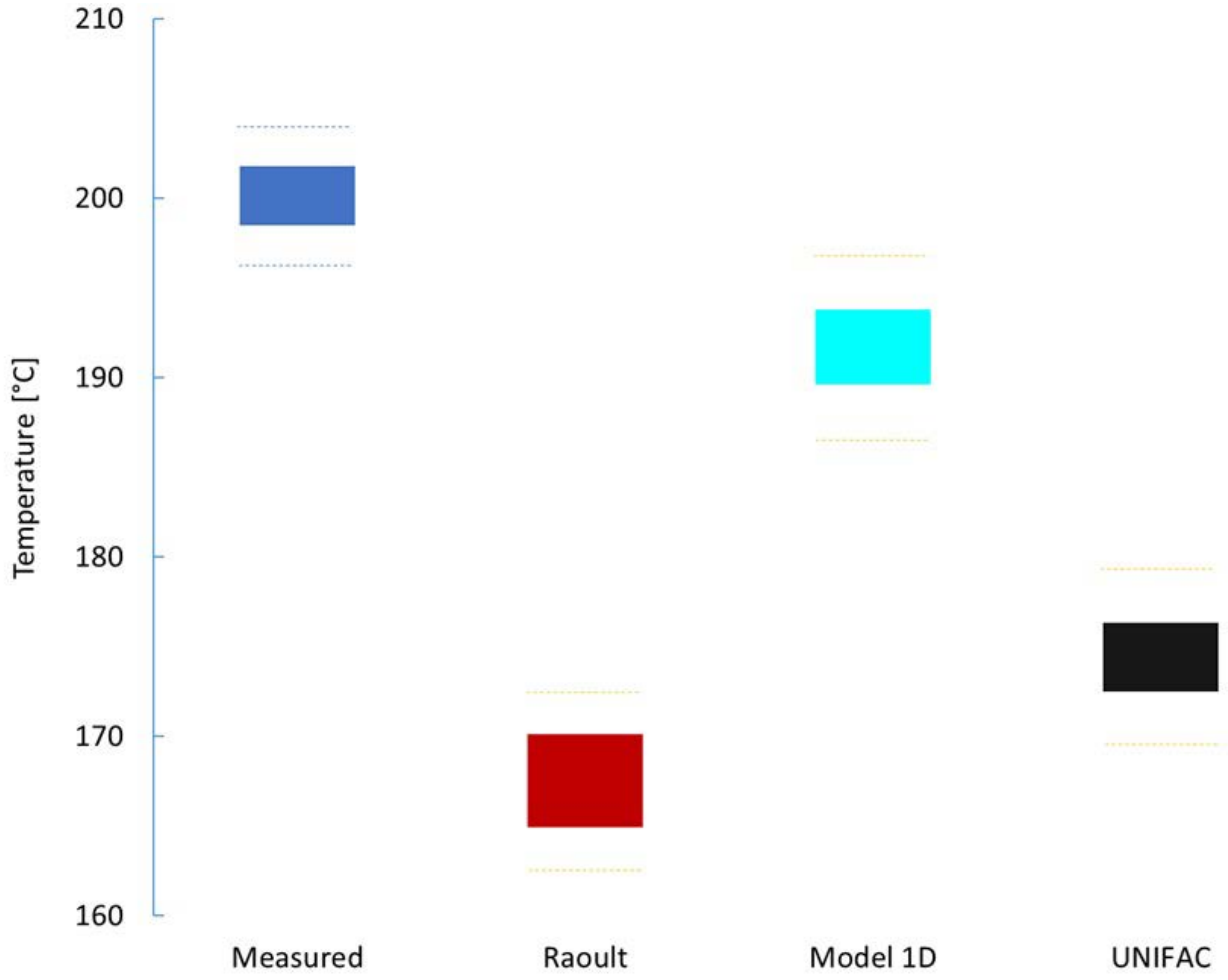


Figure 7. Measured and predicted liquid temperature of a refluxing mixture of cyclohexane and o-xylene in tetradecane. The dashed blue lines correspond to the temperature measurement uncertainty of ±2.2°C. The dashed yellow lines correspond to the predicted temperature at a vapor pressure within ±5% of lab pressure.

Literature Data

Recently, Hung et al. (2024) measured and predicted the vapor pressure of 20 different binary mixtures involving n-nonane, n-octane, methylcyclohexane or methylcyclopentane at 120°, 160°, or 200°C (see Figure 8). Their predictions were made via Aspen Plus® V11 using COSMO-SAC, UNIFAC-DMD and two additional models with coefficients of binary interactions re-tuned to their measurements and Hayden-O'Connell fugacity coefficients. A description of the UNIFAC-DMD model (highlighting modifications to UNIFAC) was provided by Gmehling et al. (1993), while a description of the COSMO-SAC model was provided by Hsieh et al. (2010). The MAREs of UNIFAC-DMD and COSM0-SAC were 1.5% and 5.1%, respectively. Comparatively, the simple two-parameter model presented here results in a MARE of 5.1% and MRE, or over-prediction, of -0.7%, considering only the data at 120°C to avoid having to account for real gas differences related to an ideal gas. Model (3d) overpredicts the vapor pressure of eleven mixtures while underpredicting the vapor pressure of nine mixtures. In contrast, Raoult's Law over-predicts the vapor pressure of all 20 mixtures, two of them by more than 40%, and has a MARE of 13.7%.

® Aspen Plus is a registered trademark of AspenTech Corporation, Bedford, Massachusetts.



It is worth noting here that the performance of model (3d) on this dataset is consistent with the authors original intent, which was to develop an algebraically simple model (suitable for hand calcs, spreadsheets or codes/applications that require vapor pressure or composition many thousands of times per run) that provides much-improved accuracy relative to Raoult's Law while remaining comparatively accurate to the more complicated and mature models used in commercially available applications that serve process engineering and industrial simulations. Model (3d) is not intended to replace models such as UNIFAC but rather to reach applications (through its simplicity) that are not currently pragmatic for UNIFAC. Specifically, this model does not address heterogeneous, real gas effects and should not be applied to conditions where such terms are expected to be important. It can be applied to our research goals, which are to support conceptual-level distillation cut-point optimization, as exemplified by Yang et al.(2023), bubble point prediction in the fuel system at chop from cruise to flight idle, preferential evaporation effects on lean blow at this same (jet engine) operating condition and evaporation rate predictions in (future) simulations of ignition in jet engines. Of these, the only one that is pragmatic for applications like ASPEN is the check on bubble point in the fuel system at the min-thrust/max-altitude (combustor) design point, but jet engine combustor designers do not generally have access to any such commercial application.

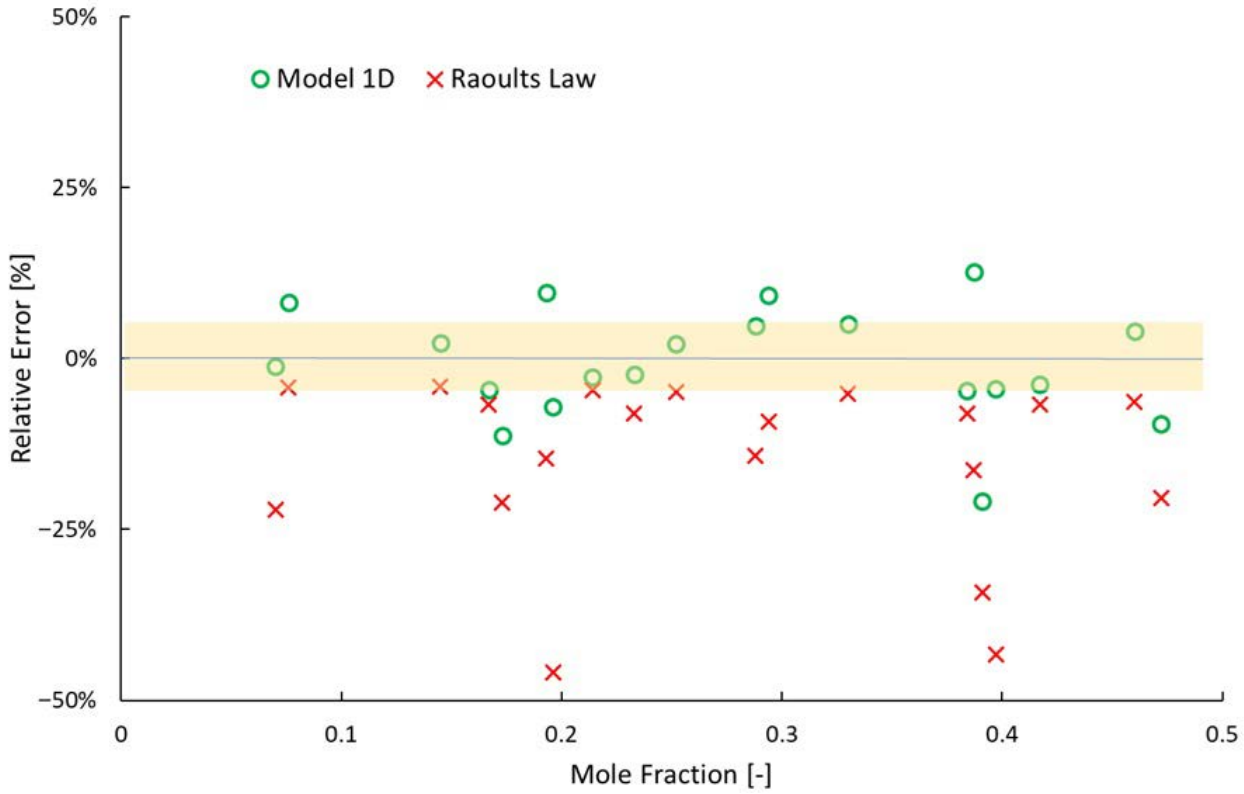


Figure 8. Relative error of vapor pressure predictions of assorted binary mixtures of n-nonane, n-octane, methylcyclohexane or methylcyclopentane. The measurements were taken from the vapor–liquid equilibrium work by Hung et al. (2024). Temperature equals 120°C and pressure equals 45.9–261.1 kPa. Relative error is defined as (measurement–prediction) divided by measurement. The shaded region corresponds to ±5%.

Modeled Distillation Validation

The final validation of the vapor pressure model compares predicted distillation curves with measured distillation curves. However, the model of the distillation process may be more important to these curves than the vapor pressure model. Figure 9 is used to compare the measured distillation curve of the ternary blend initially containing 18.2%$_{mol}$ (9.3%$_{vol}$) cyclohexane and 14.0%$_{mol}$ (7.8%$_{vol}$) o-xylene, with the balance being tetradecane. Clearly the difference resulting from the variable number of theoretical plates assumed for the distillation, one or two, has a much larger impact on the modeled

distillation curve than the choice of vapor pressure model, Raoult or model (3d). Regardless of vapor pressure model, the assumption of two theoretical plates results in a predicted distillation curve that more closely matches the measured data. Two sets of points are used to represent the measured distillation curve. One set corresponds to the measured temperature at the moment the collected distillate volume equals the first drop, 5 mL, 10 mL, 15 mL and 20 mL. The latter three points are shifted to the right to account for the distillate sample volume removed for later composition analysis. The second set of points accounts for the dynamic holdup volume, which we estimate to be 2.6 ± 1.2 mL. By comparing the curves displayed in panel a) with those displayed in panel b), it is apparent that Raoult's Law predicts more separation between the components for both distillation models; more featured and greater difference between the initial boiling point (IBP) and the temperature at 20%$_{vol}$ distilled (T_{25}). Relative to the measured data, Raoult's Law with two theoretical plates over-separates the mixture while model (3d) under-separates the mixture. An optimized linear combination of the one- and two-plate curves for Raoult's Law and model (3d), respectively, results in a rms error of 12.3 and 9.2°C. The two-plate curve weighting coefficient is 70% for Raoult's Law and 91% for model (3d).

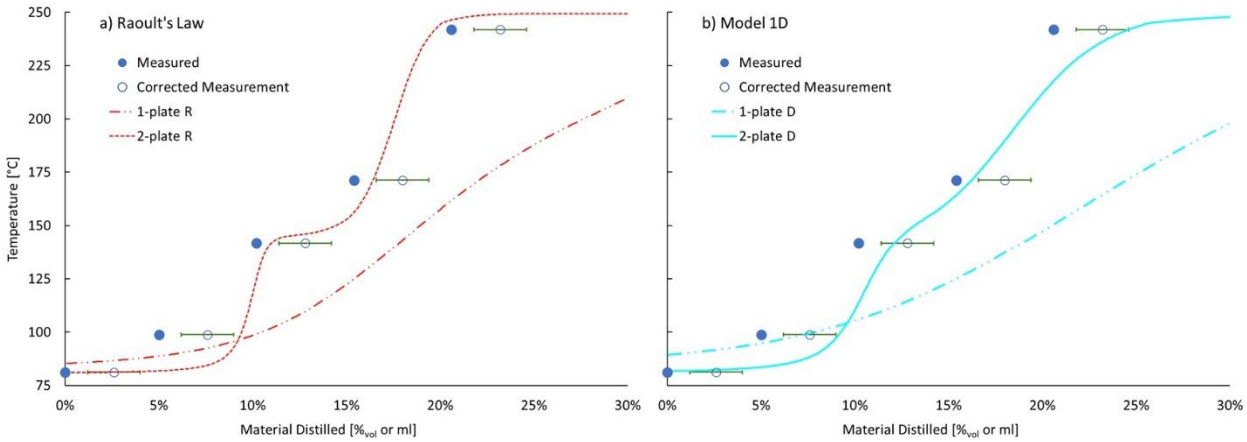


Figure 9. Measured and predicted distillation curve of a mixture of cyclohexane and o-xylene in tetradecane. Filled symbols correspond to measurements. Open symbols correspond to corrected measurements. The uncertainty bars correspond to the range of our estimated dynamic holdup volume. Curves correspond to model predictions.

To gain further insight into which vapor pressure model more accurately represents this distillation process, the measured and predicted distillate composition is compared in Figure 10. The dynamic holdup volume is not applicable to this data. The measured compositions were determined from GCxGC/FID analysis of samples drawn from the collection vessel. To account for the disconnect (1.53 mL) between the total volume of cyclohexane collected and its volume in the initial ternary mixture, we assume it was lost as vapor throughout the distillation. The open symbols in Figure 10 represent the measured data, corrected under this assumption. The vapor loss at each point is scaled by the ratio of liquid cyclohexane collected at each point divided by the final volume of cyclohexane collected. Relative to these points, it is clear that both vapor pressure models, within the two-theoretical-plate distillation model, predict greater separation at the first data point, overrepresenting cyclohexane and underrepresenting both o-xylene and n-tetradecane. By the second data point, when most of the cyclohexane is distilled, both vapor pressure models result in a predicted o-xylene concentration that matches the corrected data. Neither model captures the full extent of n-tetradecane bleed-through into the distillate. The missed n-tetradecane content may seem small in the context of vapor pressure, but the freeze point of this distillate is determined by n-tetradecane, where a mole fraction of 1% is expected result in a freeze point of -40°C (Bell et al., 2025). The difference between a measured mole fraction of 1.9% and a predicted mole fraction of 0.7% (or less) is the difference between having a product that will pass inspection or fail inspection. While model (3d) with two theoretical plates of separation is closer to reality than Raoult's Law with two theoretical plates, this distillation experiment falls somewhat short of two theoretical plates. The symbol *x* in Figure 10 corresponds to the prediction that weights a two-plate distillation by 70% and 91% for Raoult's Law and model (3d), respectively. The agreement between the measured distillate composition and its prediction based on model (3d) with two plates of separation weighted by 91% and one plate of separation weighted by 9% is remarkable at 5%, 10%, and 15% distilled, but at 20% distilled, it under-predicts o-xylene concentration while over-

predicting n-tetradecane concentration. In contrast, the modeled distillation based on Raoult's Law vapor pressures with 70% two-plate separation and 30% one-plate separation is wildly inconsistent with measured distillate composition at 15% and 20% recovered.

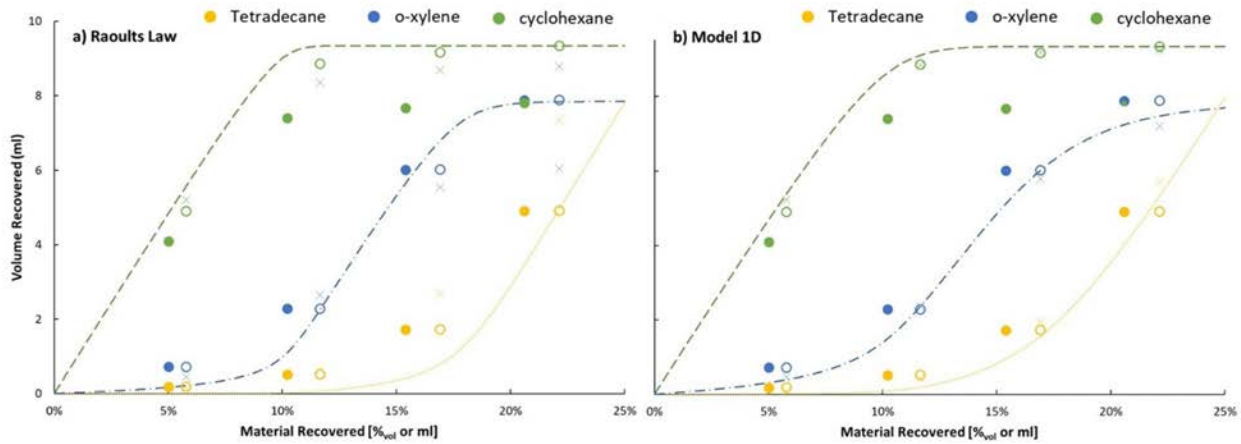


Figure 10. Measured and predicted distillate composition of a mixture of cyclohexane and o-xylene in tetradecane. Filled symbols correspond to measurements. Open symbols correspond to corrected measurements. Curves and × symbols correspond to model predictions. Green symbols and curves correspond to cyclohexane. Blue corresponds to o-xylene. Yellow corresponds to n-tetradecane.

In order to reduce the confounding effect of evaporative losses, a second ternary mixture was distilled. This mixture initially contained 15.0%$_{mol}$ (11.1%$_{vol}$) isooctane and 16.1%$_{mol}$ (8.6%$_{vol}$) o-xylene, with the balance being tetradecane. A comparison between the measured distillation curve and its prediction based on model (3d) vapor pressures and a two-plate distillation or a 96% two-plate plus 4% two-plate distillation is provided in Figure 11. The rms error of the weighted distillation curves is 10.5°C, stemming almost entirely from the big miss at 15% to 20% distilled, where the recorded temperature (130.9°C) is substantially less than the normal boiling point of o-xylene (143.8°C). The measured and modeled distillate compositions are displayed in Figure 12. Consistent with the previous result, the predicted recovery of o-xylene is noticeably under-represented by the model, while isooctane is over-represented at all four points of comparison, and n-tetradecane content is over-represented by the model at 20% recovery.

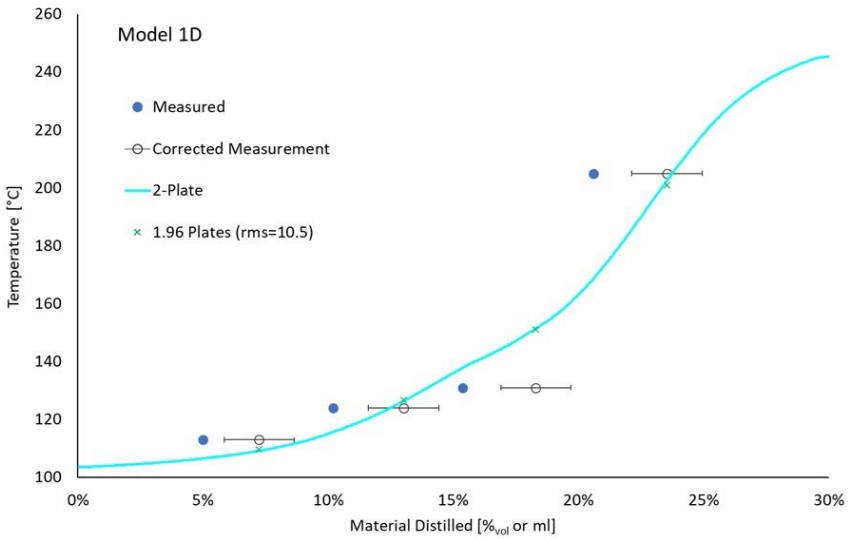


Figure 11. Measured and predicted distillation curve of a mixture of isooctane and o-xylene in tetradecane. Filled symbols correspond to measurements. Open symbols correspond to corrected measurements. The uncertainty bars correspond to the range of our estimated dynamic holdup volume. Curves and × symbols correspond to model predictions.

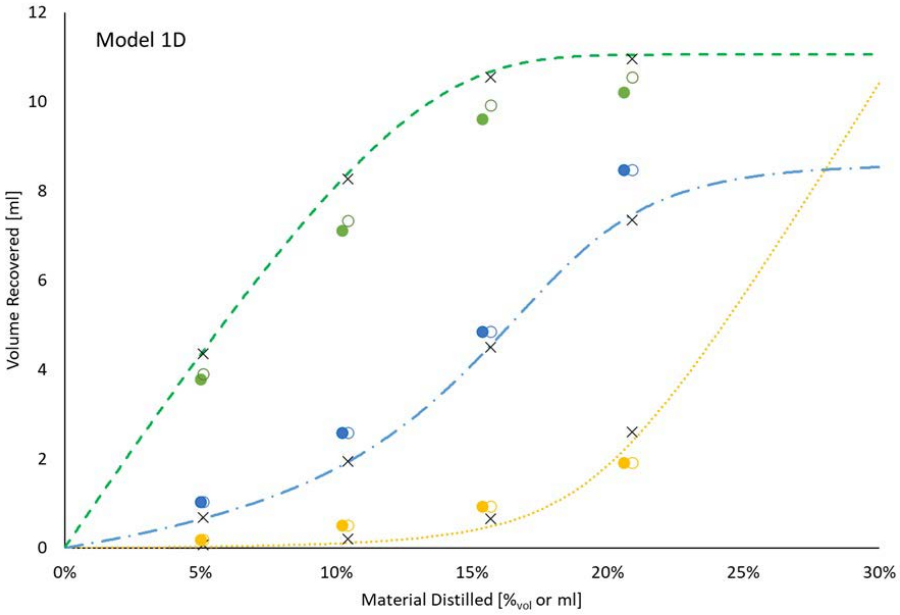


Figure 12. Measured and predicted distillate composition of a mixture of isooctane and o-xylene in tetradecane. Filled symbols correspond to measurements. Open symbols correspond to corrected measurements. Curves and × symbols correspond to model predictions. Green symbols and curves correspond to isooctane. Blue corresponds to o-xylene. Yellow corresponds to n-tetradecane.

Conclusions

A global two-parameter vapor pressure model that is rooted in our physical understanding of evaporation of hydrocarbon mixtures has been developed. Sixteen vapor pressure measurements involving two different temperatures, two binary



systems and four concentrations were used to tune the parameters, which were used to scale both the activation energy (or heat of vaporization) term and reference temperature term in the Clausius–Clapeyron equation as a function of the mole fraction.

Comparisons to 29 points ($T,P,\{x_i\}$) and four temperature curves have been presented, showing dramatically better accuracy relative to Raoult's Law and comparable accuracy relative to the UNIFAC model. Additionally, two comparisons between measured and predicted distillation curves and distillate compositions of two different ternary mixtures further demonstrate that the simple vapor pressure model presented here outperforms Raoult's Law, but these comparisons also highlight the fact that modelling the distillation process is challenging.

The confounding of distillation process modeling errors with vapor pressure (and vapor composition) modeling errors makes it difficult to validate either from data collected during a distillation experiment. To get around this issue and the uncertainty it causes, crude oil (whether synthetic or petroleum in origin) refiners may employ somewhat more fractionation than necessary, which also desensitizes the process to vapor pressure model accuracy. Alternatively, mature yet computationally extensive options available through Aspen Plus, DWSIM or ChemCAD may offer more accurate process simulations, but it would be impractical to put such tools within the inner-most loop of decision logic to select the cut points of crude oil refinement, and essentially impossible to nest them into computational fluid dynamics simulation of evaporation under combustor operating conditions near ignition, lean blow out or any other important combustor operating point. The model presented here provides dramatic improvement relative to Raoult's Law, with a very modest increase in computational complexity.

Milestone
Performed distillation optimization for eight SAF candidates from six different pathways.

Major Accomplishments
Developed a new vapor pressure model to capture molecules with low concentrations to improve distillation optimization model.

Publications
Yang, Z., Bell, D. C., Cronin, D. J., Boehm, R., Heyne, J., & Ramasamy, K. K. (2024). Volatility measurements of sustainable aviation fuels: a comparative study of D86 and D2887 methods. *ACS Sustainable Chemistry & Engineering, 12*(19), 7414-7420. https://doi.org/10.1021/acssuschemeng.4c00678

Yu, S., He H., Summers, S., Yang, Z., Si, B., Heyne, J., Zhang, Y., Yang, H. (2025). Upgrading of biocrude oil into sustainable aviation fuel using molybdenum carbide nanocatalysts, *Science Advances*. 11(26), 5777. https://doi.org/10.1126/sciadv.adu5777

Boehm, R., Parker, R., Yang, Z., Dooley, S., & Heyne, J. (2025). Blend Prediction Model for Vapor Pressure of Jet Fuel Range Hydrocarbons. *Sustainability, 17*(21), 9612. https://doi.org/10.3390/su17219612

Outreach Efforts
None.

Awards
Joshua Heyne – 2024 Energy and Fuels Rising Starts

Student Involvement
Washington State University PhD student, Alexander Kelly, leads this effort.

Plans for Next Period
- Continue improvement on the distillation optimization tool and procedure with the new vapor pressure model.
- Coordinate with novel fuel producers to optimize their distillation process.

References
Antoine, M. C. (1888). Nouvelle relation entre les tensions et les temperatures. *Seanc. Acad. Sci.,107*, 681–684.



ASTM International. (2022a). *ASTM D7566-21: Standard Specification for Aviation Turbine Fuel Containing Synthesized Hydrocarbons*. https://doi.org/10.1520/D7566-21

ASTM International. (2022b). ASTM D6378-22: Standard Test Method for Determination of Vapor Pressure (VPX) of Petroleum Products, Hydrocarbons, and Hydrocarbon-Oxygenate Mixtures (Triple Expansion Method). https://doi.org/10.1520/D6378-22

ASTM International. (2023a). *ASTM D1655-25a: Standard Specification for Aviation Turbine Fuels*. https://doi.org/10.1520/D1655-25A

ASTM International. (2023b). *ASTM D4054-22: Standard Practice for Evaluation of New Aviation Turbine Fuels and Fuel Additives*. https://doi.org/10.1520/D4054-22

ASTM International. (2024a). ASTM D86-23: Standard Test Method for Distillation of Petroleum Products and Liquid Fuels at Atmospheric Pressure. https://doi.org/10.1520/D0086-23

ASTM International. (2024b). ASTM D2887-23: Standard Test Method for Boiling Range Distribution of Petroleum Fractions by Gas Chromatography. https://doi.org/10.1520/D2887-23

Bell, D. C., Boehm, R., & Heyne, J. S. (2025). Freezing Point of Hydrocarbon Fuels from Single Species Concentrations. *Energy Fuels*, *39*, 4221–4226. https://doi.org/10.1021/acs.energyfuels.4c06091

Clapeyron, P. E. (1834). Memoire sur la Puissance Motrice De La Chaleur. J. L'école Polytech/Publié Par Le Cons D'instruction Cet Établissement. https://gallica.bnf.fr/ark:/12148/bpt6k4336791/f157

Clausius, R. (1850). Ueber die bewegende Kraft der Wärme und die Gesetze, welche sich daraus für die Wärmelehre selbst ableiten lassen. *Annalen der Physik, 155*(4), 500–524. https://doi.org/10.1002/ANDP.18501550403

Côcco, L. C., Yamamoto, C. I., & Von Meien, O. F. (2005). Study of correlations for physicochemical properties of Brazilian gasoline. *Chemometrics and Intelligent Laboratory Systems*, *76*(1), 55–63. https://doi.org/10.1016/J.CHEMOLAB.2004.09.004

Colket, M., & Heyne, J. (2021). Progress in Astronautics and Aeronautics. In *Fuel Effects on Operability of Aircraft Gas Turbine Combustors*. The American Institute of Aeronautics and Astronautics, Inc., Reston, Virginia. https://doi.org/10.2514/4.106040

Cooper, J. B., Wise, K. L., Groves, J., & Welch, W. T. (1995). Determination of Octane Numbers and Reid Vapor Pressure of Commercial Petroleum Fuels Using FT-Raman Spectroscopy and Partial Least-Squares Regression Analysis. *Analytical Chemistry*, *67*(22), 4096–4100. https://doi.org/10.1021/ac00118a011

Crozier, P. S., & Rowley, R. L. (2002). Activity coefficient prediction by osmotic molecular dynamics. *Fluid Phase Equilibria*, *193*(1-2), 53–73. https://doi.org/10.1016/S0378-3812(01)00734-8

EASC. (1974). GOST 20227-74: Medical elastic bandages, Method for determination of ductility. Euro-Asian Council for Standardization, Metrology and Certification.

Ferris, A. M., & Rothamer, D. A. (2016). Methodology for the experimental measurement of vapor–liquid equilibrium distillation curves using a modified ASTM D86 setup. *Fuel*, *182*, 467–479. https://doi.org/10.1016/j.fuel.2016.05.099

Flecher, P. E., Welch, W. T., Albin, S., & Cooper, J. B. (1997). Determination of octane numbers and Reid vapor pressure in commercial gasoline using dispersive fiber-optic Raman spectroscopy. *Spectrochimica Acta Part A: Molecular and Biomolecular Spectroscopy, 53*(2), 199–206. https://doi.org/10.1016/S1386-1425(97)83026-0

Flumignan, D. L., de Oliveira Ferreira, F., Tininis, A. G., & de Oliveira, J. E. (2008). Multivariate calibrations in gas chromatographic profiles for prediction of several physicochemical parameters of Brazilian commercial gasoline. *Chemometrics and Intelligent Laboratory Systems*, *92*(1), 53–60. https://doi.org/10.1016/J.CHEMOLAB.2007.12.003

Fredenslund, A., Jones, R. L., & Prausnitz, J. M. (1975). Group-contribution estimation of activity coefficients in nonideal liquid mixtures. *AIChE Journal, 21*(6), 1086–1099. https://doi.org/10.1002/aic.690210607

Gaudin, T., & Ma, H. (2020). The macroscopic viscosity approximation: A first-principle relationship between molecular diffusion and viscosity. *AIP Advances, 10*(3). https://doi.org/10.1063/1.5131234

Gmehling, J., Li, J., & Schiller, M. (1993). A modified UNIFAC model. 2. Present parameter matrix and results for different thermodynamic properties. *Industrial & Engineering Chemistry Research*, *32*(1), 178–193. https://doi.org/10.1021/ie00013a024

Hawkes, S. J. (1995). Raoult's law is a deception. *Journal of Chemical Education, 72*(3), 204. https://doi.org/10.1021/ed072p204

Hsieh, C.-M., Sandler, S. I., & Lin, S.-T. (2010). Improvements of COSMO-SAC for vapor–liquid and liquid–liquid equilibrium predictions. *Fluid Phase Equilibria, 297*(1), 90–97. https://doi.org/10.1016/j.fluid.2010.06.011

Hung, Y.-C., Su, S.-W., Yan, J.-W., & Hong, G.-B. (2024). Vapor-liquid equilibrium for binary systems containing n-alkanes and cycloalkanes. *Fluid Phase Equilibria*, *578*, 114004. https://doi.org/10.1016/j.fluid.2023.114004



IATA. (2025). Our Commitment to Fly Net Zero by 2050. International Air Transport Association. https://www.iata.org/en/programs/sustainability/flynetzero/?utm_source=chatgpt.com

Kroenlein, K., Muzny, C., Kazakov, A., Diky, V., Chirico, R., & Magee, J. (2012). *NIST Standard Reference 203, TRC Web Thermo Tables (WTT)*. National Institute of Standards and Technology, Gaithersburg, Maryland.

Kunz, O., & Wagner, W. (2012). The GERG-2008 Wide-Range Equation of State for Natural Gases and Other Mixtures: An Expansion of GERG-2004. *Journal of Chemical & Engineering Data, 57*(11), 3032–3091. https://doi.org/10.1021/je300655b

Lemmon, E. W., Bell, I. H., Huber, M. L., & McLinden, M. O. (2013). *NIST Standard Reference Database 23: Reference Fluid Thermodynamic and Transport Properties-REFPROP, Version 8.0, Natl Std. Ref. Data Series* (NIST NSRDS). National Institute of Standards and Technology, Gaithersburg, Maryland.

Linstrom, P. J., & Mallard, W. G. (2001). The NIST Chemistry WebBook: A Chemical Data Resource on the Internet. *ournal of Chemical & Engineering Data*, *46*(5), 1059–1063. https://doi.org/10.1021/je000236i

Lísal, M., Smith, W. R., & Nezbeda, I. (1999). Accurate Computer Simulation of Phase Equilibrium for Complex Fluid Mixtures. Application to Binaries Involving Isobutene, Methanol, Methyl tert-Butyl Ether, and n-Butane. *Journal of Physical Chemistry B*, *103*(47), 10496–10505. https://doi.org/10.1021/jp991188f

Lundberg, G. W. (1964). Thermodynamics of Solutions XI. Heats of Mixing of Hydrocarbons. *Lundberg, G. (1964). Thermodynamics of Solutions XI. Heats of Mixing of Hydrocarbons. Journal of Chemical & Engineering Data, 9, 193-198.* https://doi.org/10.1021/JE60021A013

Mendes, G., Aleme, H. G., & Barbeira, P. J. S. (2017). Reid vapor pressure prediction of automotive gasoline using distillation curves and multivariate calibration. *Fuel, 187*, 167–172. https://doi.org/10.1016/J.FUEL.2016.09.046

Miller, J. H., Tifft, S. M., Wiatrowski, M. R., Thathiana Benavides, P., Huq, N. A., Christensen, E. D., Alleman, T., Hays, C., Luecke, J., Kneucker, C. M., Haugen, S. J., Sànchez i Nogué, V., Karp, E. M., Hawkins, T. R., Singh, A., & Vardon, D. R. (2022). Screening and Evaluation of Biomass Upgrading Strategies for Sustainable Transportation Fuel Production with Biomass-Derived Volatile Fatty Acids. *iScience, 25*(11). https://doi.org/10.1016/j.isci.2022.105384

Ministry of Defence. (2025). Defence Standard 91-091: Turbine Fuel, Kerosene Type, Jet A-1; NATO Code: F-35; Joint Service Designation: AVTUR (Issue 18). United Kingdom. https://www.jig.org/documents/defstan-91-091-issue-18/

Mondragon, F., & Ouchi, K. (1984). New method for obtaining the distillation curves of petroleum products and coal-derived liquids using a small amount of sample. *Fuel*, *63*(1), 61–65. https://doi.org/10.1016/0016-2361(84)90256-4

Opacich, K. C., Peiffer, E., & Heyne, J. S. (2019). Analyzing the Relative Impact of Spray and Volatile Fuel Properties on Gas Turbine Combustor Ignition in Multiple Rig Geometries (AIAA 2019-1434). *AIAA Scitech 2019 Forum.* https://doi.org/10.2514/6.2019-1434

Poling, B. E., Prausnitz, J. M., & O'Connell, J. P. (2001). *Properties of Gases and Liquids* (5th ed). Graw-Hill Education: Columbus, Ohio.

Rauch, B. (2017). Systematic Accuracy Assessment for Alternative Aviation Fuel Evaporation Models [Doctoral Thesis, Universität Stuttgart]. Stuttgart, Germany.

State Bureau of Technical Supervision. (1997). GB/T 6539-1997: Standard test methods for electrical conductivity of aviation and distillate fuels. National Standard of the People's Republic of China. https://www.chinesestandard.net/PDF/English.aspx/GBT6539-1997

Striebich, R. C., Shafer, L. M., Adams, R. K., West, Z. J., DeWitt, M. J., & Zabarnick, S. (2014). Hydrocarbon group-type analysis of petroleum-derived and synthetic fuels using two-dimensional gas chromatography. *Energy Fuels*, *28*, 5696–5706. https://doi.org/10.1021/ef500813x

Trinklein, T. J., Prebihalo, S. E., Warren, C. G., Ochoa, G. S., & Synovec, R. E. (2020). Discovery-based analysis and quantification for comprehensive three-dimensional gas chromatography flame ionization detection data. *Journal of Chromatography A*, *1623*. https://doi.org/10.1016/j.chroma.2020.461190

Trouton, F. (1884). IV. On molecular latent heat. *The London, Edinburgh, and Dublin Philosophical Magazine and Journal of Science*, *18*(110), 54–57. https://doi.org/10.1080/14786448408627563

Wagner, W. (1973). New vapour pressure measurements for argon and nitrogen and a new method for establishing rational vapour pressure equations. *Cryogenics, 13*, 470–482. https://doi.org/10.1016/0011-2275(73)90003-9

Wilson, G. M. (1964). Vapor-Liquid Equilibrium. XI. A New Expression for the Excess Free Energy of Mixing. *Journal of the American Chemical Society, 86*(2), 127–130. https://doi.org/10.1021/ja01056a002

Yang, Z., Boehm, R. C., Bell, D. C., & Heyne, J. S. (2023). Towards sustainable aviation fuel distillation optimization. *Fuel*, *353*. https://doi.org/10.1016/j.fuel.2023.129136

Yang, Z., Kosir, S., Stachler, R., Shafer, L., Anderson, C., & Heyne, J. S. (2021). A GC × GC Tier α combustor operability prescreening method for sustainable aviation fuel candidates. *Fuel, 292.* https://doi.org/10.1016/j.fuel.2021.120345



Task 2 – Vapor Pressure Measurement for Sustainable Aviation Fuel

Washington State University

Objectives

The objectives of this task are intended to improve the current understanding of vapor pressure of approved SAF pathways and to develop and/or validate blending rules for vapor pressure.

Research Approach

There are several technical issues related to fuel vapor pressure. One key issue is the evaporation rate at temperatures below the boiling point. This rate is influenced by factors such as mass transfer rate, vapor pressure, and surface area. The evaporation rate directly affects droplet evaporation and the dry-out rate of purged staged circuits. Another concern is the pressure inside closed vessels, which can lead to "burping" and coking issues. These arise in systems such as the fuel metering unit and the fuel nozzle valve inlets during shutdown. Vapor pressure is also critical in simulated distillation modeling. During evaporation or vaporization, the composition of both liquid and gas-phase fuel evolves. This causes variations in chemical properties, such as derived cetane number (DCN) or threshold soot index (TSI), in the vapor phase. Furthermore, as the composition of lighter and heavier fractions changes, the vapor pressure and, consequently, the evaporation rate of the liquid phase will fluctuate throughout the process.

The vapor pressure measurements were performed using a PAC® Herzog HVP 972 instrument in accordance with ASTM D6378 (ASTM International, 2022). However, the instrument is currently out of order and unable to measure vapor pressure. Some experimental work has been conducted at Trinity College Dublin, and we are actively exploring the purchase of a replacement vapor pressure analyzer.

Milestone

Measured vapor pressure for two approved SAFs and two SAF candidates.

Major Accomplishments

Published new vapor pressure prediction model.

Publications

Boehm, R., Parker, R., Yang, Z., Dooley, S., & Heyne, J. (2025). Blend Prediction Model for Vapor Pressure of Jet Fuel Range Hydrocarbons. *Sustainability, 17*(21), 9612. https://doi.org/10.3390/su17219612

Outreach Efforts

None.

Awards

Joshua Heyne – 2024 Energy and Fuels Rising Starts

Student Involvement

Washington State University PhD student, Zhibin (Harrison) Yang, leads this effort. Joshua Ledezma, an undergraduate student at Washington State University, participated in this effort.

Plans for Next Period

- Continue measurements for vapor pressure of neat molecules, blends, and SAFs.
- Looking into a new vapor pressure machine for low temperature vapor pressure measurements.

Reference

ASTM International. (2022). ASTM D6378-22: Standard Test Method for Determination of Vapor Pressure (VPX) of Petroleum Products, Hydrocarbons, and Hydrocarbon-Oxygenate Mixtures (Triple Expansion Method). https://doi.org/10.1520/D6378-22



Project 104(A) Methodology for Assessing Changes in Soil Organic Carbon

The Pennsylvania State University

Project Lead Investigator

Lara Fowler
Professor of Teaching, Penn State Dickinson Law
Affiliate Faculty, Penn State School of International Affairs
The Pennsylvania State University
231 Katz Building
University Park, PA 16802
814-865-4806
Lbf10@psu.edu

University Participants

The Pennsylvania State University (Penn State)

- P.I.s: Lara Fowler, Professor of Teaching, Penn State Dickinson Law; Armen R. Kemanian, Professor of Production Systems and Modeling, College of Agricultural Sciences (starting with funding period beginning December 12, 2024).
  - Researchers: Yuning Shi, Associate Research Professor, Penn State; Emmy Wang, MS Candidate, Agricultural and Environmental Plant Science, Penn State; Alicia Costello, MS Candidate, Ecology, Penn State.
- FAA Award Number: 13-C-AJFE-PSU, RISK-INFORMED ALTERNATIVE JET FUEL (AJF)
- Periods of Performance: December 12, 2024, to September 30, 2026 (time period extended to 2026 through no-cost extension).
- Tasks:
  1. Soil Organic Carbon
     1.1. Work with ASCENT Project 001 team to identify stakeholder engagement opportunities
  2.
     2.1. Complete an analysis of the return of fermentation byproducts to the soil including collaboration with colleagues from Dartmouth College.
     2.2. Analysis of the return of fermentation byproducts to the soil using a carbon balance model and an experimental approach.
     2.3. Apply Cycles-A to the task of fitting sustainable aviation fuel (SAF) crops in the current agricultural matrix of the United States, with focus on oil crops, specifically pennycress, camelina, and *Brassica, carinata* as examples.

Project Funding Level

Federal Aviation Administration (FAA) funding: $163,195 (for December 12, 2024, to September 30, 2026)
Matching from Penn State: $165,814
Total funding: $329,009

Investigation Team

Period July 1, 2023, to September 30, 2026:

- Task 4.1 (Kemanian, Fowler, Wang, & Costello): Accounting for SOC and annual oil crops incorporation using agroecosystem model



Task 1 – Soil Organic Carbon

The Pennsylvania State University

Objective

Incorporate Penn State expertise on soil carbon and nitrogen cycling in the context of the calculation of the carbon intensity of SAF. This includes incorporating carbon cycling modeling and the inclusion of uncertainty bounds, methods for standardizing calculations that encompass baseline (or reference) scenarios and SAF production scenarios. These methods need to be applicable worldwide, but the initial focus is the Contiguous United States (CONUS). In addition, it is expected that similar work accounting for the nitrogen cycle including the carbon footprint associated with the use of fertilizers and an accounting for the emissions of nitrous oxide, whose equivalent carbon footprint can surpass that of soil organic carbon (SOC) both as a positive or negative climate forcing.

Establish the soil carbon balance when amending the soil with byproducts of fermentation for the generation of the alcohol-to-jet (ATJ) fuel. This work will combine experimental and modeling work.

Use an automatic crop sequencer, Cycles-A, to identify opportunities to incorporate oil crops for SAF as winter crops in annual crop rotations across CONUS. The analysis will allow us to access tradeoffs in yield and carbon intensity at the county level. This work contributes to quantifying the uncertainty of fertilization requirements and resulting nitrous oxide emissions, as well as changes in SOC arising from the intensification of SAF production.

Research Approach

The research approach for this task includes developing a standard method to account for land use and SAF production using Earth Stats and level three Global Administrative Areas (GADM) to report calculations on a field basis but also on political units of relevance that are standardized around the world. This task also includes overlaying the North American Land Data Assimilation System (NLDAS) (reanalysis) climate databases, and International Soil Reference and Information Centre (ISRIC) soils, so that the model Cycles (developed in Dr. Kemanian's lab) can be operated through the cropland domain. Finally, this task includes using machine learning combined with a standard initialization procedure to estimate steady state soil carbon stocks under business as usual (BAU) and alternative SAF production scenarios.

Establish both the theoretical framework and model as well as an experimental set up to evaluate the soil carbon balance when the soil is used to produce feedstock for jet fuel. Specifically, we are exploring the path from ATJ fuel, under the assumption that the alcohol is of cellulosic origin and that the fermentation byproducts are returned to the soil.

We will use Cycles-A to generate crop sequences for a representative field from each county for the rainfed area of United States (U.S.). To integrate novel oil crops, we will calibrate a crop profiles using multi-location field trial data and develop a winter-crop phenology algorithm for Cycles-A.

Milestones

The team established a stable database of land use, weather data, and soils, along with automated methods to run simulations with Cycles, and downloaded and curated the U.S. Department of Agriculture-Natural Resources Conservation Service (NRCS) pedon database for machine learning analysis. The team continues systematically updating the information required for a publication reporting expected changes in SOC. The proper allocation of biomass to rainfed and irrigated land, as well as carbon inputs from manure have been resolved. We next aim to obtain accurate estimations of carbon inputs from crop residues.

Additional steps included setting up a soil incubation method to resolve standing questions on SOC storage when amending the soil with byproducts of fermentation.

We also developed an automated mixing model to separate respiration (carbon dioxide [CO_2]) from native soil organic matter and decomposition residue using the isotopic signature. This model, now in a spreadsheet, will allow model inversion via optimization to parameterize the carbon stabilization (SOC storage) parameters.

Finally, we assembled a dataset for winter crop phenology to develop algorithms and parameters to realistically and automatically schedule the planting of winter crops.



Major Accomplishments

Dr. Yuning Shi updated the global weather data from the Global Land Data Assimilation System (GLDAS) reanalysis database, to allow simulation of any crop rotation worldwide. Dr. Yuning Shi and Dr. Armen Kemanian started developing a two-dimensional (2D) version of the model Cycles that will allow simulation of nitrous oxide fluxes in systems with banding of nitrogen fertilizer or manure. Banding is a common practice in crop production. Ignoring nitrogen banding can lead to gross underestimations of nitrogen uptake by crops and alter nitrous oxide emission estimates. The 2D version relies on the use of C-language Variable-coefficients ODE solver (CVODE), a solver for a system of ordinary differential equations maintained by the Lawrence Livermore National Laboratory. So far, water transport in 2D is still being tested, including infiltration that is resolved using a modification of the Green and Ampt method, and water redistribution using Richard's equation. This system will be now incorporated into Cycles-A.

Student Alicia Costello successfully set up an automatic incubation method to measure soil respiration from native soil organic matter versus that from decomposing fresh residues or digestate. The system that is now operational includes retooling an existing CO_2 isotopic analyzer from Picarro, Inc. (Model G2121-i) and adding incubation jars that can be sampled automatically through the incubation period. This experimental setup will provide data of exceptional quality to investigate the carbon balance of soils amended with residues from fermentation in the path from ATJ fuel. The system has been tested and works as expected; it will start yielding results through 2026.

Student Emmy Wang successfully set up and ran Cycles-A simulations at one location using the Penn State Roar Colab cluster (Penn State's high performance computer cluster), successfully generating a response curve about the ratio of pennycress to winter wheat in Darke County, Ohio. For this purpose, Wang created a winter wheat planting and flowering database that was used to modify and calibrate the module handling crop phenology. The phenology module is now generic and includes pennycress as well.

Publications

None. A publication on this topic has been reported through ASCENT Project 001.

Outreach Efforts

Presentations

None. A presentation on this topic has been reported through ASCENT Project 001.

Posters

Costello, A., Montes, F., & Kemanian, A. (2025, October). *Carbon stabilization during incubation of fermentation byproducts* [Poster presentation]. Fall 2025 ASCENT Meeting, Alexandria, Virginia.

Costello, A., Montes, F., & Kemanian, A. (2025, November). *Carbon stabilization during incubation of fermentation byproducts* [Poster presentation]. Science Societies CANVAS conference, Salt Lake City, Utah.

Wang, E., Shi, Y., Fowler, L., Kemanian, A. (2025, October). *Algorithm-based exploration of double cropping with oilseed crops for SAF* [Poster presentation]. Fall 2025 ASCENT Meeting, Alexandria, Virginia.

Wang, E., Shi, Y., White, C., & Kemanian, A. (2025, November). *Algorithm-based exploration of double cropping with oilseed crops* [Poster presentation]. Science Societies CANVAS conference, Salt Lake City, Utah.

Awards

Poster won the 3rd place award for the Climatology and Modeling Section, "Wang, E., Shi, Y., White, C., Kemanian, A. (2025, November). *Algorithm-based exploration of double cropping with oilseed crops* [Poster presentation]. Science Societies CANVAS conference, Salt Lake City, Utah."

Student Involvement

Emmy Wang, MS Candidate, Agricultural and Environmental Plant Science, and Alicia Costello, MS Candidate, Ecology, contributed to this research. Both presented posters at the ASCENT October 2025 Fall Meeting in Alexandria, Virginia; and at the Science Societies CANVAS (formerly Tri-society meeting involving the Agronomy, Crop Science, and Soil Science Society of America in November) 2025 Annual Meeting in Salt Lake City, Utah.

Plans for Next Period

As a joint-effort by the Penn State team working on ASCENT Projects 001 and 104, the top-down modeling of the SOC balance at the county level presented in the ASCENT meeting in Alexandria, Virginia, in October 2024 is being refined and



the results will be summarized in a draft article for publication. Specifically, the analysis to date used SOC from the STATSGO (U.S. General Soil Map) database; it will be replaced (or duplicated) with the global Soil Grids database from the ISRIC. Carbon input, which were estimated using only grain yield and forage yield, will be updated with a longer statistical time series from the National Agricultural Statistical Service and parsed for rainfed and irrigated land, although the analysis will only focus on rainfed soils. As reported before, the analysis has been completed for corn, and we are proceeding with estimates of carbon inputs from other crops. The target journals are *Global Change Biology – Bioenergy* (University of Oxford) and *Energy Advances* (Royal Society of Chemistry). This manuscript will complete the transition of SOC and nitrogen work from ASCENT Project 001 to Project 104.

Experimental and modeled soil carbon balance when adding corn residue to soils as compared to adding high lignin byproducts of fermentation for alcohol or its best known surrogate, digestate that are the byproducts of anaerobic digestion. This task will be part of the MS program of Alicia Costello.

Simulation of oil crops in all areas that include rainfed annual crops using Cycles-A in CONUS. The Cycles-A algorithm finds crop sequences that maximize economic output based on the expected price of grain and forage crops in the menu for a given location, and the cost of production. A system to include weather stochasticity allows generating independent crop sequence for a region that, when analyzed collectively, identify the sequence that maximizes yield or reduces the SAF carbon footprint.



Project 104(B) Methodology for Assessing Changes in Soil Organic Carbon

Purdue University

Project Lead Investigator

Farzad Taheripour
Research Professor
Department of Agricultural Economics
Purdue University
403 Mitch Daniels Blvd.
West Lafayette, IN 47906-2056
765-494-4612
tfarzad@purdue.edu

University Participants

Purdue University

- P.I.: Farzad Taheripour, Research Professor
- FAA Award Number: 13-C-AJFE-PU-058
- Period of Performance: December 3, 2024, through December 31, 2025
- Tasks:
  1. Review the literature and data sources and establish benchmark datasets for land cover and soil carbon content by land types at a global scale by country.
  2. Improve the agro-ecological zone emission factor (AEZ-EF) model and continue to investigate potential gains in soil carbon content due to improvements in land management practices. Special attention will be made to improvements in soil carbon content due to new technologies that improve crop plants root systems to sequester more carbon into soils.

Project Funding Level

This project received funding from the Federal Aviation Administration (FAA) as follows:
Amendment 58: $426,323.00

Current cost sharing for this project year was provided by Neste US, Inc.

Investigation Team

Prof. Farzad Taheripour (P.I.), All Tasks
Prof. Dominique van der Mensbrugghe (co-P.I.), Tasks 2, 3
Prof. Qianlai Zhuang (co-P.I.), All Tasks
Research Assistant Prof. Maksym Chepeliev, (co-P.I.), Tasks 1 and 2
Research Associate Prof. Uris Baldos (co-P.I.), All Tasks
Angel Aguiar (research economist), Tasks 1 and 2
Associate Prof. Mohsen Mohammadi (co-P.I.), Task 3
Shuo Chen (PhD student), Tasks 1 and 2
Xiangyu Liu (PhD student), Tasks 3
Ye Yuan (PhD student), Tasks 1 and 2
Lauren Benavidez (PhD student), All Tasks

Project Overview

The project focused on various activities including updating the AEZ-EF model to adopt the 2019 Intergovernmental Panel on Climate Change (IPCC) guidelines in assessing lands use emission factors, assessing the existing data and approaches that provide land use emission factors used in the AEZ-EF model; and studying and proposing a methodology to measure, check, and verify changes in the soil carbon content of cropland including soil organic carbon (SOC) at the farm level due to production of sustainable aviation fuels (SAF) or other biofuels. It also considers impacts of improvements in crop roots on soil carbon content.

Task 1 – Review the Literature and Data Sources and Establish Benchmark Datasets for Land Cover and Soils Carbon Content by Land Types at a Global Scale by Country

Purdue University

Objectives

The objectives of this task are to review the existing data sources that have been commonly used in determining land use emissions factors in assessing indirect land use change (ILUC) emissions for biofuels, including SAF, and to develop a database that traces land use changes at the global scale by country at 500 m between 2001 and 2020. Use the results of these activities to establish a benchmark dataset that represents SOCs by land types at a global scale by country and review the existing methodologies that have been used by the regulatory agencies across the world to measure, check, and verify changes in SOC at a farm level due to changes in agricultural practices.

Research Approach

This task will study the existing research in this field and find the relevant available data including satellite data sources and their content. Additionally, this task will develop proper cods to read the available data and process and analyze them.

Milestones

- Review of various satellite data on land cover has been accomplished,
- Review of global datasets on SOC data has been accomplished,
- Several papers have been developed.

Major Accomplishments

- Prepared a land cover dataset for 2001 to 2020 to be used in the Global Trade Analysis Project (GTAP)-BIO model.
- Provided the required data to update the AEZ-EF model.

Publications

Chen, S., Zhuang, Q., Taheripour, F., Yuan, Y., & Benavidez, L. (2025). Assessment of global land cover changes using satellite data: intermittent and long-term land cover changes from 2001 to 2020. *Environmental Research Letters*, *20*(3). http://dx.doi.org/10.1088/1748-9326/adb5a3

Chen, S., Taheripour, F., Baldos, U. L., Zhuang, Q., Yuan, Y., & Benavidez Hernandez, L. (2025, December 15-19). *Global pastureland changes from 2001 to 2020* [Conference presentation]. AGU Fall Meeting 2025, New Orleans, Louisiana.

Yuan, Y., Taheripour, F., Baldos, U. L., Chen, S., & Zhuang, Q. (2025, December 15-19). *Improving forest carbon accounting in economic models: Updating GTAP land cover with recent remote sensing products* [Conference presentation]. AGU Fall Meeting 2025, New Orleans, Louisiana.

Liu, X., Zhuang, Q., Taheripour, F., & Benavidez, L. (2025, December 15-19). *Global Marginal Land Mapping and Impact of Agricultural Management Practices on Marginal Land Soil Organic Carbon* [Conference presentation]. AGU Fall Meeting 2025, New Orleans, Louisiana.

Outreach Efforts

The results of this research will be used in ILUC assessment for Carbon Offsetting and Reduction Scheme for International Aviation (CORSIA) and other national and state biofuel policies.



Awards
None.

Student Involvement
- EhsanReza Sajedinia, current PhD student Purdue University, for data collection and running simulations.
- Lauren Benavidez, current PhD student, Purdue University, for data collection and working with land use data, emission data, and models.
- Shuo Chen, current PhD student, Purdue University, for data collection and working with land use data, emission data, and models.
- Xiangyu Liu, current PhD student, Purdue University, for data collection and working with land use data, emission data, and models.
- Ye Yuan, current PhD student, Purdue University, for data collection and working with land use data, emission data, and models.

Plans for Next Period
- Finish the soil and vegetation carbon assessments at the global scale using satellite data sources to update this data component of the AEZ-EF model.
- Complete the Threat and Error Management (TEM) simulations in (1) measuring the impacts of the land management practices on the SOC content of cropland and (2) measuring the consequences of plants' root improvements on the soil carbon content of cropland.

Task 2 – Improve the AEZ-EF model and Continue to Investigate Potential Gains in Soil Carbon Content due to Improvements in Land Management Practices
Purdue University

Objectives
The objectives of this task are to (1) improve the AEZ-EF model to operate based on the most recent available databases using the results of Task 1 to provide more accurate ILUC assessments, (2) use the TEM model to investigate potential gains in soil carbon content due to implementation of advanced land management practices, and (3) evaluate carbon savings due to improvements in crops root systems using the TEM model.

Research Approach
This task will convert the results of task 1 to the AEZ-EF format to update this model. It also calibrates the TEM model to the collected datasets in task 1 and runs various simulations to achieve the goals of this project.

Milestone
- Updated the AEZ-EF model to follow the IPCC 2019 guidelines and use the most recent version of the Harmonized World Soil Database and several national maps. The first revision has been already adopted by the Working Group 5 (WG5) of CORSIA in ILUC assessment. The second revision is expected to be approved by the WG5 in 2026 to be used in the next round of ILUC assessment.

Major Accomplishments
- Implemented the results of this work to revise the ILIUC values for about 50 regional and global SAF pathways of CORSIA. The results of this work have also been used in calculating several ILUC values for the 45Z provision of the Inflation Reduction Act of 2022.

Publications
Peer Reviewed Journal Publications

Benavidez-Brouk, L., Taheripour, F., Baldos, U., Zhuang, Q., & Chen, S. (2026). Updates in assessing soil organic carbon and their implications for evaluating land use change emissions. Environmental Research Communications, 8(2). https://doi.org/10.1088/2515-7620/ae3d84



Liu, X., Taheripour, F., Zhuang, Q., & Benavidez Hernandez, L. (2026, under review). Global marginal land mapping and the impact of agricultural management practices on marginal land soil organic carbon. *Environmental Research Letters*.

Outreach Efforts

- Dr. Taheripour has reviewed many academic papers for various journals that provide publications in research areas associated with Task 2.
- Dr. Taheripour, Dr. Chepeliev, Dr. Aguiar, Sajedinia, Chen, and Yuan attended the ASCENT Advisory Group meetings in Spring 2025 and Fall 2025 and discussed the findings of this task with members of this community.

Awards

None.

Student Involvement

See the list under Task 1.

Plans for Next Period

- Finalize the modifications in the AEZ-EF model.
- Complete the TEM simulations.



Project 104(C) Methodology for Assessing Changes in Soil Organic Carbon

University of Tennessee

Project Lead Investigator

Timothy Rials
Professor and Associate Dean
AgResearch, University of Tennessee
2506 Jacob Dr., Knoxville, TN 37996
865-946-1130
trials@utk.edu

University Participants

University of Tennessee (UT)

- P.I.: T. Edward Yu
- FAA Award Number: 13-C-AJFE-UTenn-025
- Period of Performance: December 3, 2024, through December 31, 2025
- Tasks:
  1. Enhance Soil Organic Carbon (SOC) Mapping Across the Continental United States (CONUS)
  2. Assess the direct and spatial spillover impact of agricultural management practices on agricultural productivity and sustainability
  3. Collaborate with other members in ASCENT Project 104 for SOC research (supporting role)

Project Funding Level

The Federal Aviation Administration (FAA) provided $314,999 in funding; matching funding is provided by UT ($317,753), including personnel salaries and benefits, software license, publication costs, soil sample data, and tuition remission.

Investigation Team

Timothy Rials (Project Director – PD), Task 3
T. Edward Yu (P.I.), Tasks 1-3
Joshua S. Fu (co-PI), Tasks 1 and 3
Le Chen (faculty), Task 2
Virginia Sykes (faculty), Task 1
Forbes Walker (faculty), Task 1
Robert Florence (faculty), Task 1
Hannah Williams (Research Associate), Task 2
Hannah Rubin (PhD student), Task 1
Xinxin Zhang (PhD student), Task 1

Project Overview

Utilizing sustainable aviation fuel (SAF) from agricultural and forestry feedstock has been considered the major means to meet the carbon reduction targets of the Carbon Offsetting and Reduction Scheme for International Aviation (CORSIA) and the United States (U.S.) SAF Grand Challenge. It is crucial to have a well-designed life cycle analysis (LCA) for the SAF supply chain to align with the proposed carbon credit system to expedite SAF implementation. To make an adequate estimate of SOC in the SAF LCA, a systematic approach that *integrates spatial and temporal variations and continuity* is important. Most current soil carbon properties, flux, and storage databases are not spatially or temporally continuous. Thus, the goal of this study is to improve SOC estimates and investigate long-term trends in the U.S. using in-situ measurements from soil carbon networks and previous studies and incorporating satellite imagery and machine learning methods for more



complete spatial and temporal coverage. The impact of land use changes on SOC and agricultural sustainability is also the focus of this study.

Task 1 – Enhance Soil Organic Carbon (SOC) Mapping Across the Continental United States (CONUS)

University of Tennessee, Knoxville

Objectives

This task aims to develop improved estimates of SOC across the United States to support national soil health assessments and SAF LCAs. This year, our objectives are to refine SOC data inputs, rebuild the baseline modeling framework, and lay the foundation for transitioning from traditional machine learning methods to deep learning approaches.

Research Approach

Removing Duplicates/Outliers and Standardizing the Datasets from Various Sources

This year, we removed duplicate records and outliers, and standardized SOC observations across multiple datasets (Rapid Carbon Assessment [RaCA], National Cooperative Soil Survey [NCSS], International Soil Carbon Network [ISCN], World Soil Information Service [WOSIS], SOils DAta Harmonization [SoDaH], and Sanderman et al. (2018). All soil profiles were harmonized to a consistent 0–30 cm depth and standardized for units, geographic coordinates, sampling year, and layer structure. The resulting harmonized dataset in Figure 1 provides a uniform, credible foundation for producing aggregated SOC estimates and supporting future model development.

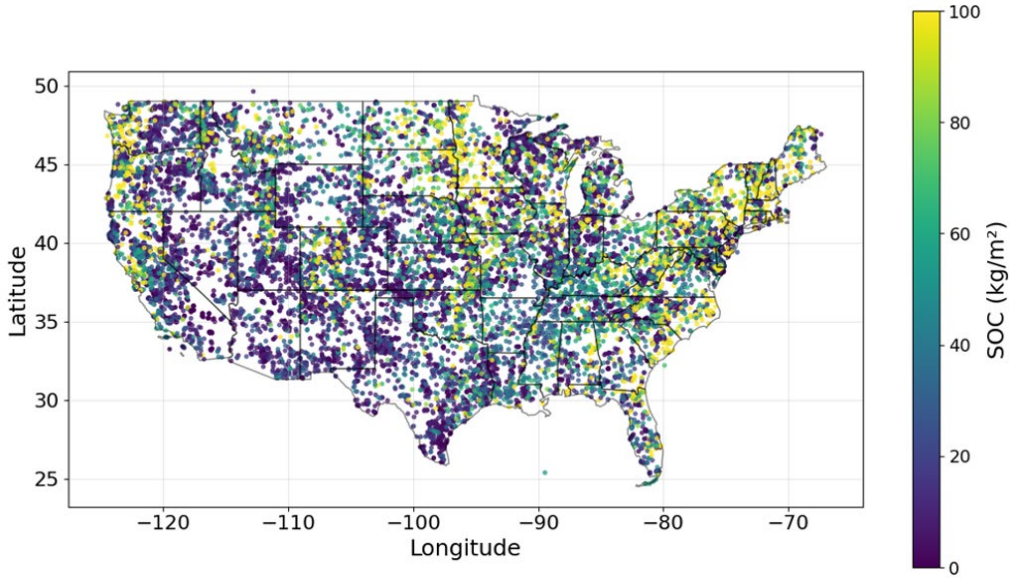


Figure 1. Spatial distribution of combined soil organic carbon (SOC) observations across all datasets (CONUS).

Environmental Covariates and Predictor Design

We compiled an expanded suite of environmental covariates, including vegetation indices (Normalized Difference Vegetation Index [NDVI], Enhanced Vegetation Index [EVI], Normalized Burn Ratio [NBR], Normalized Difference Moisture Index [NDMI], near-infrared [NIR], Short-wave infrared (SWIR)1/2 and red reflectance), topography indices (elevation, slope, aspect, Topographic Wetness Index [TWI], Topographic Position Index [TPI], and geology), climate variables (temperature and precipitation), soil properties (pH, texture, drainage class, soil moisture), and land use indicators. All predictors were spatially aligned with SOC observations using their geographic coordinates and sampling years. Together, these covariates form a robust foundation for improving existing machine learning models and enabling the development of forthcoming



deep learning approaches. Figure 2 summarizes vegetation, topographic, climate, soil, and land-use covariates, along with the SOC observations used as the target variable.

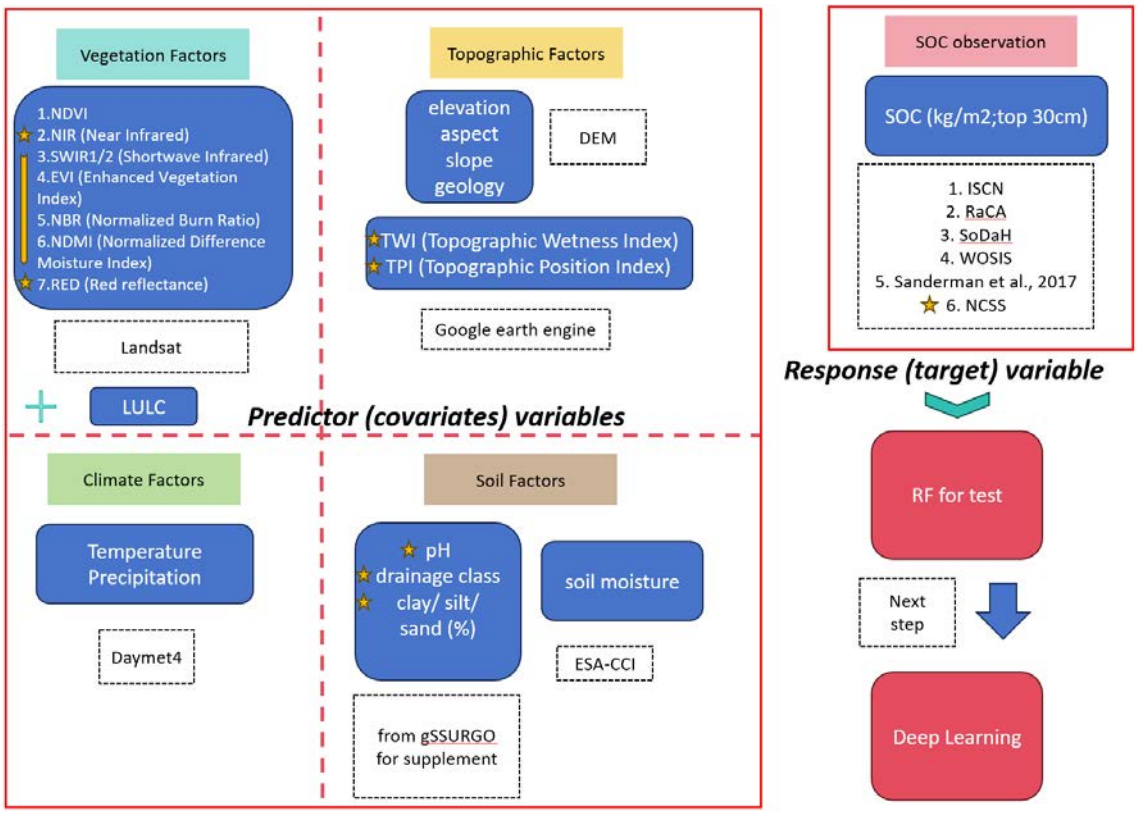


Figure 2. Overview of SOC predictor variables (blue boxes) and their corresponding data sources (dashed boxes) in model.

Machine-Learning Baseline and Model Improvement

We rebuilt the Random Forest (RF) baseline model using the cleaned SOC dataset and the expanded predictor set of predictor variables. A five-fold spatial cross-validation framework was implemented to evaluate model performance and assess its ability to generalize across different regions and environmental gradients.

To address the limitations of traditional machine-learning methods in handling large, high-dimensional SOC datasets, we also began laying the groundwork for transitioning to deep-learning approaches.

Reference

Sanderman, J. et al. (2018) A global map of mangrove forest soil carbon at 30 m spatial resolution. Environ. Res. Lett. 13, 55002.

Milestones

- Completed the compilation and standardization of SOC datasets from multiple sources.
- Mapped and evaluated the national spatial distribution of SOC observations.
- Established an updated SOC modeling framework incorporating an expanded set of predictor variables.
- Generated a preliminary 30-m SOC prediction for the year 2020.
- Prepared data structures and modeling routes for future deep-learning development.

Major Accomplishments

All SOC datasets were reprocessed by removing duplicates and standardizing units, sampling depths, and geographic coordinates. This effort substantially increased the number of usable, harmonized SOC observations and ensured consistent representation of 0–30 cm SOC stocks across all sources. The improved data foundation directly supports more robust modeling for both current machine-learning applications and future deep-learning development.

The updated SOC dataset led to a substantial improvement in model performance compared with earlier versions. Applying the RF model to the harmonized dataset increased the validation R^2 (coefficient of determination) from 0.59 (previous baseline) to 0.74, highlighting the benefits of both data cleaning and the expanded predictor set. Using this enhanced modeling framework, we generated a refined 2020 SOC stock estimate of approximately 70.45 Pg C, higher than the previous baseline estimate of 60.4 Pg C reported in the earlier SOC mapping study. This increase reflects the strengthened data foundation and improved modeling capability, rather than any temporal change in SOC. The 2020 map in Figure 3 serves as a test-year product that demonstrates the enhanced predictive capacity of the updated workflow.

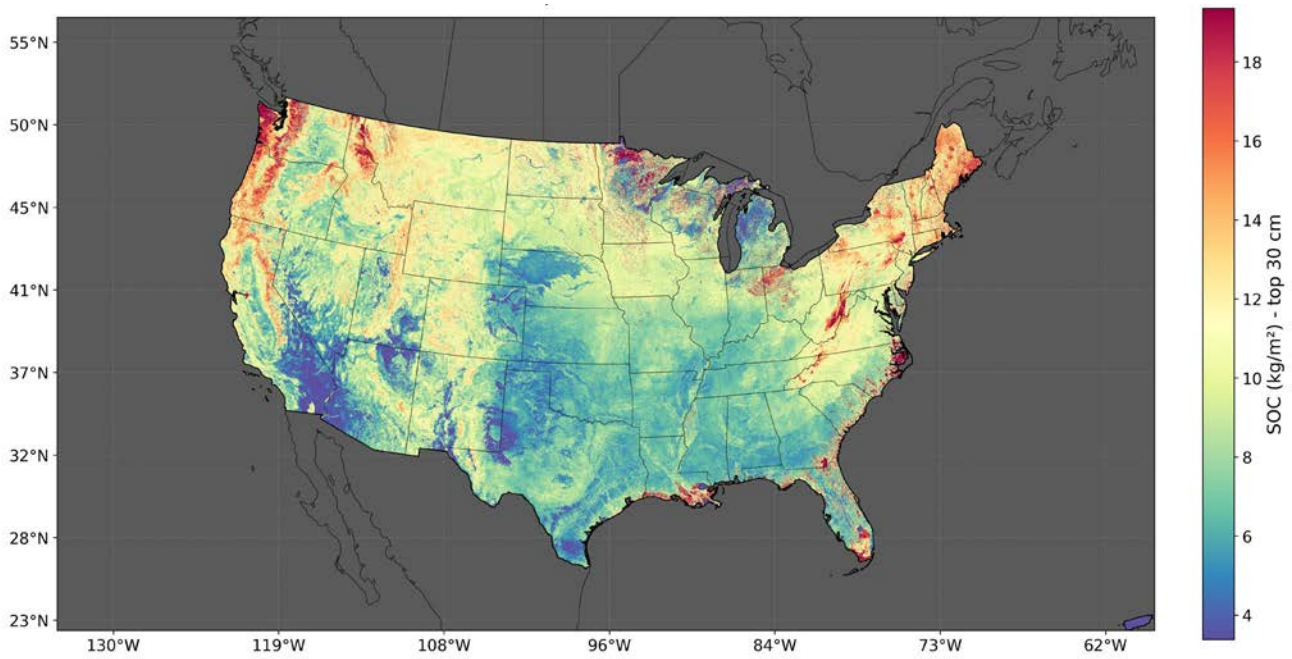


Figure 3. Estimated SOC stock for the year 2020 in the top 30 cm of soil (kg/m^2).

Publications

Rubin, H. J., Fu, J. S., & Yu, T. E. (2025). Mapping historical soil carbon in the United States with machine learning. *Manuscript under review.*

Outreach Efforts

None.

Awards

None.

Student Involvement

Hannah Rubin, a previous Ph.D. student, conducted the earlier phases of SOC analysis and graduated in May 2025. She is no longer involved in the project.



Xinxin Zhang, a Ph.D. student, took over Hannah Rubin's work and led the SOC-related work this year, including reorganizing SOC datasets, expanding predictor variables, running the updated RF model, and preparing data inputs for future deep learning applications.

Plans for Next Period

In the next reporting period, we will focus on advancing the SOC modeling framework beyond the current RF implementation. To support this transition, we will refine the predictor set by evaluating variable importance and reducing noise from less informative covariates. We will also incorporate additional satellite-derived indices and phenological variables to further enhance spatial and temporal coverage.

Building on the improved data foundation established this year, we will initiate the development of deep learning models to better capture the nonlinear, high-dimensional relationships that influence SOC formation. These models will be evaluated alongside traditional machine-learning approaches within a unified spatial cross-validation framework. Our goal is to produce more robust and reliable SOC prediction products that can support future soil-health assessments and SAF life-cycle analyses.

Task 2 - Assess the Direct and Spatial Spillover Impact of Farm Practices on Agricultural Productivity and Sustainability

University of Tennessee

Objective

Soil erosion has increasingly become a major concern in agricultural sustainability and environmental conservation. It is recognized as one of the most serious environmental challenges affecting global agriculture, as it adversely affects on-site crop productivity by reducing the availability of water, nutrients, and organic matter. Given the potential impact of soil erosion on agricultural productivity, there is extensive literature investigating the effects of soil erosion levels on crop yields. Studies have suggested that some farm practices, such as cover crops or no-tillage, could mitigate the soil erosion issue. However, little research has examined its spillover effects on surrounding agricultural fields. Soil erosion is inherently a spatial process, wherein displaced soil, nutrients, and sediments move beyond the eroded site, affecting adjacent farmlands. The objective of this study is to fill this gap by addressing the impact of soil erosion on crop yield using spatial statistical analysis, with an emphasis on both direct and spillover effects.

Research Approach

In this period, we conducted two studies to examine the related issue: first, we estimated the spatial spillover effect of soil erosion on crop productivity; and second, we explored the potential spillover effect of farm practices on SOC.

Study 1: The Impact of Soil Erosion on Corn Yields

We utilized unique county-level data for annual soil loss caused by erosion (in tons/acre) from the NRI program of the U.S. Department of Agriculture (USDA) Natural Resources Conservation Service (NRCS) and county-level data on corn yield from the USDA National Agricultural Statistics Service (NASS) for the census years 1992, 1997, 2002, 2007, 2012, and 2017. The resulting panel dataset used in the study covers 559 counties over eight states in the U.S. Corn Belt. We then applied a spatial regression approach to this panel dataset to assess the broader influence of soil erosion on crop yield beyond the area where it occurred, accounting for how erosion-induced changes in soil quality affect neighboring areas.

Study 2: The Impact of Cover Crops and No-Till Systems on Soil Organic Carbon

We used SOC data from 1990 to 2022 within the CONUS from Task 1. The fine-resolution SOC estimates (30 m) for the top 30 cm of soil are aggregated to the county level to match the farming management data. Satellite-based county-level adoption data for cover crops and no-till are then collected from the Operational Tillage Information System (OpTIS) database and compiled with the SOC data. The resulting dataset covers sixteen states (Colorado, Illinois, Indiana, Iowa, Kansas, Kentucky, Michigan, Minnesota, Missouri, Nebraska, North Dakota, Ohio, Oklahoma, South Dakota, Tennessee, and Wisconsin) from 2005 to 2020.

Milestones

- Completed the spatial regression analysis of the impact of soil erosion on corn yield in the Midwest for study 1.



- Disseminated the findings of the soil erosion analysis at the 2025 Southern Agricultural Economics Association annual meeting and developed a manuscript, which is accepted for publication in *Agrosystems, Geosciences & Environment*.
- Made a preliminary analysis of the impact of farm practices on SOC in study 2.
- Presented the preliminary analysis of study 2 at the 2025 Agricultural and Applied Economics Association annual meeting.

Major Accomplishments

Study 1: The Impact of Soil Erosion on Corn Yields

Table 1 summarizes the estimated coefficients of the explanatory variables and their direct, indirect (i.e., spatial spillover), and total effects. The results indicate that water erosion has a statistically significant and negative effect on corn yield, both within a county and in neighboring counties. The direct effects of water erosion on corn yield generally suggest that counties with higher levels of water erosion tend to have statistically lower corn yield, and this productivity effect is not explained by climate. Specifically, we find that each additional ton of soil loss per acre due to water erosion in a county can lead to a statistically significant decrease of 0.48 bushels (BU) per acre in its corn yield.

In addition to the direct effect, there is also a spillover effect of water erosion on corn yield in adjacent counties: each additional ton per acre of soil loss due to water erosion can lead to a statistically significant decrease of 1.22 BU/ac in corn yield. Thus, considering the direct and spillover effects of water erosion on corn yield, the total effect of water erosion indicates that each additional ton per acre of water erosion would result in a 1.70 BU/ac decrease in corn yield, suggesting a substantial overall regional impact of water erosion on corn yield in the U.S. Midwest. These findings imply that water erosion is not only a localized phenomenon but also has spatial externalities that affect surrounding agricultural productivity. Our study provides new empirical evidence that soil erosion is inherently a spatial phenomenon, whereby displaced soil, nutrients, and sediments are transported beyond the site of origin, impacting agricultural productivity in neighboring areas.

Table 1. Estimated coefficient and effect of explanatory variables on corn yield.

	Corn Yield			
	Coefficient	Direct Effect	Indirect Effect	Total Effect
Water Erosion	-0.3880* (0.2097)	-0.4815* (0.2537)	-1.2175* (0.6503)	-1.6990* (0.9208)
GDD	0.0023 (0.0051)	0.0031 (0.0066)	0.0079 (0.0166)	0.0110 (0.0232)
HDD	-0.2766*** (0.0212)	-0.3459*** (0.0240)	-0.8726*** (0.0610)	-1.2185*** (0.0799)
Precipitation	0.0365*** (0.0125)	0.0471*** (0.0149)	0.1191*** (0.0385)	0.1663*** (0.0533)
Precipitation squared	-0.0000*** (0.0000)	-0.0000*** (0.0000)	-0.0001*** (0.0000)	-0.0001*** (0.0000)
ρ	0.7720*** (0.0606)			
λ	0.8964*** (0.0424)			
County FE	Yes	Yes	Yes	Yes
Time FE	Yes	Yes	Yes	Yes
Observations	3354	3354	3354	3354

Note: *p<0.1, **p<0.05, *** p<0.01

FE: fixed effects; GDD: growing degree days; HDD: harmful degree days



Study 2: The Impact of Cover Crops and No-Till Systems on Soil Organic Carbon
Table 2 presents preliminary results on the effects of cover crops and no-till adoption on SOC using linear panel fixed effects (FE) estimation. Our parameter estimates suggest that counties with higher acres under no-till tend to have significantly higher SOC levels. Specifically, our results show that a 1% increase in acres under no-till adoption in a county can increase its SOC level by 0.0005%, indicating that no-tillage adoption has a positive effect on SOC by potentially promoting higher SOC accumulation over time. In contrast, the coefficient on the acreage of corn planted with cover crops is positive, but statistically insignificant. This suggests that cover crops may not have a measurable effect on SOC accumulation.

Table 2. Estimated coefficient of the explanatory variables on SOC. CC_ac: percent of cover crops per acre; FE: fixed effects; GDD: growing degree days; HDD: harmful degree days; NT_ac: percent of no-tillage per acre.

	0.00ln (Soil Organic Carbon)
ln (CC_ac)	0.0001 (0.0002)
ln (NT_ac)	0.0005* (0.0003)
GDD	-0.0076 (0.0056)
HDD	-0.0026 (0.0197)
Precipitation	0.0001*** (0.0000)
Precipitation squared	-0.0000***
County FE	Yes
Year FE	Yes
Adjusted R^2	0.050
Observations	11744

Standard error in parenthesis
*** p<0.10, **p<0.05, ***p<0.010**

Publications

Chen, L., T.E. Yu, and H. Williams. (2025). The Impact of Soil Erosion on Corn Yields: A Spatial Regression Analysis. *Agrosystems, Geosciences & Environment*, Accepted.

Outreach Efforts

Presentations

Chen, L., Yu, T.E., Rubin, H., Fu, J.S., & Rejesus, R. (2025, July 27-29). *The Impact of Adopting Cover Crops and No-Till Systems on U.S. Soil Organic Carbon* [Conference presentation]. 2025 Agricultural and Applied Economics Association (AAEA) Annual Meeting, Denver, Colorado. https://doi.org/10.22004/ag.econ.361059

Chen, L., Yu, T.E., & Williams, H. (2025, February 1-4). *Impact of Water and Wind Erosion on Corn and Soybean Yields: A Spatial Regression Analysis* [Conference presentation]. Southern Agricultural Economics Association (SAEA) 2025 Annual Meeting, Irving, Texas.

Awards

None.

Student Involvement

None.



Plans for Next Period

- Use satellite image data to further examine the impact of farm practices on SOC, as county-level data are too coarse to represent individual farm operations.
- Plan to incorporate spatial heterogeneity in both studies 1 and 2 to enhance the understanding of the variations in the impacts.

Task 3 - Collaborate with other Members in ASCENT Project 104 for SOC Research (supporting role)

University of Tennessee

Objective

Provide support to other members of the ASCENT Project 104 as requested.

Research Approach

Provide necessary input through research efforts in SOC estimates. The approach will differ as questions surface from other teams.

Milestone

Shared SOC estimates at the ASCENT fall and spring meetings.

Major Accomplishments

See Task 1 above.

Publications

None.

Outreach Efforts

None.

Awards

None.

Student Involvement

None.

Plans for Next Period (Year)

Enhance the SOC estimates and comparison.



Project 105 Quantification of Trace Levels of Sulfur Using ICP-MS

University of Dayton Research Institute

Project Lead Investigator

Zachary West, PhD
Principal Research Engineer
Group Leader, Fuel Science
University of Dayton
300 College Park
Dayton, OH 45458
937-255-4062
zachary.west@udri.udayton.edu

University Participants

University of Dayton Research Institute (UDRI)

- P.I.: Zachary West, PhD
- FAA award number: 13-C-AJFE-UD-059
- Period of Performance: January 21, 2025, through January 20, 2026
- Tasks:
  1. Background Information Collection and Method Development
  2. Formalization and Documentation of Final Method
  3. Conduct Robustness Study

Project Funding Level

Amendent	Funding
Amendment No. 59	$150,014.00

Investigation Team

Dr. Zachary West (P.I.)
Dr. Joe Gord (Staff Scientist)
Dr. Amanda Mae Arts (Staff Scientist)

Project Overview

Existing sulfur quantitation methods (Table 1) have a lower quantitation limit of approximately 1 parts per million by weight (ppm wt) of sulfur. As more synthetic aviation turbine fuel (SATF) producers enter the market and the industry considers lower sulfur specification limits, a method for accurately measuring low-level sulfur is needed. Lower sulfur is desirable in fuels because it affords decreased soot production which supports improved equipment robustness, reduced aircraft signature, and improved air quality. This effort aims to develop a relatively accessible method using inductively coupled plasma – mass spectrometry (ICP-MS) for the quantitation of sulfur at the tens to hundreds of parts per billion by weight (ppb wt) level in middle distillate fuels to include SATF, synthetic blend components (SBC), and traditional jet fuel (e.g., Jet A/A-1).



Table 1. List of existing Sulfur test methods and inductively coupled plasma (ICP) methods for testing jet fuels. UV: ultraviolet; N/A: not applicable.

Method	Lower Limit (Sulfur)	Measurement Technique	Use Case (Sulfur)
ASTM D5453	1 mg/kg	UV Fluorescence	D1655, D7566
ASTM D2622	3 mg/kg	Wavelength Dispersive X-Ray Fluorescence (XRF)	D1655, D7566
ASTM D4294	16 mg/kg	Energy Dispersive XRF	D1655, D7566
ASTM D1266	100 (5*) mg/kg	Lamp	Withdrawn 2025
IP 336	300 mg/kg	Energy Dispersive XRF	D1655, D7566
ASTM D7111	N/A	ICP-Atomic Emission Spectroscopy	N/A – Metals
ASTM D8110	N/A	ICP-Mass Spec	N/A – Metals

Task 1. - Background Information Collection and Method Development

University of Dayton Research Institute

Objective

Develop an ICP-MS method capable of quantitating low levels of sulfur in the middle distillate fuels.

Research Approach

Existing methods for both sulfur detection and application of inductively coupled plasma (ICP) were considered (Table 1) as models/benchmarks to guide this project. Additionally, a literature search was conducted, focused on applications of ICP for measuring sulfur in a variety of sample matrices by several different experimental methods. Measuring low-level sulfur in jet fuel samples by ICP is difficult for several reasons. Sulfur has a low ionization efficiency at the energy of an argon plasma, which is the plasma most often used with ICP techniques. There is a high coking potential for fuel samples because of the high-carbon character of the matrix. To prevent coking, oxygen gas is added to the plasma. Oxygen gas is a source of barometric interference for sulfur. Several approaches were tested to overcome these challenges. Such methods included monitoring of ^{34}S, SO^+ ion formation using collision cell technology, and application of xenon gas for kinetic energy discrimination to filter $^{16}O_2$ signal from the m/z = 32 mass channel.

After testing these different approaches in the laboratory, it was determined that formation and detection of SO^+ provided the best performance given the target concentrations and the sample matrices involved. Efforts then revolved around establishing a consistent test method, determining performance metrics of the calibration, applying the method across a wide range of fuels, and evaluating the limits of detection achievable given under the test conditions.

Method development has been completed with testing results in the low hundreds of ppb sulfur. Figure 1 shows a typical calibration curve covering a concentration range from 100 ppb wt to 3000 ppb wt of sulfur. This range was selected to overlap with the low end of existing test methods.

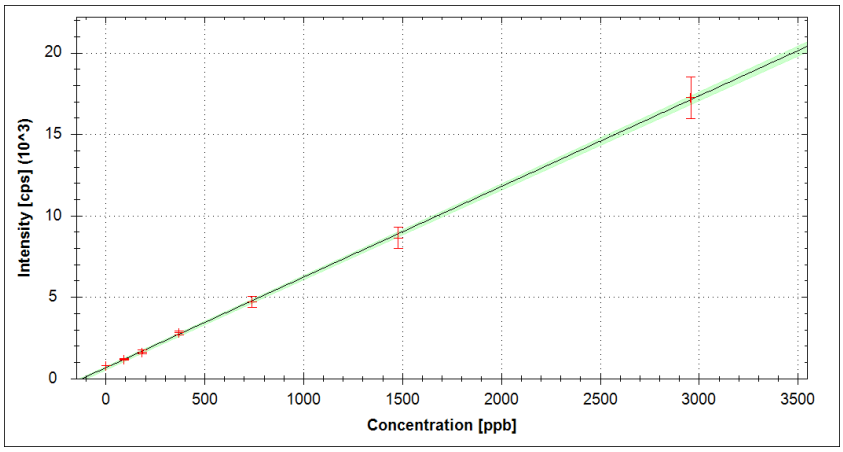


Figure 1. Inductively coupled plasma – mass spectrometry (ICP-MS) sulfur calibration curve from 100 to 3000 ppb wt sulfur in kerosene.

Initial assessments of the accuracy and precision of the method were determined using spiked kerosene samples. Figure 2 (left panel) shows the measured sulfur concentration values vs known (prepared) concentrations for a set of test samples. Samples were prepared and tested over the course of two separate days. The measured data correspond reasonably well with the known concentration values over much of the test range. The inset on the left panel reports the percent error as a function of sulfur concentration. It can be seen from the inset that the percent error increases significantly as the total concentration decreases. The percent error improves to ≤10% at concentrations at or above about two times the background equivalent concentration (BEC). There also appears to be a positive bias to the measured values compared to the prepared concentrations, however, it is yet unclear what might be causing this bias. The right-hand panel of Figure 2 shows that for all test concentrations precision is very good with relative standard deviation (%RSD) below 7% at the lowest concentrations and otherwise below 5%.

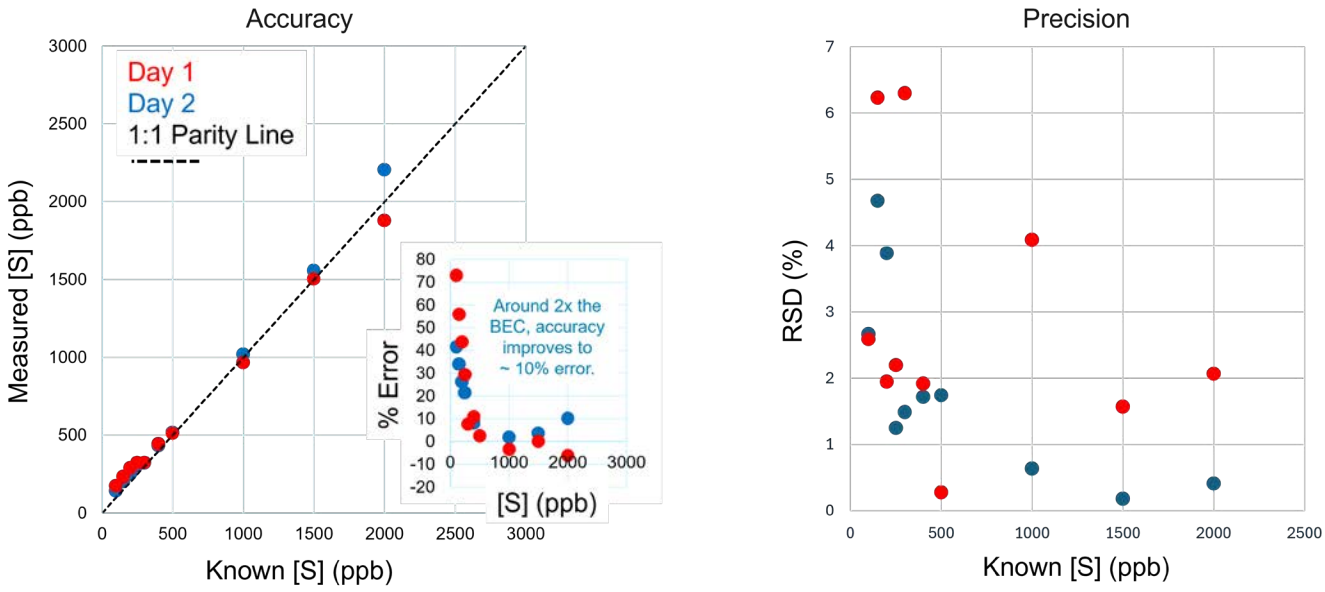


Figure 2. (Left) Measured vs known sulfur concentrations with parity line, showing accuracy of the test method. (Inset) % Error vs Sulfur concentration. (Right) %RSD vs known sulfur concentration reporting on precision of the method.

A selection of samples—three SBCs (including one hydroprocessed esters and fatty acids synthetic paraffinic kerosine [HEFA-SPK]), a low sulfur Jet A, a nominal Jet A (POSF 10325), and a kerosene spiked at 1000 ppb wt—were evaluated using this test method to demonstrate method robustness. Due to the low levels of sulfur, e.g., ≤5 ppm wt, in some of the samples a high confidence reference value for sulfur concentration was not always available. Regardless, Figure 3 shows the measured values, number of replicates (n), volumetric dilution factors (DF), and +/- 2σ error bars for each sample tested. Similar to the results seen in Figure 2, analysis of these six samples showed good precision across a large range of absolute concentrations. Even sample POSF-10325, which has a nominal sulfur content well outside of the intended target range for this method (ca. 500 ppm wt) exhibited reasonable precision (i.e., %RSD = 3%) after significant dilution to get the sample within the target range of linearity for the method (i.e., 100 – 300 ppb wt). In the next performance period, additional fuels will be procured for expanded testing.

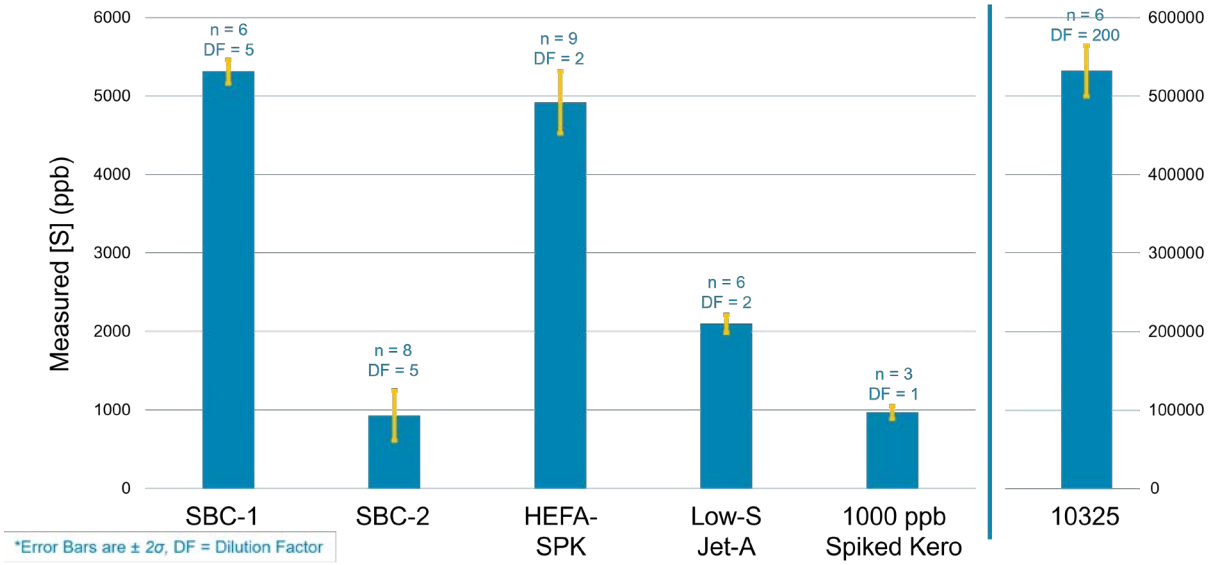


Figure 3. Measured sulfur values for real fuel samples. n: number of replicates; DF: dilution factor.

Finally, a series of fuels with available reference data (by ASTM D5453 [ASTM, 2025]) was tested using this ICP-MS method. All fuels received a two-times dilution to ensure they were within the calibration range of the current test method under development. The samples included low-sulfur Jet-A fuel and HEFA-SPK samples (yellow and green, respectively). In all instances the ICP-MS determined values were found to be higher than the reported values by ASTM D5453. The lower limit for reference data is 1000 ppb, so samples with "<1000ppb" values reported are plotted *at* 1000 ppb in Figure 4. Data reported by ICP-MS have +/- 2σ values (vertical error bars) that are significantly lower than the reproducibility values (horizontal error bars) for the D5453-determined data.

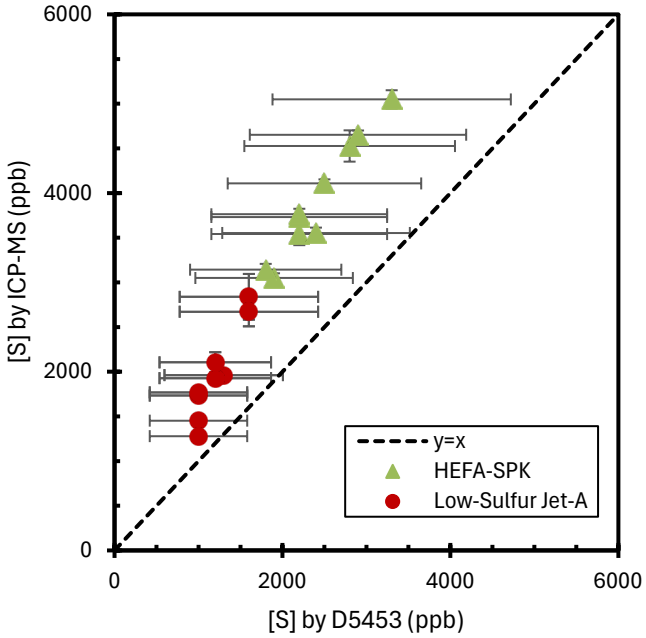


Figure 4. Inductively coupled plasma – mass spectrometry (ICP-MS) vs ASTM D5453 for a selection of low-sulfur Jet-A fuel (red markers) and hydroprocessed esters and fatty acids synthetic paraffinic kerosine (HEFA-SPK) (green markers) samples. Dashed line is a 1:1 parity line. Horizontal error bars are reproducibility values as determined by ASTM D5453. Vertical error bars are +/- 2σ.

Milestones

- Engage literature. **Complete.**
- Select Method Approach. **Complete.**
- Develop Calibration/Cal Curve. **Complete.**
- Test with "model" samples. **Complete.**
- Test with "real" samples. Ongoing.
- Solicit Partners for robustness study. Next period.
- Finalize Method. Next period.
- Complete report. Next period.

Major Accomplishments

- Completed method development phase.
- Established calibration range from 100 to 3000 ppb of sulfur.
- Achieved significant progress into method finalization and performance determination.

Publications

None.

Outreach Efforts

Presented at the Fall 2025 ASCENT Meeting.

Awards

None.



Student Involvement

None.

Plans for Next Period

- Finalize preliminary method for robustness study.
- Procure additional low-sulfur fuels for robustness testing.
- Identify robustness-testing partners.
- Conduct robustness study of preliminary method to confirm method applicability (with other labs).
- Compile report.

Reference

ASTM International. (2025). *ASTM D5453-24: Standard Test Method for Determination of Total Sulfur in Light Hydrocarbons, Spark Ignition Engine Fuel, Diesel Engine Fuel, and Engine Oil by Ultraviolet Fluorescence.* https://doi.org/10.1520/D5453-24



Project 106(A) Integration of Turbine Operational Parameters into Aerothermal System Analyses

Georgia Institute of Technology

Project Lead Investigator

Professor Dimitri N. Mavris
Director, Aerospace Systems Design Laboratory
School of Aerospace Engineering
Georgia Institute of Technology
Phone: (404) 894-1557
Fax: (404) 894-6596
Email: dimitri.mavris@ae.gatech.edu

University Participants

Georgia Institute of Technology (Georgia Tech)

- P.I.: Dr. Dimitri N. Mavris
- FAA Award Number: 13-C-AJFE-GIT-173
- Period of Performance: January 21, 2025, through January 20, 2026
- Tasks:
    1. Develop Baseline Models and Turbine Modeling Framework
    2. Integrate Experimental Data
    3. Demonstrate Impact of New Models

Project Funding Level

The Federal Aviation Administration (FAA) provided funding of $200,000. Georgia Tech agreed to a total of $200,000 in matching funds. This total includes salaries for the project director, research engineers, and graduate research assistants, as well as computing, financial, and administrative support, including meeting arrangements. Georgia Tech has also agreed to provide tuition remission for the students, paid for by state funds. During the period of performance, in-kind cost sharing is also obtained for cost share.

Investigation Team

Georgia Institute of Technology
Research Faculty:
Dimitri Mavris, P.I.
Jonathan Gladin, Co-Investigator
Russell Denney, Technical Lead
James Kenny, Project Manager
Metin Ozcan, Technical Contributor
Graduate Students:
Anand Iyer—Task 1, turbine loss model development
Niharika Akula—Task 1, turbine disk structural modeling and optimization
Esteban Pais—Task 1, turbine cooling model development
Sindhu Belki—Task 1, turbine size effects modeling and analysis
Jessica Tang—Task 1, turbine modeling framework development
Undergraduate Students (not funded):
Charles Howard—Task 1, turbine cooling model development
Ethan Cordeiro—Task 1, turbine loss model literature review



Project Overview

Gas turbine engines will continue to be the propulsion power plant of choice for large single- and twin-aisle aircraft in the foreseeable future because of their high power and energy density capabilities. However, these engines produce 90% of today's carbon dioxide emissions in the aviation sector. While turbine engines are ubiquitous in propulsion, many advances made stem from improvements in individual component efficiencies rather than system-level approaches which can quantify the inter-relations of engine operations. These operational impacts are particularly important as new architectures are explored and designed. One key component where there is a lack of information to improve operational models and thus difficult to predict thermal efficiency trends, is the turbine; here the complexities of cooling and leakages make this task exceptionally challenging. The goal of this task was to acquire data from the test turbine in The Pennsylvania State University (Penn State) Steady Thermal Aero Research Turbine (START) Lab (researchers under ASCENT Project 106B), under carefully controlled conditions to build a library of specific operational impacts on thermal efficiencies and then integrate this library of data into the modeling tools of Georgia Tech's Aerospace Systems Design Laboratory (ASDL). This effort intended to result in accurate operational trade-offs with cooled turbines whereby the modeling tools can be widely used by industry to assess sustainability concepts.

Key to being able to identify new turbine architectures is to understand thermal efficiency losses that result from blade cooling, tip clearances, purge flows, manufacturing variability, and stage gaps. Missing, however, are data on each specific loss mechanisms under carefully controlled and well-documented turbine operations. The primary reason for this lack of data is the rarity of test facilities capable of independently assessing turbine operational parameters and even fewer facilities that are able to make highly accurate thermodynamic efficiency measurements. Penn State's START Lab not only has developed a measurement capability which provides highly accurate stage efficiency measurements but also has the ability to independently vary turbine airfoil cooling flowrates; locations of where this coolant in injected back into the main hot gas path, i.e., trailing edge, blade tip, etc.; blade tip gaps; inlet temperature and turbulence profiles; under-platform sealing flowrates needed to minimize hot gas ingestion; airfoil manufacturing methods; and gap sizes between the vane and blade. All of these operational features significantly impact thermal efficiencies, as has been previously shown through preliminary measurements taken in the START Lab. Through National Aeronautics and Space Administration (NASA) University Leadership Initiative (ULI) collaborations, the START Lab and ASDL have identified a gap in data available that benchmarks thermodynamic efficiency losses of specific features. This project intended to leverage the use of several available test turbines including the START Lab's National Experimental Turbine (NExT) to do detailed efficiency measurements by controlling specific turbine operational features.

Georgia Tech's ASDL worked with the Penn State START Lab to collaborate on creating an aero- thermodynamic model of a high-pressure turbine capable of integrating the operational parameters library from the START lab. This endeavor aims to develop detailed design algorithms, systems of equations, and Numerical Propulsion System Simulation (NPSS) code to calculate the necessary turbine operational parameters for a given cycle while interfacing with the experimentally determined library. The approach was intended to be refined using an example engine model based on a state-of-the-art engine for calibration purposes. Additionally, several other "future" cycle models were intended to be developed to assess the significance of incorporating these impacts in future sustainable aircraft studies. These future cycles to be considered were sought to be selected to align with past and future FAA studies, such as the International Civil Aviation Organization (ICAO) Long Term Aspirational Goal (LTAG) analysis and other pertinent research. Following the development of the approach and integration of the operational parameter library from the START lab, a "before and after" benchmark study was planned to be conducted to demonstrate the impact of the work across the spectrum of included cycle models.

Georgia Tech has experience in creating detailed cycle models of gas turbine engines for aviation applications. These models are typically calibrated to public domain data and used to perform technology assessments to support government investment decisions, international (ICAO) goal setting and stringency exploration exercises and other relevant studies. Examples of this kind include the FAA Continuous Lower Energy, Emissions and Noise system assessment (ASCENT Project 037), and the long-term aspirational goals study with ICAO (ASCENT Project 064). Georgia Tech's models have been central in conducting these studies, in particular the use of the environmental design space (EDS). This tool has been used to create a database of notional engine models of current best in class vehicles for both short, medium, and long-haul applications. The model results have been approved by various members of industry who participated in these studies and deemed the results to be fit for the purpose of conducting high-level technology exercises. EDS is also used to support many studies for other aviation partners such as NASA, Air Force Research Laboratory, and various industrial partners.



While these achievements are significant, the development of the EDS engine model database relies upon constant development of the physics-based models operating in the background. Key features of these models play important roles during the design process and selection phases that ultimately impact the technology selection. A more recent part of the process engages the parametric design space and optimization capabilities that have been developed using the EDS tool. This means that future study results will be even more sensitive to having accurate parametric representations of detailed components within the baseline model, thus motivating the improvement of various component models.

Under prior work with the NASA ULI program, topics of small core scaling effects have been evaluated, and the results are illustrated qualitatively in Figure 1. In Figure 1, an ideal scaling curve represents the effect on high pressure turbine (HPT) efficiency, assuming a geometric scaling approach. However, many of the scaling effects are non-ideal, which is represented by the steep drop of efficiency when small core effects are taken into consideration. From a high-level perspective, some of the driving influences of these efficiency debits have been identified and are also summarized with qualitative influence in Figure 1. One of the most important effects (#1, tip gap effects) is under separate analysis in the prior ULI program. However, other significant driving parameters were modeled and sought to be evaluated as part of this effort specifically for purposes of building modeling approaches to benefit future engine designs. Accurately modeling these effects is very important in defining and deciding on future engine cycles and determining appropriate goals for carbon dioxide emission reductions.

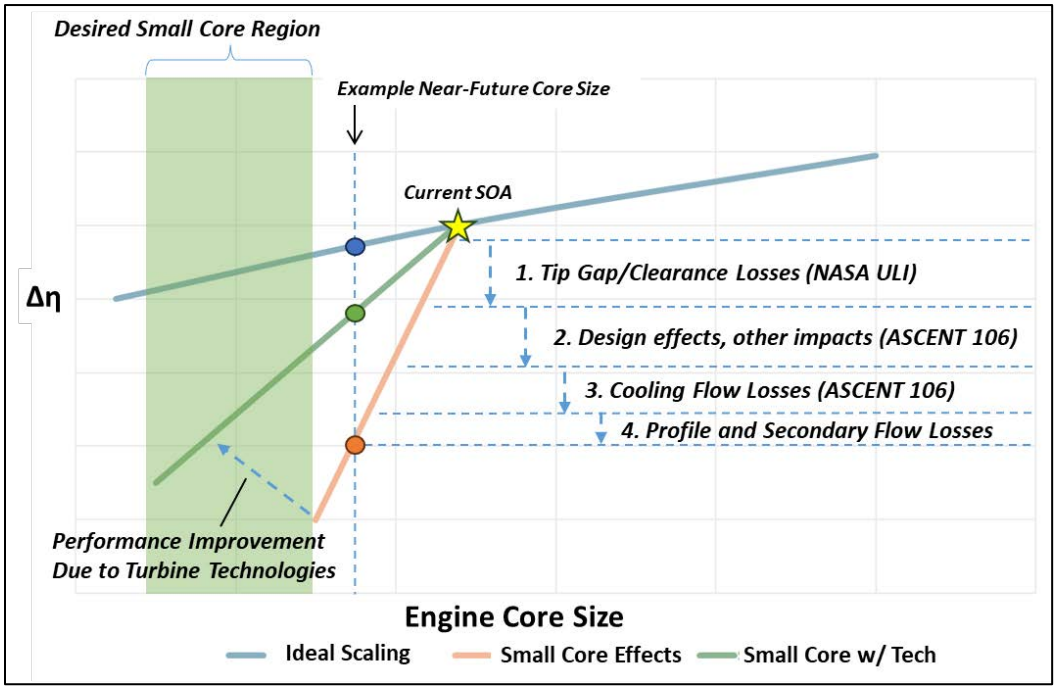


Figure 1. Small core scaling effects on high pressure turbine (HPT) efficiency. NASA: National Aeronautics and Space Administration, SOA: State of the Art, ULI: University Leadership Initiative.

The overall project scope and plan consist of three years of proposed effort. The work has been completed in partnership with the Penn State University START lab, who has performed partner tasks to perform experimental investigations of parametric turbine performance. The work pursued in the Year 1 effort focused on building a modeling framework for a baseline geometry and coordinating data analysis and integration with the team at Penn State START through their experimental measurements.

In Year 1, the project team worked to create a calibrated stage loss model of the turbine based on experiments from the NExT turbine at the Penn State START lab. A baseline turbine model was developed for the first stage of a HPT. This design was intended to map the overall flow-path geometry (i.e., scaled hub/tip radii, etc.) and scaled flow rates. A literature review was conducted to define a turbine stage loss model that is parametric to the design parameters of the turbine



stage. This loss model includes geometry and aero-thermal design impacts, small feature impacts, and cooling flow impacts. The theoretical aspects of the model were documented in detail across the development effort. The development of the model was out using the open-source turbine analysis code, Turboflow, as its basis, and the modified model can be shared with other partners who carry out extensions of the turbine analysis.

In Year 1, measurements conducted at Penn State were documented by the START team, with the intent to share these data packages with the Georgia Tech ASDL to complete Task 2, which included calibrating the baseline model developed in Task 1. Looking ahead, in Year 2, comparisons of the baseline turbine model with the measured efficiencies from the Year 1 experiments were planned to be completed. A detailed effort to calibrate these models was planned, with an effort made to parse out specific components of the loss models that contribute to the error. It was then intended to include an analysis of the impact of cooling flows on efficiency, as well. The model was planned to be integrated into a state-of-the-art calibrated engine model to determine differences between current model calibration. In Year 3, Georgia Tech then expected to integrate models for small core features to be tested in Year 2 and geometric sensitivities to be conducted in Year 3. The model was intended to be integrated into several different cycle models that have been used for FAA studies in the past to demonstrate differences in the cycle model parametric optimization. The final version of the turbine component modeling framework was planned to be delivered and documented in Year 3. A full technical schedule which was planned for ASCENT Project 106A is provided in Table 1, and a list of the ASCENT Project 106A Plan of Actions and Milestones is shown in Table 2.

Table 1. Overall plan for the ASCENT Project 106A program.

Project Year	Year 1				Year 2				Year 3			
Calendar Year Quarter	Q1	Q2	Q3	Q4	Q1	Q2	Q3	Q4	Q1	Q2	Q3	Q4
Calendar Year	2025				2026				2027			
Task 1: Develop Baseline Models												
1.1: Literature review												
1.2: Coordinate model and turbine experiments												
1.3: Develop baseline turbine model												
Task 2: Integrate experimental data												
2.1: Integrate baseline data												
2.2: Integrate cooling sensitivities												
2.3: Integrate small core impacts												
2.4: Integrate alternate geometry experiments												
Task 3: Demonstrate impact of new model												
3.1: Integration into selected cycle models												
3.2:Evaluation of impacts on selected models												
3.3:Optimization studies with final version of model												



Table 2. ASCENT Project 106A proposed plan of actions and milestones.

Milestone	Planned Due Date
Literature review and definition of model structure and theory	March 31, 2025
Define experimental "hooks" into the model with Penn State (Experiments planned in coordination with the model)	June 31, 2025
Creation of initial parametric turbine model framework with loss effects from literature – Define boundary conditions from a sample cycle model	December 31, 2025
Year 1 summary report	December 31, 2025
Integration of year 1 experimental results into the model	March 31, 2026
Integrate cooling flow sensitivities	September 30, 2026
Integrate small core impacts and finalize cycle model implementation	December 31, 2026
Year 2 summary report	December 31, 2026
Studies to validate and evaluate impact of the new models	September 30, 2027
Perform alternate turbine design geometry hardware assessments	September 30, 2027
Optimization study with the new model integrated	December 31, 2027
Year 3 summary report	December 31, 2027

While ASCENT Project 106A was ultimately not approved for continuation into Years 2 and 3, the development completed and groundwork laid for increased fidelity parametric turbine modeling will provide the FAA and project partners with a strong stepping stone which can be used to continue turbine modeling work for applications of interest to the FAA and federal government more broadly.

Task 1 - Develop Baseline Models and Turbine Modeling Framework

Georgia Institute of Technology

Objectives

The objectives of this task were to identify best practices for modeling aircraft turbines, and ultimately develop an increased fidelity, parametric modeling framework which could allow users to understand the implications of complex aerothermodynamic losses illustrated in Figure 1, above. Typically, individual losses and complex phenomena have been explored by experimentalists and disciplinary groups, but the collective knowledge of these investigations has not been compiled into a modeling tool which was available for researchers to leverage to understand component and geometry-level impacts of turbines on engine and aircraft scale studies. Task 1 sought to develop a parametric turbine modeling framework which could capture complex effects and the inputs of which could be readily input into engine modeling codes such as NPSS in the form of performance maps and extended to include other capabilities and features.

Research Approach

The development of the baseline modeling framework and a baseline single stage turbine, which could be calibrated to reflect the geometry and produce the performance results of the Penn State START NExT turbine were pursued through a methodical and systematic process. First, researchers performed an extensive literature review in several main categories to understand several critical components which were important to the framework development process.

After the completion of the initial literature review, a baseline open-source turbine modeling code was found from which to be developed, this code was investigated for missing features which were necessary to include to meet the desired needs and requirements of the parametric turbine modeling framework being developed by Georgia Tech's ASDL. Upon extensive testing and investigation, several key features were identified to be missing, and those individual features were assigned to researchers and developed throughout the second part of Year 1, with a goal to have them developed and integrated into



the framework before receiving the experimental data from Penn State for calibration and validation. To this end, throughout Year 1, Georgia Tech's ASDL worked with Penn State START Lab members to ensure hooks in the code existed to allow for easy validation and calibration (different datasets) for the baseline modeling framework against the NExT turbine data. Additionally, bi-weekly meetings with the FAA Technical Advisor were performed with ASCENT Projects 106A and 106B teams, when possible, throughout the period of performance.

Literature Review

As mentioned above, the start of Year 1 was primarily an extensive literature review of over 100 articles and papers was performed to understand the current state of the art with regards to three main categories, which were critical to understanding what the turbine design and analysis code needed to encompass and which loss models and aerothermal effects needed to be included:

1. Current turbine modeling approaches and frameworks (including software)
2. Aerothermodynamic turbine phenomena contributing to efficiency losses and operation
3. Axial turbine design methodologies and approaches

With regards to the first topic, many published papers and turbine modeling codes were identified, obtained, and investigated for appropriateness to the development task outlined as the objective for Year 1. These turbine modeling codes explored include NASA's TURBAN (Glassman, 1994a), TD-2 (Glassman, 1992), Turbo-Design (GitHub, 2025), AXOD (Glassman, 1994b), and open-source codes such as T-AXI (Turner et al., 2025) and Turboflow (Anderson et al., 2025). The exploration of and experimentation with these codes ultimately showed that the Turboflow code developed by Norwegian University of Science and Technology held the most promise for future development, and the most flexibility to be adapted to a fully parametric axial design code which could leverage modern optimization methods. While the available code holds several features which make it more desirable for use than the others (open source, high levels of parameterization, ability to use only simple input datasets if desired, meanline code), it was apparent that it was developed for terrestrial applications when it was found that certain key elements needed to be developed and integrated into the model for aircraft-focused axial turbines (i.e., cooling models and efficiency impacts, size effects, etc.). An investigation into the comparison between modeling fidelity for turbines, from meanline analyses to computational fluid dynamics resulted in the conclusion that a meanline approach was the most appropriate for conceptual level design and allowed for rapid design space exploration and provided a firm foundation for future two- and three-dimensional modeling developments, which were planned for the code.

Additionally, it was important to identify and understand the most recent literature regarding complex turbine phenomena that contribute to operational limitations and losses. As a result, many of the losses seen from the contributing factors, as illustrated in Figure 1, needed to be captured in the turbine modeling framework. This required a sufficient capture of modern literature regarding turbine loss contributors, including those introduced by cooling flows, smaller core geometries, and secondary losses, to name a few. Some significant papers which influenced the development of capabilities in the model include Young and Wilcock (2002) (cooling efficiency and modeling), Young and Horlock (2006) (cooling efficiency and modeling), Tournier and El-Genk (2010) (axial turbine modeling), Sjodin (2019) (meanline method analysis), Lakshminarayana (1970), Kofskey and Nusbaum (1968), (tip clearance effects), Bertini et al., (2013) (loss models and Smith charts), Benner et al. (2006) (secondary losses), Kacker and Okapuu (1982) (cooling efficiency and meanline modeling), and others. As mentioned previously, due to the complex nature of developing turbine models, the literature review which investigated turbine losses continued for the duration of Year 1, as required, to support model development.

Lastly, despite technical leads holding notable experience in turbomachinery analysis, it was important for the team to learn the fundamentals of how turbines are designed, and their resulting performance characteristics, prior to developing complex turbine models in code. Literature in this realm included Gambini and Vellini (2021), Kurzke and Halliwell (2018), Baskharone (2006), Aungier (2006), and others. The initial literature review provided researchers with the necessary understanding to develop their respective component models, and identification of new resources and articles were consistently found throughout Year 1 to support research efforts. Georgia Tech ASDL researchers were required to read selections from Gambini and Vellini and Kurzke and Halliwell to form a common understanding of the object of modeling.

Physics-based Turbine Modeling Framework Development

Although the selected baseline code, Turboflow, held many desirable features, it required modification for the ultimate purposes of being extended to design and optimize aircraft turbines. As mentioned above, several capabilities and the refinement or development of physics-based models to benefit the Turboflow-based design framework being pursued under Task 1 were created and implemented.



1) Cooling Model Development – A study was performed to investigate how to model the performance and calculate the efficiency for a multistage cooled turbine and develop calculations to be incorporated into the Turboflow code. The team ultimately selected to follow the procedure described in *Performance Modeling Methodology: Efficiency Definitions for Cooled Single and Multistage Turbines* (Kurzke, 2002). Due to the fact that Turboflow did not organically incorporate turbine cooling flows in efficiency calculations, a means for adding the necessary intermediate flow stations to perform efficiency calculations and addition of cooling flows was necessary. Illustrations of the conceptual cascade cooling model and modifications to the turbine cascade station numbering can be seen below in Figure 2 and Figure 3, respectively. A key problem which is still being solved by the Georgia Tech ASDL researchers is the ability to effectively model cooling and working fluid flows at the new cascade stations.

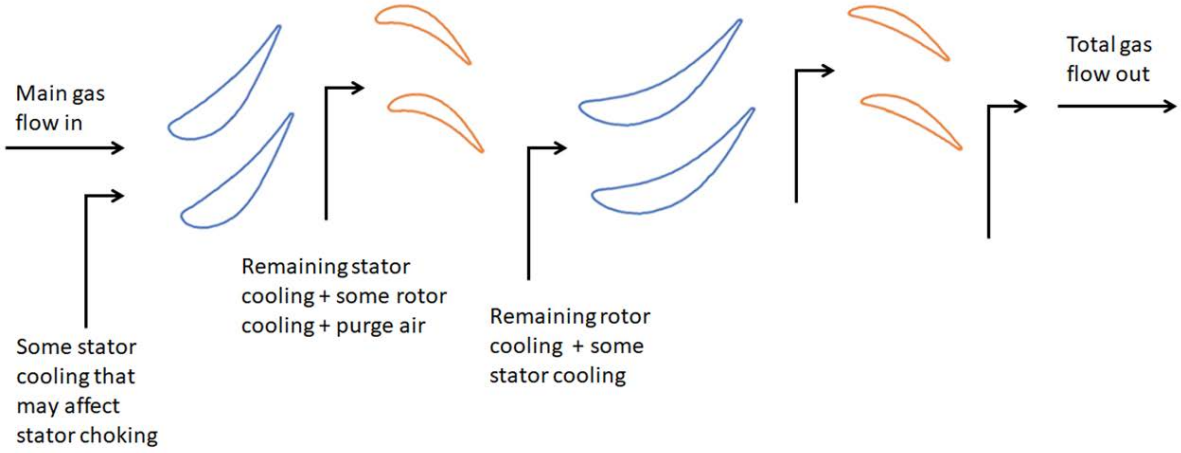


Figure 2. Addition of flows in turbine cascade, seen in cooled turbines.

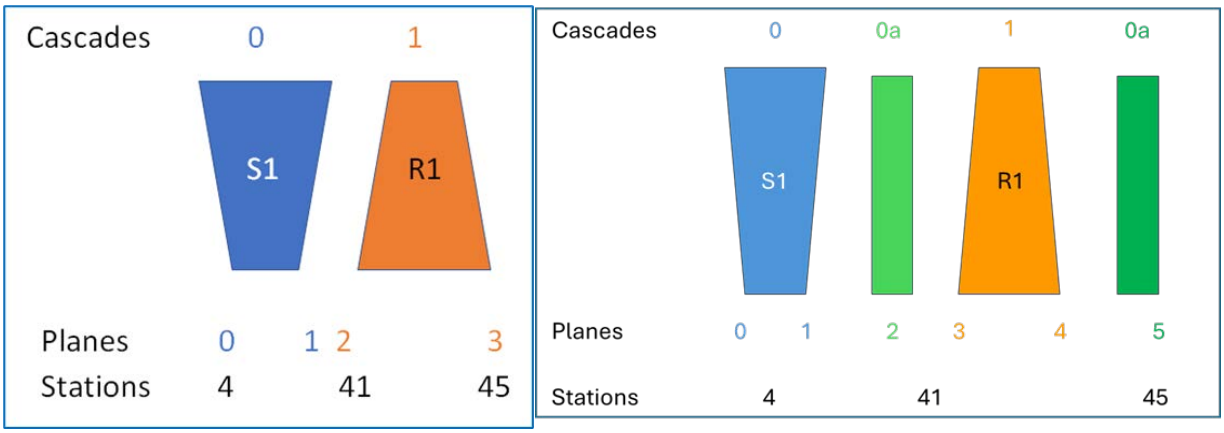


Figure 3. Turboflow cascade numbering (left) vs. modified cascade numbering (right).

Ultimately, the turbine cooling model methodology was developed and is being implemented and validate against Kurzke's published data as of November of Year 1.

2) Size Effects Study – An investigation into the capability of Turboflow to predict the change in design point efficiency with reduction in the turbine design mass flow yielded mixed results. Using the Kacker-Okapuu loss model (Kacker & Okapuu, 1982), the results appeared to be generally similar to other published data, but using the Benner et al. (2006) loss model produced incorrect and discontinuous trends. Upon further iterations of the study, working to compare Turboflow's



inherent size effects model against the turbine size effects identified in Bettner (1990), closer similarities were identified between the Turboflow code and published literature. In Year 2, it was intended to attempt to modify Turboflow's size effects to reflect modern turbine geometries and their performance. A comparison of Turboflow's performance against the results published in Bettner (1990) are shown below in Figure 4. An important finding from this study includes that the code produces a similar trend, which reinforces the understanding that Turboflow can capture size effects; however, Turboflow is more optimistic for the same turbine design.

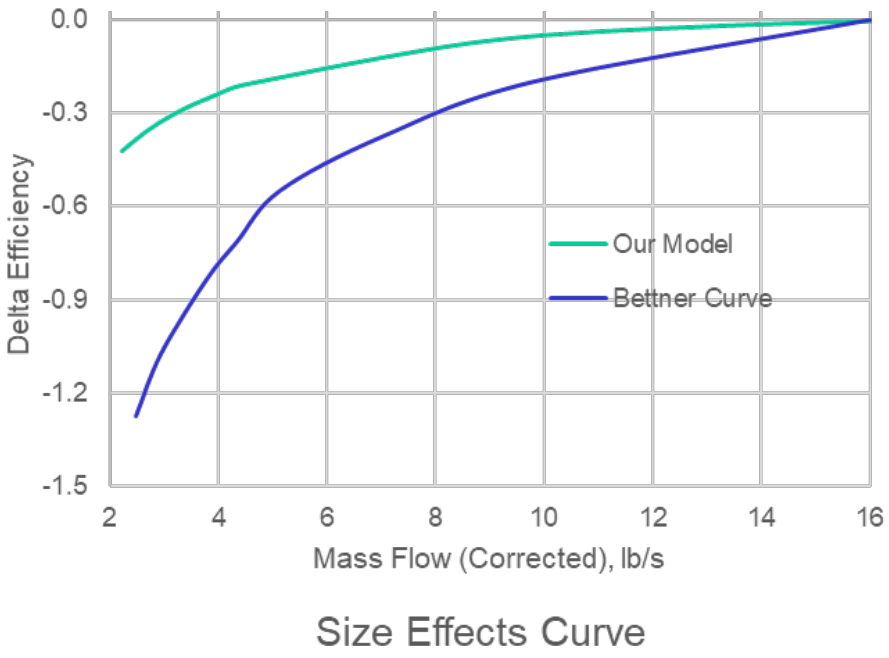


Figure 4. Turboflow size effects compared to Bettner performance.

3) Smith Chart Study – This study was a preliminary investigation of the capability to use Turboflow to reproduce a classical Smith Chart, i.e., a plot of work coefficient vs. flow coefficient with contour lines of constant efficiency, led to realization that a new "geometry tool" to estimate preliminary design geometry must be developed before proceeding with this study to provide the appropriate inputs. The new tool was also expected to help resolve some of the questions raised during the preliminary size effects study described above. Due to the need for a geometry code, that task was pursued before the ability to generate a Smith Chart was realized, and the Smith Chart task was shifted to Year 2. Further progress was made on the preliminary geometry design code and was implemented in the modified Turboflow code to achieve low-fidelity turbine geometry results, but improvements are being pursued for reliability.

4) Disk Design Study – The purpose of this study was to develop a procedure to design a turbine disk using lower-order analytical methods. The disk design is required to provide realistic design constraints for future turbine designs. A finite element method (FEM) approach for disk sizing and analysis has been developed and validated as a standalone code for accurate determination of disk geometry based on allowable stresses for provided geometry types. The analytical code was matched closely to FEM analysis and capable of identifying optimized disk geometries; it was implemented into the Turboflow code to perform disk design in October of the first year.

The capabilities of the code are illustrated by the following figures. Figure 5 illustrates two common disk designs which the code is able to analyze. Figure 6 presents an example of the disk stress analysis results provided by the code. Figure 7 presents an example comparing the temperature prediction results of the code to those obtained with Abaqus, a commercial finite element analysis code.

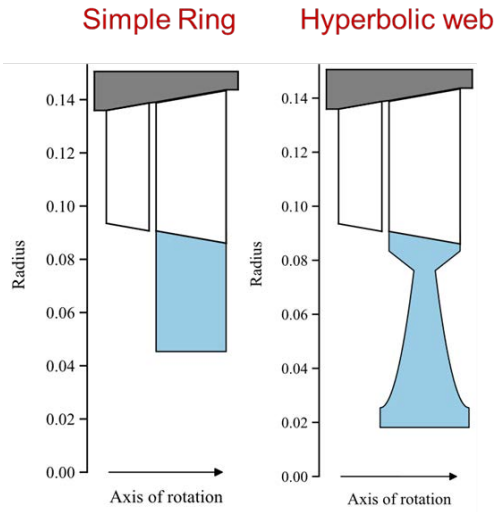


Figure 5. Turbine disk design code geometry design outputs.

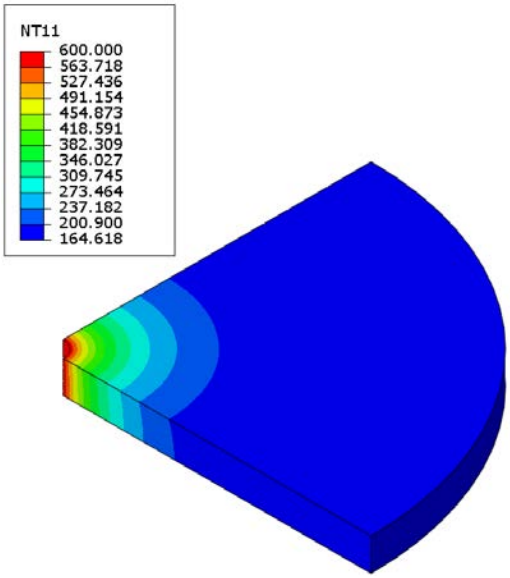


Figure 6. Turbine disk design stress analysis output.

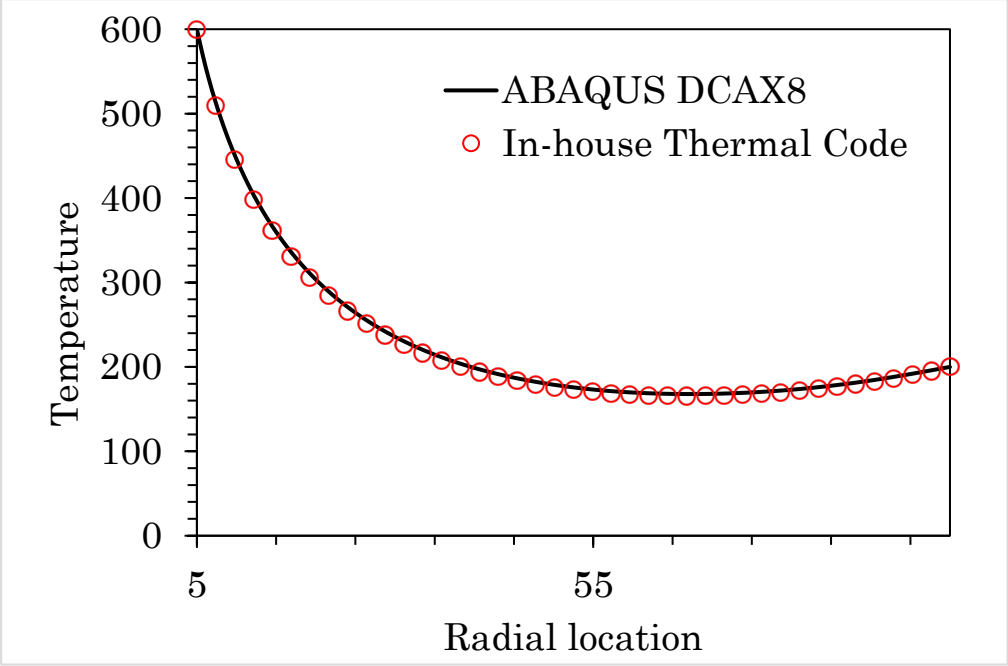


Figure 7. Finite element method vs. Georgia Tech Aerospace Systems Design Laboratory disk thermal stress analysis comparison.

5) Limit Load Study – For this study, Turboflow was examined to understand where turbine loading limits existed for turbine designs with regards to pressure ratios which contribute to the onset of turbine choking. In conjunction with subtask 6, below, Turboflow's limits for choking were identified as part of the process of developing a turbine map generator to create maps for any given Turbodesign input to the code.

6) Map Generation/NPSS output – The ability to generate new turbine maps representative of new turbine designs was completed and implemented into the Turboflow framework. The subroutine which performs this task allows for the sampling of Turboflow model performance at various rotational speed and turbine exit static pressure combinations. In addition, this code was extended to produce NPSS-format maps for the arbitrary turbine design provided to the Turboflow framework. This functionality was tested with a turbofan model which had been previously developed in NPSS and proven to be successful. An example set of turbine maps can be seen below in Figure 8.

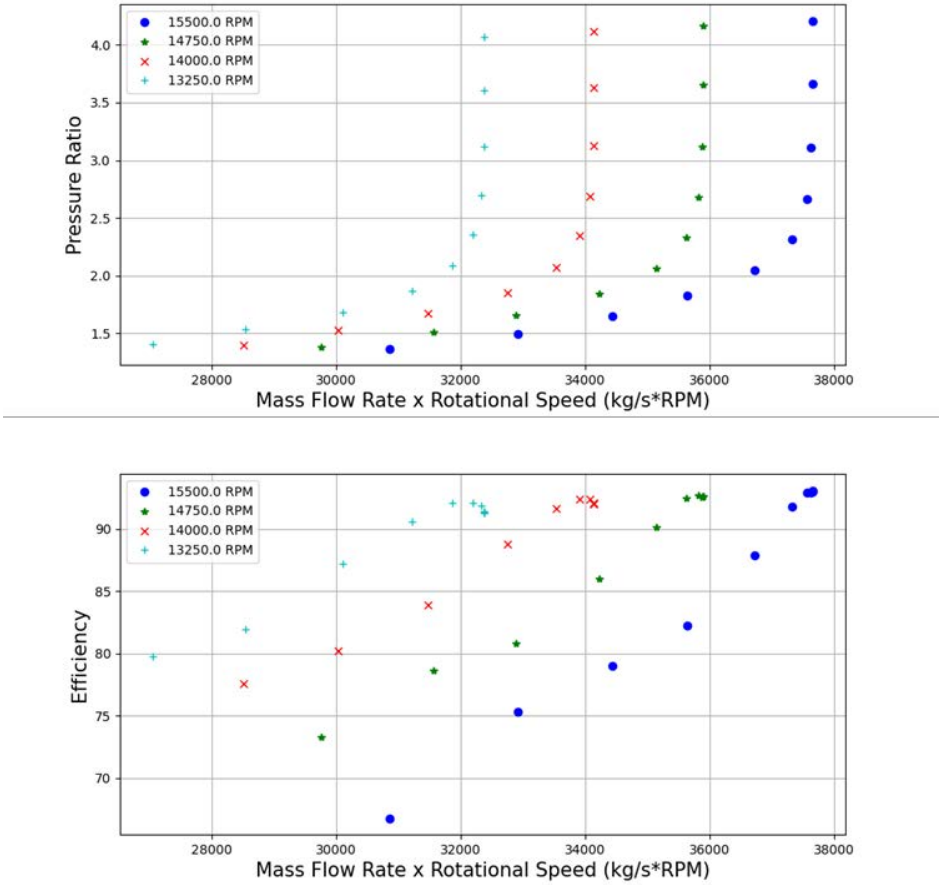


Figure 8. Example turbine maps generated from the new Turboflow map subroutine.

7) Preliminary Geometry Design Code – To address the requirements for a Smith chart creation subroutine, a preliminary geometry design code was pursued, seeking to follow the design algorithm outlined in Gambini and Vellini (2021), seen below in Figure 9. The development and integration of this algorithm into the framework is still in progress and incomplete as of the submission of this report but is expected to be completed by the end of the year.

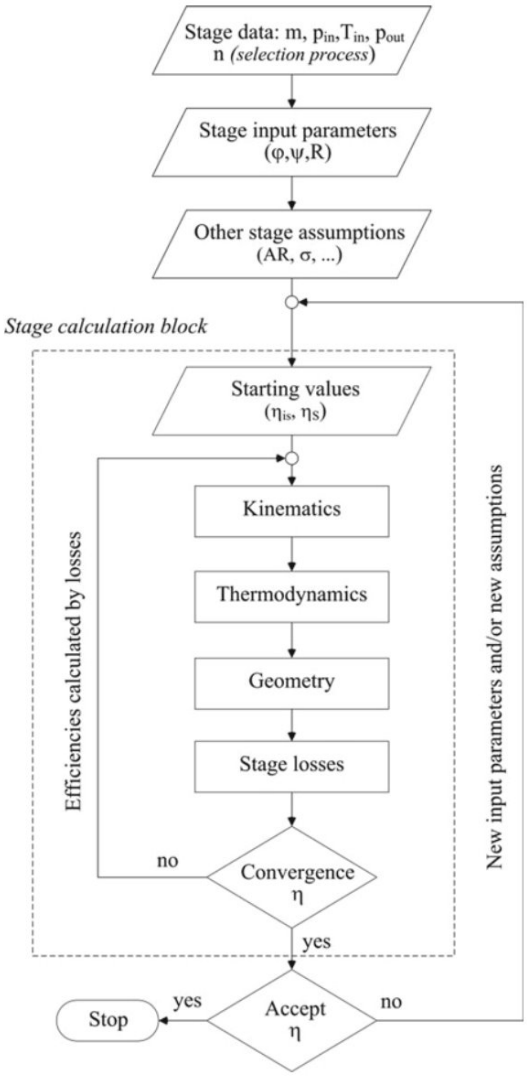


Figure 9. Preliminary geometry design code algorithm (Gambini & Vellini, 2021).

8) Thermodynamics Package Investigation – To support the project extension into the domain of gas turbine engine design and component co-optimization, a Python®-based thermodynamics package which allows for modeling of combustion products was sought in the open literature. Additionally, the desire to model chemical equilibrium was desired for combustion byproduct definition.

9) Integration of Tools into Georgia Tech Turboflow Framework – Upon the completion of the subroutines and their validation and verification, the tools were integrated into the Georgia Tech Turboflow framework for its improvement.

Experimental Data Integration
The researchers at the Georgia Tech ASDL collaborated with Penn State to discuss experimentation plans, using biweekly calls for the purposes of sharing information pertaining to research progress and coordinating future experimentation

® Python is a registered trademark of Python Software Foundation, Beaverton, Oregon.



efforts. Penn State and the Georgia Tech ASDL worked on an information sharing agreement to allow the Georgia Tech ASDL access to detailed NExT turbine geometry and performance data for the purposes of validating and training the physics-based turbine model. While NExT turbine geometry data have been requested from Penn State to support the development of a turbine rig-based analytical model for use in the verification and validation for the physics-based M&S tool outlined in Task 1.3, the data transfer took an extended period of time due to legal requirements, and was not usable by the modeling team at the Georgia Tech ASDL for use before the end of the project.

Milestones

Milestones accomplished according to the Table 2 Plan of Actions and milestones is primarily limited to the completion of Task 1.1, the literature review for modeling. Significant work into Task 1.3 took the majority of the effort for the researchers, and the milestone to complete the baseline parametric turbine model is not yet complete, but the tasks accomplished are listed above and below.

Major Accomplishments

Many notable accomplishments were achieved by the Georgia Tech ASDL team in pursuit of completion of Task 1 during Year 1, as the effort comprised the majority of the work defining the Year 1 efforts. The efforts performed in support of completing Task 1 during this year are listed below:

1. Developed disk structural and design modeling code and integrated into Turboflow.
2. Developed cooling flow modeling approach, but integration and validation of the code remain.
3. Surveyed and performed analytical comparison of loss models for capability gap identification.
4. Performed preliminary studies to generate Smith chart.
5. Developed baseline geometry design code, which is still in progress.
6. Performed preliminary exploration of Python-based thermodynamics packages for use with code able to model combustion products for gas turbine modeling.
7. Developed off-design map generation tool and integrated into Turboflow framework.
8. Extended map generation tool to integrate with NPSS cycle modeling code and related limit load study.
9. Performed size effects modeling study to understand Turboflow limitations with regards to modeling reduced core size turbines.

Publications

None.

Outreach Efforts

None.

Awards

None.

Student Involvement

The following graduate students were involved in ASCENT Project 106A:

- Anand Iyer—Worked to identify turbine loss models and code development
- Niharika Akula—Developed turbine disk structural modeling and optimization code
- Esteban Pais—Assisted in the completion of the turbine cooling methodology identification
- Sindhu Belki—Performed turbine size effects modeling and analysis
- Jessica Tang—Worked on turbine modeling framework development and preliminary geometry modeling capability. Worked to connect the Turboflow meanline modeling code to the two-dimensional streamline code Turbo-Design (GitHub, 2025) for Master's Special Problem topic

The following undergraduate students (not funded) were involved in ASCENT Project 106A:

- Charles Howard—Task 1, Developed alternate cooling modeling approach, which is currently being verified for functionality
- Ethan Cordeiro—Task 1, Assisted with the turbine loss model literature review



Plans for Next Period

The project will end at the end of this period of performance; as a result, plans for following years of work will not be pursued.

References

Anderson, L., Agromayor, R., Haglind, F., & Nord, L. (2025). Turboflow: Meanline Modeling of Axial Turbines. *Journal of Open Source Software, 10*(111), 7588. https://doi.org/10.21105/joss.07588

Aungier, R. (2006). *Turbine Aerodynamics: Axial-flow and Radial-Inflow Turbine Design and Analysis.* ASME Press.

Baskharone, E. (2006). *Principles of Turbomachinery in Air-breathing Engines*. Cambridge University Press.

Benner, M., Sjolander, S., & Moustapha, S. (2006). An Empirical Prediction Method for Secondary Losses in Turbines—Part 1: A new Loss Breakdown Scheme and Penetration Depth Correlation. *Journal of Turbomachinery, 128*(2), 273-280. https://doi.org/10.1115/1.2162593

Bertini, F., Ampellio, E., Marconcini, M., & Giovannini, M. (2013, June 3-7). A Critical Numerical Review of Loss Correlation Models and Smith Diagram for Modern Low Pressure Turbine Stages. *Proceedings of the ASME Turbo Expo 2013: Turbine Technical Conference and Exposition. Volume 6B: Turbomachinery*. San Antonio, Texas. https://doi.org/10.1115/GT2013-94849

Bettner, J. (1990, Jul 16-18). *Component Arrangement Studies for an 8000 SHP Turboshaft High Technology Core* (AIAA 1990-2398) [Conference paper]. 26th Joint Propulsion Conference, Orlando, Florida. https://doi.org/10.2514/6.1990-2398

Gambini, M., & Vellini, M. (2021). *Turbomachinery : fundamentals, selection and preliminary design* (1st Ed). Springer,

GitHub. (2025). *Radial Equilibrium Code to design Turbomachinery.* https://github.com/nasa/turbo-design

Glassman, A. (1992).*Users Manual and Modeling Improvements for Axial Turbine Design and Performance Computer Code TD2-2* (CR-189118). National Aeronautics and Space Administration.

Glassman, A. (1994a). *Enhanced Capabilities and Updated Users Manual for Axial-Flow Turbine Preliminary Sizing Code TURBAN* (CR-195405). National Aeronautics and Space Administration.

Glassman, A. (1994b). *Modeling Improvements and Users Manual for Axial-Flow Turbine Off-design Computer Code AXOD* (CR-195370). National Aeronautics and Space Administration.

Kacker, S., & Okapuu, U. (1982). A Mean Line Prediction Method for Axial Flow Turbine Efficiency. *Journal of Engineering for Power, 104*(1), 111-119. https://doi.org/10.1115/1.3227240

Kofskey, M., & Nusbaum, W. (1968). *Performance Evaluation of a Two-Stage Axial-Flow Turbine for Two Values of Tip Clearance* (TN-D-4388). National Aeronautics and Space Administration.

Kurzke, J. (2002, June 3-6). Performance Modeling Methodology: Efficiency Definitions for Cooled Single and Multistage Turbines. *Proceedings of the ASME Turbo Expo 2002: Power for Land, Sea, and Air. Volume 1: Turbo Expo 2002*. Amsterdam, The Netherlands. https://doi.org/10.1115/GT2002-30497

Kurzke, J., & Halliwell, I. (2018). *Propulsion and Power: An Exploration of Gas Turbine Performance Modeling*. Springer.

Lakshminaryana, B. (1970). Methods of Predicting the Tip Clearance Effects in Axial Flow Turbomachinery. *Journal of Basic Engineering, 92*(3), 467-480. https://doi.org/10.1115/1.3425036

Sjodin, J. (2019). *Meanline Method for Design and Off-design Turbine Performance Predictions* [Master's Thesis, Lunds University]. Lund University Publications. https://lup.lub.lu.se/luur/download?func=downloadFile&recordOId=8981907&fileOId=8981917

Tournier, J., El-Genk, M. (2010). Axial Flow, Multi-Stage Turbine and Compressor Models. *Journal of Energy Conversion and Management, 51*(1), 16-29. https://doi.org/10.1016/j.enconman.2009.08.005

Turner, M. G., Merchant, A., & Burna, D. (2025). *Turbomachinery Axisymmetric Design System T-AXI*. University of Cincinnati. https://www.downingdesign.net/gtsl/codes/taxi/

Young, J., & Horlock, J. (2006).Defining the Efficiency of a Cooled Turbine. *Journal of Turbomachinery, 128*(4), 658-667. https://doi.org/10.1115/1.2218890

Young, J., & Wilcock, R. (2002). Modeling the Air-Cooled Gas Turbine: Part 2: Coolant Flows and Losses. *Journal of Turbomachinery, 124*(2), 214-221. https://doi.org/10.1115/1.1415038



Project 106(B) Integration of Turbine Operational Parameters into Aerothermal System Analyses

The Pennsylvania State University

Project Lead Investigator

Reid A. Berdanier
Associate Professor
Department of Mechanical Engineering
The Pennsylvania State University
NARCO Building, CATO Park, Room 148
3127 Research Drive
State College, PA 16801
(814) 863-3972
rberdanier@psu.edu

University Participants

The Pennsylvania State University (Penn State)

- P.I.: Prof. Reid Berdanier
- FAA Award Number: 13-C-AJFE-PSU-129
- Period of Performance: January 21, 2025, to September 30, 2026
- Task:
  1. Define program and baseline measurements

Project Funding Level

The Federal Aviation Administration (FAA) has provided $200,000 of funding to date. In-kind cost-sharing of $200,000 has been provided by Penn State and Siemens.

Investigation Team

Prof. Reid A. Berdanier, All Tasks
Asst. Res. Prof. Matthew Meier, (staff scientist), All Tasks
Assoc. Res. Prof. Michael Barringer, (staff scientist), Task 1
Justin Brumberg, (staff scientist), Task 1
Tom Houck (project manager), Task 1
Jeremiah Bunch, (laboratory technician), Task 1
Matthew Stuber, (graduate student), Task 1

Project Overview

Gas turbine engines will continue to be the propulsion power plant of choice for large single- and twin-aisle aircraft in the foreseeable future because of their high power and energy density capabilities. However, these engines produce 90% of today's carbon dioxide (CO_2) emissions in the aviation sector. While turbine engines are ubiquitous in propulsion, many of the advances that have been made stem from improvements component efficiencies rather than system level approaches that quantify the interrelations of engine operations. These operational impacts are particularly important as new architectures are designed. One key component where there is a lack of information to improve operational models to predict thermal efficiency trends is the turbine where the complexities of leakages and cooling make this challenging. The goal of this task is to acquire data from the test turbine in Penn State's Steady Thermal Aero Research Turbine (START) Lab under carefully controlled conditions to build a library of specific operational impacts on thermal efficiencies and then integrate this library of data into the modeling tools of the Georgia Institute of Technology (GT) Aerospace Systems Design Laboratory (ASDL). This effort will result in accurate operational trade-offs with cooled turbines whereby the modeling tools can be widely used by the industry to assess sustainability concepts.



Key to being able to identify new turbine architectures is to understand thermal efficiency losses that result from blade cooling, tip clearances, purge flows, manufacturing variability, and stage gaps. Missing, however, are data on each specific loss mechanism under carefully controlled and well-documented turbine operations. There are reasons for this lack of data: there are few test facilities that can independently control turbine operational parameters and even fewer facilities that are able to make highly accurate thermodynamic efficiency measurements. The START Lab not only has developed a measurement capability that provide highly accurate stage efficiency measurements but also has the ability to independently vary turbine airfoil cooling flowrates, locations of where this coolant in injected back into the main hot gas path (i.e., trailing edge, blade tip, etc.) blade tip gaps, inlet temperature and turbulence profiles, underplatform sealing flowrates needed to minimize hot gas ingestion, airfoil manufacturing methods, and gap sizes between the vane and blade. All of these operational features significantly impact thermal efficiencies as has already been shown through preliminary measurements taken in the START Lab. Through National Aeronautics and Space Administration (NASA) University Leadership Initiative (ULI) collaborations, the START Lab and ASDL have identified a gap in data available that benchmark thermodynamic efficiency losses of specific features. This proposed project entails the use of several available test turbines including the START Lab's National Experimental Turbine (NExT) to do detailed efficiency measurements by controlling specific turbine operational features.

GT-ASDL will collaborate on creating an aero- thermodynamic model of a high-pressure turbine capable of integrating the operational parameters library from the START lab. This endeavor aims to develop detailed design algorithms, systems of equations, and Numerical Propulsion System Simulation (NPSS) code to calculate the necessary turbine operational parameters for a given cycle while interfacing with the experimentally determined library. The approach will be refined using an example engine model based on a state-of-the-art engine for calibration purposes. Additionally, several other "future" cycle models will be developed to assess the significance of incorporating these impacts in future sustainable aircraft studies. These future cycles will be selected to align with past and future FAA studies, such as the International Civil Aviation Organization (ICAO) Long Term Aspirational Goal (LTAG) analysis or other pertinent research. Following the development of the approach and integration of the operational parameter library from the START lab, a "before and after" benchmark study will be conducted to demonstrate the impact of the work across the spectrum of included cycle models.

Task 1 – Define Program and Baseline Measurements

The Pennsylvania State University

Objective

The objective of this task is to utilize NExT geometry to measure performance metrics such as stage efficiency. The turbine will be operated over a range of test conditions sweeping up to three separate cooling flow rates independently. In this way, the relative merit of each cooling flow can be independently evaluated for system-level modeling. Detailed measurements of efficiency-driving parameters such as blade tip clearances will also be monitored during the test program to serve as primary variables in the modeling approaches developed at ASDL. Measurements conducted at Penn State will be processed and curated by the START team prior to sharing data packages with GT-ASDL. The measured data, along with knowledge of the detailed geometry definition pertaining to the NExT turbine, will be packaged into system-level analysis approaches developed at ASDL and create a baseline reference case.

Research Approach

Define program and baseline measurements

The START team initiated this program by upgrading the hardware and software for START Lab inlet and exit traverse instrumentation systems to improve thermal efficiency measurement capabilities. Inlet radial traverse systems were equipped with backshaft quadrature encoders for accurate spanwise positioning of probes. With the new encoders, the START Lab can resolve spatial measurements within 0.001-in. Motor control hardware and software upgrades for the inlet radial traverse systems were completed to replace end-of-life third-party control systems with off-the-shelf motor control hardware and custom in-house software. The new hardware and a view of the control system software are depicted in Figure 1. With the new software upgrades, multiple traverses can be run simultaneously which will increase measurement accuracy through larger sample sizes. In addition, the new software updates make START Lab inlet traverses versatile to support a suite of flow measurements which will be employed through the upcoming test campaign for this ASCENT Project 106B project.

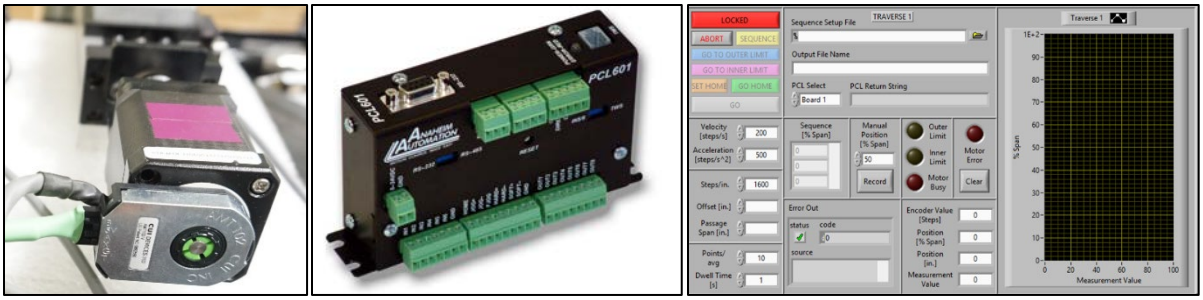


Figure 1. Left: Backshaft encoder on radial traverse. Middle: Off the shelf Anaheim Automation stepper motor controller. Right: Custom, in-house radial traverse control software.

The START Lab exit traverse, which is used to collect total pressure and total temperature measurements across the full 360-degree annulus at the turbine's exit plane, was upgraded with new hardware for improved sensor cable management. New winding ring guide rails were designed, manufactured, and installed to decrease the probability of sensor cables interfering with traverse movement and halting operation. The new hardware and cable routing are shown in Figure 2. The new guide rails restrict the motion of the cables, preventing them from crossing into different groves which would create interference with the outer diameter of the traverse cavity. Without the modifications, this interference could have resulted in damage to the traverse or a stoppage in test operations. These hardware improvements will improve the efficiency of test operations and result in more data acquisition during the ASCENT Project 106B test program.

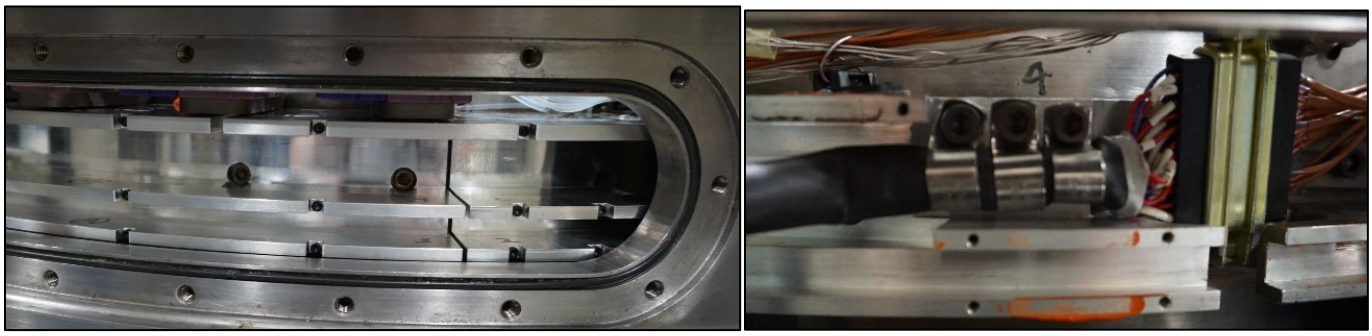


Figure 2. Left: Exit traverse winding right with new guide rails installed. Right: Thermocouple sensor cable showing how the cable is situated in the traverse groove during normal operation.

A preliminary test matrix was developed in reporting period quarter (Q)2 for the ASCENT Project 106B test campaign. Three primary turbine operating parameters (vane trailing edge flow, cavity purge flow, and blade cooling flow) have been identified as the primary variables in this test matrix. This will be optimized through collaboration with the GT team to identify additional or different parameters which will be addressed to provide model inputs. Test matrix development will continue through the next reporting period.

The START team is actively working with the Penn State Office of Research Administration Services to establish a data use agreement (DUA). This DUA will provide the legal framework for sharing test data and relevant geometric parameters of the NExT test article with the GT-ASDL team. The initial draft of this document is complete and under review. This DUA will allow the START team to share the required turbine design parameters for NExT with ASDL to incorporate into their turbine meanline model. Penn State is awaiting feedback on the document from GT, and then data transmission can begin. This process is illustrated in Figure 3.



Figure 3. Flow chart representation of the data use agreement for sharing National Experimental Turbine (NExT) design parameters with Aerospace Systems Design Laboratory (ASDL).

A separate test program was conducted which included efficiency data acquisition. Examples of several measured efficiency trends due to turbine cooling flow rate are illustrated in Figure 4. This data acquisition process was leveraged to optimize the post-processing format which will be used in the ASCENT Project 106B test program. The optimization will ensure a streamlined transfer of processed data to the GT-ASDL team for incorporation into their meanline model. Data was leveraged to refine the test matrix for the upcoming ASCENT Project 106B test program. Various turbine operational parameters (blade cooling flow rate, vane trailing edge flow rate, and tip clearance) were adjusted to determine which would have the largest influence on stage efficiency. This information has been used by the START team to refine the test matrix to represent a series of test points which will provide the largest value to the gas turbine community through this ASCENT Project 106B test campaign.

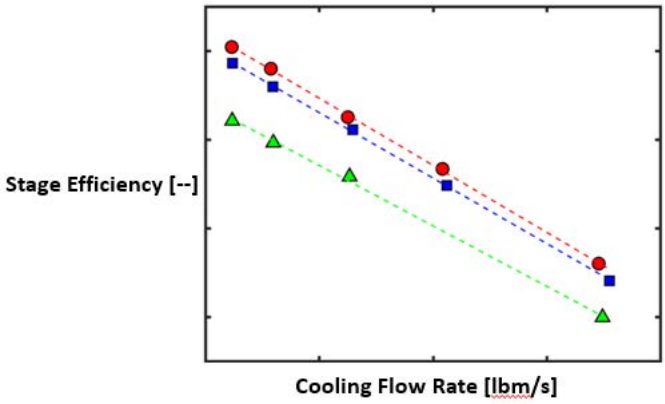


Figure 4. Example turbine efficiency trends acquired during a separate test program. These data were used to optimize the data processing format.

The START team finalized the test matrix that will yield the efficiency data pertaining to ASCENT Project 106B in reporting period Q4, and it is graphically outlined in Figure 5. This test matrix is designed to provide detailed datasets to develop turbine stage efficiency trends based on varied vane trailing edge (VTE), cavity purge, and blade cooling flow rates. Previous test program learnings were leveraged to determine stage operational parameters which resulted in significant

influence on stage efficiency, and this led to the selection of these parameters. These data will be of great importance to aircraft engine designers, as each of these test matrix parameters are critical to the design of a new turbine stage.

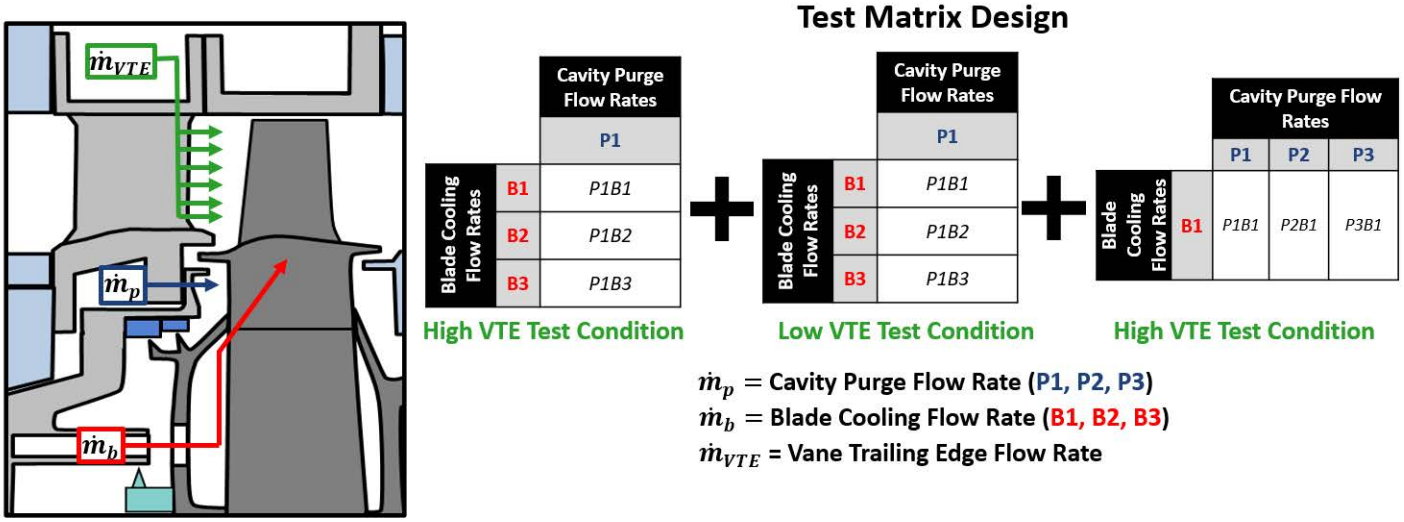


Figure 5. Test matrix for ASCENT Project 106B turbine efficiency testing.

This test program started at the end of this annual reporting period and will continue through the majority of the next quarter. Efficiency data will be processed to determine stage efficiency sensitivities, which will be shared with the GT-ASDL team for incorporation in their model. Initial data will be shared with the GT team when the aforementioned DUA is executed by both research teams.

Milestones

Milestone	Due date	Estimated date of completion	Actual date of completion	Status
Workplan	2/21/2025	2/21/2025	2/21/2025	Completed
COE meeting 1	5/31/2025	5/31/2025	5/7/2025	Completed
COE meeting 2	10/31/2025	10/31/2025	10/14 – 10/16/2025	Completed
Annual report	12/31/2025	12/31/2025		
Project closeout	9/30/2026	9/30/2026		

Major Accomplishments

- Executed a kickoff meeting with all individuals from the Penn State, GT, and FAA teams.
- Shared a presentation at the annual ASCENT meeting to share project status with the entire community.
- Completed final test hardware preparations and started the test campaign near the end of the annual reporting period.

Publications

None.

Outreach Efforts

The results reported in this document have been shared internally with the project team (Penn State and GT-ASDL) and will eventually result in a publication when testing is complete. Initial project goals were reviewed through an industry-government-academic partnership review meeting associated with the National Experimental Turbine in November 2024. Participants included the Department of Energy—National Energy Technology Laboratory, Office of Naval Research, Air Force Research Laboratory, National Aeronautics and Space Administration, Pratt & Whitney, Solar Turbines, Siemens



Energy, Honeywell Aerospace, and Agilis Engineering. Project updates and program goals were shared with Pratt & Whitney during a bi-annual industry-academic Center of Excellence partnership meeting in December 2024 and June 2025. In May 2025, updates on the overall ASCENT Project 106 program were shared during the annual ASCENT meeting and during a dedicated discussion as part of a bi-annual industry-academic Center of Excellence relationship. Additionally, goals and results were shared in a dedicated discussion in January 2025 and September 2025 as part of a bi-annual industry-academic Center of Excellence relationship with Solar Turbines.

Awards
None.

Student Involvement
An early career graduate student (Matthew Stuber) has been leading the efforts to optimize the data processing format, and he is now leading the effort to execute the test campaign. This has led to leadership development of this student through data analysis, meeting presentation skills, and team communication. Additional support has also been provided by a new graduate student (Dan Strobel) starting in August 2025.

Plans for Next Period
- Continue to coordinate & optimize the data delivery process and format for the GT-ASDL modeling tools.
- Complete the test program during the next reporting period, which will enable data analysis to proceed toward developing efficiency sensitivities to turbine operational parameters.

Disclaimer
This research was funded by the FAA Office of Environment and Energy through ASCENT, the FAA Center of Excellence for Alternative Jet Fuels and the Environment, Project 106B through FAA Award Number 13-C-AJFE-PSU-129 under the supervision of Pierre Mulgrave. Any opinions, findings, conclusions or recommendations expressed in this material are those of the authors and do not necessarily reflect the views of the FAA.

Publications Index

Project 001

Thirteen graduate students and four undergraduate students involved.

Publications

- Brandt, K., Martinez-Valencia, L., Camenzind, D., Martulli, A., Malina, R., Allroggen, F., & Wolcott, M. (2025). Pragmatic assessment of meeting the 2030 U.S. sustainable aviation fuel goal. *Biomass and Bioenergy, 206*. https://10.1016/j.biombioe.2025.108516
- Bolakhe, K., Yu, T. E., Sykes, V., Smith, A., & Boyer, C. N. (Manuscript revised and resubmitted for publication). *Assessing a Sustainable Aviation Fuel Supply Chain from Winter Canola and Its Carbon Intensity Considering Feedstock Yield Variations*.
- Li, P., Yu, T.E., Labbé, N., Abdoulmoumine, N., Garcia-Perez, M., Hoyt, K.P., & English, B.C. (2026). Spatial Optimization of the Sustainable Aviation Fuel Supply Chains from Forest Residues via Fast Pyrolysis/Hydrotreatment Considering Feedstock Ash Content Variability. *Biomass and Bioenergy*, 208:108793. https://doi.org/10.1016/j.biombioe.2025.108793
- Trejo-Pech, C. O., Bista, B., Yu, T. E., & Larson, J. A. (2025). An Analysis of the Risk Narrative Disclosed by Publicly Traded Biofuel Firms. *Energy Strategy Reviews, 62*, 101927. https://doi.org/10.1016/j.esr.2025.101927
- Martulli, A., Brandt, K., Allroggen, F., & Malina, R. (2025). The potential scale-up of sustainable aviation fuels production capacity to meet global and EU policy targets. *Nature Communications, 16*, 11619. https://www.nature.com/articles/s41467-025-66686-9

Reports

- Menefee, A., Helbing, M. (2025). *Carbon Capture and Storage in Sustainable Aviation Fuel Supply Chains* [White paper]. PennState Center for Energy Law and Policy. https://celp.psu.edu/wp-content/uploads/2025/01/SAF-CCS-white-paper-final-January-2025.pdf
- ANL. (2024). *Expansion of Carbon Calculator for Land Use and Land Management Change from Biofuels Production (CCLUB) to Address Induced Land Use Changes and Other Indirect Effects of Clean Fuel Production for R&D GREET2024*. Argonne National Laboratory (ANL).
- MIT, CAEP14/WG05_02/WP14: Proposal to the FTG Board on a default LCA value for POME HEFA.
- MIT, CAEP14_WP5_1_WP03: Update of the work of the CLCA subgroup, May 2025
- MIT, CAEP14_WP5_2_WP09: Update of the work of the CLCA subgroup
- MIT, CAEP14_WP5_2_WP13: Proposal to the WG5 Board on feedstock classification
- MIT, CAEP14_WP5_2_WP20: Work Program of the Electricity Sourcing AHG in the CAEP 14 cycle.
- MIT, CAEP14_WG5_PlenaryMeeting 1_WP01: SAF Short-term Production Projections Update, April 2025
- MIT, CAEP14_WG5_1_IP09: SAF Short-term Projections Update, May 2025
- MIT, CAEP14_WG5_1_IP08: SAF Short-term Production Projections Methodology Updates, October 2025
- Taheripour F., Purdue, CAEP/14-WG5_1-WP05 – ILUC value estimation, May 12-16, 2025, Virtual.
- Taheripour F., Purdue, CAEP/14-WG5_1-WP06 – Model Improvement and modelling time, May 12-16, 2025, Virtual.
- Taheripour F., Purdue, CAEP/14-WG5_2_IP05 – Standard GTAP, GTAP-BIO, and CORSIA GTAP-BIO models and their databases, October 27-37, 2025, São Paulo, Brazil.
- Taheripour F., Purdue, CAEP/14-WG5_2-WP015 – Progress ILUC values determination, October 27-37, 2025, São Paulo, Brazil.

Presentations

- Helbing, M. (2024, October). *Flying into the Future: Sustainable Aviation Fuel and the Policies Impacting its Development* [Oral presentation]. Penn State Earth and Environmental Systems Institute EarthTalks Series.
- Helbing, M. (2024, November). *Session 5: Discussion of other policy options that might merit review under the SAFGCR Action Area 4 - Policy Valuation and Analysis, Workstream PA.3 – Inform SAF Policy* [Panelist in oral presentation] Alternative Fuels & Chemicals Coalition's SAF Workshop, Oxon Hill, MD.



- Johnson, M., Helbing, M., & Fowler, L. (2025, May). *A 50-state Survey of Sustainable Aviation Fuel Policy.* [Poster]. Penn State Climate Solutions Symposium.
- Yu, T. E. (2024, September 30 – October 3). *Biomass Feedstock Supply Chain Modeling and Decision Tools for Sustainable Aviation Fuels* [Conference presentation]. 2024 Frontiers in Biorefining 7th International Conference, St. Simons Island, Georgia.
- Yu, T. E., Li, P., Labbé, N., Abdoulmoumine, N., Garcia-Perez, M., & Hoyt, K. (2024, November 20-22) *Sustainable Aviation Fuel Supply Chains Optimization from Forest Residues Considering Feedstock Ash Content Variability* [Conference presentation]. 2024 AFCC Global Biobased Economy Conference, Washington DC.
- Yu, T. E., Meyer, E., & Chen, X. (2025, July 9-11). *Consumers' Perception and Knowledge of Sustainable Aviation Fuel and Their Willingness to Pay a Premium* [Conference presentation]. The 1st International Conference on Sustainable Aviation Research, Dublin, Ireland.

Project 002

One graduate student and four undergraduate students involved.

Presentations

- Achterberg, A, Whitefield, P., & Woelk, K. (2025, October 8). *Gulfstream Ground Test Campaign October 2024* [Oral Presentation]. ICAO CAEP WG3 Meeting.

Project 003

No students involved.

Presentations

- Grady, S., Ngyuen, D. & Peters, J. (2025). Characterizing temporal trends in populations exposed to aircraft noise around U.S. airports: 1995–2015. Oral presentation at the Aviation Noise and Emissions Symposium (March 11-12, 2025)
- Grady, S.T., Mehta, U., Yi, L., Okereke, O.I., Hart, J.E., Laden, F., Roscoe, C., Costello, J., Bozigar, M., Whitsel, E., Kaufman, J.D., Levy, J.I., & Peters, J.L. (2025). Residential exposure to aircraft noise and depression risk in a U.S. prospective cohort. Oral presentation at the Joint Annual Meeting of ISES and ISEE 2025 (August 17-20, 2025).

Project 018

Three graduate students and three undergraduate students involved.

Publications

- Mueller, S., Patil, P., Levy, J., Hudda, N., Durant, J. L., Gause, E., van Loenen, B. D., Bermudez, M., Geddes, J. A., & Lane, K. J. (2025). Quantifying Aviation-Related Contributions to Ambient Ultrafine Particle Number Concentrations Using Interpretable Machine Learning. *Environmental Science & Technology, 59*(37), 19942-19952. doi: 10.1021/acs.est.5c07989.
- van Loenen, B. D., Black-Ingersoll, F., Durant, J. L., Levy, J. I., Patil, P., Mueller, S., Gause, E., Hudda, N., Bermudez, M., & Lane, K. J. (2025). Aircraft Arrival and Departure Contributions to Ultrafine Particle Size Distribution in a Near-Airport Community. *Environmental Science & Technology, 59*(25), 12853-12864. doi:10.1021/acs.est.5c04799.

Presentations

Mueller, S., Patil, P., Levy, J. I., Hudda, N., Durant, J. L., Gause, E., Loenen, B. V., & Lane, K. J. (2024, October 20-24). *Examining Impacts of Cross-Validation Approaches on Machine Learning Model Performance for Ultrafine Particle Exposure Assessment* [Oral presentation]. International Society for Exposure Science 2024 Annual Meeting, Montreal, Canada.



Project 019

One graduate student involved.

Project 022

No students involved.

Publications

- Singh, D. K., & Wuebbles, D. J. (2025). Aviation contrail climate forcing through 2035: Implications for sustainable aviation pathways. *Earth's Future,* submitted.
- Sanyal, S., Oh, L. J., Kulkarni, R., Eastham, S., and Wuebbles, D.J. (2025) Ozone and Climate Impacts of Future Supersonic Aircraft: A Multimodel Evaluation with WACCM and GEOS-Chem. *Earth's Future,* submitted.

Project 023

Two graduate students involved.

Publications

- Cezairli, M., Salgueiro, S., & Hansman, R. J. (2025). Implementation Analysis of Low-Noise Performance-Based Navigation Flight Procedures at Boston Logan Airport. *Journal of Air Transportation, 33*(3), 274-284. https://doi.org/10.2514/1.D0475

Project 025

One graduate student involved.

Project 031

Two undergraduate students involved.

Project 033

One graduate student involved.

- Database made accessible through https://altjetfuels.illinois.edu/

Project 37

Nineteen graduate students involved.

Project 038

One graduate student and one undergraduate student involved.



Publications

- Mukherjee, B. (2025). *Noise of Multirotor Electric Aircraft* [Doctoral dissertation, The Pennsylvania State University]. The Pennsylvania State University. https://etda.libraries.psu.edu/catalog/22433bxm437

Project 044

Four graduate and one undergraduate student involved.

Publications

- Salguiero, S., Huynh, J. & Hansman. R. J. (2025). Aircraft Takeoff and Landing Weight Estimation from Surveillance Data. *Journal of Air Transportation, 33*(1). https://doi.org/10.2514/1.D0370
- Cezairli, M., Salgueiro, S., & Hansman, R. J. (2024). Implementation Analysis of Low-Noise Performance-Based Navigation Flight Procedures at Boston Logan Airport. *Journal of Air Transportation, 33*(3), 274-284. https://doi.org/10.2514/1.D0475
- Lepe, M., Homola, M., Li, C., Lee, T., Hood, P., Huynh, J. L., & Hansman, R. J. (2025, January). Multifactor Analysis of Operational Factors Contributing to Aircraft Overflight Noise Variation. AIAA 2025-2004. AIAA SciTech 2025 Forum. https://doi.org/10.2514/6.2025-2004
- Homola, M., Lepe, M., Trávník, M., Huynh, J. L., & Hansman, R. J. (2025, July). *Take-Off and Landing Weight Estimation From ADS-B Airspeed Profiles*. AIAA 2025-3309. AIAA AVIATION Forum and ASCEND 2025. https://doi.org/10.2514/6.2025-3309
- Lee, T. (2025). A Data-Driven Approach to Aircraft Noise Variation and Operational Efficiency Analysis. *UC Irvine Masters Thesis*. ProQuest ID: Lee_uci_0030M_19549. Merritt ID: ark:/13030/m5mt5fxm. Retrieved from https://escholarship.org/uc/item/6tf709kc

Presentations

- Lepe, M., Homola, M., Li, C., Lee, T., Hood, P., Huynh, J. L., & Hansman, R. J. (2025, January). Multifactor Analysis of Operational Factors Contributing to Aircraft Overflight Noise Variation. Presented at AIAA SciTech 2025 Forum.
- Homola, M., Lepe, M., Trávník, M., Huynh, J. L., & Hansman, R. J. (2025, July). *Take-Off and Landing Weight Estimation From ADS-B Airspeed Profiles*. Presented at AIAA AVIATION Forum and ASCEND 2025.

Project 049

Two graduate students involved.

Publications

- Mukherjee, B. (2025). *Noise of Multirotor Electric Aircraft* [Doctoral dissertation, The Pennsylvania State University]. Penn State University Libraries, University Park, Pennsylvania.
- Gan, Z. F. (2025). *Time-Varying Noise of Electric Multirotor Aircraft* [Doctoral dissertation, The Pennsylvania State University]. Penn State University Libraries, University Park, Pennsylvania.

Project 051

One graduate student involved.

Project 052

One graduate student involved.



Publications

- Gomez-Vega, N., Tan, D. Y., Prashanth, P., Barrett, S. R., Speth, R. L., & Allroggen, F. (2025, January). *Influence of Fuel Tank Design on the Energy Demand of Hydrogen Aircraft* [Conference presentation paper]. AIAA SCITECH 2025 Forum, Orlando, Florida, 1243. https://doi.org/10.2514/6.2025-1243
- Gomez-Vega, N., Prashanth, P., Speth, R. L., & Allroggen, F. (2025, January). *Hydrogen Aircraft Design With Heat-Exchanger-Enhanced Turbofan Engines* [Conference presentation paper]. AIAA SCITECH 2025 Forum, Orlando, Florida, 0089. https://doi.org/10.2514/6.2025-0089

Presentations

- Gomez-Vega, N., Tan, D. Y., Prashanth, P., Barrett, S. R., Speth, R. L., & Allroggen, F. (2025, January). *Influence of Fuel Tank Design on the Energy Demand of Hydrogen Aircraft* [Conference presentation paper]. AIAA SCITECH 2025 Forum, Orlando, Florida.
- Gomez-Vega, N., Prashanth, P., Speth, R. L., & Allroggen, F. (2025, January). *Hydrogen Aircraft Design With Heat-Exchanger-Enhanced Turbofan Engines* [Conference presentation paper]. AIAA SCITECH 2025 Forum, Orlando, Florida.

Project 053

No students involved.

Project 054

Eleven graduate students involved.

Project 055

Five graduate students involved.

Publications

- Ha, S & Lieuwen, T. (2025). Direct combustion noise: Nearfield and non-compactness influences on pressure–heat release coherence, *Combustion and Flame,* Vol. 138, 113811.
- Ganesh, G.C., Ansari, N., Orsino, S., Xia, Y., & Acharya, V. (2025). *Analysis of Entropy Production Mechanisms in Turbulent Diffusion Flames.* AIAA SciTech Forum 2025, AIAA 2025-0594.
- Kastenberg, L. M., Panchal, A., & Menon, S. (2025). Direct and Indirect Combustion Noise Prediction in a Rich-Quench-Lean Combustor Using a Large Eddy Simulation. *AIAA SciTech Forum*, AIAA 2025-2489.
- Patki, P. A., Ek, H., Acharya, V., & Emerson, B. L. (2025, March 16-19). *Reduced order modeling and validation of hydrodynamic modes of reacting, swirling jets.* 14th U.S. National Combustion Meeting, Boston, Massachusetts.

Presentations

- Ganesh, G.C., Ansari, N., Orsino, S., Xia, Y., & Acharya, V. (2025). *Analysis of Entropy Production Mechanisms in Turbulent Diffusion Flames.* AIAA SciTech Forum 2025, January 6-10, Orlando, Florida.
- Kastenberg, L. M., Panchal, A., & Menon, S. (2025). Direct and Indirect Combustion Noise Prediction in a Rich-Quench-Lean Combustor Using a Large Eddy Simulation. *AIAA SciTech Forum,* January 6-10, Orlando, FL.
- Patki, P. A., Ek, H., Acharya, V., & Emerson, B. L. (2025, March 16-19). *Reduced order modeling and validation of hydrodynamic modes of reacting, swirling jets.* 14th U.S. National Combustion Meeting, Boston, Massachusetts.

Project 056

Four graduate students involved.



Project 057

One graduate student involved.

Publications

- Kapcsos, J. L., & Sparrow, V. W. (2025). Developments on ground blocking implementation in turbulence tool for sonic boom propagation. *Noise Control Engineering Journal, 73(3)*, 407-412. https://doi.org/10.3397/1/377331

Project 058

Two graduate students involved.

Publications

- Shreya Sharma, Prakash Prashanth, Raymond Speth. Regional Differences in Surface Ozone and $PM_{2.5}$ due to Aviation in Growing Markets. ESS Open Archive. March 05, 2025. DOI: 10.22541/essoar.174120418.84924481/v1

Project 059

Seven graduate students involved.

Project 060

One graduate student involved.

Project 061

Five graduate students involved.

Publications

- Ali, H. E., Ravikanti, B., Balchanos, M. G., Harrison, E., & Mavris, D. (2025). MBSE Enabled Requirement Verification for a Traceable Regulatory Analysis Framework of UAS Noise Certification Standards. *AIAA SCITECH 2025 Forum* (p. 0367).
- Mali, H., Geneti, N. F., Balchanos, M. G., Harrison, E., & Mavris, D. (2025). A Process Evaluation and Visualization Framework for Unmanned Aerial System (UAS) Noise Certification Testing. *AIAA SCITECH 2025 Forum* (p. 0368).

Presentations

- Ali, H. E., Ravikanti, B., Balchanos, M. G., Harrison, E., & Mavris, D. (2025). MBSE Enabled Requirement Verification for a Traceable Regulatory Analysis Framework of UAS Noise Certification Standards. *AIAA SCITECH 2025 Forum,* January 6-10, Orlando, FL.
- Mali, H., Geneti, N. F., Balchanos, M. G., Harrison, E., & Mavris, D. (2025). A Process Evaluation and Visualization Framework for Unmanned Aerial System (UAS) Noise Certification Testing. *AIAA SCITECH 2025 Forum,* January 6-10, Orlando, FL.

Project 062

Two graduate students involved.



Project 064

Eleven graduate students involved.

Publications

- Cheng, Y., Ergan, T., Cocoves, N., Xie, J., Cai, Y., Kirby, M., and Mavris, D. (2026, January 12-16). *Rapid Fuselage and Cabin Sizing Method for Commercial Transport Aircraft Design*. Accepted in AIAA SciTech 2026 Forum. To be published.
- Cheng, Y., Ergan, T., Xie, J., Kirby, M., Gladin, J., & Mavris, D. (2026, June 8-12). *Fleet-Level Assessment of Mission-Optimized Next-Generation Single-Aisle Aircraft with Varying Payload*. Submitted to AIAA Aviation 2026 Forum.
- Cocoves, N., Ergan, T., Benhissoune, S., Cai, Y., Gladin, J., & Mavris, D. (2026, June 8-12). *Assessing Impacts of Design Range and Payload on Next-Generation Single-Aisle Transport Fuel Burn and Noise*. Submitted to AIAA Aviation 2026 Forum
- Ergan, T., Parashar, A., Xie, J., Cai, Y., Kirby, M., Gladin, J., & Mavris, D. (in review). Design and Fleet-Level Assessment of Next-Generation Single-Aisle Aircraft with Reduced Range and Cruise Speed. Submitted to *Journal of Aircraft*.
- Ergan, T., Parashar, A., Xie, J., Kirby, M., & Mavris, D. (2025, January). Fleet-level and global emissions impact analysis of mission-optimized next-generation single-aisle aircraft. *AIAA SciTech 2025 Forum*, AIAA 2025-2168. https://doi.org/10.2514/6.2025-2168
- Patel, D., Ergan, T., Cai, Y., Gladin, J., & Mavris, D. (2025, January). Performance assessment and mission-based optimization for next-generation single-aisle aircraft conceptual design. *AIAA SciTech 2025 Forum*, AIAA 2025-0001. https://doi.org/10.2514/6.2025-0001
- Tan, Y. T., Kondur, N., Zurtia, F., Xie, J., Cai, Y., Kirby, M., & Mavris, D. (2026, June 8-12). *Development of Advanced Concept Aircraft Model in Aviation Environmental Design Tool*. Submitted to AIAA Aviation 2026 Forum.

Presentations

- Ergan, T., Parashar, A., Xie, J., Kirby, M., & Mavris, D. (2025, January). Fleet-level and global emissions impact analysis of mission-optimized next-generation single-aisle aircraft. *AIAA SciTech 2025 Forum*, January 6-10, Orlando.
- Patel, D., Ergan, T., Cai, Y., Gladin, J., and Mavris, D. (2025). Performance Assessment and Mission-Based Optimization for Next-Generation Single-Aisle Aircraft Conceptual Design, *AIAA SciTech Forum 2025,* January 6-10, Orlando.

Project 065

Two graduate and one undergraduate student involved.

Publications

- Bell, D. C., Boehm, R. C., & Heyne, J. S. (2025). Freezing Point of Hydrocarbon Fuels from Single Species Concentrations. *Energy and Fuels, 39*(9), 4221-4226. https://doi.org/10.1021/acs.energyfuels.4c06091
- Luecke, J., Naser, N., Yang, Z., Heyne, J., & McCormick, R. L. (2025). Measurement of Spray Chamber Ignition Delay and Cetane Numbers for Aviation Turbine Fuels. *ACS Energt & Fuel, 39*(22), 10479-10487. https://doi.org/10.1021/acs.energyfuels.5c01350
- O'Brien, C. J., Kang, K., Wood, E. J., Yoon, J., Mayhew, E. K., Kastengren, A., Kweon, C. M., & Lee, T. (2026). Time-resolved spray characterization via unified optical flow and binarization technique. *Fuel, 407*(C), doi: 137433. https://doi.org/10.1016/j.fuel.2025.137433
- Yang, Z., Faulhaber, C., Boehm, R. C., & Heyne, J. S. (2025). Geometric and Positional Isomer Effects on Ignition Behavior of Cycloalkanes: Implications for Sustainable Aviation Fuels. *ACS Energy & Fuel,* 39(38), 18641-18648. https://doi.org/10.1016/j.fuel.2024.133230
- Yu, S., He, H., Summers, S., Yang, Z., Si, B., Gao, R., Song, A., Heyne, J. S., Zhang, Y., & Yang, H. (2025). Upgrading biocrude oil into sustainable aviation fuel using zeolite-supported iron-molybdenum carbide nanocatalysts. *Science Advances, 11*(26), 5777. https://doi.org/10.1126/sciadv.adu5777



Project 066

One graduate and two undergraduate students involved.

Project 067

Four graduate students involved.

Publications

- Hodge, A. J., Shahin, T. T., Gejji, R. M., Philo, J. J., Lucht, R. P., & Slabaugh, C. D. (2025). Fuel temperature effects on combustion stability of a high-pressure liquid-fueled swirl flame. *Journal of Propulsion and Power, 41*(1), 53-63. https://doi.org/10.2514/1.B39592
- McDonald, C. T., Shahin, T. T., Philo, J. J., Gejji, R. M., Fish, D. D., Slabaugh, C. D., & Lucht, R. P. (2025). Combustion product measurements in a liquid-fueled aviation gas turbine combustor with heated fuels. *ASME Journal of Engineering for Gas Turbines and Power, to be submitted.*
- McLean, T. N., Koenig, K. C., Murdock, B. K., Shahin, T. T., Hodge, A. J., Gejji, R. M., Slabaugh, C. D., & Lucht, R. P. (2025, January 6-10). *Laser-induced incandescence measurements in a high-pressure swirl-stabilized flame.* In proceedings of AIAA SciTech 2025 Forum, Orlando, Florida. https://doi.org/10.2514/6.2025-1580

Presentations

- McLean, T. N., Koenig, K. C., Murdock, B. K., Shahin, T. T., Hodge, A. J., Gejji, R. M., Slabaugh, C. D., & Lucht, R. P. (2025, January 6-10). *Laser-induced incandescence measurements in a high-pressure swirl-stabilized flame* [Conference presentation]. AIAA SciTech 2025 Forum, Orlando, Florida.

Project 068

Four graduate students involved.

Publications

- McFerran, K., Thole, K. A., & Lynch, S. P. (2025). Dirt ingestion impacts on cooling within a double-walled combustor liner. *ASME Journal of Turbomachinery, 147*(8), 081019. https://doi.org/10.1115/1.4067464
- McFerran, K., Thole, K. A., Lynch, S. P., Boardman, G., Lundgreen, R., Kramer, S., and Joshi, D., (2025), "A Novel Approach to Dirt Mitigation for Combustor Walls," ASME Turbo Expo 2025. https://doi.org/10.1115/GT2025-154071
- Schaeffer, C. B., Barringer, M. D., Lynch, S. P., & Thole, K. A. (2025). Influence of dilution and effusion flows in generating variable inlet profiles for a high-pressure turbine. *ASME Journal of Turbomachinery, 147*(3), 031003. https://doi.org/10.1115/1.4066560
- Schaeffer, C., Barringer, M., Lynch, S., & Thole, K. (2025, under review) Comparison of Predicted and Measured Combustor-Relevant Flow Fields. *Journal of Turbomachinery.*
- Schaeffer, C., Barringer, M., & Thole, K. (2026, June 15-19). *Large Eddy Simulation of a Non-Reacting Profile Simulator for the First-Stage Vane* [Abstract accepted]. ASME Turbo Expo 2026, Milan, Italy.

Presentations

- McFerran, K., Thole, K. A., Lynch, S. P., Boardman, G., Lundgreen, R., Kramer, S., and Joshi, D., (2025), "A Novel Approach to Dirt Mitigation for Combustor Walls," ASME Turbo Expo 2025.
- Schaeffer, C., Barringer, M., Lynch, S., & Thole, K. (2025, June 15-19). *Comparison of Predicted and Measured Combustor-Relevant Flow Fields* [Poster presentation]. ASME Turbo Expo 2025, Memphis, Tennessee.
- Schaeffer, C., Barringer, M., & Thole, K. (2026, June 15-19). *Large Eddy Simulation of a Non-Reacting Profile Simulator for the First-Stage Vane* [Abstract accepted]. ASME Turbo Expo 2026, Milan, Italy.



Project 069

No students involved.

Publications

- Mehri, R., Nishida, R. T., Sipkens, T. A., Smallwood, G. J., Corbin, J. C., Whitefield, P., Achterberg, S., Miake-Lye, R. C., Nault, B. A., Howard, R., & Olfert, J. S. (2025). Quantification of the repeatability and reproducibility of the CPMA-electrometer reference mass standard for in-situ calibration of mass concentration aerosol instruments. *Aerosol Science and Technology, 60*(3), 230-244. https://doi.org/10.1080/02786826.2025.2568694

Project 070

Four graduate students involved.

Publications

- Juergensmeyer, J., Miller, J., Bond, R., Mcgrath, R., Wehe, S., Sun, W., Mazumdar, Y. C., & Steinberg, A. (2025, June 16–20). Measurement of Particulate Matter and Its Oxidation in a Multi-Sector Rich-Quench-Lean Combustor. *Proceedings of the ASME Turbo Expo 2025: Turbomachinery Technical Conference and Exposition*. Memphis, Tennessee. https://doi.org/10.1115/GT2025-153181
- Vishwanath, R., Bibik, O., Olimid, D., Douglas, E., Wehe, S., Mazumdar, Y. C., Steinberg, A., & Sun, W. (2025, January 6-10). Drop-size measurements using phase doppler particle anemometry in a confined high-pressure sector combustor (AIAA 2025-1519). *AIAA SCITECH 2025 Forum*, Orlando, Florida. https://doi.org/10.2514/6.2025-1519
- Vishwanath, R., Douglas, E., Wehe, S., Mazumdar, Y. C., Steinberg, A., & Sun, W. (2026). *Spray measurements in a sector combustor operating with conventional and sustainable fuels at elevated conditions*. Submitted to ASME Turbo Expo 2026.

Presentations

- Juergensmeyer, J., Miller, J., Bond, R., Mcgrath, R., Wehe, S., Sun, W., Mazumdar, Y. C., & Steinberg, A. (2025, June 16–20). Measurement of Particulate Matter and Its Oxidation in a Multi-Sector Rich-Quench-Lean Combustor. *ASME Turbo Expo 2025: Turbomachinery Technical Conference and Exposition*. Memphis, Tennessee.
- Vishwanath, R., Bibik, O., Olimid, D., Douglas, E., Wehe, S., Mazumdar, Y. C., Steinberg, A., & Sun, W. (2025, January 6-10). Drop-size measurements using phase doppler particle anemometry in a confined high-pressure sector combustor. *AIAA SCITECH 2025 Forum*, Orlando, Florida.

Project 071

One graduate student involved.

Publications

- Baranwal, M., Saldinger, J. C., Kim, D., Elvati, P., Hero, A. O., & Violi, A. (2024). SPIN: A data-driven model to reduce large chemical reaction networks. *Fuel*, *367*, 131299.
- Di Liddo, L., Saldinger, J. C., Jadidi, M., Elvati, P., Violi, A., & Dworkin, S. B. (2022). Exploring soot inception rate with stochastic modelling and machine learning. *Combustion & Flame, 258,* 112375.
- He, T., Kim, D., Dillstrom, T., Cai, K., Zhang, P., Liu, C., He, X., Wang, Z. & Violi, A. (2021). Oxidation of 2,6-dimethylheptane at low temperature: Kinetic modeling and experimental study. *Fuel*, 287, 119220.
- Karpe, S., & Menon, S. (2023, January). Model Simulations of Soot Formation due to PAH Kinetics from Mixing Layers of Jet-A Fuels. (AIAA-2023-2690). *AIAA SciTech 2023 Forum*, National Harbor, Maryland.
- Karpe, S., & Menon, S. (2025, January). Large-Eddy Simulations of Soot Formation and Dispersion in Rich-Burn Quick-Mix Lean-Burn (RQL) Spray Combustor (AIAA-2025-2484). *AIAA SciTech 2025 Forum*, Orlando, Florida.



- Karpe, S., & Menon, S. (2025). Modeling uncertainties in primary zones soot predictions for rich-quench-lean combustion system. *Proceedings of Combustion Institute, 41,* 105805.
- Kim, D., & Violi, A. (2021). On the importance of species selection for the formulation of fuel surrogates. *Proceedings of the Combustion Institute, 38*(4), 5615-5624.
- Kim, D., & Violi, A. (2022). Uncertainty-based weight determination for surrogate optimization. *Combustion and Flame, 237*, 111850.
- Saldinger, J. C., Elvati, P., & Violi, A. (2021). Stochastic and network analysis of polycyclic aromatic growth in a coflow diffusion flame. *Physical Chemistry Chemical Physics, 23*(7), 4326-4333.
- Saldinger, J.C., Elvati, P., & Violi, A. (2023). A machine learning framework to predict the aggregation of polycyclic aromatic compounds. *Proceedings of the Combustion Institute*, 39(1),1009-1017.
- Saldinger, J. C., Elvati, P., Alrawi, K., & Violi, A. (2024). Predicting aggregation rates of polycyclic aromatics through machine learning. *Fuel*, *364*, 131031.
- Shao, C., Wang, Q., Zhang, W., Bennett, A., Li, Y., Guo, J., Im, H. G., Roberts, W. L., Violi, A. & Sarathy, S. M. (2023). Elucidating the polycyclic aromatic hydrocarbons involved in soot inception. *Communications Chemistry*, *6*(1), 223.
- Shi, X., Wang, Q., & Violi, A. (2021). Reaction pathways for the formation of five-membered rings onto polyaromatic hydrocarbon framework. *Fuel*, 283, 119023.
- Wang, Q., Saldinger, J. C., Elvati, P., & Violi, A. (2021). Molecular structures in flames: A comparison between SNapS2 and recent AFM results. *Proceedings of the Combustion Institute, 38*(1), 1133-1141.

Presentations

- Karpe, S., & Menon, S. (2022). Numerical Simulations of Soot Formation in Turbulent Premixed Flames of Jet Fuels. *75th Annual Meeting of the APS Division of Fluid Dynamics, 67*(19).
- Karpe, S., & Menon, S. (2023, January). Model Simulations of Soot Formation due to PAH Kinetics from Mixing Layers of Jet-A Fuels. *AIAA SciTech 2023 Forum*, National Harbor, Maryland.
- Karpe, S., & Menon, S. (2025, January). Large-Eddy Simulations of Soot Formation and Dispersion in Rich-Burn Quick-Mix Lean-Burn (RQL) Spray Combustor. *AIAA SciTech 2025 Forum*, Orlando, Florida.
- Karpe, S., & Menon, S. (2026). Large-Eddy Simulations of dilution jet effects on rich-quench-lean spray flame. *AIAA SciTech 2026 Forum*.

Project 072

One graduate student involved.

Publications

- Allroggen, F., Knittel, C. R., Hansman, R. J., Li, J., Wan, X., & Wang, J. (2025). *Planes Overhead: How Airplane Noise Impacts Home Values* (No. w34431). National Bureau of Economic Research. https://doi.org/10.3386/w34431

Project 073

One undergraduate student involved.

Project 075

One graduate student and two undergraduate students involved.

Publications

- Li, N., & Grace, S. M. (2025). Low-Order, Data-Driven Method for Analysis of Impact of Fan Design on Fan Stage Broadband Interaction Noise (AIAA 2025-3650). *AIAA AVIATION 2025 Forum*, Las Vegas, Nevada.



Presentations

- Li, N., & Grace, S. M. (2025). Low-Order, Data-Driven Method for Analysis of Impact of Fan Design on Fan Stage Broadband Interaction Noise (AIAA 2025-3650). *AIAA AVIATION 2025 Forum*, Las Vegas, Nevada.
- Li, N., Winkler, J., Reinmann, C. A., Mendoza, J., & Grace, S. M. On the Use of a Low-Order Model for Rig and Full-Scale Turbofan Broadband Noise Predictions. *Being developed for the AIAA/CEAS Aeroacoustics Conference (2026).*

Project 077

Three graduate students involved.

Publications

- Valente, V. T., Greenwood, E., & Johnson, E. N. (2025). An Experimental Evaluation of an Electronic Rotor Phase Synchronization System for Multirotor Aircraft Noise Control. *Journal of American Helicopter Society, 70*(4). https://doi.org/10.4050/JAHS.70.042008
- Valente, V. T., Greenwood, E., & Johnson, E. N. (2026). Multirotor Noise Control using Synchrophasing Under Nonstationary Conditions. *Journal of Sound and Vibration, 629*. https://doi.org/10.1016/j.jsv.2026.119673

Presentations

- Valente, V. T., Chaudhary, R., Greenwood, E., Johnson, E. N., & Brentner, K.S. (2026, May 26-29). Predictions and Measurements of Noise Control via Synchophasing for a Fixed Wing Distributed Electric Propulsion Aircraft in Free Flight [Abstract submitted]. 32nd AIAA/CEAS Aeroacoustics Conference, Brussels, Belgium.

Project 078

One graduate student involved.

Publications

- Euchenhofer, M. V. (2025). *An investigation into contrail observability from different satellite platforms* [Master's thesis, Massachusetts Institute of Technology]. Massachusetts Institute of Technology. https://hdl.handle.net/1721.1/162925
- Euchenhofer, M. V., Prashanth, P., Parke, S. A., Eastham, S. D., & Waitz, I. A. (2025). Contrail observation limitations using geostationary satellites. *Geophysical Research Letters, 52*, e2025GL118386. https://doi.org/10.1029/2025GL118386

Project 079

Two graduate students involved.

Publications

- Packer, A., Reimann, C. A., Winkler, J., Homma, K., Mendoza, J., Greenwood, E., Manahan, M., & Meisel, N. A. (2025) Evaluating the Performance of Novel TPMS-Based Acoustic Liner Designs Suitable for Additive Manufacturing. *Proceedings of the Annual International Solid Freeform Fabrication Symposium*, in press.
- Windows, J., Packer, A., Nelson, E., Chowaniec, J., Mendoza, J., Reimann, C. A., Winkler, J., Homma, K., & Meisel, N. A. (2025). Identification of Stochastic Manufacturing Defects Within Additively Manufactured Acoustic Liners. *Proceedings of the Annual International Solid Freeform Fabrication Symposium*, in press.

Presentations

- Packer, A., Reimann, C. A., Winkler, J., Homma, K., Mendoza, J., Greenwood, E., Manahan, M., & Meisel, N. A. (2025) Evaluating the Performance of Novel TPMS-Based Acoustic Liner Designs Suitable for Additive Manufacturing. *International Solid Freeform Fabrication Symposium, Austin, TX, 8/10/2025*



- Windows, J., Packer, A., Nelson, E., Chowaniec, J., Mendoza, J., Reimann, C. A., Winkler, J., Homma, K., & Meisel, N. A. (2025). Identification of Stochastic Manufacturing Defects Within Additively Manufactured Acoustic Liners. *International Solid Freeform Fabrication Symposium, Austin, TX, 8/10/2025*.

Project 080

Three graduate students involved.

Publications

- Sierra, V., Wolcott, M., Zhang, X., Ha, S., Male, J., Garcia, A., Brandt, K., Garcia-Perez, M., Drennan, C., & Holladay, J. (Under review). *Evaluating Hydrogen Production Through Techno-Economic, Carbon Intensity, and Policy Perspectives in the U.S.* Pending submission.
- Housen, T., (2024). *Climate impact analysis of direct air capture deployment* [Master's thesis, Massachusetts Institute of Technology]. MIT Libraries. https://hdl.handle.net/1721.1/155419

Presentations

- Sierra-Jimenez, V., Brandt, K., Wolcott, M., Male, J., Garcia-Perez, M. (2024, November 20-21). *Hydrogen Production Techno-economic and Carbon Intensity Insights for a Sustainable Energy Transition in the U.S.* [Poster presentation]. Re+CHARGE H_2 Conference (PNWH2 Hub), Seattle, Washington.
- Garcia, A., Sierra-Jimenez, V., Garcia-Perez, M. (2024, October 15-16) *Screening and Optimization of Sustainable Aviation Fuel (SAF) Technologies in an Evolving Hydrogen Market* [Poster presentation]. Northwest Bioenergy Summit, Spokane, Washington.

Project 082

Four graduate students involved.

Publications

- Prashanth, P., Gomez-Vega, N., He, S., Shukla, A., Gonzalez, J. J., Bobadilla, D. S., Lee, K., Ranjan, P., Zahid, S. S., Abel, J., Drela, M., & Speth, R. (2025). TASOPT.jl: A Julia package for conceptual commercial transport aircraft design. *Journal of Open Source Software, 10*(113), 8521. https://doi.org/10.21105/joss.08521
- Shukla, A., Prashanth, P., & Speth, R. L. (2025, July). Impact of Efficiency-Driven Aircraft Technology Improvements on Climate and Air Quality (AIAA 2025-3502). *AIAA AVIATION FORUM AND ASCEND 2025*. https://doi.org/10.2514/6.2025-3502

Presentations

- Shukla, A., Prashanth, P., & Speth, R. L. (2025, July). Impact of Efficiency-Driven Aircraft Technology Improvements on Climate and Air Quality (AIAA 2025-3502). Presented at AIAA AVIATION Conference, Las Vegas, NV.

Project 083

Two graduate students involved.

Publications

- Reider, S. (2025). *Stochastic Methods for Setting Effective Aviation NO_x Policies* [Master's thesis, Massachusetts Institute of Technology]. MIT Libraries. https://dspace.mit.edu/handle/1721.1/163033



Project 084

Three graduate students involved.

Publications

- Gonzalez, V. (2025). *A Methodology for Integrating Vehicle Performance into Traffic Flow Management Analysis for AAM Airspace Integration* [Doctoral Dissertation, University of California, Irvine]. California Digital Library. https://escholarship.org/content/qt3sb9w403/qt3sb9w403.pdf
- Pellerito, V., Yeung, N., Huynh, j., & Hansman, R. J. (2025). Impact of flight trajectory design on performance and noise for AAM aircraft. *AIAA Journal of Aircraft*, 1-16. https://doi.org/10.2514/1.C038248

Project 085

Six graduate students involved.

Project 086

Six undergraduate students involved.

Project 088

No students involved.

Project 089

Two undergraduate students involved.

Publications

- Nicely, T., Nesbit, C. J., Kosir, S., Steinecker, W. H., & West, Z. (In process). Influence of Additives and Impurities on the Dielectric Properties of Jet Fuel. *Energy & Fuels.*

Project 090

Two undergraduate students involved.

Publications

- Kosir, S., Arts, A. M., Nicely, T., Nesbit, C. J., Mueller, S., Landsaw, A., Baker, M., Brown, L., Thompson, J., Anderson, C., Shafer, L., Steinecker, W. H., Zabarnick, S., & West, Z. J. (2025). *World Jet Fuel Survey Part 1: 2023-2024* (CRC AV-33-22). Coordinating Research Council (CRC), Atlanta, Georgia. In press.

Project 091

No graduate students involved.

Publications

- Kulkarni, R., Sanyal, S., Ma, C. Z., McDonald, H., Speth, R. L., Ross, M., & Wuebbles, D. J. (2025). *Effects of Potential Future Emissions from Different Rocket Fuel Types on Climate and Stratospheric Ozone*. *AGU Advances*, submitted.



Project 092

No graduate students involved.

Project 093

Seven graduate students involved.

Presentations

- Presented the results at the International Conference on Sustainable Aviation Research (ICSAR) 2025.

Project 094

Six graduate students involved.

Project 095

Four graduate students involved.

Publications

- Terzi, B., Decroix, J., Wattebled, L. A., Jazzini, A. S., Tai, J. C., & Mavris, D. (2025). Modeling Methodology for PEM Fuel Cells as Auxiliary Power Units in Aircraft Applications. In *AIAA AVIATION FORUM AND ASCEND 2025* (p. 3373).

Presentations

- Terzi, B., Decroix, J., Wattebled, L. A., Jazzini, A. S., Tai, J. C., & Mavris, D. (2025). Modeling Methodology for PEM Fuel Cells as Auxiliary Power Units in Aircraft Applications. *AIAA AVIATION FORUM AND ASCEND 2025*.

Project 096

Eight graduate students involved.

Project 097

Nine graduate students involved.

Project 098

Three graduate students involved.

Project 099

No students involved.



Project 100

No students involved.

Project 101

One graduate and two undergraduate students involved.

Project 102

Three graduate students involved.

Project 103

One graduate student and one undergraduate student involved.

Publications

- Yu, S., He H., Summers, S., Yang, Z., Si, B., Heyne, J., Zhang, Y., Yang, H. (2025). Upgrading of biocrude oil into sustainable aviation fuel using molybdenum carbide nanocatalysts, *Science Advances*. 11(26), 5777. https://doi.org/10.1126/sciadv.adu5777
- Boehm, R., Parker, R., Yang, Z., Dooley, S., & Heyne, J. (2025). Blend Prediction Model for Vapor Pressure of Jet Fuel Range Hydrocarbons. *Sustainability, 17*(21), 9612. https://doi.org/10.3390/su17219612

Project 104

Nine graduate students involved.

Publications

- Benavidez-Brouk, L., Taheripour, F., Baldos, U., Zhuang, Q., & Chen, S. (2026). Updates in assessing soil organic carbon and their implications for evaluating land use change emissions. Environmental Research Communications, 8(2). https://doi.org/10.1088/2515-7620/ae3d84
- Chen, L., T.E. Yu, and H. Williams. (2025). The Impact of Soil Erosion on Corn Yields: A Spatial Regression Analysis. *Agrosystems, Geosciences & Environment*, Accepted.
- Chen, S., Zhuang, Q., Taheripour, F., Yuan, Y., & Benavidez, L. (2025). Assessment of global land cover changes using satellite data: intermittent and long-term land cover changes from 2001 to 2020. *Environmental Research Letters*, *20*(3). http://dx.doi.org/10.1088/1748-9326/adb5a3
- Liu, X., Taheripour, F., Zhuang, Q., & Benavidez Hernandez, L. (2026, under review). Global marginal land mapping and the impact of agricultural management practices on marginal land soil organic carbon. *Environmental Research Letters.*
- Rubin, H. J., Fu, J. S., & Yu, T. E. (2025). Mapping historical soil carbon in the United States with machine learning. *Manuscript under review.*

Presentations

- Chen, L., Yu, T.E., Rubin, H., Fu, J.S., & Rejesus, R. (2025, July 27-29). *The Impact of Adopting Cover Crops and No-Till Systems on U.S. Soil Organic Carbon* [Conference presentation]. 2025 Agricultural and Applied Economics Association (AAEA) Annual Meeting, Denver, Colorado. https://doi.org/10.22004/ag.econ.361059
- Chen, L., Yu, T.E., & Williams, H. (2025, February 1-4). *Impact of Water and Wind Erosion on Corn and Soybean Yields: A Spatial Regression Analysis* [Conference presentation]. Southern Agricultural Economics Association (SAEA) 2025 Annual Meeting, Irving, Texas.



- Chen, S., Taheripour, F., Baldos, U. L., Zhuang, Q., Yuan, Y., & Benavidez Hernandez, L. (2025, December 15-19). *Global pastureland changes from 2001 to 2020* [Conference presentation]. AGU Fall Meeting 2025, New Orleans, Louisiana.
- Costello, A., Montes, F., & Kemanian, A. (2025, November). *Carbon stabilization during incubation of fermentation byproducts* [Poster presentation]. Science Societies CANVAS conference, Salt Lake City, Utah.
- Liu, X., Zhuang, Q., Taheripour F., & Benavidez, L. (2025, December 15-19). *Global Marginal Land Mapping and Impact of Agricultural Management Practices on Marginal Land Soil Organic Carbon* [Conference presentation]. AGU Fall Meeting 2025, New Orleans, Louisiana.
- Wang, E., Shi, Y., White, C., & Kemanian, A. (2025, November). *Algorithm-based exploration of double cropping with oilseed crops* [Poster presentation]. Science Societies CANVAS conference, Salt Lake City, Utah.
- Yuan, Y., Taheripour, F., Baldos, U. L., Chen, S., & Zhuang, Q. (2025, December 15-19). *Improving forest carbon accounting in economic models: Updating GTAP land cover with recent remote sensing products* [Conference presentation]. AGU Fall Meeting 2025, New Orleans, Louisiana.

Project 105

No students involved.

Project 106

Seven graduate and two undergraduate students involved.

Project Funding Allocations by Federal Fiscal Year

Breakout by Project*

Project		Funding Based on award date												
		2014	2015	2016	2017	2018	2019	2020	2021	2022	2023	2024	2025	Total
001	Alternative Jet Fuel Supply Chain Analysis	$1,599,943	$1,425,000	$1,498,749	$1,855,461	$1,102,865	$1,034,039	$3,214,455	$1,412,313	$1,569,136	$936,344	$2,688,115	-	$18,336,420
002	Ambient Conditions Corrections for Non-Volatile PM Emissions Measurements	$2,800,000	$750,000	-$147,766	$725,500	-	$1,217,221	-	$521,246	-	$3,050,812	$2,513,003	-	$11,430,016
003	Cardiovascular Disease and Aircraft Noise Exposure	$200,000	$200,000	$200,000	$340,000	-	$1,729,286	-	-	-	$1,999,608	$162,001	-	$4,830,895
004	Estimate of Noise Level Reduction	$150,000	-	-	-	-$ 8,845	-	-	-	-	-	-	-	$141,155
005	Noise Emission and Propagation Modeling	$212,000	$200,000	-	-	-	-	-	-	-	-	-	-	$412,000
006	Rotorcraft Noise Abatement Operating Conditions Modeling	$250,326	-	-	-	-	-	-	-	-	-	-	-	$250,326
007	Civil, Supersonic Over Flight, Sonic Boom (Noise) Standards Development	$100,000	$200,000	-	-	-	-	-	-	-	-	-	-	$300,000
008	Noise Outreach	$ 30,000	$ 50,000	$ 75,000	$ 25,000	-	$ 30,000	-	-	-	-	-	-	$210,000
009	Geospatially Driven Noise Estimation Module	-	-	-	-	-	-	$250,000	$249,999	-	-	-	-	$499,999
010	Aircraft Technology Modeling and Assessment	$549,979	$550,000	$310,000	$669,567	$764,185	-	$2,747,116	$700,000	-	$200,000	-	-	$6,490,847
011	Rapid Fleet-wide Environmental Assessment Capability	$600,000	$270,000	$299,999	-	-	-	-	-	-	-	-	-	$1,169,999
012	Aircraft Design and Performance Assessment Tool Enhancement	$ 90,000	-	-	-	-	-	-	-	-	-	-	-	$90,000

Project		Funding Based on award date												
		2014	2015	2016	2017	2018	2019	2020	2021	2022	2023	2024	2025	Total
013	Micro-Physical Modeling & Analysis of ACCESS 2 Aviation Exhaust Observations	$200,000	-	-	-	-	-	-	-	-	-	-	-	$200,000
014	Analysis to Support the Development of an Aircraft CO2 Standard	$520,000	-	-	-	-	-	-	-	-	-	-	-	$520,000
017	Pilot Study on Aircraft Noise and Sleep Disturbance	$154,000	$343,498	$266,001	$134,924	-	-	-	-	-	-	-	-	$898,423
018	Health Impacts Quantification for Aviation Air Quality Tools	$150,000	$150,000	$200,000	$270,000	-	-	$1,299,991	$599,371	$549,921	-	$649,915	-	$3,869,198
019	Development of Aviation Air Quality Tools for Airport-Specific Impact Assessment: Air Quality Modeling	$320,614	$369,996	-	$625,378	-	$300,000	$919,064	$650,000	-	$650,000	$300,000	-	$4,135,052
020	Development of NAS wide and Global Rapid Aviation Air Quality	$150,000	$200,000	$250,000	$250,000	-	-	-	-	-	-	-	-	$850,000
021	Improving Climate Policy Analysis Tools	$150,000	$150,000	$150,000	$150,000	-	-	-	-	-	-	-	-	$600,000
022	Evaluation of FAA Climate Tools	$150,000	$30,000	$ 75,000	$100,000	-	-	$200,000	$150,000	$199,999	-	$200,000	-	$1,104,999
023	Analytical Approach for Quantifying Noise from Advanced Operational Procedures	-	$286,711	$250,000	$250,000	-	$250,000	$500,000	-	-	$125,000	$125,000	-	$1,786,711
024	Emissions Data Analysis for CLEEN, ACCESS, and Other Recent Tests	$244,975	-	$ 75,000	-	-	-	-	-	-	-	-	-	$319,975
025	National Jet Fuels Combustion Program – Area #1: Chemical Kinetics Combustion Experiments	-	$615,000	$210,000	$200,000	$ 2,556	$110,000	$300,000	$200,000	$200,000	-	$300,000	$400,000	$2,537,556
026	National Jet Fuels Combustion Program – Area #2: Chemical Kinetics Model Development and Evaluation	-	$200,000	-	-	-$ 2,556	-	-	-	-	-	-	-	$197,444

Project		Funding Based on award date												
		2014	2015	2016	2017	2018	2019	2020	2021	2022	2023	2024	2025	Total
027	National Jet Fuels Combustion Program – Area #3: Advanced Combustion Tests	-	$1,010,000	$580,000	$265,000	-	$ 30,000	-	-	-	-	-	-	$1,885,000
028	National Jet Fuels Combustion Program – Area #4: Combustion Model Development and Evaluation	-	$470,000	$ 55,000	-	-	-	-	-	-	-	-	-	$525,000
029	National Jet Fuels Combustion Program – Area #5: Atomization Tests and Models	-	$640,000	$360,000	$150,000	-	$120,000	-	-	-	-	-	-	$1,270,000
030	National Jet Fuels Combustion Program – Area #6: Referee Swirl-Stabilized Combustor Evaluation/Support	-	$349,949	-	-	-	-	-	-	-	-	-	-	$349,949
031	Alternative Jet Fuels Test and Evaluation	-	$489,619	$744,891	$999,512	$183,019	-	$2,976,134	$499,784	$1,499,940	-	$2,101,722	$122,534	$9,617,155
032	Worldwide LCA of GHG Emissions from Petroleum Jet Fuel	-	$150,000	-	-	-	-	-	-		-	-	-	$150,000
033	Alternative Fuels Test Database Library	-	$199,624	$119,794	$165,000	-	$163,584	$330,000	$150,000	$150,000	-	$150,000	-	$1,428,002
034	National Jet Fuels Combustion Program – Area #7: Overall Program Integration and Analysis	-	$234,999	$635,365	$192,997	$374,978	-	$582,983	-	-	-	-$101,888	-	$1,919,434
035	Airline Flight Data Examination to Improve flight Performance Modeling	-	$150,001	-	-	-	-	-	-	-	-	-	-	$150,001
036	Parametric Uncertainty Assessment for AEDT2b	-	$ 65,000	$175,000	$380,000	-	$300,000	-	-	-	-	-	-	$920,000
037	CLEEN II Technology Modeling and Assessment	-	$200,000	$150,000	$170,000	-	$170,000	$490,000	-	$250,000	-	$472,000	$425,000	$2,327,000
038	Rotorcraft Noise Abatement Procedures Development	-	$150,000	$150,000	$150,000	$150,000	-	$300,000	$150,000	-	$170,000	$181,000	-	$1,401,000
039	Naphthalene Removal Assessment	-	-	$200,000	$290,000	-	$350,000	-	-	-	-	-	-	$840,000

Project		Funding Based on award date												
		2014	2015	2016	2017	2018	2019	2020	2021	2022	2023	2024	2025	Total
040	Quantifying Uncertainties in Predicting Aircraft Noise in Real-world Situations	-	-	$218,426	$200,000	-	$255,000	-		-	-	-	-	$673,426
041	Identification of Noise Acceptance Onset for Noise Certification Standards of Supersonic Airplane	-	-	$160,000	$221,000	-	$390,000	-	-	-	-	-	-	$771,000
042	Acoustical Model of Mach Cut-off	-	-	$255,000	$150,000	$170,000	-	-$120	-	-	-	-	-	$574,880
043	Noise Power Distance Re-Evaluation	-	-	$150,000	$ 75,000	-	$220,000	$400,000	-	-	-	-	-	$845,000
044	Aircraft Noise Abatement Procedure Modeling and Validation	-	-	-	-	$350,000	-	$370,000	-	-	$125,000	$150,000	-	$995,000
045	Takeoff/Climb Analysis to Support AEDT APM Development	-	-	$250,000	$ 75,000	$ 8,845	$175,000	-	-	-	-	-	-	$508,845
046	Surface Analysis to Support AEDT APM Development	-	-	$ 75,000	$ 75,000	$ 75,000	-	$400,000	-	$75,000	-	-	-	$700,000
047	Clean Sheet Supersonic Engine Design and Performance	-	-	-	-	-	$250,000	$800,000	$200,000	-	$400,000	-	-	$1,650,000
048	Analysis to Support the Development of an Engine nvPM Emissions Standards	-	-	$150,000	$200,000	-	$200,000	$200,000	$200,000	-	-	-	-	$950,000
049	Urban Air Mobility Noise Reduction Modeling	-	-	-	-	-	-	$560,000	$280,000	-	$280,000	$305,000	-	$1,425,000
050	Over-Wing Engine Placement Evaluation	-	-	-	-	-	-	$590,000	-	-	$300,000	-	-	$890,000
051	Combustion Concepts for Next-Generation Aircraft Engines	-	-	-	-	-	-	$600,000	-	$300,000	-	$350,000	-	$1,250,000
052	Comparative Assessment of Electrification Strategies for Aviation	-	-	-	-	-	-	$600,000	-	$460,000	-	$600,00	$525,000	$2,185,000

Project		Funding Based on award date												
		2014	2015	2016	2017	2018	2019	2020	2021	2022	2023	2024	2025	Total
053	Validation of Low Exposure Noise Modeling by Open Source Data Management and Visualization Systems Integrated with AEDT	-	-	-	-	-	-	$569,903	-	$90,000	$250,000	-	-	$909,903
054	AEDT Evaluation and Development Support	-	-	-	-	-	-	$1,400,000	-	$900,000	-	$700,000	$700,000	$3,700,000
055	Noise Generation and Propagation from Advanced Combustors	-	-	-	-	-	-	$2,999,984	-	$500,000	$1,000,000	$500,000	-	$4,999,984
056	Turbine Cooling through Additive Manufacturing	-	-	-	-	-	-	$800,000	-	$400,000	-	$300,000	$300,00	$1,800,000
057	Support for Supersonic Aircraft En-route Noise Efforts in ICAO CAEP	-	-	-	-	-	-	$420,000	-	$110,000	$220,000	$400,000	$400,000	$1,550,000
058	Improving Policy Analysis Tools to Evaluate Higher-Altitude Aircraft Operations	-	-	-	-	-	-	$500,000	$150,000	$500,000	-	$570,000	$450,000	$2,170,000
059	Modeling and Measurements of Supersonic Civil Transport Jet Noise	-	-	-	-	-	-	$849,956	$849,999	-	$850,000	$499,999	-	$3,049,954
060	Analytical Methods for Expanding the AEDT Aircraft Fleet Database	-	-	-	-	-	-	$150,000	$150,001	$150,000	-	-	-	$450,001
061	Noise Certification Streamlining	-	-	-	-	-	-	$250,000	$250,000	$250,000	-	$250,000	-	$1,000,000
062	Noise Model Validation for AEDT	-	-	-	-	-	-	$350,000	$375,000	$375,000	-	$375,000	-	$1,475,000
063	Parametric Noise Modeling for Boundary Layer Ingesting Propulsors	-	-	-	-	-	-	$300,000	-	-	-	-	-	$300,000
064	Alternative Design Configurations to Meet Future Demand	-	-	-	-	-	-	$250,000	$1,199,999	$500,000	-	$600,000	$600,000	$3,149,999
065	Fuel Testing Approaches for Rapid Jet Fuel Prescreening	-	-	-	-	-	-	$559,998	$150,000	$345,000	$300,000	$550,000	-	$1,904,998
066	Evaluation of High Thermal Stability Fuels	-	-	-	-	-	-	$284,997	$100,000	-	$200,000	$350,000	-122,534	$812,463

Project		Funding Based on award date												
		2014	2015	2016	2017	2018	2019	2020	2021	2022	2023	2024	2025	Total
067	Impact of Fuel Heating on Combustion and Emissions	-	-	-	-	-	-	$250,000	$250,000	$250,000	-	$200,000		$950,000
068	Combustor Wall Cooling with Dirt Mitigation	-	-	-	-	-	-	$150,000	$150,000	-	$800,000	$150,000	$150,000	$1,400,000
069	Transitioning a Research nvPM Mass Calibration Procedure to Operations	-	-	-	-	-	-	$846,707	$100,853	$99,999	-	-	-	$1,047,559
070	Reduction of nvPM Emissions from Aero-engine Fuel Injectors	-	-	-	-	-	-	$500,000	$500,000	$500,000	-	$500,000	-	$2,000,000
071	Predictive Simulation of nvPM Emissions in Aircraft Combustors	-	-	-	-	-	-	$500,000	$500,000	-	$500,000	-	-	$1,500,000
072	Aircraft Noise Exposure and Market Outcomes in the United States	-	-	-	-	-	-	$380,000	-	$100,000	$300,000	$300,000	-	$1,080,000
073	Fuel Composition Impact on Combustor Durability	-	-	-	-	-	-	$299,148	$199,865	$200,000	-	$130,000	-	$829,013
074	Low Emissions Pre-Mixed Combustion Technology for Supersonic Civil Transport	-	-	-	-	-	-	$1,000,000	$999,995	-	$1,099,999	-	-	$3,099,994
075	Improved Engine Fan Broadband Noise Prediction Capabilities	-	-	-	-	-	-	$300,000	$300,000	-	$400,160	$201,044	$219,980	$1,421,184
076	Improved Open Rotor Noise Prediction Capabilities	-	-	-	-	-	-	$300,000	$300,00	-	-	-	-	$600,000
077	Measurements to Support Noise Certification for UAS/UAM Vehicles and Identify Noise Reduction	-	-	-	-	-	-	$500,000	$500,000	-	$500,000	$500,000	-	$2,000,000
078	Contrail Avoidance Decision Support & Evaluation	-	-	-	-	-	-	-	$550,000	$550,000	-	$500,000	$650,000	$2,250,000
079	Novel Noise Liner Development Enabled by Advanced Manufacturing	-	-	-	-	-	-	-	$299,867	-	$900,000	$1,200,000	-	$2,399,867
080	Hydrogen Production Alternatives for Sustainable Aviation Fuel (SAF) Production	-	-	-	-	-	- 1340	-	$600,000	$758,026	-	$758,026	$200,000	$2,316,052

Project		Funding Based on award date												
		2014	2015	2016	2017	2018	2019	2020	2021	2022	2023	2024	2025	Total
081	Measurement and Prediction of nvPM size and number emissions from sustainable and convention al aviation fuels	-	-	-	-	-	-	-	-	$2,050,000	-$2,050,000	-	-	-
082	CAEP Stringency Analysis Modeling	-	-	-	-	-	-	-	-	$1,890,000	-	$1,662,938	-	$3,552,938
083	NOx Cruise/Climb Metric System Development	-	-	-	-	-	-	-	-	$250,000	-	$250,000	$400,000	$900,000
084	Noise Modeling of Advanced Air Mobility Flight Vehicles	-	-	-	-	-	-	-	-	-	$315,000	$300,000	-	$615,000
085	Strategies for Improving En-Route Fuel Efficiency	-	-	-	-	-	-	-	-	-	-	$400,000	$400,000	$800,000
086	Study on the Use of Broadband Sounds to Mitigate Sleep Disruption Due to Aircraft Noise	-	-	-	-	-	-	-	-	-	$1,077,621	-	-	$1,077,621
088	A Method for Rapidly Assessing Jet Fuel Compatibility with non-Metallic Materials	-	-	-	-	-	-	-	-	-	$350,000	$350,000	-	$700,000
089	Characterization of Compositional Effects on Dielectric Constant	-	-	-	-	-	-	-	-	-	$500,000	$110,607	-	$610,607
090	World Fuel Survey	-	-	-	-	-	-	-	-	-	$749,887	$999,998	-	$1,749,885
091	Environmental Impacts of High Altitude and Space Vehicle Emissions	-	-	-	-	-	-	-	-	-	$433,775	$435,000	-	$868,775
092	Advanced Two-Stage Turbine Rig Development	-	-	-	-	-	-	-	-	-	$1,100,000	$2,000,000	$2,800,000	$5,900,000
093	Collaborative Research Network for Global SAF Supply Chain Development	-	-	-	-	-	-	-	-	-	$1,131,586	$1,175,000	-	$2,306,586
094	Probabilistic Unmanned Aircraft Systems (UAS) Trajectory and Noise Estimation Tool	-	-	-	-	-	-	-	-	-	$300,000	$335,000	-	$635,000

Project		Funding Based on award date												
		2014	2015	2016	2017	2018	2019	2020	2021	2022	2023	2024	2025	Total
095	Assessment of Fuel Cells for Powering Modern Business Jets	-	-	-	-	-	-	-	-	-	-	$200,000	$200,000	$400,000
096	Future Transportation System Opportunities and Constraints	-	-	-	-	-	-	-	-	-	-	$400,000	$400,000	$800,000
097	FAST-Tech System Level Assessment	-	-	-	-	-	-	-	-	-	-	$200,000	$250,000	$450,000
098	Low Emissions Lean Pre-Mixed Pre-Vaporized Combustion Technology for Subsonic Civil Transport	-	-	-	-	-	-	-	-	-	-	$999,979	-	$999,979
099	Conceptual Analysis of Cryogenic Hydrogen Distribution to Airports	-	-	-	-	-	-	-	-	-	-	$199,911	-	$199,911
100	U.S.-Canada Cross-Border SAF Supply Chain Analysis	-	-	-	-	-	-	-	-	-	-	$200,000	-	$200,000
101	Sustainable Aviation Fuel Repository	-	-	-	-	-	-	-	-	-	-	$2,000,000	-	$2,000,000
102	Assessment on Contrail Formation via Combustion of SAF	-	-	-	-	-	-	-	-	-	-	$250,000	-	$250,000
103	Pareto Efficient SAF Yield and Blending	-	-	-	-	-	-	-	-	-	-	$350,000	-	$350,000
104	Methodology for Assessing Changes in Soil Organic Carbon	-	-	-	-	-	-	-	-	-	-	-	$904,514	$904,514
105	Quantification of Trace Levels of Sulfur Using ICP-MS	-	-	-	-	-	-	-	-	-	-		$150,014	$150,014
106	Integration of Turbine Operational Parameters into Aerothermal System Analyses												$400,000	$400,000
	Total	**$105,000**	**$9,304,992**	**$10,598,440**	**$8,620,458**	**$9,754,341**	**$3,170,047**	**$7,685,041**	**$34,159,207**	**$14,438,292**	**$16,022,021**	**$19,464,791**	**$11,343,471**	**$178,648,445**

Breakout by University*

	Funding Based on award year													
University	**2013**	**2014**	**2015**	**2016**	**2017**	**2018**	**2019**	**2020**	**2021**	**2022**	**2023**	**2024**	**2025**	**Total**
Boston University	$5,000	$350,000	$350,000	$400,000	$610,000	-	$1,729,286	$1,599,962	$899,371	$549,921	$2,399,768	$1,012,960	$219,980	$10,126,249
Georgia Institute of Technology	$5,000	$1,310,000	$1,975,001	$1,434,999	$1,468,500	$650,000	$895,000	$12,264,984	$5,434,994	$4,275,000	$3,749,999	$6,954,917	$3,175,000	$43,593,394
Massachusetts Institute of Technology	$10,000	$1,153,927	$1,169,073	$1,855,000	$1,690,000	$1,000,000	$1,050,000	$5,250,000	$1,700,000	$3,885,000	$2,098,775	5,305,000	$2,225,000	$28,391,775
Missouri University of Science and Technology	$5,000	$2,800,000	$750,000	-$147,766	$725,500	-	$1,217,221	$846,707	$622,099	$2,149,999	$1,000,812	$2,513,003	-	$12,482,575
Oregon State University	$5,000	-	$160,000	$80,000	$59,000	-	-	-	-	-	-	-	-	$304,000
Pennsylvania State University	$5,000	$862,301	$766,711	$958,426	$890,424	$320,000	$797,623	$2,945,000	$1,619,867	$750,000	$4,220,000	$5,476,000	4,013,192	$23,624,544
Purdue University	$5,000	$389,979	$1,030,000	$763,750	$747,067	$114,185	$605,000	$1,220,116	$600,000	600,000	$394,844	$599,865	$426,323	$7,496,129
Stanford University	$5,000	$380,000	$1,155,000	$345,000	$200,000	-	$110,000	$1,069,903	$400,000	$290,000	$450,000	$499,999	$400,000	$5,304,902
University of Dayton	$5,000	-	$906,196	$1,349,087	$1,192,509	$574,944	-	$4,553,260	$799,649	$1,894,940	$1,599,886	$3,590,439	$150,014	$16,615,924
University of Hawaii	$10,000	-	$75,000	$100,000	$125,000	-	$200,000	$200,000	$100,00	-	$400,000	$400,000	-	$1,610,000
University of Illinois	$5,000	$349,943	$553,000	$375,000	$265,000	-	$130,000	$879,956	$649,999	$499,999	$375,000	$1,125,000	-	$5,207,897
University of North Carolina	$5,000	$320,614	$369,996	-	$625,378	-	$300,000	$919,064	$650,000	-	$650,000	$300,000	-	$4,140,052
University of Pennsylvania	$5,000	$154,000	$343,498	$266,001	$134,924	-	-	-	-	-	$1,077,621	-	-	$1,981,044
University of Tennessee	$5,000	$200,000	$100,000	$100,000	$225,000	-	$260,000	$500,000	$100,000	$200,000	$241,500	$200,000	$314,999	$2,446,499

	Funding Based on award year													
University	**2013**	**2014**	**2015**	**2016**	**2017**	**2018**	**2019**	**2020**	**2021**	**2022**	**2023**	**2024**	**2025**	**Total**
University of Washington	$5,000	$60,000	$29,997	$15,000	-	-	-	-$120.15	-	-	-	-	-	$109,877
Washington State University	$20,000	$974,228	$864,968	$725,961	$796,039	$510,918	$390,911	$1,910,374	$862,313	$927,162	$806,586	$6,005,161	$418,963	$15,213,584

Breakout by State*

	Funding Based on award year													
State	**2013**	**2014**	**2015**	**2016**	**2017**	**2018**	**2019**	**2020**	**2021**	**2022**	**2023**	**2024**	**2025**	**Total**
California	$5,000	$380,000	$1,155,000	$345,000	$200,000	-	$110,000	$1,069,903	$400,000	$290,000	$450,000	$499,999	$400,000	$5,304,902
Georgia	$5,000	$1,310,000	$1,975,001	$1,434,999	$1,468,500	$650,000	$895,000	$12,264,984	$5,434,994	$4,275,000	$3,749,999	$6,954,917	$3,175,000	$43,593,394
Hawaii	$10,000	-	$75,000	$100,000	$125,000	-	$200,000	$200,000	$100,000	-	$400,000	$400,000	-	$1,610,000
Illinois	$5,000	$349,943	$553,000	$375,000	$265,000	-	$130,000	$879,956	$649,999	$499,999	$375,000	$1,125,000	-	$5,207,897
Indiana	$5,000	$389,979	$1,030,000	$763,750	$747,067	$114,185	$605,000	$1,220,116	$600,000	600,000	$394,844	$599,865	$426,323	$7,496,129
Massachusetts	$15,000	$1,503,927	$1,529,073	$2,255,000	$2,300,000	$1,000,000	$2,779,286	$6,849,963	$2,599,371	$4,434,921	$4,498,543	$6,317,960	$2,444,980	$38,518,024
Missouri	$5,000	$2,800,000	$750,000	-$147,766	$725,500	-	$1,217,221	$846,707	$622,099	$2,149,999	$1,000,812	$2,513,003	-	$12,482,575
North Carolina	$5,000	$320,614	$369,996	-	$625,378	-	$300,000	$919,064	$650,000	-	$650,000	$300,000	-	$4,140,052
Ohio	$5,000	-	$906,196	$1,349,087	$1,192,509	$574,944	-	$4,553,260	$799,649	$1,894,940	$1,599,886	$3,590,439	$150,014	$16,615,924
Oregon	$5,000	-	$160,000	$80,000	$59,000	-	-	-	-	-	-	-	-	$304,000
Pennsylvania	$10,000	$1,016,301	$1,110,209	$1,224,427	$1,025,348	$320,000	$797,623	$2,945,000	$1,619,867	$750,000	$5,297,621	$5,475,000	$4,013,192	$25,605,588
Tennessee	$5,000	$200,000	$100,000	$100,000	$225,000	-	$260,000	$500,000	$100,000	$200,000	$241,500	$200,000	$314,999	$2,446,499
Washington	$25,000	$1,034,228	$894,965	$740,961	$796,039	$510,918	$390,911	$1,910,254	$862,313	$927,162	$806,586	$6,005,161	$418,963	$15,323,461

*Totals include administrative funds not associated with specific NFOs